Differential Diagnosis in Neuroimaging: Brain and Meninges

Steven P. Meyers

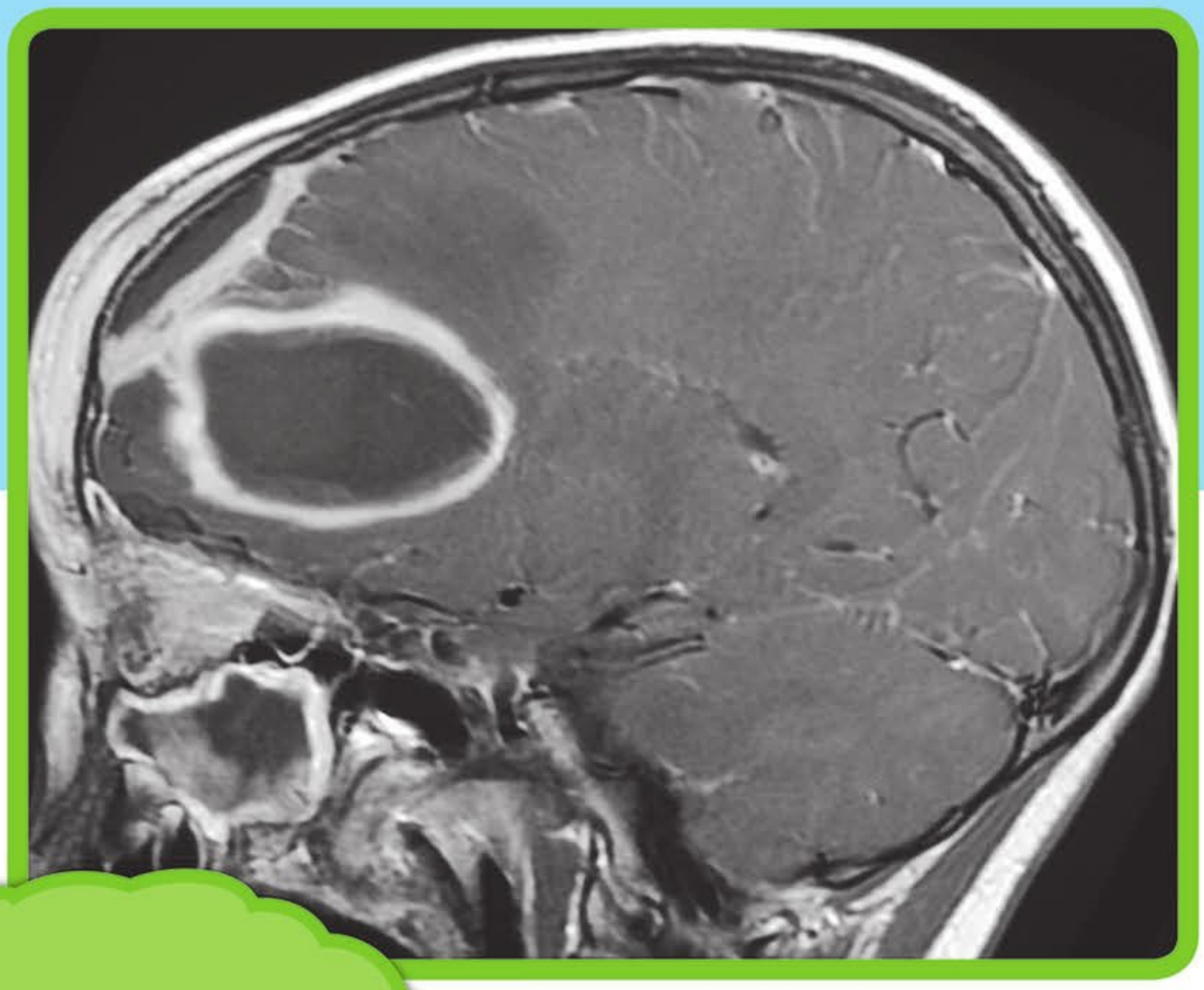

Thieme

Differential Diagnosis in Neuroimaging

Brain and Meninges

Steven P. Meyers, MD, PhD, FACR
Professor of Radiology/Imaging Sciences, Neurosurgery, and Otolaryngology
Director, Radiology Residency Program
University of Rochester School of Medicine and Dentistry
Rochester, New York

1952 illustrations

Thieme
New York • Stuttgart • Delhi • Rio de Janeiro

Executive Editor: William Lamsback
Managing Editor: J. Owen Zurhellen IV
Director, Editorial Services: Mary Jo Casey
Editorial Consultant: Judith Tomat
Production Editor: Kenneth L. Chumbley
International Production Director: Andreas Schabert
Vice President, Editorial and E-Product Development: Vera Spillner
International Marketing Director: Fiona Henderson
International Sales Director: Louisa Turrell
Director of Sales, North America: Mike Roseman
Senior Vice President and Chief Operating Officer: Sarah Vanderbilt
President: Brian D. Scanlan

Library of Congress Cataloging-in-Publication Data
Names: Meyers, Steven P., author.
Title: Differential diagnosis in neuroimaging. Brain and meninges / Steven P. Meyers.
Description: New York : Thieme, [2016] | Includes bibliographical references.
Identifiers: LCCN 2016013145 | ISBN 9781604067002 (alk. paper) | ISBN 9781604067026 (eISBN)
Subjects: | MESH: Neuroimaging | Brain Diseases—diagnosis | Magnetic Resonance Imaging | Diagnosis, Differential
Classification: LCC RC349.D52 | NLM WL 141.5.N47 | DDC 616.8/04754—dc23
LC record available at https://lccn.loc.gov/2016013145

© 2017 Thieme Medical Publishers, Inc.
Thieme Publishers New York
333 Seventh Avenue, New York, NY 10001 USA
+1 800 782 3488, customerservice@thieme.com

Thieme Publishers Stuttgart
Rüdigerstrasse 14, 70469 Stuttgart, Germany
+49 [0]711 8931 421, customerservice@thieme.de

Thieme Publishers Delhi
A-12, Second Floor, Sector-2, Noida-201301
Uttar Pradesh, India
+91 120 45 566 00, customerservice@thieme.in

Thieme Publishers Rio de Janeiro, Thieme Publicações Ltda.
Edifício Rodolpho de Paoli, 25º andar
Av. Nilo Peçanha, 50 – Sala 2508
Rio de Janeiro 20020-906, Brasil
+55 21 3172 2297

Cover design: Thieme Publishing Group
Typesetting by Prairie Papers

Printed in China by Asia Pacific Offset 5 4 3 2 1

ISBN 978-1-60406-700-2

Also available as an e-book:
eISBN 978-1-60406-702-6

Important note: Medicine is an ever-changing science undergoing continual development. Research and clinical experience are continually expanding our knowledge, in particular our knowledge of proper treatment and drug therapy. Insofar as this book mentions any dosage or application, readers may rest assured that the authors, editors, and publishers have made every effort to ensure that such references are in accordance with the state of knowledge at the time of production of the book.

Nevertheless, this does not involve, imply, or express any guarantee or responsibility on the part of the publishers in respect to any dosage instructions and forms of applications stated in the book. Every user is requested to examine carefully the manufacturers' leaflets accompanying each drug and to check, if necessary in consultation with a physician or specialist, whether the dosage schedules mentioned therein or the contraindications stated by the manufacturers differ from the statements made in the present book. Such examination is particularly important with drugs that are either rarely used or have been newly released on the market. Every dosage schedule or every form of application used is entirely at the user's own risk and responsibility. The authors and publishers request every user to report to the publishers any discrepancies or inaccuracies noticed. If errors in this work are found after publication, errata will be posted at www.thieme.com on the product description page.

Some of the product names, patents, and registered designs referred to in this book are in fact registered trademarks or proprietary names even though specific reference to this fact is not always made in the text. Therefore, the appearance of a name without designation as proprietary is not to be construed as a representation by the publisher that it is in the public domain.

This book, including all parts thereof, is legally protected by copyright. Any use, exploitation, or commercialization outside the narrow limits set by copyright legislation without the publisher's consent is illegal and liable to prosecution. This applies in particular to photostat reproduction, copying, mimeographing or duplication of any kind, translating, preparation of microfilms, and electronic data processing and storage.

To my parents, for their unwavering encouragement and support along my long journey through formal education.

And to my wife, Barbara, and son, Noah, for their continuous love, support, and patience during this project.

Contents

Preface ix
Acknowledgments x
Abbreviations xi

Prologue, Intracranial Abnormalities 1

1 Brain (Intra-Axial Lesions) **3**
Introduction 4
Table 1.1 Congenital and histogenic malformations of the brain 11
Table 1.2 Supratentorial solitary intra-axial mass lesions 36
Table 1.3 Solitary intra-axial lesions in the posterior cranial fossa (infratentorial) 94
Table 1.4 Multiple intra-axial lesions in the brain 128
Table 1.5 Multiple or diffuse lesions involving white matter in children 185
Table 1.6 Bilateral lesions involving the basal ganglia and/or thalami 219
Table 1.7 Neurodegenerative disorders 262
Table 1.8 Ischemia and infarction involving the brain and/or brainstem in adults 298
Table 1.9 Ischemia and infarction involving the brain and/or brainstem in children 318
Table 1.10 Intrasellar and juxtasellar lesions 348
Table 1.11 Lesions in the pineal region 386
References 400

2 Ventricles and Cisterns 421
Introduction 422
Table 2.1 Lateral ventricles—common masses 423
Table 2.2 Common third ventricular masses 425
Table 2.3 Fourth ventricular lesions 425
Table 2.4 Excessively small ventricles 426
Table 2.5 Dilated ventricles 428
Table 2.6 Abnormal or altered configuration of the ventricles 456
Table 2.7 Solitary intraventricular lesions in children 468
Table 2.8 Solitary intraventricular lesions in adults 488
Table 2.9 Contrast-enhancing ventricular margins 510
References 516

3 Extra-Axial Lesions 517
Introduction 518
Table 3.1 Solitary extra-axial mass lesions 518
Table 3.2 Multifocal extra-axial lesions 548
References 558

4 Meninges 561
Introduction 562
Table 4.1 Abnormalities involving the dura 563
Table 4.2 Multifocal and/or diffuse leptomeningeal abnormalities 583
References 596

5 Vascular Abnormalities 597
Introduction 598
Table 5.1 Congenital and developmental vascular anomalies/variants 607
Table 5.2 Acquired vascular disease 620
References 638

Index 641

Preface

As an academic neuroradiologist who has had the privilege of working at a university medical center for the past twenty-five years, I have had many opportunities to continuously learn and be involved in the education of medical students, as well as residents and fellows in radiology, neurosurgery, neurology, otolaryngology, and orthopedics. During my training, I had the opportunity to work with outstanding professors who served as role models for teaching and research. I learned from them that excellent teaching cases are invaluable in the education of our specialty. For the past three decades, I have been collecting and organizing a large teaching file for lectures, as well as an educational resource that can be utilized at the workstation. It is from this large data base that I began writing this three-volume series in my specialty of neuroradiology ten years ago.

The goal of these books is to present the imaging features of neuroradiological abnormalities in an easy-to-use resource, with extensive utilization of figures for illustration. This first volume of the series—*Differential Diagnosis in Neuroimaging: Brain and Meninges*—covers lesions involving the brain, ventricles, meninges, and neurovascular system in both children and adults.

The second volume of this series—*Differential Diagnosis in Neuroimaging: Head and Neck*—contains chapters describing lesions located in the skull and temporal bone, orbits, paranasal sinuses and nasal cavity, suprahyoid neck, infrahyoid neck, and brachial plexus.

The third volume—*Differential Diagnosis in Neuroimaging: Spine*—includes differential diagnosis tables, such as congenital and developmental abnormalities, intradural intramedullary lesions (spinal cord lesions), dural and intradural extramedullary lesions, extradural lesions, solitary osseous lesions involving the spine, multifocal lesions and/or poorly-defined signal abnormalities involving the spine, traumatic lesions, and lesions involving the sacrum.

The organization of these books focuses on lists of differential diagnoses of lesions based on anatomic locations in a tabular format. Brief introductory summaries with illustrations are provided at the beginning of most chapters to succinctly provide relevant information, after which the tables are presented. Each of the lesions listed in the tables has a column summarizing the pertinent Imaging findings associated with images for illustration, and a Comments column summarizing key clinical data. References are provided in alphabetical order at the end of each chapter. For the reader's convenience, some of the diagnoses are listed in two or more tables. The purpose of this is to minimize or eliminate the need to page back to the same entries in other tables in order to find the desired information.

These books' unique organization helps the reader obtain information efficiently and quickly. Because of the heavy emphasis on providing illustrative images over text, this book's format can be an effective guide in narrowing the differential diagnoses of lesions based on their locations and imaging findings.

I hope these texts will be a valuable resource for practicing radiologists, neurosurgeons, neurologists, otolaryngologists, and orthopedic spine surgeons. They are intended to become a "well-thumbed text" at the PACS station and clinics. They should also serve as a useful review and teaching guide for trainees in radiology, neurosurgery, neurology, orthopedics, otolaryngology, and other medical specialties preparing for board examinations.

Steven P. Meyers, MD, PhD, FACR

Acknowledgments

I wish to acknowledge the Thieme staff, in particular J. Owen Zurhellen IV, Judith Tomat, William Lamsback, and Kenny Chumbley, for their dedication, hard work, and attention to detail. I thank Ms. Colleen Cottrell for her outstanding secretarial work with this project. I also thank Nadezhda D. Kiriyak, BFA, and Katie Tower, BFA, for their creative talents in making illustrations for this book. I thank Sarah Klingenberger and Margaret Kowaluk for helping me optimize the MRI and CT images of this book.

In addition, I wish to acknowledge the following for their contribution of interesting cases: Jeevak Almast, MBBS, Allan Bernstein, MD, Gary M. Hollenberg, MD, Edward Lin, MD, BBA, Michael Potchen, MD, Peter Rosella, MD, David Shrier, MD, Eric P. Weinberg, MD, and Andrea Zynda-Weiss, MD.

I extend my appreciation and thanks to my coworkers and physician colleagues (Drs. Bernstein, Hollenberg, Rosella, Shrier, Weinberg, and Zynda-Weiss) at University Medical Imaging, the Outpatient Diagnostic Imaging Facility of the University of Rochester, for making an ideal collaborative environment for teaching and clinical service.

Last, I would like to give thanks to my former teachers and mentors for their guidance, encouragement, and friendship.

Illustrations by:

Katie Tower, Figs. 1.1, 1.2, 1.3, 1.4, 1.5, 1.408, 4.1, 5.3, 5.6, 5.9, 5.10, 5.12, 5.13, 5.19

Nadezhda D. Kiriyak, Figs. 1.6, 5.1

Abbreviations

ACA Anterior cerebral artery

ACOM Anterior communicating artery

ADC Apparent diffusion coefficent

ADEM Acute disseminated encephalomyelitis

AML Acute myelogenous leukemia

ANA Antinuclear antibodies

AP Anteroposterior

AS Ankylosing spondylitis

AT/RT Atypical teratoid/rhabdoid tumor

AVF Arteriovenous fistula

AVM Arteriovenous malformation

Ca Calcium/calcification

CADASIL Cerebral autosomal dominant arteriopathy with subcortical infarcts and leukoencephalopathy

CARASIL Cerebral autosomal recessive arteriopathy with subcortical infarcts and leukoencephalopathy

Cho Choline

CISS Constructive interference steady state

CLL Chronic lymphocytic leukemia

CML Chronic myelogenous leukemia

CMV Human cytomegalovirus

CNS Central nervous system

CPPD Calcium pyrophosphate dihydrate deposition

CSF Cerebrospinal fluid

CT Computed tomography

DISH Diffuse idiopathic skeletal hyperostosis

DNET Dysembryoplastic neuroectodermal tumor

DTI Diffusion tensor imaging

DWI Diffusion weighted imaging

EG Eosinophilic granuloma

EMA Epithelial membrane antigen

FIESTA Fast imaging employing steady state acquisition

FLAIR Fluid attenuation inversion recovery

FS Frequency selective fat signal suppression

FSE Fast spin echo

FS-PDWI Fat-suppressed proton density weighted imaging

FSPGR Fast spoiled gradient echo Imaging

FS-T1WI Fat-suppressed T1-weighted imaging

FS-T2WI Fat-suppressed T2-weighted imaging

Gd-contrast Gadolinium-chelate contrast

GRE Gradient echo imaging

HIV Human immundeficiency virus

HMB-45 Human melanoma black monoclonal antibody

HPF High power field

HPV Human papilloma virus

HSV Herpes simplex virus

HU Hounsfield unit

ICA Internal carotid artery

IRIS Immune reconstitution inflammatory syndrome

JIA Juvenile idiopathic arthritis

LCH Langerhans cell histiocytosis

MCA Middle cerebral artery

MDS Myelodysplastic syndrome

MELAS Mitochondrial encephalopathy, lactic acidosis, and stroke-like events

MERRF Myoclonic epilepsy with ragged red fibers

MIP Maximum intensity projection

MPNST Malignant peripheral nerve sheath tumor

MRA MR angiography

MRV MR venography

MRS MR spectroscopy

MS Multiple Sclerosis

NAA N-acetylaspartate

NF1 Neurofibromatosis Type 1

NF2 Neurofibromatosis Type 2

NSAID Non-steroidal anti-inflammatory drug

NSE Neuron specific enloase

PC Phase contrast

PCA Posterior cerebral artery

PCV Polycythemia vera

PCOM Posterior communicating artery

PDWI Proton density weighted imaging

PEDD Proton-electron dipole-dipole interaction

PML Progressive multifocal leukoencephalopathy

PNET Primitive neuroectodermal tumor

PRES Posterior reversible encephalopathy syndrome

PVNS Pigmented villondular synovitis

RF Radiofrequency

SLE Systemic lupus erythematosus

SMA Smooth muscle actin antibodies

STIR Short TI inversion recovery imaging

SWI Susceptibility weighted imaging

S-100 Cellular calcium binding protein in cytoplasm and/or nuceus

T1 Spin-lattice or longitudinal relaxation time (coefficient)

T2 Spin-spin or transverse relaxation time (coefficient)

T2* Effective spin-spin relaxation time using GRE pulse sequence

T2-PRE T2-proton relaxation enhancement

T1WI T1-weighted imaging

T2WI T2-weighted imaging

TE Time to echo

TR Pulse repetition time interval

TOF Time of flight

2D 2 Dimensional

3D 3 Dimensional

WHO World Health Organization

Prologue

Intracranial Abnormalities

Brain, Ventricles, Meninges, Skull, and Vascular Structures

Major advantages of magnetic resonance imaging (MRI) include excellent soft tissue contrast resolution, multiplanar imaging capabilities, dynamic rapid data acquisition, and the available contrast agents. MRI has proven to be a powerful imaging modality in the evaluation of congenital anomalies of the brain; disorders of histogenesis; neoplasms of the central nervous system, cranial nerves, pituitary gland, meninges, and skull base; traumatic lesions; intracranial hemorrhage; ischemia and infarction; infectious and noninfectious diseases; metabolic disorders; and dysmyelinating and demyelinating diseases.

Computed tomography (CT) has been used in the evaluation of neoplasms of the central nervous system, meninges, calvarium, and skull base; traumatic lesions; intracranial hemorrhage; ischemia and infarction (particularly using CT perfusion studies); infectious and noninfectious diseases; and metabolic disorders. Because of its widespread availability and rapid imaging capability, CT plays an important role in the evaluation of acutely injured patients in emergency departments. Multidetector CT is an excellent imaging modality for evaluation of the skull base, orbits, nasopharynx, oropharynx, and floor of the mouth. CT is a useful method for imaging the location and extent of osseous lesions at the skull base, such as metastatic tumors, myeloma, chordomas, and chondrosarcomas.

MRI and CT data can also be used to generate images of arteries and veins (MR angiography and CT angiography) in displays similar to conventional angiography. Other options with clinical MRI scanners include the acquisition of spectral data to characterize the biochemical properties of selected regions of interest in the brain (magnetic resonance spectroscopy), detection of water proton diffusion in brain and meninges (diffusion-weighted imaging and mapping of apparent diffusion coefficients), and evaluation of differing ratios of deoxyhemoglobin to oxyhemoglobin at sites of brain activation (functional MRI).

Appearance of Normal Brain Tissue on CT and MRI

The appearance of brain tissue depends on the CT technique and MRI pulse sequences used, as well as the age of the patient. Myelination of the brain begins in the fifth fetal month and progresses rapidly during the first 2 years of life. The degree of myelination affects the appearance of the brain parenchyma on MRI and CT. In adults, the cerebral cortex has an intermediate signal on T1-weighted images and is lower or hypointense relative to normal white matter. On T2-weighted images, gray matter has an intermediate signal that is higher in signal (hyperintense) relative to white matter. For infants less than 6 months old, the MRI pattern is reversed due to the immature myelination of their brain tissue. Maturation or myelination of the brain tissue, as seen on T1-weighted versus T2-weighted images, occurs at different rates. The myelination proceeds in a predictable and characteristic pattern with regard to location and timing. The changes on T1-weighted images become most evident during the first 6 months of postnatal life, whereas the changes on T2-weighted images are most apparent from 6 to 18 months. At around 6 months of age, the adult MRI signal pattern of the gray and white matter begins to progressively emerge. After 18 months, the brain has a mature MRI appearance with regard to the gray and white matter signal patterns.

On CT, the appearance of brain tissue depends on the mAs and kVp used. Immature myelin in neonates and infants has lower attenuation than myelin in older children. In adults, the cerebral cortex has an intermediate attenuation that is slightly higher relative to normal white matter. The imaging changes seen with myelin maturation are more optimally seen with MRI than with CT.

In addition to the commonly used standard fast spin echo sequences for evaluation of brain parenchyma, other MRI pulse sequences or imaging options are commonly used, such as inversion recovery (short TI inversion recovery [STIR] for fat suppression, T1-weighted or T2-weighted fluid attenuated inversion recovery [FLAIR], etc.), gradient recall echo T2* imaging, spoiled gradient recall echo T1-weighted imaging, steady-state free precession imaging, magnetic transfer, diffusion/perfusion MRI, and frequency selective chemical saturation. Detailed discussions of these sequences and options can be found elsewhere.

Appearance of Abnormal Brain Parenchyma on MRI and CT

Most pathologic processes decrease the CT attenuation values of the involved tissue and increase the MRI T1 and T2 relaxation coefficients, resulting in decreased signal on T1-weighted images and increased signal on T2-weighted images relative to adjacent normal tissue. Such processes include ischemia, infarction, inflammation, infection, demyelination, dysmyelination, metabolic or toxic encephalopathy, trauma, neoplasms, gliosis, radiation injury, and

encephalomalacia-related changes. Other processes that can result in zones of low attenuation on CT include dermoids (intact or ruptured), teratomas, lipomas, and cystic structures with high protein concentration or cholesterol, as well as Pantopaque.

Areas where there is breakdown of the blood–brain barrier can be also evaluated with iodinated intravenous contrast on CT and with gadolinium-based intravenous contrast agents on MRI. Leakage of contrast agents through the blood–brain barrier results in increased attenuation on CT (contrast enhancement) and high signal on T1-weighted images. The high signal seen on MRI after contrast administration results from reduction of the T1 and T2 values of the hydrogen nuclei in brain tissue adjacent to the intraparenchymal contrast that leaked through the damaged blood–brain barrier. Contrast-enhanced CT and MR images are important portions of most imaging examinations of the head. In addition to the contrast enhancement in pathologically altered intracranial tissues, CT and MRI contrast enhancement can be seen normally in veins, the choroid plexus, the anterior pituitary gland, the pituitary infundibulum, the pineal gland, and the area postrema.

Intracranial Hemorrhage on MRI

Intraparenchymal hemorrhage on MRI can have varying appearances in the brain depending on the age of the hematoma, oxidation states of the iron in hemoglobin, hematocrit, protein concentration, clot formation and retraction, hemorrhage location, and hemorrhage size. Oxyhemoglobin in a hyperacute blood clot has ferrous iron and is diamagnetic. Oxyhemoglobin does not significantly alter the T1 and T2 values of the tissue environment, other than causing possible localized edema. After a few hours during the acute phase of the hematoma, the oxyhemoglobin loses its oxygen and forms deoxyhemoglobin. Deoxyhemoglobin also has ferrous iron, although it has unpaired electrons and becomes paramagnetic. As a result, deoxyhemoglobin shortens the T2 value of the acute clot but does not significantly change the T1 value. On MRI, deoxyhemoglobin in the clot will have an intermediate T1 signal and a low signal on T2-weighted spin echo or gradient echo images. Later, in the early subacute phase of the hematoma, deoyxhemoglobin becomes oxidized to the ferric state, methemoglobin, which is strongly paramagnetic. Methemoglobin shortens the T1 value of hydrogen nuclei, resulting in high signal on T1-weighted images. While the red blood cells in the clot are intact, with intracellular methemoglobin, the T2 values will also be decreased, resulting in a low signal on T2-weighted images. In the late subacute phase, breakdown of the membranes of the red blood cells results in extracellular methemoglobin, which causes high signal on both T1- and T2-weighted images. In the chronic phase, methemoglobin becomes further oxidized and broken down by macrophages into hemosiderin, which has a prominent low signal on T2-weighted images and a low-intermediate signal on T1-weighted images.

The MRI features of *subdural hematomas* are variable, although the appearances can progress in patterns similar to those for intraparenchymal hematomas. Chronic subdural hematomas often have a low-intermediate signal on T1-weighted images and a high signal on T2-weighted images. *Subarachnoid hemorrhage* is often difficult to see on T1- and T2-weighted images, although it can be sometimes identified on long TR/short TE (proton density-weighted images) or FLAIR images.

In the differential diagnosis of intracranial hemorrhage, other processes that can result in zones of high signal on T1-weighted images are fat, dermoids (intact or ruptured), teratomas, lipomas, and cystic structures with high protein concentration or cholesterol, as well as Pantopaque.

Intracranial Hemorrhage on CT

An *intraparenchymal hemorrhage* on CT can have varying appearances in the brain depending on the age of the hematoma, hematocrit, protein concentration, clot formation and retraction, hemorrhage location, and hemorrhage size. In the first week, intraparenchymal hematomas typically have high attenuation.

In the late subacute phase (> 7 days to 6 weeks) *intracerebral hematomas* decrease 1.5 Hounsfield units (HU) per day and become isodense to hypodense. Chronic hematomas have low attenuation with localized encephalomalacia. The CT features of *subdural hematomas* are variable, although the appearances can progress in patterns similar to those for intraparenchymal hematomas. Acute subdural hematomas often have high attenuation. CT is the optimal exam in the diagnosis of acute *subarachnoid hemorrhage* and is more reliable than MRI. Also, CT is the optimal exam to diagnose acute *epidural and subdural hematomas* because of wide scanner availability and fast imaging acquisition, as well as capability for the evaluation of commonly associated skull injuries and fractures.

Chapter 1

Brain (Intra-Axial Lesions)

Introduction 4

1.1 Congenital and histogenic malformations of the brain 11

1.2 Supratentorial solitary intra-axial mass lesions 36

1.3 Solitary intra-axial lesions in the posterior cranial fossa 94

1.4 Multiple intra-axial lesions in the brain 128

1.5 Multiple or diffuse lesions involving white matter in children 185

1.6 Bilateral lesions involving the basal ganglia and/or thalami 219

1.7 Neurodegenerative disorders 262

1.8 Ischemia and infarction involving the brain and/or brainstem in adults 298

1.9 Ischemia and infarction involving the brain and/or brainstem in children 318

1.10 Intrasellar and juxtasellar lesions 348

1.11 Lesions in the pineal region 386

References 400

1 Brain (Intra-Axial Lesions)

Table 1.1 Congenital and histogenic malformations of the brain

Table 1.2 Supratentorial solitary intra-axial mass lesions

Table 1.3 Solitary intra-axial lesions in the posterior cranial fossa

Table 1.4 Multiple intra-axial lesions in the brain

Table 1.5 Multiple or diffuse lesions involving white matter in children

Table 1.6 Bilateral lesions involving the basal ganglia and/or thalami

Table 1.7 Neurodegenerative disorders

Table 1.8 Ischemia and infarction involving the brain and/or brainstem in adults

Table 1.9 Ischemia and infarction involving the brain and/or brainstem in children

Table 1.10 Intrasellar and juxtasellar lesions

Table 1.11 Lesions in the pineal region

Introduction

Overview of Embryonic and Fetal Brain Development

Neural Plate and Neural Tube Formation

A. Neural Plate Formation

a. At 5 to 15 days' gestation, proliferating ectodermal cells on the dorsal surface of the embryo form the primitive streak (**Fig. 1.1**).

b. A group of proliferating cells at the cephalic end of the primitive streak form a pit called Hensen's node.

c. At 15 to 16 days' gestation, cells enter Hensen's node and migrate rostrally toward the cephalic end of the embryo to form the notochord process and eventually the notochord.

d. The notochord induces the overlying dorsal ectoderm into forming neuroectoderm, which becomes the neural plate (this is the process of *neurulation*).

e. At 17 days' gestation, the lateral portions of the neural plate thicken to produce the neural folds. The neural folds elevate laterally and contract centrally to form the neural groove.

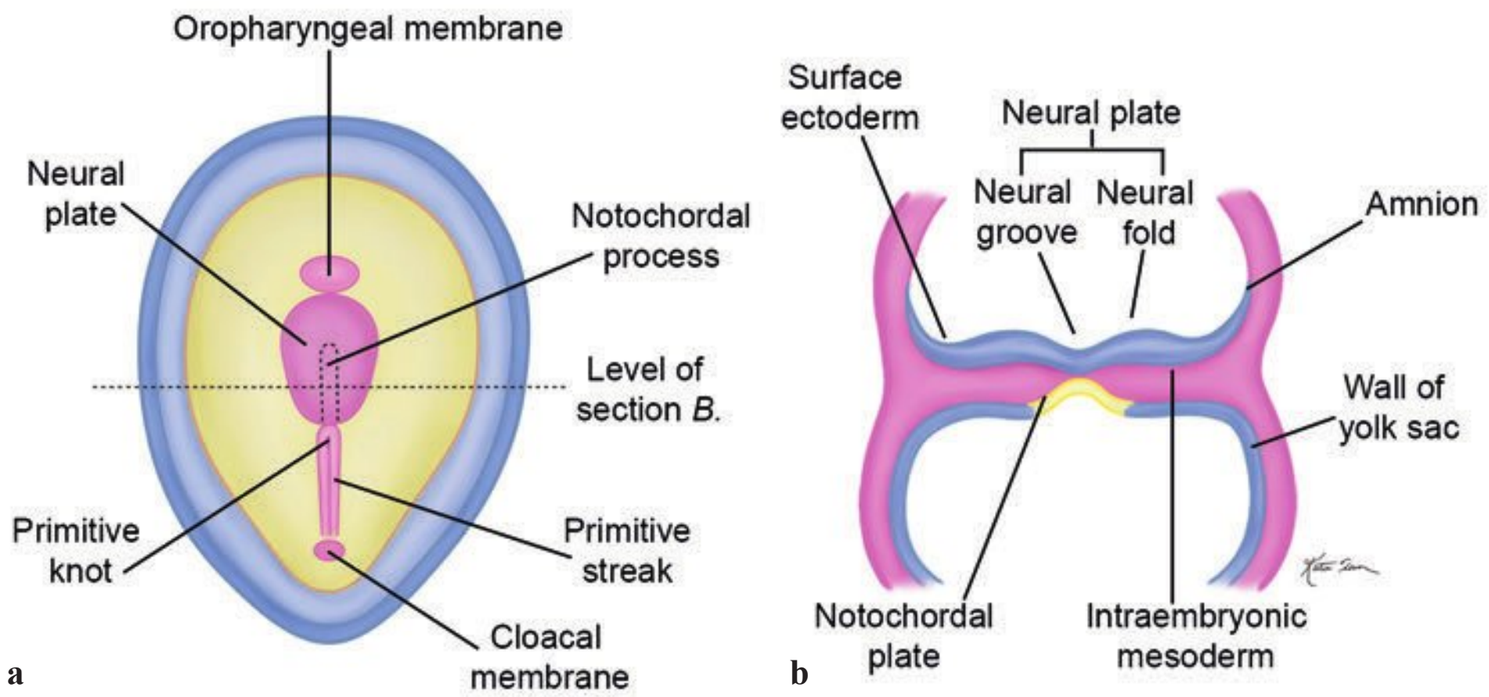

Fig. 1.1 **(a)** Dorsal and **(b)** coronal diagrams of the developing embryo.

B. Neural Tube Formation

a. At 20 days' gestation, the mesenchyme adjacent to the neural folds expands, in association with progressive approximation and eventual merger of neural folds in the midline dorsally to form the neural tube (**Fig. 1.2**). Progressive closure of the neural tube begins at two or three sites.

The neuroectoderm of the developing neural tube is covered by cutaneous ectoderm. Separation (*disjunction*) of the neuroectoderm and cutaneous ectoderm occurs as the neural folds fuse to form the neural tube. The neural tube forms the central nervous system, and the cutaneous ectoderm becomes the skin. Mesenchyme migrates between the separated cutaneous ectoderm and neuroectoderm to eventually form the meninges, vertebrae, and paraspinal muscles.

b. At 25 days' gestation, closure of the neural tube occurs at the cephalic end (anterior neuropore).

c. At 27 to 28 days' gestation, closure of the neural tube occurs at the caudal end (posterior neuropore).

d. Neuroectodermal cells at the lateral dorsal margins of the closing neural tube separate to form the neural crest cells.

Abnormalities of neural tube closure include cephaloceles, myeloceles, and Chiari malformations.

Vesicles

a. At 35 days' gestation, three fluid-filled primary expansions or vesicles form at the cephalic (rostral) end of the neural tube: the *prosencephalon, mesencephalon*, and *rhombencephalon* (**Fig. 1.3**). The prosencephalon (forebrain) will bend and constrict to form the *telencephalon* (cerebral hemispheres, basal ganglia, and lateral ventricles) and *diencephalon* (thalamus, hypothalamus, and third ventricle). The mesencephalon (midbrain) will form the midbrain and cerebral aqeduct and the rhombencephalon (hindbrain) will eventually become the metencephalon (pons, cerebellum, and upper portion of the fourth ventricle) and myelencephalon (medulla and lower portion of the fourth ventricle).

b. At 42 days' gestation, lateral protrusions of the prosencephalon begin formation of the cerebral hemispheres (**Fig. 1.4** and **Fig. 1.5**).

Abnormal formation of the vesicles causes the congenital cleavage anomalies, such as holoprosencephalies (alobar holoprosencephaly, semilobar holoprosencephaly, lobar holoprosencephaly, syntelencephaly), septo-optic dysplasia, and arrhinencephaly.

Neuronal Migration

a. At 49 days' gestation to 22 weeks, neuronal progenitor cells and stem cells arise at the innermost layer of the fetal cerebral hemisphere, which is referred to as the *ventricular zone* or *germinal zone*. At the *basal (ventral) portions* of the ventricular zone, neurons of the basal ganglia, some thalamic neurons, and GABAergic cortical interneurons develop at regional thickening of the ventricular zone, referred to as the *ganglionic germinal zone* (ganglionic eminence). This region of the ventricular germinal zone is referred to as the *subpallium*. The caudate nucleus develops at the rostral end of the ganglionic eminence. GABAergic cortical interneurons are produced in the medial ganglionic eminences of the subpallium and migrate tangentially.

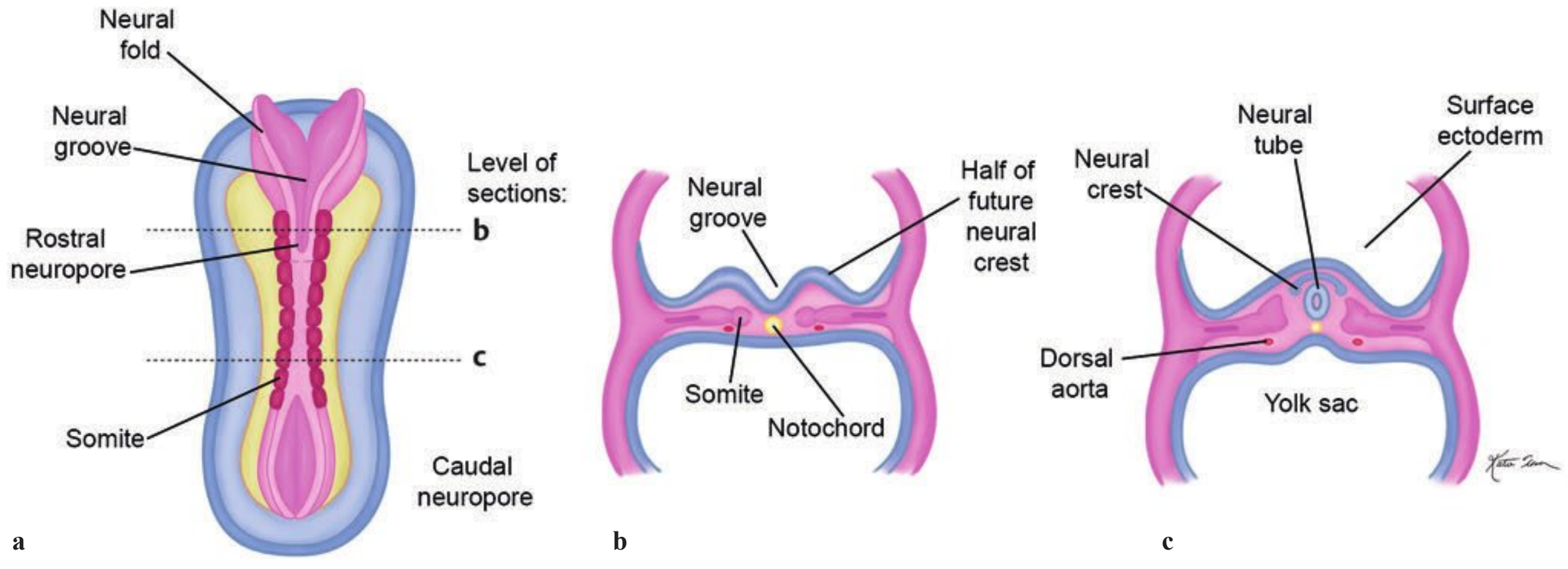

Fig. 1.2 **(a)** Dorsal view of the embryo shows closure of the neural tube, except at the rostral and caudal neuropores. **(b)** Coronal view shows infolding of the neural folds at the neural groove that eventually close to form the neural tube **(c)**.

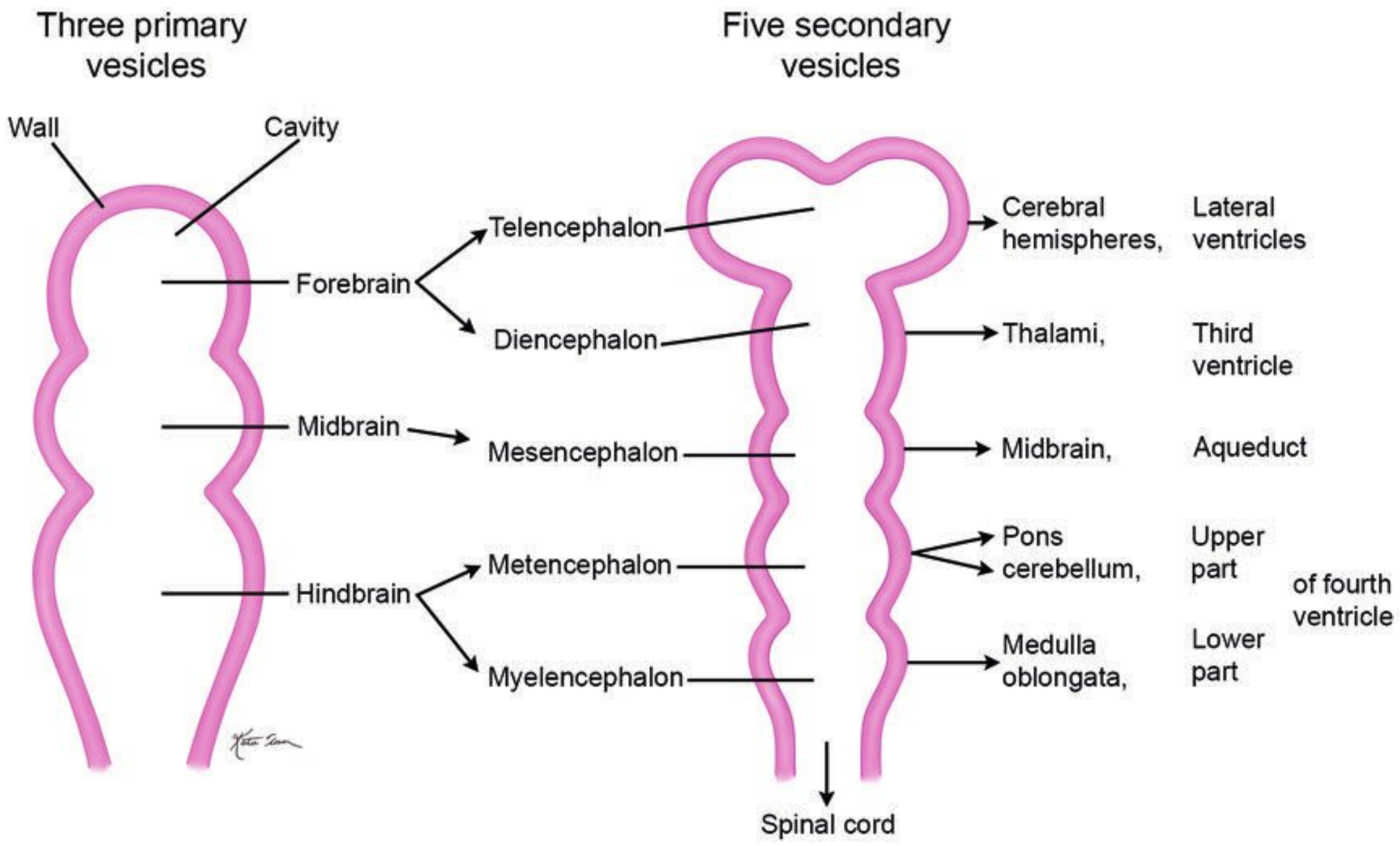

Fig. 1.3 Coronal diagram of the rostral neural tube shows initial formation of the primary vesicles, followed by the secondary vesicles and corresponding mature neural structures.

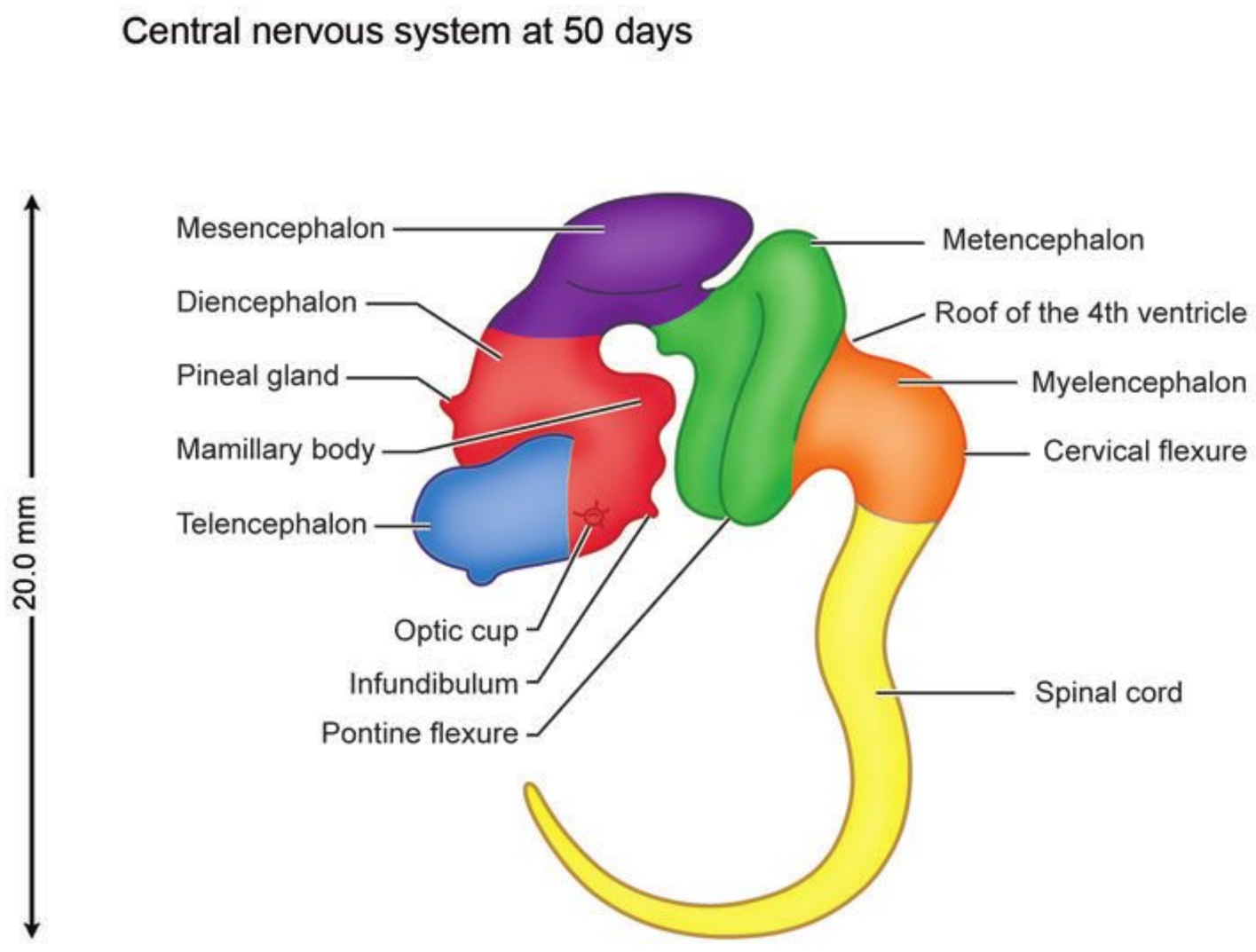

Fig. 1.4 Lateral diagram shows the CNS at 50 days' gestation.

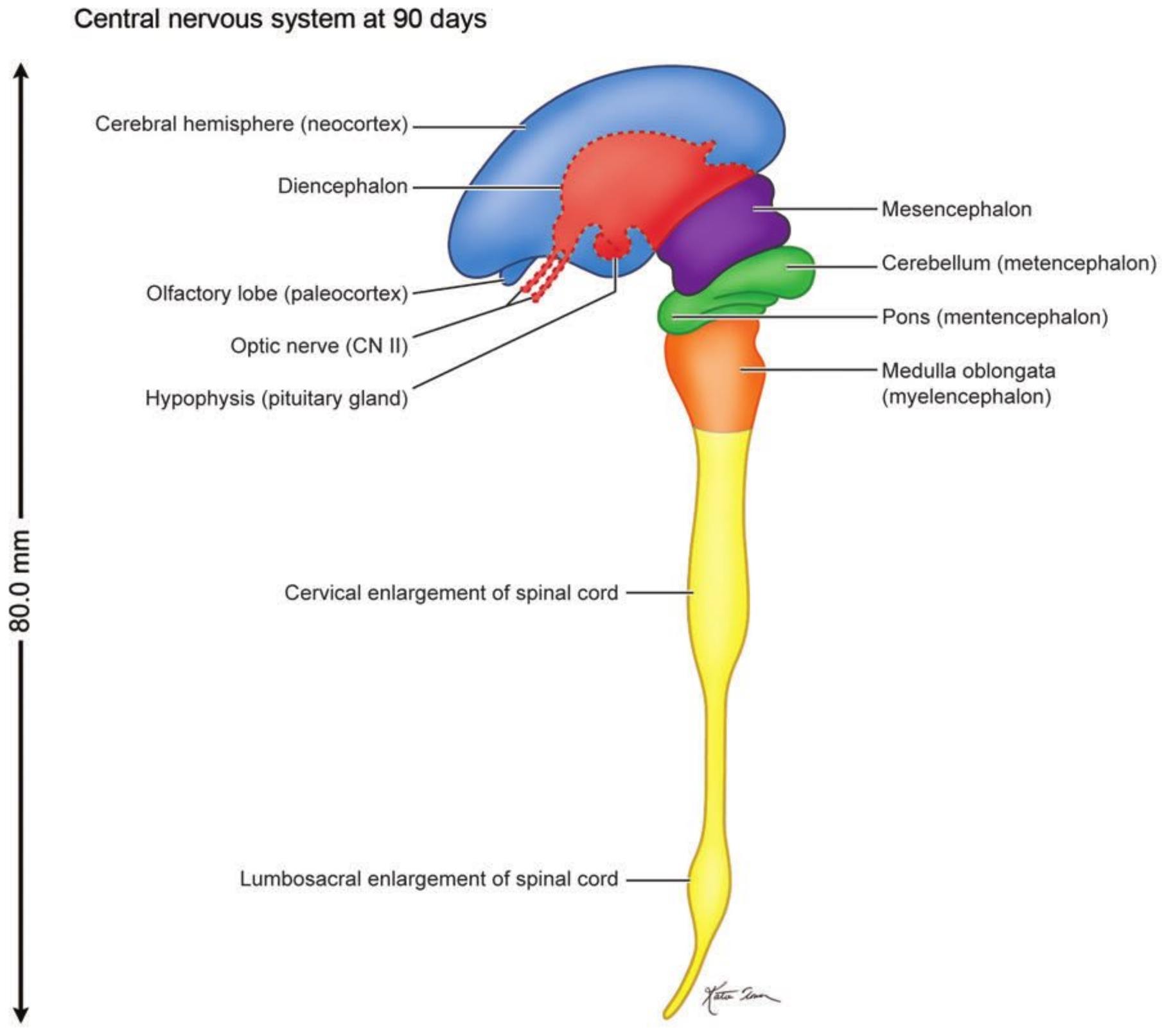

Fig. 1.5 Lateral diagram shows the CNS at 3 months' gestation.

In the other portions of the ventricular zone (VZ), pyramidal neurons that will eventually form the cerebral cortex and white matter arise in the germinal zone referred to as the *pallium*. Next to the inner wall of the closed neural tube at the ventricular side, a germinal layer of dividing neuroepithelial cells in the VZ occurs deep to the eventual site of the cerebral cortex near the meningeal surface of the neural tube, which is referred to as the primordial plexiform layer or preplate (PP). The PP will subsequently form the cortical plate and cerebral cortex. In early gestation, the VZ, including the ganglionic eminences and cortical plate, have low signal on T2-weighted imaging and high signal on T1-weighted imaging.

b. At 7 to 11 weeks of gestation, the first neurons from the *ventricular zone* migrate to the *PP layer* via nucleokinesis to form *cerebral cortical cell layer 6*, which is the deepest layer of the cortical plate. At the end of the seventh week of gestation, the PP layer divides into a superficial marginal zone next to the meningeal surface (containing neurons and reelin-positive Cajal-Retzius cells) and the subcortical layer or subplate that contains reelin-negative neurons. The Cajal-Retzius cells are involved with the regulation of neuronal migration from the germinal zone to the cortical plate and developing cerebral cortex. The radial migration of neurons from the germinal zone to the cortical plate is guided by specialized cells, referred to as the radial glia, which differentiate from neuroepithelial cells (**Fig. 1.6**). A subventricular zone (SVZ) separates from the ventricular germinal zone (VZ) and produces GABAergic neurons and short neural precursor cells.

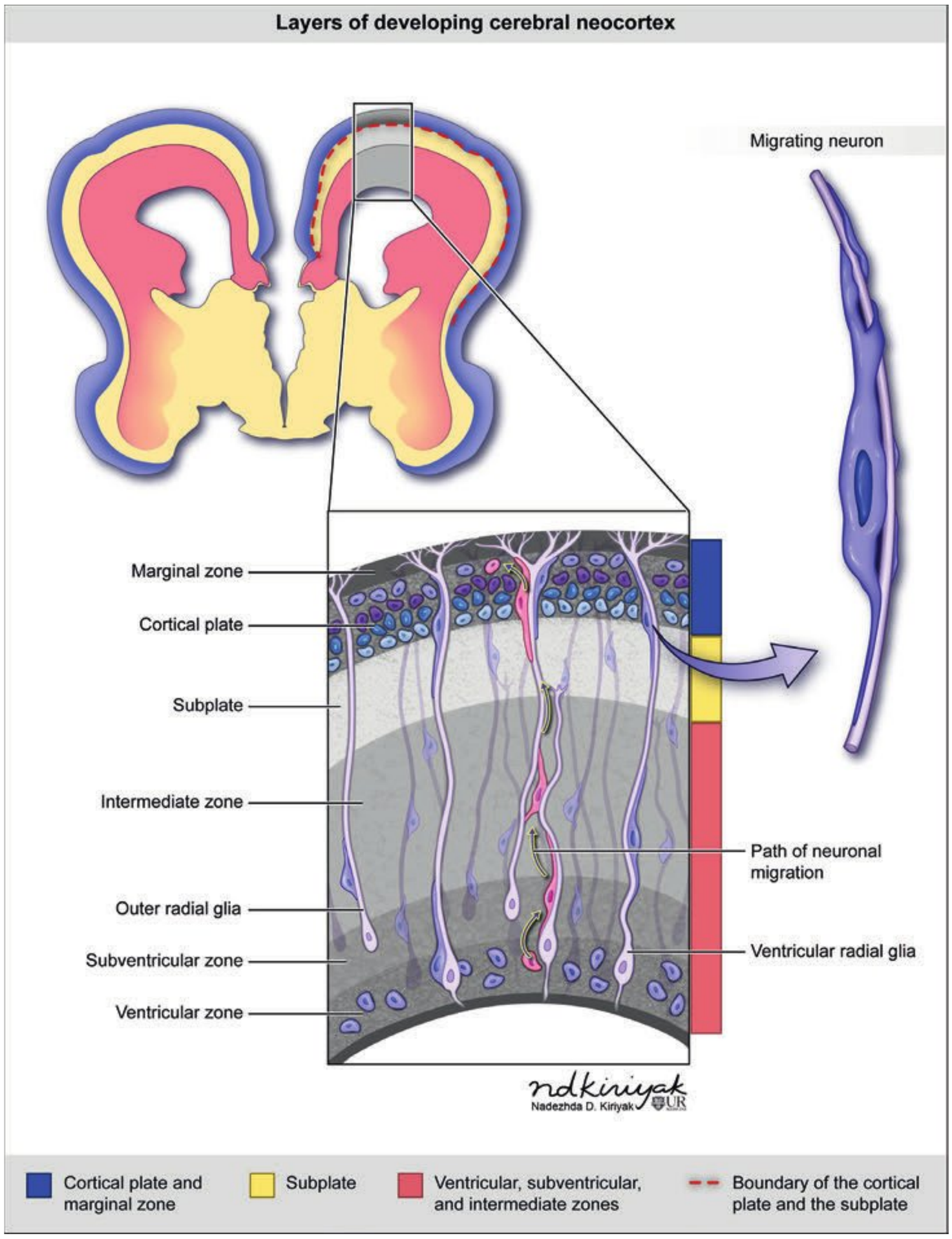

Fig. 1.6 Diagram shows layers of developing neocortex.

c. At 12 to 16 weeks of gestation, a second wave of neurons migrate from the VZ along radial glia to form *cerebral cortical layers 5 and 4*.
d. At 16 to 22 weeks of gestation, a third wave of neurons migrate to form *cerebral cortical layers 3, 2, and 1*. Cerebral cortical layer 1 is the most superficial layer. Neuronal migration to the cortical plate thus occurs in an "inside out" progressive pattern during gestation.
e. At 22 to 26 weeks of gestation, the end of neuronal migration occurs. Primary and secondary sulcal formation is observed. Radial glia lose contact with the ventricle and migrate to the cortex, forming astrocytes. The *pallial VZ* involutes at 25 weeks, but the SVZ remains and contains stem cells that may persist into adulthood. The germinal zone of the *subpallial ganglionic eminence* persists as the *germinal matrix* until the late third trimester.

Abnormalities of neuronal migration include lissencephaly and pachygyria.

Neuronal and Glial Cell Proliferation and Apoptosis

The number of neurons peaks at 28 weeks. Apoptosis is an important regulatory mechanism of brain development. Apoptosis is associated with activation of the caspase cascade, leading to programmed cell death. Antenatal apoptosis usually occurs mainly in the VZ, from weeks 7 to 13, and in the cortical plate, from weeks 19 and 23.

Microcephaly (head circumference that is three standard deviations below the mean for age and sex) can result from insufficient development and proliferation of neuronal progenitor cells and radial glia and/or increased apoptosis secondary to genetic mutations; or it may be caused by acquired (secondary) disorders, such as hypoxic-ischemic encephalopathy, prenatal infection (TORCH), and hemorrhagic, traumatic, or degenerative disorders. Rare genetic or other disorders that increase brain cell proliferation or reduce normal apoptosis can result in abnormally increased brain size (*macrocephaly*—head circumference more than two to three standard deviations above the mean for age and sex).

Abnormalities related to decreased or abnormal stem cell proliferation and/or increased apoptosis cause *decreased brain size*, such as microcephaly with simplified gyral pattern, microlissencephaly, autosomal recessive primary microcephaly, autosomal dominant microcephaly, and X-linked microcephaly. Decreased apoptosis or increased cell proliferation causes increased cerebral hemisphere and brain size, such as unilateral hemimegalencephaly, Sotos syndrome, and familial megalencephaly.

Cortical Organization

At 22 weeks of gestation, neuronal proliferation and migration are mostly complete. After 22 weeks of gestation, synaptogenesis occurs between neurons, which results in tangential growth of the cerebral cortex, as well as sulcal and gyral formation. Progressive organization of cerebral cortex layer 6 occurs. Development of the white matter is related to the formation of the cerebral cortex and occurs in the subcortical zone or subplate. Each neuron develops one axon, which makes many dendritic connections to other axons. Axonal connections progress from the deep layers (corticospinal, corticothalamic, thalamocortical) to the superficial layers (long association and commissural tracts, and short association tracts).

Abnormalities of cortical organization include polymicrogyria and focal cortical dysplasia.

Malformation Related to Abnormal Pial Basement Membrane Formation (Dystroglycanopathies)

Dystroglycanopathies are related to the congenital muscular dystrophies and result from mutations of genes that encode glycosyltransferases, causing deficient production of glycosylated α-dystroglycan. Defective or deficient α-dystroglycan results in reduced neuronal proliferation in the VZ portion of the germinal zone of the developing brain and severely alters the function of the radial glia and their attachment to the pial limiting membrane, causing abnormal neuronal migration and cortical organization. Involved genes that have been identified include *FKTN* on 9q31, *FKRP* on 19q13.3, *POMT1* on 9q34.1, *POMT2* on 14q24, *POMGnT1* on 1p33–34, and *LARGE* on 22q12.3-q13.1

Abnormalities related to pial basement membrane formation include the Walker-Warburg phenotype, muscle-eye-brain phenotype, and the Fukuyama congenital muscular dystrophy phenotype.

Cerebellar Hypoplasia and Malformations

At 4 weeks of gestation, the rhombencephalon subdivides into the metencephalon, which forms the cerebellum, and the myelencephalon, which forms the medulla oblongata. Also at 4 weeks, the rhombencephalon divides into eight transient compartments (rhombomeres), which control patterns of neuronal migration and organization of the hindbrain. Rhombomere 1 forms the cerebellum and rhombomeres 2 to 8 form the other portions of the hindbrain.

Pontine Flexure At 5 weeks of gestation, proliferating cells occur in the alar plate at the rostral and dorsolateral portions of the metencephalon in the most rostral rhombomere (first rhombomere), at the edges of the developing fourth ventricle.

The alar plate hypertrophies medially to form the rhombic lips. The rhombic lips fuse dorsally to form the cerebellar primordium or tuberculum cerebelli, which includes the cerebellar germinal matrix at the roof of the fourth ventricle (occurs from 6 to 15 weeks).

At 7 weeks, progenitor cerebellar neurons migrate tangentially from the fusing rhombic lips to the cerebellar surface, producing the temporary external granular layer, which will form the external molecular layer. Progenitor neurons and Purkinje cells migrate laterally from the cerebellar germinal matrix to form the deep cerebellar nuclei and Purkinje cell layer in the cerebellar hemispheres. Some of the cells in the external molecular layer will migrate internally to form the internal granular layer. At birth, the cerebellar cortex has three layers (outer molecular layer, middle Purkinje cell layer, and internal granular layer). Granule cells from the external molecular layer will continue to migrate to the inner granular layer up to 20 months after birth. Cellular differentiation and organization in the cerebellar cortex also continue after birth up to 20 months.

Flocculonodular Lobe At 2 months of gestation (oldest phylogenetically, archicerebellum) this develops from the tuberculum cerebelli.

Vermis and Paravermian Hemispheres (anterior or paleo-cerebellum) This develops at 4 months gestation.

Fourth Ventricle The mature configuration is observed at 24 weeks.

Cerebellar Hemispheres (Neocerebellum) The cerebellar hemispheres are first seen at 5 to 6 months of gestation and continue to develop 1 year after birth. The adult number of folia is seen at 7 months after birth.

Malformations are caused by prolonged time and phases of cerebellar development. Abnormalities include cerebellar agenesis, Chiari II with vanishing cerebellum, hypoplasia of cerebellar hemisphere, Dandy-Walker malformation, and vermian hypoplasia, also referred to as Dandy-Walker variant.

Cerebellar Dysplastic Malformations

Abnormalities include Joubert syndrome, rhombencephalosynapsis, Lhermitte-Duclos disease, and focal cerebellar cortical dysplasia.

Sulci and Fissures

At 16 to 17 weeks' gestation, *parieto-occipital and calcarine sulci and fssures* can be first seen, and they are fully developed by 24 weeks. At 24 weeks' gestation, the *central sulcus* is first seen, and it is fully developed by 35 weeks. At 26 weeks' gestation, the *precentral sulcus* is first seen, and it is developed by 35 weeks. At 28 weeks' gestation, the *postcentral sulcus* is first seen, and it is developed by 35 weeks.

Fetal Brain MRI

At ~ 14 weeks, the trilaminar appearance of the fetal brain can be seen with MRI. The innermost (ventricular zone) and outermost (cortical plate) layers have low signal on T2-weighted images and high signal on T1-weighted images. The intervening zone has high signal on T2-weighted images and low signal on T1-weighted images.

From 15 to 23 weeks, five layers of the fetal brain can be seen. The innermost layer is the *ventricular zone* (VZ), including the *germinal matrix,* and it has a high signal on T1-weighted images and low signal on T2-weighted images. Immediately superficial to the VZ and germinal matrix, a high signal zone on T2-weighted images is the *periventricular zone.* Superficial to the periventricular zone is a low signal layer on T2-weighted images that represents the *subventricular and intermediate zones.* The ventricular/germinal matrix and subventricular zones are regions where most of the cellular proliferation of the cerebrum occurs. Superficial to the subventricular and intermediate zones is the *subplate zone,* which has low signal on T1-weighted images and high signal on T2-weighted images. The most superficial layer is the *cortical plate,* which has low signal on T2-weighted images and high signal on T1-weighted images, similar to the ventricular zone/germinal matrix.

Table 1.1 Congenital and histogenic malformations of the brain

- Disorders of Neural Tube Closure
  - Cephaloceles (meningoceles or meningoencephaloceles)
  - Atretic cephaloceles
  - Chiari I malformation
  - Chiari II malformation (Arnold Chiari)
  - Chiari III malformation
- Disorders of Diverticulation (formation of cerebral hemispheres and ventricles)
  - Alobar holoprosencephaly
  - Semilobar holoprosencephaly
  - Lobar holoprosencephaly
  - Syntelencephaly
  - Septo-optic dysplasia (de Morsier syndrome)
  - Arhinia/Arrhinenecephaly
- Neuronal Migration Disorders
  - Lissencephaly (agyria or "smooth brain")
  - Pachygyria (incomplete lissencephaly)
  - Gray matter heterotopia
  - Schizencephaly (split brain)
  - Unilateral hemimegalencephaly
  - Dysgenesis of the corpus callosum
- Malformations from Abnormal Neuronal and Glial Proliferation, Apoptosis, or Neonatal Ischemia
  - Microcephaly with simplified gyral pattern; microlissencephaly
  - Microcephaly from neonatal ischemia or infection
  - Sotos syndrome (megalencephaly, cerebral gigantism)
  - Benign familial megalencephaly
- Malformations in Cortical Development
  - Polymicrogyria
  - Focal cortical dysplasia without "balloon" cells
  - Transmantle cortical dysplasia with "balloon" cells
  - Hemispheric dysplasia
- CNS Malformations Related to Abnormal Pial Basement Membrane Formation (anomalies involving muscles, eye, and brain)
  - Walker-Warburg phenotype
  - Muscle eye-brain phenotype
  - Fukuyama congenital muscular dystrophy phenotype
- Cerebellar Malformations: Hypoplasia Syndromes
  - Cerebellar agenesis
  - Chiari II with vanishing cerebellum
  - Hypoplasia of cerebellar hemisphere
  - Dandy-Walker malformation
  - Vermian hypoplasia, also referred to as Dandy Walker variant
- Cerebellar Dysplastic Malformations
  - Joubert syndrome
  - Rhombencephalosynapsis
  - Lhermitte-Duclos disease
  - Focal cerebellar cortical dysplasia

Table 1.1 Congenital and histogenic malformations of the brain

Lesions	Imaging Findings	Comments
Disorders of Neural Tube Closure		
Cephalocele (meningocele or meningoencephalocele) (**Fig. 1.7, Fig. 1.8**, and **Fig. 1.9**)	Defect in skull through which there is herniation of either meninges and CSF (meningocele) or meninges, CSF, and brain tissue (meningoencephalocele).	Congenital malformation involving lack of separation of neuroectoderm from surface ectoderm, with resultant localized failure of bone formation. Occipital location most common in Western Hemisphere, frontoethmoidal location most common site in Southeast Asians. Other sites include parietal and sphenoid bones and between the frontal and nasal bones. Cephalocele can also result from trauma or surgery.
Atretic cephalocele (**Fig. 1.10**)	Subcutaneous scalp nodule that often contains high T2 signal with thin, low-signal fibrous bands. The nodule is adjacent to a skull defect and may involve intracranial dural venous sinuses. Can result in elevation of the torcular herophili and fenestration of the superior sagittal sinus.	Small defect in the skull (usually parietal bone) through which a small (5–15) cephalocele extends, resulting in an elevated, hairless, skin-covered scalp lesion. The atretic cephalocele connects to the intracranial space via fibrous bands. May be associated with other anomalies (Dandy-Walker malformation, callosal dysgenesis, others).

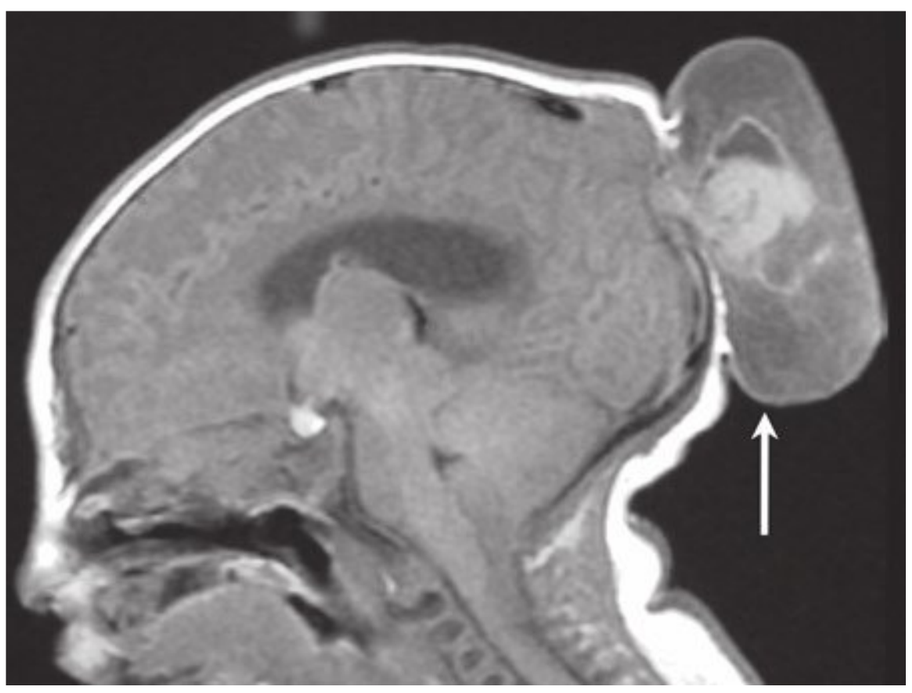

Fig. 1.7 Parietal meningoencephalocele. Sagittal T1-weighted imaging shows a localized skull defect through which damaged brain and meninges extend (arrow).

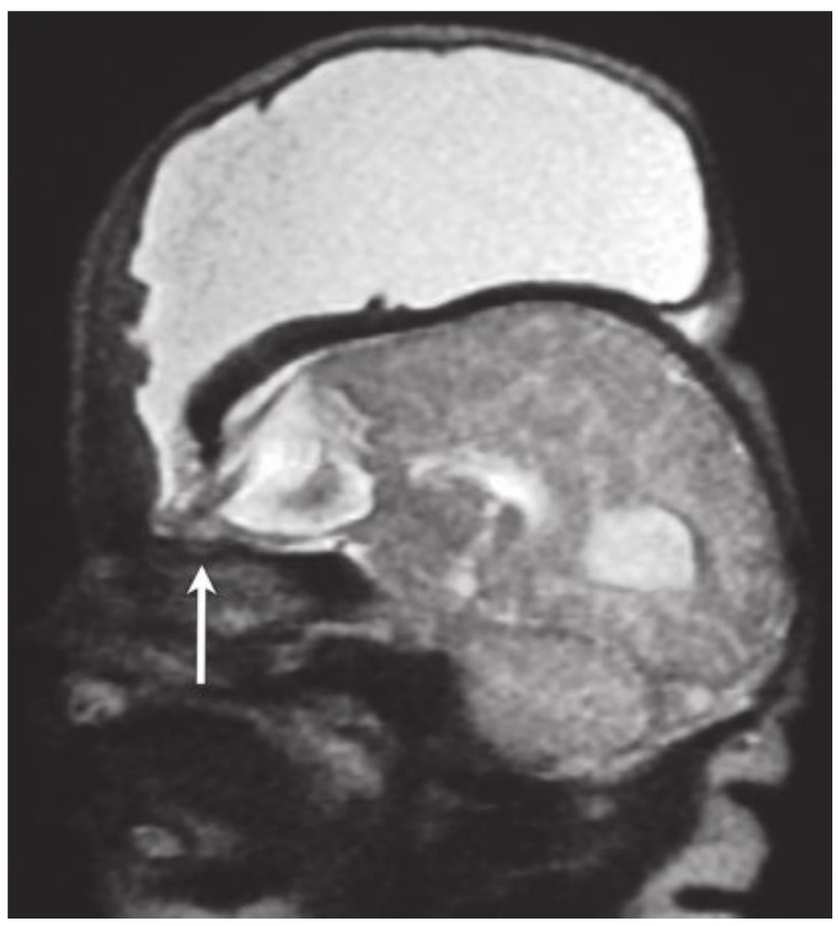

Fig. 1.8 Frontal gliocele. Sagittal T2-weighted imaging shows a localized skull defect in the frontal bone (arrow) through which damaged brain tissue and meninges extend. A large gliocele (glia-lined cyst) is seen overlying the upper calvarium.

Lesions	Imaging Findings	Comments
Chiari I malformation (**Fig. 1.11**)	Cerebellar tonsils extend more than 5 mm below the foramen magnum in adults, and 6 mm in children less than 10 years old. Syringohydromyelia in 20 to 40% Hydrocephalus in 25% Basilar impression in 25% Less common associations: Klippel-Feil syndrome, atlanto-occipital assimilation.	Cerebellar tonsillar ectopia. Most common anomaly of CNS. Not associated with myelomeningocele.
Chiari II malformation (Arnold-Chiari malformation) (**Fig. 1.12**)	Small posterior cranial fossa with gaping foramen magnum through which there is an inferiorly positioned vermis associated with a cervicomedullary kink. Beaked dorsal margin of the tectal plate. Myelomeningocele in nearly all patients. Hydrocephalus and syringomyelia common. Dilated lateral ventricles posteriorly (colpocephaly).	Complex anomaly involving the cerebrum, cerebellum, brainstem, spinal cord, ventricles, skull, and dura. Failure of fetal neural folds to develop properly, resulting in altered development affecting multiple sites of the CNS.
Chiari III malformation (**Fig. 1.13**)	Features of Chiari II plus lower occipital or high cervical encephalocele.	Rare anomaly associated with high mortality.

(continued on page 15)

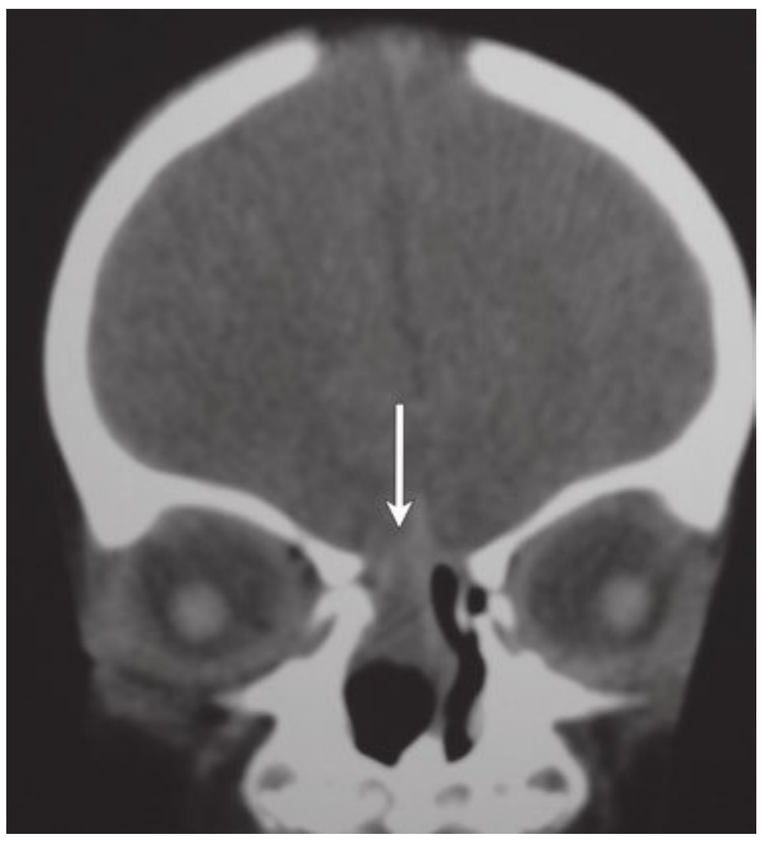

Fig. 1.9 Cephalocele. Coronal CT image shows a defect at the right cribiform plate with inferior extension of brain and meninges (arrow).

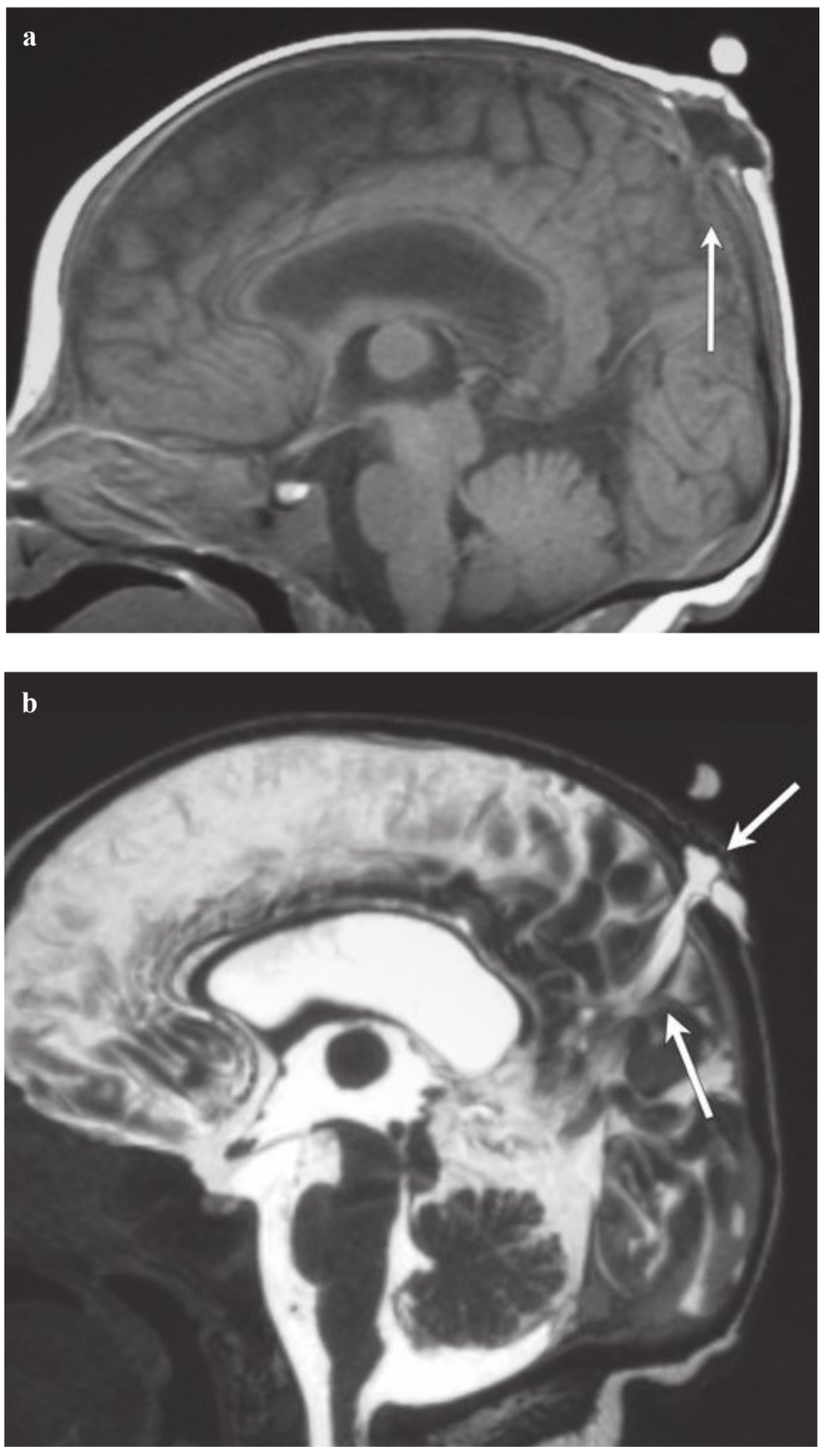

Fig. 1.10 Atretic cephalocele. **(a)** Sagittal T1-weighted imaging and **(b)** T2-weighted imaging show a subcutaneous scalp nodule with low signal on T1-weighted imaging (**a**, arrow) and high signal on T2-weighted imaging (**b**, arrows). The nodule extends intracranially through a small skull defect and then extends into a obliquely oriented straight venous sinus.

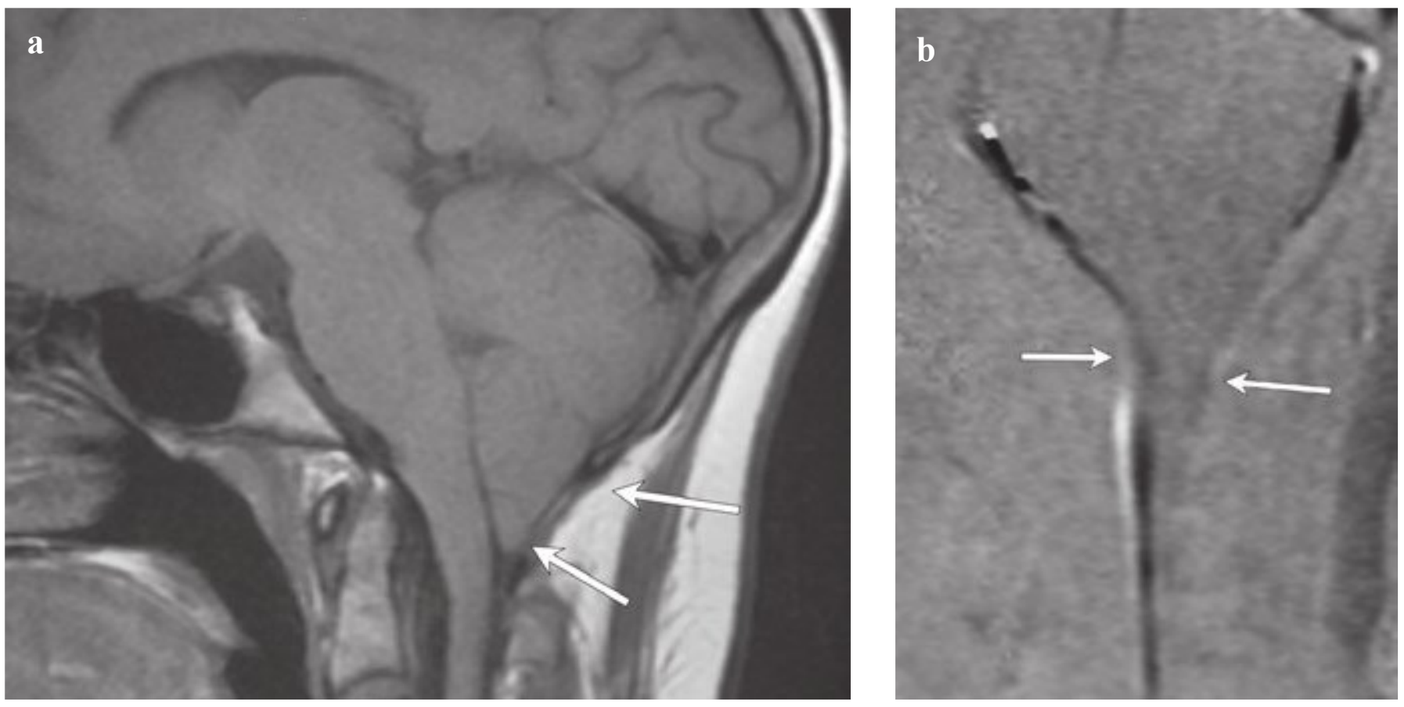

Fig. 1.11 Chiari I malformation. **(a)** Sagittal T1-weighted imaging shows the cerebellar tonsils extending below the foramen magnum to the level of the posterior arch of C1 (arrows). **(b)** CSF cine phase contrast image shows moderate-severe impedance of CSF flow ventrally at the foramen magnum and severe impedance of flow dorsally secondary to the Chiari I malformation (arrows).

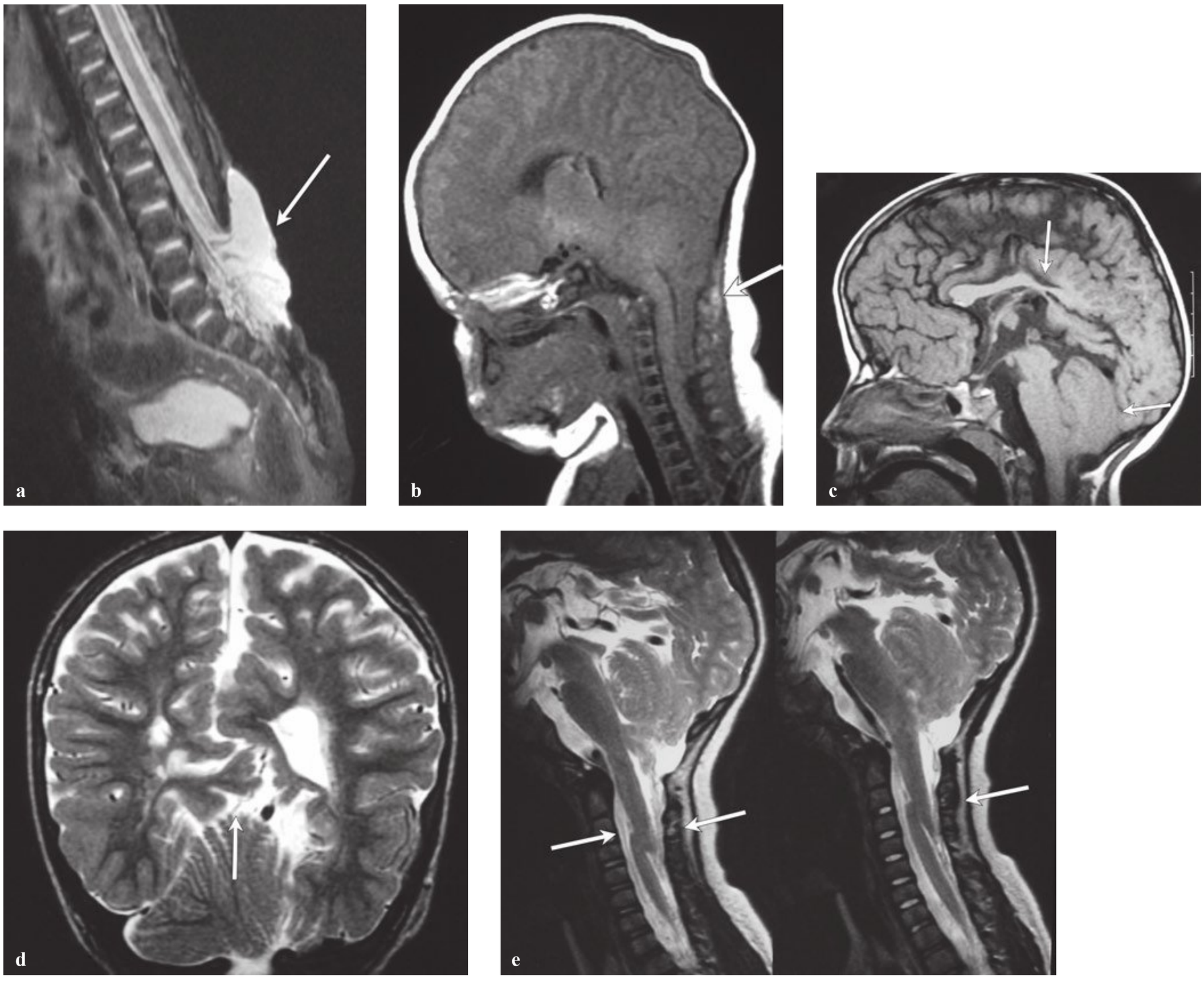

Fig. 1.12 Chiari II malformation. **(a)** Sagittal T2-weighted imaging shows a myelocele at the lumbosacral region where the unfolded neural tube (neural placode) extends through a zone of spina bifida where it is not covered by skin (arrow). **(b)** Sagittal T1-weighted imaging shows a small posterior cranial fossa and extension of the cerebellum through a widened foramen magnum, as well as a malformed fourth ventricle (arrow). **(c)** Sagittal T1-weighted imaging and **(d)** coronal T2-weighted imaging in another patient show dysgenesis of the corpus callosum, beaked shape of the tectal plate, and fenestrated falx with close approximation of medial gyri of both cerebral hemispheres (arrow). **(e)** Sagittal T2-weighted imaging shows a cervicomedullary kink in another patient (arrows).

Table 1.1 (cont.) Congenital and histogenic malformations of the brain

Lesions	Imaging Findings	Comments
Disorders of Diverticulation (Formation of Cerebral Hemispheres and Ventricles)		
Holoprosencephaly (**Fig. 1.14, Fig. 1.15, Fig. 1.16**, and **Fig. 1.17**)	Alobar: Large monoventricle with posterior midline cyst, lack of hemisphere formation, with absence of falx, corpus callosum, and septum pellucidum. Fused thalami. Can be associated with facial anomalies (facial clefts, arhinia, hypotelorism, cyclopia). Semilobar: Anterior frontal portions of brain fused across midline, lacking interhemispheric fissure anteriorly. Partial formation of interhemispheric fissure posteriorly and occipital and temporal horns of ventricles, with partially fused thalami. Absent corpus callosum anteriorly but splenium is present. Absent septum pellucidum. Associated with mild craniofacial anomalies. Lobar: Nearly complete formation of interhemispheric fissure and ventricles. Fused inferior portions of frontal lobes, dysgenesis of corpus callosum with formation of posterior portion without anterior portion, malformed frontal horns of lateral ventricles, absence of septum pellucidum, separate thalami, and neuronal migration disorders. Syntelencephaly (middle interhemispheric variant): Partial formation of interhemispheric fissure in the anterior and posterior regions, with fusion of the portions of the upper frontal and/or parietal lobes. Genu and splenium of the corpus callosum can be observed with localized absence/defect of the central body of the corpus callosum. Septum pellucidum is often absent.	Holoprosencephaly: Spectrum of diverticulation disorders that occur during weeks 4 to 6 of gestation; characterized by absent or partial cleavage and differentiation of the embryonic forebrain cerebrum (prosencephalon) into hemispheres and lobes. Causes include maternal diabetes, teratogens, and fetal genetic abnormalities, such as trisomy 16 (Patau syndrome) and trisomy 18 (Edwards syndrome). Familial holoprosencephaly: mutations of HPE1 on chromosome 21q22.3, HPE2 on 2p21, HPE3 on 7q36, HPE4 on 18p, HPE5 on 13q32, HPE6 on 2q37, HPE7 on 9q22.3, HPE8 on 14q13, and HPE9 on 2q14, the genes related to ventral and dorsal induction of the prosencephalon. ZIC2 mutations are also associated with holoprosencephaly. Clinical manifestations depend on severity of malformation and include early death, seizures, mental retardation, facial dysmorphism, and developmental delay. Patients with syntelencephaly often have mild to moderate cognitive dysfunction, spasticity, and mild visual impairment.

(continued on page 18)

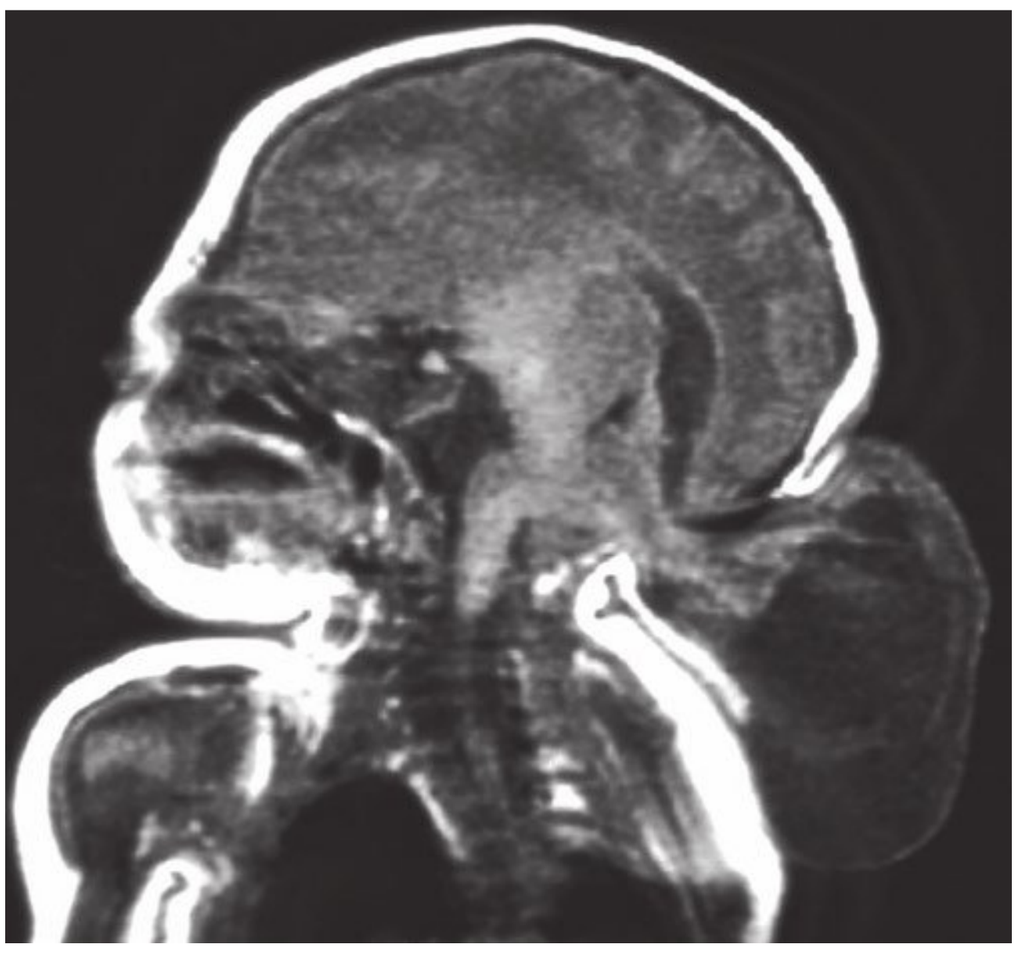

Fig. 1.13 Chiari III. Sagittal T1-weighted imaging shows a low occipital meningoencephalocele in this patient with a lumbosacral myelomeningocele and other findings of a Chiari II malformation.

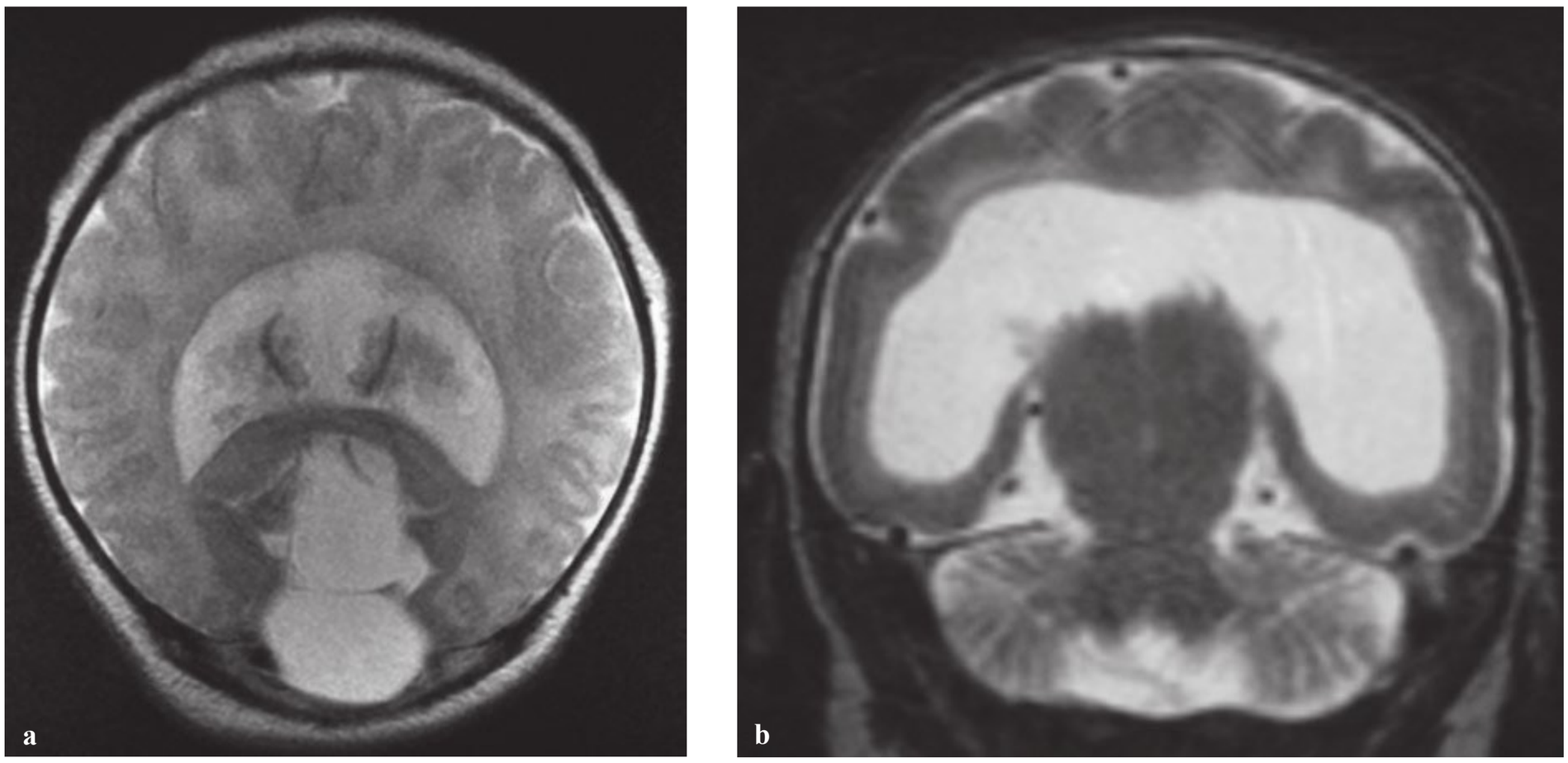

Fig. 1.14 Alobar holoprosencephaly. **(a)** Axial and **(b)** coronal T2-weighted imaging in two patients with alobar holoprosencephaly show a monoventricle, fused thalami, and absence of interhemispheric fissure and corpus callosum, as well as lack of cerebral lobe formation.

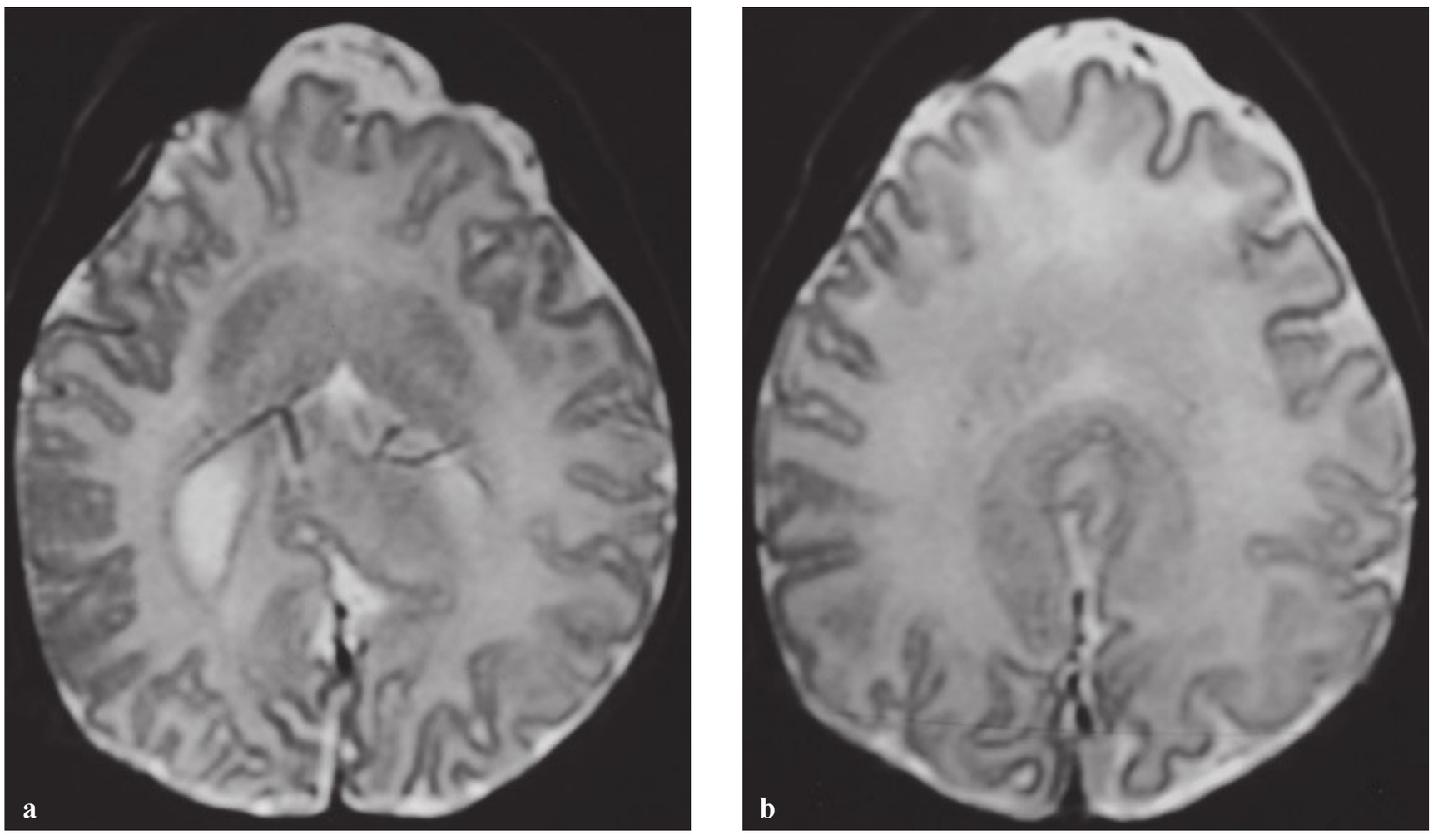

Fig. 1.15 Semilobar holoprosencephaly. **(a,b)** Axial T2-weighted imaging shows fusion of the anterior portion of the brain with presence of only the posterior portion of the interhemispheric fissure. Only the mid and posterior portions of the corpus callosum are present, with absent formation of the anterior portion.

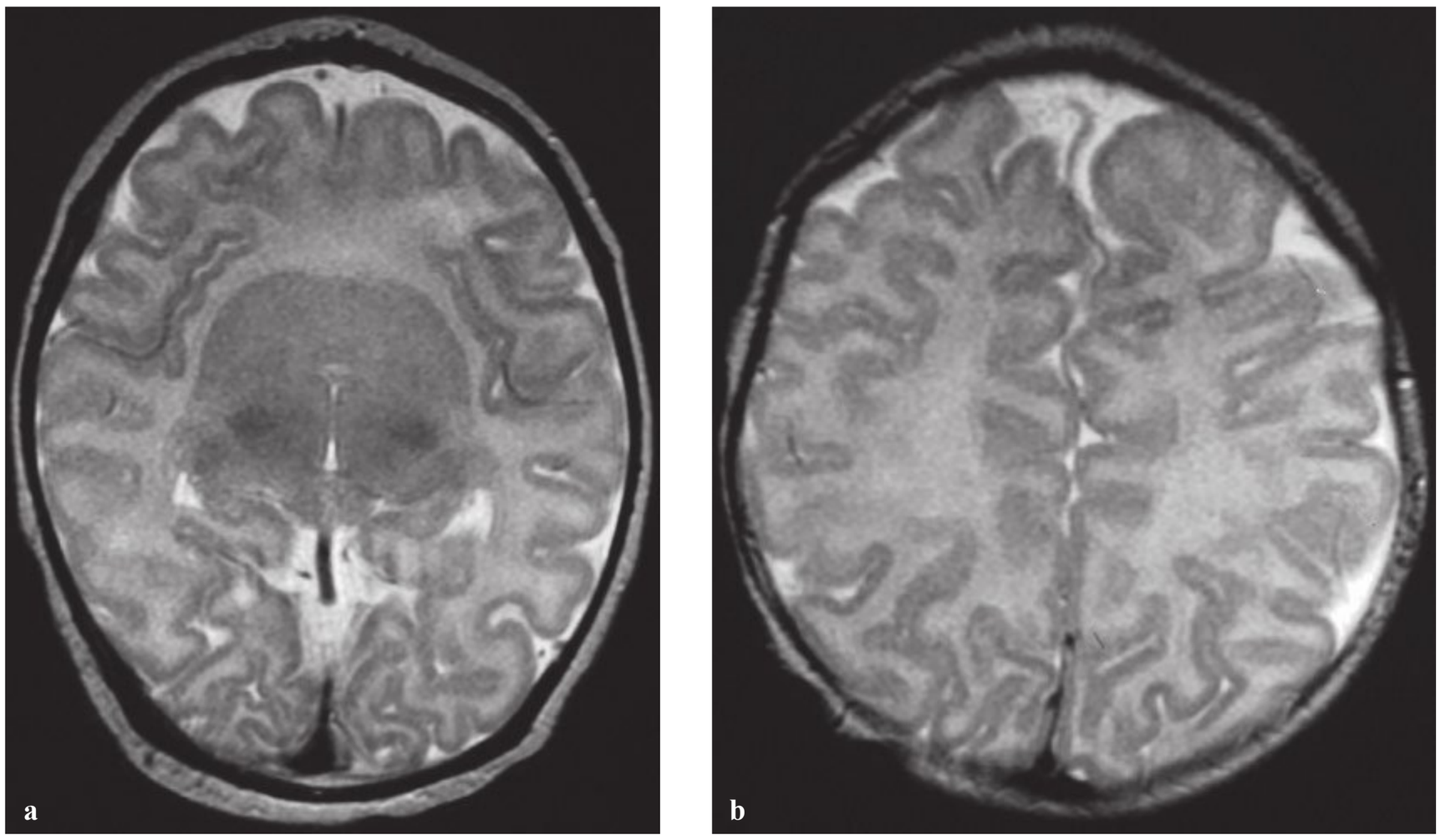

Fig. 1.16 Lobar holoprosencephaly. **(a,b)** Axial T2-weighted imaging show fusion of the inferior portions of the frontal lobes. The other portions of the frontal lobes are separated, as are the parietal and occipital lobes. Only the mid and posterior portions of the corpus callosum are present, with absent formation of the anterior portion.

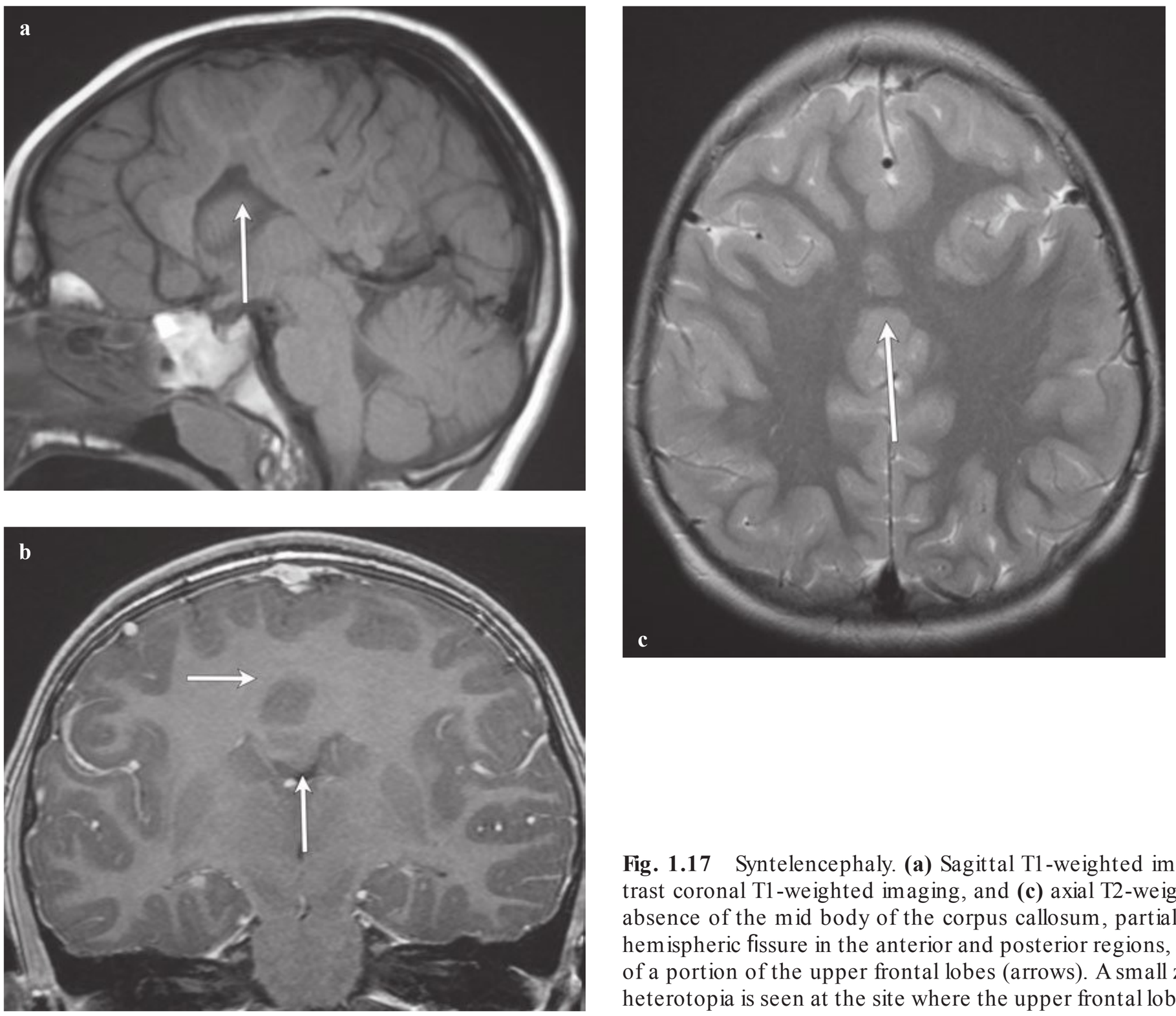

Fig. 1.17 Syntelencephaly. **(a)** Sagittal T1-weighted imaging, **(b)** postcontrast coronal T1-weighted imaging, and **(c)** axial T2-weighted imaging show absence of the mid body of the corpus callosum, partial formation of interhemispheric fissure in the anterior and posterior regions, and localized fusion of a portion of the upper frontal lobes (arrows). A small zone of gray matter heterotopia is seen at the site where the upper frontal lobes are fused.

Table 1.1 (cont.) Congenital and histogenic malformations of the brain

Lesions	Imaging Findings	Comments
Septo-optic dysplasia (de Morsier syndrome) (**Fig. 1.18**)	Dysgenesis/hypoplasia or agenesis of septum pellucidum, optic nerve hypoplasia, squared frontal horns, associated with schizencephaly in 50% Optic canals are often small. May be associated with gray matter heterotopia and polymicrogyria.	Patients can have nystagmus, decreased visual acuity, and hypothalamic-pituitary disorders (decreased thyroid-stimulating hormone and/or growth hormone). Clinical exam shows small optic discs. May be sporadic (from in utero insults) or caused by mutation-related abnormal gene expression during formation of the basal prosencephalon (HESX1 gene on chromosome 3p21.1–3p21.2 accounts for less than 1% of cases). Some findings overlap those of mild lobar holoprosencephaly.
Arhinia/Arrhinencephaly (**Fig. 1.19**)	Absence of olfactory lobes, olfactory sulci, and olfactory bulbs confirmed on coronal T1-weighted images or T2-weighted images. Anomalies of the corpus callosum, hypothalamus, and pituitary gland may also be seen.	Arhinia refers to absence of nose formation, and arrhinencephaly refers to congenital absence of the olfactory lobes. Typically associated with other congenital craniofacial anomalies, such as cleft palate/lip, hypertelorism, and hypoplasia of the nasal cavity. Considered to result from insult in utero or genetic mutation affecting formation of the embryonic prosencephalon and cerebral vesicles at 42 days' gestation.

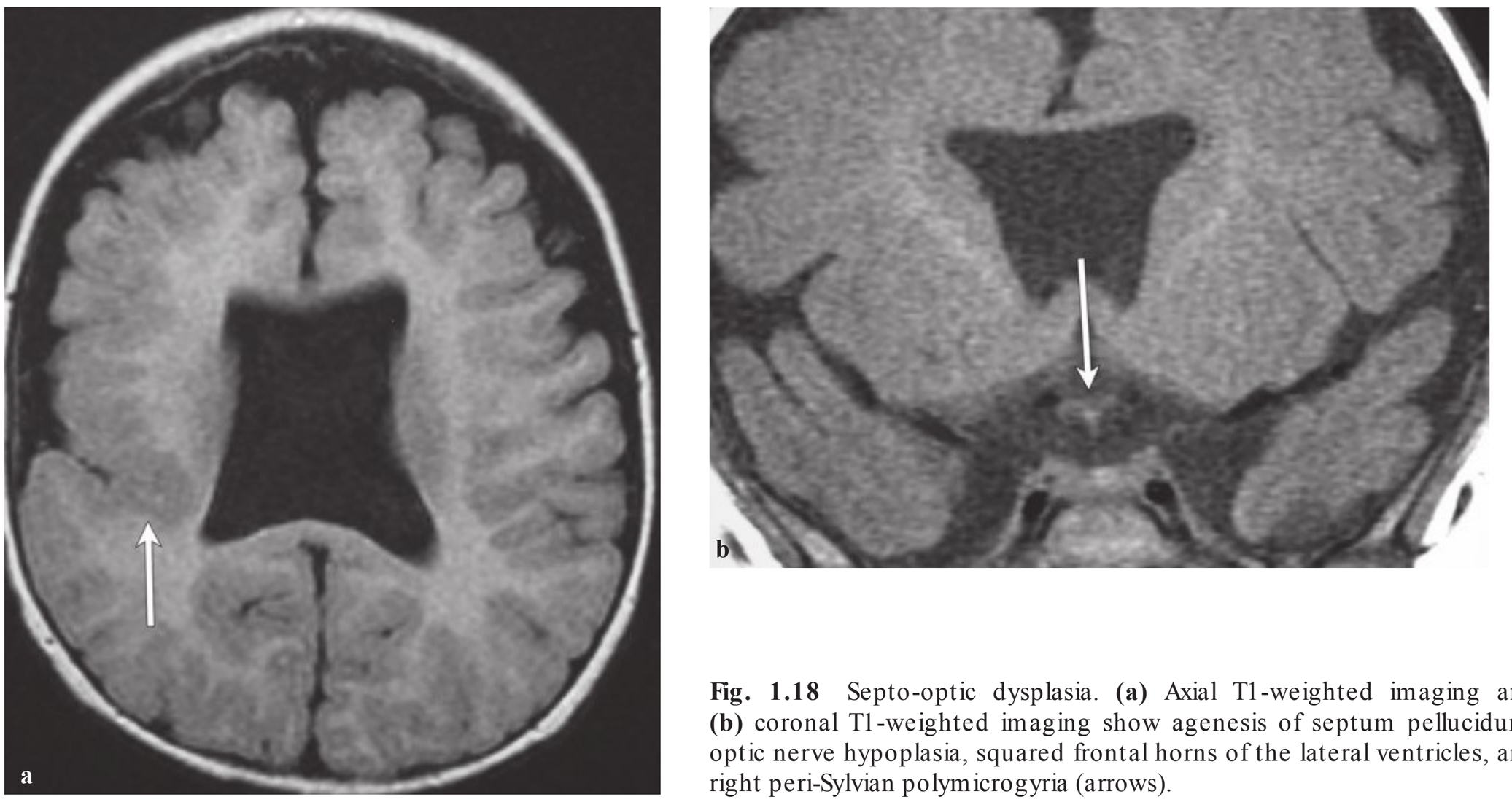

Fig. 1.18 Septo-optic dysplasia. **(a)** Axial T1-weighted imaging and **(b)** coronal T1-weighted imaging show agenesis of septum pellucidum, optic nerve hypoplasia, squared frontal horns of the lateral ventricles, and right peri-Sylvian polymicrogyria (arrows).

Lesions	Imaging Findings	Comments
Neuronal Migration Disorders		
Lissencephaly (agyria or "smooth brain") (**Fig. 1.20**)	Absent or incomplete formation of gyri and sulci, with shallow sylvian fissures and "figure 8" appearance of brain on axial images, abnormally thick cortex, and gray matter heterotopia with smooth gray–white matter interface.	Severe disorder of neuronal migration (occurs during weeks 7 to 16 of gestation) with absent or incomplete formation of gyri, sulci, and sylvian fissures. Typically in association with microcephaly (defined as head circumference three standard deviations below the mean for age and sex). Associated with severe mental retardation, developmental delay, seizures, and early death. Other associated CNS anomalies include dysgenesis of corpus callosum, hypoplastic thalami, and cephalocele. Associated with mutations of LIS gene at 17p13.3 on chromosome 17 (Miller-Dieker syndrome), DCX gene at Xq22.3-q23, and RELN gene at 7q22.

(continued on page 20)

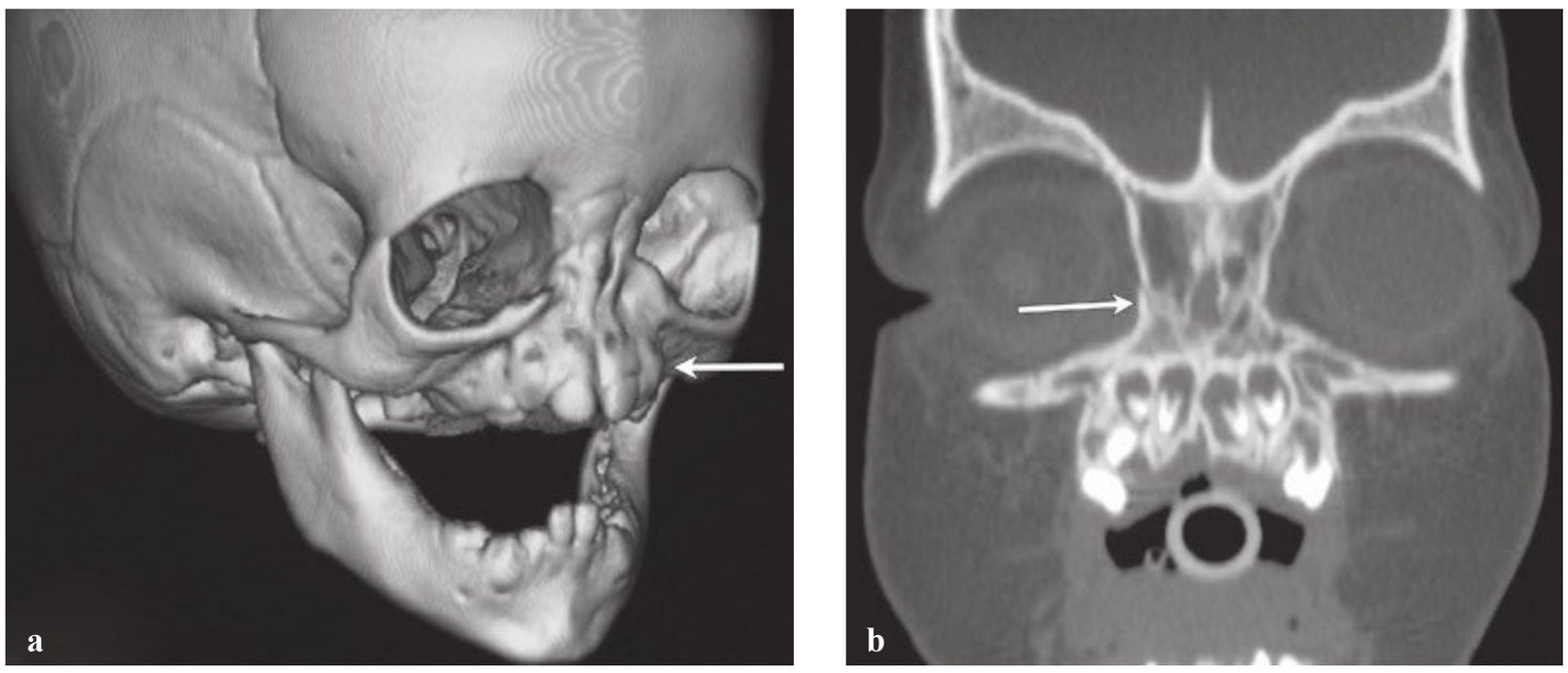

Fig. 1.19 Arhinia. **(a)** Oblique coronal volume-rendered CT image and **(b)** coronal CT image show lack of formation of the nasal bones and nasal cavity (arrows).

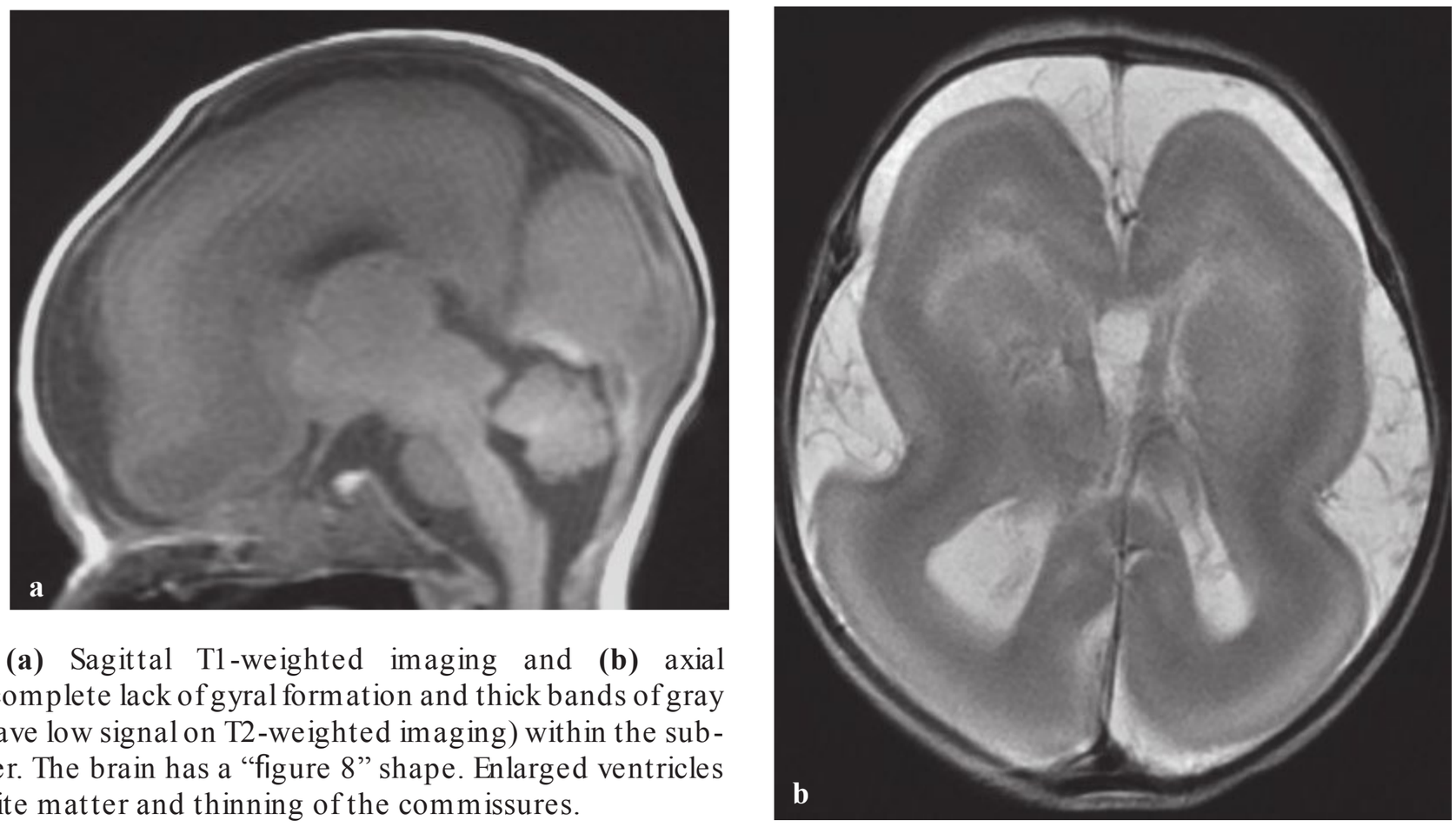

Fig. 1.20 Lissencephaly. **(a)** Sagittal T1-weighted imaging and **(b)** axial T2-weighted imaging show complete lack of gyral formation and thick bands of gray matter heterotopia (which have low signal on T2-weighted imaging) within the subcortical cerebral white matter. The brain has a "figure 8" shape. Enlarged ventricles are seen, with paucity of white matter and thinning of the commissures.

Table 1.1 (cont.) Congenital and histogenic malformations of the brain

Lesions	Imaging Findings	Comments
Pachygyria (incomplete lissencephaly) (**Fig. 1.21**)	Thick gyri with shallow sulci involving all or portions of the brain. Thickened cortex with relatively smooth gray–white interface; may have areas of high signal in the white matter (gliosis) on T2-weighted images.	Severe disorder of neuronal migration with etiologies similar to lissencephaly. Clinical findings related to extent and severity of the malformation.
Gray matter heterotopia (**Fig. 1.22, Fig. 1.23**, and **Fig. 1.24**)	Laminar heterotopia appears as a band or bands of MRI signal isointense to gray matter within the cerebral white matter (**Fig. 1.22**). Nodular heterotopia appears as one or more nodules of MRI signal isointense to gray matter along the ventricles or within the cerebral white matter (**Fig. 1.23**). Focal subcortical heterotopia can be seen as irregular nodular or multinodular masslike zones in subcortical regions with MRI signal isointense to gray matter (**Fig. 1.24**).	Disorder of neuronal migration (at 7 to 22 weeks of gestation) where a collection or layer of neurons is located between the ventricles and cerebral cortex. Can have a bandlike (laminar) or nodular appearance; typically, MRI signal is isointense to gray matter, and may be unilateral or bilateral. Associated with seizures and schizencephaly.

(continued on page 22)

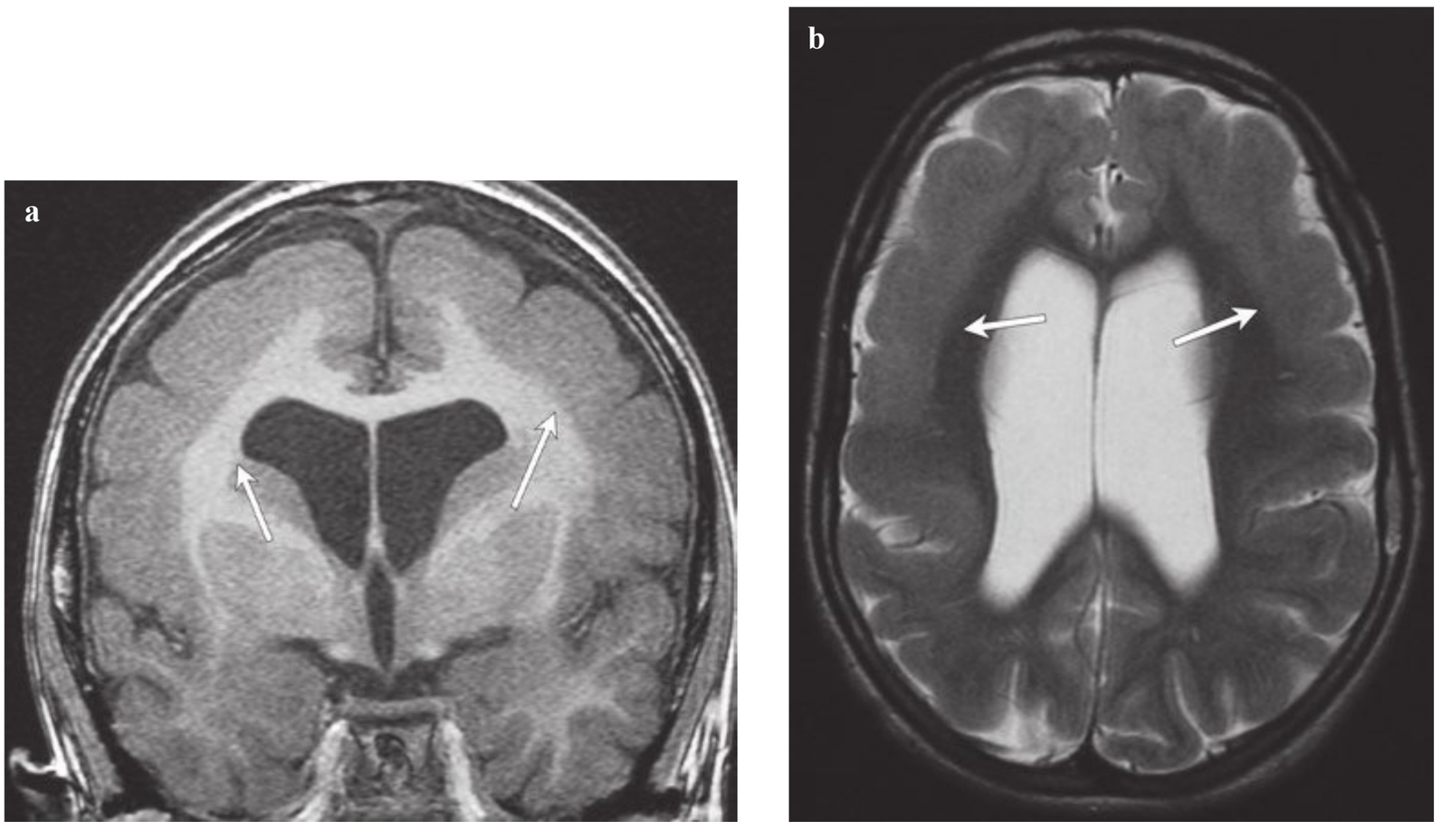

Fig. 1.21 Pachygyria. **(a)** Coronal T1-weighted imaging and **(b)** axial T2-weighted imaging show thick gyri with shallow sulci involving frontal lobes (arrows). The thickened cortex has a smooth gray–white interface.

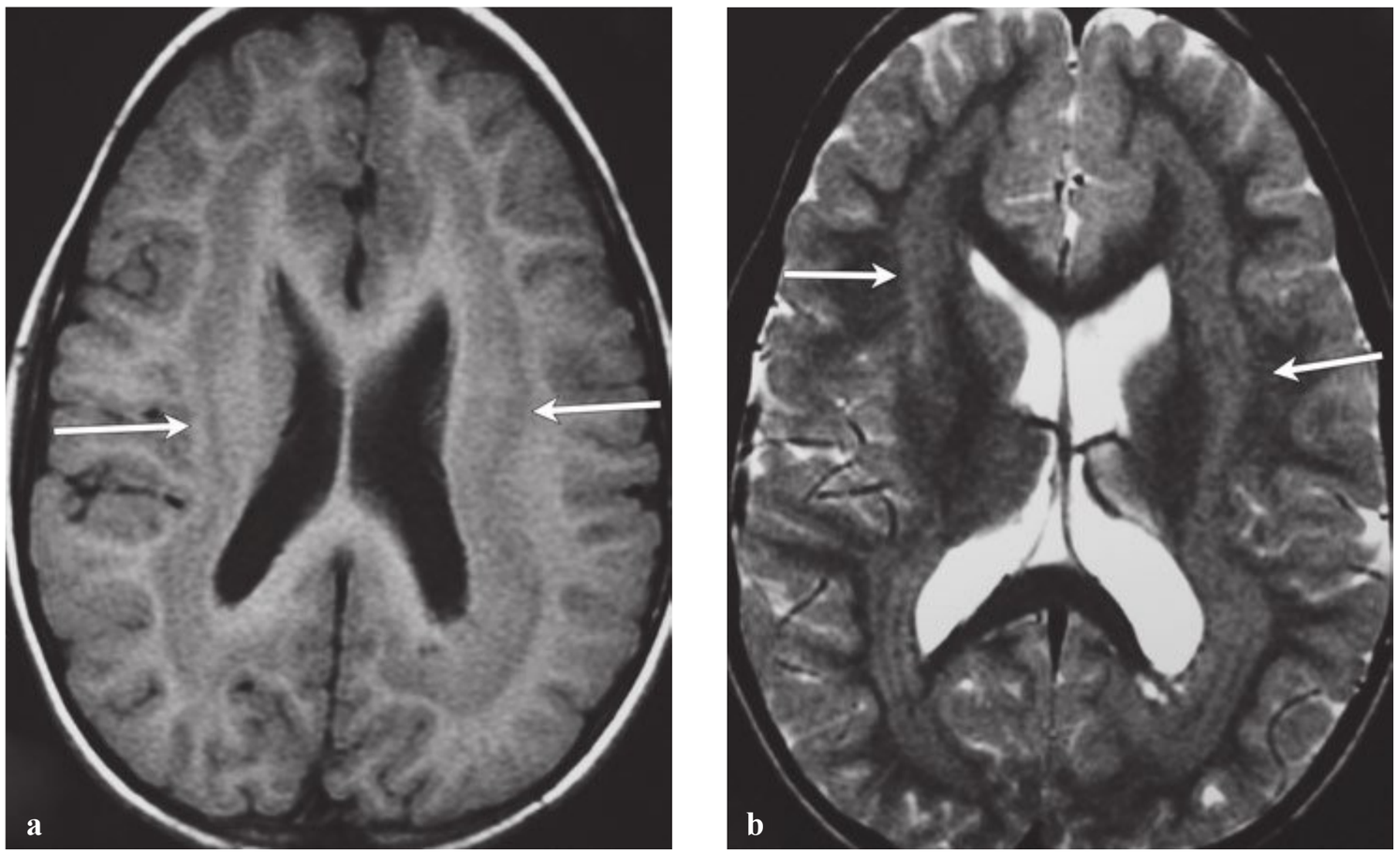

Fig. 1.22 Gray matter heterotopia, band (laminar) type. **(a)** Axial T1-weighted imaging and **(b)** axial T2-weighted imaging show bands with intermediate signal in the cerebral white matter that have an isointense signal relative to cortical gray matter (arrows), representing gray matter heterotopia.

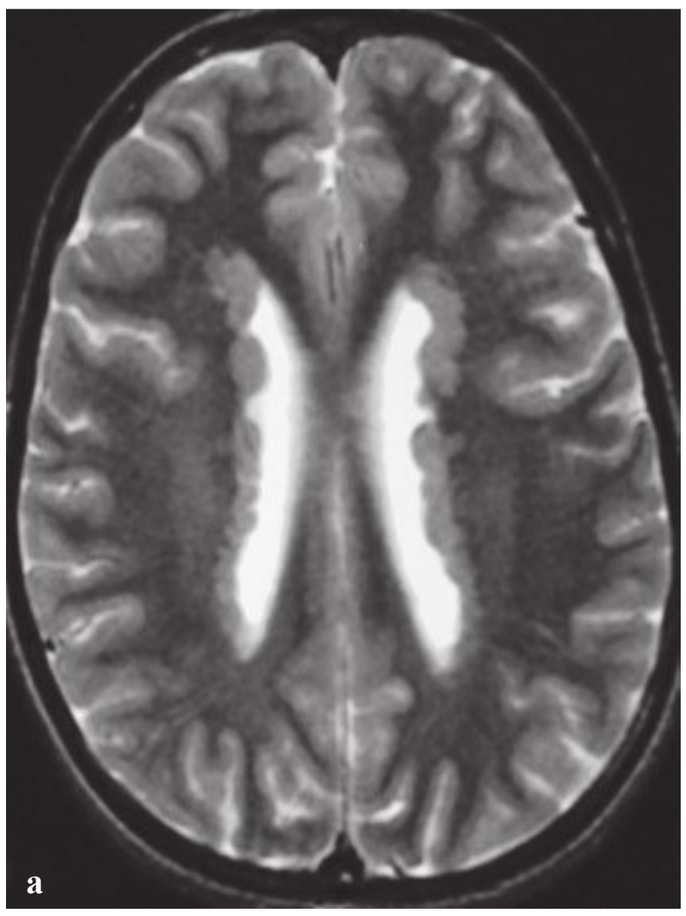

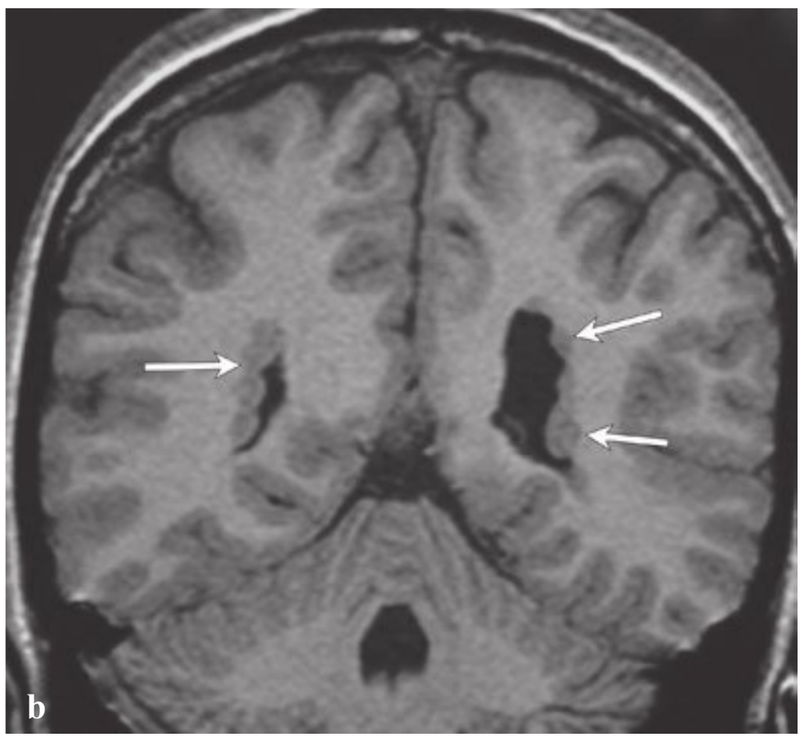

Fig. 1.23 Gray matter heterotopia, nodular ependymal type. **(a)** Axial T2-weighted imaging and **(b)** coronal T1-weighted imaging show nodular zones along the margins of the lateral ventricles that have intermediate signal that is isointense to gray matter (arrows).

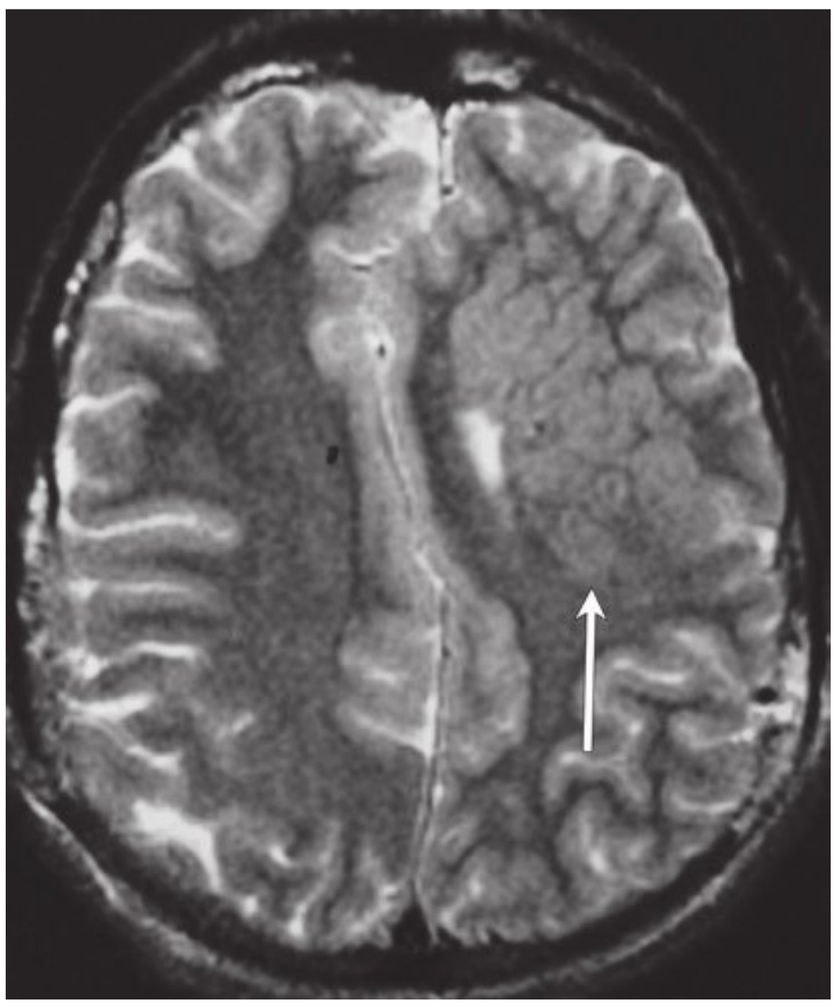

Fig. 1.24 Gray matter heterotopia, subcortical masslike type. Axial T2-weighted imaging shows a masslike zone with gray matter signal involving the anterior left frontal lobe (arrow).

Table 1.1 (cont.) Congenital and histogenic malformations of the brain

Lesions	Imaging Findings	Comments
Schizencephaly (split brain) (**Fig. 1.25** and **Fig. 1.26**)	Uni- or bilateral clefts in brain extending from ventricle to cortical surface lined by gray matter heterotopia, which may be polymicrogyric. The clefts may be narrow (closed lips, **Fig. 1.25**) or wide (open lips, **Fig. 1.26**).	Association with seizures, blindness, retardation, and other CNS anomalies (septo-optic dysplasia, etc.). Clinical manifestations related to severity of malformation. Cause is ischemia or insult to portion of germinal matrix before hemisphere formation.
Unilateral hemimegalencephaly (**Fig. 1.27** and **Fig. 1.28**)	Complex hypertrophic congenital anomaly with enlargement of all or a portion of one cerebral hemisphere, with nodular or multinodular regions of gray matter heterotopia, cortical dysplasia, and enlargement of the ipsilateral lateral ventricle. Zones with high signal on T2-weighted images may occur in the white matter.	Heterogeneous sporadic disorder with hamartomatous overgrowth of one cerebral hemisphere secondary to disturbances in neuronal proliferation and migration and in cortical organization. May be associated with unilateral hemihypertrophy and/or cutaneous abnormalities. Can occur in multisystem disorders with overgrowth of various tissues, such as Proteus syndrome, caused by mosaic mutation of the AKT1 gene, CLOVES syndrome (congenital lipomatous overgrowth, vascular malformation, epidermal nevi, scoliosis and spine deformities), and MCAP (megalencephaly-capillary malformation), caused by somatic mutations of the PIK3CA gene.

(continued on page 24)

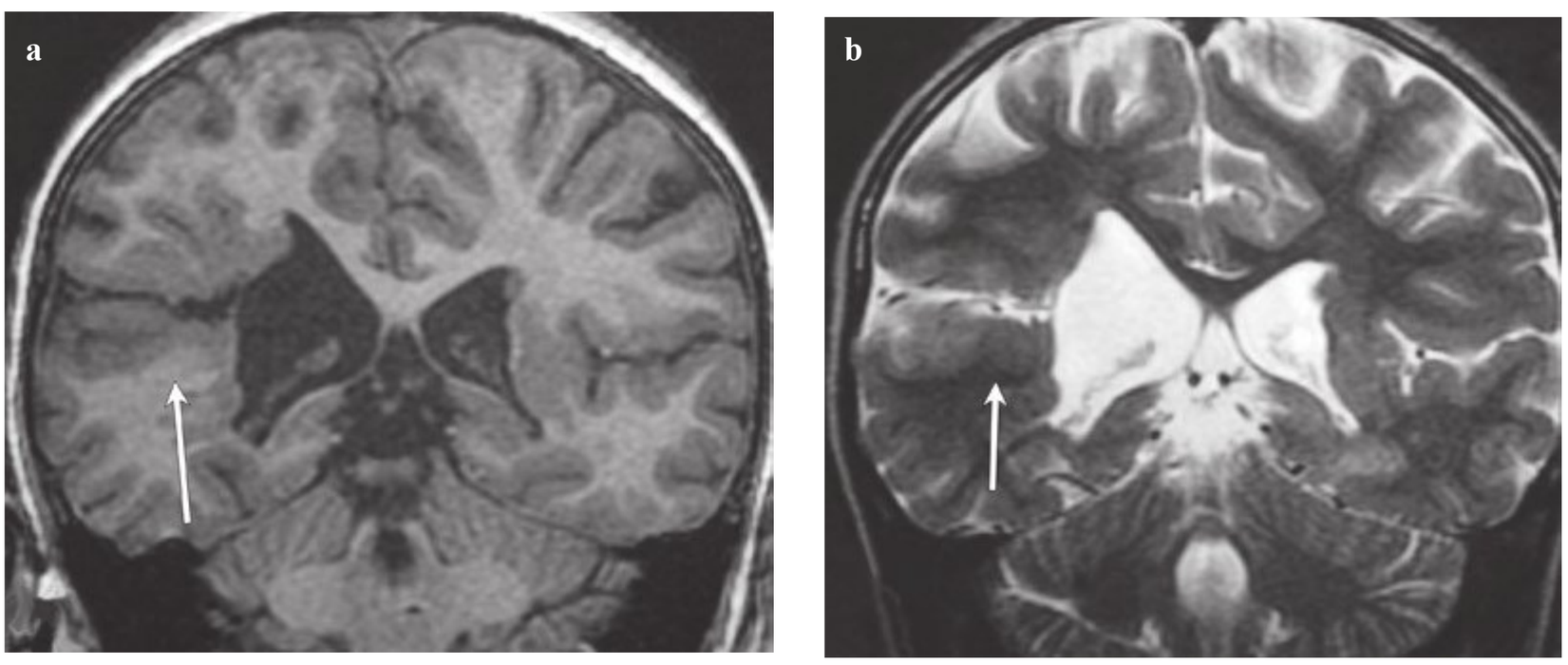

Fig. 1.25 Schizencephaly, closed-lip type. **(a)** Coronal T1-weighted imaging and **(b)** coronal T2-weighted imaging show a cleft extending from the ventricle to the pial surface that is lined by gray matter heterotopia (arrows). Also present is bilateral nodular gray matter heterotopia along the lateral ventricles.

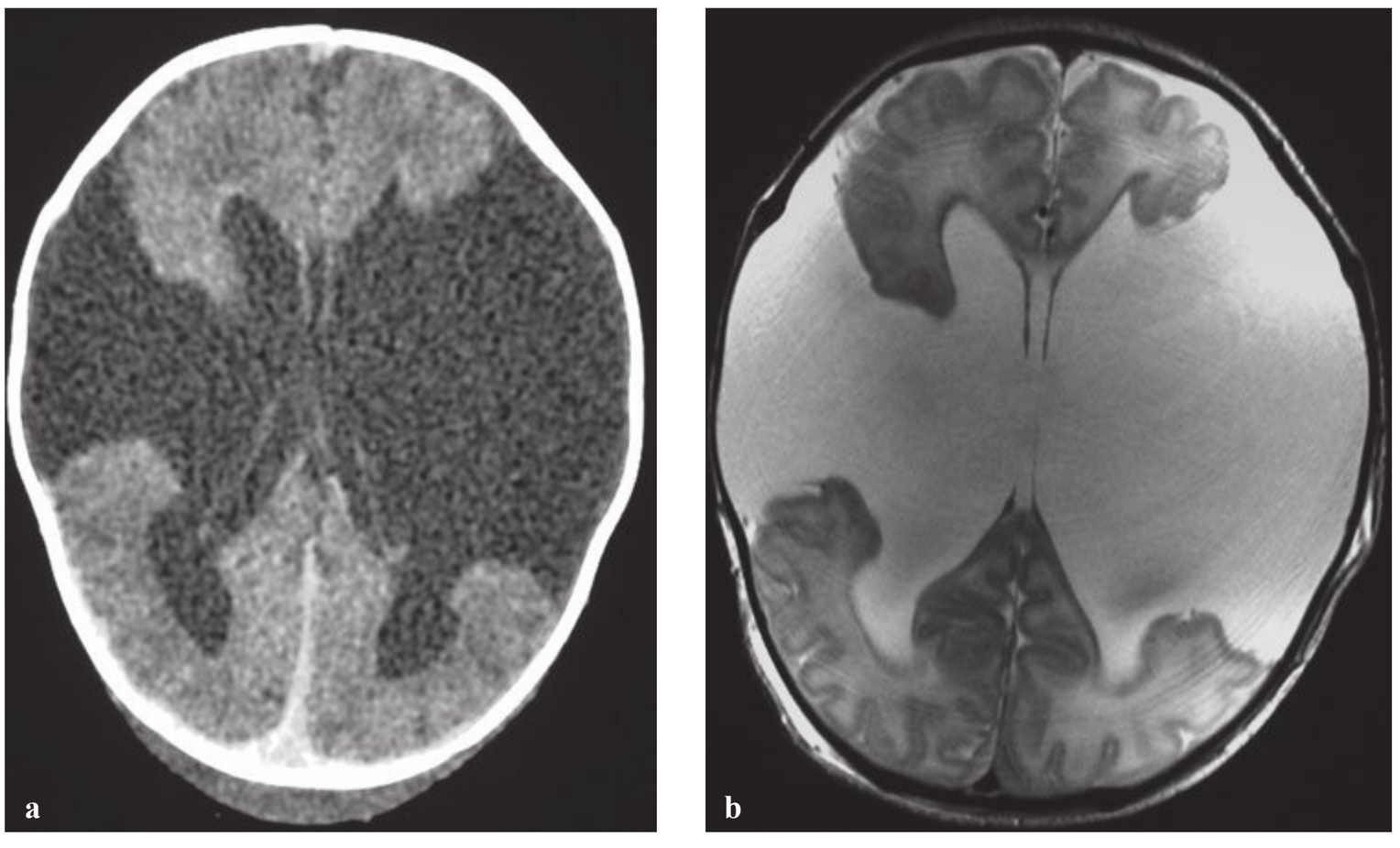

Fig. 1.26 Schizencephaly, open-lip type. **(a)** Axial CT image and **(b)** axial T2-weighted imaging show bilateral defects in the brain, with large zones of communication between the lateral ventricles and subarachnoid space that are lined with gray matter.

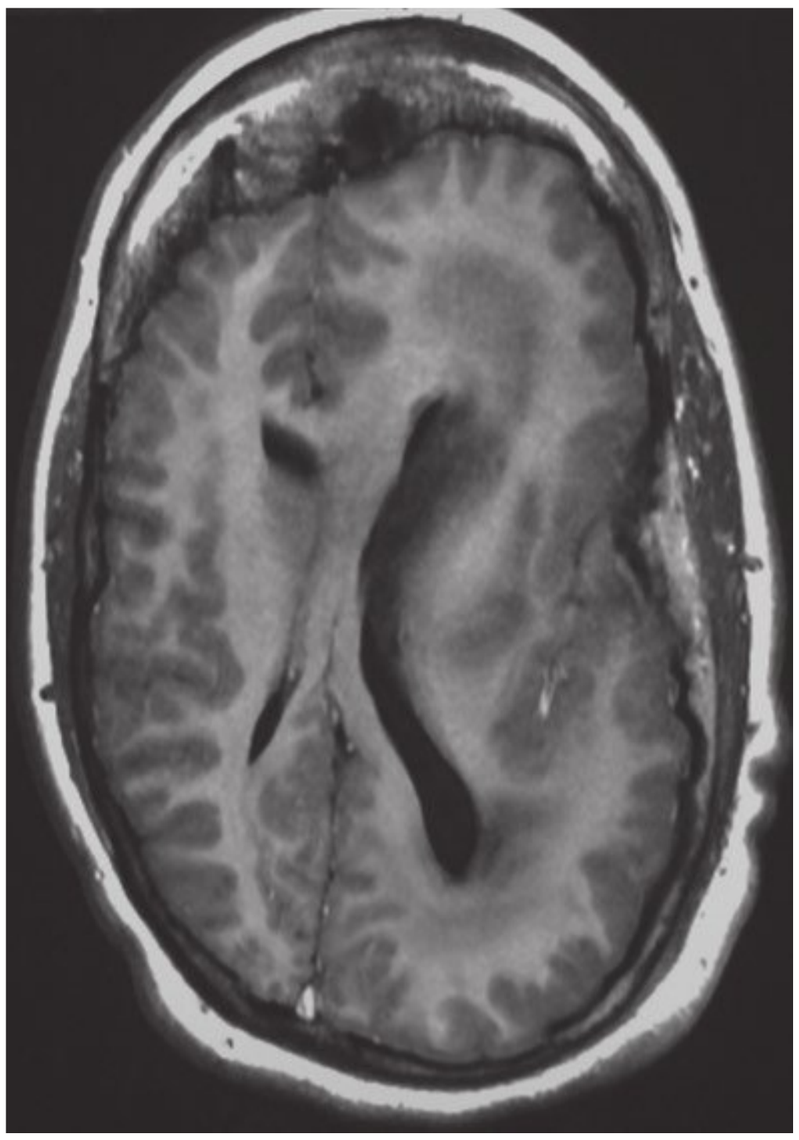

Fig. 1.27 Unilateral hemimegalencephaly. Axial T1-weighted imaging shows enlargement of the left cerebral hemisphere, which has abnormal thickened cerebral cortex and gyri, and a slightly enlarged left lateral ventricle.

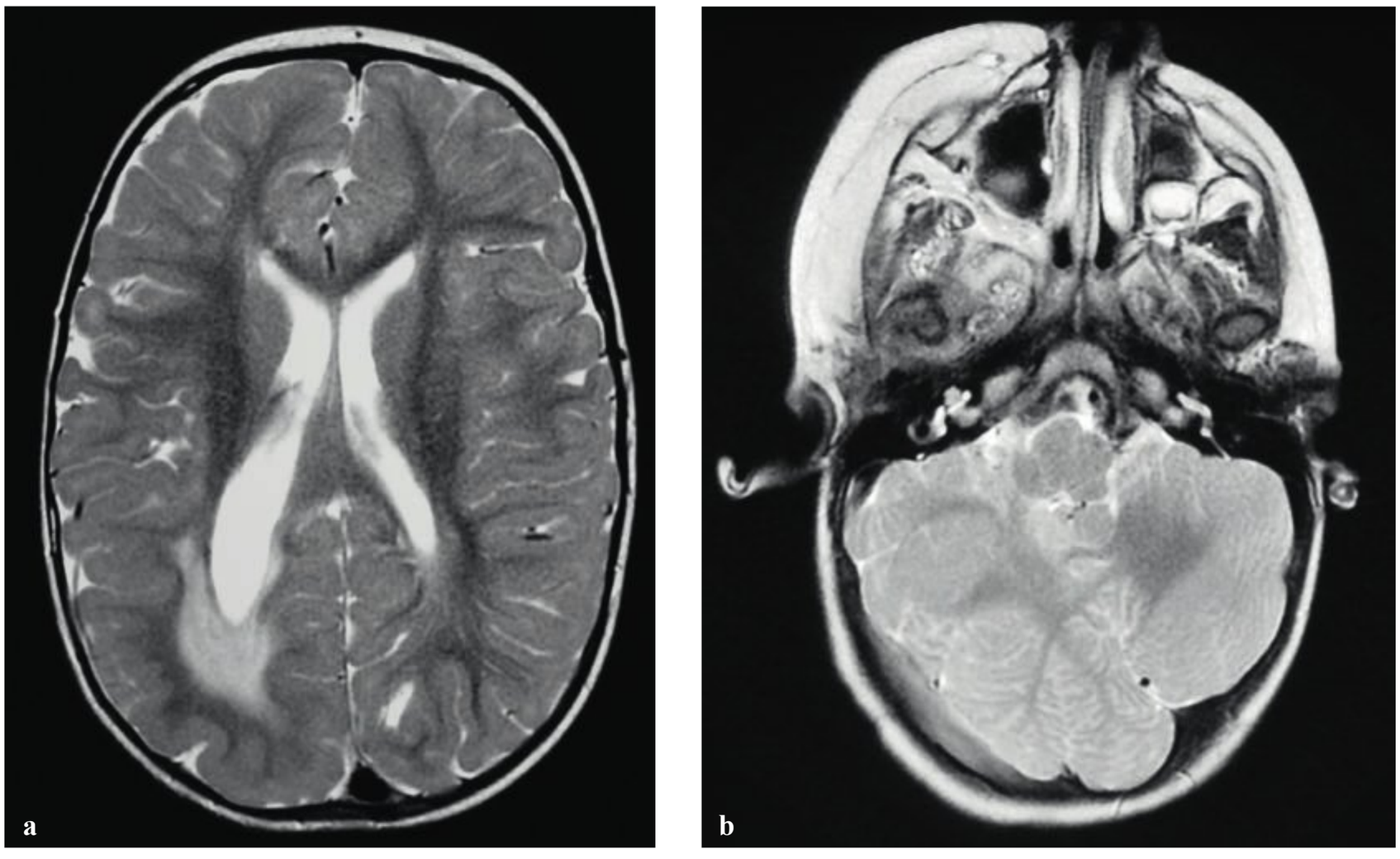

Fig. 1.28 Unilateral hemimegalencephaly in an 18-month-old male with CLOVES syndrome. **(a)** Axial T2-weighted imaging shows asymmetric enlargement of the right cerebral hemisphere with abnormal irregular and thickened cerebral cortex and gyri, dilated right lateral ventricle, and high-signal gliosis in the white matter. **(b)** Axial T2-weighted imaging shows asymmetric abnormal enlargement of the right cerebellar hemisphere, which has an abnormal irregular gyral pattern. Also seen is abnormal lipomatous overgrowth at the right side of the face.

Table 1.1 (cont.) Congenital and histogenic malformations of the brain

Lesions	Imaging Findings	Comments
Dysgenesis of the corpus callosum (**Fig. 1.29** and **Fig. 1.30**)	Spectrum of abnormalities ranging from complete to partial absence of the corpus callosum. Widely separated and parallel orientations of frontal horns and bodies of lateral ventricles, high position of third ventricle in relation to interhemispheric fissure, and colpocephaly. Associated with interhemispheric cysts, lipomas, and anomalies like Chiari II, gray matter heterotopia, Dandy-Walker malformation, holoprosencephaly, azygous anterior cerebral artery, cephalocele, and others.	Failure or incomplete formation of corpus callosum (7 to 18 weeks of gestation). Axons that normally cross from one hemisphere to the other are aligned parallel along the medial walls of lateral ventricles (bundles of Probst).

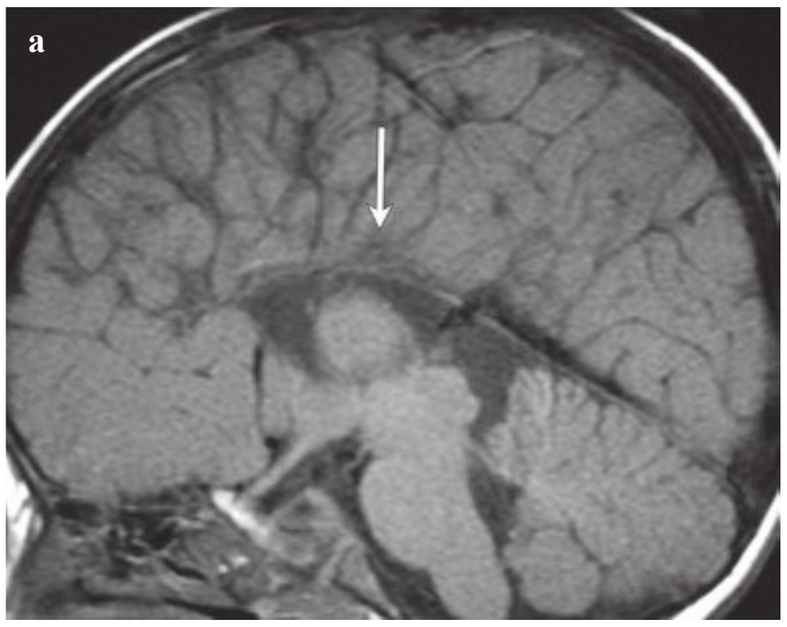

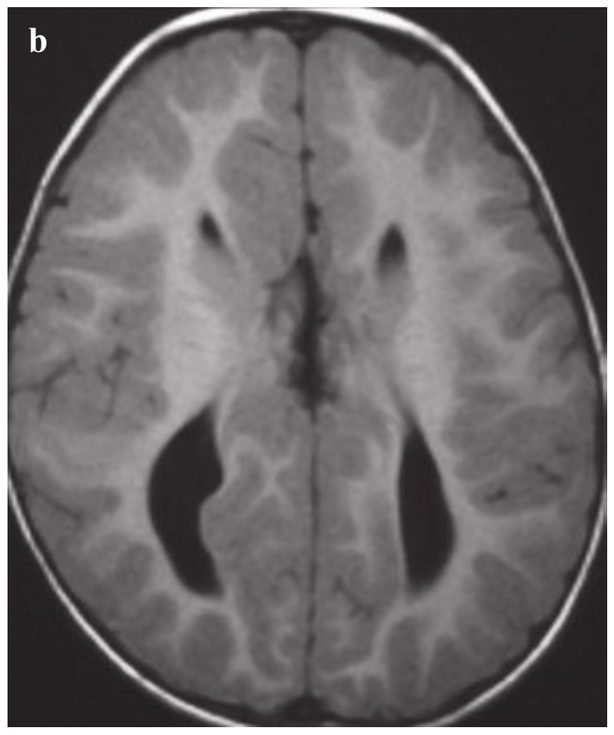

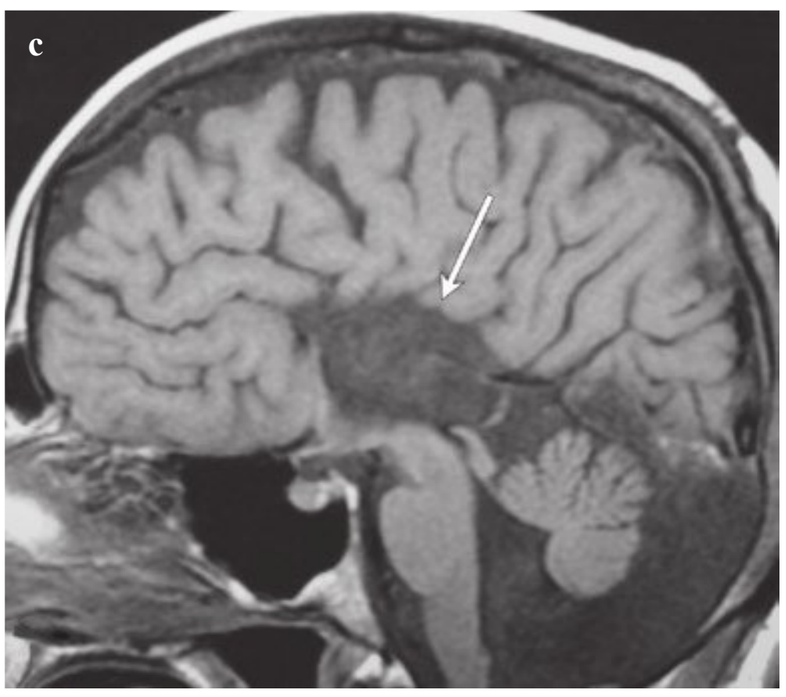

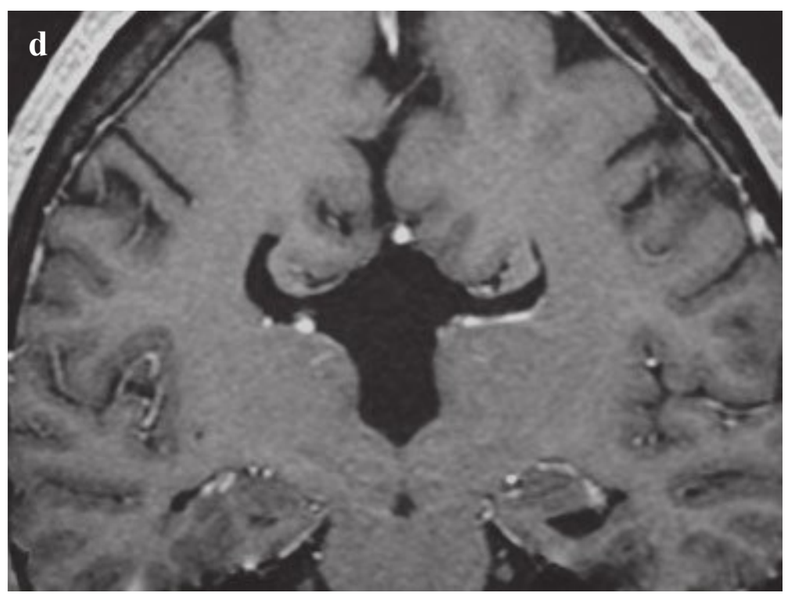

Fig. 1.29 Dysgenesis of the corpus callosum. **(a)** Sagittal and **(b)** axial T1-weighted imaging shows near-complete absence of the corpus callosum, with only a thin portion of the body present (**a**, arrow). **(c)** Sagittal and **(d)** coronal T1-weighted imaging in another patient shows complete absence of the corpus callosum (**c**, arrow). The lateral ventricles are positioned more laterally than normal and have a shape sometimes referred to as the bull or Texas steer shape.

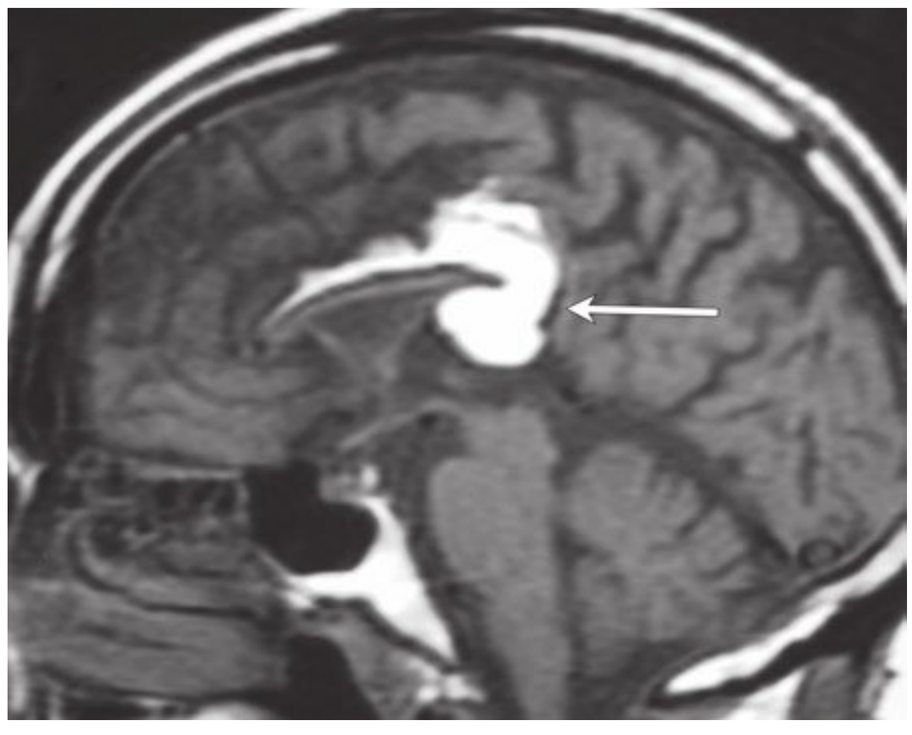

Fig. 1.30 Dysgenesis of the corpus callosum. Sagittal T1-weighted imaging shows hypoplasia of the corpus callosum with adjacent lipoma superiorly and dorsally (arrow).

Lesions	Imaging Findings	Comments
Malformations from Abnormal Neuronal and Glial Proliferation, Abnormal Apoptosis, or Neonatal Ischemia		
Microcephaly with simplified gyral pattern; microlissencephaly (**Fig. 1.31**)	Small brain size associated with simplified gyral pattern (usually less than seven to eight per hemisphere), shallow sulci, and thin cerebral cortex. Corpus callosum may be thin, deformed, or absent.	Head circumference more than three standard deviations below mean for age and sex secondary to reduced proliferation of neurons and glial cells. The severity of microcephaly is related to the degree of gyral simplification and severity of corpus callosal anomalies. Children are usually severely impaired clinically and often die in the first year of life.
Microcephaly from neonatal ischemia or infection (**Fig. 1.32**)	Microcephaly with small brain that often shows zones of gliosis and encephalomalacia.	Microcephaly can result from a neonatal destructive process, such as hypoxic-ischemic encephalopathy or infection (e.g., TORCH).
Sotos syndome (megalencephaly, cerebral gigantism)	Enlarged brain, often with asymmetric hemispheres, prominent ventricles, thin corpus callosum, cavum septi pellucidi, cavum vergae, and/or cavum velum interpositum, ± Chairi I malformation.	Most common type of megalencephaly. Sporadic or autosomal dominant mutation of NSD1 gene on chromosome 5q35.3. Patients typically have tall stature, dysmorphic facial features, developmental mental delay, and advanced bone age. Increased risk of tumorigenesis.
Benign familial megalencephaly	Enlarged brain with bulky gyri and increased thickness of cerebral cortex and cerebral white matter. Cerebellum is typically enlarged and often fills the foramen magnum, which may impede CSF outflow into the spinal canal, resulting in hydrosyringomyelia.	Familial syndrome with overproduction of brain cells (reduced apoptosis) resulting in head circumferences more than two to three times normal for age. No associated neurologic or neurocognitive dysfunction.

(continued on page 26)

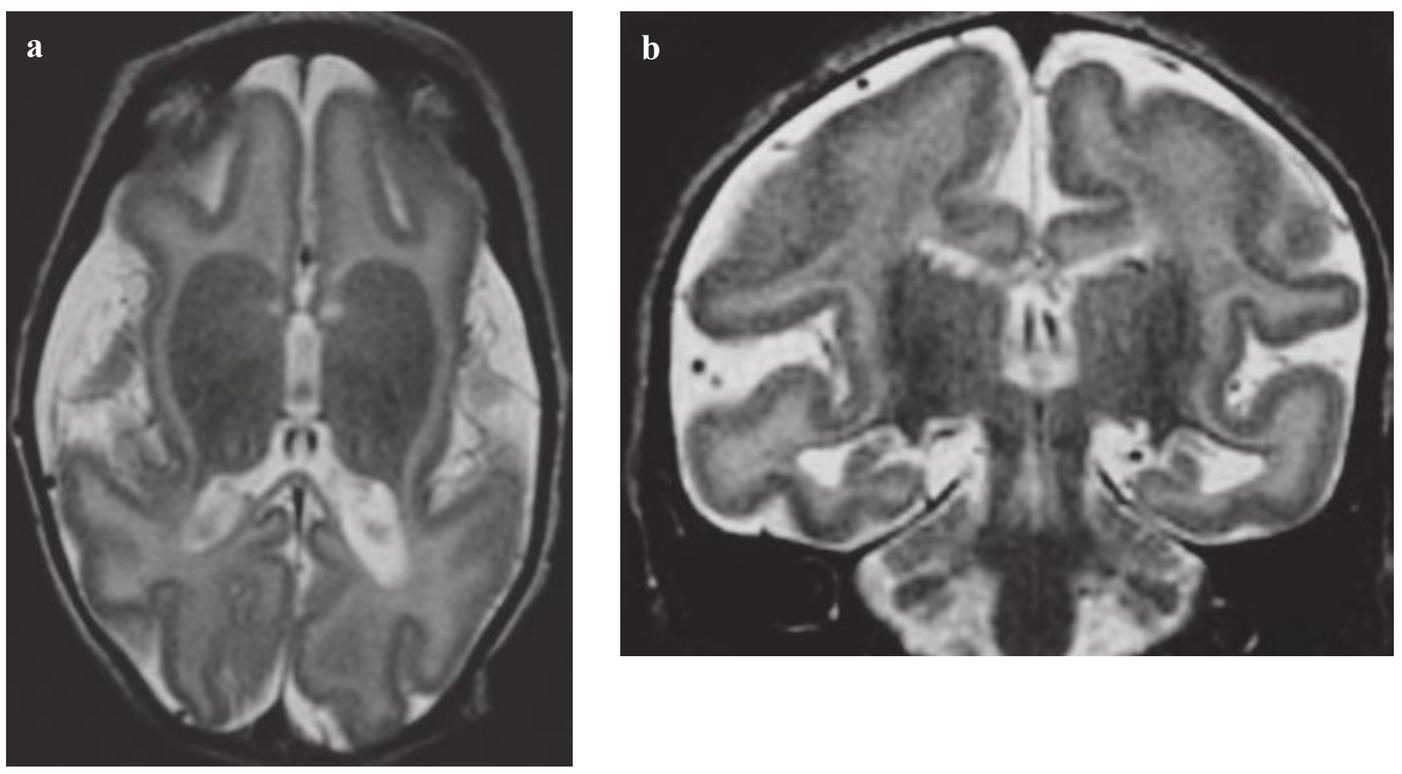

Fig. 1.31 Microcephaly with simplified gyral pattern. **(a)** Axial and **(b)** coronal T2-weighted imaging shows a small brain with simplified gyral pattern. The corpus callosum is absent.

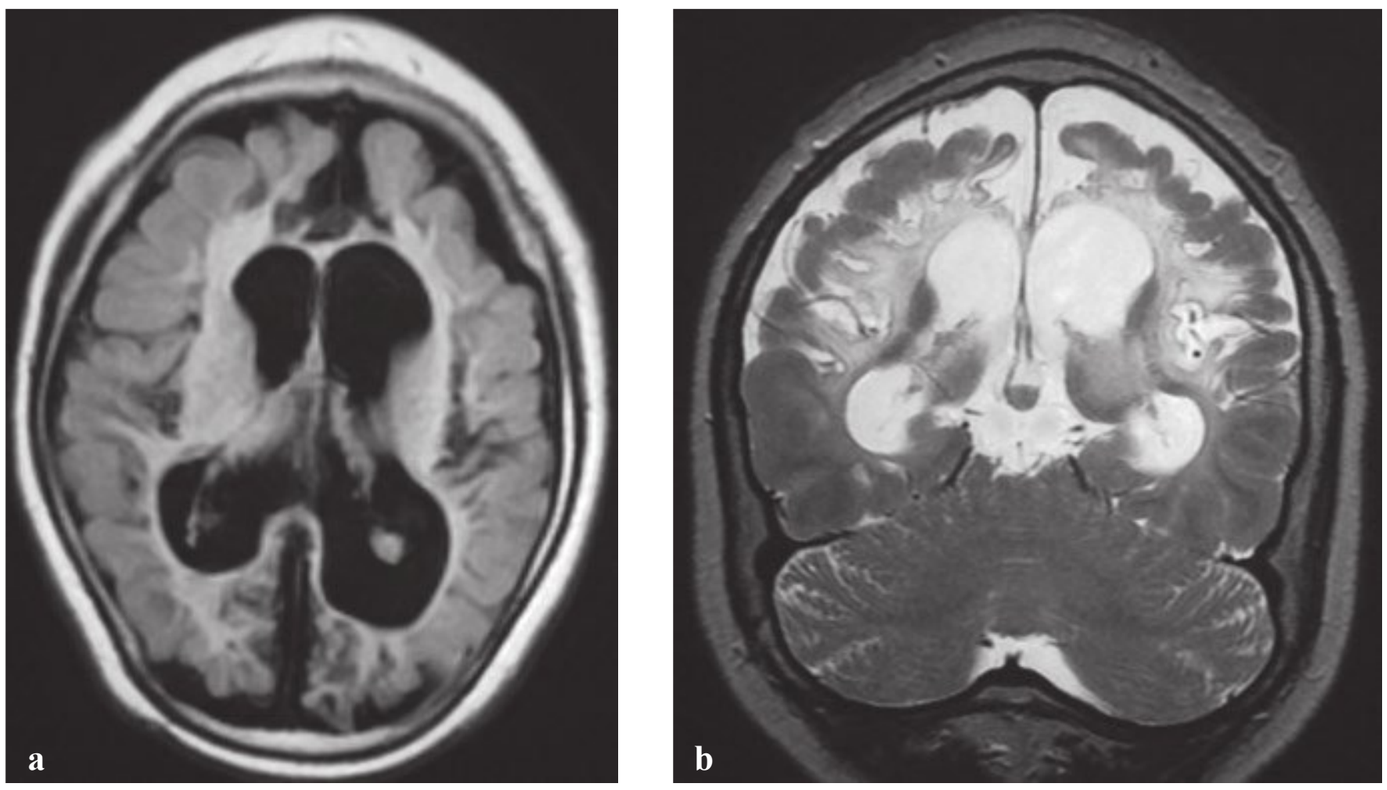

Fig. 1.32 Microcephaly due to severe neonatal ischemia. **(a)** Coronal T2-weighted imaging and **(b)** axial FLAIR image 5 years after hypoxic injury show a microcephalic brain with zones of gliosis and encephalomalacia in the cerebrum and sparing the cerebellum.

Table 1.1 (cont.) Congenital and histogenic malformations of the brain

Lesions	Imaging Findings	Comments
Malformations in Cortical Development		
Polymicrogyria (**Fig. 1.33, Fig. 1.34,** and **Fig. 1.35**)	Mutiple small gyri occur unilaterally (40%) or bilaterally (60%), most often in both sylvian fissures, followed by unilateral hemispheric and other locations. Multiple small gyri can be seen on MRI. On CT, the small gyri may appear as zones of thickened cortex.	Malformation in late stages of neuronal migration, resulting in abnormal neuronal organization of cerebral cortex. Sites involved lack normal six-layered cortex and have multiple small gyri and abnormal sulcation. Patients can present with epilepsy, developmental delay, and focal neurologic signs and symptoms that vary depending on the extent and location of the developmental anomaly.
Focal cortical dysplasia without "balloon" cells (**Fig. 1.36**)	Localized and/or diffuse zones of thinning of the cerebral cortex with signal similar to gray matter on MRI, localized blurring of the gray–white matter junction, occasionally with increased signal on T2-weighted MRI in the underlying white matter; attenuation on CT similar to gray matter.	Malformation of cerebral cortical organization with combinations of abnormal cortical lamination and giant and/or dysplastic neurons. Can be associated with dysembryoplastic neuroepithelial tumors (DNET), gangliogliomas, and mesial temporal sclerosis.

(continued on page 28)

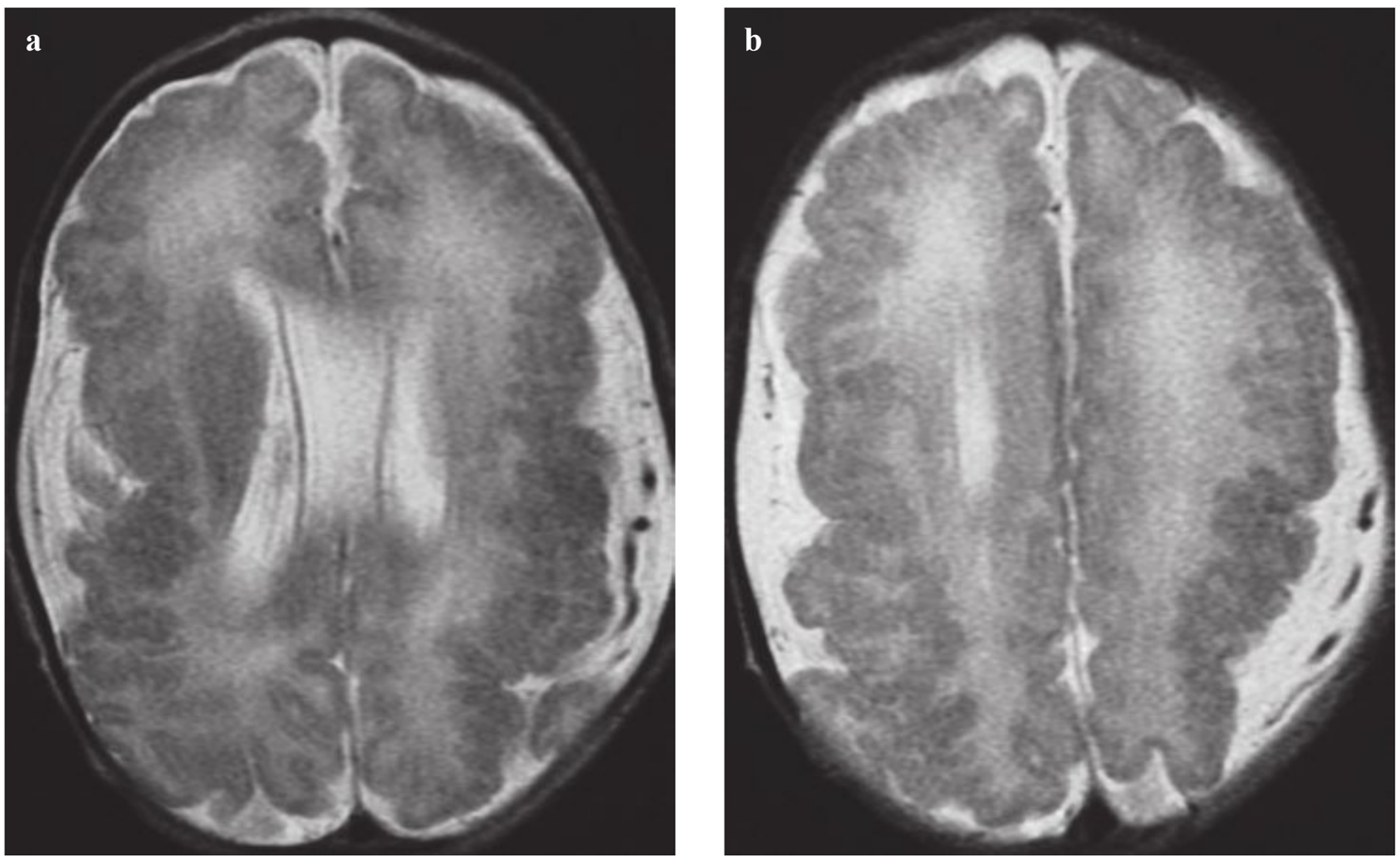

Fig. 1.33 Polymicrogyria. **(a,b)** Axial T2-weighted imaging shows mutiple small gyri bilaterally in most of the frontal and parietal lobes.

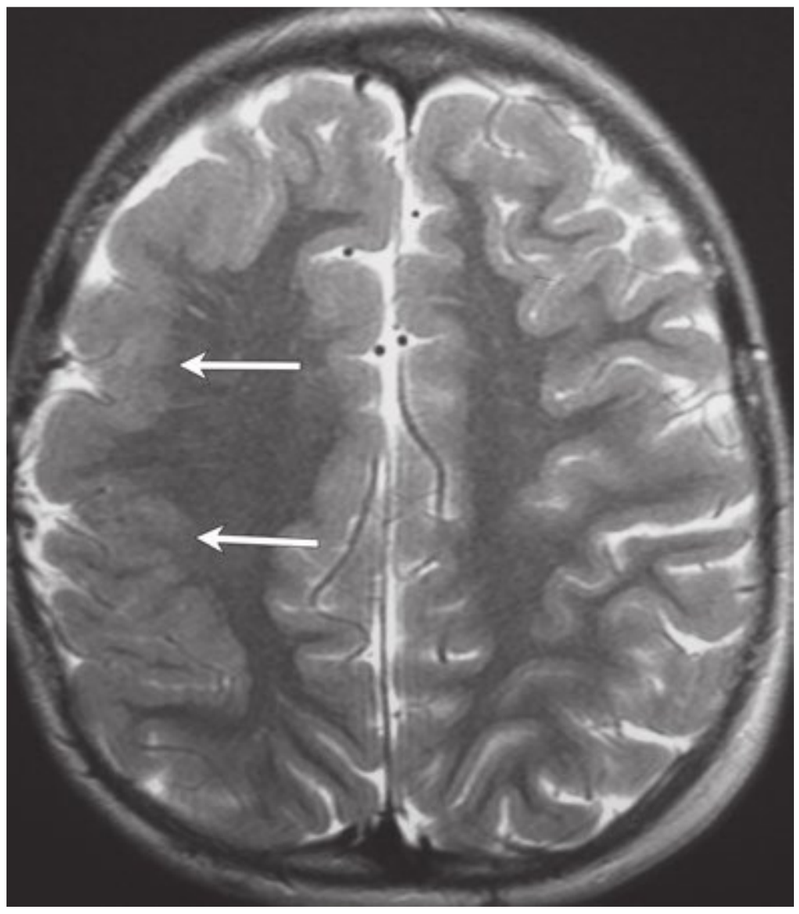

Fig. 1.34 Polymicrogyria. Axial T2-weighted imaging shows multiple small gyri in the right frontal lobe that have a "coarse or thickened" pattern (arrows).

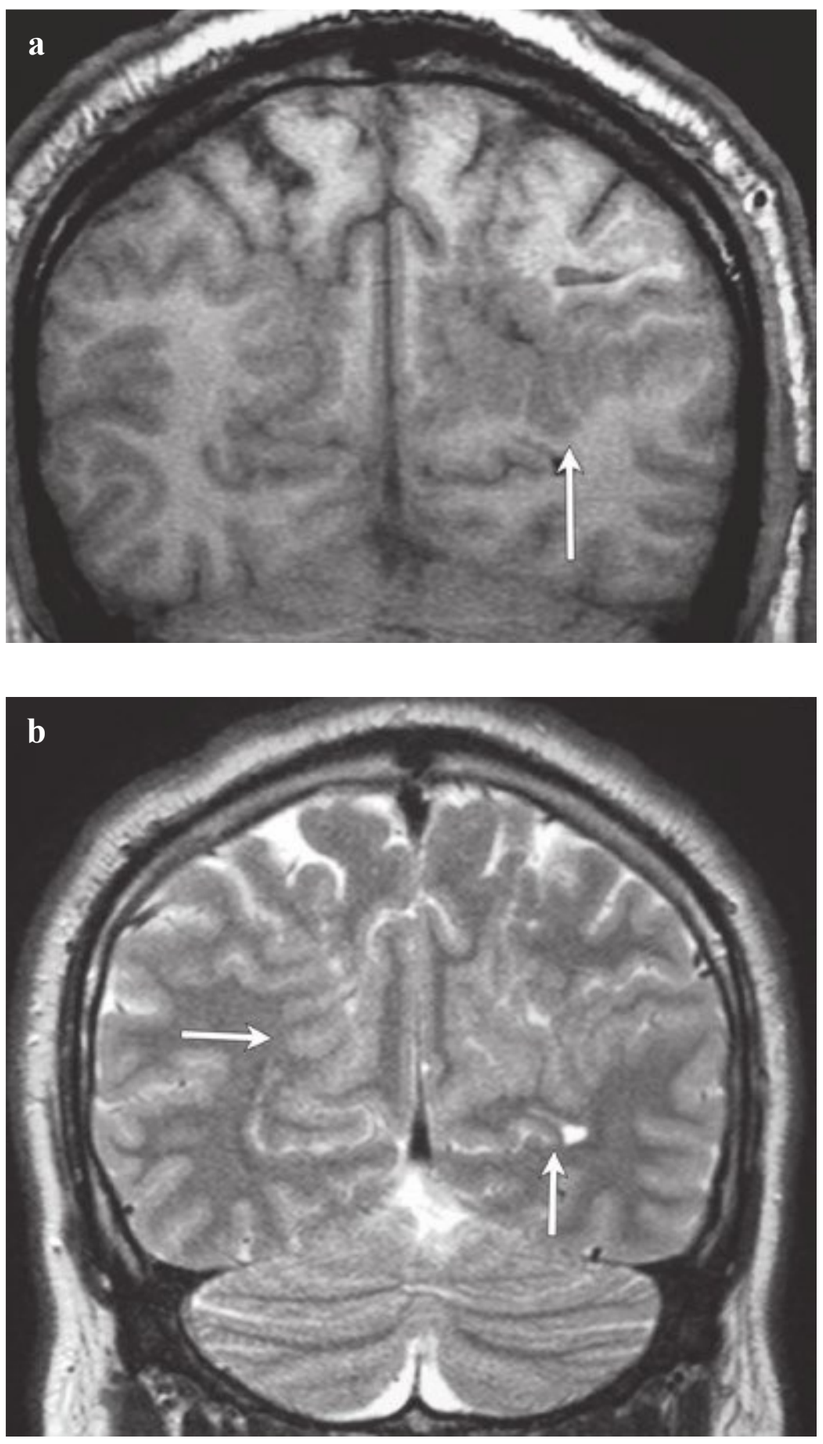

Fig. 1.35 Polymicrogyria. **(a)** Coronal T1-weighted imaging and **(b)** coronal T2-weighted imaging show multiple small gyri involving both parietal and occipital lobes (arrows).

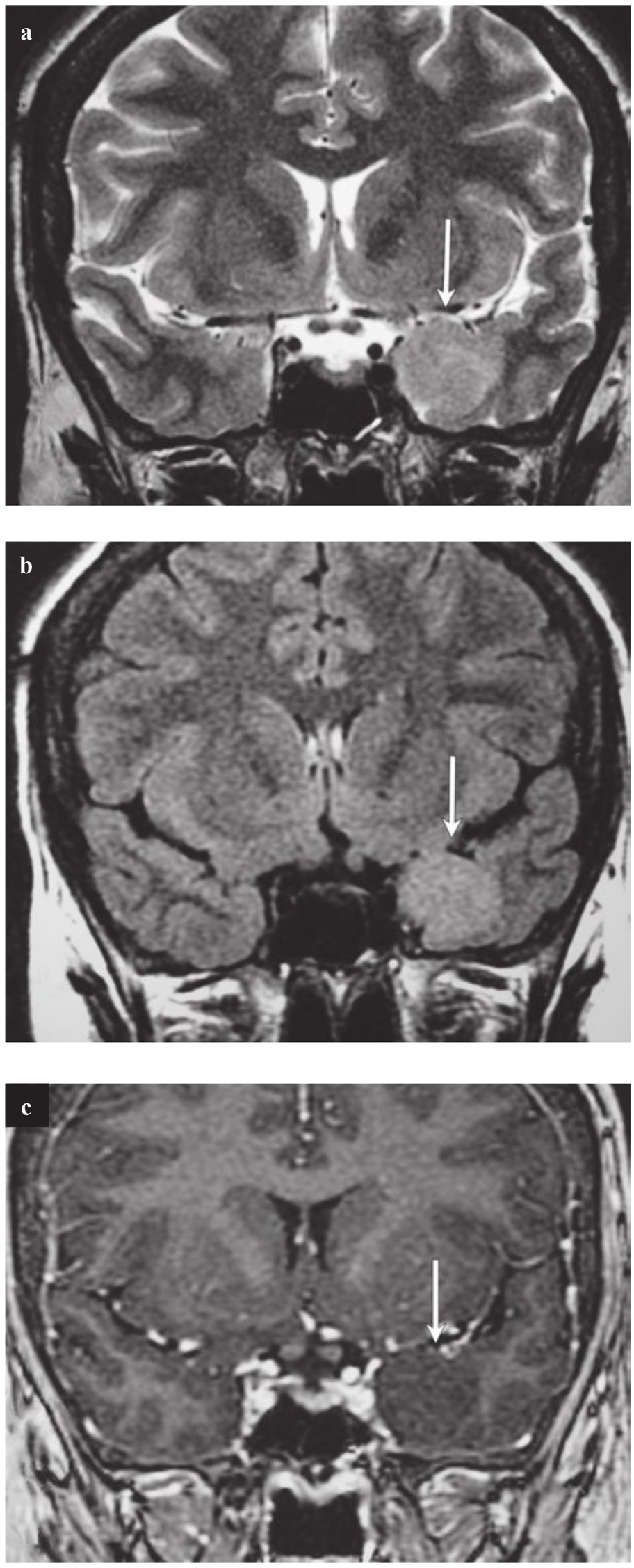

Fig. 1.36 Focal cortical dysplasia without balloon cells. **(a)** Coronal T2-weighted imaging, **(b)** FLAIR, and **(c)** coronal postcontrast T1-weighted imaging show a nodular zone of cortical dysplasia in the medial left temporal lobe that has signal similar to gray matter and shows no gadolinium contrast enhancement (arrows).

Table 1.1 (cont.) Congenital and histogenic malformations of the brain

Lesions	Imaging Findings	Comments
Transmantle cortical dysplasia with "balloon" cells (**Fig. 1.37**)	Thickened cortical gyri with disordered pattern of sulci and blurring or lack of normal gray–white matter junction. Abnormal increased signal in white matter on T2-weighted MRI.	Malformation that extends from the ventricle to the periphery resulting from abnormal lamination with dysplastic neurons, atypical glial cells, and "balloon" cells. Also referred to as Taylor type of cortical dysplasia. Typically associated with seizures in first decade. Lesions vary in extent, with large lesions associated with motor and/or sensory signs and symptoms.
Hemispheric dysplasia	One cerebral hemisphere is typically involved, with thickened cortical gyri, disordered pattern of sulci, blurring or lack of normal gray–white matter junctions, gray matter heterotopia, polymicrogyria, enlarged ipsilateral ventricle, and reduced brain volume. The latter finding differentiates hemispheric dysplasia from unilateral hemimegaencephalopathy, which typically has increased brain volume in the involved hemisphere compared with the normal contralateral cerebral hemisphere. Abnormal increased signal on T2-weighted MRI may be seen in white matter.	Hemispheric dysplasia is a complex malformation of a cerebral hemisphere that results from abnormalities involving neuronal migration and post-migrational cerebral cortical development. Abnormalities include combinations of gray matter heterotopia, cortical dysplasia, pachygyria, and polymicrogyria. Histopathologic findings often include "balloon" cells, gray matter heterotopia, demylination, and gliosis. Patients typically present with seizures and developmental delay in the first years of life.

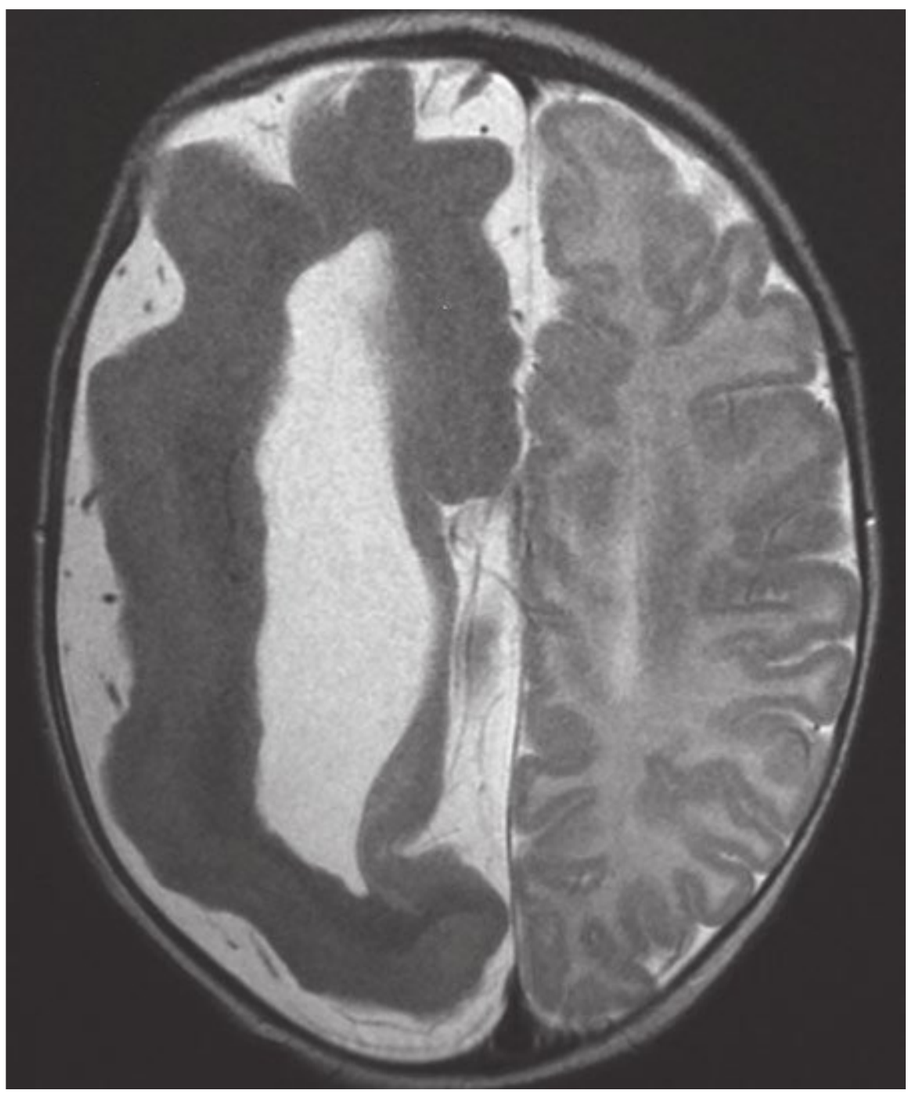

Fig. 1.37 Hemispheric dysplasia. Axial T2-weighted imaging shows a hypoplastic right cerebral hemisphere with abnormal thickened cerebral cortex and cortical gyri with disordered pattern of sulci, as well as slight blurring of the normal gray–white matter junction.

Lesions	Imaging Findings	Comments
CNS Malformations Related to Abnormal Pial Basement Membrane Formation (Anomalies involving Muscles, Eye, and Brain)		
Walker-Warburg phenotype (**Fig. 1.38**)	Ventriculomegaly with very thin cortex and white matter, absent corpus callosum and septum pellucidum, hypoplastic brainstem with posterior concavity, hypoplastic cerebellum. Cerebral cortex can have a "cobblestone" dysplastic appearance and heterotopic neurons.	Dystroglycanopathy with severe congenital muscular dystrophy, muscle weakness, and abnormal fetal brain development that result from mutations of genes encoding glycosyltransferases. Lack of these enzymes reduces glycosylation and causes defective linkage of α-dystroglycan with laminin α-2, which is necessary for functioning of the radial glia for neuronal migration from the ventricular zone of the fetal brain as well as cerebral cortical organization. Six gene mutations have been identified that can result in the Walker-Warburg phenotype, which is the most severe dystroglycanopathy; death usually occurs by age 3 years.

(continued on page 30)

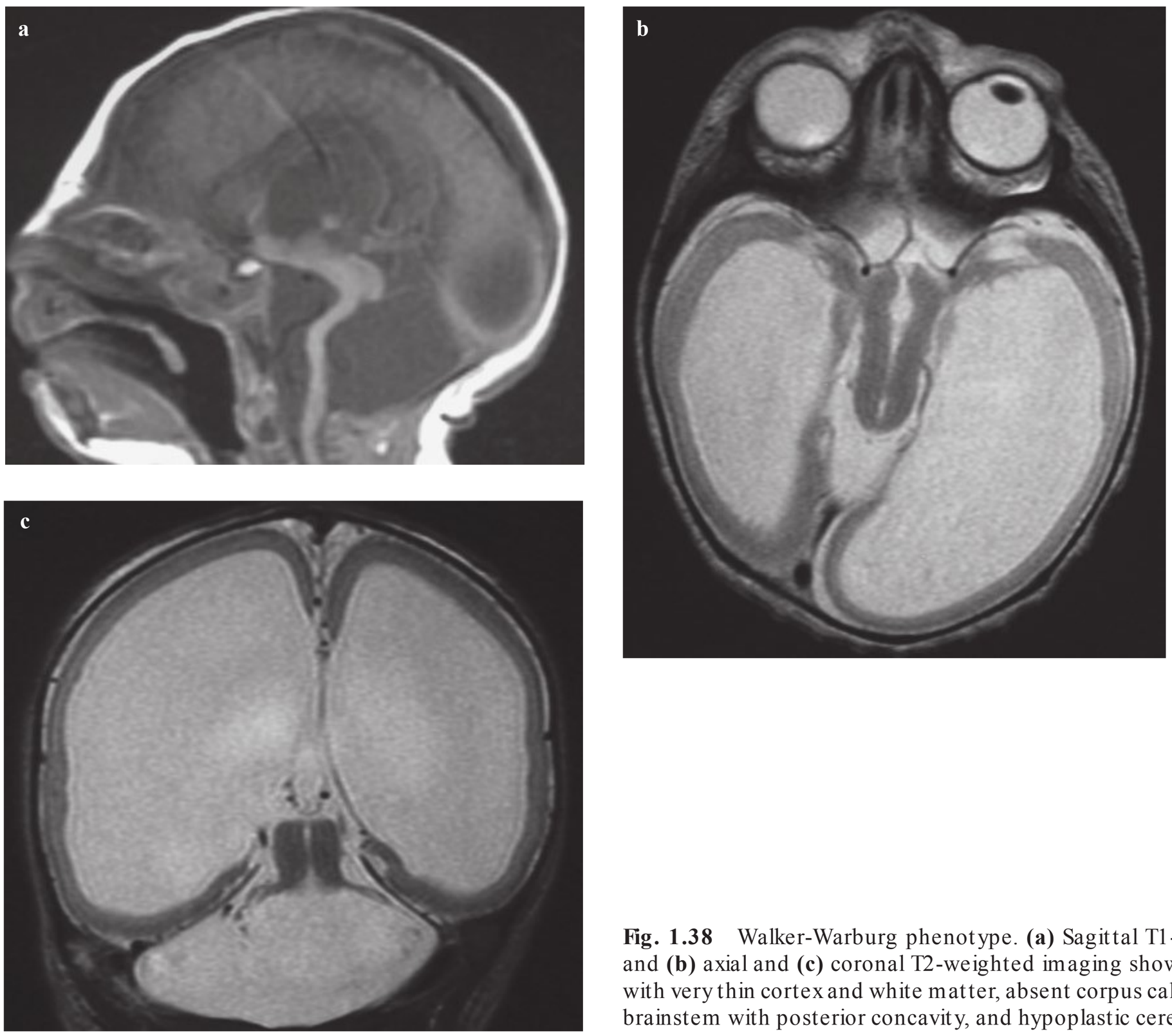

Fig. 1.38 Walker-Warburg phenotype. **(a)** Sagittal T1-weighted imaging and **(b)** axial and **(c)** coronal T2-weighted imaging show ventriculomegaly with very thin cortex and white matter, absent corpus callosum, hypoplastic brainstem with posterior concavity, and hypoplastic cerebellum.

Table 1.1 (cont.) Congenital and histogenic malformations of the brain

Lesions	Imaging Findings	Comments
Muscle-eye-brain phenotype **(Fig. 1.39)**	Cerebral cortex can have zones of agyria, pachygyria, and/or polymicrogyria; abnormal increased signal involving the cerebral white matter on T2-weighted MRI, and hypoplasia and/or microcystic changes involving the cerebellum.	Dystroglycanopathy with severe congenital muscular dystrophy and abnormal fetal brain development resulting from mutations of genes encoding glycosyltransferases. Lack of these enzymes reduces glycosylation and causes defective linkage of α-dystroglycan with laminin α-2, which is necessary for functioning of the radial glia for neuronal migration from the ventricular zone as well as cortical organization. FKRP, FKTN, POMT1, and POMT2 gene mutations have been identified with this phenotype.
Fukuyama congenital muscular dystrophy phenotype	Polymicrogyria in cerebrum and cerebellum, hypoplasia of corticospinal tracts, transient abnormal increased signal in cerebral white matter on T2-weighted MRI, ± cerebellar and pontine hypoplasia, ± cerebellar cysts.	In the Japanese population, dystroglycanopathy with severe congenital muscular dystrophy and abnormal fetal brain development resulting from mutation of the FKTN gene encoding glycosyltransferase. Lack of the enzyme reduces glycosylation and causes defective linkage of α-dystroglycan with laminin α-2, which is necessary for functioning of the radial glia for neuronal migration from the ventricular zone as well as cortical organization.

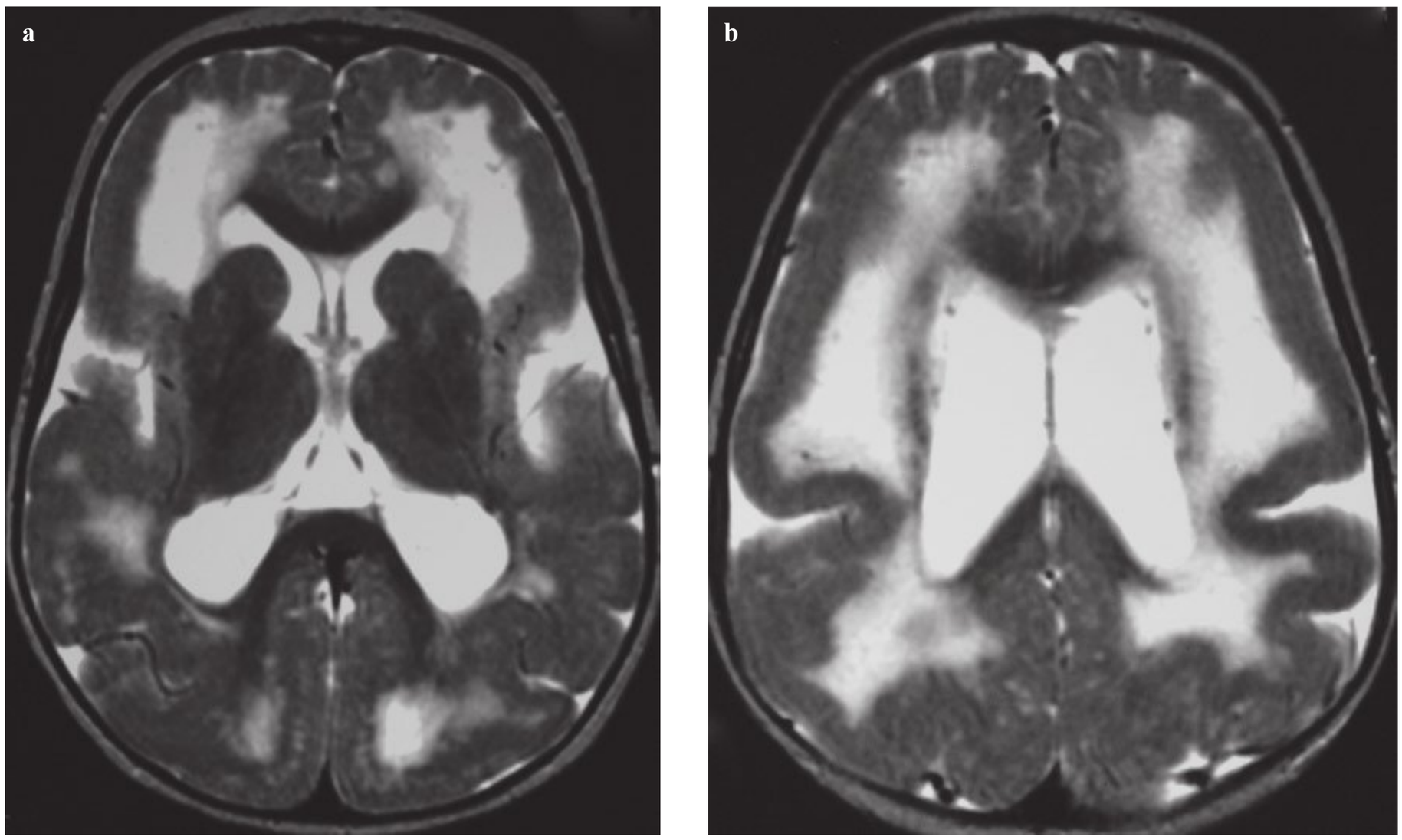

Fig. 1.39 Muscle-eye-brain phenotype. **(a,b)** Axial T2-weighted imaging shows that the cerebral cortex can have zones of agyria, pachygyria, and polymicrogyria. Extensive poorly defined zones with abnormal increased signal are seen in the cerebral white matter.

Lesions	Imaging Findings	Comments
Cerebellar Malformations: Hypoplasia Syndromes		
Cerebellar agenesis (**Fig. 1.40**)	Complete or near-complete absence of the cerebellum without associated Chiari II malformation.	Rare anomaly with congenital absence of the cerebellum.
Chiari II with vanishing cerebellum	Intracranial findings of Chiari II with complete or near-complete absence of the cerebellum.	Myeloceles in Chiari II malformations may rarely be associated with in utero destruction of the fetal cerebellum.
Hypoplasia of cerebellar hemisphere (**Fig. 1.41**)	Hypoplasia or absence of a cerebellar hemisphere.	In utero insult causing loss of formative cerebellar cells from ischemia or apoptosis.

(continued on page 32)

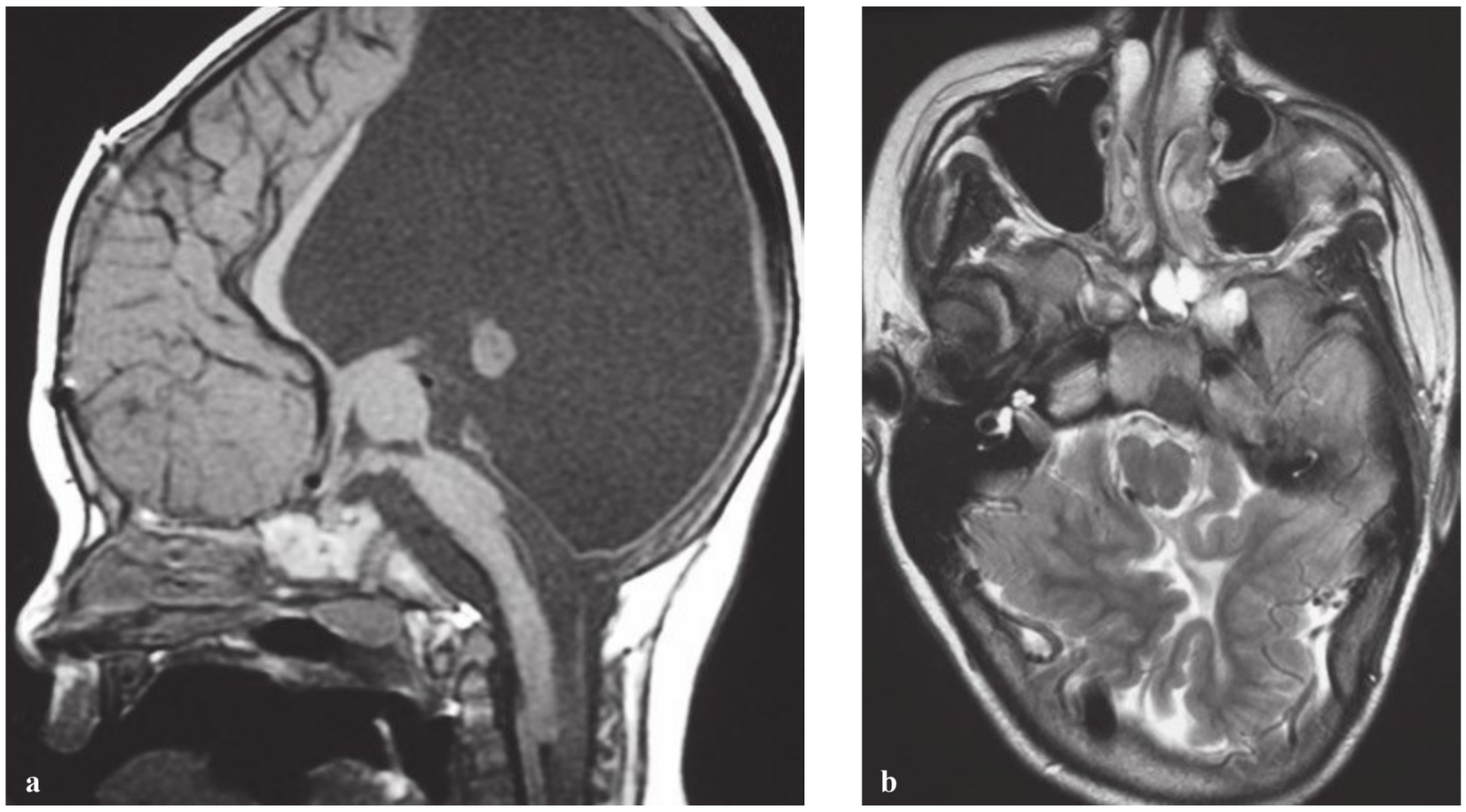

Fig. 1.40 Cerebellar agenesis. An 11-year-old male with Chiari II malformation, repaired spinal myelomeningocele, and cerebellar agenesis as seen on **(a)** sagittal T1-weighted imaging and **(b)** axial T2-weighted imaging. The sagittal image shows a cervicomedullary kink and porencephalic changes of the posterior portions of the cerebral hemispheres. Axial T2-weighted imaging shows close approximation of the medial portions of both occipital lobes in the posterior cranial fossa.

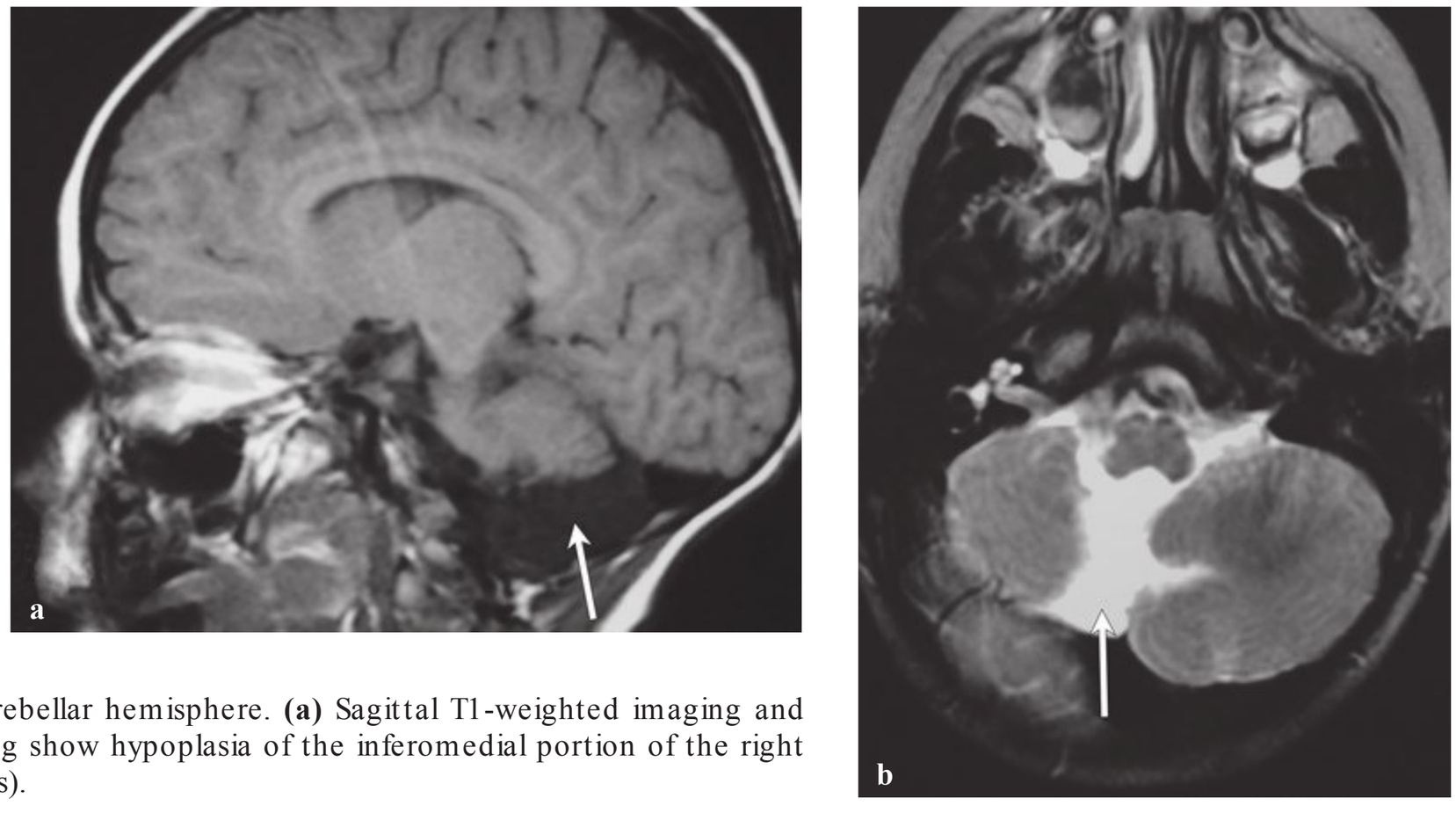

Fig. 1.41 Hypoplasia of cerebellar hemisphere. **(a)** Sagittal T1-weighted imaging and **(b)** axial T2-weighted imaging show hypoplasia of the inferomedial portion of the right cerebellar hemisphere (arrows).

Table 1.1 (cont.) Congenital and histogenic malformations of the brain

Lesions	Imaging Findings	Comments
Dandy-Walker malformation (**Fig. 1.42**)	Vermian aplasia or severe hypoplasia, communication of fourth ventricle with retrocerebellar cyst, enlarged posterior fossa, high position of tentorium and transverse venous sinuses. Hydrocephalus common. Associated with other anomalies, such as dysgenesis of the corpus callosum, gray matter heterotopia, schizencephaly, holoprosencephaly, cephalocele, and others.	Abnormal formation of roof of fourth ventricle, with absent or near-incomplete formation of cerebellar vermis.

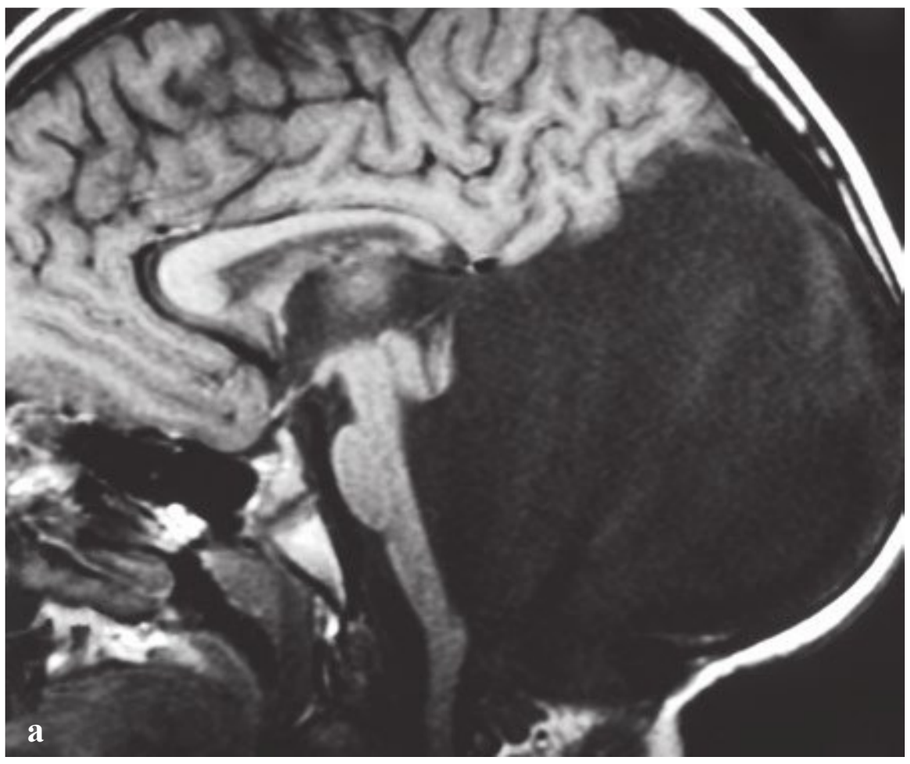

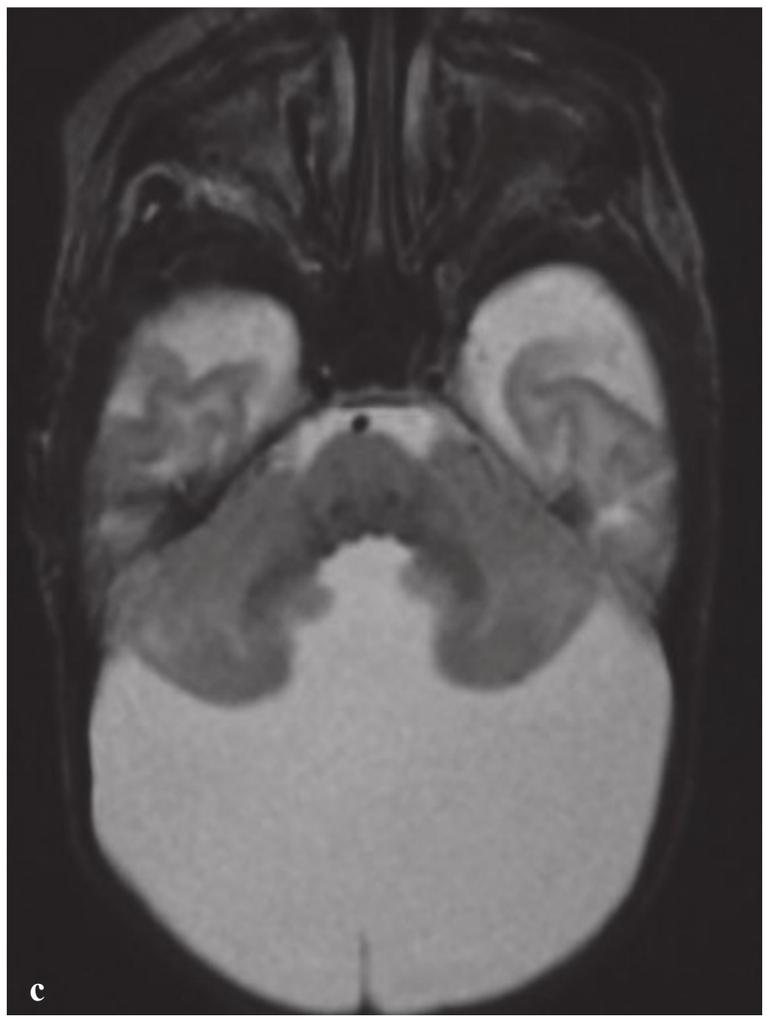

Fig. 1.42 Dandy-Walker malformation. **(a,b)** Sagittal T1-weighted imaging in two patients shows absence of the cerebellar vermis and communication of fourth ventricle with a retrocerebellar cyst, enlarged posterior cranial fossa, and high position of tentorium and transverse venous sinuses. **(c)** Axial T2-weighted imaging shows hypoplasia of the cerebellar hemispheres.

Lesions	Imaging Findings	Comments
Vermian hypoplasia, also referred to as Dandy-Walker variant (**Fig. 1.43**)	Mild vermian hypoplasia with communication of posteroinferior portion of the fourth ventricle with cisterna magna. No associated enlargement of the posterior cranial fossa.	Occasionally associated with hydrocephalus, dysgenesis of corpus callosum, gray matter heterotopia, and other anomalies.

(continued on page 34)

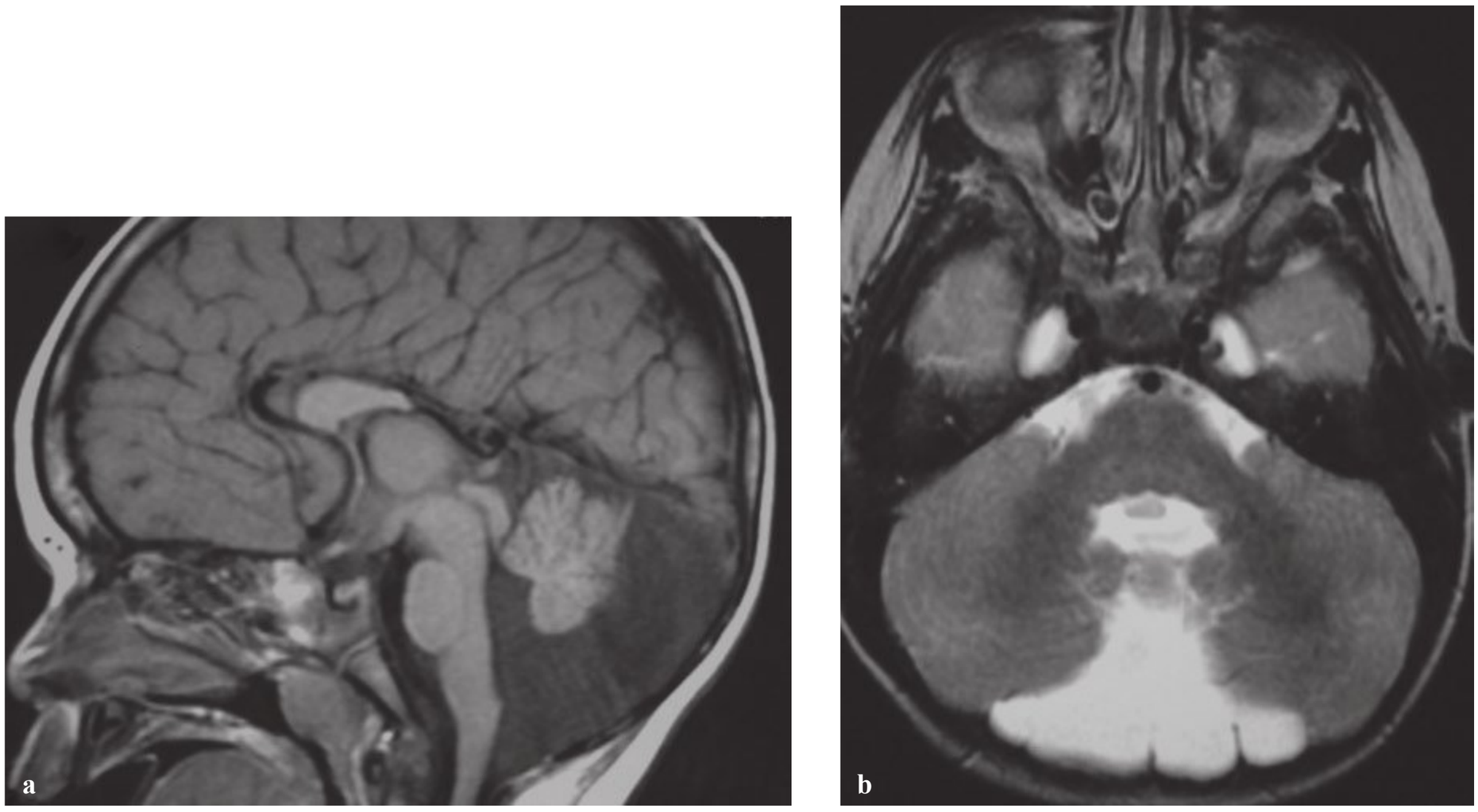

Fig. 1.43 Vermian hypoplasia, also referred to as Dandy-Walker variant/spectrum. **(a)** Sagittal T1-weighted imaging and **(b)** axial T2-weighted imaging show vermian hypoplasia with communication of the posteroinferior portion of the fourth ventricle with the cisterna magna. There is no associated abnormal enlargement of the posterior cranial fossa.

Table 1.1 (cont.) Congenital and histogenic malformations of the brain

Cerebellar Dysplastic Malformations		
Joubert syndrome (**Fig. 1.44**)	Small dysplastic vermis with midline cleft between apposing cerebellar hemispheres, "molar tooth" axial appearance from small midbrain and thickened superior cerebellar peduncles.	Malformation with hypoplasia of vermis, dysplasia, and heterotopia of cerebellar nuclei, lack of decussation of superior cerebellar peduncles, and near-complete absence of medullary pyramids. Clinical findings include ataxia, mental retardation, and abnormal eye movements.
Rhombencephalosynapsis (**Fig. 1.45**)	Dysmorphic cerebellum with no apparent separation of cerebellar hemispheres and aplasia or severe hypoplasia of vermis.	Malformation with fusion of cerebellar hemispheres, dentate nuclei, and superior cerebellar peduncles; absent or hypoplastic vermis. Clinical findings include truncal ataxia, cerebral palsy, mental retardation, and seizures.
Lhermitte-Duclos disease (**Fig. 1.46**)	Poorly defined nodular zone with low and/or intermediate signal on T1-weighted MRI, mixed high signal with laminated zones of intermediate signal on T2-weighted images, and localized mass effect located in the cerebellum. Minimal to no gadolinium contrast enhancement.	Rare, slow-growing cerebellar dysplasia (also referred to as dysplastic cerebellar gangliocytoma) that has gross thickening of cerebellar folia and disorganized cellular structure. Considered a complex hamartoma with features somewhat similar to a gangliocytoma. Can be associated with Cowden syndrome (multiple hamartomas, thyroid cancer, breast ductal carcinoma).
Focal cerebellar cortical dysplasia (**Fig. 1.47**)	Focal or diffuse polymicrogyria, cerebellar cortical dyplasia, and/or abnormal folial pattern with adjacent enlarged subarachnoid space.	Focal or diffuse malformation of cerebellar cortex and folia, often as cerebellar polymicrogyria involving cerebellar hemisphere(s) and/or vermis. May not have associated clinical signs.

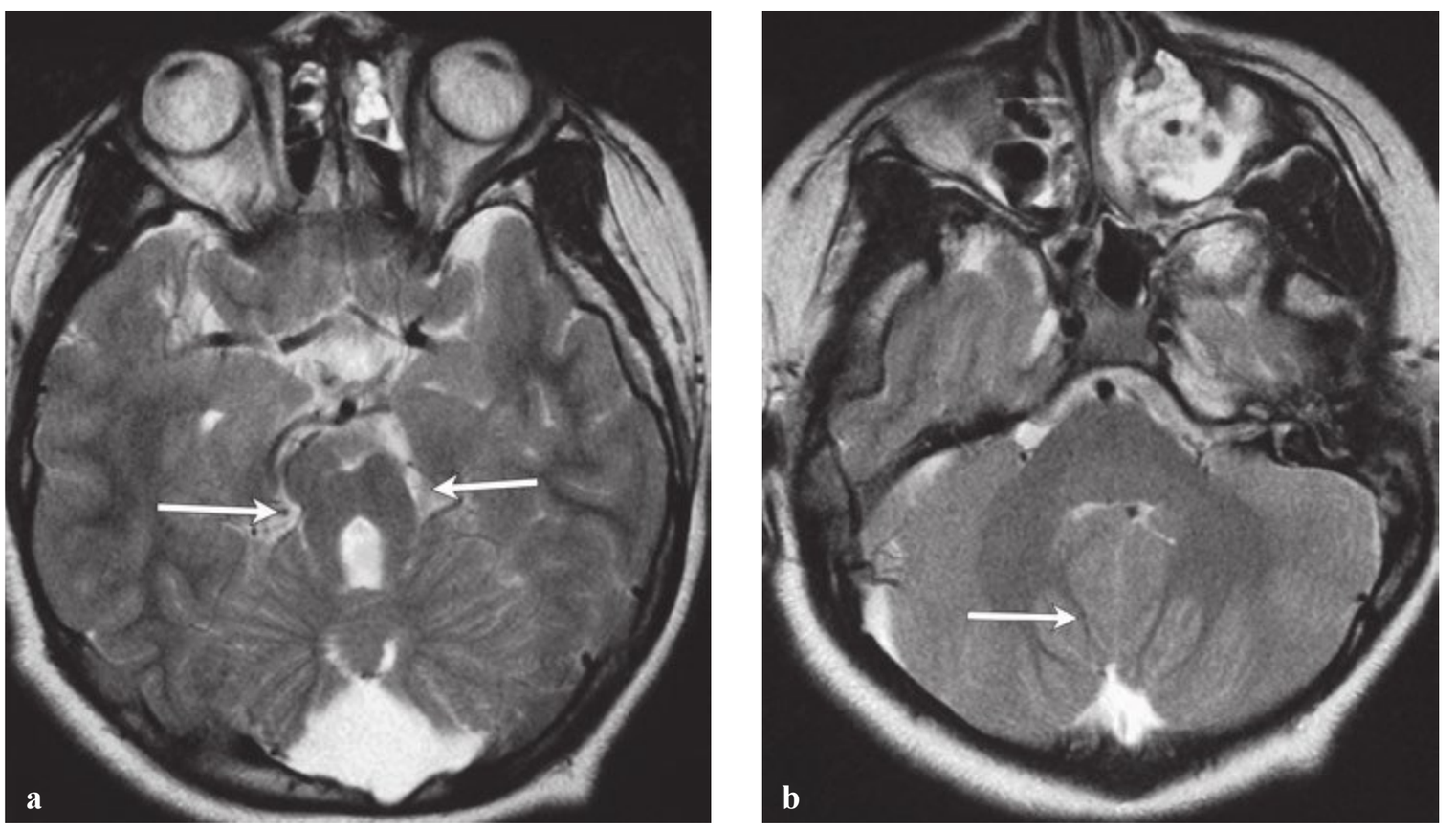

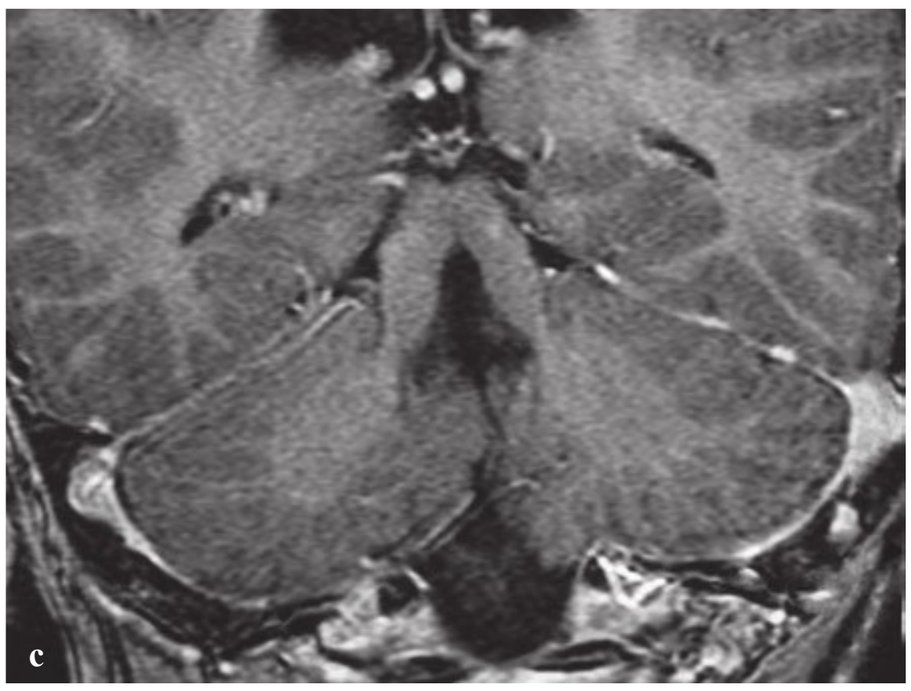

Fig. 1.44 Joubert syndrome. **(a,b)** Axial T2-weighted imaging and **(c)** coronal postcontrast T1-weighted imaging show a small dysplastic vermis with midline cleft between apposing cerebellar hemispheres, molar tooth axial appearance from small midbrain and thickened superior cerebellar peduncles (arrows).

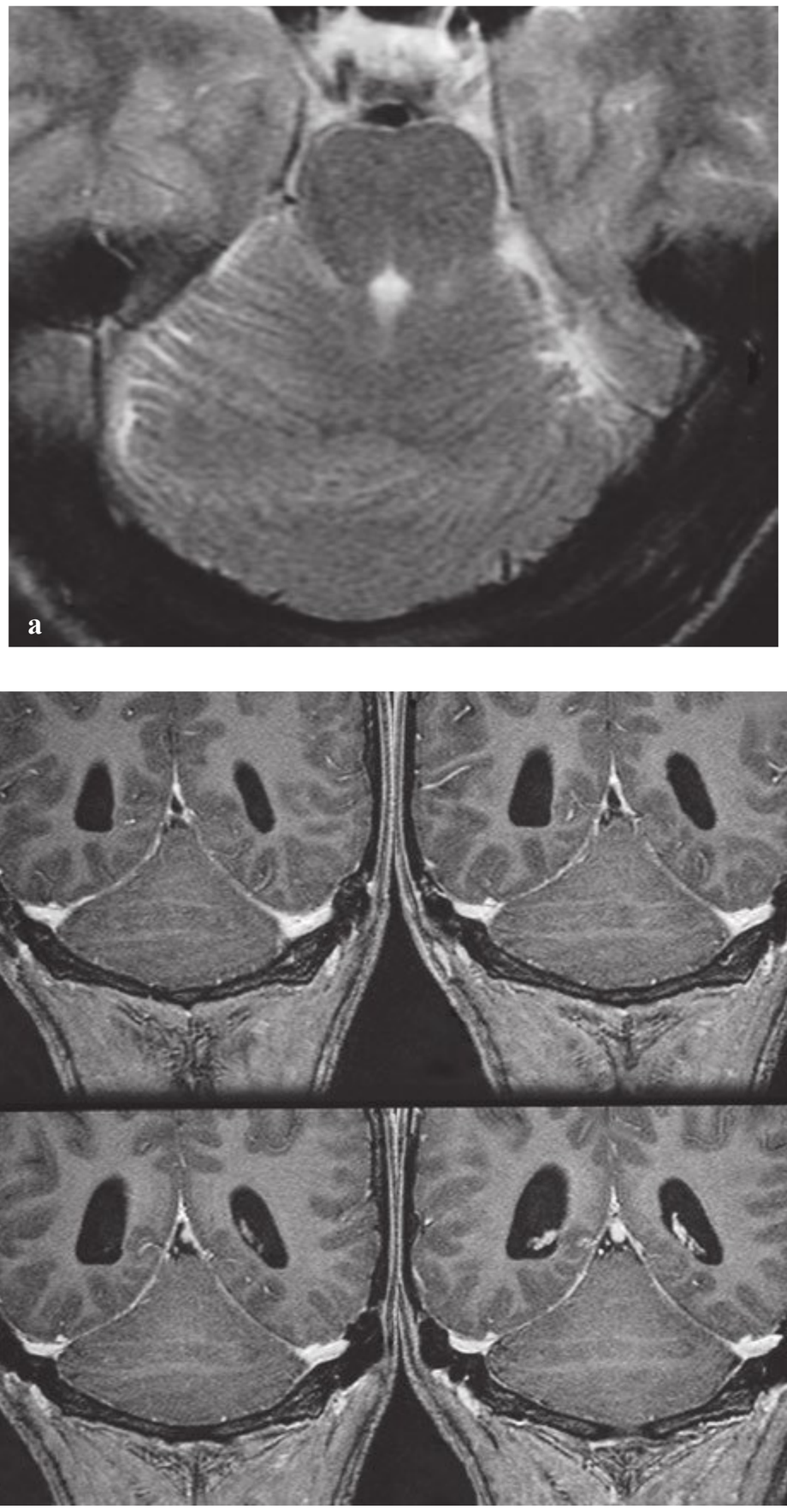

Fig. 1.45 Rhombencephalosynapsis. **(a)** Axial T2-weighted imaging shows a dysmorphic cerebellum that has no apparent separation of cerebellar hemispheres. The vermis is aplastic. **(b)** Coronal T1-weighted imaging shows no abnormal gadolinium contrast enhancement.

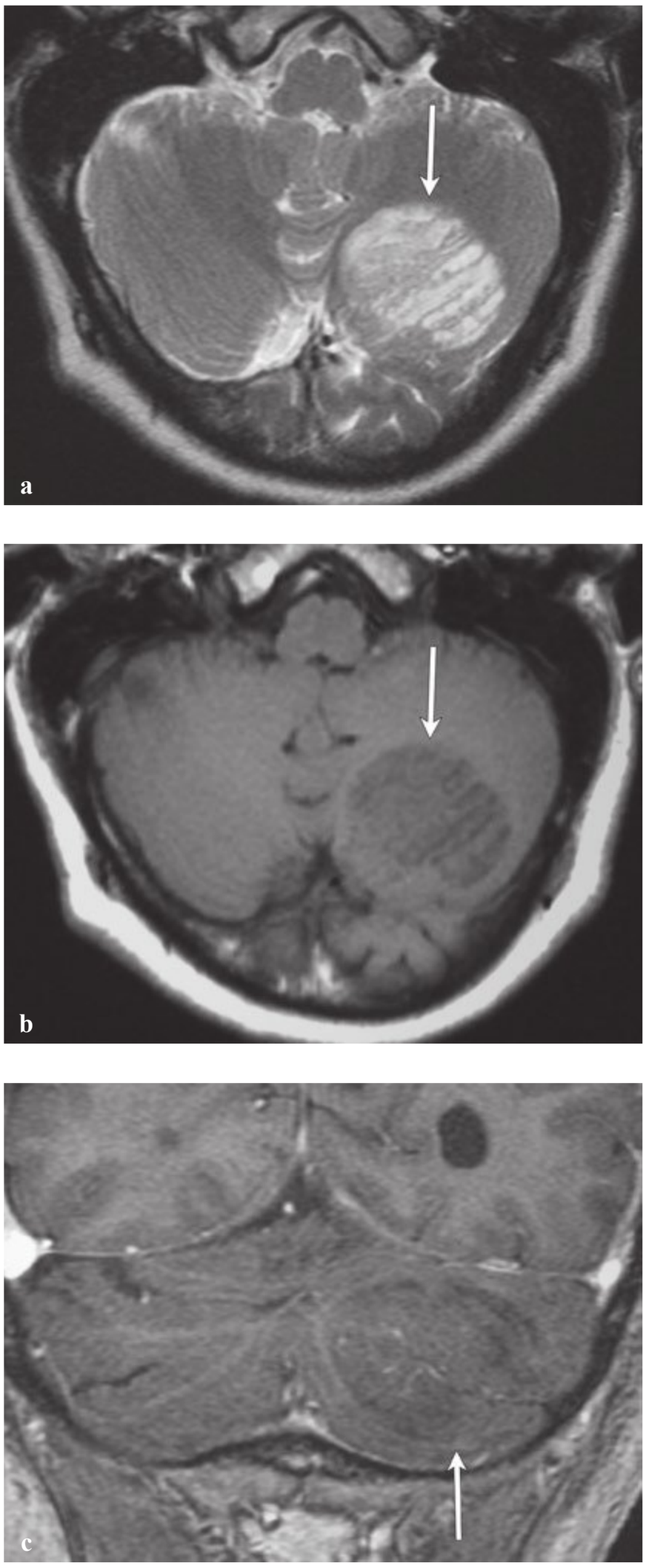

Fig. 1.46 Lhermitte-Duclos disease. **(a)** Axial T2-weighted imaging shows a nodular lesion in the left cerebellar hemisphere that has heterogeneous slightly high signal with thin bands of intermediate signal (arrow). **(b)** The lesion has intermediate signal on axial T1-weighted imaging (arrow) and **(c)** shows only small linear zones with contrast enhancement on coronal T1-weighted imaging (arrow).

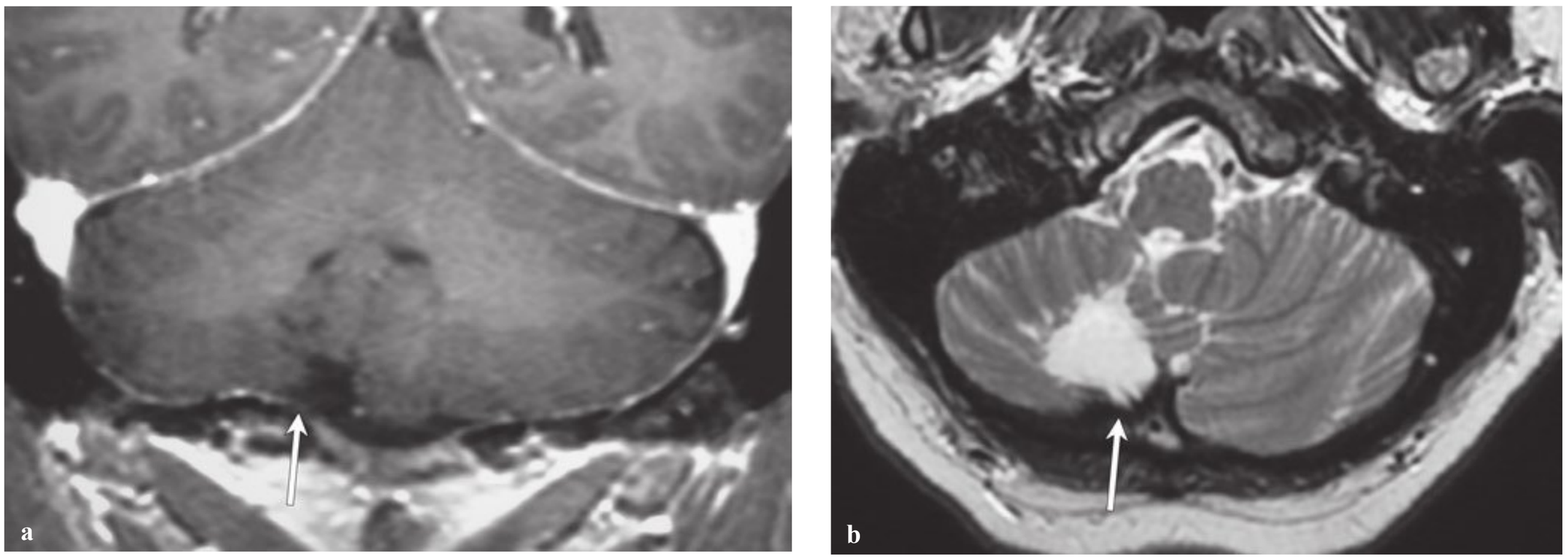

Fig. 1.47 Focal cerebellar cortical dysplasia. **(a)** Coronal postcontrast T1-weighted imaging and **(b)** axial T2-weighted imaging show localized hypoplastic dysplasia involving the inferomedial portion of the right cerebellar hemisphere, as well as aplasia of the right cerebellar tonsil (arrows). Malformed, thin cerebellar gyri are seen without evidence of gliosis or abnormal gadolinium contrast enhancement.

Table 1.2 Supratentorial solitary intra-axial mass lesions

- Congenital
  - Gray matter heterotopia
  - Unilateral hemimegalencephaly
- Neoplasms: Astrocytic Tumors
  - Pilocytic astrocytoma
  - Subependymal giant cell astrocytoma
  - Pilomyxoid astrocytoma
  - Diffuse astrocytoma
  - Pleomorphic xanthoastrocytoma
  - Gliomatosis cerebri
  - Anaplastic astrocytoma
  - Glioblastoma multiforme
  - Giant cell glioblastoma
  - Gliosarcoma
  - Astroblastoma
- Neoplasms: Oligodendroglial Tumors
  - Oligodendroglioma
  - Anaplastic oligodendroglioma
- Neoplasms: Oligoastrocytic Tumors
  - Oligoastrocytoma
  - Anaplastic oligoastrocytoma
- Neoplasms: Ependymal Tumors
  - Ependymoma
  - Subependymoma
  - Anaplastic ependymoma
- Neuronal and Mixed Neuronal-Glial Tumors
  - Ganglioglioma
  - Gangliocytoma
  - Anaplastic ganglioglioma
  - Desmoplastic infantile astrocytoma (DIA) and ganglioglioma (DIG)
  - Dysembryoplastic neuroepithelial tumor
  - Central neurocytoma
  - Papillary glioneuronal tumor
- Neoplasms: Embryonal
  - Primitive neuroectodermal tumor
  - Atypical teratoid/rhabdoid tumor
- Neoplasms: Pineal Tumors
  - Pineocytoma
  - Pineal parenchymal tumor of intermediate differentiation
  - Papillary tumor of the pineal region
  - Pineoblastoma
  - Germ cell tumors
- Other Neoplasms and Tumorlike Lesions
  - Metastases
  - Lymphoma
  - Leukemia (myeloid sarcoma, granulocytic sarcoma, chloroma)
  - Hamartoma (tuberous sclerosis)
  - Cortical-subcortical hamartomas (tubers)
  - Subependymal hamartomas
  - Hypothalamic hamartoma

  - Calcifying pseudoneoplasm of the neuraxis (CAPNON)
  - Meningioangiomatosis
  - Neurocutaneous melanosis
- Inflammatory Lesions: Infections
  - Cerebritis
  - Pyogenic brain abscess
  - Fungal brain infection
  - Encephalitis/viral infections
  - Herpes simplex
  - Cytomegalovirus (CMV)
  - Japanese encephalitis
  - Progressive multifocal leukoencephalopathy
  - Rabies
  - Acute measles encephalitis
  - Subacute sclerosing panencephalitis from measles
  - West Nile virus
  - Prion disease
  - Tuberculoma
  - Toxoplasmosis
  - Cysticercosis
  - Hydatid cyst
  - Echinococcus granulosus
  - Echinococcus multilocularis
- Inflammatory Lesions: Noninfectious
  - Demyelinating disease: multiple sclerosis, acute disseminated encephalomyelitis
  - Neurosarcoid
- Hemorrhage
  - Intra-axial hemmorhage
  - Hyperacute intra-axial hematoma hyperacute phase (0–6 hours)
  - Acute intra-axial hematoma acute phase (6 hours to 2–3 days)
  - Early subacute intra-axial hematoma early subacute phase (3–7 days)
  - Late subacute intra-axial hematoma late subacute phase (4 days to 1 month)
  - chrinic intra-axial hemorrhage chronic phase (1 month to years)
  - Cerebral contusion
  - Hemorrhage metastatic lesion
  - Hemorrhage from arteriovenous malformation (AVM)
  - Intra-axial hemorrhage from a ruptured aneurysm (saccular aneurysm, fusiform aneurysm, dissecting aneurysms [internal hematoma])
  - Hemorrhage from cavernous hemangioma
  - Venous angioma/developmental venous anomaly
- Cerebral Ischemia/Infarction
- Other Lesions
  - Cerebral infarction from arterial occlusion
  - Hyperacute infarch (< 12 hours)
  - Acute infarct (12–24 hours)
  - Early subacute infarct (24 hours to 3 days)
  - Late subacute infarct (4 days to 2 weeks)
  - Post subacute infarct (2 weeks to 2 months)
  - Remove infarct (> 2 months)
  - Cerebral infarction from venous occlusion
  - Radiation necrosis
  - Tumor pseudoprogression within 3 months after completion of chemoradiation
  - Amyloidoma
  - Lipoma
  - Neuroepithelial/neuroglial cyst
  - Porencephalic cyst

Table 1.2 Supratentorial solitary intra-axial mass lesions

Lesions	Imaging Findings	Comments
Congenital		
Gray matter heterotopia (See **Fig. 1.22, Fig. 1.23,** and **Fig. 1.24**)	Laminar heterotopia appears as a band or bands of gray matter attenuation on CT and MRI signal isointense to gray matter within the cerebral white matter (**Fig. 1.22**). Nodular heterotopia appears as one or more nodules of gray matter attenuation on CT, and MRI signal isointense to gray matter along the ventricles (**Fig. 1.23**) or within the cerebral white matter. Focal subcortical heterotopia can be seen as irregular nodular or multinodular masslike zones in subcortical regions with gray matter attenuation on CT and MRI signal isointense to gray matter (**Fig. 1.24**).	Disorder of neuronal migration (at 7 to 22 weeks of gestation) where a collection or layer of neurons is located between the ventricles and cerebral cortex. Can have a bandlike (laminar) or nodular appearance isointense to gray matter and may be unilateral or bilateral. Associated with seizures and schizencephaly.
Unilateral hemimegalencephaly (**Fig. 1.27** and **Fig. 1.28**)	Nodular or multinodular region of gray matter heterotopia involving all or part of a cerebral hemisphere, with associated enlargement of the ipsilateral lateral ventricle and hemisphere.	Neuronal migration disorder associated with hamartomatous overgrowth of the involved hemisphere.
Neoplasms: Astrocytic Tumors		
Pilocytic astrocytoma (**Fig. 1.48**)	MRI: Solid/cystic focal lesion with low-intermediate signal on T1-weighted imaging, high signal on T2-weighted imaging and FLAIR, usually showing gadolinium contrast enhancement. Lesions commonly located in cerebellum, hypothalamus, optic chiasm, adjacent to third or fourth ventricle, and brainstem. Some (30%) can have more aggressive MRI features, such as inhomogeneous gadolinium contrast enhancement, central necrotic zones, and irregular margins. Diffusion-weighted imaging: Usually no evidence of restricted diffusion. Diffusion tensor imaging (DTI) can show tumor displacement of cortical spinal tracts. Magnetic resonance spectroscopy: With these low-grade tumors in children, a paradoxic pattern associated with more aggressive tumors—elevated choline/N-acetylaspartate (NAA) and lactate levels—may be seen. CT: Solid/cystic focal lesion with low-intermediate attenuation, usually with prominent contrast enhancement.	Most common glioma in children and accounts for 6% of all gliomas. Slow-growing, solid/cystic WHO grade I astrocytoma with biphasic pattern of compacted bipolar cells, Rosenthal fibers, multipolar cells, microcysts, and eosinophilic granular bodies. Associated with BRAF mutations involving the MAPK signaling pathway. Usually lack IDH mutations. Immunoreactive to glial fibrillary acidic protein (GFAP) and apolipoprotein D. Can occur in cerebrum, cerebellum, brainstem, and optic chiasm. The majority (67%) occur in the cerebellum of children, usually with a favorable prognosis if totally resected. Increased occurrence in patients with neurofibromatosis type 1 (NF1). Leptomeningeal tumor dissemination is rare (< 3%).
Subependymal giant cell astrocytoma (**Fig. 1.49**)	MRI: Circumscribed lesion located near the foramen of Monro with mixed low-intermediate signal on T1-weighted imaging and mixed high signal on T2-weighted imaging, ± cysts and/or calcifications, + heterogeneous gadolinium contrast enhancement. Diffusion-weighted imaging: Subependymal giant cell astrocytomas usually do not have restricted diffusion. Magnetic resonance spectroscopy: Subependymal giant cell astrocytomas can have elevated choline and reduced N-acetylaspartate (NAA). CT: Circumscribed lesion with mixed low-intermediate attenuation, ± cysts and/or calcifications, and heterogeneous contrast enhancement.	Subependymal giant cell astrocytoma near foramen of Monro occurs in 6 to 18% of patients with tuberous sclerosis. Patients are usually younger than 20 years (mean age = 11 years) and have slow-growing lesions composed of neoplastic astrocytes of varying sizes, with nuclear pleomorphism and low K_i-67/MIB-1 proliferation index ranging from 1.5 to 7.4%. Immunoreactive to glial fibrillary acidic protein (GFAP), S-100 protein, neurofilament proteins, and class III b-tubulin. Enlarging lesions can progressively cause obstruction of CSF flow through the foramen of Monro. Autosomal dominant mutations involving TSC1 gene on chromosome 9q34 and TSC2 gene on chromosome 16p13.3. Prevalence of tuberous sclerosis = 1/6000 newborns. Long-term survival is common if tumor is resected.

(continued on page 40)

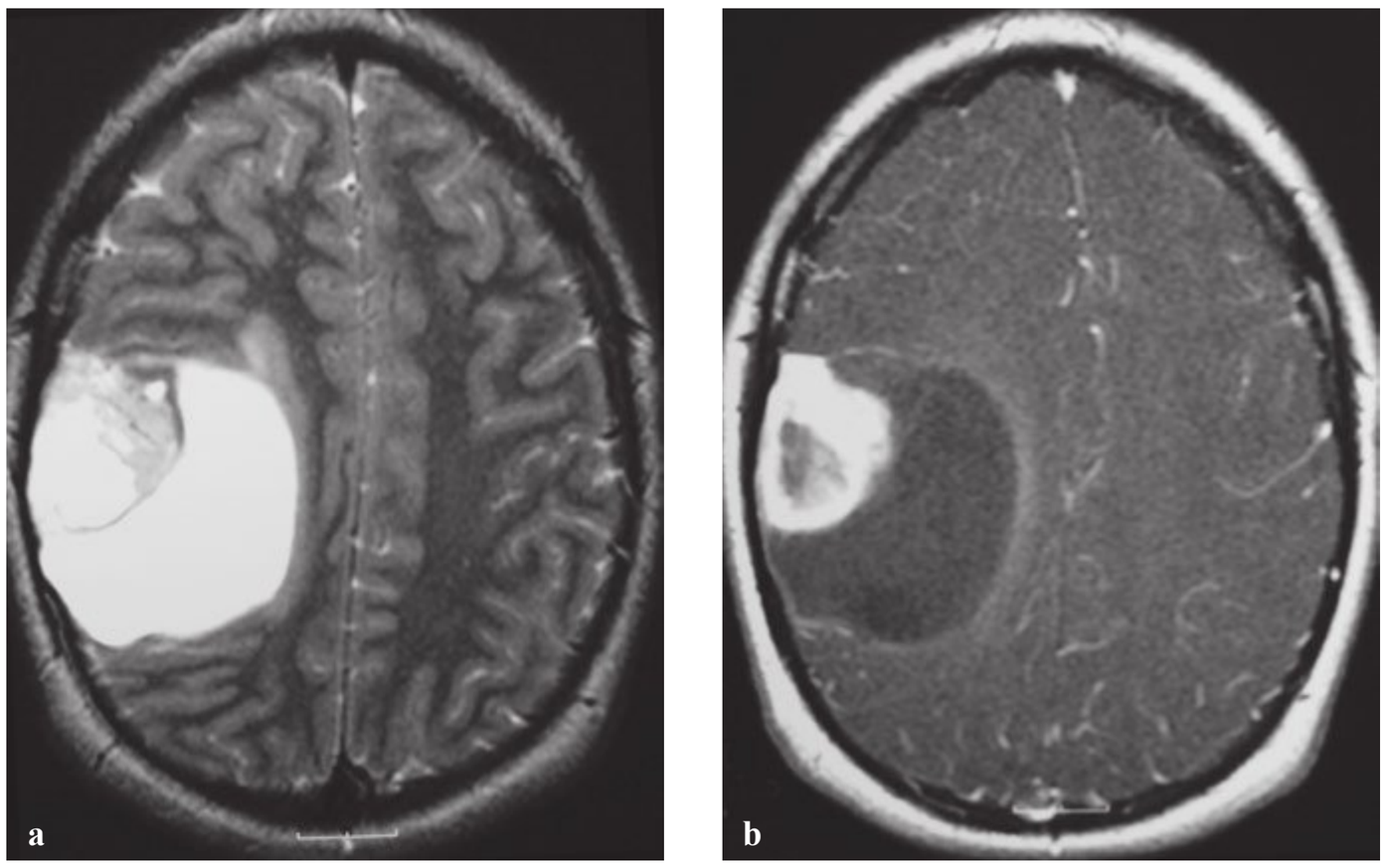

Fig. 1.48 A 17-year-old male with a pilocytic astrocytoma in the right frontal lobe. **(a)** A solid and cystic focal lesion is seen on axial T2-weighted imaging. **(b)** The solid nodular portion of the lesion shows gadolinium contrast enhancement on axial T1-weighted imaging.

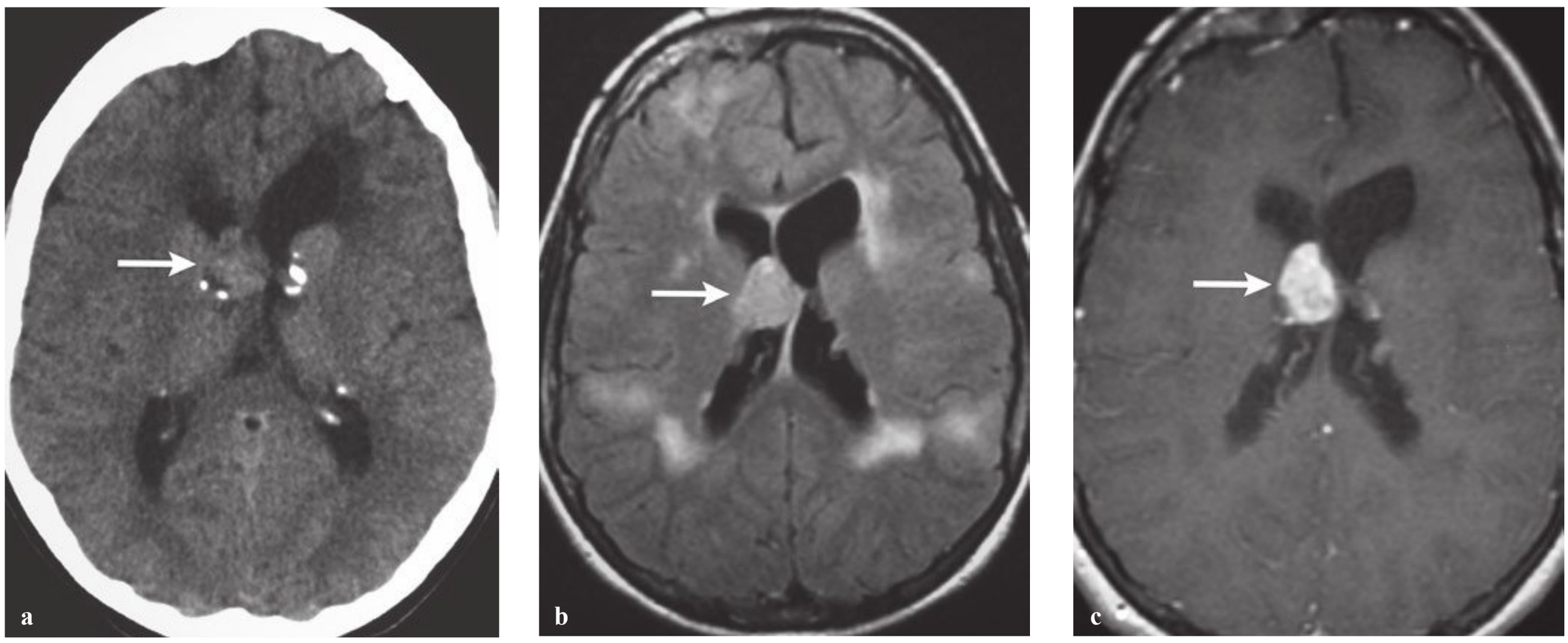

Fig. 1.49 Subependymal giant cell astrocytoma in an 18-year-old woman with tuberous sclerosis. **(a)** Axial CT shows multiple ependymal hamartomas with calcifications as well as a nodular lesion at the right foramen of Monro (arrow) representing a giant cell astrocytoma, which has **(b)** slightly high signal on FLAIR (arrow) and **(c)** shows gadolinium contrast enhancement on axial T1-weighted imaging (arrow). Other findings associated with tuberous sclerosis include slightly high signal on FLAIR at cortical tubers and peri-atrial white matter, and ependymal hamartomas.

Table 1.2 (cont.) Supratentorial solitary intra-axial mass lesions

Lesions	Imaging Findings	Comments
Pilomyxoid astrocytoma (**Fig. 1.50**)	MRI: Solid/cystic focal lesion with low-intermediate signal on T1-weighted imaging, and high signal on T2-weighted imaging and FLAIR. Tumor shows variable gadolinium contrast enhancement. Some solid portions may show minimal or no contrast enhancement. Gadolinium contrast enhancement can be uniform or in a heterogeneous peripheral pattern. Intratumoral hemorrhage can occur in 25% Lesions are commonly located in cerebellum, hypothalamus, suprasellar cistern, and thalamus. Diffusion-weighted imaging: Tumors can have increased ADC values. CT: Solid/cystic focal lesion with low-intermediate attenuation and variable contrast enhancement.	Pilomyxoid astrocytomas (WHO grade II) are rare neoplasms that contain prominent mucoid matrix and an angiocentric pattern of bipolar neoplastic astrocytes. Absence of Rosenthal fibers. Typically occur in children in first and second decades (9 months to 46 years, mean age = 7 years). Common locations include hypothalamus/suprasellar cistern, thalamus, cerebellum, brainstem, temporal lobe, and spinal cord. Tumors are more aggressive than pilocytic astrocytoma, with a higher rate of local recurrence. Leptomeningeal dissemination of tumor has been reported to occur with a higher frequency than with pilocytic astrocytomas.
Diffuse astrocytoma (**Fig. 1.51** and **Fig. 1.52**)	MRI: Intra-axial lesion with slightly ill-defined margins or diffuse mass lesion in white matter with low-intermediate signal on T1-weighted imaging, high signal on T2-weighted imaging, ± mild gadolinium contrast enhancement. Relative cerebral blood volume (rCBV) is usually low. Minimal associated mass effect, usually lacks peritumoral edema and hemorrhage. Diffusion-weighted imaging: Tumors typically do not show restricted diffusion. CT: Focal or diffuse mass lesion usually located in white matter, with low-intermediate attenuation, ± mild contrast enhancement. Minimal associated mass effect.	Low-grade astrocytomas (WHO grade II) that account for 10 to 15% of astrocytic brain tumors. Often occur in children and adults (age 20 to 40 years). Can also occur in older adults. Tumors comprised of well-differentiated fibrillary or gemistocytic neoplastic astrocytes. Association with TP53, isocitrate dehydrogenase-IDH1 and IDH2, and telomere maintenance protein-ATRX mutations. Mean survival is 6 to 8 years, and tumor may undergo malignant progression to anaplastic astrocytoma or glioblastoma. Tumors with IDH mutations have a better prognosis than those without.

(continued on page 42)

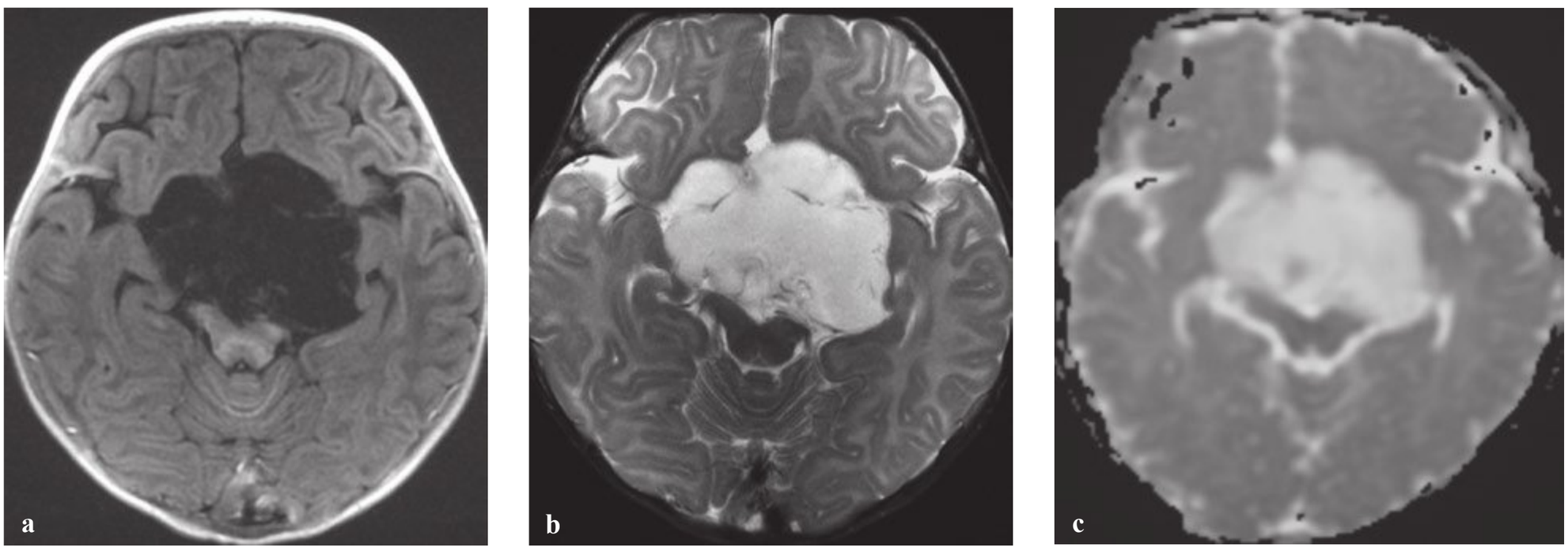

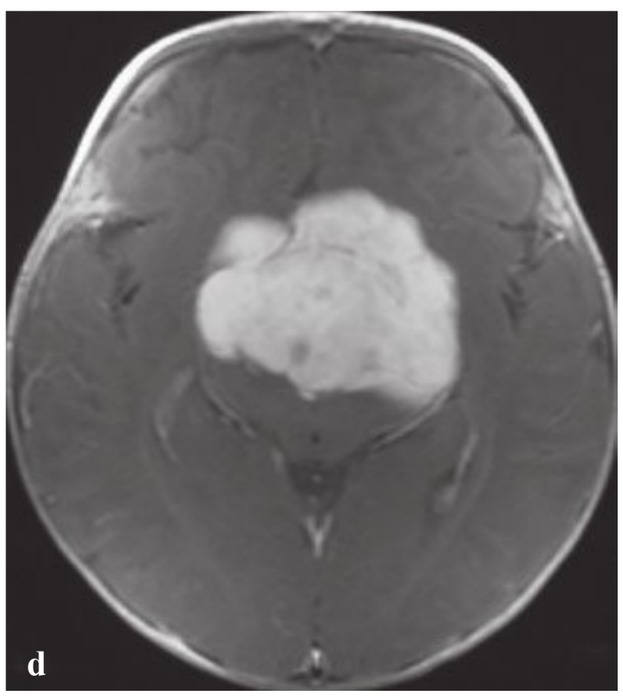

Fig. 1.50 A 4-month-old female with a pilomyxoid astrocytoma in the suprasellar cistern that has **(a)** low signal on axial T1-weighted imaging and **(b)** high signal on T2-weighted imaging and **(c)** ADC. **(d)** The large lesion shows prominent gadolinium contrast enhancement on axial T1-weighted imaging.

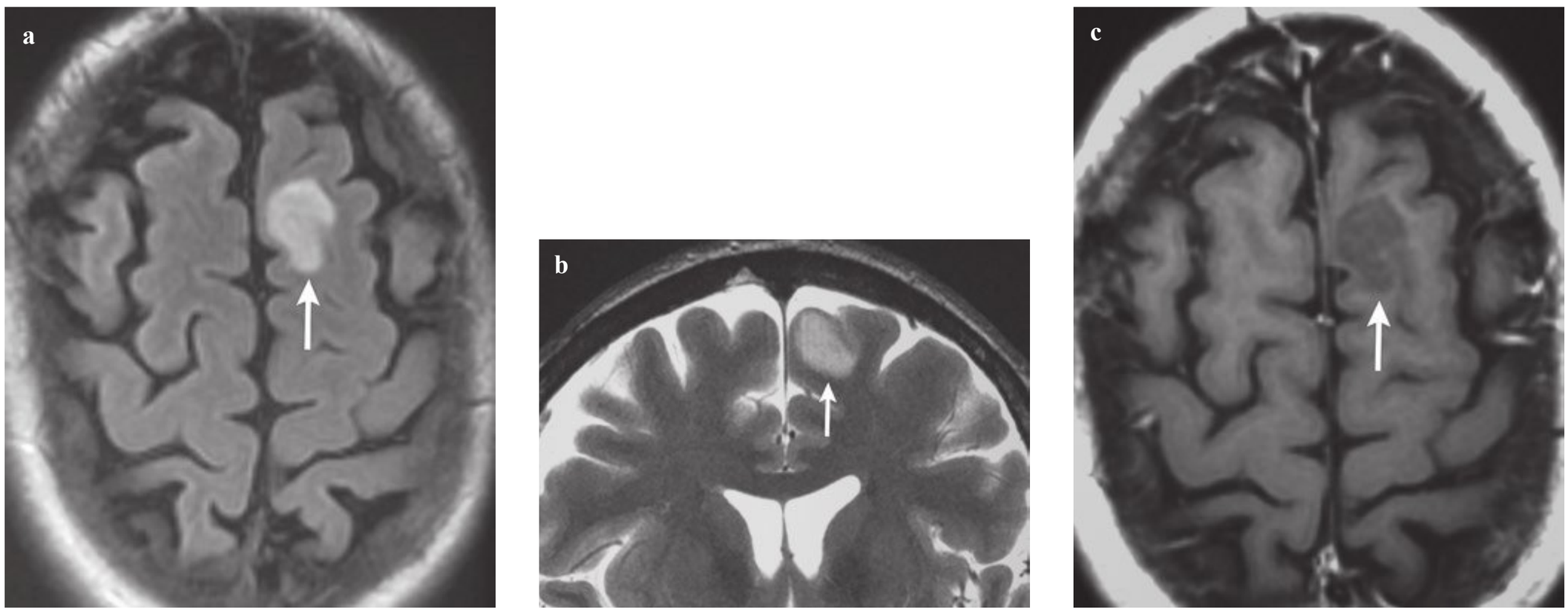

Fig. 1.51 A 48-year-old woman with a diffuse-type astrocytoma in the left frontal lobe that has high signal on **(a)** axial FLAIR (arrow) and **(b)** T2-weighted imaging (arrow). **(c)** The tumor shows no gadolinium contrast enhancement on axial T1-weighted imaging (arrow).

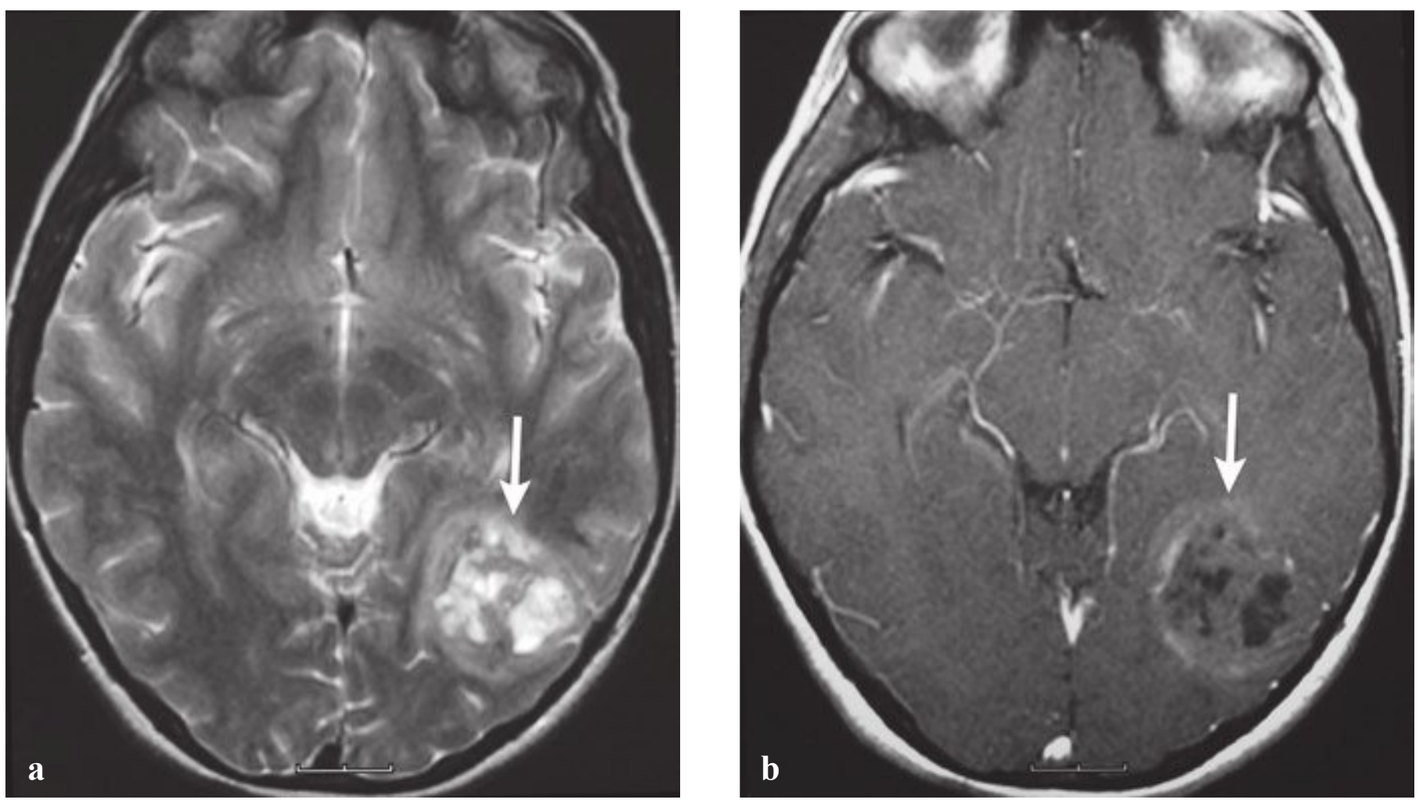

Fig. 1.52 **(a)** A 14-year-old female with a diffuse astrocytoma in the left cerebral hemisphere that has mixed intermediate and high signal on axial T2-weighted imaging (arrow) and **(b)** shows minimal heterogeneous gadolinium contrast enhancement on axial T1-weighted imaging (arrow).

Table 1.2 (cont.) Supratentorial solitary intra-axial mass lesions

Lesions	Imaging Findings	Comments
Pleomorphic xanthoastrocytoma (**Fig. 1.53**)	MRI: Circumscribed and/or poorly marginated lesion involving cerebral cortex and white matter with extension to the leptomeninges, low-intermediate signal on T1-weighted imaging, intermediate-high signal on T2-weighted imaging, ± cyst(s), ± hemorrhage, heterogeneous gadolinium contrast enhancement, ± enhancing mural nodule associated with cyst. Diffusion-weighted imaging: Tumors typically do not show restricted diffusion. CT: Circumscribed lesion involving cerebral cortex and white matter, low-intermediate attenuation, ± cyst(s), heterogeneous contrast enhancement, ± enhancing mural nodule associated with cyst.	Rare type of astrocytoma (WHO grade II) that accounts for less than 1% of astrocytic tumors. Occurs in young adults and children and is associated with seizure history. Tumors consist of mono- or multinucleated giant astrocytes with nuclei of varying sizes, xanthomatous cells containing lipids, granular eosinophilic bodies, and occasional lymphocytes. Usually, lack mutation of IDH gene. Immunoreactive to glial fibrillary acidic protein (GFAP), S-100 protein, and CD34. Tumors are supratentorial (temporal and frontal lobes are the most common locations, followed by parietal and occipital lobes). Tumors involve a superficial portion of brain and extend to leptomeninges. Survival after surgery is 81% at 5 years and 70% at 10 years. Tumors are typically resistant to chemotherapy and radiation.
Gliomatosis cerebri (**Fig. 1.54**)	MRI: Infiltrative lesion in the cerebral white matter with poorly defined margins, low-intermediate signal on T1-weighted imaging, high signal on T2-weighted imaging and FLAIR, usually minimal or no gadolinium contrast enhancement, and decreased relative cerebral blood volume (rCBV). Diffusion-weighted imaging: Tumors typically do not show restricted diffusion. Magnetic resonance spectroscopy shows elevated choline/creatine (Cho/Cr) and Cho/NAA ratios at sites with abnormal high signal on T2-weighted imaging. CT: Infiltrative lesion with low-intermediate attenuation. Usually no contrast enhancement until late in disease.	Diffusely infiltrating astrocytoma (WHO grade III) that often involves at least three cerebral lobes, including the basal nuclei. Can involve the cerebellum and brainstem. Peak age of occurrence between 40 and 50 years. Tumor consists of infiltrating small neoplastic glial cells with elongated fusiform nuclei as well as larger neoplastic cells with pleomorphic nuclei. Imaging appearance may be more prognostic than histologic grade, with approximate 2-year survival.

(continued on page 44)

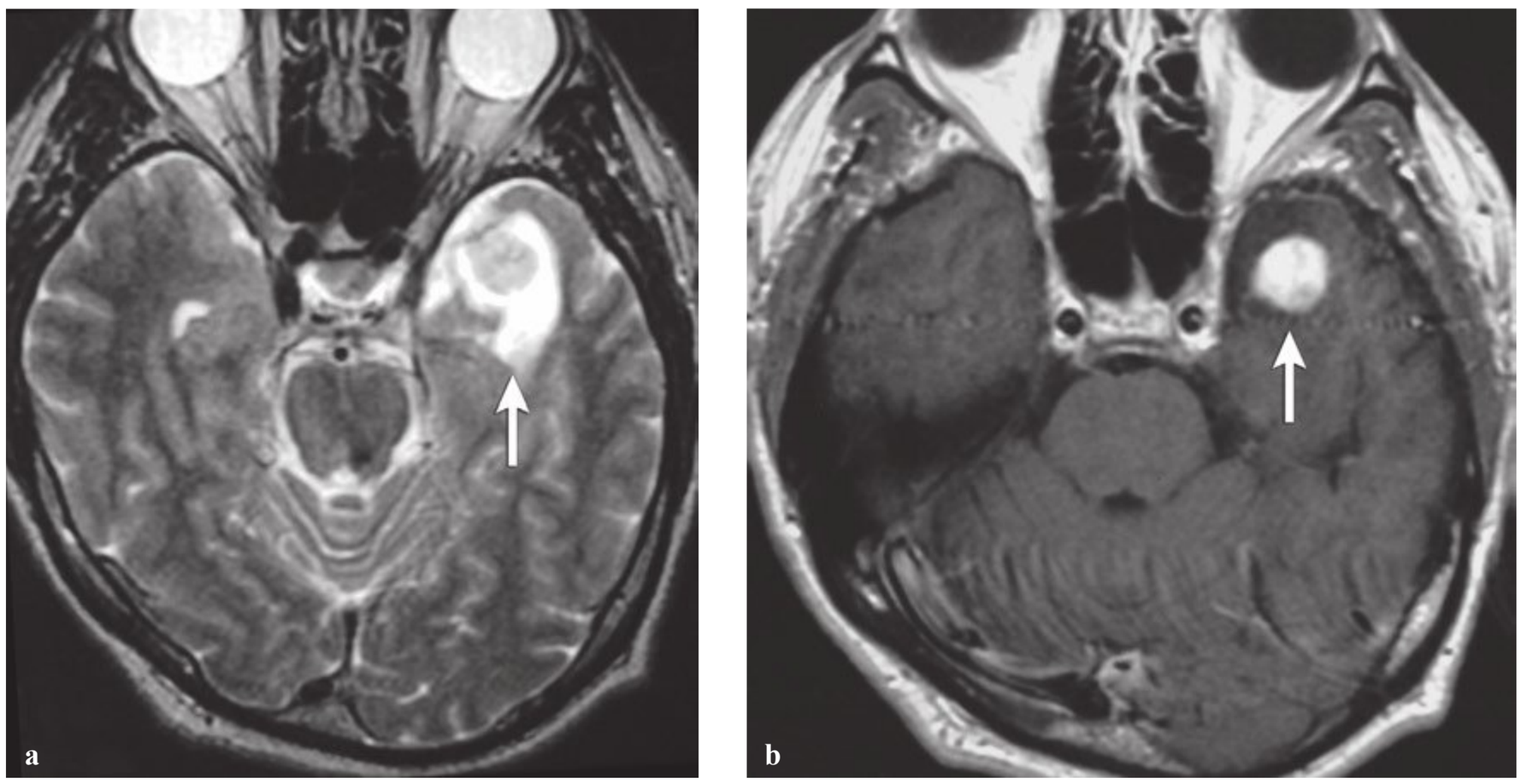

Fig. 1.53 A 42-year-old man with a pleomorphic xanthoastrocytoma in the anterior left temporal lobe. **(a)** Axial T2-weighted imaging shows a mixed nodular and cystic lesion (arrow). **(b)** The nodular portion of the tumor shows gadolinium contrast enhancement on axial T1-weighted imaging (arrow).

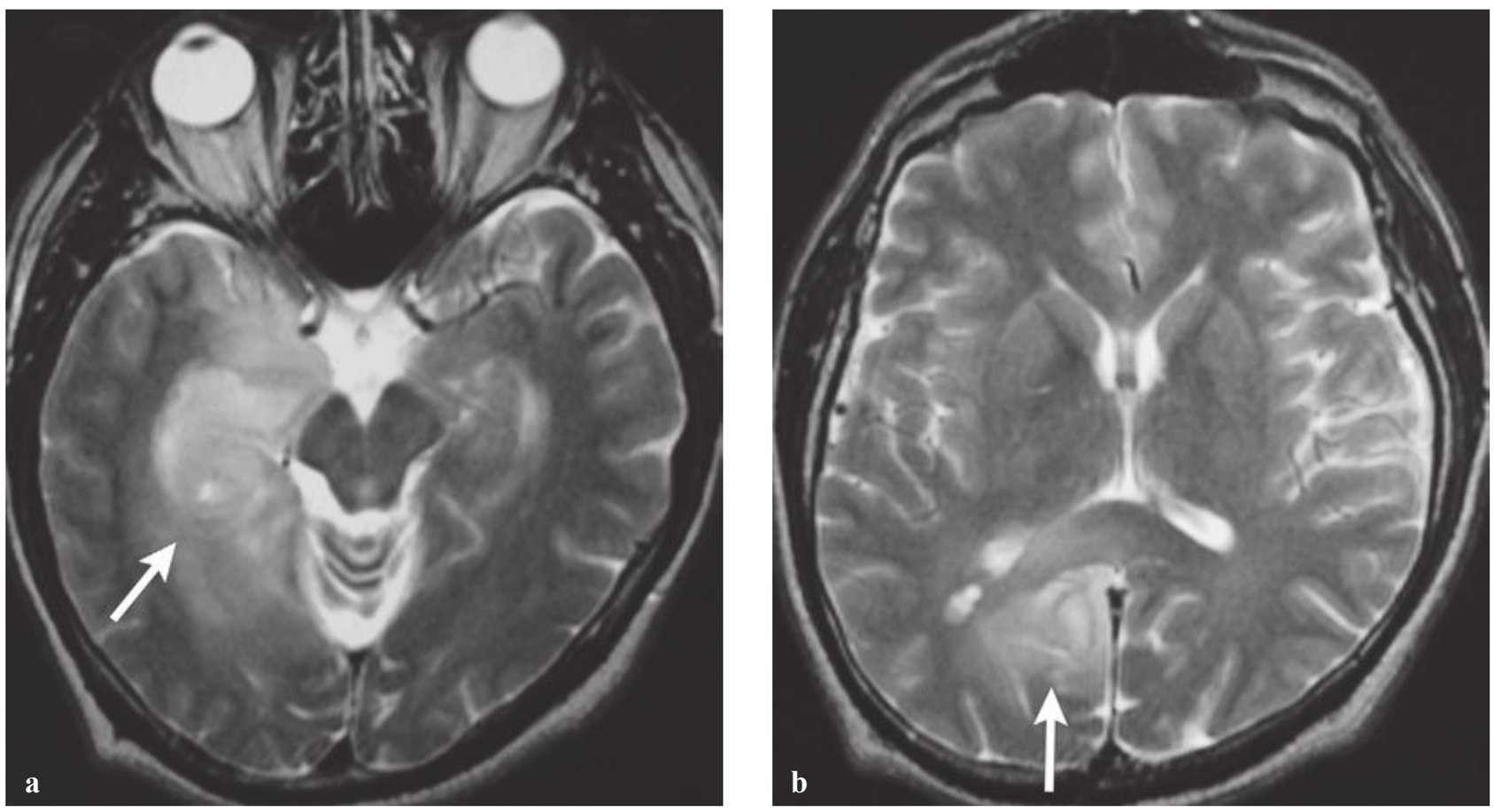

Fig. 1.54 **(a,b)** A 39-year-old man with gliomatosis cerebri, seen as poorly defined intra-axial zones with high signal on T2-weighted imaging in the right temporal and occipital lobes extending into the splenium of the corpus callosum (arrows).

Table 1.2 (cont.) Supratentorial solitary intra-axial mass lesions

Lesions	Imaging Findings	Comments
Anaplastic astrocytoma (**Fig. 1.55** and **Fig. 1.56**)	MRI: Often irregularly marginated lesion located in white matter with low-intermediate signal on T1-weighted imaging, high signal on T2-weighted imaging, ± gadolinium contrast enhancement. Tumors can have elevated relative cerebral blood volume (rCBV). Diffusion-weighted imaging: Tumors typically do not show restricted diffusion. Magnetic resonance spectroscopy: Tumor shows decreased N-acetylaspartate (NAA) and high levels of choline. CT: Irregularly marginated mass lesion with mixed low and intermediate attenuation, ± hemorrhage, prominent heterogeneous contrast enhancement, and peripheral edema. Can cross corpus callosum.	Malignant astrocytic tumor (WHO grade III) between diffuse astrocytoma and glioblastoma multiforme. Malignant astrocytes have nuclear atypia and mitotic activity. K_i-67/MIB-1 proliferation index ranges from 5 to 10% Can progress to glioblastoma. Approximate 2-year survival. Promotor methylation inactivates the effects of the DNA repair enzyme MGMT enabling improved tumor response to alkylating chemotherapy agents. Patients with IDH mutations, as well as those who have MGMT promotor methylation, have improved responses to chemotherapy.
Glioblastoma multiforme (**Fig. 1.57** and **Fig. 1.58**)	MRI: Irregularly and poorly marginated mass lesion with necrosis or cyst, mixed signal on T1-weighted imaging, heterogeneous high signal on T2-weighted imaging, ± hemorrhage, prominent heterogeneous gadolinium contrast enhancement. Increased relative cerebral blood volume (rCBV) is associated with high-grade gliomas and tumor-induced angiogenesis. Other findings include peripheral edema and tumor extension across the corpus callosum. Diffusion-weighted imaging: Tumors typically do not show restricted diffusion. Magnetic resonance spectroscopy shows decreased N-acetylaspartate (NAA) and high levels of choline. CT: Irregularly marginated mass lesion with necrosis or cyst, mixed low and intermediate attenuation, ± hemorrhage, prominent heterogeneous contrast enhancement, and peripheral edema. Can cross corpus callosum.	Most common primary CNS tumor (WHO grade IV), accounts for 15%of intracranial tumors and up to 75%of astrocytic neoplasms, with an incidence of 3 per 100,000. Most patients are over 50 years old. These highly malignant astrocytic neoplasms have nuclear atypia, with mitotic activity, cellular pleomorphism, necrosis, microvascular proliferation and invasion. K_i-67/MIB-1 proliferation index ranges from 15 to 20% Associated with mutations involving RTK/phosphatase–PTEN/PI3K signal pathway, TERT, and p53 and Rb1 tumor suppressor genes. Promotor methylation resulting in inactivation of the MGMT DNA repair enzyme enables improved malignant tumor response to chemotherapy in patients lacking IDH mutations. The extent of the lesion is underestimated by MRI. Survival is often < 1 year. Patients with secondary type glioblastoma who have IDH mutations can have a better response to chemotherapy and prognosis than those without.
Giant cell glioblastoma (**Fig. 1.59**)	MRI: Intra-axial mass lesion with necrosis and/or cysts, mixed signal on T1-weighted imaging, heterogeneous slightly high and high signal on T2-weighted imaging and FLAIR, ± hemorrhage, prominent heterogeneous gadolinium contrast enhancement, and peripheral edema. CT: Irregularly marginated mass lesion with necrosis or cyst, mixed low and intermediate attenuation, ± hemorrhage, prominent heterogeneous contrast enhancement, and peripheral edema. Can cross corpus callosum.	Subtype (5%) of glioblastoma, often involving frontal and temporal lobes. Tumors may have circumscribed margins, may contain bizarre multinucleated giant cells with a reticulin network, may have malignant astrocytes, and can have a high frequency of p53 mutations. Prognosis is poor, although slightly better in children than in adults.

(continued on page 47)

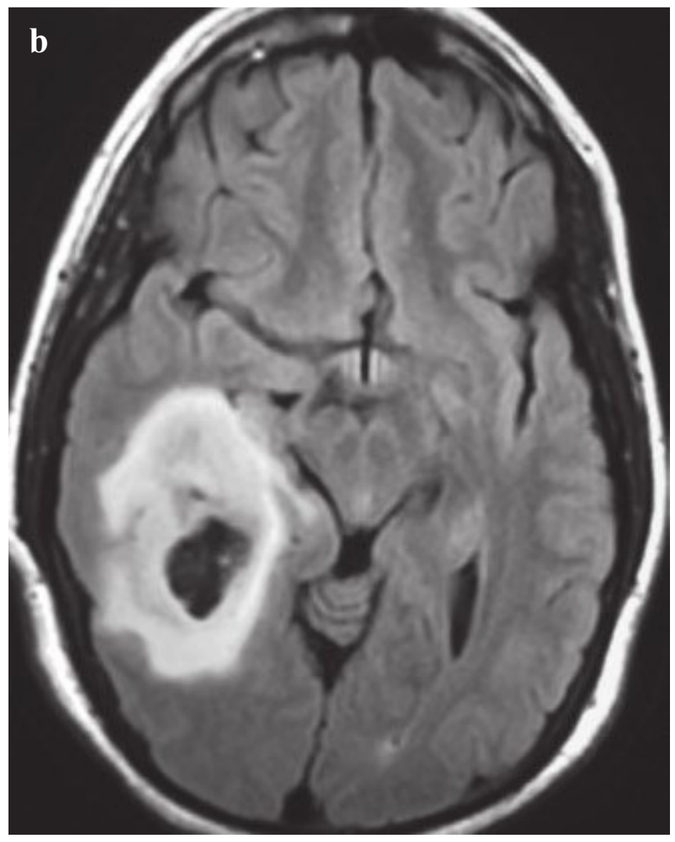

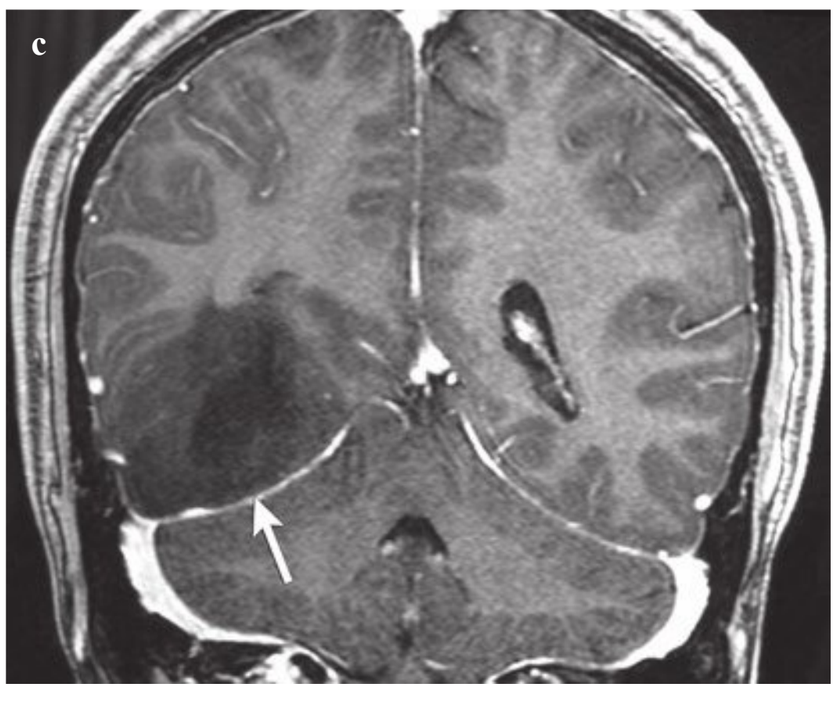

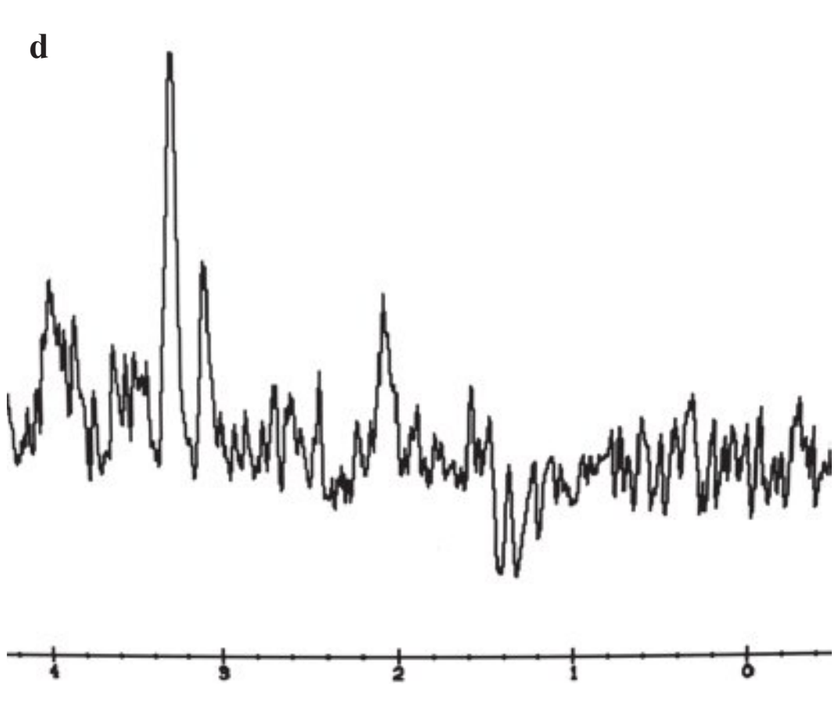

Fig. 1.55 A 72-year-old man with an anaplastic astrocytoma in the right temporal lobe that has **(a)** irregular margins and low attenuation on postcontrast CT (arrow), **(b)** heterogeneous mostly high signal on axial FLAIR, and **(c)** no gadolinium contrast enhancement on coronal T1-weighted imaging. **(d)** Magnetic resonance spectroscopy with TE of 144 ms shows a markedly abnormal decreased peak of N-acetylaspartate (NAA) at 2 ppm, abnormal increased peak of choline at 3.2 ppm, and elevated level of lactate, which has a double downward peak at 1.44 ppm.

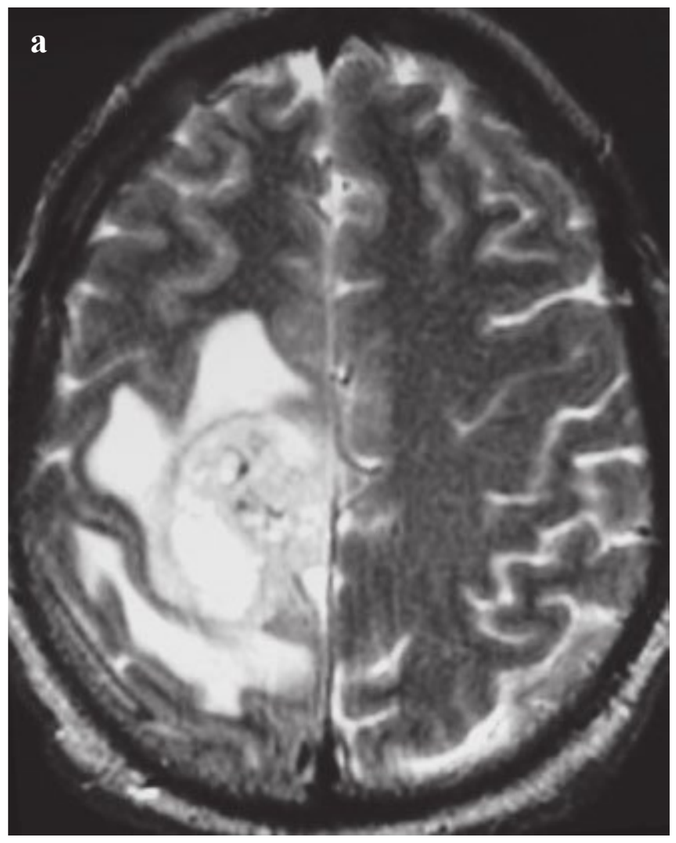

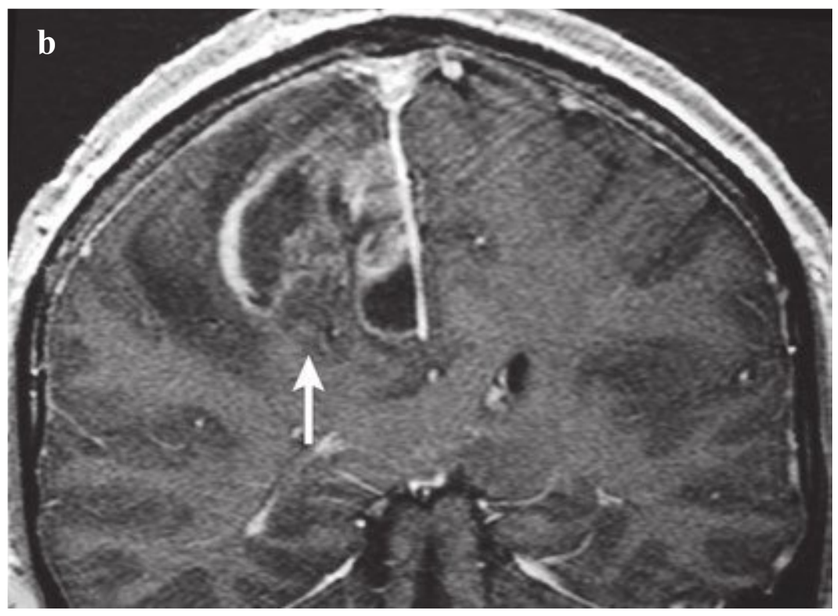

Fig. 1.56 A 44-year-old man with an anaplastic astrocytoma in the right cerebral hemisphere that has **(a)** irregular margins, heterogeneous mostly high signal on axial T2-weighted imaging, and **(b)** heterogeneous gadolinium contrast enhancement on coronal T1-weighted imaging (arrow).

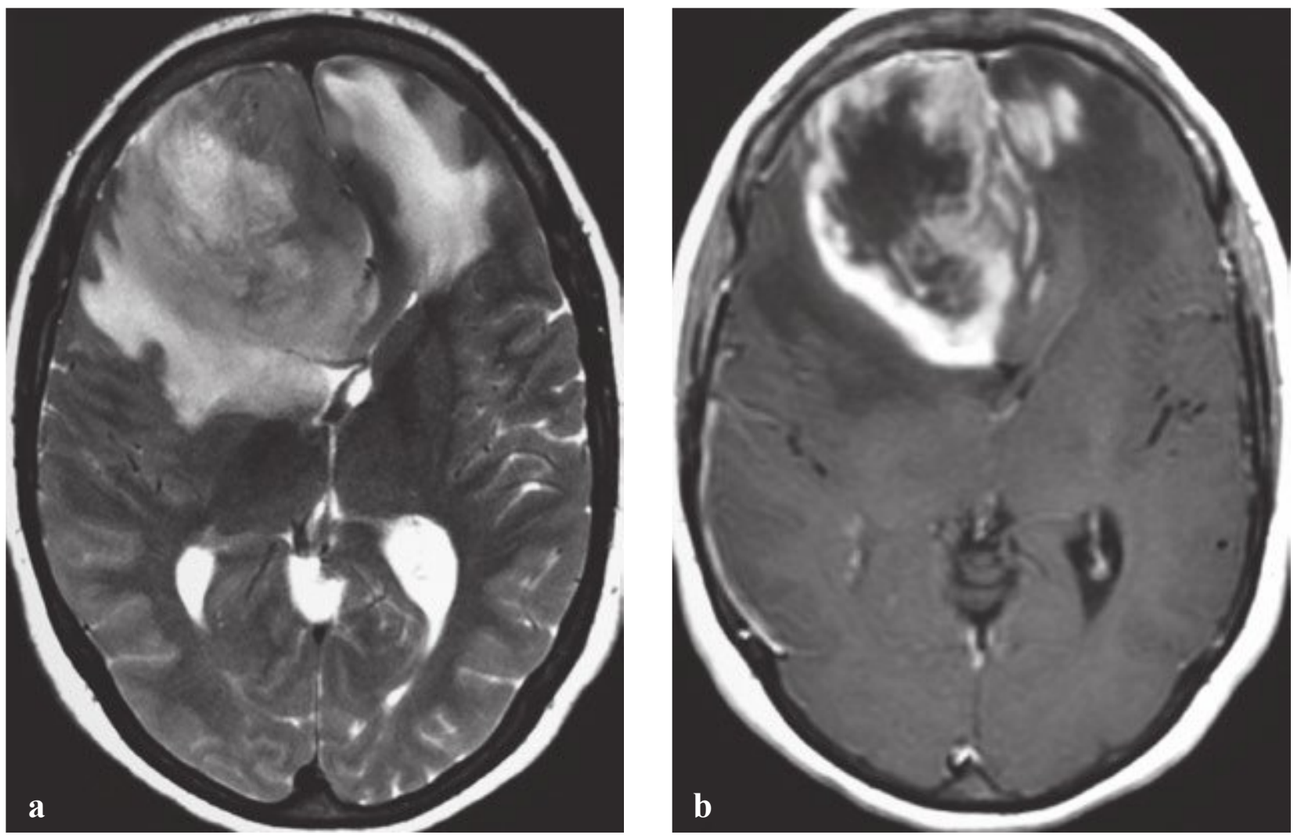

Fig. 1.57 A 64-year-old man with a glioblastoma multiforme in the right frontal lobe that has **(a)** irregular margins, heterogeneous mixed intermediate and high signal on axial T2-weighted imaging, and **(b)** heterogeneous and mostly peripheral irregular gadolinium contrast enhancement on axial T1-weighted imaging. The tumor extends into the left frontal lobe and has abnormal mass effect, resulting in subfalcine herniation to the left.

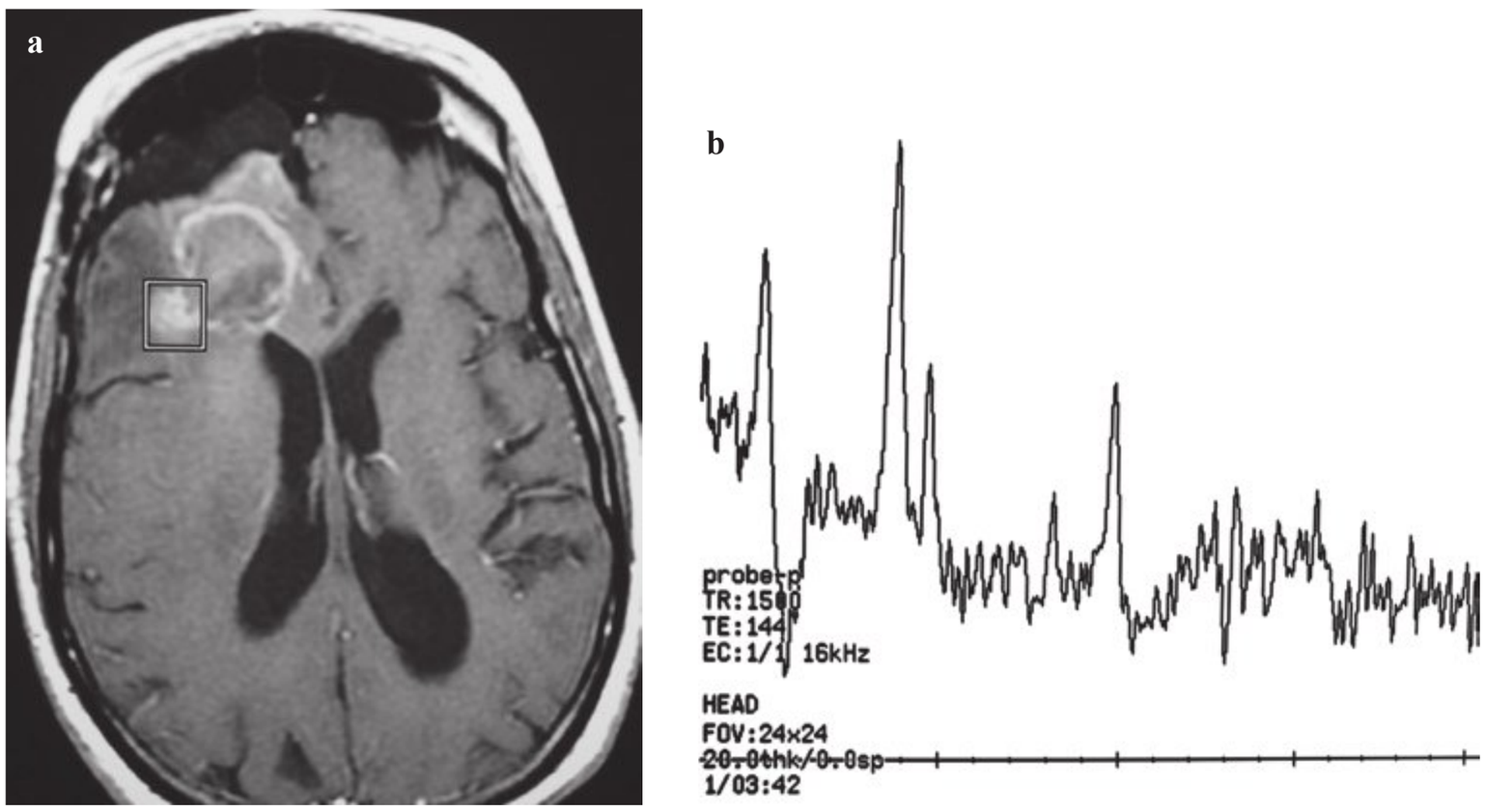

Fig. 1.58 A 34-year-old man with a glioblastoma multiforme in the right frontal lobe. **(a)** Axial T1-weighted imaging shows a gadolinium contrast-enhancing tumor in the right frontal lobe. **(b)** A square voxel used for magnetic resonance spectroscopy (MRS) is shown. MRS shows abnormal decreased peak of N-acetylaspartate (NAA) at 2 ppm and abnormal increased peak of choline at 3.2 ppm, consistent with a malignant neoplasm.

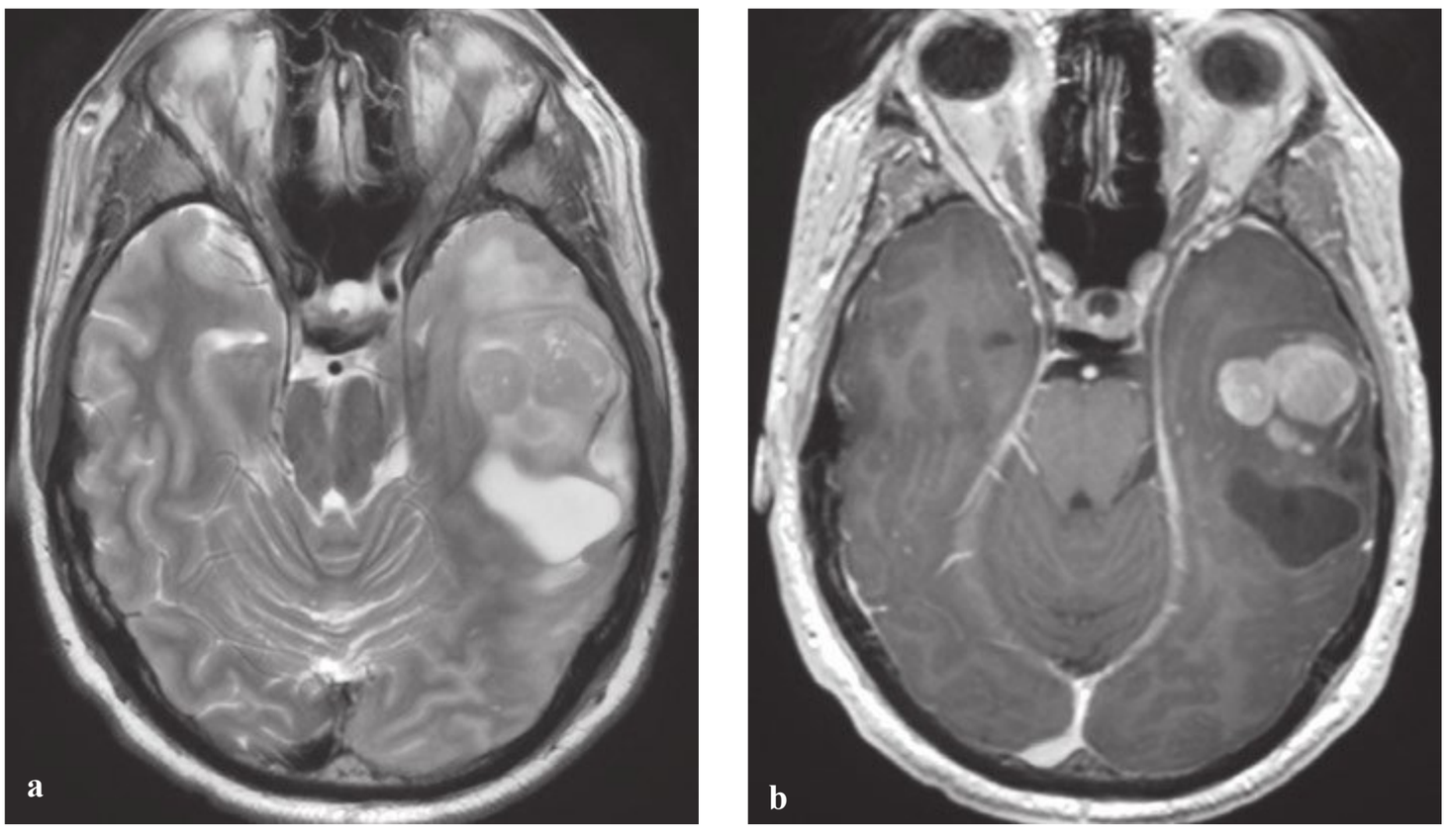

Fig. 1.59 A 30-year-old man with a giant cell glioblastoma in the left temporal lobe that has **(a)** heterogeneous intermediate and high signal on axial T2-weighted imaging, and **(b)** heterogeneous gadolinium contrast enhancement on axial T1-weighted imaging.

Table 1.2 (cont.) Supratentorial solitary intra-axial mass lesions

Lesions	Imaging Findings	Comments
Gliosarcoma (**Fig. 1.60**)	MRI: Irregularly marginated mass lesion with necrosis or cysts, mixed signal on T1-weighted imaging, heterogeneous high signal on T2-weighted imaging, peritumoral edema, ± hemorrhage, prominent heterogeneous gadolinium contrast enhancement, and peripheral edema. Can cross corpus callosum. Magnetic resonance spectroscopy shows elevated choline and decreased N-acetylaspartate (NAA) peaks. CT: Tumors have mixed low and intermediate attenuation, ± hemorrhage, prominent heterogeneous contrast enhancement, and peripheral edema.	Rare subset (2 to 3%) of glioblastoma (WHO grade IV) with biphasic tissue pattern containing malignant glial and mesenchymal cells. Peak ages are between 40 and 60 years, mean age = 52 to 61 years. Usually in a supratentorial location (temporal > frontal > parietal, occipital lobes), with only 3% in cerebellum. Associated with poor prognosis similar to glioblastoma.
Astroblastoma (**Fig. 1.61**)	MRI: Circumscribed lesion that can have cystic components, mixed signal on T1-weighted imaging, heterogeneous high signal on T2-weighted images; ± peritumoral edema, hemorrhage, and fibrosis or necrosis. Usually has heterogeneous gadolinium contrast enhancement. CT: Circumscribed lesion that can have cystic components and mixed attenuation, ± peritumoral edema, hemorrhage, fibrosis, or necrosis. Usually has heterogeneous contrast enhancement.	Rare glial neoplasm that occurs in patients ranging from 1 to 58 years old, median age = 11 to 20 years. Tumors are comprised of glial fibrillary acidic protein (GFAP)-positive neoplastic cells with broad or tapered cellular processes that extend toward blood vessels, resulting in papillary, ribboned, or radial angiocentric configurations. Also commonly immunoreactive to vimentin and S-100. Usually occur in cerebral hemispheres (parietal and frontal lobes most common). Can be low grade or high grade, with variable prognosis.

(continued on page 48)

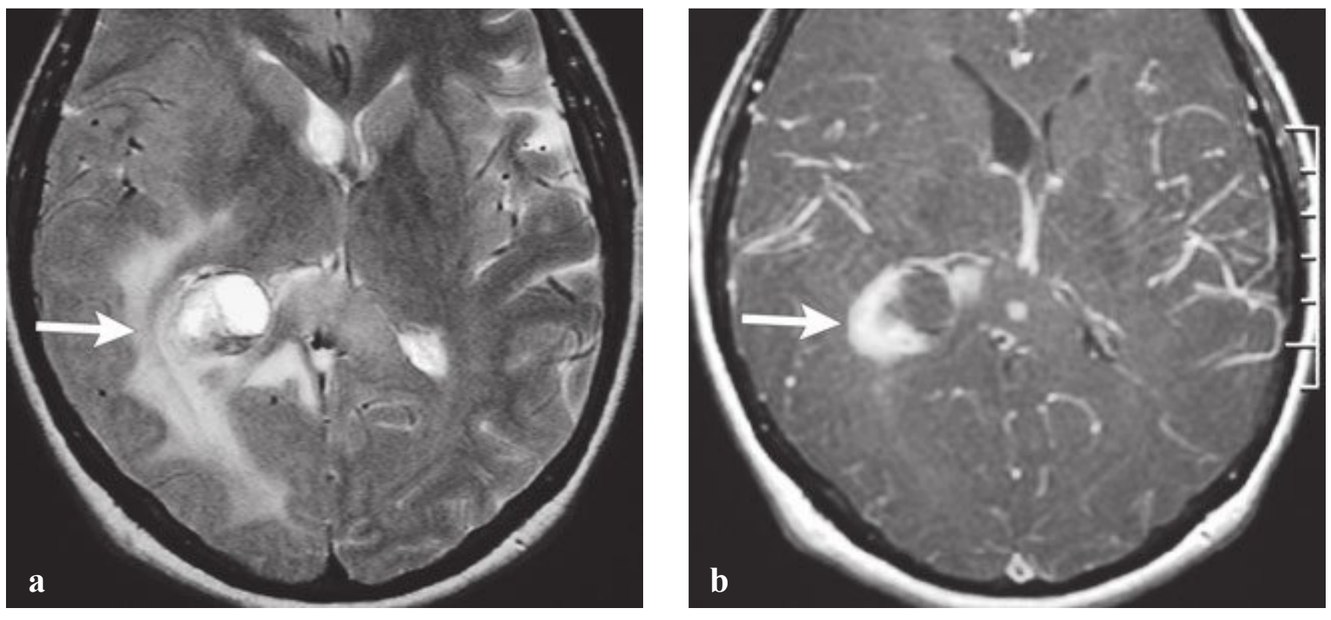

Fig. 1.60 **(a)** A 54-year-old woman with a gliosarcoma involving the right cerebral hemisphere with extension across the splenium of the corpus callosum, seen as heterogeneous high signal on axial T2-weighted imaging (arrow). **(b)** The tumor shows irregular heterogeneous gadolinium contrast enhancement on axial T1-weighted imaging (arrow).

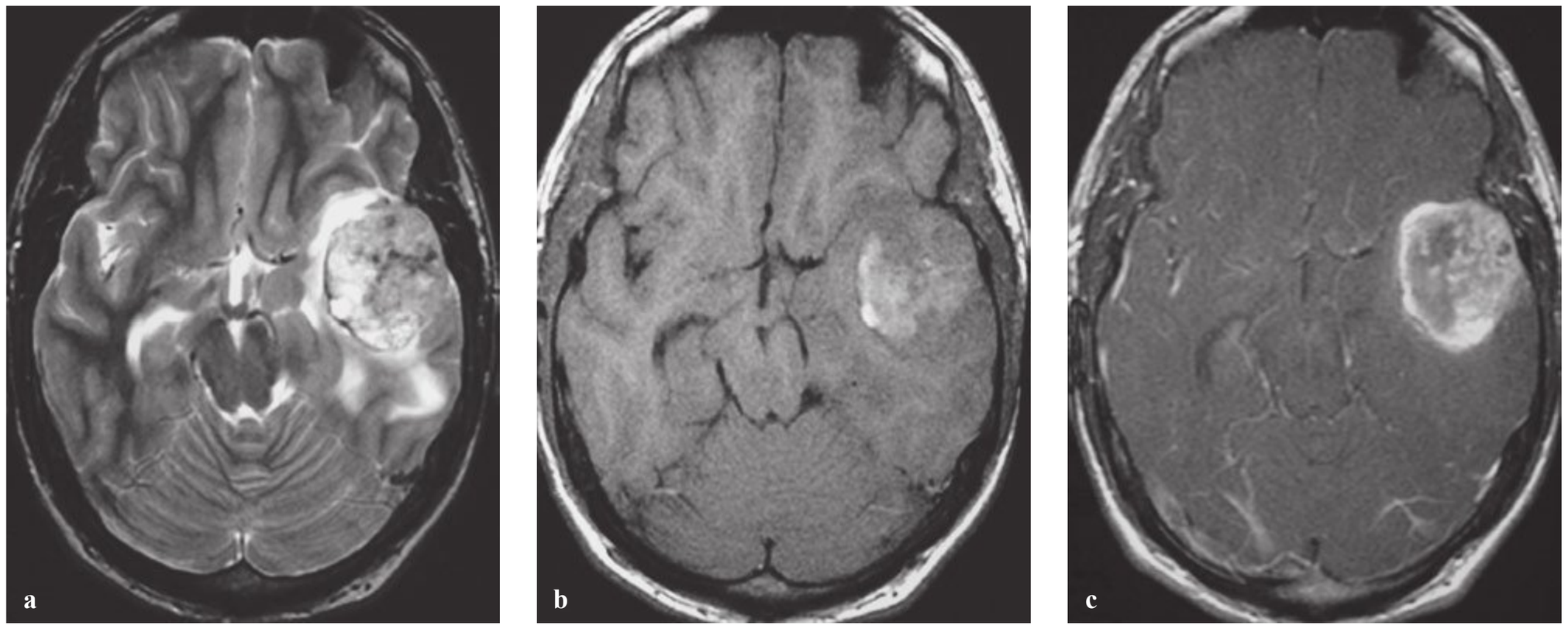

Fig. 1.61 **(a)** A 21-year-old man with an astroblastoma in the left temporal lobe that has heterogeneous slightly high and high signal on axial T2-weighted imaging. **(b)** Irregular zones with high signal on axial T1-weighted imaging from sites of intratumoral hemorrhage are present. **(c)** The tumor shows irregular heterogeneous gadolinium contrast enhancement on axial T1-weighted imaging.

Table 1.2 (cont.) Supratentorial solitary intra-axial mass lesions

Lesions	Imaging Findings	Comments
Neoplasms: Oligodendroglial Tumors		
Oligodendroglioma (**Fig. 1.62**)	MRI: Circumscribed lesion with mixed low-intermediate signal on T1-weighted imaging and mixed intermediate-high signal on T2-weighted imaging, areas of signal void at sites of clumplike calcification, and heterogeneous gadolinium contrast enhancement. Involves white matter and cerebral cortex, relative cerebral blood volume (rCBV) is often elevated, and the tumor can cause chronic erosion of the inner table of calvarium. Diffusion-weighted imaging: Usually no restricted diffusion. Magnetic resonance spectroscopy: Can show elevated choline and reduced N-acetylaspartate (NAA). CT: Circumscribed lesion with mixed low-intermediate attenuation, sites of clumplike calcification, and heterogeneous contrast enhancement. Involves white matter and cerebral cortex and can cause chronic erosion of the inner table of calvarium.	Oligodendrogliomas account for 2.5% of primary brain tumors and 6% of all gliomas, with an incidence of 0.3 per 100,000. Usually occur in adults, with the peak age between 40 and 45 years. These diffusely infiltrating, well-differentiated gliomas (WHO grade II) are comprised of neoplastic monomorphic cells with round nuclei, resembling oligodendrocytes. The majority (85%) are supratentorial. Associated with translocation involving chromosomes 1 and 19, [t(1,19) (q10;p10)], deletions of chromosome arms 1p and 19q, and IDH mutations. Oligodendrogliomas typically lack ATRX mutations allowing distinction from fibrillary and diffuse astrocytomas. If the tumor is low grade, 5-year survival is 75%; higher-grade lesions have a worse prognosis.
Anaplastic oligodendroglioma (**Fig. 1.63**)	MRI: Irregularly marginated mass lesion with necrosis or cyst, mixed signal on T1-weighted imaging, heterogeneous high signal on T2-weighted imaging, ± hemorrhage, heterogeneous gadolinium contrast enhancement, and peripheral edema. CT: Irregularly marginated mass lesion with necrosis or cyst, mixed attenuation, ± hemorrhage, heterogeneous contrast enhancement, and peripheral edema.	Oligodendroglioma containing portions with WHO grade III malignant cells. Peak ages between 45 and 50 years. Commonly occurs in frontal and temporal lobes. Associated with total losses of 1p and 19q. Survival ranges from less than 1 year to 4 years.

(continued on page 50)

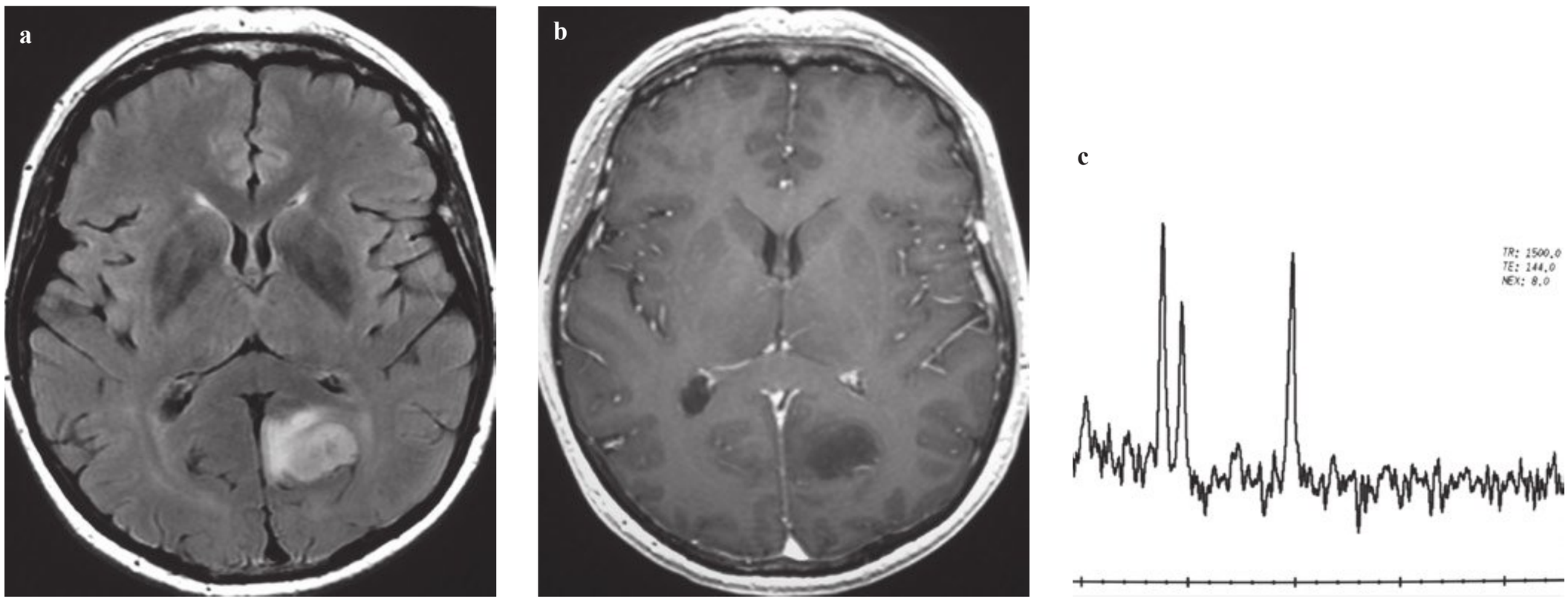

Fig. 1.62 A 57-year-old woman with a low-grade oligodendroglioma in the left occipital lobe that has **(a)** high signal on axial FLAIR and **(b)** shows no gadolinium contrast enhancement on axial T1-weighted imaging. **(c)** Magnetic resonance spectroscopy shows a slightly decreased peak of N-acetylaspartate (NAA) at 2 ppm and a slightly increased peak of choline at 3.2 ppm, consistent with a low-grade neoplasm.

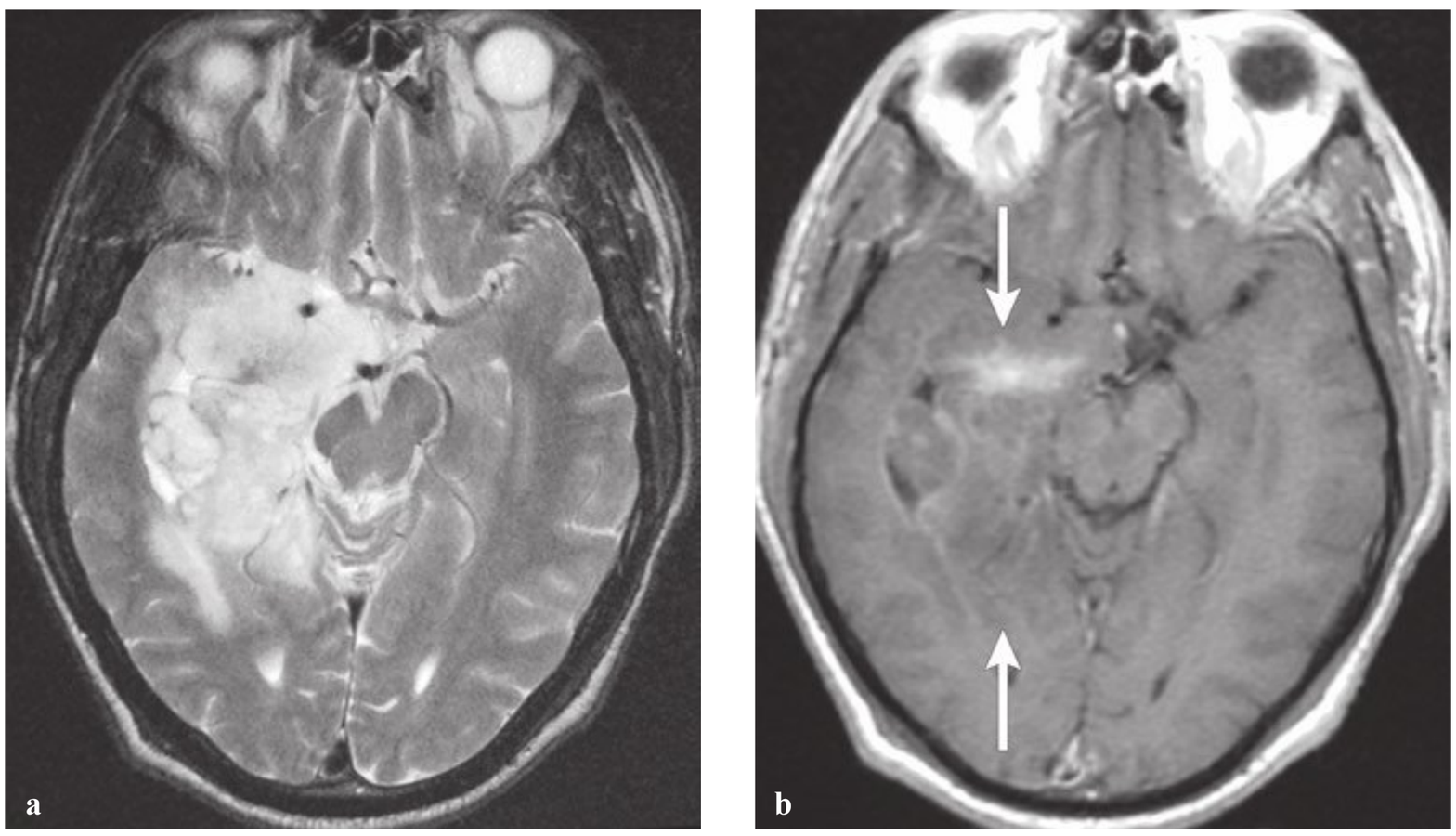

Fig. 1.63 A 51-year-old man with an anaplastic oligodendroglioma in the right temporal lobe that has **(a)** heterogeneous high signal on axial T2-weighted imaging (T2WI) and **(b)** irregular mild heterogeneous gadolinium contrast enhancement on axial T1-weighted imaging (T1WI) (arrows).

Table 1.2 (cont.) Supratentorial solitary intra-axial mass lesions

Lesions	Imaging Findings	Comments
Neoplasms: Oligoastrocytic Tumors		
Oligoastrocytoma (**Fig. 1.64**)	MRI: Irregularly marginated mass lesion with low-intermediate signal on T1-weighted imaging, heterogeneous high signal on T2-weighted imaging, and heterogeneous gadolinium contrast enhancement in half of cases. CT: Irregularly marginated mass lesion with low-intermediate attenuation and heterogeneous contrast enhancement in half of cases.	Diffusely infiltrating glioma (WHO grade II) comprised of both neoplastic astrocytes and oligodendrocytes. Recent research suggests that oligoastrocytomas can be categorized as astrocytomas when IDH and ATRX mutations are present, or oligodendrogliomas when IDH mutations occur as well as 1p/19q codeletions. Median age of occurrence is between 35 and 45 years, and tumor usually occurs in cerebral hemispheres. Annual incidence is 0.1 per 100,000. Median survival is 6.3 years, 5-year survival is 58%, and 10-year survival is 32%
Anaplastic oligoastrocytoma (**Fig. 1.65**)	MRI: Irregularly marginated mass lesion with necrosis or cyst, mixed signal on T1-weighted imaging, heterogeneous high signal on T2-weighted imaging, ± hemorrhage, heterogeneous gadolinium contrast enhancement, and peripheral edema. CT: Irregularly marginated mass lesion with necrosis or cyst, mixed attenuation, ± hemorrhage, heterogeneous contrast enhancement, and peripheral edema.	Oligoastrocytoma with increased pleomorphic cellularity, nuclear atypia, and increased mitotic activity. Mean age of patients is 44 years. Associated with loss of 1p/19q, and/or TP53. Median survival is 2.8 years, 5-year survival is 36%, and 10-year survival is 9%

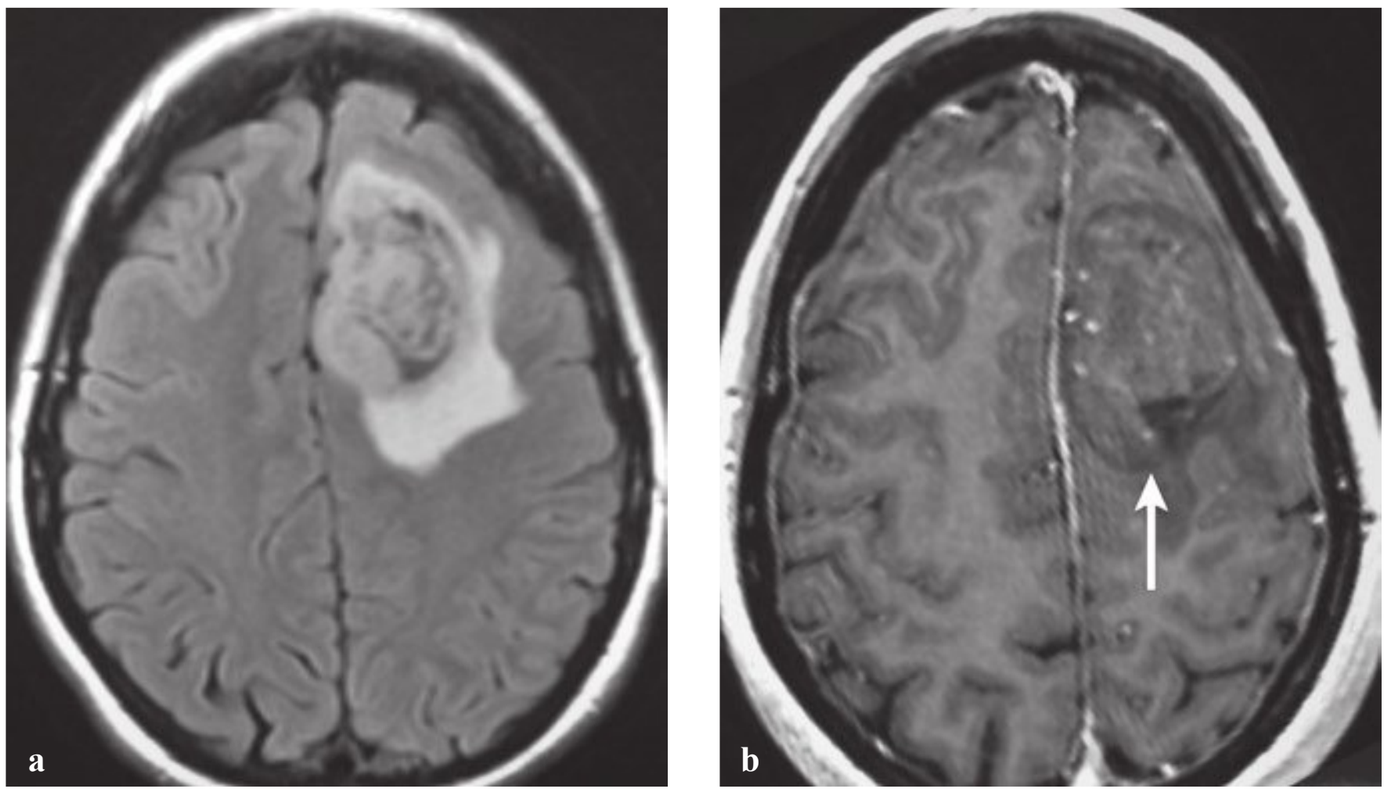

Fig. 1.64 A 30-year-old woman with an oligoastrocytoma in the left frontal lobe that has **(a)** heterogeneous slightly high and high signal on axial FLAIR and **(b)** irregular mild heterogeneous gadolinium contrast enhancement on axial T1-weighted imaging (arrow).

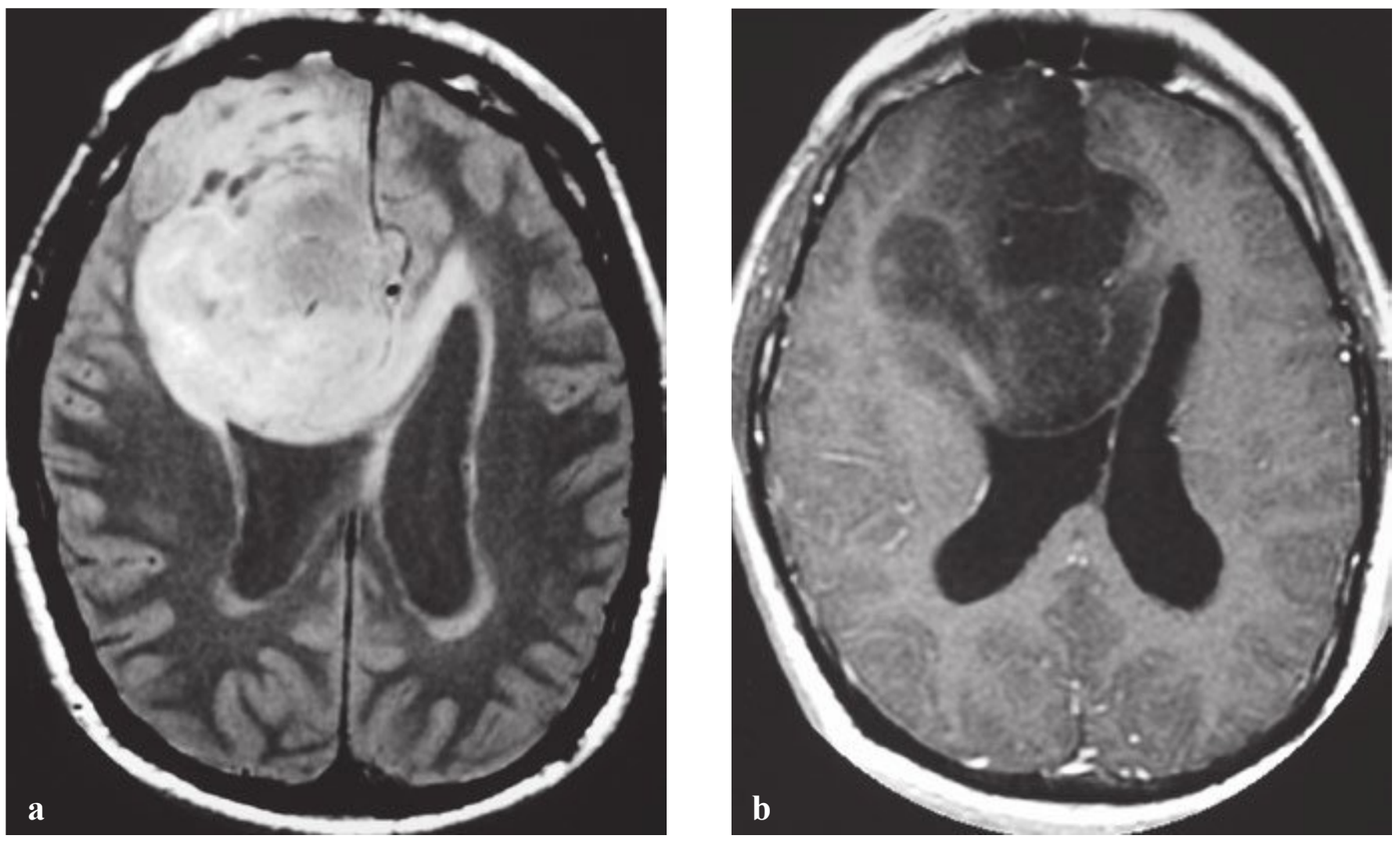

Fig. 1.65 A 41-year-old man with an anaplastic oligoastrocytoma in the right frontal lobe with extension along the corpus callosum into the left frontal lobe. **(a)** The tumor has heterogeneous high signal on axial FLAIR and **(b)** only minimal to no gadolinium contrast enhancement on axial T1-weighted imaging.

Lesions	Imaging Findings	Comments
Neoplasms: Ependymal Tumors		
Ependymoma (**Fig. 1.66**)	MRI: Circumscribed, lobulated supratentorial lesion, often extraventricular, ± cysts, calcifications, and/or hemorrhage. Low-intermediate signal on T1-weighted imaging, intermediate-high signal on T2-weighted imaging, variable gadolinium contrast enhancement. Tumors have elevated relative cerebral blood volume (rCBV) as well as delayed contrast retention secondary to intratumoral fenestrated blood vessels. Diffusion-weighted imaging: Usually no restricted diffusion. Magnetic resonance spectroscopy: Elevated choline and decreased N-acetylaspartate (NAA), similar to other neoplasms. CT: Circumscribed, lobulated, supratentorial lesion, often extraventricular, ± cysts and/or calcifications (up to 50%), low-intermediate attenuation, and variable contrast enhancement.	Slow-growing tumor (WHO grade II) comprised of neoplastic cells with monomorphic round/oval nuclei containing speckled chromatin, perivascular pseudorosettes, and ependymal rosettes. Zones of myxoid degeneration, hyalinization of blood vessels, hemorrhage, and/or calcifications may occur within the tumor. Ependymoma accounts for 6 to 12%of intracranial tumors, with an incidence of 0.22 to 0.29 per 100,000. Occurs more commonly in children than in adults. One-third of ependymomas are supratentorial, two-thirds are infratentorial. Children with infratentorial ependymomas range in age from 2 months to 16 years (mean age = 6.4 years). Supratentorial ependymomas occur in children and adults. Immunoreactive to glial fibrillary acidic protein (GFAP), S-100, vimentin, and/or epithelial membrane antigen (EMA). Associated with neurofibromatosis (NF2) and genetic mutations involving chromosomes 22, 9, 6, and 3. Usually lack mutation of IDH gene. Survival is 57%at 5 years and 45%at 10 years.

(continued on page 52)

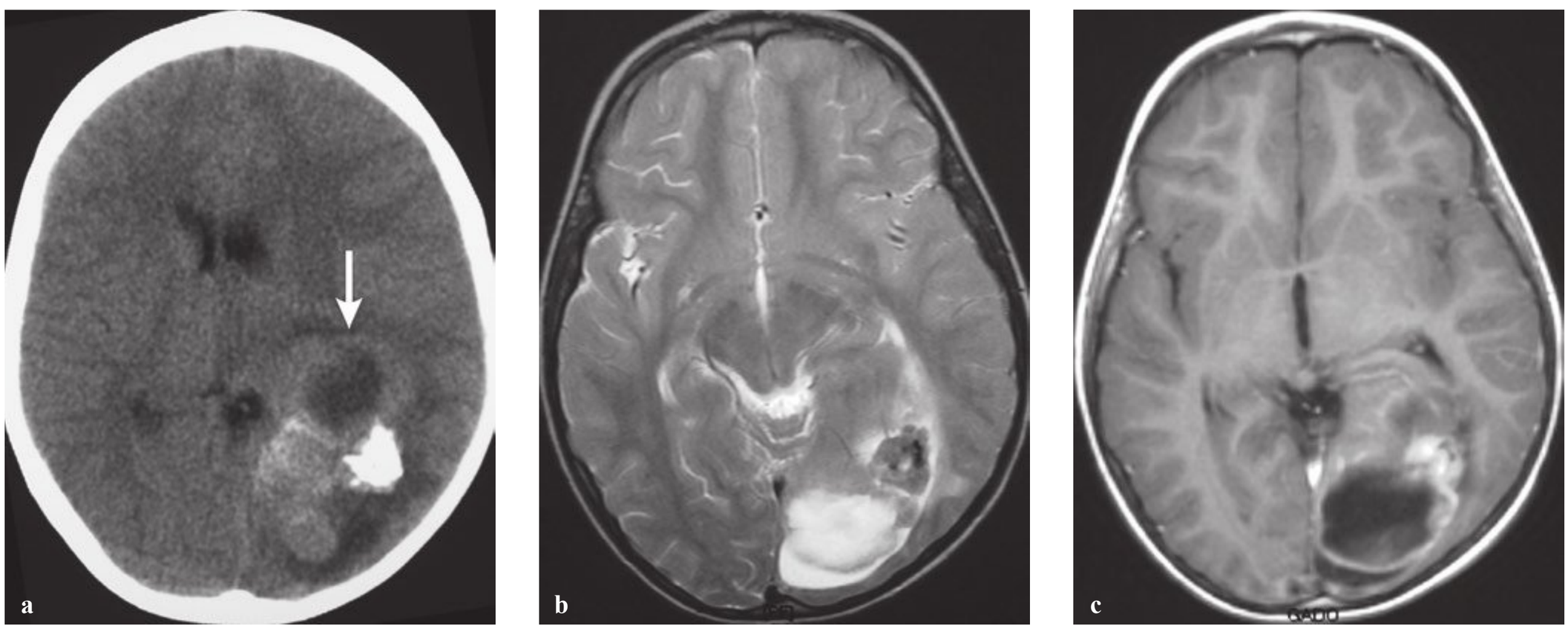

Fig. 1.66 **(a)** A 4-year-old boy with an ependymoma in the left occipital lobe that contains solid, cystic, and calcified portions on axial CT (arrow). **(b)** The tumor has heterogeneous mixed high, low, and intermediate signal on axial T2-weighted imaging and **(c)** irregular mostly peripheral gadolinium contrast enhancement on axial T1-weighted imaging.

Table 1.2 (cont.) Supratentorial solitary intra-axial mass lesions

Lesions	Imaging Findings	Comments
Subependymoma (**Fig. 1.67**)	MRI: Tumors typically attached to ventricular walls (fourth ventricle, 40–50%; lateral ventricle, 30–40%; third ventricle, 10%). Lesions have circumscribed margins, low-intermediate signal on T1-weighted imaging, and heterogeneous slightly high to high signal on T2-weighted imaging. May contain sites of hemorrhage or calcification. Variable degrees of gadolinium contrast enhancement. CT: Lesions have circumscribed margins and low-intermediate attenuation. May contain sites of hemorrhage or calcification. Variable degrees of contrast enhancement.	Slow-growing low-grade (WHO grade I) glial neoplasms comprised of clusters of tumor cells with isomorphic nuclei within a dense matrix of cell processes. Mitotic activity is absent or rare. Immunoreactive to glial fibrillary acidic protein (GFAP). Account for 8% of ependymal tumors. Complete resection can be curative.
Anaplastic ependymoma (**Fig. 1.68**)	MRI: Irregularly marginated mass lesion with necrosis or cyst, mixed signal on T1-weighted imaging, heterogeneous high signal on T2-weighted imaging, ± hemorrhage, calcifications, heterogeneous gadolinium contrast enhancement, and peripheral edema. Can disseminate within the CSF. CT: Irregularly marginated mass lesion with necrosis or cyst, mixed attenuation, ± hemorrhage, calcifications, heterogeneous contrast enhancement, and peripheral edema. Can disseminate within the CSF.	Malignant glioma (WHO grade III) with ependymal differentiation, high mitotic activity, microvascular proliferation, and pseudopalisading necrosis. Associated with poor prognosis in patients with prominent anaplastic features, CSF metastases, and incomplete resection.

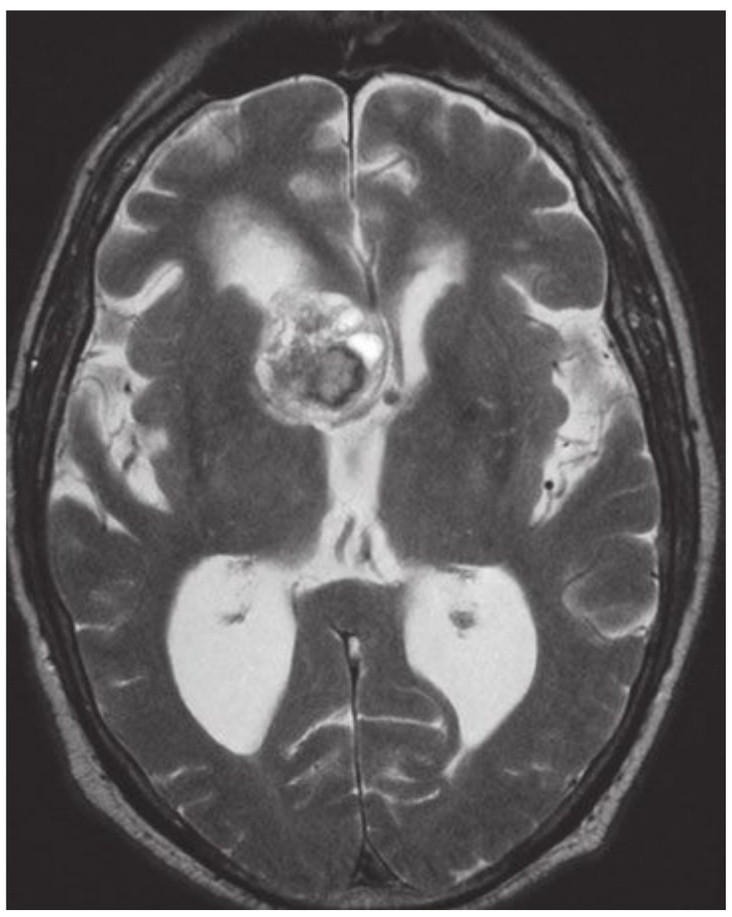

Fig. 1.67 A 75-year-old man with a subependymoma at the foramen of Monro causing obstruction of CSF outflow from the right lateral ventricle. The lesion has heterogeneous mixed high, low, and intermediate signal on axial T2-weighted imaging.

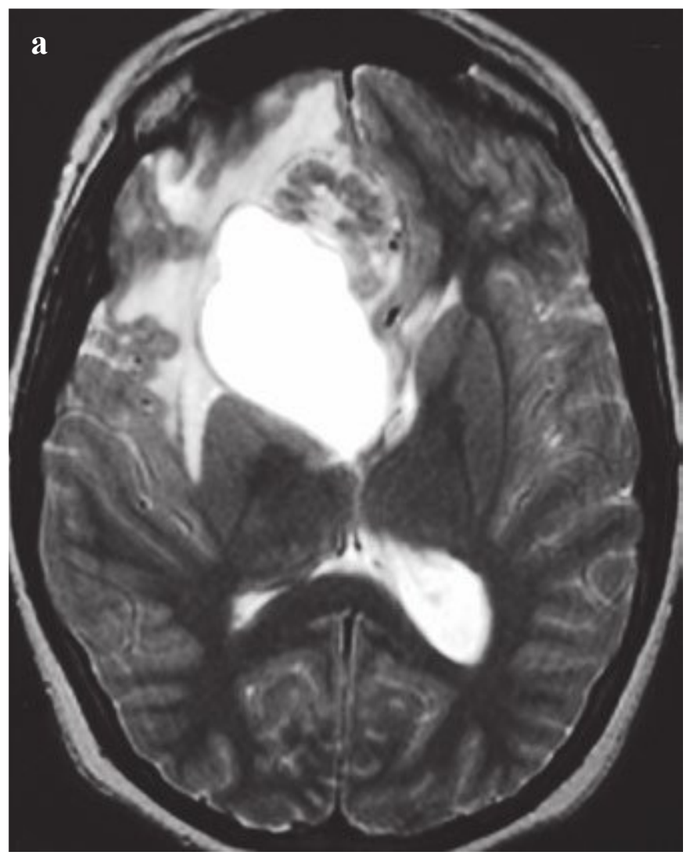

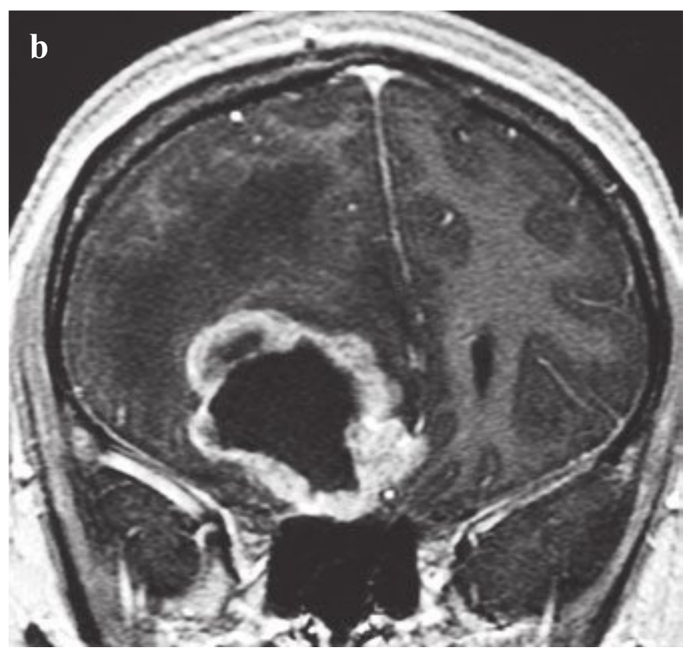

Fig. 1.68 A 20-year-old woman with an anaplastic ependymoma in the right frontal lobe with extension along the corpus callosum into the left frontal lobe. The tumor is associated with mass effect and subfalcine herniation leftward. The tumor contains solid and cystic/necrotic portions. **(a)** The tumor has heterogeneous mixed high, low, and intermediate signal on axial T2-weighted imaging and **(b)** irregular mostly peripheral gadolinium contrast enhancement on coronal T1-weighted imaging.

Lesions	Imaging Findings	Comments
Neuronal and Mixed Neuronal-Glial Tumors		
Ganglioglioma (**Fig. 1.69**)	MRI: Circumscribed tumor, usually supratentorial, often in temporal or frontal lobes, with low-intermediate signal on T1-weighted imaging and intermediate-high signal on T2-weighted imaging, ± cysts (up to 40%), calcifications (up to 30%), ± gadolinium contrast enhancement. Diffusion-weighted imaging: Usually no restricted diffusion. CT: Lesions have low-intermediate attenuation, ± cysts, ± calcifications, ± contrast enhancement.	Rare, well-differentiated neuroepithelial tumors (WHO grade I) that occur in patients with mean ages ranging from 8.5 to 26 years. Slow-growing neoplasms that account for 1.3% of brain tumors. Ganglioglioma contains glial and neuronal elements, and ganglioneuroma contains only ganglion cells. Immunoreactive to neurofilaments, synaptophysin, neuronal nuclear protein (NeuN), MAP2, and CD34. Patients are usually < 30 years old, with seizure presentation. Gangliocytoma contains only neoplastic ganglion cells and dysplastic brain tissue. Favorable prognosis if completely resected, with 7.5-year recurrence-free survival.

(continued on page 54)

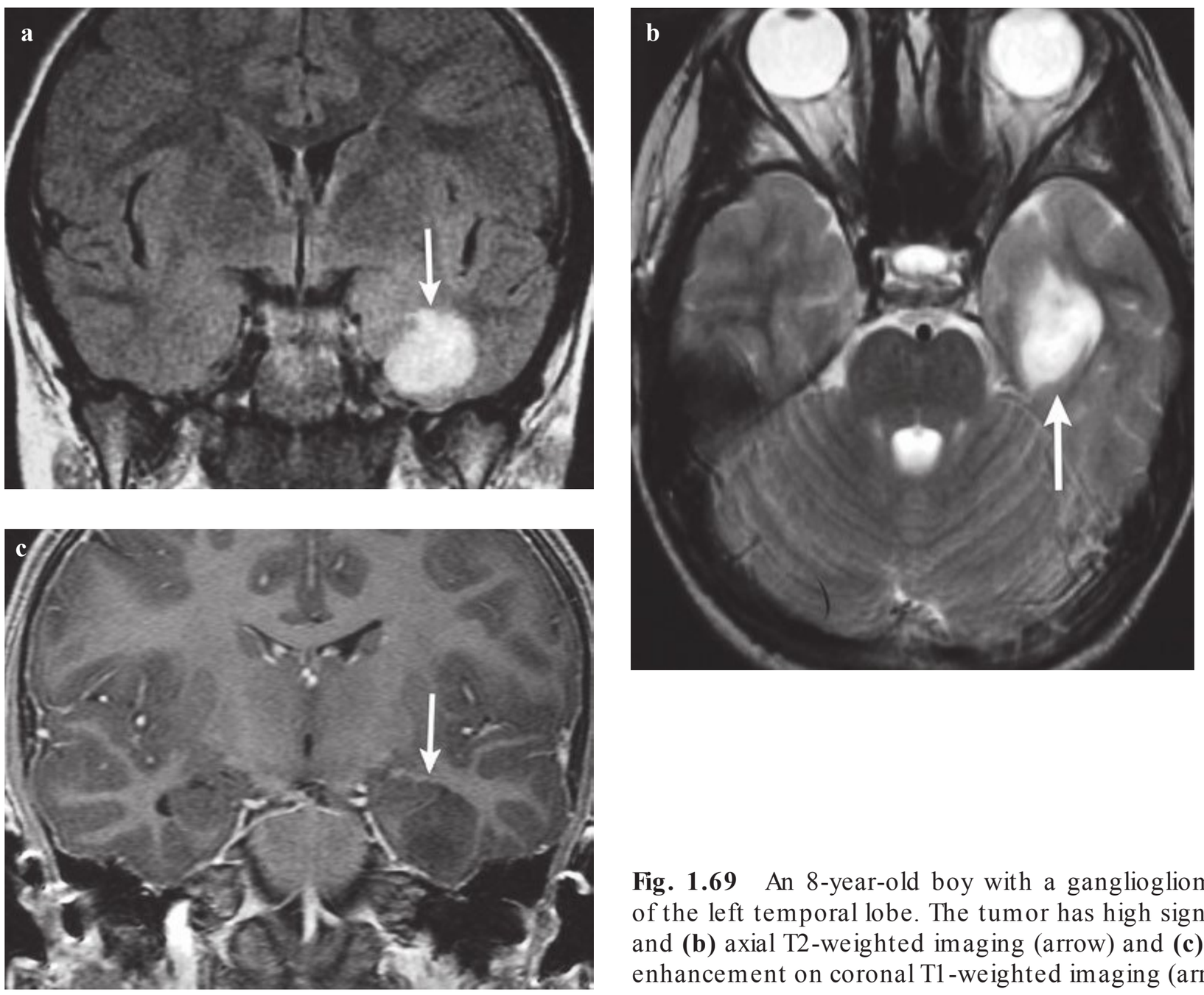

Fig. 1.69 An 8-year-old boy with a ganglioglioma in the inferomedial portion of the left temporal lobe. The tumor has high signal on **(a)** coronal FLAIR (arrow) and **(b)** axial T2-weighted imaging (arrow) and **(c)** shows no gadolinium contrast enhancement on coronal T1-weighted imaging (arrow).

Table 1.2 (cont.) Supratentorial solitary intra-axial mass lesions

Lesions	Imaging Findings	Comments
Gangliocytoma (**Fig. 1.70**)	MRI: Circumscribed tumor, usually supratentorial, often in temporal or frontal lobes, with low-intermediate signal on T1-weighted imaging and intermediate to high signal on T2-weighted imaging, ± cysts, ± gadolinium contrast enhancement. CT: Lesions have low-intermediate attenuation, ± cysts, ± contrast enhancement.	Uncommon tumors. Patients are usually < 30 years old, with seizure presentation. Slow-growing neoplasms, gangliocytomas contain only mature neoplastic ganglion cells and dysplastic brain tissue. Favorable prognosis if completely resected.
Anaplastic ganglioglioma (**Fig. 1.71**)	MRI: Irregularly marginated mass lesion with necrosis or cyst, mixed signal on T1-weighted imaging, heterogeneous high signal on T2-weighted imaging, ± hemorrhage, calcifications, heterogeneous gadolinium contrast enhancement, and peripheral edema. CT: Irregularly marginated mass lesion with necrosis or cyst, mixed attenuation, ± hemorrhage, calcifications, heterogeneous contrast enhancement, and peripheral edema.	Ganglioglioma that contains anaplastic changes in glial components, with increased mitotic activity, microvascular proliferation, and necrosis.
Desmoplastic infantile astrocytoma (DIA) and ganglioglioma (DIG) (**Fig. 1.72**)	MRI: Large cystic and solid lesions that have mixed low, intermediate, and/or high signal on T1-weighted imaging and T2-weighted imaging, and gadolinium contrast enhancement in solid portions that can extend superficially to involve the meninges. Usually, there is absence of edema in adjacent brain tissue. Mild elevated relative cerebral blood volume (rCBV). Magnetic resonance spectroscopy: May show decreased N-acetylaspartate (NAA) and elevated choline, no change in myoinositol. CT: Large lesions with low and intermediate attenuation and a contrast-enhancing component involving the superficial portion of the brain and extending to the meninges.	Rare, large, cystic/solid tumors (WHO grade I) involving the superficial portions of the brain and leptomeninges in infants, (age range, 1 to 24 months; male/female ratio = 2/1). Lesions consist of a desmoplastic leptomeningeal portion with whorls and fascicles of spindle-shaped cells and pleomorphic neoplastic neuroepithelial cells with eosinophilic cytoplasm, surrounded by reticulin network. Neoplastic astrocytes in the brain are seen with DIA, and neoplastic neurons are seen with DIG, both with low mitotic activity. Immunoreactive to glial fibrillary acidic protein (GFAP) and type IV collagen. Gross total resection typically results in long-term survival.

(continued on page 56)

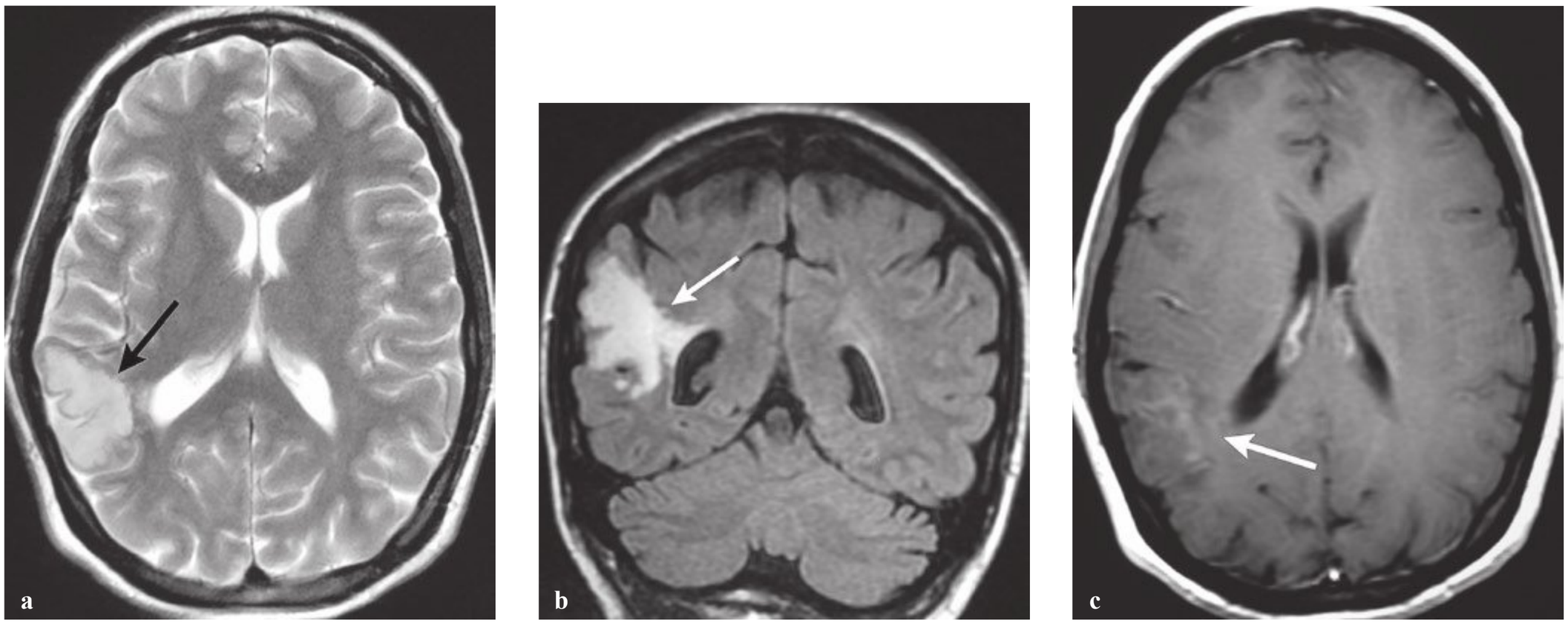

Fig. 1.70 A 35-year-old woman with a gangliocytoma in the right cerebral hemisphere that has high signal on **(a)** axial T2-weighted imaging (arrow) and **(b)** coronal FLAIR (arrow), and shows only minimal gadolinium contrast enhancement on **(c)** axial T1-weighted imaging (arrow).

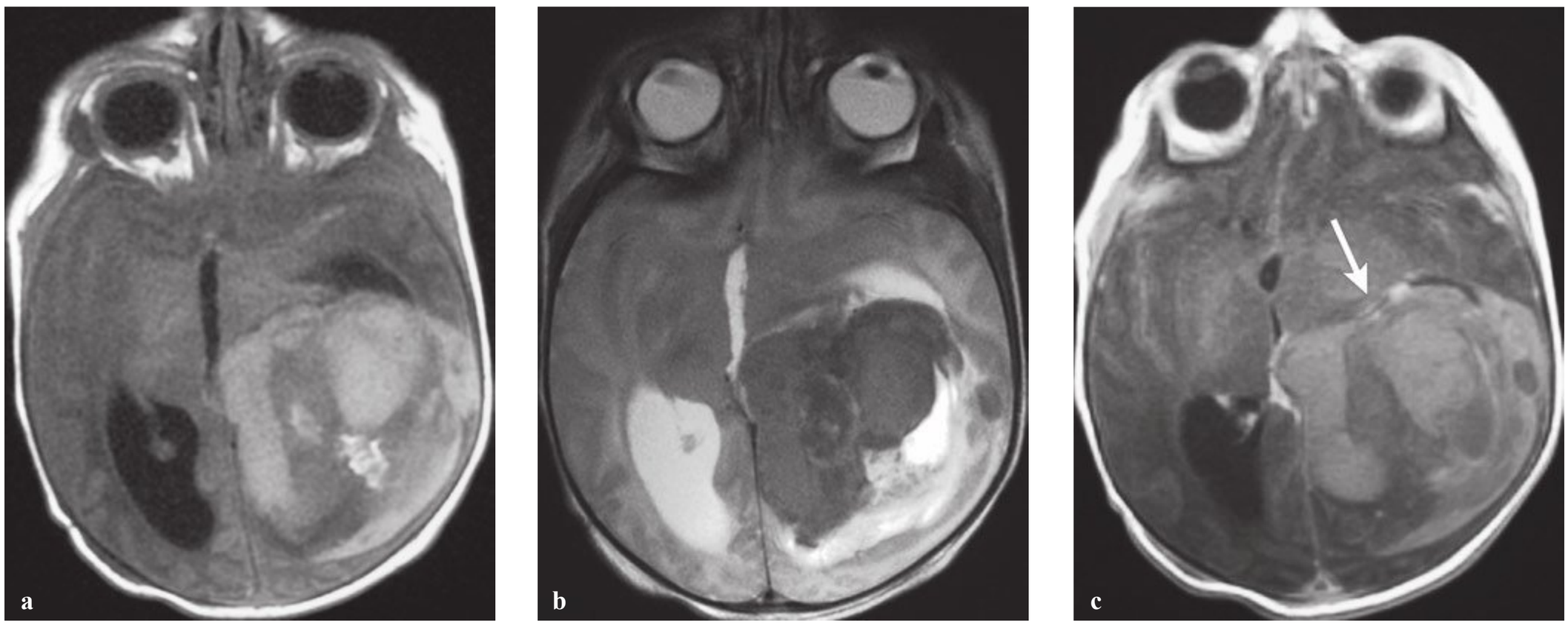

Fig. 1.71 A 1-day-old male neonate with an anaplastic ganglioglioma in the left cerebral hemisphere. This large tumor has mixed low, intermediate, and high signal on **(a)** axial T1-weighted imaging and **(b)** T2-weighted imaging, related to intratumoral portions with hemorrhage. **(c)** The tumor shows minimal heterogeneous gadolinium contrast enhancement in the nonhemorrhagic portions on axial T1-weighted imaging (arrow).

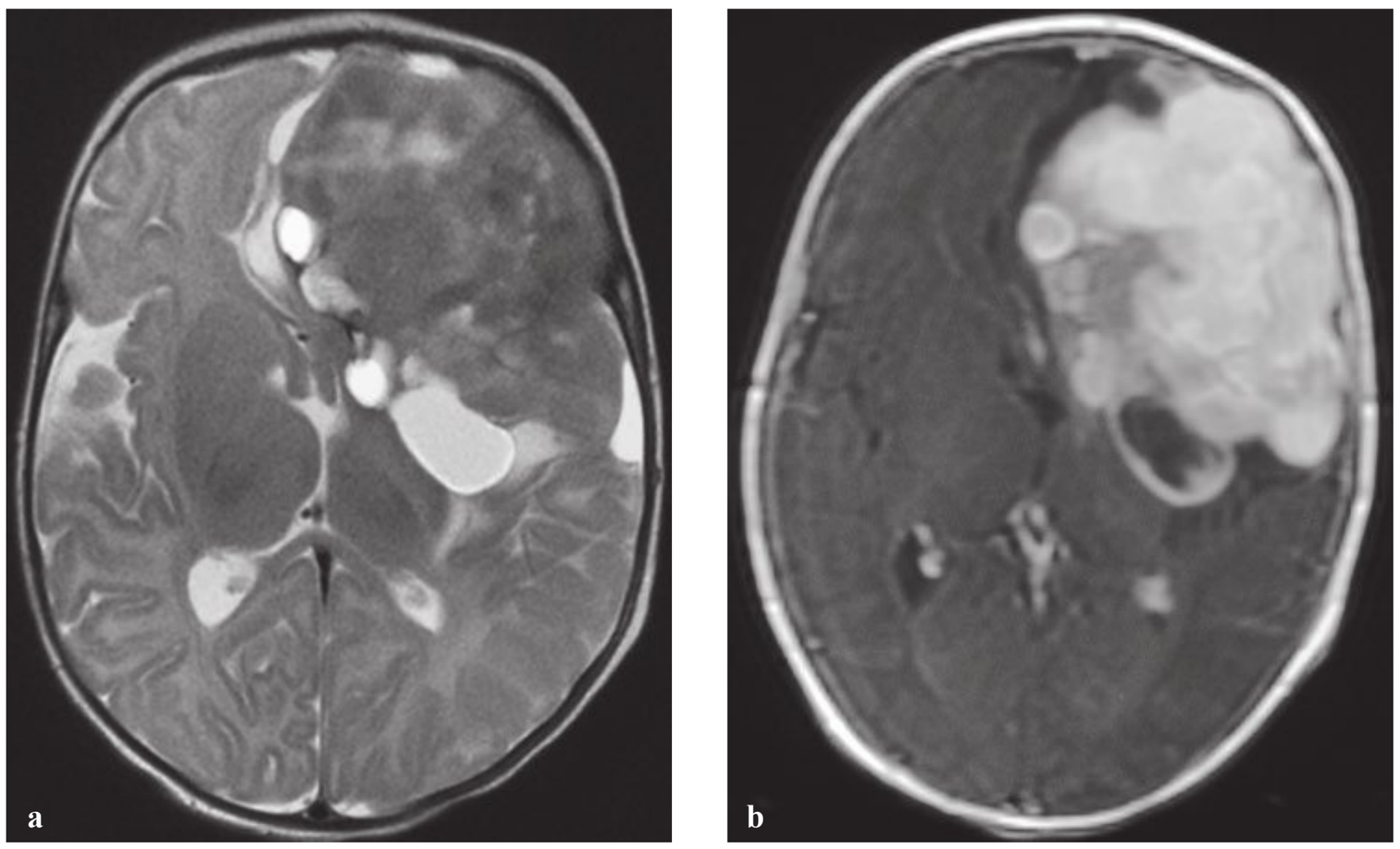

Fig. 1.72 A 2-month-old female with a desmoplastic infantile astrocytoma in the left frontal lobe. **(a)** This large tumor has mixed low, intermediate, and high signal on axial T2-weighted imaging and **(b)** shows prominent, slightly heterogeneous gadolinium contrast enhancement on axial T1-weighted imaging.

Table 1.2 (cont.) Supratentorial solitary intra-axial mass lesions

Lesions	Imaging Findings	Comments
Dysembryoplastic neuroepithelial tumor (**Fig. 1.73**)	MRI: Circumscribed and often large lesions involving the cerebral cortex and subcortical white matter, with low-intermediate signal on T1-weighted imaging, high signal on T2-weighted imaging, high signal rim on FLAIR, ± small cysts, usually no gadolinium contrast enhancement, low relative cerebral blood volume (rCBV). Typically no edema, minimal or no associated mass effect. Diffusion-weighted imaging: Usually have high ADC values. Magnetic resonance spectroscopy may show an elevated lactate level. CT: Circumscribed lesions involving the cerebral cortex and subcortical white matter, low-intermediate attenuation, ± small cysts, usually no contrast enhancement.	Benign, superficial, slow-growing glial-neuronal neoplasms (WHO grade I) commonly located in the temporal or frontal lobes. Tumors consist of bundles and columns of axons lined by small oligodendroglia-like cells oriented perpendicular to the cerebral cortex. Neurons and scattered stellate glial fibrillary acidic protein (GFAP)-staining astrocytes are also present. Associated cortical dysplasia occurs in 80%of cases. Usually occurs in patients between 10 and 30 years old. Accounts for 1.2%of intracranial tumors in patients less than 20 years old and 0.2%in patients older than 20 years. More common in males than in females. Commonly associated with seizures in young adults. Lesions are benign and have a favorable prognosis after surgery. Malignant transformation is extemely rare.
Central neurocytoma (**Fig. 1.74**)	MRI: Circumscribed lesion typically located at margin of lateral ventricle or septum pellucidum with intraventricular protrusion, heterogeneous low and intermediate signal on T1-weighted imaging, heterogeneous intermediate-high signal on T2-weighted imaging, ± calcifications and/or small cysts, heterogeneous gadolinium contrast enhancement. Diffusion-weighted imaging: Lesions can show reduced ADC values. Magnetic resonance spectroscopy: Elevated glycine (3.55 ppm), choline and alanine levels, and decreased N-acetylaspartate (NAA) in these lesions. Rare extraventricular neurocytomas have been reported in the frontal and parietal lobes and sellar region. CT: Circumscribed lesion located at margin of lateral ventricle or septum pellucidum with intraventricular protrusion, heterogeneous low and intermediate attenuation, ± calcifications and/or small cysts, heterogeneous contrast enhancement.	Slow-growing rare neuroepithelial tumor (WHO grade II) composed of uniform round cells with neuronal differentiation. Immunoreactive to synaptophysin and neuronal nuclear protein (NeuN). Represent ~ 0.5%of intracranial tumors, Patients range from 8 days to 67 years old; mean age = 29 years. Imaging appearance similar to intraventricular oligodendrogliomas. Typically benign tumors with favorable prognosis after surgery.
Papillary glioneuronal tumor	MRI: Circumscribed lesions in the cerebral hemispheres with heterogeneous low and intermediate signal on T1-weighted imaging, heterogeneous intermediate-high signal on T2-weighted imaging, heterogeneous gadolinium contrast enhancement. CT: Circumscribed lesions in the cerebral hemispheres with heterogeneous low and intermediate attenuation, heterogeneous contrast enhancement.	Rare, low-grade tumor (WHO grade I) composed of pseudostratified layers of small cuboidal glial cells with round nuclei, hyalinized blood vessels, collections of neurocytes and ganglion cells. Immunoreactive to glial fibrillary acidic protein (GFAP), neuronal nuclear protein (NeuN), synaptophysin, NSE, and class III b-tubulin. Patients range from 4 to 75 years old; mean age = 27 years. Long-term survival is typical after surgical resection.

(continued on page 58)

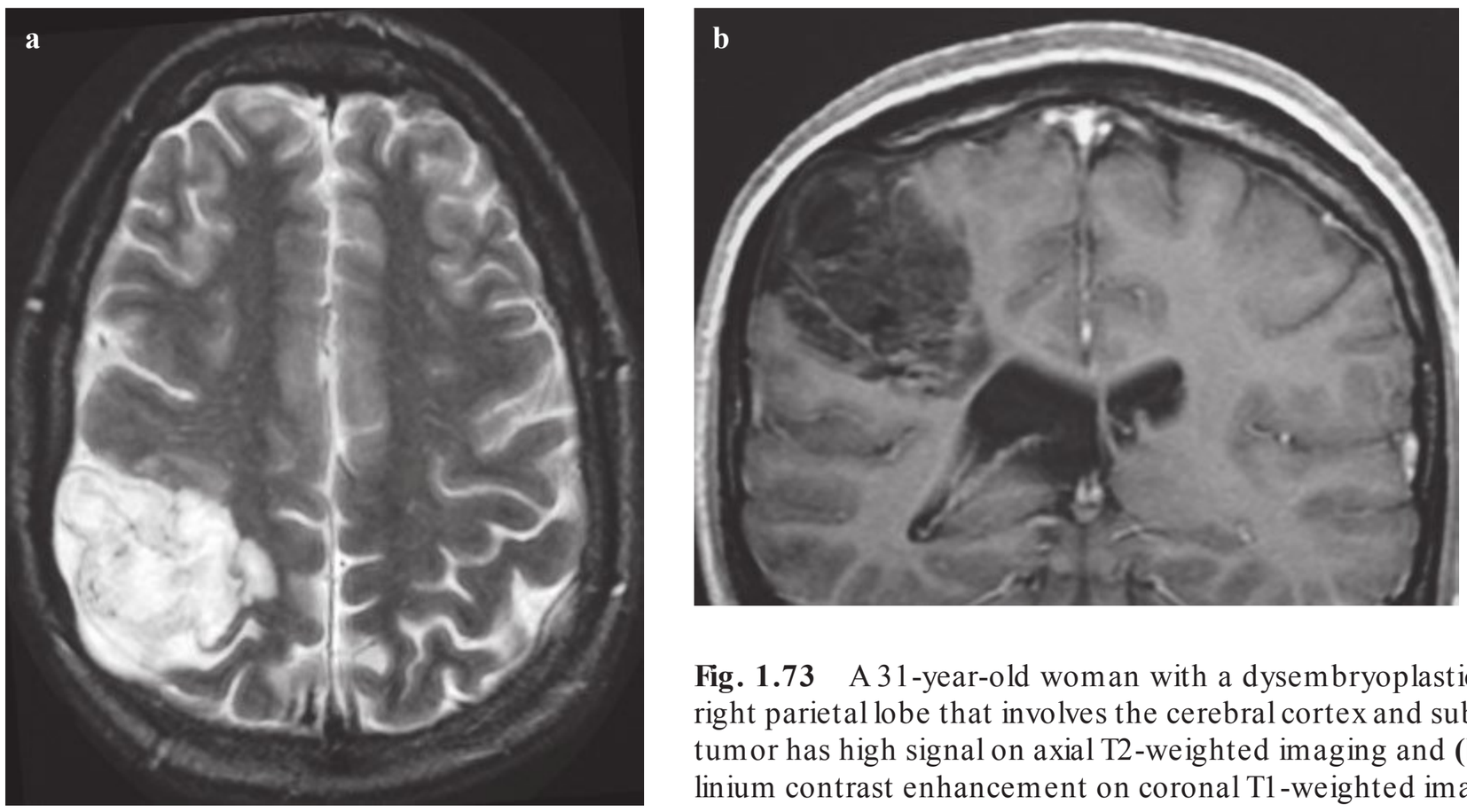

Fig. 1.73 A 31-year-old woman with a dysembryoplastic neuroepithelial tumor in the right parietal lobe that involves the cerebral cortex and subcortical white matter. **(a)** The tumor has high signal on axial T2-weighted imaging and **(b)** shows minimal to no gadolinium contrast enhancement on coronal T1-weighted imaging.

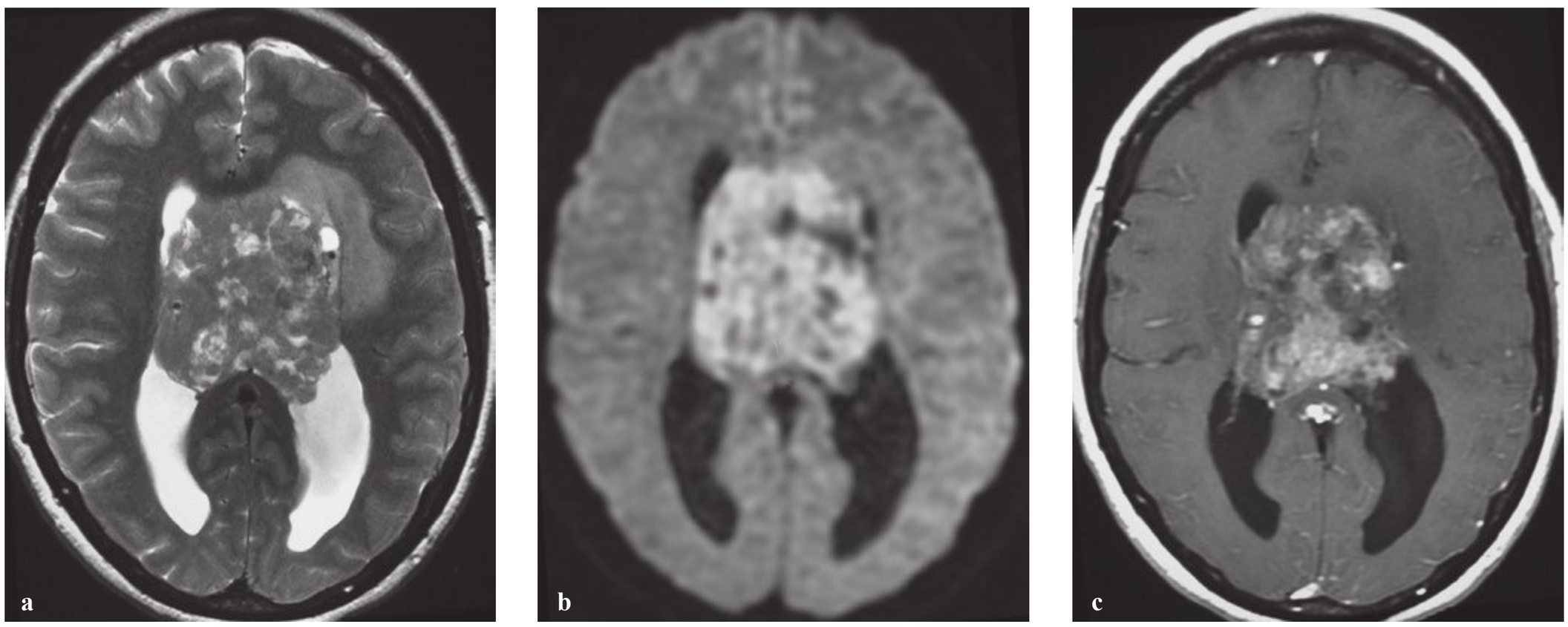

Fig. 1.74 A 60-year-old woman with a central neurocytoma centered at the septum pellucidum. The tumor has mixed intermediate and high signal on **(a)** axial T2-weighted imaging and **(b)** axial diffusion-weighted imaging (DWI) and **(c)** shows heterogeneous gadolinium contrast enhancement on axial T1-weighted imaging.

Table 1.2 (cont.) Supratentorial solitary intra-axial mass lesions

Lesions	Imaging Findings	Comments
Neoplasms: Embryonal		
Primitive neuroectodermal tumor (**Fig. 1.75**)	MRI: Circumscribed or invasive lesions, with low-intermediate signal on T1-weighted imaging, intermediate-high signal on T2-weighted imaging; ± cystic or necrotic zones, solid portions can have restricted diffusion, variable gadolinium contrast enhancement, usually high relative cerebral blood volume (rCBV), ± gadolinium contrast enhancement in the leptomeninges and/or ventricles from tumor dissemination. Diffusion-weighted imaging: Solid portions can have restricted diffusion. Magnetic resonance spectroscopy: Usually show elevated choline, lipid, and taurine peaks, and decreased N-acetylaspartate (NAA) levels. CT: Circumscribed or invasive lesions, with low-intermediate attenuation, variable contrast enhancement, and frequent dissemination into the leptomeninges.	Highly malignant tumors (WHO grade IV) located in the cerebrum, pineal gland, and cerebellum that frequently disseminate along CSF pathways. Tumors are composed of poorly differentiated or undifferentiated cells with divergent differentiation along neuronal, astrocytic, or ependymal lines. Typically occur in patients from 4 weeks to 20 years old; mean age = 5.5 years. Prognosis is poorer than that for medulloblastoma.
Atypical teratoid/ rhabdoid tumor (**Fig. 1.76**)	MRI: Circumscribed or invasive mass lesions with intermediate signal on T1-weighted imaging, ± zones of high signal from hemorrhage on T1-weighted imaging; variable mixed low, intermediate, and/or high signal on T2-weighted imaging. Solid portions can have restricted diffusion, usually prominent gadolinium contrast enhancement ± heterogeneous pattern. Gadolinium contrast enhancement in the leptomeninges and/or ventricles is caused by tumor dissemination. Diffusion-weighted imaging: Solid portions can have restricted diffusion. Magnetic resonance spectroscopy: Usually shows elevated choline, lipid, and lactate peaks and decreased N-acetylaspartate (NAA) levels. CT: Circumscribed mass lesions with intermediate or mixed low and intermediate attenuation, ± zones of hemorrhage, cystic degeneration, and/or necrosis. Calcifications occasionally occur and usually contrast enhancement is ± heterogeneous pattern. Contrast enhancement in the leptomeninges and/or ventricles is from tumor dissemination.	Rare malignant tumors involving the CNS, usually occurring in the first decade, and patients are usually < 3 years old. K_i-67/MIB-1 proliferation index often is high, > 50%. Associated with mutations of the INI1 (hSNF5/SMARCB1) gene on chromosome 22q11.2. Histologically appear as solid tumors ± necrotic areas, similar to malignant rhabdoid tumors of the kidney. Associated with a very poor prognosis.

(continued on page 60)

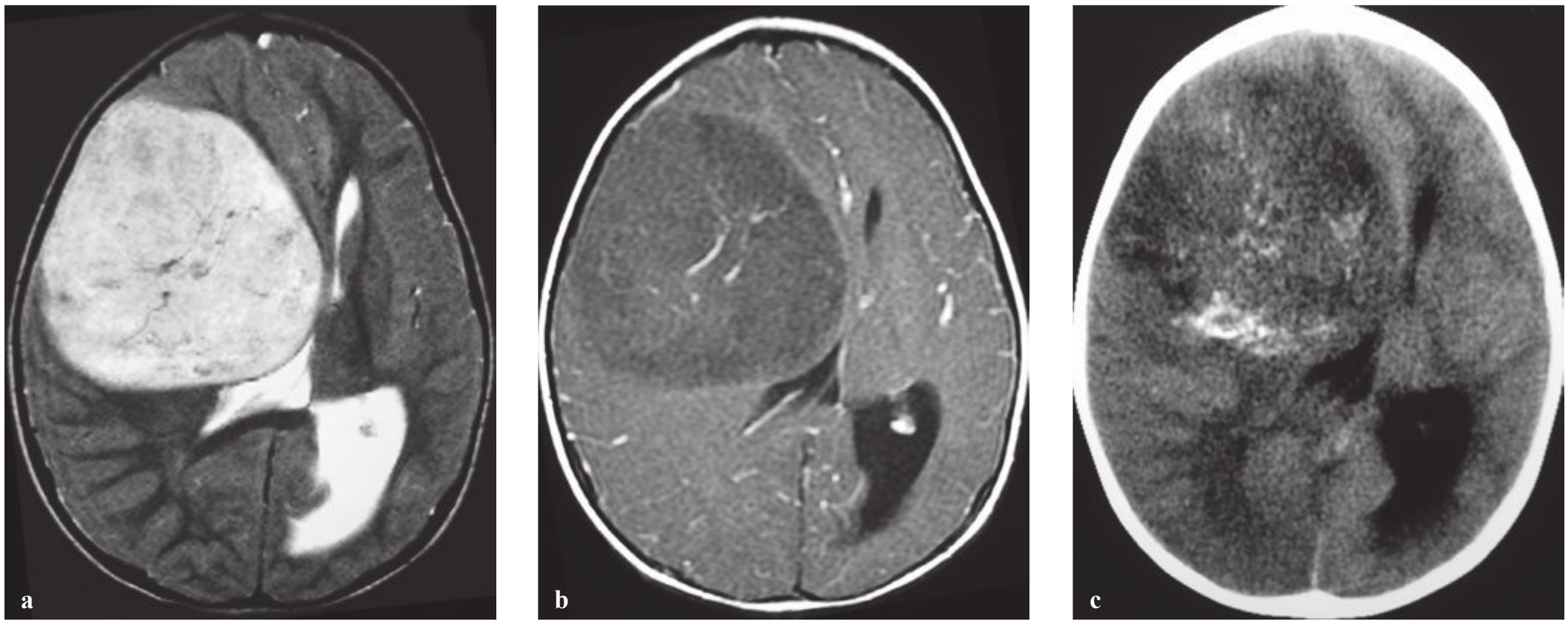

Fig. 1.75 A 1-year-old female with a large primitive neuroectodermal tumor in the right frontal lobe. **(a)** The tumor has mildly heterogeneous high signal on axial T2-weighted imaging and **(b)** shows minimal irrregular gadolinium contrast enhancement on axial T1-weighted imaging. **(c)** The tumor contains dystrophic calcifications on axial CT and has mass effect, resulting in subfalcine herniation leftward.

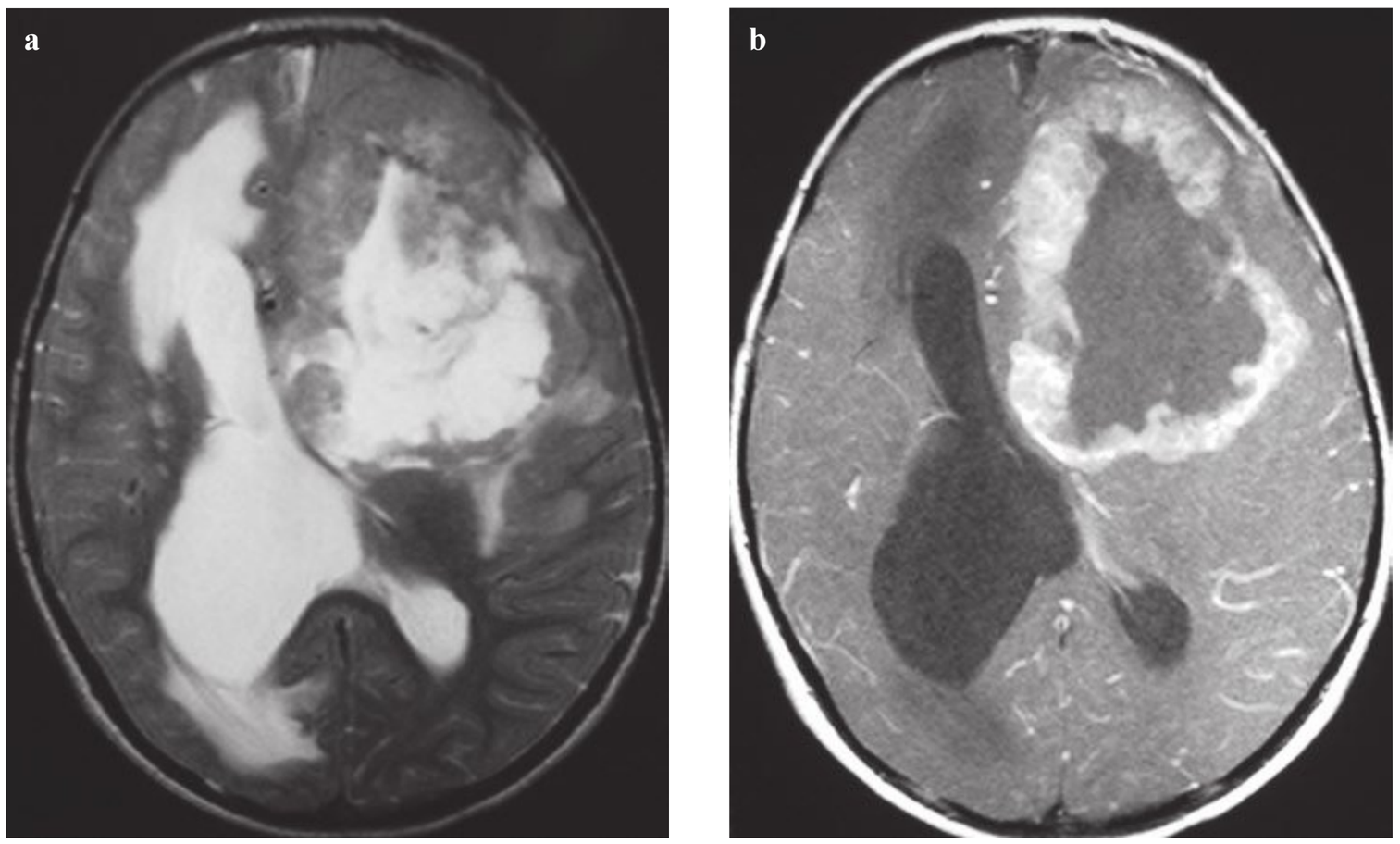

Fig. 1.76 A 3-year-old male with atypical teratoid/rhabdoid tumor in the left frontal lobe. The large tumor has irregular margins, with **(a)** heterogeneous mixed intermediate and high signal on axial T2-weighted imaging, and **(b)** heterogeneous and mostly peripheral irregular gadolinium contrast enhancement on axial T1-weighted imaging. The tumor has mass effect, resulting in subfalcine herniation rightward.

Table 1.2 (cont.) Supratentorial solitary intra-axial mass lesions

Lesions	Imaging Findings	Comments
Neoplasms: Pineal Tumors		
Pineocytoma (**Fig. 1.77**)	MRI: Tumors have low-intermediate signal on T1-weighted imaging and slightly high to high signal on T2-weighted imaging and can show gadolinium contrast enhancement. CT: Lesions have low-intermediate attenuation, ± peripheral calcifications.	Pineocytomas have circumscribed margins and usually measure less than 3 cm. They are rare, slow-growing pineal parenchymal tumors (WHO grade I) composed of sheets, lobules, or pineocytomatous rosettes of well-differentiated small cells with round-oval nuclei in moderate eosinophilic cytoplasm, and minimal to absent mitotic activity. They are immunoractive to synaptophysin, NSE, and NFP. Account for less than 1%of intracranial neoplasms. Usually occur in adults; mean age = 38 years. Five-year survival ranges from 86 to 100%
Pineal parenchymal tumor of intermediate differentiation (**Fig. 1.78**)	MRI: Tumors often have low-intermediate signal on T1-weighted imaging and slightly high to high signal on T2-weighted imaging and show gadolinium contrast enhancement. CT: Tumors often have intermediate attenuation.	Pineal parenchymal tumors of intermediate differentiation often have circumscribed margins and usually measure less than 3 cm. They are intermediate-grade pineal tumors (WHO grades II or III) consisting of uniform neoplastic cells with mild-moderate nuclear atypia, ± small rosettes, and low-moderate mitotic activity. Occur in patients from 1 to 69 years old; mean age = 38 years. Five-year survival ranges from 39 to 74%
Papillary tumor of the pineal region (**Fig. 1.79**)	MRI: Tumors often have intermediate signal on T1-weighted imaging and slightly high to high signal on T2-weighted imaging and show gadolinium contrast enhancement, ± cysts. Tumors can have mixed signal on T1- and T2-weighted imaging secondary to the presence of cysts, hemorrhage, and/or calcifications CT: Circumscribed tumors with intermediate to slightly increased attenuation.	Rare neuroepithelial tumor of the pineal gland (WHO grades II or III) composed of both papillary zones with large pale eosinophilic columnar cells overlying blood vessels, and cellular regions with vacuolated cytoplasm and round or oval nuclei. The cellular regions may show rosettelike configurations similar to ependymomas. Tumors are immunoreactive to keratins in papillary portions. Occur in children and adults; mean age = 32 years. Variable mitotic rates in tumors. Overall 5-year survival is 73%, although tumors with high mitotic activity have a much poorer prognosis.
Pineoblastoma (**Fig. 1.80**)	MRI: Tumors have low-intermediate signal on T1-weighted imaging and intermediate to slightly high and/or high signal on T2-weighted imaging, ± hemorrhage or necrotic changes. Tumors usually show prominent gadolinium contrast enhancement. Disseminated enhancing tumor in the leptomeninges and/or ventricles is not uncommon. Diffusion-weighted imaging: Solid portions can have restricted diffusion. CT: Tumors have intermediate to slightly high attenuation, ± hemorrhage, and necrotic/cystic changes. Disseminated enhancing tumor in the leptomeninges is not uncommon.	Pineoblastomas are large tumors (> 3 cm) that often have lobulated irregular margins. They are malignant embryonal tumors (WHO grade IV) consisting of diffuse dense sheets of cells with round irregular nuclei within scant cytoplasm, + neuroblastic differentiation, hemorrhage, and necrosis. Immunoreactive to synaptophysin, NSE, NFP, class III β-tubulin, and chromogranin A. Tumors occur most commonly in the first two decades; mean age = 18.5 years. Associated with familial bilateral retinoblastoma, which has a poor prognosis. Prognosis is poor when there is a documented disseminated tumor in the leptomeninges. Overall 5-year survival is 58%
Germ cell tumors (**Fig. 1.81**)	MRI: Tumors often have intermediate signal on T1-weighted images and slightly high to high signal on T2-weighted images and show gadolinium contrast enhancement, ± cysts, ± gadolinium contrast-enhancing disseminated subarachnoid and/or intraventricular tumor. Some germ cell tumors can have mixed signal on T1- and T2-weighted images secondary to the presence of cysts, hemorrhage, and/or calcifications. CT: Circumscribed tumors with intermediate to slightly increased attenuation, ± disseminated contrast-enhancing leptomeningeal and/or intraventricular tumor.	Extragonadal germ cell tumors include germinoma (most common), mature teratoma, malignant teratoma, yolk sac tumor, embryonal carcinoma, and choriocarcinoma. Germ cell tumors account for 0.6% of primary intracranial tumors, with an incidence of 0.09 per 100,000. Peak incidence is between 10 and 14 years, and 90%occur in patients less than 25 years old. Occur more frequently in males than in females. Prognosis depends on histologic subtype; 10-year survival for geminomas is > 85% Other germ cell tumors have lower survival rates, particularly those containing nongerminomatous malignant cells.

(continued on page 63)

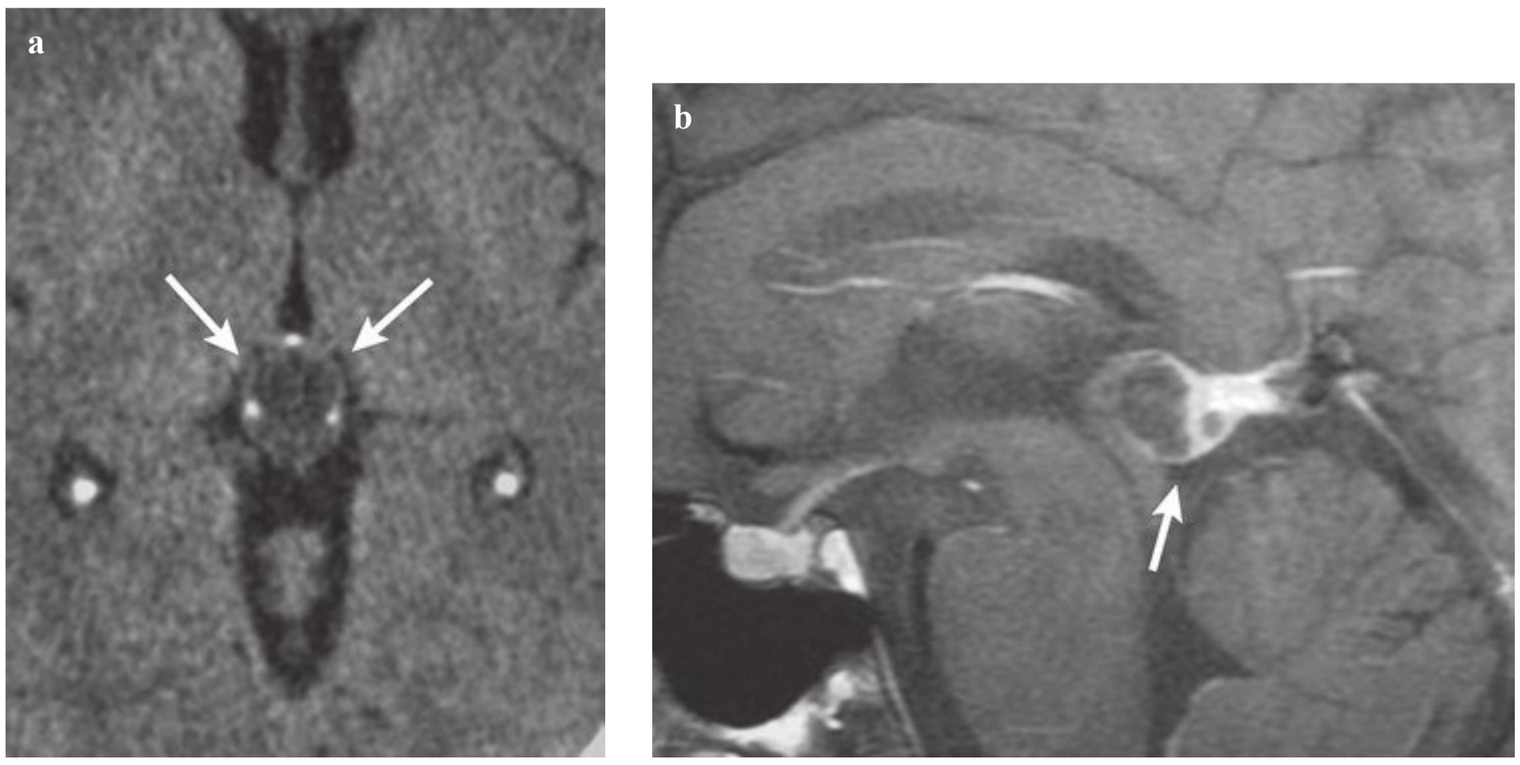

Fig. 1.77 Pineocytoma. **(a)** Axial CT shows the pineal lesion to have low-intermediate attenuation centrally with peripheral calcifications (arrows). **(b)** The lesion shows heterogeneous gadolinium contrast enhancement on sagittal fat-suppressed T1-weighted imaging (arrow).

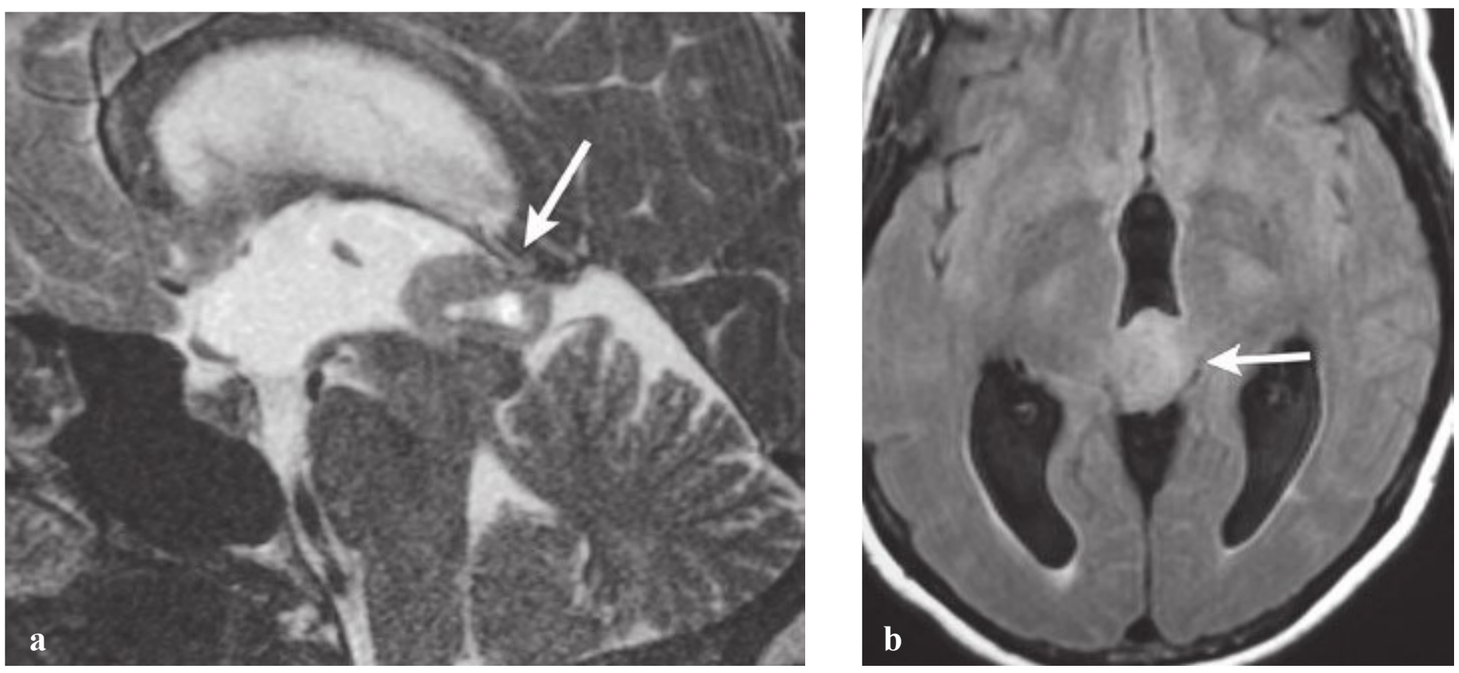

Fig. 1.78 A45-year-old woman with a pineal parenchymal tumor of intermediate differentiation that has **(a)** mixed intermediate and high signal on sagittal T2-weighted imaging (arrow) and **(b)** slightly high to high signal on axial FLAIR (arrow).

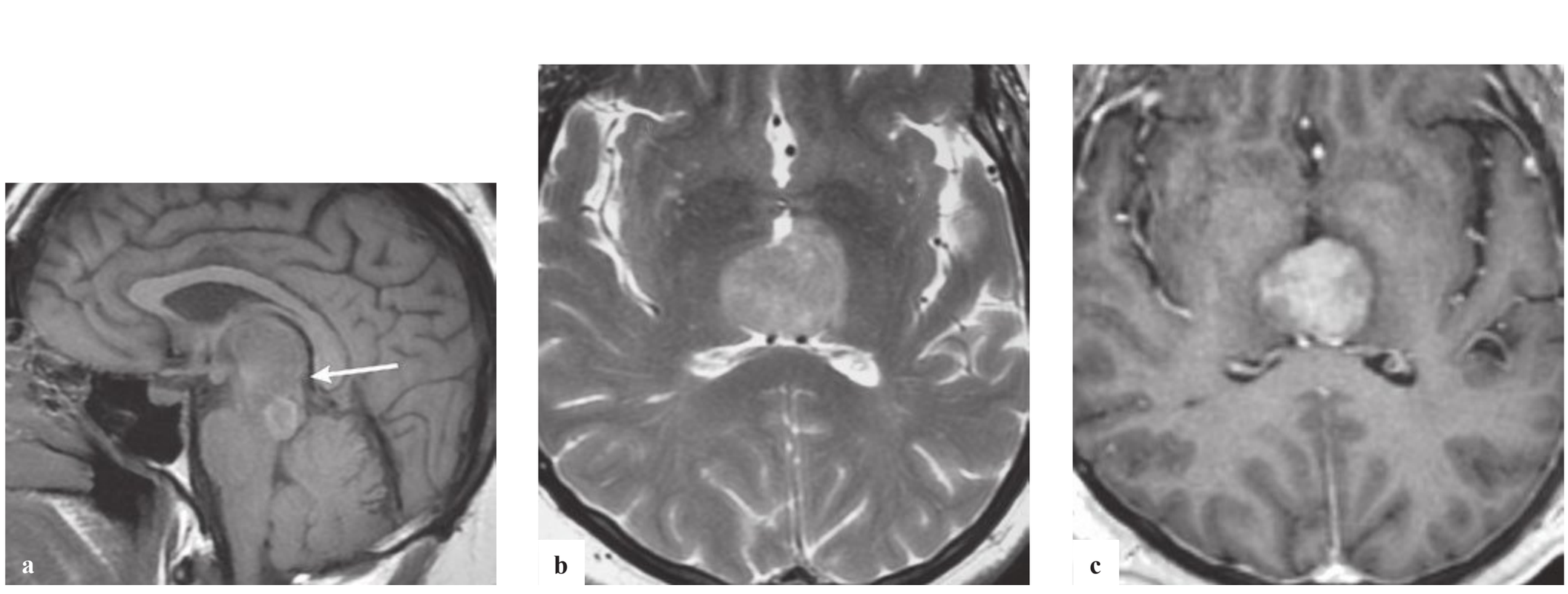

Fig. 1.79 A62-year-old man with a papillary tumor of the pineal region that has slightly ill-defined margins, with **(a)** mostly intermediate signal as well as zones of high signal on sagittal T1-weighted imaging (arrow), and **(b)** slightly high signal on axial T2-weighted imaging. **(c)** The tumor shows gadolinium contrast enhancement on axial T1-weighted imaging.

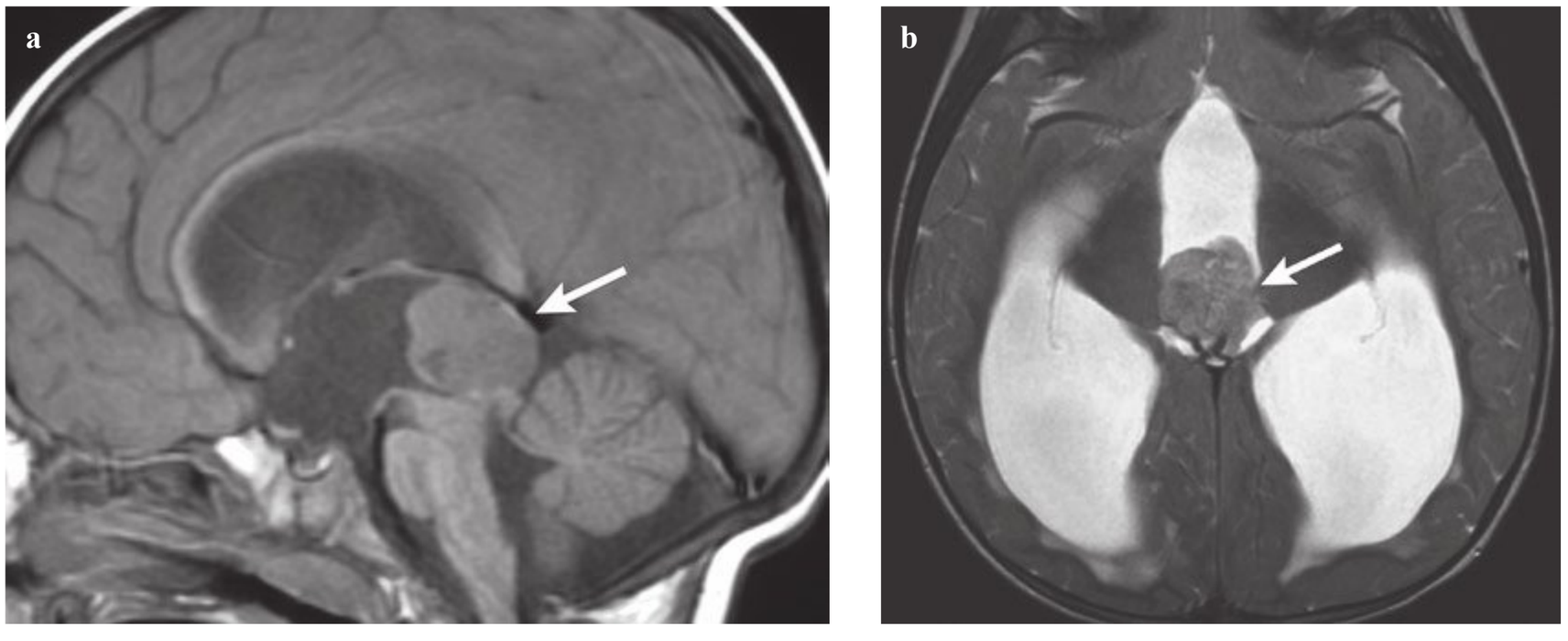

Fig. 1.80 An 18-month-old boy with a pineoblastoma that has intermediate signal on **(a)** sagittal T1-weighted imaging (arrow) and **(b)** axial T2-weighted imaging (arrow). Tumor shows **(c)** gadolinium contrast enhancement on axial T1-weighted imaging and **(d)** restricted diffusion on axial DWI (arrow).

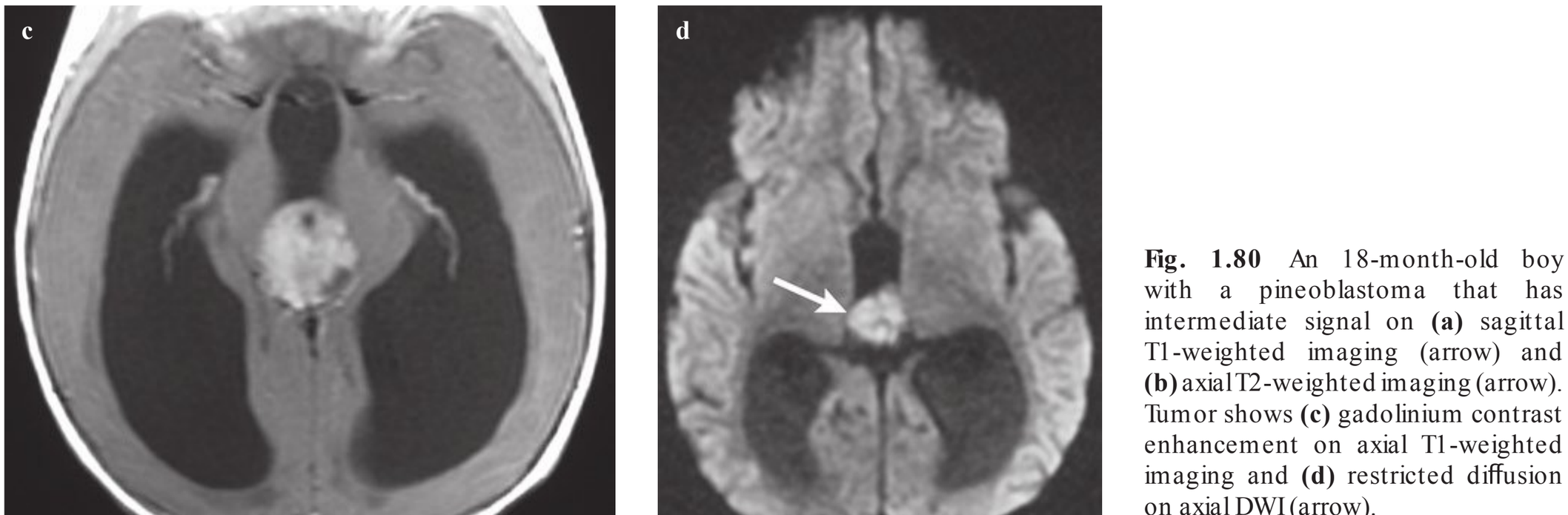

Fig. 1.81 A 15-year-old male with a germ cell tumor (germinoma) in the pineal gland that has ill-defined margins and shows gadolinium contrast enhancement (arrows) on **(a)** sagittal and **(c)** axial T1-weighted imaging. The tumor has intermediate signal on **(b)** axial FLAIR, as well as high signal in the adjacent thalami from tumor invasion.

Table 1.2 (cont.) Supratentorial solitary intra-axial mass lesions

Lesions	Imaging Findings	Comments
Other Neoplasms and Tumorlike Lesions		
Metastases (**Fig. 1.82**)	MRI: Circumscribed spheroid lesions in brain, can have various intra-axial locations, often at gray–white matter junctions, usually with low-intermediate signal on T1-weighted imaging and intermediate-high signal on T2-weighted imaging, ± hemorrhage, calcifications, and cysts. Variable gadolinium contrast enhancement, and often high signal on T2-weighted imaging peripheral to nodular enhancing lesion representing axonal edema. CT: Lesions usually have low-intermediate attenuation, ± hemorrhage, calcifications, and cysts, and variable contrast enhancement, often associated with adjacent low attenuation from axonal edema.	Metastases represent ~ 33% of intracranial tumors, usually from extracranial primary neoplasm in adults > 40 years old. Primary tumor source: lung > breast > GI > GU > melanoma.

(continued on page 64)

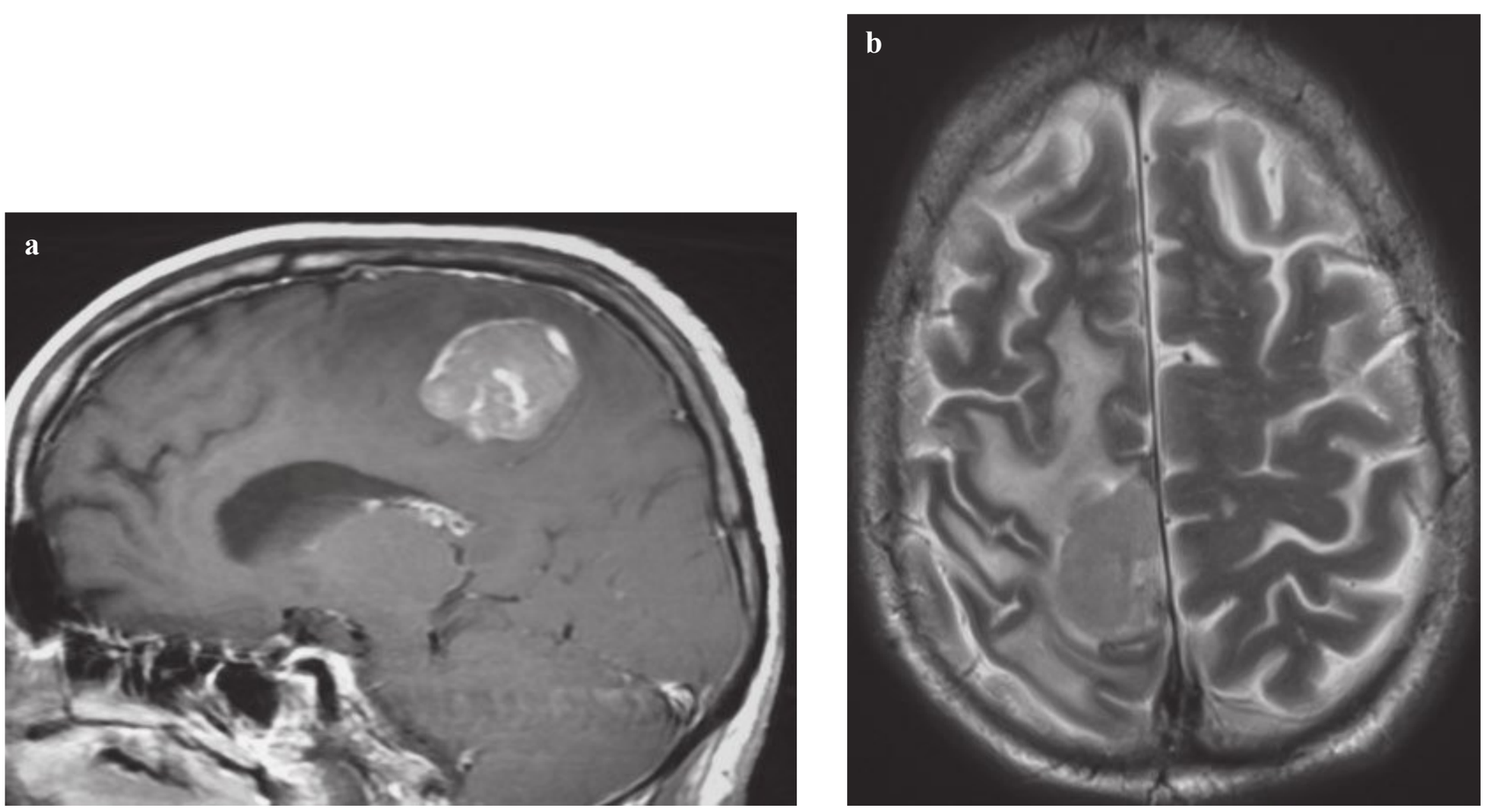

Fig. 1.82 Solitary metastatic lesion in the brain from lung carcinoma that shows **(a)** gadolinium contrast enhancement on sagittal T1-weighted imaging and **(b)** slightly high signal on axial T2-weighted imaging with surrounding high signal from axonal edema.

Table 1.2 (cont.) Supratentorial solitary intra-axial mass lesions

Lesions	Imaging Findings	Comments
Lymphoma (**Fig. 1.83**)	MRI: Primary CNS lymphoma (PCNSL) in immunocompetent patients occurs as a solitary focal or infiltrating lesion in 65% PCNSL is located in the cerebral hemispheres, basal ganglia, thalami, cerebellum, and brainstem. PCNSL can involve and cross the corpus callosum. PCNSL can be multifocal in 35% of immunocompetent patients, and is multifocal in 60% of immunocompromised patients. Tumors often have low-intermediate signal on T1-weighted imaging, intermediate-slightly high signal on T2-weighted imaging, ± perilesional edema, ± hemorrhage/necrosis in immunocompromised patients or after treatment. PCNSL in immunocompetent patients usually shows homogeneous gadolinium contrast enhancement, whereas gadolinium contrast enhancement in immunocompromised patients often has an irregular peripheral pattern. Diffuse leptomeningeal and dural gadolinium contrast enhancement are other, less common patterns of intracranial lymphoma. PCNSL typically lacks tumor neovascularization and has lower cerebral perfusion and relative cerebral blood volume (rCBV) maximum values compared with high-grade astrocytomas. PCNSL can show restricted diffusion. PCNSL ADC values (0.7 to 0.9×10^{-3} mm^2/s) are lower than those for glioblastomas and high-grade astrocytomas. MR spectroscopy of PCNSL shows decreased N-acetylaspartate (NAA) and elevated choline and lipid peaks. CT: CNS lymphoma can have intermediate attenuation, or it can be hyperdense related to a high nuclear/cytoplasm ratio, ± hemorrhage/necrosis in immunocompromised patients. It usually shows contrast enhancement. Diffuse leptomeningeal contrast enhancement is another pattern of intracranial lymphoma. PET/CT: PET/CT can show elevated FDG uptake in PCNSL and can be used in immunocompromised patients to distinguish lymphoma from toxoplasmosis, which has decreased FDG uptake.	Primary CNS lymphoma is more common than secondary, and it usually occurs in adults > 40 years old. PCNSL accounts for 5% of primary brain tumors. Incidence currently ranges from 0.8 to 1.5% of primary intracranial tumors. Former elevated incidence of 6% in patients with AIDS has been reduced with effective antiviral therapy. B cell lymphoma is more common than T cell lymphoma. MRI features of primary and secondary lymphoma of brain overlap. Intracranial lymphoma can involve the leptomeninges in secondary lymphoma > primary lymphoma.

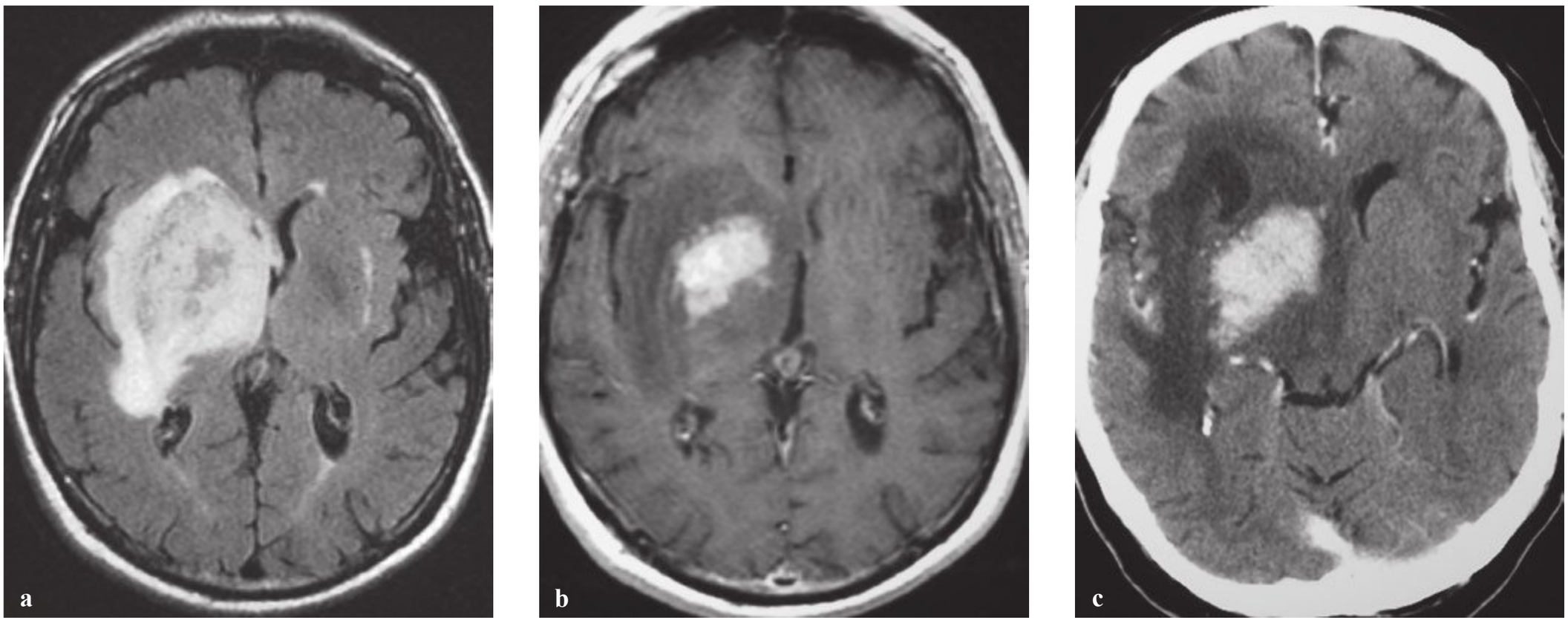

Fig. 1.83 A 66-year-old man with lymphoma in the right basal ganglia and thalamus that shows **(a)** high signal on axial FLAIR and contrast enhancement on **(b)** axial T1-weighted imaging and **(c)** axial CT.

Lesions	Imaging Findings	Comments
Leukemia (myeloid sarcoma, granulocytic sarcoma, chloroma)	MRI: Lesions often have intermediate signal on T1-weighted imaging and intermediate to slightly high signal on T2-weighted imaging and FLAIR. Small zones with low signal on GRE may be seen from sites of hemorrhage within the lesion. Lesions can have restricted diffusion on diffusion-weighted imaging (ADC values of 0.50×10^{-3} mm^2/s). Lesions usually show gadolinium contrast enhancement. Magnetic resonance spectroscopy can show reduced N-acetylaspartate (NAA) and markedly elevated choline peaks. CT: Lesions can have low-intermediate to slightly high attenuation and can show contrast enhancement.	Leukemias are neoplastic proliferations of hematopoietic cells. Myeloid sarcomas (also referred to as chloromas or granulocytic sarcomas) are focal tumors composed of myeloblasts and neoplastic granulocyte precursor cells and occur in 2% of patients with acute myelogenous leukemia. These lesions can involve the dura, leptomeninges, and brain. Intracranial lesions can be solitary or multiple.
Hamartoma (tuberous sclerosis) (**Fig. 1.84**) Cortical-subcortical hamartomas (tubers) Subependymal hamartomas	MRI: Cortical-subcortical lesions (tubers) usually have high signal on T1-weighted imaging and low signal on T2-weighted imaging in neonates and infants; signal changes to low-intermediate on T1-weighted imaging and high signal on T2-weighted imaging in older children and adults. Calcifications are seen in 50% of older children, and gadolinium contrast enhancement is uncommon. Diffusion-weighted imaging: Cortical tubers can have elevated ADC values. CT: Cortical-subcortical lesions (tubers) have variable attenuation. Calcifications are seen in 50% of older children, and contrast enhancement is uncommon. MRI: Subependymal hamartomas are small nodules located along and projecting into the lateral ventricles. Signal on T1-weighted and T2-weighted images is similar to that for cortical tubers. Calcification and gadolinium contrast enhancement are common. CT: Subependymal hamartomas appear as small nodules located along and projecting into the lateral ventricles. Calcification of nodules commonly begins early in childhood.	Cortical hamartomas (tubers), subcortical glioneuronal hamartomas, subependymal glial hamartomas (nodules), and subependymal giant cell astrocytomas are nonmalignant lesions associated with tuberous sclerosis. Tuberous sclerosis is an autosomal dominant disorder associated with hamartomas in multiple organs. Extraneural lesions include: cutaneous angiofibromas (adenoma sebaceum), subungual fibromas, visceral cysts, renal angioleiomyomas, intestinal polyps, cardiac rhabdomyomas, and pulmonary lymphangioleiomyomatosis. Caused by mutations of TSC1 gene on 9q or the TSC2 gene on 16p. Occurs in 1 in 6,000 newborns.

(continued on page 66)

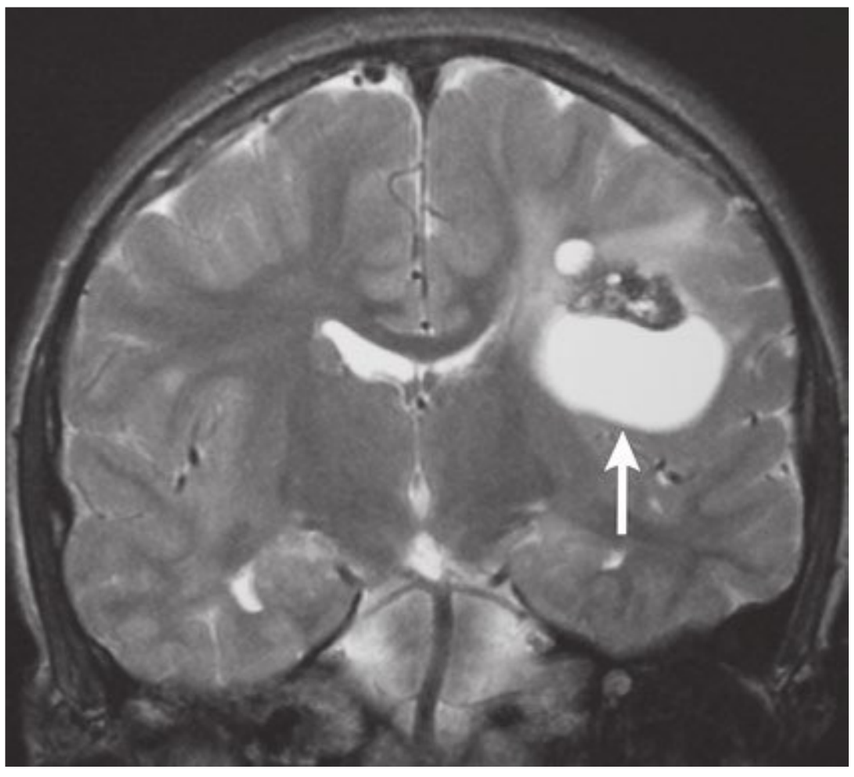

Fig. 1.84 Calcified hamartoma with cyst (arrow) involving the left cerebral hemisphere in a patient with tuberous sclerosis on coronal T2-weighted imaging.

Table 1.2 (cont.) Supratentorial solitary intra-axial mass lesions

Lesions	Imaging Findings	Comments
Hypothalamic hamartoma (**Fig. 1.85**)	MRI: Sessile or pedunculated lesions at the tuber cinereum of the hypothalamus, often with intermediate signal on T1- and T2-weighted imaging similar to gray matter, occasionally with slightly high signal on T2-weighted imaging, usually no gadolinium contrast enhancement, rarely contain cystic and/or fatty portions. Ictal FDG-PET and SPECT have shown hyperperfusion during seizures. Diffusion-weighted imaging: No restricted diffusion. Magnetic resonance spectroscopy may show elevated myoinositol. CT: Lesions often have intermediate attenuation similar to gray matter, typically with no contrast enhancement, and rarely contain cystic and/or fatty portions.	Rare, congenital/developmental heterotopia/hamartoma (nonneoplastic lesions) involving the tuber cinerum, inferior hypothalamus, and/or mamillary bodies, composed of clusters of small (< 12 microns) neuronal cells within a neutropil-like stroma and scattered fibrillary astrocytes. Immunoreactive to neuronal specific nuclear protein (NeuN) and GAD67, not immunoreactive to glial fibrillary acidic protein (GFAP). Usually occur in children with isosexual precocious puberty (0–8 years old) or seizures (gelastic or partial complex) in second decade. Can be treated with surgery or stereotactic radiosurgery.
Calcifying pseudoneoplasm of the neuraxis (CAPNON) (**Fig. 1.86**)	MRI: Lesions have low signal on T1-weighted images. On T2-weighted imaging, low signal is related to dense zone of calcification seen on CT, ± peripheral slightly high signal. There may be a peripheral rim of gadolinium contrast enhancement. CT: Lesions have varying amounts of calcification and soft tissue attenuation.	CAPNONs are rare, slow-growing, nonneoplastic, calcified lesions (also referred to as fibro-osseous lesions), which can occur anywhere in the central nervous system, as well as involve bone and/or dura. Lesions contain variable amounts of fibrous stroma, chondromyxoidlike matrix associated with palisading spindle, epthelioid, and/or multinucleated cells, and ossifications.
Meningioangiomatosis (**Fig. 1.87**)	MRI: Lesions usually involve the superficial brain tissue and leptomeninges and have low-intermediate signal on T1-weighted imaging, high signal on T2-weighted imaging, and gyriform high signal on FLAIR, ± low signal from calcifications. Typically show gadolinium contrast enhancement. Magnetic resonance spectroscopy: Choline peaks can be elevated. CT: Nodular lesions with low-intermediate attenuation involving the superficial brain, ± calcifications, ± perilesional edema. Usually show contrast enhancement.	Rare, benign, hamartomatous lesions involving the leptomeninges and adjacent cerebral cortex. Lesions contain numerous thickened blood vessels surrounded by sheaths of well-differentiated meningothelial cells and concentric layers of collagen bundles, ± psammoma bodies, low MIB-1 proliferative rate (< 1%). Mean age = 18 years. Most common locations are temporal lobe and frontal lobe. Lesions are solitary in sporadic cases, and multiple in patients with neurofibromatosis type 2.

(continued on page 68)

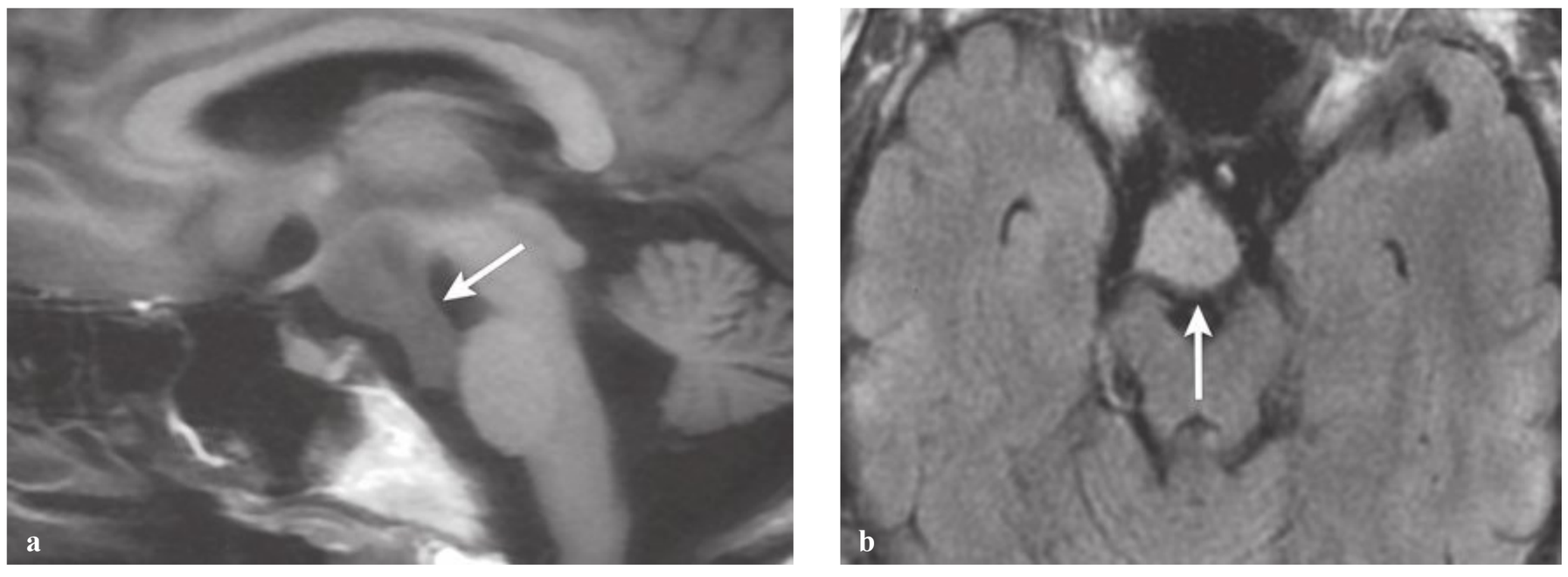

Fig. 1.85 **(a)** A 36-year-old woman with gelastic seizures from a hypothalamic hamartoma that has low-intermediate signal on sagittal T1-weighted imaging (arrow) and **(b)** slightly high signal on axial FLAIR (arrow).

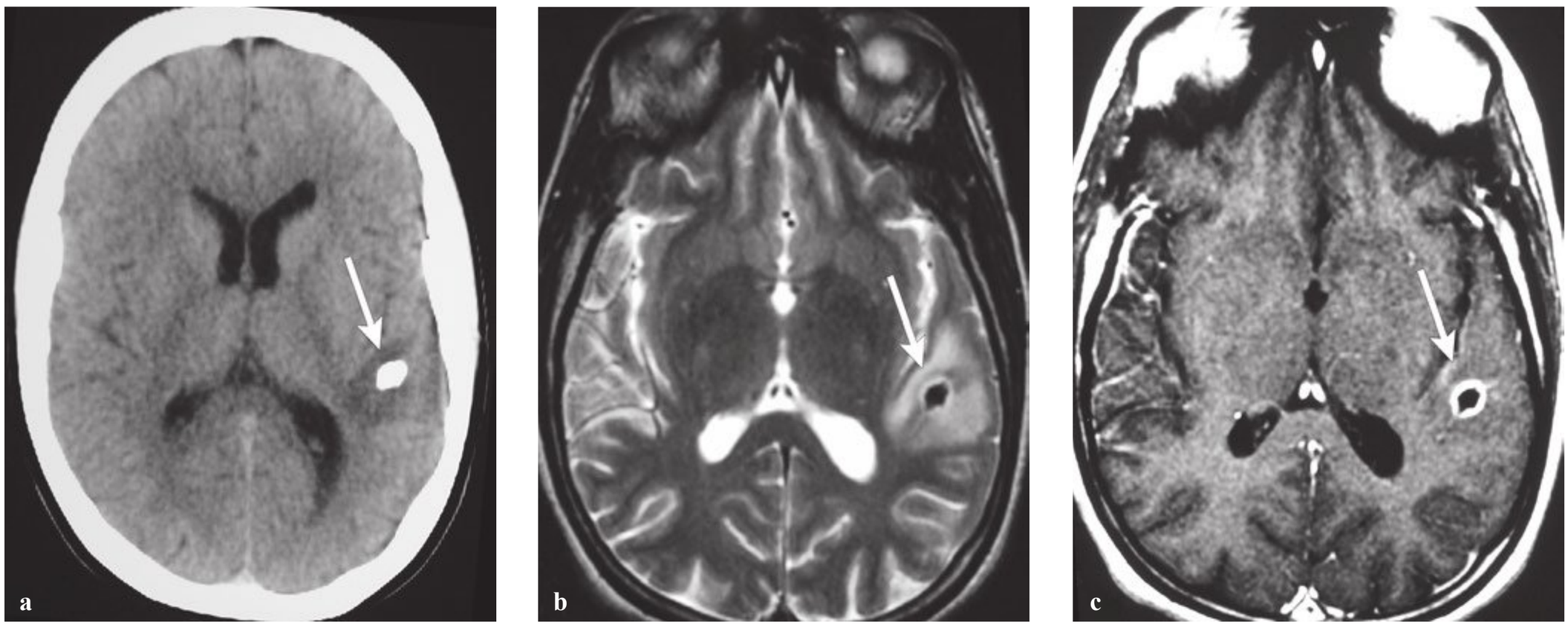

Fig. 1.86 **(a)** A 32-year-old woman with a calcifying pseudoneoplasm of the neuraxis in the left cerebral hemisphere that is seen as a nodular calcification surrounded by low attenuation (arrow) on axial CT. **(b)** The lesion (arrow) has low signal centrally surrounded by high signal edema on axial T2-weighted imaging. **(c)** A thin peripheral rim of gadolinium contrast enhancement is seen surrounding the calcified lesion (arrow) on axial T1-weighted imaging.

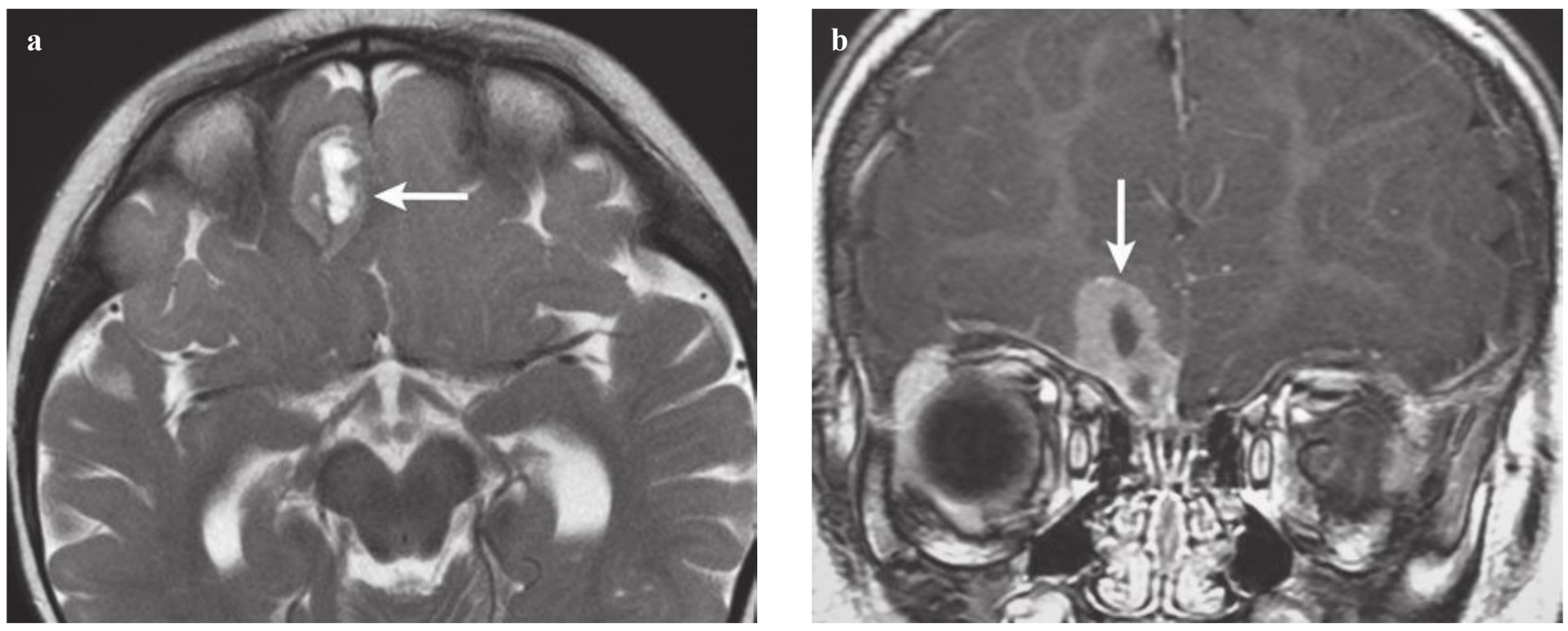

Fig. 1.87 A 1-year-old female with meningioangiomatosis. **(a)** A lesion with mixed intermediate and high signal on axial T2-weighted imaging (arrow) is seen in the inferomedial gyri of the right frontal lobe and adjacent meninges. **(b)** The lesion (arrow) shows heterogeneous gadolinium contrast enhancement on coronal T1-weighted imaging.

Table 1.2 (cont.) Supratentorial solitary intra-axial mass lesions

Lesions	Imaging Findings	Comments
Neurocutaneous melanosis (**Fig. 1.88**)	MRI: Intra-axial lesions usually < 3 cm in brain parenchyma/brainstem (anterior temporal lobes, cerebellum, thalami, inferior frontal lobes). Intra-axial lesions have intermediate-slightly high signal on T1-weighted imaging secondary to increased melanin, ± decreased signal on T2-weighted imaging, ± gadolinium contrast enhancement. Leptomeningeal lesions have irregular margins, low-intermediate or high signal on T1-weighted imaging in the sulci, intermediate-slightly high signal on T2-weighted imaging, high signal on FLAIR, and leptomeningeal gadolinium contrast enhancement. ± hydrocephalus, ± vermian hypoplasia, ± arachnoid cysts, ± Dandy-Walker malformation. CT: May show subtle hyperdensity secondary to increased melanin, ± vermian hypoplasia, ± arachnoid cysts.	Neuroectodermal dysplasia and melanosis is a rare nonfamilial disorder with focal and/or diffuse proliferation of melanocytes in leptomeninges associated with large and/or numerous cutaneous nevi. Presents in infants and young children. Immunoreactive to HMB-45, MART-1, and S-100. Cutaneous nevi are typically benign. Melanocytes in the leptomeninges in patients with neurocutaneous melanosis can change into CNS melanoma in 40 to 50% of patients.
Inflammatory Lesions: Infections		
Cerebritis	MRI: Poorly defined zone or focal area of low-intermediate signal on T1-weighted imaging, intermediate-high signal on T2-weighted imaging and FLAIR, restricted diffusion, minimal or no gadolinium contrast enhancement. Involves cerebral cortex and white matter in bacterial and fungal infections. CT: Poorly defined zone or focal area of decreased attenuation, minimal or no contrast enhancement. Involves cerebral cortex and white matter in bacterial and fungal infections.	Focal infection/inflammation of brain tissue from bacteria or fungi, secondary to sinusitis, meningitis, surgery, hematogenous source (cardiac and other vascular shunts), and/or immunocompromised status. Can progress to brain abscess formation.

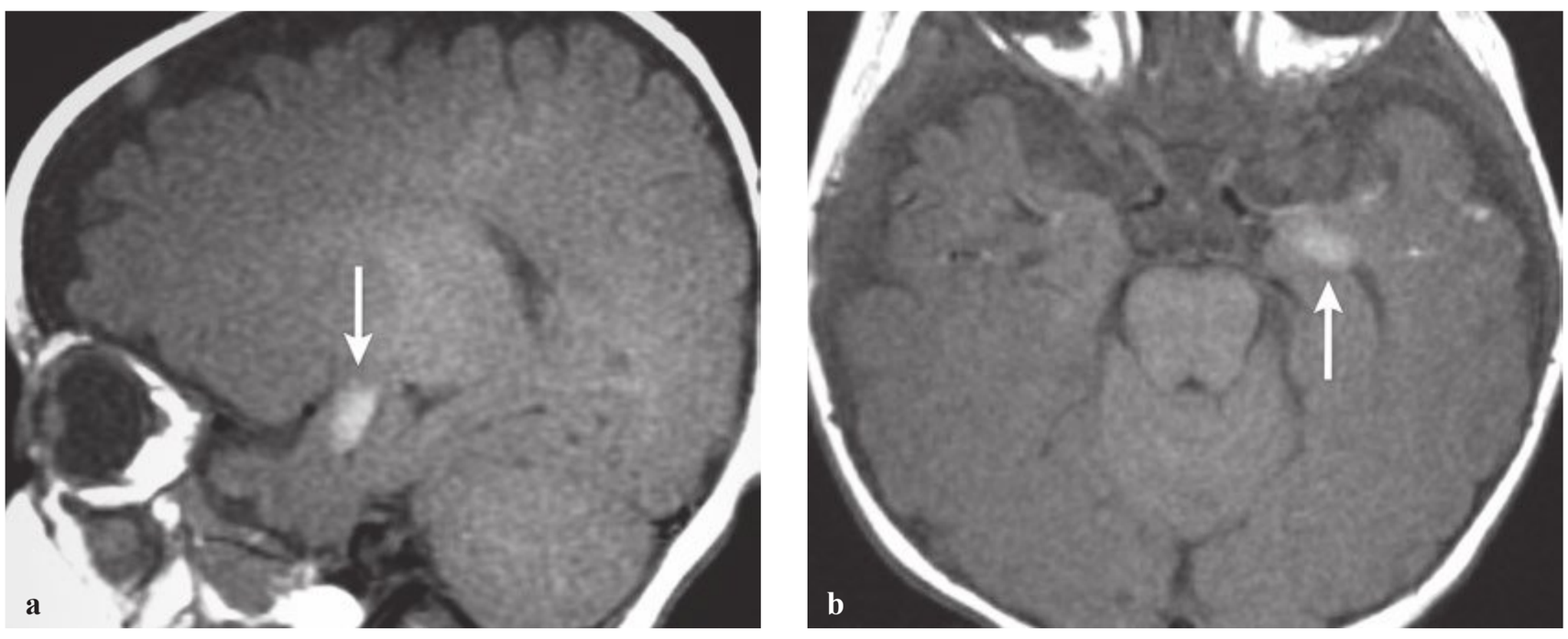

Fig. 1.88 A 3-month-old female with neurocutaneous melanosis that is seen as a zone of high signal in the left hippocampus (arrows) on **(a)** sagittal and **(b)** axial T1-weighted imaging.

Lesions	Imaging Findings	Comments
Pyogenic brain abscess (**Fig. 1.89**)	MRI: Circumscribed lesion with low signal on T1-weighted imaging, central zone of high signal on T2-weighted imaging (± air–fluid level) surrounded by a thin rim with intermediate-low signal. T2-weighted imaging shows ringlike gadolinium contrast enhancement that is sometimes thicker laterally than medially. Peripheral poorly defined zone of high signal on T2-weighted imaging represents edema. Diffusion-weighted imaging: Abscess contents typically have restricted diffusion. Mean ADC values for abscesses are significantly lower (0.63 to 1.12 × 10^{-3} mm^2/s) than those for necrotic or cystic neoplasms (2.45 × 10^{-3} mm^2/s). Magnetic resonance spectroscopy shows decreased N-acetylaspartate (NAA) from destruction of neurons, elevated lactate peak at 1.44 ppm, and amino acid peaks (valine, leucine, and isoleucine) at 0.9 ppm secondary to proteolytic enzymes. CT: Circumscribed lesion with a central zone of low attenuation (± air–fluid level) surrounded by a thin rim of intermediate attenuation, peripheral poorly defined zone of decreased attenuation representing edema, and ringlike contrast enhancement that is sometimes thicker laterally than medially.	Formation of brain abscess occurs 2 weeks after cerebritis, with liquefaction and necrosis centrally surrounded by a capsule and peripheral edema. Restricted diffusion of abscess contents is related to the combination of the high protein content and viscosity of pus, necrotic debris, and bacteria. Can be multiple, but more than 50% are solitary. Pyogenic abscess can be a complication of meningitis and/or sinusitis, septicemia, trauma, surgery, or cardiac shunt. Abscesses account for 2% and 8% of intra-axial mass lesions in developed and developing countries, respectively.

(continued on page 70)

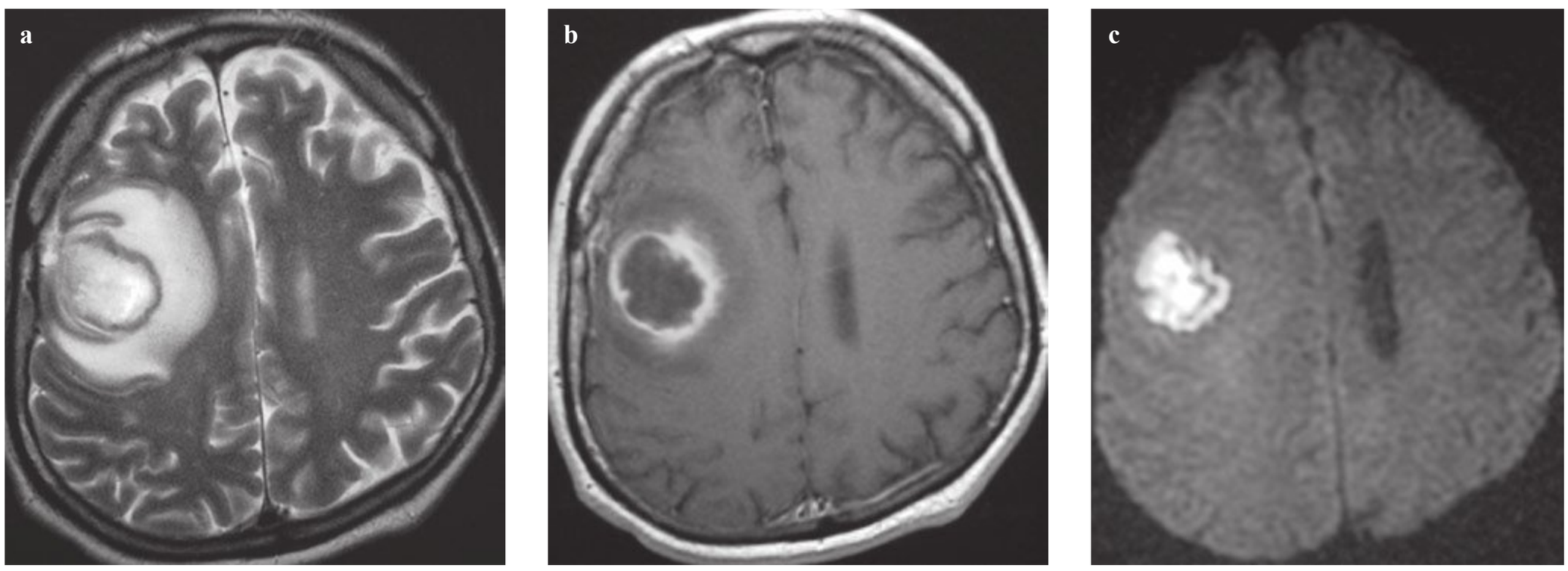

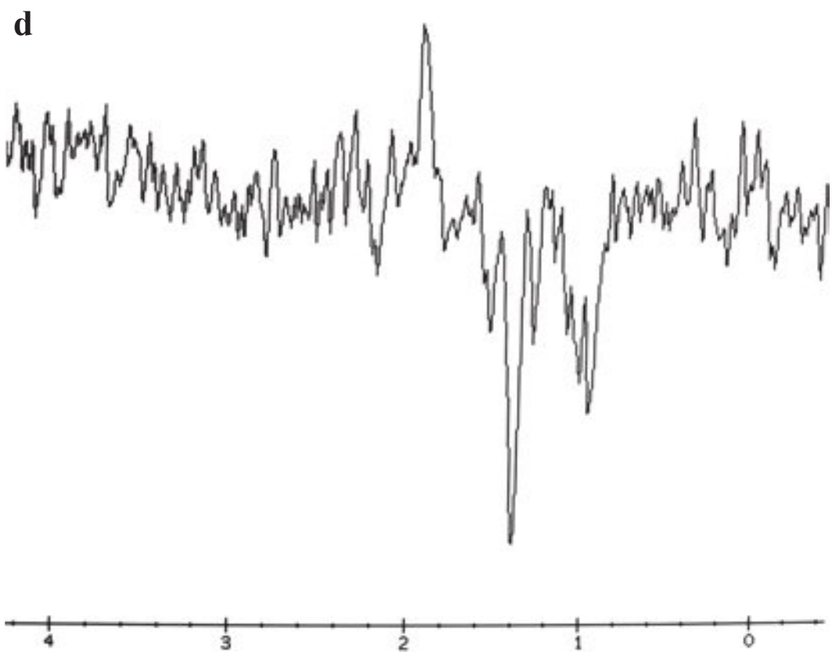

Fig. 1.89 **(a)** A 56-year-old man with a pyogenic brain abscess in the right cerebral hemisphere that has high signal centrally (purulent abscess cavity contents) surrounded by a rim of low-intermediate signal (abscess wall) and peripheral high signal edema on axial T2-weighted imaging. **(b)** The wall of the abscess shows irregular gadolinium contrast enhancement on axial T1-weighted imaging. The abscess contents show restricted diffusion on **(c)** axial DWI, and **(d)** a downward lactate peak at 1.44 ppm peak on magnetic resonance spectroscopy with a TE of 144 msec.

Table 1.2 (cont.) Supratentorial solitary intra-axial mass lesions

Lesions	Imaging Findings	Comments
Fungal brain infection (**Fig. 1.90**)	MRI: Findings vary depending on organism. Infection can occur in meninges and/or brain parenchyma; lesions are solid or cystic, with low-intermediate signal on T2-weighted imaging, high signal on T2-weighted imaging and FLAIR, nodular or ring-shaped gadolinium contrast enhancement, and peripheral high signal on T2-weighted imaging (edema). Diffusion-weighted imaging: Infected tissue may have restricted diffusion at the walls of the lesions without reduced ADC values in the central cavities of the lesions. Low signal on T2-weighted imaging and GRE at the walls of the lesions may occur from paramagnetic iron and magnesium within hyphae of the fungi. Magnetic resonance spectroscopy can show elevated lipid, lactate, and amino acid peaks, as well as multiple peaks between 3.6 and 3.8 ppm from trehalose. CT: Infection can occur in meninges and brain parenchyma. Solid or cystic-appearing lesions have decreased attenuation, a nodular or ring pattern of contrast enhancement, and a peripheral zone with decreased attenuation (edema).	Fungal brain infections occur in immunocompromised or diabetic patients, with resultant granulomas in meninges and brain parenchyma. Cryptococcus involves the basal meninges and extends along perivascular spaces into the basal ganglia. Aspergillosis and Mucor spread via direct extension through paranasal sinuses or hematogenously, invading blood vessels and resulting in hemorrhagic lesions and/or cerebral infarcts. Coccidioidomycosis usually involves the basal meninges. Candidiasis is often a nocosomial infection related to complications from surgery and/or indwelling catheters.
Encephalitis/viral infections (**Fig. 1.91**) Herpes simplex	MRI: Herpes simplex encephalitis typically involves the temporal lobes/limbic system, ± hemorrhage, with poorly defined zone or zones of low-intermediate signal on T1-weighted imaging and intermediate-high signal on T2-weighted imaging and FLAIR. Restricted diffusion can occur in early stages of infection; there is minimal or no gadolinium contrast enhancement; infection involves cerebral cortex and/or white matter, with minimal localized mass effect. CT: Poorly defined zone or zones of decreased attenuation, with minimal or no contrast enhancement.	In immunocompromised patients, encephalitis is infection/inflammation of brain tissue caused by viruses like herpes simplex, cytomegalovirus (CMV), and HIV, or by progressive multifocal leukoencephalopathy from JC polyoma virus infection of oligodendrocytes; in immunocompetent patients, it can be caused by St. Louis encephalitis virus, Eastern or Western equine encephalitis virus, measles (RNA Paramyxovirus), Epstein-Barr virus, Japanese encephalitis (Flavivirus), West Nile virus (Flavivirus), or rabies (Lyssavirus).

(continued on page 72)

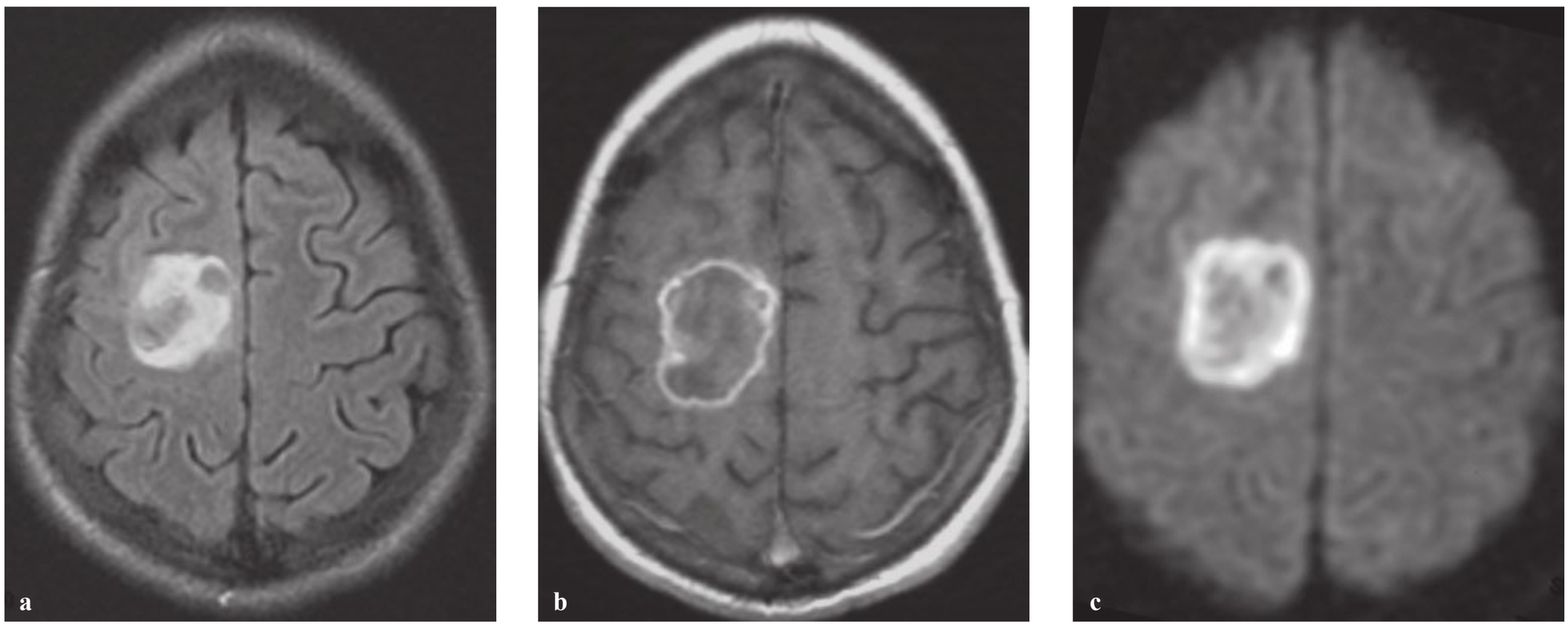

Fig. 1.90 **(a)** A 16-year-old male with Mucor fungal brain lesion/abscess in the right frontal lobe that has mixed high and intermediate signal on axial FLAIR, **(b)** irregular peripheral gadolinium contrast enhancement on axial T1-weighted imaging, and **(c)** heterogeneous mostly peripheral restricted diffusion on axial DWI.

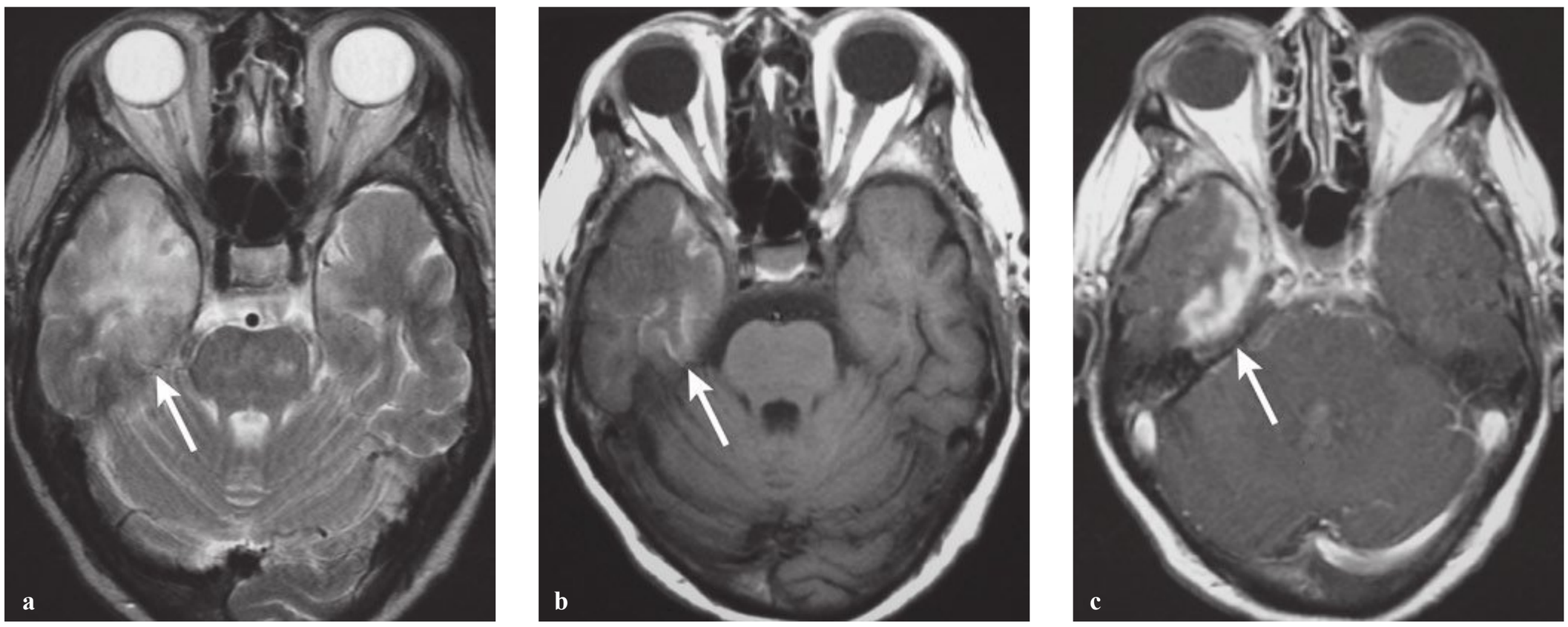

Fig. 1.91 A 67-year-old woman with encephalitis from herpes simplex 1 in the anteromedial right temporal lobe that has **(a)** high signal with poorly defined margins on axial T2-weighted imaging (arrow) and **(b)** low-intermediate signal and zones of hemorrhage with high signal on axial T1-weighted imaging (arrow). **(c)** Irregular gadolinium contrast enhancement is seen at the lesion on axial T1-weighted imaging (arrow).

Table 1.2 (cont.) Supratentorial solitary intra-axial mass lesions

Lesions	Imaging Findings	Comments
Cytomegalovirus (CMV) Japanese encephalitis Progressive multifocal leukoencephalopathy Rabies Acute measles encephalitis Subacute sclerosing panencephalitis from measles West Nile virus	CMV MRI: Periventricular/subependymal zones with high signal on T2-weighted imaging and FLAIR. HIV often involves periatrial white matter. CT: Neonatal cytomegalovirus (CMV) infections can result in localized destruction of brain with dystrophic calcifications. Japanese encephalitis often involves the thalami, basal ganglia, hippocampi, and substantia nigra, and less commonly involves the cerebral cortex, brainstem, and cerebellum. MRI: Single or multifocal zones in the cerebral white matter, including the arcuate/U-fibers, with abnormal increased signal on T2-weighted imaging and FLAIR, ± cerebral cortical involvement, ± mild localized mass effect, reduced ADC values and fractional anisotropy (FA) in acute phases, and increased ADC in late phases. Magnetic resonance spectroscopy shows decreased N-acetylaspartate (NAA) and increased choline and lactate. Rabies MRI: Poorly defined zones with increased signal on T2-weighted imaging can be seen in the cerebral white matter, cerebral cortex, basal ganglia, brainstem, and hypothalamus; ± gadolinium contrast enhancement. Acute Measles Encephalitis MRI: Increased signal on T2-weighted imaging can be seen in the cerebral white matter, cerebral cortex, basal ganglia, + restricted diffusion, ± petechial hemorrhage, ± gadolinium contrast enhancement in cerebral cortex and leptomeninges. Subacute Sclerosing Panencephalitis from Measles MRI: Zones with abnormal increased signal on T2-weighted imaging and FLAIR are seen in the cerebral and cerebellar white matter and brainstem. Increased ADC values and no gadolinium contrast enhancement. West Nile Virus MRI: Zones with abnormal increased signal on T2-weighted imaging and FLAIR are seen in the cerebral and cerebellar white matter and brainstem. Typically, there is no gadolinium contrast enhancement.	
Prion disease	MRI: Zones with high signal on T2-weighted imaging and FLAIR can be seen in the basal ganglia (caudate, putamen, and/or thalami bilaterally) and/or cerebral cortex, with corresponding restricted diffusion. Typically, no abnormal gadolinium contrast is seen with these abnormalities.	Transmissible spongiform encephalopathies are caused by prions and result in progressive neurodegeneration. Creutzfeldt-Jakob disease is the most common prion disease and has four forms (sporadic form accounts for 85% of cases, genetic form for 10–15%, and the iatrogenic and new variant forms for the remainder).

Lesions	Imaging Findings	Comments
Tuberculoma (**Fig. 1.92**)	MRI: Intra-axial lesions in cerebral hemispheres and basal ganglia (adults) and cerebellum (children), with low-intermediate signal on T1-weighted images, central zone of high signal on T2-weighted images with a thin peripheral rim of low signal, and occasionally low signal on T2-weighted images; + solid or rim gadolinium contrast enhancement; ± calcification, ± restricted or increased diffusion. Meningeal lesions: Nodular or cystic zones of basilar meningeal gadolinium contrast enhancement. Meningitis can be associated with intracranial arterial or venous thrombosis, leading to brain infarction with restricted diffusion. CT: Intra-axial lesions occur in the cerebral hemispheres, basal ganglia, and brainstem (adults), and cerebellum (children). Lesions can have decreased attenuation, central zone of low attenuation with a thin peripheral rim of intermediate attenuation, + solid or rim pattern of contrast enhancement, ± calcification. Meningeal lesions: Nodular or cystic zones of basilar meningeal enhancement.	Tuberculoma occurs in immunocompromised patients and in immunocompetent patients in developing countries. Caseating intracranial granulomas form via hematogenous dissemination. Meningitis is the most common intracranial manifestation of tuberculosis, more common than intra-axial tuberculomas in the brain.
Toxoplasmosis	MRI: Single or multiple solid and/or cystic lesions located in basal ganglia and/or corticomedullary junctions in cerebral hemispheres, with low-intermediate signal on T1-weighted images with or without high-signal peripheral rims; high signal on T2-weighted images and FLAIR with or without a central zone of low-intermediate signal, or three layers of high central signal region surrounded by a peripheral rim of low-intermediate signal, which is in turn surrounded by high signal; nodular or rim pattern of gadolinium contrast enhancement as well as an "eccentric target pattern" with a peripheral ring-shaped zone of gadolinium contrast enhancement and a small, eccentric, enhancing nodule along the wall; ± peripheral high T2 signal (edema). Diffusion-weighted imaging shows high-signal rims surrounding low-signal centers. CT: Lesions can have low or intermediate attenuation, ± peripheral rim or nodular patterns of contrast enhancement.	Most common opportunistic CNS infection in AIDS patients, caused by ingestion of food contaminated with parasites (Toxoplasma gondii). T. gondii is an intracellular protozoan with a worldwide distribution. Also occurs in immunocompetent patients. Acute lesions contain: a central zone comprised of necrotic and cellular debris, histiocytes and neutrophils; an intermediate zone of vascular congestion and tachyzoites; and an outer zone with microglial nodules, T. gondii organisms and tachyzoites, mild inflammation, and vascular congestion. FDG-PET/CT shows decreased uptake in T. gondii lesions and can be used to distinguish these lesions from lymphoma, which has increased FDG uptake.

(continued on page 74)

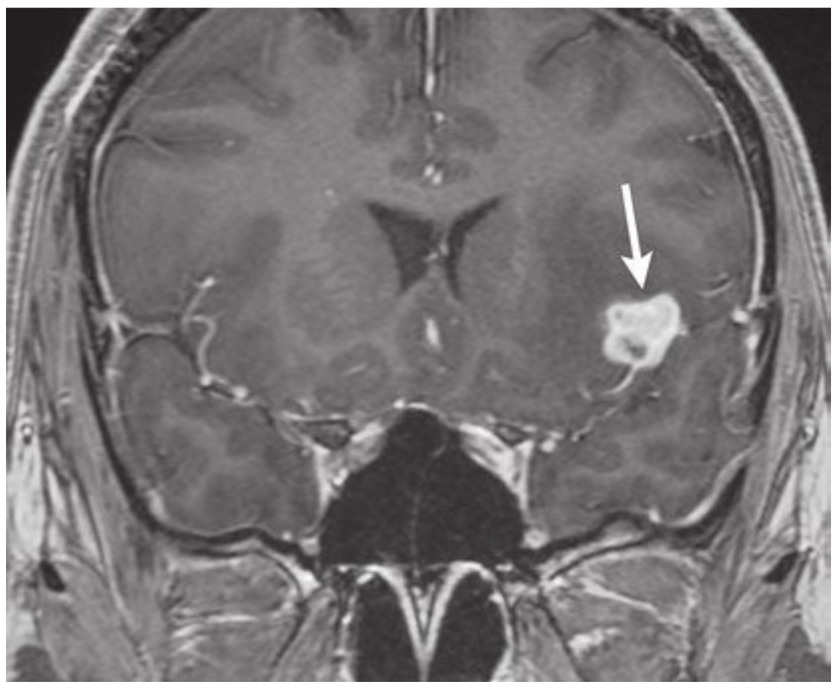

Fig. 1.92 A 21-year-old man with a tuberculoma in the right frontal lobe that shows gadolinium contrast enhancement on coronal T1-weighted imaging (arrow).

Table 1.2 (cont.) Supratentorial solitary intra-axial mass lesions

Lesions	Imaging Findings	Comments
Cysticercosis (**Fig. 1.93**)	MRI: Single or multiple cystic lesions in brain or meninges. Active vesicular phase: Cystic-appearing lesions containing a small 2–4 mm nodule (scolex) with low signal on T1-weighted images, FLAIR, and diffusion-weighted imaging, thin peripheral rim with high signal on FLAIR, and high signal on T2-weighted images; minimal peripheral rim or no gadolinium contrast enhancement; no peripheral edema on T2-weighted images and FLAIR. Active colloidal vesicular phase: Cystic-appearing lesion with low-intermediate signal on T1-weighted images, high signal on T2-weighted images, and rim and/or nodular pattern of gadolinium contrast enhancement, ± peripheral signal (edema) on T2-weighted images. Active granular nodular phase: Cyst retracts into a more solid gadolinium contrast-enhancing granulomatous nodule. Chronic non-active phase: Calcified nodular granulomas.	Caused by ingestion of encysted larva of the tapeworm Taenia solium in contaminated food (undercooked pork). Involves meninges—subarachnoid space and cisterns > brain parenchyma > ventricles. Most common parasitic disease of the CNS, usually in patients from 15 to 40 years old. Most common cause of acquired epilepsy in endemic regions. Complications include intracranial hypertension from CSF obstruction, arachnoiditis, meningitis, and vascular occlusion.
Hydatid cyst (**Fig. 1.94**) Echinococcus granulosus Echinococcus multilocularis	Echinococcus granulosus MRI: Single or rarely multiple cystic lesions with low signal on T1-weighted imaging and high signal on T2-weighted imaging surrounded by a thin wall with low signal on T2-weighted imaging, typically no gadolinium contrast enhancement or peripheral edema unless superinfected, often located in vascular territory of the middle cerebral artery. Rupture of the hydatid cyst may be contained when only the endocyst ruptures and the pericyst remains intact. In these cases, thickened high signal on T2-weighted imaging is seen in the pericyst from edema and inflammatory reaction, which can show gadolinium contrast enhancement. The ruptured endocyst can have a floating membrane sign or "scroll appearance," with low signal on T1-weighted imaging and T2-weighted imaging within the fluid deep to the pericyst. Rupture of the hydatid cyst beyond the pericyst can result in an inflammatory host response with complications based on the sites involved. Echinococcus multilocularis MRI: Cystic (± multilocular) and/or solid lesions, with a central zone of intermediate-high signal on T2-weighted images surrounded by a slightly thickened rim of low signal, + gadolinium contrast enhancement, and a peripheral zone of high signal on T2-weighted images (edema). Calcifications are common.	Rare intracranial lesions caused by the parasites Echinococcus granulosus (South America, Middle East, Australia, and New Zealand) and Echinococcus multilocularis (North America, Europe, Turkey, and China). There is CNS involvement in 1 to 4% of hydatid infections. Humans are intermediate hosts from ingestion of tapeworm eggs in fecally contaminated food or by contact with infected animal tissue. Lesions are often large before becoming symptomatic from raised intracranial pressure. The hydatid cyst has three layers. The outermost layer is the pericyst, which is a thin, compressed layer of adjacent host tissue composed of fibrous and inflammatory host cells and which usually lacks gadolinium contrast enhancement. The middle later is the acellular laminated membrane, and the inner layer is the germinative epithelium. The acellular laminated membrane and germinative layer represent the true wall of the cyst, which is referred to as the endocyst. Superinfected hydatid cysts often contain purulent material from Staphylococcus aureus infection and are typically surrounded by an inflammatory reaction in the adjacent brain tissue and/or meninges.

(continued on page 76)

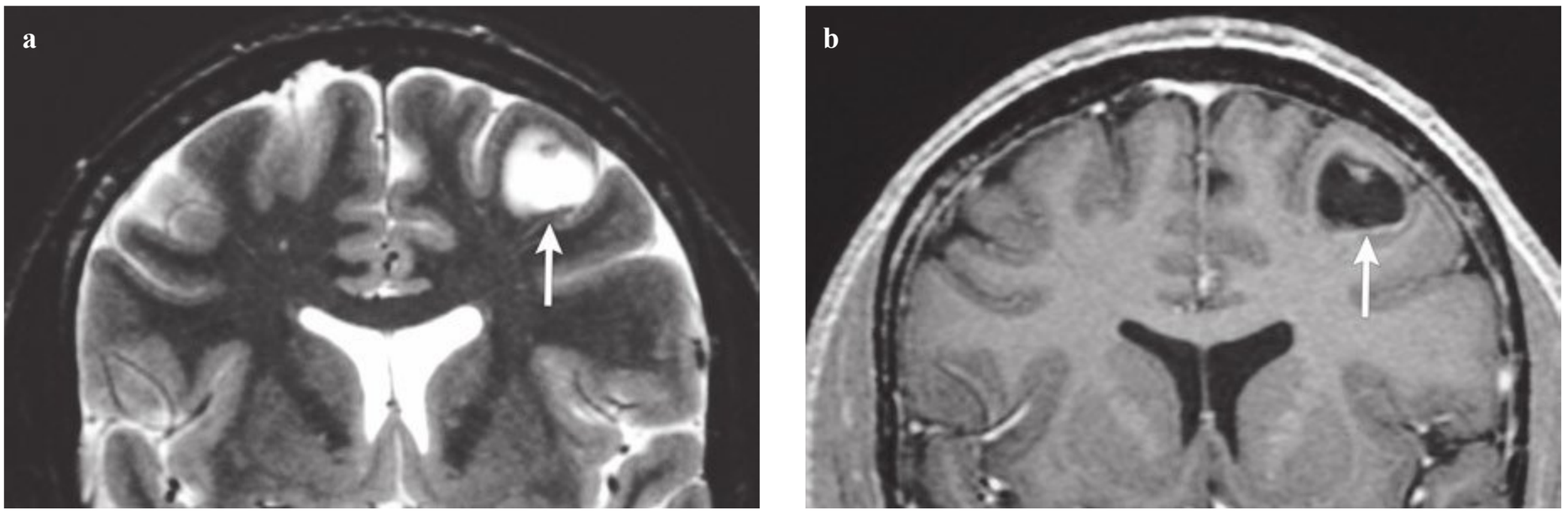

Fig. 1.93 A 36-year-old man with cysticercosis. **(a)** The cystic lesion in the left frontal lobe has circumscribed margins and high signal on coronal T2-weighted imaging (arrow). A small nodule (scolex) is seen at the upper inner margin of the cystic lesion. **(b)** The scolex and margins of the lesion show mild gadolinium contrast enhancement on coronal T1-weighted imaging (arrow).

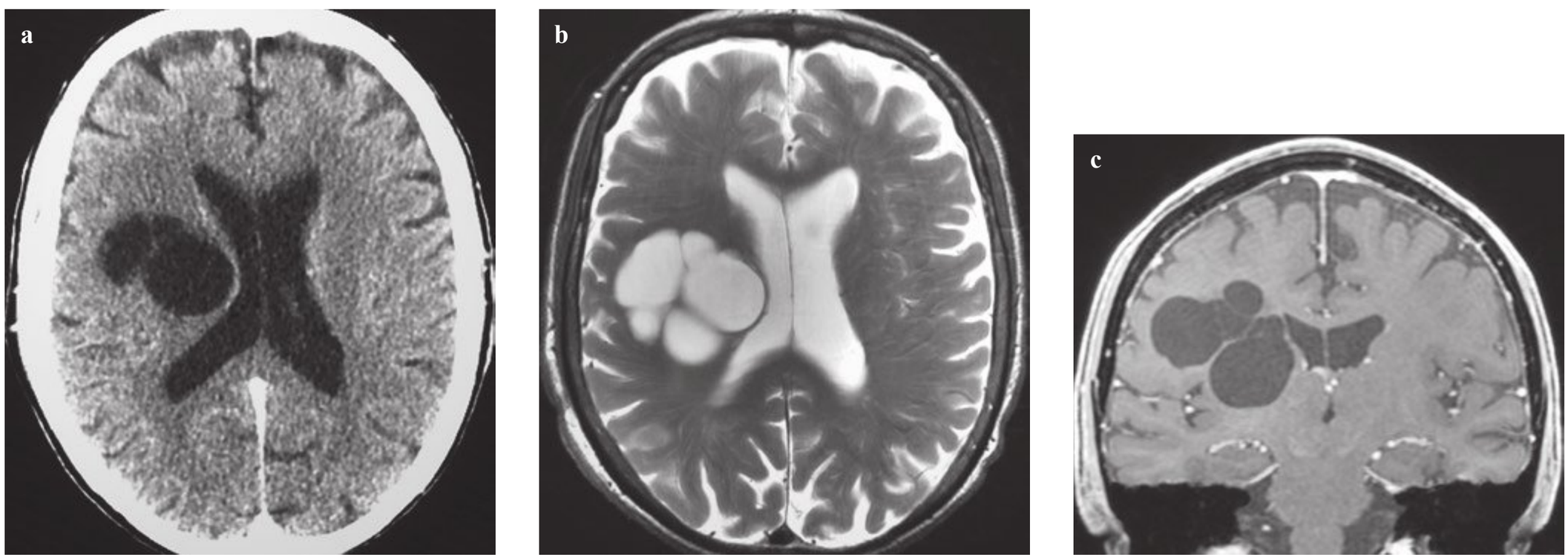

Fig. 1.94 A 78-year-old woman with hydatid cysts in the right cerebral hemisphere. There are multiple circumscribed cystic lesions with **(a)** low attenuation on axial CT and **(b)** high signal on axial T2-weighted imaging. The lesions are surrounded by thin walls without peripheral edema. **(c)** No gadolinium contrast enhancement is seen at the lesions on coronal T1-weighted imaging.

Table 1.2 (cont.) Supratentorial solitary intra-axial mass lesions

Lesions	Imaging Findings	Comments
Inflammatory Lesions: Noninfectious		
Demyelinating disease: multiple sclerosis, acute disseminated encephalomyelitis (**Fig. 1.95**)	MRI: Lesions located in cerebral or cerebellar white matter, brainstem, basal ganglia; lesions usually have low-intermediate signal on T1-weighted imaging and high signal on T2-weighted imaging, ± gadolinium contrast enhancement. Gadolinium contrast enhancement can be nodular, ringlike, or in a C shape (incomplete ring) usually in acute/ early subacute phase of demyelination, ± restricted diffusion. Acute demyelinating lesions can have localized mass effect simulating neoplasms. CT: Zones of active demyelination may show contrast enhancement and mild localized swelling.	Multiple sclerosis is the most common acquired demyelinating disease. It usually affects women, and 20 to 40 years are peak ages. Other demyelinating diseases include acute disseminated encephalomyelitis, an immune-mediated demyelination after viral infection; toxin-related conditions (environmental exposure or ingestion, such as alcohol, solvents, etc.; or endogenous toxins in metabolic disorders, such as leukodystrophies, mitochondrial encephalopathies, etc.); demyelination due to radiation injury; trauma-related demyelination; and vascular disease.
Neurosarcoid (**Fig. 1.96**)	MRI: Poorly marginated intra-axial zone or zones with low-intermediate signal on T1-weighted images and slightly high to high signal on T2-weighted images and FLAIR. Usually shows gadolinium contrast enhancement, + localized mass effect and peripheral edema. Often associated with gadolinium contrast enhancement in the leptomeninges and/or dura. CT: Poorly marginated intra-axial zone with low-intermediate attenuation. Usually shows contrast enhancement, + localized mass effect and peripheral edema. Often associated with contrast enhancement in the leptomeninges.	Sarcoidosis is a multisystem non-caseating granulomatous disease of uncertain cause that can involve the CNS in 5 to 15% of cases. If untreated, it is associated with severe neurologic deficits, such as encephalopathy, cranial neuropathies, and myelopathy. Diagnosis of neurosarcoid may be difficult when the neurologic complications precede other systemic manifestations involving the lungs, lymph nodes, skin, bone, and/or eyes.

(continued on page 78)

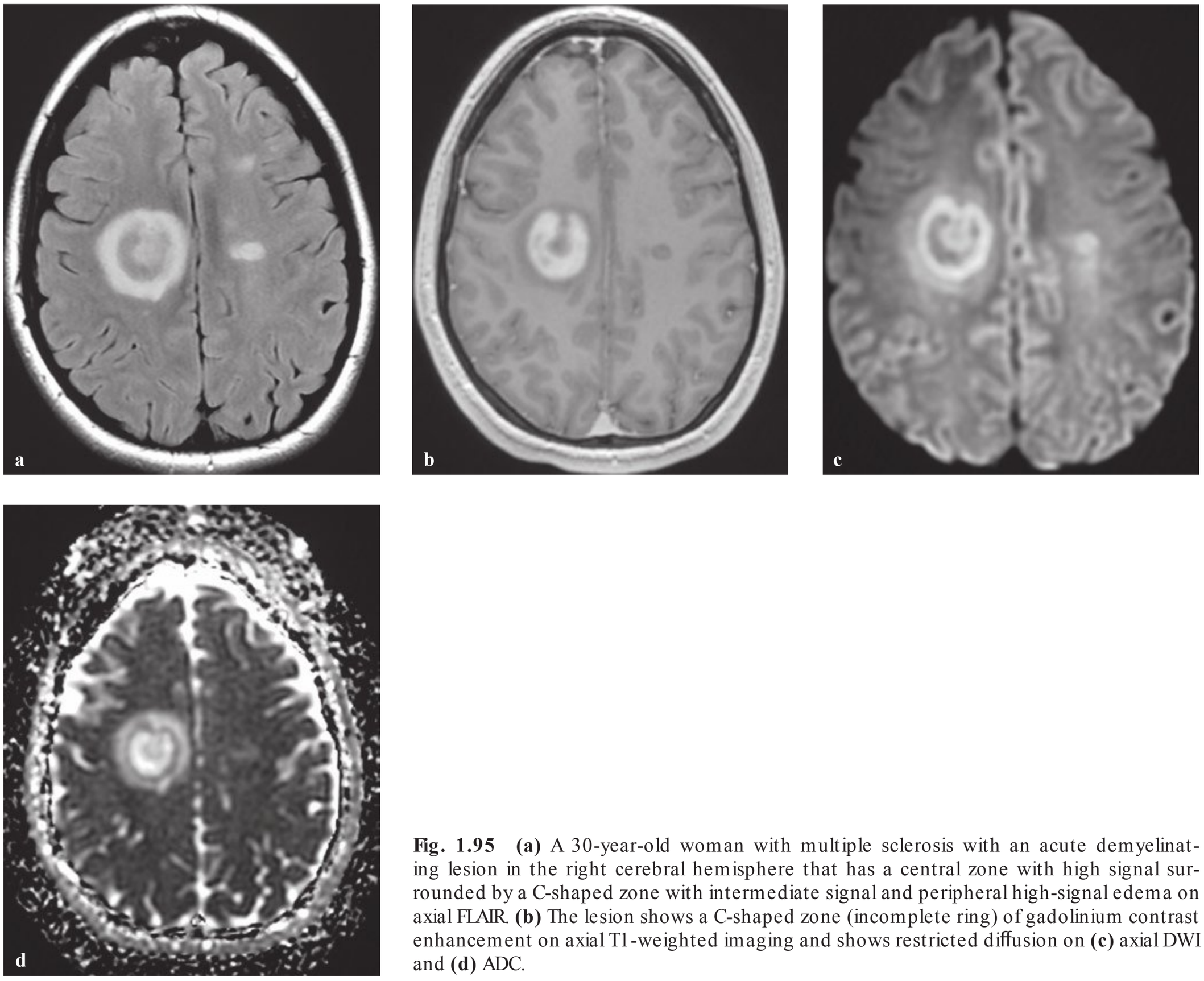

Fig. 1.95 **(a)** A 30-year-old woman with multiple sclerosis with an acute demyelinating lesion in the right cerebral hemisphere that has a central zone with high signal surrounded by a C-shaped zone with intermediate signal and peripheral high-signal edema on axial FLAIR. **(b)** The lesion shows a C-shaped zone (incomplete ring) of gadolinium contrast enhancement on axial T1-weighted imaging and shows restricted diffusion on **(c)** axial DWI and **(d)** ADC.

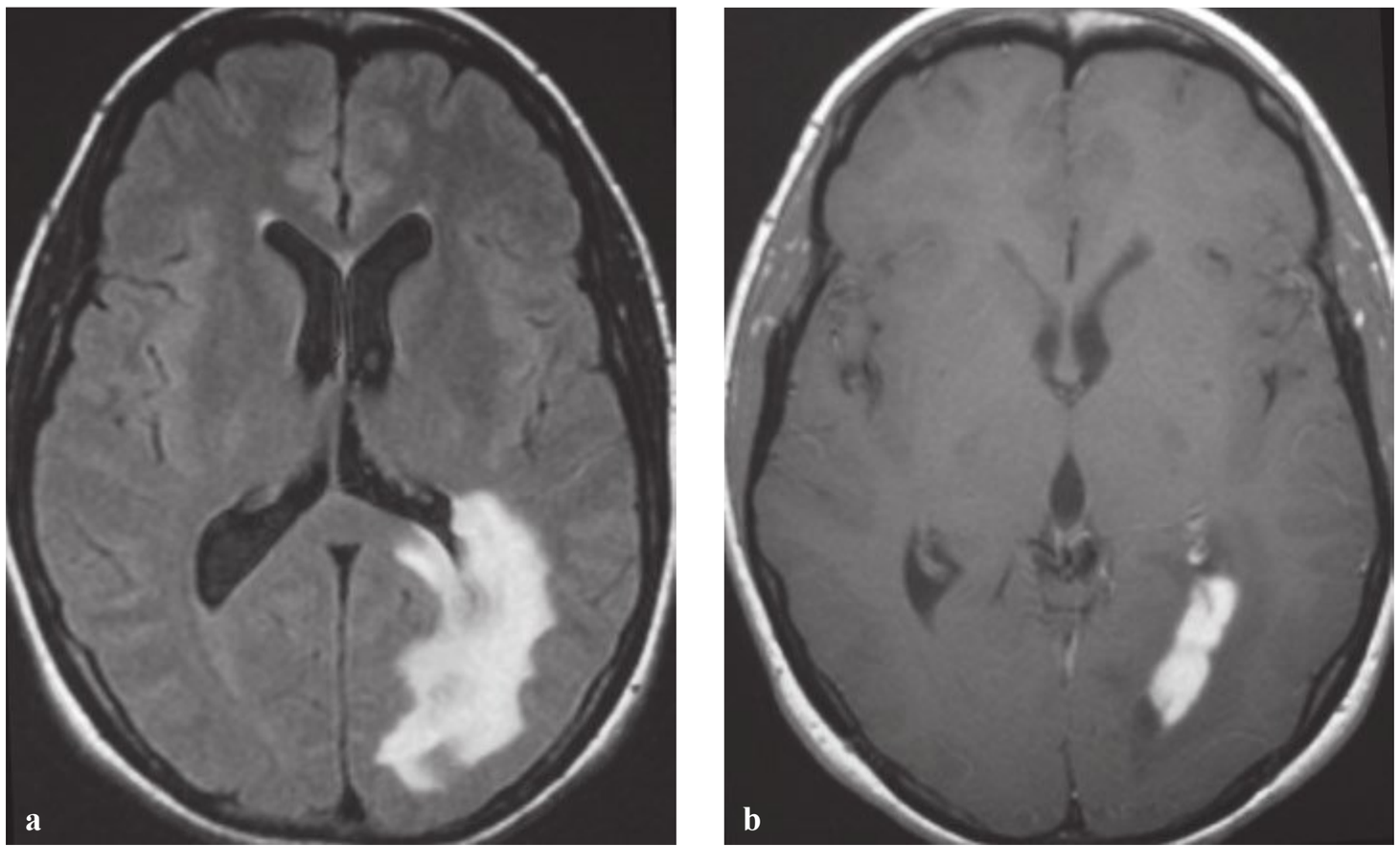

Fig. 1.96 A 40-year-old woman with sarcoidosis who has a left peri-atrial lesion with **(a)** high signal on axial FLAIR and **(b)** gadolinium contrast enhancement on axial T1-weighted imaging.

Table 1.2 (cont.) Supratentorial solitary intra-axial mass lesions

Lesions	Imaging Findings	Comments
Hemorrhage		
Intra-axial hemorrhage (**Fig. 1.97, Fig. 1.98, Fig. 1.99, Fig. 1.100,** and **Fig. 1.101**)	CT: A linear relationship exists between CT attenuation and hematocrit, hemoglobin, and protein content. MRI: The signal of the hematoma depends on its age, size, location, hematocrit, oxidation state of the iron in hemoglobin, degree of clot retraction, extent of edema, and MRI pulse sequence.	Can result from trauma, ruptured aneurysms, vascular malformations, coagulopathy, hypertension, adverse drug reaction, amyloid angiopathy, hemorrhagic transformation of cerebral infarction, metastases, abscesses, and viral infections (herpes simplex, CMV). The magnetic properties and MRI signal of intracranial hemorrhage are related to the oxidative state of the iron in hemoglobin and the presence of unpaired electrons—the paramagnetic property. Paramagnetic substances with unpaired electrons cause localized magnetic field inhomogeneities due to their interaction with adjacent hydrogen nuclei (protons) in a mechanism referred to as proton-electron dipole-dipole interaction (PEDD). PEDD is inversely proportional to the sixth power of the distance between the electrons and protons. PEDD reduces the T1 values and, to a lesser extent, the T2 values of adjacent protons. Another paramagnetic property is T2-proton relaxation enhancement (T2-PRE), which occurs when paramagnetic substances are placed in a high magnetic field, resulting in local magnetic field distortion with reduction of T2 values without altering the T1 values of adjacent protons. T2-PRE and PEDD cause low signal alteration on T2-weighted imaging only when red blood cell membranes are intact. Oxyhemoglobin contains ferrous iron (Fe^{2+}), and has no unpaired electrons (it is diamagnectic) because of the partial transfer of the outer electrons from hemoglobin to the oxygen molecules. Deoxyhemoglobin contains ferrous iron although it has four unpaired electrons and is paramagnetic. With time, when the iron becomes oxidized to the ferrous state (Fe^{3+}), the hemoglobin is referred to as methemoglobin, which has five unpaired electrons and is paramagnetic.
Hyperacute intra-axial hematoma (**Fig. 1.97**) Hyperacute phase (0–6 hours)	MRI: Hemoglobin is primarily diamagnetic oxyhemoglobin (iron Fe^{2+} state), with intermediate signal on T1-weighted images and slightly high signal on T2-weighted images. CT: High attenuation of hematoma from 40 to 90 HU. A horizontal fluid-fluid level may occur from sedimentation of cellular blood components from the serum.	Complex of extravasated blood consisting of red blood cells, white blood cells, platelets, and protein-rich serum. Progressive deposition of fibrin fibrils also occurs. The attenuation of the hematoma increases from 60 to 90 HU, mostly due to the hemoglobin protein concentration and blood clot retraction.
Acute intra-axial hematoma (**Fig. 1.98**) Acute phase (6 hours to 2–3 days)	MRI: Intracellular hemoglobin primarily is paramagnetic deoxyhemoglobin (iron Fe^{2+} state), with intermediate signal on T1-weighted images, low signal on T2-weighted images, and surrounded by a peripheral zone of high signal (edema) on T2-weighted images. CT: Attenuation of intra-axial hematoma can be up to 80–100 HU secondary to clot retraction, ± fluid-fluid level, ± peripheral halo of low attenuation from edema and/or serum extrusion.	Deoxygenation of hemoglobin within intact red blood cell membranes results in deoxyhemoglobin, which has four unpaired electrons and is paramagnetic. The 3D configuration of deoxyhemoglobin does not allow contact of the water protons with the paramagnetic center, eliminating the PEDD effect. The low signal of deoxyhemoglobin on T2-weighted images is primarily due to T2-PRE.

(continued on page 81)

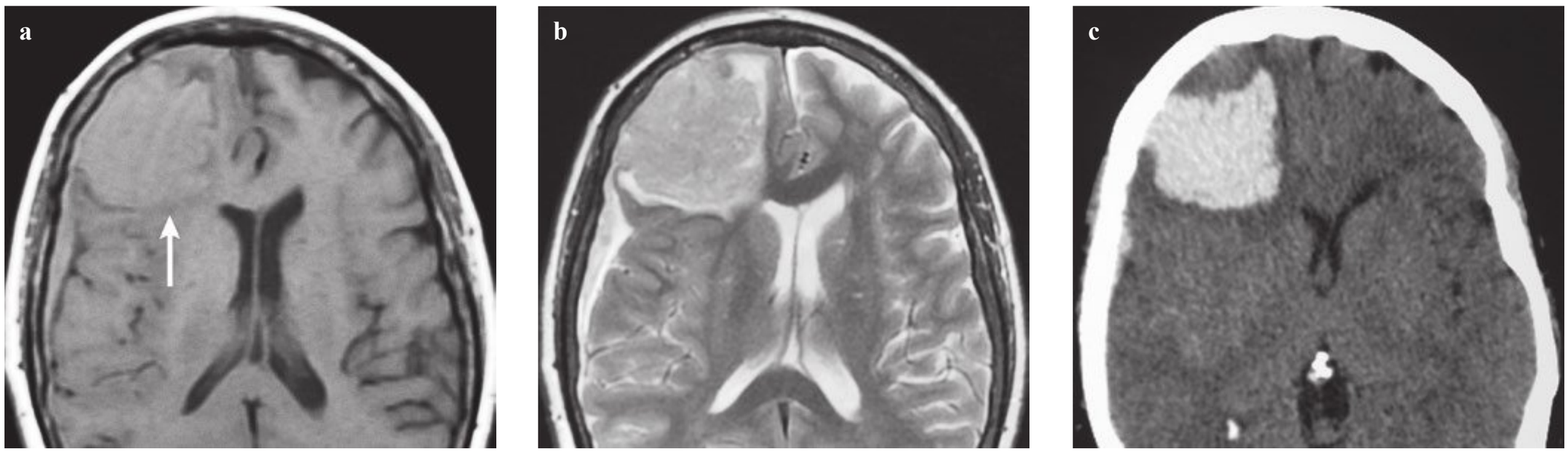

Fig. 1.97 Hyperacute intra-axial hematoma (0–6 hours) in a patient 2 hours after a normal head CT exam. The hyperacute hematoma has **(a)** intermediate signal on axial T1-weighted imaging (arrow) and **(b)** slightly high signal on axial T2-weighted imaging (arrow). **(c)** CT obtained 2 hours later shows the hematoma to have high attenuation.

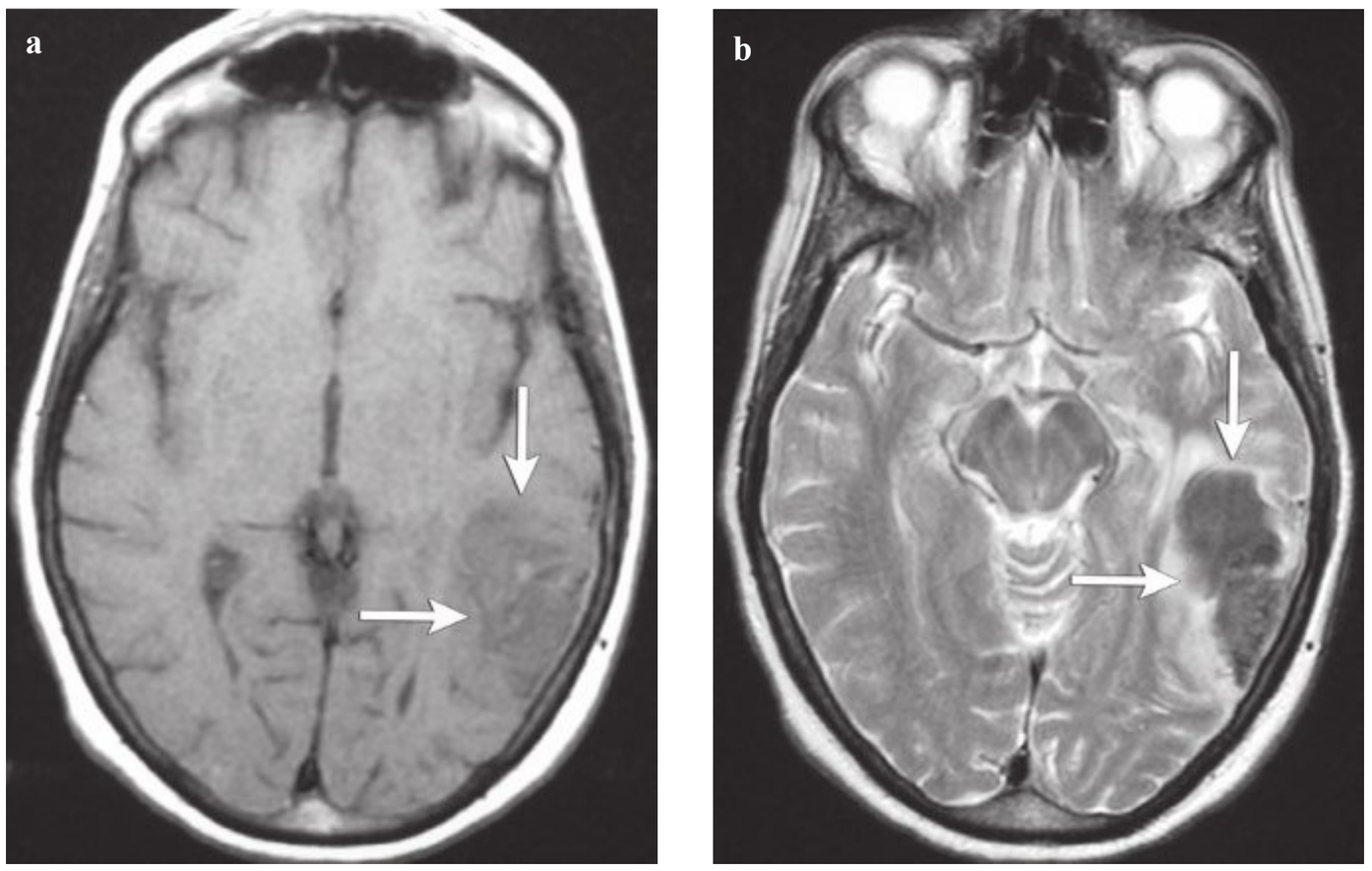

Fig. 1.98 Acute intra-axial hematoma (6 hours to 2–3 days) that has **(a)** intermediate signal on axial T1-weighted imaging (arrows) and **(b)** low signal on T2-weighted imaging (arrows) from paramagnetic deoxyhemoglobin surrounded by a peripheral zone of high signal (edema).

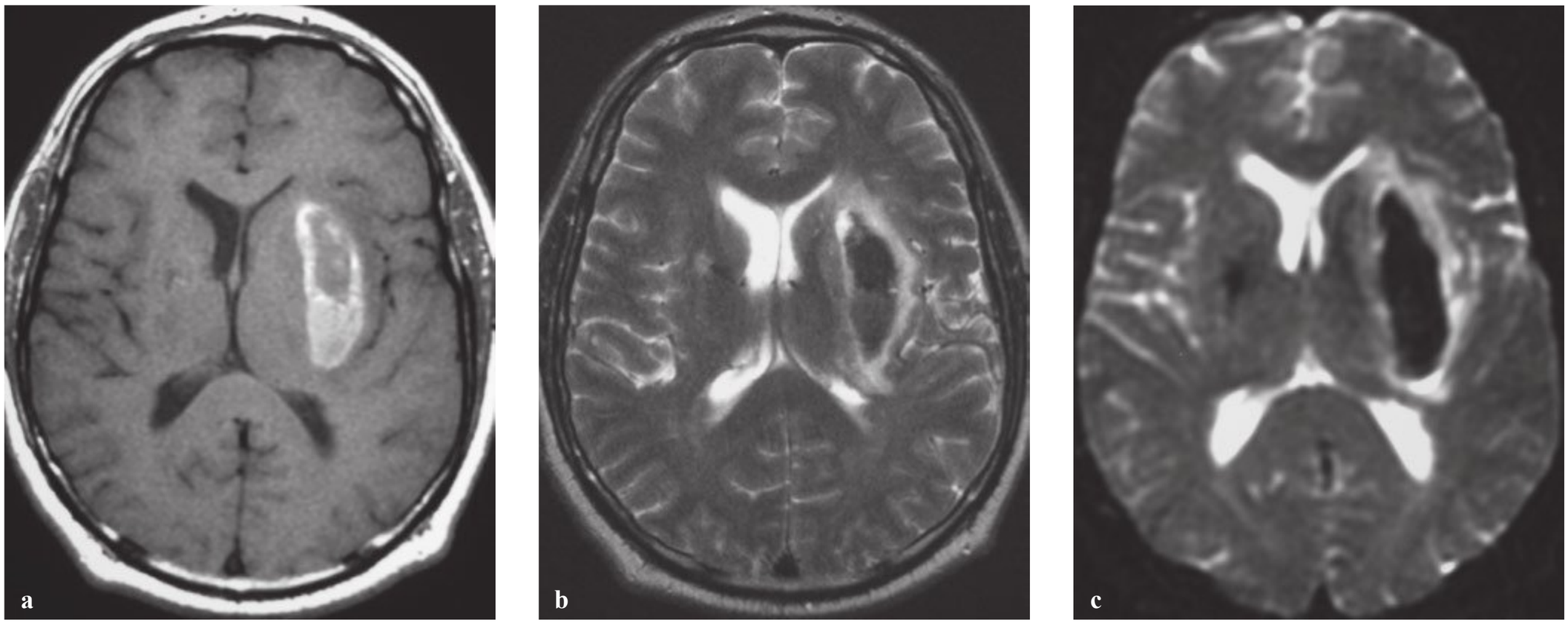

Fig. 1.99 **(a)** Early subacute intra-axial hematoma (3–7 days) that has high signal on axial T1-weighted imaging from methemoglobin (iron Fe^{3+} state). Methemoglobin is primarily intracellular and has low signal on **(b)** T2-weighted imaging and **(c)** axial GRE. **(d)** The hematoma has high attenuation on CT.

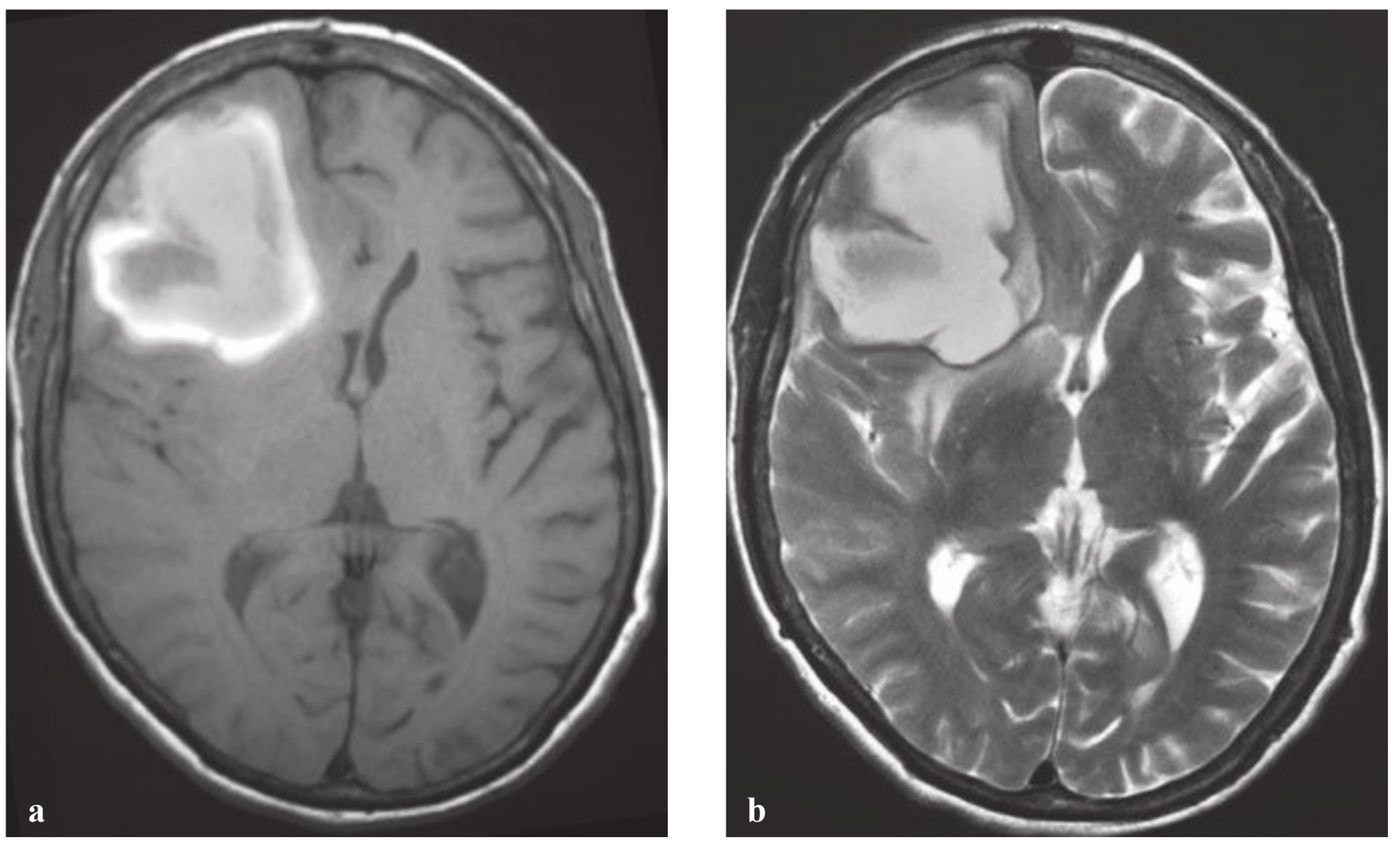

Fig. 1.100 Late subacute intra-axial hematoma (4 days to 1 month) has **(a)** high signal on axial T1-weighted imaging and **(b)** high signal on axial T2-weighted imaging from extracellular methemoglobin and increased proton density.

Table 1.2 (cont.) Supratentorial solitary intra-axial mass lesions

Lesions	Imaging Findings	Comments
Early subacute intra-axial hematoma (**Fig. 1.99**) Early subacute phase (3–7 days)	MRI: Hemoglobin becomes oxidized to the iron Fe^{3+} state—methemoglobin. Methemoglobin is primarily intracellular, with high signal on T1-weighted images from PEDD and low signal on T2-weighted images from PEDD and T2-PRE. CT: Attenuation of intra-axial hematoma can be up to 80–100 HU secondary to clot retraction, ± fluid-fluid level, ± peripheral halo of low attenuation from edema and/or serum extrusion.	Clot retraction within the hematoma progresses. The ferrous iron in the hematoma becomes oxidized to the ferric state (Fe^{3+}), forming methemoglobin, which has five unpaired electrons and is paramagnetic.
Late subacute intra-axial hematoma (**Fig. 1.100** and **Fig. 1.101**) Late subacute phase (4 days to 1 month)	Methemoglobin eventually becomes primarily extracellular. The hematoma has high signal on T1-weighted images from PEDD and high signal on T2-weighted images from increased proton density and loss of the T2-PRE effect secondary to membrane lysis.	Lysis of membranes of red blood cells occurs resulting in extracellular methemoglobin. Proteolysis of the globin and fibrin protein in the hematoma from macrophages results in a progressive centripetal decrease in attenuation of 0.7 to 1.5 HU/day. Edema and mass effect associated with the hematoma also decrease.

(continued on page 82)

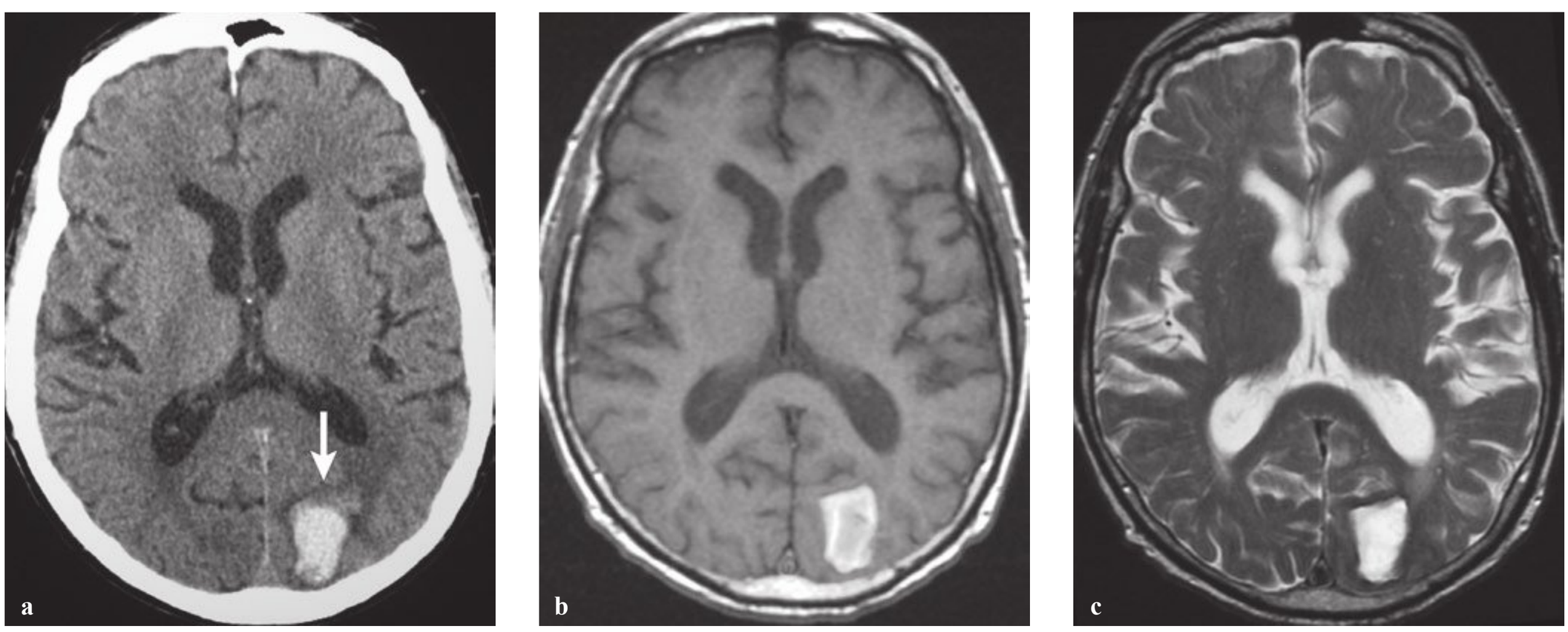

Fig. 1.101 Late subacute hematoma (4 days to 1 month) has **(a)** high attenuation on axial CT (arrow), **(b)** high signal on axial T1-weighted imaging, and **(c)** high signal on axial T2-weighted imaging.

Table 1.2 (cont.) Supratentorial solitary intra-axial mass lesions

Lesions	Imaging Findings	Comments
Chronic intra-axial hemorrhage (**Fig. 1.102**) Chronic phase (1 month to years)	The hematoma progresses from a lesion with high signal on T1- and T2-weighted images, with a peripheral rim of low signal on T2-weighted images and gradient recalled echo (GRE) imaging due to superparamagnetic hemosiderin, which results in low signal on T2-weighted images and GRE imaging. Chronic hematomas can eventually have low or slightly high signal on T1-weighted images.	Extracellular methemoglobin is progressively degraded to hemosiderin, which has many unpaired electrons and is superparamagnetic. Superparamagnetic substances typically have a high T2-PRE effect and cause decreased signal on T2-weighted images and GRE imaging.
Cerebral contusion (**Fig. 1.103**)	The MRI appearance of contusions is focal hemorrhage involving the cerebral cortex and subcortical white matter. The MRI signal of the contusion depends on its age and presence of oxyhemoglobin, deoxyhemoglobin, methemoglobin, hemosiderin, etc. Surrounding the hematoma is a zone of edema with high signal on T2-weighted images and FLAIR.	Contusions are superficial brain injuries involving the cerebral cortex and subcortical white matter that result from skull fracture and/or trauma due to acceleration/deceleration of the brain onto the inner table of the skull. Lesions consist of capillary injury, edema, and hemorrhage, and often involve the anterior portions of the temporal and frontal lobes and the inferior portions of the frontal lobes.
Hemorrhagic metastatic lesion (**Fig. 1.104**)	The MRI appearance of a hemorrhagic metastatic lesion is one of an intracerebral hematoma involving a portion or all of the neoplasm, usually associated with peripheral edema (high signal on T2-weighted imaging). Lesions are often multiple.	Metastatic intra-axial tumors associated with hemorrhage include bronchogenic carcinoma, renal cell carcinoma, melanoma, choriocarcinoma, and thyroid carcinoma. May be difficult to distinguish from hemorrhage related to other etiologies, such as vascular malformations and amyloid angiopathy.

(continued on page 84)

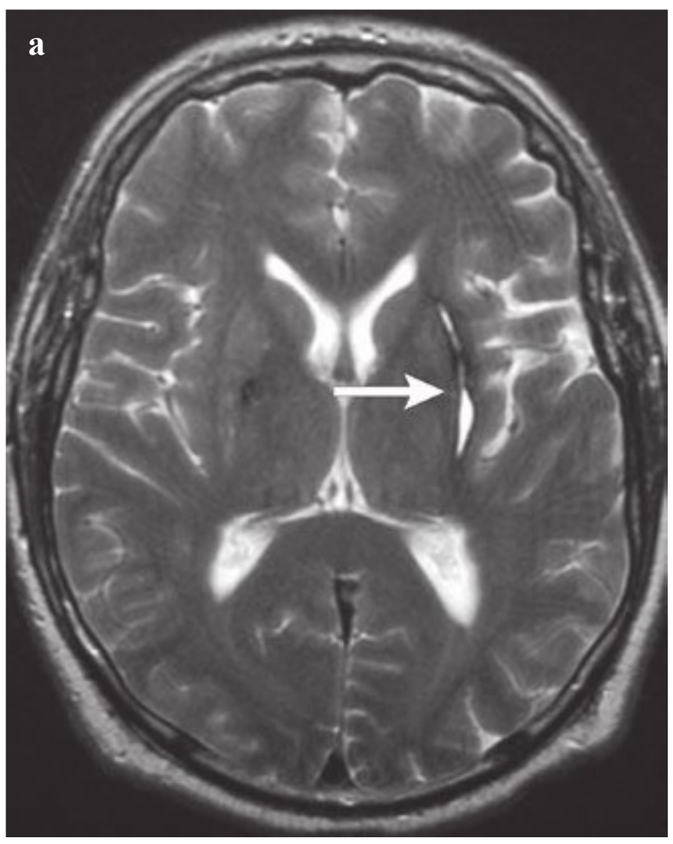

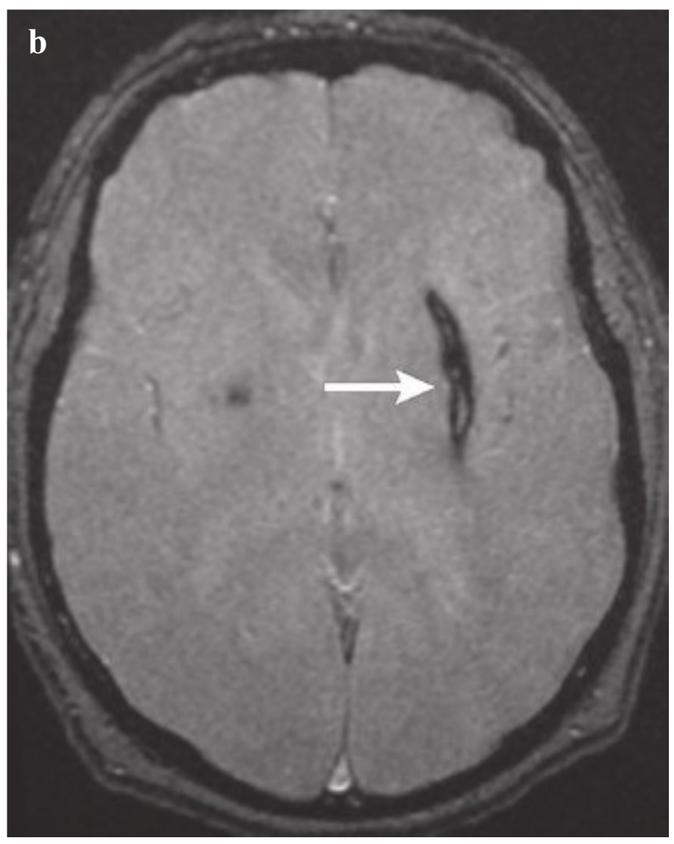

Fig. 1.102 Chronic intra-axial hematoma (1 month to years) has **(a)** high signal centrally on T2-weighted imaging (arrow), with **(b)** a peripheral rim of low signal on T2-weighted imaging and GRE due to the presence of superparamagnetic hemosiderin (arrow).

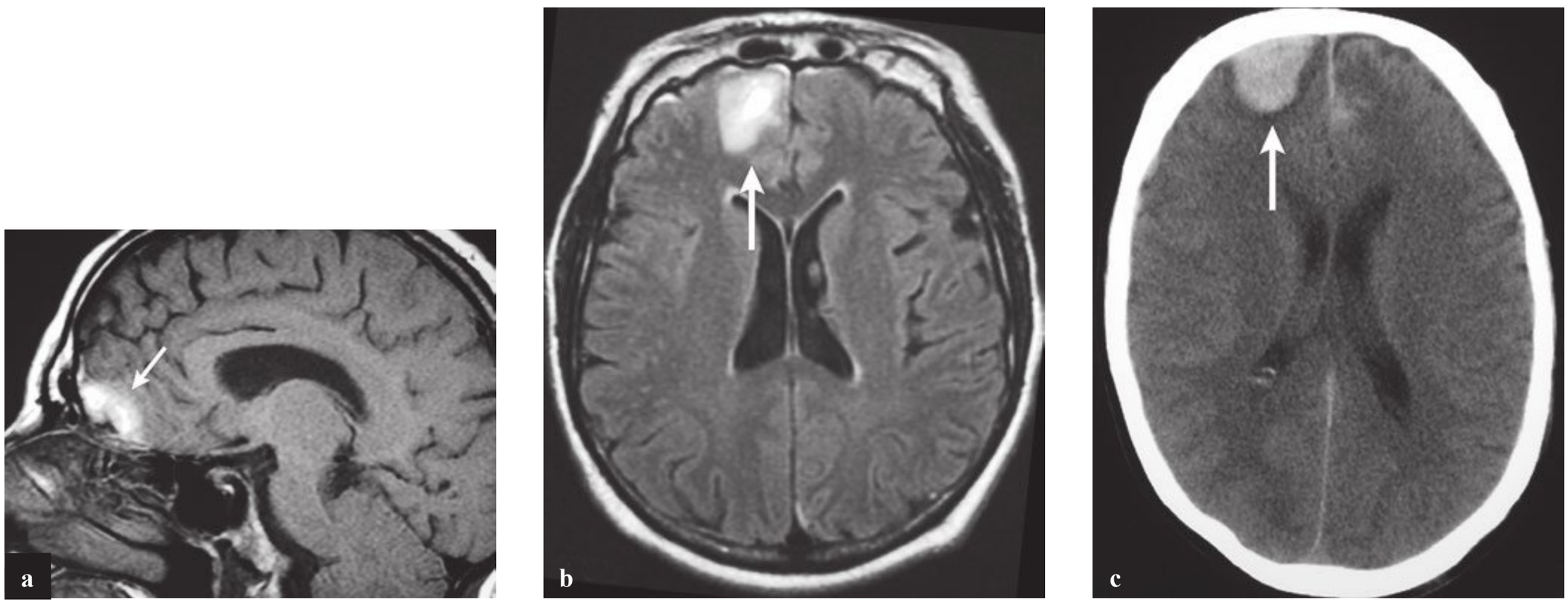

Fig. 1.103 A 60-year-old man with a cerebral contusion in the superficial portion of the right frontal lobe that has high signal on **(a)** sagittal T1-weighted imaging (arrow) and **(b)** axial FLAIR (arrow), as well as **(c)** high attenuation on axial CT (arrow).

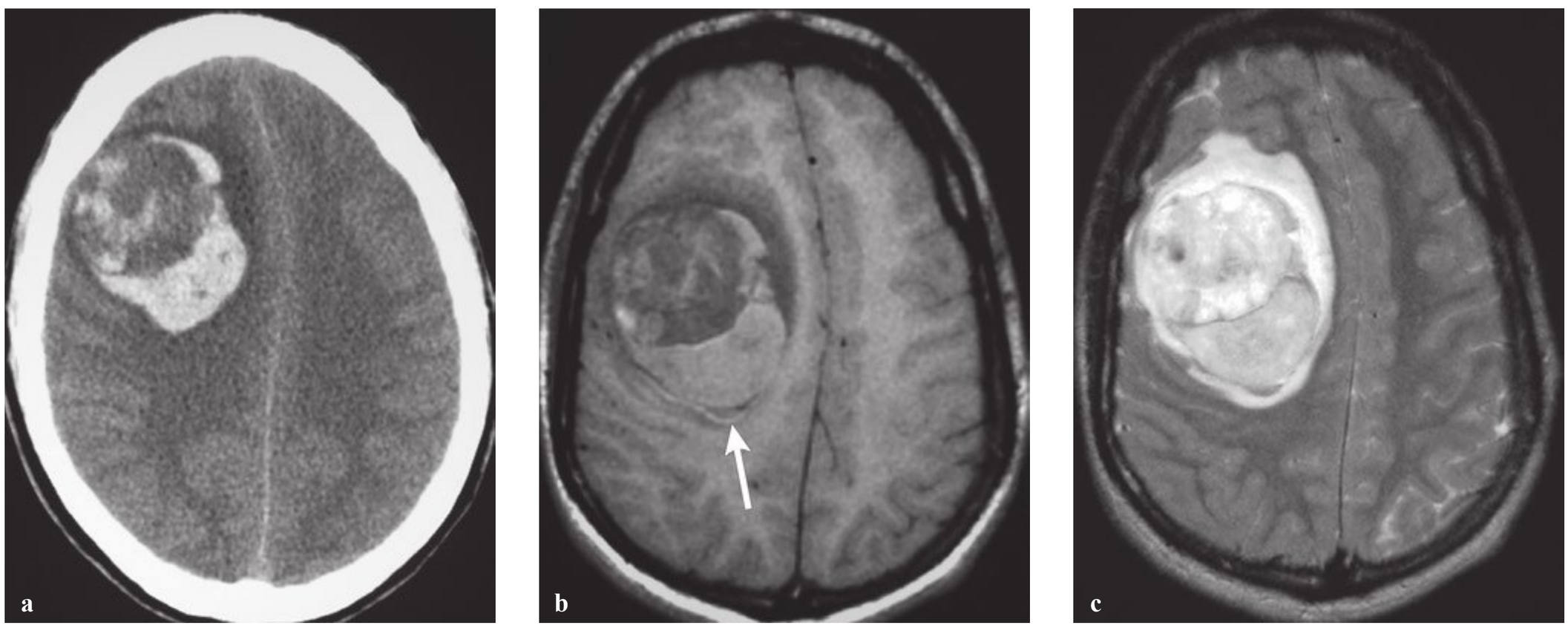

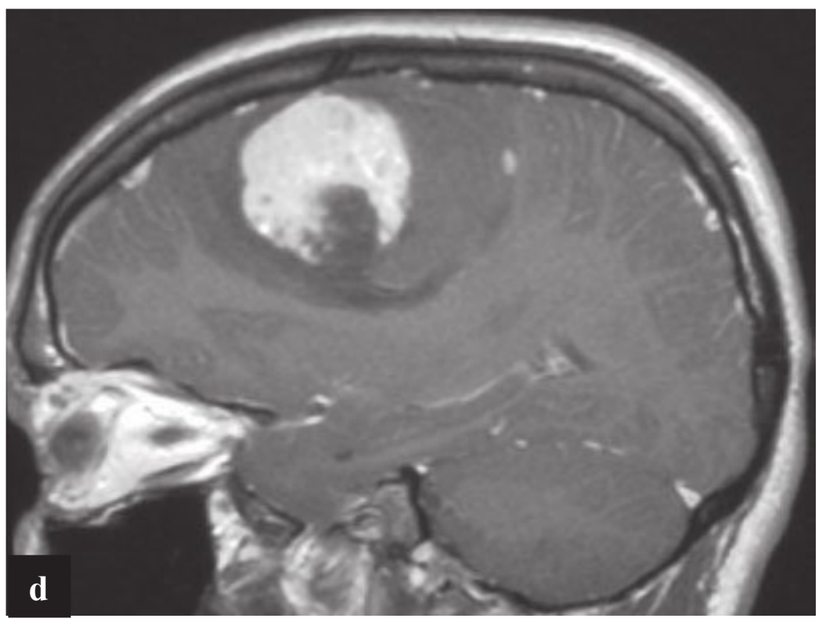

Fig. 1.104 A 16-year-old male with a metastatic lesion in the right frontal lobe from embryonal yolk sac tumor that is associated with a peripheral hyperacute hemorrhage, seen as **(a)** a high attenuation zone on axial CT, **(b)** intermediate signal (arrow) on axial T1-weighted imaging, and **(c)** heterogeneous high signal on axial T2-weighted imaging. **(d)** The tumor shows gadolinium contrast enhancement on sagittal T1-weighted imaging.

Table 1.2 (cont.) Supratentorial solitary intra-axial mass lesions

Lesions	Imaging Findings	Comments
Hemorrhage from arteriovenous malformation (AVM) (**Fig. 1.105**)	MRI: Lesions with irregular margins that can be located in the brain parenchyma—pia, dura, and/or ventricles. AVMs contain multiple, tortuous, tubular flow voids on T1- and T2-weighted images secondary to patent arteries with high blood flow, as well as thrombosed vessels with variable signal and areas of hemorrhage in various phases. Gradient echo MRI shows flow-related enhancement (high signal) in patent arteries and veins of the AVM. Magnetic resonance angiography using time-of-flight or phase-contrast techniques can provide additional detailed information about the nidus, feeding arteries, and draining veins, as well as presence of associated aneurysms. Usually not associated with mass effect unless there is recent hemorrhage or venous occlusion. CT: Lesions with irregular margins that can be located in the brain parenchyma—pia, dura, and/or ventricles. AVMs contain multiple tortuous vessels, ± calcifications. The venous portions often show contrast enhancement. Usually not associated with mass effect unless there is recent hemorrhage or venous occlusion. CT angiography can show the nidus and arterial and venous portions of the AVMs.	Supratentorial AVMs occur more frequently (80–90%) than infratentorial AVMs (10–20%). Annual risk of hemorrhage. AVMs can be sporadic, congenital, or associated with a history of trauma. Multiple AVMs can be seen in Rendu-Osler-Weber syndrome (AVMs in brain and lungs and mucosal capillary telangiectasias) and Wyburn-Mason syndrome (AVMs in brain and retina, + cutaneous nevi).

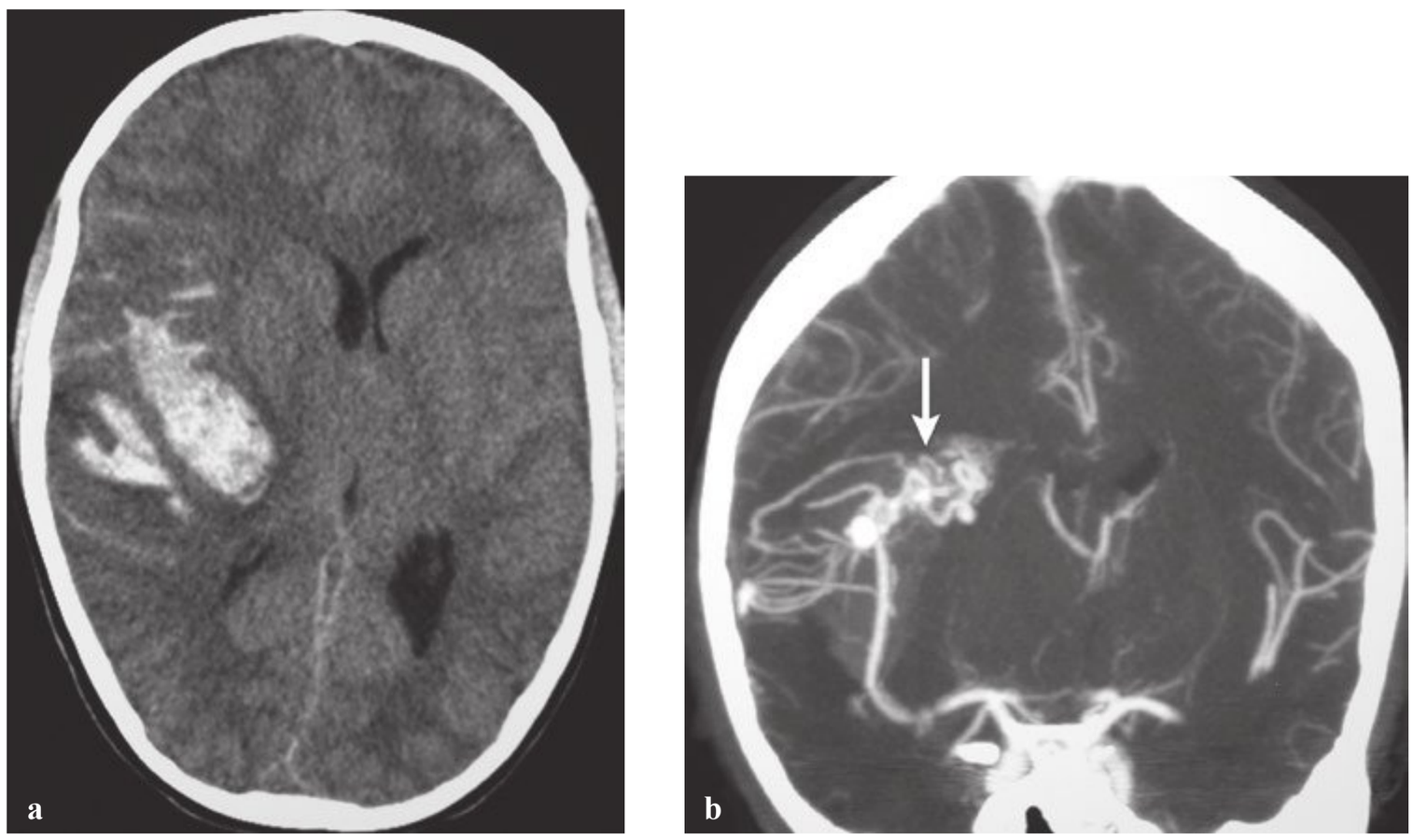

Fig. 1.105 **(a)** Axial CT shows an intra-axial hemorrhage in the right cerebral hemisphere, as well as subarachnoid blood in the sulci that resulted from **(b)** an arteriovenous malformation (arrow) seen on CTA.

Lesions	Imaging Findings	Comments
Intra-axial hemorrhage from a ruptured aneurysm (**Fig. 1.106**) Saccular aneurysm Fusiform aneurysm Dissecting aneurysms (intramural hematoma)	Saccular aneurysm Focal, well-circumscribed zone of contrast enhancement (**Fig. 1.106**). Fusiform aneurysm Tubular dilatation of involved artery. Dissecting aneurysm Initially, the involved arterial wall is thickened in a circumferential or semilunar configuration and has intermediate attenuation with luminal narrowing. Evolution of the intramural hematoma can lead to focal dilatation of the arterial wall hematoma.	Abnormal fusiform or focal saccular dilatation of artery secondary to acquired/degenerative etiology, polycystic disease, connective tissue disease, atherosclerosis, trauma, infection (mycotic), edema (oncotic), arteriovenous malformation, vasculitis, and drugs. Focal aneurysms are also referred to as saccular aneurysms, typically occur at arterial bifurcations, and are multiple in 20% of cases. The chance of rupture of a saccular aneurysm causing subarachnoid hemorrhage is related to the size of the aneurysm. Saccular aneurysms > 2.5 cm in diameter are referred to as giant aneurysms. Fusiform aneurysms are often related to atherosclerosis or collagen vascular disease (Marfan syndrome, Ehlers-Danlos syndrome, etc.). With dissecting aneurysms, hemorrhage occurs in the arterial wall from incidental or significant trauma.
Hemorrhage from cavernous malformation (**Fig. 1.107**)	MRI: Single or multiple multilobulated intra-axial lesions that have a peripheral rim or irregular zone of low signal on T2-weighted images secondary to hemosiderin, surrounding a central zone of variable signal (low, intermediate, high, or mixed) on T1- and T2-weighted images depending on ages of hemorrhagic portions. Gradient echo and magnetic susceptibility-weighted techniques are useful for detecting multiple lesions. Gadolinium contrast enhancement is usually absent, although some lesions may show mild heterogeneous enhancement. CT: Lesions have intermediate to slightly increased attenuation, ± calcifications.	Cavernous malformations are hamartomas composed of thin-walled sinusoids and blood vessels without intervening neural tissue. Can occur in many different locations. Supratentorial cavernous malformations occur more frequently than infratentorial lesions. Lesions consist of epithelium-lined vascular channels within a collagenous stroma. Zones of thrombus and remote hemorrhage with hemosiderin are often present. Dystrophic calcifications may be present. Developmental venous anomalies occur in 25% Hereditary syndromes in which multiple cavernous malformations occur are associated with mutations of the CCM1/KRIT1, CCM2/MGC4608, and CCM3 PDCD10 genes, and have a higher risk of hemorrhage (up to 5% per year) than sporadic cavernous malformations.
Venous angioma/ developmental venous anomaly	MRI: Gadolinium contrast-enhanced T1-weighted imaging shows a group of small veins in a “Medusa head” configuration that connect and drain into a slightly prominent, enhancing vein. CT: No abnormality or small, slightly hyperdense zone prior to contrast administration. Contrast enhancement seen in a slightly prominent vein draining a collection of small veins.	Considered an anomalous venous formation typically not associated with hemorrhage; usually an incidental finding, except when associated with cavernous hemangioma. Lesions consist of thin-walled venous channels within normal neural tissue. Can occur in association with cavernous malformations. Account for more than 50% of cerebrovascular malformations.

(continued on page 87)

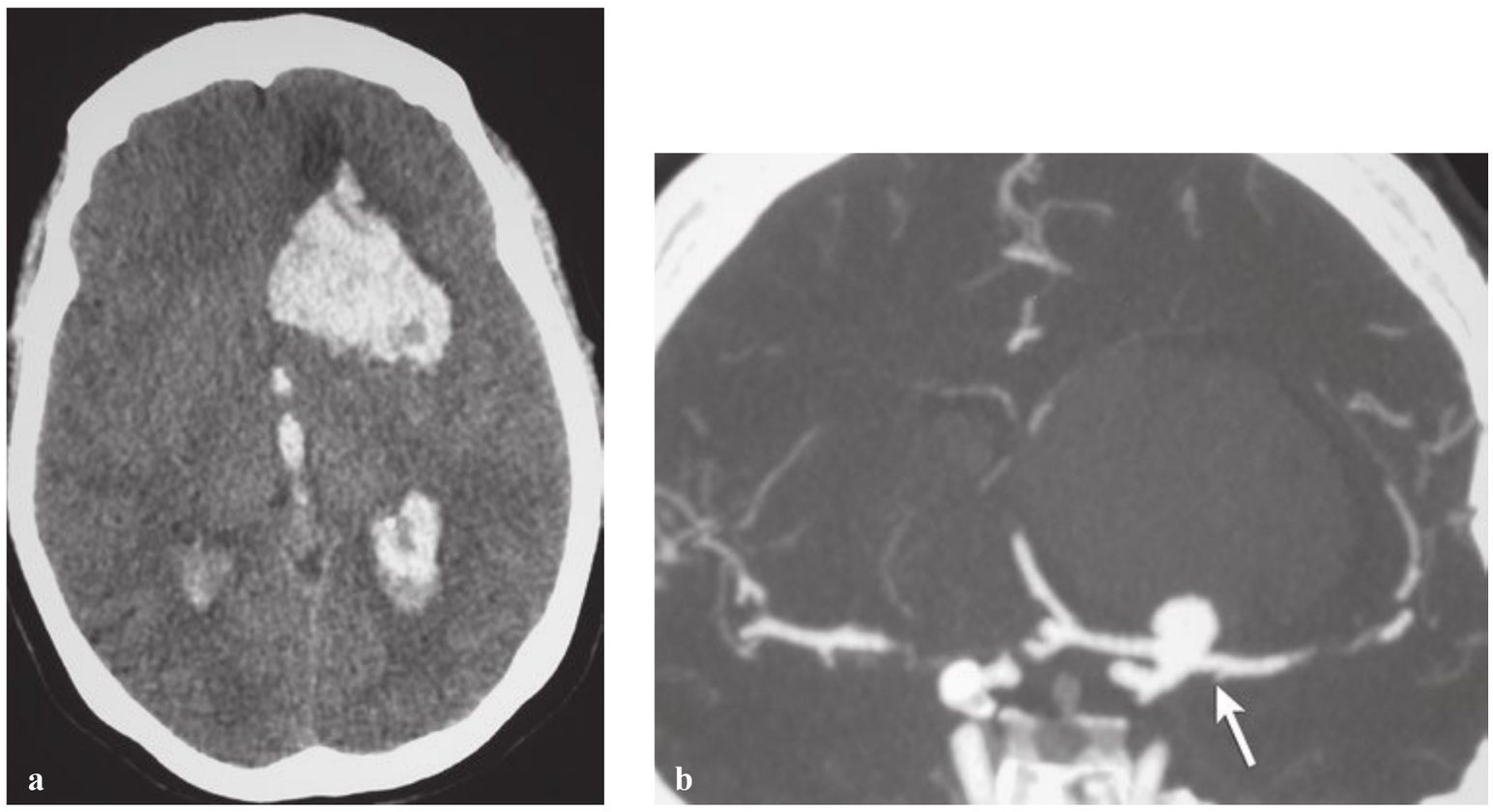

Fig. 1.106 **(a)** Axial CT shows an intra-axial hemorrhage in the left frontal lobe as well as intraventricular blood in the third and lateral ventricles that resulted from **(b)** a ruptured aneurysm (arrow) as seen on CTA in a 51-year-old woman.

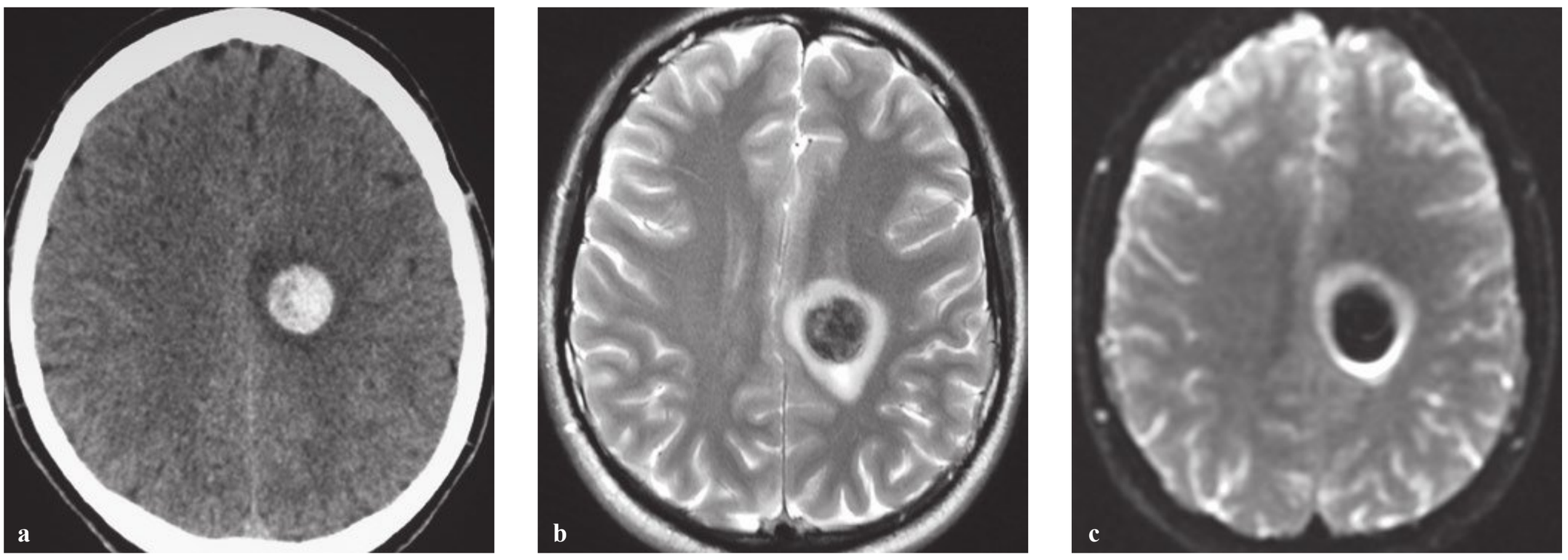

Fig. 1.107 **(a)** A 22-year-old man with recent hemorrhage from a cavernous malformation in the left cerebral hemisphere as seen on axial CT. **(b)** Axial T2-weighted imaging and **(c)** axial GRE show low signal centrally surrounded by high signal.

Table 1.2 (cont.) Supratentorial solitary intra-axial mass lesions

Lesions	Imaging Findings	Comments
Cerebral Ischemia/Infarction		
Cerebral infarction from arterial occlusion (**Fig. 1.108**)	MRI and CT features of cerebral and cerebellar infarcts depend on age of infarct relative to time of examination.	Cerebral infarcts usually result from occlusive vascular disease involving large, medium, or small arteries.

(continued on page 88)

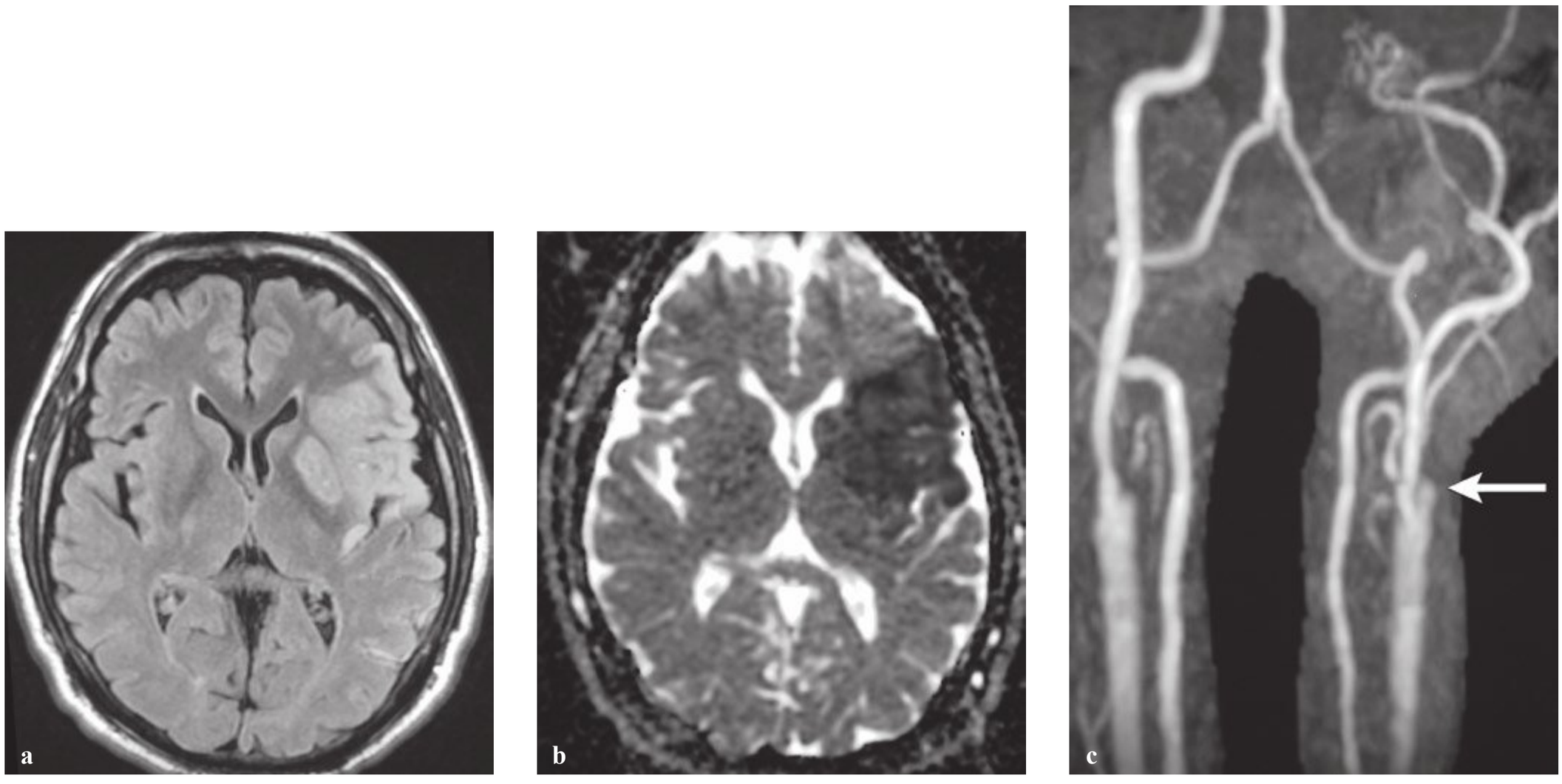

Fig. 1.108 Acute cerebral infarction in the left cerebral hemisphere in the vascular distribution of the left middle cerebral artery, seen as **(a)** high signal on axial FLAIR and **(b)** low signal on axial ADC. **(c)** Coronal MRA shows abrupt tapering and occlusion of the proximal left internal carotid artery (arrow).

Table 1.2 (cont.) Supratentorial solitary intra-axial mass lesions

Lesions	Imaging Findings	Comments
Hyperacute infarct (< 12 hours) Acute infarct (12–24 hours) Early subacute infarct (24 hours to 3 days) Late subacute infarct (4 days to 2 weeks)	Hyperacute infarct MRI: Localized edema, usually isointense signal to normal brain on T1- and T2-weighted imaging. Diffusion-weighted imaging (DWI) shows positive findings related to decreased apparent diffusion coefficients secondary to cytotoxic edema, and absence of arterial flow void or arterial enhancement in the vascular distribution of the infarct. CT: No abnormality in 50%, decreased attenuation and blurring of lentiform nuclei and hyperdense artery in remainder Acute infarct MRI: Intermediate signal on T1-weighted imaging, high signal on T2-weighted imaging and DWI, with localized edema. Signal abnormalities commonly involve the cerebral cortex, subcortical white matter, and/or basal ganglia. CT: Blurring of junction between the cerebral cortex and white matter, decreased attenuation in the basal ganglia. Early subacute infarct MRI: Low-intermediate signal on T1-weighted images, high signal on T2-weighted images and DWI, localized edema, ± hemorrhage, ± gadolinium contrast enhancement. CT: Localized swelling at sites of decreased attenuation involving gray and white matter (often wedge-shaped) with or without hemorrhage. Late subacute infarct MRI: Low-intermediate signal on T1-weighted imaging, high signal on T2-weighted imaging, edema/mass effect diminishing, ± hemorrhage, ± gadolinium contrast enhancement. High signal on DWI and low signal on ADC maps resolve ("pseudonormalize") at 10 days to 2 weeks. CT: Localized swelling increases, then decreases; low attenuation at lesion becomes more conspicuous, with or without gyral contrast enhancement.	Vascular occlusion may be secondary to atheromatous arterial disease, cardiogenic emboli, neoplastic encasement, hypercoagulable states, dissection, or congenital anomalies. Cerebral infarcts usually result from arterial occlusion involving specific vascular territories, although occasionally they are caused by metabolic disorders (mitochondrial encephalopathies, etc.) or intracranial venous occlusion—thrombophlebitis, hypercoagulable states, dehydration, etc., which do not correspond to arterial distributions.
Post-subacute infarct (2 weeks to 2 months) Remote infarct (> 2 months)	Post-subacute infarct MRI: Low-intermediate signal on T1-weighted imaging, high signal on T2-weighted imaging, edema resolves, ± hemorrhage, ± gadolinium contrast enhancement eventually declines. CT: Localized mass effect at site of low attenuation resolves, ± gyral contrast enhancement. Remote infarct MRI: Low signal on T1-weighted imaging, high signal on T2-weighted imaging, encephalomalacic changes, ± calcification, hemosiderin. CT: Zone of low attenuation associated with encephalomalacia.	

Lesions	Imaging Findings	Comments
Cerebral infarction from venous occlusion (**Fig. 1.109**)	MRI: Poorly defined intra-axial zone in the subcortical white matter that has high signal on T2-weighted images and FLAIR, + localized mass effect and restricted diffusion in acute phase, ± hemorrhage, ± gadolinium contrast enhancement. Lesions do not correspond to an arterial vascular distribution. CT: Poorly defined intra-axial zone in the subcortical white matter that has low-intermediate attenuation, + localized mass effect and restricted diffusion in acute phase, ± hemorrhage. CTA/MRA: Absent contrast enhancement on CTA and absent flow signal on MRA in the intracranial venous sinuses or large intracranial veins.	Infarction of brain tissue in the venous distribution that results from thrombosis of the corresponding vein or venous sinus secondary to venous hypertension. Occlusion of the superficial venous system (superior and inferior sagittal sinuses and cortical veins) typically causes infarction of the adjacent cerebral cortex and subcortical white matter. Venous occlusion can be related to coagulopathy (sickle-cell disease, thalassemia, etc.), dehydration, polycythemia, and medications, such as oral contraceptives.

(continued on page 90)

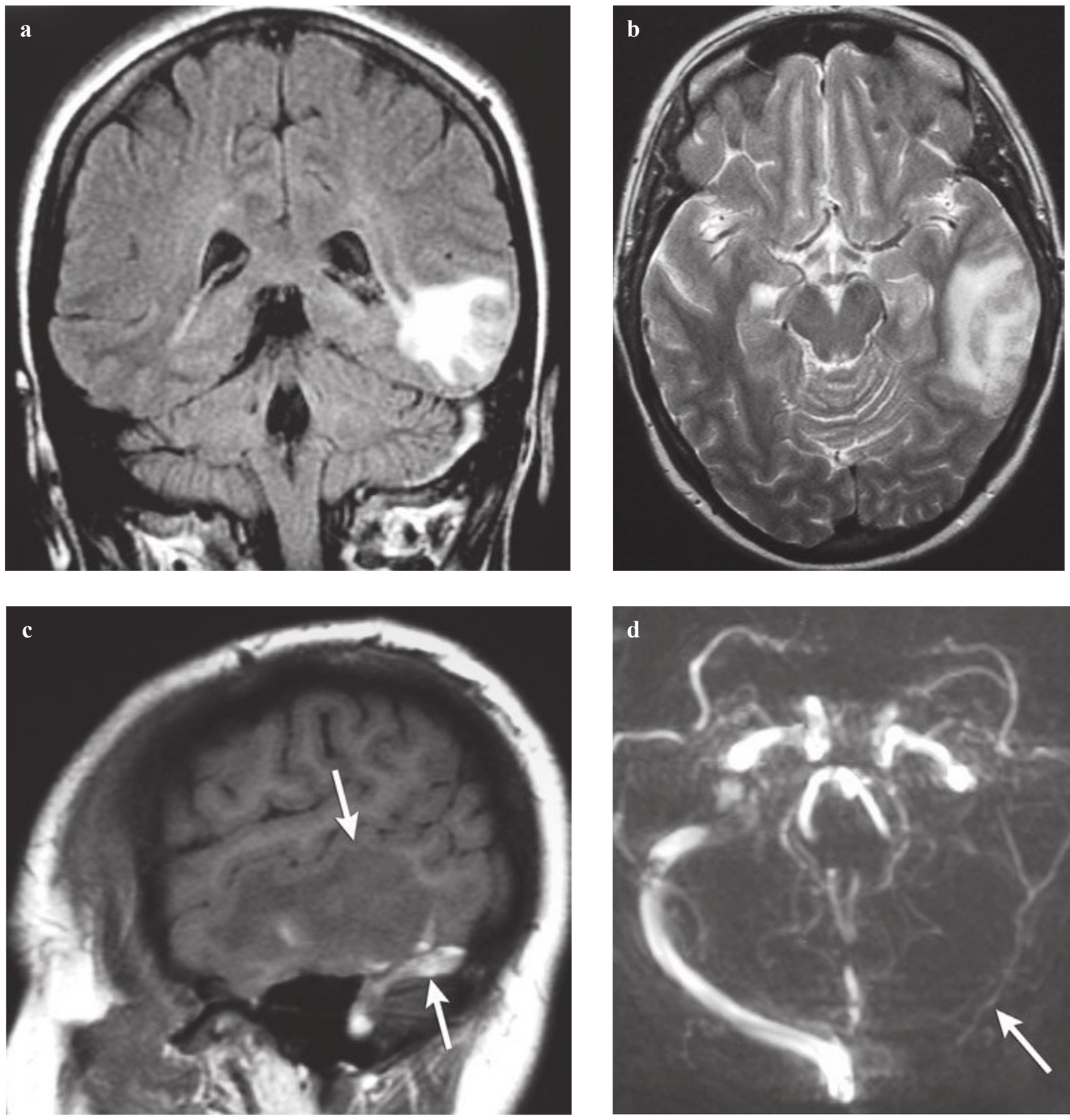

Fig. 1.109 A 33-year-old woman with cerebral infarction in the left temporal lobe from thrombosis of the left transverse venous sinus. The infarct has high signal on **(a)** coronal FLAIR and **(b)** axial T2-weighted imaging and **(c)** low-intermediate signal (upper arrow) on sagittal T1-weighted imaging. The thrombus in the left transverse venous sinus has high signal on FLAIR and sagittal T1-weighted imaging (lower arrow in **c**). **(d)** Axial 2D phase-contrast MRV shows no flow signal in the occluded left transverse venous sinus (arrow).

Table 1.2 (cont.) Supratentorial solitary intra-axial mass lesions

Lesions	Imaging Findings	Comments
Other Lesions		
Radiation necrosis (**Fig. 1.110**)	MRI: Focal lesion ± mass effect or poorly defined, intra-axial zone of low-intermediate signal on T1-weighted imaging, intermediate-high signal on T2-weighted imaging, ± gadolinium contrast enhancement involving tissue (white matter and/or gray matter) in the field of radiation treatment. Relative cerebral blood volume (rCBV) value for radiation necrosis (0.6) has been shown to be significantly lower than that for recurrent high-grade gliomas. Radiation necrosis at sites of surgically resected metastatic lesions may show a three-layer pattern on diffusion-weighted imaging consisting of an inner liquefied portion with high ADC, a middle layer with decreased ADC and without gadolinium contrast enhancement, and an outer layer with gadolinium contrast enhancement and high ADC. CT: Focal lesion ± mass effect or poorly defined zone of low-intermediate attenuation, ± contrast enhancement involving tissue (gray matter and/or white matter) in field of treatment.	Severe local tissue reaction to radiation treatment, related to doses over 65 Gy. Occurs 3–6 months to 12 months, and occasionally up to10 years, after radiation treatment. Occurrence is up to three times higher when chemotherapy is given concurrently with radiation treatment. Results from vascular endothelial injury and apoptosis leading to thrombosis, fibrinous exudates, hyalinization with luminal stenosis, and fibrinoid and vascular necrosis, as well as glial and white matter damage. May be difficult to distinguish from neoplasm. Using dynamic susceptibility contrast-enhanced perfusion MRI, $rCBV_{max}$ and $rCBV_{mean}$ values for recurrent tumor have been shown to be significantly higher than tumor necrosis, aiding in distinguishing between these two diagnoses. Similar findings have been found with perfusion CT. Perfusion MRI has been shown to be superior to ^{18}F-FDG PET and ^{11}C-methionine PET in distinguishing high-grade gliomas from radiation necrosis. Magnetic resonance hydrogen spectroscopy shows decreased N-acetylaspartate (NAA) and choline peaks at sites of radiation necrosis, whereas residual and recurrent tumor shows elevated choline peaks and choline/creatine ratio > 2.
Tumor pseudoprogression within 3 months after completion of chemoradiation	MRI: Gadolinium contrast enhancement within the tumor resection cavity and surrounding edema can be seen within the first 3 months after chemoradiation, but they eventually have progressive resolution.	Increasing contrast enhancement within the tumor resection cavity and surrounding edema can be seen in 15 to 20%of patients during the first 3 months after chemoradiation, but these findings subsequently stabilize and regress. Pseudoprogression results from transient attenuation of the blood–brain barrier. Histologic evaluation of the enhancing tissue shows no evidence of tumor. Pseudoprogression has been associated with a better treatment response and longer survival. Pseudoprogression is correlated with O-6-methylguanine-DNA methyltransferase (MGMT) activity in tumors, which is associated with positive response to radiation treatment in combination with the chemotherapeutic agent temozolomide (TMZ).
Amyloidoma (**Fig. 1.111**)	Amyloidomas can occur as solitary or multifocal lesions with ill-defined margins involving the supratentorial cerebral white matter and extending to the ventricular surface. MRI: Lesions can have low-intermediate or slightly high signal on T1-weighted imaging, and variable heterogeneous slightly high to high signal with or without low signal zones on T2-weighted imaging. Variable degrees of gadolinium contrast enhancement can be seen. Magnetic resonance spectroscopy may show decreased N-acetylaspartate (NAA) and increased choline and lactate peaks. CT: Lesions can have low, intermediate, and/or high attenuation, as well as contrast enhancement.	Amyloidosis is a disease complex that results from the extracellular deposition of insoluble eosinophilic fibrillar protein with a β-pleated configuration. Deposits of amyloid protein can occur in a systemic distribution or as localized lesions. The systemic form often results from plasma cell dyscrasias and hereditary diseases, or it is related to chronic diseases. The systemic amyloid form involving the brain can occur as cerebral amyloid angiopathy with deposits in blood vessel walls, senile plaques in Alzheimer's disease, or in spongiform encephalopathy, such as Creutzfeldt-Jakob disease and kuru. Localized amyloid deposits or amyloidomas in the brain are rare and are often not associated with an underlying disease.

(continued on page 92)

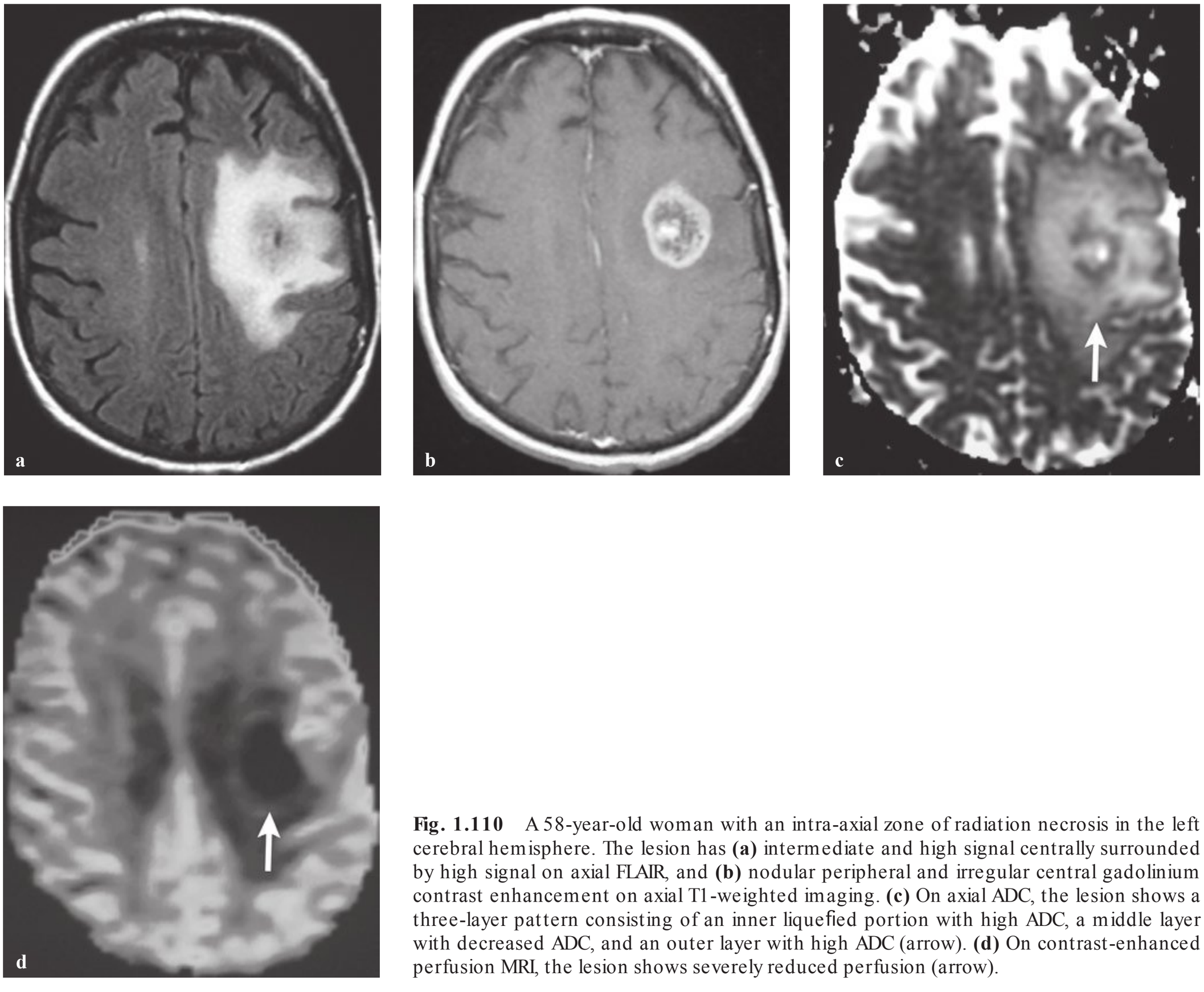

Fig. 1.110 A 58-year-old woman with an intra-axial zone of radiation necrosis in the left cerebral hemisphere. The lesion has **(a)** intermediate and high signal centrally surrounded by high signal on axial FLAIR, and **(b)** nodular peripheral and irregular central gadolinium contrast enhancement on axial T1-weighted imaging. **(c)** On axial ADC, the lesion shows a three-layer pattern consisting of an inner liquefied portion with high ADC, a middle layer with decreased ADC, and an outer layer with high ADC (arrow). **(d)** On contrast-enhanced perfusion MRI, the lesion shows severely reduced perfusion (arrow).

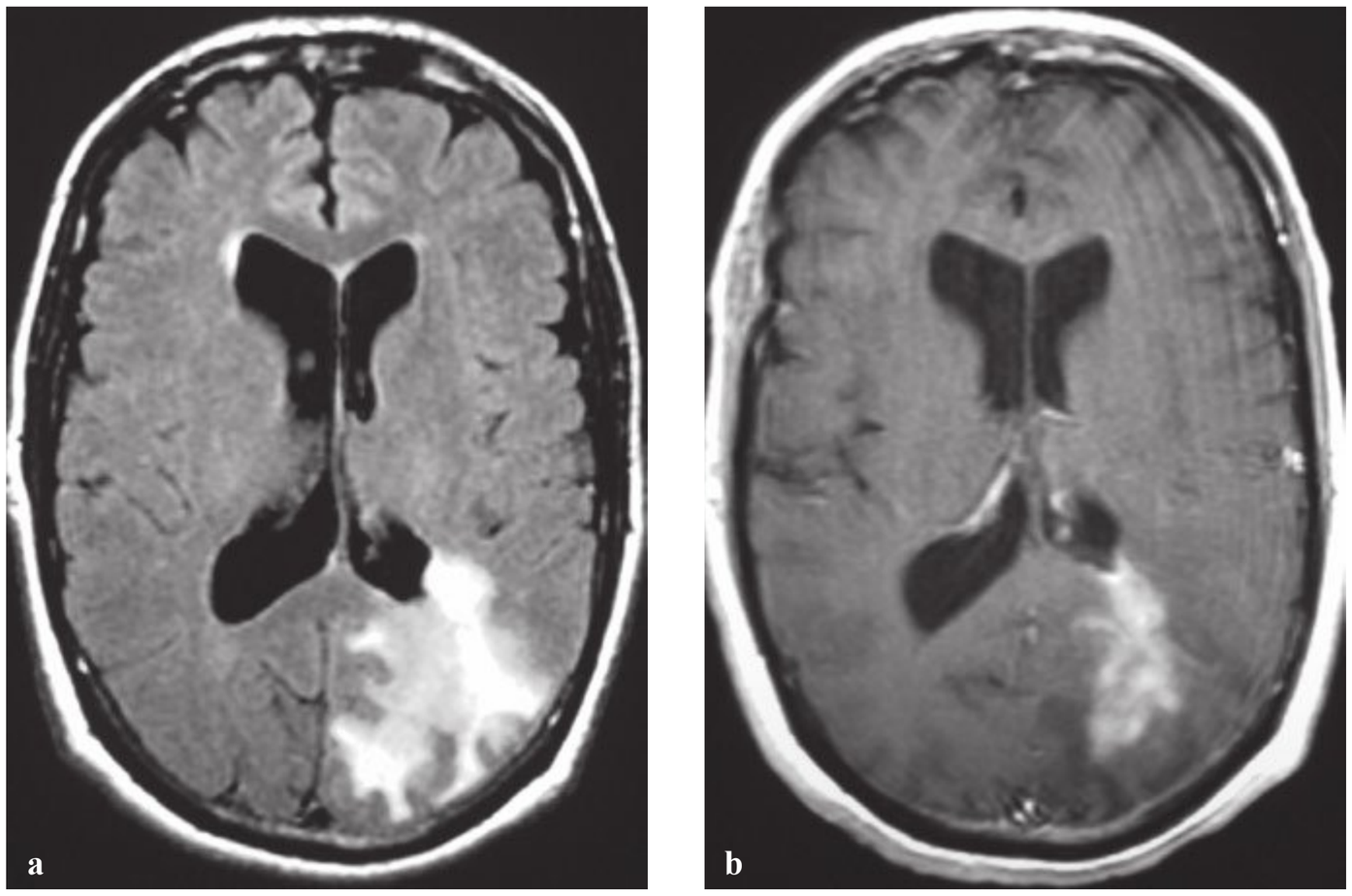

Fig. 1.111 **(a)** A 58-year-old man with an amyloidoma in the posterior cerebral hemisphere that has high signal and poorly defined margins on axial FLAIR. **(b)** The lesion has localized mass effect, with compression of the occipital horn of the left lateral ventricle, and shows gadolinium contrast enhancement on axial T1-weighted imaging.

Table 1.2 (cont.) Supratentorial solitary intra-axial mass lesions

Lesions	Imaging Findings	Comments
Lipoma (**Fig. 1.112**)	MRI: Signal isointense to subcutaneous fat on T1-weighted imaging (high signal), and on T2-weighted imaging, signal suppression occurs with frequency-selective fat saturation techniques or with a short time to inversion recovery (STIR) method. Typically, there is no gadolinium contrast enhancement or peripheral edema. Lipomas can be tubulonodular or curvilinear. CT: Lipomas have attenuation equal to fat (–40 HU to –100 HU), ± calcifications or ossifications.	Lipomas are rare, benign fatty lesions within the subarachnoid space resulting from congenital malformation involving differentiation of the menix primitive, often are located in or near the midline, and may contain calcifications and/or traversing blood vessels. Lipomas account for less than 0.1%of all intracranial tumors. They can occur in many locations: corpus callosum, pericallosum, cerebellopontine angle cistern, quadrigeminal cistern, interpeduncular cistern, tectal plate, sylvian fissure, interhemispheric fissure, choroid plexus, and intercerebellar fissure. They occur in children and adults 5 months to 76 years old; mean age = 38.6 years. Can be associated with dysgenesis of the corpus callosum. Lipomas are usually asymptomatic except for an increased incidence of intracranial aneurysms, seizures with lipomas in the sylvian fissure, and hearing loss with cerebellopontine angle lipomas > 8 mm.
Neuroepithelial/ neuroglial cyst (**Fig. 1.113**)	MRI: Well-circumscribed unilocular cysts with low signal on T1-weighted images, FLAIR, and diffusion-weighted imaging (DWI), high signal on T2-weighted and ADC images, thin walls, and no gadolinium contrast enhancement or peripheral edema. CT: Well-circumscribed cysts with low attenuation, no contrast enhancement.	Rare, congenital, benign intra-axial lesions containing CSF that result from sequestered embryonic cells within developing white matter. Represent < 1%of intracranial cysts and are typically asymptomatic. Cyst walls contain cells with histopathologic features of low cuboidal epithelium similar to choroid plexus or columnar epithelial cells similar to ependyma. Neuroepithelial cysts can occur anywhere within the brain but are most common in the frontal lobes.
Porencephalic cyst (**Fig. 1.114**)	MRI: Irregular, relatively well-circumscribed zone with low signal on T1-weighted imaging, FLAIR, and diffusion-weighted imaging (DWI), and high signal on T2-weighted imaging similar to CSF, surrounded by poorly defined thin zone of high T2 signal in adjacent brain tissue, no gadolinium contrast enhancement or peripheral edema. CT: Irregular, relatively well-circumscribed zone with low attenuation similar to CSF and no contrast enhancement or peripheral edema.	Represent remote sites of brain injury (trauma, infarction, infection, hemorrhage) with evolution into a cystic zone with CSF MRI signal characteristics, surrounded by gliosis in adjacent brain parenchyma. Gliosis (high T2 signal) allows differentiation from schizencephaly.

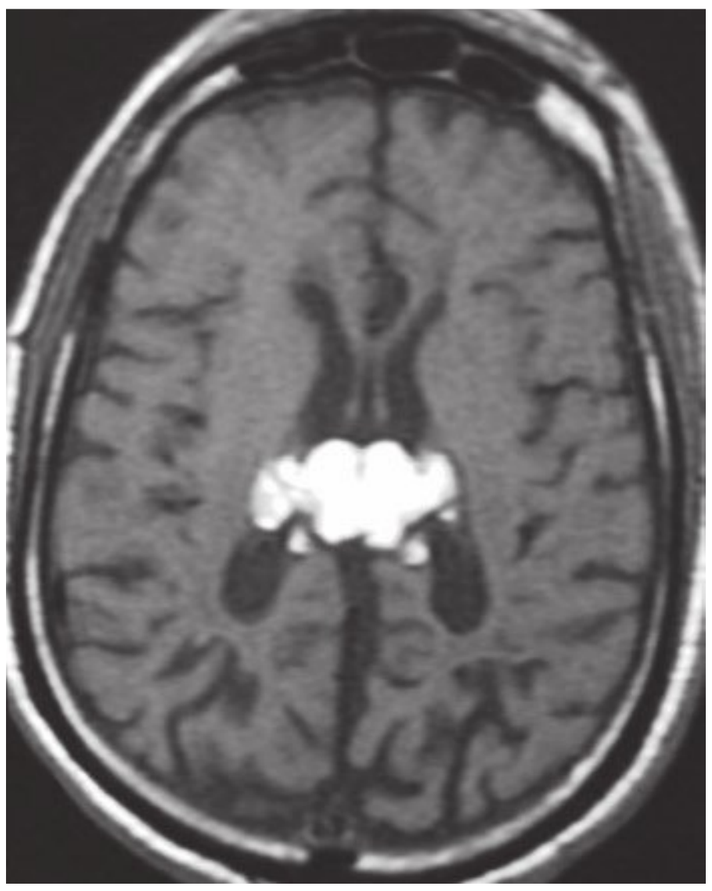

Fig. 1.112 A 62-year-old man with dysgenesis of the corpus callosum associated with a midline lipoma that has high signal on axial T1-weighted imaging.

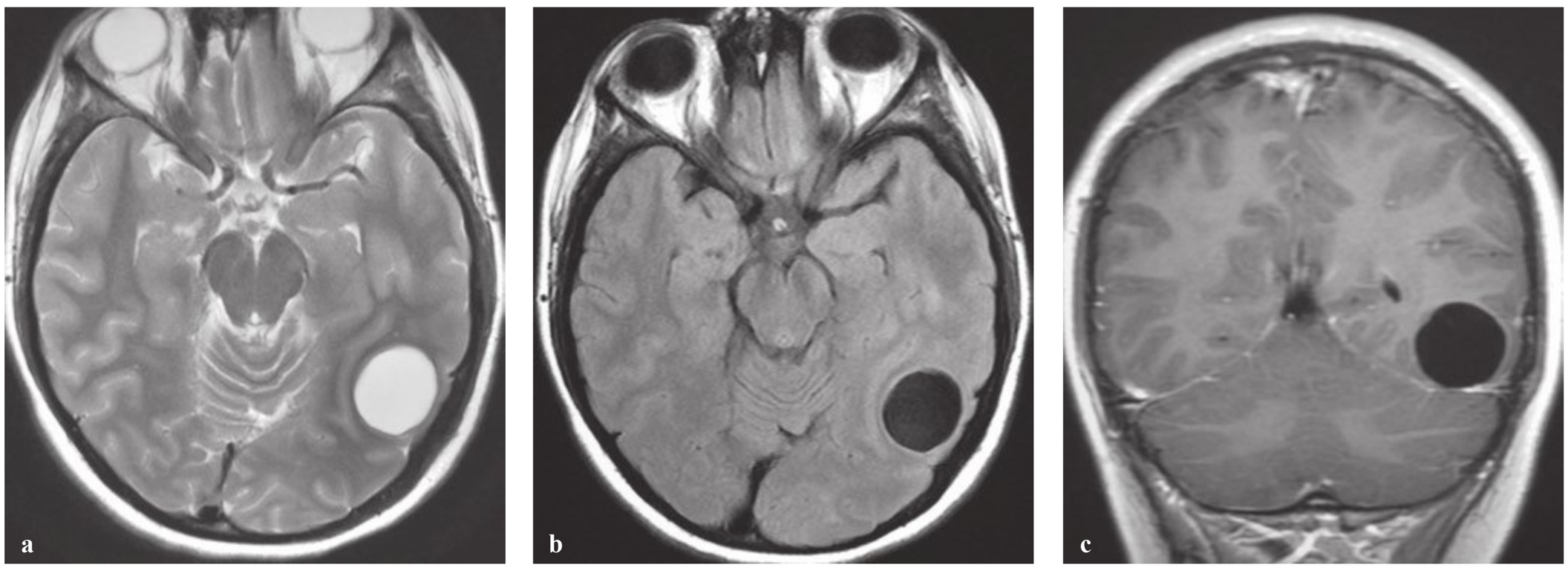

Fig. 1.113 A 20-year-old woman with a neuroepithelial cyst in the posterior left temporal lobe. The cyst has **(a)** high signal on axial T2-weighted imaging, and low signal on **(b)** axial FLAIR and **(c)** coronal postcontrast T1-weighted imaging.

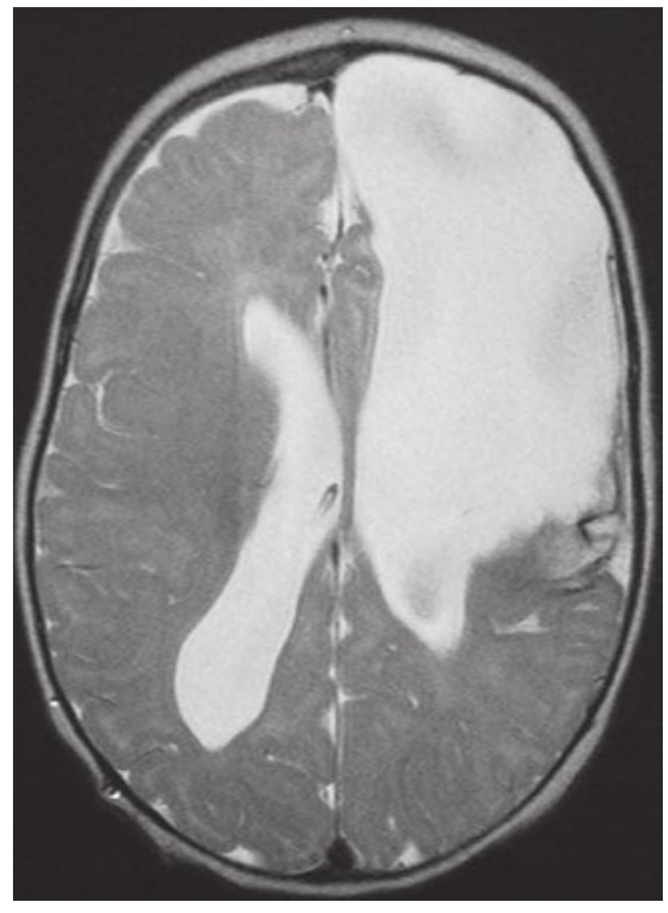

Fig. 1.114 A 6-month-old female with a large porencephalic cyst in the left frontal lobe that communicates with the frontal horn of the left lateral ventricle on axial T2-weighted imaging.

Table 1.3 Solitary intra-axial lesions in the posterior cranial fossa (infratentorial)

- Neoplasms: Intra-axial Lesions
  - Pilocytic astrocytoma
  - Diffuse astrocytoma
  - Gliomatosis cerebri
  - Anaplastic astrocytoma
  - Glioblastoma multiforme
  - Oligodendroglioma
  - Oligoastrocytoma
  - Ependymoma
  - Subependymoma
  - Ganglioglioma
  - Gangliocytoma
  - Dysplastic cerebellar gangliocytoma (Lhermitte-Duclos disease)
  - Medulloblastoma (PNET)
  - Atypical teratoid/rhabdoid tumors
  - Metastatic lesion
  - Lymphoma
  - Leukemia (myeloid sarcoma, granulocytic sarcoma, chloroma)
  - Hemangioblastoma
  - Neurofibromatosis type 1 (von Recklinghausen disease)
  - Hamartoma (tuberous sclerosis)
- Inflammatory Lesions: Infectious
  - Pyogenic brain abscess
  - Tuberculoma
  - Fungal brain infection
  - Encephalitis
  - Acute cerebellitis
- Parasitic Brain Lesions
  - Toxoplasmosis
  - Cysticercosis
  - Hydatid cyst
  - Echinococcus granulosus
  - Echinococcus multilocularis
- Inflammatory Lesions: Noninfectious
  - Demyelinating disease: multiple sclerosis, acute disseminated encephalomyelitis
  - Chronic lymphocytic infiltration with pontine perivascular enhancement responsive to steroids (CLIPPERS)
  - Neurosarcoid
- Hemorrhage and Vascular Lesions
  - Cerebellar hemorrhage
  - Cerebellar contusion
  - Hemorrhagic metastatic tumor
- Vascular
  - Hemorrhage from intracranial aneurysm
  - Saccular aneurysm
  - Fusiform aneurysm
  - Dissecting aneurysm (intramural hematoma)
  - Hemorrhage from arteriovenous malformation (AVM)
  - Cavernous hemangioma/malformation
  - Venous angioma/developmental venous anomaly
  - Capillary telangiectasia
- Cerebellar Ischemia/Infarction
  - Cerebellar/brainstem infarction
- Other Lesions
  - Central pontine myelinolysis/osmotic myelinolysis
  - Hypertensive encephalopathy (posterior reversible encephalopathy syndrome/PRES)
  - Radiation injury/necrosis
  - Lipoma

Table 1.3 Solitary intra-axial lesions in the posterior cranial fossa (infratentorial)

Lesions	Imaging Findings	Comments
Neoplasms: Intra-axial Lesions		
Pilocytic astrocytoma (**Fig. 1.115**)	MRI: Solid/cystic focal lesion with low-intermediate signal on T1-weighted images, high signal on T2-weighted images and FLAIR, usually showing gadolinium contrast enhancement. Large cyst with enhancing mural nodule seen in 46%. Lesions commonly located in cerebellum, hypothalamus, optic chiasm, adjacent to third or fourth ventricle, and brainstem. Some (30%) can have more aggressive MRI features, such as inhomogeneous gadolinium contrast enhancement, central necrotic zones, and irregular margins. Diffusion-weighted imaging (DWI): Usually no evidence of restricted diffusion. Diffusion tensor imaging (DTI) can show tumor displacement of cortical spinal tracts. Magnetic resonance spectroscopy: Although these are low-grade tumors, a paradoxic pattern associated with more aggressive tumors—elevated choline/N-acetylaspartate (NAA) and lactate levels—may be seen. CT: Solid/cystic focal lesion with low-intermediate attenuation, usually with prominent contrast enhancement.	Most common glioma in children and accounts for 6% of all gliomas and 30% of all posterior fossa neoplasms in children. Slow-growing cystic-solid WHO grade I astrocytoma with biphasic pattern of compacted bipolar cells, Rosenthal fibers, multipolar cells, microcysts, and eosinophilic granular bodies. Associated with BRAF mutations involving the MAPK signaling pathway. Usually lack IDH mutations. Immunoreactive to glial fibrillary acidic protein (GFAP) and apolipoprotein D. Can occur in cerebrum, cerebellum, brainstem, and optic chiasm. The majority (67%) occur in the cerebellum of children, usually with a favorable prognosis if totally resected. Increased occurrence in patients with neurofibromatosis type 1 (NF1). Leptomeningeal tumor dissemination is rare (< 3%).

(continued on page 96)

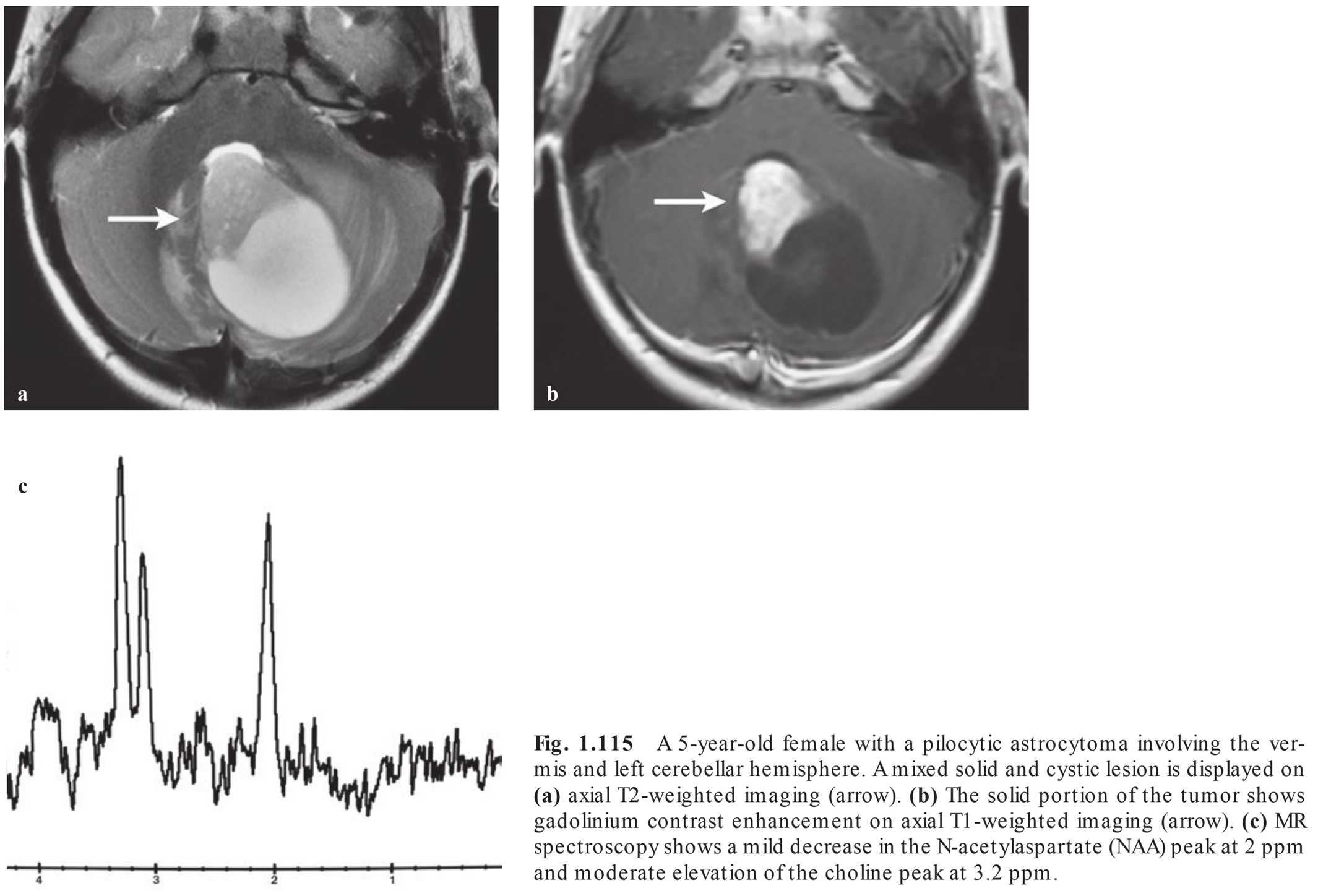

Fig. 1.115 A 5-year-old female with a pilocytic astrocytoma involving the vermis and left cerebellar hemisphere. A mixed solid and cystic lesion is displayed on **(a)** axial T2-weighted imaging (arrow). **(b)** The solid portion of the tumor shows gadolinium contrast enhancement on axial T1-weighted imaging (arrow). **(c)** MR spectroscopy shows a mild decrease in the N-acetylaspartate (NAA) peak at 2 ppm and moderate elevation of the choline peak at 3.2 ppm.

Table 1.3 (cont.) Solitary intra-axial lesions in the posterior cranial fossa (infratentorial)

Lesions	Imaging Findings	Comments
Diffuse astrocytoma (**Fig. 1.116** and **Fig. 1.117**)	MRI: Intra-axial lesion with slightly ill-defined margins or diffuse mass lesion in white matter or brainstem with low-intermediate signal on T1-weighted imaging, high signal on T2-weighted imaging, ± mild gadolinium contrast enhancement. Minimal associated mass effect. Diffusion-weighted imaging: Tumors typically do not show restricted diffusion. CT: Focal or diffuse mass lesion usually located in white matter or brainstem with low-intermediate attenuation, ± mild contrast enhancement. Minimal associated mass effect.	Low-grade astrocytomas (WHO grade II) that account for 10 to 15% of astrocytic brain tumors. Often occur in children and adults (20–40 years old). Can also occur in older adults. Brainstem gliomas usually occur in children less than 10 years old. Tumors are comprised of well-differentiated fibrillary or gemistocytic neoplastic astrocytes. Can occur in the cerebellum or brainstem. Associated with TP53, isocitrate dehydrogenase-IDH1 and IDH2, and telomere maintenance protein-ATRX mutations. Mean survival is 6 to 8 years, and tumor may undergo malignant progression to anaplastic astrocytoma or glioblastoma. Tumors with IDH mutations have a better prognosis than those without. Patients with neurofibromatosis type 1 (NF1) have an increased incidence of brainstem gliomas involving the medulla.
Gliomatosis cerebri	MRI: Infiltrative lesion in the cerebral white matter with poorly defined margins, low-intermediate signal on T1-weighted imaging, high signal on T2-weighted imaging and FLAIR, usually minimal or no gadolinium contrast enhancement, and decreased relative cerebral blood volume (rCBV). Magnetic resonance spectroscopy shows elevated choline/creatine (Cho/Cr) and Cho/NAA ratios at sites with abnormal high signal on T2-weighted imaging. CT: Infiltrative lesion with low-intermediate attenuation. Usually no contrast enhancement until late in disease.	Diffusely infiltrating astrocytoma (WHO grade III) that often involves at least three cerebral lobes, including the basal nuclei. Can involve the cerebellum and brainstem. Peak age of occurrence between 40 and 50 years. Tumor consists of infiltrating small neoplastic glial cells with elongated fusiform nuclei as well as larger neoplastic cells with pleomorphic nuclei. Imaging appearance may be more prognostic than histologic grade, and there is an approximate 2-year survival.
Anaplastic astrocytoma (**Fig. 1.118**)	MRI: Often irregularly marginated lesion located in white matter, with low-intermediate signal on T1-weighted imaging, high signal on T2-weighted imaging, ± gadolinium contrast enhancement. Tumors can have elevated relative cerebral blood volume (rCBV). Diffusion-weighted imaging: Tumors typically do not show restricted diffusion. Magnetic resonance spectroscopy: Tumors show decreased N-acetylaspartate (NAA) and high levels of choline. CT: Irregularly marginated mass lesion with mixed low and intermediate attenuation, ± hemorrhage, prominent heterogeneous contrast enhancement, and peripheral edema. Can cross corpus callosum.	Malignant astrocytic tumor (WHO grade III) between diffuse astrocytoma and glioblastoma multiforme. Malignant astrocytes have nuclear atypia and mitotic activity. K_i-67 /MIB-1 proliferation index ranges from 5 to 10% Can progress to glioblastoma. Approximate 2-year survival. Promotor methylation inactivates the effects of the DNA repair enzyme MGMT enabling improved tumor response to alkylating chemotherapy agents. Patients with IDH mutations as well as those who have MGMT promotor methylation have improved responses to chemotherapy.

(continued on page 98)

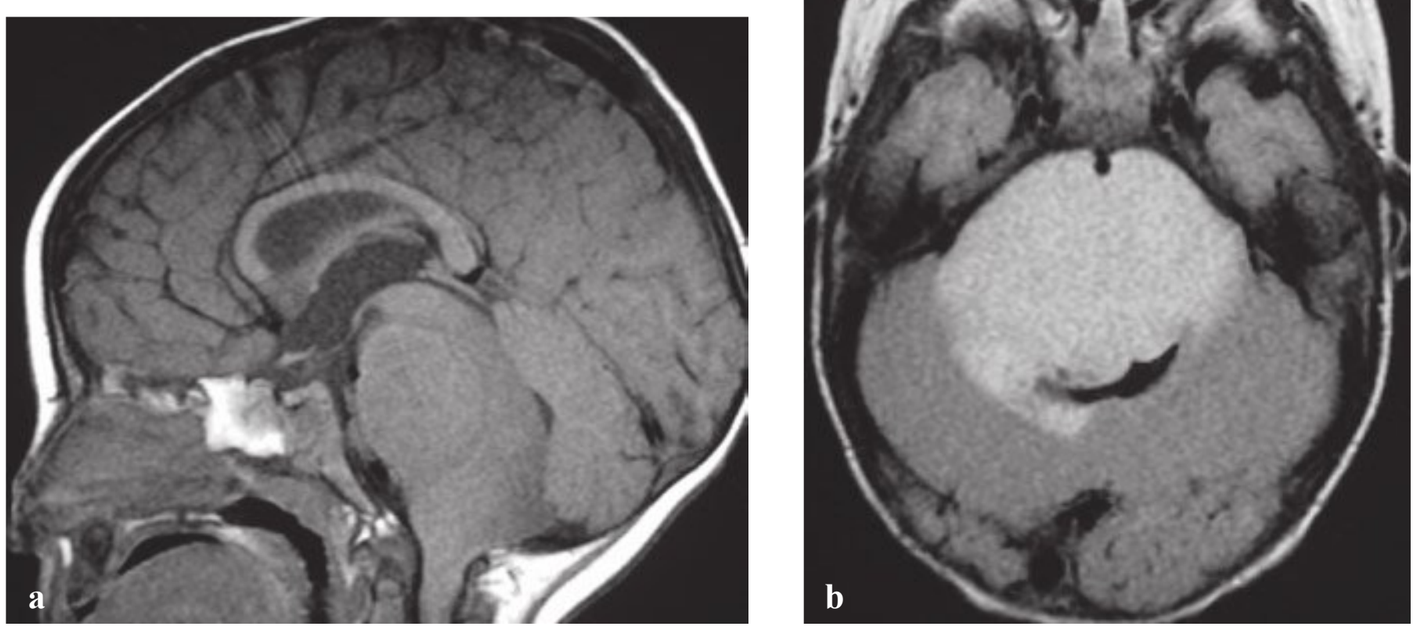

Fig. 1.116 An 18-month-old male with a diffuse astrocytoma in the pons that has **(a)** intermediate signal on sagittal T1-weighted imaging and **(b)** high signal on axial FLAIR. The tumor enlarges the pons and compresses the fourth ventricle.

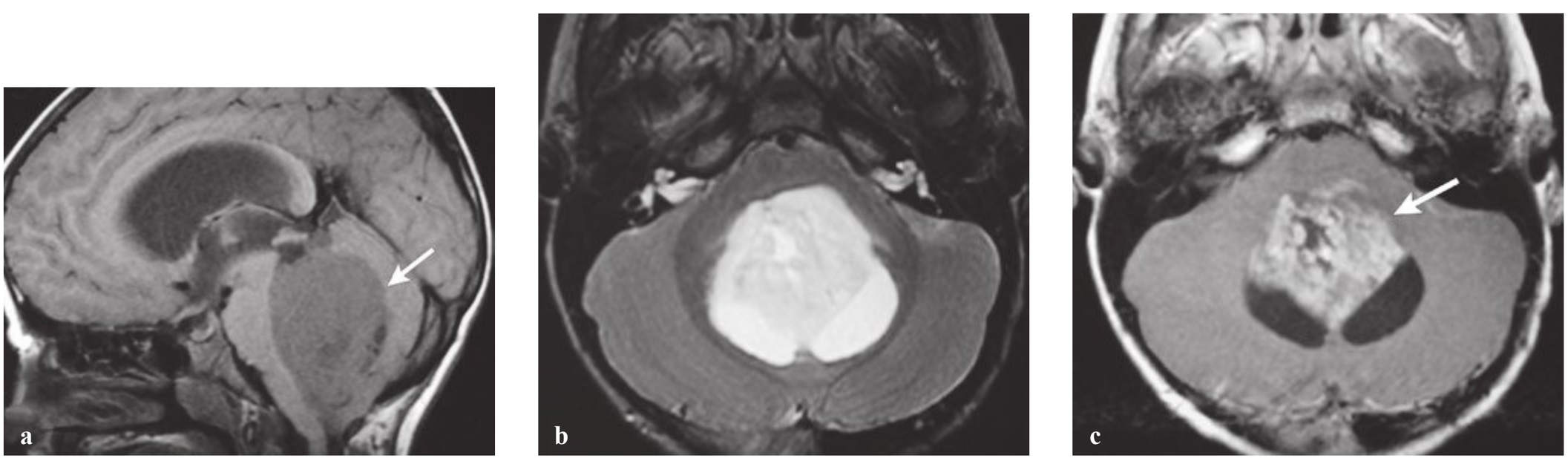

Fig. 1.117 A 5-year-old male with a diffuse astrocytoma in the vermis that has **(a)** low-intermediate signal on sagittal T1-weighted imaging (arrow) and **(b)** high signal on axial T2-weighted imaging. **(c)** The tumor show heterogeneous gadolinium contrast enhancement on axial T1-weighted imaging (arrow).

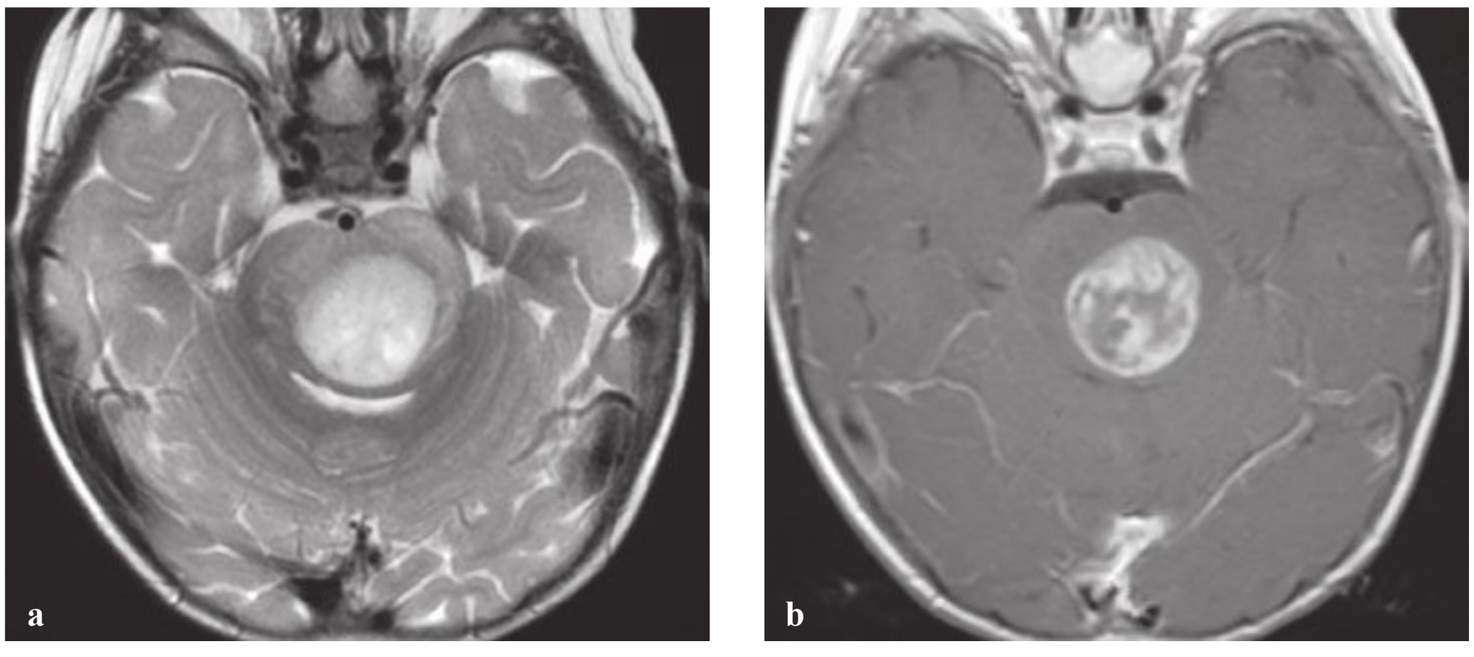

Fig. 1.118 (a) A 15-month-old female with an anaplastic astrocytoma that has high signal on axial T2-weighted imaging with surrounding edema. **(b)** The tumor shows heterogeneous gadolinium contrast enhancement on axial T1-weighted imaging and has mass effect compressing the fourth ventricle.

Table 1.3 (cont.) Solitary intra-axial lesions in the posterior cranial fossa (infratentorial)

Lesions	Imaging Findings	Comments
Glioblastoma multiforme (**Fig. 1.119**)	MRI: Irregularly and poorly marginated mass lesion with necrosis or cyst, mixed signal on T1-weighted imaging, heterogeneous high signal on T2-weighted imaging, ± hemorrhage, prominent heterogeneous gadolinium contrast enhancement. Increased relative cerebral blood volume (rCBV) is associated with high-grade gliomas and tumor-induced angiogenesis. Other findings include peripheral edema and tumor extension across the corpus callosum. Diffusion-weighted imaging: Tumors typically do not show restricted diffusion. Magnetic resonance spectroscopy shows decreased N-acetylaspartate (NAA) and high levels of choline. CT: Irregularly marginated mass lesion with necrosis or cyst, mixed low and intermediate attenuation, ± hemorrhage, prominent heterogeneous contrast enhancement, and peripheral edema. Can cross corpus callosum.	Most common primary CNS tumor (WHO grade IV), glioblastoma multiforme accounts for 15% of intracranial tumors and up to 75% of astrocytic neoplasms. Incidence is 3 per 100,000. Most patients are over 50 years old. These highly malignant astrocytic neoplasms have nuclear atypia, with mitotic activity, cellular pleomorphism, necrosis, microvascular proliferation, and invasion. K_i-67 /MIB-1 proliferation index ranges from 15 to 20% Associated with mutations involving RTK/phosphatase–PTEN/PI3K signal pathway, TERT, and p53 and Rb1 tumor suppressor genes. Promotor methylation resulting in inactivation of the MGMT DNA repair enzyme enables improved malignant tumor response to chemotherapy in patients lacking IDH mutations. The extent of lesion is underestimated by MRI. Survival is often < 1 year. Patients with secondary type glioblastoma who have IDH mutations can have a better response to chemotherapy and prognosis than those without.
Oligodendroglioma (**Fig. 1.120**)	MRI: Circumscribed lesion with mixed low-intermediate signal on T1-weighted imaging and mixed intermediate-high signal on T2-weighted imaging, areas of signal void at sites of clumplike calcification, and heterogeneous gadolinium contrast enhancement. Involves white matter and cerebral cortex. Relative cerebral blood volume (rCBV) is often elevated, and the tumor can cause chronic erosion of the inner table of calvarium. Diffusion-weighted imaging: Usually no restricted diffusion. Magnetic resonance spectroscopy: Can show elevated choline and reduced N-acetylaspartate (NAA). CT: Circumscribed lesion with mixed low-intermediate attenuation, sites of clumplike calcification (up to 40%), and heterogeneous contrast enhancement. Involves white matter and cerebral cortex and can cause chronic erosion of the inner table of calvarium.	Accounts for 2.5% of primary brain tumors and 6% of all gliomas. Incidence of 3 to 4 per 100,000. Usually occurs in adults, with peak age between 40 and 45 years. These diffusely infiltrating, well-differentiated gliomas (WHO grade II) are comprised of neoplastic monomorphic cells with round nuclei, resembling oligodendrocytes. The majority (85%) are supratentorial. Associated with translocation involving chromosomes 1 and 19 [t(1,19) (q10;p10)], deletions of chromosome arms 1p and 19q, and IDH mutations. Oligodendrogliomas typically lack ATRX mutations allowing distinction from fibrillary and diffuse astrocytomas. If the tumor is low grade, 5-year survival is 75%; higher-grade lesions have a worse prognosis.
Oligoastrocytoma	MRI: Irregularly marginated mass lesion with low-intermediate signal on T1-weighted imaging, heterogeneous high signal on T2-weighted imaging, and heterogeneous gadolinium contrast enhancement in half of cases. CT: Irregularly marginated mass lesion with low-intermediate attenuation and heterogeneous contrast enhancement in half of cases.	Diffusely infiltrating glioma (WHO grade II) comprised of both neoplastic astrocytes and oligodendrocytes. Recent research suggests that oligoastrocytomas can be categorized as astrocytomas when IDH and ATRX mutations are present, or oligodendrogliomas when IDH mutations occur as well as 1p/19q codeletions. Median age between 35 and 45 years, and tumor usually occurs in cerebral hemispheres. Annual incidence is 0.1 per 100,000. Median survival is 6.3 years, 5-year survival is 58%, and 10-year survival is 32%

(continued on page 100)

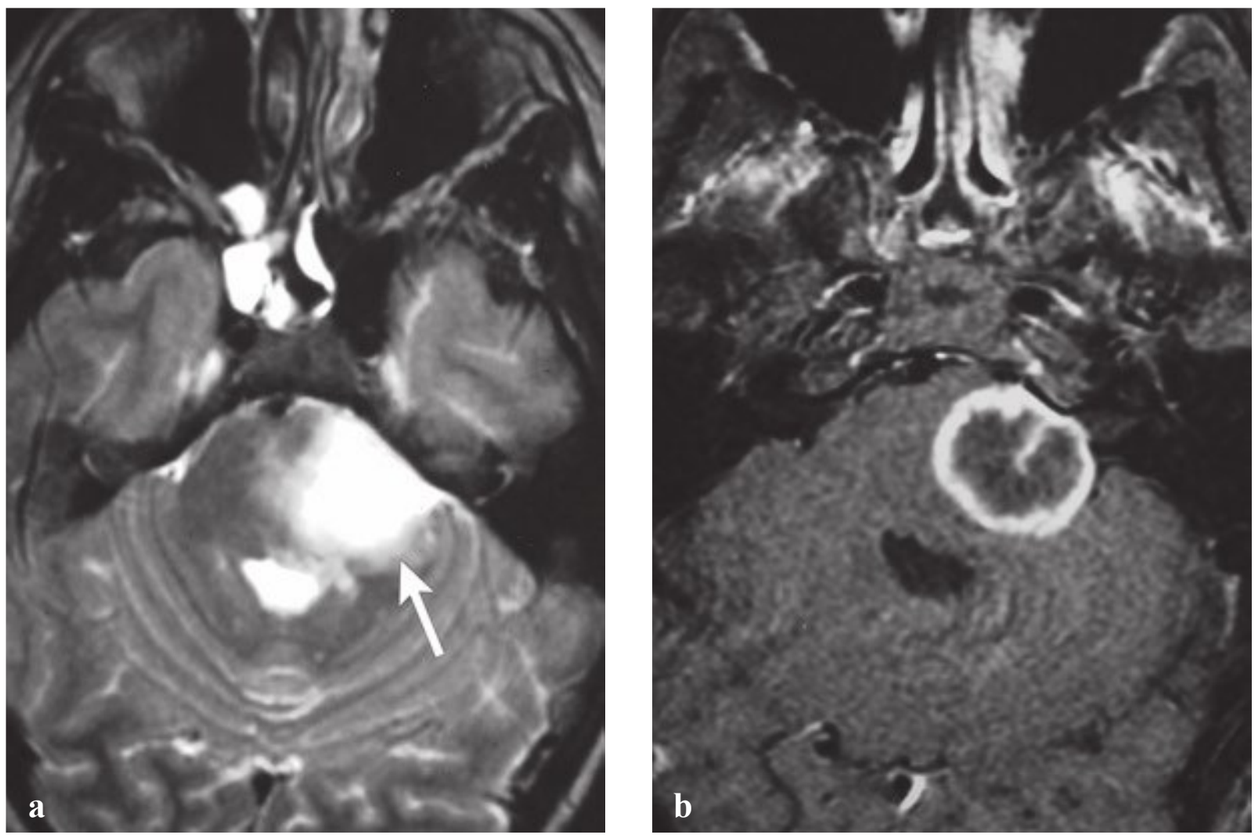

Fig. 1.119 An 11-year-old male with a glioblastoma multiforme in the left side of the pons that **(a)** has heterogeneous mostly high signal on axial T2-weighted imaging (arrow) and **(b)** shows irregular, peripheral, ring-shaped gadolinium contrast enhancement on axial T1-weighted imaging.

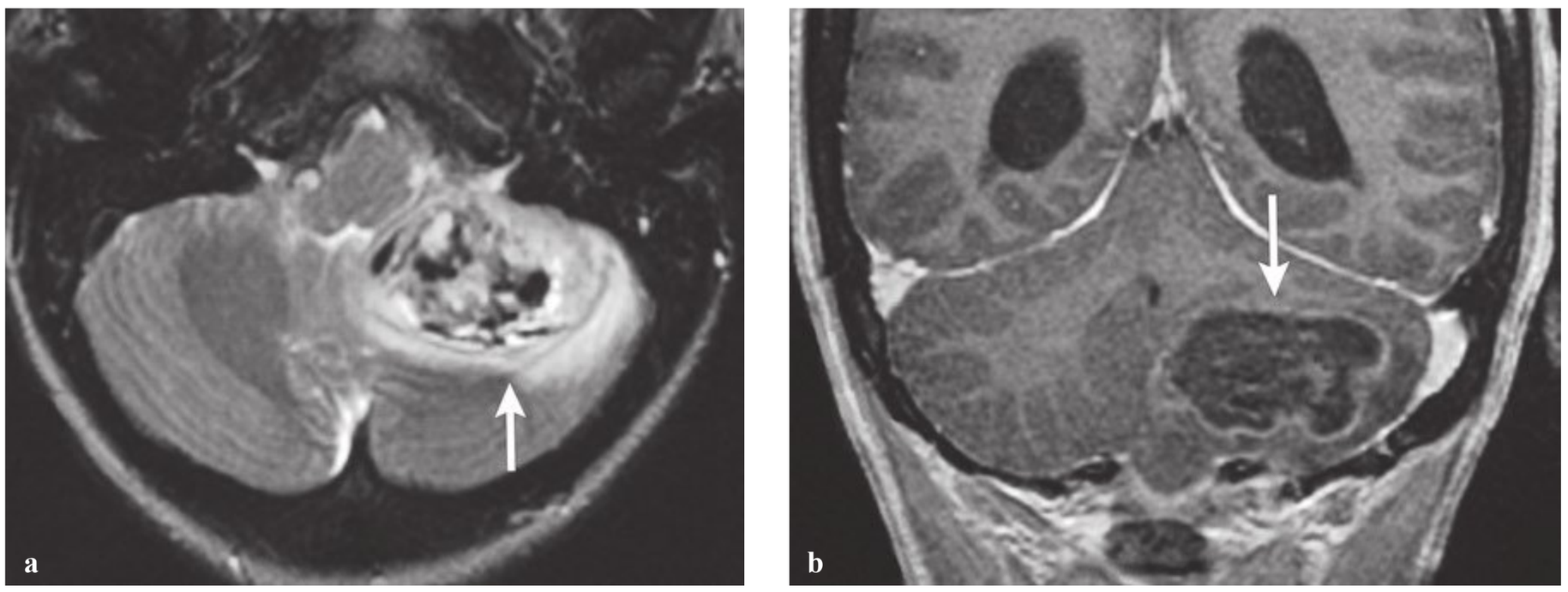

Fig. 1.120 **(a)** A 37-year-old woman with a malignant oligodendroglioma in the inferior left cerebellar hemisphere that has mixed high, low, and intermediate signal on axial T2-weighted imaging (arrow). **(b)** The tumor shows heterogeneous mild gadolinium contrast enhancement on coronal T1-weighted imaging (arrow).

Table 1.3 (cont.) Solitary intra-axial lesions in the posterior cranial fossa (infratentorial)

Lesions	Imaging Findings	Comments
Ependymoma (**Fig. 1.121** and **Fig. 1.122**)	MRI: Circumscribed, lobulated, supratentorial lesion, often extraventricular, ± cysts, calcifications, and/or hemorrhage. Low-intermediate signal on T1-weighted imaging, intermediate-high signal on T2-weighted imaging, and variable gadolinium contrast enhancement. Tumors have elevated relative cerebral blood volume (rCBV) as well as delayed contrast retention secondary to intratumoral fenestrated blood vessels. Diffusion-weighted imaging: Usually no restricted diffusion. Magnetic resonance spectroscopy: Elevated choline and decreased N-acetylaspartate (NAA), similar to other neoplasms. CT: Circumscribed, lobulated, supratentorial lesion, often extraventricular, ± cysts and/or calcifications (up to 50%), low-intermediate attenuation, and variable contrast enhancement.	Slow-growing tumor (WHO grade II) comprised of neoplastic cells with monomorphic round/oval nuclei containing speckled chromatin, perivascular pseudorosettes, and ependymal rosettes. Zones of myxoid degeneration, hyalinization of blood vessels, hemorrhage, and/or calcifications may occur within tumors. Ependymoma accounts for 6 to 12% of intracranial tumors, with an incidence of 0.22 to 0.29 per 100,000. Occurs more commonly in children than in adults. One-third of ependymomas are supratentorial, and two-thirds are infratentorial. Children with infratentorial ependymomas range in age from 2 months to 16 years (mean age = 6.4 years). Supratentorial ependymomas occur in children and adults. Tumors usually lack IDH mutations. Immunoreactive to glial fibrillary acidic protein (GFAP), S-100, vimentin, and/or epithelial membrane antigen (EMA). Associated with neurofibromatosis type 2 (NF2) and genetic mutations involving chromosomes 22, 9, 6, and 3. Five-year survival is 57%, and 10-year survival is 45%
Subependymoma (**Fig. 1.123**)	MRI: Tumors typically attached to ventricular walls (fourth ventricle, 40–50%; lateral ventricle, 30–40%; third ventricle, 10%). Lesions have circumscribed margins, low-intermediate signal on T1-weighted imaging and heterogeneous slightly high to high signal on T2-weighted imaging. May contain sites of hemorrhage or calcification. Variable degrees of gadolinium contrast enhancement. CT: Lesions have circumscribed margins and low-intermediate attenuation. May contain sites of hemorrhage or calcification. Variable degrees of contrast enhancement.	Slow-growing low-grade (WHO grade I) glial neoplasms comprised of clusters of tumor cells with isomorphic nuclei within a dense matrix of cell processes. Mitotic activity is absent or rare. Immunoreactive to glial fibrillary acidic protein (GFAP). Account for 8% of ependymal tumors. Complete resection can be curative.

(continued on page 102)

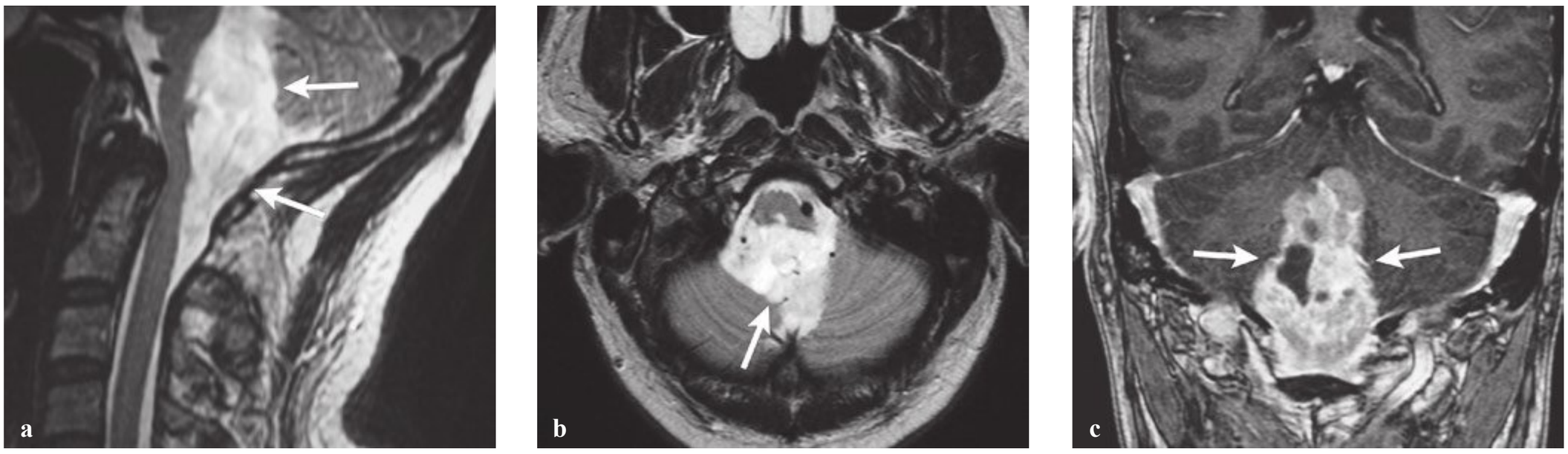

Fig. 1.121 A 34-year-old man with an ependymoma in the fourth ventricle that extends inferiorly through the foramen of Magendie. The tumor (arrows) has high signal on **(a)** sagittal and **(b)** axial T2-weighted imaging and **(c)** shows gadolinium contrast enhancement (arrows) on coronal T1-weighted imaging. The tumor extends from the fourth ventricle though the foramina of Luschka on axial T2-weighted imaging **(b)**.

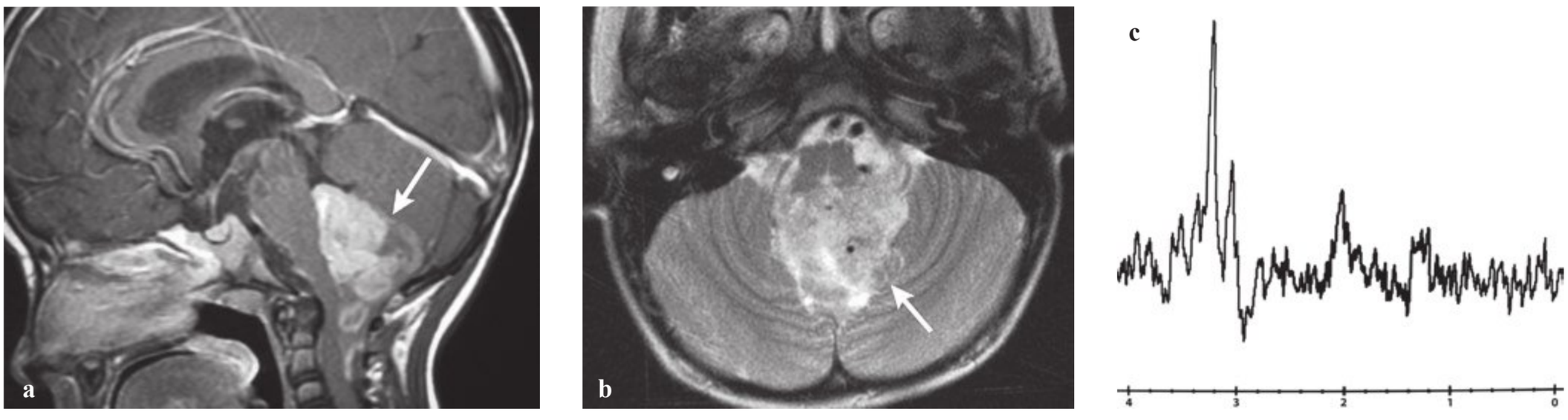

Fig. 1.122 A 30-month-old female with a grade II–III ependymoma in the fourth ventricle that shows **(a)** heterogeneous, prominent gadolinium contrast enhancement on sagittal T1-weighted imaging (arrow) and **(b)** heterogeneous slightly high and high signal on axial T2-weighted imaging (arrow). **(c)** Magnetic resonance spectroscopy shows a large decrease in the N-acetylaspartate (NAA) peak at 2 ppm and an elevated choline peak at 3.2 ppm.

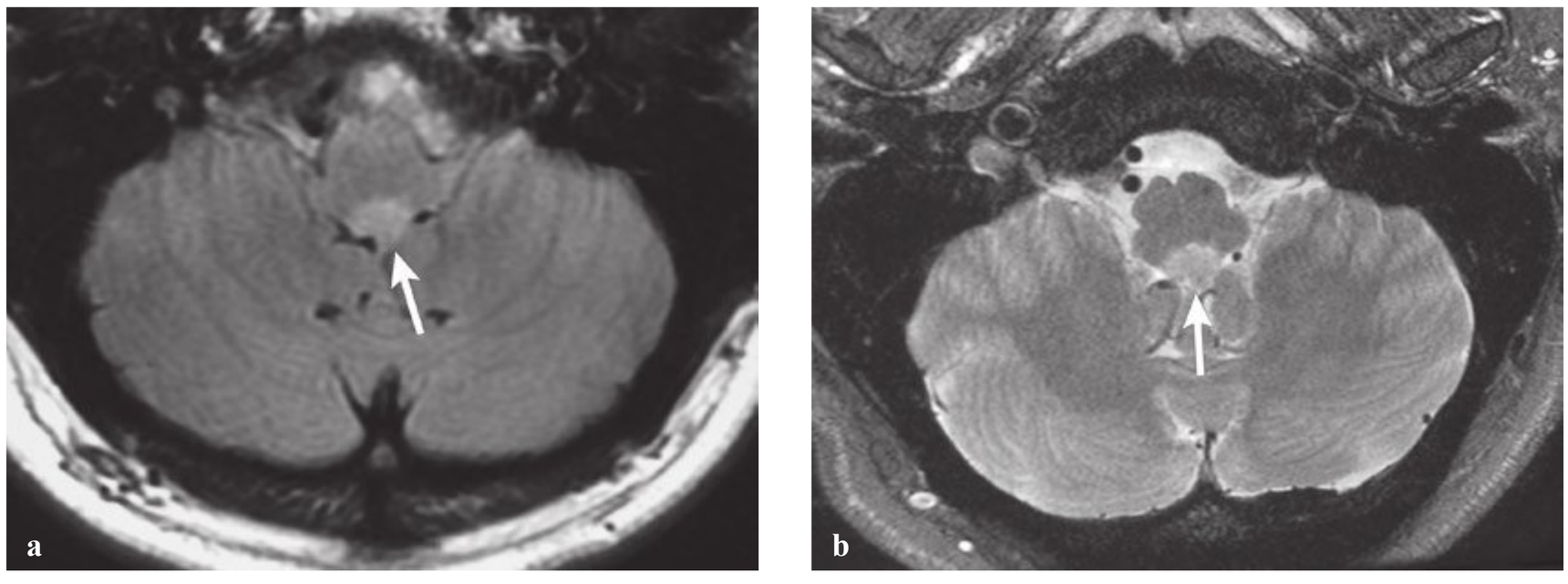

Fig. 1.123 A 43-year-old man with a subependymoma in the lower fourth ventricle that has slightly high signal on **(a)** axial FLAIR (arrow) and **(b)** axial T2-weighted imaging (arrow).

Table 1.3 (cont.) Solitary intra-axial lesions in the posterior cranial fossa (infratentorial)

Lesions	Imaging Findings	Comments
Ganglioglioma (**Fig. 1.124**)	MRI: Circumscribed tumor, usually supratentorial, often in temporal or frontal lobes, but 15% occur in the cerebellum or brainstem. Low-intermediate signal on T1-weighted imaging and intermediate-high signal on T2-weighted imaging, ± cysts (up to 40%), calcifications (up to 30%), ± gadolinium contrast enhancement. Diffusion-weighted imaging: Usually no restricted diffusion. CT: Lesions have low-intermediate attenuation, ± cysts, ± contrast enhancement.	Rare, well-differentiated neuroepithelial tumors (WHO grade I) that occur in patients with mean ages ranging from 8.5 to 26 years. Slow-growing neoplasms, gangliogliomas account for 1.3% of brain tumors and 4% of pediatric brain tumors. Ganglioglioma contains glial and neuronal elements, and ganglioneuroma contains only ganglion cells. Immunoreactive to neurofilaments, synaptophysin, neuronal nuclear protein (NeuN), MAP2, and CD34. Patients are usually < 30 years old, with seizure presentation. Favorable prognosis if completely resected, with 7.5-year recurrence-free survival.
Gangliocytoma	MRI: Circumscribed tumor, usually supratentorial, often in temporal or frontal lobes, occasionally in the cerebellum or brainstem. Tumors have low-intermediate signal on T1-weighted imaging and intermediate to high signal on T2-weighted imaging, ± cysts, ± gadolinium contrast enhancement. Diffusion-weighted imaging: Usually there is no restricted diffusion. CT: Lesions have low-intermediate attenuation, ± cysts, ± contrast enhancement.	Uncommon tumors. Patients are usually < 30 years old, with seizure presentation. Slow-growing neoplasms, gangliocytomas contain only mature neoplastic ganglion cells and dysplastic brain tissue. Favorable prognosis if completely resected.
Dysplastic cerebellar gangliocytoma (Lhermitte-Duclos disease) (**Fig. 1.125**)	MRI: Nodular lesions, usually located in the cerebellar hemispheres, and which usually have low-intermediate signal bands on T1-weighted images and adjacent bands of low-intermediate signal with bands of slightly high signal on T2-weighted images. The cerebellar folia at the lesion are enlarged. Lesions usually lack gadolinium contrast enhancement except for enhancement of veins between enlarged cerebellar folia. Diffusion-weighted imaging: ± restricted diffusion. Magnetic resonance spectroscopy: Normal or slightly decreased N-acetylaspartate (NAA), normal choline/creatine (Cho/Cr) ratios. CT: Nodular lesion with low-intermediate attenuation, and typically lacking contrast enhancement, calcification, or necrosis.	Rare benign cerebellar lesion (WHO grade I) comprised of dysplastic ganglion cells causing diffuse enlargement of the molecular and internal granular layers of the cerebellum. Lesions have absent or very low mitotic activity and lack necrosis. The disease usually occurs in young adults 20 to 40 years old, although it can occur in patients from 3 to 70 years old, and 40% of cases occur in patients with Cowden syndrome, which is an autosomal dominant disorder involving the PTEN (phosphatase and tensin) gene on chromosome 10, resulting in multiple hamartomas of the skin (trichilemmomas—benign neoplasms of lower outer root epithelial sheath of the hair follicle), intestines, and other organs, as well as cancers of the breast, thyroid (medullary type), and endometrium. Incidence is 1 per 250,000.

(continued on page 104)

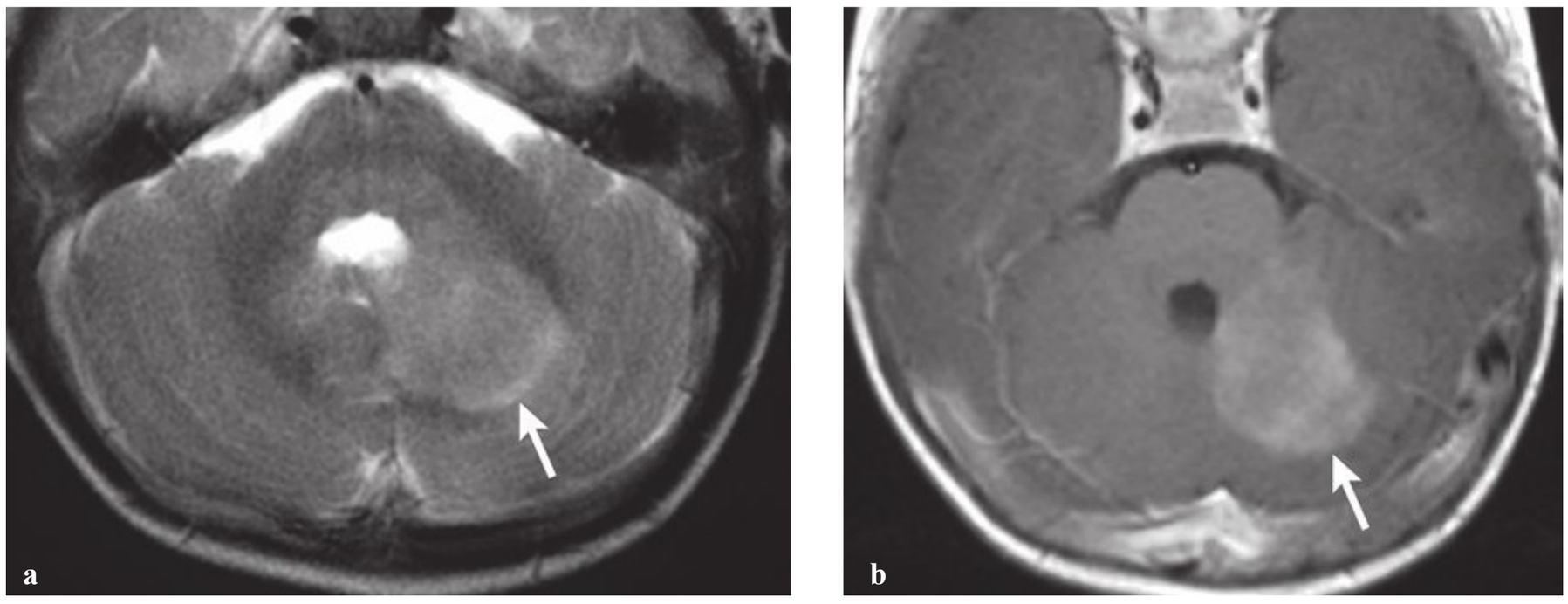

Fig. 1.124 **(a)** A ganglioglioma in the medial left cerebellar hemisphere with heterogeneous intermediate signal on axial T2-weighted imaging (arrow) and **(b)** heterogeneous mild gadolinium contrast enhancement on axial T1-weighted imaging (arrow).

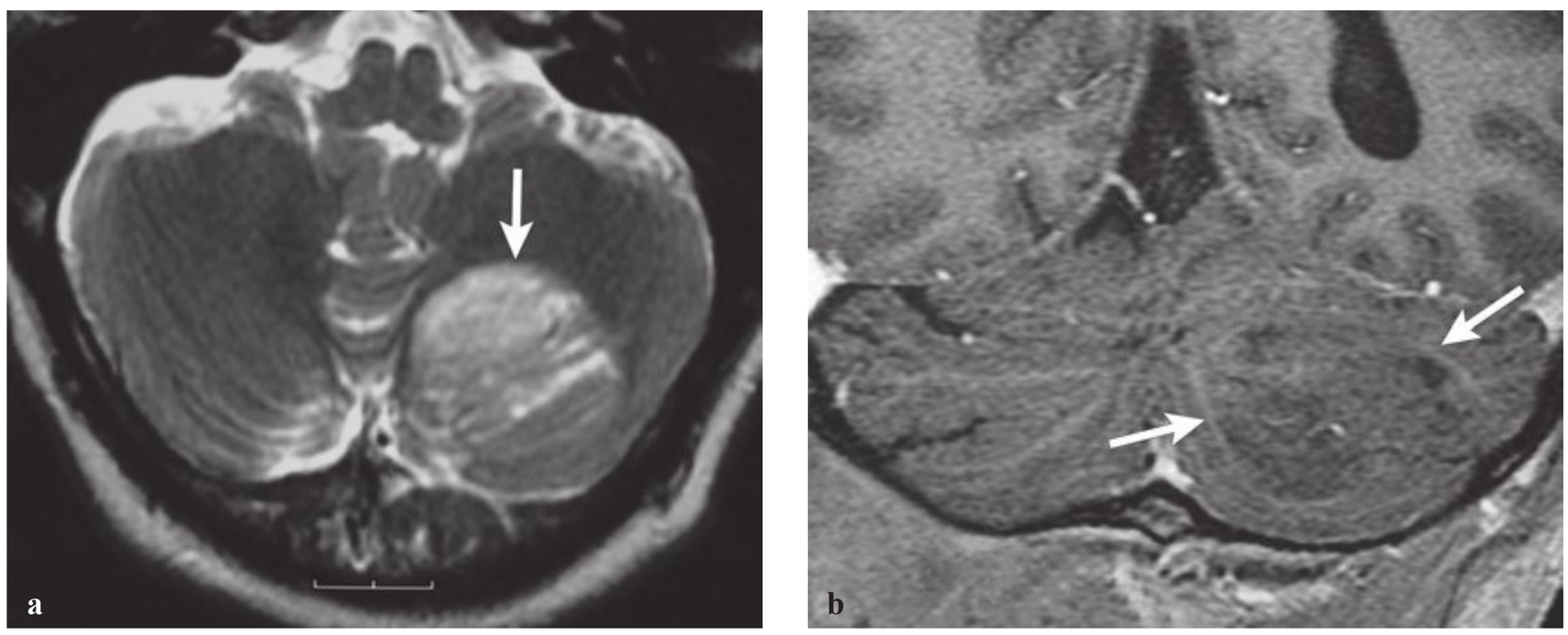

Fig. 1.125 **(a)** Dysplastic cerebellar gangliocytoma (Lhermitte-Duclos disease) seen as a nodular lesion in the left cerebellar hemisphere consisting of adjacent bands of low-intermediate signal with bands of slightly high signal on axial T2-weighted imaging (arrow). **(b)** The lesion lacks gadolinium contrast enhancement except for enhancement of veins between enlarged cerebellar folia on coronal T1-weighted imaging (arrows).

Table 1.3 (cont.) Solitary intra-axial lesions in the posterior cranial fossa (infratentorial)

Lesions	Imaging Findings	Comments
Medulloblastoma (PNET) (**Fig. 1.126** and **Fig. 1.127**)	MRI: Circumscribed or invasive lesions involving the cerebellum, with low-intermediate signal on T1-weighted imaging and intermediate-high signal on T2-weighted imaging, ± cystic or necrotic zones. Variable gadolinium contrast enhancement, usually high relative cerebral blood volume (rCBV), ± gadolinium contrast enhancement in the leptomeninges and/or ventricles from tumor dissemination. Diffusion-weighted imaging: Solid portions can have restricted diffusion. Magnetic resonance spectroscopy: Usually shows elevated choline, lipid, and taurine peaks and decreased N-acetylaspartate (NAA) levels. CT: Circumscribed or invasive lesions with intermediate to slightly high attenuation, variable contrast enhancement, and frequent dissemination into the leptomeninges.	Highly malignant tumors (WHO grade IV) located in the cerebellum and that frequently disseminate along CSF pathways. Tumors are composed of poorly differentiated or undifferentiated cells with divergent differentiation along neuronal, astrocytic, or ependymal lines. Histologic subtypes include classic, desmoplastic, large cell (LC), anaplastic, and medulloblastoma with extensive nodularity. LC and anaplastic types have the worst prognoses. Medulloblastoma typically occurs in patients 4 weeks to 20 years old, with a mean age = 5.5 years. Can also occur in adults.
Atypical teratoid/ rhabdoid tumors (**Fig. 1.128**)	MRI: Circumscribed or invasive mass lesions with intermediate signal on T1-weighted imaging, ± zones of high signal from hemorrhage on T1-weighted imaging and variable mixed low, intermediate, and/or high signal on T2-weighted imaging. Solid portions can have restricted diffusion with associated prominent gadolinium contrast enhancement ± heterogeneous pattern. Gadolinium contrast enhancement in the leptomeninges and/or ventricles is caused by tumor dissemination. Diffusion-weighted imaging: Solid portions can have restricted diffusion. Magnetic resonance spectroscopy: Usually shows elevated choline, lipid, and lactate peaks and decreased N-acetylaspartate (NAA) levels. CT: Circumscribed mass lesions with intermediate or mixed low and intermediate attenuation, ± zones of hemorrhage, cystic degeneration, and/or necrosis. Calcifications occasionally occur, usually there is contrast enhancement ± heterogeneous pattern, ± contrast enhancement in the leptomeninges and/or ventricles from tumor dissemination.	Rare malignant tumors (WHO grade IV) involving the CNS usually occurring in the first decade, usually in patients < 3 years old. K_i-67/MIB-1 proliferation index is often high, > 50% Associated with mutations of the INI1 (hSNF5/SMARCB1) gene on chromosome 22q11.2. Histologically appear as solid tumors ± necrotic areas, similar to malignant rhabdoid tumors of the kidney. Nearly all are intra-axial and can occur in supra- and/or infratentorial locations. Associated with a very poor prognosis.
Metastatic lesion (**Fig. 1.129**)	MRI: Circumscribed spheroid lesions in brain, can have various intra-axial locations, often at gray–white matter junctions, usually with low-intermediate signal on T1-weighted imaging and intermediate-high signal on T2-weighted imaging, ± hemorrhage, calcifications, and cysts. Variable gadolinium contrast enhancement, and often high signal on T2-weighted imaging peripheral to nodular enhancing lesion representing axonal edema. CT: Lesions usually have low-intermediate attenuation, ± hemorrhage, calcifications, and cysts, and variable contrast enhancement, often associated with adjacent low attenuation from axonal edema.	Metastasis represents ~ 33% of intracranial tumors, usually from extracranial primary neoplasm in adults > 40 years old. Primary tumor source: lung > breast > GI > GU > melanoma. Metastatic lesions in the cerebellum can present with obstructive hydrocephalus/neurosurgical emergency.

(continued on page 107)

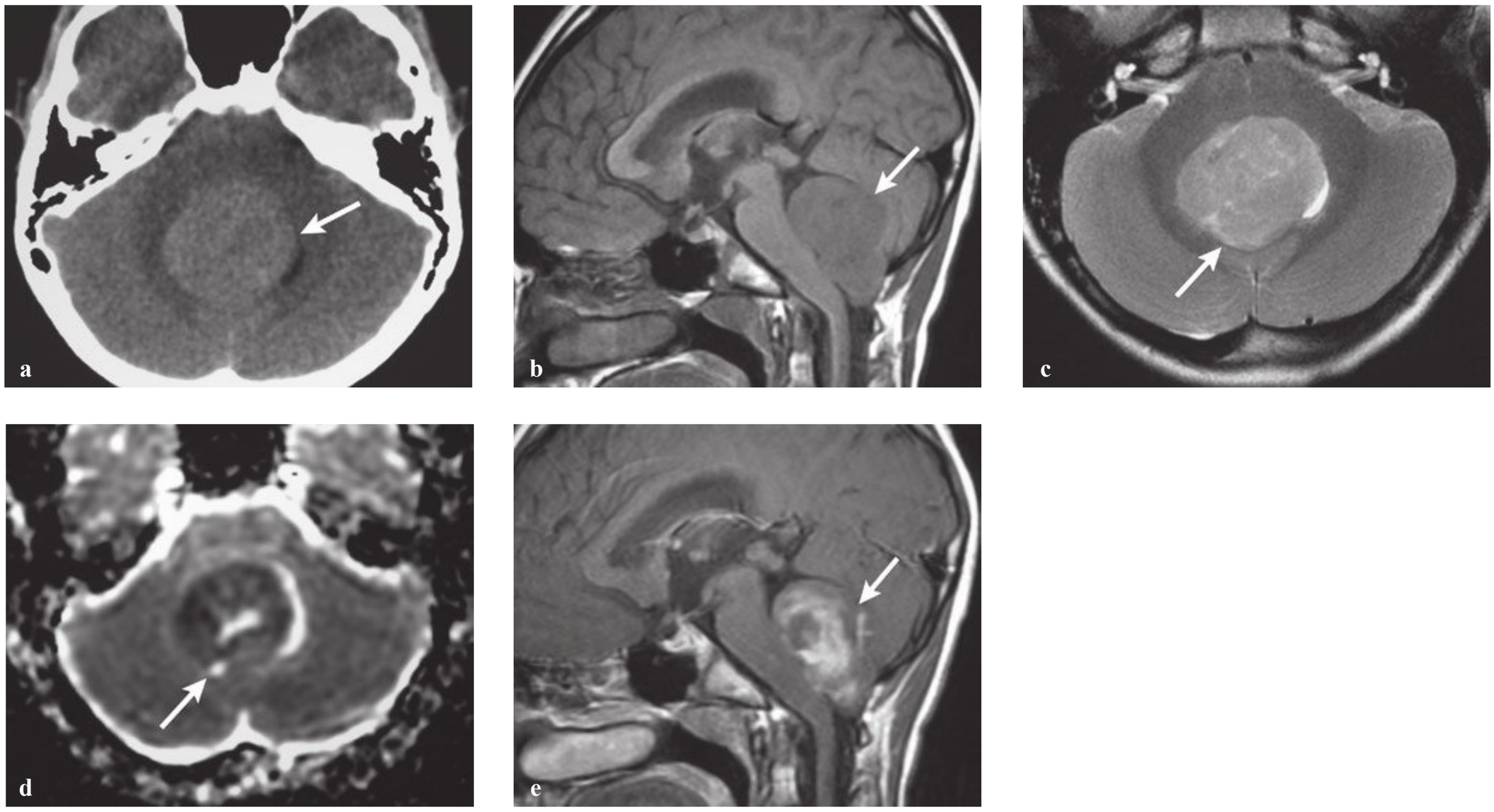

Fig. 1.126 A 12-year-old boy with a medulloblastoma in the vermis that has **(a)** intermediate attenuation on CT (arrow), **(b)** intermediate signal on sagittal T1-weighted imaging (arrow), **(c)** heterogeneous intermediate to slightly high signal on axial T2-weighted imaging (arrow), **(d)** restricted diffusion on axial ADC (arrow), and **(e)** heterogeneous gadolinium contrast enhancement on sagittal T1-weighted imaging (arrow).

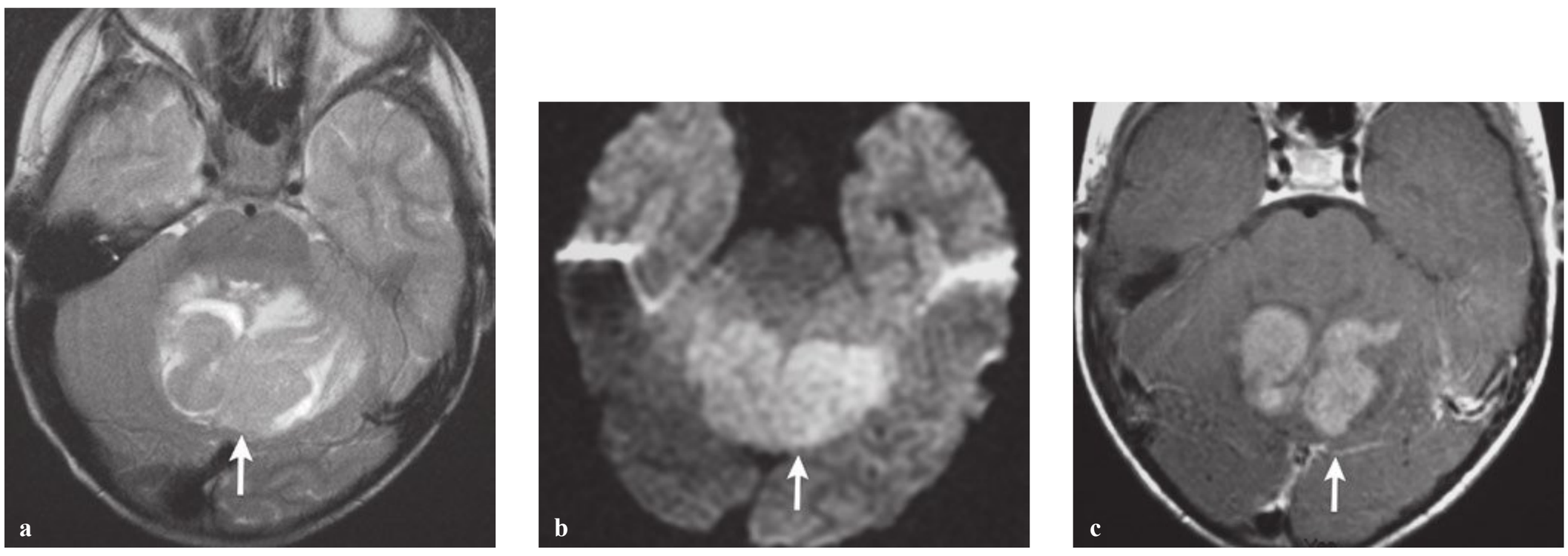

Fig. 1.127 A 4-year-old boy with a medulloblastoma in the upper vermis that has **(a)** heterogeneous intermediate to slightly high signal on axial T2-weighted imaging (arrow), **(b)** restricted diffusion on axial diffusion-weighted imaging (DWI) (arrow), and **(c)** heterogeneous gadolinium contrast enhancement on axial T1-weighted imaging (arrow).

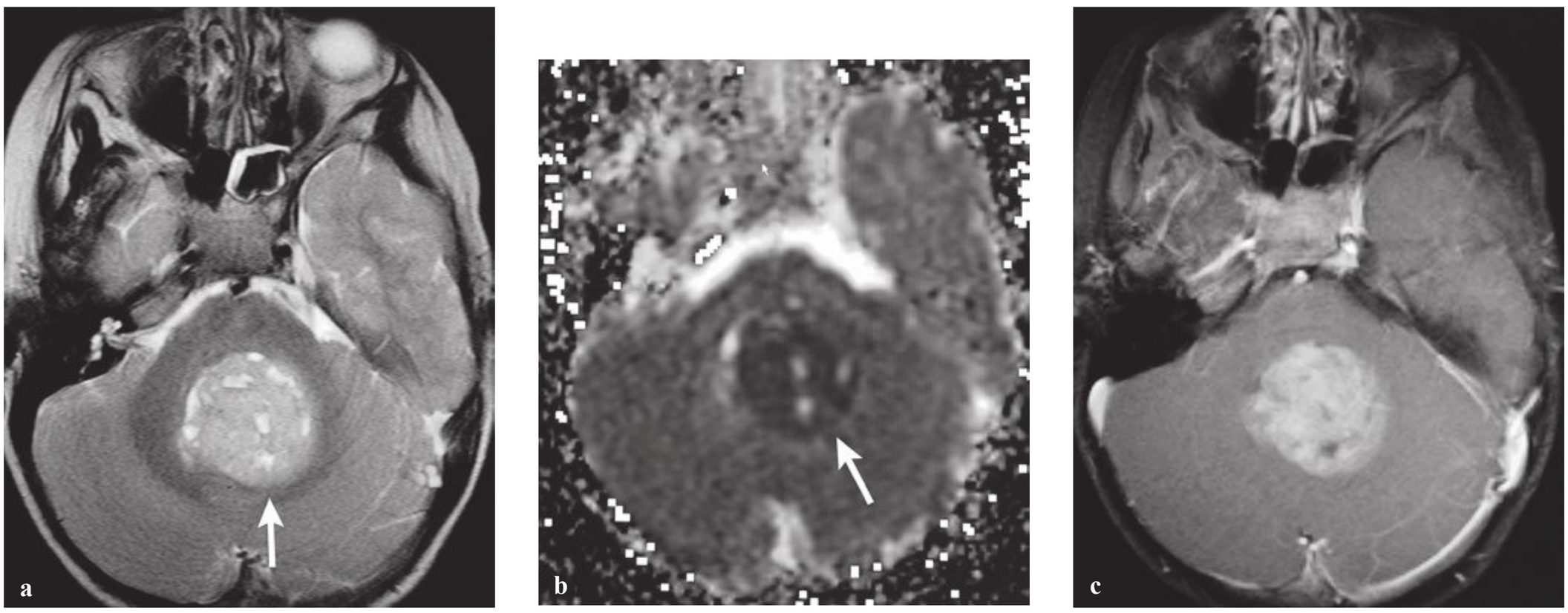

Fig. 1.128 A 4-year-old male with an atypical teratoid/rhabdoid tumor in the vermis that has **(a)** heterogeneous intermediate to slightly high signal on axial T2-weighted imaging (arrow), **(b)** restricted diffusion on axial ADC (arrow), and **(c)** gadolinium contrast enhancement on axial fat-suppressed T1-weighted imaging.

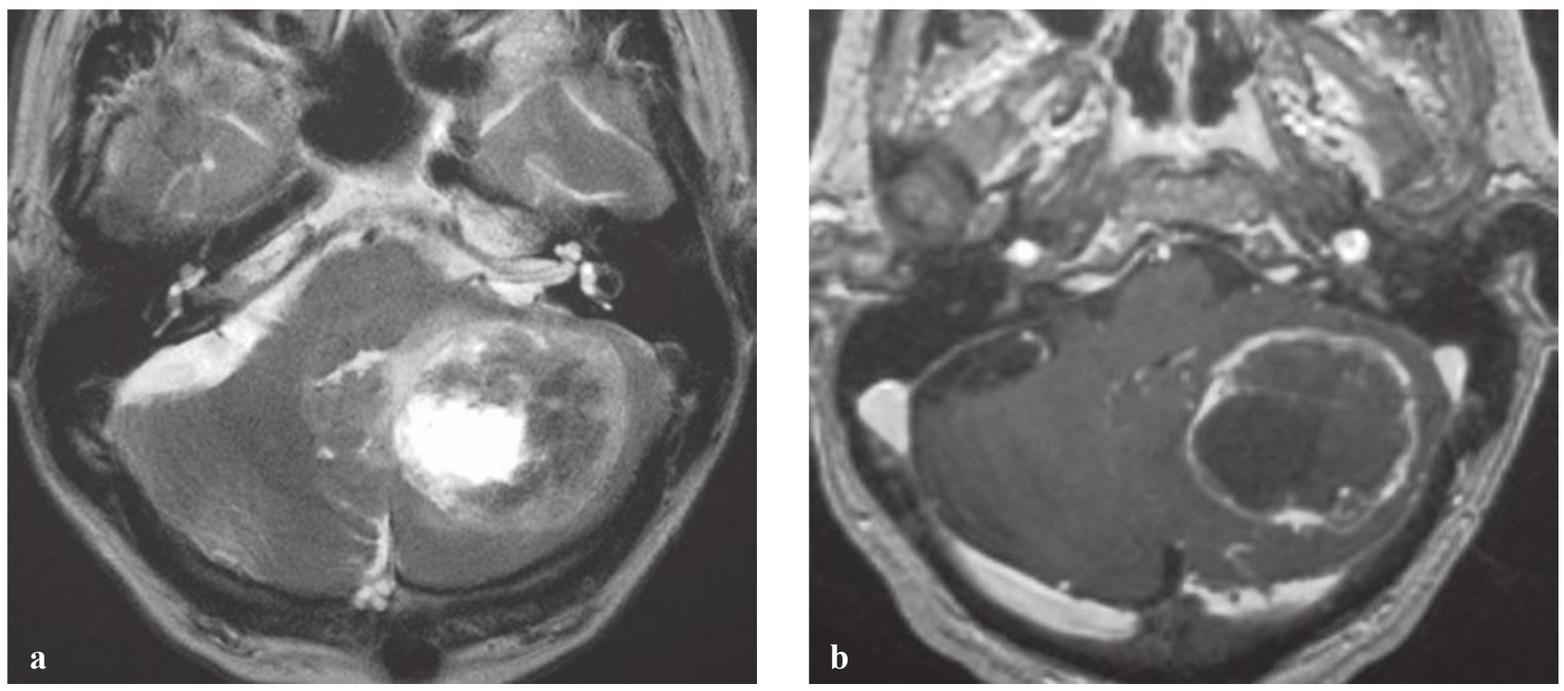

Fig. 1.129 A 67-year-old man with lung carcinoma and a metastatic lesion in the left cerebellar hemisphere that has **(a)** mixed low, intermediate, and high signal on axial T2-weighted imaging, and **(b)** peripheral gadolinium contrast enhancement on axial T1-weighted imaging. The lesion has mass effect with axonal edema and causes compression of the fourth ventricle.

Table 1.3 (cont.) Solitary intra-axial lesions in the posterior cranial fossa (infratentorial)

Lesions	Imaging Findings	Comments
Lymphoma (**Fig. 1.130**)	MRI: Primary CNS lymphoma (PCNSL) in immunocompetent patients occurs as a solitary focal or infiltrating lesion in 65%. Tumors often have low-intermediate signal on T1-weighted imaging, intermediate-slightly high signal on T2-weighted imaging, ± perilesional edema; ± hemorrhage/necrosis in immunocompromised patients or after treatment. PCNSL in immunocompetent patients usually shows homogeneous gadolinium contrast enhancement, whereas gadolinium contrast enhancement in immunocompromised patients often has an irregular peripheral pattern. Diffuse leptomeningeal and dural gadolinium contrast enhancement are other less common patterns of intracranial lymphoma. Diffusion-weighted imaging: PCNSL can show restricted diffusion. CT: CNS lymphoma can have intermediate attenuation, or it can be hyperdense related to a high nuclear/cytoplasm ratio, ± hemorrhage/necrosis in immunocompromised patients. PCNSL usually shows contrast enhancement. Diffuse leptomeningeal contrast enhancement is another pattern of intracranial lymphoma.	Primary CNS lymphoma is more common than secondary lymphoma and usually occurs in adults > 40 years old. PCNSL accounts for 5% of primary brain tumors. Incidence currently ranges from 0.8 o 1.5% of primary intracranial tumors. Former elevated incidence of 6% in patients with AIDS has been reduced with effective antiviral therapy. B cell lymphoma is more common than T cell lymphoma. MRI features of primary and secondary lymphoma of brain overlap. Intracranial lymphoma can involve the leptomeninges in secondary lymphoma more often than in primary lymphoma.
Leukemia (myeloid sarcoma, granulocytic sarcoma, chloroma)	MRI: Lesions often have intermediate signal on T1-weighted imaging and intermediate to slightly high signal on T2-weighted imaging and FLAIR. Small zones with low signal on GRE may be seen from sites of hemorrhage within the lesion. Lesions can have restricted diffusion on diffusion-weighted imaging (DWI) (ADC values of 0.50×10^{-3} mm^2/s). Lesions usually show gadolinium contrast enhancement. Magnetic resonance spectroscopy: Lesions can have reduced N-acetylaspartate (NAA) and markedly elevated choline peaks. CT: Lesions can have low-intermediate to slightly high attenuation and can show contrast enhancement.	Leukemias are neoplastic proliferations of hematopoietic cells. Myeloid sarcomas (also referred to as chloromas or granulocytic sarcomas) are focal tumors composed of myeloblasts and neoplastic granulocyte precursor cells, and they occur in 2% of patients with acute myelogenous leukemia. These lesions can involve the dura, leptomeninges, and brain. Intracranial lesions can be solitary or multiple.

(continued on page 108)

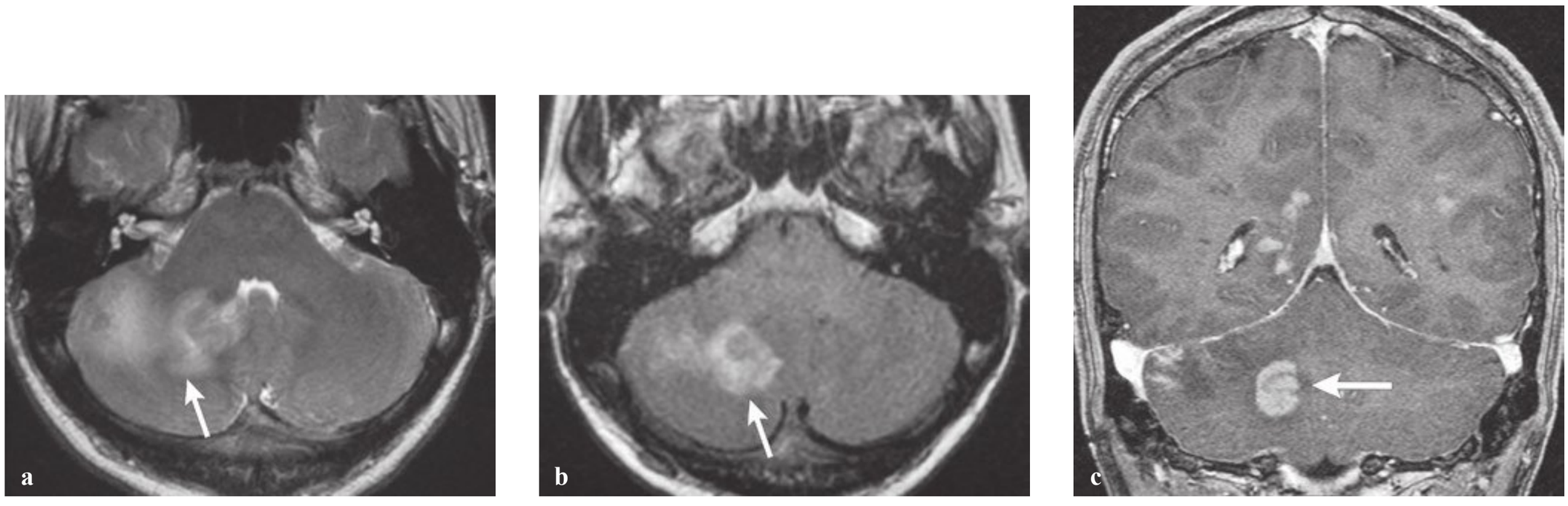

Fig. 1.130 A 27-year-old man with large B cell lymphoma with an intra-axial lesion in the right cerebellar hemisphere that has high signal on **(a)** axial T2-weighted imaging (arrow) and **(b)** axial FLAIR (arrow), and **(c)** shows gadolinium contrast enhancement on coronal T1-weighted imaging (arrow). Abnormal gadolinium contrast enhancement is also seen in the cerebral and cerebellar leptomeninges.

Table 1.3 (cont.) Solitary intra-axial lesions in the posterior cranial fossa (infratentorial)

Lesions	Imaging Findings	Comments
Hemangioblastoma (**Fig. 1.131** and **Fig. 1.132**)	Circumscribed tumors, usually located in the cerebellum and/or brainstem. MRI: Small gadolinium contrast-enhancing nodule ± cyst, or larger lesion with prominent heterogeneous enhancement ± flow voids within lesion or at the periphery. Intermediate signal on T1-weighted imaging, intermediate-high signal on T2-weighted imaging, and occasionally evidence of recent or remote hemorrhage. Relative cerebral blood volume (rCBV) of lesions is high. CT: Small contrast-enhancing nodule ± cyst, or larger lesion with prominent heterogeneous enhancement, ± hemorrhage.	Slow-growing, vascular tumors (WHO grade I) that involve the cerebellum, brainstem, and/or spinal cord. Hemangioblastomas account for 1–3% of intracranial neoplasms and usually occur in middle-aged adults. They rarely occur in children, except for patients with von Hippel-Lindau disease (VHL disease). Tumors consist of numerous thin-walled vessels as well as large, lipid-containing vacuolated stromal cells that have variably sized and hyperchromatic nuclei. Mitotic figures are rare. Stromal cells are immunoreactive to VEGF, vimentin, CXCR4, aquaporin 1, carbonic anhydrase, S-100, CD56, neuron specific enolase, and D2–40. Vessels typically react to a reticulin stain. Reactive astrocytic gliosis can ocur in adjacent tissue. Tumors occur as sporadic mutations of the VHL gene or as an autosomal dominant germline mutation of the VHL gene on chromosome 3p25–26 resulting in VHL disease. In VHL disease, multiple hemangioblastomas involving the central nervous system occur, as well as clear-cell renal carcinoma, pheochromocytoma, endolymphatic sac tumor, neuroendocrine tumor, adenoma of the pancreas, and epididymal cystadenoma. VHL disease occurs in adolescents and young and middle-aged adults.
Neurofibromatosis type 1 (von Recklinghausen disease) (**Fig. 1.133**)	MRI: In addition to neoplasms of the central nervous system (astrocytomas, grades I to IV, and optic gliomas), nonneoplastic lesions can occur in the white matter that have high signal on T2-weighted imaging and lack gadolinium contrast enhancement. Can be solitary or multiple. Lesions occur in the cerebral and/or cerebellar white matter, basal ganglia, and brainstem. Lesions can increase in size in the first decade and then usually regress and resolve by the third decade.	Autosomal dominant disorder (1/2500 births) from mutations involving the neurofibromin gene on chromosome 17q11.2. NF1 represents the most common type of neurocutaneous syndrome and is associated with neoplasms of the central and peripheral nervous systems (optic gliomas, astrocytomas, and plexiform and solitary neurofibromas) and skin (café-au-lait spots, axillary and inguinal freckling). NF1 is also associated with meningeal and skull dysplasias, as well as hamartomas of the iris (Lisch nodules).
Hamartoma (tuberous sclerosis) (**Fig. 1.134**)	MRI: Cortical-subcortical lesions (tubers) usually have high signal on T1-weighted imaging and low signal on T2-weighted imaging in neonates and infants; changes to low-intermediate signal on T1-weighted imaging and high signal on T2-weighted imaging in older children and adults. Calcifications occur in 50% in older children, and gadolinium contrast enhancement is uncommon. Diffusion-weighted imaging: Cortical tubers can have elevated ADC values. Subependymal giant cell astrocytomas usually do not have restricted diffusion. Magnetic resonance spectroscopy: Subependymal giant cell astrocytomas can have elevated choline and reduced N-acetylaspartate (NAA). CT: Cortical-subcortical lesions (tubers) have variable attenuation. Calcifications are seen in 50% of older children. Contrast enhancement is uncommon.	Cortical hamartomas (tubers), subcortical glioneuronal hamartomas, subependymal glial hamartomas (nodules), and subependymal giant cell astrocytomas are nonmalignant lesions associated with tuberous sclerosis. Tuberous sclerosis is an autosomal dominant disorder associated with hamartomas in multiple organs. Extraneural lesions include cutaneous angiofibromas (adenoma sebaceum), subungual fibromas, visceral cysts, renal angioleiomyomas, intestinal polyps, cardiac rhabdomyomas, and pulmonary lymphangioleiomyomatosis. Caused by mutations of the TSC1 gene on 9q or the TSC2 gene on 16p. Occurs in 1 in 6,000 newborns.

(continued on page 110)

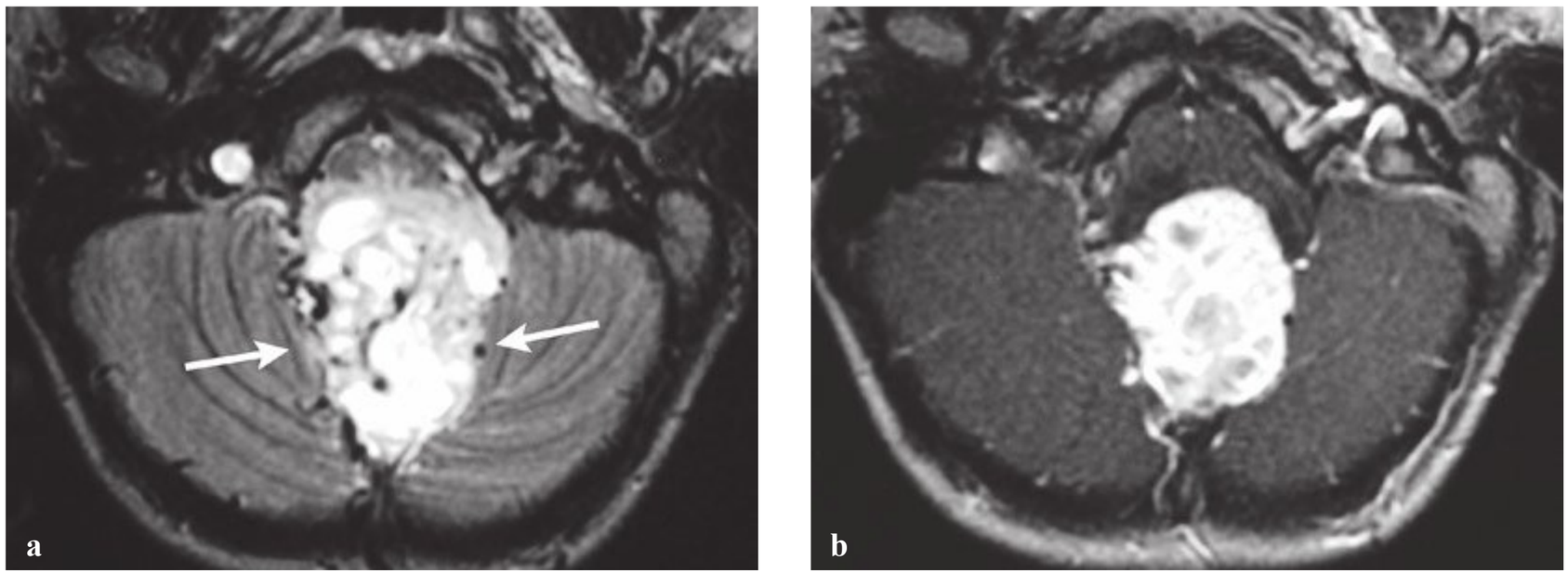

Fig. 1.131 **(a)** A 16-year-old male with von Hippel-Lindau disease and a hemangioblastoma in the inferior vermis and fourth ventricle that has high signal on axial T2-weighted imaging, as well as blood vessels with flow voids (arrows). **(b)** The lesion shows prominent gadolinium contrast enhancement on axial T1-weighted imaging.

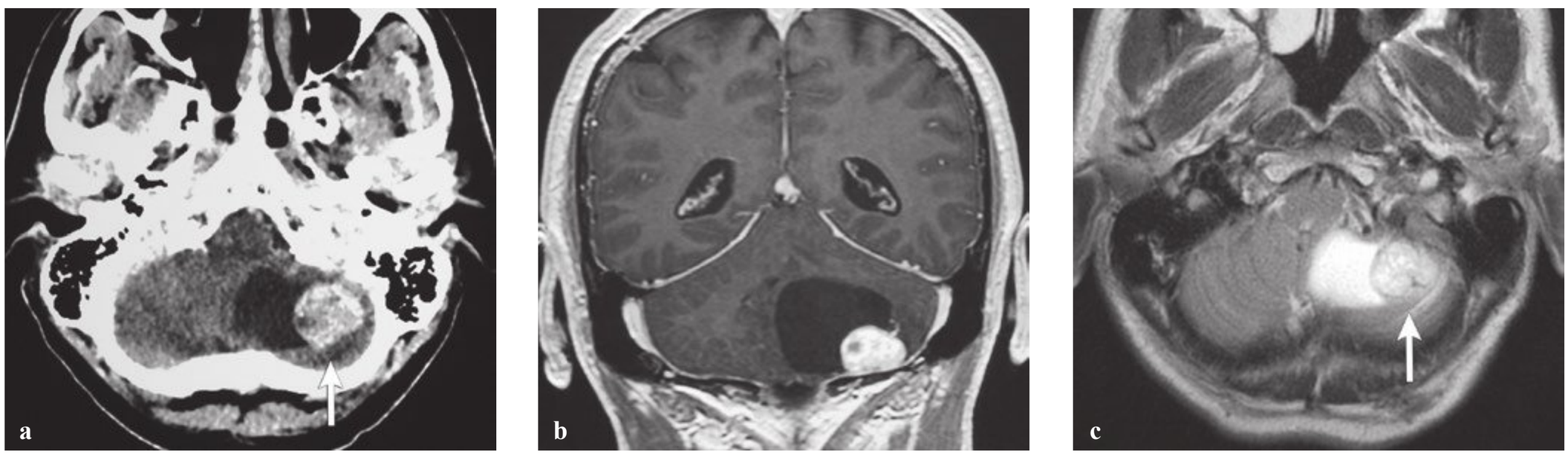

Fig. 1.132 A 51-year-old man with a hemangioblastoma in the left cerebellar hemisphere that is seen as a nodular enhancing lesion associated with a cyst on **(a)** axial CT (arrow) and **(b)** coronal T1-weighted imaging. **(c)** The solid portion of the lesion has slightly high to high signal on axial T2-weighted imaging (arrow).

Fig. 1.133 A 4-year-old male with neurofibromatosis type 1 and multiple intra-axial zones with dysplastic white matter lesions (arrows) with high signal on axial T2-weighted imaging.

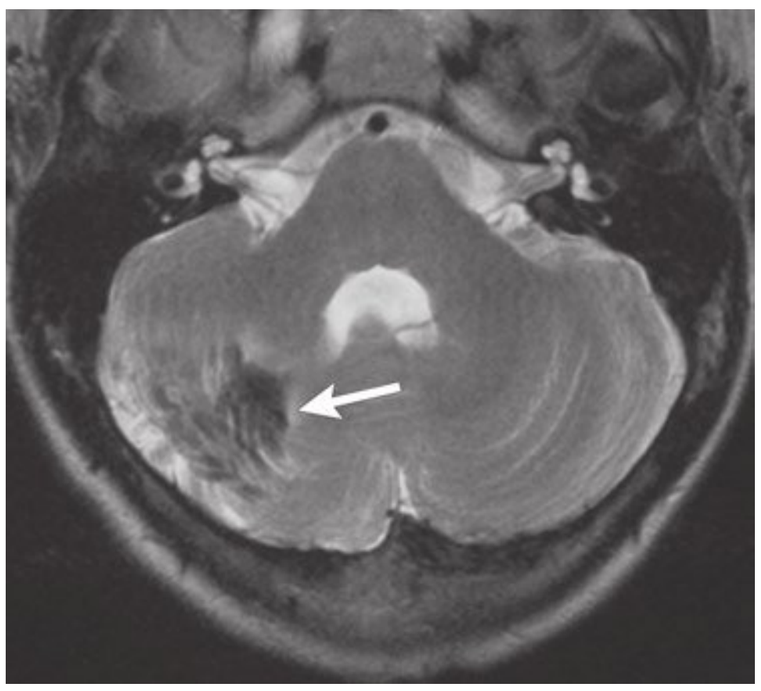

Fig. 1.134 Calcified hamartoma with low signal on axial T2-weighted imaging in the right cerebellar hemisphere (arrow) in a patient with tuberous sclerosis.

Table 1.3 (cont.) Solitary intra-axial lesions in the posterior cranial fossa (infratentorial)

Lesions	Imaging Findings	Comments
Inflammatory Lesions: Infectious		
Pyogenic brain abscess (**Fig. 1.135** and **Fig. 1.136**)	MRI: Circumscribed lesion with low signal on T1-weighted imaging, central zone of high signal on T2-weighted imaging (± air–fluid level) surrounded by a thin rim with intermediate-low signal on T2-weighted imaging that shows ringlike gadolinium contrast enhancement that is sometimes thicker laterally than medially. Peripheral poorly defined zone of high signal on T2-weighted imaging is typically seen that represents edema. Diffusion-weighted imaging: Abscess contents typically have restricted diffusion. Mean ADC values for abscesses are significantly lower (0.63 to 1.12 × 10^{-3} mm^2/s) than those for necrotic or cystic neoplasms (2.45 × 10^{-3} mm^2/s). Magnetic resonance spectroscopy: Decreased N-acetylaspartate (NAA) from destruction of neurons and elevated lactate and amino acid peaks (valine, leucine, and isoleucine) at 0.9 ppm secondary to proteolytic enzymes. CT: Circumscribed lesion with a central zone of low attenuation (± air–fluid level) surrounded by a thin rim of intermediate attenuation; peripheral poorly defined zone of decreased attenuation representing edema; ringlike contrast enhancement that is sometimes thicker laterally than medially.	Formation of brain abscess occurs 2 weeks after cerebritis, with liquefaction and necrosis centrally surrounded by a capsule and peripheral edema Restricted diffusion of abscess contents is related to the combination of the high protein content and viscosity of pus, necrotic debris, and bacteria. Can be multiple, but more than 50%are solitary. Abscess can be a complication of meningitis and/or sinusitis, septicemia, trauma, surgery, or cardiac shunt. Accounts for 2%and 8%of intra-axial mass lesions in developed and developing countries, respectively.

(continued on page 112)

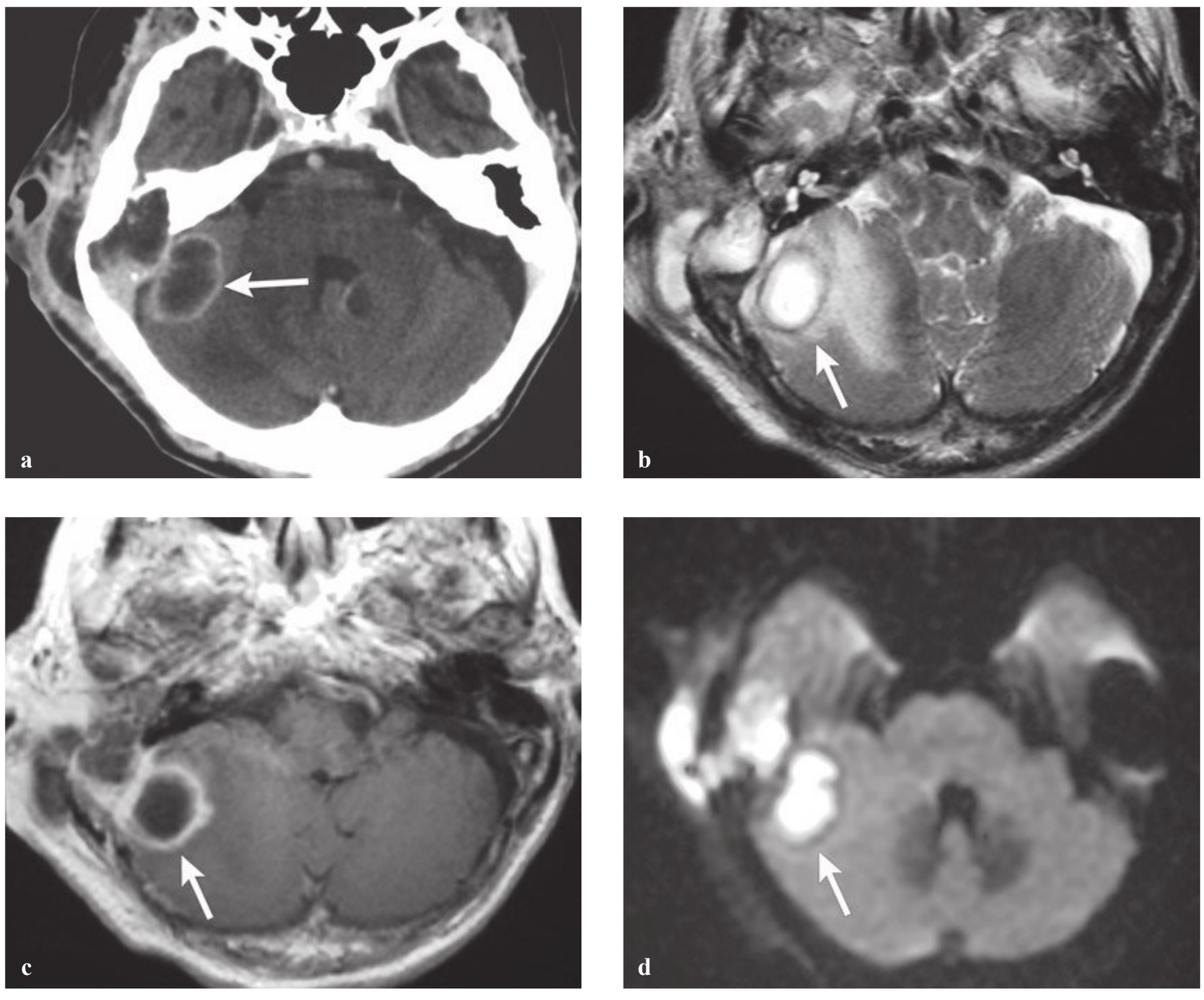

Fig. 1.135 Multifocal infection with abscesses in subcutaneous soft tissue, mastoid bone, and adjacent right cerebellar hemisphere. The abscesses are **(a)** low-attenuation collections with peripheral contrast enhancement on axial CT (arrow) and **(b)** on MRI appear as central zones of high signal on T2-weighted imaging (arrow) surrounded by a thin rim with intermediate-low signal (arrow) that shows **(c)** corresponding ringlike gadolinium contrast enhancement on axial T1-weighted imaging (arrow). Peripheral poorly defined high-signal edema on T2-weighted imaging is also seen. **(d)** The abscesses show restricted diffusion (arrow) on axial DWI.

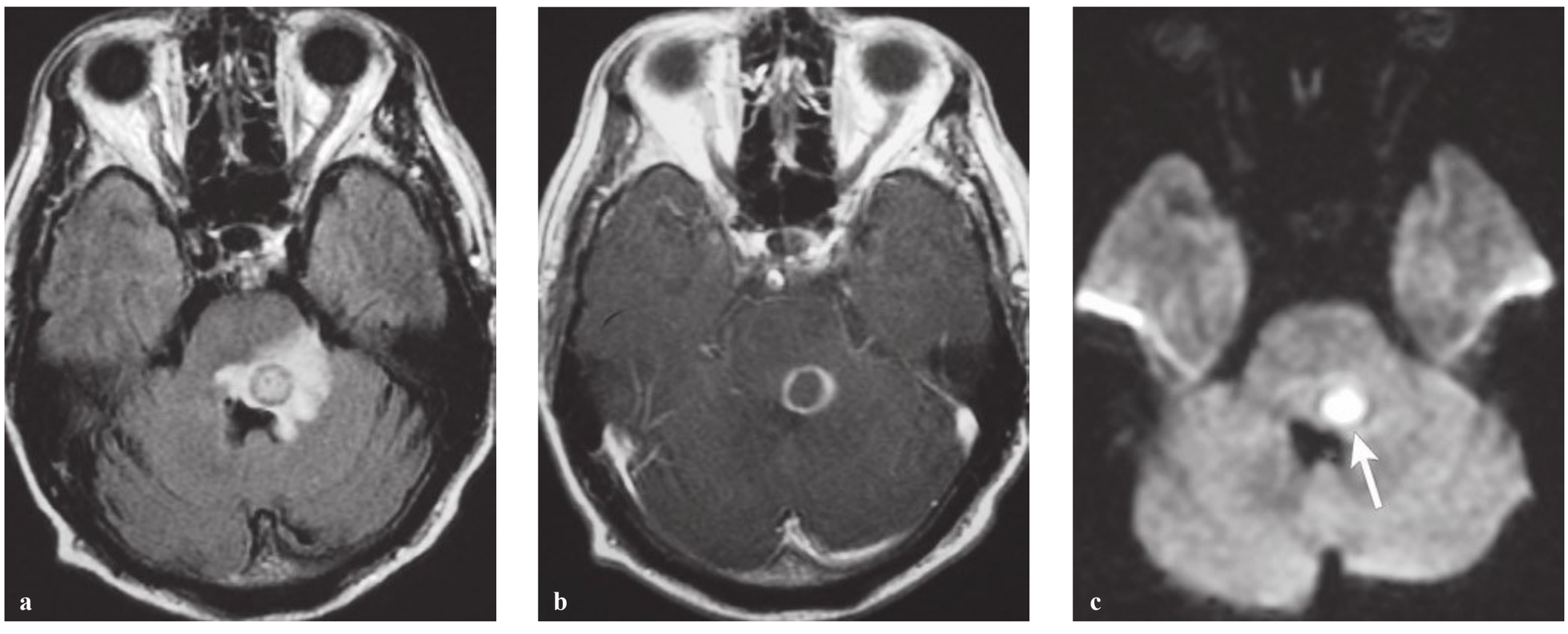

Fig. 1.136 A 70-year-old man with an abscess (arrows) in the pons and left middle cerebellar peduncle. **(a)** The abscess has a central zone of high signal on axial FLAIR surrounded by a thin rim with intermediate signal that shows **(b)** ringlike gadolinium contrast enhancement on axial T1-weighted imaging. Peripheral poorly defined high-signal edema on FLAIR is also seen. **(c)** The abscess shows restricted diffusion on axial DWI (arrow).

Table 1.3 (cont.) Solitary intra-axial lesions in the posterior cranial fossa (infratentorial)

Lesions	Imaging Findings	Comments
Tuberculoma (**Fig. 1.137**)	MRI: Intra-axial lesions in cerebral hemispheres and basal ganglia (adults) and cerebellum (children): Low-intermediate signal on T1-weighted imaging, central zone of high signal on T2-weighted imaging, with a thin peripheral rim of low signal, occasionally low signal on T2-weighted images; + solid or rim gadolinium contrast enhancement; ± calcification, ± restricted or increased diffusion. Meningeal lesions: Nodular or cystiz zones of basilar meningeal gadolinium contrast enhancement. Meningitis can be associated with intracranial arterial or venous thrombosis leading to brain infarction with restricted diffusion.	Occurs in immunocompromised patients and in immunocompetent patients in developing countries. Caseating intracranial granulomas form via hematogenous dissemination; meningitis is the most common intracranial manifestation compared with intra-axial tuberculomas in brain.
Fungal brain infection	MRI: Findings vary depending on organism. Infection can occur in meninges and/or brain parenchyma. Fungal infection can appear as solid or cystic lesion with low-intermediate signal on T2-weighted imaging and high signal on T2-weighted imaging and FLAIR, with nodular or ring-shaped gadolinium contrast enhancement. Peripheral high signal on T2-weighted imaging represents edema. Diffusion-weighted imaging: Infected tissue may have restricted diffusion. Magnetic resonance spectroscopy: Spectroscopy can show elevated lipid, lactate, and amino acid peaks as well as multiple peaks between 3.6 and 3.8 ppm from trehalose. CT: Infection can occur in meninges and brain parenchyma. Solid or cystic-appearing lesions have decreased attenuation, nodular or ring-shaped pattern of contrast enhancement, and a peripheral zone with decreased attenuation that represents edema.	Fungal infections occur in immunocompromised or diabetic patients, with resultant granulomas in meninges and brain parenchyma. Cryptococcus involves the basal meninges and extends along perivascular spaces into the basal ganglia. Aspergillosis and Mucor spread via direct extension through paranasal sinuses or hematogenously, invading blood vessels and resulting in hemorrhagic lesions and/or cerebral or cerebellar infarcts. Coccidioidomycosis usually involves the basal meninges.
Encephalitis (**Fig. 1.138** and **Fig. 1.139**)	MRI: Poorly defined zone or zones of low-intermediate signal on T1-weighted imaging, intermediate-high signal on T2-weighted imaging, and minimal or no gadolinium enhancement. Encephalitis involves cerebellar cortex and/or white matter, with minimal localized mass effect. CT: Poorly defined zone or zones of low-intermediate attenuation, typically with no contrast enhancement.	In immunocompromised patients, encephalitis is infection/inflammation of brain tissue caused by viruses like herpes simplex, cytomegalovirus (CMV), and HIV, or by progressive multifocal leukoencephalopathy from JC polyoma virus infection of oligodendrocytes; in immunocompetent patients, it can be caused by St. Louis encephalitis virus, Eastern or Western equine encephalitis virus, measles (RNA Paramyxovirus) virus, Epstein-Barr virus, Japanese encephalitis (Flavivirus), West Nile virus (Flavivirus), or rabies (Lyssavirus).

(continued on page 114)

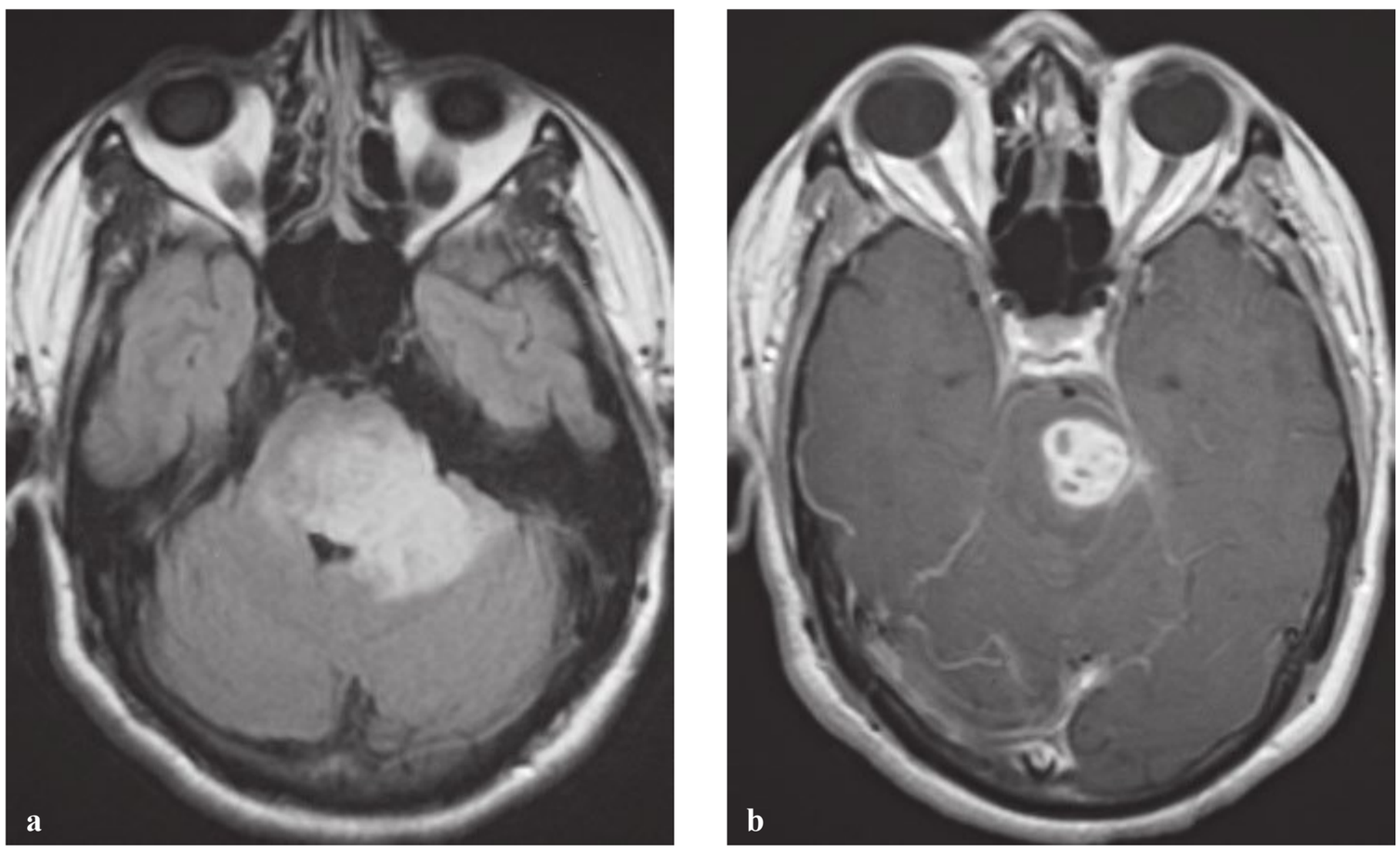

Fig. 1.137 A 21-year-old man with a tuberculoma in the pons and left middle cerebellar peduncle that has **(a)** poorly defined high signal on axial FLAIR and **(b)** gadolinium contrast enhancement on axial T1-weighted imaging.

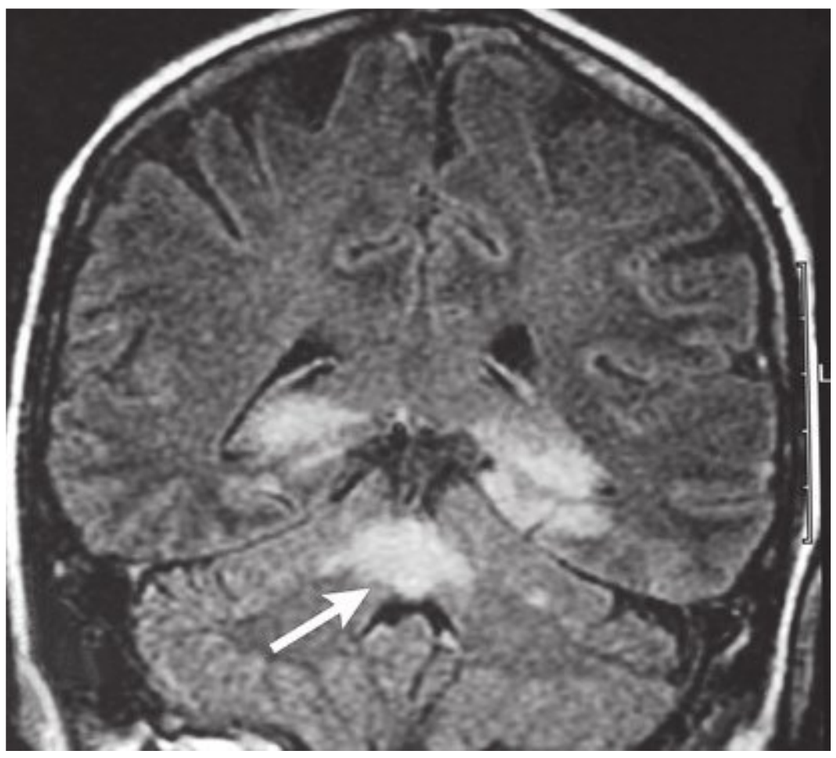

Fig. 1.138 A 64-year-old man with limbic encephalitis from herpes simplex 1 infection. Abnormal high signal is seen in the cerebellar white matter and medial temporal gyri, including the hippocampi, on coronal FLAIR (arrow).

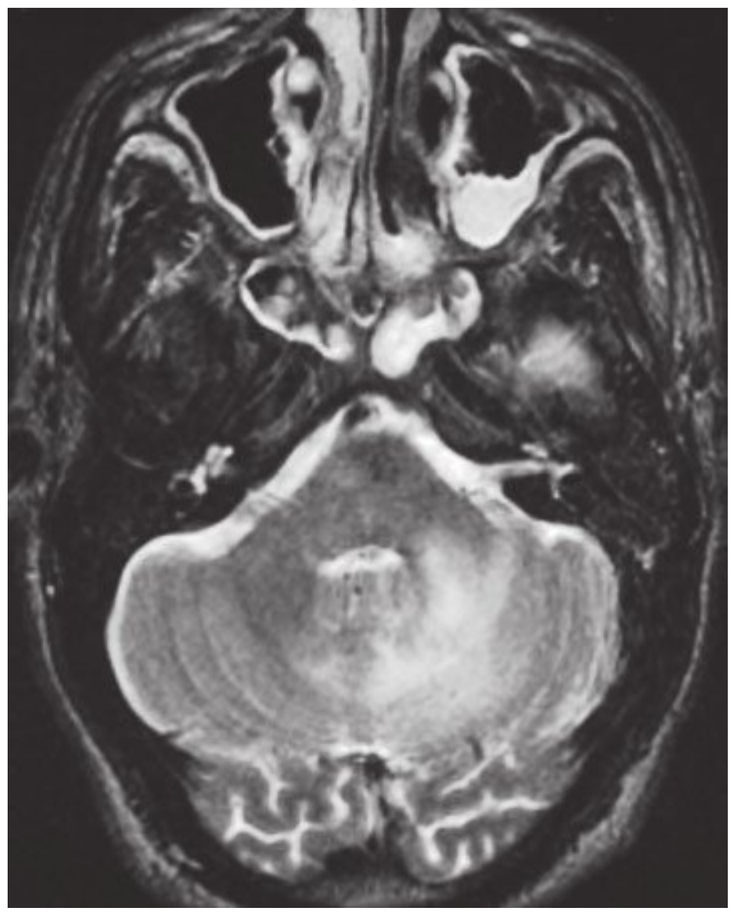

Fig. 1.139 A 32-year-old woman with progressive multifocal leukoencephalopathy (PML) and abnormal poorly defined high signal in the white matter of the left cerebellar hemisphere and left middle cerebellar peduncle on axial T2-weighted imaging.

Table 1.3 (cont.) Solitary intra-axial lesions in the posterior cranial fossa (infratentorial)

Lesions	Imaging Findings	Comments
Acute cerebellitis (**Fig. 1.140**)	MRI: Poorly defined zone or focal area of low-intermediate signal on T1-weighted imaging, intermediate-high signal on T2-weighted imaging, and minimal or no gadolinium contrast enhancement. Cerebellitis involves cerebellar cortex and adjacent white matter. Edema may result in hydrocephalus from compression of the fourth ventricle. CT: Poorly defined zone or focal area of low-intermediate attenuation, and no contrast enhancement.	Acute cerebellitis (acute cerebellar ataxia) is a rare inflammatory disorder associated with cerebellar dysfunction (acute ataxia, dysmetria, and opsoclonus/myoclonus). Can result from infection (Coxsackie virus, rubeola, typhoid fever, poliovirus, pertussis, diphtheria, varicella-zoster virus, Epstein-Barr virus, herpes virus, rubella, rotavirus), or can occur as a post-inflammatory/infectious or postvaccination syndrome. Definitive cause is rarely confirmed. Occurs in patients from 1 to 64 years old, although usually occurs in young patients (mean age = 13 years; median age = 11 years).
Parasitic Brain Lesions		
Toxoplasmosis	MRI: Single or multiple solid and/or cystic lesions located in basal ganglia and/or corticomedullary junctions in cerebral hemispheres, with low-intermediate signal on T1-weighted imaging with or without high signal in peripheral rims; high signal on T2-weighted imaging and FLAIR with or without a central zone of low-intermediate signal, or three layers of high central signal region surrounded by a peripheral rim of low-intermediate signal that is in turn surrounded by high signal; nodular or rim pattern of gadolinium contrast enhancement as well as an "eccentric target pattern" with a peripheral ring-shaped zone of gadolinium contrast enhancement and a small eccentric enhancing nodule along the wall; ± peripheral high T2 signal representing edema. Diffusion-weighted imaging: High signal rims surrounding low signal centers. CT: Lesions can have low or intermediate attenuation, ± peripheral rim or nodular patterns of contrast enhancement.	Most common opportunistic CNS infection in AIDS patients, caused by ingestion of food contaminated with parasites (Toxoplasma gondii). T. gondii is an intracellular protozoan with a worldwide distribution. Also occurs in immunocompetent patients. Acute lesions contain a central zone comprised of necrotic and cellular debris, histiocytes, and neutrophils; an intermediate zone of vascular congestion and tachyzoites; and an outer zone with microglial nodules, T. gondii organisms, and tachyzoites, mild inflammation and vascular congestion. PET/CT shows decreased FDG uptake in T. gondii lesions and can be used to distinguish toxoplasmosis from lymphoma, which has increased FDG uptake.
Cysticercosis (**Fig. 1.141**)	MRI: Single or multiple cystic lesions in brain or meninges. In the active vesicular phase, there are cystic-appearing lesions containing a small 2–4 mm nodule (scolex) with low signal on T1-weighted imaging, FLAIR, and DWI, thin peripheral rim with high signal on FLAIR, and high signal on T2-weighted imaging with minimal peripheral rim or no gadolinium contrast enhancement. No peripheral edema on T2-weighted imaging and FLAIR. In the active colloidal vesicular phase, there is a cystic-appearing lesion with low-intermediate signal on T1-weighted imaging, high signal on T2-weighted imaging, rim and/or nodular pattern of gadolinium contrast enhancement, ± peripheral signal (edema) on T2-weighted imaging. In the active granular nodular phase, the cyst retracts into a more solid gadolinium contrast-enhancing granulomatous nodule. The chronic non-active phase is characterized by calcified nodular granulomas. CT: Chronic phase shows calcified granulomas.	Caused by ingestion of encysted larva of the tapeworm Taenia solium in contaminated food (undercooked pork), cysticercosis involves meninges, subarachnoid space, and cisterns > brain parenchyma > ventricles. It is the most common parasitic disease of the CNS, usually in patients from 15 to 40 years old, and the most common cause of acquired epilepsy in edemic regions. Complications include intracranial hypertension from CSF obstruction, arachnoiditis, meningitis, and vascular occlusion.

Lesions	Imaging Findings	Comments
Hydatid cyst Echinococcus granulosus Echinococcus multilocularis	Echinococcus granulosus MRI: Single or rarely multiple cystic lesions with low signal on T1-weighted imaging and high signal on T2-weighted imaging surrounded by a thin wall with low signal on T2-weighted imaging, typically no gadolinium contrast enhancement or peripheral edema unless superinfected, often located in vascular territory of the middle cerebral artery. Rupture of the hydatid cyst may be contained by the pericyst, causing an inflammation and gadolinium contrast enhancement of the pericyst as well as perilesional edema. Floating germinal membranes with low signal on T1- and T2-weighted imaging can be seen within the fluid deep in the pericyst. Rupture of the hydatid cyst beyond the pericyst can also result in an inflammatory host response. Echinococcus multilocularis MRI: Cystic (± multilocular) and/or solid lesions, with a central zone of intermediate-high signal on T2-weighted imaging surrounded by a slightly thickened rim of low signal, + gadolinium contrast enhancement, and a peripheral zone of high signal on T2-weighted imaging (edema). Calcifications are common.	Rare intracranial lesions caused by parasites Echinococcus granulosus (South America, Middle East, Australia, and New Zealand) or Echinococcus multilocularis (North America, Europe, Turkey, and China). There is CNS involvement in 1 to 4% of cases of hydatid infections. Humans are intermediate hosts from ingestion of tapeworm eggs in fecally contaminated food or by contact with infected animal tissue. Lesions are often large before becoming symptomatic from raised intracranial pressure. The enlarging cystic lesion results in a thin, compressed layer of adjacent host tissue (pericyst) which can show increased vascularity and gliosis, but without gadolinium contrast enhancement. Superinfected hydatid cysts can contain purulent material, often with Staphylococcus aureus, and are typically surrounded by an inflammatory reaction in the adjacent brain tissue and/or meninges.

(continued on page 116)

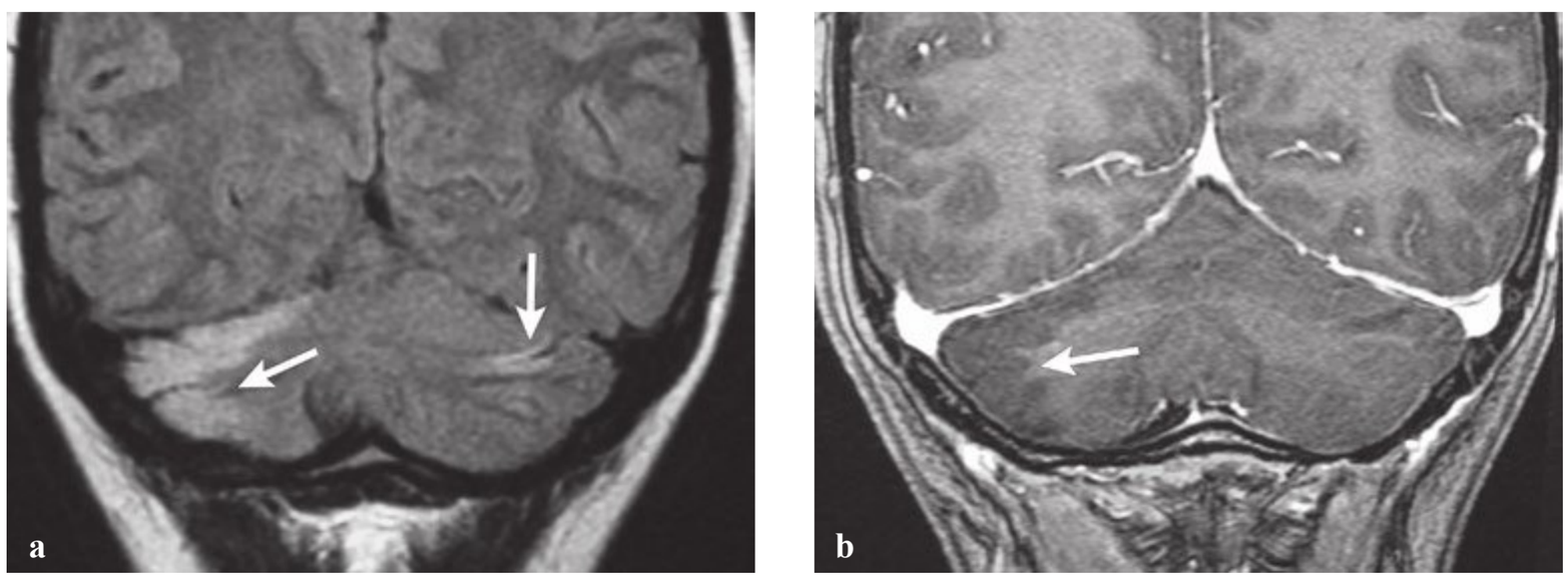

Fig. 1.140 An 18-year-old woman with cerebellitis. **(a)** Abnormal high signal is seen in cerebellar cortex and adjacent white matter (arrows) on coronal FLAIR, but **(b)** there is no gadolinium contrast enhancement on coronal T1-weighted imaging (arrow).

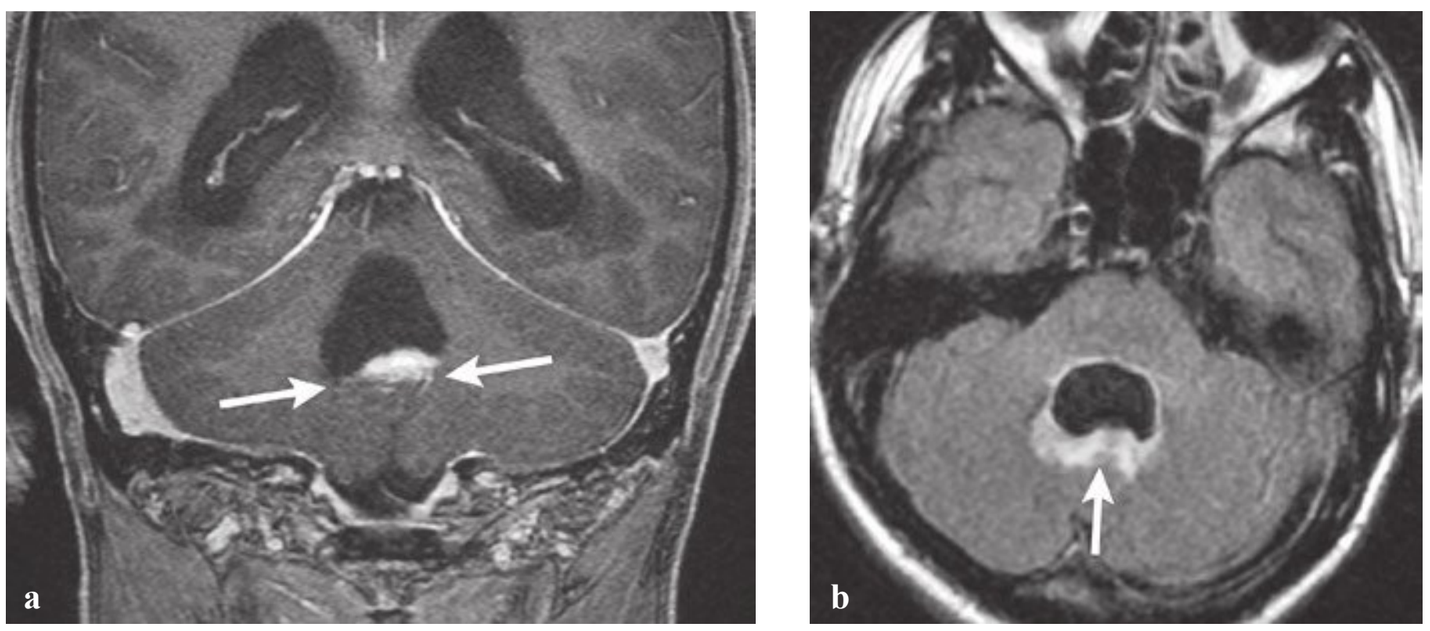

Fig. 1.141 A 35-year-old man with cysticercosis. **(a)** The lesion in the fourth ventricle has both nodular gadolinium contrast-enhancing and cystic portions that result in ventricular obstruction on coronal T1-weighted imaging (arrows). **(b)** The nodular portion of the lesion has high signal on axial FLAIR (arrow).

Table 1.3 (cont.) Solitary intra-axial lesions in the posterior cranial fossa (infratentorial)

Lesions	Imaging Findings	Comments
Inflammatory Lesions: Noninfectious		
Demyelinating disease: multiple sclerosis, acute disseminated encephalomyelitis (**Fig. 1.142** and **Fig. 1.143**)	MRI: Lesions located in cerebral or cerebellar white matter, brainstem, basal ganglia; lesions usually have low-intermediate signal on T1-weighted imaging and high signal on T2-weighted imaging, ± gadolinium contrast enhancement. Gadolinium contrast enhancement can be ringlike or nodular, usually in acute/early subacute phase of demyelination, ± restricted diffusion. Acute demyelinating lesions can have localized mass effect simulating neoplasms. CT: Zones of active demyelination may show contrast enhancement and mild localized swelling.	Multiple sclerosis is the most common acquired demyelinating disease, usually affecting women 20 to 40 years old. Other demyelinating diseases include acute disseminated encephalomyelitis, an immune-mediated demyelination after viral infection; toxin-induced demyelination (from environmental exposure or ingestion, such as alcohol, solvents, etc.; or endogenous toxins in metabolic disorders, such as leukodystrophies, mitochondrial encephalopathies, etc.), radiation injury, trauma, and vascular disease.
Chronic lymphocytic infiltration with pontine perivascular enhancement responsive to steroids (CLIPPERS) (**Fig. 1.144**)	MRI: Poorly defined zones with high signal on T2-weighted imaging and FLAIR involving the pons, midbrain, middle cerebellar peduncles, and/or cerebellum. Small, low-signal foci and slightly prominent veins can be seen on susceptibility weighted imaging. Lesions usually show foci of gadolinium contrast enhancement. Lesions show regression with immunosuppressive treatment.	CLIPPERS is a rare chronic immune-mediated inflammatory disorder involving the central nervous system (pons and cerebellum) with predominant mature T cell perivascular infiltrates. Myelin and vessel walls remain intact. Patients often present with diplopia, nystagmus, facial parathesia, dizziness, and/or ataxia. Lesions are responsive to immunosuppressive treatment with steroids and cyclophosphamide
Neurosarcoid	MRI: Poorly marginated intra-axial zone or zones with low-intermediate signal on T1-weighted imaging, slightly-high to high signal on T2-weighted imaging and FLAIR, usually show gadolinium contrast enhancement, ± localized mass effect and peripheral edema. Often associated with gadolinium contrast enhancement in the leptomeninges and/or dura. CT: Poorly marginated intra-axial zone with low-intermediate attenuation, usually shows contrast enhancement, ± localized mass effect and peripheral edema. Often associated with contrast enhancement in the leptomeninges.	Sarcoidosis is a multisystem noncaseating granulomatous disease of uncertain cause that can involve the CNS in 5 to 15% of cases. If untreated, it is associated with severe neurologic deficits, such as encephalopathy, cranial neuropathies, and myelopathy. Diagnosis of neurosarcoid may be difficult when the neurologic complications precede other systemic manifestations involving the lungs, lymph nodes, skin, bone, and/or eyes.

(continued on page 118)

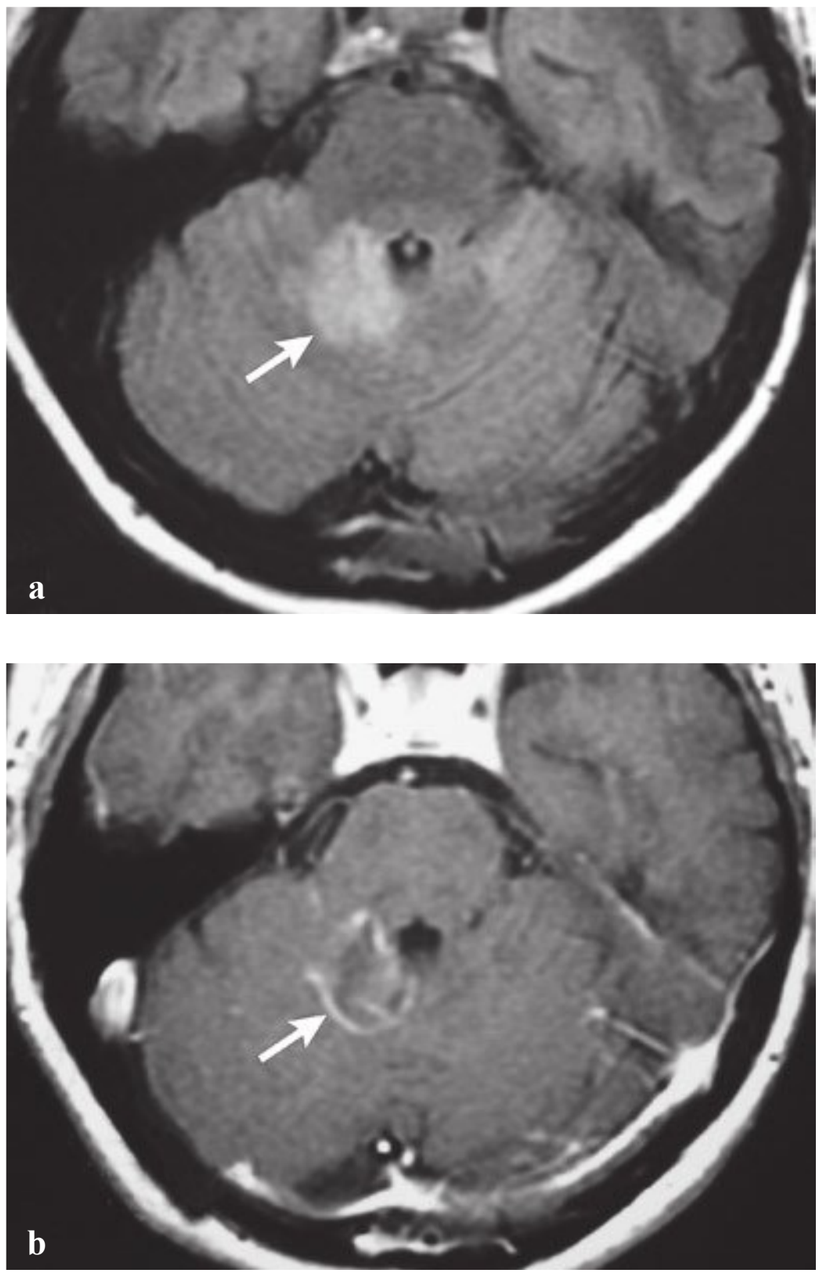

Fig. 1.142 A 50-year-old woman with multiple sclerosis and a zone of acute demyelination in the right cerebellar white matter that has **(a)** high signal on axial FLAIR (arrow) and **(b)** peripheral gadolinium contrast enhancement on axial T1-weighted imaging (arrow).

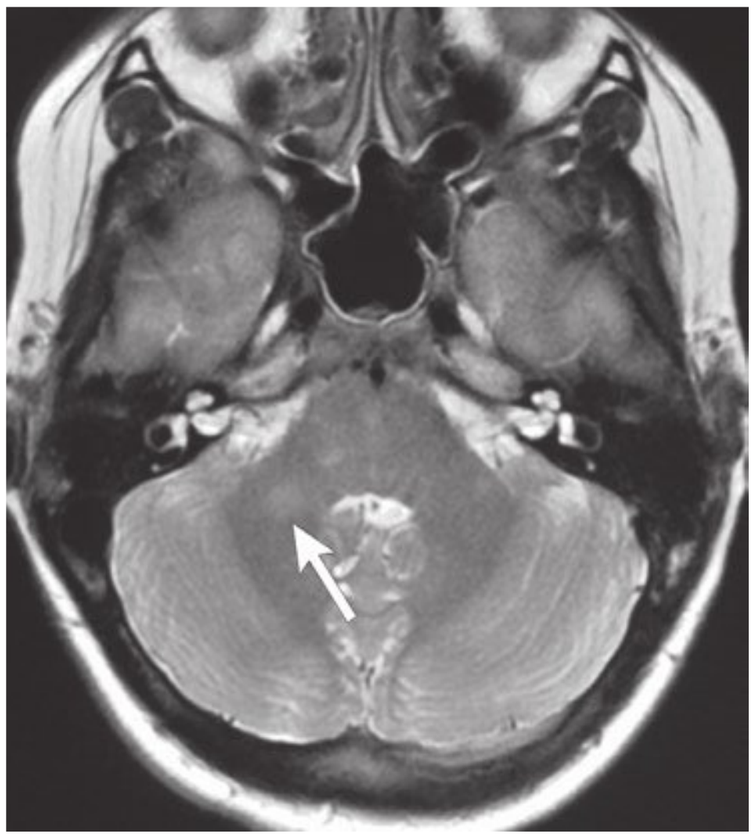

Fig. 1.143 A 12-year-old female with acute disseminated encephalomyelitis (ADEM) and a zone of demyelination (arrow) in the right middle cerebellar peduncle that has high signal on axial T2-weighted imaging.

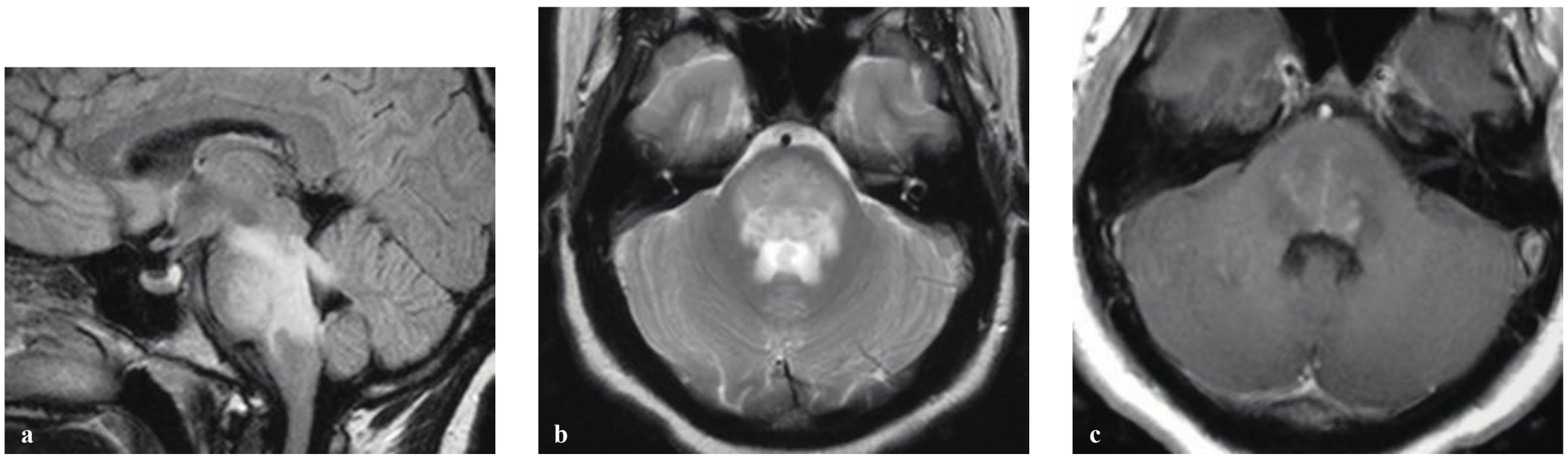

Fig. 1.144 Patient with CLIPPERS. A poorly defined zone with high signal on **(a)** sagittal FLAIR and **(b)** axial T2-weighted imaging is seen in the pons, midbrain, and middle and superior cerebellar peduncles. **(c)** The lesion shows small foci and a thin linear zone of gadolinium contrast enhancement on axial T1-weighted imaging.

Table 1.3 (cont.) Solitary intra-axial lesions in the posterior cranial fossa (infratentorial)

Lesions	Imaging Findings	Comments
Hemorrhage and Vascular Lesions		
Cerebellar hemorrhage (**Fig. 1.145**) Hyperacute hematoma (0–6 hours) Acute phase (6 hours to 2–3 days) Early subacute phase (3–7 days) Late subacute phase (4 days to 1 month)	Hyperacute hematoma MRI: Hemoglobin primarily as diamagnetic oxyhemoglobin (iron Fe^{2+} state), intermediate signal on T1-weighted imaging, and slightly high signal on T2-weighted imaging. CT: A linear relationship exists between CT attenuation and hematocrit, hemoglobin, and protein content. High attenuation of hematoma from 40 to 90 Hounsfield units (HU). A horizontal fluid–fluid level may occur from sedimentation of cellular blood components from the serum. Acute hematoma MRI: Intracellular hemoglobin primarily is paramagnetic deoxyhemoglobin (iron, Fe^{2+} state). Intermediate signal on T1-weighted imaging, low signal on T2-weighted imaging, surrounded by a peripheral zone of high signal (edema) on T2-weighted imaging. CT: Attenuation of intra-axial hematoma can be up to 80–100 HU secondary to clot retraction, ± fluid–fluid level, ± peripheral halo of low attenuation from edema and/or serum extrusion. Early subacute hematoma Hemoglobin becomes oxidized to the iron Fe^{3+} state, methemoglobin. Methemoglobin is primarily intracellular, with high signal on T1-weighted imaging from PEDD and low signal on T2-weighted imaging from PEDD and T2-PRE. CT: Attenuation of intra-axial hematoma can be up to 80–100 HU secondary to clot retraction, ± fluid–fluid level, ± peripheral halo of low attenuation from edema and/or serum extrusion. Late subacute hematoma Methemoglobin eventually becomes primarily extracellular: The hematoma has high signal on T1-weighted imaging from PEDD and high signal on T2-weighted imaging from increased proton density and loss of the T2-PRE effect secondary to membrane lysis.	Can result from trauma, ruptured aneurysms or vascular malformations, coagulopathy, hypertension, adverse drug reaction, amyloid angiopathy, hemorrhagic transformation of cerebral infarction, metastases, abscesses, and viral infections (herpes simplex, CMV). The signal of the hematoma depends on its age, size, location, hematocrit, oxidation state of iron in hemoglobin, degree of clot retraction, extent of edema, and MRI pulse sequence. Hyperacute phase: Complex of extravasated blood consisting of red blood cells, white blood cells, platelets and protein-rich serum. A progressive deposition of fibrin fibrils also occurs. The attenuation of the hematoma increases from 60 to 90 HU, mostly due to the hemoglobin protein concentration and blood clot retraction. Acute phase: Deoxygenation of hemoglobin occurs within intact red blood cell membranes and results in deoxyhemoglobin, which has four unpaired electrons (paramagnetic). The 3D configuration of deoxyhemoglobin does not allow contact of the water protons with the paramagnetic center, eliminating the PEDD effect. The low signal of deoxyhemoglobin on T2-weighted imaging is primarily due to T2-PRE. Early subacute phase: Clot retraction within the hematoma progresses. The ferrous iron in the hematoma becomes oxidized to the ferric state (Fe^{3+}), methemoglobin, which has five unpaired electrons and is paramagnetic. Late subacute phase: Lysis of membranes of red blood cells occurs, resulting in extracellular methemoglobin. Proteolysis of the globin and fibrin protein in the hematoma from macrophages results in a progressive centripetal decrease in attenuation of 0.7 to 1.5 HU/day. Edema and mass effect associated with the hematoma also decrease.
Cerebellar contusion	MRI: Signal of the contusion depends on its age and presence of oxyhemoglobin, deoxyhemoglobin, methemoglobin, hemosiderin, etc. Surrounding the hematoma is a zone of edema with high signal on T2-weighted imaging and FLAIR that has decreased relative cerebral blood volume (rCBF). Contusions eventually appear as focal superficial zones of encephalomalacia with high signal on T2-weighted imaging, ± small zones of low signal on T2-weighted imaging from hemosiderin. CT: Acute contusions have high attenuation from hemorrhage involving the superficial portions of the brain. Remote contusions arppear as localized zones of encephalomalacia.	Contusions are superficial brain injuries involving the cerebellar cortex and subcortical white matter that result from skull fracture and/or acceleration–deceleration trauma to the inner table of the skull.

Lesions	Imaging Findings	Comments
Hemorrhagic metastatic tumor	MRI: Circumscribed spheroid lesions in brain, can have various intra-axial locations, often at gray–white matter junctions, with usually low-intermediate signal on T1-weighted imaging, intermediate-high signal on T2-weighted imaging, ± hemorrhage, calcifications, and cysts. Variable gadolinium contrast enhancement, often high signal on T2-weighted imaging peripheral to nodular enhancing lesion representing axonal edema. CT: Lesions usually have low-intermediate attenuation, ± hemorrhage, calcifications, and cysts. Variable contrast enhancement, often associated with adjacent low attenuation from axonal edema.	Metastatic tumors represent ~ 33%of intracranial tumors, usually from extracranial primary neoplasm in adults > 40 years old. Primary tumor source: lung > breast > GI > GU > melanoma. Metastatic intra-axial tumors associated with hemorrhage include bronchogenic carcinoma, renal cell carcinoma, melanoma, choriocarcinoma, and thyroid carcinoma. May be difficult to distinguish from hemorrhage related to other etiologies.
Vascular		
Hemorrhage from intracranial aneurysm Saccular aneurysm Fusiform aneurysm Dissecting aneurysm (intramural hematoma)	Saccular aneurysm Focal well-circumscribed zone of contrast enhancement. Fusiform aneurysm Tubular dilatation of involved artery. Dissecting aneurysm Initially, the involved arterial wall is thickened in a circumferential or semilunar configuration and has intermediate attenuation with luminal narrowing. Evolution of the intramural hematoma can lead to focal dilatation of the arterial wall.	Abnormal fusiform or focal saccular dilatation of artery secondary to: acquired/degenerative etiology, polycystic disease, connective tissue disease, atherosclerosis, trauma, infection (mycotic), oncotic lesion, arteriovenous malformation, vasculitis, and/or drugs. Focal aneurysms are also referred to as saccular aneurysms, which typically occur at arterial bifurcations and are multiple in 20%of cases. The chance of rupture of a saccular aneurysm causing subarachnoid hemorrhage is related to the size of the aneurysm. Saccular aneurysms > 2.5 cm in diameter are referred to as giant aneurysms. Fusiform aneurysms are often related to atherosclerosis or collagen vascular disease (Marfan syndrome, Ehlers-Danlos syndrome, etc.). With dissecting aneurysms, hemorrhage occurs in the arterial wall from incidental or significant trauma.

(continued on page 120)

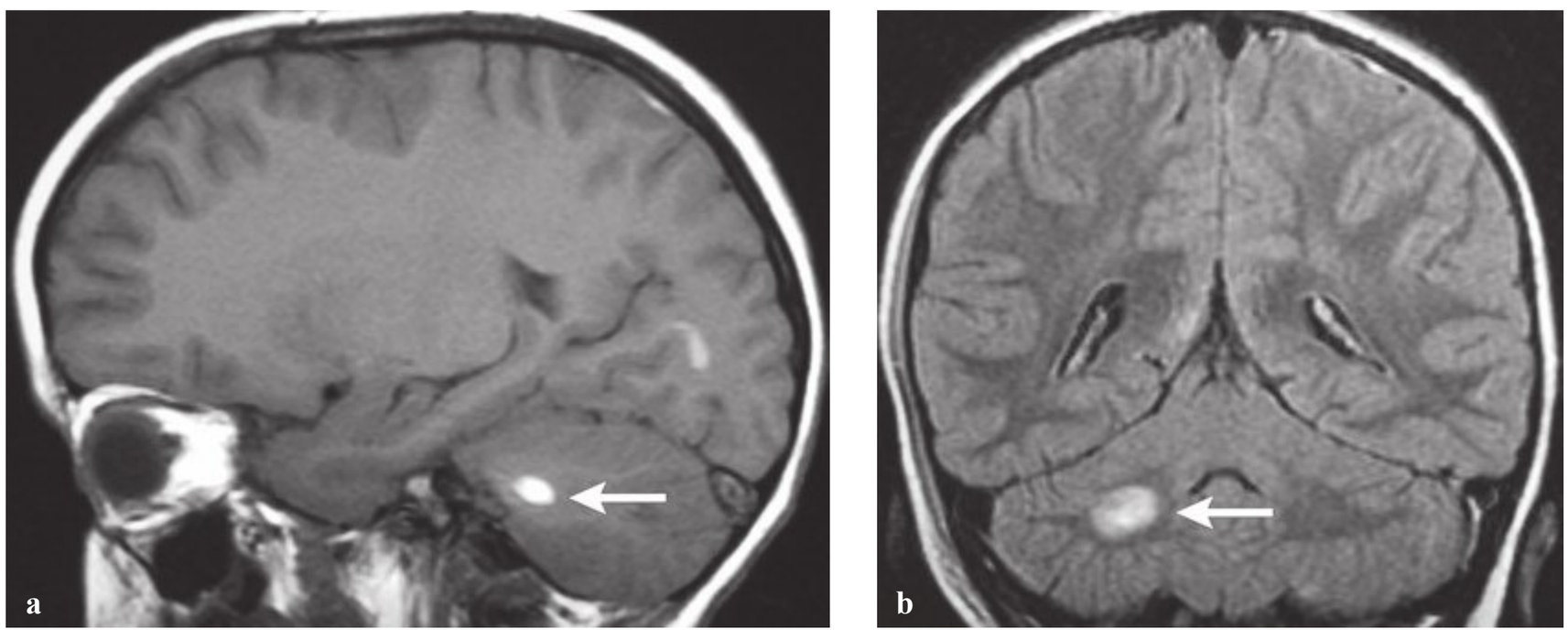

Fig. 1.145 A 6-year-old female with history of trauma resulting in diffuse axonal injury seen as hemorrhagic foci with high signal on **(a)** sagittal T1-weighted imaging (arrow) and **(b)** coronal FLAIR (arrow).

Table 1.3 (cont.) Solitary intra-axial lesions in the posterior cranial fossa (infratentorial)

Lesions	Imaging Findings	Comments
Hemorrhage from arteriovenous malformation (AVM) (**Fig. 1.146**)	MRI: AVMs contain multiple, tortuous, tubular flow voids on T1- and T2-weighted imaging secondary to patent arteries with high blood flow, as well as thrombosed vessels with variable signal, and areas of hemorrhage in various phases. The venous portions often show gadolinium contrast enhancement. Gradient echo MRI shows flow-related enhancement (high signal) in patent arteries and veins of the AVM. MRA using time-of-flight or phase-contrast techniques can provide additional detailed information about the nidus, feeding arteries and draining veins, and presence of associated aneurysms. AVMs are usually not associated with mass effect unless there is recent hemorrhage or venous occlusion. CT: Lesions can be located in the brain parenchyma, pia, dura, or both locations. AVMs contain multiple tortuous vessels. The venous portions often show contrast enhancement. AVMs are usually not associated with mass effect unless there is recent hemorrhage or venous occlusion. CTA can show the arterial, nidus, and venous portions of the AVM in various phases.	Infratentorial AVMs are much less common than supratentorial AVMs.
Cavernous hemangioma/ malformation (**Fig. 1.147**)	MRI: Single or multiple multilobulated intra-axial lesions that have a peripheral rim or irregular zone of low signal on T2-weighted imaging secondary to hemosiderin, surrounding a central zone of variable signal (low, intermediate, high, or mixed) on T1- and T2-weighted imaging depending on ages of hemorrhagic portions. Gradient echo techniques useful for detecting multiple lesions. CT: Lesions have intermediate to slightly increased attenuation, ± calcifications.	Can be located in many different locations. Supratentorial cavernous angiomas occur more frequently than infratentorial lesions. Lesions consist of epithelium-lined vascular channels within a collagenous stroma. Zones of thrombus and remote hemorrhage with hemosiderin are often present. Dystrophic calcifications may be present. Developmental venous anomalies occur in 25% of cases. Hereditary syndromes in which multiple cavernous malformations occur are associated with mutations of the CCM1/KRIT1, CCM2/MGC4608, and CCM3PDCD10 genes and have a higher risk of hemorrhage (up to 5% per year) than sporadic cavernous malformations.

(continued on page 122)

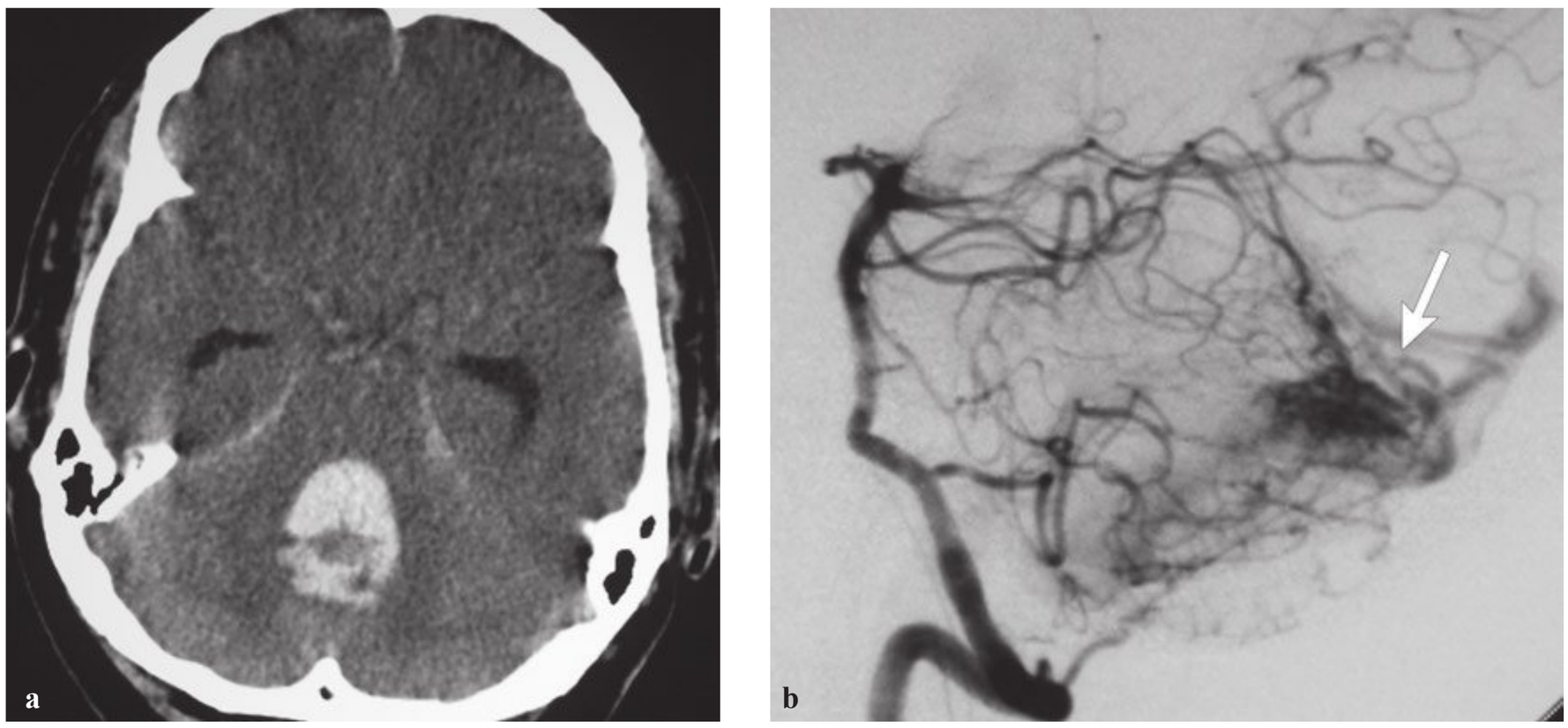

Fig. 1.146 A 53-year-old man with hemorrhage in the vermis and fourth ventricle on **(a)** axial CT that resulted from an arteriovenous malformation, as seen on **(b)** conventional arteriogram (arrow).

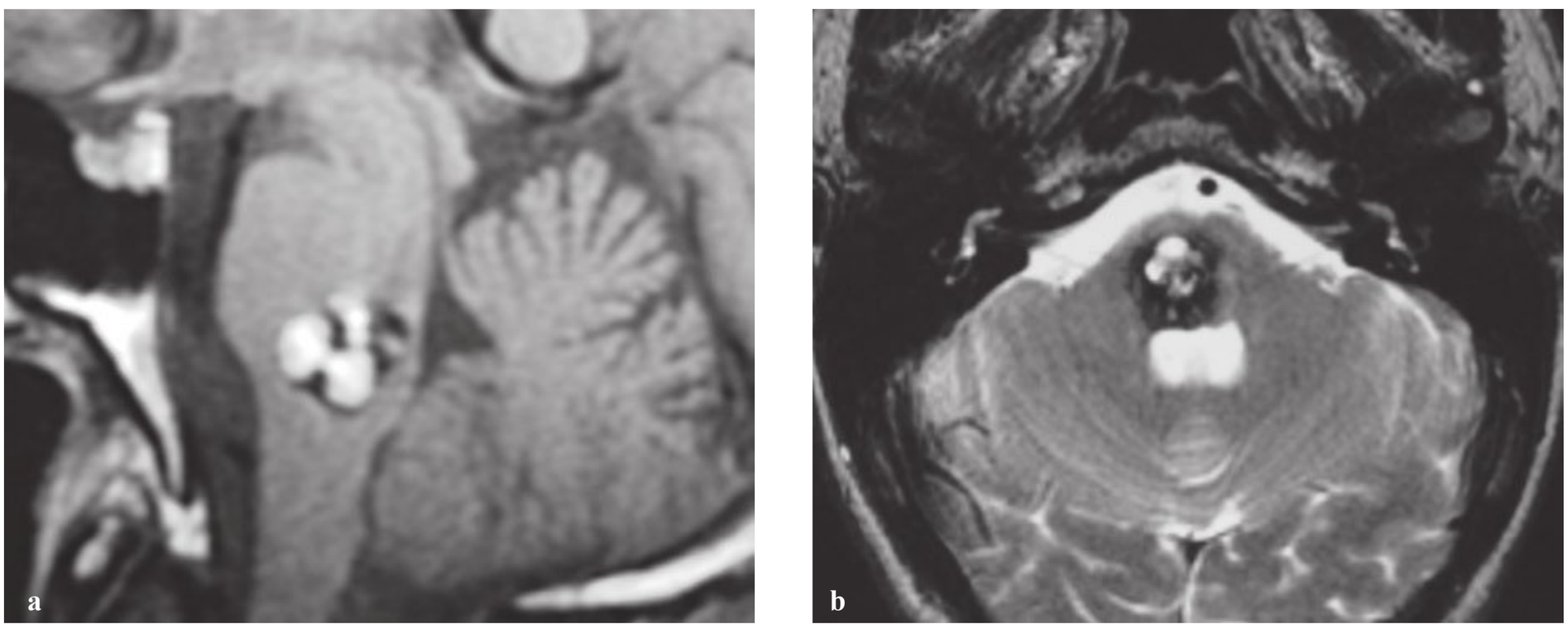

Fig. 1.147 A 36-year-old man with a cavernous malformation in the pons that has **(a)** mixed high and low signal on sagittal T1-weighted imaging and **(b)** a central zone with high signal surrounded by an irregular rim of low signal on axial T2-weighted imaging.

Table 1.3 (cont.) Solitary intra-axial lesions in the posterior cranial fossa (infratentorial)

Lesions	Imaging Findings	Comments
Venous angioma/ developmental venous anomaly (**Fig. 1.148**)	MRI: Gadolinium contrast-enhanced T1-weighted imaging shows a group of small veins in a "Medusa head" configuration that connect and drain into a slightly prominent enhancing vein. CT: No abnormality or small, slightly hyperdense zone prior to contrast administration. Contrast enhancement seen in a slightly prominent vein draining a collection of small veins.	Considered an anomalous venous formation typically not associated with hemorrhage, usually an incidental finding except when associated with cavernous malformation. Lesions consist of thin-walled venous channels within normal neural tissue. Can occur in association with cavernous malformations. Account for more than 50% of cerebrovascular malformations.
Capillary telangiectasia (**Fig. 1.149**)	MRI: Postcontrast MRI shows a small zone with enhancement without abnormal mass effect. Lesions are typically inconspicuous on precontrast T1- and T2-weighted imaging. CT: Not usually seen on pre- or postcontrast examinations.	Asymptomatic, often incidental findings on gadolinium contrast-enhanced MRI, which shows enhancement of a group of thin-walled vessels and capillaries within normal neural tissue in the brain or brainstem. Most are less than 1 cm in diameter. Can occur 10 years after radiation therapy. Common locations include the pons and cerebellum. Account for up to 20% of vascular malformations in brain.

(continued on page 124)

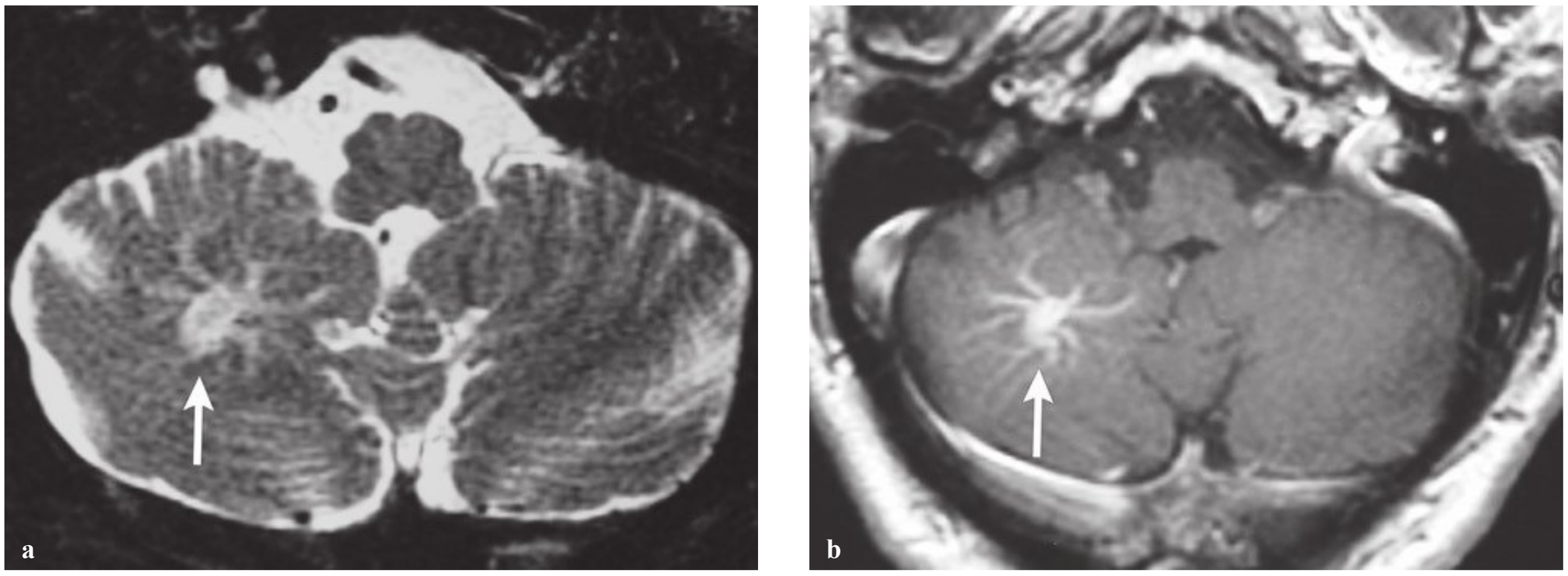

Fig. 1.148 **(a)** A developmental venous anomaly (venous angioma) is seen in the right cerebellar hemisphere with high signal on axial T2-weighted imaging (arrow) and **(b)** shows gadolinium contrast enhancement of a group of small veins in a "Medusa head" configuration that connect and drain into a slightly prominent, enhancing vein on axial T1-weighted imaging (arrow).

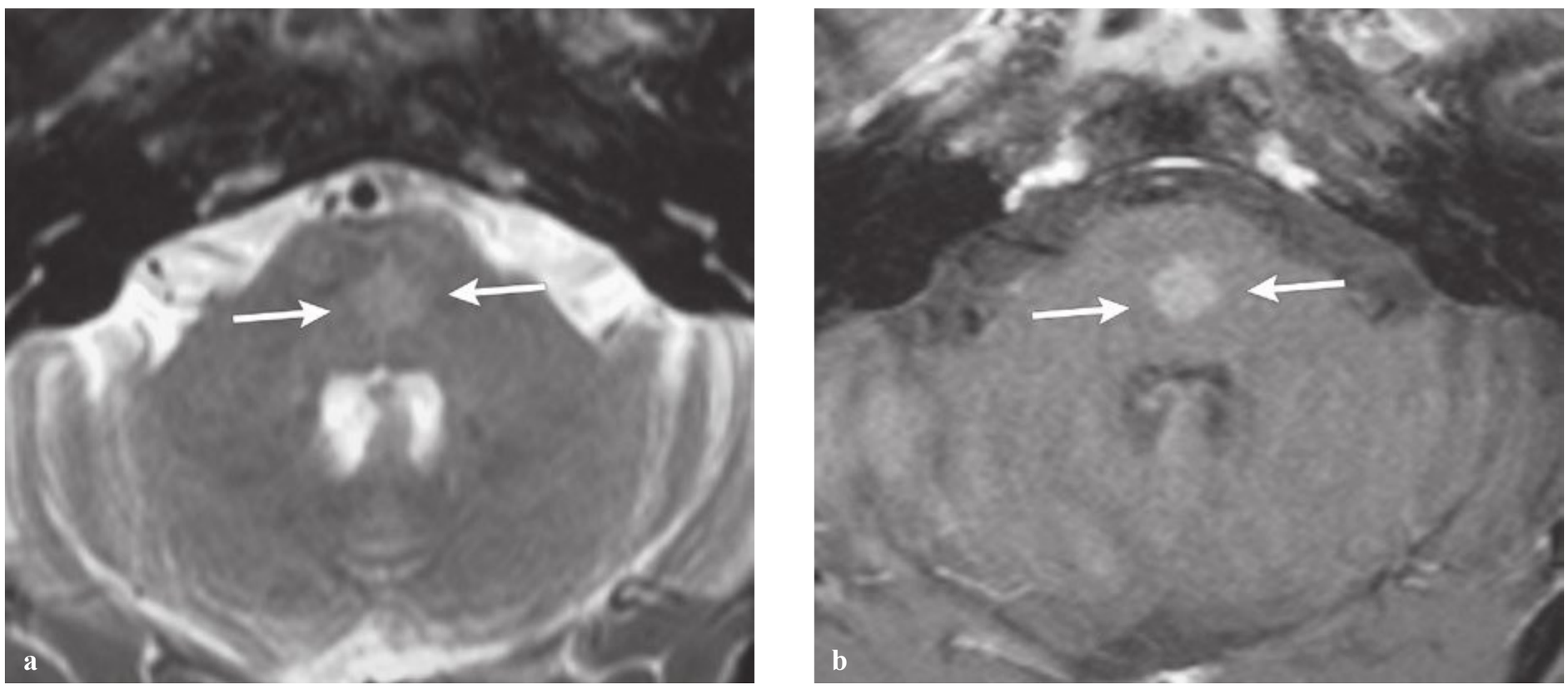

Fig. 1.149 A 79-year woman with a capillary telangiectasia in the pons that is seen as **(a)** a poorly defined zone of slightly high signal on axial T2-weighted imaging (arrows) and **(b)** mild gadolinium contrast enhancement on axial T1-weighted imaging (arrows).

Table 1.3 (cont.) Solitary intra-axial lesions in the posterior cranial fossa (infratentorial)

Lesions	Imaging Findings	Comments
Cerebellar Ischemia/Infarction		
Cerebellar/brainstem infarction (**Fig. 1.150** and **Fig. 1.151**) Hyperacute (< 12 hours) Acute (12–24 hours) Early subacute (24 hours to 3 days) Late subacute (4 days to 2 weeks) Post-subacute infarct (2 weeks to 2 months) Remote infarct (> 2 months)	CT and MRI features of cerebral, cerebellar, and brainstem infarcts depend on age of infarct relative to time of examination. Hyperacute infarction CT: No abnormality (50%), decreased attenuation and blurring of lentiform nuclei, hyperdense artery in up to 50% MRI: Localized edema, usually isointense signal to normal brain on T1- and T2-weighted imaging. Diffusion-weighted images can show positive findings related to decreased apparent diffusion coefficients secondary to cytotoxic edema, and absence of arterial flow void or arterial enhancement in the vascular distribution of the infarct. Acute infarction CT: Zones with decreased attenuation in brainstem, blurring of junction between cerebellar cortex and white matter, sulcal effacement. MRI: Intermediate signal on T1-weighted imaging, high signal on T2-weighted imaging, localized edema. Signal abnormalities commonly involve the cerebellar cortex and subcortical white matter, and/or basal ganglia. Early subacute infarction CT: Localized swelling at sites with low attenuation involving gray and white matter (often wedge-shaped), ± hemorrhage. MRI: Zones with low-intermediate signal on T1-weighted imaging, high signal on T2-weighted imaging, localized edema, ± hemorrhage, ± gadolinium contrast enhancement. Late subacute infarction CT: Localized swelling increases and then decreases, low attenuation at lesion can become more prominent, ± gyral contrast enhancement. MRI: Low-intermediate signal on T1-weighted imaging, high signal on T2-weighted imaging, edema/mass effect diminishing, ± hemorrhage, ± contrast enhancement. Post-subacute infarct CT: ± Gyral contrast enhancement, localized mass effect resolves. MRI: Low-intermediate signal on T1-weighted imaging, high signal on T2-weighted imaging, edema resolves, ± hemorrhage, ± enhancement eventually declines. Remote infarct CT: Zone of low attenuation associated with encephalomalacia. MRI: Low signal on T1-weighted imaging, high signal on T2-weighted imaging, encephalomalacic changes, ± calcification, hemosiderin.	Cerebellar infarcts usually result from occlusive vascular disease involving branches from the basilar artery (PICA, AICA). Vascular occlusion may be secondary to atheromatous arterial disease, cardiogenic emboli, neoplastic encasement, hypercoagulable states, dissection, or congenital anomalies. Cerebellar infarcts usually result from arterial occlusion involving specific vascular territories, although occasionally they may occur due to metabolic disorders (mitochondrial encephalopathies, etc.) or intracranial venous occlusion (thrombophlebitis, hypercoagulable states, dehydration, etc.), and the latter do not correspond to arterial distributions.

(continued on page 126)

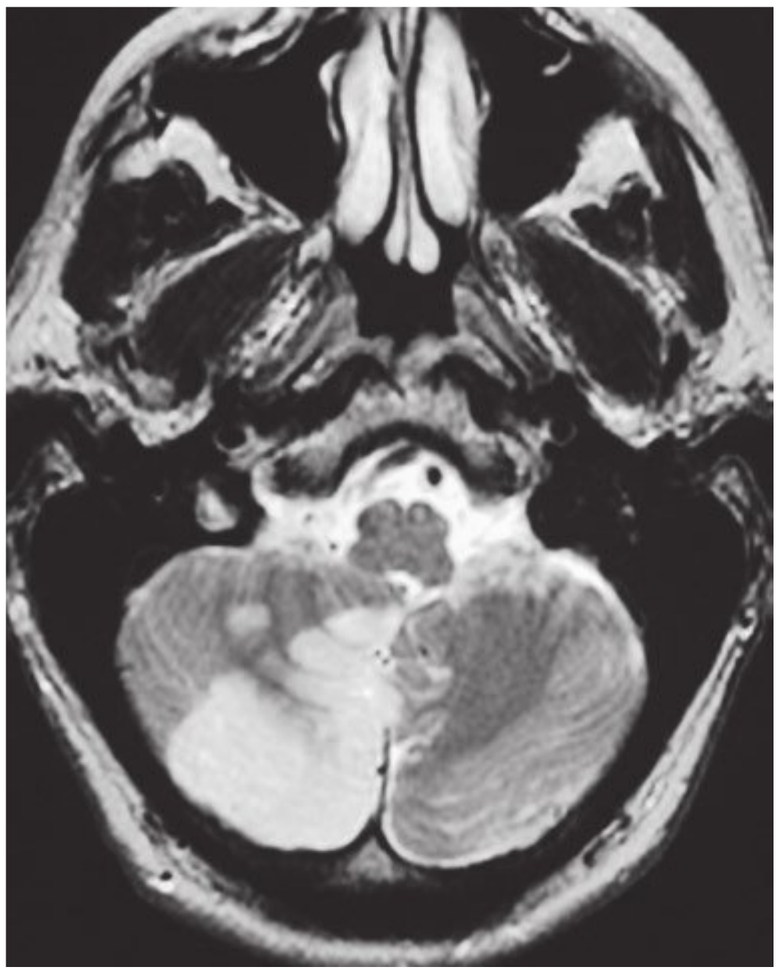

Fig. 1.150 A 64-year-old man with an infarct in the inferior and posterior portions of the right cerebellar hemisphere in the vascular distribution of the right posterior inferior cerebellar artery. The wedge-shaped infarct has high signal on axial T2-weighted imaging and involves both cerebellar cortex and white matter.

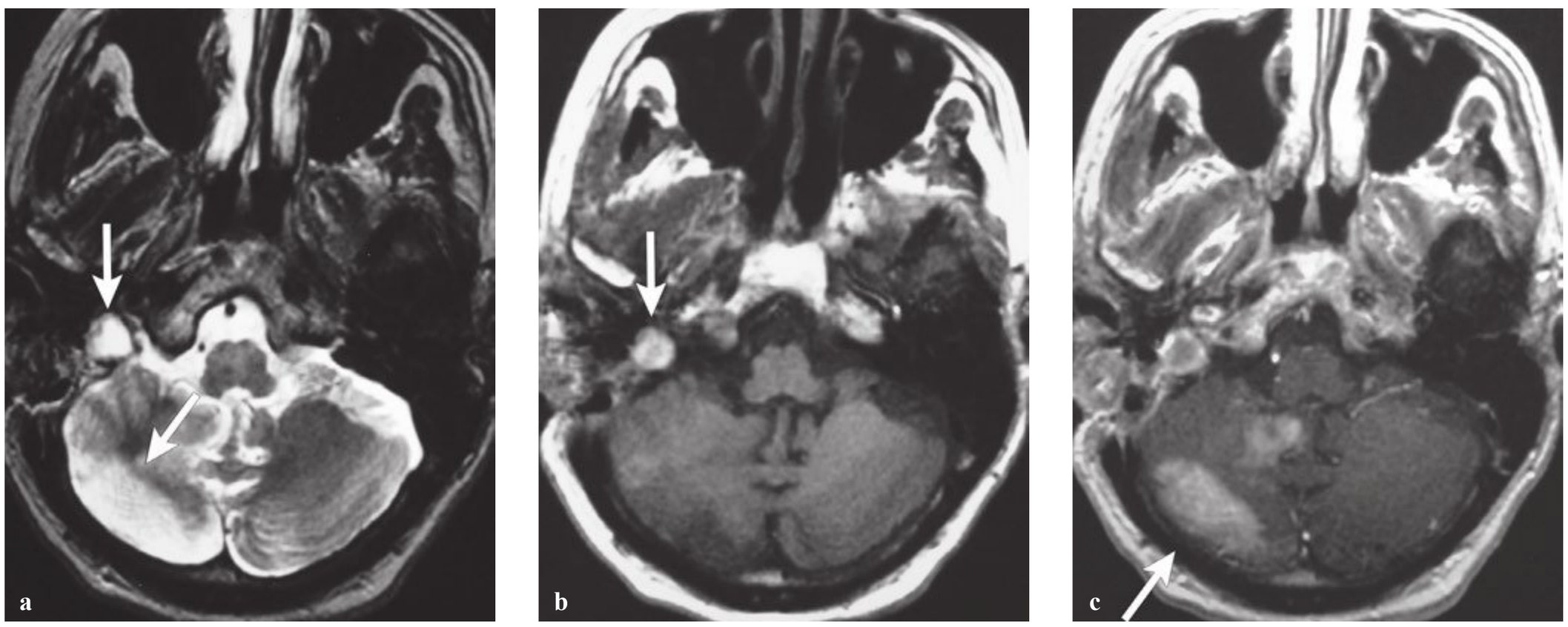

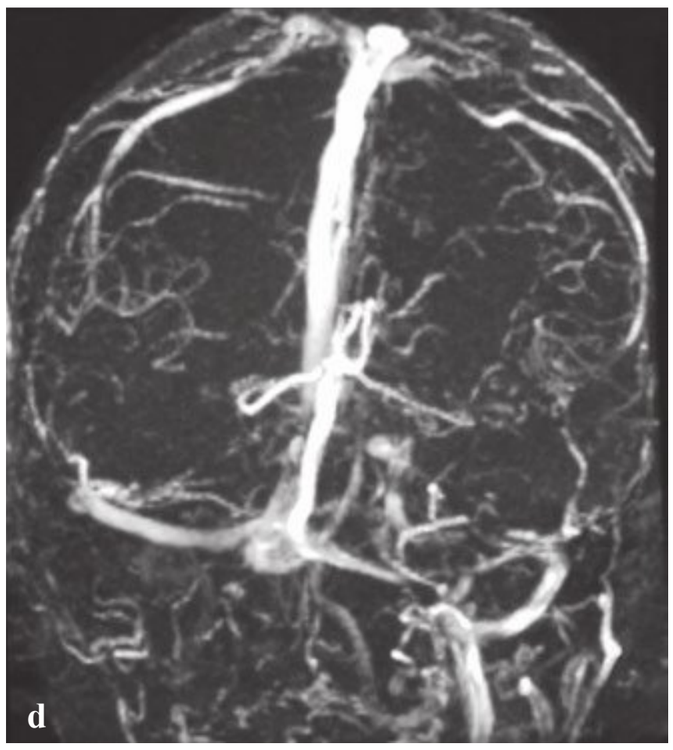

Fig. 1.151 A 64-year-old man with mastoiditis causing thrombosis of the right jugular vein that has high signal on **(a)** axial T2-weighted imaging (arrow), and on **(b)** axial T1-weighted imaging (arrow). A gadolinium contrast-enhancing venous infarct (arrow) is seen in the right cerebellar hemisphere on **(c)** axial T1-weighted imaging (arrow), which also has high signal on axial T2-weighted imaging **(a)**. **(d)** Coronal MRV shows lack of flow in the occluded right sigmoid venous sinus and right jugular vein.

Table 1.3 (cont.) Solitary intra-axial lesions in the posterior cranial fossa (infratentorial)

Lesions	Imaging Findings	Comments
Other Lesions		
Central pontine myelinolysis/osmotic myelinolysis (**Fig. 1.152**)	MRI: Poorly defined zone of low-intermediate signal and high signal on T2-weighted imaging involving the central portion of the pons (central pontine myelinolysis). Extrapontine myelinolysis occurs as zones with high signal on T2-weighted imaging in the cerebral white matter, external capsules, basal ganglia. thalami, midbrain, and middle cerebellar peduncles, ± small areas of gadolinium contrast enhancement in the first 4 weeks. ADC values are low in the acute phase. CT: Poorly defined zone of decreased attenuation involving the central portion of the pons (central pontine myelinolysis). Extrapontine myelinolysis occurs as zones with decreased attenuation in the cerebral white matter, external capsules, basal ganglia. thalami, midbrain, and middle cerebellar peduncles, ± occasional contrast enhancement.	Demyelinating disorder resulting from rapid correction of hyponatremia in chronically ill, malnourished, or alcoholic patients. Associated with diabetes mellitus, hepatitis, and chronic disease of the lungs, liver, and/or kidneys. Damage occurs to the myelin sheaths, without initial destruction of axons. Can result in spastic tetraparesis, quadraparesis, pseudobulbar paralysis, seizures, coma, and locked-in syndrome. Clinical findings can regress or progress, and the disease is occasionally fatal.
Hypertensive encephalopathy (posterior reversible encephalopathy syndrome/PRES) (**Fig. 1.153**)	MRI: Zones of low-intermediate signal on T1-weighted imaging and high signal on T2-weighted imaging in subcortical white matter, ± cerebral cortex, ± gadolinium contrast enhancement. Findings can be reversed if eliciting cause is corrected. CT: Foci and/or confluent zones of decreased attenuation in subcortical white matter, ± cerebral cortex, ± contrast enhancement.	Occurs with elevations in blood pressure above the upper limit in cerebral vascular autoregulation, resulting in capillary leakage of fluid in the brain, often in arterial boundary zones. Associated with immunosuppressant drugs (tacrolimus/FK506, cyclosporine) chemotherapy (cisplatin, L-asparaginase, others), acute onset of hypertension, pre-eclampsia, eclampsia, renal dysfunction, and fluid overload. Neurologic symptoms include confusion, headaches, seizures, visual loss, dysarthria, and coma. Cortical abnormalities may be related to cortical laminar necrosis due to hypoperfusion injury.
Radiation injury/necrosis	MRI: Focal lesion ± mass effect or poorly defined, intra-axial zone of low-intermediate signal on T1-weighted imaging, intermediate-high signal on T2-weighted imaging, ± gadolinium contrast enhancement involving tissue (white matter and/or gray matter) in the field of radiation treatment. Relative cerebral blood volume (rCBV) values for radiation necrosis (0.6) have been shown to be significantly lower than those for recurrent high-grade gliomas (2.6). Radiation necrosis at sites of surgically resected metastatic lesions may show a three-layer pattern on diffusion-weighted imaging consisting of an inner liquefied portion with high apparent diffusion coefficient (ADC), a middle layer with decreased ADC without gadolinium contrast enhancement, and an outer layer with gadolinium contrast enhancement with high ADC. CT: Focal lesion ± mass effect or poorly defined zone of low-intermediate attenuation, ± contrast enhancement involving tissue (gray matter and/or white matter) in field of treatment.	Severe local tissue reaction to radiation treatment, related to doses over 65 Gy. Occurs from 3–6 months to 12 months, and occasionally up to 10 years, after radiation treatment. Occurrence is up to three times higher when chemotherapy is given concurrently with radiation treatment. Results from vascular endothelial injury and apoptosis, leading to thrombosis, fibrinous exudates, hyalinization with luminal stenosis, and fibrinoid and vascular necrosis, as well as glial and white matter damage. May be difficult to distinguish from neoplasm. Using dynamic susceptibility contrast-enhanced perfusion MRI, $rCBV_{max}$ and $rCBV_{mean}$ values for recurrent tumor have been shown to be significantly higher than tumor necrosis, which aids in distinguishing between these two diagnoses. Similar findings have been found with perfusion computed tomography. Perfusion MRI has been shown to be superior to ^{18}F-FDG PET and ^{11}C-methionine PET in distinguishing high-grade gliomas from radiation necrosis. MR hydrogen spectroscopy shows decreased N-acetylaspartate (NAA) and choline peaks at sites of radiation necrosis, whereas residual and recurrent tumors show elevated choline peaks and choline/creatine (Cho/Cr) ratio > 2.

Lesions	Imaging Findings	Comments
Lipoma (**Fig. 1.154**)	MRI: Signal isointense to subcutaneous fat on T1-weighted imaging (high signal), and on T2-weighted imaging, signal suppression occurs with frequency-selective fat saturation techniques or with short T1 inversion recovery (STIR) method. Typically there is no gadolinium contrast enhancement or peripheral edema. Lipomas can be tubulonodular or curvilinear. CT: Lipomas have attenuation equal to fat (-40 HU to -100 HU), ± calcifications or ossifications.	Benign fatty lesions resulting from congenital malformation often located in or near the midline may contain calcifications and/or traversing blood vessels. Common locations in the posterior cranial fossa include cerebellopontine angle cisterns and tectal plate.

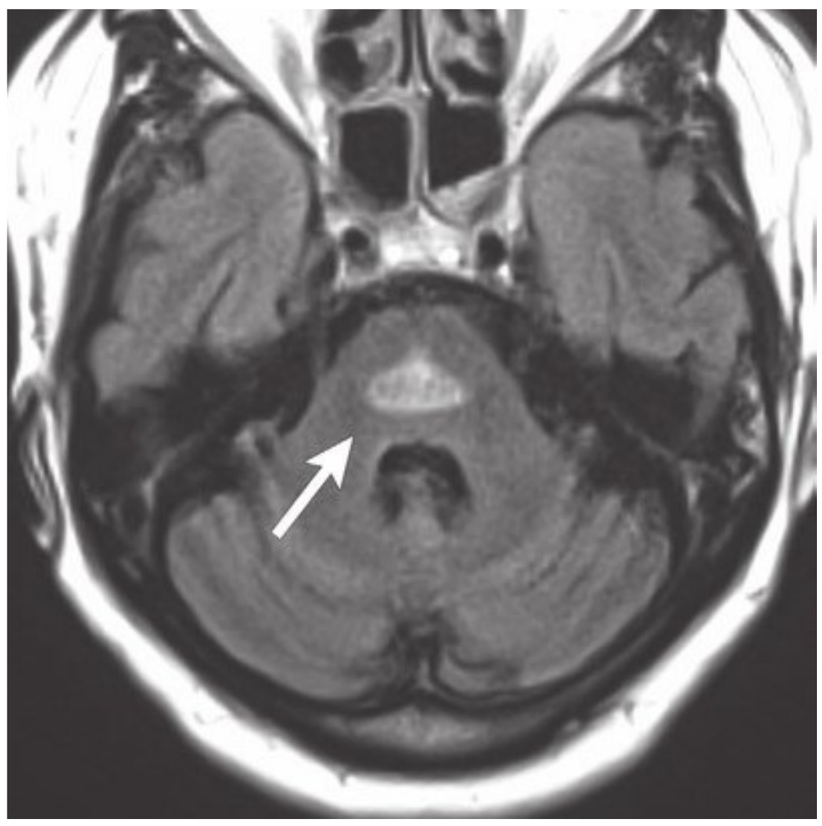

Fig. 1.152 A 44-year-old man with osmotic myelinolysis that is seen as a zone of high signal on axial T2-weighted imaging in the central portion of the pons (arrow).

Fig. 1.154 A 52-year-old woman with a lipoma (arrow) located at the pial surface of the left middle cerebellar peduncle in the left cerebellopontine angle cistern, which has high signal on axial T1-weighted imaging.

Fig. 1.153 A 60-year-old woman with a history of bone marrow transplant and immunosuppression with FK506/tacrolimus complicated by posterior reversible encephalopathy syndrome. A poorly defined zone with high signal is seen in the central portion of the pons on **(a)** axial T2-weighted imaging (arrow) and **(b)** coronal FLAIR. Additional zones with high signal are seen in the subcortical cerebral white matter and thalami representing extrapontine myelinolysis.

Table 1.4 Multiple intra-axial lesions in the brain

- Congenital
  - Gray matter heterotopia
  - Unilateral hemimegalencephaly
- Neoplasms
  - Metastatic disease
  - Lymphoma
  - Leukemia (myeloid sarcoma, granulocytic sarcoma, chloroma)
  - Gliomatosis cerebri
  - Glioblastoma multiforme
- Other Neoplasms or Tumorlike Lesions
  - Neurofibromatosis type 1 (NF1): vacuolated myelin/dysplastic white matter lesions
  - Hamartomas: tuberous sclerosis
  - Cortical hamartomas (tubers)
  - Subependymal hamartomas
  - Hemangioblastomas (von Hippel-Lindau disease)
  - Neurocutaneous melanosis
- Inflammatory Lesions: Infection
  - Cerebritis
  - Pyogenic brain abscess
  - Lyme disease (spirochete infection)
  - Syphilis (spirochete infection)
  - Rickettsial infection—Rocky Mountain spotted fever (RMSF)
  - Tuberculomas
  - Fungal brain lesions
  - Herpes simplex virus infection
  - Cytomegalovirus (CMV)
  - Human immunodeficiency virus (HIV) infection
  - Progressive multifocal leukoencephalopathy
  - Japanese encephalitis virus infection
  - Rabies virus infection
  - Acute measles encephalitis
  - Subacute sclerosing panencephalitis from measles virus
  - Progressive multifocal leukoencephalopathy (PML)—immune reconstitution inflammatory syndrome (IRIS)
  - Prion disease
- Inflammatory Lesions: Parasitic Infections
  - Toxoplasmosis
  - Cysticercosis
  - Hydatid cysts
  - Echinococcus granulosus
  - Echinococcus multilocularis
  - Amebiasis
  - Granulomatous amebic encephalitis
  - Primary amebic meningoencephalitis
  - Malaria
  - Schistosomiasis
  - Trypanosomiasis
  - Paragonimiasis
  - Sparganosis
- Inflammatory Lesions: Noninfectious
  - Demyelinating disease—Multiple sclerosis
  - Acute disseminated encephalomyelitis
  - Neurosarcoid
  - Brain contusions
  - Diffuse axonal injury
  - Hemorrhagic metastatic lesions
  - Amyloid angiopathy
- Vascular Malformations
  - Arteriovenous malformations (AVMs)
  - Cavernous malformations
  - Capillary telangiectasias
  - Venous angioma/developmental venous anomaly
- Cerebral Ischemia/Infarction
  - Ischemic disease related to occlusion of small vessels (small-vessel disease)
  - Periventricular leukomalacia
  - Brain infarcts from embolic disease
  - Brain infarcts from vasculitis
  - CADASIL
  - CARASIL
  - Susac syndrome (retinocochleocerebral vasculopathy)
  - Systemic lupus erythematosus (SLE)
  - Antiphospholipid syndrome
  - Behçet's syndrome
  - Hypoxic-ischemic injury
  - Neurologic decompressive sickness
- Metabolic Disorders
  - Seizure
  - MELAS/MERRF
  - Leigh's disease
  - Kearns-Sayre syndrome
  - Fabry disease
  - Hyperglycemia
  - Hypoglycemia
  - Disorders of amino acid and urea cycle metabolism: lysosomal enzyme defects: Tay-Sachs disease and Sandhoff disease (gangliosidoses)
  - Lysosomal enzyme defects: Neuronal ceroid lipofuscinosis
  - Lysosomal enzyme defects: mucopolysaccharidoses
  - Carbon monoxide poisoning
  - Heroin toxicity
  - Cocaine toxicity
- Other Lesions
  - Radiation necrosis
  - Pontine and extrapontine osmotic myelinolysis
  - Hypertensive encephalopathy (posterior reversible encephalopathy syndrome [PRES])
  - Reversible cerebral vasoconstriction syndrome
  - Paraneoplastic syndrome

Table 1.4 Multiple intra-axial lesions in the brain

Lesions	Imaging Findings	Comments
Congenital		
Gray matter heterotopia (**Fig. 1.155**)	Nodular heterotopia appears as one or more nodules of gray matter attenuation on CT, and as MRI signal isointense to gray matter along the ventricles or within the cerebral white matter (**Fig. 1.155a**). Focal subcortical heterotopia can be seen as irregular nodular or multinodular masslike zones in subcortical regions with gray matter attenuation on CT, and as MRI signal isointense to gray matter (**Fig. 1.155b**). Laminar heterotopia appears as a band or bands of MRI signal isointense to gray matter within the cerebral white matter (**Fig. 1.155c**).	Disorder of neuronal migration (at 7 to 22 weeks of gestation) where a collection or layer of neurons is located between the ventricles and cerebral cortex. Can have a bandlike (laminar) or nodular appearance isointense to gray matter and may be unilateral or bilateral. Associated with seizures and schizencephaly.

(continued on page 130)

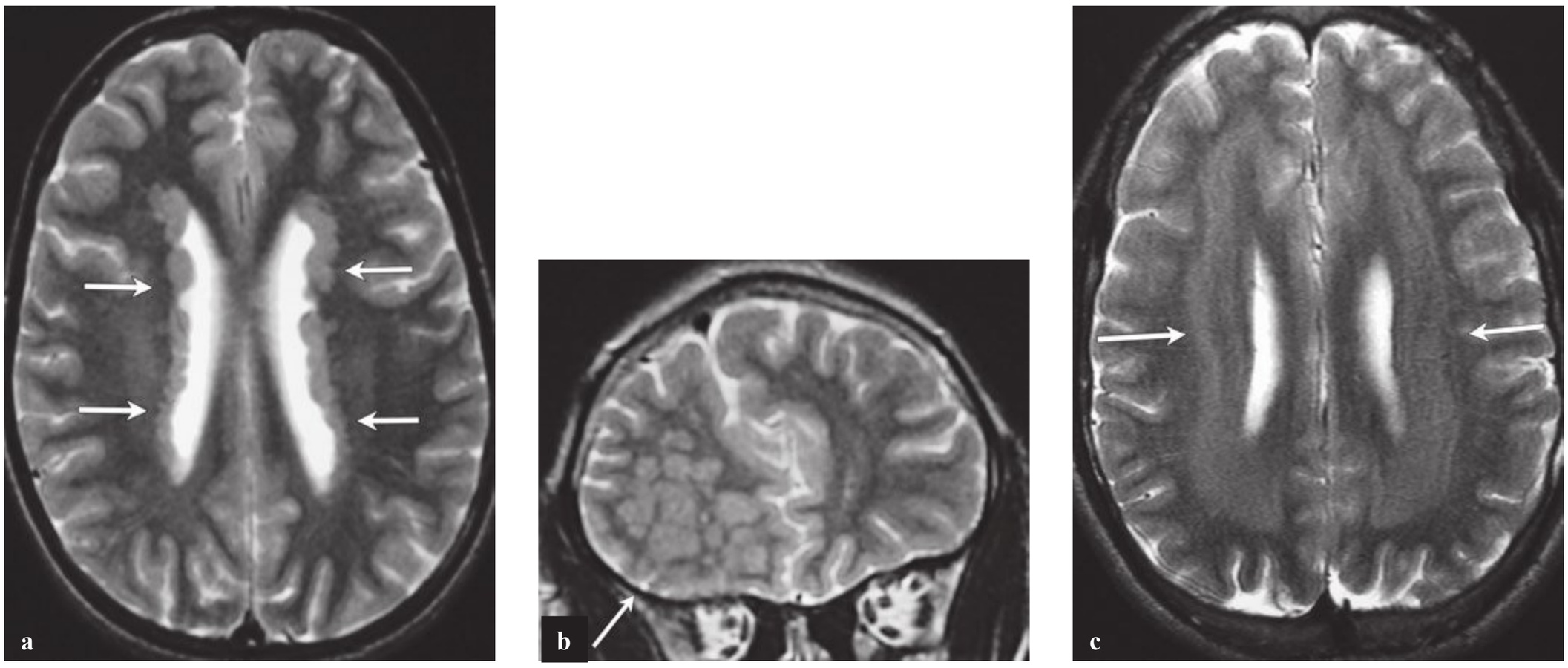

Fig. 1.155 Three patients with gray matter heterotopia that has signal isointense to cerebral cortex on axial T2-weighted imaging. **(a)** Multiple nodules of gray matter heterotopia are seen along the ependymal surface of the lateral ventricles (arrows). **(b)** Subcortical nodules of gray matter heterotopia are seen in the right frontal lobe (arrow). **(c)** Laminar (bandlike) gray matter heterotopia is seen bilaterally in the cerebral white matter (arrows).

Table 1.4 (cont.) Multiple intra-axial lesions in the brain

Lesions	Imaging Findings	Comments
Unilateral hemimegalencephaly (**Fig. 1.156**)	Complex hypertrophic congenital anomaly with enlargement of all or a portion of one cerebral hemisphere, with nodular or multinodular regions of gray matter heterotopia, and associated enlargement of the ipsilateral lateral ventricle. Zones with high signal on T2-weighted imaging may occur in the white matter.	Heterogeneous sporadic disorder with hamartomatous overgrowth of one cerebral hemisphere secondary to disturbances in neuronal proliferation and migration and in cortical organization. May be associated with unilateral hemihypertrophy and/or cutaneous abnormalities.
Neoplasms		
Metastatic disease (**Fig. 1.157**)	MRI: Circumscribed spheroid lesions in brain, can have various intra-axial locations (often at gray–white matter junctions), usually with low-intermediate signal on T1-weighted imaging and intermediate-high signal on T2-weighted imaging; ± hemorrhage, calcifications, and cysts. Variable gadolinium contrast enhancement, and high signal on T2-weighted imaging peripheral to nodular enhancing lesion represents axonal edema. CT: Lesions usually have low-intermediate attenuation, ± hemorrhage, calcifications, and cysts. Variable contrast enhancement, often associated with adjacent low attenuation from axonal edema.	Metastases represent ~ 33% of intracranial tumors, usually from extracranial primary neoplasm in adults > 40 years old. Primary tumor source: lung > breast > GI > GU > melanoma.
Lymphoma (**Fig. 1.158**)	MRI: Primary CNS lymphoma (PCNSL) in immunocompetent patients occurs as a solitary focal or infiltrating lesion in 65% PCNSL is located in the cerebral hemispheres, basal ganglia, thalami, cerebellum, and brainstem. PCNSL can involve and cross the corpus callosum. PCNSL in immunocompetent patients can be multifocal in 35% Multifocal PCNSL occurs in 60% of immunocompromised patients. Tumors often have low-intermediate signal on T1-weighted imaging, intermediate-slightly high signal on T2-weighted imaging, ± perilesional edema; ± hemorrhage/necrosis in immunocompromised patients or after treatment. PCNSL in immunocompetent patients usually shows homogeneous gadolinium contrast enhancement, whereas gadolinium contrast enhancement in immunocompromised patients often has an irregular peripheral pattern. Diffuse leptomeningeal or dural gadolinium contrast enhancement are other less common patterns of intracranial lymphoma. PCNSL typically lacks tumor neovascularization and has lower cerebral perfusion and relative cerebral blood volume (rCBV) maximum values than high-grade astrocytomas. PCNSL can show restricted diffusion. PCNSL ADC values (0.7 to 0.9 × 10^{-3} mm^2/s) are lower than those for glioblastomas and high-grade astrocytomas. MR spectroscopy of PCNSL shows decreased N-acetylaspartate (NAA) and elevated choline and lipid peaks. CT: CNS lymphoma can have intermediate attenuation, or it can be hyperdense related to a high nuclear/cytoplasm ratio, ± hemorrhage/necrosis in immunocompromised patients. Usually shows contrast enhancement. Diffuse leptomeningeal contrast enhancement is another pattern of intracranial lymphoma. PET/CT: PET/CT can show elevated FDG uptake in PCNSL and can be used to distinguish lymphoma from toxoplasmosis, which has decreased FDG uptake.	Primary CNS lymphoma is more common than secondary, usually in adults > 40 years old. Accounts for 5% of primary brain tumors. Currently accounts for 0.8 to 1.5% of primary intracranial tumors. Prior elevated incidence of 6% in patients with AIDS has been reduced with effective antiviral therapy. B cell lymphoma is more common than T cell lymphoma. MRI features of primary and secondary lymphoma of brain overlap. Intracranial lymphoma can involve the leptomeninges in secondary lymphoma > primary lymphoma.

(continued on page 132)

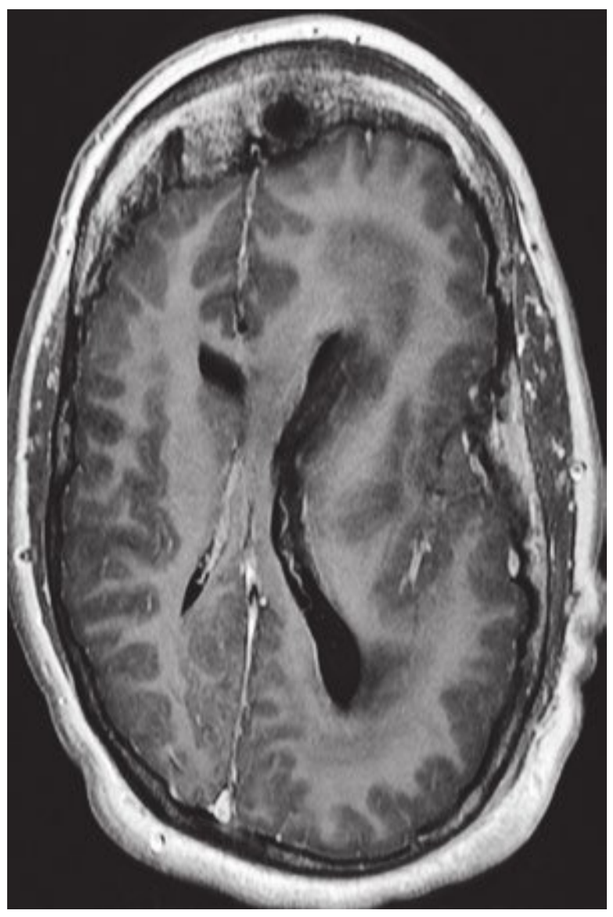

Fig. 1.156 Unilateral hemimegalencephaly. Axial T1-weighted imaging shows enlargement of the left cerebral hemisphere with nodular or regions of gray matter heterotopia within the left cerebral white matter, cortical dysplasia, and enlargement of the ipsilateral lateral ventricle.

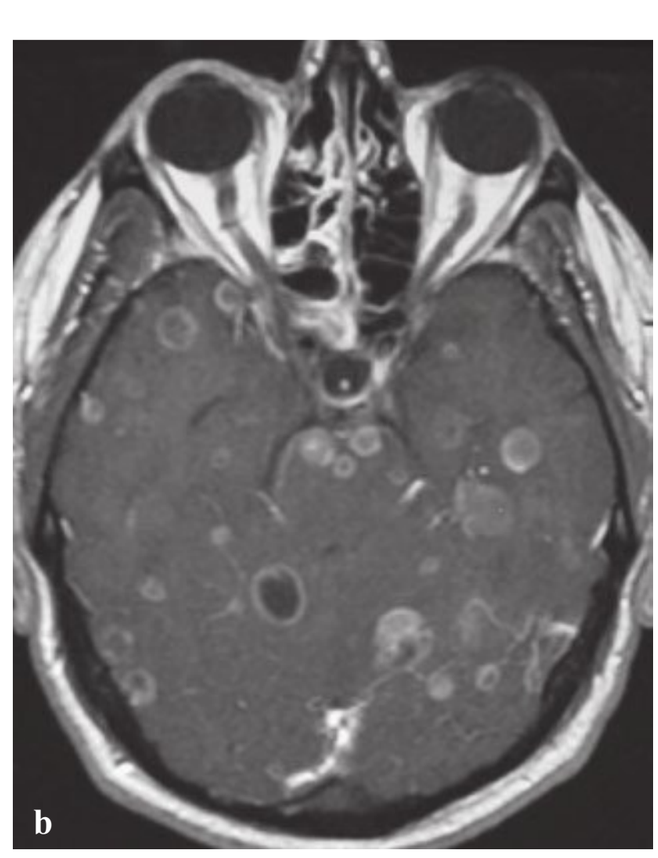

Fig. 1.157 Multiple metastatic lesions from lung carcinoma in the cerebrum and cerebellum that have **(a)** high signal on axial T2-weighted imaging and **(b)** ring and solid patterns of gadolinium contrast enhancement on axial T1-weighted imaging.

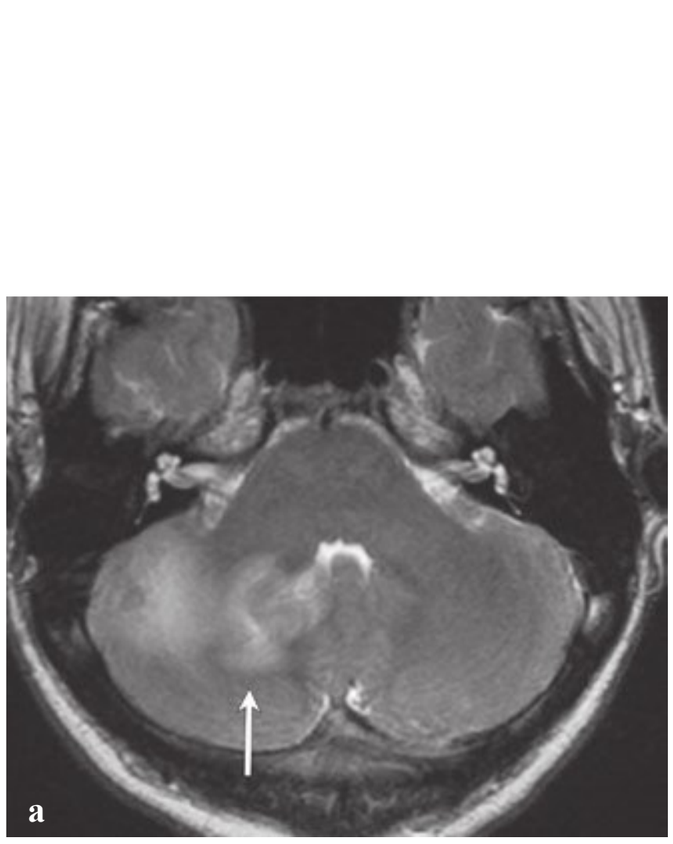

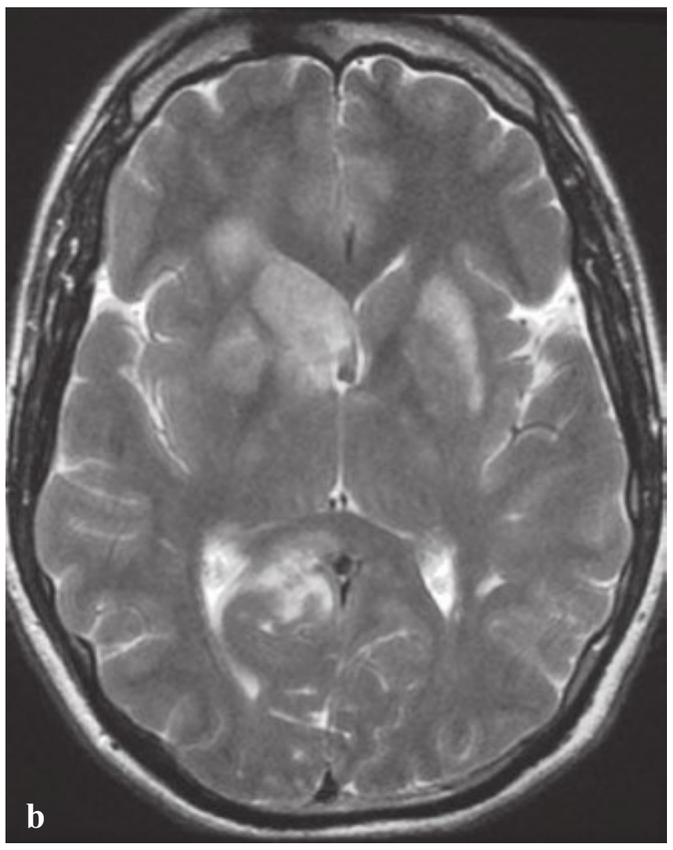

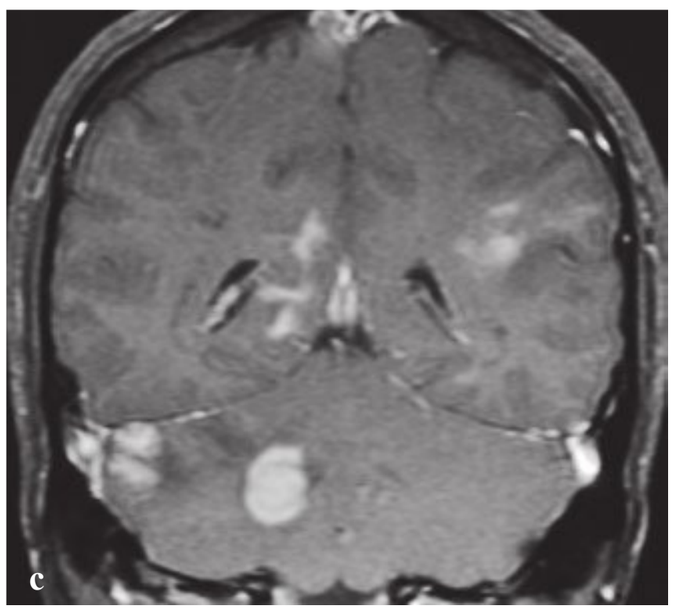

Fig. 1.158 **(a,b)** B cell non-Hodgkin lymphoma that is seen as multiple intra-axial zones with high signal on axial T2-weighted imaging (arrow) and **(c)** shows gadolinium contrast enhancement on coronal fat-suppressed T1-weighted imaging.

Table 1.4 (cont.) Multiple intra-axial lesions in the brain

Lesions	Imaging Findings	Comments
Leukemia (myeloid sarcoma, granulocytic sarcoma, chloroma)	MRI: Lesions often have intermediate signal on T1-weighted imaging, intermediate to slightly high signal on T2-weighted imaging and FLAIR. Small zones with low signal on GRE may be seen from sites of hemorrhage within the lesion. Lesions can have restricted diffusion on diffusion-weighted imaging (ADC values of 0.50×10^{-3} mm^2/s). Lesions usually show gadolinium contrast enhancement. Magnetic resonance spectroscopy: Can have reduced N-acetylaspartate (NAA) and markedly elevated choline peaks. CT: Lesions can have low-intermediate to slightly high attenuation, can show contrast enhancement.	Leukemias are neoplastic proliferations of hematopoietic cells. Myeloid sarcomas (also referred to as chloromas or granulocytic sarcomas) are focal tumors composed of myeloblasts and neoplastic granulocyte precursor cells and occur in 2% of patients with acute myelogenous leukemia. These lesions can involve the dura, leptomeninges, and brain. Intracranial lesions can be solitary or multiple.
Gliomatosis cerebri (**Fig. 1.159**)	MRI: Infiltrative lesion in the cerebral white matter with poorly defined margins, low-intermediate signal on T1-weighted imaging, high signal on T2-weighted imaging and FLAIR, usually minimal or no gadolinium contrast enhancement, and decreased relative cerebral blood volume (rCBV). Magnetic resonance spectroscopy shows elevated choline/creatine (Cho/Cr) and Cho/NAA ratios at sites with abnormal high signal on T2-weighted imaging. CT: Infiltrative lesion with low-intermediate attenuation. Usually no contrast enhancement until late in disease.	Diffusely infiltrating astrocytoma (WHO grade III) that often involves at least three cerebral lobes, including the basal nuclei. Can involve the cerebellum and brainstem. Peak age of occurrence is between 40 and 50 years. Tumor consists of infiltrating, small, neoplastic glial cells with elongated fusiform nuclei as well as larger neoplastic cells with pleomorphic nuclei. Imaging appearance may be more prognostic than histologic grade, with approximate 2-year survival.

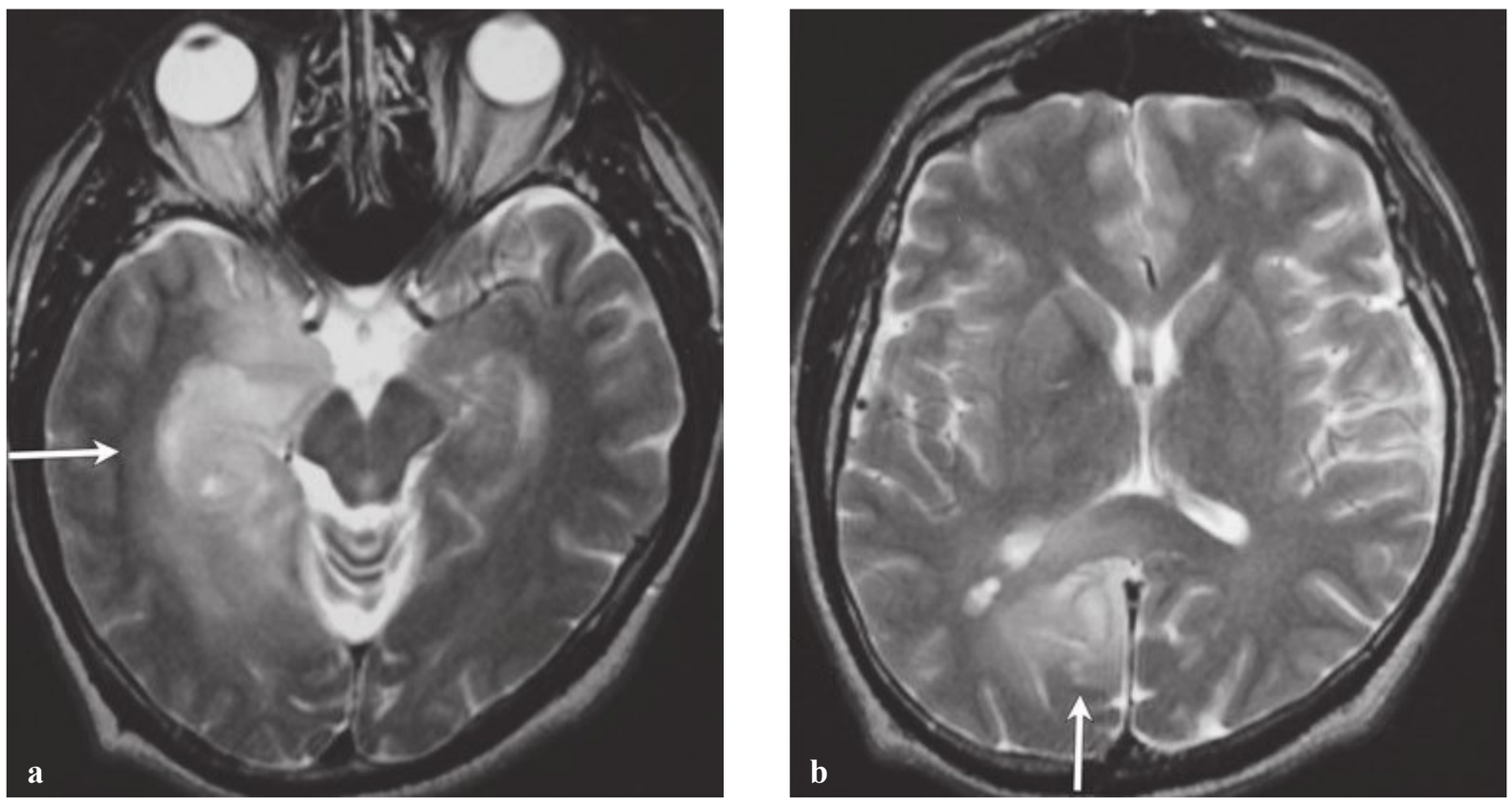

Fig. 1.159 Gliomatosis cerebri seen as poorly defined intra-axial lesions with high signal on axial T2-weighted imaging in **(a)** the right temporal lobe (arrow) and **(b)** right occipital lobe and splenium of the corpus callosum (arrow).

Lesions	Imaging Findings	Comments
Glioblastoma multiforme	MRI: Irregularly and poorly marginated mass lesion with necrosis or cyst, mixed signal on T1-weighted imaging, heterogeneous high signal on T2-weighted imaging and FLAIR, ± hemorrhage, and prominent heterogeneous gadolinium contrast enhancement. Increased relative cerebral blood volume (rCBV) is asssociated with high-grade gliomas from tumor-induced angiogenesis. Other findings include peripheral edema and tumor extension across the corpus callosum. Magnetic resonance spectroscopy shows decreased N-acetylaspartate (NAA) and high levels of choline. CT: Irregularly marginated mass lesion with necrosis or cyst, mixed low and intermediate attenuation, ± hemorrhage, prominent heterogeneous contrast enhancement, and peripheral edema. Can cross corpus callosum.	Most common primary CNS tumor (WHO grade IV), accounts for 15%of intracranial tumors and up to 75% of astrocytic neoplasms, with an incidence of 3 per 100,000. Most patients are over 50 years old. These highly malignant astrocytic neoplasms have nuclear atypia, with mitotic activity, cellular pleomorphism, necrosis, and microvascular proliferation and invasion. K_i-67/MIB-1 proliferation index ranges from 15 to 20% Associated with mutations involving RTK/phosphatase–PTEN/PI3K signal pathway, TERT, and p53 and Rb1 tumor suppressor genes. Promotor methylation resulting in inactivation of the MGMT DNA repair enzyme enables improved malignant tumor response to chemotherapy in patients lacking IDH mutations. The extent of lesion is underestimated by MRI. Survival is often < 1 year. Patients with secondary type glioblastoma who have IDH mutations can have a better response to chemotherapy and prognosis than those without.
Other Neoplasms or Tumorlike Lesions		
Neurofibromatosis type 1 (NF1): vacuolated myelin/ dysplastic white matter lesions (**Fig. 1.160**)	In addition to CNS neoplasms (e.g., astrocytomas, grades II to IV, and optic gliomas), NF1 can have nonneoplastic lesions related to vacuolated myelin in the basal ganglia, thalamus, brainstem, internal capsules, corpus callosum, and/or cerebellar white matter. These lesions have high signal on T2-weighted imaging and FLAIR ± increased diffusion on DWI. They typically lack gadolinium contrast enhancement and can be solitary or multiple.	NF1 is an autosomal dominant disorder (1/2500 births) from mutations involving the neurofibromin gene on chromosome 17q11.2. It is the most common type of neurocutaneous syndrome. Associated with neoplasms of central and peripheral nervous system (optic gliomas, astrocytomas, plexiform and solitary neurofibromas) and skin (café-au-lait spots, axillary and inguinal freckling). Also associated with meningeal and skull dysplasias and hamartomas of the iris (Lisch nodules). Single or multiple zones of vacuolated myelin with high signal on T2-weighted imaging can occur in the basal ganglia, thalamus, brainstem, cerebellar white matter, and/or corpus callosum. The lesions increase in size in the first decade and then usually regress and resolve by the third decade.

(continued on page 134)

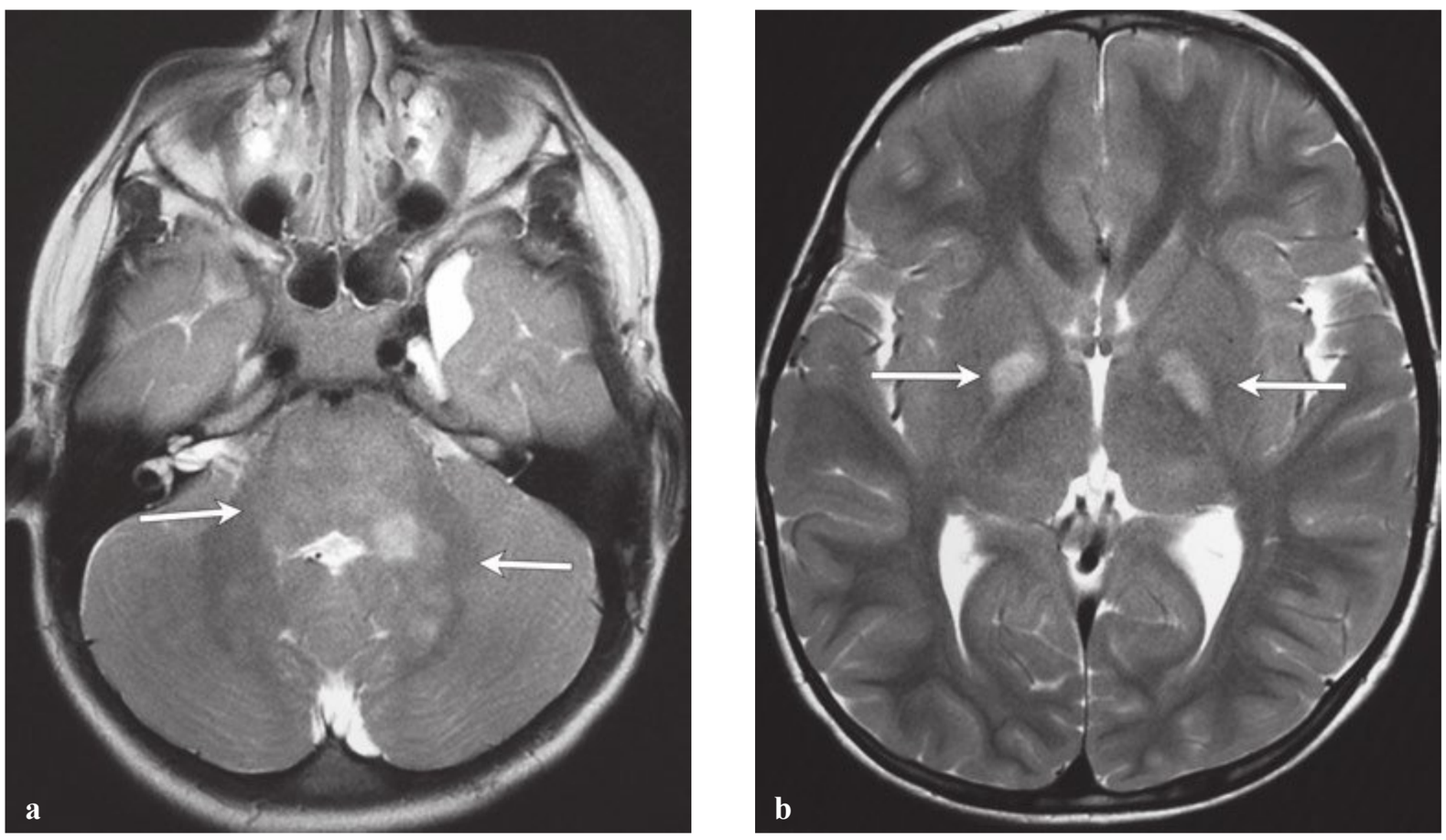

Fig. 1.160 Neurofibromatosis type 1. Dysplastic white matter abnormalities with high signal on axial T2-weighted imaging are seen in **(a)** the pons, middle cerebellar peduncles, and cerebellar white matter (arrows) and **(b)** globi pallidi (arrows).

Table 1.4 (cont.) Multiple intra-axial lesions in the brain

Lesions	Imaging Findings	Comments
Hamartomas: tuberous sclerosis (**Fig. 1.161**) Cortical hamartomas (tubers) Subependymal hamartomas	Cortical hamartomas (tubers) MRI: Cortical-subcortical lesions (tubers) usually have high signal on T1-weighted imaging and low signal on T2-weighted imaging and FLAIR in neonates and infants; changes to low-intermediate signal on T1-weighted imaging and high signal on T2-weighted imaging and FLAIR in older children and adults, calcifications in 50% of older children, gadolinium contrast enhancement uncommon. Cortical tubers can have elevated ADC values. CT: Cortical-subcortical lesions (tubers) have variable attenuation and calcifications in 50% of older children; contrast enhancement is uncommon. Subependymal hamartomas MRI: Subependymal hamartomas are small nodules located along, and projecting into, the lateral ventricles, with signal on T1- and T2-weighted imaging and FLAIR similar to cortical tubers. Calcification and gadolinium contrast enhancement are common. CT: Subependymal hamartomas appear as small nodules located along, and projecting into, the lateral ventricles. Calcification of nodules commonly begins to occur early in childhood.	Cortical hamartomas (tubers), subcortical glioneuronal hamartomas, subependymal glial hamartomas (nodules), and subependymal giant cell astrocytomas are nonmalignant lesions associated with tuberous sclerosis. Tuberous sclerosis is an autosomal dominant disorder associated with hamartomas in multiple organs. Extraneural lesions include cutaneous angiofibromas (adenoma sebaceum), subungual fibromas, visceral cysts, renal angioleiomyomas, intestinal polyps, cardiac rhabdomyomas, and pulmonary lymphangioleiomyomatosis. Caused by mutations of TSC1 gene on 9q or the TSC2 gene on 16p. Prevalence is 1 in 6,000 newborns.
Hemangioblastomas (von Hippel-Lindau disease) (**Fig. 1.162**)	Circumscribed tumors usually located in the cerebellum and/or brainstem. MRI: Small gadolinium-enhancing nodule ± cyst, or larger lesion with prominent heterogeneous enhancement ± flow voids within lesion or at the periphery. Intermediate signal on T1-weighted imaging, intermediate-high signal on T2-weighted imaging, and occasionally lesions have evidence of recent or remote hemorrhage. CT: Small contrast-enhancing nodule ± cyst, or larger lesion with prominent heterogeneous enhancement, ± hemorrhage.	Slow-growing, vascular tumors (WHO grade I) that involve the cerebellum, brainstem, and/or spinal cord. Tumors consist of numerous thin-walled vessels as well as large, lipid-containing vacuolated stromal cells that have variably sized and hyperchromatic nuclei. Mitotic figures are rare. Stromal cells are immunoreactive to VEGF, vimentin, CXCR4, aquaporin 1, carbonic anhydrase, S-100, CD56, neuron specific enolase, and D2–40. Vessels typically react to a reticulin stain. Reactive astrocytic gliosis can ocur in adjacent tissue. Tumors occur as sporadic mutations of the VHL gene or as an autosomal dominant germline mutation of the VHL gene on chromosome 3p25–26, resulting in von Hippel-Lindau disease (VHL disease). In VHL disease, multiple hemangioblastomas involving the central nervous system occur, as well as clear-cell renal carcinoma, pheochromocytoma, endolymphatic sac tumor, neuroendocrine tumor, adenoma of the pancreas, and epididymal cystadenoma. Occurs in adolescents and young and middle-aged adults.

(continued on page 136)

Fig. 1.161 Tuberous sclerosis. **(a)** Axial CT shows small nodules representing subependymal hamartomas located along and projecting into the lateral ventricles, some of which are calcified. **(b)** The noncalcified subependymal hamartomas have slightly high to high signal on FLAIR. **(c)** Also seen are cortical-subcortical lesions (tubers) and poorly defined white matter lesions that have high signal on FLAIR.

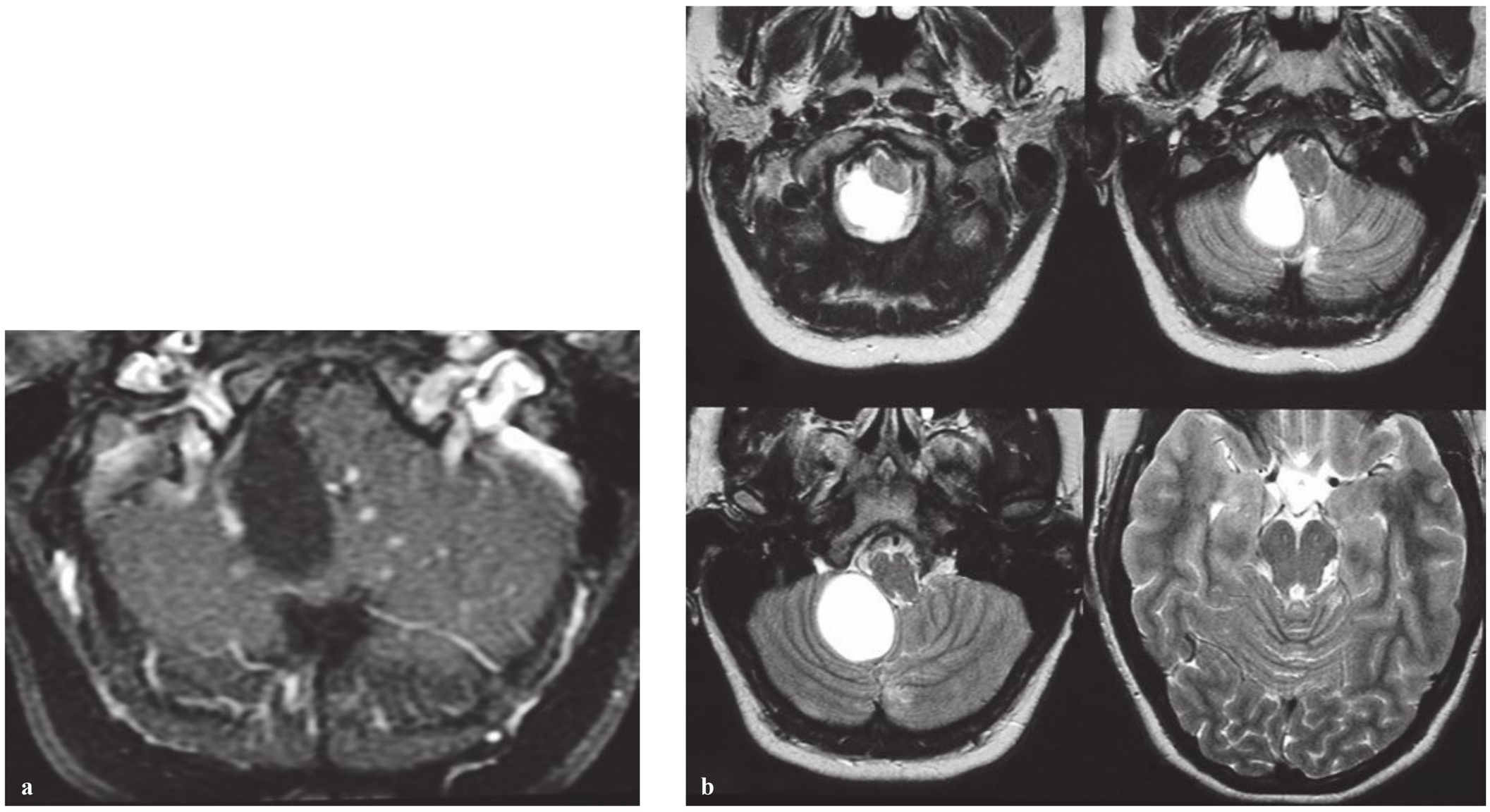

Fig. 1.162 Von Hippel-Lindau disease. **(a)** Multiple small gadolinium contrast-enhancing lesions are seen in the cerebellum on axial fat-suppressed T1-weighted imaging. **(b)** The lesions have high signal on axial T2-weighted imaging. One hemangioblastoma is seen as a cystic lesion with a gadolinium contrast-enhancing mural nodule.

Table 1.4 (cont.) Multiple intra-axial lesions in the brain

Lesions	Imaging Findings	Comments
Primary melanocytic tumors of the central nervous system (**Fig. 1.163**)	MRI: Neurocutaneous melanosis: Intra-axial lesions usually < 3 cm in brain parenchyma/brainstem (anterior temporal lobes, cerebellum, thalami, inferior frontal lobes). Intra-axial lesions have intermediate-slightly high signal on T1-weighted imaging secondary to increased melanin, ± decreased signal on T2-weighted imaging, ± gadolinium contrast enhancement. Leptomeningeal lesions have irregular margins, intermediate and/or high signal on T1-weighted imaging in the sulci, intermediate-slightly high signal on T2-weighted imaging, high signal on FLAIR, and leptomeningeal gadolinium contrast enhancement. ± hydrocephalus, ± vermian hypoplasia, ± arachnoid cysts, ± Dandy-Walker malformation. CT: May show subtle hyperdensity secondary to increased melanin, ± vermian hypoplasia, ± arachnoid cysts.	Primary melanocytic tumors of the CNS represents a spectrum of benign to malignant pigmented tumors in adults and children. In children, neurocutaneous melanosis or melanocytosis is a rare nonfamilial disorder with focal and/or diffuse proliferation of melanocytes in leptomeninges associated with large and/or numerous cutaneous nevi. Presents in infants and young children. Rarely occurs in adults. Immunoreactive to HMB-45, MART-1, and S-100. Cutaneous nevi are typically benign. Melanocytes in the leptomeninges change to CNS melanoma in 40 to 50% of cases in patients with neurocutaneous melanosis. Meningeal melanocytoma is a benign rare pigmented tumor consisting of leptomeningeal melanocytes which typically occur in the posterior cranial fossa or spinal canal in patients with a mean age of 42 years.
Inflammatory Lesions: Infection		
Cerebritis (**Fig. 1.164**)	MRI: Poorly defined zone or focal area of low-intermediate signal on T1-weighted imaging, intermediate-high signal on T2-weighted imaging and FLAIR, restricted diffusion, and minimal or no gadolinium contrast enhancement. Involves cerebral cortex and white matter in bacterial and fungal infections. CT: Poorly defined zone or focal area of decreased attenuation, and minimal or no contrast enhancement. Involves cerebral cortex and white matter in bacterial and fungal infections.	Focal infection/inflammation of brain tissue from bacteria or fungi, secondary to sinusitis, meningitis, surgery, hematogenous source (cardiac and other vascular shunts), and/or immunocompromised status. Can progress to brain abscess formation.
Pyogenic brain abscess (**Fig. 1.165**)	MRI: Circumscribed lesions with low signal on T1-weighted imaging, central zone of high signal on T2-weighted imaging (± air–fluid level) surrounded by a thin rim with intermediate-low signal on T2-weighted imaging that shows ringlike gadolinium contrast enhancement that is sometimes thicker laterally than medially, and peripheral poorly defined zone of high signal on T2-weighted imaging representing edema. Abscess contents typically have restricted diffusion. Mean ADC values for abscesses are significantly lower (0.63 to 1.12 × 10^{-3} mm^2/s) than those for necrotic or cystic neoplasms (2.45 × 10^{-3} mm^2/s). MR spectroscopy shows decreased N-acetylaspartate (NAA) from destruction of neurons, and elevated lactate and amino acid peaks (valine, leucine, and isoleucine) at 0.9 ppm secondary to proteolytic enzymes. CT: Circumscribed lesion with a central zone of low attenuation (± air–fluid level) surrounded by a thin rim of intermediate attenuation, peripheral poorly defined zone of decreased attenuation representing edema, and ringlike contrast enhancement that is sometimes thicker laterally than medially.	Formation of brain abscess occurs 2 weeks after cerebritis, with liquefaction and necrosis centrally surrounded by a capsule and peripheral edema. Restricted diffusion of abscess contents is related to the combination of the high protein content and viscosity of pus, necrotic debris, and bacteria. Can be multiple, but more than 50%are solitary. Complication from meningitis and/or sinusitis, septicemia, trauma, surgery, and cardiac shunt. Accounts for 2%and 8%of intra-axial mass lesions in developed and developing countries, respectively.

(continued on page 138)

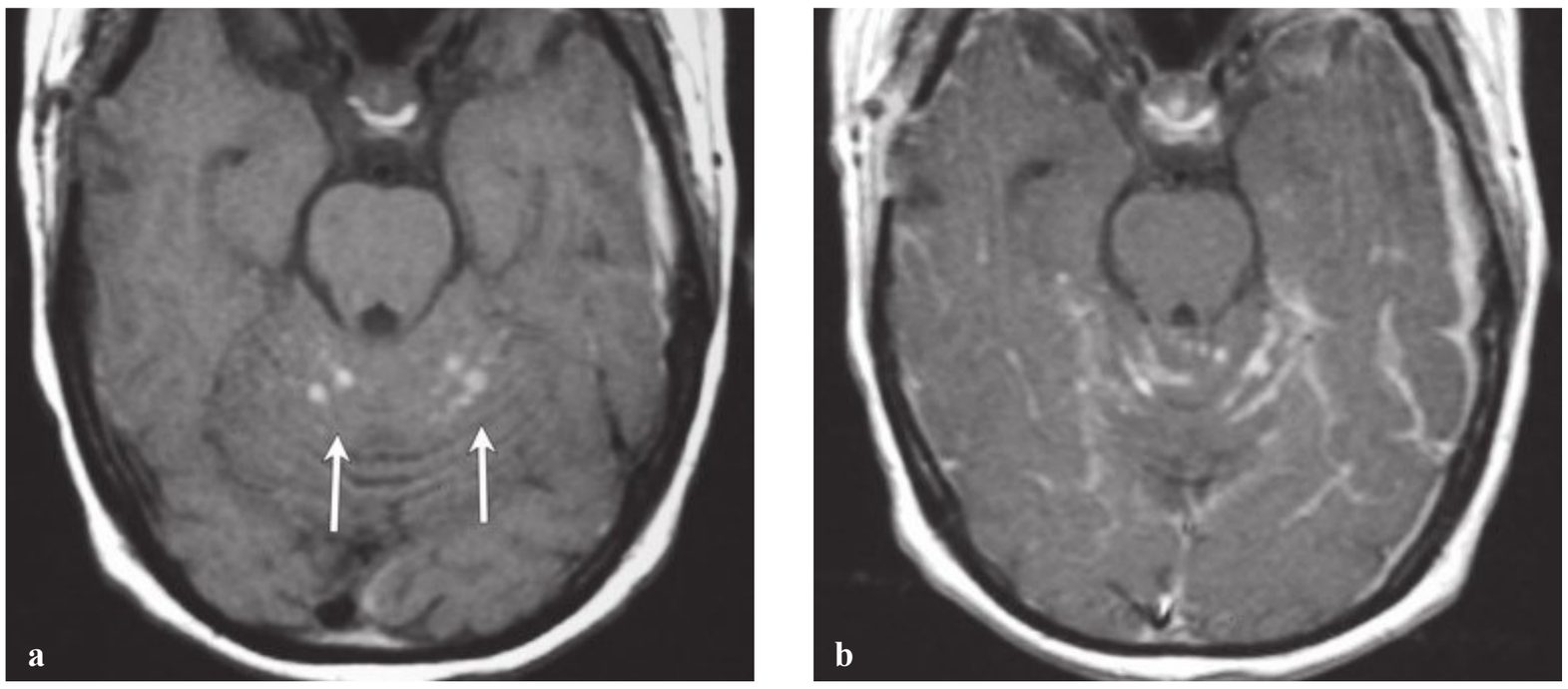

Fig. 1.163 Neurocutaneous melanosis. **(a)** Small nodules with high signal on T1-weighted imaging are seen along the surface of the upper cerebellum (arrows). **(b)** Nodular and diffuse gadolinium contrast enhancement is seen in the leptomeninges, as well as left dural enhancement on axial T1-weighted imaging.

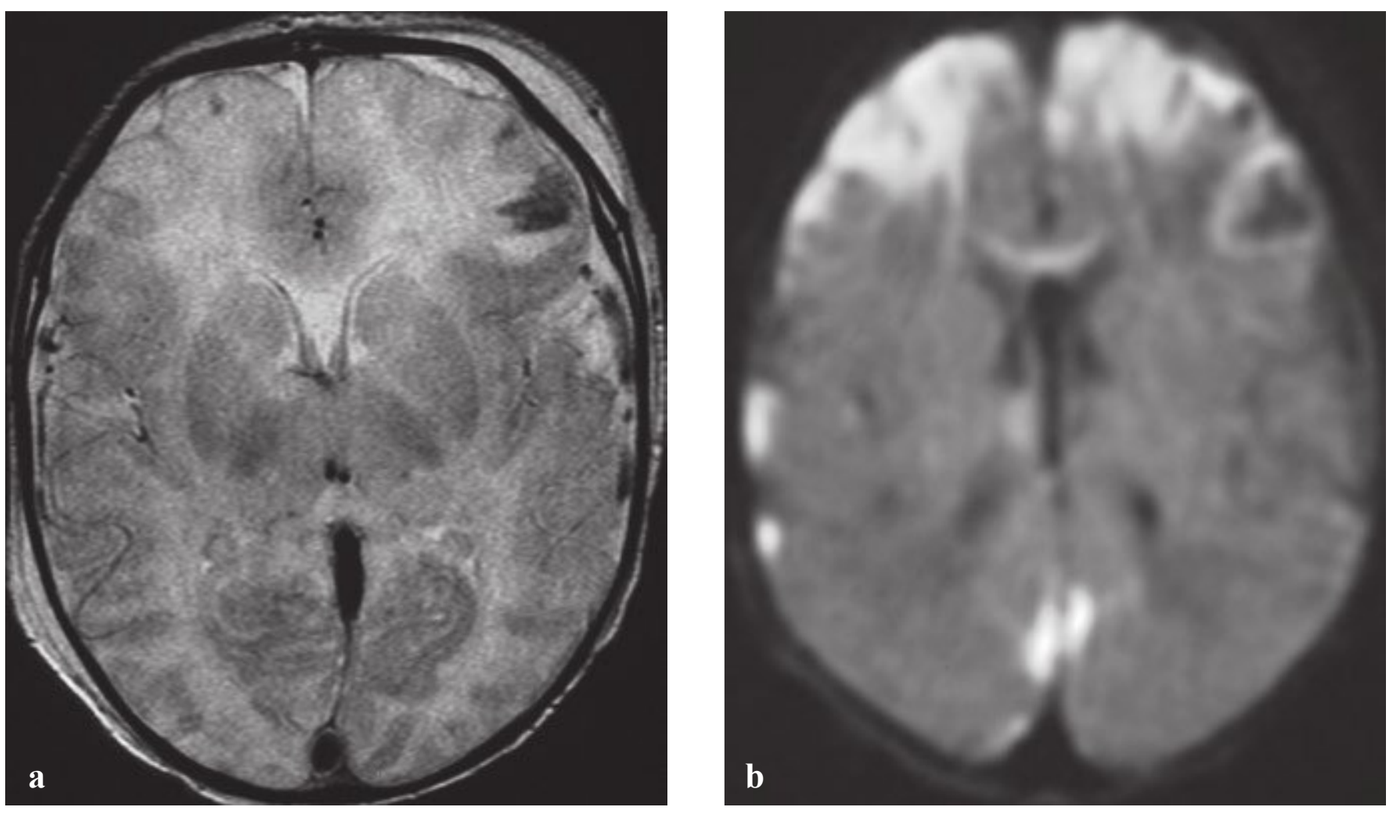

Fig. 1.164 Neonatal cerebritis. **(a)** Poorly defined zones with high signal on axial T2-weighted imaging are seen in the frontal lobes, with loss of differentiation of the cerebral cortex and subcortical white matter, which have **(b)** restricted diffusion on axial DWI.

Fig. 1.165 Pyogenic brain abscesses in a patient with a right-to-left cardiac shunt. **(a)** T2-weighted imaging shows circumscribed lesions with central zones of high signal surrounded by thin rims with intermediate-low signal, as well as peripheral edema. **(b)** Ringlike zones of gadolinium contrast enhancement are seen in the abscess walls on axial T1-weighted imaging.

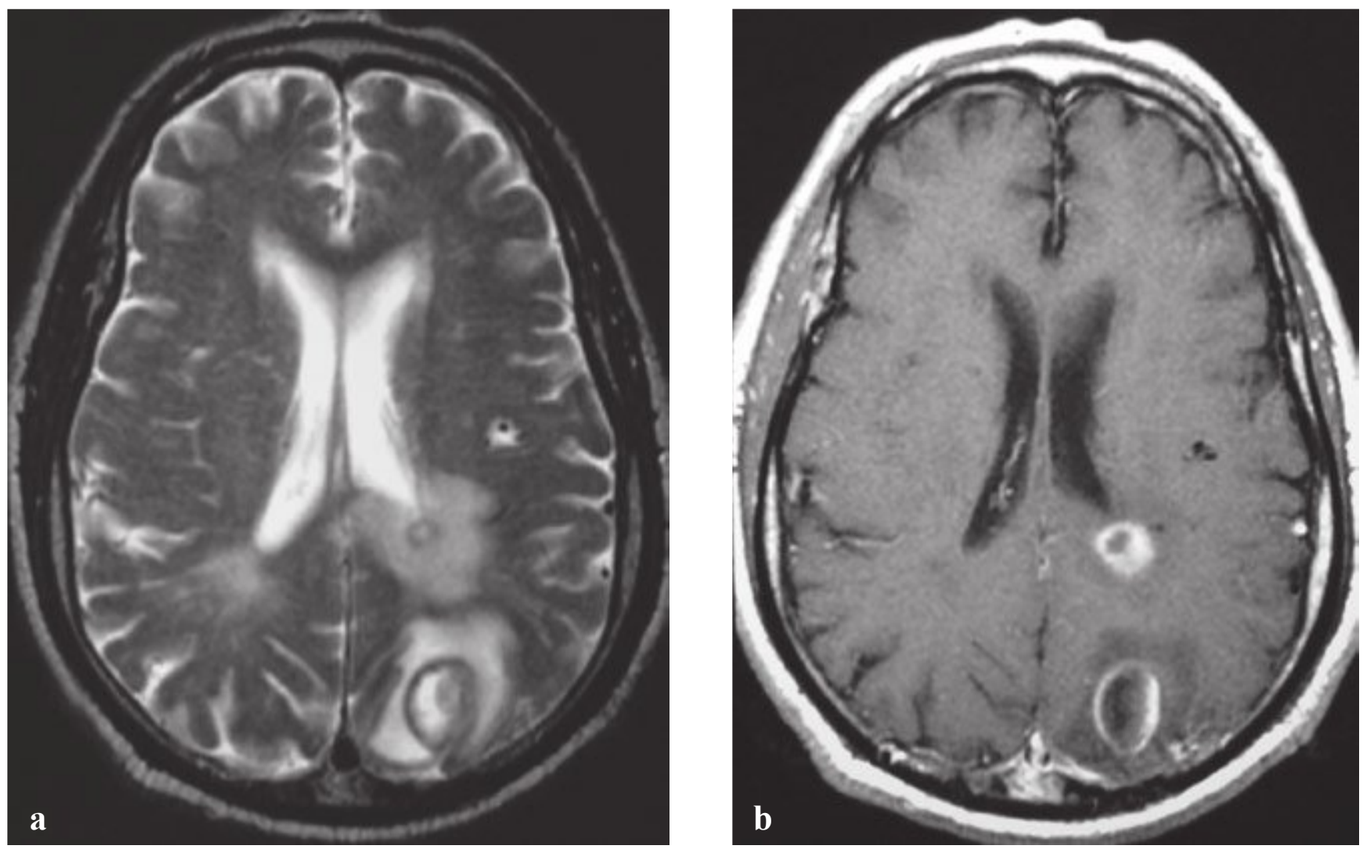

Table 1.4 (cont.) Multiple intra-axial lesions in the brain

Lesions	Imaging Findings	Comments
Lyme disease (spirochete infection) (**Fig. 1.166**)	MRI: Foci (2 to 8 mm) with high signal on T2-weighted imaging and FLAIR in cerebral and/or cerebellar white matter, ± restricted diffusion, ± contrast enhancement of intra-axial lesions and/or leptomeninges and cranial nerves III, V, VII, and/or VIII. CT: Foci of decreased attenuation in cerebral and/or cerebellar white matter, ± contrast enhancement.	CNS manifestations presumed to occur from immune-related demyelination due to Lyme disease (infection by the spirochete Borrelia burgdoferi) transmitted to humans via bites from Ixodes ticks that have been infected by primary hosts (mice and deer). Most cases in the United States occur in the Mid-Atlantic region. Patients can present with headaches, malaise, fevers, myalgias, and erythema migrans.
Syphilis (spirochete infection)	MRI: Findings include gadolinium contrast enhancement of thickened dura and leptomeninges, cranial nerves, and cochlea. Nodular lesions with solid or rim patterns of gadolinium contrast enhancement (gummas) can be seen involving superficial brain tissue adjacent to the meninges, ± restricted diffusion, often with peripheral edema with high signal on T2-weighted imaging and FLAIR. Vascular neurosyphilis also occurs with tertiary disease and results in cerebral infarcts from vasculitis, causing arterial narrowing and occlusions.	Spirochetes are gram-negative bacteria that have flagella between the cell wall and outer membrane that cause spiral motions resulting in movement. Syphilis is caused by Treponema pallidum, which is spread by sexual contact via skin lesions. Can also occur from transplacental transmission. Can be sporadic or in association with AIDS. Late phases of infection (tertiary phase after 5 years) involve the CNS (neurosyphilis) or cardiovascular system.
Rickettsial infection—Rocky Mountain spotted fever (RMSF) (**Fig. 1.167**)	MRI: RMSF can be associated with infarcts in the basal ganglia, prominent perivascular spaces (starry sky sign) in the cerebral white matter, cerebellum and pons, white matter infarcts, ± restricted diffusion from perivascular inflammation, ± cerebral edema, ± meningeal gadolinium contrast enhancement. CT: RMSF can show foci of decreased attenuation in the basal ganglia or white matter, ± meningeal contrast enhancement.	Infections caused by gram-negative rickettsial bacteria in humans. The most common rickettsial infections are Rocky Mountain spotted fever (RMSF), epidemic typhus, and Q fever. RMSF, caused by Rickettsia rickettsii, is a tick-borne disease that often occurs in the Southeast United States. Organisms invade blood vessels, causing endothelial injury. Associated with maculopapular rash involving the wrists, hands, feet, and ankles and which can become ecchymotic. Epidemic typhus is caused by Rickettsia prowazekii via lice. Q fever is caused by Coxiella burnetii via inhalation of dust contaminated with endospores and has a worldwide distribution.

(continued on page 140)

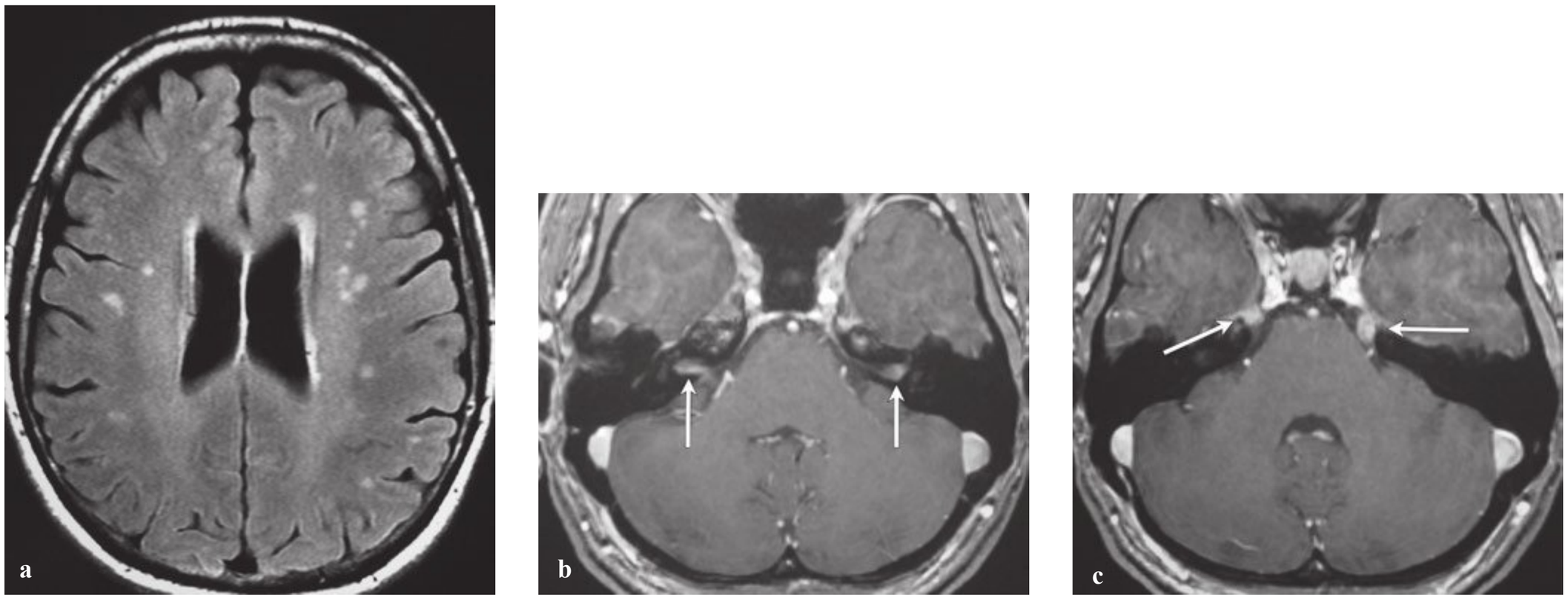

Fig. 1.166 Lyme disease. **(a)** Multiple small foci with high signal on axial FLAIR are seen in the cerebral white matter. **(b,c)** Gadolinium contrast enhancement of cranial nerves V, VII, and VIII is seen on axial T1-weighted imaging (arrows).

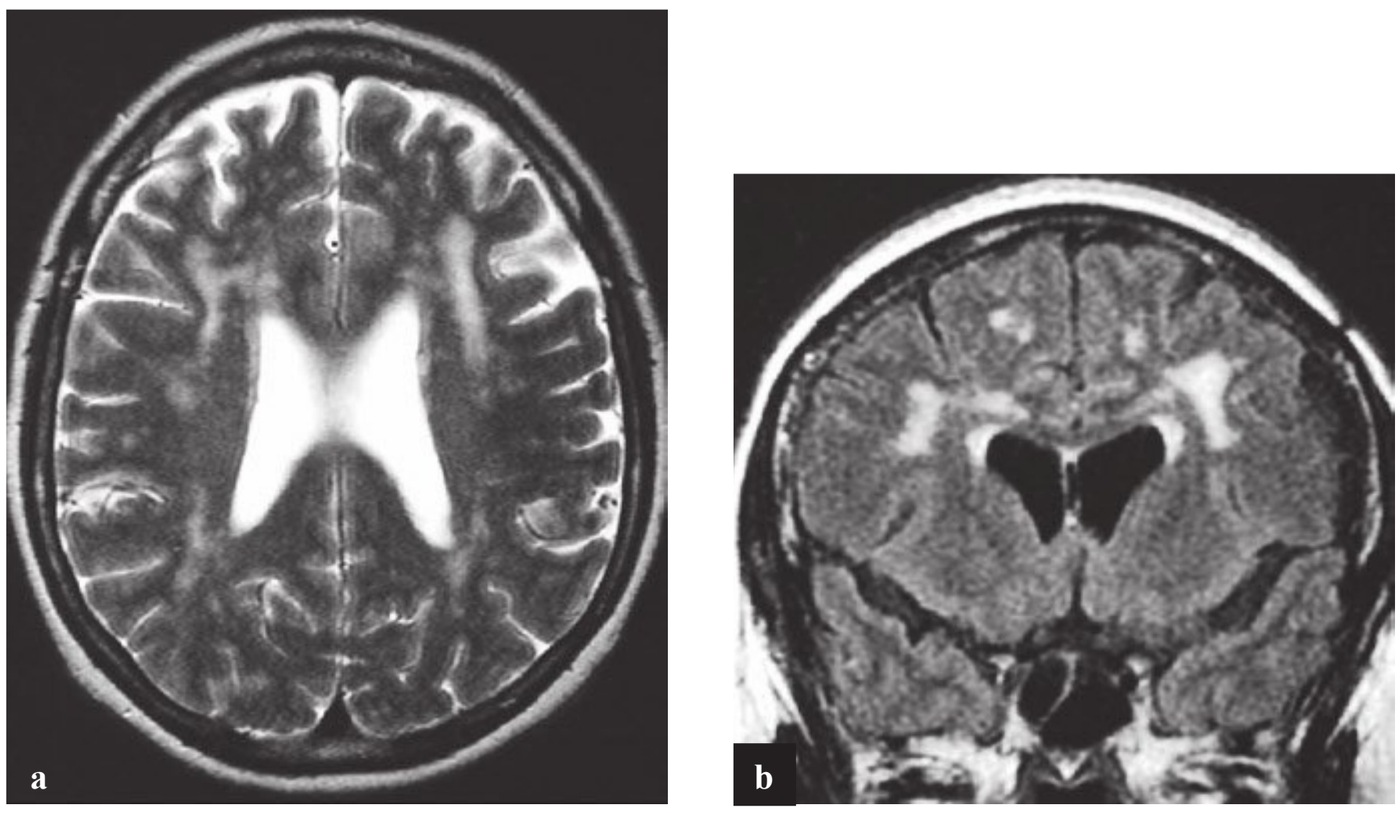

Fig. 1.167 Rocky Mountain spotted fever. Foci and confluent zones with high signal on **(a)** axial T2-weighted imaging and **(b)** coronal FLAIR are seen in the cerebral white matter bilaterally.

Table 1.4 (cont.) Multiple intra-axial lesions in the brain

Lesions	Imaging Findings	Comments
Tuberculomas (**Fig. 1.168**)	MRI: Intra-axial lesions in cerebral hemispheres and basal ganglia (adults) and cerebellum (children): Low-intermediate signal on T1-weighted imaging, central zone of high signal on T2-weighted imaging with a thin peripheral rim of low signal, occasionally low signal on T2-weighted imaging, + solid or rim gadolinium contrast enhancement, ± calcification, ± restricted or increased diffusion. Meningeal lesions: Nodular or cystic zones of basilar meningeal gadolinium contrast enhancement. Meningitis can be associated with intracranial arterial or venous thrombosis, leading to brain infarction with restricted diffusion. CT: Intra-axial lesions in cerebral hemispheres, basal ganglia, and brainstem (adults), and cerebellum (children): Lesions can have decreased attenuation, central zone of low attenuation with a thin peripheral rim of intermediate attenuation, + solid or rim pattern of contrast enhancement, ± calcification. Meningeal lesions can have nodular or cystic zones of basilar meningeal enhancement.	Infection by Mycobacterium tuberculosis from human to human transmisssion. Occurs in immunocompromised patients and in immunocompetent patients in developing countries. Caseating intracranial granulomas form via hematogenous dissemination. Meningitis is the most common intracranial manifestation compared with intra-axial tuberculomas in brain. Infection occurs in up to 10 million patients per year; CNS infection occurs in 2 to 5% of cases.
Fungal brain lesions (**Fig. 1.169**)	MRI: Findings vary depending on organism. Infection can occur in meninges and/or brain parenchyma, forming solid or cystic lesions with low-intermediate signal on T2-weighted imaging, high signal on T2-weighted imaging and FLAIR, nodular or ring-shaped gadolinium contrast enhancement, and peripheral high signal on T2-weighted imaging (edema). Infected tissue may have restricted diffusion at the walls of the lesions without reduced ADC values in the central cavities. Low signal on T2-weighted imaging and GRE at the walls of the lesions may occur from paramagnetic iron and magnesium within hyphae of the fungi. Magnetic resonance spectroscopy can show elevated lipid, lactate, and amino acid peaks, as well as multiple peaks between 3.6 and 3.8 ppm from trehalose. CT: Infection can occur in meninges and brain parenchyma, forming solid or cystic-appearing lesions with decreased attenuation, nodular or ring-pattern of contrast enhancement, and a peripheral zone with decreased attenuation (edema).	Occur in immunocompromised or diabetic patients, with resultant granulomas in meninges and brain parenchyma. Cryptococcus involves the basal meninges and extends along perivascular spaces into the basal ganglia. Aspergillosis and Mucor spread via direct extension through paranasal sinuses or hematogenously, invading blood vessels and resulting in hemorrhagic lesions and/or cerebral infarcts. Coccidioidomycosis usually involves the basal meninges. Candidiasis is often a nocosomial infection related to complications from surgery and/or indwelling catheters.

(continued on page 142)

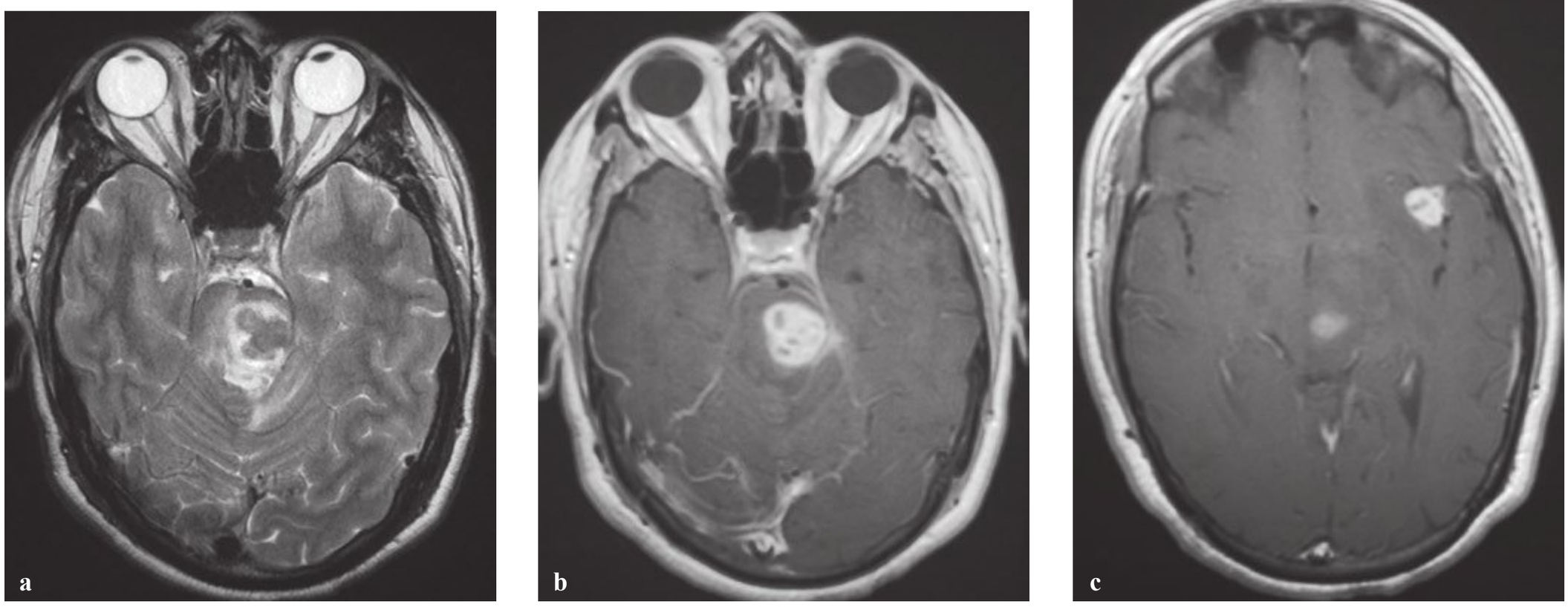

Fig. 1.168 **(a)** Pontine tuberculoma that has intermediate and high signal on axial T2-weighted imaging, with surrounding edema. **(b,c)** The pontine lesion and additional left frontal lobe lesion show gadolinium contrast enhancement on axial T1-weighted imaging.

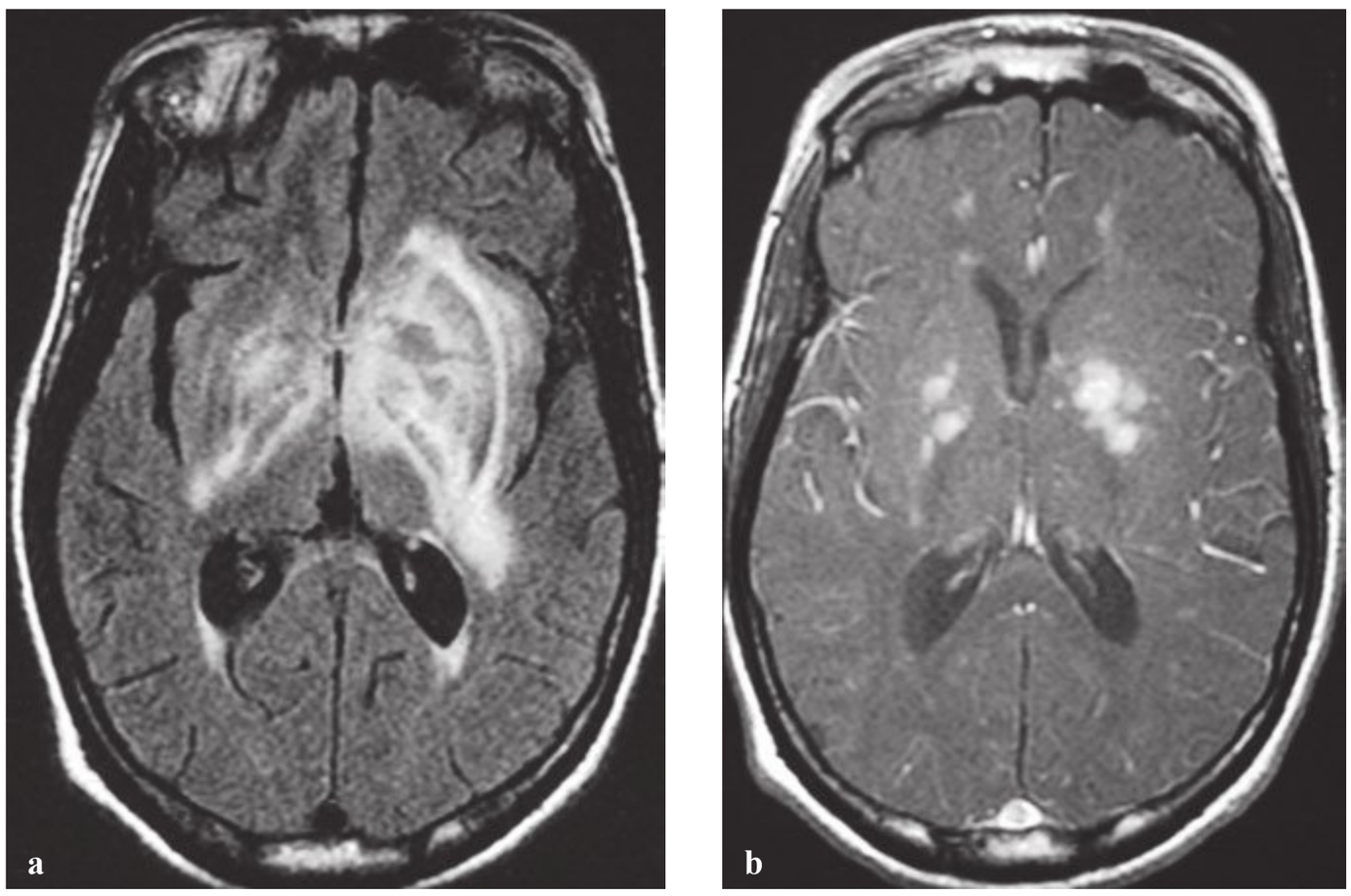

Fig. 1.169 A 37-year-old immunocompromised man with Cryptococcus infection. **(a)** Poorly defined zones with abnormal, asymmetric, high signal in the basal ganglia bilaterally on axial FLAIR are associated with **(b)** multiple intra-axial foci of gadolinium contrast enhancement on axial T1-weighted imaging.

Table 1.4 (cont.) Multiple intra-axial lesions in the brain

Lesions	Imaging Findings	Comments
Encephalitis/viral infections (**Fig. 1.170, Fig. 1.171, Fig. 1.172, Fig. 1.173, Fig. 1.174, Fig. 1.175**, and **Fig. 1.176**) Herpes simplex	Herpes simplex MRI: Typically involves the temporal lobes/limbic system, ± hemorrhage. Poorly defined zone or zones of low-intermediate signal on T1-weighted imaging, and intermediate-high signal on T2-weighted imaging and FLAIR. Restricted diffusion can occur in early stages of infection. Minimal or no gadolinium contrast enhancement, involvement of cerebral cortex and/or white matter, and minimal localized mass effect. CT: Poorly defined zone or zones of decreased attenuation, minimal or no contrast enhancement.	Encephalitis is infection/inflammation of brain tissue by viruses. In immunocompromised patients, encephalitis is caused by herpes simplex, cytomegalovirus (CMV), HIV, and progressive multifocal leukoencephalopathy from JC polyoma virus infection of oligodendrocytes. In immunocompetent patients, infections are caused by St. Louis encephalitis, Eastern or Western equine encephalitis, measles (RNA Paramyxovirus), Epstein-Barr virus, Japanese encephalitis (Flavivirus), West Nile virus (Flavivirus), and rabies (Lyssavirus).

(continued on page 145)

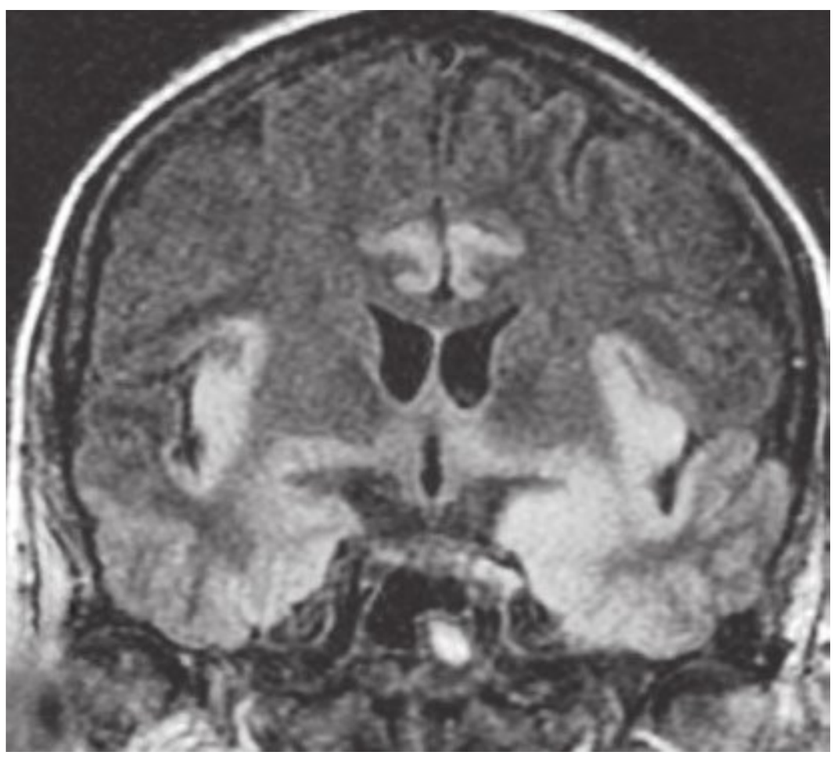

Fig. 1.170 Herpes simplex 1 encephalitis in a 64-year-old man seen as bilateral intra-axial zones with abnormal high signal in cerebral cortex and subcortical white matter in both temporal lobes, inferior frontal lobes, both insula, and cingulate gyri on coronal FLAIR.

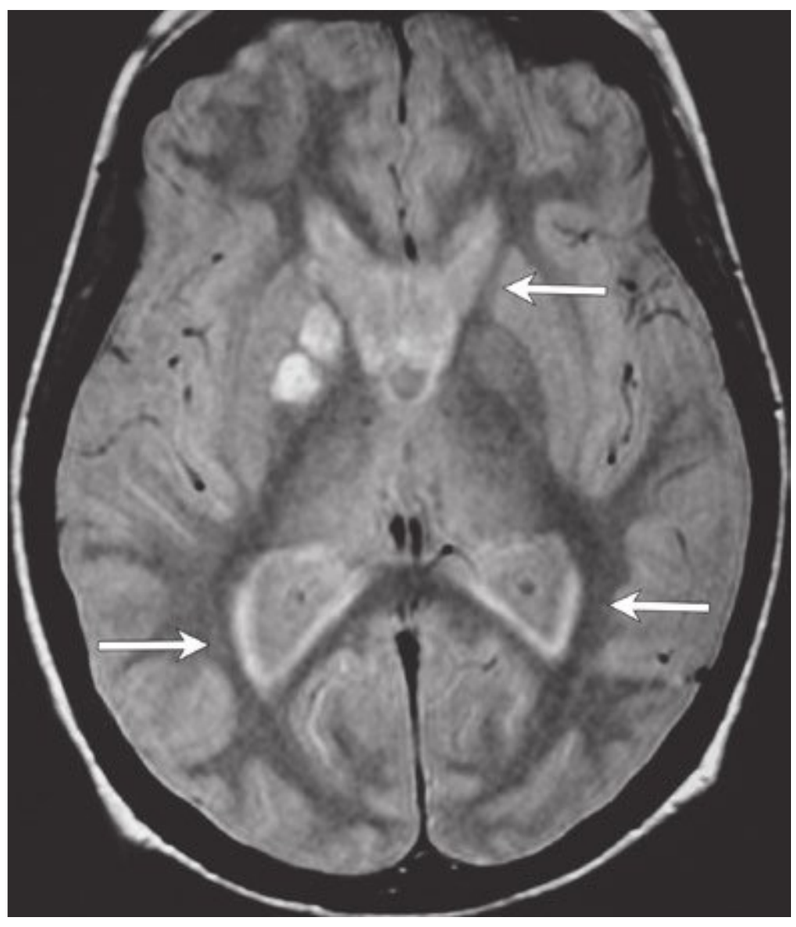

Fig. 1.171 Cytomegalovirus infection in a 33-year-old immunocompromised woman seen as abnormal, linear, high signal along the ependyma of the lateral ventricles (arrows) on axial FLAIR. Also seen are two foci with high signal in the right basal ganglia.

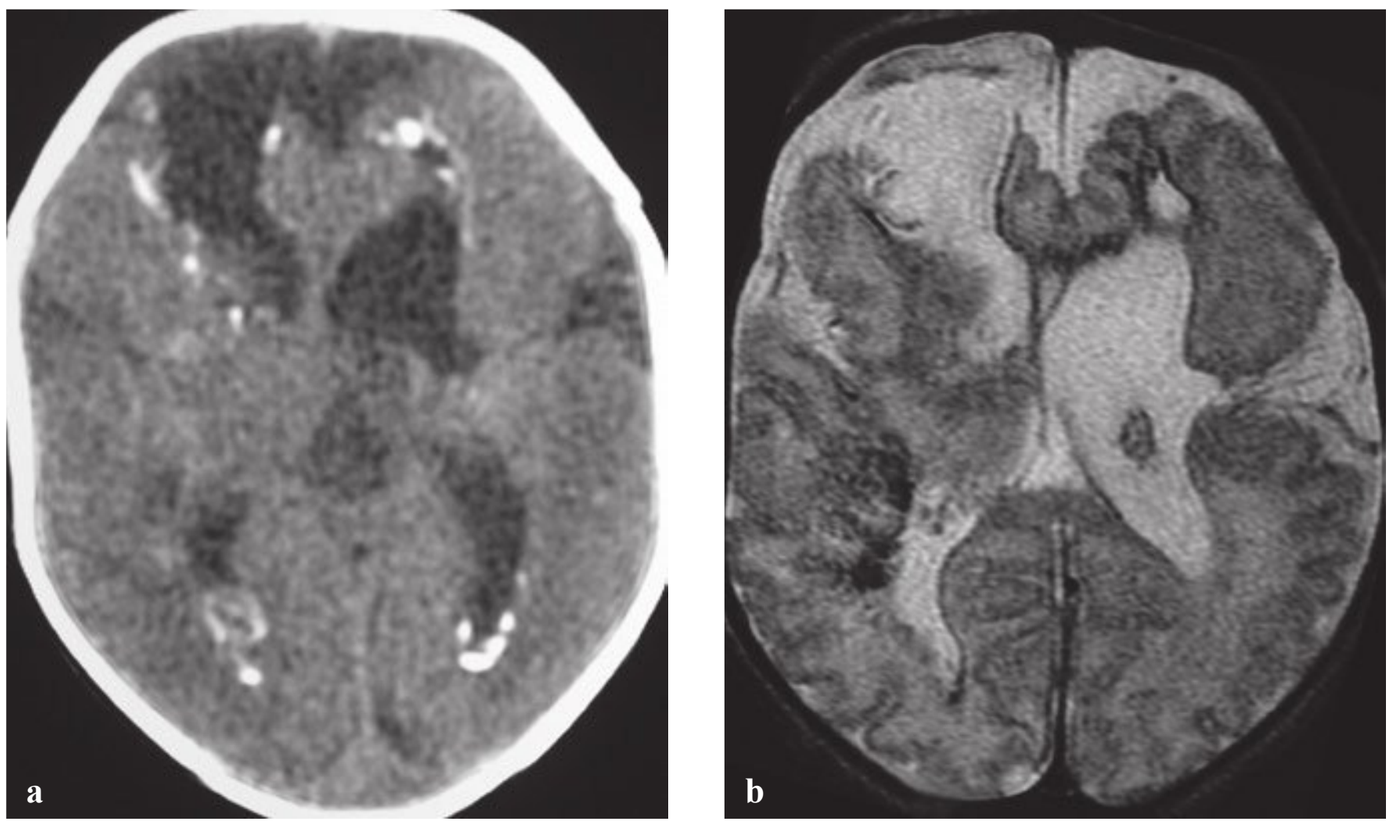

Fig. 1.172 An 8-day-old male neonate with prenatal cytomegalovirus (CMV) infection resulting in diffuse and focal zones of brain encephalomalacia, porencephaly in the right frontal lobe, schizencephaly in the left cerebral hemisphere, and multiple intra-axial calcifications as seen on **(a)** axial CT and **(b)** axial T2-weighted imaging.

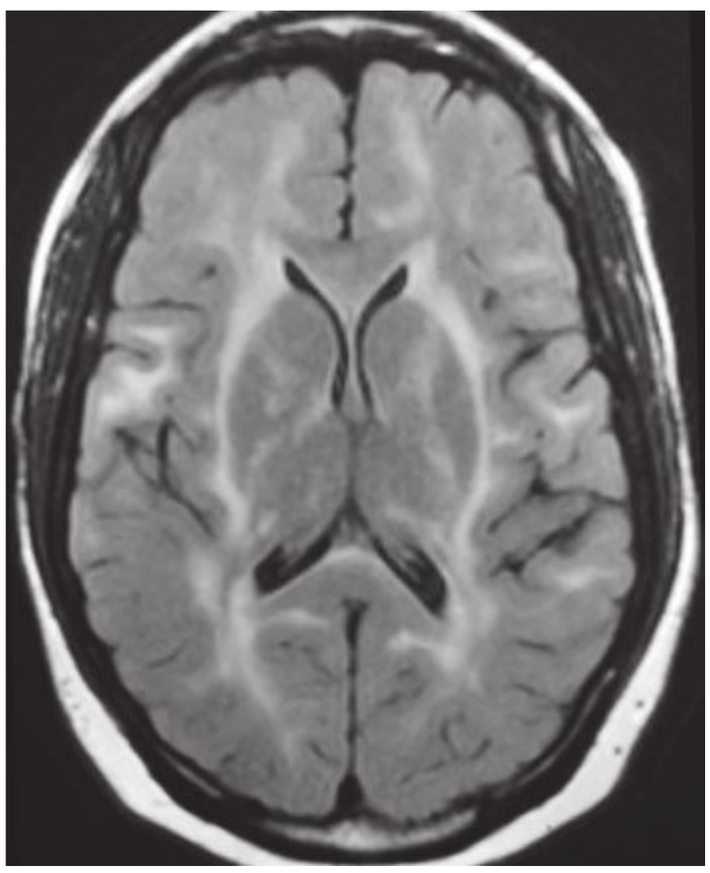

Fig. 1.173 Primary human immunodeficiency virus (HIV) infection of the brain that shows diffuse abnormal high signal, mostly in the central cerebral white matter bilaterally, as seen on axial FLAIR.

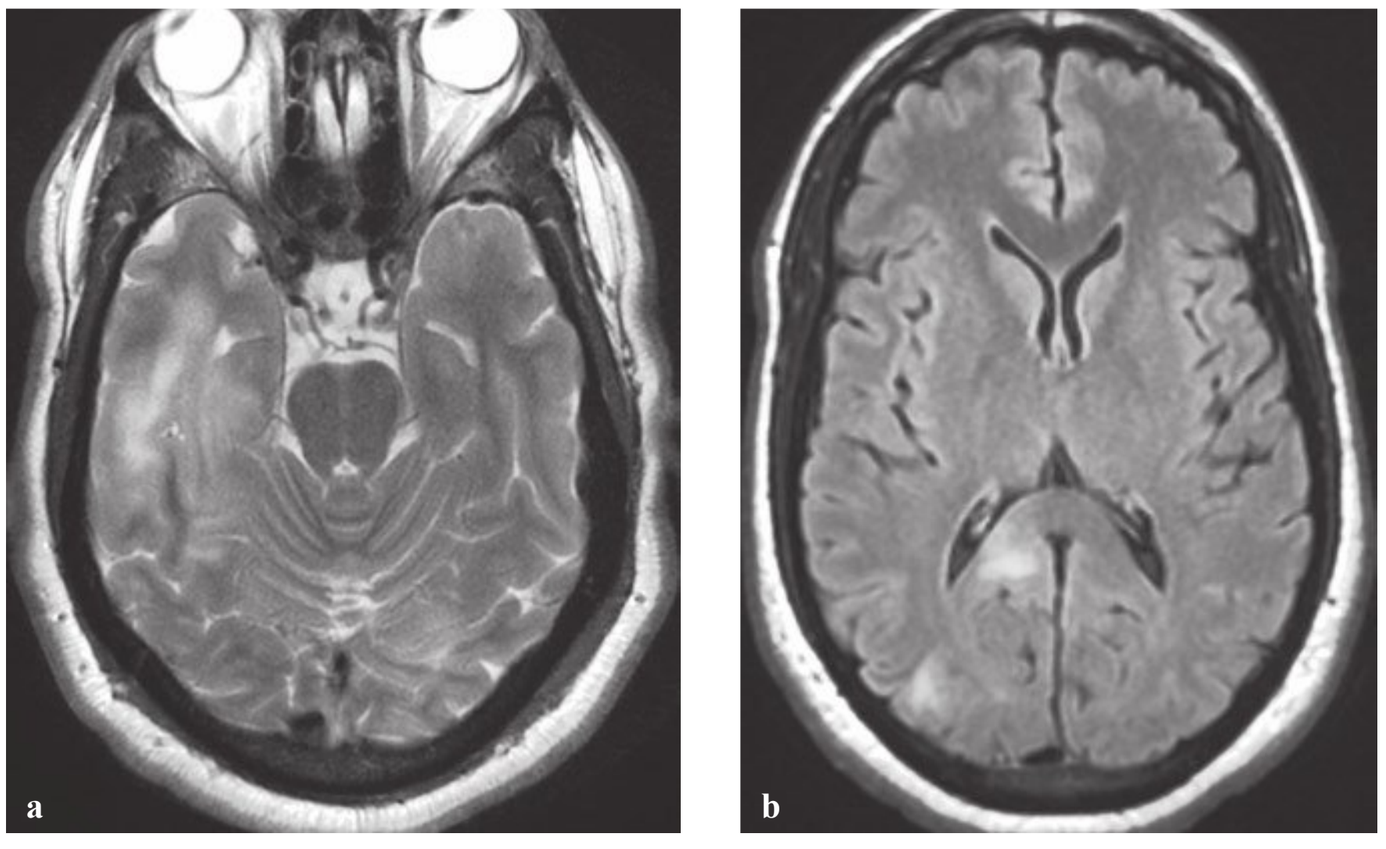

Fig. 1.174 Progressive multifocal leukoencephalopathy (PML) in an immunocompromised patient shows poorly defined zones with abnormal high signal in **(a)** the right temporal lobe on axial T2-weighted imaging and **(b)** right occipital lobe and splenium of the corpus callosum on axial FLAIR.

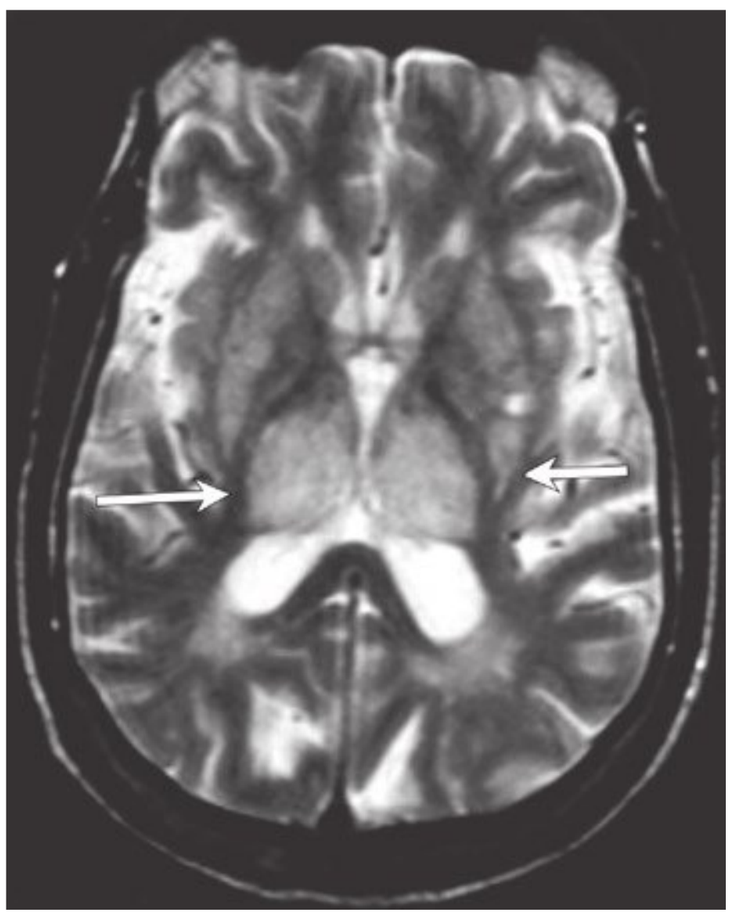

Fig. 1.175 Japanese encephalitis seen as bilateral zones of abnormal high signal in the bilateral thalami, basal ganglia, and peri-atrial white matter on axial T2-weighted imaging (arrows).

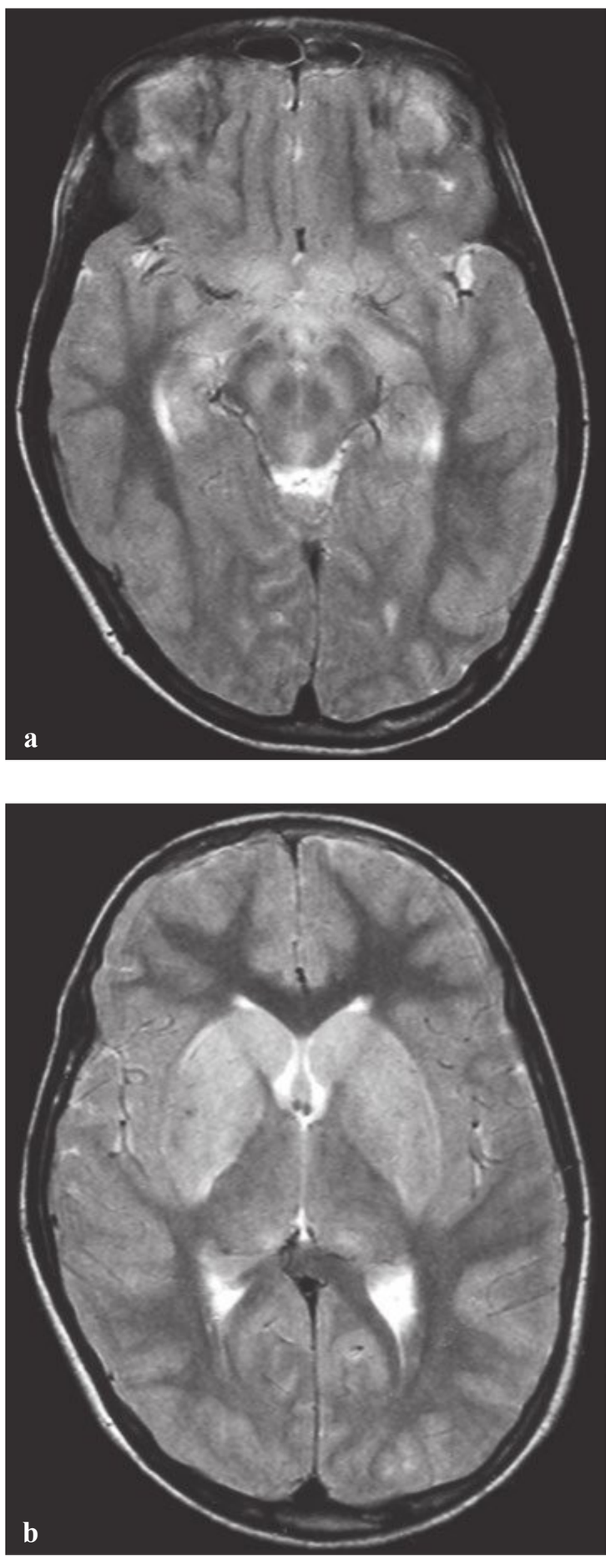

Fig. 1.176 Rabies infection with poorly defined zones with increased signal on axial T2-weighted imaging in **(a)** the infero-medial portions of the frontal and temporal lobes and **(b)** bilateral basal ganglia.

Table 1.4 (cont.) Multiple intra-axial lesions in the brain

Lesions	Imaging Findings	Comments
Cytomegalovirus (CMV) Human immunodeficiency virus (HIV) infection Progressive multifocal leukoencephalopathy Japanese encephalitis Rabies Acute measles encephalitis Subacute sclerosing panencephalitis from measles virus	CMV MRI: Periventricular/subependymal zones with high signal on T2-weighted imaging and FLAIR. CT: Neonatal CMV infections can result in localized destruction of brain, with dystrophic calcifications. HIV MRI: Confluent zones with high signal on T2-weighted imaging and FLAIR in the deep and peripheral cerebral white matter, ± sparing the subcortical U-fibers. Atrophy of cerebral white matter and progressive global brain atrophy. Typically no gadolinium contrast enhancement. Increased diffusion on diffusion tensor imaging (DTI) in cerebral white matter in patients with AIDS dementia complex. CT: Confluent zones with decreased attenuation in cerebral white matter, ± basal ganglia calcifications in up to one-third of children with HIV infection, and cerebral atrophy. PML MRI: Single or multifocal zones in the cerebral white matter, including the arcuate/U-fibers, with abnormal increased signal on T2-weighted imaging and FLAIR, ± cerebral cortical involvement, ± mild localized mass effect. Reduced ADC values and fractional anisotropy (FA) in acute phases, increased ADC in late phases. Magnetic resonance spectroscopy shows decreased N-acetylaspartate (NAA) and increased choline and lactate. Japanese encephalitis often involves the thalami, basal ganglia, hippocampi, and substantia nigra, and less commonly involves the cerebral cortex, brainstem, and cerebellum. MRI: Poorly defined zones with increased signal on T2-weighted imaging can be seen in the cerebral white matter, cerebral cortex, basal ganglia, brainstem, and hypothalamus, ± gadolinium contrast enhancement. Rabies MRI: Increased signal on T2-weighted imaging can be seen in the cerebral white matter, cerebral cortex, and basal ganglia, + restricted diffusion, ± petechial hemorrhage, ± gadolinium contrast enhancement in cerebral cortex and leptomeninges. Acute measles encephalitis MRI: Zones with abnormal increased signal on T2-weighted imaging and FLAIR are seen in the cerebral and cerebellar white matter and brainstem, with increased ADC values and no gadolinium contrast enhancement. Subacute sclerosing panencephalitis from measles virus MRI: Zones with abnormal increased signal on T2-weighted imaging and FLAIR are seen in the cerebral and cerebellar white matter, deep gray matter, brainstem, and or spinal cord, ± intra-axial, leptomeningeal, and/or spinal cord gadolinium contrast enhancement.	

(continued on page 146)

Table 1.4 (cont.) Multiple intra-axial lesions in the brain

Lesions	Imaging Findings	Comments
Progressive multifocal leukoencephalopathy (PML)—immune reconstitution inflammatory syndrome (IRIS) (**Fig. 1.177**)	MRI: Single or multiple intra-axial lesions involving white matter, including subcortical U-fibers, with high signal on T2-weighted imaging and FLAIR, with mass effect, but usually no restricted diffusion. PML usually shows no gadolinium contrast enhancement; gadolinium contrast enhancement can be seen with PML-IRIS, ± localized mass effect. CT: Multiple intra-axial lesions with decreased attenuation and mass effect.	Treatment of multiple sclerosis with monoclonal antibodies can result in PML and PML-IRIS. One such agent is natalizumab, which is directed against α4-β1 and α4-β7 integrins, which prevent inflammatory cells from binding to brain endothelial cells and moving into the brain, resulting in decreased host inflammatory reaction, which may cause reactivation of the JC polyoma virus. Diagnosis can be made by quantitative PCR analysis for JC viral DNA in CSF or brain tissue samples. Detection of viral DNA in CSF may be delayed by up to 1 month after the onset of seizures and MRI findings. Treatment of PML involves cessation of natalizumab, plasma exchange, and medications (such as maraviroc, mefloquine, and mirtazapine). IRIS occurs after cessation of natalizumab, with restoration of the immune response in the brain, which can be excessive, leading to neurologic deterioration, coma, and/or death from influx of activated lymphocytes into the brain. Steroids have been used for treatment of PML-IRIS.
Prion disease (**Fig. 1.178** and **Fig. 1.179**)	MRI: Zones with high signal on T2-weighted imaging and FLAIR can be seen in the basal ganglia (caudate, putamen, and/or thalami bilaterally) and/or cerebral cortex, with corresponding restricted diffusion. Typically no abnormal gadolinium contrast enhancement is seen with these abnormalities. CT: Usually no findings in the early phases of the disease.	Prion disease causes transmissible spongiform encephalopathies, resulting in progressive neurodegeneration. Creutzfeldt-Jakob disease is the most common type and has four forms (the sporadic form accounts for 85%, the genetic form for 10–15%, and the iatrogenic and new variant forms for the remainder).

(continued on page 148)

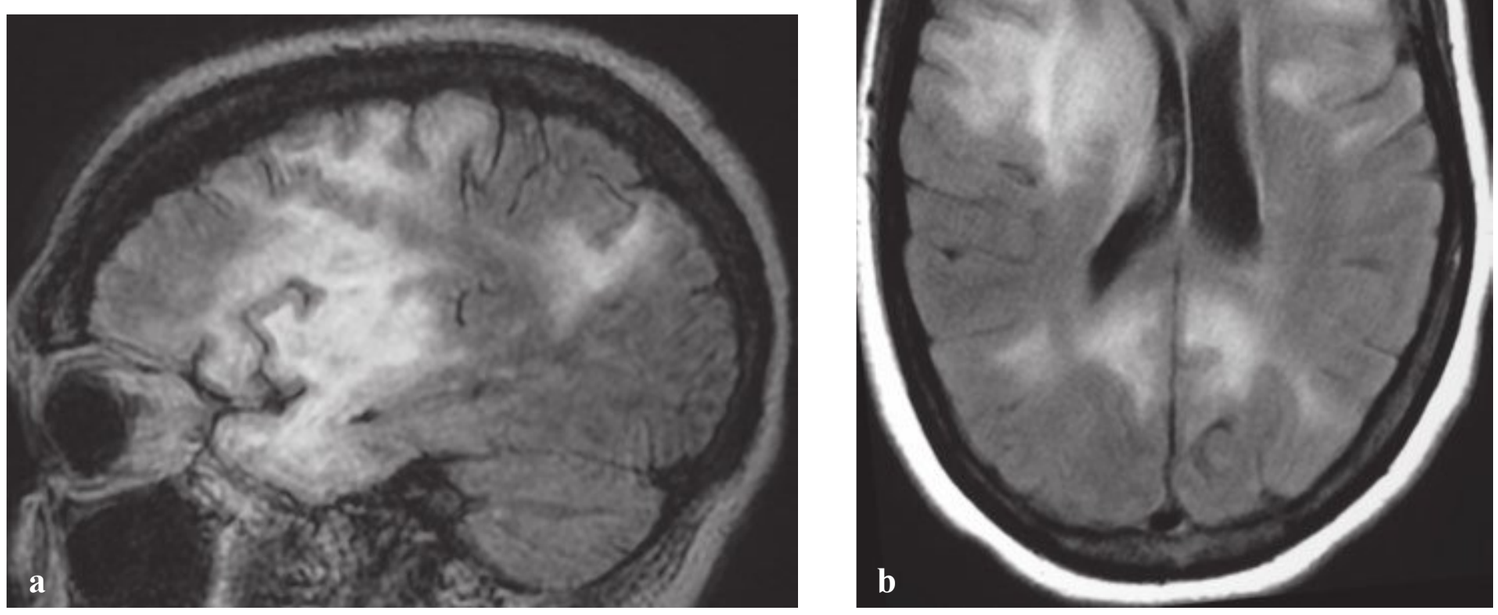

Fig. 1.177 Patient with progressive multifocal leukoencephalopathy (PML) and IRIS. Multiple, poorly defined, intra-axial lesions with high signal and localized mass effect are seen in the cerebral whiter matter bilaterally on **(a)** sagittal and **(b)** axial FLAIR.

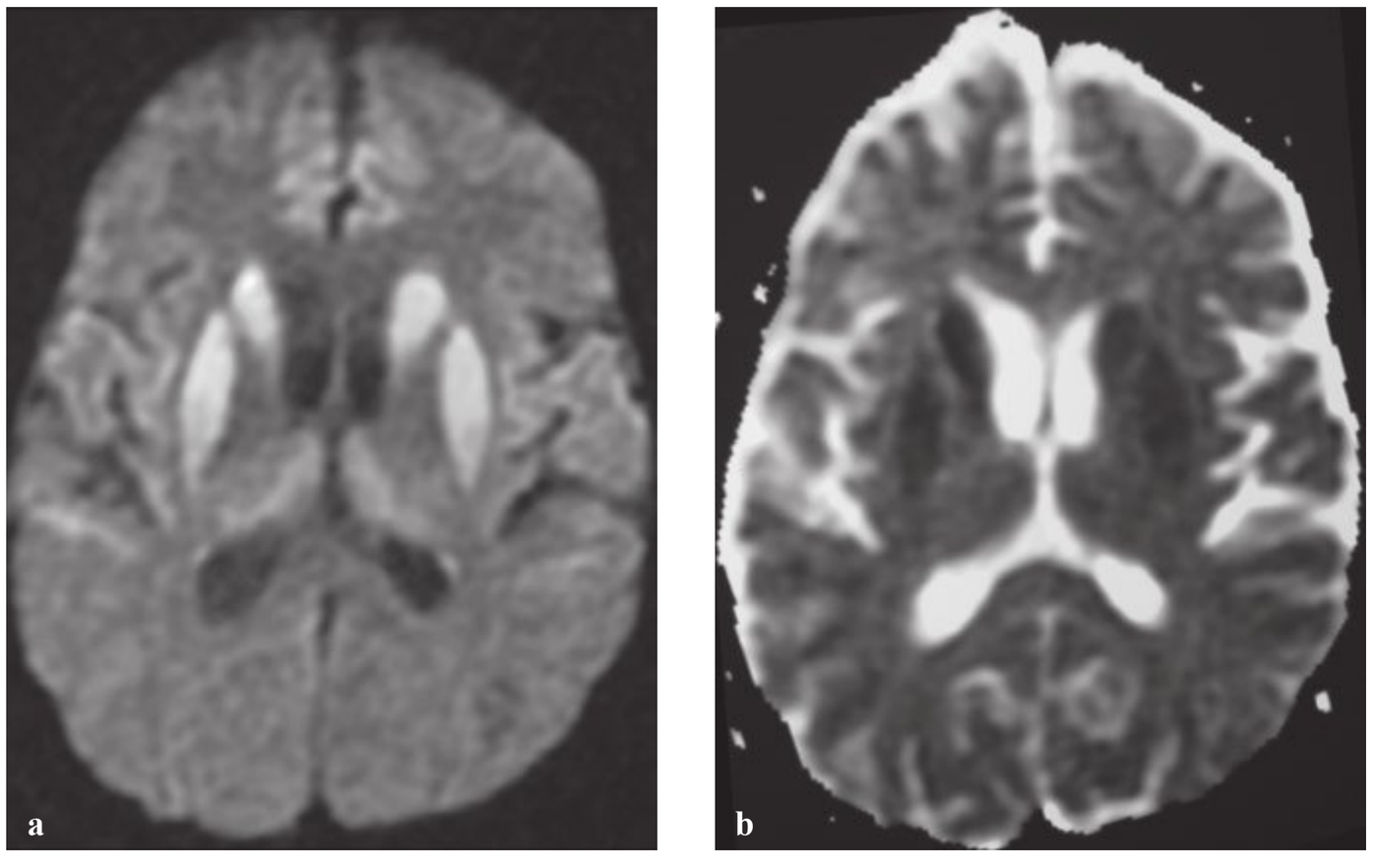

Fig. 1.178 Prion disease (Creutfeld-Jakob disease) in a 55-year-old man with progressive dementia. Restricted diffusion is seen in the bilateral caudate nuclei and putamina on **(a)** axial DWI and **(b)** ADC.

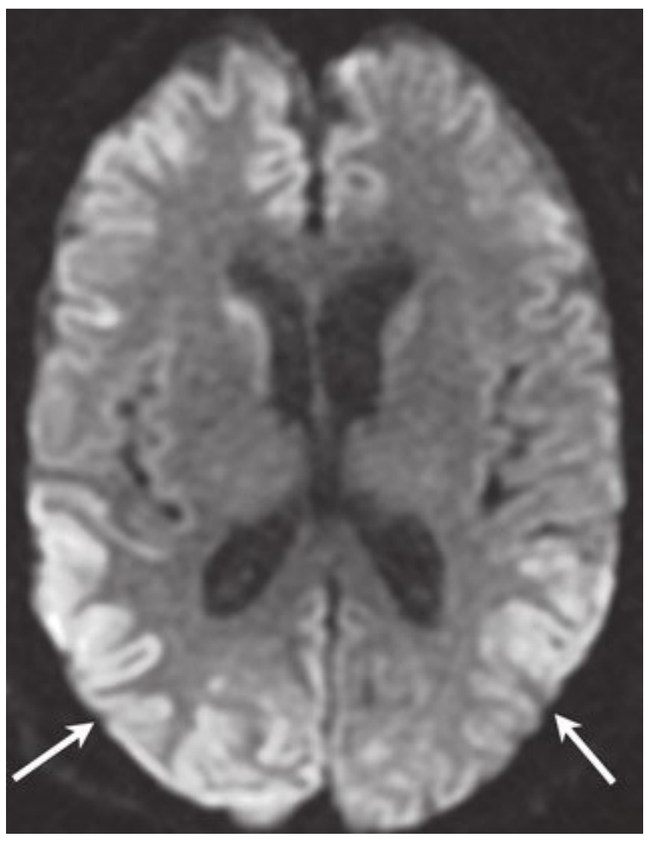

Fig. 1.179 Prion disease (Creutfeld-Jakob disease) with restricted diffusion in the parietal cerebral cortex bilaterally (arrows) on axial DWI.

Table 1.4 (cont.) Multiple intra-axial lesions in the brain

Lesions	Imaging Findings	Comments
Inflammatory Lesions: Parasitic Infections		
Toxoplasmosis (**Fig. 1.180** and **Fig. 1.181**)	MRI: Single or multiple solid and/or cystic lesions located in basal ganglia and/or corticomedullary junctions in cerebral hemispheres, with low-intermediate signal on T1-weighted imaging with or without high-signal peripheral rims; high signal on T2-weighted imaging and FLAIR with or without a central zone of low-intermediate signal, or three layers of high central signal region surrounded by a peripheral rim of low-intermediate signal, which is in turn surrounded by high signal; nodular or rim pattern of gadolinium contrast enhancement as well as an "eccentric target pattern" with a peripheral ring-shaped zone of gadolinium contrast enhancement with a small eccentric enhancing nodule along the wall; ± peripheral high T2 signal (edema). Diffusion-weighted imaging shows high-signal rims surrounding low-signal centers. CT: Lesions can have low or intermediate attenuation, ± peripheral rim or nodular patterns of contrast enhancement.	Most common opportunistic CNS infection in AIDS patients, caused by ingestion of food contaminated with parasites (Toxoplasma gondii). T. gondii is an intracellular protozoan with a worldwide distribution. Also occurs in immunocompetent patients. Acute lesions contain a central zone comprised of necrotic and cellular debris, histiocytes, and neutrophils; an intermediate zone of vascular congestion and tachyzoites; and an outer zone with microglial nodules, T. gondii organisms, and tachyzoites, mild inflammation, and vascular congestion. FDG-PET/CT shows decreased FDG uptake in T. gondii lesions and can be used to distinguish toxoplasmosis from lymphoma, which has increased FDG uptake.
Cysticercosis (**Fig. 1.182**)	MRI: Single or multiple cystic lesions in brain or meninges. Active vesicular phase: Cystic-appearing lesions containing a small 2–4 mm nodule (scolex), with low signal on T1-weighted imaging, FLAIR, and diffusion-weighted imaging, a thin peripheral rim with high signal on FLAIR, and a high signal on T2-weighted imaging; minimal peripheral rim or no gadolinium contrast enhancement; no peripheral edema on T2-weighted imaging and FLAIR. Active colloidal vesicular phase: Cystic-appearing lesion with low-intermediate signal on T1-weighted imaging, high signal on T2-weighted imaging, rim and/or nodular pattern of gadolinium contrast enhancement, ± peripheral signal (edema) on T2-weighted imaging. Active granular nodular phase: Cyst retracts into a more solid gadolinium contrast-enhancing granulomatous nodule. CT: Single or multiple cystic-appearing lesions in brain or meninges. In the acute/subacute phase there is low-intermediate attenuation, rim ± nodular pattern of contrast enhancement, ± peripheral low attenuation (edema). The chronic phase is characterized by calcified granulomas.	Cysticercosis is caused by ingestion of encysted larva of the tapeworm Taenia solium in contaminated food (undercooked pork). It involves meninges, subarachnoid space, and cisterns > brain parenchyma > ventricles. It is the most common parasitic disease of the CNS, usually in patients from 15 to 40 years old, and the most common cause of acquired epilepsy in endemic regions. Complications include intracranial hypertension from CSF obstruction, arachnoiditis, meningitis, and vascular occlusion.

(continued on page 150)

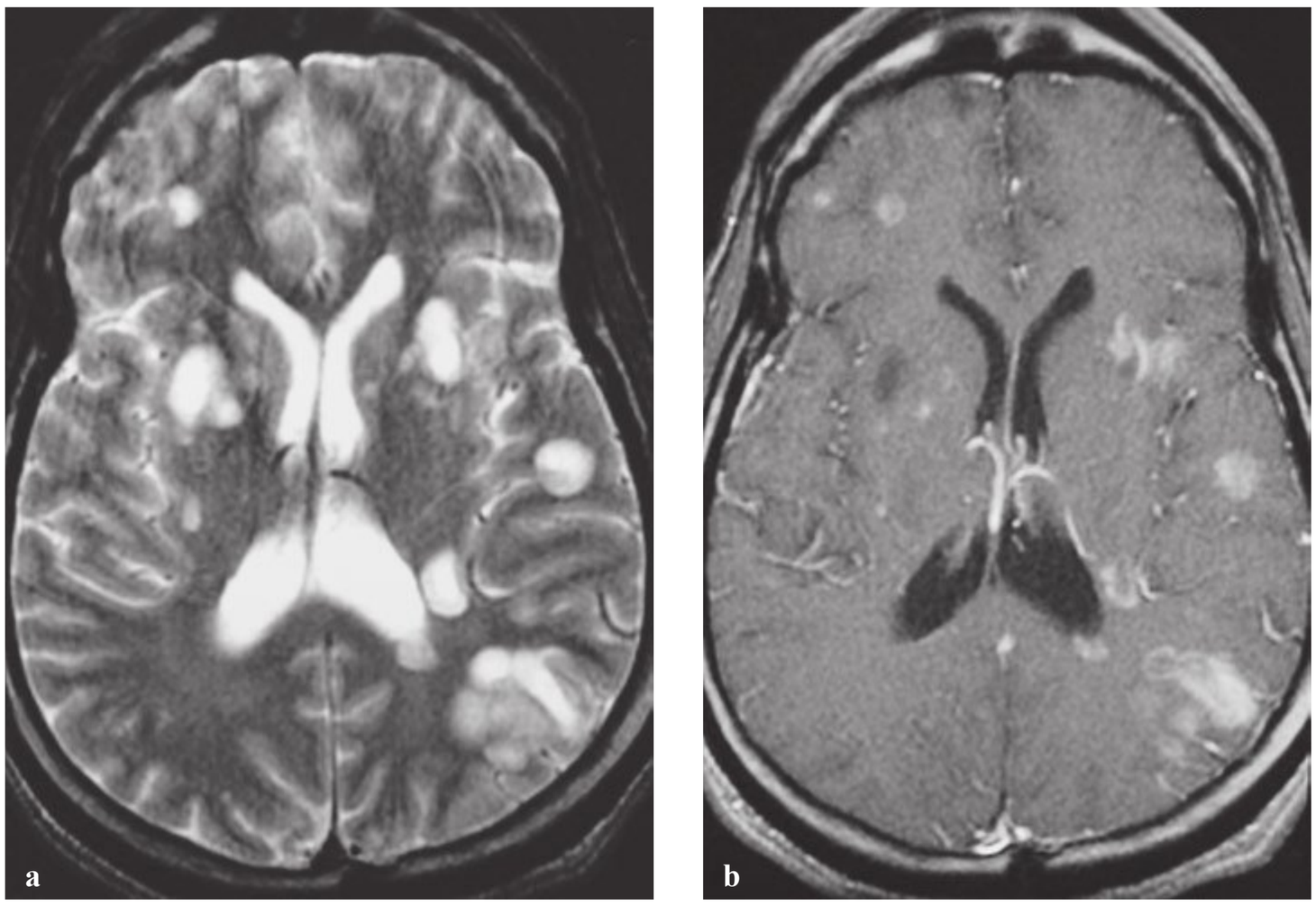

Fig. 1.180 **(a)** Toxoplasmosis in an immunocompromised patient seen as multiple cystic lesions located in basal ganglia and corticomedullary junctions in cerebral hemispheres that have high signal on axial T2-weighted imaging. **(b)** Lesions show a nodular or rim pattern of gadolinium contrast enhancement, as well as an eccentric target pattern with a peripheral ring-shaped zone of gadolinium contrast enhancement and a small eccentric enhancing nodule along the wall on axial T1-weighted imaging.

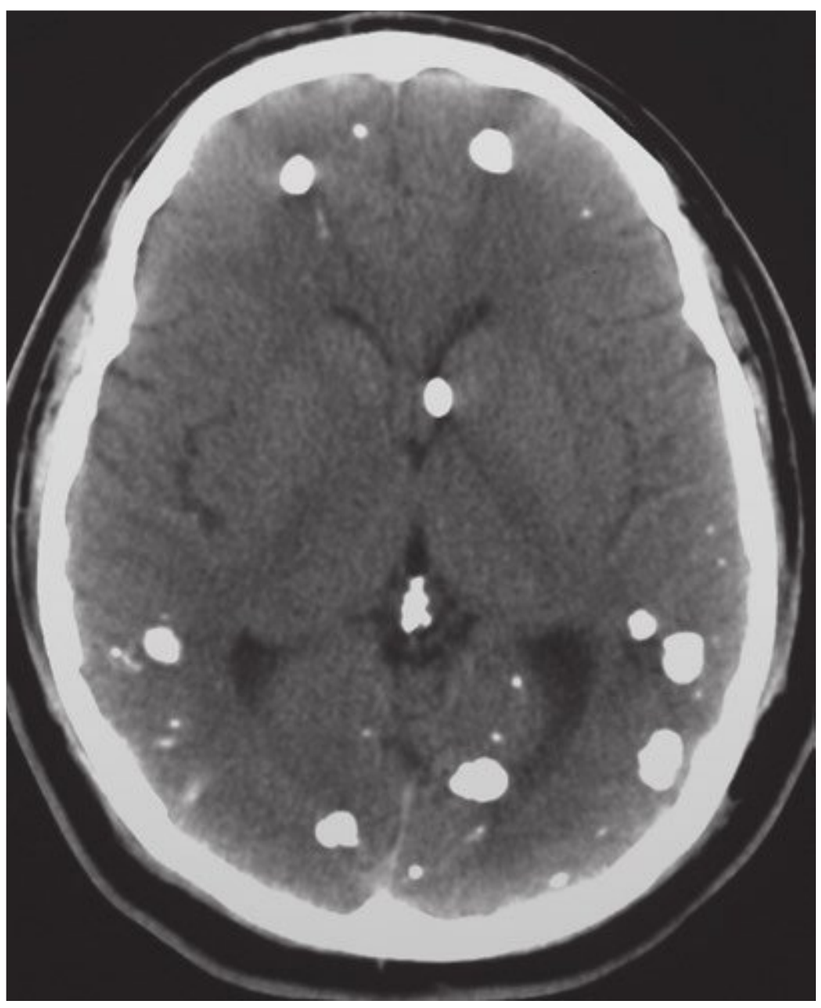

Fig. 1.181 An 18-year-old man with a history of congenital toxoplasmosis and multiple calcifications seen in the brain on axial CT.

Fig. 1.182 Patient with a remote history of intracranial cysticercosis and multiple small calcified granulomas in the brain seen on axial CT.

Table 1.4 (cont.) Multiple intra-axial lesions in the brain

Lesions	Imaging Findings	Comments
Hydatid cysts (**Fig. 1.183**) Echinococcus granulosus Echinococcus multilocularis	Echinococcus granulosus MRI: Single or rarely multiple cystic lesions with low signal on T1-weighted imaging and high signal on T2-weighted imaging surrounded by a thin wall with low signal on T2-weighted imaging. Typically there is no gadolinium contrast enhancement or peripheral edema unless superinfected. Cysts are often located in the territory of the middle cerebral artery. Rupture of the hydatid cyst may be contained by the pericyst, causing an inflammation and gadolinium contrast enhancement of the pericyst as well as perilesional edema. Floating germinal membranes with low signal on T1- and T2-weighted images can be seen within the fluid deep in the pericyst. Rupture of the hydatid cyst beyond the pericyst can also result in an inflammatory host response. Echinococcus multilocularis MRI: Cystic (± multilocular) and/or solid lesions, with a central zone of intermediate-high signal on T2-weighted imaging surrounded by a slightly thickened rim of low signal, + gadolinium contrast enhancement. Peripheral zone of high signal on T2-weighted images (edema) and calcifications are common.	Rare intracranial lesions caused by Echinococcus granulosus (South America, Middle East, Australia, and New Zealand) and Echinococcus multilocularis (North America, Europe, Turkey, and China). CNS involvement in 1 to 4% of cases of hydatid infections. Humans are intermediate hosts from ingestion of tapeworm eggs in fecally contaminated food or by contact with infected animal tissue. Lesions are often large before becoming symptomatic from raised intracranial pressure. The enlarging cystic lesion results in a thin, compressed layer of adjacent host tissue (pericyst) that can show increased vascularity and gliosis, but without gadolinium contrast enhancement. Superinfected hydatid cysts often contain purulent material, often with Staphylococcus aureus, and are typically surrounded by an inflammatory reaction in the adjacent brain tissue and/or meninges.
Amebiasis (**Fig. 1.184**) Granulomatous amebic encephalitis Primary amebic meningoencephalitis	MRI: Nodular lesions can be seen in the brain, ± hemorrhage related to necrotizing angiitis, and adjacent poorly defined zones with high signal on T2-weighted imaging. Lesions can show variable gadolinium contrast enhancement, ± gyriform leptomeningeal contrast enhancement. Postcontrast MRI shows gadolinium contrast enhancement of the leptomeninges, with or without abnormal high signal on T2-weighted imaging and gadolinium contrast enhancement of the adjacent brain and/or brainstem.	Cerebral amebiasis is rare, accounting for 0.8% of CNS infections. Usually occurs in patients from 10 to 30 years old, and in males more frequently than in females. Amebic organisms that cause infection of the CNS include Acanthamoeba species, Balamuthia mandrillaris, and Sappinia diploidea, which cause subacute or chronic granulomatous CNS infections (meningoencephalitis and occasionally cerebral abscesses). Another ameba, Entamoeba histolytica, infects the colon primarily and is associated with secondary brain and hepatic abscesses. Amebic brain abscesses can be solitary or multiple, and often involve the frontal lobes and basal ganglia. Primary amebic meningoencephalitis from infection by Naegleria fowleri, which can have acute onset of symptoms within 3 days, has extensive purulent leptomeningeal exudate that results in necrosis and hemorrhage of the brain and brainstem.
Malaria (**Fig. 1.185**)	MRI: Focal and/or poorly defined zones with high signal on T2-weighted imaging in the cerebral white matter and/or cerebral cortex, corpus callosum, basal ganglia, thalami, and cerebellum, ± cerebral edema with effacement of sulci and basal cisterns, ± uncal herniation, ± hemorrhage, ± restricted diffusion related to ischemic injury. Usually no gadolinium contrast enhancement of lesions. CT: Focal and/or poorly defined zones with decreased attenuation in the cerebral white matter, basal ganglia, and/or thalami.	Malaria results from infection by protozoan parasites from the genus Plasmodium. Transmission of the parasite to humans occurs via bites from female mosquitoes (Anopheles genus) containing the Plasmodium organisms. Malaria involving the CNS occurs in 2% of patients infected with Plasmodium falciparum. Occurs commonly in children and visitors to endemic regions (sub-Saharan Africa, other tropical zones with altitudes less than 1500 m). Aggregation of infected erythrocytes in cerebral blood vessels results in perivascular hemorrhage, myelin damage, and necrosis of white matter. Inflammatory reaction, with cytokine release, vasodilation, and vascular engorgement, can result in cerebral edema and increased intracranial pressure, which may be reversible. Severe malaria results in ~ 1 million deaths per year.

(continued on page 152)

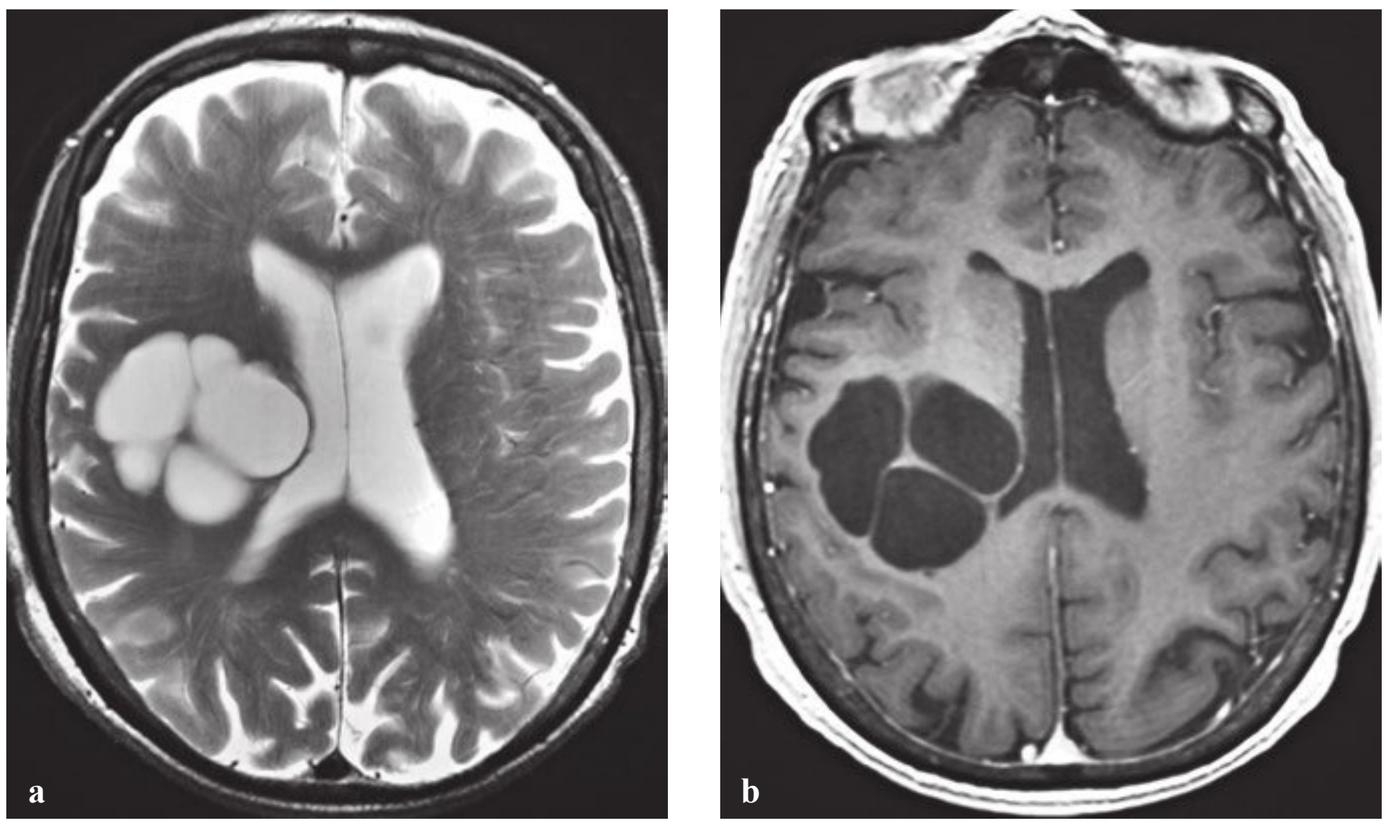

Fig. 1.183 Patient with intracranial hydatid cysts that are well-circumscribed lesions with **(a)** high signal on axial T2-weighted imaging and **(b)** low signal without gadolinium contrast enhancement on axial T1-weighted imaging.

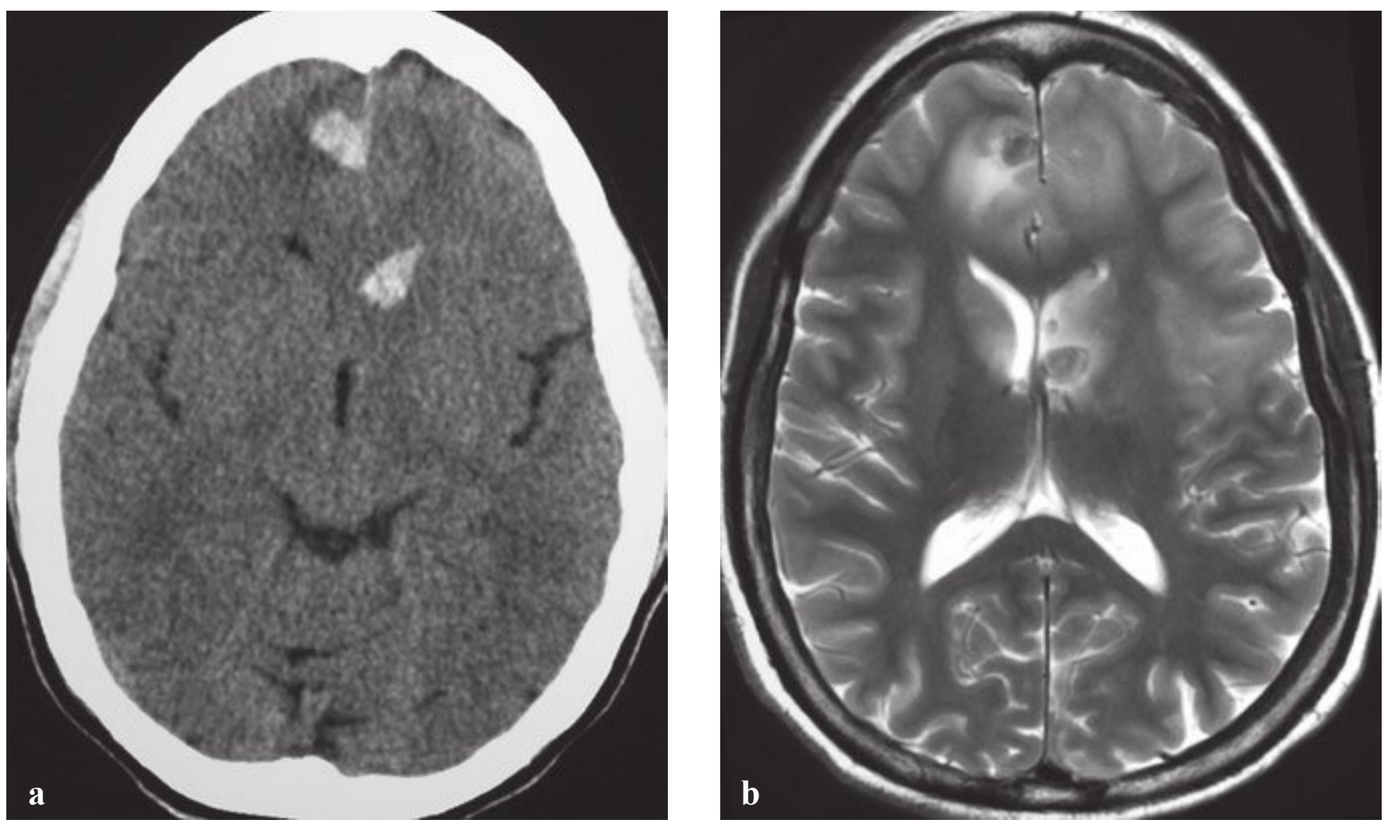

Fig. 1.184 A 29-year-old woman with intracranial amebiasis. **(a)** On axial CT, nodular lesions are seen in both frontal lobes with hemorrhage related to necrotizing angiitis. **(b)** The hemorrhagic lesions have low signal and adjacent poorly defined zones with high signal on T2-weighted imaging.

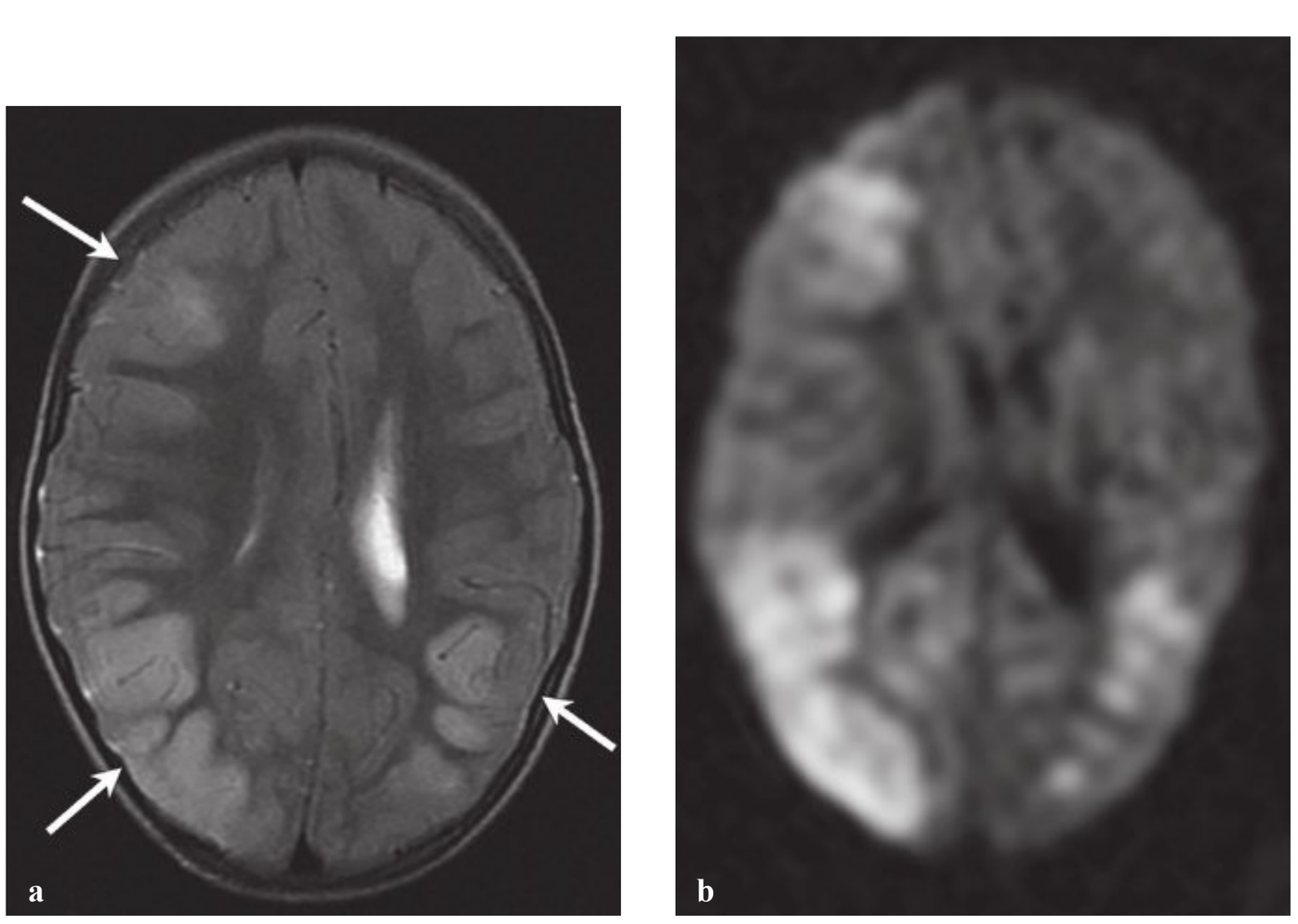

Fig. 1.185 Young child from Malawi with cerebral malaria. **(a)** Poorly defined zones with abnormal slightly high signal on axial T2-weighted imaging are seen in cerebral cortex bilaterally (arrows) with associated localized gyral swelling. **(b)** The involved sites have corresponding restricted diffusion on axial DWI.

Table 1.4 (cont.) Multiple intra-axial lesions in the brain

Lesions	Imaging Findings	Comments
Schistosomiasis	MRI: Foci with low signal on T1-weighted imaging and high signal on T2-weighted imaging in the cerebrum, cerebellum, and/or brainstem, which usually show gadolinium contrast enhancement. Gadolinium contrast enhancement in the cranial and spinal leptomeninges and lower spinal cord can also be seen. CT: Foci with slightly increased attenuation surrounded by decreased attenuation (edema) in the cerebrum, cerebellum, and/or brainstem.	Parasitic disease caused by Schistosoma mansoni (Africa, Southwest Asia, South America), Schistosoma haematobium (Africa and Southwest Asia), and Schistosoma japonicum (Asia). Schistosoma cercariae released by infected snails into freshwater can enter humans via the skin and can migrate to the lungs, liver, and portal venous system. Embolization of the eggs into the pulmonary arteries or into Batson's venous plexus can spead to involve the brain. Treatment can lead to complete resolution after 6 months.
Trypanosomiasis	MRI: Focal and/or poorly defined zones with high signal on T2-weighted imaging in the cerebral white matter, corpus callosum, internal capsules, basal ganglia, and cerebral peduncles, ± gadolinium contrast enhancement of brain lesions. Dural and/or leptomeningeal gadolinium contrast enhancement can be seen. CT: Focal and/or poorly defined zones with decreased attenuation in the cerebral white matter and basal ganglia.	In Africa, infection of humans results from bites from infected tsetse flies that transmit Trypanosoma brucei rhodesiense or Trypanosoma brucei gambiense. Lesions involve the brain and meninges via hematogenous spread to the choroid plexus into the CSF and directly through capillaries in the brain. In the Americas, infection of humans results from bites from infected Triatominae insects that transmit Trypanosoma cruzi. Also referred to as Chagas disease, infection usually involves the heart, esophagus, and colon and rarely involves the CNS.
Paragonimiasis	MRI: Aggregates of nodular zones with high signal on T2-weighted imaging in the cerebral white matter, ± zones of low signal from calcification, ± zones of hemorrhage, ± peripheral gadolinium contrast enhancement. Fusiform tunnellike zones with high signal on T2-weighted imaging can be seen. CT: Multiple intra-axial calcifications can be seen surrounded by zones with decreased attenuation, ± localized cerebral atrophy.	Occurs in Asia (China, Korea, and Japan) from infection of humans by ingestion of food contaminated with the parasite Paragonimus westermani. Granulomatous reaction and aseptic inflammation occur in host in response to ingested parasites and/or eggs. Infection of brain results in granulomatous reaction, cerebral hemorrhage, and/or brain infarction.
Sparganosis	MRI: Fusiform tunnellike zones with low signal on T1-weighted imaging and slightly high signal on T2-weighted imaging can be seen in the brain, and they have peripheral gadolinium contrast enhancement. Nodular zones with slightly high signal are seen on T2-weighted imaging surrounded by a low signal wall, and peripheral or solid gadolinium contrast enhancement is another pattern that can be seen in the cerebral white matter. Acute lesions can have peripheral edema and chronic lesions may show localized gliosis and encephalomalacia, ± zones of low signal from calcification, ± zones of hemorrhage. CT: Multiple intra-axial calcifications can be seen surrounded by zones with decreased attenuation, ± localized cerebral atrophy.	Occurs in China, Korea, Japan, and other sites in Southeast Asia from infection of humans by ingestion of water and/or food contaminated with the parasite Spirometra mansoni. Larvae of parasite or live worms measuring 5 to 8 cm tunnel through and migrate within host and can pass intracranially through skull base foramina in up to 25% of infections. Can be a chronic disease lasting up to 30 years.

Lesions	Imaging Findings	Comments
Inflammatory Lesions: Noninfectious		
Demyelinating disease—Multiple sclerosis (**Fig. 1.186**)	MRI: Lesions located in cerebral or cerebellar white matter, brainstem, basal ganglia; lesions usually have low-intermediate signal on T1-weighted imaging and high signal on T2-weighted imaging, ± gadolinium contrast enhancement. Gadolinium contrast enhancement can be ringlike or nodular, usually in acute/early subacute phase of demyelination, ± restricted diffusion. Acute demyelinating lesions can have localized mass effect simulating neoplasms. CT: Zones of active demyelination may show contrast enhancement and mild localized swelling.	Multiple sclerosis (MS) is the most common acquired demyelinating disease in young and middle-aged adults (peak ages = 20–40 years). MS affects 400,000 people in the United States and 2,000,000 worldwide. Women are affected twice as frequently as men. MS is most common in people with northern European heritage. MS is not inherited in a Mendelian fashion, although it can cluster in families. Diagnosis is made based on clinical history and findings, results from MRI examinations (lesions with high signal on T2-weighted imaging or FLAIR seen in brain white matter, spinal cord, and optic nerves), abnormal visual evoked potentials, and isoelectric focusing evidence of oligoclonal bands and/or increased IgG index in CSF samples. Demyelinating disease occurs wherever myelin is present, including deep brain nuclei (caudate, putamen, globus pallidus, and/or thalamus). The disease is typically multi-episodic. Treament includes monoclonal antibodies and steroids.

(continued on page 154)

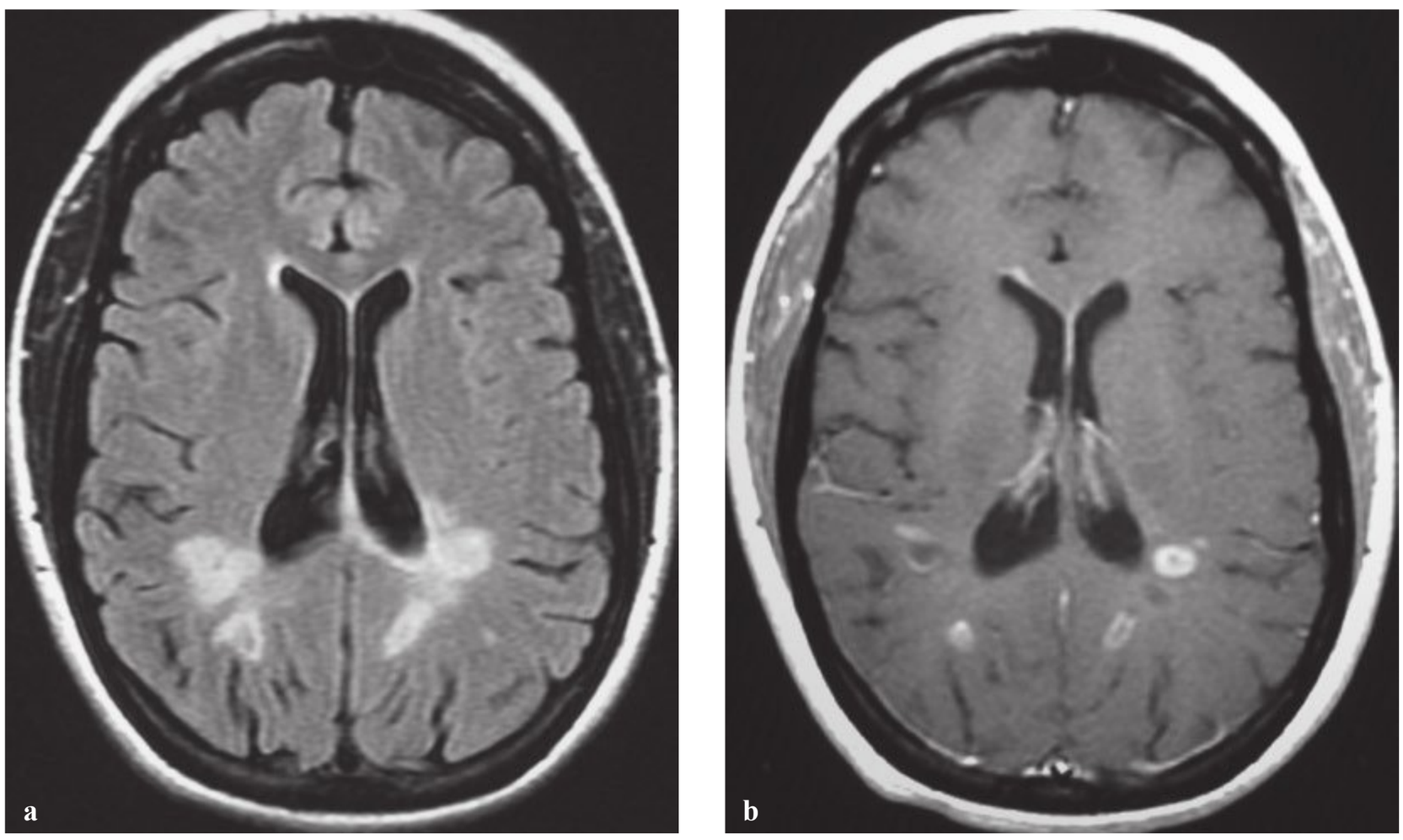

Fig. 1.186 Patient with multiple sclerosis. **(a)** Lesions with high signal on axial FLAIR are seen in the periventricular white matter. **(b)** Some of the lesions show ringlike or nodular gadolinium contrast enhancement on axial T1-weighted imaging.

Table 1.4 (cont.) Multiple intra-axial lesions in the brain

Lesions	Imaging Findings	Comments
Acute disseminated encephalomyelitis (**Fig. 1.187** and **Fig. 1.188.** See also **Fig. 1.260.**)	MRI: Lesions located in cerebral or cerebellar white matter, brainstem, basal ganglia; lesions usually have low-intermediate signal on T1-weighted imaging and high signal on T2-weighted imaging, ± gadolinium contrast enhancement. Gadolinium contrast enhancement can be ringlike or nodular, usually in acute/early subacute phase of demyelination, ± restricted diffusion. Acute demyelinating lesions can have localized mass effect simulating neoplasms. CT: Zones of active demyelination may show contrast enhancement and mild localized swelling.	Acute disseminated encephalomyelitis is an immune-mediated demyelination occurring after viral infection or due to toxin exposure (environmental exposure or ingestion, such as alcohol or solvents).
Neurosarcoid (**Fig. 1.189**)	MRI: Poorly marginated intra-axial zone or zones with low-intermediate signal on T1-weighted imaging, slightly-high to high signal on T2-weighted imaging and FLAIR, usually with gadolinium contrast enhancement, + localized mass effect and peripheral edema. Often associated with gadolinium contrast enhancement in the leptomeninges and/or dura. CT: Poorly marginated intra-axial zone with low-intermediate attenuation, usually showing contrast enhancement, + localized mass effect and peripheral edema. Often associated with contrast enhancement in the leptomeninges.	Sarcoidosis is a multisystem noncaseating granulomatous disease of uncertain cause that can involve the CNS in 5 to 15% of cases. If untreated, it is associated with severe neurologic deficits, such as encephalopathy, cranial neuropathies, and myelopathy. Diagnosis of neurosarcoid may be difficult when the neurologic complications precede other systemic manifestations involving the lungs, lymph nodes, skin, bone, and/or eyes.
Brain contusions (**Fig. 1.190**)	MRI: The MR appearance of contusions is focal hemorrhage involving the cerebral cortex and subcortical white matter. The signal of the contusion depends on its age and presence of oxyhemoglobin, deoxyhemoglobin, methemoglobin, hemosiderin, etc. Surrounding the hematoma is a zone of edema with high signal on T2-weighted imaging and FLAIR and decreased relative cerebral blood volume (rCBF). Contusions eventually appear as zones of focal superficial encephalomalacia with high signal on T2-weighted imaging, ± small zones of low signal on T2-weighted imaging from hemosiderin. CT: The CT appearance of contusions is initially one of focal hemorrhage involving the cerebral cortex and subcortical white matter. Contusions eventually appear as zones of focal superficial encephalomalacia.	Contusions are superficial brain injuries involving the cerebral cortex and subcortical white matter that result from skull fracture and/or acceleration-deceleration trauma of the brain impacting onto the inner table of the skull. Lesions consist of capillary injury, edema, and hemorrhage, and often involve the anterior portions of the temporal and frontal lobes, as well as the inferior portions of the frontal lobes.

(continued on page 156)

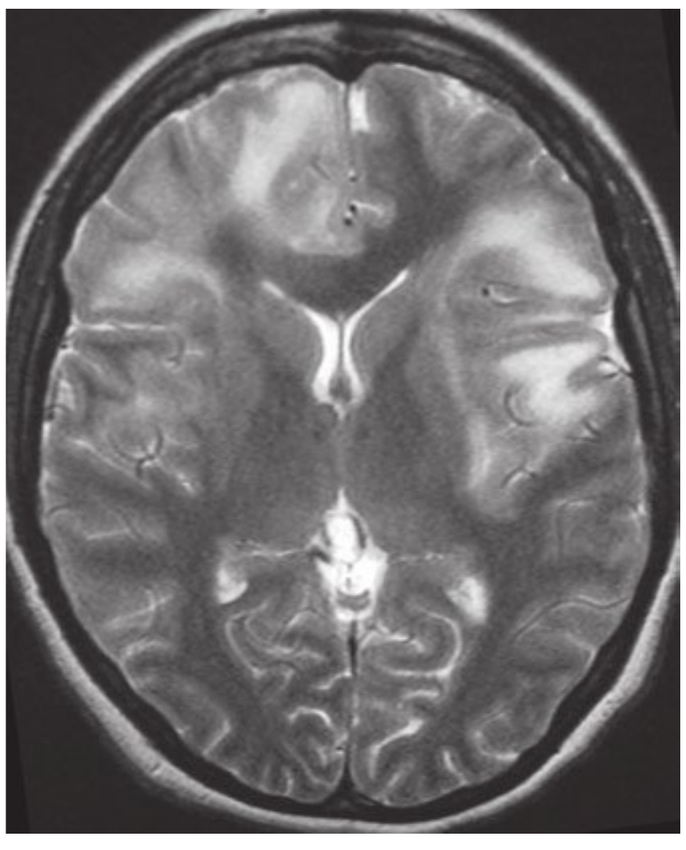

Fig. 1.187 A 35-year-old woman with acute disseminated encephalomyelitis. Multiple, poorly defined zones with abnormal high signal are seen in the cerebral white matter on axial T2-weighted imaging.

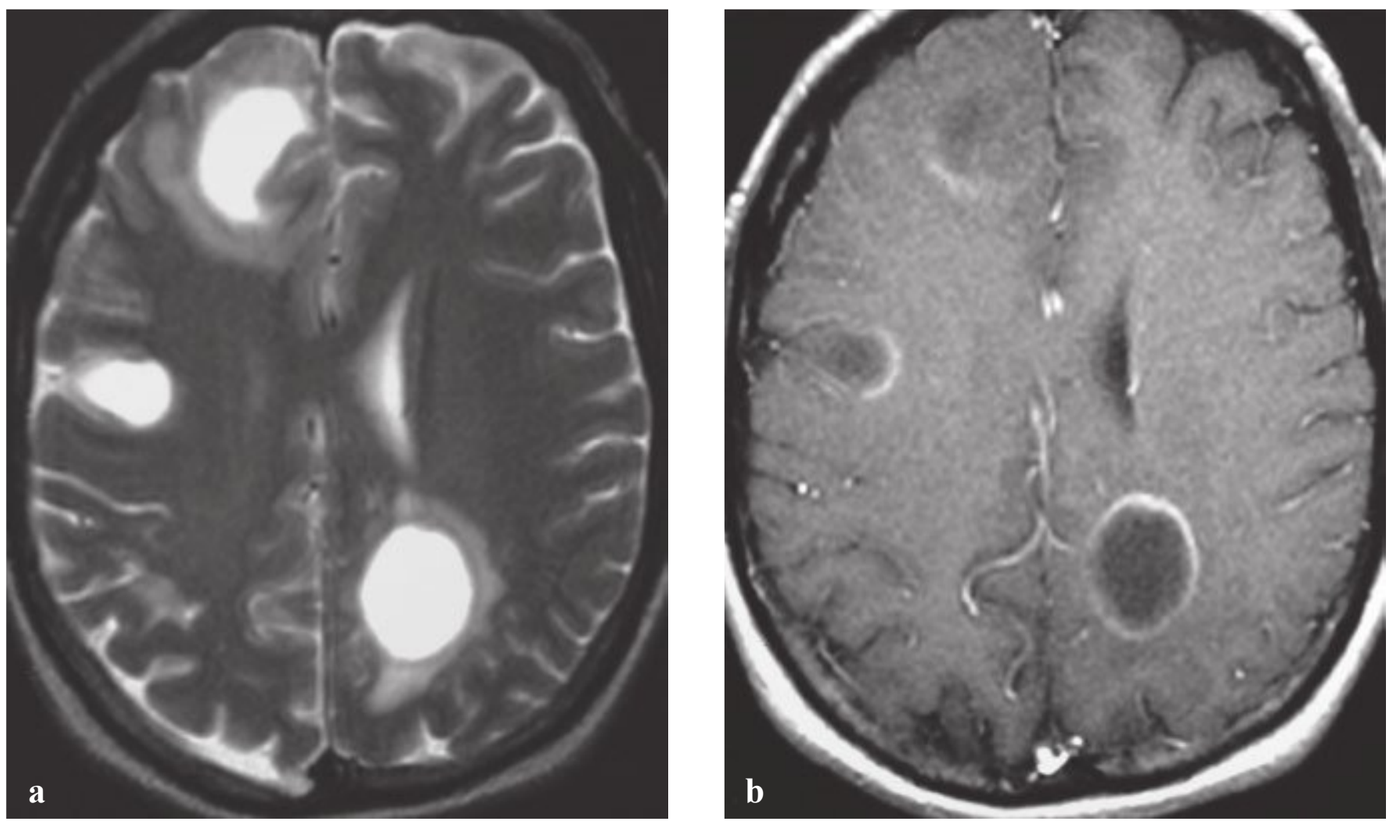

Fig. 1.188 A 24-year-old man with acute disseminated encephalomyelitis. **(a)** Multiple tumefactive lesions with high signal and localized mass effect are seen in the cerebral white matter on axial T2-weighted imaging. **(b)** Lesions show partial, thin, rim patterns of gadolinium contrast enhancement on axial T1-weighted imaging.

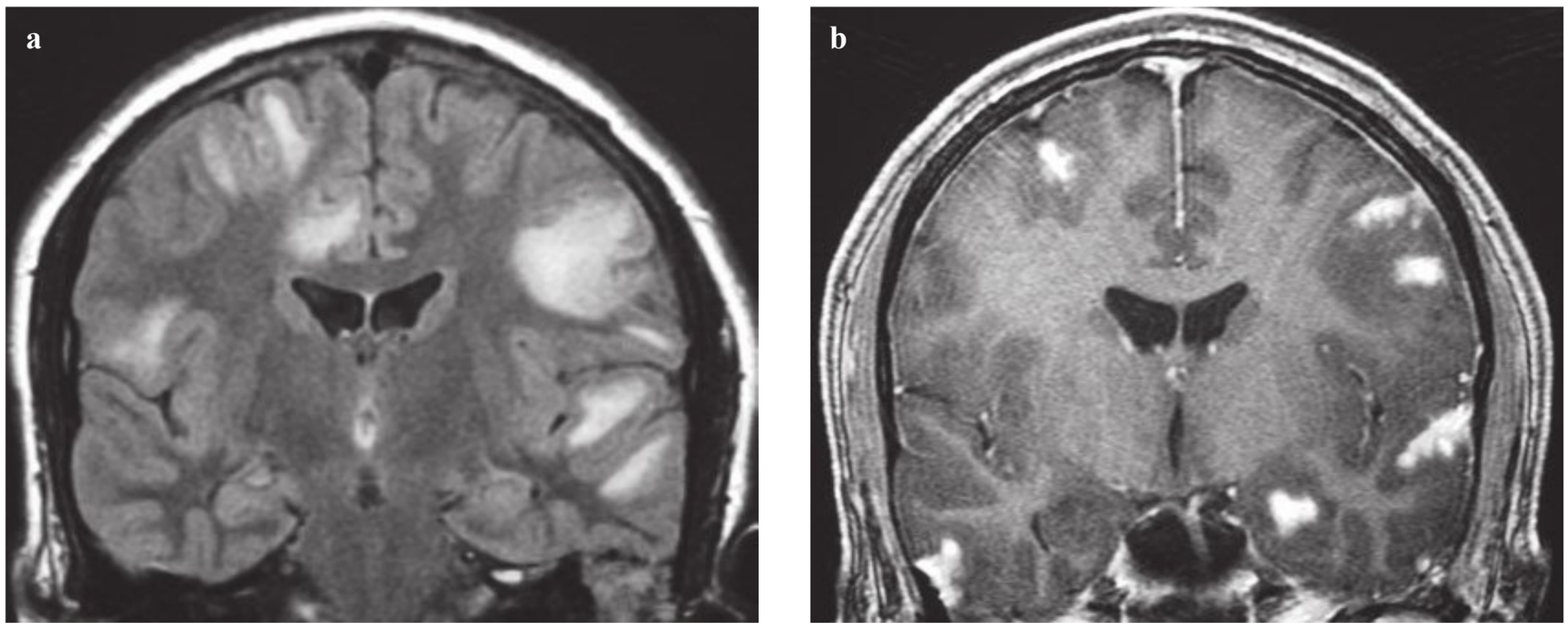

Fig. 1.189 A 30-year-old man with neurosarcoid. Multiple subcortical and cortical zones with abnormal high signal are seen on **(a)** coronal FLAIR that show irregular gadolinium contrast enhancement on **(b)** coronal T1-weighted imaging.

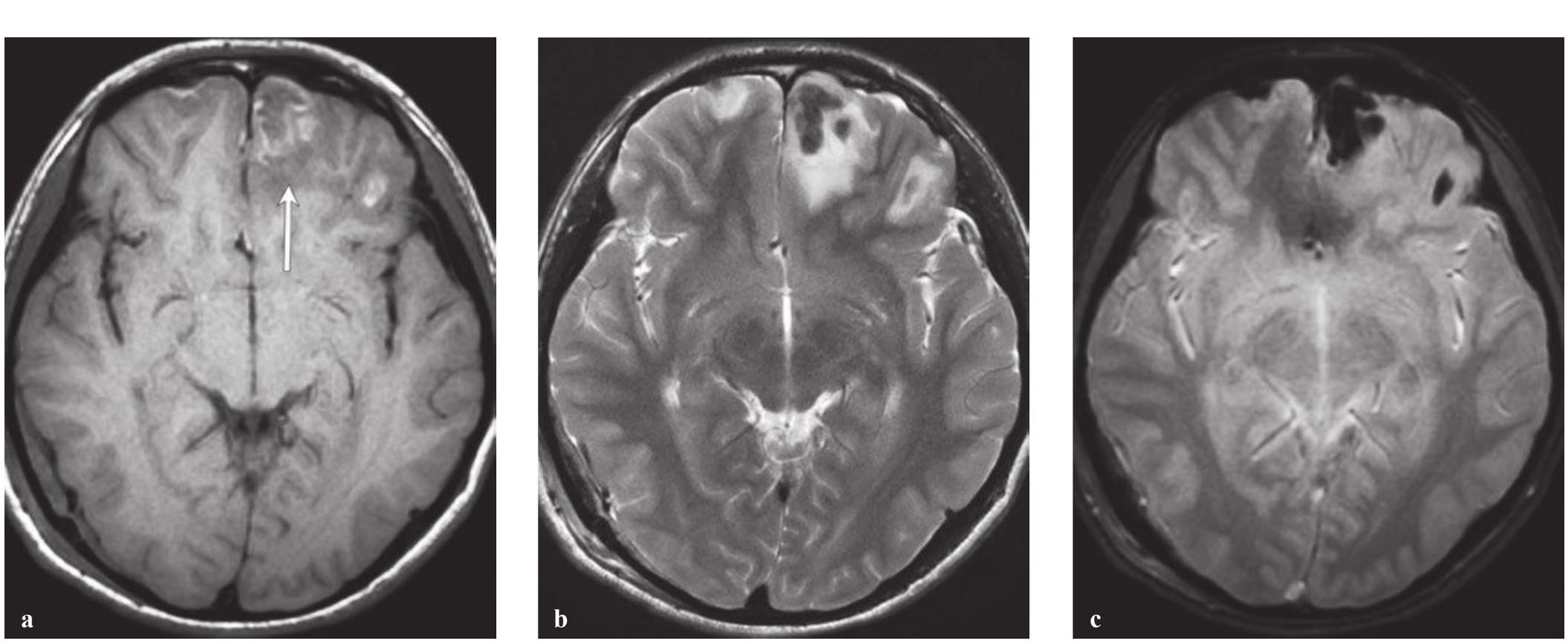

Fig. 1.190 Traumatic cerebral contusions are seen in the anterior portions of both frontal lobes as poorly defined zones of **(a)** low-intermediate and high signal on axial T1-weighted imaging (arrow) and **(b)** low and high signal on axial T2-weighted imaging. **(c)** The sites of hemorrhage also have low signal on axial GRE.

Table 1.4 (cont.) Multiple intra-axial lesions in the brain

Lesions	Imaging Findings	Comments
Diffuse axonal injury (**Fig. 1.191**)	MRI: One or multiple sites within the brain with intermediate or high signal on T1-weighted imaging, low, intermediate, and/or high signal on T2-weighted imaging and FLAIR, and low signal on gradient echo imaging. CT: With acute injuries, one or multiple sites of hemorrhage with high attenuation are seen and commonly occur at the corpus callosum, cerebral cortical–white matter junctions, basal ganglia, and brainstem.	Brain injury caused by deceleration and rotational shear forces, which result in disruption of axons and blood vessels. The degree of axonal injury is related to a poorer prognosis.
Hemorrhagic metastatic lesions (**Fig. 1.192**)	The MR appearance of a hemorrhagic metastatic lesion is one of an intracerebral hematoma involving a portion or all of the neoplasm, usually associated with peripheral edema (high signal on T2-weighted imaging). Lesions are often multiple.	Metastatic intra-axial tumors associated with hemorrhage include bronchogenic carcinoma, renal cell carcinoma, melanoma, choriocarcinoma, and thyroid carcinoma. May be difficult to distinguish from hemorrhage related to other etiologies, such as vascular malformations and amyloid angiopathy.
Amyloid angiopathy (**Fig. 1.193**)	MRI: Lesions can have low-intermediate or slightly high signal on T1-weighted imaging, and variable heterogeneous slightly high to high signal with or without low signal zones on T2-weighted imaging. Variable degrees of gadolinium contrast enhancement can be seen. Magnetic resonance spectroscopy may show decreased N-acetylaspartate (NAA) and increased choline and lactate peaks. Severe vasculopathic changes occur in association with apolipoprotein alleles E epsilon-4 or E-epsilon 2. Lobar hemorrhages usually occur in the cerebrum > cerebellum in patients older than 55 years. Silent intra-axial and subarachnoid microhemorrhages can occur that have low signal on T2-weighted imaging, GRE, and susceptibility-weighted imaging (SWI). CT: Lesions can have low, intermediate, and/or high attenuation, as well as contrast enhancement.	Amyloidosis is a disease complex that results from the extracellular deposition of insoluble eosinophilic fibrillar protein with a β-pleated configuration. Deposits of amyloid protein can occur in a systemic distribution or as localized lesions. The systemic form results often from plasma cell dyscrasias and hereditary diseases or is related to chronic diseases. The systemic amyloid form involving the brain can occur as cerebral amyloid angiopathy with deposits in blood vessel walls, senile plaques in Alzheimer's disease, or in spongiform encephalopathy, such as Creutzfeldt-Jakob disease and kuru. Localized amyloid deposits or amyloidomas in the brain are rare and are often not associated with an underlying disease.

(continued on page 158)

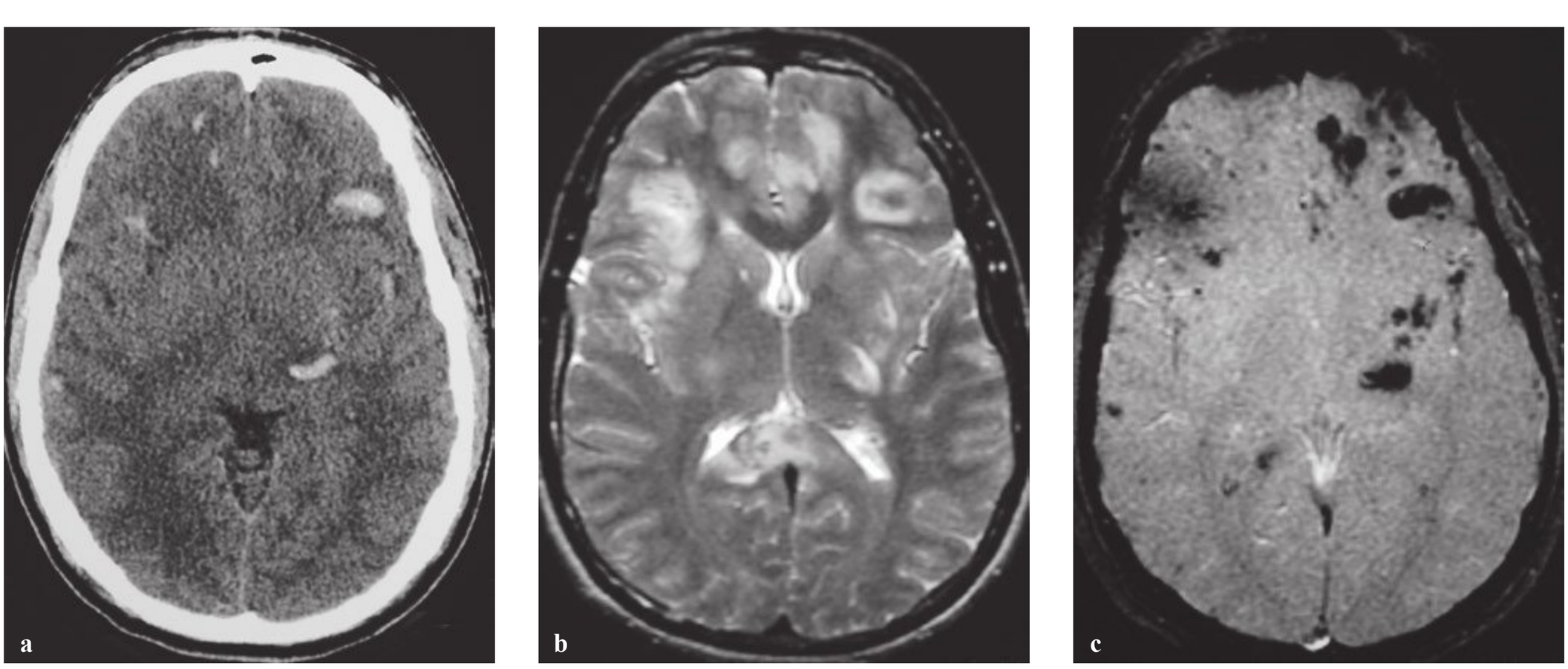

Fig. 1.191 A 19-year-old man with traumatic head injury resulting in diffuse axonal injury, which is seen as multiple subcortical and other intra-axial zones of hemorrhage with **(a)** high attenuation on axial CT, **(b)** mixed low and high signal on axial T2-weighted imaging, and **(c)** low signal on axial GRE.

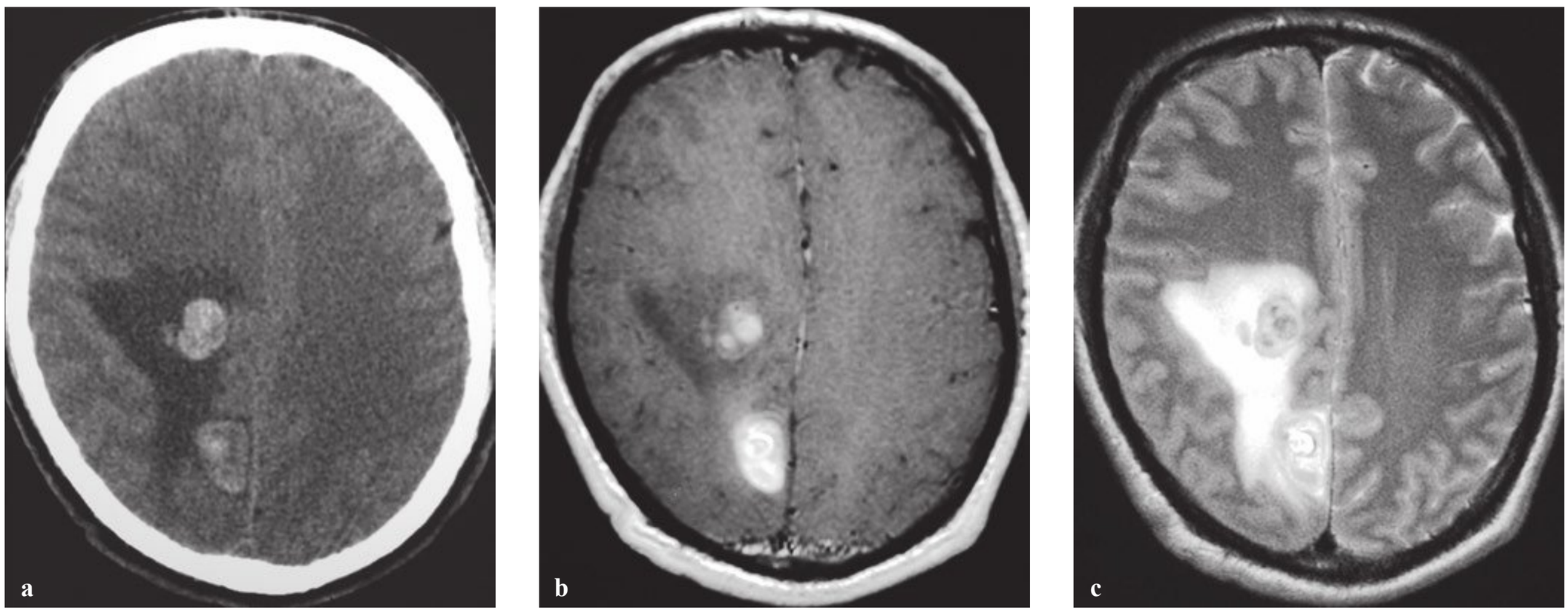

Fig. 1.192 A 47-year-old man with hemorrhagic metastatic lesions in the brain from renal cell carcinoma that have **(a)** high attenuation with surrounding edema on axial CT, **(b)** high signal on axial T1-weighted imaging, and **(c)** intermediate to slightly high signal on axial T2-weighted imaging with surrounding high-signal axonal edema.

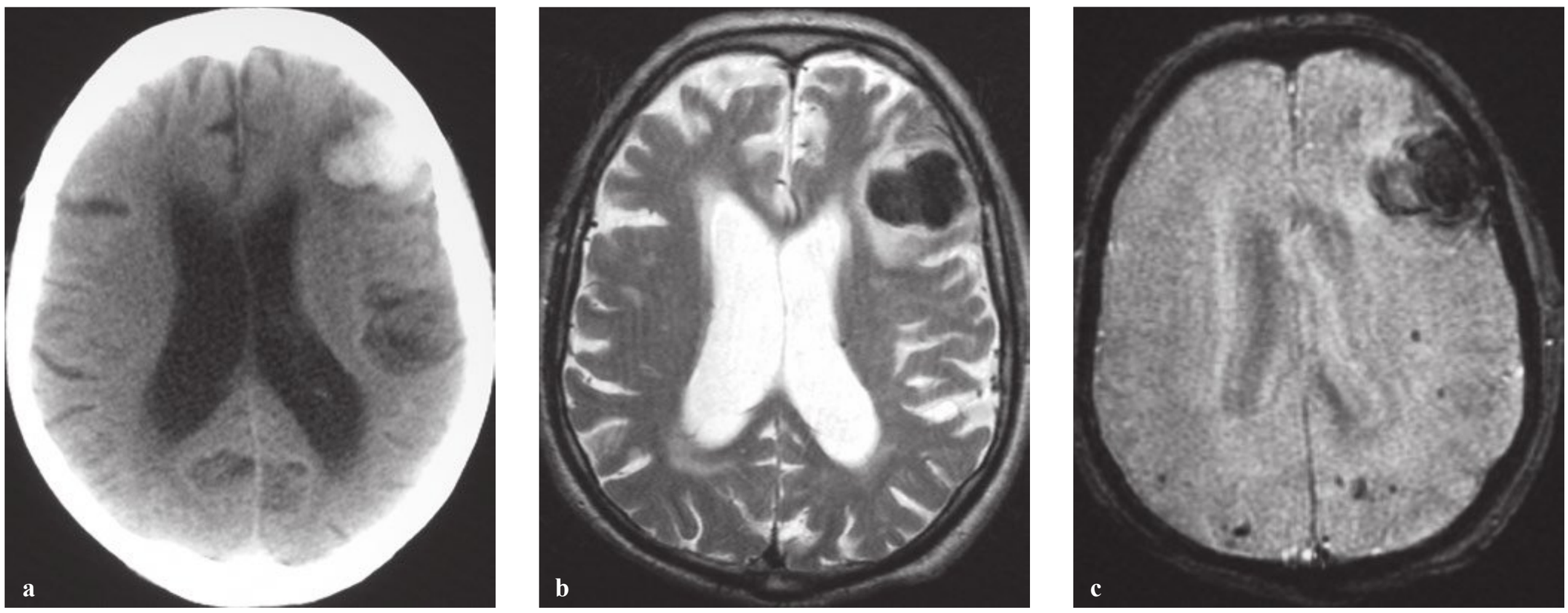

Fig. 1.193 An 84-year-old man with amyloid angiopathy seen as an intra-axial hematoma in the left frontal lobe that has **(a)** high attenuation on axial CT and **(b)** low signal centrally with surrounding high signal on axial T2-weighted imaging. **(c)** In addition to the low signal of the hematoma on axial GRE, multiple foci with low signal are also seen in the brain.

Table 1.4 (cont.) Multiple intra-axial lesions in the brain

Lesions	Imaging Findings	Comments
Vascular Malformations		
Arteriovenous malformations (AVMs)	MRI: Lesions with irregular margins that can be located in the brain parenchyma, pia, dura, or both locations. AVMs contain multiple, tortuous, tubular flow voids on T1- and T2-weighted imaging secondary to patent arteries with high blood flow, as well as thrombosed vessels with variable signal, and areas of hemorrhage in various phases. CT: Lesions with irregular margins that can be located in the brain parenchyma, pia, dura, or both locations. AVMs contain multiple tortuous vessels. The venous portions often show contrast enhancement. Usually not associated with mass effect unless there is recent hemorrhage or venous occlusion. CTA can show the arterial, nidus, and venous portions of the AVMs, calcifications, and gliosis. The venous portions often show gadolinium enhancement. Gradient echo MRI shows flow-related enhancement (high signal) in patent arteries and veins of the AVM. MRA using time-of-flight or phase-contrast techniques can provide additional detailed information about the nidus, feeding arteries and draining veins, and presence of associated aneurysms. Usually not associated with mass effect unless there is recent hemorrhage or venous occlusion.	Supratentorial AVMs occur more frequently (80–90%) than infratentorial AVMs (10–20%). Annual risk of hemorrhage. AVMs can be sporadic, congenital, or associated with a history of trauma. Multiple AVMs can be seen in Rendu-Osler-Weber syndrome (AVMs in brain and lungs, as well as capillary telangectasias) and Wyburn-Mason syndrome (AVMs in brain and retina, + cutaneous nevi).
Cavernous malformations (**Fig. 1.194**)	MRI: Single or multiple multilobulated intra-axial lesions that have a peripheral rim or irregular zone of low signal on T2-weighted imaging secondary to hemosiderin, surrounding a central zone of variable signal (low, intermediate, high, or mixed) on T1- and T2-weighted imaging depending on ages of hemorrhagic portions. Gradient echo and magnetic susceptibility-weighted techniques are useful for detecting multiple lesions. Gadolinium contrast enhancement is usually absent, although some may show mild heterogeneous enhancement. CT: Lesions have intermediate to slightly increased attenuation, ± calcifications.	Can be found in many different locations. Supratentorial cavernous angiomas occur more frequently than infratentorial lesions. Lesions consist of epithelium-lined vascular channels within a collagenous stroma. Zones of thrombus and remote hemorrhage with hemosiderin are often present. Dystrophic calcifications may be present. Developmental venous anomalies occur in 25% Hereditary syndromes in which multiple cavernous malformations occur are associated with mutations of the CCM1/KRIT1, CCM2/MGC4608, and CCM3PDCD10 genes, and have a higher risk of hemorrhage (up to 5% per year) than sporadic cavernous malformations.
Capillary telangiectasias (**Fig. 1.195**)	MRI: Postcontrast MRI shows a small zone with enhancement without abnormal mass effect. Lesions are typically inconspicuous on precontrast T1- and T2-weighted imaging. CT: Not usually seen on pre-or postcontrast examinations.	Asymptomatic, often incidental findings on gadolinium contrast-enhanced MRI, which shows enhancement of a group of thin-walled vessels and capillaries within normal neural tissue of the brain or brainstem. Most are less than 1 cm in diameter. Can occur 10 years after radiation therapy. Common locations include the pons and cerebellum. Account for up to 20%of vascular malformations in brain.
Venous angioma/ developmental venous anomaly	MRI: Gadolinium contrast-enhanced T1-weighted imaging shows a group of small veins in a "Medusa head" configuration that connect and drain into a slightly prominent enhancing vein. Can have low signal on axial susceptibility-weighted imaging, CT: No abnormality or small, slightly hyperdense zone prior to contrast administration. Contrast enhancement seen in a slightly prominent vein draining a collection of small veins.	Considered an anomalous venous formation typically not associated with hemorrhage, usually an incidental finding except when associated with cavernous malformation. Lesions consist of thin-walled venous channels within normal neural tissue. Can occur in association with cavernous malformations. Account for more than 50%of cerebrovascular malformations.

(continued on page 160)

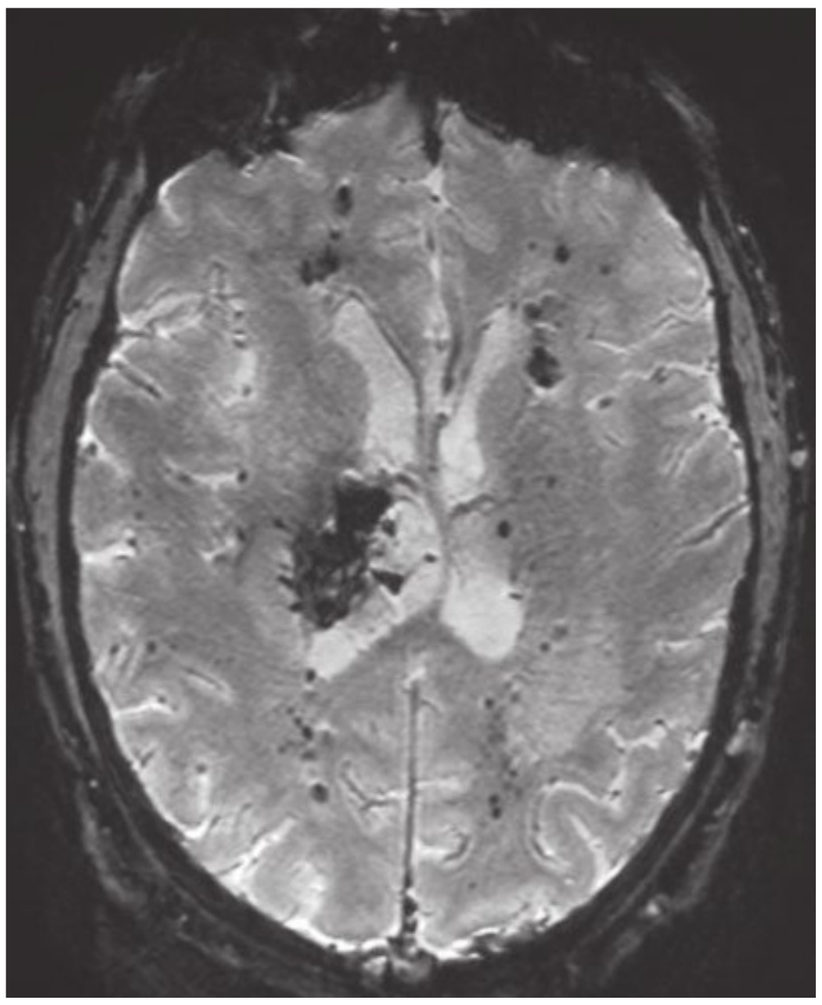

Fig. 1.194 Multiple cavernous malformations are seen in the brain that have low signal on axial susceptibility weighted imaging (SWI) .

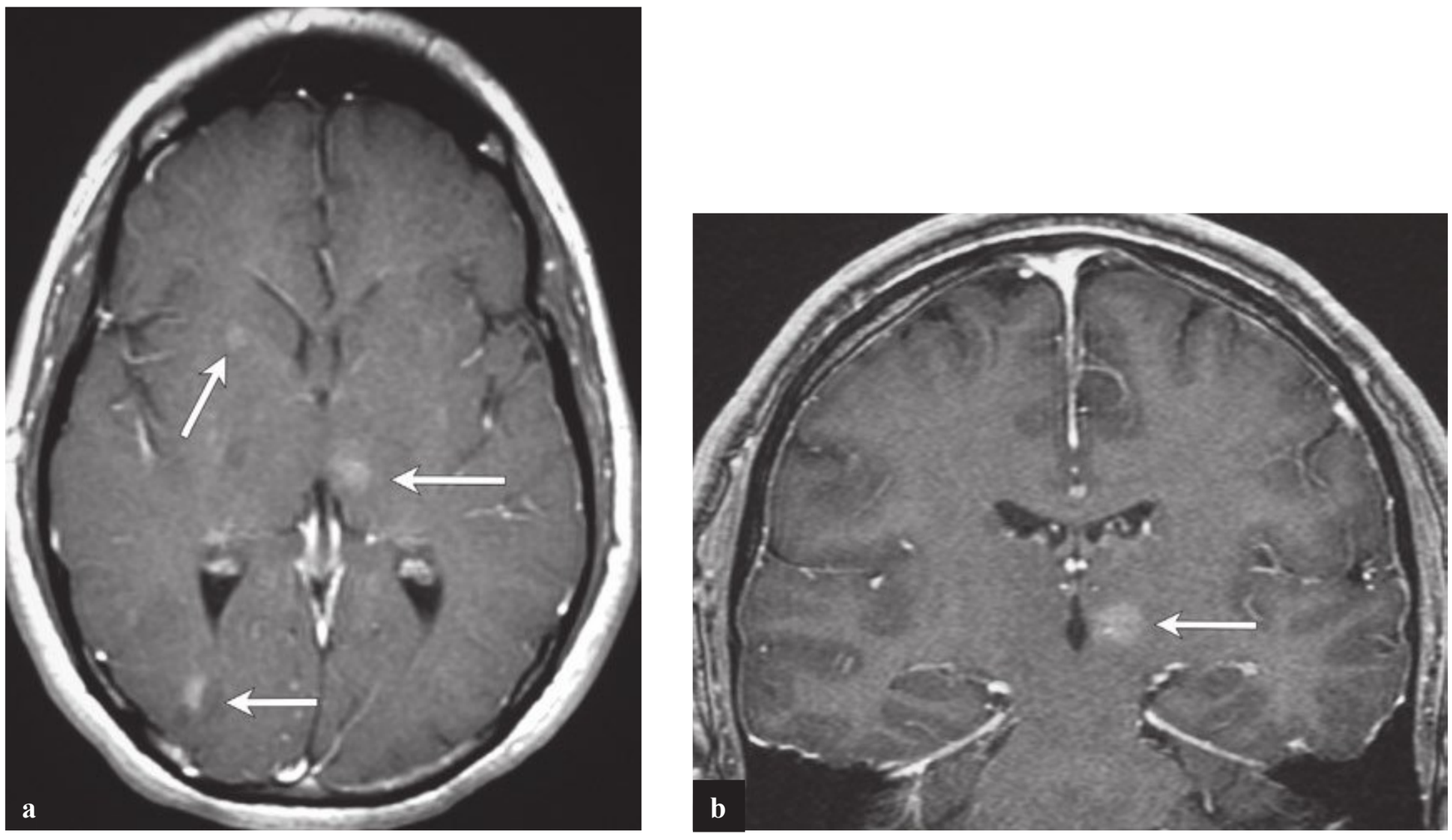

Fig. 1.195 A 40-year-old man with multiple capillary telangiectasias in the brain that are small gadolinium contrast-enhancing intra-axial lesions with ill-defined margins on **(a)** axial and **(b)** coronal T1-weighted imaging (arrows).

Table 1.4 (cont.) Multiple intra-axial lesions in the brain

Lesions	Imaging Findings	Comments
Cerebral Ischemia/Infarction		
Ischemic disease related to occlusion of small vessels (small-vessel disease) (**Fig. 1.196**)	MRI: Multiple foci and/or confluent zones of decreased signal on T1-weighted imaging and high signal on T2-weighted imaging and FLAIR involving the subcortical and periventricular cerebral white matter, basal ganglia, and brainstem. No associated mass effect, typically no restricted diffusion and no gadolinium contrast enhancement. CT: Multiple foci and/or confluent zones of decreased attenuation involving the subcortical and periventricular cerebral white matter, basal ganglia, and brainstem. No associated mass effect, and typically no contrast enhancement.	Lesions in white matter and/or brainstem related to occlusive disease involving perforating arteries associated with hypertension, atherosclerosis, diabetes, vasculitis, and aging. Unlike multiple sclerosis, ischemic small-vessel disease does not usually involve the corpus callosum because of its abundant blood supply from multiple branches of the adjacent pericallosal arteries.
Periventricular leukomalacia (**Fig. 1.197**)	MRI: Multiple foci and/or confluent zones of decreased signal on T1-weighted imaging and high signal on T2-weighted imaging and FLAIR involving the subcortical and periventricular white matter, basal ganglia, and brainstem. No associated mass effect, no gadolinium contrast enhancement, irregular ventricular margins and ventricular enlargement related to cerebral volume loss. CT: Multiple foci and/or confluent zones of decreased attenuation involving the subcortical and periventricular white matter, basal ganglia, and brainstem. No associated mass effect, no contrast enhancement, irregular ventricular margins and ventricular enlargement related to cerebral volume loss.	Ischemic injury involving fetal brain/premature infants with gliosis and resultant encephalomalacic changes involving periventricular white matter (fetal watershed vascular zones). Associated neurologic deficits depend on severity of injuries, e.g., cerebral palsy.
Brain infarcts from embolic disease (**Fig. 1.198**)	MRI: Multiple small infarcts are seen at the cortical–subcortical borders of multiple arterial territories that have low-intermediate signal on T1-weighted imaging and high signal on T2-weighted imaging and FLAIR, ± restricted diffusion, ± hemorrhage. Multiple small foci of gadolinium contrast enhancement may be seen at zones of recent infarction. Septic emboli may have a ring pattern of gadolinium contrast enhancement. CT: Multiple small zones with low attenuation are seen at the cortical–subcortical borders of multiple arterial territories, ± hemorrhage. Multiple small foci of contrast enhancement may be seen at zones of recent infarction.	Septic or aseptic emboli often originate from cardiac vegetations or result from ventricular or atrial septal defects. The other major source for emboli is atherosclerotic plaque.

(continued on page 162)

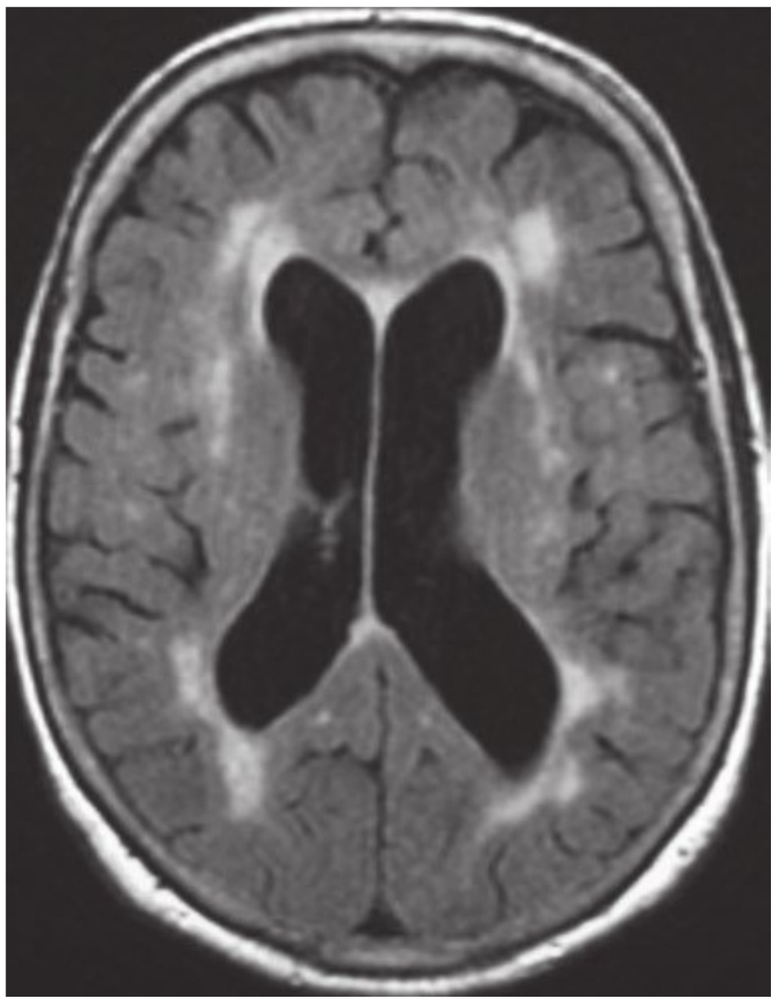

Fig. 1.196 An 83-year-old woman with small-vessel ischemic disease in the cerebral white matter that is seen as multiple foci and confluent zones with high signal on axial FLAIR.

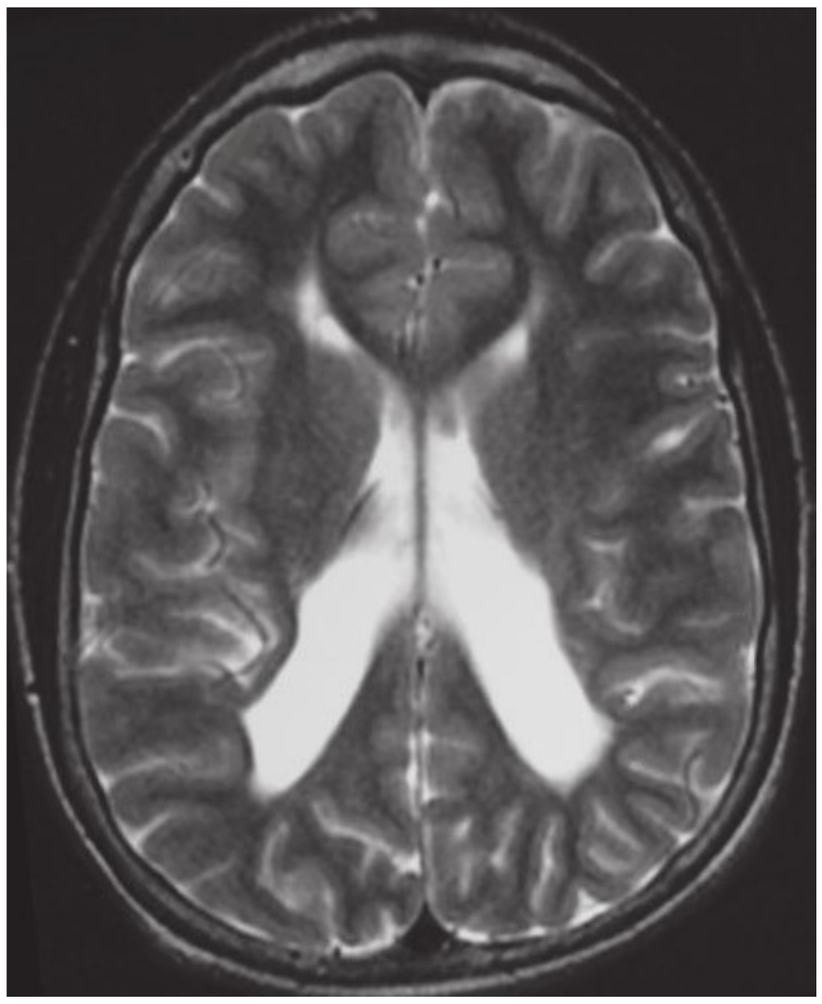

Fig. 1.197 A 17-year-old male with periventricular leukomalacia, with small zones of high signal on axial T2-weighted imaging in the cerebral white matter that are associated with diminished white matter volume and compensatory ventricular dilatation.

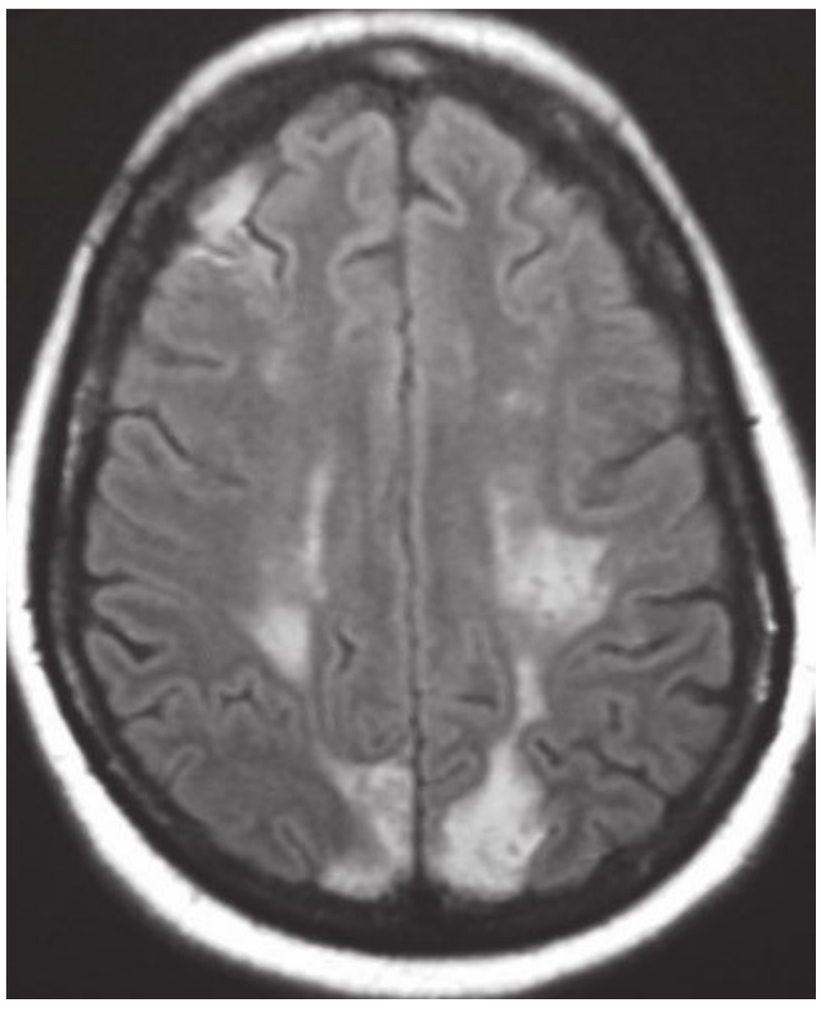

Fig. 1.198 Brain infarcts from aseptic emboli (Libman-Sachs endocarditis). Intra-axial zones with high signal on axial FLAIR are seen in the cerebral cortex and adjacent white matter in both cerebral hemispheres.

Table 1.4 (cont.) Multiple intra-axial lesions in the brain

Lesions	Imaging Findings	Comments
Brain infarcts from vasculitis (**Fig. 1.199**)	MRI/MRA: Zones of arterial occlusion and/or foci of stenosis and poststenotic dilatation can be seen involving large, medium, or small intracranial and extracranial arteries. Cerebral and/or cerebellar infarcts can be seen in cortex and subcortical white matter and/or basal ganglia and have high signal on T2-weighted imaging and FLAIR, ± small zones of hemorrhage, with low T2* signal on gradient echo imaging. Linear zones or foci of gadolinium contrast enhancement may be seen at the lesions. Gadolinium contrast enhancement of arterial walls can be seen with active inflammation. Acute lesions usually have restricted diffusion. CT/CTA: Zones of arterial occlusion and/or foci of stenosis and poststenotic dilatation can be seen involving intracranial and extracranial arteries. Multiple foci and/or confluent zones of decreased attenuation involving the subcortical and periventricular white matter, basal ganglia, and brainstem. No associated mass effect, minimal or no contrast enhancement. Conventional arteriography shows zones of arterial occlusion and/or foci of stenosis and poststenotic dilatation. May involve large, medium, or small intracranial and extracranial arteries.	Uncommon mixed group of inflammatory diseases/disorders involving the walls of cerebral blood vessels. Can involve small arteries (CNS vasculitis), small and medium-sized arteries (polyarteritis nodosa, Kawasaki disease), or large arteries with diameters of 7 to 35 mm, such as the aorta and its main branches (Takayasu's arteritis, giant cell arteritis). Vasculitis can be a primary disease in which biopsies of meninges and brain show transmural inflammation of vessels in the leptomeninges and brain parenchyma. Vasculitis can occur as a secondary disease in association with other disorders, such as systemic disease (polyarteritis nodosa, granulomatosis with polyangiitis, giant cell arteritis, Takayasu's arteritis, sarcoid, Behçet's disease, systemic lupus erythematosus, Sjögren's disease, dermatomyositis, mixed connective tissue disease), drugs (amphetamine, ephedrine, phenylpropaline, cocaine), or infections (viruses, bacteria, fungi, or parasites).
CADASIL (**Fig. 1.200**)	MRI: Multiple zones of decreased signal on T1-weighted imaging and high signal on T2-weighted imaging and FLAIR in the subcortical and periventricular white matter, basal ganglia, thalami, and brainstem. Usually there is no restricted diffusion unless recent ischemic event (uncommon), no associated mass effect, and typically no gadolinium contrast enhancement. CT: Multiple zones of decreased attenuation involving the subcortical and periventricular white matter, basal ganglia, thalami, and brainstem. No associated mass effect, and no contrast enhancement.	Cerebral autosomal dominant arteriopathy with subcortical infarcts and leukoencephalopathy (CADASIL) is an inherited abnormality with mutations involving the NOTCH3 gene on chromosome 19q12, which results in angiopathy of small and medium arteries, with granular osmiophilic deposits in the basement membrane. Symptoms and signs begin in the fourth decade, with headaches, transient ischemic attacks, strokes, and subcortical dementia.
CARASIL	MRI: Multiple zones of decreased signal on T1-weighted imaging and high signal on T2-weighted imaging and FLAIR in the cerebral white matter, basal ganglia, and thalami. Usually there is no restricted diffusion unless recent ischemic event (uncommon), no associated mass effect, and typically no gadolinium contrast enhancement. CT: Multiple zones of decreased attenuation in the subcortical and periventricular white matter, basal ganglia, and thalami. No associated mass effect, no contrast enhancement.	Cerebral autosomal recessive arteriopathy with subcortical infarcts and leukoencephalopathy (CARASIL) is a rare inherited abnormality involving mutations of the HTRA1 gene on chromosome 10q26 encoding HtrA serine peptidase/protease 1. Most patients are from Japan, with a male/female ratio of 3/1. Clinical findings often include multiple ischemic strokes before the age of 40 years, progressive dementia, premature baldness in the second decade, and severe low back pain. Histopathologic findings include progressive atherosclerosis, with fibrous intimal proliferation and hyaline wall degeneration resulting in luminal stenosis of small penetrating arteries without amyloid deposition or osmiophilic deposits.

(continued on page 164)

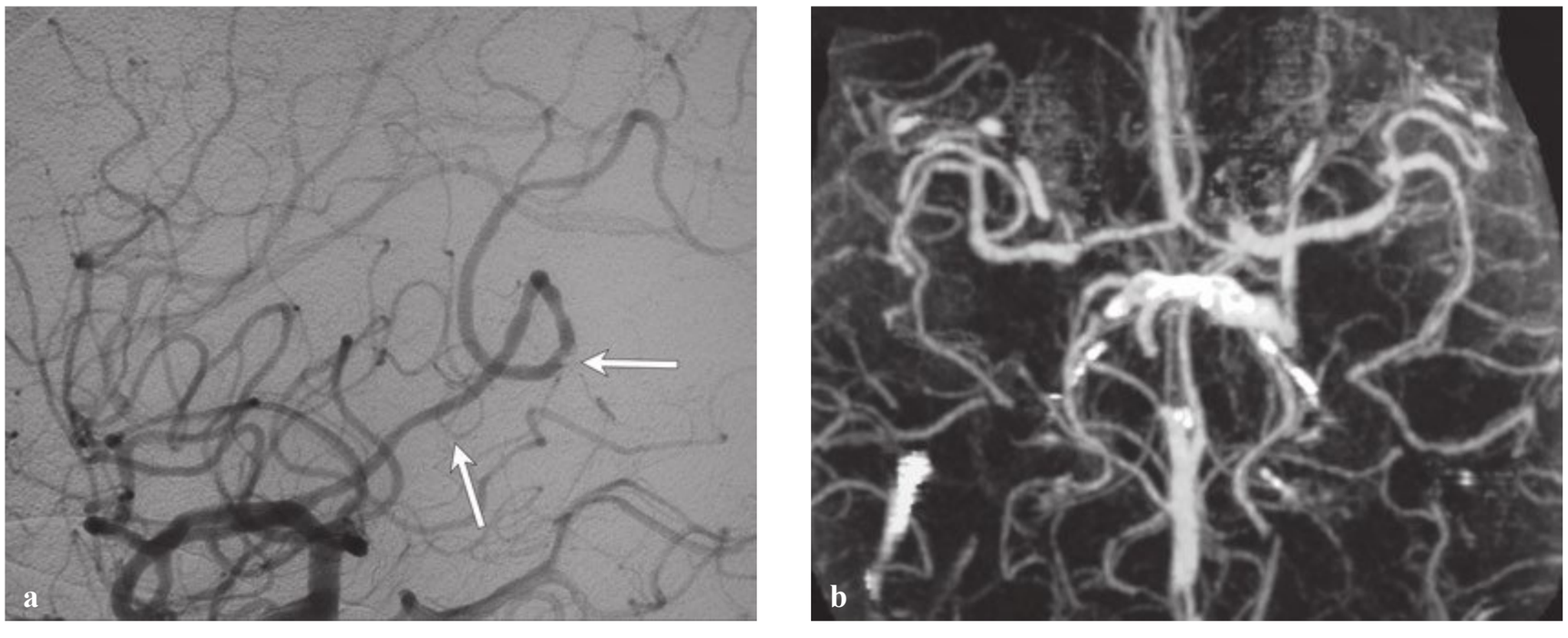

Fig. 1.199 A 50-year-old man with intracranial vasculitis causing multiple small brain infarcts. **(a)** Conventional arteriography and **(b)** axial CTA show zones of stenosis and poststenotic dilatation (arrows) of branches of the middle cerebral arteries. **(c)** Multiple small foci with high signal on axial FLAIR are seen in the cerebral hemispheres, **(d)** including two with restricted diffusion (arrow) on axial DWI.

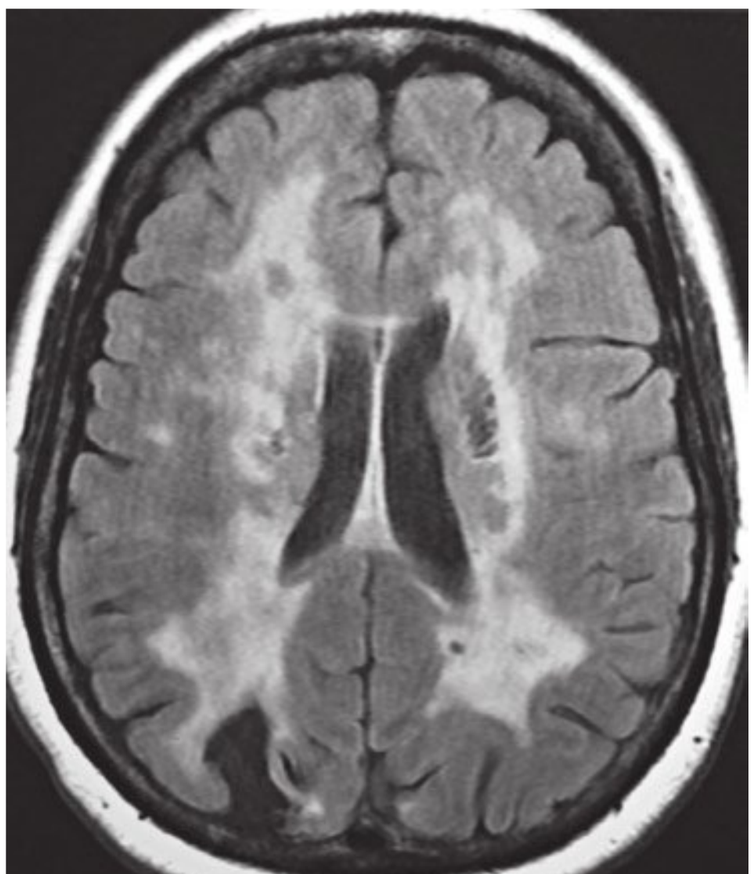

Fig. 1.200 A 50-year-old woman with CADASIL. Extensive zones with abnormal high signal on axial FLAIR are seen in the cerebral white matter, as well as a zone of cortical infarction in the posterior right parietal lobe.

Table 1.4 (cont.) Multiple intra-axial lesions in the brain

Lesions	Imaging Findings	Comments
Susac syndrome (retinocochleocerebral vasculopathy) (**Fig. 1.201**)	MRI: Multiple zones (usually less than 10 mm) with high signal on T2-weighted imaging in the cerebral white matter and within the central portion of the corpus callosum. Zones of high signal on T2-weighted imaging may also occur in the basal ganglia (two-thirds of patients). Leptomeningeal gadolinium contrast enhancement may be seen in one-third of patients. CT: Multiple zones (usually less than 10 mm) with decreased attenuation in the cerebral white matter and within the central portion of the corpus callosum. Zones of low attenuation may also occur in the basal ganglia (two-thirds of patients). Leptomeningeal contrast enhancement may be seen in one-third of patients.	Immune-mediated, small-vessel vasculitis of unknown etiology resulting in arteriolar occlusion and microinfarction in cerebral white matter, retina, and cochlea. Patients often have headaches, cognitive changes, confusion, and memory impairment. Female/male ratio of 3/1; age range = 16 to 58 years.
Systemic lupus erythematosus (SLE) (**Fig. 1.202**)	MRI: Multiple foci and/or confluent zones with high signal on T2-weighted imaging and FLAIR in the cerebral white matter, basal ganglia, and brainstem, usually without restricted diffusion on diffusion-weighted imaging unless acute ischemia, and typically no gadolinium contrast enhancement unless during acute or subacute ischemic event. Intracranial venous thrombosis occurs in 25%of cases. Cortical and central brain atrophy can be seen in severe cases. CT: Multiple zones with decreased attenuation in the cerebral white matter.	SLE is an autoimmune disease with autoantibodies produced that react against various organs and tissues including the CNS, respiratory, cardiovascular, gastrointestinal, genitourinary, and musculoskeletal systems. Most patients have anitinuclear antibodies (ANA), and many have antibodies to double stranded DNA (anti-dsDNA), anti-Sm, and/or anti-U1RNP. Activation of the complement system and autoantibodies can result in angiopathy, thromboembolism, brain ischemia and infarction, demyelination, and/or hemorrhage. CNS involvement can present with neuropsychiatric signs and symptoms. Peak ages at onset are 10 to 40 years. SLE occurs more commonly in females than in males.
Antiphospholipid syndrome	MRI: Multiple foci and/or confluent zones with high signal on T2-weighted imaging and FLAIR in the cerebral white matter, basal ganglia, and brainstem, usually without restricted diffusion on diffusion-weighted imaging unless acute ischemia, and typically no gadolinium contrast enhancement. Cerebral infarcts can be seen in some patients. Intracranial venous thrombosis occurs in 25%of cases. Cortical and central brain atrophy can be seen in severe cases. CT: Multiple zones with decreased attenuation in the cerebral white matter.	Automimmune prothrombotic syndrome from the production of antiphospholid antibodies (anticardiolipin antibodies, lupus anticoagulant), which cause microangiopathic disease and endothelial damage in various tissues and organs, such as the brain, heart, lungs, kidneys, and skin. Can occur as primary disorder or in association with systemic lupus erythematosus. Patients can have arterial and venous thromboses and neuropschiatric disorders. Usually occurs in adults older than 50 years, and in females more than in males. CNS disease is associated with stroke, transient ischemic attacks, and seizures.
Behçet's syndrome (**Fig. 1.203**)	MRI: Multiple foci and/or confluent zones with high signal on T2-weighted imaging and FLAIR in the brainstem, diencephalon, and periventricular and subcortical cerebral white matter, usually without restricted diffusion on diffusion-weighted imaging, and typically no gadolinium contrast enhancement. Lesions may regress or become less conspicuous over time, possibly related to status as acute inflammatory vasogenic edematous lesions. CT: Multiple zones with decreased attenuation in the cerebral white matter.	Chronic, relapsing, multisystem, vascular inflammatory disease that is associated with mucocutaneous oral and genital aphthous ulcers, uveitis, erythema nodosum, pseudofolliculitis, mono- or oligoarthritis, arterial aneurysms, and deep venous thrombosis. CNS involvement occurs in 5 to 13%of cases and includes venous sinus thrombosis (10–12%). Diagnosis is made by the pathergy test.

(continued on page 166)

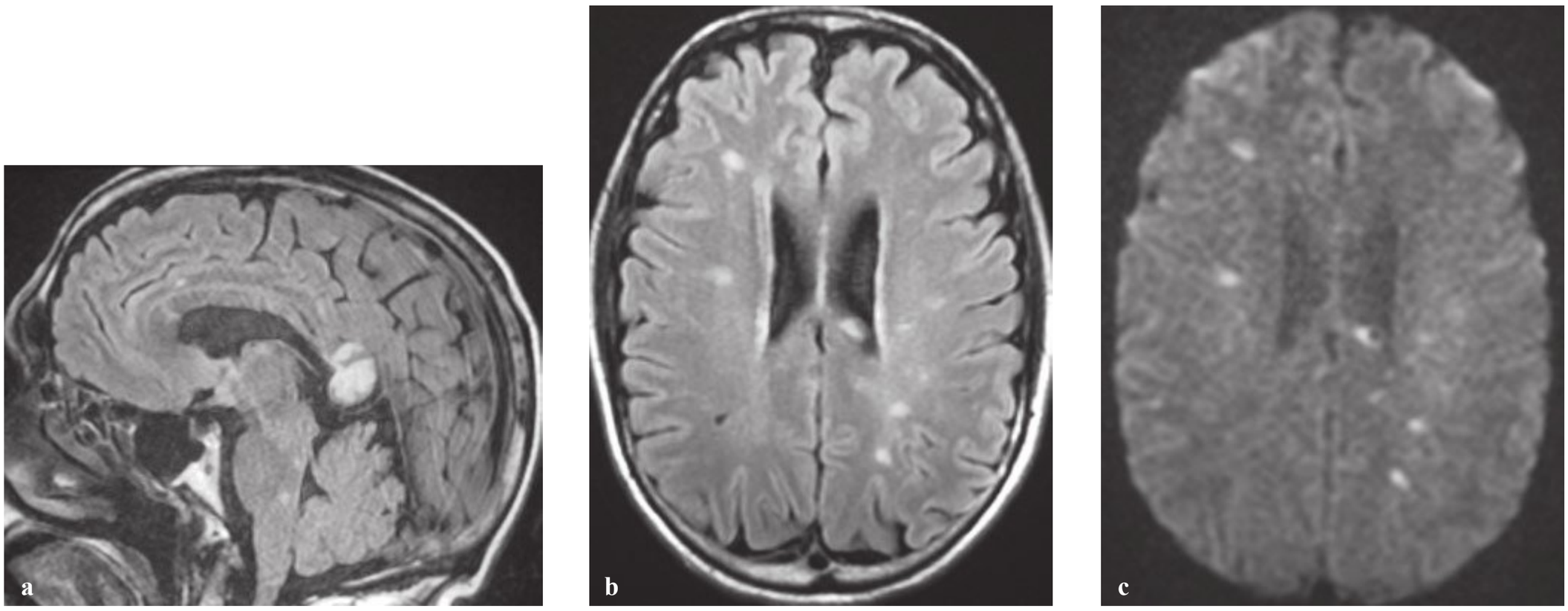

Fig. 1.201 Susac syndrome. Multiple small zones with high signal on **(a)** sagittal and **(b)** axial FLAIR are seen in the cerebral white matter, including the corpus callosum. **(c)** Many of the foci also have restricted diffusion on axial DWI.

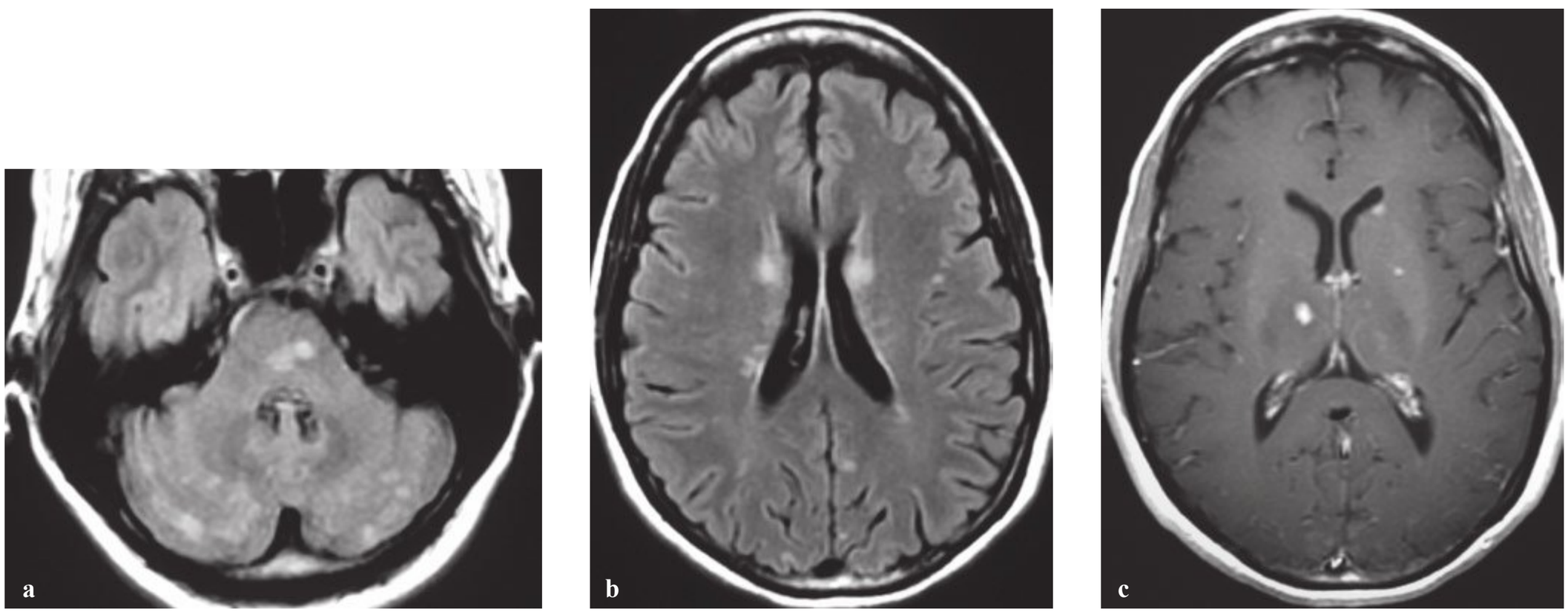

Fig. 1.202 **(a,b)** Patient with systemic lupus erythematosus who has multiple foci with high signal on axial FLAIR in the cerebral and cerebellar white matter and brainstem. **(c)** Some of the foci have associated gadolinium contrast enhancement on axial T1-weighted imaging.

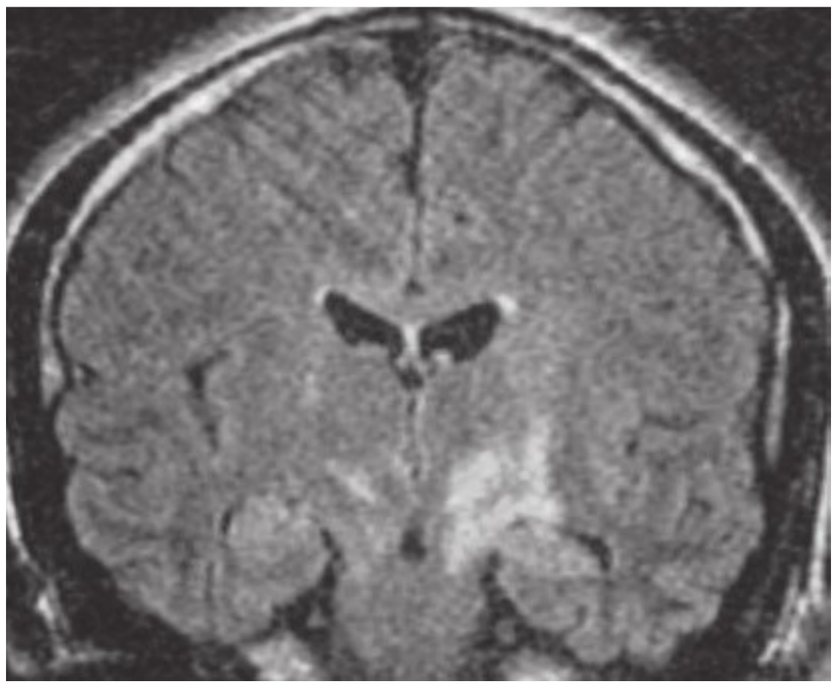

Fig. 1.203 Patient with Behçet's syndrome and bilateral zones with high signal in the thalami and midbrain on coronal FLAIR.

Table 1.4 (cont.) Multiple intra-axial lesions in the brain

Lesions	Imaging Findings	Comments
Hypoxic-ischemic injury (**Fig. 1.204, Fig. 1.205, Fig. 1.206**, and **Fig. 1.207**)	CT: Bilateral zones of low attenuation in the basal ganglia, caudate nuclei, thalami, brainstem, and/or perisylvian cerebral cortex. MRI: Bilateral zones of high signal on T2-weighted imaging, FLAIR, and diffusion-weighted imaging (low signal on ADC maps) in the basal ganglia, caudate nuclei, thalami, brainstem, and/or perisylvian cerebral and cerebellar cortex and at watershed vascular distribution sites.	Prolonged hypotension and anoxia result in ischemia and infarction in portions of the brain with selective vulnerability to hypoxia and impairment of aerobic metabolism. Can result from drowning, asphyxiation, and cardiac arrest. In less severe cases of hypotension in adults, zones of infarction can occur between the distal distributions of two arteries, as watershed infarcts.

(continued on page 168)

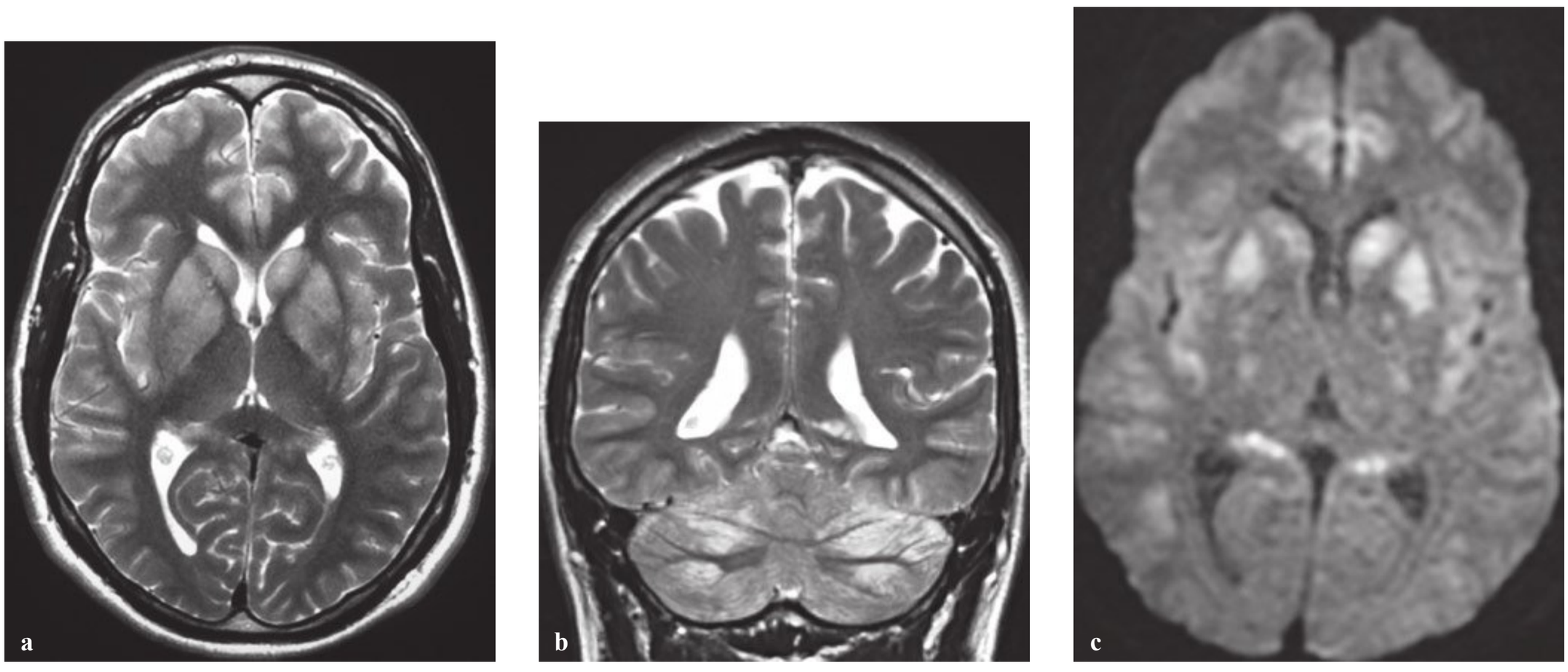

Fig. 1.204 A 45-year-old man with hypoperfusion/hypoxic-ischemic injury from cardiac arrest resulting in abnormal high signal on **(a)** axial and **(b)** coronal T2-weighted imaging in the basal ganglia and cerebellar cortex. **(c)** Restricted diffusion is seen in the basal ganglia bilaterally on axial DWI.

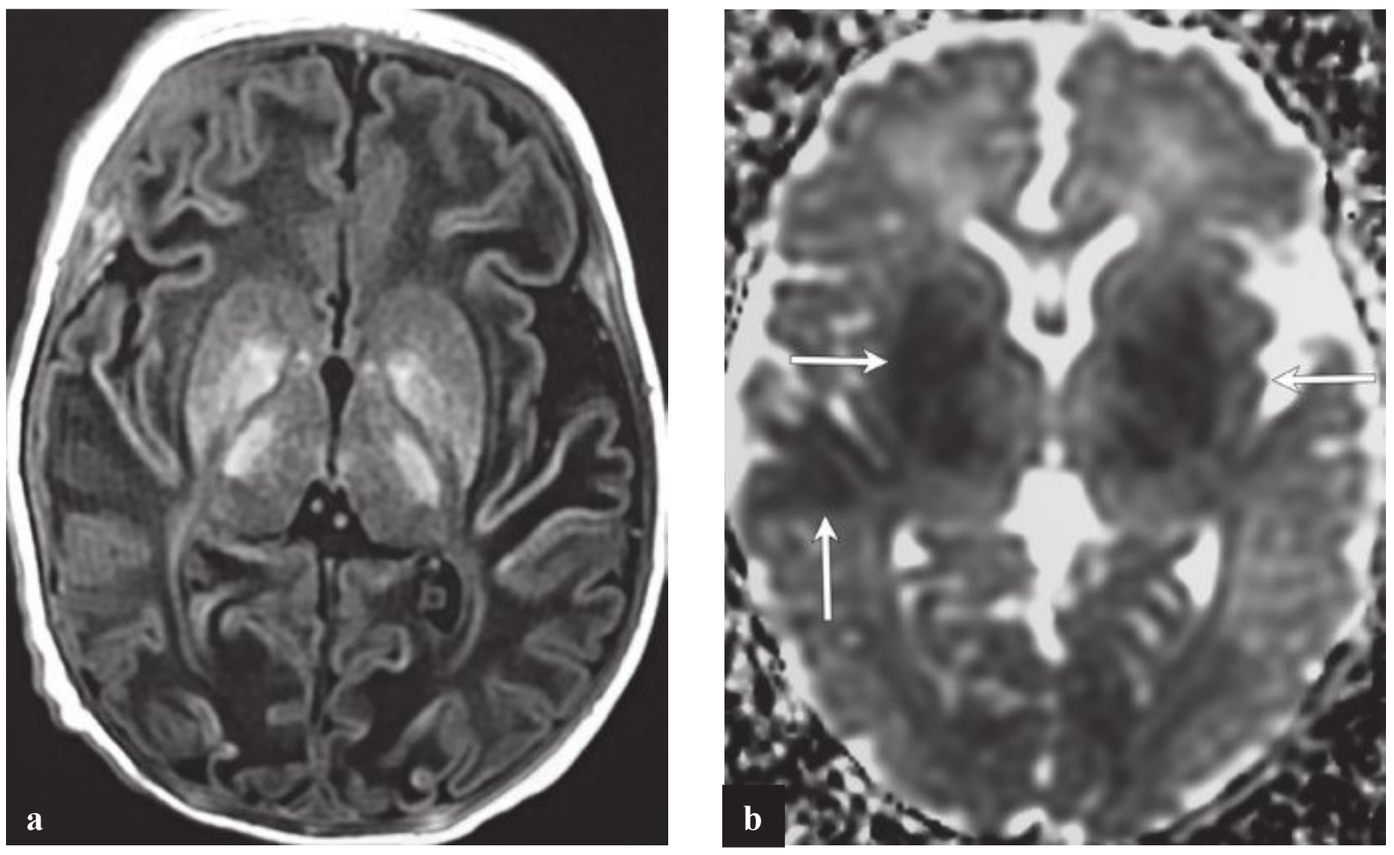

Fig. 1.205 **(a)** A 7-day-old term neonate with severe hypoperfusion/hypoxic-ischemic injury that is seen as abnormal high signal in the putamina and thalami relative to the internal capsules on axial T1-weighted imaging, with **(b)** corresponding restricted diffusion (arrows) on axial ADC.

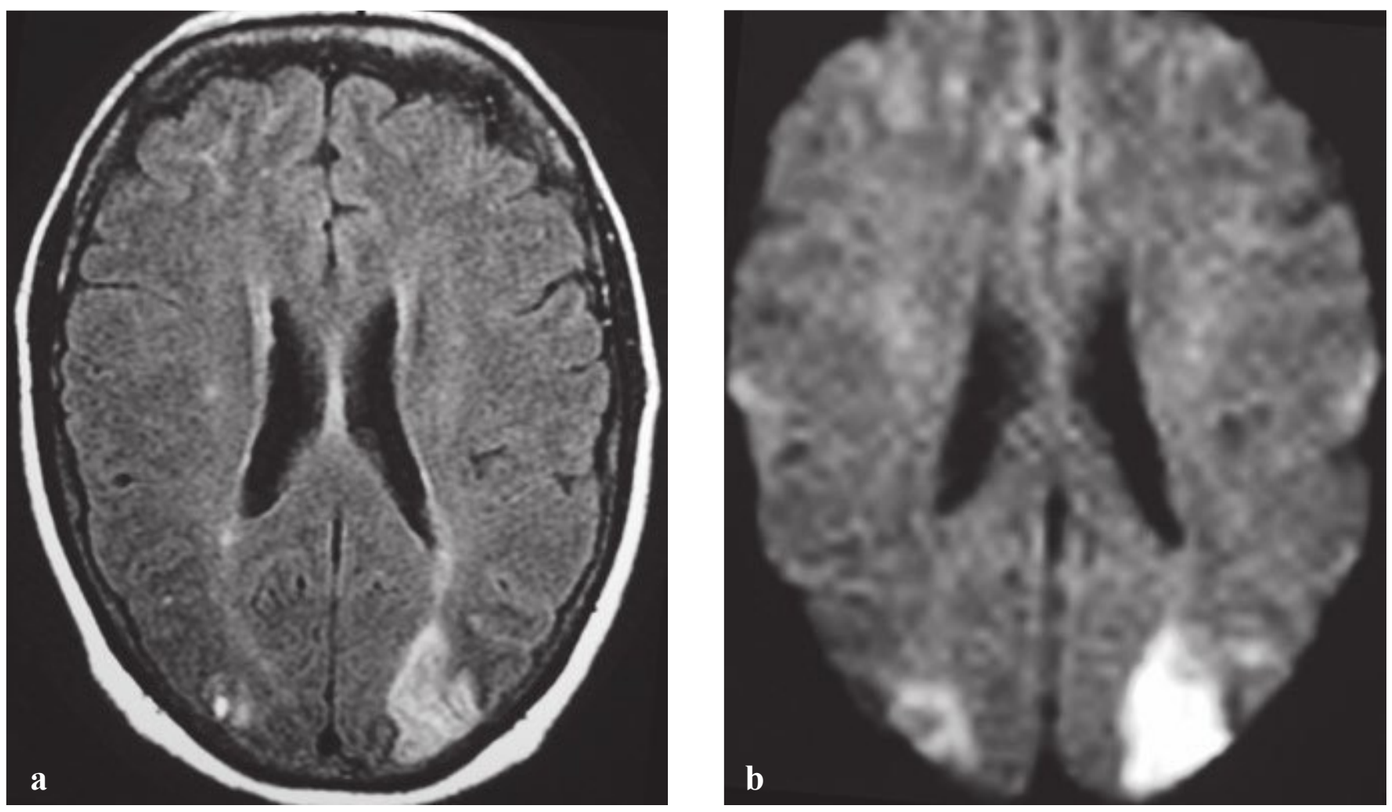

Fig. 1.206 Infarcts from hypotension in the watershed vascular distributions between the middle and posterior cerebral arteries, which have high signal on **(a)** axial FLAIR and **(b)** axial DWI.

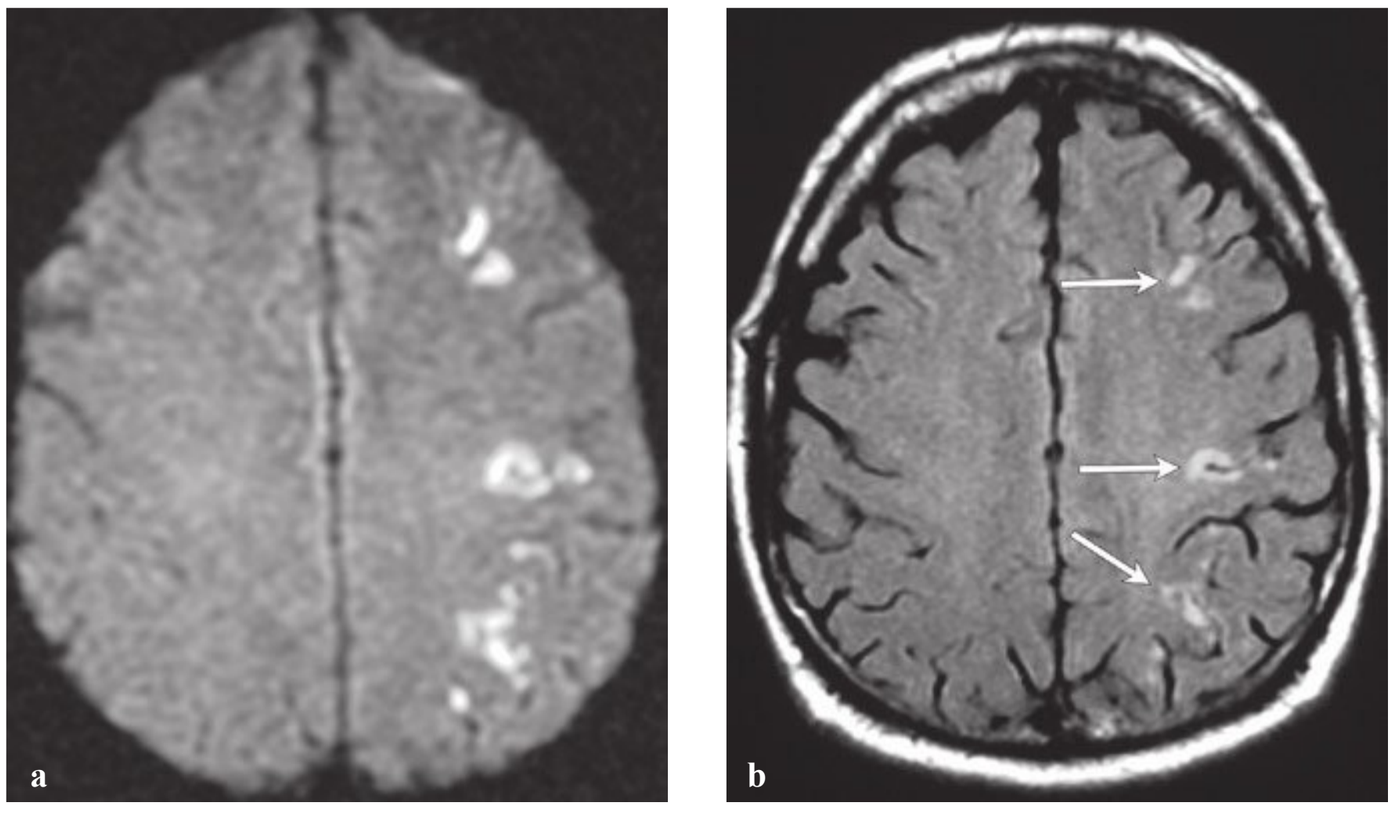

Fig. 1.207 Multiple small sites of acute infarction from hypoperfusion in the watershed vascular distributions between the left anterior and middle cerebral arteries, which have high signal on **(a)** axial DWI and **(b)** axial FLAIR (arrows).

Table 1.4 (cont.) Multiple intra-axial lesions in the brain

Lesions	Imaging Findings	Comments
Neurologic decompressive sickness (**Fig. 1.208**)	CT: Foci of air can be seen in the intracranial CSF, and/or cerebral arteries. MRI: Bilateral zones of high signal on T2-weighted imaging, FLAIR, and diffusion-weighted imaging (low signal on ADC maps) may be seen in the cerebral cortex, basal ganglia, caudate nuclei, thalami, and/or brainstem.	Rapid decompression or barotrauma can result in arterial gas embolism causing occlusion of intracerebral arteries with infarcts. Treatment is recompression with hyperbaric oxygen treatment.
Metabolic Disorders		
Seizure (**Fig. 1.209**)	MRI: Zones with restricted diffusion (high signal on diffusion-weighted imaging and low signal on ADC maps) typically occur in the hippocampus (69%), pulvinar-thalamus (26%), and cerebral cortex in patients with status epilepticus, generalized seizures, and febrile seizures. Abnormal increased signal on T2-weighted imaging and FLAIR, as well as gyral swelling can also be seen in the peri-ictal period.	Patients with complex partial seizures and generalized seizures, including status epilepticus, have localized ictal and peri-ictal sites in the brain with increased energy metabolism, hyperperfusion, and cell swelling, which typically show restricted diffusion that can be transient. Abnormalities are often bilateral in patients with generalized seizures and status epilepticus, and unilateral in patients with complex partial seizures.
MELAS/MERRF (**Fig. 1.210** and **Fig. 1.211**)	CT: Symmetric zones of low attenuation in the basal ganglia, and cerebral cortical infarction that is not limited to one vascular distribution, ± dystrophic calcifications in basal ganglia. MRI: High signal on T2-weighted imaging and FLAIR in basal ganglia that is usually symmetric, high signal on T2-weighted imaging and FLAIR in cerebral and cerebellar cortex and subcortical white matter that often has restricted diffusion. Findings do not correspond to a specific large arterial territory. Signal abnormalities may resolve and reappear.	MELAS (mitochondrial encephalopathy, lactic acidosis, and stroke-like events) is a maternally inherited disease affecting transfer RNA in mitochondria. MERRF (myoclonic epilepsy with ragged red fibers) is a mitochondrial encephalopathy associated with muscle weakness and myoclonic epilepsy, short stature, ophthalmoplegia, and cardiac disease.

(continued on page 170)

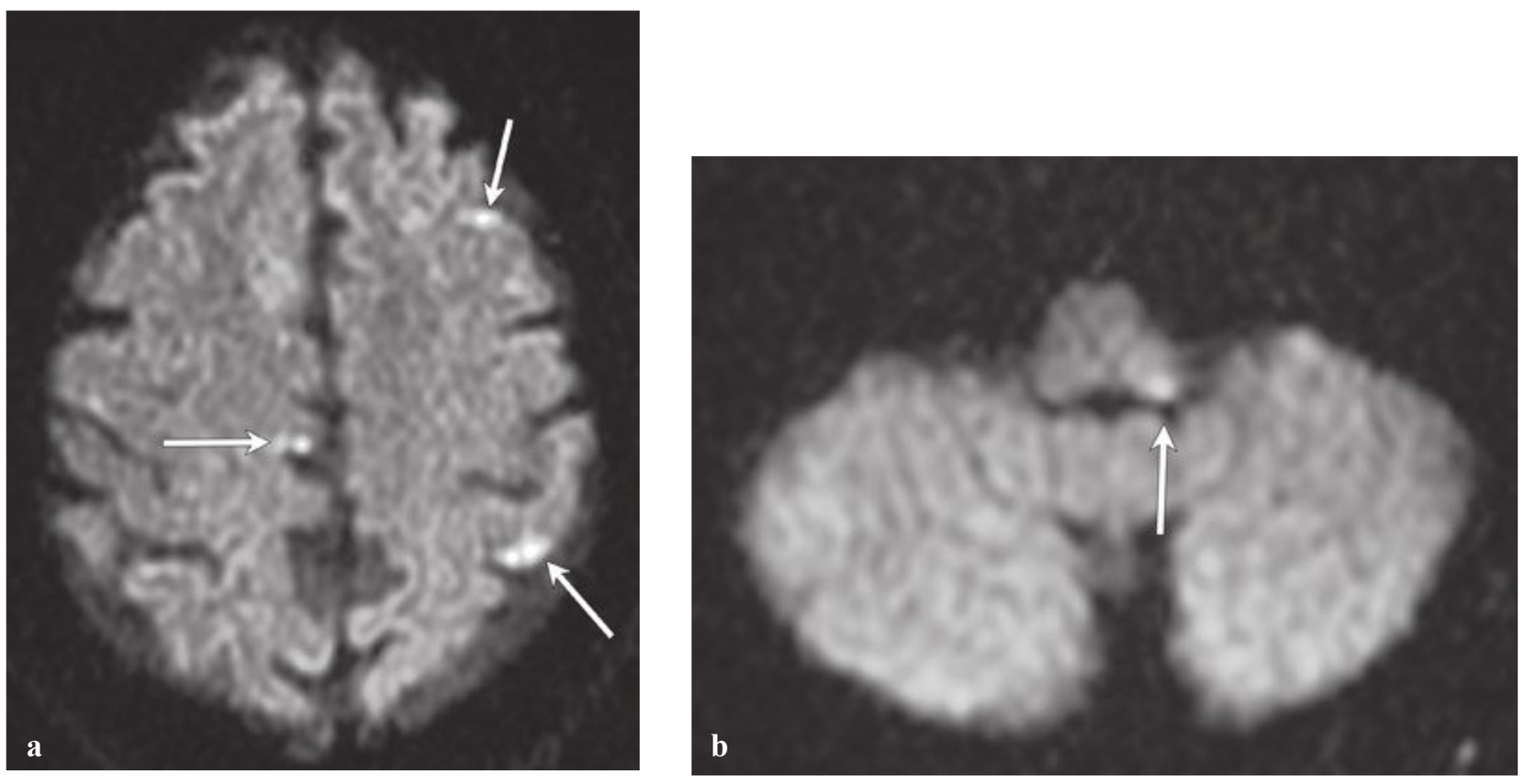

Fig. 1.208 **(a,b)** Small zones of restricted diffusion (arrows) are seen in the cerebral cortex and posterior left medulla on axial DWI.

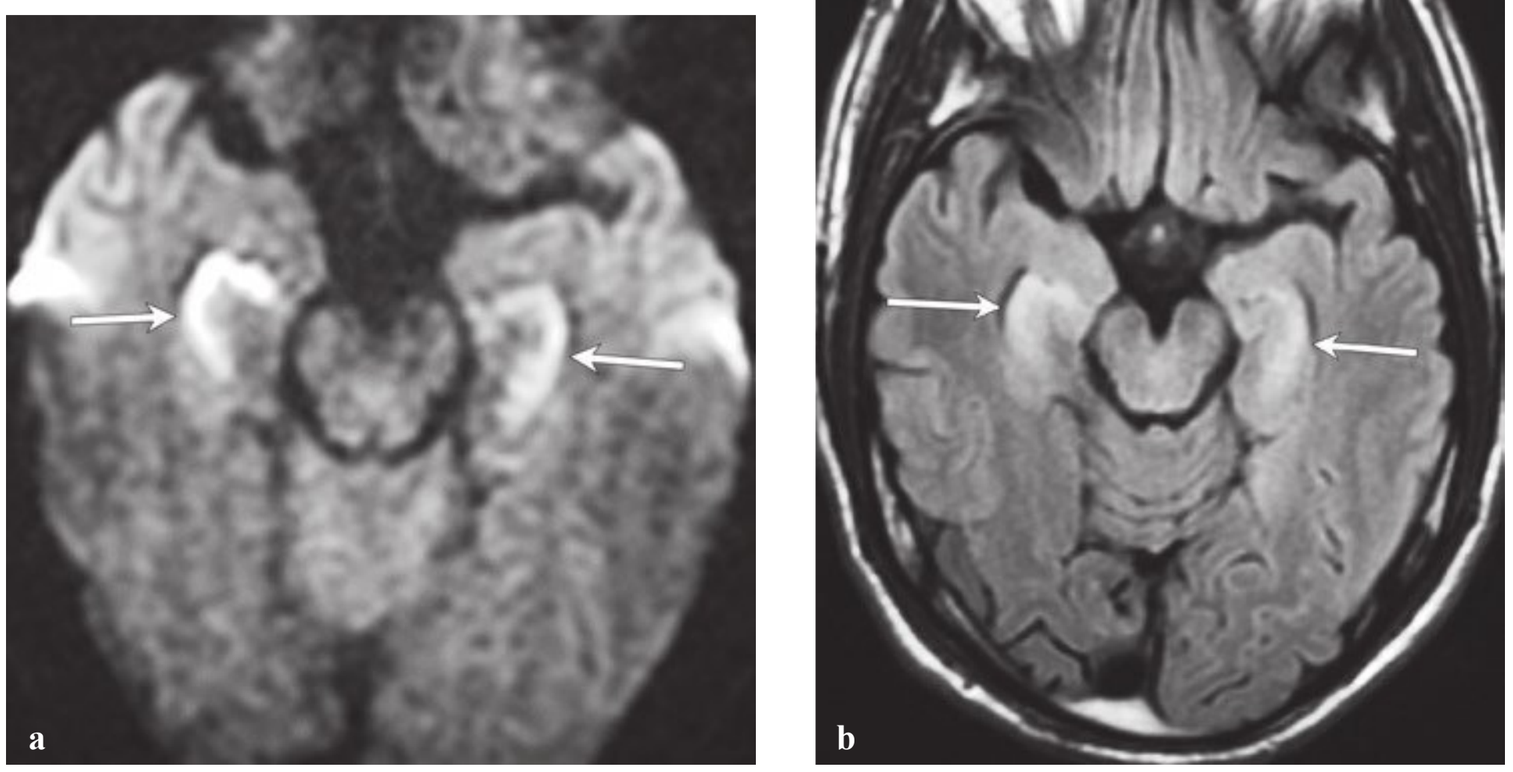

Fig. 1.209 **(a)** Patient with recent seizures who has restricted diffusion in both hippocampi (arrows) on axial DWI, with **(b)** corresponding high signal on axial FLAIR (arrows).

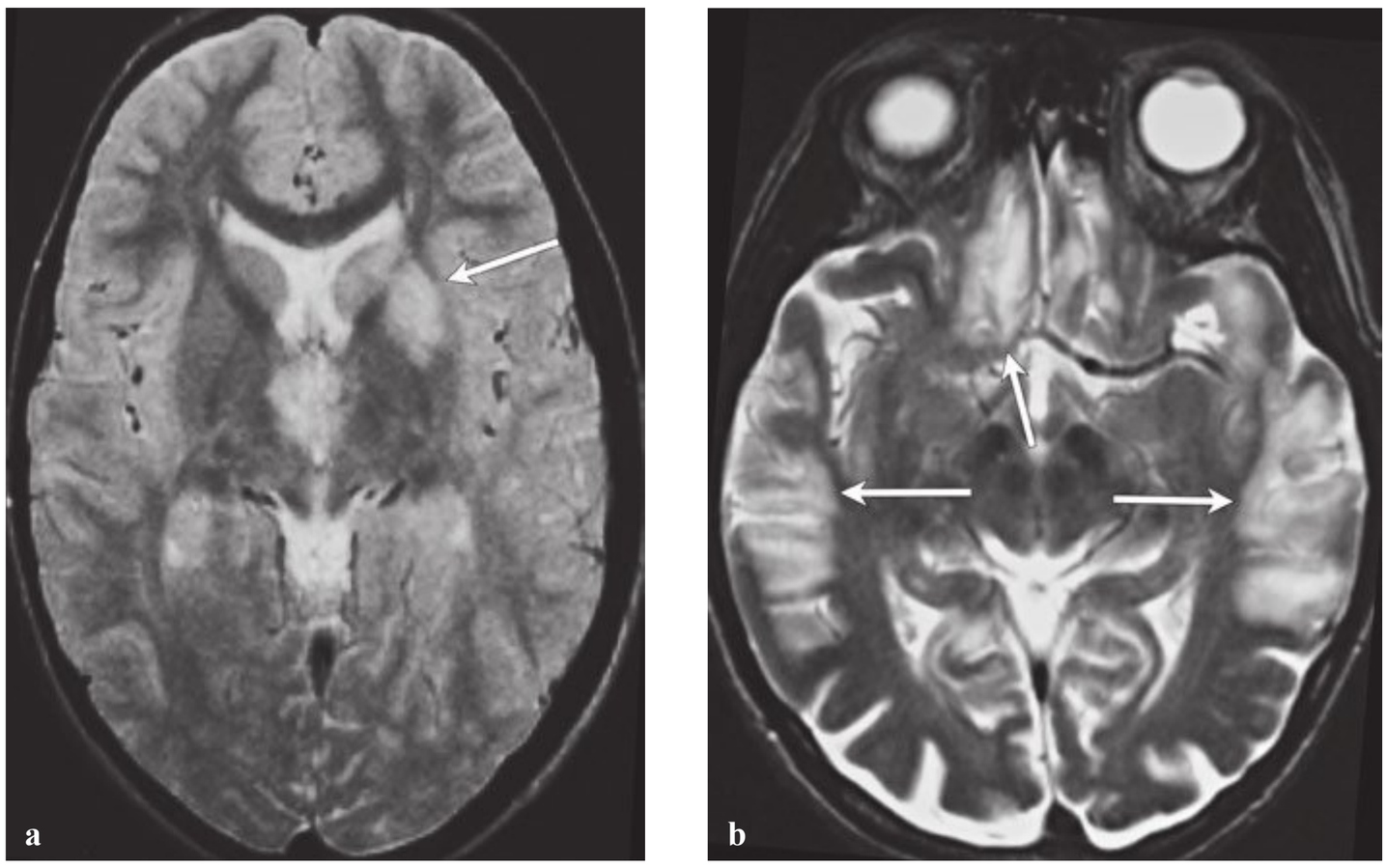

Fig. 1.210 Two patients with MELAS. **(a)** A6-year-old female has abnormal high signal in the left caudate nucleus and left putamen (arrow) on axial T2-weighted imaging. **(b)** A 45-year-old woman has bilateral high signal in the cerebral cortex and adjacent white matter (arrows) on axial T2-weighted imaging.

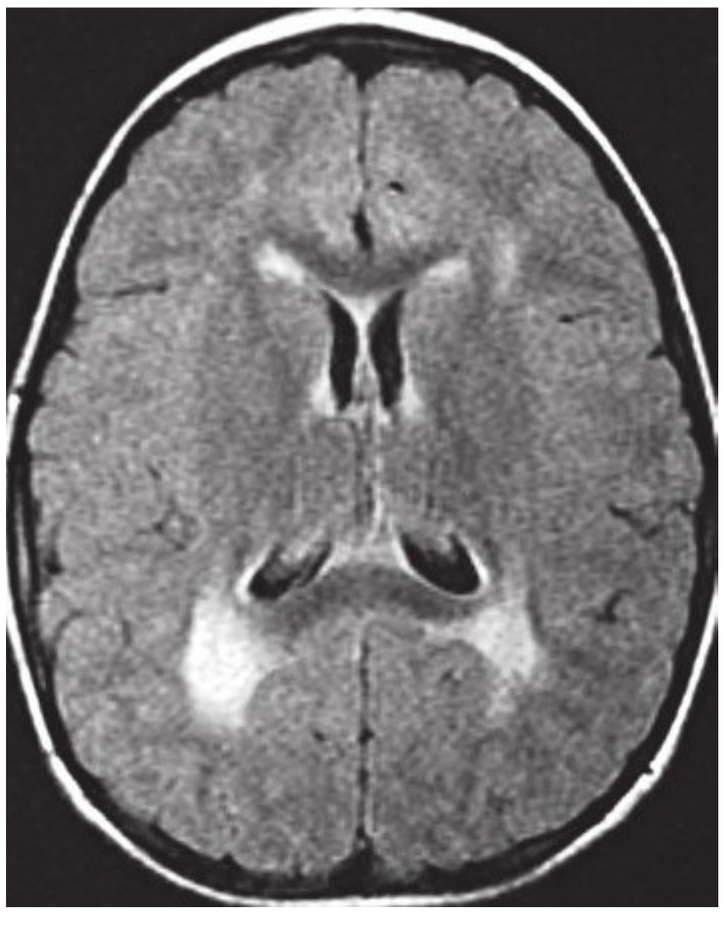

Fig. 1.211 An 8-year-old male with MERRF who has abnormal high signal on axial FLAIR in the peri-atrial and frontal periventricular white matter.

Table 1.4 (cont.) Multiple intra-axial lesions in the brain

Lesions	Imaging Findings	Comments
Leigh's disease (**Fig. 1.212**)	CT: Zones of low attenuation in both caudate nuclei and putamina, ± decreased attenuation in white matter, typically with no contrast enhancement. MRI: Symmetric high signal on T2-weighted imaging and FLAIR in globi pallidi, putamina, and caudate nuclei, as well as high signal on T2-weighted imaging in thalami, cerebral and cerebellar white matter, cerebellar cortex, brainstem, and spinal cord gray matter, + restricted diffusion for acute ischemia. Typically there is no gadolinium contrast enhancement. Magnetic resonance spectroscopy can show elevated lactate peaks during metabolic decompensation with lactic acidosis.	Autosomal recessive disorder, also referred to as subacute necrotizing encephalopathy, occurs in three forms (infantile type, juvenile type, and adult-onset type). Etiology is related to abnormalities in oxidative metabolism in mitochondria due to one of several enzyme deficiencies from mutations of mitochondrial and/or nuclear genes (coenzyme Q10, pyruvate carboxylase, pyruvate dehydrogenase complex, others). Progressive neurodegenerative disease with deterioration of cognitive and motor functions. Lesions in brainstem are associated with loss of respiratory control.
Kearns-Sayre syndrome (**Fig. 1.213**)	MRI: Zones with high signal on T2-weighted imaging and FLAIR in globi pallidi, putamina, and caudate nuclei, as well as high signal on T2-weighted imaging in thalami, subcortical cerebral and cerebellar white matter, posterior brainstem, and corticospinal tracts, + restricted diffusion for acute ischemia. Typically there is no gadolinium contrast enhancement. CT: Zones with decreased attenuation can be seen in the cerebral white matter, ± calcifications in globi pallidi and caudate nuclei.	Sporadic deletions of mitochondrial DNA involving genes that encode proteins of the respiratory chain and/or tRNA. Results in mitochondrial dysfunction and spongiform changes of the cerebral and cerebellar white matter and basal ganglia, as well as progressive external ophthalmoplegia, pigmentary degeneration of the retina, and cardiac conduction blocks.
Fabry disease (**Fig. 1.214**)	CT: Zones of low attenuation in the thalami, basal ganglia, and white matter, ± calcifications in basal ganglia and thalami. Typically there is no contrast enhancement. MRI: Multiple foci with high signal on T2-weighted imaging and FLAIR in basal ganglia, thalami, and cerebral and cerebellar white matter, ± low signal foci on GRE from microbleeds in 10% of cases. Typically there is no gadolinium contrast enhancement.	X-linked lysosomal disorder from mutations involving the gene encoding the enzyme α-galactosidase. Dysfunction of this enzyme leads to abnormal accumulation of glycosphingolipids in multiple tissues, including the heart, kidneys, and blood vessels, causing arteriopathy, emboli, and strokes (in patients < 30 years old and older adults).

(continued on page 172)

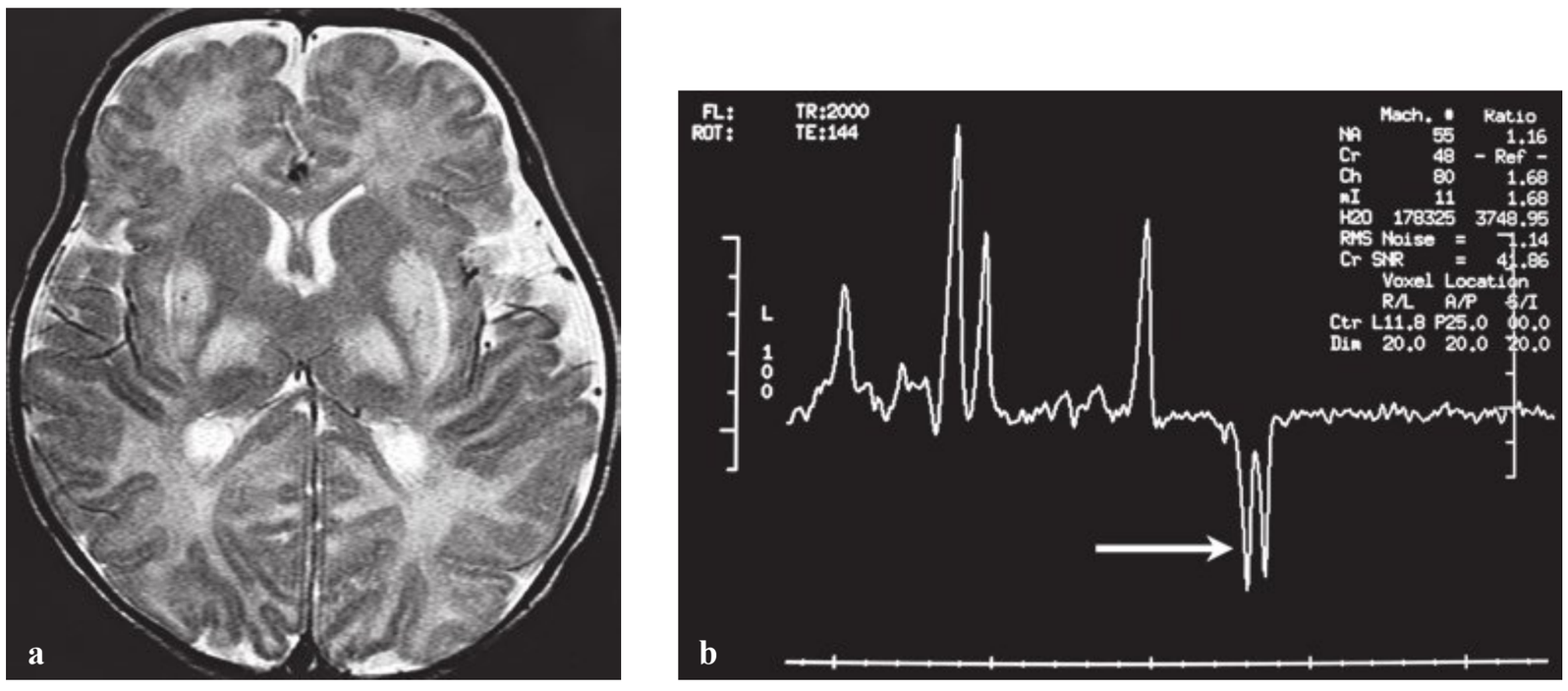

Fig. 1.212 **(a)** A 2-month-old female with Leigh's disease who has abnormal high signal in the putamina and thalami on axial T2-weighted imaging. **(b)** Magnetic resonance spectroscopy shows an abnormal lactate peak at 1.44 ppm (arrow) from lactic acidosis.

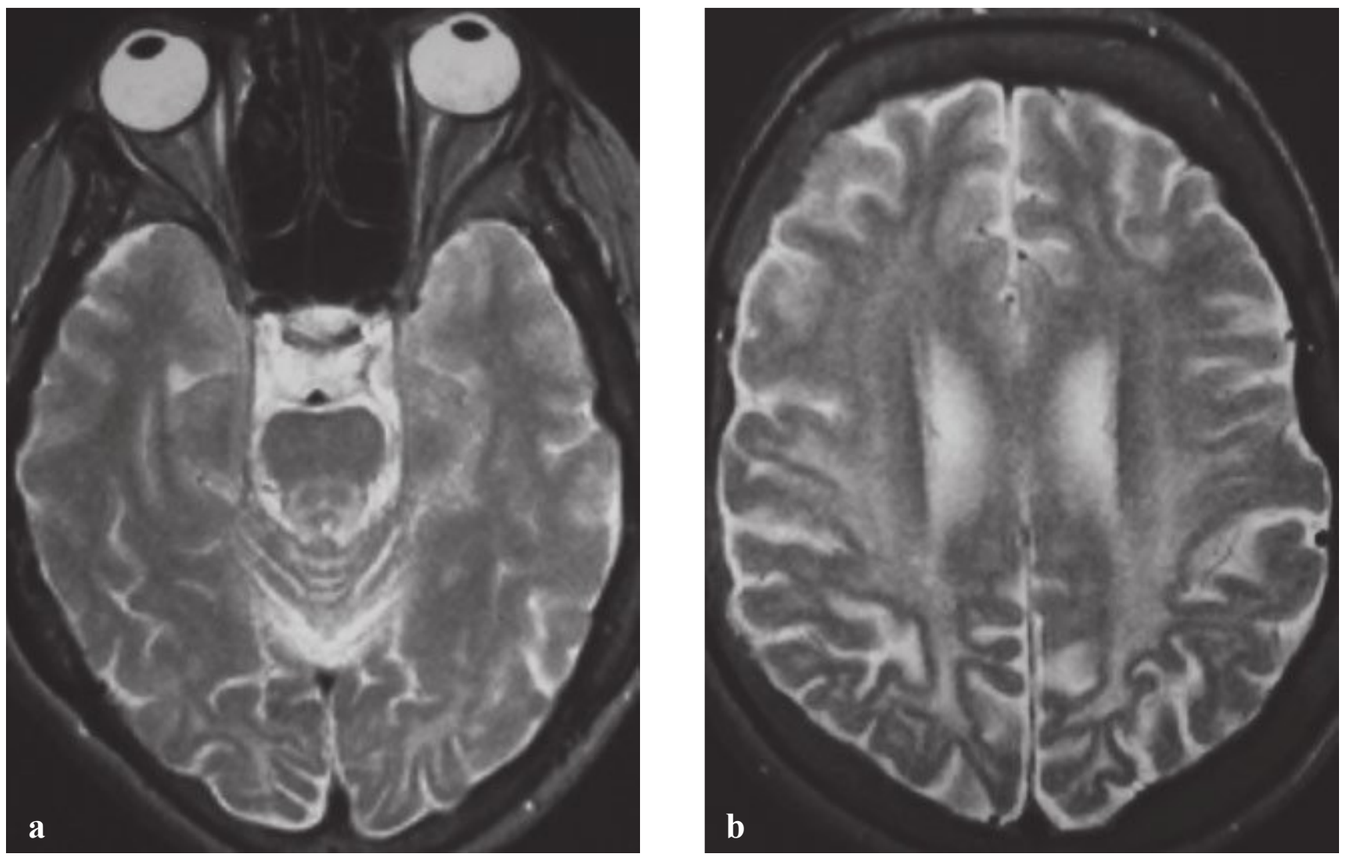

Fig. 1.213 Kearns-Sayre syndrome. **(a,b)** Zones with high signal on axial T2-weighted imaging are seen in the cerebral white matter and posterior brainstem.

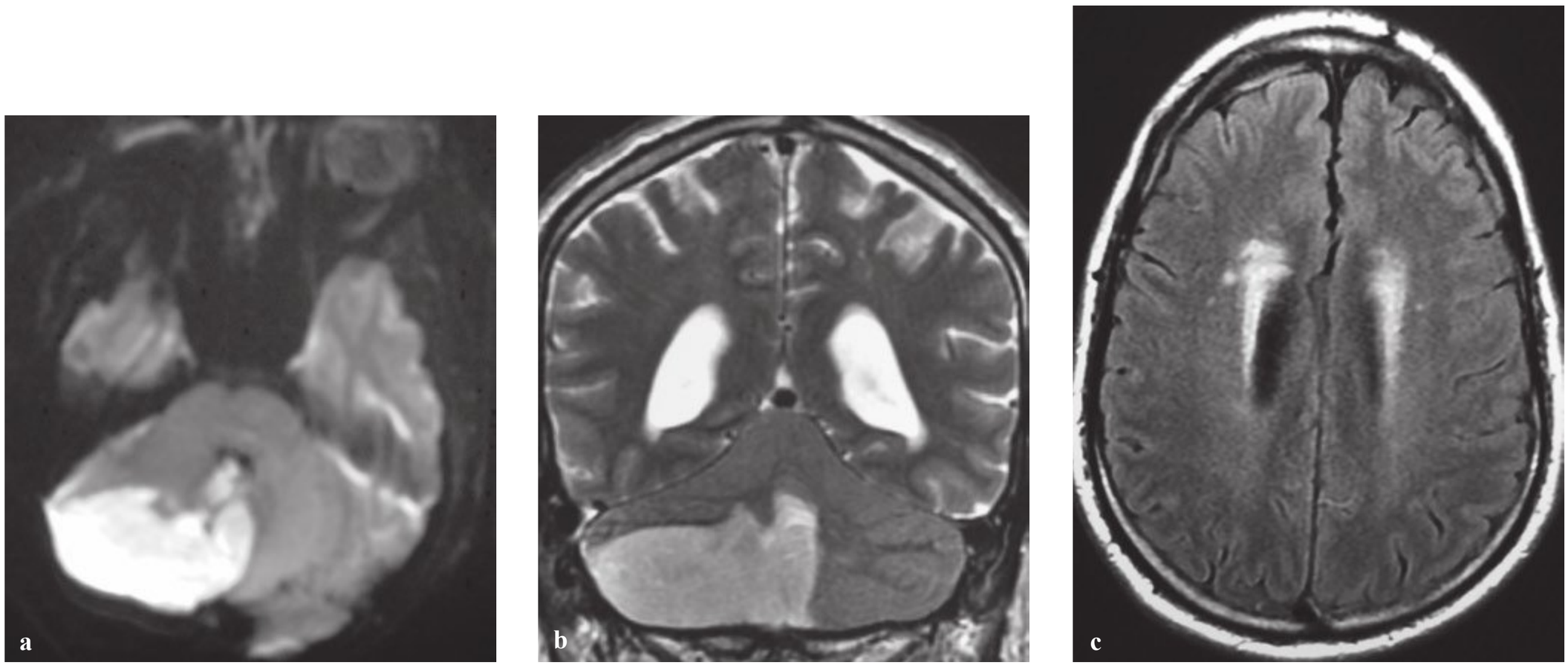

Fig. 1.214 A 50-year-old man with Fabry disease and acute infarction of the inferior right cerebellar hemisphere and vermis that has **(a)** restricted diffusion on DWI and **(b)** high signal on coronal T2-weighted imaging. **(c)** Multiple zones with high signal on axial FLAIR are also seen in the periventricular white matter.

Table 1.4 (cont.) Multiple intra-axial lesions in the brain

Lesions	Imaging Findings	Comments
Hyperglycemia (**Fig. 1.215**)	CT: Patients with nonketotic hyperglycemia in type 2 diabetes have zones with increased attenuation in the caudate and putamen, which can be unilateral or bilateral. In patients with insulin-dependent diabetes (type 1) with hyperglycemia and ketoacidosis, diffuse cerebral edema with effacement of sulci and cisterns can occur. MRI: In patients with nonketotic hyperglycemia in type 2 diabetes, zones with increased signal on T1-weighted imaging and variable signal changes on T2-weighted imaging and FLAIR in the caudate and putamen can occur, and they may be unilateral or bilateral. Restricted diffusion on diffusion-weighted imaging has also been reported in the involved sites. In patients with type 1 diabetes, diffuse cerebral edema with effacement of sulci and cisterns can occur. Complications from the brain swelling include central brain herniation with brain infarcts.	Nonketotic hyperglycemia (blood glucose generally over 350 mg/dL) can occur in patients with insulin-resistant (type 2) diabetes because of poor medical control, and may be associated with abnormalities involving the caudate, putamen, and subthalamic nuclei. May result in chorea ballismus. In patients with insulin-dependent diabetes (type 1), hyperglycemia can occur with ketoacidosis, leading to generalized brain swelling and central brain herniation.
Hypoglycemia (**Fig. 1.216**)	CT: Zones with decreased attenuation in the brain; they can be unilateral or bilateral and symmetric. MRI: Zones with abnormal increased signal T2-weighted imaging, FLAIR, and diffusion-weighted imaging (DWI) in the brain (cerebral cortex, hippocampi, internal capsules, basal ganglia, cerebral peduncles, pons); they may be unilateral or bilateral and symmetric. The lesions do not correspond to a specific arterial vascular territory. Treatment to correct hypoglycemia can result in resolution of high signal abnormalities on DWI within hours. With severe, prolonged hypoglycemia, poorly defined zones with increased signal on T2-weighted imaging, FLAIR, and DWI can be seen in the cerebral white matter and are often associated with a poor prognosis. Generalized cerebral swelling also may be seen, followed by cerebral atrophy.	Hypoglycemia is defined as blood glucose levels less than 45 mg/dL. Severe hypoglycemia (< 20 mg/dL) for more than 4 hours results in irreversible brain injury. Causes include overdose of insulin or other medications used by diabetic patients, insulin-secreting tumors, Addison's disease, severe sepsis, and hepatic or renal failure. If hypoglycemia is not corrected promptly, symptoms like drowsiness, personality changes, seizures, and hemiplegia occur. Severe prolonged hypoglycemia can result in coma and death. Lack of adequate glucose can result in impaired cerebral oxidative metabolism, leading to massive release of excitatory amino acid neurotransmitters, causing cytotoxic edema in neuronal and glial cells that can progress to cell death.

(continued on page 174)

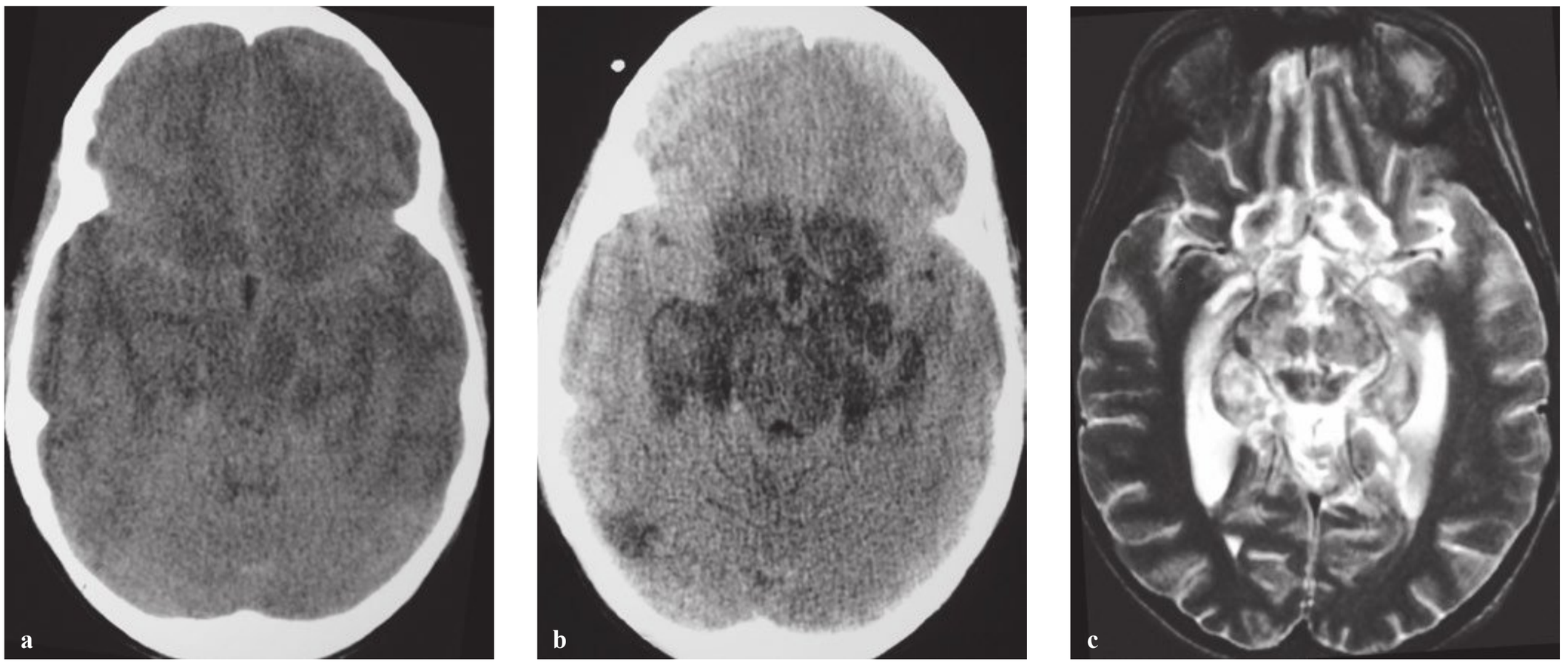

Fig. 1.215 A 9-year-old female with hyperglycemia and diabetic ketoacidosis. **(a)** Axial CT shows brain swelling with effacement of sulci and basal cisterns, as well as diffuse low attenuation in the cerebral white matter. **(b)** Follow-up CT exam 2 days later shows ischemic necrosis with low attenuation in the central portions of the brain and brainstem on axial CT from central brain herniation, with **(c)** corresponding abnormal high signal on axial T2-weighted imaging obtained 22 days later.

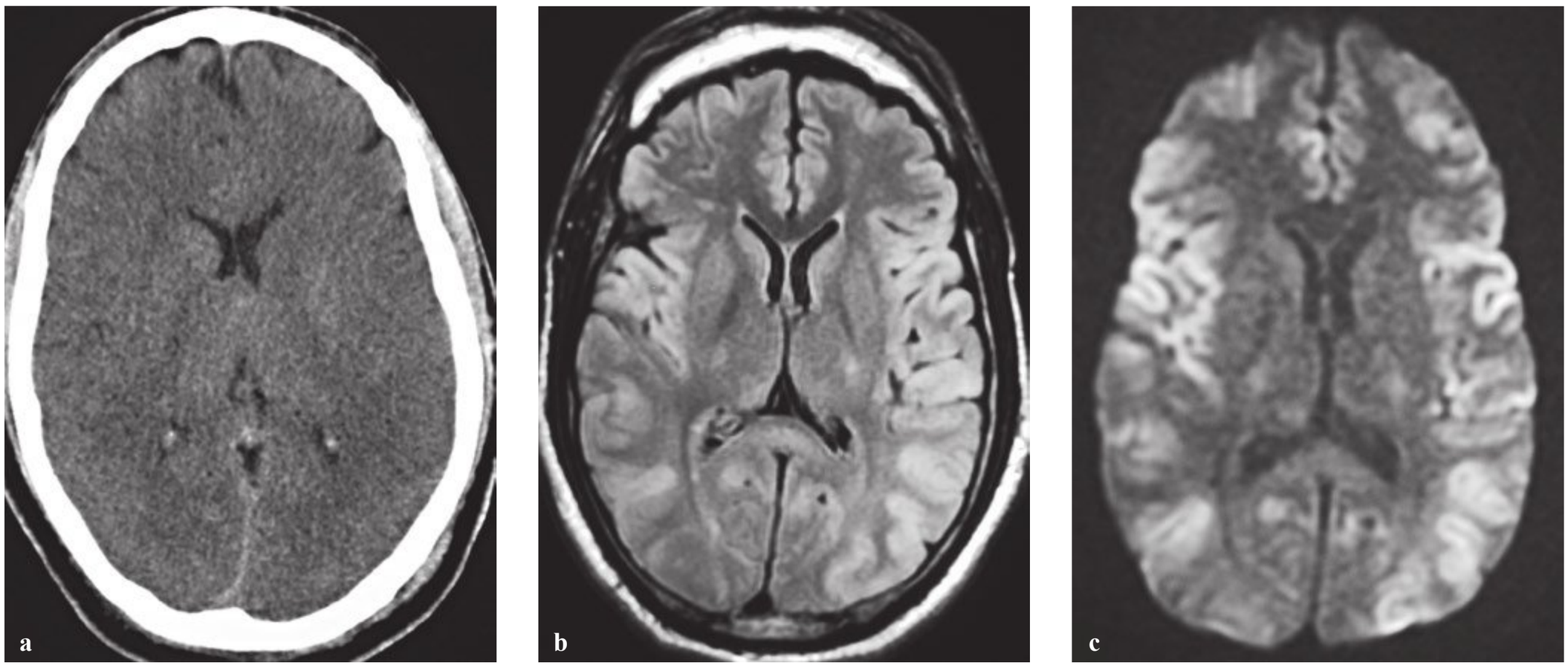

Fig. 1.216 A 42-year-old man with prolonged hypoglycemia. **(a)** Axial CT shows diffuse brain swelling with effacement of sulci and diffuse decreased attenuation in the brain. **(b)** Axial FLAIR and **(c)** axial DWI show abnormal increased signal in the cerebral cortex bilaterally. **(d)** Axial CT obtained 6 months later shows diffuse cerebral atrophy.

Table 1.4 (cont.) Multiple intra-axial lesions in the brain

Lesions	Imaging Findings	Comments
Disorders of amino acid and urea cycle metabolism: phenylketonuria, propionic acidemia, methylmalonic aciduria, homocystinuria, ornithine transcarbamylase deficiency, citrullinemia, arginosuccinic aciduria, leucinosis (maple syrup urine disease [MSUD]), glutaric acidemia/aciduria, others (**Fig. 1.217, Fig. 1.218, Fig. 1.219, Fig. 1.220**, and **Fig. 1.221**)	CT: Zones with decreased attenuation in cerebral and/or cerebellar white matter, ± zones with decreased attenuation in globi pallidi, putamina, caudate nuclei, thalami, and brainstem. MRI: Zones with increased signal on T2-weighted imaging and FLAIR in cerebral and/or cerebellar white matter, ± zones with increased signal on T2-weighted imaging in globi pallidi, putamina, caudate nuclei, thalami, and brainstem. Restricted diffusion can be seen with metabolic decompensation, ketoacidosis, and ischemia.	Autosomal recessive or X-linked disorders involving defective enzymes affecting mitochondrial function. These disorders can cause toxic accumulation of metabolites, resulting in mitochondrial dysfunction, ketoacidosis, and/or hyperammonemia, as well as alteration of myelin formation. Phenylketonuria: Autosomal recessive mutation of gene causing deficiency of phenylalanine hydroxylase, with toxic accumulation of phenyalanine. Propionic acidemia: Autosomal recessive mutation causing deficiency of propionyl-CoA carboxylase, with toxic accumulation of propionate, 3-hydroxybutyrate, methylcitrate, and 3-hydroxypropionate. Methylmalonic aciduria/homocystinuria: Autosomal recessive mutations causing lack of normal conversion of methylmalonyl-CoA to succinyl-CoA via defects of the apoenzyme methylmalonyl-CoA mutase or deficiency of the coenzyme adenosylcobalamine, resulting in accumulation and urinary excretion of methylmalonic acid, methylcitric acid, and 3-hydroxyproprionic acid. Ornithine transcarbamylase deficiency: X-linked mutation causing deficiency of ornithine transcarbamylase, which results in toxic accumulation of ammonia. Leucinosis (maple syrup urine disease): Autosomal recessive mutation involving the a-ketoacid dehydrogenase complex that results in toxic accumulation of branched-chain amino acids (leucine, isoleucine, and valine). Glutaric acidemia/aciduria type1: Autosomal recessive mutation causing deficiency of glutaryl-CoA dehydrogenase, with toxic accumulation of glutaric acid. Normal activity is needed for metabolism of lysine, hydroxylysine, and tryptophan. Glutaric acidemia/aciduria type 2: Autosomal recessive mutation causing deficiency of acyl coenzyme A dehydrogenase activity, resulting in impairment in mitochondrial electron transport related to electron transport flavoprotein or ubiquinone oxidoreductase.
Lysosomal enzyme defects: Tay-Sachs disease and Sandhoff disease (gangliosidoses)	CT: Increased, slightly high attenuation in the thalami, and decreased attenuation in the cerebral white matter, followed by progressive cerebral and cerebellar atrophy. MRI: Increased signal on T2-weighted imaging and FLAIR in the basal ganglia and cerebral white matter, no gadolinium contrast enhancement. Magnetic resonance spectroscopy: Decreased ratio of NAA/creatine, elevated ratios of choline/creatine (Cho/Cr) and myoinositol/creatine consistent with neuronal loss and gliosis.	Functional defects (usually autosomal recessive) involving lysosomal catabolic enzymes. Tay-Sachs disease: Functional N-acetyl hexosaminidase A deficiency from mutation at HEXA gene on chromosome 15q-23–24. Sandhoff disease: Functional N-acetyl hexosaminidase A and B deficiency from mutation at HEXB gene on chromosome 5q-13.
Lysosomal enzyme defects: neuronal ceroid lipofuscinosis	CT: Progressive cerebral and cerebellar atrophy, ± zones of decreased attenuation in white matter. MRI: Progressive cerebral and cerebellar atrophy, ± zones of increased signal on T2-weighted imaging and FLAIR in the periventricular white matter, and decreased signal on T2-weighted imaging in the globi pallidi and thalami. Typically no gadolinium contrast enhancement.	NCL is a progressive neurodegenerative encephalopathy in children (1/25,000 births) with toxic cytosomal accumulation of autofluorescent pigment (lipofuscin). Associated with progressive cerebral and cerebellar atrophy, retinal degeneration, epilepsy, and movement disorders. Congenital type: mutations of CLN10 gene (chromosome 11p15). Infantile type: mutations of the CLN1 gene (1p32). Late-infantile type: mutations of genes CLN1 to CLN8. Juvenile type (Batten disease): mutations involving CLN1, CLN3, or CLN5. Adult type (Kufs disease): mutations of CLN1, CLN4, or CLN6. Mutations result in absence of cathepsin D, PPT1, or TPP1 enzyme activities.

(continued on page 178)

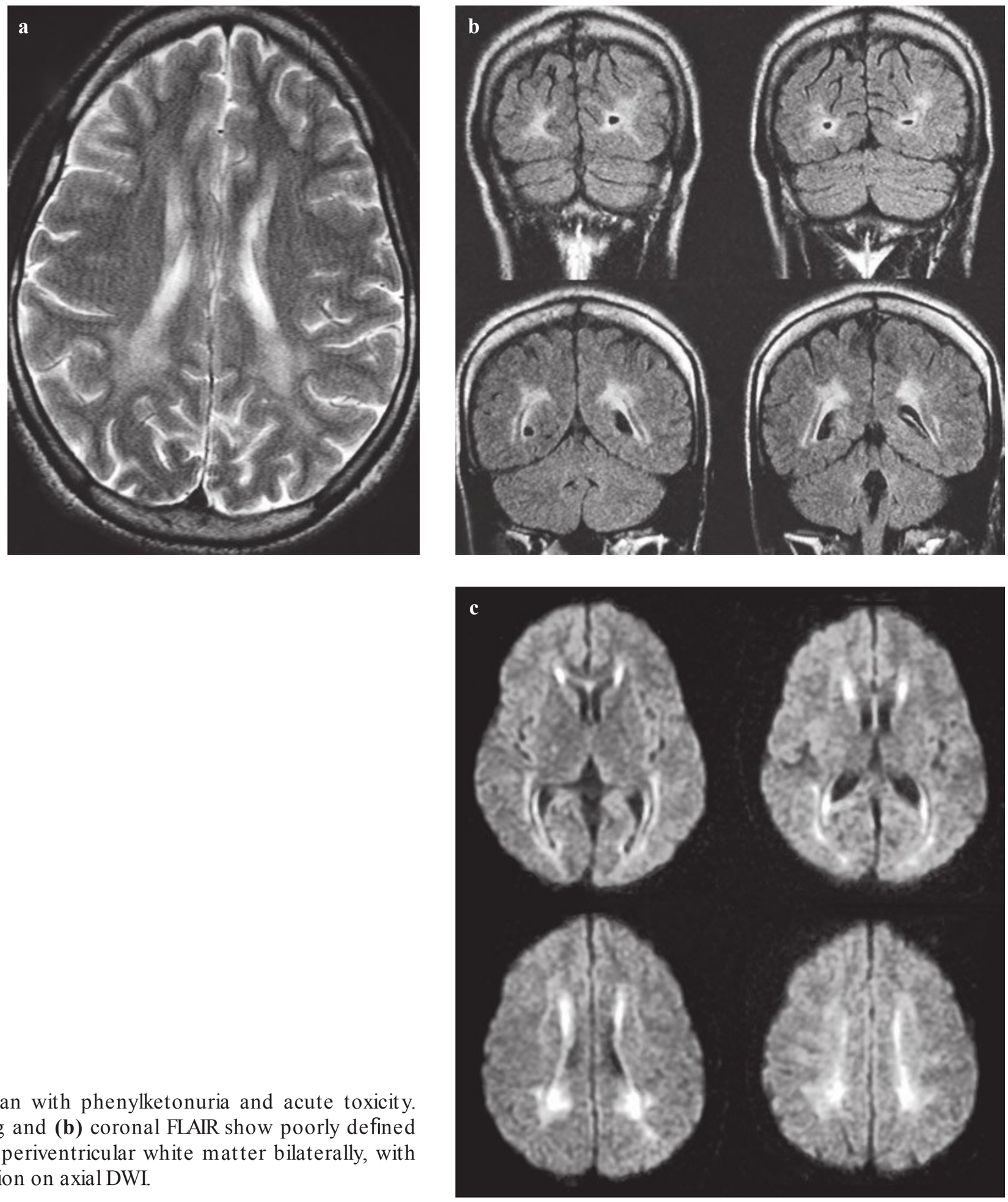

Fig. 1.217 A 22-year-old man with phenylketonuria and acute toxicity. **(a)** Axial T2-weighted imaging and **(b)** coronal FLAIR show poorly defined zones with high signal in the periventricular white matter bilaterally, with **(c)** associated restricted diffusion on axial DWI.

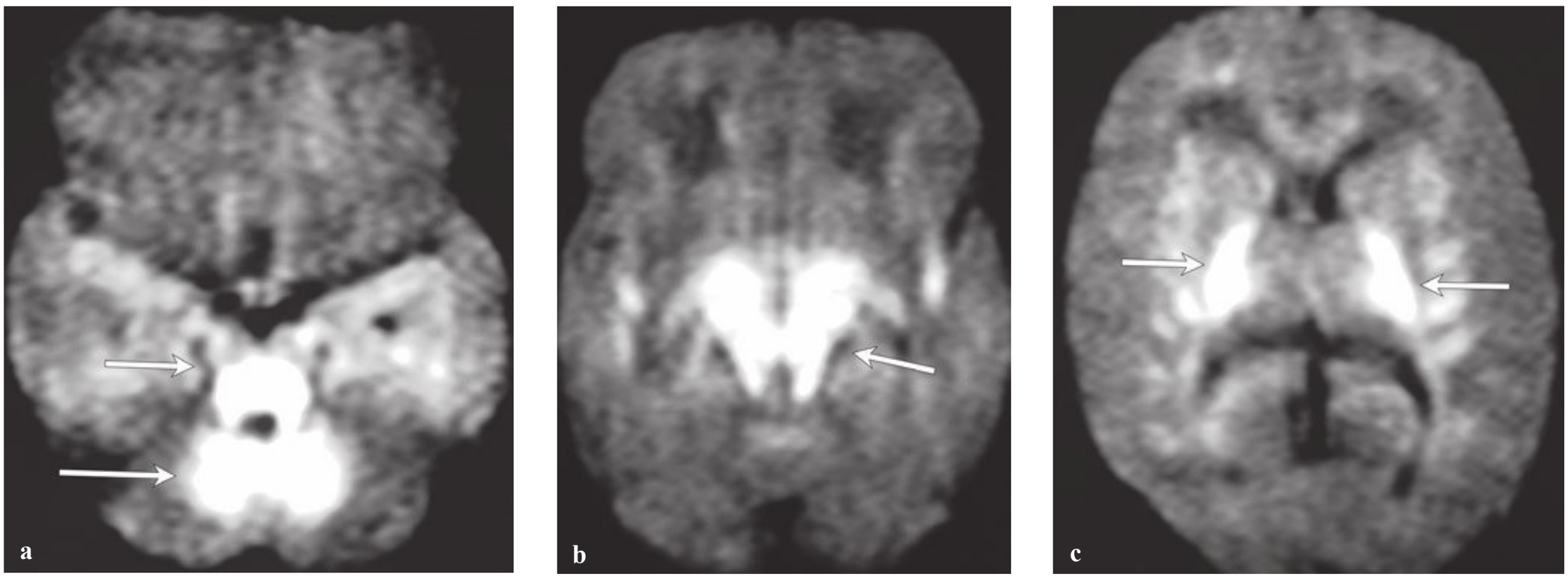

Fig. 1.218 A 1-week-old male neonate with methylmalonic aciduria and metabolic decompensation with acute toxicity. **(a–c)** Restricted diffusion (arrows) is seen in the brainstem, deep cerebellar white matter, internal capsules, and thalami on axial DWI.

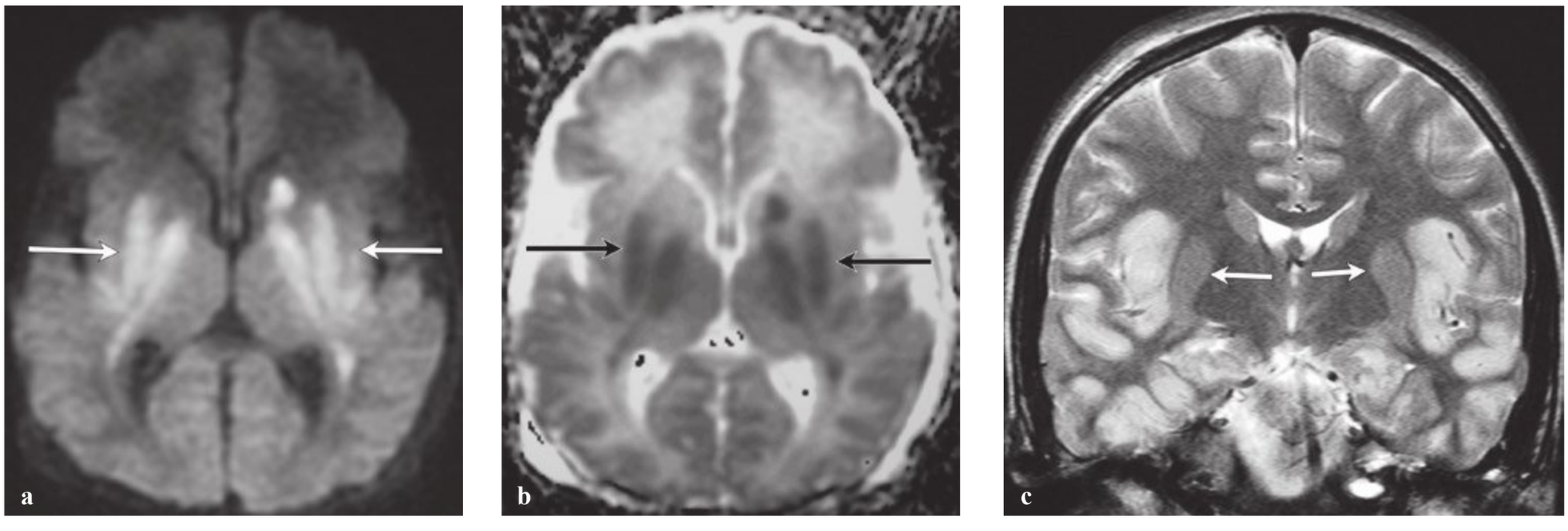

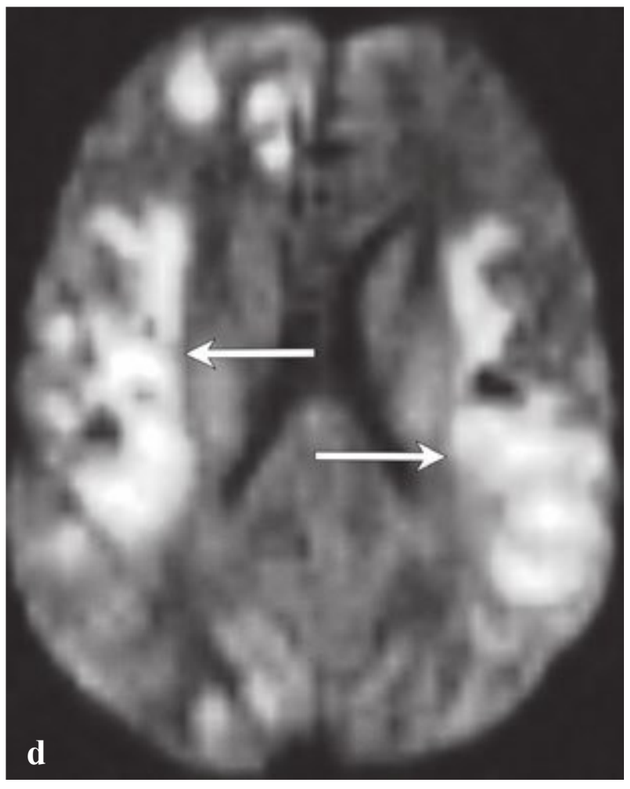

Fig. 1.219 Ornithine transcarbamylase deficiency. A 9-day-old male with restricted diffusion in the left caudate nucleus, putamina, and thalami on **(a)** axial DWI (arrows) and **(b)** ADC (arrows) from ammonia toxicity. **(c)** A 14-year-old male with metabolic ketoacidosis and abnormal high signal in the cerebral cortex bilaterally (arrows) on coronal T2-weighted imaging, with **(d)** corresponding restricted diffusion (arrows) on axial DWI.

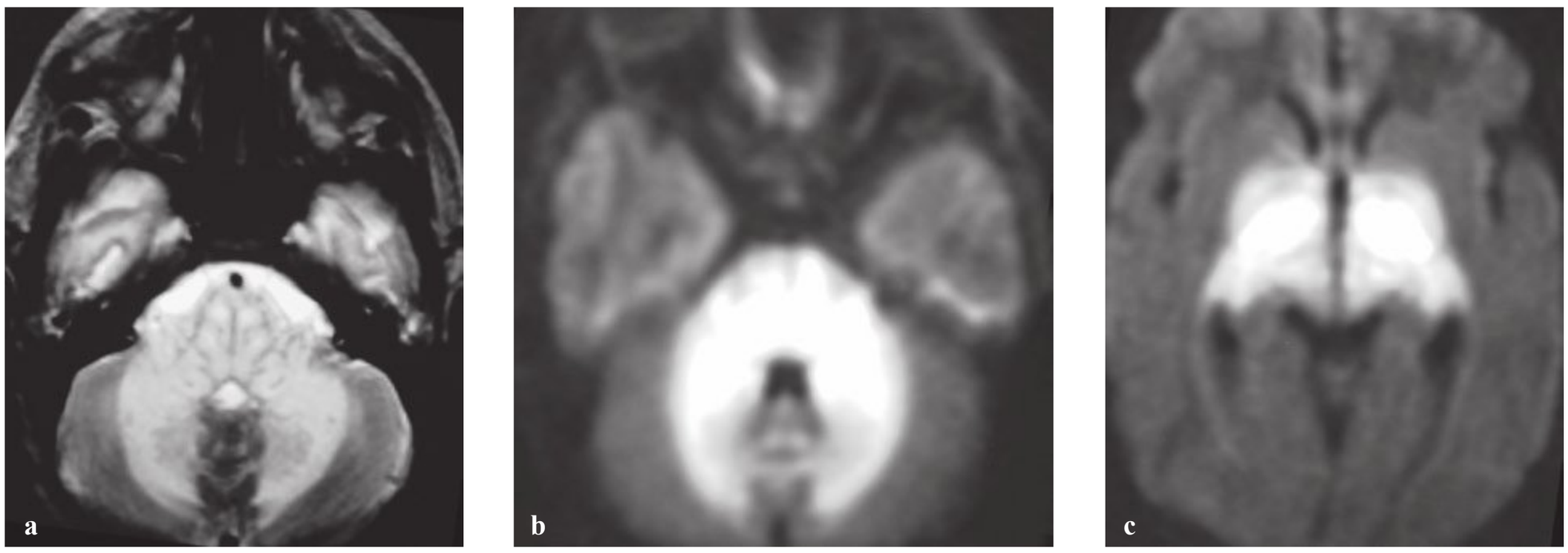

Fig. 1.220 A 2-week-old female with MSUD and metabolic decompensation with abnormal high signal in the brainstem, middle cerebellar peduncles, and deep cerebellar white matter on **(a)** axial T2-weighted imaging and **(b–d)** corresponding restricted diffusion on axial DWI that also involves the thalami and pre- and postcentral gyri. **(e)** Magnetic resonance spectroscopy with TE of 35 msec shows elevated lactate at 1.4 ppm and 0.9 ppm from the methyl group of branched-chain amino acids and α-keto acids.

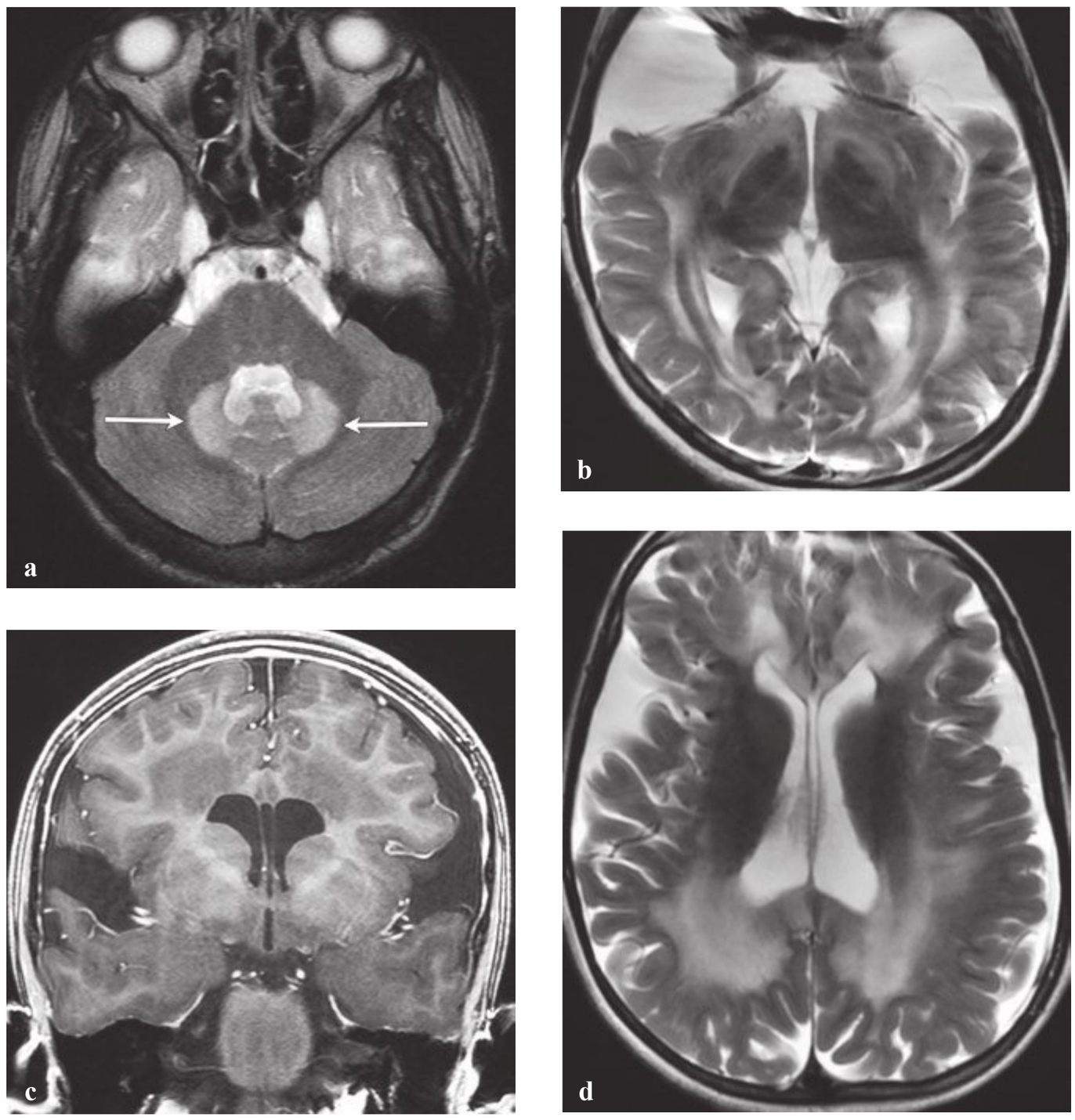

Fig. 1.221 Glutaric acidemia/aciduria type 1. **(a)** A 13-year-old male with abnormal increased signal in the dentate nuclei on T2-weighted imaging (arrows). **(b)** An 11-year-old female with expanded subarachnoid spaces in the middle cranial fossa and widened enlarged sylvian fissures on axial T2-weighted imaging and **(c)** coronal T1-weighted imaging. **(d)** Bilateral frontal-temporal lobe hypoplasia/atrophy and abnormal increased signal on T2-weighted imaging are seen in the cerebral white matter secondary to dysmyelination/demyelination from neurotoxic effects of abnormal metabolites.

Table 1.4 (cont.) Multiple intra-axial lesions in the brain

Lesions	Imaging Findings	Comments
Lysosomal enzyme defects: mucopolysaccharidoses (**Fig. 1.222** and **Fig. 1.223**)	CT: Poorly defined zones of decreased attenuation in white matter, cerebral and cerebellar atrophy, ± foci of low attenuation in corpus callosum and basal ganglia (prominent perivascular spaces). MRI: Poorly defined zones of decreased signal on T1-weighted imaging and increased signal on T2-weighted imaging and FLAIR in white matter, cerebral and cerebellar atrophy, ± foci of low signal on T1-weighted imaging in corpus callosum and basal ganglia (prominent perivascular spaces), cerebral cortical/subcortical infarcts, ± macrocephaly, communicating hydrocephalus, ± meningeal thickening.	Mucopolysaccharidoses are autosomal recessive or X-linked disorders related to abnormal metabolism of mucopolysaccharides (glycosaminoglycans) in lysosomes due to enzymatic defects. Hurler phenotype syndrome (MPS IH), Hurler-Scheie phenotype syndrome (MPS IH/S), and Scheie phenotype syndrome (MPS IS): abnormal iduronate 2-sulfatase; San*fi*lippo syndrome (MPS type III): abnormal heparan N-sulfatase, α-N-acetylglucosaminidase, acetyl-CoA:α-glucosaminidine acyltransferase, or N-acetylglucosamine 6-sulfatase; Morquio syndrome (MPS type IV): abnormal galactose 6-sulfatase or β-galactosidase. Abnormal accumulation of mucopolysaccharides (glycosaminoglycans) results in axonal loss and demyelination.
Carbon monoxide poisoning (**Fig. 1.224**)	CT: Acute poisoning shows symmetric decreased attenuation in the globi pallidi. MRI: Low signal on T1-weighted imaging and high signal on T2-weighted imaging in putamen and globus pallidus bilaterally, ± patchy contrast enhancement in necrotic zones. Diffusion-weighted imaging shows restricted diffusion from acute necrosis. Similar but less pronounced findings are seen in the brainstem and cerebellum.	Toxic effects of CO result in selective necrosis of basal ganglia bilaterally, and also, to a lesser degree, the brainstem and cerebellum. Atrophic changes involving the brain can be seen later and may be associated with cognitive impairment. The binding of CO to the heme protein is 250 times greater than the binding to oxygen, resulting in tissue hypoxia.
Heroin toxicity (**Fig. 1.225** and **Fig. 1.226**)	CT: Inhalation of heroin can result in symmetric abnormal decreased attenuation involving the cerebellar white matter, middle cerebellar peduncles, brainstem, and temporo-occipital white matter. MRI: Inhalation of heroin vapor can result in symmetric abnormal increased signal on T2-weighted imaging and FLAIR in the cerebellar white matter, middle cerebellar peduncles, brainstem, temporo-occipital white matter, and internal capsules, with no abnormal gadolinium contrast enhancement. In the acute phase, restricted diffusion can occur at the involved white matter. In the subacute and chronic stages, increased diffusion with increased ADC values is typically seen. Intravenous heroin can cause infarcts in the globus pallidus, as well as in the cerebral white matter, related to small-vessel disease.	Heroin-induced leukoencephalopathy (chasing the dragon) is toxic spongiform encephalopathy from inhalation of heroin vapor. Intravenous heroin can cause acute neurovascular complications, such as embolic events, vasospasm, and vasculitis resulting in brain infarcts. In the acute phase of spongiform leukoencephalopathy, restricted diffusion can be seen at the involved sites related to the presence of small vacuoles in myelin. In the subacute and later phases, the vacuoles within myelin progressively become larger, resulting in increased diffusion.
Cocaine toxicity	CT: Findings include cerebral infarcts and intra-axial or extra-axial hemorrhages. CTA shows zones of arterial narrowing from vasoconstriction, often in association with brain infarcts in the affected vascular territory. MRI: Findings include cerebral infarcts with high signal on T2-weighted imaging and FLAIR, restricted diffusion for acute infarcts, ± intra-axial or extra-axial hemorrhages.	Cocaine can be inhaled as powdered cocaine hydrochloride through nasal mucous membranes or as a vapor in the alkaloid combined form of cocaine hydrochloride with sodium bicarbonate or ammonia ("crack cocaine"). Results in blockage of uptake of monoamines, causing vasoconstriction of blood vessels, hypertension, tachycardia, intracranial hemorrhage (brain and subarachnoid), and stroke.

(continued on page 182)

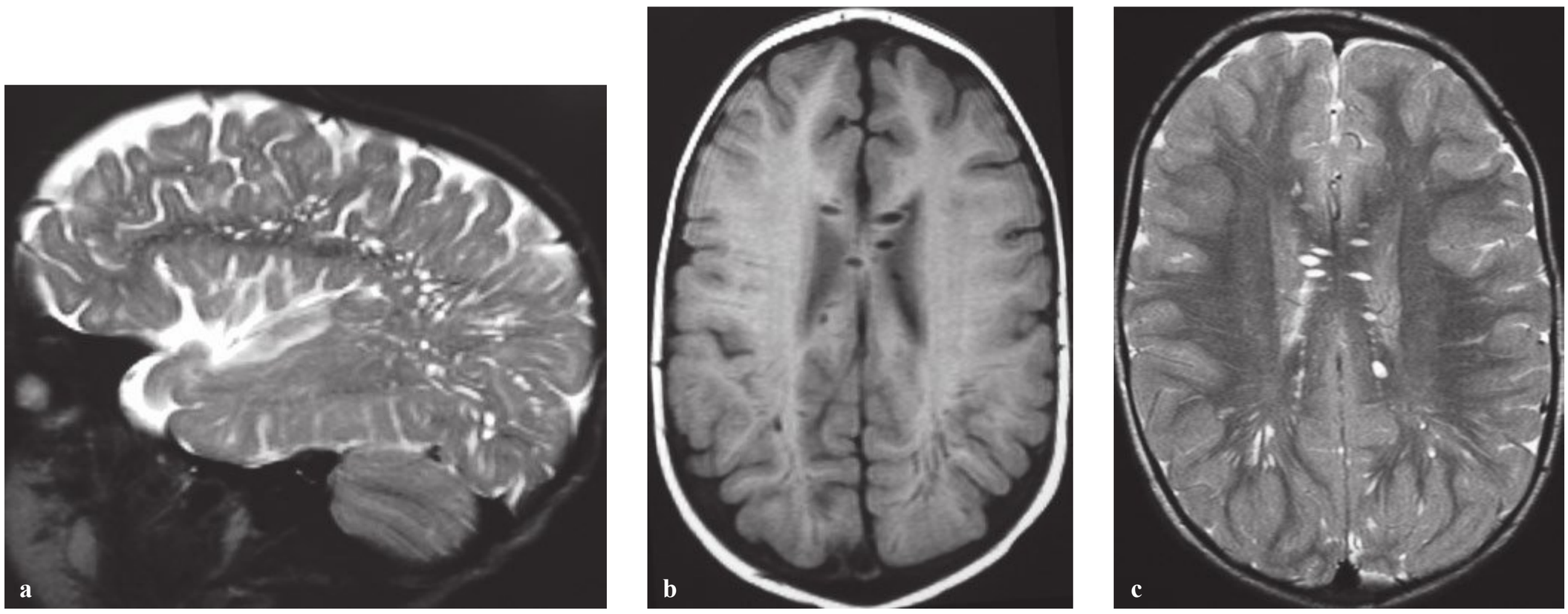

Fig. 1.222 Lysosomal enzyme defect (mucopolysacharidosis, MPS type I). **(a)** Axial T2-weighted imaging and **(b)** axial T1-weighted imaging in a 2.5-year-old child with Hurler syndrome (MPS IH) shows foci of high signal on T2-weighted imaging and low signal on T1-weighted imaging in the corpus callosum and periventricular white matter. **(c)** Similar findings are seen in a 5-year-old male with Hurler-Scheie (MPS IH/S) on axial T2-weighted imaging.

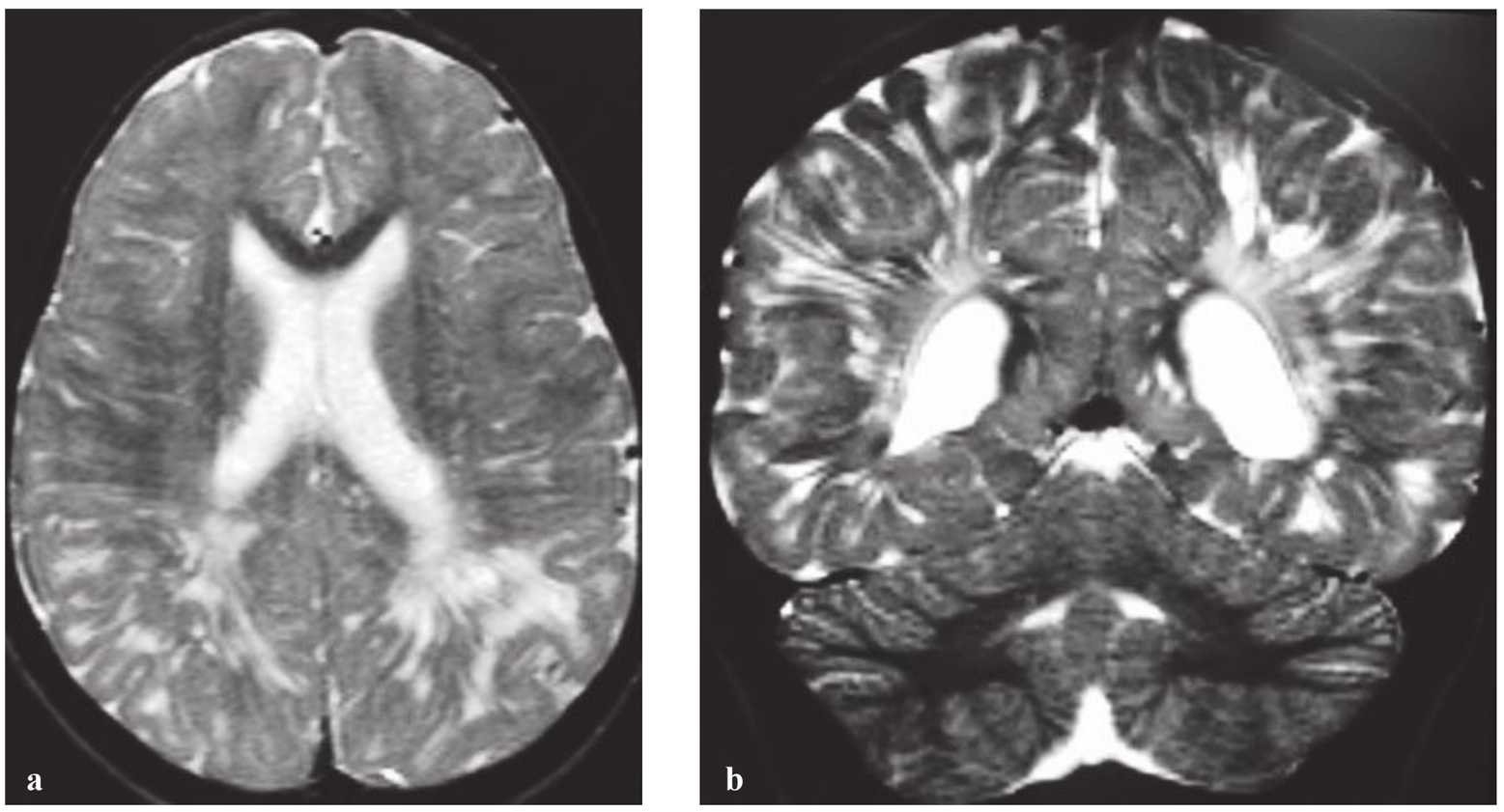

Fig. 1.223 Lysosomal enzyme defect. A 4-year-old child with Hunter syndrome (MPS type II) who has poorly defined zones of high signal on **(a)** axial and **(b)** coronal T2-weighted imaging in cerebral white matter, as well as high signal foci representing prominent perivascular spaces.

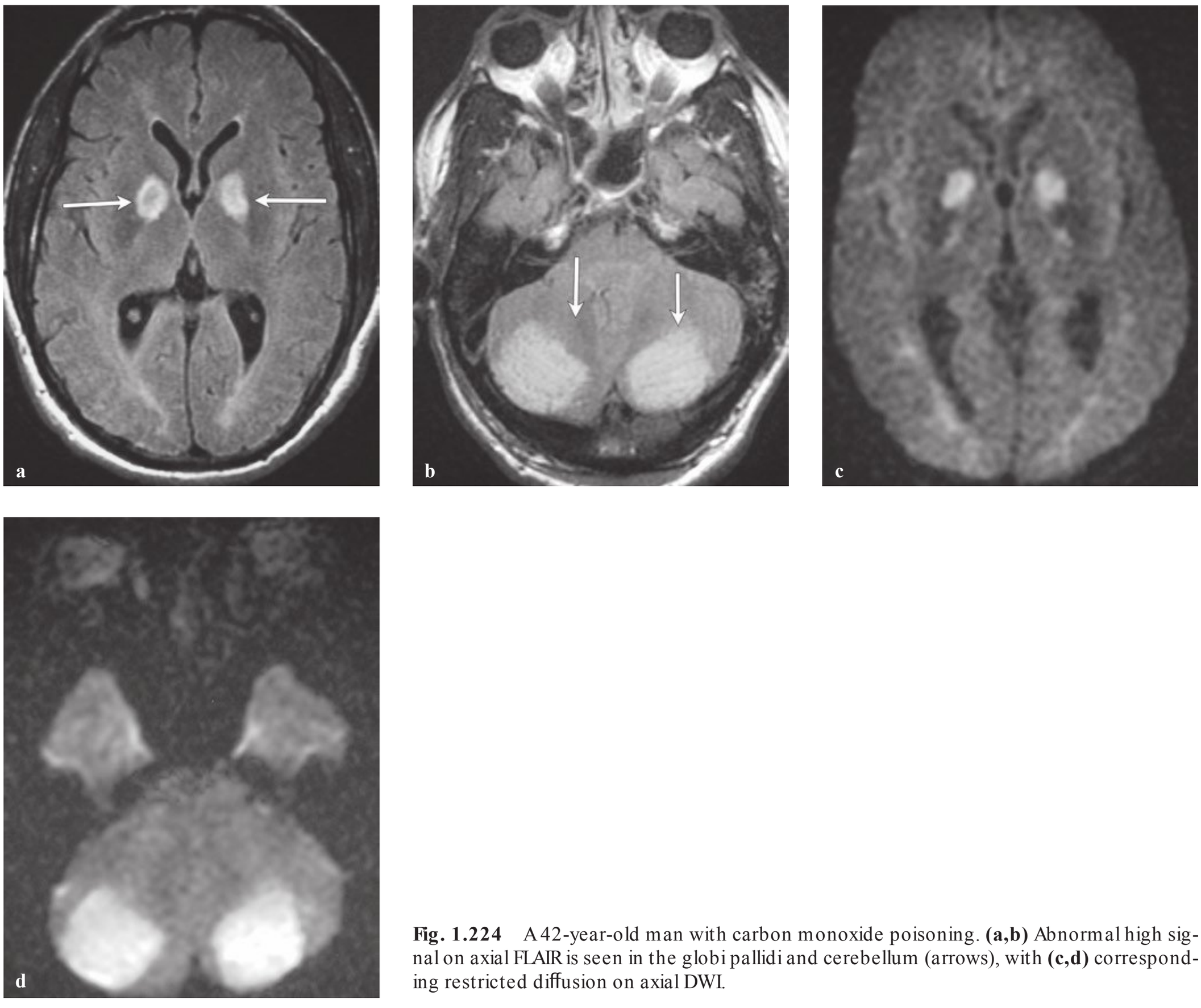

Fig. 1.224 A 42-year-old man with carbon monoxide poisoning. **(a,b)** Abnormal high signal on axial FLAIR is seen in the globi pallidi and cerebellum (arrows), with **(c,d)** corresponding restricted diffusion on axial DWI.

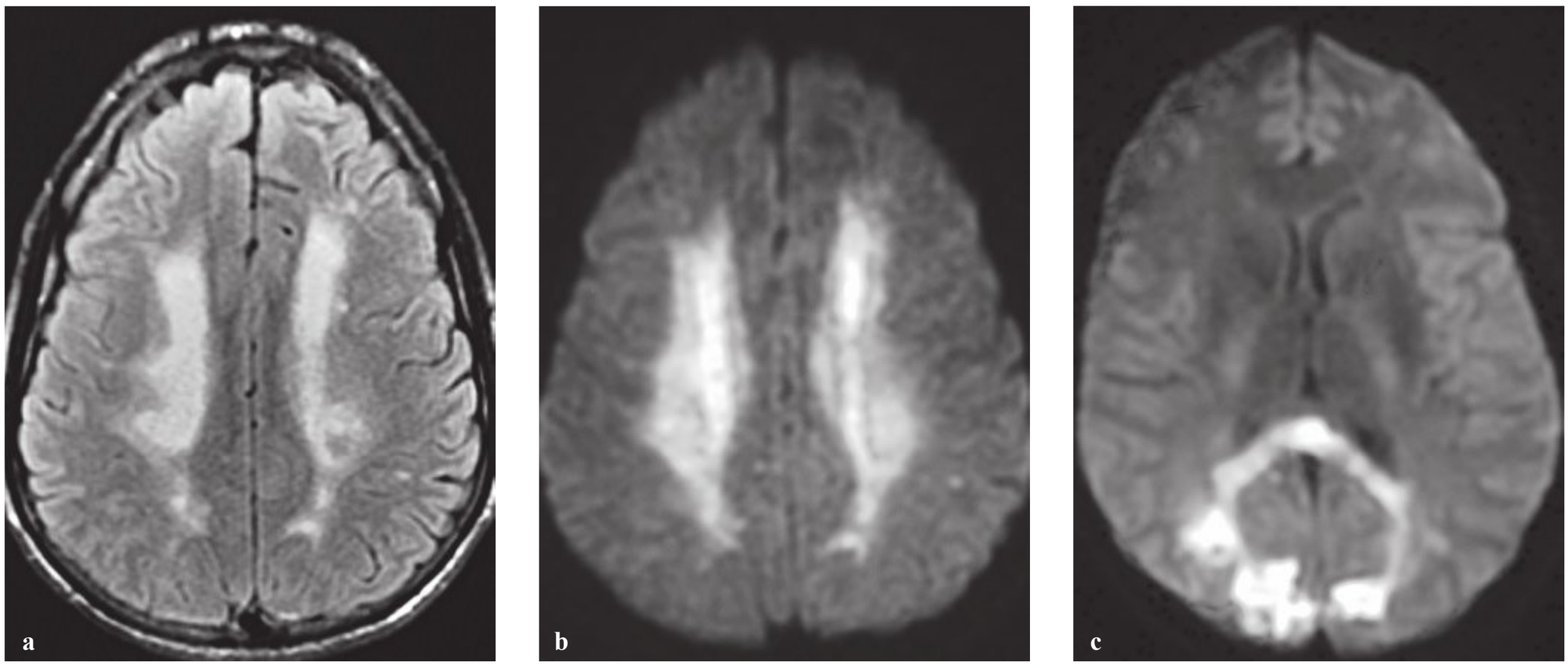

Fig. 1.225 Acute toxicity from inhalation of heroin ("chasing the dragon"). **(a)** A 32-year-old woman with abnormal increased signal on axial FLAIR in the cerebral white matter and corpus callosum, with **(b,c)** associated restricted diffusion on axial DWI.

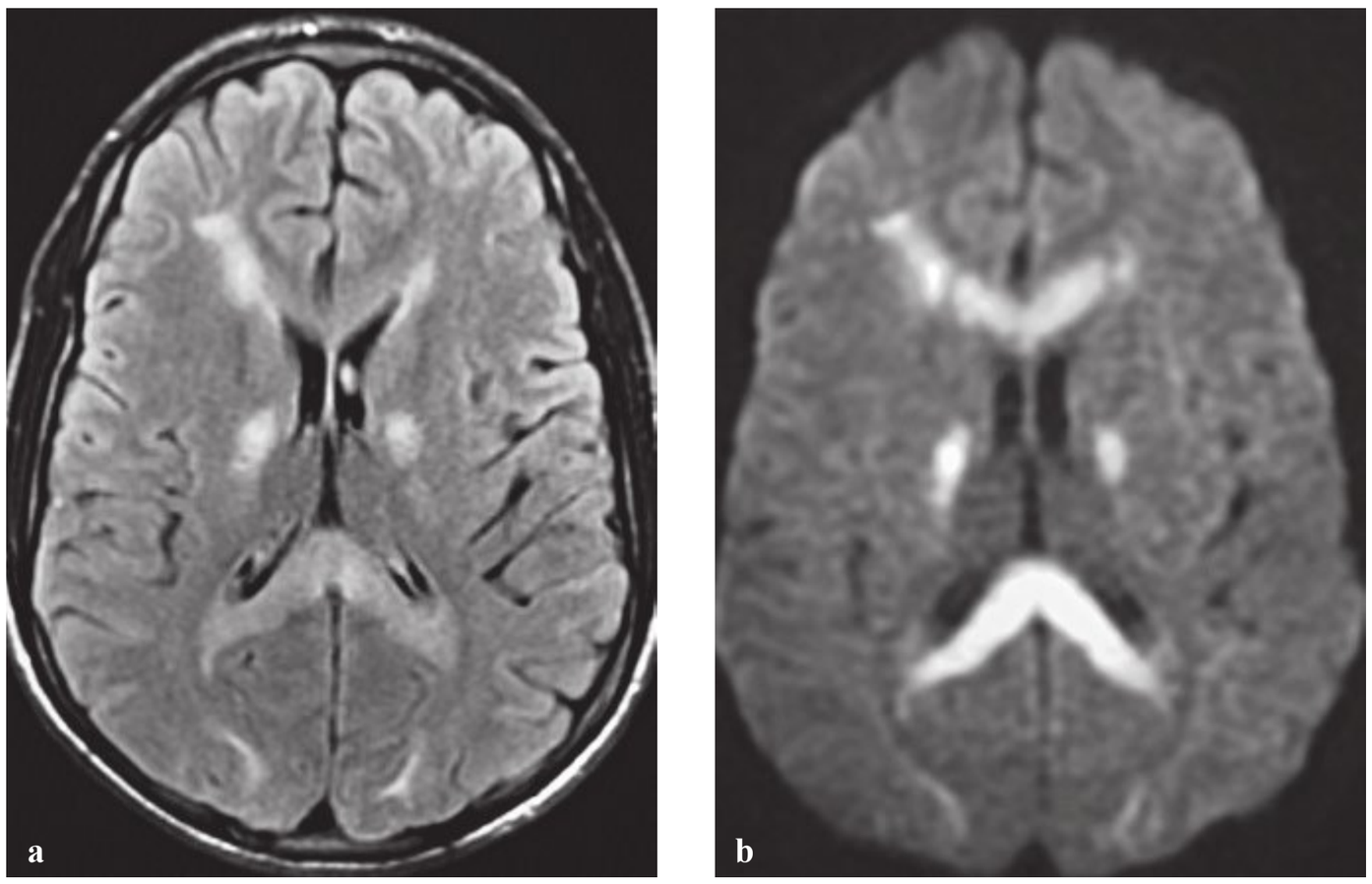

Fig. 1.226 A 17-year-old man with toxicity from intravenous heroin. Abnormal high signal is seen in the globi pallidi, corpus callosum, and periventricular white matter on **(a)** axial FLAIR, with **(b)** corresponding restricted diffusion on axial DWI.

Table 1.4 (cont.) Multiple intra-axial lesions in the brain

Lesions	Imaging Findings	Comments
Other Lesions		
Radiation necrosis (**Fig. 1.227** and **Fig. 1.228**)	MRI: Focal lesion ± mass effect or poorly defined, intra-axial zone of low-intermediate signal on T1-weighted imaging, intermediate-high signal on T2-weighted imaging, ± gadolinium contrast enhancement in tissue (white matter and/or gray matter) in the field of radiation treatment. Relative cerebral blood volume (rCBV) values for radiation necrosis (0.6) have been shown to be significantly lower than those for recurrent high-grade gliomas (2.6). Radiation necrosis at sites of surgically resected metastatic lesions may show a three-layer pattern on diffusion-weighted imaging consisting of an inner liquefied portion with high ADC, a middle layer with decreased ADC without gadolinium contrast enhancement, and an outer layer with gadolinium contrast enhancement with high ADC. CT: Focal lesion ± mass effect or poorly defined zone of low-intermediate attenuation, ± contrast enhancement in tissue (gray matter and/or white matter) in field of treatment.	Severe local tissue reaction to radiation treatment, related to doses over 65 Gy. Occurs from 3–6 months to 12 months, and occasionally up to 10 years, after radiation treatment. Occurrence rate is up to three times higher when chemotherapy is given concurrently with radiation treatment. Results from vascular endothelial injury and apoptosis, leading to thrombosis, fibrinous exudates, hyalinization with luminal stenosis, and fibrinoid and vascular necrosis, as well as glial and white matter damage. May be difficult to distinguish from neoplasm. Using dynamic susceptibility contrast-enhanced perfusion MRI, $rCBV_{max}$ and $rCBV_{mean}$ values for recurrent tumor have been shown to be significantly higher than those for tumor necrosis, aiding in distinguishing between these two diagnoses. Similar findings have been found with perfusion computed tomography. Perfusion MRI has been shown to be superior to ^{18}F-FDG PET and ^{11}C-methionine PET in distinguishing high-grade gliomas from radiation necrosis. MR hydrogen spectroscopy shows decreased N-acetylaspartate and choline peaks at sites of radiation necrosis, whereas residual and recurrent tumor show elevated choline peaks and a choline/creatine ratio > 2.
Pontine and extrapontine osmotic myelinolysis (**Fig. 1.152**)	MRI: Poorly defined zone of low-intermediate signal and high signal on T2-weighted imaging involving the central portion of the pons (central pontine myelinolysis). Extrapontine myelinolysis occurs as zones with high signal on T2-weighted imaging in the cerebral white matter, external capsules, basal ganglia. thalami, midbrain, and middle cerebellar peduncles, ± small areas of gadolinium contrast enhancement in the first 4 weeks. ADC values are low in the acute phase. CT: Poorly defined zone of decreased attenuation involving the central portion of the pons (central pontine myelinolysis). Extrapontine myelinolysis occurs as zones with decreased attenuation in the cerebral white matter, external capsules, basal ganglia. thalami, midbrain, and middle cerebellar peduncles, ± occasional contrast enhancement.	Demyelinating disorder resulting from rapid correction of hyponatremia in chronically ill, malnourished, or alcoholic patients. Associated with diabetes mellitus, hepatitis, and chronic disease of the lungs, liver, and/or kidneys. Damage occurs to the myelin sheaths, without initial destruction of axons. Can result in spastic tetraparesis, quadraparesis, pseudobulbar paralysis, seizures, coma, and locked-in syndrome. Clinical findings can regress or progress; the disorder is occasionally fatal.
Hypertensive encephalopathy (posterior reversible encephalopathy syndrome [PRES]) (**Fig. 1.229**)	MRI: Zones of low-intermediate signal on T1-weighted imaging and high signal on T2-weighted imaging in subcortical white matter, ± cerebral cortex, ± gadolinium contrast enhancement. Findings can be reversed if eliciting cause is corrected. Progression to cerebral infarction can sometimes occur. CT: Foci and/or confluent zones of decreased attenuation in subcortical white matter, ± cerebral cortex, ± contrast enhancement.	Occurs with elevations in blood pressure above the upper limit of cerebral vascular autoregulation, resulting in capillary leakage of fluid in the brain, often in arterial boundary zones. Associated with immunosuppressant drugs (tacrolimus/FK506, cyclosporine), chemotherapy (cisplatin, L-asparaginase, others), acute onset of hypertension, pre-eclampsia, eclampsia, renal dysfunction, and fluid overload. Neurologic symptoms include confusion, headaches, seizures, visual loss, dysarthria, and coma. Cortical abnormalities may be related to cortical laminar necrosis due to hypoperfusion injury.

(continued on page 184)

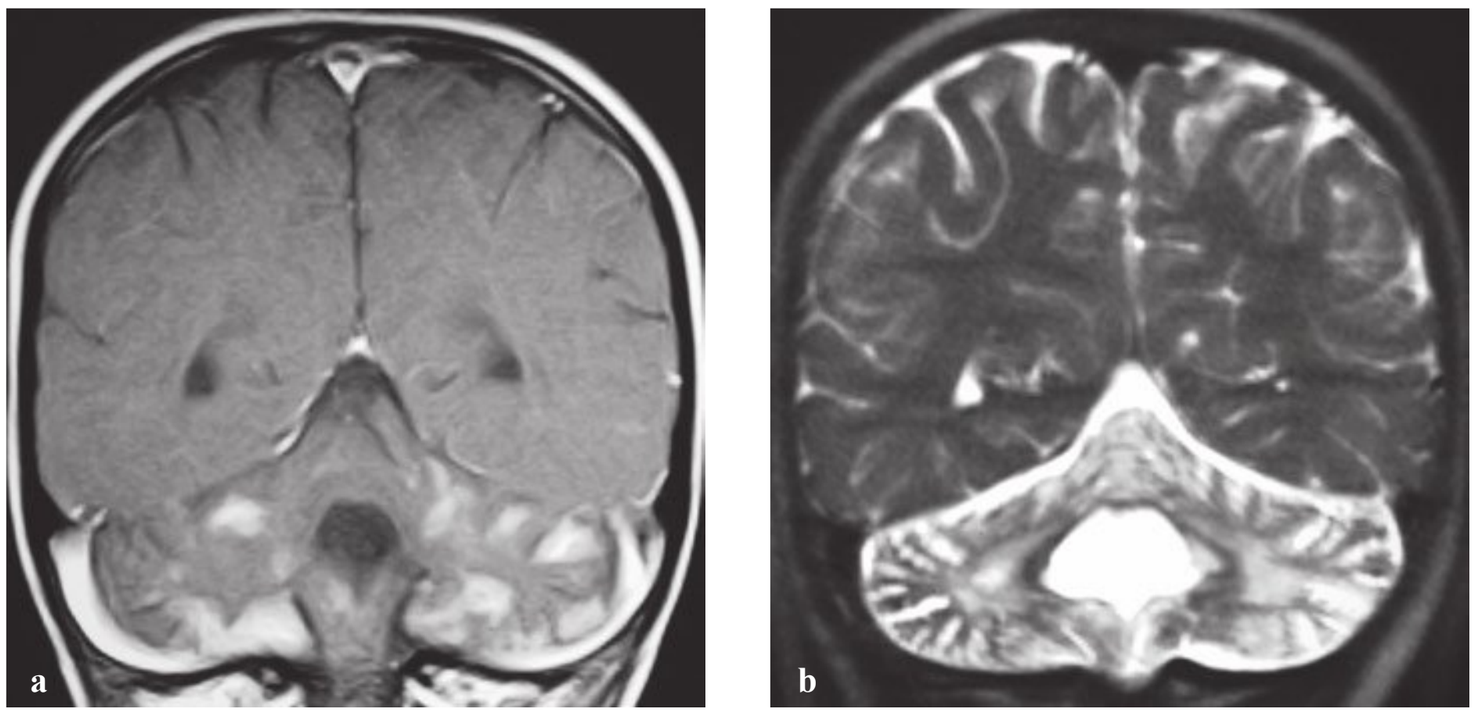

Fig. 1.227 Radiation necrosis 7 months after surgery and radiation treatment of medulloblastoma. **(a)** Multiple, poorly defined zones of gadolinium contrast enhancement are seen in the cerebellum on coronal T1-weighted imaging. **(b)** Encephalomalacia and gliosis are seen in the cerebellum on subsequent T2-weighted imaging.

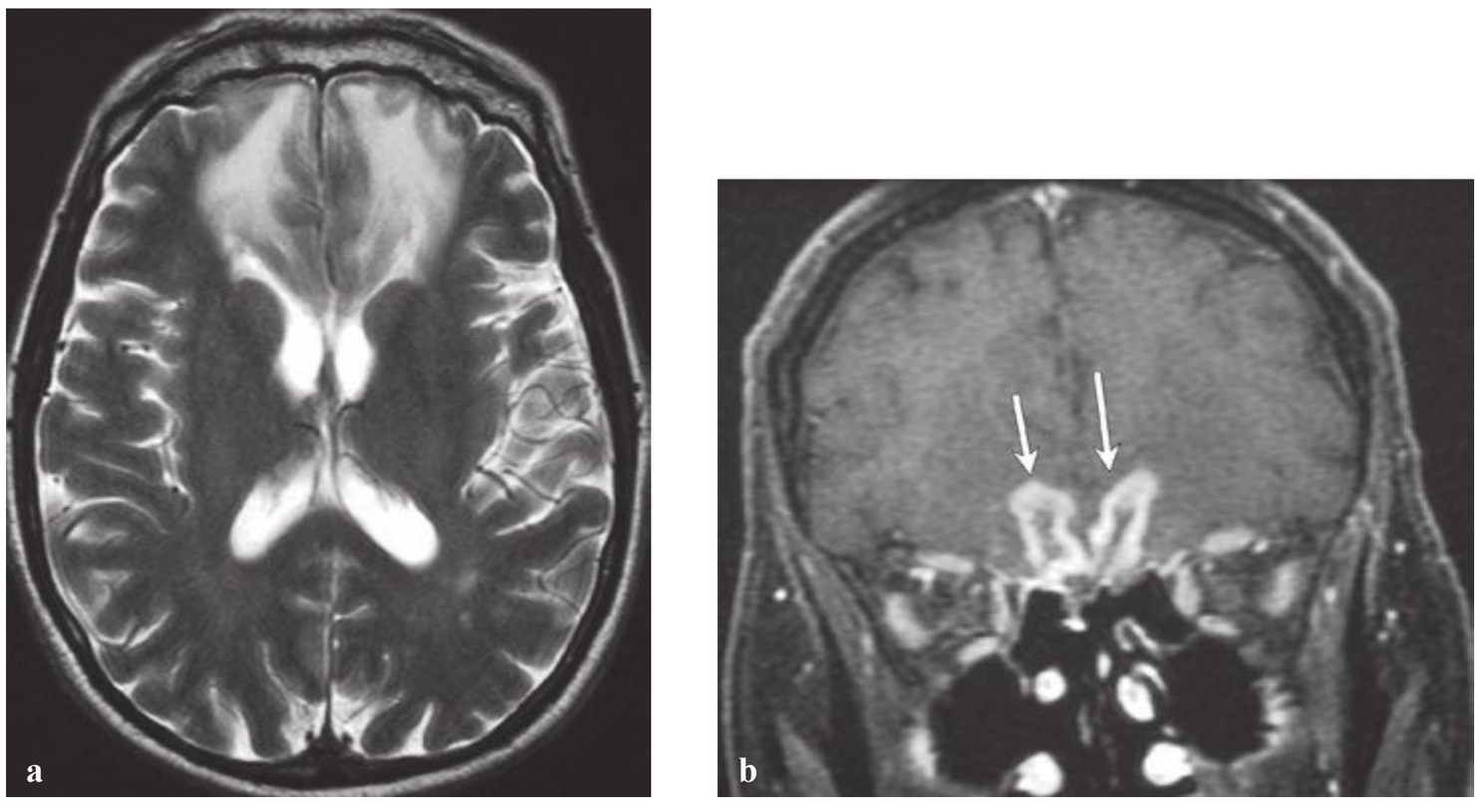

Fig. 1.228 A 55-year-old man with radiation necrosis in the frontal lobes after treatment for squamous cell carcinoma in the ethmoid sinuses. **(a)** Poorly defined zones with high signal are seen in the inferior portions of both frontal lobes on axial T2-weighted imaging, with **(b)** corresponding irregular peripheral patterns of gadolinium contrast enhancement on coronal fat-suppressed T1-weighted imaging (arrows).

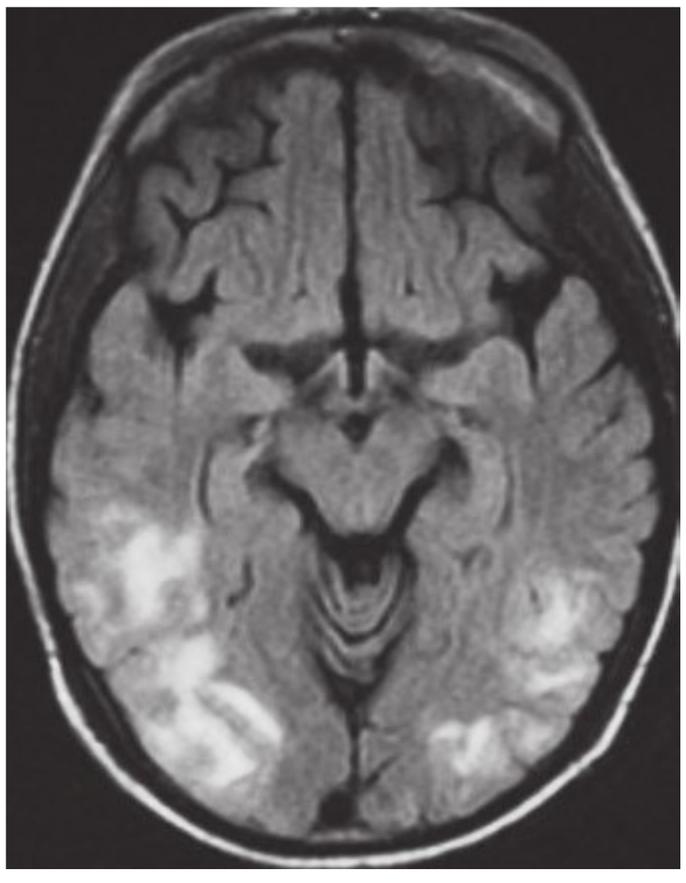

Fig. 1.229 Patient with posterior reversible encephalopathy syndrome (PRES). Poorly defined zones of high signal on axial FLAIR are seen predominantly in the subcortical white matter of the posterior portions of the temporal lobes and occipital lobes.

Table 1.4 (cont.) Multiple intra-axial lesions in the brain

Lesions	Imaging Findings	Comments
Reversible cerebral vasoconstriction syndrome	MRI: Zones of low-intermediate signal on T1-weighted imaging and high signal on T2-weighted imaging, FLAIR, and ADC in subcortical white matter, ± brainstem, ± cerebral cortex, ± gadolinium contrast enhancement. Progression to cerebral infarction can sometimes occur. CT: Foci and/or confluent zones of decreased attenuation in subcortical white matter, ± cerebral cortex, ± contrast enhancement. CTA/MRA: Segmental vasoconstriction of intracranial arteries seen as multifocal narrowing of mid and distal cerebral arteries. Conventional arteriography: Segmental vasoconstriction of intracranial arteries that resolves over 1–3 months.	Clinical and radiologic syndrome consisting of thunderclap headaches and segmental vasoconstriction that resolves by 3 months. Occurs in patients 20 to 50 years old, with mean age of 42 to 45 years, and a female/male ratio of 2.4/1. No histologic evidence of vasculitis. CSF protein content and white blood cells in CSF are typically within normal limits. Can be associated with sympathomimetic drugs, cannabis, 1–3 weeks in postpartum state, and history of migraine headaches. Transient or permanent neurologic deficits can occur, such as hemiplegia, aphasia, numbness, and visual impairment. Intra-axial hemorrhage can occur in up to 20% of cases.
Paraneoplastic syndrome	MRI: Findings include abnormal high signal on T2-weighted images and FLAIR in the limbic system, cerebral white matter, and/or brainstem. Cerebellar degeneration with atrophy is another finding. PET/CT: May show hypermetabolic activity at sites of encephalitis as well as primary malignant tumor.	Rare neurologic syndromes that result from peripheral immune-mediated responses against autoantigens expressed in tumors (occurs in < 1% of cancers of the lung, breast, ovaries, testicles, and thymus). The effects on the brain are not directly from tumor invasion or metastatic disease. Neural specific autoantibodies include ANNA-1, PCA-1, CRMP-5IgG, VGKC,complex proteins, NDMA, and GABA-B receptors. Paraneoplastic disorders involving the brain include limbic and extra-limbic encephalitis, brainstem encephalitis, and/or cerebellar degeneration. Antibodies against VKKC complex protein result in muscle weakness (Lambert-Eaton myasthenic syndrome).

Table 1.5 Multiple or diffuse lesions involving white matter in children

- Congenital Neuronal Migration Disorders
  - Lissencephaly
  - Pachygyria (nonlissencephalic cortical dysplasia)
  - Gray matter heterotopia
  - Schizencephaly (split brain)
  - Unilateral hemimegalencephaly
- Disorders of Histogenesis
  - Neurofibromatosis type 1 (NF1)
  - Tuberous sclerosis
- Inherited Metabolic Disorders Involving White Matter
  - Lysosomal disorders
    - Metachromatic leukodystrophy
    - Krabbe disease (globoid cell leukodystrophy)
    - Mucopolysaccharidoses
    - Gangliosidoses—Tay-Sachs disease and Sandhoff disease
    - Neuronal ceroid lipofuscinosis
  - Peroxisomal disorders from mutations affecting normal peroxisomal enzyme function: X-linked adrenal leukodystrophy, adrenomyeloneuropathy, adult Refsum disease, acyl-CoA oxidase 1 deficiency, and D-bifunctional protein deficiency
  - Peroxisomal disorders related to abnormal formation of peroxisomes: Zellweger syndrome (cerebrohepatorenal syndrome), infantile Refsum disease, and neonatal adrenoleukodystrophy
  - Disorders of amino acid and urea cycle metabolism: phenylketonuria, propionic acidemia, methylmalonic aciduria, homocystinuria, ornithine transcarbamylase deficiency, citrullinemia, arginosuccinic aciduria, leucinosis (maple syrup urine disease), glutaric acidemia/aciduria, others
- Other Inherited Metabolic Disorders
  - Leukoencephalopathy with vanishing white matter disease (VWMD), also referred to as childhood ataxia with central nervous system hypomyelination (CACH)
  - Megalencephalic leukodystrophy with subcortical cysts (MLC), also referred to as van der Knaap disease
  - Pelizaeus-Merzbacher disease (PMD)
  - Alexander disease
  - Canavan disease, also known as Canavan-van Bogaert-Bertrand disease
  - Cockayne syndrome
  - Kearns-Sayre syndrome
- Malformations Related to Abnormal Pial Basement Membrane Formation
  - Walker-Warburg phenotype, muscle-eye-brain phenotype, Fukuyama congenital muscular dystrophy phenotype
  - Muscle-eye-brain phenotype
  - Fukuyama congenital muscular dystrophy phenotype
- Trauma-related Lesions
  - Diffuse axonal injury
  - Non-accidental head injury (child abuse)
  - Diffuse axonal injury
  - Hypoxic-ischemic injury (HII)
- Ischemic Injury
  - Small-vessel ischemic injury: Sickle-cell disease
  - Periventricular leukomalacia
  - Hypoxic-ischemic injury in preterm neonates
  - Hypoxic-ischemic injury in term neonates
- Infections
  - Pyogenic brain abscess
  - Spirochete infection: Lyme disease
  - Fungal brain lesions
  - Encephalitis/viral infections
  - Herpes simplex
  - Cytomegalovirus (CMV)
  - Acute measles encephalitis
  - Subacute sclerosing panencephalitis from measles
  - West Nile virus
  - Cysticercosis
  - Malaria
- Inflammatory Disease: Noninfectious
  - Acute disseminated encephalomyelitis
  - Multiple sclerosis
  - Hemophagocytic lymphohistiocytosis
- Neoplasms
  - Metastases
  - Lymphoma
  - Leukemia (myeloid sarcoma, granulocytic sarcoma, chloroma)
  - Posttransplant lymphoproliferative disorder (PTLD)
- Other Abnormalities
  - Radiation injury/necrosis
  - Acute toxic leukoencephalopathy
  - Hypertensive encephalopathy (posterior reversible encephalopathy syndrome/PRES)

Table 1.5 Multiple or diffuse lesions involving white matter in children

Lesions	Imaging Findings	Comments
Congenital Neuronal Migration Disorders		
Lissencephaly (**Fig. 1.20**)	MRI: Absent or incomplete formation of gyri and sulci, with shallow sylvian fissures and "figure 8" appearance of brain on axial images, abnormally thick cortex, and gray matter heterotopia with smooth gray–white matter interface.	Severe disorder of neuronal migration (7–16 weeks of gestation) with absent or incomplete formation of gyri, sulci, and sylvian fissures. Associated with severe mental retardation and seizures, as well as early death. Other associated CNS anomalies include dysgenesis of corpus callosum, microcephaly, hypoplastic thalami, and cephaloceles.
Pachygyria (nonlissencephalic cortical dysplasia) (**Fig. 1.21**)	MRI: Thick gyri with shallow sulci in all or portions of the brain. Thickened cortex with relatively smooth gray–white interface, may have areas of signal on T2-weighted imaging in the white matter (gliosis).	Severe disorder of neuronal migration. Clinical findings related to extent of the malformation.
Gray matter heterotopia (**Fig. 1.22, Fig. 1.23**, and **Fig. 1.24**)	MRI: Laminar heterotopia appears as a band or bands of isointense gray matter within the cerebral white matter. Nodular heterotopia appears as one or more nodules of isointense gray matter along the ventricles or within the cerebral white matter.	Disorder of neuronal migration (7–22 weeks of gestation) where a collection or layer of neurons is located between the ventricles and cerebral cortex. Can have a bandlike (laminar) or nodular appearance isointense to gray matter, and may be unilateral or bilateral. Associated with seizures and schizencephaly.
Schizencephaly (split brain) (**Fig. 1.25**)	MRI: Cleft in brain extending from ventricle to cortical surface lined by heterotopic gray matter. The cleft may be narrow (closed lip) or wide (open lip).	Association with seizures, blindness, retardation, and other CNS anomalies (septo-optic dysplasia, etc). Clinical manifestations related to severity of malformation. Ischemia or insult to portion of germinal matrix before hemisphere formation.
Unilateral hemimegalencephaly (**Fig. 1.27** and **Fig. 1.28**)	MRI: Nodular or multinodular region of gray matter heterotopia involving all or part of a cerebral hemisphere, with associated enlargement of the ipsilateral lateral ventricle and hemisphere.	Neuronal migration disorder associated with hamartomatous overgrowth of the involved hemisphere.
Disorders of Histogenesis		
Neurofibromatosis type 1 (NF1) (**Fig. 1.160**)	MRI: Poorly defined zones of high signal on T2-weighted images located in cerebral and/or cerebellar white matter and globus pallidus and intermediate or slightly high signal on T1-weighted images. Typically no gadolinium contrast enhancement, associated edema, or mass effect.	Autosomal dominant disorder (1/2500 births) from mutations involving the neurofibromin gene on chromosome 17q11.2. Represents the most common type of neurocutaneous syndrome. NF1 is associated with neoplasms of the central and peripheral nervous systems (optic gliomas, astrocytomas, and plexiform and solitary neurofibromas) and skin (café-au-lait spots, axillary and inguinal freckling). Also associated with meningeal and skull dysplasias. Benign lesions with high signal on T2-weighted images can be seen in cerebral or cerebellar white matter (sometimes they are referred to as "hamartomas") and show histologic findings of spongiotic or vacuolar changes. They may regress over time, as shown by serial MRI.

Lesions	Imaging Findings	Comments
Tuberous sclerosis (**Fig. 1.161**)	MRI: Foci and/or confluent zones of high signal on T2-weighted imaging in cerebral white matter. Gadolinium contrast enhancement seen in ~ 10% CT: Foci and/or confluent zones of decreased attenuation in cerebral white matter.	Autosomal dominant disorder caused by mutations of TSC1 gene on 9q or the TSC2 gene on chromosome 16p. Prevalence of 1 in 6,000 newborns. Nonmalignant lesions in white matter associated with tuberous sclerosis, consisting of areas of demyelination and/or dysplastic white matter with high signal on T2-weighted imaging along pathways of radial glial fibers during neuronal migration. Other CNS nonmalignant lesions include cortical hamartomas (tubers), subcortical glioneuronal hamartomas, subependymal glial hamartomas (nodules), and subependymal giant cell astrocytomas. Extraneural lesions include cutaneous angiofibromas (adenoma sebaceum), subungual fibromas, visceral cysts, renal angioleiomyomas, intestinal polyps, cardiac rhabdomyomas, and pulmonary lymphangioleiomyomatosis.
Inherited Metabolic Disorders Involving White Matter		
Lysosomal disorders: metachromatic leukodystrophy, Krabbe disease, mucopolysaccharidoses, gangliosidoses, and neuronal ceroid lipofuscinosis		Lysosomes are intracellular organelles measuring from 0.1 up to 1.2 microns containing hydrolytic enzymes at a pH of 4.8, and are involved in breakdown of metabolic waste products and phagocytosed microbes. Mutations causing enzymatic defects result in toxic accumulation of metabolites, which can damage oligodendrocytes (which form myelin) and alter mitochondrial function.
Metachromatic leukodystrophy (**Fig. 1.230**)	MRI: Symmetric diffuse zones of low signal on T1-weighted images and high signal on T2-weighted images in deep cerebral/periventricular white matter, with progression of abnormal signal peripherally to involve the subcortical white matter and with late involvement of subcortical U-fibers. Initial asymmetric lesser demyelination adjacent to medullary veins may give a "tiger" pattern of relatively normal low signal on T2-weighted imaging adjacent to zones with high signal on T2-weighted imaging in the abnormal cerebral white matter, + high signal on T2-weighted imaging in cerebellar white matter, ± low signal on T2-weighted imaging in the thalami. Typically no gadolinium contrast enhancement; progressive atrophy. CT: Symmetric diffuse zones of decreased attenuation in deep cerebral/periventricular white matter and in the cerebellar white matter. No contrast enhancement.	Prevalence is 1 per 100,000, incidence is 1 in 40,000 births. Autosomal recessive disease involving the ARSA gene on chromosome 22q13.31-qter, with deficiency of arylsulfatase A in lysosomes resulting in toxic accumulation of ceramide sulfatide (myelin breakdown product) in macrophages and Schwann cells. Three subtypes depending on onset (late infantile form [80%], juvenile form, and adult form). Demyelination is seen in both the central and peripheral nervous systems. Progressive neurologic deterioration with peripheral neuropathy, gait disorders, and cognitive dysfunction, leading to death.

(continued on page 188)

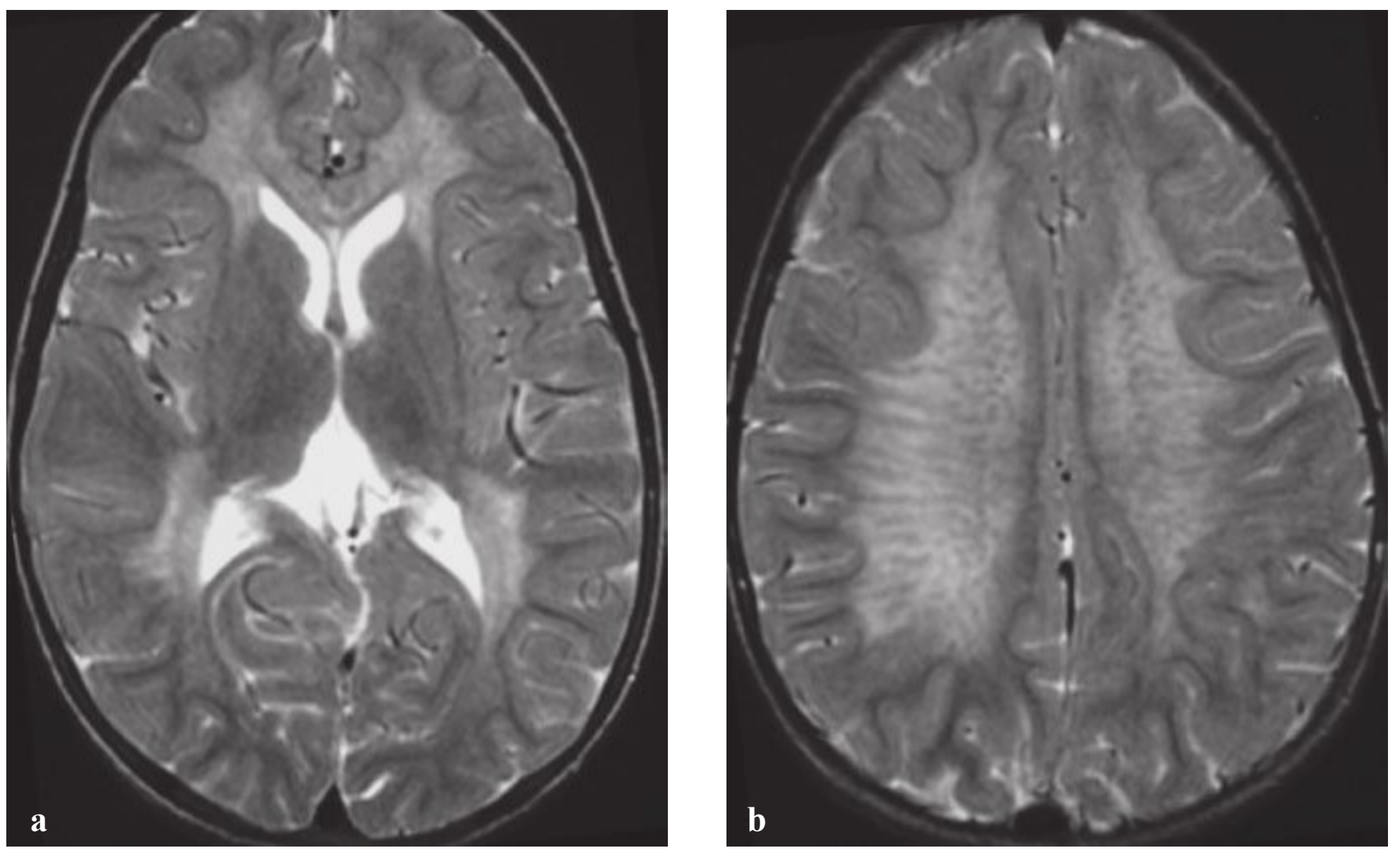

Fig. 1.230 A 4-year-old boy with metachromatic leukodystrophy. **(a)** Symmetric, diffuse zones of high signal on axial T2-weighted imaging are seen in the cerebral white matter without involvement of the subcortical U-fibers. **(b)** Asymmetric, lesser demyelination adjacent to medullary veins results in a "tiger" pattern of relatively normal low signal adjacent to zones with high signal on T2-weighted imaging of the abnormal cerebral white matter.

Table 1.5 (cont.) Multiple or diffuse lesions involving white matter in children

Lesions	Imaging Findings	Comments
Krabbe disease (globoid cell leukodystrophy) (**Fig. 1.231**)	MRI: Symmetric confluent zones of high signal on T2-weighted imaging involving the periventricular white matter, with progressive involvement toward the subcortical white matter, usually sparing the subcortical U-fibers. Cerebral white matter is involved more often than cerebellar white matter. + high signal involving corticospinal tracts on T2-weighted imaging, with decreased fractional anisotropy on diffusion tensor imaging (DTI), and usually no gadolinium contrast enhancement. Progressive cerebral atrophy, ± enlargement of cranial and spinal nerves. CT: Symmetric confluent zones of decreased attenuation involving the periventricular white matter, ± increased attenuation in thalami and basal ganglia from globoid cells, ± calcification in basal ganglia, thalami and dentate nuclei.	Incidence of 1–2 per 100,000. Also known as globoid cell leukodystrophy, Krabbe disease is an autosomal recessive disorder involving mutations of the GLAC gene on chromosome 14q24.3–32.1 causing deficiency of the lysosomal enzyme galactosylcerebroside β-galactosidase, resulting in toxic accumulation of cerebroside and psychosine in "globoid cells," which causes destruction of oligodendrocytes and myelin as well as decreased myelin production. There are three subtypes: infantile (most common), late infantile, and adult-onset. Clinical findings include seizures, psychomotor dysfunction, optic atrophy, and progressive neurologic deterioration leading to death.
Lysosomal enzyme defects: mucopolysaccharidoses (**Fig. 1.232, Fig. 1.233**, and **Fig. 1.234**)	CT: Poorly defined zones of decreased attenuation in white matter, cerebral and cerebellar atrophy, ± foci of low attenuation in corpus callosum and basal ganglia (prominent perivascular spaces). MRI: Poorly defined zones of decreased signal on T1 WI and increased signal on T2 WI and FLAIR in white matter, cerebral and cerebellar atrophy, ± foci of low signal on T1 WI in corpus callosum and basal ganglia (prominent perivascular spaces with thickened adventitia of blood vessels containing large cells filled with glycosaminoglycans), cerebral cortical/subcortical infarcts, ± macrocephaly, communicating hydrocephalus, ± meningeal thickening.	Mucopolysaccharidoses are autosomal recessive or X-linked disorders related to abnormal metabolism of mucopolysaccharides (glycosaminoglycans) in lysosomes from enzymatic defects. Hurler syndrome (MPS IH), Hurler-Scheie phenotype syndrome (MPS IH/S), and Scheie phenotype syndrome (MPS IS): autosomal recessive mutation of IDUA gene with abnormal α-L-iduronidase; Hunter syndrome (MPS type II): X-linked mutation of IDS gene causing abnormal iduronate 2-sulfatase; San*fi*lippo syndrome (MPS type III): autosomal recessive mutations causing abnormalities of one of four of the following enzymes involved in the breakdown of the glycosaminoglycan heparan sulfate: heparan N-sulfatase, α-N-acetylglucosaminidase, acetyl-CoA:α-glucosaminidine acyltransferase, or N-acetylglucosamine 6-sulfatase; Morquio syndrome (MPS type IV): autosomal recessive mutations of GALNS gene resulting in abnormal activity of galactosamine 6-sulfatase or β-galactosidase. Abnormal accumulation of metabolites—mucopolysaccharides, glycosaminoglycans—results in axonal loss and demyelination. Patients with Hurler syndrome rarely survive more than 16 years. With the severe form of Hunter syndrome, patients usually die between the ages of 8 and 15 years. With Sanfilippo syndrome, patients often die by the third decade.
Lysosomal enzyme defects: Gangliosidoses—Tay-Sachs disease and Sandhoff disease (**Fig. 1.235**)	CT: Increased, slightly high attenuation in the thalami and decreased attenuation in the cerebral white matter, followed by progressive cerebral and cerbellar atrophy. MRI: Increased signal on T2-weighted imaging and FLAIR in the basal ganglia, cerebral white matter, and posteromedial thalami (Tay-Sachs disease). No gadolinium contrast enhancement. Magnetic resonance spectroscopy: Decreased NAA/creatine ratio, elevated ratios of choline/creatine and myoinositol/creatine consistent with neuronal loss and gliosis.	Functional defects (usually autosomal recessive) involving lysosomal catabolic enzymes. Tay-Sachs disease: Functional N-acetyl hexosaminidase A deficiency from mutation of HEXA gene on chromosome 15q-23–24. Carrier frequency in Ashkenazi Jews is 1 in 30, versus 1 in 380 for other groups. After 6 months, neurologic deterioration begins and progresses for the next 2 years, leading to death by 3–4 years. Sandho*ff* disease: Functional N-acetyl hexosaminidase A and B deficiency from mutation of HEXB gene on chromosome 5q-13.

(continued on page 191)

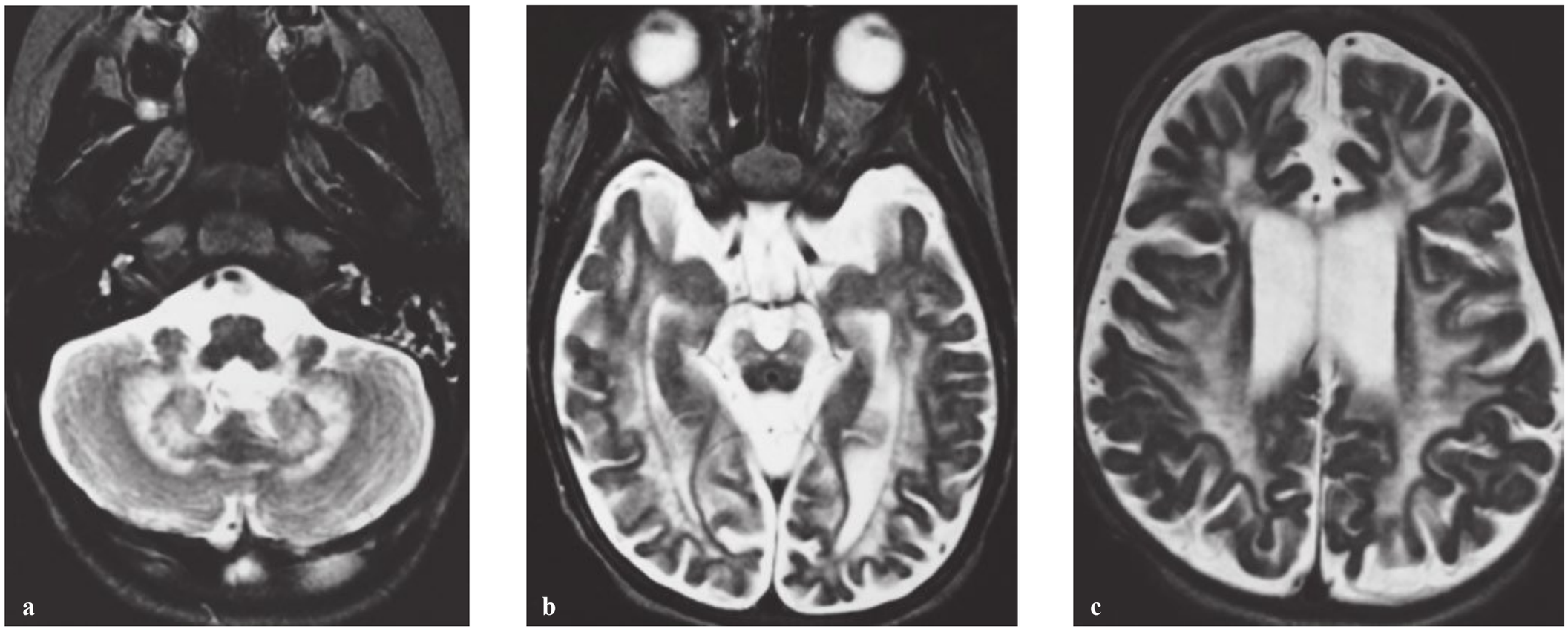

Fig. 1.231 A 4-year-old female with Krabbe disease. **(a–c)** Symmetric confluent zones of high signal on T2-weighted imaging are seen in the cerebral and cerebellar white matter, with progressive involvement toward the subcortical white matter. Also seen is abnormal high signal in the brainstem, including the corticospinal tracts. Prominent atrophy is seen in the brain and brainstem.

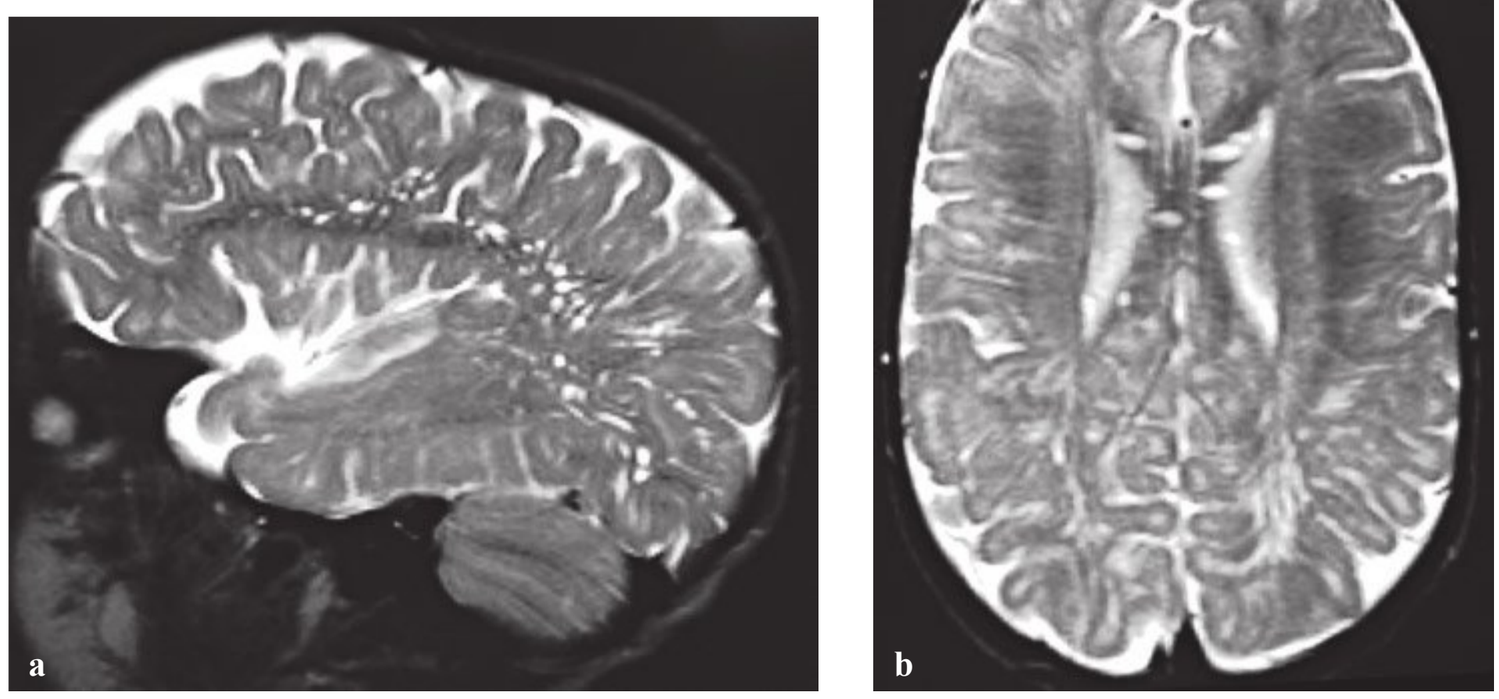

Fig. 1.232 A 2.5-year-old child with Hurler syndrome (MPS IH) shows foci of high signal on **(a)** sagittal and **(b)** axial T2-weighted imaging in the periventricular white matter and corpus callosum. Diffuse brain atrophy is seen.

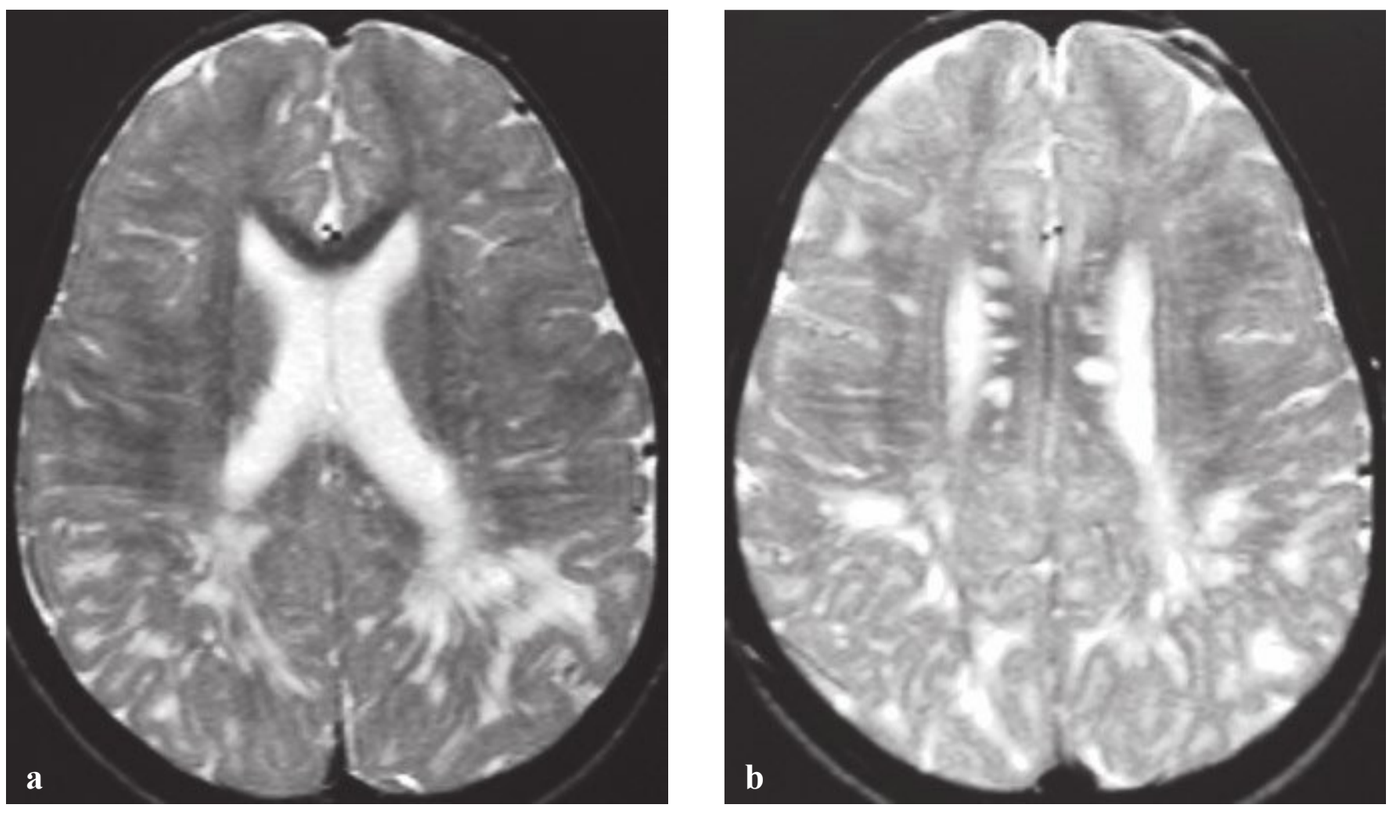

Fig. 1.233 **(a,b)** A 4-year-old child with Hunter syndrome (MPS type II) who has poorly defined zones of high signal on axial T2-weighted imaging in cerebral white matter, as well as high-signal foci representing prominent perivascular spaces.

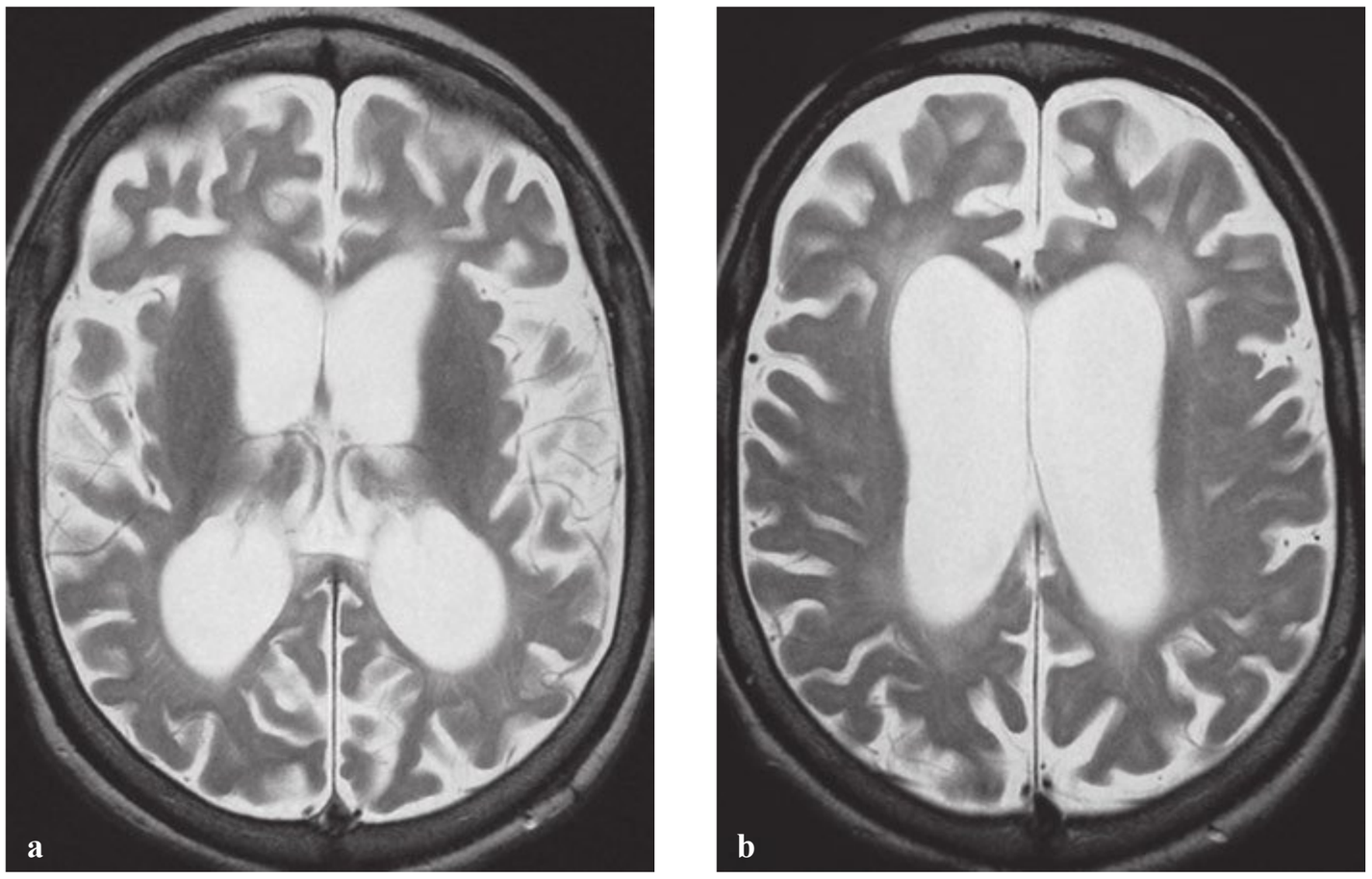

Fig. 1.234 **(a,b)** A 6-year-old girl with Sanfilippo syndrome (MPS type III). Axial T2-weighted imaging shows poorly defined zones of high signal in the periventricular cerebral white matter, as well as prominent atrophic changes.

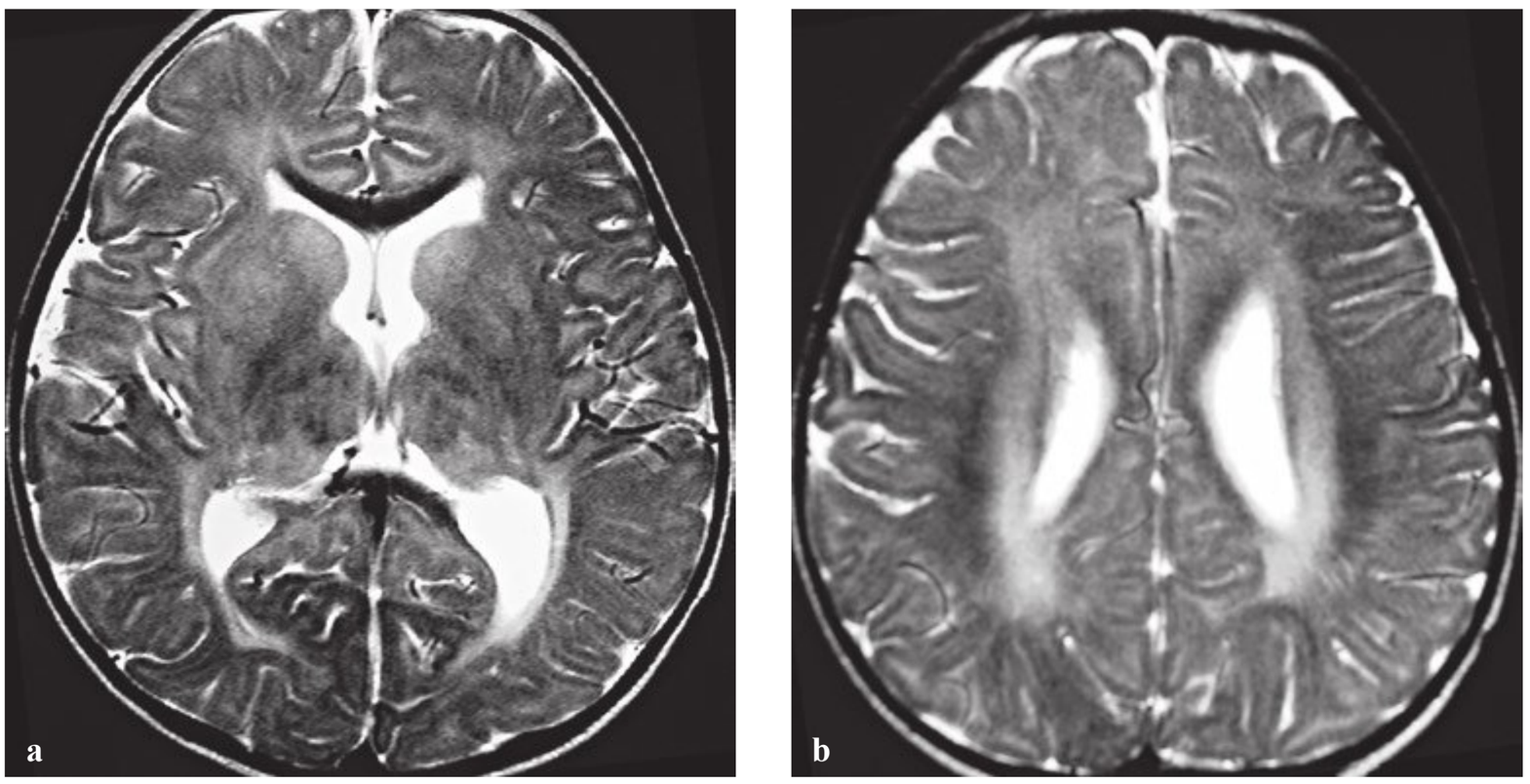

Fig. 1.235 **(a,b)** An 18-month-old female with Tay-Sachs disease. Poorly defined zones with abnormal high signal on axial T2-weighted imaging are seen in the periventricular white matter. Abnormal high signal is also seen in the caudate nuclei, putamina, and posterior thalami.

Table 1.5 (cont.) Multiple or diffuse lesions involving white matter in children

Lesions	Imaging Findings	Comments
Lysosomal enzyme defects: Neuronal ceroid lipofuscinosis (**Fig. 1.236**)	CT: Progressive cerebral and cerebellar atrophy, ± zones of decreased attenuation in white matter. MRI: Progressive cerebral and cerebellar atrophy, ± zones of increased signal on T2-weighted imaging and FLAIR in the periventricular white matter, decreased signal on T2-weighted imaging in the globi pallidi and thalami, and typically no gadolinium contrast enhancement. Increases in ADC values occur at involved sites after 5 years.	Neuronal ceroid lipofuscinosis is a progressive type of neurodegenerative encephalopathy in children (1/25,000 births; incidence of 1 in 10,000 in the United States and Europe) secondary to the toxic cytosomal accumulation of an autofluorescent pigment referred to as lipofuscin. Results in progressive cerebral and cerebellar atrophy. Clinical findings include retinal degeneration in the pediatric types, epilepsy, and movement disorders. Associated with nine mutations involving the CLN gene. Congenital type: mutations involving CLN10 gene on chromosome 11p15. Infantile type (Haltia-Santavuori disease): mutations involving the CLN1 gene on 1p32. Late-infantile type (Jansky-Bielschowsky disease): mutations involving genes CLN1 to CLN8. Juvenile type (Batten disease): mutations involving CLN1, CLN3, or CLN5. Adult type (Kufs disease): mutations involving CLN1, CLN4, or CLN6. Mutations result in absence of cathepsin D, PPT1, or TPP1 enzyme activities.
Peroxisomal disorders resulting from mutations affecting normal peroxisomal enzyme function: X-linked adrenoleukodystrophy, adrenomyeloneuropathy, adult Refsum disease, acyl-CoA oxidase 1 deficiency, and D-bifunctional protein deficiency. Peroxisomal disorders related to abnormal formation of peroxisomes: Zellweger syndrome (cerebrohepatorenal syndrome), infantile Refsum disease, and neonatal adrenoleukodystrophy		Disorders involving peroxisomes, organelles ranging in size from 0.2 to 1 micron and which contain enzymes that metabolize long-chain fatty acids by β-oxidation, branched-chain fatty acids, D-amino acids, and polyamines. Biosynthesis of plasmalogens (ether phospholipids), which are involved in myelin formation, occurs in peroxisomes. Normal organelle function is needed for cellular metabolism, growth, and development.

(continued on page 192)

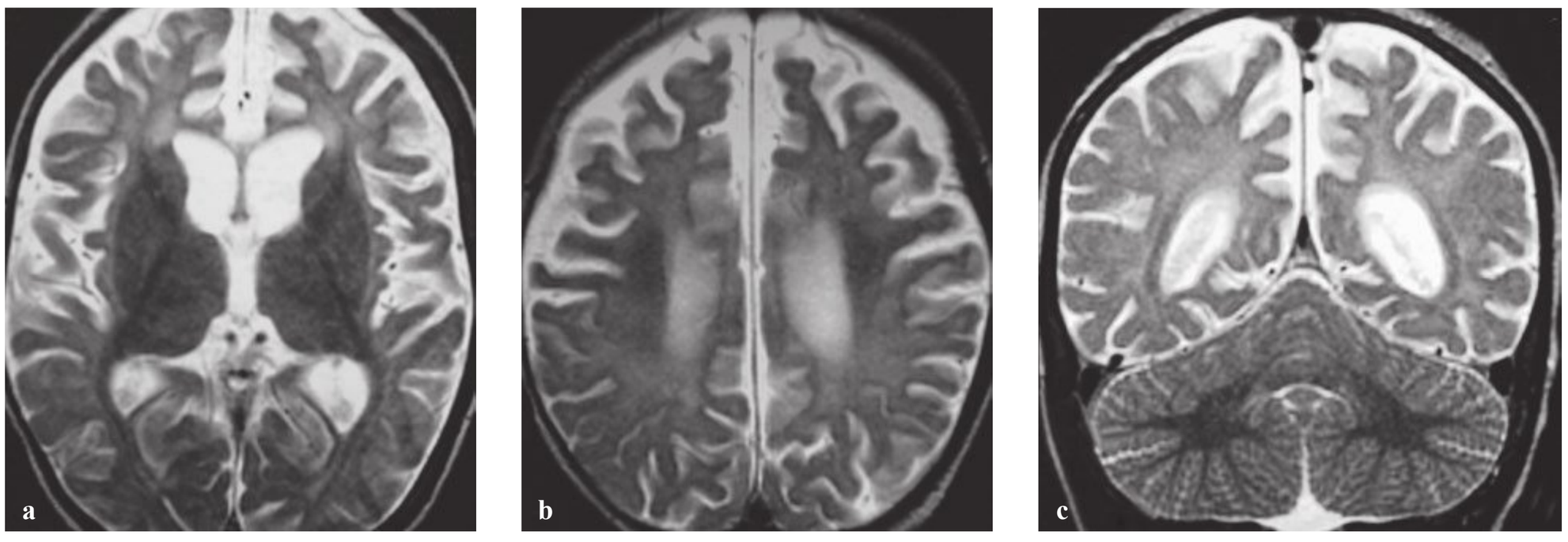

Fig. 1.236 A 19-month-old male with neuronal ceroid lipofuscinosis. Poorly defined zones of high signal on **(a,b)** axial and **(c)** coronal T2-weighted imaging are seen in the periventricular white matter, with decreased signal in the thalami. Prominent cerebral atrophy is also seen.

Table 1.5 (cont.) Multiple or diffuse lesions involving white matter in children

Lesions	Imaging Findings	Comments
X-linked adrenoleukodystrophy (**Fig. 1.237** and **Fig. 1.238**)	MRI: Diffuse abnormal high signal on T2-weighted imaging, usually with corresponding low signal on T1-weighted imaging in parieto-occipital white matter and corpus callosum (85%), and progression of signal abnormality to the remaining cerebral white matter. Less common variant involves the frontal white matter initially (15%), ± gadolinium contrast enhancement at regions of active demyelination/inflammation, ± high signal on T2-weighted imaging in lateral geniculate bodies and corticospinal tracts. Adrenomyeloneuropathy: Findings in cerebral white matter are less prominent than in pediatric ALD. CT: Zones with decreased attenuation, usually in parieto-occipital periventricular white matter and corpus callosum, progression of abnormality to the remaining cerebral white matter, ± contrast enhancement at regions of active demyelination/inflammation.	Incidence: 1 in 16,800 males. X-linked adrenoleukodystrophy (ALD) results from mutations of the ABCD1 gene on chromosome Xq28, with functional deficiency of the peroxisomal ATP-binding cassette trans-membrane transporter ALDP that would normally transport very-long-chain fatty acids (VLCFA) (C24:0, C26:0) into peroxisomes for degradation. Lack of this normal membrane protein results in abnormal toxic accumulation of the VLCFA in tissues, including the brain, with resultant demyelination, inflammation, gliosis, and necrosis. In the childhood cerebral form, clinical onset occurs from 3 to 10 years with psychomotor retardation, seizures, hypotonia, facial dysmorphism, and progressive deterioration. There are also other subtypes: neonatal-onset and adult-onset. X-linked ALD in adults (adrenomyeloneuropathy) has a slow, progressive clinical course, with spastic paraparesis, myelopathy with altered vibration sense in the lower extremities, and sphincter dysfunction with voiding problems.
Zellweger syndrome (**Fig. 1.239**)	MRI: Poorly defined zones with abnormal high signal on T2-weighted imaging, usually with corresponding low signal on T1-weighted imaging in cerebral white matter. Abnormal gyral patterns—pachygyria (usually frontoparietal) and/or polymicrogyria (perisylvian or generalized)—and germinolytic cysts in the caudate nuclei that protrude into the ventricles. CT: Zones with decreased attenuation in cerebral white matter, pachygyria.	Incidence is 1 per 100,000 live births. Autosomal recessive disorder with abnormal formation of peroxisomes from mutations of one of the peroxisomal assembly (PEX) genes. Zellweger syndrome spectrum includes: Zellweger syndrome, neonatal adrenoleukodystrophy, and infantile Refsum disease. Clinical findings include hypotonia, seizures, facial dysmorphism (hypertelorism, large fontanelles, wide sutures), psychomotor retardation, cataracts, retinitis pigmentosa, hepatomegaly, and liver fibrosis.

(continued on page 194)

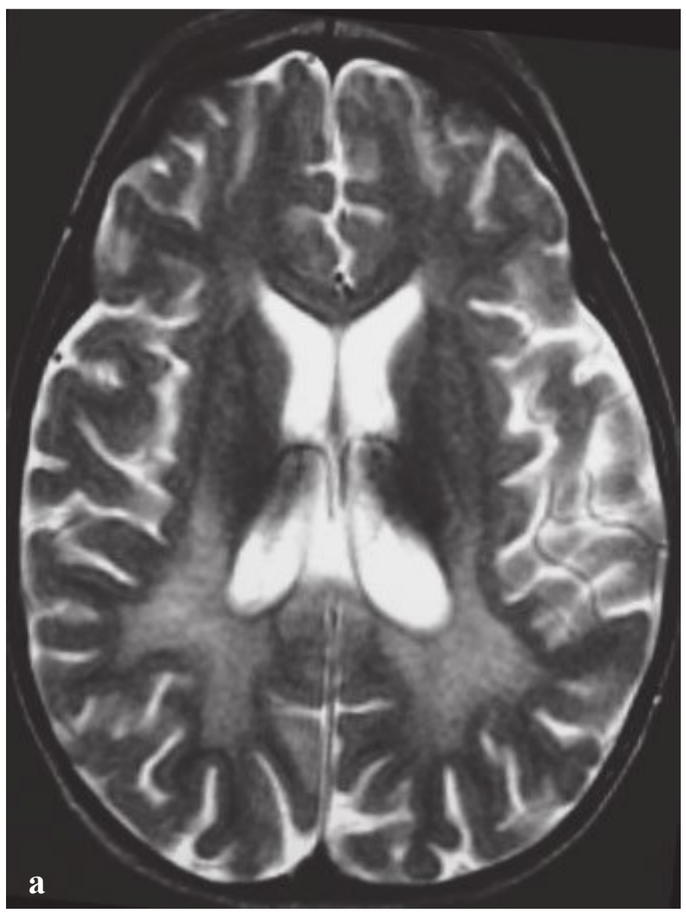

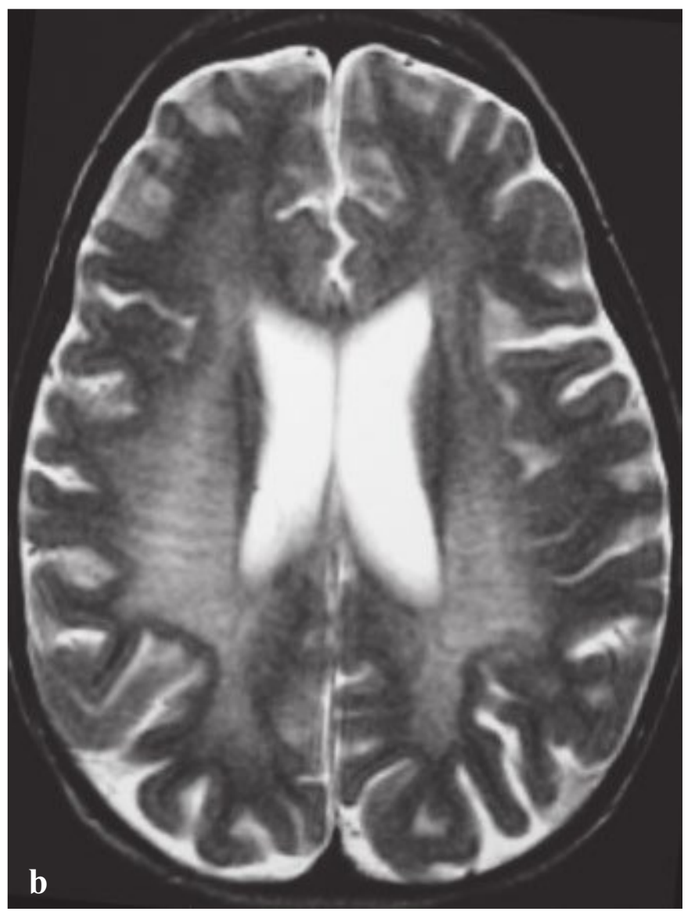

Fig. 1.237 (a,b) A 2-year-old male with X-linked adrenoleukodystrophy. Abnormal high signal on axial T2-weighted imaging is seen in the parieto-occipital white matter and corpus callosum in association with mild-moderate cerebral atrophy.

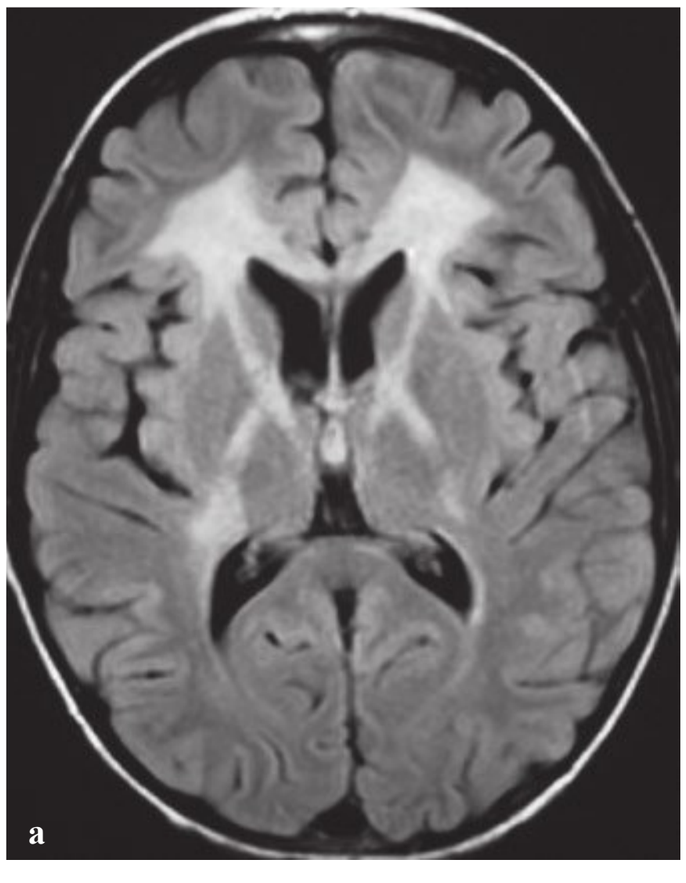

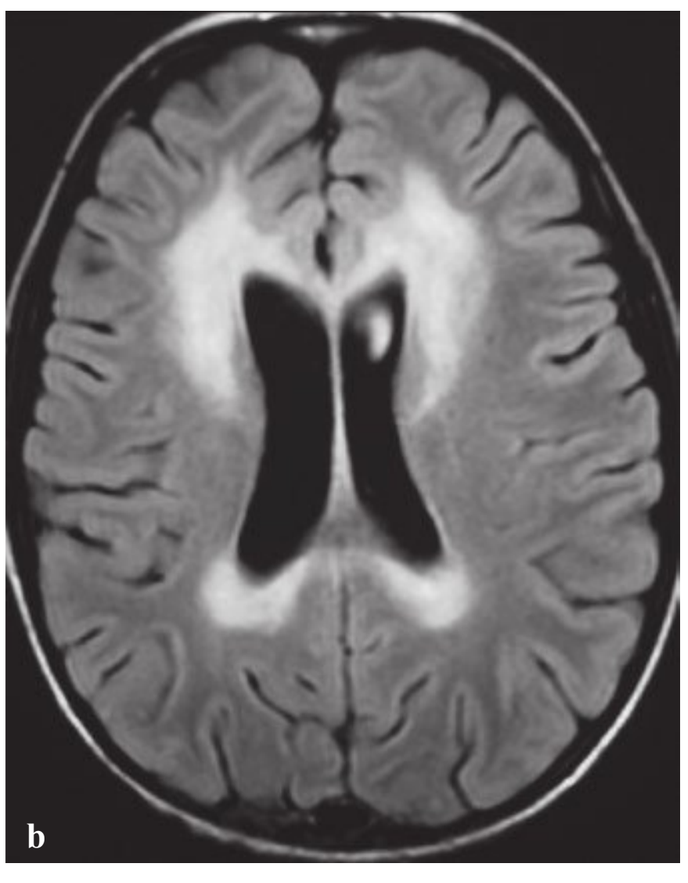

Fig. 1.238 (a,b) An 11-year-old male with X-linked adrenoleukodystrophy (anterior predominant demyelination type). Abnormal high signal on axial FLAIR is seen in the periventricular white matter of both frontal lobes and internal capsules, and to a lesser extent the parieto-occipital white matter.

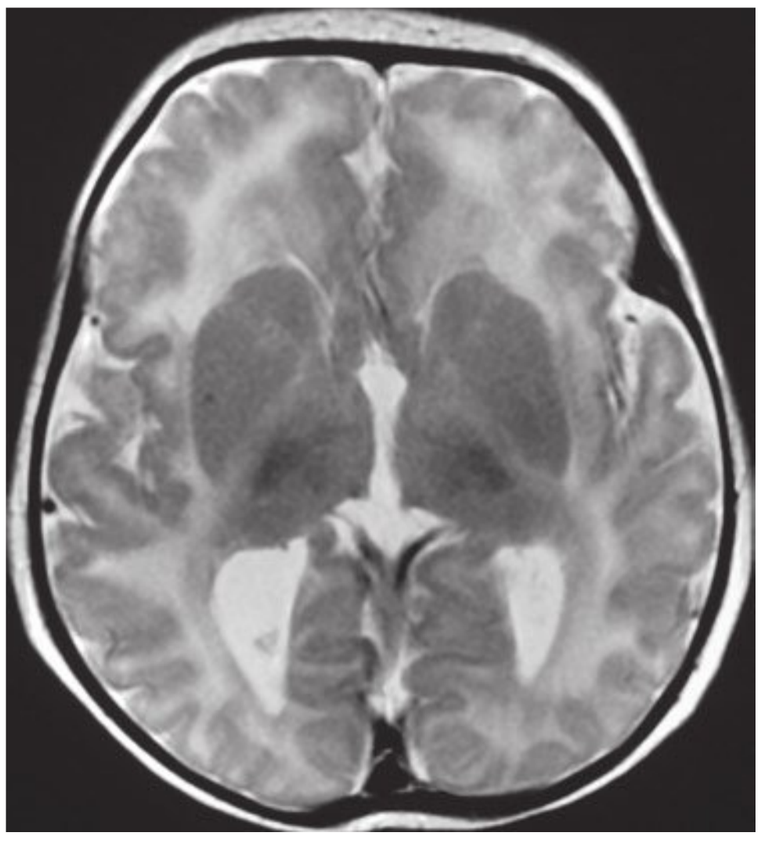

Fig. 1.239 A 1-month-old female with Zellweger syndrome. Axial T2-weighted imaging shows poorly defined zones with abnormal high signal in the cerebral white matter associated with abnormal gyral patterns, including polymicrogyria.

Table 1.5 (cont.) Multiple or diffuse lesions involving white matter in children

Lesions	Imaging Findings	Comments
Disorders of amino acid and urea cycle metabolism: phenylketonuria, propionic acidemia, methylmalonic aciduria, homocystinuria, ornithine transcarbamylase deficiency, citrullinemia, arginosuccinic aciduria, leucinosis (maple syrup urine disease), glutaric acidemia/aciduria, others (**Fig. 1.240, Fig. 1.241**, and **Fig. 1.242**)	CT: Zones with decreased attenuation in cerebral and/or cerebellar white matter, ± zones with decreased attenuation in globi pallidi, putamina, caudate nuclei, thalami, and brainstem. MRI: Zones with increased signal on T2-weighted imaging and FLAIR in cerebral and/or cerebellar white matter, ± zones with increased signal on T2-weighted imaging in globi pallidi, putamina, caudate nuclei, thalami, and brainstem. Restricted diffusion can be seen with metabolic decompensation, ketoacidosis, and ischemia.	Autosomal recessive or X-linked disorders involving defective enzymes regulating amino acid metabolism and mitochondrial function. These disorders can cause toxic accumulation of metabolites resulting in mitochondrial dysfunction, ketoacidosis, and/or hyperammonemia, as well as alteration of myelin formation. Phenylketonuria: autosomal recessive mutation of gene causing deficiency of phenylalanine hydroxylase with toxic accumulation of phenyalanine. Propionic acidemia: autosomal recessive mutation causing deficiency of propionyl-CoA carboxylase, with toxic accumulation of propionate, 3-hydroxybutyrate, methylcitrate, and 3-hydroxypropionate. Methylmalonic aciduria/ homocystinuria: autosomal recessive mutations causing lack of normal conversion of methylmalonyl-CoA to succinyl-CoA via defects of the apoenzyme methylmalonyl-CoA mutase or deficiency of the coenzyme adenosylcobalamine, resulting in accumulation and urinary excretion of methylmalonic acid, methylcitric acid, and 3-hydroxypropionic acid. Ornithine transcarbamylase deficiency: X-linked mutation causing deficiency of ornithine transcarbamylase, which results in toxic accumulation of ammonia. Leucinosis (maple syrup urine disease): autosomal recessive mutation involving the a-ketoacid dehydrogenase complex, which results in toxic accumulation of branched-chain amino acids (leucine, isoleucine, and valine). Glutaric acidemia/ aciduria type 1: autosomal recessive mutation causing deficiency of glutaryl-CoA dehydrogenase, with toxic accumulation of glutaric acid. Normal activity is needed for metabolism of lysine, hydroxylysine, and tryptophan. Glutaric acidemia/aciduria type 2: autosomal recessive mutation causing deficiency of acyl coenzyme A dehydrogenase activity, resulting in impairment in mitochondrial electron transport related to electron transport flavoprotein, or ubiquinone oxidoreductase.

(continued on page 196)

Fig. 1.240 A 2-week-old female with leucinosis (maple syrup urine disease) and metabolic decompensation. **(a,c)** Abnormal high signal on axial T2-weighted imaging is seen in the pons, middle cerebellar peduncles, cerebellar white matter, and cerebral peduncles, with **(b)** corresponding restricted diffusion on axial DWI.

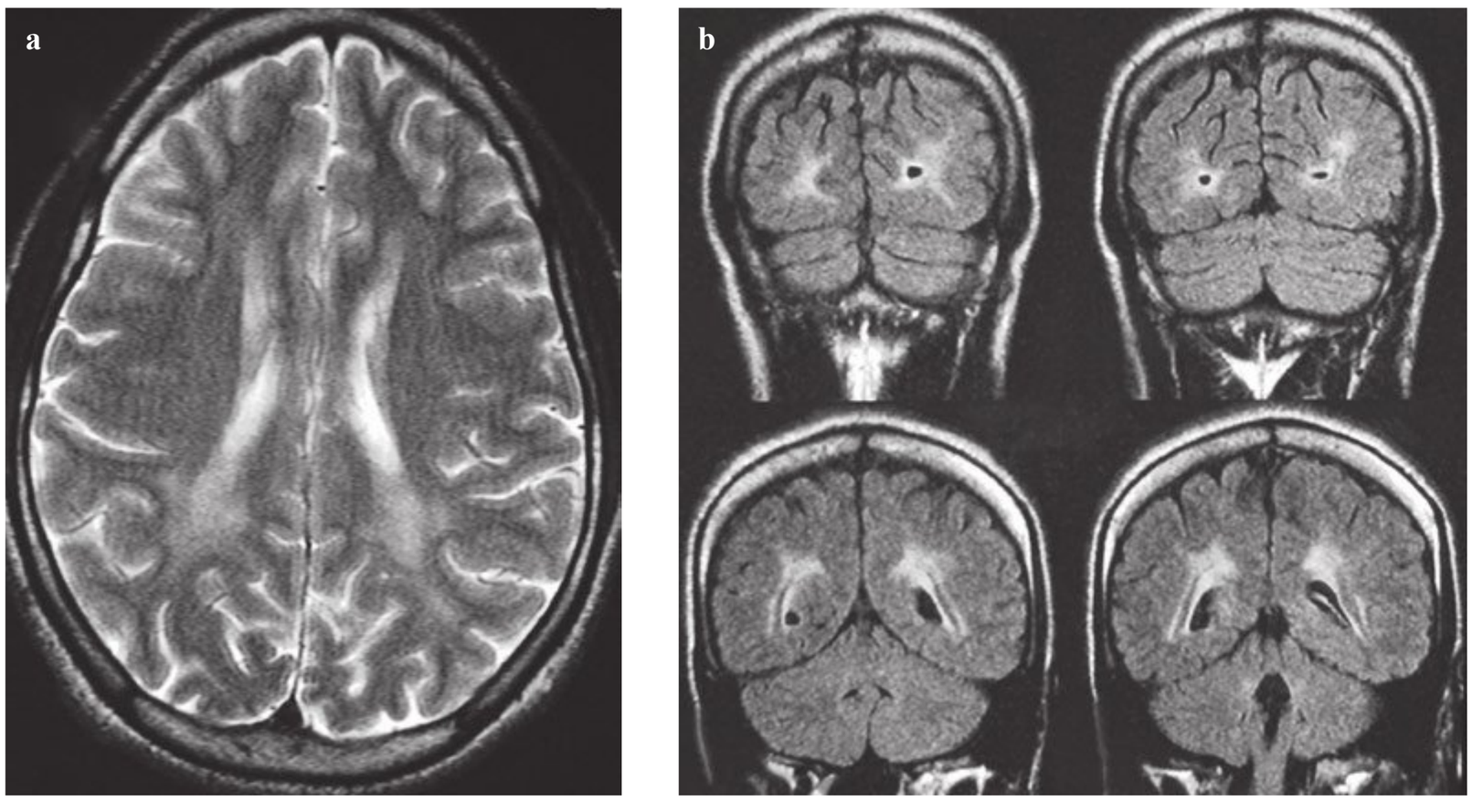

Fig. 1.241 A 22-year-old man with phenylketonuria. **(a)** Axial T2-weighted imaging and **(b)** coronal FLAIR show poorly defined zones with high signal in the periventricular white matter bilaterally.

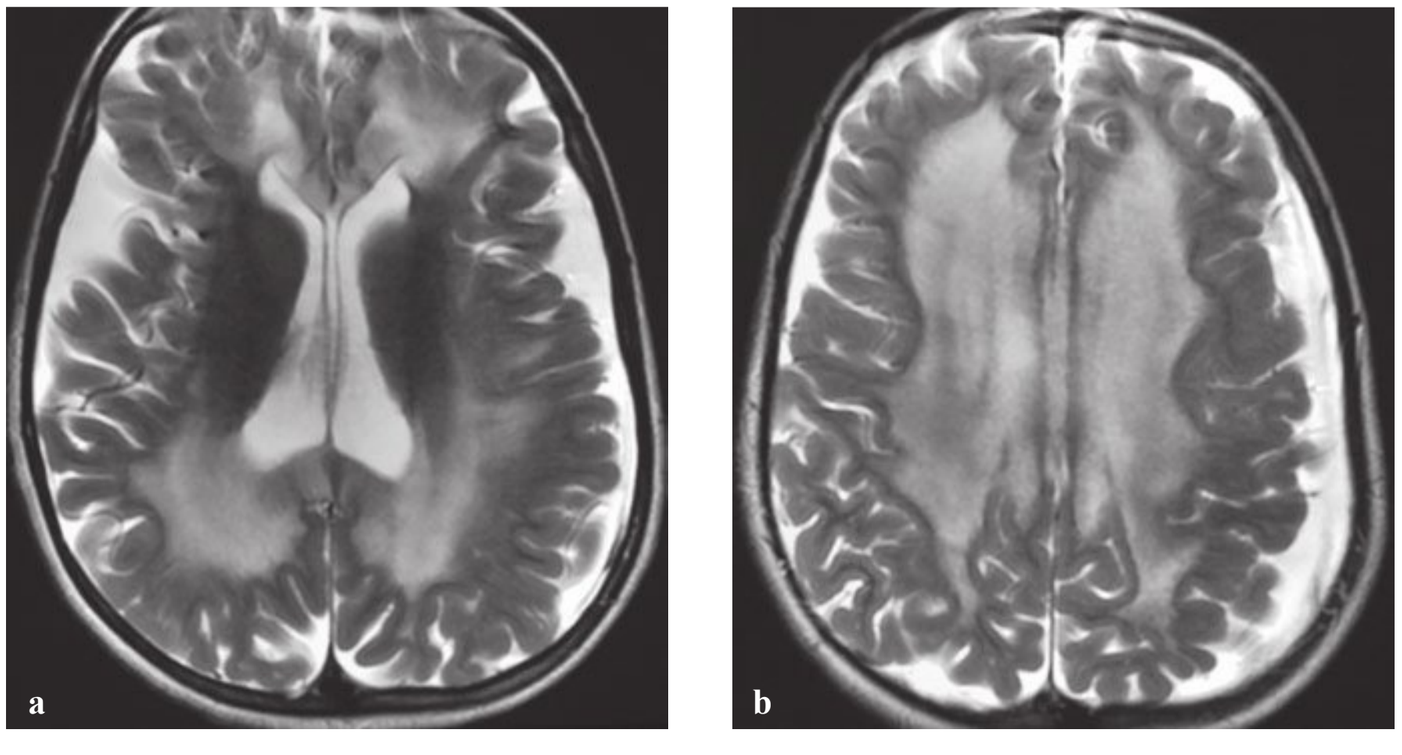

Fig. 1.242 An 11-year-old female with glutaric acidemia/aciduria type 1. **(a,b)** Expanded subarachnoid spaces in the middle cranial fossa with enlarged sylvian fissures and bilateral frontal lobe hypoplasia/atrophy are seen on axial T2-weighted imaging. Abnormal increased signal is also seen in the cerebral white matter secondary to dysmyelination/demyelination from neurotoxic effects of abnormal metabolites.

Table 1.5 (cont.) Multiple or diffuse lesions involving white matter in children

Lesions	Imaging Findings	Comments
Other Inherited Metabolic Disorders		
Leukoencephalopathy with vanishing white matter disease (VWMD), also referred to as childhood ataxia with central nervous system hypomyelination (CACH) (**Fig. 1.243**)	MRI: Diffuse abnormal high signal on T2-weighted imaging and FLAIR in the cerebral white matter and sparing the cerebral cortex, basal ganglia, and thalami. Limited involvement of the cerebellum initially. Findings secondary to vacuolation and loss of myelin and degenerative cystic changes. Eventual progressive disappearance of the white matter, which is replaced by fluid. CT: Symmetric diffuse zones of decreased attenuation involving the cerebral white matter, with progressive involvement of the subcortical white matter. Cerebral white matter is involved more often than cerebellar white matter. There is no contrast enhancement; there is progressive cerebral and cerebellar atrophy.	Leukoencephalopathy with vanishing white matter disease (VWMD), also referred to as childhood ataxia with central nervous system hypomyelination (CACH), is an autosomal recessive disease related to mutations in genes encoding the translation initiation factor eIF2B, which is involved in initiation of translation of mRNA in association with ribosomes. eFI2B has five subunits encoded by genes on five different chromosomes (12q24.3, 14q24, 1p34.1, 2p23.3, and 3q27). Mutations of any one of these genes can cause VWMD, with inhibition of protein synthesis. Clinical presentation is between 2 and 6 years of age, with progressive neurologic deterioration, cerebellar ataxia, mild spasticity, mild mental decline, and epilepsy, ± vision loss. Stress (trauma, infection, etc.) can cause episodes of rapid neurologic decline.
Megalencephalic leukodystrophy with subcortical cysts (MLC), also referred to as van der Knaap disease (**Fig. 1.244**)	MRI: Large brain with diffuse abnormal high signal on T2-weighted imaging and FLAIR in the cerebral white matter but sparing the cerebral cortex, basal ganglia, and thalami, ± signal changes involving the corpus callosum and internal capsules. Limited involvement of the cerebellum initially. Findings secondary to vacuolation and loss of myelin, and degenerative cystic changes. Eventual progressive disappearance of the white matter, which is replaced by fluid. Subcortical cysts typically develop in the anterior temporal lobes, as well as in the frontal and parietal lobes. Magnetic resonance spectroscopy can show reduced N-acetylaspartate (NAA) and NAA/Cr ratio. CT: Symmetric diffuse zones of decreased attenuation involving the cerebral white matter, with progressive involvement of the subcortical white matter. Cerebral white matter is involved more often than cerebellar white matter. There is no contrast enhancement; there is progressive cerebral and cerebellar atrophy.	Also referred to as leukoencephalopathy with macrocephaly, MLC is a rare autosomal recessive disease with slow progressive clinical deterioration in the first two decades. The majority of cases (75%) are caused by mutations of the MLC1 gene on chromosome 22qtel, which normally encodes a membrane protein at astrocyte–astrocyte junctions. Another mutation associated with MLC involves the HEPCAM gene, which encodes a glial adhesion protein (GLIALCAM). Mutated genes result in intramyelinic vacuolation and fibrillary astrogliosis.
Pelizaeus-Merzbacher disease (PMD) (**Fig. 1.245**)	MRI: Heterogeneneous, diffuse, or "patchy-tigroid' patterns of abnormal high signal on T2-weighted imaging in cerebral white matter, initially involving the subcortical white matter, with progression to the other remaining white matter, including the internal capsules, ± involvement of cerebellum and brainstem (pons, pyramidal tracts). No contrast enhancement; progressive cerebral and cerebellar atrophy with cavitary changes in the white matter. Diffusion-weighted imaging: Involved white matter can have elevated ADC values. Magnetic resonance spectroscopy: Reduced levels of N-acetylaspartate (NAA) and choline have been observed. CT: Heterogeneneous or diffuse decreased attenuation in cerebral white matter, initially involving the subcortical white matter with progression to the other remaining white matter, ± involvement of cerebellum and brainstem. There is no contrast enhancement; there is progressive cerebral and cerebellar atrophy.	Incidence is 1–10 per million. PMD is an X-linked (type 1) or autosomal recessive (type 2) leukodystrophy. There are five subtypes, characterized by deficiency or abnormality of major myelin proteins. Mutations (gene duplication, insertions, deletions, and missense mutations) of the PLP1 gene on chromosome Xq22 affect the production of proteolipid protein (PLP) and its isoform DM20, which results in lack of myelin and apoptosis of oligodendrocytes in the brain and brainstem. Cranial and peripheral nerves are often myelinated. Presentation is during the neonatal period for connatal PMD (type 2); for the most common, classic type of PMD (type 1), presentation is during the first year of life. Patients with the classic type have abnormal eye movements, nystagmus, hypotonia, delayed psychomotor development, growth retardation, ataxia, and seizures, neurologic often occurs by 10–12 years. With the connatal type, severe hypotonia, nystagmus, feeding impairment, and failure to meet developmental milestones begin in the neonatal period, with progressive deterioration leading to death in the first decade. As an X-linked disease, PMD affects males, but female carriers exhibit features of the disease as well.

(continued on page 198)

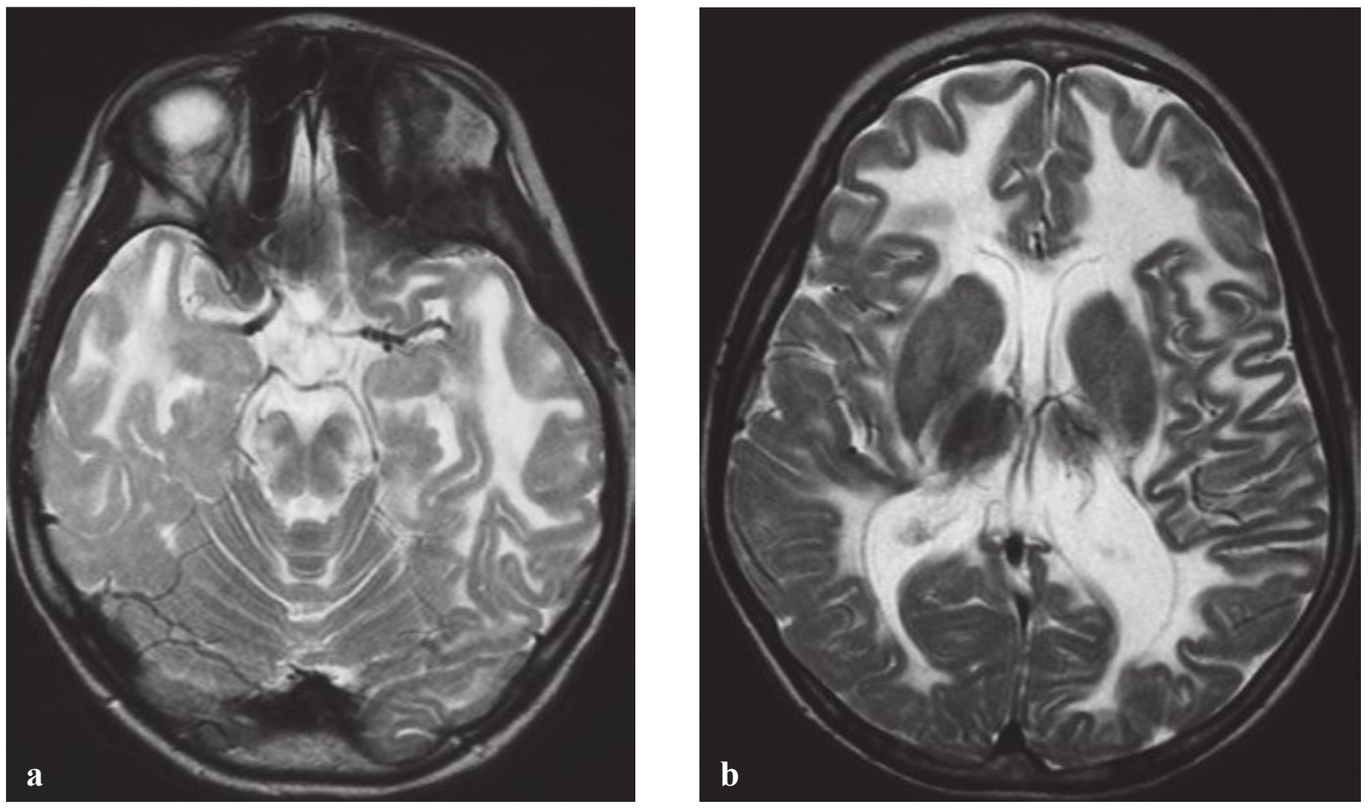

Fig. 1.243 A 2-year-old male with leukoencephalopathy with vanishing white matter disease (VWMD). **(a,b)** Diffuse abnormal high signal on axial T2-weighted imaging is seen in the cerebral white matter, sparing the cerebral cortex, basal ganglia, and thalami.

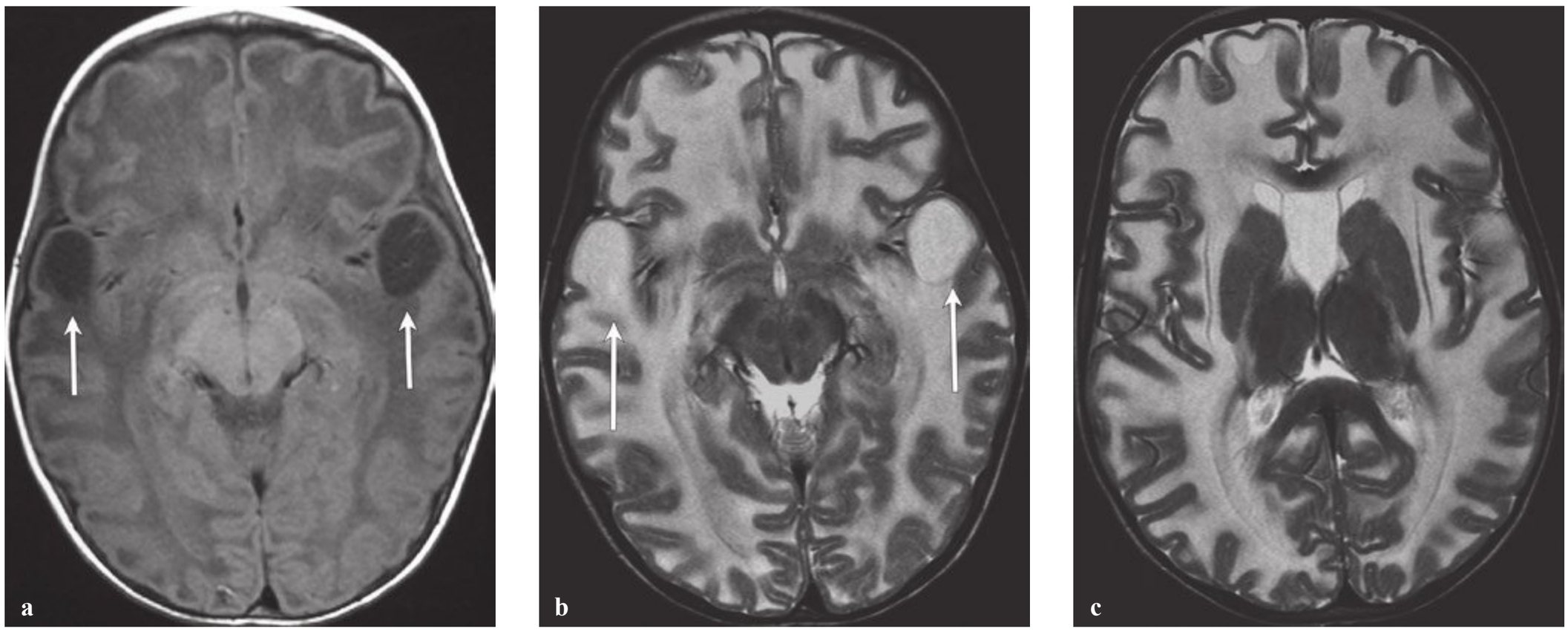

Fig. 1.244 A 10-month-old male with an enlarged brain from megalencephalic leukodystrophy with subcortical cysts (MLC). **(a)** Subcortical cysts are seen in the anterior portions of both temporal lobes, which have low signal on axial T1-weighted imaging (arrows) and **(b)** high signal on axial T2-weighted imaging (arrows). **(b,c)** Diffuse abnormal high signal on T2-weighted imaging is seen in the cerebral white matter, sparing the cerebral cortex, basal ganglia, and thalami. Limited abnormal signal changes are seen in the corpus callosum and internal capsules.

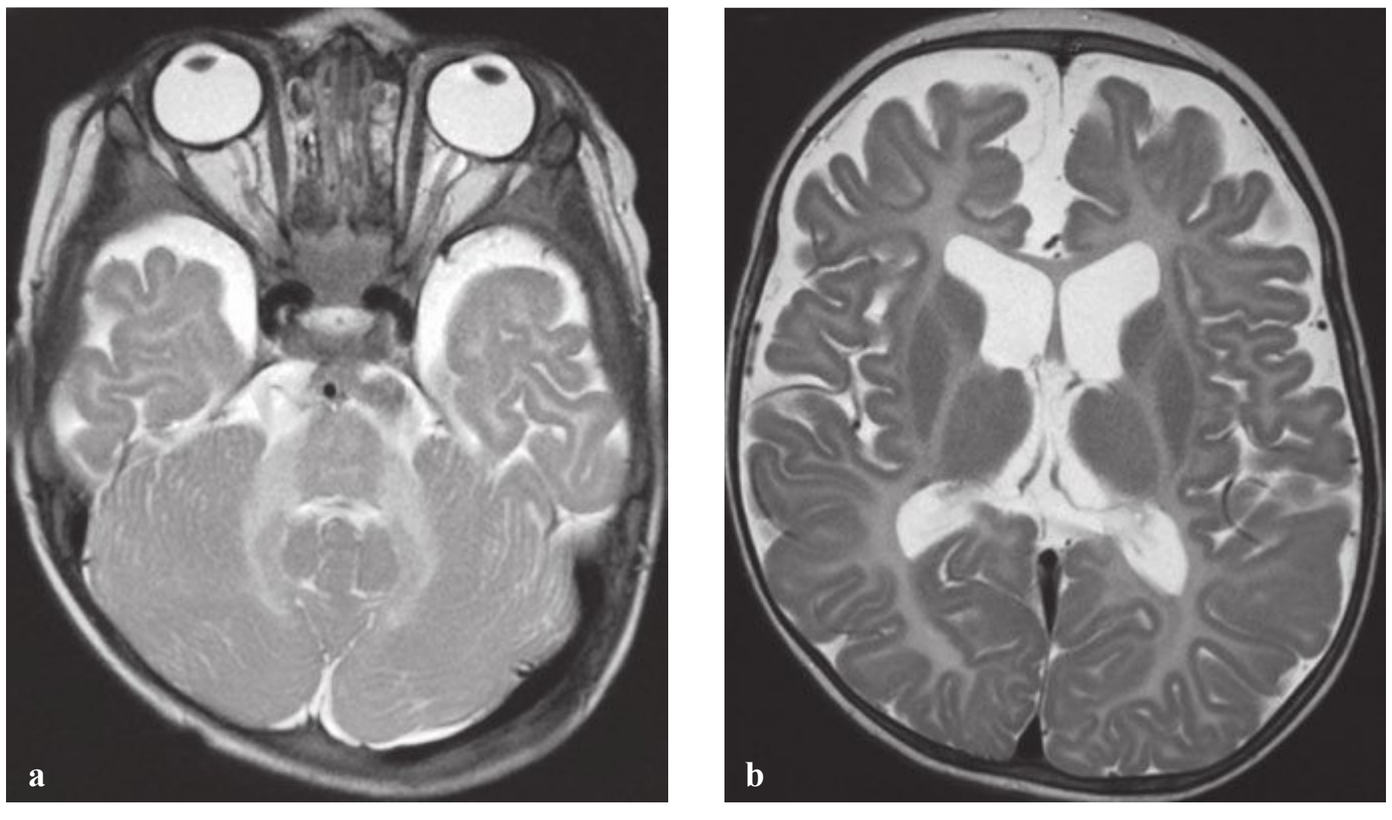

Fig. 1.245 A 10-month-old male with Pelizaeus-Merzbacher disease. **(a,b)** Diffuse abnormal high signal on axial T2-weighted imaging is seen in the cerebral and cerebellar white matter, internal capsules, brainstem, and middle cerebellar peduncles. Also seen is moderate brain atrophy.

Table 1.5 (cont.) Multiple or diffuse lesions involving white matter in children

Lesions	Imaging Findings	Comments
Alexander disease (**Fig. 1.246** and **Fig. 1.247**)	MRI: High signal on T2-weighted imaging and decreased signal on T1-weighted imaging involving the peripheral frontal white matter, including the subcortical U-fibers, with progressive involvement of the white matter posteriorly and centrally (internal and external capsules), ± caudate nuclei, brainstem, medulla, middle cerebellar peduncles, and dentate nuclei. Periventricular rims of high signal on T1-weighted imaging and low signal on T2-weighted imaging may be seen surrounding the frontal horns of the lateral ventricles. Gadolinium contrast enhancement occurs at sites of active demyelination in involved white matter—usually periventricular locations, ± caudate nuclei and brainstem. Increased size and weight of brain tissue initially. ADC values of involved white matter may be increased. Magnetic resonance spectroscopy can show elevated myoinositol and increased choline from astrocytosis and demyelination, increased lactate from infiltrating macrophages, and decreased N-acetylaspartate from neuroaxonal degeneration. CT: Zones with decreased attenuation involving the peripheral frontal white matter, with progressive involvement of the white matter posteriorly and centrally (internal and external capsules). Can show a marginal pattern of contrast enhancement.	Rare, sporadic leukoencephalopathy also referred to as fibrinoid leukoencephalopathy. The infantile type (most common form) presents in the first 2 years of life with macrocephaly and progressive psychomotor retardation, usually resulting in death during early childhood 8 years after diagnosis. Other, less severe types are the juvenile (onset 4 to 14 years) and adult forms. Caused by mutations of a gene on chromosome 17q21 resulting in abnormal function and levels of the intermediate filament protein (GFAP) in astrocytes. Histopathologic findings include numerous Rosenthal fibers (elongated or round eosinophilic structures 50 microns or less in length) arrayed adjacent to blood vessels within white matter, aggregates of enlarged fibrillary astrocytes, and progressive loss of myelin.

(continued on page 200)

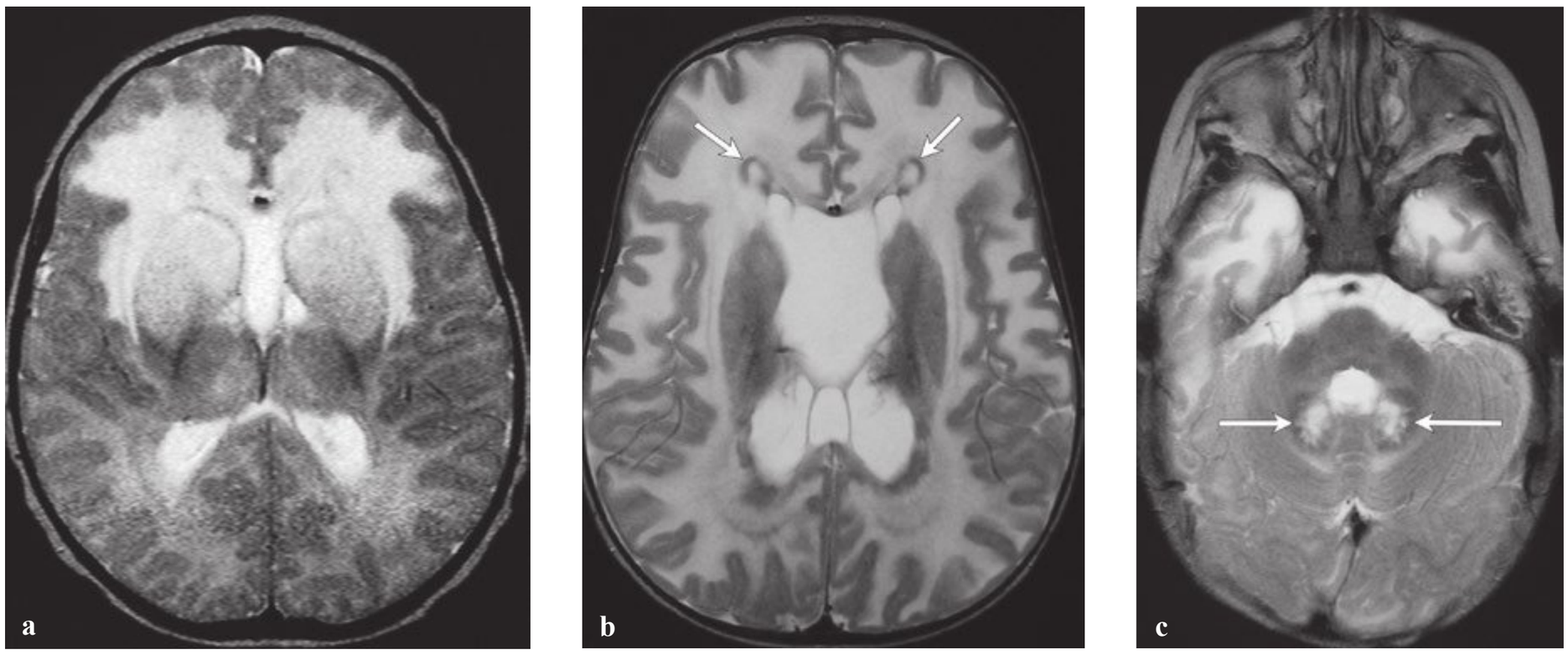

Fig. 1.246 Alexander disease, infantile type. **(a)** A 3-month-old male with abnormal high signal on axial T2-weighted imaging in the frontal white matter bilaterally, caudate nuclei, and putamina and associated with brain swelling. **(b,c)** An 11-month-old female with diffuse abnormal high signal on axial T2-weighted imaging in the cerebral white matter with frontal predominance, subcortical U-fibers, brainstem, middle cerebellar peduncles, and dentate nuclei (arrows). **(b)** Periventricular rims of low signal (arrows) on T2-weighted imaging are seen surrounding the frontal horns of the lateral ventricles, which show **(d)** corresponding gadolinium contrast enhancement (arrows) on axial fat-suppressed T1-weighted imaging representing sites of active demyelination. **(e)** Gadolinium contrast enhancement is also seen in the medial portions of both cerebellar hemispheres.

Table 1.5 (cont.) Multiple or diffuse lesions involving white matter in children

Lesions	Imaging Findings	Comments
Canavan disease, also known as Canavan-van Bogaert-Bertrand disease (**Fig. 1.248** and **Fig. 1.249**)	MRI: High signal on T2-weighted imaging involving the peripheral cerebral and cerebellar white matter diffusely, with progressive involvement of the white matter centrally (internal capsules, corpus callosum), ± involvement of the globus pallidus, thalamus, hypothalamus, and brainstem. Typically no gadolinium contrast enhancement. Associated with increased size and weight of brain tissue. Can have restricted diffusion in involved white matter initially, and elevated ADC later in disease. Magnetic resonance spectroscopy shows an enlarged N-acetylaspartate (NAA) peak. CT: Zones with decreased attenuation involving the peripheral cerebral and cerebellar white matter diffusely, with progressive involvement of the white matter centrally and subsequent atrophy.	Rare autosomal recessive disease (common in Ashkenazi Jews), with spongy degeneration of the brain caused by deficiency of aspartoacyclase in oligodendrocytes, microglia, and brainstem neurons that results from mutations of the ASPA gene on chromosome 17p13-ter. Mutations of the gene that encodes for aspartoacyclase result in lack of breakdown of N-acetyl aspartic acid (NAA) into aspartic acid and acetate. NAA accumulates in brain and plasma, with elevated levels in urine. Excess NAA in brain causes injury to oligodendrocytes and spongiform and vacuolation changes with myelin destruction. Presents in infancy (3–6 months) with macrocephaly, hypotonia, seizures, spasticity, optic atrophy, and visual loss. Death often occurs by the fourth year. Gene therapy with an adeno-associated viral vector carrying the ASPA gene has shown promising early results.

(continued on page 202)

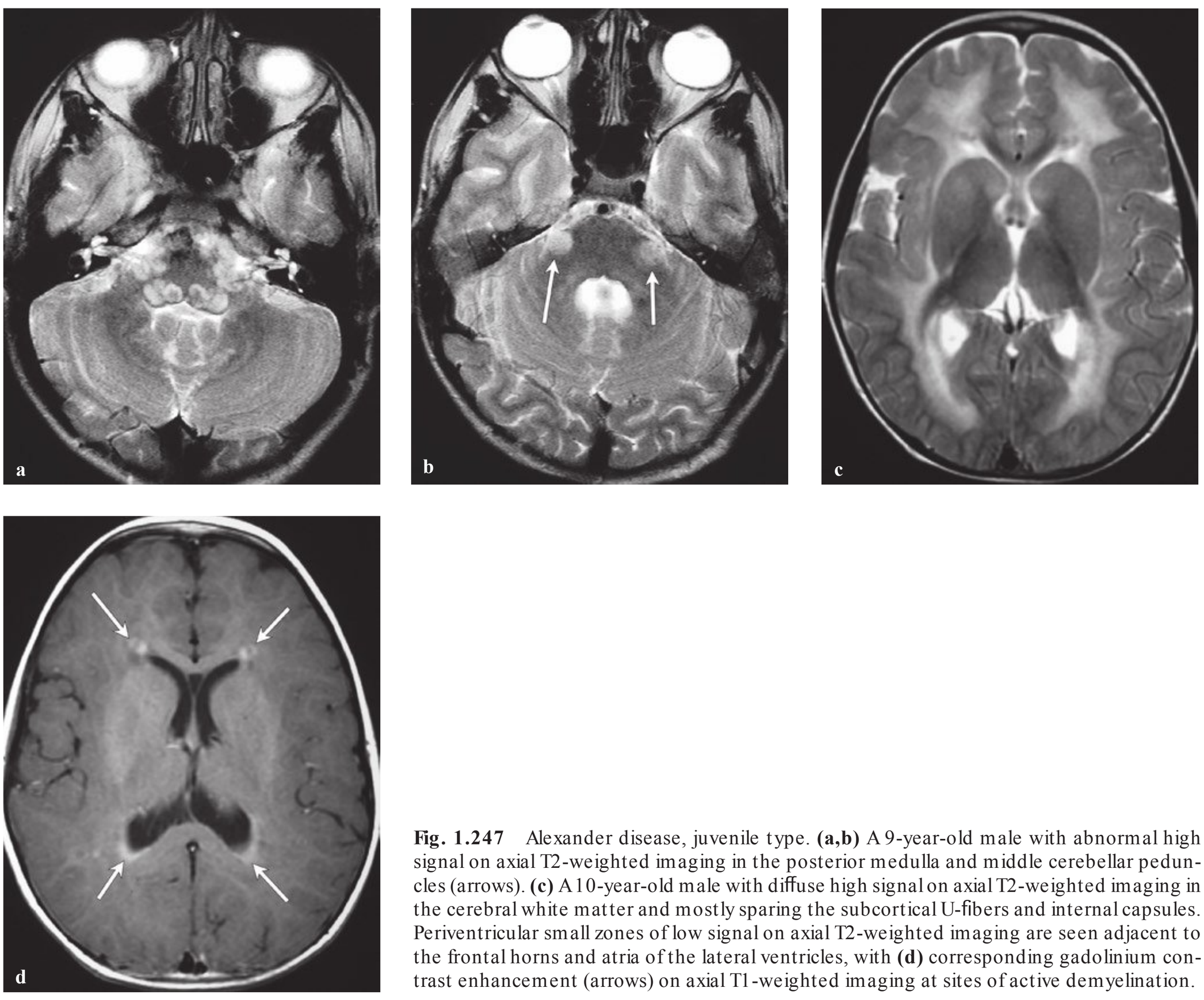

Fig. 1.247 Alexander disease, juvenile type. **(a,b)** A 9-year-old male with abnormal high signal on axial T2-weighted imaging in the posterior medulla and middle cerebellar peduncles (arrows). **(c)** A 10-year-old male with diffuse high signal on axial T2-weighted imaging in the cerebral white matter and mostly sparing the subcortical U-fibers and internal capsules. Periventricular small zones of low signal on axial T2-weighted imaging are seen adjacent to the frontal horns and atria of the lateral ventricles, with **(d)** corresponding gadolinium contrast enhancement (arrows) on axial T1-weighted imaging at sites of active demyelination.

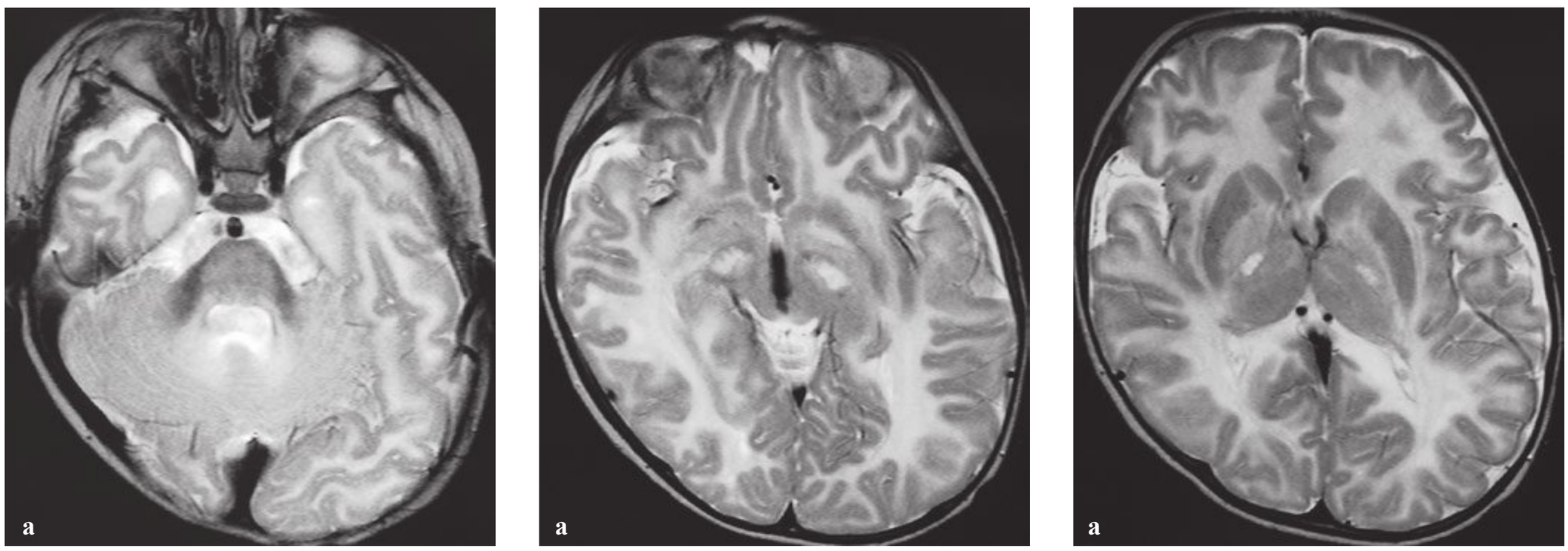

Fig. 1.248 Canavan-van Bogaert disease. **(a–c)** A 14-month-old female with diffuse abnormal high signal on axial T2-weighted imaging in the cerebral and cerebellar white matter, internal capsules including the corticospinal tracts, corpus callosum, globi pallidi, thalami, and brainstem.

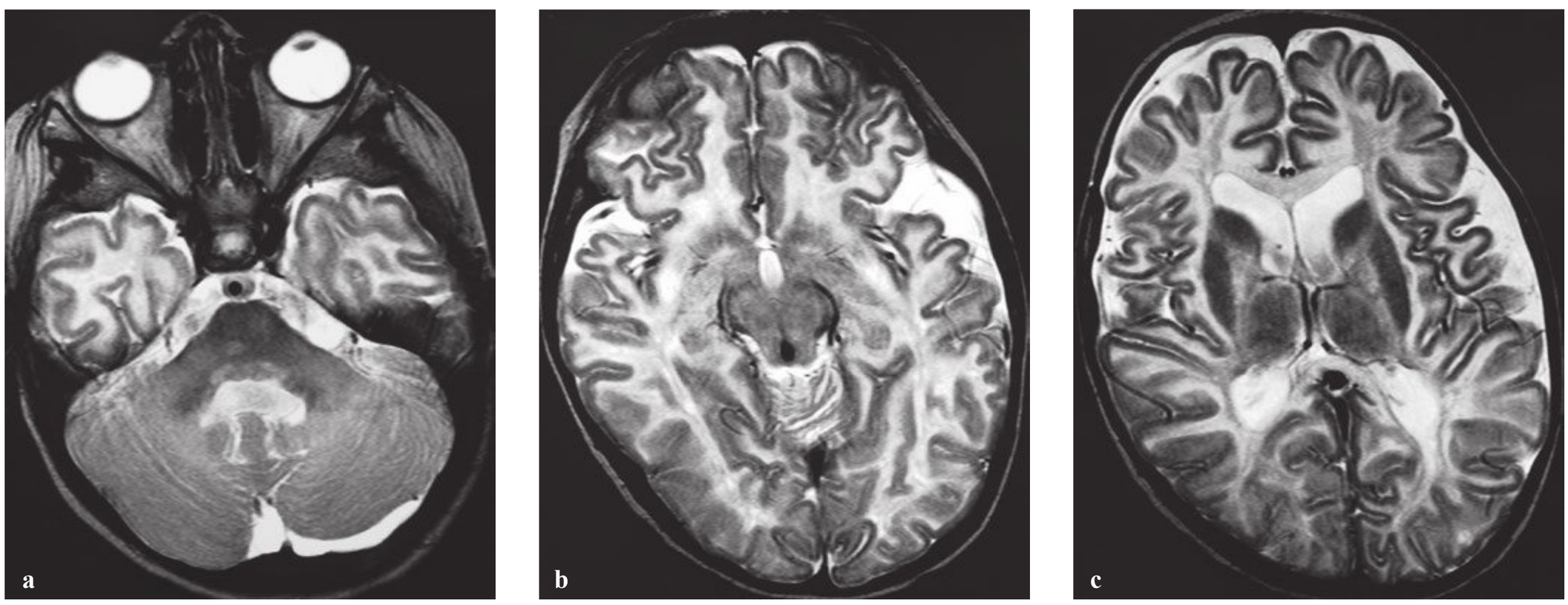

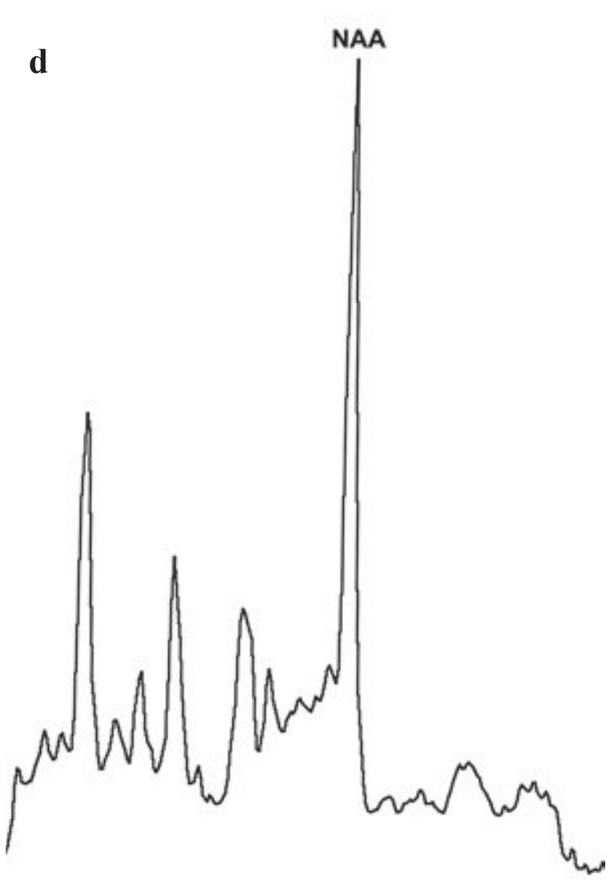

Fig. 1.249 Canavan-van Bogaert disease. **(a–c)** A 4-year-old male with diffuse abnormal high signal on T2-weighted imaging in the cerebral and cerebellar white matter, internal capsules, corpus callosum, globi pallidi, brainstem, and middle cerebellar peduncles. **(d)** Magnetic resonance spectroscopy shows an enlarged N-acetylaspartate (NAA) peak.

Table 1.5 (cont.) Multiple or diffuse lesions involving white matter in children

Lesions	Imaging Findings	Comments
Cockayne syndrome (**Fig. 1.250**)	MRI: High signal on T2-weighted imaging in the periventricular white matter, basal ganglia, and dentate nuclei; low signal on T2-weighted imaging from calcifications in basal ganglia, dentate nuclei, and white matter; progressive cerebral and cerebellar atrophy; microcephaly. Magnetic resonance spectroscopy can show decreased N-acetylaspartate (NAA) and choline peaks and slightly elevated lactate. CT: Progressive cerebral and cerebellar atrophy, calcifications in basal ganglia and dentate nuclei.	Autosomal recessive disorder involving mutations of the CSA (CKN1 or ERCC8) gene, CSB (CKN2 or ERCC6) gene, or xeroderma pigmentosa (XP) gene. Mutations alter nucleotide excision-repair pathways, resulting in defective repair of DNA damage caused by ultraviolet radiation. The syndrome presents in the first decade with progressive neurologic dysfunction, cataracts, cutaneous photosensitivity, optic atrophy, and dwarfism. There are four overlapping subgroups with decreasing severity: COFS, CSI, CSII, and CSIII. Pathologic findings include hypomyelination, myelin loss and degradation involving cerebral and cerebellar white matter, cerebral and cerebellar atrophy, and intra-axial calcifications.
Kearns-Sayre syndrome (**Fig. 1.251**)	MRI: Zones with high signal on T2-weighted imaging and FLAIR in globi pallidi, putamina, and caudate nuclei, as well as high signal on T2-weighted imaging in thalami, subcortical cerebral and cerebellar white matter, posterior brainstem, and corticospinal tracts, + restricted diffusion for acute ischemia. Typically no gadolinium contrast enhancement. CT: Zones with decreased attenuation can be seen in the cerebral white matter, ± calcifications involving globi pallidi and caudate nuclei.	Sporadic deletions of mitochondrial DNA involving genes that encode proteins of the respiratory chain and/or tRNA. Results in mitochondrial dysfunction, spongiform changes of the cerebral and cerebellar white matter and basal ganglia, as well as progressive external ophthalmoplegia, pigmentary degeneration of the retina (retinitis pigmentosa), and cardiac conduction blocks. Onset of clinical muscular and neurologic signs before the age of 20 years.
Malformations Related to Abnormal Pial Basement Membrane Formation:		
Walker-Warburg phenotype, muscle-eye-brain phenotype, Fukuyama congenital muscular dystrophy phenotype		Dystroglycanopathies are related to the congenital muscular dystrophies and result from mutations of genes that encode glycosyltransferase enzymes, causing deficient production of glycosylated α-dystroglycan. Defective or deficient α-dystroglycan results in reduced neuronal proliferation in the ventricular zone portion of the germinal zone of the developing brain and severely alters the function of the radial glia and their attachment to the pial limiting membrane, resulting in abnormal neuronal migration and cortical organization. Genes that have been identified include FKTN on 9q31, FKRP on 19q13.3, POMT1 on 9q34.1, POMT2 on 14q24, POMGnT1 on 1p33–34, and LARGE gene on 22q12.3-q13.1.
Muscle-eye-brain phenotype (**Fig. 1.252**)	MRI: Cerebral cortex can have zones of agyria, pachygyria, and/or polymicrogyria; abnormal increased signal involving the cerebral white matter on T2WI, hypoplasia and/or microcystic changes involving the cerebellum.	Dystroglycanopathies with severe congenital muscular dystrophy and abnormal fetal brain development that result from mutations of genes encoding glycosyltransferase enzymes. Lack of these enzymes reduces glycosylation and causes defective linkage of α-dystroglycan with laminin α-2, which is necessary for functioning of the radial glia for neuronal migration from the ventricular zone as well as cortical organization. Mutations of the FKRP, FKTN, POMT1, and POMT2 genes have been identified with this phenotype.
Fukuyama congenital muscular dystrophy phenotype	MRI: Polymicrogyria in cerebrum and cerebellum, hypoplasia of corticospinal tracts, transient abnormal increased signal in cerebral white matter on T2-weighted imaging, ± cerebellar and pontine hypoplasia, ± cerebellar cysts.	In the Japanese population, dystroglycanopathy with severe congenital muscular dystrophy and abnormal fetal brain development resulting from mutation of the FKTN gene encoding glycosyltransferase. Lack of this enzyme reduces glycosylation and causes defective linkage of α-dystroglycan with laminin α-2, which is necessary for functioning of the radial glia for neuronal migration from the ventricular zone as well as cortical organization.

(continued on page 204)

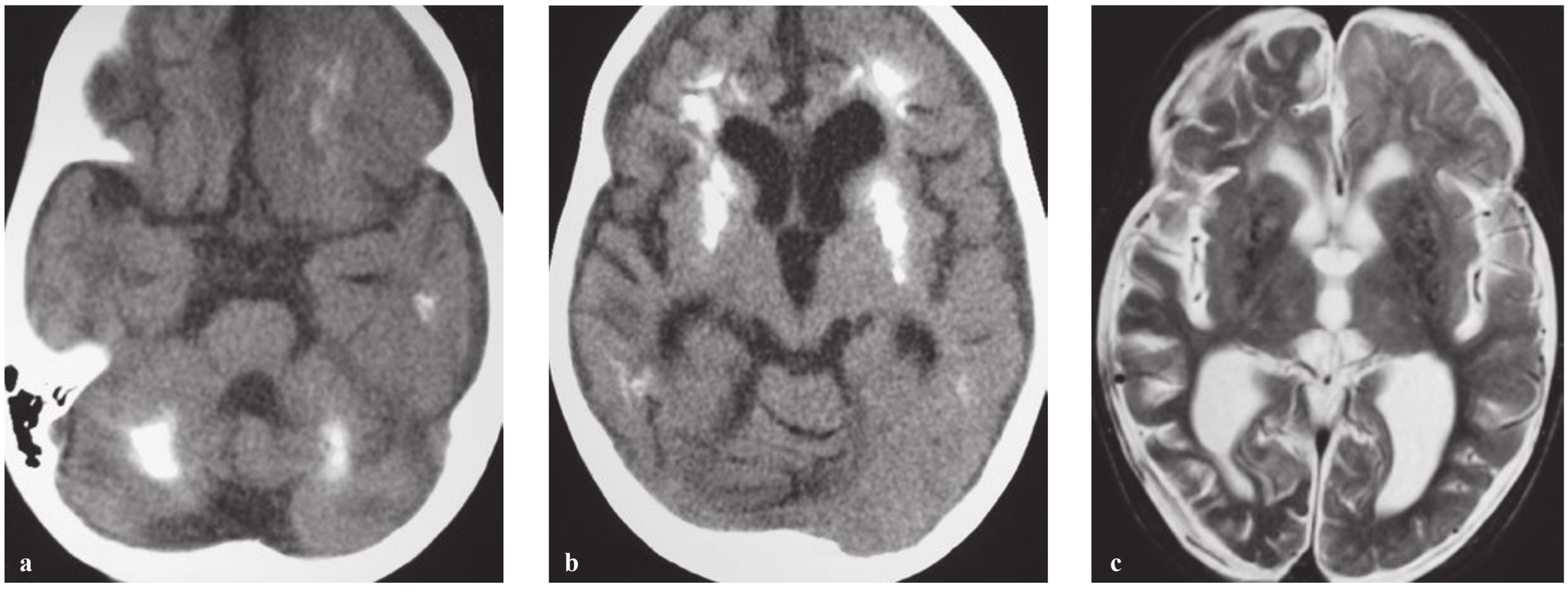

Fig. 1.250 An 11-year-old male with Cockayne syndrome. **(a,b)** Calcifications are seen in the frontal and temporal white matter, caudate nuclei, putamina and dentate nuclei on axial CT. Cerebral and cerebellar atrophy are also present. **(c)** Poorly defined zones with high signal on axial T2-weighted imaging are seen in the cerebral white matter.

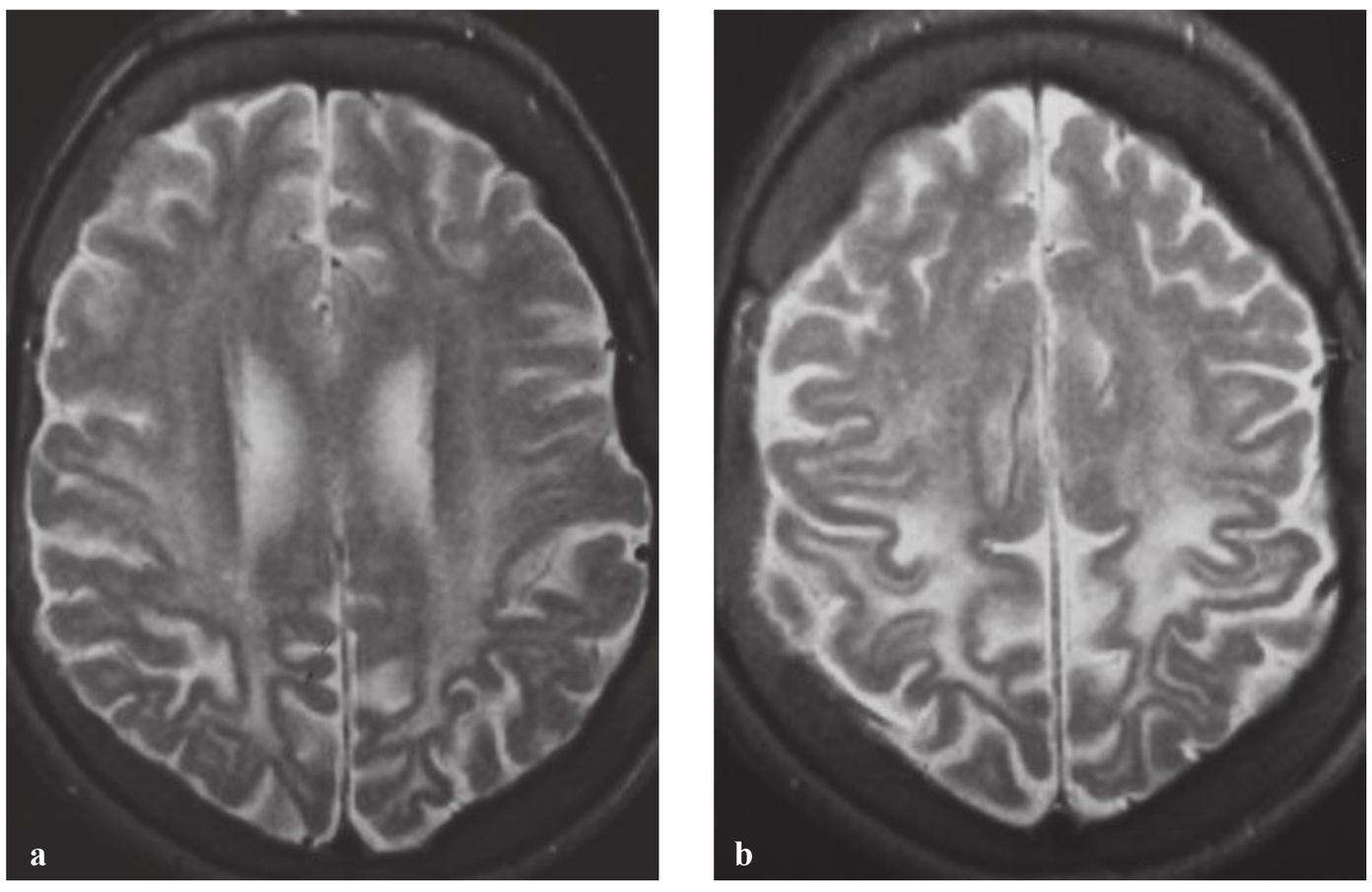

Fig. 1.251 Kearns-Sayre syndrome. **(a,b)** Zones with high signal on axial T2-weighted imaging are seen in the subcortical cerebral white matter and are associated with brain volume loss.

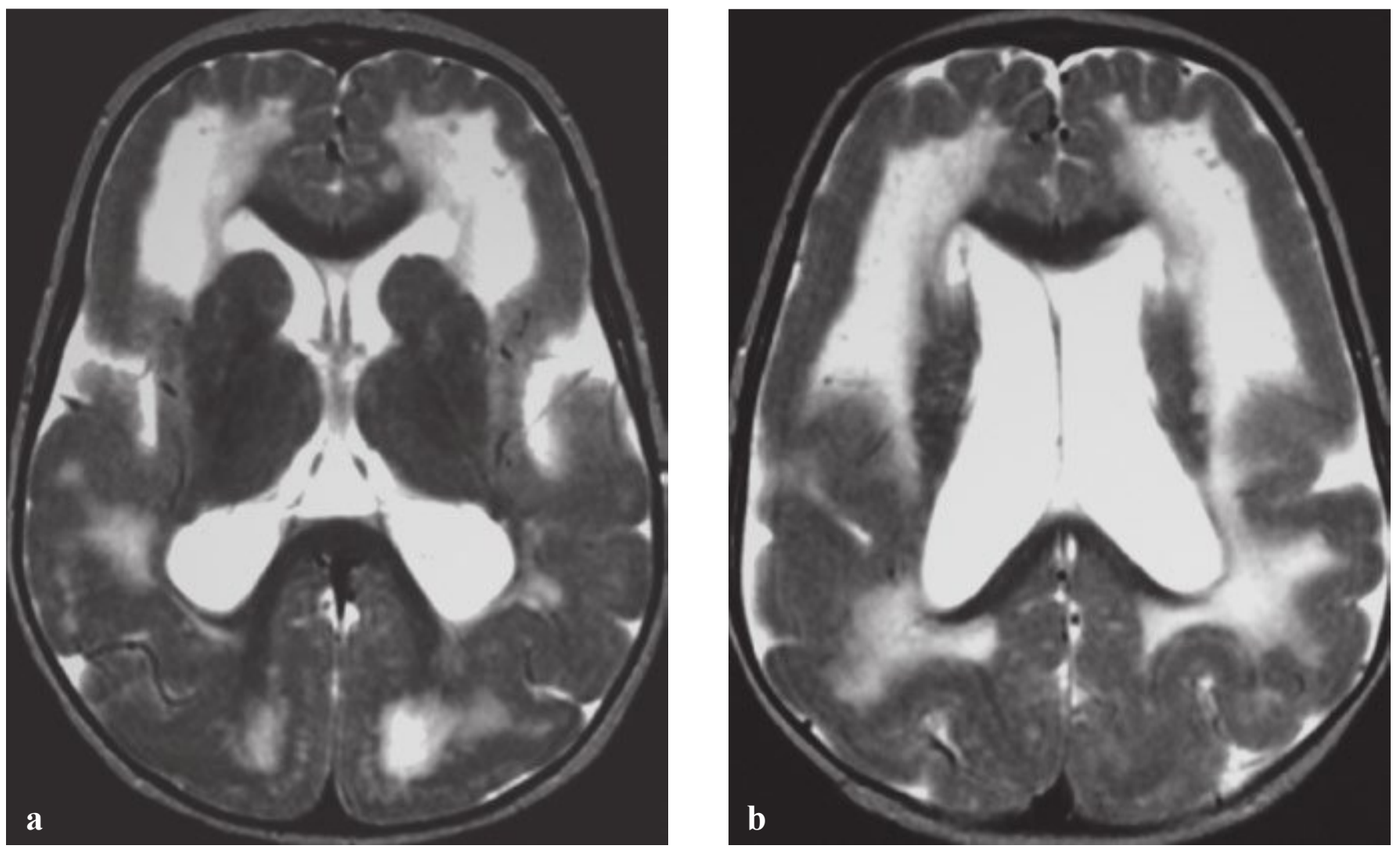

Fig. 1.252 A 14-month-old female with muscle-eye-brain phenotype. **(a,b)** Diffuse abnormal high signal on axial T2-weighted imaging is seen in the cerebral white matter in association with cerebral atrophy and polymicrogyria in the frontal lobes.

Table 1.5 (cont.) Multiple or diffuse lesions involving white matter in children

Lesions	Imaging Findings	Comments
Trauma-related Lesions		
Diffuse axonal injury (**Fig. 1.253** and **Fig. 1.254**)	MRI: One or multiple sites within the brain with intermediate or high signal on T1-weighted imaging; low, intermediate, and/or high signal on T2-weighted imaging and FLAIR; and low signal on gradient echo imaging or susceptibility-weighted imaging. CT: With acute injuries, one or multiple sites of high-attenuation hemorrhage are seen, commonly at the corpus callosum, cerebral cortical–white matter junctions, basal ganglia, and brainstem.	Brain injury caused by deceleration and rotational shear forces, which result in disruption of axons and blood vessels. The degree of axonal injury is related to a poorer prognosis. Often associated with other intracranial injuries, such as traumatic subarachnoid or parenchymal hemorrhage and cerebral contusions.
Non-accidental head injury (child abuse) (**Fig. 1.255**) Diffuse axonal injury Hypoxic-ischemic injury (HII)	Diffuse axonal injury MRI: One or multiple sites within the brain with intermediate or high signal on T1-weighted imaging; low, intermediate, and/or high signal on T2-weighted imaging and FLAIR; and low signal on gradient echo imaging or susceptibility-weighted imaging. CT: With acute injuries, one or multiple sites of high-attenuation hemorrhage are seen, commonly at the corpus callosum, cerebral cortical–white matter junctions, basal ganglia, and brainstem. Hypoxic ischemic injury MRI: HII usually involves the cerebrum and often spares the cerebellum. Zones with restricted diffusion can be seen in the subcortical white matter (often involving the posterior portions of the brain). Restricted diffusion with edema/brain swelling often involves the watershed vascular distribution zones of the brain between two vascular territories. Zones with restricted diffusion in the brain are usually bilateral, but can be unilateral. CT: Diffuse decreased attenuation involving the cerebral cortex and white matter of the cerebrum, often without initial abnormal attenuation of the thalamus, basal ganglia, and cerebellum.	Non-accidental head injury (NAHI) refers to child abuse from shaking and/or head impact upon a hard surface. Can result in various brain abnormalities, such as brain contusions, traumatic clefts, diffuse axonal injuries, and hypoxic-ischemic injury (HII). HII results from apnea caused by traumatic stretching of the brainstem and spinal cord that affects the respiratory centers or it results from arterial injury. HII is associated with a poor prognosis and occurs in 37% of patients with NAHI, compared with 9%of patients with accidental injuries. Subdural hemorrhage with or without skull fractures occurs in up to 81%of children with NAHI. Mixed attenuation subdural hematomas occur more commonly with NAHI than with accidental head trauma. Most NAHI occur in children less than 2 years old (24 per 100,000 below the age of 1 year; and 3.8 per 100,000 in children between 1 and 2 years old). Other findings associated with child abuse include retinal hemorrhage and rib and long bone fractures.

(continued on page 206)

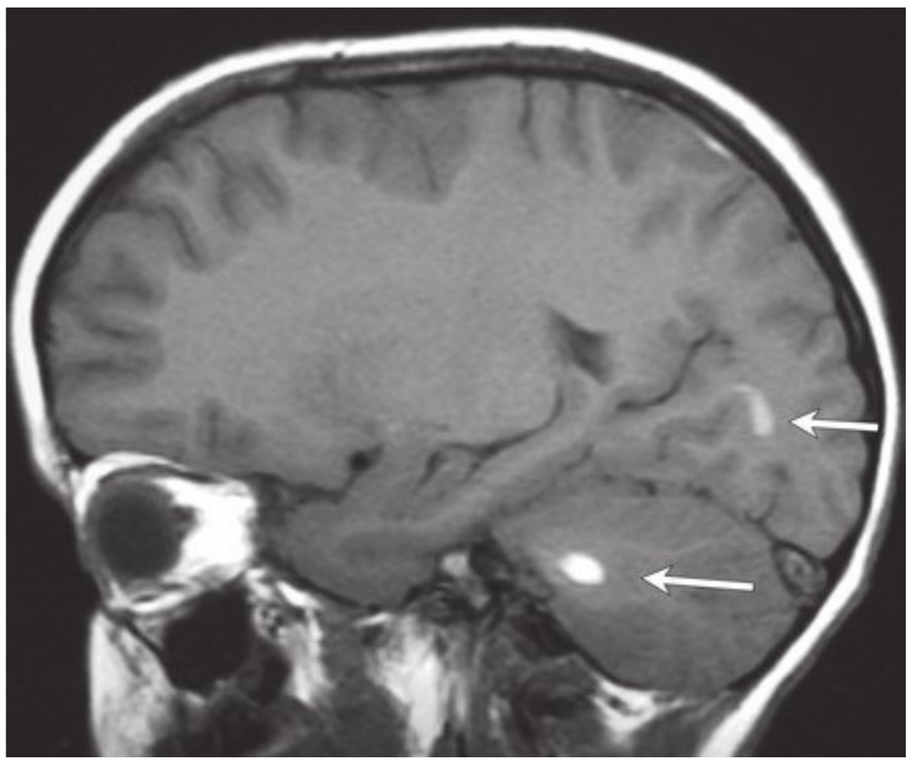

Fig. 1.253 A 6-year-old female with head trauma resulting in diffuse axonal injury. Sagittal T1-weighted imaging shows foci with high signal (arrows) in the cerebral and cerebellar white matter.

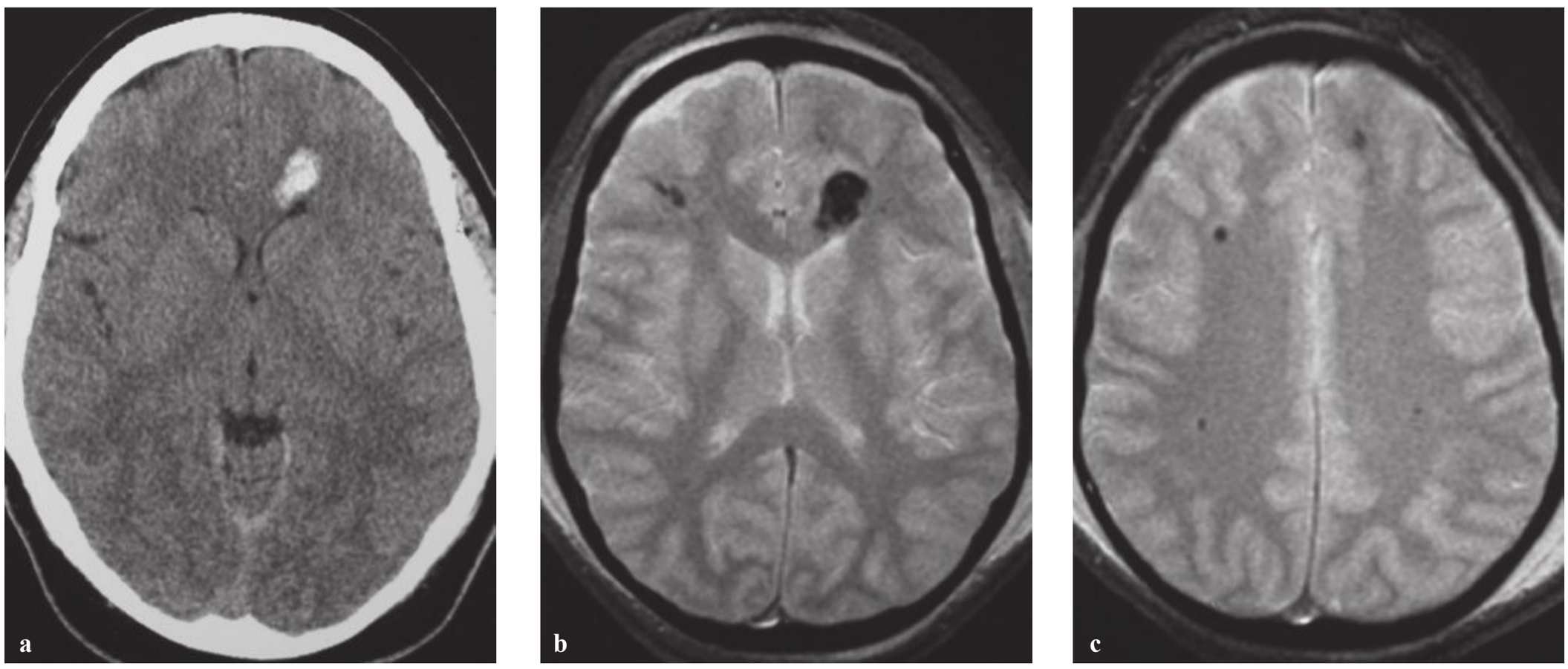

Fig. 1.254 A 17-year-old female with head trauma resulting in diffuse axonal injury. **(a)** Axial CT shows a zone of hemorrhage with high attenuation in the left frontal white matter that has **(b)** corresponding low signal on axial GRE. **(b,c)** Additional foci of low signal seen on axial GRE in the cerebral white matter represent small sites of hemorrhage below the resolution of CT.

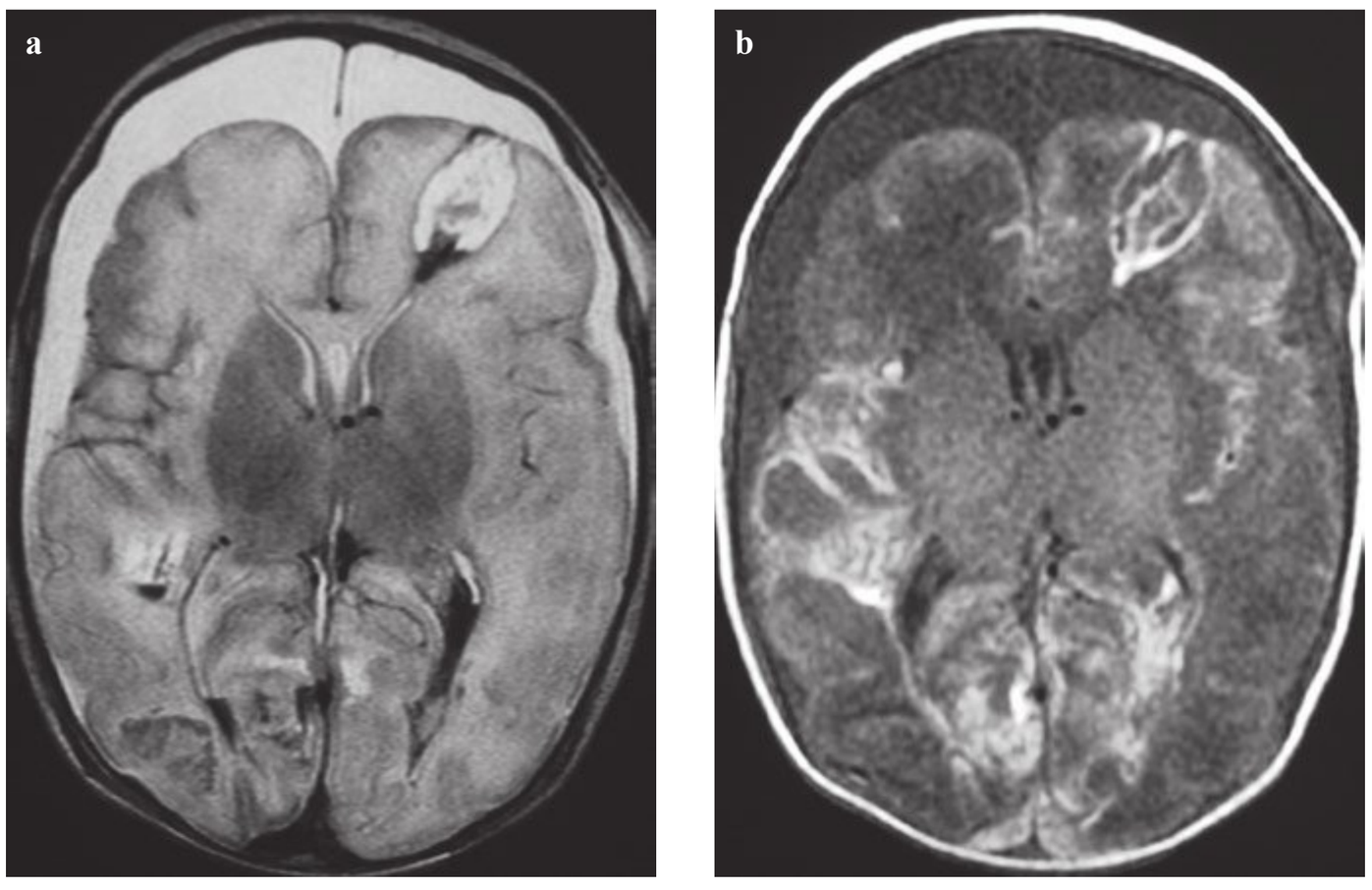

Fig. 1.255 A 2-month-old child with non-accidental head injury (child abuse). Multiple intrial-axial sites of hemorrhage of varying ages are seen that have mixed high and low signal on **(a)** axial T2-weighted imaging and **(b)** axial T1-weighted imaging. Enlarged intracranial subarachnoid spaces are also present.

Table 1.5 (cont.) Multiple or diffuse lesions involving white matter in children

Lesions	Imaging Findings	Comments
Ischemic Injury		
Small-vessel ischemic injury: Sickle-cell disease	MRI: Multiple foci and/or confluent zones of high signal on T2-weighted images in the subcortical and periventricular white matter, basal ganglia, and brainstem, with associated mass effect and typically no contrast enhancement. Chronic lesions may have low signal on T1-weighted imaging. CT: Zones of decreased attenuation involving the cerebral white matter, basal ganglia, and brainstem. No associated mass effect.	Lesions in white matter and/or brainstem related to occlusive disease involving perforating arteries associated with sickle-cell disease, thalassemia, and vasculitis. Unlike multiple sclerosis, ischemic small-vessel disease does not usually involve the corpus callosum because of its abundant blood supply from multiple branches of the adjacent pericallosal arteries.
Periventricular leukomalacia (**Fig. 1.256**)	MRI: Multiple foci and/or confluent zones of high signal on T2-weighted images in the subcortical and periventricular white matter, basal ganglia, and brainstem. No associated mass effect, no gadolinium contrast enhancement, ± low signal on T1-weighted images, and irregular ventricular margins and ventricular enlargement related to cerebral volume loss. CT: Multiple zones of decreased attenuation involving the cerebral white matter, basal ganglia, and brainstem. No associated mass effect, no contrast enhancement, and irregular ventricular margins and ventricular enlargement.	Ischemic injury involving fetal brain/premature infants, with gliosis and resultant encephalomalacia in periventricular white matter (fetal watershed vascular zones). Associated with neurologic deficits depending on severity of injuries (e.g., cerebral palsy).
Hypoxic-ischemic injury in preterm neonates	MRI: Confluent zones of high signal on T2-weighted imaging and FLAIR in the periventricular and/or subcortical white matter, + restricted diffusion on diffusion-weighted imaging in acute and early subacute phases. Typically there is no gadolinium contrast enhancement, eventually there is a decrease in volume of white matter and periventricular leukomalacia. CT: In late phases, zones of decreased attenuation in the cerebral white matter associated with volume loss and periventricular leukomalacia.	Within the developing cerebral white matter, sites of selective vulnerability to hypoxia are related to the locations of pre-oligodendrocytes (late oligodendrocyte precursor cells), and watershed vascular zones between the periventricular and subcortical white matter. The sensitive pre-oligodendrocytes show progressive maturity by 32 weeks, after which hypoxic lesions in the white matter decline in frequency. The watershed vascular border zones in the cerebral white matter also change in location based on maturity. Watershed vascular zones in immature cerebral white matter migrate from a periventricular location to a more subcortical location in the third trimester. The repositioning of the watershed vascular zones is related to the developing arterial supply to the immature white matter, with progressive shifting from ventriculopetal arteries from the outer brain surface to ventriculofugal arteries. Hypoxic injuries to cerebral white matter in preterm neonates involve the watershed vascular zones in the periventricular white matter in the late second trimester and early third trimester and are observed later in locations closer to the cortex where the watershed vascular zone has shifted centrifugally. The hypoxic and hypoperfused lesions involving the immature cerebral white matter result in periventricular leukomalacia, also referred to as white matter injury of prematurity.

Lesions	Imaging Findings	Comments
Hypoxic-ischemic injury in term neonates	MRI: Within the first 24 hours, ischemic changes from mild-moderate hypoxia can be seen as zones with high signal on diffusion-weighted imaging (DWI) and low signal on ADC maps (secondary to cytotoxic edema with restricted diffusion) in the cerebral cortex and subcortical white matter at watershed vascular boundary zones of the cerebrum (frontal lobes and parieto-occipital regions) and cerebellum. After the first week, abnormal ADC values associated with severe hypoxic injury "pseudonormalize," and they may be increased after the second week. Signal abnormalities on T1- and T2-weighted imaging may be absent in the first 24 hours. At 2 days, loss of distinction between cortical gray and white matter occurs on T2-weighted imaging secondary to increased abnormal signal of the cortex. The signal abnormalities on T2-weighted imaging usually underestimate the extent of ischemia in the white matter as seen on DWI. Edema in white matter may be better seen on T1-weighted imaging than on T2-weighted imaging. With mild-moderate hypoxia, signal abnormalities are often not seen in the basal ganglia or thalami. Magnetic resonance spectroscopy: Elevation of choline relative to creatine, decreased N-acetylaspartate (NAA), and presence of a lactate peak within the first 48 hours after birth in the cerebral cortex and subcortical white matter in the watershed zones, as well as to a much lesser extent in the deep gray matter. The lactate peak is often maximal at 5 days. CT: Cerebral edema associated with effacement of sulci may be seen. Abnormal attenuation of the cerebral cortex in the watershed vascular zones may not be apparent in the acute phase, and MRI is preferred for evaluation.	With mild-moderate hypoxia, a peripheral pattern (also referred to as "watershed predominant pattern") of restricted diffusion and signal abnormality is seen that involves the cortex and adjacent white matter but spares the ventrolateral thalamus, corticospinal tracts, and perirolandic cortex. With mild-moderate hypoxia, blood flow is shunted from the anterior to posterior circulation to maintain adequate perfusion of the basal ganglia, thalami, cerebellum, and brainstem. Hypoperfusion hypoxic injuries then occur at the cortex and subcortical white matter in the watershed vascular boundary zones of the cerebrum and cerebellum. These watershed vascular zones occur between the anterior and middle cerebral arteries, and between the middle and posterior cerebral arteries, and have been referred to as "parasagittal watershed zones." These sites of restricted diffusion occur at vulnerable watershed vascular zones located in the cortical and subcortical regions in full-term and near-full-term neonates. In neonates with lesser gestational ages, the vulnerable watershed vascular zones are located in the white matter closer to the ventricles, the locations of which are related to the immature development of centrifugal arteries and/or increased vulnerability of these regions to hypoxia.

(continued on page 208)

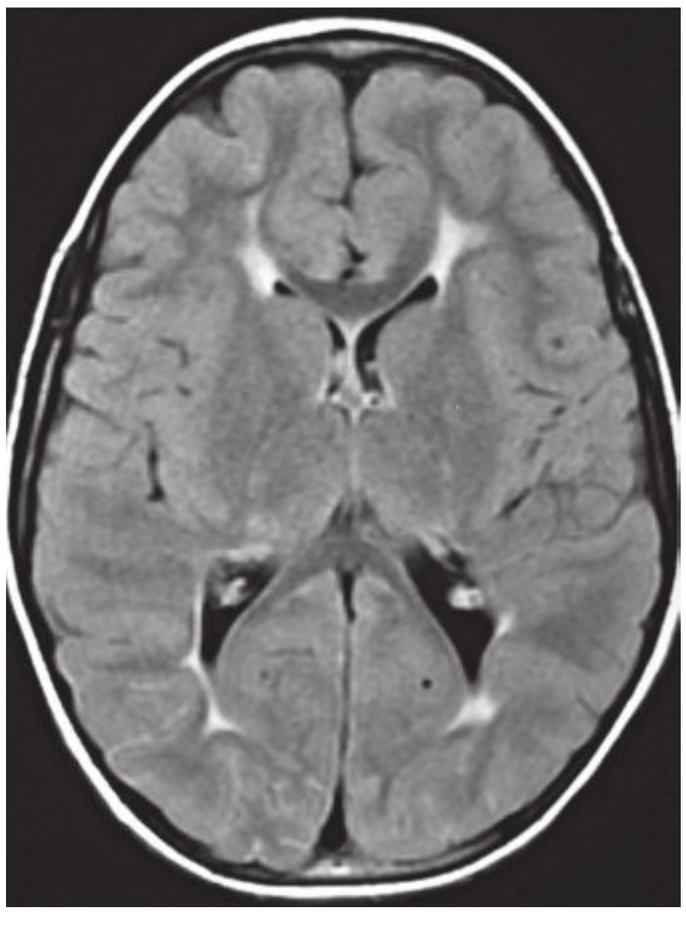

Fig. 1.256 A 5-year-old boy with cerebral palsy and periventricular leukomalacia. Zones of high signal on axial FLAIR are seen in the periventricular cerebral white matter with no associated mass effect. Mild loss of cerebral volume is seen in the peri-atrial white matter adjacent to the sites of gliosis from remote injury.

Table 1.5 (cont.) Multiple or diffuse lesions involving white matter in children

Lesions	Imaging Findings	Comments
Infections		
Pyogenic brain abscess (**Fig. 1.257**)	MRI: Circumscribed lesions with low signal on T1-weighted imaging; central zone of high signal on T2-weighted imaging (± air–fluid level) surrounded by a thin rim with intermediate-low signal on T2-weighted imaging that shows ring-like gadolinium contrast enhancement that is sometimes thicker laterally than medially; and peripheral poorly defined zone of high signal on T2-weighted imaging representing edema. Abscess contents typically have restricted diffusion. Mean ADC values for abscesses are significantly lower (0.63 to 1.12 × 10^{-3} mm^2/s) than those for necrotic or cystic neoplasms (2.45 × 10^{-3} mm^2/s). Magnetic resonance spectroscopy shows decreased N-acetylaspartate (NAA) from destruction of neurons, and elevated lactate and amino acid peaks (valine, leucine, and isoleucine) at 0.9 ppm secondary to proteolytic enzymes. CT: Circumscribed lesion with a central zone of low attenuation (± air–fluid level) surrounded by a thin rim of intermediate attenuation; peripheral poorly defined zone of decreased attenuation representing edema; ringlike contrast enhancement that is sometimes thicker laterally than medially.	Formation of brain abscess occurs 2 weeks after cerebritis with liquefaction and necrosis centrally surrounded by a capsule and peripheral edema. Restricted diffusion of abscess contents is related to the combination of the high protein content and viscosity of pus, necrotic debris, and bacteria. Can be multiple, but more than 50%are solitary. Complication from meningitis and/or sinusitis, septicemia, trauma, surgery, and cardiac shunt. Accounts for 2%and 8%of intra-axial mass lesions in developed and developing countries, respectively.
Spirochete infection: Lyme disease (**Fig. 1.166**)	MRI: Foci (2 to 8 mm) with high signal on T2-weighted imaging and FLAIR in cerebral and/or cerebellar white matter, ± restricted diffusion, ± contrast enhancement of intra-axial lesions and/or leptomeninges and cranial nerves III, V, and/or VII. CT: Foci of decreased attenuation in cerebral and/or cerebellar white matter, ± contrast enhancement.	CNS manifestations presumed to occur from immune-related demyelination from Lyme disease (infection by spirochete Borrelia burgdoferi) transmitted to humans via bites from Ixodes ticks that have been infected by primary hosts (mice and deer). Most cases in the United States occur in the Mid-Atlantic region. Patients can present with headaches, malaise, fevers, myalgias, and erythema migrans.

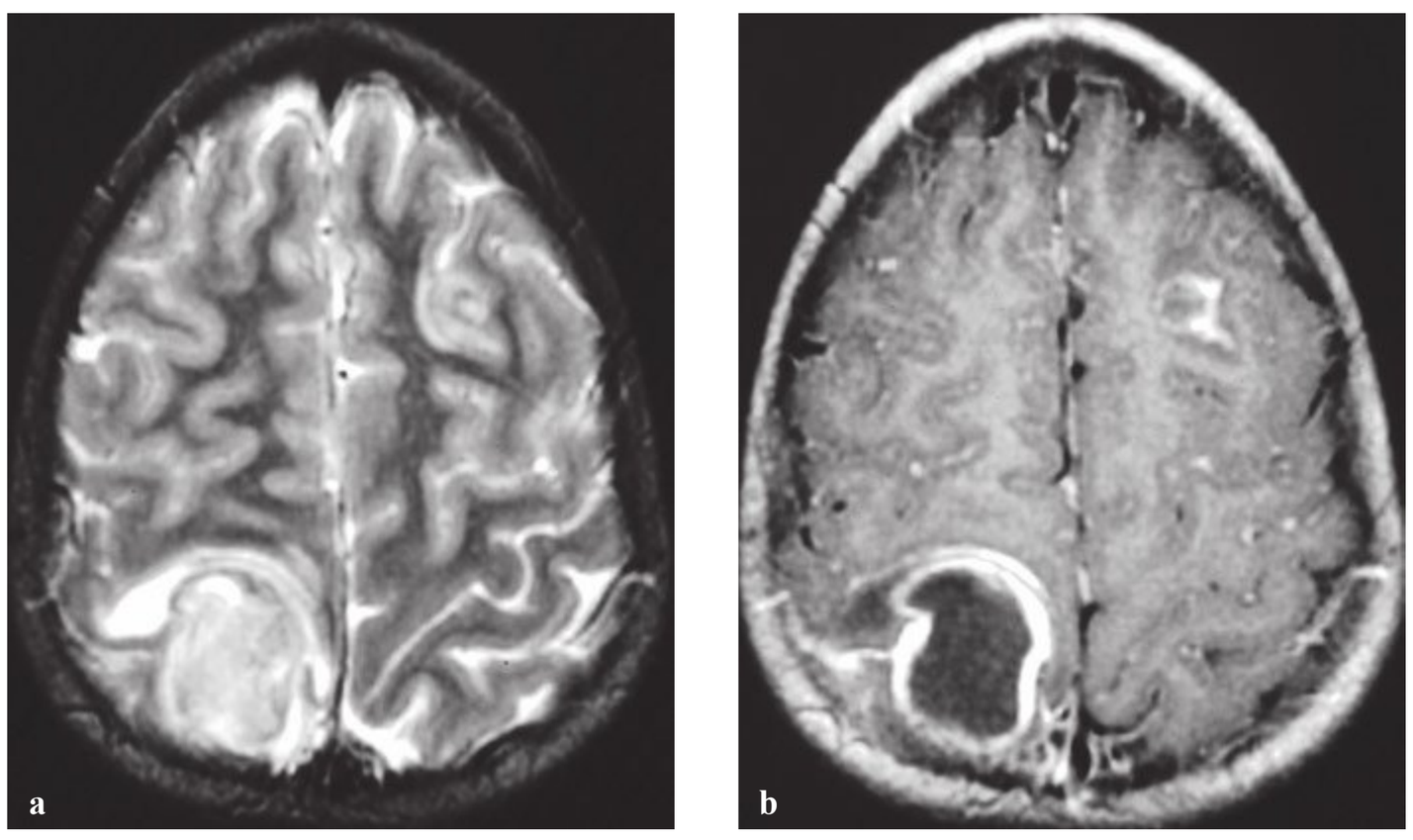

Fig. 1.257 A 9-year-old boy with a right-to-left-to-right cardiac shunt associated with two pyogenic brain abscesses as seen on **(a)** axial T2-weighted imaging and **(b)** axial postcontrast T1-weighted imaging.

Lesions	Imaging Findings	Comments
Fungal brain lesions (**Fig. 1.169**)	MRI: Findings vary depending on organism. Infection can occur in meninges and/or brain parenchyma, with solid or cystic lesions and low-intermediate signal on T2-weighted imaging, high signal on T2-weighted imaging and FLAIR, nodular or ring-shaped gadolinium contrast enhancement, and peripheral high signal in brain lesions on T2-weighted imaging (edema). Infected tissue may have restricted diffusion at the walls of the lesions without reduced ADC values in the central cavities of the lesions. Low signal on T2-weighted imaging and GRE at the walls of the lesions may occur from paramagnetic iron and magnesium within hyphae of the fungi. Magnetic resonance spectroscopy can show elevated lipid, lactate and amino acid peaks as well as multiple peaks between 3.6 and 3.8 ppm from trehalose. CT: Infection can occur in meninges and brain parenchyma, with solid or cystic-appearing lesions with decreased attenuation, nodular or ring pattern of contrast enhancement, and a peripheral zone with decreased attenuation.	Occur in immunocompromised or diabetic patients, with resultant granulomas in meninges and brain parenchyma. Cryptococcus involves the basal meninges and extends along perivascular spaces into the basal ganglia. Aspergillosis and Mucor spread via direct extension through paranasal sinuses or hematogenously, invading blood vessels and resulting in hemorrhagic lesions and/or cerebral infarcts. Coccidioidomycosis usually involves the basal meninges. Candidiasis is often a nocosomial infection related to complications from surgery and/or indwelling catheters.
Encephalitis/viral infections (**Fig. 1.258**) Herpes simplex Cytomegalovirus (CMV) Acute measles encephalitis Subacute sclerosing panencephalitis from measles (SSPE) West Nile virus	Herpes simplex MRI: typically involves the temporal lobes/limbic system ± hemorrhage. Poorly defined zone or zones of low-intermediate signal on T1WI, intermediate-high signal on T2WI and FLAIR, restricted diffusion can occur in early stages of infection, minimal or no gadolinium contrast enhancement, involves cerebral cortex and/or white matter, minimal localized mass effect. CT: Poorly defined zone or zones of decreased attenuation, minimal or no contrast enhancement. CMV MRI: Periventricular/subependymal zones with high signal on T2-weighted imaging and FLAIR. HIV often involves periatrial white matter. CT: Neonatal CMV infections can result in localized destruction of brain with dystrophic calcifications. Acute measles encephalitis MRI: increased signal on T2-weighted imaging can be seen in the cerebral white matter, cerebral cortex, and basal ganglia, + restricted diffusion, ± petechial hemorrhage, ± gadolinium contrast enhancement in cerebral cortex and leptomeninges. SSPE Zones with abnormal increased signal on T2-weighted imaging and FLAIR are seen in the cerebral and cerebellar white matter and brainstem, with increased ADC values and no gadolinium contrast enhancement. West Nile virus Zones with abnormal increased signal on T2-weighted imaging and FLAIR are seen in the cerebral and cerebellar white matter and brainstem. Typically there is no gadolinium contrast enhancement.	Encephalitis is an infection/inflammation of brain tissue from viruses. In immunocompromised patients, encephalitis is caused by herpes simplex, cytomegalovirus (CMV), human immunodeficiency virus (HIV), and progressive multifocal leukoencephalopathy from JC polyoma virus infection of oligodendrocytes. In immunocompetent patients, the causes are St. Louis encephalitis virus, Eastern or Western equine encephalitis virus, measles (RNA Paramyxovirus) virus, Epstein-Barr virus, Japanese encephalitis (Flavivirus), West Nile virus (Flavivirus), and rabies (Lyssavirus).

(continued on page 210)

Table 1.5 (cont.) Multiple or diffuse lesions involving white matter in children

Lesions	Imaging Findings	Comments
Cysticercosis (**Fig. 1.141**)	MRI: Single or multiple cystic lesions in brain or meninges. In the active vesicular phase, there are cystic-appearing lesions containing a small 2–4 mm nodule (scolex) with low signal on T1-weighted imaging, FLAIR, and diffusion-weighted imaging (DWI), a thin peripheral rim with high signal on FLAIR, high signal on T2-weighted imaging, minimal peripheral rim or no gadolinium contrast enhancement, and no peripheral edema on T2-weighted imaging and FLAIR. In the active colloidal vesicular phase, there are cystic-appearing lesions with low-intermediate signal on T1-weighted imaging, high signal on T2-weighted imaging, rim and/or nodular pattern of gadolinium contrast enhancement, ± peripheral signal (edema) on T2-weighted imaging. In the active granular nodular phase, the cyst retracts into a more solid gadolinium contrast-enhancing granulomatous nodule. CT: Single or multiple cystic-appearing lesions in brain or meninges. In the acute/subacute phase, there is low-intermediate attenuation, rim ± nodular pattern of contrast enhancement, ± peripheral low attenuation (edema). The chronic phase is characterized by calcified granulomas.	Cysticercosis is caused by ingestion of encysted larva of the tapeworm Taenia solium in contaminated food (undercooked pork) and involves meninges, subarachnoid space, and cisterns > brain parenchyma > ventricles. It is the most common parasitic disease of the CNS, usually in patients from 15 to 40 years old, and it is the most common cause of acquired epilepsy in endemic regions. Complications include intracranial hypertension from CSF obstruction, arachnoiditis, meningitis, and vascular occlusion.

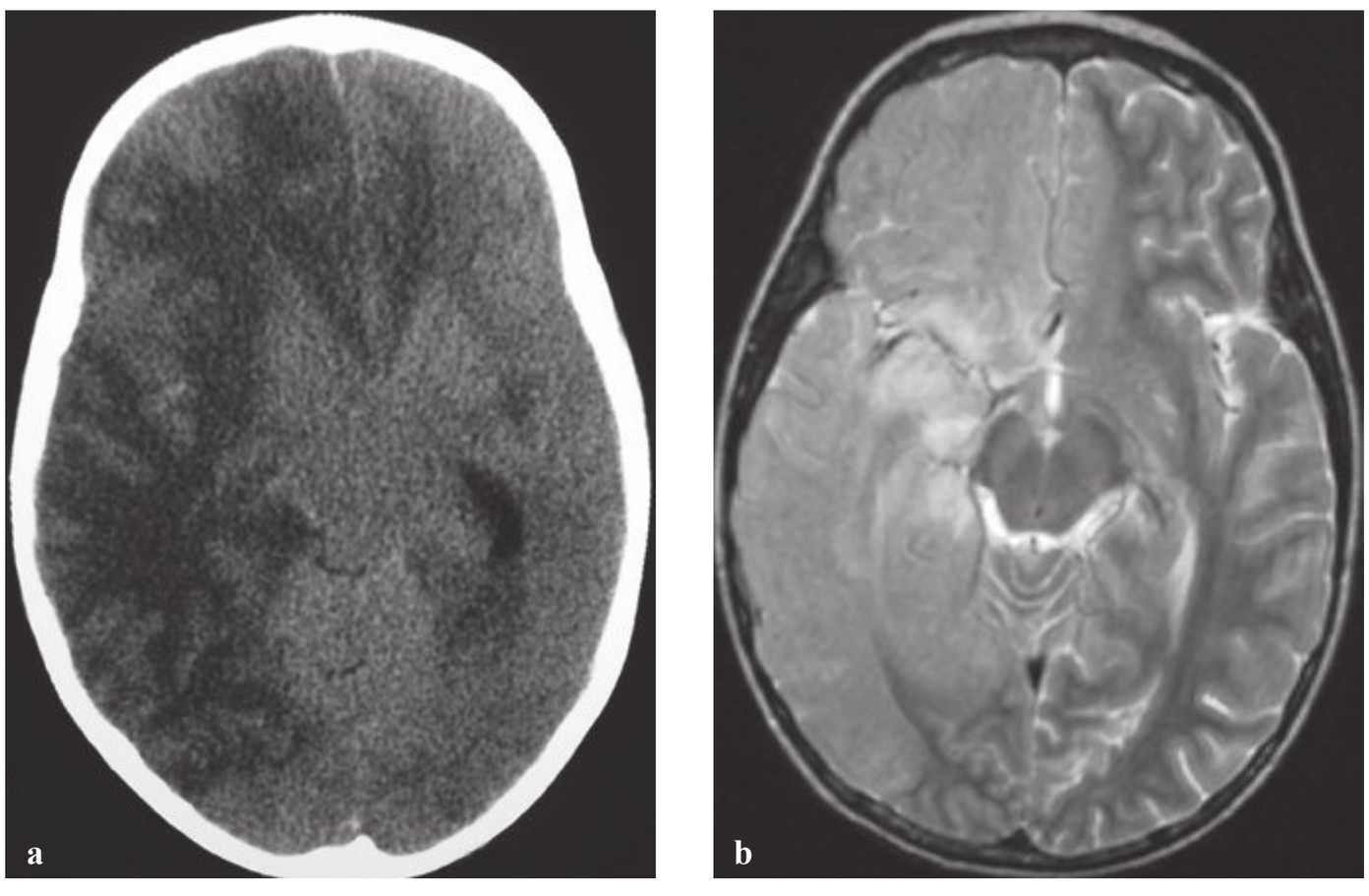

Fig. 1.258 A 3-year-old boy with cerebral herpes simplex 1 virus infection. **(a)** Diffuse, poorly defined zones with abnormal decreased attenuation on axial CT are seen in the right cerebral hemisphere and are associated with mass effect causing subfalcine herniation to the left and effacement of sulci and basal cisterns. **(b)** Diffuse abnormal increased signal on axial T2-weighted imaging is seen in the most of the right cerebral hemisphere, including gray and white matter.

Lesions	Imaging Findings	Comments
Malaria (**Fig. 1.259**)	MRI: Focal and/or poorly defined zones with high signal on T2-weighted imaging in the cerebral white matter and/or cerebral cortex, corpus callosum, basal ganglia, thalami, and cerebellum, ± cerebral edema with effacement of sulci and basal cisterns, ± uncal herniation, ± hemorrhage, ± restricted diffusion related to ischemic injury. Usually no gadolinium contrast enhancement of lesions. CT: Focal and/or poorly defined zones with decreased attenuation in the cerebral white matter, basal ganglia, and/or thalami.	Malaria results from infection by protozoan parasites from the genus Plasmodium. Transmission of the parasite to humans occurs via bites from female mosquitoes (Anopheles genus) containing the Plasmodium organisms. Malaria involving the CNS occurs in 2%of patients infected with Plasmodium falciparum. Malaria occurs commonly in children and visitors to endemic regions (sub-Saharan Africa, other tropical zones with altitudes less than 1500 m). Aggregation of infected erythrocytes in brain blood vessels results in perivascular hemorrhage, myelin damage, and necrosis of white matter. Inflammatory reaction with cytokine release, vasodilation and vascular engorgement can result in cerebral edema and increased intracranial pressure.

(continued on page 212)

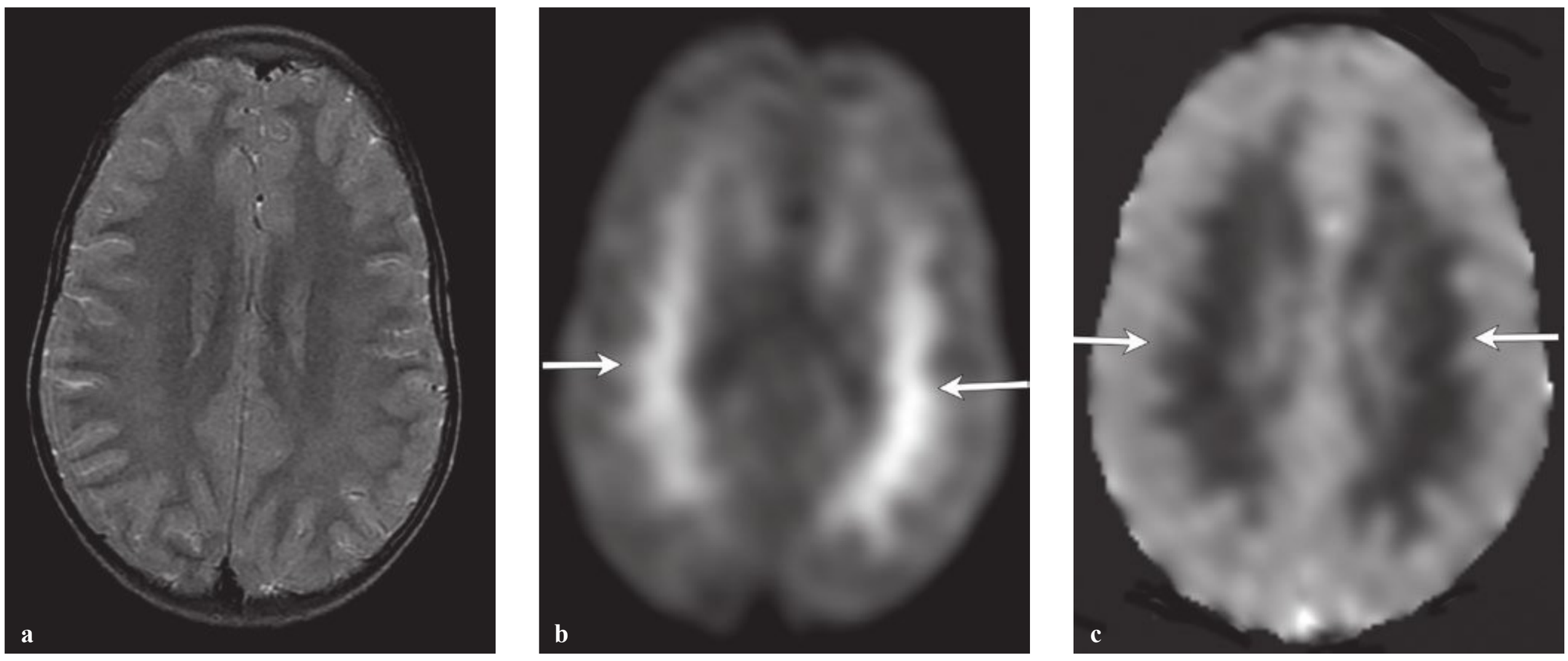

Fig. 1.259 Young child from Malawi with cerebral malaria. **(a)** Poorly defined zones with abnormal slightly high signal on axial T2-weighted imaging are seen in the cerebral white matter bilaterally that have corresponding restricted diffusion on **(b)** axial DWI (arrows) and **(c)** ADC (arrows).

Table 1.5 (cont.) Multiple or diffuse lesions involving white matter in children

Lesions	Imaging Findings	Comments
Inflammatory Disease: Noninfectious		
Acute disseminated encephalomyelitis (**Fig. 1.260**)	MRI: Lesions located in cerebral or cerebellar white matter, brainstem, basal ganglia; lesions usually have low-intermediate signal on T1-weighted imaging and high signal on T2-weighted imaging, ± gadolinium contrast enhancement. Gadolinium contrast enhancement can be ringlike or nodular, usually in acute/early subacute phase of demyelination, ± restricted diffusion. Acute demyelinating lesions can have localized mass effect simulating neoplasms. CT: Zones of active demyelination may show contrast enhancement and mild localized swelling.	Acute disseminated encephalomyelitis is an immune-mediated demyelination occurring after viral infection or due to toxins (exogenous toxins from environmental exposure or ingestion, such as alcohol, solvents).
Multiple sclerosis (**Fig. 1.261**)	MRI: Lesions located in cerebral or cerebellar white matter, brainstem, and basal ganglia. Lesions usually have low-intermediate signal on T1-weighted imaging and high signal on T2-weighted imaging, ± gadolinium contrast enhancement. Gadolinium contrast enhancement can be ringlike or nodular, usually in acute/early subacute phase of demyelination, ± restricted diffusion. Acute demyelinating lesions can have localized mass effect simulating neoplasms. CT: Zones of active demyelination may show contrast enhancement and mild localized swelling.	Multiple sclerosis (MS) is the most common acquired demyelinating disease in young and middle-aged adults (peak ages are 20 to 40 years). Can also occur in pediatric patients in the second decade. Affects 400,000 in the United States and 2,000,000 worldwide. Women are affected twice as frequently as men. Most common in people with northern European heritage. MS is not inherited in a Mendelian fashion, although it can cluster in families. Diagnosis is made based on clinical history and findings, results from MRI examinations (lesions with high signal on T2-weighted imaging or FLAIR seen in brain white matter, spinal cord, and optic nerves), abnormal visual evoked potentials, and isoelectric focusing evidence of oligocloncal bands and/or increased IgG index in CSF samples. Demyelinating disease occurs wherever myelin is present, including in deep brain nuclei (caudate, putamen, globus pallidus, and/or thalamus). The disease is typically multi-episodic.
Hemophagocytic lymphohistiocytosis (**Fig. 1.262**)	MRI: Foci and/or confluent zones with high signal on T2-weighted imaging and FLAIR are seen in the cerebral and/or cerebellar white matter, basal ganglia, and/or thalami, ± gadolinium contrast enhancement in brain and/or leptomeninges. Serial imaging can show progressive brain atrophy.	Rare multisystem primary immunodeficiency disorders in children, with accumulation of histiocytes and lymphocytes in the CNS, lymph nodes, bone, liver, and/or spleen. Patients range in age from 1 month to 14 years; median age = 2.5 to 21 months. Includes familial hemophagocytic lymphohistiocytosis types 1–5, Griscelli syndrome type 2, Chediak-Higashi syndrome, X-linked lymphoproliferative syndrome, and Hermansky-Pudlak syndrome type 2. Patients can present with seizures, impaired consciousness, meningismus, fever, hepatomegaly, splenomegaly, and/or lymphadenopathy. Hematopoietic stem cell transplantation can be curative.

(continued on page 214)

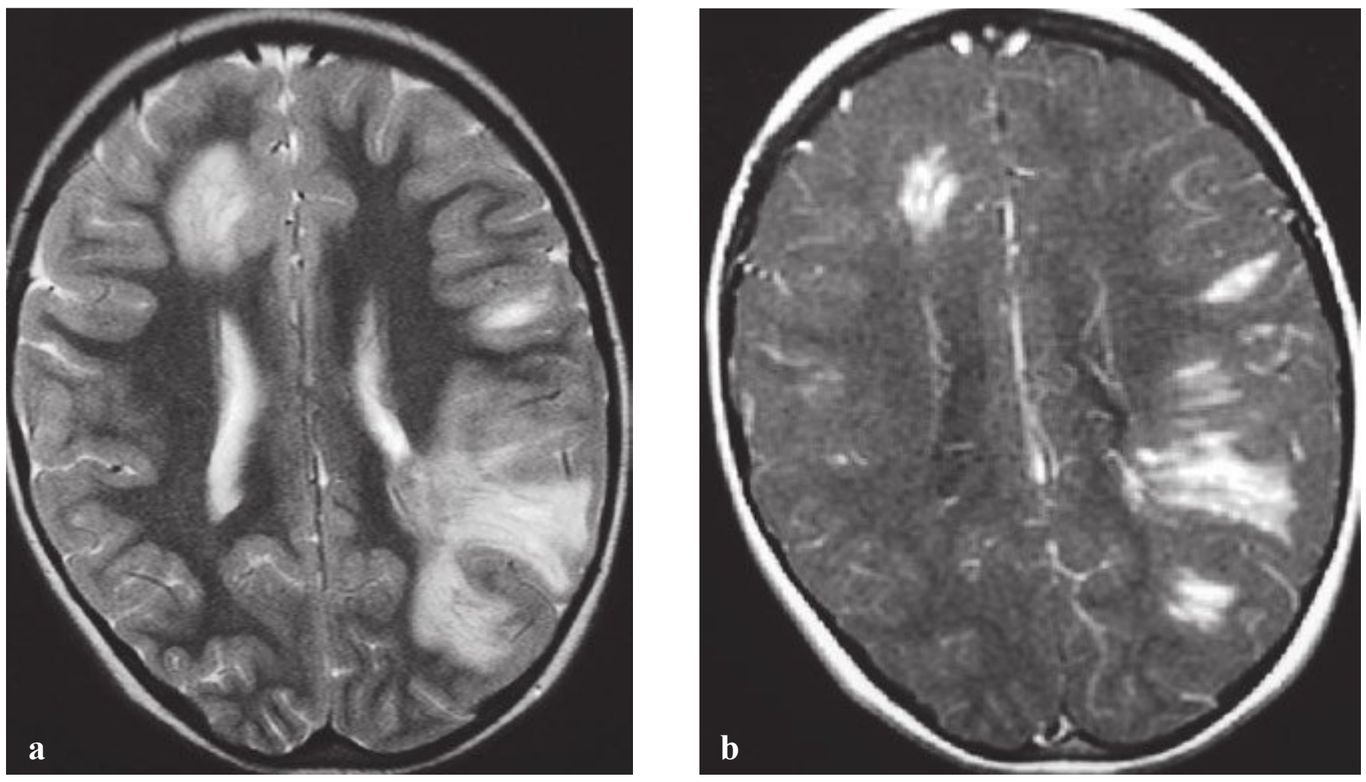

Fig. 1.260 A 5-year-old girl with acute disseminated encephalomyelitis 3 weeks after a viral illness. **(a)** Poorly defined zones with abnormal high signal on axial T2-weighted imaging are seen in the cerebral white matter bilaterally that have **(b)** corresponding gadolinium contrast enhancement on axial T1WI.

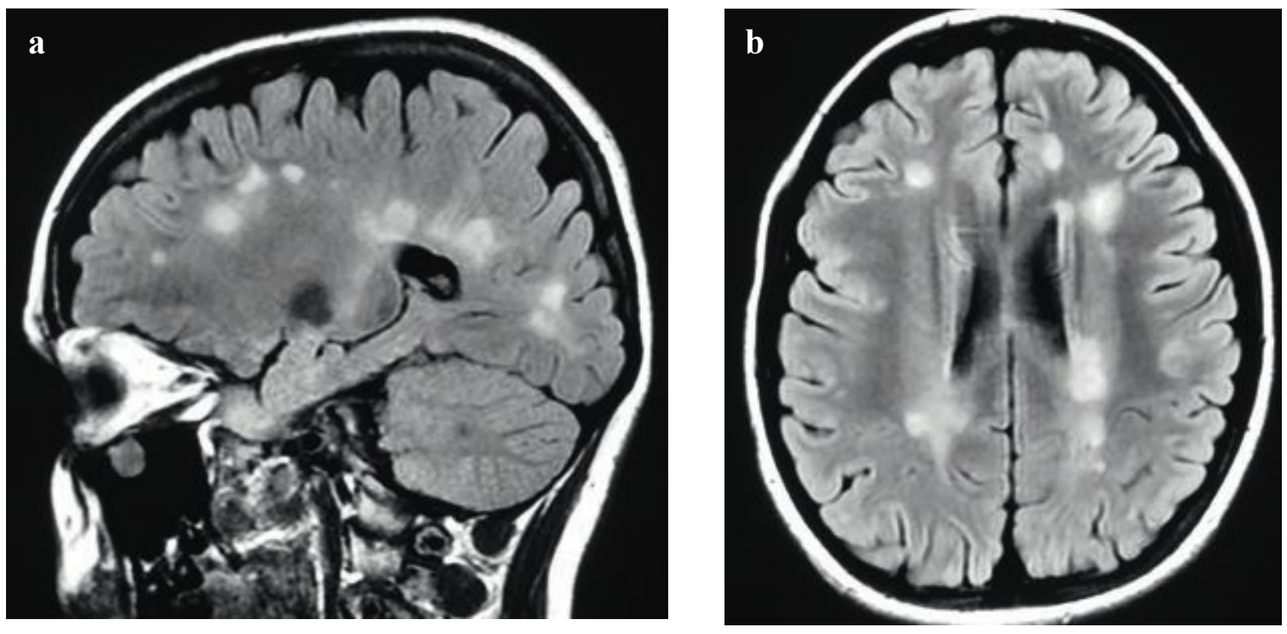

Fig. 1.261 A 17-year-old female with multiple sclerosis. **(a)** Sagittal and **(b)** axial FLAIR images show multiple zones with high signal in the periventricular white matter bilaterally.

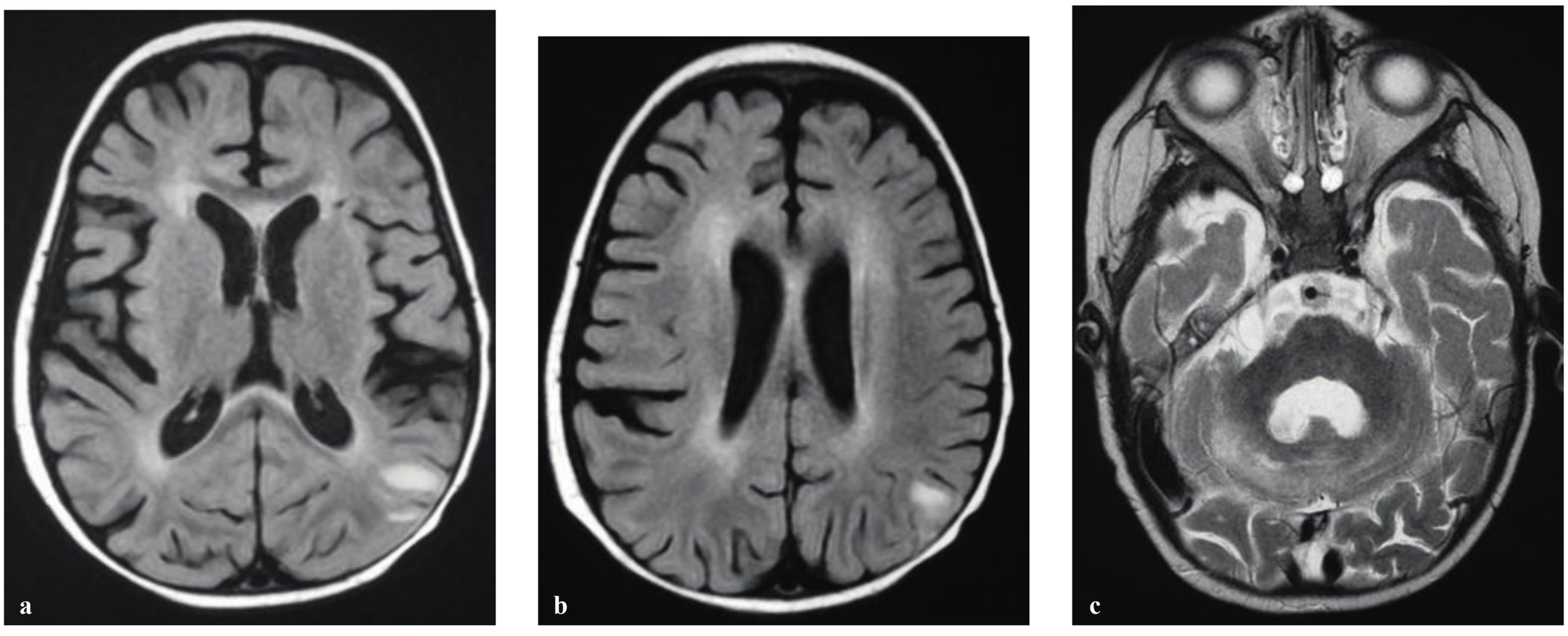

Fig. 1.262 A 17-month-old male with hemophagic lymphohistiocytosis. **(a,b)** Poorly defined zones with high signal on axial FLAIR and **(c)** axial T2-weighted imaging are seen in the cerebral and cerebellar white matter bilaterally and are associated with brain volume loss.

Table 1.5 (cont.) Multiple or diffuse lesions involving white matter in children

Lesions	Imaging Findings	Comments
Neoplasms		
Metastases	MRI: Circumscribed spheroid lesions in brain, can have various intra-axial locations (often at gray–white matter junctions), usually low-intermediate signal on T1-weighted imaging; intermediate-high signal on T2-weighted imaging; ± hemorrhage, calcifications, and cysts. Variable gadolinium contrast enhancement, and often high signal on T2-weighted imaging peripheral to nodular enhancing lesion representing axonal edema. CT: Lesions usually have low-intermediate attenuation; ± hemorrhage, calcifications, and cysts; and variable contrast enhancement, often associated with adjacent low attenuation from axonal edema.	Rare in children, can result from extracranial sarcomas (osteosarcoma, rhabdomyosarcoma), and neuroblastoma. In adults, metastatic lesions in brain account for 33% of intracranial tumors, usually from extracranial primary neoplasm in adults more than 40 years old. Primary tumor source: lung > breast > GI > GU > melanoma.
Lymphoma	MRI: Primary CNS lymphoma (PCNSL) in immunocompetent patients occurs as a solitary focal or infiltrating lesion in 65% of cases. PCNSL is located in the cerebral hemispheres, basal ganglia, thalami, cerebellum, and brainstem. PCNSL can involve and cross the corpus callosum. PCNSL in immunocompetent patients can be multifocal in 35% of cases, whereas multifocal PCNSL occurs in 60% of immunocompromised patients. Tumors often have low-intermediate signal on T1-weighted imaging, intermediate-slightly high signal on T2-weighted imaging, ± perilesional edema; ± hemorrhage/necrosis in immunocompromised patients or after treatment. PCNSL in immunocompetent patients usually shows homogeneous gadolinium contrast enhancement, whereas gadolinium contrast enhancement in immunocompromised patients often has an irregular peripheral pattern. Diffuse leptomeningeal and dural gadolinium contrast enhancement are other less common patterns of intracranial lymphoma. PCNSL can show restricted diffusion. Magnetic resonance spectroscopy of PCNSL shows decreased N-acetylaspartate (NAA) and elevated choline and lipid peaks. CT: CNS lymphoma can have intermediate attenuation, or can be hyperdense related to a high nuclear/cytoplasm ratio, ± hemorrhage, calcification, and necrosis in immunocompromised patients. Usually shows contrast enhancement.	Rarely occurs in children. Primary CNS lymphoma is more common than secondary, and typically occurs in adults > 40 years old. B cell lymphoma is more common than T cell lymphoma. MR imaging features of primary and secondary lymphoma of brain overlap. Intracranial lymphoma can involve the leptomeninges in secondary lymphoma > primary lymphoma.
Leukemia (myeloid sarcoma, granulocytic sarcoma, chloroma)	MRI: Lesions often have intermediate signal on T1-weighted imaging, intermediate to slightly high signal on T2-weighted imaging and FLAIR. Small zones with low signal on GRE may be seen from sites of hemorrhage within the lesion. Lesions can have restricted diffusion on diffusion-weighted imaging (ADC values of 0.50×10^{-3} mm^2/s). Lesions usually show gadolinium contrast enhancement. Magnetic resonance spectroscopy can show reduced N-acetylaspartate (NAA) and markedly elevated choline peaks. CT: Lesions can have low-intermediate to slightly high attenuation and can show contrast enhancement.	Leukemias are neoplastic proliferations of hematopoietic cells. Myeloid sarcomas (also referred to as chloromas or granulocytic sarcomas) are focal tumors composed of myeloblasts and neoplastic granulocyte precursor cells and occur in 2% of patients with acute myelogenous leukemia. These lesions can involve the dura, leptomeninges, and brain. Intracranial lesions can be solitary or multiple.

Lesions	Imaging Findings	Comments
Posttransplant lymphoproliferative disorder (PTLD)	MRI: PTLD can occur as multiple gadolinium contrast-enhancing intra-axial lesions with slightly high to high signal on T2-weighted imaging and FLAIR. Lesions can occur in the periventricular white matter and basal ganglia (63%) as well as other intra-axial locations.	PTLD is a complication of solid organ or hematopoietic stem cell transplantation, with lymphoid or plasmacytic cell aggregates occurring in one or multiple organs. The incidence ranges from 1% for renal transplants to 20% for small bowel transplants. Most common lesions are of B cell origin, and 90% are associated with Epstein-Barr virus. More common in children than in adults. Isolated involvement of the CNS occurs in 7% of PTLD. Within the brain, 61% of PTLD is seen as multifocal lesions.
Other Abnormalities		
Radiation injury/necrosis (**Fig. 1.263**)	MRI: Focal lesion ± mass effect or poorly defined, intra-axial zone of low-intermediate signal on T1-weighted imaging, intermediate-high signal on T2-weighted imaging, ± gadolinium contrast enhancement involving tissue (white matter and/or gray matter) in the field of radiation treatment. Relative cerebral blood volume (rCBV) values for radiation necrosis (0.6) have been shown to be significantly lower than those for recurrent high-grade gliomas (2.6). Radiation necrosis at sites of surgically resected metastatic lesions may show a three-layer pattern on diffusion-weighted imaging (DWI) consisting of an inner liquefied portion with high ADC, a middle layer with decreased ADC without gadolinium contrast enhancement, and an outer layer with gadolinium contrast enhancement with high ADC. CT: Focal lesion ± mass effect or poorly defined zone of low-intermediate attenuation, ± contrast enhancement involving tissue (gray matter and/or white matter) in field of treatment.	Severe local tissue reaction to radiation treatment, related to doses over 65 Gy. Occurs from 3–6 months to 12 months, and occasionally up to 10 years, after radiation treatment. Occurrence rate is up to three times higher when chemotherapy is given concurrently with radiation treatment. Results from vascular endothelial injury and apoptosis, leading to thrombosis, fibrinous exudates, hyalinization with luminal stenosis, and fibrinoid and vascular necrosis, as well as glial and white matter damage. May be difficult to distinguish from neoplasm. Using dynamic susceptibility contrast-enhanced perfusion MRI, $rCBV_{max}$ and $rCBV_{mean}$ values for recurrent tumor have been shown to be significantly higher than those for tumor necrosis, aiding in distinguishing between the two diagnoses. Similar findings have been found with perfusion computed tomography. Perfusion MRI has been shown to be superior to ^{18}F-FDG PET and ^{11}C-methionine PET in distinguishing high-grade gliomas from radiation necrosis. Magnetic resonance hydrogen spectroscopy shows decreased N-acetylaspartate (NAA) and choline peaks at sites of radiation necrosis, whereas residual and recurrent tumor show elevated choline peaks and a choline/creatine (Cho/Cr) ratio > 2.
Acute toxic leukoencephalopathy (**Fig. 1.264**)	MRI: Symmetric bilateral zones of high signal on T2-weighted imaging involving the periventricular cerebral white matter, including the centrum semiovale and corona radiata, ± involvement of the corpus callosum, thalami, globus pallidus, and dentate nuclei, usually with associated restricted diffusion. Findings on diffusion-weighted imaging (DWI) may be earlier and more prominent than the degree of abnormal high signal on T2-weighted imaging. Findings can be reversed if eliciting cause is removed.	Can result from effects of medications (vigabatrin for seizures, high doses of metronidazole for infections), chemotherapeutic agents (intrathecal methotrexate), immunosuppressive therapy, exposure to environmental toxins or illicit drugs, or infectious agents. Pathologic changes include intramyelinic vacuolation, demyelination, cell death, and capillary endothelial damage.
Hypertensive encephalopathy (posterior reversible encephalopathy syndrome/PRES) (**Fig. 1.265**)	MRI: Zones of low-intermediate signal on T1-weighted imaging and high signal on T2-weighted imaging in subcortical white matter, ± cerebral cortex, ± gadolinium contrast enhancement. Findings can be reversed if eliciting cause is corrected. CT: Foci and/or confluent zones of decreased attenuation in subcortical white matter, ± cerebral cortex, ± contrast enhancement.	Occurs with elevations in blood pressure above the upper limit for cerebral vascular autoregulation, resulting in capillary leakage of fluid in the brain, often in arterial boundary zones. Associated with immunosuppressant drugs (tacrolimus/FK506, cyclosporine), chemotherapy (cisplatin, L-asparaginase, others), acute onset of hypertension, pre-eclampsia, eclampsia, renal dysfunction, and fluid overload. Neurologic symptoms include confusion, headaches, seizures, visual loss, dysarthria, and coma. Cortical abnormalities may be necrosis related to hypoperfusion injury.

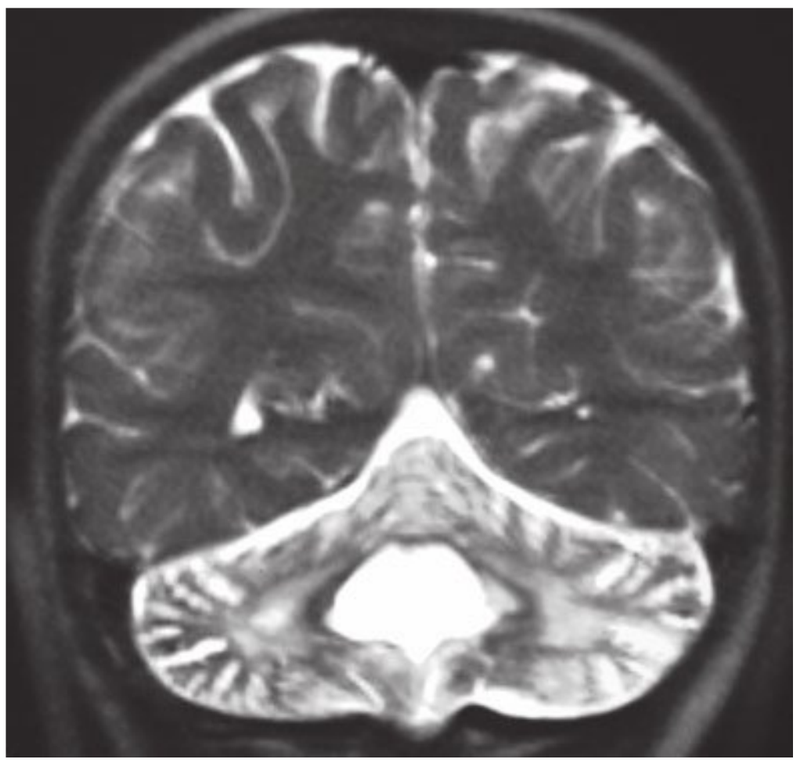

Fig. 1.263 Postoperative and post-treatment T2-weighted imaging of a patient who had medulloblastoma and subsequent radiation injury/necrosis in the cerebellum. There is diffuse abnormal high signal in the cerebellar white matter associated with prominent atrophic change.

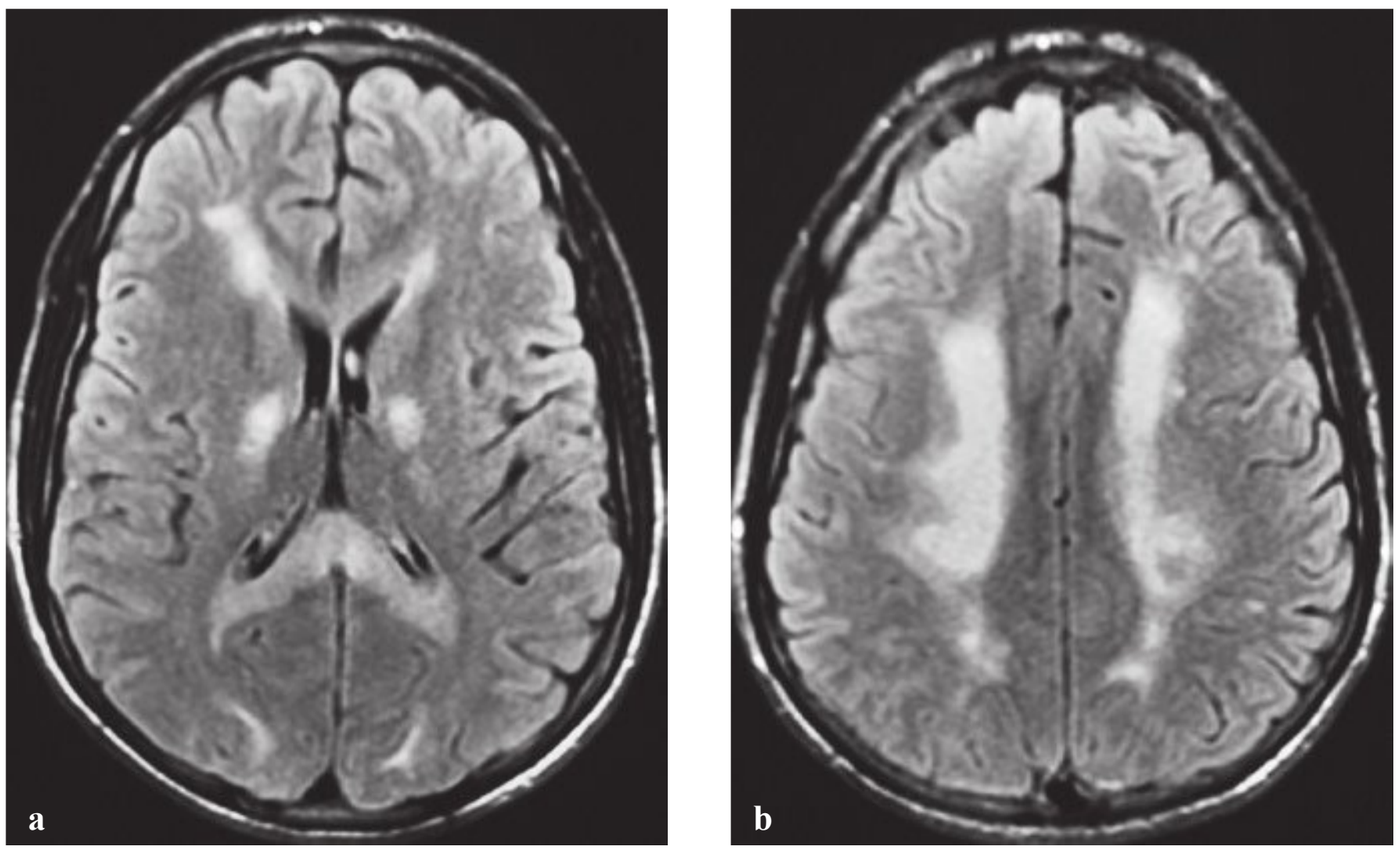

Fig. 1.264 **(a,b)** A 17-year-old male with toxicity from intravenous heroin. Abnormal high signal is seen in the globi pallidi, corpus callosum, and periventricular white matter on axial FLAIR.

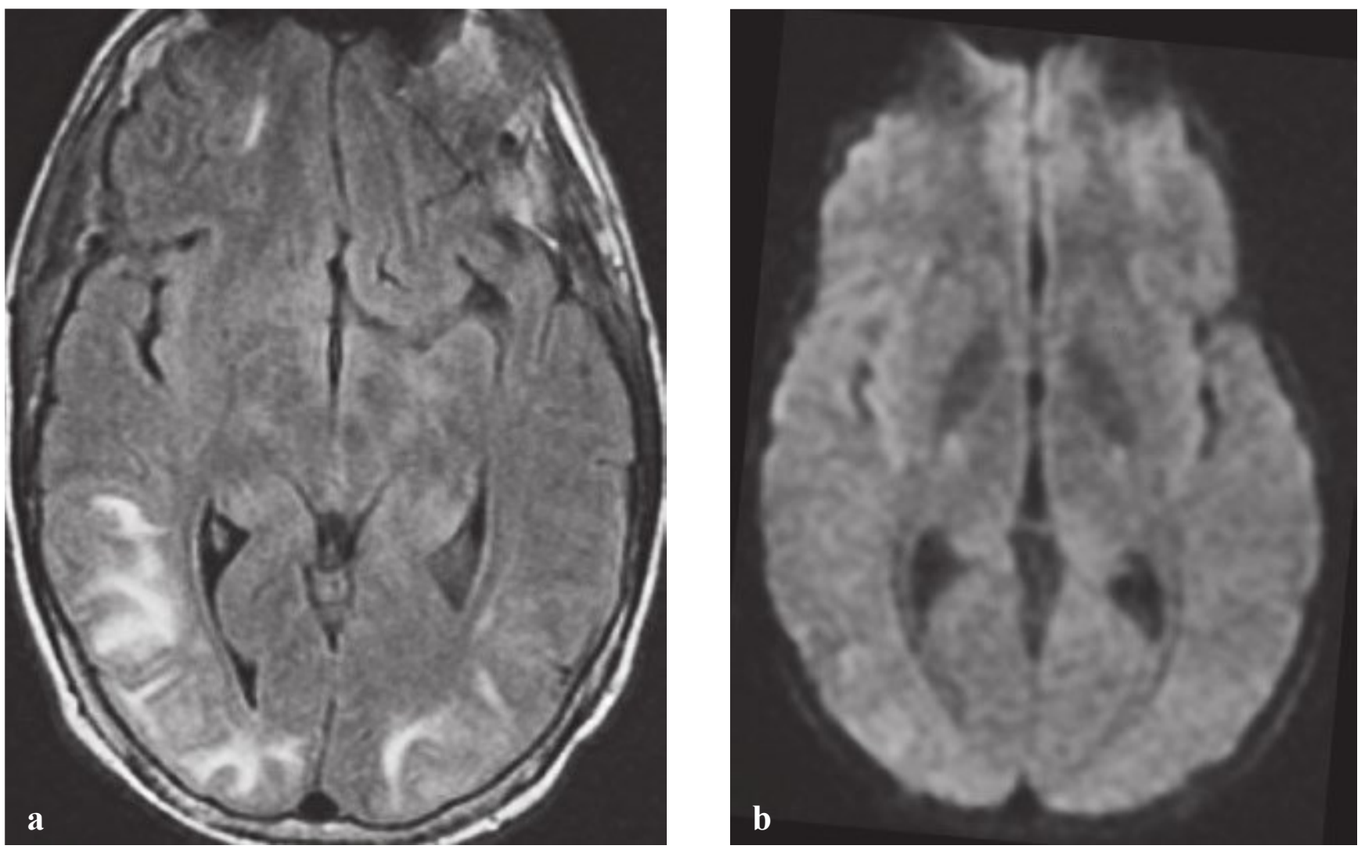

Fig. 1.265 A 12-year-old female who had chemotherapy for acute lymphocytic leukemia (ALL) complicated by posterior reversible encephalopathy syndrome (PRES). **(a)** Axial FLAIR shows asymmetric abnormal high signal in the posterior cerebral white matter, with **(b)** no restricted diffusion on axial DWI.

1.6 Basal Ganglia and Thalami

Basal Ganglia

The basal ganglia includes the *corpus striatum* (*caudate* and *putamen*), *globus pallidus, subthalamic nucleus*, and *substantia nigra* **(Fig. 1.266** and **Fig. 1.267)**. The corpus striatum is derived from the telencephalon (neostriatum) and consists of the putamen and caudate. The caudate is a C-shaped structure that consists of a large head that borders the floor and lateral margin of the frontal horn of the lateral ventricle, a narrow body posteriorly, and a contiguous thin tail that extends anteriorly along the upper margin of the temporal horn of the lateral ventricle until its termination into the amygdala. The medial border of the head and body of the caudate is the lateral ventricle, and the lateral margin of the caudate head is the anterior limb of the internal capsule. The putamen is located medial to the external capsule, posterolateral to the anterior limb of the internal capsule, and lateral to the globus pallidus. The caudate connects to the putamen via thin bands of gray matter that pass through the internal capsule. The globus pallidus is derived from the diencephalon/paleostriatum. The lateral border of the globus pallidus is the putamen, and the medial border is the posterior limb of the internal capsule. The combination of the putamen and globus pallidus is referred to as the lentiform (lens-shaped) nucleus. The subthalamic nucleus is a small gray matter/nucleus positioned between the midbrain inferiorly and diencephalon superiorly. The subthalamic nucleus is located superior to the low-signal substantia nigra on T2-weighted imaging, and inferomedial to the internal capsule. The substantia nigra is located in the ventral tegmentum of the midbrain anterolateral to the red nuclei and consists of the pars compacta and pars reticularis.

The corpus striatum is involved in control of motor movements by mediation via the pyramidal system through interactions with the motor cortex, globus pallidus, subthalamic nucleus, and substantia nigra **(Fig. 1.268)**. There is, however, no direct ouput from the basal ganglia to the spinal cord. In addition to a role in control of motor movements, the basal ganglia is involved in various neuronal pathways, including associative and cognitive functions, emotions, and motivation. Abnormalities involving the corpus striatum can result in movement disorders, such as Huntington disease and multisystem atrophy (MSA-P).

The globus pallidus is involved with control of fine motor movement via interaction with the caudate, putamen, substantia nigra, and thalamus. The globus pallidus often has lower signal than the putamen on T2-weighted imaging because of age-related iron deposition, and it can have higher signal on T1-weighted imaging because of a relatively greater proportion of myelin. High signal on T1-weighted imaging can be seen in the globus pallidus with hepatic dysfunction, hyperalimentation, and manganese deposition. High signal on T2-weighted imaging in the globus pallidus can be seen with carbon monoxide poisoning and in neurodegeneration with brain iron accumulation (PKAN disease).

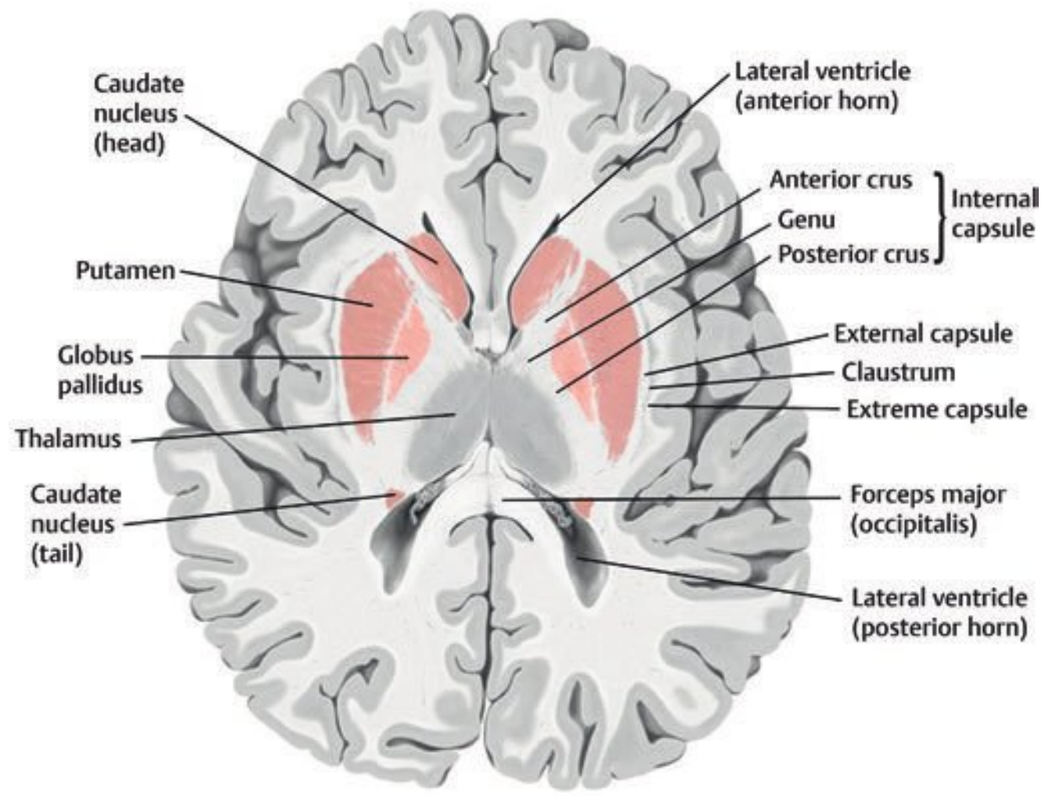

Fig. 1.266 Axial diagram shows basal ganglia, thalami, and adjacent structures. From THIEME Atlas of Anatomy, Neck and Internal Organs, © Thieme 2006, Illustration by Karl Wesker.

Subthalamic Nucleus

The subthalamic nucleus has functional interaction with the globus pallidus and substantia nigra within the latero-pallido-subthalamic system that is affected in Parkinson's disease. The subthalamic nucleus is a treatment placement site for deep brain stimulation in patients with Parkinson's disease.

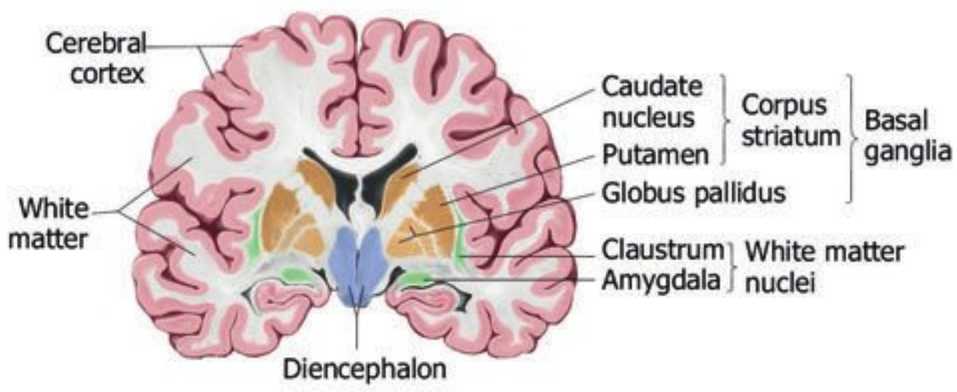

Fig. 1.267 Coronal diagram shows basal ganglia, thalami, and adjacent structures. From THIEME Atlas of Anatomy, Neck and Internal Organs, © Thieme 2006, Illustration by Karl Wesker.

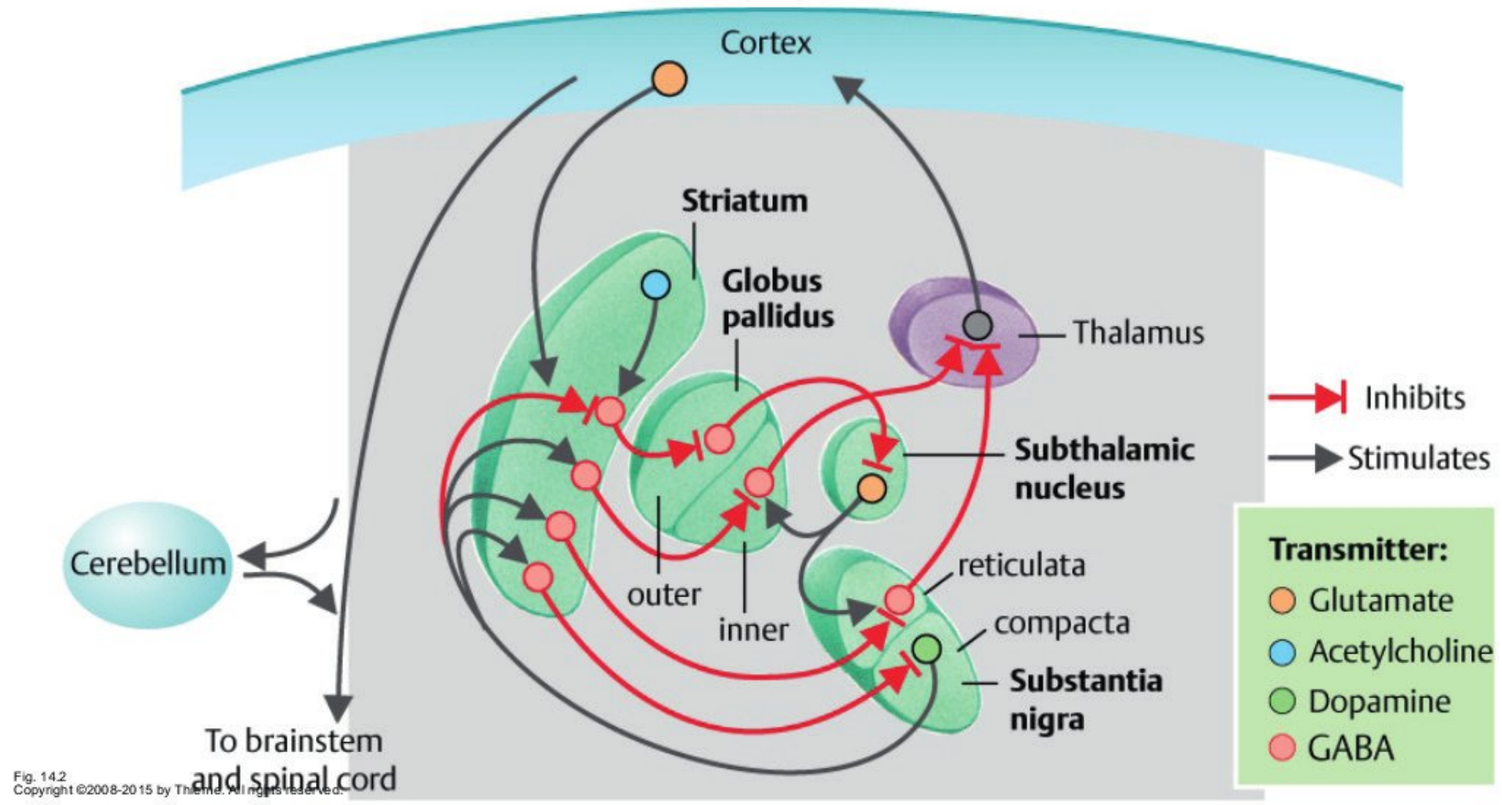

Fig. 14.2
Copyright ©2008-2015 by Thieme. All rights reserved.

Fig. 1.268 Diagram shows neurotransmitter pathways in the basal ganglia, thalamus, subthalamic nucleus, cerebral cortex, brainstem, and spinal cord. Used with permission from Simmons MA. Pharmacology: An Illustrated Review. New York, NY: Thieme; 2012.

Substantia Nigra

The pars reticularis of the substantia nigra has elevated iron deposition, resulting in a low signal on T2-weighted imaging and GRE relative to the pars compacta. The pars compacta usually has a higher signal on T2-weighted imaging relative to the pars reticularis. The pars compacta contains dopaminergic neurons with melanin that can result in gross specimens having dark pigmentation, accounting for the "nigra" in substantia nigra. Parkinson's disease is associated with degeneration of the pars compacta, resulting in decreased dopaminergic input to the corpus striatum and globus pallidus.

Thalamus

The thalamus is derived from the diencephalon and is located at the dorsal upper end of the brainstem. The thalamus is bordered by the internal capsules laterally, the third ventricle medially, and the corpus callosum and lateral ventricles superiorly. Each side of the thalamus is connected via the massa intermedia that crosses the third ventricle. The thalamus has an MRI signal similar to gray matter, and contains up to 60 nuclei. The thalamic nuclei are divided into groups based on location, such as the medial, lateral, and anterior groups. The thalamus is involved in the relay of sensory and motor input between the cerebral cortex and spinal cord. Deep brain stimulation has been used for treatment of essential tremors by placement of probes into the ventral intermediate nucleus of the thalamus.

Table 1.6 Bilateral lesions involving the basal ganglia and/or thalami

- Calcifications
  - Idiopathic basal ganglia calcifications
  - Hypothyroidism
  - Hyperparathyroidism
  - Hypoparathyroidism
  - Pseudohypoparathyroidism
  - Pseudo-pseudohypopara-thyroidism (Pseudo-PHP)
  - Fahr disease
  - Cockayne syndrome
- Cerebral Ischemia/Infarction
  - Hypoxic-ischemic injury
  - Arterial occlusion/brain infarction
  - Moyamoya disease
  - Venous occlusion/cerebral infarction
  - Small-vessel ischemic disease
  - CADASIL
  - Vasculitis
  - Acute hypertensive crisis (malignant hypertension)
- Inherited Metabolic Disorders
  - MELAS and MERRF
  - Leigh's disease
  - Kearns-Sayre syndrome
  - Disorders of amino acid and urea cycle metabolism: Phenylketonuria, propionic acidemia, methylmalonic aciduria, homocystinuria, ornithine transcarbamylase deficiency, citrullinemia, arginosuccinic aciduria, leucinosis (maple syrup urine disease), glutaric acidemia/aciduria, others
  - Neurodegeneration with brain iron accumulation: Pantothenate kinase-associated neurodegeneration (PKAN disease)
  - Wilson's disease
  - Menkes' syndrome (trichopoliodystrophy)
  - Lysosomal enzyme defects:mucopolysaccharidoses
  - Canavan disease, also known as Canavan-van Bogaert-Bertrand disease
- Other Metabolic Disorders
  - Acquired hepatocerebral degeneration
  - Hypoglycemia
  - Nonketotic hyperglycemia
  - Wernicke's encephalopathy
  - Seizure
- Toxic Encephalopathy
  - Carbon monoxide poisoning
  - Methanol intoxication
  - Ethylene glycol toxicity
  - Cyanide
  - Cocaine
  - Heroin
- Neurodegenerative Disease
  - Huntington disease
  - Multiple system atrophy (striatonigral degeneration [MSA-P], olivopontocerebellar atrophy [MSA-C], Shy-Drager syndrome [MSA-A])
  - Pallidotomy
  - Wallerian degeneration
  - Prominent perivascular spaces
- Infection
  - Pyogenic brain abscess
  - Fungal brain lesions
  - Viral encephalitis
  - Herpes simplex
  - Cytomegalovirus (CMV)
  - Progressive multifocal leukoencephalopathy
  - Japanese encephalitis
  - Rabies
  - Acute measles encephalitis
  - Subacute sclerosing panencephalitis from measles
  - West Nile virus
  - Parasitic disease: Toxoplasmosis
  - Parasitic disease: Cysticercosis
  - Prion disease
- Demyelinating Disease
  - Multiple sclerosis
  - Acute disseminated encephalomyelitis
  - Neurosarcoid
- Trauma
  - Diffuse axonal injury
- Hemorrhage
  - Deep venous occlusion with hemorrhagic infarction
  - Preterm neonates with hemorrhage involving the germinal matrix
- Vascular Malformations
  - Cavernous malformations
  - Capillary telangiectasias
- Neoplasms
  - Metastases
  - Lymphoma
  - Gliomatosis cerebri
  - Anaplastic astrocytoma
  - Glioblastoma multiforme
  - Pilocytic astrocytoma
- Tumorlike Lesions
  - Neurofibromatosis type 1 (NF1): Vacuolated myelin/dysplastic white matter lesions
  - Neurofibromatosis type 1 (NF1): High signal on T1-weighted images involving the globus pallidus and internal capsules bilaterally
  - Neuroepithelial cyst

Table 1.6 Bilateral lesions involving the basal ganglia and/or thalami

Lesions	Imaging Findings	Comments
Calcifications		
Idiopathic basal ganglia calcifications (**Fig. 1.269**)	CT: Punctate calcifications in the caudate nuclei, thalami, putamina, and/or globi pallidi bilaterally. MRI: Calcifications usually have low signal on T2-weighted images, gradient echo imaging, and susceptibility weighted imaging.	The basal ganglia are involved in the intiation and modulation of movement. Physiologic and nonpathologic calcifications involving the caudate nuclei, putamen, and/or globus pallidus bilaterally occur in adults over the age of 30 years. They occur in 1 to 2% of the population, usually in adults, and increase in frequency with age. Idiopathic calcifications account for 75% of basal ganglia calcifications. Calcifications in these locations can also occur with disorders of calcium and phosphate metabolism (hypoparathyroidism, pseudohypoparathyroidism, pseudo-pseudohypoparathyroidism, hyperparathyroidism, and carbonic anhydrase II deficiency).
Hypothyroidism	CT: Punctate calcifications in the caudate nuclei, thalami, putamina, and/or globi pallidi bilaterally. MRI: Calcifications usually have low signal on T2-weighted imaging, gradient echo imaging, and susceptibility weighted imaging.	Disorder resulting from insufficient amount of thyroid hormone that can be congenital and associated with developmental abnormalities (cretinism) or resulting from loss of thyroid tissue (autoimmune diseases that produce antithyroid antibodies or antibodies that block the TSH receptor, surgery, or radioiodine ablation for treatment of Graves disease).
Hyperparathyroidism	CT: Punctate calcifications in the caudate nuclei, thalami, putamina, and/or globi pallidi bilaterally. MRI: Calcifications usually have low signal on T2-weighted imaging, gradient echo imaging, and susceptibility weighted imaging.	Primary type results from excess production of parathyroid hormone (PTH) from hyperplasia or adenomas of the parathyroid gland(s). PTH regulates calcium and phosphate blood levels. Excessive PTH secretion results in hypercalcemia and hypophosphatemia. Secondary hyperparathyroidism occurs with elevated PTH levels in response to low calcium levels from disorders such as chronic renal disease or vitamin D deficiency. Calcium levels in blood are low or normal, and phosphate levels are usually elevated.
Hypoparathyroidism	CT: Punctate calcifications in the caudate nuclei, thalami, putamina, and/or globi pallidi bilaterally. MRI: Calcifications usually have low signal on T2-weighted imaging, gradient echo imaging, and susceptibility weighted imaging.	Hypoparathroidism occurs when there is a deficiency in formation of parathyroid hormone (PTH), which regulates metabolism of calcium, phosphorus, and vitamin D. Deficiency of PTH from the parathyroid glands results in decreased blood calcium levels and elevated blood phosphorus levels. Can result from injury to the parathyroid glands during head and neck surgery or radioactive iodine treatment for hyperthyroidism. DiGeorge syndrome of hypoparathyroidism occurs because of congenital absence of the parathyroid glands. Familial hypoparathyroidism occurs with other endocrine diseases, such as adrenal insufficiency in a syndrome called type I polyglandular autoimmune syndrome (PGA-I).

Lesions	Imaging Findings	Comments
Pseudohypoparathyroidism	CT: Punctate calcifications in the caudate nuclei, thalami, putamina, and/or globi pallidi bilaterally. MRI: Calcifications usually have low signal on T2-weighted imaging, gradient echo imaging, and susceptibility weighted imaging.	Pseudohypoparathyroidism is a rare syndrome in which there is resistance to the effects of PTH in the body, resulting in low blood calcium levels and high blood phosphate levels. Associated with dysfunctional G proteins (Gs-α subunit) due to mutation in the GNAS1 gene. PTH levels are often elevated. Type Ia (also called Albright's hereditary osteodystrophy) is autosomal dominant and results in short stature, round face, and short fourth and fifth metacarpal bones. Type Ib involves resistance to PTH only in the kidneys and is associated with a methylation defect; it lacks the physical features of type Ia. Type II pseudohypoparathyroidism is very similar to type I but the events that take place in the kidneys are different. Type II is associated with low blood calcium and high blood phosphate levels, but the physical characteristics associated with type Ia are absent.
Pseudo-pseudohypopara-thyroidism (Pseudo-PHP)	CT: Punctate calcifications in the caudate nuclei, thalami, putamina, and/or globi pallidi bilaterally. MRI: Calcifications usually have low signal on T2-weighted imaging, gradient echo imaging, and susceptibility weighted imaging.	Pseudo-pseudohypoparathyroidism has skeletal features similar to pseudohypoparathyroidism Ia without abnormal serum levels of PTH, calcium, phosphate, or calcitrol. It is related to mutation of the GNAS gene inherited from the father. Punctate calcifications are seen in the caudate nuclei, thalami, putamina, and/or globi pallidi bilaterally.

(continued on page 222)

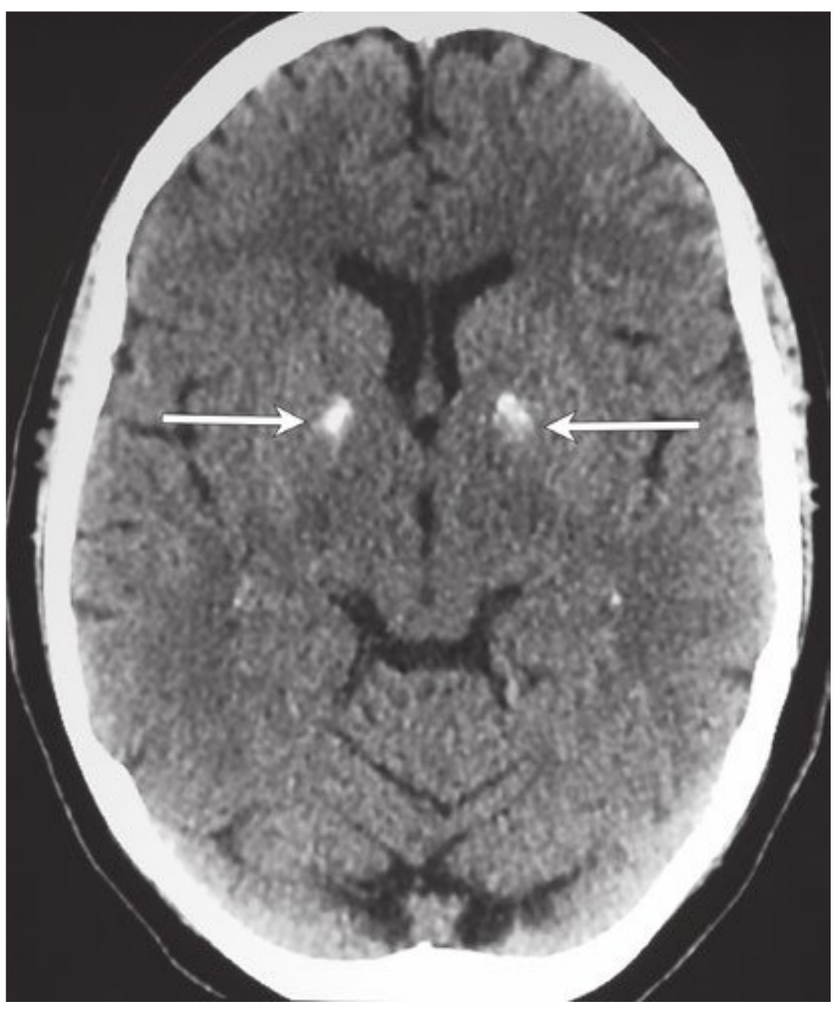

Fig. 1.269 Idiopathic calcifications (arrows) are seen in the basal ganglia bilaterally on axial CT.

Table 1.6 (cont.) Bilateral lesions involving the basal ganglia and/or thalami

Lesions	Imaging Findings	Comments
Fahr disease (**Fig. 1.270**)	CT: Intra-axial calcifications occur in the basal ganglia, dentate nuclei, and cerebral white matter. MRI: Calcifications usually have low signal on T2-weighted imaging, gradient echo imaging, and susceptibility weighted imaging. Calcifications in brain usually have low signal on T1-weighted imaging, but occasionally, when calcified particles in brain are small and/or have high relative surface areas, T1 relaxation times of adjacent protons can be reduced, resulting in high signal on T1-weighted imaging.	Fahr disease, also known as familial cerebrovascular ferrocalcinosis or idiopathic basal ganglia calcification (IBGC), is a group of disorders with deposition of calcification in the brain. Patients can present with dystonia, parkinsonism, ataxia, and behavioral and cognitive impairment. Autosomal dominant inheritance of IBGC has been linked to a locus on chromosome 14.
Cockayne syndrome (**Fig. 1.271**)	MRI: High signal on T2-weighted imaging in the periventricular white matter, basal ganglia, and dentate nuclei; low signal on T2-weighted imaging from calcifications in basal ganglia, dentate nuclei, and white matter; progressive cerebral and cerebellar atrophy; microcephaly. Magnetic resonance spectroscopy can show decreased N-acetylaspartate (NAA) and choline peaks, and slightly elevated lactate. CT: Progressive cerebral and cerebellar atrophy, with calcifications in basal ganglia and dentate nuclei.	Autosomal recessive disorder involving mutations of the CSA (CKN1 or ERCC8) gene, CSB (CKN2 or ERCC6) gene, or xeroderma pigmentosa (XP) gene. Mutations alter nucleotide excision-repair pathways, resulting in defective repair of DNA damage caused by ultraviolet radiation. The syndrome presents in the first decade with progressive neurologic dysfunction, cataracts, cutaneous photosensitivity, optic atrophy, and dwarfism. Four overlapping subgroups with decreasing severity: COFS, CSI, CSII, and CSIII. Pathologic findings include hypomyelination, myelin loss and degradation involving cerebral and cerebellar white matter, cerebral and cerebellar atrophy, and intra-axial calcifications.

(continued on page 224)

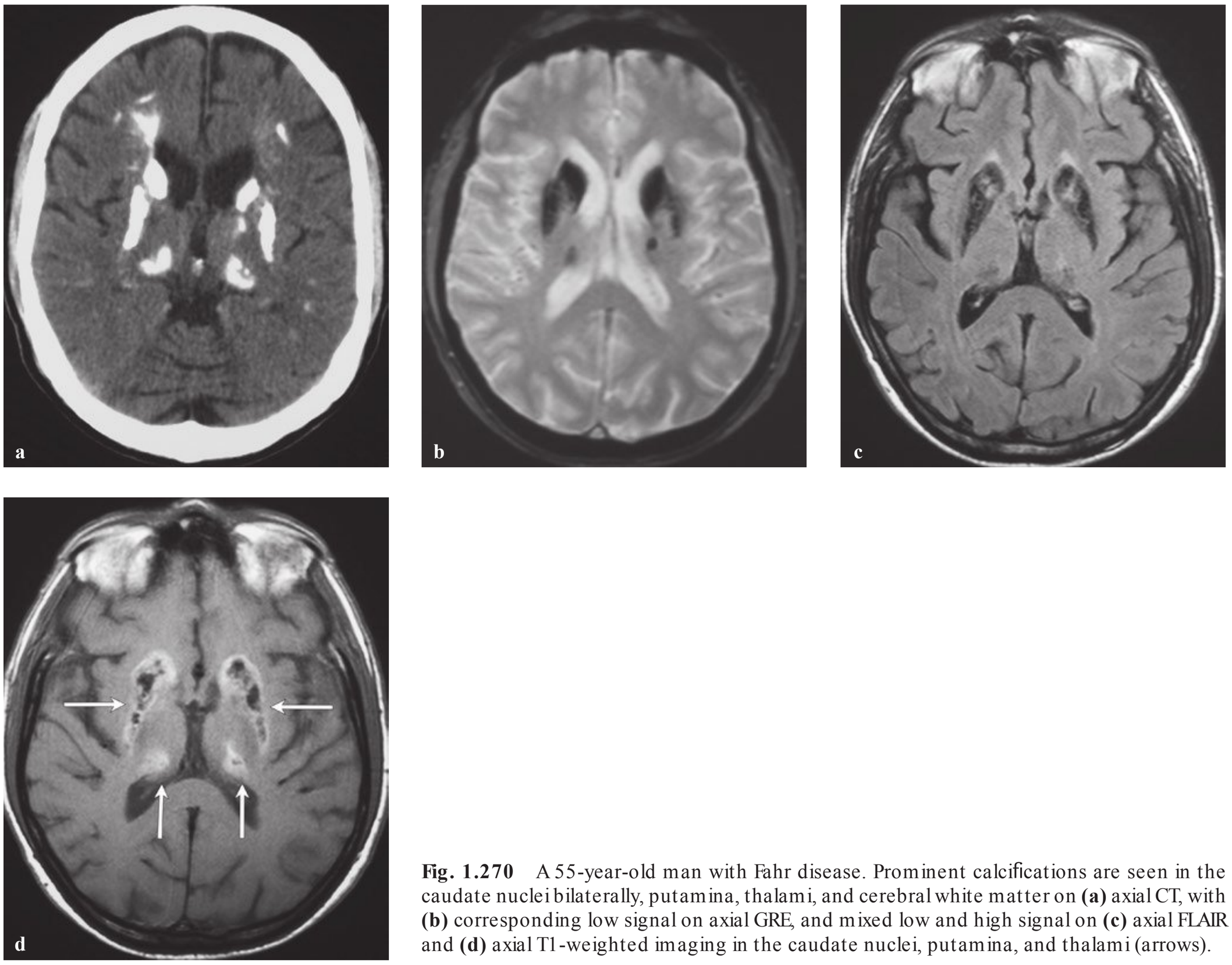

Fig. 1.270 A 55-year-old man with Fahr disease. Prominent calcifications are seen in the caudate nuclei bilaterally, putamina, thalami, and cerebral white matter on **(a)** axial CT, with **(b)** corresponding low signal on axial GRE, and mixed low and high signal on **(c)** axial FLAIR and **(d)** axial T1-weighted imaging in the caudate nuclei, putamina, and thalami (arrows).

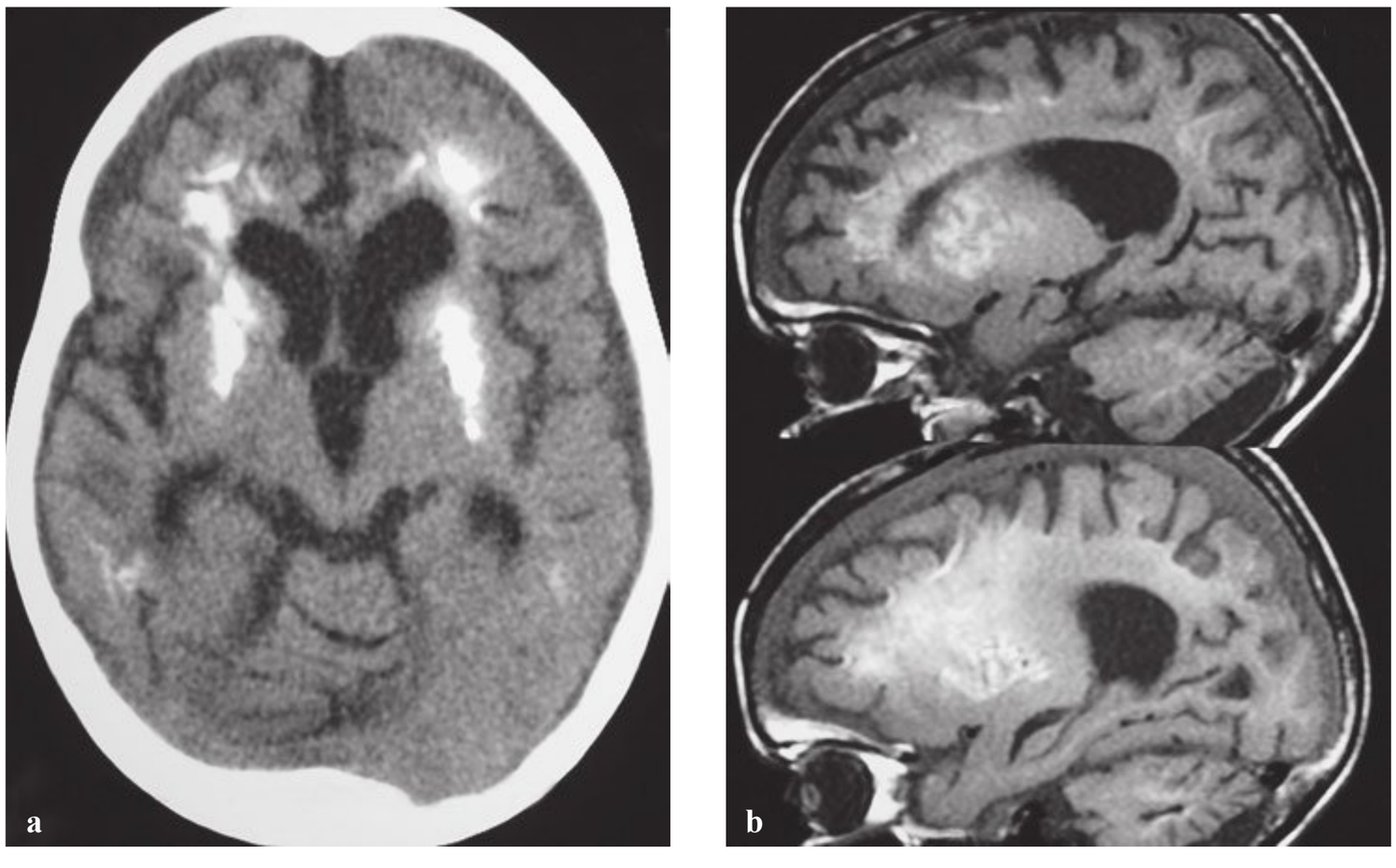

Fig. 1.271 **(a)** An 11-year-old male with Cockayne disease who has multiple calcifications in the caudate nuclei, putamina, and white matter bilaterally on axial CT that **(b)** have high signal on sagittal T1-weighted imaging.

Table 1.6 (cont.) Bilateral lesions involving the basal ganglia and/or thalami

Lesions	Imaging Findings	Comments
Cerebral Ischemia/Infarction		
Hypoxic-ischemic injury (**Fig. 1.272** and **Fig. 1.273**)	CT: Bilateral zones of low attenuation in the basal ganglia, caudate nuclei, thalami, brainstem, and/or perisylvian cerebral cortex. MRI: Bilateral zones of high signal on T2-weighted imaging, FLAIR, and diffusion-weighted imaging (low signal on ADC maps) in the basal ganglia, caudate nuclei, thalami, brainstem, and/or perisylvian cerebral cortex.	Prolonged hypotension and anoxia result in ischemia and infarction in portions of the brain with selective vulnerability to hypoxia and impairment of aerobic metabolism. Can result from drowning, asphyxiation, and cardiac arrest. In less severe cases of hypotension in adults, zones of infarction can occur between the distal vascular distributions of two arteries, "watershed infarcts."
Arterial occlusion/brain infarction (**Fig. 1.274**) Hyperacute infarct (< 12 hours) Acute infarct (12–24 hours) Early subacute infarct (24 hours to 3 days) Late subacute infarct (4 days to 2 weeks) Post-subacute infarct (2 weeks to 2 months) Remote infarct (> 2 months)	MRI and CT features of cerebral and cerebellar infarcts depend on age of infarct relative to time of examination. Hyperacute infarct MRI: Localized edema, usually isointense signal to normal brain on T1- and T2-weighted imaging. Diffusion-weighted imaging (DWI) shows positive findings related to decreased apparent diffusion coefficients secondary to cytotoxic edema, and absence of arterial flow void or arterial enhancement in the vascular distribution of the infarct. CT: No abnormality in 50%, decreased attenuation and blurring of lentiform nuclei and hyperdense artery in remainder. Acute infarct MRI: Intermediate signal on T1-weighted imaging, high signal on T2-weighted imaging, FLAIR, and DWI, localized edema. Signal abnormalities commonly involve the cerebral cortex and subcortical white matter, and/or basal ganglia. CT: Blurring of junction between the cerebral cortex and white matter, decreased attenuation in the basal ganglia. Early subacute infarct MRI: Low-intermediate signal on T1-weighted imaging, high signal on T2-weighted imaging, FLAIR, and DWI, localized edema, ± hemorrhage, ± gadolinium contrast enhancement. CT: Localized swelling at sites of decreased attenuation with or without hemorrhage. Late subacute infarct MRI: Low-intermediate signal on T1-weighted imaging, high signal on T2-weighted imaging and FLAIR, edema/mass effect diminishing, ± hemorrhage, ± gadolinium contrast enhancement. High signal on DWI and low signal on ADC maps resolve ("pseudonormalize") at 10 days to 2 weeks. CT: Localized swelling increases, then decreases; low attenuation at lesion becomes more conspicuous. Post-subacute infarct MRI: Low-intermediate signal on T1-weighted imaging, high signal on T2-weighted imaging and FLAIR, edema resolves, ± hemorrhage CT: Localized mass effect at site of low attenuation resolves. Remote infarct MRI: Low signal on T1-weighted imaging, high signal on T2-weighted imaging, encephalomalacic changes, ± calcification, hemosiderin. CT: Zone of low attenuation associated with encephalomalacia.	Brain infarcts usually result from occlusive vascular disease involving large, medium, or small arteries. The basal ganglia (caudate nucleus, putamen, and globus pallidus) receive their blood supply from the medial lenticulostriate arteries (anterior cerebral artery) and the lateral lenticulostriate arteries (middle cerebral artery). The thalamus receives its blood supply from branches off the P1 and P2 segments of the posterior cerebral artery as well as from branches off the posterior communicating artery. A relevant anatomic vascular variant is the artery of Percheron, which is an artery that arises from the proximal portion of one posterior cerebral artery and provides blood supply to both thalami as well as both sides of the midbrain. Occlusion of this artery can result in infarction of the paramedian portions of both the thalami and the midbrain.

(continued on page 226)

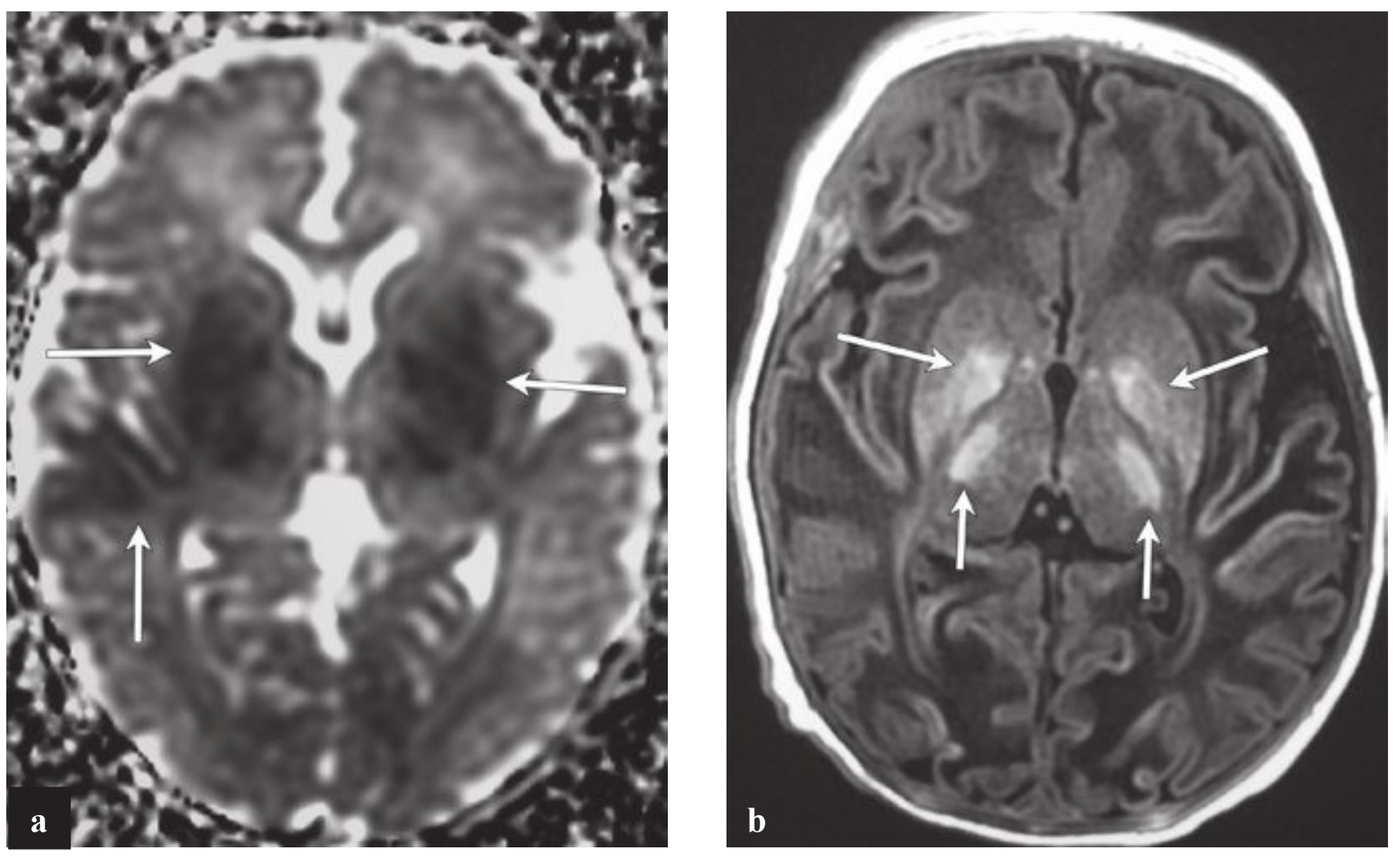

Fig. 1.272 A 2-month-old male infant with an episode of severe hypoxic-ischemic encephalopathy. **(a)** Axial ADC shows restricted diffusion in the basal ganglia and thalami bilaterally (arrows), as well as right temporal cerebral cortex. **(b)** Abnormal high signal on axial T1-weighted imaging is seen in the putamina and thalami (arrows), which are higher than the internal capsules.

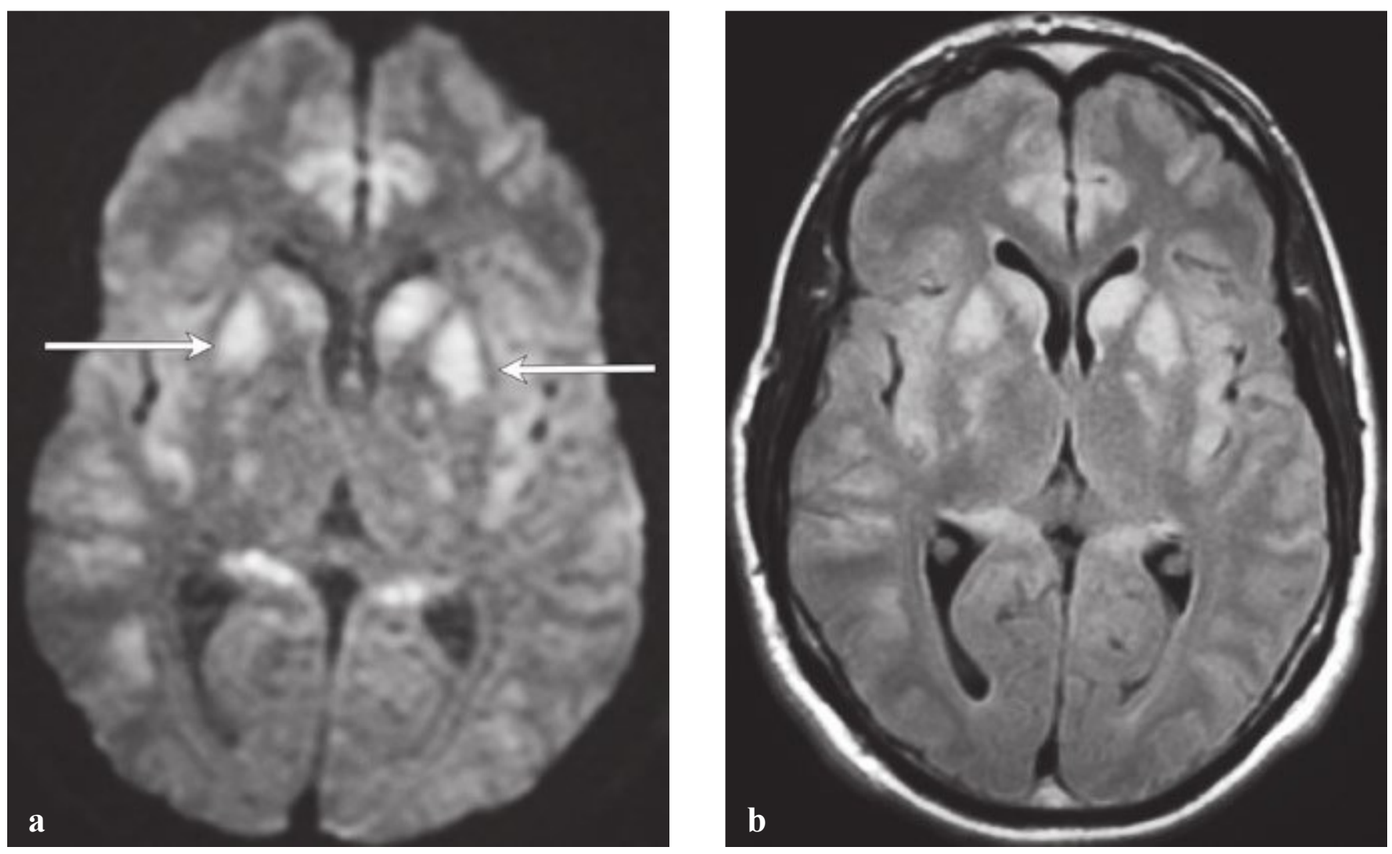

Fig. 1.273 A45-year-old man resuscitated man after cardiac arrest complicated by hypoxic-ischemic encephalopathy. **(a)** Axial DWI shows restricted diffusion in the caudate nuclei, putamina, and thalami (arrows), with **(b)** corresponding high signal on axial FLAIR.

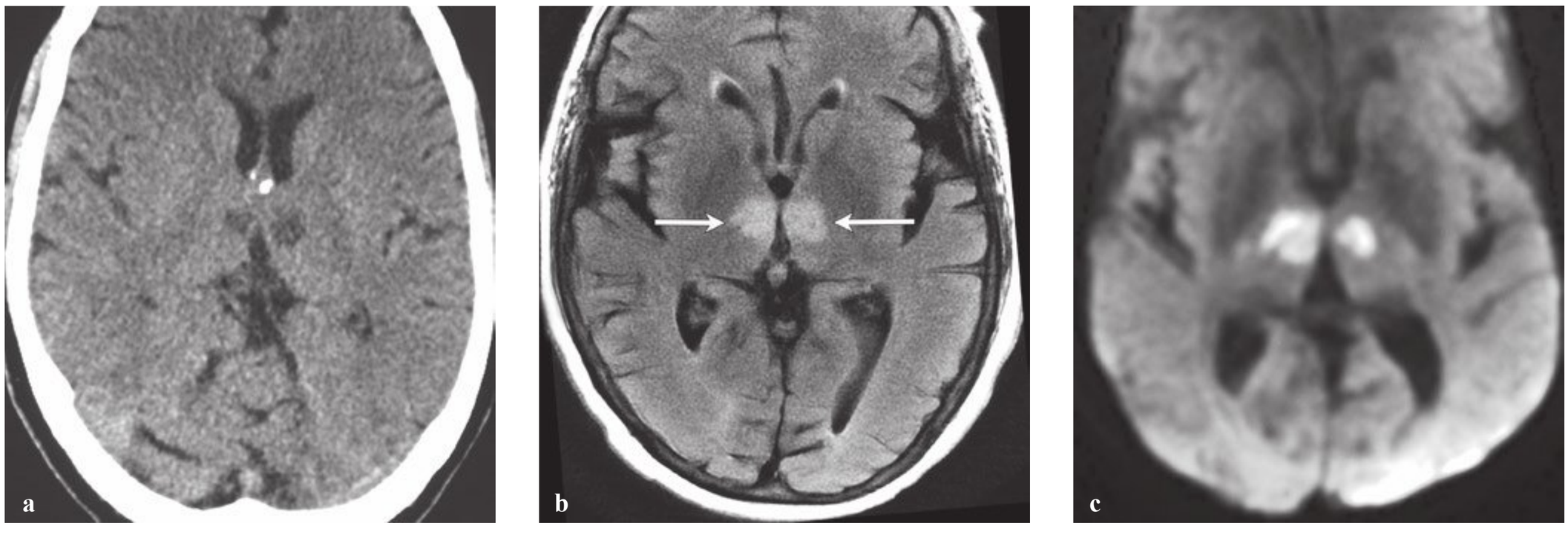

Fig. 1.274 Bilateral acute infarcts in thalami from occlusion of the artery of Percheron in a 76-year-old woman seen as **(a)** bilateral zones with low attenuation on axial CT, **(b)** high signal (arrows) on axial FLAIR, and **(c)** restricted diffusion on axial DWI.

Table 1.6 (cont.) Bilateral lesions involving the basal ganglia and/or thalami

Lesions	Imaging Findings	Comments
Moyamoya disease (**Fig. 1.275**)	Multiple, tortuous, tubular vessels seen in the basal ganglia and thalami secondary to dilated collateral arteries. CT and MRI can show contrast enhancement of these arteries related to slow flow within the collateral arteries versus normal-size arteries. Often + contrast enhancement of the leptomeninges related to pial collateral vessels. Decreased or absent caliber of contrast-enhanced supraclinoid portions of the internal carotid arteries and proximal middle and anterior cerebral arteries. MRA and CTA show stenosis and occlusion of the distal internal carotid arteries with collateral arteries (lenticulostriate, thalamoperforate, and leptomeningeal) best seen after contrast administration, enabling detection of slow blood flow.	Progressive occlusive disease of the intracranial portions of the internal carotid arteries, with resultant numerous dilated collateral arteries arising from the lenticulostriate and thalamoperforate arteries as well as other parenchymal, leptomeningeal, and transdural arterial anastomoses. Moyamoya translates from Japanese as "puff of smoke," which refers to the angiographic appearance of the collateral arteries (lenticulostriate, thalamoperforate). There is often a nonspecific etiology but the disease can be associated with neurofibromatosis, radiation angiopathy, atherosclerosis, and sickle-cell disease. It usually occurs in Asia, and in children more than in adults.
Venous occlusion/ cerebral infarction (**Fig. 1.276**)	MRI: Intra-axial zones with high signal on T2-weighted imaging and FLAIR, + localized mass effect and restricted diffusion in acute phase, ± hemorrhage, ± gadolinium contrast enhancement. Lesions do not correspond to an arterial distribution. CT: Intra-axial zones with low-intermediate attenuation, + localized mass effect in acute phase, ± hemorrhage. CTA/MRA: Absent contrast enhancement on CTA and absent flow signal on MRA in the intracranial venous sinuses or large intracranial veins.	Infarction of brain tissue in the venous distribution that results from thrombosis of the corresponding vein or venous sinus secondary to venous hypertension. Occlusion of the deep venous system (internal cerebral veins, vein of Galen, and straight sinus) can result in infarcts involving both thalami and basal ganglia. Venous occlusion be related to coagulopathy (sickle-cell disease, thalassemia, etc.), dehydration, polycythemia, and medications, such as oral contraceptives.
Small-vessel ischemic disease (**Fig. 1.277**)	MRI: Multiple foci and/or confluent zones of decreased signal on T1-weighted imaging and high signal on T2-weighted imaging and FLAIR in the subcortical and periventricular cerebral white matter, basal ganglia, and brainstem. There is no associated mass effect, and typically no restricted diffusion and no gadolinium contrast enhancement. CT: Multiple foci and/or confluent zones of decreased attenuation involving the subcortical and periventricular cerebral white matter, basal ganglia, and brainstem. There is no associated mass effect, and typically no contrast enhancement.	Lesions in white matter and/or brainstem related to occlusive disease involving perforating arteries and associated with hypertension, atherosclerosis, diabetes, vasculitis, and aging. Unlike multiple sclerosis, ischemic small-vessel disease does not usually involve the corpus callosum because of its abundant blood supply from multiple branches of the adjacent pericallosal arteries.

(continued on page 228)

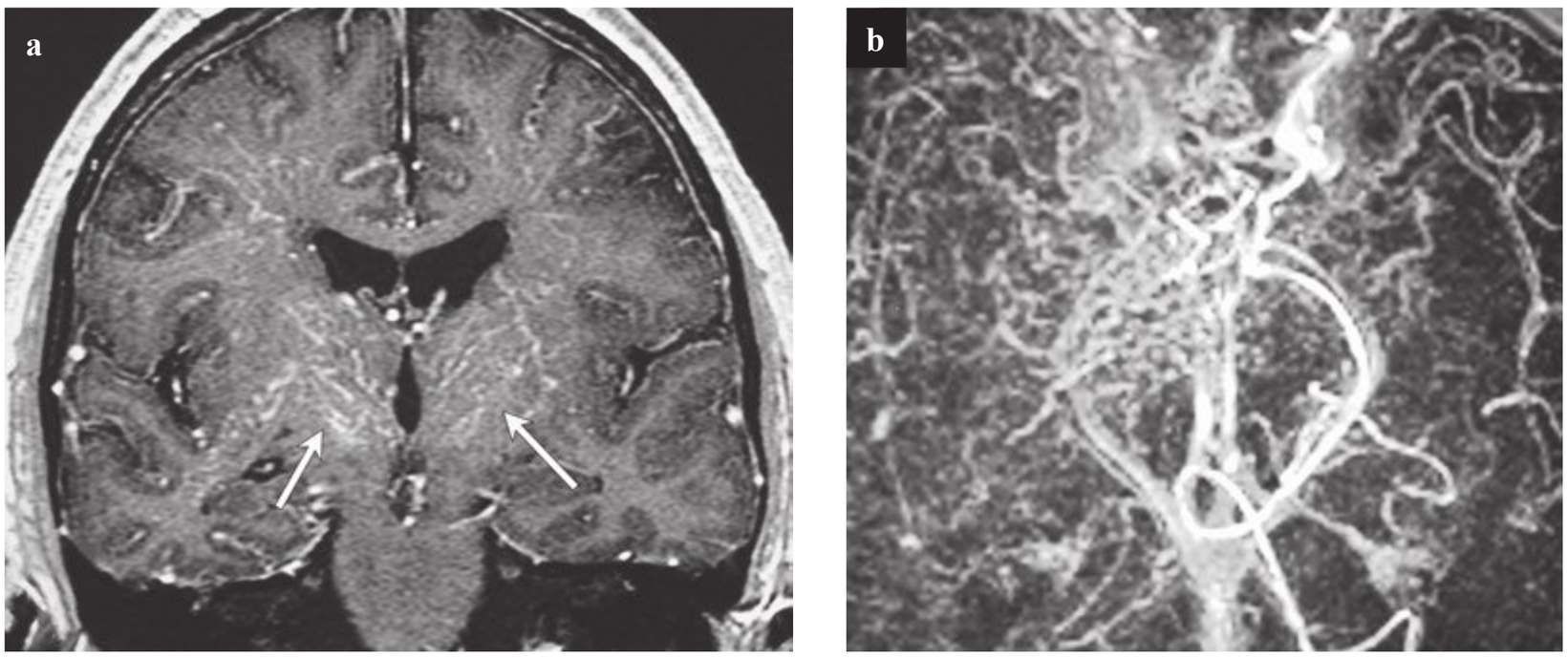

Fig. 1.275 A 31-year-old man with moyamoya disease. **(a)** Postcontrast coronal T1-weighted imaging shows multiple enhancing lenticulostriate collateral blood vessels in the basal ganglia (arrows). **(b)** Postcontrast axial MRA shows multiple small enhancing leptomenigeal and lecticulostriate collateral blood vessels.

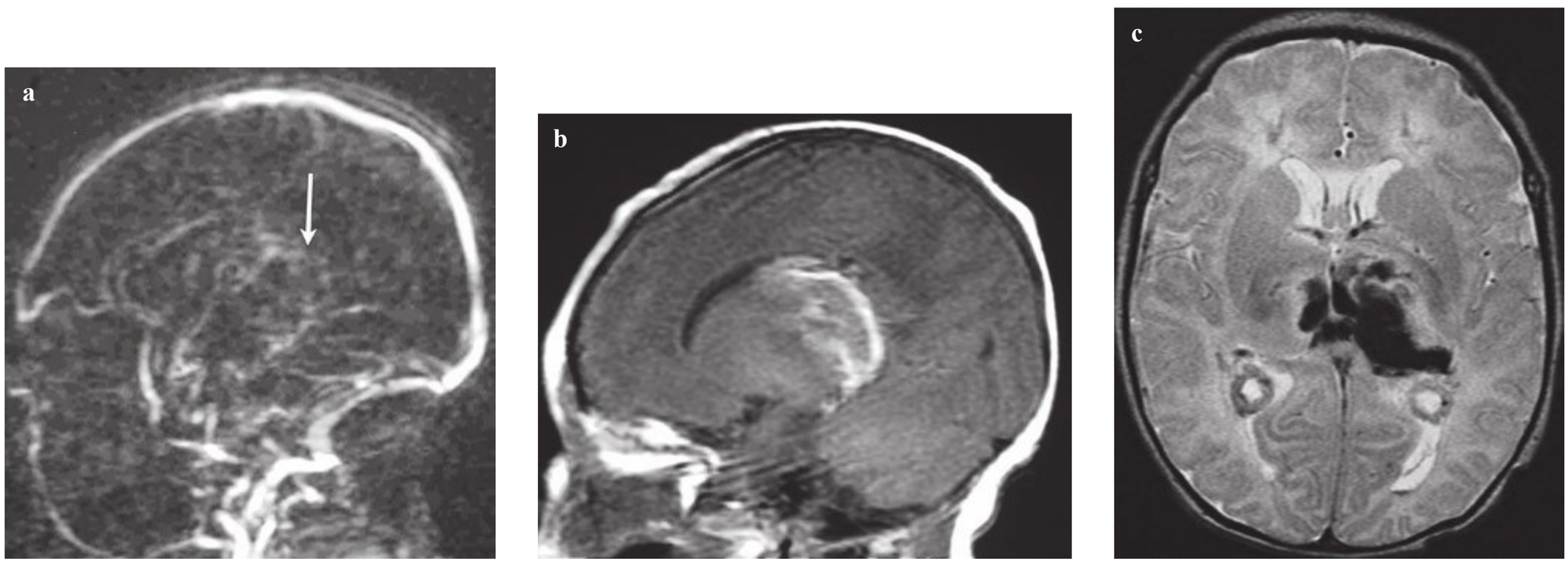

Fig. 1.276 **(a)** A 5-day-old neonate with occlusion of the internal cerebral veins, vein of Galen, and straight venous sinus with lack of flow signal (arrow) on sagittal 2D phase contrast MRV. The occluded vein has high signal on sagittal T1-weighted imaging and **(c)** is associated with hemorrhage in the thalami with high signal on **(b)** T1-weighted imaging and low signal on **(c)** axial T2-weighted imaging.

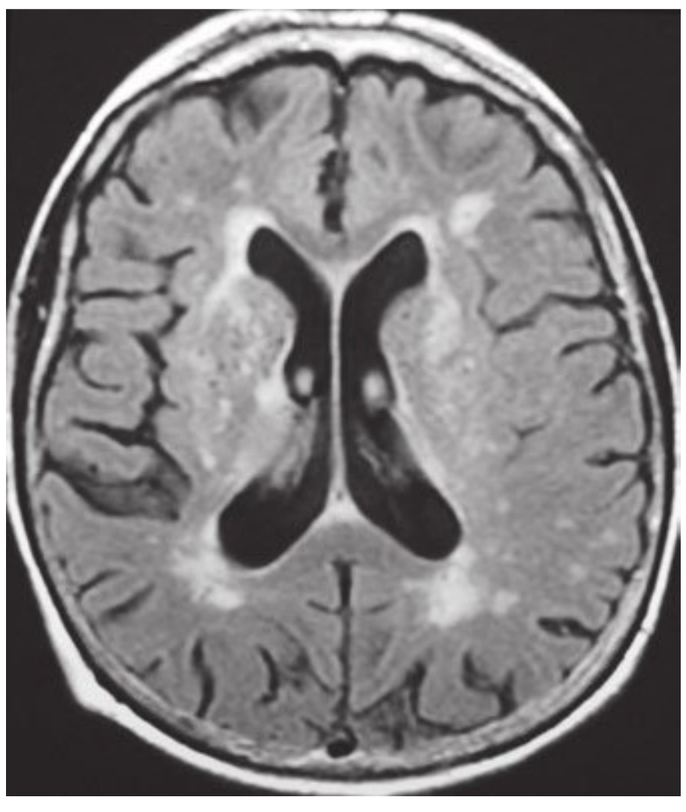

Fig. 1.277 An 85-year-old woman with small-vessel ischemic disease that is seen as multiple zones with abnormal high signal on axial FLAIR in the cerebral white matter and basal ganglia bilaterally without abnormal mass effect.

Table 1.6 (cont.) Bilateral lesions involving the basal ganglia and/or thalami

Lesions	Imaging Findings	Comments
CADASIL (**Fig. 1.278**)	MRI: Multiple zones of decreased signal on T1-weighted imaging and high signal on T2-weighted imaging in the subcortical and periventricular white matter, basal ganglia, thalami, and brainstem. Usually no restricted diffusion unless recent ischemic event (uncommon), no associated mass effect, and typically no gadolinium contrast enhancement. CT: Multiple zones of decreased attenuation in the subcortical and periventricular white matter, basal ganglia, thalami, and brainstem. There is no associated mass effect, and no contrast enhancement.	CADASIL (cerebral autosomal dominant arteriopathy with subcortical infarcts and leukoencephalopathy) is an inherited abnormality with mutations involving the NOTCH3 gene on chromosome 19q12, which results in angiopathy of small and medium arteries. Symptoms and signs begin in the fourth decade with headaches, transient ischemic attacks, strokes, and subcortical dementia.
Vasculitis (**Fig. 1.279**)	Zones of arterial occlusion, and/or foci of stenosis and poststenotic dilatation. May involve large, medium, or small intracranial and extracranial arteries. Can result in single or multiple cerebral and/or cerebellar infarcts seen with CT and/or MRI.	Uncommon mixed group of inflammatory diseases/disorders involving the walls of cerebral blood vessels. Can result from noninfectious etiology (polyarteritis nodosa, Wegener's granulomatosis, giant cell arteritis, Takayasu's arteritis, sarcoid, drug-induced vasculitis, etc.) or can be related to an infectious cause (bacteria, fungi, tuberculosis, syphilis, viruses).
Acute hypertensive crisis (malignant hypertension) (**Fig. 1.280**)	CT: Bilateral zones of low attenuation in the basal ganglia, caudate nuclei, thalami, brainstem, and cerebral white matter. MRI: Bilateral poorly defined zones of high signal on T2-weighted imaging, FLAIR, and diffusion–weighted imaging (low signal on ADC maps) in the basal ganglia, caudate nuclei, thalami, brainstem, and cerebral white matter.	Acute severe hypertension with mean arterial blood pressure > 160 mm/Hg can cause headaches, visual disturbances, nausea and vomiting, and altered mental status. Pathologic changes include edema with proteinaceous exudates in the cerebrum and brainstem, intravascular hemolysis, and thrombotic microangiopathy. Clinical findings can resolve with restoration of normal blood pressure. Uncorrected acute severe hypertension can progress to cerebral infarction, coma, and death.

(continued on page 230)

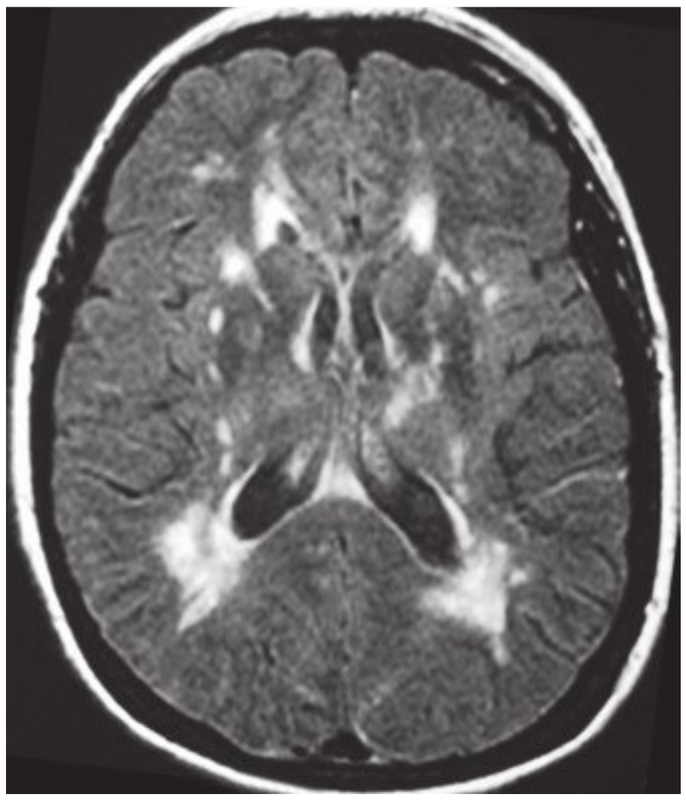

Fig. 1.278 A 47-year-old woman with CADASIL who has multiple zones with abnormal high signal on axial FLAIR in the cerebral white matter, basal ganglia, and thalami bilaterally without abnormal mass effect.

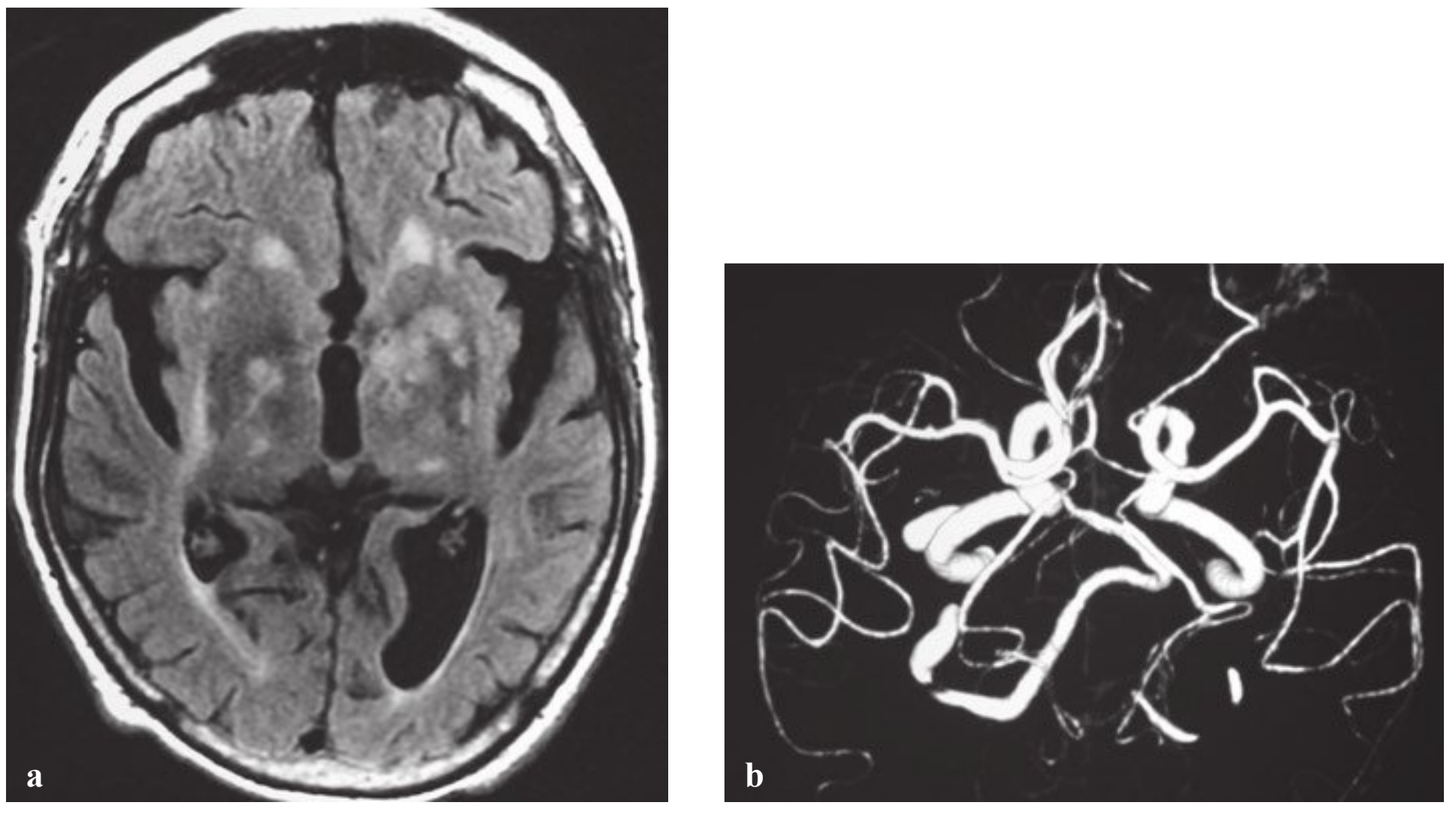

Fig. 1.279 A 78-year-old man with polyarteritis nodosa. **(a)** Multiple zones with abnormal high signal on axial FLAIR are seen in the cerebral white matter, basal ganglia, and thalami bilaterally without abnormal mass effect. **(b)** Axial MRA shows multiple sites of focal stenosis in the middle and anterior cerebral arteries.

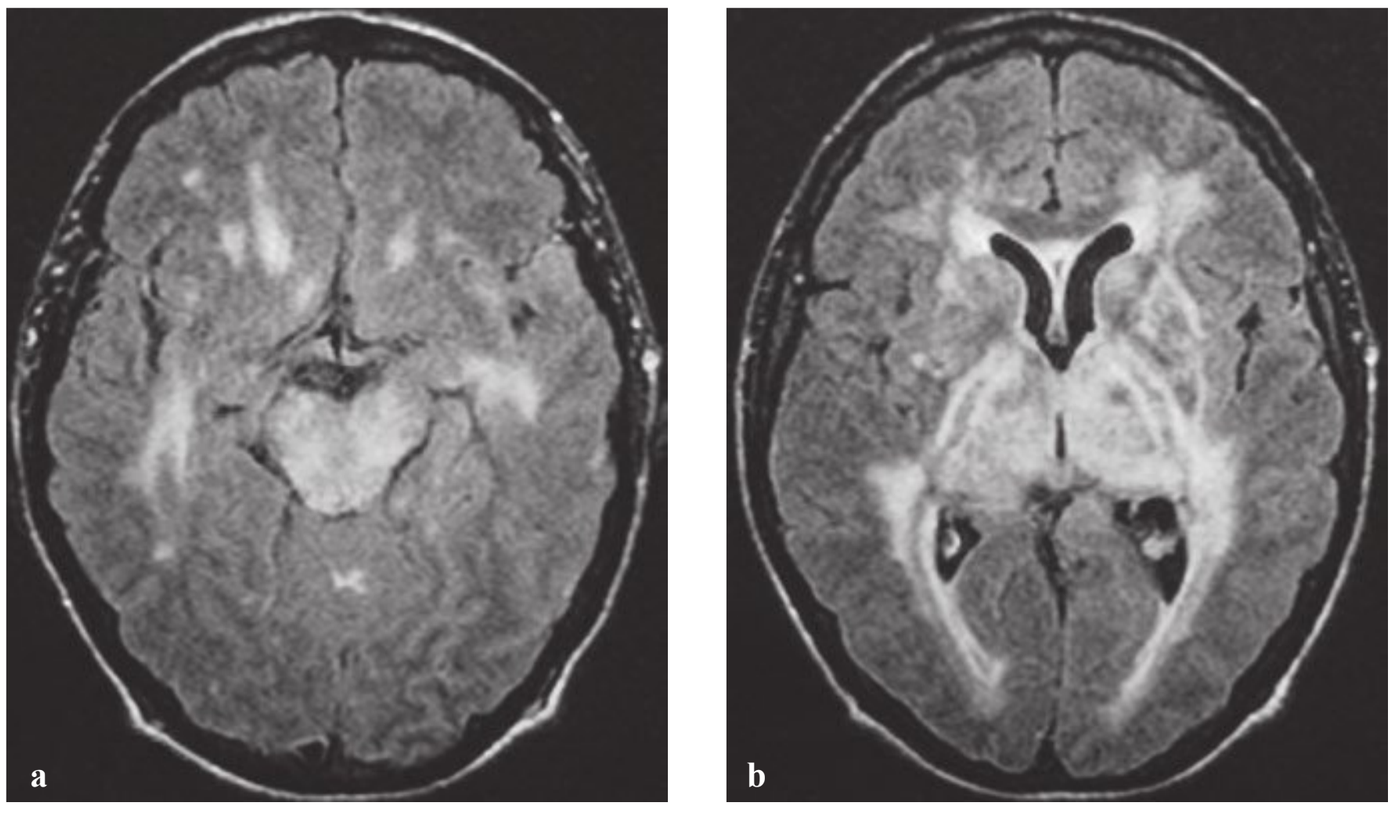

Fig. 1.280 A 49-year-old woman with uncontrolled malignant hypertension. **(a,b)** Axial FLAIR shows diffuse abnormal high signal in the brainstem, thalami, basal ganglia, and central cerebral white matter. The patient died hours after the MRI exam.

Table 1.6 (cont.) Bilateral lesions involving the basal ganglia and/or thalami

Lesions	Imaging Findings	Comments
Inherited Metabolic Disorders		
MELAS and MERRF (**Fig. 1.281**)	CT: Symmetric zones of low attenuation in the basal ganglia, and cerebral infarction that is not limited to one vascular distribution. MRI: High T2-weighted signal in basal ganglia, usually symmetric, and high T2-weighted signal in cerebral and cerebellar cortex and subcortical white matter not corresponding to a specific large arterial territory. Signal abnormalities may resolve and reappear.	Mitochondrial encephalomyopathy, lactic acidosis, and stroke-like episodes (MELAS) is a maternally inherited disease affecting transfer RNA in mitochondria. Myoclonic epilepsy with ragged red fibers (MERRF) is a mitochondrial encephalopathy associated with muscle weakness and myoclonic epilepsy, short stature, ophthalmoplegia, and cardiac disease.
Leigh's disease (**Fig. 1.282**)	CT: Zones of low attenuation in both caudate nuclei and putamina, ± decreased attenuation in white matter. Typically no contrast enhancement. MRI: Symmetric high signal on T2-weighted images in globus pallidus, putamen, and caudate, as well as high signal on T2-weighted images in thalami, cerebral and cerebellar white matter, cerebellar cortex, brainstem, and spinal cord gray matter. Typically there is no gadolinium contrast enhancement. Magnetic resonance spectroscopy can show elevated lactate peaks during metabolic decompensation with lactic acidosis.	Autosomal recessive disorder, also referred to as subacute necrotizing encephalopathy, occurs in three forms (infantile type, juvenile type, and adult-onset type). Etiology is related to abnormalities in oxidative metabolism in mitochondria due to one of several enzyme deficiencies from mutations of mitochondrial and/or nuclear genes (coenzyme Q10, pyruvate carboxylase, pyruvate dehydrogenase complex, others). Lesions in brainstem are associated with loss of respiratory control.
Kearns-Sayre syndrome	MRI: Zones with high signal on T2-weighted imaging and FLAIR in globi pallidi, putamina, and caudate nuclei, as well as high signal on T2-weighted imaging in thalami, subcortical cerebral and cerebellar white matter, posterior brainstem, and corticospinal tracts, + restricted diffusion for acute ischemia. Typically there is no gadolinium contrast enhancement. CT: Zones with decreased attenuation can be seen in the cerebral white matter, ± calcifications in globi pallidi and caudate nuclei.	Sporadic deletions of mitochondrial DNA involving genes that encode proteins of the respiratory chain and/or tRNA. Results in mitochondrial dysfunction, spongiform changes of the cerebral and cerebellar white matter, basal ganglia, as well as progressive extrernal ophthalmoplegia, pigmentary retinopathy, and cardiac conduction blocks. Mitochondrial disorder associated with external ophthalmoplegia, retinitis pigmentosa, and onset of clinical muscular and neurologic signs < 20 years.

(continued on page 232)

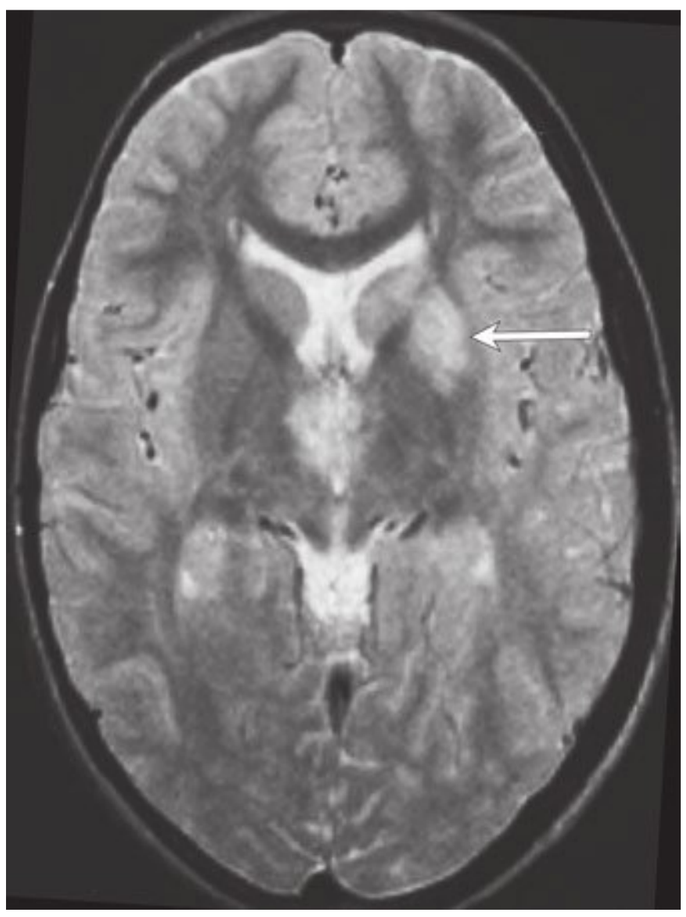

Fig. 1.281 A 6-year-old girl with MELAS. Axial T2-weighted imaging shows abnormal high signal in the left caudate nucleus and putamen (arrow).

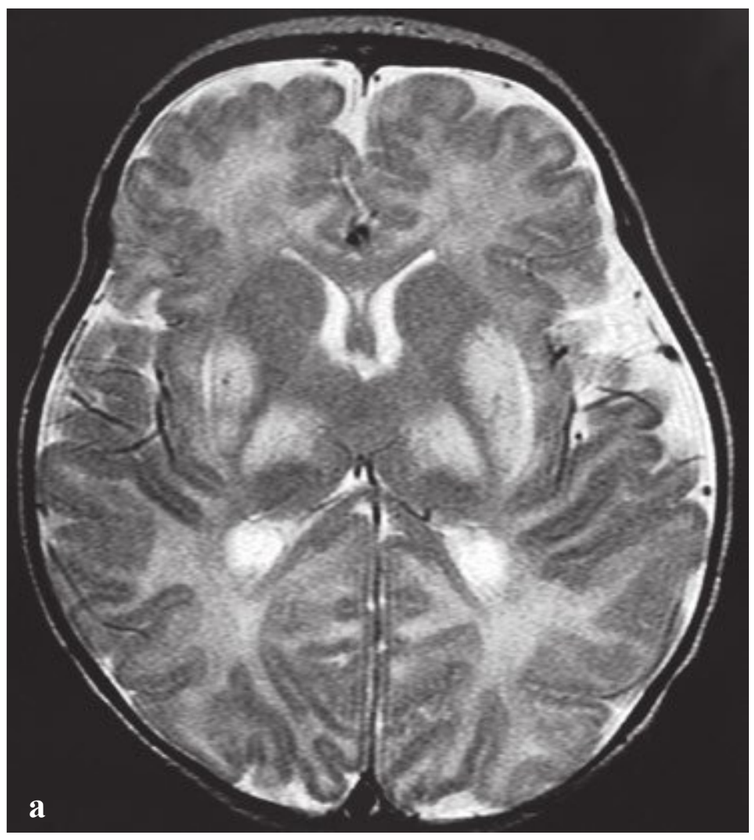

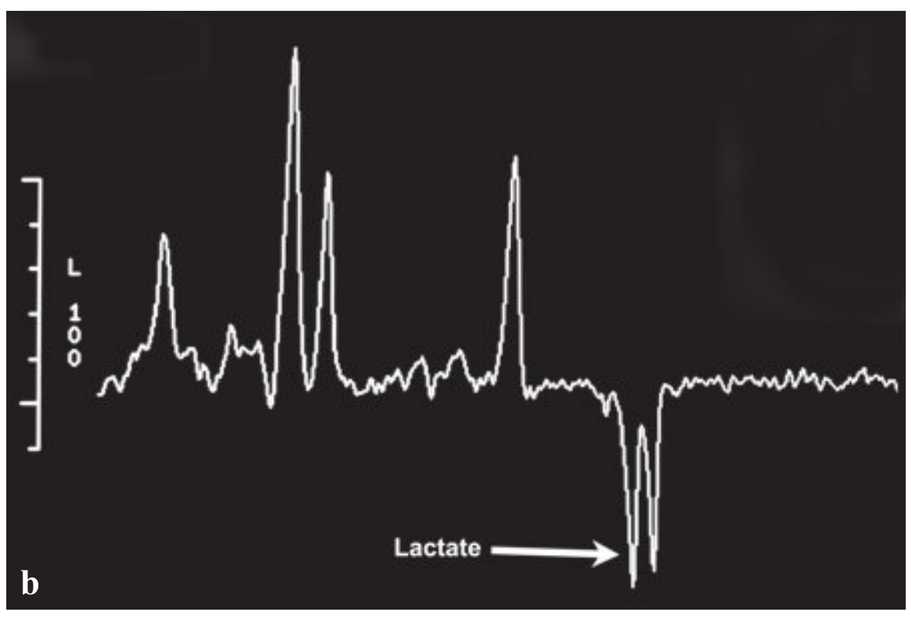

Fig. 1.282 **(a)** A 2-month-old female with Leigh's disease who has abnormal high signal in the putamina and thalami on axial T2-weighted imaging. **(b)** Magnetic resonance spectroscopy with a TE of 144 msec shows an abnormal lactate peak (arrow) from lactic acidosis.

Table 1.6 (cont.) Bilateral lesions involving the basal ganglia and/or thalami

Lesions	Imaging Findings	Comments
Disorders of Amino Acid and Urea Cycle Metabolism: Phenylketonuria, propionic acidemia, methylmalonic aciduria, homocystinuria, ornithine transcarbamylase deficiency, citrullinemia, arginosuccinic aciduria, leucinosis (maple syrup urine disease), glutaric acidemia/aciduria, others (**Fig. 1.283, Fig. 1.284, Fig. 1.285, Fig. 1.286**, and **Fig. 1.287**)	CT: Zones with decreased attenuation in cerebral and/or cerebellar white matter, ± zones with decreased attenuation in globi pallidi, putamina, caudate nuclei, thalami, brainstem. MRI: Zones with increased signal on T2WI and FLAIR in cerebral and/or cerebellar white matter, ± zones with increased signal on T2WI in globi pallidi, putamina, caudate nuclei, thalami, brainstem. Restricted diffusion can be seen with metabolic decompensation-ketoacidosis, ischemia.	Autosomal recessive or X-linked disorders involving defective enzymes affecting mitochondrial function. These disorders can cause toxic accumulation of metabolites, resulting in mitochondrial dysfunction, ketoacidosis, and/or hyperammonemia, as well as alteration of myelin formation. Phenylketonuria: autosomal recessive mutation of gene causing deficiency of phenylalanine hydroxylase with toxic accumulation of phenyalanine. Propionic acidemia: autosomal recessive mutation causing deficiency of propionyl-CoA carboxylase with toxic accumulation of propionate, 3-hydroxybutyrate, methylcitrate, and 3-hydroxypropionate. Methylmalonic aciduria/homocystinuria: autosomal recessive mutations causing lack of normal conversion of methylmalonyl-CoA to succinyl-CoA via defects of the apoenzyme methylmalonyl-CoA mutase or deficiency of the coenzyme adenosylcobalamine, resulting in accumulation and urinary excretion of methylmalonic acid, methylcitric acid, and 3-hydroxypropionic acid. Ornithine transcarbamylase deficiency: X-linked mutation causing deficiency of ornithine transcarbamylase, which results in toxic accumulation of ammonia. Leucinosis (maple syrup urine disease): autosomal recessive mutation involving the α-ketoacid dehydrogenase complex, which results in toxic accumulation of branched-chain amino acids (leucine, isoleucine, and valine). Glutaric acidemia/aciduria type 1: autosomal recessive mutation causing deficiency of glutaryl-CoA dehydrogenase, with toxic accumulation of glutaric acid. Normal activity is needed for metabolism of lysine, hydroxylysine, and tryptophan. Glutaric acidemia/aciduria type 2: autosomal recessive mutation causing deficiency of acyl coenzyme A dehydrogenase activity, resulting in impairment in mitochondrial electron transport related to electron transport flavoprotein or ubiquinone oxidoreductase.
Neurodegeneration with brain iron accumulation: Pantothenate kinase-associated neurodegeneration (PKAN disease) (**Fig. 1.288**)	CT: Zones of low attenuation in the globus pallidus bilaterally. MRI: Low signal ± areas of high signal on T2-weighted imaging in the globus pallidus bilaterally, giving the eye of the tiger sign. No gadolinium contrast enhancement.	Rare autosomal recessive metabolic disorder from mutations in the pantothenate kinase 2 (PANK2) gene. Onset is usually in childhood, with progressive limb rigidity, gait dysfunction, dysarthria, and mental deterioration. Increased iron deposition and destruction of globus pallidus and substantia nigra bilaterally.

(continued on page 235)

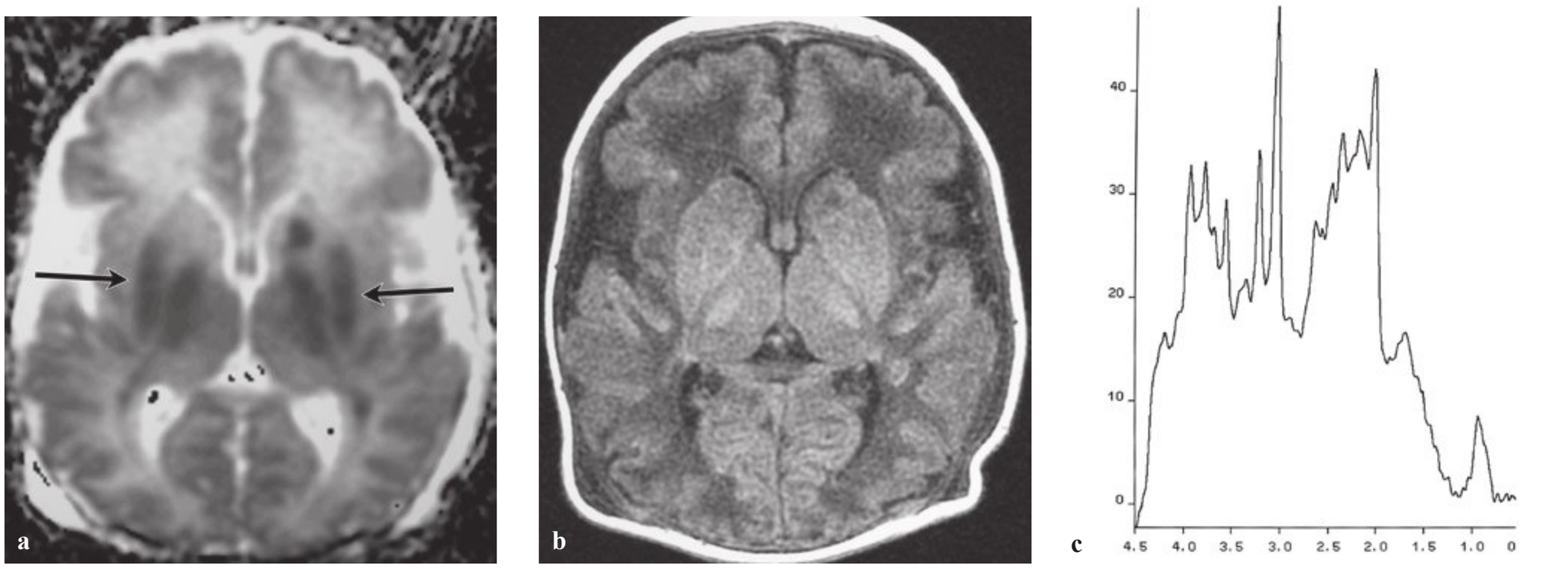

Fig. 1.283 A 9-day-old male neonate with ornithine transcarbamylase deficiency who has **(a)** restricted diffusion in the left caudate nucleus and bilateral putamina (arrows) and thalami on axial ADC and **(b)** abnormal high signal on axial T1-weighted imaging relative to the internal capsules from ammonia toxicity. **(c)** Magnetic resonance spectroscopy (TE of 35 msec) of the basal ganglia shows elevated glutamate/glutamine complex peaks at 2.05 to 2.55 and 3.7 to 3.9 ppm, and elevated lipid-lactate complex at 0.8 to 1.5 ppm.

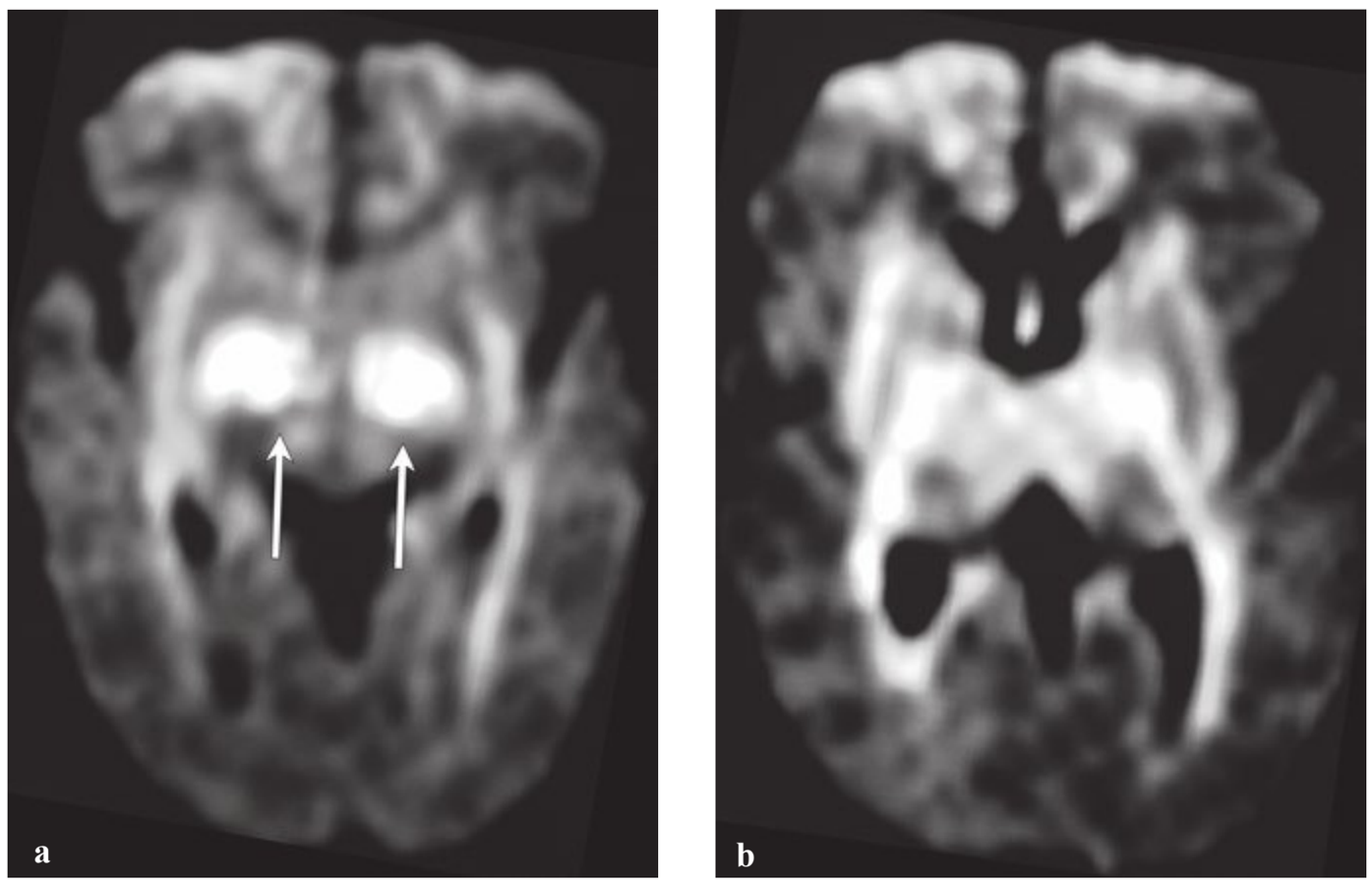

Fig. 1.284 **(a,b)** A 3-week-old male with propionic acidemia who has restricted diffusion in the thalami, basal ganglia, and central cerebral white matter (arrows) on axial DWI.

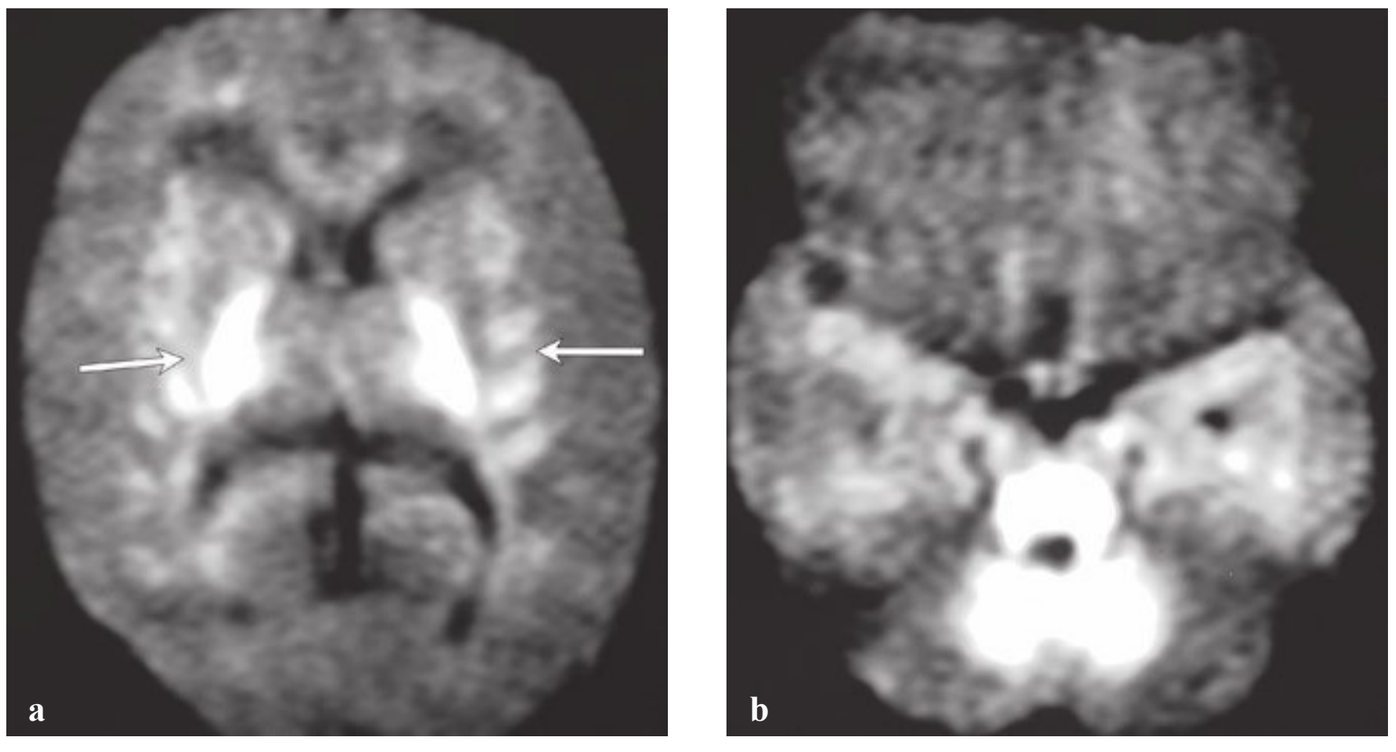

Fig. 1.285 **(a,b)** A 1-week-old male with methylmalonic aciduria who has restricted diffusion on axial DWI in the thalami, internal capsules, deep cerebral white matter, pons, and cerebellar white matter (arrows).

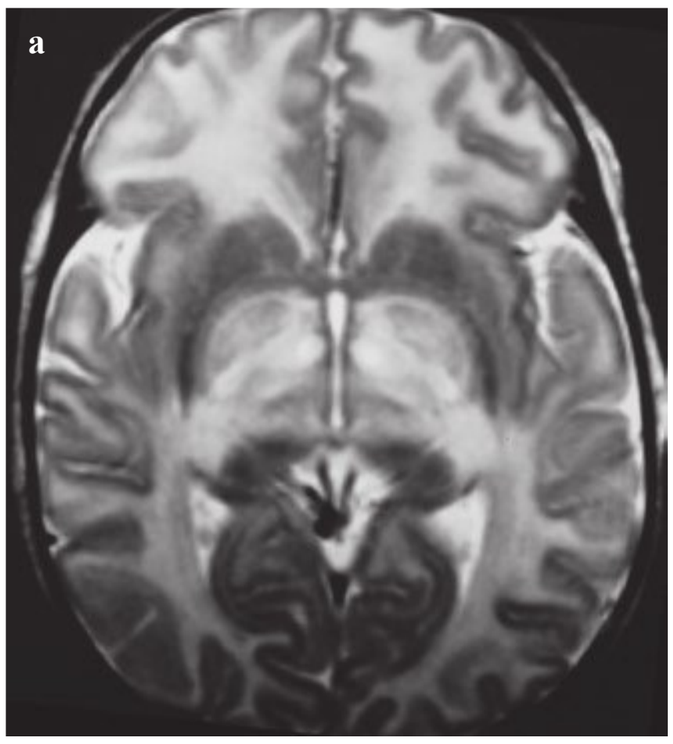

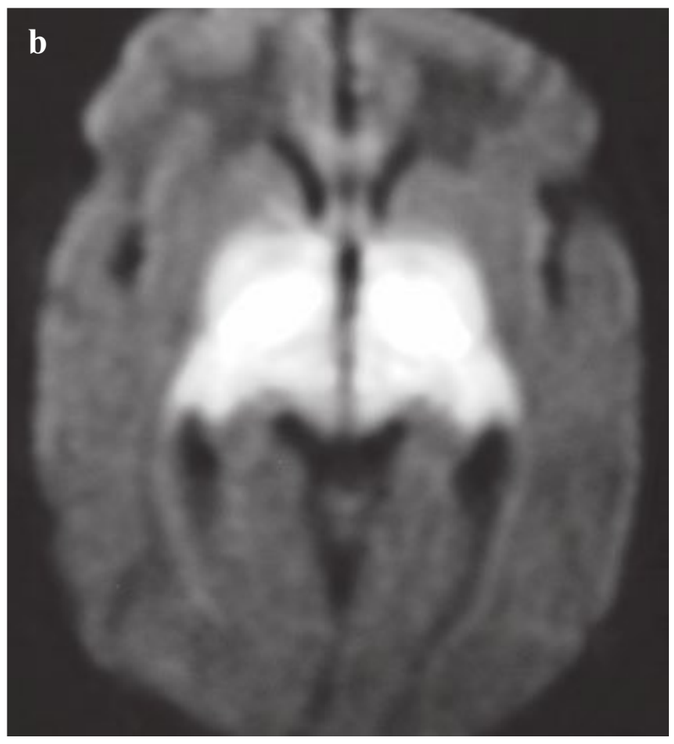

Fig. 1.286 A 2-week-old female with leucinosis (maple syrup urine disease) and metabolic decompensation with **(a)** abnormal high signal in the thalami, internal capsules, and cerebral white matter on axial T2-weighted imaging and **(b)** corresponding restricted diffusion on axial DWI.

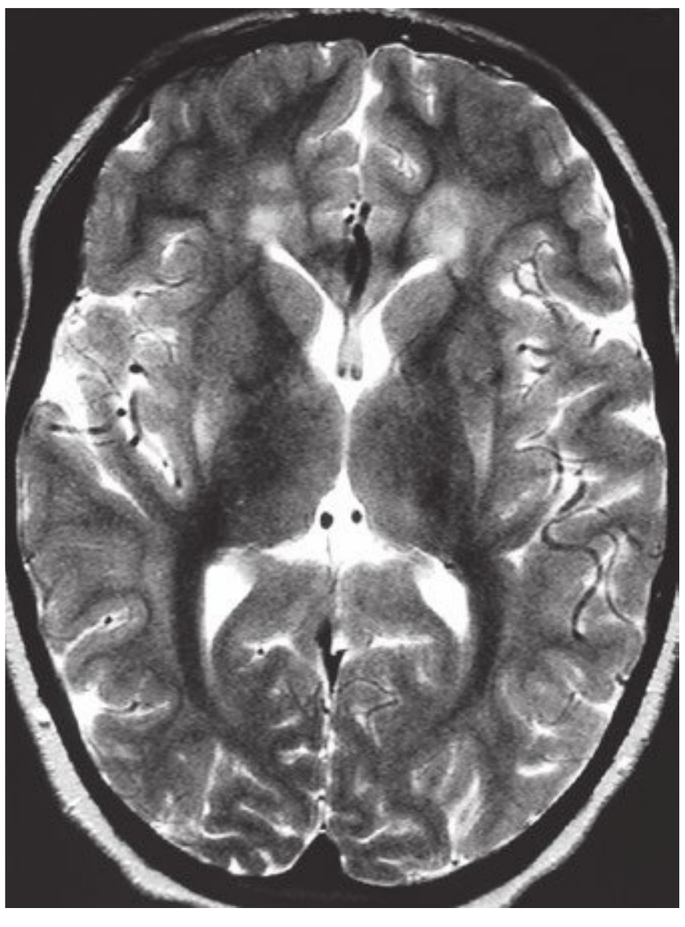

Fig. 1.287 An 8-year-old girl with glutaric acidemia/aciduria who has abnormal high signal in the periventricular frontal white matter and posterior portions of the putamina on axial T2-weighted imaging.

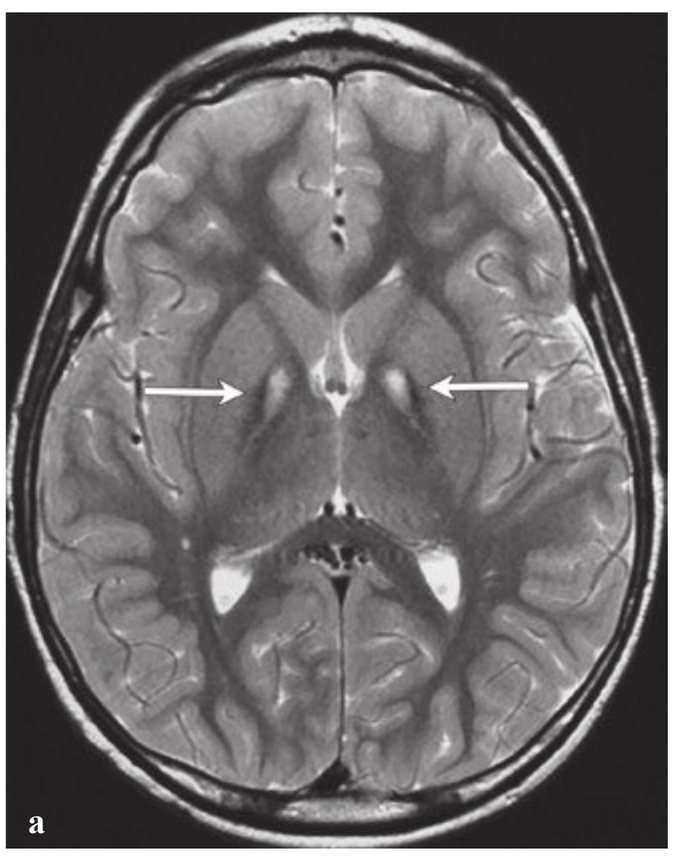

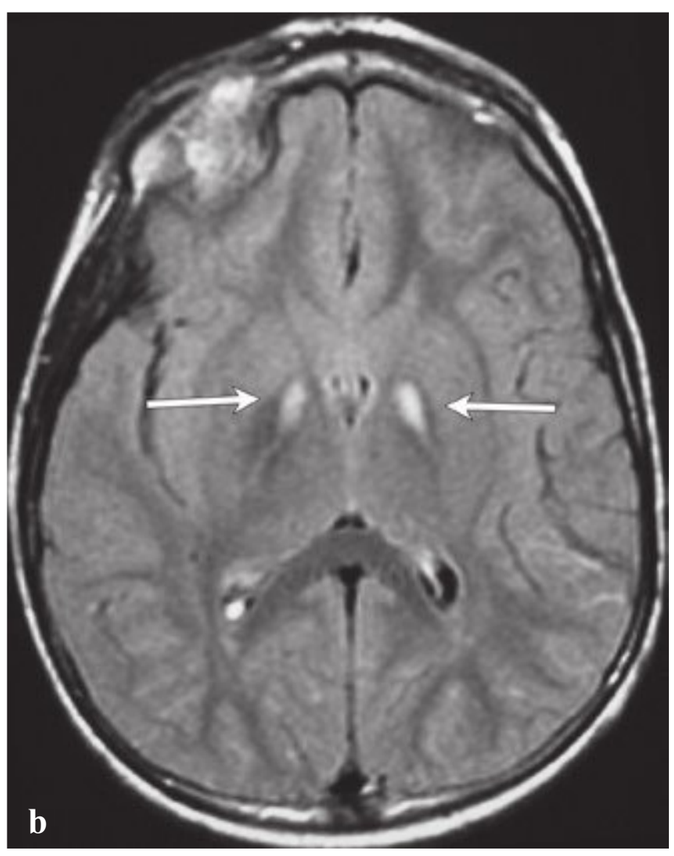

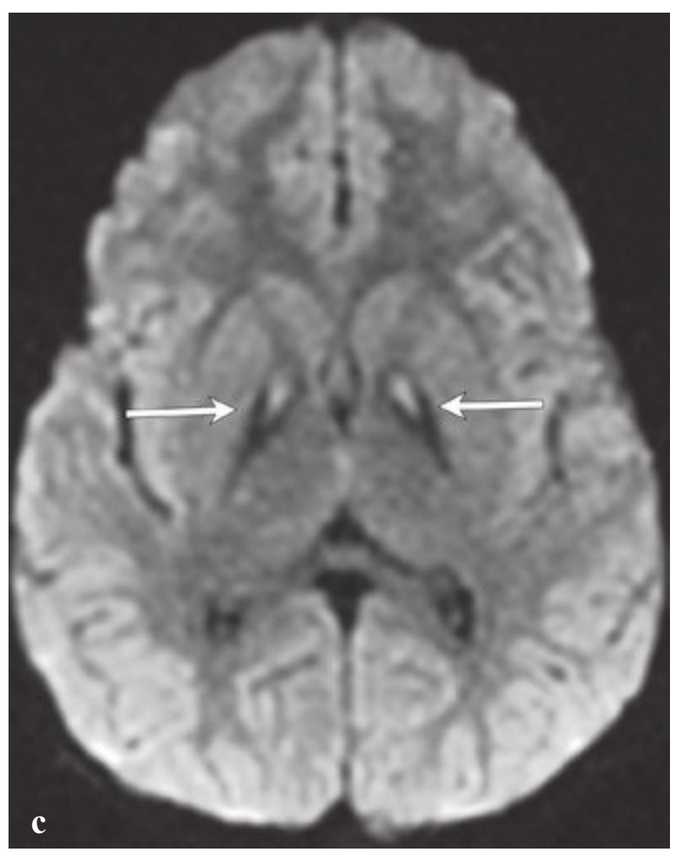

Fig. 1.288 A 6-year-old male with neurodegeneration with brain iron accumulation (PKAN disease). Low signal with central foci with high signal in the globus pallidus bilaterally is seen on **(a)** axial T2-weighted imaging (arrows), **(b)** axial FLAIR (arrows), and **(c)** axial GRE (arrows), giving the eye of the tiger sign.

Table 1.6 (cont.) Bilateral lesions involving the basal ganglia and/or thalami

Lesions	Imaging Findings	Comments
Wilson's disease (**Fig. 1.289**)	CT: Zones of low attenuation in the basal ganglia and thalami. No abnormal contrast enhancement seen. Progressive atrophy of the cerebrum, cerebellum, and brainstem. MRI: High signal on T2-weighted imaging in the putamen bilaterally as well as in the thalami, caudate nuclei, dentate nuclei, and brainstem (periaqueductal zone). Low signal on T2-weighted imaging can also be seen in the caudate and putamen. Some patients have high signal on T1-weighted imaging in the globi pallidi and dorsal midbrain related to hepatic dysfunction. Low signal on T1-weighted imaging may also be seen in the putamina, globi pallidi, and both thalami. Progressive atrophy of the cerebrum, cerebellum, and brainstem.	Autosomal recessive disease involving the ATP7B gene on chromosome 13q14.3–21.1, which encodes for the copper-transporting ATPase protein in hepatocytes. Loss of the normal copper-transporting ATPase protein results in reduced hepatic biliary copper excretion and reduced incorporation of copper into ceruloplasmin. Patients have abnormal hepatic levels of copper and increased abnormal urinary excretion of copper. The disease usually presents in childhood with abnormal toxic copper deposition in tissues, resulting in cirrhosis and degenerative changes in the basal ganglia (lentiform nuclei) and brainstem. Patients can have dysarthria, tremors, choreoathetosis, dystonia, and Kayser-Fleischer rings on ophthalmologic examination.
Menkes' syndrome (trichopoliodystrophy)	CT: Rapid, progressive brain atrophy with large bilateral subdural hematomas. MRI: High signal on T2-weighted imaging can be seen in the cerebral white matter, putamen bilaterally, and/or caudate nuclei with or without restricted diffusion. Delayed myelination involving the posterior limb of the internal capsules can be seen. Progressive atrophy of the cerebrum, cerebellum, and brainstem. Small zones with high signal on T1-weighted imaging may be seen in the cerebral cortex. Large bilateral subdural hematomas can be seen with mixed signal on T1- and T2-weighted imaging. MRA and CTA show tortuous "corkscrew" arteries.	X-linked recessive disorder from mutations involving the ATP7A gene on Xq13.3, which encodes for the copper-transporting ATPase protein necessary for intestinal uptake of copper. Lack of adequate copper results in defective cytochrome c oxidase activity in mitochondria. Patients often have seizures, truncal hypotonia, hypothermia, failure to thrive, failure to reach developmental milestones, hypermobile joints, hypopigmentation, and coarse, stiff, and broken hair ("kinky hair disease").

(continued on page 236)

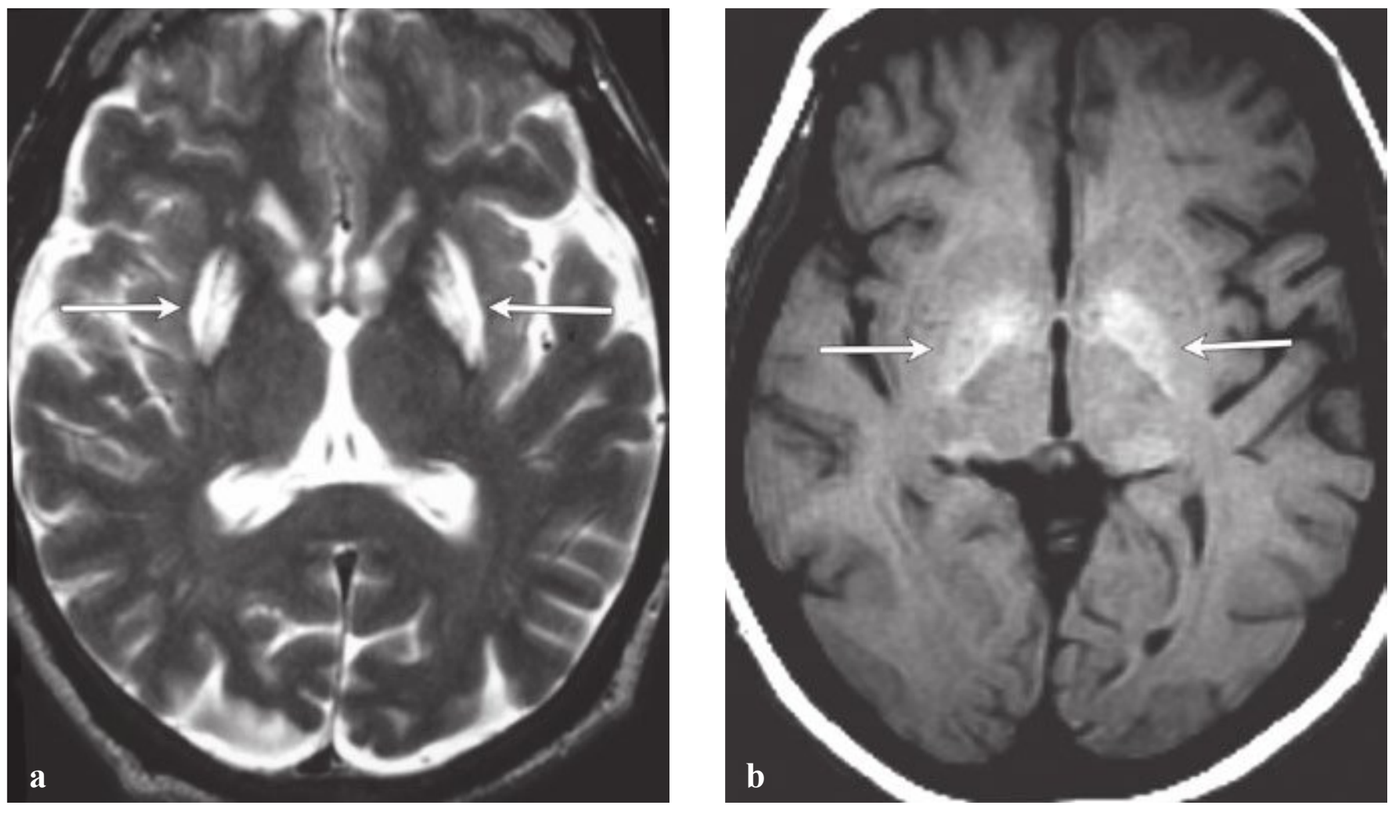

Fig. 1.289 **(a)** A 46-year-old man with Wilson's disease has abnormal high signal in the putamina on axial T2-weighted imaging (arrows). **(b)** A 49-year-old woman with Wilson's disease has abnormal high signal in the putmina and globi pallidi (arrows) on axial T1-weighted imaging.

Table 1.6 (cont.) Bilateral lesions involving the basal ganglia and/or thalami

Lesions	Imaging Findings	Comments
Lysosomal enzyme defects: mucopolysaccharidoses (**Fig. 1.290**)	CT: Poorly defined zones of decreased attenuation in white matter, cerebral and cerebellar atrophy, ± foci of low attenuation in corpus callosum and basal ganglia (prominent perivascular spaces). MRI: Poorly defined zones of decreased signal on T1 WI and increased signal on T2 WI and FLAIR in white matter, cerebral and cerebellar atrophy, ± foci of low signal on T1 WI in corpus callosum and basal ganglia (prominent perivascular spaces with thickened adventitia of blood vessels containing large cells filled with glycosaminoglycans), cerebral cortical/subcortical infarcts, ± macrocephaly, communicating hydrocephalus, ± meningeal thickening.	Mucopolysaccharidoses are autosomal recessive or X-linked disorders related to abnormal metabolism of mucopolysaccharides (glycosaminoglycans) in lysosomes due to enzymatic defects. Hurler syndrome (MPS type I): autosomal recessive mutation of IDUA gene with abnormal a-L-iduronidase. Hunter syndrome (MPS type II): X-linked mutation of IDS gene causing abnormal iduronate 2-sulfatase. San*fi*lippo syndrome (MPS type III): autosomal recessive mutations causing abnormalities of one of four of the following enzymes involved in the breakdown of the glycosaminoglycan heparan sulfate: heparan N-sulfatase, α-N-acetylglucosaminidase, acetyl-CoA:α-glucosaminidine acyltransferase, or N-acetylglucosamine 6-sulfatase. Morquio syndrome (MPS type IV): autosomal recessive mutations of GALNS gene resulting deficient activity of galactosamine 6-sulfatase or β-galactosidase. Abnormal accumulation of metabolite mucopoly-saccharides (glycosaminoglycans) results in axonal loss and demyelination. Patients with Hurler syndrome rarely survive longer than 16 years. With the severe form of Hunter syndrome, patients usually die between the ages of 8 and 15 years. With Sanfilippo syndrome, patients often die by the third decade.
Canavan disease, also known as Canavan-van Bogaert-Bertrand disease (**Fig. 1.291**)	MRI: High signal on T2-weighted imaging in the peripheral cerebral and cerebellar white matter diffusely, with progressive involvement of the white matter centrally (internal capsules, corpus callosum), ± involvement of the globus pallidus, thalamus, hypothalamus, and brainstem. Typically no gadolinium contrast enhancement. Associated with increased size and weight of brain tissue. Can have restricted diffusion in involved white matter initially, and elevated ADC later in disease. Magnetic resonance spectroscopy: Enlarged N-acetylaspartate (NAA) peak. CT: Zones with decreased attenuation involving the peripheral cerebral and cerebellar white matter diffusely, with progressive involvement of the white matter centrally and subsequent atrophy.	Rare autosomal recessive disease (common in Ashkenazi Jews) with spongy degeneration of the brain caused by deficiency of aspartoacyclase in oligodendrocytes, microglia, and brainstem neurons that results from mutations of the ASPA gene on chromosome 17p13-ter. Mutations involving this gene, which encodes for aspartoacyclase, result in lack of breakdown of N-acetylaspartate (NAA) into aspartic acid and acetate. NAA accumulates in brain and plasma, with elevated levels in urine. Excess NAA in brain causes injury to oligodendrocytes, and spongiform and vacuolation changes with myelin destruction. Presents in infancy (3–6 months) with macrocephaly, hypotonia, seizures, spasticity, optic atrophy, and visual loss. Death often occurs by the fourth year. Gene therapy with an adenoassociated viral vector carrying the ASPA gene has shown promising early results.
Other Metabolic Disorders		
Acquired hepatocerebral degeneration (**Fig. 1.292**)	CT: No zones with definite abnormal attenuation seen in the basal ganglia, ± cerebral and cerebellar atrophy. MRI: High signal on T1-weighted imaging in basal ganglia/globi pallidi and anterior midbrain. No abnormal gadolinium contrast enhancement. Magnetic resonance spectroscopy: Decreased choline and myo-inositol levels and elevated glutamine/glutamate peaks related to toxic effects of hyperammonemia.	Signal hyperintensity on T1-weighted imaging secondary to hepatic dysfunction (alcoholic cirrhosis, hepatitis, portal-systemic shunts) is related to increased serum ammonia and manganese levels. The signal hyperintensity on T1-weighted imaging may reverse after liver transplantation.

(continued on page 238)

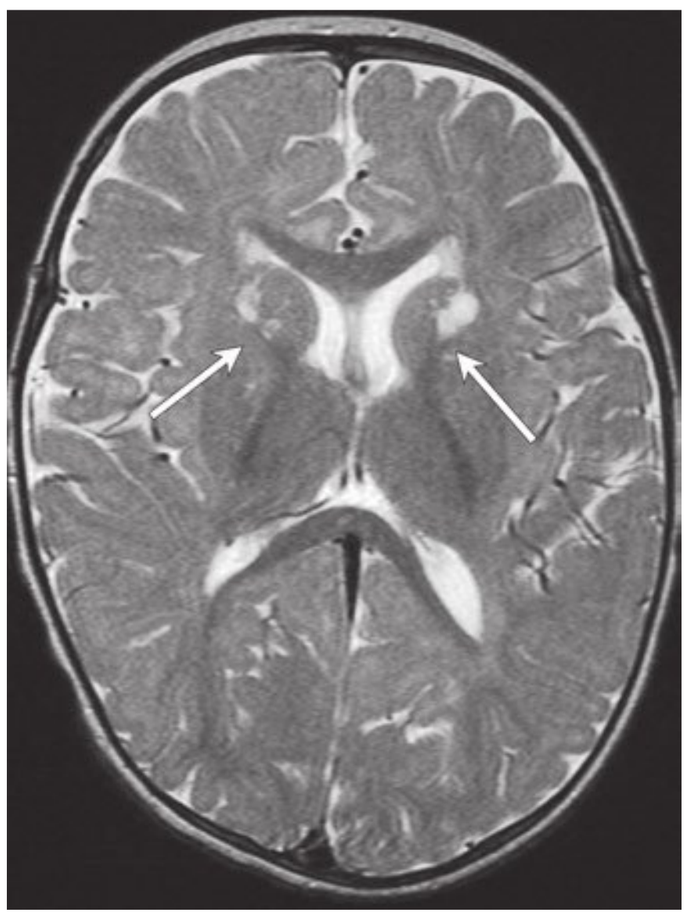

Fig. 1.290 A 1-year-old male with mucopolysaccharidosis with abnormal high signal foci in the anterior limbs of the internal capsules bordering the caudate nuclei (arrows) on axial T2-weighted imaging.

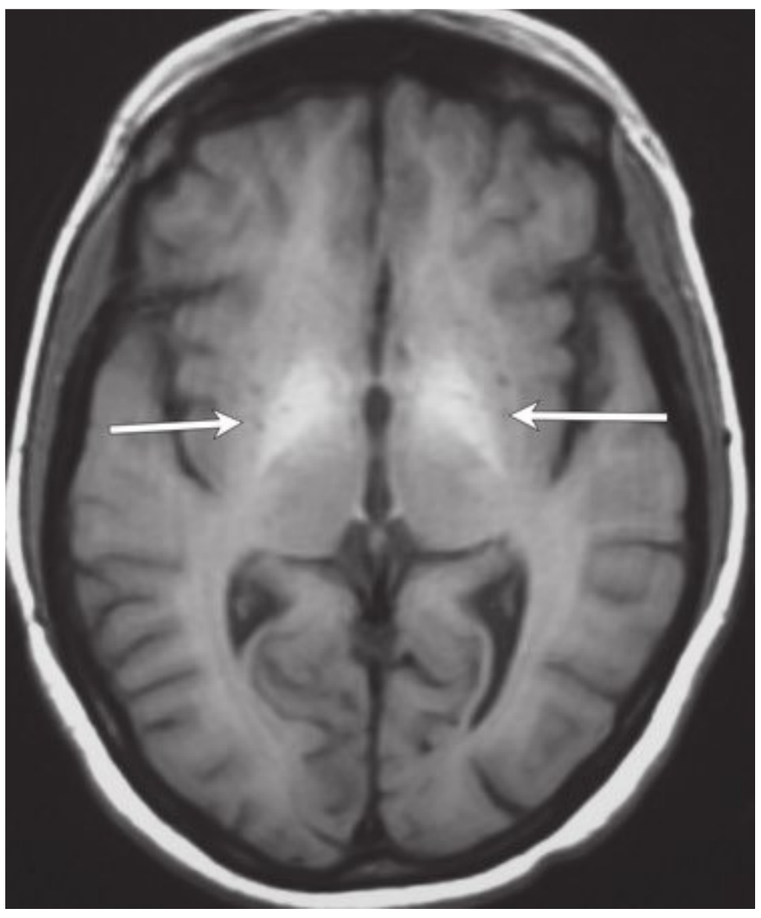

Fig. 1.292 Patient with acquired hepatocellular degeneration and abnormal high signal on axial T1-weighted imaging in the basal ganglia bilaterally (arrows).

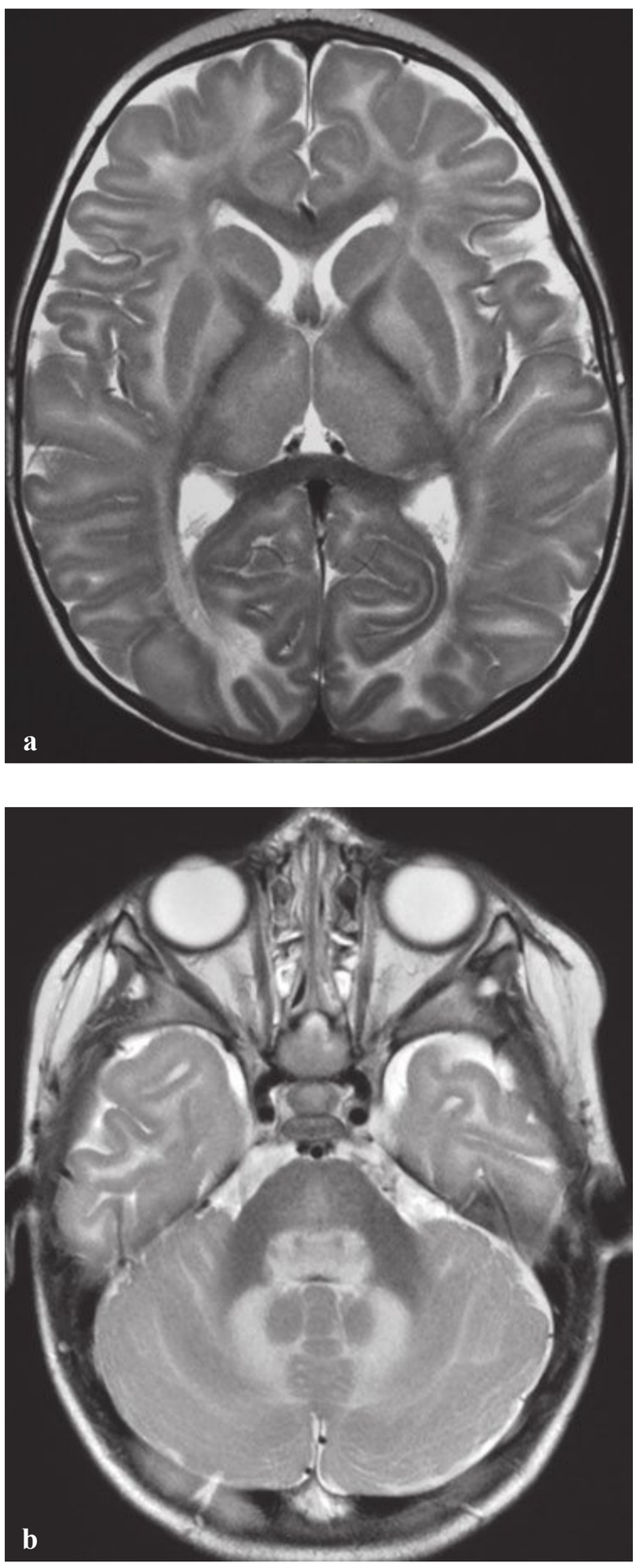

Fig. 1.291 **(a,b)** A 9-month-old male with Canavan-van Bogaert disease who has abnormal high signal on axial T2-weighted imaging in the cerebral and cerebellar white matter, globi pallidi, thalami, and pons.

Table 1.6 (cont.) Bilateral lesions involving the basal ganglia and/or thalami

Lesions	Imaging Findings	Comments
Hypoglycemia	CT: Zones with decreased attenuation in the brain that can be unilateral or bilateral and symmetric. MRI: Zones with abnormal increased signal on T2-weighted imaging, FLAIR, and diffusion-weighted imaging (DWI) can occur in the brain (cerebral cortex, hippocampi, internal capsules, basal ganglia, cerebral peduncles, pons), and they may be unilateral or bilateral and symmetric. The lesions do not correspond to a specific arterial territory. Treatment to correct hypoglycemia can result in resolution of high signal abnormalities on DWI within hours. With severe, prolonged hypoglycemia, poorly defined zones with increased signal on T2-weighted imaging, FLAIR, and DWI can be seen in the cerebral white matter and are often associated with a poor prognosis. Generalized cerebral swelling may be also seen, followed by cerebral atrophy.	Hypoglycemia is defined as plasma glucose levels less than 45 mg/dL. Severe hypoglycemia (< 20 mg/dL) for more than 4 hours results in irreversible brain injury. Causes include overdose of insulin or other medications used by diabetic patients, insulin-secreting tumors, Addison's disease, severe sepsis, and hepatic or renal failure. If hypoglycemia is not corrected promptly, symptoms like drowsiness, personality changes, seizures, and hemiplegia occur. Severe prolonged hypoglycemia can result in coma and death. Lack of adequate glucose can result in impaired oxidative brain metabolism, leading to massive release of excitatory amino acid neurotransmitters, causing cytotoxic edema in neuronal and glial cells that can progress to cell death.
Nonketotic hyperglycemia	CT: In patients with nonketotic hyperglycemia in type 2 diabetes, there are zones with increased attenuation in the caudate and putamen, which can be unilateral or bilateral. In patients with type 1 diabetes (insulin-dependent diabetes) with hyperglycemia and ketoacidosis, diffuse cerebral edema with effacement of sulci and cisterns can occur. MRI: In patients with nonketotic hyperglycemia in type 2 diabetes, zones with increased signal on T1-weighted imaging and variable signal changes on T2-weighted imaging and FLAIR can occur in the caudate and putamen, and may be unilateral or bilateral. Restricted diffusion on diffusion-weighted imaging (DWI) has also been reported in the involved sites. In patients with type 1 diabetes, diffuse cerebral edema with effacement of sulci and cisterns can occur. Complications from the brain swelling include central brain herniation with brain infarcts.	Nonketotic hyperglycemia (blood glucose levels generally over 350 mg/dL) can occur in patients with type 2 diabetes (insulin-resistant diabetes) because of poor medical control and may be associated with abnormalities involving the caudate, putamen, and subthalamic nuclei. May result in chorea ballismus. In patients with type 1 diabetes (insulin-dependent diabetes), hyperglycemia can occur with ketoacidosis, leading to generalized brain swelling and central brain herniation.
Wernicke's encephalopathy (**Fig. 1.293**)	MRI: Symmetric lesions with abnormal increased signal on T2-weighted imaging and FLAIR in the medial thalami (70–80%), periventricular regions adjacent to the third ventricle (80%), periaqueductal area (59%), mamillary bodies (45%), and/or tectal plate (13–36%). In nonalcoholics, lesions may also be seen in the cerebral cortex, caudate nuclei, splenium, cerebellum, and brainstem. Lesions in the mamillary bodies and thalamus often show gadolinium contrast enhancement in alcoholic patients with thiamine deficiency. Uncommon findings of restricted diffusion on diffusion-weighted imaging (DWI), and magnetic resonance spectroscopy findings of increased lactate and decreased NAA/Cr have been associated with irreversible brain injury and poor prognosis.	Severe neurologic disorder resulting from vitamin B_1 (thiamine) deficiency. Thiamine reserves in the body can be depleted in 3 weeks. Thiamine is an important cofactor for enzymes in the Krebs cycle and pentose phosphate pathway. Lack of thiamine results in injury to regions of the brain with high metabolic requirements. Usually occurs in alcoholics from dietary deficiency, but it can also occur in patients with malabsorption from surgical procedures, gastrointestinal malignancies, chemotherapy, hyperemesis, and chronic malnutrition/starvation. Clinical findings include altered consciousness, ocular dysfunction/ophthalmoplegia, and ataxia.
Seizure (**Fig. 1.294**)	MRI: Zones with restricted diffusion (high signal on diffusion-weighted imaging and low signal on ADC maps) typically occur in the hippocampus (69%), pulvinar-thalamus (26%), and cerebral cortex in patients with status epilepticus, generalized seizures, and febrile seizures. Abnormal increased signal on T2-weighted imaging and FLAIR can also be seen in these locations, as well as localized swelling.	Patients with complex partial seizures and generalized seizures, including status epilepticus, have localized ictal and peri-ictal sites in the brain with increased energy metabolism, hyperperfusion, and cell swelling, which typically show restricted diffusion that can be transient. Abnormalities are often bilateral in patients with generalized seizures and status epilepticus, and unilateral in patients with partial complex seizures.

(continued on page 240)

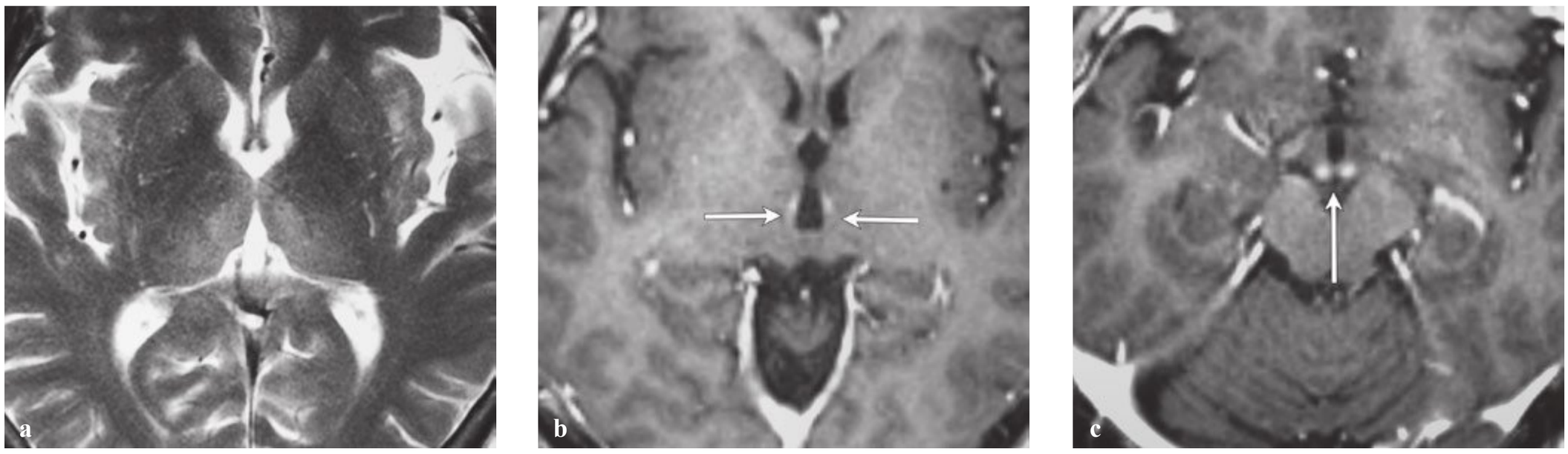

Fig. 1.293 A 73-year-old man with Wernicke's encephalopathy. **(a)** Symmetric zones with abnormal increased signal on axial T2-weighted imaging are seen in the medial thalami. **(b,c)** Bilateral foci with gadolinium contrast enhancement (arrows) are seen in the thalami and mamillary bodies on axial T1-weighted imaging.

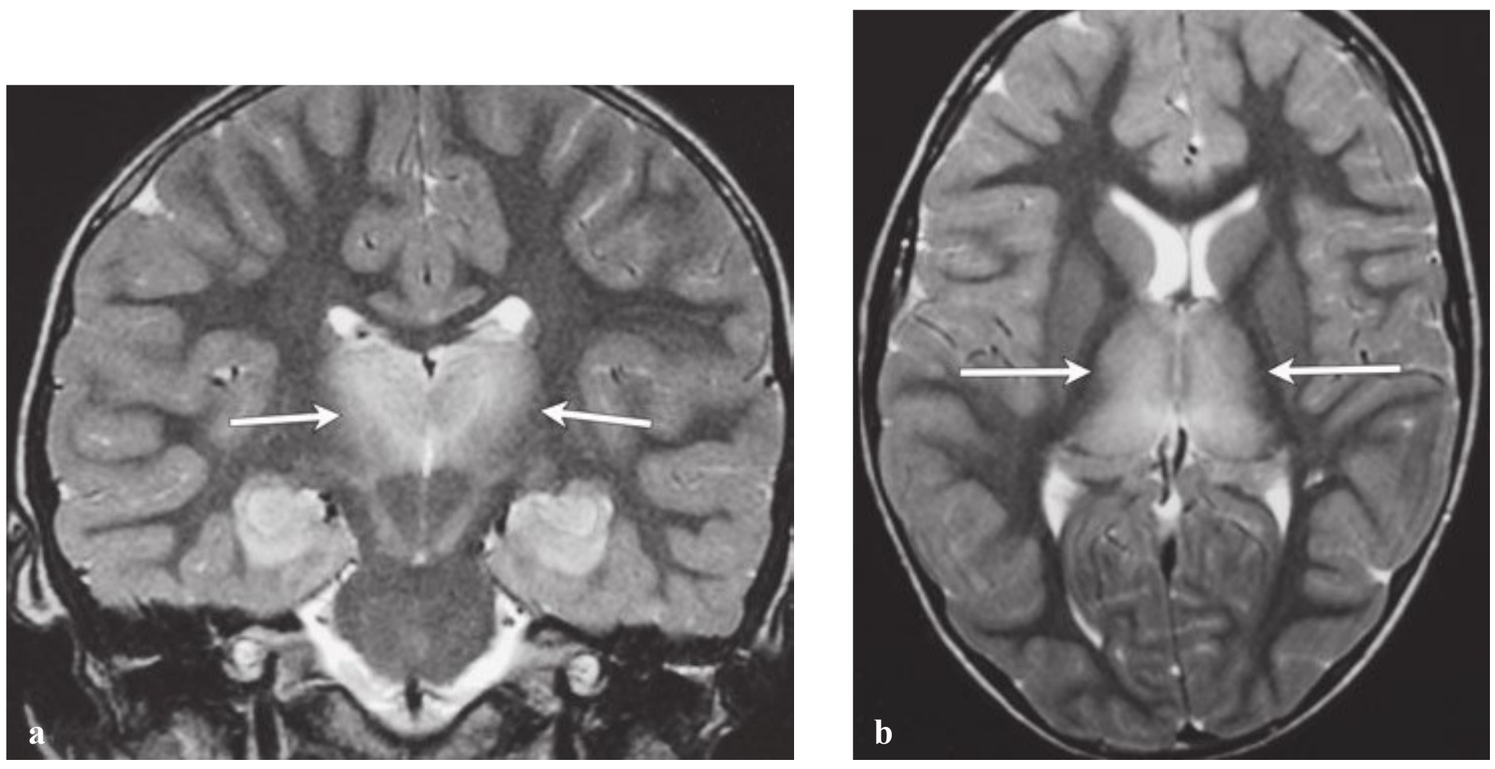

Fig. 1.294 A 5-year-old male with status epilepticus. Zones with abnormal high signal on **(a)** coronal and **(b)** axial T2-weighted imaging are seen in both hippocampi, and pulvinar-thalami (arrows). Localized swelling is associated with the signal abnormalities.

Table 1.6 (cont.) Bilateral lesions involving the basal ganglia and/or thalami

Lesions	Imaging Findings	Comments
Toxic Encephalopathy		
Carbon monoxide poisoning (**Fig. 1.295**)	CT: Acute poisoning shows symmetric decreased attenuation in the globi pallidi. MRI: Low signal on T1-weighted imaging and high signal on T2-weighted imaging in putamen and globus pallidus bilaterally, ± patchy gadolinium contrast enhancement in necrotic zones. Diffusion-weighted imaging (DWI) shows restricted diffusion from acute necrosis. Similar but less pronounced findings are seen in the brainstem and cerebellum. Delayed effects that consist of progressive demyelination of cerebral white matter with high signal on T2-weighted imaging and FLAIR can occur 1 to 2 weeks after CO exposure.	The binding of CO to the heme protein is 250 times greater than the binding to oxygen, resulting in tissue hypoxia. Toxic effects of CO result in selective necrosis of basal ganglia bilaterally, and also to a lesser degree the brainstem and cerebellum. Atrophic changes involving the brain can be seen later and may be associated with cognitive impairment. Clinical findings include headache, nausea, altered consciousness, seizures, coma, and death.
Methanol intoxication	CT: Acute poisoning shows symmetric decreased attenuation in the basal ganglia and subcortical white matter, ± hemorrhage. MRI: High signal on T2-weighted imaging and FLAIR in putamen and globus pallidus bilaterally, with restricted diffusion in the acute phase, ± high signal on T2-weighted imaging in subcortical cerebral white matter, ± hemorrhage, necrosis, ± gadolinium contrast enhancement.	Methanol is rapidly absorbed by the GI tract, with peak plasma levels reached within 1 hour. Methanol can also be absorbed through the skin. Metabolic conversion of methanol to formic acid by hepatic alcohol dehydrogenase and aldehyde dehydrogenase causes severe metabolic acidosis, resulting in selective necrosis of the basal ganglia/putamina bilaterally and subcortical white matter 12 to 24 hours after accidental or suicidal ingestion. Clinical findings include visual disturbances, drowsiness, seizures, coma, and death.
Ethylene glycol toxicity (**Fig. 1.296**)	MRI: Zones with high signal on T2-weighted imaging and FLAIR are seen in the basal ganglia, thalamus, midbrain, pons, medulla, cerebellum, and/or cerebral white matter, ± restricted diffusion in the acute phase. Putaminal necrosis can be seen weeks afterward. CT: Zones with decreased attenuation are seen in the basal ganglia, thalamus, midbrain, pons, medulla, cerebellum, and/or cerebral white matter.	Ethylene glycol is absorbed by the GI tract with peak plasma levels occurring between 1 and 4 hours. Metabolic conversion of ethylene glycol by hepatic enzymes (alcohol dehydrogenase, aldehyde dehydrogenase, glyoxalase I and II, α-oxoaldehyde dehydrogenase, and glycolate oxidase) results in toxic accumulation of glycolic, glyoxylic, and oxalic acid, causing severe metabolic acidosis. This results in selective necrosis of the basal ganglia/putamina bilaterally and subcortical white matter 12 to 24 hours after accidental or suicidal ingestion. Clinical findings can occur 30 minutes after ingestion and include headache, dizziness, abdominal pain, and vomiting. After 12 hours, clinical findings progress, including seizures, coma, respiratory distress, and death.
Cyanide	MRI: Zones with high signal on T2-weighted imaging and FLAIR can be seen in the caudate nuclei, putamina, and globi pallidi, ± sensorimotor cortex, ± gadolinium contrast enhancement. Late findings include high signal on T1-weighted imaging in the caudate and lentiform nuclei and sensorimotor cortex from hemorrhagic necrosis and cortical laminar necrosis, respectively. CT: Zones with decreased attenuation are seen in the basal ganglia.	Toxic exposure to cyanide can occur from ingestion, inhalation, or skin absorption. Cyanide causes inactivation of mitochondrial cytochrome oxidase which normally has a critical function in the cellular respiratory chain. Clinical findings include altered mental status, dyspnea, lactic acidosis, seizures, hypotension, cardiac arrythymias, and death.
Cocaine	CT: Findings include cerebral infarcts, intra-axial or extra-axial hemorrhages. CTA shows zones of arterial narrowing from vasoconstriction, often in association with brain infarcts in the affected vascular territory. MRI: Findings include cerebral infarcts with high signal on T2-weighted imaging and FLAIR, restricted diffusion for acute infarcts, ± intra-axial or extra-axial hemorrhages.	Cocaine can be inhaled as powdered cocaine hydrochloride through nasal mucous membranes or as a vapor in the alkaloid combined form of cocaine hydrochloride with sodium bicarbonate or ammonia ("crack cocaine"). Results in blockage of uptake of monoamines, causing vasoconstriction, hypertension, tachycardia, intracranial hemorrhage (brain and subarachnoid), and stroke.

(continued on page 242)

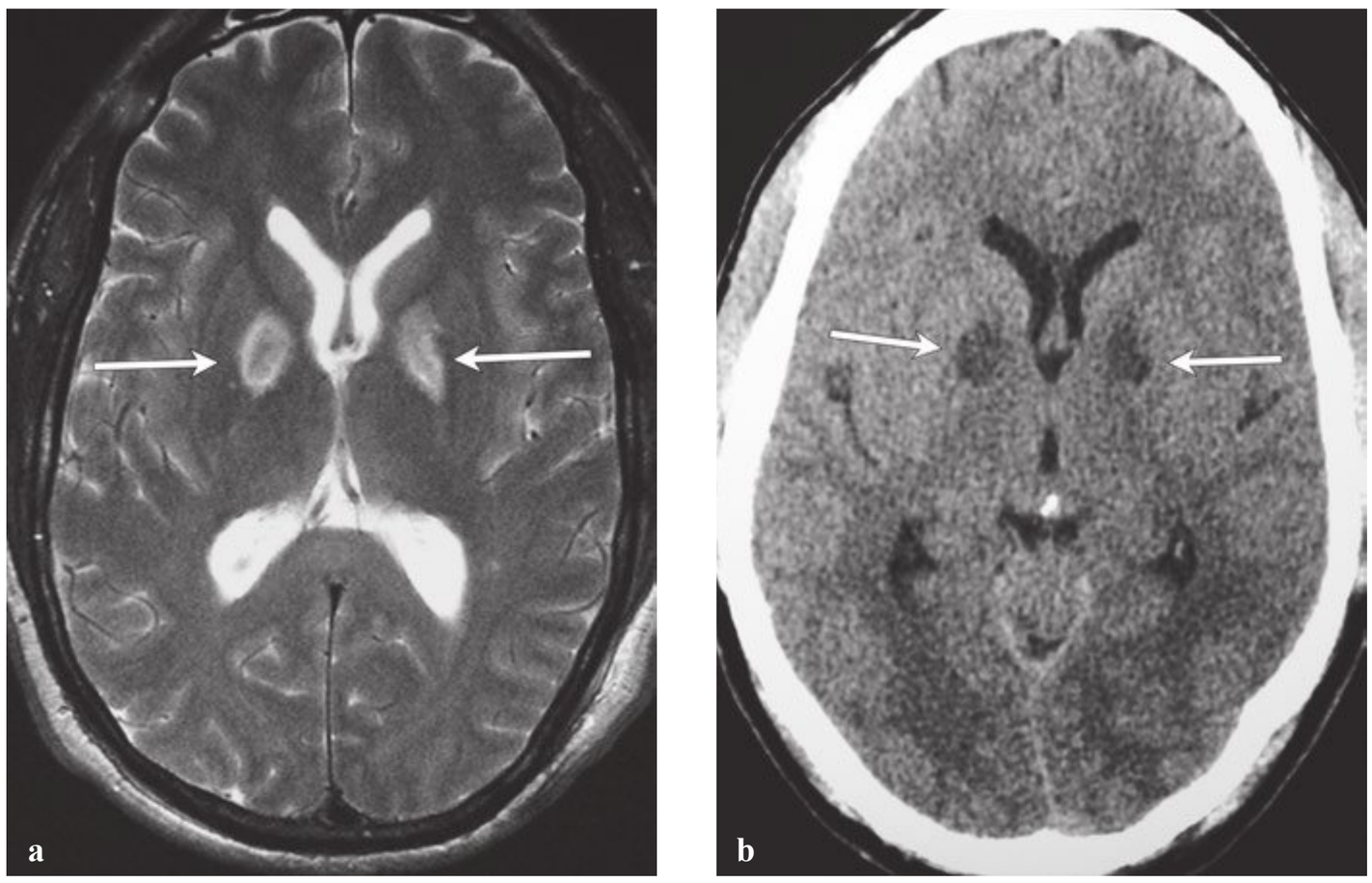

Fig. 1.295 Patient with toxic exposure to carbon monoxide who has **(a)** abnormal high signal on axial T2-weighted imaging (arrows) and **(b)** low attenuation on axial CT in the globus pallidus bilaterally (arrows).

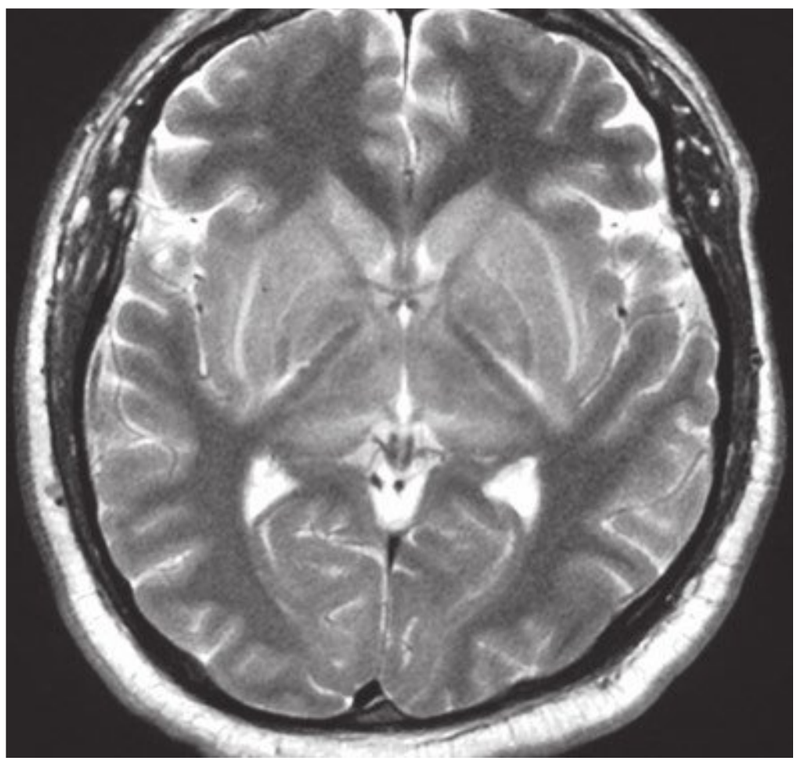

Fig. 1.296 A 34-year-old man who ingested ethylene glycol. Poorly defined zones with high signal on axial T2-weighted imaging are seen in the basal ganglia, thalami, and cerebral white matter.

Table 1.6 (cont.) Bilateral lesions involving the basal ganglia and/or thalami

Lesions	Imaging Findings	Comments
Heroin (**Fig. 1.297**)	CT: Inhalation of heroin can result in symmetric abnormal decreased attenuation involving the cerebellar white matter, middle cerebellar peduncles, brainstem, and temporo-occipital white matter. MRI: Inhalation of heroin vapor can result in symmetric abnormal increased signal on T2-weighted imaging and FLAIR in the cerebellar white matter, middle cerebellar peduncles, brainstem, temporo-occipital white matter, and internal capsules. There is no abnormal gadolinium contrast enhancement. In the acute phase, restricted diffusion can occur at the involved white matter. In the subacute and chronic stages, increased diffusion with increased ADC values is typically seen. Intravenous heroin can cause infarcts in the globus pallidus as well as in the cerebral white matter related to small-vessel disease.	Heroin-induced leukoencephalopathy (chasing the dragon) is toxic spongiform encephalopathy from inhalation of heroin vapor. Intravenous heroin can cause acute neurovascular complications, such as embolic events, vasospasm, and vasculitis, resulting in brain infarcts. In the acute phase of spongiform leukoencephalopathy, restricted diffusion can be seen at the involved sites related to the presence of small vacuoles in myelin. In the subacute and later phases, the vacuoles within myelin progressively become larger, resulting in increased diffusion.
Neurodegenerative Disease		
Huntington disease (**Fig. 1.298**)	Disproportionate atrophy of basal ganglia (caudate > putamen > cerebellum/brainstem). CT: Progressive atrophy of caudate and putamen bilaterally. MRI: Variable low signal (iron deposition) or high signal (gliosis) changes on T2-weighted imaging in the caudate nuclei and putamen bilaterally and associated with atrophy. Usually there is no abnormal gadolinium contrast enhancement.	Autosomal dominant neurodegenerative disease in adults related to abnormal segment (CAG repeats) of DNA on chromosome 4 involving the huntingtin gene. Usually presents after 40 years with progressive movement disorders (choreoathetosis, rigidity, hypokinesia), behavioral abnormalities, and progressive mental dysfunction (dementia). Juvenile Huntington disease also occurs in a small number of patients in the second decade. Patients present with rigidity, hypokinesia, seizures, and progressive mental dysfunction.
Multiple system atrophy (striatonigral degeneration [MSA-P], olivopontocerebellar atrophy [MSA-C], Shy-Drager syndrome [MSA-A])	CT: Progressive atrophy of the brainstem, cerebellum, and/or cerebrum. MRI: In MSA-P, low signal on T2-weighted imaging in small putamina equal to or more pronounced than in the globus pallidus. Atrophy of the brainstem, cerebellum, and/or cerebrum.	Multiple system atrophy (MSA) encompasses progressive adult-onset neurodegenerative disorders that are referred to as Parkinson-plus syndromes. In MSA, there is degeneration of the substantia nigra, striatum, pons, middle cerebellar peduncles, cerebellum, and inferior olivary nuclei. The syndromes have the dyskinetic features of Parkinson disease (muscle rigidity, tremors, slow movement), as well as additional clinical findings of autonomic dysfunction (orthostatic hypotension), poor response to levodopa, cerebellar ataxia, extrapyramidal signs, and urogenital dysfunction. MSA-P (previously referred to as striatonigral degeneration) has mostly Parkinsonian features; MSA-C (previously referred to as olivopontocerebellar atrophy) has ataxia; and MSA-A (previously referred to as Shy-Drager syndrome) has autonomic dysfunction with orthostatic hypotension, urogenital dysfunction, and anhydrosis.

(continued on page 244)

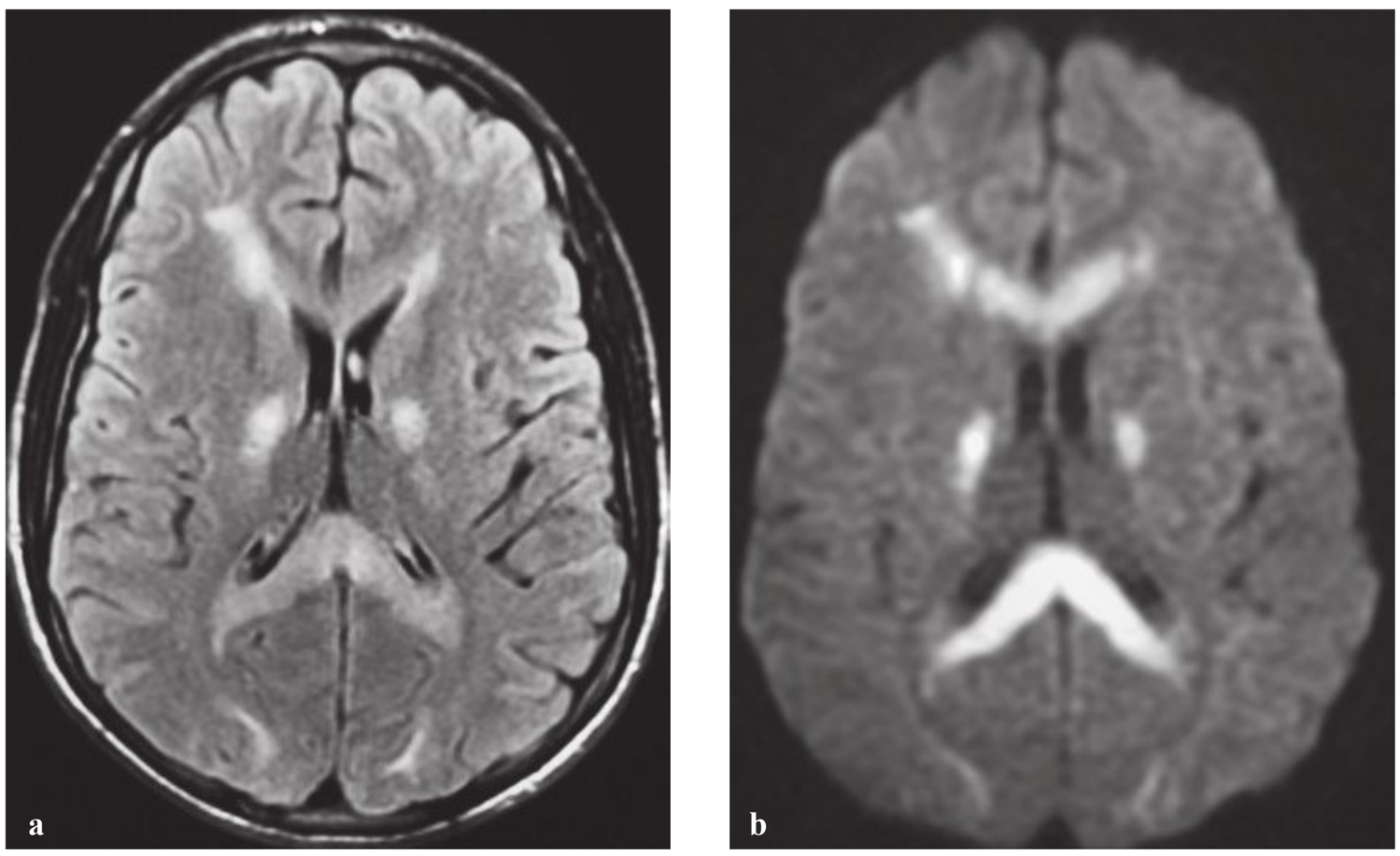

Fig. 1.297 A 17-year-old male with toxicity from intravenous heroin. **(a)** Abnormal high signal is seen in the globi pallidi, corpus callosum, and periventricular white on axial FLAIR, with **(b)** corresponding restricted diffusion on axial DWI.

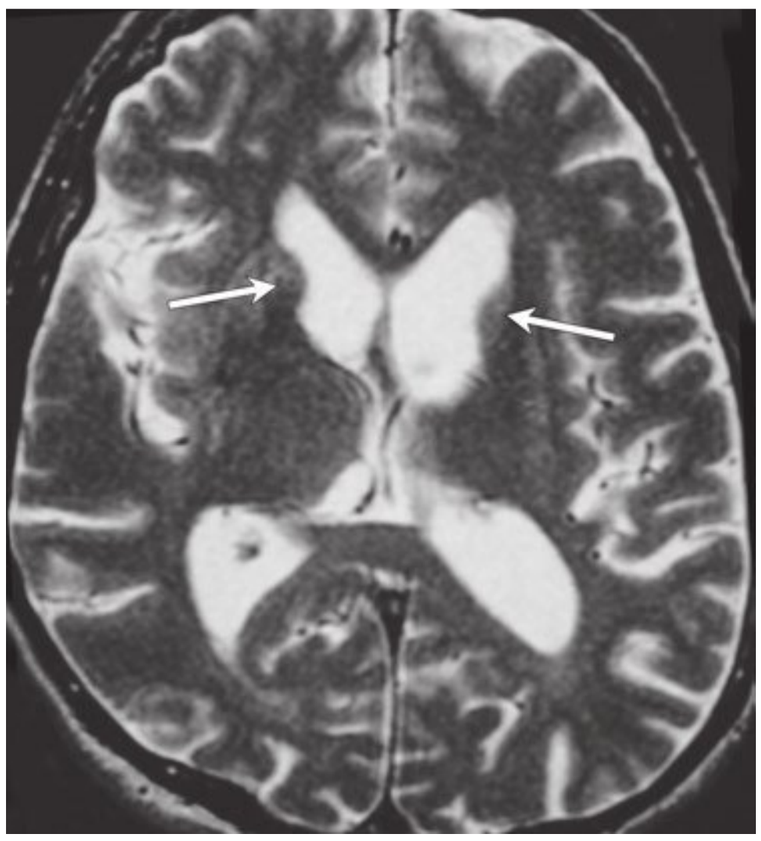

Fig. 1.298 A 64-year-old man with Huntington disease. Slightly high signal on axial T2-weighted imaging is seen in both atrophied caudate nuclei (arrows). Mixed low signal (iron deposition) and slightly high signal changes are seen in the putamen bilaterally and are associated with atrophy.

Table 1.6 (cont.) Bilateral lesions involving the basal ganglia and/or thalami

Lesions	Imaging Findings	Comments
Pallidotomy (**Fig. 1.299**)	MRI: Chronic changes from pallidotomy include zones of signal alteration in one or both globi pallidi consisting of low signal on T1-weighted imaging; high signal on T2-weighted imaging; low, intermediate, or high signal on FLAIR; and low signal on diffusion-weighted imaging (DWI). Typically there is no gadolinium contrast enhancement. CT: Zones of low signal can be seen in one or both globi pallidi.	Treatment for Parkinson disease includes medication with levodopa as well as pallidotomy or placement of electrodes for deep brain stimulation.
Wallerian degeneration	Corticospinal tract involvement from infarct or injury at motor cortex or posterior limb of internal capsule. CT: Hemiatrophy of brainstem (midbrain, pons) ipsilateral to cerebral lesion. MRI: Linear zone of high signal on T2-weighted imaging in ipsilateral corticospinal tract of brainstem (high signal on T2-weighted imaging 5–12 weeks after). Injury results from edema, > 12 weeks secondary to gliosis, ± associated atrophy in brainstem at ipsilateral corticospinal tract. Extensive unilateral cerebral cortical atrophy can result in atrophy of the contralateral middle cerebellar peduncle and cerebellum from interruption of the corticopontocerebellar pathway (which connects the cerebral cortex to the contralateral middle cerebellar peduncle via pontine nuclei).	Refers to pathologic changes (degeneration, myelin degradation, atrophy) in axons secondary to injuries involving the cell bodies of neurons (hemorrhage, cerebral infarction, contusion, surgery, etc.).
Prominent perivascular spaces (**Fig. 1.300**)	MRI: Focus or foci with signal similar to CSF on FLAIR and high signal on T2-weighted imaging, usually not apparent on FLAIR images, low signal on diffusion-weighted imaging (DWI) and T1-weighted imaging, with no gadolinium contrast enhancement. Located in the basal ganglia, and high subcortical cerebral white matter/centrum semiovale.	Pia-lined spaces filled with CSF containing arteries supplying brain parenchyma, also referred to as Virchow-Robin spaces. Perivascular spaces increase in size and number with aging.

(continued on page 246)

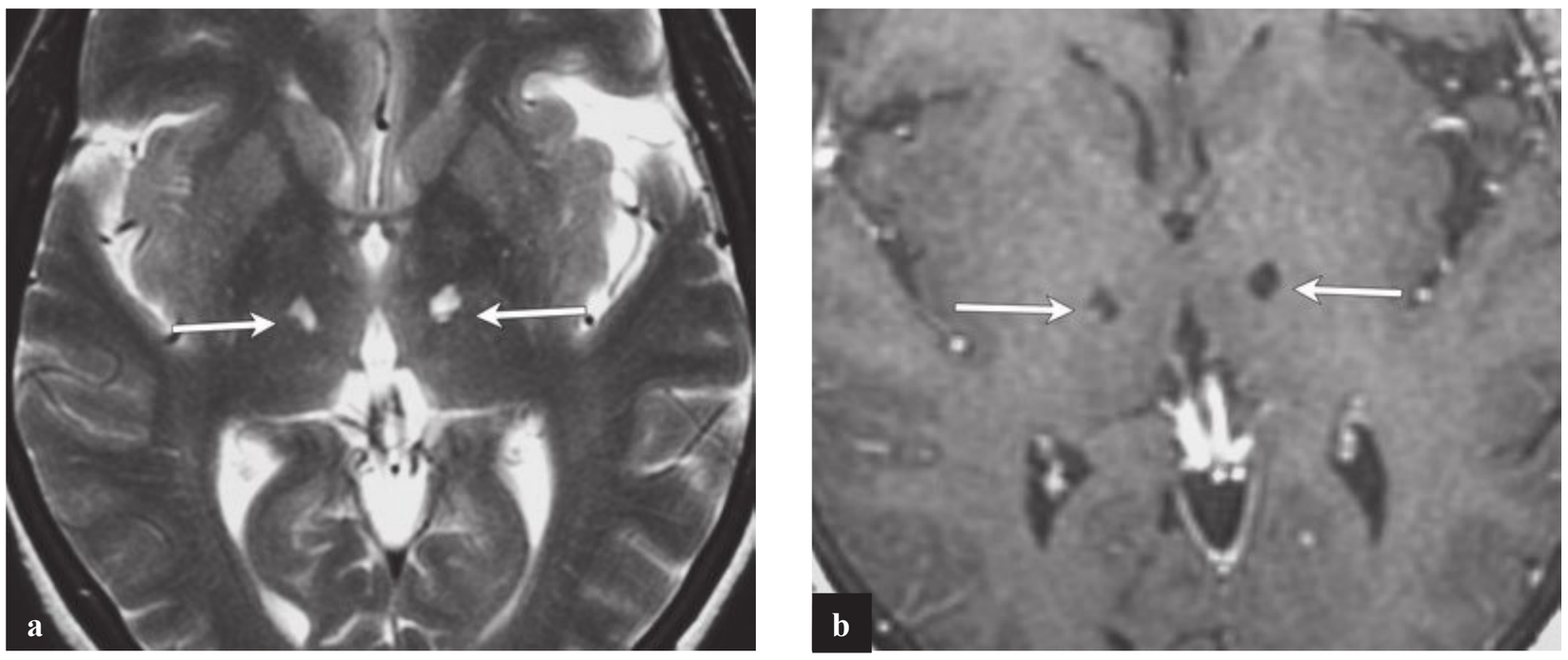

Fig. 1.299 A 62-year-old man with history of pallidotomy. **(a)** Small zones of high signal on axial T2-weighted imaging (arrows) and **(b)** low signal on T1-weighted imaging are seen in the region of both globi pallidi and subthalami nuclei (arrows).

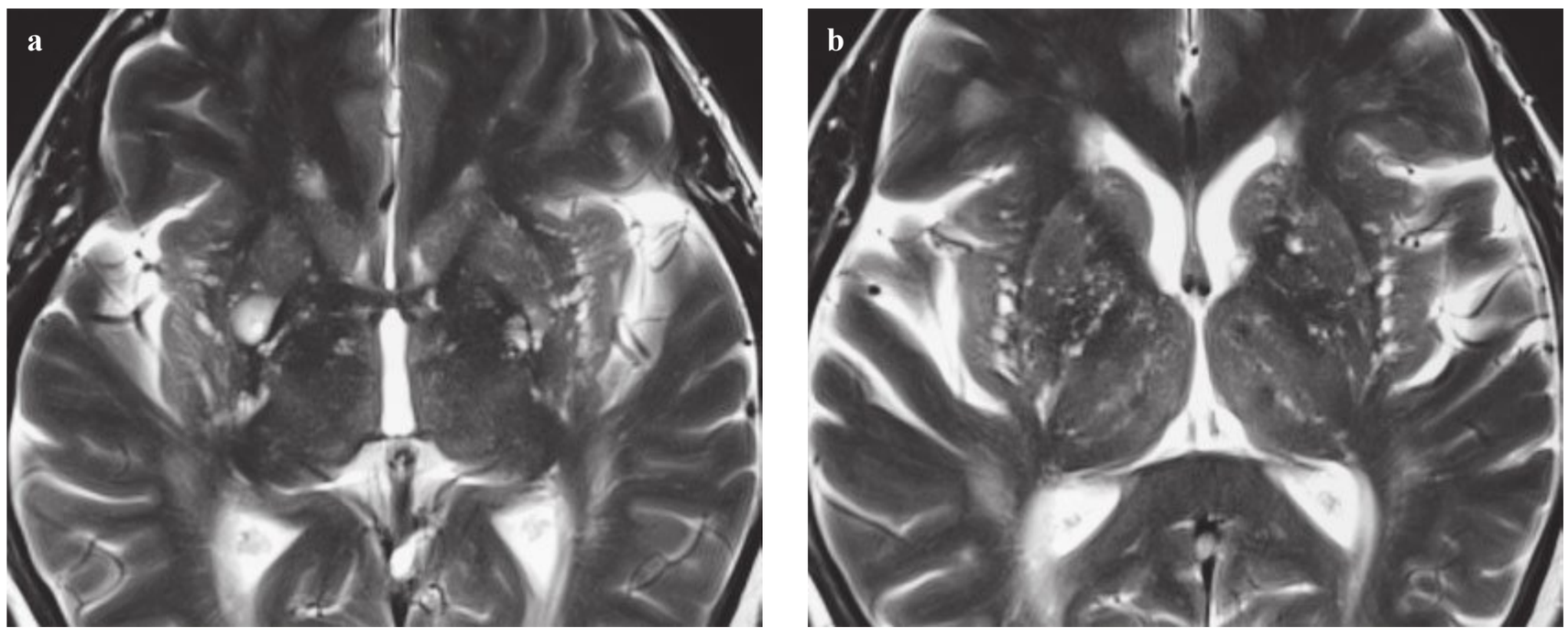

Fig. 1.300 **(a,b)** An 81-year-old woman with prominent perivascular spaces seen as foci with high signal on axial T2-weighted imaging in the basal ganglia bilaterally.

Table 1.6 (cont.) Bilateral lesions involving the basal ganglia and/or thalami

Lesions	Imaging Findings	Comments
Infection		
Pyogenic brain abscess	MRI: Circumscribed lesions with low signal on T1-weighted imaging; central zone of high signal on T2-weighted imaging (± air–fluid level) surrounded by a thin rim with intermediate-low signal on T2-weighted imaging that shows ringlike gadolinium contrast enhancement that is sometimes thicker laterally than medially; and peripheral poorly defined zone of high signal on T2-weighted imaging representing edema. Abscess contents typically have restricted diffusion. Mean ADC values for abscesses are significantly lower (0.63 to 1.12 × 10^{-3} mm^2/s) than those for necrotic or cystic neoplasms (2.45 × 10^{-3} mm^2/s). MR spectroscopy shows decreased N-acetylaspartate (NAA) due to destruction of neurons, and elevated lactate, and amino acid peaks (valine, leucine, and isoleucine) at 0.9 ppm secondary to proteolytic enzymes. CT: Circumscribed lesion with a central zone of low attenuation (± air–fluid level) surrounded by a thin rim of intermediate attenuation; peripheral poorly defined zone of decreased attenuation representing edema; and ringlike contrast enhancement that is sometimes thicker laterally than medially.	Formation of brain abscess occurs 2 weeks after cerebritis, with liquefaction and necrosis centrally surrounded by a capsule and peripheral edema. Restricted diffusion of abscess contents is related to the combination of the high protein content and viscosity of pus, necrotic debris, and bacteria. Can be multiple, but more than 50%are solitary. Complication from meningitis and/or sinusitis, septicemia, trauma, surgery, and cardiac shunt. Abscesses account for 2% and 8%of intra-axial mass lesions in developed and developing countries, respectively.
Fungal brain lesions (**Fig. 1.301**)	MRI: Findings vary depending on organism. Infection can occur in meninges and/or brain parenchyma, as solid or cystic lesions with low-intermediate signal on T2-weighted imaging, high signal on T2-weighted imaging and FLAIR, nodular or ring-shaped gadolinium contrast enhancement, and peripheral high signal in brain lesions on T2-weighted imaging (edema). Infected tissue may have restricted diffusion at the walls of the lesions without reduced ADC values in the central cavities of the lesions. Low signal on T2-weighted imaging and GRE at the walls of the lesions may occur from paramagnetic iron and magnesium within hyphae of the fungi. Magnetic resonance spectroscopy can show elevated lipid, lactate, and amino acid peaks, as well as multiple peaks between 3.6 and 3.8 ppm from trehalose. CT: Infection can occur in meninges and brain parenchyma, with solid or cystic-appearing lesions with decreased attenuation, nodular or ring pattern of contrast enhancement, and a peripheral zone with decreased attenuation (edema).	Occur in immunocompromised or diabetic patients, with resultant granulomas in meninges and brain parenchyma. Cryptococcus involves the basal meninges and extends along perivascular spaces into the basal ganglia. Aspergillosis and Mucor spread via direct extension through paranasal sinuses or hematogenously, invading blood vessels and resulting in hemorrhagic lesions and/or cerebral infarcts. Coccidioidomycosis usually involves the basal meninges. Candidiasis is often a nocosomial infection related to complications from surgery and/or indwelling catheters.

(continued on page 248)

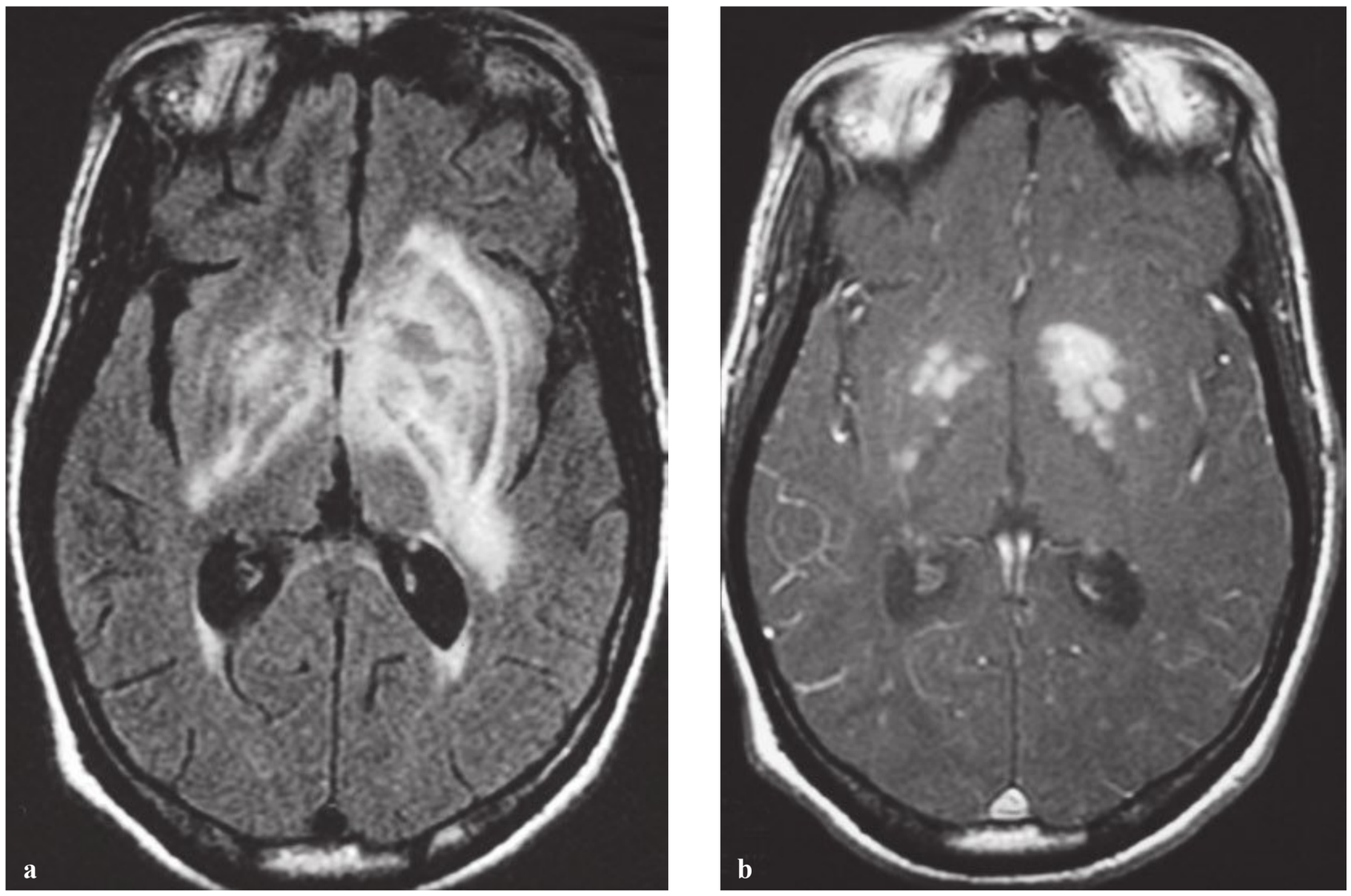

Fig. 1.301 A 37-year-old immunocompromised man with Cryptococcus infection in the CNS. **(a)** Poorly defined zones with abnormal asymmetric high signal in the basal ganglia bilaterally on axial FLAIR that are associated with **(b)** multiple intra-axial foci of gadolinium contrast enhancement on axial T1-weighted imaging.

Table 1.6 (cont.) Bilateral lesions involving the basal ganglia and/or thalami

Lesions	Imaging Findings	Comments
Viral encephalitis (**Fig. 1.302** and **Fig. 1.303**) Herpes simplex Cytomegalovirus (CMV) Progressive multifocal leukoencephalopathy Japanese encephalitis Rabies Acute measles encephalitis Subacute sclerosing panencephalitis from measles (SSPE) West Nile virus	Herpes simplex MRI: Typically involves the temporal lobes/limbic system ± hemorrhage. Poorly defined zone or zones of low-intermediate signal on T1-weighted imaging and intermediate-high signal on T2-weighted imaging and FLAIR. Restricted diffusion can occur in early stages of infection. Minimal or no gadolinium contrast enhancement, involves cerebral cortex and/or white matter, and minimal localized mass effect. CT: Poorly defined zone or zones of decreased attenuation, minimal or no contrast enhancement. CMV MRI: Periventricular/subependymal zones with high signal on T2-weighted imaging and FLAIR. HIV often involves periatrial white matter. CT: Neonatal CMV infections can result in localized destruction of brain with dystrophic calcifications. PML MRI: Single or multifocal zones in the cerebral white matter, including the arcuate/U-fibers, with abnormal increased signal on T2-weighted imaging and FLAIR, ± cerebral cortical involvement, ± mild localized mass effect, reduced ADC values and fractional anisotropy (FA) in acute phases, increased ADC in late phases. Magnetic resonance spectroscopy shows decreased N-acetylaspartate (NAA) and increased choline and lactate. Japanese encephalitis MRI: Abnormal increased signal on T2-weighted imaging and FLAIR involving the thalami, basal ganglia, hippocampi, and substantia nigra, and less commonly the cerebral cortex, brainstem, and cerebellum. Rabies MRI: Poorly defined zones with increased signal on T2-weighted imaging can be seen in the cerebral white matter, cerebral cortex, basal ganglia, brainstem, and hypothalamus; ± gadolinium contrast enhancement. Acute measles MRI: Increased signal on T2-weighted imaging can be seen in the cerebral white matter, cerebral cortex, basal ganglia, + restricted diffusion, ± petechial hemorrhage, ± gadolinium contrast enhancement in cerebral cortex and leptomeninges. SSPE MRI: Zones with abnormal increased signal on T2-weighted imaging and FLAIR are seen in the cerebral and cerebellar white matter and brainstem, with increased ADC values and no gadolinium contrast enhancement. West Nile virus MRI: Zones with abnormal increased signal on T2-weighted imaging and FLAIR are seen in the cerebral and cerebellar white matter and brainstem. Typically there is no gadolinium contrast enhancement.	Encephalitis is infection/inflammation of brain tissue from viruses. In immunocompromised patients, causative viruses include herpes simplex, cytomegalovirus (CMV), human immunodeficiency virus (HIV), and progressive multifocal leukoencephalopathy from JC polyoma virus infection of oligodendrocytes. In immunocompetent patients, causes include St. Louis encephalitis virus, Eastern or Western equine encephalitis virus, measles (RNA Paramyxovirus) virus, Epstein-Barr virus, Japanese encephalitis (Flavivirus), West Nile virus (Flavivirus), and rabies (Lyssavirus).

(continued on page 250)

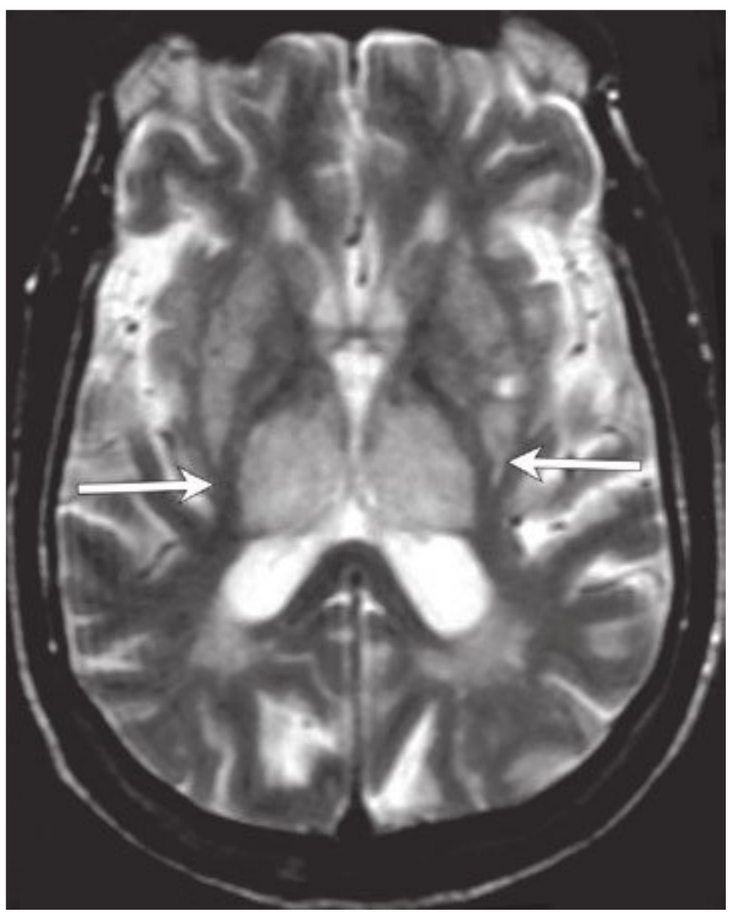

Fig. 1.302 Patient with Japanese encephalitis who has abnormal increased signal on axial T2-weighted imaging in both thalami (arrows).

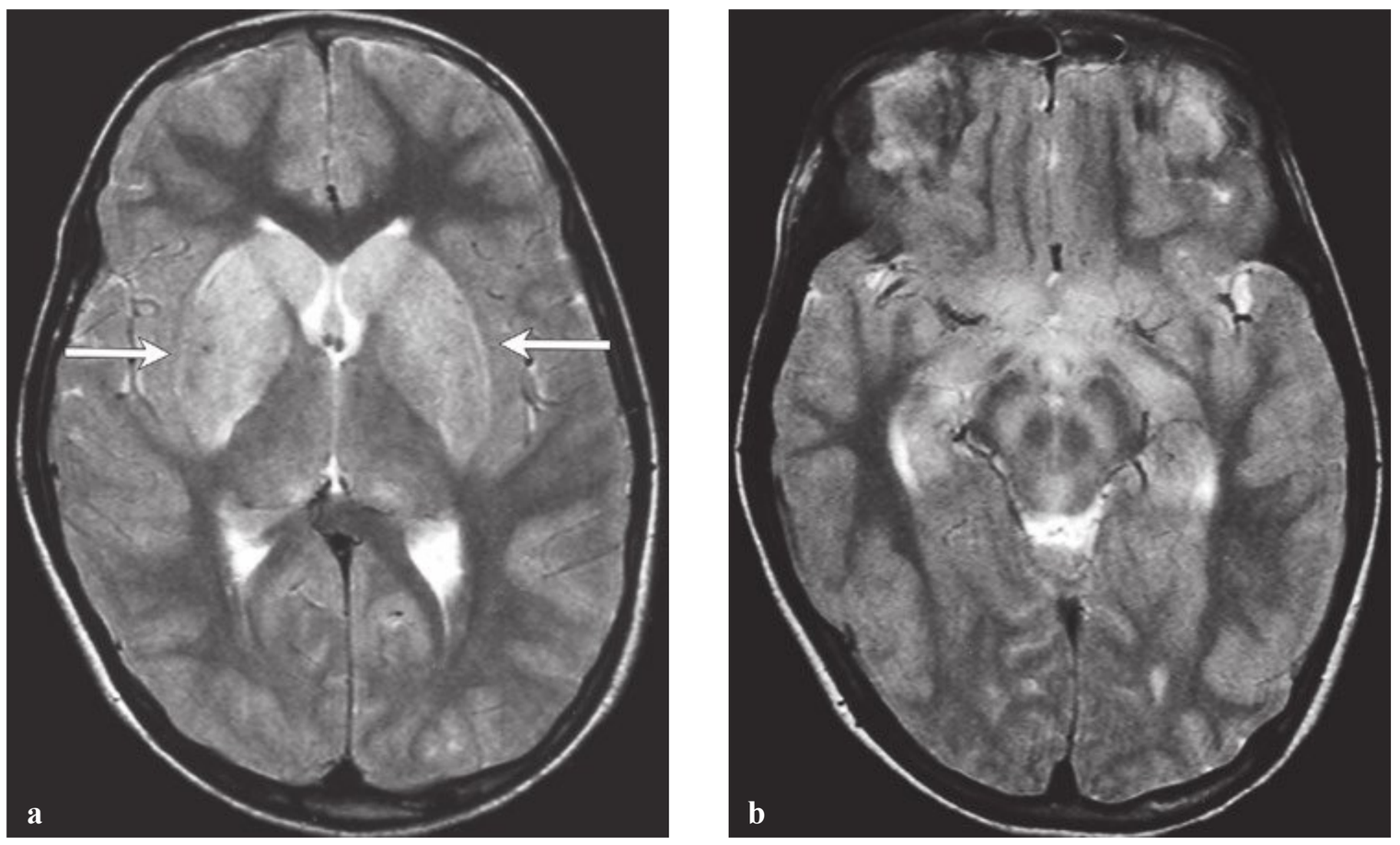

Fig. 1.303 **(a,b)** Patient with rabies who has poorly defined zones with abnormal increased signal on axial T2-weighted imaging in the basal ganglia (arrows), thalami, brainstem, cerebral white matter, and cerebral cortex.

Table 1.6 (cont.) Bilateral lesions involving the basal ganglia and/or thalami

Lesions	Imaging Findings	Comments
Parasitic disease: Toxoplasmosis (**Fig. 1.304**)	MRI: Single or multiple solid and/or cystic lesions located in basal ganglia and/or corticomedullary junctions in cerebral hemispheres, low-intermediate signal on T1-weighted imaging with or without high-signal peripheral rims; high signal on T2-weighted imaging and FLAIR with or without a central zone of low-intermediate signal, or three layers of high central signal region surrounded by a peripheral rim of low-intermediate signal that is in turn surrounded by high signal; nodular or rim pattern of gadolinium contrast enhancement as well as an "eccentric target pattern" with a peripheral ring-shaped zone of gadolinium contrast enhancement and a small, eccentric, enhancing nodule along the wall; ± peripheral high T2 signal (edema). Diffusion-weighted imaging (DWI) shows high-signal rims surrounding low-signal centers. CT: Lesions can have low or intermediate attenuation, ± peripheral rim or nodular patterns of contrast enhancement.	Most common opportunistic CNS infection in AIDS patients, caused by ingestion of food contaminated with parasites (Toxoplasma gondii). T. gondii is an intracellular protozoan with a worldwide distribution. Also occurs in immunocompetent patients. Acute lesions contain a central zone comprised of necrotic and cellular debris, histiocytes, and neutrophils; an intermediate zone of vascular congestion and tachyzoites; and an outer zone with microglial nodules, T. gondii organisms, and tachyzoites, mild inflammation, and vascular congestion. 18F-Fluorodeoxyglucose (18F-FDG) PET/CT shows decreased uptake in T. gondii lesions and can be used to distinguish toxoplasmosis from lymphoma, which has increased FDG uptake.
Parasitic disease: Cysticercosis	MRI: Single or multiple cystic lesions in brain or meninges. In the active vesicular phase, there are cystic-appearing lesions containing a small 2–4 mm nodule (scolex) with low signal on T1-weighted imaging, FLAIR, and diffusion-weighted imaging (DWI), a thin peripheral rim with high signal on FLAIR, and high signal on T2-weighted imaging, minimal peripheral rim or no gadolinium contrast enhancement, and no peripheral edema on T2-weighted imaging and FLAIR. In the active colloidal vesicular phase, there are cystic-appearing lesions with low-intermediate signal on T1-weighted imaging, high signal on T2-weighted imaging, and rim and/or nodular pattern of gadolinium contrast enhancement, ± peripheral signal (edema) on T2-weighted imaging. In the active granular nodular phase, the cyst retracts into a more solid gadolinium contrast-enhancing granulomatous nodule. CT: Single or multiple cystic-appearing lesions in brain or meninges. In the acute/subacute phase, there is low-intermediate attenuation, rim ± nodular pattern of contrast enhancement, ± peripheral low attenuation (edema). The chronic phase is characterized by calcified granulomas.	Caused by ingestion of encysted larva of the tapeworm Taenia solium in contaminated food (undercooked pork). Cysticercosis involves meninges, subarachnoid space, and cisterns > brain parenchyma > ventricles. Most common parasitic disease of the CNS, usually in patients from 15 to 40 years old, and the most common cause of acquired epilepsy in endemic regions. Complications include intracranial hypertension from CSF obstruction, arachnoiditis, meningitis, and vascular occlusion.
Prion disease (**Fig. 1.305**)	MRI: Zones with high signal on T2-weighted imaging and FLAIR can be seen in the basal ganglia (caudate, putamen, and/or thalami bilaterally) and/or cerebral cortex with corresponding restricted diffusion. Typically no abnormal gadolinium contrast enhancement is seen with these abnormalities. CT: Usually no findings in the early phases of the disease.	Transmissible spongiform encephalopathies resulting in progressive neurodegeneration caused by infection with prions. Creutzfeldt-Jakob disease is the most common type and has four forms (sporadic form accounts for 85%, genetic for 10–15%, and the iatrogenic and new variant forms for the remainder).

(continued on page 252)

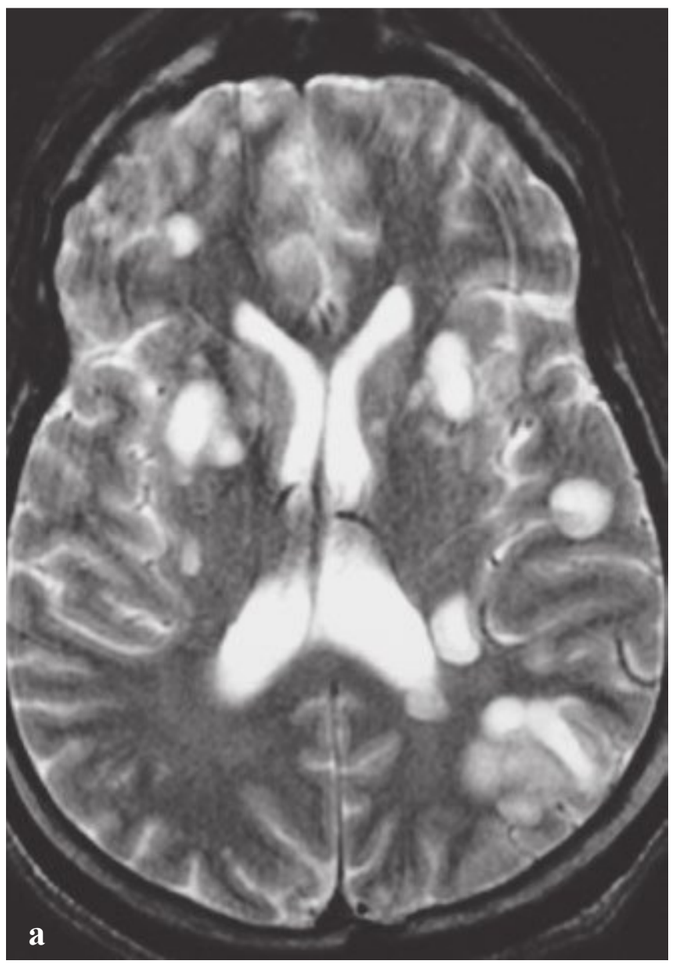

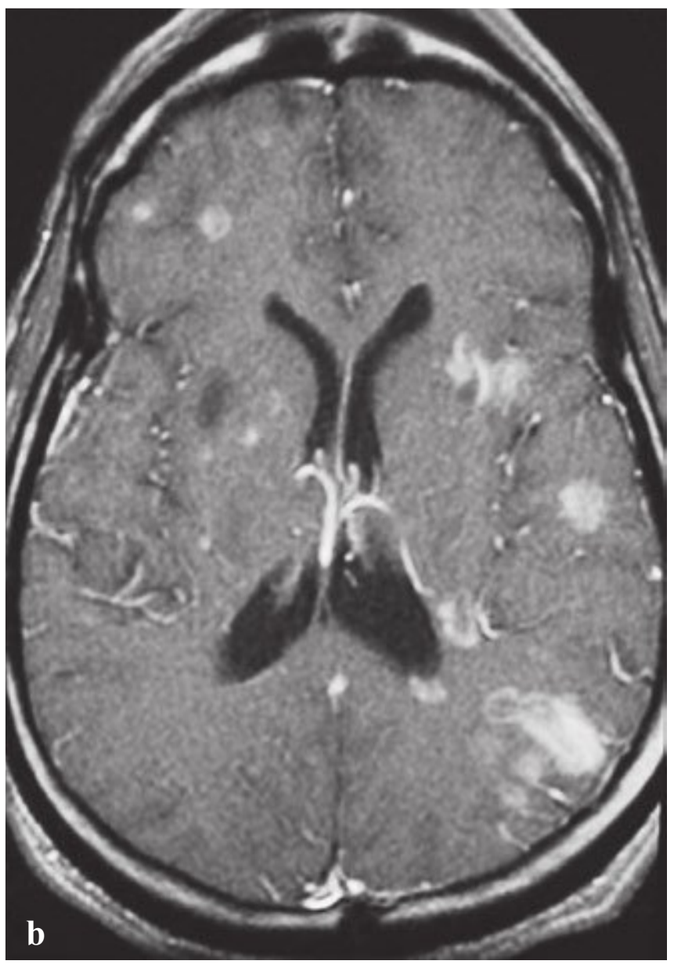

Fig. 1.304 **(a)** Toxoplasmosis in an immunocompromised 31-year-old man seen as multiple cystic lesions located in basal ganglia and corticomedullary junctions in the cerebral hemispheres, which have high signal on axial T2-weighted imaging. **(b)** Lesions show a nodular or rim pattern of gadolinium contrast enhancement as well as an eccentric target pattern with a peripheral ring-shaped zone of gadolinium contrast enhancement and a small eccentric enhancing nodule along the wall on axial T1-weighted imaging.

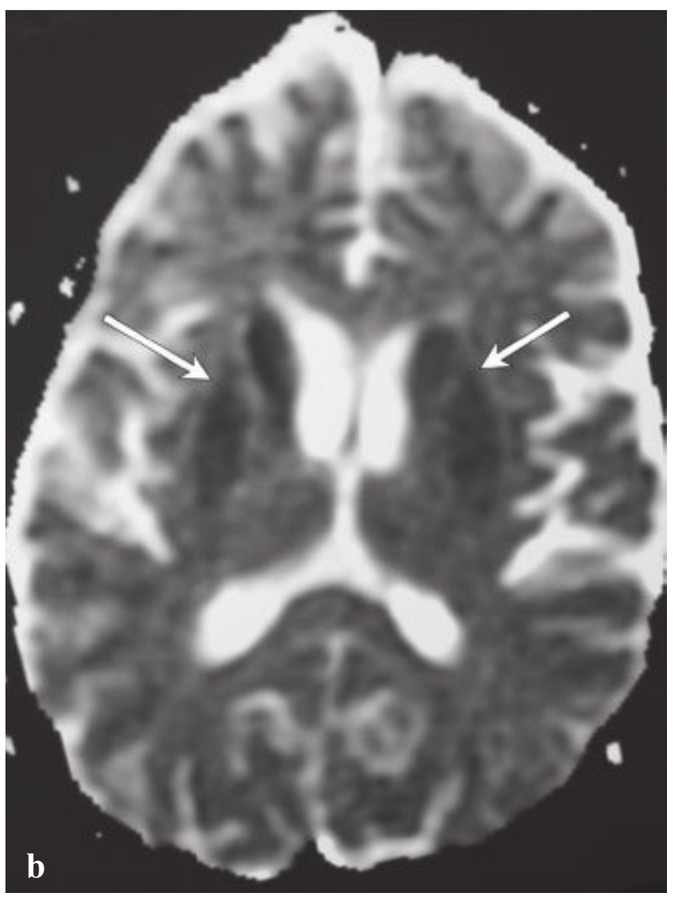

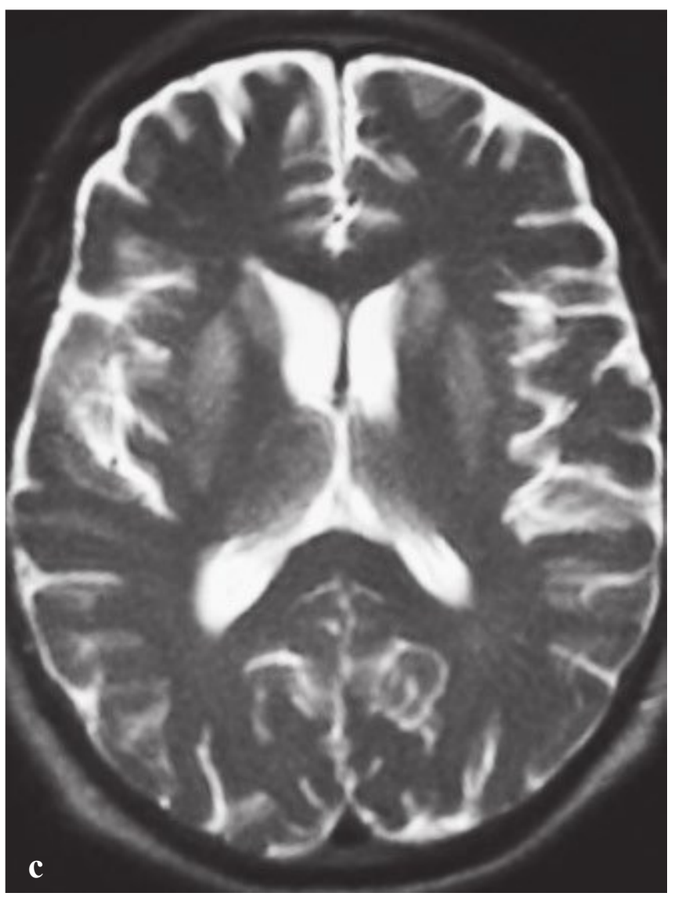

Fig. 1.305 A 60-year-old man with Creutzfeldt-Jakob disease. Restricted diffusion is seen in the caudate nuclei bilaterally and and putamina on **(a)** axial DWI and **(b)** ADC (arrows). **(c)** Corresponding increased signal is seen on axial T2-weighted imaging.

Table 1.6 (cont.) Bilateral lesions involving the basal ganglia and/or thalami

Lesions	Imaging Findings	Comments
Demyelinating Disease		
Multiple sclerosis	MRI: Lesions located in cerebral or cerebellar white matter, brainstem, and basal ganglia. Lesions usually have low-intermediate signal on T1-weighted imaging and high signal on T2-weighted imaging, ± gadolinium contrast enhancement. Gadolinium contrast enhancement can be ringlike or nodular, usually in acute/ early subacute phase of demyelination, ± restricted diffusion. Acute demyelinating lesions can have localized mass effect simulating neoplasms. CT: Zones of active demyelination may show contrast enhancement and mild localized swelling.	Multiple sclerosis (MS) is the most common acquired demyelinating disease in young and middle-aged adults (peak ages = 20–40 years). MS affects 400,000 people in the United States and 2,000,000 worldwide. Women are affected twice as frequently as men. Most common in people with northern European heritage. MS is not inherited in a Mendelian fashion, although it can cluster in families. Diagnosis is made based on clinical history and findings, results from MRI examinations (lesions with high signal on T2-weighted imaging or FLAIR seen in brain white matter, spinal cord, and optic nerves), abnormal visual evoked potentials, and isoelectric focusing evidence of oligocloncal bands and/or increased IgG index in CSF samples. Demyelinating disease occurs wherever myelin is present, including deep brain nuclei (caudate, putamen, globus pallidus and/or thalamus). The disease is typically multi-episodic. Treatment includes monoclonal antibodies and steroids.
Acute disseminated encephalomyelitis (**Fig. 1.306**)	MRI: Lesions located in cerebral or cerebellar white matter, brainstem, and basal ganglia. Lesions usually have low-intermediate signal on T1-weighted imaging and high signal on T2-weighted imaging, ± gadolinium contrast enhancement. Gadolinium contrast enhancement can be ringlike or nodular, usually in acute/ early subacute phase of demyelination, ± restricted diffusion. Acute demyelinating lesions can have localized mass effect simulating neoplasms. CT: Zones of active demyelination may show contrast enhancement and mild localized swelling.	Acute disseminated encephalomyelitis is an immune-mediated demyelination occurring after viral infection or toxin exposure (environmental or ingested, such as alcohol or solvents).
Neurosarcoid (**Fig. 1.307**)	MRI: Poorly marginated intra-axial zone or zones with low-intermediate signal on T1-weighted imaging, slightly high to high signal on T2-weighted imaging and FLAIR, usually with gadolinium contrast enhancement, + localized mass effect and peripheral edema. Often associated with gadolinium contrast enhancement in the leptomeninges and/or dura. CT: Poorly marginated intra-axial zone with low-intermediate attenuation, usually shows contrast enhancement, + localized mass effect and peripheral edema. Often associated with contrast enhancement in the leptomeninges.	Sarcoidosis is a multisystem noncaseating granulomatous disease of uncertain cause that can involve the CNS in 5 to 15% of cases. If untreated, it is associated with severe neurologic deficits, such as encephalopathy, cranial neuropathies, and myelopathy. Diagnosis of neurosarcoid may be difficult when the neurologic complications precede other systemic manifestations in the lungs, lymph nodes, skin, bone, and/or eyes.
Trauma		
Diffuse axonal injury (**Fig. 1.308**)	MRI: One or multiple sites within the brain with intermediate or high signal on T1-weighted imaging, low, intermediate and/or high signal on T2-weighted imaging and FLAIR, and low signal on gradient echo imaging. CT: With acute injuries, one or multiple sites of high-attenuation hemorrhage are seen, commonly at the corpus callosum, cerebral cortical–white matter junctions, basal ganglia, and brainstem.	Brain injury caused by deceleration and rotational shear forces, which result in disruption of axons and blood vessels with hemorrhage. The degree of axonal injury is related to a poorer prognosis.

(continued on page 254)

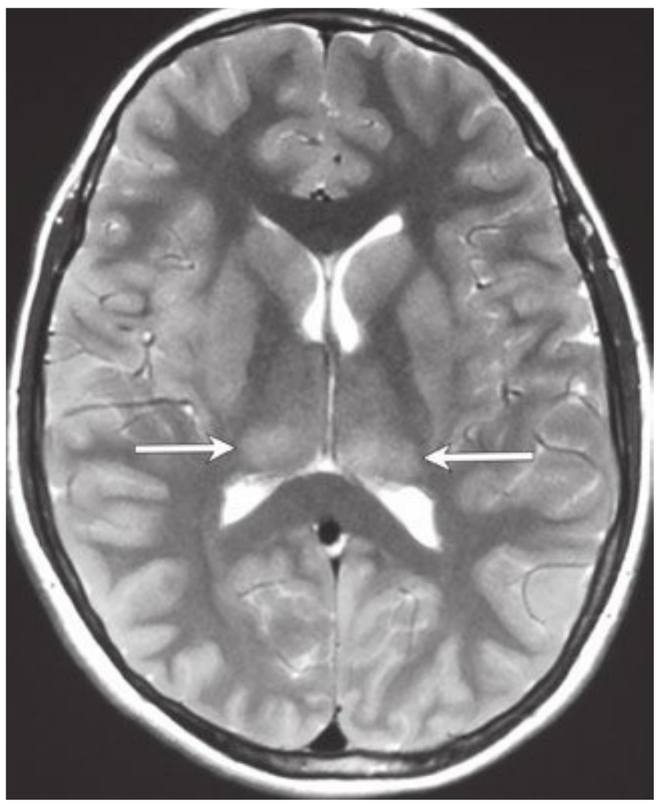

Fig. 1.306 A 12-year-old male with acute disseminated encephalomyelitis 3 weeks after a viral illness. Abnormal high signal on axial T2-weighted imaging is seen in both thalami (arrows).

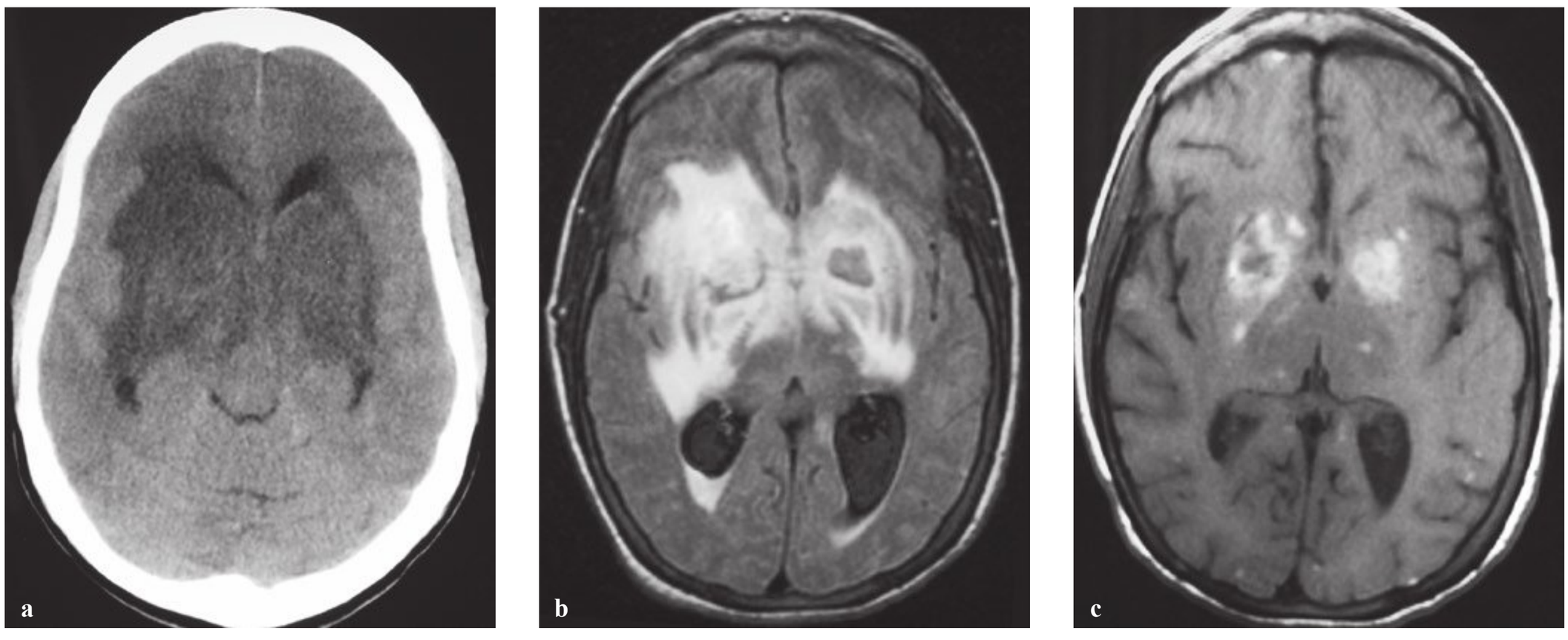

Fig. 1.307 A 42-year-old woman with neurosarcoidosis. **(a)** Extensive, diffuse, abnormal low attenuation on axial CT is seen in the basal ganglia, thalami, and adjacent deep white matter bilaterally that **(b)** has corresponding high signal on axial FLAIR. **(c)** Axial T1-weighted imaging shows multiple, irregular, intra-axial zones of gadolinium contrast enhancement in the basal ganglia, thalami, and deep white matter, as well as small extra-axial enhancing foci within the sulci along the pial surface.

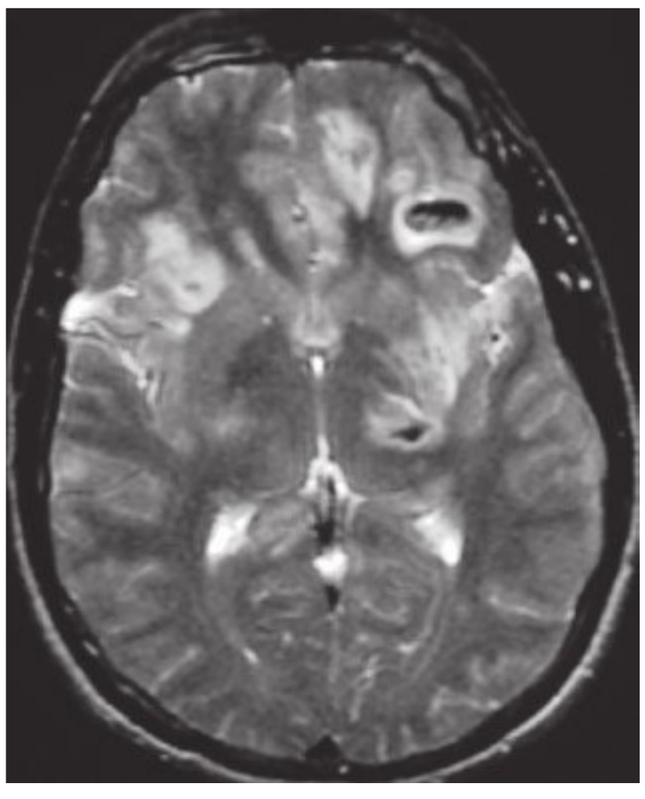

Fig. 1.308 A 19-year-old man with traumatic head injury resulting in diffuse axonal injury that is seen as multiple subcortical and other intra-axial zones of hemorrhage that have mixed low and high signal on axial T2-weighted imaging.

Table 1.6 (cont.) Bilateral lesions involving the basal ganglia and/or thalami

Lesions	Imaging Findings	Comments
Hemorrhage		
Deep venous occlusion with hemorrhagic infarction Hyperacute hematoma (0–6 hours) Acute phase (6 hours to 2–3 days) Early subacute phase (3 to 7 days) Late subacute phase (4 days to 1 month)	Hyperacute hematoma MRI: Hemoglobin primarily as diamagnetic oxyhemoglobin (iron in Fe^{2+} state), with intermediate signal on T1-weighted imaging, and slightly high signal on T2-weighted imaging. CT: A linear relationship exists between CT attenuation and hematocrit, hemoglobin, and protein content. High attenuation of hematoma from 40 to 90 HU. A horizontal fluid–fluid level may occur from sedimentation of cellular blood components from the serum. Acute hematoma MRI: Intracellular hemoglobin primarily is paramagnetic deoxyhemoglobin (iron in Fe^{2+} state), with intermediate signal on T1-weighted imaging, low signal on T2-weighted imaging, surrounded by a peripheral zone of high signal (edema) on T2-weighted imaging. CT: Attenuation of intra-axial hematoma can be up to 80–100 HU secondary to clot retraction, ± fluid–fluid level, ± peripheral halo of low attenuation from edema and/or serum extrusion. Early subacute hematoma MRI: Hemoglobin becomes oxidized to the iron Fe^{3+} state, becoming methemoglobin, which is primarily intra-cellular, with high signal on T1-weighted imaging from PEDD and low signal on T2-weighted imaging from PEDD and T2-PRE. CT: Attenuation of intra-axial hematoma can be up to 80–100 HU secondary to clot retraction, ± fluid–fluid level, ± peripheral halo of low attenuation from edema and/or serum extrusion. Late subacute hematoma MRI: When methemoglobin eventually becomes primarily extracellular, the hematoma has high signal on T1-weighted imaging from PEDD and high signal on T2-weighted imaging from increased proton density and loss of the T2-PRE effect secondary to membrane lysis. CTA/MRA: Absent contrast enhancement on CTA and absent flow signal on MRA in the intracranial venous sinuses or large intracranial veins.	Occlusion of the deep venous system (internal cerebral veins, vein of Galen, and straight sinus) can result in infarcts with hemorrhage involving both thalami and basal ganglia. Venous occlusion can be related to coagulopathy (sickle-cell disease, thalassemia, etc.), dehydration, polycythemia, and medications, such as oral contraceptives. The signal of the hematoma depends on its age, size, location, hematocrit, oxidation state of iron in hemoglobin, degree of clot retraction, extent of edema, and MRI pulse sequence.

Lesions	Imaging Findings	Comments
Preterm neonates with hemorrhage involving the germinal matrix (**Fig. 1.309**)	MRI: In the early phases, germinal matrix hemorrhage has intermediate to high signal on T1-weighted imaging from methemoglobin and low signal on T2-weighted imaging from intracellular methemoglobin. Hemorrhage within the ventricles is often also seen. By the second week, tissue loss at the hemorrhage results in localized secondary ex vacuo ventricular dilatation. CT: Recent germinal matrix hemorrhages typically have increased attenuation. Intraventicular hemorrhage, when present, shows high attenuation. Ventricular dilatation may be seen. By the second week, tissue loss at the hemorrhage results in localized secondary ex vacuo ventricular dilatation. Ultrasonography: In the early phases, zones of increased echogenicity are seen at the caudate heads, along the caudothalamic grooves, and within the ventricles, particularly anterior to the foramen of Monro, where there is no confounding echogenic choroid plexus.	Premature or preterm neonates at less than 34 weeks of gestation and weighing less than 2,000 g have a 25%risk of periventricular and/or intraventricular hemorrhage that occurs within the first 24 hours after birth in 40%and within 4 days in 90% Most of these hemorrhages are associated with the germinal matrix. The germinal matrix contains a rich network of capillaries that are lined only by a simple endothelium lacking muscular or collagenous support. The vascularity of the germinal matrix is greater than in the other portions of the brain. The endothelial cells lining the capillaries of the germinal matrix also have three to five times the number of mitochondria per cell compared with the endothelial cells of systemic capillaries, and they have an increased selective vulnerability to hypoxia because of their high demand for oxidative phosphorylation. Hypoxia and ischemia in the preterm neonate result in damage to the capillaries of the germinal matrix. If reperfusion occurs, the injured germinal matrix is prone to hemorrhage. The severity of the germinal matrix hemorrhage is grouped into four grades: Grade I: Subependymal hemorrhage occurs without, or with only minimal, intraventricular extension. Grade II: The subependymal hemorrhage extends into the ventricles without ventricular dilatation. Grade III: The subependymal hemorrhage extends into the ventricles with associated ventricular dilatation. Grade IV: Periventricular hemorrhages secondary to venous infarction extending into the ventricles. Survival for grades III and IV hemorrhages is ~ 26%, whereas for grades I and II it is ~ 67%

(continued on page 256)

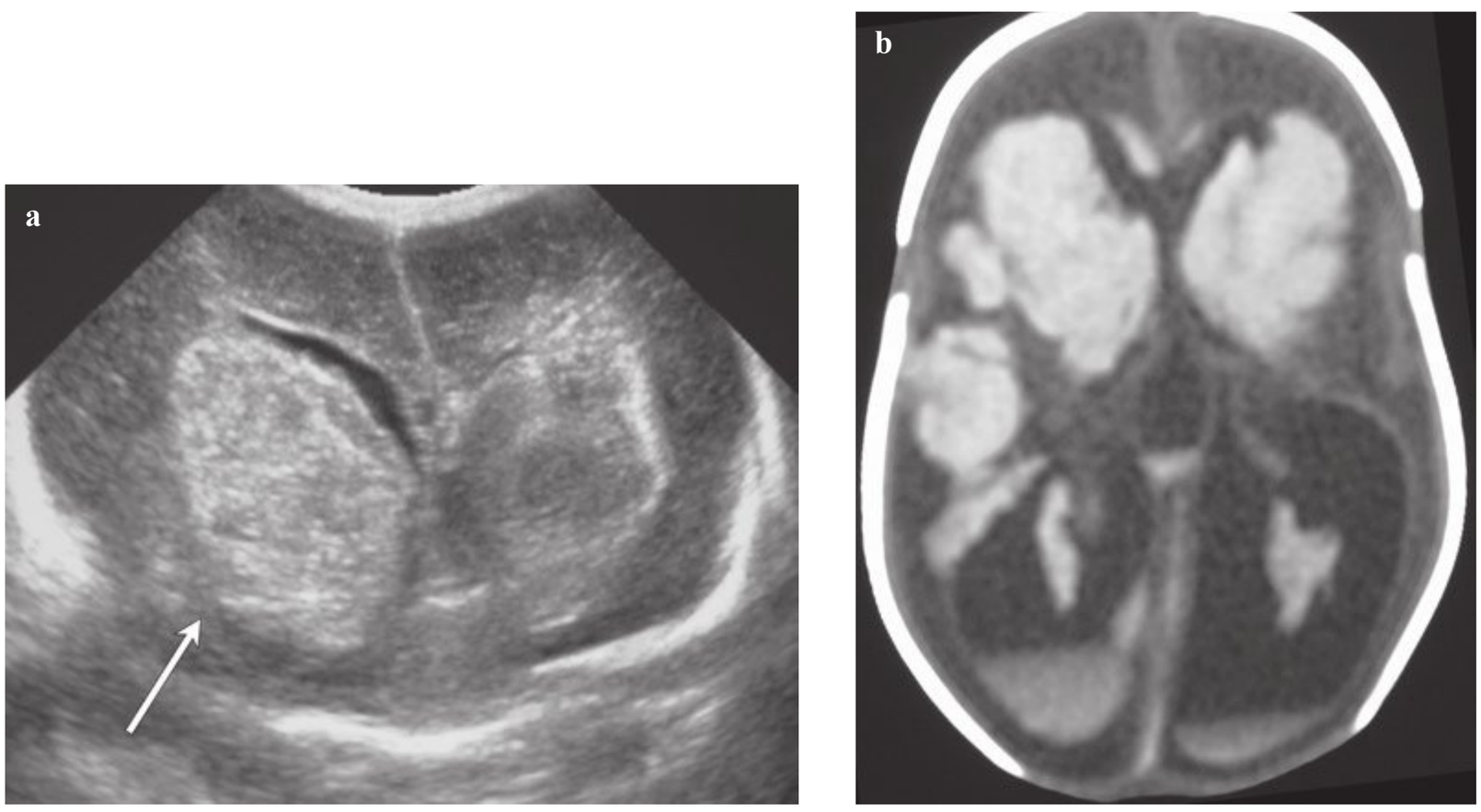

Fig. 1.309 **(a)** Preterm neonate with hemorrhage in the germinal matrix bilaterally seen as large echogenic zones on sonographic exam in the basal ganglia, larger on the right (arrow) than the left. **(b)** Subsequent axial CT shows hemorrhage with high attenuation in the basal ganglia bilaterally and rupture into the ventricles causing hydrocephalus.

Table 1.6 (cont.) Bilateral lesions involving the basal ganglia and/or thalami

Lesions	Imaging Findings	Comments
Vascular Malformations		
Cavernous malformations (**Fig. 1.194**)	MRI: Single or multiple multilobulated intra-axial lesions that have a peripheral rim or irregular zone of low signal on T2-weighted imaging secondary to hemosiderin, surrounding a central zone of variable signal (low, intermediate, high, or mixed) on T1- and T2-weighted imaging depending on age of hemorrhagic portions. Gradient echo and magnetic susceptibility weighted techniques are useful for detecting multiple lesions. Gadolinium contrast enhancement is usually absent, although some may show mild heterogeneous enhancement. CT: Lesions have intermediate to slightly increased attenuation, ± calcifications.	Can be found in many different locations. Supratentorial cavernous malformations occur more frequently than infratentorial lesions. Lesions consist of epithelium-lined vascular channels within a collagenous stroma. Zones of thrombus and remote hemorrhage with hemosiderin are often present. Dystrophic calcifications may be present. Developmental venous anomalies occur in 25% Hereditary syndromes in which multiple cavernous malformations occur are associated with mutations of the CCM1/KRIT1, CCM2/MGC4608, and CCM3PDCD10 genes, and have a higher risk of hemorrhage (up to 5% per year) than sporadic cavernous malformations.
Capillary telangiectasias (**Fig. 1.195**)	MRI: Postcontrast MRI shows a small zone with enhancement, without abnormal mass effect. Lesions are typically inconspicuous on precontrast T1- and T2-weighted imaging. CT: Not usually seen on pre- or postcontrast examinations.	Asymptomatic, often incidental findings on gadolinium contrast-enhanced MRI, which shows enhancement of a group of thin-walled vessels and capillaries within normal neural tissue in the brain or brainstem. Most are less than 1 cm in diameter. Can occur 10 years after radiation therapy. Common locations include the pons and cerebellum. Account for up to 20%of vascular malformations in the brain.
Neoplasms		
Metastases	MRI: Circumscribed spheroid lesions in brain, can have various intra-axial locations (often at gray–white matter junctions), usually with low-intermediate signal on T1-weighted imaging, intermediate-high signal on T2-weighted imaging, ± hemorrhage, calcifications, and cysts. Variable gadolinium contrast enhancement, often high signal on T2-weighted imaging peripheral to nodular enhancing lesion representing axonal edema. CT: Lesions usually have low-intermediate attenuation, ± hemorrhage, calcifications, and cysts. Variable contrast enhancement, often associated with adjacent low attenuation from axonal edema.	Represent ~ 33%of intracranial tumors, usually from extracranial primary neoplasm in adults > 40 years old. Primary tumor source: lung > breast > GI > GU > melanoma.

Lesions	Imaging Findings	Comments
Lymphoma (**Fig. 1.310**)	MRI: Primary CNS lymphoma (PCNSL) in immunocompetent patients occurs as a solitary focal or infiltrating lesion in 65% PCNSL is located in the cerebral hemispheres, basal ganglia, thalami, cerebellum, and brainstem. PCNSL can involve and cross the corpus callosum. PCNSL in immunocompetent patients can be multifocal in 35% of cases. Multifocal PCNSL occurs in 60% of immunocompromised patients. Tumors often have low-intermediate signal on T1-weighted imaging, intermediate-slightly high signal on T2-weighted imaging, ± perilesional edema, ± hemorrhage/necrosis in immunocompromised patients or after treatment. PCNSL in immunocompetent patients usually show homogeneous gadolinium contrast enhancement, whereas gadolinium contrast enhancement in immunocompromised patients often has an irregular peripheral pattern. Diffuse leptomeningeal and dural gadolinium contrast enhancement are other less common patterns of intracranial lymphoma. PCNSL typically lacks neovascularization and has lower cerebral perfusion and relative cerebral blood volume (rCBV) maximum values than high-grade astrocytomas. PCNSL can show restricted diffusion. PCNSL ADC values ($0.7–0.9 \times 10^{-3}$ mm^2/s) are lower than those for glioblastomas and high-grade astrocytomas. Magnetic resonance spectroscopy of PCNSL shows decreased N-acetylaspartate (NAA) and elevated choline and lipid peaks. CT: CNS lymphomas can have intermediate attenuation or can be hyperdense related to a high nuclear/cytoplasm ratio, ± hemorrhage/necrosis in immunocompromised patients. Usually shows contrast enhancement. Diffuse leptomeningeal contrast enhancement is another pattern of intracranial lymphoma. PET/CT: FDG can show elevated uptake in PCNSL, and in immunocompromised patients can be used to distinguish lymphoma from toxoplasmosis brain lesions, which have decreased FDG uptake.	Primary CNS lymphoma is more common than secondary, usually in adults > 40 years old, and lymphoma accounts for 5% of primary brain tumors. Currently, PCNSL accounts for 0.8 to 1.5% of primary intracranial tumors. Prior elevated incidence of 6% in patients with AIDS has been reduced with effective antiviral therapy. B cell lymphoma is more common than T cell lymphoma. MR imaging features of primary and secondary lymphoma of brain overlap. Intracranial lymphoma can involve the leptomeninges in secondary lymphoma > primary lymphoma.

(continued on page 258)

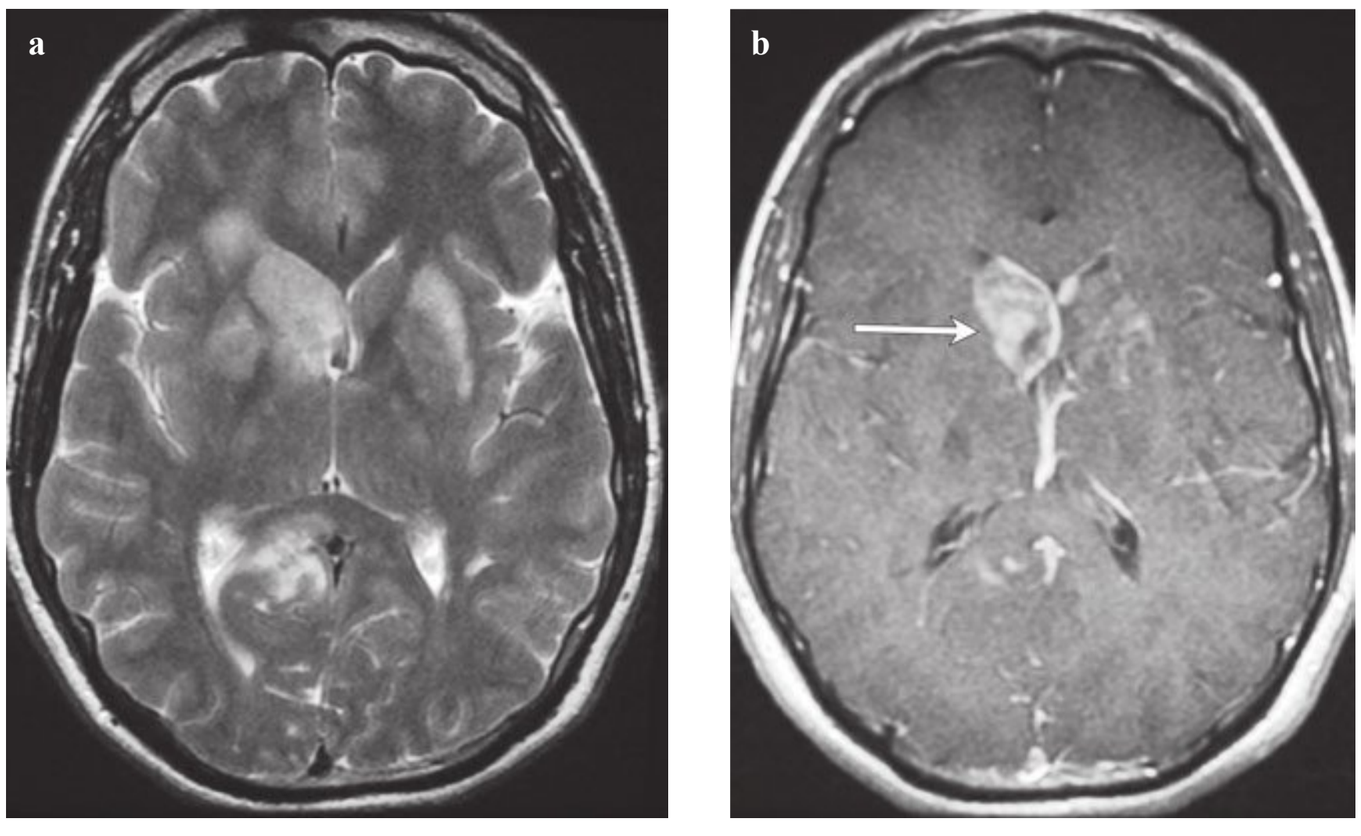

Fig. 1.310 A 27-year-old man with CNS lymphoma. **(a)** Abnormal high signal on axial T2WI is seen in the right caudate nucleus with localized mass effect, right putamen, right frontal white matter, and left putamen. **(b)** Abnormal gadolinium contrast enhancement (arrow) is seen in the right caudate nucleus on axial T1WI.

Table 1.6 (cont.) Bilateral lesions involving the basal ganglia and/or thalami

Lesions	Imaging Findings	Comments
Gliomatosis cerebri	MRI: Infiltrative lesion in the cerebral white matter with poorly defined margins, low-intermediate signal on T1-weighted images, high signal on T2-weighted images and FLAIR, usually minimal or no gadolinium contrast enhancement, and decreased relative cerebral blood volume (rCBV). MR spectroscopy shows elevated choline/creatine (Cho/Cr) and Cho/NAA ratios at sites with abnormal high signal on T2-weighted imaging. CT: Infiltrative lesion with low-intermediate attenuation. Usually no contrast enhancement until late in disease.	Diffusely infiltrating astrocytoma (WHO grade III) that often involves at least three cerebral lobes, including the basal nuclei. Can involve the cerebellum and brainstem. Peak age of occurrence is between 40 and 50 years. Tumor consists of infiltrating, small, neoplastic glial cells with elongated fusiform nuclei as well as larger neoplastic cells with pleomorphic nuclei. Imaging appearance may be more prognostic than histologic grade, with approximate 2-year survival.
Anaplastic astrocytoma	MRI: Often irregularly marginated lesion located in white matter with low-intermediate signal on T1-weighted imaging, high signal on T2-weighted imaging, ± gadolinium contrast enhancement. Magnetic resonance spectroscopy shows decreased N-acetylaspartate (NAA) and high levels of choline. CT: Irregularly marginated mass lesion with mixed low and intermediate attenuation, ± hemorrhage, prominent heterogeneous contrast enhancement, and peripheral edema. Can cross corpus callosum.	Malignant astrocytic tumor (WHO grade III) between diffuse astrocytoma and glioblastoma multiforme. Malignant astrocytes have nuclear atypia and increased mitotic activity. K_i-67/MIB-1 proliferation index ranges from 5 to 10% Can progress to glioblastoma. Approximate 2-year survival.
Glioblastoma multiforme	MRI: Irregularly and poorly marginated mass lesion with necrosis or cystic degeneration, mixed signal on T1-weighted imaging, heterogeneous high signal on T2-weighted imaging and FLAIR, ± hemorrhage, prominent heterogeneous gadolinium contrast enhancement, and peripheral edema. Increased relative cerebral blood volume (rCBV) is associated with high-grade gliomas and tumor-induced angiogenesis. Can cross corpus callosum. Magnetic resonance spectroscopy shows decreased N-acetylaspartate (NAA) and high levels of choline. CT: Irregularly marginated mass lesion with necrosis or cystic degeneration, mixed low and intermediate attenuation, ± hemorrhage, prominent heterogeneous contrast enhancement, and peripheral edema. Can cross corpus callosum.	Most common primary CNS tumor (WHO grade IV), accounts for 15%of intracranial tumors and up to 75%of astrocytic neoplasms, with an incidence of 3 per 100,000. Most patients are over 50 years old. These highly malignant astrocytic neoplasms have nuclear atypia, with increased mitotic activity, cellular pleomorphism, necrosis, and microvascular proliferation and invasion. K_i-67/MIB-1 proliferation index ranges from 15 to 20% Associated with mutations in RTK/phosphatase–PTEN/PI3K signal pathway and p53 and Rb1 tumor suppressor genes. The extent of lesion is underestimated by MRI. Survival is often < 1 year.

Lesions	Imaging Findings	Comments
Pilocytic astrocytoma (**Fig. 1.311**)	MRI: Solid/cystic focal lesion with low-intermediate signal on T1-weighted imaging, high signal on T2-weighted imaging and FLAIR, usually showing gadolinium contrast enhancement. Lesions commonly located in cerebellum, hypothalamus, optic chiasm, optic pathways, adjacent to third or fourth ventricle, and brainstem (medulla is the most common site). Some (30%) can have more aggressive MRI features, such as inhomogeneous gadolinium contrast enhancement, central necrotic zones, and irregular margins. Diffusion-weighted imaging: Usually no evidence of restricted diffusion. Diffusion tensor imaging (DTI) can show tumor displacement of corticospinal tracts. Magnetic resonance spectroscopy: In children with these low-grade tumors, a paradoxic pattern associated with more aggressive tumors (elevated choline/NAA and lactate levels) may be seen. CT: Solid/cystic focal lesion with low-intermediate attenuation, usually with prominent contrast enhancement.	Most common glioma in children and accounts for 6% of all gliomas. Slow-growing, solid/cystic WHO grade I astrocytoma with a biphasic pattern of compacted bipolar cells, Rosenthal fibers, multipolar cells, microcysts, and eosinophilic granular bodies. Immunoreactive to glial fibrillary acidic protein (GFAP) and apolipoprotein D. Can occur in cerebrum, cerebellum, brainstem, or optic chiasm. The majority (67%) occur in the cerebellum of children, usually with a favorable prognosis if totally resected. Increased occurrence in patients with neurofibromatosis type 1 (NF1). Leptomeningeal tumor dissemination is rare (< 3%).

(continued on page 260)

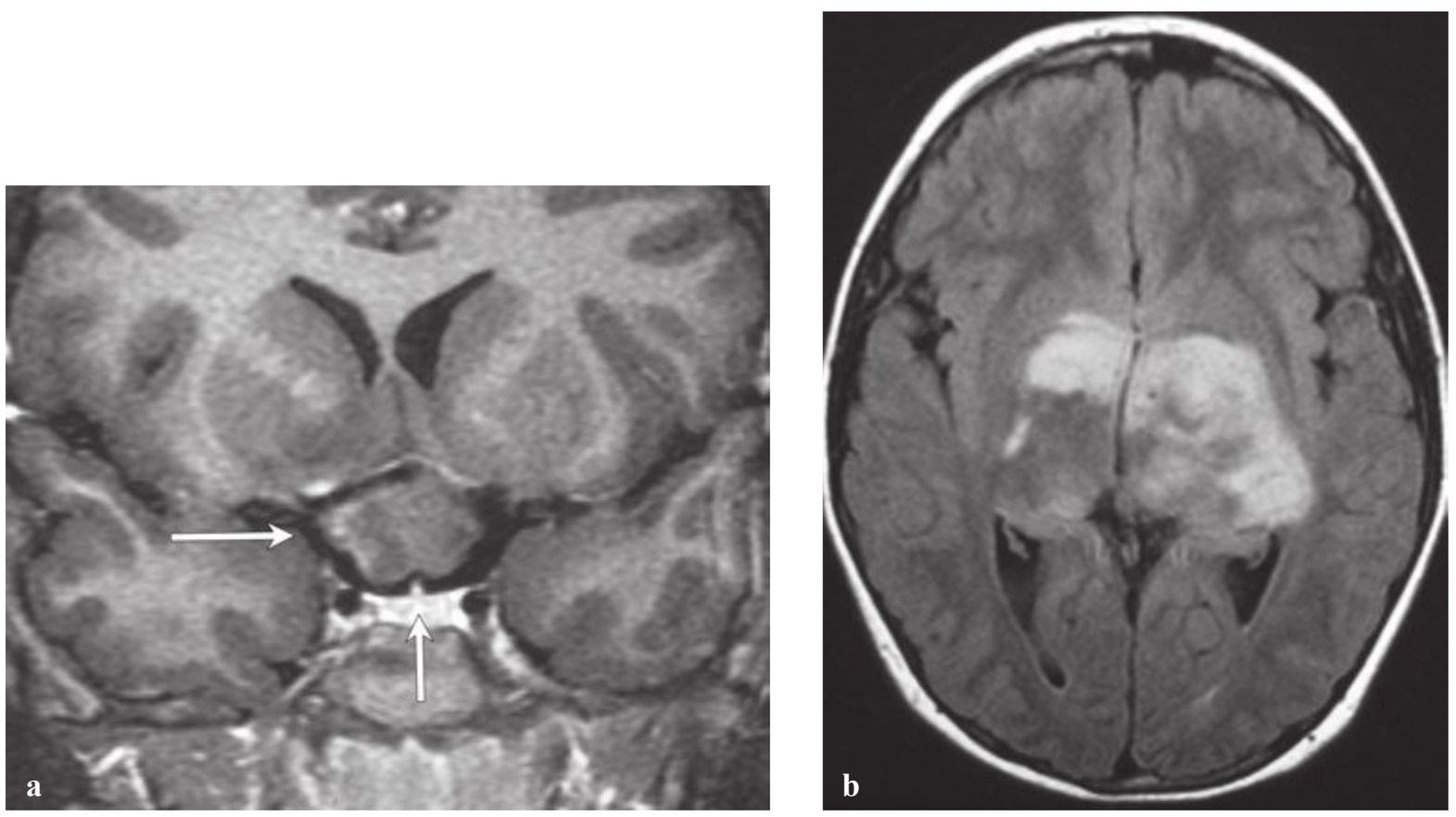

Fig. 1.311 A 10-year-old female with neurofibromatosis type 1 and a pilocytic astrocytoma in the optic chiasm as seen on **(a)** coronal T1 WI (arrows), which extends into the globi pallidi, thalami, and optic radiations on **(b)** axial FLAIR.

Table 1.6 (cont.) Bilateral lesions involving the basal ganglia and/or thalami

Lesions	Imaging Findings	Comments
Tumorlike Lesions		
Neurofibromatosis type 1 (NF1): Vacuolated myelin/ dysplastic white matter lesions (**Fig. 1.312**)	In NF1, in addition to CNS neoplasms (astrocytomas, grades II to IV, and optic gliomas), nonneoplastic lesions related to vacuolated myelin can occur in the basal ganglia, thalamus, brainstem, internal capsules, corpus callosum, and/or cerebellar white matter. These lesions have high signal on T2-weighted images and FLAIR, ± increased diffusion on diffusion-weighted imaging. They typically lack gadolinium contrast enhancement and can be solitary or multiple.	Autosomal dominant disorder (1/2500 births) from mutations involving the neurofibromin gene on chromosome 17q11.2. Represents the most common type of neurocutaneous syndrome. Associated with neoplasms of central and peripheral nervous systems (optic gliomas, astrocytomas, plexiform and solitary neurofibromas) and skin (café-au-lait spots, axillary and inguinal freckling). Also associated with meningeal and skull dysplasias, as well as hamartomas of the iris (Lisch nodules). Single or multiple zones of vacuolated myelin with high signal on T2-weighted imaging can occur in the basal ganglia, thalamus, brainstem, cerebellar white matter, and/or corpus callosum. The lesions increase in size in the first decade and then usually regress and resolve by the third decade.
Neurofibromatosis type 1 (NF1): High signal on T1-weighted images involving the globus pallidus and internal capsules bilaterally (**Fig. 1.313**)	MRI: Zones with high signal on T1-weighted imaging can be seen involving the globus pallidus and internal capsules bilaterally, ± high signal on T2-weighted imaging and FLAIR.	High signal on T1-weighted imaging involving the globus pallidus and internal capsules occurs in 20% of patients with NF1. Possible causes include Schwann cell heterotopia, melanin, remyelination, and/or microcalcifications. Findings persist longer than those seen with vacuolated myelin (high signal on T2-weighted imaging) in patients with NF1.
Neuroepithelial cyst (See **Fig. 1.113**)	MRI: Well-circumscribed cysts with low signal on T1-weighted imaging and high signal on T2-weighted imaging, thin walls, and no gadolinium contrast enhancement or peripheral edema. Cysts occur in the white matter and have high signal on T2-weighted imaging and FLAIR. Can be solitary or multiple. Occur in the cerebral and/or cerebellar white matter, basal ganglia, and brainstem. Lesions can increase in size in first decade, and then usually regress and resolve by the third decade.	Cyst walls have histopathologic features similar to epithelium. Neuroepithelial cysts are located in choroid plexus > choroidal fissure > ventricles > brain parenchyma.

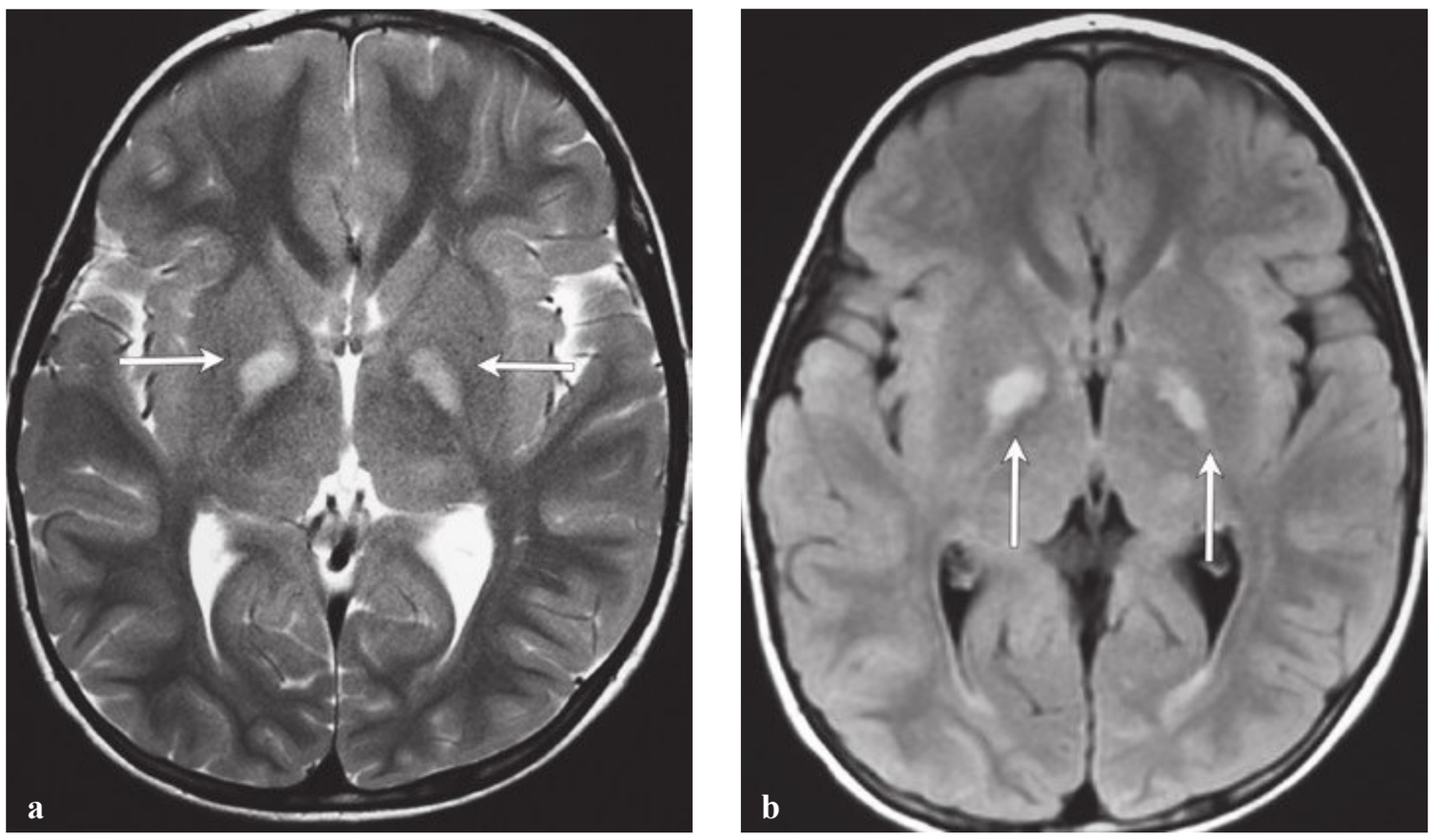

Fig. 1.312 A 4-year-old female with neurofibromatosis type 1 with vacuolated myelin in the globi pallidi of both basal ganglia that have high signal on **(a)** axial T2WI (arrows) and **(b)** FLAIR (arrows).

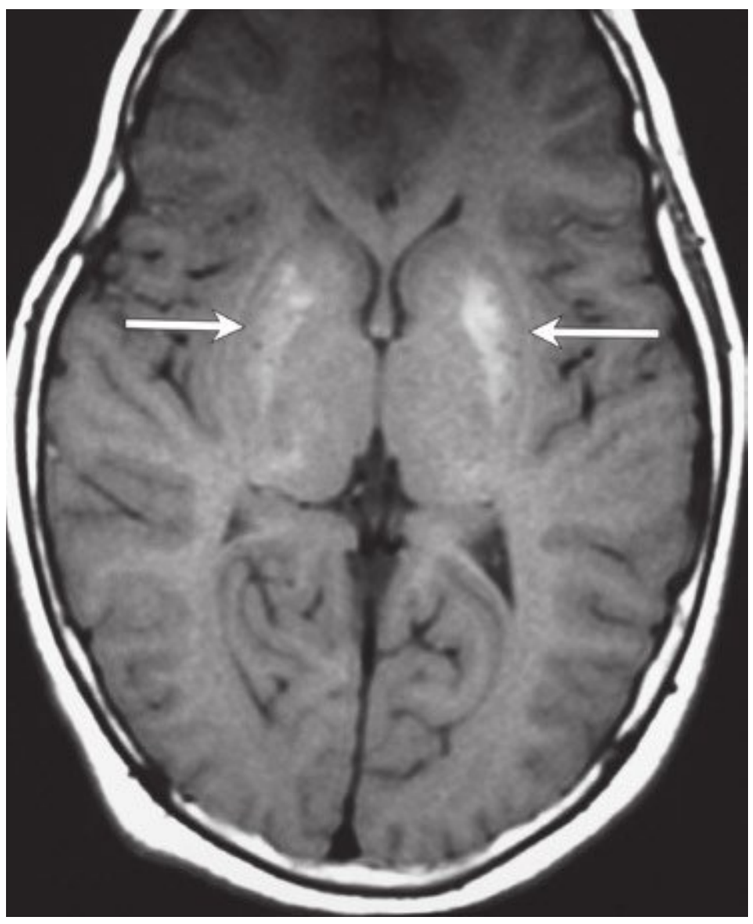

Fig. 1.313 A 12-year-old male with neurofibromatosis type 1 who has high signal (arrows) on axial T1WI in both putamina.

Table 1.7 Neurodegenerative disorders

- Dementia
  - Alzheimer's disease
  - Frontotemporal lobar degeneration (FTLD), Frontotemporal dementia (FTD)
  - Dementia with Lewy bodies
  - Posterior cortical atrophy, Benson dementia
  - Vascular or multi-infarct dementia
  - Corticobasal degeneration
  - Prion disease
- Movement/Motor Disorders
  - Parkinson's disease
  - Parkinson-plus syndromes: Multiple system atrophy (striatonigral degeneration [MSA-P], olivopontocerebellar atrophy [MSA-C], Shy-Drager syndrome [MSA-A])
  - Progressive supranuclear palsy
  - Amyotrophic lateral sclerosis
- Postinfectious Degenerative Disorders
  - TORCH and neonatal infections
- Noninfectious Inflammatory Disorders
  - Multiple sclerosis
  - Vasculitis
  - Rasmussen encephalitis
- Developmental Disorder
  - Sturge-Weber syndrome
- Post-Injury Degenerative Changes in Young Children
  - Germinal matrix hemorrhage
  - Hydranencephaly
  - Hypoxic-ischemic encephalopathy
  - Porencephalic cyst
  - Periventricular leukomalacia
  - Dyke-Davidoff-Masson syndrome
- Post-Injury Degenerative Changes in Older Children and Adults
  - Wallerian degeneration
  - Crossed cerebellar diaschisis
  - Hypertrophic olivary degeneration (HOD)
  - Posttraumatic gliosis and encephalomalacia from brain contusions
- Inherited Neurodegenerative Disorders
  - Neurodegeneration with brain iron accumulation (pantothenate kinase–associated neurodegeneration: PKAN disease)
  - Wilson's disease
  - Menkes' syndrome (trichopoliodystrophy)
  - Fahr disease
  - Huntington disease
  - Ataxia telangiectasia
  - Friedreich's ataxia
  - Spinocerebellar ataxia/degeneration
  - Mitochondrial disorders: MELAS/MERRF
- Acquired Neurodegenerative Disorders
  - Acquired hepatocerebral degeneration
  - Alcohol (ETOH) abuse
  - Wernicke's encephalopathy
  - Osmotic pontine myelinolysis
  - Multiple seizures
  - Phenytoin-related cerebellar atrophy
  - Paraneoplastic syndrome
  - Radiation necrosis
  - Toxic encephalopathy, late effects
  - Superficial siderosis

Table 1.7 Neurodegenerative disorders

Disorders	Imaging Findings	Comments
Alzheimer's disease (**Fig. 1.314**)	MRI: Brain atrophy, often most pronounced in the hippocampi and entorhinal cortex of the temporal lobes; thinned gyri; and sulcal and ventricular prominence. Atophic changes also can involve the posterior portion of the corpus callosum. Diffusion tensor imaging (DTI): Decreased fractional anisotropy in splenium of the corpus callosum and superior longitudinal fasciculus. Magnetic resonance spectroscopy shows a decreased NAA/myo-inositol ratio. PET/CT: Reduced FDG activity/glucose metabolism in the superior/posterior temporal lobes, posterior cingulate cortex, precuneus, and parietal lobes. Increased activity of ^{11}C–or ^{18}F–labeled amyloid-binding radionuclide agents can be seen with PET/CT in the cerebral cortex of the frontal, temporal, parietal, and occipital lobes as well as corpus striatum and subcortical white matter compared with healthy controls.	Alzheimer's disease is the most common form of progressive dementia and accounts for up to 60% of cases in patients older than 65 years. Pathologic changes include: neurofibrillary tangles from abnormal phosphorylation of microtubule-associated tau protein (tauopathy); senile plaques in gray matter, consisting of neurotoxic deposits of amyloid–β 42 protein, which also occur in blood vessels; and decreased neurons from neuronal death. Damage begins in the entorhinal cortex, and then involves the hippocampus before involving the rest of the cortex. Increased familial risk in 10%of patients related to PSEN1, PSEN2, and APOE*E4 genes. Clinical findings include poor recent memory; disorientation to time and place; impaired recall, recognition, and working memory; word retrieval difficulty; impaired conversational speech; and impaired object and space perception.

(continued on page 264)

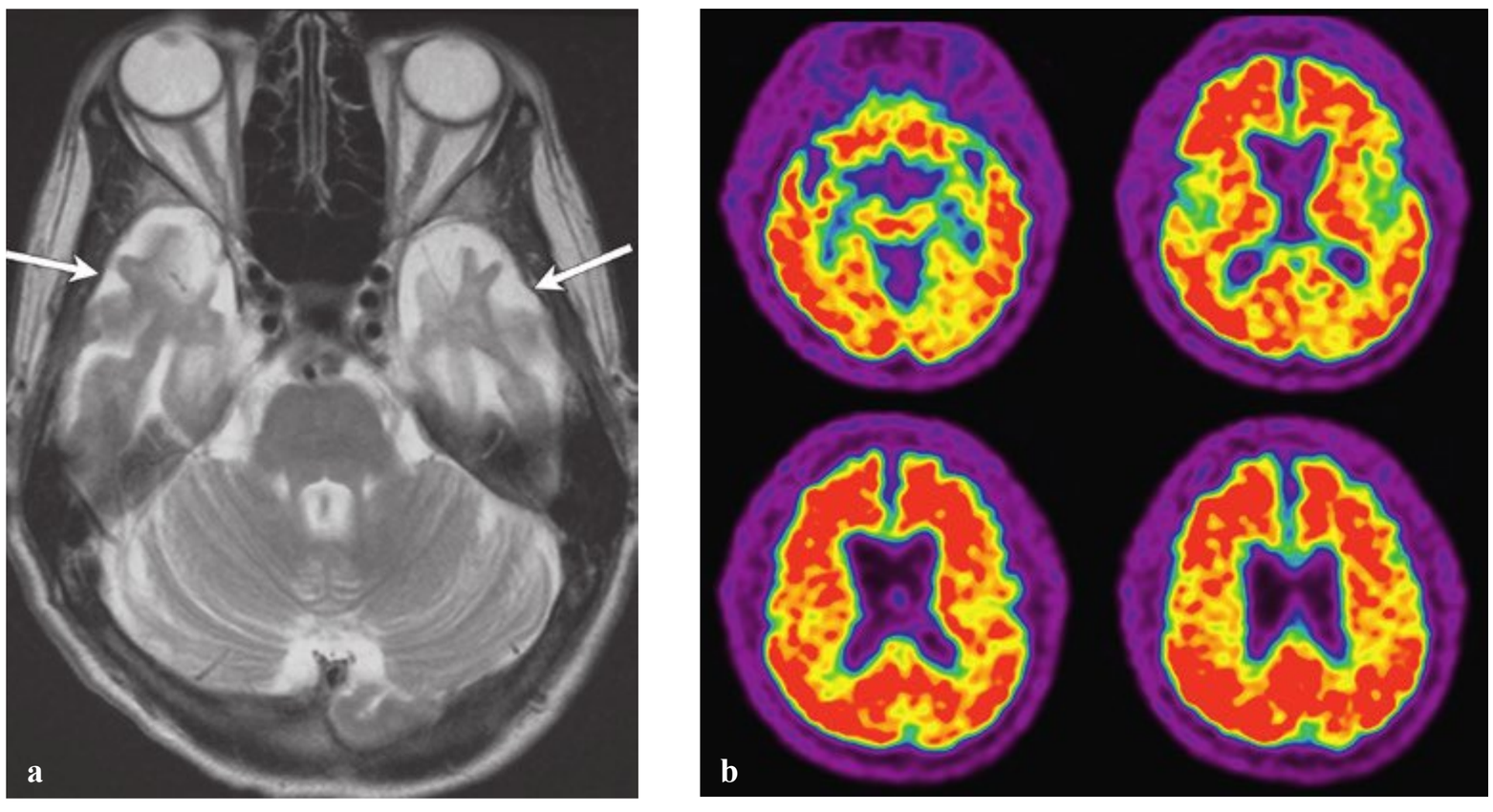

Fig. 1.314 Alzheimer's disease. **(a)** Axial T2-weighted image shows atrophy in both temporal lobes (arrows). **(b)** Axial PET CT images using 18F-florbetaben amyloid binding radiopharmaceutical show abnormal increased uptake in the cerebral white matter greater than normal with extension to the outer gray matter as compared with **(c)** a normal study with PET data merged onto MRI.

Table 1.7 (cont.) Neurodegenerative disorders

Disorders	Imaging Findings	Comments
Frontotemporal lobar degeneration (FTLD), Frontotemporal dementia (FTD) (**Fig. 1.315** and **Fig. 1.316**)	MRI: Progressive brain atrophy often most pronounced in frontal and temporal lobes, hippocampi, and both amygdala; sulcal and ventricular prominence. Cortical atrophic changes common. Abnormal increased signal on T2-weighted imaging can be seen in the subcortical white matter of the atrophied gyri. Atophy of the anterior portion of the corpus callosum can be seen. Behavioral variant FTD: Atrophy initially involves the gray matter of the frontal lobes (dorsolateral, medial-frontal and orbital gyral cortex) and anterior temporal cortex). FDG PET shows frontal hypometabolism. Semantic dementia: Atrophy initially involves the gray matter of the anterior temporal lobes (left usually greater than the right). FDG-PET shows temporal lobe hypometabolism. Progressive non*fl*uent aphasia: Selective atrophy initially involves the inferior left frontal lobe and insula and left perisylvian region FDG-PET shows left perisylvian hypometabolism. Pick disease: Gray matter atrophy involving predominantly the prefrontal cortex and to a lesser degree the temporal lobes, insula. and anterior cingulate gyri. Atrophy can be symmetric or greater on the left than right cerebral hemispheres. Typically does not involve the parietal lobes.	Frontotemporal lobar degeneration (FTLD) is a heterogeneous group of interrelated neurodegenerative disorders that can be associated with the clinical diagnosis of frontotemporal dementia (FTD). FTD is less common than Alzheimer's disease, with a prevalence of 15 per 100,000 and incidence of 2.2 to 8.9 per 100,000. Clinical subtypes include: Behavioral variant (bvFTD), characterized by abnormal affect, apathy or social disinhibition, loss of empathy, and neglect of self care. Semantic dementia (SD), characterized by difficulty remembering words, impaired word comprehension with semantic errors, and preserved spatial skills. Progressive non*fl*uent aphasia (PNFA), which includes difficulty in expressive language (with anomia, speech apraxia, and agrammatism) and impaired verbal memory, but no spatial impairment. FTD with motor neuron disease presents with personality and behavioral changes, executive dysfunction, fasciculations, muscle weakness, and/or swallowing difficulty. Other, related types include progressive supranuclear palsy and corticobasilar syndrome. Pathologic changes include neuronal loss and gliosis as well as deposition of three proteins in the cytoplasm of brain neurons: 1) microtubule-associated protein tau (FTLD-tau), 2) transactive response DNA-binding protein 43 (TDP-43, FTLD-TDP), and 3) fused in sarcoma protein (FUS, FTLD-FUS). bvFTD is associated with FTLD-TDP, FLTD-tau, or FTLD-FUS deposits. SD is associated with deposition of FTLD-TDP, and PFNA is associated with FTLD-TDP. FTD with motor neuron disease is associated with deposits of TDP. Pick disease is associated with FTLD-tau (agyrophilic and 3R tau-positive inclusions, "classic Pick bodies").
Dementia with Lewy bodies	MRI: Mild, diffuse cerebral cortical atrophy. SPECT: Can show reduced uptake of dopamine (ioflupane I-123 dopamine transporter) in the corpus striatum. PET/CT: No significant amyloid plaque demonstrated in cerebral cortex using Florbetapir (^{18}F-labeled amyloid-binding radionuclide agent), unlike in Alzheimer's disease, ± decreased ^{18}F-FDG uptake in the occipital cortex.	Progressive cognitive decline involving memory and visuospatial and executive functions; may be associated with rapid-eye-movement sleep disorder and/or visual hallucinations. Pathologic findings include neuronal inclusions of α-synuclein-positive Lewy bodies in the cerebral cortex, substantia nigra, and brainstem. Results in neuronal loss and dopamine depletion in the substantia nigra, and cholinergic neuronal loss in nucleus basalis of Meynert. Usually occurs in elderly, with a median age of death = 78 years.

(continued on page 266)

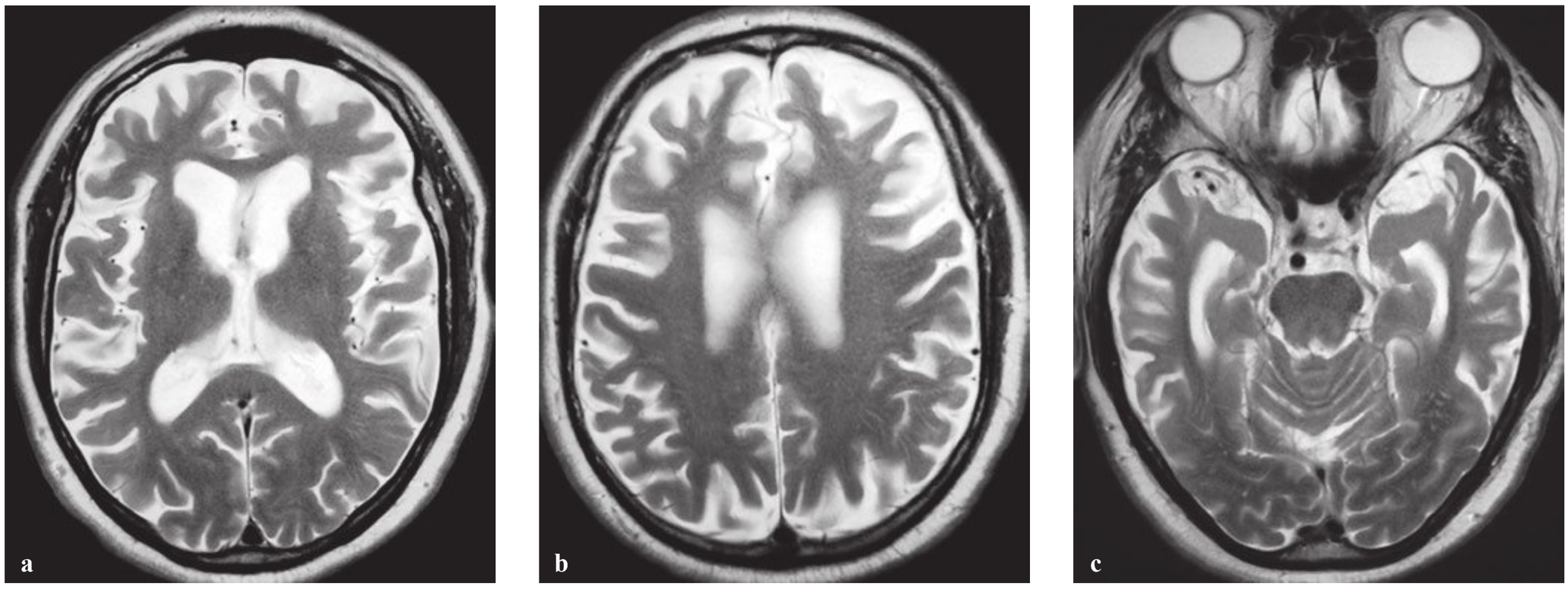

Fig. 1.315 A 59-year-old man with frontotemporal dementia. Asymmetric greater atrophy is seen in both **(a,b)** frontal and **(c)** temporal lobes relative to other portions of the brain as seen on axial T2WI.

Fig. 1.316 A 59-year-old woman with Pick disease. Asymmetric greater atrophy is seen in both frontal lobes relative to other portions of the brain as seen on axial T2WI.

Table 1.7 (cont.) Neurodegenerative disorders

Disorders	Imaging Findings	Comments
Posterior cortical atrophy, Benson dementia (**Fig. 1.317**)	MRI: Focal or asymmetric parietal-occipital cortical atrophy. Diffusion-weighted imaging/diffusion tensor imaging (DWI/DTI): Reduced fractional anisotropy (FA) in the occipital lobes in early phases of disease. Reduced FA also occurs in the parietal lobes. PET and SPECT: Hypoperfusion and hypometabolism involving the parietal and occipital lobes.	Rare, slowly progressive degenerative disorder with progressive decrease of visuospatial and visual-perceptual abilities before onset of memory impairment. Occurs in adults more than 50 years old.
Vascular or multi-infarct dementia (**Fig. 1.318**)	MRI: Multiple punctuate and/or confluent zones of decreased signal on T1-weighted imaging and high signal on T2-weighted imaging and FLAIR involving the subcortical and periventricular white matter, basal ganglia, thalami, and brainstem, usually no restricted diffusion unless recent ischemic event (uncommon), no associated mass effect, ± foci of low signal on GRE or SWI from microhemorrhages involving the cerebral cortex and/or white matter (up to 65% of cases). Typically no gadolinium contrast enhancement. CT: Multiple zones of decreased attenuation involving the subcortical and periventricular white matter, basal ganglia, thalami, and brainstem. No associated mass effect, no contrast enhancement.	Accounts for up to 10% of dementia cases and results from accumulation of brain infarcts, usually related to occlusion of small > large arteries. Can also occur in patients with CADASIL (cerebral autosomal dominant arteriopathy with subcortical infarcts and leukoencephalopathy), an inherited abnormality with mutations in the NOTCH3 gene on chromosome 19q12, which results in angiopathy of small and medium-size arteries.
Corticobasal degeneration	MRI: Can show asymmetric atrophy involving the perirolandic, frontal, and parietal lobes. Zones with high signal on T2-weighted imaging and FLAIR can be seen in the subcortical white matter of atrophic gyri. PET/CT: Can show asymmetric hypometabolism involving the caudate and thalamus, as well as prefrontal, parietotemporal, cingulate, and motor cortex contralateral to clinically affected side.	Uncommon neurodegenerative disorder that presents with progressive asymmetric cortical symptoms, such as abnormal speech and language, hemineglect, other visuospatial deficits, and motor apraxia. Histopathologic findings include FTLD-tau inclusions in neurons and glia. Gliosis and neuronal loss occur in the cerebral cortex and basal ganglia. Swollen achromatic neurons ("ballooned cells") occur in the cerebral cortex, striatum, and substantia nigra.
Prion disease (**Fig. 1.305**)	MRI: Zones with high signal on T2-weighted imaging and FLAIR can be seen in the basal ganglia (caudate, putamen, and/or thalami bilaterally) and/or cerebral cortex, with corresponding restricted diffusion. Typically no abnormal gadolinium contrast enhancement is seen with these abnormalities. CT: Usually no findings in the early phases of the disease.	Transmissible spongiform encephalopathies resulting in progressive neurodegeneration caused by infection with prions. Creutzfeldt-Jakob disease is the most common type and has four forms (sporadic form accounts for 85%, genetic for 10–15%, and the iatrogenic and new variant forms for the remainder).

(continued on page 268)

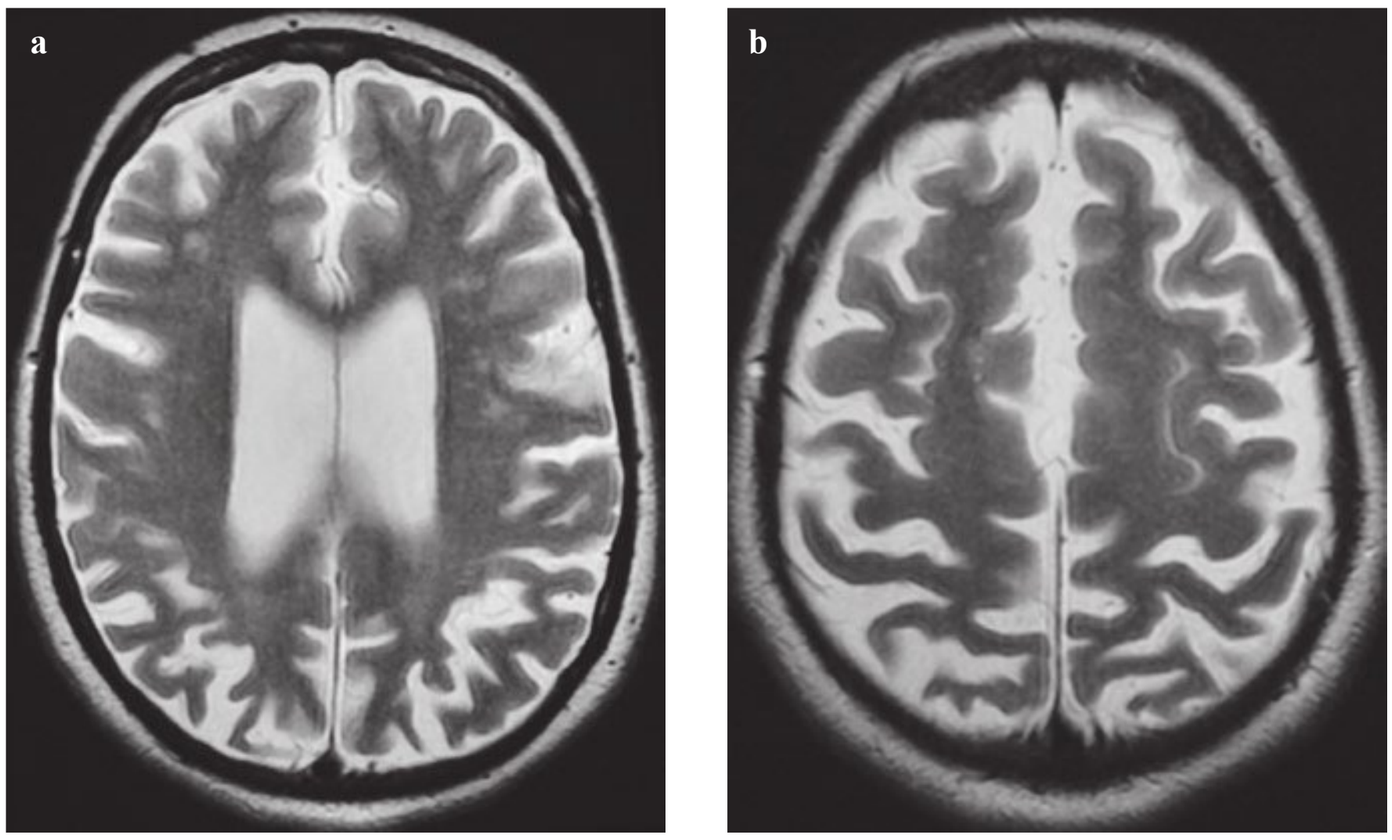

Fig. 1.317 A 57-year-old woman with posterior cortical atrophy. **(a,b)** Asymmetric greater atrophy is seen in both parietal and occipital lobes relative to other portions of the brain as seen on axial T2WI.

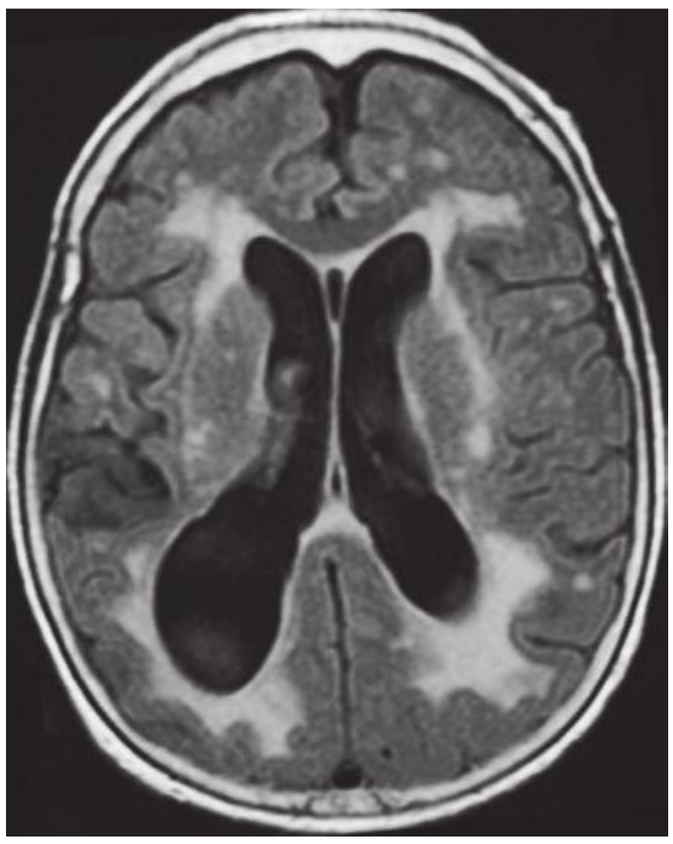

Fig. 1.318 A 78-year-old woman with multi-infarct dementia. Axial FLAIR shows foci and confluent intra-axial zones with abnormal high signal in the cerebral white associated with parenchymal volume loss and compensatory dilatation of the lateral ventricles.

Table 1.7 (cont.) Neurodegenerative disorders

Disorders	Imaging Findings	Comments
Movement/Motor Disorders		
Parkinson's disease (**Fig. 1.319**)	MRI: Usually no specific findings seen with conventional MRI. Medial temporal lobe atrophy may be seen in patients with memory deficits. Diffusion tensor imaging (DTI) can show reduced fractional anisotropy (FA) in the caudal portion of the substantia nigra. PET/CT: Abnormal reduced striatal uptake of ^{18}F-dopa secondary to impaired striatal dopamine terminal function. Reduced dopamine transporter function can also be seen with decreased uptake of ^{11}C-CFT, ^{18}F-FP-CIT, and ^{11}C-RTI-32 on PET/CT. SPECT: Assessment of impaired presynaptic dopamine transporters in the corpus striatum of Parkinsonian patients based on decreased uptake/activity of ^{123}I-Ioflupane, ^{123}I-b-CIT, ^{123}I-FP-CIT, ^{123}I-IPT, ^{123}I-altropane, and ^{99m}Tc-TRODAT in the corpus striatum.	Chronic and progressive degenerative neurologic disorder in adults with clinical findings of rest tremors, bradykinesia, and rigidity. Prevalence is ~ 200 per 100,000, with slight male predominance. Cognitive deterioration with executive dysfunction and memory problems related to retrieval deficits can also occur. Pathologic findings include degeneration of dopamine neurons in the substantia nigra compacta as well as intraneuronal proteinaceous inclusions of α-synuclein (Lewy bodies). Lewy bodies initially occur in the medulla oblongata, pontine tegmentum, olfactory bulbs, and anterior olfactory nuclei (Braak preclinical stages 1–2). In stages 3–4, which are associated with clinical findings, deposition of Lewy bodies occurs in the midbrain (substantia nigra, other nuclei) and forebrain. In stages 5 and 6, Lewy bodies can occur in the neocortex. Genetic abnormalities associated with Parkinson's disease include mutations of the LRRK2 gene, as well as mutations involving the SNCA, PINK1, PARK2, PARK7, PLA2G6, FBX07, and ATP13A2 genes.
Parkinson-plus syndromes: Multiple system atrophy (striatonigral degeneration [MSA-P], olivopontocerebellar atrophy [MSA-C], Shy-Drager syndrome [MSA-A]) (**Fig. 1.320, Fig. 1.321**, and **Fig. 1.322**)	CT: Progressive atrophy of the brainstem, cerebellum, and/or cerebrum. MRI: Atrophy of the brainstem, cerebellum, and/or cerebrum. In the axial plane, a thin cross with slightly high signal on T2-weighted imaging can be seen in the pons (hot cross bun sign). High signal on T2-weighted imaging can be seen in both middle cerebellar peduncles (MCP sign). In MSA-P, high signal on T1-weighted imaging and high signal ± low signal on T2-weighted imaging can be seen in small atrophic putamina and is equal to or more pronounced than in the globi pallidi. PET/CT: Symmetric hypometabolism involving the cerebellum and putamen, as well as the frontal, temporal, and occipital lobes, can be seen.	Multiple system atrophy (MSA) encompasses progressive adult-onset neurodegenerative disorders that are referred to as Parkinson-plus syndromes. In MSA, there is degeneration of the substantia nigra, striatum, pons, middle cerebellar peduncles, cerebellum, and inferior olivary nuclei. These syndromes have the dyskinetic features of Parkinson's disease (muscle rigidity, tremors, slow movement), as well as additional clinical findings of autonomic dysfunction (orthostatic hypotension), poor response to levodopa, cerebellar ataxia, extra-pyramidal signs, and urogenital dysfunction. MSA-P (previously referred to as striatonigral degeneration) has mostly Parkinsonian features. MSA-C (previously referred to as olivopontocerebellar atrophy) has ataxia. MSA-A (previously referred to as Shy-Drager syndrome) has autonomic dysfunction with orthostatic hypotension, urogenital dysfunction, and anhydrosis. Histopathologic findings include synuclein-positive glial cytoplasmic inclusions in oligodendroglia, glia, and neurons of the inferior olivary nuclei, pons, substantia nigra, putamina, locus ceruleus, medullary pyramids, and interomedial columns of the thoracic spinal cord, as well as lower motor neurons.
Progressive supranuclear palsy (**Fig. 1.323**)	MRI: Atrophy of the midbrain, tegmentum, and periaqueductal gray with reduced AP dimension to < 15–17 mm. On sagittal images, atrophy of the midbrain results in a hummingbird sign. Also seen is concavity of the lateral margins of the midbrain tegmentum on axial images, resulting in a morning glory sign. Also observed is atrophy of superior cerebellar peduncles and frontal and parietal cerebral cortex. Dilatation of the third ventricle can be seen. PET/CT: Decreased metabolic activity seen in the prefrontal cortex, thalamus, and midbrain.	Neurodegenerative disease involving the midbrain, subthalamus, globus pallidus, dentate nucleus, and frontal lobes. Patients present with difficulty in vertical eye movements as well as postural instability. Deposits of insoluble FTLD-tau-proteins are seen in the neurons of the substantia nigra, periaqueductal gray matter, and quadrigeminal plate, as well as within neurons and glia of the basal ganglia and frontal cortex.

(continued on page 271)

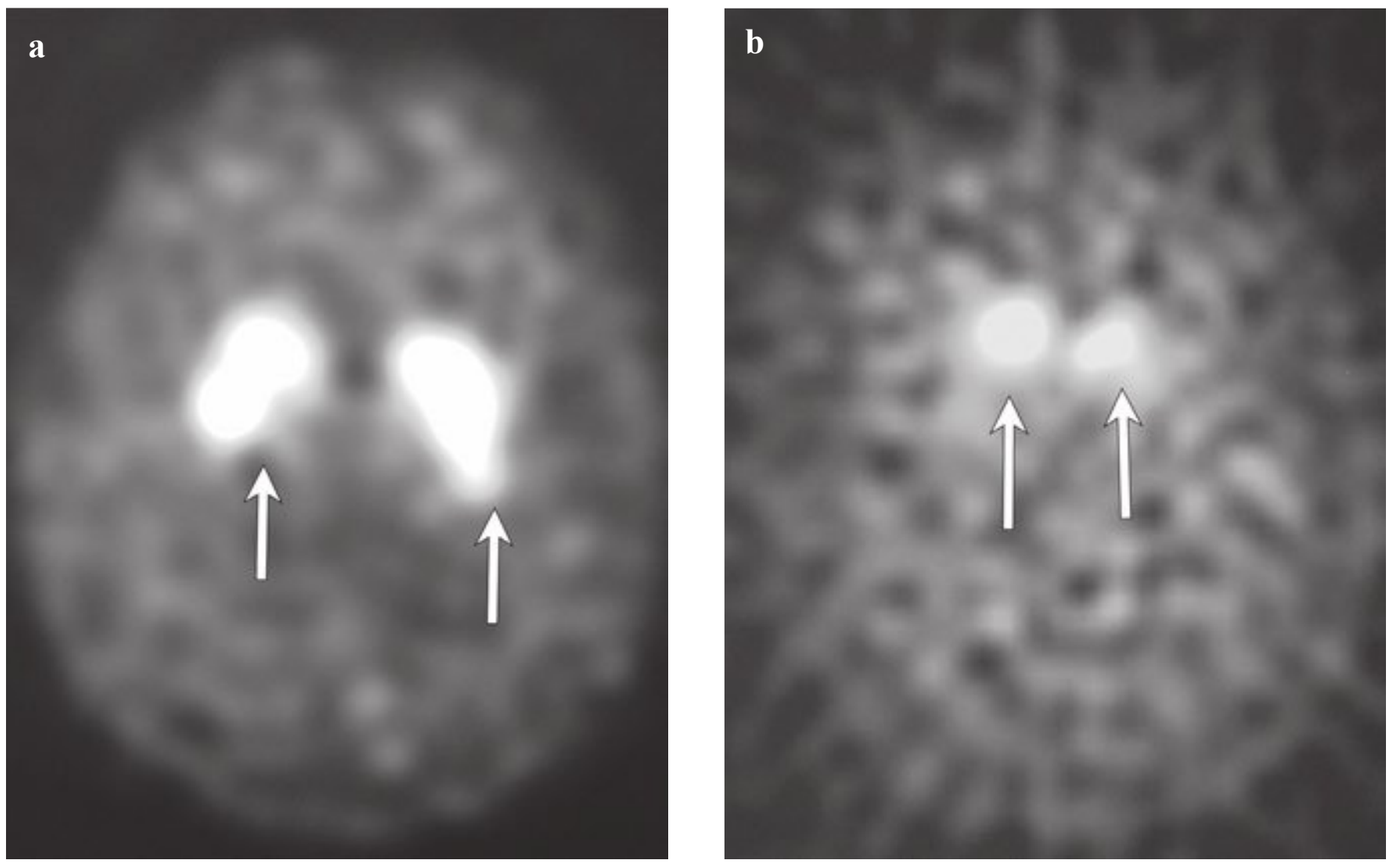

Fig. 1.319 Ioflupane 123-I (DaTSCAN) for Parkinson's disease. **(a)** Normal uptake of Ioflupane 123-I in the basal ganglia (arrows) is seen on axial SPECT. **(b)** Patient with Parkinson's disease has markedly reduced uptake (arrows) in the basal ganglia.

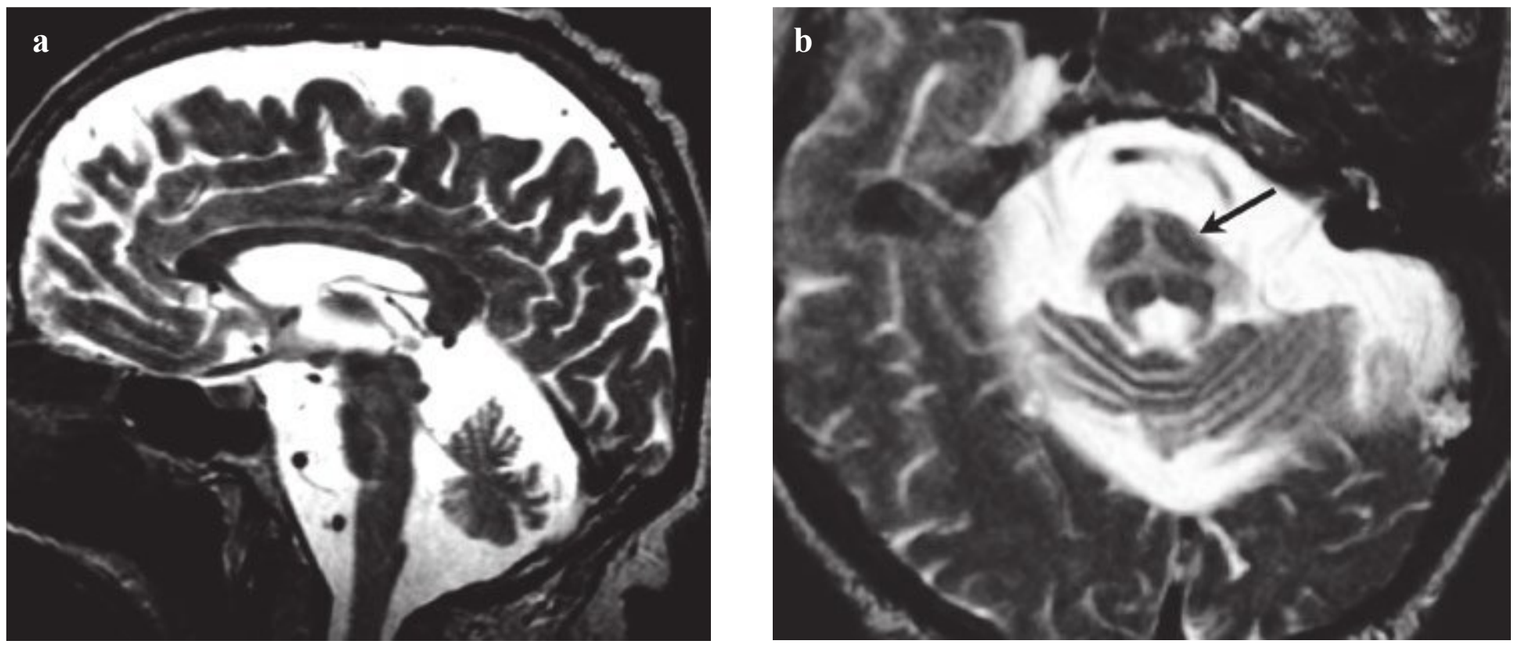

Fig. 1.320 A 64-year-old woman with multiple system atrophy-C. **(a)** Sagittal and **(b)** axial T2WI shows an atrophied pons, medulla, cerebellum and middle cerebellar peduncles. In the axial plane, a thin cross with slightly high signal on T2WI (arrow) is seen in the pons ("hot cross bun" sign).

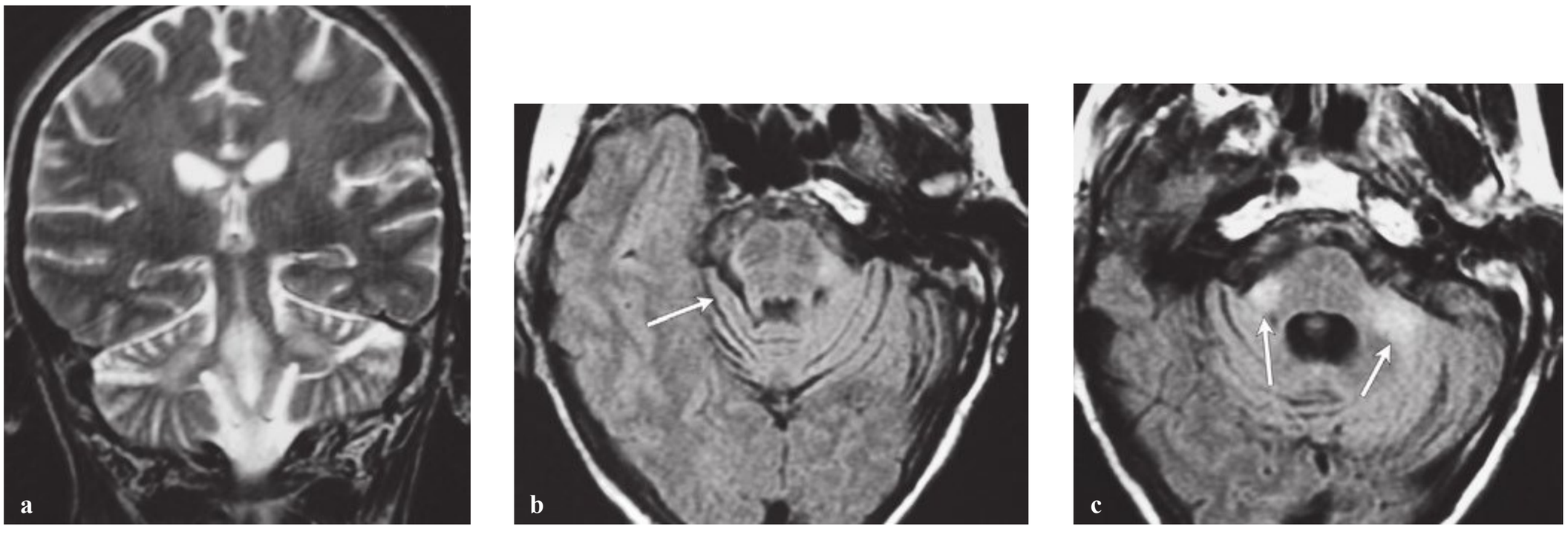

Fig. 1.321 A 52-year-old woman with multisystem atrophy-C. **(a)** Coronal T2WI and **(b,c)** axial FLAIR shows an atrophied pons, medulla, cerebellum, and middle cerebellar peduncles. In the axial plane, a thin cross with slightly high signal on FLAIR (arrow) is seen in the pons ("hot cross bun" sign). **(c)** High signal is seen in both middle cerebellar peduncles ("MCP" sign) on axial FLAIR (arrows).

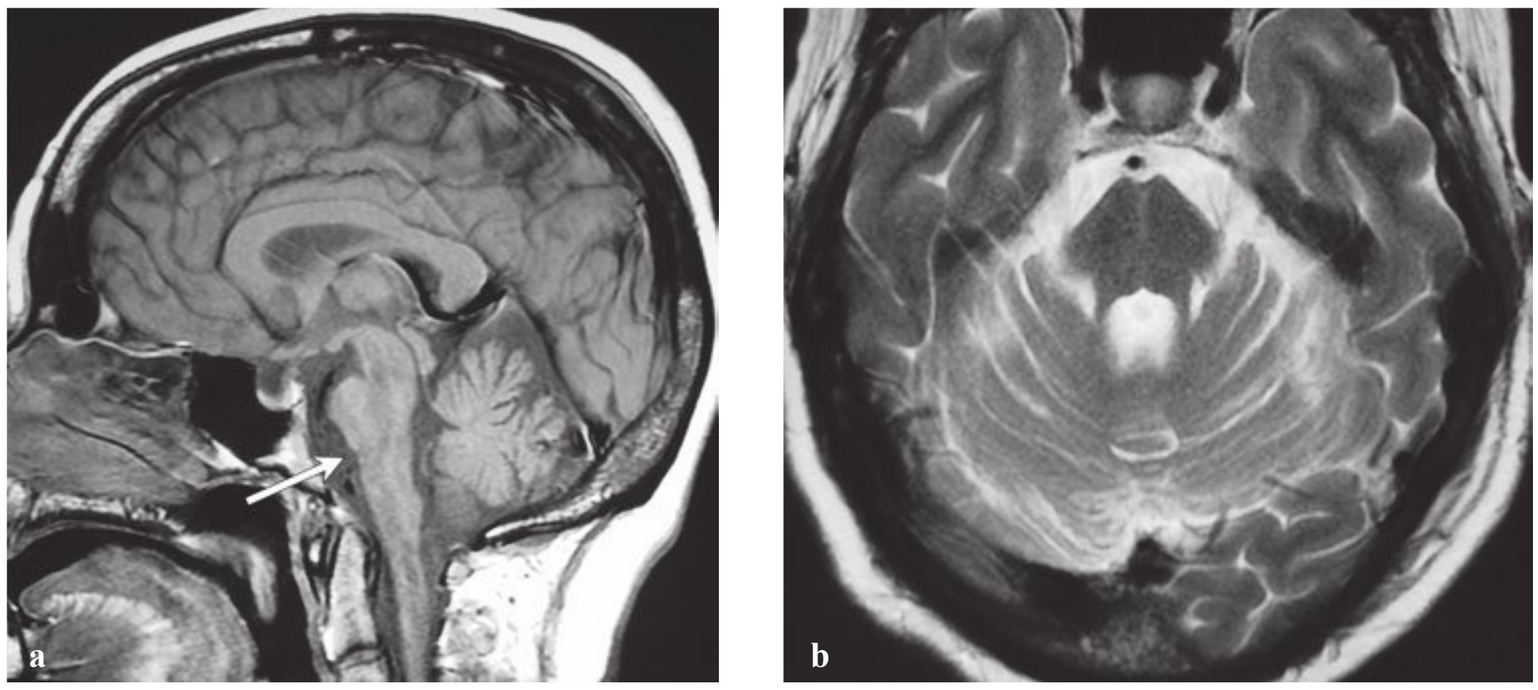

Fig. 1.322 A 45-year-old woman with multisystem atrophy-P. **(a)** Sagittal T1WI and **(b)** axial T2WI show an atrophied pons (arrow) and medulla. In the axial plane, a thin cross with slightly high signal on T2WI **(b)** is seen in the pons ("hot cross bun" sign). High signal on **(c)** axial FLAIR (arrows) and **(d)** axial T1WI (arrows) is seen in atrophied putamina.

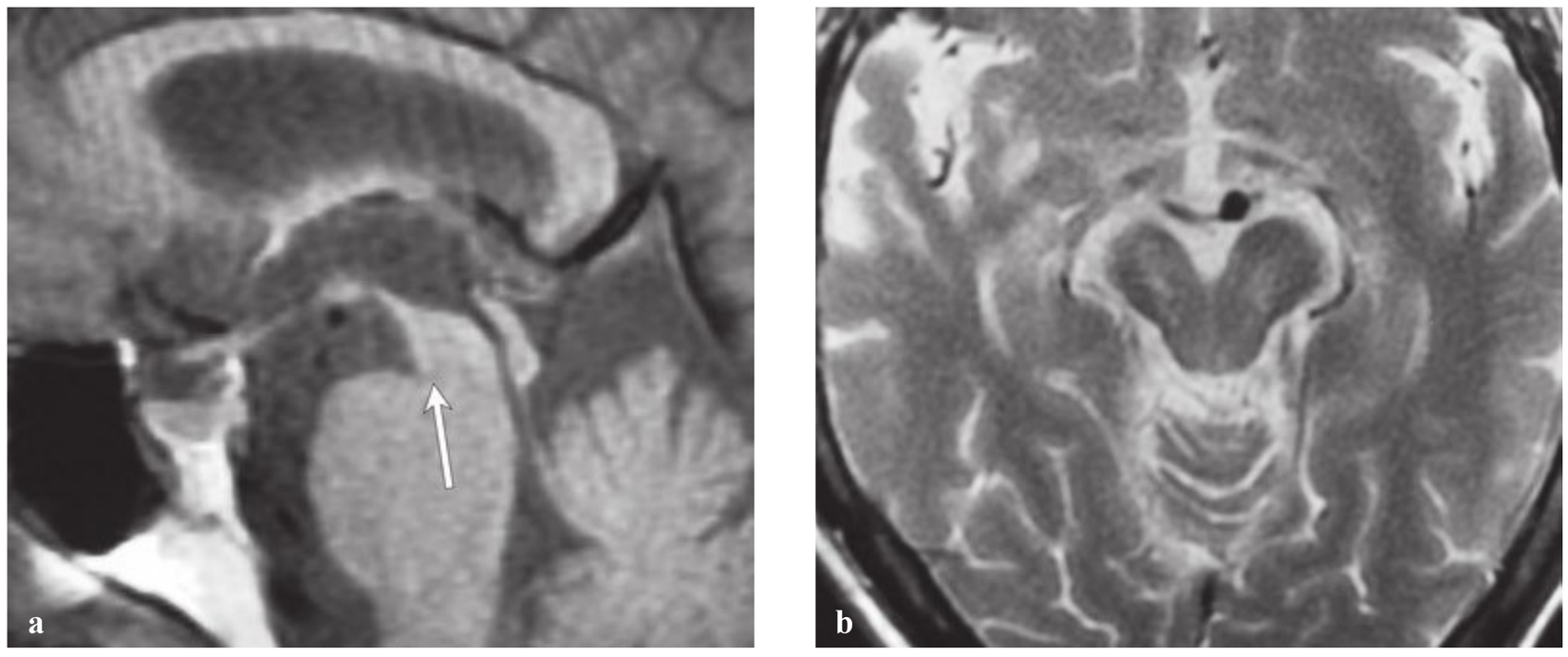

Fig. 1.323 An 82-year-old woman with progressive supranuclear palsy. **(a)** Sagittal T1WI shows atrophy of the midbrain resulting in a "hummingbird sign" appearance (arrow). **(b)** On axial T2WI, concavity of the lateral margins of the midbrain is seen resulting in a "morning glory" sign.

Table 1.7 (cont.) Neurodegenerative disorders

Disorders	Imaging Findings	Comments
Amyotrophic lateral sclerosis (**Fig. 1.324**)	MRI: Foci with high signal on T2-weighted imaging and FLAIR can occasionally be seen involving the corticospinal tracts in the posterior limbs of the internal capsules, brainstem, and spinal cord, ± low signal on T2-weighted imaging involving the motor cortex due to iron deposition. No gadolinium contrast enhancement. Diffusion tensor imaging (DTI): Progressive decreases occur in the fractional anisotropy (FA) at the corticospinal tracts and corpus callosum secondary to myelin damage.	Progressive and often rapid degeneration of upper motor neurons of the primary motor cortex and corticospinal tracts (CST), medullary brainstem nuclei, and lower motor neurons at the anterior horns of the spinal cord. Histologic findings include loss of pyramidal motor neurons in the primary motor cortex, axonal degeneration in the CST, proliferation of glial cells, and expansion of the extracellular matrix. Degeneration also involves neurons in the frontal and temporal lobes.

(continued on page 272)

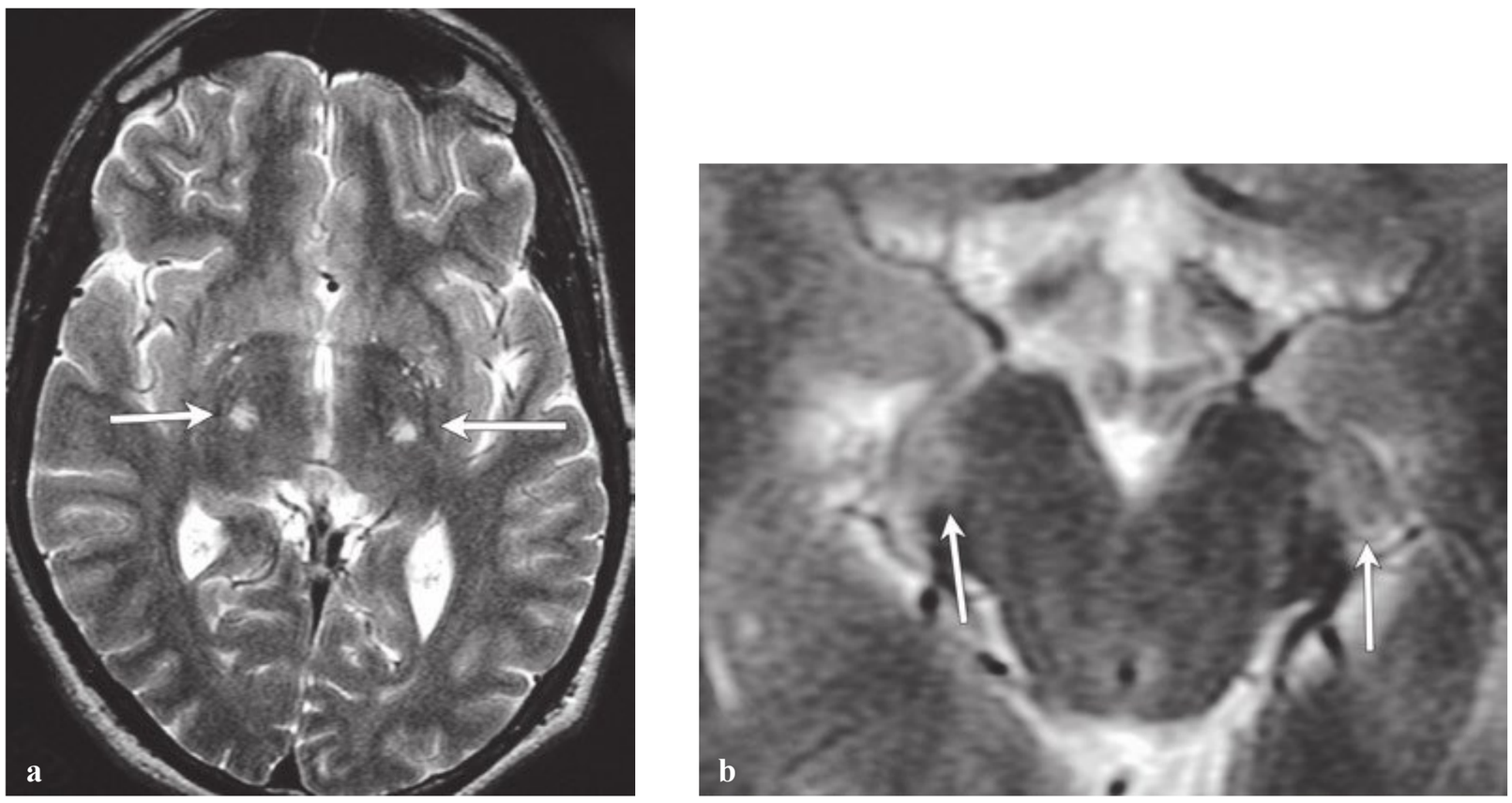

Fig. 1.324 A 45-year-old man with amyotrophic lateral sclerosis. **(a)** Foci with high signal on axial T2WI are seen in the corticospinal tracts (arrows) in the posterior limbs of the internal capsules and **(b)** cerebral peduncles (arrows).

Table 1.7 (cont.) Neurodegenerative disorders

Disorders	Imaging Findings	Comments
Postinfectious Degenerative Disorders		
TORCH and neonatal infections (**Fig. 1.325, Fig. 1.326,** and **Fig. 1.327**)	CT and MRI: Prenatal and neonatal infections often result in intra-axial calcifications. Prenatal infection by cytomegalovirus and rubella can result in microcephaly, schizencephaly, gray matter heterotopia, transmantle clefts, porencephalic cysts, and/or periventricular leukomalacia. Herpes simplex and rubella often cause extensive encephaloclastic changes that result in multicystic encephalomalacia.	TORCH is an acronym applied to congenital infections from toxoplasmosis, rubella, cytomegalovirus, and herpes.
Noninfectious Inflammatory Disorders		
Multiple sclerosis (**Fig. 1.328**)	MRI: Lesions located in cerebral or cerebellar white matter, corpus callosum, brainstem, and basal ganglia. Lesions usually have low-intermediate signal on T1-weighted imaging and high signal on T2-weighted imaging, ± gadolinium contrast enhancement. Gadolinium contrast enhancement can be ringlike or nodular, usually in acute/early subacute phase of demyelination, ± restricted diffusion. Acute demyelinating lesions can have localized mass effect simulating neoplasms. CT: Zones of active demyelination may show contrast enhancement and mild localized swelling.	Multiple sclerosis (MS) is the most common acquired demyelinating disease in young and middle-aged adults (peak ages = 20–40 years). MS can also occur in pediatric patients in the second decade. MS affects 400,000 people in the United States and 2,000,000 worldwide. Women are affected twice as frequently as men. Most common in people with northern European heritage. MS is not inherited in a Mendelian fashion, although it can cluster in families. Diagnosis is made based on clinical history and findings, results from MRI examinations (lesions with high signal on T2-weighted imaging or FLAIR seen in brain white matter, spinal cord, and optic nerves), abnormal visual evoked potentials, and isoelectric focusing evidence of oligocloncal bands and/or increased IgG index in CSF samples. Demyelinating disease occurs wherever myelin is present, including deep brain nuclei (caudate, putamen, globus pallidus and/or thalamus). The disease is typically multi-episodic.

(continued on page 275)

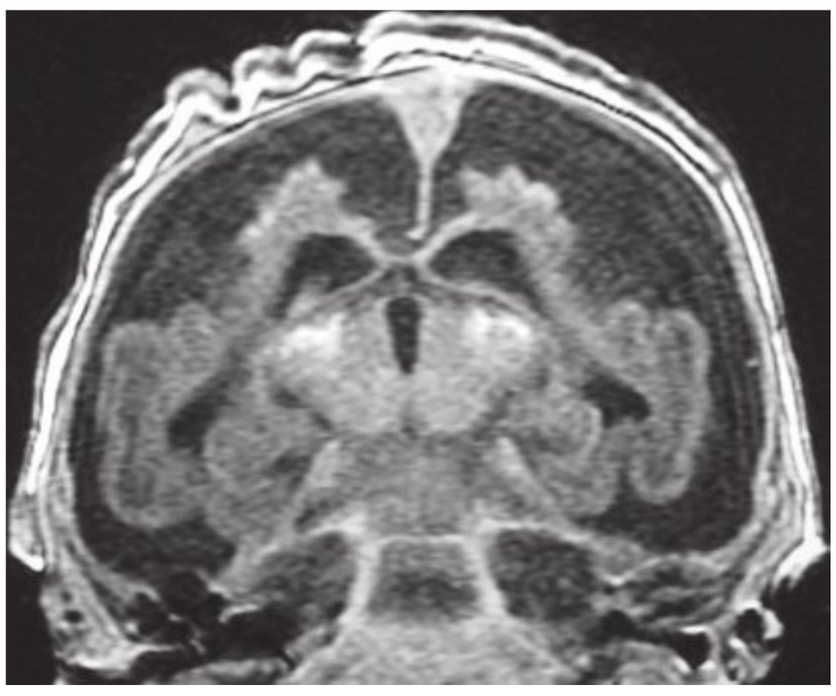

Fig. 1.325 A 2-day-old male neonate with extensive encephalomalacia related to prenatal infection (TORCH) as seen on coronal T1 WI.

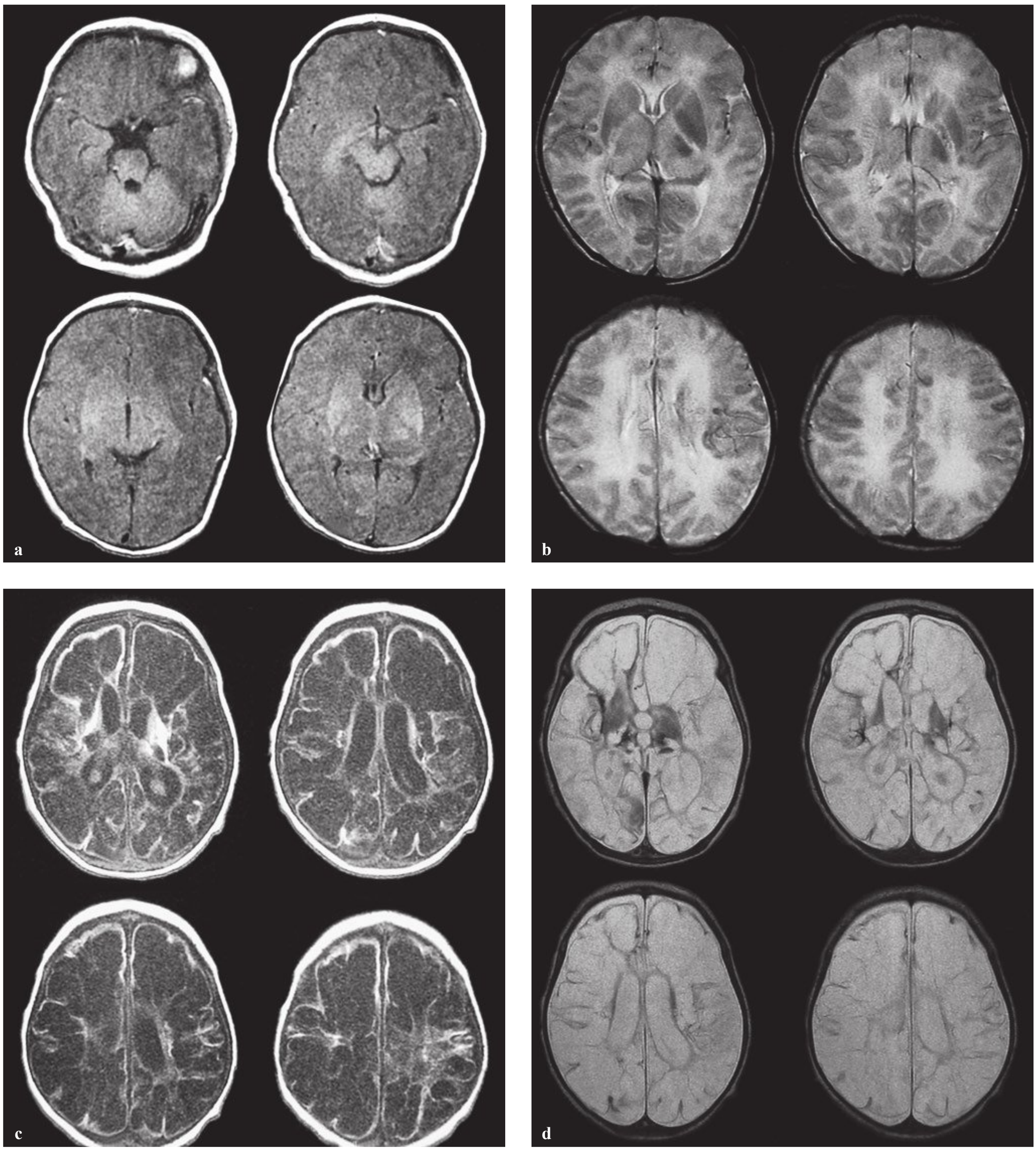

Fig. 1.326 **(a)** Axial T1WI and **(b)** T2WI of a 1-week-old male neonate exposed to herpes simplex 2 during delivery shows zones with abnormal cerebral cortical signal and blurring of the gray-white matter junctions bilaterally as well as abnormal increased signal on T1WI in the basal ganglia. **(c)** Axial T1WI and **(d)** T2WI six weeks later shows extensive destruction of brain parenchyma resulting in multicystic encephalomalacia.

Fig. 1.327 A 6-week-old male with postnatal cerebritis from Enterococcus that resulted in extensive destruction of brain parenchyma and cystic encphalomalacia as seen on axial postcontrast T1WI. Abnormal contrast enhancement is seen along the inner margins of the dilated ventricles.

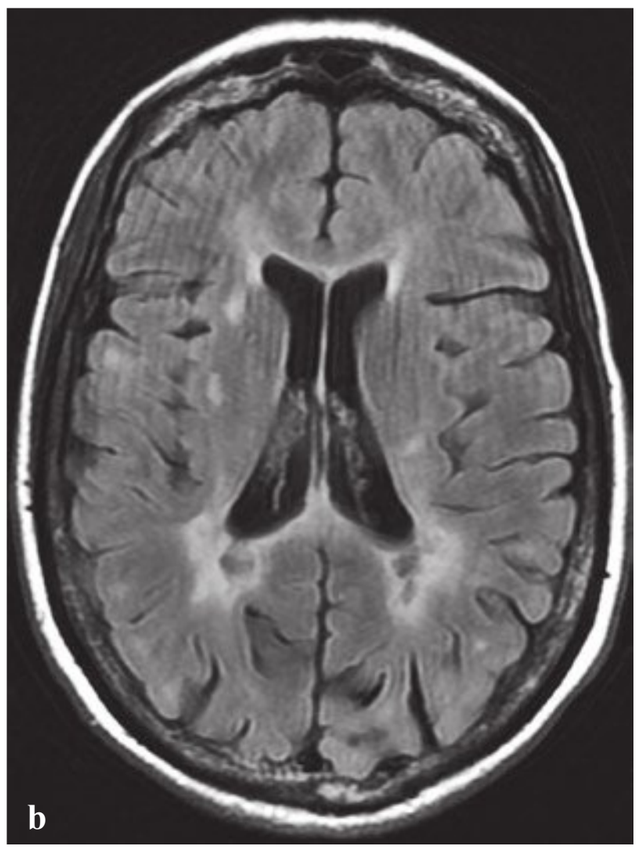

Fig. 1.328 A 32-year-old woman with multiple sclerosis. **(a)** Sagittal and **(b)** axial FLAIR shows zones with abnormal high signal in the cerebral white matter including the corpus callosum associated with brain volume loss.

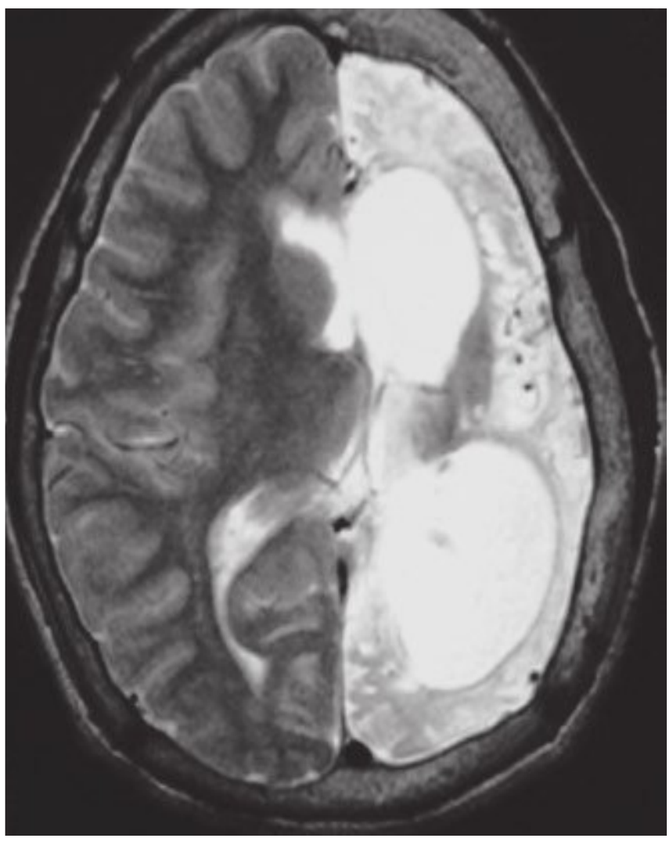

Fig. 1.329 A12-year-old male with Rasmussen encephalitis. Diffuse abnormal high signal on axial T2WI is seen in the left cerebral hemisphere associated with brain volume loss, compensatory dilatation of the lateral ventricle and expansion of the diploic marrow space of the left side of the calvarium.

Table 1.7 (cont.) Neurodegenerative disorders

Disorders	Imaging Findings	Comments
Vasculitis	Zones of arterial occlusion and/or foci of stenosis and poststenotic dilatation. May involve large, medium, or small intracranial and extracranial arteries. Can result in single or multiple cerebral and/or cerebellar infarcts seen with CT and/or MRI.	Uncommon mixed group of inflammatory diseases/disorders involving the walls of cerebral blood vessels. Can result from noninfectious etiology (polyarteritis nodosa, Wegener's granulomatosis, giant cell arteritis, Takayasu's arteritis, sarcoid, drug-induced vasculitis, etc.) or can be related to infectious cause (bacteria, fungi, tuberculosis, syphilis, viruses).
Rasmussen encephalitis (**Fig. 1.329**)	MRI: Progressive atrophy of one cerebral hemisphere involving the white matter, basal ganglia, and cortex, with prominent sulci and dilated ipsilateral lateral ventricle. Abnormal high signal on T2-weighted imaging and FLAIR can be seen in the gray and white matter. Usually no gadolinium contrast enhancement.	Uncommon chronic T cell-mediated immune disorder usually seen in children < 10 years old who have severe and progressive epilepsy and unilateral neurologic deficits, including hemiplegia and psychomotor deterioration. Biopsies show T cell-dominated encephalitis with activated microglial cells and absence of macrophages, B-cells, or plasma cells, and viral inclusion bodies. Treatment is hemispherectomy.
Developmental Disorder		
Sturge-Weber syndrome (**Fig. 1.330**)	MRI: Prominent, localized, leptomeningeal gadolinium contrast enhancement, usually in parietal and/or occipital regions in children. Unilateral in 80% Low signal on T2-weighted imaging is often seen at the involved gyri due to dystrophic calcifications, ± gyral gadolinium contrast enhancement, localized atrophic changes in brain adjacent to the pial angioma, ± prominent medullary and/or subependymal veins, ± ipsilateral prominence of choroid plexus. CT: Gyral calcifications > 2 years, progressive cerebral atrophy in region of pial angioma.	Also known as encephalotrigeminal angiomatosis, Sturge-Weber syndrome is a non-inherited sporadic neurocutaneous syndrome associated with ipsilateral port wine cutaneous lesion, seizures, glaucoma, and hemiparesis. Results from persistence of primitive leptomeningeal venous drainage (pial angioma) and developmental lack of normal cortical veins, producing chronic venous congestion and brain ischemia. Patients often present with progressive neurologic impairment.

(continued on page 276)

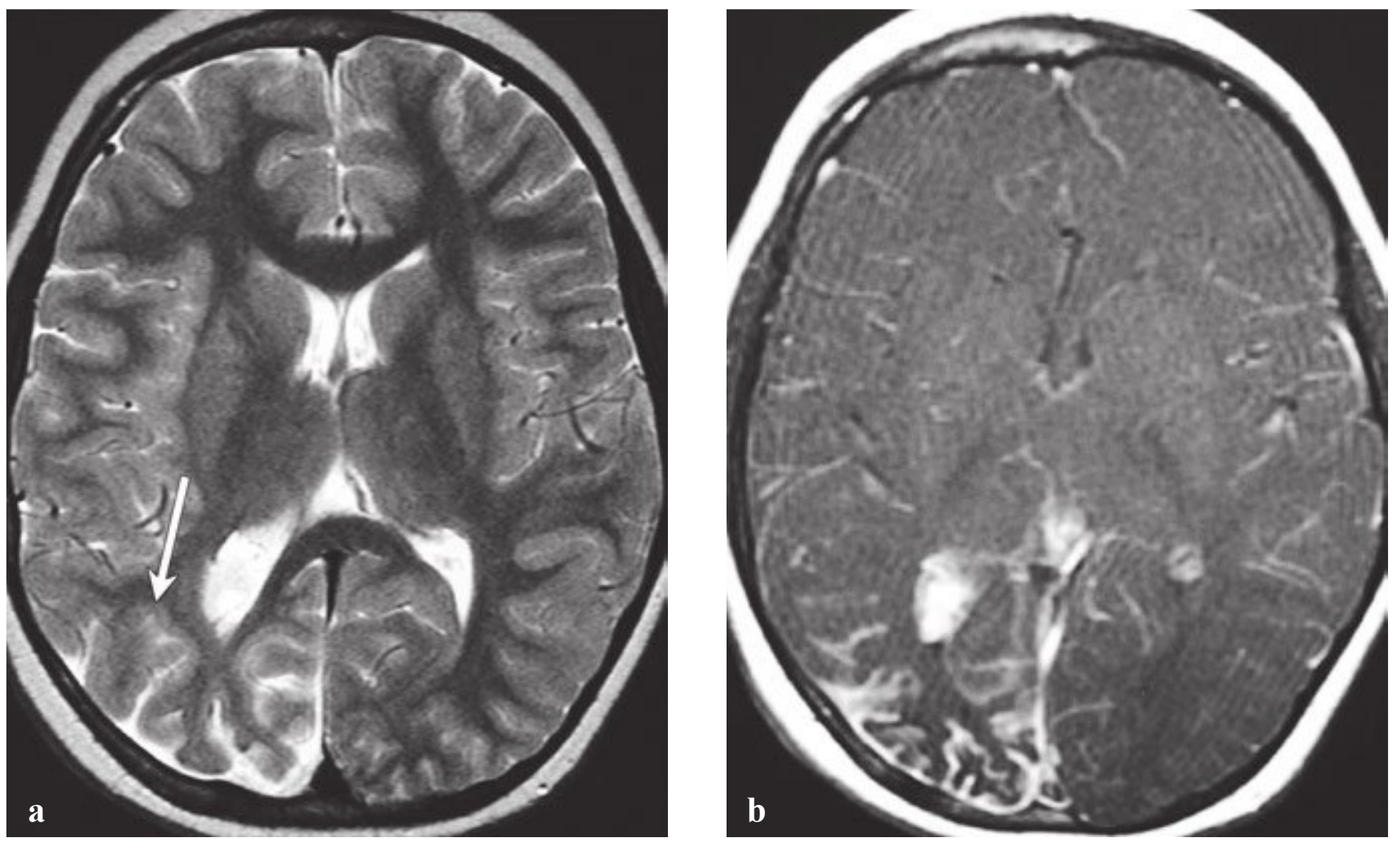

Fig. 1.330 **(a)** Axial T2WI of a patient with Sturge-Weber syndrome shows gyral atrophy in the right occipital lobe (arrow), which is associated with diffuse sulcal gadolinium contrast enhancement of the pial angioma on **(b)** axial T1WI.

Table 1.7 (cont.) Neurodegenerative disorders

Disorders	Imaging Findings	Comments
Post-Injury Degenerative Changes in Young Children		
Germinal matrix hemorrhage (**Fig. 1.331**)	MRI: In the early phases, germinal matrix hemorrhage has intermediate to high signal on T1-weighted imaging from methemoglobin and low signal on T2-weighted imaging from intracellular methemoglobin. Hemorrhage within the ventricles is often also seen. By the second week, tissue loss at the hemorrhage results in localized secondary ex vacuo ventricular dilatation. CT: Recent germinal matrix hemorrhages typically have increased attenuation. Intraventicular hemorrhage, when present, shows high attenuation. Ventricular dilatation may be seen. By the second week, tissue loss at the hemorrhage results in localized secondary ex vacuo ventricular dilatation. Ultrasonography: In the early phases, zones of increased echogenicity at the caudate heads, along the caudothalamic grooves, and within the ventricles, particularly anterior to the foramen of Monro, where there is no confounding echogenic choroid plexus.	Premature or preterm neonates less than 34 weeks' gestation and weighing less than 2,000 g have a 25%risk of periventricular and/or intraventricular hemorrhage that occurs within the first 24 hours after birth in 40%of cases and within 4 days in 90%of cases. Most of the hemorrhages are associated with the germinal matrix. The germinal matrix contains a rich network of capillaries that are lined by only a simple endothelium and are lacking muscular or collagenous support. The vascularity of the germinal matrix is greater than that in the other portions of the brain. The endothelial cells lining the capillaries of the germinal matrix also have three to five times the number of mitochondria per cell compared with the endothelial cells of systemic capillaries, and they have an increased selective vulnerability to hypoxia because of their high demand for oxidative phosphorylation. Hypoxia and ischemia in the preterm neonate damage the capillaries of the germinal matrix. If reperfusion occurs, the injured germinal matrix is prone to hemorrhage. The severity of the germinal matrix hemorrhage is grouped into four grades: Grade I: Subependymal hemorrhage occurs without, or with only minimal, intraventricular extension. Grade II: The subependymal hemorrhage extends into the ventricles without ventricular dilatation. Grade III: The subependymal hemorrhage extends into the ventricles with associated ventricular dilatation. Grade IV: Periventricular hemorrhages secondary to venous infarction extending into the ventricles. Survival for grades III and IV hemorrhages is ~ 26%, whereas for grades I and II it is ~ 67%
Hydranencephaly (**Fig. 1.332**)	Replacement of substantial portions of cerebral tissue with thin-walled sacs containing CSF, inferomedial portions of frontal and temporal lobes often preserved, cerebellum and thalami usually have a normal appearance.	In utero destruction of cerebral parenchyma from vascular injury or infection (e.g., CMV or toxoplasmosis). Patients may be normocephalic, microcephalic, or macrocephalic. Children are developmentally delayed.
Hypoxic-ischemic encephalopathy (**Fig. 1.333**)	CT: Bilateral zones of low attenuation in the basal ganglia, caudate nuclei, thalami, brainstem, and/or perisylvian cerebral cortex. MRI: Bilateral zones of high signal on T2-weighted imaging, FLAIR, and diffusion-weighted imaging (low signal on ADC maps) in the basal ganglia, caudate nuclei, thalami, brainstem, and/or perisylvian cerebral cortex.	Prolonged hypotension and anoxia result in ischemia and infarction in portions of the brain with selective vulnerability to hypoxia and impairment of aerobic metabolism. Can result from drowning, asphyxiation, and cardiac arrest. In less severe cases of hypotension in adults, zones of infarction can occur between the distal distributions of two arteries, as "watershed infarcts."

(continued on page 278)

Fig. 1.331 Premature neonate (25 weeks' gestation) with a grade IV germinal matrix hemorrhage seen as a hyperechoic lesion on **(a)** coronal sonographic image (arrow). **(b)** Sonogram and **(c)** CT 2 months later show ventriculomegaly and a porencephalic cyst contiguous with the frontal horn of the right lateral ventricle at the former site of hemorrhage.

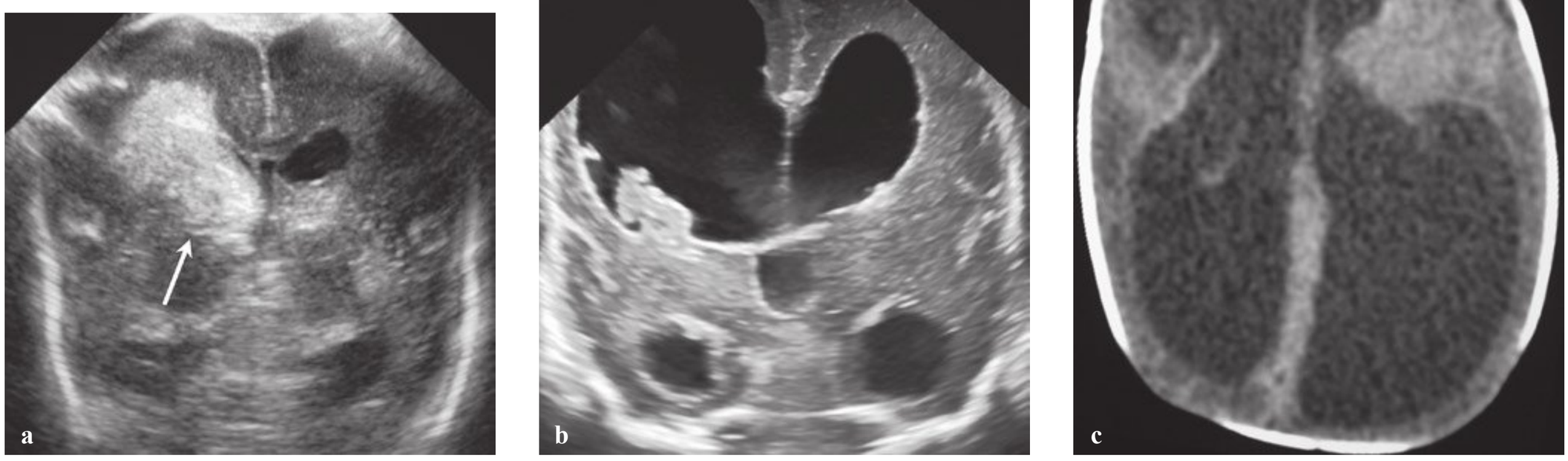

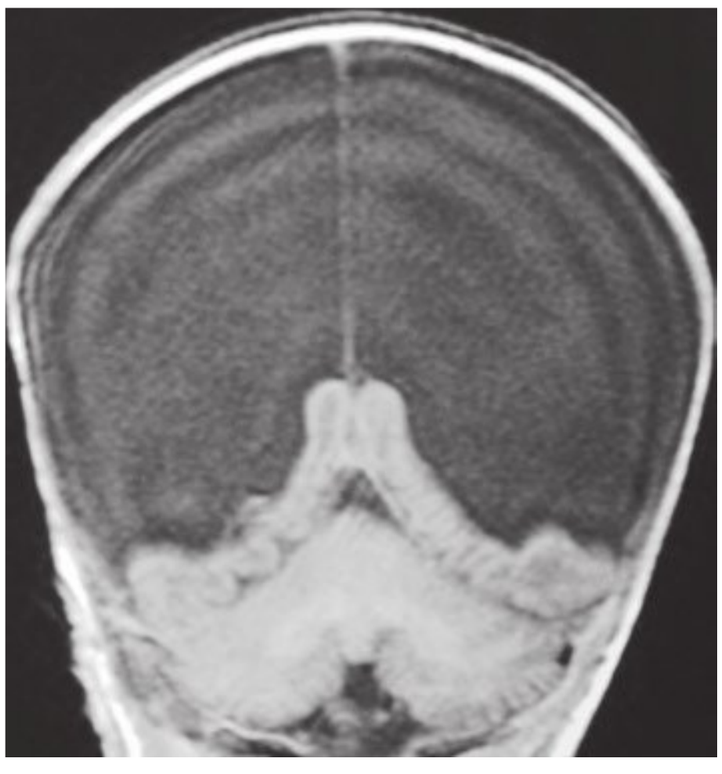

Fig. 1.332 A 5-week-old male with hydranencephaly. Coronal T1 WI shows replacement of the upper portions of cerebral tissue with thin-walled sacs containing CSF with relative preservation of inferomedial portions of the cerebral hemispheres. The falx cerebi is present and the cerebellar hemispheres have a normal appearance.

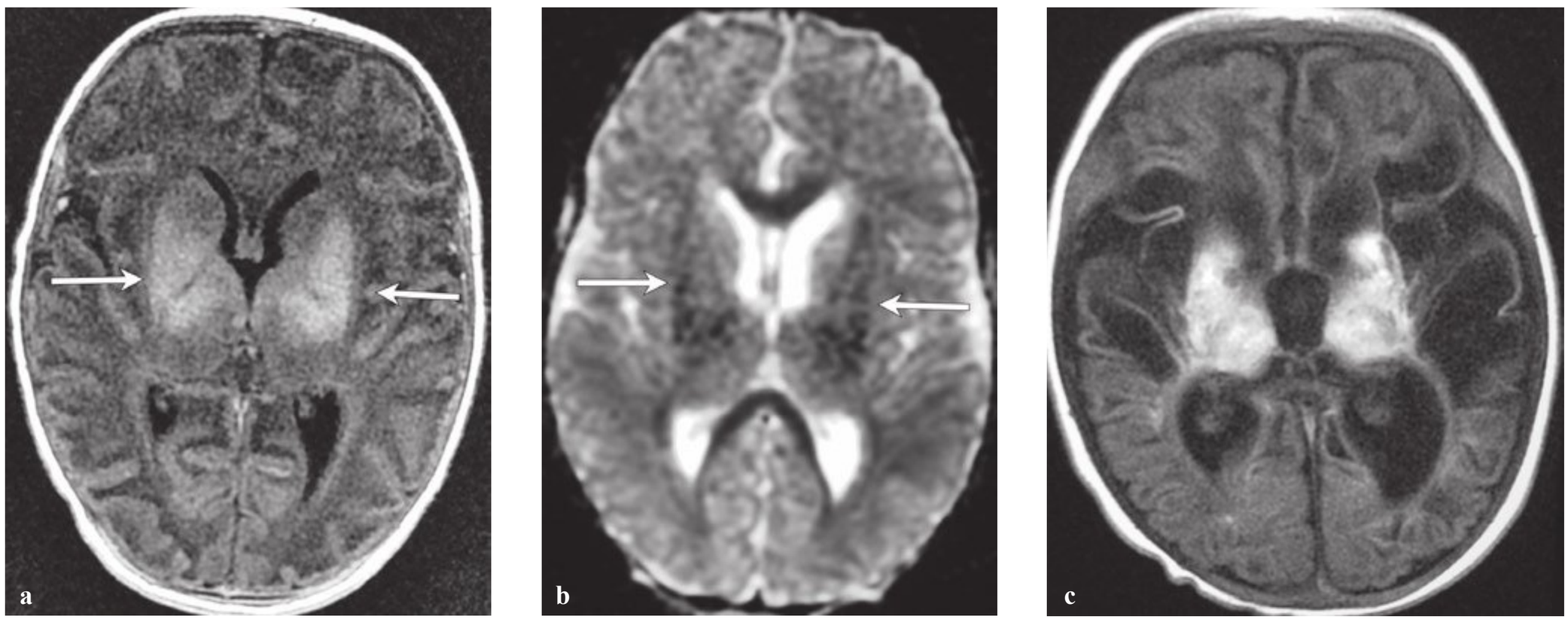

Fig. 1.333 An 8-day-old full-term neonate with severe hypoxic–ischemic encephalopathy. **(a)** Axial T1 WI shows abnormal high signal in the putamina and thalami relative to the internal capsules (arrows) with **(b)** corresponding restricted diffusion on axial ADC (arrows). **(c)** Axial T1 WI 5 weeks later shows denaturation necrosis with high signal in the basal ganglia and thalami, and internal capsules with associated atrophy and adjacent cystic encephalomalacia.

Table 1.7 (cont.) Neurodegenerative disorders

Disorders	Imaging Findings	Comments
Porencephalic cyst (**Fig. 1.334**)	MRI: Irregular, relatively well-circumscribed zone with high signal on T2-weighted imaging, and low signal on T1-weighted imaging and diffusion-weighted imaging (DWI) similar to CSF, surrounded by poorly defined thin zones of increased signal on FLAIR in adjacent brain tissue representing gliosis. No gadolinium contrast enhancement or peripheral edema. CT: Irregular, relatively well-circumscribed zone with low attenuation similar to CSF, surrounded by poorly defined thin zone of decreased attenuation in adjacent brain tissue. No contrast enhancement or peripheral edema.	Porencephalic cysts represent remote sites of brain injury (trauma, infarction, infection, hemorrhage) occurring in late second trimester, with evolution by an encephaloclastic process into a cystic zone with CSF MR signal characteristics surrounded by zones of gliosis in adjacent brain parenchyma. Gliosis (high T2 signal) allows differentiation from schizencephaly.
Periventricular leukomalacia (**Fig. 1.335**)	MRI: Multiple foci and/or confluent zones of high signal on T2-weighted imaging in the subcortical and periventricular white matter, basal ganglia, and brainstem, with associated mass effect, – enhancement, ± low signal on T1-weighted imaging, irregular ventricular margins, and ventricular enlargement related to cerebral volume loss. CT: Multiple zones of decreased attenuation involving the cerebral white matter, basal ganglia, and brainstem. No associated mass effect, no contrast enhancement, irregular ventricular margins, and ventricular enlargement.	Ischemic injury in fetal brain/premature infants with gliosis and resultant encephalomalacic changes in periventricular white matter (fetal watershed vascular zones). Associated with neurologic deficits depending on severity of injuries (e.g., cerebral palsy).
Dyke-Davidoff-Masson syndrome (**Fig. 1.336**)	Atrophy/encephalomalacia of one cerebral hemisphere with compensatory dilatation of ipsilateral lateral ventricle, midline shift, unilateral ipsilateral decrease in size of cranial fossa associated with thickened calvarium, ± enlargement of ipsilateral pneumatized paranasal sinuses and mastoid air cells.	Rare disorder in adolescents that presents with seizures, mental retardation, and hemiparesis or hemiplegia. Can result from congenital injury, such as cerebral infarction due to occlusion of the middle cerebral artery, or from postnatal trauma, hemorrhage, ischemia, or infection.

(continued on page 280)

Fig. 1.334 Axial CT shows a large porencephalic cyst contiguous with frontal horn of the right lateral ventricle.

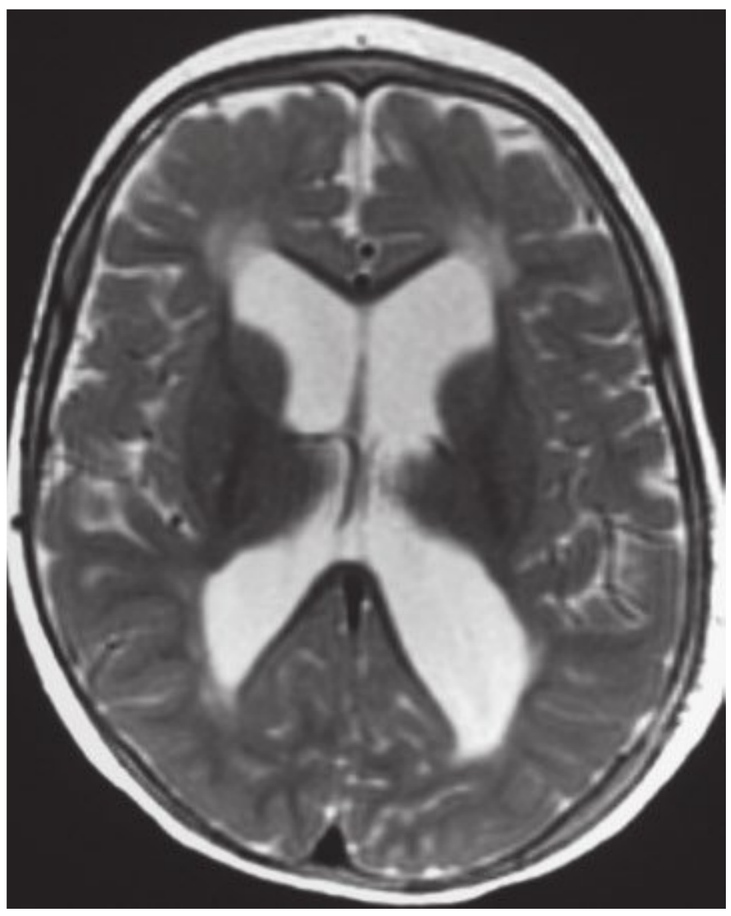

Fig. 1.335 An 18-month-old male with periventricular leukomalacia. Axial T2WI shows periventricular gliosis with high signal and decreased volume of white matter with compensatory dilatation of the lateral ventricles.

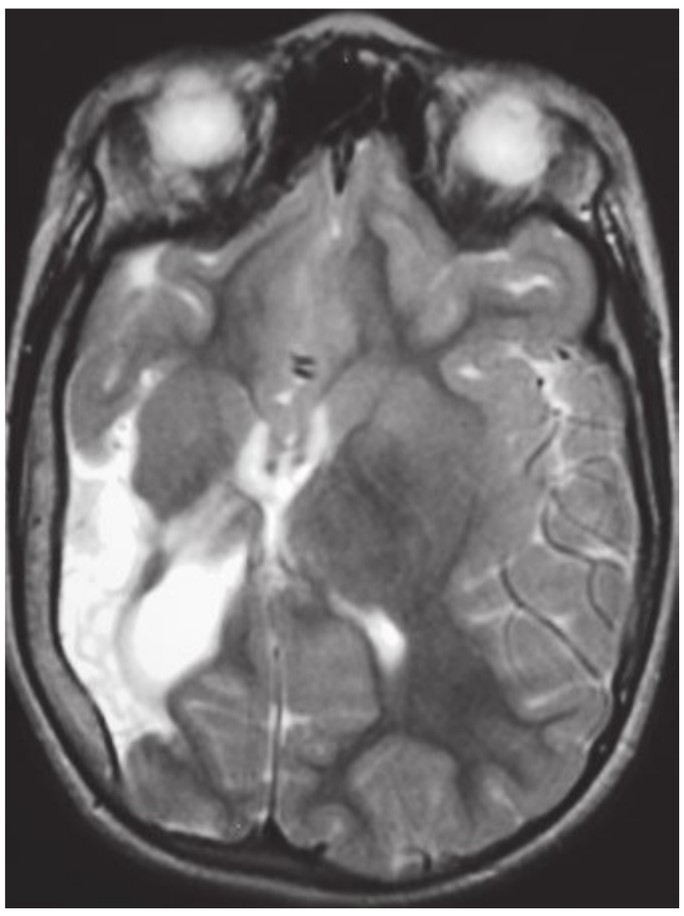

Fig. 1.336 A 7-year-old female with Dyke-Davidoff-Masson syndrome. Axial T2WI shows encephalomalacia of the right cerebral hemisphere with compensatory dilatation of the right lateral ventricle, midline shift, and unilateral ipsilateral decrease in size of the right cranial fossa associated with thickened calvarium.

Table 1.7 (cont.) Neurodegenerative disorders

Disorders	Imaging Findings	Comments
Post-Injury Degenerative Changes in Older Children and Adults		
Wallerian degeneration (**Fig. 1.337**)	CT: Corticospinal tract involvement from infarct or injury at motor cortex or posterior limb of internal capsule can result in hemiatrophy of brainstem (midbrain, pons) ipsilateral to cerebral lesion. MRI: Cerebral injury can result in a linear zone of high signal on T2-weighted imaging in ipsilateral corticospinal tract of brainstem, high signal on T2-weighted imaging 4–12 weeks after injury resulting from edema, > 12 weeks secondary to gliosis, ± associated atrophy in brainstem at ipsilateral corticospinal tract. Extensive unilateral cerebral cortical atrophy can result in atrophy of the contralateral middle cerebellar peduncle and cerebellum from interruption of the cerebropontocerebellar pathway (which connects the cerebral cortex to the contralateral middle cerebellar peduncle via pontine nuclei—crossed cerebellar diaschisis). Symmetric high signal on T2-weighted imaging can also be seen in both middle cerebellar peduncles 23 days after pontine injury (infarction, hemorrhage, or osmotic myelinolysis) from Wallerian degeneration involving the fibers of the pontocerebellar tract. Diffusion-weighted imaging (DWI) and Diffusion tensor imaging (DTI): Transient reduced ADC can be seen at the corticospinal tract ipsilateral to acute cerebral stroke within 3 days. Progressive decrease of fractional anisotropy (FA) also occurs. Thirty days after stroke, reduced FA at the involved corticospinal tract can be correlated with motor deficits.	Refers to pathologic changes (degeneration, myelin degradation, atrophy) in axons secondary to injuries involving the cell bodies and/or proximal portions of neurons (hemorrhage, cerebral infarction, contusion, neoplasm, and surgery). Most frequently involves the corticospinal tract from injuries to the cerebral motor cortex. Can involve other axons of the optic radiations, corpus callosum, limbic system, brainstem, and spinal cord.
Crossed cerebellar diaschisis (**Fig. 1.338** and **Fig. 1.339**)	MRI: In the acute phase, diffusion-weighted imaging (DWI) can show restricted diffusion in a cerebellar hemisphere and contralateral cerebral hemisphere. Contrast-enhanced perfusion MRI can show decreased perfusion (prolonged TTP and decreased cerebral blood volume) of involved cerebellar hemisphere. Late findings include unilateral atrophy of a cerebellar hemisphere contralateral to a lesion involving one cerebral hemisphere. PET/CT and SPECT: Hypoperfusion and hypometabolism in involved cerebellar hemisphere.	Disorder in which unilateral cerebellar hypoperfusion and hypometabolism occur from injury (infarct, hemorrhage, infection, or seizures) in the contralateral suparatentorial brain. Results from interruption of afferent associative, sensory, paralimbic, and motor input into the cerebropontocerebellar pathway, causing a decline in synaptic cerebellar Purkinje function coupled with hypometabolism, decreased perfusion, and decreased oxygen consumption.

(continued on page 282)

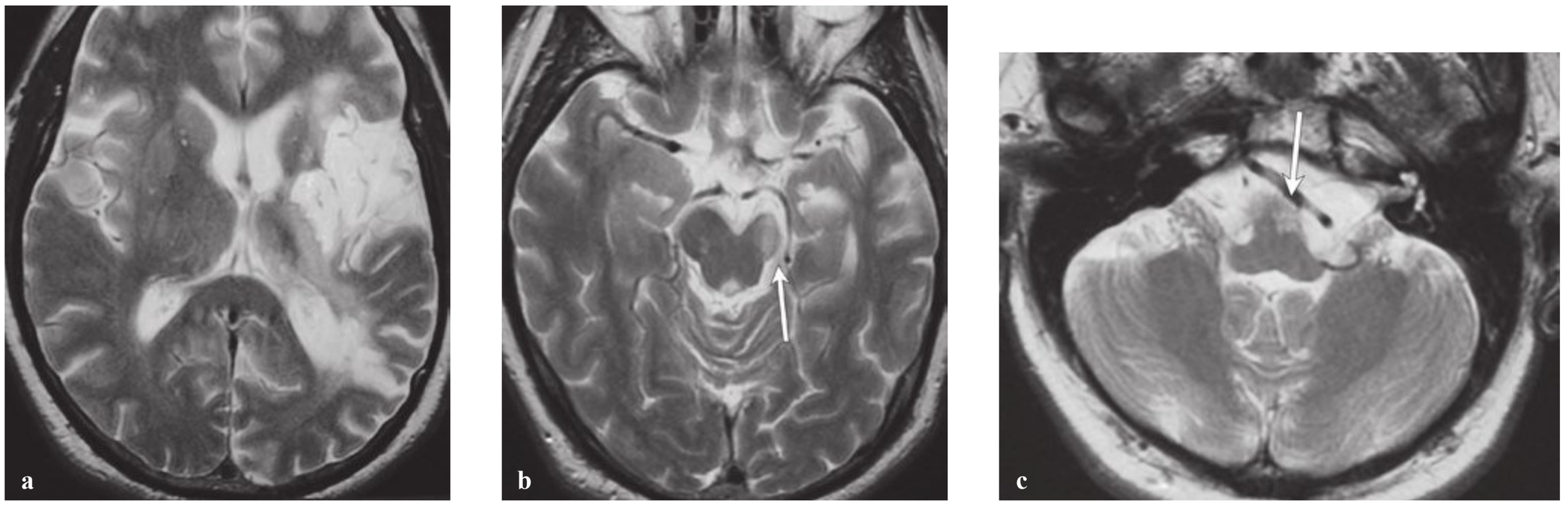

Fig. 1.337 Encephalomalacia and gliosis are seen in the left cerebral hemisphere secondary to cerebral infarction on **(a)** axial T2WI that occurred 1.5 years earlier in the vascular distribution of the right middle cerebral artery. **(b,c)** Axial T2WI through the brainstem show Wallerian degeneration with atrophy and high signal gliosis in the left cerebral peducle and upper left anterior medulla (arrows).

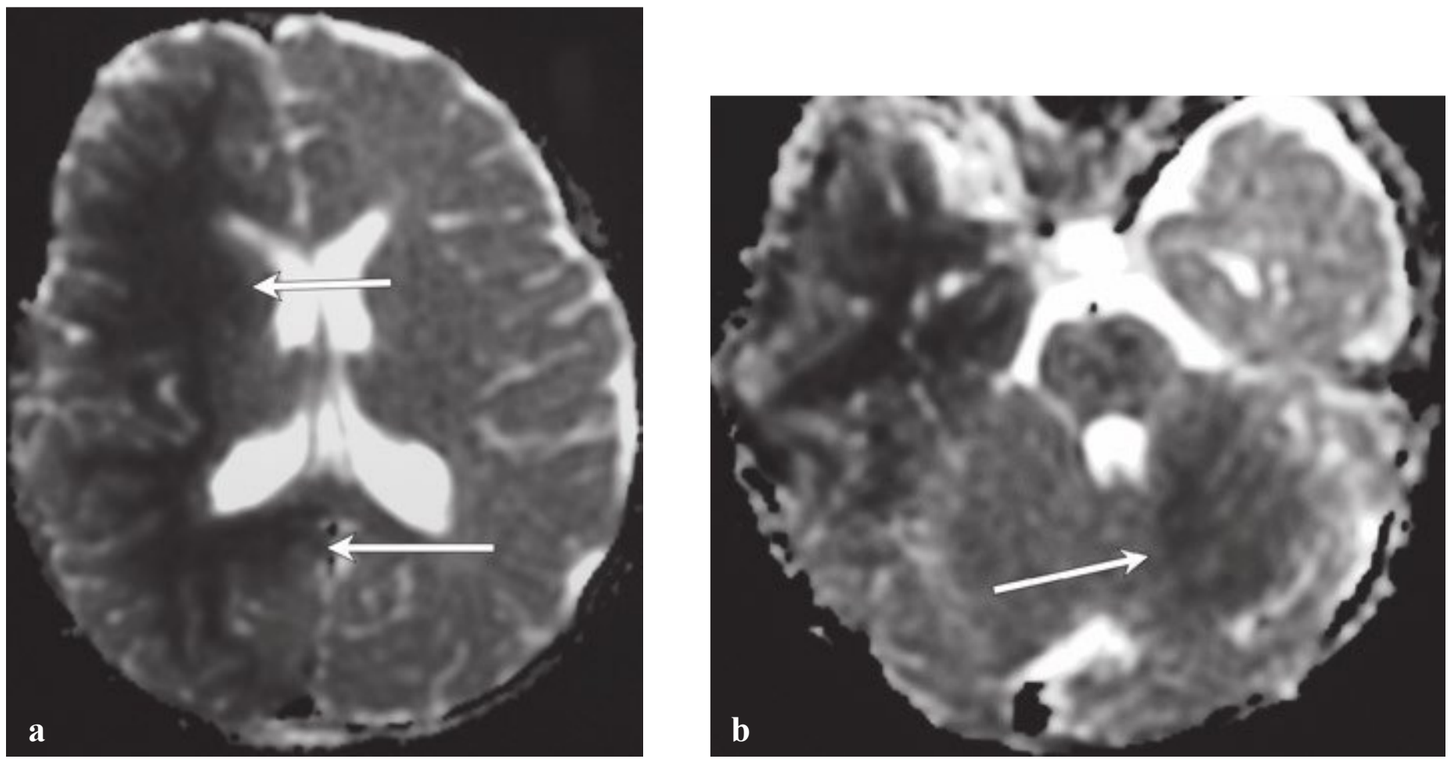

Fig. 1.338 A 9-month-old female with acute large infarct in the right cerebral hemisphere with low signal on **(a)** axial ADC associated with acute-phase crossed cerebellar diaschisis seen as restricted diffusion (arrow) in the left cerebellar hemisphere on **(b)** axial ADC (arrow).

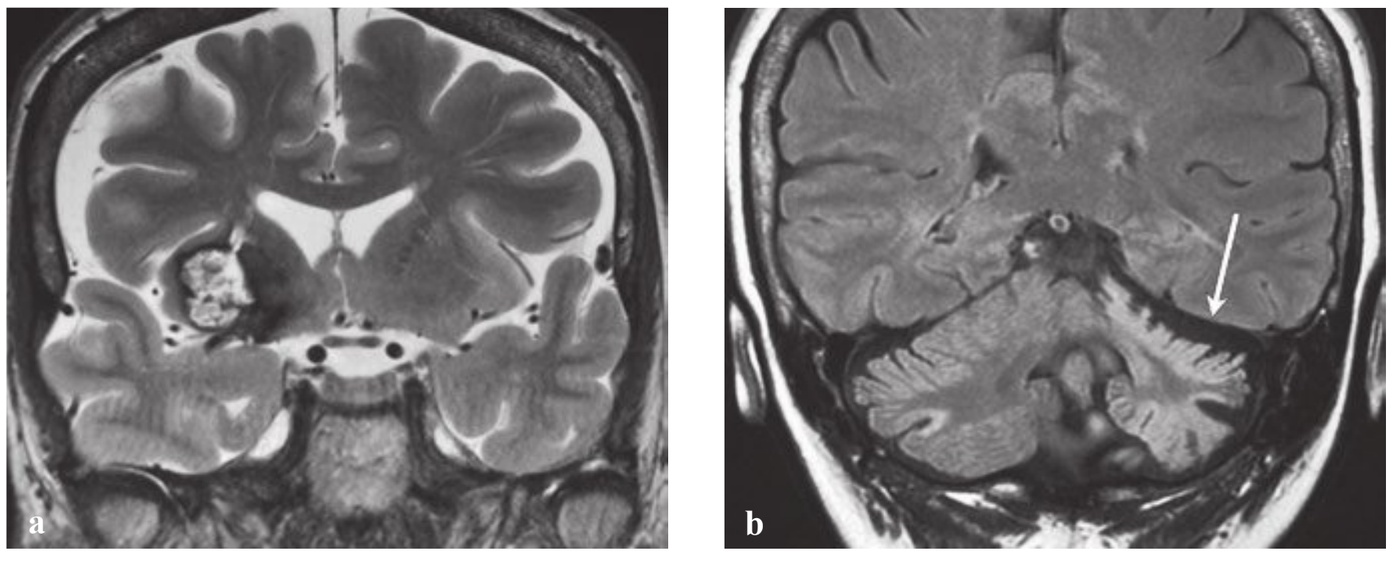

Fig. 1.339 A 52-year-old woman with a cavernous malformation in the inferior right frontal lobe seen on **(a)** coronal T2WI associated with late-phase crossed cerebellar diaschisis (arrow) in **(b)** the left cerebellar hemisphere on coronal FLAIR (arrow).

Table 1.7 (cont.) Neurodegenerative disorders

Disorders	Imaging Findings	Comments
Hypertrophic olivary degeneration (HOD) (**Fig. 1.340** and **Fig. 1.341**)	MRI: Zone of high signal on T2-weighted imaging and FLAIR in the inferior olivary nucleus without enlargement in first 4 months after injury. Abnormalities of the inferior olivary nuclei can be unilateral or bilateral. After 6 months, enlargement of the involved inferior olivary nucleus can occur. Typically, no gadolinium contrast enhancement. Susceptibility-weighted imaging (SWI) can show lack of normal low signal in both red nuclei of the midbrain without corresponding abnormal high signal on T2-weighted imaging, possibly due to Wallerian degeneration. PET/CT may show hypermetabolism in acute phase. SPECT may show hyperperfusion in early phases.	Disorder that occurs from injury to the dentato-rubro-olivary (DROP) pathway (also referred to as the Guillain-Mollaret triangle/GMT). The GMT consists of the ipsilateral red nucleus (RN), ipsilateral inferior olivary nucleus (ION), and the contralateral dentate nucleus (DN). The RN connects to the ipsilateral ION via the central tegmental tract. The ION connects to the contralateral DN via the olivocerebellar tract through the inferior cerebellar peduncle. The DN connects to the contralateral RN via the efferent dentatorubral tract, which passes through the superior cerebellar peduncle. Injuries that disconnect this pathway result in hypertrophy and enlargement of the inferior olivary nuclei secondary to trans-synaptic vacuolar degeneration with glial hypertrophy and proliferation of gemistocytic astrocytes. Most lesions can be seen 4 to 12 months after injury, and occasionally after 3 weeks. The clinical finding of palatal myoclonus has been associated with HOD.
Posttraumatic gliosis and encephalomalacia from brain contusions (**Fig. 1.342**)	MRI: In the acute phase, signal of the contusion depends on its age and presence of oxyhemoglobin, deoxyhemoglobin, methemoglobin, hemosiderin, etc. Surrounding the hematoma is a zone of edema with high signal on T2-weighted imaging and FLAIR and that has decreased rCBF. Contusions eventually appear as zones of focal superficial encephalomalacia with high signal on T2-weighted imaging, ± small zones of low signal on T2-weighted imaging and GRE from hemosiderin. Zones of high signal on FLAIR are seen in the adjacent brain tissue from gliosis.	Contusions are superficial brain injuries involving the cerebral cortex and subcortical white matter that result from skull fracture and/or acceleration deceleration trauma of the brain onto the inner table of the skull. Lesions consist of capillary injury, edema, and hemorrhage, and often involve the anterior portions of the temporal and frontal lobes, and inferior portions of the frontal lobes.

(continued on page 284)

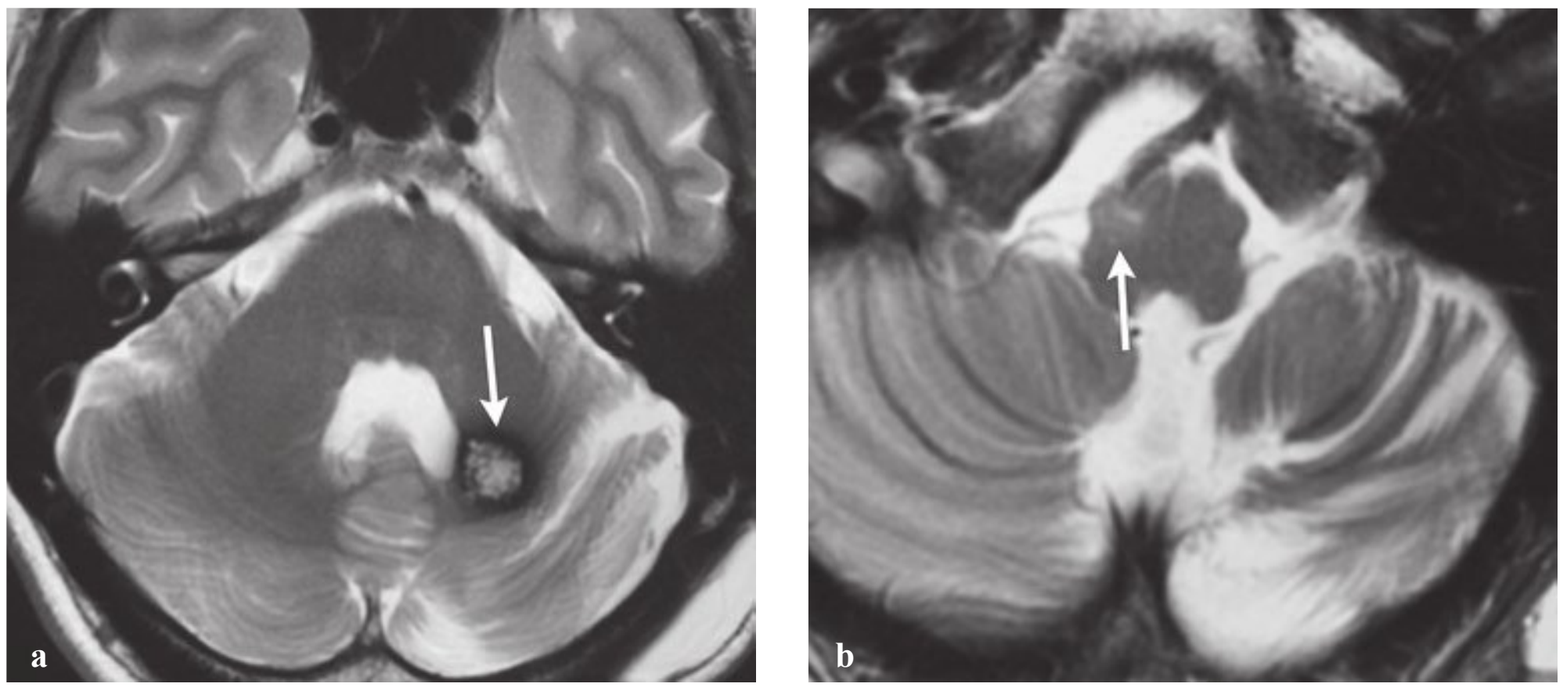

Fig. 1.340 A 50-year-old man with a cavernous malformation in the left dentate nucleus on **(a)** axial T2WI (arrow) resulting in hypertrophic olivary degeneration with high signal on **(b)** axial T2WI at the contralateral anterior right medulla (arrow).

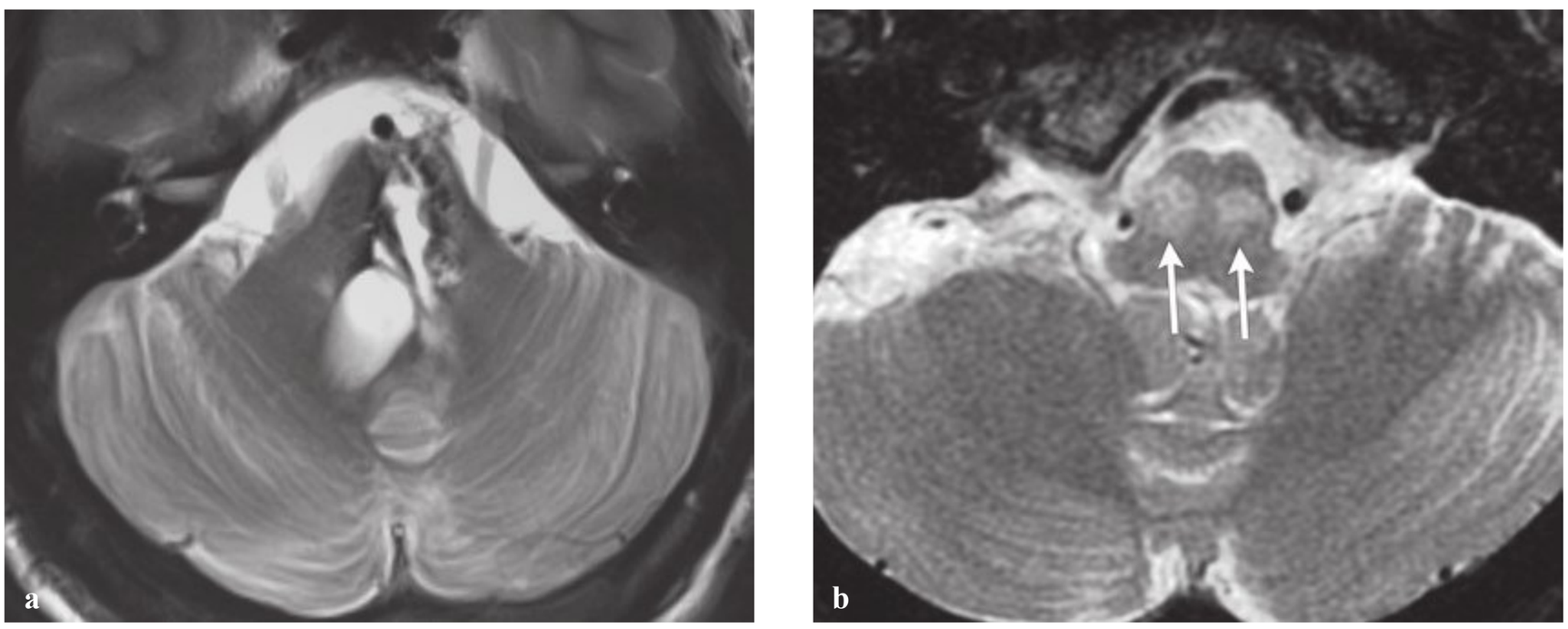

Fig. 1.341 A 33-year-old woman with a vascular malformation in the pons on **(a)** axial T2WI associated with bilateral hypertrophic olivary degeneration on **(b)** axial T2WI (arrows).

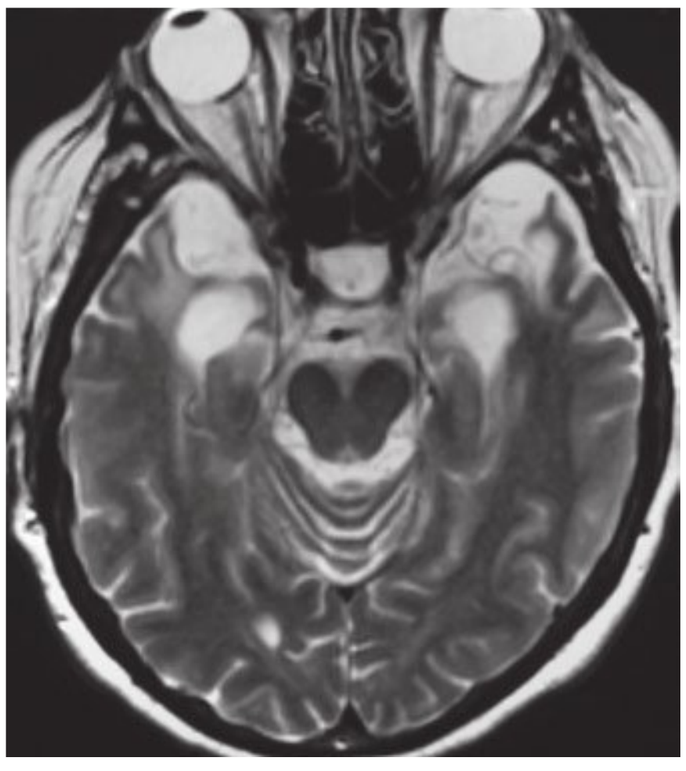

Fig. 1.342 A 61-year-old woman with posttraumatic gliosis and encephalomalacia from brain contusions as seen on axial T2WI.

Table 1.7 (cont.) Neurodegenerative disorders

Disorders	Imaging Findings	Comments
Inherited Neurodegenerative Disorders		
Neurodegeneration with brain iron accumulation (pantothenate kinase–associated neurodegeneration: PKAN disease) (**Fig. 1.343**)	CT: Zones of low attenuation in the globus pallidus bilaterally MRI: Low signal ± areas of high signal on T2-weighted imaging in the globus pallidus bilaterally giving the eye of the tiger sign. No gadolinium contrast enhancement.	Rare autosomal recessive metabolic disorder from mutations in the pantothenate kinase 2 (PANK2) gene. Onset is usually in childhood, with progressive limb rigidity and gait dysfunction, dysarthria, and mental deterioration. Increased iron deposition and destruction of globus pallidus and substantia nigra bilaterally.
Wilson's disease (**Fig. 1.344**)	CT: Zones of low attenuation in the basal ganglia and thalami. No abnormal contrast enhancement seen. Progressive atrophy of the cerebrum, cerebellum, and brainstem. MRI: High signal on T2-weighted imaging in the putamen bilaterally as well as in the thalami, caudate nuclei, dentate nuclei, middle cerebellar peduncles, and brainstem (periaqueductal zone). Low signal on T2-weighted imaging can also be seen in the caudate and putamen. Some patients have high signal on T1-weighted imaging in the globi pallidi and dorsal midbrain related to hepatic dysfunction. Low signal on T1-weighted imaging may also be seen in the putamina, globi pallidi, and both thalami. Progressive atrophy of the cerebrum, cerebellum, and brainstem.	Autosomal recessive disease involving the ATP7B gene on chromosome 13q14.3–21.1, which encodes for the copper-transporting ATPase protein in hepatocytes. Loss of the normal copper-transporting ATPase protein results in reduced hepatic biliary copper excretion and reduced incorporation of copper into ceruloplasmin. Patients have abnormal hepatic levels of copper and abnormally increased urinary excretion of copper. Usually presents in childhood with abnormal toxic copper deposition in tissues, resulting in cirrhosis and degenerative changes in the basal ganglia (lentiform nuclei) and brainstem. Patients can have dysarthria, tremors, choreoathetosis, dystonia, and Kayser-Fleischer rings on ophthalmologic examination.
Menkes' syndrome (trichopoliodystrophy)	CT: Rapid, progressive brain atrophy with large bilateral subdural hematomas. MRI: High signal on T2-weighted imaging can be seen in the cerebral white matter, putamen bilaterally, and/or caudate nuclei with or without restricted diffusion. Delayed myelination involving the posterior limb of the internal capsules can be seen. Progressive atrophy of the cerebrum, cerebellum, and brainstem. Small zones with high signal on T1-weighted imaging may be seen in the cerebral cortex. Large, bilateral subdural hematomas can be seen with mixed signal on T1- and T2-weighted imaging. MRA and CTA show tortuous "corkscrew" arteries.	X-linked recessive disorder from mutations of the ATP7A gene on Xq13.3, which encodes for the copper-transporting ATPase protein necessary for intestinal uptake of copper. Lack of adequate copper results in defective cytochrome c oxidase activity in mitochondria. Patients often have seizures, truncal hypotonia, hypothermia, failure to thrive, failure to reach developmental milestones, hypermobile joints, hypopigmentation, and coarse, stiff, and broken hair—"kinky hair disease."

(continued on page 286)

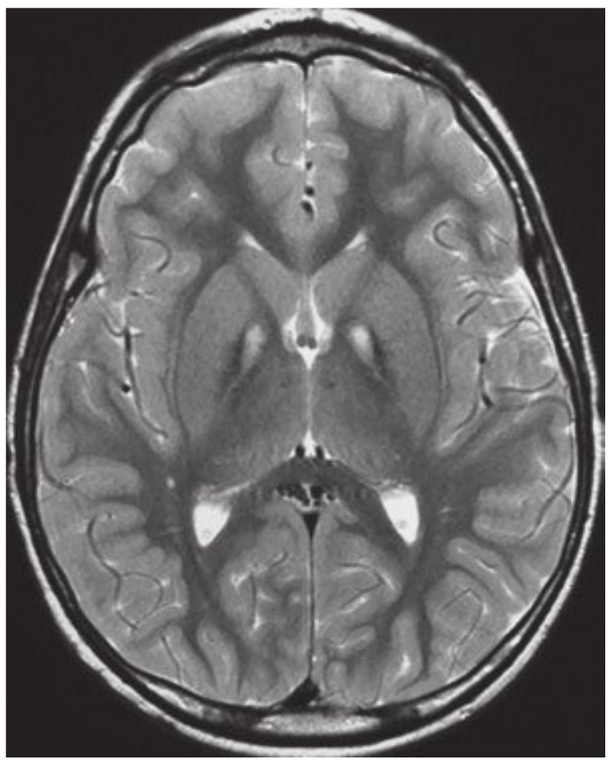

Fig. 1.343 A 6-year-old male with neurodegeneration with brain iron accumulation (PKAN disease). Axial T2WI shows bilateral foci with high signal in the globus pallidus bilaterally giving the "eye of the tiger" sign.

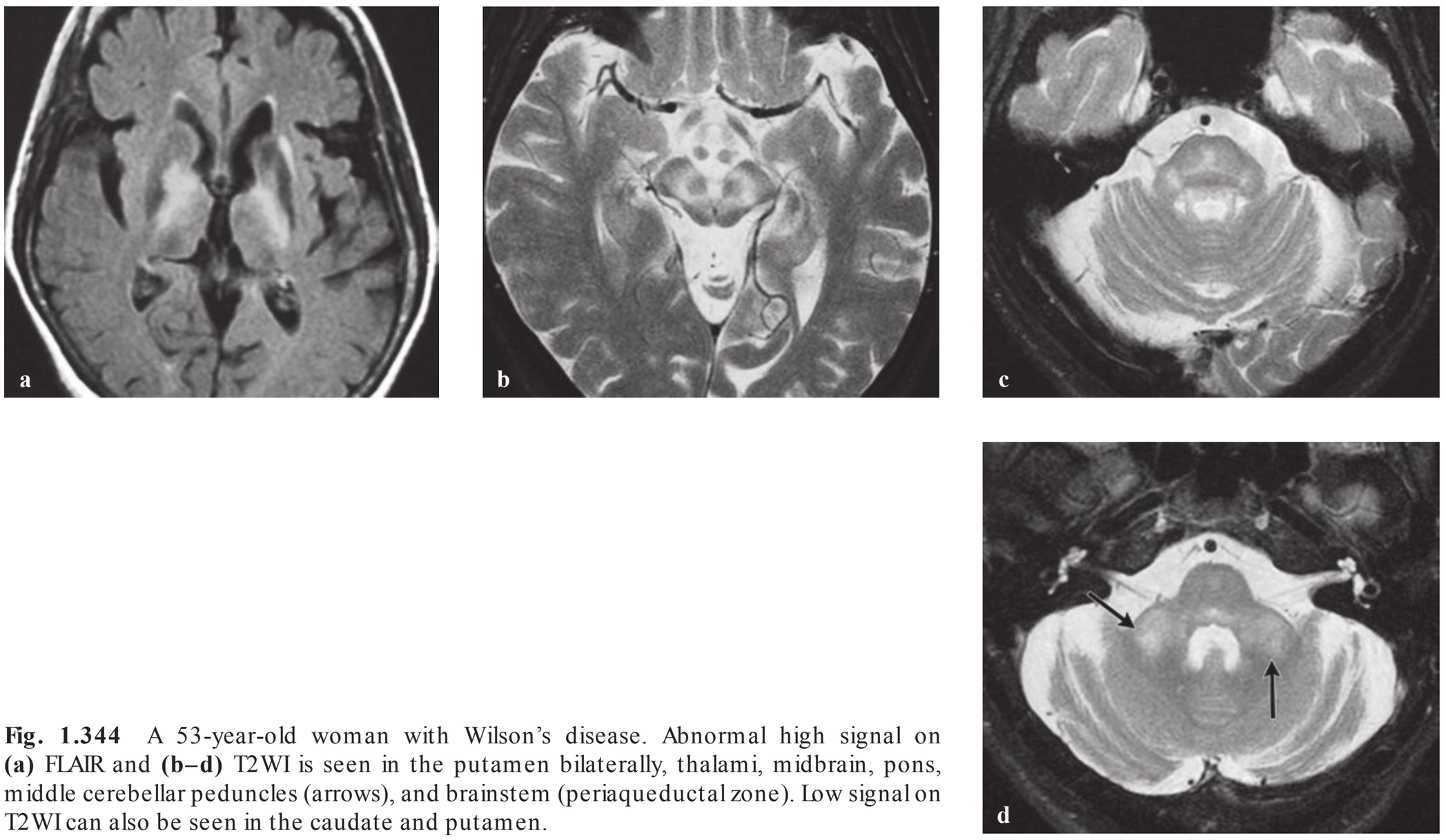

Fig. 1.344 A 53-year-old woman with Wilson's disease. Abnormal high signal on **(a)** FLAIR and **(b–d)** T2WI is seen in the putamen bilaterally, thalami, midbrain, pons, middle cerebellar peduncles (arrows), and brainstem (periaqueductal zone). Low signal on T2WI can also be seen in the caudate and putamen.

Table 1.7 (cont.) Neurodegenerative disorders

Disorders	Imaging Findings	Comments
Fahr disease (**Fig. 1.345**)	CT: Intra-axial calcifications occur in the basal ganglia, dentate nuclei, and cerebral white matter. MRI: Calcifications usually have low signal on T2-weighted imaging, gradient echo imaging and susceptibility-weighted imaging. Calcifications in brain usually have low signal on T1-weighted imaging. In occasional situations when calcified particles in brain are small and/or have high relative surface areas, T1 relaxation times of adjacent protons can be reduced, resulting in high signal on T1-weighted imaging.	Fahr disease, also known as familial cerebrovascular ferrocalcinosis or idiopathic basal ganglia calcification (IBGC), is a group of disorders with deposition of calcium in the brain. Patients can present with dystonia, parkinsonism, ataxia, and behavioral and cognitive impairment. An autosomal dominant inheritance pattern of IBGC has been linked to a locus on chromosome 14.
Huntington disease (**Fig. 1.346**)	Disproportionate atrophy of basal ganglia (caudate > putamen > cerebellum/brainstem). CT: Progressive atrophy of caudate and putamen bilaterally. MRI: Atrophy of caudate and putamen bilaterally. Variable low signal (iron deposition) or high signal (gliosis) changes on T2-weighted imaging in the putamen bilaterally. Usually no abnormal contrast enhancement.	Autosomal dominant neurodegenerative polyglutamine disease in adults related to abnormal segment (CAG repeats) of DNA on chromosome 4 involving the huntingtin gene. Results in increased synthesis of huntingtin protein, which causes neuronal damage and brain atrophy. Neuronal loss, astrogliosis, and increased oligodentrocytes within a loose textured neuropil are seen in the striatum. Usually presents after the age of 40 years with progressive movement disorders (choreoathetosis, rigidity, hypokinesia), behavioral abnormalities, and progressive mental dysfunction (dementia). Juvenile Huntington disease also occurs in a small number of patients in their second decade. Patients present with rigidity, hypokinesia, seizures, and progressive mental dysfunction.
Ataxia telangiectasia (**Fig. 1.347**)	MRI: Progressive atrophy of the cerebellar vermis and cerebellar hemispheres that occurs in children and young adults. Intra-axial zones with high signal on T2-weighted imaging and FLAIR can be seen in the cerebral white matter as well as multiple foci with low signal on gradient echo and susceptibility-weighted imaging. Small gadolinium contrast-enhancing capillary telangectasias can be seen in the cerebrum. Diffusion-weighted imaging: Increased ADC values in involved cerebellum compared with controls. Magnetic resonance spectroscopy: Decreased NAA/choline and increased choline/creatine (Cho/Cr) in the cerebellum can occur.	Autosomal recessive neurodegenerative disorder resulting from mutations in the AT gene on chromosome 11q22–23. Frequency of 1–2.5 per 100,000. Onset of symptoms between ages of 2 and 4 years. Patients often require a wheelchair by age 10 years and may survive up to their 50s. The AT gene encodes for a serine-threonine kinase that plays a role in cell cycle regulation and DNA damage control. Clinical findings include telangiectatic vessels in the brain, conjunctiva, and skin; cell-mediated and humoral immunodeficiency; progressive cerebellar ataxia; oculomotor signs; hypogonadism; and α-fetoprotein elevated above 10 ng/mL. Pathologic findings include the marked loss of Purkinje and granule cells from the cerebellar cortex. Patients often have dysarthria, choreoathetosis, decreased deep tendon reflexes, oculomotor disturbances, and sensorimotor polyneuropathy.

(continued on page 288)

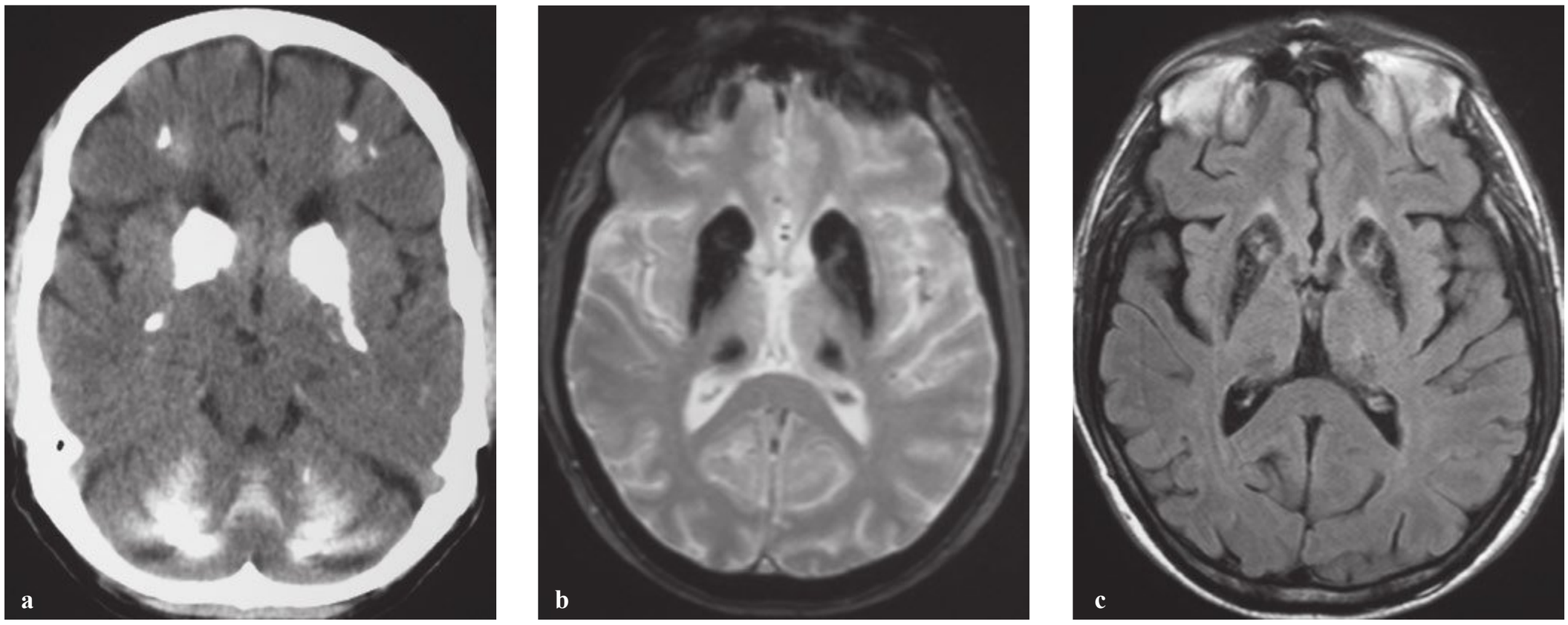

Fig. 1.345 A 55-year-old man with Fahr disease. Calcifications are seen in the basal ganglia, thalami, cerebral and cerebellar white matter, and dentate nuclei as seen on **(a)** axial CT, and which have low signal on **(b)** axial GRE and **(c)** axial FLAIR.

Fig. 1.346 A 64-year-old man with Huntington disease. Bilateral atrophied caudate nuclei (arrows) are seen on coronal T1 WI with compensatory enlargement of the frontal horns of the lateral ventricles.

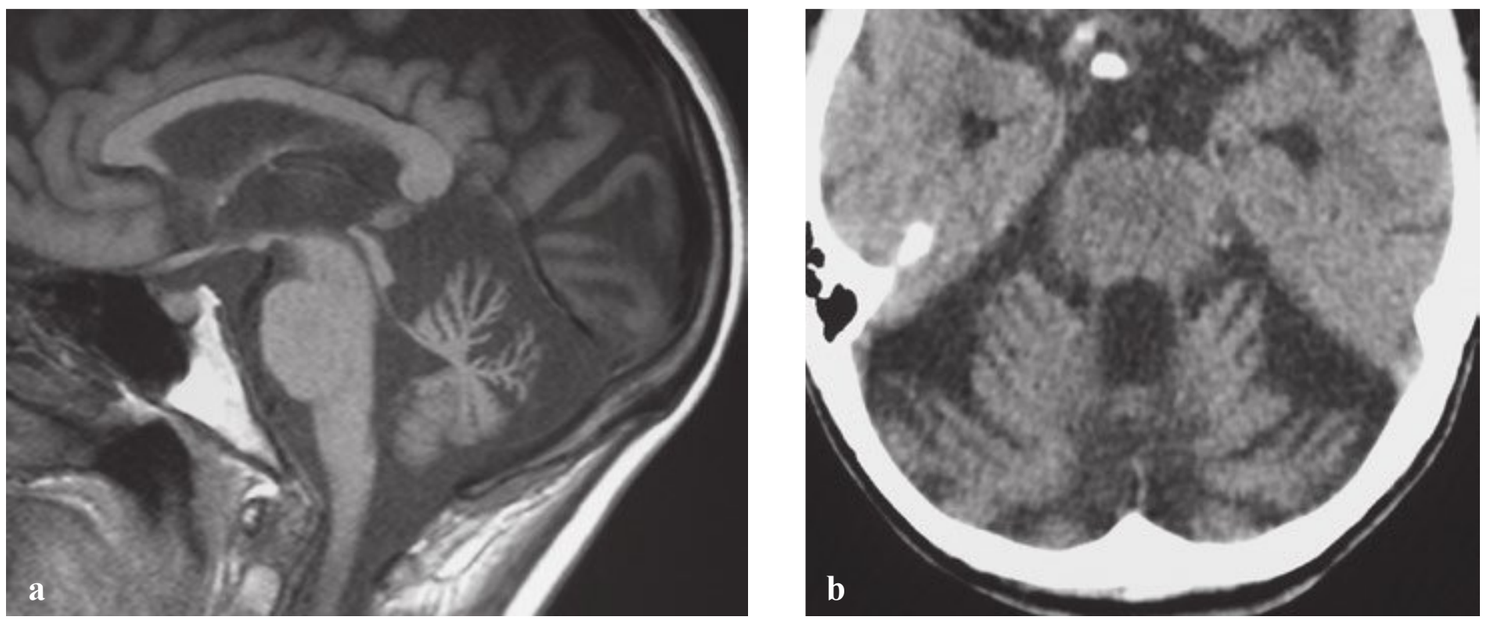

Fig. 1.347 A 36-year-old woman with ataxia telangiectasia. Diffuse cerebellar atrophy is seen on **(a)** sagittal T1 WI and **(b)** axial CT.

Table 1.7 (cont.) Neurodegenerative disorders

Disorders	Imaging Findings	Comments
Friedreich's ataxia	MRI: Atrophy of the superior cerebellar peduncles, ± inferomedial portions of the cerebellar hemispheres, medulla, and cervical spinal cord. Zones with high signal on T2-weighted imaging can be seen in the lateral and posterior columns of the cervical spinal cord. Diffusion tensor imaging (DTI): White matter atrophy with increased ADC values and reduced fractional anisotropy (FA) can be seen involving the optic chiasm, midbrain, superior cerebellar peduncles, cerebellar hemispheres, and vermis, pons, and medulla.	Most common form of autosomal recessive ataxia secondary to mutations (repeats of the trinucleotide GAA sequence) involving the FRDA gene on chromosome 9q13. These mutations inhibit transcription of the mitochondrial protein frataxin. Prevalence is 2–4 per 100,000. Onset of disease usually occurs before the age of 25 years. Clinical findings can include spinocerebellar and sensory ataxia, dysarthria, pyramidal signs, hypacusia, decreased deep tendon reflexes, hypertrophic cardiomyopathy, scoliosis, and/or pes cavus. Pathologic findings include neuronal loss, degeneration of white matter in the cerebellum, brainstem, posterior columns of the spinal cord, dorsal root ganglia, and large peripheral sensory nerve fibers.
Spinocerebellar ataxia/ degeneration (**Fig. 1.348**)	MRI: Progressive atrophy of the cerebellar vermis and cerebellar hemispheres in all spinocerebellar ataxia (SCA) types; atrophy of the pons in SCA 1–3, 7, 13, and 14; atrophy of the brainstem in SCA 1–3 and 13; and cortical atrophy in SCA 1, 2, 12, and 17–19. Signal abnormalities involving the basal ganglia and posterior fossa are usually absent, except in SCA 2 and 3.	Autosomal dominant spinocerebellar ataxias (SCA) are progressive neurodegenerative disorders involving the cerebellum and are associated with symmetric midline and appendicular ataxia (ataxia of gait, stance, and limbs), dysarthria, and oculomotor disturbances. There are 31 types of SCA based on specific gene mutations that result in repeats of the trinucleotide CAG sequence (glutamine codon). Hyperkinetic movements are typically seen in SCA types 1–3, 6–8, 12, 14, 15, 17, 19–21, and 27.
Mitochondrial disorders: MELAS/MERRF (**Fig. 1.349**)	CT: Symmetric zones of low attenuation in the basal ganglia, and cerebral cortical infarction that is not limited to one vascular distribution, ± dystrophic calcifications in basal ganglia. MRI: High signal on T2-weighted imaging and FLAIR in basal ganglia, usually symmetric; and high signal on T2-weighted imaging and FLAIR in cerebral and cerebellar cortex and subcortical white matter, often with restricted diffusion. Findings do not correspond to a specific large arterial territory. Signal abnormalities may resolve and reappear. Cerebral and cerebellar atrophy can result after multiple ischemic episodes.	MELAS (mitochondrial encephalopathy, lactic acidosis, and stroke-like events) is a maternally inherited disease affecting tRNA in mitochondria. MERRF (myoclonic epilepsy with ragged red fibers) is a mitochondrial encephalopathy associated with muscle weakness and myoclonic epilepsy, short stature, ophthalmoplegia, and cardiac disease.

(continued on page 290)

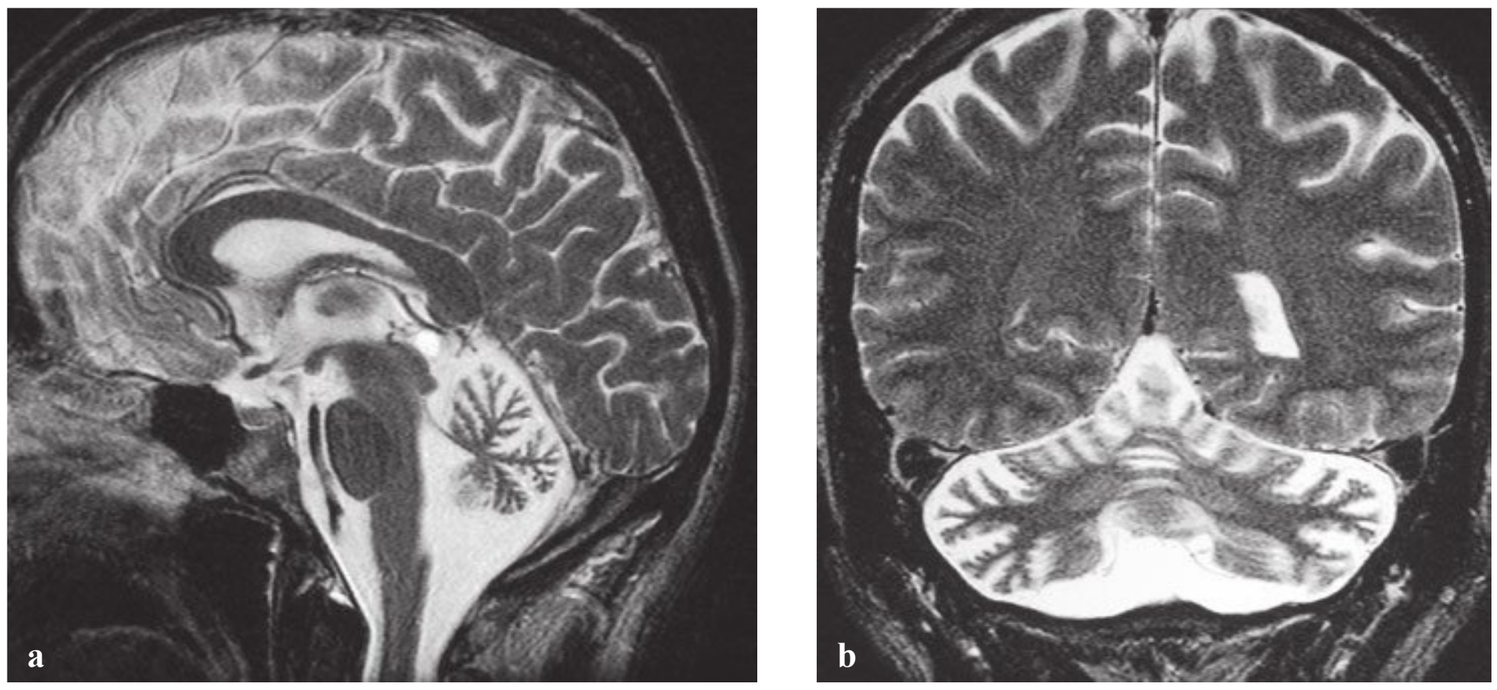

Fig. 1.348 A 40-year-old man with spinocerebellar ataxia/degeneration. **(a)** Sagittal and **(b)** coronal T2WI show diffuse atrophy of the cerebellar vermis and hemispheres.

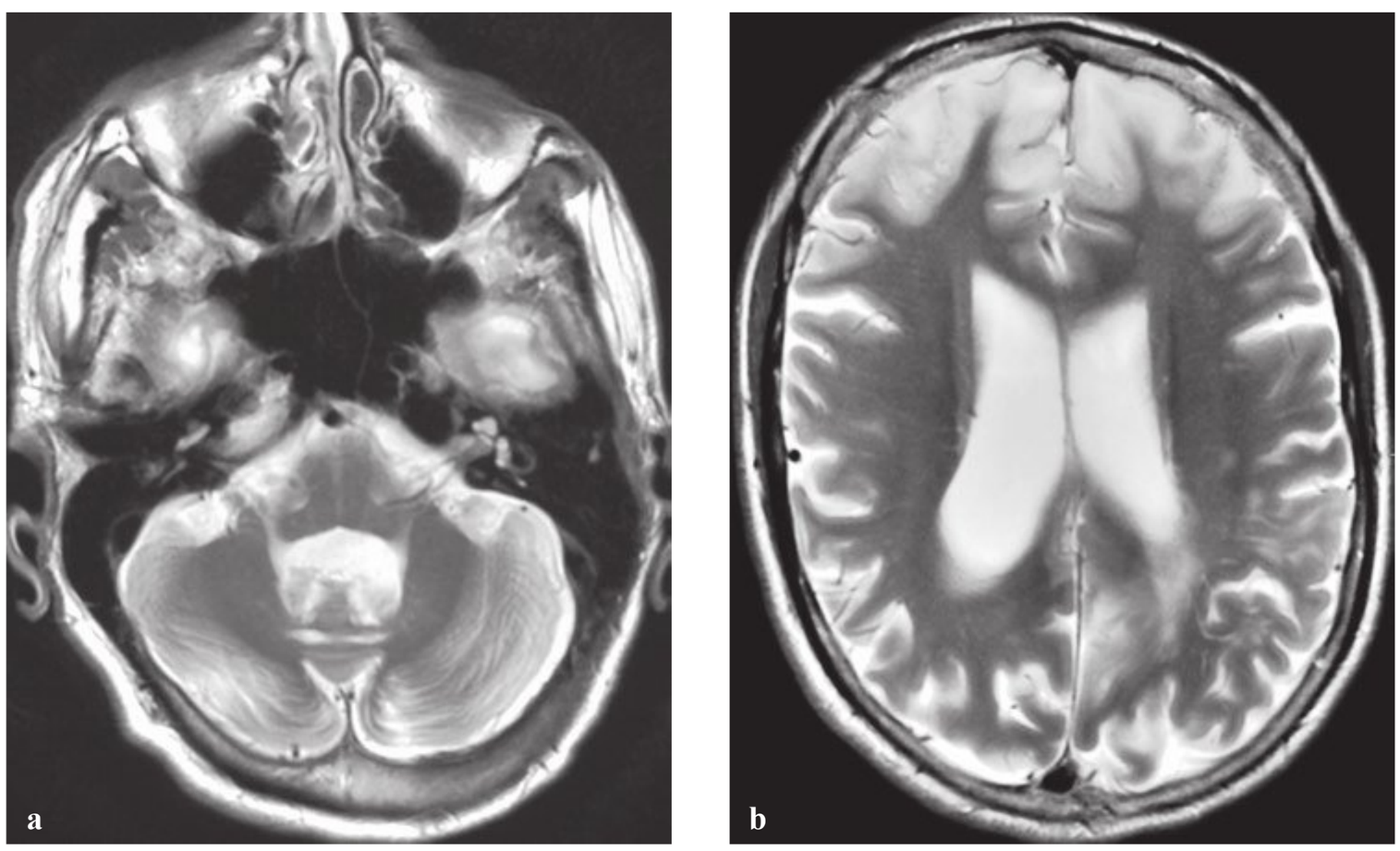

Fig. 1.349 A 47-year-old man with MELAS who has had multiple episodes of ischemia resulting in progressive **(a)** cerebral and **(b)** cerebellar atrophy on axial T2WI.

Table 1.7 (cont.) Neurodegenerative disorders

Disorders	Imaging Findings	Comments
Acquired Neurodegenerative Disorders		
Acquired hepatocerebral degeneration (See **Fig. 1.292**)	CT: No zones with definite abnormal attenuation seen in the basal ganglia, ± cerebral and cerebellar atrophy. MRI: High signal on T1-weighted imaging in basal ganglia/globi pallidi and anterior midbrain. No abnormal gadolinium contrast enhancement. Magnetic resonance spectroscopy can show decreased choline and myo-inositol levels and elevated glutamine/glutamate peaks related to toxic effects of hyperammonemia.	Signal hyperintensity on T1-weighted imaging secondary to hepatic dysfunction (alcoholic cirrhosis, hepatitis, portal-systemic shunts) is related to increased serum ammonia and manganese levels. The signal hyperintensity on T1-weighted imaging may reverse after liver transplantation.
Alcohol (ETOH) abuse (**Fig. 1.350**)	MRI and CT: Progressive atrophy of the cerebellum, pons, and frontal and temporal lobes. With Marchiafava-Bignami disease: Lesions with low signal on T1-weighted imaging and high signal on T2-weighted imaging and FLAIR occur in the corpus callosum without significant mass effect, ± hemorrhage. Gadolinium contrast enhancement and restricted diffusion in the corpus callosum can be seen in the acute phase. Diffusion tensor imaging (DTI): Decreased fractional anisotropy (FA) can be seen in the corpus callosum, inferior longitudinal fasciculus, and superior longitudinal fasciculus of the left cerebral hemisphere, as well as the forceps major tract.	Alcohol is one of the most commonly abused substances, and alcohol abuse is the third leading cause of disease in developing countries. ETOH is absorbed in the stomach and is metabolized in the liver, where it is oxidized into aldehyde by alcohol dehydrogenase, and then into acetic acid by acetaldehyde dehydrogenase, with eventual metabolic conversion to CO_2 and water via the citric acid cycle. ETOH has a primary toxic effect on neurons, resulting in brain volume loss from decreased neurotrophic factors and lipid peroxidation. Primary direct toxicity also results from altered homocysteine catabolism, with increased N-methyl-D-aspartate receptors causing impaired function of cell membrane ionic channels as well as enhanced susceptibility to neurotoxic effects of glutamate. ETOH abuse can result in progressive liver disease, with cirrhosis, coagulopathy, and hepatic encephalopathy. Other associated chronic effects related to ETOH abuse include Wernicke's encephalopathy from associated malnutrition and deficiency of vitamin B_1, osmotic myelinolysis from electrolyte disturbances, and Marchiafava-Bignami disease (primary toxic demyelination and necrosis of the central portion of the corpus callosum), resulting from deficiency of all B vitamins.
Wernicke's encephalopathy (See **Fig. 1.293**)	MRI: Symmetric lesions with abnormal increased signal on T2-weighted imaging and FLAIR in the medial thalami (70–80%), periventricular regions adjacent to the third ventricle (80%), periaqueductal area (59%), mamillary bodies (45%), and/or tectal plate (13–36%). In non-alcoholics, lesions may also be seen in the cerebral cortex, caudate nuclei, splenium, cerebellum, and brainstem. Lesions in the mamillary bodies and thalamus often show gadolinium contrast enhancement in alcoholic patients with thiamine deficiency. Uncommon findings of restricted diffusion on diffusion-weighted imaging (DWI), and magnetic resonance spectroscopy findings of increased lactate and decreased NAA/Cr have been associated with irreversible brain injury and poor prognosis.	Severe neurologic disorder resulting from vitamin B_1 (thiamine) deficiency. Thiamine reserves in the body can be depleted in 3 weeks. Thiamine is an important cofactor for enzymes in the Krebs cycle and pentose phosphate pathway. Lack of thiamine results in injury to regions of the brain with high metabolic requirements. Usually occurs in alcoholics from dietary deficiency, but can also occur in patients with malabsorption from surgical procedures, gastrointestinal malignancies, chemotherapy, hyperemesis, and chronic malnutrition/starvation. Clinical findings include altered consciousness, ocular dysfunction/ophthalmoplegia, and ataxia.

Disorders	Imaging Findings	Comments
Osmotic pontine myelinolysis (**Fig. 1.351**)	MRI: Poorly defined zone of low-intermediate signal on T1-weighted imaging and high signal on T2-weighted imaging involving the central portion of the pons (central pontine myelinolysis). Extrapontine myelinolysis occurs as zones with high signal on T2-weighted imaging in the cerebral white matter, external capsules, basal ganglia, thalami, midbrain, and middle cerebellar peduncles, ± small areas of gadolinium contrast enhancement in the first 4 weeks. Wallerian degeneration involving the fibers of the pontocerebellar tract can result in high signal on T2-weighted imaging in both middle cerebellar peduncles 23 days after pontine injury from osmotic myelinolysis. Diffusion-weighted imaging: ADC values are low in the acute phase. CT: Poorly defined zone of decreased attenuation involving the central portion of the pons (central pontine myelinolysis). Extrapontine myelinolysis occurs as zones with decreased attenuation in the cerebral white matter, external capsules, basal ganglia. thalami, midbrain, and middle cerebellar peduncles, ± occasional contrast enhancement.	Demyelinating disorder resulting from rapid correction of hyponatremia in chronically ill, malnourished, or alcoholic patients. Associated with diabetes mellitus, hepatitis, and chronic disease of the lungs, liver, and/or kidneys. Damage occurs to the myelin sheaths, without initial destruction of axons. Can result in spastic tetraparesis, quadraparesis, pseudobulbar paralysis, seizures, coma, and locked-in syndrome. Clinical findings can regress or progress, and the disease is occasionally fatal.

(continued on page 292)

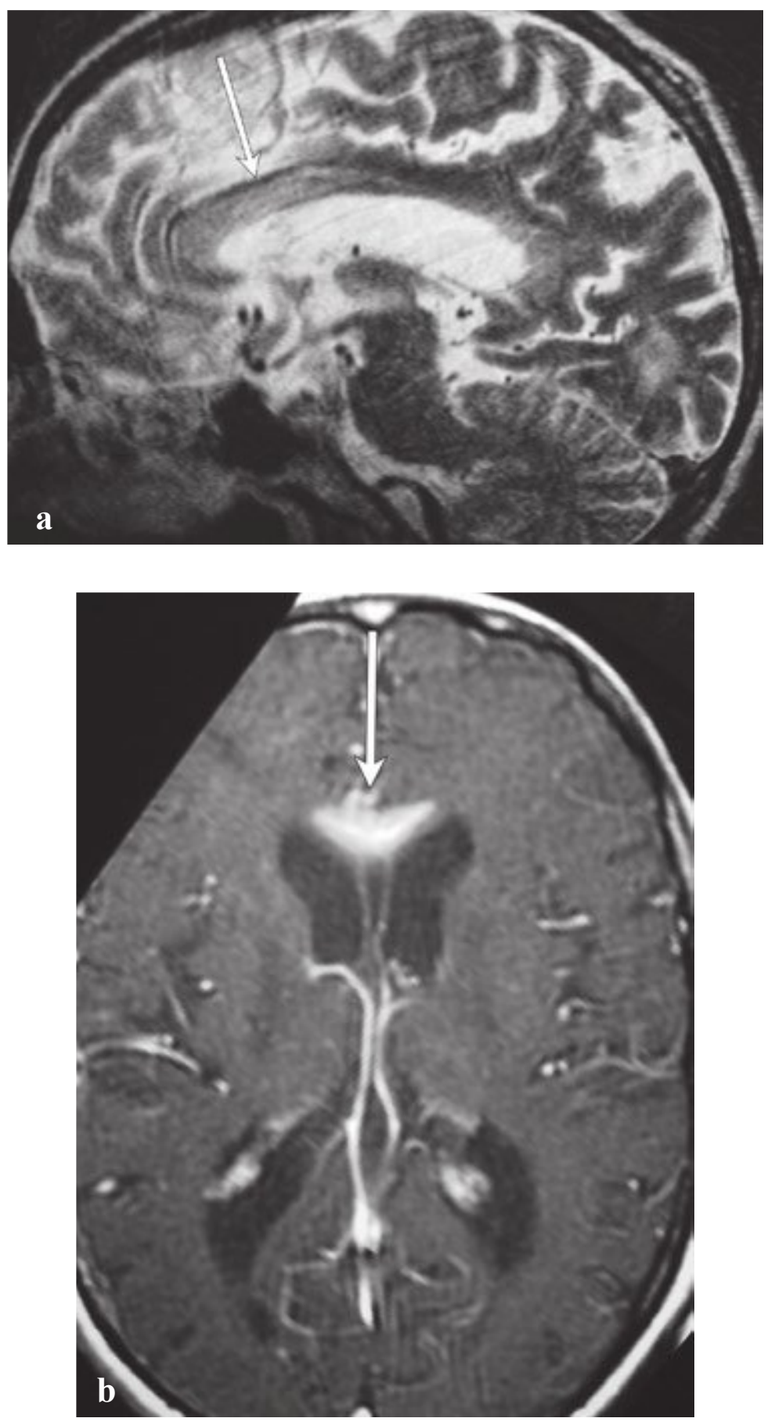

Fig. 1.350 A 59-year-old alcoholic man with Marchiafava-Bignami disease. Poorly defined zones with abnormal high signal on **(a)** sagittal T2WI are seen in the corpus callosum (arrow), with corresponding gadolinium contrast enhancement on **(b)** axial T1WI (arrow).

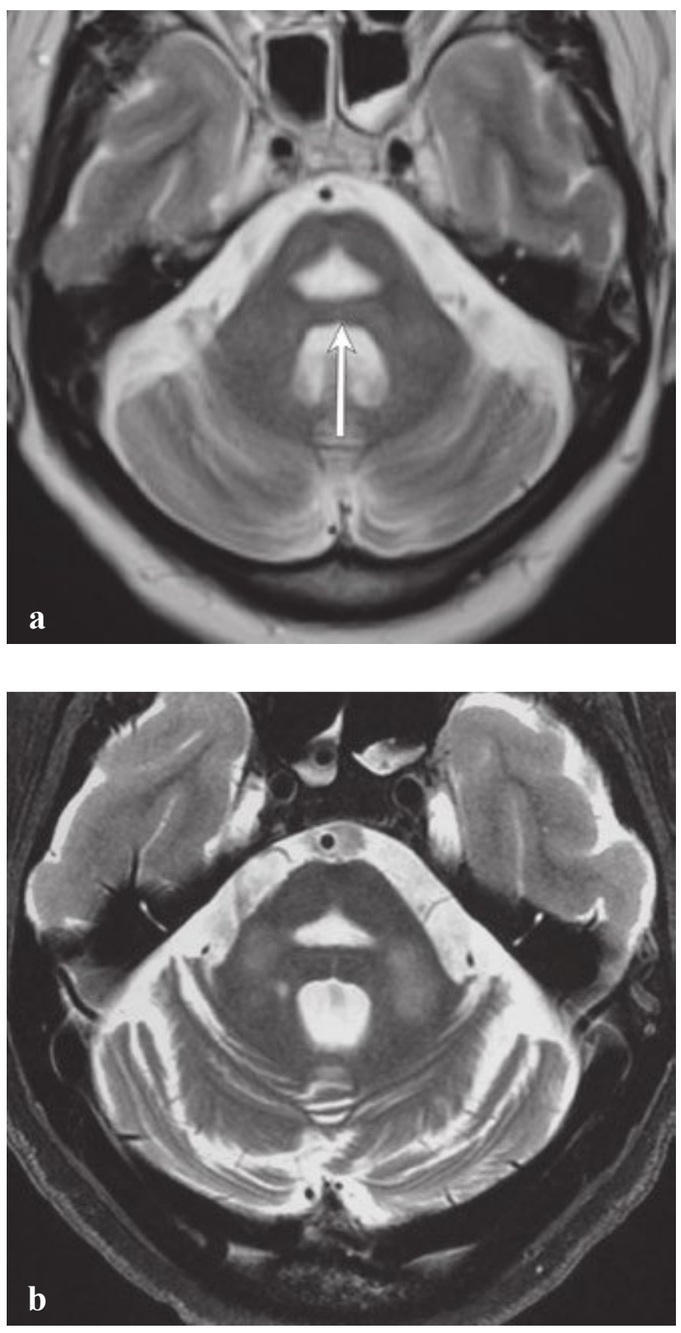

Fig. 1.351 Abnormal high signal on **(a)** axial T2WI is seen in the central portion of the pons (arrow) in a patient with osmotic pontine myelinolysis. **(b)** Axial T2WI obtained 4 weeks later shows persistent abnormal signal in the pons as well as high signal in both middle cerebellar peduncles from Wallerian degeneration involving the fibers of the pontocerebellar tract.

Table 1.7 (cont.) Neurodegenerative disorders

Disorders	Imaging Findings	Comments
Multiple seizures (**Fig. 1.352** and **Fig. 1.353**)	MRI: Zones with restricted diffusion (high signal on diffusion-weighted imaging and low signal on ADC maps) typically occur in the hippocampus (70%), pulvinar-thalamus (25%), and cerebral cortex in patients with status epilepticus, generalized seizures, and febrile seizures. Abnormal increased signal on T2-weighted imaging and FLAIR, as well as gyral swelling, can also be seen in the peri-ictal period. Multiple seizures can result in neuronal degeneration at involved sites, with progressive atrophic changes. Patients with temporal lobe epilepsy and multiple seizures can have mesial temporal sclerosis with hippocampal atrophy (80%unilateral) and abnormal high signal on T2-weighted imaging and FLAIR.	Patients with complex partial seizures and generalized seizures, including status epilepticus, have localized ictal and peri-ictal sites in the brain with increased energy metabolism, hyperperfusion, and cell swelling that typically show restricted diffusion that can be transient. Abnormalities are often bilateral in patients with generalized seizures and status epilepticus, and unilateral in patients with complex partial seizures. Multiple seizures can result in apoptosis and degeneration of neurons with localized atrophy. Multiple seizures involving the temporal lobes can result in mesial temporal sclerosis.
Phenytoin-related cerebellar atrophy (**Fig. 1.354**)	Diffuse, variable degrees of cerebellar atrophy can be seen. Diffusion tensor imaging (DTI) shows no abnormal fractional anisotropy (FA) involving the middle cerebellar peduncles, cerebellum, or transverse pontine fibers.	Long-term use of the antiepileptic drug phenytoin can cause cerebellar atrophy, which can be exacerbated in patients with CYP2C9 mutations, which reduce metabolism of phenytoin.
Paraneoplastic syndrome (**Fig. 1.355**)	MRI: Findings include abnormal high signal on T2-weighted imaging and FLAIR in the limbic system, cerebral white matter, and/or brainstem. Cerebellar degeneration with atrophy is another finding. PET/CT may show hypermetabolic activity at sites of encephalitis as well as primary malignant tumor.	Rare neurological syndromes that result from peripheral immune-mediated responses against autoantigens expressed in tumors (occurs in < 1% of cancers of the lung, breast, ovaries, testicles, and thymus). The effects on the brain are not directly from tumor invasion or metastatic disease. Neural specific autoantibodies include those directed toward ANNA-1, PCA-1, CRMP-5 IgG, VGKC complex proteins, NDMA, and GABA-B receptors. Paraneoplastic disorders involving the brain include limbic and extralimbic encephalitis, brainstem encephalitis, and/or cerebellar degeneration. Antibodies against VGKC complex proteins result in muscle weakness (Lambert-Eaton myasthenic syndrome).

(continued on page 294)

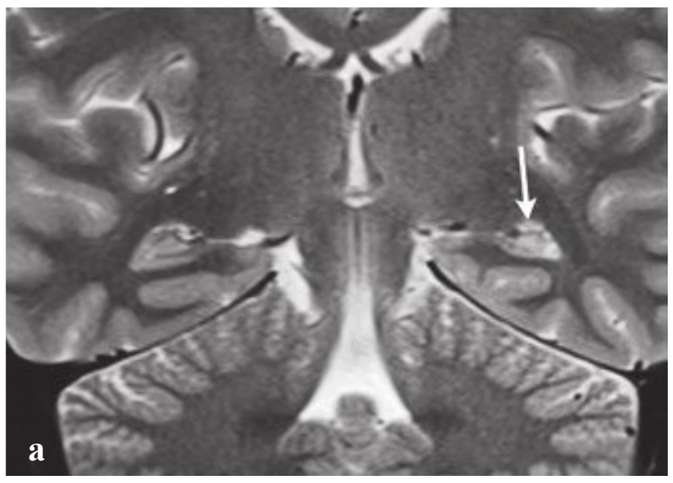

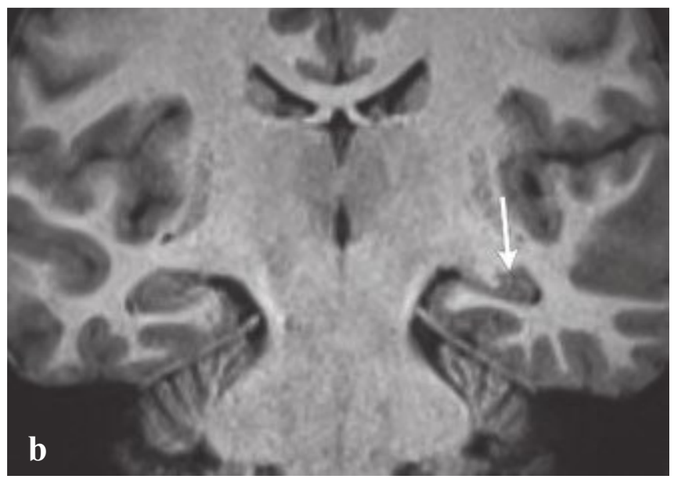

Fig. 1.352 A 49-year-old woman with a history of temporal lobe epilepsy with multiple seizures resulting in left mesial temporal sclerosis. **(a)** Coronal T2WI shows abnormal high signal in the left hippocampus (arrow), which is also smaller relative to the right hippocampus as seen on **(b)** coronal T1WI (arrow).

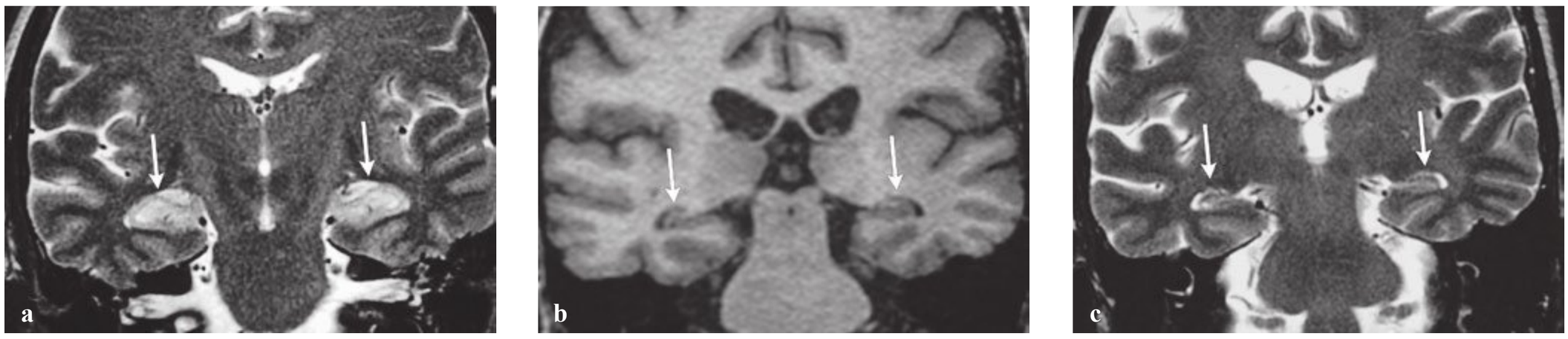

Fig. 1.353 A 56-year-old woman with status epilepticus seen as swelling and diffuse abnormal high signal in both hippocampi on **(a)** coronal T2WI (arrows). Six months later, both hippocampi are atrophied on **(b)** coronal T1WI (arrows) and have persistent high signal on **(c)** coronal T2WI (arrows).

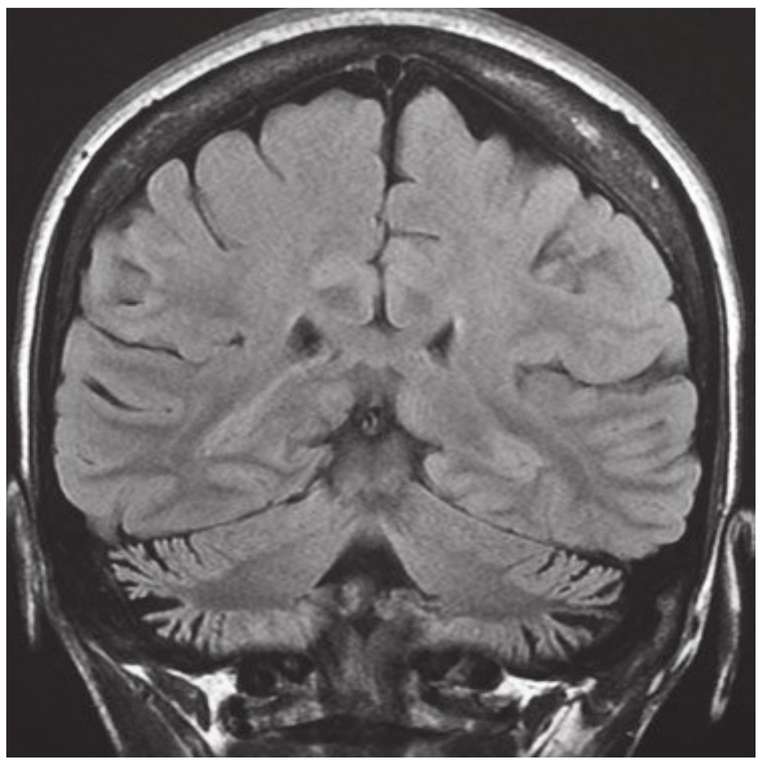

Fig. 1.354 A 39-year-old woman with phenytoin-related cerebellar atrophy as seen on coronal FLAIR.

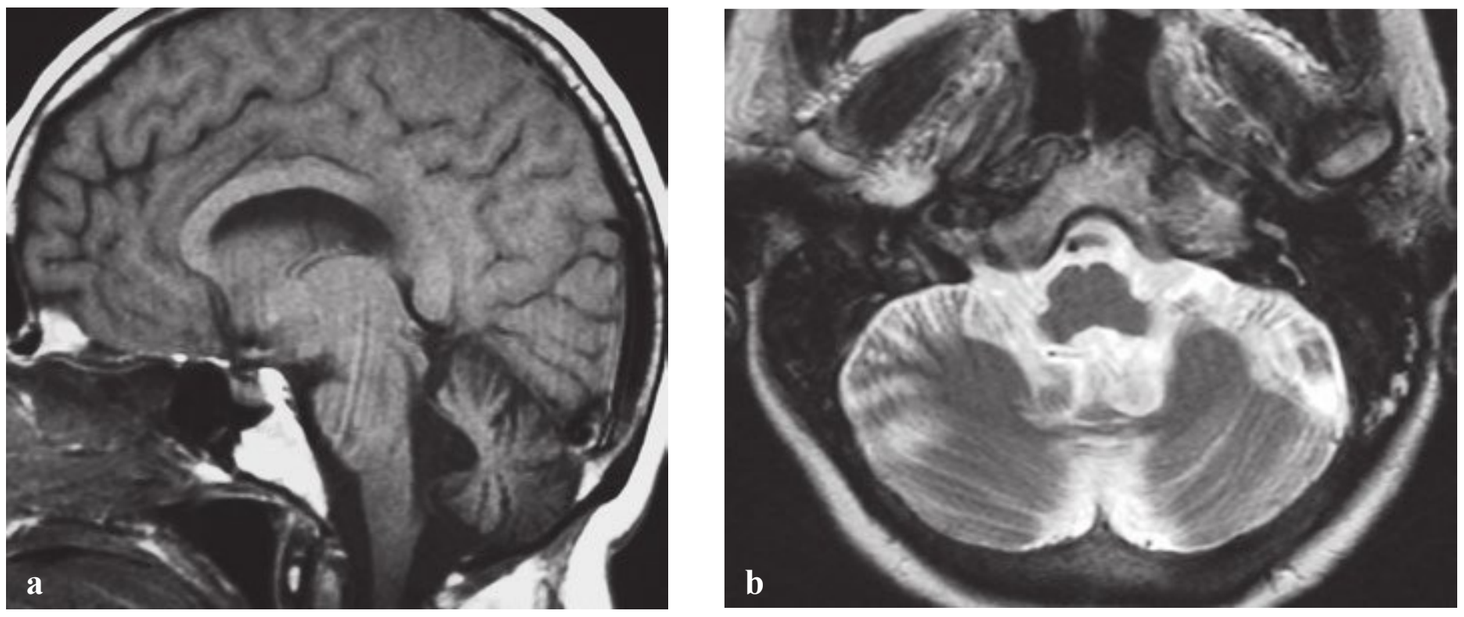

Fig. 1.355 Patient with lung carcinoma and paraneoplastic syndrome resulting in cerebellar atrophy on **(a)** sagittal T1WI and **(b)** axial T2WI.

Table 1.7 (cont.) Neurodegenerative disorders

Disorders	Imaging Findings	Comments
Radiation necrosis (**Fig. 1.356**)	MRI: Focal lesion ± mass effect or poorly defined, intra-axial zone of low-intermediate signal on T1-weighted imaging, intermediate-high signal on T2-weighted imaging, ± gadolinium contrast enhancement involving tissue (white matter and/or gray matter) in the field of radiation treatment. Relative cerebral blood volume (rCBV) values for radiation necrosis (0.6) have been shown to be significantly lower than those for recurrent high-grade gliomas (2.6). Radiation necrosis at sites of surgically resected metastatic lesions may show a three-layer pattern on diffusion-weighted imaging (DWI) consisting of an inner liquefied portion with high ADC, a middle layer with decreased ADC without gadolinium contrast enhancement, and an outer layer with gadolinium contrast enhancement with high ADC. CT: Focal lesion ± mass effect or poorly defined zone of low-intermediate attenuation, ± contrast enhancement involving tissue (gray matter and/or white matter) in field of treatment.	Severe local tissue reaction to radiation treatment, related to doses over 65 Gy. Occurs from 3–6 months to 12 months, and occasionally up to 10 years, after radiation treatment. Occurrence rate is up to three times higher when chemotherapy is given concurrently with radiation treatment. Results from vascular endothelial injury and apoptosis, leading to thrombosis, fibrinous exudates, hyalinization with luminal stenosis, and fibrinoid and vascular necrosis, as well as glial and white matter damage. May be difficult to distinguish from neoplasm. Using dynamic susceptibility contrast-enhanced perfusion MRI, $rCBV_{max}$ and $rCBV_{mean}$ values for recurrent tumor have been shown to be significantly higher than those for tumor necrosis, aiding in distinguishing between the two diagnoses. Similar findings have been found with perfusion computed tomography. Perfusion MRI has been shown to be superior to ^{18}F-FDG PET and ^{11}C-methionine PET in distinguishing high-grade gliomas from radiation necrosis. Magnetic resonance hydrogen spectroscopy shows decreased N-acetylaspartate (NAA) and choline peaks at sites of radiation necrosis, whereas residual and recurrent tumor shows elevated choline peaks and a choline/creatine ratio > 2.
Toxic encephalopathy, late effects (**Fig. 1.357**)	MRI: Symmetric bilateral zones of high signal on T2-weighted imaging in the periventricular cerebral white matter, including the centrum semiovale and corona radiata, ± involvement of the corpus callosum, thalami, globus pallidus, and dentate nuclei. Can progress to brain volume loss.	Can result from effects of medications (vigabatrin for seizures, high doses of metronidazole for infections), chemotherapeutic agents (intrathecal methotrexate), immunosuppressive therapy (tacrolimus, cyclosporine A, etc.), exposure to environmental toxins or illicit drugs, or infectious agents. Pathologic changes include intramyelinic vacuolation, demyelination, cell death, capillary endothelial damage, and encephalomalacia.
Superficial siderosis (**Fig. 1.358**)	MRI: Low signal on T2-weighted imaging, GRE, and susceptibility-weighted imaging along the pial surfaces of the brain, brainstem, and cranial nerves, ± ependymal lining. May be associated with brain atrophy, which often involves the cerebellum.	Deposition of hemosiderin along the pial surfaces of the brain and brainstem results from episodes of hemorrhage within the subarachnoid spaces. Can be secondary to vascular malformations, amyloid angiopathy, trauma, hemorrhagic vasculopathy, hemorrhagic neoplasms, and ruptured aneurysms. Results in toxic effects on brain and cochleovestibular nerves, and can be associated with cranial neuropathies, including hearing loss, gait ataxia, and dysarthria.

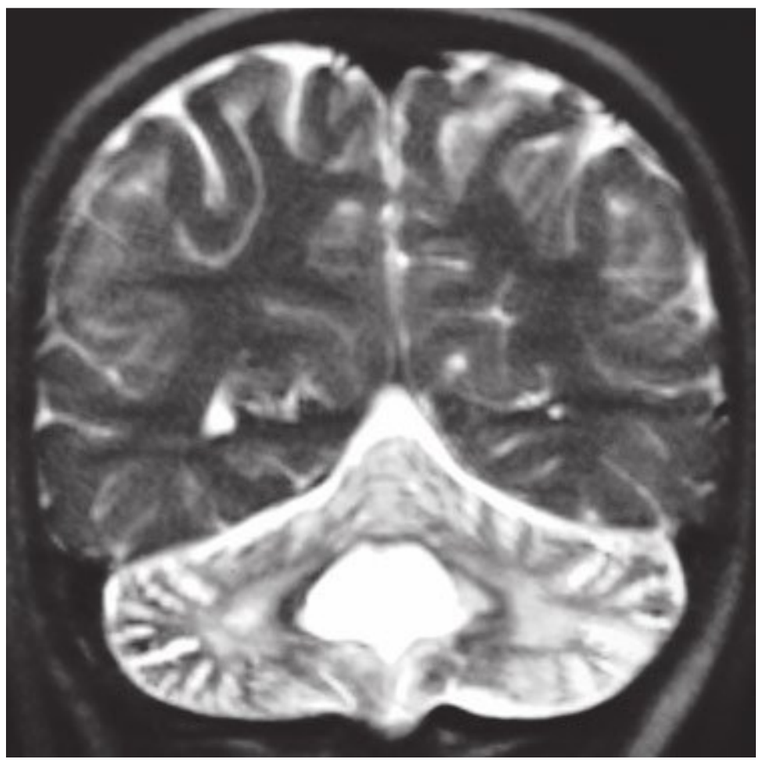

Fig. 1.356 Coronal T2WI shows abnormal high signal in cerebellar white matter associated with encephalomalacia resulting from the late effects of radiation necrosis in this patient who had surgery and radiation treatment for medulloblastoma.

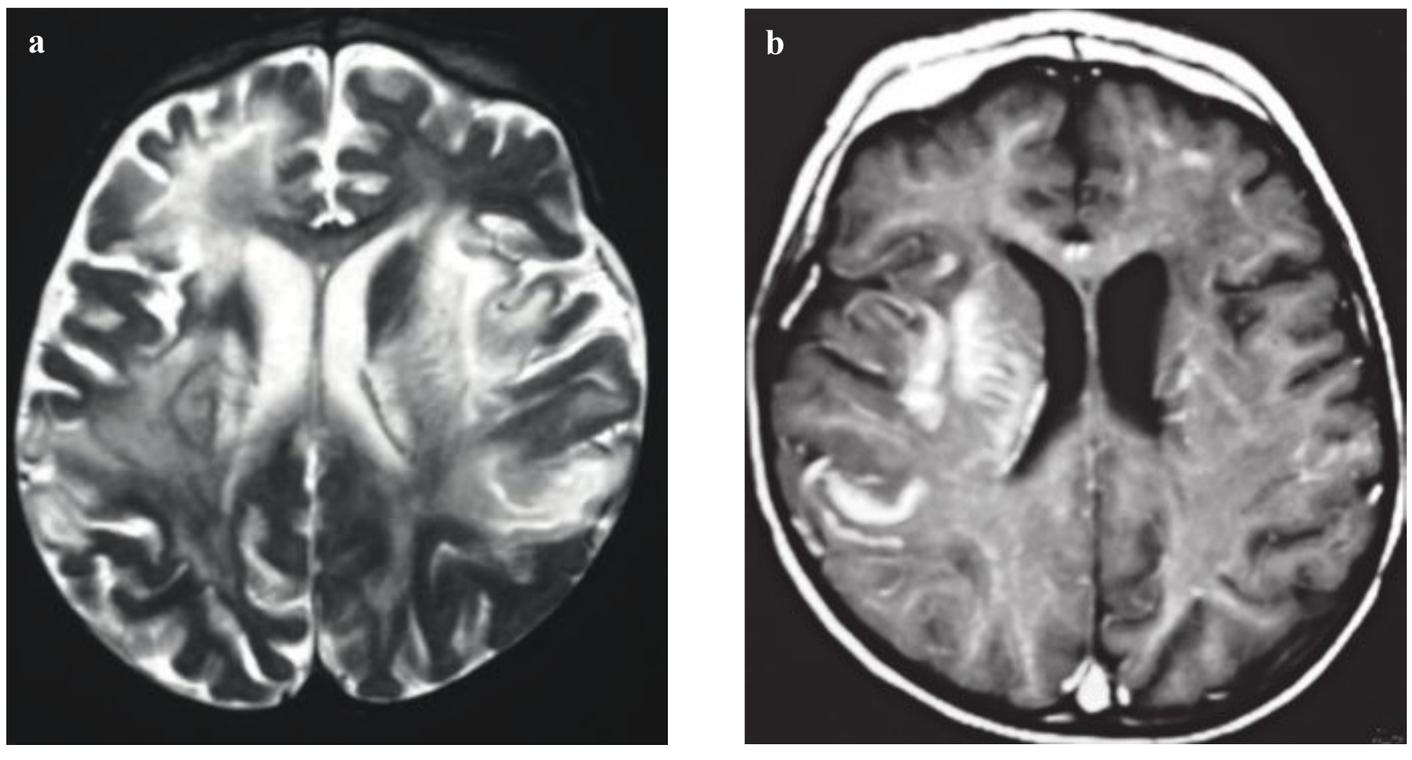

Fig. 1.357 Toxic encephalopathy from cyclosporin A. Poorly defined zones with abnormal high signal on **(a)** axial T2WI and gadolinium contrast enhancement on **(b)** axial T1WI are seen in the cerebral white matter bilaterally in association with cerebral atrophy.

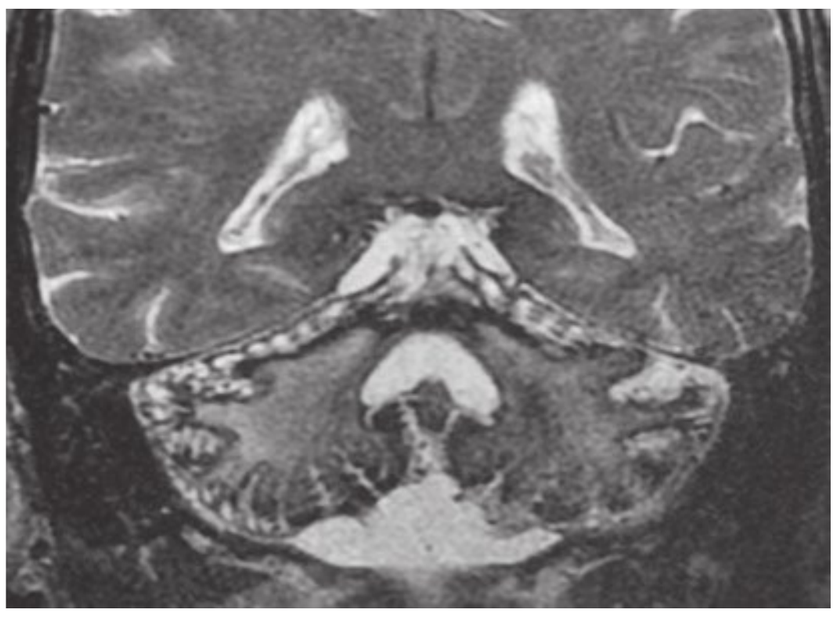

Fig. 1.358 Coronal T2WI in a patient with superficial siderosis shows low signal along the pial and ependymal surfaces of the cerebellum associated with encephalomalacia.

1.8 Ischemia and Infarction Involving the Brain and/or Brainstem in Adults

Overview of Cerebral Blood Flow and Perfusion

Of the various human body tissues, the brain is the least tolerant of ischemia. Lack of sufficient blood flow to the brain for ~ 5 seconds results in loss of consciousness, and after several minutes it can result in irreversible cerebral ischemia and infarction. For normal brain function, cerebral blood flow must be maintained at a constant rate to deliver oxygen and glucose as well as to remove CO_2 and metabolic waste products. Constant blood flow to the brain can be defined using cerebral perfusion pressure (CPP), which is the mean arterial pressure (MAP), defined as diastolic blood pressure plus ⅓ (systolic blood pressure – diastolic pressure), minus the intracranial pressure (ICP, pressure within the skull): CPP = MAP – ICP. Normal CPP values for adults are 70 to 100 mm Hg, and for children, 40 to 60 mm Hg. Normal values for ICP are < 10 to 15 mm Hg in adults, 3 to 7.5 mm Hg in children, 1.5 to 6 mm Hg in infants, and 0.7 to 1.5 mm Hg in neonates. In adults, when CPP is abnormally reduced below 50 mm Hg, cerebral ischemia occurs, with progressive loss of neuronal electrical activity.[1,2,3]

Terminology needed in clinical practice for measuring cerebral perfusion, cerebral blood volume (CBV), cerebral blood flow (CBF), and mean transit time (MTT) is defined below:

- Cerebral perfusion is a generic term describing the amount or level of blood flow to and within the brain. Intracranial blood flow can be further characterized using parameters like CBV, CBF, and MTT.[1]
- Cerebral blood volume (CBV) is defined as the total volume of blood in a volume of brain tissue, including arterioles, capillaries, and venules, as well as arteries and veins (milliliters of blood per 100 g of brain tissue).[1,3]
- Cerebral blood flow (CBF) is the volume of blood moving though a volume of brain tissue per unit time (milliliters of blood per 100 g of brain tissue per minute). Normal CBF ranges from 50 to 60 mL/100 g/min.[1,2,3]
- Mean transit time (MTT) is defined as the average transit time of blood through a region of brain tissue (in seconds).[3]

The relationship of CBF to CBV and MTT can be shown by the equation

$$CBF = CBV/MTT.$$

The relationship of CBF to CPP is shown by the equation

$$CBF = CPP/CVR$$

where CVR is cerebrovascular resistance. CVR is related to myogenic resistance of blood vessels (mostly those 100 to 250 microns in diameter), neurogenic factors related to sympathetic and parasympathic innervation of cerebral blood vessels, metabolic factors (blood levels of CO_2, O_2, lactate) and ICP, which is related to jugular venous pressure and CBV.[3]

Normal blood perfusion parameters for brain tissue			
	CBF	CBV	MTT
Gray matter	60 mL/100 g/min	4 mL/100 g	4 s
White matter	25 mL/100 g/min	2 mL/100 g	4.8 s

Maintenance of Cerebral Blood Flow by Cerebrovascular Reactivity

Constant rates of cerebral blood flow (CBF), enabling proper neurochemical function and neurologic electrical activity, are maintained over various systemic blood pressures by mechanisms referred to as autoregulation or cerebrovascular reactivity.[3,4] As described previously, CBF = CPP/CVR (cerebrovascular resistance). Cerebral autoregulation is mediated by three mechanisms (*myogenic, metabolic,* and *neurogenic)* that modulate CVR, allowing maintainance of CBF over a range of CPPs and MAPs.[3] Resistance to blood flow in the brain mediated by myogenic mechanisms predominantly involves the reaction of small arterioles (100 to 250 microns in diameter) in the brain to changes in intracranial pressure. When systemic blood pressure decreases, vascular resistance in these small blood vessels also decreases due to vasodilatation, resulting in maintenance of CBF and CPP, as well as increased cerebral blood volume (CBV).[4] Myogenic control has been proposed to be secondary to changes in activation states of K and Ca channels in cell membranes affecting cell membrane polarization with changes in blood pressure as well as alterations in activity of phospholipases and protein kinase C.[3]

The second mechanism, metabolic changes that can directly affect the myogenic tone of arterioles, causing vasodilatation, include: elevated CO_2 levels in blood; reduced O_2 levels, causing increased membrane potentials of smooth muscle via opening of Ca-activated K and ATP-K membrane channels; elevated levels of lactate and decreased pH; elevated levels of nitric oxide produced by endothelial cells, causing smooth muscle relaxation; and elevated adenosine levels from ATP catabolism.[3] Conversely, decreased levels of CO_2 result in vasoconstriction.

The neurogenic mechanism of intracranial vasodilatation or vasoconstriction functions by synchronized and balanced vasoactive mechanisms involving the extracerebral pial arteries (sympathetic fibers from the superior cervical ganglion mediated by norepinephrine and neuropeptide Y, which is predominantly involved in vasoconstriction; parasympathetic fibers from the sphenopalatine and otic ganglia stimulated by vasoactive intestinal peptide, acetylcholine, and nitric oxide and primarily involved in vasodilatation; as well as sensory fibers from the trigeminal ganglion affecting release of calcitonin gene-related peptide, causing vasodilatation). An additional neurogenic mechanism of cerebrovascular resistance involves the intracerebral arterioles through function of a neurovascular unit composed of intracranial arteries, arterioles, capillaries, nerves, astrocytes, and pericytes.[3] This intracerebral

neurovascular unit is innervated by subcortical neurons that project to the intracerebral arterioles and surrounding astrocytes from the raphe nucleus of the brainstem (associated with serotonin-induced vasoconstriction), basal forebrain (with gamma-aminobutyric acid–mediated vasodilatation), thalamus, and locus ceruleus (with noradrenergic neurons on perivascular astrocytes).[3] Vasoactive neurotransmitters (acetylcholine, gamma-aminobutyric acid, and dopamine) can also cause localized vasodilatation at the neurovascular unit of the intracerebral arterioles.[3] These protective mechanisms of cerebrovascular reactivity maintain CBF and CPP when MAP ranges from 50 to 60 mm Hg up to 150 to 160 mm Hg.[1,2,3] In hypotension and mildly decreased CPP, additional compensatory mechanisms, such as increased nutrient and oxygen extraction from blood, maintain cellular function.[3,4] When CPP has decreased beyond the limit of maximal oxygen extraction and maximal vessel dilatation, continued decreased systemic blood pressure results in decreased oxygen consumption by, and nutrient delivery to, the brain, causing syncope and loss of cellular viability.[4]

In the opposite situation, when systemic blood pressure increases, vascular resistance in small blood vessels increases, resulting in maintenance of CBF and CPP, as well as decreased CBV.[3,4] When MAP exceeds 150 to 160 mm Hg, there is, however, abnormal alteration in the permeability of the blood–brain barrier, resulting in cerebral edema. In the early phases of cerebral arterial hypertension, edematous changes predominantly involve the white matter supplied by the posterior circulation, often referred to as posterior reversible encephalopathy syndrome (PRES).[5] The greater earlier involvement of the posterior compared with the anterior circulation seen with PRES is related to a lesser degree of sympathetic innervation in the vertebrobasilar system than in the anterior circulation, allowing a lower capacity for cerebrovascular autoregulation with cerebral arterial hypertension.[5] Continued increases in cerebral arterial hypertension cause eventual edematous changes in the anterior circulation structures.[5]

Levels of Impaired Cerebral Blood Flow Causing Brain Ischemia and Infarction

Maintenance of CBF is critical for neuronal function. With arterial occlusion, loss of normal neuronal electrical activity occurs within seconds.[2] Cell death is dependent on the duration and magnitude of ischemia, metabolic vulnerability of specific anatomic sites, and the oxygen content of blood.[4] Normal CBF ranges from 50 to 60 mL/100 g/min. When the CBF is reduced to 15 to 20 mL/100 g/min for several hours (mild–moderate hypoxia), spontaneous and evoked neuronal electrical activity decreases significantly secondary to ischemia, although it can be reversed by reperfusion with CBF above 50 mL/100 g/min.[2,3] With severe hypoxia/anoxia resulting from CBF below 10 mL/100 g/min, cellular membrane depolarization and ischemia leading to brain infarction may occur in several minutes.[2,3] In these cases of severe hypoxia, brain ischemia occurs from the switch of effective energy utilization within cells from oxidative phosphorylation to the inefficient process of anaerobic metabolism, resulting in depletion of cellular ATP.[2,3,6] Depletion of ATP within cells results in lactate accumulation as well as loss of membrane electrical potential (depolarization).[2,6] Cellular membrane depolarization causes a cascade of adverse events (release of glutamate into the extracellular space; activation of membrane receptors, such as *N*-methyl-D-aspartate receptors, α-amino-3-hydroxy-5-methyl-4-isoxazole proprionic acid, and kainite; influx of calcium and sodium ions associated with cytotoxic edema; activation of proteolytic enzymes; production of free radicals; disruption of mitochondrial membranes; lipolysis; and proteolysis) that eventually leads to necrosis and/or apoptosis (programmed cell death).[2,6] After the initial drop in CBF below 10 mL/100 g/min, impairment of the Na,K-ATPase pump within cellular membranes, causing membrane depolarization, results in cytotoxic edema that is associated with an exponential decrease in ADC within a few minutes and later with an increase in net water content (ischemic edema) after 30 minutes.[7] On CT, the early ischemic signs of net water content in infarcts occur later and appear smaller in extent than they do in infarcts visualized by MRI using ADC maps.[7]

When thrombotic or embolic arterial occlusions occur, CBF in the involved brain tissue is usually heterogeneous, with a central core showing the greatest reductions in CBF and causing irreversible cell damage and infarction, and a surrounding zone (referred to as the *salvageable penumbra*) that may have moderate reduction in CBF, resulting in ischemia that may be reversible with reperfusion. The penumbra typically shows loss of neuronal electrical activity without immediate anoxic depolarization, as well as loss of autoregulation.[2,7] If reperfusion does not occur, the penumbra will progress to infarction.[2,7] An *oligemic zone* of mildly reduced CBF may also be seen surrounding the penumbra; the oligemic zone is less vulnerable to infarction than the penumbra. Thrombolytic medication can be useful and beneficial when it results in timely reperfusion of the penumbra and oligemic zone. Estimating the sizes of the penumbra and oligemic zone can be done with dynamic contrast-enhanced CT and/or MRI perfusion techniques.[1,2] CT perfusion uses iodinated contrast delivered as an intravenous bolus; the linear relationship between contrast concentration and attenuation allows direct calculation and quantification of CBF, CBV, and MTT.[1,2] MRI perfusion techniques use intravenous infusion of paramagnetic gadolinium contrast agents; measurement of the dynamics of the T2* shortening enhancement effects as the contrast agent passes through the capillary bed allows indirect estimation of the relative values of CBF, CBV, and MTT.[1,2] Therefore, there is no easy and reliable way to calculate CBF and CBV from perfusion MRI, unlike with perfusion CT.[1,2]

Stages of pathologic changes associated with cerebral infarction have been described.[2] In the first 2 days, no gross pathologic changes are seen. The infarcted cells, however, show pyknosis and swelling. Diffusion-weighted imag-

ing (DWI) MRI shows restricted diffusion due to cytotoxic edema caused by intracellular accumulation of sodium and water related to the cellular membrane depolarization that occurs minutes after infarction.[2] Overall tissue water content at the site of infarction increases ~ 3 to 5%[2] From 4 to 6 hours to 3 to 5 days after the ischemic insult, the capillary endothelium of the brain vasculature loses its ability to maintain the blood–brain barrier, which results in vasogenic edema at the infarct.[2] After ~ 2 days, necrosis of the full thickness of the cerebral cortex occurs, resulting in protein denaturation, paramagnetic compounds (such as manganese ions), and macrophage-produced free radicals.[8] From 3 to 10 days after infarction, swelling and softening of the infarcted brain tissue is observed in gross specimens. Maximal edema is seen at 3 to 5 days. Neurons, microglia cells, astrocytes, and oligodendrocytes show cellular and membrane breakdown. Encephalomalacia and gliosis are seen weeks to months afterward.

References

1. Shetty SK, Lev MH. CT perfusion in acute stroke. Neuroimaging Clin N Am 2005;15(3):481–501, ix
2. Marks MP. Cerebral ischemia and infarction. In: Atlas SW, ed. Magnetic Resonance Imaging of the Brain and Spine. 4th ed. Philadelphia: Lippincott Williams & Wilkins; 2009:772–825
3. Franco Folino A. Cerebral autoregulation and syncope. Prog Cardiovasc Dis 2007;50(1):49–80
4. Eskey CJ, Sanelli PC. Perfusion imaging of cerebrovascular reserve. Neuroimaging Clin N Am 2005;15(2):367–381, xi
5. Covarrubias DJ, Luetmer PH, Campeau NG. Posterior reversible encephalopathy syndrome: prognostic utility of quantitative diffusion-weighted MR images. AJNR Am J Neuroradiol 2002;23(6):1038–1048
6. Huang BY, Castillo M. Hypoxic-ischemic brain injury: imaging findings from birth to adulthood. Radiographics 2008;28(2):417–439, quiz 617
7. Kucinski T. Unenhanced CT and acute stroke physiology. Neuroimaging Clin N Am 2005;15(2):397–407, xi–xii
8. Kinoshita T, Ogawa T, Yoshida Y, Tamura H, Kado H, Okudera T. Curvilinear T1 hyperintense lesions representing cortical necrosis after cerebral infarction. Neuroradiology 2005;47(9):647–651

Table 1.8 Ischemia and infarction involving the brain and/or brainstem in adults

- Adults
  - Ischemic strokes from arterial stenosis or occlusion
- Infarcts from Occlusion of Large and Medium-Size Arteries
  - Atherosclerotic-thrombotic and embolic hyperacute and acute infarcts
  - Atherosclerotic-thrombotic and embolic subacute infarcts
  - Remote atherosclerotic-thrombotic and embolic infarcts
  - Cardioembolic stroke
- Small-Vessel or Lacunar Infarction
- Hypoxic-Ischemic Injuries in Adults
  - Severe hypoxic-ischemic injuries in adults
  - Mild-moderate hypoxic-ischemic injuries in adults
- Sinovenous Infarction in Adults

Table 1.8 Ischemia and infarction involving the brain and/or brainstem in adults

Lesion/Disorder	Imaging Findings	Comments
Ischemic strokes from arterial stenosis or occlusion		In adults, cerebral and cerebellar infarcts most frequently result from stenosis or occlusion of arteries (in atheromatous or cardioembolic disease) that causes absent or severely reduced blood flow to selected portions of brain tissue, producing focal or regional ischemia/infarction. Approximately 80% of strokes in adults are ischemic cerebral infarctions caused by arterial occlusions or stenoses. Risk factors include hypertension, cardiac and peripheral vascular disease, diabetes mellitus, tobacco smoke exposure, hyperlipemia, and hypercholesterolemia. There are three major categories of stroke caused by arterial disease: infarction from atherosclerotic stenosis/occlusion of large and/or medium arteries, accounting for 15 to 40%; cardioembolic infarctions, accounting for 15 to 30%; and small-vessel or lacunar infarctions, accounting for 15 to 30%. In adults, brain hypoperfusion from cardiac arrest and/or severe prolonged hypotension can also result in ischemia that involves most of the brain, which is referred to as global ischemia. Cell death from ischemia typically results from ischemic necrosis.

Lesion/Disorder	Imaging Findings	Comments
Infarcts from Occlusion of Large and Medium-Size Arteries		
Atherosclerotic-thrombotic and embolic hyperacute and acute infarcts (**Fig. 1.359, Fig. 1.360, Fig. 1.361, Fig. 1.362**, and **Fig. 1.363**) Hyperacute infarct (< 12 hours on CT) Acute infarct (12–24 hours on CT) Hyperacute infarct (< 3 hours on MRI) Acute infarct (< 12 hours on MRI) Acute infarct (12–24 hours on MRI)	CT: Hyperacute infarct (< 12 hours): • Decreased attenuation in lentiform nuclei from edema associated with loss of definition at margins with the internal and external capsules (**Fig. 1.360a**), and involving the insular cortex, loss of the insular ribbon sign (thickening with obscuration and decreased attenuation of the thin, hyperdense band of insular cerebral cortex relative to the adjacent external capsule [**Fig. 1.360b**]). • Hyperdense artery (25 to 50%) secondary to intravascular blood clot, red thrombus, which has HU values of 60 to 90, compared with unclotted blood with HU values of 30 to 60 (**Fig. 1.360c**). Sensitivity of this sign has been reported to range from 5 to 50%. • No apparent findings on CT in some cases. • On CT cerebral perfusion, CBF is reduced to 15 to 20 mL/100 g/min for several hours or is below 10 mL/100 g/min for several minutes (**Fig. 1.361**). Acute infarct (12–24 hours): • Decreased attenuation in the basal ganglia. • Indistinctness at borders between cerebral cortex and adjacent white matter. • Subtle decrease in attenuation in brain involving the vascular distribution of the infarct, with or without localized edema and sulcal effacement. MRI: Hyperacute infarct (< 3 hours): • Exponential decrease in ADC at infarct after several minutes, with high signal on diffusion-weighted imaging and low signal on ADC maps. • Absence of flow void in occluded artery. • Intravascular contrast enhancement. • Magnetic resonance spectroscopy can show elevated lactate peak at 1.32 ppm, with or without a slight decrease in N-acetylaspartate (NAA) at 2.02 ppm. Acute infarct (< 12 hours) • High signal on diffusion-weighted imaging and low signal on ADC maps (**Fig. 1.359** and **Fig. 1.363**). • Slightly decreased signal on T1-weighted imaging at infarct in an arterial distribution. • Indistinctness at borders between cerebral cortex and adjacent white matter. • Subtle localized edema and sulcal effacement. Acute infarct (12–24 hours): • High signal on diffusion-weighted imaging and low signal on ADC maps. • Increase in signal at infarct on proton density-weighted imaging, T2-weighted imaging, and FLAIR. • Localized mass effect. • Gadolinium contrast enhancement at adjacent leptomeninges (**Fig. 1.362**).	Atherosclerotic plaques are the most common cause of large-artery strokes, which result from thrombotic occlusion locally or from embolic plaque that lodges downstream. Atherosclerotic plaques are commonly located at the upper common carotid arteries in the neck, carotid artery bifurcations, proximal portions of the internal carotid arteries, carotid artery siphons, proximal portions of the anterior and middle cerebral arteries, upper portions of the vertebral arteries, and basilar artery. Infarcts secondary to occlusion of large arteries most frequently involve the middle cerebral artery. These infarcts usually result from atheromatous emboli or cardiac emboli. Other etiologies for large-artery strokes include infectious arteritis (bacterial, tuberculous, fungal, viral), noninfectious arteritis or vasculopathy (systemic lupus erythomatosus, scleroderma, systemic necrotizing vasculitis, rheumatoid arthritis, sarcoid, giant cell arteritis, and Wegener's granulomatosis), arterial dissection (traumatic, fibromuscular dysplasia, connective tissue disorders, such as Marfan syndrome, Ehlers-Danlos syndrome, etc.), and hypercoagulable states (deficiencies of protein C, protein S, or antithrombin III; sickle-cell disease; dehydration; paraneoplastic syndromes; leukemia).

(continued on page 302)

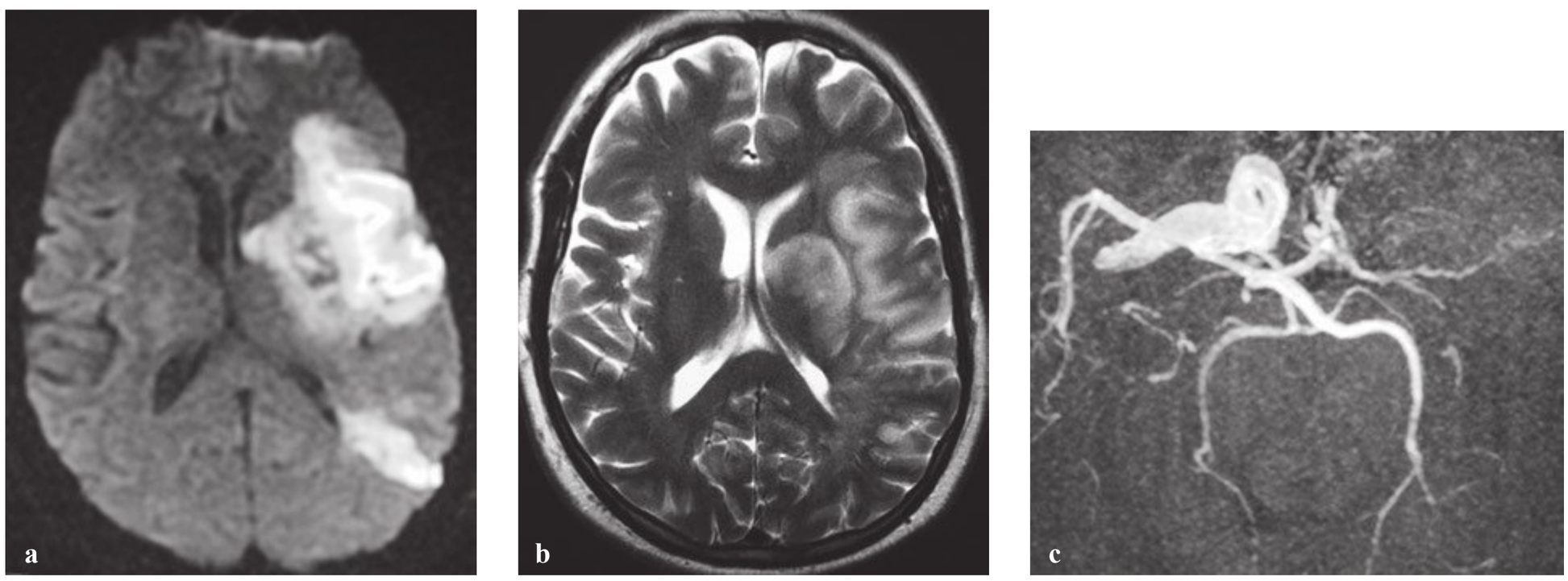

Fig. 1.359 A 57-year-old man with an acute infarct in the left cerebral hemisphere in the vascular distribution of the left middle cerebral artery seen as restricted diffusion on **(a)** axial DWI and **(b)** high signal on T2WI secondary to occlusion of the left middle cerebral artery on **(c)** axial 3D time-of-flight (TOF) magnetic resonance angiography (MRA).

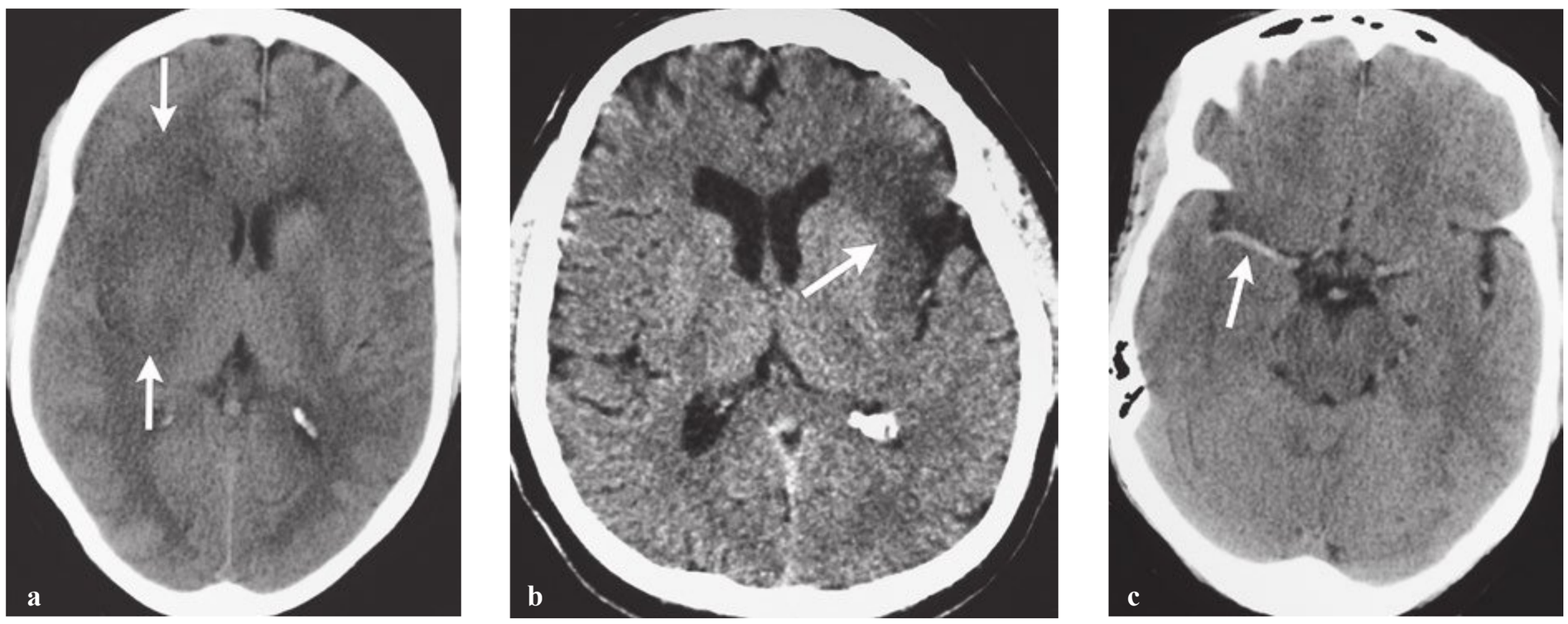

Fig. 1.360 CT findings of acute cerebral infarction. **(a)** Axial CT shows poorly defined decreased attenuation in the right frontal lobe with loss of differentiation of the basal ganglia from the adjacent white matter (arrows). **(b)** CT shows the insula ribbon sign on the left (arrow). **(c)** CT shows a hyperdense right middle cerebral artery (arrow).

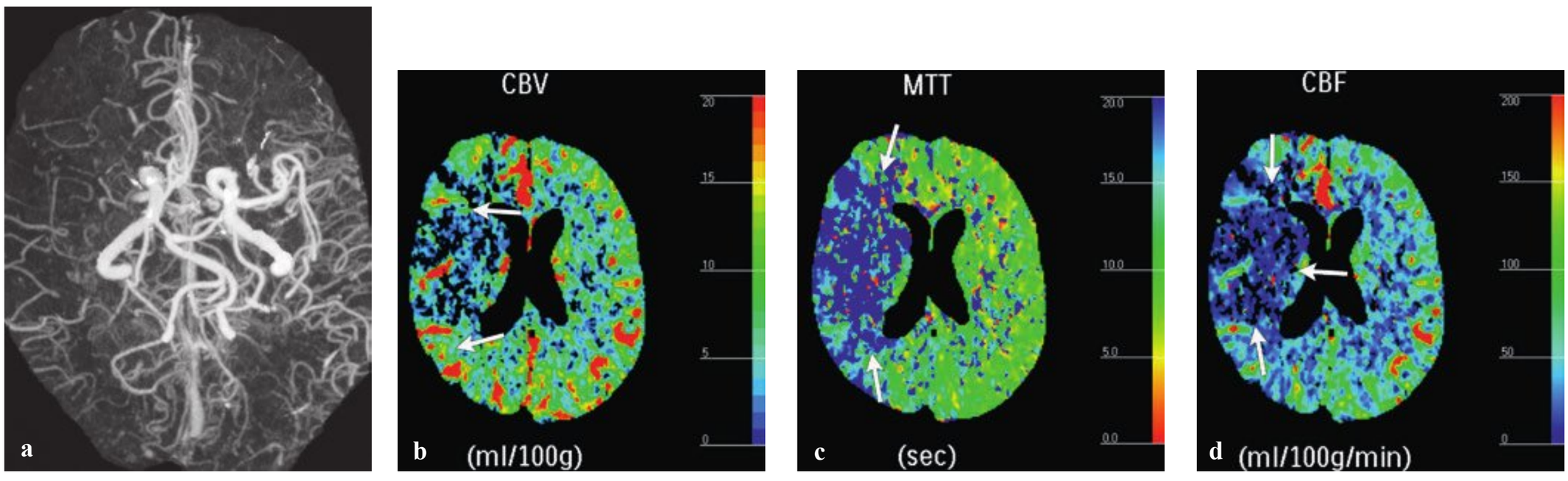

Fig. 1.361 A 69-year-old man with right cerebral infarct from near complete occlusion of the right middle cerebral artery as seen on **(a)** axial CTA with only minimal blood flow in only some of the sylvian branches. Cerebral perfusion study shows **(b)** reduced CBV, **(c)** increased MTT, and **(d)** reduced CBF at the site of infarction (arrows).

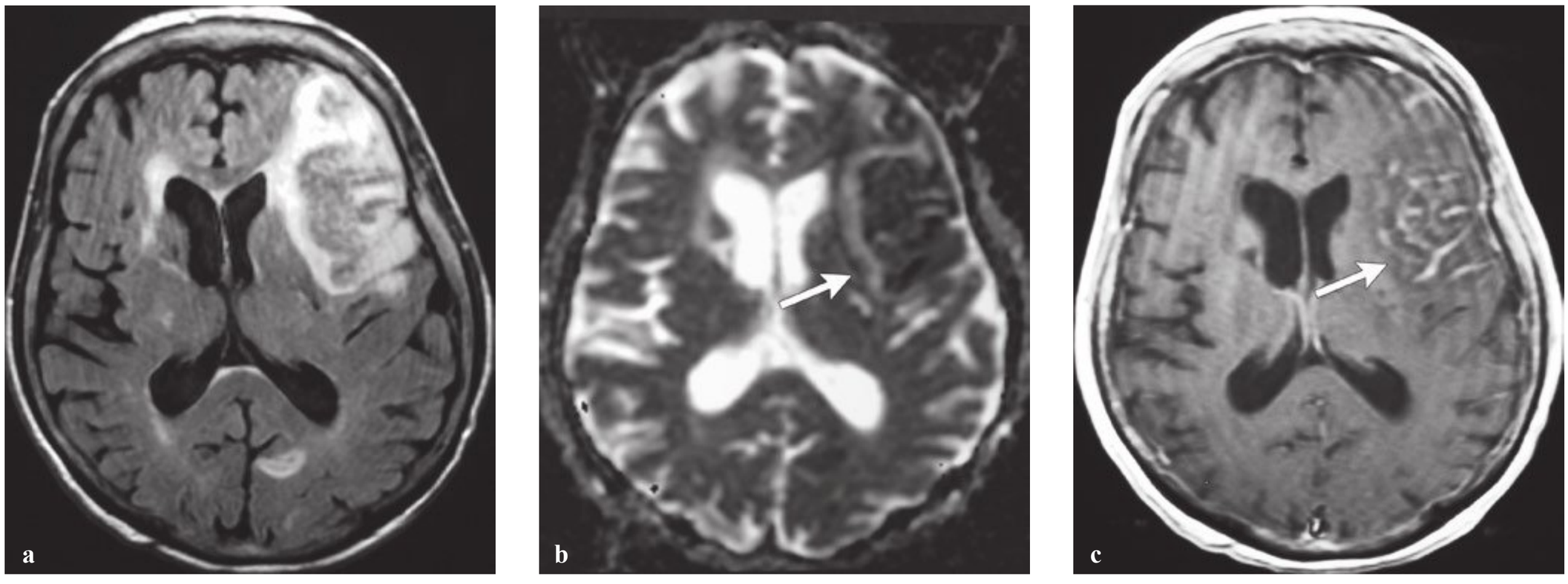

Fig. 1.362 Acute left cerebral infarct that has high signal on **(a)** axial FLAIR, restricted diffusion (arrow) on **(b)** axial ADC, and leptomeningeal gadolinium contrast enhancement (arrow) on **(c)** axial T1 WI (arrow).

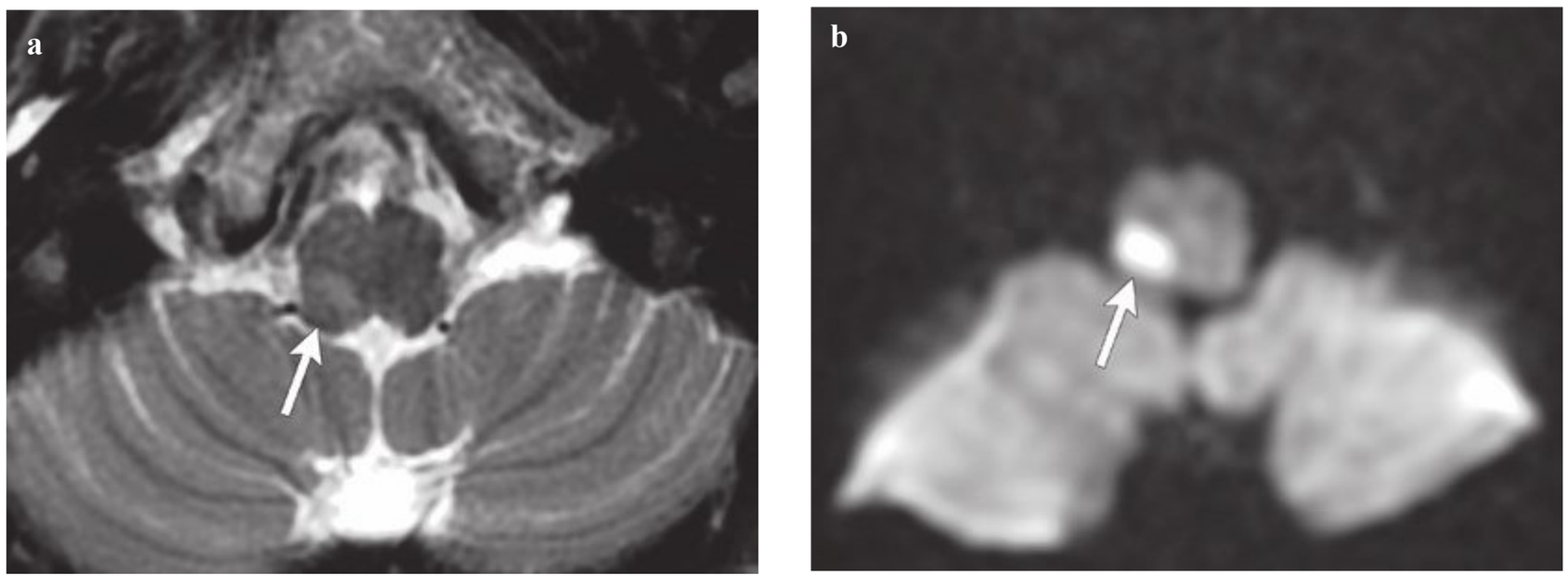

Fig. 1.363 A 58-year-old woman with acute infarct in the posterior-lateral right medulla that has high signal on **(a)** axial T2 WI (arrow) and restricted diffusion on **(b)** axial DWI (arrow).

Table 1.8 (cont.) Ischemia and infarction involving the brain and/or brainstem in adults

Lesion/Disorder	Imaging Findings	Comments
Atherosclerotic-thrombotic and embolic subacute infarcts (**Fig. 1.364, Fig. 1.365, Fig. 1.366, Fig. 1.367, Fig. 1.368, Fig. 1.369**, and **Fig. 1.370**) Early subacute infarct (1–3 days on CT) Subacute infarct (4–7 days on CT) Late subacute infarct (1–7 weeks on CT) Early subacute infarct (1–3 days on MRI) Subacute infarct (4–7 days on MRI) Late subacute infarct (1 to 3–4 weeks on MRI)	CT: Early subacute infarct (1–3 days): • Zone of decreased attenuation at infarct becomes more conspicuous. • Increase in edema and localized mass effect associated with infarct (peaks at 3–4 days). • Hemorrhagic transformation may occur at infarct. Subacute infarct (4–7 days): • Mass effect and edema associated with infarct persist. • Hemorrhagic transformation may occur at infarct. • Gyral pattern of contrast enhancement may be seen (**Fig. 1.365**). Late subacute infarct (1–7 weeks): • Progressive decrease of localized mass effect and edema. • Slight increase in attenuation of hypodense lesion and blurring of margins; fogging effect secondary to macrophage invasion and proliferation of capillaries. • Persistence of contrast enhancement at the infarct. • Dystrophic calcifications may be seen, more commonly in children than in adults. • High attenuation along cortex secondary to laminar necrosis (**Fig. 1.370**). MRI: Early subacute infarct (1–3 days): • High signal on diffusion-weighted imaging and low signal on ADC maps. • Progressive increase in abnormal signal at infarct on proton density-weighted imaging, T2-weighted imaging, and FLAIR. • Increase in edema and localized mass effect associated with infarct (peaks at 3–4 days). • Early gadolinium contrast enhancement may be seen at the infarct. • Hemorrhagic transformation may occur at infarct (**Fig. 1.364**). • Gadolinium contrast enhancement at meninges and within blood vessels declines. Subacute infarct (4–7 days): • Infarct has high signal on proton density-weighted imaging, T2-weighted imaging, FLAIR, and diffusion-weighted imaging, and low signal on ADC maps. • Increased gadolinium contrast enhancement may be seen at infarct (**Fig. 1.366, Fig. 1.367**, and **Fig. 1.368**). • Progressive decrease in localized mass effect and edema. • Hemorrhage may be seen in 25% of cases. • Resolution of intravascular and meningeal gadolinium contrast enhancement. Late subacute infarct (1 to 3–4 weeks): • Infarct has high signal on proton density-weighted imaging, T2-weighted imaging, and FLAIR. At 2 weeks, diffusion-weighted imaging may show high signal from T2 shine-through effects, and ADC maps do not show low signal at infarcts, indicating absence of restricted diffusion that was seen during the first 2 weeks. • Progressive decrease in localized mass effect and edema. • Persistence of contrast enhancement at the infarct. • After 2 weeks, curvilinear thin zones in the cerebral cortex can be seen with high signal on T1-weighted imaging; they represent cortical laminar necrosis (**Fig. 1.369**), which can become progressively more prominent at 1 to 2 months and persist up to 1.5 years. The high signal may be secondary to cortical necrotic changes of protein denaturation, paramagnetic compounds (such as manganese ions), and macrophage-produced free radicals. • Dystrophic calcifications may be seen as zones of low signal on T2-weighted imaging, more commonly in children than in adults (**Fig. 1.370**).	

(continued on page 306)

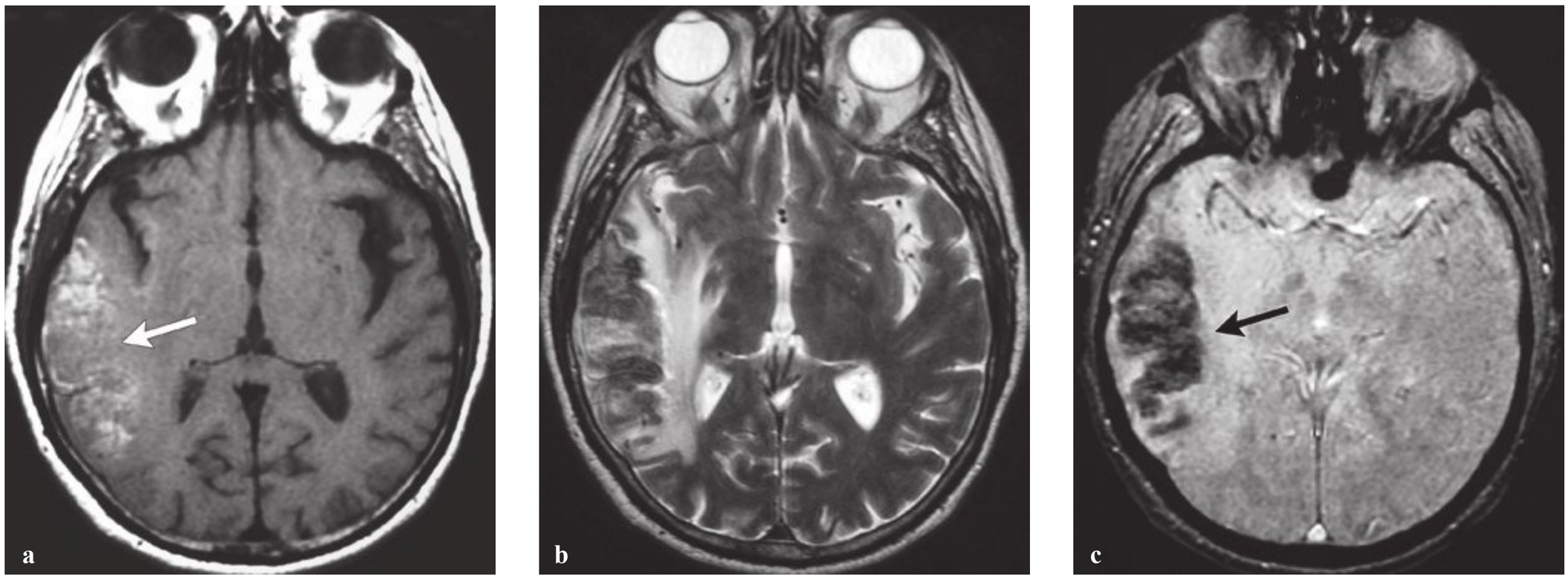

Fig. 1.364 Hemorrhagic transformation of an early subacute infarct in the right temporal lobe with high signal on **(a)** axial T1 WI (arrow), mixed low and high signal on **(b)** axial T2 WI, and **(c)** axial GRE (arrow).

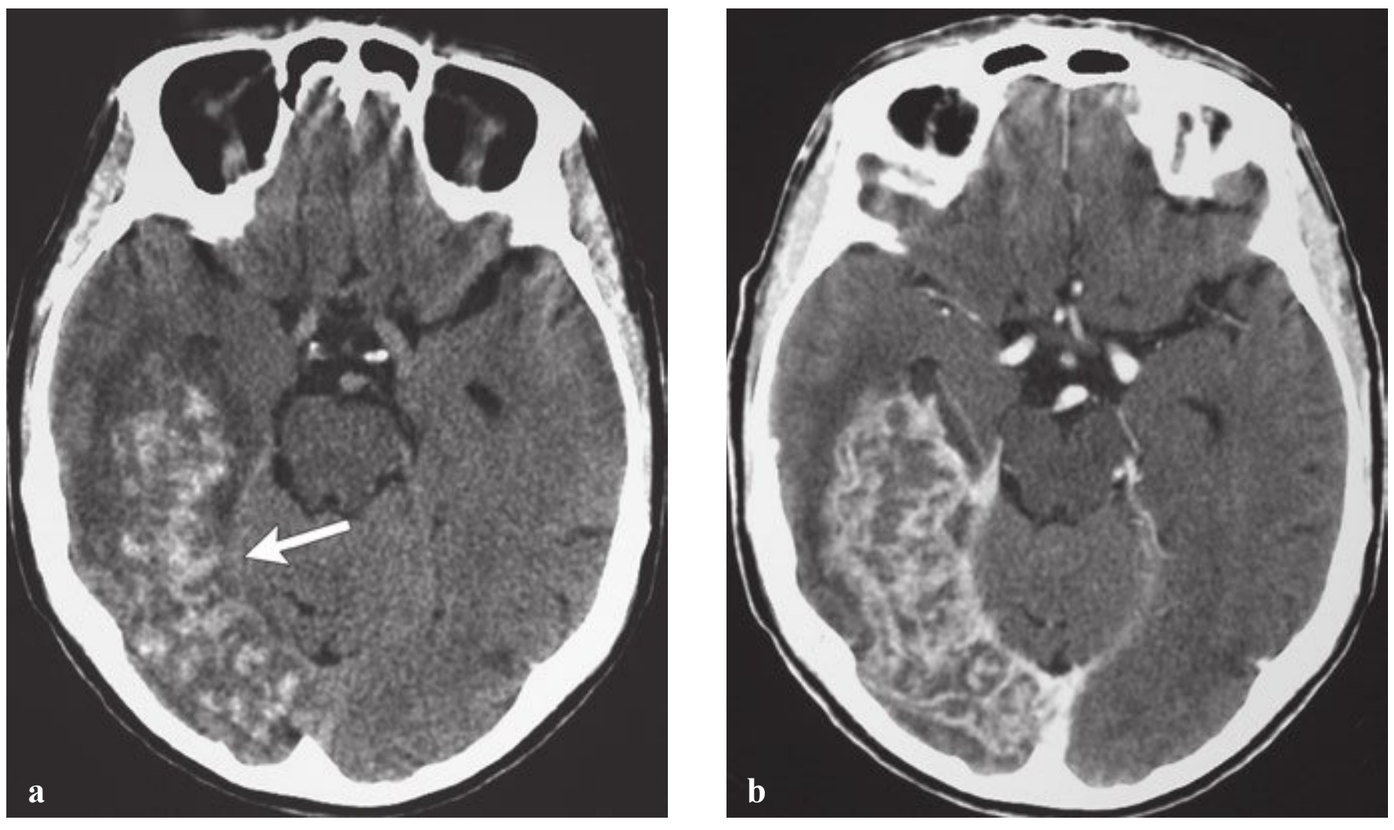

Fig. 1.365 Hemorrhagic transformation of a subacute infarct in the right cerebral hemisphere in a 61-year-old man. **(a)** Axial CT shows irregular zones with abnormal high and low attenuation in the right temporal and occipital lobes (arrow). **(b)** Contrast enhancement is also seen in portions of the hemorrhagic infarct.

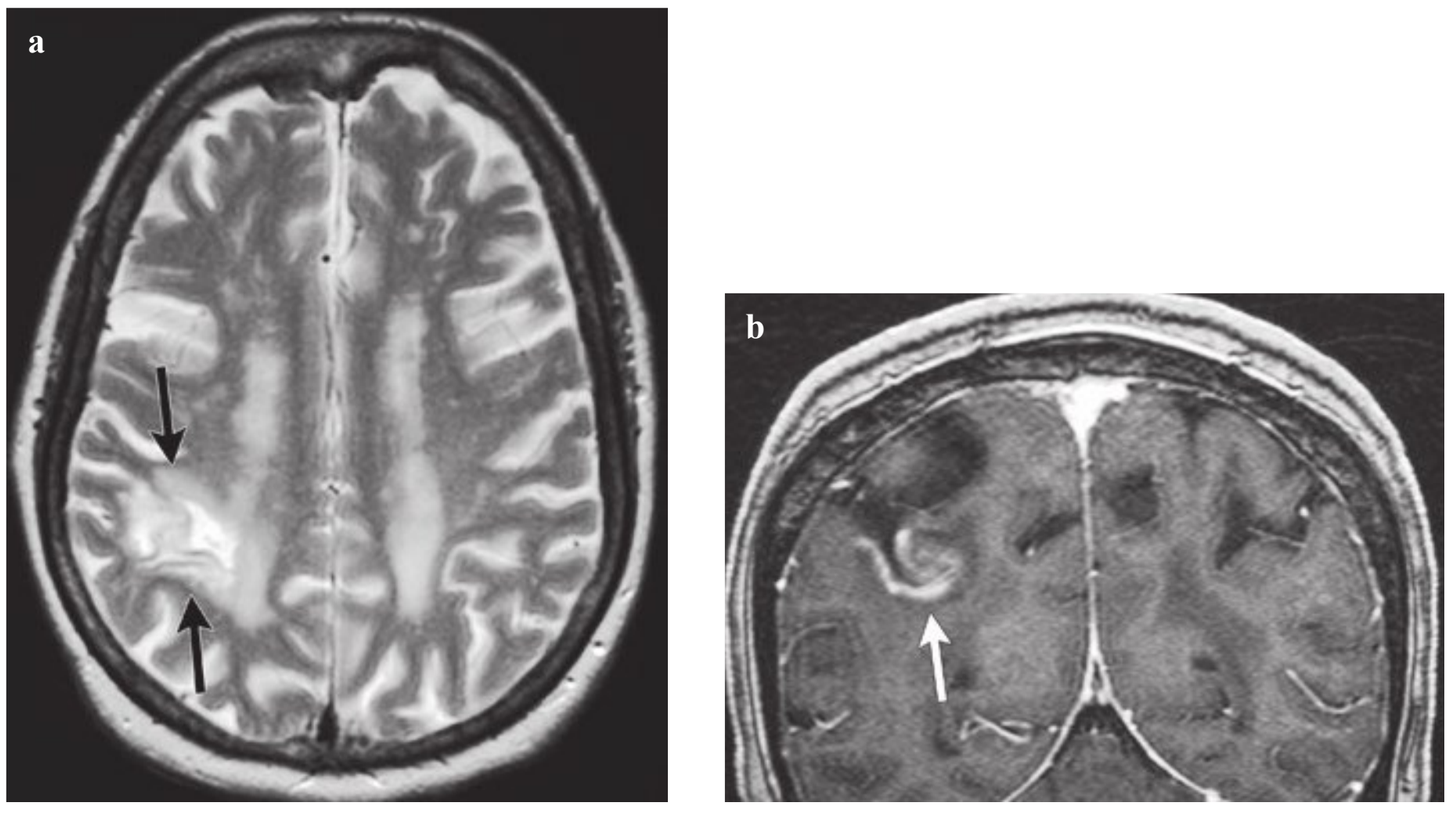

Fig. 1.366 An 80-year-old woman with a subacute infarct in the upper right parietal lobe that has high signal on **(a)** axial T2 WI (arrows). A gyriform pattern of gadolinium contrast enhancement is seen at the subacute infarct on **(b)** coronal T1 WI (arrow).

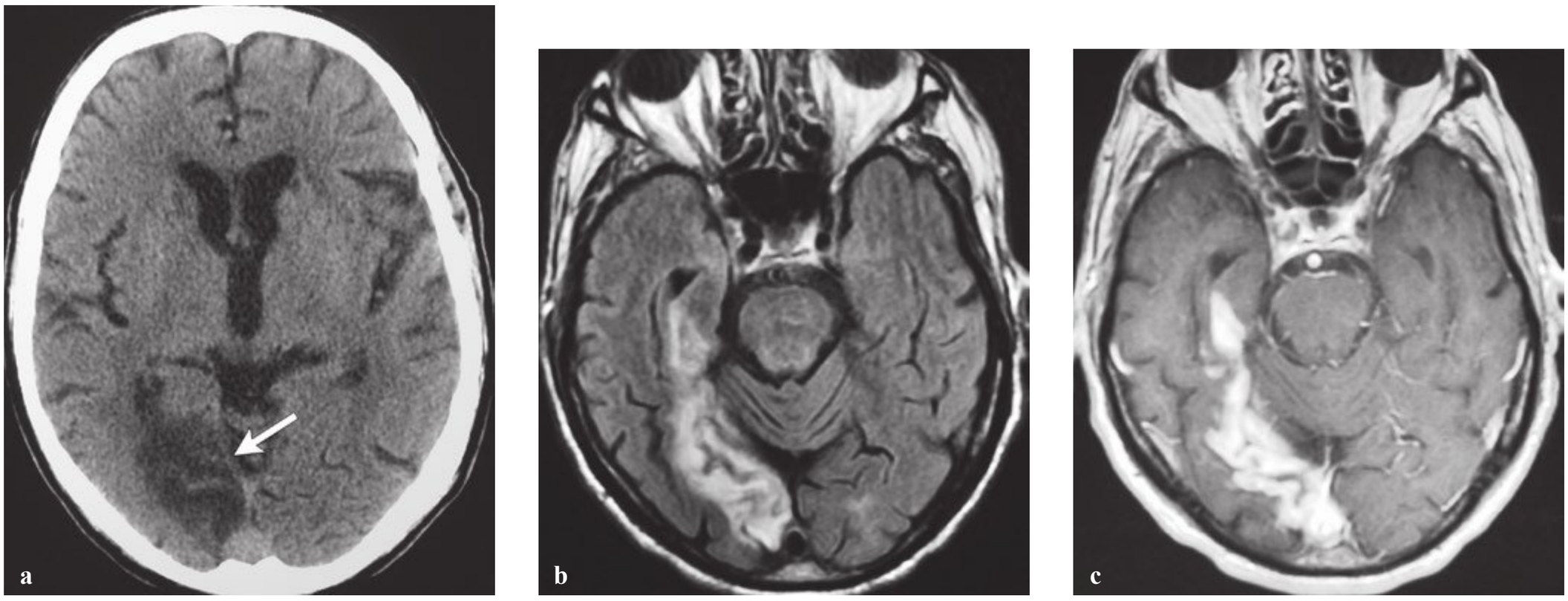

Fig. 1.367 A 78-year-old man with a zone of subacute cerebral infarction in the medial portions of the right temporal and occipital lobes in the vascular distribution of the right posterior cerebral artery. The subacute infarct has low attenuation on **(a)** axial CT (arrow), high signal on **(b)** axial FLAIR, and shows gadolinium contrast enhancement on **(c)** axial T1WI.

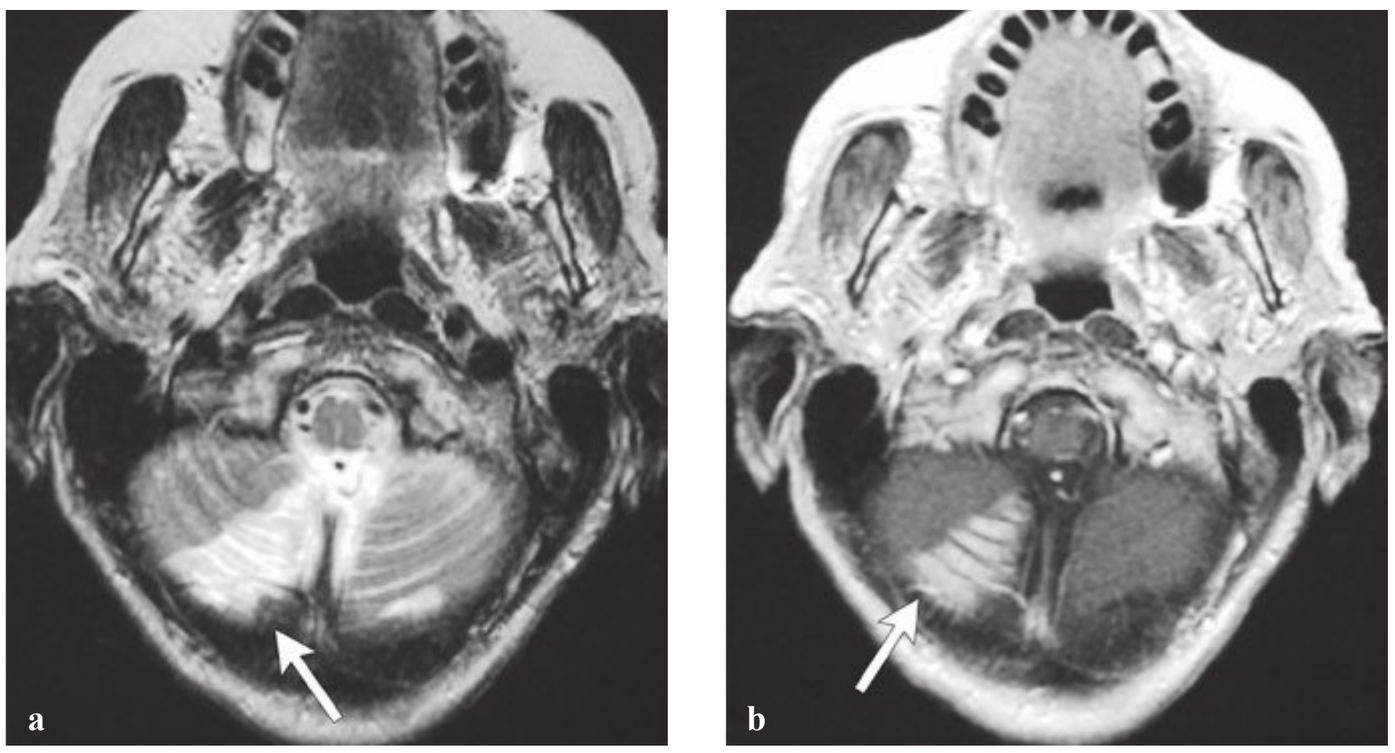

Fig. 1.368 An 85-year-old man with a subacute infarct in the inferomedial portion of the right cerebellar hemisphere in the vascular distribution of the right posterior inferior cerebellar artery that has high signal on **(a)** axial T2WI (arrow) and shows gadolinium contrast enhancement on **(b)** axial T1WI (arrow).

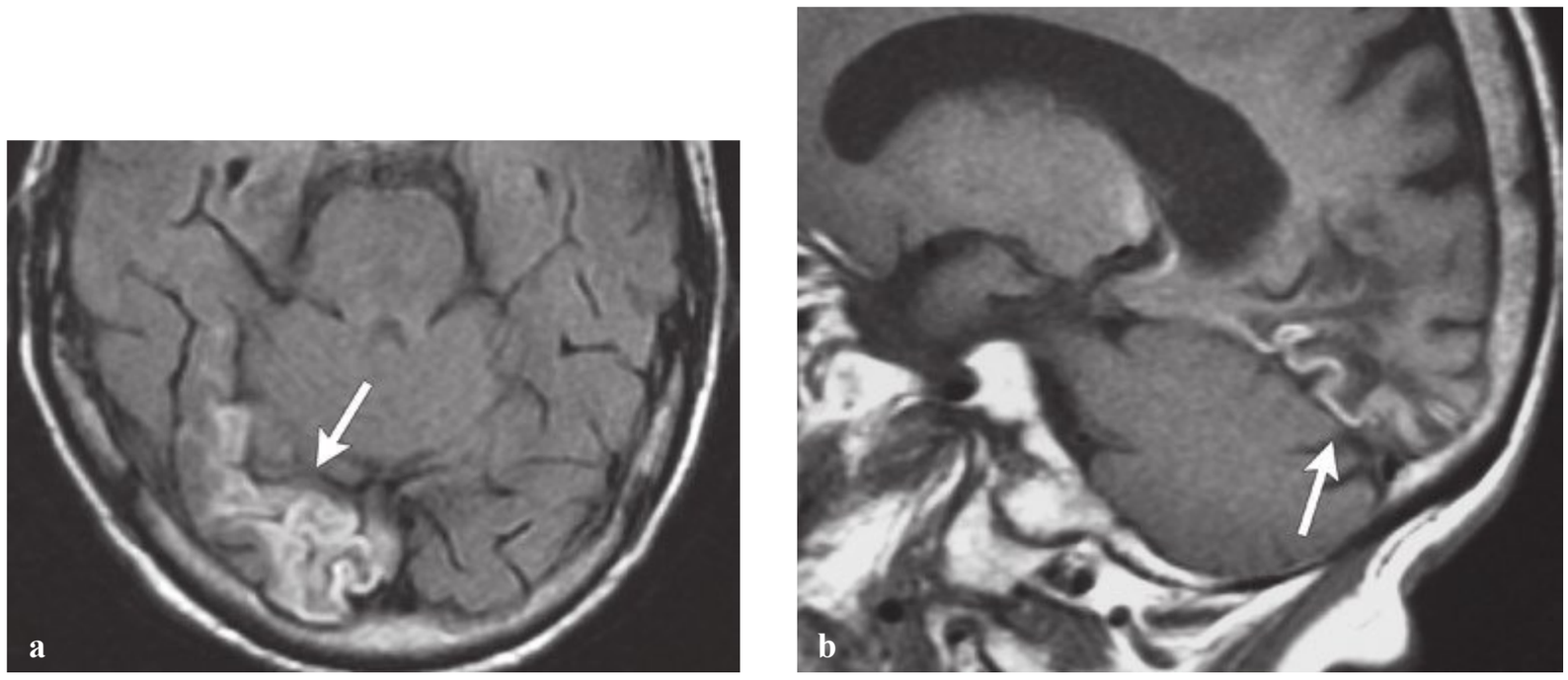

Fig. 1.369 Late subacute infarct in the right occipital lobe that has high signal on **(a)** axial FLAIR (arrow), and gyriform zones with high signal on **(b)** sagittal T1 WI (arrow) representing sites of cortical laminar necrosis.

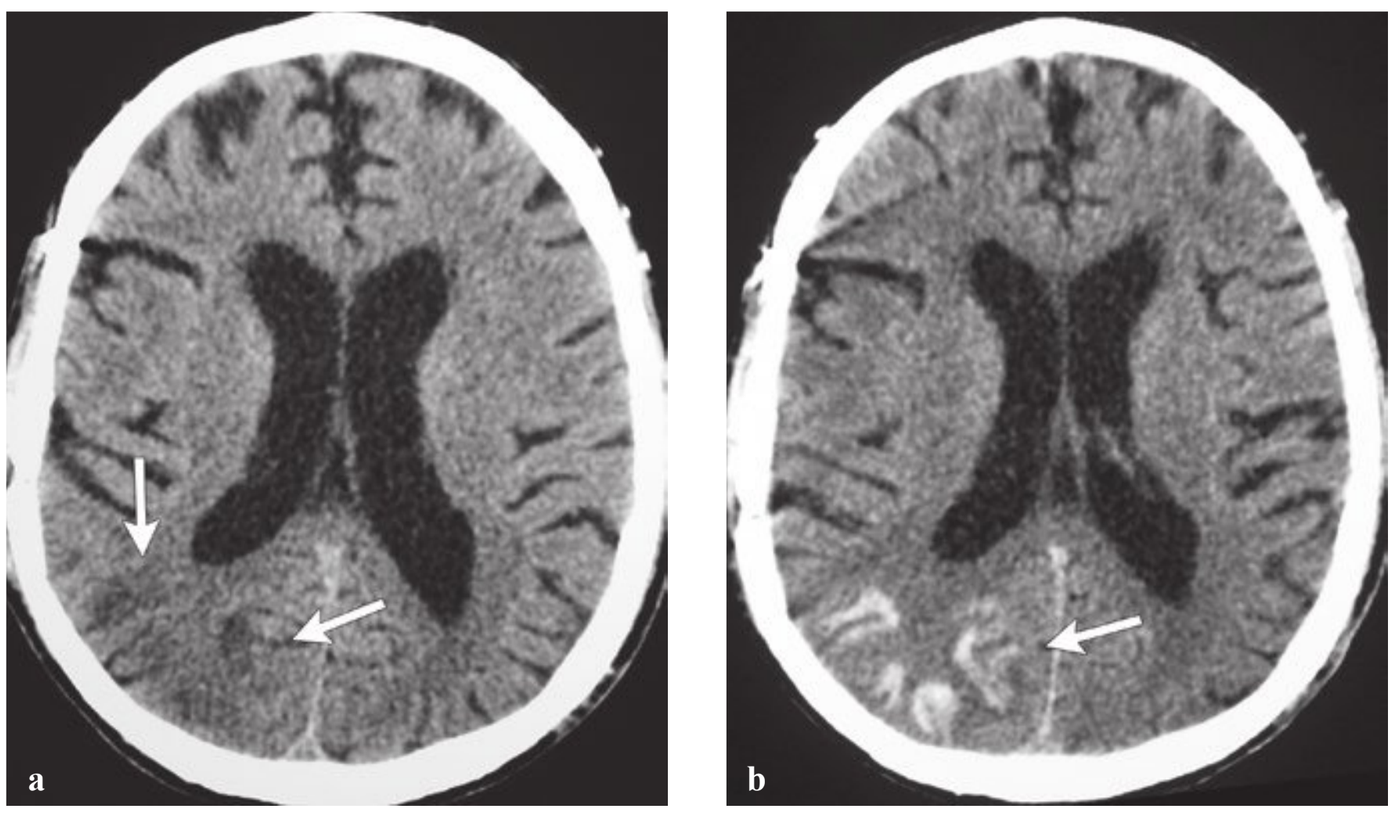

Fig. 1.370 **(a)** CT of an acute cerebral infarct (arrows) in the posterior right cerebral hemisphere. **(b)** CT 4 weeks later shows gyriform cortical zones with high attenuation (arrow) representing cortical laminar necrosis.

Table 1.8 (cont.) Ischemia and infarction involving the brain and/or brainstem in adults

Lesion/Disorder	Imaging Findings	Comments
Remote atherosclerotic-thrombotic and embolic infarcts (**Fig. 1.371** and **Fig. 1.372**) Months to years (chronic/old infarct)	CT: Localized encephalomalacia and ipsilateral atrophy of brainstem (Wallerian degeneration). MRI: Localized encephalomalacia and increased signal on T2-weighted imaging, proton density-weighted imaging, and FLAIR at infarct. Low signal on T1-weighted imaging and diffusion-weighted imaging and high signal on ADC maps. Presence of zones of low T2 and T2* signal secondary to hemosiderin. Ipsilateral atrophy of brainstem (Wallerian degeneration).	
Cardioembolic stroke (**Fig. 1.373** and **Fig. 1.374**)	CT: Up to 26% of patients with strokes have associated hemorrhage detected with CT. Hemorrhagic transformation occurs more frequently with cardioembolic infarcts than atheroma-related strokes. MRI: Sensitive method for detecting hemorrhage associated with strokes. In the first 2 days, T2*WI using gradient-echo and susceptibility weighted MRI can detect low signal from magnetic susceptibility effects at sites of acute hemorrhage in areas of infarction. In addition, MRI is also more sensitive than CT for detecting small petechial hemorrhages at infarcts. Diffusion-weighted imaging may be useful for differentiating hemorrhagic transformation of stroke from other causes of intra-axial hemorrhage by demonstrating restricted diffusion in adjacent nonhemorrhagic infarcted brain tissue. The presence of hemorrhage within strokes seen with CT and/or MRI usually precludes thrombolytic therapy.	Cardioembolic strokes can occur from emboli that result from disordered or slow blood flow caused by myocardial infarction, cardiomyopathy, atrial fibrillation or flutter, ventricular aneurysm, valvular vegetations related to bacterial endocarditis or nonbacterial endocarditis (such as Libman-Sacks endocarditis associated with systemic lupus erythematosus), congenital heart disease with right-to-left shunts, and hypercoagulable states. In these situations, localized clot formation occurs along a vessel wall, with production of emboli that lodge downstream, causing infarction. Hemorrhagic transformation of strokes occurs more frequently with cardioembolic infarcts than with atheromatous strokes. The mechanism for hemorrhagic transformation of strokes is related to subsequent reperfusion to the injured and impaired vascular endothelium, leading to blood extravasation that ranges from petechial hemorrhage to large hematomas at sites of infarction. Reperfusion with resultant hemorrhage may occur from lysis and fragmentation of the embolus causing the stroke or from collateral blood flow. In patients with initially "bland" (nonhemorrhagic infarcts), thrombolytic therapy also increases the risk for hemorrhage.

(continued on page 308)

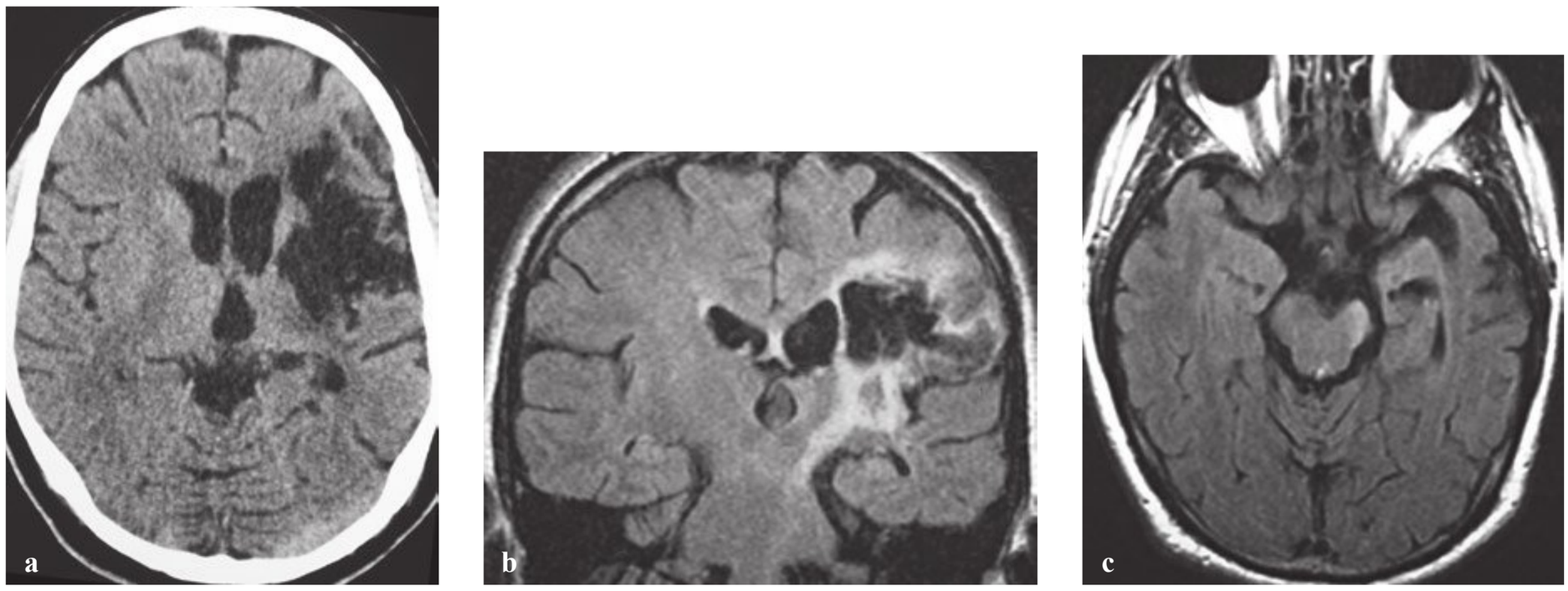

Fig. 1.371 Chronic/remote infarct in patient from **Fig. 1.359** 18 months later showing encephalomalacia and Wallerian degeneration on **(a)** axial CT and **(b)** coronal and **(c)** axial FLAIR.

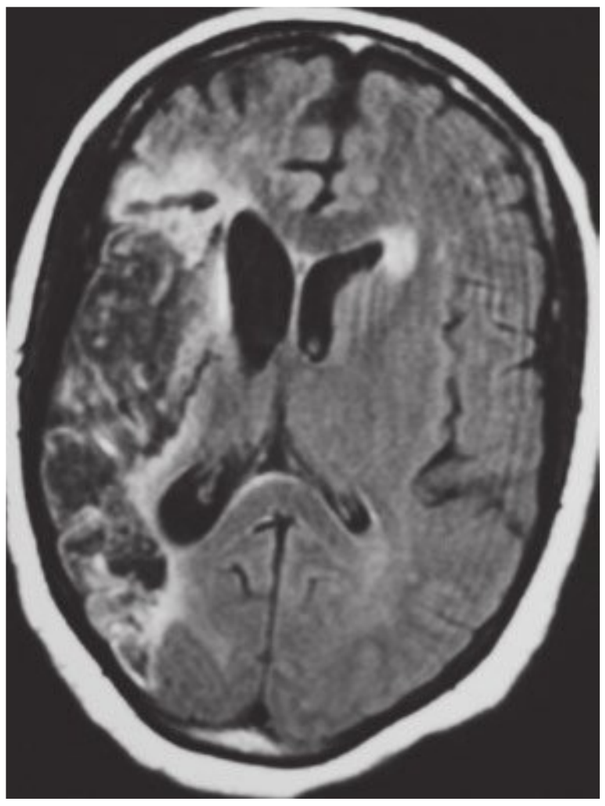

Fig. 1.372 A 47-year-old woman with a history of cerebral infarction 7 months earlier shows gliosis and encephalomalacia in the right cerebral hemisphere on axial FLAIR.

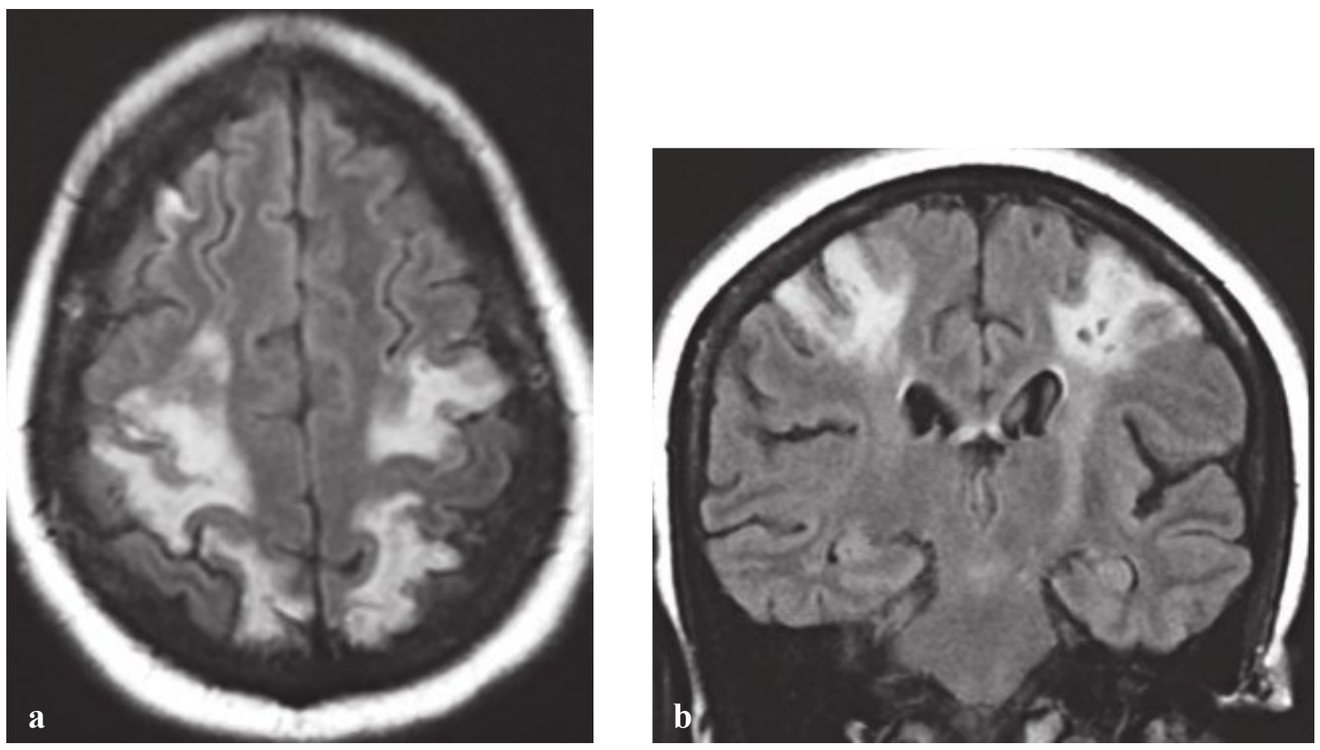

Fig. 1.373 Bilateral cerebral infarcts are seen on **(a)** axial and **(b)** coronal FLAIR from non-bacterial emboli from cardiac vegetations composed of fibrin, lymphocytes, histiocytes, and neutrophils in a patient with systemic lupus erythematosus (Libman-Sacks endocarditis).

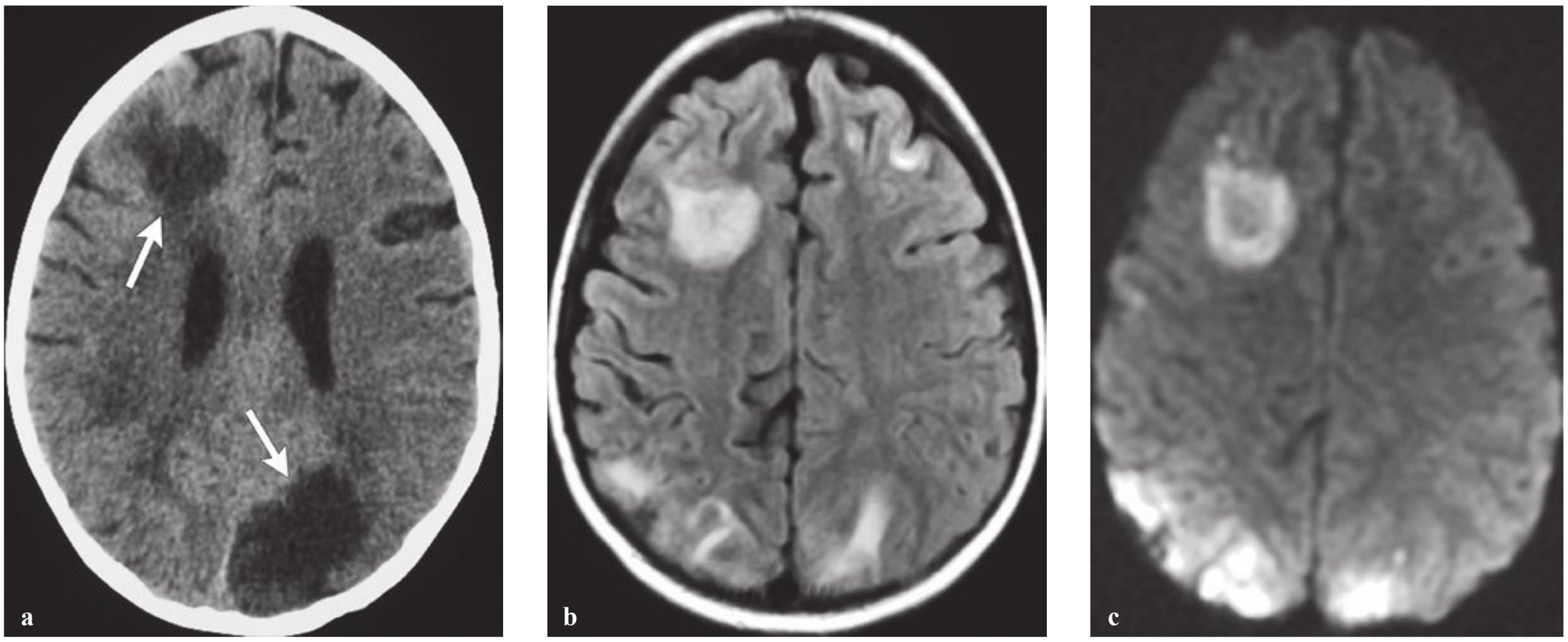

Fig. 1.374 A 12-year-old immunocompromised male with fungal embolic infarcts in the brain that have low attenuation on **(a)** axial CT (arrows), high signal on **(b)** axial FLAIR, and restricted diffusion on **(c)** axial DWI.

Table 1.8 (cont.) Ischemia and infarction involving the brain and/or brainstem in adults

Lesion/Disorder	Imaging Findings	Comments
Small-vessel or lacunar infarction (**Fig. 1.375, Fig. 1.376, Fig. 1.377**, and **Fig. 1.378**)	CT: • Acute lacunar infarcts may be seen as irregular zones of decreased attenuation in basal ganglia, periventricular and subcortical white matter, brainstem, and cerebellum and often measure less than 15 mm. • Non-acute small-vessel infarcts become more conspicuous over time, with low attenuation approximating CSF and circumscribed margins. MRI: • Acute lacunar infarcts can be seen as zones with high signal on diffusion-weighted imaging secondary to restricted diffusion as seen with ADC maps. They typically show high signal on T2-weighted imaging and FLAIR. • Subacute lacunar infarcts usually have high signal on T2-weighted imaging and FLAIR and may show mild gadolinium contrast enhancement. • Old lacunar infarcts typically have low signal on T1-weighted imaging, FLAIR, and diffusion-weighted imaging, high signal on T2-weighted imaging, and ADC maps, and lack gadolinium contrast enhancement. • Lesions typically involve the cerebral white matter bilaterally.	Occlusions of small arteries result in small lacunar infarctions, which are typically less than 15 mm in diameter. The vessels involved are the small perforating arteries (lenticulostriate arteries from the anterior circulation, thalamoperforating arteries, and perforating basilar artery branches from the posterior circulation), which supply the basal ganglia, internal capsules, deep cerebral white matter, and brainstem. Risk factors include hypertension, diabetes mellitus with elevated HgbA1c levels, tobacco smoke exposure, and elevated blood levels of homocysteine. Pathologic changes seen in the walls of the small perforating arteries include fibrinoid necrosis, lipohyalinosis, and microatheroma. In addition to atherosclerotic hypertensive-related changes, occlusion of the small vessels can also result from infectious arteritis (bacterial, tuberculous, fungal, viral); noninfectious arteritis or vasculopathy, such as polyarteritis nodosa, systemic lupus erythomatosus, scleroderma, systemic necrotizing vasculitides, rheumatoid arthritis, sarcoid, giant cell arteritis, granulomatosis with polyangiitis (Wegener's granulomatosis), and amphetamine-related arteritis; arterial dissection (traumatic, fibromuscular dysplasia, connective tissue disorders like Marfan syndrome, Ehlers-Danlos syndrome, etc.); hypercoagulable states (deficiencies of protein C, protein S, or antithrombin III; sickle-cell disease; dehydration; paraneoplastic syndromes); meningitis; cerebral autosomal dominant arteriopathy with subcortical infarcts and leukoencephalopathy (CADASIL); cerebral autosomal recessive arteriopathy with subcortical infarcts and leukoencephalopathy (CARASIL); and Fabry disease. The clinical features of acute lacunar infarcts depend on where the lesions are located. Patients may present with a motor deficit (hemiplegia) without loss of neurologic function, unilateral weakness with ipsilateral loss of proprioceptive and pain sensation, ataxic hemiparesis, dysarthria-clumsy hand syndrome, or pure sensory deficit.

(continued on page 310)

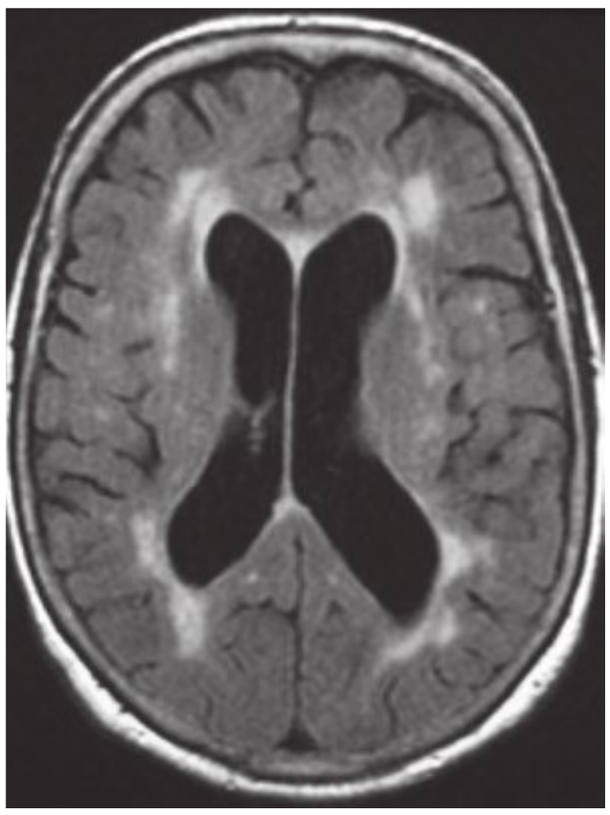

Fig. 1.375 An 83-year-old woman with multiple intra-axial zones with high signal on axial FLAIR in the cerebral white matter from small vessel ischemic disease.

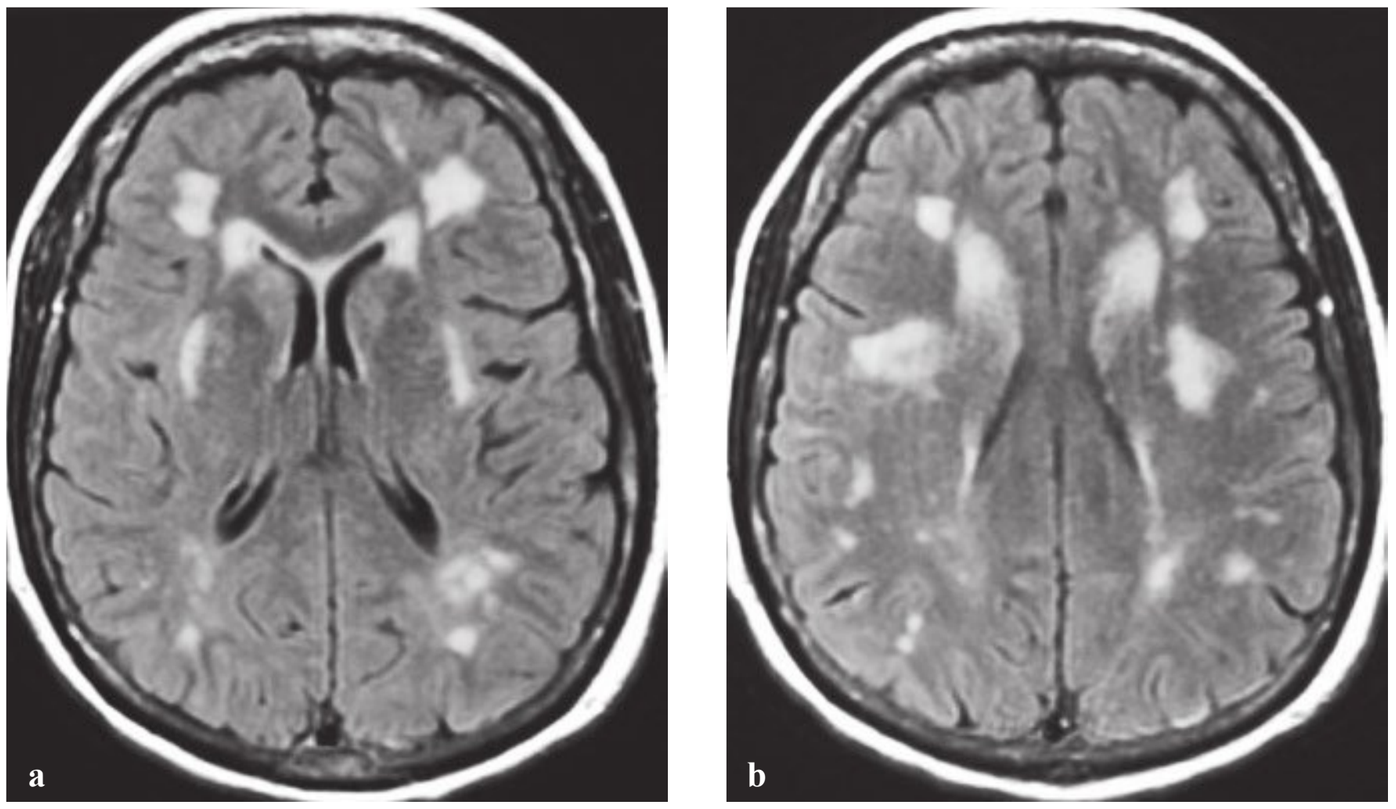

Fig. 1.376 (a,b) A 54-year-old woman with CADASIL who has multiple zones with high signal in the cerebral white matter bilaterally on axial FLAIR.

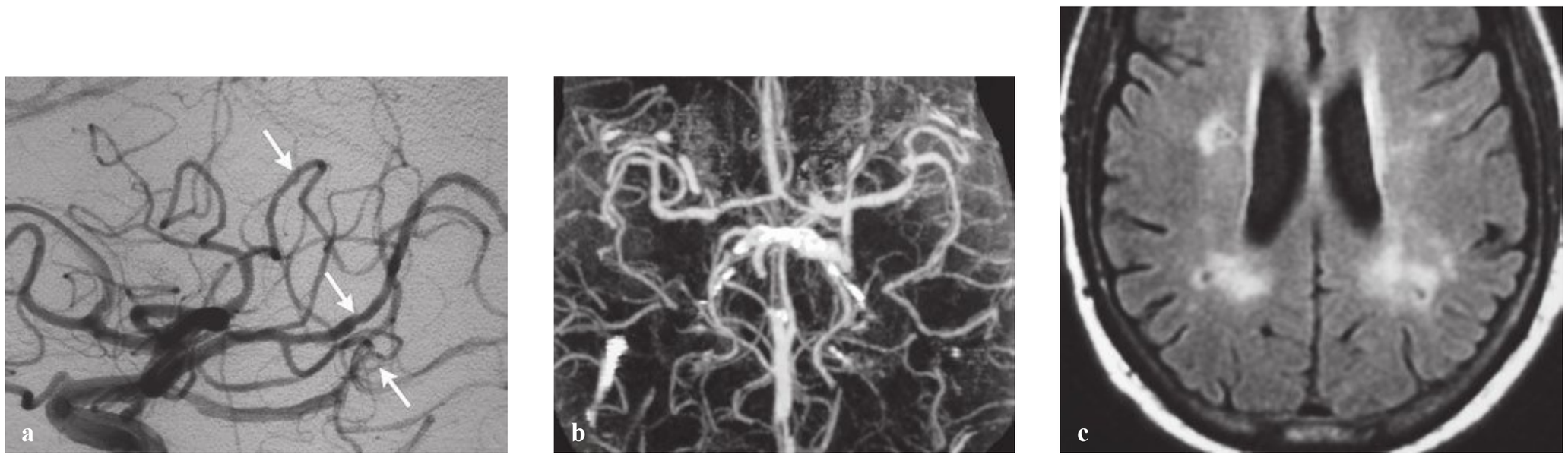

Fig. 1.377 A 50-year-old woman with vasculitis seen as sites of stenosis and beaded appearance of the middle cerebral artery branches on **(a)** conventional arteriogram (arrows) and **(b)** axial CTA. Intra-axial zones with high signal on **(c)** FLAIR are seen in the cerebral white matter secondary to ischemia related to the vasculitis.

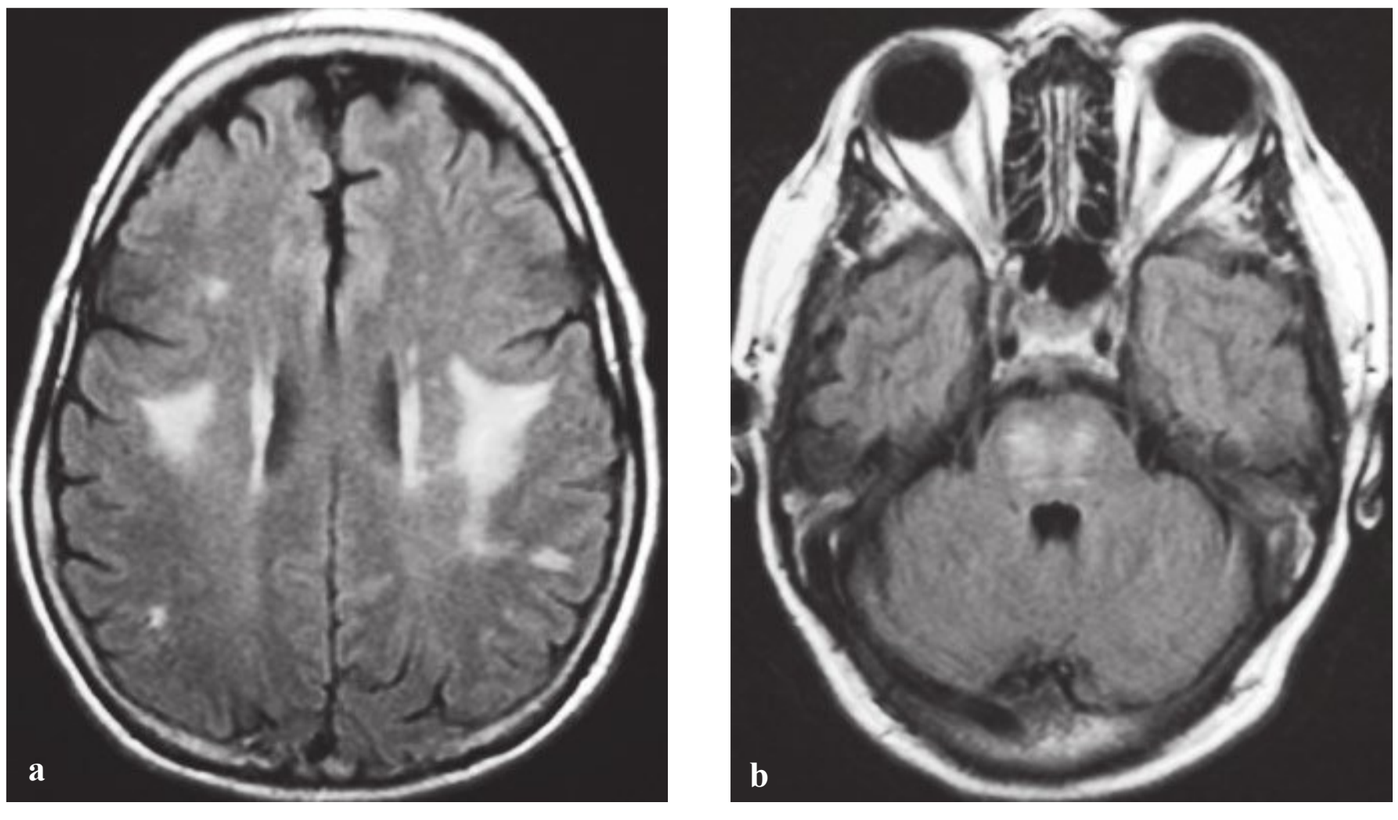

Fig. 1.378 A 41-year-old woman with lupus with multiple sites of infarcts in the **(a)** cerebral white matter and **(b)** pons on axial FLAIR.

Table 1.8 (cont.) Ischemia and infarction involving the brain and/or brainstem in adults

Lesion/Disorder	Imaging Findings	Comments
Hypoxic-Ischemic Injuries in Adults		Global hypoxic-ischemic injuries to the brain occur from lack of oxygen (asphyxia, drowning, carbon monoxide poisoning, etc.) and/or hypoperfusion (cardiac arrest with resuscitation, cardiac arrhythmia, prolonged hypotension). Hypoxic ischemia in the brain causes varying degrees and locations of injuries to the brain, depending on the duration and severity of the hypoxia and hypotension.
Severe hypoxic-ischemic injuries in adults **(Fig. 1.379)**	CT: Zones with decreased attenuation in the basal ganglia, as well as involving the cerebral and cerebellar cortex, with blurring of the gray–white matter junction. Diffuse cerebral edema associated with effacement of sulci. MRI: • Within the first 24 hours, ischemic changes from severe hypoxia can be seen as zones with high signal on diffusion-weighted imaging in the basal ganglia, cerebral cortex (notably in the occipital lobes and perirolandic cortex), thalami, hippocampi, cerebellar hemispheres, and brainstem. Curvilinear thin zones of restricted diffusion can be seen in the cerebral cortex within 24 hours, and persist for up to 2 weeks. • After 24 hours, zones with high signal on proton density-weighted imaging, T2-weighted imaging, and FLAIR can be seen at the involved sites of ischemic change. Echoplanar gradient-echo T2* images may show low signal from small zones of hemorrhage. • After ~ 2 weeks, curvilinear thin zones with high signal on T1-weighted imaging can be seen in the cerebral cortex, representing cortical laminar necrosis (pseudolaminar cortical necrosis). The high signal on T1-weighted imaging in the cerebral cortex occurs from necrosis, resulting in protein denaturation, paramagnetic compounds such as manganese ions, and macrophage-produced free radicals. • In 3%of patients with hypoxia, delayed imaging findings of high signal on T2-weighted imaging and FLAIR in the cerebral white matter associated with restricted diffusion may be seen 1 week after hypoxia, followed by acute neurologic decline (intellectual impairment, delirium, movement disorders, seizures) 2–3 weeks after the hypoxic event. This variant of delayed post-anoxic leukoencephalopathy may show persistent signal abnormalities and cerebral atrophy. The etiology for this type of delayed encephalopathy may be secondary to apoptosis (programmed cell death). • On magnetic resonance spectroscopy, poor outcome after resuscitation is related to a large decrease in the NAA:creatine ratio and elevated lactate levels.	Severe hypoxic-ischemic injuries occur when cerebral blood flow is below 10 mL/100 g/min, which is associated with cellular membrane depolarization and ischemia, leading to brain infarction in several minutes. In adults, the gray matter tends to show high selective vulnerability to hypoxia because of its high metabolic activity with associated increased energy requirements relative to white matter. Within gray matter, there are high densities of dendrites with postsynaptic glutamate receptors, causing increased vulnerability to glutamate excitotoxicity that occurs from massive release of glutamate and other neurotransmitters from depolarized presynaptic neuronal cell membranes secondary to insufficient cellular ATP production from hypoxia and/or ischemia. Severe hypoxic-ischemic lesions involve the basal ganglia (caudate and putamen bilaterally), thalami, hippocampi, and cerebellum.

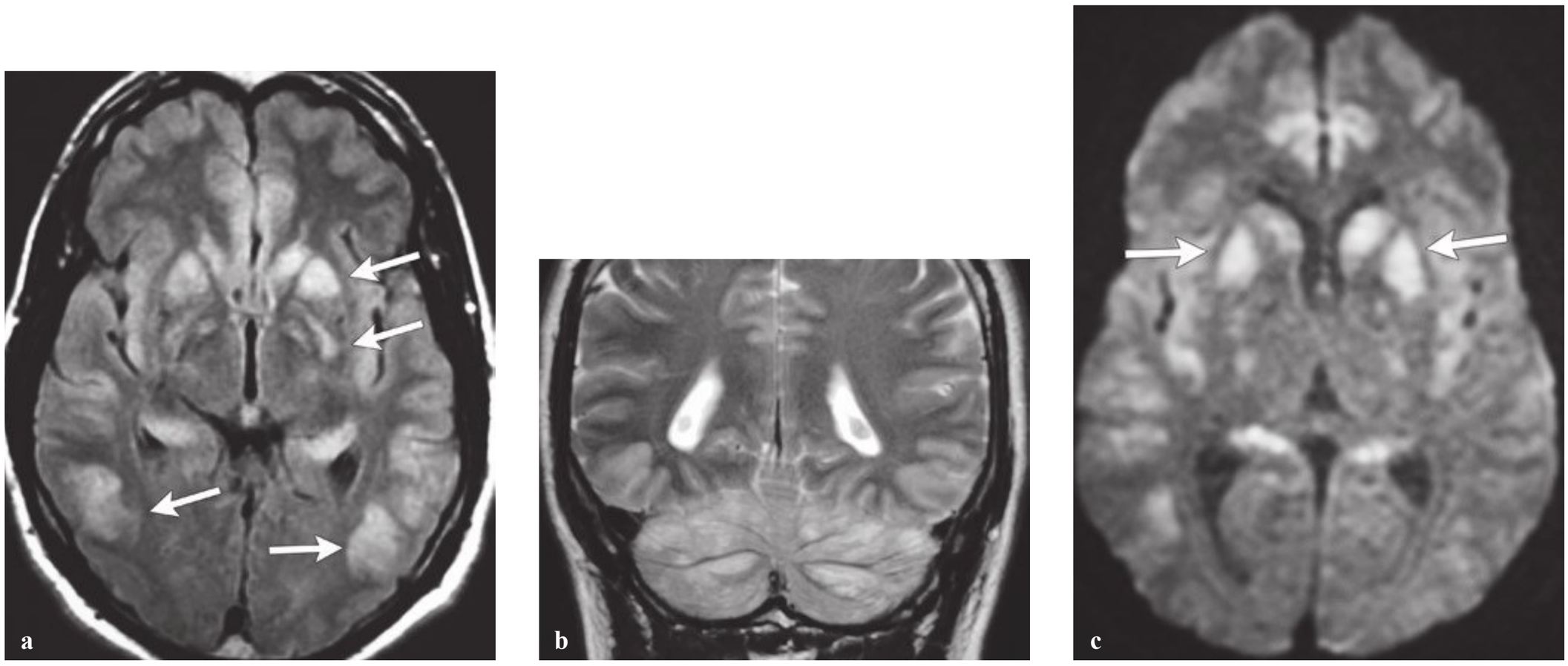

Fig. 1.379 A 46-year-old resuscitated man after cardiac arrest complicated with global hypoxic brain injury seen as abnormal high signal on **(a)** axial FLAIR (arrows) and **(b)** coronal T2WI in the caudate nuclei, putamina, globi pallidi, cerebral and cerebellar cortex. Restricted diffusion is also seen in the basal ganglia and cerebral cortex on **(c)** axial DWI (arrows).

Lesion/Disorder	Imaging Findings	Comments
Mild-moderate hypoxic-ischemic injuries in adults (**Fig. 1.380, Fig. 1.381,** and **Fig. 1.382**)	CT: Mild-moderate hypoxic-ischemic and hypoperfusion injuries result in ischemic lesions at the arterial border (watershed) zones between the distributions of the major cerebral arteries (anterior, middle, and posterior cerebral arteries), and between the distributions of the cerebellar arteries. MRI: With mild-moderate hypoxia, ischemic lesions can be seen at arterial border (watershed) zones between the distributions of the major cerebral arteries. Wedge-shaped zones of restricted diffusion for acute infarcts and high signal on T2-weighted imaging and FLAIR after 12 hours can be seen in cerebral cortex and subcortical white matter at the watershed vascular zone between the middle and posterior cerebral arteries. Multiple foci of restricted diffusion and high signal on T2-weighted imaging can be seen in the cerebral white matter in the watershed vascular zones between the middle and anterior cerebral arteries. Curvilinear thin zones of restricted diffusion can be seen in the cerebral cortex within 24 hours and persist for up to 2 weeks. Watershed zone infarcts can occur in the deep cerebral white matter between the distributions of the lenticulostriate arteries from the proximal middle cerebral artery and the penetrating superficial cortical branches from the M2, M3, and M4 segments of the middle cerebral artery. Signal abnormalities can also be seen at the cortex between the leptomeningeal distributions of the anterior and middle cerebral arteries, and between the middle and posterior cerebral arteries, as well as between the distributions of the cerebellar arteries.	Mild-moderate hypoxic-ischemic injuries occur when cerebral blood flow is reduced to 15–20 mL/100 g/min for several hours. Spontaneous and evoked neuronal electrical activity decreases significantly secondary to ischemia, although this can be reversed with reperfusion with cerebral blood flow above 50 mL/100 g/min. Mild-moderate hypoxic-ischemic injuries in adults can be seen as: lesions at the arterial border (watershed) zones in the brain between the distributions of the major cerebral arteries (anterior, middle, and posterior cerebral arteries), and between the distributions of the cerebellar arteries; and as signal abnormalities involving the third, fifth, and sixth cerebral cortical layers (commonly involving the sensorimotor and visual cortex), resulting in cortical laminar necrosis, also referred to as pseudolaminar cortical necrosis, since only three cortical layers are involved, unlike the full-thickness cortical necrosis that is seen with strokes from occlusion of large or medium-size arteries.

(continued on page 314)

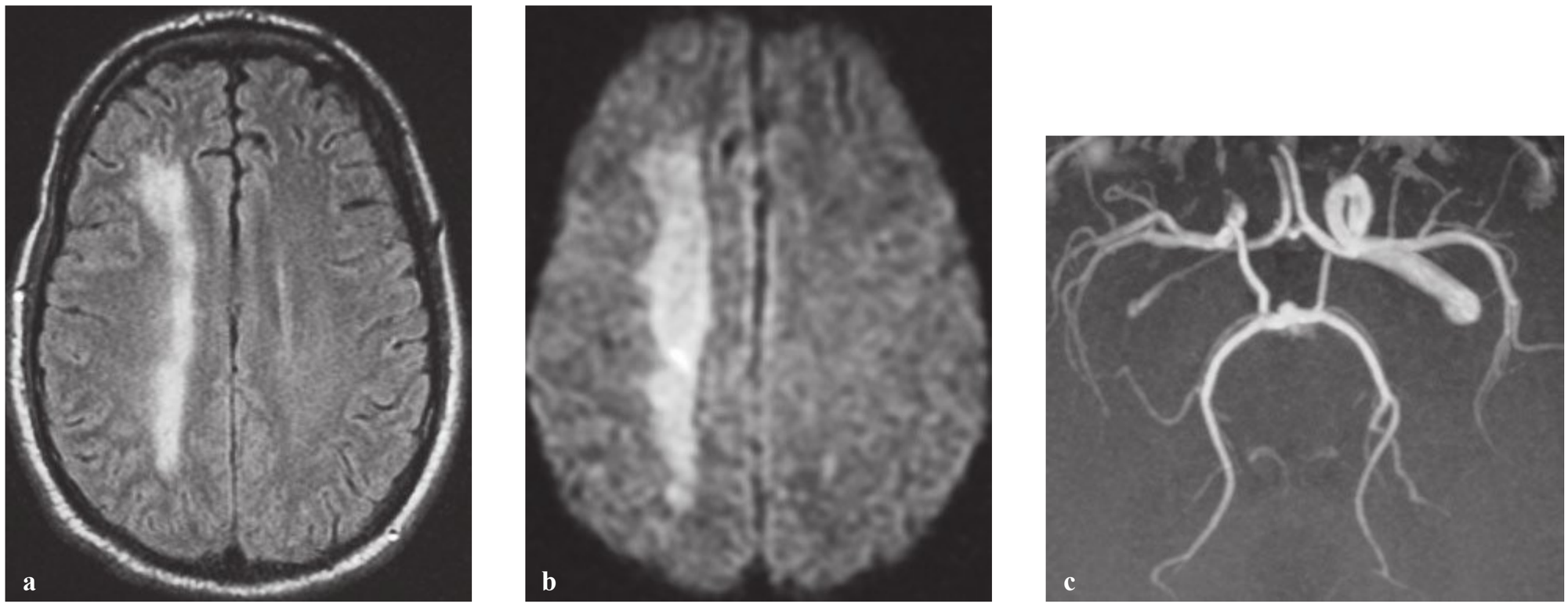

Fig. 1.380 Acute cerebral infarct in the watershed vascular distribution zone between the distal branches of the right middle and anterior cerebral arteries seen as high signal on **(a)** axial FLAIR and restricted diffusion on **(b)** DWI. The patient has occlusion of the right internal carotid artery with collateral blood flow to the right middle cerebral artery via a patent anterior communicating artery and a right posterior communicating artery on **(c)** axial MRA. The flow signal in the right middle cerebral artery is less than the left middle cerebral artery related to inadequacy of collateral blood flow. **(d)** Axial FLAIR shows gliosis and localized encephalomalacia at the zone of infarction 2 years later.

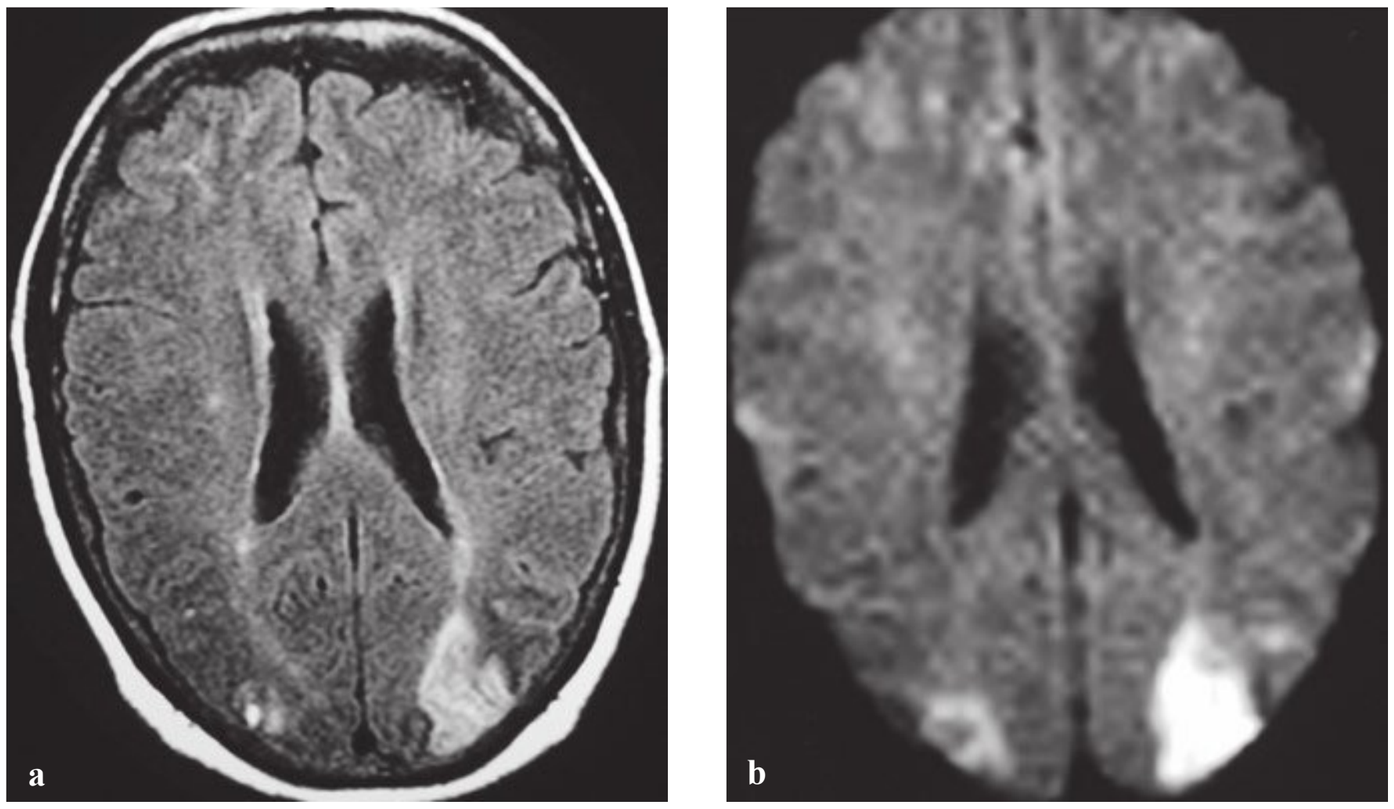

Fig. 1.381 A 62-year-old woman with bilateral acute infarcts in the watershed vascular distribution zone between the distal branches of both the middle and posterior cerebral arteries seen as high signal on **(a)** axial FLAIR and restricted diffusion on **(b)** DWI.

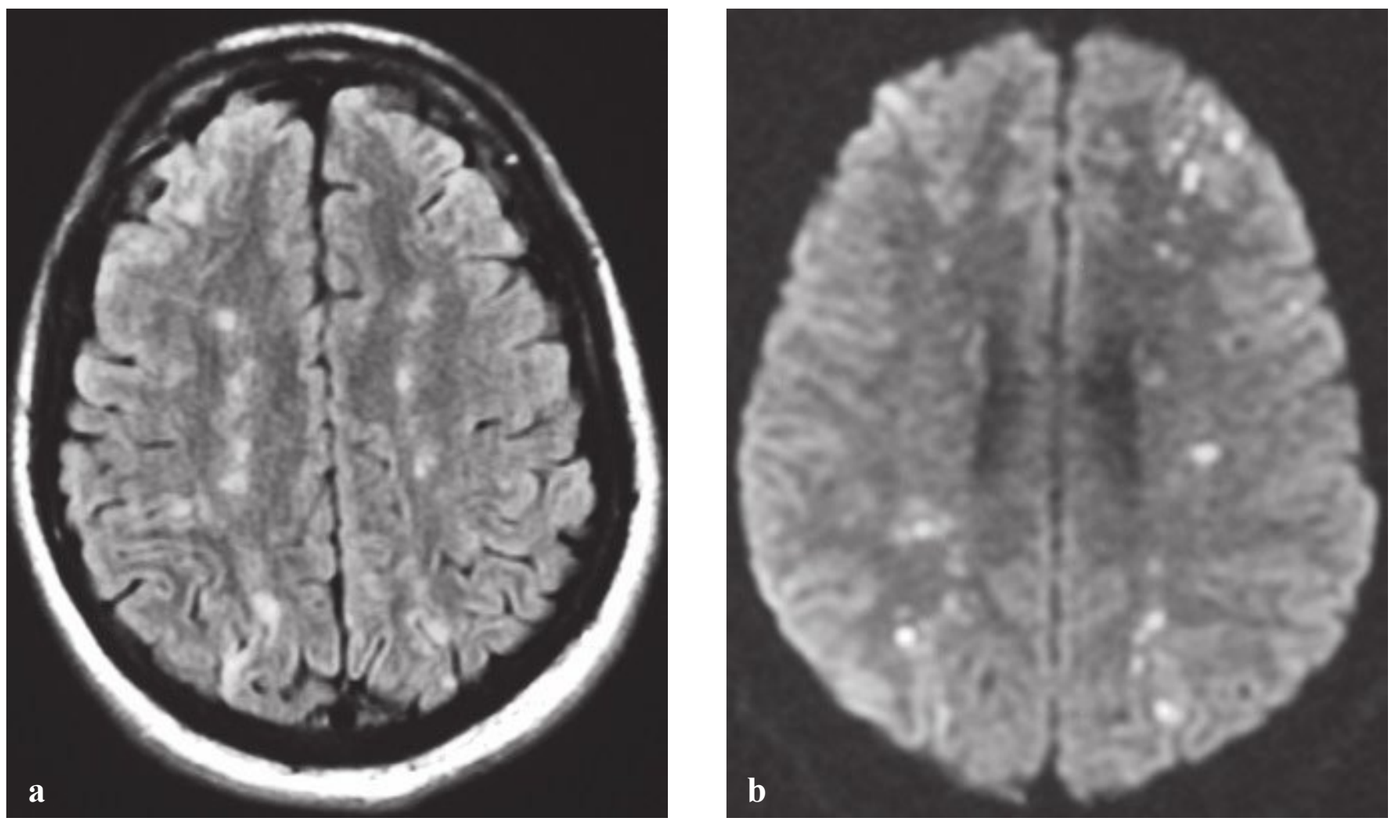

Fig. 1.382 A 26-year-old man with idiopathic hypereosinophilic syndrome who has acute infarcts in the watershed vascular distribution zones between the distal branches of the anterior and middle cerebral arteries, and between the deep and superficial branches of both middle cerebral arteries as seen as high signal on **(a)** axial FLAIR and restricted diffusion on **(b)** DWI. Patients with this disorder have persistent eosinophilia of more than 1500 per microliter for more than 6 months, which is associated with blood hyperviscosity, microthromboembolism or thromboembolism related to endomyocardial fibrosis, and/or localized thrombosis.

Table 1.8 (cont.) Ischemia and infarction involving the brain and/or brainstem in adults

Lesion/Disorder	Imaging Findings	Comments
Sinovenous Infarction in Adults (**Fig. 1.383, Fig. 1.384,** and **Fig. 1.385**)	CT: • Venous infarcts secondary to occlusion of the dural venous sinuses are seen as poorly marginated zones with low or mixed low and intermediate attenuation in the subcortical white matter, with or without regions of high attenuation from hemorrhage. Hemorrhage associated with venous infarcts is seen in 10–50%. Venous infarcts involving the central deep veins (internal cerebral veins, vein of Galen, straight venous sinus) are usually located in the basal ganglia and thalami, with or without localized or intraventicular hemorrhage. • Curvilinear and/or round zones of contrast enhancement can be seen at venous infarcts on CT. • Thrombus may be seen on non-contrast-enhanced CT as a dense vessel sign, and/or dense cord sign. • On contrast-enhanced CT, an empty delta sign can be seen, with a zone lacking enhancement within a dural venous sinus. • On CT angiography, the venous thrombus shows a zone with minimal enhancement relative to normal venous enhancement. • Enlargement of collateral patent veins and dural venous sinuses is seen on contrast-enhanced CT. • Pseudotumor cerebri (benign intracranial hypertension) may occur when sinovenous thrombosis occurs in a slow fashion with progressive impairment of CSF resorption through the arachnoid granulations at the thrombosed venous sinuses. • Dilatation of ventricles may occur from a rapidly progressive impairment of CSF resorption.	Venous infarcts are rare, and represent only 0.1% of strokes. They result from occlusion and/or thrombosis of the dural venous sinuses, superficial cortical veins, or deep veins, which causes elevation of the venous pressure above the arterial perfusion pressure. Venous occlusion can result acutely from infections (meningitis, sinusitis, mastoiditis), hypercoaguable states (dehydration, pregnancy, leukemia, sickle-cell disease, thalassemia, homocystinemia, nephrotic syndrome, anticardiolipin antibodies, lupus anticoagulant, factor V Leiden, prothrombin gene mutations, and decreased levels of protein C, antithrombin, protein S, fibrinogen, and plasminogen), and/or trauma, or, in a more chronic progressive sequence, by neoplastic infiltration or external compression of the dural venous sinuses. The most frequently occluded/thrombosed dural venous sinus is the superior sagittal sinus, followed by the transverse, straight, and cavernous sinuses. With venous occlusion, there is an increase in venous and capillary pressure in the zone of affected venous drainage that can result in decreased resorption of interstitial CSF, interstitial edema, and congestion, leading to eventual venous infarction. Venous infarctions commonly occur in the subcortical white matter and are associated with hemorrhage in 10–50% of cases. Locations of venous infarcts are related to the drainage territory of the occluded vein or dural venous sinus. Occlusions involving the superior sagittal sinus cause parasagittal infarcts in the white matter of the upper frontal and parietal lobes, with or without cerebral cortical involvement; occlusions of the vein of Galen and/or straight sinus result in thalamic and basal ganglia infarcts; and occlusions of the vein of Labbe and transverse and/or sigmoid venous sinuses cause infarcts in the lateral portions of the temporal lobes. Zones of hemorrhage can be seen at these sites and should raise the suspicion for venous infarction. Patients with sinovenous infarction can present with headaches (70–91%), papilledema (32%), emesis, focal motor deficits (34–79%), altered levels of consciousness (26–63%), and seizures (29–63%). The signs and symptoms may occur acutely within 48 hours in 28–54% of cases. Pseudotumor cerebri as a complication of intracranial venous thrombosis can be seen in 10 to 40% of cases. The prognosis depends upon the extent of venous thrombosis. Patients with thrombus in cortical veins and associated venous infarcts have a much better prognosis than those with deep venous occlusions and infarctions.

Lesion/Disorder	Imaging Findings	Comments
Sinovenous Infarction in Adults (cont.) (**Fig. 1.383, Fig. 1.384,** and **Fig. 1.385**)	MRI: • Venous infarcts are seen as poorly defined zones with decreased signal on T1-weighted imaging and increased signal on T2-weighted imaging and FLAIR. Lesions secondary to superficial venous obstruction usually involve the subcortical white matter more than the cortex. Occlusions of the internal cerebral veins, vein of Galen, and/or straight sinus result in thalamic and basal ganglia venous infarcts. • Thrombus within veins or dural venous sinuses can have intermediate signal on T1-weighted imaging in the first 3 days; intermediate signal on T1-weighted imaging, low signal on FLAIR, and low signal on T2-weighted imaging from deoxyhemoglobin in the late acute phase (3–5 days); and high signal on T1- and T2-weighted imaging from methemoglobin in the subacute phase (6–30 days). In the chronic phase (> 30 days), thrombus can have intermediate signal on T1-weighted imaging and intermediate or high signal on T2-weighted imaging. • In the first 7 days, T2* gradient echo (GRE) images and T2* susceptibility-weighted images (SWI) show low signal at the venous thrombus secondary to the paramagnetic effects of deoxyhemoglobin. • Heterogeneous mixed signal may seen on diffusion-weighted imaging (DWI) and ADC maps at acute venous infarcts related to sites with restricted diffusion from cytotoxic edema, hemorrhage, and interstitial or vasogenic edema. • Impaired resorption of CSF at the arachnoid granulations may result from dural venous thrombosis. The extent of venous infarction may be related to the degree of abnormal dural venous pressures associated with venous thrombosis. • Hemorrhage at venous infarcts may be seen in varying degrees and extent within the subcortical white matter. • MR venography using 2D and 3D phase contrast, 2D time-of-flight techniques, and contrast-enhanced time-resolved 3D time-of-flight techniques can show occlusion of the dural venous sinuses. Treatment usually consists of anticoagulation. • Contrast-enhanced magnetic resonance angiography can show multiple, small, collateral vessels at the recanalized venous sinus.	

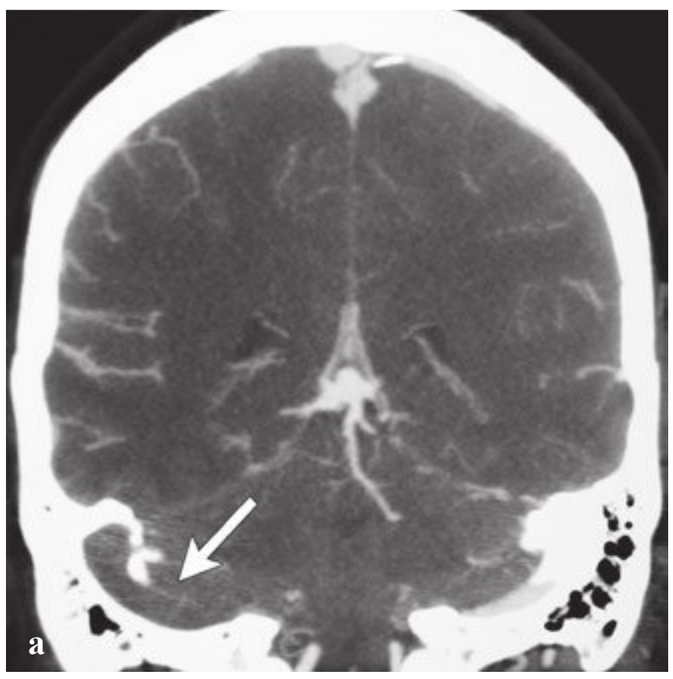

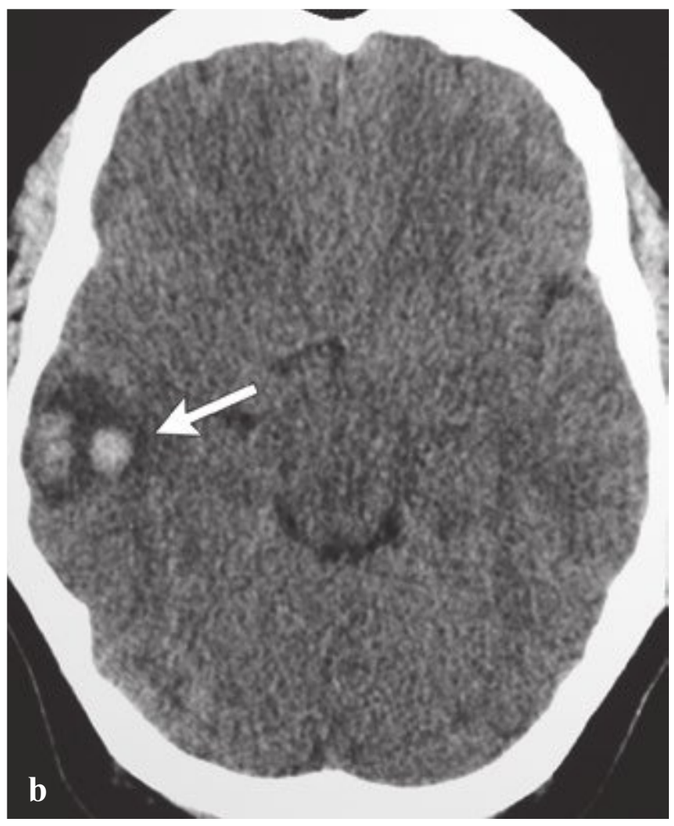

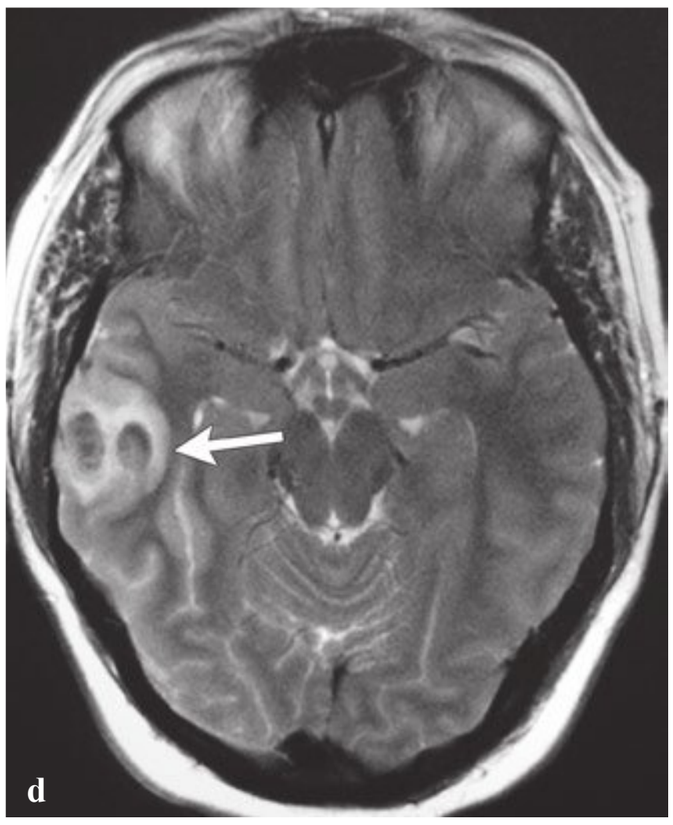

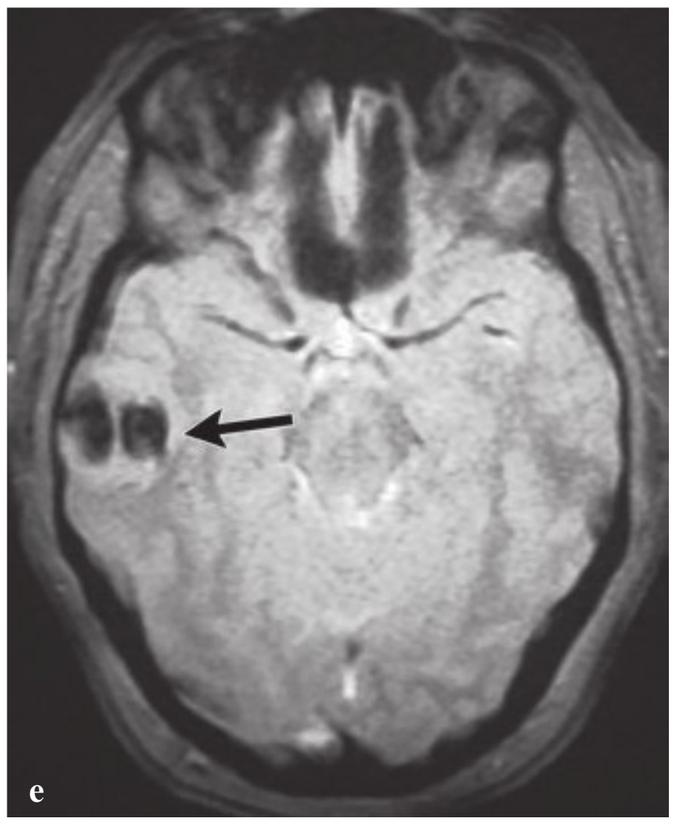

Fig. 1.383 Hemorrhagic venous infarct in the right temporal lobe from thrombus occluding the right transverse sinus on **(a)** coronal CTA (arrow), **(b)** axial CT (arrow), and **(c)** axial T1WI (arrow). The hemorrhagic venous infarct has mixed low and high signal on **(d)** axial T2WI (arrow) and **(e)** GRE (arrow).

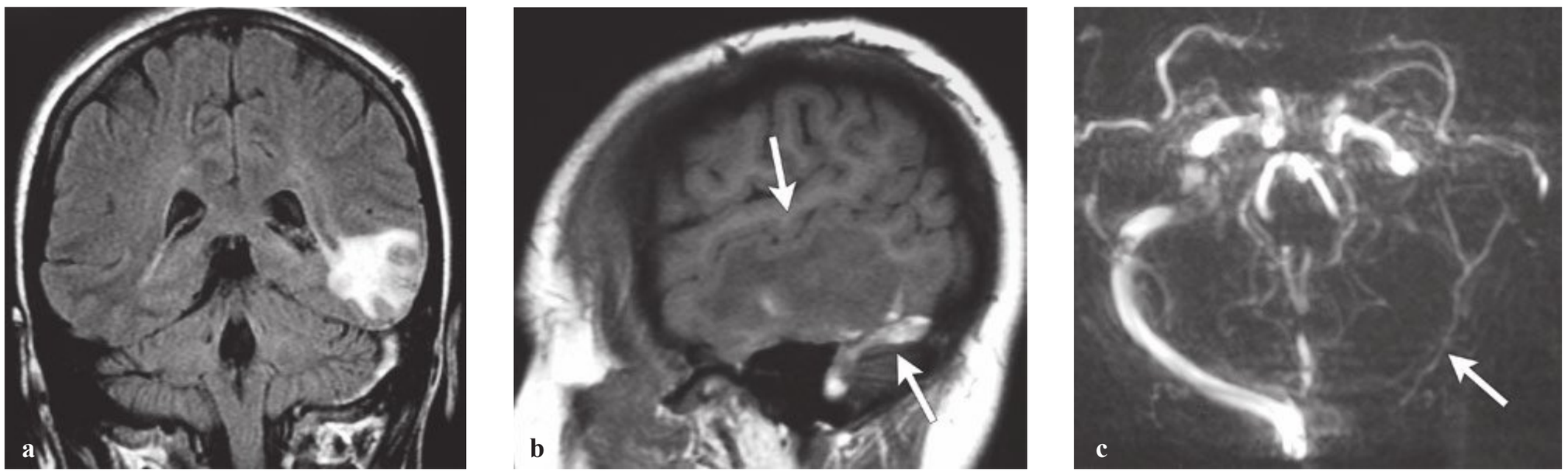

Fig. 1.384 A 33-year-old woman with a venous infarct in the left temporal lobe from thrombus occluding the left transverse sinus. The venous infarct has high signal on **(a)** coronal FLAIR, and contains small sites of hemorrhage with high signal (upper arrow) on **(b)** sagittal T1 WI. The thrombus has high signal on both **(a)** FLAIR and **(b)** T1 WI (lower arrow). **(c)** MRV shows absence of flow signal (arrow) in the occluded left transverse venous sinus.

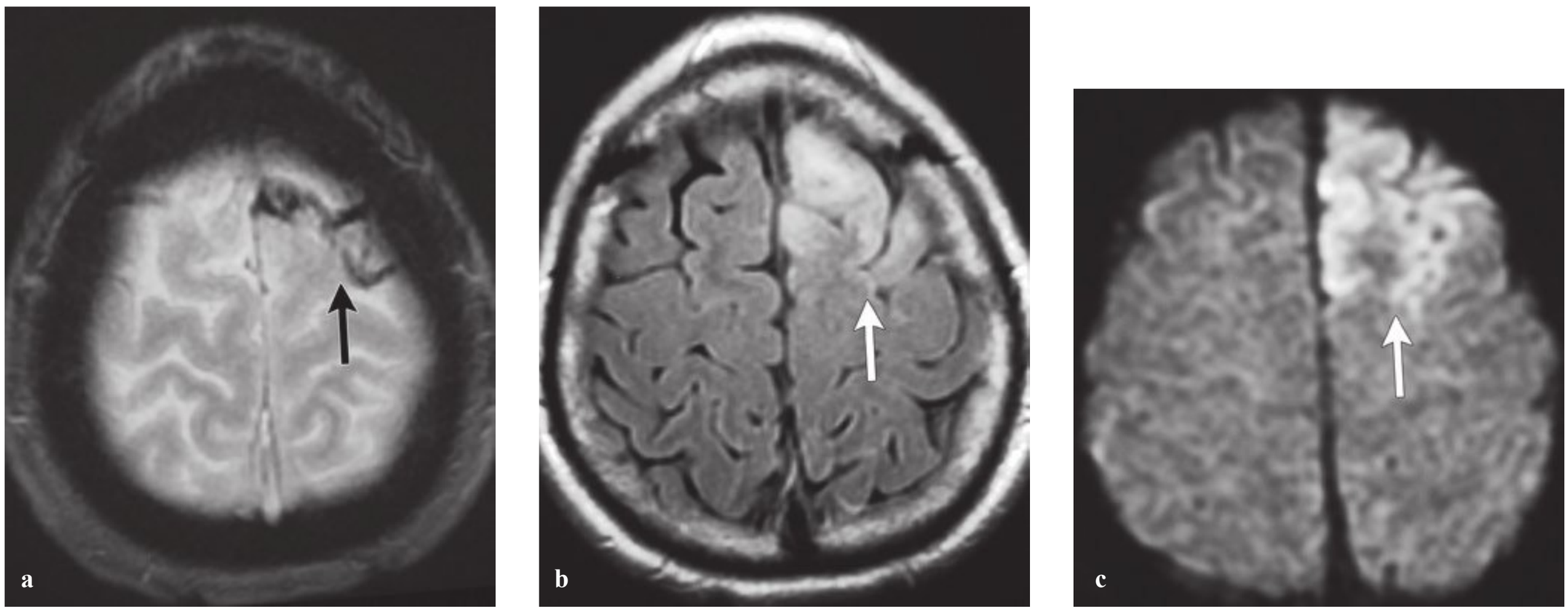

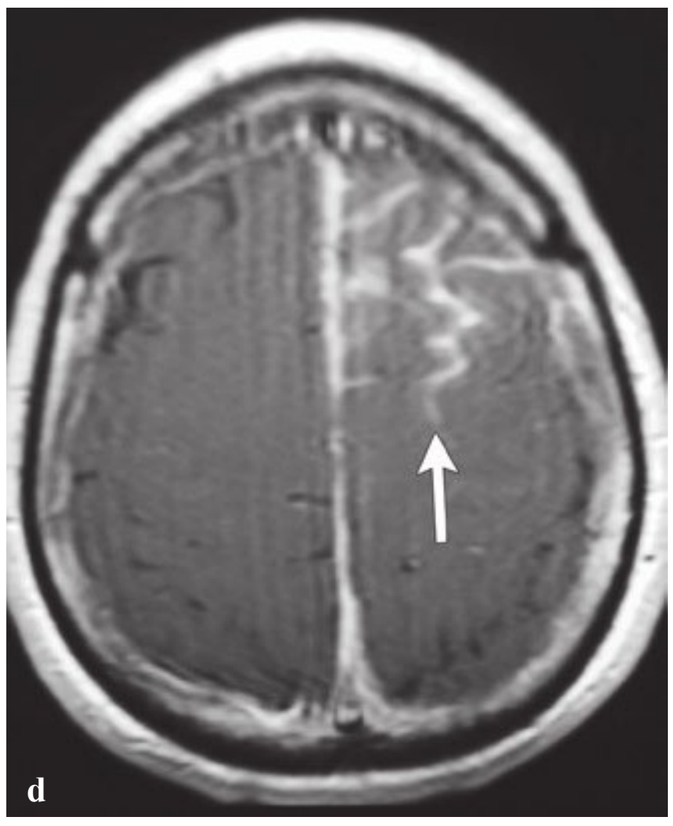

Fig. 1.385 A 49-year-old man with thrombosis of a cortical vein resulting in localized acute venous infarction of the upper anterior left frontal lobe. The thrombosed vein has low signal on **(a)** axial GRE (arrow). The acute infarct has high signal on **(b)** axial FLAIR (arrow) and **(c)** DWI (arrow), and is associated with leptomeningeal gadolinium contrast enhancement on **(d)** axial T1 WI (arrow).

1.9 Ischemia and Infarction in Children

Pediatric strokes are defined as cerebrovascular injuries that occur between 14 weeks of gestation and 18 years of life. Cerebral infarction seen in the pediatric population is subcategorized based on the timing of the cerebrovascular injury: *fetal strokes* occur between 14 weeks of gestation and the onset of labor, *perinatal-neonatal strokes* occur in neonates (> 28 weeks' gestational age) and in the first 28 days of postnatal life, and *childhood strokes* occur between 29 days and 18 years after birth. Pediatric strokes occur with a frequency of 8 per 100,000 children per year. Neurologic and cognitive impairment occurs in 50% of cases, and death occurs in up to 10% Approximately 30% of patients have subsequent cerebrovascular events. Pediatric strokes can result from arterial occlusions (focal lesions—infarcts), global hypotension (cardiac arrhythmia/cardiac arrest, asphyxia resulting in hypoxic-ischemic and hypoperfusion injuries), and sinovenous thrombosis/occlusions. Most arterial occlusions causing strokes in children involve the anterior arterial circulation and rarely involve the posterior circulation. Infarcts involving the posterior circulation may be secondary to traumatic injuries to the vertebrobasilar system, migraine-associated vasospasm, or metabolic disorders, such as mitochondrial-related encephalopathies.

Table 1.9 Ischemia and infarction involving the brain and/or brainstem in children

- Fetal stroke
- Perinatal/neonatal stroke

• Preterm Neonates
- Severe hypoxic-ischemic injuries
- Mild-moderate hypoxic-ischemic injuries
- Germinal matrix hemorrhage
- Periventricular leukomalacia (PVL; white matter injury of prematurity)

• Term Neonates
- Severe hypoxic injuries
- Moderate-severe hypoxic injuries
- Mild-moderate hypoxic injuries
- Neonatal ischemia from anoxia followed by hypoperfusion
- Hyperacute and acute infarcts from arterial occlusion
- Subacute infarcts from arterial occlusion
- Remote infarcts from arterial occlusion
- Neonatal sinovenous thrombosis and venous infarction

• Stroke in Children
- Childhood strokes: hyperacute and acute infarction from arterial occlusion
- Subacute infarction from arterial occlusion
- Remote infarction from arterial occlusion
- Small-vessel ischemic injury: sickle-cell disease
- Severe anoxic/hypoxic-ischemic injuries in children
- Mild-moderate anoxic/hypoxic-ischemic injuries in children
- Sinovenous infarction in children

• Inherited Metabolic Disorders Associated with Strokes in Children
- MELAS/MERRF
- Leigh's disease
- Kearns-Sayre syndrome
- Fabry disease

Table 1.9 Ischemia and infarction involving the brain and/or brainstem in children

Lesion/Disorder	Imaging Findings	Comments
Fetal stroke (**Fig. 1.386** and **Fig. 1.387**)	Fetal strokes may be seen on ultrasound. On diffusion-weighted imaging, restricted diffusion can be seen with acute and early subacute cerebral infacts in utero. In the second trimester, arterial infarcts can cause alterations in the cortical organization of neuroblasts, resulting in polymicrogyria and/or schizencephaly. Because of the lack of fetal astroglial reaction to brain injuries during the first 27 weeks of gestation, early fetal cerebral infarcts can result in encephaloclastic porencephaly. After 27 weeks of gestation, cerebral infarcts may be seen as zones of encephalomalacia with varying degrees of gliosis and/or cystic changes. In addition to focal arterial occlusions causing stroke, hypoperfusion related to mild-moderate hypotension in the fetal circulation from 28 to 36 weeks of gestation typically results in periventricular leukomalacia with sparing of cerebral cortex and subcortical white matter, as seen on MRI and CT. Prenatal episodes of severe hypoperfusion/hypoxia can result in extensive cystic encephalomalacia and abnormal high signal on T1-weighted imaging in the basal ganglia and thalami seen on postnatal MRI.	Fetal strokes occur between 14 weeks of gestation and the onset of labor. Most occur between 24 and 34 weeks of gestation. Fetal arterial strokes are usually clinically silent, with no maternal symptoms. Most fetal infarcts result from focal arterial occlusion, commonly involving the middle cerebral artery. Maternal risk factors include alloimmune thrombocytopenia, diabetic ketoacidosis, anticoagulation, antiepileptic therapy, trauma, and placental infarction, hemorrhage, or thrombosis adversely affecting fetal cerebral blood flow, as well as placental abruption and placenta previa. In more than 50%of fetal cerebral infarcts, no definite cause is found. Prognosis is dependent on the size of the fetal stroke, presence of hemorrhage, and ventricular dilatation. Prenatal hypoxia/hypoperfusion episodes can result in varying degrees of brain injuries that can be seen on postnatal MRI.
Perinatal/neonatal stroke	Color-flow Doppler can be used to detect arterial occlusions in the circle of Willis region. Hypoxic-ischemic injuries in neonates can result in different locations and degrees of damage to the brain and brainstem, depending on the severity of the insult (mild-moderate or severe hypoxia and duration of hypoxia) as well as the relevant developmental stage of the brain in relation to gestational age (i.e, preterm versus term neonates).	Perinatal/neonatal strokes occur in 1 in 4,000 live births per year. A common presentation for perinatal stroke is an unexpected focal seizure in a neonate within 3 days of birth. Perinatal/neonatal strokes can result from global hypoxic-ischemic injuries or from focal arterial occlusions.

(continued on page 320)

Fig. 1.386 A 6-year-old boy with porencephaly secondary to fetal stroke as seen on axial T1 WI.

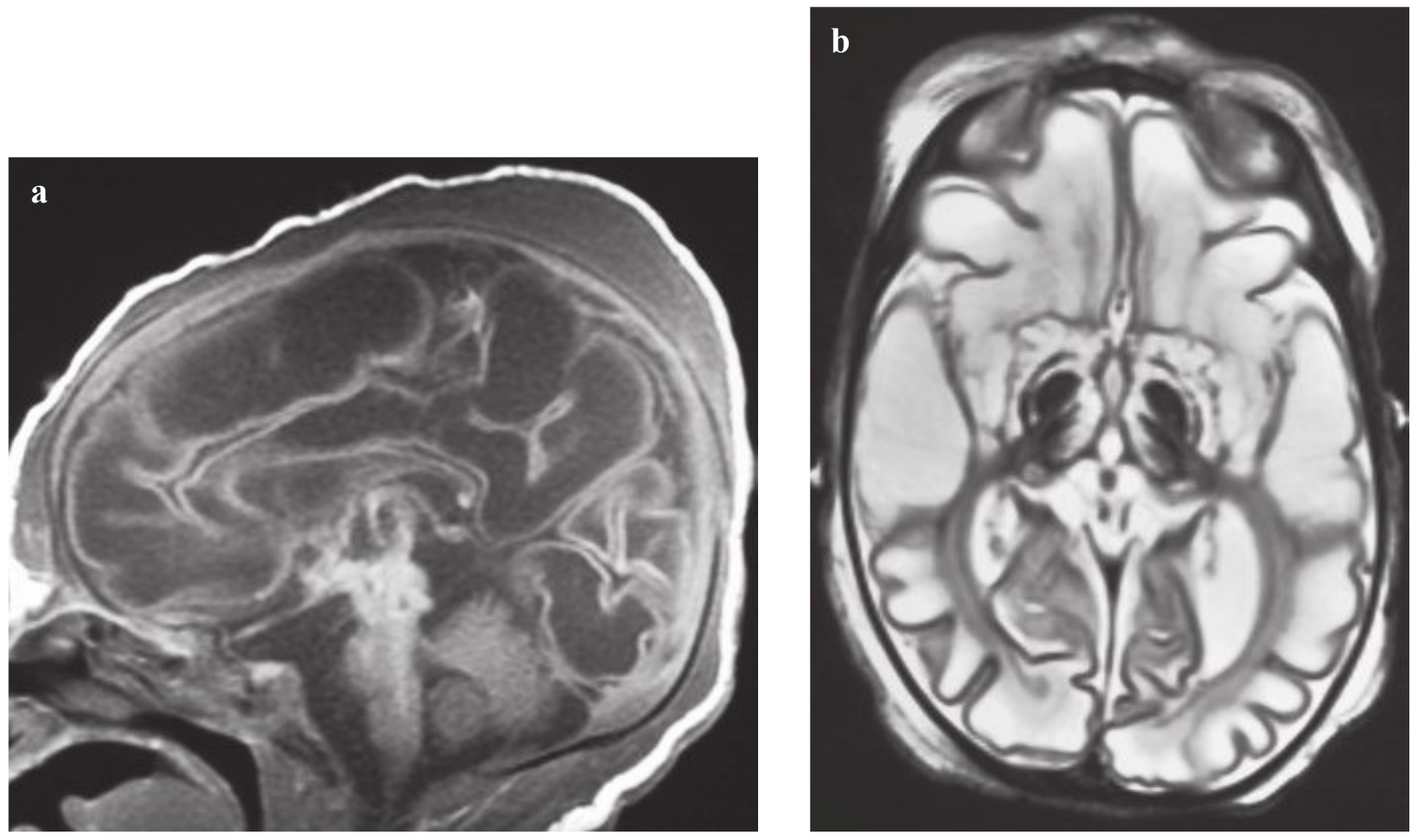

Fig. 1.387 A 1-day-old male with prenatal episode of severe hypoxia/hypoperfusion resulting in extensive cystic encephalomalacia on **(a)** sagittal T1WI and **(b)** axial T2WI.

Table 1.9 (cont.) Ischemia and infarction involving the brain and/or brainstem in children

Lesion/Disorder	Imaging Findings	Comments
Preterm Neonates		Hypoxic-ischemic injuries vary depending on the duration and severity of the hypoxia and hypotension, as well as the neonate's gestational age. Areas in the brain with maximal selective vulnerability vary based on gestational age. In brains of preterm neonates, areas with high metabolic demand associated with increased selective vulnerability to hypoxia tend to occur at sites that have relatively advanced myelination. The thalamus and globus pallidus are myelinated by 24–25 weeks of gestation and show selective vulnerability to hypoxia after this time, whereas the caudate and putamen (corpus striatum) and perirolandic cortex myelinate at 35–36 weeks and show susceptibility to hypoxic injury afterward. Another site of selective vulnerability to hypoxia related to high metabolic demand is the germinal matrix, from 8 to 28 weeks of gestation. Sites of selective vulnerability to hypoxia that occur with the developing cerebral white matter are related to the locations of pre-oligodendrocytes (late oligodendrocyte precursor cells) and watershed vascular zones between the periventricular and subcortical white matter.

Lesion/Disorder	Imaging Findings	Comments
Preterm neonates: Severe hypoxic-ischemic injuries (**Fig. 1.388**)	CT: • Severe hypoxic-ischemic injuries may be seen as zones with decreased attenuation in the basal ganglia and thalami, as well as in the cerebral and cerebellar cortex, with blurring of the gray–white matter junctions. • Diffuse cerebral edema is associated with effacement of sulci. MRI: • Within the first 24 hours, ischemic changes from severe hypoxia can be seen as zones with high signal on diffusion-weighted imaging and low signal on ADC maps secondary to cytotoxic edema, with restricted diffusion involving the thalami > basal ganglia, cerebellum, and brainstem. In the first week, abnormal ADC values associated with severe hypoxic injury involving the thalami and basal ganglia typically measure less than 0.8×10^{-3} mm^2/s, pseudonormalize after the first week, and may be increased after the second week. • With diffusion tensor imaging (DTI), fractional anisotropy in the thalami and basal ganglia is typically decreased significantly for at least 3 weeks after birth, even after pseudonormalization of ADC values. • On magnetic resonance spectroscopy, poor outcome in neonates after resuscitation (within 48 hours) is related to a large decrease in the NAA:creatine ratio, elevated lactate:NAA ratios greater than 0.5, and a lactate:choline ratio of greater than 1. • Increased signal on T1-weighted imaging in the ventrolateral thalami and to a lesser extent in the putamina can also be seen 2–3 days after birth, and often persists for 2–4 months. This signal alteration may be secondary to mineralization, lipid release from myelin degradation, paramagnetic effects of localized free radicals, and hemorrhage. • Decreased signal on T2-weighted imaging may be seen in these regions after 7–10 days. • Later in the chronic phase of the injury, bilateral zones with high signal on T2-weighted imaging can be seen in the posterior ventrolateral thalami, putamina, and corticospinal tracts.	With severe hypoxic/hypotensive ischemic injuries involving preterm neonates, a central pattern of abnormal restricted diffusion can be seen from cytotoxic edema in the ventrolateral thalami, basal ganglia, hippocampi, cerebellum, and corticospinal tracts. The central pattern of restricted diffusion and signal abnormality in neonatal ischemia is associated with a severe lack of oxygen (hypoxia) and blood flow (hypoperfusion) to the brain over a relatively short time period (several minutes) that results in damage to sites with high metabolic demand. This pattern occurs with severe cerebral hypotension and markedly reduced or absent cerebral blood flow to the level where shunting of blood to the sites with high metabolic demand (basal ganglia, thalami, and brainstem) no longer occurs. The abnormal increased signal on diffusion-weighted imaging (DWI) at these locations can be seen within the first 24 hours after birth, with progressively greater restricted diffusion seen on ADC maps over the next 4–5 days. In most cases, restricted diffusion is not seen after 10–12 days, and in some cases after only 4 days. The pathophysiology associated with severe hypoxia at these vulnerable sites in neonates has been suggested to be related to abnormally high toxic concentrations of excitatory neurotransmitters (glutamate, aspartate) causing depolarization of neuronal membranes with high neonatal metabolic activity. This hyperexcitatory state produces a cascade of adverse metabolic events that progresses to neuronal cell death. Active neonatal myelination also occurs at these sites, where there are pre-oligodendrocytes and oligodendrocyte progenitor cells containing levels of glutamate receptors associated with increased vulnerability to glutaminergic excitatory toxicity, which also makes them prone to ischemic injury from acute severe hypoxia.
Preterm neonates: Mild-moderate hypoxic-ischemic injuries		In preterm neonates exposed to episodes of mild-moderate hypoxia, two types of injuries to the brain can be seen, those causing germinal matrix hemorrhage and those involving the immature white matter, resulting in periventricular leukomalacia.

(continued on page 323)

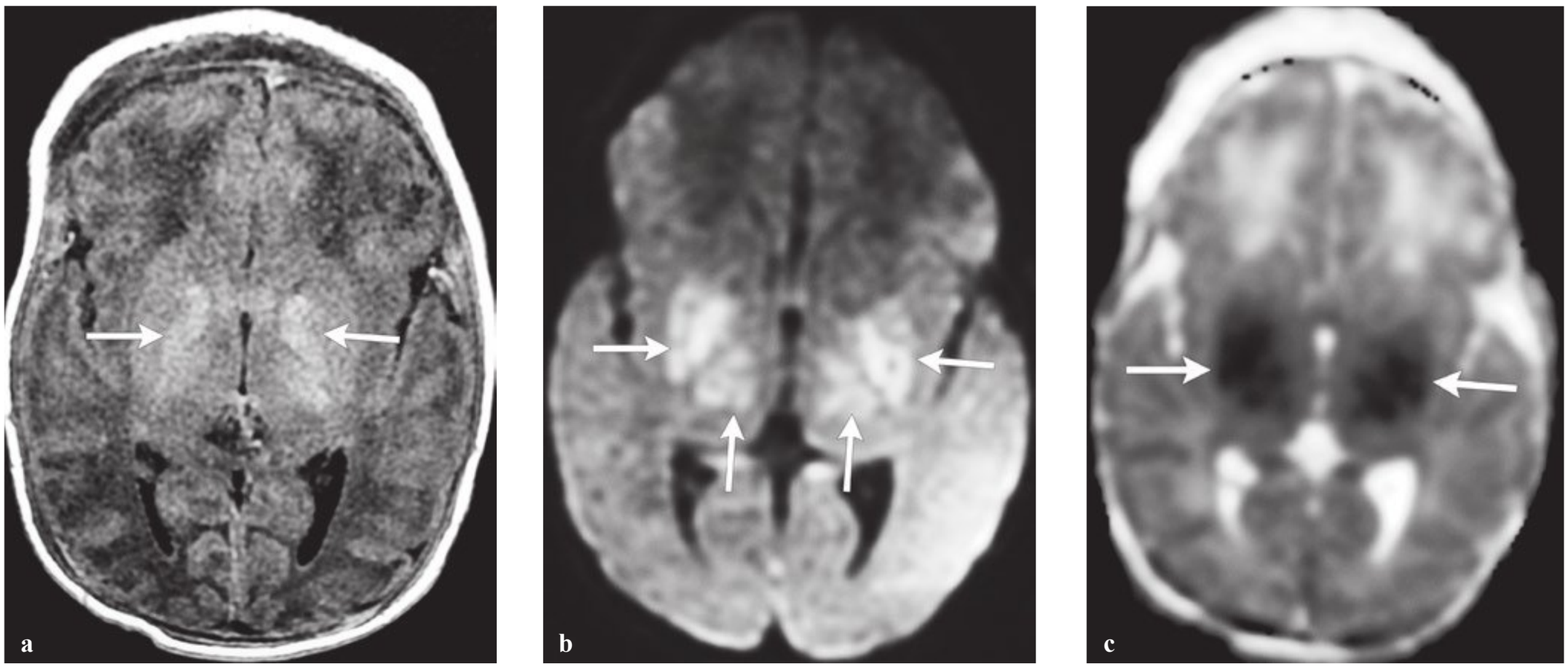

Fig. 1.388 A 4-day-old preterm neonate with perinatal episode of severe hypoxic-ischemic injury. Abnormal high signal on **(a)** axial T1 WI is seen in the putamina (arrows) and ventrolateral thalami with associated restricted diffusion on **(b)** axial DWI (arrows) and **(c)** axial ADC (arrows).

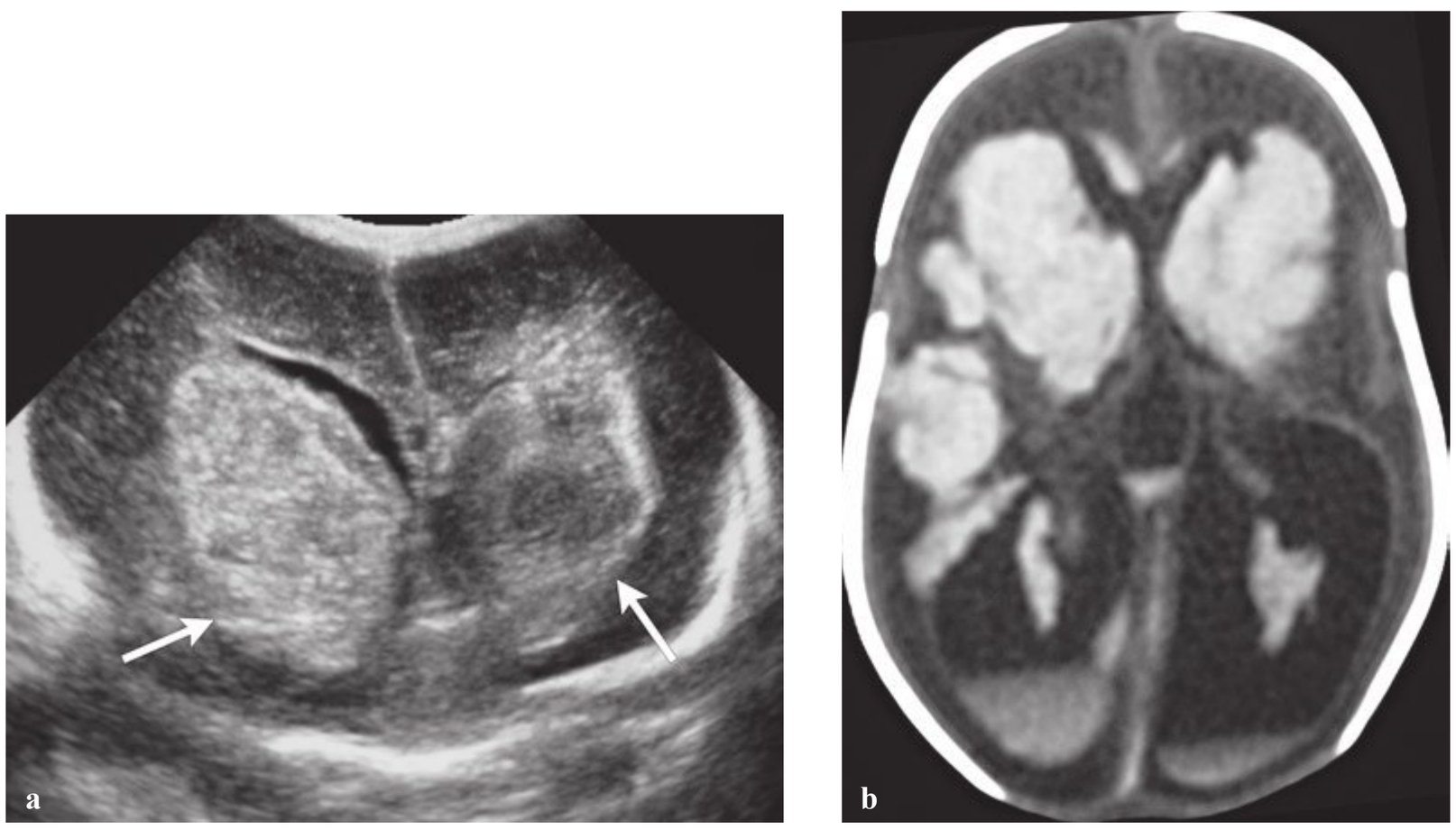

Fig. 1.389 Preterm neonate (26 weeks' gestation) who had a mild-moderate hypoxic-ischemic injury resulting in bilateral germinal matrix hemorrhages as seen on **(a)** coronal sonogram (arrows) and **(b)** subsequent axial CT.

Table 1.9 (cont.) Ischemia and infarction involving the brain and/or brainstem in children

Lesion/Disorder	Imaging Findings	Comments
Preterm neonates: Germinal matrix hemorrhage (**Fig. 1.389**)	Ultrasonography: In the early phases, zones of increased echogenicity at the caudate heads, along the caudothalamic grooves, and within the ventricles—particularly anterior to the foramen of Monro, where there is no confounding echogenic choroid plexus. Can be grouped into four grades of hemorrhage. CT: • Recent germinal matrix hemorrhages typically have increased attenuation. • Intraventicular hemorrhage, when present, shows high attenuation. • Ventricular dilatation may be seen. • By the second week, tissue loss at the hemorrhage results in localized secondary ex vacuo ventricular dilatation. MRI: • In the early phases, germinal matrix hemorrhage has intermediate to high signal on T1-weighted images from methemoglobin and low signal on T2-weighted images from intracellular methemoglobin. • Hemorrhage within the ventricles also is often seen. • By the second week, tissue loss at the hemorrhage results in localized secondary ex vacuo ventricular dilatation.	The germinal matrix is a site of selective vulnerability to hypoxia related to high metabolic demand. The germinal matrix, which is located along the caudothalamic groove and at the external granular layer of the cerebellum, consists of cells that give rise to neurons and glial cells of the developing brain from 8 to 28 weeks of gestation. The germinal matrix regresses after 28 weeks of gestation, with complete involution by 34 weeks. Premature or preterm neonates of less than 34 weeks' gestation and weighing less than 2,000 g have a 25%risk of periventricular and/or intraventricular hemorrhage that occurs within the first 24 hours after birth in 40% of cases and within 4 days in 90%of cases. Most of these hemorrhages are associated with the germinal matrix. The germinal matrix contains a rich network of capillaries that are lined by only a simple endothelium and lack muscular or collagenous support. The vascularity of the germinal matrix is greater than that of the other portions of the brain. The endothelial cells lining the capillaries of the germinal matrix also have 3–5 times the number of mitochondria per cell compared with the endothelial cells of systemic capillaries and have an increased selective vulnerability to hypoxia because of their high demand for oxidative phosphorylation. Hypoxia and ischemia in the preterm neonate results in damage to the capillaries of the germinal matrix. If reperfusion occurs, the injured germinal matrix is prone to hemorrhage. The severity of the germinal matrix hemorrhage can be grouped into four grades: Grade I: subependymal hemorrhage occurs without, or with only minimal, intraventricular extension. Grade II: the subependymal hemorrhage extends into the ventricles without ventricular dilatation. Grade III: the subependymal hemorrhage extends into the ventricles with associated ventricular dilatation. Grade IV: periventricular hemorrhages secondary to venous infarction extend into the ventricles. Survival for grades III and IV hemorrhages is ~ 26%, whereas survival for grades I and II is ~ 67%

(continued on page 324)

Table 1.9 (cont.) Ischemia and infarction involving the brain and/or brainstem in children

Lesion/Disorder	Imaging Findings	Comments
Periventricular leukomalacia (PVL; white matter injury of prematurity) (**Fig. 1.390** and **Fig. 1.391**)	Ultrasonography: • In the first 24 hours, irregular or globular zones of echogenicity are seen in the periventricular white matter. • At 2–4 weeks, pseudonormalization of damaged brain parenchyma may be observed. • At 2–6 weeks, anechoic to hypoechoic zones representing periventricular cystic zones may be seen at the damaged tissue. • By 6 months, periventricular cystic zones progress to tissue loss and associated ventricular enlargement (end-stage PVL). CT: • Useful in confirming the presence or exclusion of recent germinal matrix hemorrhage. • May not show definite findings in first 4 weeks. • Can show zones of decreased attenuation in periventricular cystic zones in subacute phases. • Shows ex vacuo ventricular dilatation in end-stage PVL. MRI: • In the early phases, signal abnormalities can be seen in the immature white matter as poorly defined zones with increased signal on T2-weighted images, with or without foci with intermediate or slightly high signal on T1-weighted images at 3–4 days. Small zones of decreased signal on T2-weighted images may be seen after 6–7 days from small sites of hemorrhage or mineralization. • In the first week after birth, acute changes of PVL can be seen on diffusion-weighted images (DWI) with ADC maps as zones with restricted diffusion in the cerebral white matter and are less than 1.10^{-3} mm^2/s. ADC values often "normalize" (referred to as pseudonormalization) after the first week, and may be increased after the second week. • With diffusion tensor imaging (DTI), fractional anisotropy (FA) values in cerebral white matter are decreased for at least 3 weeks after delivery, even after pseudonormalization of ADC values on DWI. • At 2–6 weeks, evolve into periventricular cystic zones may be seen at the damaged tissue. • By 6 months, periventricular cystic zones evolve into gliosis and localized encephalomalacia in the damaged white matter associated with secondary ventricular enlargement (end-stage PVL).	Within the developing cerebral white matter, sites of selective vulnerability to hypoxia are related to the locations of pre-oligodendrocytes (late oligodendrocyte precursor cells), and watershed vascular zones between the periventricular and subcortical white matter. The sensitive pre-oligodendrocytes show progressive maturity by 32 weeks, after which hypoxic lesions in the white matter decline in frequency. The watershed vascular border zones in the cerebral white matter also change in location based on maturity. Watershed vascular zones in immature cerebral white matter migrate from a periventricular location to a more subcortical location in the third trimester. The repositioning of the watershed vascular zones is related to the developing arterial supply to the immature white matter, with progressive shifting from ventriculopetal arteries from the outer brain surface to ventriculofugal arteries. Hypoxic injuries to cerebral white matter in preterm neonates involve the watershed vascular zones in the periventricular white matter in the late second trimester and early third trimester and are observed later in locations closer to the cortex, where the watershed vascular zone has shifted centrifugally. These hypoxic and hypoperfused lesions involving the immature cerebral white matter result in periventricular leukomalacia, also referred to as white matter injury of prematurity.
Term Neonates		MRI is a useful in the detection of acute perinatal/neonatal strokes from focal arterial occlusions and/or hypoxic-ischemic injuries. In neonates with strokes, three patterns of restricted diffusion and signal abnormality are seen with MRI: a focal pattern secondary to an arterial occlusion, and central and peripheral patterns of restricted diffusion and signal abnormality secondary to severe and mild-moderate hypoxia, respectively. In some cases, mixed central and peripheral patterns of restricted diffusion may be seen in neonates with severe hypoxia.

(continued on page 326)

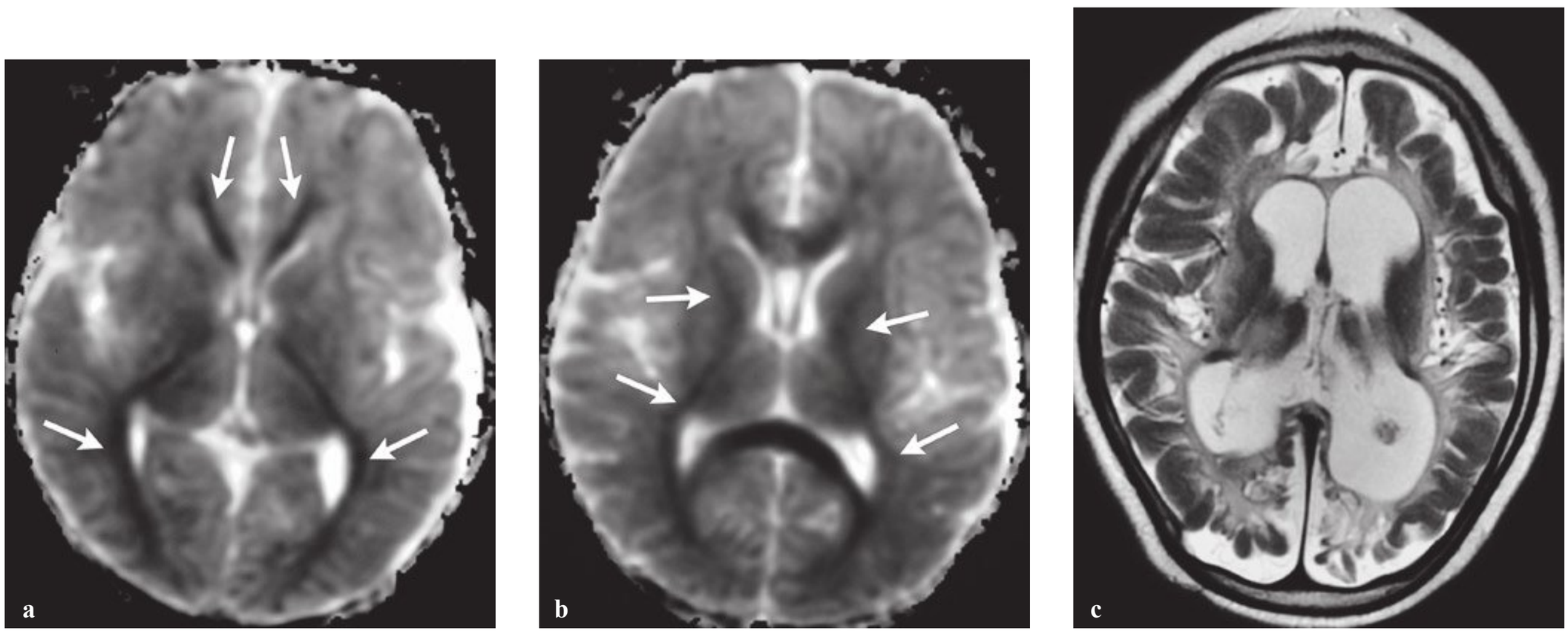

Fig. 1.390 Neonate (31 weeks' gestation) with white matter ischemic injury of prematurity. Zones with restricted diffusion are seen in the cerebral white matter bilaterally (arrows) on **(a,b)** axial ADC. **(c)** Axial T2WI 5 years later shows periventricular leukomalacia with gliosis and encephalomalacia in the damaged white matter associated with secondary ventricular enlargement (end-stage PVL).

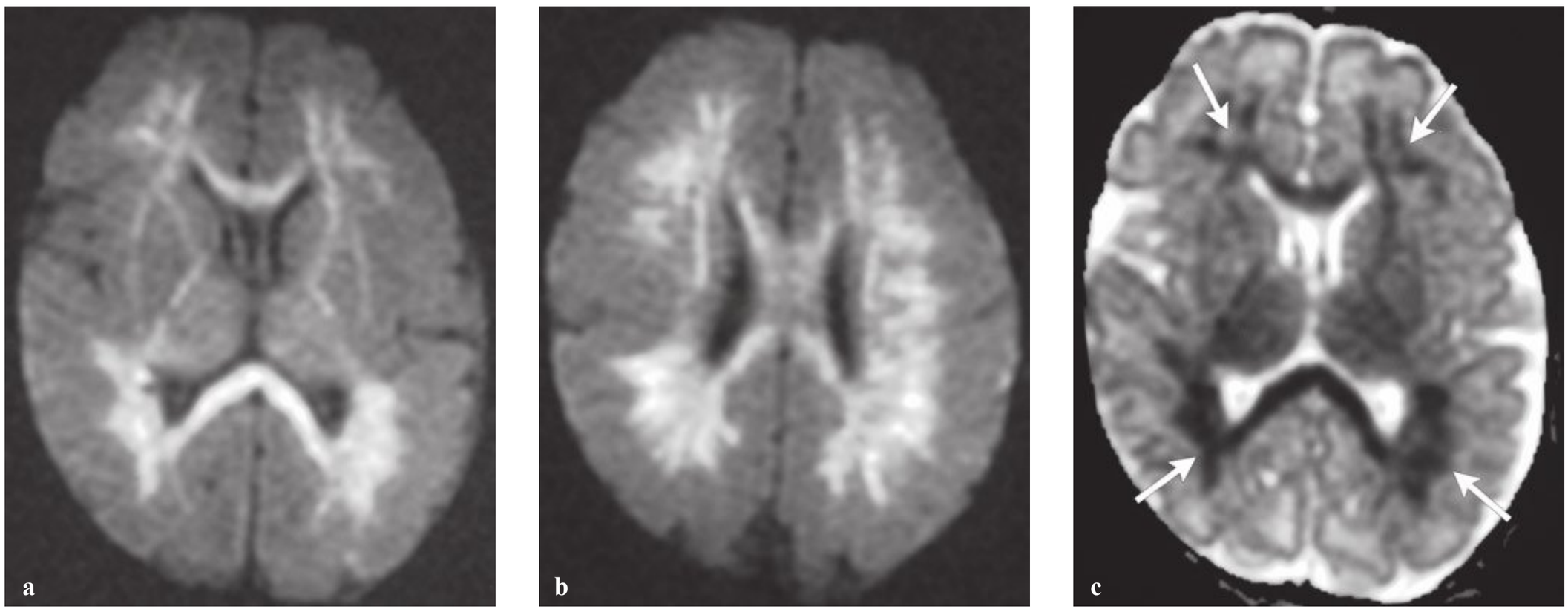

Fig. 1.391 Premature neonate with extensive white matter injury of prematurity as seen as large zones with restricted diffusion in the cerebral white matter on **(a,b)** axial DWI and **(c)** ADC (arrows).

Table 1.9 (cont.) Ischemia and infarction involving the brain and/or brainstem in children

Lesion/Disorder	Imaging Findings	Comments
Term neonates: Severe hypoxic injuries (**Fig. 1.392** and **Fig. 1.393**)	CT: • Severe hypoxic-ischemic injuries may be seen as zones with decreased attenuation in the basal ganglia and thalami 1–7 days after injury, as well as in the cerebral and cerebellar cortex with blurring of the gray–white matter junctions. • Diffuse cerebral edema associated with effacement of sulci. MRI: • Within the first 24 hours, ischemic changes from severe hypoxia can be seen as zones with high signal on diffusion-weighted imaging and low signal on ADC maps (secondary to cytotoxic edema with restricted diffusion) in the ventrolateral thalamus, putamina, corticospinal tracts, and/or perirolandic cortex. In the first week, abnormal ADC values associated with severe hypoxic injury in the thalami and basal ganglia typically drop to less than 50%of normal values and measure less than 0.8×10^{-3} mm^2/s. The ADC values pseudonormalize after the first week and may be increased after the second week. Significantly abnormal ADC values can be seen in the basal ganglia and thalami in the first week, even when there are minimal or no apparent signal abnormalities seen on diffusion-weighted imaging MRI. • With diffusion tensor imaging (DTI), fractional anisotropy (FA) in the thalami and basal ganglia is typically decreased significantly for at least 3 weeks after birth, even after pseudonormalization of ADC values. • Slightly high to high signal on T1-weighted images can be seen in the putamina and ventrolateral thalami 2–3 days after birth, and often persists for 2–4 months. These signal changes may be related to the effects of mineralization, lipid release from myelin degradation, paramagnetic effects of localized free radicals, and hemorrhage. • Decreased signal on T2-weighted images may be seen in these regions after 7–10 days. • Absence of the normal linear zone of high signal on T1-weighted images and loss of the normal low signal on T2-weighted images at the posterior limbs of the internal capsules in neonates with gestational ages greater than 36–37 weeks, and who are imaged more than 48 hours after the hypoxic injury. • Use of gadolinium contrast does not contribute to the diagnosis of hypoxic-ischemic injury, and its use is not necessary for these ill newborn patients. • Later in the chronic phase of the injury, bilateral zones with high signal on T2-weighted images can be seen in the posterior putamina, ventrolateral thalami, and corticospinal tracts. • Findings of hypoxic-ischemic injuries on hydrogen magnetic resonance spectroscopy include: elevation of the ratio of choline to creatine, decreased N-acetylaspartate (NAA), and presence of a lactate peak within the first 48 hours after birth. Abnormally elevated lactate peaks in the basal ganglia and cerebral white matter can be seen within the first 24 hours and are often maximal at 5 days. Abnormal lactate levels are associated with a poor prognosis. • FLAIR can be useful for detecting glial scar in the late phase of hypoxic-ischemic injuries, although it has minimal value in the initial neonatal evalution for hypoxic injuries because of its insensitivity to acute edema in the newborn.	With severe hypoxic/hypotensive ischemic injuries in neonates, a central pattern (also referred to as the basal nuclei-predominant pattern) of restricted diffusion is seen in the ventrolateral thalamus, putamina, corticospinal tracts, and/or perirolandic cortex. The central pattern of restricted diffusion and signal abnormality is associated with a severe lack of oxygen (hypoxia) and blood flow (hypoperfusion) to the brain over a relatively short time period (several minutes) that results in damage to sites with high metabolic demand, such as the ventrolateral thalami, putamina, hippocampi, lateral geniculate nuclei, posterior limbs of the internal capsule, and dorsal mesencephalon. This pattern occurs with severe cerebral hypotension and markedly reduced or absent cerebral blood flow to the level where shunting of blood to the sites with high metabolic demand (basal ganglia, thalami, brainstem, sensorimotor cortex) no longer occurs. The abnormal increased signal on diffusion-weighted imaging at these locations can be seen within the first 24 hours after birth, with progressively greater restricted diffusion seen on ADC maps over the next 4–5 days. In most cases, restricted diffusion is not seen after 10–12 days, and in some cases in only 4 days. The pathophysiology associated with severe hypoxia at these vulnerable sites in neonates has been suggested to be related to abnormally high concentrations of excitatory neurotransmitters (glutamate, aspartate) associated with N-methyl-D-aspartate membrane receptors in these locations, causing depolarization of neuronal membranes with high neonatal metabolic activity. This hyperexcitatory state produces a cascade of adverse metabolic events (abnormal increased calcium influx, activation of second messenger systems, activation of proteases and lipases, release of intracellular stores of calcium, mitochondrial dysfunction, formation of free radicals and free fatty acids) that progresses to neuronal cell death. Active neonatal myelination also occurs at these sites, where there are pre-oligodendrocytes and oligodendrocyte progenitor cells containing levels of glutamate receptors associated with increased vulnerability to glutaminergic excitatory toxicity, which also makes them prone to ischemic injury from acute severe hypoxia.

(continued on page 328)

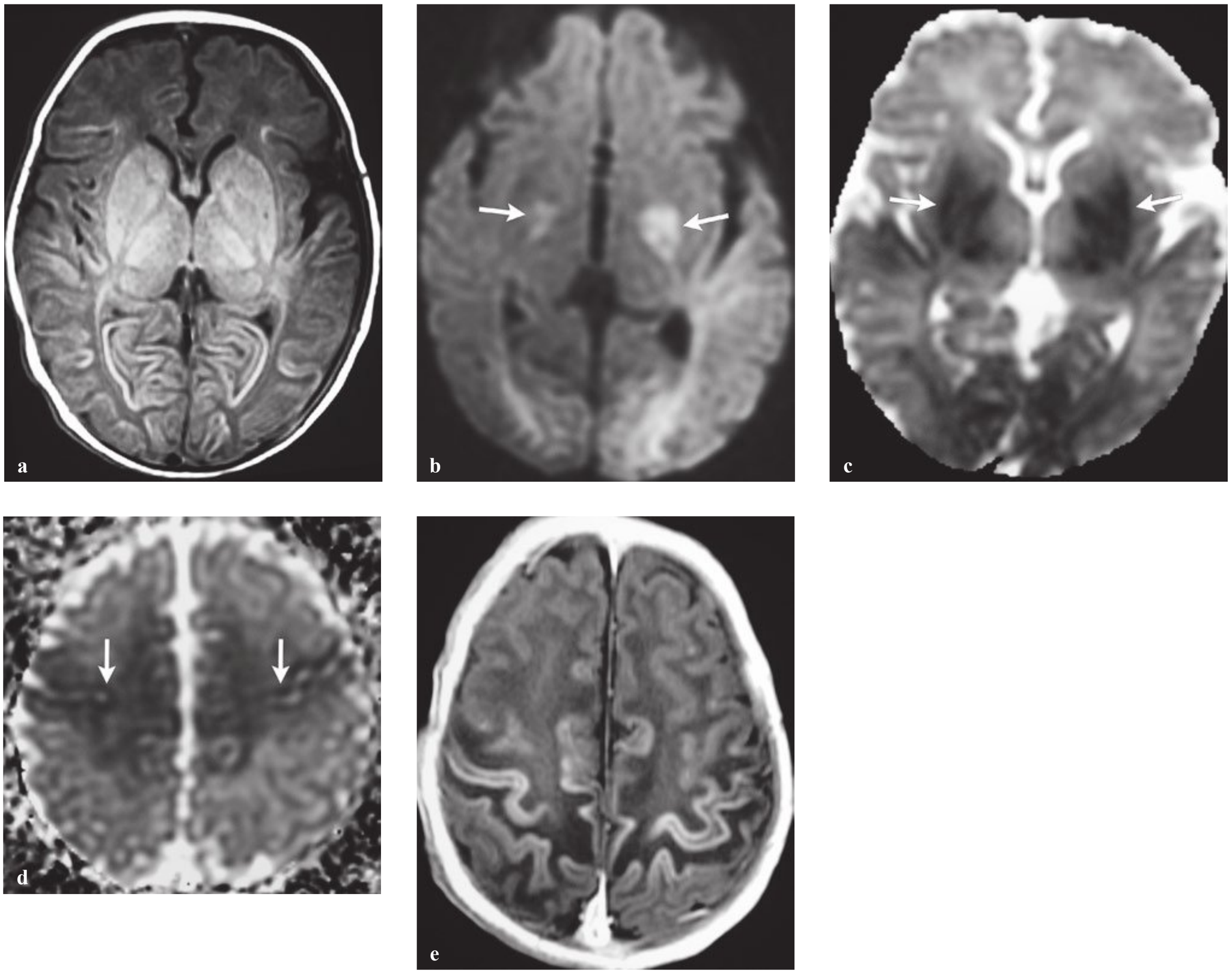

Fig. 1.392 Severe hypoxic injury in a 7-day-old term neonate. Abnormal high signal on **(a)** axial T1 WI is seen in the putamina and thalami relative to the internal capsules. Corresponding restricted diffusion is seen in the putamina, thalami (arrows), and occipital lobes on **(b)** axial DWI and **(c)** ADC, as well as in the perirolandic cortex (arrows) on **(d)** axial ADC. 2 weeks later, cortical laminar necrosis is seen as high signal on **(e)** axial T1 WI in the perirolandic cortex.

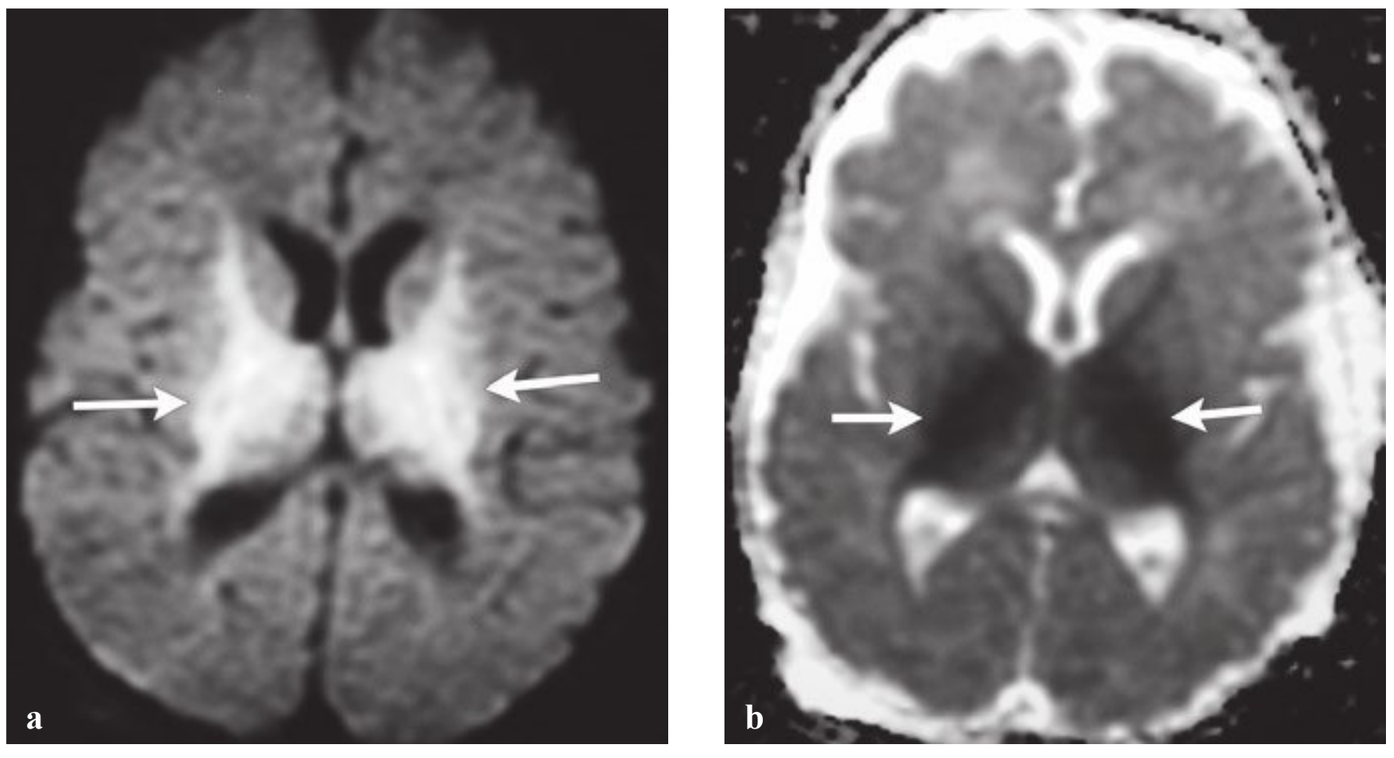

Fig. 1.393 Severe hypoxic-ischemic injury in a 27-day-old term neonate with restricted diffusion in the thalamus, putamina, and internal capsules on **(a)** axial DWI (arrows) and **(b)** ADC (arrows).

Table 1.9 (cont.) Ischemia and infarction involving the brain and/or brainstem in children

Lesion/Disorder	Imaging Findings	Comments
Term neonates: Moderate-severe hypoxic injuries (**Fig. 1.394**)	CT: Diffuse decreased attenuation can be seen in the brain, with blurring of the gray–white matter junction; it can also involve the basal ganglia and thalami 1 to 7 days after injury. There is diffuse brain swelling with narrowing of ventricles and sulci. MRI: • Within the first 24 hours, ischemic changes from moderate-severe hypoxia can be seen as zones with high signal on diffusion-weighted imaging and low signal on ADC maps in the cerebral cortex and subcortical white matter, ± basal ganglia and thalami. • Slightly high to high signal on T1-weighted images can be seen diffusely in the putamina and ventrolateral thalami 2–3 days after birth, and often persists for 2–4 months. • Diffuse abnormal increased signal on T2-weighted images is seen involving both the gray and white matter, often without involving the ventrolateral thalami and putamina. • Extensive cystic encephalomalacia can be seen on subsequent imaging.	With moderate-severe hypoxic/hypotensive ischemic injuries in neonates, extensive diffuse injury can involve the cerebral and cerebellar cortex, seen as restricted diffusion, as well as having varying degrees of involvement of the basal ganglia, thalami, and white matter. Abnormal increased signal on diffusion-weighted imaging at these locations can be seen within the first 24 hours after birth, with progressively greater restricted diffusion seen on ADC maps over the next 4–5 days. In most cases, restricted diffusion is not seen after 10–12 days.

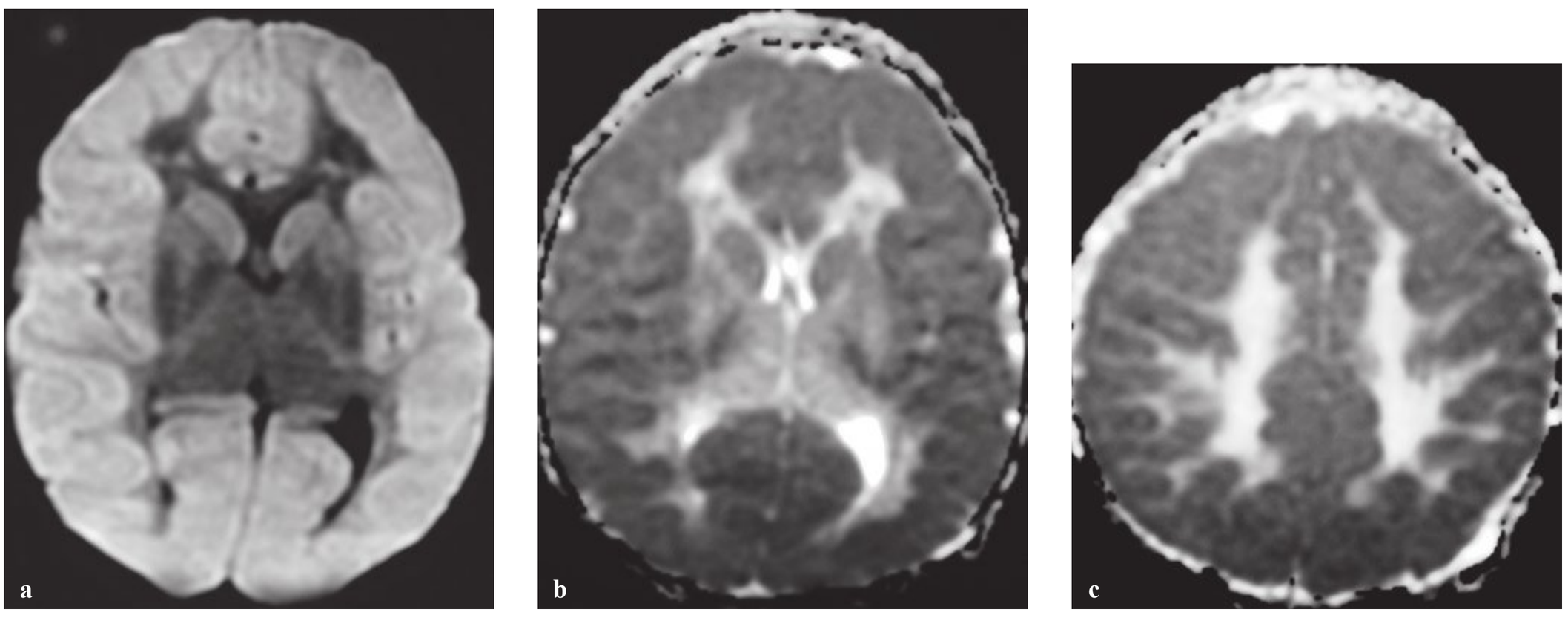

Fig. 1.394 Moderate-severe hypoxic injury in a neonate seen as zones with high signal on **(a)** DWI and low signal on **(b,c)** ADC in the cerebral cortex and subcortical white matter.

Lesion/Disorder	Imaging Findings	Comments
Term neonates: Mild-moderate hypoxic injuries (**Fig. 1.395** and **Fig. 1.396**)	CT: • Cerebral edema associated with effacement of sulci may be seen. • Abnormal attenuation of the cerebral cortex in the watershed vascular zones may not be apparent in the acute phase, and MRI is preferred for evaluation. MRI: • Within the first 24 hours, ischemic changes from mild-moderate hypoxia can be seen as zones with high signal on diffusion-weighted imaging and low signal on ADC maps (secondary to cytotoxic edema with restricted diffusion) in the cerebral cortex and subcortical white matter at watershed vascular boundary zones of the cerebrum (frontal lobes and parieto-occipital regions) and cerebellum. In the first week, abnormal ADC values associated with hypoxic injury pseudonormalize, and may be increased after the second week. • Signal abnormalities on T1- and T2-weighted images may be absent in the first 24 hours. • At 2 days, loss of distinction between cortical gray and white matter occurs on T2-weighted images secondary to increased abnormal signal of the cortex. The signal abnormalities on T2-weighted images usually underestimate the extent of ischemia in the white matter as seen on diffusion-weighted imaging. Edema in white matter may be better seen on T1- than on T2-weighted images. • With mild-moderate hypoxia, signal abnormalities are often not seen in the basal ganglia or thalami. • Magnetic resonance hydrogen spectroscopy shows elevation of choline relative to creatine, decreased N-acetylaspartate (NAA), and presence of a lactate peak within the first 48 hours after birth in the cerebral cortex and subcortical white matter in the watershed zones, as well as, to a much lesser extent, the deep gray matter. The lactate peak is often maximal at 5 days. Poor outcome after resuscitation is related to a large decrease in the NAA:creatine ratio and elevation of the lactate:creatine ratio in the first day. • In the late stages, decreased white matter volume and cortical thinning are seen at the sites of injury in the watershed vascular zones. The extent of glial scar from reactive astroglial cells in the white matter is often best seen near the end of the first year relative to the contrast of gliosis from the signal of myelination in unaffected tissue. • Use of gadolinium contrast does not contribute to the diagnosis of hypoxic-ischemic injury, and its use is not necessary in ill newborn patients. • Late phases may show ulegyria, in which there is asymmetrically greater gliosis and volume loss in the deeper subgyral white matter adjacent to the sulcus than in the more peripherally located subcortical white matter, producing a malformed, “mushroom-shaped” gyrus. This is secondary to the more robust vascular supply to the superficial portion of the gyrus than to the deeper portions in neonates. Ulegyria is most frequently seen in the watershed vascular zones between the major cerebral arteries. FLAIR can be useful for detecting glial scar in the late phase of hypoxic-ischemic injuries, although it has minimal value in the initial neonatal evaluation for acute hypoxic injuries because of its insensitivity to acute edema in the newborn.	With mild-moderate hypoxia, a peripheral pattern (also referred to as watershed-predominant pattern) of restricted diffusion and signal abnormality is seen that involves the cerebral cortex and adjacent white matter but spares the ventrolateral thalamus, corticospinal tracts, and perirolandic cortex. Unlike in adults, where hypoxic injuries result in quick cell death from ischemic necrosis, similar hypoxic injuries in neonates can result not only in immediate cell death from ischemic necrosis, but also in cell death from three other pathways (delayed necrosis, delayed apoptosis, and/or delayed apoptosis/necroapoptosis) that result in delayed but eventual cell death. Delayed necrosis results from hypoxia followed by transient recovery after reperfusion, although with subsequent eventual cell death by ischemic necrosis from malfunctioning of ATP production secondary to the initial injury. Delayed apoptosis occurs due to transient hypoxia and ischemia that activates caspase and caspase-independent mechanisms of programmed cell death (apoptosis) without malfunctioning of cellular ATP production. Delayed apoptosis or necroapoptosis represents both activation of programmed cell death (apoptotic) pathways and ischemic necrosis. These mechanisms of delayed cell death can affect the timing and extent of zones with restricted diffusion seen with MRI in neonates with hypoxic-ischemic injuries.

(continued on page 331)

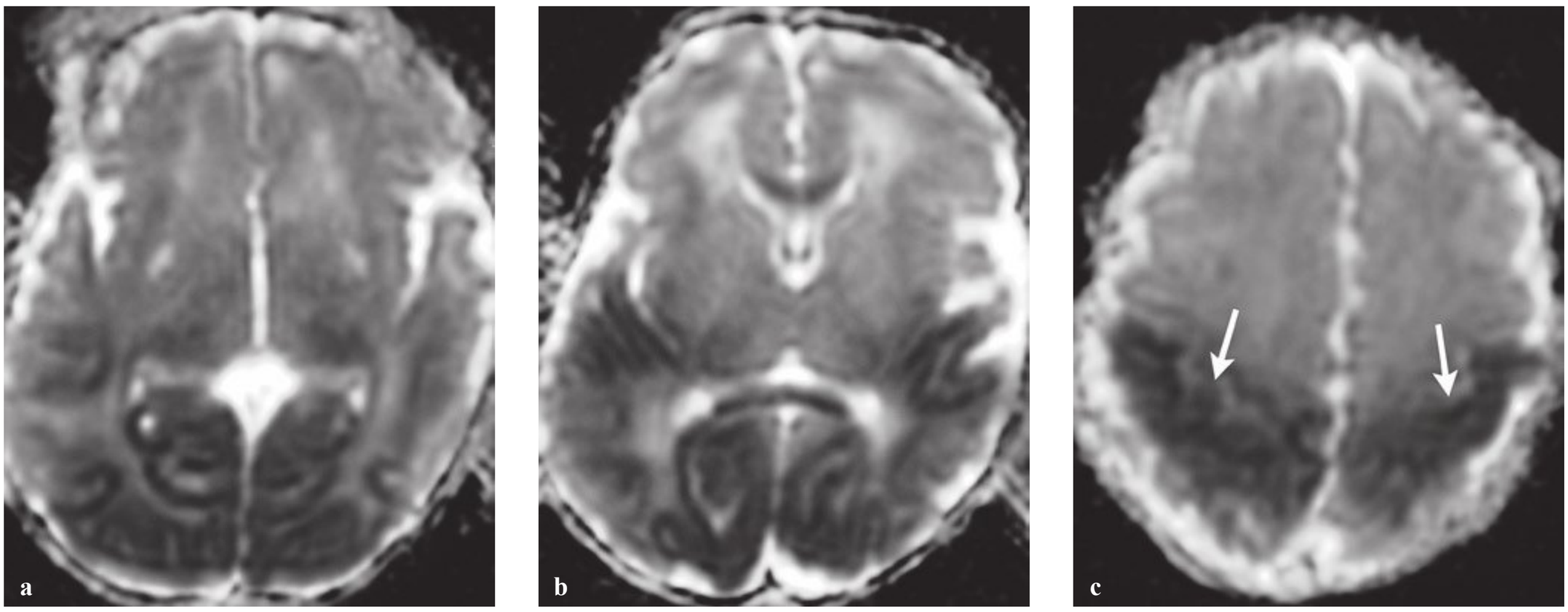

Fig. 1.395 Mild-moderate hypoxic injuries in a 3-day-old term neonate. Zones with restricted diffusion with low signal on **(a,b)** ADC are seen in the cerebral cortex and subcortical white matter of the cerebrum between the frontal and parietal lobes, and **(c)** between the parietal and occipital lobes (arrows).

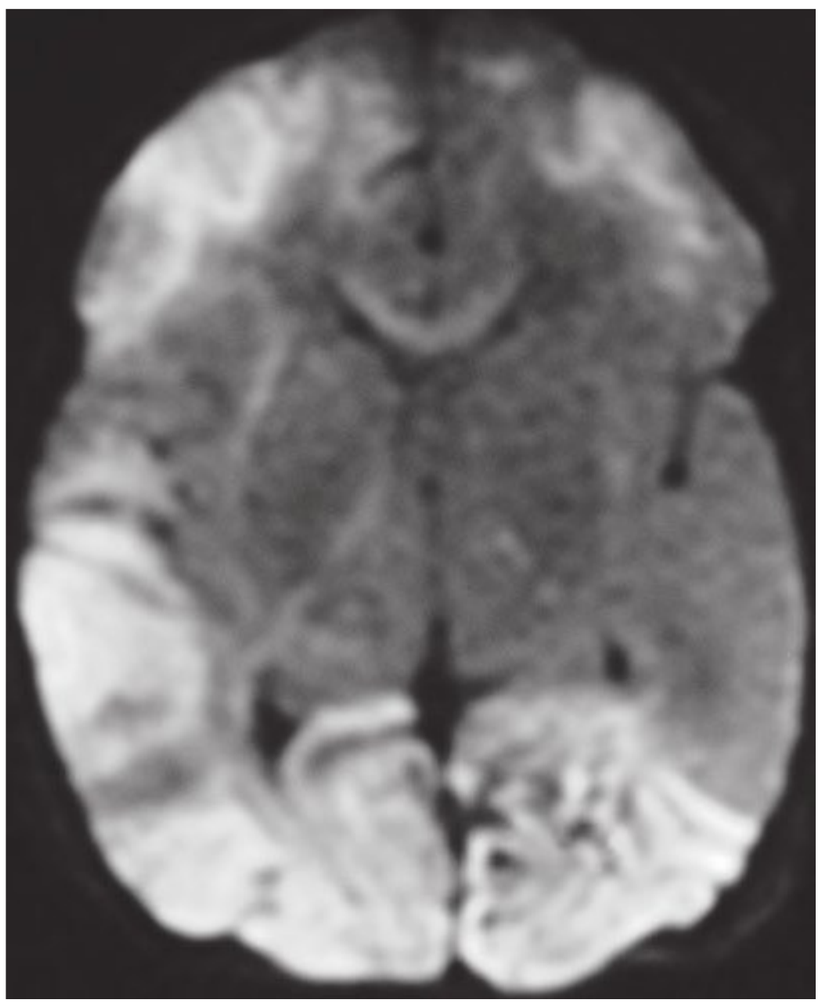

Fig. 1.396 Mild-moderate hypoxic injuries in a 5-day-old term neonate. Multiple zones with high signal from restricted diffusion on axial DWI are seen in the cerebral cortex and subcortical white matter in the frontal, parietal, and occipital lobes.

Table 1.9 (cont.) Ischemia and infarction involving the brain and/or brainstem in children

Lesion/Disorder	Imaging Findings	Comments
Term neonates: Neonatal ischemia from anoxia followed by hypoperfusion	Hypoperfusion injuries show two types of MRI findings. In term infants, hypoperfusion ischemic changes are seen in the centrum semiovale between the lateral ventricle and cortex. Hypoperfusion ischemic changes also occur at the watershed vascular zones between the anterior and middle cerebral arteries, and between the middle and posterior cerebral arteries. Lesions appear as symmetric zones with abnormal high signal on T2-weighted images and restricted diffusion at the watershed vascular zones (anterior and posterior quadrants).	In neonates with asphyxia and anoxia, cardiopulmonary arrest can occur, causing hypoperfusion ischemic injuries in addition to the hypoxic-ischemic injuries.
Term neonates: Hyperacute and acute infarcts from arterial occlusion (**Fig. 1.397**) Hyperacute infarct (< 12 hours) Acute infarct (12 to 24 hours) Acute infarct (< 24 hours)	CT: Hyperacute infarct (< 12 hours): • Zone of decreased attenuation in cerebral cortex and adjacent white matter at the site of infarction. • Some cases can have no apparent findings on CT. Acute infarct (12–24 hours): • Decreased attenuation in the basal ganglia. • Indistinctness at borders between cerebral cortex and adjacent white matter. • Subtle decrease in attenuation in brain in the vascular distribution of the infarct, with or without localized edema and sulcal effacement. MRI: Hyperacute and acute infarct: • High signal on diffusion-weighted imaging and low signal on ADC maps at infarct from restricted diffusion. • Absence of flow void in occluded artery. • Intravascular contrast enhancement. • Magnetic resonance hydrogen spectroscopy can show elevated lactate peak at 1.32 ppm, with or without a slight decrease in N-acetylaspartate (NAA) at 2.02 ppm.	Neonatal strokes caused by an arterial occlusion result in a focal pattern of restricted diffusion and signal abnormality at the involved vascular territory. The arterial occlusion may result from emboli, thrombosis, or vasospasm, or it may be idiopathic. Neonatal stroke may be related to pre-eclampsia, chorioamnionitis, or prolonged rupture of membranes. Neonates with focal strokes usually have normal Apgar scores and often present with focal seizures 2–3 days after birth. Most focal arterial neonatal strokes likely occur during birth. Restricted diffusion is seen in the involved territory of the occluded artery. On T2-weighted images, the infarcted cerebral cortex becomes isointense to the unmyelinated white matter after 24 hours, which is referred to as the missing cortex sign. No signal abnormalities may be observed on T2-weighted FLAIR images for focal infarcts in neonates because of the signal of the immature myelin. Subacute focal arterial infarcts in neonates can have increased signal on T1-weighted images and decreased signal on T2-weighted images secondary to petechial hemorrhages, calcifications, or altered myelin metabolites. On CT, focal neonatal cerebral infarcts are seen as zones of abnormal decreased attenuation similar in appearance to infarcts seen in older children and adults.

(continued on page 332)

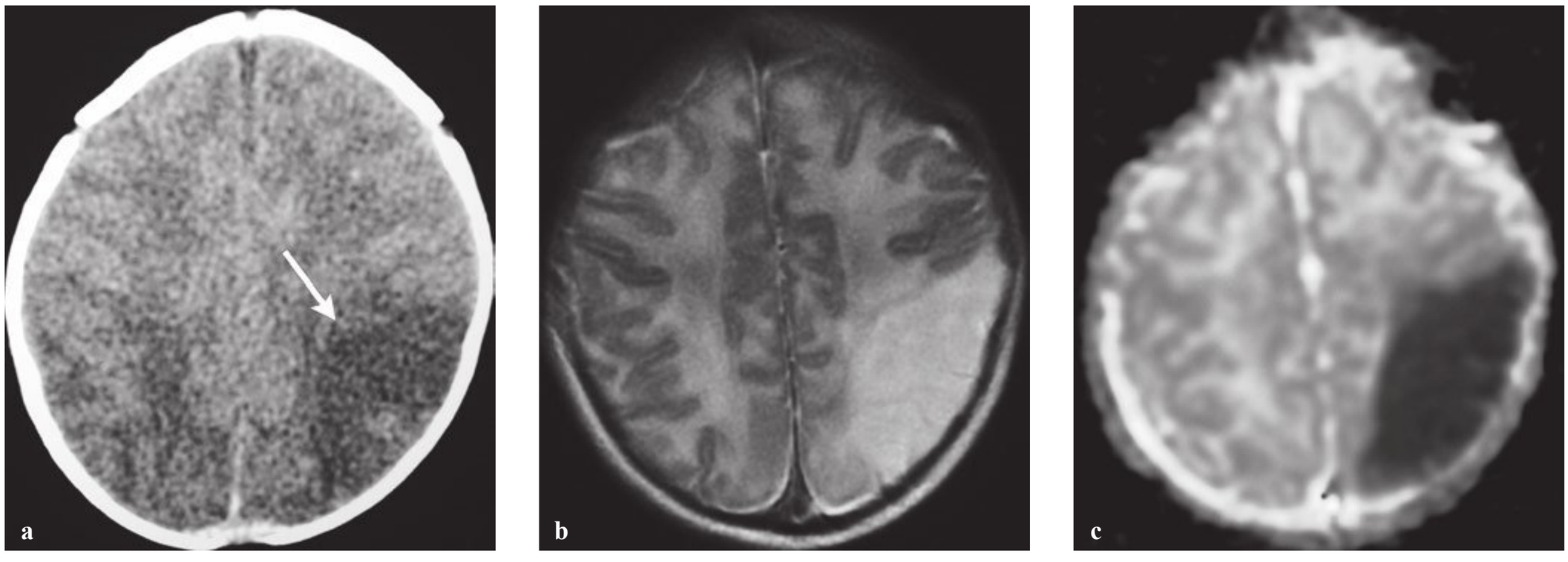

Fig. 1.397 A 2-day-old full-term neonate with acute arterial infarct in the left cerebral hemisphere in the vascular distribution of the left middle cerebral artery. The infarct has low attenuation on **(a)** axial CT (arrow), high signal on **(b)** axial T2WI, and restricted diffusion with low signal on **(c)** ADC.

Table 1.9 (cont.) Ischemia and infarction involving the brain and/or brainstem in children

Lesion/Disorder	Imaging Findings	Comments
Term neonates: Subacute infarcts from arterial occlusion (**Fig. 1.398**) Early subacute infarct (1–3 days on CT) Subacute infarct (4–7 days on CT) Late subacute infarct (1–7 weeks on CT) Early subacute infarct (1–3 days on MRI) Subacute infarct (4–7 days on MRI) Late subacute infarct (1 to 3–4 weeks on MRI)	CT: Early subacute infarct (1–3 days): • Zone of decreased attenuation at infarct becomes more conspicuous. • Increase in edema and localized mass effect associated with infarct (peaks at 3–4 days). • Hemorrhagic transformation may occur at infarct. Subacute infarct (4–7 days): • Mass effect and edema associated with infarct persist. • Gyral pattern of contrast enhancement may be seen. Late subactue infarct (1–7 weeks): • Progressive decrease in localized mass effect and edema. • Slight increase in attenuation of hypodense lesion and blurring of margins, with fogging effect secondary to macrophage invasion and capillary proliferation. • Persistence of contrast enhancement at the infarct. • Dystrophic calcifications may be seen, more commonly in children than in adults. MRI: Early subacute infarct (1–3 days): • High signal on diffusion-weighted imaging, low signal on ADC maps. • Zones with progressive increase in abnormal signal at the involved cortex and/or basal ganglia on T2-weighted images. FLAIR may not show the infarct in neonates because of lack of discrimination of infarct from the signal of adjacent immature white matter. • Involved basal ganglia may show increased signal on T1-weighted images secondary to petechial hemorrhage, release of myelin lipids, and/or mineralization. • Increase in edema and localized mass effect associated with infarct (peaks at 3–4 days). • Early gadolinium contrast enhancement may be seen at the infarct. • . Hemorrhagic transformation may occur at infarct. • Gadolinium contrast enhancement at meninges and within blood vessels declines. Subacute infarct (4–7 days): • Infarct has high signal on T2-weighted imaging and diffusion-weighted imaging, and low signal on ADC maps. • Increase in degree of gadolinium contrast enhancement at infarct may be seen. • Progressive decrease in localized mass effect and edema. • Hemorrhage may be seen. • Resolution of intravascular and meningeal gadolinium contrast enhancement. Late subacute infarct (1 to 3–4 weeks): • Infarct has high signal on T2-weighted imaging. At 2 weeks, diffusion-weighted imaging may show high signal from T2 shine-through effects. ADC maps do not show low signal at infarcts, indicating absence of restricted diffusion that was seen during the first 2 weeks. • Progressive decrease in localized mass effect and edema. • Persistence of contrast enhancement at the infarct. • Dystrophic calcifications may be seen as zones of low signal on T2-weighted imaging, more commonly in children than in adults.	

Lesion/Disorder	Imaging Findings	Comments
Term neonates: Remote infarcts from arterial occlusion Months to years (chronic/old infarct)	CT: • Localized encephalomalacia. • Ipsilateral atrophy of brainstem (Wallerian degeneration). MRI: • Localized encephalomalacia. • Increased signal on T2-weighted imaging and FLAIR at infarct. • Low signal on T1-weighted imaging and diffusion-weighted imaging and high signal on ADC maps. • Presence of zones of low T2 and T2* signal secondary to hemosiderin. • Ipsilateral atrophy of brainstem (Wallerian degeneration).	

(continued on page 334)

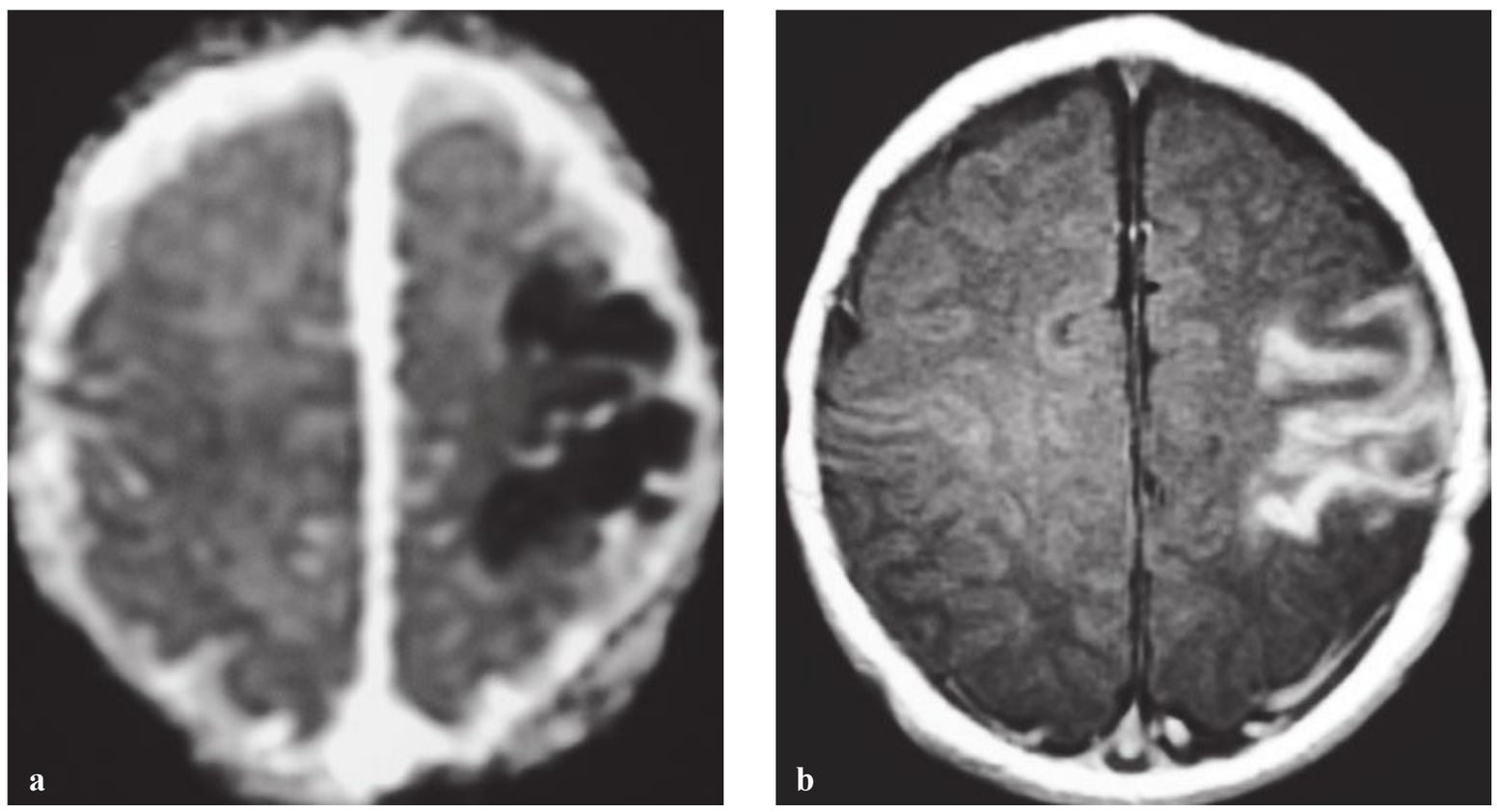

Fig. 1.398 Focal subacute arterial ischemic infarct in a 5-day-old full-term neonate is seen in the left cerebral hemisphere that has restricted diffusion on **(a)** axial ADC, and shows gadolinium contrast enhancement on **(b)** axial T1 WI**.**

Table 1.9 (cont.) Ischemia and infarction involving the brain and/or brainstem in children

Lesion/Disorder	Imaging Findings	Comments
Neonatal sinovenous thrombosis and venous infarction (**Fig. 1.399**)	CT: • Venous infarcts secondary to occlusion of the dural venous sinuses are seen as poorly marginated zones with low or mixed low and intermediate attenuation located in the subcortical white matter with or without regions of high attenuation from hemorrhage. Hemorrhage associated with venous infarcts is seen in 10–50% of cases. Venous infarcts involving the central deep veins (internal cerebral veins, vein of Galen, straight venous sinus) are usually located in the basal ganglia and thalami, and are often associated with intraventicular or thalamic hemorrhage. • Curvilinear and/or round zones of contrast enhancement can be seen at venous infarcts on CT. • Thrombus may be seen on non-contrast-enhanced CT as a dense vessel sign, and/or dense cord sign. • On contrast-enhanced CT, an empty delta sign can be seen with a zone lacking enhancement within a dural venous sinus. • On CT angiography/venography, the venous thrombus shows a zone with minimal enhancement relative to normal venous enhancement. • Enlargement of collateral patent veins and dural venous sinuses on contrast-enhanced CT. • Dilatation of ventricles may occur from a rapidly progressive impairment of CSF resorption. MRI: • Venous infarcts may be seen as poorly defined zones with decreased signal on T1-weighted images and increased signal on T2-weighted images. Lesions secondary to superficial venous obstruction usually involve the subcortical white matter more than the cortex. Occlusions of the internal cerebral veins, vein of Galen, and/or straight sinus result in thalamic and basal ganglia venous infarcts as well as intraventricular hemorrhage and thalamic hemorrhage. • Thrombus within veins or dural venous sinuses can have intermediate signal on T1-weighted images in the first 3 days, intermediate signal on T1-weighted images and low signal on T2-weighted images from deoxyhemoglobin in the late acute phase (3–5 days), and high signal on T1-weighted images and T2-weighted images from methemoglobin in the subacute phase (6–30 days). • In the first 7 days, T2* gradient echo (GRE) images and T2* susceptibility-weighted images (SWI) show low signal at the venous thrombus secondary to the paramagnetic effects of deoxyhemoglobin, as well as sites of venous hemorrhage. • Heterogeneous mixed signal may be seen on diffusion-weighted imaging and ADC maps at acute venous infarcts related to sites with restricted diffusion from cytotoxic edema, hemorrhage, and interstitial or vasogenic edema. • Impaired resorption of CSF at the arachnoid granulations may result from dural venous thrombosis. The extent of venous infarction may be related to the degree of abnormal dural venous pressures associated with venous thrombosis. • Hemorrhage at venous infarcts may be seen in varying degrees and extent within the subcortical white matter. • MR venography using methods like 2D phase contrast, 2D time-of-flight, and contrast-enhanced time-resolved 3D time-of-flight techniques can show occlusion of the dural venous sinuses. Treatment usually consists of anticoagulation.	Intracranial venous infarctions in neonates are rare (~ 4 per million children). Venous infarcts occur from occlusion and/or thrombosis of the dural venous sinuses and/or superficial or deep intracranial veins, which results in elevation of the venous pressure above the arterial perfusion pressure. Intracranial venous occlusion in neonates can result acutely from prolonged rupture of membranes, maternal gestational diabetes, maternal infections, neonatal asphyxia at birth, neonatal dehydration, sepsis, and neonatal prothrombotic disorders (anticardiolipin antibodies, lupus anticoagulant, factor V Leiden, prothrombin gene mutations, and decreased levels of protein C, antithrombin, protein S, fibrinogen, and plasminogen). The most frequently occluded/thrombosed dural venous sinus is the superior sagittal sinus, followed by the transverse venous sinus, straight venous sinus, torcula, sigmoid venous sinus, vein of Galen, internal cerebral veins, cortical veins, and jugular veins. Multiple venous sinus thromboses are seen in 71% of cases. With venous occlusion, there is an increase in venous and capillary pressure in the zone of affected venous drainage that can result in decreased resorption of interstitial CSF, interstitial edema, and congestion leading to eventual venous infarction. Venous infarctions commonly occur in the subcortical white matter and occur in 54% of neonatal venous occlusions. Intracranial hemorrhage is also seen in 42% Locations of venous infarcts are related to drainage territory of the occluded vein or dural venous sinus. Occlusions involving the superior sagittal sinus cause parasagittal infarcts in the white matter of the upper frontal and parietal lobes, with or without cerebral cortical involvement; occlusions of the vein of Galen and/or straight sinus result in thalamic and basal ganglia infarcts; and occlusions involving the vein of Labbe and transverse and/or sigmoid venous sinuses cause infarcts in the lateral portions of the temporal lobes. Zones of hemorrhage can be seen at these sites and should raise the suspicion for venous infarction. Venous thrombosis involving the deep veins (internal cerebral veins, vein of Galen, straight venous sinus) in term neonates (36 weeks' gestational age) is associated with intraventicular hemorrhage and choroid plexus hemorrhage, as well as thalamic hemorrhage. Neonates with sinovenous infarction usually present within 48 hours of birth and may have clinical findings of seizures, respiratory distress, hypoxia, poor muscle tone, low Apgar scores, bulging fontanel, poor oral intake, lethargy, and irritability.

(continued on page 336)

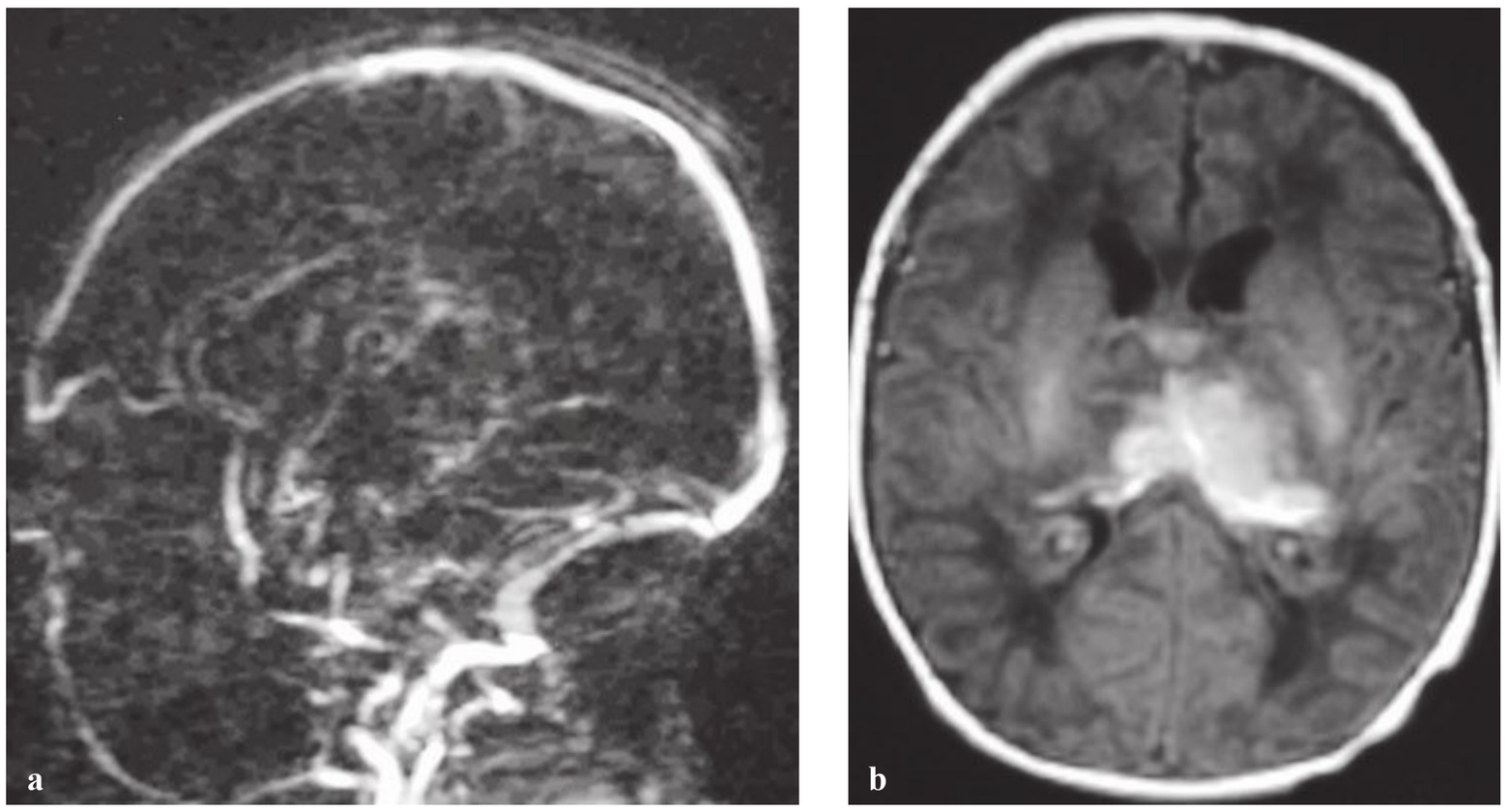

Fig. 1.399 A 5-day-old male neonate with thrombosis of the internal cerebral veins, vein of Galen, and straight venous sinus with absent flow signal on **(a)** sagittal magnetic resonance venography (MRV). Hemorrhagic venous infarction is seen in both thalami on **(b)** axial T1 WI.

Table 1.9 (cont.) Ischemia and infarction involving the brain and/or brainstem in children

Lesion/Disorder	Imaging Findings	Comments
Stroke in Children		Strokes in children between the ages of 29 days and 18 years are uncommon and occur in ~ 40 per million children per year. Childhood strokes can result from arterial occlusions (thrombotic or embolic), anoxic/hypoxic episodes, and sinovenous thrombosis.
Stroke in Children: hyperacute and acute infarction from arterial occlusion (**Fig. 1.400**) Hyperacute infarct (< 12 hours on CT) Acute infarct (12–24 hours on CT) Hyperacute infarct (< 3 hours on MRI) Acute infarct (< 12 hours on MRI) Acute infarct (12–24 hours on MRI)	CT: Hyperacute infarct (< 12 hours): • Edema-related decreased attenuation in the lentiform nuclei, associated with loss of definition at margins with the internal and external capsules, and involving the insular cortex—loss of the insular ribbon sign (thickening and obscuration of the thin hyperdense band of insular cerebral cortex relative to the adjacent external capsule). • Hyperdense artery (25 to 50%) secondary to intravascular blood clot: red thrombus, which has HU values of 60 to 90, compared with unclotted blood with HU values of 30 to 60. Sensitivity of this sign has been reported to range from 5 to 50% • In some cases, there are no apparent findings on CT. • On CT cerebral perfusion, cerebral blood flow is reduced to 15–20 mL/100 g/min for several hours or is below 10 mL/100 g/min for several minutes. Acute infarct (12–24 hours): • Decreased attenuation in the basal ganglia. • Indistinctness at borders between cerebral cortex and adjacent white matter. • Subtle decrease in attenuation in brain in the vascular distribution of the infarct, with or without localized edema and sulcal effacement. MRI: Hyperacute infarct (< 3 hours): • Exponential decrease in ADC at infarct after several minutes, with high signal on diffusion-weighted imaging and low signal on ADC maps. • Absence of flow void in occluded artery. • Intravascular contrast enhancement. • Magnetic resonance hydrogen spectroscopy can show elevated lactate peak at 1.32 ppm, with or without a slight decrease in N-acetylaspartate (NAA) at 2.02 ppm. Acute infarct (< 12 hours): • High signal on diffusion-weighted imaging, low signal on ADC maps. • Slightly decreased signal on T1-weighted images at infarct in an arterial distribution. • Indistinctness at borders between cerebral cortex and adjacent white matter. • Subtle localized edema and sulcal effacement. Acute infarct (12–24 hours): • High signal on diffusion-weighted imaging (DWI), low signal on ADC maps. • Increase in signal at infarct on DWI, T2- weighted imaging, and FLAIR. • Localized mass effect. • Gadolinium contrast enhancement at adjacent leptomeninges.	The focal pattern of stroke in children caused by arterial occlusions or stenoses may result from emboli, thrombosis, hematologic abnormalities (polycythemia, sickle-cell disease, antiphospholipid antibodies, and deficiencies of factor V Leiden, protein S, or protein C), vasospasm, cardiac abnormalities (cyanotic congenital heart disease, mitral valve prolapse, cardiomyopathy, or endocarditis), or arterial dissection, or they may be idiopathic. Approximately two-thirds of focal cerebral infarcts in children involve the supraclinoid portion of the internal carotid artery or proximal M1 segment of the middle cerebral artery. Abnormal increased signal on T2-weighted imaging and FLAIR is seen in the involved territory of the occluded artery, and restricted diffusion is observed 1 hour after the event and usually persists for up to 14 days. Long-term prognosis for children with focal cerebral infarcts with no underlying medical disorder tends to be better than in adults with similar sized strokes. Neurologic deficits vary depending on the size of the infarct, location (eloquent versus less eloquent regions of the involved brain tissue), and patient age at the time of infarction. Due to the greater functional plasticity of pediatric brains, younger patients tend to have lesser neurologic deficits from focal regional strokes than older children, adolescents, and adults with similar-sized strokes.

(continued on page 338)

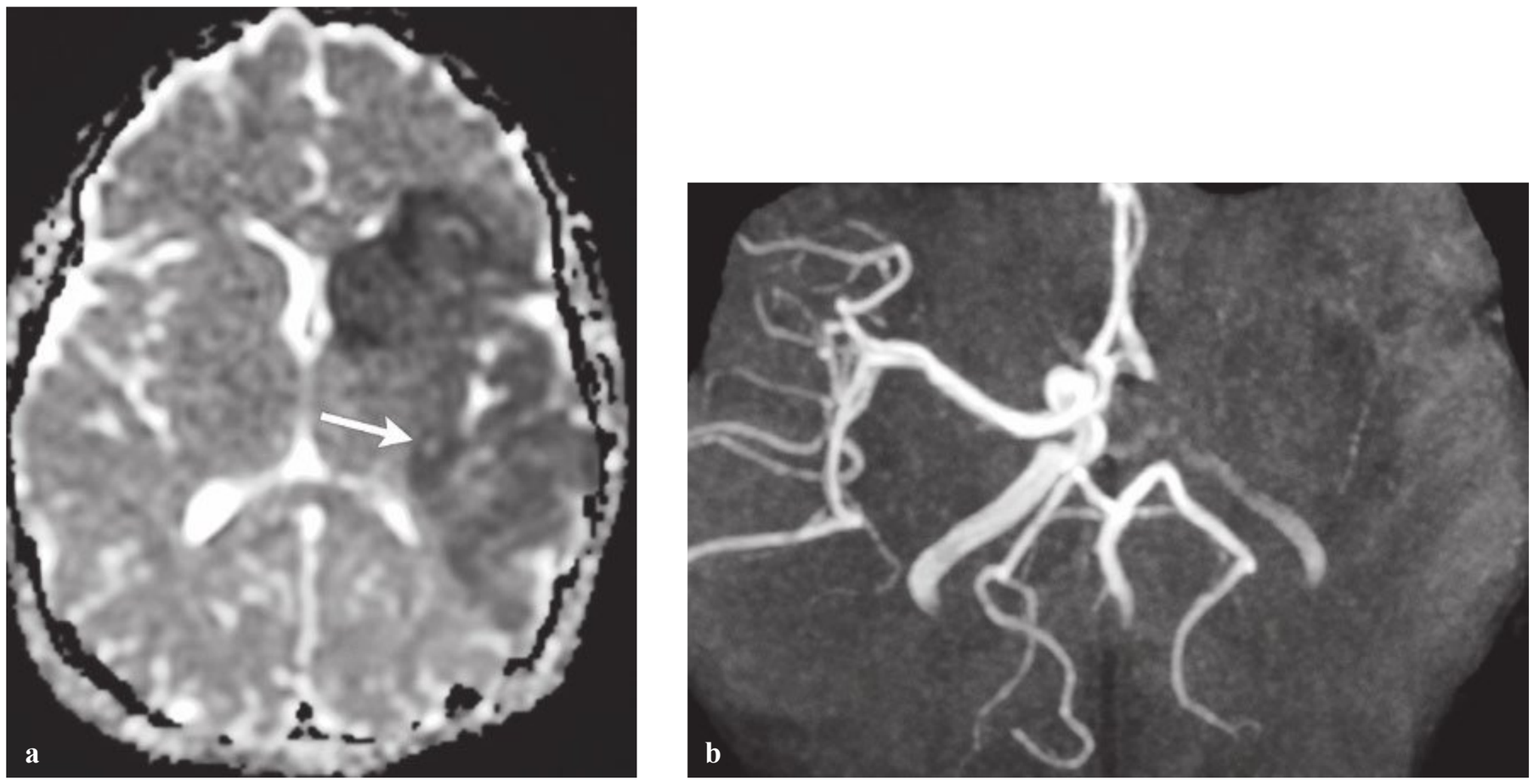

Fig. 1.400 A 14-year-old female with an acute arterial infarction in the left cerebral hemisphere as seen on **(a)** axial ADC (arrow) that resulted from occlusion of the left internal carotid artery from arterial dissection with absent flow signal on **(b)** axial MRA.

Table 1.9 (cont.) Ischemia and infarction involving the brain and/or brainstem in children

Lesion/Disorder	Imaging Findings	Comments
Subacute infarction from arterial occlusion (**Fig. 1.401**) Early subacute infarct (1–3 days on CT) Subacute infarct (4–7 days on CT) Late subacute infarct (1–7 weeks on CT) Early subacute infarct (1–3 days on MRI) Subacute infarct (4–7 days on MRI) Late subacute infarct (1 to 3–4 weeks on MRI)	CT: Early subacute infarct (1–3 days): • Zone of decreased attenuation at infarct becomes more conspicuous. • Increase in edema and localized mass effect associated with infarct (peaks at 3–4 days). • Hemorrhagic transformation may occur at infarct. Subacute infarct (4–7 days): • Mass effect and edema associated with infarct persist. • Gyral pattern of contrast enhancement may be seen. Late subacute infarct (1–7 weeks): • Progressive decrease in localized mass effect and edema. • Slight increase in attenuation of hypodense lesion and blurring of margins; fogging effect secondary to macrophage invasion and proliferation of capillaries. • Persistence of contrast enhancement at the infarct. • Dystrophic calcifications may be seen, more commonly in children than in adults. • High attenuation along cortex secondary to laminar necrosis. MRI: Early subacute infarct (1–3 days): • High signal on diffusion-weighted imaging, low signal on ADC maps. • Progressive increase in abnormal signal at infarct on proton density-weighted imaging, T2-weighted imaging, and FLAIR. • Increase in edema and localized mass effect associated with infarct (peaks at 3–4 days). • Early gadolinium contrast enhancement may be seen at the infarct. • Hemorrhagic transformation may occur at infarct. • Gadolinium contrast enhancement at meninges and within blood vessels declines. Subacute infarct (4–7 days): • Infarct has high signal on proton density-weighted imaging, T2-weighted imaging, FLAIR, and diffusion-weighted imaging. Low signal on ADC maps. • Increase in degree of gadolinium contrast enhancement at infarct may be seen. • Progressive decrease in localized mass effect and edema. • Hemorrhage may be seen in 25% • Resolution of intravascular and meningeal gadolinium contrast enhancement. Late subacute infarct (1 to 3–4 weeks): • Infarct has high signal on proton density-weighted imaging, T2-weighted imaging, and FLAIR. At 2 weeks, diffusion-weighted imaging may show high signal from T2 shine-through effects, and ADC maps do not show low signal at infarcts, indicating absence of restricted diffusion that was seen previously during the first 2 weeks. • Progressive decrease in localized mass effect and edema. • Persistence of contrast enhancement at the infarct. • Dystrophic calcifications may be seen as zones of low signal on T2-weighted images, more commonly in children than in adults. • After 2 weeks, curvilinear thin zones with high signal on T1-weighted imaging can be seen in the cerebral cortex and represent cortical laminar necrosis. This can become progressively more prominent at 1 to 2 months and persist up to 1.5 years. The high signal may be secondary to cortical necrotic changes of protein denaturation, paramagnetic compounds (e.g., manganese ions), and macrophage-produced free radicals.	

Lesion/Disorder	Imaging Findings	Comments
Remote infarction from arterial occlusion (**Fig. 1.402**) Months to years (chronic/old infarct)	CT: • Localized encephalomalacia. • Ipsilateral atrophy of brainstem (Wallerian degeneration). MRI: • Localized encephalomalacia. • Increased signal on T2-weighted imaging and FLAIR at infarct. • Low signal on T1-weighted imaging and diffusion-weighted imaging, and high signal on ADC maps. • Presence of zones of low T2 and T2* signal secondary to hemosiderin. • Ipsilateral atrophy of brainstem (Wallerian degeneration).	

(continued on page 340)

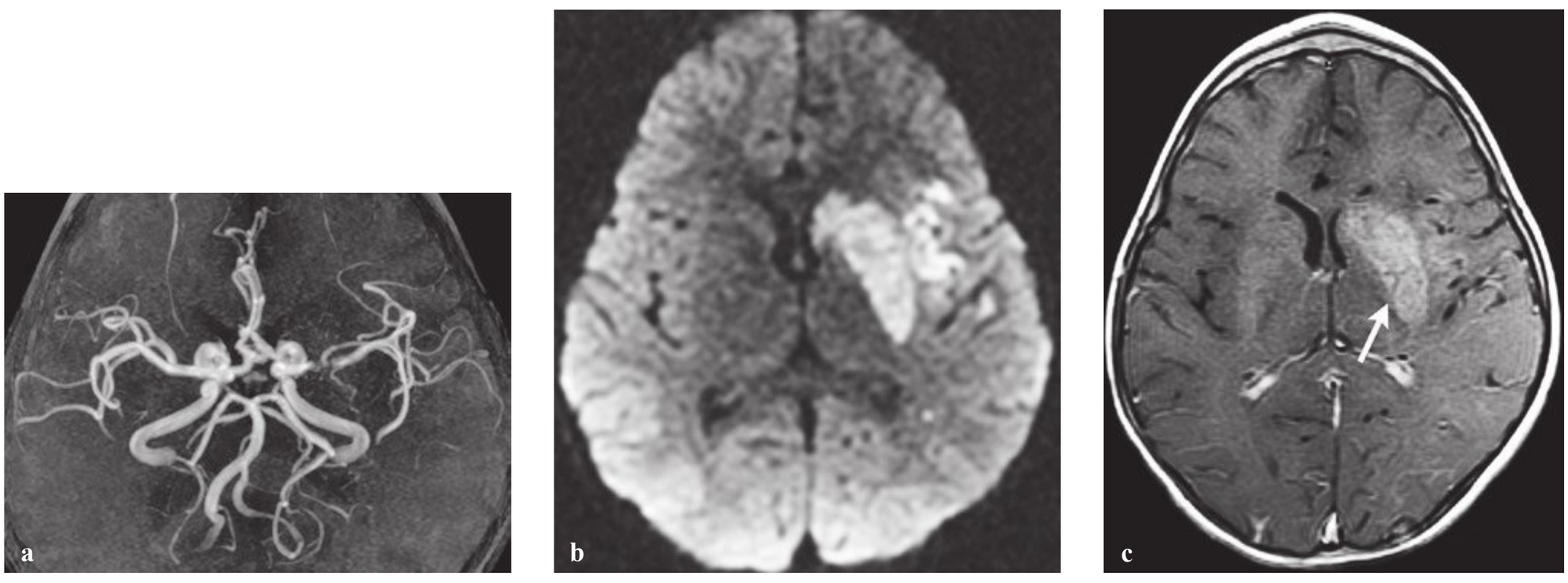

Fig. 1.401 A 3-year-old male with sickle-cell disease who has severe narrowing of the M1 segment of the left middle cerebral artery as seen on **(a)** axial MRA, with corresponding findings of subacute infarction with restricted diffusion on **(b)** axial DWI, and gadolinium contrast enhancement in the left basal ganglia and adjacent brain parenchyma on **(c)** axial T1 WI (arrow).

Fig. 1.402 A 7-year-old male imaged 4 years after the exam in **Fig. 1.401** shows gliosis and localized encephalomalacia at the site of infarction in the left cerebral hemisphere on axial T2WI that was seen on the prior exam.

Table 1.9 (cont.) Ischemia and infarction involving the brain and/or brainstem in children

Lesion/Disorder	Imaging Findings	Comments
Small-vessel ischemic injury: sickle-cell disease (**Fig. 1.403**)	MRI: On T2-weighted images, multiple foci and/or confluent zones of high signal in the subcortical and periventricular white matter, basal ganglia, and brainstem, without associated mass effect, and typically no contrast enhancement. Chronic lesions may have low signal on T1-weighted imaging. CT: Zones of decreased attenuation in the cerebral white matter, basal ganglia, and brainstem, with no associated mass effect.	Lesions in white matter and/or brainstem are related to occlusive disease involving perforating arteries and are associated with sickle-cell disease, thalassemia, and vasculitis. Unlike multiple sclerosis, ischemic small-vessel disease does not usually involve the corpus callosum because of its abundant blood supply from multiple branches of the adjacent pericallosal arteries.

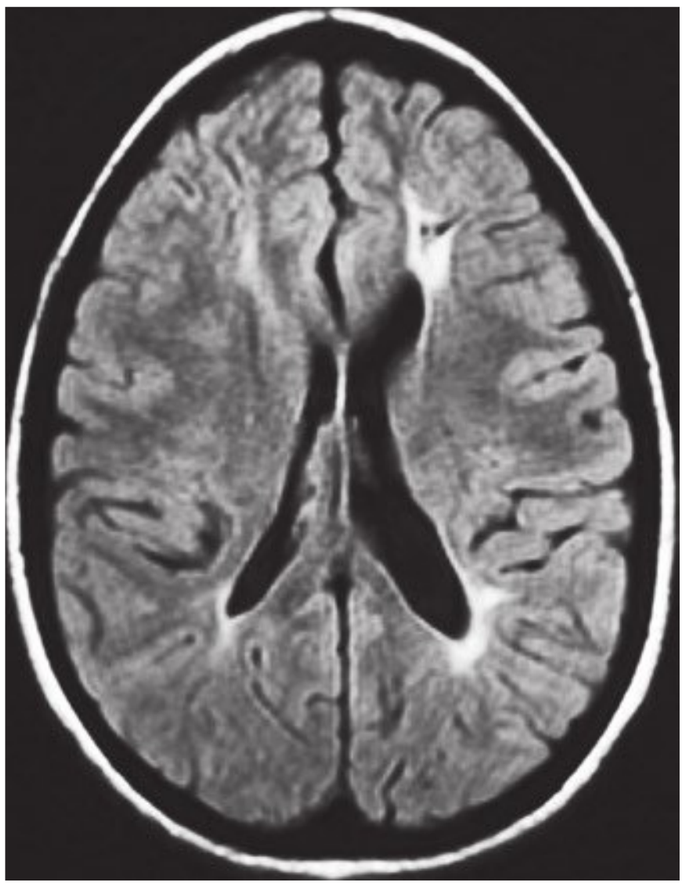

Fig. 1.403 A 10-year-old male with sickle-cell disease and intra-axial zones with high signal on axial FLAIR in the cerebral white matter from small vessel ischemic disease.

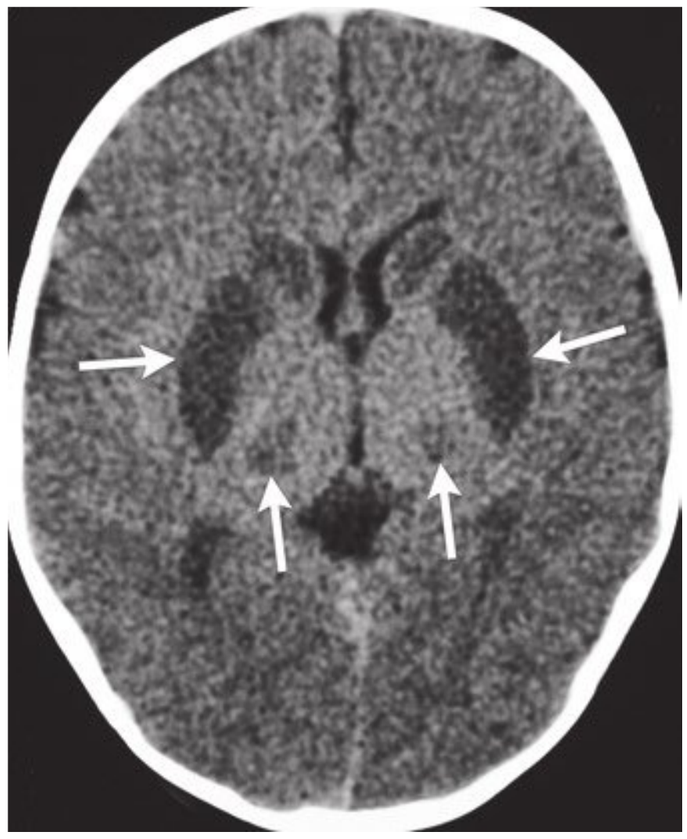

Fig. 1.404 A 2-year-old male with severe hypoxic-ischemic injury from cardiac arrest. Axial CT shows abnormal low attenuation within the basal ganglia and thalami (arrows).

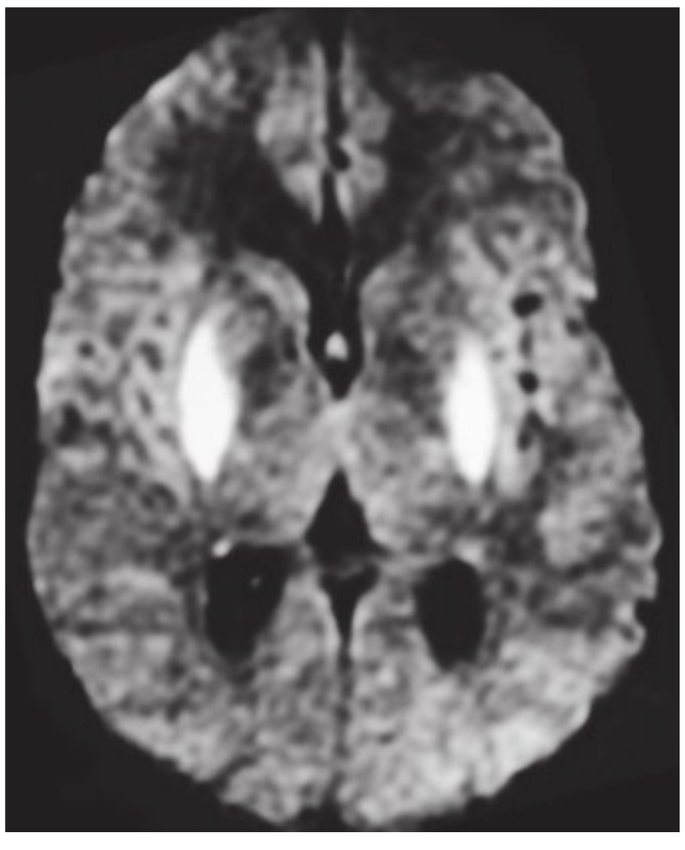

Fig. 1.405 A 16-year-old male with severe hypoxic-ischemic injury from cardiac arrest. Axial DWI shows restricted diffusion in the putamina.

Lesion/Disorder	Imaging Findings	Comments
Severe anoxic/hypoxic-ischemic injuries in children (**Fig. 1.404** and **Fig. 1.405**)	CT: • Severe hypoxic-ischemic injuries may be seen as zones with decreased attenuation in the basal ganglia and insular cortex within 24 hours. • From 1 to 3 days, diffuse edema with blurring of the gray–white matter junctions and effacement of sulci and cisterns can be seen; these findings are associated with decreased attenuation in the basal ganglia and cerebral cortex. • From 4 to 6 days, hemorrhage may be seen in the basal ganglia and involved cerebral cortex. • Reversed attenuation sign, with the cerebral white matter having abnormal higher attenuation relative to the cerebral cortex secondary to venous stasis in the white matter. If present, this sign is associated with a poor prognosis. MRI: • Within the first 24 hours, ischemic changes from severe hypoxia can be seen as zones with high signal on diffusion-weighted imaging in the basal ganglia, cerebral cortex (notably in the occipital lobes and perirolandic cortex), thalami, hippocampi, cerebellar hemispheres, and brainstem. • After 24 hours, zones with high signal on proton density-weighted imaging, T2-weighted imaging, and FLAIR can be seen at the sites of ischemic change. • Echoplanar gradient echo T2* images may show low signal from small zones of hemorrhage. • After ~ 2 weeks, curvilinear thin zones with high signal on T1-weighted imaging can be seen in the cerebral cortex, representing cortical laminar necrosis (pseudolaminar cortical necrosis). The high signal on T1-weighted imaging in the cerebral cortex is caused by necrosis, resulting in protein denaturation, paramagnetic compounds (e.g., manganese ions), and macrophage-produced free radicals. • In 3%of patients with hypoxia, delayed imaging findings of high signal on T2-weighted imaging and FLAIR in the cerebral white matter and associated with restricted diffusion may be seen 1 week after hypoxia, followed by acute neurologic decline (intellectual impairment, delirium, movement disorders, seizures) 2–3 weeks after the hypoxic event. This variant of delayed post-anoxic leukoencephalopathy may show persistent signal abnormalities and cerebral atrophy. The delayed encephalopathy may be secondary to apoptosis (programmed cell death). • On magnetic resonance spectroscopy, poor outcome after resuscitation is related to a large decrease in the NAA/creatine ratio and elevated lactate levels.	In children, nonaccidental trauma, choking, and drowning are common causes of brain injury. Other clinical conditions that may lower the threshold for hypoxic-ischemic injuries include acquired metabolic disorders (dehydration, anemia/blood volume depletion) and congenital metabolic disorders (MELAS, Leigh's disease, etc.). With resuscitation, reversal of mild hypoxic changes can occur after reoxygenation. In cases with more prolonged hypoxia, cardiac insufficiency or arrest can occur resulting in hypoxic brain injuries combined with hypoperfusion injuries. In children with severe anoxia and subsequent cardiopulmonary arrest, poor outcomes (death or neurovegetative state) have been associated with restricted diffusion on diffusion-weighted imaging in the ventrolateral thalami (as seen in neonates) and posterior lateral lentiform nuclei within 12 to 24 hours after injury and prior to signal changes seen on T1- and T2-weighted imaging. In children with poor outcomes, progression of the restricted diffusion is seen in the basal ganglia, thalami, perirolandic cortex, and visual cortex at 48 hours, and by 72 hours the entire cortex has abnormal signal associated with diffuse cerebral swelling.
Mild-moderate anoxic/hypoxic-ischemic injuries in children	CT: Mild-moderate hypoxic-ischemic and hypoperfusion injuries result in lesions at the arterial border (watershed) zones between the distributions of the major cerebral arteries (anterior, middle, and posterior cerebral arteries), and between the distributions of the cerebellar arteries. MRI: With mild-moderate hypoxia, ischemic lesions can be seen at arterial border (watershed) zones between the distributions of the major cerebral arteries. Curvilinear thin zones of restricted diffusion can be seen in the cerebral cortex within 24 hours and persist for up to 2 weeks. Signal abnormalities are seen at the cortex between the leptomeningeal distributions of the anterior and middle cerebral arteries, and between the middle and posterior cerebral arteries, as well as between the distributions of the cerebellar arteries. Additional watershed infarcts can occur in the deep cerebral white matter between the distributions of the lenticulostriate arteries from the proximal middle cerebral artery and the penetrating superficial cortical branches from the M2, M3, and M4 segments of the middle cerebral artery.	

(continued on page 342)

Table 1.9 (cont.) Ischemia and infarction involving the brain and/or brainstem in children

Lesion/Disorder	Imaging Findings	Comments
Sinovenous infarction in children (**Fig. 1.406**)	CT: • Venous infarcts secondary to occlusion of the dural venous sinuses are seen as poorly marginated zones with low or mixed low and intermediate attenuation located in the subcortical white matter, with or without regions of high attenuation from hemorrhage. Hemorrhage associated with venous infarcts is seen in 10–50% of cases. Infarcts in the central deep veins (internal cerebral veins, vein of Galen, straight venous sinus) are usually located in the basal ganglia and thalami and are often associated with intraventicular or thalamic hemorrhage. • Curvilinear and/or round zones of contrast enhancement can be seen at venous infarcts on CT. • Thrombus may be seen on non-contrast-enhanced CT as a dense vessel sign, and/or dense cord sign. • On contrast-enhanced CT, an empty delta sign can be seen, with a zone lacking enhancement within a dural venous sinus. • On CT angiography/venography, the venous thrombus shows a zone with minimal enhancement relative to normal venous enhancement. • Enlargement of collateral patent veins and dural venous sinuses is seen on contrast-enhanced CT. • Dilatation of ventricles may occur from a rapidly progressive impairment of CSF resorption. MRI: • Venous infarcts may be seen as poorly defined zones with decreased signal on T1-weighted imaging and increased signal on T2-weighted imaging. Lesions secondary to superficial venous obstruction usually involve the subcortical white matter more than the cortex. Occlusions of the internal cerebral veins, vein of Galen, and/or straight sinus result in thalamic and basal ganglia venous infarcts as well as intraventricular and thalamic hemorrhage. • Thrombus within veins or dural venous sinuses can have intermediate signal on T1-weighted imaging in the first 3 days; intermediate signal on T1-weighted imaging, low signal on FLAIR, and low signal on T2-weighted imaging from deoxyhemoglobin in the late acute phase (3–5 days); and high signal on T1- and T2-weighted imaging from methemoglobin in the subacute phase. In the chronic phase (> 30 days), thrombus can have intermediate signal on T1-weighted imaging and intermediate or high signal on T2-weighted imaging. • In the first 7 days, T2* gradient echo (GRE) images and T2* susceptibility-weighted images (SWI) show low signal at the venous thrombus secondary to the paramagnetic effects of deoxyhemoglobin as well as sites of venous hemorrhage. • Heterogeneous mixed signal may seen on diffusion-weighted imaging and ADC maps at acute venous infarcts related to sites with restricted diffusion from cytotoxic edema, hemorrhage, and interstitial or vasogenic edema. • Impaired resorption of CSF at the arachnoid granulations may result from dural venous thrombosis. The extent of venous infarction may be related to the degree of abnormal dural venous pressures associated with venous thrombosis. • Hemorrhage at venous infarcts may be seen in varying degrees and extent within the subcortical white matter. • MR venography using 2D phase contrast, 2D time-of-flight, and contrast-enhanced time-resolved 3D time-of-flight techniques can show occlusion of the dural venous sinuses.	Intracranial venous infarctions in children are rare (~ 3 per million children). Venous infarcts occur from occlusion and/or thrombosis of the dural venous sinuses and/or superficial or deep intracranial veins, which results in elevation of the venous pressure above the arterial perfusion pressure. Intracranial venous occlusion in children can result acutely from dehydration, mastoiditis, sepsis, anemia (sickle-cell disease, thalassemia, iron deficiency) and prothrombotic disorders (anticardiolipin antibodies, lupus anticoagulant, factor V Leiden, prothrombin gene mutations, and decreased levels of protein C, antithrombin, protein S, fibrinogen, and plasminogen). Intracranial venous thrombosis can also occur in association with trauma, indwelling catheters, connective tissue disorders (i.e., lupus), cardiac surgery, infection related to immunosuppression, and diabetes. The most frequently occluded/thrombosed dural venous sinuses or veins in children are the transverse venous sinuses, followed by the superior sagittal venous sinus, straight venous sinus, torcula, sigmoid venous sinus, vein of Galen, internal cerebral veins, cortical veins, and jugular veins. Multiple venous sinus thrombosis is seen in 71% of cases. In children with sinovenous thrombosis, associated brain infarction occurs in ~ 40% of cases. Hemorrhage associated with venous infarction is seen in up to 42% Locations of venous infarcts are related to drainage territory of the occluded vein or dural venous sinus. Occlusions involving the superior sagittal sinus cause parasagittal infarcts in the white matter of the upper frontal and parietal lobes, with or without cerebral cortical involvement; occlusions of the vein of Galen and/or straight sinus result in thalamic and basal ganglia infarcts; and occlusions involving the vein of Labbe and transverse and/or sigmoid venous sinuses cause infarcts in the lateral portions of the temporal lobes. Venous thrombosis involving the deep veins (internal cerebral veins, vein of Galen, straight venous sinus) is associated with intraventicular hemorrhage and choroid plexus hemorrhage, as well as thalamic hemorrhage. Treatment of patients without intracranial hemorrhage usually is anticoagulation.

(continued on page 344)

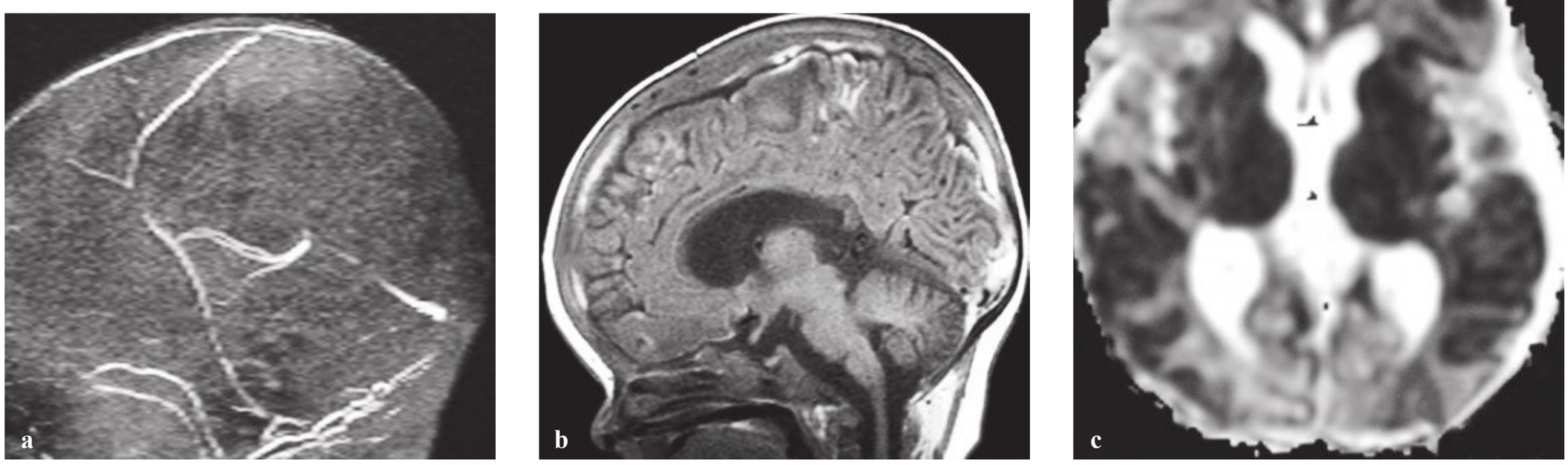

Fig. 1.406 **(a)** A 2-month-old female infant with sinovenous thrombus occluding the superior sagittal sinus and most of the straight venous and transverse venous sinuses seen as lack of flow signal on sagittal MRV. **(b)** The sinovenous thrombus has high signal on sagittal T1-weighted imaging. **(c)** Extensive central and peripheral brain ischemia is seen as restricted diffusion with low signal on axial ADC.

Table 1.9 (cont.) Ischemia and infarction involving the brain and/or brainstem in children

Lesion/Disorder	Imaging Findings	Comments
Inherited Metabolic Disorders Associated with Strokes in Children		
MELAS/MERRF (See **Fig. 1.210** and **Fig. 1.211**)	CT: Symmetric zones of low attenuation in the basal ganglia, cerebral cortical infarction that is not limited to one vascular distribution, ± dystrophic calcifications in basal ganglia. MRI: High signal on T2-weighted imaging and FLAIR in basal ganglia, usually symmetric; high signal on T2-weighted imaging and FLAIR in cerebral and cerebellar cortex and subcortical white matter, often with restricted diffusion. Findings do not correspond to a specific large arterial territory. Signal abnormalities may resolve and reappear.	MELAS (mitochondrial encephalopathy, lactic acidosis, and stroke-like events) is a maternally inherited disease affecting transfer RNA in mitochondria. MERRF (myoclonic epilepsy with ragged red fibers) is a mitochondrial encephalopathy associated with muscle weakness and myoclonic epilepsy, short stature, ophthalmoplegia, and cardiac disease.
Leigh's disease (See **Fig. 1.212**)	CT: Zones of low attenuation in both caudate nuclei and putamina, ± decreased attenuation in white matter, typically with no contrast enhancement. MRI: Symmetric high signal on T2-weighted imaging and FLAIR in globi pallidi, putamina, and caudate nuclei, as well as high signal on T2-weighted imaging in thalami, cerebral and cerebellar white matter, cerebellar cortex, brainstem, and spinal cord gray matter, + restricted diffusion for acute ischemia. Typically, there is no gadolinium contrast enhancement. Magnetic resonance spectroscopy can show elevated lactate peaks during metabolic decompensation with lactic acidosis.	An autosomal recessive disorder also referred to as subacute necrotizing encephalopathy, Leigh's disease occurs in three forms (infantile type, juvenile type, and adult-onset type). Progressive neurodegenrative disease whose etiology is related to abnormalities in oxidative metabolism in mitochondria due to one of several enzyme deficiencies from mutations of mitochondrial and/or nuclear genes (coenzyme Q10, pyruvate carboxylase, pyruvate dehydrogenase complex, others). Lesions in the brainstem are associated with loss of respiratory control.
Kearns-Sayre syndrome (See **Fig. 1.213**)	MRI: Zones with high signal on T2-weighted imaging and FLAIR in globi pallidi, putamina, and caudate nuclei, as well as high signal on T2-weighted imaging in thalami, subcortical cerebral and cerebellar white matter, posterior brainstem, and corticospinal tracts, + restricted diffusion for acute ischemia. Typically, there is no gadolinium contrast enhancement. CT: Zones with decreased attenuation can be seen in the cerebral white matter, ± calcifications involving globi pallidi and caudate nuclei.	Sporadic deletions of mitochondrial DNA involving genes that encode proteins of the respiratory chain and/or tRNA. Results in mitochondrial dysfunction, spongiform changes of the cerebral and cerebellar white matter and basal ganglia, progressive external ophthalmoplegia, pigmentary degeneration of the retina, and cardiac conduction blocks.
Fabry disease (See **Fig. 1.214**)	CT: Zones of low attenuation in the thalami, basal ganglia, and white matter, ± calcifications in basal ganglia and thalami. Typically there is no contrast enhancement. MRI: Multiple foci with high signal on T2-weighted imaging and FLAIR in basal ganglia, thalami, and cerebral and cerebellar white matter, ± low signal foci on gradient echo imaging (GRE) from microbleeds in 10% Typically there is no gadolinium contrast enhancement.	X-linked lysosomal disorder involving mutations of the gene encoding α-galactosidase. Dysfunction of this enzyme leads to abnormal accumulation of glycosphingolipids in multiple tissues, including the heart, kidneys, and blood vessels, causing arteriopathy, emboli, and strokes (in patients < 30 years old and older adults).

1.10 Pituitary Gland and Hypothalamus

The pituitary gland is an important endocrine gland that is located within the sella turcica of the sphenoid bone. The pituitary gland is composed of two lobes, the anteriorly located adenohypophysis and the posterior neurohypophysis. Hormones secreted by the adenohypophysis include the growth hormone, thyroid-stimulating hormone, prolactin, corticotropin, follicle-stimulating hormone, and luteinizing hormone. Release of hormones from the adenohypophysis is regulated by the small parvocellular neurosecretory cells of the paraventricular nucleus, periventricular, arcuate, and supra-optic nuclei of the hypothalamus. The axons of the parvocellular neurons extend inferiorly to the median eminence at the base of the brain, where the nerve terminals release messenger peptides into the small blood vessels of the hypothalamic-hypophyseal portal system. These peptides are transported inferiorly via the hypothalamic-hypophyseal portal system into the capillaries around the anterior pituitary gland, causing hormone release from the adenohypophysis. Peptide hormones secreted from the neurohypophysis include oxytocin and vasopressin. Large magnocellular neurosecretory cells from the hypothalamic supraoptic and paraventricular nuclei extend directly into the neurohypophysis via the hypothalamic infundibulum (pituitary stalk), where axon terminals in the posterior pituitary (pars nervosa) release the hormones into the bloodstream **(Fig. 1.407)**.

The adenohypophysis develops from Rathke's pouch, which is an ectodermal protusion of stomodeum rostral to the oropharyngeal membrane beginning at 24 days of gestation **(Fig. 1.408)**. The neurohypophysis begins as an inferior protusion (infundibulum) at the floor of the diencephalon. Rathke's pouch progressively extends posteriorly and superiorly, with eventual separation from the stomodeum. The infundibulum extends inferiorly and anteriorly and eventually merges with the migrating Rathke's pouch. Rathke's pouch differentiates into the adenohypophysis, and the distal portion of the infundibulum differentiates into the neurohypophysis.

At birth, both the adenohypophysis and neurohypophysis have high signal on T1-weighted imaging. By 6 weeks, the adenohypophysis has intermediate signal on T1-weighted imaging. The neurohypophysis typically retains high signal, which is attributed to the presence of neurosecretory granules and the protein neurophysin. The adenohypophysis and pituitary stalk normally show gadolinium contrast enhancement on T1-weighted imaging. Pituitary height remains unchanged for the first 2 years of life in full-term children. In preterm infants, the adenohypophysis is often taller than in full-term infants, which is attributed to higher levels of growth hormone and reduced insulin-like growth factor 1. For the first decade, the pituitary gland measures between 2 and 6 mm in height; during puberty, it measures up to 10 mm in height.

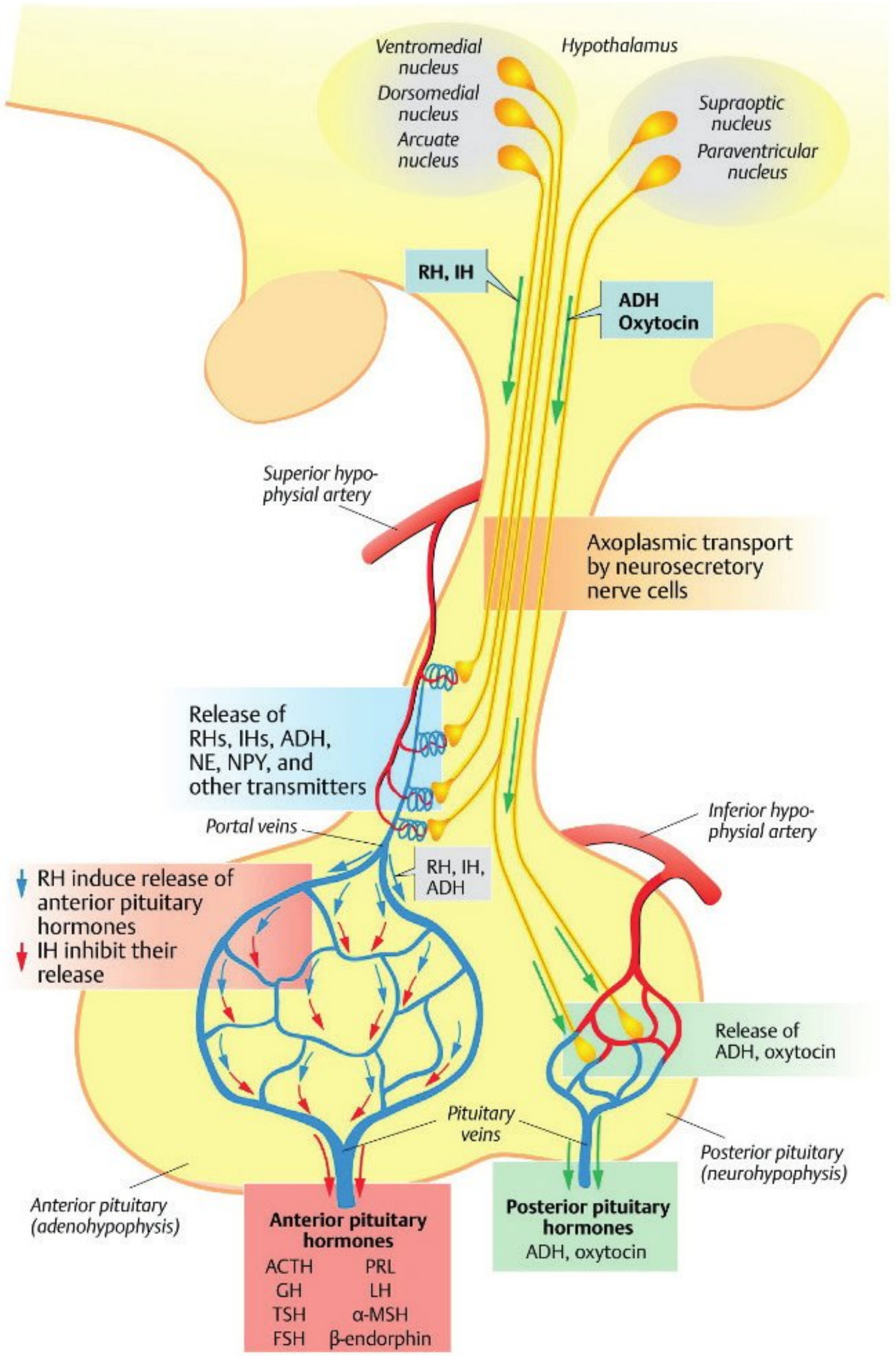

Fig. 1.407 Anatomic diagram of hormone regulation in the anterior and posterior lobes of the pituitary gland in relation to the hypothalamus. Used with permission from TannerThies R. Physiology: An Illustrated Review. New York, NY: Thieme; 2012.

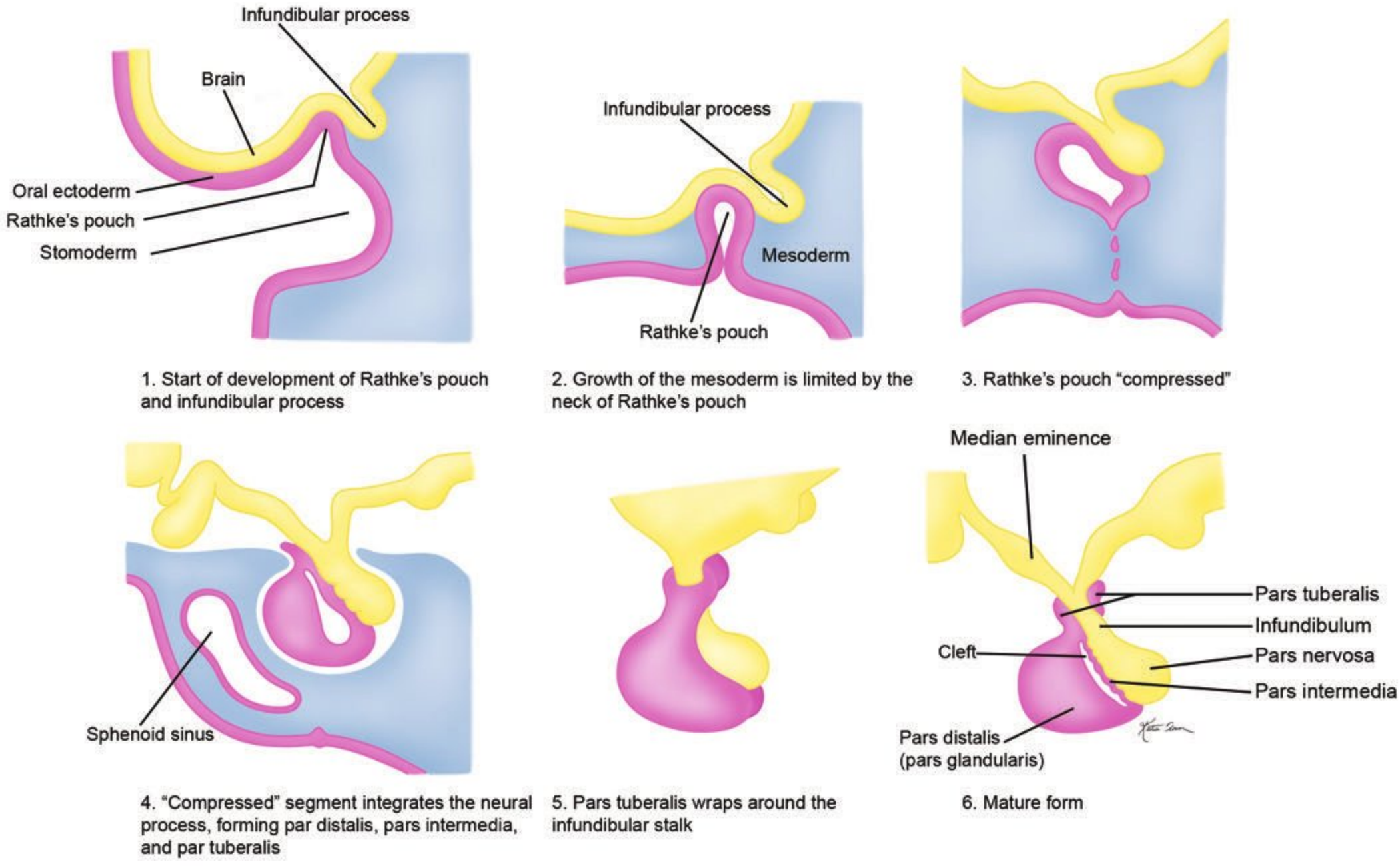

Fig. 1.408 Diagram shows progressive developmental pattern of the pituitary gland.

Table 1.10 Intrasellar and juxtasellar lesions

- Developmental Anomalies
  - Agenesis of the anterior pituitary lobe (adenohypophysis)
  - Hypoplasia of the anterior pituitary lobe
  - Ectopic posterior pituitary
  - Pituitary duplication
  - Hypothalamic hamartoma
  - Persistent craniopharyngeal canal
  - Rathke's cleft cyst
  - Pars intermedia cyst
  - Cephalocele (meningocele or meningoencephalocele)
  - Epidermoid (congenital cholesteatoma)
  - Dermoid
  - Colloid cyst
  - Lipoma of the sellar/hypothalamic region
  - Empty sella
- Pituitary Lesions
  - Pituitary hypertrophy/hyperplasia
  - Diabetes insipidus
- Neoplasms
  - Pituitary adenoma
  - Invasive pituitary adenoma
  - Pituitary carcinoma
  - Pituicytoma
  - Granular cell tumor (choristoma, or glioma of the neurohypophysis)
  - Spindle-cell oncocytoma of the adenohypophysis
  - Metastatic lesions involving the pituitary gland
- Suprasellar Lesions
  - Craniopharyngioma
  - Glioma (optic chiasm, hypothalamus)
  - Pilomyxoid astrocytoma
  - Meningioma
  - Schwannoma
  - Paraganglioma
  - Germ cell tumors
  - Teratoma
- Suprasellar Lesions
  - Arterial aneurysm
  - Saccular aneurysm
  - Giant aneurysm
  - Fusiform aneurysm
  - Dissecting aneurysms
  - Carotid-cavernous fistula
  - Arteriovenous malformations (AVMs)
  - Cavernous malformation
  - Cavernous sinus hemangioma
  - Arachnoid cyst—sellar/suprasellar
- Osseous Lesions: Neoplasm
  - Metastatic tumor involving the sphenoid bone and suprasellar cistern
  - Myeloma/plasmacytoma
  - Lymphoma
  - Chordoma
  - Chondrosarcoma
  - Osteogenic sarcoma
  - Ewing's sarcoma
  - Sinonasal squamous cell carcinoma
  - Nasopharyngeal carcinoma
  - Adenoid cystic carcinoma
  - Esthesioneuroblastoma
- Nonneoplastic Osseous Abnormalities
  - Fibrous dysplasia
  - Osteoma
  - Paget disease
- Infection
  - Leptomeningeal infection
- Inflammation
  - Langerhans' cell histiocytosis
  - Lymphocytic hypophysitis
  - Granulomatous hypophysitis
  - Sarcoidosis
  - Granulomatosis with polyangiitis (Wegener's granulomatosis)
  - Rosai-Dorfman disease

Table 1.10 Intrasellar and juxtasellar lesions

Lesions	Imaging Findings	Comments
Developmental Anomalies		
Agenesis of the anterior pituitary lobe (adenohypophysis) (**Fig. 1.409**)	MRI: Absence of anterior pituitary lobe, shallow sella, and variable length of infundibulum and position of posterior pituitary ranging from the hypothalamus to the sella. The infundibulum may be thinned and terminate into a partially formed bulbous posterior pituitary gland. CT: Small sella.	Rare congenital anomaly with neonatal presentation (metabolic acidosis, thyroid and adrenal insufficiency, hypoglycemia, and/or seizures). Often associated with other anomalies of the forebrain and midline craniofacial bones. Treatment includes replacement of growth hormone, thyroid hormone, and glucocorticoids.
Hypoplasia of the anterior pituitary lobe (**Fig. 1.410**)	MRI: Varying degrees of hypoplasia of the anterior pituitary lobe. Variable size and length of the infundibulum. The position of the posterior pituitary can range from the hypothalamus to the sella.	Rare anomaly with hypoplasia of the anterior pituitary lobe, infundibulum, and posterior pituitary lobe; associated with varying degrees of endocrine dysfunction, including panhypopituitarism, as well as with other congenital anomalies.

(continued on page 350)

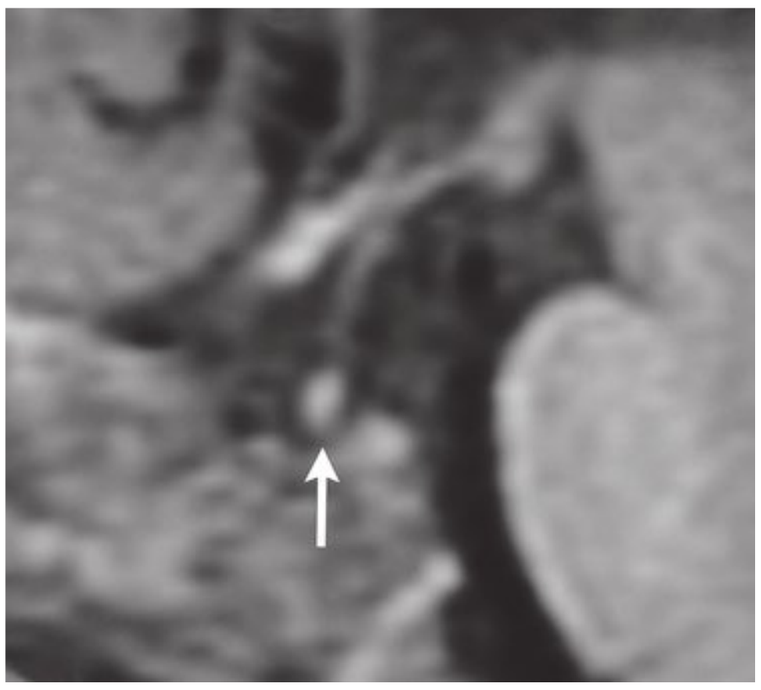

Fig. 1.409 Agenesis of the anterior pituitary lobe in an infant with hypopituitarism. Absence of the adenohypophysis is seen on sagittal T1-weighted imaging. The pituitary stalk terminated inferiorly into a bulbous neurohypophysis (arrow) with high signal in the dorsal portion of the sella.

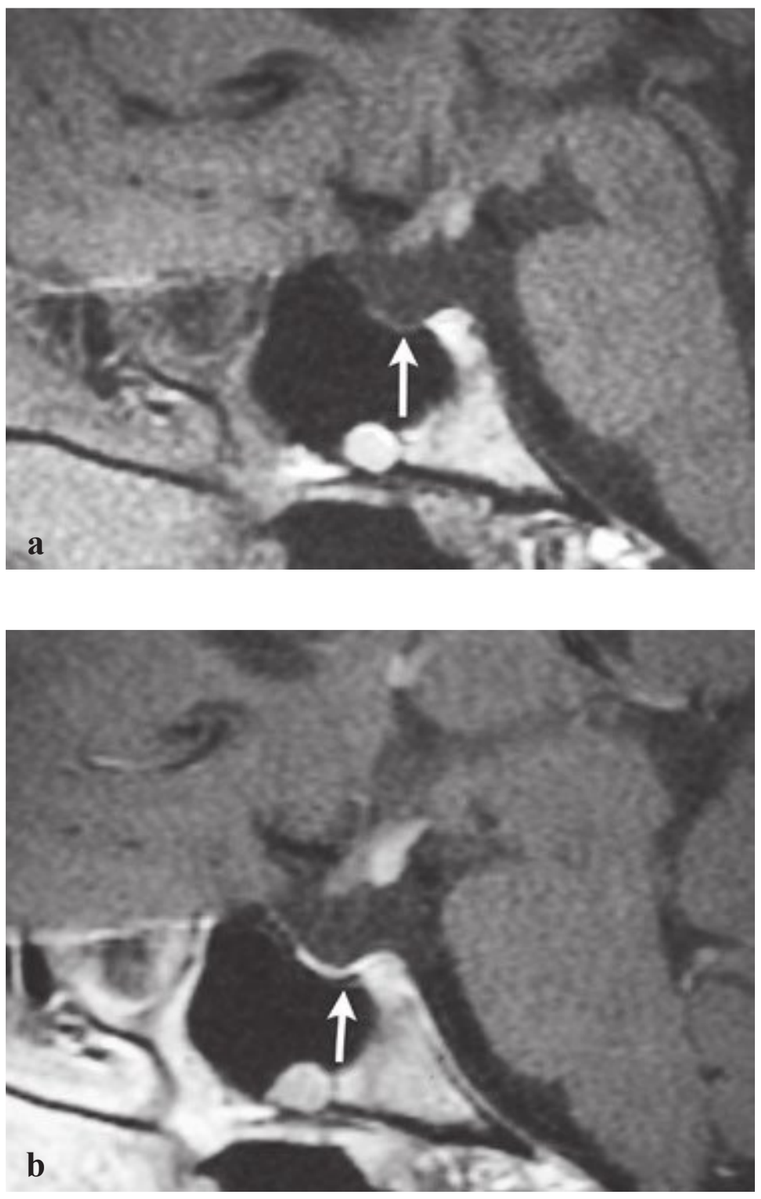

Fig. 1.410 Severe hypoplasia of the adenohypophysis. **(a)** Precontrast and **(b)** postcontrast sagittal T1-weighted imaging shows hypoplasia of the anterior pituitary gland (**a**, arrow) along the floor of the sella, which shows gadolinium contrast enhancement (**b**, arrow).

Table 1.10 (cont.) Intrasellar and juxtasellar lesions

Lesions	Imaging Findings	Comments
Ectopic posterior pituitary (**Fig. 1.411**)	MRI: Posterior "bright spot" of pituitary gland (neurohypophysis) on T1-weighted imaging located at upper portion of infundibulum or undersurface of hypothalamus instead of dorsal portion of the sella. Variable degree of hypoplasia of the anterior pituitary lobe.	Congenital anomaly with the aberrant position of the neurohypophysis (posterior pituitary), often at undersurface of hypothalamus, associated with pituitary dwarfism, delayed skeletal maturation, Kallmann syndrome, septo-optic dysplasia, dysgenesis of the corpus callosum, lobar holoprosencephaly, Chiari I malformation, or persistent/enlarged craniopharyngeal canal. Seen in males more often than in females.
Pituitary duplication (**Fig. 1.412**)	MRI: Duplicated pituitary stalks and glands within separate pituitary fossa in the sphenoid bone. There is often abnormal thickening ("pseudohamartoma") of the hypothalamus with duplication of the infundibular recess of the third ventricle. Also, duplication of the basilar artery may be seen.	Rare congenital anomaly related to abnormal separation of the anterior portion of the notochord and prechordal plate during embryogenesis. May be related to teratogens. Clinical findings include precocious puberty, facial dysmorphism, hypothyroidism, and/or increased prolactin level. May be associated with other anomalies, such as dysgenesis of the corpus callosum, absent olfactory bulbs, cerebellar hypoplasia, midline defects, and teratomas.
Hypothalamic hamartoma (**Fig. 1.413** and **Fig. 1.414**)	MRI: Sessile or pedunculated lesions at the tuber cinereum of the hypothalamus, often intermediate signal on T1- and T2-weighted imaging similar to gray matter, occasionally slightly high signal on T2-weighted imaging, usually no gadolinium contrast enhancement, and rarely contain cystic and/or fatty portions. Ictal FDG PET and SPECT have shown hyperperfusion during seizures. Diffusion-weighted imaging: No restricted diffusion. Magnetic resonance spectroscopy may show elevated myo-inositol. CT: Lesions often have intermediate attenuation similar to gray matter, typically no contrast enhancement, and rarely contain cystic and/or fatty portions, similar to brain.	Rare, congenital/developmental heterotopia/hamartoma (nonneoplastic lesions) in the tuber cinereum, inferior hypothalamus, and/or mamillary bodies composed of clusters of small (< 12 microns) neuronal cells within a neutropil-like stroma and scattered fibrillary astrocytes. Immunoreactive to NeuN and GAD67, not immunoreactive to glial fibrillary acidic protein (GFAP). Usually occur in children with isosexual precocious puberty (0–8 years old) or seizures (gelastic or partial complex) in second decade. Can be treated with surgery or stereotactic radiosurgery.

(continued on page 352)

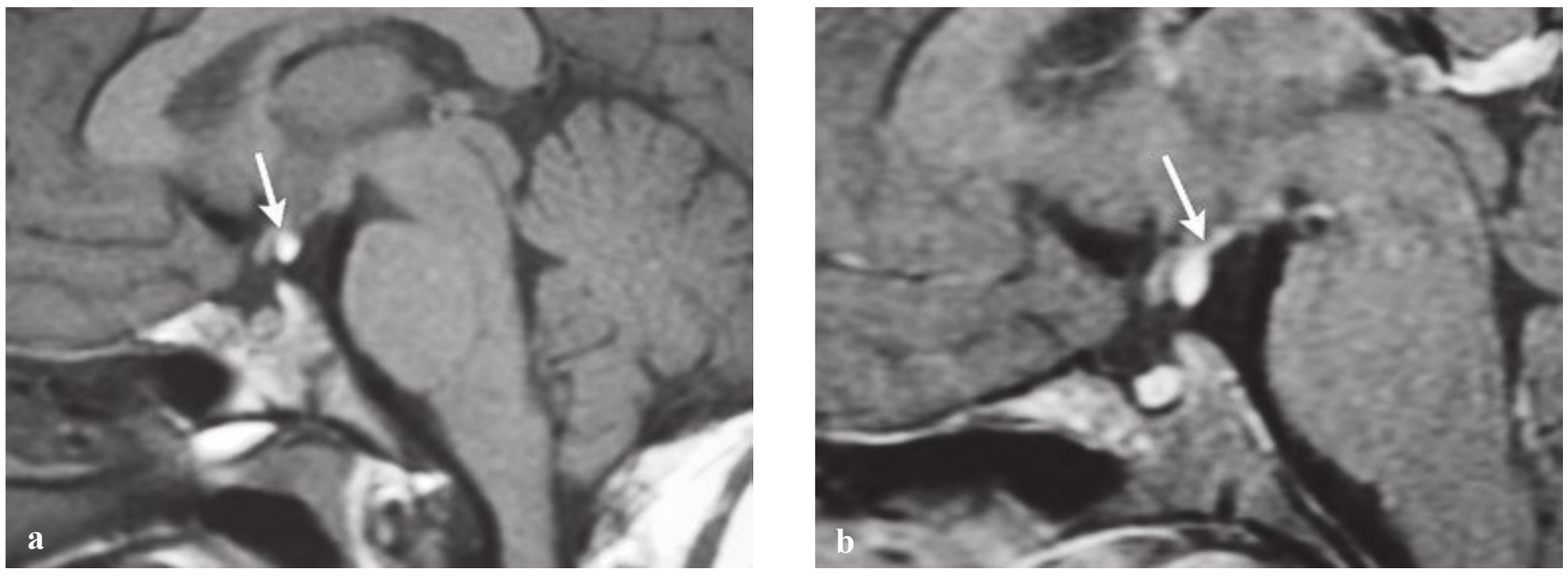

Fig. 1.411 Ectopic posterior pituitary gland. **(a)** Precontrast and **(b)** postcontrast sagittal T1-weighted imaging shows the normal appearance of the anterior pituitary gland, and an ectopic posterior pituitary gland (arrows) with high signal on both **(a)** precontrast and **(b)** postcontrast T1-weighted imaging adjacent to the optic chiasm.

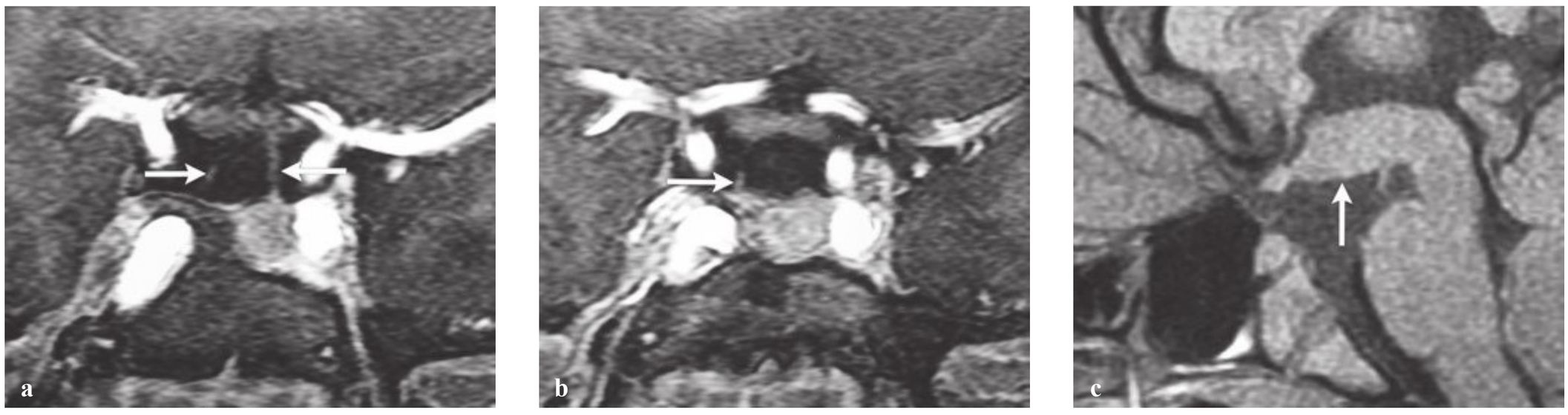

Fig. 1.412 Pituitary duplication. **(a,b)** Coronal postcontrast T1-weighted imaging shows two pituitary stalks (arrows) that extend inferiorly into duplicated pituitary glands. **(c)** Sagittal T1-weighted imaging shows marked enlargement of the hypothalamus (arrow), representing a pseudohamartoma, which did not show gadolinium contrast enhancement (not shown).

Fig. 1.413 Sagittal T1-weighted imaging in a child with precocious puberty shows a sessile type of hypothalamic hamartoma (arrow) that has intermediate signal that is isointense to gray matter.

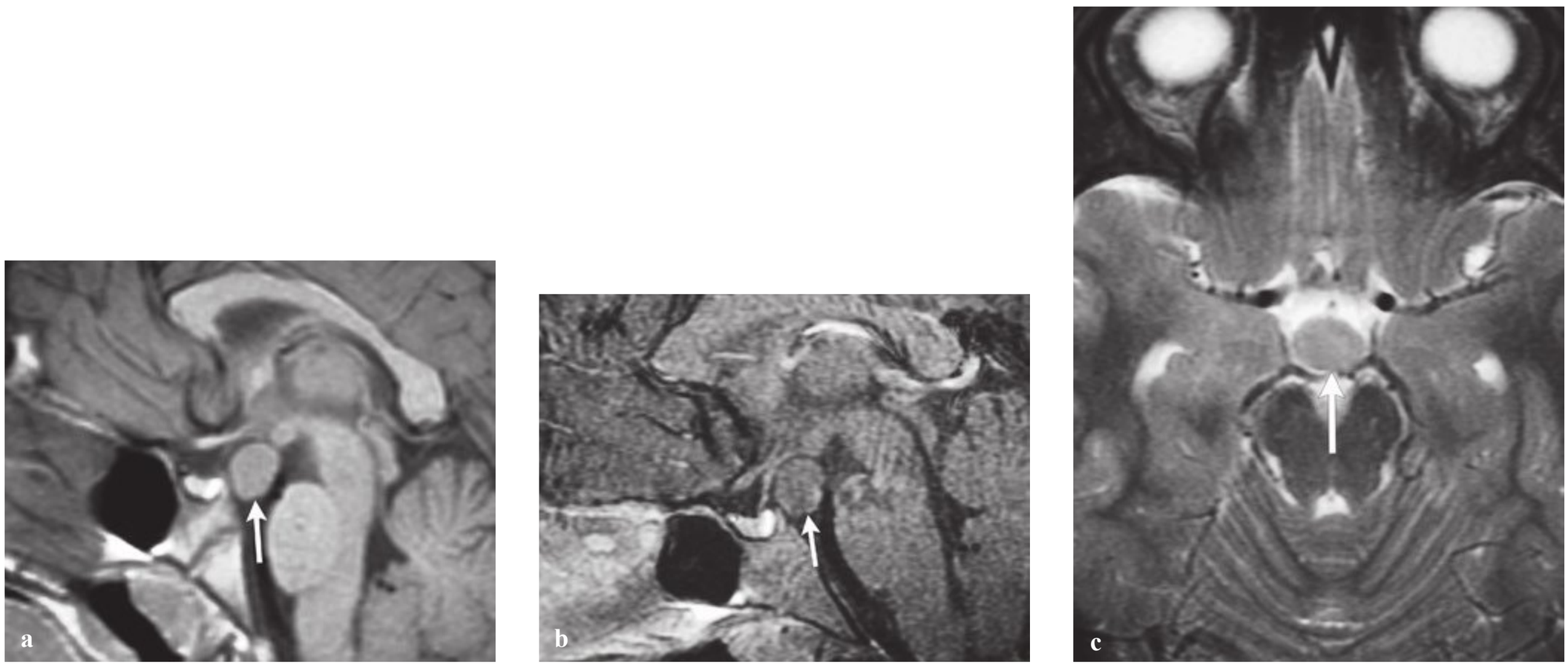

iFig. 1.414 Sagittal **(a)** precontrast T1-weighted image and **(b)** postcontrast T1-weighted image in a child with precocious puberty who has a pedunculated hypothalamic hamartoma that has intermediate signal (**a**, arrow) and shows no gadolinium contrast enhancement (**b**, arrow). **(c)** The lesion (arrow) has intermediate signal on axial T2-weighted imaging similar to gray matter.

Table 1.10 (cont.) Intrasellar and juxtasellar lesions

Lesions	Imaging Findings	Comments
Persistent craniopharyngeal canal (**Fig. 1.415**)	CT: Can range in diameter from 1 to15 mm and extend from the anterior portion of the sella to the junction of the soft palate and nasal septum. MRI: Persistent craniopharyngeal canal can be associated with transsphenoidal meningoencephaloceles, ectopic pituitary tissue, sphenoid teratoma, and infrasellar craniopharyngioma.	The anterior lobe (adenohypophysis) of the pituitary gland develops from evagination of ectodermal cells at the upper posterior portion of primitive oropharynx (Rathke's pouch) at 4–5 weeks of gestation. Rathke's pouch passes between the developing presphenoid and basisphenoid chondrification centers at the upper clivus and sella, where it associates with the descending neuroectoderm of the infundibulum, which will go on to form the posterior lobe (neurohypophysis). The pathway of Rathke's pouch is the craniopharyngeal canal, which progressively involutes by 6–7 weeks of gestation. Lack of involution results in a persistent craniopaharyngeal canal, which can contain pituitary tissue.
Rathke's cleft cyst (**Fig. 1.416** and **Fig. 1.417**)	MRI: Well-circumscribed lesion with variable low, intermediate, or high signal on T1- and T2-weighted imaging. On T1-weighted imaging, two-thirds have high signal, one-third have low signal; on T2-weighted imaging, one-half have high signal, one-fourth have low signal, and one-fourth have intermediate signal. On T2-weighted imaging, a small low-signal nodule may be seen within the predominant high signal of the lesion. Lesions show no gadolinium contrast enhancement centrally, only occasionally showing a thin peripheral rim of enhancement from associated inflammation. Lesion locations: half are intrasellar, one-fourth are suprasellar, and one-fourth are intra- and suprasellar. CT: Lesions can have low or intermediate attenuation.	Uncommon sellar/juxtasellar benign cystic lesion containing fluid with variable amounts of protein, mucopolysaccharide, and/or cholesterol. Rathke's cleft cysts arise from epithelial rests of the craniopharyngeal canal and are two to three times more common in women than in men. Occasionally, the cyst becomes symptomatic due to compression of adjacent structures.

(continued on page 354)

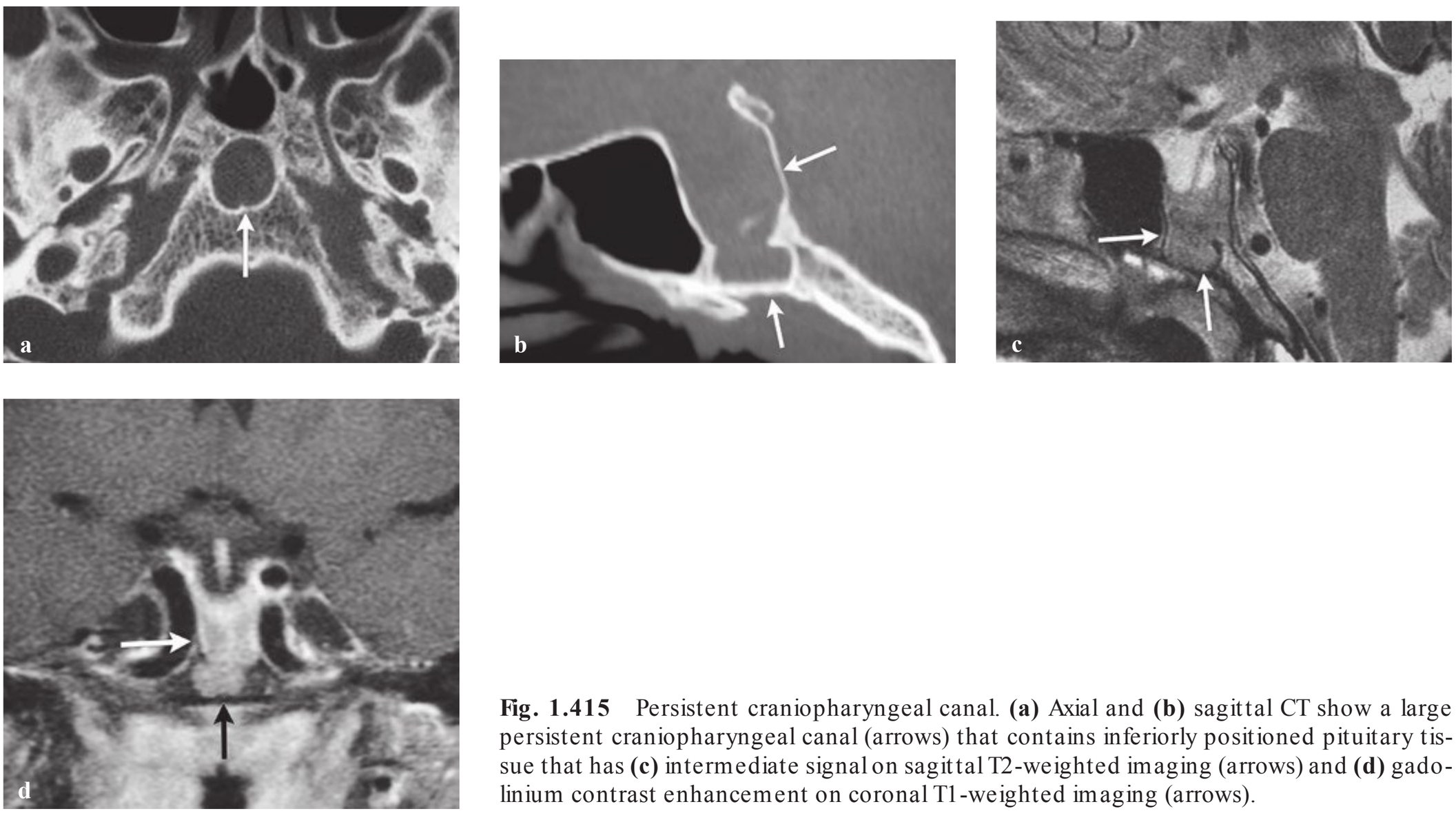

Fig. 1.415 Persistent craniopharyngeal canal. **(a)** Axial and **(b)** sagittal CT show a large persistent craniopharyngeal canal (arrows) that contains inferiorly positioned pituitary tissue that has **(c)** intermediate signal on sagittal T2-weighted imaging (arrows) and **(d)** gadolinium contrast enhancement on coronal T1-weighted imaging (arrows).

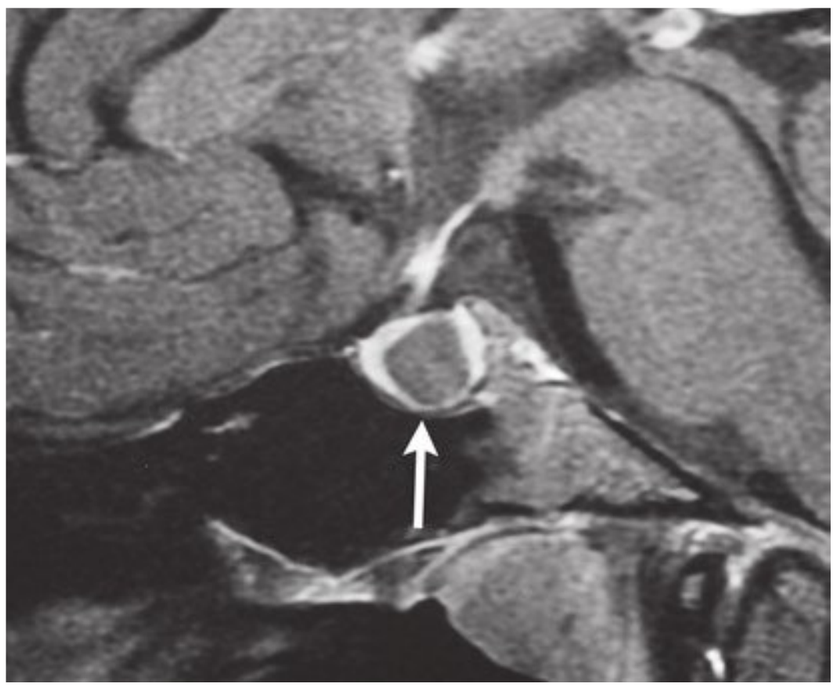

Fig. 1.416 Rathke's cleft cyst. Sagittal postcontrast T1-weighted imaging shows a nonenhancing cyst (arrow) in the mid portion of the pituitary gland between the adenohypophysis and neurohypophysis.

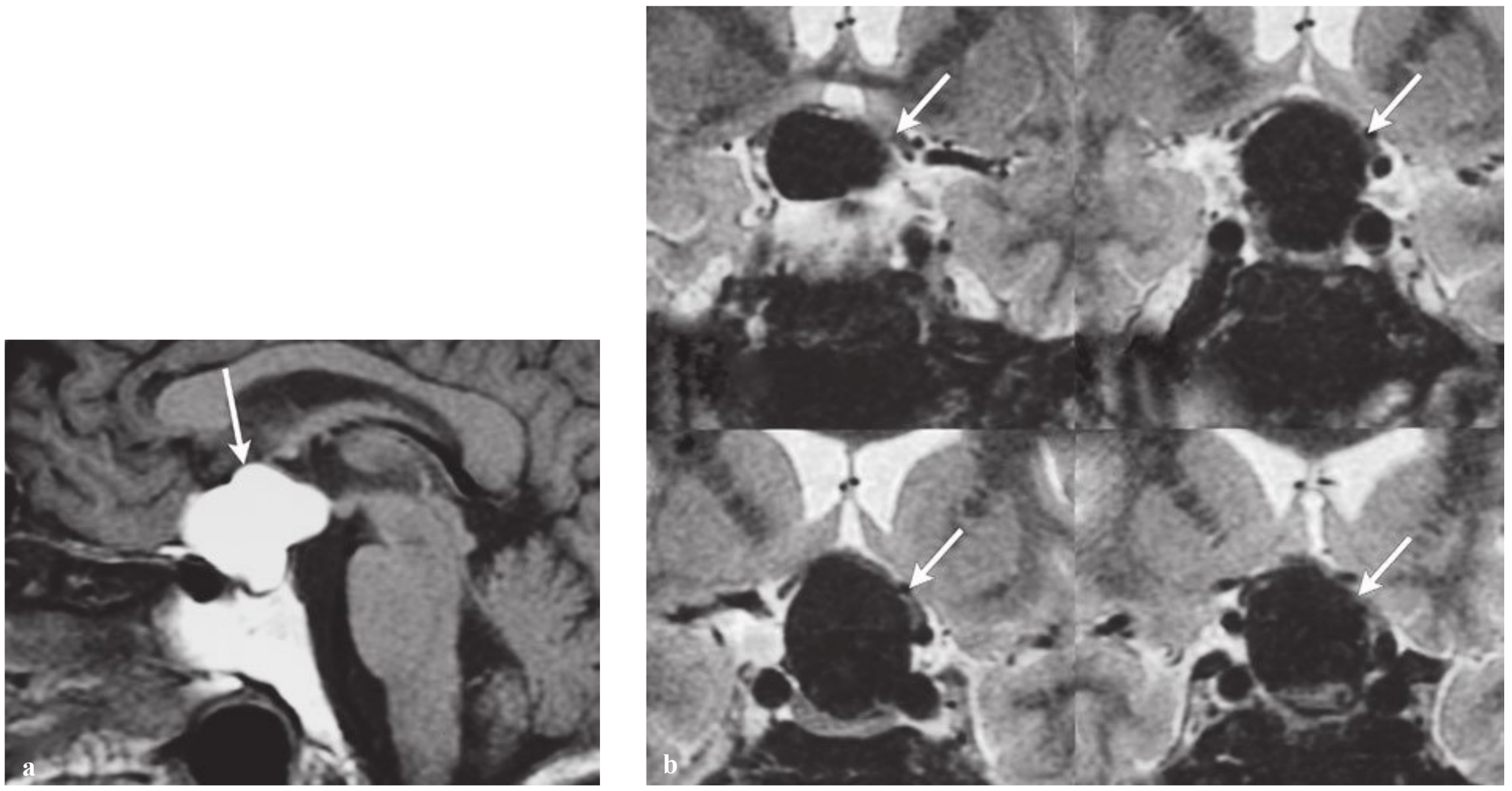

Fig. 1.417 A 60-year-old woman with a Rathke's cleft cyst that has **(a)** high signal on sagittal T1-weighted imaging (arrow) and **(b)** low signal on coronal T2-weighted imaging (arrows).

Table 1.10 (cont.) Intrasellar and juxtasellar lesions

Lesions	Imaging Findings	Comments
Pars intermedia cyst (**Fig. 1.418**)	MRI: Circumscribed small structure within the pituitary gland that usually measures less than 3 mm. Can have variable low, intermediate, and/or high signal on T1-weighted imaging, slightly high or high signal on T2-weighted imaging. No gadolinium contrast enhancement. CT: Small zone within the pituitary gland lacking contrast enhancement.	Small, 2–3 mm cystic remnants of Rathke's cleft located in the pars intermedia. The inner lining of the cysts is comprised of a single layer of columnar or cuboidal cells. Cyst contents include proteinaceous fluid and debris. Considered an incidental finding.
Cephalocele (meningocele or meningoencephalocele) (**Fig. 1.419**)	CT and MRI: Defect in skull through which there is either herniation of meninges and CSF (meningocele) or meninges, CSF, and brain tissue (meningoencephalocele).	Congenital malformation involving lack of separation of neuroectoderm from surface ectoderm, with resultant localized failure of bone formation. Can involve the sphenoid bone with extension into the sella, sphenoid bone and sinus, and nasopharynx. Incidence of transsphenoidal meningoencephaloceles is 1 per 700,000 live births. Clinical findings include difficulty in feeding and nasal obstruction in the first year, and potential for CSF leaks and meningitis.
Epidermoid (congenital cholesteatoma) (**Fig. 1.420**)	MRI: Well-circumscribed spheroid or multilobulated extra-axial ectodermal inclusion cystic lesions with low-intermediate signal on T1-weighted imaging, and high signal on T2-weighted imaging and diffusion-weighted imaging, and low signal on ADC maps. Mixed low, intermediate, or high signal on FLAIR images, and no gadolinium contrast enhancement. More commonly located in posterior cranial fossa (cerebellopontine angle cistern) than in parasellar/middle cranial fossa. CT: Extra-axial lesions with low-intermediate attenuation, no contrast enhancement, ± bone erosion/destruction.	Nonneoplastic congenital or acquired extra-axial off-midline lesions filled with desquamated cells and keratinaceous debris, usually with mild mass effect on adjacent brain, ± related clinical symptoms, with infratentorial > supratentorial locations. In adults, seen equally in males and females.

(continued on page 356)

Fig. 1.418 Pars intermedia cyst. **(a)** Sagittal T1-weighted imaging (arrow) and **(b)** axial T2-weighted imaging (arrow) show a small cyst between the anterior and posterior pituitary lobes that **(c)** lacks gadolinium contrast enhancement on axial T1-weighted imaging (arrow).

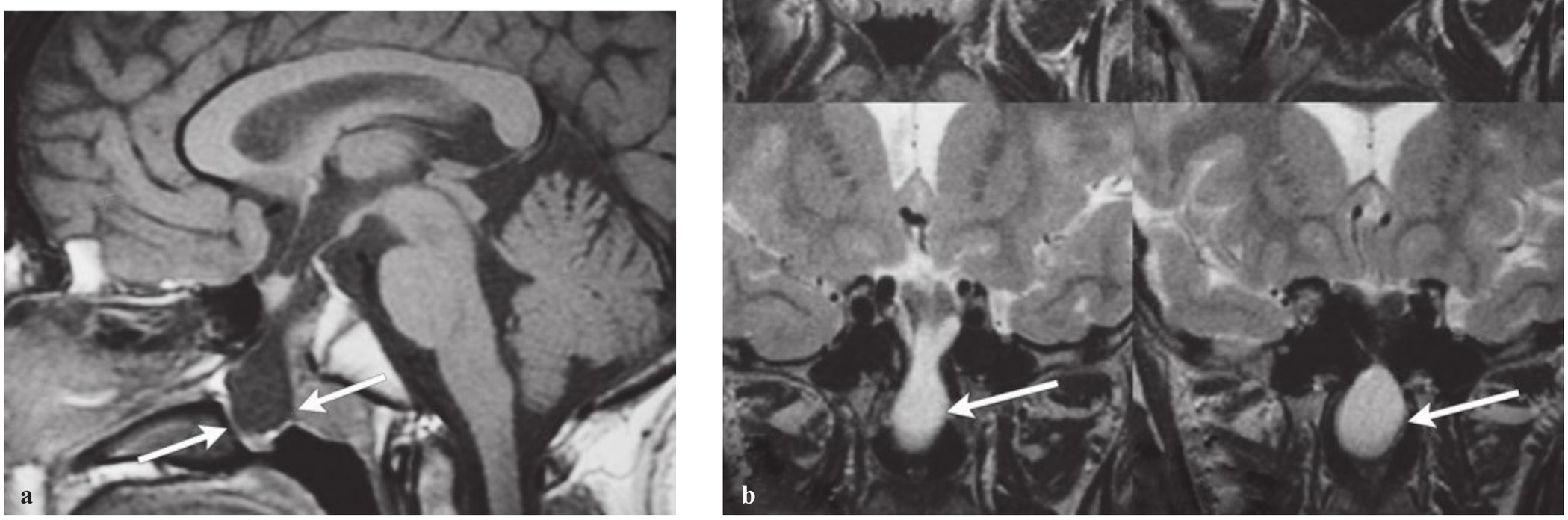

Fig. 1.419 A 17-year-old female with a meningocele extending inferiorly into the nasopharynx through an osseous defect in the sphenoid bone located posterior to the pituitary gland, as seen on **(a)** sagittal T1-weighted imaging (arrow) and **(b)** coronal T2-weighted imaging (arrows).

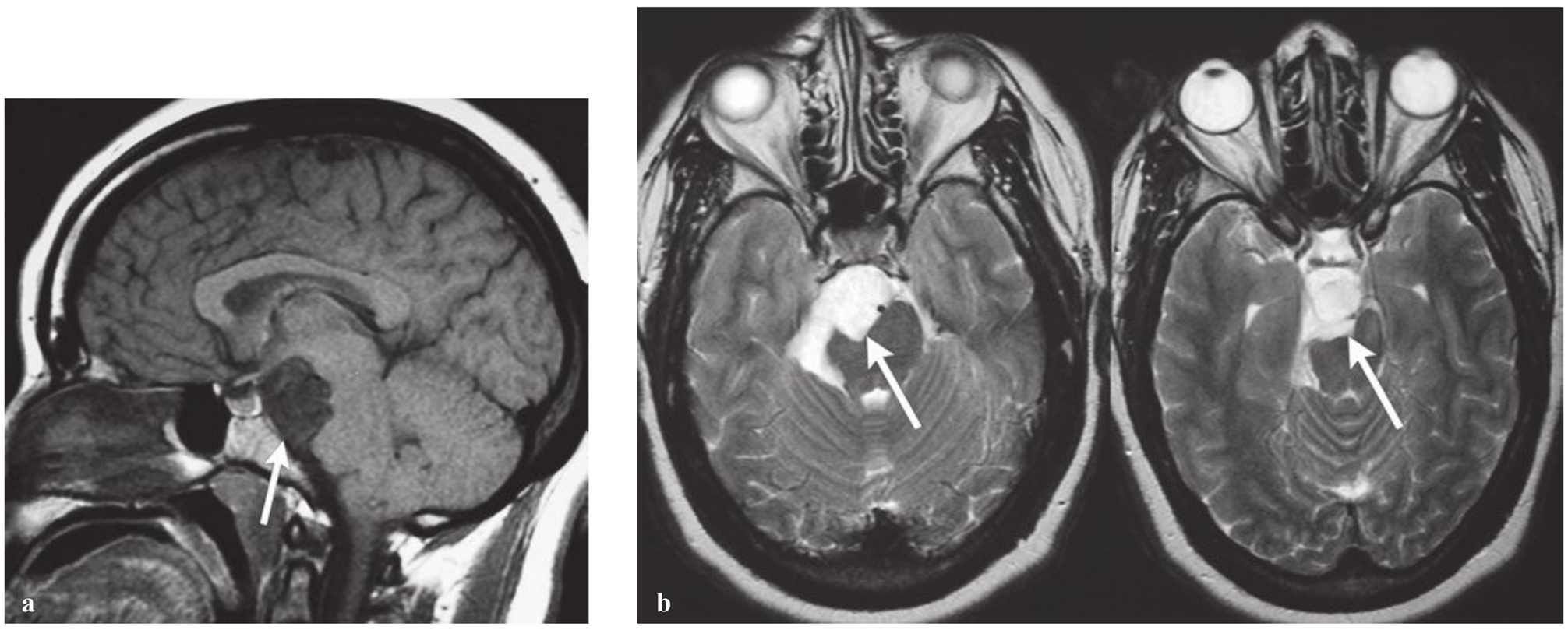

Fig. 1.420 Epidermoid. **(a)** Sagittal T1-weighted imaging shows an extra-axial lesion with mostly low signal along the endocranial surface of the clivus (arrow) that has **(b)** high signal (arrows) on axial T2-weighted imaging.

Table 1.10 (cont.) Intrasellar and juxtasellar lesions

Lesions	Imaging Findings	Comments
Dermoid (**Fig. 1.421**)	MRI: Well-circumscribed spheroid or multilobulated extra-axial lesions, usually with high signal on T1-weighted imaging and variable low, intermediate, and/or high signal on T2-weighted imaging, no gadolinium contrast enhancement, ± fluid–fluid or fluid–debris levels. Can cause chemical meningitis if dermoid cyst ruptures into the subarachnoid space. Commonly located at or near the midline, supratentorial more often than infratentorial. CT: Spheroid or multilobulated extra-axial lesion with variable low, intermediate, and/or high attenuation and no contrast enhancement, ± fluid–fluid or fluid–debris levels.	Nonneoplastic congenital or acquired ectodermal inclusion cystic lesions filled with lipid material, cholesterol, desquamated cells, and keratinaceous debris, usually with mild mass effect on adjacent brain. Congenital dermoid and epidermoid cysts result from inclusion of surface ectoderm before the closure of the neural tube at 4 weeks of gestation. In adults, found slightly more often in males than in females, ± related clinical symptoms.
Colloid cyst	MRI: Well-circumscribed spheroid lesion located at the anterior upper portion of the third ventricle, with variable signal (low, intermediate, or high) on T1- and T2-weighted imaging, and often high signal on T1-weighted imaging and low signal on T2-weighted imaging. No gadolinium contrast enhancement. CT: Spheroid lesions located at the anterior upper portion of the third ventricle, with variable attenuation (low, intermediate, or high), and no contrast enhancement.	Slow-growing, benign, cystic lesions whose wall contains a single layer of epithelial cells. Cyst contents can include cholesterol granules, various blood products, macrophages, and various minerals and/or ions. Most colloid cysts occur in the anterosuperior portion of the third ventricle, and rarely in the sella or suprasellar cistern. Usually found in adults (50–60 years old).
Lipoma of the sellar/hypothalamic region (**Fig. 1.422**)	MRI: Lipomas in the sellar region are usually found in the suprasellar cistern more often than intrasellar. MR signal is isointense to subcutaneous fat on T1-weighted imaging (high signal), and on T2-weighted imaging, fat signal suppression occurs with frequency-selective fat saturation techniques or with a short time to inversion recovery (STIR) method. Typically there is no gadolinium contrast enhancement. CT: Low attenuation similar to subcutaneous fat.	These lipomas are benign fatty lesions resulting from congenital malformation, often located in or near the midline, that may contain calcifications and/or traversing blood vessels. Usually asymptomatic unless they cause mass effect.
Empty sella (**Fig. 1.423**)	MRI: Pituitary gland is thinned and flattened along floor of sella, with infundibulum in midline. The flattened pituitary gland has normal MRI signal characteristics and gadolinium contrast enhancement. CT: Expansion and thinning of the bony margins of the sella. CSF attenuation within the sella.	Common incidental finding involving the pituitary gland and sella. Can result from a weakened or fenestrated diaphragma sella allowing CSF pulsations to flatten the pituitary gland. Occurs five times more frequently in women than in men. Can be associated with hydrocephalus and pseudotumor cerebri. A secondary empty sella can result from peripartum pituitary necrosis or injury from radiation/surgery.

(continued on page 358)

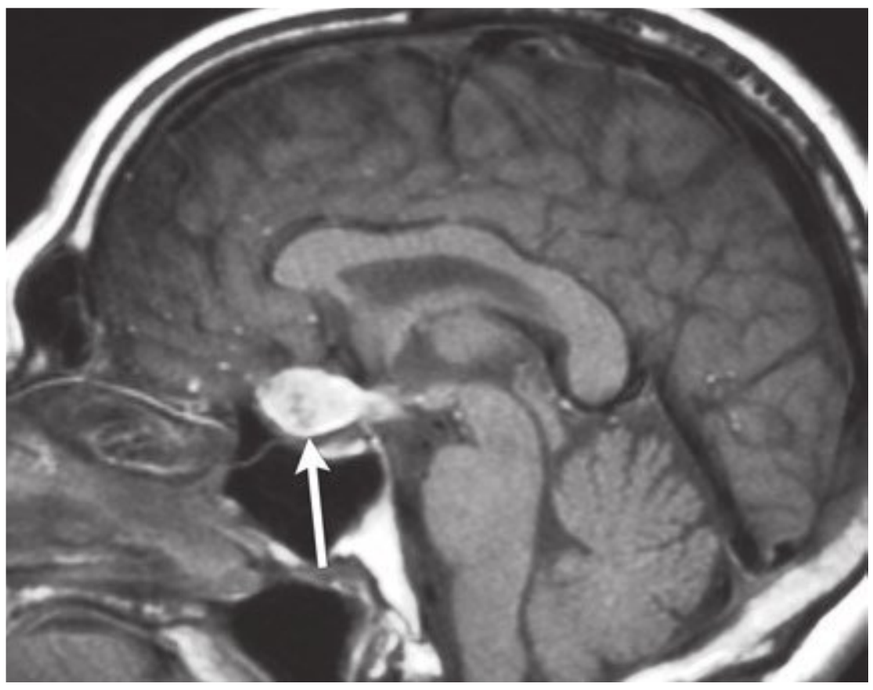

Fig. 1.421 Dermoid. Sagittal T1-weighted imaging shows an extra-axial lesion (arrow) in the suprasellar cistern that has high signal. Multiple small foci with high signal are seen in the subarachnoid space, representing ruptured dermoid contents.

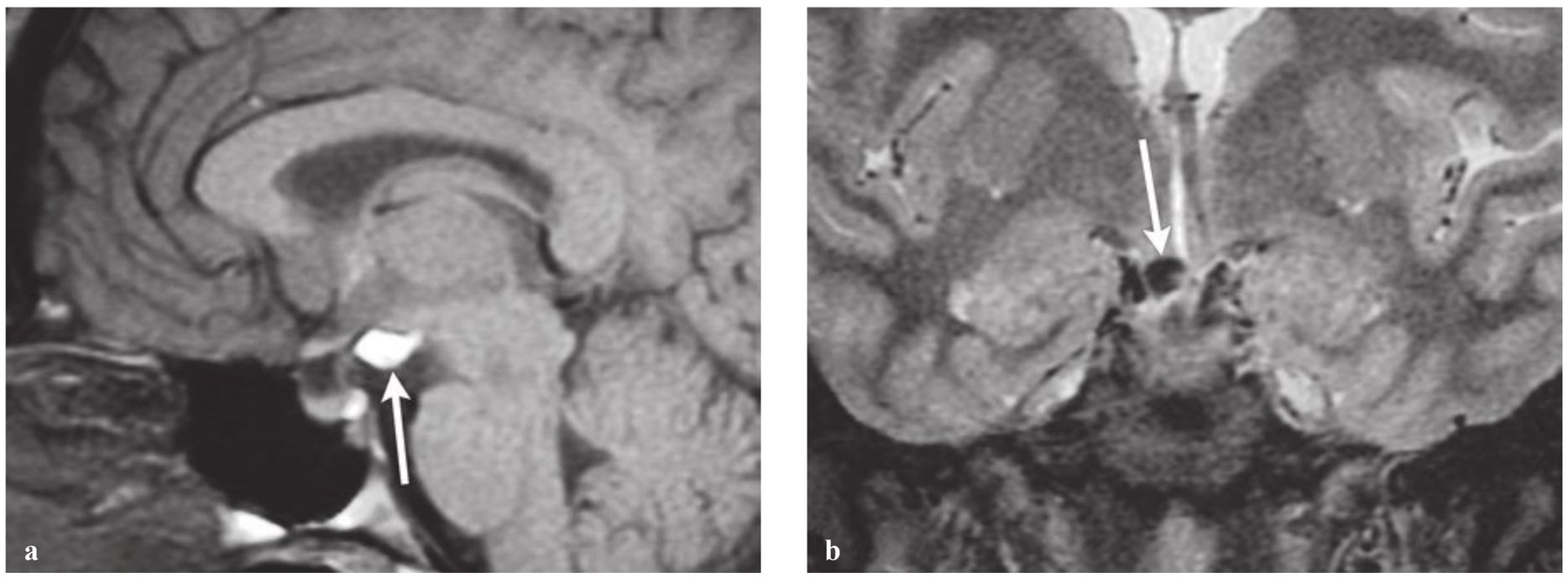

Fig. 1.422 Hypothalamic lipoma. **(a)** Sagittal T1-weighted imaging shows a lipoma (arrow) with high signal along the inferior surface of the hypothalamus. **(b)** The high signal of the lipoma is nulled (arrow) on coronal fat-suppressed T2-weighted imaging.

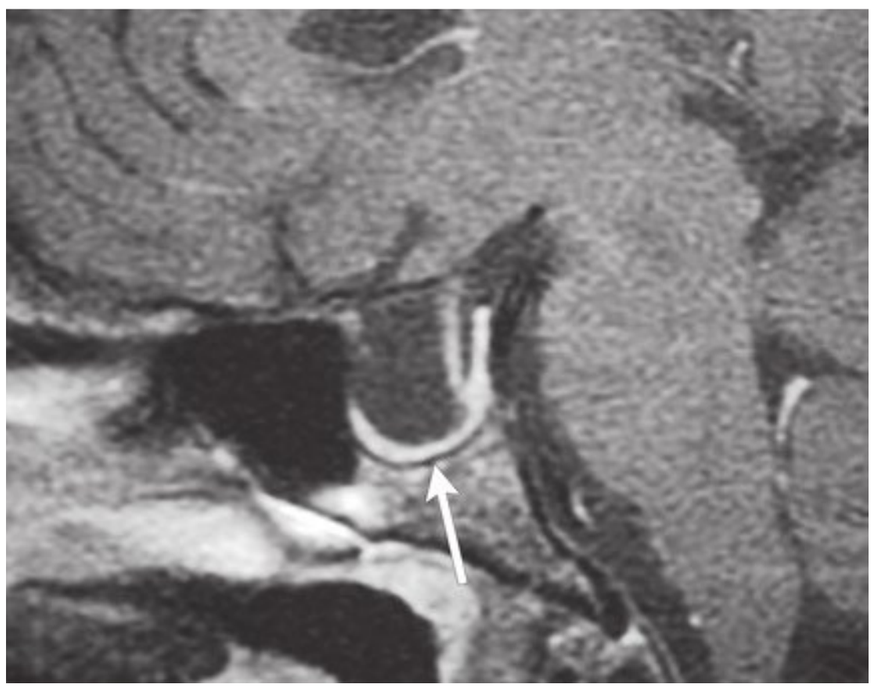

Fig. 1.423 Empty sella. Sagittal postcontrast fat-suppressed T1-weighted imaging shows an enlarged sella filled mostly with CSF. The gadolinium contrast-enhancing flattened pituitary tissue (arrow) is located along the floor of the sella.

Table 1.10 (cont.) Intrasellar and juxtasellar lesions

Lesions	Imaging Findings	Comments
Pituitary Lesions		
Pituitary hypertrophy/ hyperplasia (**Fig. 1.424**)	MRI: In pituitary hyperplasia/hypertrophy, there is enlargement of the pituitary gland without focal abnormalities in MRI signal characteristics or enhancement pattern. The normal pituitary gland in adults measures up to 10 mm in height. During puberty in girls, the gland can measure up to 12 mm in height with a slightly convex upper margin. In the early postpartum period, the gland measures up to 12 mm in height, and this is referred to as physiologic hypertrophy. During late pregnancy and in the early postpartum period, the pituitary gland also has slightly high signal on T1-weighted imaging. Pituitary hypertrophy can also be seen with hypothyroidism.	In addition to puberty and pregnancy, pituitary hyperplasia/hypertrophy can be associated with endocrine end-organ failure, such as hypothyroidism and central precocious puberty. The pituitary gland can increase by 30 to 100%in size during the third trimester of pregnancy.
Diabetes insipidus	MRI: The neurohypophysis or posterior pituitary lobe is seen as a zone of high signal (bright spot) on T1-weighted imaging in almost all healthy patients. The normal high signal of the neurohypophysis on T1-weighted imaging is secondary to the presence of neurophysin-vasopressin complex in lipid-rich secretory vesicles. In patients with central diabetes insipidus, this bright spot is usually absent.	Diabetes insipidus is a disorder of water balance, with excretion of abnormally large volumes of dilute urine. Central diabetes insipidus results from inadequate secretion of antidiuretic hormone due to hypothalamic/pituitary dysfunction resulting from trauma, surgery, neoplasm (germinoma, astrocytoma), and inflammatory diseases like Langerhans' cell histiocytosis, sarcoid, etc.

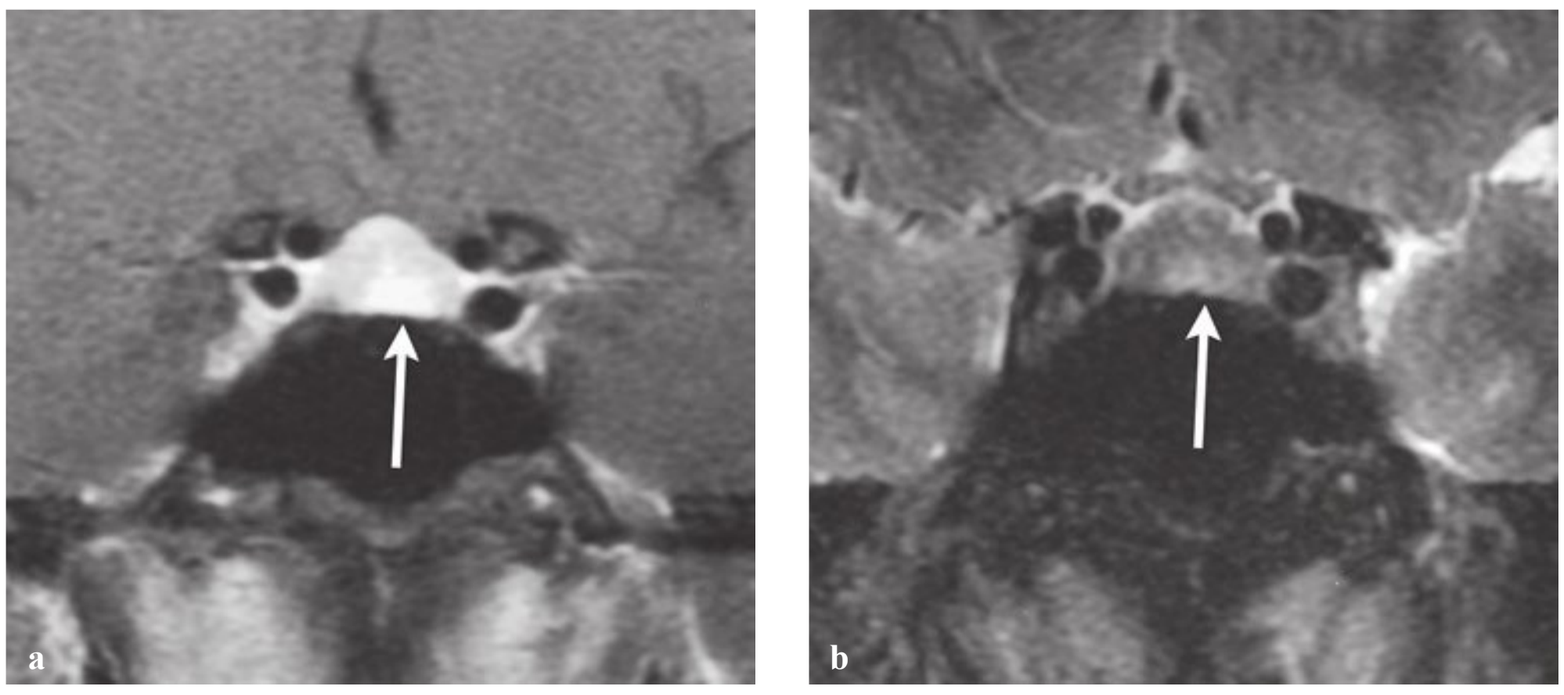

Fig. 1.424 An 8-year-old female with pituitary hypertrophy/hyperplasia. **(a)** Coronal fat-suppressed T1-weighted imaging shows gadolinium contrast enhancement of a slightly enlarged pituitary gland (arrow) that has **(b)** slightly heterogeneous intermediate and slightly high signal (arrow) on coronal T2-weighted imaging.

Lesions	Imaging Findings	Comments
Neoplasms		
Pituitary adenoma (**Fig. 1.425, Fig. 1.426, Fig. 1.427**, and **Fig. 1.428**) Microadenomas (< 10 mm) Macroadenomas (> 10 mm)	MRI: Microadenoma: Commonly have intermediate signal on T1- and T2-weighted imaging, ± cyst, ± hemorrhage, ± necrosis. Typically show less gadolinium contrast enhancement than normal pituitary tissue—often best seen with dynamic early phase imaging. Macroadenoma: Commonly have intermediate signal on T1- and T2-weighted imaging similar to gray matter, ± necrosis, ± cyst, ± hemorrhage, usually with prominent gadolinium contrast enhancement, extension into suprasellar cistern with waist at diaphragma sella, ± extension into cavernous sinus, occasionally invading skull base.	Common, benign, slow-growing tumors account for 50%of sellar/parasellar neoplasms in adults, and up to 15%of primary intracranial neoplasms. Microadenomas can be associated with endocrine abnormalities related to oversecretion of hormones (prolactin > nonsecretory type > growth hormone > ACTH > thyrotropin). Prolactinomas: females > males, growth hormone tumors: males > females. Macroadenomas with suprasellar extension can cause compression and displacement of the optic chiasm, with associated visual distrurbance (bitemporal hemianopia). Most pituitary tumors arise from sporadic mutations. Five percent of tumors can be associated with inherited disorders, such as McCune-Albright syndrome, Carney complex, and multiple endocrine neoplasia type 1. Rarely, extensive hemorrhage involving a pituitary adenoma can result in a rapid severe rise in intrasellar pressure, resulting in decreased blood flow in portal vessels and leading to acute ischemic necrosis of the adenohypophysis with hypopituitarism (pituitary apoplexy, Sheehan syndrome) if not treated promptly with steroids ± transsphenoidal surgical decompression. Patients often present with acute, severe headaches, altered consciousness, hypopituitarism, and/or ophthalmoplegia.

(continued on page 361)

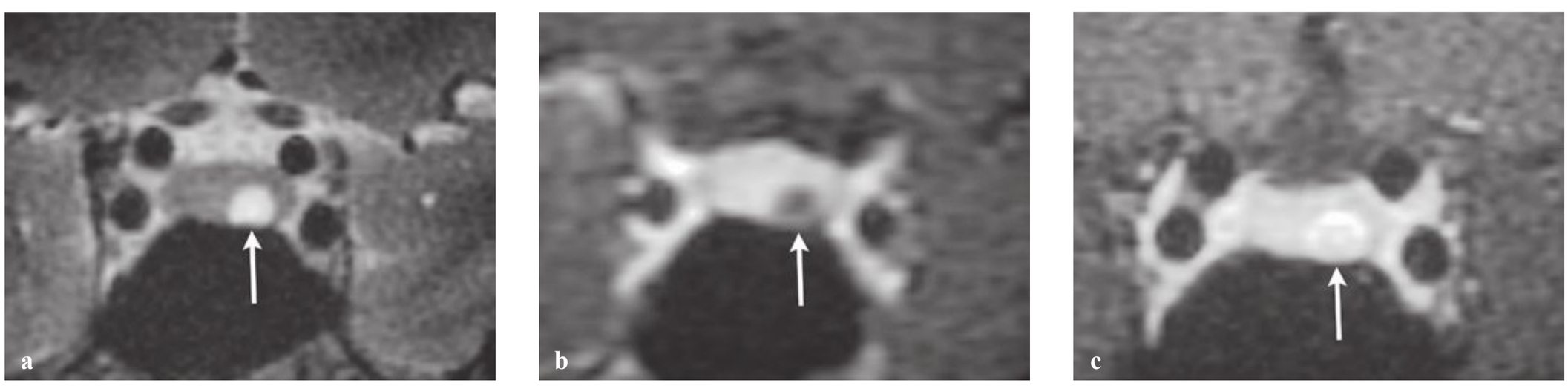

Fig. 1.425 A 19-year-old female with a pituitary microadenoma. **(a)** Coronal T2-weighted imaging shows the lesion to have high signal (arrow), **(b)** lesser gadolinium contrast enhancement (arrow) on coronal T1-weighted imaging relative to normal tissue during early serial acquisitions, and **(c)** slightly greater enhancement (arrow) than normal tissue on delayed T1-weighted imaging.

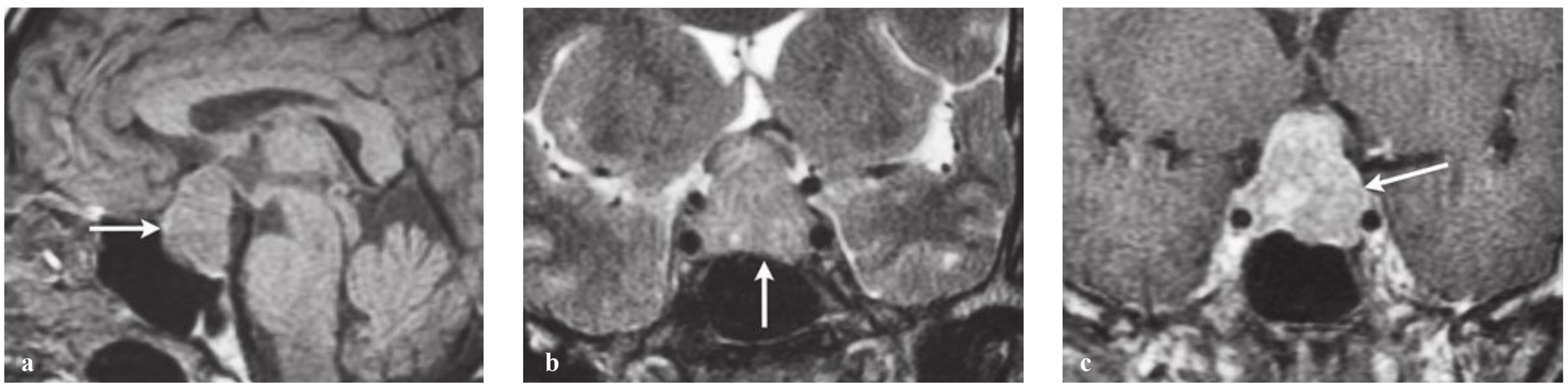

Fig. 1.426 A 52-year-old man with a pituitary macroadenoma. **(a)** Sagittal T1-weighted imaging shows the tumor to have intermediate signal (arrow) and **(b)** slightly high signal on coronal T2-weighted imaging (arrow). **(c)** The tumor shows gadolinium contrast enhancement (arrow) on coronal T1-weighted imaging.

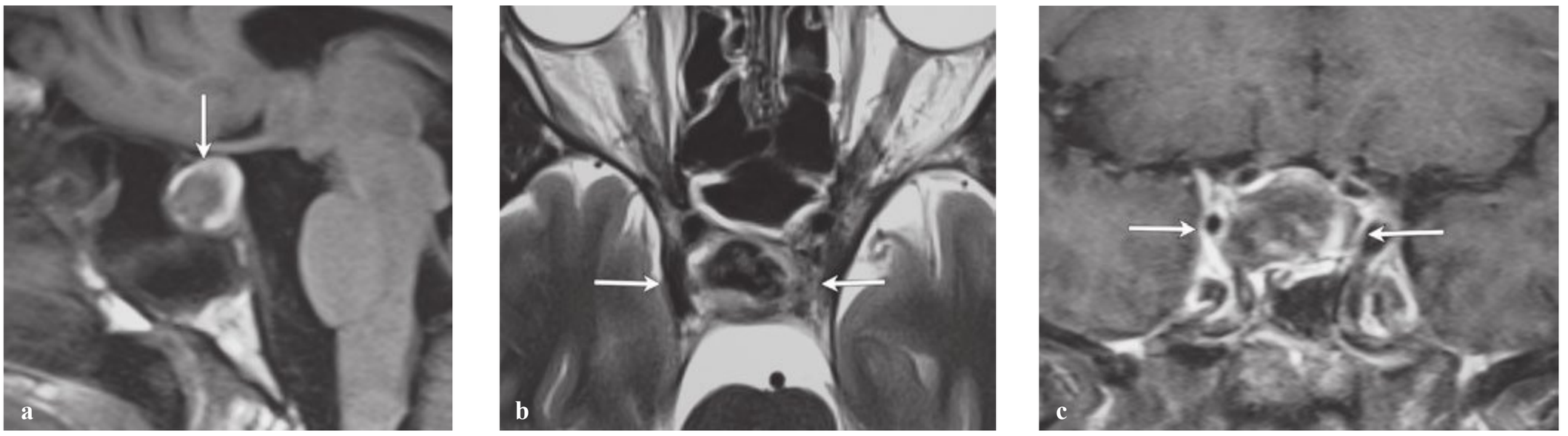

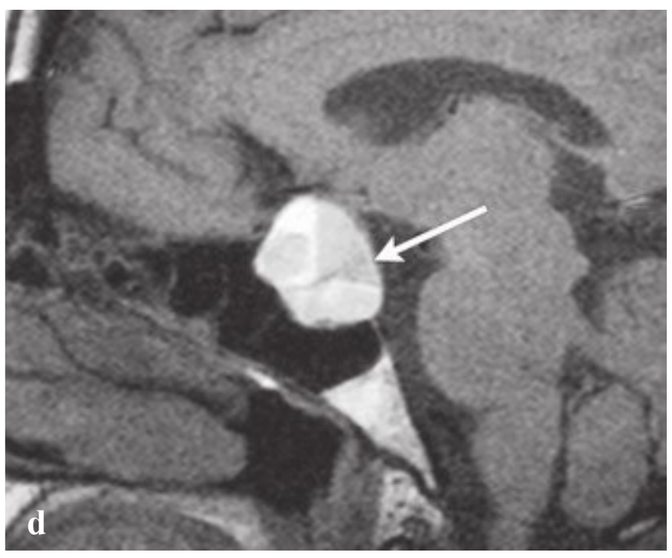

Fig. 1.427 A 63-year-old man with pituitary apoplexy. Acute hemorrhage within the abnormally enlarged pituitary gland has **(a)** mixed intermediate and high signal (arrow) on sagittal T1 WI, **(b)** mixed low and slightly high signal on axial T2-weighted imaging (arrows), and irregular mostly peripheral gadolinium contrast enhancement on coronal T1-weighted imaging (arrows). **(d)** Sagittal T1-weighted imaging of a 50-year-old woman shows hemorrhage with high signal within pituitary macroadenoma (arrow).

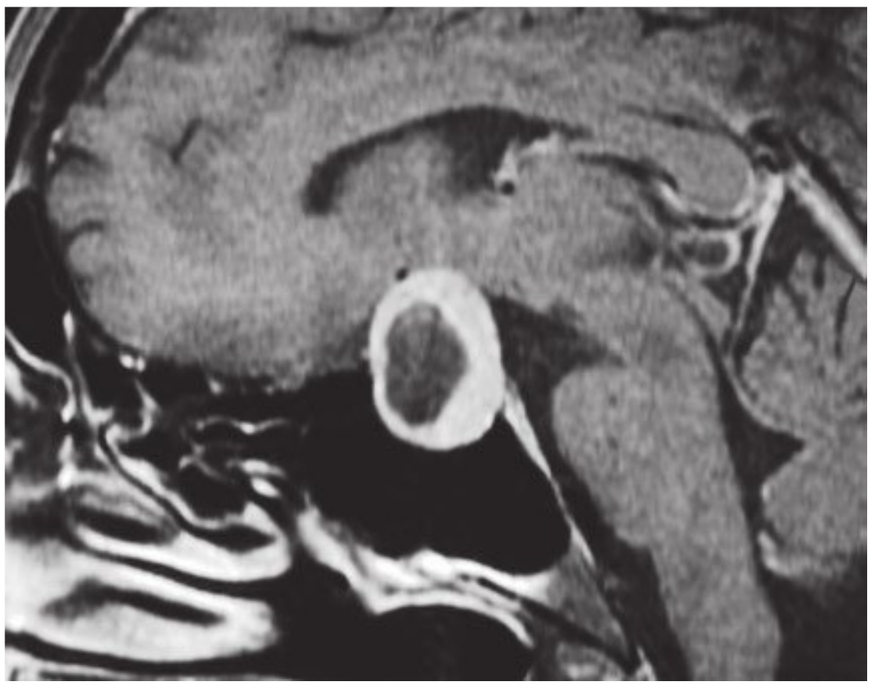

Fig. 1.428 Pituitary macroadenoma with cystic degeneration seen as a non-enhancing zone within the tumor on sagittal T1-weighted imaging.

Table 1.10 (cont.) Intrasellar and juxtasellar lesions

Lesions	Imaging Findings	Comments
Invasive pituitary adenoma (**Fig. 1.429**)	MRI: Often have intermediate signal on T1- and T2-weighted imaging and often similar to gray matter, ± necrosis, ± cyst, ± hemorrhage. Usually show prominent gadolinium contrast enhancement, extension into suprasellar cistern with waist at diaphragma sella, ± extension into cavernous sinus, occasionally invading skull base. CT: Often have intermediate attenuation, ± necrosis, ± cyst, ± hemorrhage, usually show contrast enhancement, extension into suprasellar cistern with waist at diaphragma sella, ± extension into cavernous sinus, and can invade the skull base.	Histologically benign pituitary macroadenomas can occasionally have an invasive growth pattern with extension into the sphenoid bone, clivus, ethmoid sinus, orbits, and/or interpeduncular cistern.
Pituitary carcinoma (**Fig. 1.430**)	MRI: Commonly has intermediate signal on T1- and T2-weighted imaging and often similar to gray matter, ± necrosis, ± cyst, ± hemorrhage, usually with prominent gadolinium contrast enhancement. Extension into suprasellar cistern with waist at diaphragma sella, ± extension into cavernous sinus, can invade skull base, ± leptomeningeal gadolinium contrast enhancement. CT: Commonly has intermediate attenuation, ± necrosis, ± cyst, ± hemorrhage, usually with contrast enhancement. Extension into suprasellar cistern with waist at diaphragma sella, ± extension into cavernous sinus, and can invade the skull base.	Rare malignant pituitary tumors involving the adenohypophysis. Account for 0.5%of pituitary tumors. In addition to locally invasive disease and subarachnoid tumor dissemination, hematogenous metastatic spread has been reported to bone, liver, lungs, lymph nodes, pancreas, heart, ovaries, and myometrium.

(continued on page 362)

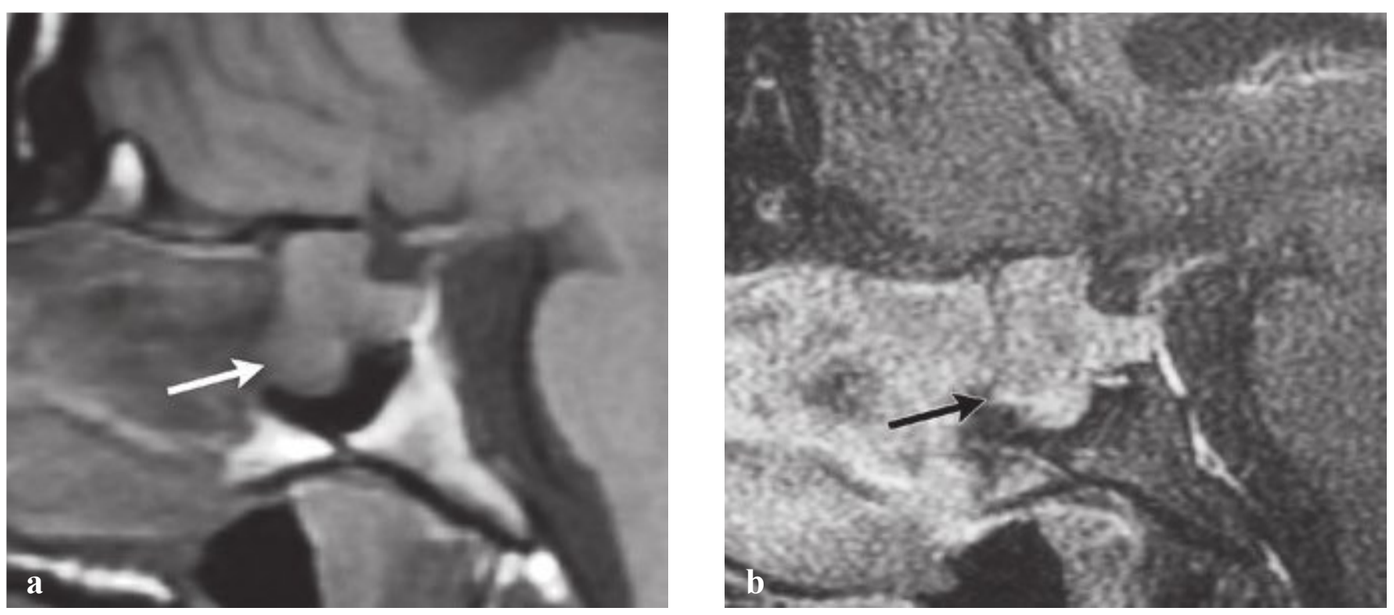

Fig. 1.429 A 47-year-old woman with an invasive pituitary adenoma (arrows) that is seen extending into the sphenoid sinus on sagittal **(a)** precontrast T1-weighted imaging and **(b)** postcontrast T1-weighted imaging.

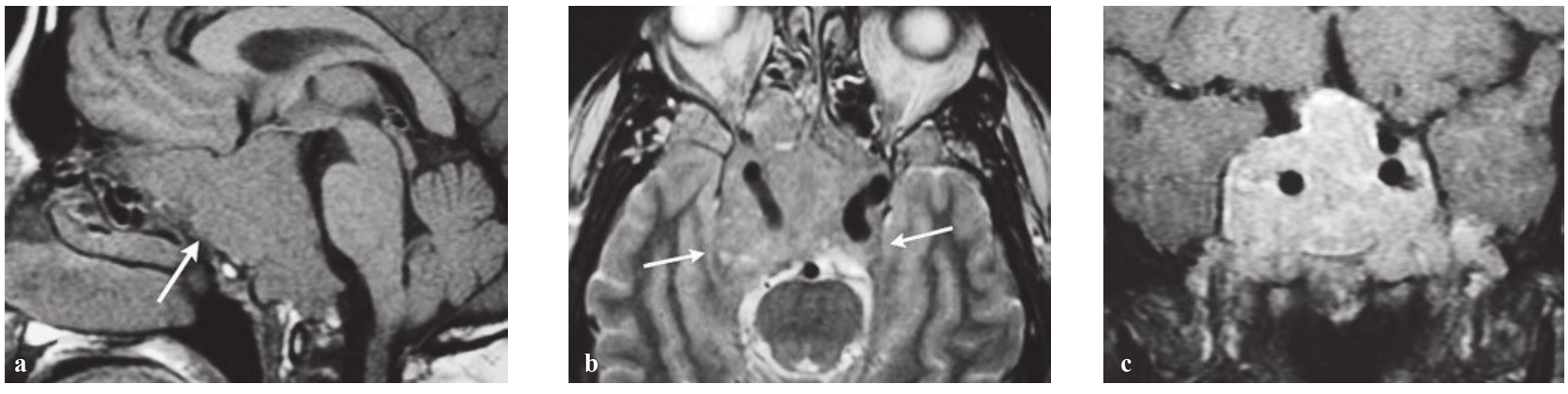

Fig. 1.430 A 44-year-old man with an aggressive pituitary carcinoma invading the sphenoid and occipital portions of the clivus, cavernous sinuses, and sphenoid sinus. The tumor has **(a)** intermediate signal on sagittal T1-weighted imaging (arrow), **(b)** intermediate to slightly high signal on axial T2-weighted imaging (arrows), and **(c)** gadolinium contrast enhancement on coronal fat-suppressed T1-weighted imaging.

Table 1.10 (cont.) Intrasellar and juxtasellar lesions

Lesions	Imaging Findings	Comments
Pituicytoma (**Fig. 1.431**)	MRI: Round/ovoid lesions or diffuse abnormal enlargement of pituitary stalk and/or posterior pituitary. Most lesions are suprasellar or within both the sella and suprasellar cistern. Lesions usually have intermediate signal on T1-weighted imaging, and intermediate to slightly high signal on T2-weighted imaging that may be isointense to brain tissue. Typically show gadolinium contrast enhancement (homogeneous > heterogeneous pattern). Lesions range in size from 1.5 to 6 cm. CT: Lesions usually have attenuation similar to brain.	Rare, low-grade spindle-cell glial neoplasms that originate in the infundibulum and/or neurohypophysis. Arise from glial cells of the neurohypophysis (pituicytes). Typically occur in adults (average age = 50 years). Imunoreactive to S-100 protein, vimentin, and glial fibrillary acidic protein (GFAP). Symptoms related to compression of adjacent optic chiasm (visual disturbances) and pituitary dysfunction (amenorrhea, elevated prolactin).
Granular cell tumor (choristoma or glioma of the neurohypophysis) (**Fig. 1.432**)	MRI: Round/ovoid lesions or diffuse abnormal enlargement of pituitary stalk and/or posterior pituitary. Most lesions are suprasellar or within both the sella and suprasellar cistern. Lesions have low-intermediate signal on T1-weighted imaging and intermediate to slightly high signal on T2-weighted imaging that may be isointense to brain tissue. Typically show gadolinium contrast enhancement (heterogeneous or homogeneous pattern). CT: Lesions often have attenuation slightly higher than brain and usually show contrast enhancement.	Rare, slow-growing, benign primary neoplasms that arise from the neurohypophysis and/or infundibulum. Tumors are composed of groups of large polygonal cells with granular eosinophilic cytoplasm. Immunoreactive to CD68, S-100 protein, α-1-antitrypsin, α-1-antichymotrypsin, and cathepsin B. Usually occur in patients older than 30 years (age range = 26 to 73 years, average age = 49 years), and female/male ratio is 2/1. Symptoms related to compression of adjacent optic chiasm (visual disturbances) and pituitary dysfunction (amenorrhea, elevated prolactin).
Spindle-cell oncocytoma of the adenohypophysis	MRI: Diffuse abnormal enlargement of anterior pituitary gland. Lesions have low-intermediate signal on T1-weighted imaging that may be isointense to brain tissue. Typically show gadolinium contrast enhancement (heterogeneous > homogeneous pattern).	Rare benign tumor of the adenohypophysis composed of fascicles of spindle and/or epithelioid cells with eosinophilic cytoplasm. Mitotic activity is less than 1 per 10 high-power fields (HPF). Immunoreactive to S-100 protein, vimentin, EMA, and antimitochondrial antibody 113–1. May originate from folliculo-stellate cells of the adenohypophysis. Usually occur in adults (average age = 59 years).
Metastatic lesions involving the pituitary gland (**Fig. 1.433**)	MRI: Focal gadolinium contrast-enhancing lesion in the pituitary gland with or without enlargement of the pituitary gland and bone destruction. CT: Can show sites of bone destruction at the sella and skull base.	Metastatic lesions to the pituitary gland can occur hematogenously or by direct extension from CSF, dural, or osseous tumor. Hematogenous metastatic tumor usually involves the posterior lobe and/or infundibulum initially (related to the arterial supply to the posterior pituitary compared with the predominant hypothalamic portal blood supply to the anterior pituitary) with eventual extension to the anterior lobe. Most common primary neoplasms are carcinomas of the lung, breast, and thyroid. Only 15% of patients have symptoms related to the pituitary metastases.

(continued on page 364)

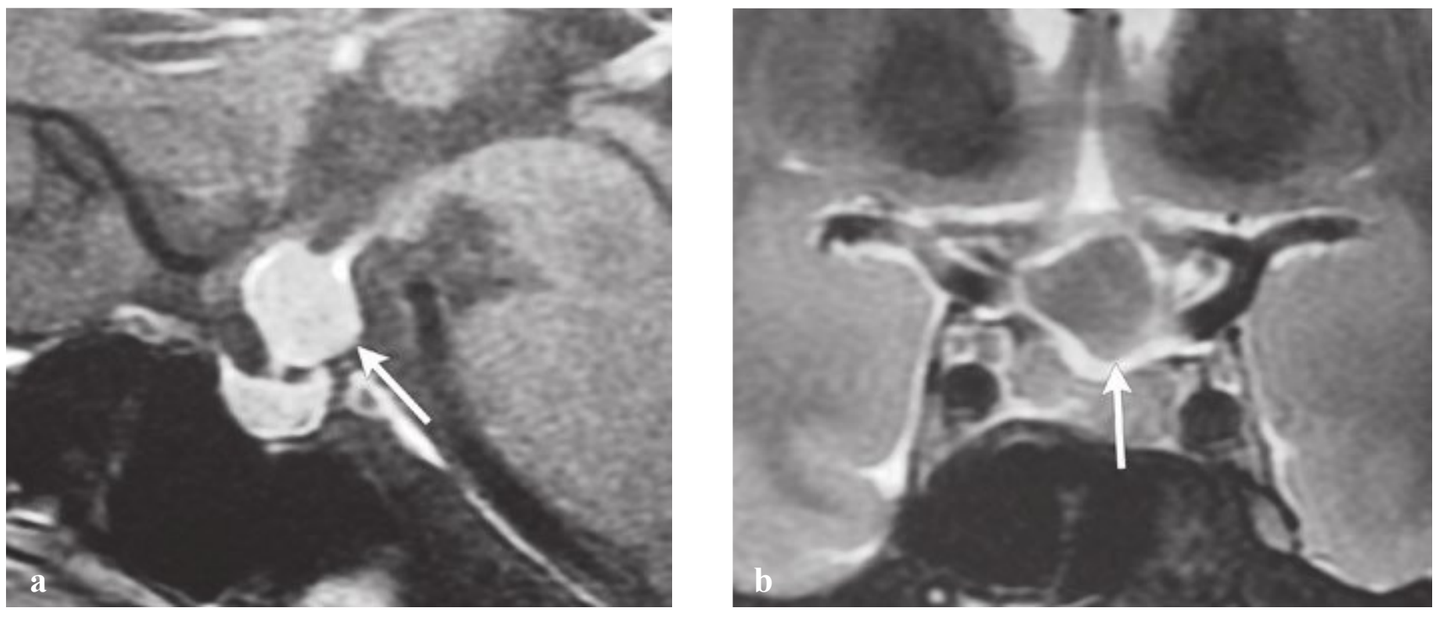

Fig. 1.431 A 57-year-old woman with pituicytoma that is seen as a gadolinium contrast-enhancing lesion in the pituitary stalk on **(a)** sagittal fat-suppressed T1-weighted imaging (arrow) and that **(b)** also has intermediate signal on coronal T2-weighted imaging (arrow).

Fig. 1.432 A 72-year-old woman with granular cell tumor (choristoma) of the pituitary stalk and hypothalamus. The tumor has **(a)** intermediate signal on sagittal T1-weighted imaging (arrow), **(b)** mixed intermediate and slightly high signal on coronal T2-weighted imaging (arrow), and **(c)** prominent gadolinium contrast enhancement on sagittal fat-suppressed T1-weighted imaging (arrow).

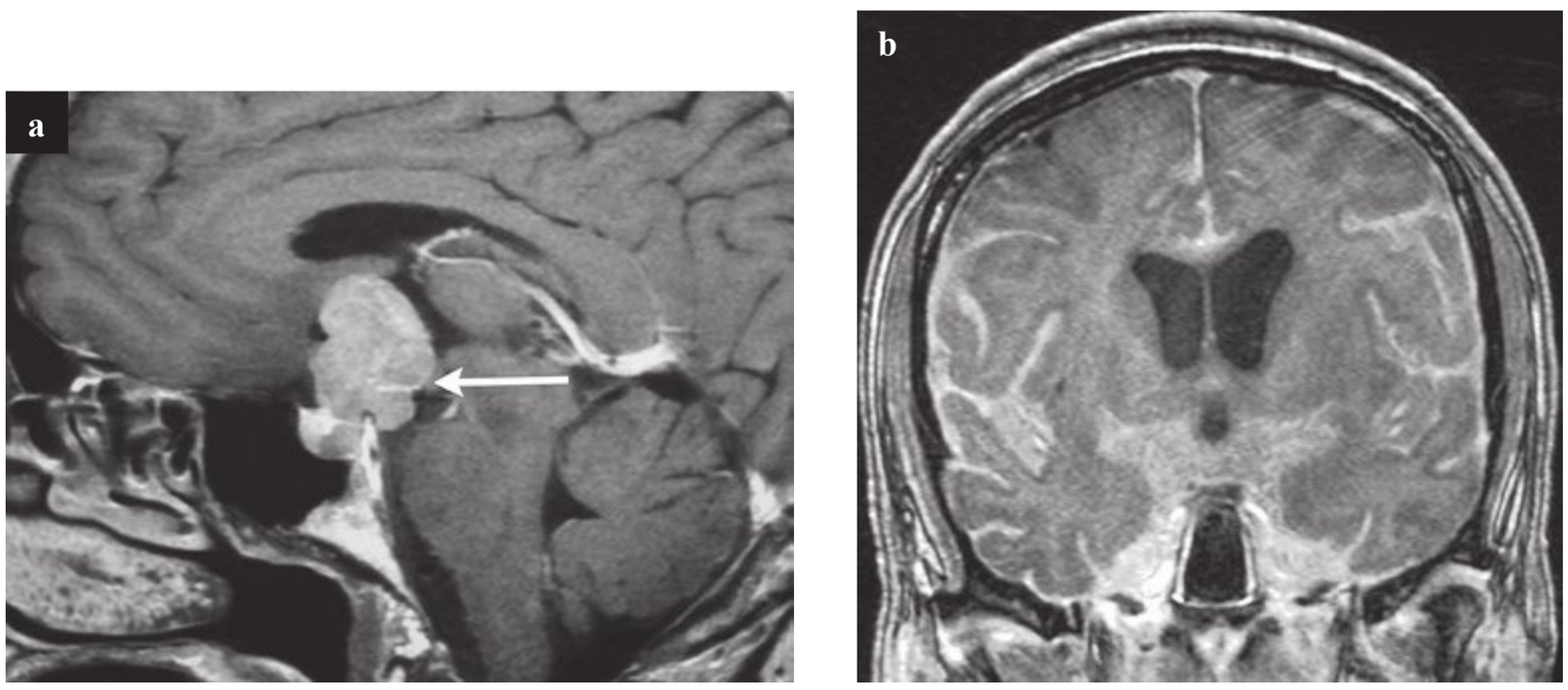

Fig. 1.433 **(a)** A 55-year-old woman with metastatic breast carcinoma in the posterior pituitary gland, pituitary stalk, and hypothalamus that is seen as a gadolinium contrast-enhancing lesion on sagittal T1-weighted imaging (arrow). **(b)** Disseminated subarachnoid tumor from melanoma in another patient seen on coronal T1-weighted imaging as diffuse abnormal gadolinium contrast enhancement in the leptomeninges, including the suprasellar cistern.

Table 1.10 (cont.) Intrasellar and juxtasellar lesions

Lesions	Imaging Findings	Comments
Suprasellar Lesions		
Craniopharyngioma (**Fig. 1.434** and **Fig. 1.435**)	MRI: The adamantinomatous type usually has circumscribed lobulated margins, occurs in both suprasellar and intrasellar locations > suprasellar > intrasellar (10%) sites; with variable low, intermediate, and/or high signal on T1- and T2-weighted imaging, ± nodular or rim gadolinium contrast enhancement. May contain cysts, lipid components, and calcifications. The squamous-papillary type can occur as a solid lesion with intermediate signal on T1-weighted imaging that shows gadolinium contrast enhancement. CT: Circumscribed lobulated lesions with variable low, intermediate, and/or high attenuation, ± nodular or rim contrast enhancement. May contain cysts, lipid components, and calcifications. Calcifications often occur in the adamantinomatous type.	Craniopharyngiomas are usually histologically benign but locally aggressive lesions arising from squamous epithelial rests along Rathke's cleft. They occur in children (10 years old) and adults (> 40 years old) and in males and females equally often. Account for 3% of all intracranial tumors. Can be categorized into adamantinomatous and squamous-papillary types. The adamantinomatous type is more common and has a bimodal age distribution, occurring in children and adults, whereas the squamous-papillary type usually occurs in adults. Craniopharyngiomas have an insinuating pattern of growth that makes complete surgical excision very difficult and not often possible.
Glioma (optic chiasm, hypothalamus) (**Fig. 1.436** and **Fig. 1.437**)	MRI: Fusiform and/or nodular enlargement of optic chiasm and/or optic nerves, usually with low-intermediate signal on T1-weighted imaging, intermediate-high signal on T2-weighted imaging, variable gadolinium contrast enhancement, ± cystic components in large lesions. CT: Usually intermediate attenuation, variable or no contrast enhancement, ± cystic components in large lesions.	In children, usually associated with neurofibromatosis type 1 (~ 10% of patients with NF1). Most tumors are slow-growing grade I astrocytomas (often pilocytic type). High signal abnormality on T2-weighted imaging can extend along optic radiations from neoplastic extension.

(continued on page 366)

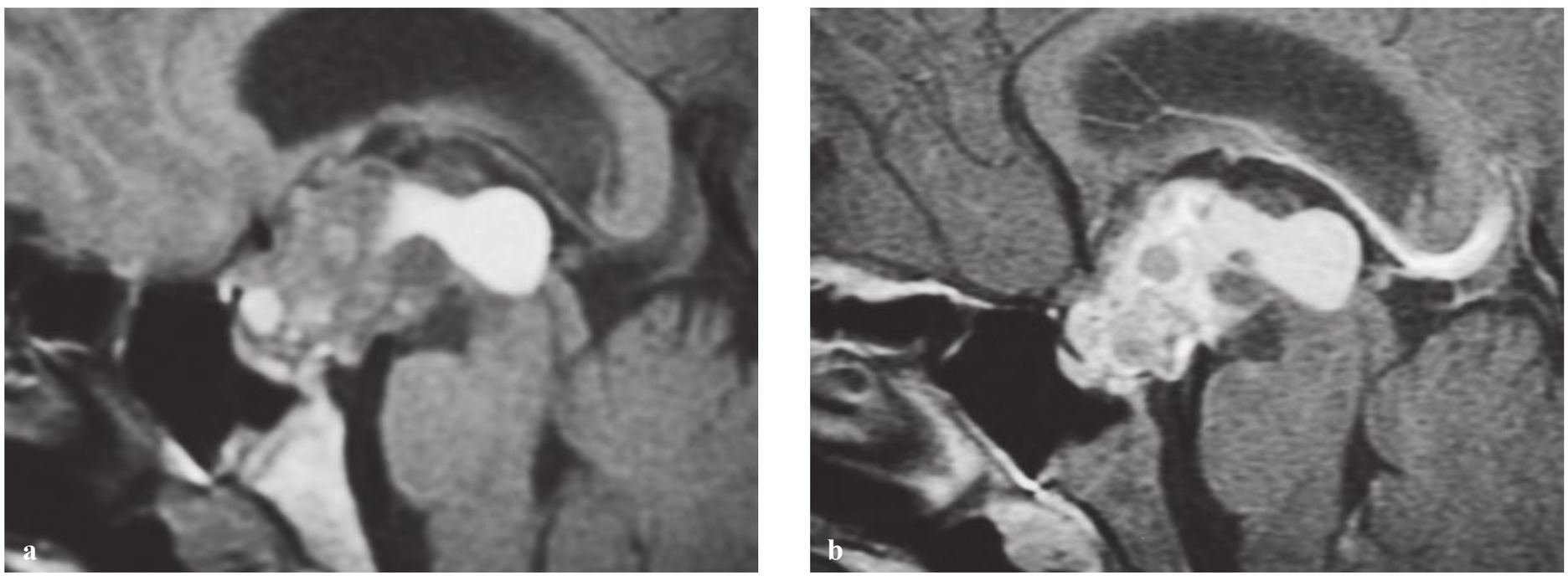

Fig. 1.434 A 17-year-old male with an adamantinomatous type of craniopharyngioma. **(a)** Sagittal T1-weighted imaging shows a lobulated lesion filling the suprasellar cistern and containing zones with low, intermediate, and high signal. **(b)** Sagittal postcontrast T1-weighted imaging shows the lesion to have heterogeneous contrast enhancement.

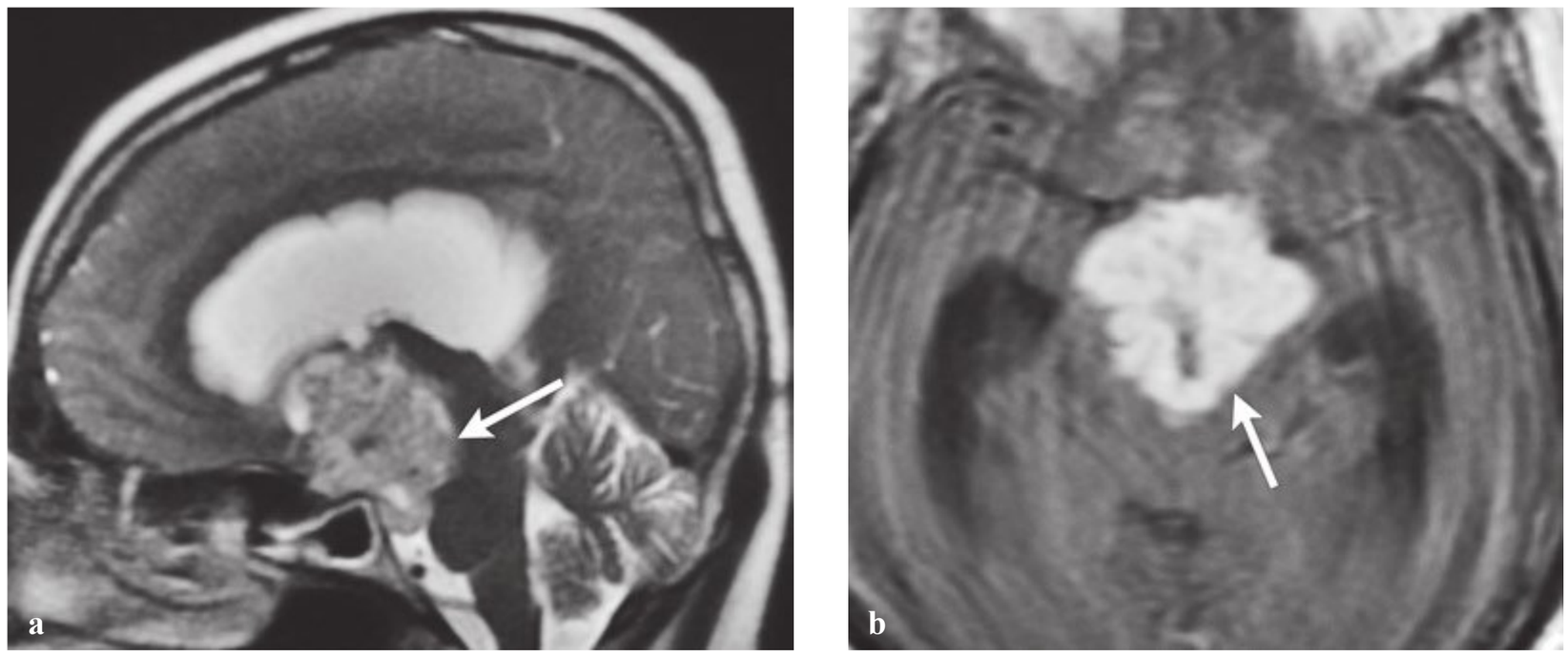

Fig. 1.435 A 49-year-old man with a squamous-papillary type of craniopharyngioma. **(a)** Sagittal T2-weighted imaging shows a lobulated lesion (arrow) filling the suprasellar, interpeduncular, and prepontine cisterns and containing zones with low, intermediate, slightly high, and high signal. The extra-axial lesion involves the hypothalamus and third ventricle and indents the ventral margin of the brainstem. **(b)** Axial postcontrast T1-weighted imaging shows the lesion to have prominent gadolinium contrast enhancement (arrow).

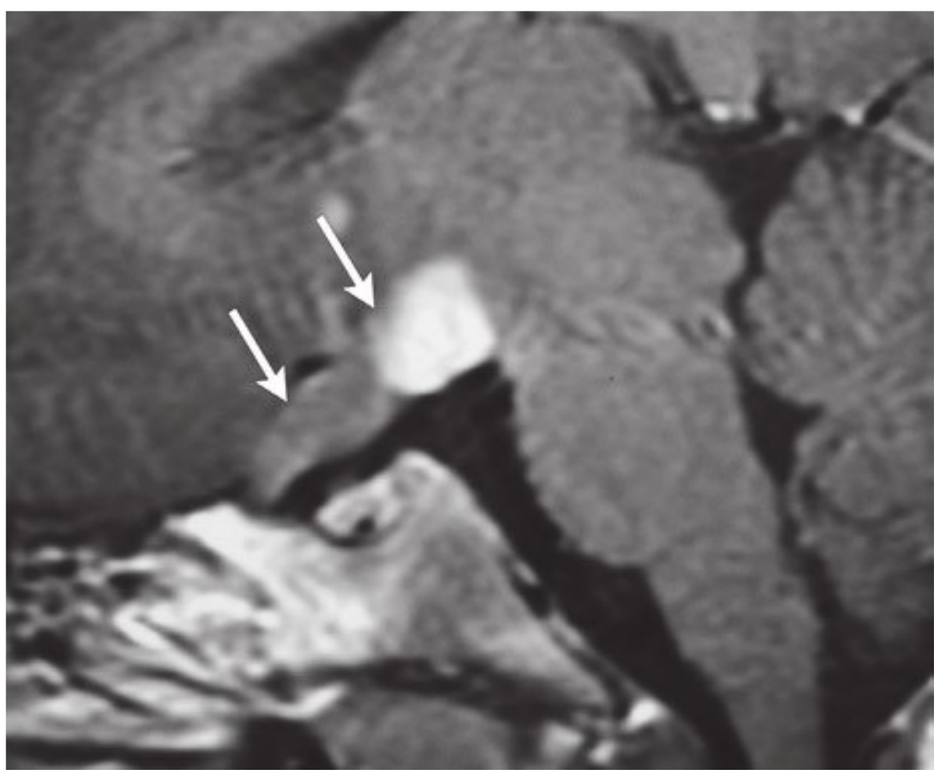

Fig. 1.436 A 2-year-old female with neurofibromatosis type 1 and a pilocytic astrocytoma involving the optic chiasm. Postcontrast sagittal T1-weighted imaging shows a partially enhancing tumor (arrows) enlarging the optic chiasm and proximal optic nerves.

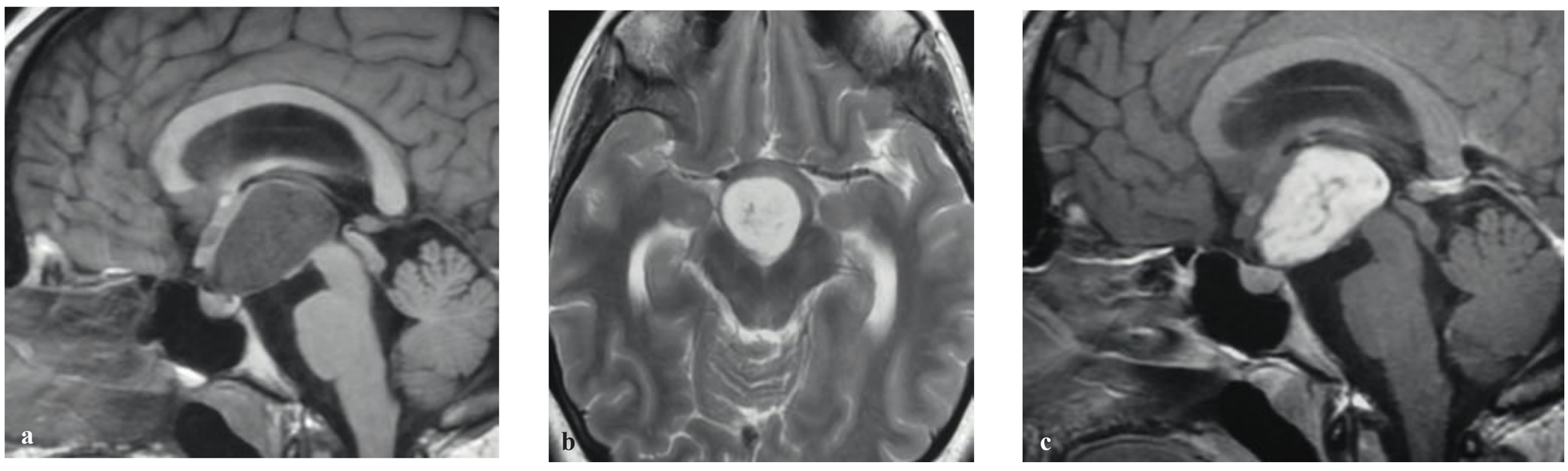

Fig. 1.437 A 1-year-old female with a hypothalamic astrocytoma that extends superiorly, filling the third ventricle, and inferiorly into the suprasellar cistern. The tumor has **(a)** low-intermediate signal on sagittal T1-weighted imaging, **(b)** high signal on axial T2-weighted imaging, and **(c)** gadolinium contrast enhancement on sagittal T1-weighted imaging.

Table 1.10 (cont.) Intrasellar and juxtasellar lesions

Lesions	Imaging Findings	Comments
Pilomyxoid astrocytoma (**Fig. 1.438**)	MRI: Solid/cystic focal lesion with low-intermediate signal on T1-weighted imaging, high signal on T2-weighted imaging and FLAIR, and variable gadolinium contrast enhancement. Some solid portions may show minimal or no contrast enhancement. Gadolinium contrast enhancement can be uniform or in a heterogeneous peripheral pattern. Intratumoral hemorrhage can occur in 25% of cases. Lesions commonly located in cerebellum, hypothalamus, suprasellar cistern, and thalamus. Diffusion-weighted imaging: Tumors can have increased ADC values. CT: Solid/cystic focal lesion with low-intermediate attenuation, variable contrast enhancement.	Pilomyxoid astrocytomas (WHO grade II) are rare neoplasms that contain prominent mucoid matrix and an angiocentric pattern of bipolar neoplastic astrocytes. Absence of Rosenthal fibers. Typically occur in children in first and second decades (9 months to 46 years, mean age = 7 years). Common locations include hypothalamus/ suprasellar cistern, thalamus, cerebellum, brainstem, temporal lobe, and spinal cord. Pilomyxoid astrocytomas are more aggressive than pilocytic astrocytomas, with a higher rate of local recurrence. Leptomeningeal dissemination of tumor has been reported to occur at a higher frequency than with pilocytic astrocytomas.
Meningioma (**Fig. 1.439**)	MRI: Extra-axial dural based lesions, well-circumscribed, supra- > infratentorial, with intermediate signal on T1-weighted imaging, intermediate-slightly high signal on T2-weighted imaging, usually prominent gadolinium contrast enhancement, ± calcifications. CT: Lesions often have intermediate attenuation, usually prominent contrast enhancement, ± calcifications, ± hyperostosis of adjacent bone.	Most common extra-axial tumor, usually benign neoplasms composed of neoplastic meningothelial (arachnoidal or arachnoid cap) cells. Typically occurs in adults (> 40 years old), women > men. In neurofibromatosis type 2, multiple meningiomas can result in compression of adjacent brain parenchyma, encasement of arteries, and compression of dural venous sinuses. Rarely invasive/malignant types.
Schwannoma (**Fig. 1.440**)	MRI: Circumscribed or lobulated extra-axial lesions, with low-intermediate signal on T1-weighted imaging, intermediate-high signal on T2-weighted imaging, + prominent gadolinium contrast enhancement. High signal on T2-weighted imaging and gadolinium contrast enhancement can be heterogeneous in large lesions. CT: Ovoid or fusiform lesions with low-intermediate attenuation. Lesions can show contrast enhancement. Often erode adjacent bone.	Schwannomas are benign encapsulated tumors that contain differentiated neoplastic Schwann cells. Acoustic (vestibular nerve) schwannomas account for 90% of intracranial schwannomas and represent 75% of lesions in the cerebellopontine angle cisterns; trigeminal schwannomas are the next most common intracranial schwannoma, followed by facial nerve schwannomas, and multiple schwannomas seen with neurofibromatosis type 2. Schwannomas can involve cranial nerves III, IV, V, and VI within the cavernous sinus and/or orbit.

(continued on page 368)

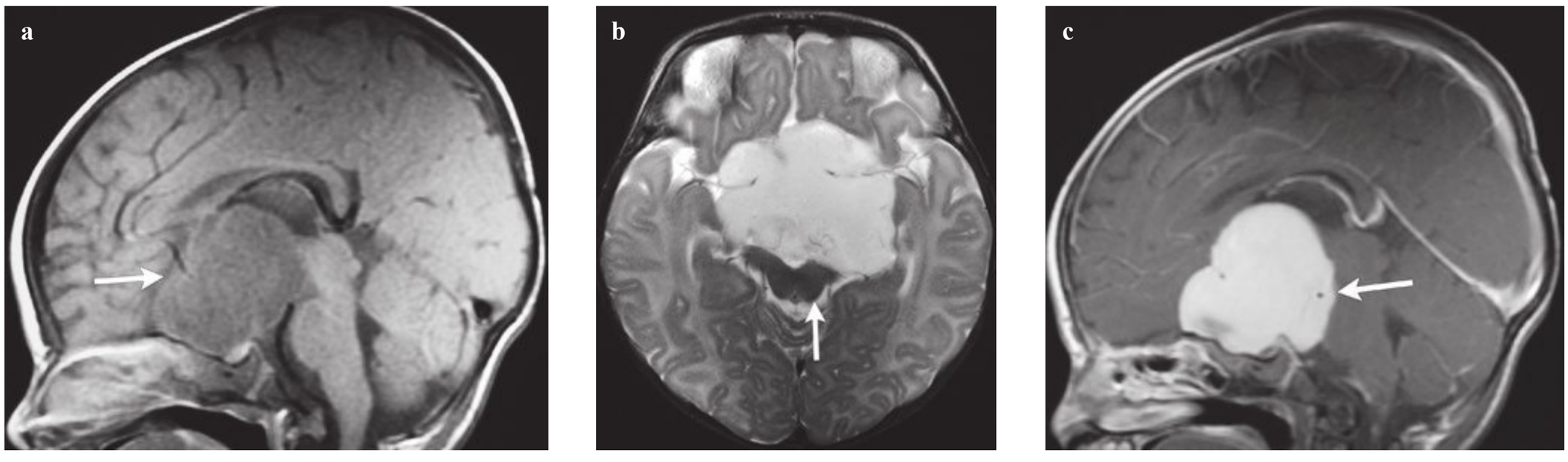

Fig. 1.438 A 4-month-old female with a pilomyxoid astrocytoma in the hypothalamus, third ventricle, and suprasellar cistern that has **(a)** intermediate signal on sagittal T1-weighted imaging (arrow), **(b)** high signal on axial T2-weighted imaging (arrow), and **(c)** prominent gadolinium contrast enhancement on sagittal T1-weighted imaging (arrow).

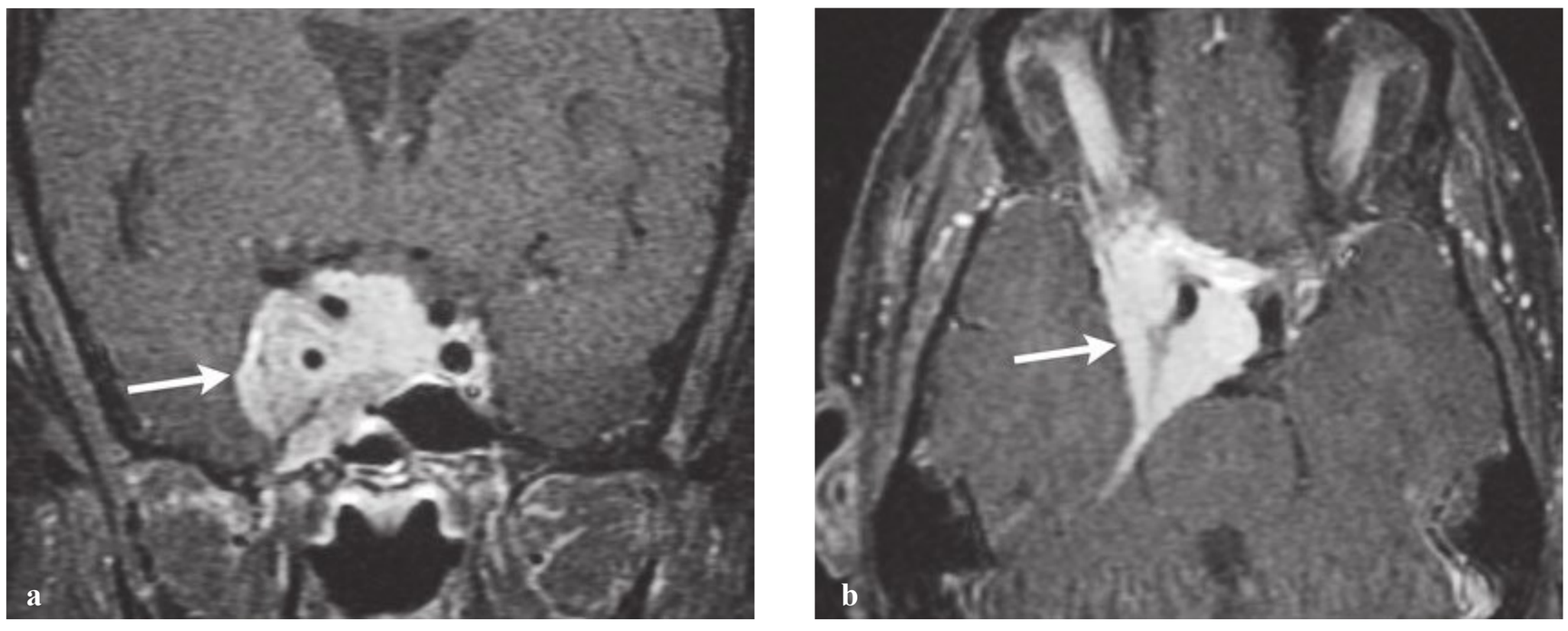

Fig. 1.439 A 55-year-old woman with a gadolinium contrast-enhancing meningioma (arrows) in the right cavernous sinus, suprasellar cistern, anteromedial right middle cranial fossa, and right tentorial incisura on **(a)** coronal and **(b)** axial fat-suppressed T1-weighted imaging. The meningioma encases and narrows the flow void of the right internal carotid artery.

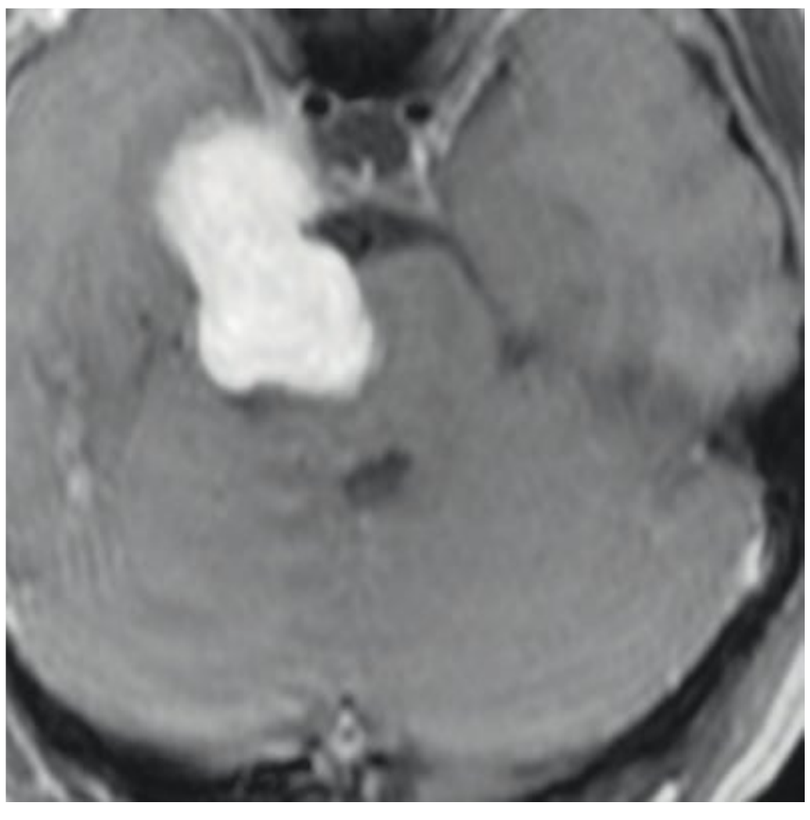

Fig. 1.440 A 30-year-old man with a gadolinium contrast-enhancing trigeminal schwannoma extending along the right lateral aspect of the suprasellar cistern on axial fat-suppressed T1-weighted imaging.

Table 1.10 (cont.) Intrasellar and juxtasellar lesions

Lesions	Imaging Findings	Comments
Paraganglioma	MRI: Lobulated lesion involving the pituitary gland and/or pituitary stalk, with intermediate signal on T1-weighted imaging, high signal on T2-weighted imaging with tubular zones of flow voids, + prominent gadolinium contrast enhancement. CT: Extra-axial mass lesions, often well circumscribed, with intermediate attenuation and contrast enhancement.	Paragangliomas, also referred to as chemodectomas, arise from paraganglia of neural crest origin in multiple sites in the body and are named accordingly (glomus jugulare, tympanicum, vagale, etc.). Rarely occur in suprasellar cistern or sella as well as pineal gland and cauda equina. Paragangliomas are typically well-differentiated neoplasms composed of biphasic collections of chief cells (type 1) arranged in nests or lobules (zellballen) surrounded by single layers of sustentacular cells (type 2). Present in patients from 24 to 70 years old (mean age = 47 years).
Germ cell tumors (**Fig. 1.441**)	MRI: Tumors often have intermediate signal on T1-weighted imaging, slightly high to high signal on T2-weighted imaging, and show gadolinium contrast enhancement, ± cysts, ± gadolinium contrast-enhancing disseminated subarachnoid and/or intraventricular tumor. Other germ cell tumors can have mixed signal on T1- and T2-weighted imaging secondary to the presence of cysts, hemorrhage, and/or calcifications CT: Circumscribed tumors with intermediate to slightly increased attenuation, ± disseminated contrast-enhancing leptomeningeal and/or intraventricular tumor.	Extragonadal germ cell tumors include germinoma (most common), mature teratoma, malignant teratoma, yolk sac tumor, embryonal carcinoma, and choriocarcinoma. They account for 0.6%of primary intracranial tumors, with an incidence of 0.09 per 100,000. Peak age of incidence is between 10 and 14 years, and 90%occur in patients less than 25 years old. Occur more frequently in males than in females. Prognosis depends on histologic subtype.Ten-year survival for geminomas is > 85% Other germ cell tumors have lower survival rates, particularly those containing nongerminomatous malignant cells.
Teratoma (**Fig. 1.442**)	MRI: Circumscribed lesions; pineal region > suprasellar region > third ventricle; variable low, intermediate, and/or high signal on T1- and T2-weighted imaging; ± gadolinium contrast enhancement. May contain calcifications with low signal on T1- and T2-weighted imaging, as well as fatty components with high signal on T1-weighted imaging. CT: May contain calcifications and zones with intermediate and fat attenuation.	Second most common type of germ cell tumor; occurs in children, males > females. Benign or malignant types, composed of derivatives of ectoderm, mesoderm, and/or endoderm.

(continued on page 370)

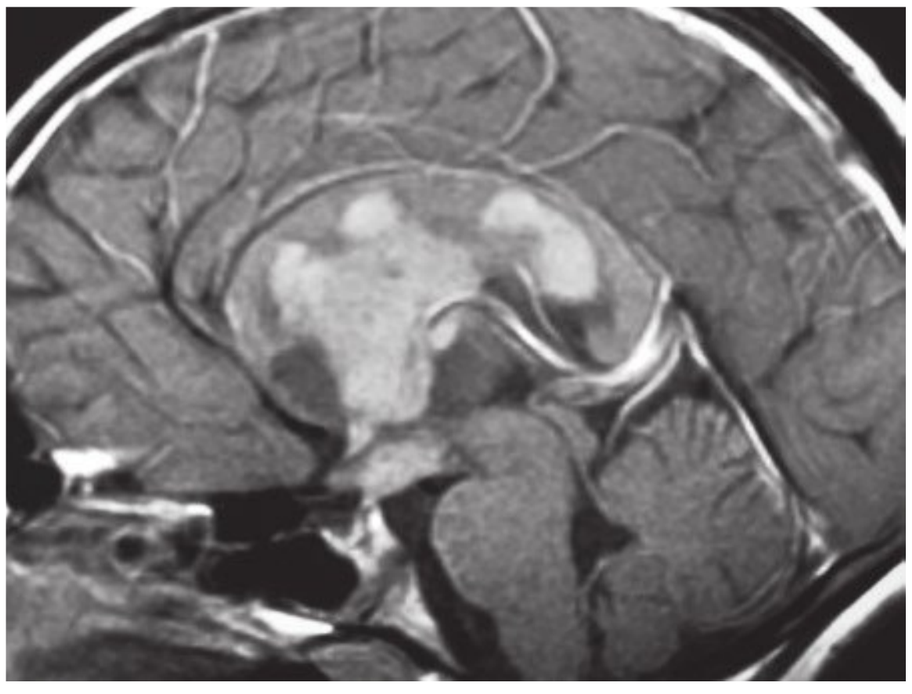

Fig. 1.441 A 12-year-old female shows gadolinium contrast-enhancing disseminated germinoma in the suprasellar cistern and third and lateral ventricles, with involvement of the optic chiasm and corpus callosum on sagittal T1-weighted imaging.

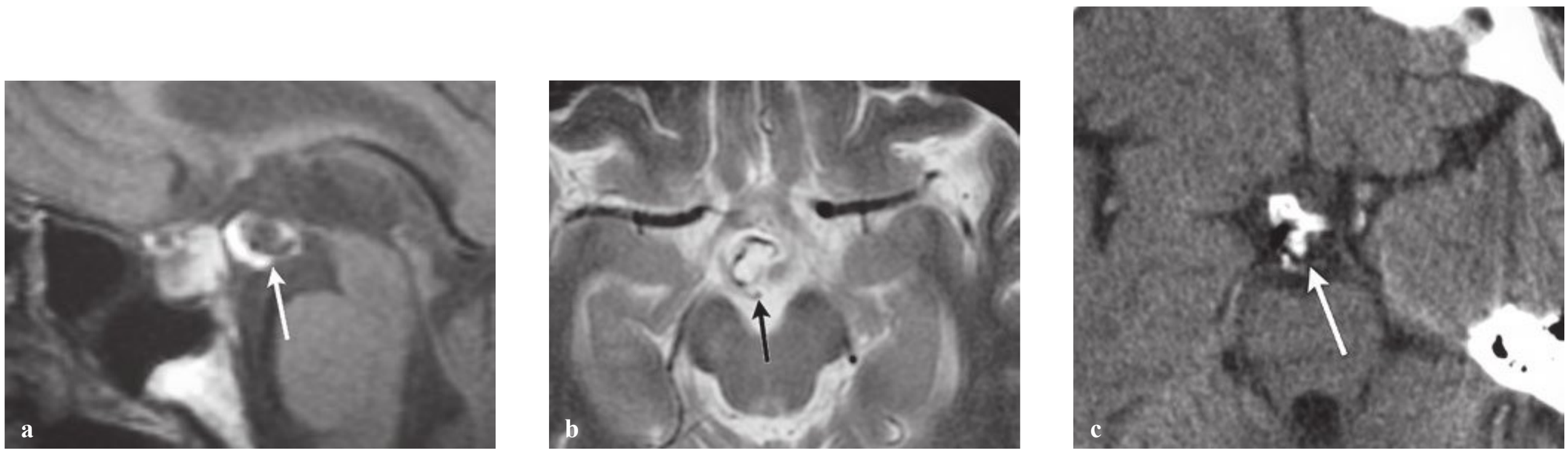

Fig. 1.442 Teratoma. **(a)** Sagittal T1-weighted imaging and **(b)** axial T2-weighted imaging show a lesion (arrows) at the undersurface of the hypothalamus that has mixed low, intermediate, and high signal. **(c)** Axial CT shows the lesion containing calcifications, fat, and intermediate soft tissue attenuation (arrow).

Table 1.10 (cont.) Intrasellar and juxtasellar lesions

Lesions	Imaging Findings	Comments
Suprasellar Lesions		
Arterial aneurysm (**Fig. 1.443**) Saccular aneurysm Giant aneurysm Fusiform aneurysm Dissecting aneurysms	MRI: Saccular aneurysm: Focal well-circumscribed zone of signal void on T1- and T2-weighted imaging, variable mixed signal if thrombosed. Giant aneurysm: Saccular aneurysms > 2.5 cm in diameter are referred to as giant aneurysms. Focal well-circumscribed structure with layers of low, intermediate, and high signal on T2-weighted imaging secondary to layers of thrombus of different ages, as well a zone of signal void representing a patent lumen if present. On T1-weighted imaging, layers of intermediate and high signal can be seen as well as a zone of signal void. Fusiform aneurysm: Elongated and ectatic arteries, variable intraluminal MR signal related to turbulent or slowed blood flow or partial/complete thrombosis. Dissecting aneurysms: The involved arterial wall is thickened and has intermediate-high signal on T1- and T2-weighted imaging, and the signal void representing the patent lumen is narrowed.	Abnormal fusiform or focal dilatation of artery secondary to acquired/degenerative etiology, polycystic disease, connective tissue disease, atherosclerosis, trauma, infection (mycotic), oncotic lesions, arteriovenous malformation, vasculitis, and drugs.
Carotid-cavernous fistula (**Fig. 1.444**)	CTA and MRA show marked dilatation of the cavernous sinuses as well as the superior and inferior ophthalmic veins and facial veins. Multiple flow voids can be seen in both cavernous sinuses.	Carotid artery to cavernous sinus fistulas usually occur as a result of blunt trauma causing dissection or laceration of the cavernous portion of the internal carotid artery. Patients can present with pulsating exophthalmos.
Arteriovenous malformations (AVMs) (**Fig. 1.445**)	MRI: Lesions with irregular margins that can be located in the brain parenchyma—pia, dura, or both locations. AVMs contain multiple tortuous tubular flow voids on T1- and T2-weighted imaging secondary to patent arteries with high blood flow, as well as thrombosed vessels with variable signal, areas of hemorrhage in various phases, calcifications, and gliosis. The venous portions often show gadolinium contrast enhancement. Gradient echo MRI shows flow-related enhancement (high signal) in patent arteries and veins of the AVM. MRA using time-of-flight or phase-contrast techniques can provide additional detailed information about the nidus, feeding arteries, and draining veins and presence of associated aneurysms. Dural AVMs contain multiple, tortuous, small vessels at the site of a recanalized thrombosed dural venous sinus. CTA can show patent portions of the vascular malformation and areas of venous sinus occlusion or recanalization in dural AVMs.	Supratentorial AVMs occur more frequently (80–90%) than infratentorial AVMs (10–20%). Annual risk of hemorrhage. AVMs can be sporadic, congenital, or associated with a history of trauma. Dural AVMs are usually acquired lesions resulting from thrombosis or occlusion of an intracranial venous sinus with subsequent recanalization resulting in direct arterial to venous sinus communications. Transverse, sigmoid venous sinuses > cavernous sinus > straight, superior sagittal sinuses. Usually not associated with mass effect unless there is recent hemorrhage or venous occlusion.

(continued on page 372)

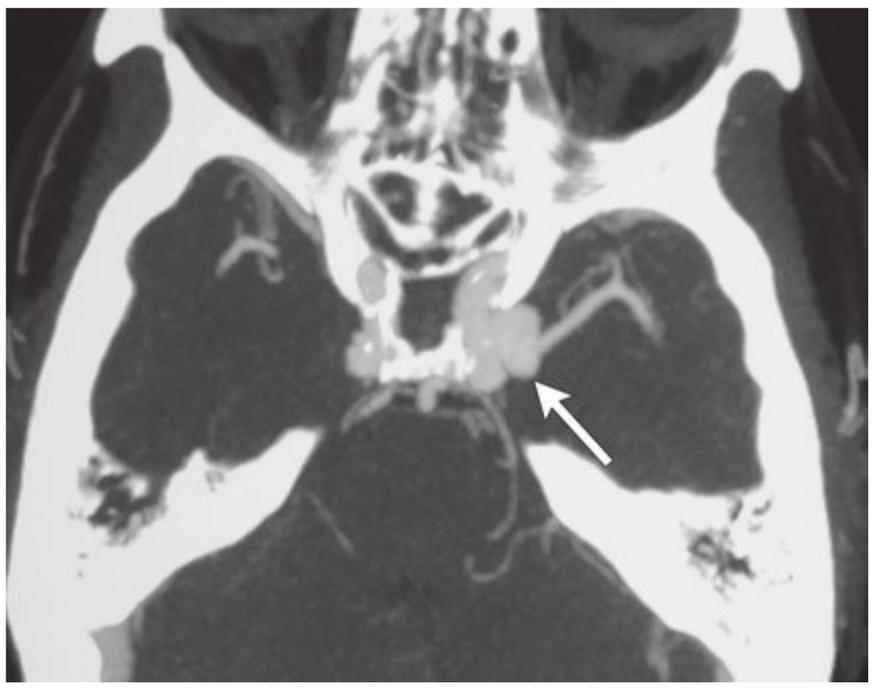

Fig. 1.443 Axial CTA shows a parasellar aneurysm (arrow) of the left internal carotid artery.

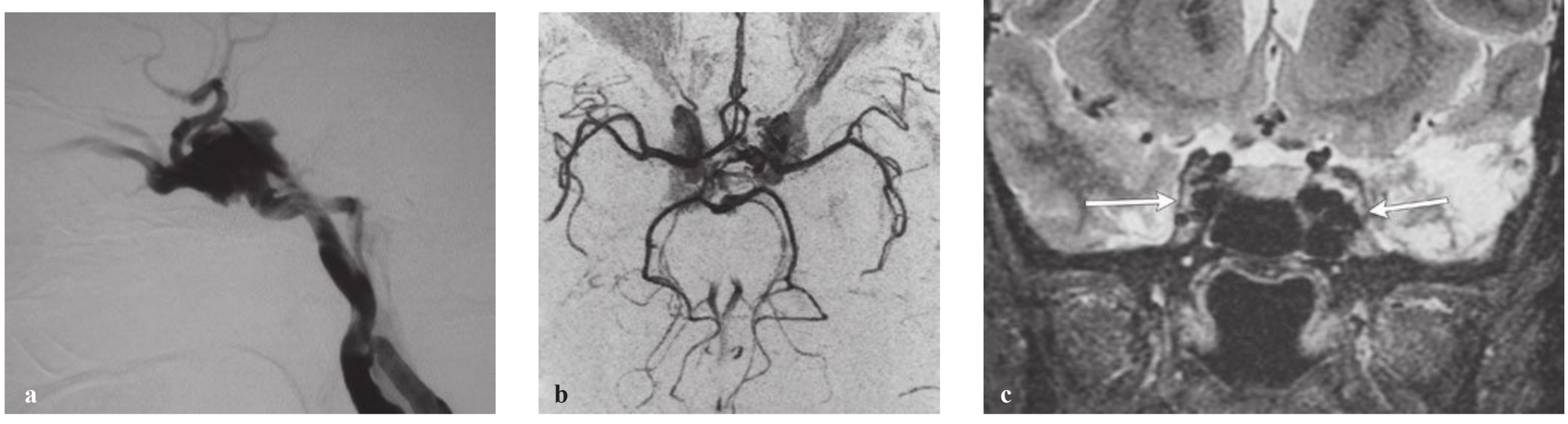

Fig. 1.444 Posttraumatic carotid cavernous fistula in a 50-year-old woman. **(a)** Lateral view arteriogram shows early arterial-phase contrast filling the cavernous sinus. **(b)** Axial MRA shows faint flow signal in both cavernous sinuses and retrograde flow signal into both orbits. **(c)** Coronal STIR shows multiple flow voids (arrows) within both enlarged cavernous sinuses. Brain contusions with high signal are also seen at the anterior portions of both temporal lobes.

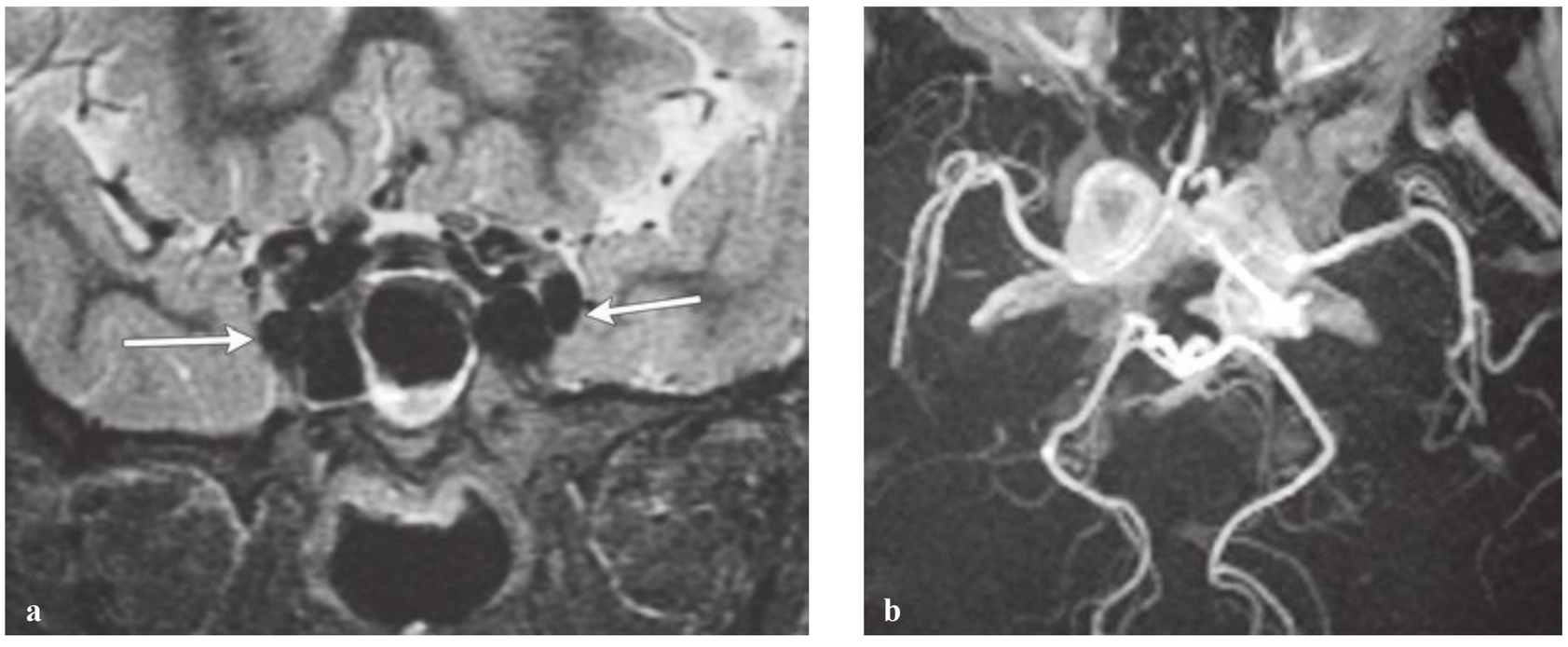

Fig. 1.445 **(a)** A 23-year-old woman with a dural arteriovenous malformation with multiple flow voids seen within both enlarged cavernous sinuses (arrows) on coronal STIR. **(b)** Axial MRA shows faint flow signal in both cavernous sinuses.

Table 1.10 (cont.) Intrasellar and juxtasellar lesions

Lesions	Imaging Findings	Comments
Cavernous malformation (**Fig. 1.446**)	MRI: Single or multiple multilobulated intra-axial lesions that have a peripheral rim or irregular zone of low signal on T2-weighted images secondary to hemosiderin, surrounding a central zone of variable signal (low, intermediate, high, or mixed) on T1- and T2-weighted imaging depending on ages of the hemorrhagic portions. Gradient echo and magnetic susceptibility-weighted techniques are useful for detecting multiple lesions. Gadolinium contrast enhancement is usually absent, although some lesions may show mild heterogeneous enhancement. CT: Lesions have intermediate to slightly increased attenuation, ± calcifications.	Cavernous malformations are hamartomas composed of thin-walled sinusoids lined by a single layer of endothelium lacking smooth muscle and elastic fibers that can be separated by fibrous connective tissue, without intervening neural tissue. Hemosiderin-laden macrophages and various phases of thrombosis within the sinusoids are commonly present. Supratentorial lesions occur more frequently than infratentorial lesions. Can be located in many different locations, with multiple lesions in more than 50% of cases. Association with venous angiomas (developmental venous anomalies) in 25% of cases and increased risk for hemorrhage. Hereditary syndromes in which multiple cavernous malformations occur are associated with mutations of the CCM1/KRIT1, CCM2/MGC4608, and CCM3PDCD10 genes, and have a higher risk of hemorrhage (up to 5% per year) than sporadic cavernous malformations (0.25 to 2.3%).
Cavernous sinus hemangioma (**Fig. 1.447**)	MRI: Solitary extra-axial lesion in the cavernous sinus that has intermediate signal on T1-weighted imaging and slightly high and/or high signal on T2-weighted imaging. Lesions usually show prominent gadolinium contrast enhancement. CT: Lesions have intermediate to slightly increased attenuation, show contrast enhancement, and have no calcifications. Can show erosion of adjacent bone.	Rare, benign, solitary extra-axial vascular tumors that occur in the cavernous sinus and can slowly grow and compress adjacent structures. These lesions have a capsule or pseudocapsule related to adjacent dura that surrounds thin-walled sinusoids lined by a single layer of endothelium lacking smooth muscle and elastic fibers. The sinusoids can be separated by varying amounts of fibrous connective tissue. Unlike cavernous malformations, these lesions typically lack areas of thrombosis or calcifications. Can be associated with increased risk of severe intraoperative bleeding.
Arachnoid cyst—sellar/suprasellar (**Fig. 1.448**)	MRI: Well-circumscribed extra-axial lesions with low signal on T1-weighted imaging, FLAIR, and diffusion-weighted imaging and high signal on T2-weighted imaging similar to CSF. No gadolinium contrast enhancement. CT: Circumscribed extra-axial lesions with low attenuation similar to CSF. May be associated with chronic erosion of adjacent bone.	Nonneoplastic congenital, developmental, or acquired extra-axial lesions filled with CSF, usually with mild mass effect on adjacent brain, in supratentorial more often than infratentorial locations, males > females, ± related clinical symptoms.

(continued on page 374)

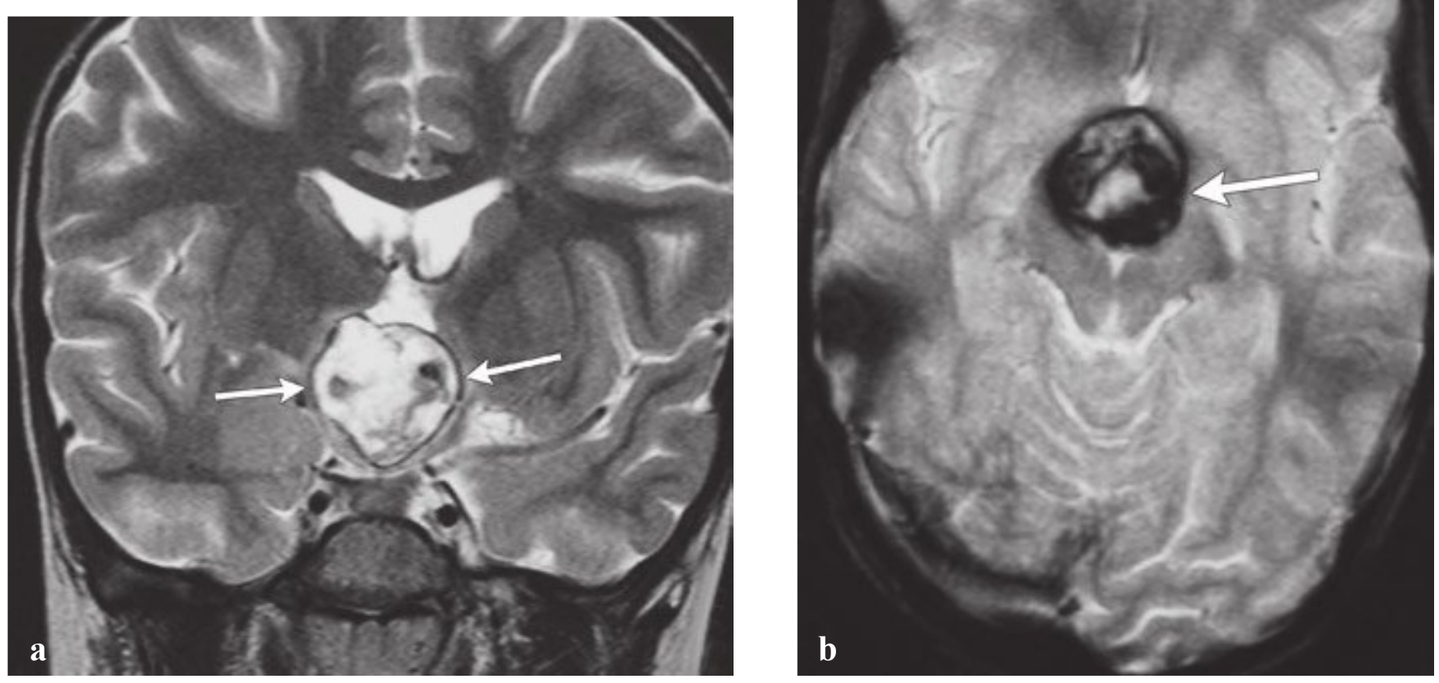

Fig. 1.446 **(a)** A 5-year-old female with a hypothalamic cavernous malformation (arrows) that has mixed high and low signal centrally, surrounded by a rim of low signal on coronal T2-weighted imaging. **(b)** Prominent low T2* signal is seen at the lesion on axial GRE (arrow).

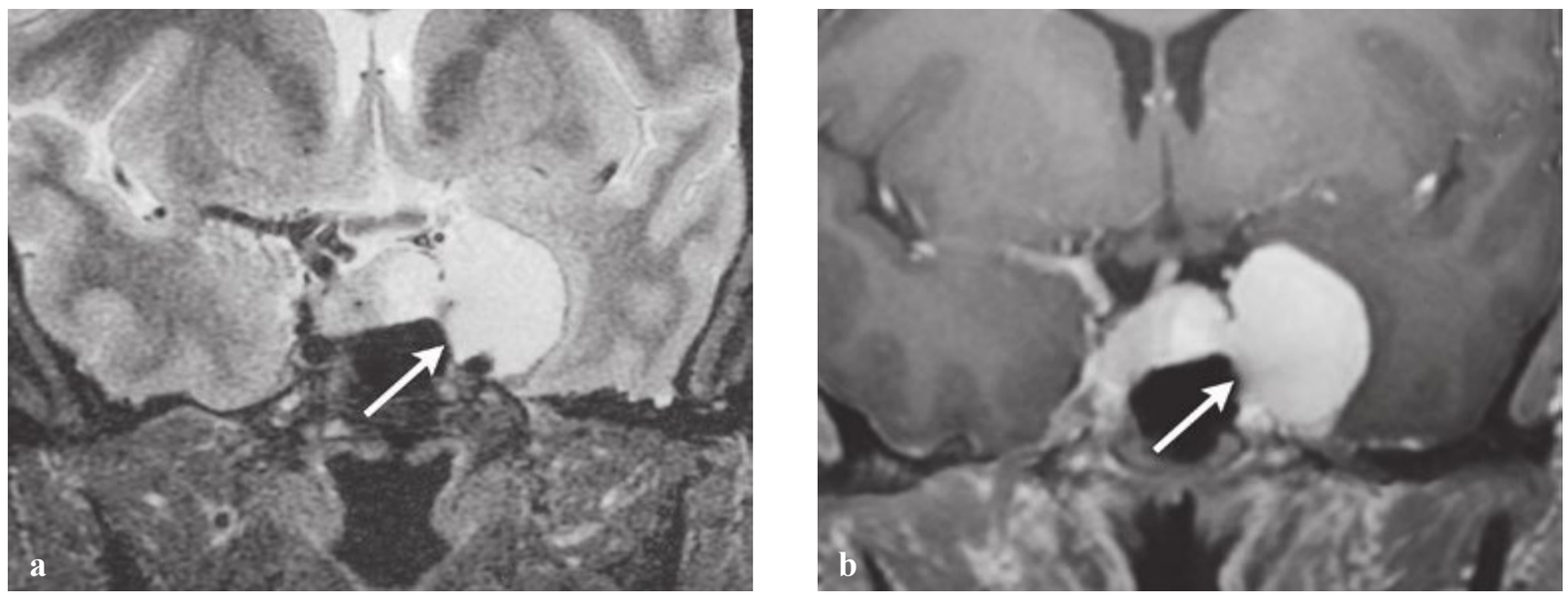

Fig. 1.447 A 47-year-old woman with a cavernous sinus hemangioma that has **(a)** high signal on coronal fat-suppressed T2-weighted imaging (arrow) and **(b)** prominent gadolinium contast enhancement on coronal T1-weighted imaging (arrow).

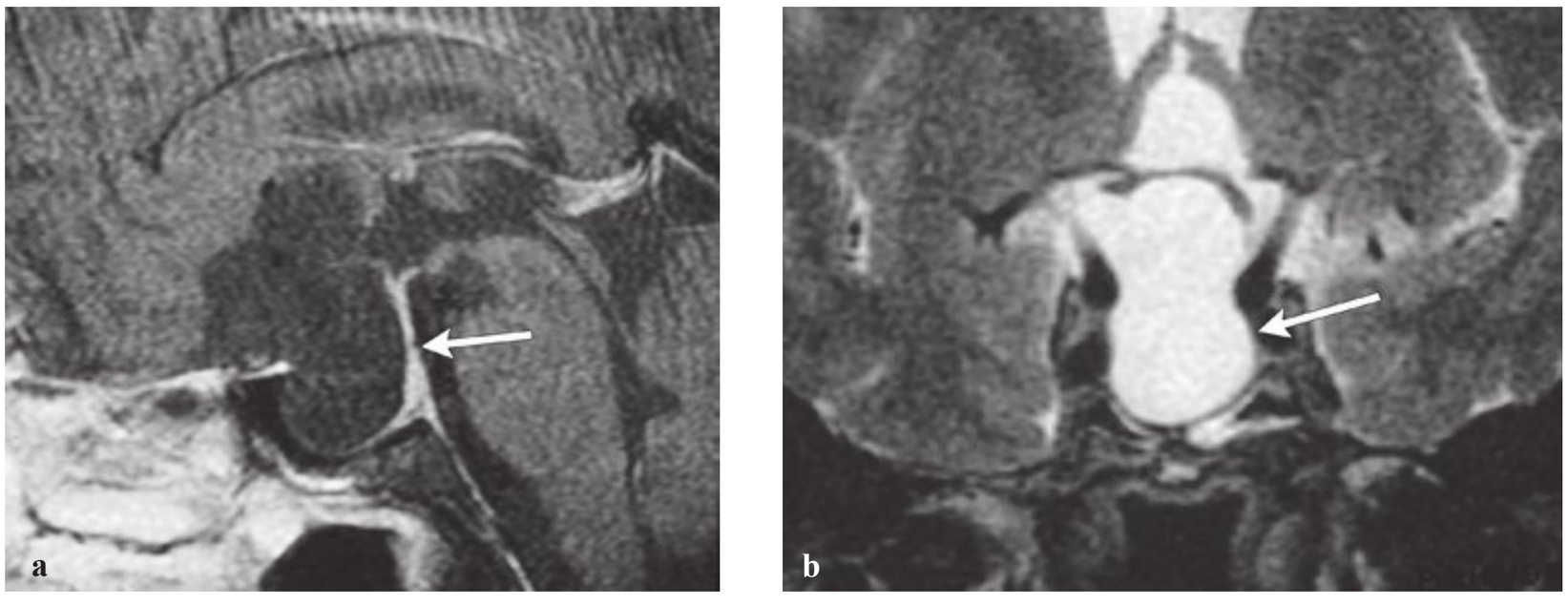

Fig. 1.448 Arachnoid cyst. **(a)** Sagittal T1-weighted imaging and **(b)** coronal T2-weighted imaging show a well-defined cystic lesion (arrows) that is located in the sella and suprasellar cistern.

Table 1.10 (cont.) Intrasellar and juxtasellar lesions

Lesions	Imaging Findings	Comments
Osseous Lesions: Neoplasm		
Metastatic tumor involving the sphenoid bone and suprasellar cistern (**Fig. 1.449**)	MRI: Single or multiple well-circumscribed or poorly defined lesions involving the skull, dura, leptomeninges, choroid plexus, or CSF. Lesions have low-intermediate signal on T1-weighted imaging, intermediate-high signal on T2-weighted imaging, and usually show gadolinium contrast enhancement, ± bone destruction, ± compression of neural tissue or vessels. Leptomeningeal tumor often best seen on postcontrast images. CT: Lesions involving bone are typically associated with zones of bone destruction.	Metastatic lesions represent proliferating neoplastic cells that are located in sites or organs separated or distant from their origins. Metastatic lesions can disseminate hematogenously via arteries or veins, along CSF pathways, along surgical tracts, and along lymphatic structures. Metastatic carcinoma is the most frequent malignant tumor involving bone. In adults, metastatic lesions to bone occur most frequently from carcinomas of the lung, breast, prostate, kidney, and thyroid, as well as from sarcomas. Primary malignancies of the lung, breast, and prostate account for 80% of bone metastases. Metastatic tumor may have variable destructive or infiltrative changes in single or multiple sites of involvement.
Myeloma/plasmacytoma (**Fig. 1.450**)	MRI: Multiple (myeloma) or single (plasmacytoma) well-circumscribed or poorly defined lesions involving the skull and dura with low-intermediate signal on T1-weighted imaging, intermediate-high signal on T2-weighted imaging, usually + gadolinium contrast enhancement, + bone destruction. CT: Lesions have low-intermediate attenuation, usually + contrast enhancement, + bone destruction.	Multiple myeloma is malignancy comprised of proliferating antibody-secreting plasma cells derived from single clones. Multiple myeloma is primarily located in bone marrow. A solitary myeloma or plasmacytoma is an infrequent variant in which a neoplastic mass of plasma cells occurs at a single site of bone or soft tissues. In the United States, 14,600 new cases occur each year. Multiple myeloma is the most common primary malignant neoplasm of bone in adults. Median age at presentation = 60 years. Most patients are older than 40 years.
Lymphoma (**Fig. 1.451**)	MRI: Primary CNS lymphoma can be seen as a focal or infiltrating lesion in the basal ganglia or posterior fossa/brainstem, with low-intermediate signal on T1-weighted imaging, intermediate-slightly high signal on T2-weighted imaging, ± hemorrhage/necrosis in immunocompromised patients. Usually shows gadolinium enhancement. Diffuse leptomeningeal contrast enhancement is another pattern of intracranial lymphoma. CT: Lesions have low-intermediate attenuation, may show contrast enhancement, ± bone destruction.	Primary CNS lymphoma is more common than secondary, usually in adults > 40 years old. B cell lymphoma is more common than T cell lymphoma, with an increasing incidence related to the number of immunocompromised patients in the population. MRI features of primary and secondary lymphoma of brain overlap. Intracranial lymphoma can involve the leptomeninges in secondary lymphoma more often than in primary lymphoma.

(continued on page 376)

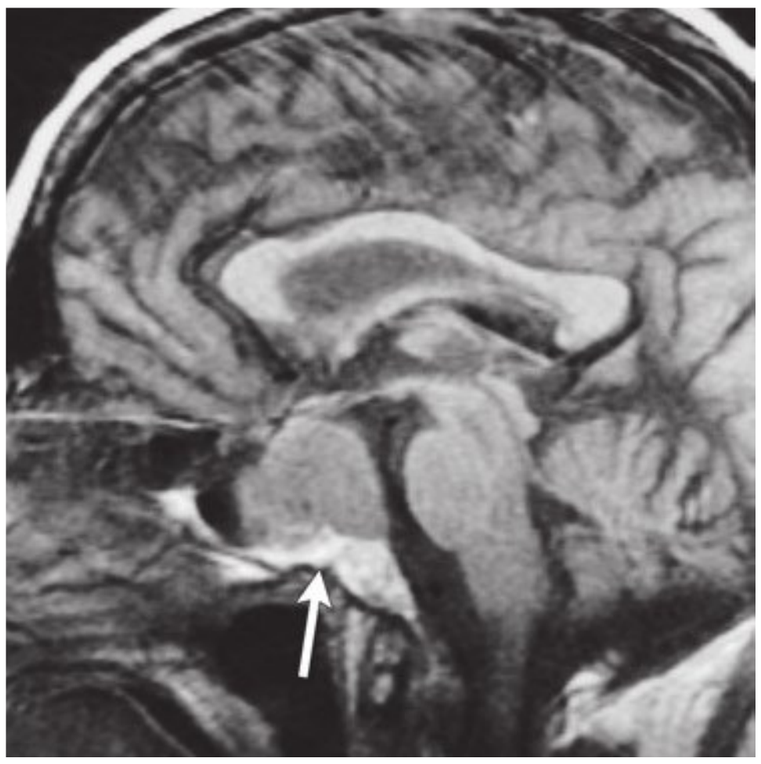

Fig. 1.449 Metastatic breast carcinoma (arrow) in the upper clivus and sella that has intermediate signal on sagittal T1-weighted imaging.

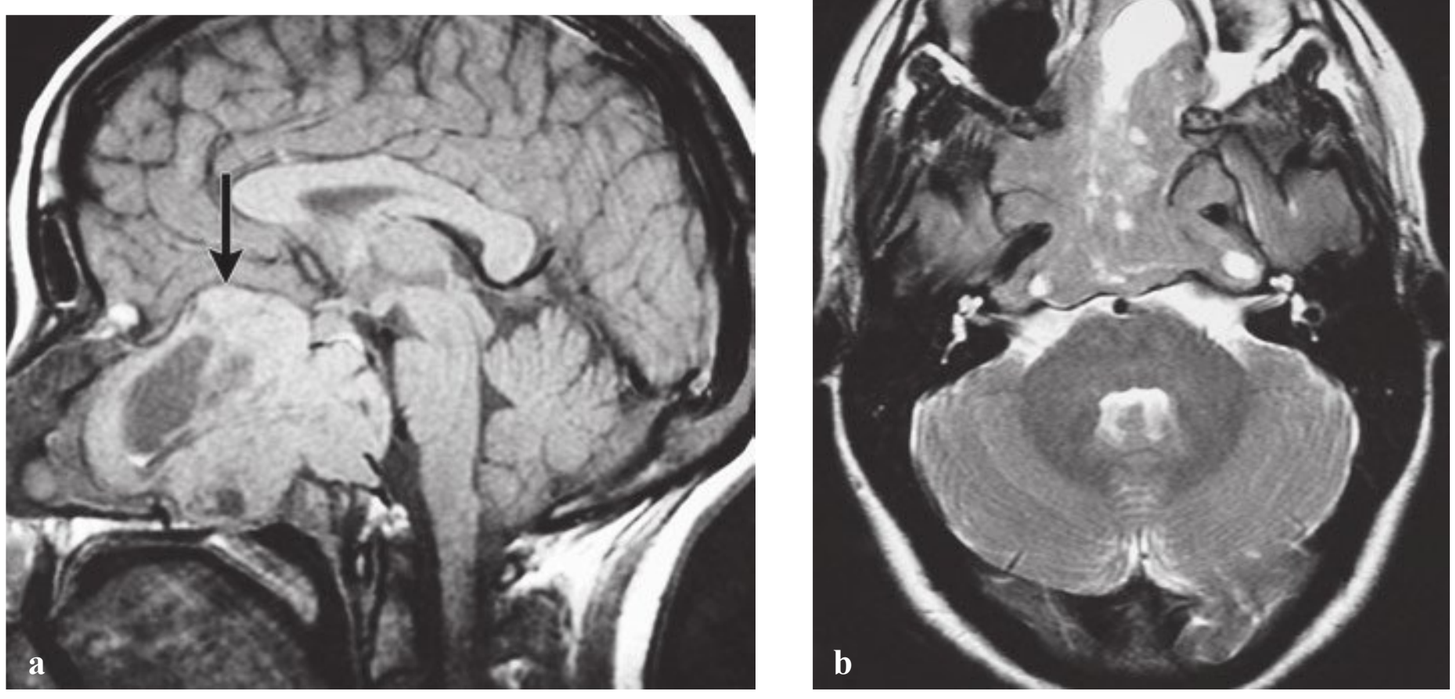

Fig. 1.450 A 28-year-old woman with a large plasmacytoma in the nasal cavity, nasopharynx, ethmoid and sphenoid sinuses, clivus, and sella on **(a)** sagittal T1-weighted imaging (arrow) and **(b)** axial T2-weighted imaging.

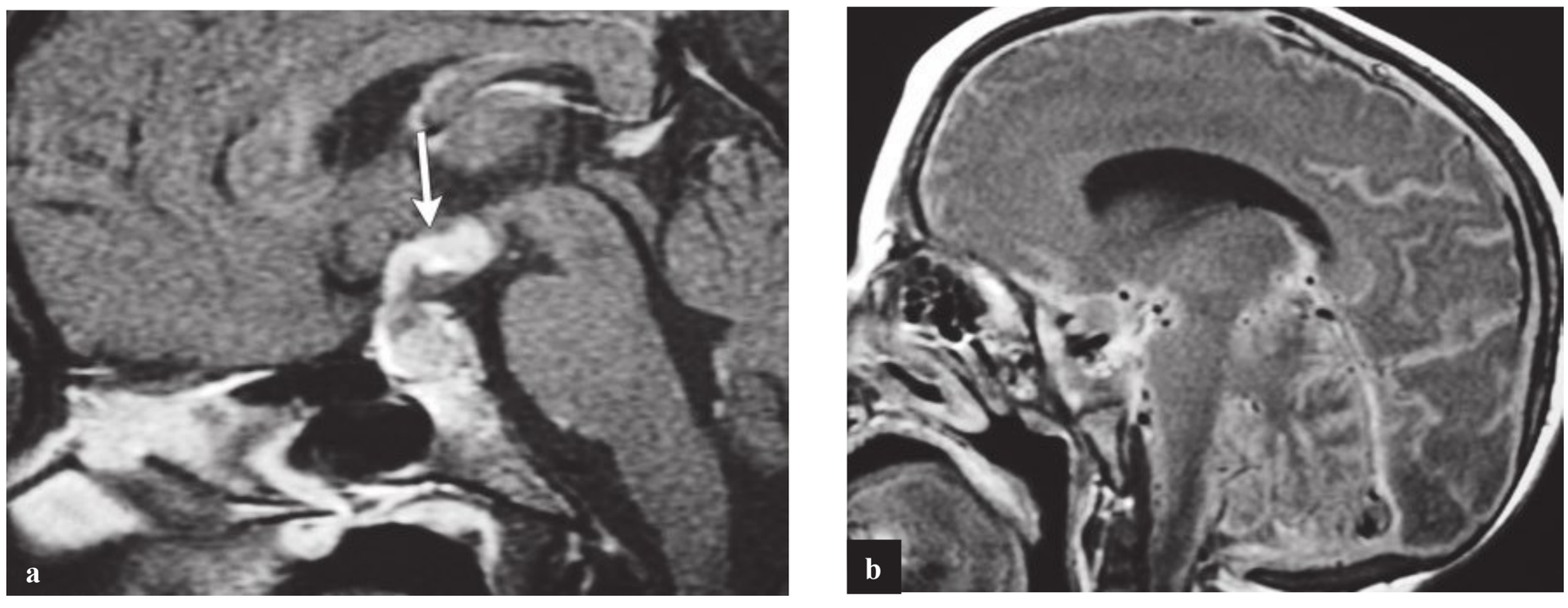

Fig. 1.451 Intracranial lymphoma. **(a)** A 36-year-old HIV-positive man with gadolinium contrast-enhancing lymphoma in the hypothalamus and suprasellar cistern on sagittal T1-weighted imaging (arrow). **(b)** A 2-year-old male with lymphoma who has extensive leptomeningeal gadolinium contrast enhancement on sagittal T1-weighted imaging.

Table 1.10 (cont.) Intrasellar and juxtasellar lesions

Lesions	Imaging Findings	Comments
Chordoma (**Fig. 1.452**)	MRI: Well-circumscribed lobulated lesions with low-intermediate signal on T1-weighted images, high signal on T2-weighted imaging, + gadolinium contrast enhancement (usually heterogeneous). Locally invasive lesions are associated with bone erosion/destruction and encasement of vessels and nerves. Skull base-clivus is a common location, usually in the midline for conventional chordomas, which account for 80%of skull base chordomas. Chondroid chordomas tend to be located off midline near skull base synchondroses. CT: Lesions have low-intermediate attenuation, ± calcifications from destroyed bone carried away by tumor, + contrast enhancement.	Chordomas are rare, locally aggressive, slow-growing, low to intermediate grade malignant tumors derived from ectopic notochordal remnants along the axial skeleton. Chondroid chondromas (5 to 15% of all chordomas) have both chordomatous and chondromatous differentiation. Chordomas that contain sarcomatous components are referred to as dedifferentiated chordomas or sarcomatoid chordomas (5%of all chordomas). Chordomas account for 2–4%of primary malignant bone tumors, 1–3%of all primary bone tumors, and less than 1%of intracranial tumors. The annual incidence has been reported to be 0.18 to 0.3 per million. Dedifferentiated chordomas or sarcomatoid chordomas account for less than 5%of all chordomas. Patients' mean age = 37 to 40 years for cranial chordomas.
Chondrosarcoma (**Fig. 1.453**)	MRI: Lobulated lesions with low-intermediate signal on T1-weighted imaging, high signal on T2-weighted imaging, ± matrix mineralization and low signal on T2-weighted imaging, + gadolinium contrast enhancement (usually heterogeneous). Locally invasive chondrosarcoma is associated with bone erosion/destruction and encasement of vessels and nerves. Skull base petro-occipital synchondrosis is a common location, usually off midline. CT: Lesions have low-intermediate attenuation associated with localized bone destruction, ± chondroid matrix calcifications, + contrast enhancement.	Chondrosarcomas are malignant tumors containing cartilage formed within sarcomatous stroma. Chondrosarcomas can contain areas of calcification/mineralization, myxoid material, and/or ossification. Chondrosarcomas rarely arise within synovium. Chondrosarcomas represent from 12 to 21%of malignant bone lesions, 21 to 26%of primary sarcomas of bone, 9 to 14%of all bone tumors, 6%of skull base tumors, and 0.15%of all intracranial tumors.
Osteogenic sarcoma	MRI: Destructive lesions involving the skull base, with low-intermediate signal on T1-weighted imaging, and mixed low, intermediate, and high signal on T2-weighted imaging, usually + matrix mineralization/ossification with low signal on T2-weighted imaging, + gadolinium contrast enhancement (usually heterogeneous). CT: Tumors have low-intermediate attenuation, usually + matrix mineralization/ossification, and often show contrast enhancement (usually heterogeneous).	Rare malignant bone tumors comprised of proliferating neoplastic spindle cells, which produce osteoid and/or immature tumoral bone. Osteogenic sarcomas usually involve the endochondral bone-forming portions of the skull base, and they are more common than chondrosarcomas and Ewing's sarcoma. Tumors are locally invasive, causing bone destruction, and have high metastatic potential. Occur in children as primary tumors, and in adults they can be associated with Paget disease, irradiated bone, chronic osteomyelitis, osteoblastoma, giant cell tumor, and fibrous dysplasia.

(continued on page 378)

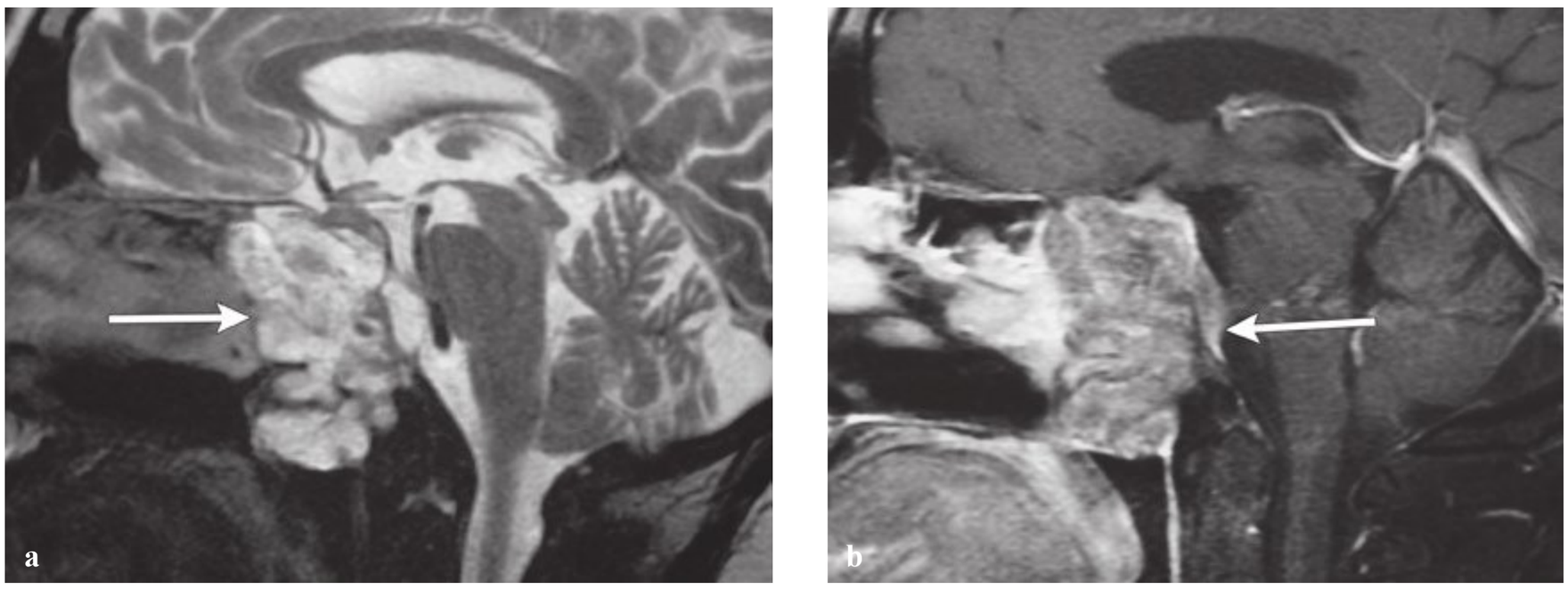

Fig. 1.452 A 77-year-old woman with a chordoma in the clivus and sella with extension into the sphenoid sinus, nasopharynx, and prepontine cistern. **(a)** The tumor has mostly high signal on sagittal T2-weighted imaging (arrow) and **(b)** shows heterogeneous gadolinium contrast enhancement on fat-suppressed sagittal T1-weighted imaging (arrow).

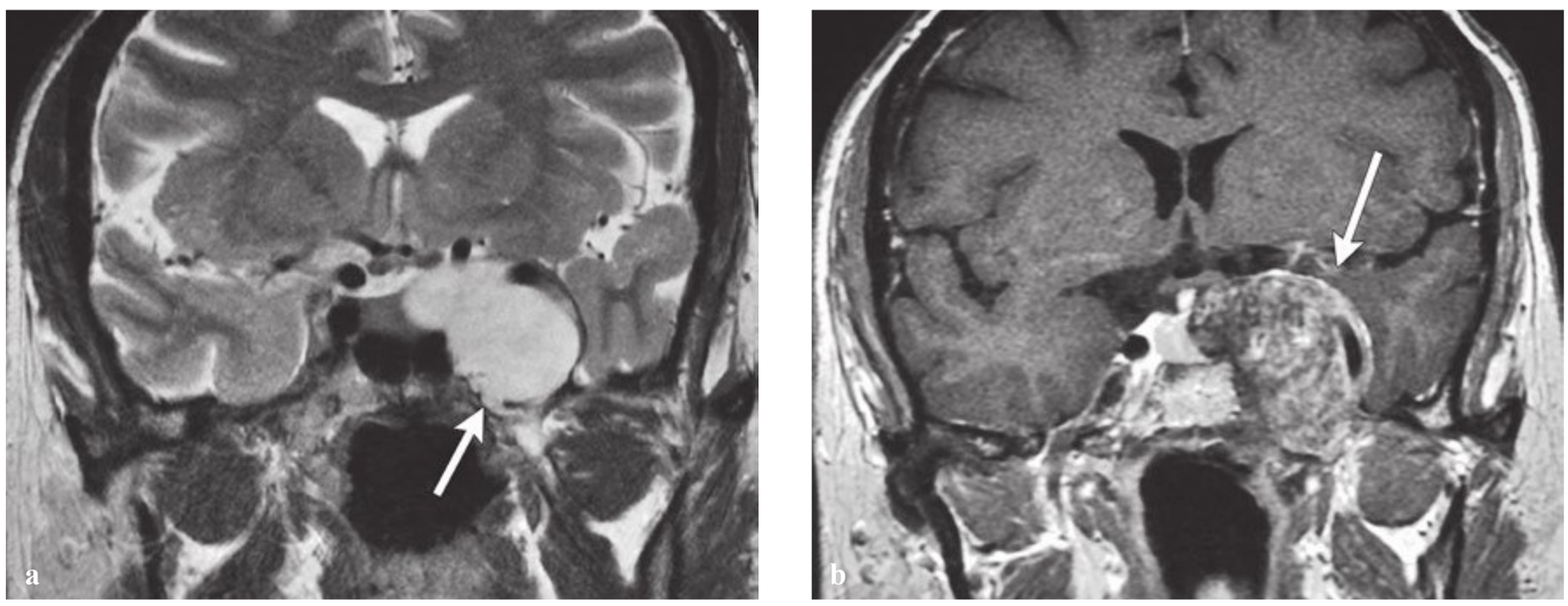

Fig. 1.453 Chondrosarcoma in the sphenoid bone with involvement of the left cavernous sinus and extension into the left side of the sella. **(a)** The tumor has high signal on coronal T2-weighted imaging (arrow) and **(b)** shows heterogeneous gadolinium contrast enhancement on coronal T1-weighted imaging (arrow). The tumor displaces, but does not narrow, the flow void of the left internal carotid artery.

Table 1.10 (cont.) Intrasellar and juxtasellar lesions

Lesions	Imaging Findings	Comments
Ewing's sarcoma	MRI: Destructive lesions involving the skull base, with low-intermediate signal on T1-weighted images and mixed low, intermediate, and high signal on T2-weighted images, ± matrix mineralization with low signal on T2-weighted images, + gadolinium contrast enhancement (usually heterogeneous). CT: Bone destruction without matrix mineralization, usually associated with extraosseous tumor extension.	Malignant primitive tumor of bone comprised of undifferentiated small cells with round nuclei. Accounts for 6 to 11% of primary malignant bone tumors, 5 to 7% of primary bone tumors. Ewing's sarcomas commonly have translocations involving chromosomes 11 and 22: t(11;22) (q24:q12) which results in fusion of the FL1-1 gene at 11q24 to the EWS gene at 22q12. Ewing's sarcoma usually occurs between the ages of 5 and 30 years, in males more than in females. It is a rare lesion involving the skull base and is locally invasive, with high metastatic potential.
Sinonasal squamous cell carcinoma (**Fig. 1.454**)	MRI: Destructive lesions in the nasal cavity, paranasal sinuses, and nasopharynx, ± intracranial extension via bone destruction or perineural spread. Intermediate signal on T1-weighted images, intermediate-slightly high signal on T2-weighted images, and mild gadolinium contrast enhancement. Large lesions ± necrosis and/or hemorrhage. CT: Tumors have intermediate attenuation and mild contrast enhancement. Large lesions ± necrosis and/or hemorrhage.	Malignant epithelial tumors originating from the mucosal epithelium of the paranasal sinuses (maxillary, 60%; ethmoid, 14%; sphenoid and frontal sinuses, 1%) and nasal cavity (25%). Includes both keratinizing and nonkeratinizing types. Accounts for 3% of malignant tumors of the head and neck. Occurs in adults, usually more than 55 years old, and in males more often than in females. Associated with occupational or other exposure to tobacco smoke, nickel, chlorophenols, chromium, mustard gas, radium, and material in the manufacture of wood products.
Nasopharyngeal carcinoma (**Fig. 1.455**)	MRI: Invasive lesions in the nasopharynx (lateral wall/fossa of Rosenmuller and posterior upper wall), ± intracranial extension via bone destruction or perineural spread. Intermediate signal on T1-weighted images and intermediate-slightly high signal on T2-weighted images. Lesion often shows gadolinium contrast enhancement. Large lesions ± necrosis and/or hemorrhage. CT: Tumors have intermediate attenuation and mild contrast enhancement. Large lesions ± necrosis and/or hemorrhage.	Carcinomas arising from the nasopharyngeal mucosa with varying degrees of squamous differentiation. Subtypes include squamous cell carcinoma, nonkeratinizing carcinoma (differentiated and undifferentiated), and basaloid squamous cell carcinoma. Occurs at higher frequency in Southern Asia and Africa than in Europe and the Americas. Peak ages: 40–60 years. Occurs two to three times more frequently in men than in women. Associated with Epstein-Barr virus, diets containing nitrosamines, and chronic exposure to tobacco smoke, formaldehyde, chemical fumes, and dust.
Adenoid cystic carcinoma (**Fig. 1.456**)	MRI: Destructive lesions with intracranial extension via bone destruction or perineural spread. Tumors have intermediate signal on T1-weighted images, intermediate-high signal on T2-weighted images, and variable mild, moderate, or prominent gadolinium contrast enhancement. CT: Tumors have intermediate attenuation, variable mild, moderate, or prominent contrast enhancement.	Basaloid tumor comprised of neoplastic epithelial and myoepithelial cells. Morphologic tumor patterns include tubular, cribriform, and solid. Accounts for 10% of epithelial salivary neoplasms. Most commonly involves the parotid, submandibular, and minor salivary glands (palate, tongue, buccal mucosa, and floor of the mouth, other locations). Perineural tumor spread common, ± facial nerve paralysis. Usually occurs in adults > 30 years old. Solid type has the worst prognosis. Up to 90% of patients die within 10–15 years after diagnosis.
Esthesioneuroblastoma (**Fig. 1.457**)	MRI: Locally destructive lesions with low-intermediate signal on T1-weighted images, intermediate-high signal on T2-weighted images, + prominent gadolinium contrast enhancement. Locations are superior nasal cavity and ethmoid air cells, with occasional extension into the other paranasal sinuses, orbits, anterior cranial fossa, and cavernous sinuses. CT: Tumors have intermediate attenuation and variable mild, moderate, or prominent contrast enhancement. PET/CT: FDG is useful for staging of disease and detection of metastases.	Also referred to as olfactory neuroblastoma, these malignant neoplasms of neuroectodermal origin arise from olfactory epithelium in the upper nasal cavity and cribriform region. Tumors consist of immature neuroblasts with variable nuclear pleomorphism, mitoses, and necrosis. Tumor cells occur in a neurofibrillary intercellular matrix. Bimodal age of occurrence in adolescents (11 to 20 years) and adults (50 to 60 years), more often in males than in females.

(continued on page 380)

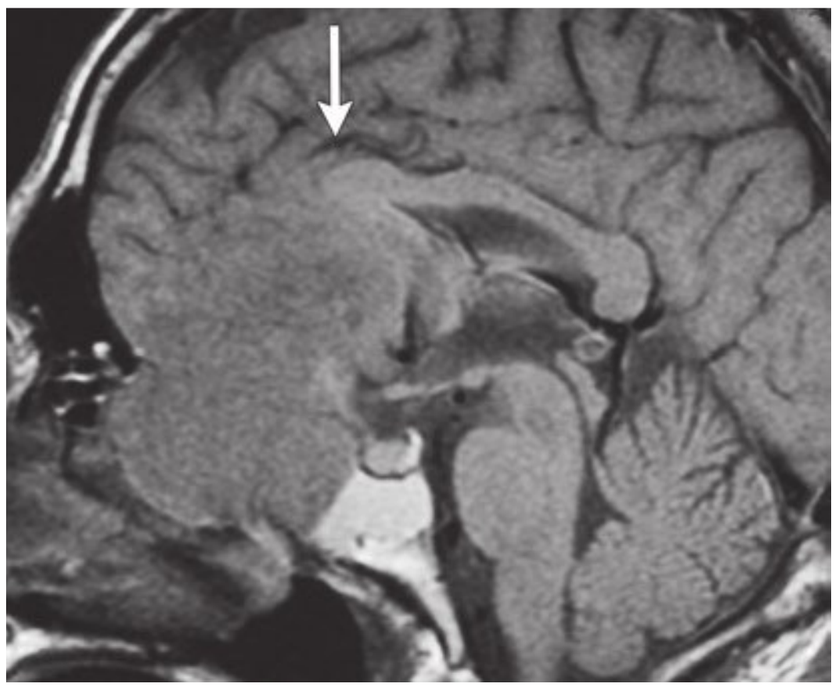

Fig. 1.454 A 48-year-old woman with sinonasal squamous cell carcinoma (arrow) in the ethmoid and sphenoid bones, including the anterior margin of the sella, as well as intracranial tumor extension seen on sagittal T1-weighted imaging.

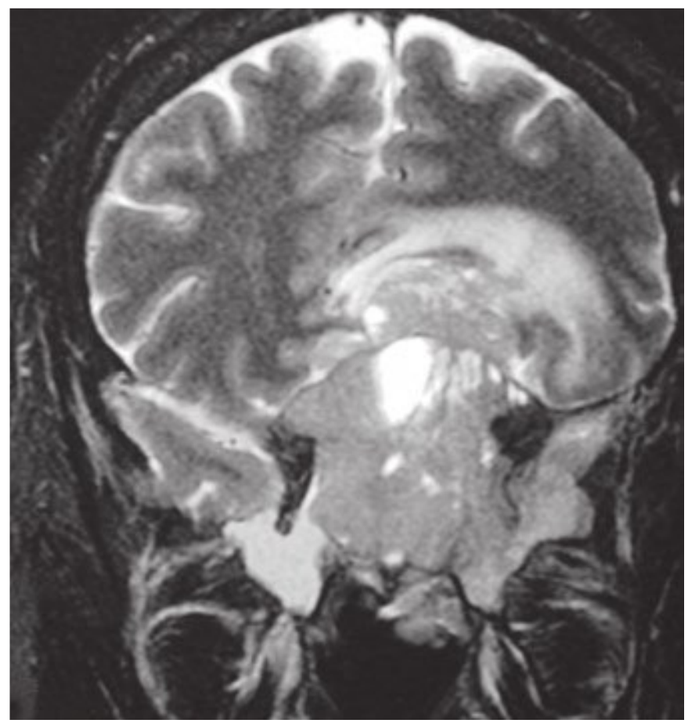

Fig. 1.455 A 49-year-old man with nasopharyngeal carcinoma in the sphenoid bone, sella, and nasopharynx, as well as intracranial tumor extension seen on coronal fat-suppressed T2-weighted imaging.

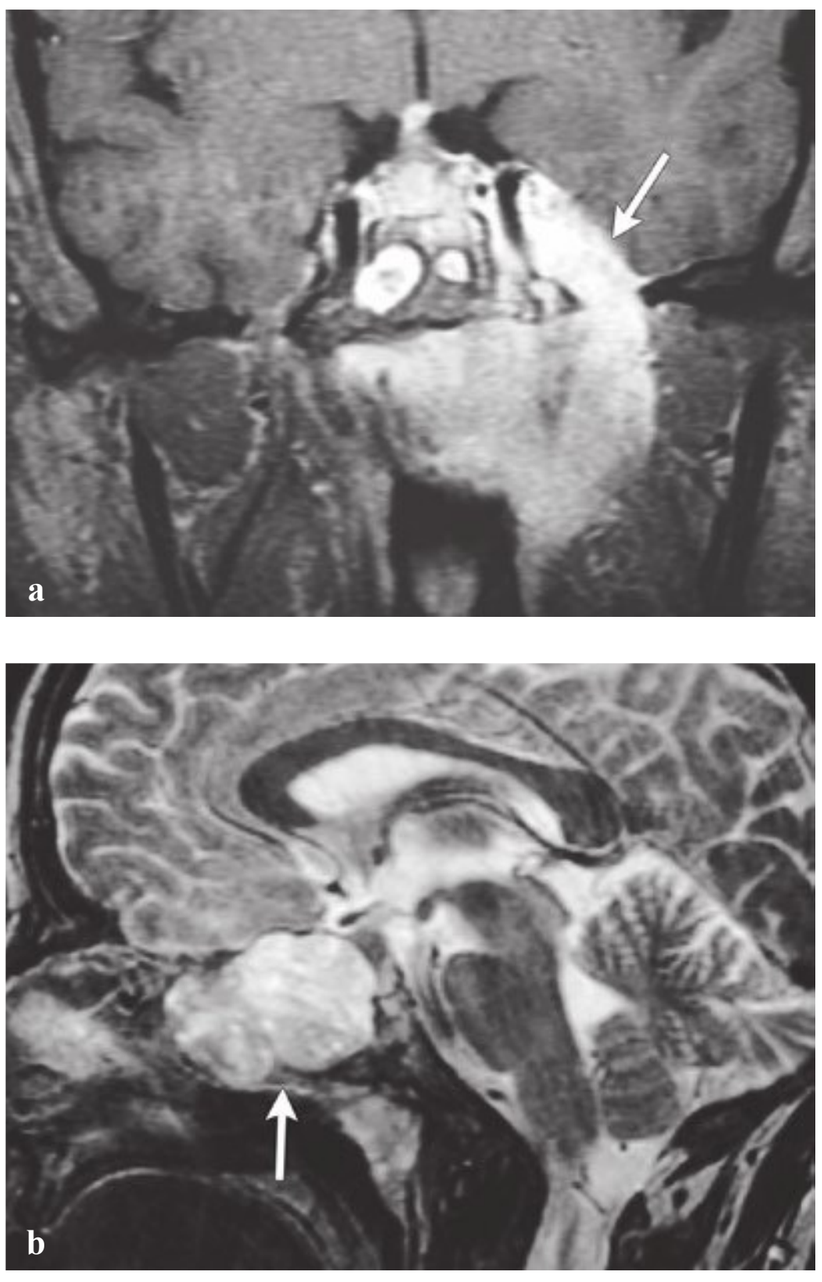

Fig. 1.456 Adenoid cystic carcinoma. **(a)** Fat-suppressed coronal T1-weighted imaging shows gadolinium contrast-enhancing tumor (arrow) within the nasopharynx extending through a widened left foramen ovale is associated with invasion of the sphenoid bone, sella, left trigeminal cistern, and left cavernous sinus. **(b)** The tumor (arrow) has high signal on sagittal fat-suppressed T2-weighted imaging.

Fig. 1.457 Esthesioneuroblastoma. **(a)** Sagittal T1-weighted imaging and **(b)** postcontrast T1-weighted imaging show a destructive tumor with intermediate signal (arrows) in the sphenoid bone, with invasion of the sphenoid sinus and sella. **(b)** The tumor shows mildly heterogeneous gadolinium contrast enhancement on sagittal fat-suppressed T1-weighted imaging.

Table 1.10 (cont.) Intrasellar and juxtasellar lesions

Lesions	Imaging Findings	Comments
Nonneoplastic Osseous Abnormalities		
Fibrous dysplasia (**Fig. 1.458**)	MRI: Features depend on the proportions of bony spicules, collagen, fibroblastic spindle cells, hemorrhagic and/or cystic changes, and associated pathologic fracture if present. Lesions are usually well circumscribed and have low or low-intermediate signal on T1-weighted images and proton density-weighted images. On T2-weighted images, lesions have variable mixtures of low, intermediate, and/or high signal, often surrounded by a low signal rim of variable thickness. Internal septations and cystic changes are seen in a minority of lesions. Bone expansion with thickened and/or thinned cortex can be seen. Lesions show gadolinium contrast enhancement that varies in degree and pattern. CT: Expansile bone changes with mixed-intermediate and high attenuation, often with a "ground glass" appearance. Can show contrast enhancement.	Benign medullary fibro-osseous lesion that can involve a single site (monostotic) or multiple locations (polyostotic). Results from developmental failure in the normal process of remodeling primitive bone to mature lamellar bone, with resultant zone or zones of immature trabeculae within dysplastic fibrous tissue. Accounts for ~ 10% of benign bone lesions. Patients range in age from < 1 year to 76 years, and 75% of patients present before the age of 30 years. McCune-Albright syndrome refers to an uncommon disorder in which polyostotic fibrous dysplasia is associated with pigmented cutaneous macules with irregular indented borders (sometimes referred to as café-au-lait spots), precocious puberty, and/or other endocrine disorders, such as acromegaly, hyperthyroidism, hyerparathyroidism, and/or Cushing's syndrome. The complete clinical triad of polyostotic fibrous dysplasia, café-au-lait spots, and precocious puberty associated with McCune-Albright syndrome is uncommon and occurs in 3% of patients with polyostotic fibrous dysplasia.
Osteoma (**Fig. 1.459**)	MRI: Well-circumscribed lesions in the skull, with low-intermediate signal on T1- and T2-weighted imaging, typically showing no significant gadolinium contrast enhancement. CT: Well-circumscribed lesions in the skull, with high attenuation, and typically show contrast enhancement.	Benign primary bone tumors composed of dense lamellar, woven, and/or compact cortical bone. The periosteal surface of osteomas usually has layers of lamellar bone, whereas deeper portions may contain a coarse mosaic pattern of lamellar bone. Haversian systems and cement lines similar to Paget disease may be present in osteomas. Osteomas are usually covered by a thin layer of spindle cells without cellular atypia. No cartilage is present in osteomas. Located in the skull or paranasal sinuses (frontal > ethmoid > maxillary > sphenoid).
Paget disease	CT: Lesions often have mixed intermediate high attenuation. Irregular/indistinct borders between marrow and inner margins of the outer and inner tables of the skull. MRI: The MRI features of Paget disease vary based on the phases of the disease. Most cases involving the skull are the late or inactive phases. Findings include osseous expansion and cortical thickening with low signal on T1- and T2-weighted imaging. The inner margins of the thickened cortex can be irregular and indistinct. Zones of low signal on T1- and T2-weighted imaging can be seen in the diploic marrow secondary to thickened bone trabeculae. Marrow in late or inactive phases of Paget disease can have signal similar to normal marrow, can contain focal areas of fat signal, can have low signal on T1- and T2-weighted imaging secondary to regions of sclerosis, can have areas of high signal on fat-suppressed (FS) T2-weighted imaging from edema or persistent fibrovascular tissue, or can show various combinations of the aforementioned.	Paget disease is a chronic skeletal disease in which there is disordered bone resorption and woven bone formation, resulting in osseous deformity. A paramyxovirus may be an etiologic agent. Paget disease is polyostotic in up to 66% of patients. Paget disease is associated with a < 1% risk of developing secondary sarcomatous changes. Occurs in 2.5 to 5% of Caucasians older than 55 years, and 10% of those over the age of 85 years. Can result in narrowing of neuroforamina, with cranial nerve compression and basilar impression, ± compression of brainstem.

(continued on page 382)

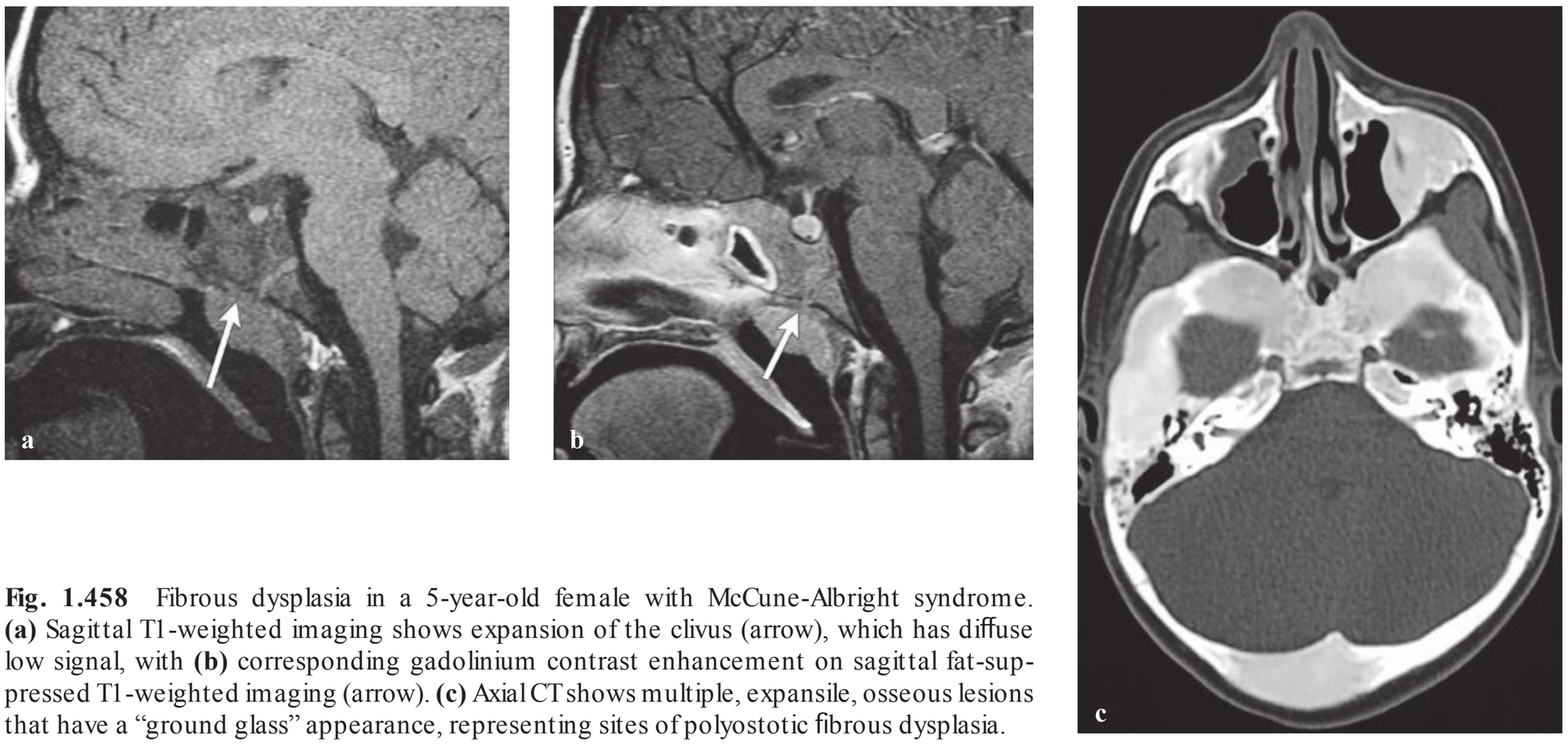

Fig. 1.458 Fibrous dysplasia in a 5-year-old female with McCune-Albright syndrome. **(a)** Sagittal T1-weighted imaging shows expansion of the clivus (arrow), which has diffuse low signal, with **(b)** corresponding gadolinium contrast enhancement on sagittal fat-suppressed T1-weighted imaging (arrow). **(c)** Axial CT shows multiple, expansile, osseous lesions that have a "ground glass" appearance, representing sites of polyostotic fibrous dysplasia.

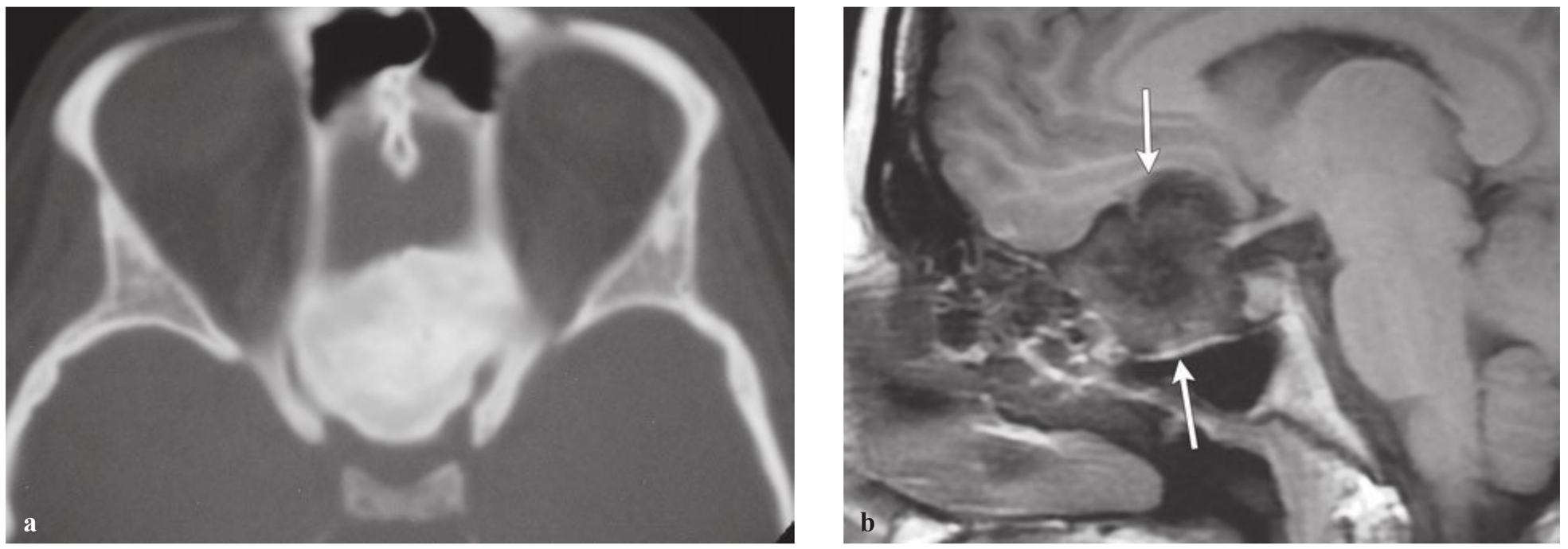

Fig. 1.459 A 26-year-old woman with an osteoma at the planum sphenoidale that has **(a)** high attenuation on axial CT and **(b)** heterogeneous mostly low signal (arrows) on sagittal T1-weighted imaging.

Table 1.10 (cont.) Intrasellar and juxtasellar lesions

Lesions	Imaging Findings	Comments
Infection		
Leptomeningeal infection (**Fig. 1.460**)	MRI: Single or multiple nodular enhancing lesions and/or focal or diffuse abnormal subarachnoid enhancement in suprasellar cistern ± intrasellar extension. Low-intermediate signal on T1-weighted imaging and intermediate-high signal on T2-weighted imaging and FLAIR. Leptomeningeal inflammation often best seen on postcontrast images. CT: Single or multiple nodular enhancing lesions and/or focal or diffuse abnormal subarachnoid enhancement.	Gadolinium contrast enhancement in the intracranial subarachnoid space (leptomeninges) usually is associated with significant pathology (inflammation and/or infection versus neoplasm). Inflammation and/or infection of the leptomeninges can result from pyogenic, fungal, or parasitic diseases, as well as tuberculosis. Neurosarcoid results in granulomatous disease in the leptomeninges, producing similar patterns of subarachnoid enhancement.
Inflammation		
Langerhans' cell histiocytosis (**Fig. 1.461**)	MRI: Fusiform or lobulated lesion with intermediate signal on T1- and T2-weighted imaging involving the pituitary stalk. Pituitary stalk is usually > 3 mm in thickness, often associated with loss of high signal on T1-weighted imaging of the posterior pituitary. Lesions involving the pituitary usually show gadolinium contrast enhancement. CT: Thickening of the pituitary stalk may be seen. Intraosseous lesions are typically associated with localized bone destruction.	Disorder of reticuloendothelial system in which bone marrow–derived dendritic Langerhans' cells infiltrate various organs as focal lesions or in diffuse patterns. Langerhans' cells have eccentrically located ovoid or convoluted nuclei within pale to eosinophilic cytoplasm. Lesions often consist of Langerhans' cells, macrophages, plasma cells, and eosinophils. Lesions are immunoreactive to S-100, CD1a, CD207, HLA-DR, and β_2-microglobulin. Prevalence is 2 per 100,000 children < 15 years old; only a third of lesions occur in adults. Localized lesions (eosinophilic granuloma) can be single or multiple in the skull, usually at the skull base. Intradural lesions occur at pituitary stalk/hypothalamus and can present with diabetes insipidus. Lesions rarely occur in brain tissue (< 4% of patients with Langerhans' cell histiocytosis).
Lymphocytic hypophysitis (**Fig. 1.462**)	MRI: Slightly lobulated lesion with intermediate signal on T1-weighted imaging and heterogeneous low-intermediate and high signal on T2-weighted imaging. Lesion involves the pituitary gland, with thickened pituitary stalk, and there is prominent abnormal homogeneous or heterogeneous gadolinium contrast enhancement in the pituitary gland and often the pituitary stalk and dura. CT: Enlarged pituitary gland with thickened stalk.	Rare autoimmune inflammatory process involving the pituitary gland, confirmed by biopsy showing varying degrees of lymphocytic infiltration and plasma cells with fibrotic changes without multinucleated giant cells. Usually occurs in adults, and in women (80%) more often than in men. Clinical findings include headaches and pituitary hormonal dysfunction (such as diabetes insipidus) that responds to steroid medication. Can be associated with Hashimoto thyroiditis, polymyositis, pernicious anemia, atrophic gastritis, psoriasis, systemic lupus erythematosus, adrenalitis, and/or ovarian failure.
Granulomatous hypophysitis	MRI: Lesion involving the pituitary gland with intermediate signal on T1-weighted imaging, heterogeneous low-intermediate and high signal on T2-weighted imaging, with or without cystic changes, hemorrhage, ± thickened pituitary stalk, and abnormal homogeneous or heterogeneous or rimlike gadolinium contrast enhancement in the pituitary gland. Gadolinium contrast enhancement may also be seen in the dura, bone, and sphenoid sinus mucosa. CT: Enlarged pituitary gland with thickened stalk.	The primary form is a rare chronic inflammatory disease with nonnecrotizing granulomas, histiocytes, lymphocytes, plasma cells, and multinucleated giant cells involving the pituitary gland. The secondary form occurs with necrotizing granulomatous involvement of the pituitary gland related to systemic disorders, such as sarcoidosis, Langerhans' cell histiocytosis, Erdheim-Chester disease, Takayasu's disease, Crohn disease, granulomatosis with polyangiitis (Wegener's granulomatosis), and infections in immunocompromised patients (fungal organisms, tuberculosis, or toxoplasmosis).

(continued on page 384)

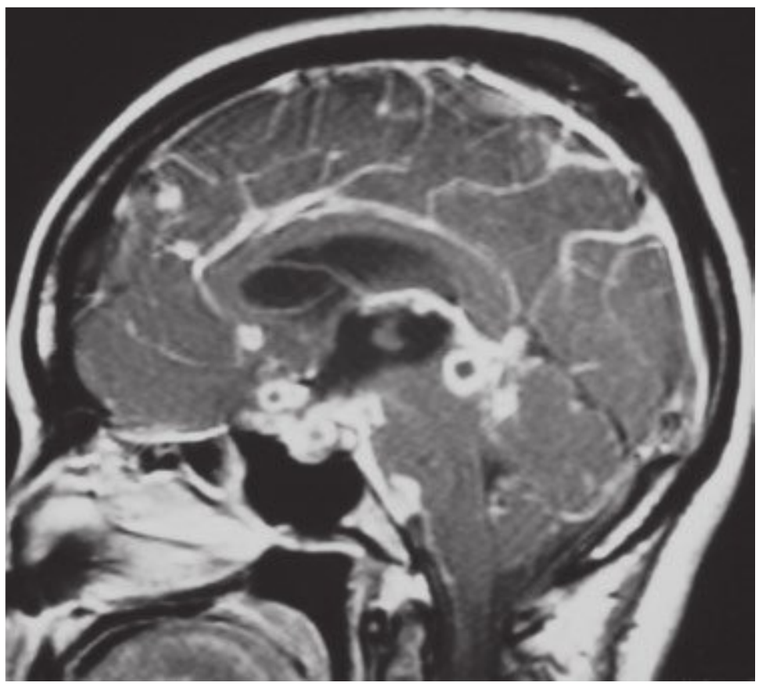

Fig. 1.460 Meningitis from tuberculosis seen as ring-shaped and irregular zones with abnormal subarachnoid gadolinium contrast enhancement, including the suprasellar cistern, on sagittal T1-weighted imaging.

Fig. 1.461 An 8-year-old female with Langerhans' cell histiocytosis and abnormal gadolinium contrast enhancement involving the pituitary stalk (arrow) and hypothalamus on sagittal T1-weighted imaging.

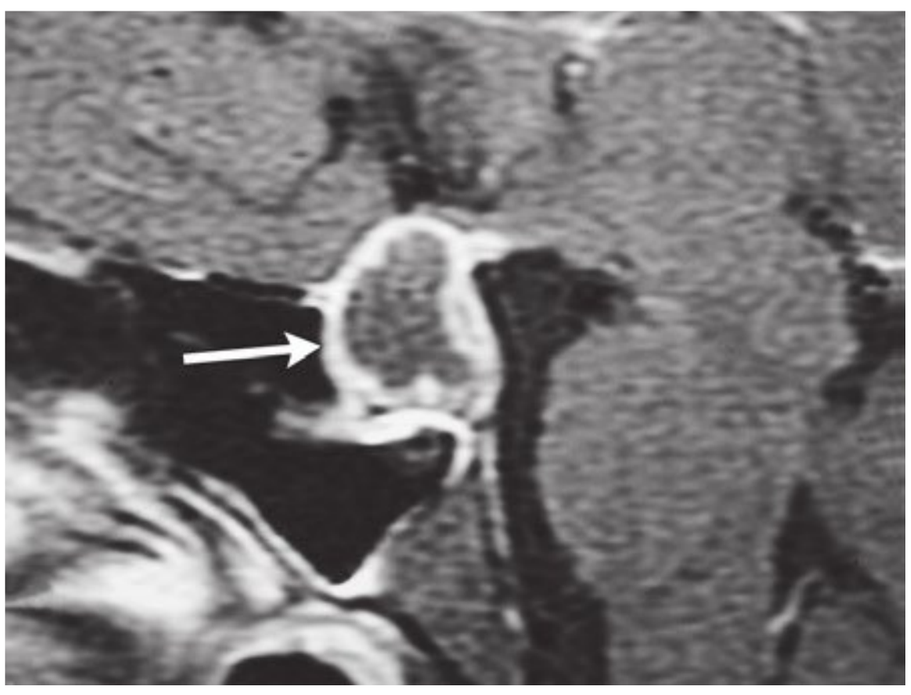

Fig. 1.462 A 40-year-old woman with lymphocytic adenohypophysitis. Sagittal fat-suppressed T1-weighted imaging shows marked enlargement of the pituitary gland, which has irregular peripheral gadolinium contrast enhancement (arrow).

Table 1.10 (cont.) Intrasellar and juxtasellar lesions

Lesions	Imaging Findings	Comments
Sarcoidosis (**Fig. 1.463**)	MRI: Lesions can be extra-axial, involving the leptomeninges, intra-axial, or both. Lesions can have low to intermediate signal on T1-weighted imaging and slightly high to high signal on T2-weighted imaging and fat-suppressed (FS) proton density-weighted imaging and FS T2-weighted imaging. Erosions and zones of destruction involving adjacent bone cortex can occur. Extraosseous extension of the granulomatous process can also occur from primary osseous involvement. After gadolinium contrast administration, intra-axial lesions and leptomeningeal disease typically show moderate to prominent enhancement. CT: Intra-axial lesions often have low-intermediate attenuation and usually show contrast enhancement. Extra-axial disease involving the meninges can be seen as leptomeningeal contrast enhancement. Intraosseous lesions usually appear as intramedullary radiolucent zones, and rarely are sclerotic with high attenuation.	Multisystem noncaseating granulomatous disease of uncertain cause that can involve the CNS in 5 to 15% of cases and bone in 1 to 15%. Associated with severe neurologic deficits if CNS lesions are untreated.
Granulomatosis with polyangiitis (Wegener's granulomatosis)	MRI: Enlargement of pituitary gland, with intermediate signal on T1-weighted imaging, heterogeneous low-intermediate and high signal on T2-weighted imaging with or without thickened pituitary stalk, and loss of high signal of posterior pituitary on T1-weighted imaging. Abnormal homogeneous or heterogeneous gadolinium contrast enhancement in the pituitary gland. Gadolinium contrast enhancement may also be seen in the dura and bone.	Multisystem necrotizing granulomatous disease with small-vessel vasculitis that is associated with antineutrophil cytoplasmic antibodies (ANCA). Usually involves lungs, upper respiratory tract, and kidneys. Involves the pituitary gland in 1% of patients (female/male ratio = 3/1) and can result in panhypopituitarism and/or diabetes insipidus.
Rosai-Dorfman disease	MRI: Lesions can be suprasellar or both intrasellar and supasellar. Other intracranial lesions involve the dura, midbrain, or cerebellum. Lesions have intermediate signal on T1-weighted imaging, variable intermediate and/or slightly high signal on T2-weighted imaging, and homogeneous gadolinium contrast enhancement.	Rare benign histiocytosis (also referred to as sinus histiocytosis with massive lymphadenopathy) that usually occurs in children and young adults. The male/female ratio = 3/2. Patients typically present with painless adenopathy and one or more extranodal sites. Involvement of the CNS occurs in 4% and usually involves the intracranial or spinal dura. Rarely occurs in the sella and suprasellar region. Patients may present with headaches, seizures, visual disturbance, numbness, and/or paraplegia.

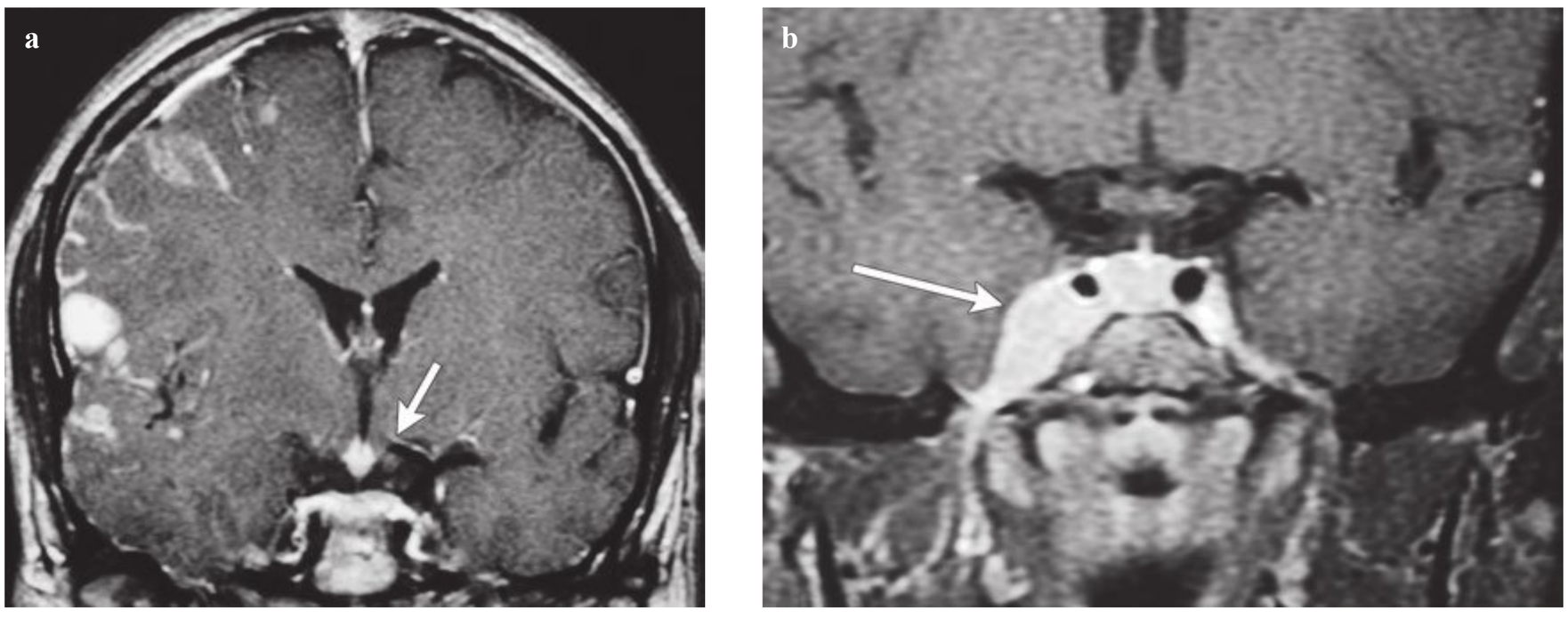

Fig. 1.463 Intracranial sarcoidosis. **(a)** A 33-year-old man with irregular zones of abnormal intracranial subarachnoid gadolinium contrast enhancement, including the suprasellar cistern (arrow), on coronal T1-weighted imaging. **(b)** A 49-year-old woman with abnormal gadolinium contrast enhancement filling the right trigeminal cistern (Meckel's cave), with extension into the right cavernous sinus associated with narrowing of the flow void of the right internal carotid artery (arrow).

1.11 Pineal Gland

The pineal gland is a small, ovoid endocrine gland measuring between 10 and 14 mm that is attached to the posterior border of the third ventricle above the superior colliculi and inferior to the splenium of the corpus callosum (**Fig. 1.464**). The pineal gland produces melatonin, a serotonin-type hormone that has a major role in regulating the wake–sleep cycles as well as having photoperiodic/seasonal functions. Melatonin also affects release of other hormones, such as follicle-stimulating hormone and luteinizing hormone.

The pineal gland has a central core with lobules composed mostly of pinealocytes, which produce and secrete melatonin. The pinealocytes, which account for over 90% of pineal gland cells, have a prominent nucleus with a granulated appearance, lightly basophilic cytoplasm, and cytoplasmic processes that extend to connective septa and adjacent fenestrated capillaries. The other, less common types of pineal cells include neuroglia (fibrous astrocytes and microglia), perivascular phagocytes, and pineal neurons. Granular calcium deposits are present in the pineal gland at birth, and their accumulation increases during childhood and becomes visible on CT. The deposits occur between and within pineal cells as layered concretions of calcium and magnesium salts and hydroxyapatite. Glial or benign ependymal cysts frequently occur in the pineal gland.

The pineal gland develops as an evagination of ependymal cells at the caudal roof portion of the third ventricle during the seventh week of gestation. Developing pineal parenchyma progressively fills this evagination to form the solid pineal gland. After birth, the pineal gland increases in size up to age 2 years and remains relatively constant in size from 2 to 20 years. After puberty, there is a slight gradual increase in weight of the pineal gland. Blood supply to the pineal gland is primarily from the posterior choroidal arteries, and venous drainage is into the internal cerebral veins and basal vein of Rosenthal. Arteries and veins extend into the hila of the pineal gland and connect to capillaries in the septae between the lobules containing the pinealocytes within the central core of the gland. No blood–brain barrier exists for the pineal gland.

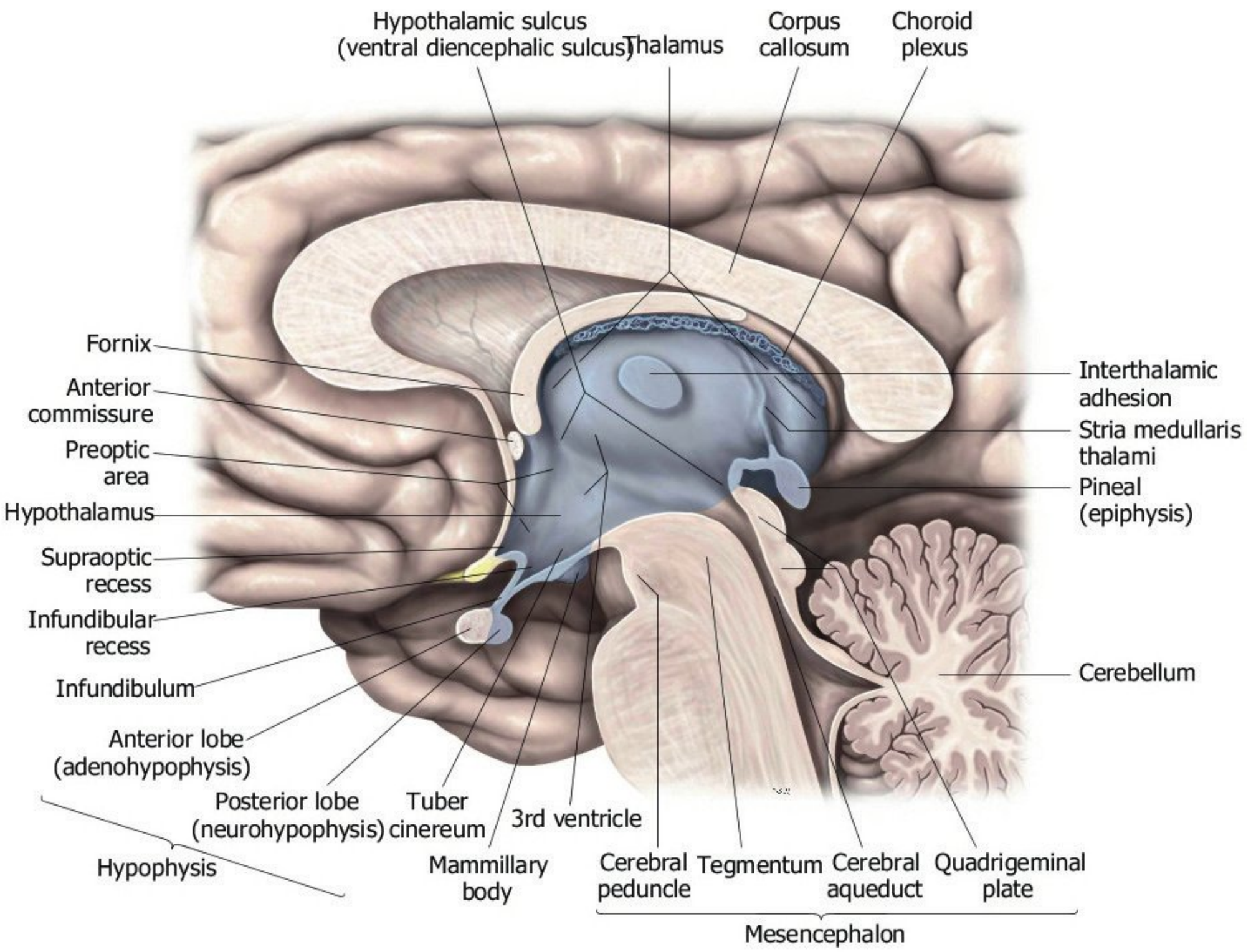

Fig. 1.464 Sagittal diagram shows the pineal gland and adjacent structures. From THIEME Atlas of Anatomy, Neck and Internal Organs, © Thieme 2006, Illustration by Karl Wesker.

Table 1.11 Lesions in the pineal region

- Pineal Parenchymal Lesions
  - Pineocytoma
  - Pineal parenchymal tumor of intermediate differentiation
  - Papillary tumor of the pineal region
  - Pineoblastoma
- Germ Cell Tumors
  - Germinoma
  - Teratoma
  - Choriocarcinoma
  - Yolk sac tumor
  - Embryonal carcinoma
- Other Lesions Within or Adjacent to the Pineal Gland
  - Pineal cyst
  - Metastatic disease
  - Pineal melanoma
  - Meningioma
  - Primitive neuroectodermal tumor (PNET)
  - Atypical teratoid/rhabdoid tumor (AT/RT)
  - Ependymoma
  - Arachnoid cyst
  - Epidermoid cyst
  - Dermoid cyst
  - Lipoma

Table 1.11 Lesions in the pineal region

Lesions	Imaging Findings	Comments
Pineal Parenchymal Lesions		
Pineocytoma (**Fig. 1.465**)	MRI: Tumors have low-intermediate signal on T1-weighted imaging, slightly high to high signal on T2-weighted imaging, and can show gadolinium contrast enhancement. CT: Lesions have low-intermediate attenuation, ± peripheral calcifications.	Pineocytomas have circumscribed margins and usually measure less than 3 cm. Rare, slow-growing pineal parenchymal tumors (WHO grade I) composed of sheets, lobules, or pineocytomatous rosettes of well-differentiated small cells with round-oval nuclei in moderate eosinophilic cytoplasm, with minimal to absent mitotic activity, and immunoreactive to synaptophysin, NSE, and NFP. Account for less than 1% of intracranial neoplasms. Usually occur in adults (mean age = 38 years). Five-year survival ranges from 86 to 100%
Pineal parenchymal tumor of intermediate differentiation (**Fig. 1.466** and **Fig. 1.467**)	MRI: Tumors often have low-intermediate signal on T1-weighted imaging, slightly high to high signal on T2-weighted imaging, and show gadolinium contrast enhancement. Disseminated enhancing tumor in the leptomeninges and/or ventricles may be seen with grade III neoplasms. CT: Tumors often have intermediate attenuation.	Pineal parenchymal tumors of intermediate differentiation often have circumscribed margins and usually measure less than 3 cm. They are intermediate-grade pineal tumors (WHO grades II–III) consisting of uniform neoplastic cells with mild-moderate nuclear atypia, ± small rosettes, and low-moderate mitotic activity. Occur in patients from 1 to 69 years old (mean age = 38 years). Five-year survival ranges from 39 to74%

(continued on page 388)

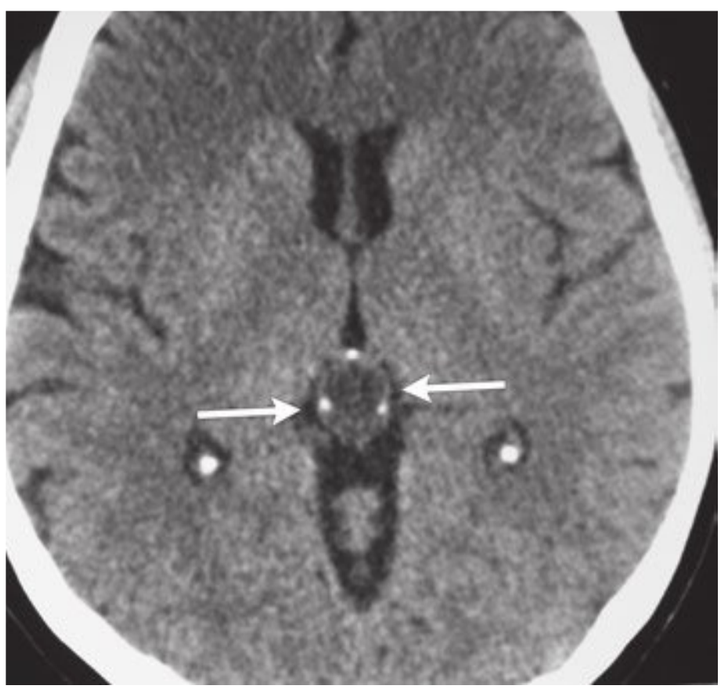

Fig. 1.465 A35-year-old woman with a pineocytoma. Axial CT shows a circumscribed low attenuation lesion within the pineal gland (arrows) with a characteristic “explosion” of pineal calcifications at the periphery.

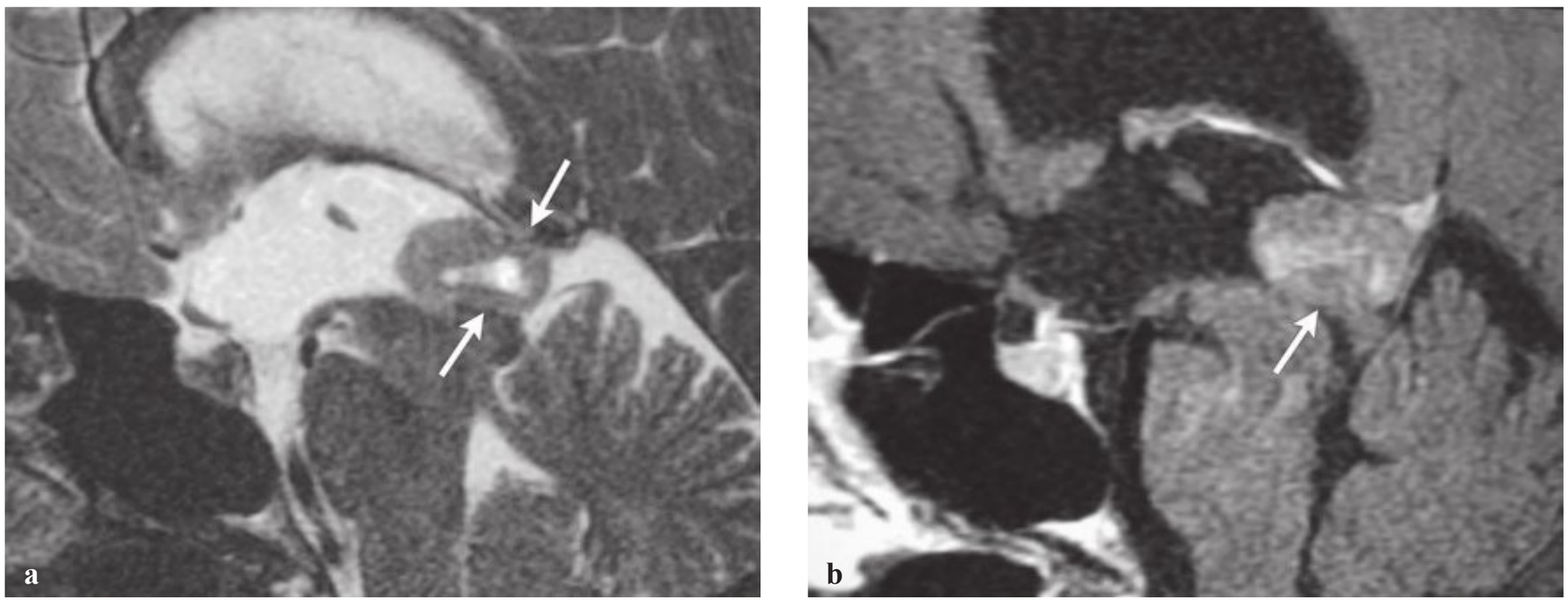

Fig. 1.466 A 33-year-old woman with a pineal parenchymal tumor of intermediate differentiation (PPTID). **(a)** The tumor has mixed intermediate and high signal on sagittal T2-weighted imaging (arrows), and **(b)** shows mild heterogeneous gadolinium contrast enhancement (arrow) on sagittal T1-weighted imaging.

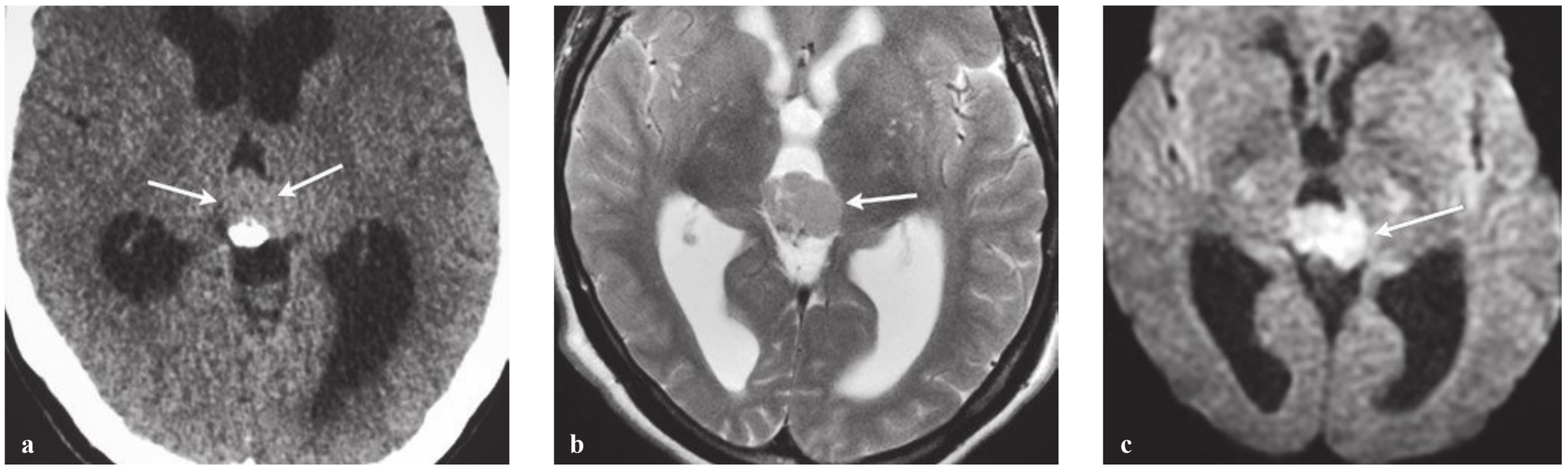

Fig. 1.467 A 66-year-old woman with a grade III pineal parenchymal tumor of intermediate differentiation (PPTID). **(a)** The tumor (arrows) has intermediate attenuation and a posterior calcification on axial CT, **(b)** intermediate to slightly high signal on axial T2-weighted imaging (arrow), **(c)** restricted diffusion on axial DWI (arrow), and **(d)** gadolinium contrast enhancement on sagittal T1-weighted imaging (arrow). **(e)** Magnetic resonance spectroscopy shows the tumor to have an elevated choline peak at 3.2 ppm and low N-acetylaspartate (NAA) at 2 ppm.

Table 1.11 (cont.) Lesions in the pineal region

Lesions	Imaging Findings	Comments
Papillary tumor of the pineal region (**Fig. 1.468**)	MRI: Tumors often have intermediate signal on T1-weighted imaging, slightly high to high signal on T2-weighted imaging, and show gadolinium contrast enhancement, ± cysts. Tumors can have mixed signal on T1- and T2-weighted imaging secondary to the presence of cysts, hemorrhage, and/or calcifications CT: Circumscribed tumors with intermediate to slightly increased attenuation.	Rare neuroepithelial tumor of the pineal gland (WHO grades II or III) composed of both papillary zones with large, pale, eosinophilic columnar cells overlying blood vessels and cellular regions with vacuolated cytoplasm and round or oval nuclei. The cellular regions may show rosettelike configurations similar to ependymomas. Tumors are immunoreactive to keratins in papillary portions. Occur in children and adults (mean age = 32 years). Variable mitotic rates in tumors. Overall 5-year survival is 73%, although tumors with high mitotic activity have a much poorer prognosis.
Pineoblastoma (**Fig. 1.469** and **Fig. 1.470**)	MRI: Tumors have low-intermediate signal on T1-weighted imaging, and intermediate to slightly high and/or high signal on T2-weighted imaging, ± hemorrhage or necrotic changes. Tumors usually show prominent gadolinium contrast enhancement. Disseminated enhancing tumor in the leptomeninges and/or ventricles is not uncommon. Diffusion-weighted imaging: Solid portions can have restricted diffusion. Magnetic resonance spectroscopy: Tumors show decreased N-acetylaspartate (NAA) and high levels of choline. CT: Tumors have intermediate to slightly high attenuation, ± hemorrhage, and necrotic/cystic changes. Disseminated enhancing tumor in the leptomeninges is not uncommon.	Pineoblastomas are large tumors (> 3 cm) that often have lobulated irregular margins. They are malignant embryonal tumors (WHO grade IV) consisting of diffuse, dense sheets of cells with round, irregular nuclei within scant cytoplasm, + neuroblastic differentiation, hemorrhage, and necrosis. Immunoreactive to synaptophysin, NSE, NFP, class III β-tubulin, and chromogranin A. Occur most commonly in first two decades (mean age = 18.5 years). Associated with familial bilateral retinoblastoma, which has a poor prognosis. Prognosis is poor when there is documented disseminated tumor in the leptomeninges. Overall 5-year survival is 58%

(continued on page 390)

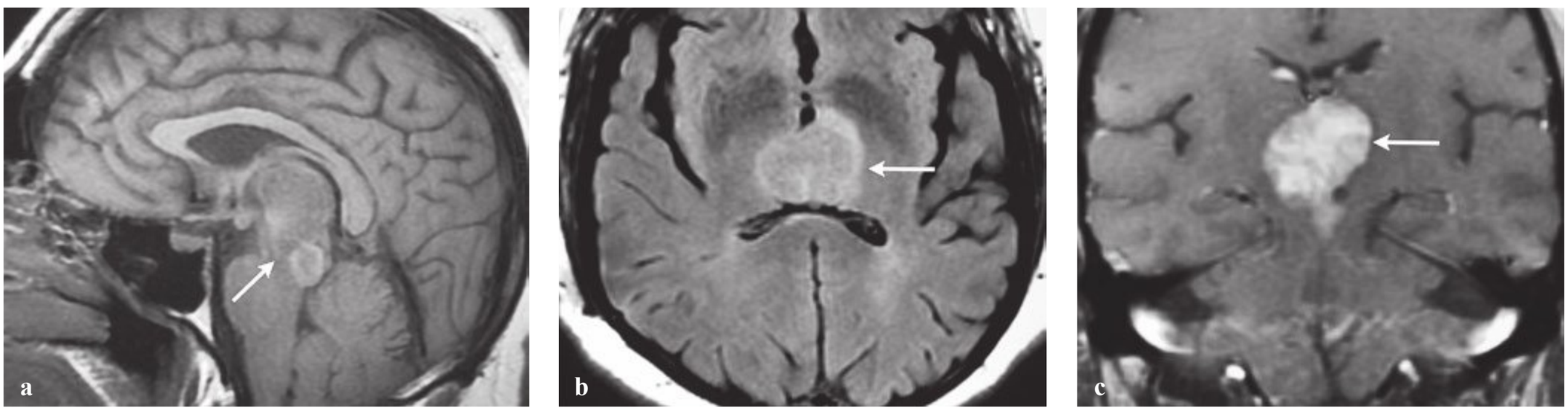

Fig. 1.468 Papillary tumor of the pineal region. A lesion is seen involving the pineal gland with irregular margins and mass effect on the tectal plate and with extension into the third ventricle. **(a)** The lesion has mixed intermediate and slightly high signal on sagittal T1-weighted imaging (arrow), **(b)** slightly high to high signal on axial FLAIR (arrow), and **(c)** gadolinium contrast enhancement on coronal fat-suppressed T1-weighted imaging (arrow).

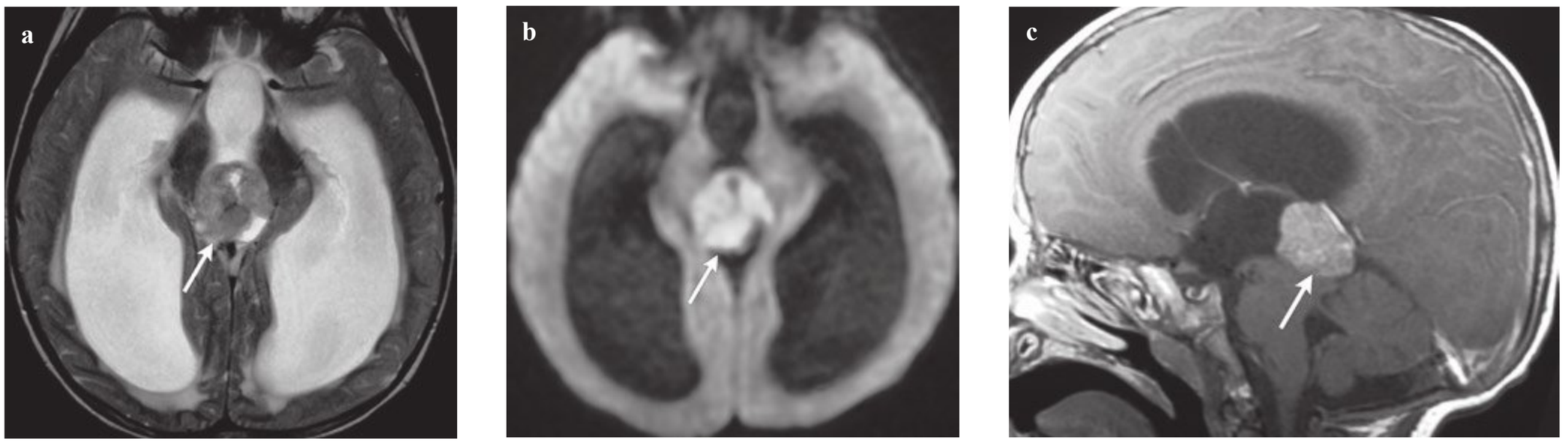

Fig. 1.469 An 18-month-old male with a pineoblastoma that has **(a)** mixed intermediate to slightly high, high, and low signal on axial T2-weighted imaging (arrow), **(b)** restricted diffusion on DWI (arrow), and **(c)** gadolinium contrast enhancement on sagittal T1-weighted imaging (arrow). **(d)** Magnetic resonance spectroscopy shows an elevated choline peak (*) at 3.2 ppm and decreased N-acetylaspartate (**) at 2 ppm.

Fig. 1.470 A 4-year-old girl with a disseminated pineoblastoma seen as poorly defined contrast enhancement in the pineal recess and posterior sulci.

Table 1.11 (cont.) Lesions in the pineal region

Lesions	Imaging Findings	Comments
Germ Cell Tumors		Extragonadal germ cell tumors include germinoma (most common), mature teratoma, malignant teratoma, yolk sac tumor, embryonal carcinoma, and choriocarcinoma. Germ cell tumors account for 1% of primary intracranial tumors, with an incidence of 0.09 per 100,000. Peak age of incidence is between 10 and 14 years, and 90%occur in patients less than 25 years old. Occur more frequently in males than in females. Immunoreactive to α-fetoprotein and β-HCG. Prognosis depends on histologic subtype; 10-year survival for geminomas is > 85% Other germ cell tumors have lower survival rates, particulary those containing nongerminomatous malignant cells.
Germinoma (**Fig. 1.471, Fig. 1.472,** and **Fig. 1.473**)	MRI: Tumors often have intermediate signal on T1-weighted imaging, slightly high to high signal on T2-weighted imaging, and show gadolinium contrast enhancement, ± cysts, ± gadolinium contrast-enhancing disseminated subarachnoid and/or intraventricular tumor. CT: Circumscribed tumors with intermediate to slightly increased attenuation, ± disseminated contrast-enhancing leptomeningeal and/or intraventricular tumor.	Germinomas account for up to 70%of all pineal neoplasms, 5%of pediatric intracranial tumors, and < 1%of adult intracranial tumors. Tumors contain large undifferentiated neoplastic cells that resemble primordial elements. Neoplastic cells have central round nuclei, prominent nucleoli, and clear cytoplasm from glycogen deposits. Mitotic activity is usually seen. Necrosis is uncommon. Immunoreactive to c-kit and OCT4.
Teratoma (**Fig. 1.474**)	MRI: Circumscribed lesions with variable low, intermediate, and/or high signal on T1- and T2-weighted imaging; ± gadolinium contrast enhancement. May contain calcifications with low signal on T1- and T2-weighted imaging, as well as fatty/lipid components (with high signal on T1-weighted imaging) that can cause chemical meningitis if ruptured. CT: May contain calcifications, and zones with intermediate and fat attenuation.	The second most common type of germ cell tumor, teratomas occur in children, and in males more than in females. They are benign or malignant, and are composed of derivatives of ectoderm, mesoderm, and/or endoderm. Mature teratomas have differentiated cells from ectoderm (brain, skin, and/or choroid plexus), mesoderm (cartilage, bone, muscle, and/or fat), and endoderm (cysts with enteric or respiratory epithelia). Immature teratomas contain partially differentiated ectodermal, mesodermal, or endodermal cells.

(continued on page 392)

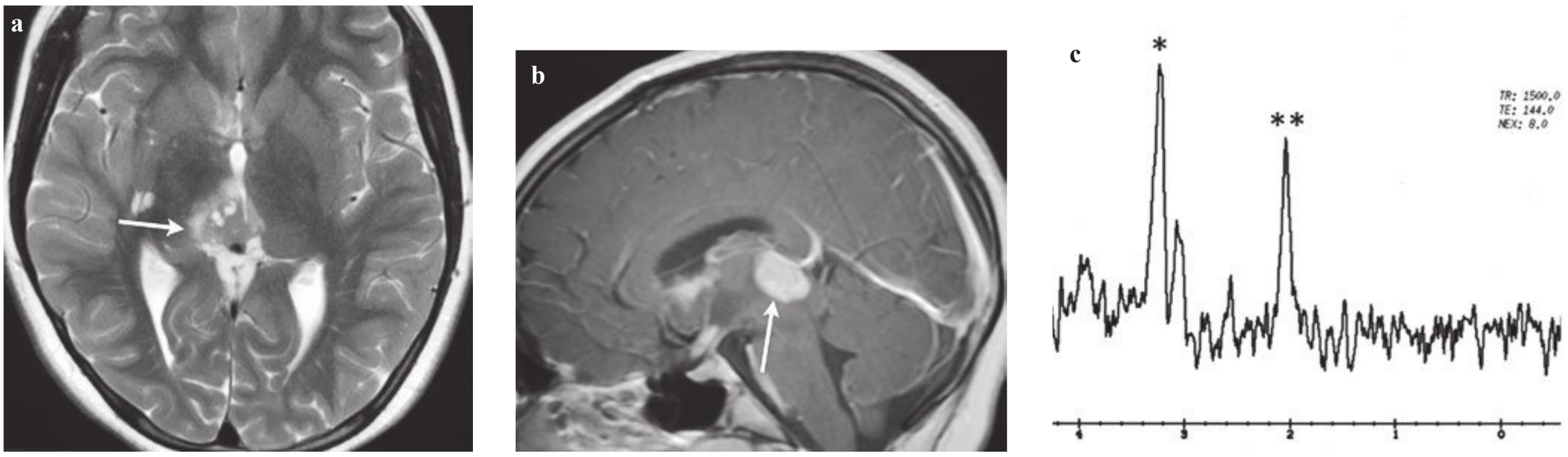

Fig. 1.471 **(a)** A 12-month-old female with a pineal germinoma that has ill-defined margins, mixed intermediate, slightly high, and high signal on axial T2-weighted imaging (arrow). **(b)** The pineal tumor (arrow) shows gadolinium contrast enhancement on sagittal T1-weighted imaging (arrow), and contrast-enhancing disseminated tumor is also seen along the floor of the lateral ventricle and anteroinferior portion of the third ventricle. **(c)** Magnetic resonance spectroscopy shows an elevated choline peak (*) at 3.2 ppm and slightly decreased N-acetylaspartate (**) at 2 ppm.

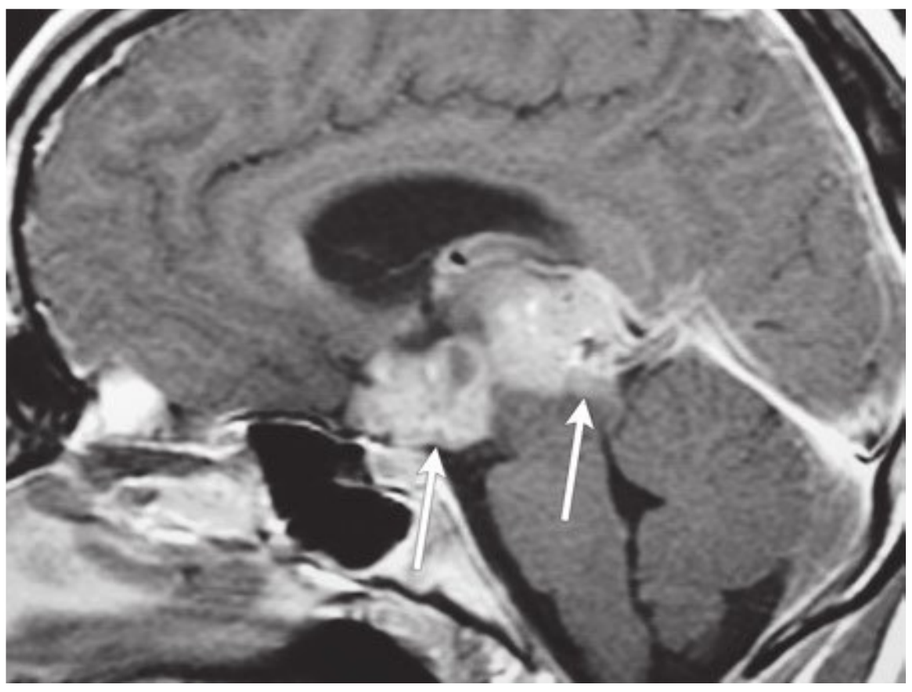

Fig. 1.472 A 20-year-old man with an intracranial germinoma seen as gadolinium contrast-enhancing mass lesions (arrows) with irregular margins in both the pineal recess and suprasellar cistern on sagittal T1-weighted imaging.

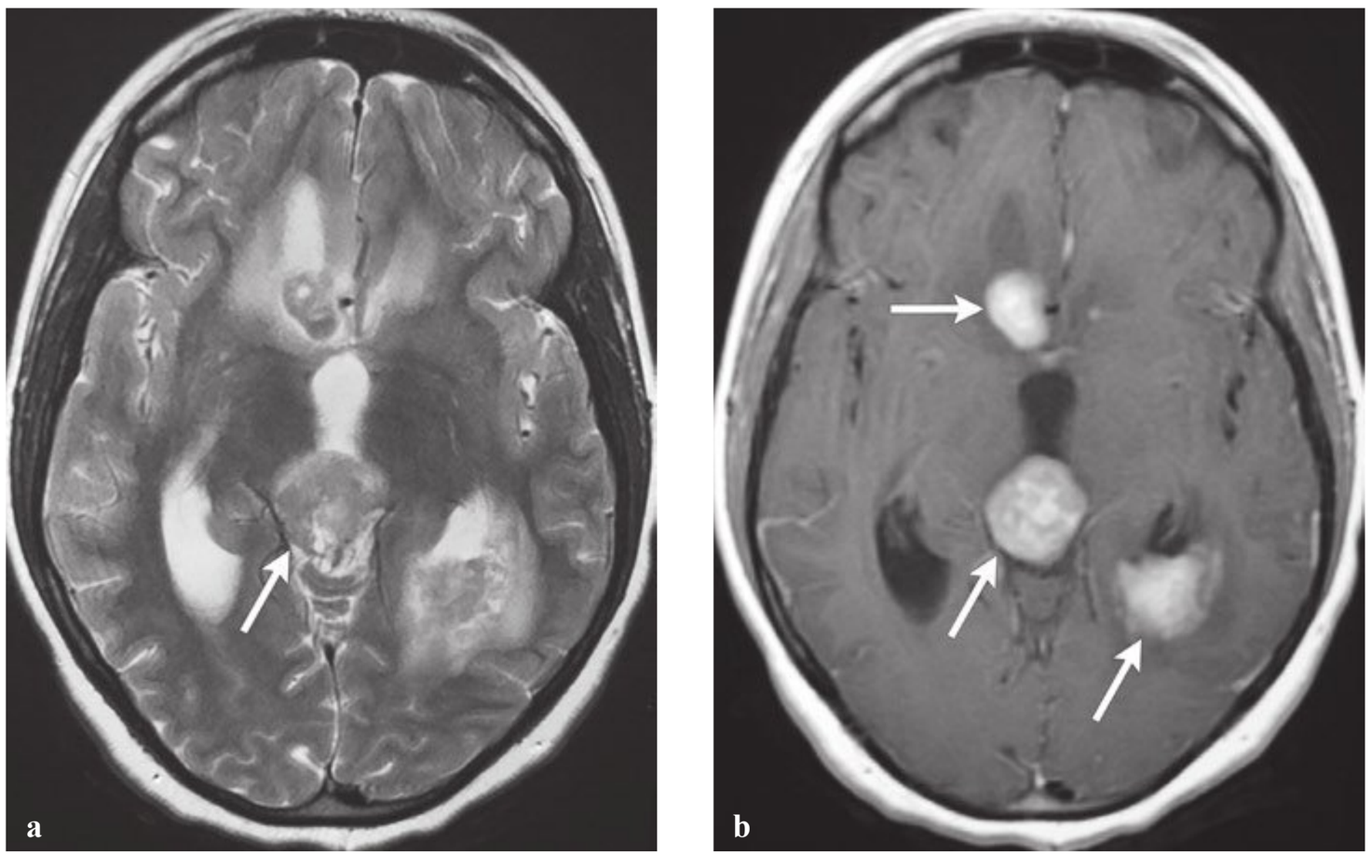

Fig. 1.473 **(a)** A 23-year-old woman with a pineal germinoma that has mixed intermediate to slightly high signal on axial T2-weighted imaging (arrow). **(b)** In addition to the pineal tumor, disseminated intraventricular nodular lesions with ependymal invasion are seen that show gadolinium contrast enhancement (arrows) on axial T1-weighted imaging.

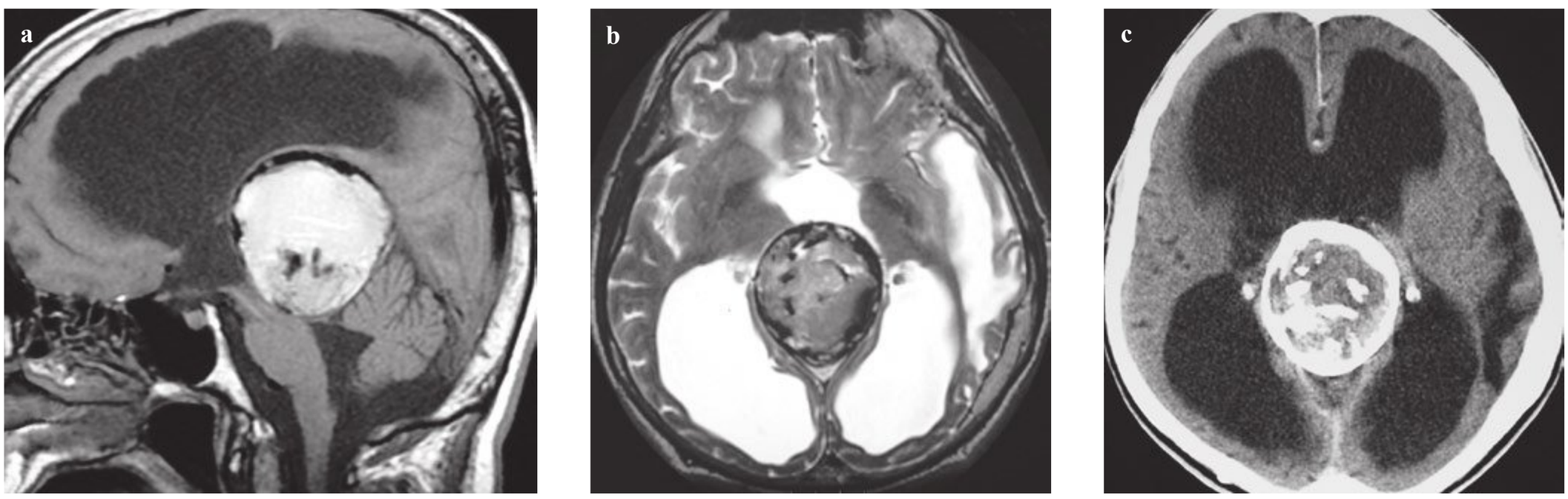

Fig. 1.474 A 56-year-old man with a pineal teratoma that has **(a)** mixed high, slightly high, and low signal on sagittal T1-weighted imaging and **(b)** mixed intermediate and low signal on axial T2-weighted imaging. **(c)** Internal foci and peripheral rim with low signal on T1- and T2-weighted imaging correspond to calcifications on axial CT.

Table 1.11 (cont.) Lesions in the pineal region

Lesions	Imaging Findings	Comments
Choriocarcinoma	MRI: Tumors often have intermediate signal on T1-weighted imaging, slightly high to high signal on T2-weighted imaging, and show gadolinium contrast enhancement, ± cysts, hemorrhage. CT: Circumscribed tumors with intermediate to slightly increased attenuation.	Tumors contain cytotrophoblastic cells and syncytiotrophoblastic giant cells that contain multiple hyperchromatic nuclei and basophilic cytoplasm. Immunoreactive to β-HCG and human placental lactogen (HPL). Elevated CSF and plasma levels of HCG.
Yolk sac tumor (**Fig. 1.475**)	MRI: Tumors often have intermediate signal on T1-weighted imaging, slightly high to high signal on T2-weighted imaging, and show gadolinium contrast enhancement, ± cysts, hemorrhage. CT: Circumscribed tumors with intermediate to slightly increased attenuation.	Tumors contain primitive epithelial cells that may contain PAS-positive eosinophilic foci within the cytoplasm. Neoplastic cells usually occur within a myxoid matrix. Immunoreactive to α-fetoprotein (AFP). Elevated serum and CSF levels of AFP.
Embryonal carcinoma (**Fig. 1.476**)	MRI: Tumors often have intermediate signal on T1-weighted imaging, slightly high to high signal on T2-weighted imaging, and show gadolinium contrast enhancement, ± cysts, ± gadolinium contrast-enhancing disseminated subarachnoid and/or intraventricular tumor. Other germ cell tumors can have mixed signal on T1- and T2-weighted imaging secondary to the presence of cysts, hemorrhage, and/or calcifications. CT: Circumscribed tumors with intermediate to slightly increased attenuation, ± disseminated contrast-enhancing leptomeningeal and/or intraventricular tumor.	Tumors contain large neoplastic cells with enlarged nucleoli, violet cytoplasm, high mitotic activity, and zones of necrosis. Immunoreacttive to cytokeratins, PLAP, and OCT4. Usually lack elevated serum and CSF levels of α-fetoprotein (AFP) and HCG.
Other Lesions Within or Adjacent to the Pineal Gland		
Pineal cyst (**Fig. 1.477**)	MRI: Spheroid or ovoid thin-walled uniloculated or multiloculated lesions that contain fluid with low signal on T1-weighted imaging and high signal on T2-weighted imaging. Fluid within the cyst can have elevated protein, which can result in intermediate to slightly high signal on T1- and T2-weighted imaging and FLAIR. Typically, no restricted diffusion. A thin rim of gadolinium contrast enhancement may be seen at the cyst wall. Delayed images may show layering of contrast within the cyst. CT: Circumscribed lesions with low attenuation, ± calcifications at cyst wall.	Cyst wall consists of an inner layer of gliotic tissue, middle layer of pineal parenchymal tissue, and outer layer of connective tissue. Seen in up to 4% of MRI examinations and 30% of autopsies. Large lesions may compress the dorsal margin of the midbrain. Most pineal cysts are asymptomatic usually when measuring less than 10 mm in diameter, but occasionally, larger cysts can be associated with headaches, hydrocephalus, abnormal extraocular movements, and Parinaud syndrome. Surgical excision is typically performed only for symptomatic patients.

(continued on page 394)

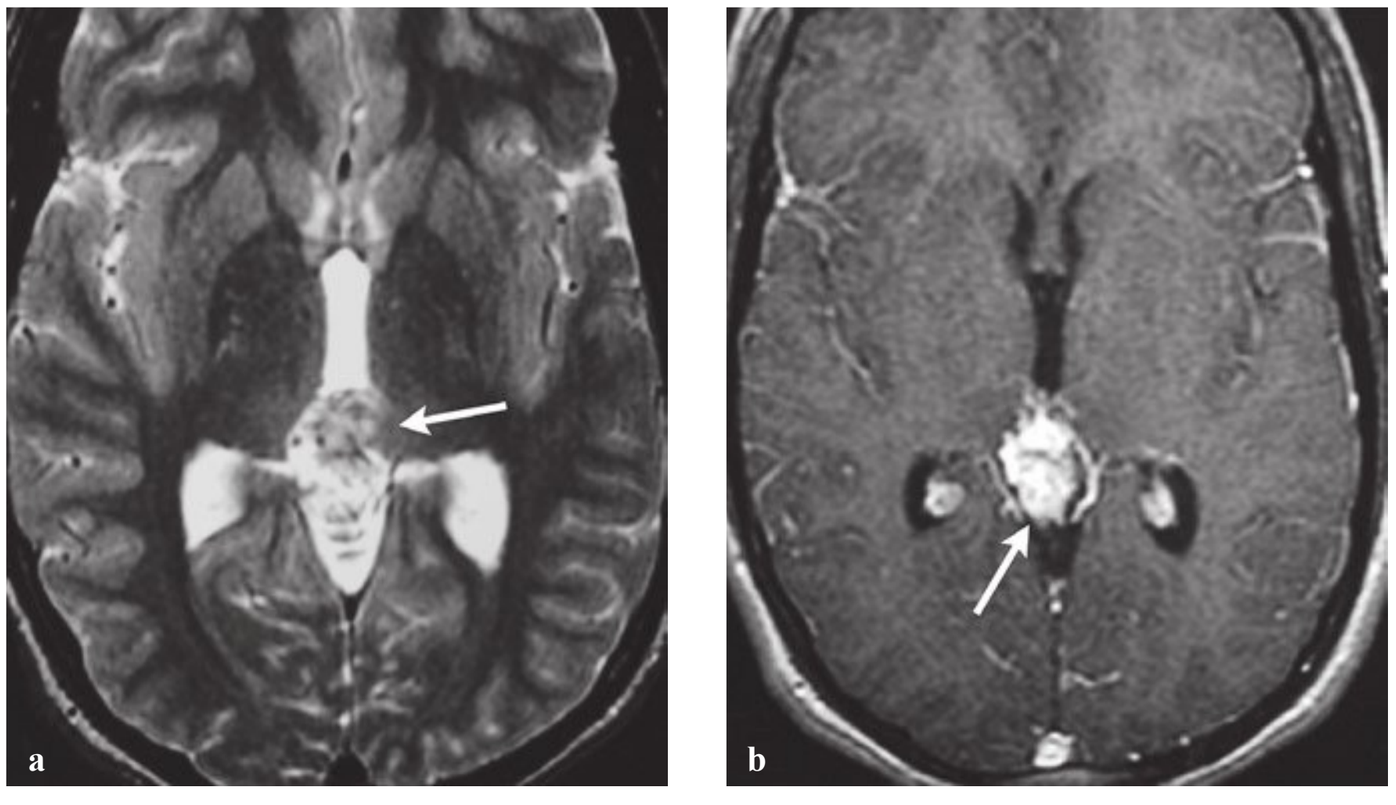

Fig. 1.475 A 15-year-old male with a pineal yolk sac tumor that has slightly lobulated margins, **(a)** mixed slightly high, high, and low signal on axial T2-weighted imaging (arrow), and **(b)** gadolinium contrast enhancement on axial T1-weighted imaging (arrow).

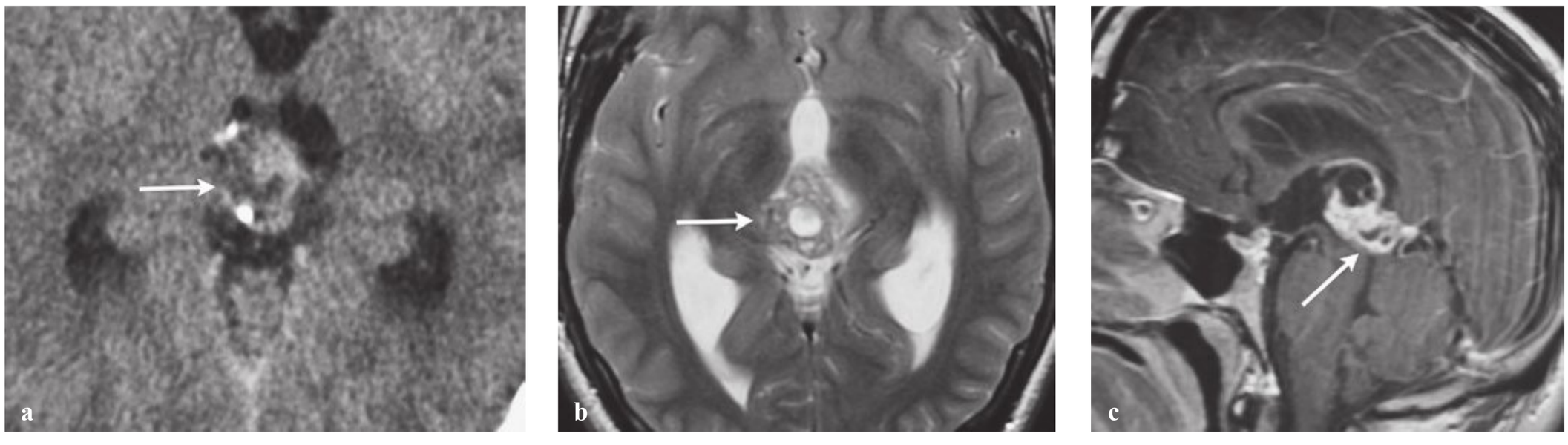

Fig. 1.476 A 34-year-old man with a pineal embryonal carcinoma that has **(a)** mixed low and intermediate attenuation with calcifications on axial CT (arrow), **(b)** mixed slightly high and high signal on axial T2-weighted imaging (arrow), and **(c)** heterogeneous gadolinium contrast enhancement on sagittal T1-weighted imaging (arrow).

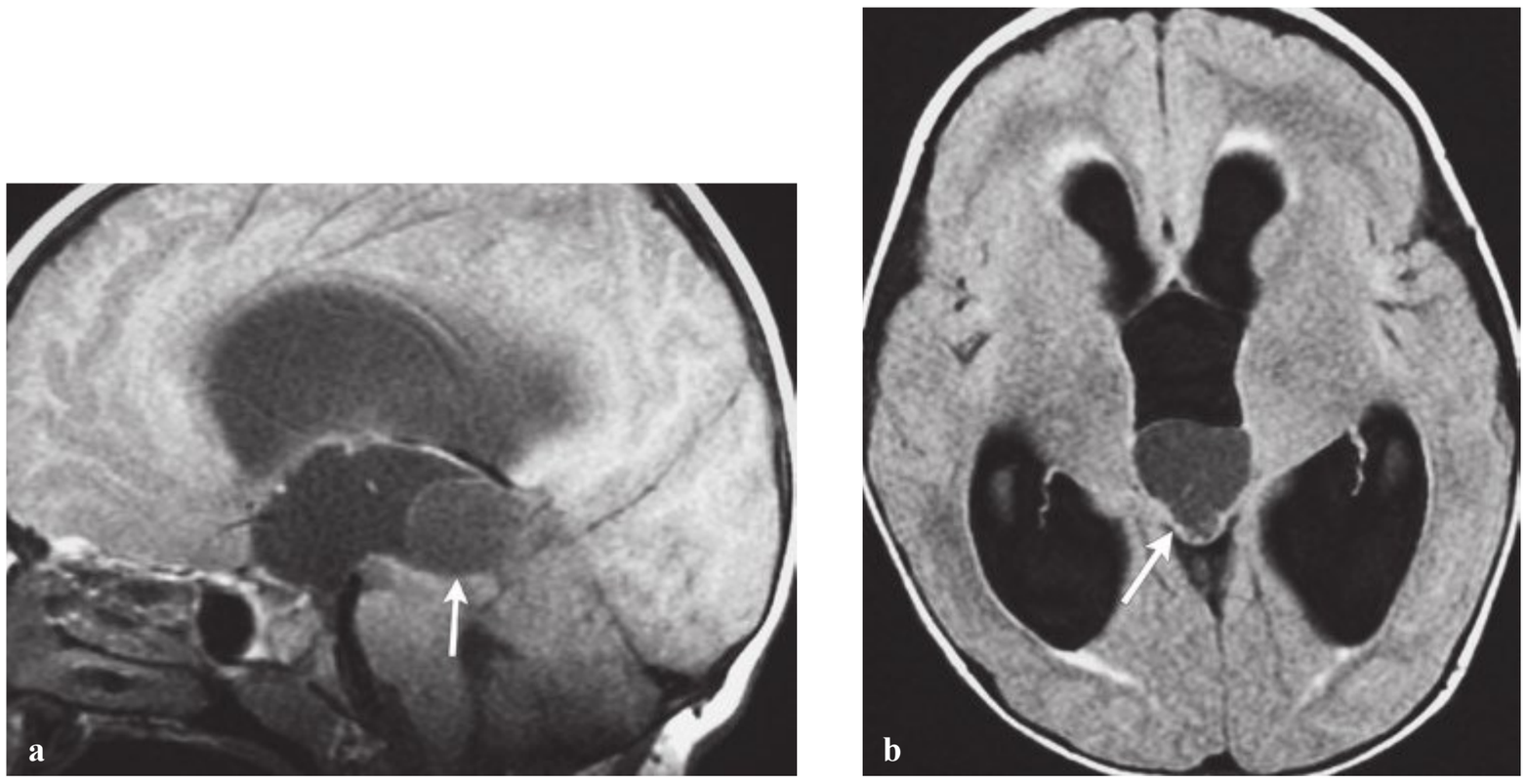

Fig. 1.477 A 4-year-old girl with a large pineal cyst compressing the tectal plate that has signal similar to CSF on **(a)** sagittal T1-weighted imaging (arrow) and **(b)** axial FLAIR (arrow). This large pineal cyst caused obstructive hydrocephalus.

Table 1.11 (cont.) Lesions in the pineal region

Lesions	Imaging Findings	Comments
Metastatic disease (**Fig. 1.478**)	MRI: Circumscribed spheroid lesions in brain, can have various intra-axial locations—often at gray–white matter junctions, usually with low-intermediate signal on T1-weighted imaging, and intermediate-high signal on T2-weighted imaging, ± hemorrhage, calcifications, and cysts. Variable gadolinium contrast enhancement, often high signal on T2-weighted imaging peripheral to nodular enhancing lesion representing axonal edema. Can occur as subarachnoid neoplastic disease seen as leptomeningeal gadolinium contrast enhancement. CT: Lesions usually have low-intermediate attenuation, ± hemorrhage, calcifications, and cysts. Variable contrast enhancement, often associated with adjacent low attenuation from axonal edema.	Metastases represent ~ 33% of intracranial tumors, usually from extracranial primary neoplasm in adults more than 40 years old. Primary tumor source: lung > breast > GI > GU > melanoma.
Pineal melanoma (**Fig. 1.479**)	MRI: Melanin-containing tumors can have slightly high to high signal on T1-weighted imaging related to the presence of melanin free radicals, which cause T1 shortening, and low to intermediate signal on T2-weighted imaging. Tumor-related hemorrhage can occur with metastatic disease. Amelanotic melanomas often have low-intermediate signal on T1-weighted imaging and slightly high to high signal on T2-weighted imaging. These neoplasms typically show gadolinium contrast enhancement, ± gadolinium contrast-enhancing disseminated subarachnoid and/or intraventricular tumor.	Malignant melanoma involving the pineal gland can result from metastatic disease, or rarely arises from melanocytic cells within the leptomeninges that are adjacent to the pineal gland. Most melanomas (90%) contain melanin, rather than being amelanotic. Patients range in age from 20 to 70 years, and more commonly are women. Prognosis is typically poor.
Meningioma (**Fig. 1.480**)	MRI: Extra-axial dural based lesions, well-circumscribed, more often supratentorial than infratentorial, with intermediate signal on T1-weighted imaging and intermediate to slightly high signal on T2-weighted imaging. Usually prominent gadolinium contrast enhancement, ± calcifications. CT: Lesions often have intermediate attenuation, usually prominent contrast enhancement, ± calcifications, ± hyperostosis of adjacent bone.	Most common extra-axial tumor, usually benign neoplasms composed of neoplastic meningothelial (arachnoidal or arachnoid cap) cells. Typically occur in adults (> 40 years old), women > men. Multiple meningiomas are seen in neurofibromatosis type 2, and can result in compression of adjacent brain parenchyma, encasement of arteries, and compression of dural venous sinuses. Rarely, meningiomas are invasive/malignant.

(continued on page 396)

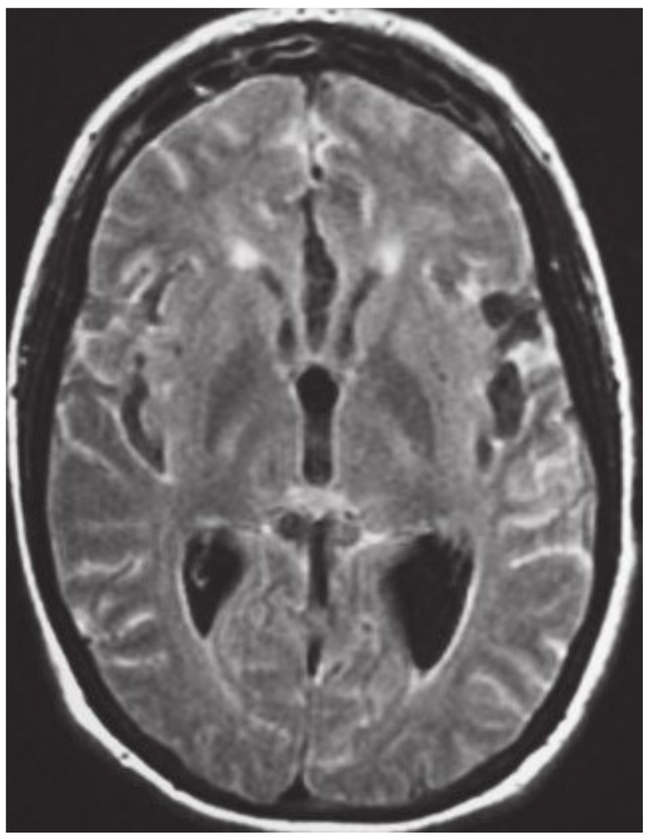

Fig. 1.478 A 27-year-old woman with disseminated intracranial melanoma seen as diffuse abnormal gadolinium contrast enhancement within the leptomeninges, ventricles, and pineal recesss.

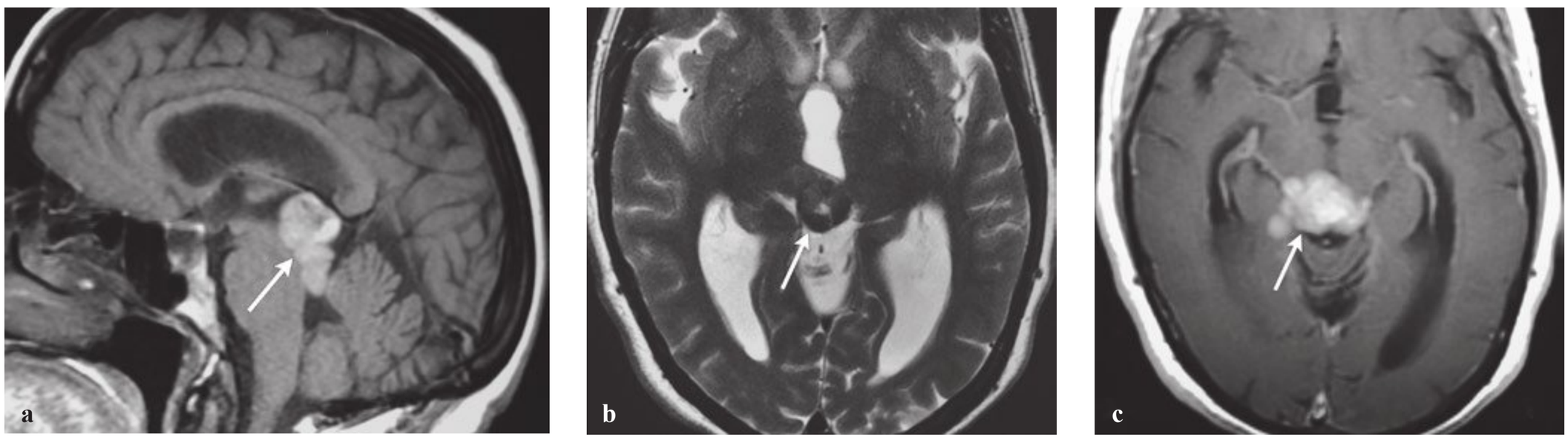

Fig. 1.479 A 65-year-old woman with a pineal melanoma that has **(a)** heterogenous high signal on sagittal T1-weighted imaging (arrow) and **(b)** mixed low and intermediate signal on axial T2-weighted imaging (arrow). **(c)** Extension of gadolinium-contrast enhancing tumor (arrow) into the medial portion of the right temporal lobe is seen on axial T1-weighted imaging (arrow).

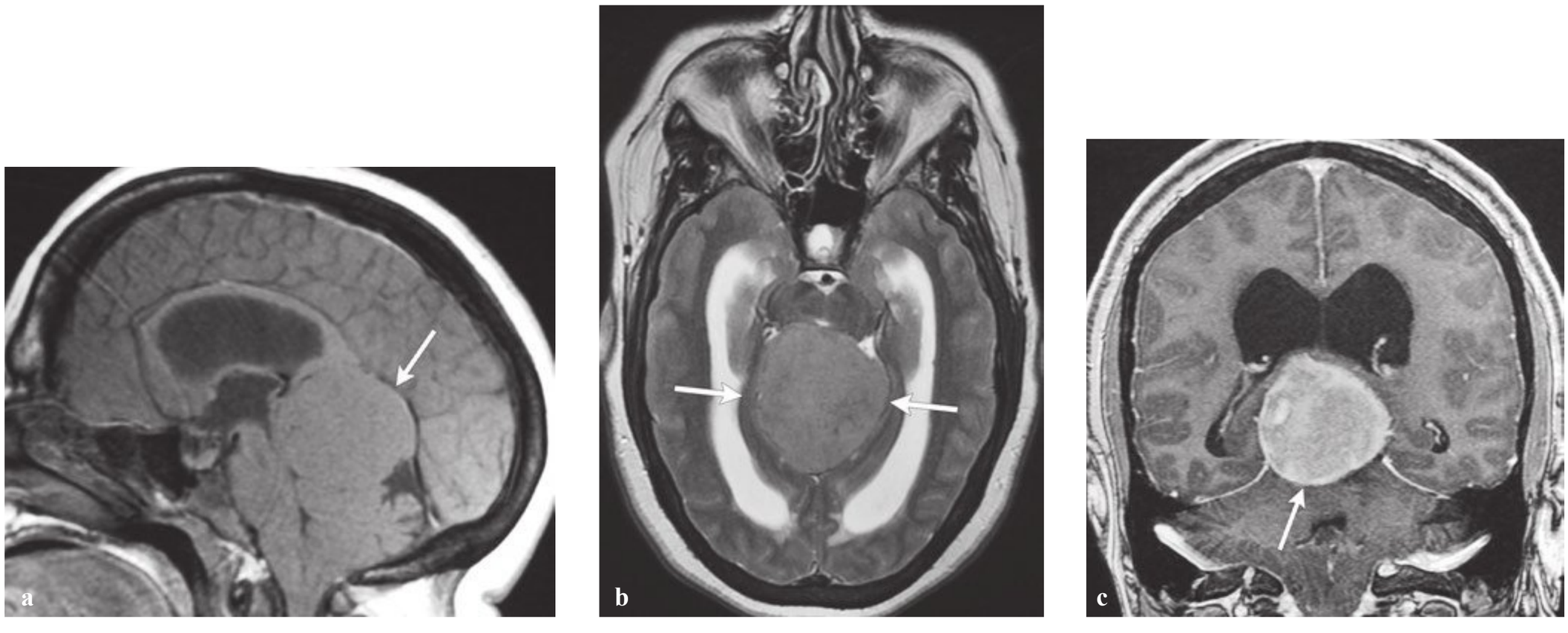

Fig. 1.480 A 45-year-old woman with a tentorial meningioma (arrows) extending into the pineal recess and compressing the tectal plate and upper cerebellar vermis, with associated cerebellar tonsilar herniation below the foramen magnum. The meningioma has intermediate signal on **(a)** sagittal T1-weighted imaging (arrow) and **(b)** axial T2-weighted imaging (arrows) and **(c)** shows gadolinium contrast enhancement on coronal T1-weighted imaging (arrow).

Table 1.11 (cont.) Lesions in the pineal region

Lesions	Imaging Findings	Comments
Primitive neuroectodermal tumor (PNET) (**Fig. 1.481**)	MRI: Circumscribed or invasive lesions with low-intermediate signal on T1-weighted imaging and intermediate-high signal on T2-weighted imaging, ± cystic or necrotic zones. Variable gadolinium contrast enhancement, usually high relative cerebral blood volume (rCBV), ± gadolinium contrast enhancement in the leptomeninges and/or ventricles from tumor dissemination. Diffusion-weighted imaging: Solid portions can have restricted diffusion. Magnetic resonance spectroscopy usually shows elevated choline, lipid, and taurine peaks and decreased N-acetylaspartate (NAA) levels. CT: Circumscribed or invasive lesions, with intermediate to slightly high attenuation, variable contrast enhancement, and frequent dissemination into the leptomeninges	Highly malignant tumors (WHO grade IV) located in the cerebrum, pineal gland, and cerebellum that frequently disseminate along CSF pathways. Tumors are composed of poorly differentiated or undifferentiated cells with divergent differentiation along neuronal, astrocytic, or ependymal lines. Typically occur in patients from 4 weeks to 20 years old; mean age = 5.5 years. Prognosis is poorer than that for medulloblastoma.
Atypical teratoid/rhabdoid tumor (AT/RT) (**Fig. 1.482**)	MRI: Circumscribed or invasive mass lesions with intermediate signal on T1-weighted imaging, ± zones of high signal from hemorrhage; variable mixed low, intermediate, and/or high signal on T2-weighted imaging. Usually prominent gadolinium contrast enhancement, ± heterogeneous pattern, ± gadolinium contrast enhancement in the leptomeninges and/or ventricles from tumor dissemination. Diffusion-weighted imaging: Solid portions can have restricted diffusion. Magnetic resonance spectroscopy usually shows elevated choline, lipid, and lactate peaks and decreased N-acetylaspartate (NAA) levels. CT: Circumscribed mass lesions with intermediate or mixed low and intermediate attenuation, ± zones of hemorrhage, cystic degeneration, and/or necrosis. Calcifications in tumors occasionally occur. Usually there is contrast enhancement, ± heterogeneous pattern, ± contrast enhancement in the leptomeninges and/or ventricles from tumor dissemination.	Rare malignant tumors (WHO grade IV) involving the CNS and usually occurring in the first decade, usually before 3 years of age. K_i-67/MIB-1 proliferation index is often high, > 50%. Associated with mutations of the INI1 (hSNF5/SMARCB1) gene on chromosome 22q11.2. Histologically appear as solid tumors ± necrotic areas, similar to malignant rhabdoid tumors of the kidney. Nearly all are intra-axial and can occur in supra- and/or infratentorial locations. Associated with a very poor prognosis.
Ependymoma (**Fig. 1.483**)	MRI: Circumscribed, lobulated lesion, ± ill-defined margins, extraventricular or intraventricular, ± cysts, calcifications, and/or hemorrhage; with low-intermediate signal on T1-weighted imaging and intermediate-high signal on T2-weighted imaging; variable gadolinium contrast enhancement. Tumors have elevated relative cerebral blood volume (rCBV) as well as delayed contrast retention secondary to intratumoral fenestrated blood vessels. Diffusion-weighted imaging: Usually no restricted diffusion. Magnetic resonance spectroscopy: Elevated choline and decreased N-acetylaspartate (NAA), similar to other neoplasms. CT: Circumscribed, lobulated lesion, extraventricular or intraventricular, ± cysts and/or calcifications (up to 50%), low-intermediate attenuation, and variable contrast enhancement.	Slow-growing tumor (WHO grade II) comprised of neoplastic cells with monomorphic round/oval nuclei containing speckled chromatin, perivascular pseudorosettes, and ependymal rosettes. Zones of myxoid degeneration, hyalinization of blood vessels, hemorrhage, and/or calcifications may occur within tumors. Account for 6 to 12% of intracranial tumors, with an incidence of 0.22 to 0.29 per 100,000. Occur more commonly in children than in adults. One-third are supratentorial, two-thirds are infratentorial. Children with infratentorial ependymomas range in age from 2 months to 16 years (mean age = 6.4 years). Supratentorial ependymomas occur in children and adults. Immunoreactive to glial fibrillary acidic protein (GFAP), S-100, vimentin, and/or EMA. Associated with neurofibromatosis type 2 and genetic mutations in chromosomes 22, 9, 6, and 3. Five-year survival is 57%; 10-year survival is 45%.

(continued on page 398)

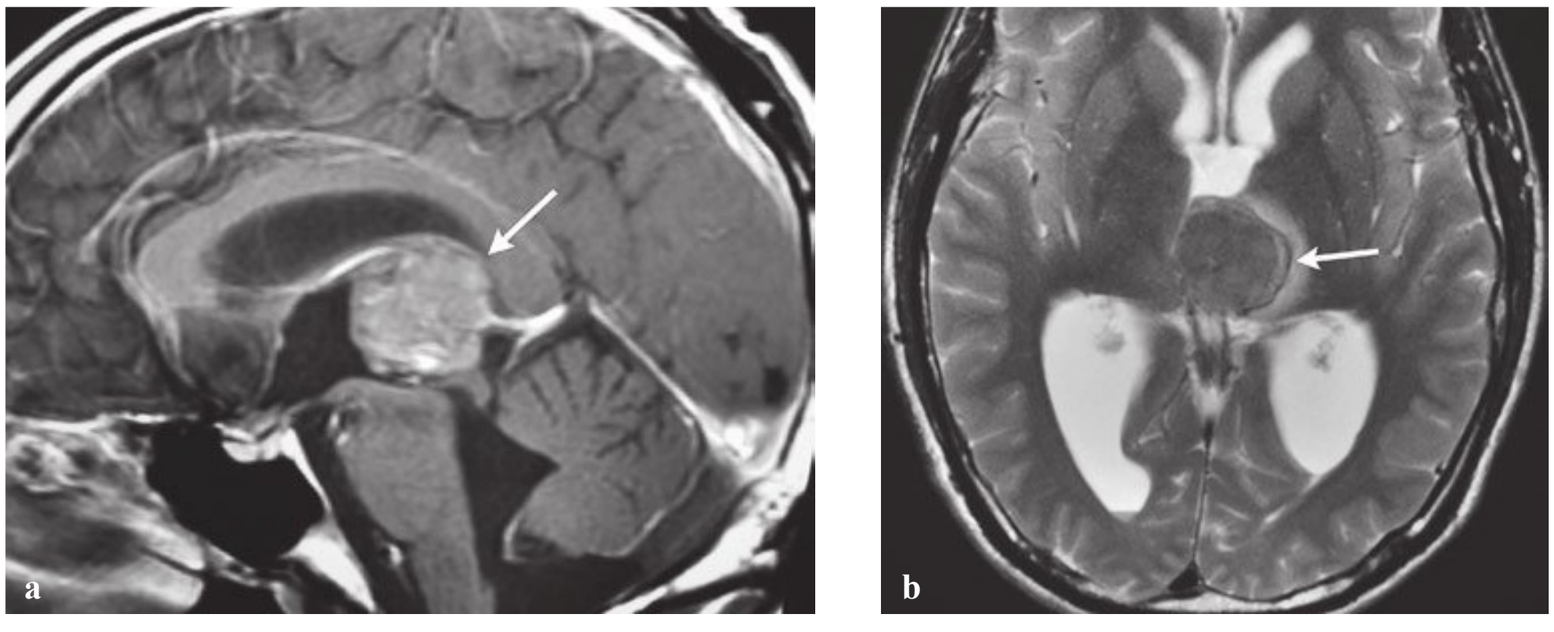

Fig. 1.481 Primitive neuroectodermal tumor (PNET) in the pineal gland in a 3-year-old boy. The tumor shows **(a)** gadolinium contrast enhancement on sagittal T1-weighted imaging (arrow) and **(b)** mostly intermediate signal on axial T2-weighted imaging (arrow). The tumor causes obstructive hydrocephalus by compression of the tectal plate and cerebral aqueduct.

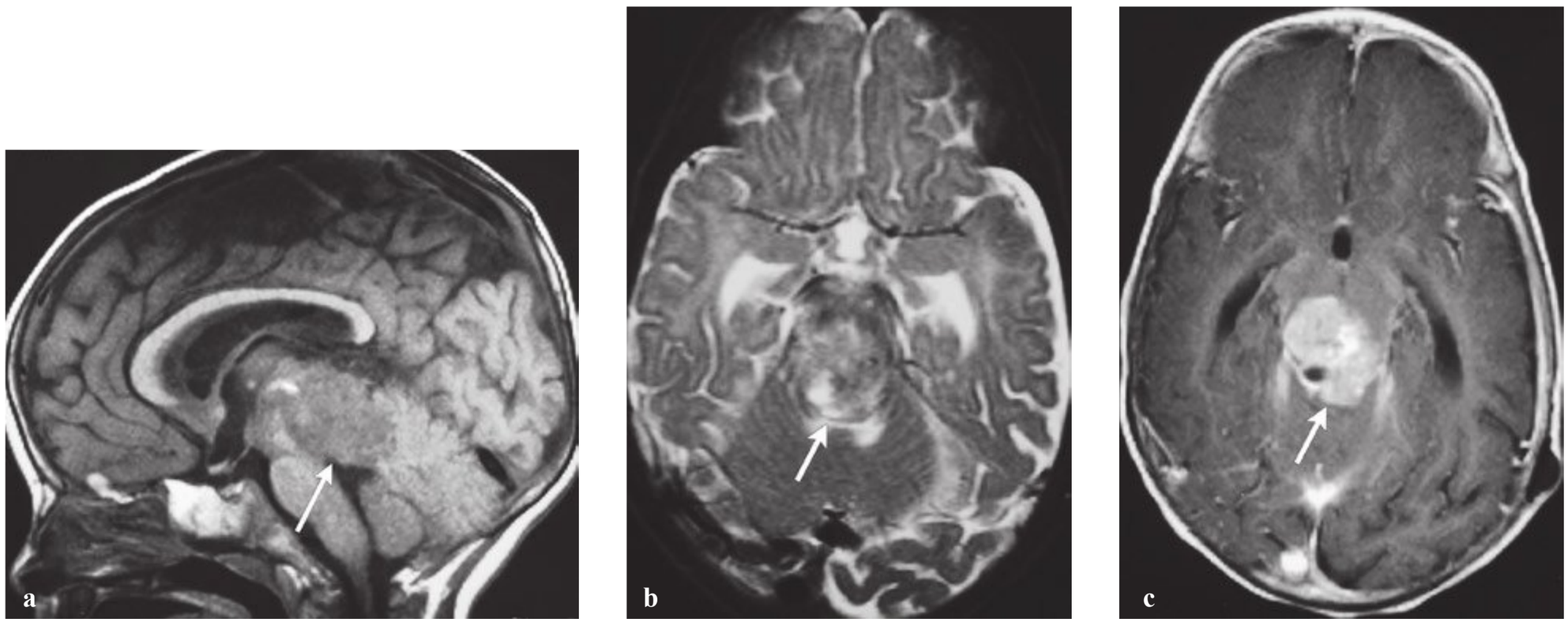

Fig. 1.482 Atypical teratoid/rhabdoid tumor (AT/RT) in the pineal gland and midbrain in a 10-month-old male. **(a)** The tumor has ill-defined margins and has mostly intermediate signal on sagittal T1-weighted imaging (arrow), **(b)** mixed intermediate, high, and low signal on axial T2-weighted imaging (arrow), and **(c)** gadolinium contrast enhancement on axial T1-weighted imaging (arrow).

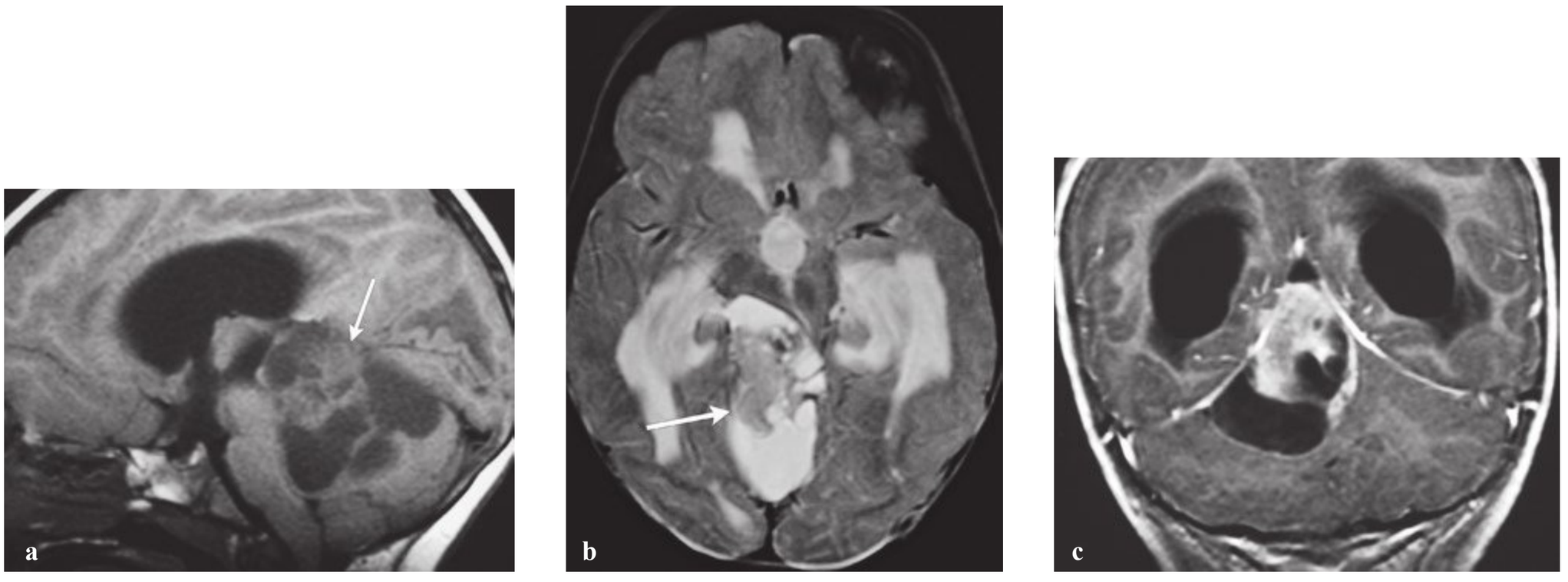

Fig. 1.483 Ependymoma in the pineal region that contains zones with **(a)** low and intermediate signal on sagittal T1-weighted imaging (arrow), **(b)** mixed slightly high and high signal on axial T2-weighted imaging (arrow), and **(c)** heterogeneous gadolinium contrast enhancement on coronal T1-weighted imaging.

Table 1.11 (cont.) Lesions in the pineal region

Lesions	Imaging Findings	Comments
Arachnoid cyst (**Fig. 1.484**)	MRI: Well-circumscribed extra-axial lesions with low signal on T1-weighted imaging, FLAIR, and diffusion-weighted imaging, and high signal on T2-weighted imaging similar to CSF. No gadolinium contrast enhancement. CT: Circumscribed extra-axial lesions with low attenuation similar to CSF. May be associated with chronic erosion of adjacent bone.	Nonneoplastic congenital, developmental, or acquired extra-axial lesions filled with CSF, usually with mild mass effect on adjacent brain, occurring in supratentorial more than in infratentorial locations, in males more than in females, ± related clinical symptoms.
Epidermoid cyst	MRI: Well-circumscribed spheroid or multilobulated extra-axial ectodermal-inclusion cystic lesions with low-intermediate signal on T1-weighted imaging, high signal on T2-weighted imaging and diffusion-weighted imaging, and low signal on ADC maps. Mixed low, intermediate, or high signal on FLAIR images. No gadolinium contrast enhancement. Commonly located in posterior cranial fossa (cerebellopontine angle cistern) more than in parasellar/middle cranial fossa. CT: Extra-axial lesions with low-intermediate attenuation, no contrast enhancement, ± bone erosion/destruction.	Nonneoplastic congenital or acquired extra-axial off-midline lesions filled with desquamated cells and keratinaceous debris, usually with mild mass effect on adjacent brain, occurring in infratentorial locations more often than in supratentorial locations; more common in adults; found equally often in males and females; ± related clinical symptoms.
Dermoid cyst	MRI: Well-circumscribed spheroid or multilobulated extra-axial lesion, usually with high signal on T1-weighted imaging and variable low, intermediate, and/or high signal on T2-weighted imaging. No gadolinium contrast enhancement, ± fluid–fluid or fluid–debris levels. Can cause chemical meningitis if dermoid cyst ruptures into the subarachnoid space. Commonly located at or near midline, more often supratentorial than infratentorial. CT: Spheroid or multilobulated extra-axial lesions, which have variable low, intermediate, and/or high attenuation and no contrast enhancement, ± fluid–fluid or fluid–debris levels.	Nonneoplastic congenital or acquired ectodermal inclusion cystic lesions filled with lipid material, cholesterol, desquamated cells, and keratinaceous debris, usually with mild mass effect on adjacent brain. Congenital dermoid and epidermoid cysts result from inclusion of surface ectoderm before the closure of the neural tube at 4 weeks of gestation. Found in adults, in males slightly more often than in females, ± related clinical symptoms.
Lipoma (**Fig. 1.485**)	MRI: Lipomas have MR signal isointense to subcutaneous fat on T1-weighted imaging (high signal), and on T2-weighted imaging, fat signal suppression occurs with frequency-selective fat saturation techniques or with a short time to inversion recovery (STIR) method. Typically there is no gadolinium contrast enhancement. CT: Low attenuation similar to subcutaneous fat.	Lipomas are benign fatty lesions resulting from congenital malformation, are often located in or near the midline, and may contain calcifications and/or may traverse blood vessels. They are usually asymptomatic unless they cause mass effect.

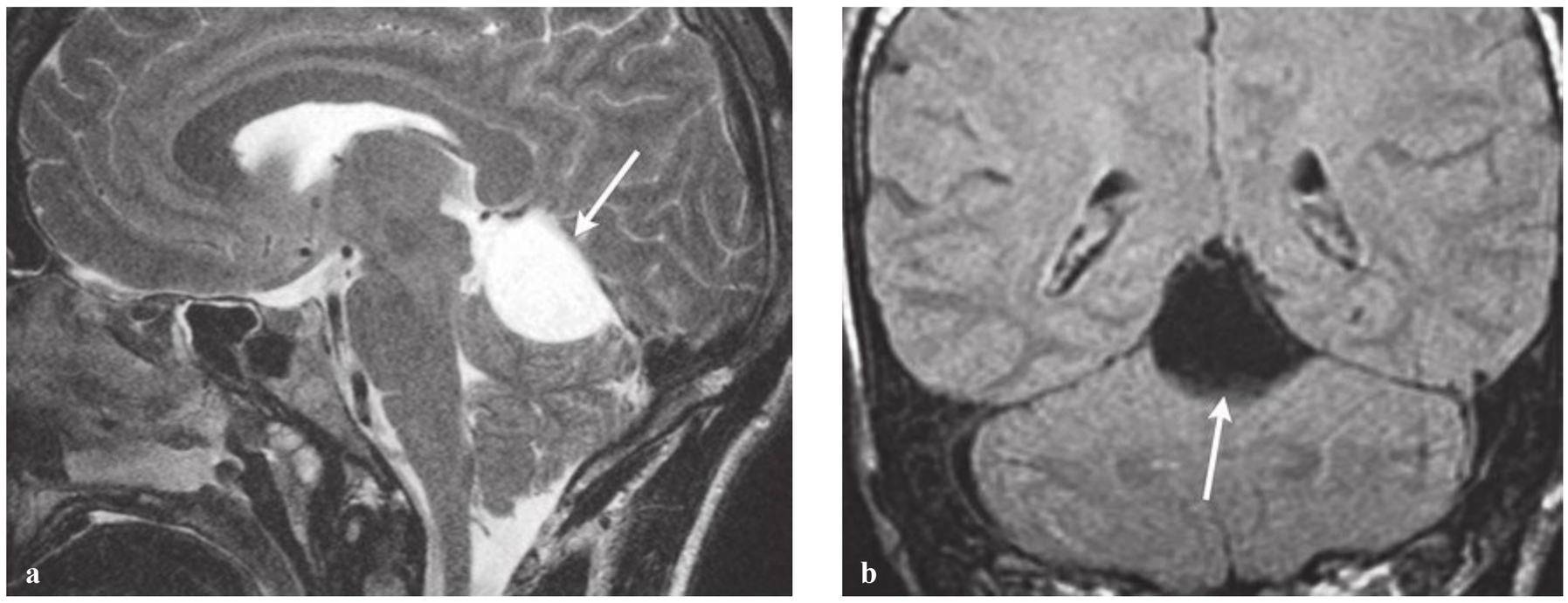

Fig. 1.484 A 23-year-old man with an arachnoid cyst in the pineal recess that has signal equal to CSF on **(a)** sagittal T2-weighted imaging (arrow) and **(b)** coronal FLAIR (arrow).

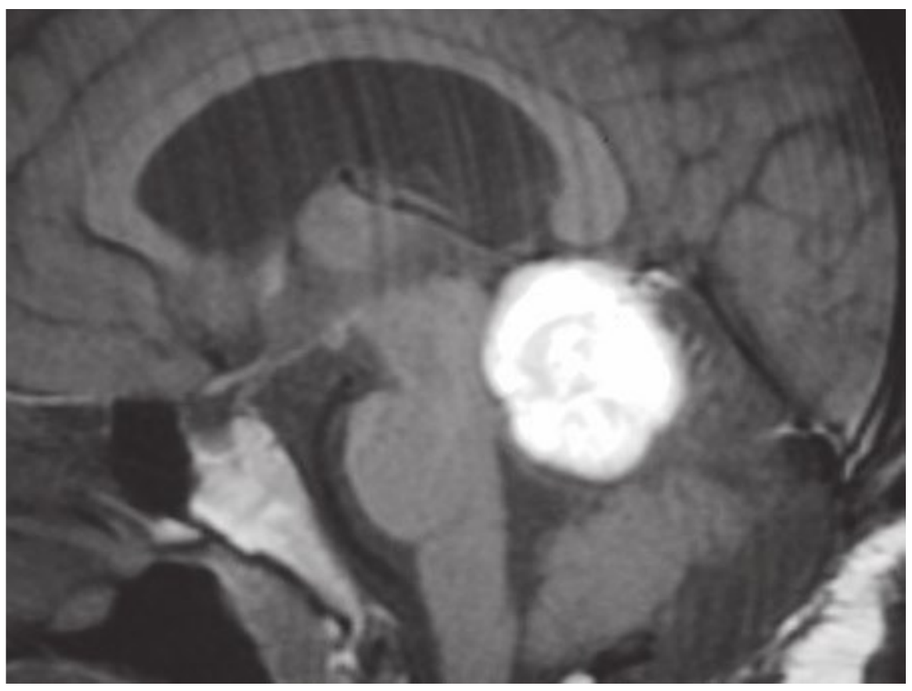

Fig. 1.485 A 40-year-old woman with a lipoma involving the pineal gland that has high signal on sagittal T1-weighted imaging.

References

Acute Demyelination—Acute Disseminated Encephalomyelitis

1. Absoud M, Lim MJ, Chong WK, et al; UK and Ireland Childhood CNS Inflammatory Demyelination Working Group. Paediatric acquired demyelinating syndromes: incidence, clinical and magnetic resonance imaging features. Mult Scler 2013;19(1):76–86
2. Rossi A. Imaging of acute disseminated encephalomyelitis. Neuroimaging Clin N Am 2008;18(1):149–161, ix ix
3. Lim CC. Neuroimaging in postinfectious demyelination and nutritional disorders of the central nervous system. Neuroimaging Clin N Am 2011;21(4):843–858, viii
4. Tenembaum S, Chitnis T, Ness J, Hahn JS; International Pediatric MS Study Group. Acute disseminated encephalomyelitis. Neurology 2007;68(16, Suppl 2):S23–S36

Acute Demyelination—Multiple Sclerosis

5. Lucchinetti CF, Gavrilova RH, Metz I, et al. Clinical and radiographic spectrum of pathologically confirmed tumefactive multiple sclerosis. Brain 2008;131(Pt 7):1759–1775
6. Saini J, Chatterjee S, Thomas B, Kesavadas C. Conventional and advanced magnetic resonance imaging in tumefactive demyelination. Acta Radiol 2011;52(10):1159–1168

Adrenoleukodystrophy

7. Barkovich AJ, Ferriero DM, Bass N, Boyer R. Involvement of the pontomedullary corticospinal tracts: a useful finding in the diagnosis of X-linked adrenoleukodystrophy. AJNR Am J Neuroradiol 1997;18(1):95–100
8. Dubey P, Fatemi A, Huang H, et al. Diffusion tensor-based imaging reveals occult abnormalities in adrenomyeloneuropathy. Ann Neurol 2005;58(5):758–766
9. Eichler FS, Itoh R, Barker PB, et al. Proton MR spectroscopic and diffusion tensor brain MR imaging in X-linked adrenoleukodystrophy: initial experience. Radiology 2002;225(1):245–252
10. Eichler FS, Barker PB, Cox C, et al. Proton MR spectroscopic imaging predicts lesion progression on MRI in X-linked adrenoleukodystrophy. Neurology 2002;58(6):901–907
11. Hung KL, Wang JS, Keng WT, et al. Mutational analyses on X-linked adrenoleukodystrophy reveal a novel cryptic splicing and three missense mutations in the ABCD1 gene. Pediatr Neurol 2013;49(3):185–190
12. Kim JH, Kim HJ. Childhood X-linked adrenoleukodystrophy: clinical-pathologic overview and MR imaging manifestations at initial evaluation and follow-up. Radiographics 2005;25(3):619–631
13. Loes DJ, Fatemi A, Melhem ER, et al. Analysis of MRI patterns aids prediction of progression in X-linked adrenoleukodystrophy. Neurology 2003;61(3):369–374
14. Mo YH, Chen YF, Liu HM. Adrenomyeloneuropathy, a dynamic progressive disorder: brain magnetic resonance imaging of two cases. Neuroradiology 2004;46(4):296–300
15. Öz G, Tkác I, Charnas LR, et al. Assessment of adrenoleukodystrophy lesions by high field MRS in non-sedated pediatric patients. Neurology 2005;64(3):434–441
16. Schneider JFL, Il'yasov KA, Boltshauser E, Hennig J, Martin E. Diffusion tensor imaging in cases of adrenoleukodystrophy: preliminary experience as a marker for early demyelination? AJNR Am J Neuroradiol 2003;24(5):819–824
17. Sener RN. Atypical X-linked adrenoleukodystrophy: new MRI observations with FLAIR, magnetization transfer contrast, diffusion MRI, and proton spectroscopy. Magn Reson Imaging 2002;20(2):215–219
18. van der Knaap M, Valk J. X-linked adrenoleukodystrophy. In: van der Knaap MS, Valk J, eds. Magnetic Resonance of Myelination and Myelin Disorders. 3rd ed. New York: Springer; 2005:176–190
19. Wiesinger C, Kunze M, Regelsberger G, Forss-Petter S, Berger J. Impaired very long-chain acyl-CoA b-oxidation in human X-linked adrenoleukodystrophy fibroblasts is a direct consequence of ABCD1 transporter dysfunction. J Biol Chem 2013;288(26):19269–19279

Adrenomyeloneuropathy

20. Mo YH, Chen YF, Liu HM. Adrenomyeloneuropathy, a dynamic progressive disorder: brain magnetic resonance imaging of two cases. Neuroradiology 2004;46(4):296–300
21. Powers JM, DeCiero DP, Cox C, et al. The dorsal root ganglia in adrenomyeloneuropathy: neuronal atrophy and abnormal mitochondria. J Neuropathol Exp Neurol 2001;60(5):493–501

Alcohol-Induced Changes

22. Gass JT, Olive MF. Neurochemical and neurostructural plasticity in alcoholism. ACS Chem Neurosci 2012;3(7):494–504
23. Geibprasert S, Gallucci M, Krings T. Alcohol-induced changes in the brain as assessed by MRI and CT. Eur Radiol 2010;20(6):1492–1501
24. Hill SY, Terwilliger R, McDermott M. White matter microstructure, alcohol exposure, and familial risk for alcohol dependence. Psychiatry Res 2013;212(1):43–53
25. Hillbom M, Saloheimo S, Fujioka S, et al. Diagnosis and management of Marchiafava-Bignami disease: a review of CT/MRI confirmed cases. J Neurol Neurosurg Psychiatry 2014;85(2):168–173
26. Konrad A, Vucurevic G, Lorscheider M, et al. Broad disruption of brain white matter microstructure and relationship with neuropsychological performance in male patients with severe alcohol dependence. Alcohol Alcohol 2012;47(2):118–126

Alexander Disease

27. Barkovich AJ, Messing A. Alexander disease: not just a leukodystrophy anymore. Neurology 2006;66(4):468–469
28. Bassuk AG, Joshi A, Burton BK, Larsen MB, Burrowes DM, Stack C. Alexander disease with serial MRS and a new mutation in the glial fibrillary acidic protein gene. Neurology 2003;61(7):1014–1015
29. Brockmann K, Dechent P, Meins M, et al. Cerebral proton magnetic resonance spectroscopy in infantile Alexander disease. J Neurol 2003;250(3):300–306
30. Johnson AB, Brenner M. Alexander's disease: clinical, pathologic, and genetic features. J Child Neurol 2003;18(9):625–632
31. Moser HW. Alexander disease: combined gene analysis and MRI clarify pathogenesis and extend phenotype. Ann Neurol 2005;57(3):307–308
32. Ni Q, Johns GS, Manepalli A, Martin DS, Geller TJ. Infantile Alexander's disease: serial neuroradiologic findings. J Child Neurol 2002;17(6):463–466
33. Pareyson D, Fancellu R, Mariotti C, et al. Adult-onset Alexander disease: a series of eleven unrelated cases with review of the literature. Brain 2008;131(Pt 9):2321–2331
34. Poloni CB, Ferey S, Haenggeli CA, et al. Alexander disease: early presence of cerebral MRI criteria. Eur J Paediatr Neurol 2009;13(6):556–558
35. Probst EN, Hagel C, Weisz V, et al. Atypical focal MRI lesions in a case of juvenile Alexander's disease. Ann Neurol 2003;53(1):118–120
36. van der Knaap MS, Ramesh V, Schiffmann R, et al. Alexander disease: ventricular garlands and abnormalities of the medulla and spinal cord. Neurology 2006;66(4):494–498
37. van der Knaap MS, Salomons GS, Li R, et al. Unusual variants of Alexander's disease. Ann Neurol 2005;57(3):327–338
38. van der Knaap MS, Naidu S, Breiter SN, et al. Alexander disease: diagnosis with MR imaging. AJNR Am J Neuroradiol 2001;22(3):541–552
39. van der Knaap M, Valk J. Alexander disease In: van der Knaap MS, Valk J, eds. Magnetic Resonance of Myelination and Myelin Disorders. 3rd ed. New York: Springer; 2005:416–435

Alzheimer Disease

40. Adlard PA, Tran BA, Finkelstein DI, et al. A review of b-amyloid neuroimaging in Alzheimer's disease. Front Neurosci 2014;8:327
41. Becker GA, Ichise M, Barthel H, et al. PET quantification of 18F-florbetaben binding to b-amyloid deposits in human brains. J Nucl Med 2013;54(5):723–731
42. Benzinger TLS. Radiologic approach to Alzheimer's disease and other dementias: the emerging role of diffusion tensor magnetic resonance imaging. Appl Radiol 2005;34(1):25–33
43. Goto H, Ishii K, Uemura T, et al. Differential diagnosis of dementia with Lewy Bodies and Alzheimer Disease using combined MR imaging and brain perfusion single-photon emission tomography. AJNR Am J Neuroradiol 2010;31(4):720–725
44. Karantzoulis S, Galvin JE. Distinguishing Alzheimer's disease from other major forms of dementia. Expert Rev Neurother 2011;11(11):1579–1591
45. Nelson PT, Alafuzoff I, Bigio EH, et al. Correlation of Alzheimer disease neuropathologic changes with cognitive status: a review of the literature. J Neuropathol Exp Neurol 2012;71(5):362–381

46. Sabri O, Seibyl J, Rowe C, Barthel H. Beta-amyloid imaging with florbetaben. Clin Transl Imaging 2015;3(1):13–26
47. Vallabhajosula S. Positron emission tomography radiopharmaceuticals for imaging brain Beta-amyloid. Semin Nucl Med 2011; 41(4):283–299
48. Whitwell JL, Shiung MM, Przybelski SA, et al. MRI patterns of atrophy associated with progression to AD in amnestic mild cognitive impairment. Neurology 2008;70(7):512–520

Amyloidoma

49. Foreid H, Barroso C, Evangelista T, Campos A, Pimentel J. Intracerebral amyloidoma: case report and review of the literature. Clin Neuropathol 2010;29(4):217–222
50. Gallucci M, Caulo M, Splendiani A, Russo R, Ricci A, Galzio R. Neuroradiological findings in two cases of isolated amyloidoma of the central nervous system. Neuroradiology 2002;44(4):333–337
51. Gandhi D, Wee R, Goyal M. CT and MR imaging of intracerebral amyloidoma: case report and review of the literature. AJNR Am J Neuroradiol 2003;24(3):519–522
52. Nossek E, Bashat DB, Artzi M, et al. The role of advanced MR methods in the diagnosis of cerebral amyloidoma. Amyloid 2009;16(2): 94–98
53. Ragel BT, Blumenthal DT, Browd SR, Salzman KL, Jensen RL. Intracerebral amyloidoma can mimic high-grade glioma on magnetic resonance imaging and spectroscopy. Arch Neurol 2006;63(6):906–907
54. Renard D, Campello C, Rigau V, de Champfleur N, Labauge P. Primary brain amyloidoma: long-term follow-up. Arch Neurol 2008;65(7):979–980
55. Tabatabai G, Baehring J, Hochberg FH. Primary amyloidoma of the brain parenchyma. Arch Neurol 2005;62(3):477–480
56. Vital A, Ellie E, Loiseau H. A 61-year-old man with instability of gait and right hand clumsiness. Brain Pathol 2010;20(1):273–274

Amyotrophic Lateral Sclerosis (ALS)

57. Ciccarelli O, Behrens TE, Johansen-Berg H, et al. Investigation of white matter pathology in ALS and PLS using tract-based spatial statistics. Hum Brain Mapp 2009;30(2):615–624
58. Charil A, Corbo M, Filippi M, et al. Structural and metabolic changes in the brain of patients with upper motor neuron disorders: a multiparametric MRI study. Amyotroph Lateral Scler 2009;10(5-6):269–279
59. da Rocha AJ, Oliveira ASB, Fonseca RB, Maia ACM Jr, Buainain RP, Lederman HM. Detection of corticospinal tract compromise in amyotrophic lateral sclerosis with brain MR imaging: relevance of the T1-weighted spin-echo magnetization transfer contrast sequence. AJNR Am J Neuroradiol 2004;25(9):1509–1515
60. Iwata NK. [Objective markers for upper motor neuron involvement in amyotrophic lateral sclerosis]. Brain Nerve 2007;59(10):1053–1064
61. Turner MR, Agosta F, Bede P, Govind V, Lulé D, Verstraete E. Neuroimaging in amyotrophic lateral sclerosis. Biomarkers Med 2012;6(3):319–337
62. Wang S, Poptani H, Woo JH, et al. Amyotrophic lateral sclerosis: diffusion-tensor and chemical shift MR imaging at 3.0 T. Radiology 2006;239(3):831–838

Anaplastic Astrocytoma

63. Faehndrich J, Weidauer S, Pilatus U, Oszvald A, Zanella FE, Hattingen E. Neuroradiological viewpoint on the diagnostics of space-occupying brain lesions. Clin Neuroradiol 2011;21(3):123–139
64. Holodny AI, Makeyev S, Beattie BJ, Riad S, Blasberg RG. Apparent diffusion coefficient of glial neoplasms: correlation with fluorodeoxyglucose-positron-emission tomography and gadolinium-enhanced MR imaging. AJNR Am J Neuroradiol 2010;31(6):1042–1048
65. Kleihues P, Burger PC, Rosenblum MK, Paulus W, Scheithauer BW. Anaplastic astrocytoma. In: Louis DN, Ohgaki H, Wiestler OD, Cavenee WK, eds. World Health Organization Classification of Tumours of the Central Nervous System. 4th ed. Geneva: IARC Press; 2007:30–32

Anaplastic Ependymoma

66. Alexiou GA, Panagopoulos D, Moschovi M, Stefanaki K, Sfakianos G, Prodromou N. Supratentorial extraventricular anaplastic ependymoma in a 10-year-old girl. Pediatr Neurosurg 2010;46(6):480–481
67. McLendon RE, Wiestler OD, Kros JM, Korshunov A, Ng HK. Anaplastic ependymoma. In: Louis DN, Ohgaki H, Wiestler OD, Cavenee WK, eds. World Health Organization Classification of Tumours of the Central Nervous System. 4th ed. Geneva: IARC Press; 2007:79–80 Anaplastic Oligoastrocytoma
68. Reifenberger G, Kros JM, Louis DN, Collins VP. Anaplastic oligodendroglioma. In: Louis DN, Ohgaki H, Wiestler OD, Cavenee WK, eds. World Health Organization Classification of Tumours of the Central Nervous System. 4th ed. Geneva: IARC Press; 2007:60–62
69. von Deimling A, Reifenberger G, Kros JM, Louis DN, Collins VP. Anaplastic oligoastrocytoma. In: Louis DN, Ohgaki H, Wiestler OD, Cavenee WK, eds. World Health Organization Classification of Tumours of the Central Nervous System. 4th ed. Geneva: IARC Press; 2007:66–67

Anaplastic Oligodendroglioma

70. Reifenberger G, Kros JM, Louis DN, Collins VP. Anaplastic oligodendroglioma. In: Louis DN, Ohgaki H, Wiestler OD, Cavenee WK, eds. World Health Organization Classification of Tumours of the Central Nervous System. 4th ed. Geneva: IARC Press; 2007:60–62 Arhinia
71. Brusati R, Donati V, Marelli S, Ferrari M. Management of a case of arhinia. J Plast Reconstr Aesthet Surg 2009;62(7):e206–e210
72. Sato D, Shimokawa O, Harada N, et al. Congenital arhinia: molecular-genetic analysis of five patients. Am J Med Genet A 2007;143A(6): 546–552
73. Zhang MM, Hu YH, He W, Hu KK. Congenital arhinia: A rare case. Am J Case Rep 2014;15:115–118

Arterial Ischemic Stroke in Adults

74. Adams HP Jr, Bendixen BH, Kappelle LJ, et al. Classification of subtype of acute ischemic stroke. Definitions for use in a multicenter clinical trial. TOAST. Trial of Org 10172 in Acute Stroke Treatment. Stroke 1993;24(1):35–41
75. Allmendinger AM, Tang ER, Lui YW, Spektor V. Imaging of stroke: Part 1, Perfusion CT—overview of imaging technique, interpretation pearls, and common pitfalls. AJR Am J Roentgenol 2012;198(1):52–62
76. Eastwood JD, Lev MH, Provenzale JM. Perfusion CT with iodinated contrast material. AJR Am J Roentgenol 2003;180(1):3–12
77. Eskey CJ, Sanelli PC. Perfusion imaging of cerebrovascular reserve. Neuroimaging Clin N Am 2005;15(2):367–381, xi
78. Grant PE, Yu D. Acute injury to the immature brain with hypoxia with or without hypoperfusion. Magn Reson Imaging Clin N Am 2006;14(2):271–285
79. Huang BY, Castillo M. Hypoxic-ischemic brain injury: imaging findings from birth to adulthood. Radiographics 2008;28(2):417–439, quiz 617
80. Kanekar SG, Zacharia T, Roller R. Imaging of stroke: Part 2, Pathophysiology at the molecular and cellular levels and corresponding imaging changes. AJR Am J Roentgenol 2012;198(1):63–74
81. Kucinski T. Unenhanced CT and acute stroke physiology. Neuroimaging Clin N Am 2005;15(2):397–407, xi–xii
82. Lee LJ, Kidwell CS, Alger J, Starkman S, Saver JL. Impact on stroke subtype diagnosis of early diffusion-weighted magnetic resonance imaging and magnetic resonance angiography. Stroke 2000; 31(5):1081–1089
83. Marks MP. Cerebral ischemia and infarction. In: Atlas SW, ed. Magnetic Resonance Imaging of the Brain and Spine. 4th ed. Philadelphia: Lippincott Williams & Wilkins; 2009:772–825
84. Ratai EM, Gonzalez RG. Magnetic resonance spectroscopy and the biochemical basis of neurologic disease. In: Atlas SW, ed. Magnetic Resonance Imaging of the Brain and Spine. 4th ed. Philadelphia: Lippincott Williams & Wilkins; 2009:1836–1870
85. Shetty SK, Lev MH. CT perfusion in acute stroke. Neuroimaging Clin N Am 2005;15(3):481–501, ix
86. Wessels T, Wessels C, Ellsiepen A, et al. Contribution of diffusion-weighted imaging in determination of stroke etiology. AJNR Am J Neuroradiol 2006;27(1):35–39

Arterial Ischemic Stroke in Children

87. Barkovich AJ. Brain and spine injuries in infancy and childhood. In: Pediatric Neuroimaging. 4th ed. Philadelphia: Lippincott Williams & Wilkins; 2005:190–290
88. Husson B, Lasjaunias P. Radiological approach to disorders of arterial brain vessels associated with childhood arterial stroke-a comparison between MRA and contrast angiography. Pediatr Radiol 2004;34(1):10–15
89. Kimchi TJ, Agid R, Lee SK, Ter Brugge KG. Arterial ischemic stroke in children. Neuroimaging Clin N Am 2007;17(2):175–187

Astroblastoma

90. Aldape KD, Rosenblum MK. Astroblastoma. In: Louis DN, Ohgaki H, Wiestler OD, Cavenee WK, eds. World Health Organization Classification of Tumours of the Central Nervous System. 4th ed. Geneva: IARC Press; 2007:88–89
91. Bell JW, Osborn AG, Salzman KL, Blaser SI, Jones BV, Chin SS. Neuroradiologic characteristics of astroblastoma. Neuroradiology 2007;49(3):203–209
92. Kantar M, Ertan Y, Turhan T, et al. Anaplastic astroblastoma of childhood: aggressive behavior. Childs Nerv Syst 2009;25(9):1125–1129
93. Salvati M, D'Elia A, Brogna C, et al. Cerebral astroblastoma: analysis of six cases and critical review of treatment options. J Neurooncol 2009;93(3):369–378

Ataxia-Telangiectasia

94. Firat AK, Karakaş HM, Firat Y, Yakinci C. Quantitative evaluation of brain involvement in ataxia telangiectasia by diffusion weighted MR imaging. Eur J Radiol 2005;56(2):192–196
95. Lin DDM, Barker PB, Lederman HM, Crawford TO. Cerebral abnormalities in adults with ataxia-telangiectasia. AJNR Am J Neuroradiol 2014;35(1):119–123
96. Palau F, Espinós C. Autosomal recessive cerebellar ataxias. Orphanet J Rare Dis 2006;1:47
97. Tavani F, Zimmerman RA, Berry GT, Sullivan K, Gatti R, Bingham P. Ataxia-telangiectasia: the pattern of cerebellar atrophy on MRI. Neuroradiology 2003;45(5):315–319
98. Wallis LI, Griffiths PD, Ritchie SJ, Romanowski CAJ, Darwent G, Wilkinson ID. Proton spectroscopy and imaging at 3T in ataxia-telangiectasia. AJNR Am J Neuroradiol 2007;28(1):79–83

Atypical Teratoid/Rhabdoid Tumor

99. Han L, Qiu Y, Xie C, et al. Atypical teratoid/rhabdoid tumors in adult patients: CT and MR imaging features. AJNR Am J Neuroradiol 2011;32(1):103–108
100. Judkins AR, Eberhart CG, Wesseling P. Atypical teratoid/rhabdoid tumour. In: Louis DN, Ohgaki H, Wiestler OD, Cavenee WK, eds. World Health Organization Classification of Tumours of the Central Nervous System. 4th ed. Geneva: IARC Press; 2007:147–149
101. Meyers SP, Khademian ZP, Biegel JA, Chuang SH, Korones DN, Zimmerman RA. Primary intracranial atypical teratoid/rhabdoid tumors of infancy and childhood: MRI features and patient outcomes. AJNR Am J Neuroradiol 2006;27(5):962–971
102. Warmuth-Metz M, Bison B, Dannemann-Stern E, Kortmann R, Rutkowski S, Pietsch T. CT and MR imaging in atypical teratoid/rhabdoid tumors of the central nervous system. Neuroradiology 2008;50(5):447–452

Basal Ganglia and Thalami—Functional Anatomy

103. Arsalidou M, Duerden EG, Taylor MJ. The centre of the brain: topographical model of motor, cognitive, affective, and somatosensory functions of the basal ganglia. Hum Brain Mapp 2013;34(11):3031–3054
104. Herrero MT, Barcia C, Navarro JM. Functional anatomy of thalamus and basal ganglia. Childs Nerv Syst 2002;18(8):386–404
105. Telford R, Vattoth S. MR anatomy of deep brain nuclei with special reference to specific diseases and deep brain stimulation localization. Neuroradiol J 2014;27(1):29–43

Behçet's Syndrome

106. Siva A, Saip S. The spectrum of nervous system involvement in Behçet's syndrome and its differential diagnosis. J Neurol 2009;256(4):513–529

Brain Abscess

107. Gupta RK, Kumar S. Central nervous system tuberculosis. Neuroimaging Clin N Am 2011;21(4):795–814, vii–viii
108. Husain N, Kumar P. Pathology of tropical diseases. Neuroimaging Clin N Am 2011;21(4):757–775, vii
109. Lai PH, Hsu SS, Ding SW, et al. Proton magnetic resonance spectroscopy and diffusion-weighted imaging in intracranial cystic mass lesions. Surg Neurol 2007;68(Suppl 1):S25–S36
110. Luthra G, Parihar A, Nath K, et al. Comparative evaluation of fungal, tubercular, and pyogenic brain abscesses with conventional and diffusion MR imaging and proton MR spectroscopy. AJNR Am J Neuroradiol 2007;28(7):1332–1338
111. Morais LT, Zanardi VdeA, Faria AV. Magnetic resonance spectroscopy in the diagnosis and etiological definition of brain bacterial abscesses. Arq Neuropsiquiatr 2007;65(4B):1144–1148
112. Rath TJ, Hughes M, Arabi M, Shah GV. Imaging of cerebritis, encephalitis, and brain abscess. Neuroimaging Clin N Am 2012;22(4):585–607
113. Satishchandra P, Sinha S. Relevance of neuroimaging in the diagnosis and management of tropical neurologic disorders. Neuroimaging Clin N Am 2011;21(4):737–756, vii

CADASIL

114. Chabriat H, Joutel A, Dichgans M, Tournier-Lasserve E, Bousser MG. Cadasil. Lancet Neurol 2009;8(7):643–653
115. Choi JC. Cerebral autosomal dominant arteriopathy with subcortical infarcts and leukoencephalopathy: a genetic cause of cerebral small vessel disease. J Clin Neurol 2010;6(1):1–9
116. Choi J, Song SK, Lee JS, et al. Diversity of stroke presentation in CADASIL: study from patients harboring the predominant NOTCH3 mutation R544C. J Stroke Cerebrovasc Dis 2013;22(2):126–131
117. Federico A, Di Donato I, Bianchi S, Di Palma C, Taglia I, Dotti MT. Hereditary cerebral small vessel diseases: a review. J Neurol Sci 2012;322(1-2):25–30
118. Chabriat H, Joutel A, Dichgans M, Tournier-Lasserve E, Bousser MG. Cadasil. Lancet Neurol 2009;8(7):643–653

Calcifying Pseudoneoplasm of the Neuraxis

119. Aiken AH, Akgun H, Tihan T, Barbaro N, Glastonbury C. Calcifying pseudoneoplasms of the neuraxis: CT, MR imaging, and histologic features. AJNR Am J Neuroradiol 2009;30(6):1256–1260
120. Hodges TR, Karikari IO, Nimjee SM, et al. Calcifying pseudoneoplasm of the cerebellopontine angle: case report. Neurosurgery 2011;69(1, Suppl Operative):E117–E120
121. Mohapatra I, Manish R, Mahadevan A, Prasad C, Sampath S, Shankar SK. Calcifying pseudoneoplasm (fibro osseous lesion) of neuraxis (CAPNON)—a case report. Clin Neuropathol 2010;29(4):223–226
122. Park P, Schmidt LA, Shah GV, Tran NK, Gandhi D, La Marca F. Calcifying pseudoneoplasm of the spine. Clin Neurol Neurosurg 2008;110(4):392–395
123. Shrier DA, Melville D, Millet D, et al. Fibro-osseous lesions involving the brain: MRI. Neuroradiology 1999;41(1):18–21

Canavan Disease

124. Bekiesinska-Figatowska M, Mierzewska H, Jurkiewicz E. Basal ganglia lesions in children and adults. Eur J Radiol 2013;82(5):837–849
125. Cakmakci H, Pekcevik Y, Yis U, Unalp A, Kurul S. Diagnostic value of proton MR spectroscopy and diffusion-weighted MR imaging in childhood inherited neurometabolic brain diseases and review of the literature. Eur J Radiol 2010;74(3):e161–e171
126. Leone P, Shera D, McPhee SWJ, et al. Long-term follow-up after gene therapy for canavan disease. Sci Transl Med 2012;4(165):165ra163
127. Michel SJ, Given CA II. Case 99: Canavan disease. Radiology 2006;241(1):310–314
128. Sener RN. Canavan disease: diffusion magnetic resonance imaging findings. J Comput Assist Tomogr 2003;27(1):30–33
129. Srikanth SG, Chandrashekar HS, Nagarajan K, Jayakumar PN. Restricted diffusion in Canavan disease. Childs Nerv Syst 2007;23(4):465–468
130. van der Knaap M, Valk J. Canavan disease In: van der Knaap MS, Valk J, eds. Magnetic Resonance of Myelination and Myelin Disorders. 3rd ed. New York: Springer; 2005:326–333

CARASIL

131. Fukutake T. Cerebral autosomal recessive arteriopathy with subcortical infarcts and leukoencephalopathy (CARASIL): from discovery to gene identification. J Stroke Cerebrovasc Dis 2011;20(2):85–93

Carbon Monoxide Poisoning

132. Lo CP, Chen SY, Lee KW, et al. Brain injury after acute carbon monoxide poisoning: early and late complications. AJR Am J Roentgenol 2007;189(4):W205-11

Cavernous Sinus Hemangioma

133. Gonzalez LF, Lekovic GP, Eschbacher J, Coons S, Porter RW, Spetzler RF. Are cavernous sinus hemangiomas and cavernous malformations different entities? Neurosurg Focus 2006;21(1):e6
134. Tannouri F, Divano L, Caucheteur V, et al. Cavernous haemangioma in the cavernous sinus: case report and review of the literature. Neuroradiology 2001;43(4):317–320
135. Wang X, Liu X, Mei G, Dai J, Pan L, Wang E. Phase II study to assess the efficacy of hypofractionated stereotactic radiotherapy in patients with large cavernous sinus hemangiomas. Int J Radiat Oncol Biol Phys 2012;83(2):e223–e230

Central Neurocytoma

136. Figarella-Branger D, Söylemezoglu F, Burger PC. Central neurocytoma and extraventricular neurocytoma. In: Louis DN, Ohgaki H, Wiestler OD, Cavenee WK, eds. World Health Organization Classification of Tumours of the Central Nervous System. 4th ed. Geneva: IARC Press; 2007:106–109
137. Jaiswal S, Vij M, Rajput D, et al. A clinicopathological, immunohistochemical and neuroradiological study of eight patients with central neurocytoma. J Clin Neurosci 2011;18(3):334–339
138. Kocaoglu M, Ors F, Bulakbasi N, Onguru O, Ulutin C, Secer HI. Central neurocytoma: proton MR spectroscopy and diffusion weighted MR imaging findings. Magn Reson Imaging 2009;27(3):434–440
139. Peltier J, Baroncini M, Le Gars D, Lejeune JP. [Central neurocytomas of the lateral ventricle. A series of 35 cases with review of the literature]. Neurochirurgie 2011;57(4-6):215–219
140. Shah T, Jayasundar R, Singh VP, Sarkar C. MRS characterization of central neurocytomas using glycine. NMR Biomed 2011;24(10):1408–1413
141. Yang GF, Wu SY, Zhang LJ, Lu GM, Tian W, Shah K. Imaging findings of extraventricular neurocytoma: report of 3 cases and review of the literature. AJNR Am J Neuroradiol 2009;30(3):581–585
142. Yeh IB, Xu M, Ng WH, Ye J, Yang D, Lim CC. Central neurocytoma: typical magnetic resonance spectroscopy findings and atypical ventricular dissemination. Magn Reson Imaging 2008;26(1):59–64

Central Pontine Myelinolysis/Osmotic Myelinolysis

143. Guzmán-De-Villoria JA, Ferreiro-Argüelles C, Fernández-García P. Differential diagnosis of T2 hyperintense brainstem lesions: Part 2. Diffuse lesions. Semin Ultrasound CT MR 2010;31(3):260–274
144. Ranger AM, Chaudhary N, Avery M, Fraser D. Central pontine and extrapontine myelinolysis in children: a review of 76 patients. J Child Neurol 2012;27(8):1027–1037

Cerebellar Atrophy in Children

145. Poretti A, Wolf NI, Boltshauser E. Differential diagnosis of cerebellar atrophy in childhood. Eur J Paediatr Neurol 2008;12(3):155–167

Cerebellitis

146. De Bruecker Y, Claus F, Demaerel P, et al. MRI findings in acute cerebellitis. Eur Radiol 2004;14(8):1478–1483
147. Desai J, Mitchell WG. Acute cerebellar ataxia, acute cerebellitis, and opsoclonus-myoclonus syndrome. J Child Neurol 2012;27(11):1482–1488
148. Takanashi J, Miyamoto T, Ando N, et al. Clinical and radiological features of rotavirus cerebellitis. AJNR Am J Neuroradiol 2010;31(9):1591–1595

Cerebral Cortical Dysplasia

149. Barkovich AJ, Guerrini R, Kuzniecky RI, Jackson GD, Dobyns WB. A developmental and genetic classification for malformations of cortical development: update 2012. Brain 2012;135(Pt 5):1348–1369
150. Crino PB. Focal cortical dysplasia. Semin Neurol 2015;35(3):201–208
151. Gaitanis JN, Donahue J. Focal cortical dysplasia. Pediatr Neurol 2013;49(2):79–87
152. Raybaud C, Widjaja E. Development and dysgenesis of the cerebral cortex: malformations of cortical development. Neuroimaging Clin N Am 2011;21(3):483–543, vii
153. Widjaja E, Geibprasert S, Mahmoodabadi SZ, Brown NE, Shannon P. Corroboration of normal and abnormal fetal cerebral lamination on postmortem MR imaging with postmortem examination. AJNR Am J Neuroradiol 2010;31(10):1987–1993

Cerebritis

154. Gasparetto EL, Cabral RF, da Cruz LC Jr, Domingues RC. Diffusion imaging in brain infections. Neuroimaging Clin N Am 2011;21(1):89–113, viii

Chiari Malformations

155. Chiapparini L, Saletti V, Solero CL, Bruzzone MG, Valentini LG. Neuroradiological diagnosis of Chiari malformations. Neurol Sci 2011;32(Suppl 3):S283–S286
156. Di Rocco C, Frassanito P, Massimi L, Peraio S. Hydrocephalus and Chiari type I malformation. Childs Nerv Syst 2011;27(10):1653–1664
157. McVige JW, Leonardo J. Imaging of Chiari type I malformation and syringohydromyelia. Neurol Clin 2014;32(1):95–126
158. Duprez TP, Sindic CJM. Contrast-enhanced magnetic resonance imaging and perfusion-weighted imaging for monitoring features in severe CLIPPERS. Brain 2011;134(Pt 8):e184, author reply e186
159. Jones JL, Dean AF, Antoun N, Scoffings DJ, Burnet NG, Coles AJ. 'Radiologically compatible CLIPPERS' may conceal a number of pathologies. Brain 2011;134(Pt 8):e187
160. Kastrup O, van de Nes J, Gasser T, Keyvani K. Three cases of CLIPPERS: a serial clinical, laboratory and MRI follow-up study. J Neurol 2011;258(12):2140–2146
161. Limousin N, Praline J, Motica O, et al. Brain biopsy is required in steroid-resistant patients with chronic lymphocytic inflammation with pontine perivascular enhancement responsive to steroids (CLIPPERS). J Neurooncol 2012;107(1):223–224
162. Sempere AP, Mola S, Martin-Medina P, Bernabeu A, Khabbaz E, Lopez-Celada S. Response to immunotherapy in CLIPPERS: clinical, MRI, and MRS follow-up. J Neuroimaging 2013;23(2):254–255
163. Simon NG, Parratt JD, Barnett MH, et al. Expanding the clinical, radiological and neuropathological phenotype of chronic lymphocytic inflammation with pontine perivascular enhancement responsive to steroids (CLIPPERS). J Neurol Neurosurg Psychiatry 2012;83(1):15–22
164. Taieb G, Duflos C, Renard D, et al. Long-term outcomes of CLIPPERS (chronic lymphocytic inflammation with pontine perivascular enhancement responsive to steroids) in a consecutive series of 12 patients. Arch Neurol 2012;69(7):847–855

CLOVES Syndrome

165. Bloom J, Upton J III. CLOVES syndrome. J Hand Surg Am 2013;38(12):2508–2512
166. Gucev ZS, Tasic V, Jancevska A, et al. Congenital lipomatous overgrowth, vascular malformations, and epidermal nevi (CLOVE) syndrome: CNS malformations and seizures may be a component of this disorder. Am J Med Genet A 2008;146A(20):2688–2690
167. Mirzaa G, Conway R, Graham JM, Dobyns WB. *PIK3CA*-related segmental overgrowth. In: Paragon RA, Adam MP, Ardinger HH, et al, eds. GeneReviews. Seattle, WA: University of Washington; 2013:Aug 15
168. Uller W, Fishman SJ, Alomari AI. Overgrowth syndromes with complex vascular anomalies. Semin Pediatr Surg 2014;23(4):208–215

Cockayne Syndrome

169. Koob M, Laugel V, Durand M, et al. Neuroimaging in Cockayne syndrome. AJNR Am J Neuroradiol 2010;31(9):1623–1630
170. van der Knaap M, Valk J. Cockayne syndrome In: van der Knaap MS, Valk J, eds. Magnetic Resonance of Myelination and Myelin Disorders. 3rd ed. New York: Springer; 2005:259–267
171. Weidenheim KM, Dickson DW, Rapin I. Neuropathology of Cockayne syndrome: Evidence for impaired development, premature aging, and neurodegeneration. Mech Ageing Dev 2009;130(9):619–636

Coenzyme Q10 Deficiency

172. Lamperti C, Naini A, Hirano M, et al. Cerebellar ataxia and coenzyme Q10 deficiency. Neurology 2003;60(7):1206–1208
173. Musumeci O, Naini A, Slonim AE, et al. Familial cerebellar ataxia with muscle coenzyme Q10 deficiency. Neurology 2001;56(7):849–855
174. Salviati L, Sacconi S, Murer L, et al. Infantile encephalomyopathy and nephropathy with CoQ10 deficiency: a CoQ10-responsive condition. Neurology 2005;65(4):606–608

Congenital and Developmental Abnormalities of the Pituitary Gland

175. Akin L, Kendirci M, Doğanay S, Kurtoğlu S, Tucer B, Coskun A. Pituitary duplication: a rare cause of precocious puberty. Childs Nerv Syst 2011;27(7):1157–1160
176. Delman BN. Imaging of pediatric pituitary abnormalities. Endocrinol Metab Clin North Am 2009;38(4):673–698
177. Hamilton BE, Salzman KL, Osborn AG. Anatomic and pathologic spectrum of pituitary infundibulum lesions. AJR Am J Roentgenol 2007;188(3):W223-32
178. Di Iorgi N, Allegri AEM, Napoli F, et al. The use of neuroimaging for assessing disorders of pituitary development. Clin Endocrinol (Oxf) 2012;76(2):161–176
179. de Penna GC, Pimenta MP, Drummond JB, et al. Duplication of the hypophysis associated with precocious puberty: presentation of two cases and review of pituitary embryogenesis. Arq Bras Endocrinol Metabol 2005;49(2):323–327
180. Shields R, Mangla R, Almast J, Meyers S. Magnetic resonance imaging of sellar and juxtasellar abnormalities in the paediatric population: an imaging review. Insights Imaging 2015;6(2):241–260
181. Spampinato MV, Castillo M. Congenital pathology of the pituitary gland and parasellar region. Top Magn Reson Imaging 2005; 16(4):269–276

Congenital Anomalies of the Brain

182. Barkovich AJ, Guerrini R, Kuzniecky RI, Jackson GD, Dobyns WB. A developmental and genetic classification for malformations of cortical development: update 2012. Brain 2012;135(Pt 5):1348–1369
183. Barkovich AJ, Raybaud C. Congenital malformation of the brain and skull. In: Barkovich AJ, Raybaud C, eds. Pediatric Neuroimaging. 5th ed. New York, NY: Wolters-Kluwer/Lippincott Williams & Wilkins; 2012:367–568
184. Guerrini R, Dobyns WB. Malformations of cortical development: clinical features and genetic causes. Lancet Neurol 2014;13(7):710–726
185. Nuñez S, Mantilla MT, Bermúdez S. Midline congenital malformations of the brain and skull. Neuroimaging Clin N Am 2011;21(3):429–482, vii

Cortical Laminar Necrosis (Pseudolaminar Cortical Necrosis)

186. Huang BY, Castillo M. Hypoxic-ischemic brain injury: imaging findings from birth to adulthood. Radiographics 2008;28(2):417–439, quiz 617
187. Kinoshita T, Ogawa T, Yoshida Y, Tamura H, Kado H, Okudera T. Curvilinear T1 hyperintense lesions representing cortical necrosis after cerebral infarction. Neuroradiology 2005;47(9):647–651
188. Komiyama M, Nakajima H, Nishikawa M, Yasui T. Serial MR observation of cortical laminar necrosis caused by brain infarction. Neuroradiology 1998;40(12):771–777
189. Kucinski T. Unenhanced CT and acute stroke physiology. Neuroimaging Clin N Am 2005;15(2):397–407, xi–xii
190. McKinney AM, Teksam M, Felice R, et al. Diffusion-weighted imaging in the setting of diffuse cortical laminar necrosis and hypoxic-ischemic encephalopathy. AJNR Am J Neuroradiol 2004;25(10): 1659–1665
191. Siskas N, Lefkopoulos A, Ioannidis I, Charitandi A, Dimitriadis AS. Cortical laminar necrosis in brain infarcts: serial MRI. Neuroradiology 2003;45(5):283–288

Corticobasal Degeneration

192. Armstrong MJ, Litvan I, Lang AE, et al. Criteria for the diagnosis of corticobasal degeneration. Neurology 2013;80(5):496–503
193. Dickson DW, Bergeron C, Chin SS, et al; Office of Rare Diseases of the National Institutes of Health. Office of Rare Diseases neuropathologic criteria for corticobasal degeneration. J Neuropathol Exp Neurol 2002;61(11):935–946
194. Whitwell JL, Jack CR Jr, Boeve BF, et al. Imaging correlates of pathology in corticobasal syndrome. Neurology 2010;75(21):1879–1887

Craniopharyngeal Canal

195. Chen CJ. Suprasellar and infrasellar craniopharyngioma with a persistent craniopharyngeal canal: case report and review of the literature. Neuroradiology 2001;43(9):760–762
196. Kaushik C, Ramakrishnaiah R, Angtuaco EJ. Ectopic pituitary adenoma in persistent craniopharyngeal canal: case report and literature review. J Comput Assist Tomogr 2010;34(4):612–614

Craniopharyngioma

197. Curran JG, O'Connor E. Imaging of craniopharyngioma. Childs Nerv Syst 2005;21(8-9):635–639
198. Rushing EJ, Giangaspero F, Paulus W, Burger PC. Craniopharyngioma. In: Louis DN, Ohgaki H, Wiestler OD, Cavenee WK, eds. World Health Organization Classification of Tumours of the Central Nervous System. 4th ed. Geneva: IARC Press; 2007:238–240
199. Zada G, Lin N, Ojerholm E, Ramkissoon S, Laws ER. Craniopharyngioma and other cystic epithelial lesions of the sellar region: a review of clinical, imaging, and histopathological relationships. Neurosurg Focus 2010;28(4):E4

Crossed Cerebellar Diaschisis

200. Cianfoni A, Luigetti M, Bradshaw ML, Welsh CT, Edwards J, Glazier S. MRI findings of crossed cerebellar diaschisis in a case of Rasmussen's encephalitis. J Neurol 2010;257(10):1748–1750
201. Lin DDM, Kleinman JT, Wityk RJ, et al. Crossed cerebellar diaschisis in acute stroke detected by dynamic susceptibility contrast MR perfusion imaging. AJNR Am J Neuroradiol 2009;30(4):710–715
202. Liu Y, Karonen JO, Nuutinen J, Vanninen E, Kuikka JT, Vanninen RL. Crossed cerebellar diaschisis in acute ischemic stroke: a study with serial SPECT and MRI. J Cereb Blood Flow Metab 2007;27(10): 1724–1732
203. Miller NG, Reddick WE, Kocak M, et al. Cerebellocerebral diaschisis is the likely mechanism of postsurgical posterior fossa syndrome in pediatric patients with midline cerebellar tumors. AJNR Am J Neuroradiol 2010;31(2):288–294
204. Samaniego EA, Stuckert E, Fischbein N, Wijman CAC. Crossed cerebellar diaschisis in status epilepticus. Neurocrit Care 2010;12(1):88–90
205. Tien RD, Ashdown BC. Crossed cerebellar diaschisis and crossed cerebellar atrophy: correlation of MR findings, clinical symptoms, and supratentorial diseases in 26 patients. AJR Am J Roentgenol 1992;158(5):1155–1159

Cyanide

206. Geller RJ, Barthold C, Saiers JA, Hall AH. Pediatric cyanide poisoning: causes, manifestations, management, and unmet needs. Pediatrics 2006;118(5):2146–2158
207. Rachinger J, Fellner FA, Stieglbauer K, Trenkler J. MR changes after acute cyanide intoxication. AJNR Am J Neuroradiol 2002;23(8): 1398–1401

Dementia with Lewy Bodies

208. Kantarci K. Magnetic resonance spectroscopy in common dementias. Neuroimaging Clin N Am 2013;23(3):393–406
209. Kantarci K, Ferman TJ, Boeve BF, et al. Focal atrophy on MRI and neuropathologic classification of dementia with Lewy bodies. Neurology 2012;79(6):553–560
210. Taylor JP, O'Brien J. Neuroimaging of dementia with Lewy bodies. Neuroimaging Clin N Am 2012;22(1):67–81, viii

Desmoplastic Infantile Astrocytoma and Ganglioglioma

211. Borja MJ, Plaza MJ, Altman N, Saigal G. Conventional and advanced MRI features of pediatric intracranial tumors: supratentorial tumors. AJR Am J Roentgenol 2013;200(5):W483-503
212. Brat DJ, VandenBerg SR, Figarella-Branger D, Taratuto AL. Desmoplastic infantile astrocytoma and ganglioglioma. In: Louis DN, Ohgaki H, Wiestler OD, Cavenee WK, eds. World Health Organization Classification of Tumours of the Central Nervous System. 4th ed. Geneva: IARC Press; 2007:96–98
213. Tamburrini G, Colosimo C Jr, Giangaspero F, Riccardi R, Di Rocco C. Desmoplastic infantile ganglioglioma. Childs Nerv Syst 2003;19(5-6): 292–297
214. Trehan G, Bruge H, Vinchon M, et al. MR imaging in the diagnosis of desmoplastic infantile tumor: retrospective study of six cases. AJNR Am J Neuroradiol 2004;25(6):1028–1033

Diffuse Axonal Injury

215. Anzalone N, Scotti R, Riva R. Neuroradiologic differential diagnosis of cerebral intraparenchymal hemorrhage. Neurol Sci 2004; 25(Suppl 1):S3–S5
216. Hijaz TA, Cento EA, Walker MT. Imaging of head trauma. Radiol Clin North Am 2011;49(1):81–103
217. Kubal WS. Updated imaging of traumatic brain injury. Radiol Clin North Am 2012;50(1):15–41

218. Parizel PM, Makkat S, Van Miert E, Van Goethem JW, van den Hauwe L, De Schepper AM. Intracranial hemorrhage: principles of CT and MRI interpretation. Eur Radiol 2001;11(9):1770–1783
219. Tong KA, Ashwal S, Obenaus A, Nickerson JP, Kido D, Haacke EM. Susceptibility-weighted MR imaging: a review of clinical applications in children. AJNR Am J Neuroradiol 2008;29(1):9–17

Dyke-Davidoff-Masson Syndrome

220. Atalar MH, Icagasioglu D, Tas F. Cerebral hemiatrophy (Dyke-Davidoff-Masson syndrome) in childhood: clinicoradiological analysis of 19 cases. Pediatr Int 2007;49(1):70–75
221. Chand G, Goel R, Kapur R. Dyke-Davidoff-Masson syndrome. Arch Neurol 2010;67(8):1026–1027
222. Tasdemir HA, Incesu L, Yazicioglu AK, Belet U, Güngör L. Dyke-Davidoff-Masson syndrome. Clin Imaging 2002;26(1):13–17

Dysembryoplastic Neuroepithelial Tumor

223. Bulakbasi N, Kocaoglu M, Sanal TH, Tayfun C. Dysembryoplastic neuroepithelial tumors: proton MR spectroscopy, diffusion and perfusion characteristics. Neuroradiology 2007;49(10):805–812
224. Campos AR, Clusmann H, von Lehe M, et al. Simple and complex dysembryoplastic neuroepithelial tumors (DNT) variants: clinical profile, MRI, and histopathology. Neuroradiology 2009;51(7):433–443
225. Daumas-Duport C, Pietsch T, Hawkins C, Shankar SK. Dysembryoplastic neuroepithelial tumour. In: Louis DN, Ohgaki H, Wiestler OD, Cavenee WK, eds. World Health Organization Classification of Tumours of the Central Nervous System. 4th ed. Geneva: IARC Press; 2007:99–102
226. Fernandez C, Girard N, Paz Paredes A, Bouvier-Labit C, Lena G, Figarella-Branger D. The usefulness of MR imaging in the diagnosis of dysembryoplastic neuroepithelial tumor in children: a study of 14 cases. AJNR Am J Neuroradiol 2003;24(5):829–834
227. Ozlen F, Gunduz A, Asan Z, et al. Dysembryoplastic neuroepithelial tumors and gangliogliomas: clinical results of 52 patients. Acta Neurochir (Wien) 2010;152(10):1661–1671
228. Parmar HA, Hawkins C, Ozelame R, Chuang S, Rutka J, Blaser S. Fluid-attenuated inversion recovery ring sign as a marker of dysembryoplastic neuroepithelial tumors. J Comput Assist Tomogr 2007;31(3):348–353
229. Thom M, Toma A, An S, et al. One hundred and one dysembryoplastic neuroepithelial tumors: an adult epilepsy series with immunohistochemical, molecular genetic, and clinical correlations and a review of the literature. J Neuropathol Exp Neurol 2011;70(10):859–878
230. Yu AH, Chen L, Li YJ, Zhang GJ, Li KC, Wang YP. Dysembryoplastic neuroepithelial tumors: magnetic resonance imaging and magnetic resonance spectroscopy evaluation. Chin Med J (Engl) 2009;122(20):2433–2437

Dysplastic Cerebellar Gangliocytoma (Lhermitte-Duclos Disease)

231. Eberhart CG, Wiestler OD, Eng C. Cowden disease and dysplastic gangliocytoma of the cerebellum/Lhermitte-Duclos disease. In: Louis DN, Ohgaki H, Wiestler OD, Cavenee WK, eds. World Health Organization Classification of Tumours of the Central Nervous System. 4th ed. Geneva: IARC Press; 2007:226–228
232. Kumar R, Vaid VK, Kalra SK. Lhermitte-Duclos disease. Childs Nerv Syst 2007;23(7):729–732
233. Shinagare AB, Patil NK, Sorte SZ. Case 144: Dysplastic cerebellar gangliocytoma (Lhermitte-Duclos disease). Radiology 2009;251(1):298–303
234. Yağci-Küpeli B, Oguz KK, Bilen MA, Yalçin B, Akalan N, Büyükpamukçu M. An unusual cause of posterior fossa mass: Lhermitte-Duclos disease. J Neurol Sci 2010;290(1-2):138–141

Encephalitis/Viral Infections

235. Ali M, Safriel Y, Sohi J, Llave A, Weathers S. West Nile virus infection: MR imaging findings in the nervous system. AJNR Am J Neuroradiol 2005;26(2):289–297
236. Bag AK, Curé JK, Chapman PR, Roberson GH, Shah R. JC virus infection of the brain. AJNR Am J Neuroradiol 2010;31(9):1564–1576
237. Buckle C, Castillo M. Use of diffusion-weighted imaging to evaluate the initial response of progressive multifocal leukoencephalopathy to highly active antiretroviral therapy: early experience. AJNR Am J Neuroradiol 2010;31(6):1031–1035
238. Debiasi RL, Tyler KL. West Nile virus meningoencephalitis. Nat Clin Pract Neurol 2006;2(5):264–275
239. Gupta RK, Soni N, Kumar S, Khandelwal N. Imaging of central nervous system viral diseases. J Magn Reson Imaging 2012;35(3):477–491
4. Handique SK. Viral infections of the central nervous system. Neuroimaging Clin N Am 2011;21(4):777–794, vii
240. Petropoulou KA, Gordon SM, Prayson RA, Ruggierri PM. West Nile virus meningoencephalitis: MR imaging findings. AJNR Am J Neuroradiol 2005;26(8):1986–1995
241. Sahraian MA, Radue EW, Eshaghi A, Besliu S, Minagar A. Progressive multifocal leukoencephalopathy: a review of the neuroimaging features and differential diagnosis. Eur J Neurol 2012;19(8):1060–1069
242. Sureka J, Jakkani RK. Clinico-radiological spectrum of bilateral temporal lobe hyperintensity: a retrospective review. Br J Radiol 2012;85(1017):e782–e792

Ependymoma

243. McLendon RE, Rosenblum MK, Schiffer D, Wiestler OD. Myxopapillary ependymoma. In: Louis DN, Ohgaki H, Wiestler OD, Cavenee WK, eds. World Health Organization Classification of Tumours of the Central Nervous System. 4th ed. Geneva: IARC Press; 2007:72–73
244. McLendon RE, Wiestler OD, Kros JM, Korshunov A, Ng HK. Ependymoma. In: Louis DN, Ohgaki H, Wiestler OD, Cavenee WK, eds. World Health Organization Classification of Tumours of the Central Nervous System. 4th ed. Geneva: IARC Press; 2007:74–78
245. Yuh EL, Barkovich AJ, Gupta N. Imaging of ependymomas: MRI and CT. Childs Nerv Syst 2009;25(10):1203–1213

Fabry Disease

246. Ginsberg L, Manara R, Valentine AR, Kendall B, Burlina AP. Magnetic resonance imaging changes in Fabry disease. Acta Paediatr Suppl 2006;95(451):57–62
2. Viana-Baptista M. Stroke and Fabry disease. J Neurol 2012;259(6):1019–1028

Fahr Disease

247. Henkelman RM, Watts JF, Kucharczyk W. High signal intensity in MR images of calcified brain tissue. Radiology 1991;179(1):199–206
248. Oliveira JRM, Spiteri E, Sobrido MJ, et al. Genetic heterogeneity in familial idiopathic basal ganglia calcification (Fahr disease). Neurology 2004;63(11):2165–2167

Fetal Brain Anomalies

249. Glenn OA, Barkovich AJ. Magnetic resonance imaging of the fetal brain and spine: an increasingly important tool in prenatal diagnosis, part 1. AJNR Am J Neuroradiol 2006;27(8):1604–1611
250. Glenn OA, Barkovich J. Magnetic resonance imaging of the fetal brain and spine: an increasingly important tool in prenatal diagnosis: part 2. AJNR Am J Neuroradiol 2006;27(9):1807–1814

Fetal Stroke

251. Brobeck BR, Grant PE. Pediatric stroke: the child is not merely a small adult. Neuroimaging Clin N Am 2005;15(3):589–607, xi
252. Miller SP. Newborn brain injury: looking back to the fetus. Ann Neurol 2007;61(4):285–287

Fragile X Syndrome (FraX)

253. Hallahan BP, Craig MC, Toal F, et al. In vivo brain anatomy of adult males with Fragile X syndrome: an MRI study. Neuroimage 2011;54(1):16–24

Friedreich Ataxia

254. Pagani E, Ginestroni A, Della Nave R, et al. Assessment of brain white matter fiber bundle atrophy in patients with Friedreich ataxia. Radiology 2010;255(3):882–889
255. Rizzo G, Tonon C, Valentino ML, et al. Brain diffusion-weighted imaging in Friedreich's ataxia. Mov Disord 2011;26(4):705–712

Frontotemporal Degeneration/Dementia

256. Josephs KA, Hodges JR, Snowden JS, et al. Neuropathological background of phenotypical variability in frontotemporal dementia. Acta Neuropathol 2011;122(2):137–153
257. Mackenzie IRA, Neumann M, Baborie A, et al. A harmonized classification system for FTLD-TDP pathology. Acta Neuropathol 2011;122(1):111–113
258. Rohrer JD, Lashley T, Schott JM, et al. Clinical and neuroanatomical signatures of tissue pathology in frontotemporal lobar degeneration. Brain 2011;134(Pt 9):2565–2581

259. Whitwell JL, Josephs KA. Neuroimaging in frontotemporal lobar degeneration—predicting molecular pathology. Nat Rev Neurol 2011;8(3):131–142

Fungal Infections

260. Mathur M, Johnson CE, Sze G. Fungal infections of the central nervous system. Neuroimaging Clin N Am 2012;22(4):609–632
261. Patiroglu T, Unal E, Karakukcu M, et al. Multiple fungal brain abscesses in a child with acute lymphoblastic leukemia. Mycopathologia 2012;174(5-6):505–509

Ganglioglioma, Gangliocytoma, and Anaplastic Ganglioglioma

262. Becker AJ, Wiestler OD, Figarella-Branger D, Blümcke I. Ganglioglioma and gangliocytoma. In: Louis DN, Ohgaki H, Wiestler OD, Cavenee WK, eds. World Health Organization Classification of Tumours of the Central Nervous System. 4th ed. Geneva: IARC Press; 2007:103–105
263. Castillo M, Davis PC, Takei Y, Hoffman JC Jr. Intracranial ganglioglioma: MR, CT, and clinical findings in 18 patients. AJNR Am J Neuroradiol 1990;11(1):109–114
264. DeMarchi R, Abu-Abed S, Munoz D, Loch Macdonald R. Malignant ganglioglioma: case report and review of literature. J Neurooncol 2011;101(2):311–318
265. Lagares A, Gómez PA, Lobato RD, Ricoy JR, Ramos A, de la Lama A. Ganglioglioma of the brainstem: report of three cases and review of the literature. Surg Neurol 2001;56(5):315–322, discussion 322–324
266. Löbel U, Ellison DW, Shulkin BL, Patay Z. Infiltrative cerebellar ganglioglioma: conventional and advanced MRI, proton MR spectroscopic, and FDG PET findings in an 18-month-old child. Clin Radiol 2011;66(2):194–201
267. Milligan BD, Giannini C, Link MJ. Ganglioglioma in the cerebellopontine angle in a child. Case report and review of the literature. J Neurosurg 2007;107(4, Suppl):292–296
268. Safavi-Abbasi S, Di Rocco F, Chantra K, et al. Posterior cranial fossa gangliogliomas. Skull Base 2007;17(4):253–264

Gangliosidosis

269. van der Knaap M, Valk J. GM2, gangliosidosis. In: van der Knaap MS, Valk J, eds. Magnetic Resonance of Myelination and Myelin Disorders. 3rd ed. New York: Springer; 2005:103–111

Germ Cell Tumors

270. Rosenblum MK, Nakazato Y, Matsutani M. CNS Germ cell tumours. In: Louis DN, Ohgaki H, Wiestler OD, Cavenee WK, eds. World Health Organization Classification of Tumours of the Central Nervous System. 4th ed. Geneva: IARC Press; 2007:198–204

Glioblastoma Multiforme

271. Belden CJ, Valdes PA, Ran C, et al. Genetics of glioblastoma: a window into its imaging and histopathologic variability. Radiographics 2011;31(6):1717–1740
272. Calli C, Kitis O, Yunten N, Yurtseven T, Islekel S, Akalin T. Perfusion and diffusion MR imaging in enhancing malignant cerebral tumors. Eur J Radiol 2006;58(3):394–403
273. Kleihues P, Burger PC, Aldape KD, et al. Glioblastoma. In: Louis DN, Ohgaki H, Wiestler OD, Cavenee WK, eds. World Health Organization Classification of Tumours of the Central Nervous System. 4th ed. Geneva: IARC Press; 2007:33–49
274. Zipp L, Schwartz KM, Hewer E, Yu Y, Stippich C, Slopis JM. Magnetic resonance imaging and computed tomography findings in pediatric giant cell glioblastoma. Clin Neuroradiol 2012;22(4):359–363

Gliomatosis cerebri

275. Desclée P, Rommel D, Hernalsteen D, Godfraind C, de Coene B, Cosnard G. Gliomatosis cerebri, imaging findings of 12 cases. J Neuroradiol 2010;37(3):148–158
276. Fuller GN, Kros JM. Gliomatosis cerebri. In: Louis DN, Ohgaki H, Wiestler OD, Cavenee WK, eds. World Health Organization Classification of Tumours of the Central Nervous System. 4th ed. Geneva: IARC Press; 2007:50–52
277. Guzmán-de-Villoria JA, Sánchez-González J, Muñoz L, et al. 1H MR spectroscopy in the assessment of gliomatosis cerebri. AJR Am J Roentgenol 2007;188(3):710–714
278. Yu A, Li K, Li H. Value of diagnosis and differential diagnosis of MRI and MR spectroscopy in gliomatosis cerebri. Eur J Radiol 2006;59(2):216–221

Gliosarcoma

279. Han SJ, Yang I, Ahn BJ, et al. Clinical characteristics and outcomes for a modern series of primary gliosarcoma patients. Cancer 2010;116(5):1358–1366
280. Kleihues P, Burger PC, Aldape KD, et al. Gliosarcoma. In: Louis DN, Ohgaki H, Wiestler OD, Cavenee WK, eds. World Health Organization Classification of Tumours of the Central Nervous System. 4th ed. Geneva: IARC Press; 2007:48–49
281. Zhang BY, Chen H, Geng DY, et al. Computed tomography and magnetic resonance features of gliosarcoma: a study of 54 cases. J Comput Assist Tomogr 2011;35(6):667–673

Globoid Cell Leukodystrophy (GLD)

282. Beslow LA, Schwartz ES, Bönnemann CG. Thickening and enhancement of multiple cranial nerves in conjunction with cystic white matter lesions in early infantile Krabbe disease. Pediatr Radiol 2008;38(6):694–696
283. Brockmann K, Dechent P, Wilken B, Rusch O, Frahm J, Hanefeld F. Proton MRS profile of cerebral metabolic abnormalities in Krabbe disease. Neurology 2003;60(5):819–825
284. Guo AC, Petrella JR, Kurtzberg J, Provenzale JM. Evaluation of white matter anisotropy in Krabbe disease with diffusion tensor MR imaging: initial experience. Radiology 2001;218(3):809–815
285. Loes DJ, Peters C, Krivit W. Globoid cell leukodystrophy: distinguishing early-onset from late-onset disease using a brain MR imaging scoring method. AJNR Am J Neuroradiol 1999;20(2):316–323
286. Nagar VA, Ursekar MA, Krishnan P, Jankharia BG. Krabbe disease: unusual MRI findings. Pediatr Radiol 2006;36(1):61–64
287. Patel B, Gimi B, Vachha B, Agadi S, Koral K. Optic nerve and chiasm enlargement in a case of infantile Krabbe disease: quantitative comparison with 26 age-matched controls. Pediatr Radiol 2008;38(6):697–699
288. van der Knaap M, Valk J. Globoid cell leukodystrophy: Krabbe disease. In: van der Knaap MS, Valk J, eds. Magnetic Resonance of Myelination and Myelin Disorders. 3rd ed. New York: Springer; 2005:87–95

Glutaric Acidemia/Aciduria Type 1

289. Elster AW. Glutaric aciduria type I: value of diffusion-weighted magnetic resonance imaging for diagnosing acute striatal necrosis. J Comput Assist Tomogr 2004;28(1):98–100
290. Hedlund GL, Longo N, Pasquali M. Glutaric acidemia type 1. Am J Med Genet C Semin Med Genet 2006;142C(2):86–94
291. Mellerio C, Marignier S, Roth P, et al. Prenatal cerebral ultrasound and MRI findings in glutaric aciduria Type 1: a de novo case. Ultrasound Obstet Gynecol 2008;31(6):712–714
292. Neumaier-Probst E, Harting I, Seitz A, Ding C, Kölker S. Neuroradiological findings in glutaric aciduria type I (glutaryl-CoA dehydrogenase deficiency). J Inherit Metab Dis 2004;27(6):869–876
293. Oguz KK, Ozturk A, Cila A. Diffusion-weighted MR imaging and MR spectroscopy in glutaric aciduria type 1. Neuroradiology 2005;47(3):229–234
294. Santos CC, Roach ES. Glutaric aciduria type I: a neuroimaging diagnosis? J Child Neurol 2005;20(7):588–590
295. Twomey EL, Naughten ER, Donoghue VB, Ryan S. Neuroimaging findings in glutaric aciduria type 1. Pediatr Radiol 2003;33(12):823–830

Glutaric Acidemia/Aciduria Type 2

296. Mumtaz HA, Gupta V, Singh P, Marwaha RK, Khandelwal N. MR imaging findings of glutaric aciduria type II. Singapore Med J 2010;51(4):e69–e71
297. Takanashi J, Fujii K, Sugita K, Kohno Y. Neuroradiologic findings in glutaric aciduria type II. Pediatr Neurol 1999;20(2):142–145

GM-2 Gangliosidosis

298. Koelfen W, Freund M, Jaschke W, Koenig S, Schultze C. GM-2 gangliosidosis (Sandhoff's disease): two year follow-up by MRI. Neuroradiology 1994;36(2):152–154

Granular Cell Tumor

299. Cohen-Gadol AA, Pichelmann MA, Link MJ, et al. Granular cell tumor of the sellar and suprasellar region: clinicopathologic study of 11 cases and literature review. Mayo Clin Proc 2003;78(5):567–573
300. Fuller GN, Wesseling P. Granular cell tumour of the neurohypophysis. In: Louis DN, Ohgaki H, Wiestler OD, Cavenee WK, eds. World Health

Organization Classification of Tumours of the Central Nervous System. 4th ed. Geneva: IARC Press; 2007:241–242

301. Wilkinson MD, Fulham MJ, Besser M. Neuroimaging findings in a suprasellar granular cell tumor. J Comput Assist Tomogr 2003;27(1): 26–29

Hemangioblastoma

302. Aldape KD, Plate KH, Vortmeyer AO, Zagzag D, Neumann HPH. Hemangioblastoma. In: Louis DN, Ohgaki H, Wiestler OD, Cavenee WK, eds. World Health Organization Classification of Tumours of the Central Nervous System. 4th ed. Geneva: IARC Press; 2007:184–186

303. Plate KH, Vortmeyer AO, Zagzag D, Neumann HPH. Von Hippel-Lindau disease and haemangioblastoma. In: Louis DN, Ohgaki H, Wiestler OD, Cavenee WK, eds. World Health Organization Classification of Tumours of the Central Nervous System. 4th ed. Geneva: IARC Press; 2007:215–217

304. Torreggiani WC, Keogh C, Al-Ismail K, Munk PL, Nicolaou S. Von Hippel-Lindau disease: a radiological essay. Clin Radiol 2002;57(8): 670–680

Hemimegalencephaly

305. Mirzaa GM, Poduri A. Megalencephaly and hemimegalencephaly: breakthroughs in molecular etiology. Am J Med Genet C Semin Med Genet 2014;166C(2):156–172

306. Santos AC, Escorsi-Rosset S, Simao GN, et al. Hemispheric dysplasia and hemimegalencephaly: imaging definitions. Childs Nerv Syst 2014;30(11):1813–1821

Hemophagocytic Lymphohistiocytosis

307. Deiva K, Mahlaoui N, Beaudonnet F, et al. CNS involvement at the onset of primary hemophagocytic lymphohistiocytosis. Neurology 2012;78(15):1150–1156

308. Guandalini M, Butler A, Mandelstam S. Spectrum of imaging appearances in Australian children with central nervous system hemophagocytic lymphohistiocytosis. J Clin Neurosci 2014;21(2):305–310

309. Jovanovic A, Kuzmanovic M, Kravljanac R, et al. Central nervous system involvement in hemophagocytic lymphohistiocytosis: a single-center experience. Pediatr Neurol 2014;50(3):233–237

Hemorrhage and Vascular Lesions

310. Anzalone N, Scotti R, Riva R. Neuroradiologic differential diagnosis of cerebral intraparenchymal hemorrhage. Neurol Sci 2004;25(Suppl 1): S3–S5

311. Dainer HM, Smirniotopoulos JG. Neuroimaging of hemorrhage and vascular malformations. Semin Neurol 2008;28(4):533–547

312. Kubal WS. Updated imaging of traumatic brain injury. Radiol Clin North Am 2012;50(1):15–41

313. Leblanc GG, Golanov E, Awad IA, Young WL; Biology of Vascular Malformations of the Brain NINDS Workshop Collaborators. Biology of vascular malformations of the brain. Stroke 2009;40(12):e694–e702

314. Parizel PM, Makkat S, Van Miert E, Van Goethem JW, van den Hauwe L, De Schepper AM. Intracranial hemorrhage: principles of CT and MRI interpretation. Eur Radiol 2001;11(9):1770–1783

315. Riant F, Cecillon M, Saugier-Veber P, Tournier-Lasserve E. CCM molecular screening in a diagnosis context: novel unclassified variants leading to abnormal splicing and importance of large deletions. Neurogenetics 2013;14(2):133–141

Hemorrhagic Transformation of Stroke

316. Smith EE, Rosand J, Greenberg SM. Hemorrhagic stroke. Neuroimaging Clin N Am 2005;15(2):259–272, ix

Hepatic Encephalopathy

317. Bindu PS, Sinha S, Taly AB, Christopher R, Kovoor JME. Cranial MRI in acute hyperammonemic encephalopathy. Pediatr Neurol 2009; 41(2):139–142

318. Rovira A, Alonso J, Córdoba J. MR imaging findings in hepatic encephalopathy. AJNR Am J Neuroradiol 2008;29(9):1612–1621

319. Sharma P, Eesa M, Scott JN. Toxic and acquired metabolic encephalopathies: MRI appearance. AJR Am J Roentgenol 2009;193(3): 879–886

Heroin/Cocaine Toxicity

320. Bartlett E, Mikulis DJ. Chasing "chasing the dragon" with MRI: leukoencephalopathy in drug abuse. Br J Radiol 2005;78(935):997–1004

321. Geibprasert S, Gallucci M, Krings T. Addictive illegal drugs: structural neuroimaging. AJNR Am J Neuroradiol 2010;31(5):803–808

322. Offiah C, Hall E. Heroin-induced leukoencephalopathy: characterization using MRI, diffusion-weighted imaging, and MR spectroscopy. Clin Radiol 2008;63(2):146–152

323. Tamrazi B, Almast J. Your brain on drugs: imaging of drug-related changes in the central nervous system. Radiographics 2012;32(3):701–719

HIV Encephalitis

324. Donald KA, Walker KG, Kilborn T, et al. HIV Encephalopathy: pediatric case series description and insights from the clinic coalface. AIDS Res Ther 2015;12(1):2

325. Masters MC, Ances BM. Role of neuroimaging in HIV-associated neurocognitive disorders. Semin Neurol 2014;34(1):89–102

326. Miller RF, Isaacson PG, Hall-Craggs M, et al. Cerebral CD8+ lymphocytosis in HIV-1 infected patients with immune restoration induced by HAART. Acta Neuropathol 2004;108(1):17–23

327. Senocak E, Oğuz KK, Ozgen B, et al. Imaging features of CNS involvement in AIDS. Diagn Interv Radiol 2010;16(3):193–200

328. Sibtain NA, Chinn RJS. Imaging of the central nervous system in HIV infection. Imaging 2002;14:48–59

329. Tucker KA, Robertson KR, Lin W, et al. Neuroimaging in human immunodeficiency virus infection. J Neuroimmunol 2004;157(1-2): 153–162

Hydatid Cyst

330. Duishanbai S, Jiafu D, Guo H, et al. Intracranial hydatid cyst in children: report of 30 cases. Childs Nerv Syst 2010;26(6):821–827

331. El-Shamam O, Amer T, El-Atta MA. Magnetic resonance imaging of simple and infected hydatid cysts of the brain. Magn Reson Imaging 2001;19(7):965–974

332. Ghonge NP, Rajan S, Aggarwal B, Sahu AK. Imaging of ruptured endocyst in an isolated intramuscular hydatid cyst—the Scroll appearance. J Radiol Case Rep 2012;6(8):17–21

333. Rumboldt Z, Jednacak H, Talan-Hranilović J, Rumboldt T, Kalousek M. Unusual appearance of a cisternal hydatid cyst. AJNR Am J Neuroradiol 2003;24(1):112–114

Hyperglycemia

334. Bathla G, Hegde AN. MRI and CT appearances in metabolic encephalopathies due to systemic diseases in adults. Clin Radiol 2013; 68(6):545–554

335. Cherian A, Thomas B, Baheti NN, Chemmanam T, Kesavadas C. Concepts and controversies in nonketotic hyperglycemia-induced hemichorea: further evidence from susceptibility-weighted MR imaging. J Magn Reson Imaging 2009;29(3):699–703

336. Portet F, Brickman AM, Stern Y, et al. Metabolic syndrome and localization of white matter hyperintensities in the elderly population. Alzheimers Dement 2012;8(5, Suppl):S88–95.e1

337. Shrier DA, Shibata DK, Wang HZ, Numaguchi Y, Powers JM. Central brain herniation secondary to juvenile diabetic ketoacidosis. AJNR Am J Neuroradiol 1999;20(10):1885–1888

Hypertensive Encephalopathy (Posterior reversible encephalopathy syndrome/PRES)

338. Bartynski WS. Posterior reversible encephalopathy syndrome, part 1: fundamental imaging and clinical features. AJNR Am J Neuroradiol 2008;29(6):1036–1042

339. Bartynski WS. Posterior reversible encephalopathy syndrome, part 2: controversies surrounding pathophysiology of vasogenic edema. AJNR Am J Neuroradiol 2008;29(6):1043–1049

340. Dicuonzo F, Salvati A, Palma M, et al. Posterior reversible encephalopathy syndrome associated with methotrexate neurotoxicity: conventional magnetic resonance and diffusion-weighted imaging findings. J Child Neurol 2009;24(8):1013–1018

341. Stevens CJ, Heran MKS. The many faces of posterior reversible encephalopathy syndrome. Br J Radiol 2012;85(1020):1566–1575

342. Yilmaz S, Gokben S, Arikan C, Calli C, Serdaroglu G. Reversibility of cytotoxic edema in tacrolimus leukoencephalopathy. Pediatr Neurol 2010;43(5):359–362

Hypertrophic Olivary Degeneration

343. Bruno MK, Wooten GF. Hypertrophic olivary degeneration. Arch Neurol 2012;69(2):274–275

344. Cilia R, Righini A, Marotta G, et al. Clinical and imaging characterization of a patient with idiopathic progressive ataxia and palatal tremor. Eur J Neurol 2007;14(8):944–946
345. Goyal M, Versnick E, Tuite P, et al. Hypertrophic olivary degeneration: metaanalysis of the temporal evolution of MR findings. AJNR Am J Neuroradiol 2000;21(6):1073–1077
346. Kim SJ, Lee JH, Suh DC. Cerebellar MR changes in patients with olivary hypertrophic degeneration. AJNR Am J Neuroradiol 1994;15(9):1715–1719
347. Kitajima M, Korogi Y, Shimomura O, et al. Hypertrophic olivary degeneration: MR imaging and pathologic findings. Radiology 1994;192(2):539–543
348. Palacios E, Wasilewska E, Alvernia JE, Figueroa RE. Palatal myoclonus secondary to hypertrophic olivary degeneration. Ear Nose Throat J 2009;88(7):989–991
349. Sanverdi SE, Oguz KK, Haliloglu G. Hypertrophic olivary degeneration in children: four cases and a review of the literature. Br J Radiol 2012;85:511–516
350. Shah R, Markert J, Bag AK, Curé JK. Diffusion tensor imaging in hypertrophic olivary degeneration. AJNR Am J Neuroradiol 2010;31(9):1729–1731
351. Vossough A, Ziai P, Chatzkel JA. Red nucleus degeneration in hypertrophic olivary degeneration after pediatric posterior fossa tumor resection: use of susceptibility-weighted imaging (SWI). Pediatr Radiol 2012;42(4):481–485

Hypoglycemia

352. Atay M, Aralasmak A, Sharifov R, Kilicarslan R, Asil T, Alkan A. Transient cytotoxic edema caused by hypoglycemia: follow-up diffusion-weighted imaging features. Emerg Radiol 2012;19(5):473–475
353. Johkura K, Nakae Y, Kudo Y, Yoshida TN, Kuroiwa Y. Early diffusion MR imaging findings and short-term outcome in comatose patients with hypoglycemia. AJNR Am J Neuroradiol 2012;33(5):904–909
354. Yong AW, Morris Z, Shuler K, Smith C, Wardlaw J. Acute symptomatic hypoglycaemia mimicking ischaemic stroke on imaging: a systemic review. BMC Neurol 2012;12:139

Hypothalamic Hamartoma

355. Amstutz DR, Coons SW, Kerrigan JF, Rekate HL, Heiserman JE. Hypothalamic hamartomas: Correlation of MR imaging and spectroscopic findings with tumor glial content. AJNR Am J Neuroradiol 2006;27(4):794–798
356. Freeman JL, Coleman LT, Wellard RM, et al. MR imaging and spectroscopic study of epileptogenic hypothalamic hamartomas: analysis of 72 cases. AJNR Am J Neuroradiol 2004;25(3):450–462
357. Maixner W. Hypothalamic hamartomas—clinical, neuropathological and surgical aspects. Childs Nerv Syst 2006;22(8):867–873
358. Mathieu D, Deacon C, Pinard CA, Kenny B, Duval J. Gamma Knife surgery for hypothalamic hamartomas causing refractory epilepsy: preliminary results from a prospective observational study. J Neurosurg 2010;113(Suppl):215–221
359. Parvizi J, Le S, Foster BL, et al. Gelastic epilepsy and hypothalamic hamartomas: neuroanatomical analysis of brain lesions in 100 patients. Brain 2011;134(Pt 10):2960–2968

Hypopthalamus

360. Saleem SN, Said AHM, Lee DH. Lesions of the hypothalamus: MR imaging diagnostic features. Radiographics 2007;27(4):1087–1108

Hypoxic Ischemic Injuries in Adults

361. Franco Folino A. Cerebral autoregulation and syncope. Prog Cardiovasc Dis 2007;50(1):49–80
362. Huang BY, Castillo M. Hypoxic-ischemic brain injury: imaging findings from birth to adulthood. Radiographics 2008;28(2):417–439, quiz 617
363. Kanekar SG, Zacharia T, Roller R. Imaging of stroke: Part 2, Pathophysiology at the molecular and cellular levels and corresponding imaging changes. AJR Am J Roentgenol 2012;198(1):63–74
364. Kucinski T. Unenhanced CT and acute stroke physiology. Neuroimaging Clin N Am 2005;15(2):397–407, xi–xii

Idiopathic Hypereosinophilic Syndrome

365. Lee EJ, Lee YJ, Lee SR, Park DW, Kim HY. Hypereosinophilia with multiple thromboembolic cerebral infarcts and focal intracerebral hemorrhage. Korean J Radiol 2009;10(5):511–514
366. Kono Y, Itoh Y. Diffusion-weighted imaging of encephalopathy related to idiopathic hypereosinophilic syndrome. Clin Neurol Neurosurg 2009;111(6):551–553

Inflammatory and Infectious Diseases of the Pituitary Gland

367. Lury KM. Inflammatory and infectious processes involving the pituitary gland. Top Magn Reson Imaging 2005;16(4):301–306
368. Santoro SG, Guida AH, Furioso AE, Glikman P, Rogozinski AS. Panhypopituitarism due to Wegener's granulomatosis. Arq Bras Endocrinol Metabol 2011;55(7):481–485
369. Yong TY, Li JYZ, Amato L, et al. Pituitary involvement in Wegener's granulomatosis. Pituitary 2008;11(1):77–84

Intra-axial Hemorrhage

370. Anzalone N, Scotti R, Riva R. Neuroradiologic differential diagnosis of cerebral intraparenchymal hemorrhage. Neurol Sci 2004;25(Suppl 1):S3–S5
371. Dainer HM, Smirniotopoulos JG. Neuroimaging of hemorrhage and vascular malformations. Semin Neurol 2008;28(4):533–547
372. Kubal WS. Updated imaging of traumatic brain injury. Radiol Clin North Am 2012;50(1):15–41
373. Leblanc GG, Golanov E, Awad IA, Young WL; Biology of Vascular Malformations of the Brain NINDS Workshop Collaborators. Biology of vascular malformations of the brain. Stroke 2009;40(12):e694–e702
374. Parizel PM, Makkat S, Van Miert E, Van Goethem JW, van den Hauwe L, De Schepper AM. Intracranial hemorrhage: principles of CT and MRI interpretation. Eur Radiol 2001;11(9):1770–1783
375. Riant F, Cecillon M, Saugier-Veber P, Tournier-Lasserve E. CCM molecular screening in a diagnosis context: novel unclassified variants leading to abnormal splicing and importance of large deletions. Neurogenetics 2013;14(2):133–141
376. Smith EE, Rosand J, Greenberg SM. Hemorrhagic stroke. Neuroimaging Clin N Am 2005;15(2):259–272, ix

Kearns-Sayre Syndrome

378. Duning T, Deppe M, Keller S, Mohammadi S, Schiffbauer H, Marziniak M. Diffusion tensor imaging in a case of Kearns-Sayre syndrome: striking brainstem involvement as a possible cause of oculomotor symptoms. J Neurol Sci 2009;281(1-2):110–112
379. Saneto RP, Friedman SD, Shaw DW. Neuroimaging of mitochondrial disease. Mitochondrion 2008;8(5-6):396–413
380. van der Knaap M, Valk J. Kearns-Sayre syndrome. In: van der Knaap MS, Valk J, eds. Magnetic Resonance of Myelination and Myelin Disorders. 3rd ed. New York: Springer; 2005:215–220

Langerhans Cel Histiocytosis

381. Paulus W, Perry A. Histiocytic tumours. In: Louis DN, Ohgaki H, Wiestler OD, Cavenee WK, eds. World Health Organization Classification of Tumours of the Central Nervous System. 4th ed. Geneva: IARC Press; 2007:193–196

Leigh's Disease

382. Baertling F, Rodenburg RJ, Schaper J, et al. A guide to diagnosis and treatment of Leigh syndrome. J Neurol Neurosurg Psychiatry 2014;85(3):257–265

Leukemia (Myeloid Sarcoma)

383. Akhaddar A, Zyani M, Mikdame M, Boucetta M. Acute myeloid leukemia with brain involvement (chloroma). Intern Med 2011;50(5):535–536
384. Cho SF, Liu TC, Chang CS. Isolated central nervous system relapse presenting as myeloid sarcoma of acute myeloid leukemia after allogeneic peripheral blood stem cell transplantation. Ann Hematol 2013;92(1):133–135
385. Grier DD, Al-Quran SZ, Gray B, Li Y, Braylan R. Intracranial myeloid sarcoma. Br J Haematol 2008;142(5):681
386. Hakyemez B, Yildirim N, Taskapilioglu O, et al. Intracranial myeloid sarcoma: conventional and advanced MRI findings. Br J Radiol 2007;80(954):e109–e112
387. Laningham FH, Kun LE, Reddick WE, Ogg RJ, Morris EB, Pui CH. Childhood central nervous system leukemia: historical perspectives, current therapy, and acute neurological sequelae. Neuroradiology 2007;49(11):873–888

Leukodystrophies

388. Barkovich AJ, Patay Z. Metabolic, toxic and inflammatory brain disorders. In: Barkovich AJ, Raybaud C, eds. Pediatric Neuroimaging. 5th ed. New York, NY: Wolters-Kluwer/Lippincott Williams & Wilkins; 2012:81–239
389. Bizzi A, Castelli G, Bugiani M, et al. Classification of childhood white matter disorders using proton MR spectroscopic imaging. AJNR Am J Neuroradiol 2008;29(7):1270–1275
390. Engelbrecht V, Scherer A, Rassek M, Witsack HJ, Mödder U. Diffusion-weighted MR imaging in the brain in children: findings in the normal brain and in the brain with white matter diseases. Radiology 2002;222(2):410–418
391. Kaye EM, Moser H. Where has all the white matter gone? Unraveling the mysteries of leukoencephalopathies. Neurology 2004;62(9):1464–1465
392. Lyon G, Fattal-Valevski A, Kolodny EH. Leukodystrophies: clinical and genetic aspects. Top Magn Reson Imaging 2006;17(4):219–242
393. Osborn AG. Inherited metabolic disorders. In: Osborn AG. Osborn's Brain: Imaging, Pathology, and Anatomy. Salt Lake City, UT: Amirsys; 2013: 853–905
394. Perlman SJ, Mar S. Leukodystrophies. In: Ahmad SI, ed. Neurodegenerative Diseases. Austin TX: Landes Bioscience/Springer Science; 2012:154–171
395. Phelan JA, Lowe LH, Glasier CM. Pediatric neurodegenerative white matter processes: leukodystrophies and beyond. Pediatr Radiol 2008;38(7):729–749
396. van der Knaap MS, Naidu S, Pouwels PJW, et al. New syndrome characterized by hypomyelination with atrophy of the basal ganglia and cerebellum. AJNR Am J Neuroradiol 2002;23(9):1466–1474
397. van der Knapp MS, Valk J. Leukoencephalopathy with vanishing white matter. In: van der Knaap MS, Valk J, eds. Magnetic Resonance of Myelination and Myelin Disorders. 3rd ed. New York: Springer; 2005:481–485
398. van der Voorn JP, Pouwels PJW, Hart AAM, et al. Childhood white matter disorders: quantitative MR imaging and spectroscopy. Radiology 2006;241(2):510–517

Lipoma

399. Jabot G, Stoquart-Elsankari S, Saliou G, Toussaint P, Deramond H, Lehmann P. Intracranial lipomas: clinical appearances on neuroimaging and clinical significance. J Neurol 2009;256(6):851–855
400. Mukherjee P, Street I, Irving RM. Intracranial lipomas affecting the cerebellopontine angle and internal auditory canal: a case series. Otol Neurotol 2011;32(4):670–675
401. Sommet J, Schiff M, Evrard P, Blanc R, Elmaleh-Bergès M. Pericallosal lipoma and middle cerebral artery aneurysm: a coincidence? Pediatr Radiol 2010;40(8):1417–1420
402. Yildiz H, Hakyemez B, Koroglu M, Yesildag A, Baykal B. Intracranial lipomas: importance of localization. Neuroradiology 2006;48(1): 1–7

Low grade Astrocytoma

403. Khayal IS, Vandenberg SR, Smith KJ, et al. MRI apparent diffusion coefficient reflects histopathologic subtype, axonal disruption, and tumor fraction in diffuse-type grade II gliomas. Neuro-oncol 2011;13(11):1192–1201
404. Poretti A, Meoded A, Huisman TAGM. Neuroimaging of pediatric posterior fossa tumors including review of the literature. J Magn Reson Imaging 2012;35(1):32–47
405. Rumboldt Z, Camacho DLA, Lake D, Welsh CT, Castillo M. Apparent diffusion coefficients for differentiation of cerebellar tumors in children. AJNR Am J Neuroradiol 2006;27(6):1362–1369
406. Siegal T. Clinical impact of molecular biomarkers in gliomas. J Clin Neurosci 2015;22:437–444
407. von Deimling A, Burger PC, Nakazato Y, Ohgaki H, Kleihues P. Diffuse astrocytoma. In: Louis DN, Ohgaki H, Wiestler OD, Cavenee WK, eds. World Health Organization Classification of Tumours of the Central Nervous System. 4th ed. Geneva: IARC Press; 2007:25–29

Lyme Disease

408. Hildenbrand P, Craven DE, Jones R, Nemeskal P. Lyme neuroborreliosis: manifestations of a rapidly emerging zoonosis. AJNR Am J Neuroradiol 2009;30(6):1079–1087

Lymphoma

409. Deckert M, Paulus W. Malignant lymphomas. In: Louis DN, Ohgaki H, Wiestler OD, Cavenee WK, eds. World Health Organization Classification of Tumours of the Central Nervous System. 4th ed. Geneva: IARC Press; 2007:188–192
410. Doskaliyev A, Yamasaki F, Ohtaki M, et al. Lymphomas and glioblastomas: differences in the apparent diffusion coefficient evaluated with high b-value diffusion-weighted magnetic resonance imaging at 3T. Eur J Radiol 2012;81(2):339–344
411. Lueth M, Stein H, Spors B, Henze G, Driever PH. First case report of a peripheral T-cell lymphoma, not otherwise specified, of the central nervous system in a child. J Pediatr Hematol Oncol 2012;34(2): e66–e68
412. Tang YZ, Booth TC, Bhogal P, Malhotra A, Wilhelm T. Imaging of primary central nervous system lymphoma. Clin Radiol 2011;66(8): 768–777
413. Toh CH, Castillo M, Wong AM, et al. Primary cerebral lymphoma and glioblastoma multiforme: differences in diffusion characteristics evaluated with diffusion tensor imaging. AJNR Am J Neuroradiol 2008;29(3):471–475
414. Villano JL, Koshy M, Shaikh H, Dolecek TA, McCarthy BJ. Age, gender, and racial differences in incidence and survival in primary CNS lymphoma. Br J Cancer 2011;105(9):1414–1418
415. Zhu JQ, Hao NX, Bao WQ, Wu XR. Multiple calcified primary central nervous system lymphoma with immunodeficiency in a child. World J Pediatr 2011;7(3):277–279

Malaria

416. Potchen MJ, Kampondeni SD, Seydel KB, et al. Acute brain MRI findings in 120 Malawian children with cerebral malaria: new insights into an ancient disease. AJNR Am J Neuroradiol 2012;33(9): 1740–1746
417. Seydel KB, Kampondeni SD, Valim C, et al. Brain swelling and death in children with cerebral malaria. N Engl J Med 2015;372(12): 1126–1137

Malignant Hypertension

418. Choi JH, Choi KD, Kim JS, Kim HJ, Lee JE, An SJ. Simultaneous posterior ischemic optic neuropathy, cerebral border zone infarction, and spinal cord infarction after correction of malignant hypertension. J Neuroophthalmol 2008;28(3):198–201
419. Cruz-Flores S, de Assis Aquino Gondim F, Leira EC. Brainstem involvement in hypertensive encephalopathy: clinical and radiological findings. Neurology 2004;62(8):1417–1419
420. Eguchi K, Kasahara K, Nagashima A, et al. Two cases of malignant hypertension with reversible diffuse leukoencephalopathy exhibiting a reversible nocturnal blood pressure "riser" pattern. Hypertens Res 2002;25(3):467–473
421. Elliott WJ. Clinical features and management of selected hypertensive emergencies. J Clin Hypertens (Greenwich) 2004;6(10): 587–592
422. Feldstein C. Management of hypertensive crises. Am J Ther 2007; 14(2):135–139
423. Garewal M, Yahya S, Ward C, Singh N, Cruz-Flores S. MRI changes in thrombotic microangiopathy secondary to malignant hypertension. J Neuroimaging 2007;17(2):178–180
424. Seet RCS, Lim ECH. Images in cardiovascular medicine. Hypertensive brainstem encephalopathy. Circulation 2007;115(9):e310–e311

Maple Syrup Urine Disease

425. Ha JS, Kim TK, Eun BL, et al. Maple syrup urine disease encephalopathy: a follow-up study in the acute stage using diffusion-weighted MRI. Pediatr Radiol 2004;34(2):163–166
426. Jan W, Zimmerman RA, Wang ZJ, Berry GT, Kaplan PB, Kaye EM. MR diffusion imaging and MR spectroscopy of maple syrup urine disease during acute metabolic decompensation. Neuroradiology 2003;45(6):393–399
427. Parmar H, Sitoh YY, Ho L. Maple syrup urine disease: diffusion-weighted and diffusion-tensor magnetic resonance imaging findings. J Comput Assist Tomogr 2004;28(1):93–97
428. Sakai M, Inoue Y, Oba H, et al. Age dependence of diffusion-weighted magnetic resonance imaging findings in maple syrup urine disease encephalopathy. J Comput Assist Tomogr 2005;29(4):524–527

Medulloblastoma

429. Giangaspero F, Eberhart CG, Haapasalo H, et al. Medulloblastoma. In: Louis DN, Ohgaki H, Wiestler OD, Cavenee WK, eds. World Health Organization Classification of Tumours of the Central Nervous System. 4th ed. Geneva: IARC Press; 2007:132–140
430. Isaacs H. Fetal brain tumors: a review of 154 cases. Am J Perinatol 2009;26(6):453–466
431. Koeller KK, Rushing EJ. From the archives of the AFIP: medulloblastoma: a comprehensive review with radiologic-pathologic correlation. Radiographics 2003;23(6):1613–1637
432. McLendon RE, Judkins AR, Eberhart CG, Fuller GN, Sarkar C, Ng HK. Central nervous system primitive neuroectodermal tumours. In: Louis DN, Ohgaki H, Wiestler OD, Cavenee WK, eds. World Health Organization Classification of Tumours of the Central Nervous System. 4th ed. Geneva: IARC Press; 2007:141–146
433. Mehrotra N, Shamji MF, Vassilyadi M, Ventureyra EC. Intracranial tumors in first year of life: the CHEO experience. Childs Nerv Syst 2009;25(12):1563–1569
434. Meyers SP, Wildenhain SL, Chang JK, et al. Postoperative evaluation for disseminated medulloblastoma involving the spine: contrast-enhanced MR findings, CSF cytologic analysis, timing of disease occurrence, and patient outcomes. AJNR Am J Neuroradiol 2000;21(9):1757–1765
435. Meyers SP, Wildenhain S, Chess MA, Tarr RW. Postoperative evaluation for intracranial recurrence of medulloblastoma: MR findings with gadopentetate dimeglumine. AJNR Am J Neuroradiol 1994;15(8):1425–1434
436. Meyers SP, Kemp SS, Tarr RW. MR imaging features of medulloblastomas. AJR Am J Roentgenol 1992;158(4):859–865
437. Yeom KW, Mobley BC, Lober RM, et al. Distinctive MRI features of pediatric medulloblastoma subtypes. AJR Am J Roentgenol 2013;200(4):895–903

Megalencephalic Leukodystrophy with Subcortical Cysts

438. Barkovich AJ, Patay Z. Metabolic, toxic and inflammatory brain disorders. In: In: Barkovich AJ, Raybaud C, eds. Pediatric Neuroimaging. 5th ed. New York, NY: Wolters-Kluwer/Lippincott Williams & Wilkins; 2012:81–239
439. López-Hernández T, Sirisi S, Capdevila-Nortes X, et al. Molecular mechanisms of MLC1 and GLIALCAM mutations in megalencephalic leukoencephalopathy with subcortical cysts. Hum Mol Genet 2011;20(16):3266–3277
440. Osborn AG. Inherited metabolic disorders. In: Osborn AG. Osborn's Brain: Imaging, Pathology, and Anatomy. Salt Lake City, UT: Amirsys; 2013:853–905
441. van der Knaap MS, Boor I, Estévez R. Megalencephalic leukoencephalopathy with subcortical cysts: chronic white matter oedema due to a defect in brain ion and water homoeostasis. Lancet Neurol 2012;11(11):973–985
442. van der Knaap M, Valk J. Megalencephalic leukoencephalopathy with subcortical cysts. In: van der Knaap MS, Valk J, eds. Magnetic Resonance of Myelination and Myelin Disorders. 3rd ed. New York: Springer; 2005: 442–450

MELAS/MERRF

443. Diogo L, Cordeiro M, Garcia P, et al. Value of brain magnetic resonance imaging in mitochondrial respiratory chain disorders. Pediatr Neurol 2010;42(3):196–200
444. Sofou K, Steneryd K, Wiklund LM, Tulinius M, Darin N. MRI of the brain in childhood-onset mitochondrial disorders with central nervous system involvement. Mitochondrion 2013;13(4):364–371

Meningioangiomatosis

445. Kashlan ON, Laborde DV, Davison L, et al. Meningioangiomatosis: a case report and literature review emphasizing diverse appearance on different imaging modalities. Case Rep Neurol Med 2011;2011: 361203
446. Rokes C, Ketonen LM, Fuller GN, Weinberg J, Slopis JM, Wolff JE. Imaging and spectroscopic findings in meningioangiomatosis. Pediatr Blood Cancer 2009;53(4):672–674
447. Yao Z, Wang Y, Zee C, Feng X, Sun H. Computed tomography and magnetic resonance appearance of sporadic meningioangiomatosis correlated with pathological findings. J Comput Assist Tomogr 2009;33(5):799–804

Menkes Disease

448. Barnerias C, Boddaert N, Guiraud P, et al. Unusual magnetic resonance imaging features in Menkes disease. Brain Dev 2008;30(7):489–492
449. Bekiesińska-Figatowska M, Rokicki D, Walecki J, Gremida M. Menkes' disease with a Dandy-Walker variant: case report. Neuroradiology 2001;43(11):948–950
450. Ito H, Mori K, Sakata M, Naito E, Harada M, Kagami S. Transient left temporal lobe lesion in Menkes disease may influence the generation of tonic spasms. Brain Dev 2011;33(4):345–348
451. Jaspan T. Current controversies in the interpretation of non-accidental head injury. Pediatr Radiol 2008;38(Suppl 3):S378–S387
452. Koprivsek K, Lucic M, Kozic D, Djordjevic M, Kravljanac R. Basal ganglia lesions in the early stage of Menkes disease. J Inherit Metab Dis 2010;33(3):301–302
453. Moser FG, Sarnat HB, Maya MM, Menkes JH. Corkscrew basilar artery as an incidental finding on neuroimaging. Pediatr Neurol 2007;37(5):375–377
454. Nassogne MC, Sharrard M, Hertz-Pannier L, et al. Massive subdural haematomas in Menkes disease mimicking shaken baby syndrome. Childs Nerv Syst 2002;18(12):729–731

Metachromatic Leukodystrophy

455. Faerber EN, Melvin J, Smergel EM. MRI appearances of metachromatic leukodystrophy. Pediatr Radiol 1999;29(9):669–672
456. Kim TS, Kim IO, Kim WS, et al. MR of childhood metachromatic leukodystrophy. AJNR Am J Neuroradiol 1997;18(4):733–738
457. Nandhagopal R, Krishnamoorthy SG. Neurological picture. Tigroid and leopard skin pattern of dysmyelination in metachromatic leucodystrophy. J Neurol Neurosurg Psychiatry 2006;77(3):344
458. Oguz KK, Anlar B, Senbil N, Cila A. Diffusion-weighted imaging findings in juvenile metachromatic leukodystrophy. Neuropediatrics 2004;35(5):279–282
459. Sener RN. Metachromatic leukodystrophy. Diffusion MR imaging and proton MR spectroscopy. Acta Radiol 2003;44(4):440–443
460. Sener RN. Metachromatic leukodystrophy: diffusion MR imaging findings. AJNR Am J Neuroradiol 2002;23(8):1424–1426
461. Toldo I, Carollo C, Battistella PA, Laverda AM. Spinal cord and cauda equina MRI findings in metachromatic leukodystrophy: case report. Neuroradiology 2005;47(8):572–575
462. van der Voorn JP, Pouwels PJ, Kamphorst W, et al. Histopathologic correlates of radial stripes on MR images in lysosomal storage disorders. AJNR Am J Neuroradiol 2005;26(3):442–446

Metastases

463. Mitsuya K, Nakasu Y, Horiguchi S, et al. Perfusion weighted magnetic resonance imaging to distinguish the recurrence of metastatic brain tumors from radiation necrosis after stereotactic radiosurgery. J Neurooncol 2010;99(1):81–88
464. Toh CH, Wei KC, Ng SH, Wan YL, Lin CP, Castillo M. Differentiation of brain abscesses from necrotic glioblastomas and cystic metastatic brain tumors with diffusion tensor imaging. AJNR Am J Neuroradiol 2011;32(9):1646–1651
465. Wang W, Steward CE, Desmond PM. Diffusion tensor imaging in glioblastoma multiforme and brain metastases: the role of p, q, L, and fractional anisotropy. AJNR Am J Neuroradiol 2009;30(1):203–208
466. Wesseling P, von Deimling A, Aldape KD. Metastatic tumours of the CNS. In: Louis DN, Ohgaki H, Wiestler OD, Cavenee WK, eds. World Health Organization Classification of Tumours of the Central Nervous System. 4th ed. Geneva: IARC Press; 2007:248–251

Metastatic Tumor

467. Kose D, Karabagli P, Yavas G, Karabagli H, Koksal Y. Intracranial metastasis of neuroblastoma: in two different areas at the same time. Childs Nerv Syst 2013;29(10):1799–1802
468. Paulino AC, Mai WY, Teh BS. Radiotherapy in metastatic ewing sarcoma. Am J Clin Oncol 2013;36(3):283–286
469. Rabah F, Al-Mashaikhi N, Beshlawi I, et al. Brain is not always the last fortress; osteosarcoma with large brain metastasis. J Pediatr Hematol Oncol 2013;35(2):e91–e93

Methanol

470. Arora V, Nijjar IB, Multani AS, et al. MRI findings in methanol intoxication: a report of two cases. Br J Radiol 2007;80(958):e243–e246

471. Bhatia R, Kumar M, Garg A, Nanda A. Putaminal necrosis due to methanol toxicity. Pract Neurol 2008;8(6):386–387
472. Kruse JA. Methanol and ethylene glycol intoxication. Crit Care Clin 2012;28(4):661–711
473. Takao H, Doi I, Watanabe T. Serial diffusion-weighted magnetic resonance imaging in methanol intoxication. J Comput Assist Tomogr 2006;30(5):742–744

Methylmalonic Aciduria / Homocystinuria

474. Burlina AP, Manara R, Calderone M, Catuogno S, Burlina AB. Diffusion-weighted imaging in the assessment of neurological damage in patients with methylmalonic aciduria. J Inherit Metab Dis 2003;26(5):417–422
475. Carrozzo R, Dionisi-Vici C, Steuerwald U, et al. SUCLA2 mutations are associated with mild methylmalonic aciduria, Leigh-like encephalomyopathy, dystonia and deafness. Brain 2007;130(Pt 3):862–874
476. Ostergaard E, Schwartz M, Batbayli M, et al. A novel missense mutation in SUCLG1 associated with mitochondrial DNA depletion, encephalomyopathic form, with methylmalonic aciduria. Eur J Pediatr 2010;169(2):201–205
477. Rossi A, Cerone R, Biancheri R, et al. Early-onset combined methylmalonic aciduria and homocystinuria: neuroradiologic findings. AJNR Am J Neuroradiol 2001;22(3):554–563
478. Yeşildağ A, Ayata A, Baykal B, et al. Magnetic resonance imaging and diffusion-weighted imaging in methylmalonic acidemia. Acta Radiol 2005;46(1):101–103

Microcephaly

479. Adachi Y, Poduri A, Kawaguch A, et al. Congenital microcephaly with a simplified gyral pattern: associated findings and their significance. AJNR Am J Neuroradiol 2011;32(6):1123–1129
480. Poulton CJ, Schot R, Kia SK, et al. Microcephaly with simplified gyration, epilepsy, and infantile diabetes linked to inappropriate apoptosis of neural progenitors. Am J Hum Genet 2011;89(2):265–276

Movement Disorders

481. Mascalchi M, Vella A, Ceravolo R. Movement disorders: role of imaging in diagnosis. J Magn Reson Imaging 2012;35(2):239–256

MRI of Fetal Brain Development

482. Chapman T, Matesan M, Weinberger E, Bulas DI. Digital atlas of fetal brain MRI. Pediatr Radiol 2010;40(2):153–162
483. Kostovic I, Vasung L. Insights from in vitro fetal magnetic resonance imaging of cerebral development. Semin Perinatol 2009;33(4):220–233
484. Manganaro L, Perrone A, Savelli S, et al. Evaluation of normal brain development by prenatal MR imaging. Radiol Med (Torino) 2007;112(3):444–455
485. Rados M, Judas M, Kostović I. In vitro MRI of brain development. Eur J Radiol 2006;57(2):187–198
486. Shekdar K, Feygin T. Fetal neuroimaging. Neuroimaging Clin N Am 2011;21(3):677–703, ix

Mucopolysaccharidoses

487. Davison JE, Hendriksz CJ, Sun Y, Davies NP, Gissen P, Peet AC. Quantitative in vivo brain magnetic resonance spectroscopic monitoring of neurological involvement in mucopolysaccharidosis type II (Hunter Syndrome). J Inherit Metab Dis 2010;33(Suppl 3):S395–S399
488. Finn CT, Vedolin L, Schwartz IV, et al. Magnetic resonance imaging findings in Hunter syndrome. Acta Paediatr 2008;97(457):61–68
489. Horovitz DDG, Magalhães TdeS, Pena e Costa A, et al. Spinal cord compression in young children with type VI mucopolysaccharidosis. Mol Genet Metab 2011;104(3):295–300
490. Iyer RS, Khanna PC. Intracranial findings of Hunter syndrome. Pediatr Radiol 2010;40(Suppl 1):S173
491. Kara S, Sherr EH, Barkovich AJ. Dilated perivascular spaces: an informative radiologic finding in Sanfilippo syndrome type A. Pediatr Neurol 2008;38(5):363–366
492. Lee C, Dineen TE, Brack M, Kirsch JE, Runge VM. The mucopolysaccharidoses: characterization by cranial MR imaging. AJNR Am J Neuroradiol 1993;14(6):1285–1292
493. Li MF, Chiu PC, Weng MJ, Lai PH. Atlantoaxial instability and cervical cord compression in Morquio syndrome. Arch Neurol 2010; 67(12):1530 (formerly Archives of Neurology)
494. Manara R, Priante E, Grimaldi M, et al. Brain and spine MRI features of Hunter disease: frequency, natural evolution and response to therapy. J Inherit Metab Dis 2011;34(3):763–780
495. Martin R, Beck M, Eng C, et al. Recognition and diagnosis of mucopolysaccharidosis II (Hunter syndrome). Pediatrics 2008;121(2): e377–e386
496. Matheus MG, Castillo M, Smith JK, Armao D, Towle D, Muenzer J. Brain MRI findings in patients with mucopolysaccharidosis types I and II and mild clinical presentation. Neuroradiology 2004;46(8):666–672
497. Rasalkar DD, Chu WCW, Hui J, Chu CM, Paunipagar BK, Li CK. Pictorial review of mucopolysaccharidosis with emphasis on MRI features of brain and spine. Br J Radiol 2011;84(1001):469–477
498. van der Knaap M, Valk J. Mucopolysaccharidoses. In: van der Knaap MS, Valk J, eds. Magnetic Resonance of Myelination and Myelin Disorders. 3rd ed. New York: Springer; 2005;123–136
499. Vedolin L, Schwartz IVD, Komlos M, et al. Brain MRI in mucopolysaccharidosis: effect of aging and correlation with biochemical findings. Neurology 2007;69(9):917–924
500. Vedolin L, Schwartz IVD, Komlos M, et al. Correlation of MR imaging and MR spectroscopy findings with cognitive impairment in mucopolysaccharidosis II. AJNR Am J Neuroradiol 2007;28(6):1029–1033
501. White KK, Karol LA, White DR, Hale S. Musculoskeletal manifestations of Sanfilippo Syndrome (mucopolysaccharidosis type III). J Pediatr Orthop 2011;31(5):594–598
502. Wraith JE, Scarpa M, Beck M, et al. Mucopolysaccharidosis type II (Hunter syndrome): a clinical review and recommendations for treatment in the era of enzyme replacement therapy. Eur J Pediatr 2008;167(3):267–277

Multiple Sclerosis

503. Filippi M. Multiple sclerosis in 2010: Advances in monitoring and treatment of multiple sclerosis. Nat Rev Neurol 2011;7(2):74–75
504. Inglese M, Petracca M. Imaging multiple sclerosis and other neurodegenerative diseases. Prion 2013;7(1):47–54
505. Milo R, Kahana E. Multiple sclerosis: geoepidemiology, genetics and the environment. Autoimmun Rev 2010;9(5):A387–A394
506. Minagar A, Barnett MH, Benedict RHB, et al. The thalamus and multiple sclerosis: modern views on pathologic, imaging, and clinical aspects. Neurology 2013;80(2):210–219
507. Sheremata W, Tornes L. Multiple sclerosis and the spinal cord. Neurol Clin 2013;31(1):55–77

Multiple System Atrophy

508. Iodice V, Lipp A, Ahlskog JE, et al. Autopsy confirmed multiple system atrophy cases: Mayo experience and role of autonomic function tests. J Neurol Neurosurg Psychiatry 2012;83(4):453–459
509. Ito S, Shirai W, Hattori T. Putaminal hyperintensity on T1-weighted MR imaging in patients with the Parkinson variant of multiple system atrophy. AJNR Am J Neuroradiol 2009;30(4):689–692
510. Massey LA, Jäger HR, Paviour DC, et al. The midbrain to pons ratio: a simple and specific MRI sign of progressive supranuclear palsy. Neurology 2013;80(20):1856–1861
511. Matsusue E, Fujii S, Kanasaki Y, Kaminou T, Ohama E, Ogawa T. Cerebellar lesions in multiple system atrophy: postmortem MR imaging-pathologic correlations. AJNR Am J Neuroradiol 2009; 30(9):1725–1730
512. Nair SR, Tan LK, Mohd Ramli N, Lim SY, Rahmat K, Mohd Nor H. A decision tree for differentiating multiple system atrophy from Parkinson's disease using 3-T MR imaging. Eur Radiol 2013;23(6):1459–1466
513. Nicoletti G, Rizzo G, Barbagallo G, et al. Diffusivity of cerebellar hemispheres enables discrimination of cerebellar or parkinsonian multiple system atrophy from progressive supranuclear palsy-Richardson syndrome and Parkinson disease. Radiology 2013;267(3):843–850
514. Okamoto K, Tokiguchi S, Furusawa T, et al. MR features of diseases involving bilateral middle cerebellar peduncles. AJNR Am J Neuroradiol 2003;24(10):1946–1954
515. Paviour DC, Price SL, Jahanshahi M, Lees AJ, Fox NC. Longitudinal MRI in progressive supranuclear palsy and multiple system atrophy: rates and regions of atrophy. Brain 2006;129(Pt 4):1040–1049
516. Savoiardo M, Strada L, Girotti F, et al. Olivopontocerebellar atrophy: MR diagnosis and relationship to multisystem atrophy. Radiology 1990;174(3 Pt 1):693–696
517. Shrivastava A. The hot cross bun sign. Radiology 2007;245(2): 606–607

518. Tsukamoto K, Matsusue E, Kanasaki Y, et al. Significance of apparent diffusion coefficient measurement for the differential diagnosis of multiple system atrophy, progressive supranuclear palsy, and Parkinson's disease: evaluation by 3.0-T MR imaging. Neuroradiology 2012;54(9):947–955

Neonatal Hypoxic-Ischemic Injury

519. Boichot C, Walker PM, Durand C, et al. Term neonate prognoses after perinatal asphyxia: contributions of MR imaging, MR spectroscopy, relaxation times, and apparent diffusion coefficients. Radiology 2006;239(3):839–848
520. Chao CP, Zaleski CG, Patton AC. Neonatal hypoxic-ischemic encephalopathy: multimodality imaging findings. Radiographics 2006;26(Suppl 1):S159–S172
521. Grant PE, Yu D. Acute injury to the immature brain with hypoxia with or without hypoperfusion. Magn Reson Imaging Clin N Am 2006; 14(2):271–285
522. Heinz ER, Provenzale JM. Imaging findings in neonatal hypoxia: a practical review. AJR Am J Roentgenol 2009;192(1):41–47
523. Huang BY, Castillo M. Hypoxic-ischemic brain injury: imaging findings from birth to adulthood. Radiographics 2008;28(2):417–439, quiz 617
524. Liauw L, Palm-Meinders IH, van der Grond J, et al. Differentiating normal myelination from hypoxic-ischemic encephalopathy on T1-weighted MR Images: a new approach. AJNR Am J Neuroradiol 2007;28(4):660–665
525. Liauw L, van der Grond J, van den Berg-Huysmans AA, Laan LAEM, van Buchem MA, van Wezel-Meijler G. Is there a way to predict outcome in (near) term neonates with hypoxic-ischemic encephalopathy based on MR imaging? AJNR Am J Neuroradiol 2008;29(9): 1789–1794
526. Liauw L, van der Grond J, van den Berg-Huysmans AA, Palm-Meinders IH, van Buchem MA, van Wezel-Meijler G. Hypoxic-ischemic encephalopathy: diagnostic value of conventional MR imaging pulse sequences in term-born neonates. Radiology 2008;247(1):204–212
527. Liauw L, van Wezel-Meijler G, Veen S, van Buchem MA, van der Grond J. Do apparent diffusion coefficient measurements predict outcome in children with neonatal hypoxic-ischemic encephalopathy? AJNR Am J Neuroradiol 2009;30(2):264–270
528. Nikas I, Dermentzoglou V, Theofanopoulou M, Theodoropoulos V. Parasagittal lesions and ulegyria in hypoxic-ischemic encephalopathy: neuroimaging findings and review of the pathogenesis. J Child Neurol 2008;23(1):51–58
529. Zarifi MK, Astrakas LG, Poussaint TY, Plessis Ad Ad, Zurakowski D, Tzika AA. Prediction of adverse outcome with cerebral lactate level and apparent diffusion coefficient in infants with perinatal asphyxia. Radiology 2002;225(3):859–870

Neurocutaneous Melanosis

530. Brat DJ, Perry A. Melanocytic lesions. In: Louis DN, Ohgaki H, Wiestler OD, Cavenee WK, eds. World Health Organization Classification of Tumours of the Central Nervous System. 4th ed. Geneva: IARC Press; 2007:181–183
531. Di Rocco F, Sabatino G, Koutzoglou M, Battaglia D, Caldarelli M, Tamburrini G. Neurocutaneous melanosis. Childs Nerv Syst 2004; 20(1):23–28
532. Hayashi M, Maeda M, Maji T, Matsubara T, Tsukahara H, Takeda K. Diffuse leptomeningeal hyperintensity on fluid-attenuated inversion recovery MR images in neurocutaneous melanosis. AJNR Am J Neuroradiol 2004;25(1):138–141
533. Peretti-Viton P, Gorincour G, Feuillet L, et al. Neurocutaneous melanosis: radiological-pathological correlation. Eur Radiol 2002; 12(6):1349–1353
534. Ramaswamy V, Delaney H, Haque S, Marghoob A, Khakoo Y. Spectrum of central nervous system abnormalities in neurocutaneous melanocytosis. Dev Med Child Neurol 2012;54(6):563–568

Neurocysticercosis

535. Lerner A, Shiroishi MS, Zee CS, Law M, Go JL. Imaging of neurocysticercosis. Neuroimaging Clin N Am 2012;22(4):659–676

Neurodegenerative Disease

536. Schuff N, Zhu XP. Imaging of mild cognitive impairment and early dementia. Br J Radiol 2007;80(Spec No 2):S109–S114
537. Snowden JS, Thompson JC, Stopford CL, et al. The clinical diagnosis of early-onset dementias: diagnostic accuracy and clinicopathological relationships. Brain 2011;134(Pt 9):2478–2492
538. Sullivan EV, Pfefferbaum A. Neuroradiological characterization of normal adult ageing. Br J Radiol 2007;80(Spec No 2):S99–S108
539. Tartaglia MC, Rosen HJ, Miller BL. Neuroimaging in dementia. Neurotherapeutics 2011;8(1):82–92
540. Vitali P, Migliaccio R, Agosta F, Rosen HJ, Geschwind MD. Neuroimaging in dementia. Semin Neurol 2008;28(4):467–483

Neuroepithelial Cyst

541. Guermazi A, Miaux Y, Majoulet JF, Lafitte F, Chiras J. Imaging findings of central nervous system neuroepithelial cysts. Eur Radiol 1998;8(4):618–623
542. Ormond DR, Omeis I, Mohan A, Murali R, Narayan P. Obstructive hydrocephalus due to a third ventricular neuroepithelial cyst. J Neurosurg Pediatr 2008;1(6):481–484
543. Uematsu Y, Kubo K, Nishibayashi T, Ozaki F, Nakai K, Itakura T. Interhemispheric neuroepithelial cyst associated with agenesis of the corpus callosum. A case report and review of the literature. Pediatr Neurosurg 2000;33(1):31–36

Neuroepithelial/Neuroglial Cyst

544. Osborn AG, Preece MT. Intracranial cysts: radiologic-pathologic correlation and imaging approach. Radiology 2006;239(3):650–664

Neurofibromatosis Type 1

545. Ginat DT, Meyers SP. Intracranial lesions with high signal intensity on T1-weighted MR images: differential diagnosis. Radiographics 2012;32(2):499–516
546. Mentzel HJ, Seidel J, Fitzek C, et al. Pediatric brain MRI in neurofibromatosis type I. Eur Radiol 2005;15(4):814–822
547. Terada H, Barkovich AJ, Edwards MSB, Ciricillo SM. Evolution of high-intensity basal ganglia lesions on T1-weighted MR in neurofibromatosis type 1. AJNR Am J Neuroradiol 1996;17(4):755–760
548. von Deimling A, Perry A. Neurofibromatosis type 1. In: Louis DN, Ohgaki H, Wiestler OD, Cavenee WK, eds. World Health Organization Classification of Tumours of the Central Nervous System. 4th ed. Geneva: IARC Press; 2007:206–209

Neurologic Decompression Sickness

549. Gao GK, Wu D, Yang Y, et al. Cerebral magnetic resonance imaging of compressed air divers in diving accidents. Undersea Hyperb Med 2009;36(1):33–41
550. Jersey SL, Jesinger RA, Palka P. Brain magnetic resonance imaging anomalies in U-2 pilots with neurological decompression sickness. Aviat Space Environ Med 2013;84(1):3–11
551. Ozdoba C, Weis J, Plattner T, Dirnhofer R, Yen K. Fatal scuba diving incident with massive gas embolism in cerebral and spinal arteries. Neuroradiology 2005;47(6):411–416
552. Tamaki H, Kohshi K, Sajima S, et al. Repetitive breath-hold diving causes serious brain injury. Undersea Hyperb Med 2010;37(1):7–11

Neuronal Ceroid Lipofuscinoses

553. Paniagua Bravo A, Forkert ND, Schulz A, et al. Quantitative t2 measurements in juvenile and late infantile neuronal ceroid lipofuscinosis. Clin Neuroradiol 2013;23(3):189–196
554. Dyke JP, Voss HU, Sondhi D, et al. Assessing disease severity in late infantile neuronal ceroid lipofuscinosis using quantitative MR diffusion-weighted imaging. AJNR Am J Neuroradiol 2007;28(7): 1232–1236
555. Kohlschütter A, Schulz A. Towards understanding the neuronal ceroid lipofuscinoses. Brain Dev 2009;31(7):499–502
556. Mink JW, Augustine EF, Adams HR, Marshall FJ, Kwon JM. Classification and natural history of the neuronal ceroid lipofuscinoses. J Child Neurol 2013;28(9):1101–1105
557. Mole SE, Cotman SL. Genetics of the neuronal ceroid lipofuscinoses (Batten disease). Biochimica et Biophysica Acta 2015;1852: 2237–2241

Neuronal Migration Disorders

558. Spalice A, Parisi P, Nicita F, Pizzardi G, Del Balzo F, Iannetti P. Neuronal migration disorders: clinical, neuroradiologic and genetics aspects. Acta Paediatr 2009;98(3):421–433

Neurosarcoid

559. Koyama T, Ueda H, Togashi K, Umeoka S, Kataoka M, Nagai S. Radiologic manifestations of sarcoidosis in various organs. Radiographics 2004;24(1):87–104
560. Spencer TS, Campellone JV, Maldonado I, Huang N, Usmani Q, Reginato AJ. Clinical and magnetic resonance imaging manifestations of neurosarcoidosis. Semin Arthritis Rheum 2005;34(4):649–661

Neurotoxicity from Chemotherapeutic Agents

561. Daams M, Schuitema I, van Dijk BW, et al. Long-term effects of cranial irradiation and intrathecal chemotherapy in treatment of childhood leukemia: a MEG study of power spectrum and correlated cognitive dysfunction. BMC Neurol 2012;12:84
562. Inaba H, Khan RB, Laningham FH, Crews KR, Pui CH, Daw NC. Clinical and radiological characteristics of methotrexate-induced acute encephalopathy in pediatric patients with cancer. Ann Oncol 2008;19(1):178–184
563. Laningham FH, Kun LE, Reddick WE, Ogg RJ, Morris EB, Pui CH. Childhood central nervous system leukemia: historical perspectives, current therapy, and acute neurological sequelae. Neuroradiology 2007;49(11):873–888
564. Wells EM, Nageswara Rao AA, Scafidi J, Packer RJ. Neurotoxicity of biologically targeted agents in pediatric cancer trials. Pediatr Neurol 2012;46(4):212–221
565. Yoshida S, Hayakawa K, Yamamoto A, Kuroda H, Imashuku S. The central nervous system complications of bone marrow transplantation in children. Eur Radiol 2008;18(10):2048–2059

Non-Accidental Head Injury in Children (Child Abuse)

567. Bode-Jänisch S, Bültmann E, Hartmann H, Schroeder G, Zajaczek JEW, Debertin AS. Serious head injury in young children: birth trauma versus non-accidental head injury. Forensic Sci Int 2012;214(1-3):e34–e38
568. Demaerel P. MR imaging in inflicted brain injury. Magn Reson Imaging Clin N Am 2012;20(1):35–44
569. Ichord RN, Naim M, Pollock AN, Nance ML, Margulies SS, Christian CW. Hypoxic-ischemic injury complicates inflicted and accidental traumatic brain injury in young children: the role of diffusion-weighted imaging. J Neurotrauma 2007;24(1):106–118
570. Kemp AM, Rajaram S, Mann M, et al; Welsh Child Protection Systematic Review Group. What neuroimaging should be performed in children in whom inflicted brain injury (iBI) is suspected? A systematic review. Clin Radiol 2009;64(5):473–483
571. Piteau SJ, Ward MGK, Barrowman NJ, Plint AC. Clinical and radiographic characteristics associated with abusive and nonabusive head trauma: a systematic review. Pediatrics 2012;130(2):315–323
572. Rajaram S, Batty R, Rittey CDC, Griffiths PD, Connolly DJA. Neuroimaging in non-accidental head injury in children: an important element of assessment. Postgrad Med J 2011;87(1027):355–361
573. Stoodley N. Radiology in non-accidental head injury. Paediatr Child Health (Oxford) 2009;19(2):90–92
574. Stoodley N. Neuroimaging in non-accidental head injury: if, when, why and how. Clin Radiol 2005;60(1):22–30
575. Tung GA, Kumar M, Richardson RC, Jenny C, Brown WD. Comparison of accidental and nonaccidental traumatic head injury in children on noncontrast computed tomography. Pediatrics 2006;118(2):626–633

Nonadenomatous Tumors of Pituitary Gland and Sella

576. Abele TA, Yetkin ZF, Raisanen JM, Mickey BE, Mendelsohn DB. Non-pituitary origin sellar tumours mimicking pituitary macroadenomas. Clin Radiol 2012;67(8):821–827
577. Huang BY, Castillo M. Nonadenomatous tumors of the pituitary and sella turcica. Top Magn Reson Imaging 2005;16(4):289–299

Oligoastrocytoma

578. Naugle DK, Duncan TD, Grice GP. Oligoastrocytoma. Radiographics 2004;24(2):598–600
579. von Deimling A, Reifenberger G, Kros JM, Louis DN, Collins VP. Oligoastrocytoma. In: Louis DN, Ohgaki H, Wiestler OD, Cavenee WK, eds. World Health Organization Classification of Tumours of the Central Nervous System. 4th ed. Geneva: IARC Press; 2007:63–65

Oligodendroglioma

580. Khalid L, Carone M, Dumrongpisutikul N, et al. Imaging characteristics of oligodendrogliomas that predict grade. AJNR Am J Neuroradiol 2012;33(5):852–857
581. Kim JW, Park CK, Park SH, et al. Relationship between radiological characteristics and combined 1p and 19q deletion in World Health Organization grade III oligodendroglial tumours. J Neurol Neurosurg Psychiatry 2011;82(2):224–227
582. Reifenberger G, Kros JM, Louis DN, Collins VP. Oligodendroglioma. In: Louis DN, Ohgaki H, Wiestler OD, Cavenee WK, eds. World Health Organization Classification of Tumours of the Central Nervous System. 4th ed. Geneva: IARC Press; 2007:54–59

Ornithine Transcarbamylase Deficiency

583. Choi CG, Yoo HW. Localized proton MR spectroscopy in infants with urea cycle defect. AJNR Am J Neuroradiol 2001;22(5):834–837
584. Gropman A. Brain imaging in urea cycle disorders. Mol Genet Metab 2010;100(Suppl 1):S20–S30
585. Gropman AL, Sailasuta N, Harris KC, Abulseoud O, Ross BD. Ornithine transcarbamylase deficiency with persistent abnormality in cerebral glutamate metabolism in adults. Radiology 2009;252(3):833–841
586. Michalak A, Butterworth RF. Ornithine transcarbamylase deficiency: pathogenesis of the cerebral disorder and new prospects for therapy. Metab Brain Dis 1997;12(3):171–182
587. Parmar H, Sitoh YY, Ho L. Maple syrup urine disease: diffusion-weighted and diffusion-tensor magnetic resonance imaging findings. J Comput Assist Tomogr 2004;28(1):93–97
588. Schwab S, Schwarz S, Mayatepek E, Hoffmann GF. Recurrent brain edema in ornithine-transcarbamylase deficiency. J Neurol 1999;246(7):609–611
589. Sener RN. Diffusion magnetic resonance imaging patterns in metabolic and toxic brain disorders. Acta Radiol 2004;45(5):561–570
590. Takanashi J, Barkovich AJ, Cheng SF, et al. Brain MR imaging in neonatal hyperammonemic encephalopathy resulting from proximal urea cycle disorders. AJNR Am J Neuroradiol 2003;24(6):1184–1187

Osmotic Pontine Myelinolysis/Osmotic Myelinolysis

591. Guzmán-De-Villoria JA, Ferreiro-Argüelles C, Fernández-García P. Differential diagnosis of T2 hyperintense brainstem lesions: Part 2. Diffuse lesions. Semin Ultrasound CT MR 2010;31(3):260–274
592. Ranger AM, Chaudhary N, Avery M, Fraser D. Central pontine and extrapontine myelinolysis in children: a review of 76 patients. J Child Neurol 2012;27(8):1027–1037

Pallidotomy

593. Blomstedt P, Hariz GM, Hariz MI. Pallidotomy versus pallidal stimulation. Parkinsonism Relat Disord 2006;12(5):296–301
594. Guridi J, Obeso JA. The subthalamic nucleus, hemiballismus and Parkinson's disease: reappraisal of a neurosurgical dogma. Brain 2001;124(Pt 1):5–19

Papillary Glioneuronal Tumor

595. Hsu C, Kwan G, Lau Q, Bhuta S. Rosette-forming glioneuronal tumour: imaging features, histopathological correlation and a comprehensive review of literature. Br J Neurosurg 2012;26(5):668–673
597. Mahajan H, Varikatt W, Dexter M, Boadle R, Ng T. Papillary glioneuronal tumor of the frontal lobe. J Clin Neurosci 2010;17(4):534–536
598. Marhold F, Preusser M, Dietrich W, Prayer D, Czech T. Clinicoradiological features of rosette-forming glioneuronal tumor (RGNT) of the fourth ventricle: report of four cases and literature review. J Neurooncol 2008;90(3):301–308
599. Nakazato Y, Figarella-Branger D, Becker AJ, Scheithauer BW, Rosenblum MK. Papillary glioneuronal tumour. In: Louis DN, Ohgaki H, Wiestler OD, Cavenee WK, eds. World Health Organization Classification of Tumours of the Central Nervous System. 4th ed. Geneva: IARC Press; 2007:113–114

Papillary Tumor of the Pineal Region

600. Buffenoir K, Rigoard P, Wager M, et al. Papillary tumor of the pineal region in a child: case report and review of the literature. Childs Nerv Syst 2008;24(3):379–384
601. Chang AH, Fuller GN, Debnam JM, et al. MR imaging of papillary tumor of the pineal region. AJNR Am J Neuroradiol 2008;29(1):187–189

602. Fèvre-Montange M, Hasselblatt M, Figarella-Branger D, et al. Prognosis and histopathologic features in papillary tumors of the pineal region: a retrospective multicenter study of 31 cases. J Neuropathol Exp Neurol 2006;65(10):1004–1011
603. Jouvet A, Nakazato Y, Scheithauer BW, Paulus W. Papillary tumour of the pineal region. In: Louis DN, Ohgaki H, Wiestler OD, Cavenee WK, eds. World Health Organization Classification of Tumours of the Central Nervous System. 4th ed. Geneva: IARC Press; 2007:128–129
604. Patel SK, Tomei KL, Christiano LD, Baisre A, Liu JK. Complete regression of papillary tumor of the pineal region after radiation therapy: case report and review of the literature. J Neurooncol 2012;107(2): 427–434
605. Júnior GV, Dellaretti M, de Carvalho GTC, Brandão RACS, Mafra A, de Sousa AA. Papillary tumor of the pineal region. Brain Tumor Pathol 2011;28(4):329–334

Paraneoplastic Syndrome

606. Basu S, Alavi A. Role of FDG-PET in the clinical management of paraneoplastic neurological syndrome: detection of the underlying malignancy and the brain PET-MRI correlates. Mol Imaging Biol 2008;10(3):131–137
607. Gilmore CP, Elliott I, Auer D, Maddison P. Diffuse cerebellar MR imaging changes in anti-Yo positive paraneoplastic cerebellar degeneration. J Neurol 2010;257(3):490–491
608. Karmon Y, Inbar E, Cordoba M, Gadoth N. Paraneoplastic cerebellar degeneration mimicking acute post-infectious cerebellitis. Cerebellum 2009;8(4):441–444
609. McKeon A, Ahlskog JE, Britton JW, Lennon VA, Pittock SJ. Reversible extralimbic paraneoplastic encephalopathies with large abnormalities on magnetic resonance images. Arch Neurol 2009;66(2):268–271
610. McKeon A, Pittock SJ. Paraneoplastic encephalomyelopathies: pathology and mechanisms. Acta Neuropathol 2011;122(4): 381–400
611. Shams'ili S, Grefkens J, de Leeuw B, et al. Paraneoplastic cerebellar degeneration associated with antineuronal antibodies: analysis of 50 patients. Brain 2003;126(Pt 6):1409–1418
612. Sioka C, Fotopoulos A, Kyritsis AP. Paraneoplastic neurological syndromes and the role of PET imaging. Oncology 2010;78(2):150–156

Parasellar Tumors

613. Smith JK. Parasellar tumors: suprasellar and cavernous sinuses. Top Magn Reson Imaging 2005;16(4):307–315

Parasitic Diseases

614. da Cunha Correia C, Ramos Lacerda H, de Assis Costa VM, Mertens de Queiroz Brainer A. Cerebral toxoplasmosis: unusual MRI findings. Clin Imaging 2012;36(5):462–465
615. Duishanbai S, Jiafu D, Guo H, et al. Intracranial hydatid cyst in children: report of 30 cases. Childs Nerv Syst 2010;26(6):821–827
616. Kimura-Hayama ET, Higuera JA, Corona-Cedillo R, et al. Neurocysticercosis: radiologic-pathologic correlation. Radiographics 2010;30(6):1705–1719
617. Kumar GGS, Mahadevan A, Guruprasad AS, et al. Eccentric target sign in cerebral toxoplasmosis: neuropathological correlate to the imaging feature. J Magn Reson Imaging 2010;31(6):1469–1472
618. Lee GT, Antelo F, Mlikotic AA. Best cases from the AFIP: cerebral toxoplasmosis. Radiographics 2009;29(4):1200–1205
619. Masamed R, Meleis A, Lee EW, Hathout GM. Cerebral toxoplasmosis: case review and description of a new imaging sign. Clin Radiol 2009;64(5):560–563
620. Mohindra S, Savardekar A, Gupta R, Tripathi M, Rane S. Varied types of intracranial hydatid cysts: radiological features and management techniques. Acta Neurochir (Wien) 2012;154(1):165–172
621. Nash TE, Garcia HH. Diagnosis and treatment of neurocysticercosis. Nat Rev Neurol 2011;7(10):584–594
622. Abdel Razek AA, Watcharakorn A, Castillo M. Parasitic diseases of the central nervous system. Neuroimaging Clin N Am 2011;21(4): 815–841, viii

Parkinson's Disease

623. Braak H, Del Tredici K, Rüb U, de Vos RA, Jansen Steur EN, Braak E. Staging of brain pathology related to sporadic Parkinson's disease. Neurobiol Aging 2003;24(2):197–211
624. Brooks DJ, Pavese N. Imaging biomarkers in Parkinson's disease. Prog Neurobiol 2011;95(4):614–628
625. Ibarretxe-Bilbao N, Junque C, Marti MJ, Tolosa E. Brain structural MRI correlates of cognitive dysfunctions in Parkinson's disease. J Neurol Sci 2011;310(1-2):70–74
626. Ibarretxe-Bilbao N, Tolosa E, Junque C, Marti MJ. MRI and cognitive impairment in Parkinson's disease. Mov Disord 2009;24(Suppl 2): S748–S753
627. Mascalchi M, Vella A, Ceravolo R. Movement disorders: role of imaging in diagnosis. J Magn Reson Imaging 2012;35(2):239–256
628. Pavese N, Brooks DJ. Imaging neurodegeneration in Parkinson's disease. Biochim Biophys Acta 2009;1792(7):722–729
629. Singleton AB, Farrer MJ, Bonifati V. The genetics of Parkinson's disease: progress and therapeutic implications. Mov Disord 2013;28(1): 14–23
630. Vaillancourt DE, Spraker MB, Prodoehl J, et al. High-resolution diffusion tensor imaging in the substantia nigra of de novo Parkinson disease. Neurology 2009;72(16):1378–1384

Pelizaeus-Merzbacher Disease

631. Hanefeld FA, Brockmann K, Pouwels PJW, Wilken B, Frahm J, Dechent P. Quantitative proton MRS of Pelizaeus-Merzbacher disease: evidence of dys- and hypomyelination. Neurology 2005;65(5):701–706
632. Hoffman-Zacharska D, Kmieć T, Poznański J, Jurek M, Bal J. Mutations in the PLP1 gene residue p. Gly198 as the molecular basis of Pelizeaus-Merzbacher phenotype. Brain Dev 2013;35(9):877–880
633. Koeppen AH, Robitaille Y. Pelizaeus-Merzbacher disease. J Neuropathol Exp Neurol 2002;61(9):747–759
634. Nezu A, Kimura S, Takeshita S, Osaka H, Kimura K, Inoue K. An MRI and MRS study of Pelizaeus-Merzbacher disease. Pediatr Neurol 1998;18(4):334–337
635. Pizzini F, Fatemi AS, Barker PB, et al. Proton MR spectroscopic imaging in Pelizaeus-Merzbacher disease. AJNR Am J Neuroradiol 2003; 24(8):1683–1689
636. Sener RN. Pelizaeus-Merzbacher disease: diffusion MR imaging and proton MR spectroscopy findings. J Neuroradiol 2004;31(2): 138–141
637. Woodward KJ. The molecular and cellular defects underlying Pelizaeus-Merzbacher disease. Expert Rev Mol Med 2008;10:e14

Perinatal / Neonatal Strokes

638. Barkovich AJ, Westmark KD, Bedi HS, Partridge JC, Ferriero DM, Vigneron DB. Proton spectroscopy and diffusion imaging on the first day of life after perinatal asphyxia: preliminary report. AJNR Am J Neuroradiol 2001;22(9):1786–1794
639. Boichot C, Walker PM, Durand C, et al. Term neonate prognoses after perinatal asphyxia: contributions of MR imaging, MR spectroscopy, relaxation times, and apparent diffusion coefficients. Radiology 2006;239(3):839–848
640. Husson B, Lasjaunias P. Radiological approach to disorders of arterial brain vessels associated with childhood arterial stroke-a comparison between MRA and contrast angiography. Pediatr Radiol 2004;34(1):10–15
641. Rutherford MA, Ward P, Malamateniou C. Advanced MR techniques in the term-born neonate with perinatal brain injury. Semin Fetal Neonatal Med 2005;10(5):445–460
642. Rutherford M, Srinivasan L, Dyet L, et al. Magnetic resonance imaging in perinatal brain injury: clinical presentation, lesions and outcome. Pediatr Radiol 2006;36(7):582–592

Periventricular Leukomalacia

643. Bozzao A, Di Paolo A, Mazzoleni C, et al. Diffusion-weighted MR imaging in the early diagnosis of periventricular leukomalacia. Eur Radiol 2003;13(7):1571–1576
644. Fu J, Xue X, Chen L, Fan G, Pan L, Mao J. Studies on the value of diffusion-weighted MR imaging in the early prediction of periventricular leukomalacia. J Neuroimaging 2009;19(1):13–18
645. Kidokoro H, Kubota T, Ohe H, et al. Diffusion-weighted magnetic resonance imaging in infants with periventricular leukomalacia. Neuropediatrics 2008;39(4):233–238

Phenylketonuria

646. Kono K, Okano Y, Nakayama K, et al. Diffusion-weighted MR imaging in patients with phenylketonuria: relationship between serum phenylalanine levels and ADC values in cerebral white matter. Radiology 2005;236(2):630–636

647. Leuzzi V, Tosetti M, Montanaro D, et al. The pathogenesis of the white matter abnormalities in phenylketonuria. A multimodal 3.0 tesla MRI and magnetic resonance spectroscopy (1H MRS) study. J Inherit Metab Dis 2007;30(2):209–216

Phenytoin-related Cerebellar Atrophy

648. De Marcos FA, Ghizoni E, Kobayashi E, Li LM, Cendes F. Cerebellar volume and long-term use of phenytoin. Seizure 2003;12(5):312–315
649. Lee SK, Mori S, Kim DJ, et al. Diffusion tensor MRI and fiber tractography of cerebellar atrophy in phenytoin users. Epilepsia 2003; 44(12):1536–1540
650. Twardowschy CA, Werneck LC, Scola RH, Borgio JG, De Paola L, Silvado C. The role of CYP2C9 polymorphisms in phenytoin-related cerebellar atrophy. Seizure 2013;22(3):194–197

Pilocytic Astrocytoma

651. Hwang JH, Egnaczyk GF, Ballard E, Dunn RS, Holland SK, Ball WS Jr. Proton MR spectroscopic characteristics of pediatric pilocytic astrocytomas. AJNR Am J Neuroradiol 1998;19(3):535–540
652. Kumar AJ, Leeds NE, Kumar VA, et al. Magnetic resonance imaging features of pilocytic astrocytoma of the brain mimicking high-grade gliomas. J Comput Assist Tomogr 2010;34(4):601–611
653. Plaza MJ, Borja MJ, Altman N, Saigal G. Conventional and advanced MRI features of pediatric intracranial tumors: posterior fossa and suprasellar tumors. AJR Am J Roentgenol 2013;200(5):1115–1124
654. Scheithauer BW, Hawkins C, Tihan T, VandenBerg SR, Burger PC. Pilocytic astrocytoma. In: Louis DN, Ohgaki H, Wiestler OD, Cavenee WK, eds. World Health Organization Classification of Tumours of the Central Nervous System. 4th ed. Geneva: IARC Press; 2007:14–21

Pilomyxoid Astrocytoma

655. Arslanoglu A, Cirak B, Horska A, et al. MR imaging characteristics of pilomyxoid astrocytomas. AJNR Am J Neuroradiol 2003;24(9): 1906–1908
656. Forbes JA, Mobley BC, O'Lynnger TM, et al. Pediatric cerebellar pilomyxoid-spectrum astrocytomas. J Neurosurg Pediatr 2011;8(1): 90–96
657. Lee IH, Kim JH, Suh YL, et al. Imaging characteristics of pilomyxoid astrocytomas in comparison with pilocytic astrocytomas. Eur J Radiol 2011;79(2):311–316
658. Linscott LL, Osborn AG, Blaser S, et al. Pilomyxoid astrocytoma: expanding the imaging spectrum. AJNR Am J Neuroradiol 2008; 29(10):1861–1866

Pineal Cyst

659. Al-Holou WN, Maher CO, Muraszko KM, Garton HJL. The natural history of pineal cysts in children and young adults. J Neurosurg Pediatr 2010;5(2):162–166
660. Engel U, Gottschalk S, Niehaus L, et al. Cystic lesions of the pineal region—MRI and pathology. Neuroradiology 2000;42(6):399–402
661. Kahilogullari G, Massimi L, Di Rocco C. Pineal cysts in children: case-based update. Childs Nerv Syst 2013;29(5):753–760

Pineal Gland

662. Macchi MM, Bruce JN. Human pineal physiology and functional significance of melatonin. Front Neuroendocrinol 2004;25(3-4): 177–195
663. Sapède D, Cau E. The pineal gland from development to function. Curr Top Dev Biol 2013;106:171–215

Pineal Parenchymal Tumor of Intermediate Differentiation

664. Nakazato Y, Jouvet A, Scheithauer BW. Pineal parenchymal tumour of intermediate differentiation. In: Louis DN, Ohgaki H, Wiestler OD, Cavenee WK, eds. World Health Organization Classification of Tumours of the Central Nervous System. 4th ed. Geneva: IARC Press; 2007:124–125

Pineal Region Lesions

665. Fang AS, Meyers SP. Magnetic resonance imaging of pineal region tumours. Insights Imaging 2013;4(3):369–382
666. Knierim DS, Yamada S. Pineal tumors and associated lesions: the effect of ethnicity on tumor type and treatment. Pediatr Neurosurg 2003;38(6):307–323
667. Smith AB, Rushing EJ, Smirniotopoulos JG. From the archives of the AFIP: lesions of the pineal region: radiologic-pathologic correlation. Radiographics 2010;30(7):2001–2020
668. Tien RD, Barkovich AJ, Edwards MSB. MR imaging of pineal tumors. AJR Am J Roentgenol 1990;155(1):143–151
669. Zee CS, Segall H, Apuzzo M, et al. MR imaging of pineal region neoplasms. J Comput Assist Tomogr 1991;15(1):56–63

Pineal Tumors

670. Fang AS, Meyers SP. Magnetic resonance imaging of pineal region tumours. Insights Imaging 2013;4(3):369–382
671. Jouvet A, Nakazato Y, Scheithauer BW, Paulus W. Papillary tumour of the pineal region. In: Louis DN, Ohgaki H, Wiestler OD, Cavenee WK, eds. World Health Organization Classification of Tumours of the Central Nervous System. 4th ed. Geneva: IARC Press; 2007:128–129
672. Nakazato Y, Jouvet A, Scheithauer BW. Pineocytoma. In: Louis DN, Ohgaki H, Wiestler OD, Cavenee WK, eds. World Health Organization Classification of Tumours of the Central Nervous System. 4th ed. Geneva: IARC Press; 2007:122–123
673. Nakazato Y, Jouvet A, Scheithauer BW. Pineal parenchymal tumour of intermediate differentiation. In: Louis DN, Ohgaki H, Wiestler OD, Cavenee WK, eds. World Health Organization Classification of Tumours of the Central Nervous System. 4th ed. Geneva: IARC Press; 2007:124–125
674. Nakazato Y, Jouvet A, Scheithauer BW. Pineoblastoma. In: Louis DN, Ohgaki H, Wiestler OD, Cavenee WK, eds. World Health Organization Classification of Tumours of the Central Nervous System. 4th ed. Geneva: IARC Press; 2007:126–127
675. Rosenblum MK, Nakazato Y, Matsutani M. CNS germ cell tumours—germinoma; mature teratoma; immature teratoma; teratoma with malignant transformation; yolk sac tumour (endodermal sinus tumour); embryonal carcinoma; choriocarcinoma. In: Louis DN, Ohgaki H, Wiestler OD, Cavenee WK, eds. World Health Organization Classification of Tumours of the Central Nervous System. 4th ed. Geneva: IARC Press; 2007:198–20
676. Smith AB, Rushing EJ, Smirniotopoulos JG. From the archives of the AFIP: lesions of the pineal region: radiologic-pathologic correlation. Radiographics 2010;30(7):2001–2020

Pineoblastoma

678. Nakazato Y, Jouvet A, Scheithauer BW. Pineoblastoma. In: Louis DN, Ohgaki H, Wiestler OD, Cavenee WK, eds. World Health Organization Classification of Tumours of the Central Nervous System. 4th ed. Geneva: IARC Press; 2007:126–127
679. Nakamura M, Saeki N, Iwadate Y, Sunami K, Osato K, Yamaura A. Neuroradiological characteristics of pineocytoma and pineoblastoma. Neuroradiology 2000;42(7):509–514

Pineocytoma

680. Deshmukh VR, Smith KA, Rekate HL, Coons S, Spetzler RF. Diagnosis and management of pineocytomas. Neurosurgery 2004;55(2):349–355, discussion 355–357
681. Nakazato Y, Jouvet A, Scheithauer BW. Pineocytoma. In: Louis DN, Ohgaki H, Wiestler OD, Cavenee WK, eds. World Health Organization Classification of Tumours of the Central Nervous System. 4th ed. Geneva: IARC Press; 2007:122–123

Pituicytoma

682. Covington MF, Chin SS, Osborn AG. Pituicytoma, spindle cell oncocytoma, and granular cell tumor: clarification and meta-analysis of the world literature since 1893. AJNR Am J Neuroradiol 2011;32(11):2067–2072
683. Hammoud DA, Munter FM, Brat DJ, Pomper MG. Magnetic resonance imaging features of pituicytomas: analysis of 10 cases. J Comput Assist Tomogr 2010;34(5):757–761
684. Ulm AJ, Yachnis AT, Brat DJ, Rhoton AL Jr. Pituicytoma: report of two cases and clues regarding histogenesis. Neurosurgery 2004;54(3):753–757, discussion 757–758
685. Wesseling P, Brat DJ, Fuller GN. Pituicytoma. In: Louis DN, Ohgaki H, Wiestler OD, Cavenee WK, eds. World Health Organization Classification of Tumours of the Central Nervous System. 4th ed. Geneva: IARC Press; 2007:243–244

Pituitary Apoplexy

686. Boellis A, di Napoli A, Romano A, Bozzao A. Pituitary apoplexy: an update on clinical and imaging features. Insights Imaging 2014; 5(6):753–762

687. Murad-Kejbou S, Eggenberger E. Pituitary apoplexy: evaluation, management, and prognosis. Curr Opin Ophthalmol 2009;20(6): 456–461

Pituitary Gland

688. Aquilina K, Boop FA. Nonneoplastic enlargement of the pituitary gland in children. J Neurosurg Pediatr 2011;7(5):510–515
689. Ouyang T, Rothfus WE, Ng JM, Challinor SM. Imaging of the pituitary. Radiol Clin North Am 2011;49(3):549–571, vii
690. Rennert J, Doerfler A. Imaging of sellar and parasellar lesions. Clin Neurol Neurosurg 2007;109(2):111–124
691. Rumboldt Z. Pituitary adenomas. Top Magn Reson Imaging 2005; 16(4):277–288

Pleomorphic Xanthoastrocytoma

692. Crespo-Rodríguez AM, Smirniotopoulos JG, Rushing EJMR. MR and CT imaging of 24 pleomorphic xanthoastrocytomas (PXA) and a review of the literature. Neuroradiology 2007;49(4):307–315
693. Giannini C, Paulus W, Louis DN, Liberski P. Pleomorphic xanthoastrocytoma. In: Louis DN, Ohgaki H, Wiestler OD, Cavenee WK, eds. World Health Organization Classification of Tumours of the Central Nervous System. 4th ed. Geneva: IARC Press; 2007:22–24
694. Yu S, He L, Zhuang X, Luo B. Pleomorphic xanthoastrocytoma: MR imaging findings in 19 patients. Acta Radiol 2011;52(2):223–228

Polymicrogyria

695. Barkovich AJ. MRI analysis of sulcation morphology in polymicrogyria. Epilepsia 2010;51(Suppl 1):17–22

Porencephalic Cyst

696. Moinuddin A, McKinstry RC, Martin KA, Neil JJ. Intracranial hemorrhage progressing to porencephaly as a result of congenitally acquired cytomegalovirus infection—an illustrative report. Prenat Diagn 2003;23(10):797–800
697. Kułak W, Sobaniec W, Kubas B, et al. Spastic cerebral palsy: clinical magnetic resonance imaging correlation of 129 children. J Child Neurol 2007;22(1):8–14

Posterior Cortical Atrophy (Benson Syndrome)

698. Duning T, Warnecke T, Mohammadi S, et al. Pattern and progression of white-matter changes in a case of posterior cortical atrophy using diffusion tensor imaging. J Neurol Neurosurg Psychiatry 2009;80(4):432–436
699. Giovagnoli AR, Aresi A, Reati F, Riva A, Gobbo C, Bizzi A. The neuropsychological and neuroradiological correlates of slowly progressive visual agnosia. Neurol Sci 2009;30(2):123–131
700. McMonagle P, Deering F, Berliner Y, Kertesz A. The cognitive profile of posterior cortical atrophy. Neurology 2006;66(3):331–338
701. Migliaccio R, Agosta F, Rascovsky K, et al. Clinical syndromes associated with posterior atrophy: early age at onset AD spectrum. Neurology 2009;73(19):1571–1578
702. Rózsa A, Szilvássy I, Kovács K, Boór K, Gács G. [Posterior cortical atrophy (Benson-syndrome)]. Ideggyogy Sz 2010;63(1-2):45–47
703. Schmidtke K, Hüll M, Talazko J. Posterior cortical atrophy: variant of Alzheimer's disease? A case series with PET findings. J Neurol 2005;252(1):27–35
704. Pantel J, Schröder J. [Posterior cortical atrophy—a new dementia syndrome or a form of Alzheimer's disease?]. Fortschr Neurol Psychiatr 1996;64(12):492–508
705. Whitwell JL, Jack CR Jr, Kantarci K, et al. Imaging correlates of posterior cortical atrophy. Neurobiol Aging 2007;28(7):1051–1061

Posterior Fossa Malformations

706. Chapman T, Mahalingam S, Ishak GE, Nixon JN, Siebert J, Dighe MK. Diagnostic imaging of posterior fossa anomalies in the fetus and neonate: part 2, Posterior fossa disorders. Clin Imaging 2015;39(2): 167–175
707. Shekdar K. Posterior fossa malformations. Semin Ultrasound CT MR 2011;32(3):228–241

Posttransplant Lymphoproliferative Disorder

708. Brennan KC, Lowe LH, Yeaney GA. Pediatric central nervous system posttransplant lymphoproliferative disorder. AJNR Am J Neuroradiol 2005;26(7):1695–1697
709. Cavaliere R, Petroni G, Lopes MB, Schiff D; International Primary Central Nervous System Lymphoma Collaborative Group. Primary central nervous system post-transplantation lymphoproliferative disorder: an International Primary Central Nervous System Lymphoma Collaborative Group Report. Cancer 2010;116(4):863–870
710. Maecker B, Jack T, Zimmermann M, et al. CNS or bone marrow involvement as risk factors for poor survival in post-transplantation lymphoproliferative disorders in children after solid organ transplantation. J Clin Oncol 2007;25(31):4902–4908
711. Traum AZ, Rodig NM, Pilichowska ME, Somers MJ. Central nervous system lymphoproliferative disorder in pediatric kidney transplant recipients. Pediatr Transplant 2006;10(4):505–512

PRES

712. Covarrubias DJ, Luetmer PH, Campeau NG. Posterior reversible encephalopathy syndrome: prognostic utility of quantitative diffusion-weighted MR images. AJNR Am J Neuroradiol 2002;23(6):1038–1048

Primitive Neuroectodermal Tumor

713. Isaacs H. Fetal brain tumors: a review of 154 cases. Am J Perinatol 2009;26(6):453–466
714. McLendon RE, Judkins AR, Eberhart CG, Fuller GN, Sarkar C, Ng HK. Central nervous system primitive neuroectodermal tumours. In: Louis DN, Ohgaki H, Wiestler OD, Cavenee WK, eds. World Health Organization Classification of Tumours of the Central Nervous System. 4th ed. Geneva: IARC Press; 2007:141–146
715. Mehrotra N, Shamji MF, Vassilyadi M, Ventureyra EC. Intracranial tumors in first year of life: the CHEO experience. Childs Nerv Syst 2009;25(12):1563–1569
716. Price SJ, Green HAL, Dean AF, Joseph J, Hutchinson PJ, Gillard JH. Correlation of MR relative cerebral blood volume measurements with cellular density and proliferation in high-grade gliomas: an image-guided biopsy study. AJNR Am J Neuroradiol 2011;32(3):501–506

Prion Disease

718. Talbott SD, Plato BM, Sattenberg RJ, Parker J, Heidenreich JO. Cortical restricted diffusion as the predominant MRI finding in sporadic Creutzfeldt-Jakob disease. Acta Radiol 2011;52(3):336–339
719. Vitali P, Maccagnano E, Caverzasi E, et al. Diffusion-weighted MRI hyperintensity patterns differentiate CJD from other rapid dementias. Neurology 2011;76(20):1711–1719
720. Young GS, Geschwind MD, Fischbein NJ, et al. Diffusion-weighted and fluid-attenuated inversion recovery imaging in Creutzfeldt-Jakob disease: high sensitivity and specificity for diagnosis. AJNR Am J Neuroradiol 2005;26(6):1551–1562

Progressive Multifocal Leukoencephalopathy (PML)-Immune Reconstitution Inflammatory Syndrome (IRIS)

721. Gheuens S, Smith DR, Wang X, Alsop DC, Lenkinski RE, Koralnik IJ. Simultaneous PML-IRIS after discontinuation of natalizumab in a patient with MS. Neurology 2012;78(18):1390–1393
722. Kleinschmidt-DeMasters BK, Miravalle A, Schowinsky J, Corboy J, Vollmer T. Update on PML and PML-IRIS occurring in multiple sclerosis patients treated with natalizumab. J Neuropathol Exp Neurol 2012;71(7):604–617
723. Sahraian MA, Radue EW, Eshaghi A, Besliu S, Minagar A. Progressive multifocal leukoencephalopathy: a review of the neuroimaging features and differential diagnosis. Eur J Neurol 2012;19(8):1060–1069

Progressive Supranuclear Palsy

724. Massey LA, Micallef C, Paviour DC, et al. Conventional magnetic resonance imaging in confirmed progressive supranuclear palsy and multiple system atrophy. Mov Disord 2012;27(14):1754–1762
725. Sitburana O, Ondo WG. Brain magnetic resonance imaging (MRI) in parkinsonian disorders. Parkinsonism Relat Disord 2009;15(3): 165–174

Propionic Acidemia

726. Bergman AJIW, Van der Knaap MS, Smeitink JAM, et al. Magnetic resonance imaging and spectroscopy of the brain in propionic acidemia: clinical and biochemical considerations. Pediatr Res 1996;40(3): 404–409
727. Brismar J, Ozand PT. CT and MR of the brain in disorders of the propionate and methylmalonate metabolism. AJNR Am J Neuroradiol 1994;15(8):1459–1473

728. Chemelli AP, Schocke M, Sperl W, Trieb T, Aichner F, Felber S. Magnetic resonance spectroscopy (MRS) in five patients with treated propionic acidemia. J Magn Reson Imaging 2000;11(6):596–600
729. Nyhan WL, Bay C, Beyer EW, Mazi M. Neurologic nonmetabolic presentation of propionic acidemia. Arch Neurol 1999;56(9): 1143–1147

Proteus Syndrome

730. Bastos H, da Silva PFS, de Albuquerque MA, et al. Proteus syndrome associated with hemimegalencephaly and Ohtahara syndrome: report of two cases. Seizure 2008;17(4):378–382
731. Cohen MM Jr. Proteus syndrome review: molecular, clinical, and pathologic features. Clin Genet 2014;85(2):111–119
732. Jamis-Dow CA, Turner J, Biesecker LG, Choyke PL. Radiologic manifestations of Proteus syndrome. Radiographics 2004;24(4): 1051–1068
733. Kaduthodil MJ, Prasad DS, Lowe AS, Punekar AS, Yeung S, Kay CL. Imaging manifestations in Proteus syndrome: an unusual multisystem developmental disorder. Br J Radiol 2012;85(1017):e793–e799

Radiation Necrosis

734. Bobek-Billewicz B, Stasik-Pres G, Majchrzak H, Zarudzki L. Differentiation between brain tumor recurrence and radiation injury using perfusion, diffusion-weighted imaging and MR spectroscopy. Folia Neuropathol 2010;48(2):81–92
735. Cha J, Kim ST, Kim H-J, et al. Analysis of the layering pattern of the apparent diffusion coefficient (ADC) for differentiation of radiation necrosis from tumour progression. Eur Radiol 2013;23(3):879–886
736. Fatterpekar GM, Galheigo D, Narayana A, Johnson G, Knopp E. Treatment-related change versus tumor recurrence in high-grade gliomas: a diagnostic conundrum—use of dynamic susceptibility contrast-enhanced (DSC) perfusion MRI. AJR Am J Roentgenol 2012;198(1):19–26
737. Kim YH, Oh SW, Lim YJ, et al. Differentiating radiation necrosis from tumor recurrence in high-grade gliomas: assessing the efficacy of 18F-FDG PET, 11C-methionine PET and perfusion MRI. Clin Neurol Neurosurg 2010;112(9):758–765
738. Mitsuya K, Nakasu Y, Horiguchi S, et al. Perfusion weighted magnetic resonance imaging to distinguish the recurrence of metastatic brain tumors from radiation necrosis after stereotactic radiosurgery. J Neurooncol 2010;99(1):81–88
739. Siu A, Wind JJ, Iorgulescu JB, Chan TA, Yamada Y, Sherman JH. Radiation necrosis following treatment of high grade glioma—a review of the literature and current understanding. Acta Neurochir (Wien) 2012;154(2):191–201, discussion 201
740. Vidiri A, Guerrisi A, Pinzi V, et al. Perfusion Computed Tomography (PCT) adopting different perfusion metrics: recurrence of brain metastasis or radiation necrosis? Eur J Radiol 2012;81(6):1246–1252

Rasmussen Encephalitis

741. Faingold R, Onyekwelu OA. MRI appearance of Rasmussen encephalitis. Pediatr Radiol 2009;39(7):756
742. Granata T, Andermann F. Rasmussen encephalitis. Handb Clin Neurol 2013;111:511–519
743. Olson HE, Lechpammer M, Prabhu SP, et al. Clinical application and evaluation of the Bien diagnostic criteria for Rasmussen encephalitis. Epilepsia 2013;54(10):1753–1760

Reversible Cerebral Vasoconstriction Syndrome

744. Miller TR, Shivashankar R, Mossa-Basha M, Gandhi D. Reversible cerebral vascoconstriction syndrome, part 1: epidemiology, pathogenesis, and clinical course. AJNR Am J Neuroradiol 2015;36(8):1392–1399
745. Miller TR, Shivashankar R, Mossa-Basha M, Gandhi D. Reversible cerebral vascoconstriction syndrome, part 2: diagnostic work-up, imaging evaluation, and differential diagnosis. AJNR Am J Neuroradiol 2015;36(9):1580–1588

Rickettsial and Spirochetal Infections

746. Akgoz A, Mukundan S, Lee TC. Imaging of rickettsial, spirochetal, and parasitic infections. Neuroimaging Clin N Am 2012;22(4):633–657
747. Crapp S, Harrar D, Strother M, Wushensky C, Pruthi S. Rocky Mountain spotted fever: 'starry sky' appearance with diffusion-weighted imaging in a child. Pediatr Radiol 2012;42(4):499–502
748. Maller VG, Agarwal AK, Choudhary AK. Diffusion imaging findings in Rocky Mountain spotted fever encephalitis: a case report. Emerg Radiol 2012;19(1):79–81

Rosai-Dorfman Disease

749. Lou X, Chen ZY, Wang FL, Ma L. MR findings of Rosai-Dorfman disease in sellar and suprasellar region. Eur J Radiol 2012;81(6):1231–1237

Sanfilippo Syndrome

750. Kara S, Sherr EH, Barkovich AJ. Dilated perivascular spaces: an informative radiologic finding in Sanfilippo syndrome type A. Pediatr Neurol 2008;38(5):363–366
751. Zafeiriou DI, Savvopoulou-Augoustidou PA, Sewell A, et al. Serial magnetic resonance imaging findings in mucopolysaccharidosis IIIB (Sanfilippo's syndrome B). Brain Dev 2001;23(6):385–389

Seizure

752. Chatzikonstantinou A, Gass A, Förster A, Hennerici MG, Szabo K. Features of acute DWI abnormalities related to status epilepticus. Epilepsy Res 2011;97(1-2):45–51
753. Förster A, Griebe M, Gass A, Kern R, Hennerici MG, Szabo K. Diffusion-weighted imaging for the differential diagnosis of disorders affecting the hippocampus. Cerebrovasc Dis 2012;33(2):104–115
754. Gross DW. Diffusion tensor imaging in temporal lobe epilepsy. Epilepsia 2011;52(Suppl 4):32–34
755. Hakami T, McIntosh A, Todaro M, et al. MRI-identified pathology in adults with new-onset seizures. Neurology 2013;81(10):920–927
756. Kato T, Okumura A, Hayakawa F, Tsuji T, Natsume J. Transient reduced diffusion in the cortex in a child with prolonged febrile seizures. Brain Dev 2012;34(9):773–775
757. Kim JA, Chung JI, Yoon PH, et al. Transient MR signal changes in patients with generalized tonicoclonic seizure or status epilepticus: periictal diffusion-weighted imaging. AJNR Am J Neuroradiol 2001;22(6):1149–1160
758. Milligan TA, Zamani A, Bromfield E. Frequency and patterns of MRI abnormalities due to status epilepticus. Seizure 2009;18(2): 104–108
759. Stanescu L, Ishak GE, Khanna PC, Biyyam DR, Shaw DW, Parisi MT. FDG PET of the brain in pediatric patients: imaging spectrum with MR imaging correlation. Radiographics 2013;33(5):1279–1303
760. Urbach H. Imaging of the epilepsies. Eur Radiol 2005;15(3): 494–500

Sinovenous Thrombosis in Adults

761. Camargo ECS, Bacheschi LA, Massaro AR. Stroke in Latin America. Neuroimaging Clin N Am 2005;15(2):283–296, x
762. Ferro JM, Canhão P, Stam J, Bousser MG, Barinagarrementeria F; ISCVT Investigators. Prognosis of cerebral vein and dural sinus thrombosis: results of the International Study on Cerebral Vein and Dural Sinus Thrombosis (ISCVT). Stroke 2004;35(3):664–670
763. Idbaih A, Boukobza M, Crassard I, Porcher R, Bousser MG, Chabriat H. MRI of clot in cerebral venous thrombosis: high diagnostic value of susceptibility-weighted images. Stroke 2006;37(4):991–995
764. Jonas Kimchi T, Lee SK, Agid R, Shroff M, Ter Brugge KG. Cerebral sinovenous thrombosis in children. Neuroimaging Clin N Am 2007;17(2):239–244
765. Leach JL, Fortuna RB, Jones BV, Gaskill-Shipley MF. Imaging of cerebral venous thrombosis: current techniques, spectrum of findings, and diagnostic pitfalls. Radiographics 2006;26(Suppl 1):S19–S41, discussion S42–S43
766. Leach JL, Strub WM, Gaskill-Shipley MF. Cerebral venous thrombus signal intensity and susceptibility effects on gradient recalled-echo MR imaging. AJNR Am J Neuroradiol 2007;28(5):940–945
767. Lin A, Foroozan R, Danesh-Meyer HV, De Salvo G, Savino PJ, Sergott RC. Occurrence of cerebral venous sinus thrombosis in patients with presumed idiopathic intracranial hypertension. Ophthalmology 2006;113(12):2281–2284
768. Poon CS. Chang Ja-Kwei, Swarnkar A, Johnson MH, Wasenko J. Radiologic diagnosis of central venous thrombosis: pictorial review. AJR Am J Roentgenol 2007;189:S64–S75
769. Ratai EM, Gonzalez RG. Magnetic resonance spectroscopy and the biochemical basis of neurologic disease. In: Atlas SW, ed. Magnetic Resonance Imaging of the Brain and Spine. 4th ed. Lippincott Williams & Wilkins; 2009: 1836–1870
770. Rodallec MH, Krainik A, Feydy A, et al. Cerebral venous thrombosis and multidetector CT angiography: tips and tricks. Radiographics 2006;26(Suppl 1):S5–S18, discussion S42–S43

771. Sagduyu A, Sirin H, Mulayim S, et al. Cerebral cortical and deep venous thrombosis without sinus thrombosis: clinical MRI correlates. Acta Neurol Scand 2006;114(4):254–260
772. Wasay M, Bakshi R, Bobustuc G, et al. Cerebral venous thrombosis: analysis of a multicenter cohort from the United States. J Stroke Cerebrovasc Dis 2008;17(2):49–54

Sinovenous Thrombosis in Children

773. deVeber G, Andrew M, Adams C, et al; Canadian Pediatric Ischemic Stroke Study Group. Cerebral sinovenous thrombosis in children. N Engl J Med 2001;345(6):417–423
774. Dlamini N, Billinghurst L, Kirkham FJ. Cerebral venous sinus (sinovenous) thrombosis in children. Neurosurg Clin N Am 2010;21(3):511–527
775. Nwosu ME, Williams LS, Edwards-Brown M, Eckert GJ, Golomb MR. Neonatal sinovenous thrombosis: presentation and association with imaging. Pediatr Neurol 2008;39(3):155–161
776. Sébire G, Tabarki B, Saunders DE, et al. Cerebral venous sinus thrombosis in children: risk factors, presentation, diagnosis and outcome. Brain 2005;128(Pt 3):477–489
777. Standridge SM, O'Brien SH. Idiopathic intracranial hypertension in a pediatric population: a retrospective analysis of the initial imaging evaluation. J Child Neurol 2008;23(11):1308–1311
778. Wasay M, Dai AI, Ansari M, Shaikh Z, Roach ES. Cerebral venous sinus thrombosis in children: a multicenter cohort from the United States. J Child Neurol 2008;23(1):26–31
779. Wu YW, Hamrick SEG, Miller SP, et al. Intraventricular hemorrhage in term neonates caused by sinovenous thrombosis. Ann Neurol 2003;54(1):123–126

SLE/Antiphospholipid Syndrome

780. Luyendijk J, Steens SCA, Ouwendijk WJN, et al. Neuropsychiatric systemic lupus erythematosus: lessons learned from magnetic resonance imaging. Arthritis Rheum 2011;63(3):722–732
781. Tektonidou MG, Varsou N, Kotoulas G, Antoniou A, Moutsopoulos HM. Cognitive deficits in patients with antiphospholipid syndrome: association with clinical, laboratory, and brain magnetic resonance imaging findings. Arch Intern Med 2006;166(20):2278–2284
782. Valdés-Ferrer SI, Vega F, Cantú-Brito C, et al. Cerebral changes in SLE with or without antiphospholipid syndrome. a case-control MRI study. J Neuroimaging 2008;18(1):62–65
783. Zivadinov R, Shucard JL, Hussein S, et al. Multimodal imaging in systemic lupus erythematosus patients with diffuse neuropsychiatric involvement. Lupus 2013;22(7):675–683 Epub ahead of print

Small Vessel or Lacunar Infarction

784. Cloonan L, Fitzpatrick KM, Kanakis AS, Furie KL, Rosand J, Rost NS. Metabolic determinants of white matter hyperintensity burden in patients with ischemic stroke. Atherosclerosis 2015;240(1):149–153
785. Conijn MMA, Kloppenborg RP, Algra A, et al; SMART Study Group. Cerebral small vessel disease and risk of death, ischemic stroke, and cardiac complications in patients with atherosclerotic disease: the Second Manifestations of ARTerial disease-Magnetic Resonance (SMART-MR) study. Stroke 2011;42(11):3105–3109
786. Erten-Lyons D, Woltjer R, Kaye J, et al. Neuropathologic basis of white matter hyperintensity accumulation with advanced age. Neurology 2013;81(11):977–983

Sotos Syndrome

787. Horikoshi H, Kato Z, Masuno M, et al. Neuroradiologic findings in Sotos syndrome. J Child Neurol 2006;21(7):614–618
788. Leventopoulos G, Kitsiou-Tzeli S, Kritikos K, et al. A clinical study of Sotos syndrome patients with review of the literature. Pediatr Neurol 2009;40(5):357–364

Spindle Cell Oncocytoma of the Adenohypophysis

789. Fuller GN, Scheithauer BW, Roncaroli F, Wesserling P. Spindle cell oncocytoma of the adenohypophysis. In: Louis DN, Ohgaki H, Wiestler OD, Cavenee WK, eds. World Health Organization Classification of Tumours of the Central Nervous System. 4th ed. Geneva: IARC Press; 2007:245–246

Spinocerebellar Ataxia/Degeneration

790. Mascalchi M. Spinocerebellar ataxias. Neurol Sci 2008;29(Suppl 3):311–313
791. Palau F, Espinós C. Autosomal recessive cerebellar ataxias. Orphanet J Rare Dis 2006;1:47
792. Perlman SL. Spinocerebellar degenerations. Handb Clin Neurol 2011;100:113–140
793. Schulz JB, Borkert J, Wolf S, et al. Visualization, quantification and correlation of brain atrophy with clinical symptoms in spinocerebellar ataxia types 1, 3 and 6. Neuroimage 2010;49(1):158–168
794. Seidel K, Siswanto S, Brunt ERP, den Dunnen W, Korf HW, Rüb U. Brain pathology of spinocerebellar ataxias. Acta Neuropathol 2012;124(1):1–21

Subependymal Giant Cell Astrocytoma

795. Clarke MJ, Foy AB, Wetjen N, Raffel C. Imaging characteristics and growth of subependymal giant cell astrocytomas. Neurosurg Focus 2006;20(1):E5
796. Goh S, Butler W, Thiele EA. Subependymal giant cell tumors in tuberous sclerosis complex. Neurology 2004;63(8):1457–1461
797. Lopes MBS, Wiestler OD, Stemmer-Rachamimov AO, Sharma MC. Tuberous sclerosis complex and subependymal giant cell astrocytoma. In: Louis DN, Ohgaki H, Wiestler OD, Cavenee WK, eds. World Health Organization Classification of Tumours of the Central Nervous System. 4th ed. Geneva: IARC Press; 2007:218–221

Subependymoma

798. Chiechi MV, Smirniotopoulos JG, Jones RV. Intracranial subependymomas: CT and MR imaging features in 24 cases. AJR Am J Roentgenol 1995;165(5):1245–1250
799. Fujisawa H, Hasegawa M, Ueno M. Clinical features and management of five patients with supratentorial subependymoma. J Clin Neurosci 2010;17(2):201–204
800. Ragel BT, Osborn AG, Whang K, Townsend JJ, Jensen RL, Couldwell WT. Subependymomas: an analysis of clinical and imaging features. Neurosurgery 2006;58(5):881–890, discussion 881–890
801. McLendon RE, Schiffer D, Rosenblum MK, Wiestler OD. Subependymoma. In: Louis DN, Ohgaki H, Wiestler OD, Cavenee WK, eds. World Health Organization Classification of Tumours of the Central Nervous System. 4th ed. Geneva: IARC Press; 2007:70–71

Superficial Siderosis

802. Kumar N. Superficial siderosis: associations and therapeutic implications. Arch Neurol 2007;64(4):491–496
803. Kumar N, Fogelson JL, Morris JM, Pichelmann MA. Superficial siderosis should be included in the differential diagnosis of motor neuron disease. Neurologist 2012;18(3):139–145
804. Sydlowski SA, Cevette MJ, Shallop J. Superficial siderosis of the central nervous system: phenotype and implications for audiology and otology. Otol Neurotol 2011;32(6):900–908

Syphilis

805. Darwish BS, Fowler A, Ong M, Swaminothan A, Abraszko R. Intracranial syphilitic gumma resembling malignant brain tumour. J Clin Neurosci 2008;15(3):308–310
806. Hama K, Ishiguchi H, Tuji T, Miwa H, Kondo T. Neurosyphilis with mesiotemporal magnetic resonance imaging abnormalities. Intern Med 2008;47(20):1813–1817
807. Soares-Fernandes JP, Ribeiro M, Maré R, Magalhães Z, Lourenço E, Rocha JF. Diffusion-weighted magnetic resonance imaging findings in a patient with cerebral syphilitic gumma. J Comput Assist Tomogr 2007;31(4):592–594

Toxic Demyelination

808. Erbetta A, Salmaggi A, Sghirlanzoni A, et al. Clinical and radiological features of brain neurotoxicity caused by antitumor and immunosuppressant treatments. Neurol Sci 2008;29(3):131–137
809. Inaba H, Khan RB, Laningham FH, Crews KR, Pui CH, Daw NC. Clinical and radiological characteristics of methotrexate-induced acute encephalopathy in pediatric patients with cancer. Ann Oncol 2008;19(1):178–184
810. Serkova NJ, Christians U, Benet LZ. Biochemical mechanisms of cyclosporine neurotoxicity. Mol Interv 2004;4(2):97–107

Toxic Encephalopathies

811. Hegde AN, Mohan S, Lath N, Lim CCT. Differential diagnosis for bilateral abnormalities of the basal ganglia and thalamus. Radiographics 2011;31(1):5–30

812. Sharma P, Eesa M, Scott JN. Toxic and acquired metabolic encephalopathies: MRI appearance. AJR Am J Roentgenol 2009;193(3): 879–886

Toxic Leukoencephalopathy

813. Iyer RS, Chaturvedi A, Pruthi S, Khanna PC, Ishak GE. Medication neurotoxicity in children. Pediatr Radiol 2011;41(11):1455–1464

Tuberculosis

814. Patkar D, Narang J, Yanamandala R, Lawande M, Shah GV. Central nervous system tuberculosis: pathophysiology and imaging findings. Neuroimaging Clin N Am 2012;22(4):677–705

Tuberous Sclerosis

815. Arulrajah S, Ertan G, Jordan L, et al. Magnetic resonance imaging and diffusion-weighted imaging of normal-appearing white matter in children and young adults with tuberous sclerosis complex. Neuroradiology 2009;51(11):781–786

816. Lopes MBS, Wiestler OD, Stemmer-Rachamimov AO, Sharma MC. Tuberous sclerosis complex and subependymal giant cell astrocytoma. In: Louis DN, Ohgaki H, Wiestler OD, Cavenee WK, eds. World Health Organization Classification of Tumours of the Central Nervous System. 4th ed. Geneva: IARC Press; 2007:218–221

817. Michelozzi C, Di Leo G, Galli F, et al. Subependymal nodules and giant cell tumours in tuberous sclerosis complex patients: prevalence on MRI in relation to gene mutation. Childs Nerv Syst 2013;29(2): 249–254

818. Piao C, Yu A, Li K, Wang Y, Qin W, Xue S. Cerebral diffusion tensor imaging in tuberous sclerosis. Eur J Radiol 2009;71(2):249–252

Urea Cycle Abnormalities

819. Choi CG, Yoo HW. Localized proton MR spectroscopy in infants with urea cycle defect. AJNR Am J Neuroradiol 2001;22(5):834–837

Venous Sinus Occlusion

820. Dlamini N, Billinghurst L, Kirkham FJ. Cerebral venous sinus (sinovenous) thrombosis in children. Neurosurg Clin N Am 2010;21(3): 511–527

821. Hegde AN, Mohan S, Lath N, Lim CCT. Differential diagnosis for bilateral abnormalities of the basal ganglia and thalamus. Radiographics 2011;31(1):5–30

822. Leach JL, Fortuna RB, Jones BV, Gaskill-Shipley MF. Imaging of cerebral venous thrombosis: current techniques, spectrum of findings, and diagnostic pitfalls. Radiographics 2006;26(Suppl 1):S19–S41, discussion S42–S43

Wallerian Degeneration

823. De Simone T, Regna-Gladin C, Carriero MR, Farina L, Savoiardo M. Wallerian degeneration of the pontocerebellar fibers. AJNR Am J Neuroradiol 2005;26(5):1062–1065

824. Fitzek C, Fitzek S, Stoeter P. Bilateral Wallerian degeneration of the medial cerebellar peduncles after ponto-mesencephalic infarction. Eur J Radiol 2004;49(3):198–203

825. Küker W, Schmidt F, Heckl S, Nägele T, Herrlinger U. Bilateral Wallerian degeneration of the middle cerebellar peduncles due to paramedian pontine infarction: MRI findings. Neuroradiology 2004;46(11): 896–899

826. Liu X, Tian W, Li L, et al. Hyperintensity on diffusion weighted image along ipsilateral cortical spinal tract after cerebral ischemic stroke: a diffusion tensor analysis. Eur J Radiol 2012;81(2):292–297

827. Musson R, Romanowski C. Restricted diffusion in Wallerian degeneration of the middle cerebellar peduncles following pontine infarction. Pol J Radiol 2010;75(4):38–43

828. Puig J, Pedraza S, Blasco G, et al. Wallerian degeneration in the corticospinal tract evaluated by diffusion tensor imaging correlates with motor deficit 30 days after middle cerebral artery ischemic stroke. AJNR Am J Neuroradiol 2010;31(7):1324–1330

829. Uchino A, Sawada A, Takase Y, Kudo S. Symmetrical lesions of the middle cerebellar peduncle: MR imaging and differential diagnosis. Magn Reson Med Sci 2004;3(3):133–140

830. Uchino A, Yuzuriha T, Murakami M, et al. Magnetic resonance imaging of sequelae of central pontine myelinolysis in chronic alcohol abusers. Neuroradiology 2003;45(12):877–880

Wernicke's Encephalopathy

831. Bathla G, Hegde AN. MRI and CT appearances in metabolic encephalopathies due to systemic diseases in adults. Clin Radiol 2013;68(6):545–554

832. Beh SC, Frohman TC, Frohman EM. Isolated mammillary body involvement on MRI in Wernicke's encephalopathy. J Neurol Sci 2013; 334(1-2):172–175

833. Elefante A, Puoti G, Senese R, et al. Non-alcoholic acute Wernicke's encephalopathy: role of MRI in non typical cases. Eur J Radiol 2012; 81(12):4099–4104

834. Zuccoli G, Santa Cruz D, Bertolini M, et al. MR imaging findings in 56 patients with Wernicke encephalopathy: nonalcoholics may differ from alcoholics. AJNR Am J Neuroradiol 2009;30(1):171–176

Wilson's Disease

835. Kim TJ, Kim IO, Kim WS, et al. MR imaging of the brain in Wilson disease of childhood: findings before and after treatment with clinical correlation. AJNR Am J Neuroradiol 2006;27(6):1373–1378

836. King AD, Walshe JM, Kendall BE, et al. Cranial MR imaging in Wilson's disease. AJR Am J Roentgenol 1996;167(6):1579–1584

837. Kitzberger R, Madl C, Ferenci P. Wilson disease. Metab Brain Dis 2005;20(4):295–302

838. Magalhaes ACA, Caramelli P, Menezes JR, et al. Wilson's disease: MRI with clinical correlation. Neuroradiology 1994;36(2):97–100

839. Rosencrantz R, Schilsky M. Wilson disease: pathogenesis and clinical considerations in diagnosis and treatment. Semin Liver Dis 2011;31(3):245–259

840. Thapa R, Ghosh A. 'Face of the giant panda' sign in Wilson disease. Pediatr Radiol 2008;38(12):1355

841. van Wassenaer-van Hall HN, van den Heuvel AG, Algra A, Hoogenraad TU, Mali WPTM. Wilson disease: findings at MR imaging and CT of the brain with clinical correlation. Radiology 1996;198(2):531–536

842. Youn J, Kim JS, Kim HT, et al. Characteristics of neurological Wilson's disease without Kayser-Fleischer ring. J Neurol Sci 2012; 323(1-2):183–186

Zellweger Syndrome

843. Lee PR, Raymond GV. Child neurology: Zellweger syndrome. Neurology 2013;80(20):e207–e210

844. van der Knaap MS, Wassmer E, Wolf NI, et al. MRI as diagnostic tool in early-onset peroxisomal disorders. Neurology 2012;78(17): 1304–1308

845. Weller S, Rosewich H, Gärtner J. Cerebral MRI as a valuable diagnostic tool in Zellweger spectrum patients. J Inherit Metab Dis 2008; 31(2):270–280

Chapter 2

Ventricles and Cisterns

Introduction 422

2.1 Lateral ventricles—common masses 423

2.2 Common third ventricular masses 425

2.3 Fourth ventricular lesions 425

2.4 Small ventricles 426

2.5 Dilated ventricles 428

2.6 Abnormal or altered configuration of the ventricles 456

2.7 Solitary intraventricular lesions in children 468

2.8 Solitary intraventricular lesions in adults 488

2.9 Contrast-enhancing ventricular margins 510

References 516

2 Ventricles and Cisterns

Table 2.1 Lateral ventricles—common masses

Table 2.2 Common third ventricular masses

Table 2.3 Fourth ventricular lesions

Table 2.4 Small ventricles

Table 2.5 Dilated ventricles

Table 2.6 Abnormal or altered configuration of the ventricles

Table 2.7 Solitary intraventricular lesions in children

Table 2.8 Solitary intraventricular lesions in adults

Table 2.9 Contrast-enhancing ventricular margins

Introduction

The embryologic development of the ventricles begins with three expansions (primary vesicles) of the rostral neural tube (weeks 4 to 5 of gestation), which are referred to as the forebrain (prosencephalon), midbrain (mesencephalon), and hindbrain (rhombencephalon) (see **Fig. 1.3**). The primary vesicles subsequently expand and bend with localized constrictions to form the five secondary vesicles (~ 7 weeks of gestation). The forebrain gives rise to the telencephalon (eventual cerebral hemispheres and lateral ventricles) and diencephalon (thalamus, hypothalamus, and third ventricle). The midbrain-primary vesicle eventually forms the secondary vesicle, also referred to as the mesencephalon, which eventually forms the tectum, midbrain portion of the brainstem, and cerebral aqueduct. The hindbrain gives rise to the metencephalon (eventual pons, cerebellum, and upper portion of the fourth ventricle) and myelencephalon (eventual medulla and lower portion of the fourth ventricle).

Abnormalities in development of the cerebral vesicles result in congenital anomalies like the holoprosencephalies, lissencephaly/pachygyria, Dandy-Walker malformations, etc. Abnormalities in the closure of the caudal neural tube with altered internal pressure dynamics have been proposed as a mechanism in malformation of the ventricles and other anomalies associated with Chiari II malformations.

The normal lateral ventricles are bilateral, elongated, C-shaped structures, each containing a contiguous frontal horn, body, atrium (trigone), occipital horn, and temporal horn (**Fig. 2.1**). The lateral ventricles are often symmetric, but varying degrees of asymmetry are not uncommon. The anterior portions of the lateral ventricles are normally separated by the septum pellucidum.

The third ventricle appears as a slitlike compartment filled with cerebrospinal fluid (CSF) between the thalami. The inferior border of the third ventricle is the hypothalamus, and the upper border is the choroid tela (fusion of pia and ependymal lining of ventricle) and choroid plexus. The anterior border is the lamina terminalis and anterior commissure. The posterior border includes the pineal gland and recess and posterior commissure. The third ventricle communicates with the lateral ventricles via the foramina of Monro located anterolaterally. The third ventricle communicates with the fourth ventricle via the cerebral aqueduct posteroinferiorly.

The fourth ventricle has a pyramidal shape in the sagittal plane and an inverted C-shape/inverted kidney-bean shape in the axial plane. The fourth ventricle is located dorsal to the pons, with its roof comprised of the cerebellar vermis. The fourth ventricle communicates with the cerebral aqueduct at its upper margin, and with the cisterna magna of the subarachnoid space via the foramen of Magendie and the paired foramina of Luschka.

Cerebrospinal fluid fills the ventricles and is produced by the choroid plexus located within the lateral, third, and fourth ventricles, as well as the foramina of Luschka and Magendie. Choroid plexus typically enhances after intravenous gadolinium contrast administration because of its lack of a blood–brain barrier. CSF from the ventricles communicates with the subarachnoid space adjacent to the brain and spinal cord through the foramina of Luschka and Magendie. CSF has the primary function of protecting the brain and spinal cord from trauma and rapid changes in venous pressure. CSF represents ~ 10% of the intracranial and intraspinal spaces. A total of ~ 150 mL of CSF is present within the ventricles and intracranial and spinal subarachnoid spaces. The choroid plexus forms 500 mL of CSF daily, allowing turnover three to four times daily. More than 90% of the CSF is normally resorbed by arach-

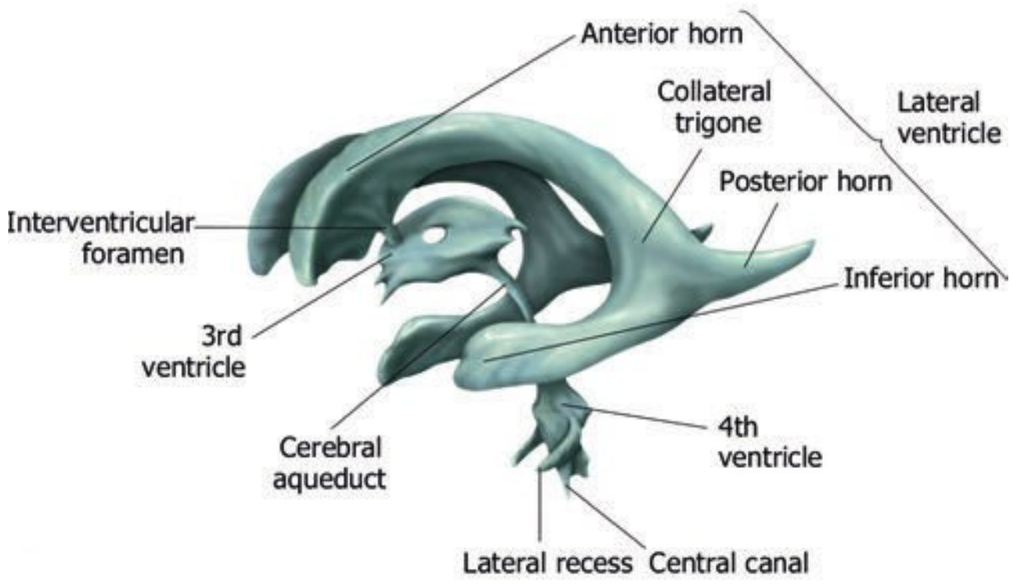

Fig. 2.1 Lateral view of the intracranial ventricular system. From THIEME Atlas of Anatomy, Neck and Internal Organs, © Thieme 2006, Illustration by Karl Wesker.

noid villi or granulations (grouping of villi), which penetrate the dura, with resultant emptying of fluid into the intracranial venous sinuses. The remaining small amount of fluid is resorbed through the ependymal linings of the ventricles. CSF normally flows from the cranial to spinal subarachnoid spaces during systole secondary to increased brain volume and in the opposite direction during diastole (**Fig. 2.2**).

Obstruction of outflow of CSF from the ventricles results in dilatation of the ventricles proximal to the site of blockage. The obstruction can result from congenital malformations (Chiari II, etc.) neoplasms/other intracranial mass lesions (colloid cyst, etc.), inflammatory lesions, hemorrhage, brain edema/swelling (ischemia, trauma), etc. In addition to ventricular dilatation, transependymal leakage of fluid can be seen with MRI. Obstructive or noncommunicating hydrocephalus can result, if untreated, in increased intracranial pressure, intracranial herniation, and death.

Communicating hydrocephalus occurs when there is overproduction of CSF (choroid plexus papilloma/carcinoma, impaired resorption of CSF through the arachnoid villi, and/or obstruction of CSF flow through the cisterns and sulci). With communicating hydrocephalus, the ventricles are disproportionately more prominent than the sulci. Subependymal edema may be seen with MRI due to the impaired resorption of CSF. Patients with communicating hydrocephalus (normal-pressure hydrocephalus) may also have clinical features of gait disturbance, incontinence, and/or progressive impairment of mental function.

Ventricular enlargement can also result from cerebral infarction, cerebral atrophy, or various neurodegenerative diseases. With these disorders, sulcal prominence is usually evident with MRI and CT.

Sulci normally vary in size, although typically increase in size with aging. Sulcal enlargement can also be seen in a child with dehydration. Congenital malformations like lissencephaly and pachygyria result in absence of sulci, or a few shallow sulci, respectively. Sulci may be asymmetrically prominent at sites of prior cerebral or cerebellar infarction, prior intra-axial hemorrhage, contusion, inflammation, or radiation injury.

The basal cisterns represent the subarachnoid compartment adjacent to the pial margins of the inferior portions of the brain and brainstem. The cisterns are named according to the adjacent neural structures. The larger of the cisterns include the cisterna magna (dorsal and inferior to the cerebellar vermis), and superior cerebellar cistern.

Approximately 10% of neoplasms in the CNS extend into, or are completely within, the ventricles. The age of the patient and the location of the tumor influence the differential diagnosis of lesions.

Table 2.1 Lateral ventricles—common masses

Age	Foramen of Monro	Trigone and atrium	Lateral ventricle—body
Adult	Colloid cyst Cysticercosis	Meningioma Choroid plexus cyst Ependymal cyst Central neurocytoma Metastasis Neuroepithelial cyst	Ependymoma Glioblastoma Metastasis Central neurocytoma Cysticercosis
Child (> 5 years)	Giant cell astrocytoma Pilocytic astrocytoma Cysticercosis	Ependymoma Ependymal cyst Choroid plexus cyst Choroid plexus papilloma Choroid plexus carcinoma Hamartoma–tuberous sclerosis Gray matter heterotopia Cysticercosis	Ependymoma Pilocytic astrocytoma Hamartoma–tuberous sclerosis Gray matter heterotopia Cysticercosis
Child (< 5 years)	Giant cell astrocytoma Pilocytic astrocytoma Cysticercosis	Choroid plexus papilloma Choroid plexus carcinoma Cysticercosis	Choroid plexus papilloma Choroid plexus carcinoma PNET Teratoma Cysticercosis

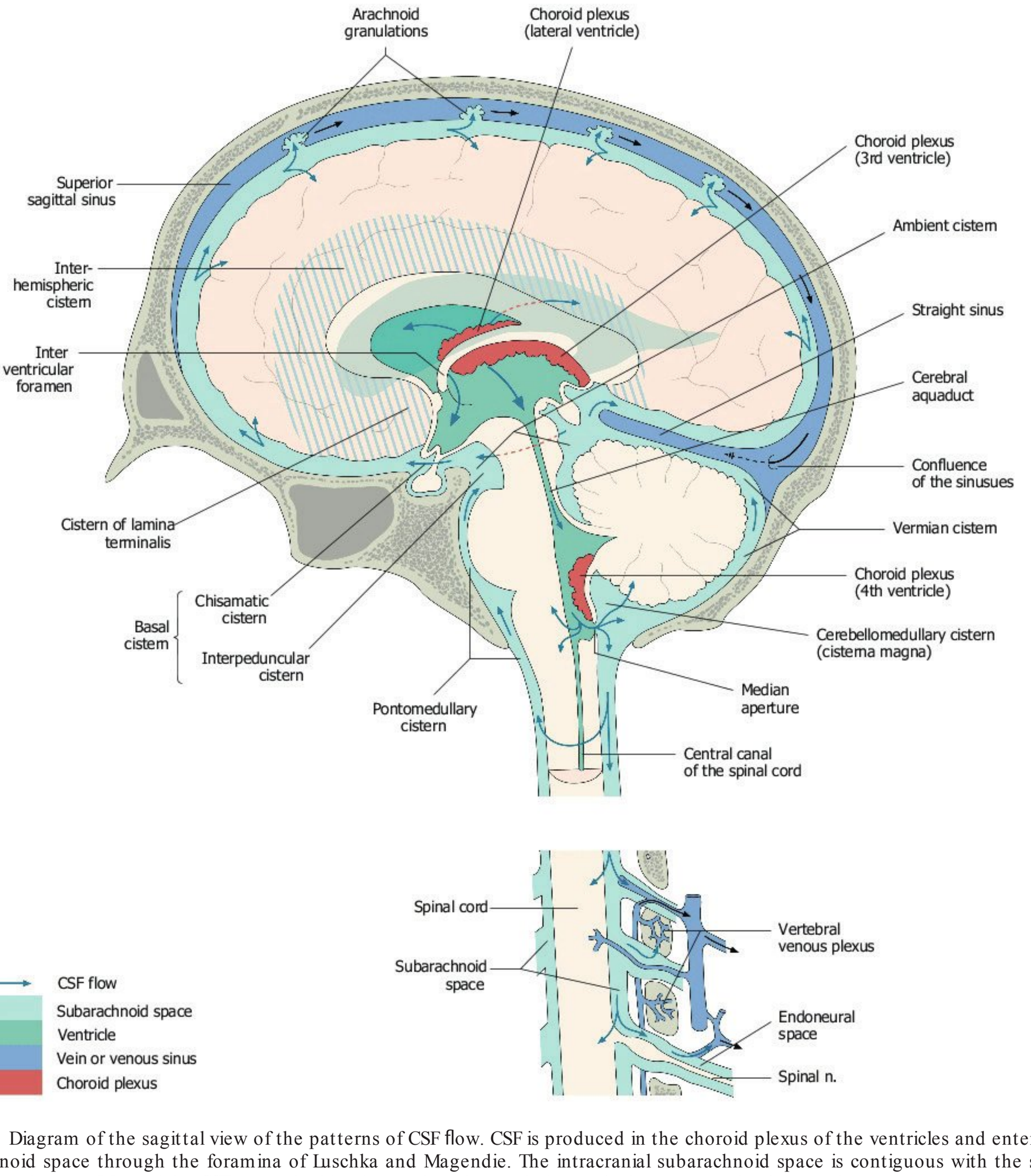

Fig. 2.2 Diagram of the sagittal view of the patterns of CSF flow. CSF is produced in the choroid plexus of the ventricles and enters the subarachnoid space through the foramina of Luschka and Magendie. The intracranial subarachnoid space is contiguous with the spinal subarachnoid space. Most of the CSF is resorbed by the arachnoid granulations, which penetrate the dura, with resultant emptying of fluid into the intracranial venous sinuses. From THIEME Atlas of Anatomy, Neck and Internal Organs, © Thieme 2006, Illustration by Karl Wesker.

Table 2.2 Common third ventricular masses

Age	Foramen of Monro	Anterior Recess	Third ventricle—body	Third ventricle—posterior
Adult	Colloid cyst Metastases Cysticercosis	Pituitary adenoma Meningioma Metastasis Aneurysm Craniopharyngioma Lymphoma Cysticercosis	Glioma Cysticercosis	Pineal tumor Glioma Vascular malformation Cysticerosis
Child	Giant cell astrocytoma Pilocytic astrocytoma Cysticercosis	Germ cell tumor Langerhans' cell histiocytosis Glioma Craniopharyngioma Cysticercosis	Choroid plexus papilloma Glioma Cysticercosis	Pineal tumor Glioma Vascular malformation Cysticercosis

Table 2.3 Fourth ventricular lesions

Age	Neoplasm	Tumorlike Lesions
Adult	Metastatic tumor Hemangioblastoma Ependymoma Astrocytoma Choroid plexus papilloma Atypical choroid plexus papilloma Choroid plexus carcinoma Meningioma	Arachnoid cyst Epidermoid Abscess Parasitic infection
Child	Astrocytoma Medulloblastoma Atypical teratoid/rhabdoid tumor Ependymoma Metastatic lesion Hemangioblastoma (von Hippel-Lindau disease) Choroid plexus papilloma Atypical choroid plexus papilloma Choroid plexus carcinoma	Abscess Parasitic infection

Table 2.4 Excessively small ventricles

- Normal variant
- Postshunt change
- Increased intracranial pressure
- Pseudotumor cerebri—idiopathic intracranial hypertension

Table 2.4 Excessively small ventricles

Lesions	MRI Findings	Comments
Normal variant	Small ventricles with normal appearance of brain parenchyma and presence of CSF in subarachnoid spaces and cisterns.	Normal variation.
Postshunt change	Small, slitlike ventricles (± shunt tube present).	Small ventricular size can result from chronic overdrainage of ventricles with shunts.
Increased intracranial pressure (**Fig. 2.3** and **Fig. 2.4**)	Small ventricles with effacement of subarachnoid spaces, ± high signal on T2-weighted imaging in brain parenchyma—cerebral edema.	Increased intracranial pressure can result from diffuse cerebral edema secondary to trauma, metabolic disorders (ketoacidosis, hepatic encephalopathy, mitochondrial encephalopathy) and acute inflammatory/infectious disease. Ventricular size usually does not correlate well with intracranial pressure.
Pseudotumor cerebri—idiopathic intracranial hypertension (**Fig. 2.5** and **Fig. 2.6**)	Normal shaped but small ventricles, ± mild prominence of intracranial subarachnoid spaces, ± empty sella configuration (prevalence up to 70%), enlarged trigeminal cisterns/Meckel caves without meningoceles (9%), and Meckel cave/petrous apex meningoceles (11%). Orbital findings include increased fluid in distended optic nerve sheath complexes (67%), flattening of the posterior sclera (prevalence of 80%, specificity of 100%), intraocular protrusion of the optic nerve head (30%), tortuosity of the optic nerves, and/or gadolinium contrast enhancement of the prelaminar optic nerve.	Idiopathic intracranial hypertension is a syndrome with elevated intracranial pressure without evidence of a mass lesion, hydrocephalus, or abnormal CSF. MRI with gadolinium contrast has a role in excluding intracranial tumors involving the brain or leptomeninges. Magnetic resonance venography is useful to exclude intracranial venous sinus thrombosis or stenosis causing increased intracranial pressure. Treatment includes medications to reduce CSF pressure or CSF diversion procedures/shunts.

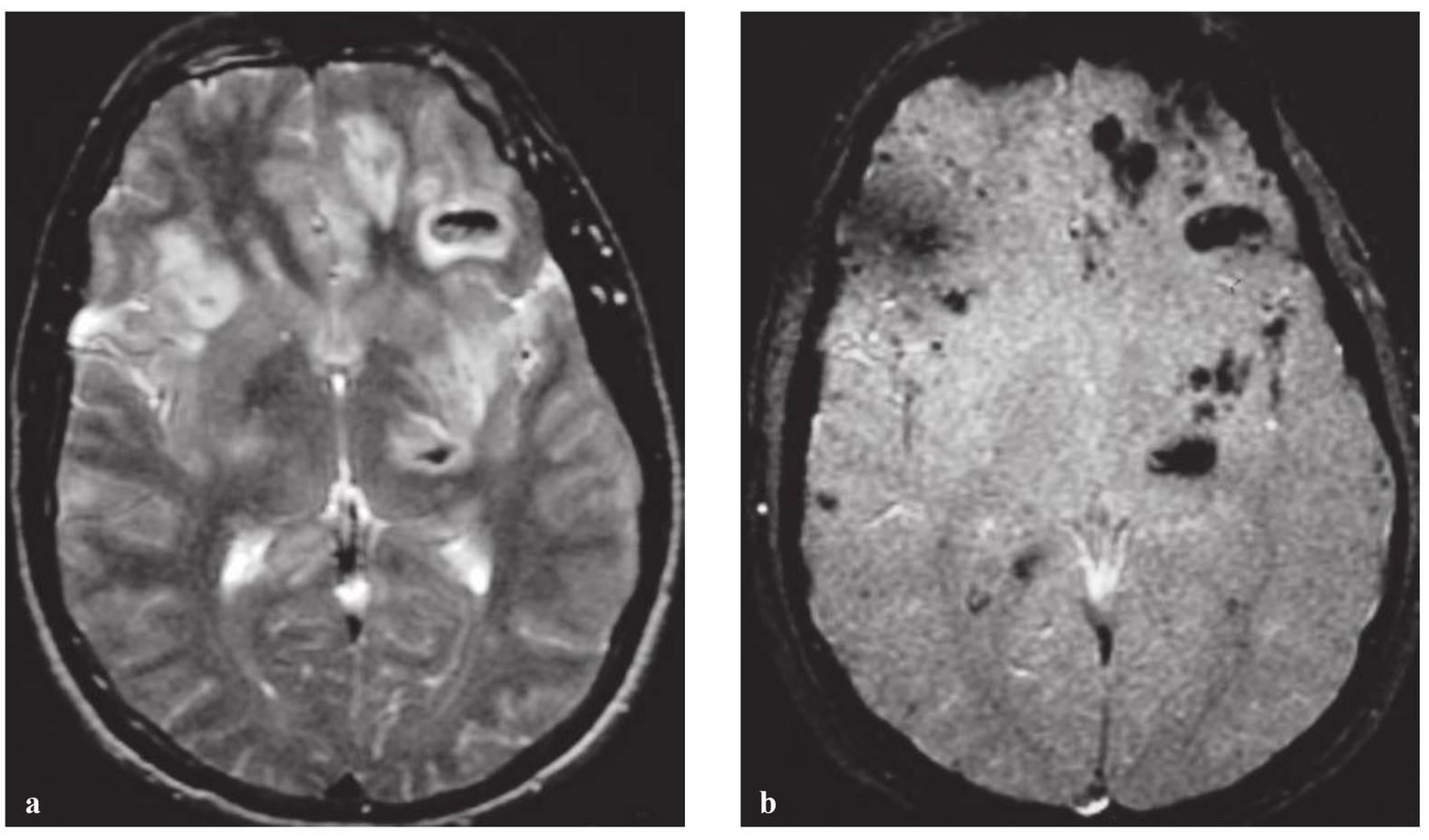

Fig. 2.3 A 19-year-old man with severe head trauma and diffuse axonal injury with brain swelling from multiple intra-axial sites of hemorrhage in the cerebral white matter that have **(a)** mixed low and high signal on axial T2-weighted imaging and **(b)** low signal on axial GRE.

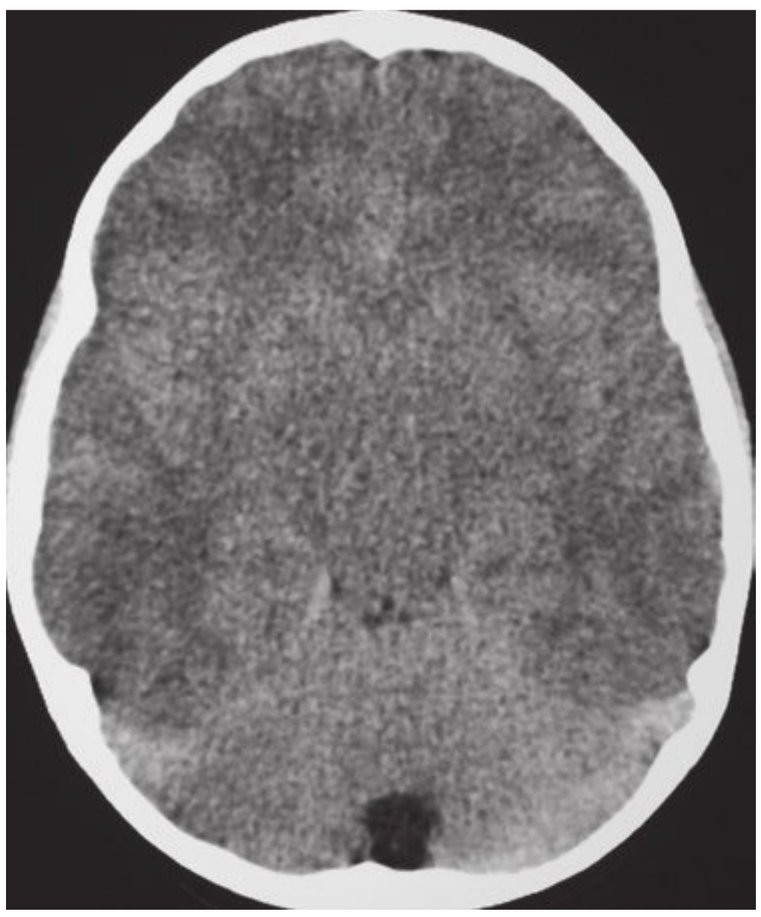

Fig. 2.4 A 7-year-old boy with diabetic ketoacidosis and cerebral edema with effacement of ventricles and sulci on axial CT.

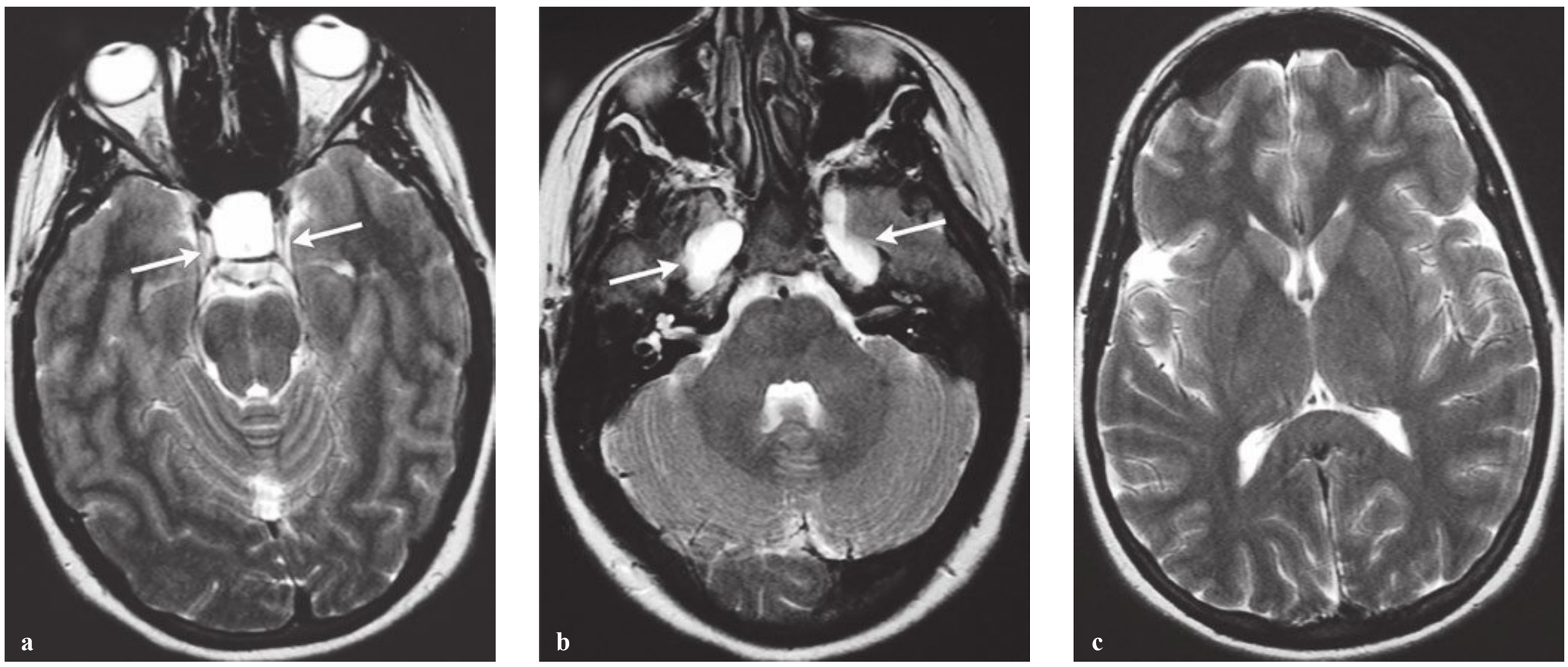

Fig. 2.5 A 25-year-old woman with pseudotumor cerebri. **(a)** Axial T2-weighted imaging shows a prominent empty sella configuration (arrows) and flattened dorsal margins of the eyes, **(b)** dilated trigeminal cisterns/Meckel's caves (arrows), and **(c)** small ventricles.

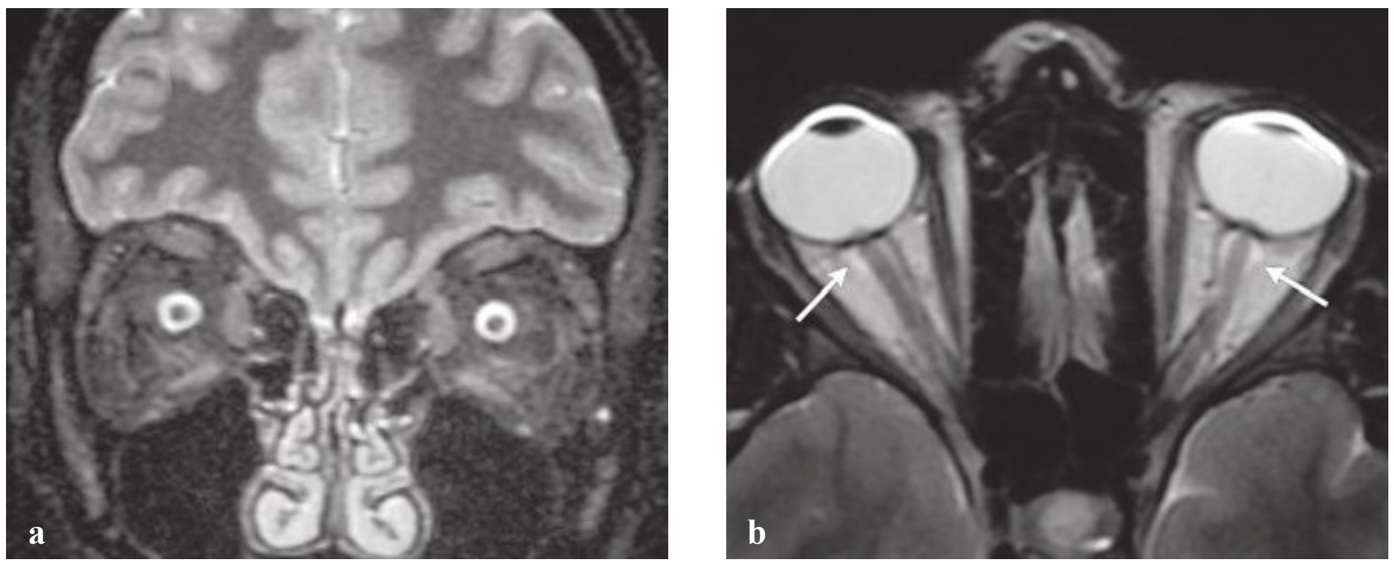

Fig. 2.6 A 23-year-old woman with pseudotumor cerebri who has **(a)** increased fluid in distended optic nerve sheath complexes as seen on coronal STIR and **(b)** flattening of the posterior sclera and intra-ocular protrusion of the optic nerve heads (arrows) as seen on axial T2-weighted imaging.

Table 2.5 Dilated ventricles

- Normal variant
- Aqueductal stenosis
- Congenital/Developmental Abnormalities
  - Chiari I malformation
  - Chairi II malformation
  - Chiari III malformation
  - Dandy-Walker malformation
  - Vermian hypoplasia (Dandy-Walker variant)
  - Colpocephaly
- Lesions Causing Obstructive Hydrocephalus
  - Metastatic tumor
  - Intra-axial primary tumors
  - Pilocytic astrocytoma
  - Diffuse astroctyoma
  - Anaplastic astrcytoma
  - Glioblastoma multiforme
  - Giant cell astrocytoma
  - Medulloblastoma
  - Atypical teratoid/rhabdoid tumor
  - Ependymoma
  - Malignant ependymoma
  - Hemangioblastoma
- Intraventricular Tumors
  - Choroid plexus papilloma
  - Atypical choroid plexus papilloma
  - Choroid plexus carcinoma
  - Subependymoma
  - Meningioma
  - Hemangiopericytoma
  - Central neurocytoma
  - Pineal region lesions and tumors
  - Intraventricular non-neoplastic lesions
  - Colloid cyst
  - Ependymal cyst
- Inflammation/Infection
  - Ependymitis/ventriculitis
  - TORCH and neonatal infections
  - Cysticercosis
  - Hydatid cyst
  - Rasmussen's encephalitis
- Neurodegeneration
  - Hydranencephaly
  - Porencephalic cyst
  - Encephalomalacia
  - Dyke-Davidoff-Mason syndrome
  - Alzheimer's disease
  - Frontal temporal degeneration
  - Huntington disease
  - Communicating hydrocephalus, normal pressure hydrocephalus
  - Ventricular shunt failure

Table 2.5 Dilated ventricles

Lesions	Imaging Findings	Comments
Normal variant	Mild ventricular enlargement can occur without associated cerebral or cerebellar abnormality.	Ventricular size usually increases with age, and it is most pronounced after 60 years.
Aqueductal stenosis (**Fig. 2.7** and **Fig. 2.8**)	MRI: Dilatation of lateral and third ventricles with normal-sized fourth ventricle, ± dilatation of only the upper portion of cerebral aqueduct and not the lower portion, ± discrete or poorly defined lesion in midbrain. Subependymal edema can be seen on FLAIR.	Aqueductal stenosis can result from a small lesion/neoplasm in the midbrain or debris or adhesions from hemorrhage or inflammatory diseases. It may also result from extrinsic compression of the tectal plate and aqueduct from massively enlarged ventricles or ventricular diverticulum. MRI can exclude other lesions causing obstruction of CSF flow through the aqueduct, such as lesions in the posterior third ventricle or posterior cranial fossa.

(continued on page 430)

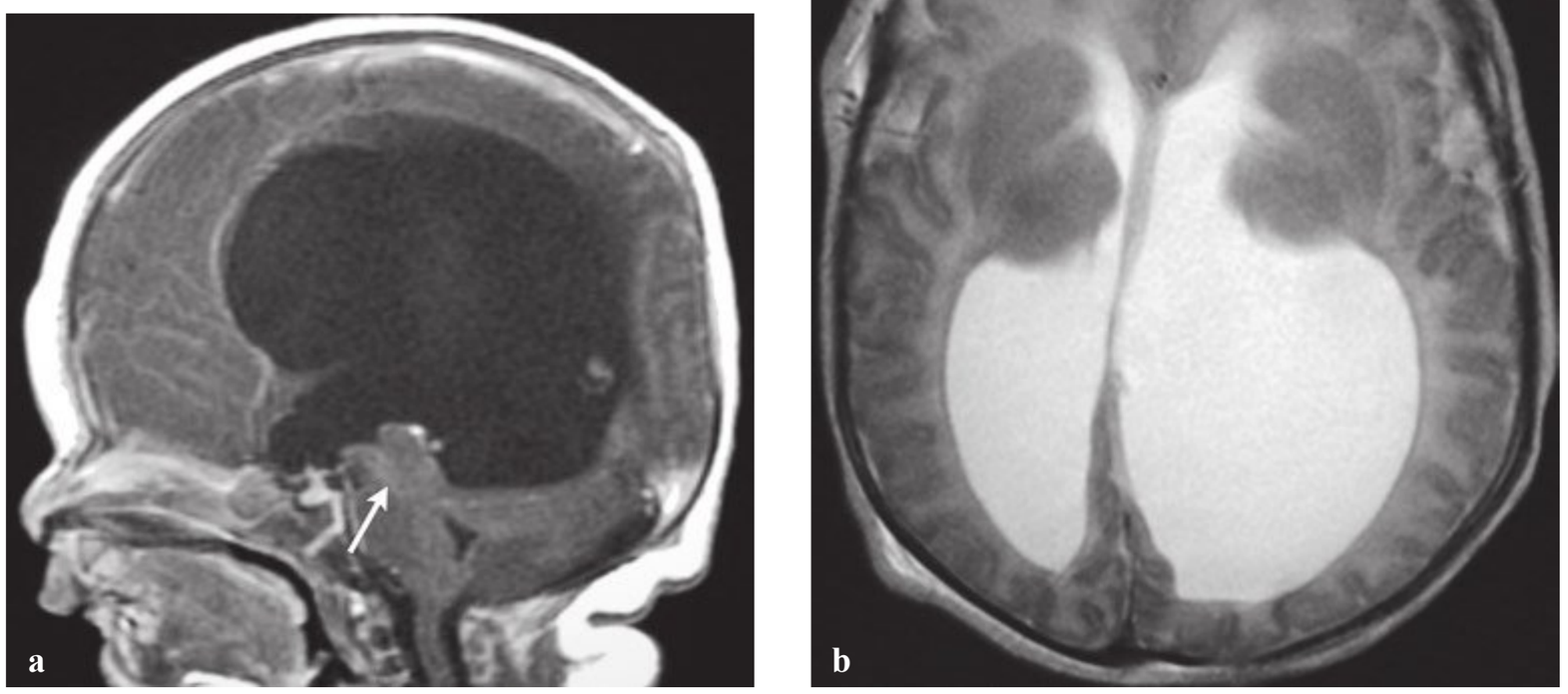

Fig. 2.7 A 4-day-old male with congenital hydrocephalus and extrinsic aqueductal stenosis. **(a)** Postcontrast sagittal T1-weighted imaging and **(b)** axial T2-weighted imaging show marked dilatation of the lateral and third ventricles. The enlarged lateral ventricles compress the cerebellum and brainstem, including the tectal plate (**a**, arrow), resulting in aqueductal occlusion.

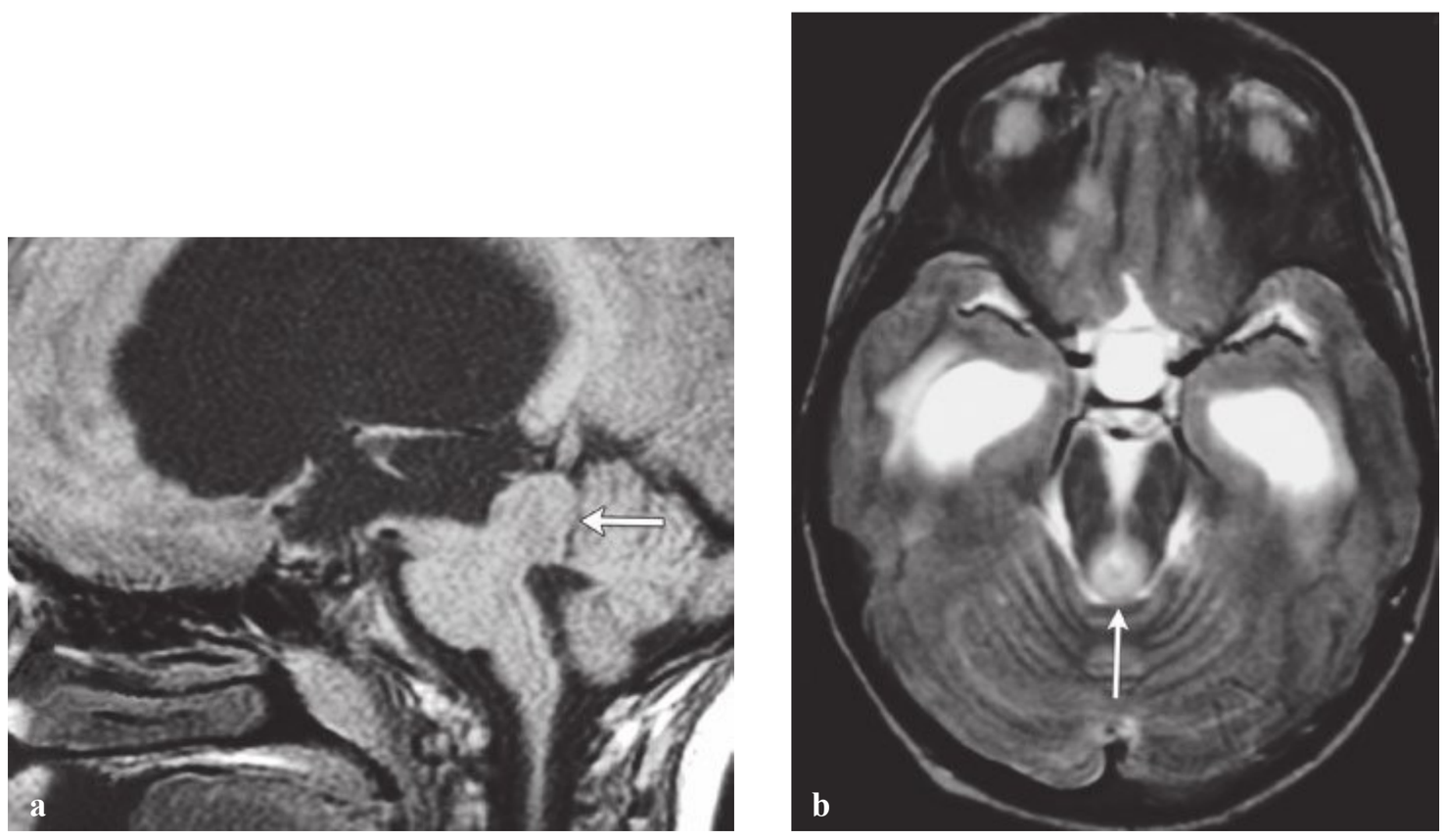

Fig. 2.8 A 7-year-old male with intrinsic aqueductal stenosis resulting from an astrocytoma involving the tectal plate as seen on **(a)** sagittal T1-weighted imaging (arrow) and **(b)** axial T2-weighted imaging (arrow).

Table 2.5 (cont.) Dilated ventricles

Congenital/Developmental Abnormalities		
Chiari I malformation (**Fig. 2.9**)	Cerebellar tonsils extend more than 5 mm below the foramen magnum in adults, 6 mm in children < 10 years old. Syringohydromyelia occurs in 20 to 40% Hydrocephalus in 25% Basilar impression in 25% Less common associations are Klippel-Feil syndrome and atlanto-occipital assimilation.	Cerebellar tonsillar ectopia. Most common anomaly of CNS. Not associated with myelomeningocele.
Chiari II malformation (Arnold-Chiari) (**Fig. 2.10, Fig. 1.12**)	Small posterior cranial fossa with gaping foramen magnum through which there is an inferiorly positioned vermis associated with a cervicomedullary kink. Beaked dorsal margin of the tectal plate. Myelomeningoceles in nearly all patients. Hydrocephalus and syringomyelia common. Dilated lateral ventricles posteriorly (colpocephaly).	Complex anomaly involving the cerebrum, cerebellum, brainstem, spinal cord, ventricles, skull, and dura. Failure of fetal neural folds to develop properly results in altered development affecting multiple sites of the CNS.
Chiari III malformation	Features of Chiari II plus lower occipital or high cervical encephalocele.	Rare anomaly associated with high mortality.

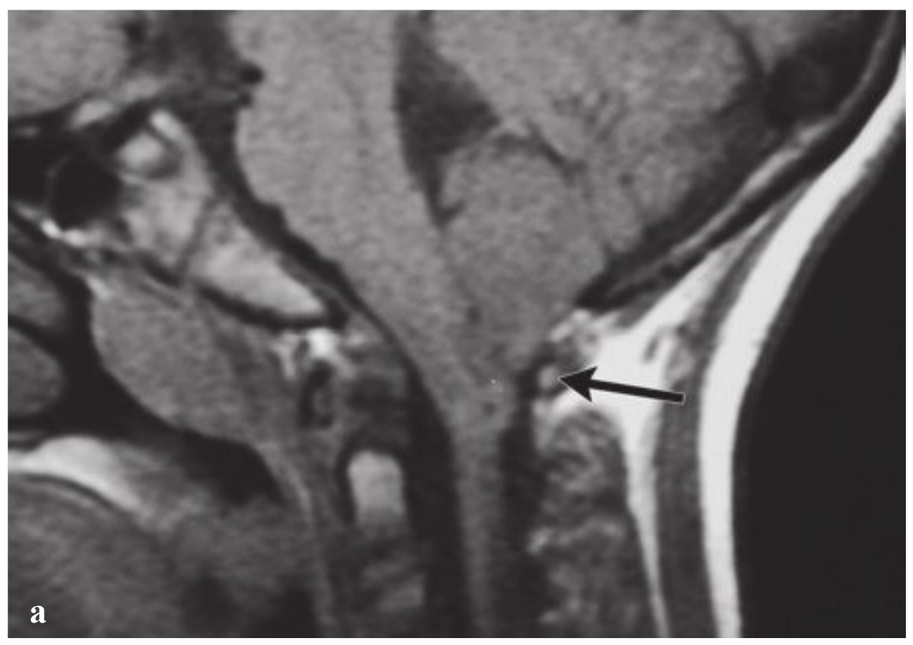

Fig. 2.9 A 14-year-old male with hydrocephalus related to a Chiari I malformation. **(a)** Sagittal T1-weighted imaging shows the cerebellar tonsils (arrow) extending below the foramen magnum down to the level of the posterior arch of C1 and **(b)** associated with dilated lateral ventricles on axial T2-weighted imaging.

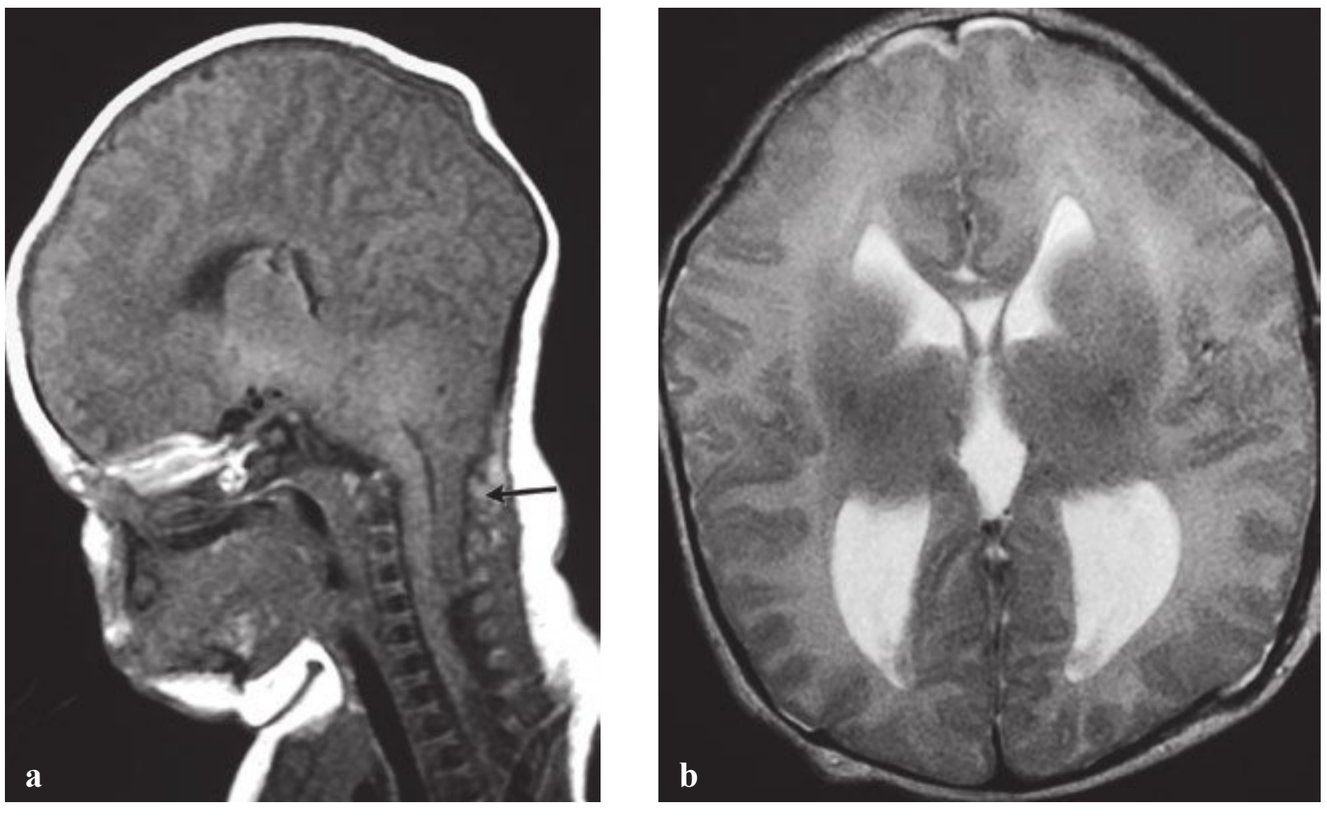

Fig. 2.10 Neonate with a Chairi II malformation. **(a)** Sagittal T1-weighted imaging shows a small posterior cranial fossa with a gaping foramen magnum through which there is an inferiorly positioned cerebellum (arrow). **(b)** Axial T2-weighted imaging shows dilatation of the lateral and third ventricles with asymmetric prominence of the occipital horns of the lateral ventricles (colpocephaly).

Lesions	Imaging Findings	Comments
Dandy-Walker malformation (**Fig. 2.11**)	Vermian aplasia or severe hypoplasia, communication of fourth ventricle with retrocerebellar cyst, enlarged posterior fossa, and high position of tentorium and transverse venous sinuses. Hydrocephalus common. Associated with other anomalies, such as dysgenesis of the corpus callosum, gray matter heterotopia, schizencephaly, holoprosencephaly, cephaloceles, and others.	Abnormal formation of roof of fourth ventricle with absent or near-incomplete formation of cerebellar vermis.
Vermian hypoplasia (Dandy-Walker variant) (**Fig. 1.43**)	Mild vermian hypoplasia with communication of posteroinferior portion of the fourth ventricle with cisterna magna. No associated enlargement of the posterior cranial fossa.	Occasionally associated with hydrocephalus, dysgenesis of corpus callosum, gray matter heterotopia, or other anomalies.
Colpocephaly (**Fig. 2.10**)	Asymmetric enlargement of the occipital horns of the lateral ventricles.	Associated with Chiari II malformation and dysgenesis of corpus callosum.

(continued on page 432)

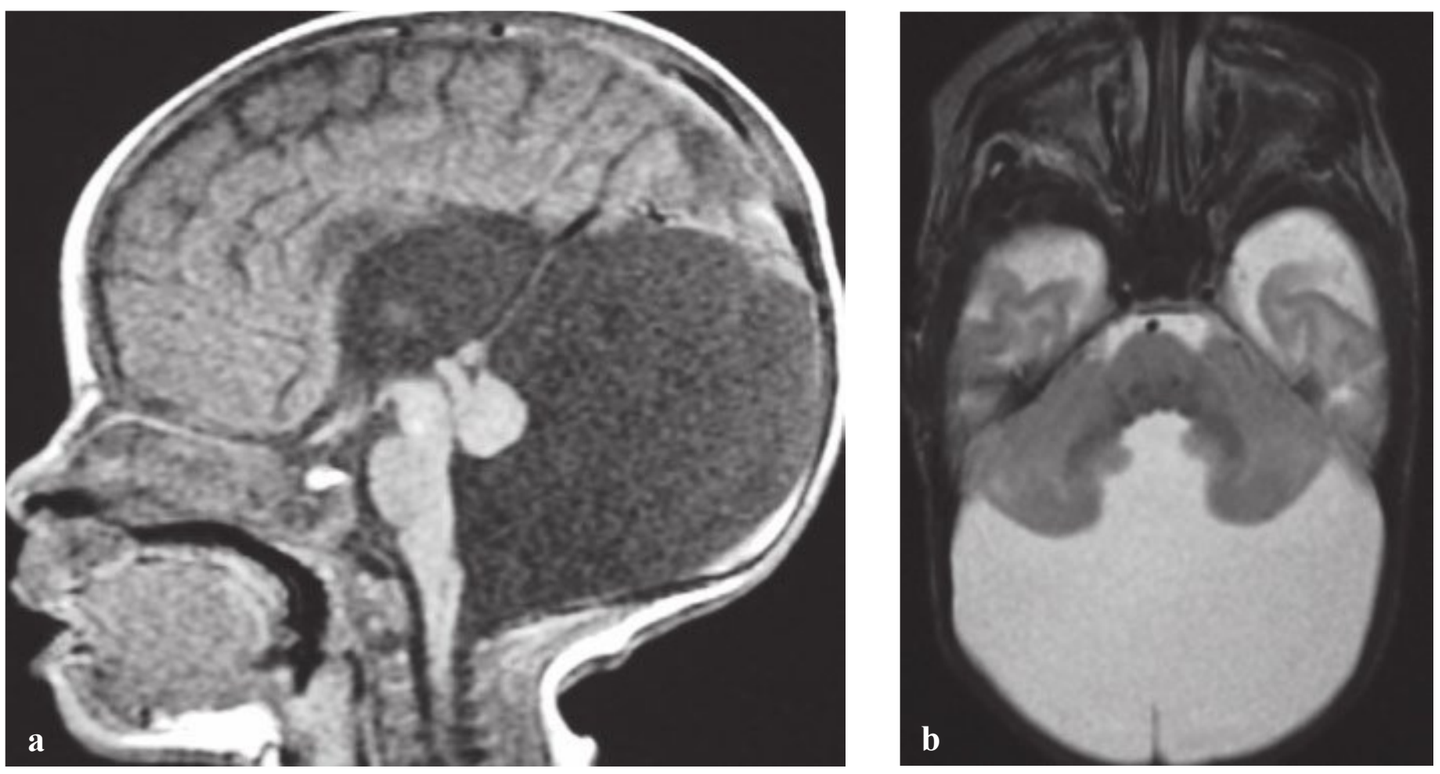

Fig. 2.11 Dandy-Walker malformation in a child. **(a)** Sagittal T1-weighted imaging and **(b)** axial T2-weighted imaging show severe vermian hypoplasia and moderate hypoplasia of the cerebellar hemispheres, communication of fourth ventricle with retrocerebellar cyst, enlarged posterior cranial fossa, high position of tentorium, dysgenesis of the corpus callosum, and hydrocephalus.

Table 2.5 (cont.) Dilated ventricles

Neoplasms (causing obstructive hydrocephalus)		
Metastatic tumor (**Fig. 2.12**)	MRI: Circumscribed spheroid lesions in brain, can have various intra-axial locations (often at gray–white matter junctions), usually low-intermediate signal on T1-weighted imaging, intermediate-high signal on T2-weighted imaging, ± hemorrhage, calcifications, and cysts. Variable gadolinium contrast enhancement, often with high signal on T2-weighted imaging peripheral to a nodular enhancing lesion representing axonal edema. Metastatic lesions can also involve the skull, dura, leptomeninges, ventricles, choroid plexus, or pituitary gland. Leptomeningeal tumor often best seen on postcontrast images. CT: Lesions usually have low-intermediate attenuation, ± hemorrhage, calcifications, or cysts. Variable contrast enhancement, often associated with adjacent low attenuation.	Represents ~ 33% of intracranial tumors, usually from extracranial primary neoplasm in adults more than 40 years old. Primary tumor source: lung > breast > GI > GU > melanoma.
Intra-axial Primary Tumors		
Pilocytic astrocytoma (**Fig. 2.13**)	MRI: Solid/cystic focal lesion with low-intermediate signal on T1-weighted imaging, high signal on T2-weighted imaging and FLAIR, usually showing gadolinium contrast enhancement. Lesions commonly are located in cerebellum, hypothalamus, optic chiasm, adjacent to third or fourth ventricles, or in brainstem. Thirty percent can have more aggressive MRI features, such as inhomogeneous gadolinium contrast enhancement, central necrotic zones, and irregular margins. Diffusion-weighted imaging: Usually no evidence of restricted diffusion. Diffusion tensor imaging can show tumor displacement of cortical spinal tracts. Magnetic resonance spectroscopy: With these low-grade tumors in children, a paradoxical pattern associated with more aggressive tumors (elevated choline/N-acetylaspartate and lactate levels) may be seen. CT: Solid/cystic focal lesion with low-intermediate attenuation, usually with prominent contrast enhancement.	Most common glioma in children and accounts for 6% of all gliomas. Slow-growing cystic-solid WHO grade I astrocytoma with biphasic pattern of compacted bipolar cells, Rosenthal fibers, multipolar cells, microcysts, and eosinophilic granular bodies. Associated with BRAF mutations involving the MAPK signaling pathway. Usually lack IDH mutations. Immunoreactive to GFAP and apolipoprotein D. Can occur in cerebrum, cerebellum, brainstem, and optic chiasm. In children, 67% occur in the cerebellum and usually have a favorable prognosis if totally resected. Increased occurrence in patients with neurofibromatosis type 1. Leptomeningeal tumor dissemination is rare (< 3%).

(continued on page 434)

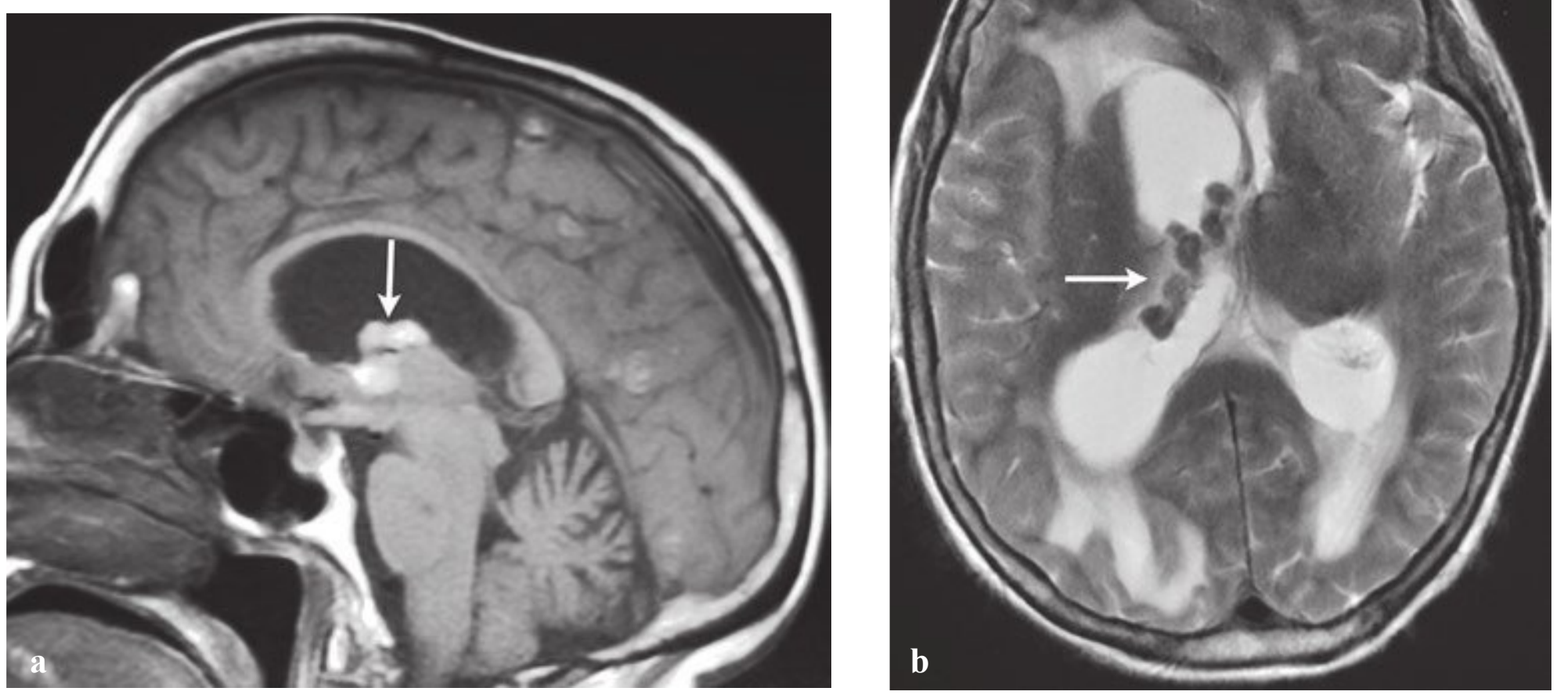

Fig. 2.12 A 56-year-old woman with intraventricular metastatic melanoma causing hydrocephalus. Nodular intraventricular lesions with **(a)** high signal on sagittal T1-weighted imaging (arrow) and **(b)** low signal on T2-weighted imaging (arrow) are seen associated with dilated ventricles and transependymal egress of CSF.

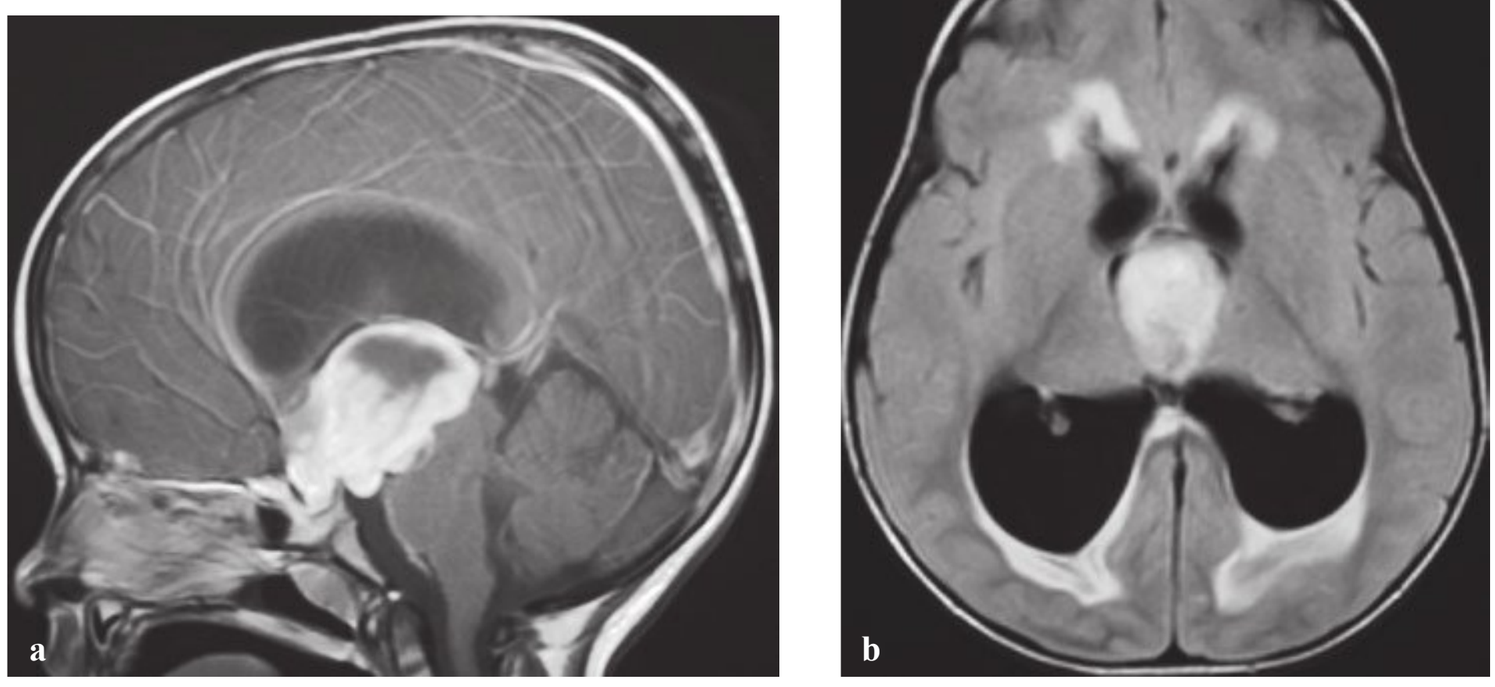

Fig. 2.13 A 3-year-old girl with **(a)** a gadolinium-enhancing pilocytic astrocytoma involving the hypothalamus on sagittal T1-weighted imaging that **(b)** extends into the third ventricle and causes obstructive hydrocephalus as seen on axial FLAIR.

Table 2.5 (cont.) Dilated ventricles

Lesions	Imaging Findings	Comments
Diffuse astrocytoma	MRI: Intra-axial lesion with slightly ill-defined margins or diffuse mass lesion in white matter with low-intermediate signal on T1-weighted imaging, high signal on T2-weighted imaging, ± mild gadolinium contrast enhancement. relative cerebral blood volume (rCBV) is usually low. There is minimal associated mass effect, and it usually lacks peritumoral edema and hemorrhage. Diffusion-weighted imaging: Tumors typically do not show restricted diffusion. CT: Focal or diffuse mass lesion usually located in white matter with low-intermediate attenuation, ± mild contrast enhancement. Minimal associated mass effect.	Low-grade astrocytoma (WHO grade II) that accounts for 10 to 15% of astrocytic brain tumors. Often occurs in children and adults (20–40 years old). Can also occur in children and older adults. Tumors comprised of well-differentiated fibrillary or gemistocytic neoplastic astrocytes. Association with TP53, isocitrate dehydogenase-IDH1 and IDH2, and telomere maintenance protein-ATRX mutation. Mean survival is 6 to 8 years; may undergo malignants progression to anaplastic astrocytoma or glioblastoma. Tumors with IDH mutations have a better prognosis than those without.
Anaplastic astrocytoma (**Fig. 2.14**)	MRI: Often irregularly marginated lesion located in white matter with low-intermediate signal on T1-weighted imaging, high signal on T2-weighted imaging, ± gadolinium contrast enhancement. Tumors can have elevated relative cerebral blood volume rCBV). Diffusion-weighted imaging: Tumors typically do not show restricted diffusion. Magnetic resonance spectroscopy shows decreased N-acetylaspartate (NAA) and high levels of choline. CT: Irregularly marginated mass lesion with mixed low and intermediate attenuation, ± hemorrhage, prominent heterogeneous contrast enhancement, and peripheral edema. Can cross corpus callosum.	Malignant astrocytic tumor (WHO grade III) between diffuse astrocytoma and glioblastoma multiforme. Malignant astrocytes have nuclear atypia and mitotic activity. Ki-67/MIB-1 ranges from 5 to 10% Can progress to glioblastoma. Approximate 2-year survival. Promotor methylation inactivates the effects of the DNA repair enzyme MGMT enabling improved tumor response to alkylating chemotherapy agents. Patients with IDH mutations as well as those who have MGMT promotor methylation have improved responses to chemotherapy.
Glioblastoma multiforme	MRI: Irregularly and poorly marginated mass lesion with necrosis or cyst, mixed signal on T1-weighted imaging, heterogeneous high signal on T2-weighted imaging, ± hemorrhage, and prominent heterogeneous gadolinium contrast enhancement. Increased relative cerebral blood volume (rCBV) is associated with high-grade gliomas from tumor-induced angiogenesis. Other findings include peripheral edema and tumor extension across the corpus callosum. Diffusion-weighted imaging: Tumors typically do not show restricted diffusion. Magnetic resonance spectroscopy shows decreased N-acetylaspartate (NAA) and high levels of choline. CT: Irregularly marginated mass lesion with necrosis or cyst, mixed low and intermediate attenuation, ± hemorrhage, prominent heterogeneous contrast enhancement, and peripheral edema. Can cross corpus callosum.	Glioblastoma multiforme is the most common primary CNS tumor and accounts for 15% of intracranial tumors and up to 75% of astrocytic neoplasms, with an incidence of 3 per 100,000. Most patients are over 50 years old. These highly malignant (WHO grade IV) astrocytic neoplasms have nuclear atypia with increased mitotic activity, cellular pleomorphism, necrosis, and microvascular proliferation and invasion. Ki-67/MIB-1 ranges from 15 to 20% Associated with mutations involving RTK/phosphatase–PTEN/PI3K signal pathway, TERT, and TP53 and Rb1 tumor suppressor genes. Promotor methylation resulting in inactivation of the MGMT DNA repair enzyme enables improved malignant tumor response to chemotherapy in patients lacking IDH mutations. The extent of lesion is underestimated by MRI; survival is often often < 1 year. Patients with secondary type glioblastoma who have IDH mutations can have a better response to chemotherapy and prognosis than those without.

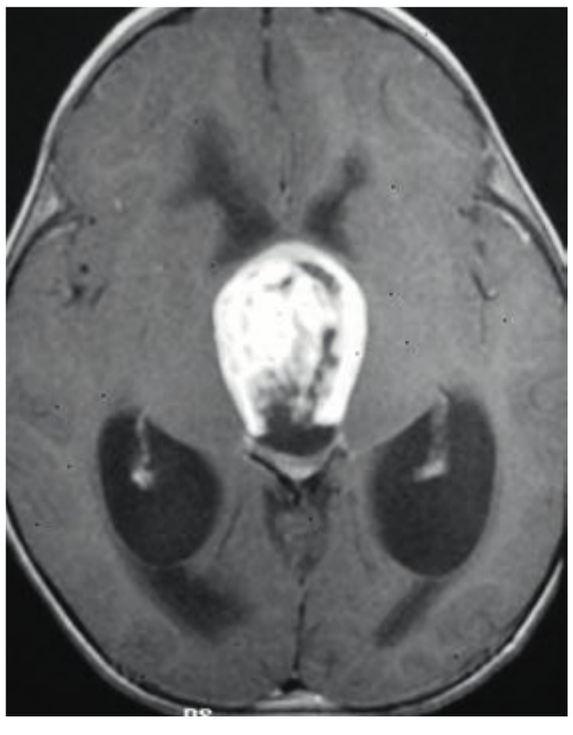

Fig. 2.14 A 2-year-old male with a gadolinium-enhancing anaplastic astrocytoma involving the hypothalamus on axial T1-weighted imaging that extends into the third ventricle and causes obstructive hydrocephalus.

Lesions	Imaging Findings	Comments
Intra-axial Primary Tumors		
Subependymal giant cell astrocytoma (tuberous sclerosis) (**Fig. 1.49**)	MRI: Circumscribed lesion located near the foramen of Monro with mixed low-intermediate signal on T1-weighted imaging and mixed high signal on T2-weighted imaging, ± cysts and/or calcifications, + heterogeneous gadolinium contrast enhancement. Diffusion-weighted imaging: Subependymal giant cell astrocytomas usually do not have restricted diffusion. Magnetic resonance spectroscopy: Subependymal giant cell astrocytomas can have elevated choline and reduced N-acetylaspartate (NAA). CT: Circumscribed lesion with mixed low-intermediate attenuation, ± cysts and/or calcifications, + heterogeneous contrast enhancement.	Subependymal giant cell astrocytoma near foramen of Monro, occurs in 6 to 18%of patients with tuberous sclerosis, patients usually younger than 20 years (mean age = 11 years), slow-growing lesions composed of neoplastic astrocytes of varying sizes with nuclear pleomorphism and low Ki-67/MIB-1 ranging from 1.5 to 7.4% Immunoreactive to GFAP, S-100 protein, neurofilament proteins, and class III b-tubulin. Enlarging lesions can progressively cause obstruction of CSF flow through the foramen of Monro. Autosomal dominant mutations involving TSC1 gene on chromosome 9q34 and TSC2 gene on chromosome 16p13.3. Prevalence of tuberous sclerosis = 1/6,000 newborns. Long-term survival is usual if the tumor is resected.
Medulloblastoma (primitive neuroectodermal tumor of the cerebellum) (**Fig. 2.15**)	MRI: Circumscribed or invasive lesions involving the cerebellum, with low-intermediate signal on T1-weighted imaging, intermediate-high signal on T2-weighted imaging, ± cystic or necrotic zones. Variable gadolinium contrast enhancement and usually high relative cerebral blood volume (rCBV), ± gadolinium contrast enhancement in the leptomeninges and/or ventricles from tumor dissemination. Can cause obstructive hydrocephalus. Diffusion-weighted imaging: Solid portions can have restricted diffusion. Magnetic resonance spectroscopy usually shows elevated choline, lipid, and taurine peaks, and decreased N-acetylaspartate (NAA) levels. CT: Circumscribed or invasive lesions with intermediate to slightly high attenuation, variable contrast enhancement, and frequent dissemination into the leptomeninges	Highly malignant tumors (WHO grade IV) located in the cerebellum and that frequently disseminate along CSF pathways. Tumors are composed of poorly differentiated or undifferentiated cells with divergent differentiation along neuronal, astrocytic, or ependymal lines. Histologic subtypes include classic, desmoplastic, large cell (LC), anaplastic, and medulloblastoma with extensive nodularity. LC and anaplastic types have the worst prognoses. Typically occurs in patients from 4 weeks to 20 years old (mean age = 5.5 years). Can also occur in adults.

(continued on page 436)

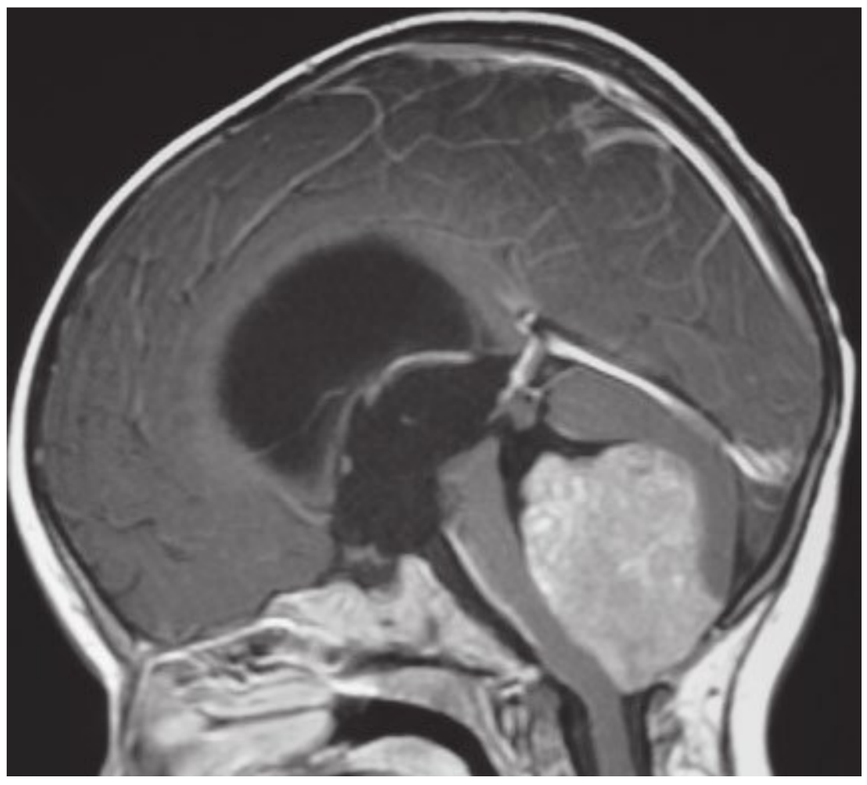

Fig. 2.15 Sagittal T1-weighted imaging shows a gadolinium-enhancing medulloblastoma in the vermis filling the fourth ventricle and resulting in obstructive hydrocephalus.

Table 2.5 (cont.) Dilated ventricles

Lesions	Imaging Findings	Comments
Atypical teratoid/rhabdoid tumors (**Fig. 2.16**)	MRI: Circumscribed or invasive mass lesions with intermediate signal on T1-weighted imaging, ± zones of high signal from hemorrhage on T1-weighted imaging, and variable mixed low, intermediate, and/or high signal on T2-weighted imaging. Solid portions can have restricted diffusion, usually with prominent gadolinium contrast enhancement ± heterogeneous pattern. Gadolinium contrast enhancement may occur in the leptomeninges and/or ventricles from tumor dissemination. Diffusion-weighted imaging: Solid portions can have restricted diffusion. Magnetic resonance spectroscopy usually shows elevated choline, lipid, and lactate peaks, and decreased N-acetylaspartate (NAA) levels. CT: Circumscribed mass lesions with intermediate or mixed low and intermediate attenuation, ± zones of hemorrhage, cystic degeneration, and/or necrosis. Calcifications in tumors occasionally occur. Usually there is contrast enhancement, ± heterogeneous pattern, ± contrast enhancement in the leptomeninges and/or ventricles from tumor dissemination.	Rare malignant tumors (WHO grade IV) involving the CNS usually occurring in the first decade, commonly before 3 years of age. Ki-67/MIB-1 is often high, > 50%. Associated with mutations of the INI1 (hSNF5/SMARCB1) gene on chromosome 22q11.2. Histologically appear as solid tumors ± necrotic areas, similar to malignant rhabdoid tumors of the kidney. Nearly all are intra-axial and can occur in supra- and/or infratentorial locations. Associated with a very poor prognosis.
Ependymoma (**Fig. 2.17**)	MRI: Circumscribed, lobulated, supratentorial lesion, often extraventricular, ± cysts, calcifications, and/or hemorrhage. Low-intermediate signal on T1-weighted imaging, intermediate-high signal on T2-weighted imaging, variable gadolinium contrast enhancement. Tumors have elevated relative cerebral blood volume (rCBV) as well as delayed contrast retention secondary to intratumoral fenestrated blood vessels. Diffusion-weighted imaging usually shows no restricted diffusion. Magnetic resonance spectroscopy: Elevated choline and decreased N-acetylaspartate (NAA), similar to other neoplasms. CT: Circumscribed, lobulated, supratentorial lesion, often extraventricular, ± cysts and/or calcifications (up to 50%), with low-intermediate attenuation and variable contrast enhancement.	Slow-growing tumor (WHO grade II) comprised of neoplastic cells with monomorphic round/oval nuclei containing speckled chromatin, perivascular pseudorosettes, and ependymal rosettes. Zones of myxoid degeneration, hyalinization of blood vessels, hemorrhage, and/or calcifications may occur within tumors. Ependymomas account for 6–12% of intracranial tumors, with an incidence of 0.22 to 0.29 per 100,000. Occur more commonly in children than in adults; one-third of tumors are supratentorial and two-thirds are infratentorial. Infratentorial ependymomas occur in children ranging in age from 2 months to 16 years (mean age = 6.4 years). Supratentorial ependymomas occur in children and adults. Immunoreactive to glial fibrillary acidic protein (GFAP), S-100, vimentin, and/or epithelial membrane antigen (EMA). Associated with neurofibromatosis type 2 and genetic mutations involving chromosomes 22, 9, 6, and 3. Usually lack mutation of IDH gene. Survival is 57% at 5 years and 45% at 10 years.
Anaplastic ependymoma (**Fig. 2.18**)	MRI: Irregularly marginated mass lesion with necrosis or cyst, mixed signal on T1-weighted imaging, heterogeneous high signal on T2-weighted imaging, ± hemorrhage, calcifications, heterogeneous gadolinium contrast enhancement, and peripheral edema. Can disseminate within the CSF. CT: Irregularly marginated mass lesion with necrosis or cyst, mixed attenuation, ± hemorrhage, calcifications, heterogeneous contrast enhancement, and peripheral edema. Can disseminate within the CSF.	Malignant glioma (WHO grade III) with ependymal differentiation and high mitotic activity, microvascular proliferation, and pseudopalisading necrosis. Associated with poor prognosis in patients with prominent anaplastic features, CSF metastases, and incomplete resection.

(continued on page 438)

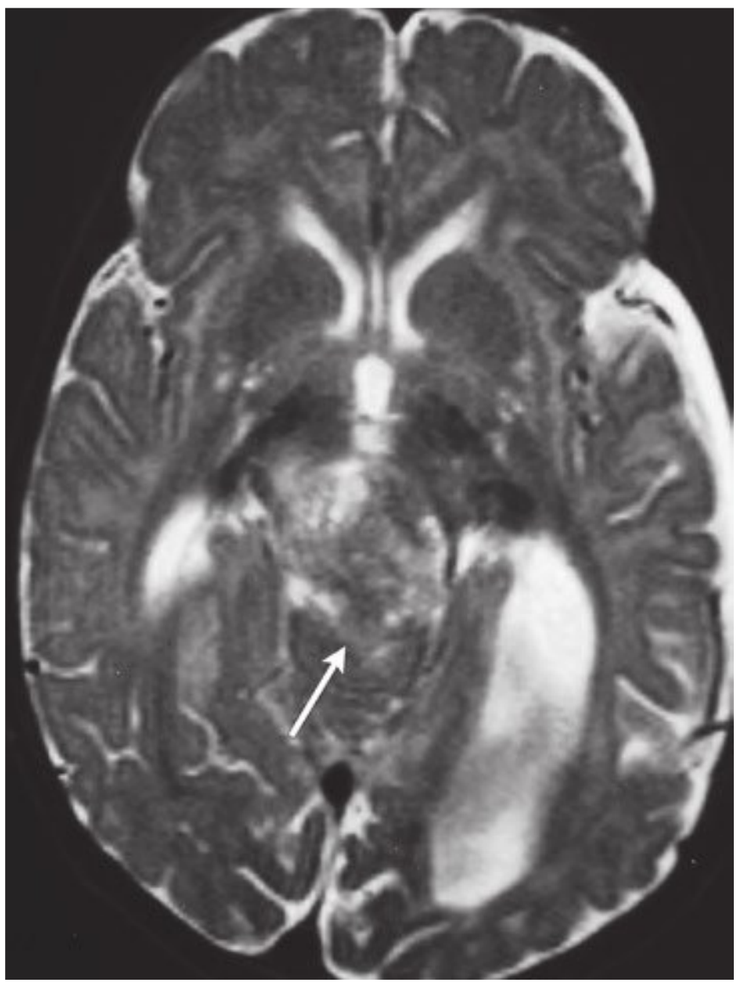

Fig. 2.16 Atypical teratoid/rhabdoid tumor in the pineal gland and midbrain in a 10-month-old male. The tumor (arrow) has ill-defined margins and has mixed intermediate, high, and low signal on axial T2-weighted imaging. Also seen are dilated lateral ventricles related to compression of the cerebral aqueduct.

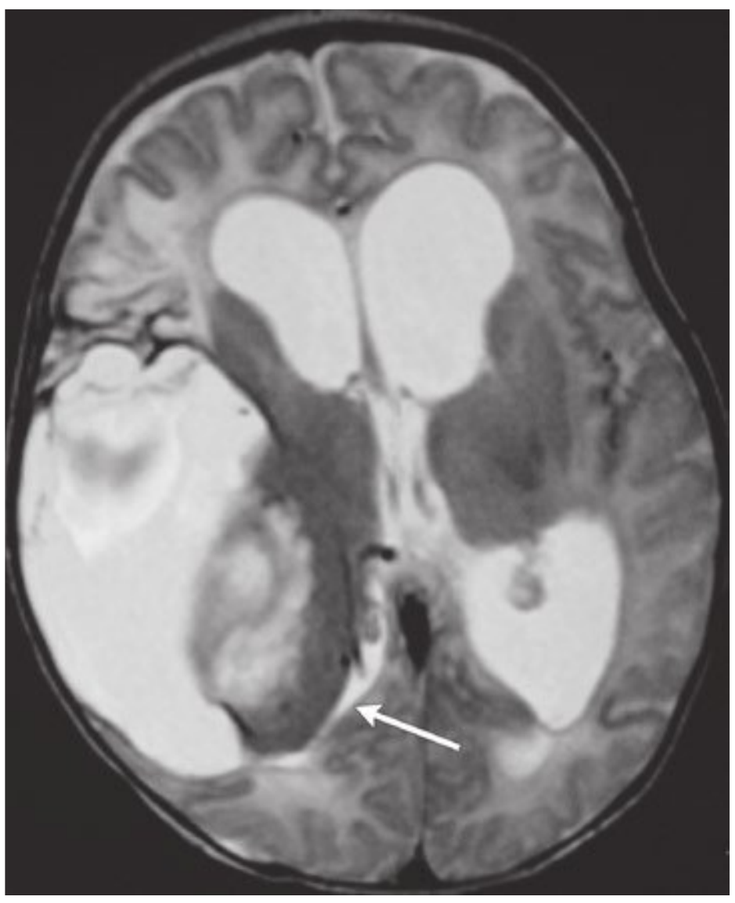

Fig. 2.18 A 2-month-old female with a malignant ependymoma (arrow) in the right cerebral hemisphere containing solid and cystic portions and associated with ventricular dilatation.

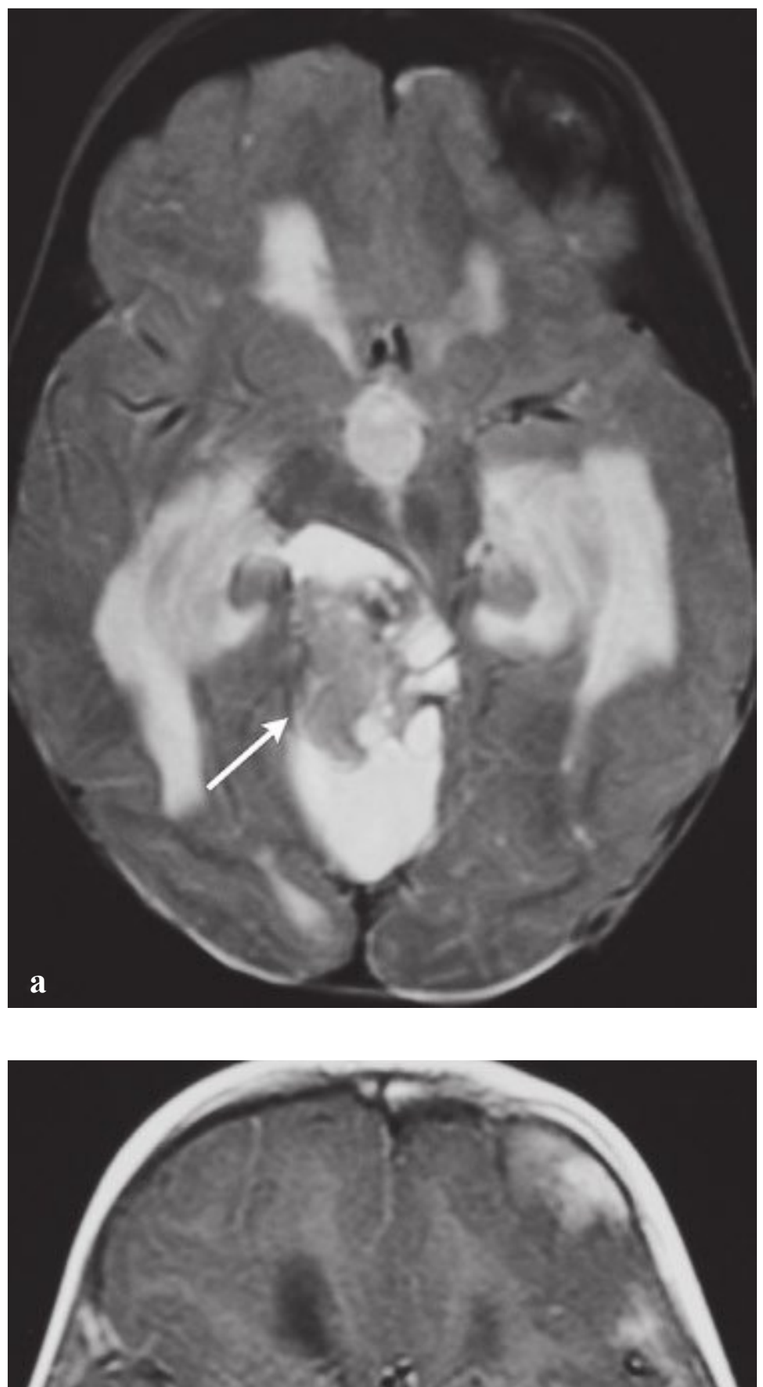

Fig. 2.17 **(a)** A 5-year-old female with obstructive hydrocephalus secondary to an ependymoma that has both cystic components and solid portions with mixed slightly high and high signal on axial T2-weighted imaging (arrow) and **(b)** that shows heterogeneous gadolinium contrast enhancement on axial T1-weighted imaging (arrow).

Table 2.5 (cont.) Dilated ventricles

Lesions	Imaging Findings	Comments
Hemangioblastoma	Circumscribed tumors usually located in the cerebellum and/or brainstem. MRI: Small gadolinium-enhancing nodule ± cyst, or larger lesion with prominent heterogeneous enhancement ± flow voids within lesion or at the periphery; as well as intermediate signal on T1-weighted imaging, intermediate-high signal on T2-weighted imaging. Occasionally, lesions have evidence of recent or remote hemorrhage. Relative cerebral blood volume (rCBV) of lesions is high. CT: Small contrast-enhancing nodule ± cyst, or larger lesion with prominent heterogeneous enhancement, ± hemorrhage.	Slow-growing, vascular tumors (WHO grade I) that involve the cerebellum, brainstem, and/or spinal cord. Account for 1–3% of intracranial neoplasms and usually occur in middle-aged adults. Rarely occur in children except for those with von Hippel-Lindau (VHL) disease. Tumors consist of numerous thin-walled vessels as well as large, lipid-containing vacuolated stromal cells that have variably sized, hyperchromatic nuclei. Mitotic figures are rare. Stromal cells are immunoreactive to VEGF, vimentin, CXCR4, aquaporin 1, carbonic anhydrase, S-100, CD56, neuron-specific enolase, and D2–40. Vessels typically react to a reticulin stain. Reactive astrocytic gliosis can occur in adjacent tissue. Tumors occur as sporadic mutations of the VHL gene or as an autosomal dominant germline mutation of the VHL gene on chromosome 3p25–26, resulting in VHL disease. In VHL disease, multiple hemangioblastomas involving the CNS occur as well as clear-cell renal carcinoma, pheochromocytoma, endolymphatic sac tumor, neuroendocrine tumor, adenoma of the pancreas, and epididymal cystadenoma. VHL disease occurs in adolescents and young and middle-aged adults.
Intraventricular Tumors		
Choroid plexus papilloma (**Fig. 2.19**)	MRI: Circumscribed and/or lobulated lesions with papillary projections, intermediate signal on T1-weighted imaging and mixed intermediate-high signal on T2-weighted imaging, usually with prominent gadolinium contrast enhancement, ± calcifications. Locations: atrium of lateral ventricle (children) > fourth ventricle (adults), rarely other locations, such as third ventricle. Associated with hydrocephalus from CSF overproduction or mechanical obstruction. CT: Circumscribed and/or lobulated lesions with papillary projections, intermediate attenuation, usually prominent contrast enhancement, ± calcifications.	Rare benign (WHO grade I) intraventricular neoplasms derived from choroid plexus epithelium in which a single layer of cuboidal or columnar epithelial cells with round/oval nuclei overlies fibrovascular connective tissue in frondlike patterns. Occurs in lateral ventricle (50%), fourth ventricle/CP angle (40%), third ventricle (5%), and multiple ventricles (5%). Occurs in children and adults. Tumors in the lateral ventricles account for up to 80% of cases in patients less than 20 years old. Lesions in the fourth ventricle are most common in adults. Tumors have very low mitotic activity. Immunoreactive to cytokeratins, vimentin, podoplanin, S-100, and transthyretin. Can be cured by surgical resection.
Atypical choroid plexus papilloma (**Fig. 2.20**)	MRI: Circumscribed and/or lobulated lesions with papillary projections, intermediate signal on T1-weighted imaging and mixed intermediate-high signal on T2-weighted imaging, usually with prominent gadolinium contrast enhancement, ± calcifications. Locations: atrium of lateral ventricle (children) > fourth ventricle (adults), rarely other locations, such as third ventricle, associated with hydrocephalus. CT: Circumscribed and/or lobulated lesions with papillary projections, intermediate attenuation, usually prominent contrast enhancement, ± calcifications.	Rare (WHO grade II) intraventricular neoplasms derived from choroid plexus that have some histologic features that overlap those of choroid plexus papillomas, although atypical papillomas can have higher mitotic activity (> 2/HPF), increased cellularity, nuclear pleomorphism, partial loss of the papillary morphology, and/or necrosis. Immunoreactive to cytokeratins, S-100. Occur in children and adults. Can be cured by surgical resection.

(continued on page 440)

Fig. 2.19 A 6-month-old male with a gadolinium-enhancing choroid plexus papilloma (arrow) on coronal T1-weighted imaging. The papilloma causes ventricular dilatation from overproduction of CSF.

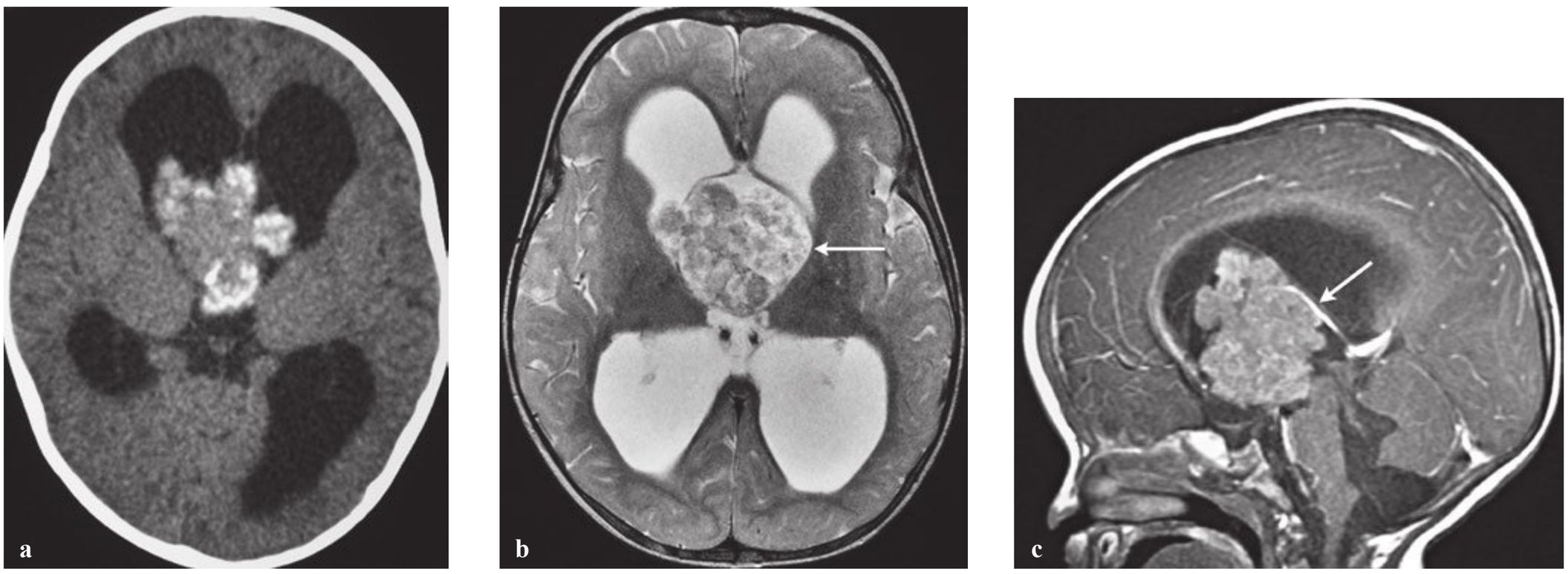

Fig. 2.20 A 1-year-old female with an atypical choroid plexus papilloma in the third ventricle causing obstructive hydrocephalus. **(a)** The tumor has lobulated margins and contains calcifications on axial CT and **(b)** mixed intermediate and high signal on axial T2-weighted imaging (arrow) and **(c)** shows gadolinium contrast enhancement on sagittal T1-weighted imaging (arrow).

Table 2.5 (cont.) Dilated ventricles

Lesions	Imaging Findings	Comments
Choroid plexus carcinoma (**Fig. 2.21**)	MRI: Large lobulated neoplasms with mean tumor size of 5 cm, often with irregular margins, ± brain invasion. On T1-weighted imaging, tumors have heterogeneous intermediate signal with foci of high signal in 45% from areas of hemorrhage. On T2-weighted imaging, solid portions of the tumor often have heterogeneous intermediate to slightly high signal. Small zones with low signal on T2-weighted imaging can occur from sites of hemorrhage or calcifications. Intratumoral cystic or necrotic zones occur in 64%and have high signal on T2-weighted imaging. Tubular flow voids representing blood vessels occur in up to 55%of tumors. Tumors typically show prominent gadolinium contrast enhancement. Nearly 75%of tumors have irregular enhancing margins from ependymal invasion. Disseminated gadolinium-enhancing tumor in the leptomeninges can occur in up to 45%. Hydrocephalus is seen in up to 80%. CT: Large intraventricular tumors with intermediate attenuation as well as foci with high attenuation from areas of hemorrhage or calcification, low attenuation zones from cystic or necrotic zones. Tumors typically show prominent contrast enhancement.	Rare malignant (WHO grade III) intraventricular neoplasms derived from choroid plexus epithelium that contain irregular sheets of neoplastic cells with nuclear pleomorphism, high mitotic activity (> 5/HPF), loss of the papillary morphology, and necrotic and/or hemorrhagic areas. Immunoreactive to cytokeratins. Account for 0.1%of all intracranial tumors and 0.6%of primary pediatric CNS neoplasms. These tumors are five times less frequent than choroid plexus papillomas. Median ages range from 12 to 32 months. Most commonly occur in the lateral ventricle, followed by the fourth and third ventricles. These tumors commonly disseminate along CSF pathways and invade brain tissue. Poor prognosis, with 5-year survival of 45%.
Subependymoma (**Fig. 2.22**)	MRI: Tumors typically attached to ventricular walls (fourth ventricle, 40–50%; lateral ventricle, 30–40%; third ventricle, 10%). Lesions have circumscribed margins, low-intermediate signal on T1-weighted imaging, and heterogeneous slightly high to high signal on T2-weighted imaging. May contain sites of hemorrhage or calcification. Variable degrees of gadolinium contrast enhancement. CT: Lesions have circumscribed margins, low-intermediate attenuation. May contain sites of hemorrhage or calcification. Variable degrees of contrast enhancement.	Slow-growing low-grade (WHO grade I) glial neoplasms comprised of clusters of tumor cells with isomorphic nuclei within a dense matrix of cell processes. Mitotic activity is absent or rare. Immunoreactive to glial fibrillary acidic protein (GFAP). Account for 8%of ependymal tumors. Complete resection can be curative.
Meningioma (**Fig. 2.23**)	Extra-axial dura-based lesions that are well circumscribed. Locations are supra- > infratentorial, parasagittal > convexity > sphenoid ridge > parasellar > posterior fossa > optic nerve sheath > intraventricular. MRI: Dura-based tumors with intermediate signal on T1-weighted imaging, intermediate to slightly high signal on T2-weighted imaging, usually prominent gadolinium contrast enhancement, often with a dural tail, ± calcifications. Intratumoral hemorrhage and cystic or necrotic foci can occur in 15%. Diffusion-weighted imaging /diffusion tensor imaging: ADC values vary among the different subtypes of meningioma. Some tumors can show restricted diffusion, although these findings can be seen with both benign and atypical tumors. Magnetic resonance spectroscopy can show elevated alanine (1.5 ppm), lactate, choline, and glutamine/glutamate levels, and reduced N-acetylaspartate (NAA). CT: Tumors have intermediate attenuation, with or without calcifications, with or without hyperostosis, and usually show prominent contrast enhancement.	Most common extra-axial tumor, accounts for up to 26%of primary intracranial tumors. Annual incidence is 6 per 100,000, typically occurs in adults (> 40 years old), women > men. Composed of neoplastic meningothelial (arachnoidal or arachnoid cap) cells. Meningiomas are usually solitary and sporadic, but can also occur as multiple lesions in patients with neurofibromatosis type 2. Eighty percent of meningiomas are benign (WHO grade I), although 15% have atypical features (WHO grade II) and ~ 5%have anaplastic histologic features (WHO grade III). Can occur secondary to radiation treatment, with latencies ranging from 19 to 35 years. Classified into different subtypes, such as: meningothelial, fibrous (fibroblastic), transitional (mixed), psammomatous, angiomatous, atypical, and anaplastic. Meningothelial, fibrous, and transitional meningiomas are the most common intracranial types. Usually show immunoreactivity to epithelial membrane antigen (EMA) and vimentin. Secretory meningiomas are typically immunoreactive to CEA. Associated cytogenetic findings of deletion of chromosome 22. Mutations in the NF2 tumor suppressor gene on chromosome 22 have been found in 60%of sporadic meningiomas.

(continued on page 442)

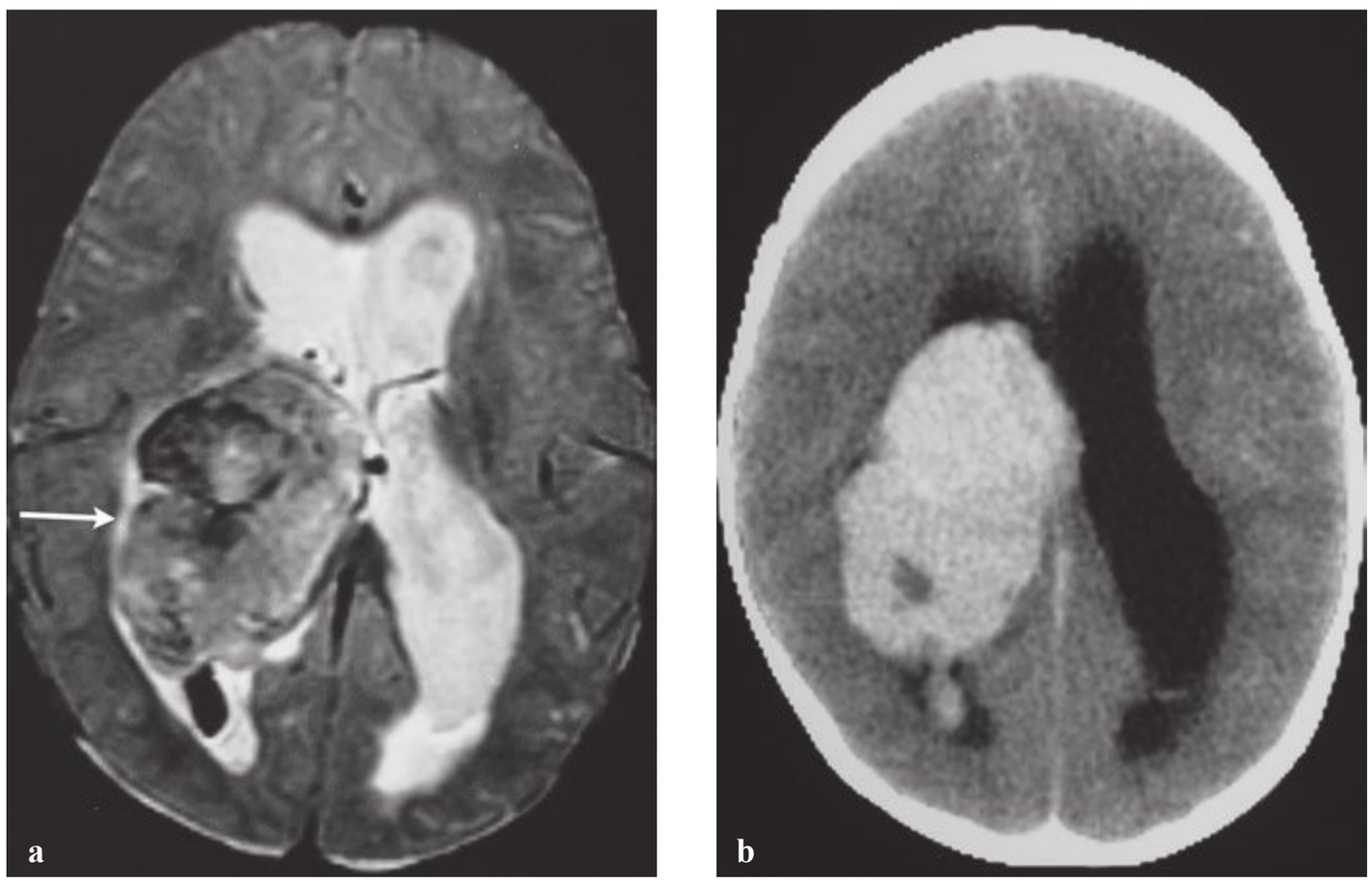

Fig. 2.21 A 17-month-old female with a choroid plexus carcinoma within the right lateral ventricle causing hydrocephalus. **(a)** The tumor has mixed intermediate, low, and high signal on axial T2-weighted imaging (arrow) and **(b)** shows prominent contrast enhancement on axial CT.

Fig. 2.22 A 75-year-old man with a subependymoma at the foramen of Monro causing obstruction of CSF outflow from the right lateral ventricle. The lesion has heterogeneous mixed high and low signal on axial FLAIR (arrow).

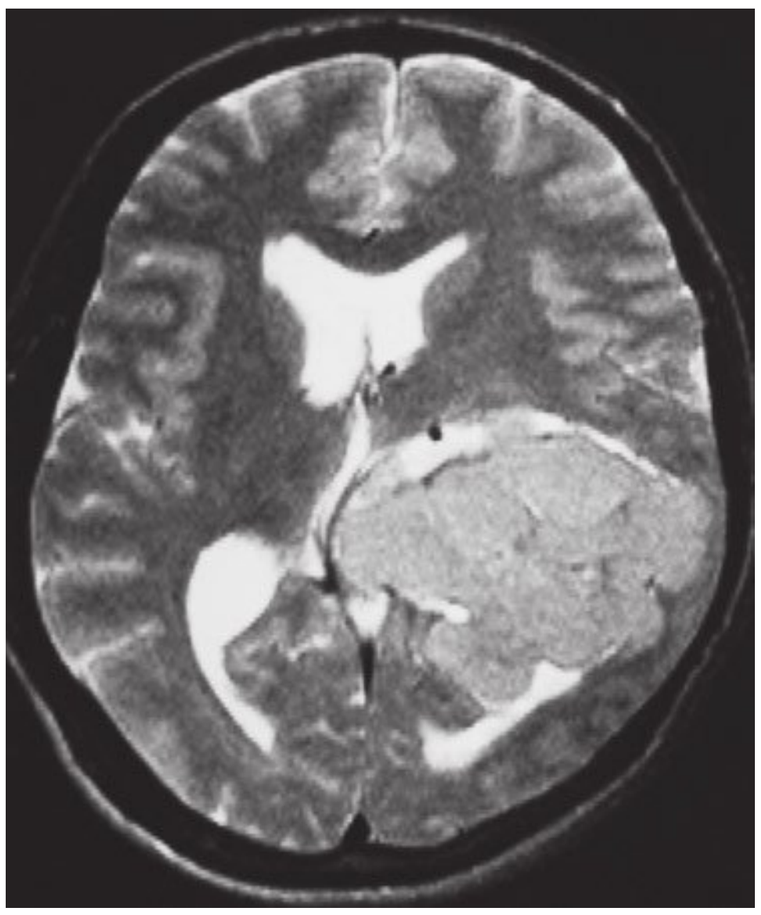

Fig. 2.23 A 36-year-old woman with a meningioma within the atrium of the left lateral ventricle associated with ventricular dilatation. The tumor has slightly lobulated margins and has slightly high signal on axial T2-weighted imaging.

Table 2.5 (cont.) Dilated ventricles

Lesions	Imaging Findings	Comments
Hemangiopericytoma	MRI: Solitary dura-based tumors ranging from 2 to 7 cm in diameter that have low-intermediate signal on T1-weighted imaging, intermediate to slightly high signal on T2-weighted imaging, usually prominent gadolinium contrast enhancement often with a dural tail, ± calcifications. Intratumoral hemorrhage and cystic or necrotic foci can occur in 30% Magnetic resonance spectroscopy: Relative ratios of myo-inositol, glucose, and glutathione with respect to glutamate are higher in hemangiopericytomas than in meningiomas. CT: Tumors have intermediate attenuation with or without calcifications and usually show prominent contrast enhancement.	Rare (WHO grade II) neoplasms that account for 0.4%of primary intracranial tumors; 50 times less frequent than meningiomas, Tumors composed of closely packed cells with scant cytoplasm and round, ovoid, or elongated nuclei with moderately dense chromatin. Numerous slitlike vascular channels are seen and are lined by flattened endothelial cells, ± zones of necrosis. Immunoreactive to vimentin (85%), factor XIIIa (80–100%), and variably to Leu-7 and CD34. Associated with abnormalities involving chromosome 12. Typically occur in young adults (mean age = 43 years), males > females. Sometimes referred to as angioblastic meningioma or meningeal hemangiopericytoma, they arise from vascular cells—pericytes. Frequency of recurrence and metastases > meningiomas.
Intraventricular Tumors		
Central neurocytoma (**Fig. 2.24**)	MRI: Circumscribed lesion typically located at margin of lateral ventricle or septum pellucidum with intraventricular protrusion, heterogeneous low and intermediate signal on T1-weighted imaging, heterogeneous intermediate-high signal on T2-weighted imaging, ± calcifications and/or small cysts, and heterogeneous gadolinium contrast enhancement. Diffusion-weighted imaging: Lesions can show reduced ADC values. Magnetic resonance spectroscopy: Elevated glycine (3.55 ppm), choline and alanine levels, and decreased N-acetylaspartate (NAA) in these lesions. Rare extraventricular neurocytomas have been reported in the frontal and parietal lobes and sellar region. CT: Circumscribed lesion located at margin of lateral ventricle or septum pellucidum with intraventricular protrusion, heterogeneous low and intermediate attenuation, ± calcifications and/or small cysts, heterogeneous contrast enhancement.	Slow-growing rare neuroepithelial tumor composed of uniform round cells with neuronal differentiation. Immunoreactive to synaptophysin and NeuN. Represent ~ 0.5%of intracranial tumors. Patients range from 8 days to 67 years old (mean age = 29 years). Imaging appearance similar to intraventricular oligodendrogliomas. Typically benign tumors (WHO grade I) with favorable prognosis after surgery.
Pineal lesions and tumors (**Fig. 2.25**)	MRI and CT findings for the lesions and tumors in the pineal region are listed in detail in **Table 1.11**.	Lesions involving the pineal gland include primary pineal tumors (pineocytoma, pineal parenchymal tumor intermediate differentiation, papillary tumor, and pineoblastoma), germ cell tumors, embryonal tumors, and ependymoma, as well as lesions in the pineal region (ependymoma, meningioma, arachnoid cyst, epidermoid, dermoid and lipoma).

(continued on page 444)

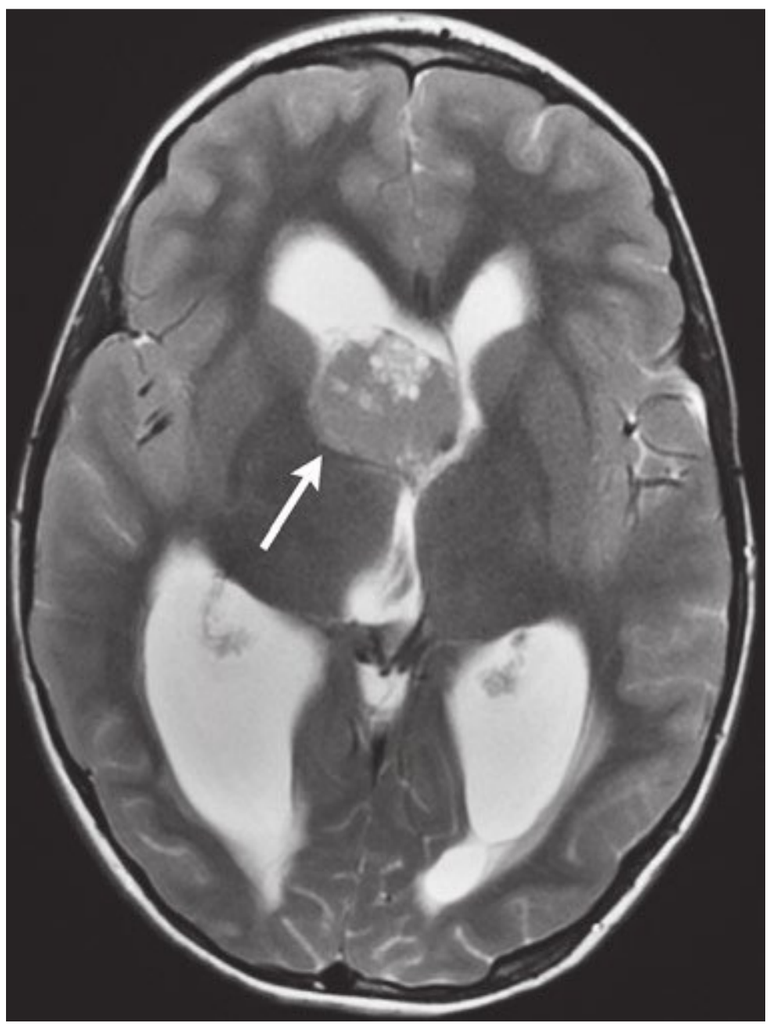

Fig. 2.24 A 15-year-old female with a central neurocytoma (arrow) involving the septum pellucidum and causing obstructive hydrocephalus. The tumor has intermediate and high signal on axial T2-weighted imaging.

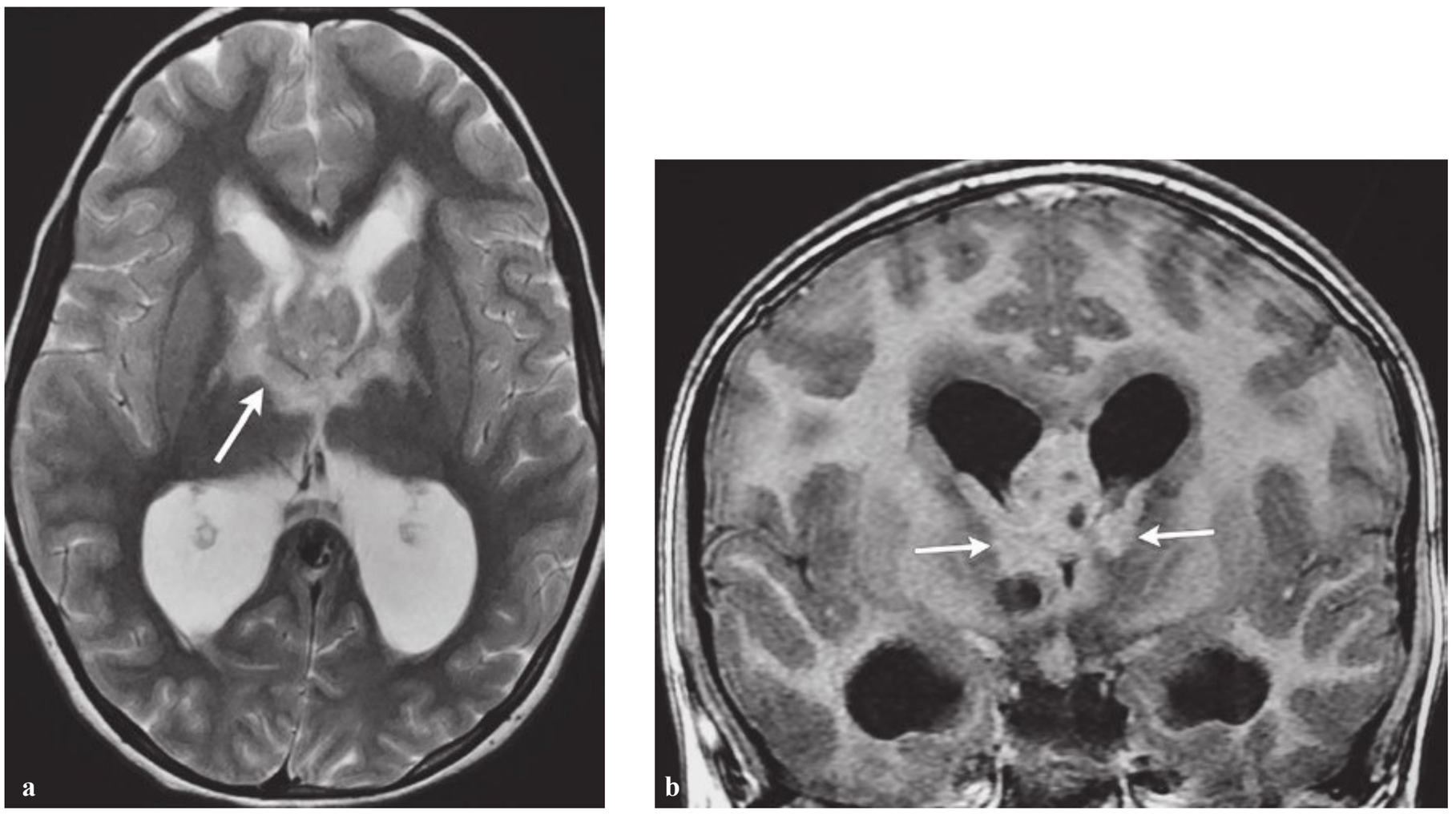

Fig. 2.25 A 14-year-old female with disseminated germinoma within the third ventricle causing obstructive hydrocephalus. **(a)** The tumor has irregular poorly defined margins and intermediate signal on axial T2-weighted imaging (arrow) and **(b)** shows gadolinium contrast enhancement on coronal T1-weighted imaging, with evidence of invasion of adjacent brain parenchyma (arrows).

Table 2.5 (cont.) Dilated ventricles

Lesions	Imaging Findings	Comments
Intraventricular Lesions		
Colloid cyst (**Fig. 2.26**)	MRI: Well-circumscribed spheroid lesion located at the anterior upper portion of the third ventricle, with variable signal (low, intermediate, or high) on T1- and T2-weighted imaging, often with high signal on T1-weighted imaging and low signal on T2-weighted imaging. No gadolinium contrast enhancement. CT: Spheroid lesions located at the anterior upper portion of the third ventricle, with variable attenuation (low, intermediate, or high) and no contrast enhancement.	Slow-growing, benign cystic lesions whose wall contains a single layer of epithelial cells. Cyst contents can include cholesterol granules, various blood products, macrophages, and various minerals and/or ions. Most colloid cysts occur in the anterosuperior portion of the third ventricle, and rarely in the sella or suprasellar cistern. Usually found in adults (50–60 years old). Can cause acute onset of hydrocephalus.
Ependymal cyst (**Fig. 2.27**)	MRI: Well-circumscribed thin-walled cyst in the lateral ventricles with low signal on T1-weighted imaging, diffusion-weighted imaging, and FLAIR and high signal on T2-weighted imaging. Usually no gadolinium contrast enhancement. CT: Thin-walled cyst in the lateral ventricles with low attenuation similar to CSF.	Benign cysts in the lateral ventricles containing serous fluid surrounded by a thin wall containing ependymal columnar cells with vesicular nuclei and eosinophilic cytoplasm. May result from neuroectoderm sequestered during development. Can cause dilation of ventricles.

(continued on page 446)

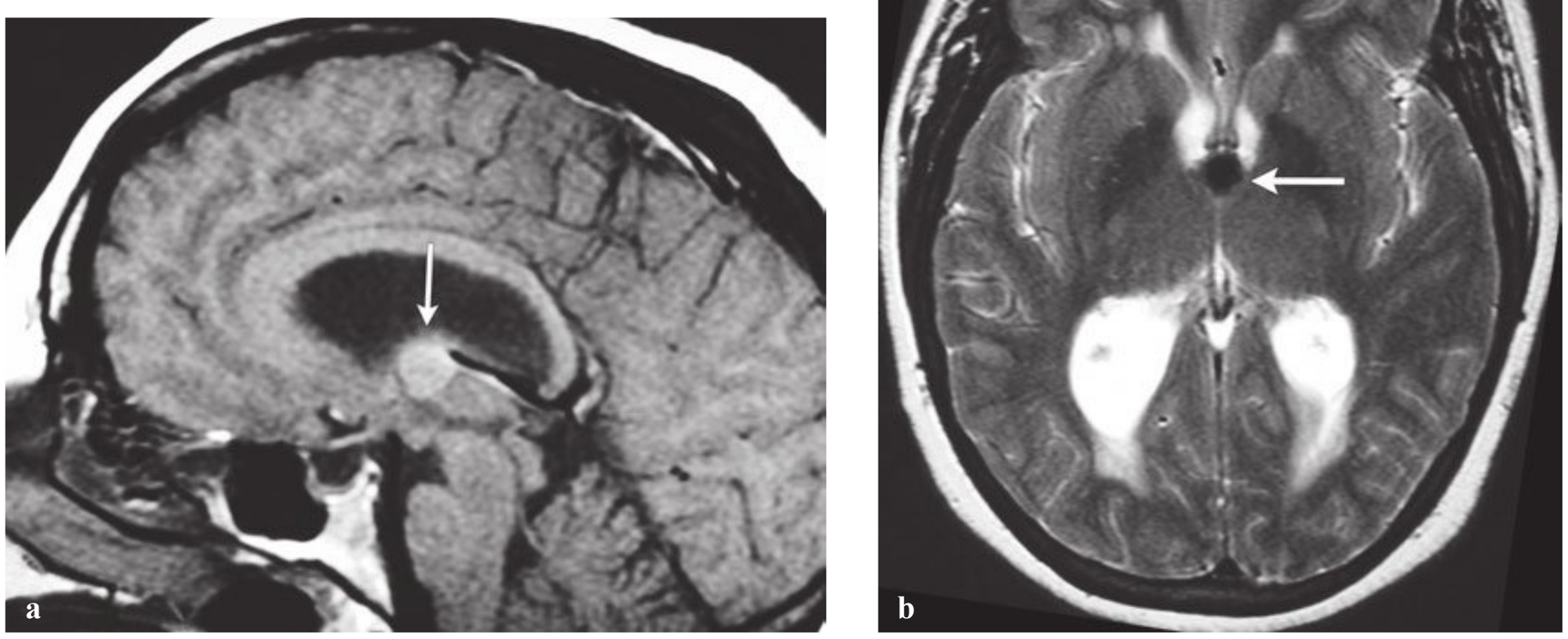

Fig. 2.26 A 34-year-old woman with a colloid cyst at the anterosuperior portion of the third ventricle that has **(a)** high signal on sagittal T1-weighted imaging (arrow) and **(b)** low signal on axial T2-weighted imaging (arrow). A mild degree of hydrocephalus is present with slight ventricular dilatation and subependymal edema adjacent to the occipital horns of the lateral ventricles.

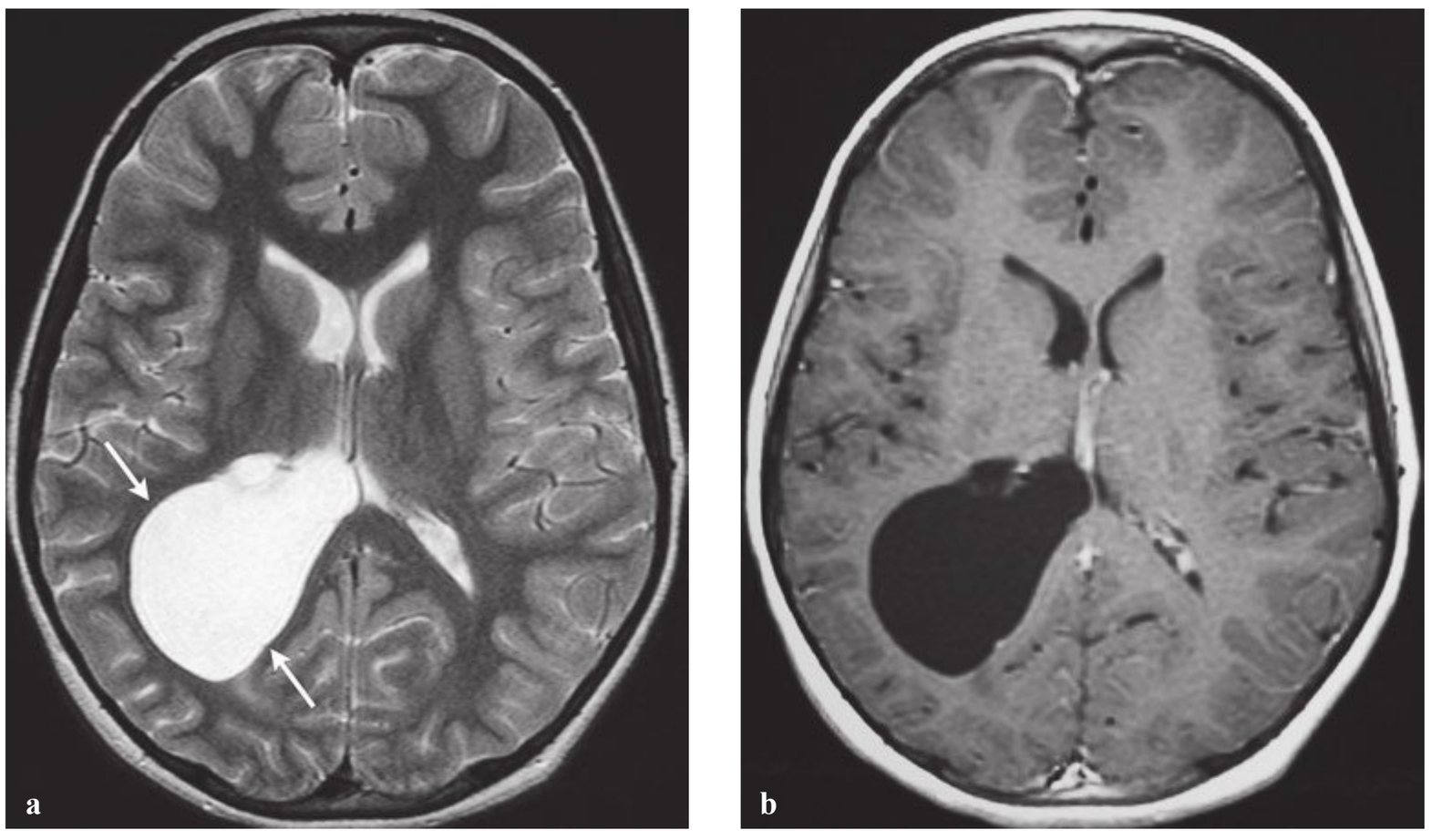

Fig. 2.27 A 10-year-old female with ependymal cyst enlarging the atrium and occipital horn of the right lateral ventricle that has **(a)** high signal on axial T2-weighted imaging (arrows) and **(b)** low signal on postcontrast T1-weighted imaging.

Table 2.5 (cont.) Dilated ventricles

Lesions	Imaging Findings	Comments
Inflammation/Infection		
Ependymitis/ventriculitis (**Fig. 2.28**)	MRI: Curvilinear and/or nodular zones of gadolinium contrast enhancement along ventricular/ependymal margins, with resultant communicating or noncommunicating hydrocephalus. Poorly defined zones with high signal on T2-weighted imaging and FLAIR are often seen in the subependymal and periventricular white matter.	Complications of intracranial inflammatory processes, such as bacterial, fungal, or viral infections, tuberculosis, and parasites. Can result from brain abscess extending into the ventricles and CSF. Noninfectious diseases like sarcoid can result in a similar pattern.
TORCH and neonatal infections (**Fig. 2.29** and **Fig. 2.30**)	CT and MRI: Prenatal and neonatal infections often result in intra-axial calcifications. Prenatal infection with cytomegalovirus and rubella can result in microcephaly, schizencephaly, gray matter heterotopia, transmantle clefts, porencephalic cysts, and/or periventricular leukomalacia. Herpes simplex virus and rubella often cause extensive encephaloclastic changes, which result in multicystic encephalomalacia.	TORCH is an acronym applied to congenital infections from toxoplasmosis, rubella, cytomegalovirus, or herpes. Postnatal viral, bacterial, and fungal infections can result in extensive destructive changes in brain tissue, with compensatory dilatation of the ventricles.
Cysticercosis (**Fig. 2.31**)	MRI: Single or multiple cystic lesions in brain or meninges. Active vesicular phase: Cystic-appearing lesions containing a small 2–4 mm nodule (scolex) with low signal on T1-weighted imaging, FLAIR, and diffusion-weighted imaging; a thin peripheral rim with high signal on FLAIR and T2-weighted imaging; minimal peripheral rim or no gadolinium contrast enhancement; and no peripheral edema on T2-weighted imaging and FLAIR. Active colloidal vesicular phase: Cystic-appearing lesion with low-intermediate signal on T1-weighted imaging, high signal on T2-weighted imaging, rim and/or nodular pattern of gadolinium contrast enhancement, ± peripheral signal (edema) on T2-weighted imaging. Active granular nodular phase: Cyst retracts into a more solid gadolinium-enhancing granulomatous nodule. Chronic non-active phase: Calcified nodular granulomas.	Caused by ingestion of encysted larva of the tapeworm Taenia solium in contaminated food (undercooked pork). Involves meninges, subarachnoid space and cisterns > brain parenchyma > ventricles. Most common parasitic disease of the CNS, usually in patients from 15 to 40 years old. Most common cause of acquired epilepsy in endemic regions. Complications include intracranial hypertension from CSF obstruction, arachnoiditis, meningitis, and vascular occlusion.

(continued on page 448)

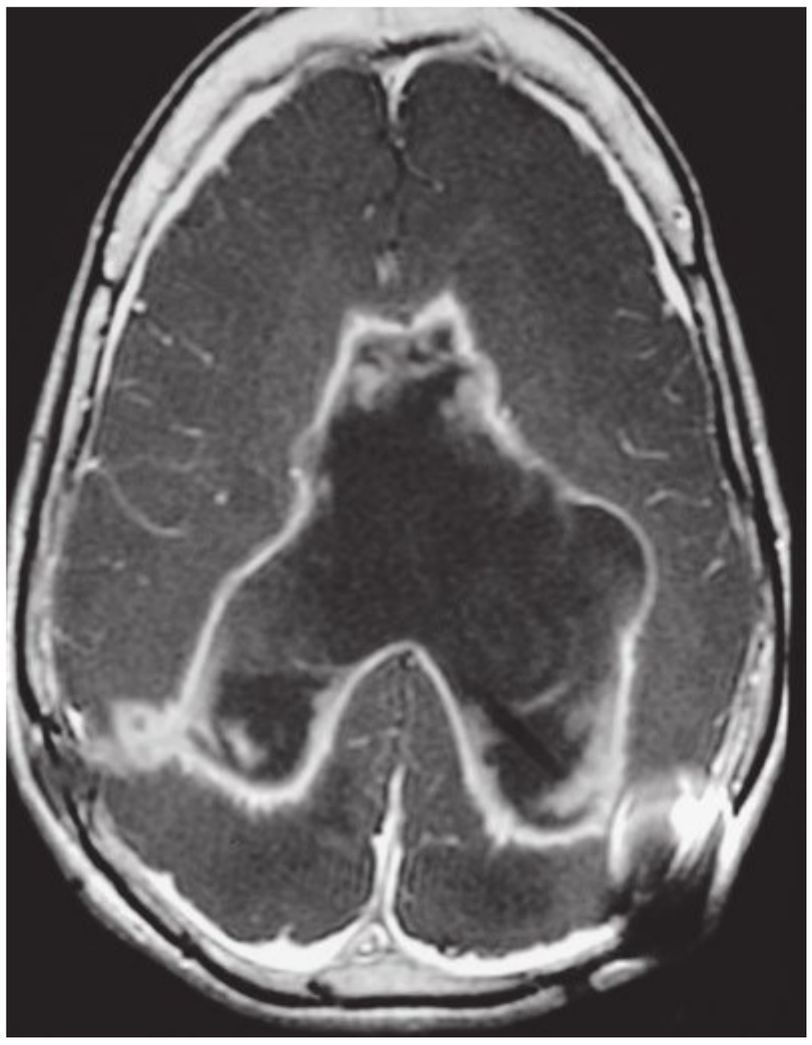

Fig. 2.28 A 29-year-old man with pyogenic ependymitis/ventriculitis related to an infected shunt. Abnormal gadolinium contrast enhancement is seen along the ependymal lining of the dilated lateral ventricles and right shunt tract on axial T1-weighted imaging.

Fig. 2.29 An 8-day-old male with prenatal cytomegalovirus infection resulting in diffuse and focal zones of brain encephalomalacia, with dilated lateral ventricles, porencephaly involving the right frontal lobe, schizencephaly involving the left cerebral hemisphere, and multiple intra-axial calcifications as seen on axial CT.

Fig. 2.30 A 6-week-old male with postnatal cerebritis from Enterococcus that resulted in extensive destruction of brain parenchyma and cystic encephalomalacia, as seen on axial postcontrast T1-weighted imaging. Abnormal contrast enhancement is seen along the inner margins of the dilated ventricles.

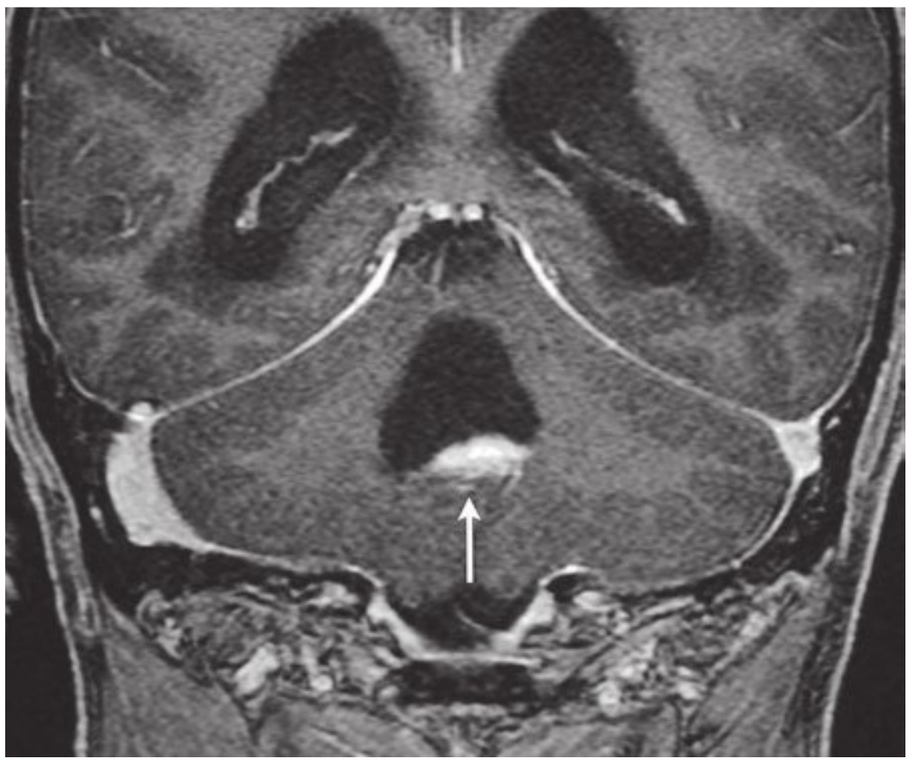

Fig. 2.31 A 35-year-old man with a cysticercosis lesion (arrow) in the fourth ventricle that has both a nodular gadolinium-enhancing and cystic portion on coronal T1-weighted imaging that results in ventricular obstruction.

Table 2.5 (cont.) Dilated ventricles

Lesions	Imaging Findings	Comments
Hydatid cyst (**Fig. 2.32**) Echinococcus granulosus Echinococcus multilocularis	Echinococcus granulosus MRI: Single or rarely multiple cystic lesions with low signal on T1-weighted imaging and high signal on T2-weighted imaging surrounded by a thin wall with low signal on T2-weighted imaging, and typically no gadolinium contrast enhancement or peripheral edema unless superinfected. Often located in vascular territory of the middle cerebral artery. Rupture of the hydatid cyst may be contained when only the endocyst ruptures and the pericyst remains intact. In these cases, thickened high signal on T2-weighted imaging is seen in the pericyst from edema and inflammatory reaction, which can show gadolinium contrast enhancement. The ruptured endocyst can have a *f*loating membrane sign or "scroll appearance" with low signal on T1- and T2-weighted imaging within the fluid deep to the pericyst. Rupture of the hydatid cyst beyond the pericyst can also result in an inflammatory host response with complications based on the sites involved. Echinococcus multilocularis MRI: Cystic (± multilocular) and/or solid lesions with central zone of intermediate-high signal on T2-weighted imaging surrounded by a slightly thickened rim of low signal, + gadolinium contrast enhancement. Peripheral zone of high signal on T2-weighted imaging (edema) and calcifications are common.	Rare intracranial lesions caused by parasites Echinococcus granulosus (South America, Middle East, Australia, and New Zealand) or Echinococcus multilocularis (North America, Europe, Turkey, and China). CNS involvement occurs in 1 to 4% of hydatid infections. Humans are intermediate hosts from ingestion of tapeworm eggs in fecally contaminated food or by contact with infected animal tissue. Lesions are often large before becoming symptomatic from raised intracranial pressure. The hydatid cyst has three layers. The outermost layer is the pericyst, which is a thin compressed layer of adjacent host tissue composed of fibrous and inflammatory host cells and usually lacks gadolinium contrast enhancement. The middle layer is the acellular laminated membrane, and the inner layer is the germinative epithelium. The acellular laminated membrane and germinative layer represent the true wall of the cyst, which is referred to as the endocyst. Superinfected hydatid cysts often contain purulent material, commonly with Staphylococcus aureus, and are typically surrounded by an inflammatory reaction in the adjacent brain tissue and/or meninges.
Rasmussen's encephalitis (**Fig. 2.33**)	MRI: Progressive atrophy of one cerebral hemisphere involving the white matter, basal ganglia, and cortex, with prominent sulci and dilated ipsilateral lateral ventricle. Abnormal high signal on T2-weighted imaging and FLAIR can be seen in the gray and white matter. Usually there is no gadolinium contrast enhancement.	Uncommon chronic T-cell–mediated immune disorder usually seen in children < 10 years old who have severe and progressive epilepsy and unilateral neurologic deficits, including hemiplegia and psychomotor deterioration. Biopsies show T-cell–dominated encephalitis with activated microglial cells and absence of macrophages, B cells, and plasma cells, and viral inclusion bodies. Treatment is hemispherectomy.

(continued on page 450)

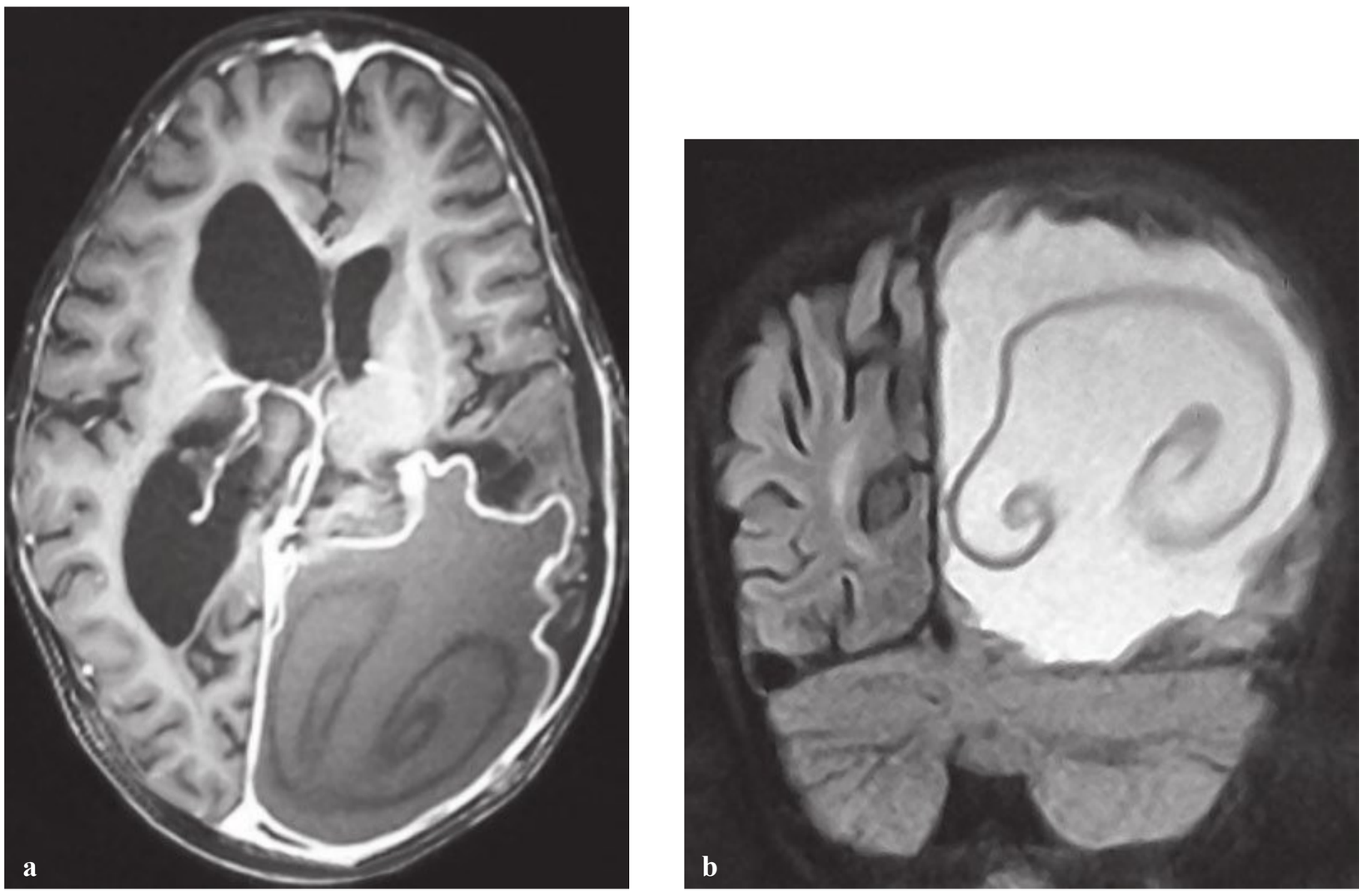

Fig. 2.32 Ruptured hydatid cyst in the left cerebral hemisphere with peripheral gadolinium contrast enhancement of the pericyst surrounding the fluid portions of the lesion on axial T1-weighted imaging. The collapsed walls of the endocyst have with low signal on **(a)** axial T1-weighted imaging and **(b)** coronal FLAIR, within the proteinaceous fluid giving the floating membrane sign. The ruptured hydatid cyst has associated mass effect causing hydrocephalus.

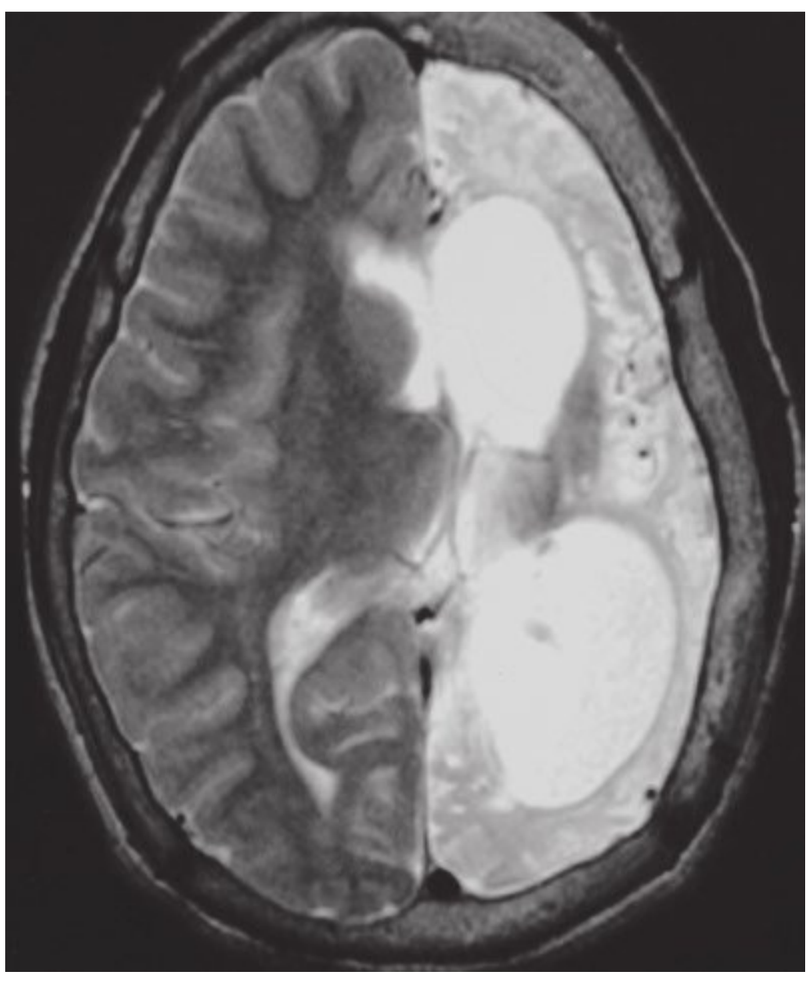

Fig. 2.33 A 12-year-old male with Rasmussen encephalitis. Diffuse abnormal high signal on axial T2-weighted imaging is seen in the left cerebral hemisphere, with compensatory dilatation of the lateral ventricle and expansion of the diploic marrow space of the left side of the calvarium.

Table 2.5 (cont.) Dilated ventricles

Lesions	Imaging Findings	Comments
Neurodegeneration		
Hydranencephaly (**Fig. 2.34**)	Replacement of substantial portions of cerebral tissue with thin-walled sacs containing CSF. Inferomedial portions of frontal and temporal lobes are often preserved, and cerebellum and thalami usually have a normal appearance.	In utero destruction of cerebral parenchyma from injury (vascular, infectious—CMV, toxoplasmosis, etc.). Patients may be normo-, micro-, or macrocephalic. Children are developmentally delayed.
Porencephalic cyst (**Fig. 2.35**)	MRI: Irregular, relatively well-circumscribed zone with high signal on T2-weighted imaging and FLAIR and low signal on T1-weighted imaging and diffusion-weighted imaging similar to CSF, surrounded by poorly defined thin zone of increased signal on FLAIR in adjacent brain tissue. No gadolinium contrast enhancement or peripheral edema. CT: Irregular, relatively well-circumscribed zone with low attenuation similar to CSF, surrounded by poorly defined thin zone of decreased attenuation in adjacent brain tissue. No contrast enhancement or peripheral edema.	Represent remote sites of brain injury (trauma, infarction, infection, hemorrhage) occurring in late second trimester with evolution by an encephaloclastic process into a cystic zone with CSF MR signal characteristics surrounded by zones of gliosis in adjacent brain parenchyma. Gliosis (high T2 signal) allows differentiation from schizencephaly.
Encephalomalacia (**Fig. 2.36**)	Poorly defined zone of high signal on T2-weighted imaging in brain tissue (gray and/or white matter) with localized volume loss and compensatory dilatation of adjacent ventricle.	Damaged residual brain tissue characterized by astrocytic proliferation related to prior infarct, hemorrhage, inflammation, infection, and/or trauma, with compensatory ipsilateral ventricular dilatation resulting from localized volume loss. Encephalomalacia can occur during late gestation, in the postnatal period, or in mature brain when an astrocytic proliferation response is possible.

(continued on page 452)

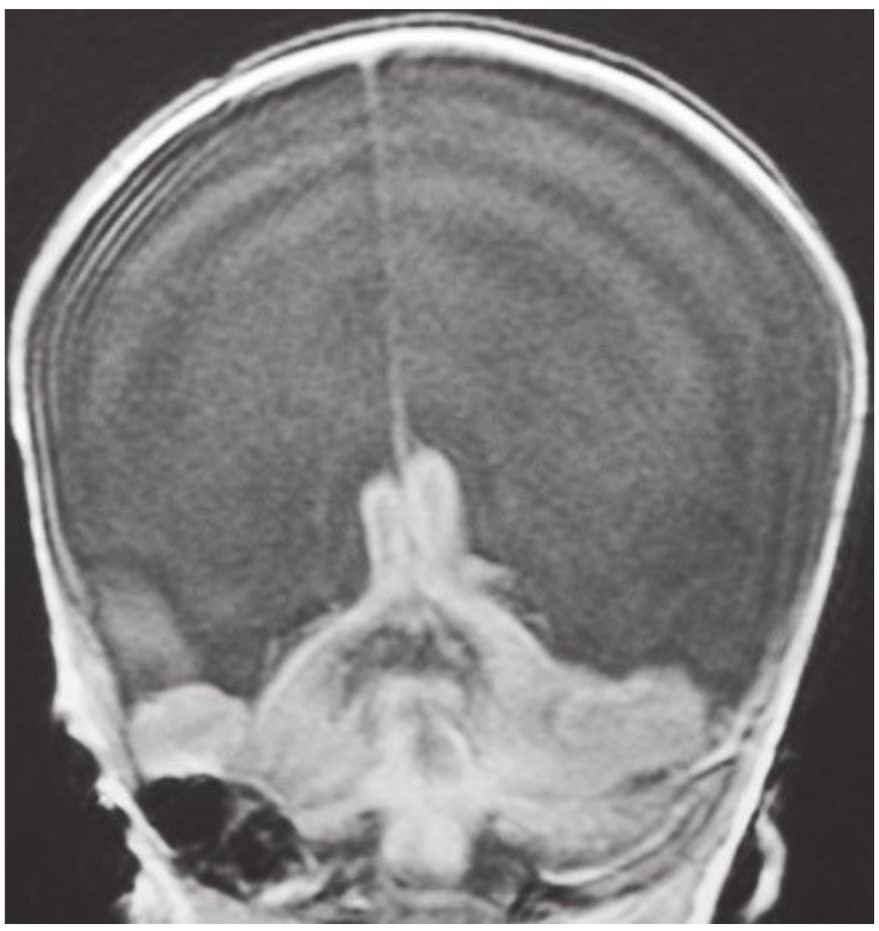

Fig. 2.34 A 5-week-old male with hydranencephaly. Coronal T1-weighted imaging shows replacement of the upper portions of cerebral tissue with thin-walled sacs containing CSF, with relative preservation of inferomedial portions of the cerebral hemispheres. The falx cerebi is present and the cerebellar hemispheres have a normal appearance.

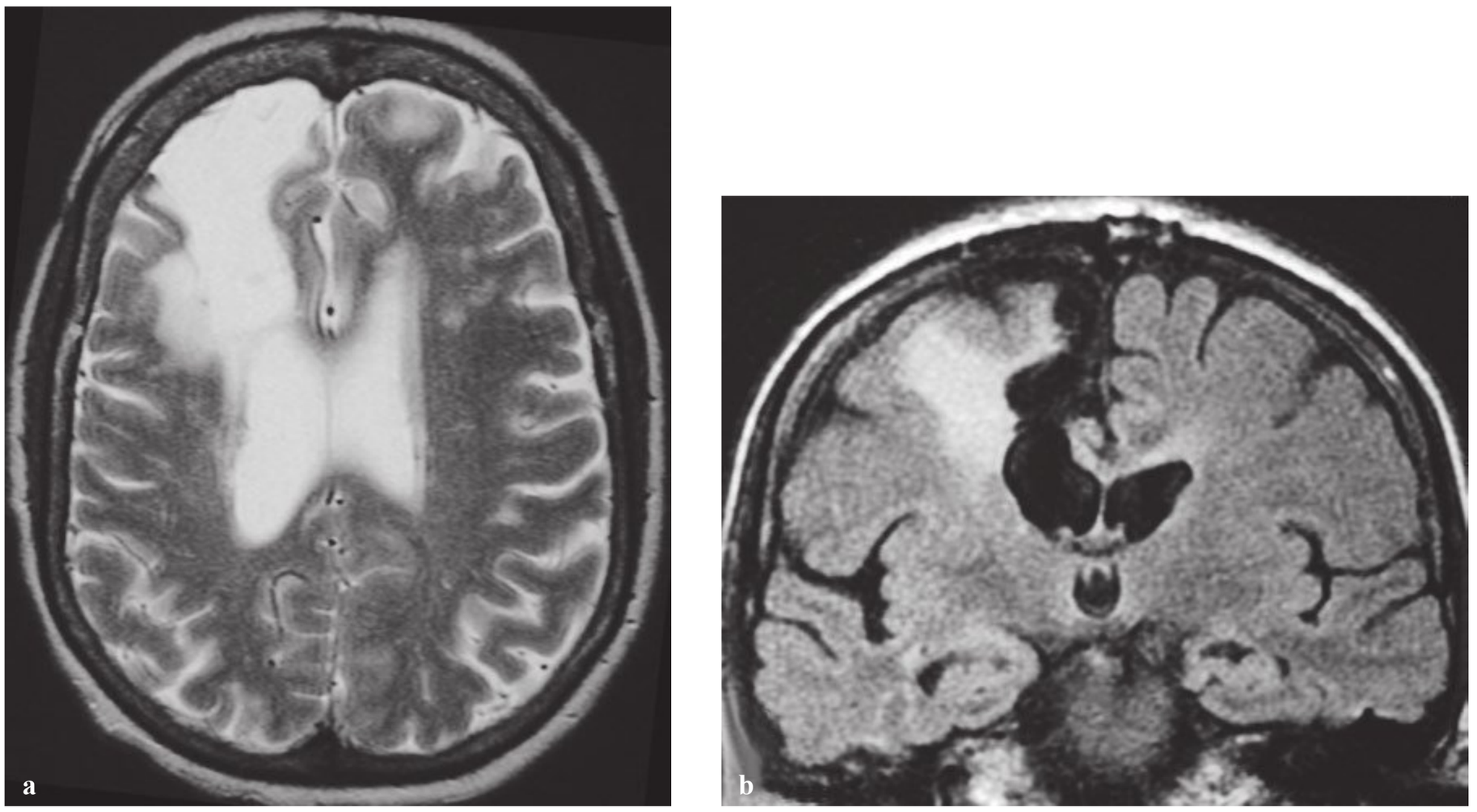

Fig. 2.35 Aporencephalic cyst is seen contiguous with frontal horn of the right lateral ventricle on **(a)** axial T2-weighted imaging and **(b)** coronal FLAIR.

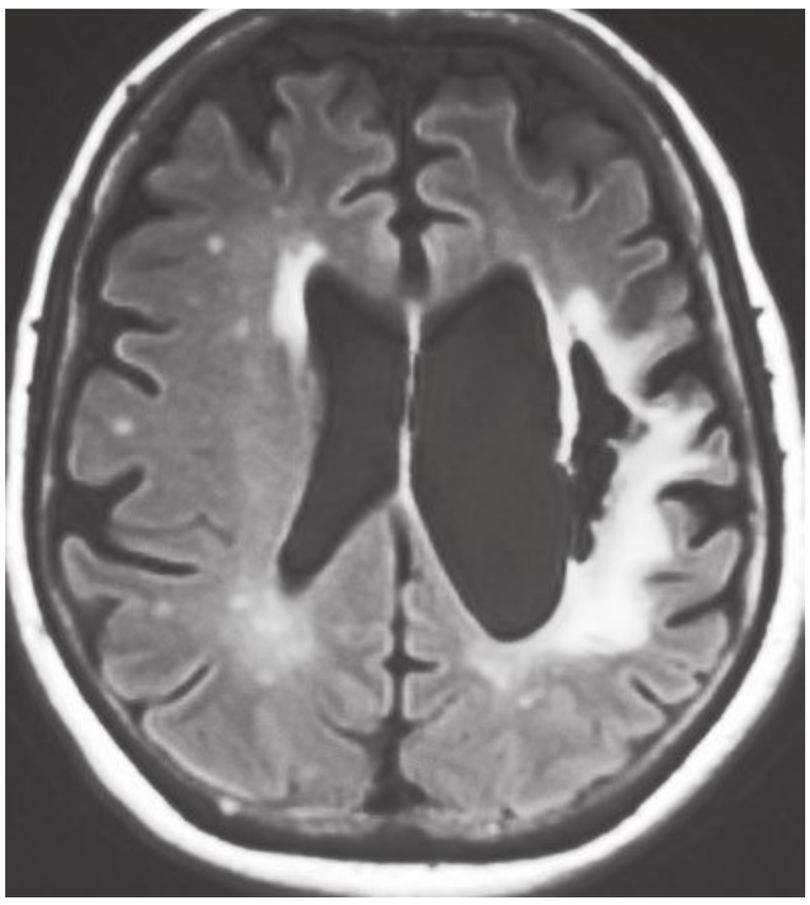

Fig. 2.36 Encephalomalacia and gliosis are seen involving the left cerebral hemisphere secondary to cerebral infarction, with associated compensatory dilatation of the left lateral ventricle on axial FLAIR.

Table 2.5 (cont.) Dilated ventricles

Lesions	Imaging Findings	Comments
Dyke-Davidoff-Mason syndrome (**Fig. 2.37**)	Atrophy/encephalomalacia of one cerebral hemisphere, with compensatory dilatation of ipsilateral lateral ventricle, midline shift, unilateral ipsilateral decrease in size of cranial fossa associated with thickened calvarium, ± enlargement of ipsilateral pneumatized paranasal sinuses and mastoid air cells.	Rare disorder in adolescents presenting with seizures, mental retardation, hemiparesis, or hemiplegia. Can result from congenital injury, such as cerebral infarction from occlusion of the middle cerebral artery, or from postnatal trauma, hemorrhage, ischemia, or infection.
Alzheimer's disease (**Fig. 2.38**)	MRI: Brain atrophy often most pronounced in the hippocampi and entorhinal cortex of the temporal lobes, thinned gyri, and sulcal and ventricular prominence. Cortical atrophic changes are common. Atrophic changes typically involve the posterior portion of the corpus callosum. Diffusion tensor imaging: Decreased fractional anisotropy in splenium of the corpus callosum and superior longitudinal fasciculus. Magnetic resonance spectroscopy: Decreased N-acetylaspartate (NAA)/myo-inositol. PET/CT: Reduced F-18 FDG activity/glucose metabolism in the parietal and superior/posterior temporal lobes, posterior cingulate cortex, and precuneus. Increased amyloid-binding radionuclide activity can be seen with PET/CT.	Alzheimer's disease is the most common form of progressive dementia and accounts for up to 60% of cases in patients older than 65 years. Pathologic changes include: neurofibrillary tangles from abnormal phosphorylation of microtubule-associated tau protein (tauopathy), senile plaques in gray matter consisting of neurotoxic deposits of amyloid–β 42 protein (deposits also occur in blood vessels), and decreased neurons from neuronal death. Damage begins in the entorhinal cortex and then involves the hippocampus before involving the rest of the cortex. Increased familial risk in 10% of patients related to PSEN1, PSEN2, and APOE*E4 genes. Clinical findings include: poor recent memory; disorientation to time and place; impaired recall, recognition, and working memory; word retrieval difficulty; impaired conversational speech; and impaired object and space perception.
Frontotemporal lobar degeneration (**Fig. 2.39**)	MRI: Progressive brain atrophy often most pronounced in frontal and temporal lobes, hippocampi, and both amygdala; sulcal and ventricular prominence. Cortical atrophic changes common. Abnormal increased signal on T2-weighted imaging can be seen in the subcortical white matter of the atrophied gyri. Atrophy of the anterior portion of the corpus callosum can be seen.	Frontotemporal lobar degeneration (FTLD) is a heterogeneous group of interrelated neurodegenerative disorders that can be associated with the clinical diagnosis of frontotemporal dementia (FTD). FTD is less common than Alzheimer's disease. Prevalence of 15 per 100,000 and incidence of 2.2 to 8.9 per 100,000. Pathologic changes include neuronal loss and gliosis as well as deposition of three proteins in the cytoplasm of brain neurons: 1) microtubule-associated protein tau (FTLD-tau), 2) transactive response DNA-binding protein 43 (TDP-43, FTLD-TDP), or 3) fused in sarcoma protein (FUS, FTLD-FUS).

(continued on page 454)

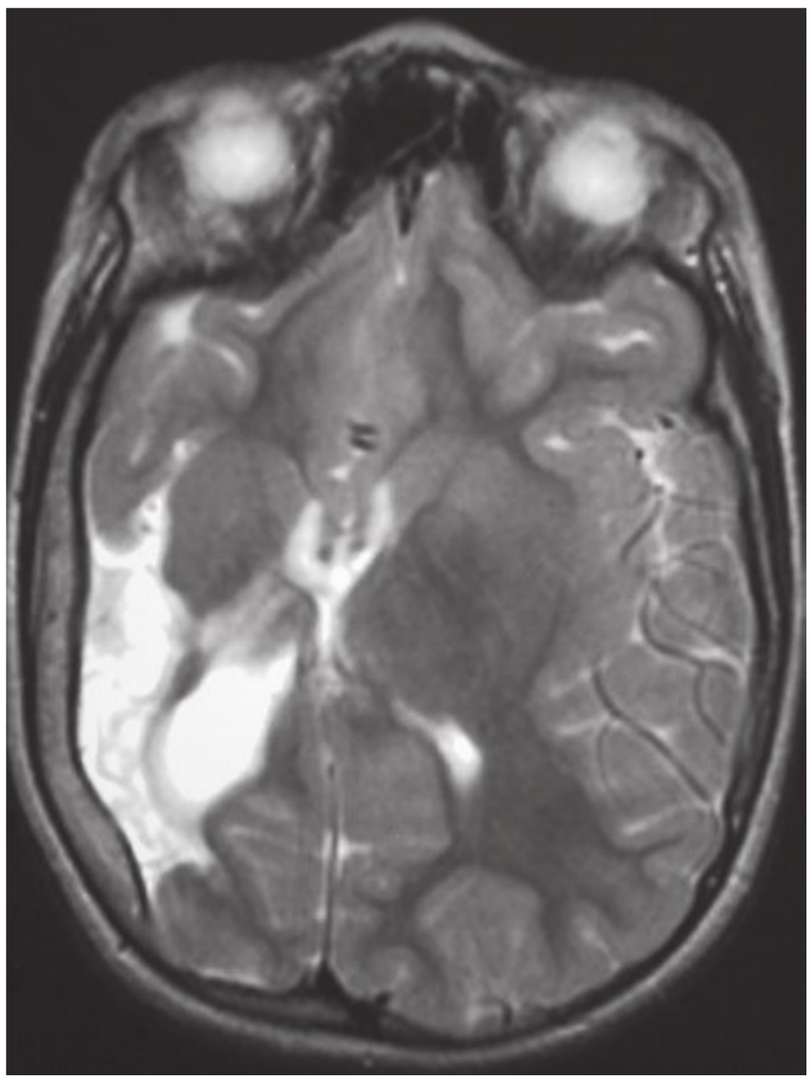

Fig. 2.37 A 7-year-old female with Dyke-Davidoff-Masson syndrome. Axial T2-weighted imaging shows encephalomalacia of the right cerebral hemisphere with compensatory dilatation of right lateral ventricle, midline shift, and unilateral ipsilateral decrease in size of right cranial fossa associated with thickened calvarium.

Fig. 2.38 An 80-year-old man with Alzheimer's disease. Axial T2-weighted imaging shows asymmetric prominent atrophy involving both the anterior portions of both temporal lobes.

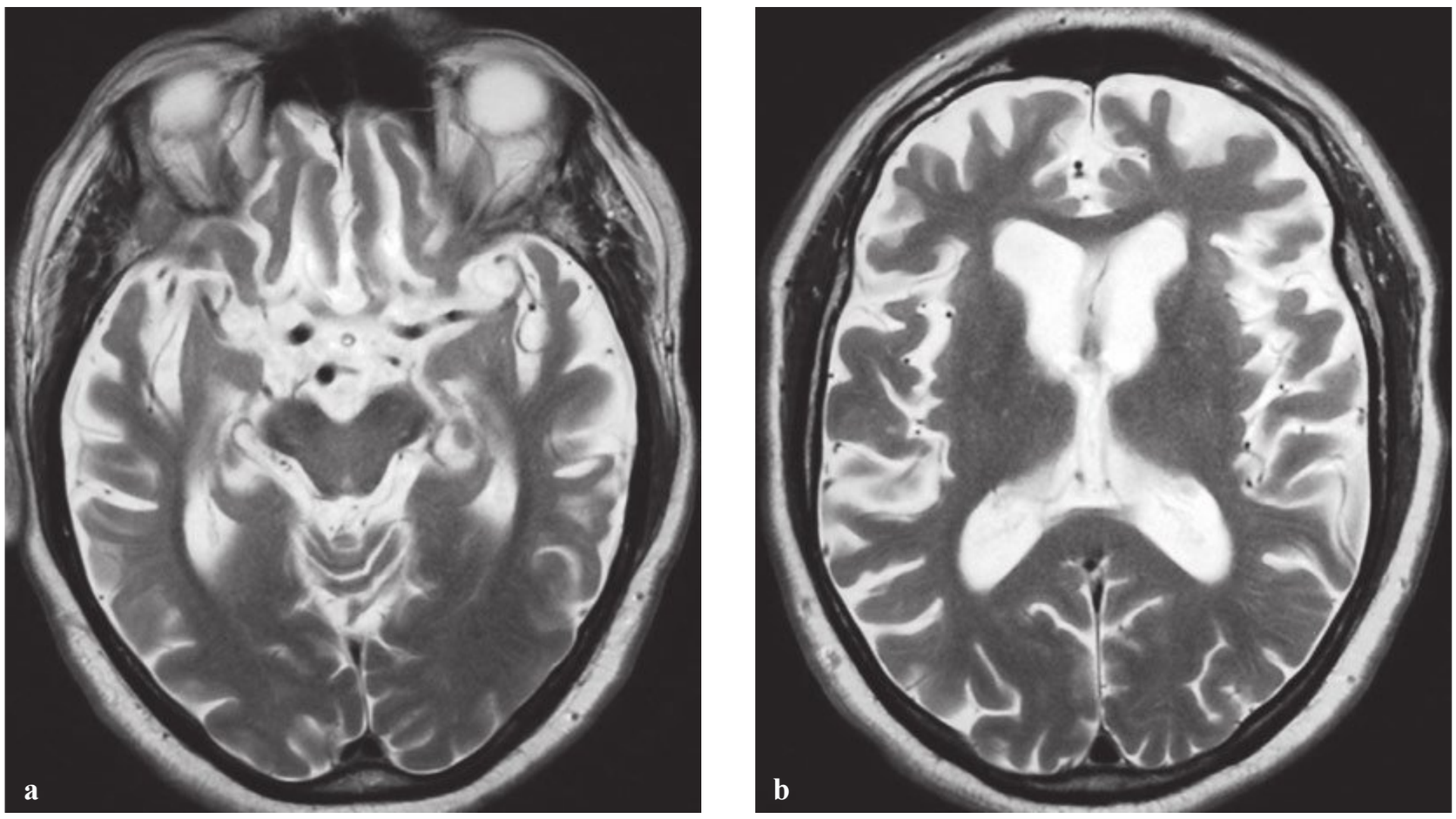

Fig. 2.39 A 59-year-old man with frontotemporal dementia. Asymmetric greater atrophy is seen involving both **(a)** frontal and **(b)** temporal lobes relative to other portions of the brain, as seen on axial T2-weighted imaging.

Table 2.5 (cont.) Dilated ventricles

Lesions	Imaging Findings	Comments
Huntington disease (**Fig. 2.40**)	Disproportionate atrophy of basal ganglia (caudate > putamen > cerebellum/brainstem). MRI: Atrophy of caudate and putamen bilaterally. Variable low signal (iron deposition) or high signal (gliosis) changes on T2-weighted imaging in the putamen bilaterally. Usually no abnormal contrast enhancement. CT: Progressive atrophy of caudate and putamen bilaterally.	Autosomal dominant neurodegenerative polyglutamine disease in adults related to abnormal segment (CAG repeats) of DNA on chromosome 4 involving the huntingtin gene. Results in increased synthesis of huntingtin protein, which causes neuronal damage and brain atrophy. Neuronal loss, astrogliosis, and increased oligodentrocytes within a loose textured neuropil are seen in the striatum. Usually presents after age 40 years with progressive movement disorders (choreoathetosis, rigidity, hypokinesia), behavioral abnormalities, and progressive mental dysfunction (dementia). Juvenile Huntington disease also occurs in a small number of patients in their second decade. Patients present with rigidity, hypokinesia, seizures, and progressive mental dysfunction.
Communicating hydrocephalus, normal-pressure hydrocephalus (**Fig. 2.41**)	MRI: Disproportionately greater prominence of the ventricles relative to the sulci, narrowed sulci at the high convexities; ± focal bulging of the roofs of the lateral ventricles; + hyperdynamic CSF flow at the third ventricle, cerebral aqueduct, and fourth ventricle as seen on 2D cine phase contrast MRI and as a flow void on T1- and T2-weighted imaging. Transependymal egress of CSF is also seen as subependymal zones with high signal in T2-weighted imaging and FLAIR. CT: Disproportionate greater prominence of the ventricles relative to the sulci, with periventricular/subependymal decreased attenuation. Nuclear medicine: In-111 DTPA cisternography can show prominent activity after 24 hours.	Usually occurs in patients older than 40 years. Dilatation of the ventricles with transependymal egress of CSF is thought to be related to impaired resorption of CSF through arachnoid granulations. Can be associated with progressive memory impairment, urinary incontinence, and gait disorders (normal-pressure hydrocephalus). Patients with normal pressure hydrocephalus have CSF opening pressures between 60 and 240 mm H_2O or between 4 and 17 mmHg. Can be idiopathic (primary type) or result from meningitis or subarachnoid hemorrhage (secondary type). Treatment is with ventricular shunting.
Ventricular shunt failure (**Fig. 2.42**)	Enlargement of ventricles above site of CSF outflow obstruction despite the presence of a ventricular shunt catheter.	Blockage of ventricular shunt catheters can result in progressive ventricular dilation.

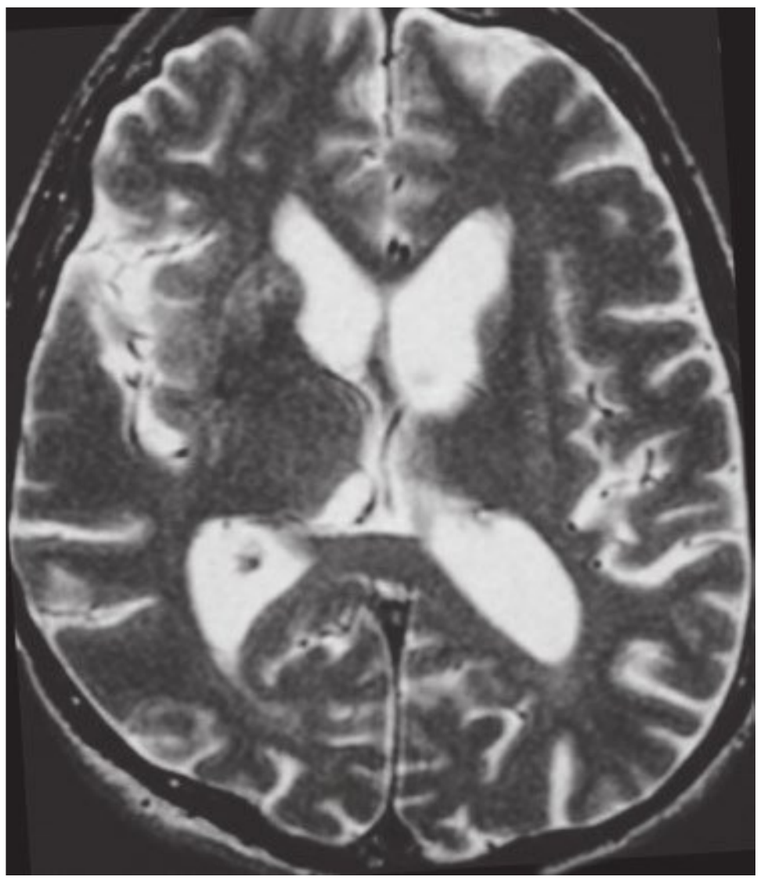

Fig. 2.40 A 64-year-old man with Huntington disease. Bilateral atrophied caudate and putamen nuclei with increased signal on axial T2-weighted imaging are seen with compensatory enlargement of the frontal horns of the lateral ventricles.

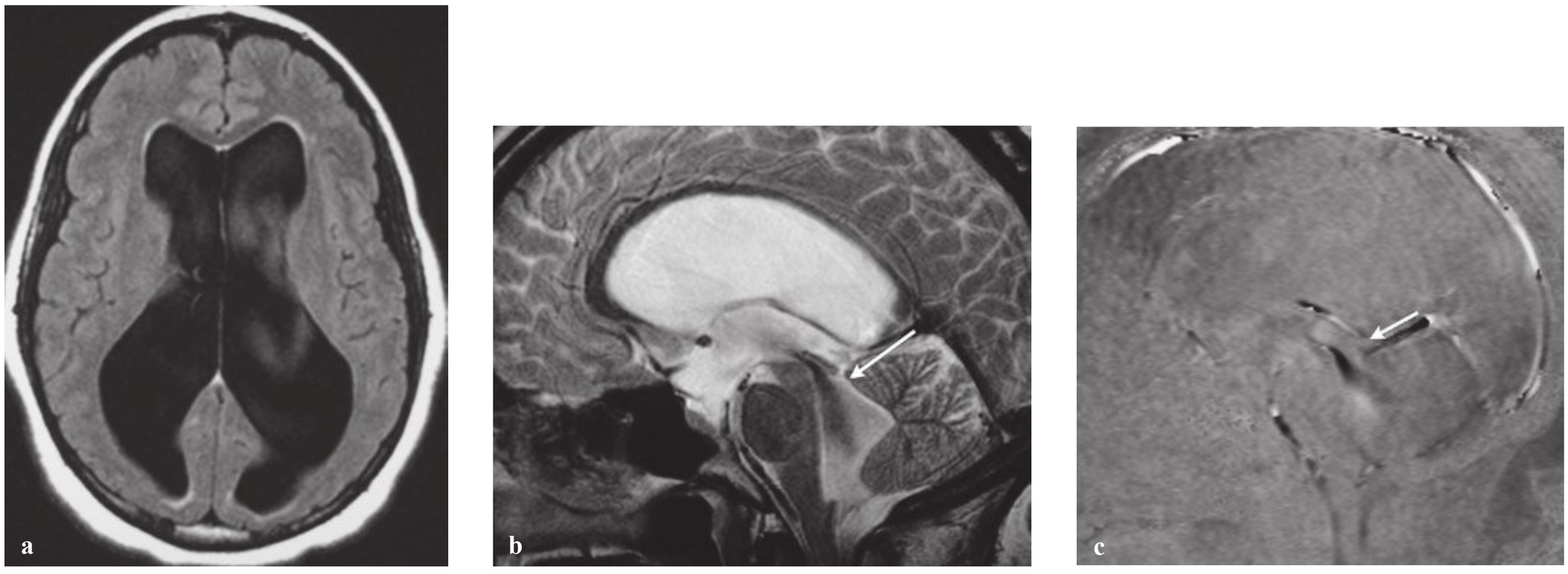

Fig. 2.41 Patient with communicating, normal-pressure hydrocephalus. **(a)** Axial FLAIR shows disproportionately greater prominence of the ventricles relative to the sulci and subependymal zones with high signal from transependymal egress of CSF. **(b)** Sagittal T2-weighted imaging shows a hyperdynamic CSF flow void (arrow) at the cerebral aqueduct, with corresponding hyperdynamic CSF flow signal on **(c)** sagittal 2D phase-contrast MRI (arrow).

Fig. 2.42 Ventricular shunt failure, seen as dilated lateral ventricles, despite the presence of a ventricular shunt catheter on axial CT.

Table 2.6 Abnormal or altered configuration of the ventricles

- Congenital/Developmental
  - Chiari II malformation (Arnold-Chiari)
  - Holoprosencephaly
  - Septo-optic dysplasia (de Morsier syndrome)
  - Gray matter heterotopia
  - Unilateral hemimegalencephaly
  - Cortical dysplasia
  - Dysgenesis of the corpus callosum
  - Dandy-Walker malformation
  - Vermian hypoplasia (also referred to as Dandy-Walker variant)
  - Joubert syndrome
  - Rhombencephalosynapsis
  - Porencephalic cyst
  - Hamartoma–tuberous sclerosis
  - Cavum septum pellucidum/cavum vergae
  - Cavum velum interpositum
- Acquired Disorders
  - Subfalcine herniation
  - Transtentorial herniation

Table 2.6 Abnormal or altered configuration of the ventricles

Lesions	Imaging Findings	Comments
Congenital/Developmental		
Chiari II malformation (Arnold-Chiari) (**Fig. 2.43** and **Fig. 2.44**)	Small posterior cranial fossa with gaping foramen magnum through which there is an inferiorly positioned vermis associated with a cervicomedullary kink. Beaked dorsal margin of the tectal plate. Myelomeningoceles in nearly all patients. Hydrocephalus and syringomyelia common. Dilated lateral ventricles posteriorly (colpocephaly).	Complex anomaly involving the cerebrum, cerebellum, brainstem, spinal cord, ventricles, skull, and dura. Failure of fetal neural folds to develop properly results in altered development affecting multiple sites of the CNS.
Holoprosencephaly (**Fig. 2.45, Fig. 2.46, Fig. 2.47,** and **Fig. 1.17**)	Alobar: Large monoventricle with posterior midline cyst, lack of hemisphere formation with absence of falx, corpus callosum, and septum pellucidum. Fused thalami. Can be associated with facial anomalies (facial clefts, arrhinia, hypotelorism, cyclops). Semilobar: Anterior frontal portions of brain fused across midline lacking interhemispheric fissure anteriorly. Partial formation of interhemispheric fissure posteriorly and occipital and temporal horns of ventricles, partially fused thalami. Absent corpus callosum anteriorly but splenium is present. Absent septum pellucidum. Associated with mild craniofacial anomalies. Lobar: Near-complete formation of interhemispheric fissure and ventricles. Fused inferior portions of frontal lobes, dysgenesis of corpus callosum with formation of posterior portion without anterior portion, malformed frontal horns of lateral ventricles, absence of septum pellucidum, separate thalami, and neuronal migration disorders. Syntelencephaly (middle interhemispheric variant): Partial formation of interhemispheric fissure in the anterior and posterior regions with fusion of the portions of the upper frontal and/or parietal lobes. Genu and splenium of the corpus callosum can be observed with localized absence/defect of the central body of the corpus callosum. Septum pellucidum is often absent.	Holoprosencephaly (HPE) is a spectrum of diverticulation disorders that occur during weeks 4 to 6 of gestation and are characterized by absent or partial cleavage and differentiation of the embryonic forebrain cerebrum (prosencephalon) into hemispheres and lobes. Causes include maternal diabetes, teratogens, and fetal genetic abnormalities, such as trisomy 16 (Patau syndrome) and trisomy 18 (Edwards syndrome). Familial HPE is caused by mutations of HPE1 on chromosome 21q22.3, HPE2 on 2p21, HPE3 on 7q36, HPE4 on 18p, HPE5 on 13q32, HPE6 on2q37, HPE7 on9q22.3, HPE8 on 14q13, and HPE9 on2q14, genes that are related to ventral and dorsal induction of the prosencephalon. ZIC2 mutations are also associated with HPE. Clinical manifestations depend on severity of malformation and include early death, seizures, mental retardation, facial dysmorphism, and developmental delay. Patients with syntelencephaly often have mild to moderate cognitive dysfunction, spasticity, and mild visual impairment.
Septo-optic dysplasia (de Morsier syndrome) (**Fig. 2.48**)	Dysgenesis/hypoplasia or agenesis of septum pellucidum, optic nerve hypoplasia, and squared frontal horns. Association with schizencephaly in 50% Optic canals are often small. May be associated with gray matter heterotopia and polymicrogyria.	Patients can have nystagmus, decreased visual acuity, and hypothalamic-pituitary disorders (decreased thyroid-stimulating hormone and/or growth hormone). Clinical exam shows small optic discs. May be sporadic from in utero insults, or from mutations (HESX1 gene on chromosome 3p21.1–3p21.2 accounts for less than 1%of cases) during formation of the basal prosencephalon. Some findings overlap those of mild lobar holoprosencephaly.

(continued on page 459)

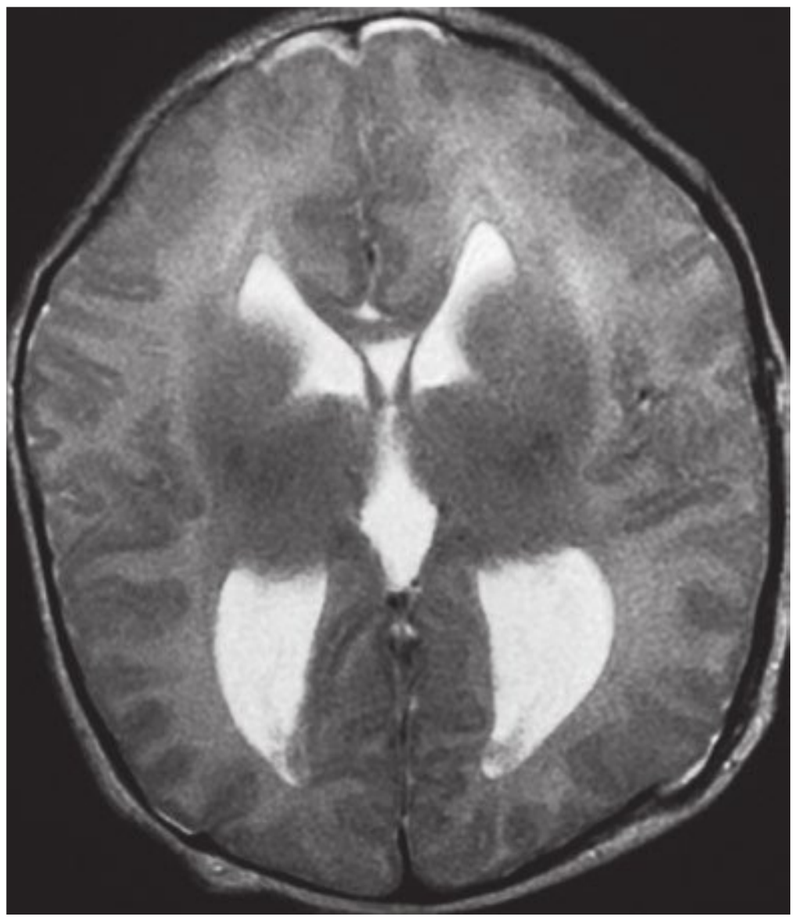

Fig. 2.43 Chiari II malformation (Arnold-Chiari malformation). Neonate with dilated ventricles on axial T2-weighted imaging. Slight disproportionate dilatation of the occipital horns of the lateral ventricles is seen (colpocephaly).

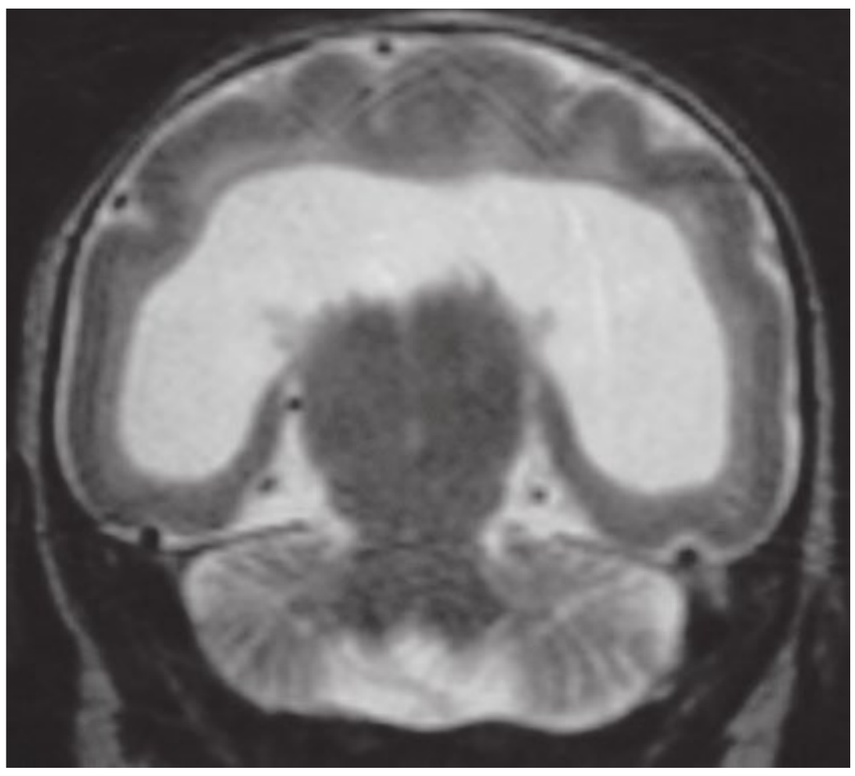

Fig. 2.45 Neonate with alobar holoprosencephaly. Coronal T2-weighted imaging shows a monoventricle and lack of interhemispheric fissure and falx.

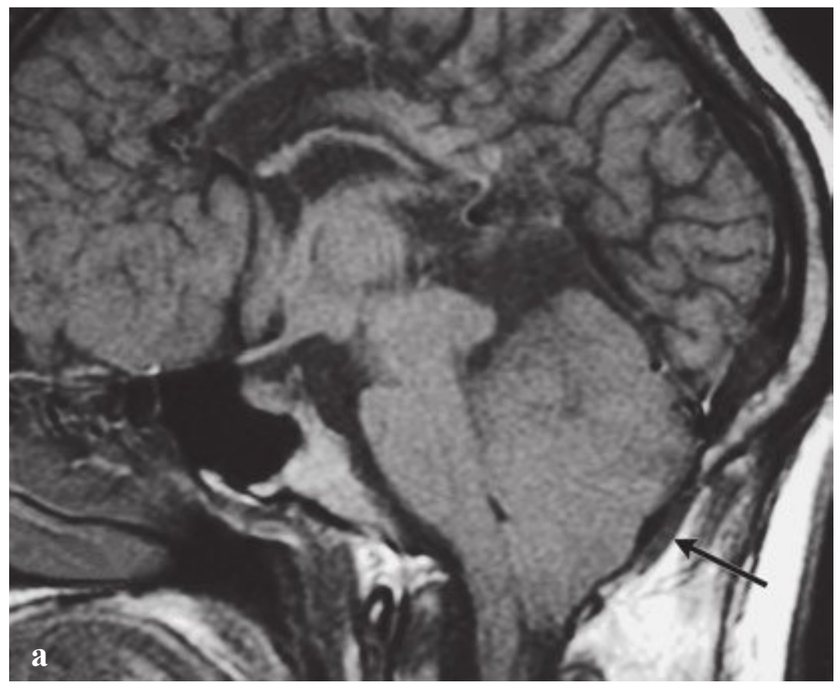

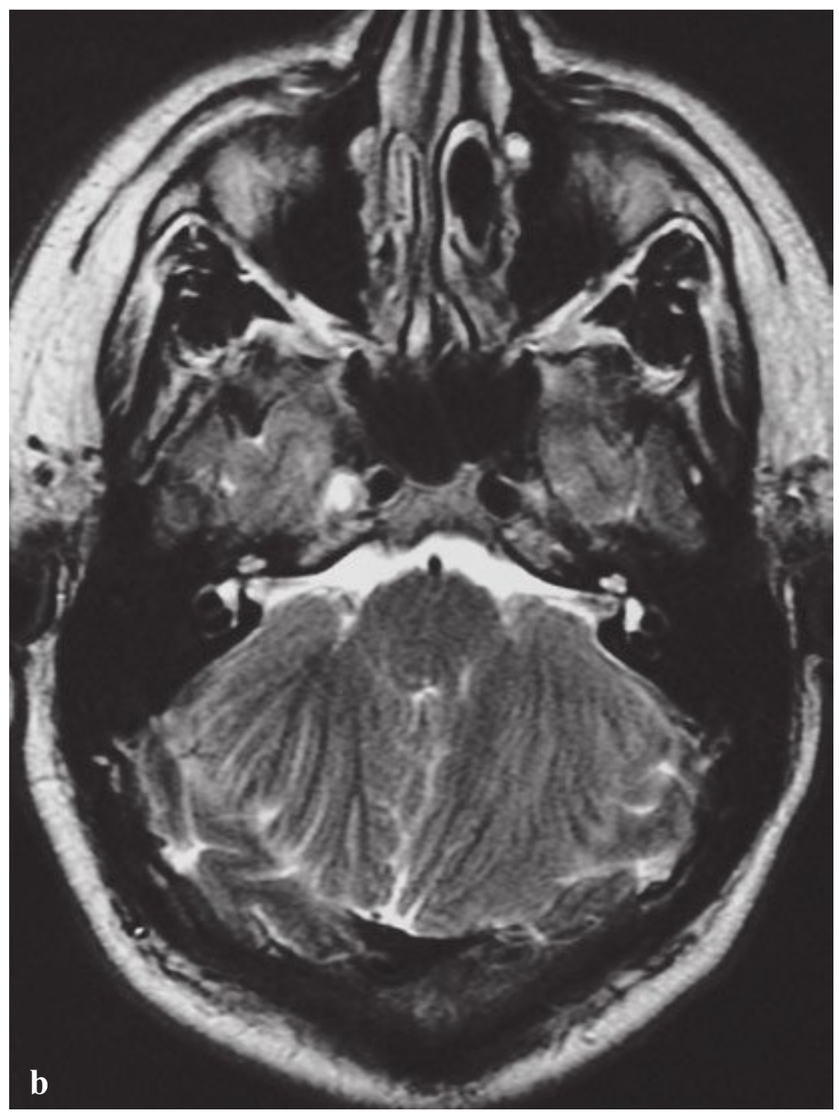

Fig. 2.44 A 25-year-old man with history of a Chiari II malformation. **(a)** Sagittal T1-weighted imaging and **(b)** axial T2-weighted imaging show a malformed a fourth ventricle as well as small posterior cranial fossa with downward position of the cerebellum through a wide foramen magnum (**a**, arrow), tectal beak, and dysgenesis of the corpus callosum.

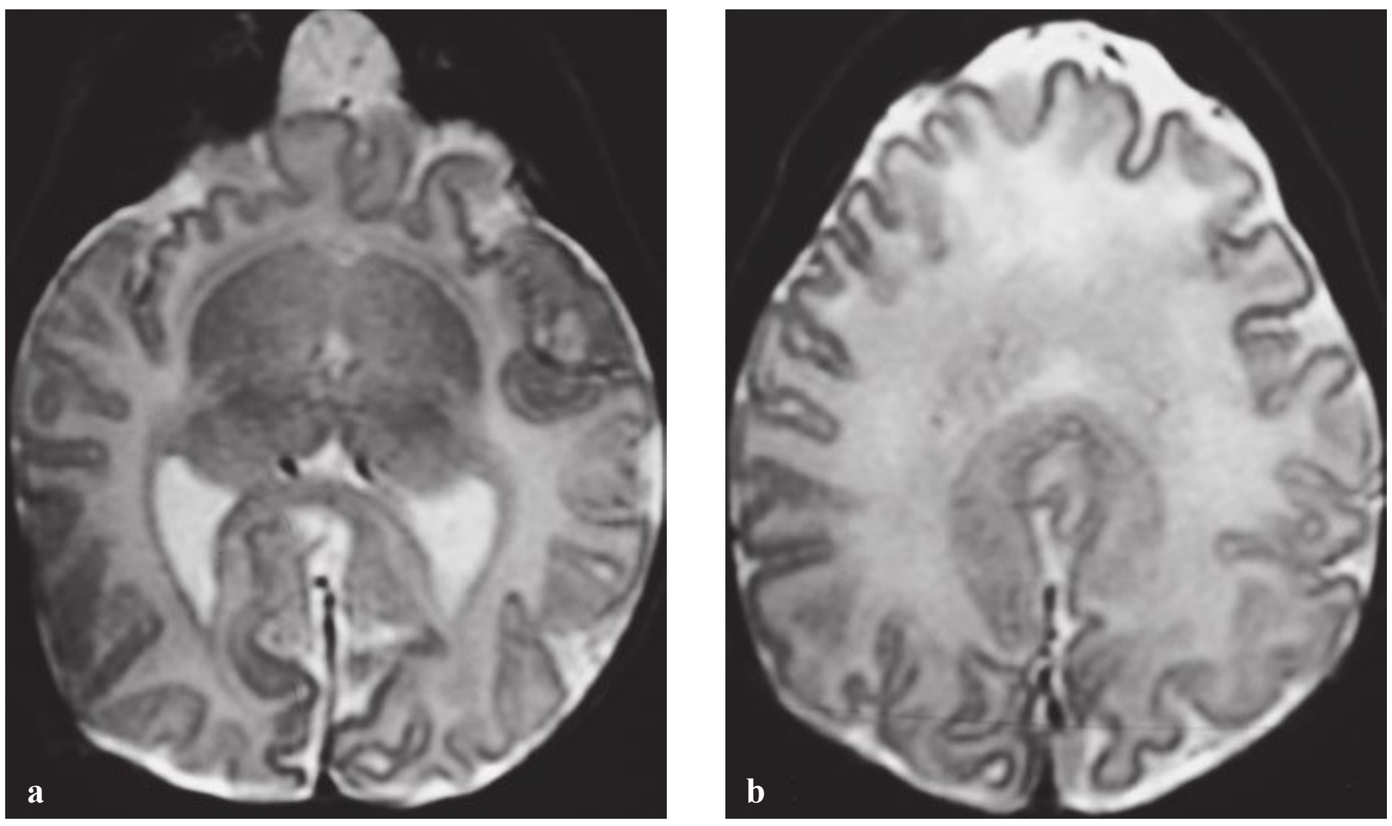

Fig. 2.46 An 8-day-old male with semilobar holoprosencephaly. **(a,b)** Axial T2-weighted imaging shows only lobar and ventricle formation in the posterior brain and lacking in the anterior brain.

Fig. 2.47 Lobar holoprosencephaly. **(a,b)** Axial T2-weighted imaging shows fusion of the anteroinferior portions of the frontal lobes and lobar development in the other portions of the brain.

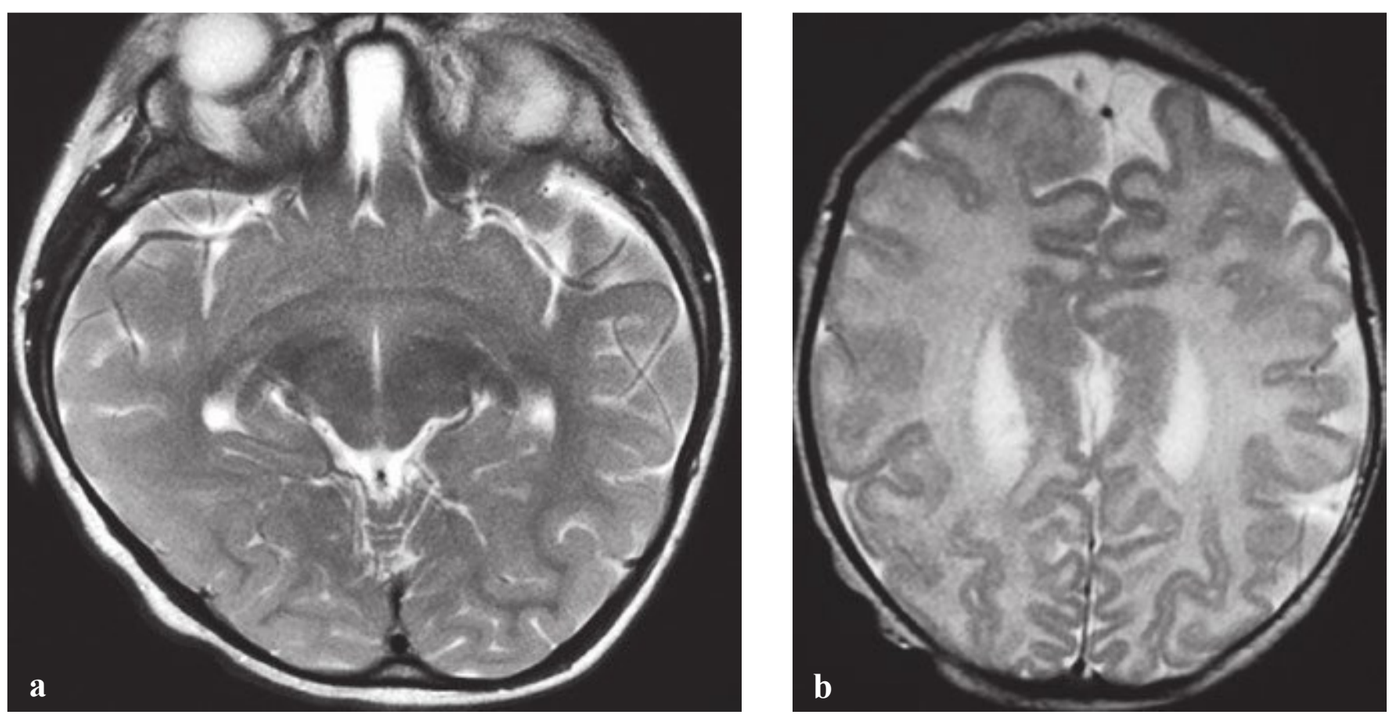

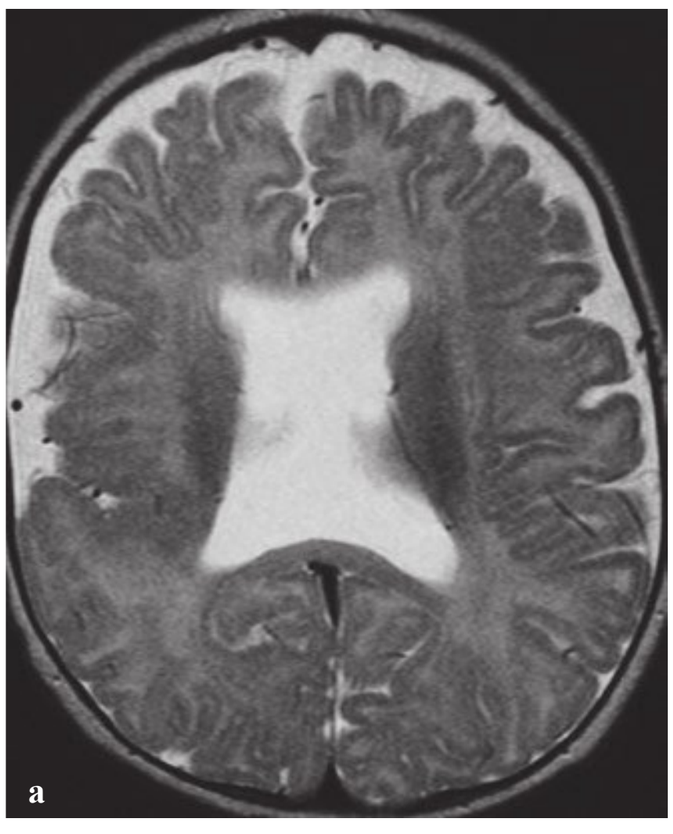

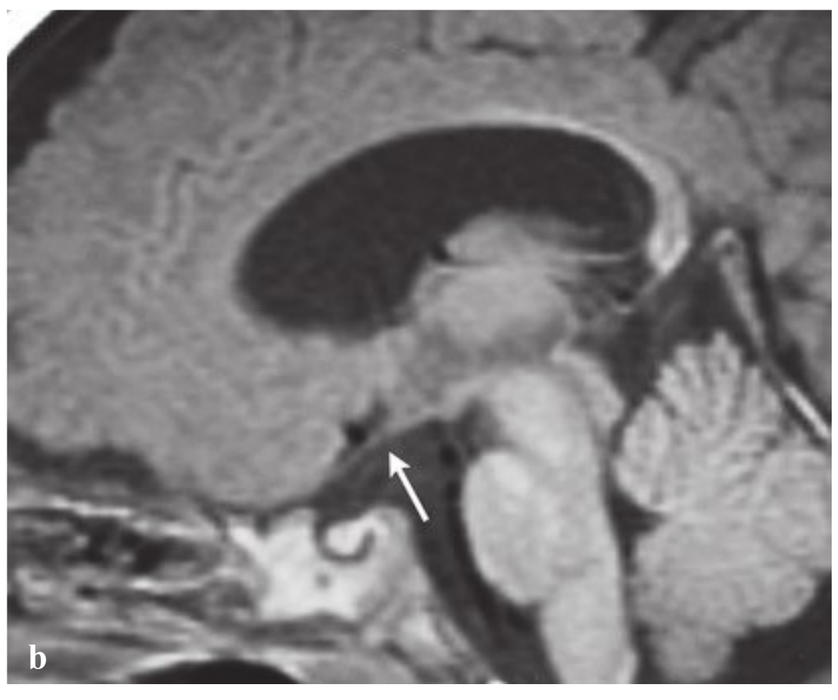

Fig. 2.48 Septo-optic dysplasia (de Morsier syndrome). **(a)** Axial T2-weighted imaging shows absence of the septum pellucidum and polymicrogyria in the right cerebral hemisphere. **(b)** Sagittal T1-weighted imaging shows hypoplasia of the optic chiasm (arrow).

Table 2.6 (cont.) Abnormal or altered configuration of the ventricles

Lesions	Imaging Findings	Comments
Gray matter heterotopia (**Fig. 2.49** and **Fig. 2.50**)	Nodular heterotopia appears as one or more nodules of isointense gray matter along the ventricles or within the cerebral white matter.	Disorder of neuronal migration (7–22 weeks of gestation) where a collection or layer of neurons is located between the ventricles and cerebral cortex. Can have a bandlike (laminar) or nodular appearance isointense to gray matter, and may be unilateral or bilateral. Associated with seizures and schizencephaly.

(continued on page 460)

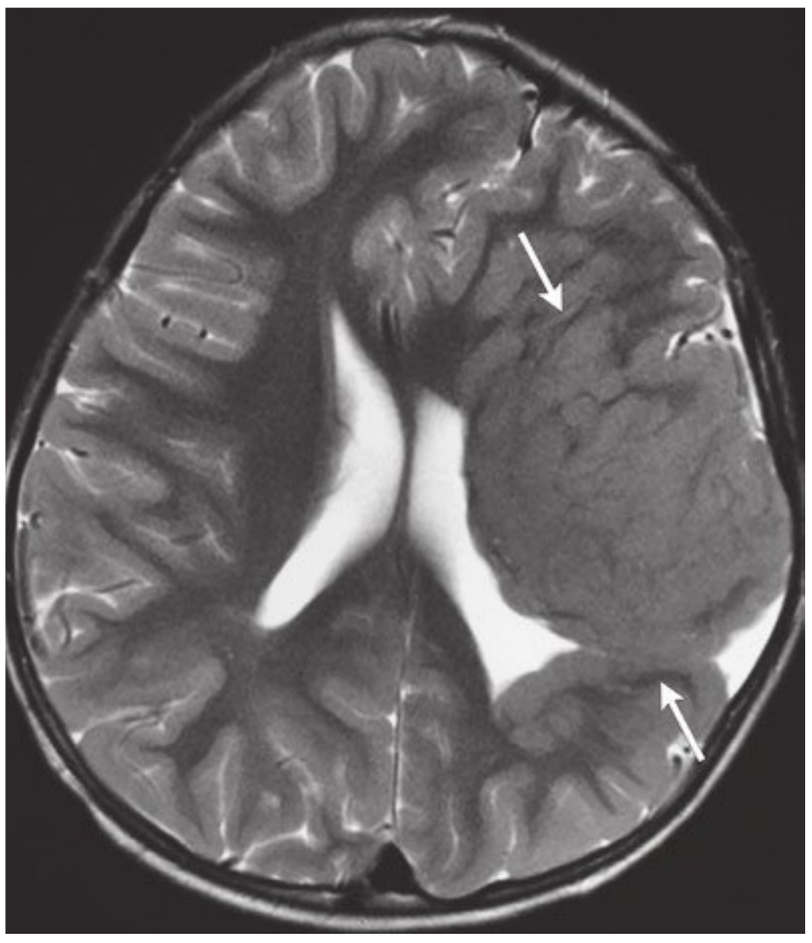

Fig. 2.49 Transmantle mass of gray matter heterotopia (arrows) involving the left cerebral hemisphere with closed-lip schizencephaly posteriorly altering the configuration of the left lateral ventricle on axial T2-weighted imaging.

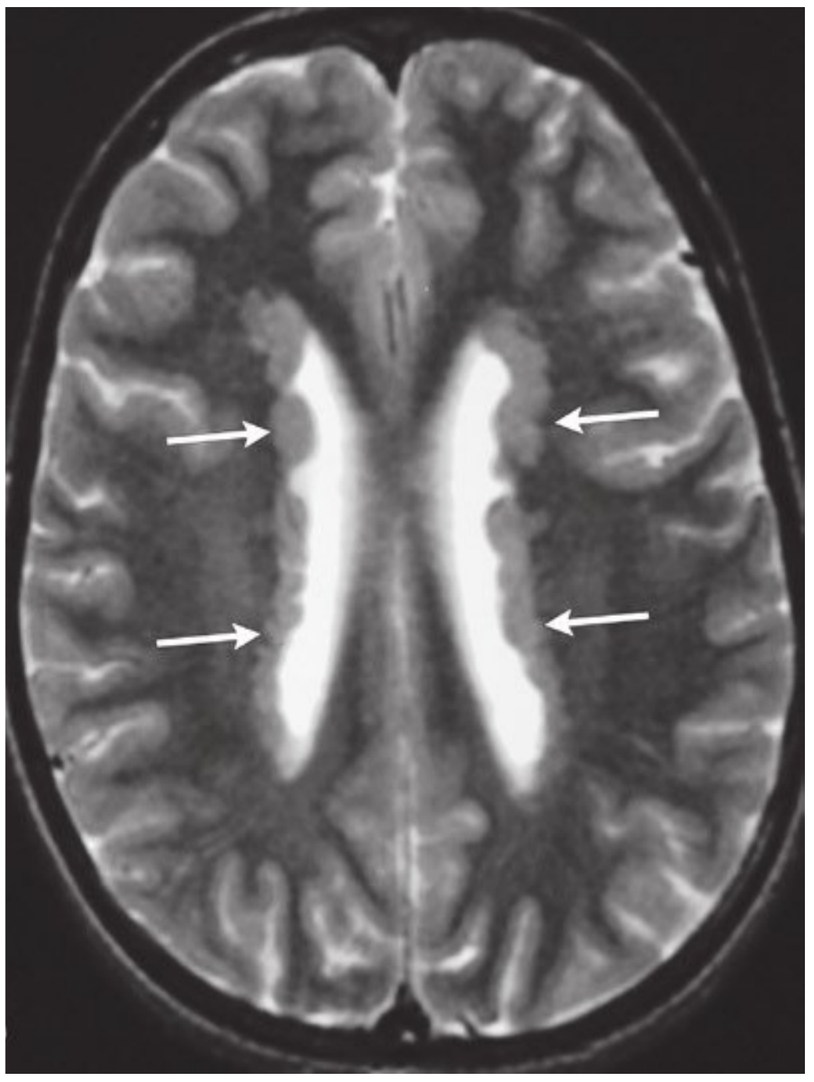

Fig. 2.50 Ependymal nodules of gray matter heterotopia (arrows) are seen on axial T2-weighted imaging.

Table 2.6 (cont.) Abnormal or altered configuration of the ventricles

Lesions	Imaging Findings	Comments
Schizencephaly (split brain) (**Fig. 2.51** and **Fig. 2.52**)	Uni- or bilateral clefts in brain extending from ventricle to cortical surface and lined by gray matter heterotopia, which may be polymicrogyric. The cleft may be narrow (closed lip) or wide (open lip).	Association with seizures, blindness, retardation, and other CNS anomalies (septo-optic dysplasia, etc). Clinical manifestations related to severity of malformation. Ischemia or insult to portion of germinal matrix before hemisphere formation.
Unilateral hemimegalencephaly (**Fig. 2.53**)	Nodular or multinodular regions of gray matter heterotopia involving all or part of a cerebral hemisphere with associated enlargement of the ipsilateral lateral ventricle and hemisphere. Zones with high signal on T2-weighted imaging may occur in the white matter.	Heterogeneous sporadic disorder with hamartomatous overgrowth of one cerebral hemisphere secondary to disturbances in neuronal proliferation and migration and cortical organization. May be associated with unilateral hemihypertrophy and/or curtaneous abnormalities.
Cortical dysplasia (**Fig. 2.54**)	Polymicrogyria: Mutiple small gyri occur unilaterally (40%) or bilaterally (60%) and most often occur in both sylvian fissures, followed by unilateral hemispheric and other locations. Multiple small gyri can be seen on MRI. On CT, the small gyri may appear as zones of thickened cortex. Focal cortical dysplasia without or with balloon cells: Localized and/or diffuse zones of thinning of the cerebral cortex with signal similar to gray matter on MRI, localized blurring of the gray–white matter junction, occasionally with increased signal in the underlying white matter on T2-weighted imaging. Attenuation on CT similar to gray matter.	Malformation in late stages of neuronal migration resulting in abnormal neuronal organization of cerebral cortex. Includes polymicrogyria, focal cortical dysplasia without "balloon" cells, and transmantle cortical dysplasia with "balloon" cells. Histologic findings include abnormal cortical lamination, dysplastic neurons, and atypical glial cells. Can be associated with dysembryoplastic neuroepithelial tumors (DNET), gangliogliomas, and mesial temporal sclerosis.
Dysgenesis of the corpus callosum (**Fig. 2.55**)	Spectrum of abnormalities ranging from complete to partial absence of the corpus callosum. Widely separated and parallel orientations of frontal horns and bodies of lateral ventricles, high position of third ventricle in relation to interhemispheric fissure, and colpocephaly. Associated with interhemispheric cysts and lipomas, and anomalies like Chiari II malformation, gray matter heterotopia, Dandy-Walker malformation, holoprosencephaly, azygous anterior cerebral artery, cephaloceles, and others.	Failure of, or incomplete, formation of corpus callosum (7–18 weeks of gestation). Axons that normally cross from one hemisphere to the other are aligned parallel along the medial walls of the lateral ventricles (bundles of Probst).

(continued on page 462)

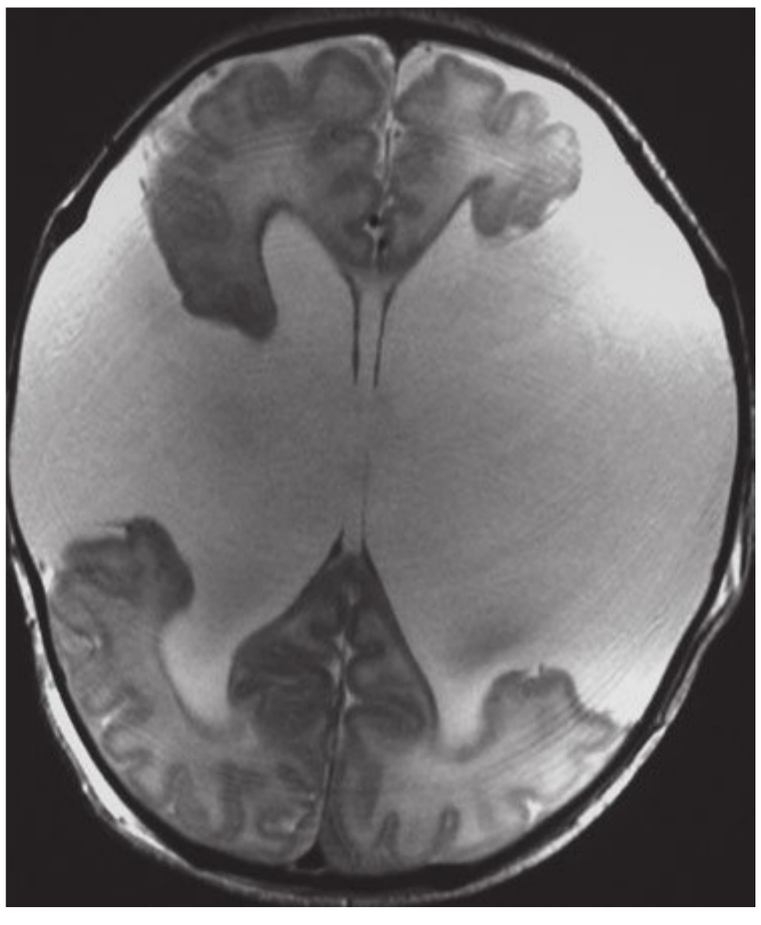

Fig. 2.51 Axial T2-weighted imaging shows open-lip schizencephaly with gray matter lining the borders of the cerebral defects.

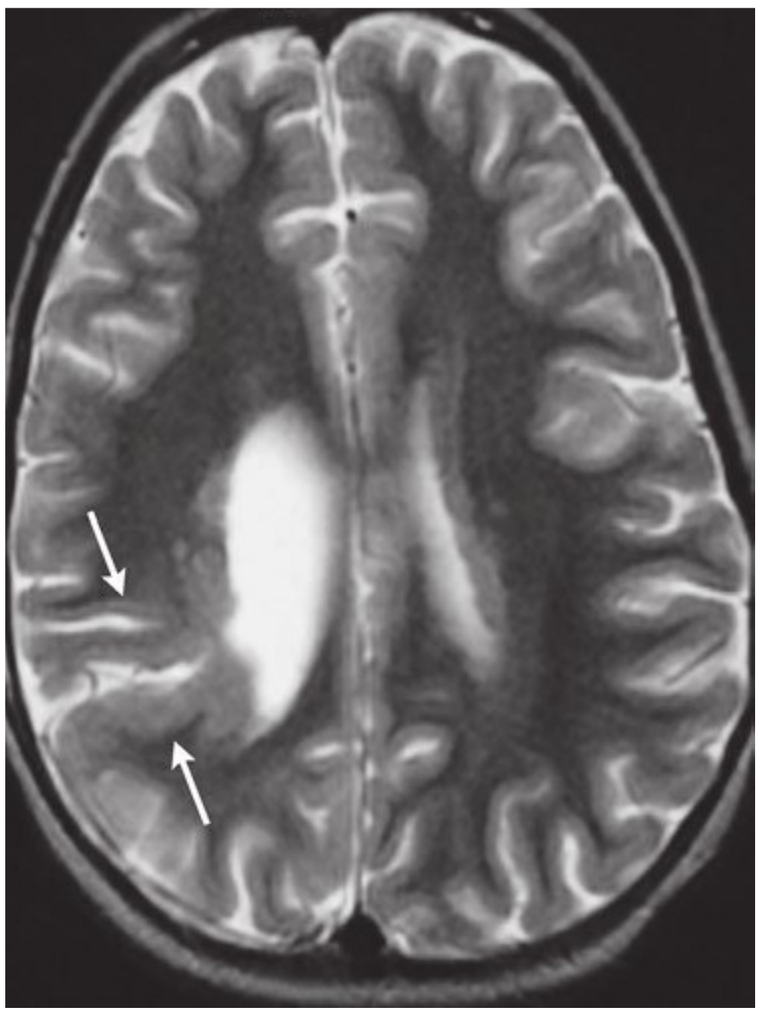

Fig. 2.52 Axial T2-weighted imaging shows closed-lip type of schizencephaly (arrows). Ependymal nodules of gray matter heterotopia are also present bilaterally.

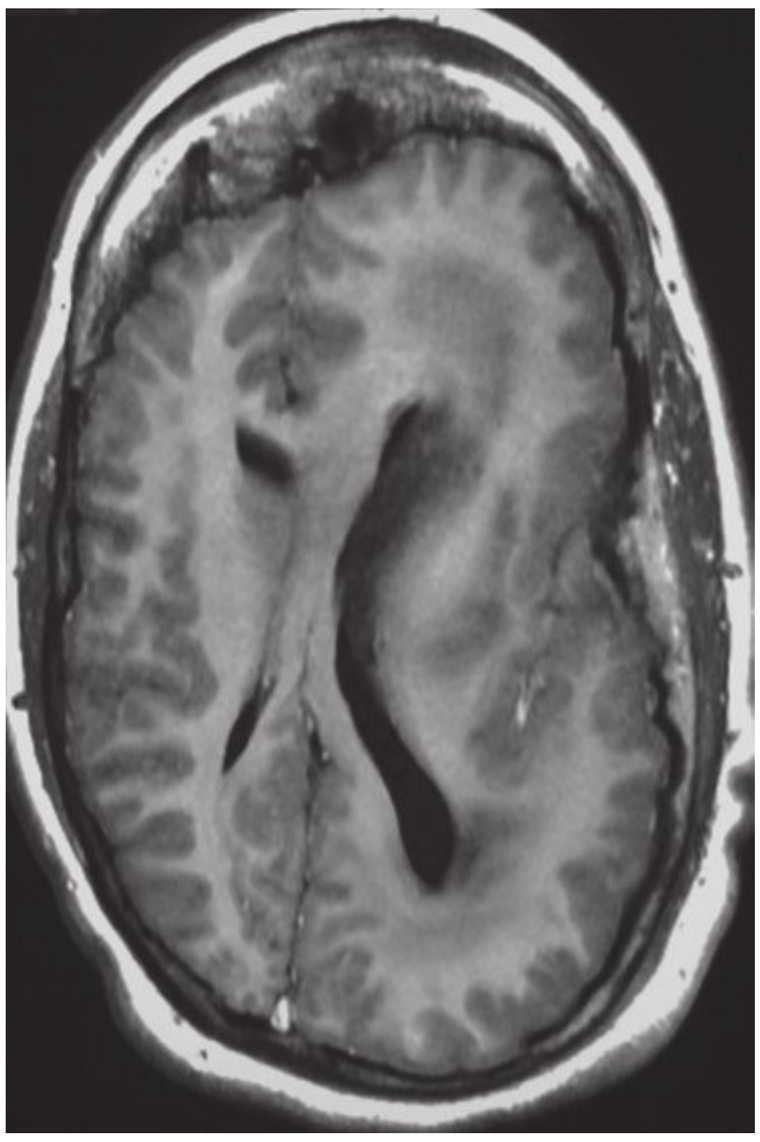

Fig. 2.53 Unilateral hemimegalencephaly. Axial T1-weighted imaging shows enlarged left cerebral hemisphere with cortical dysplasia and asymmetrically enlarged left lateral ventricle.

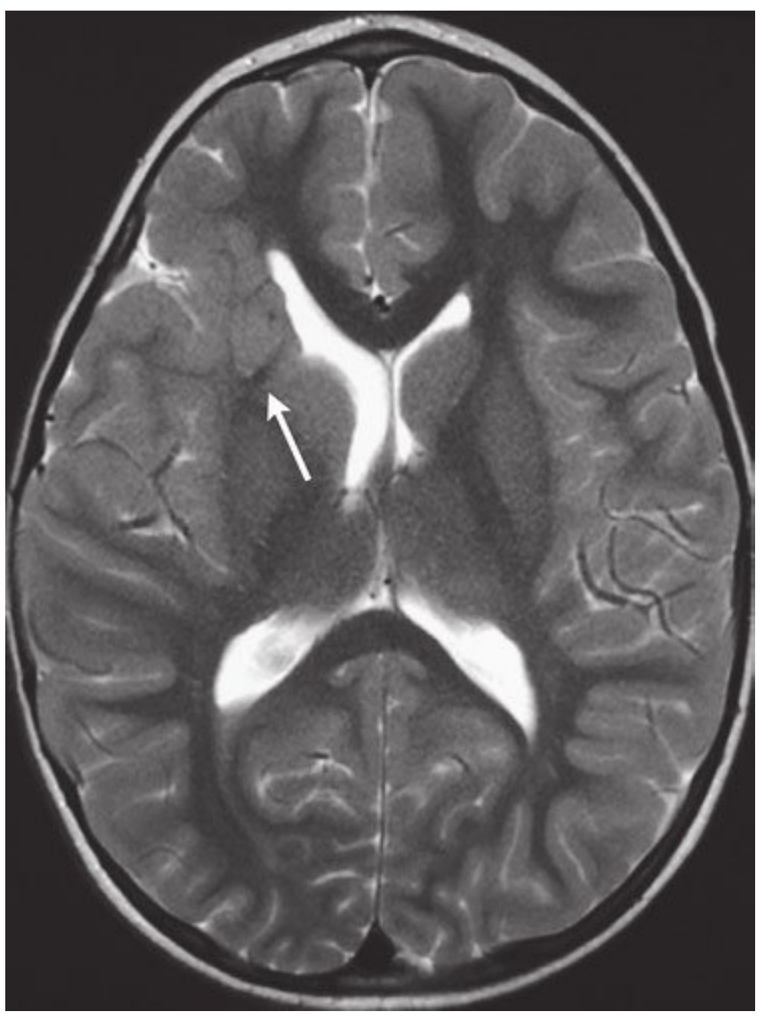

Fig. 2.54 Cortical dysplasia with localized polymicrogyria (arrow) involving the right frontal lobe on axial T2-weighted imaging and associated with deformity of the frontal horn of the right lateral ventricle.

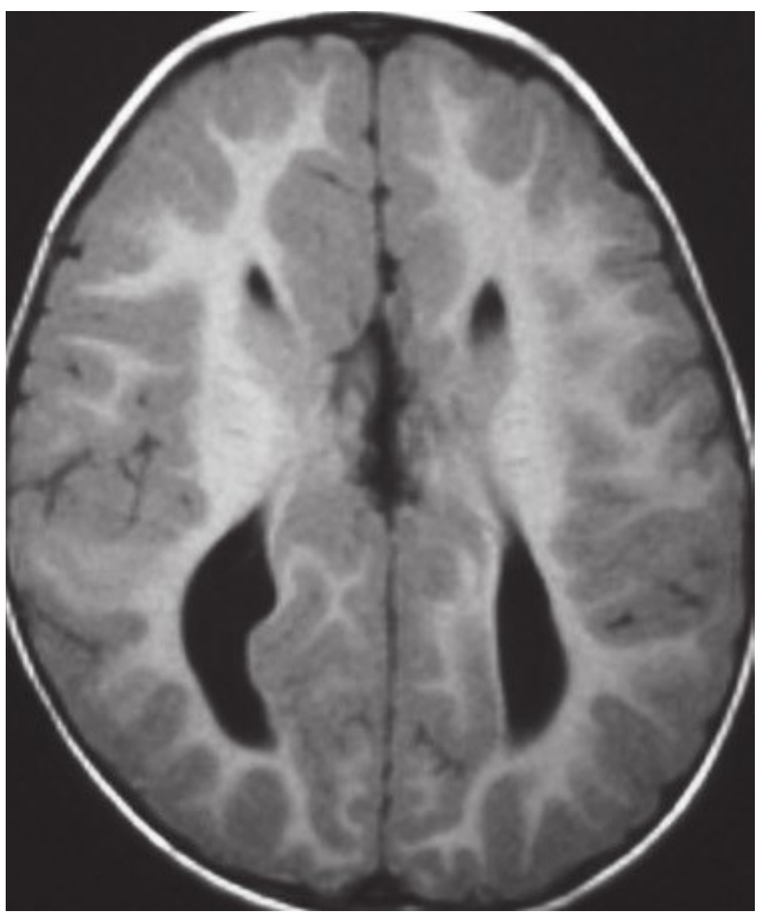

Fig. 2.55 Agenesis of the corpus callosum, with widely separated and parallel orientations of the frontal horns and bodies of lateral ventricles, as seen on axial T1-weighted imaging.

Table 2.6 (cont.) Abnormal or altered configuration of the ventricles

Lesions	Imaging Findings	Comments
Dandy-Walker malformation (**Fig. 2.56**)	Vermian aplasia or severe hypoplasia, communication of fourth ventricle with retrocerebellar cyst, enlarged posterior fossa, with high position of tentorium and transverse venous sinuses. Hydrocephalus common. Associated with other anomalies, such as dysgenesis of the corpus callosum, gray matter heterotopia, schizencephaly, holoprosencephaly, cephalocele, and others.	Abnormal formation of roof of fourth ventricle with absent or nearly incomplete formation of cerebellar vermis.
Vermian hypoplasia (also referred to as Dandy-Walker variant) (**Fig. 1.43**)	Mild vermian hypoplasia with communication of posteroinferior portion of the fourth ventricle with cisterna magna. No associated enlargement of the posterior cranial fossa.	Occasionally associated with hydrocephalus, dysgenesis of corpus callosum, gray matter heterotopia, and other anomalies.
Joubert syndrome (**Fig. 2.57**)	Small dysplastic vermis with midline cleft between apposing cerebellar hemispheres. Molar tooth axial appearance from small midbrain and thickened superior cerebellar peduncles.	Malformation with hypoplasia of vermis, dysplasia and heterotopia of cerebellar nuclei, lack of decussation of superior cerebellar peduncles, and near-complete absence of medullary pyramids. Clinical findings include ataxia, mental retardation, and abnormal eye movements.
Rhombencephalosynapsis (**Fig. 2.58**)	Dysmorphic cerebellum with no apparent separation of cerebellar hemispheres and aplasia or severe hypoplasia of vermis.	Malformation with fusion of cerebellar hemispheres, dentate nuclei, and superior cerebellar peduncles, as well as absent or hypoplastic vermis. Clinical findings include truncal ataxia, cerebral palsy, mental retardation, and seizures.
Porencephalic cyst (**Fig. 2.59**)	MRI: Irregular, relatively well-circumscribed zone with high signal on T2-weighted imaging and FLAIR, and low signal on T1-weighted imaging and diffusion-weighted imaging similar to CSF, surrounded by poorly defined thin zone of increased signal on FLAIR in adjacent brain tissue. No gadolinium contrast enhancement or peripheral edema. CT: Irregular, relatively well-circumscribed zone with low attenuation similar to CSF, surrounded by poorly defined thin zone of decreased attenuation in adjacent brain tissue. No contrast enhancement or peripheral edema.	Porencephalic cyst represents remote sites of brain injury (trauma, infarction, infection, hemorrhage) occurring in late second trimester with evolution by an encephaloclastic process into a cystic zone with CSF MRI signal characteristics surrounded by zones of gliosis in adjacent brain parenchyma. Gliosis (high T2 signal) allows differentiation from schizencephaly.

(continued on page 464)

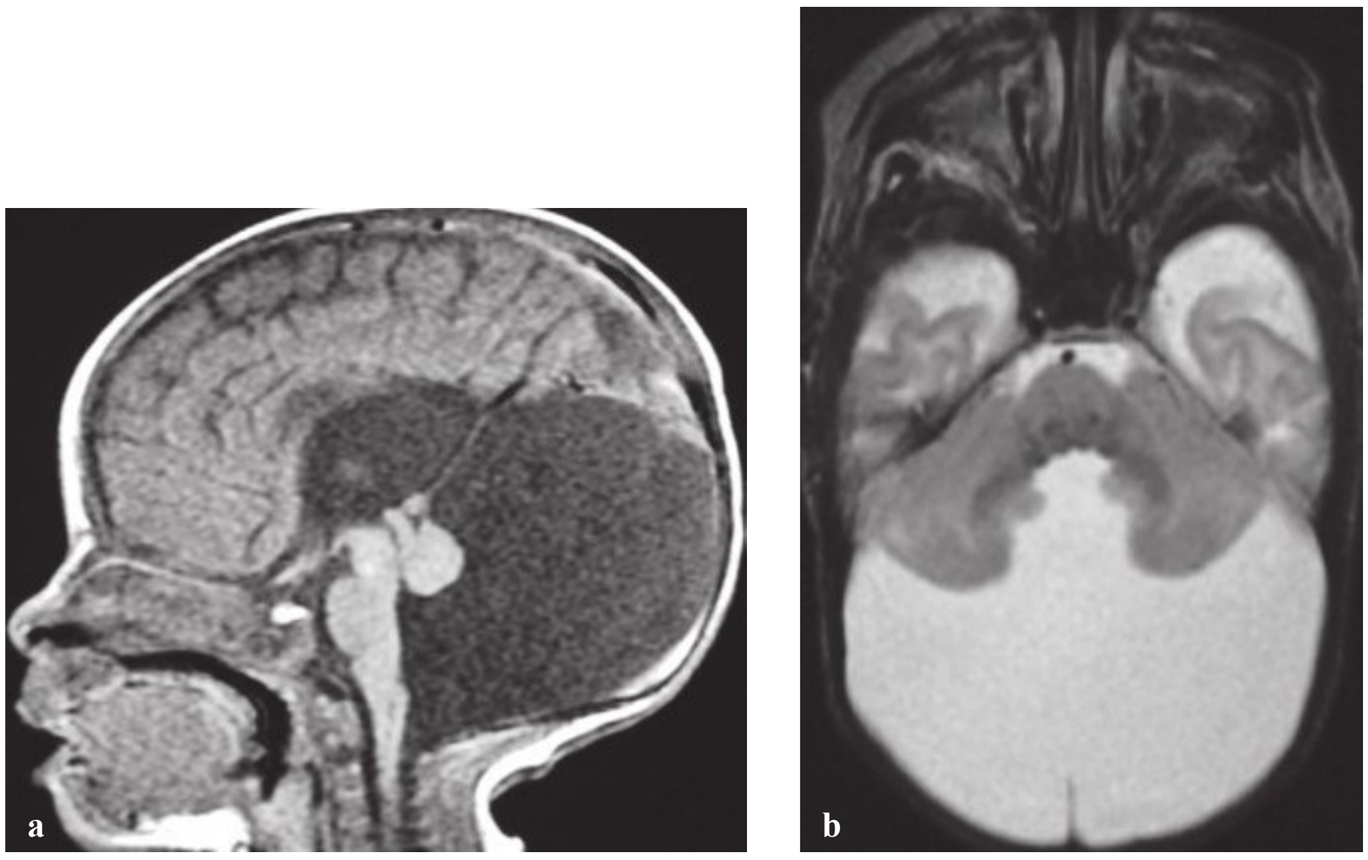

Fig. 2.56 Dandy-Walker malformation. Severe hypoplasia of the cerebellar vermis and mild hypoplasia of the cerebellar hemispheres, communication of fourth ventricle with retrocerebellar cyst, enlarged posterior fossa, high position of tentorium, and dysgenesis of the corpus callosum are seen on **(a)** sagittal T1-weighted imaging and **(b)** axial T2-weighted imaging.

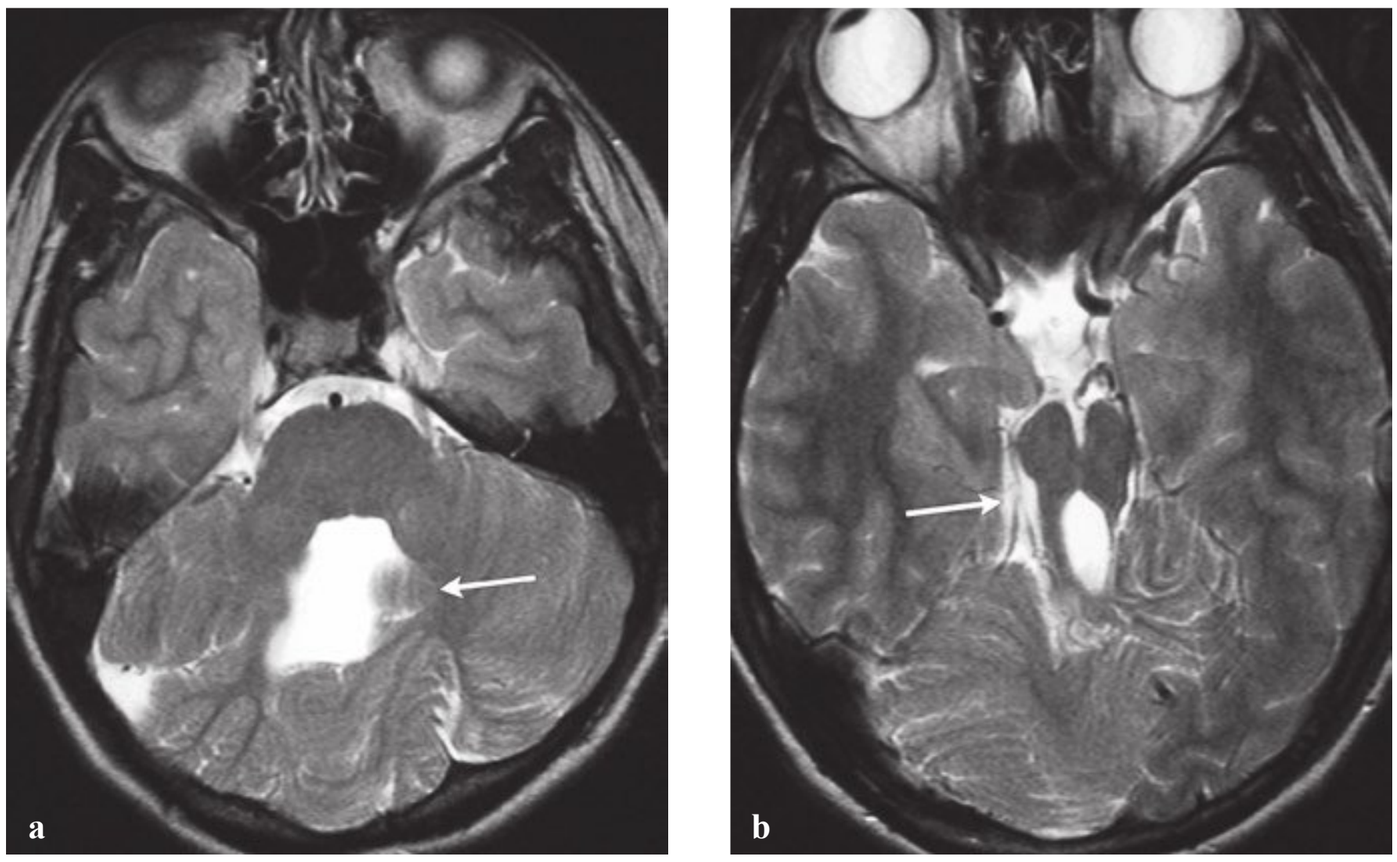

Fig. 2.57 Joubert syndrome. **(a,b)** Small dysplastic vermis with midline cleft between opposing cerebellar hemispheres, malformed fourth ventricle, molar tooth axial appearance from small midbrain and thickened superior cerebellar peduncles are seen on axial T2-weighted imaging (arrows).

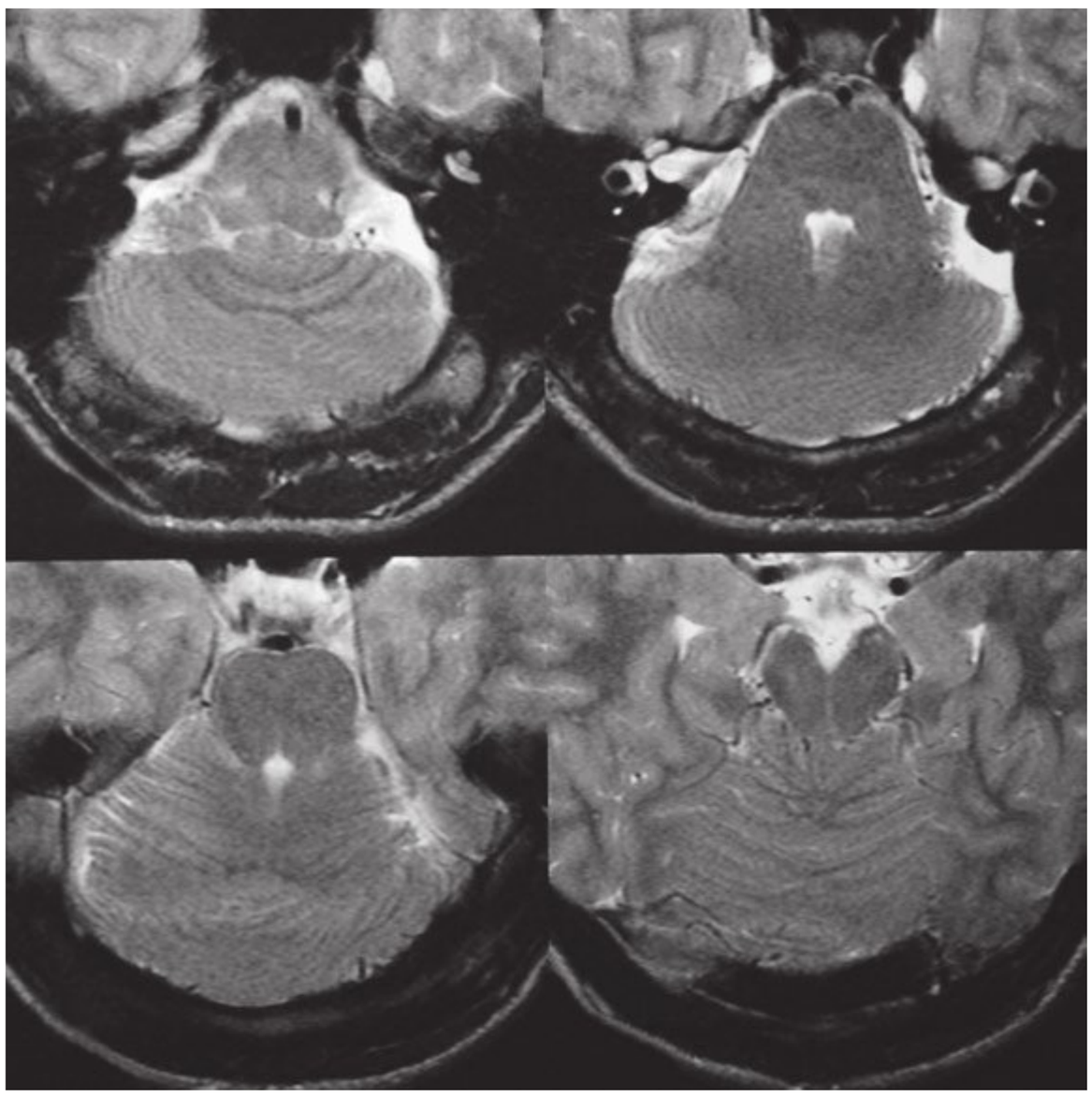

Fig. 2.58 Rhombencephalosynapsis. Axial T2-weighted imaging shows dysmorphic cerebellum lacking separation of cerebellar hemispheres and severe hypoplasia of the vermis.

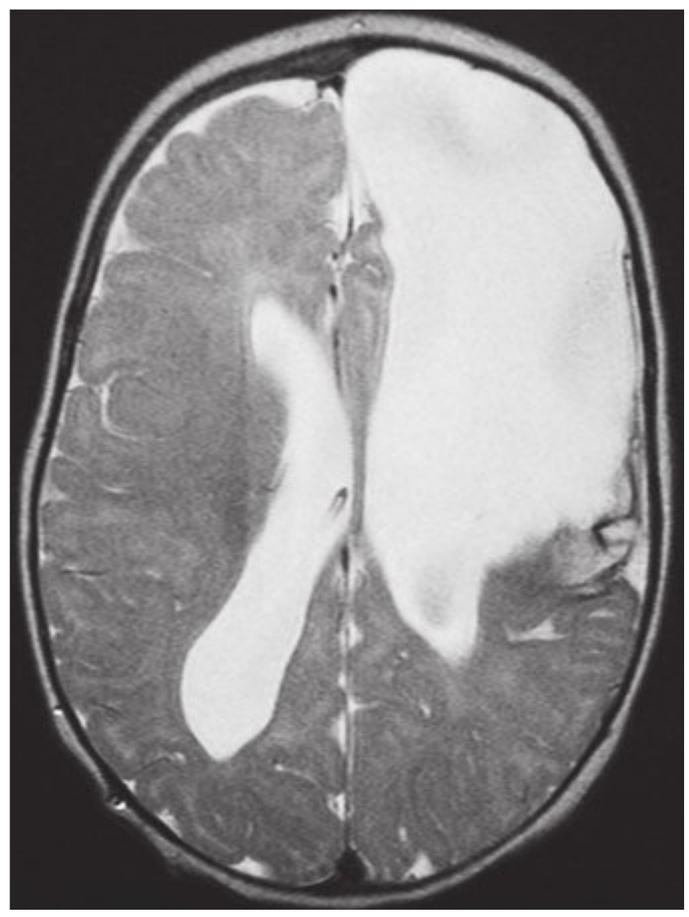

Fig. 2.59 Porencephalic cyst in an infant. Irregular, well-circumscribed, cystic zone with CSF signal communicating with the left lateral ventricle and that is surrounded by poorly defined thin zone of increased signal in adjacent brain tissue, representing gliosis, on axial T2-weighted imaging.

Table 2.6 (cont.) Abnormal or altered configuration of the ventricles

Lesions	Imaging Findings	Comments
Hamartoma–tuberous sclerosis (**Fig. 2.60**)	Subependymal hamartomas: Small nodules located along and projecting into the lateral ventricles, with signal on T1- and T2-weighted imaging similar to cortical tubers. Calcification and gadolinium contrast enhancement common.	Cortical and subependymal hamartomas are nonmalignant lesions associated with tuberous sclerosis. Tuberous sclerosis is an autosomal dominant disorder associated with hamartomas in multiple organs. Caused by mutations of TSC1 gene on 9q or the TSC2 gene on 16p. Prevalence is 1 in 6,000 newborns.
Cavum septum pellucidum/ cavum vergae (**Fig. 2.61** and **Fig. 2.62**)	Cavum septum pellucidum: CSF-containing zone between the anterior portions of the two septal leaves. Cavum vergae: Same as cavum septum pellucidum, with posterior extension of fluid-containing zone between septal leaves.	Developmental anomaly with lack of normal fusion of the two septal leaves, occurs in 3%of normal adults and has no clinical significance. Midline fusion of the posterior portions of the septal leaves usually occurs at 6 months of gestation, and fusion of the anterior portion from 3 to 6 months after birth in 85%
Cavum velum interpositum (**Fig. 2.63**)	Triangular, wedge-shaped zone with MRI signal and CT attenuation equivalent to CSF located between the bodies of the lateral ventricles posteriorly, inferior to the fused columns of the fornix, and superior to the choroid at the roof of the third ventricle. The internal cerebral veins are displaced inferiorly and laterally.	Developmental variant secondary to dilation of the potential CSF space between infolded tela choroidea at the roof of the third ventricle during fetal brain development. Results in anterior extension of the quadrigeminal plate cistern superior to the pineal gland.

(continued on page 466)

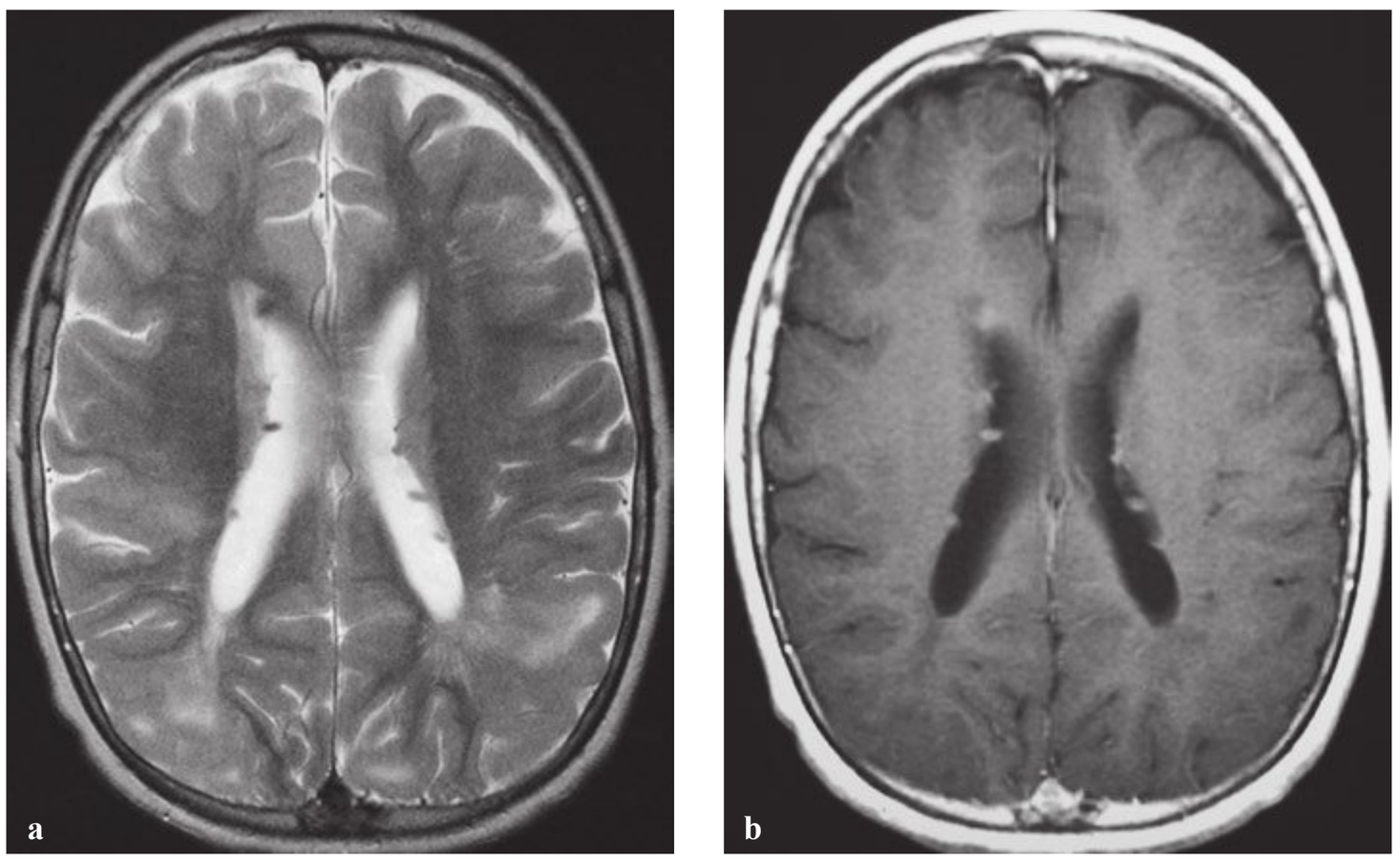

Fig. 2.60 Ependymal hamartomas in a young patient with tuberous sclerosis. Small nodules located along and projecting into the lateral ventricles **(a)** have low or intermediate signal on axial T2-weighted imaging and **(b)** show gadolinium contrast enhancement on axial T1-weighted imaging.

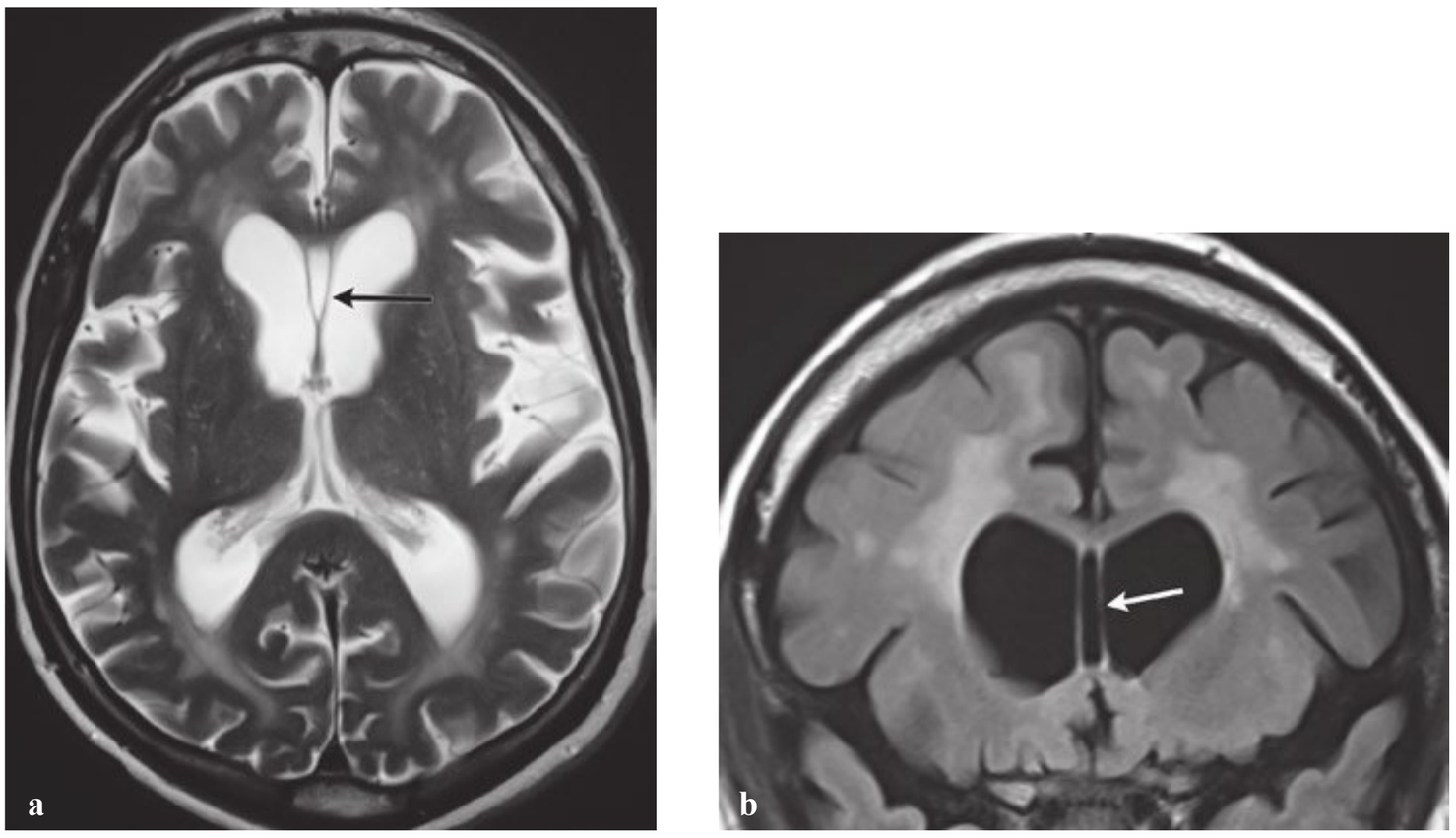

Fig. 2.61 **(a)** Axial T2-weighted imaging (arrow) and **(b)** coronal FLAIR (arrow) show a CSF-containing zone between the anterior portions of the two septal leaves.

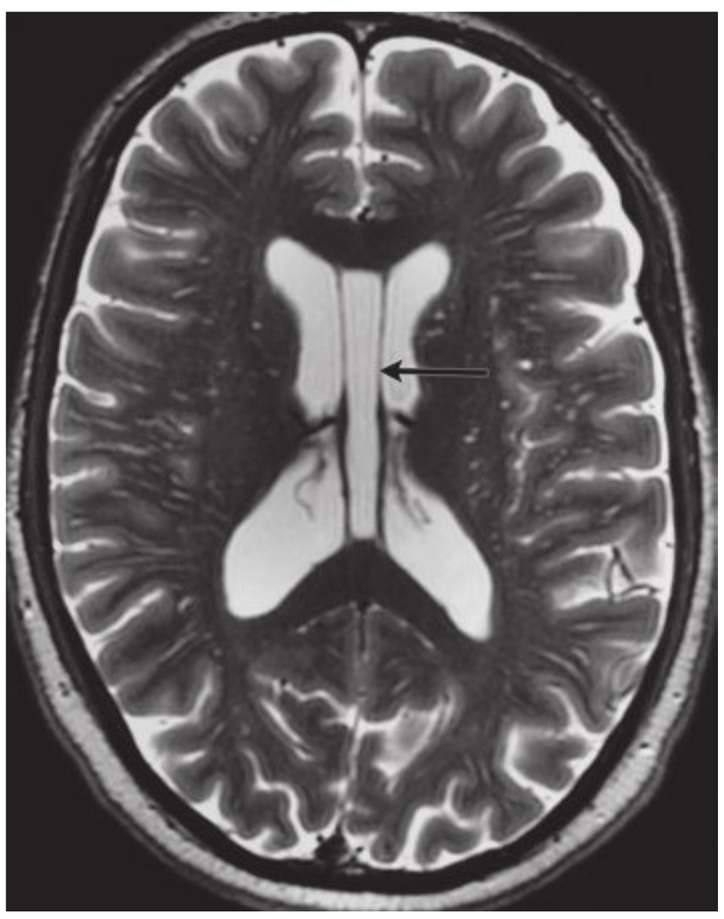

Fig. 2.62 Axial T2-weighted imaging shows a CSF zone between the two septal leaves that extends the entire anteroposterior length of the septum pellucidum (arrow).

Fig. 2.63 Cavum velum interpositum. A triangular wedge-shaped zone with MRI signal equivalent to CSF is seen **(a)** inferior to the fused columns of the fornix and superior to the choroid at the roof of the third ventricle on sagittal T1-weighted imaging (arrow) and **(b)** between the bodies of the lateral ventricles posteriorly on axial T2-weighted imaging (arrows).

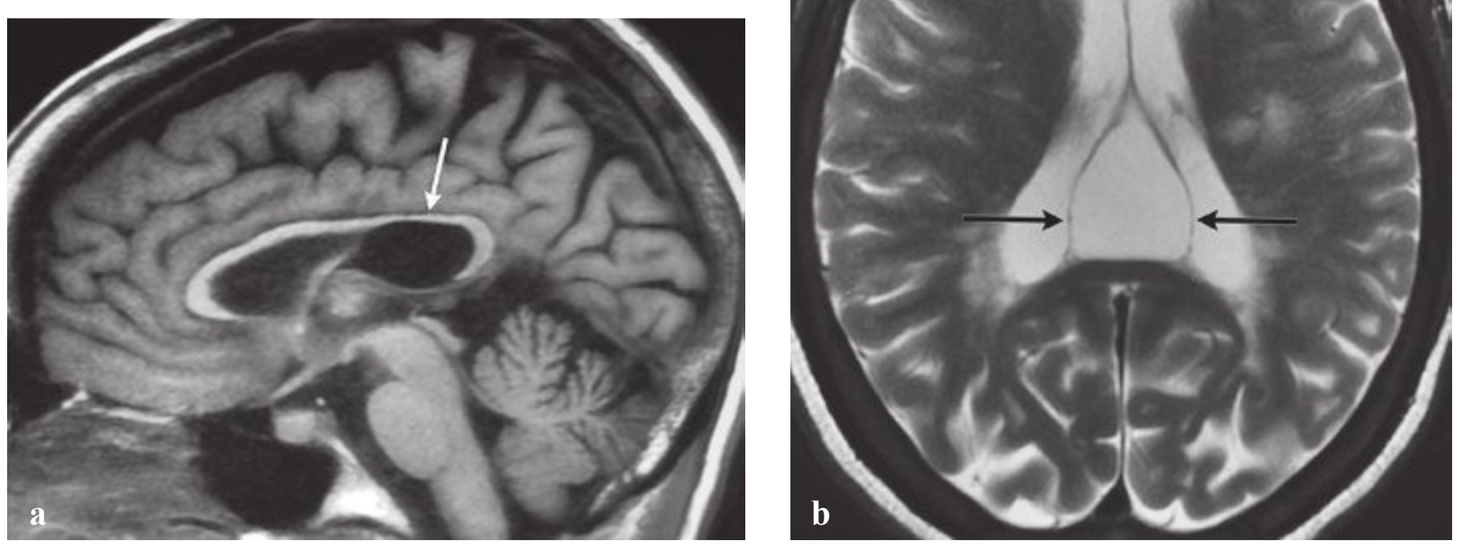

Table 2.6 (cont.) Abnormal or altered configuration of the ventricles

Lesions	Imaging Findings	Comments
Acquired Disorders		
Subfalcine herniation (**Fig. 2.64**)	Compression and shift of the lateral and third ventricles under the falx cerebri to the other side, ± dilatation of contralateral lateral ventricle because of CSF outflow obstruction from compression at contralateral foramen of Monro, ± displacement of ipsilateral anterior cerebral artery and subependymal veins.	Most often occurs from primary or metastatic intra-axial tumor or hemorrhage.
Transtentorial herniation (**Fig. 2.65**)	Ascending type: Upward herniation of cerebellar vermis and hemispheres through the tentorial incisura, resulting in compression and displacement of the cerebral aqueduct and posterior portion of the third ventricle, effacement of superior vermian cistern, compression and anterior displacement of the fourth ventricle, ± obstructive hydrocephalus. Descending type: Medial and inferior displacement of uncus and parahippocampal gyrus below the tentorium, progressive effacement of suprasellar cistern and basal cisterns, compression of ipsilateral portion of midbrain, which is displaced toward contralateral side, ± Kernohan's notch, ± Duret hemorrhage, ± inferior displacement and/or compression of anterior choroidal, posterior communicating, and posterior cerebral arteries, as well as perforating branches of the basilar artery, resulting in cerebral, cerebellar, and/or brainstem infarcts. Often results in death.	Descending type more common than ascending type. Typically results from a focal mass lesion or hemorrhage causing displacement of brain tissue across tentorium.

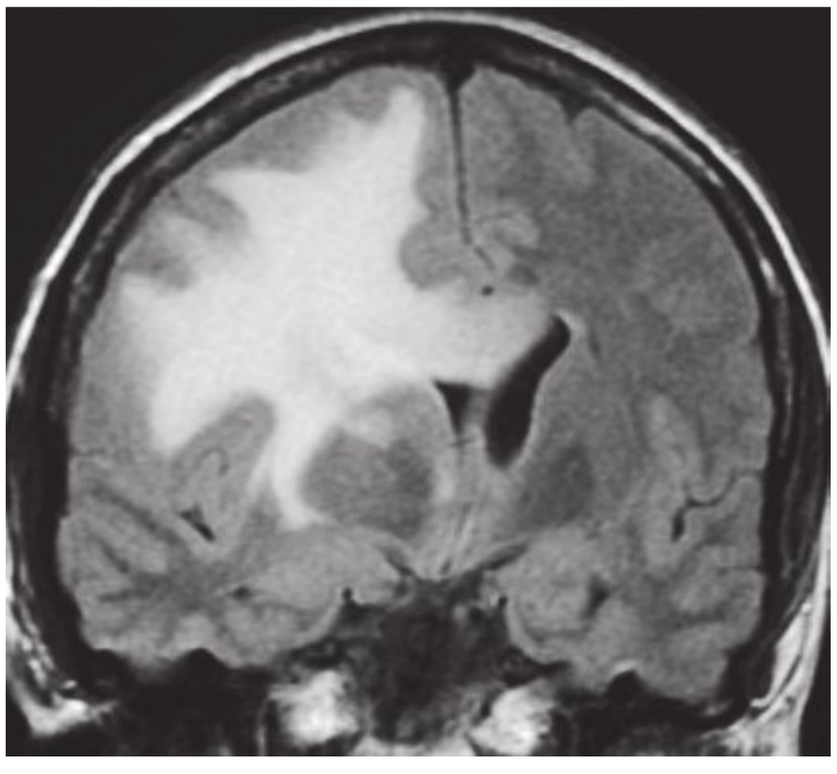

Fig. 2.64 Subfalcine herniation from an anaplastic astrocytoma. Abnormal high signal on coronal FLAIR is seen involving the right cerebral hemisphere with extension into the corpus callosum. Mass effect from the tumor causes compression and shift of the right lateral ventricle under the falx cerebri to the other side.

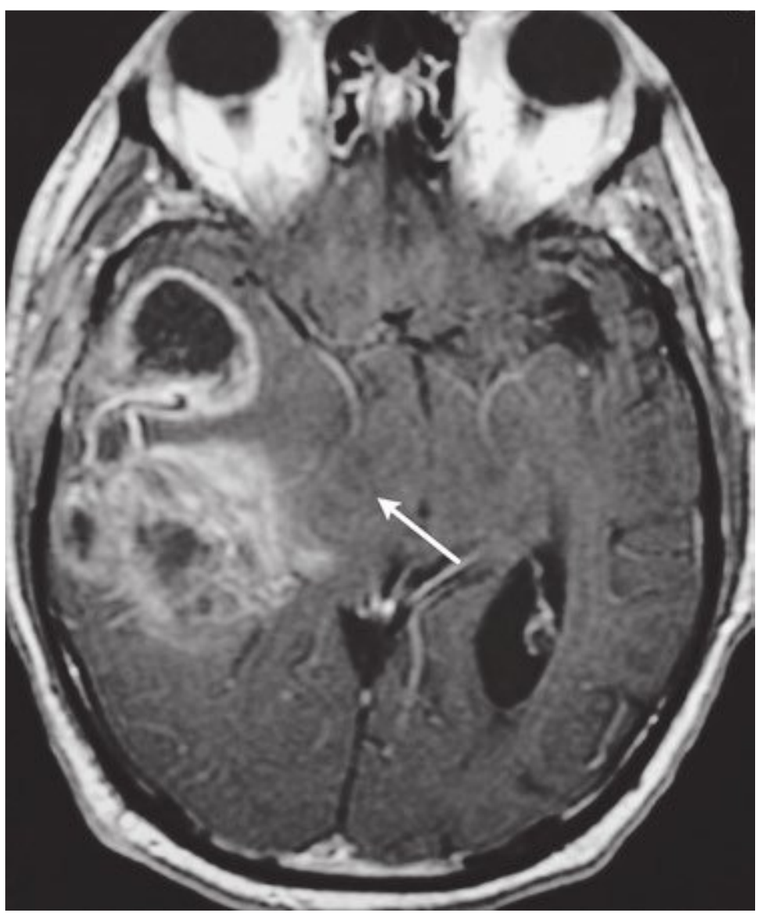

Fig. 2.65 Descending type of transtentorial herniation. Gadolinium-enhancing glioblastoma in the right temporal lobe as seen on axial T1-weighted imaging has mass effect effacing the temporal, atrial, and occipital portions of the right lateral ventricle and basal cisterns. The tumor is associated with enlargement of the right uncus (arrow), which causes compression and clockwise rotation of the midbrain, which is also displaced leftward.

Table 2.7 Solitary intraventricular lesions in children

- Neoplasms
  - Pilocytic astrocytoma
  - Diffuse astrocytoma
  - Subependymal giant cell astrocytoma
  - Anaplastic astrocytoma
  - Glioblastoma multiforme
  - Medulloblastoma (PNET)
  - Atypical teratoid/ rhabdoid tumors
  - Ependymoma
  - Metastatic tumor
  - Hemangioblastoma
  - Choroid plexus papilloma
  - Atypical choroid plexus papilloma
  - Choroid plexus carcinoma
  - Central neurocytoma
  - Craniopharyngioma
  - Germ cell tumors
  - Pineoblastoma
  - Hypothalamic hamartoma
  - Meningioma
- Tumorlike Lesions
  - Ependymal cyst
  - Choroid plexus cyst
  - Hemorrhage
- Vascular Abnormality
  - Arteriovenous malformation (AVM)
  - Vein of Galen malformation/aneurysm
  - Cavernous malformation
  - Sturge-Weber syndrome
- Infection
  - Ventriculitis
  - Parasitic infection/cysticercosis
- Inflammation
  - Langerhans' cell histiocytosis

Table 2.7 Solitary intraventricular lesions in children

Lesions	Imaging Findings	Comments
Neoplasms		
Pilocytic astrocytoma (**Fig. 2.66**)	MRI: Solid/cystic focal lesion with low-intermediate signal on T1-weighted imaging, high signal on T2-weighted imaging and FLAIR, usually showing gadolinium contrast enhancement. Large cyst with enhancing mural nodule seen in 46%. Lesions commonly located in cerebellum, hypothalamus, optic chiasm, adjacent to third or fourth ventricles, and brainstem. Thirty percent can have more aggressive MRI features, such as inhomogeneous gadolinium contrast enhancement, central necrotic zones, and irregular margins. Diffusion-weighted imaging: Usually no evidence of restricted diffusion. Diffusion tensor imaging can show tumor displacement of cortical spinal tracts. Magnetic resonance spectroscopy: With these low-grade tumors, a paradoxical pattern associated with more aggressive tumors (elevated choline/N-acetylaspartate and lactate levels) may be seen. CT: Solid/cystic focal lesion with low-intermediate attenuation, usually with prominent contrast enhancement.	Pilocytic astrocytoma is the most common glioma in children and accounts for 6% of all gliomas and 30% of all posterior fossa neoplasms in children. Slow-growing cystic-solid WHO grade I astrocytoma with biphasic pattern of compacted bipolar cells, Rosenthal fibers, multipolar cells, microcysts, and eosinophilic granular bodies. Associated with BRAF mutations involving the MAPK signaling pathway. Usually lack IDH mutations. Immunoreactive to glial fibrillary acidic protein (GFAP) and apolipoprotein D. Can occur in cerebrum, cerebellum, brainstem, and optic chiasm. In children, 67% occur in the cerebellum and usually have a favorable prognosis if totally resected. Increased occurrence in patients with neurofibromatosis type 1. Leptomeningeal tumor dissemination is rare (< 3%).
Diffuse astrocytoma (**Fig. 2.67**)	MRI: Intra-axial lesion with slightly ill-defined margins or diffuse mass lesion in white matter or brainstem with low-intermediate signal on T1-weighted imaging, high signal on T2-weighted imaging, ± mild gadolinium contrast enhancement. Minimal associated mass effect. Diffusion-weighted imaging: Tumors typically do not show restricted diffusion. CT: Focal or diffuse mass lesion usually located in white matter or brainstem with low-intermediate attenuation, ± mild contrast enhancement. Minimal associated mass effect.	Low-grade astrocytoma (WHO grade II) that accounts for 10 to 15% of astrocytic brain tumors. Often occurs in children and adults (20–40 years old). Can also occur in children and older adults. Brainstem gliomas usually occur in children less than 10 years old. Tumors are comprised of well-differentiated fibrillary or gemistocytic neoplastic astrocytes. Can occur in the cerebellum or brainstem. Association with TP53, isocitrate dehydogenase-IDH1 and IDH2, and telomere maintenance protein-ATRX mutations. Mean survival is 6–8 years, and tumors may undergo malignant progression to anaplastic astrocytoma or glioblastoma. Patients with neurofibromatosis type 1 have an increased incidence of brainstem gliomas involving the medulla. Tumors with IDH mutations have a better prognosis than those without.
Subependymal giant cell astrocytoma (**Fig. 2.68**)	MRI: Circumscribed lesion located near the foramen of Monro with mixed low-intermediate signal on T1-weighted imaging and mixed high signal on T2-weighted imaging, ± cysts and/or calcifications, + heterogeneous gadolinium contrast enhancement. Diffusion-weighted imaging: Subependymal giant cell astrocytomas usually do not have restricted diffusion. Magnetic resonance spectroscopy: Subependymal giant cell astrocytomas can have elevated choline and reduced N-acetylaspartate (NAA). CT: Circumscribed lesion with mixed low-intermediate attenuation, ± cysts and/or calcifications, + heterogeneous contrast enhancement.	Subependymal giant cell astrocytoma near foramen of Monro occurs in 6 to 18% of patients with tuberous sclerosis, and patients usually are younger than 20 years (mean age = 11 years). Slow-growing lesions composed of neoplastic astrocytes of varying sizes, with nuclear pleomorphism and low Ki-67/MIB-1 ranging from 1.5 to 7.4% Immunoreactive to glial fibrillary acidic protein (GFAP), S-100 protein, neurofilament proteins, and class III b-tubulin. Enlarging lesions can progressively cause obstruction of CSF flow through the foramen of Monro. Autosomal dominant mutations involving TSC1 gene on chromosome 9q34 and TSC2 gene on chromosome 16p13.3. Prevalence of tuberous sclerosis = 1/6,000 newborns. Long-term survival is usual if tumor is resected.

(continued on page 470)

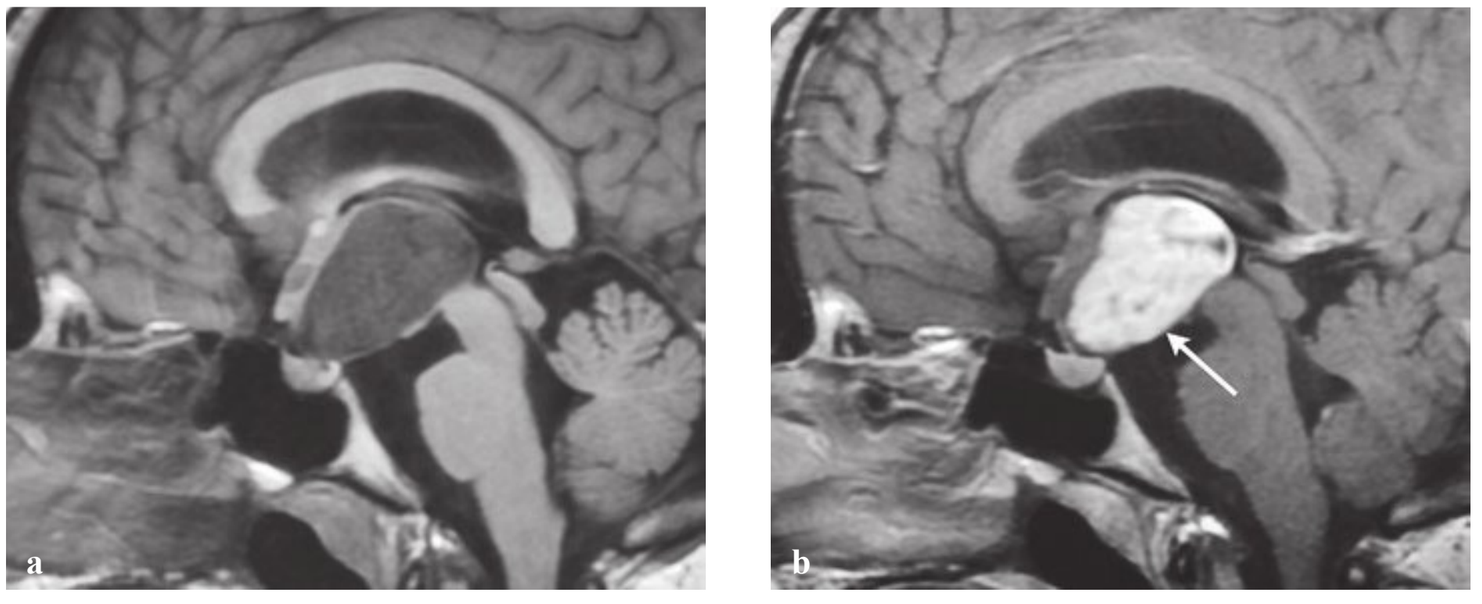

Fig. 2.66 A 1-year-old female with a pilocytic astrocytoma involving the hypothalamus and that extends superiorly into the third ventricle. The tumor **(a)** has low-intermediate signal on sagittal T1-weighted imaging and **(b)** shows prominent gadolinium contrast enhancement (arrow) on sagittal T1-weighted imaging.

Fig. 2.67 A 5-year-old boy with diffuse astrocytoma arising from the vermis and extending into the fourth ventricle and causing obstructive hydrocephalus. The tumor has **(a)** low-intermediate signal on sagittal T1-weighted imaging (arrow) and **(b)** heterogeneous high signal on axial T2-weighted imaging and **(c)** shows gadolinium contrast enhancement on axial T1-weighted imaging.

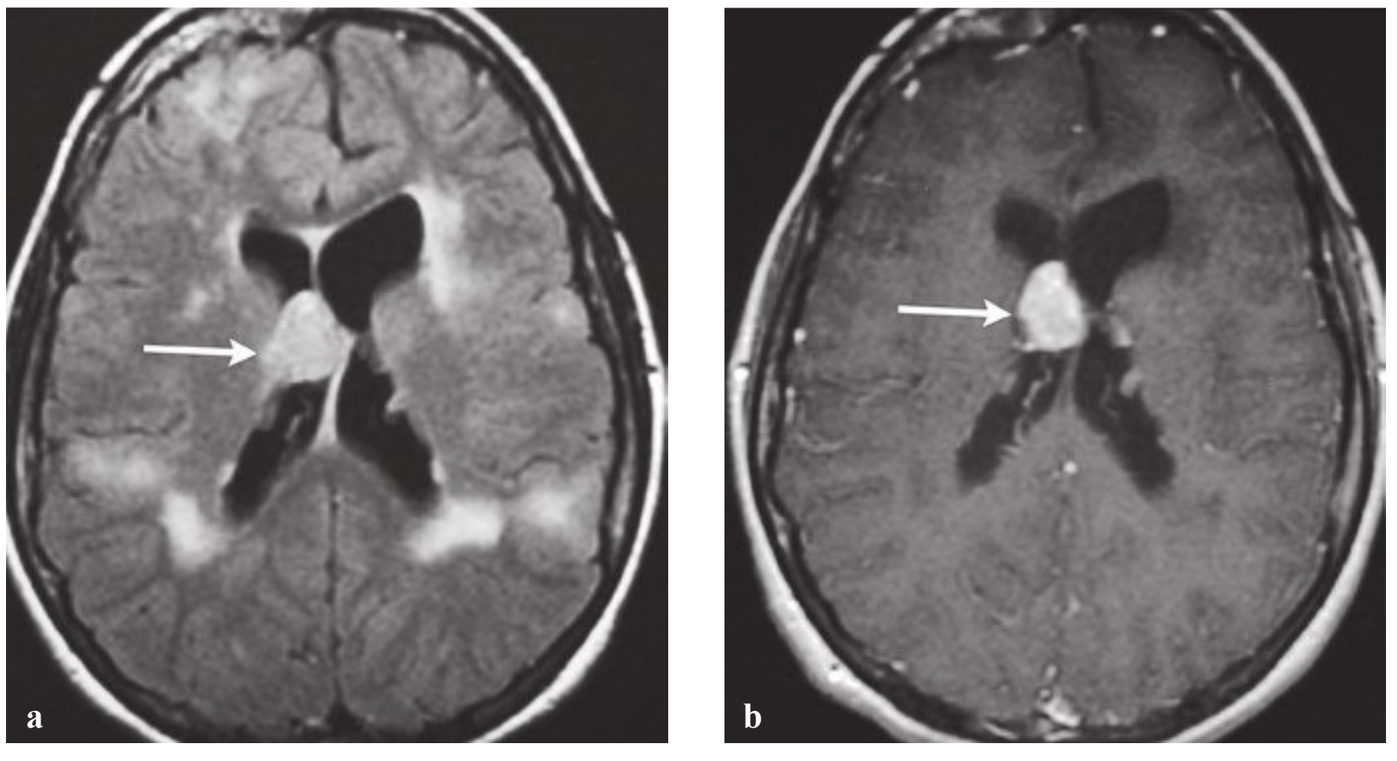

Fig. 2.68 An 18-year-old woman with tuberous sclerosis. A subependymal giant cell astrocytoma is seen at the right foramen of Monro that **(a)** has high signal on axial FLAIR (arrow) and **(b)** shows gadolinium contrast enhancement on axial T1-weighted imaging (arrow). Also seen are cortical tubers, peri-atrial white matter signal abnormalities, and ependymal hamartomas on axial FLAIR. The ependymal hamartomas also show gadolinium contrast enhancement on axial T1-weighted imaging.

Table 2.7 (cont.) Solitary intraventricular lesions in children

Lesions	Imaging Findings	Comments
Anaplastic astrocytoma (**Fig. 2.69**)	MRI: Often irregularly marginated lesion located in white matter with low-intermediate signal on T1-weighted imaging, high signal on T2-weighted imaging, ± gadolinium contrast enhancement. Tumors can have elevated relative cerebral blood volume (rCBV). Diffusion-weighted imaging: Tumors typically do not show restricted diffusion. Magnetic resonance spectroscopy shows decreased N-acetylaspartate (NAA) and high levels of choline. CT: Irregularly marginated mass lesion with mixed low and intermediate attenuation, ± hemorrhage, prominent heterogeneous contrast enhancement, and peripheral edema. Can cross corpus callosum.	Malignant astrocytic tumor (WHO grade III) between diffuse astrocytoma and glioblastoma multiforme. Malignant astrocytes have nuclear atypia and mitotic activity. Ki-67/MIB-1 ranges from 5 to 10% More common in adults than in children. Can progress to glioblastoma. Approximate 2-year survival. Promotor methylation inactivates the effects of the DNA repair enzyme MGMT enabling improved tumor response to alkylating chemotherapy agents. Patients with IDH mutations as well as those who have MGMT promotor methylation have improved responses to chemotherapy.
Glioblastoma multiforme (**Fig. 2.70**)	MRI: Irregularly and poorly marginated mass lesion with necrosis or cyst, mixed signal on T1-weighted imaging, heterogeneous high signal on T2-weighted imaging, ± hemorrhage, and prominent heterogeneous gadolinium contrast enhancement. Increased relative cerebral blood volume (rCBV) is asssociated with high-grade gliomas from tumor-induced angiogenesis. Other findings include peripheral edema and tumor extension across the corpus callosum. Diffusion-weighted imaging: Tumors typically do not show restricted diffusion. Magnetic resonance spectroscopy shows decreased N-acetylaspartate (NAA) and high levels of choline. CT: Irregularly marginated mass lesion with necrosis or cyst, mixed low and intermediate attenuation, ± hemorrhage, prominent heterogeneous contrast enhancement, and peripheral edema. Can cross corpus callosum.	Glioblastoma multiforme is the most common primary CNS tumor and accounts for 15%of intracranial tumors and up to 75%of astrocytic neoplasms, with an incidence of 3 per 100,000. Most patients are over 50 years old. Only 1%of these neoplasms occur in patients less than 20 years old. These highly malignant (WHO grade IV) astrocytic neoplasms have nuclear atypia with mitotic activity, cellular pleomorphism, necrosis, and microvascular proliferation and invasion. Ki-67/MIB-1 ranges from 15 to 20% Associated with mutations involving RTK/phosphatase– PTEN/PI3K signal pathway, TERT, and TP53 and Rb1 tumor suppressor genes. Promotor methylation resulting in inactivation of the MGMT DNA repair enzyme enables improved malignant tumor response to chemotherapy in patients lacking IDH mutations. The extent of lesion is underestimated by MRI and survival is often < 1 year. Patients with secondary type glioblastoma who have IDH mutations can have a better response to chemotherapy and prognosis than those without.
Medulloblastoma (PNET) (**Fig. 2.71**)	MRI: Circumscribed or invasive lesions involving the cerebellum, with low-intermediate signal on T1-weighted imaging, intermediate-high signal on T2-weighted imaging, ± cystic or necrotic zones. Variable gadolinium contrast enhancement, usually high relative cerebral blood volume (rCBV), ± gadolinium contrast enhancement in the leptomeninges and/or ventricles from tumor dissemination. Diffusion-weighted imaging: Solid portions can have restricted diffusion. Magnetic resonance sepctroscopy usually shows elevated choline, lipid, and taurine peaks and decreased N-acetylaspartate (NAA) levels. CT: Circumscribed or invasive lesions, with intermediate to slightly high attenuation, variable contrast enhancement, and frequent dissemination into the leptomeninges.	Highly malignant tumors (WHO grade IV) located in the cerebellum and that frequently disseminate along CSF pathways. Tumors are composed of poorly differentiated or undifferentiated cells with divergent differentiation along neuronal, astrocytic, or ependymal lines. Histologic subtypes include classic, desmoplastic, large cell (LC), anaplastic, and medulloblastoma with extensive nodularity. LC and anaplastic types have the worst prognoses. Typically occur in patients from 4 weeks to 20 years old (mean age = 5.5 years). Can also occur in adults.

(continued on page 472)

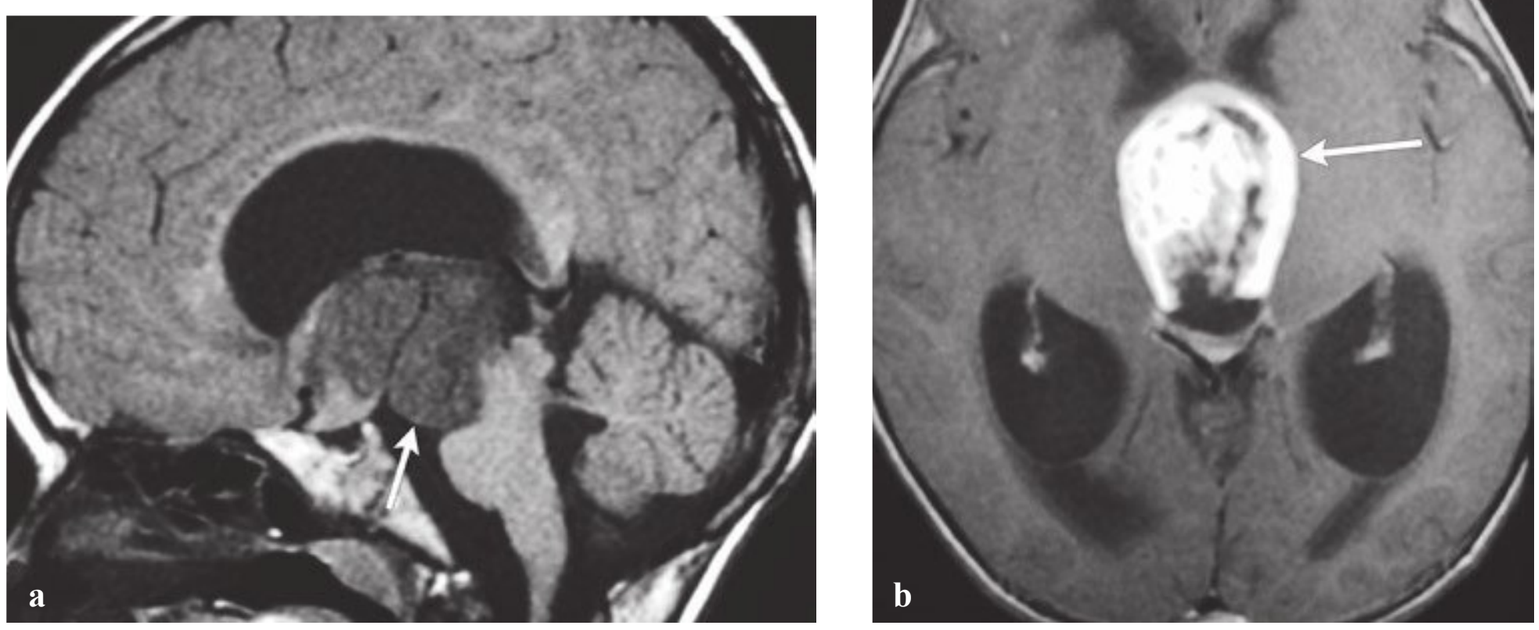

Fig. 2.69 A 2-year-old male with an anaplastic astrocytoma involving the hypothalamus that extends into the third ventricle, causing obstructive hydrocephalus. **(a)** The tumor has low-intermediate signal on sagittal T1-weighted imaging (arrow) and **(b)** shows heterogeneous prominent gadolinium contrast enhancement on axial T1-weighted imaging (arrow).

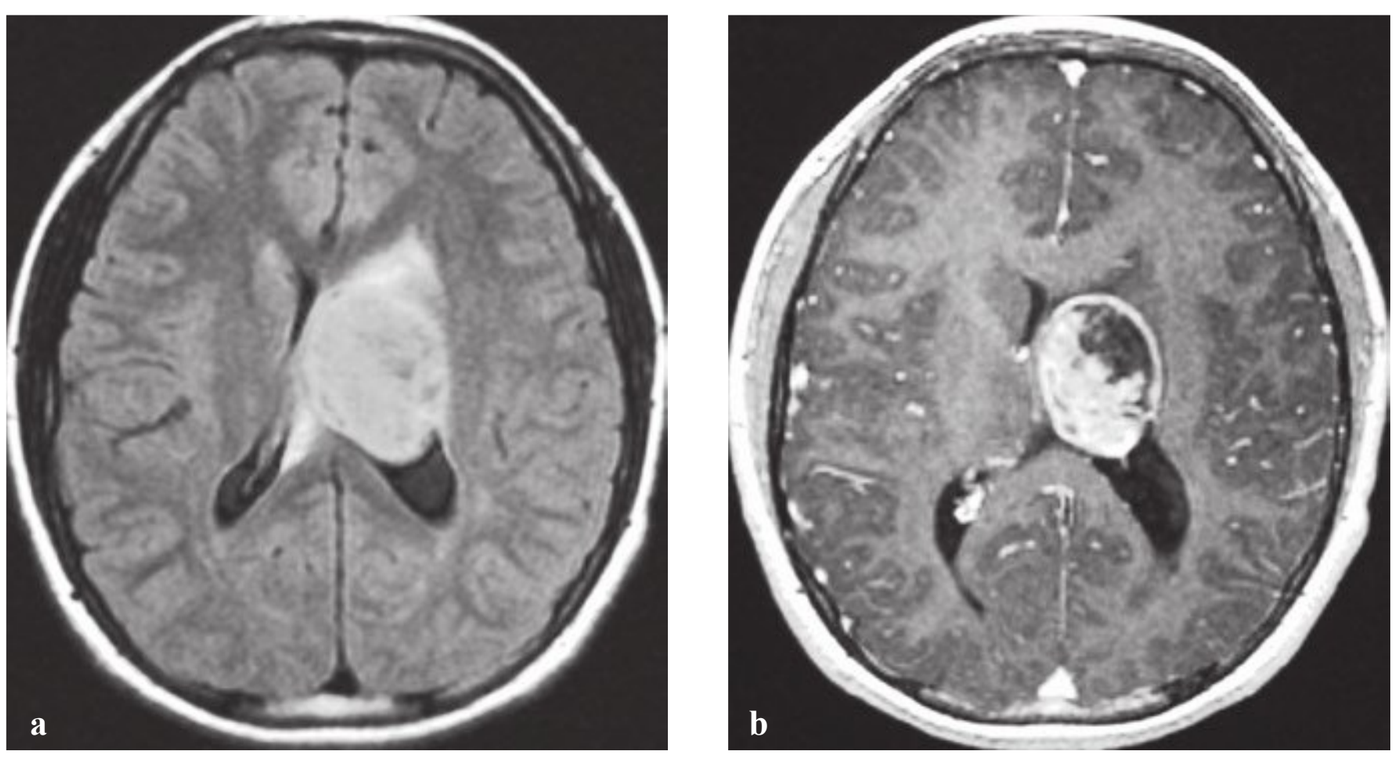

Fig. 2.70 A 13-year-old female with a glioblastoma multiforme extending into the left lateral ventricle that **(a)** has high signal on axial FLAIR and **(b)** shows heterogeneous gadolinium contrast enhancement on axial T1-weighted imaging.

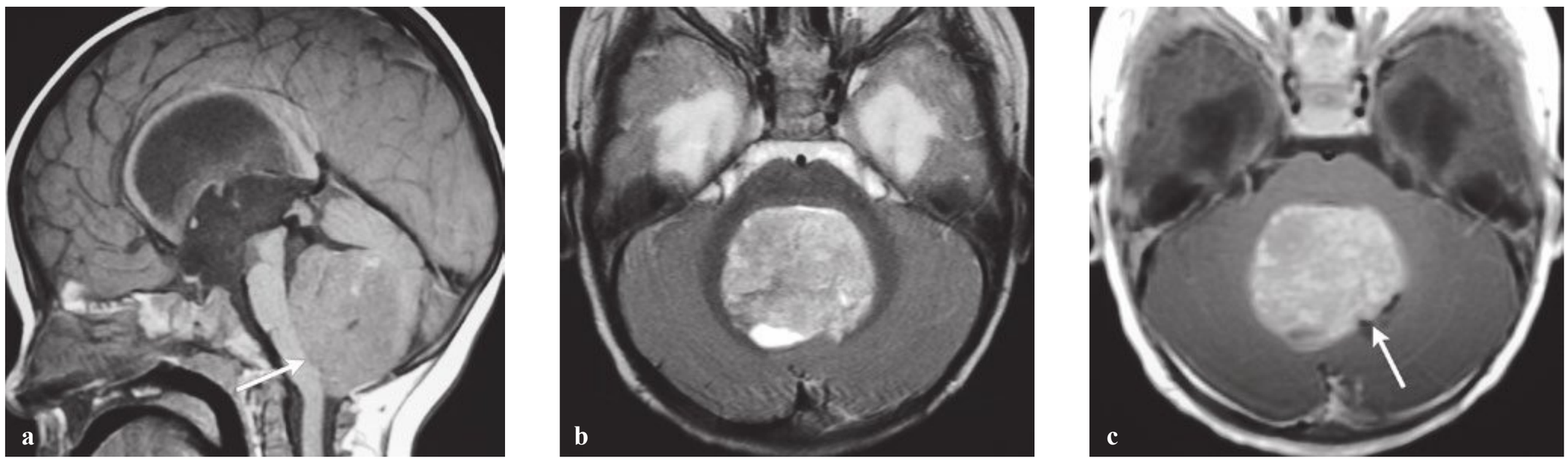

Fig. 2.71 A 5-year-old male with a medulloblastoma in the vermis extending into the fourth ventricle and causing obstructive hydrocephalus. The tumor has mostly intermediate signal as well as several small zones with high signal on **(a)** sagittal T1-weighted imaging (arrow) and heterogeneous slightly high and high signal on **(b)** axial T2-weighted imaging and shows gadolinium contrast enhancement on **(c)** axial T1-weighted imaging (arrow).

Table 2.7 (cont.) Solitary intraventricular lesions in children

Lesions	Imaging Findings	Comments
Atypical teratoid/ rhabdoid tumors (**Fig. 2.72** and **Fig. 2.73**)	MRI: Circumscribed or invasive mass lesions with intermediate signal on T1-weighted imaging, ± zones of high signal from hemorrhage on T1-weighted imaging; variable mixed low, intermediate, and/or high signal on T2-weighted imaging; solid portions can have restricted diffusion, usually prominent gadolinium contrast enhancement ± heterogeneous pattern. ± Gadolinium contrast enhancement in the leptomeninges and/or ventricles from tumor dissemination. Diffusion-weighted imaging: Solid portions can have restricted diffusion. Magnetic resonance spectroscopy usually shows elevated choline, lipid, and lactate peaks and decreased N-acetylaspartate (NAA) levels. CT: Circumscribed mass lesions with intermediate or mixed low and intermediate attenuation, ± zones of hemorrhage, cystic degeneration, and/or necrosis. Calcifications occasionally occur. Usually contrast enhancement ± heterogeneous pattern, ± contrast enhancement in the leptomeninges and/or ventricles from tumor dissemination.	Rare malignant tumors (WHO grade IV) involving the CNS usually occurring in the first decade, commonly in patients < 3 years old. Ki-67/MIB-1 is often high, > 50%. Associated with mutations of the INI1 (hSNF5/SMARCB1) gene on chromosome 22q11.2. Histologically appear as solid tumors ± necrotic areas, similar to malignant rhabdoid tumors of the kidney. Nearly all are intra-axial and can occur in supra- and/or infratentorial locations. Associated with a very poor prognosis.
Ependymoma (**Fig. 2.74**)	MRI: Circumscribed, lobulated, supratentorial lesion, often extraventricular, ± cysts, calcifications, and/or hemorrhage; low-intermediate signal on T1-weighted imaging, intermediate-high signal on T2-weighted imaging, variable gadolinium contrast enhancement. Tumors have elevated relative cerebral blood volume (rCBV) as well as delayed contrast retention secondary to intratumoral fenestrated blood vessels. Diffusion-weighted imaging: Usually there is no restricted diffusion. Magnetic resonance spectroscopy: Elevated choline and decreased N-acetylaspartate (NAA), similar to other neoplasms. CT: Circumscribed, lobulated, supratentorial lesion, often extraventricular, ± cysts and/or calcifications (up to 50%), low-intermediate attenuation, variable contrast enhancement.	Slow-growing tumor (WHO grade II) comprised of neoplastic cells with monomorphic round/oval nuclei containing speckled chromatin, perivascular pseudorosettes, and ependymal rosettes. Zones of myxoid degeneration, hyalinization of blood vessels, hemorrhage, and/or calcifications may occur within tumors. Ependymomas account for 6–12% of intracranial tumors, with an incidence of 0.22 to 0.29 per 100,000. Occur more commonly in children than in adults; one-third are supratentorial and two-thirds are infratentorial. Children with infratentorial ependymomas range in age from 2 months to 16 years (mean age = 6.4 years). Supratentorial ependymomas occur in children and adults. Immunoreactive to glial fibrillary acidic protein (GFAP), S-100, vimentin, and/or epithelial membrane antigen (EMA). Associated with neurofibromatosis type 2 and genetic mutations involving chromosomes 22, 9, 6, and 3. Survival is 57% at 5 years and 45% at 10 years.

(continued on page 474)

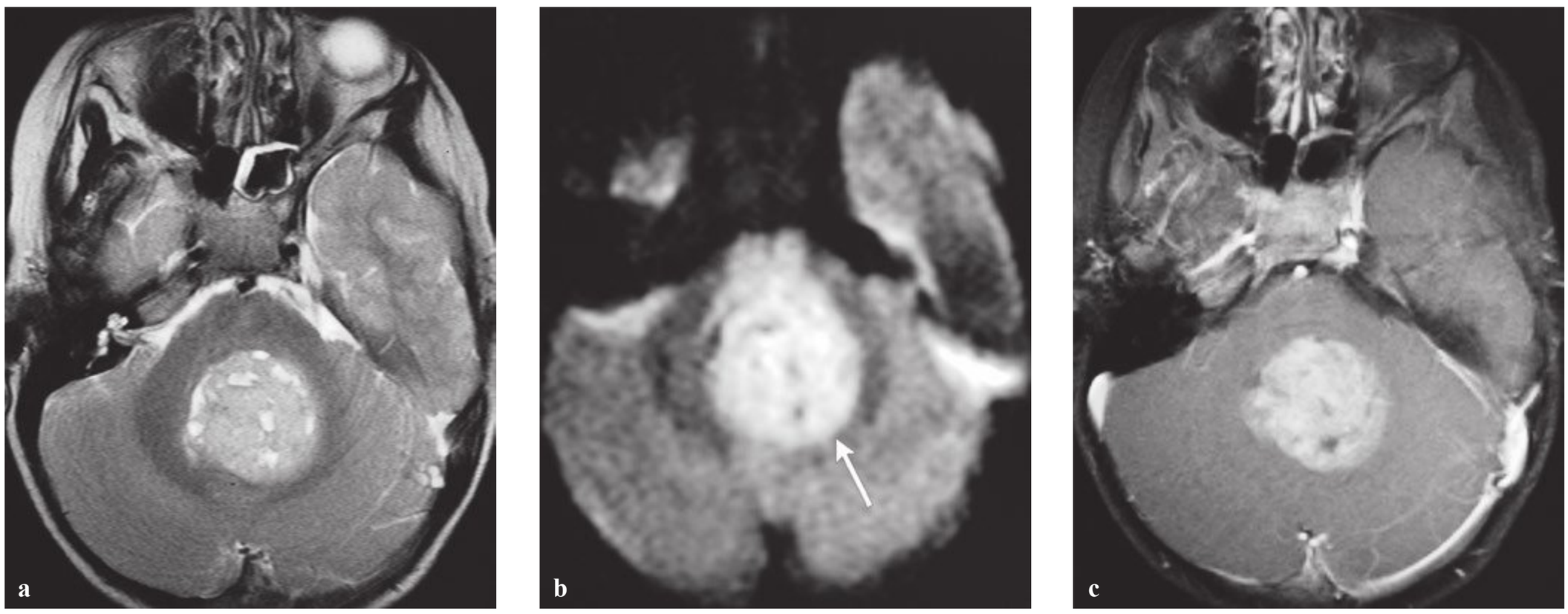

Fig. 2.72 A 4-year-old boy with an atypical teratoid/rhabdoid tumor involving the vermis and with extension into the fourth ventricle. The tumor has heterogeneous intermediate to slightly high signal on **(a)** axial T2-weighted imaging, restricted diffusion on **(b)** axial diffusion-weighted imaging (arrow), and shows gadolinium contrast enhancement on **(c)** axial FS T1-weighted imaging.

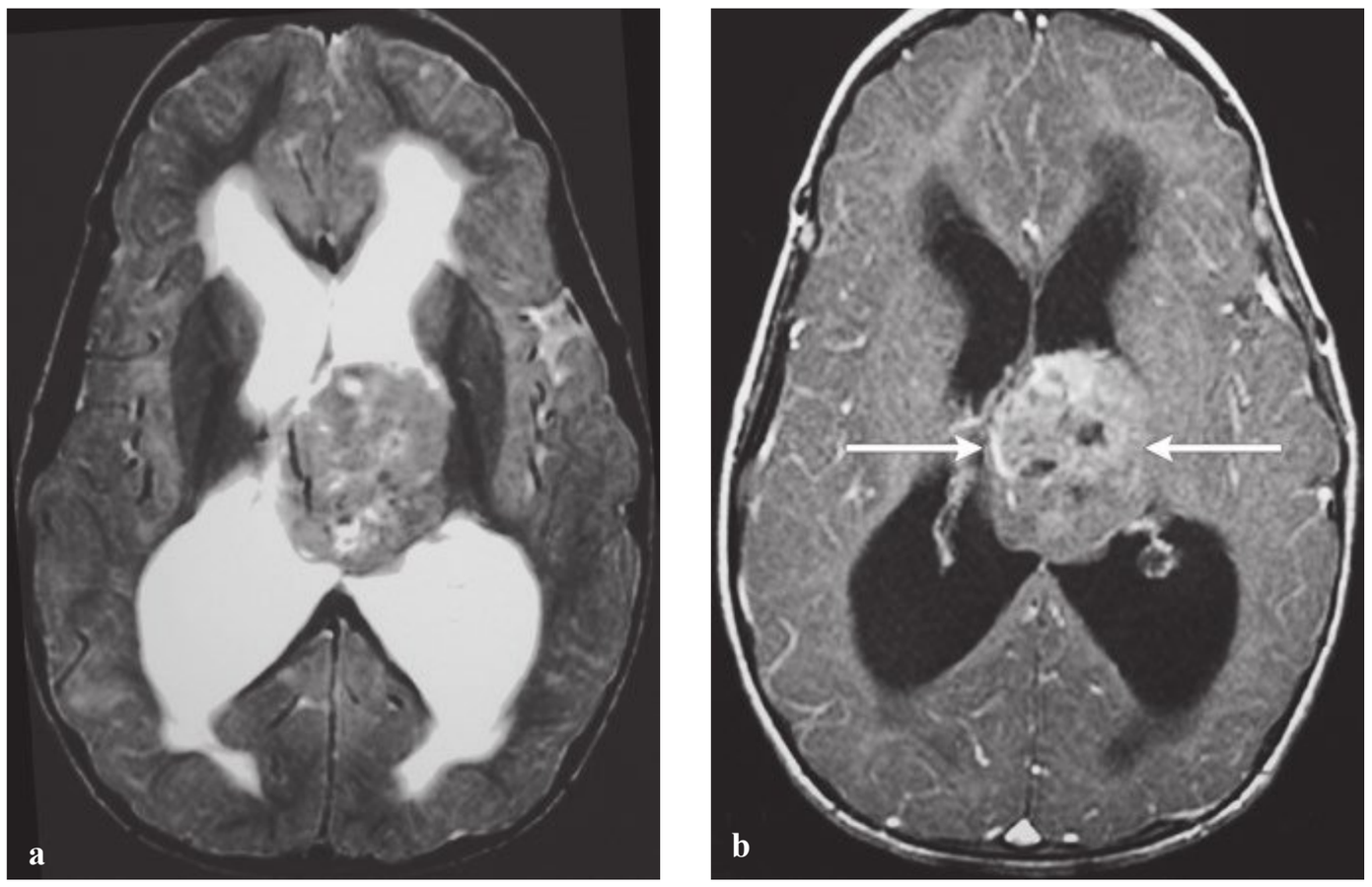

Fig. 2.73 A 4-year-old girl with an atypical teratoid/rhabdoid tumor involving the septum pellucidum and with extension into both lateral ventricles. The tumor has heterogeneous intermediate to slightly high signal on **(a)** axial T2-weighted imaging and shows heterogeneous gadolinium contrast enhancement on **(b)** axial FS T1-weighted imaging (arrows).

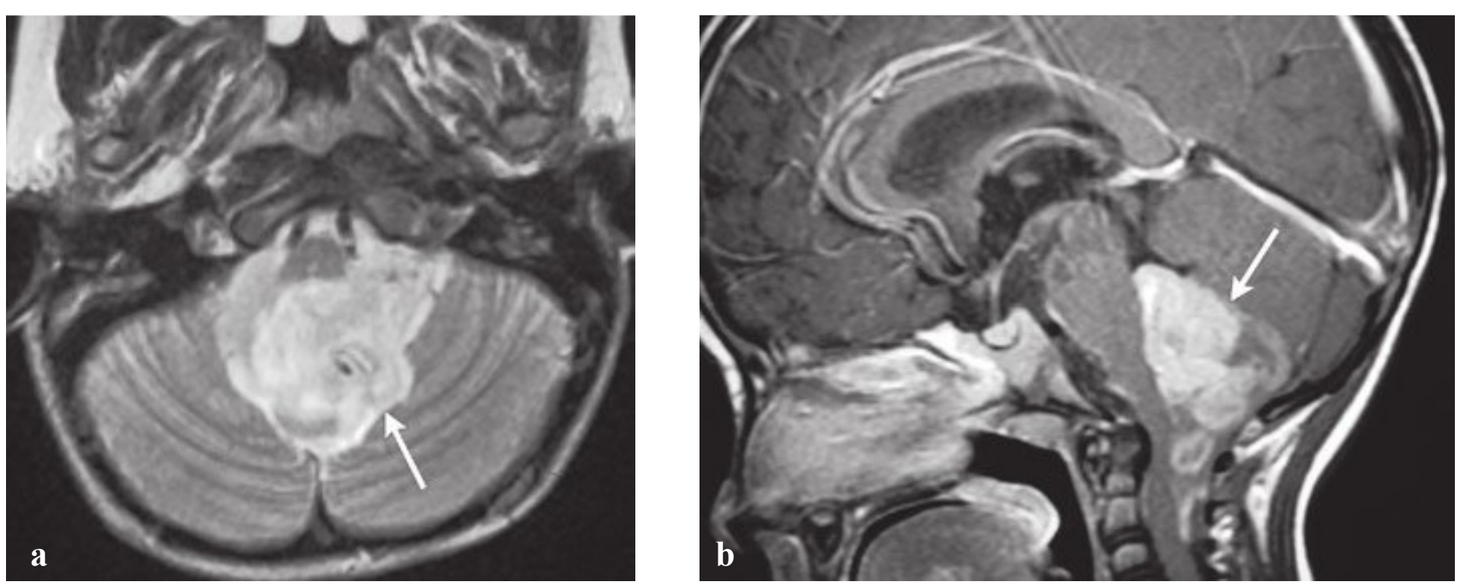

Fig. 2.74 A 30-month-old female with an ependymoma in the fourth ventricle that has heterogeneous high signal on **(a)** axial T2-weighted imaging (arrow) and shows gadolinium contrast enhancement on **(b)** sagittal T1-weighted imaging (arrow). The tumor extends into both foramina of Luschka as seen on axial T2-weighted imaging and though the foramen of Magendie on sagittal T1-weighted imaging.

Table 2.7 (cont.) Solitary intraventricular lesions in children

Lesions	Imaging Findings	Comments
Metastatic tumor (**Fig. 2.75**)	MRI: Circumscribed spheroid lesions in brain, can have various intra-axial locations, often at gray–white matter junctions, usually with low-intermediate signal on T1-weighted imaging and intermediate-high signal on T2-weighted imaging, ± hemorrhage, calcifications, and cysts. Variable gadolinium contrast enhancement. Often there is high signal on T2-weighted imaging peripheral to nodular enhancing lesion, representing axonal edema. CT: Lesions usually have low-intermediate attenuation; ± hemorrhage, calcifications, cysts; variable contrast enhancement, often associated with adjacent low attenuation from axonal edema.	Represents ~ 33% of intracranial tumors, usually from extracranial primary neoplasm in adults > 40 years old. Uncommon in children. Primary tumor source: lung > breast > GI > GU > melanoma. Metastatic lesions in the cerebellum can present with obstructive hydrocephalus/neurosurgical emergency.
Hemangioblastoma (**Fig. 2.76**)	Circumscribed tumors usually located in the cerebellum and/or brainstem. MRI: Small gadolinium-enhancing nodule ± cyst, or larger lesion with prominent heterogeneous enhancement ± flow voids within lesion or at the periphery. Intermediate signal on T1-weighted imaging, intermediate-high signal on T2-weighted imaging. Occasionally, lesions have evidence of recent or remote hemorrhage. Relative cerebral blood volume (rCBV) of lesions is high. CT: Small contrast-enhancing nodule ± cyst, or larger lesion with prominent heterogeneous enhancement, ± hemorrhage.	Slow-growing, vascular tumors (WHO grade I) that involve the cerebellum, brainstem, and/or spinal cord. Account for 1 to 3% of intracranial neoplasms and usually occur in middle-aged adults. Rarely occur in children except for those with von Hippel-Lindau (VHL) disease. Tumors consist of numerous thin-walled vessels as well as large, lipid-containing vacuolated stromal cells, which have variably sized and hyperchromatic nuclei. Mitotic figures are rare. Stromal cells are immunoreactive to VEGF, vimentin, CXCR4, aquaporin 1, carbonic anhydrase, S-100, CD56, neuron-specific enolase, and D2–40. Vessels typically react to a reticulin stain. Reactive astrocytic gliosis can ocur in adjacent tissue. Tumors occur as sporadic mutations of the VHL gene or as an autosomal dominant germline mutation of the VHL gene on chromosome 3p25–26 resulting in VHL disease. In VHL disease, multiple CNS hemangioblastomas occur, as well as clear-cell renal carcinoma, pheochromocytoma, endolymphatic sac tumor, neuroendocrine tumor, adenoma of the pancreas, and epididymal cystadenoma. VHL disease occurs in adolescents and young and middle-aged adults.

(continued on page 476)

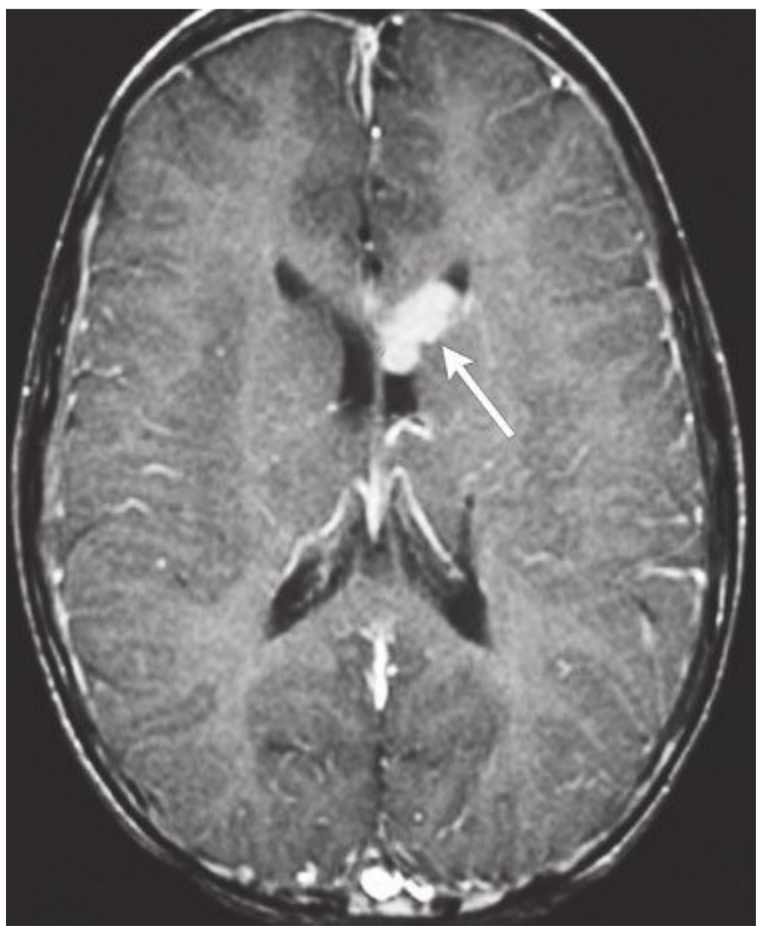

Fig. 2.75 A 10-year-old boy with medulloblastoma and a nodular gadolinium-enhancing disseminated tumor (arrow) in the frontal horn of the left lateral ventricle on axial T1-weighted imaging.

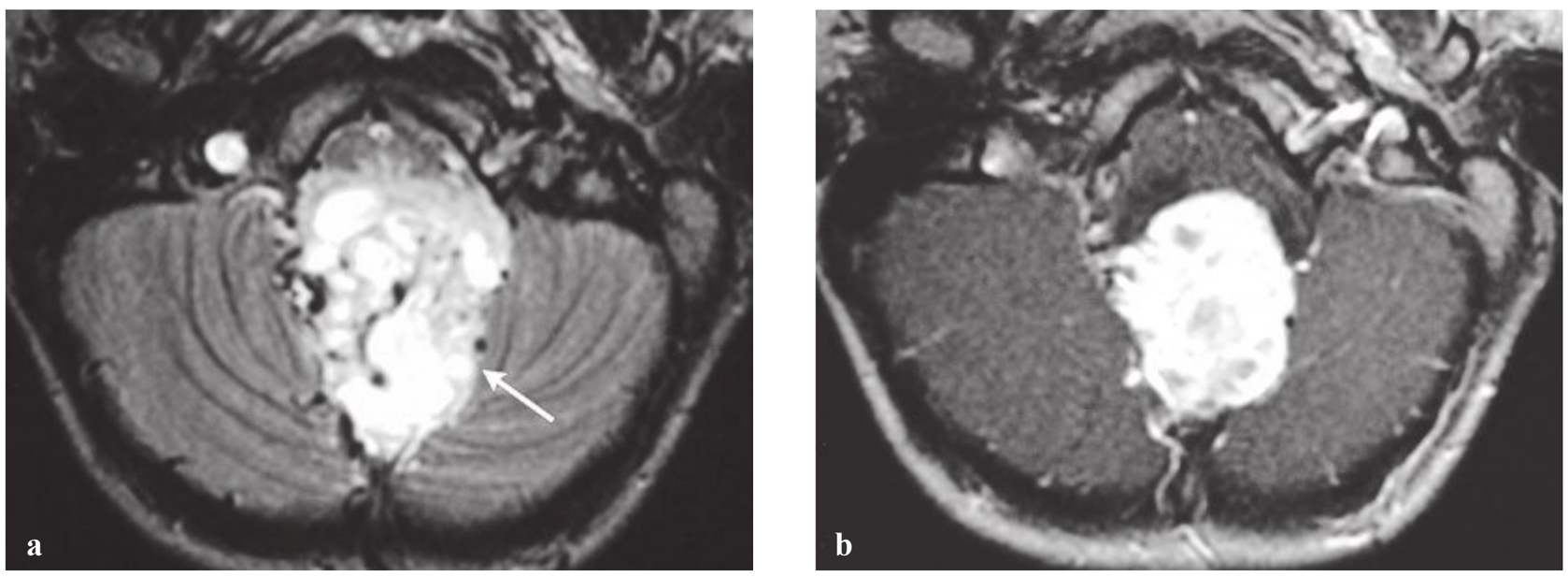

Fig. 2.76 A 16-year-old male with von Hippel-Lindau disease and a hemangioblastoma in the inferior vermis and fourth ventricle that has high signal on **(a)** axial T2-weighted imaging (arrow), as well as blood vessels with flow voids. The lesion shows prominent gadolinium contrast enhancement on **(b)** axial T1-weighted imaging.

Table 2.7 (cont.) Solitary intraventricular lesions in children

Lesions	Imaging Findings	Comments
Choroid plexus papilloma (**Fig. 2.77** and **Fig. 2.78**)	MRI: Circumscribed and/or lobulated lesions with papillary projections; intermediate signal on T1-weighted imaging and heterogeneous intermediate to high signal on T2-weighted imaging, usually with prominent gadolinium contrast enhancement, ± calcifications. Locations: atrium of lateral ventricle (children) > fourth ventricle (adults), rarely other locations, such as third ventricle. Associated with hydrocephalus from CSF overproduction or mechanical obstruction. CT: Circumscribed and/or lobulated lesions with papillary projections, intermediate attenuation, usually prominent contrast enhancement, ± calcifications.	Rare benign (WHO grade I) intraventricular neoplasms derived from choroid plexus epithelium in which a single layer of cuboidal or columnar epithelial cells with round/oval nuclei overlies fibrovascular connective tissue in frondlike patterns. Occurs in lateral ventricle (50%), fourth ventricle/CP angle (40%), third ventricle (5%), and multiple ventricles (5%). Occurs in children and adults. Tumors in the lateral ventricles account for up to 80% of cases in patients less than 20 years old. Lesions in the fourth ventricle are most common in adults. Tumors have very low mitotic activity. Immunoreactive to cytokeratins, vimentin, podoplanin, S-100, and transthyretin. Can be cured by surgical resection.
Atypical choroid plexus papilloma (**Fig. 2.79**)	MRI: Circumscribed and/or lobulated lesions with papillary projections, intermediate signal on T1-weighted imaging and mixed intermediate-high signal on T2-weighted imaging, usually with prominent gadolinium contrast enhancement, ± calcifications. Locations: atrium of lateral ventricle (children) > fourth ventricle (adults), rarely other locations, such as third ventricle. Associated with hydrocephalus. CT: Circumscribed and/or lobulated lesions with papillary projections, intermediate attenuation, usually prominent contrast enhancement, ± calcifications.	Rare (WHO grade II) intraventricular neoplasms derived from choroid plexus that have some histologic features that overlap those for choroid plexus papillomas, although can have higher mitotic activity (> 2/HPF), increased cellularity, nuclear pleomorphism, partial loss of the papillary morphology, and/or necrosis. Immunoreactive to cytokeratins and S-100. Occur in children and adults. Can be cured by surgical resection.

(continued on page 478)

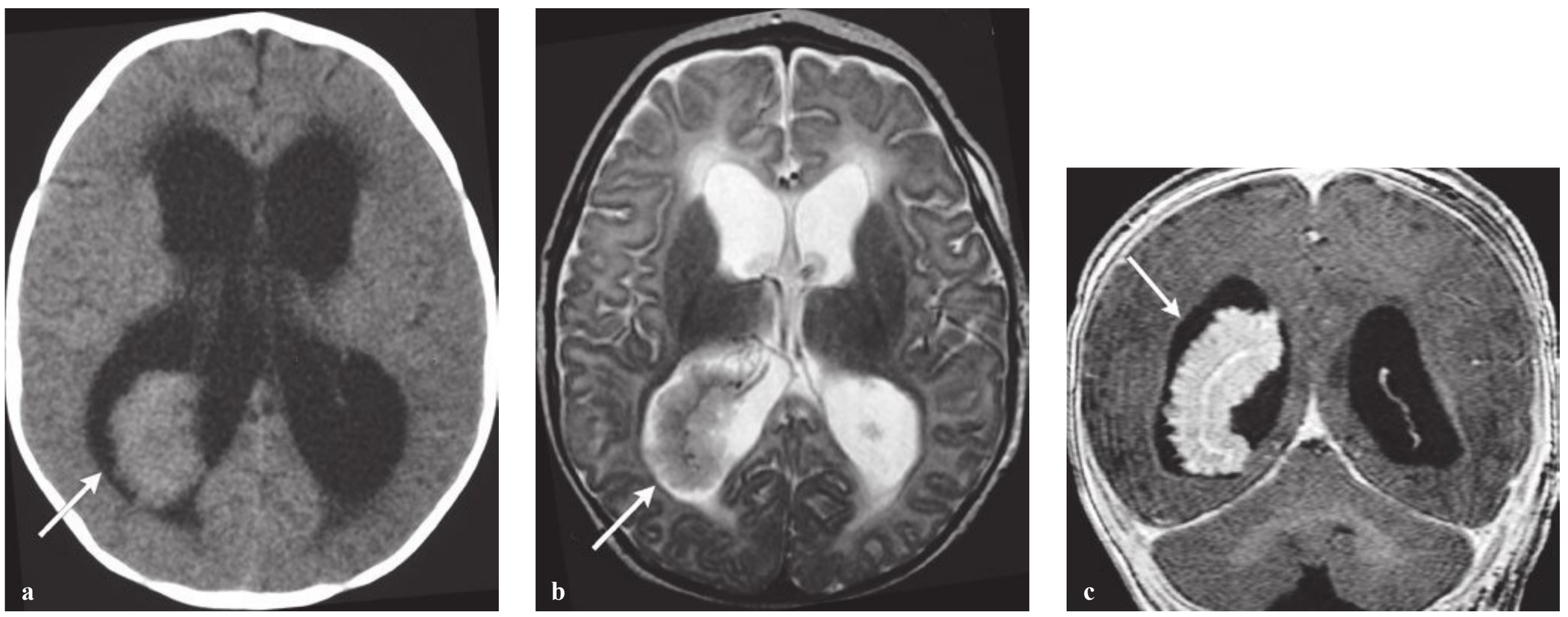

Fig. 2.77 A 3-month-old male with a choroid plexus papilloma in the right lateral ventricle that is associated with hydrocephalus from overproduction of CSF. The tumor has intermediate attenuation on **(a)** axial CT (arrow), heterogeneous intermediate and slightly high signal on **(b)** axial T2-weighted imaging (arrow), and prominent gadolinium contrast enhancement on **(c)** coronal T1-weighted imaging. The tumor has multiple, small, marginal papillary-like lobulations (arrow).

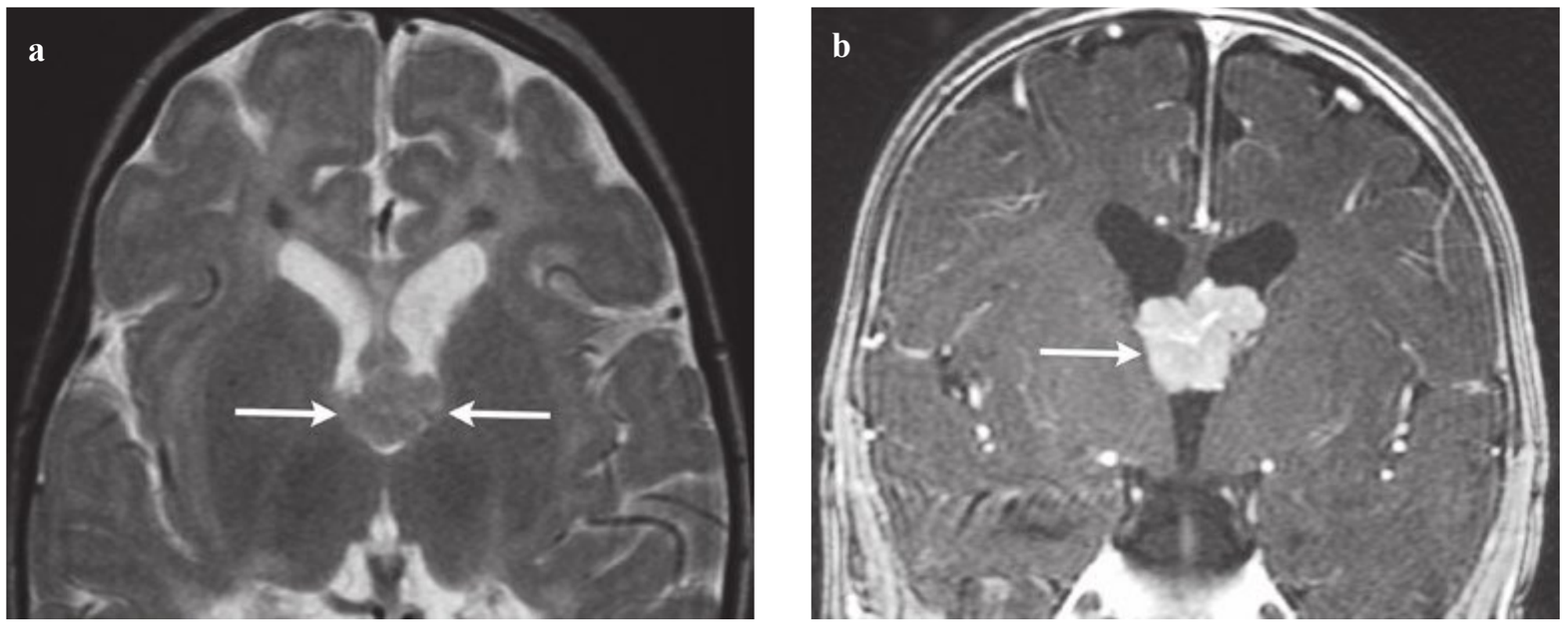

Fig. 2.78 An 11-month-old female with a choroid plexus papilloma in the third ventricle that has intermediate signal on **(a)** axial T2-weighted imaging (arrows) and shows prominent gadolinium contrast enhancement on **(b)** coronal T1-weighted imaging (arrow).

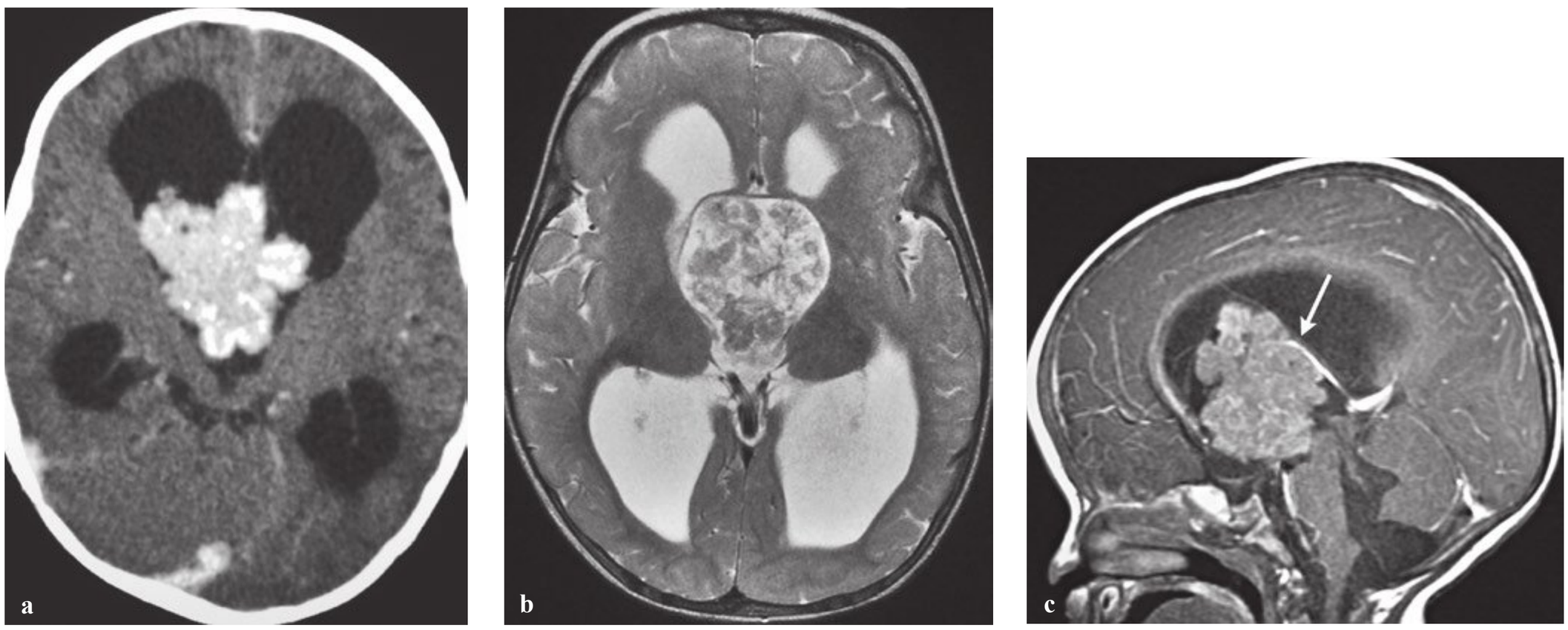

Fig. 2.79 A 1-year-old female with an atypical choroid plexus papilloma in the third ventricle causing obstructive hydrocephalus. **(a)** The tumor has lobulated margins and shows prominent contrast enhancement on axial CT. **(b)** The tumor has heterogeneous intermediate and high signal on axial T2-weighted imaging and contains many papillary-like projections. **(c)** The tumor (arrow) shows gadolinium contrast enhancement on sagittal T1-weighted imaging.

Table 2.7 (cont.) Solitary intraventricular lesions in children

Lesions	Imaging Findings	Comments
Choroid plexus carcinoma (**Fig. 2.80** and **Fig. 2.81**)	MRI: Large, lobulated neoplasms with mean tumor size of 5 cm, often with irregular margins ± brain invasion. On T1-weighted imaging, tumors have heterogeneous intermediate signal with foci of high signal in 45% from areas of hemorrhage. On T2-weighted imaging, solid portions of the tumor often have heterogeneous intermediate to slightly high signal. Small zones with low signal on T2-weighted imaging can occur from sites of hemorrhage or calcifications. Intratumoral cystic or necrotic zones occur in 64%and have high signal on T2-weighted imaging. Tubular flow voids representing blood vessels occur in up to 55%of tumors. Tumors typically show prominent gadolinium contrast enhancement. Nearly 75%of tumors have irregular enhancing margins from ependymal invasion. Disseminated gadolinium-enhancing tumor in the leptomeninges can occur in up to 45% Hydrocephalus is seen in up to 80% CT: Large intraventricular tumors with intermediate attenuation as well as foci with high attenuation from areas of hemorrhage or calcification and low attenuation zones in cystic or necrotic zones. Tumors typically show prominent contrast enhancement.	Rare malignant (WHO grade III) intraventricular neoplasms derived from choroid plexus epithelium and that contain irregular sheets of neoplastic cells with nuclear pleomorphism, high mitotic activity (> 5/HPF), loss of the papillary morphology, and necrotic and/or hemorrhagic areas. Immunoreactive to cytokeratins. Account for 0.1%of all intracranial tumors and 0.6%of primary pediatric CNS neoplasms. These tumors are five times less frequent than choroid plexus papillomas. Median ages range from 12 to 32 months. Most commonly occur in the lateral ventricle, followed by the fourth and third ventricles. These tumors commonly disseminate along CSF pathways and invade brain tissue. Poor prognosis, with 5-year survival of 45%
Central neurocytoma (**Fig. 2.82**)	MRI: Circumscribed lesion typically located at margin of lateral ventricle or septum pellucidum with intraventricular protrusion, heterogeneous low and intermediate signal on T1-weighted imaging, heterogeneous intermediate-high signal on T2-weighted imaging, ± calcifications and/or small cysts, and heterogeneous gadolinium contrast enhancement. Diffusion-weighted imaging: Lesions can show reduced ADC values. Magnetic resonance spectroscopy: Elevated glycine (3.55 ppm), choline, and alanine levels, and decreased N-acetylaspartate (NAA). Rare extraventricular neurocytomas have been reported in the frontal and parietal lobes and sellar region. CT: Circumscribed lesion located at margin of lateral ventricle or septum pellucidum with intraventricular protrusion, heterogeneous low and intermediate attenuation, ± calcifications and/or small cysts, heterogeneous contrast enhancement.	Slow-growing, rare neuroepithelial tumor (WHO grade I) composed of uniform round cells with neuronal differentiation. Immunoreactive to synaptophysin and NeuN. Represent ~ 0.5%of intracranial tumors. Patients range from 8 days to 67 years old (mean age = 29 years). Imaging appearance similar to intraventricular oligodendrogliomas. Typically benign tumors with favorable prognosis after surgery.

(continued on page 480)

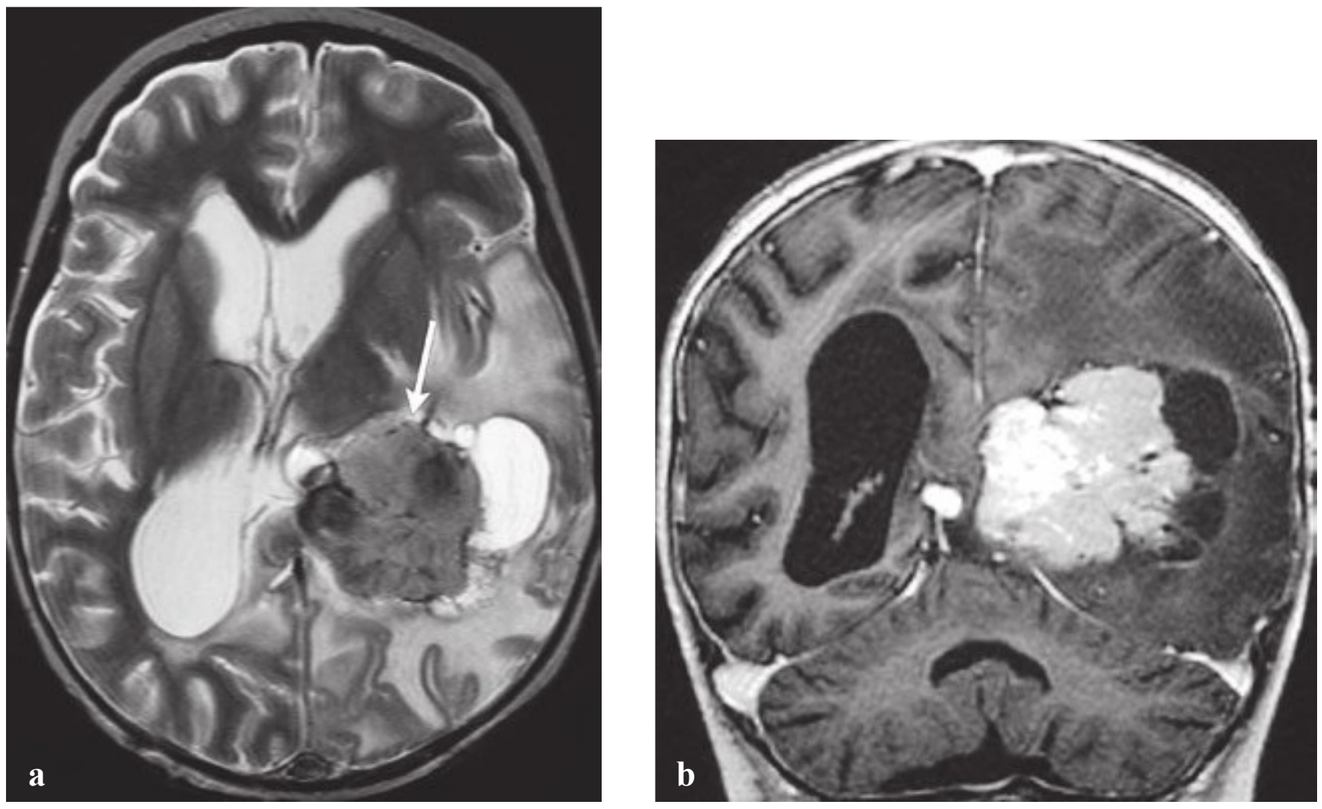

Fig. 2.80 A 4-year-old female with a choroid plexus carcinoma within the atrium of the left lateral ventricle; the tumor invades the adjacent brain parenchyma and causes obstructive hydrocephalus. **(a)** The tumor has mixed intermediate and low signal on axial T2-weighted imaging (arrow) and is associated with peripheral edema. **(b)** The tumor shows gadolinium contrast enhancement on coronal T1-weighted imaging and has irregular margins related to invasion of adjacent brain parenchyma.

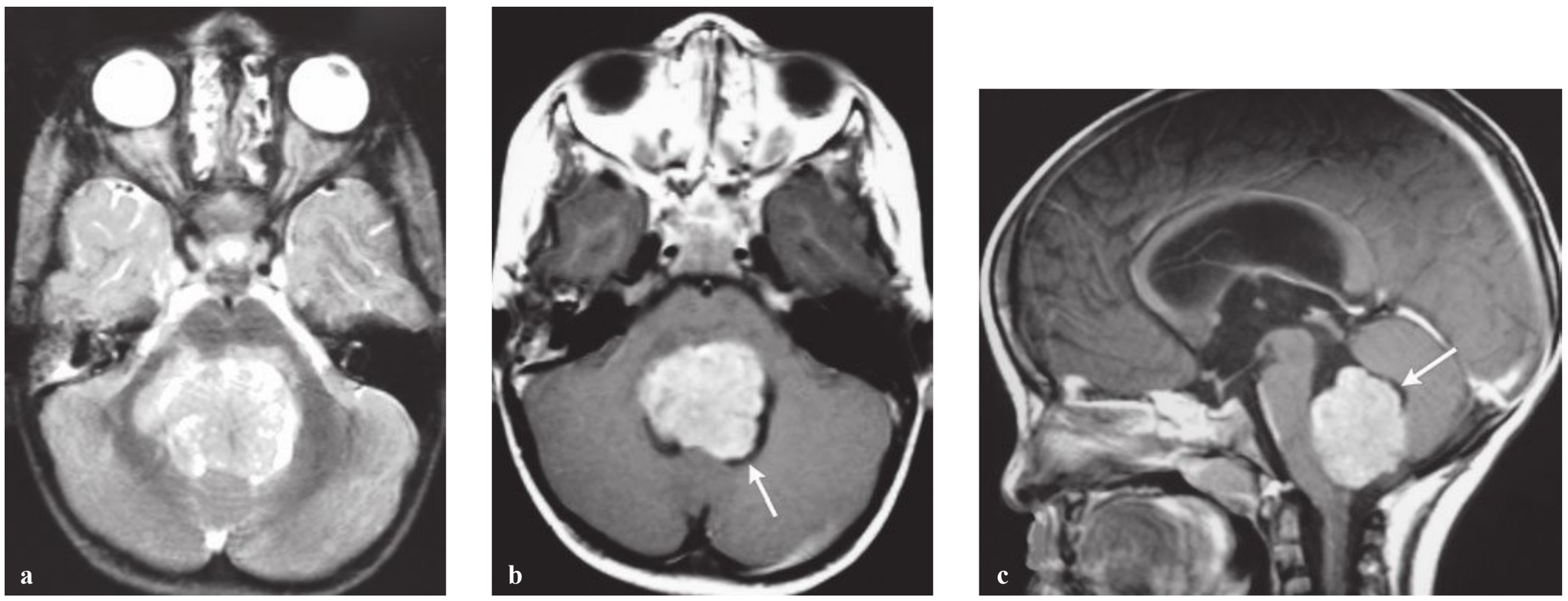

Fig. 2.81 A 3-year-old boy with a choroid plexus carcinoma in the fourth ventricle causing hydrocephalus. **(a)** The tumor has irregular margins and intermediate and high signal on axial T2-weighted imaging. Abnormal high signal is also seen in the adjacent neural tissue representing tumor invasion. The tumor shows gadolinium contrast enhancement with irregular margins on **(b)** axial and **(c)** sagittal T1-weighted imaging (arrows).

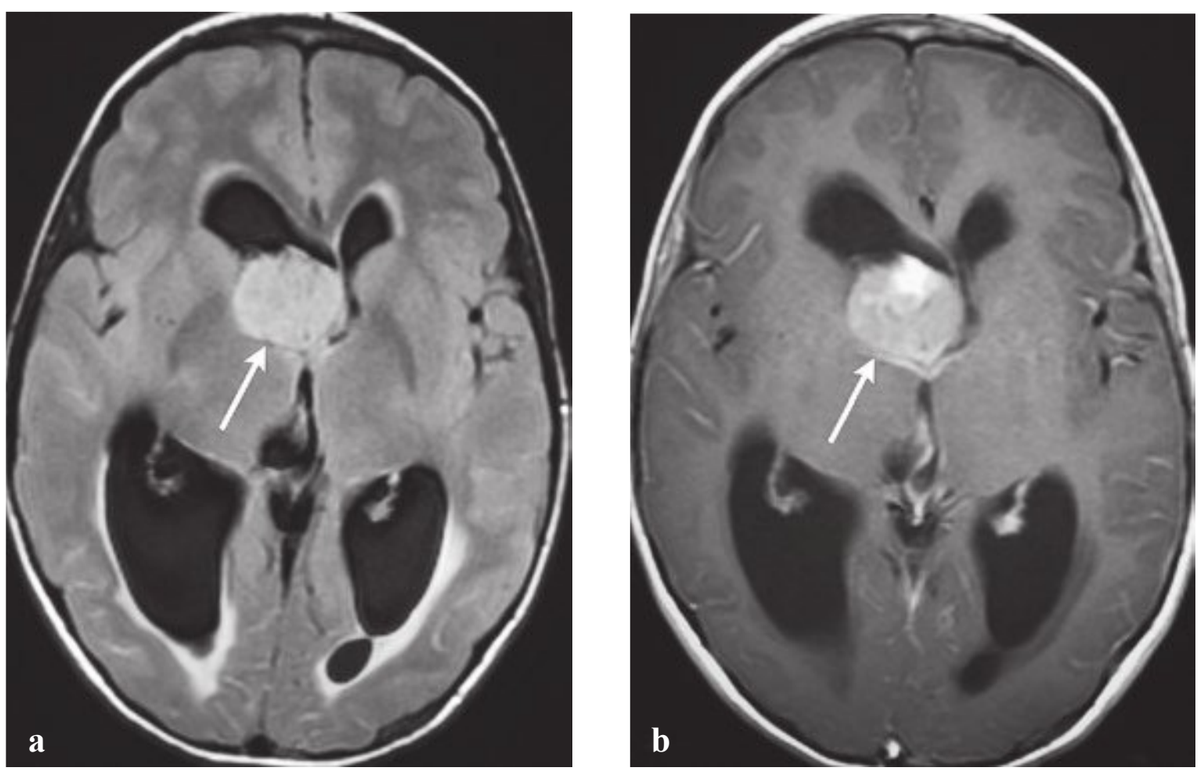

Fig. 2.82 A 15-year-old female with a central neurocytoma involving the septum pellucidum and causing obstructive hydrocephalus. The tumor has high signal on **(a)** axial FLAIR (arrow) and shows gadolinium contrast enhancement on **(b)** axial T1-weighted imaging (arrow).

Table 2.7 (cont.) Solitary intraventricular lesions in children

Lesions	Imaging Findings	Comments
Craniopharyngioma (**Fig. 2.83**)	MRI: The adamantinomatous type usually has circumscribed lobulated margins; occurs in both suprasellar and intrasellar locations > suprasellar > intrasellar (10%) sites. Variable low, intermediate, and/or high signal on T1- and T2-weighted imaging, ± nodular or rim gdolinium contrast enhancement. May contain cysts, lipid components, and calcifications. The squamous papillary type can occur as a solid lesion with intermediate signal on T1-weighted imaging that shows gadolinium contrast enhancement. CT: Circumscribed, lobulated lesions with variable low, intermediate, and/or high attenuation, ± nodular or rim contrast enhancement. May contain cysts, lipid components, and calcifications. Calcifications often occur in the adamantinomatous type.	Usually histologically benign but locally aggressive lesions arising in squamous epithelial rests along Rathke's cleft. Occur in children (10 years) and adults (> 40 years old), males = females. Account for 3% of all intracranial tumors. Can be categorized into adamantinomatous and squamous-papillary types. The adamantinomatous type is more common and has a bimodal age distribution, occurring in children and adults, whereas the squamous-papillary type usually occurs in adults. Craniopharyngiomas are histologically benign, but their insinuating pattern of growth makes complete surgical excision very difficult and not often possible.
Germ cell tumors (**Fig. 2.84**)	MRI: Tumors often have intermediate signal on T1-weighted imaging, slightly high to high signal on T2-weighted imaging, and show gadolinium contrast enhancement, ± cysts, ± gadolinium-enhancing disseminated subarachnoid and/or intraventricular tumor. Some germ cell tumors can have mixed signal on T1- and T2-weighted imaging secondary to the presence of cysts, hemorrhage, and/or calcifications. CT: Circumscribed tumors with intermediate to slightly increased attenuation, ± disseminated contrast-enhancing leptomeningeal and/or intraventricular tumor.	Extragonadal germ cell tumors include germinoma (most common), mature teratoma, malignant teratoma, yolk sac tumor, embryonal carcinoma, and choriocarcinoma. They account for 0.6%of primary intracranial tumors, with an incidence of 0.09 per 100,000. Peak incidence is between 10 and 14 years of age, and 90%occur in patients less than 25 years old. Occur more frequently in males than in females. Prognosis depends on histologic subtype. Germinomas have 10-year survival of > 85% Other germ cell tumors have lower survival rates, particularly those containing nongerminomatous malignant cells.
Pineoblastoma (**Fig. 2.85**)	Large tumors (> 3 cm) that often have lobulated, irregular margins. MRI: Tumors have low-intermediate signal on T1-weighted imaging, and intermediate to slightly high and/or high signal on T2-weighted imaging, ± hemorrhage or necrotic changes. Tumors usually show prominent gadolinium contrast enhancement. Disseminated enhancing tumor in the leptomeninges and/or ventricles is not uncommon. Diffusion-weighted imaging: Solid portions can have restricted diffusion. CT: Tumors have intermediate to slightly high attenuation, ± hemorrhage and necrotic/cystic changes. Disseminated enhancing tumor in the leptomeninges is not uncommon.	Malignant embryonal tumor (WHO grade IV) consisting of diffuse, dense sheets of cells with round, irregular nuclei within scant cytoplasm, + neuroblastic differentiation, hemorrhage, and necrosis. Immunoreactive to synaptophysin, neuron-specific enolase, NFP, class III β-tubulin, and chromogranin A. Occurs most commonly in first two decades (mean age = 18.5 years). Associated with familial bilateral retinoblastoma, which has a poor prognosis. Prognosis is poor when there is documented disseminated tumor in the leptomeninges. Overall 5-year survival is 58%

(continued on page 482)

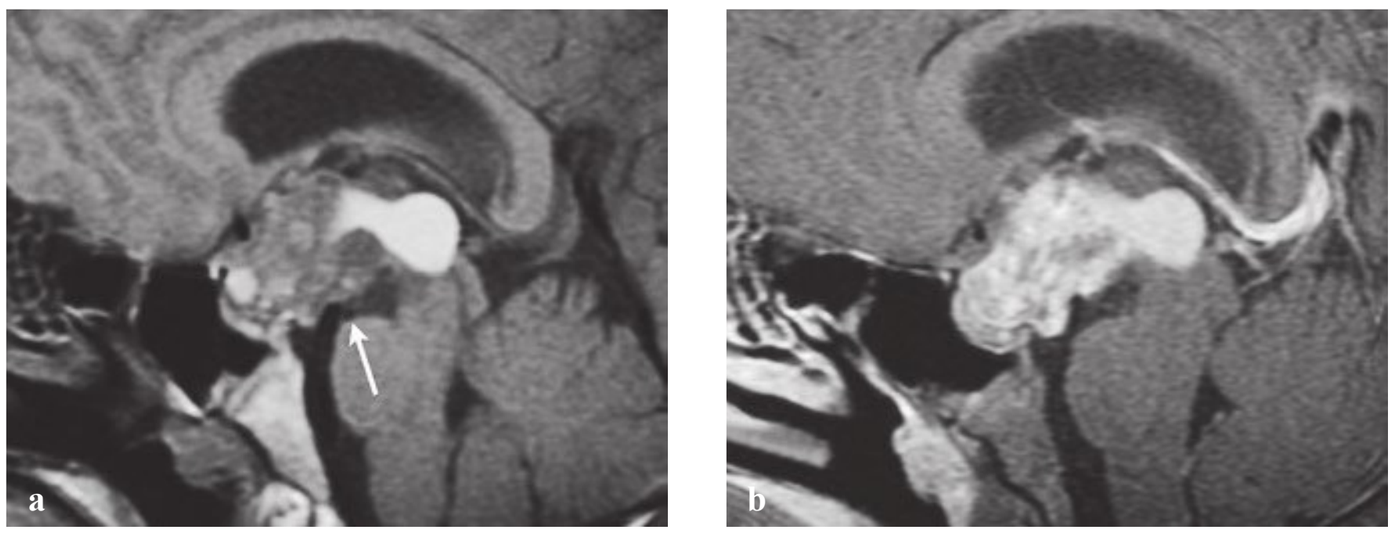

Fig. 2.83 A 17-year-old male with an adamantinomatous type of craniopharyngioma. **(a)** Sagittal T1-weighted imaging shows a lobulated lesion filling the suprasellar cistern and involving the third ventricle, which contains zones with low, intermediate, and high signal (arrow). **(b)** Sagittal postcontrast T1-weighted imaging shows the lesion to have heterogeneous contrast enhancement.

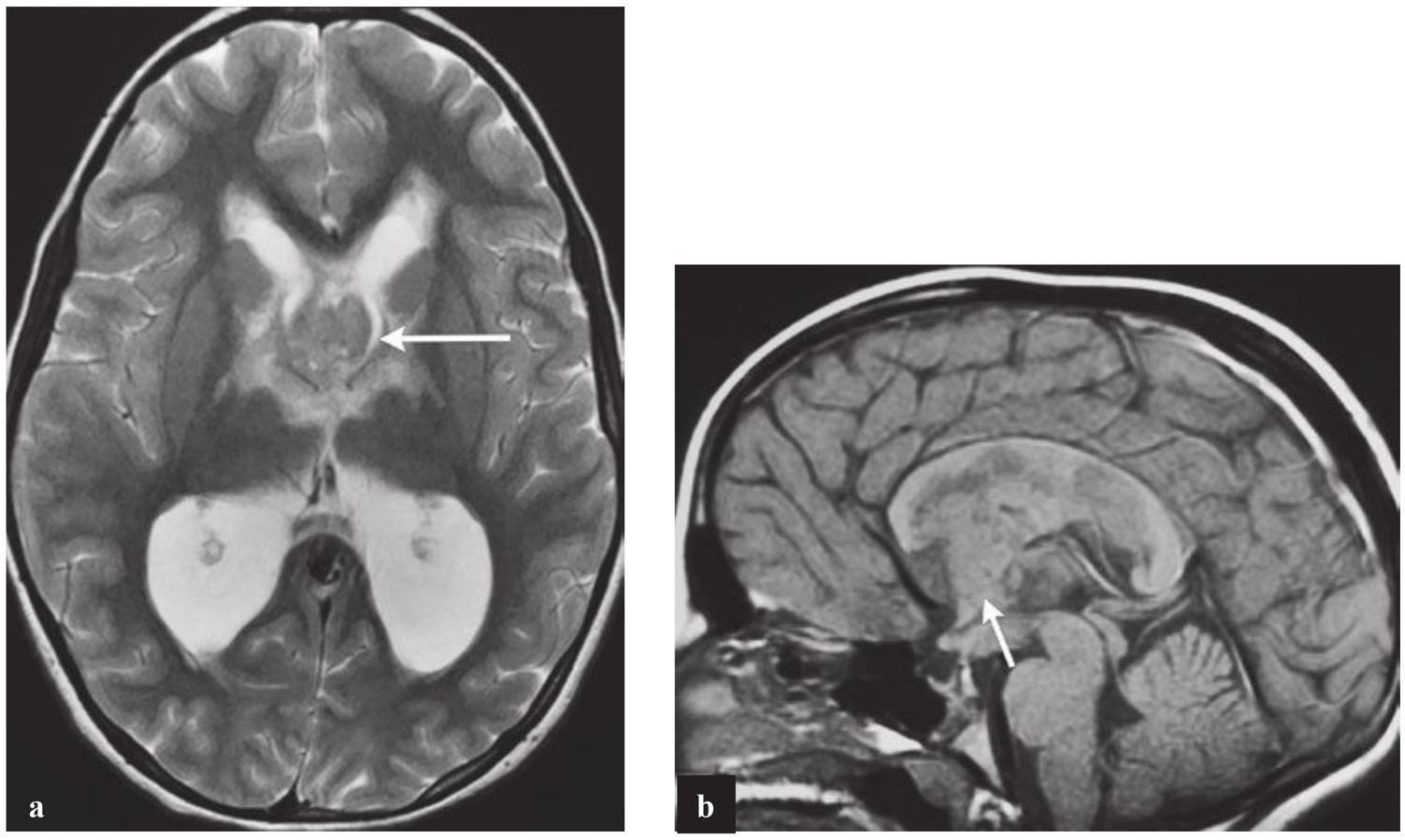

Fig. 2.84 A 14-year-old female with disseminated germinoma within the third ventricle causing obstructive hydrocephalus. **(a)** The tumor (arrow) has heterogeneous intermediate signal on axial T2-weighted imaging and poorly defined margins representing invasion of adjacent brain tissue. **(b)** The tumor (arrow) shows gadolinium contrast enhancement on sagittal T1-weighted imaging.

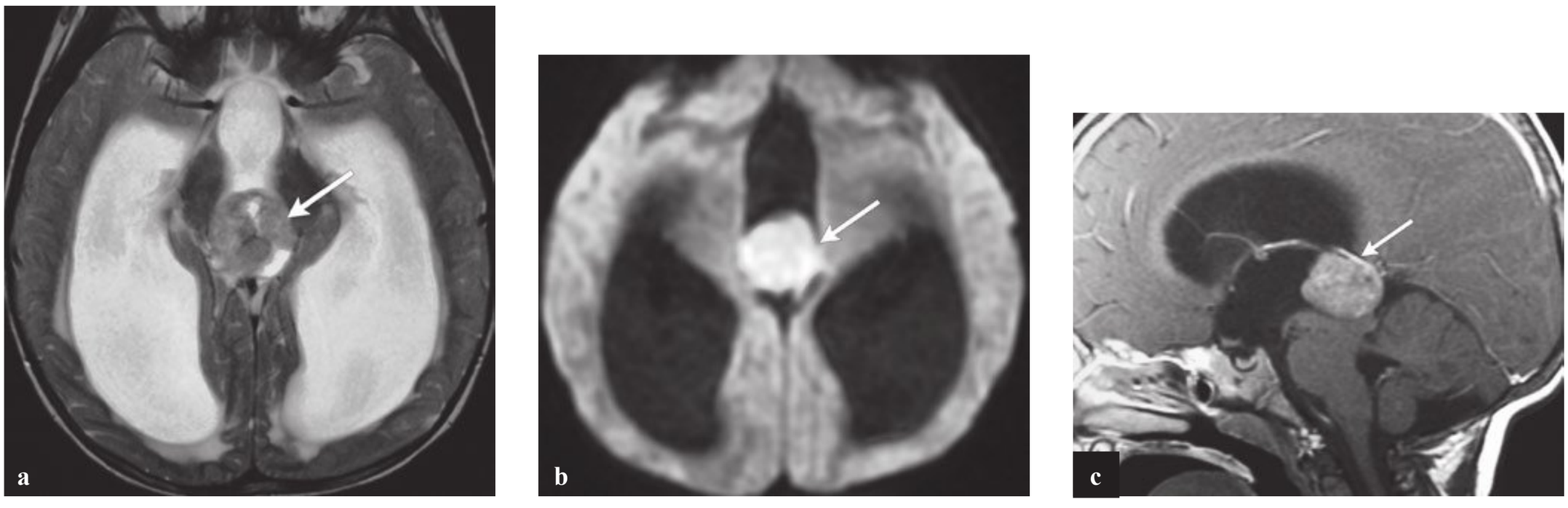

Fig. 2.85 An 18-month-old male with a pineoblastoma that extends into the posterior portion of the third ventricle, causing obstructive hydrocephalus. The tumor has **(a)** mixed intermediate to slightly high, high, and low signal on axial T2-weighted imaging (arrow), **(b)** restricted diffusion on diffusion-weighted imaging (arrow), and **(c)** gadolinium contrast enhancement on sagittal T1-weighted imaging (arrow).

Table 2.7 (cont.) Solitary intraventricular lesions in children

Lesions	Imaging Findings	Comments
Hypothalamic hamartoma (**Fig. 2.86**)	MRI: Sessile or pedunculated lesions at the tuber cinereum of the hypothalamus, often with intermediate signal on T1- and T2-weighted imaging similar to gray matter, occasionally slightly high signal on T2-weighted imaging, and usually no gadolinium contrast enhancement. Rarely contain cystic and/or fatty portions. Ictal FDG PET and SPECT have shown hyperfusion during seizures. Diffusion-weighted imaging: No restricted diffusion. Magnetic resonance spectroscopy may show elevated myo-inositol. CT: Lesions often have intermediate attenuation similar to gray matter, typically have no contrast enhancement, and rarely contain cystic and/or fatty portions similar to brain.	Rare, congenital/developmental heterotopia/hamartoma (nonneoplastic) lesions involving the tuber cinereum, inferior hypothalamus, and/or mamillary bodies composed of clusters of small (< 12 microns) neuronal cells within a neutropil-like stroma and scattered fibrillary astrocytes. Immunoreactive to NeuN and GAD67, not immunoreactive to glial fibrillary acidic protein (GFAP). Usually occur in children with isosexual precocious puberty (0–8 years old) or seizures (gelastic or partial complex) in second decade. Can be treated with surgery or stereotactic radiosurgery.
Meningioma (**Fig. 2.87**)	Extra-axial dura-based lesions that are well circumscribed. Locations are supra- > infratentorial, parasagittal > convexity > sphenoid ridge > parasellar > posterior fossa > optic nerve sheath > intraventricular. MRI: Dura-based tumors with intermediate signal on T1-weighted imaging, intermediate-slightly high signal on T2-weighted imaging, usually prominent gadolinium contrast enhancement often with a dural tail, ± calcifications. Intratumoral hemorrhage and cystic or necrotic foci can occur in 15% Diffusion-weighted imaging/diffusion tensor imaging: ADC values vary among the different subtypes of meningioma. Some tumors can show restricted diffusion, although these findings can be seen with both benign and atypical tumors. Magnetic resonance spectroscopy can show elevated alanine (1.5 ppm), lactate, choline, and glutamine/glutamate levels, as well as reduced N-acetylaspartate (NAA). CT: Tumors have intermediate attenuation with or without calcifications, with or without hyperostosis, and usually show prominent contrast enhancement.	Meningiomas are the most common extra-axial tumor and account for up to 26%of primary intracranial tumors. Annual incidence is 6 per 100,000. Meningioma typically occurs in adults (> 40 years old), and in women > men. Occasionally occurs in children, with tendency for more aggressive types than in adults. Composed of neoplastic meningothelial (arachnoidal or arachnoid cap) cells. Meningiomas are usually solitary and sporadic but can also occur as multiple lesions in patients with neurofibromatosis type 2. Eighty percent of meningiomas are benign (WHO grade I), although 15%have atypical features (WHO grade II) and ~ 5% have anaplastic histologic features (WHO grade III). Can occur secondary to radiation treatment, with latencies ranging from 19 to 35 years. Classified into different subtypes, such as meningothelial, fibrous (fibroblastic), transitional (mixed), psammomatous, angiomatous, atypical, and anaplastic. Meningothelial, fibrous, and transitional meningiomas are the most common intracranial types. Usually show immunoreactivity to epithelial membrane antigen (EMA) and vimentin. Secretory meningiomas are typically immunoreactive to CEA. Associated cytogenetic findings include deletion of chromosome 22. Mutations in the NF2 tumor suppressor gene on chromosome 22 have been found in 60%of sporadic meningiomas.

(continued on page 484)

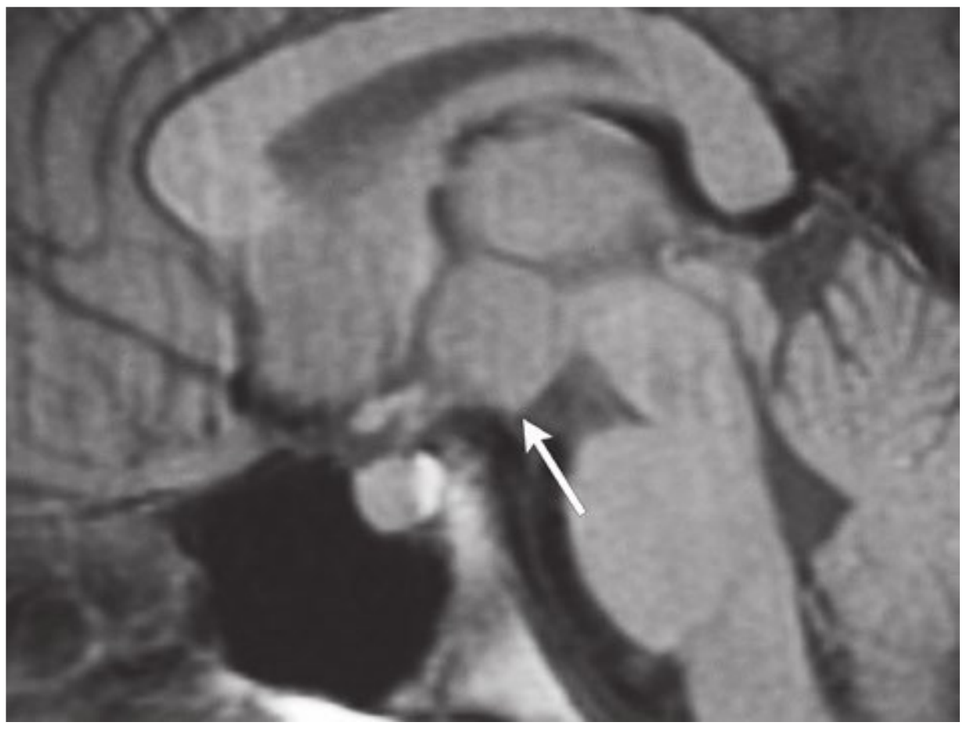

Fig. 2.86 Sagittal T1-weighted imaging shows a sessile type of hypothalamic hamartoma (arrow) in a child with precocious puberty. The hamartoma protrudes into the lower portion of the third ventricle and has intermediate signal that is isointense to gray matter.

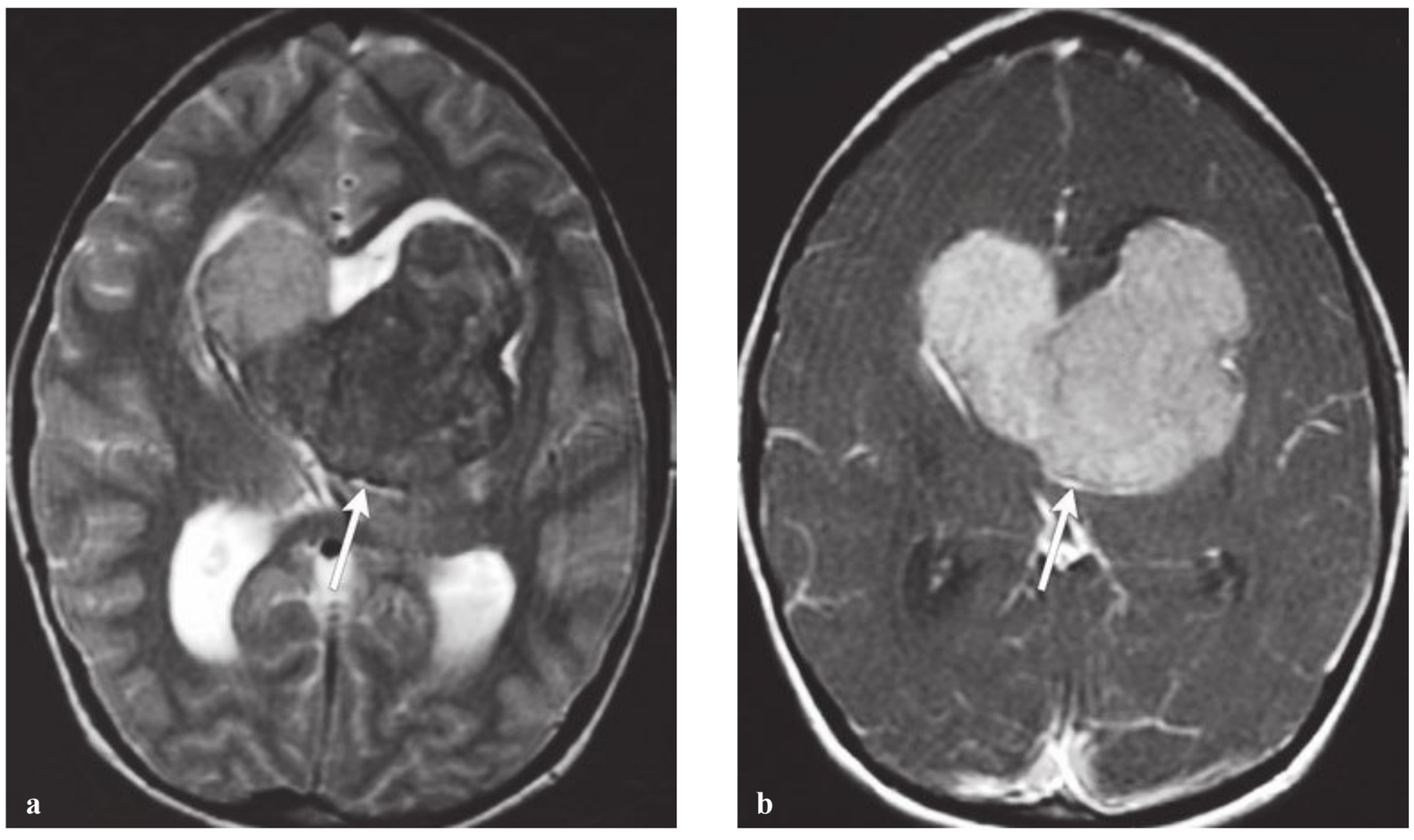

Fig. 2.87 A 9-year-old boy with a large meningioma within the third ventricle extending through the foramen of Monro into the frontal horns of both lateral ventricles, resulting in obstructive hydrocephalus. The meningioma has mixed intermediate and low signal on **(a)** axial T2-weighted imaging (arrow) and shows gadolinium contrast enhancement on **(b)** axial T1-weighted imaging (arrow).

Table 2.7 (cont.) Solitary intraventricular lesions in children

Lesions	Imaging Findings	Comments
Tumorlike Lesions		
Ependymal cyst (**Fig. 2.88**)	MRI: Well-circumscribed, thin-walled cyst in the lateral ventricles with low signal on T1-weighted imaging, diffusion-weighted imaging, and FLAIR and high signal on T2-weighted imaging. Usually no gadolinium contrast enhancement. CT: Thin-walled cyst in the lateral ventricles with low attenuation similar to CSF.	Benign cysts in the lateral ventricles containing serous fluid surrounded by a thin wall containing ependymal columnar cells with vesicular nuclei and eosinophilic cytoplasm. May result from neuroectoderm sequestered during development.
Choroid plexus cyst	MRI: Cysts often have low or intermediate signal on T1-weighted imaging, intermediate or slightly high to high signal on FLAIR, and high signal on T2-weighted imaging. Often have high signal on diffusion-weighted imaging. Can show rim or nodular patterns of gadolinium contrast enhancement. CT: Typically have low-intermediate attenuation, ± peripheral calcification.	Common epithelium-lined nonneoplastic cysts that occur in the choroid plexus, often bilaterally within the atria of the lateral ventricles. Usually range in size from 5 to 20 mm. Result from desquamating and degenerating choroid epithelium within nodular structures containing lipid-laden histiocytes, cholesterol, fluid, hemosiderin, lymphocytic and plasma cell infiltrates, cellular debris, and peripheral psammomatous calcification. Usually asymptomatic incidental finding.
Hemorrhage	CT: A linear relationship exists between CT attenuation and hematocrit and hemoglobin and protein content. MRI: The signal of the hematoma depends on its age, size, location, hematocrit, oxidation state of iron in hemoglobin, degree of clot retraction, extent of edema, and MRI pulse sequence.	Can result from trauma, ruptured aneurysms or vascular malformations, coagulopathy, hypertension, adverse drug reaction, and viral infections (herpes simplex virus or cytomegalovirus).

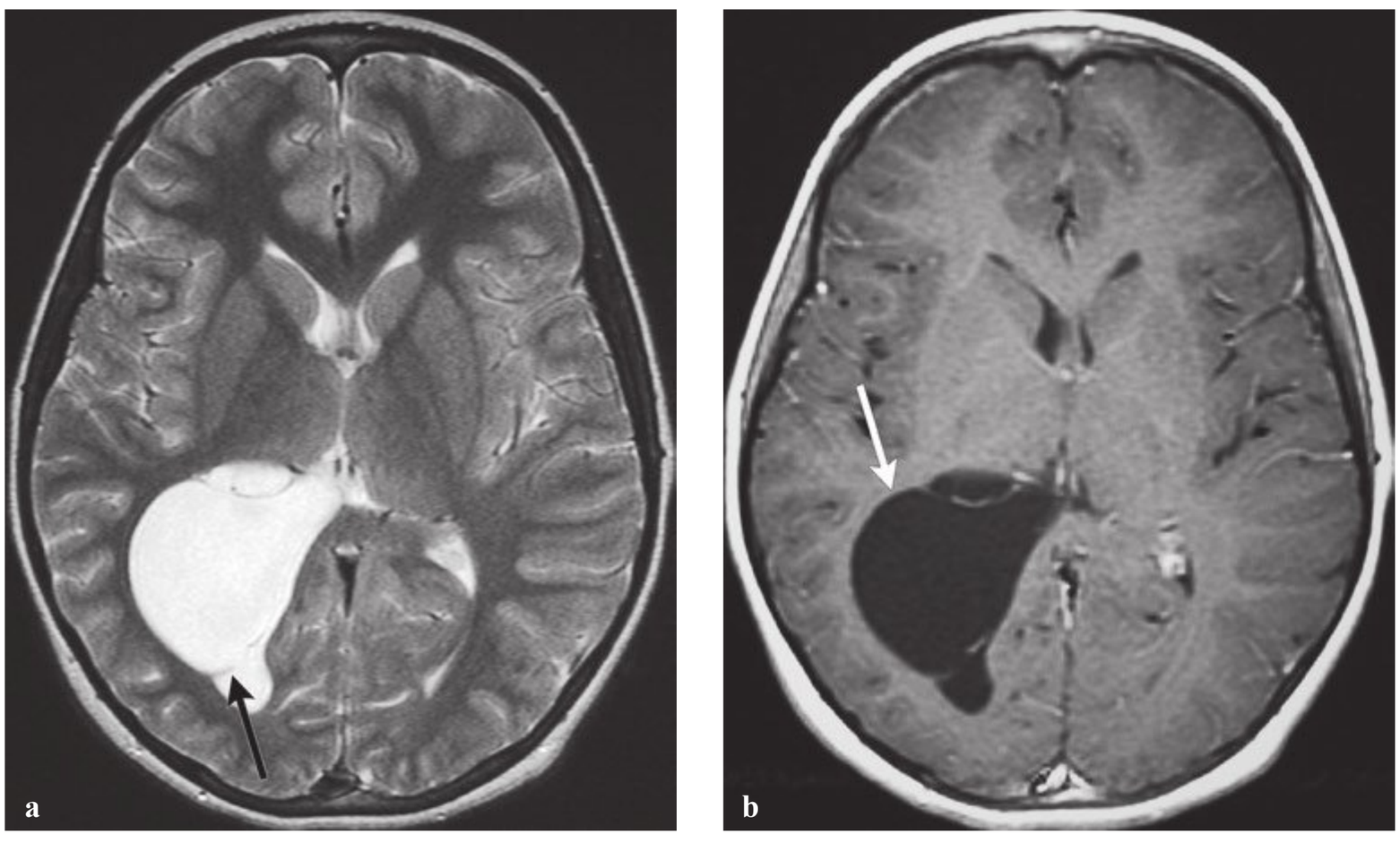

Fig. 2.88 A 10-year-old female with an ependymal cyst expanding the atrium of the right lateral ventricle. The ependymal cyst has signal equal to CSF on **(a)** axial T2-weighted imaging (arrow) and **(b)** postcontrast axial T1-weighted imaging (arrow).

Lesions	Imaging Findings	Comments
Vascular Abnormality		
Arteriovenous malformation (AVM)	MRI: Lesions with irregular margins that can be located in the brain parenchyma, pia, dura, and/or ventricles. AVMs contain multiple, tortuous, tubular flow voids on T1- and T2-weighted imaging secondary to patent arteries with high blood flow, as well as thrombosed vessels with variable signal, areas of hemorrhage in various phases. Gradient echo MRI shows flow-related enhancement (high signal) in patent arteries and veins of the AVM. MRA using time-of-flight or phase contrast techniques can provide additional detailed information about the nidus, feeding arteries and draining veins, and presence of associated aneurysms. Usually not associated with mass effect unless there is recent hemorrhage or venous occlusion. CT: Lesions with irregular margins that can be located in the brain parenchyma, pia, dura, and/or ventricles, ± calcifications. AVMs contain multiple tortuous vessels. The venous portions often show contrast enhancement. Usually not associated with mass effect unless there is recent hemorrhage or venous occlusion. CTA can show the nidus and arterial and venous portions of the AVM.	AVMs can be sporadic, congenital, or associated with a history of trauma. Supratentorial AVMs occur more frequently (80–90%) than infratentorial AVMs (10–20%). Annual risk of hemorrhage. AVMs can be sporadic, congenital, or associated with a history of trauma. Multiple AVMs can be seen in Rendu-Osler-Weber syndrome (AVMs in brain and lungs and mucosal capillary telangiectasias) and Wyburn-Mason syndrome (AVMs in brain and retina, + cutaneous nevi).
Vein of Galen malformation/ aneurysm (**Fig. 2.89**)	Multiple, tortuous, contrast-enhancing vessels involving choroidal and thalamoperforate arteries, internal cerebral veins, vein of Galen (aneurysmal formation), straight and transverse venous sinuses, and other adjacent veins and arteries. The venous portions often show contrast enhancement. CTA and MRA show contrast enhancement in patent portions of the vascular malformation.	Heterogeneous group of vascular malformations with arteriovenous shunts and dilated deep venous structures draining into and from an enlarged vein of Galen, ± hydrocephalus, ± hemorrhage, ± macrocephaly, ± parenchymal vascular malformation components, ± seizures, and high-output congestive heart failure in neonates.
Cavernous malformation (**Fig. 2.90**)	MRI: Single or multiple multilobulated intra-axial lesions that have a peripheral rim or irregular zone of low signal on T2-weighted imaging secondary to hemosiderin, surrounding a central zone of variable signal (low, intermediate, high, or mixed) on T1- and T2-weighted imaging depending on ages of hemorrhagic portions. Gradient echo and magnetic-susceptibility weighted techniques are useful for detecting multiple lesions. Gadolinium contrast enhancement is usually absent, although some lesions may show mild heterogeneous enhancement. Up to 25% of sporadic cavernous malformations are associated with a developmental venous anomaly. CT: Lesions have intermediate to slightly increased attenuation, ± calcifications.	Cavernous malformations are hamartomas composed of thin-walled sinusoids and blood vessels without intervening neural tissue. Can be found in many different locations. Supratentorial cavernous angiomas occur more frequently than infratentorial lesions. Lesions consist of epithelium-lined vascular channels within a collagenous stroma. Zones of thrombus and remote hemorrhage with hemosiderin are often present. Dystrophic calcifications may be present. Developmental venous anomalies occur in 25% Hereditary syndromes in which multiple cavernous malformations occur are associated with mutations of the CCM1/KRIT1, CCM2/MGC4608, and CCM3 PDCD10 genes, and have a higher risk of hemorrhage (up to 5% per year) than sporadic cavernous malformations.
Sturge-Weber syndrome (**Fig. 2.91**)	MRI: Prominent, localized, unilateral leptomeningeal gadolinium contrast enhancement usually in parietal and/or occipital regions in children (unilateral in 80%). Low signal on T2-weighted imaging is often seen at the involved gyri from dystrophic calcifications ± gyral gadolinium contrast enhancement, localized atrophic changes in brain adjacent to the pial angioma, ± prominent medullary and/or subependymal veins, ± ipsilateral enlargement of choroid plexus. CT: Gyral calcifications > 2 years, progressive cerebral atrophy in region of pial angioma.	Also known as encephalotrigeminal angiomatosis, Sturge-Weber syndrome is a non-inherited sporadic neurocutaneous syndrome in which a pial angioma is associated with ipsilateral port wine cutaneous lesion, seizures, glaucoma, and hemiparesis. Results from persistence of primitive leptomeningeal venous drainage (pial angioma) and developmental lack of normal cortical veins producing chronic venous congestion and ischemia. Patients often present with progressive neurologic impairment.

(continued on page 487)

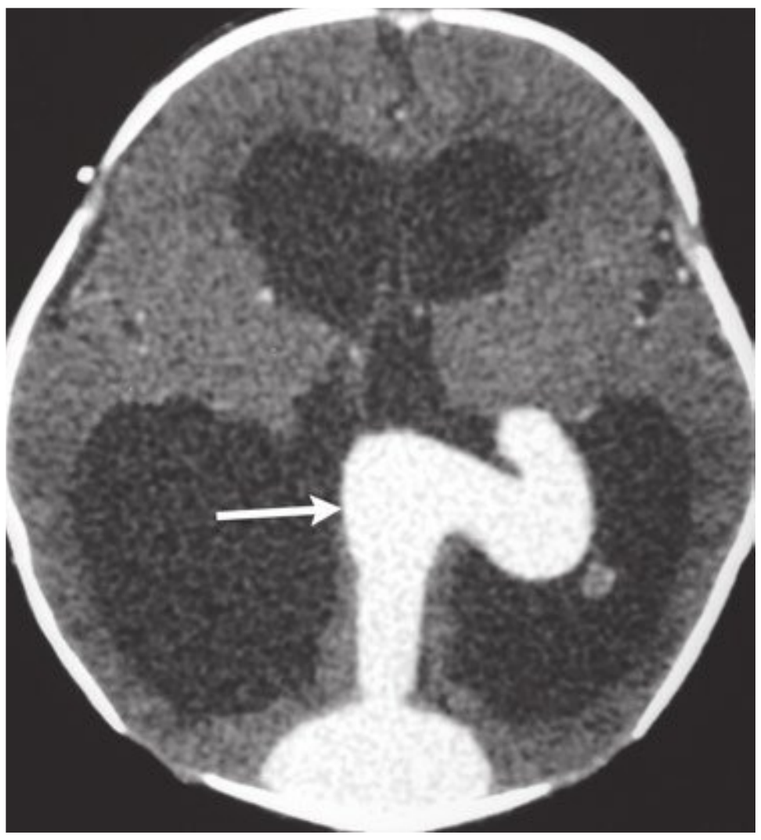

Fig. 2.89 A 1-day-old male with a vein of Galen malformation/aneurysm (arrow) associated with hydrocephalus as seen on postcontrast axial CT.

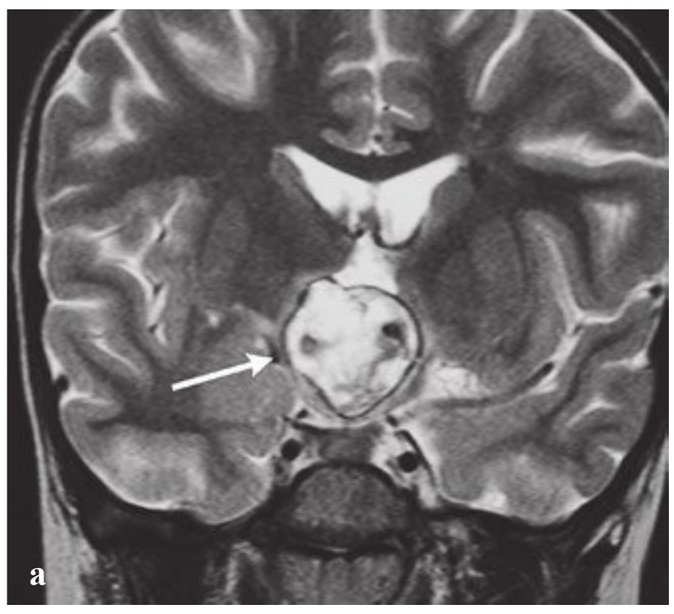

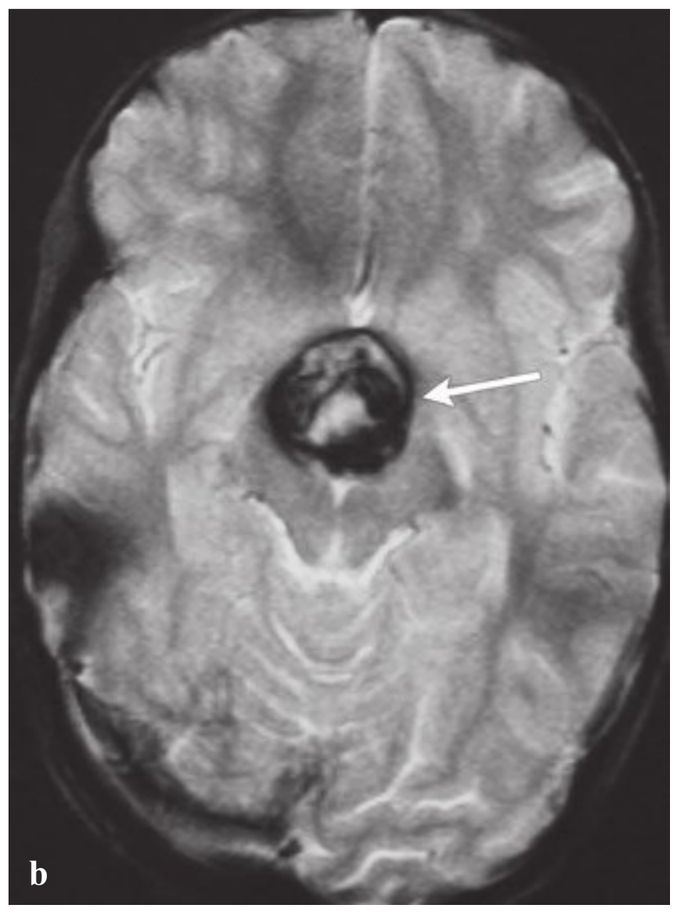

Fig. 2.90 **(a)** A 5-year-old male with a cavernous malformation in the hypothalamus extending into the third ventricle that has mixed high and low signal centrally surrounded by a rim of low signal on coronal T2-weighted imaging (arrow). **(b)** Prominent low T2* signal is seen at the lesion on axial GRE (arrow).

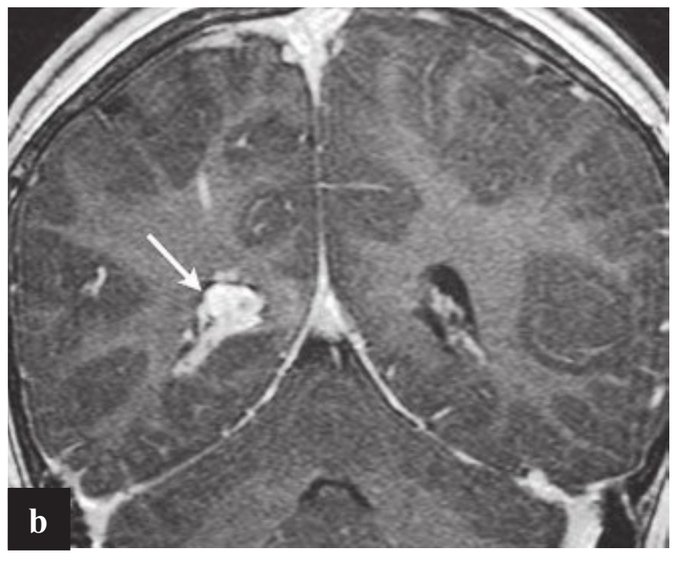

Fig. 2.91 Patient with Sturge-Weber syndrome. Prominent localized unilateral leptomeningeal gadolinium contrast enhancement on **(a)** axial (arrows) and **(b)** coronal T1-weighted imaging is seen in the posterior right parietal-occipital region and is associated with gyral atrophy and enlarged choroid plexus **(b)** in the atrium of the right lateral ventricle (arrow).

Table 2.7 (cont.) Solitary intraventricular lesions in children

Lesions	Imaging Findings	Comments
Infection		
Ventriculitis	MRI: Curvilinear and/or nodular gadolinium contrast enhancement along ventricular/ependymal margins with resultant communicating or noncommunicating types of hydrocephalus.	Complications of intracranial inflammatory processes, such as bacterial, fungal and viral (CMV) infections, tuberculosis, and parasites. Noninfectious diseases like sarcoid can result in a similar pattern.
Parasitic infection/ cysticercosis	MRI: Single or multiple cystic lesions in brain or meninges. Active vesicular phase: Cystic-appearing lesions containing a small 2–4 mm nodule (scolex) with low signal on T1-weighted imaging, FLAIR, and diffusion-weighted imaging; a thin peripheral rim with high signal on FLAIR and T2-weighted imaging; minimal peripheral rim or no gadolinium contrast enhancement; and no peripheral edema on T2-weighted imaging and FLAIR. Active colloidal vesicular phase: Cystic-appearing lesion with low-intermediate signal on T1-weighted imaging, high signal on T2-weighted imaging, rim and/or nodular pattern of gadolinium contrast enhancement, ± peripheral signal (edema) on T2-weighted imaging. Active granular nodular phase: Cyst retracts into a more solid gadolinium-enhancing granulomatous nodule. Chronic non-active phase: Calcified nodular granulomas.	Caused by ingestion of encysted larva of the tapeworm Taenia solium in contaminated food (undercooked pork). Involves meninges, subarachnoid space, and and cisterns > brain parenchyma > ventricles. Most common parasitic disease of the CNS, usually in patients from 15 to 40 years old. Most common cause of acquired epilepsy in endemic regions. Complications include intracranial hypertension from CSF obstruction, arachnoiditis, meningitis, and vascular occlusion.
Inflammation		
Langerhans' cell histiocytosis	MRI: Fusiform or lobulated lesion with intermediate signal on T1- and T2-weighted imaging involving the pituitary stalk and hypothalamus, ± third ventricle. Pituitary stalk is usually > 3 mm in thickness, often associated with loss of high signal on T1-weighted imaging of the posterior pituitary. Lesions in the pituitary usually show gadolinium contrast enhancement. CT: Thickening of the pituitary stalk may be seen. Intraosseous lesions are typically associated with localized bone destruction.	Disorder of reticuloendothelial system in which bone marrow–derived dendritic Langerhans' cells infiltrate various organs as focal lesions or in diffuse patterns. Langerhans' cells have eccentrically located ovoid or convoluted nuclei within pale to eosinophilic cytoplasm. Lesions often consist of Langerhans' cells, macrophages, plasma cells, and eosinophils. Lesions are immunoreactive to S-100, CD1a, CD-207, HLA-DR, and b_2-microglobulin. Prevalence of 2 per 100,000 in children less than 15 years old, and only a third of lesions occur in adults. Localized lesions (eosinophilic granuloma) can be single or multiple in the skull, usually at the skull base. Intradural lesions occur at pituitary stalk/hypothalamus and third ventricle. Can present with diabetes insipidus. Lesions rarely occur in brain tissue (< 4% of patients with Langerhans' cell histiocytosis).

Table 2.8 Solitary intraventricular lesions in adults

- Neoplasms
  - Metastatic tumor
  - Hemangioblastoma
  - Low-grade (diffuse) astrocytoma
  - Anaplastic astrocytoma
  - Glioblastoma multiforme
  - Lymphoma
  - Ependymoma
  - Anaplastic ependymoma
  - Subependymoma
  - Meningioma
  - Hemangiopericytoma
  - Choroid plexus papilloma
  - Atypical choroid plexus papilloma
  - Choroid plexus carcinoma
  - Central neurocytoma
  - Papillary glioneuronal tumor
  - Chordoid glioma of the third ventricle
  - Craniopharyngioma
  - Germ cell tumor
  - Teratoma
  - Pineal lesions and tumors
- Tumorlike lesions
  - Epidermoid
  - Colloid cyst
  - Ependymal cyst
  - Neuroepithelial (neuroglial) cyst
  - Choroid plexus cyst
  - Hematoma
  - Arteriovenous malformation (AVM)
  - Cavernous malformation
- Infection
  - Ventriculitis/abscess
  - Parasitic infection/cysticercosis
- Inflammation
  - Neurosarcoid

Table 2.8 Solitary intraventricular lesions in adults

Lesions	Imaging Findings	Comments
Neoplasms		
Metastatic tumor (**Fig. 2.92**)	Single or multiple well-circumscribed or poorly defined lesions involving the skull, dura, leptomeninges, brainstem, cerebellum, ventricles, choroid plexus, or pituitary gland. Lesions have low-intermediate signal on T1-weighted imaging, intermediate-high signal on T2-weighted imaging, usually + gadolinium contrast enhancement, ± bone destruction, ± compression of neural tissue or vessels. Leptomeningeal tumor often best seen on postcontrast images.	Represents ~ 33% of intracranial tumors, usually from extracranial primary neoplasm in adults > 40 years old. Uncommon in children. Primary tumor source: lung > breast > GI > GU > melanoma. Metastatic lesions in the cerebellum can present with obstructive hydrocephalus/neurosurgical emergency.
Hemangioblastoma (**Fig. 2.93**)	Circumscribed tumors usually located in the cerebellum and/or brainstem. Small gadolinium-enhancing nodule ± cyst, or larger lesion with prominent heterogeneous gadolinium contrast enhancement ± flow voids within lesion or at the periphery; intermediate signal on T1-weighted imaging, intermediate-high signal on T2-weighted imaging. Occasionally, lesions have evidence of recent or remote hemorrhage that may extend into ventricle.	Slow-growing, vascular tumors (WHO grade I) that involve the cerebellum, brainstem, and/or spinal cord. Account for 1 to 3% of intracranial neoplasms and usually occur in middle-aged adults. Rarely occur in children except for those with von Hippel-Lindau (VHL) disease. Tumors consist of numerous thin-walled vessels as well as large, lipid-containing vacuolated stromal cells, which have variably sized and hyperchromatic nuclei. Mitotic figures are rare. Stromal cells are immunoreactive to VEGF, vimentin, CXCR4, aquaporin 1, carbonic anhydrase, S-100, CD56, neuron-specific enolase, and D2–40. Vessels typically react to a reticulin stain. Reactive astrocytic gliosis can ocur in adjacent tissue. Tumors occur as sporadic mutations of the VHL gene or as an autosomal dominant germline mutation of the VHL gene on chromosome 3p25–26 resulting in VHL disease. In VHL disease, multiple CNS hemangioblastomas occur, as well as clear-cell renal carcinoma, pheochromocytoma, endolymphatic sac tumor, neuroendocrine tumor, adenoma of the pancreas, and epididymal cystadenoma. VHL disease occurs in adolescents and young and middle-aged adults.

(continued on page 490)

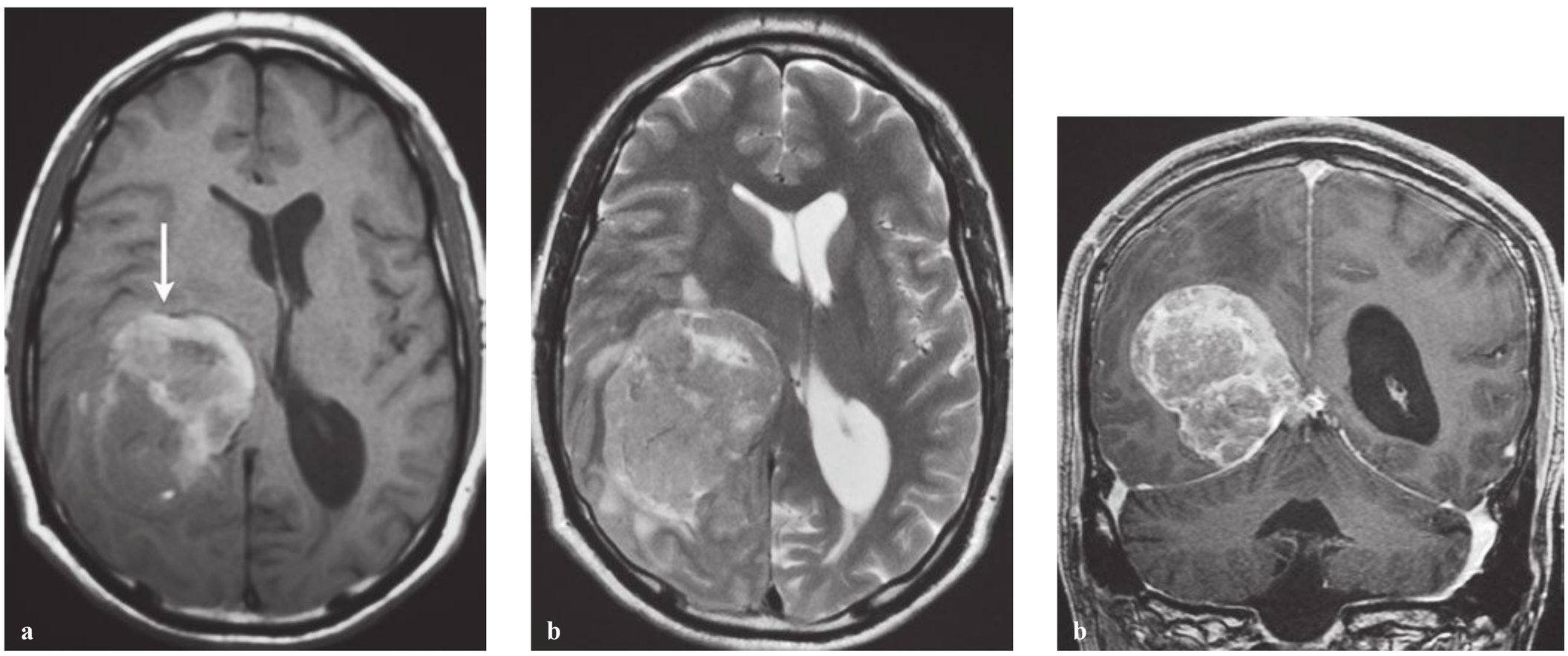

Fig. 2.92 A 57-year-old man with metastatic melanoma within the right lateral ventricle and involving the adjacent brain parenchyma that has **(a)** mixed intermediate and high signal on axial T1-weighted imaging (arrow), **(b)** mixed intermediate and high signal on axial T2-weighted imaging, and **(c)** gadolinium contrast enhancement on coronal T1-weighted imaging.

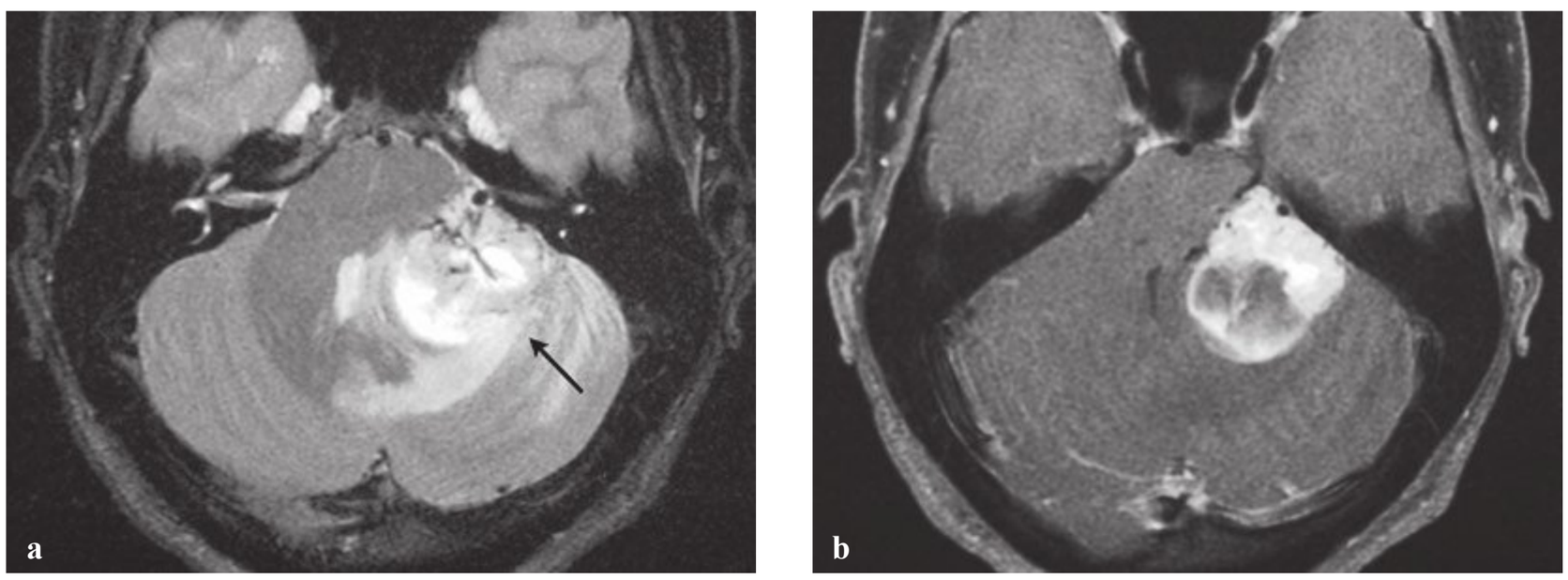

Fig. 2.93 **(a)** A 41-year-old woman with a hemangioblastoma involving the left middle cerebellar peduncle and with extension into the left side of the fourth ventricle that has mixed slightly high and high signal on axial fat-suppressed T2-weighted imaging (arrow) as well as flow voids and peripheral edema. **(b)** The lesion shows heterogeneous gadolinium contrast enhancement on axial fat-suppressed T1-weighted imaging.

Table 2.8 (cont.) Solitary intraventricular lesions in adults

Lesions	Imaging Findings	Comments
Low-grade (diffuse) astrocytoma	MRI: Intra-axial lesion with slightly ill-defined margins or diffuse mass lesion in white matter or brainstem with low-intermediate signal on T1-weighted imaging, high signal on T2-weighted imaging, ± mild gadolinium contrast enhancement. Minimal associated mass effect. Diffusion-weighted imaging: Tumors typically do not show restricted diffusion. CT: Focal or diffuse mass lesion usually located in white matter or brainstem with low-intermediate attenuation, ± mild contrast enhancement. Minimal associated mass effect.	Low-grade astrocytoma (WHO grade II) that accounts for 10 to 15% of astrocytic brain tumors. Often occur in children and adults (20–40 years old). Brainstem gliomas usually occur in children less than 10 years old. Tumors are comprised of well-differentiated fibrillary or gemistocytic neoplastic astrocytes. Can occur in the cerebellum or brainstem. Association with TP53, isocitrate dehydogenase-IDH1 and IDH2, and telomere maintenance protein-ATRX mutations. Mean survival is 6–8 years, and tumors may undergo malignant progression to anaplastic astrocytoma or glioblastoma. Patients with neurofibromatosis type 1 have an increased incidence of brainstem gliomas involving the medulla. Tumors with IDH mutations have a better prognosis than those without.
Anaplastic astrocytoma (**Fig. 2.94**)	MRI: Often irregularly marginated lesion located in white matter with low-intermediate signal on T1-weighted imaging, high signal on T2-weighted imaging, ± gadolinium contrast enhancement. Tumors can have elevated relative cerebral blood volume (rCBV). Diffusion-weighted imaging: Tumors typically do not show restricted diffusion. Magnetic resonance spectroscopy shows decreased N-acetylaspartate (NAA) and high levels of choline. CT: Irregularly marginated mass lesion with mixed low and intermediate attenuation, ± hemorrhage, prominent heterogeneous contrast enhancement, and peripheral edema. Can cross corpus callosum.	Malignant astrocytic tumor (WHO grade III) between diffuse astrocytoma and glioblastoma multiforme. Malignant astrocytes have nuclear atypia and mitotic activity. Ki-67/MIB-1 ranges from 5 to 10% Can progress to glioblastoma. Approximate 2-year survival. Promotor methylation inactivates the effects of the DNA repair enzyme MGMT enabling improved tumor response to alkylating chemotherapy agents. Patients with IDH mutations as well as those who have MGMT promotor methylation have improved responses to chemotherapy.
Glioblastoma multiforme (**Fig. 2.95**)	MRI: Irregularly and poorly marginated mass lesion with necrosis or cyst, mixed signal on T1-weighted imaging, heterogeneous high signal on T2-weighted imaging, ± hemorrhage, and prominent heterogeneous gadolinium contrast enhancement. Increased relative cerebral blood volume (rCBV) is associated with high-grade gliomas from tumor-induced angiogenesis. Other findings include peripheral edema and tumor extension across the corpus callosum. Diffusion-weighted imaging: Tumors typically do not show restricted diffusion. Magnetic resonance spectroscopy shows decreased N-acetylaspartate (NAA) and high levels of choline. CT: Irregularly marginated mass lesion with necrosis or cyst, mixed low and intermediate attenuation, ± hemorrhage, prominent heterogeneous contrast enhancement, and peripheral edema. Can cross corpus callosum.	Glioblastoma multiforme is the most common primary CNS tumor (WHO grade IV) and accounts for 15% of intracranial tumors and up to 75% of astrocytic neoplasms, with an incidence of 3 per 100,000. Most patients are over 50 years old. These highly malignant astrocytic neoplasms have nuclear atypia with mitotic activity, cellular pleomorphism, necrosis, and microvascular proliferation and invasion. Ki-67/MIB-1 ranges from 15 to 20% Associated with mutations involving RTK/phosphatase–PTEN/PI3K signal pathway, TERT, and TP53 and Rb1 tumor suppressor genes. Promotor methylation resulting in inactivation of the MGMT DNA repair enzyme enables improved malignant tumor response to chemotherapy in patients lacking IDH mutations. The extent of the lesion is underestimated by MRI, and survival is often < 1 year. Patients with secondary type glioblastoma who have IDH mutations can have a better response to chemotherapy and prognosis than those without.
Lymphoma (**Fig. 2.96**)	MRI: Primary CNS lymphoma has focal or infiltrating lesions located in the basal ganglia, posterior fossa/brainstem, ventricles, leptomeninges, and/or dura, with low-intermediate signal on T1-weighted imaging, intermediate-slightly high signal on T2-weighted imaging, ± hemorrhage/necrosis. Lesions usually show gadolinium contrast enhancement. CT: Lesions have low-intermediate attenuation and may show contrast enhancement, ± bone destruction.	Primary CNS lymphoma is more common than secondary, usually in adults > 40 years old. B-cell lymphoma is more common than T-cell lymphoma, with an increasing incidence related to the number of immunocompromised patients in the population. MRI features of primary and secondary lymphoma of brain overlap. Intracranial lymphoma can involve the brain, dura, leptomeninges, and/or ventricles.

(continued on page 492)

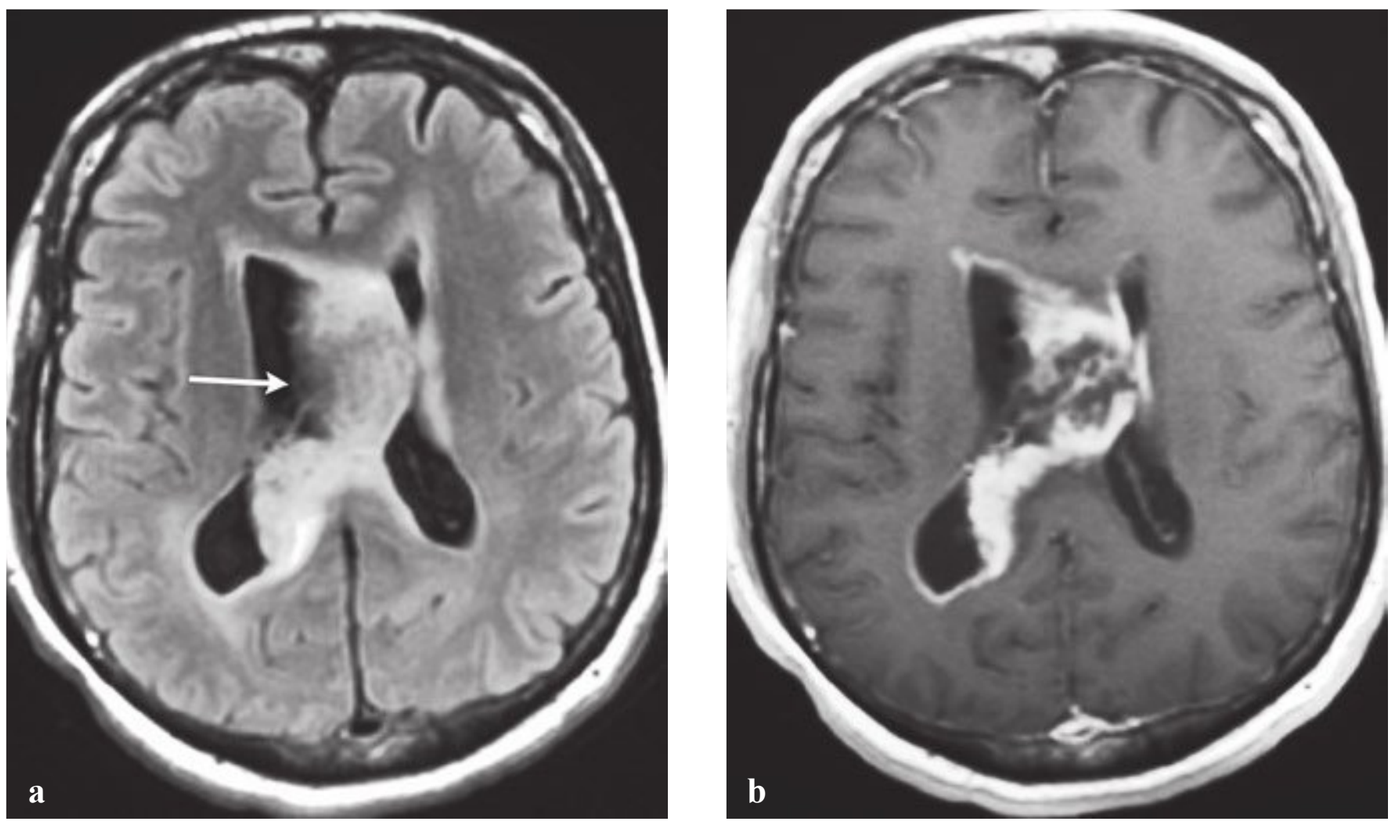

Fig. 2.94 A 51-year-old man with an anaplastic astrocytoma involving the septum pellucidum with intraventricular extension that has **(a)** high signal on axial FLAIR (arrow) and **(b)** heterogeneous gadolinium contrast enhancement on axial T1-weighted imaging. Contrast enhancement is also seen along ependymal lining of the right lateral ventricle, representing a disseminated tumor.

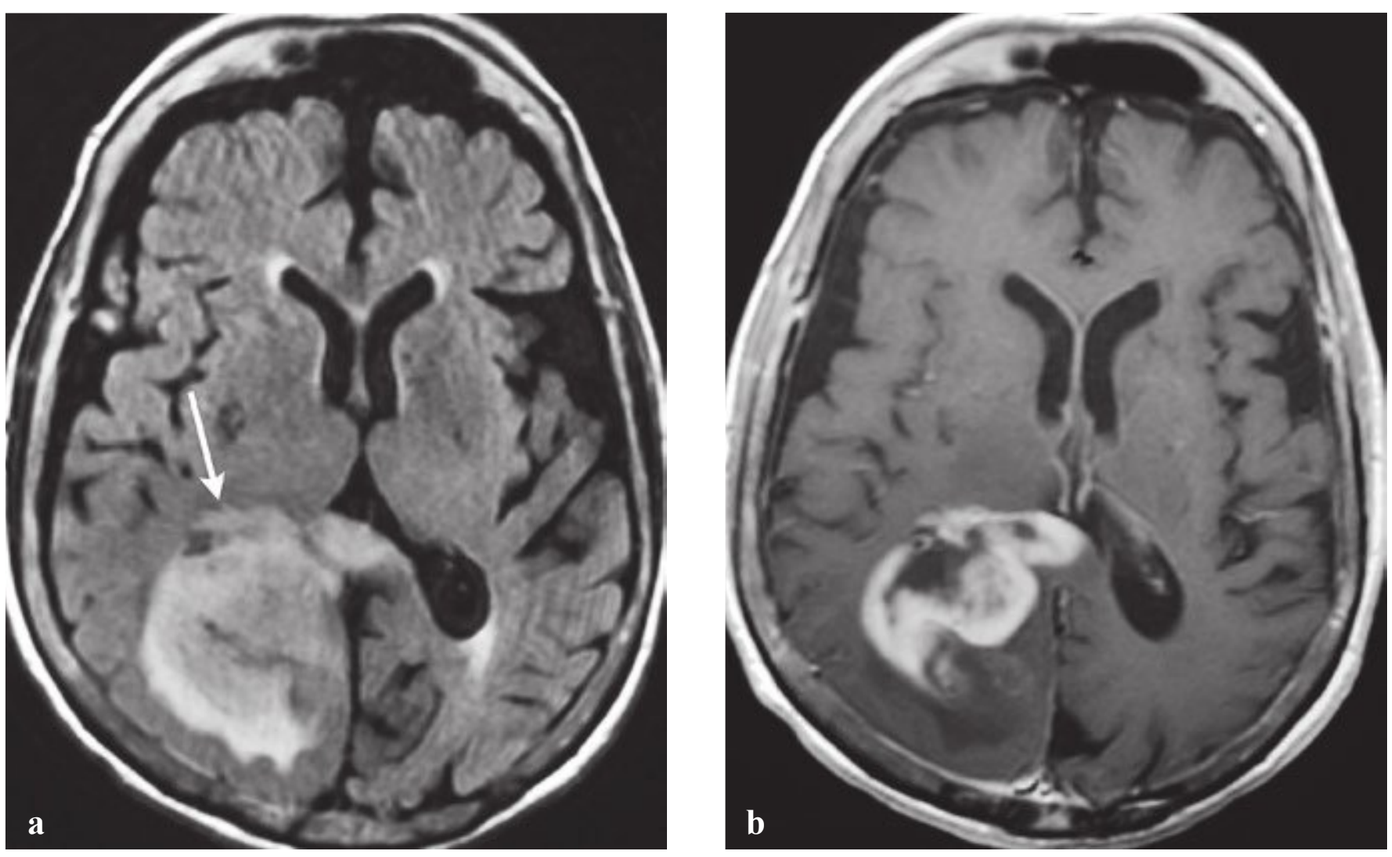

Fig. 2.95 An 81-year-old woman with glioblastoma multiforme in the posterior right cerebral hemisphere extending into the atrium of the right lateral ventricle and splenium of the corpus callosum. The tumor has ill-defined margins, **(a)** high signal on axial FLAIR (arrow), and **(b)** heterogeneous gadolinium contrast enhancement on axial T1-weighted imaging.

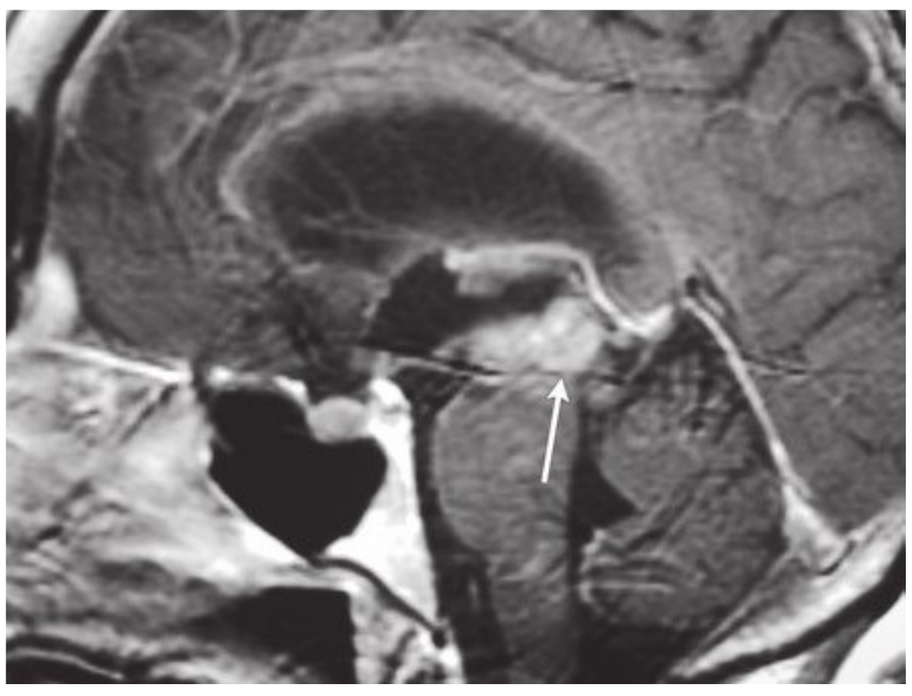

Fig. 2.96 A 62-year-old woman with large B-cell non-Hodgkin lymphoma with a gadolinium-enhancing lesion (arrow) within the third ventricle seen on sagittal T1-weighted imaging.

Table 2.8 (cont.) Solitary intraventricular lesions in adults

Lesions	Imaging Findings	Comments
Ependymoma (**Fig. 2.97**)	MRI: Circumscribed, lobulated, supratentorial lesion, often extraventricular, ± cysts, calcifications, and/or hemorrhage; low-intermediate signal on T1-weighted imaging, intermediate-high signal on T2-weighted imaging; variable gadolinium contrast enhancement. Tumors have elevated relative cerebral blood volume (rCBV) as well as delayed contrast retention secondary to intratumoral fenestrated blood vessels. Diffusion-weighted imaging: Usually there is no restricted diffusion. Magnetic resonance spectroscopy: Elevated choline and decreased N-acetylaspartate (NAA), similar to other neoplasms. CT: Circumscribed, lobulated, supratentorial lesion, often extraventricular, ± cysts and/or calcifications (up to 50%), with low-intermediate attenuation and variable contrast enhancement.	Ependymoma is a slow-growing tumor (WHO grade II) comprised of neoplastic cells with monomorphic round/oval nuclei containing speckled chromatin, perivascular pseudorosettes, and ependymal rosettes. Zones of myxoid degeneration, hyalinization of blood vessels, hemorrhage, and/or calcifications may occur within tumors. Ependymoma accounts for 6–12% of intracranial tumors, with an incidence of 0.22 to 0.29 per 100,000. Occurs more commonly in children than in adults; one-third of tumors are supratentorial and two-thirds are infratentorial. Children with infratentorial ependymomas range in age from 2 months to 16 years (mean age = 6.4 years). Supratentorial ependymomas occur in children and adults. Immunoreactive to glial fibrillary acidic protein (GFAP), S-100, vimentin, and/or epithelial mebrane antigen (EMA). Associated with neurofibromatosis type 2 and genetic mutations involving chromosomes 22, 9, 6, and 3. Usually lack mutation of IDH gene. Survival is 57% at 5 years and 45% at 10 years.
Anaplastic ependymoma (**Fig. 2.98**)	MRI: Irregularly marginated mass lesion with necrosis or cyst, mixed signal on T1-weighted imaging, heterogeneous high signal on T2-weighted imaging, ± hemorrhage, calcifications, heterogeneous gadolinium contrast enhancement, and peripheral edema. Can disseminate within the CSF. CT: Irregularly marginated mass lesion with necrosis or cyst, mixed attenuation, ± hemorrhage, calcifications, heterogeneous contrast enhancement, and peripheral edema. Can disseminate within the CSF.	Malignant glioma (WHO grade III) with ependymal differentiation and high mitotic activity, microvascular proliferation, and pseudopalisading necrosis. Associated with poor prognosis in patients with prominent anaplastic features, CSF metastases, and incomplete resection.

(continued on page 494)

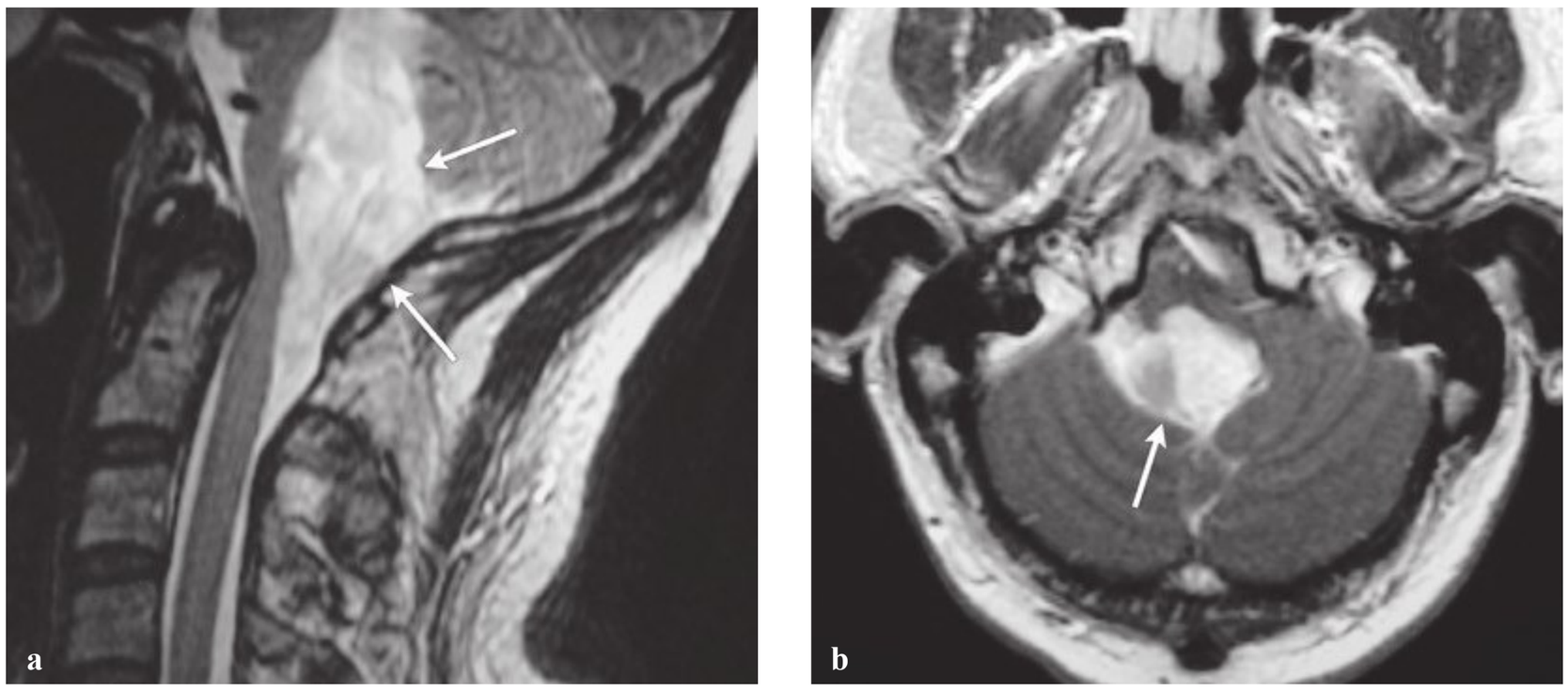

Fig. 2.97 A 34-year-old man with an ependymoma within the fourth ventricle that has **(a)** high signal on sagittal T2-weighted imaging (arrows) and **(b)** gadolinium contrast enhancement on axial T1-weighted imaging (arrow). The tumor extends inferiorly through a widened foramen of Magendie **(a)** and laterally into the right foramen of Luschka **(b)**.

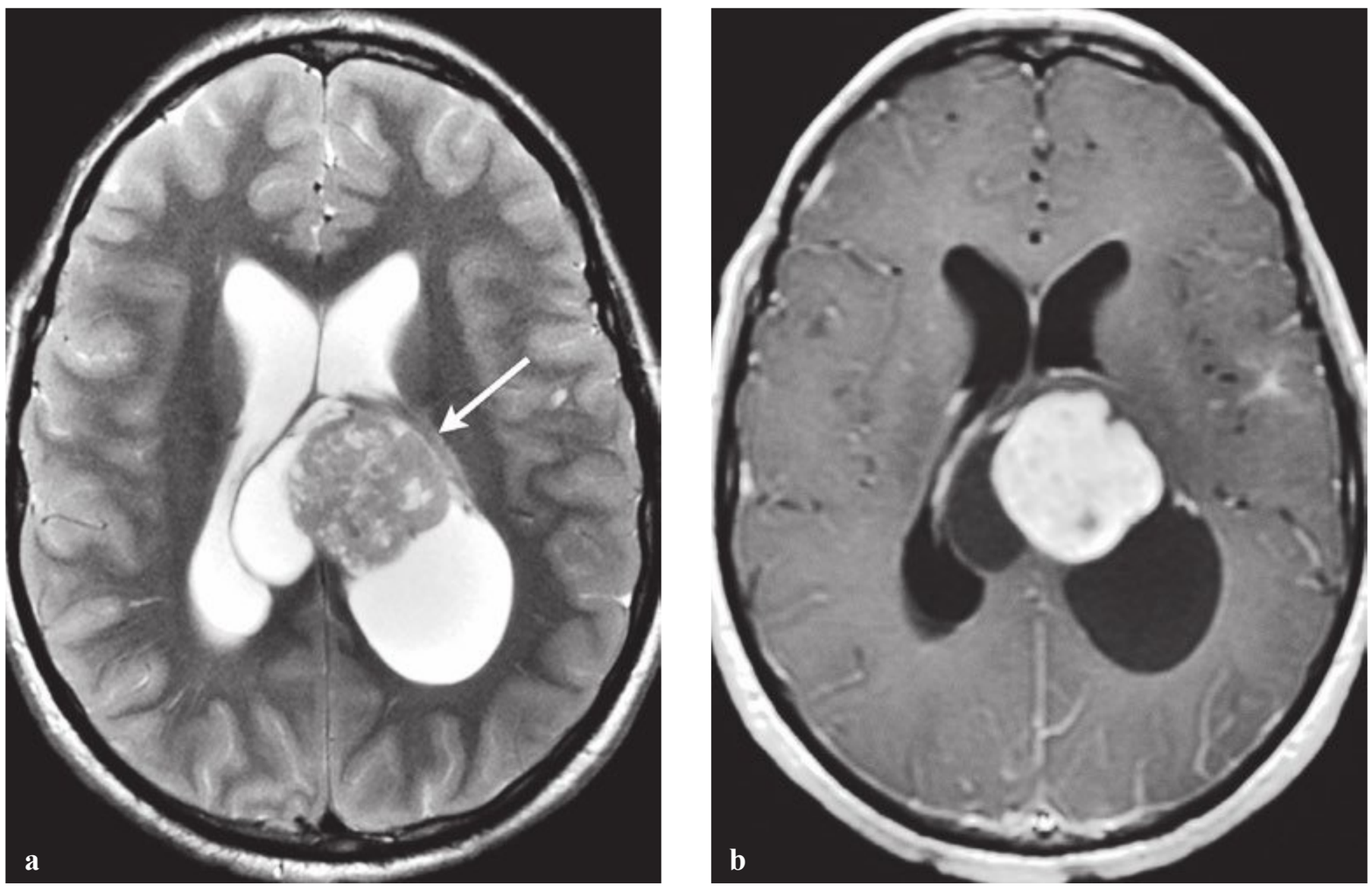

Fig. 2.98 **(a)** Anaplastic ependymoma within the left lateral ventricle has a solid portion with mixed intermediate and high signal on axial T2-weighted imaging (arrow) as well as a tumoral cyst medially. **(b)** The solid portion of the tumor shows prominent gadolinium contrast enhancement on axial T1-weighted imaging.

Table 2.8 (cont.) Solitary intraventricular lesions in adults

Lesions	Imaging Findings	Comments
Subependymoma (**Fig. 2.99, Fig. 2.100,** and **Fig. 2.101**)	MRI: Tumors typically attach to ventricular walls (fourth ventricle, 40–50%; lateral ventricle, 30–40%; third ventricle, 10%). Lesions have circumscribed margins, low-intermediate signal on T1-weighted imaging, and heterogeneous slightly high to high signal on T2-weighted imaging. May contain sites of hemorrhage or calcification. Variable degrees of gadolinium contrast enhancement. CT: Lesions have circumscribed margins and low-intermediate attenuation. May contain sites of hemorrhage or calcification. Variable degrees of contrast enhancement.	Slow-growing low-grade (WHO grade I) glial neoplasms comprised of clusters of tumor cells with isomorphic nuclei within a dense matrix of cell processes. Mitotic activity is absent or rare. Immunoreactive to glial fibrillary acidic protein (GFAP). Account for 8% of ependymal tumors. Complete resection can be curative.
Meningioma (**Fig. 2.102**)	Extra-axial dura-based lesions that are well circumscribed. Locations are supra- > infratentorial, parasagittal > convexity > sphenoid ridge > parasellar > posterior fossa > optic nerve sheath > intraventricular. MRI: Dura-based tumors with intermediate signal on T1-weighted imaging, intermediate to slightly high signal on T2-weighted imaging, usually prominent gadolinium contrast enhancement often with a dural tail, ± calcifications. Intratumoral hemorrhage and cystic or necrotic foci can occur in 15% Diffusion-weighted imaging/diffusion tensor imaging: ADC values vary among the different subtypes of meningioma. Some tumors can show restricted diffusion, although these findings can be seen with both benign and atypical tumors. Magnetic resonance spectroscopy: Can show elevated alanine (1.5 ppm), lactate, choline, and glutamine/glutamate levels and reduced N-acetylaspartate (NAA). CT: Tumors have intermediate attenuation with or without calcifications, with or without hyperostosis, and usually show prominent contrast enhancement.	Meningiomas are the most common extra-axial tumors and account for up to 26% of primary intracranial tumors. Annual incidence is 6 per 100,000. Meningioma typically occurs in adults (> 40 years old) and in women > men. Composed of neoplastic meningothelial (arachnoidal or arachnoid cap) cells. Meningiomas are usually solitary and sporadic, but they can also occur as multiple lesions in patients with neurofibromatosis type 2. Eighty percent of meningiomas are benign (WHO grade I), although 15% have atypical features (WHO grade II) and ~ 5% have anaplastic histologic features (WHO grade III). Can occur secondary to radiation treatment, with latencies ranging from 19 to 35 years. Classified into different subtypes, such as meningothelial, fibrous (fibroblastic), transitional (mixed), psammomatous, angiomatous, atypical, and anaplastic. Meningothelial, fibrous, and transitional meningiomas are the most common intracranial types. Usually show immunoreactivity to epithelial membrane antigen (EMA) and vimentin. Secretory meningiomas are typically immunoreactive to CEA. Associated cytogenetic findings of deletion of chromosome 22. Mutations in the NF2 tumor suppressor gene on chromosome 22 have been found in 60% of sporadic meningiomas.

(continued on page 496)

Fig. 2.99 A 40-year-old man with a subependymoma (arrow) with high signal on axial T2-weighted imaging within the frontal horn of the left lateral ventricle causing hydrocephalus.

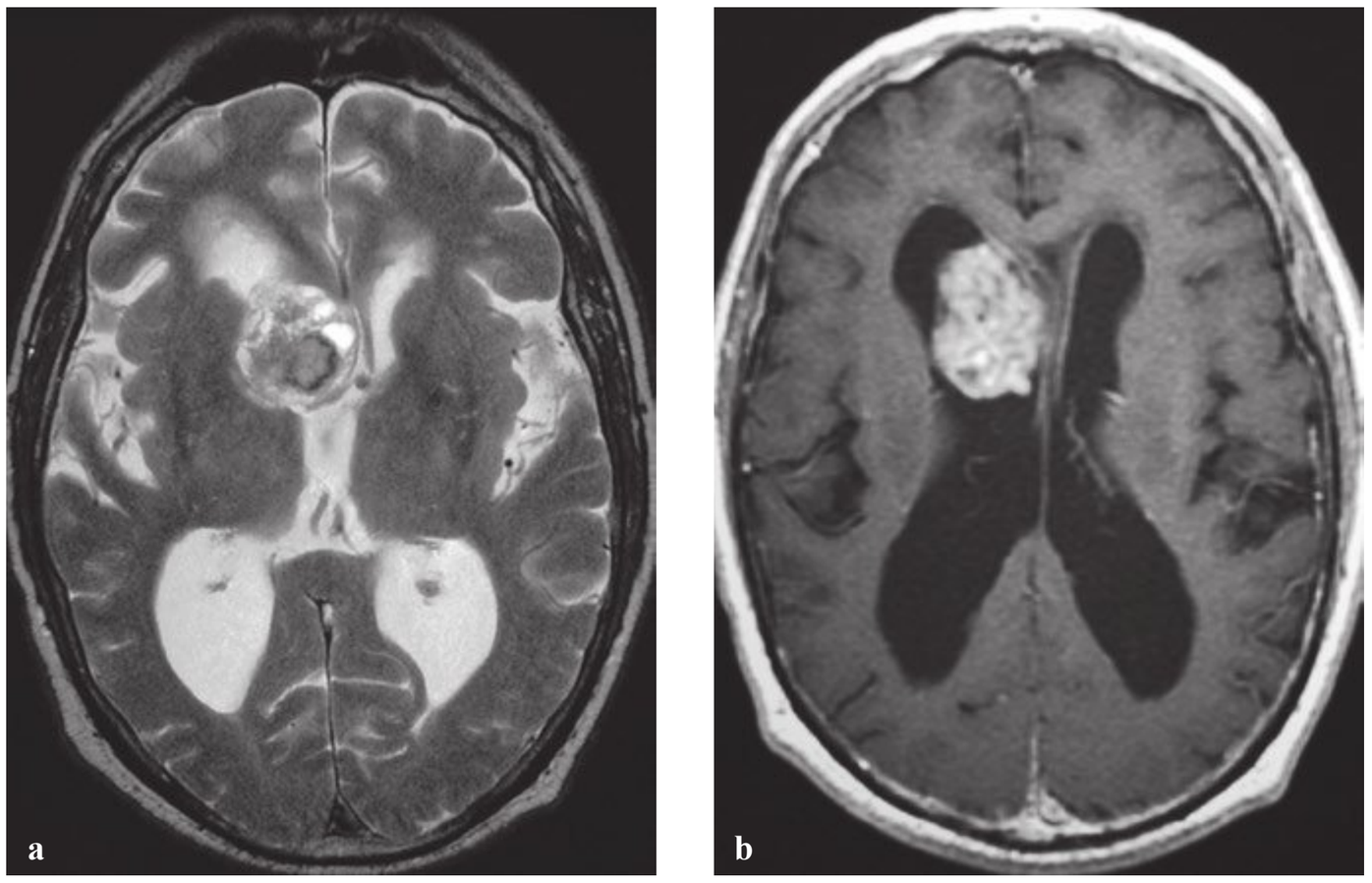

Fig. 2.100 A 75-year-old man with a subependymoma at the foramen of Monro causing obstruction of CSF outflow from the right lateral ventricle. **(a)** The lesion has heterogeneous mixed high, low, and intermediate signal on axial T2-weighted imaging and **(b)** shows gadolinium contrast enhancement on axial T1-weighted imaging.

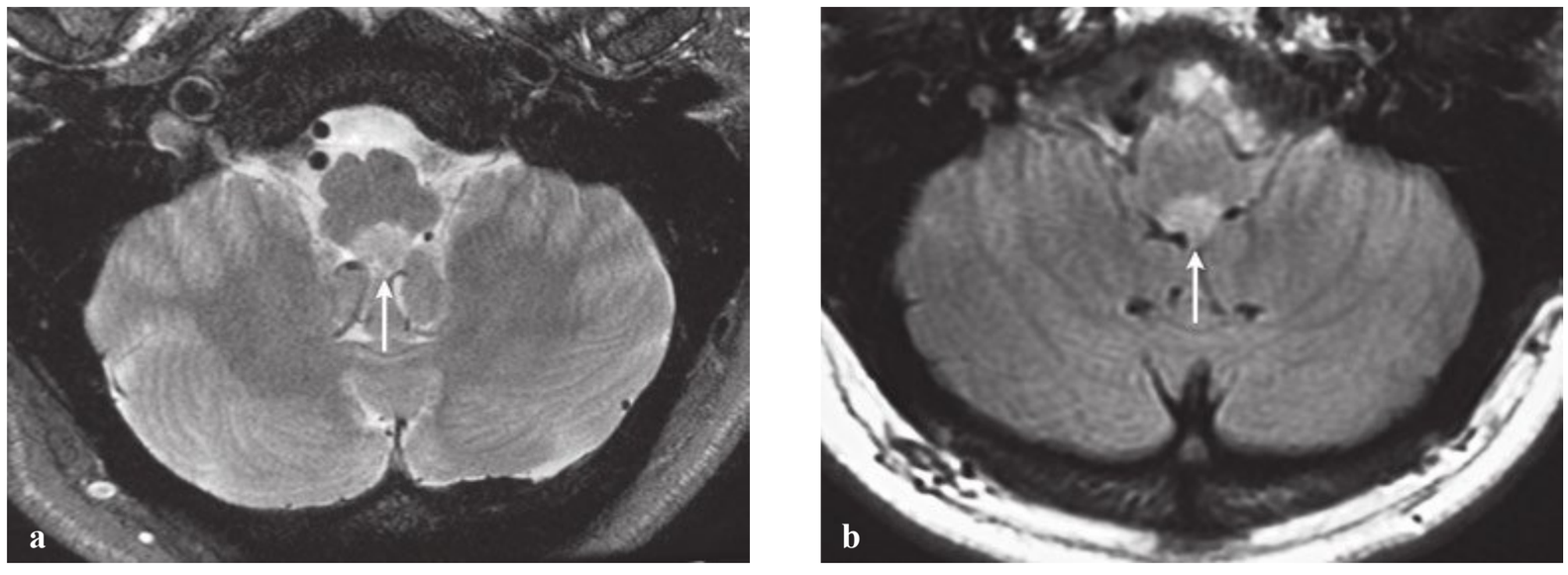

Fig. 2.101 A 43-year-old man with a subependymoma in the lower fourth ventricle that has **(a)** intermediate signal on axial T2-weighted imaging (arrow) and **(b)** slightly high signal on FLAIR imaging (arrow).

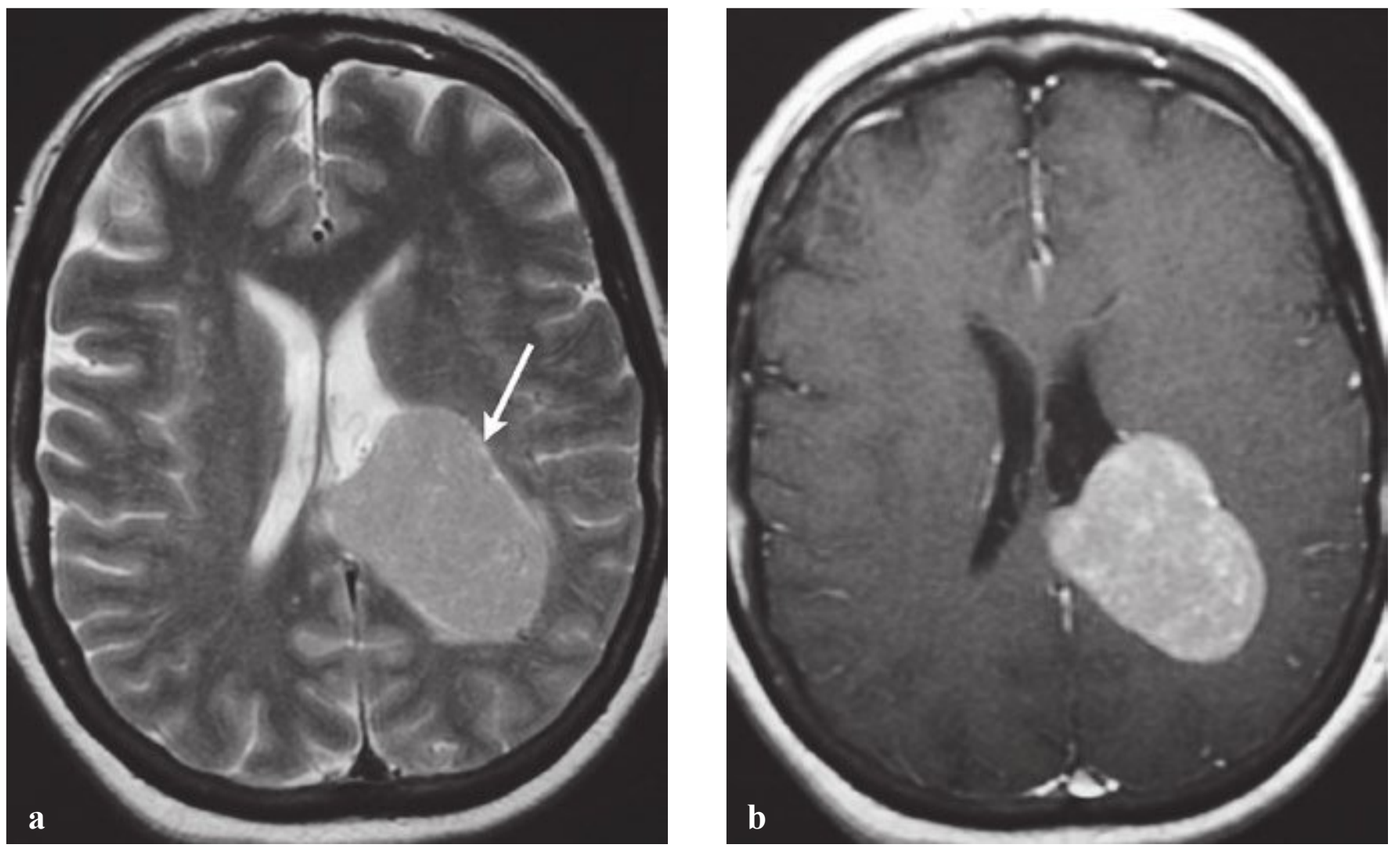

Fig. 2.102 A 62-year-old woman with an intraventricular meningioma in the left lateral ventricle that **(a)** has intermediate to slightly high signal on axial T2-weighted imaging (arrow) and **(b)** shows gadolinium contrast enhancement on axial T1-weighted imaging.

Table 2.8 (cont.) Solitary intraventricular lesions in adults

Lesions	Imaging Findings	Comments
Hemangiopericytoma (**Fig. 2.103**)	MRI: Solitary dura-based tumors ranging from 2 to 7 cm in diameter. These neoplasms can rarely occur within ventricles. Tumors usually have low-intermediate signal on T1-weighted imaging and intermediate to slightly high signal on T2-weighted imaging, ± intratumoral flow voids. Tumors usually show prominent gadolinium contrast enhancement, often with a dural tail, ± calcifications. Intratumoral hemorrhage and cystic or necrotic foci can occur in 30% Magnetic resonance spectroscopy may show elevated choline peak. Relative ratios of myo-inositol, glucose, and glutathione with respect to glutamate are higher in hemangiopericytomas than in meningiomas. CT: Tumors have intermediate attenuation with or without calcifications and usually show prominent contrast enhancement.	Hemangiopericytomas are rare (WHO grade II) neoplasms that account for 0.4%of primary intracranial tumors and are 50 times less frequent than meningiomas. Tumors are composed of closely packed cells with scant cytoplasm and round, ovoid, or elongated nuclei with moderately dense chromatin. Numerous slitlike vascular channels are seen that are lined by flattened endothelial cells, ± zones of necrosis. Immunoreactive to vimentin (85%), factor XIIIa (80–100%), and variably to Leu-7 and CD34. Associated with abnormalities involving chromosome 12. Typically occur in young adults, (mean age = 43 years) and in males > females. Sometimes referred to as angioblastic meningioma or meningeal hemangiopericytoma, they arise from vascular cells—pericytes. Recur and metastasize more frequently than meningiomas do.
Choroid plexus papilloma (**Fig. 2.104**)	MRI: Circumscribed and/or lobulated lesions with papillary projections, intermediate signal on T1-weighted imaging, mixed intermediate-high signal on T2-weighted imaging, and usually prominent gadolinium contrast enhancement, ± calcifications. Locations: atrium of lateral ventricle (children) > fourth ventricle (adults), rarely other locations, such as third ventricle. Associated with hydrocephalus from CSF overproduction or mechanical obstruction. CT: Circumscribed and/or lobulated lesions with papillary projections, intermediate attenuation, usually prominent contrast enhancement, ± calcifications.	Rare benign (WHO grade I) intraventricular neoplasms derived from choroid plexus epithelium in which a single layer of cuboidal or columnar epithelial cells with round/oval nuclei overlies fibrovascular connective tissue in frondlike patterns. Occurs in lateral ventricle (50%), fourth ventricle/CP angle (40%), third ventricle (5%), and multiple ventricles (5%). Occurs in children and adults. Tumors in the lateral ventricles account for up to 80%of cases in patients less than 20 years old. Lesions in the fourth ventricle are most common in adults. Tumors have very low mitotic activity. Immunoreactive to cytokeratins, vimentin, podoplanin, S-100, and transthyretin. Can be cured by surgical resection.
Atypical choroid plexus papilloma	MRI: Circumscribed and/or lobulated lesions with papillary projections, intermediate signal on T1-weighted imaging, mixed intermediate-high signal on T2-weighted imaging, and usually prominent gadolinium contrast enhancement, ± calcifications. Locations: atrium of lateral ventricle (children) > fourth ventricle (adults), rarely other locations, such as third ventricle. Associated with hydrocephalus. CT: Circumscribed and/or lobulated lesions with papillary projections, intermediate attenuation, usually prominent contrast enhancement, ± calcifications.	Rare (WHO grade II) intraventricular neoplasms derived from choroid plexus that have some histologic features that overlap those for choroid plexus papillomas, although atypical papillomas can have higher mitotic activity (> 2/HPF), increased cellularity, nuclear pleomorphism, partial loss of the papillary morphology, and/or necrosis. Immunoreactive to cytokeratins and S-100. Occur in children and adults. Can be cured by surgical resection.

(continued on page 498)

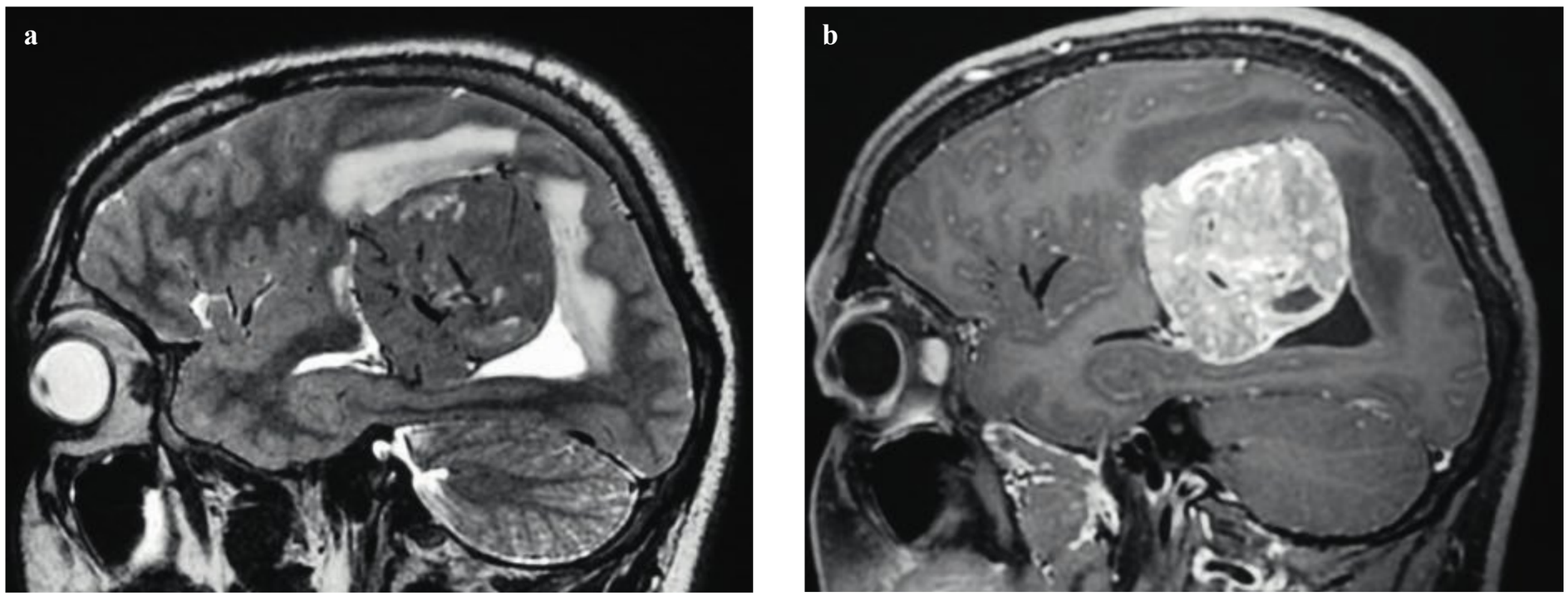

Fig. 2.103 A 24-year-old man with an intraventricular hemangiopericytoma in the left lateral ventricle causing hydrocephalus. **(a)** The tumor has circumscribed margins, heterogeneous slightly high signal on sagittal T2-weighted imaging with intratumoral flow voids, and **(b)** gadolinium contrast enhancement on sagittal T1-weighted imaging.

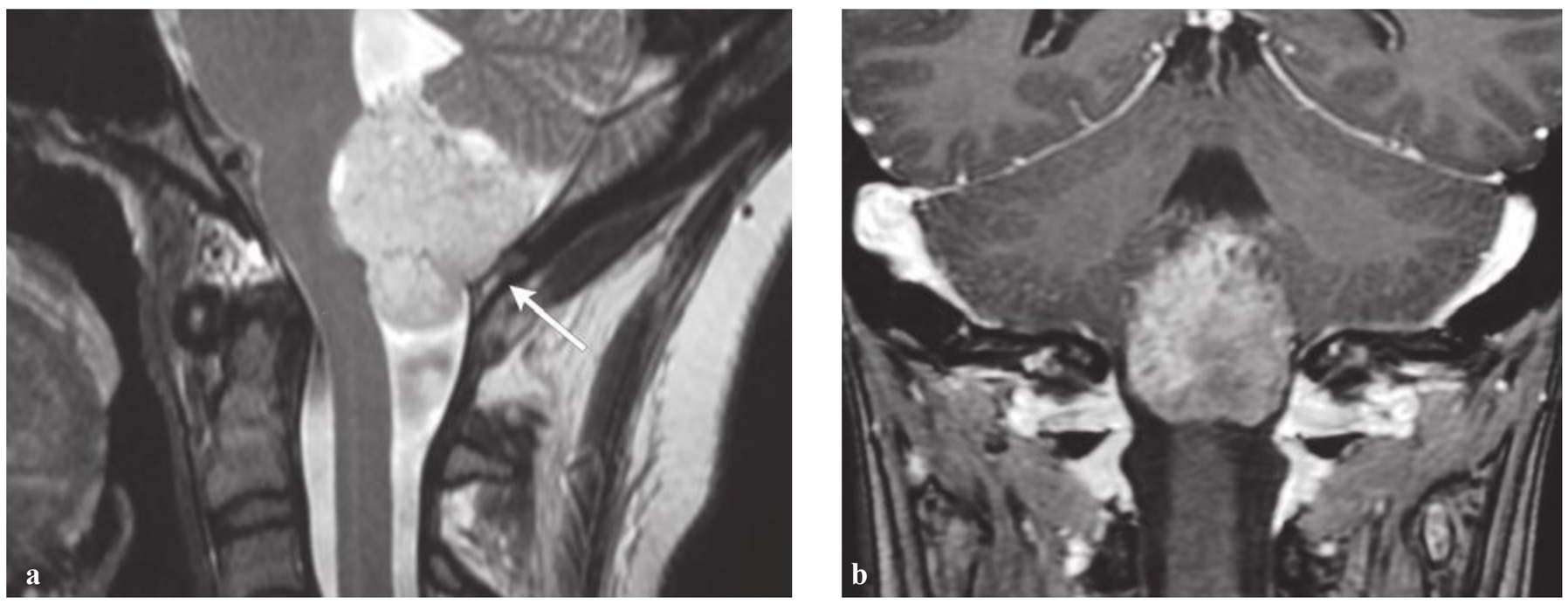

Fig. 2.104 A 25-year-old woman with a choroid plexus papilloma in the inferior portion of the fourth ventricle that **(a)** has slightly high signal on sagittal T2-weighted imaging (arrow) and **(b)** shows gadolinium contrast enhancement on coronal T1-weighted imaging.

Table 2.8 (cont.) Solitary intraventricular lesions in adults

Lesions	Imaging Findings	Comments
Choroid plexus carcinoma (**Fig. 2.105**)	MRI: Large, lobulated neoplasms with mean tumor size of 5 cm, often with irregular margins ± brain invasion. On T1-weighted imaging, tumors have heterogeneous intermediate signal with foci of high signal in 45% from areas of hemorrhage. On T2-weighted imaging, solid portions of the tumor often have heterogeneous intermediate to slightly high signal. Small zones with low signal on T2-weighted imaging can occur from sites of hemorrhage or calcifications. Intratumoral cystic or necrotic zones occur in 64%and have high signal on T2-weighted imaging. Tubular flow voids representing blood vessels occur in up to 55%of tumors. Tumors typically show prominent gadolinium contrast enhancement. Nearly 75%of tumors have irregular enhancing margins from ependymal invasion. Disseminated gadolinium-enhancing tumor in the leptomeninges can occur in up to 45% Hydrocephalus is seen in up to 80% CT: Large intraventricular tumors with intermediate attenuation as well as foci with high attenuation from areas of hemorrhage or calcification and low attenuation zones from cystic or necrotic zones. Tumors typically show prominent contrast enhancement.	Rare malignant (WHO grade III) intraventricular neoplasms derived from choroid plexus epithelium that contain irregular sheets of neoplastic cells with nuclear pleomorphism, high mitotic activity (> 5/HPF), loss of the papillary morphology, and necrotic and/or hemorrhagic areas. Immunoreactive to cytokeratins. Account for 0.1%of all intracranial tumors and 0.6% of primary pediatric CNS neoplasms. These tumors are five times less frequent than choroid plexus papillomas. Median ages range from 12 to 32 months and rarely occur in adults. Most commonly occur in the lateral ventricle, followed by the fourth and third ventricles. These tumors commonly disseminate along CSF pathways and invade brain tissue. Poor prognosis, with 5-year survival of 45%
Central neurocytoma (**Fig. 2.106**)	MRI: Circumscribed lesion typically located at the margin of lateral ventricle or septum pellucidum with intraventricular protrusion, heterogeneous low and intermediate signal on T1-weighted imaging, heterogeneous intermediate-high signal on T2-weighted imaging, ± calcifications and/or small cysts, and heterogeneous gadolinium contrast enhancement. Diffusion-weighted imaging: Lesions can show reduced ADC values. Magnetic resonance spectroscopy: Elevated glycine (3.55 ppm), choline, and alanine levels and decreased N-acetylaspartate (NAA). Rare extraventricular neurocytomas have been reported in the frontal and parietal lobes and sellar region. CT: Circumscribed lesion located at margin of lateral ventricle or septum pellucidum with intraventricular protrusion, heterogeneous low and intermediate attenuation, ± calcifications and/or small cysts, and heterogeneous contrast enhancement.	Slow-growing rare neuroepithelial tumor (WHO grade I) composed of uniform round cells with neuronal differentiation. Immunoreactive to synaptophysin and NeuN. Represent ~ 0.5%of intracranial tumors. Patients range from 8 days to 67 years old (mean age = 29 years). Imaging appearance similar to intraventricular oligodendrogliomas. Typically benign tumors with favorable prognosis after surgery.
Papillary glioneuronal tumor	MRI: Circumscribed lesions in the cerebral hemispheres and occasionally within the ventricles. Tumors have heterogeneous low and intermediate signal on T1-weighted imaging, heterogeneous intermediate-high signal on T2-weighted imaging, and heterogeneous gadolinium contrast enhancement. CT: Circumscribed lesion with heterogeneous low and intermediate attenuation and heterogeneous contrast enhancement.	Rare, low-grade tumor (WHO grade I) composed of pseudostratified layers of small cuboidal glial cells with round nuclei, hyalinized blood vessels, and collections of neurocytes and ganglion cells. Immunoreactive to glial fibrillary acidic protein (GFAP), NeuN, synaptophysin, neuron-specific enolase (NSE), and class III b-tubulin. Patients range from 4 to 75 years old (mean age = 27 years). Long-term survival is typical after surgical resection.

(continued on page 500)

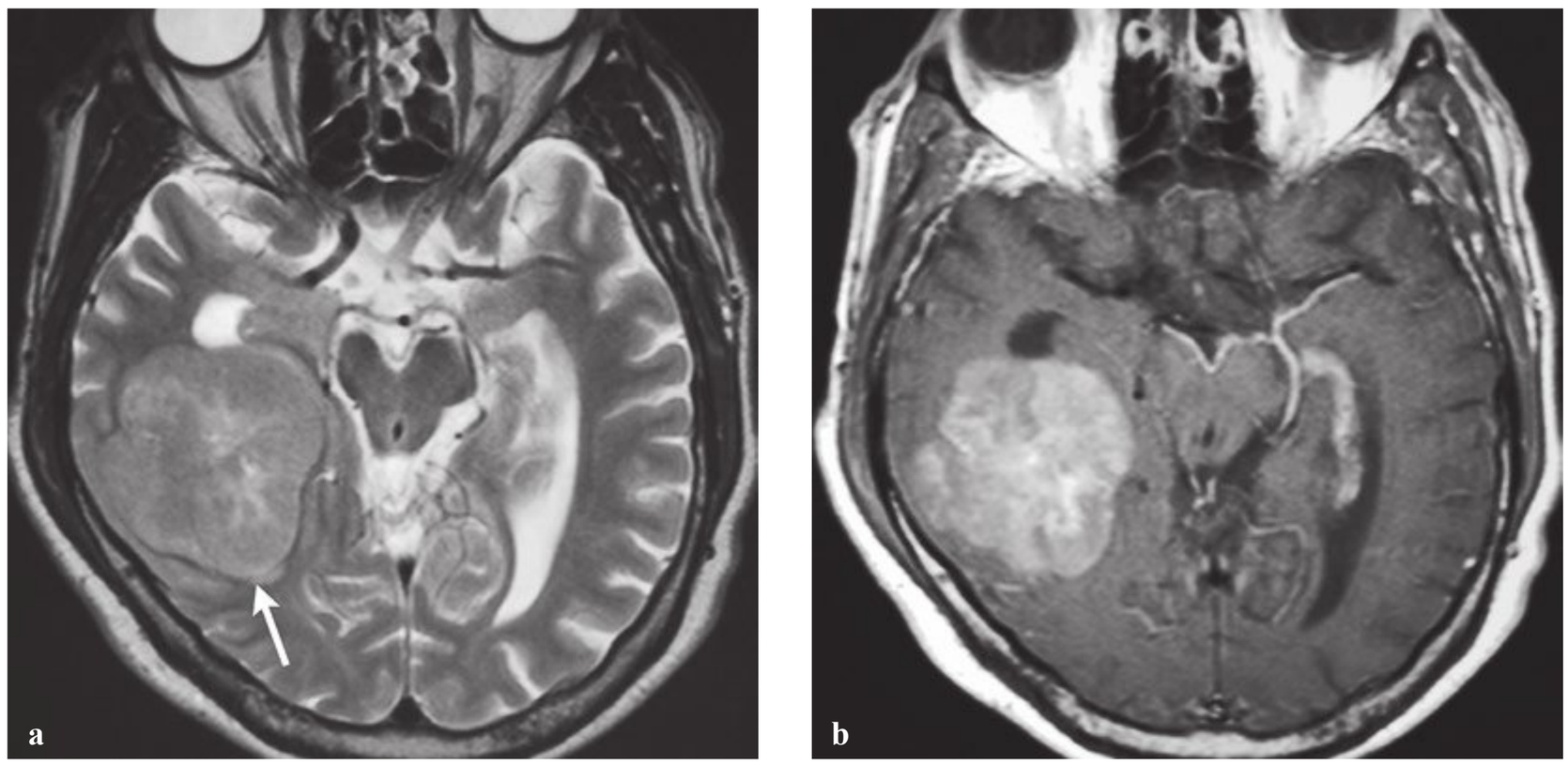

Fig. 2.105 A 49-year-old man with a choroid plexus carcinoma in the right lateral ventricle that has **(a)** slightly irregular margins, heterogeneous intermediate and slightly high signal on axial T2-weighted imaging (arrow) and **(b)** gadolinium contrast enhancement on axial T1-weighted imaging, with ill-defined margins posterolaterally representing invasion of adjacent brain parenchyma.

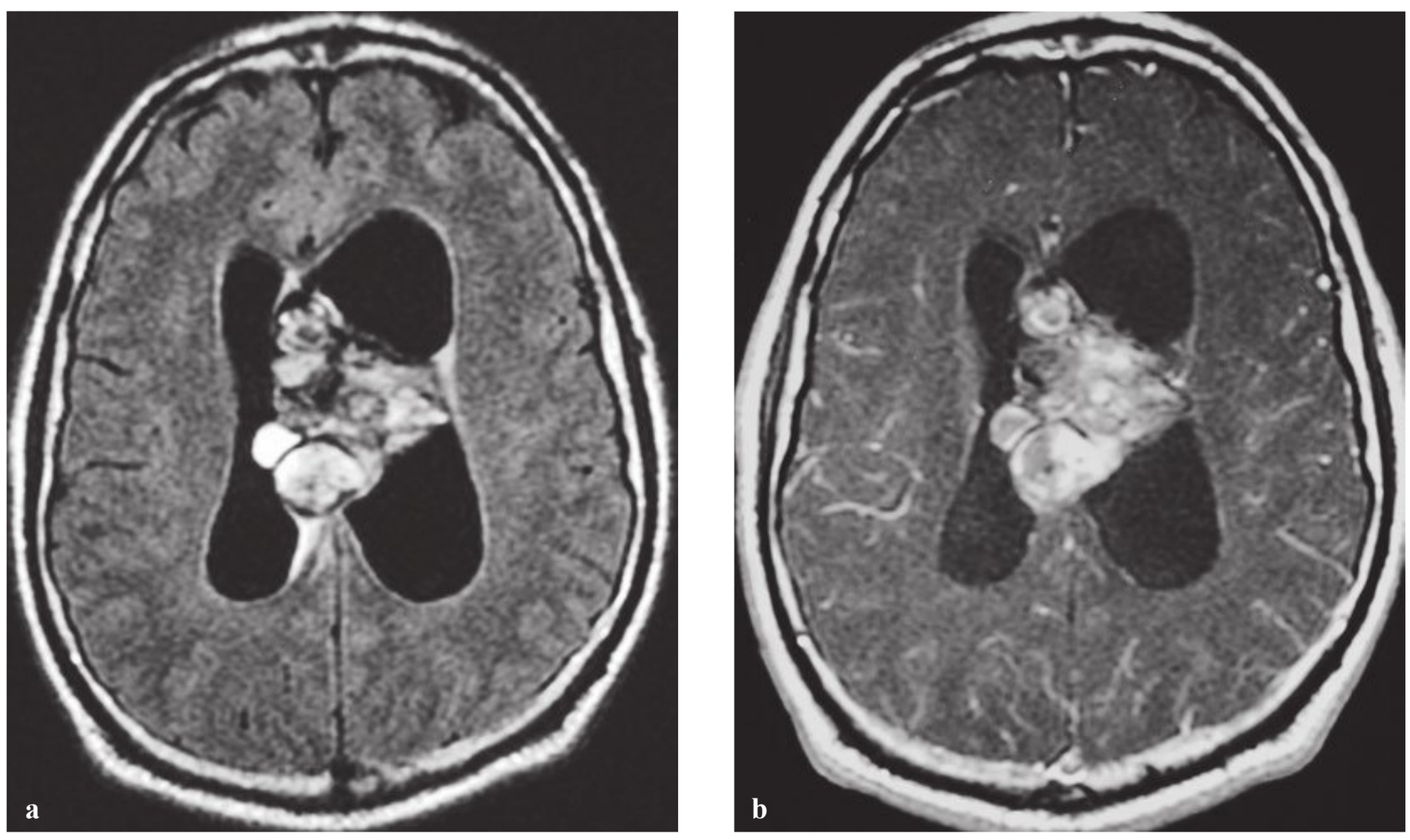

Fig. 2.106 A 38-year-old man with a central neurocytoma involving the septum pellucidum with extension into the lateral ventricles. **(a)** The tumor has lobulated margins, heterogeneous high and low signal on axial FLAIR, and **(b)** heterogeneous gadolinium contrast enhancement on axial T1-weighted imaging.

Table 2.8 (cont.) Solitary intraventricular lesions in adults

Lesions	Imaging Findings	Comments
Chordoid glioma of the third ventricle (**Fig. 2.107**)	MRI: Circumscribed lesions located at the anteroinferior portion of the third ventricle that have intermediate signal on T1-weighted imaging and intermediate to slightly high signal on T2-weighted imaging, ± cystic changes. Tumors usually show prominent gadolinium contrast enhancement. CT: Lesions often have intermediate attenuation and show contrast enhancement.	Rare slow-growing glial tumor (WHO grade II) composed of epithelioid neoplastic cells containing uniform moderate-sized nuclei (low mitotic activity, < 1/HPF) within eosinophilic cytoplasm. Neoplastic cells can be organized as clusters or cords within mucinous stroma with lymphoplasmacytic infiltrate. Immunoreactive to glial fibrillary acidic protein (GFAP), EGFR, and merlin (NF2 gene product). Usually occur in adults (mean age = 46 years), with 2:1 female predominance. Tumors typically occur at the anteroinferior portion of the third ventricle adjacent to the hypothalamus. Local recurrence and hypothalamic dysfunction can occur after surgery.
Craniopharyngioma (**Fig. 2.108**)	MRI: The adamantinomatous type usually has circumscribed, lobulated margins; occurs in both suprasellar and intrasellar locations > suprasellar > intrasellar (10%) sites; variable low, intermediate and/or high signal on T1- and T2-weighted imaging; ± nodular or rim gadolinium contrast enhancement. May contain cysts, lipid components, and calcifications. The squamous papillary type can occur as a solid lesion with intermediate signal on T1-weighted imaging that shows gadolinium contrast enhancement. CT: Circumscribed, lobulated lesions with variable low, intermediate, and/or high attenuation, ± nodular or rim contrast enhancement. May contain cysts, lipid components, and calcifications. Calcifications often occur in the adamantinomatous type.	Usually histologically benign but locally aggressive lesions arising in squamous epithelial rests along Rathke's cleft. Occur in children (10 years old) and adults (> 40 years old), males = females. Account for 3% of all intracranial tumors. Can be categorized into adamantinomatous and squamous-papillary types. The adamantinomatous type is more common and has a bimodal age distribution, occurring in children and adults, whereas the squamous-papillary type usually occurs in adults. Craniopharyngiomas are histologically benign, but their insinuating pattern of growth makes complete surgical excision very difficult or impossible.
Germ cell tumor (**Fig. 2.109**)	MRI: Tumors often have intermediate signal on T1-weighted imaging and slightly high to high signal on T2-weighted imaging and show gadolinium contrast enhancement, ± cysts, ± gadolinium-enhancing disseminated subarachnoid and/or intraventricular tumor. Some germ cell tumors can have mixed signal on T1- and T2-weighted imaging secondary to the presence of cysts, hemorrhage, and/or calcifications. CT: Circumscribed tumors with intermediate to slightly increased attenuation, ± disseminated contrast-enhancing leptomeningeal and/or intraventricular tumor.	Extragonadal germ cell tumors include germinoma (most common), mature teratoma, malignant teratoma, yolk sac tumor, embryonal carcinoma, and chroriocarcinoma. Account for 0.6% of primary intracranial tumors, with an incidence of 0.09 per 100,000. Peak incidence is between 10 and 14 years, and 90% occur in patients less than 25 years old. Occur more frequently in males than in females. Prognosis depends on histologic subtype. Ten-year survival for geminomas is > 85% Other germ cell tumors have lower survival rates, particularly those containing nongerminomatous malignant cells.

(continued on page 502)

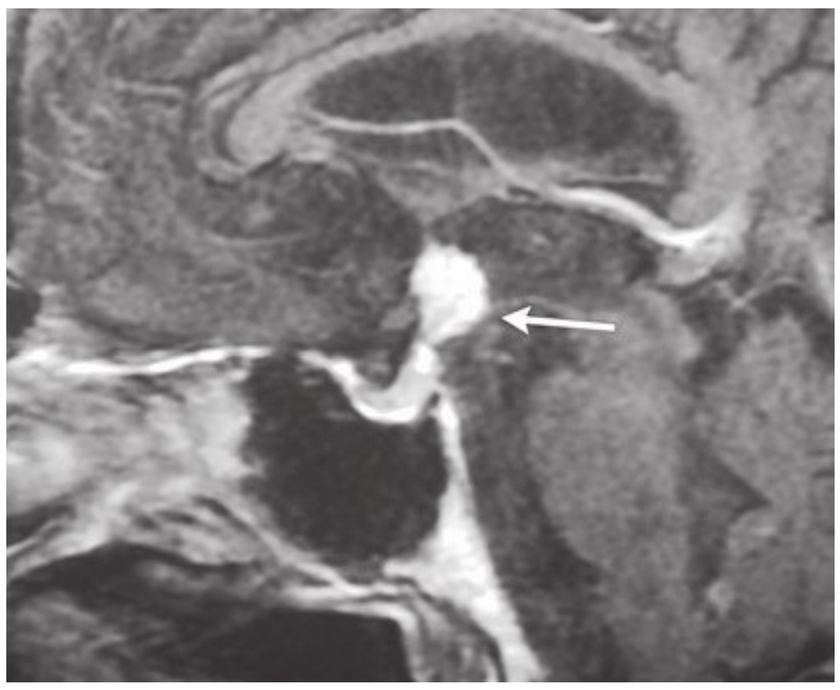

Fig. 2.107 Sagittal postcontrast T1-weighted imaging shows an enhancing chordoid glioma (arrow) at the anteroinferior portion of the third ventricle.

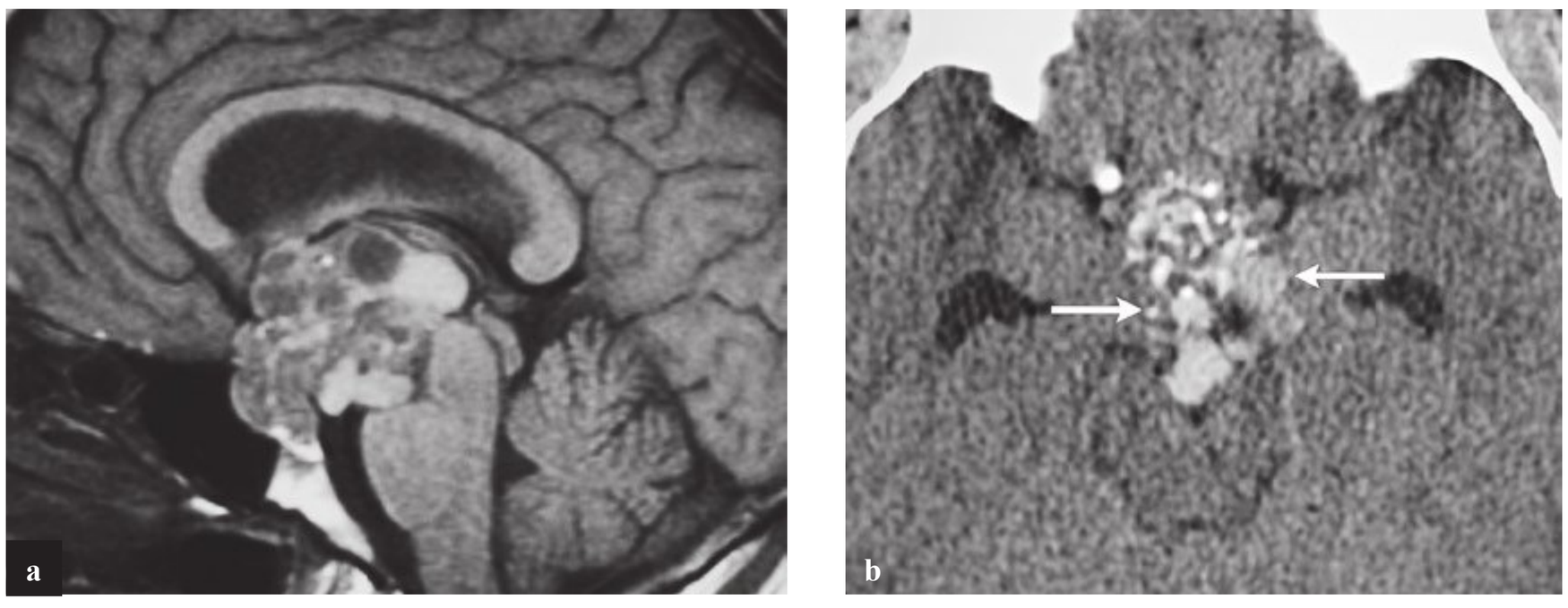

Fig. 2.108 A23-year-old man with a craniopharyngioma in the suprasellar cistern and sella with extension into the third ventricle that has **(a)** zones with low, intermediate, and high signal on sagittal T1-weighted imaging and **(b)** zones with slightly high and low attenuation on axial CT, as well as calcifications (arrows).

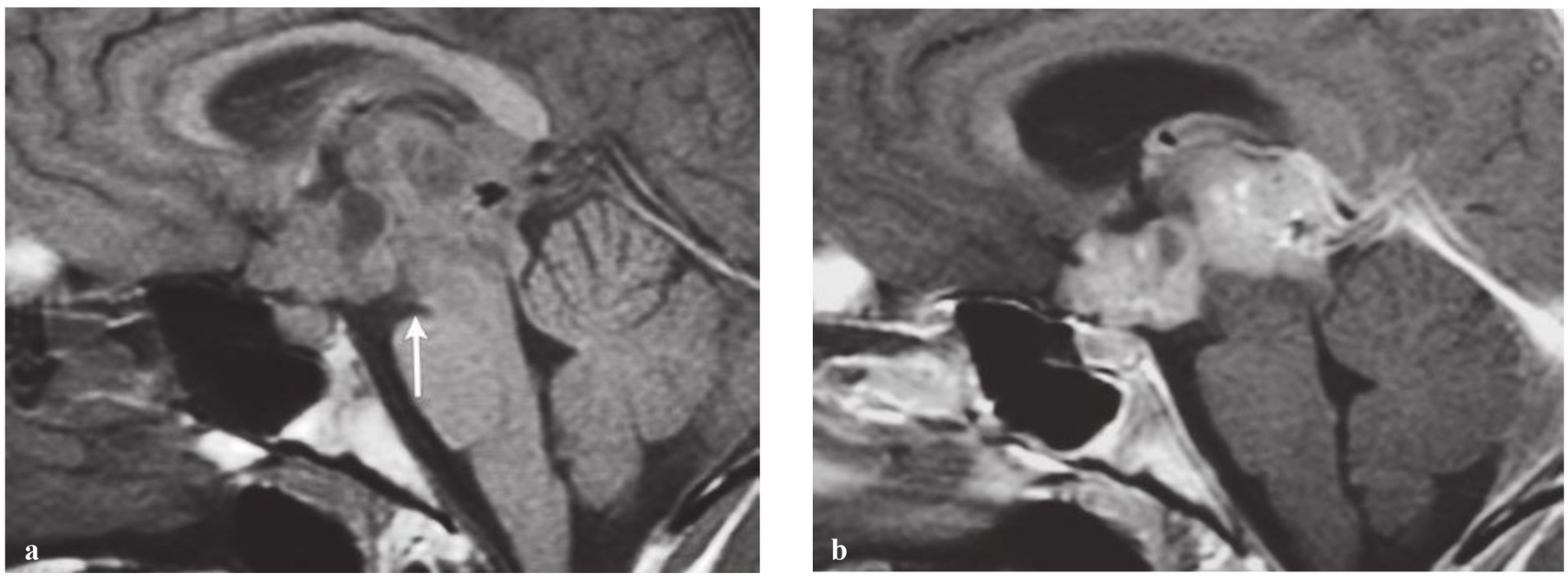

Fig. 2.109 A20-year-old man with a germinoma in the suprasellar cistern, third ventricle, and pineal recess that has **(a)** mixed intermediate and low signal on sagittal T1-weighted imaging (arrow) and **(b)** gadolinium contrast enhancement on sagittal T1-weighted imaging.

Table 2.8 (cont.) Solitary intraventricular lesions in adults

Lesions	Imaging Findings	Comments
Teratoma (**Fig. 2.110**)	MRI: Circumscribed lesions in pineal region > suprasellar region > third ventricle; variable low, intermediate, and/or high signal on T1- and T2-weighted imaging; ± gadolinium contrast enhancement. May contain calcifications with low signal on T1- and T2-weighted imaging, as well as fatty components with high signal on T1-weighted imaging that can cause chemical meningitis if ruptured. CT: May contain calcifications and zones with intermediate and fat attenuation.	Second most common type of germ cell tumor. Occurs in children and in males > females. Benign or malignant types, composed of derivatives of ectoderm, mesoderm, and/or endoderm.
Pineal lesions and tumors (See **Table 1.11**)	MRI and CT findings for the lesions and tumors in the pineal region are listed in detail in **Table 1.11**.	Lesions involving the pineal gland include primary pineal tumors (pineocytoma, pineal parenchymal tumor intermediate differentiation, papillary tumor, and pineoblastoma), germ cell tumors, embryonal tumors, and ependymoma, as well as lesions in the pineal region (ependymoma, meningioma, arachnoid cyst, epidermoid, dermoid, and lipoma).
Tumorlike lesions		
Epidermoid (**Fig. 2.111**)	MRI: Well-circumscribed spheroid or multilobulated extra-axial ectodermal-inclusion lesions with low-intermediate signal on T1-weighted imaging, high signal on T2-weighted imaging and diffusion-weighted imaging, and low signal on ADC maps. Mixed low, intermediate, or high signal on FLAIR images, and no gadolinium contrast enhancement. Commonly located in posterior cranial fossa (cerebellopontine angle cistern) > parasellar/middle cranial fossa. CT: Extra-axial lesions with low-intermediate attenuation, no contrast enhancement, ± bone erosion/destruction.	Nonneoplastic congenital or acquired extra-axial off-midline lesions filled with desquamated cells and keratinaceous debris, usually with mild mass effect on adjacent brain. Infratentorial > supratentorial locations. In adults, epidermoids occur in males = females, ± related clinical symptoms.

(continued on page 504)

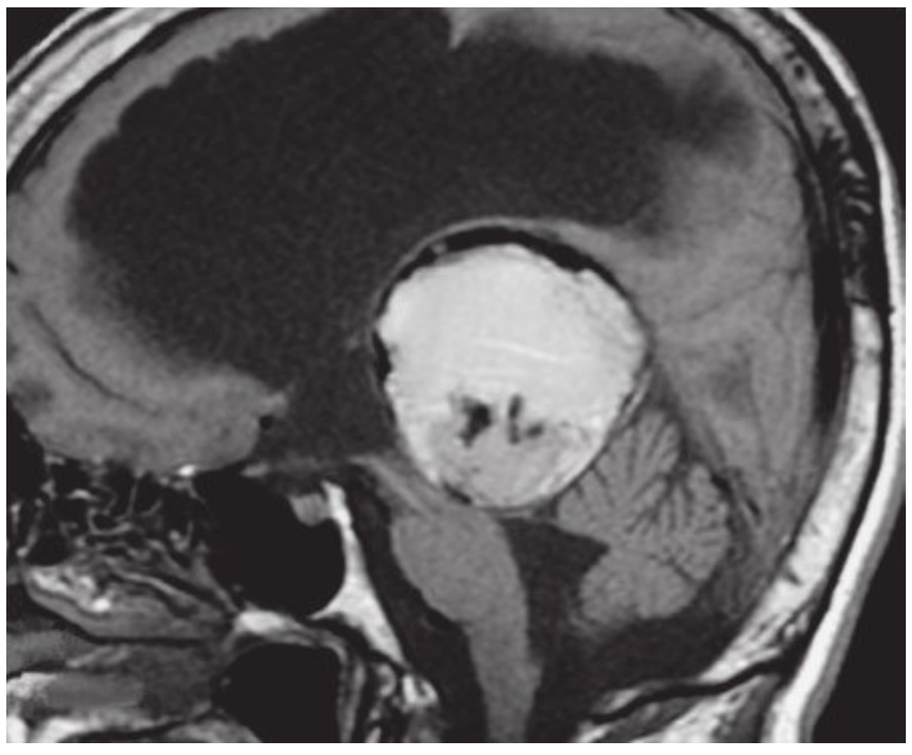

Fig. 2.110 A 50-year-old man with a teratoma in the pineal recess extending into the third ventricle that has mostly high signal on sagittal T1-weighted imaging as well as central and peripheral zones of low signal from calcifications.

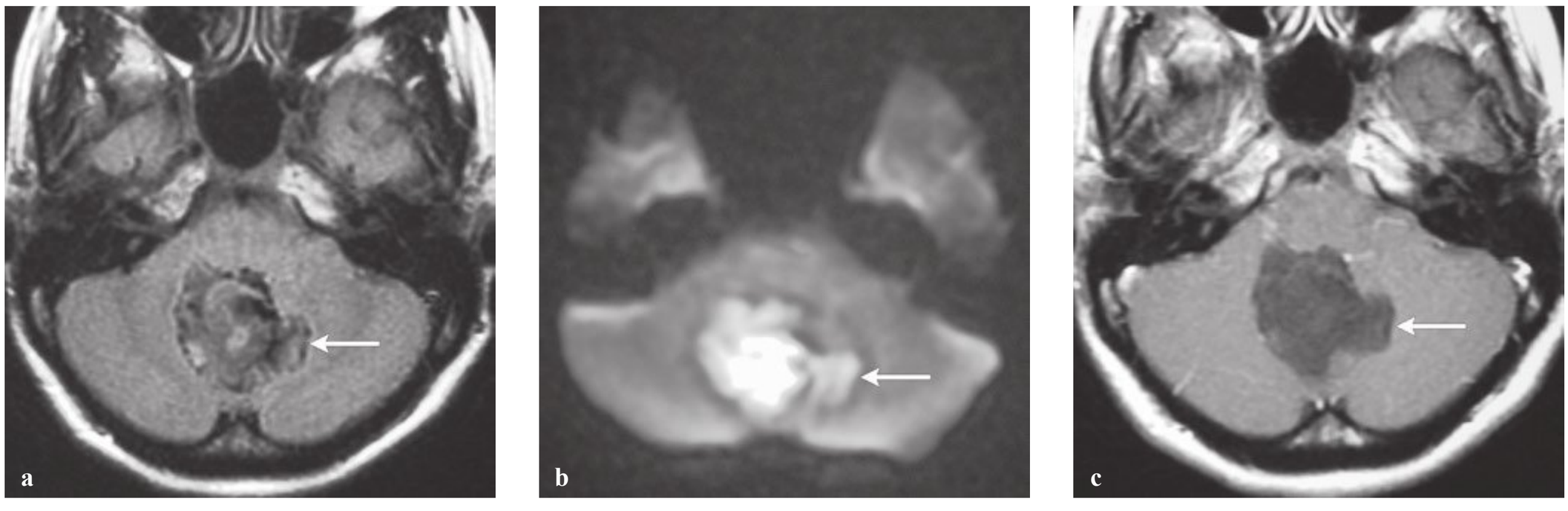

Fig. 2.111 Intraventricular epidermoid in the fourth ventricle has **(a)** mixed low, intermediate, and high signal on axial FLAIR (arrow), **(b)** restricted diffusion on axial diffusion-weighted imaging (arrow), and **(c)** low signal without gadolinium contrast enhancement on axial T1-weighted imaging (arrow).

Table 2.8 (cont.) Solitary intraventricular lesions in adults

Lesions	Imaging Findings	Comments
Colloid cyst (**Fig. 2.112, Fig. 2.113,** and **Fig. 2.114**)	MRI: Well-circumscribed spheroid lesion located at the anterior upper portion of the third ventricle, with variable signal (low, intermediate, or high) on T1- and T2-weighted imaging, and often high signal on T1-weighted imaging and low signal on T2-weighted imaging. No gadolinium contrast enhancement. CT: Spheroid lesions located at the anterior upper portion of the third ventricle, with variable attenuation (low, intermediate, or high) and no contrast enhancement.	Slow-growing, benign cystic lesions whose wall contains a single layer of epithelial cells. Cyst contents can include cholesterol granules, various blood products, macrophages, and various minerals and/or ions. Most colloid cysts occur in the anterosuperior portion of the third ventricle, and rarely in the sella or suprasellar cistern. Usually found in adults (50–60 years old).
Ependymal cyst (**Fig. 2.115**)	MRI: Well-circumscribed thin-walled cyst in the lateral ventricles with low signal on T1-weighted imaging, diffusion-weighted imaging, and FLAIR and high signal on T2-weighted imaging. Usually no gadolinium contrast enhancement. CT: Thin-walled cyst in the lateral ventricles with low attenuation similar to CSF.	Benign cysts in the lateral ventricles containing serous fluid surrounded by a thin wall containing ependymal columnar cells with vesicular nuclei and eosinophilic cytoplasm. May result from neuroectoderm sequestered during development.
Neuroepithelial (neuroglial) cyst (**Fig. 2.116**)	MRI: Well-circumscribed cysts with low signal on T1-weighted imaging, FLAIR, and diffusion-weighted imaging and high signal on T2-weighted imaging and ADC images, thin walls, and no gadolinium contrast enhancement or peripheral edema. CT: Well-circumscribed cysts with low attenuation and no contrast enhancement.	Rare, benign, cystic lesions containing CSF that are usually asymptomatic. Can be intra-axial, extra-axial, or intraventricular. Intraventricular lesions do not communicate with the ventricular CSF. Cyst walls contain cuboidal epithelial cells. Neuroepithelial cysts are found in the brain (commonly in frontal lobe) > choroidal fissure > ventricles.

(continued on page 506)

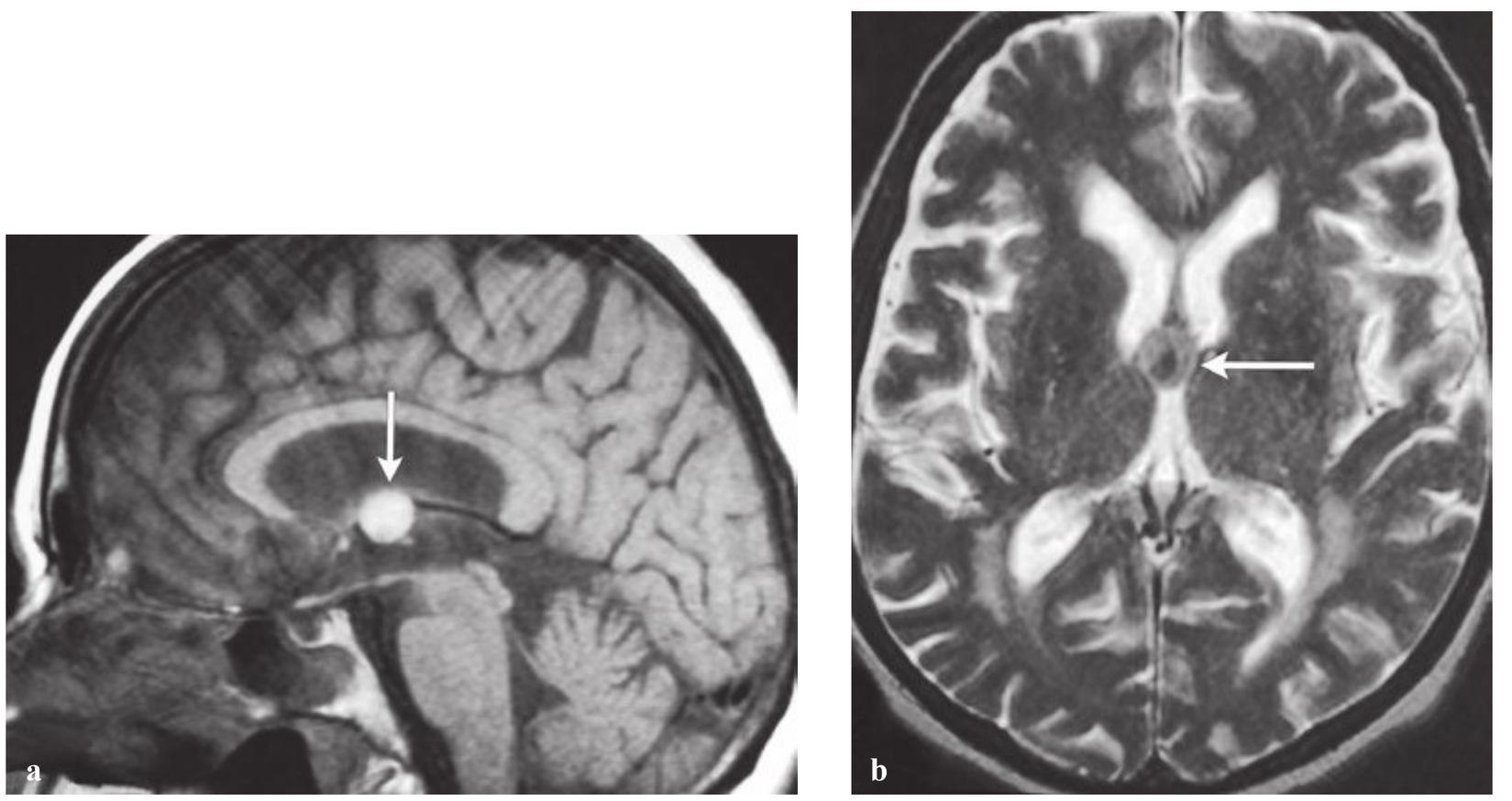

Fig. 2.112 A 67-year-old woman with colloid cyst in the upper anterior portion of the third ventricle that has **(a)** high signal on sagittal T1-weighted imaging (arrow) and **(b)** mixed intermediate and low signal on axial T2-weighted imaging (arrow).

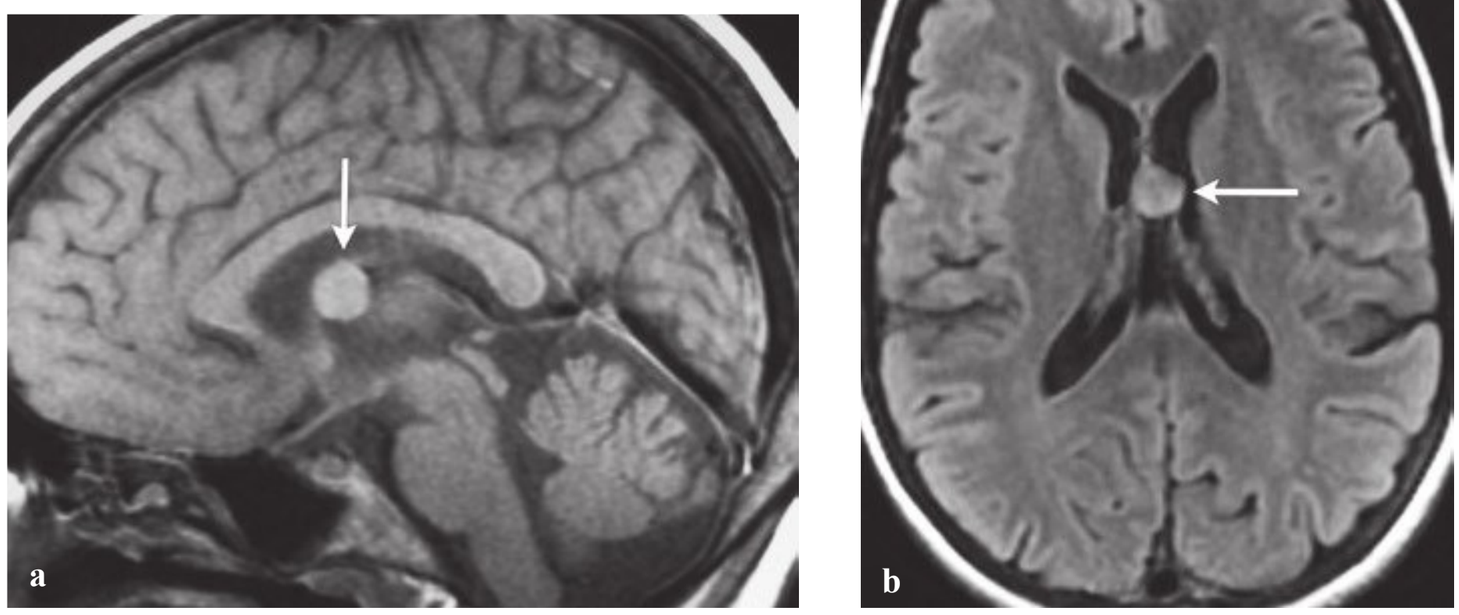

Fig. 2.113 A 32-year-old woman with a colloid cyst in the third ventricle that has **(a)** intermediate to slightly high signal on sagittal T1-weighted imaging (arrow) and **(b)** slightly high signal on axial FLAIR (arrow).

Fig. 2.114 A 25-year-old woman with a colloid cyst in the third ventricle that has high attenuation on axial CT.

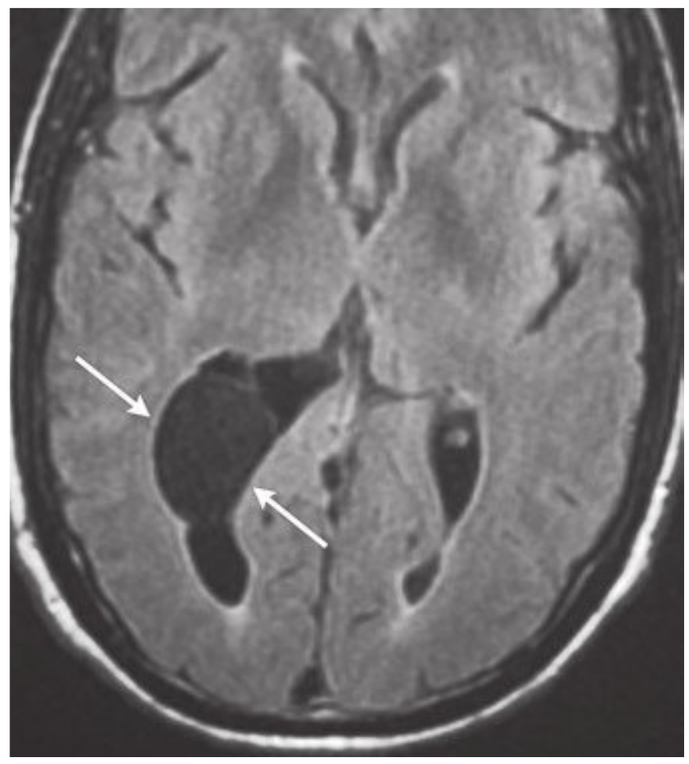

Fig. 2.115 A 55-year-old man with an ependymal cyst (arrows) in the atrium of the right lateral ventricle that has isointense signal to CSF on axial FLAIR (arrows).

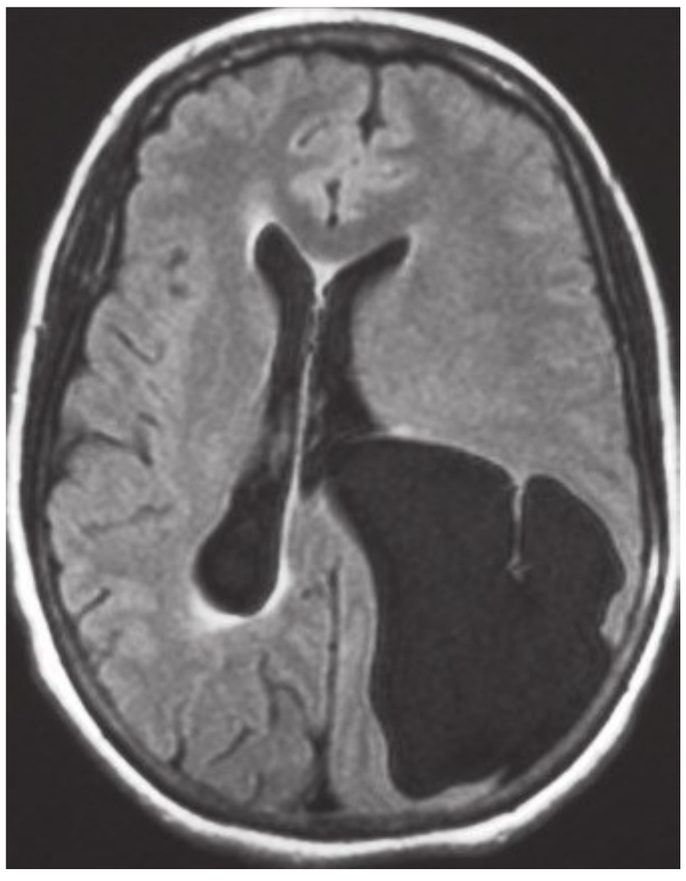

Fig. 2.116 A 51-year-old woman with an intra-axial neuroepithelial (neuroglial) cyst in the left cerebral hemisphere that protrudes into the left lateral ventricle, as seen on axial FLAIR.

Table 2.8 (cont.) Solitary intraventricular lesions in adults

Lesions	Imaging Findings	Comments
Choroid plexus cyst (**Fig. 2.117** and **Fig. 2.118**)	MRI: Cysts often have low or intermediate signal on T1-weighted imaging, intermediate signal or slightly high to high signal on FLAIR, and high signal on T2-weighted imaging. Often have high signal on diffusion-weighted imaging. Can show rim or nodular patterns of gadolinium contrast enhancement. CT: Typically have low-intermediate attenuation, ± peripheral calcification.	Common epithelium-lined nonneoplastic cysts that occur in the choroid plexus and that are often bilateral within the atria of the lateral ventricles. Usually range in size from 5 to 20 mm. Result from desquamating and degenerating choroid epithelium within nodular structures containing lipid-laden histiocytes, cholesterol, fluid, hemosiderin, lymphocytic and plasma cell infiltrates, cellular debris, and peripheral psammomatous calcifications. Usually asymptomatic incidental finding.
Hematoma (**Fig. 2.119**)	CT: A linear relationship exists between CT attenuation and hematocrit and hemoglobin and protein content. MRI: The signal of the hematoma depends on its age, size, location, hematocrit, oxidation state of iron in hemoglobin, degree of clot retraction, extent of edema, and MRI pulse sequence.	Can result from trauma, ruptured aneurysms or vascular malformations, coagulopathy, hypertension, adverse drug reaction, amyloid angiopathy, hemorrhagic transformation of cerebral infarction, metastases, abscesses, and viral infections (herpes simplex virus, cytomegalovirus).
Arteriovenous malformation (AVM)	MRI: Lesions with irregular margins that can be located in the brain parenchyma, pia, dura, and/or ventricles. AVMs contain multiple, tortuous, tubular flow voids on T1- and T2-weighted imaging secondary to patent arteries with high blood flow, as well as thrombosed vessels with variable signal and areas of hemorrhage in various phases. CT: Lesions with irregular margins that can be located in the brain parenchyma, pia, dura, or both locations. AVMs contain multiple tortuous vessels. The venous portions often show contrast enhancement. Usually not associated with mass effect unless there is recent hemorrhage or venous occlusion. CTA can show the nidus and arterial and venous portions of the AVMs.	AVMs can be sporadic, congenital, or associated with a history of trauma. Supratentorial AVMs occur more frequently (80–90%) than infratentorial AVMs (10–20%). Annual risk of hemorrhage.
Cavernous malformation	MRI: Single or multiple multilobulated intra-axial lesions that have a peripheral rim or irregular zone of low signal on T2-weighted imaging secondary to hemosiderin, surrounding a central zone of variable signal (low, intermediate, high, or mixed) on T1- and T2-weighted imaging depending on ages of hemorrhagic portions. Gradient echo and magnetic-susceptibility weighted techniques are useful for detecting multiple lesions that have low signal.. Gadolinium contrast enhancement is usually absent, although malformations may show mild heterogeneous enhancement. CT: Lesions have intermediate to slightly increased attenuation, ± calcifications.	Cavernous malformations are hamartomas composed of thin-walled sinusoids and blood vessels without intervening neural tissue. Can be found in many different locations. Supratentorial cavernous angiomas occur more frequently than infratentorial lesions. Lesions consist of epithelium-lined vascular channels within a collagenous stroma. Zones of thrombus and remote hemorrhage with hemosiderin are often present. Dystrophic calcifications may be present. Associated developmental venous anomalies occur in 25% Hereditary syndromes in which multiple cavernous malformations occur are associated with mutations of the CCM1/KRIT1, CCM2/MGC4608, and CCM3PDCD10 genes and have a higher risk of hemorrhage (up to 5%per year) than sporadic cavernous malformations.

(continued on page 508)

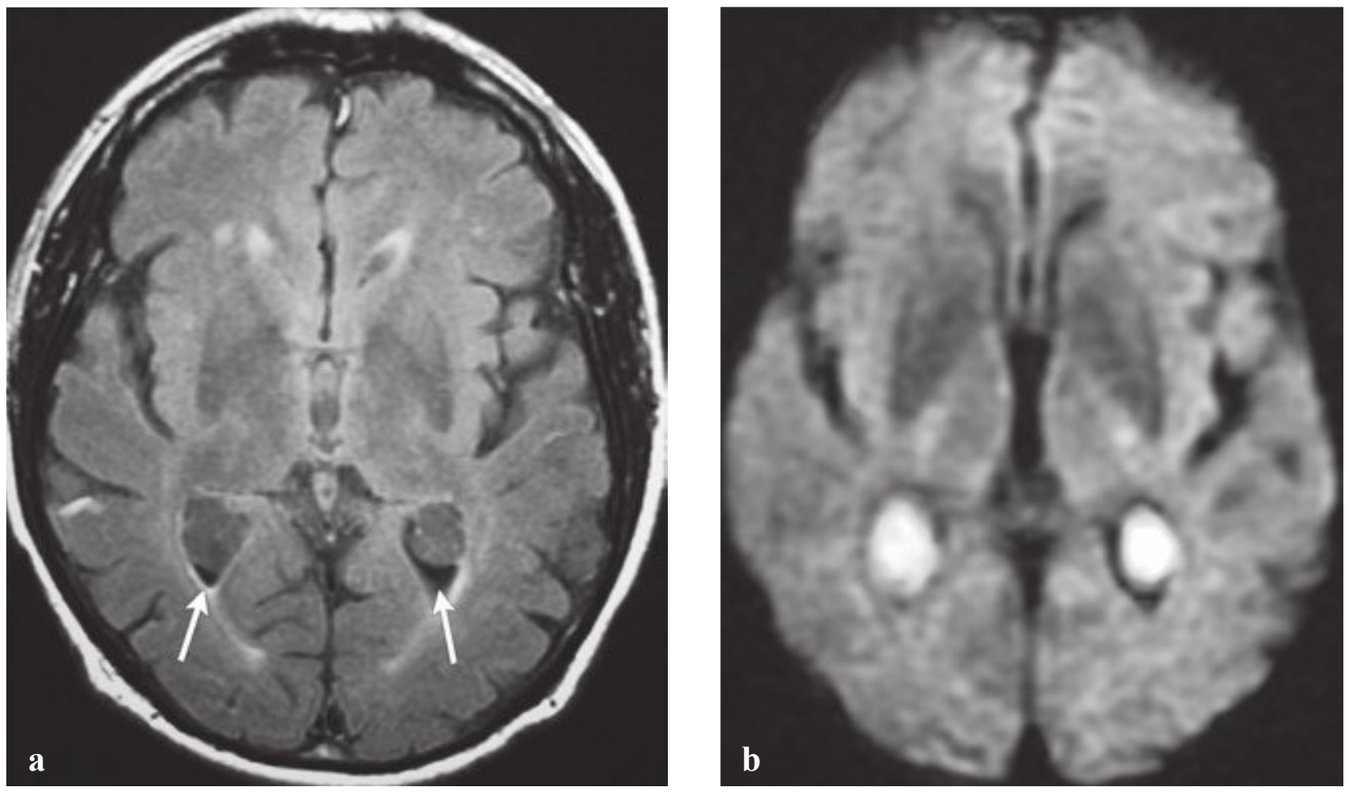

Fig. 2.117 A 77-year-old man with bilateral choroid plexus cysts in the atria of the lateral ventricles that have **(a)** low-intermediate signal on axial FLAIR (arrows) and **(b)** restricted diffusion on axial diffusion-weighted imaging.

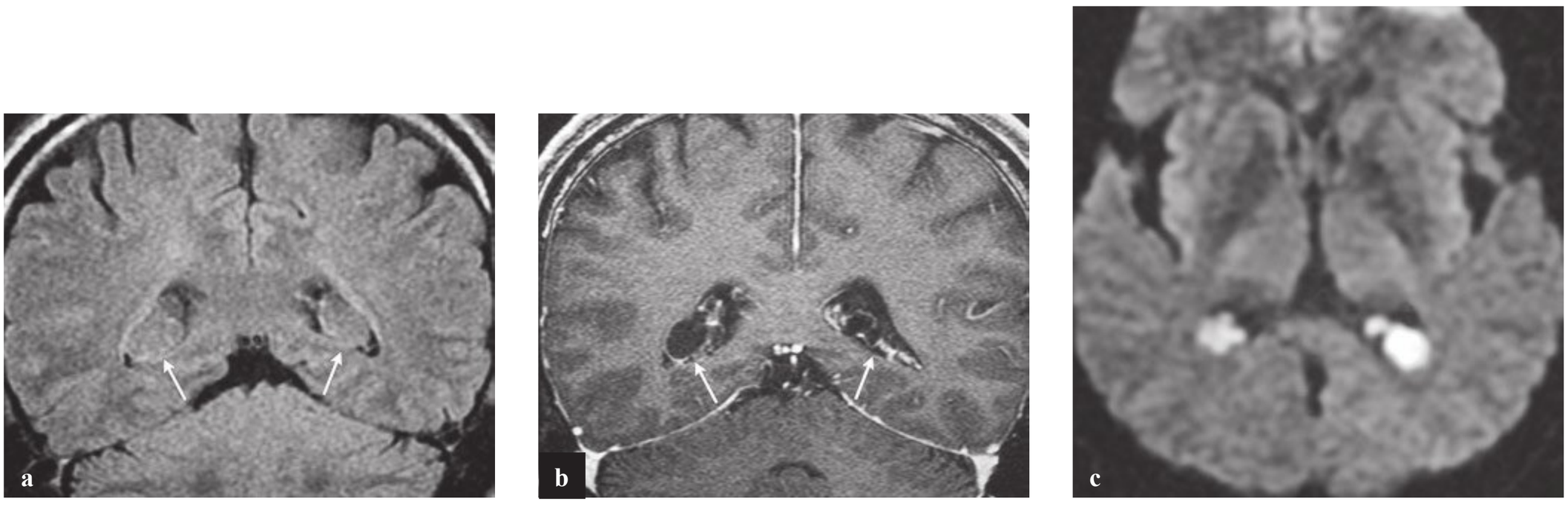

Fig. 2.118 A 58-year-old man with bilateral choroid plexus cysts that have **(a)** intermediate signal on coronal FLAIR (arrows), **(b)** low signal centrally with thin peripheral gadolinium contrast enhancement on coronal T1-weighted imaging (arrows), and **(c)** restricted diffusion on axial diffusion-weighted imaging.

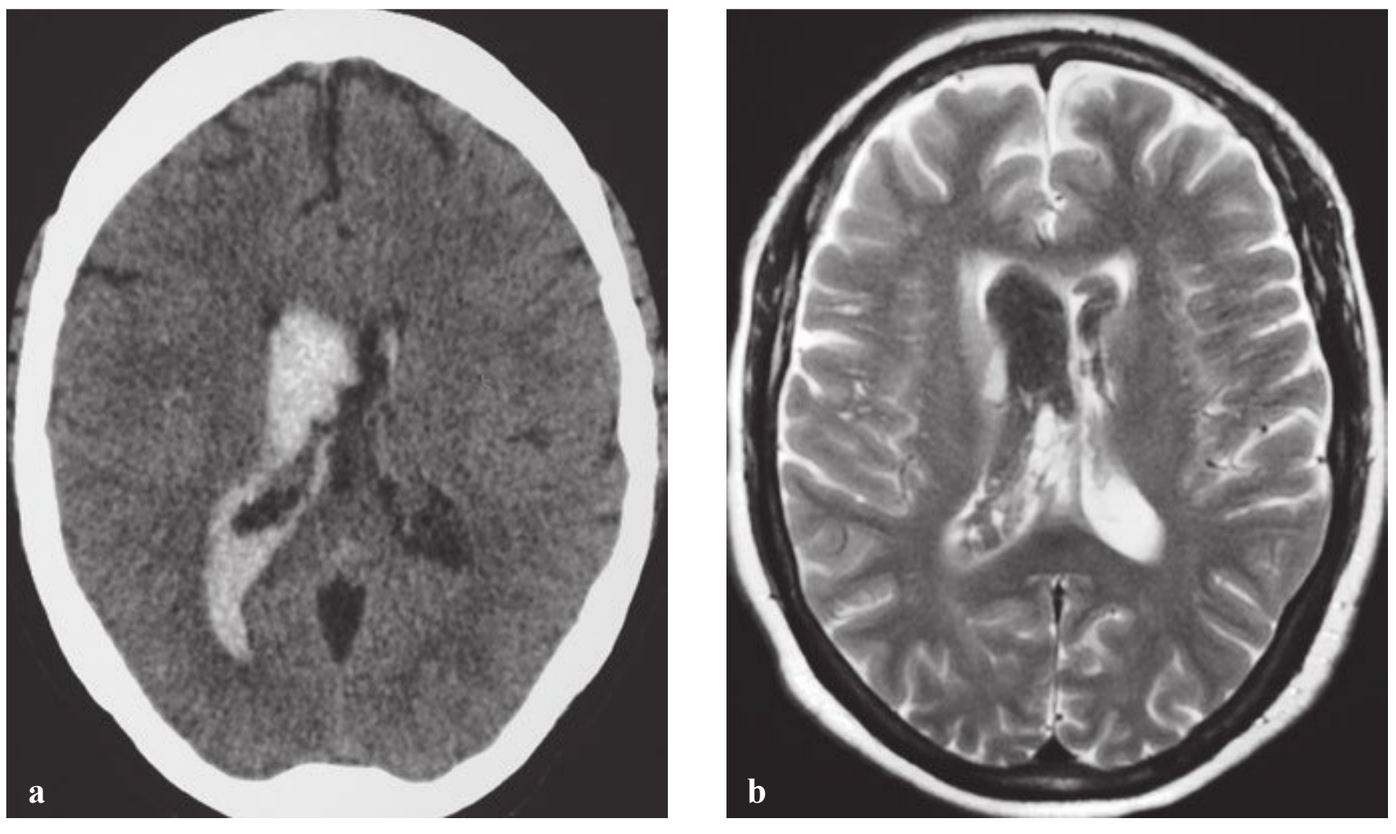

Fig. 2.119 Hemorrhage in the right lateral ventricle has **(a)** high attenuation on axial CT and **(b)** mostly low signal on axial T2-weighted imaging. A small amount of blood is also seen in the left lateral ventricle.

Table 2.8 (cont.) Solitary intraventricular lesions in adults

Lesions	Imaging Findings	Comments
Infection		
Ventriculitis/abscess (**Fig. 2.120**)	MRI: Curvilinear and/or nodular gadolinium contrast enhancement along ventricular/ependymal margins, with resultant communicating or noncommunicating types of hydrocephalus.	Complications of intracranial inflammatory processes, such as bacterial, fungal, and viral (CMV) infections, tuberculosis, and parasites. Noninfectious diseases like sarcoid can result in a similar pattern.
Parasitic infection/ cysticercosis (**Fig. 2.121**)	MRI: Single or multiple cystic lesions in brain or meninges. Active vesicular phase: Cystic-appearing lesions containing a small 2–4 mm nodule (scolex) with low signal on T1-weighted imaging, FLAIR, and diffusion-weighted imaging; a thin peripheral rim with high signal on FLAIR and T2-weighted imaging; minimal peripheral rim or no gadolinium contrast enhancement; and no peripheral edema on T2-weighted imaging and FLAIR. Active colloidal vesicular phase: Cystic-appearing lesion with low-intermediate signal on T1-weighted imaging, high signal on T2-weighted imaging, and rim and/or nodular pattern of gadolinium contrast enhancement, ± peripheral signal (edema) on T2-weighted imaging. Active granular nodular phase: Cyst retracts into a more solid gadolinium-enhancing granulomatous nodule. CT: Chronic non-active phase: Calcified nodular granulomas.	Caused by ingestion of ova (Taenia solium) in contaminated food (undercooked pork). Involves meninges > brain parenchyma > ventricles. Intra-axial lesion can be associated with seizures, and intraventricular lesions with hydrocephalus. Neurosurgical resection of lesions in the fourth ventricle is often done when there is brainstem compression.
Inflammation		
Neurosarcoid (**Fig. 2.122**)	MRI: Poorly marginated intra-axial and/or intraventricular zone or zones with low-intermediate signal on T1-weighted imaging, slightly high to high signal on T2-weighted imaging and FLAIR, usually shows gadolinium contrast enhancement, + localized mass effect and peripheral edema. Often associated with gadolinium contrast enhancement in the leptomeninges and/or dura. CT: Poorly marginated intra-axial zone with low-intermediate attenuation, usually shows contrast enhancement, + localized mass effect and peripheral edema. Often associated with contrast enhancement in the leptomeninges.	Sarcoidosis is a multisystem noncaseating granulomatous disease of uncertain cause that can involve the CNS in 5 to 15% of cases. If untreated, it is associated with severe neurologic deficits, such as encephalopathy, cranial neuropathies, and myelopathy. Diagnosis of neurosarcoid may be difficult when the neurologic complications precede other systemic manifestations in the lungs, lymph nodes, skin, bone, and/or eyes.

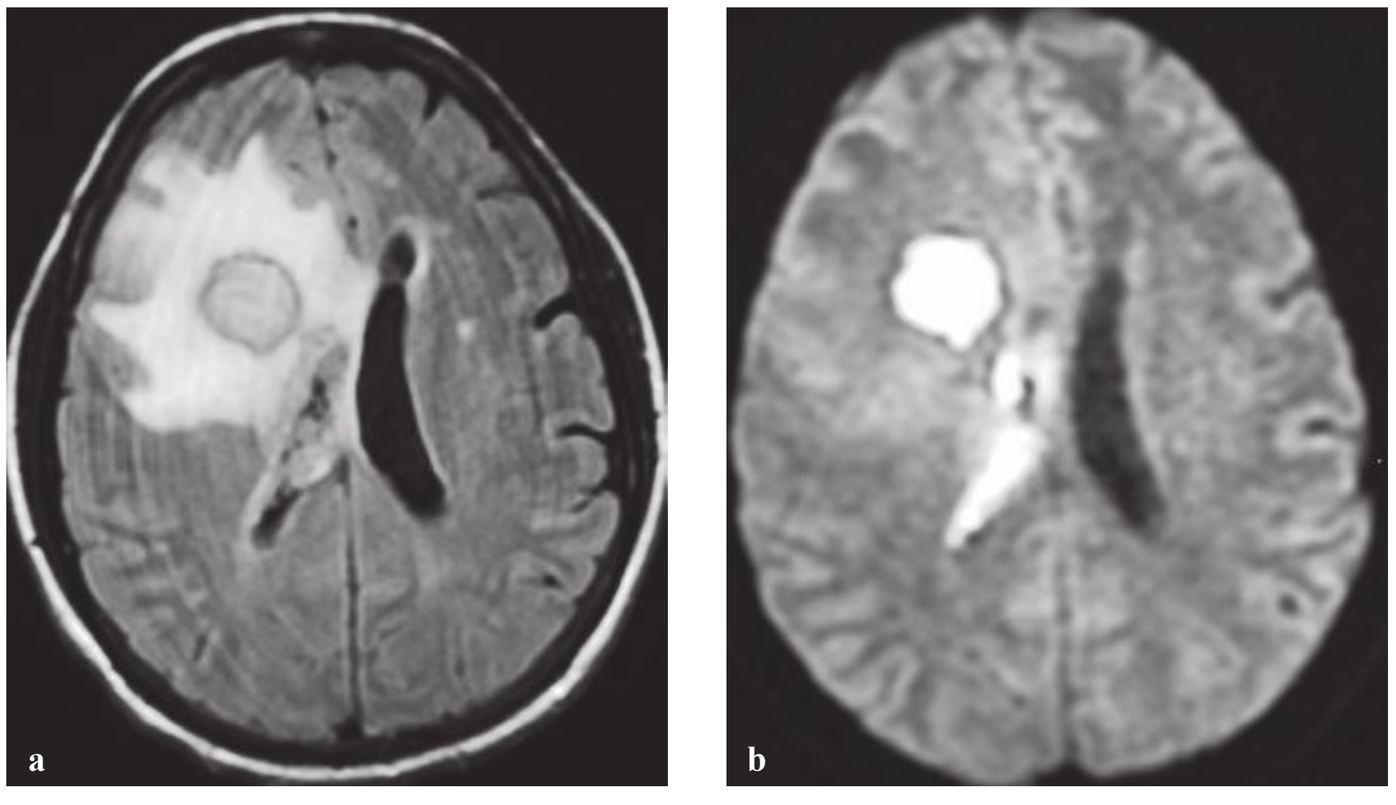

Fig. 2.120 A 53-year-old woman with a pyogenic brain abscess in the right frontal lobe with extension of infection into the right lateral ventricle. **(a)** The spheroid abscess in the right frontal lobe has surrounding high signal edema on axial FLAIR as well as high signal within the right lateral ventricle. **(b)** Restricted diffusion on axial diffusion-weighted imaging is seen in the abscess as well as within the right lateral ventricle, representing ventriculitis.

Fig. 2.121 A 35-year-old man with a cysticercosis lesion in the fourth ventricle that has both nodular gadolinium-enhancing and cystic portions on coronal T1-weighted imaging (arrows) that result in ventricular obstruction.

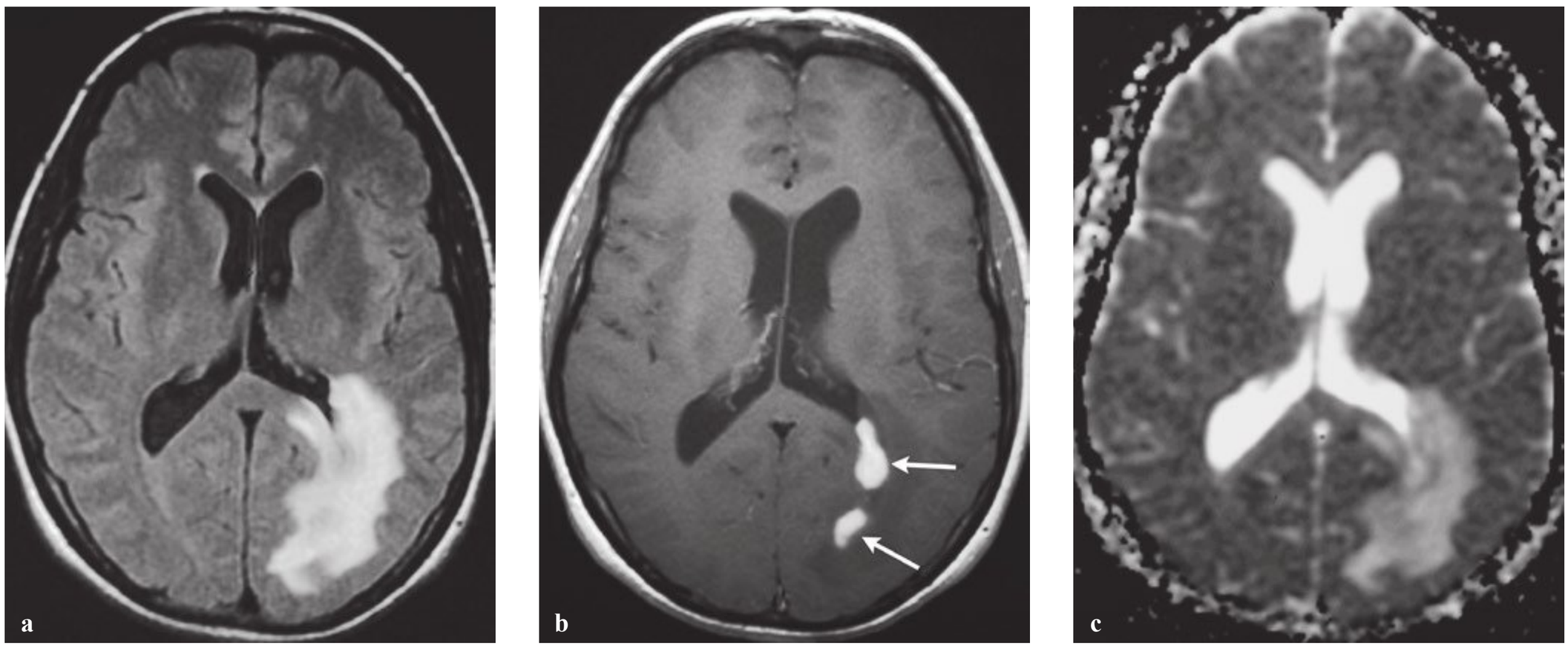

Fig. 2.122 A 40-year-old woman with sarcoidosis who has a left periatrial lesion that extends into the left lateral ventricle and has **(a)** high signal on axial FLAIR, **(b)** gadolinium contrast enhancement on axial T1-weighted imaging (arrows), and **(c)**, on axial ADC, a thin zone of restricted diffusion with low signal along the ventricular wall surrounded by high signal edema.

Table 2.9 Contrast-enhancing ventricular margins

- Normal Vascular Structures
- Neoplastic Lesions
  - Metastatic disease from primary neoplasms outside the CNS
  - Disseminated tumor from primary neoplasms of the CNS
  - Malignant brain neoplasms with direct extension into the ventricles
  - Ependymal-subependymal hamartomas–tuberous sclerosis
- Inflammatory Disease
  - Ventriculitis/ependymitis
  - Chemical ventriculitis
  - Radiation injury/necrosis
- Posttraumatic Lesions
  - Shunt placement
  - Surgery
  - Hematoma
- Vascular Lesions
  - Arteriovenous malformation (AVM)
  - Developmental venous anomaly/venous angioma
  - Sturge-Weber syndrome

Table 2.9 Contrast-enhancing ventricular margins

Lesions	Imaging Findings	Comments
Normal vascular structures	MRI and CT: Normal enhancing structures that can be seen include ependymal/subependymal veins, which have a linear tubular configuration, and choroid plexus.	Vascular structures with slow flow (veins and venous sinuses) usually enhance because of T1 shortening effects of gadolinium contrast, and choroid plexus enhances because of lack of blood–brain barrier.
Neoplastic Lesions		
Metastatic disease from primary neoplasms outside the CNS (**Fig. 2.123**)	Single or multiple well-circumscribed or poorly defined lesions in the ventricles with or without involvement of the leptomeninges, dura, and/or skull. MRI: Lesions often have low-intermediate signal on T1-weighted imaging, intermediate-high signal on T2-weighted imaging, + linear or nodular patterns of contrast enhancement, ± hydrocephalus, ± bone destruction, ± compression of neural tissue or vessels.	Intraventricular metastatic tumor can result from primary tumors outside the CNS, such as lung carcinoma, breast carcinoma, melanoma, lymphoma, and leukemia.
Disseminated tumor from primary neoplasms of the CNS (**Fig. 2.124** and **Fig. 2.125**)	Single or multiple well-circumscribed or poorly defined lesions in the ventricles with or without involvement of the leptomeninges, dura, and/or skull. MRI: Lesions often have low-intermediate signal on T1-weighted imaging, intermediate-high signal on T2-weighted imaging, + linear and/or nodular patterns of contrast enhancement, ± hydrocephalus, ± bone destruction, ± compression of neural tissue or vessels.	Disseminated tumor within the ventricles can result from malignant primary tumors of the CNS, such as primitive neuroectodermal tumors (PNET), medulloblastoma, pineoblastoma, choroid plexus carcinoma, glioblastoma multiforme, anaplastic astrocytoma, anaplastic ependymoma, anaplastic oligodendroglioma, oligoastrocytoma, primary CNS lymphoma, and other high-grade neoplasms.

(continued on page 512)

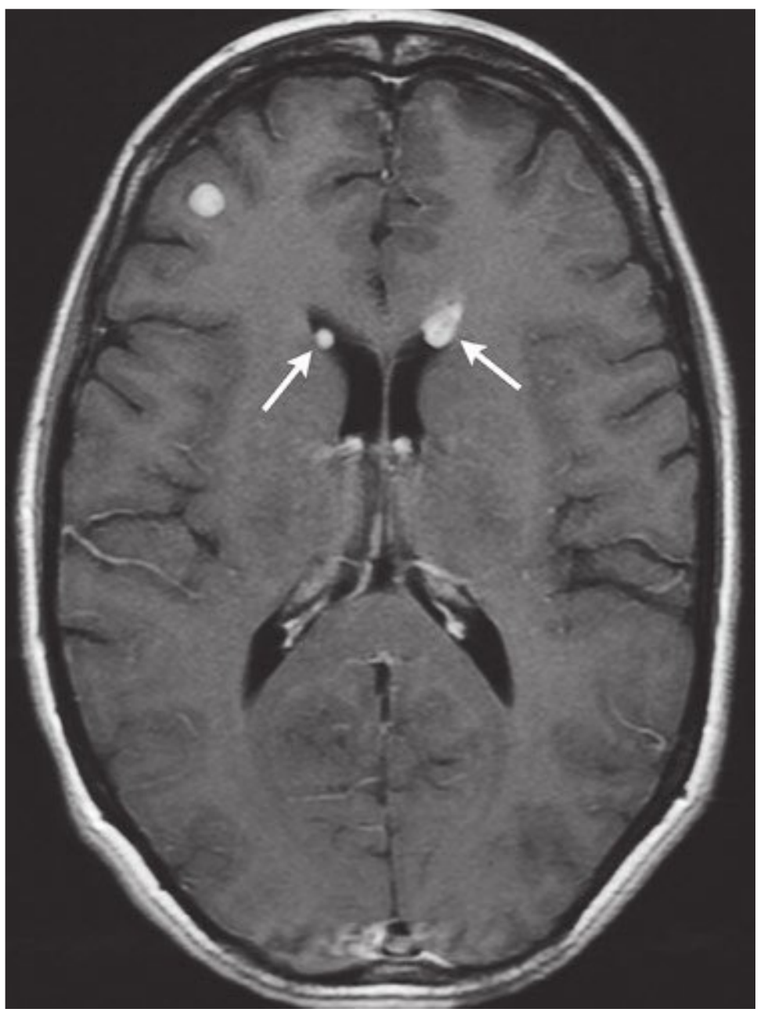

Fig. 2.123 A 31-year-old woman with melanoma and gadolinium-enhancing metastatic lesions in the lateral ventricles, as well as in the right frontal lobe (arrows), on axial T1-weighted imaging.

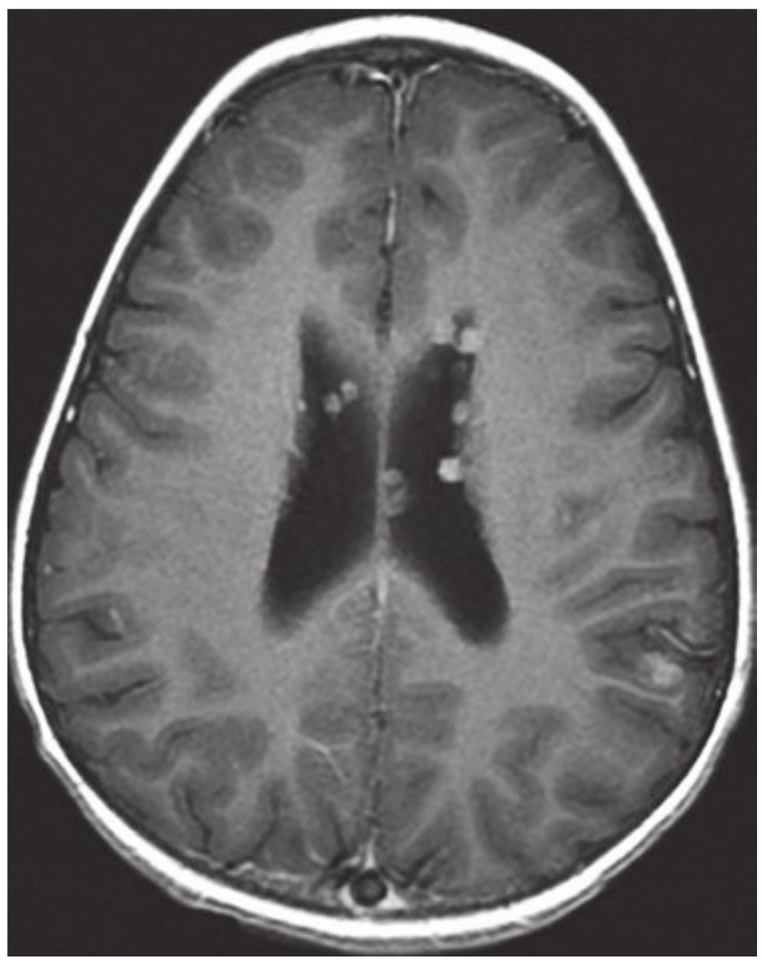

Fig. 2.124 A 5-year-old female with multiple gadolinium-enhancing nodular lesions in the lateral ventricles representing disseminated CNS ependymoma on axial T1-weighted imaging.

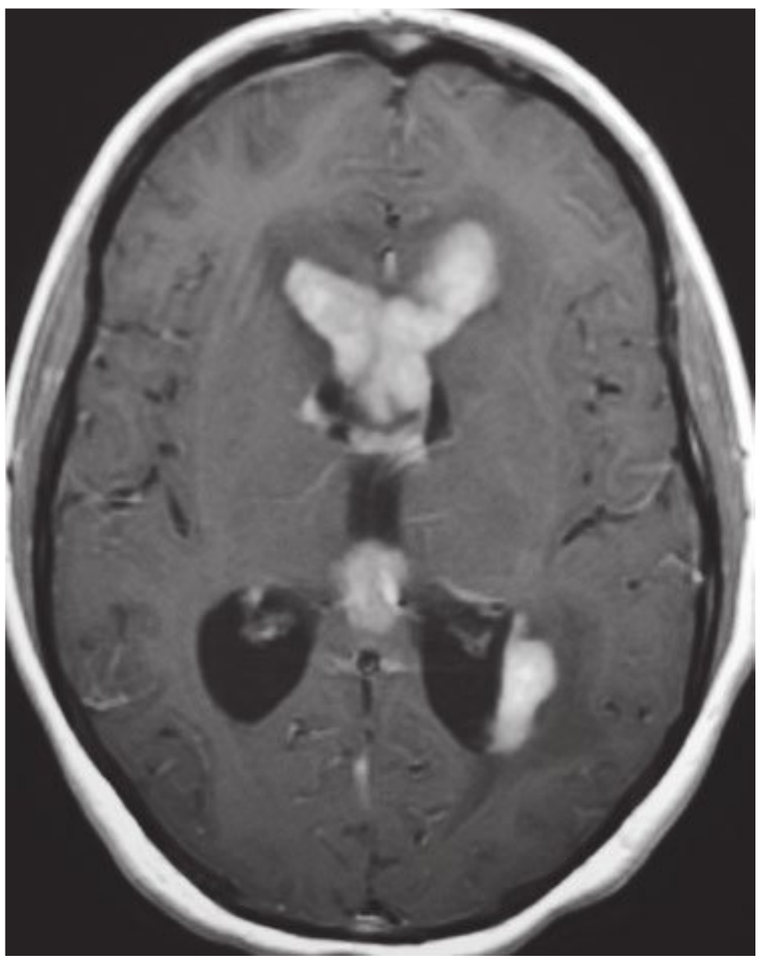

Fig. 2.125 A 23-year-old woman with a pineal germinoma and disseminated tumor, seen as multiple intraventricular lesions with gadolinium contrast enhancement on axial T1-weighted imaging.

Table 2.9 (cont.) Contrast-enhancing ventricular margins

Lesions	Imaging Findings	Comments
Malignant brain neoplasms with direct extension Into the ventricles (**Fig. 2.126** and **Fig. 2.127**)	MRI: Intra-axial lesions adjacent to the ventricles with low-intermediate signal on T1-weighted imaging, intermediate-high signal on T2-weighted imaging, and gadolinium contrast enhancement can extend into the ventricles and disseminate along the ventricles, with associated linear and/or nodular patterns of contrast enhancement.	High-grade primary or metastatic intra-axial neoplasms can extend into the ventricles, with associated contrast enhancement. Contrast enhancement within the ventricles can also occur from tumor dissemination.
Ependymal-subependymal hamartomas–tuberous sclerosis (**Fig. 2.128**)	MRI: Small nodules located along, and projecting into, the lateral ventricles, with signal on T1- and T2-weighted imaging and FLAIR similar to cortical tubers; calcification and gadolinium contrast enhancement are common. CT: Small nodules located along, and projecting into, the lateral ventricles. Calcifications of nodules commonly begin early in childhood.	Cortical and subependymal hamartomas are nonmalignant lesions associated with tuberous sclerosis. Tuberous sclerosis is an autosomal dominant disorder associated with hamartomas in multiple organs. Extraneural lesions include cutaneous angiofibromas (adenoma sebaceum), subungual fibromas, visceral cysts, renal angioleiomyomas, intestinal polyps, cardiac rhabdomyomas, and pulmonary lymphangioleiomyomatosis. Caused by mutations of TSC1 gene on 9q or the TSC2 gene on 16p. Prevalence of 1 in 6,000 newborns.
Inflammatory Disease		
Ventriculitis/ependymitis (**Fig. 2.129, Fig. 2.130,** and **Fig. 2.131**)	MRI and CT: Curvilinear and/or nodular zones of contrast enhancement along ventricular/ependymal margins, with resultant communicating or noncommunicating types of hydrocephalus. Acute infection can show corresponding restricted diffusion on diffusion-weighted imaging.	Complications of intracranial inflammatory processes, such as bacterial, fungal, or viral (CMV) infections, tuberculosis, and parasites. Noninfectious diseases like sarcoid can result in a similar pattern.

(continued on page 514)

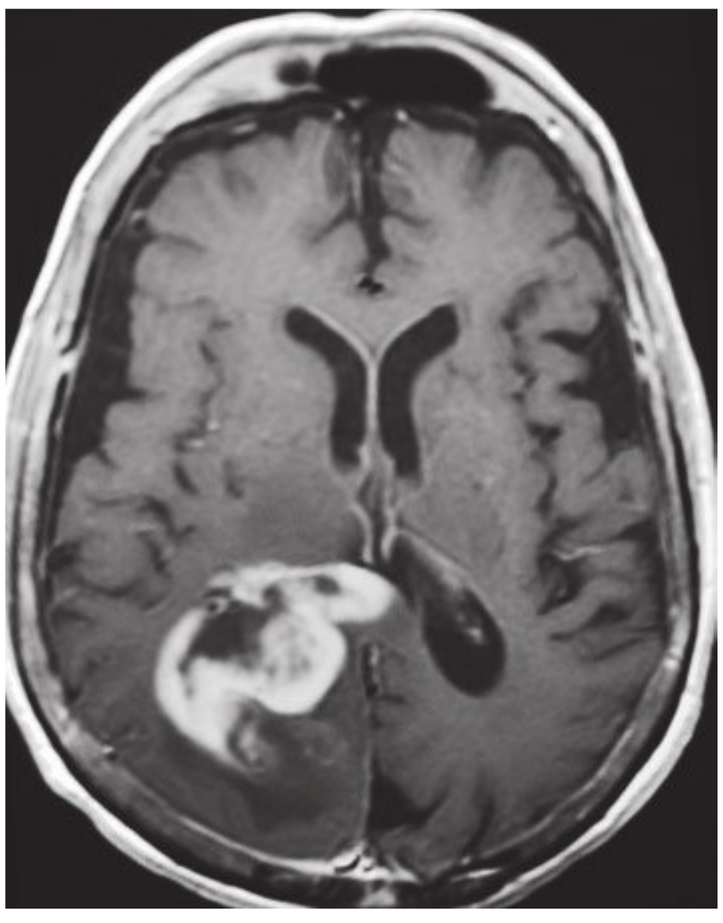

Fig. 2.126 An 81-year-old woman with a glioblastoma multiforme in the posterior right cerebral hemisphere that extends into the atrium of the right lateral ventricle and splenium of the corpus callosum, which shows heterogeneous gadolinium contrast enhancement on axial T1-weighted imaging.

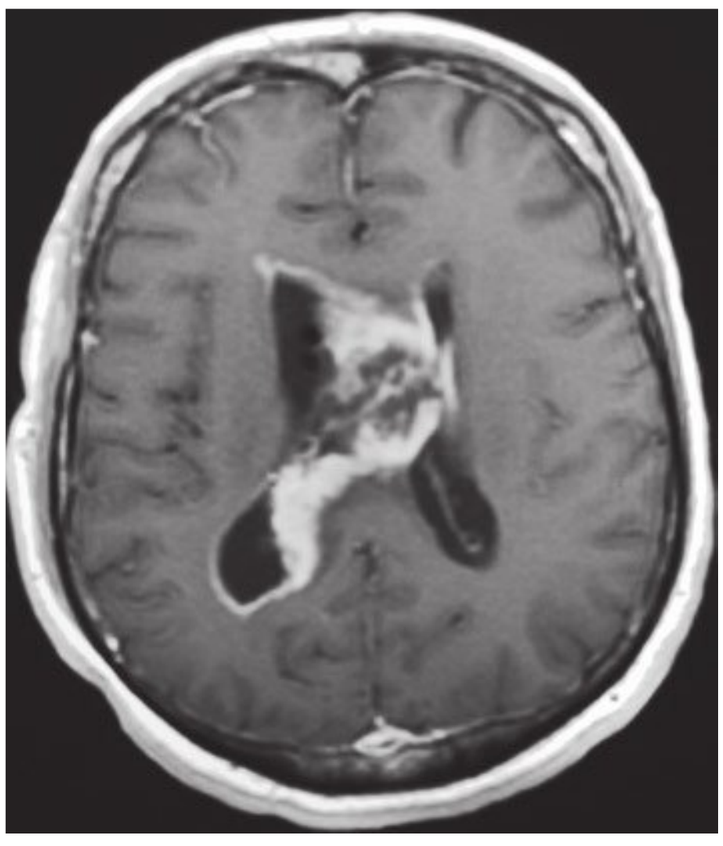

Fig. 2.127 A 51-year-old man with an anaplastic astrocytoma involving the septum pellucidum with intraventricular extension. The tumor shows heterogeneous gadolinium contrast enhancement on axial T1-weighted imaging. Contrast enhancement is also seen along the ependymal lining of the right lateral ventricle, representing disseminated tumor.

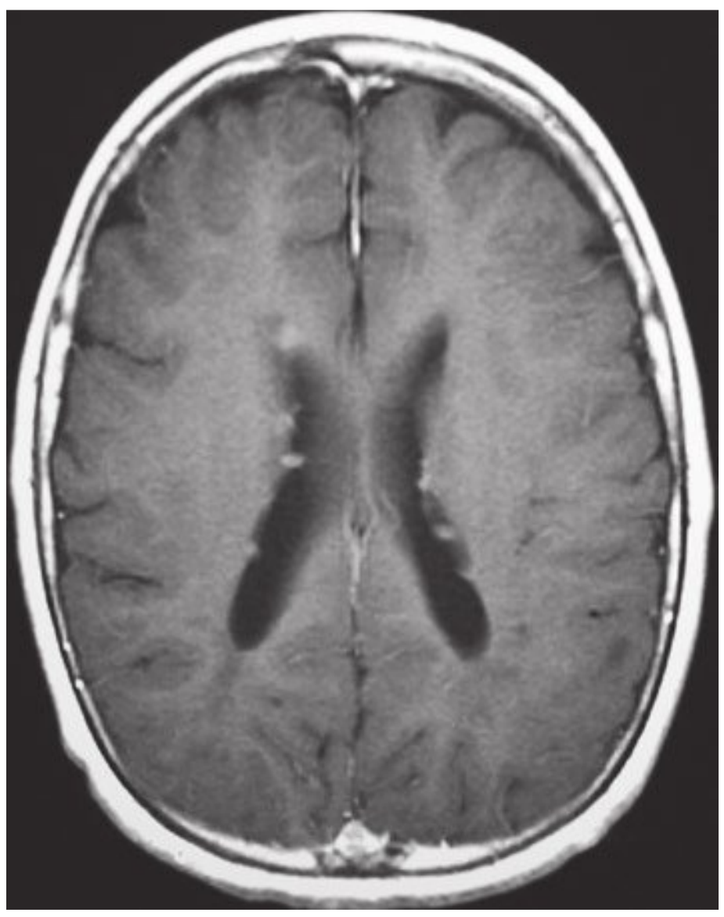

Fig. 2.128 Patient with tuberous sclerosis who has multiple, small, gadolinium-enhancing ependymal hamartomas on axial T1-weighted imaging.

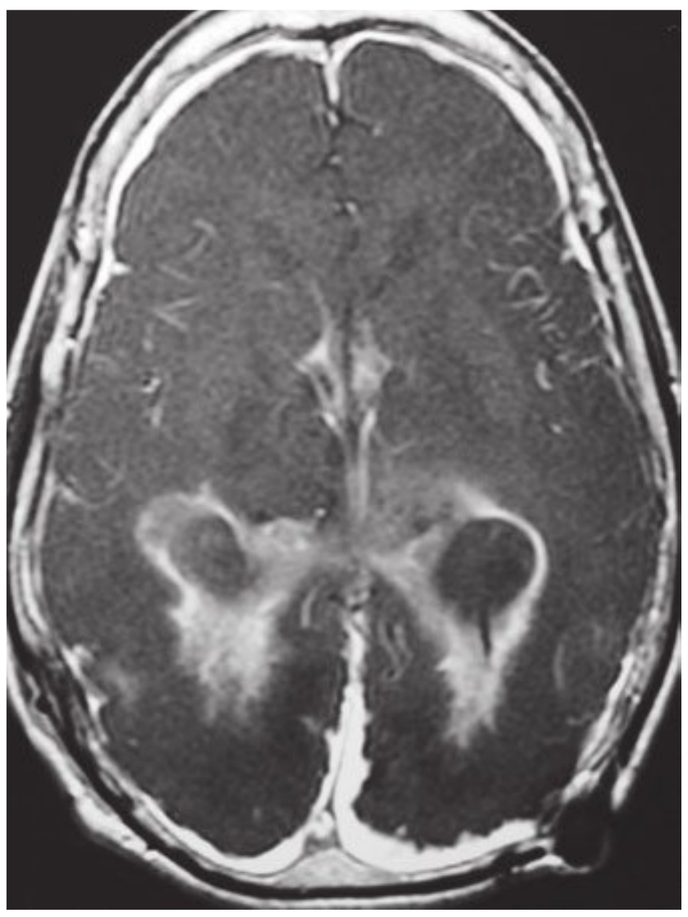

Fig. 2.129 A 29-year-old man with pyogenic ependymitis/ventriculitis related to an infected shunt. Abnormal gadolinium contrast enhancement is seen along the ependymal lining of the lateral ventricles on axial T1-weighted imaging.

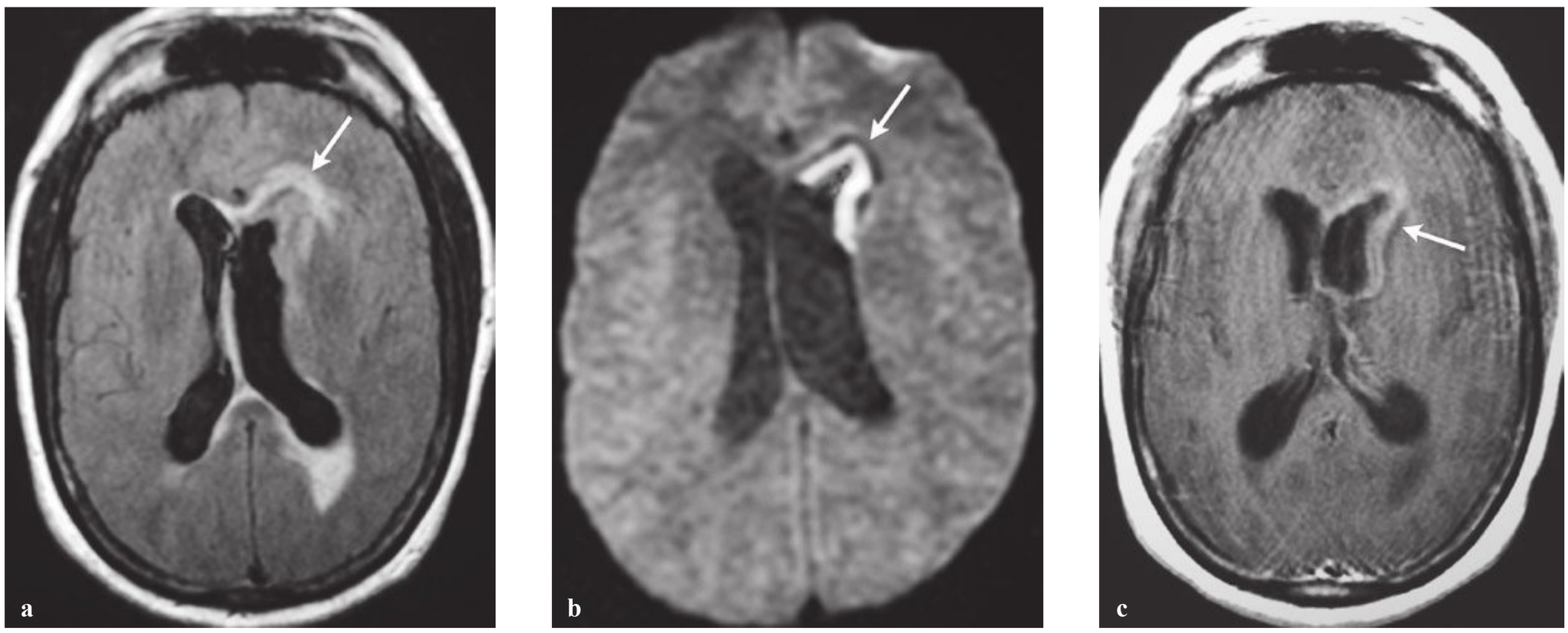

Fig. 2.130 **(a)** A 47-year old woman with pyogenic ventriculitis/ependymitis with abnormal high signal (arrow) on axial FLAIR along the wall of the left lateral ventricle, **(b)** restricted diffusion (arrow) on axial diffusion-weighted imaging at the frontal horn of the left lateral ventricle, and **(c)** associated gadolinium contrast enhancement (arrow) on axial T1-weighted imaging.

Table 2.9 (cont.) Contrast-enhancing ventricular margins

Lesions	Imaging Findings	Comments
Chemical ventriculitis	MRI and CT: Curvilinear and/or nodular contrast enhancement along ventricular/ependymal margins, with resultant communicating or noncommunicating types of hydrocephalus.	Complications relating to intrathecal administration of chemotherapeutic agents or rupture of intracranial dermoid into CSF spaces.
Radiation injury/necrosis	MRI: Focal lesion ± mass effect or poorly defined zone of low-intermediate signal on T1-weighted imaging, intermediate-high signal on T2-weighted imaging, ± contrast enhancement involving tissue (gray matter and/or white matter) in field of treatment. Lesion can extend to and involve ventricular margins.	Usually occurs from 4–6 months to 10 years after radiation treatment. May be difficult to distinguish from neoplasm. PET and magnetic resonance spectroscopy might be helpful for evaluation.
Posttraumatic Lesions		
Shunt placement	MRI: Transient curvilinear gadolinium contrast enhancement along ventricular/ependymal margins.	Transient gadolinium contrast enhancement after recent placement of ventricular shunt possibly related to mild hemorrhage.
Surgery	MRI: Transient curvilinear gadolinium contrast enhancement along ventricular/ependymal margins as well along encephalotomy margins.	Transient gadolinium contrast enhancement related to recent surgery, usually resolves after 2–3 months.
Hematoma (**Fig. 2.132**)	CT: A linear relationship exists between CT attenuation and hematocrit and hemoglobin and protein content. MRI: The signal of the hematoma depends on its age, size, location, hematocrit, oxidation state of iron in hemoglobin, degree of clot retraction, extent of edema, and MRI pulse sequence. In the early subacute phase (3 to 7 days), hemoglobin becomes oxidized to the iron Fe^{3+} state/methemoglobin. In the early phase, intracellular methemoglobin has high signal on T1-weighted imaging and low signal on T2-weighted imaging; eventually, high signal on T2-weighted imaging ` from extracellular methemoglobin that results from progressive lysis of red blood cell membranes. Gadolinium contrast may be seen at the margins of the hematoma. Inflammatory response to intraventricular blood can result in gadolinium contrast along the margins of the ventricles.	Can result from trauma, ruptured aneurysms or vascular malformations, coagulopathy, hypertension, adverse drug reaction, amyloid angiopathy, hemorrhagic transformation of cerebral infarction, metastases, abscesses, and viral infections (herpes simplex, CMV).

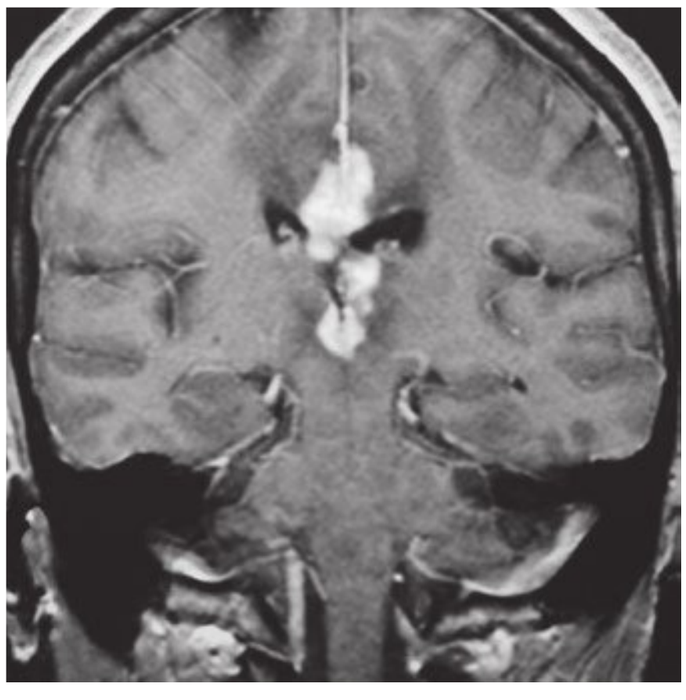

Fig. 2.131 A 53-year-old woman with neurosarcoidosis. Coronal T1-weighted imaging shows irregularly shaped zones with abnormal gadolinium contrast enhancement within the lateral and third ventricles.

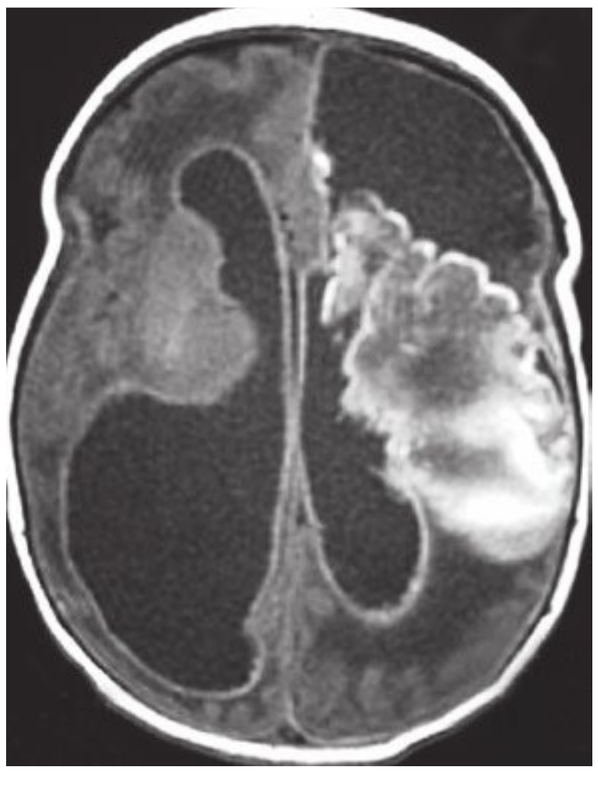

Fig. 2.132 Neonate with hemorrhagic infarction and necrosis that involves the left frontal lobe and that is associated with gadolinium contrast enhancement along the margins of the lateral ventricles on axial T1-weighted imaging.

Lesions	Imaging Findings	Comments
Vascular Lesions		
Arteriovenous malformation (AVM)	Lesions with irregular margins that can be located in the brain parenchyma, pia, dura, or both locations. MRI: AVMs contain multiple, tortuous, tubular flow voids on T1- and T2-weighted imaging secondary to patent arteries with high blood flow, as well as thrombosed vessels with variable signal, areas of hemorrhage in various phases, calcifications, and gliosis. The venous portions often show gadolinium contrast enhancement. Gradient echo MRI shows flow-related enhancement (high signal) in patent arteries and veins of the AVM. MRA using time-of-flight or phase-contrast techniques can provide additional detailed information about the nidus, feeding arteries and draining veins, and presence of associated aneurysms. Usually not associated with mass effect unless there is recent hemorrhage or venous occlusion.	Supratentorial AVMs occur more frequently (80–90%) than infratentorial AVMs (10–20%). Annual risk of hemorrhage. AVMs can be sporadic, congenital, or associated with a history of trauma. Multiple AVMs can be seen in Rendu-Osler-Weber syndrome (AVMs in brain and lungs and mucosal capillary telangectasias) and Wyburn-Mason syndrome (AVMs in brain and retina, + cutaneous nevi).
Developmental venous anomaly/venous angioma	MRI: On postcontrast T1-weighted imaging, venous angiomas are seen as a gadolinium-enhancing transcortical vein draining a collection of small medullary veins (caput medusae). The draining vein can be seen as a linear zone of low signal on T2-weighted imaging and susceptibility weighted imaging.	Considered an anomalous venous formation; typically not associated with hemorrhage, and usually an incidental finding except when associated with cavernous malformation.
Sturge-Weber syndrome **(Fig. 2.133)**	MRI: Prominent localized unilateral leptomeningeal contrast enhancement usually in parietal and/or occipital regions in children, ± gyral enhancement, slightly decreased signal on T2-weighted imaging in adjacent gyri, mild localized atrophic changes in brain adjacent to the pial angioma, ± prominent medullary and/or subependymal veins, ± ipsilateral prominence of choroid plexus. CT: Gyral calcifications > 2 years, progressive cerebral atrophy in region of pial angioma.	Also known as encephalotrigeminal angiomatosis, Sturge-Weber syndrome is a neurocutaneous syndrome in which a pial angioma is associated with ipsilateral port wine cutaneous lesion and seizures. It results from persistence of primitive leptomeningeal venous drainage (pial angioma) and developmental lack of normal cortical veins, producing chronic venous congestion and ischemia.

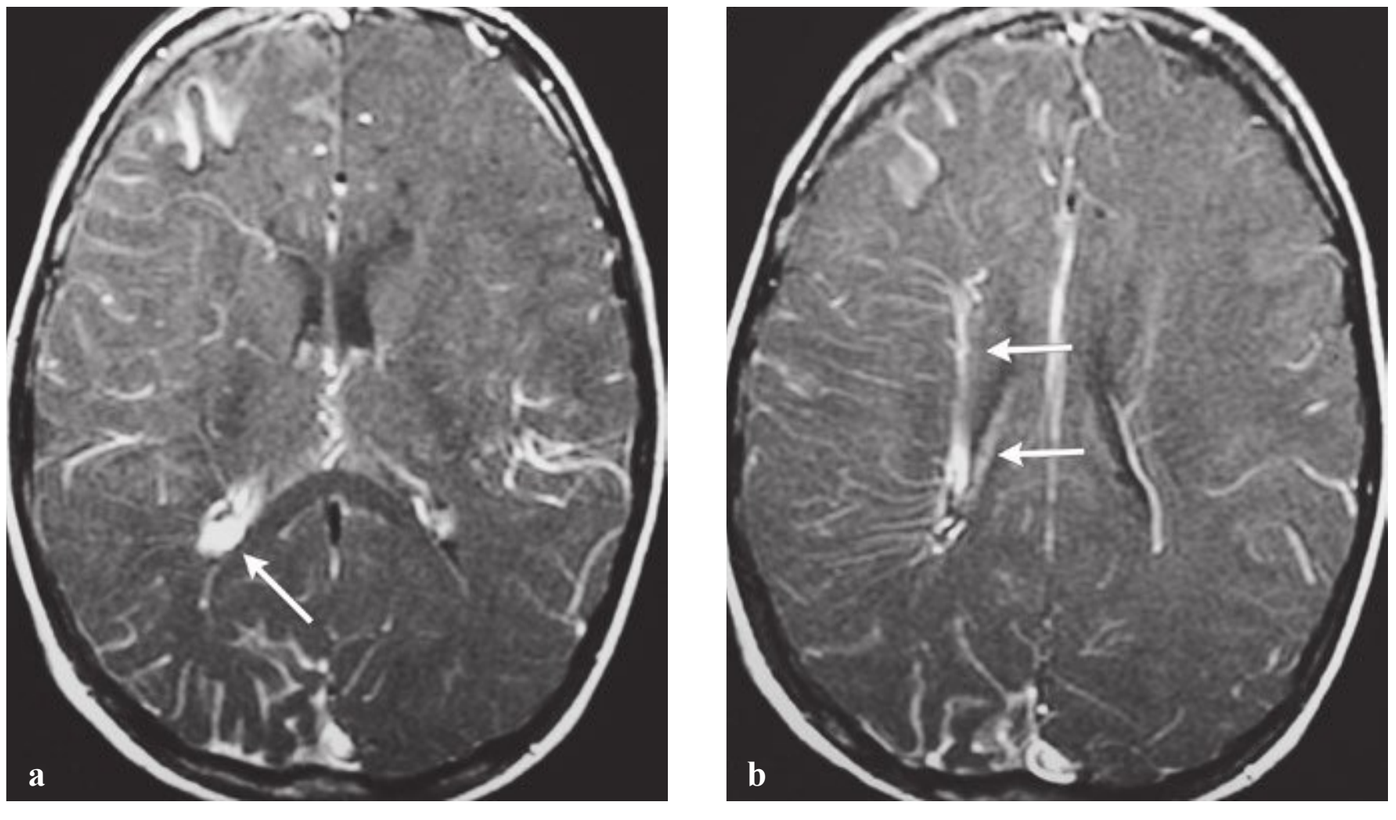

Fig. 2.133 A 6-year-old male with Sturge-Weber syndrome. **(a,b)** Axial postcontrast T1-weighted imaging shows unilateral leptomeningeal contrast enhancement adjacent to the right cerebral hemisphere with prominent medullary and subependymal veins, as well as ipsilateral prominence of choroid plexus (arrows).

References

Arachnoid Cyst

1. Westermaier T, Vince GH, Meinhardt M, Monoranu C, Roosen K, Matthies C. Arachnoid cysts of the fourth ventricle–short illustrated review. Acta Neurochir (Wien) 2010;152(1):119–124

Atypical Teratoid/Rhabdoid Tumor

2. Meyers SP, Khademian ZP, Biegel JA, Chuang SH, Korones DN, Zimmerman RA. Primary intracranial atypical teratoid/rhabdoid tumors of infancy and childhood: MRI features and patient outcomes. AJNR Am J Neuroradiol 2006;27(5):962–971

Cavernous Malformation

3. Ozgen B, Senocak E, Oguz KK, Soylemezoglu F, Akalan N. Radiological features of childhood giant cavernous malformations. Neuroradiology 2011;53(4):283–289

Cavum Septum Pellucidum and Cavum Vergae

4. Tubbs RS, Krishnamurthy S, Verma K, et al. Cavum velum interpositum, cavum septum pellucidum, and cavum vergae: a review. Childs Nerv Syst 2011;27(11):1927–1930

Central Neurocytoma

5. Kocaoglu M, Ors F, Bulakbasi N, Onguru O, Ulutin C, Secer HI. Central neurocytoma: proton MR spectroscopy and diffusion weighted MR imaging findings. Magn Reson Imaging 2009;27(3):434–440
6. Yeh IB, Xu M, Ng WH, Ye J, Yang D, Lim CC. Central neurocytoma: typical magnetic resonance spectroscopy findings and atypical ventricular dissemination. Magn Reson Imaging 2008;26(1):59–64

Chordoid Glioma

7. Brat DJ, Scheithauer BW. Chordoid glioma of the third ventricle. In: Louis DN, Ohgaki H, Wiestler OD, Cavenee WK, eds. World Health Organization Classification of Tumours of the Central Nervous System. 4th ed. Geneva: IARC Press; 2007:90–91
8. Horbinski C, Dacic S, McLendon RE, et al. Chordoid glioma: a case report and molecular characterization of five cases. Brain Pathol 2009;19(3):439–448
9. Ni HC, Piao YS, Lu DH, Fu YJ, Ma XL, Zhang XJ. Chordoid glioma of the third ventricle: four cases including one case with papillary features. Neuropathology 2013;33(2):134–139

Choroid Plexus Tumors

10. Meyers SP, Khademian ZP, Chuang SH, Pollack IF, Korones DN, Zimmerman RA. Choroid plexus carcinomas in children: MRI features and patient outcomes. Neuroradiology 2004;46(9):770–780
11. Ogiwara H, Dipatri AJ Jr, Alden TD, Bowman RM, Tomita T. Choroid plexus tumors in pediatric patients. Br J Neurosurg 2012;26(1):32–37
12. Paulus W, Brandner S. Choroid plexus tumours. In: Louis DN, Ohgaki H, Wiestler OD, Cavenee WK, eds. World Health Organization Classification of Tumours of the Central Nervous System. 4th ed. Geneva: IARC Press; 2007:82–85
13. Yan C, Xu Y, Feng J, et al. Choroid plexus tumours: classification, MR imaging findings and pathological correlation. J Med Imaging Radiat Oncol 2013;57(2):176–183

Ependymoma

14. Yuh EL, Barkovich AJ, Gupta N. Imaging of ependymomas: MRI and CT. Childs Nerv Syst 2009;25(10):1203–1213

Glioneuronal Tumor

15. Yano H, Nakayama N, Hirose Y, et al. Intraventricular glioneuronal tumor with disseminated lesions at diagnosis—a case report. Diagn Pathol 2011;6:119–125

Hemangiopericytoma

16. Hattingen E, Pilatus U, Good C, Franz K, Lanfermann H, Zanella FE. An unusual intraventricular haemangiopericytoma: MRI and spectroscopy. Neuroradiology 2003;45(6):386–389
17. Tanaka T, Kato N, Arai T, Hasegawa Y, Abe T. Hemangiopericytoma in the trigone of the lateral ventricle. Neurol Med Chir (Tokyo) 2011;51(5):378–382

Intracranial Cystic Lesions

18. Epelman M, Daneman A, Blaser SI, et al. Differential diagnosis of intracranial cystic lesions at head US: correlation with CT and MR imaging. Radiographics 2006;26(1):173–196
19. Osborn AG, Preece MT. Intracranial cysts: radiologic-pathologic correlation and imaging approach. Radiology 2006;239(3):650–664
20. Westermaier T, Vince GH, Meinhardt M, Monoranu C, Roosen K, Matthies C. Arachnoid cysts of the fourth ventricle—short illustrated review. Acta Neurochir (Wien) 2010;152(1):119–124

Intraventricular Cysts

21. Clarençon F, Bonneville F, Rousseau A, et al. Intracranial solitary fibrous tumor: imaging findings. Eur J Radiol 2011;80(2):387–394
22. Epelman M, Daneman A, Blaser SI, et al. Differential diagnosis of intracranial cystic lesions at head US: correlation with CT and MR imaging. Radiographics 2006;26(1):173–196
23. Osborn AG, Preece MT. Intracranial cysts: radiologic-pathologic correlation and imaging approach. Radiology 2006;239(3):650–664

Intraventricular Masses

24. Glastonbury CM, Osborn AG, Salzman KL. Masses and malformations of the third ventricle: normal anatomic relationships and differential diagnoses. Radiographics 2011;31(7):1889–1905
25. Paulus W, Brandner S. Choroid plexus tumours. In: Louis DN, Ohgaki H, Wiestler OD, Cavenee WK, eds. World Health Organization Classification of Tumours of the Central Nervous System. 4th ed. Geneva: IARC Press; 2007:82–85
26. Smith AB, Smirniotopoulos JG, Horkanyne-Szakaly I. From the radiologic pathology archives: intraventricular neoplasms: radiologic-pathologic correlation. Radiographics 2013;33(1):21–43

Meningioma

27. Kim EY, Kim ST, Kim HJ, Jeon P, Kim KH, Byun HS. Intraventricular meningiomas: radiological findings and clinical features in 12 patients. Clin Imaging 2009;33(3):175–180

Neurocysticercosis

28. Hanak BW, Walcott BP, Codd PJ, et al. Fourth ventricular neurocysticercosis presenting with acute hydrocephalus. J Clin Neurosci 2011;18(6):867–869

Normal-Pressure Hydrocephalus

29. Bradley WG Jr. CSF flow in the brain in the context of normal pressure hydrocephalus. AJNR Am J Neuroradiol 2015;36(5):831–838
30. Shprecher D, Schwalb J, Kurlan R. Normal pressure hydrocephalus: diagnosis and treatment. Curr Neurol Neurosci Rep 2008;8(5):371–376
31. Virhammar J, Laurell K, Cesarini KG, Larsson EM. Preoperative prognostic value of MRI findings in 108 patients with idiopathic normal pressure hydrocephalus. AJNR Am J Neuroradiol 2014;35(12):2311–2318

Small Ventricles

32. Bialer OY, Rueda MP, Bruce BB, Newman NJ, Biousse V, Saindane AM. Meningoceles in idiopathic intracranial hypertension. AJR Am J Roentgenol 2014;202(3):608–613
33. Nguyen HS, Callahan JD, Cohen-Gadol AA. Life-saving decompressive craniectomy for diffuse cerebral edema during an episode of new-onset diabetic ketoacidosis: case report and review of the literature. Childs Nerv Syst 2011;27(4):657–664
34. Piteau SJ, Ward MGK, Barrowman NJ, Plint AC. Clinical and radiographic characteristics associated with abusive and nonabusive head trauma: a systematic review. Pediatrics 2012;130(2):315–323
35. Saindane AM, Bruce BB, Riggeal BD, Newman NJ, Biousse V. Association of MRI findings and visual outcome in idiopathic intracranial hypertension. AJR Am J Roentgenol 2013;201(2):412–418
36. Zhang LJ, Zhong J, Lu GM. Multimodality MR imaging findings of low-grade brain edema in hepatic encephalopathy. AJNR Am J Neuroradiol 2013;34(4):707–715

Tuberous Sclerosis

37. Katz JS, Milla SS, Wiggins GC, Devinsky O, Weiner HL, Roth J. Intraventricular lesions in tuberous sclerosis complex: a possible association with the caudate nucleus. J Neurosurg Pediatr 2012;9(4):406–413

Ventriculitis

38. Clarençon F, Bonneville F, Rousseau A, et al. Intracranial solitary fibrous tumor: imaging findings. Eur J Radiol 2011;80(2):387–394
39. Kawaguchi T, Sakurai K, Hara M, et al. Clinico-radiological features of subarachnoid hyperintensity on diffusion-weighted images in patients with meningitis. Clin Radiol 2012;67(4):306–312
40. Mohan S, Jain KK, Arabi M, Shah GV. Imaging of meningitis and ventriculitis. Neuroimaging Clin N Am 2012;22(4):557–583

Chapter 3

Extra-Axial Lesions

Introduction 518

3.1 Solitary extra-axial mass lesions 518

3.2 Multifocal extra-axial lesions 548

References 558

3 Extra-Axial Lesions

Table 3.1 Solitary extra-axial mass lesions

Table 3.2 Multifocal extra-axial lesions

Introduction

Intracranial lesions are typically classified as being extra- or intra-axial. Extra-axial lesions arise from the skull, meninges, or tissues other than the brain parenchyma. Intra-axial lesions are located in the brain. Extra-axial lesions are characterized as being within epidural, subdural, and/or subarachnoid spaces or compartments. Lesions involving the meninges can further be categorized as involving the dura mater (such as benign postoperative dural fibrosis) or involving the leptomeninges (pia and arachnoid). Abnormalities of the meninges are often best seen after the intravenous administration of gadolinium contrast material. Dural enhancement usually has a linear configuration, whereas pathology involving the leptomeninges appears as enhancement within the sulci and basilar cisterns. Enhancement of the leptomeninges is usually related to significant pathology, such as neoplastic or inflammatory diseases.

Table 3.1 Solitary extra-axial mass lesions

- Benign Neoplasms
  - Meningioma
  - Hemangiopericytoma
  - Meningioangiomatosis
  - Schwannoma
  - Neurofibroma
  - Paraganglioma
  - Benign mesenchymal non-meningothelial tumors
  - Osteoma
  - Pituitary adenoma
  - Craniopharyngioma
  - Choroid plexus papilloma
- Malignant Neoplasms
  - Malignant meningioma
  - Anaplastic hemangiopericytoma
  - Metastatic tumor
  - Lymphoma
  - Plasmacytoma/myeloma
  - Malignant mesenchymal non-meningothelial tumors
  - Chordoma
  - Chondrosarcoma
  - Osteogenic sarcoma
  - Ewing's sarcoma
  - Sinonasal squamous cell carcinoma
  - Nasopharyngeal carcinoma
  - Adenoid cystic carcinoma
  - Esthesioneuroblastoma
- Hemorrhage
  - Epidural hematoma
  - Subdural hematoma
  - Ossified hematoma
- Infection/Inflammation
  - Epidural abscess or subdural empyema
  - Langerhans' cell histiocytosis/eosinophilic granuloma
- Vascular Lesions
  - Arterial aneurysm
  - Dural arteriovenous malformations (AVMs)
  - Vein of Galen aneurysm
- Tumorlike Lesions
  - Arachnoid cyst
  - Leptomeningeal cyst
  - Rathke's cleft cyst
  - Epidermoid
  - Dermoid
  - Neurenteric cyst
  - Lipoma
  - Dural calcification and ossification
  - Ecchordosis physaliphora

Table 3.1 Solitary extra-axial mass lesions

Lesions	Imaging Findings	Comments
Benign Neoplasms		
Meningioma (**Fig. 3.1, Fig. 3.2,** and **Fig. 3.3**)	Well-circumscribed extra-axial dura-based lesions. Locations: supra- > infratentorial, parasagittal > convexity > sphenoid ridge > parasellar > posterior fossa > optic nerve sheath > intraventricular. MRI: Dura-based tumors with intermediate signal on T1-weighted imaging, intermediate to slightly high signal on T2-weighted imaging, usually with prominent gadolinium contrast enhancement, often with a dural tail, ± calcifications. Intratumoral hemorrhage and cystic or necrotic foci can occur in 15% Can result in compression of adjacent brain parenchyma, encasement of arteries, and compression of dural venous sinuses. Rarely invasive/malignant. Diffusion-weighted imaging/diffusion tensor imaging: ADC values vary among the different subtypes of meningioma. Some tumors can show restricted diffusion, although these findings can be seen with both benign and atypical tumors. Magnetic resonance spectroscopy can show elevated alanine (1.5 ppm), lactate, choline, and glutamine/glutamate levels, and reduced N-acetylaspartate (NAA). CT: Tumors have intermediate attenuation with or without calcifications, with or without hyperostosis, and usually show prominent contrast enhancement.	Meningiomas are the most common extra-axial tumors, accounting for up to 26%of primary intracranial tumors. Annual incidence is 6 per 100,000, typically in adults (> 40 years old) and in women > men. Composed of neoplastic meningothelial (arachnoid or arachnoid cap) cells. Meningiomas are usually solitary and sporadic, but can also occur as multiple lesions in patients with neurofibromatosis type 2. Eighty percent of meningiomas are benign (WHO grade I), although 15%have atypical features (WHO grade II) and ~ 5%have anaplastic histologic features (WHO grade III). Can occur secondary to radiation treatment, with latencies ranging from 19 to 35 years. Classified into different subtypes, such as meningothelial, fibrous (fibroblastic), transitional (mixed), psammomatous, angiomatous, atypical, and anaplastic. The most common intracranial types of meningioma are meningothelial, fibrous, and transitional types. Usually show immunoreactivity to epithelial membrane antigen (EMA) and vimentin. Secretory meningiomas are typically immunoreactive to CEA. Associated cytogenetic findings of deletion of chromosome 22. Mutations in the NF2 tumor suppressor gene on chromosome 22 have been found in 60%of sporadic meningiomas.
Hemangiopericytoma (**Fig. 3.4**)	MRI: Solitary dura-based tumors ranging from 2 to 7 cm in diameter that have low-intermediate signal on T1-weighted imaging, intermediate to slightly high signal on T2-weighted imaging, and usually prominent gadolinium contrast enhancement, often with a dural tail, ± calcifications. Intratumoral hemorrhage and cystic or necrotic foci can occur in 30% Magnetic resonance spectroscopy: May show elevated choline peak. Relative ratios of myo-inositol, glucose, and glutathione with respect to glutamate are higher in hemangiopericytomas than in meningiomas. CT: Tumors have intermediate attenuation with or without calcifications and usually show prominent contrast enhancement.	Rare (WHO grade II) neoplasms that account for 0.4% of primary intracranial tumors and are 50 times less frequent than meningiomas. Tumors are composed of closely packed cells with scant cytoplasm and round, ovoid, or elongated nuclei with moderately dense chromatin. Numerous slitlike vascular channels are seen in these tumors that are lined by flattened endothelial cells, ± zones of necrosis. Immunoreactive to vimentin (85%) and factor XIIIa (80–100%), and variably to Leu-7. and CD34. Associated with abnormalities involving chromosome 12. Typically occur in young adults (mean age = 43 years) and in males > females. Sometimes referred to as angioblastic meningioma or meningeal hemangiopericytoma, these tumors arise from vascular cells—pericytes. Recur and metastasize more frequently than meningiomas.
Meningioangiomatosis (**Fig. 3.5**)	MRI: Lesions usually involve the superficial brain tissue and leptomeninges and have low-intermediate signal on T1-weighted imaging, high signal on T2-weighted imaging, and gyriform high signal on FLAIR, ± low signal from calcifications. Typically show gadolinium contrast enhancement. Magnetic resonance spectroscopy: Choline peaks can be elevated. CT: Nodular lesions with low-intermediate attenuation involving the superficial brain, ± calcifications, ± perilesional edema, and usually show contrast enhancement.	Rare benign hamartomatous lesions involving the leptomeninges and adjacent cerebral cortex. Lesions contain numerous thickened blood vessels surrounded by sheaths of well-differentiated meningothelial cells and concentric layers of collagen bundles, ± psammoma bodies, and typically have a low MIB-1 proliferative rate (< 1%). Mean age =18 years. Most common locations are temporal and frontal lobes. Lesions are solitary in sporadic cases and multiple in patients with neurofibromatosis type 2.

(continued on page 522)

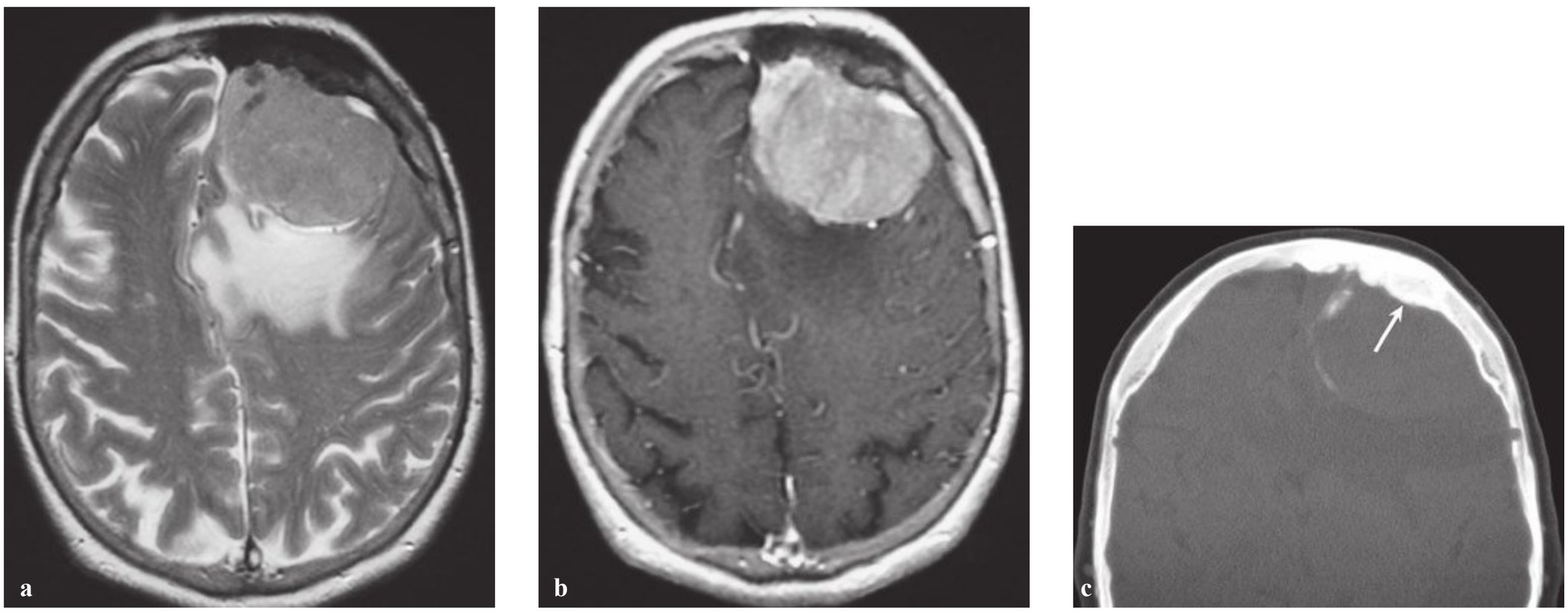

Fig. 3.1 A 75-year-old woman with a meningioma in the left frontal region that has **(a)** intermediate signal on axial T2-weighted imaging with surrounding edema; **(b)** gadolinium contrast enhancement on axial T1-weighted imaging, and **(c)** hyperostosis (arrow) on axial CT.

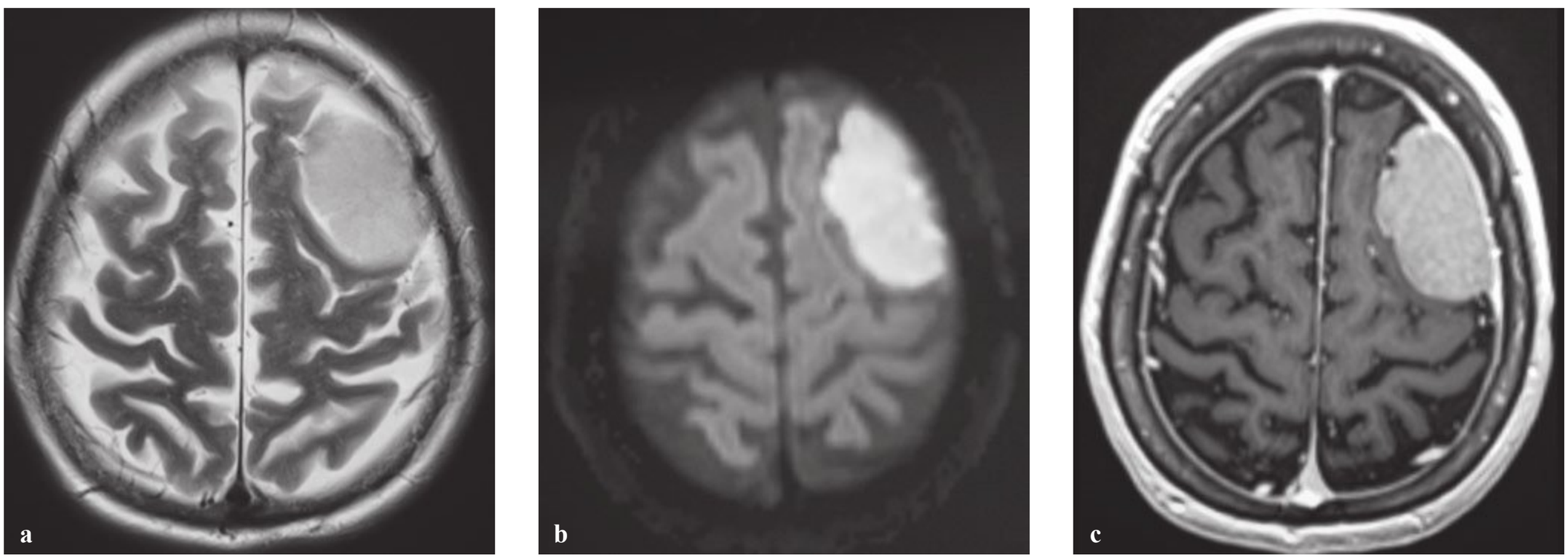

Fig. 3.2 A 76-year-old woman with a low-grade meningioma in the left frontal region that has **(a)** slightly high signal on axial T2-weighted imaging, **(b)** restricted diffusion on axial diffusion-weighted imaging, and **(c)** gadolinium contrast enhancement on axial T1-weighted imaging with dural tails.

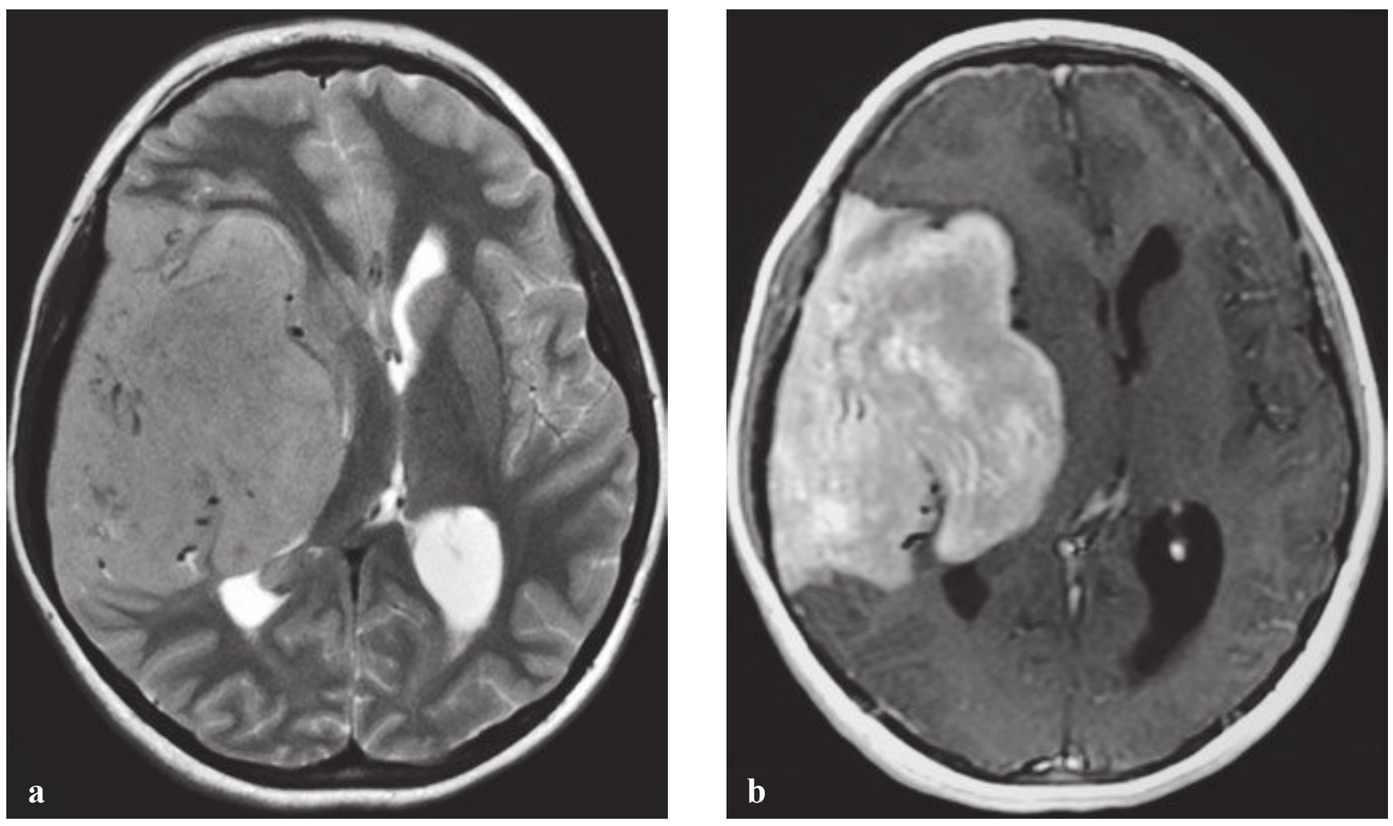

Fig. 3.3 An 11-year-old female with a papillary meningioma that has slightly lobulated margins and **(a)** intermediate to slightly high signal on axial T2-weighted imaging with internal vascular flow voids and **(b)** heterogeneous gadolinium contrast enhancement on axial T1-weighted imaging.

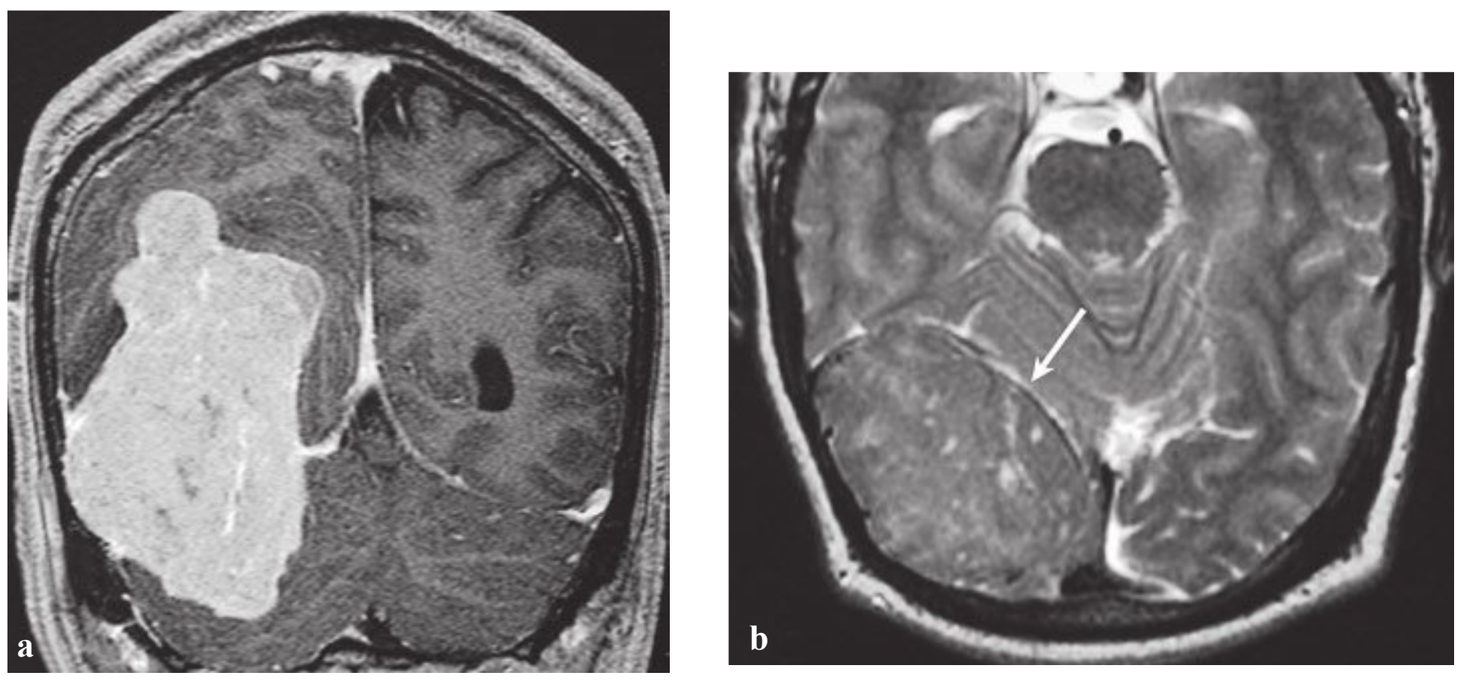

Fig. 3.4 A 32-year-old man with a hemangiopericytoma involving the tentorium with superior and inferior extension. **(a)** The gadolinium-enhancing tumor on coronal T1-weighted imaging has slightly lobulated margins and **(b)** mostly intermediate signal with high signal foci on axial T2-weighted imaging (arrow).

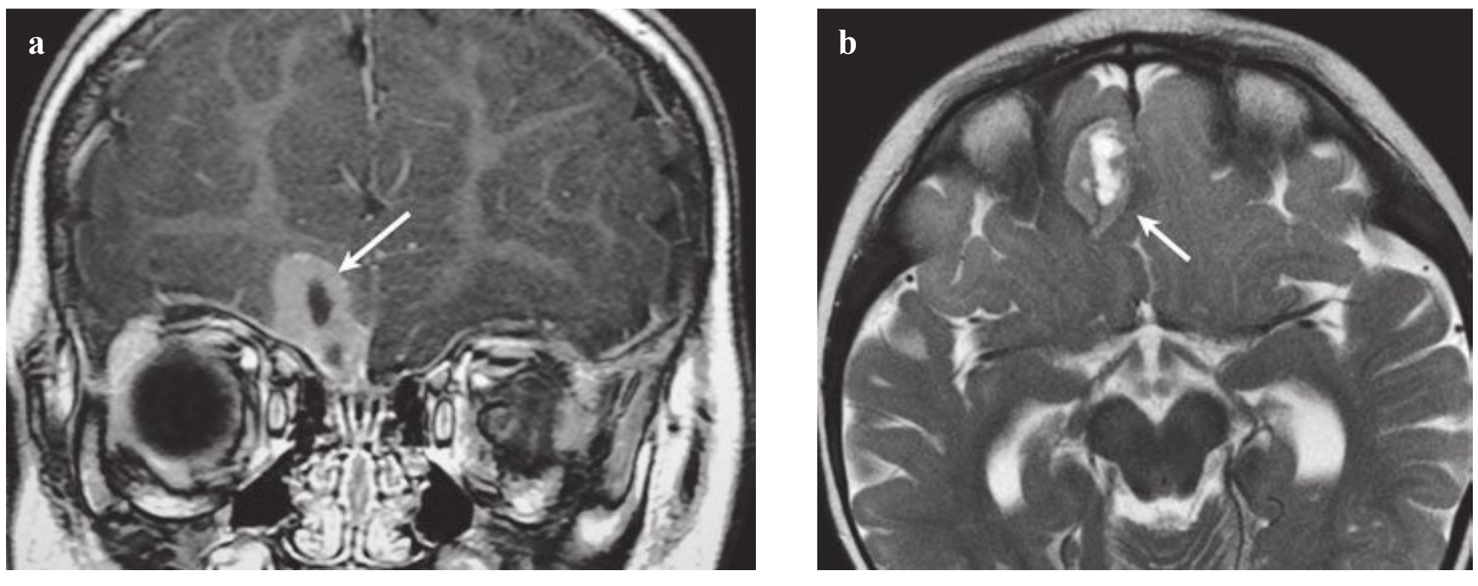

Fig. 3.5 A 1-year-old female with meningioangiomatosis at the inferomedial right frontal region that is seen as **(a)** gadolinium contrast enhancement involving the superficial brain tissue and leptomeninges (arrow) on coronal T1-weighted imaging, with **(b)** corresponding mixed slightly high and high signal (arrow) on axial T2-weighted imaging.

Table 3.1 (cont.) Solitary extra-axial mass lesions

Lesions	Imaging Findings	Comments
Schwannoma (**Fig. 3.6**)	MRI: Circumscribed or lobulated lesions with low-intermediate signal on T1-weighted imaging and high signal on T2-weighted imaging and fat-suppressed T2-weighted imaging. Usually show prominent gadolinium contrast enhancement. High signal on T2-weighted imaging and gadolinium contrast enhancement can be heterogeneous in large lesions due to cystic degeneration, fibrosis, and/or hemorrhage. Schwannomas involving the temporal bone include those from CN V (trigeminal nerve cistern/Meckel's cave), CN VI (Dorello canal), CN VII and CN VIII (IAC and CPA cistern), CN IX, CN X, and CN XI (jugular foramen). CT: Circumscribed or lobulated lesions, intermediate attenuation, + contrast enhancement. Large lesions can have cystic degeneration and/or hemorrhage.	Schwannomas are benign encapsulated tumors that contain differentiated neoplastic Schwann cells. Most commonly occur as solitary sporadic lesions. Multiple schwannomas are often associated with neurofibromatosis type 2 (NF2), which is an autosomal dominant disease involving a gene at chromosome 22q12. In addition to schwannomas, patients with NF2 can also have multiple meningiomas and ependymomas. Schwannomas represent 8% of primary intracranial tumors and 29% or primary spinal tumors. The incidence of NF2 is 1/ 37,000 to 1/50,000 newborns. Age at presentation is 22 to 72 years (mean age = 46 years). Peak incidence is in the fourth to sixth decades. In NF2, many patients present in the third decade with bilateral vestibular schwannomas.
Neurofibroma	MRI: Solitary neuro*fi*bromas appear as circumscribed or lobulated extra-axial lesions with low-intermediate signal on T1-weighted imaging and intermediate-high signal on T2-weighted imaging, + prominent gadolinium contrast enhancement. High signal on T2-weighted imaging and gadolinium contrast enhancement can be heterogeneous in large lesions. Plexiform neuro*fi*bromas appear as curvilinear and multinodular lesions involving multiple nerve branches and have low to intermediate signal on T1-weighted imaging and intermediate, slightly high to high signal on T2-weighted imaging and fat-suppressed T2-weighted imaging, with or without bands or strands of low signal. Lesions usually show gadolinium contrast enhancement. CT: Ovoid or fusiform lesions with low-intermediate attenuation. Lesions can show contrast enhancement. Often erode adjacent bone.	Benign nerve sheath tumors that contain mixtures of Schwann cells, perineural-like cells, and interlacing fascicles of fibroblasts associated with abundant collagen. Unlike schwannomas, neurofibromas lack Antoni A and B regions and cannot be separated pathologically from the underlying nerve. Most frequently occur as sporadic, localized, solitary lesions, less frequently as diffuse or plexiform lesions. Multiple neurofibromas are typically seen in neurofibromatosis type 1, which is an autosomal dominant disorder (1/2,500 births) from mutations in the neurofibromin gene on chromosome 17q11.2. Represents the most common type of neurocutaneous syndrome and is associated with neoplasms of the central and peripheral nervous systems (optic gliomas, astrocytomas, plexiform and solitary neurofibromas) and skin (café-au-lait spots, axillary and inguinal freckling). Also associated with meningeal and skull dysplasias, as well as hamartomas of the iris (Lisch nodules).
Paraganglioma (**Fig. 3.7**)	Ovoid or fusiform lesions with low-intermediate attenuation. MRI: Spheroid or lobulated lesion with intermediate signal on T1-weighted imaging and intermediate-high signal on T2-weighted imaging and fat-suppressed T2-weighted imaging, ± tubular zones of flow voids. Usually show prominent gadolinium contrast enhancement, ± foci of high signal on T1-weighted images from mucin or hemorrhage, ± peripheral rim of low signal (hemosiderin) on T2-weighted imaging. CT: Lesions can show contrast enhancement. Often erode adjacent bone.	Benign encapsulated neuroendocrine tumors that arise from neural crest cells associated with autonomic ganglia (paraganglia) throughout the body. These lesions are also referred to as chemodectomas and are named according to location (glomus jugulare, tympanicum, vagale). Paragangliomas represent 0.6% of head and neck tumors and 0.03% of all neoplasms.
Benign mesenchymal non-meningothelial tumors	MRI and CT findings of these lesions are dependent on their histologic features.	Benign mesenchymal tumors (WHO grade I) can rarely occur as solitary lesions involving the meninges and skull. Lesions include lipoma, angiolipoma, hibernoma, solitary fibrous tumor, leiomyoma, rhabdomyoma, chondroma, and osteoma.
Osteoma (**Fig. 3.8**)	MRI: Osteomas typically appear as well-circumscribed zones of dense bone with low signal on T1-weighted imaging, FLAIR imaging, T2-weighted imaging, and fat-suppressed T2-weighted imaging. CT: Dense round or ovoid lesions with well-circumscribed margins that are contiguous with cortical bone, and inner or outer table of the skull is usually smooth or lobulated.	Primary osseous tumors composed of dense lamellar, woven, and/or compact cortical bone and usually located at the surface of bones. Usually occur in Gardner's syndrome, which is an autosomal dominant disorder that is associated with intestinal polyposis, fibromas, and desmoid tumors.

(continued on page 524)

Fig. 3.6 A 17-year-old female with a gadolinium-enhancing left trigeminal schwannoma (arrow) on axial fat-suppressed T1-weighted imaging.

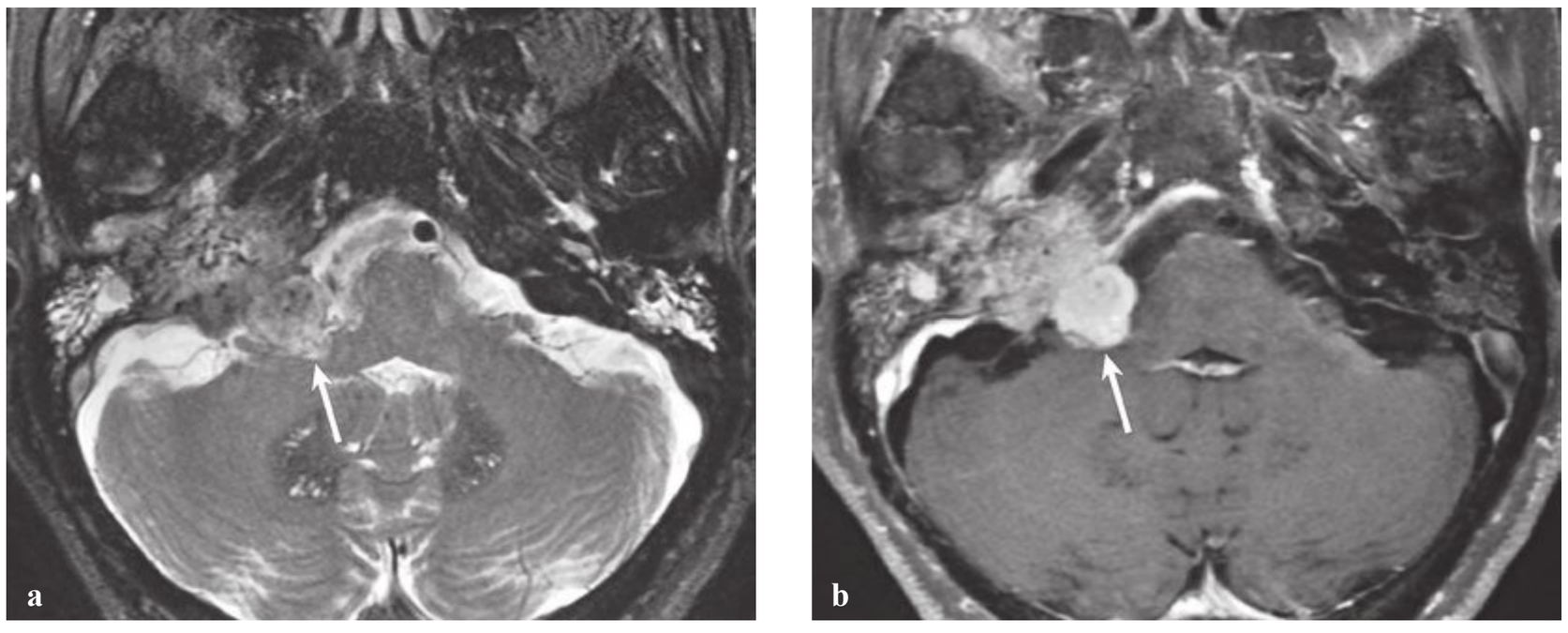

Fig. 3.7 **(a)** An 83-year-old woman with a paraganglioma/glomus jugulare eroding and invading the right jugular foramen with intracranial extension that has heterogeneous intermediate signal with multiple small vascular signal voids on axial fat-suppressed T2-weighted imaging (arrow), and **(b)** shows gadolinium contrast enhancement on axial fat-suppressed T1-weighted imaging (arrow).

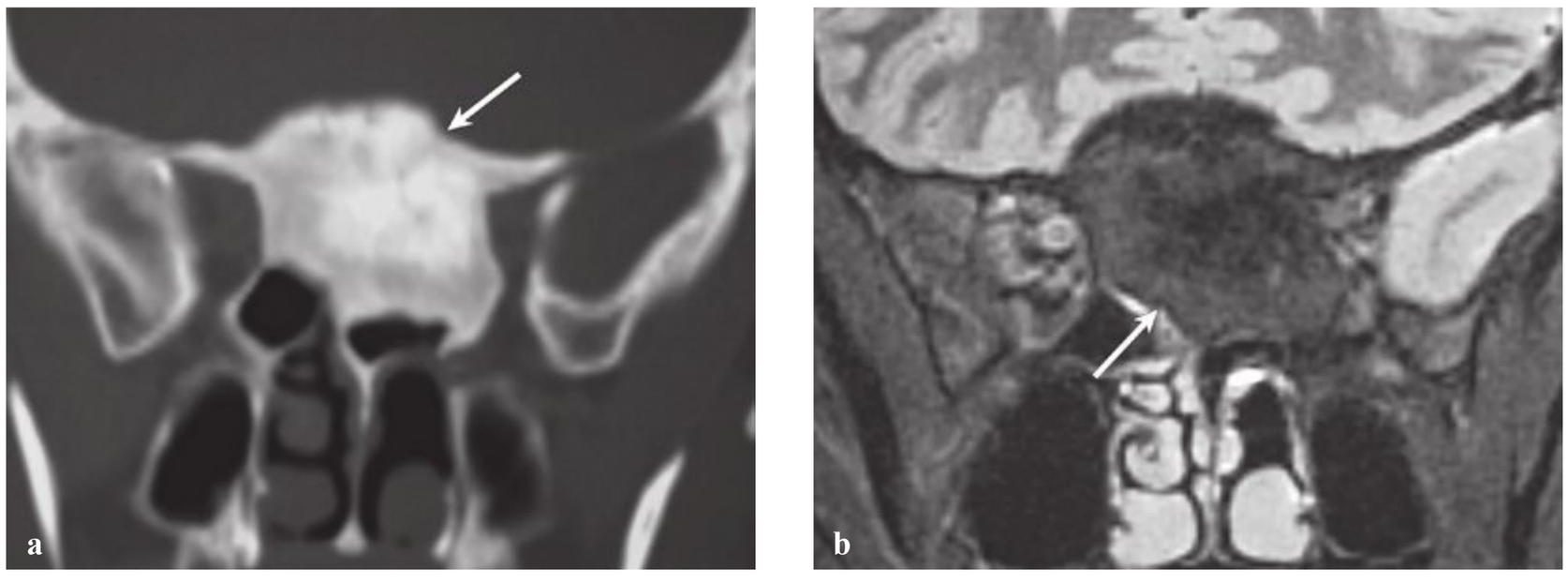

Fig. 3.8 A 26-year-old woman with an osteoma involving the ethmoid bone that extends superiorly, indenting the inferior frontal lobes. The lesion also extends laterally into the left orbit. **(a)** The osteoma has high attenuation on coronal CT (arrow) and **(b)** heterogeneous mostly low signal on coronal STIR (arrow).

Table 3.1 (cont.) Solitary extra-axial mass lesions

Lesions	Imaging Findings	Comments
Pituitary adenoma (**Fig. 3.9**)	Microadenomas (< 10 mm): Commonly have intermediate signal on T1- and T2-weighted imaging occasionally have high signal on T2-weighted imaging, ± cyst, ± hemorrhage, ± necrosis. Typically enhance less than normal pituitary tissue—often best seen with dynamic early phase imaging. Macroadenomas (> 10 mm): Commonly have intermediate signal on T1- and T2-weighted imaging similar to gray matter, ± necrosis, ± cyst, ± hemorrhage. Usually have prominent gadolinium contrast enhancement, extension into suprasellar cistern with waist at diaphragma sella, ± extension into cavernous sinus, occasionally invading skull base.	Common, benign, slow-growing tumors representing ~ 50% of sellar/parasellar neoplasms in adults. Can be associated with endocrine abnormalities related to oversecretion of hormones (prolactin > nonsecretory type > growth hormone > ACTH > others). Prolactinomas occur in females > males. Growth hormone tumors occur in males > females.
Craniopharyngioma (**Fig. 3.10**)	Circumscribed, lobulated lesions; both suprasellar and intrasellar location > suprasellar > intrasellar locations. Lesions can contain cysts, lipid components, and calcifications. MRI: Lesions can have variable low, intermediate, and/or high signal on T1- and T2-weighted imaging, ± nodular or rim patterns of gadolinium contrast enhancement. CT: Circumscribed, lobulated lesions; variable low, intermediate, and/or high attenuation; ± nodular or rim patterns of contrast enhancement ± calcifications.	Usually histologically benign but locally aggressive lesions arising from squamous epithelial rests along Rathke's cleft. Lesions contain cords and and lobules of squamous epithelium, pallisaded columnar epithelium, cystic cavities containing squamous debris and/or cholesterol, and piloid gliosis with Rosenthal fibers. Mutations of the β-catenin gene in 70% Accounts for 1.2 to 4.6% of all intracranial tumors, with an incidence of 2 cases per million per year. Occurs in children (10 years old) and adults (> 40 years old) and in males = females.
Choroid plexus papilloma (**Fig. 3.11**)	MRI: Circumscribed and/or lobulated lesions with papillary projections, intermediate signal on T1-weighted imaging and mixed intermediate-high signal on T2-weighted imaging, usually with prominent gadolinium contrast enhancement, ± calcifications. Locations: atrium of lateral ventricle (children) > fourth ventricle (adults), rarely other locations. such as third ventricle. Associated with hydrocephalus from CSF overproduction or mechanical obstruction. CT: Circumscribed and/or lobulated lesions with papillary projections, intermediate attenuation, and usually prominent contrast enhancement, ± calcifications.	Rare benign (WHO grade I) intraventricular neoplasms derived from choroid plexus epithelium in which a single layer of cuboidal or columnar epithelial cells with round/oval nuclei overlies fibrovascular connective tissue in frondlike patterns. Occur in lateral ventricle (50%), fourth ventricle/CP angle (40%), third ventricle (5%), and multiple ventricles (5%). Occur in children and adults. Tumors in the lateral ventricles account for up to 80% of cases in patients less than 20 years old. Lesions in the fourth ventricle are most common in adults. Tumors have very low mitotic activity. Immunoreactive to cytokeratins, vimentin, podoplanin, S-100, and transthyretin. Can be cured by surgical resection.

(continued on page 526)

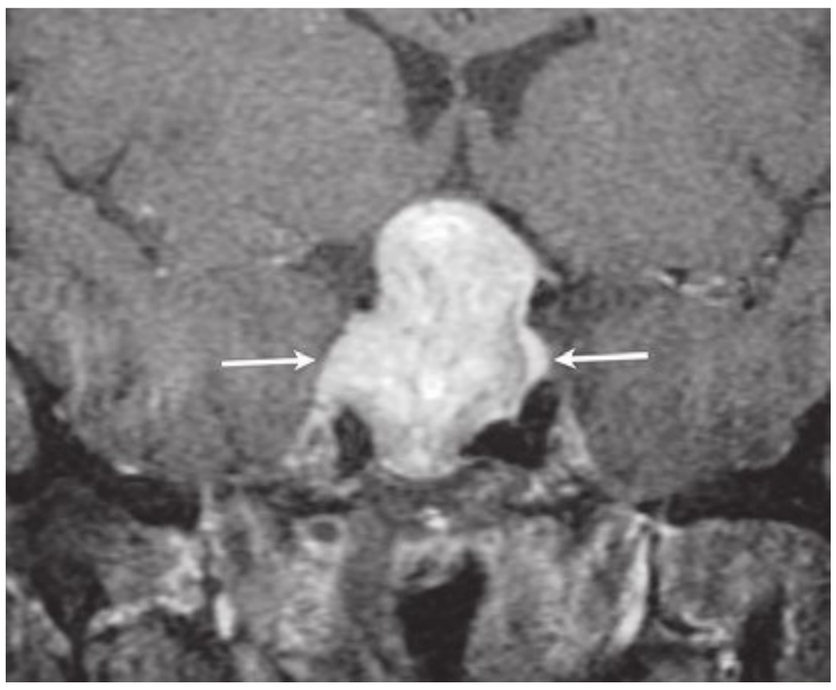

Fig. 3.9 A 67-year-old woman with a large gadolinium-enhancing pituitary macroadenoma (arrows) extending superiorly into the suprasellar cistern and elevating the optic chiasm on coronal fat-suppressed T1-weighted imaging.

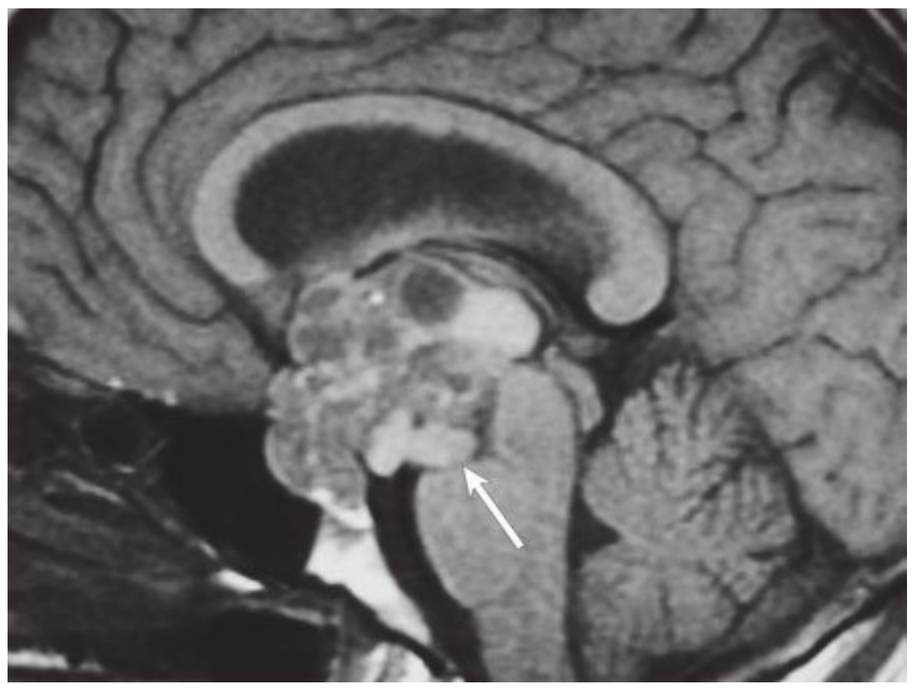

Fig. 3.10 A 23-year-old woman with a craniopharyngioma in the sella and suprasellar cistern, that has mixed low, intermediate, and high signal on sagittal T1-weighted imaging (arrow).

Fig. 3.11 A 6-month-old male with a gadolinium-enhancing choroid plexus papilloma (arrows) in the inferior left posterior cranial fossa associated with hypoplasia of the left cerebellar hemisphere, as seen on coronal T1-weighted imaging. The lesion borders the fourth ventricle and subarachnoid space. Overproduction of CSF from the tumor causes dilatation of the intracranial subarachnoid space/external hydrocephalus.

Table 3.1 (cont.) Solitary extra-axial mass lesions

Lesions	Imaging Findings	Comments
Malignant Neoplasms		
Malignant meningioma (**Fig. 3.12** and **Fig. 3.13**)	MRI: Dura-based tumors with intermediate signal on T1-weighted imaging and intermediate to slightly high signal on T2-weighted imaging, usually with prominent gadolinium contrast enhancement, ± calcifications. Malignant meningiomas are often large and may have irregular margins, with brain invasion and peritumoral edema. Difusion-weighted imaging/diffusion tensor imaging: ADC values vary among the different subtypes of meningioma. Some tumors can show restricted diffusion, although these findings can be seen with both benign and malignant tumors. Magnetic resonance spectroscopy: Can show elevated alanine (1.5 ppm), lactate, choline, and glutamine/glutamate peaks, and reduced N-acetylaspartate (NAA). MRS cannot reliably differentiate benign from malignant meningiomas. CT: Tumors have intermediate attenuation with or without calcifications, with or without hyperostosis, and usually show prominent contrast enhancement.	Eighty percent of meningiomas are benign (WHO grade I), although 15%have atypical features (WHO grade II) and ~ 5%have anaplastic/malignant histologic features (WHO grade III). Atypical and anaplastic/malignant meningiomas are associated with recurrence rates at 5 years of 40%and 50–80%, respectively.
Anaplastic hemangiopericytoma	MRI: Solitary, lobulated, dura-based tumors that have low-intermediate signal on T1-weighted imaging, mixed intermediate, slightly high, and high signal on T2-weighted imaging, and usually prominent heterogeneous gadolinium contrast enhancement. Intratumoral hemorrhage and cystic or necrotic foci are often present, ± dural tail, ± calcifications, ± bone destruction, ± peritumoral edema. CT: Tumors have intermediate attenuation with or without calcifications, and usually show prominent contrast enhancement.	Anaplastic hemangiopericytomas (WHO grade III) have high degrees of nuclear atypia with mitotic activities of greater than 5 mitoses per 10 HPF. Ki-67 activity is > 15% Recur and metastasize more frequently than WHO grade II hemangiopericytomas.
Metastatic tumor (**Fig. 3.14**)	MRI: Circumscribed spheroid lesion in bone, dura, leptomeninges, and/or choroid plexus. Often has low-intermediate signal on T1-weighted imaging and intermediate-high signal on T2-weighted imaging, ± hemorrhage, calcifications, and cysts. Variable gadolinium contrast enhancement. CT: Lesions usually have low-intermediate attenuation, ± hemorrhage, calcifications, and cysts. Variable contrast enhancement, ± bone destruction, ± compression of neural tissue or vessels. Leptomeningeal tumor often best seen on postcontrast images.	Represent ~ 33%of intracranial tumors, usually from extracranial primary neoplasm in adults > 40 years old. Primary tumor source: lung > breast > GI > GU > melanoma. Can occur as single or multiple well-circumscribed or poorly defined lesions involving the skull, dura, leptomeninges, and/or choroid plexus. Metastatic tumor may cause variable destructive or infiltrative changes in single or multiple sites.

(continued on page 528)

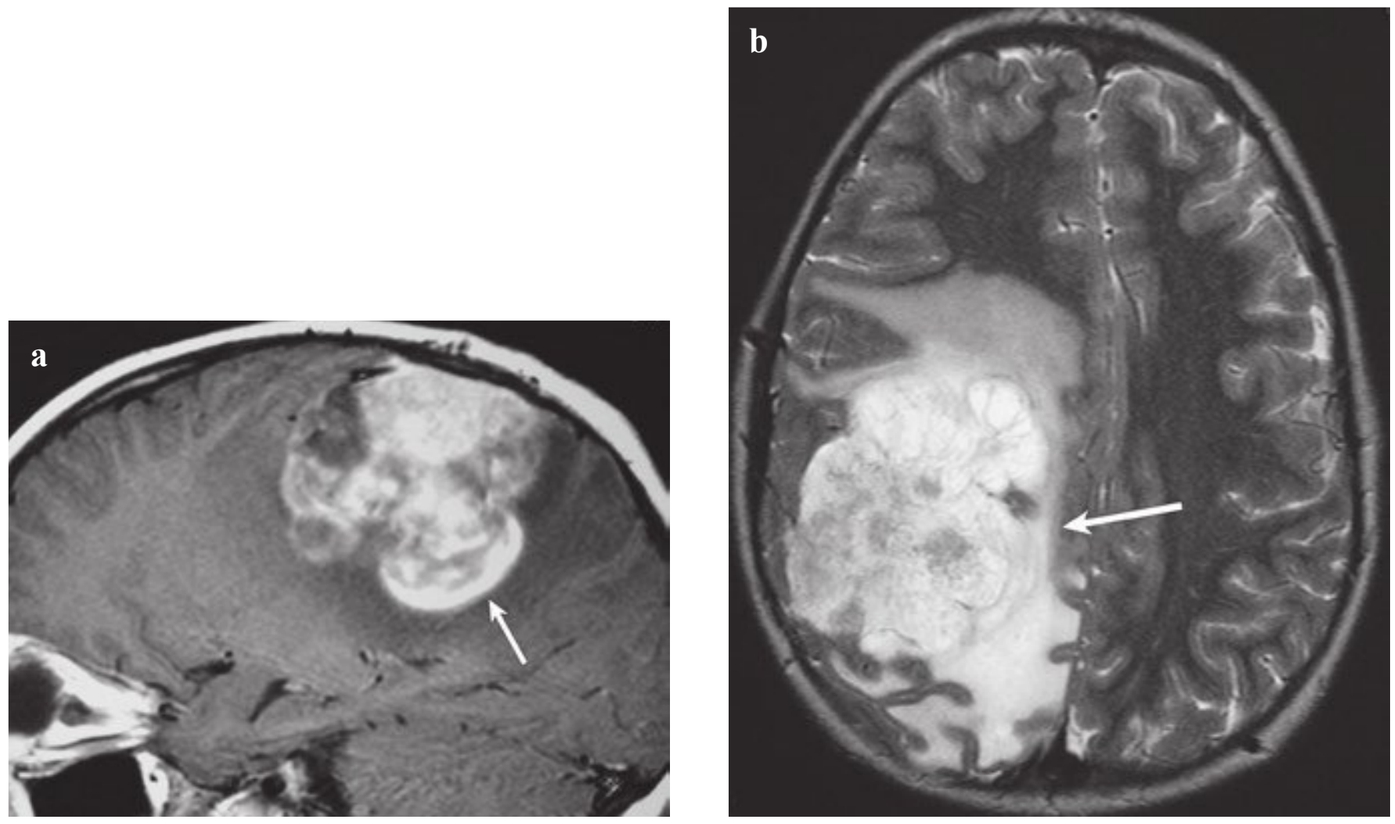

Fig. 3.12 **(a)** An 11-year-old male with a large malignant meningioma at the right convexity that shows heterogeneous gadolinium contrast enhancement (arrow) and partially indistinct margins representing invasion of adjacent brain parenchyma on sagittal T1-weighted imaging. **(b)** The tumor has mostly high signal on axial T2-weighted imaging with ill-defined margins (arrow).

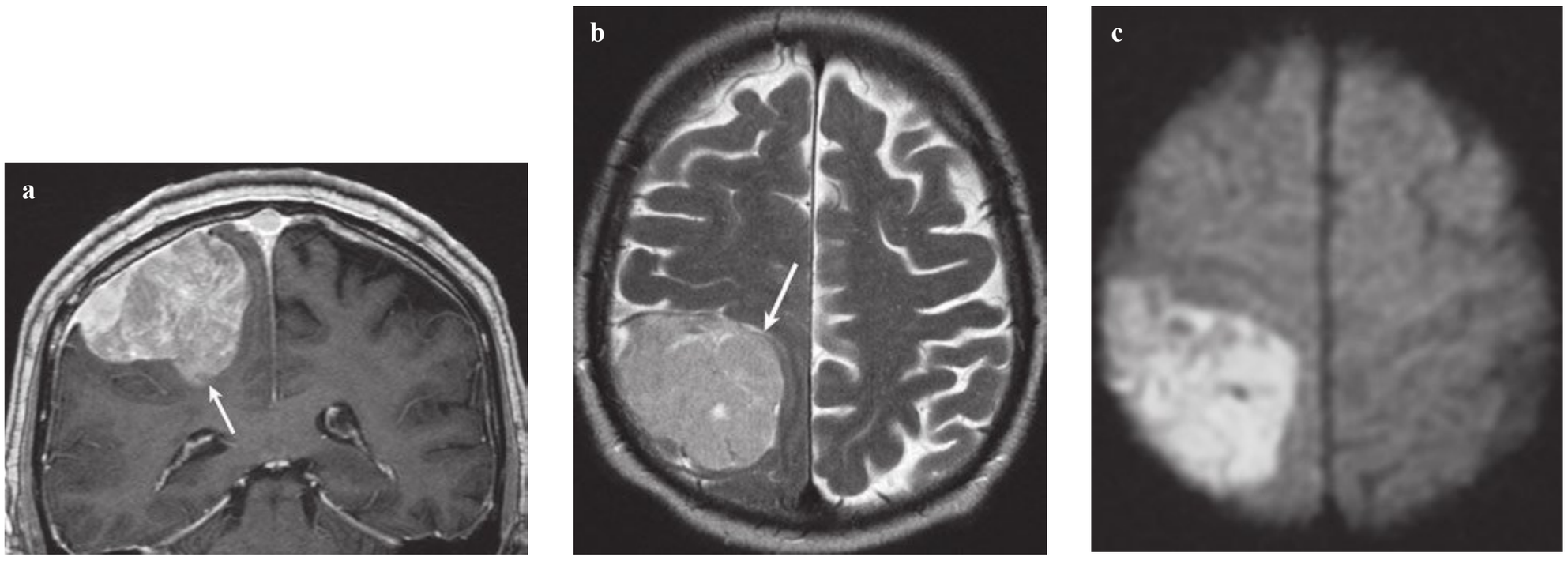

Fig. 3.13 Malignant meningioma at the right convexity that shows **(a)** slightly heterogeneous gadolinium contrast enhancement on coronal T1-weighted imaging (arrow), **(b)** slightly high signal on axial T2-weighted imaging (arrow), and **(c)** restricted diffusion on axial diffusion-weighted imaging.

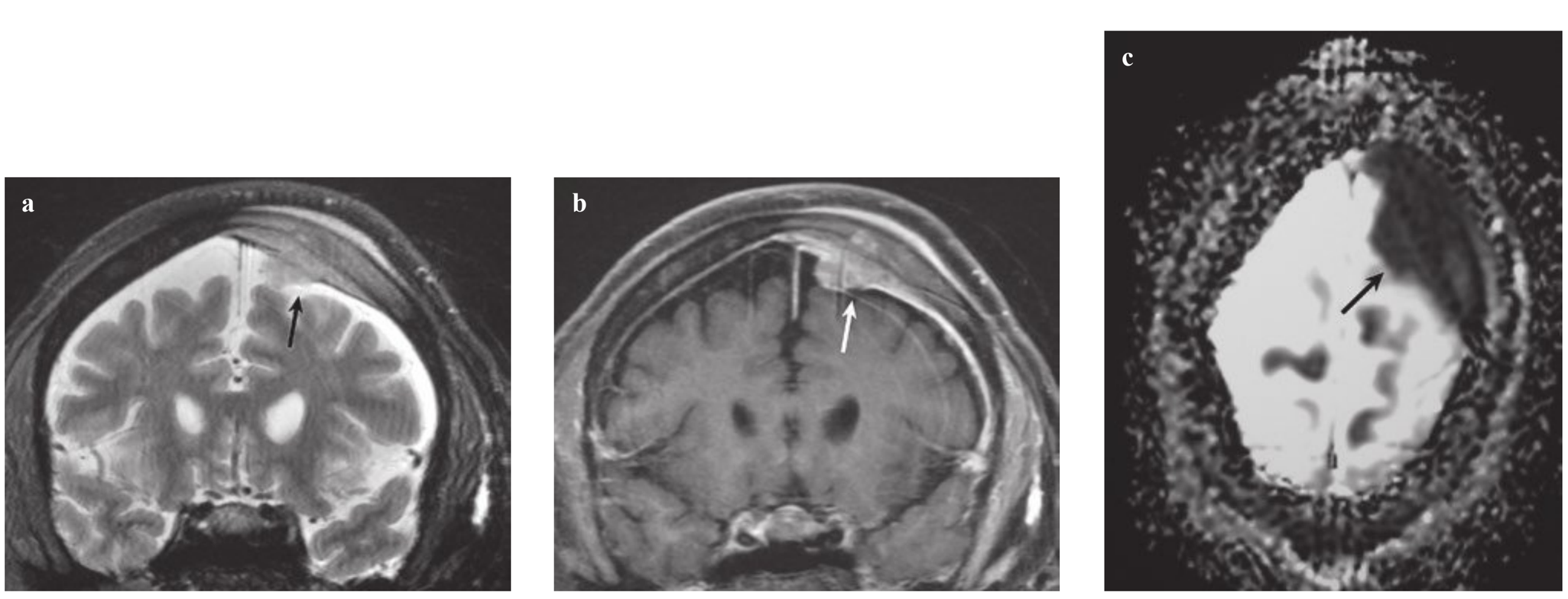

Fig. 3.14 A 68-year-old man with metastatic lung carcinoma in the marrow of the left frontal bone associated with invasion through the inner table involving the dura and epidural and subarachnoid spaces. **(a)** The tumor has intermediate signal on coronal fat-suppressed T2-weighted imaging (arrow), **(b)** gadolinium contrast enhancement on coronal T1-weighted imaging (arrow), and **(c)** restricted diffusion on axial ADC (arrow).

Table 3.1 (cont.) Solitary extra-axial mass lesions

Lesions	Imaging Findings	Comments
Lymphoma (**Fig. 3.15**)	In immunocompetent patients, primary CNS lymphoma (PCNSL) occurs as a solitary focal or infiltrating lesion in 65% of cases. MRI: Single or multiple well-circumscribed or poorly defined lesions involving the skull, dura, and/or leptomeninges; low-intermediate signal on T1-weighted imaging, intermediate-high signal on T2-weighted imaging, usually + gadolinium contrast enhancement, ± bone destruction. Leptomeningeal tumor often best seen on postcontrast images. CT: CNS lymphoma can have intermediate attenuation or can be hyperdense related to a high nuclear/cytoplasm ratio. FDG PET/CT can show elevated uptake in PCNSL and in immunocompromised patients can be used to distinguish lymphoma from toxoplasmosis brain lesions, which have decreased FDG uptake.	Primary CNS lymphoma is more common than secondary, usually in adults > 40 years old. Accounts for 5% of primary brain tumors. Incidence currently ranges from 0.8 to 1.5% of primary intracranial tumors. Prior elevated incidence of 6% in patients with AIDS has been reduced with effective antiviral therapy. B-cell lymphoma is more common than T-cell lymphoma. MRI features of primary and secondary lymphoma of brain overlap. Intracranial lymphoma can involve the leptomeninges in secondary lymphoma > primary lymphoma.
Plasmacytoma/myeloma (**Fig. 3.16**)	Multiple (myeloma) or single (plasmacytoma) well-circumscribed or poorly defined lesions involving the skull and dura. MRI: Well-circumscribed or poorly defined lesions involving the skull and dura with low-intermediate signal on T1-weighted imaging and intermediate-high signal on T2-weighted imaging. Usually show gadolinium contrast enhancement, + bone destruction. CT: Lesions have low-intermediate attenuation, usually + contrast enhancement, + bone destruction.	In multiple myeloma, the malignancy is comprised of proliferating antibody-secreting plasma cells derived from single clones. Multiple myelomas are primarily located in bone marrow. A solitary myeloma or plasmacytoma is an infrequent variant in which a neoplastic mass of plasma cells occurs at a single site of bone or soft tissue. In the United States, 14,600 new cases occur each year. Multiple myeloma is the most common primary neoplasm of bone in adults. Median age at presentation = 60 years. Most patients are older than 40 years. Tumors occur in the vertebrae > ribs > femur > iliac bone > humerus > craniofacial bones > sacrum > clavicle > sternum > pubic bone > tibia.
Malignant mesenchymal non-meningothelial tumors (**Figs. 3.17**)	MRI and CT findings of these lesions are dependent on their histologic features. Malignant tumors may be associated with invasion of adjacent brain, bone, and/or leptomeninges.	Malignant mesenchymal tumors (WHO grades III and IV) can rarely occur as solitary lesions involving the meninges and skull. Lesions include: malignant fibrous histiocytoma, fibrosarcoma, rhabdomyosarcoma, leiomyosarcoma, liposarcoma, chondrosarcoma, osteosarcoma, Ewing's sarcoma, and angiosarcoma.

(continued on page 530)

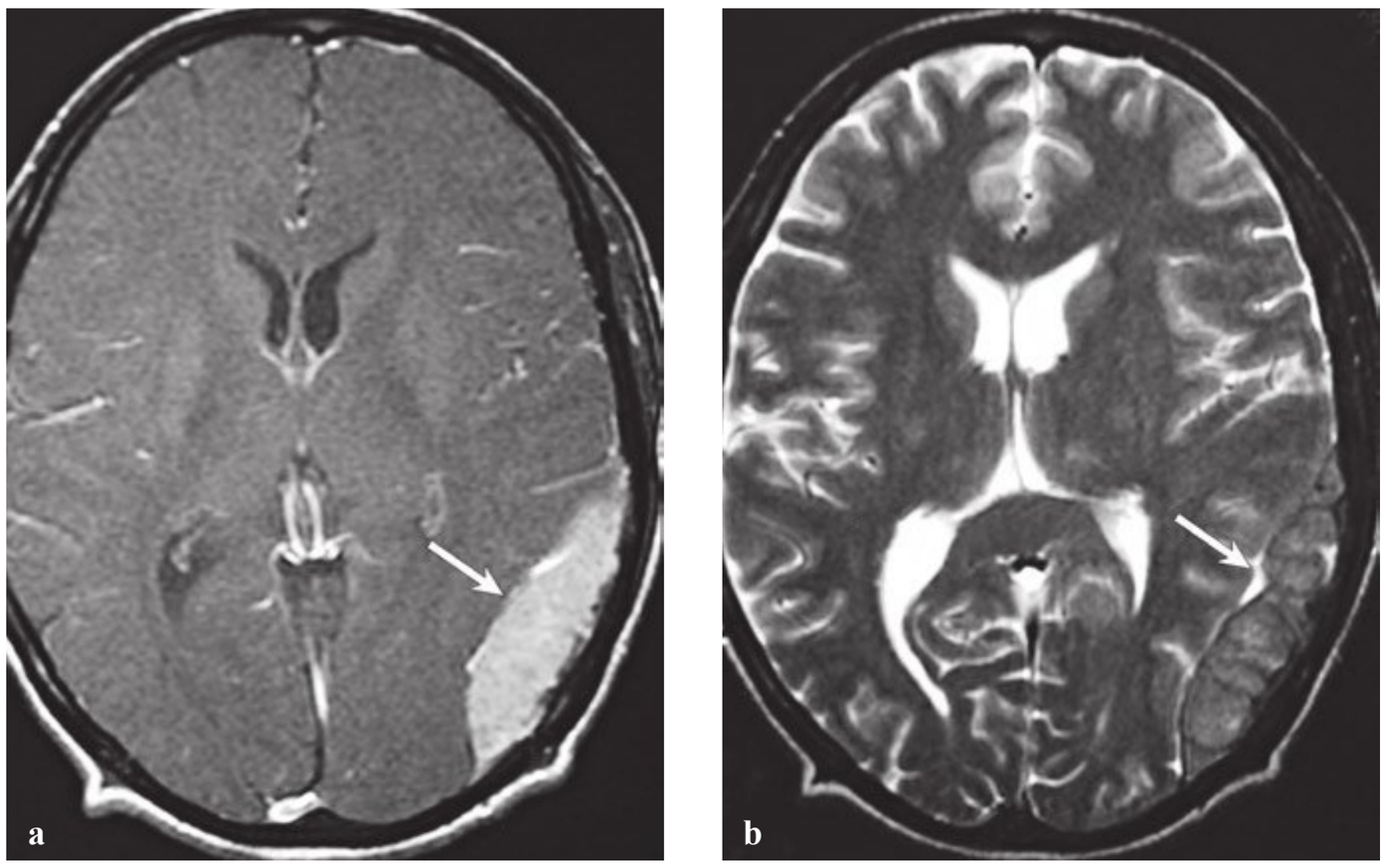

Fig. 3.15 A 25-year-old man with non-Hodgkin lymphoma involving the posterior left dura that shows **(a)** gadolinium contrast enhancement on axial T1-weighted imaging (arrow) and **(b)** mixed low and intermediate signal on axial T2-weighted imaging (arrow).

Fig. 3.16 A 65-year-old woman with a plasmacytoma in the marrow of the left parietal bone associated with destruction of both the inner and outer tables of the skull and with extraosseous extension. **(a)** The tumor shows gadolinium contrast enhancement on coronal fat-suppressed T1-weighted imaging (arrow), and **(b)** heterogeneous high signal on axial T2-weighted imaging (arrow).

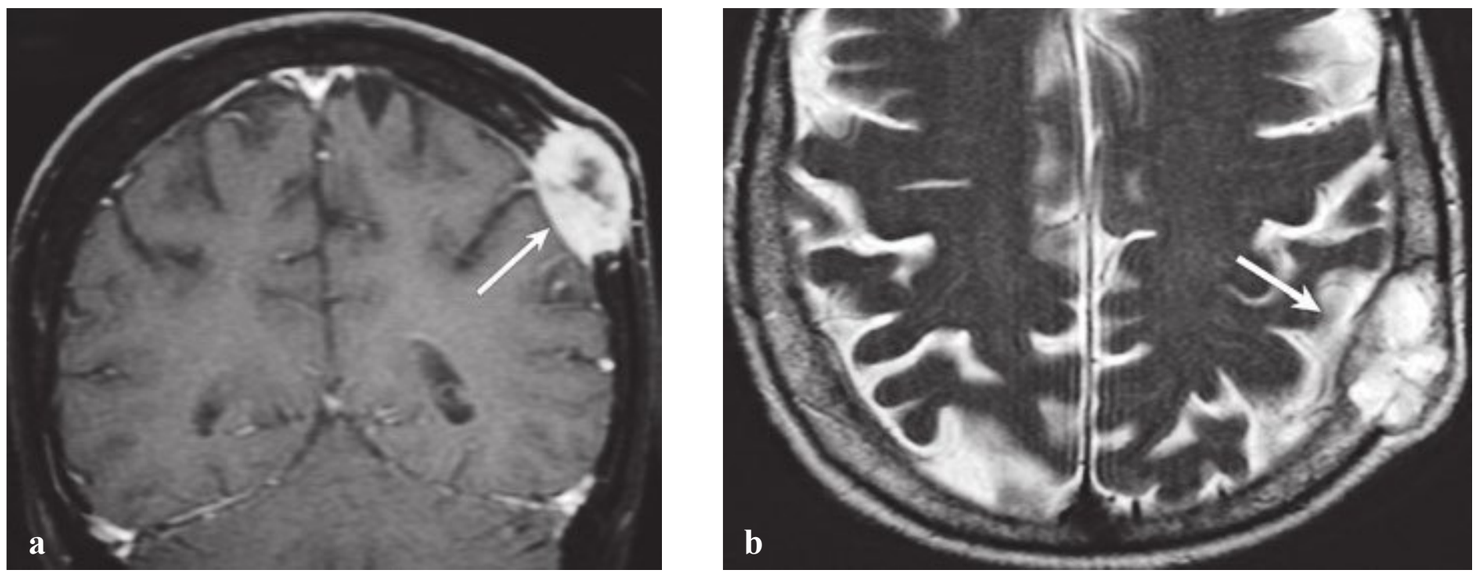

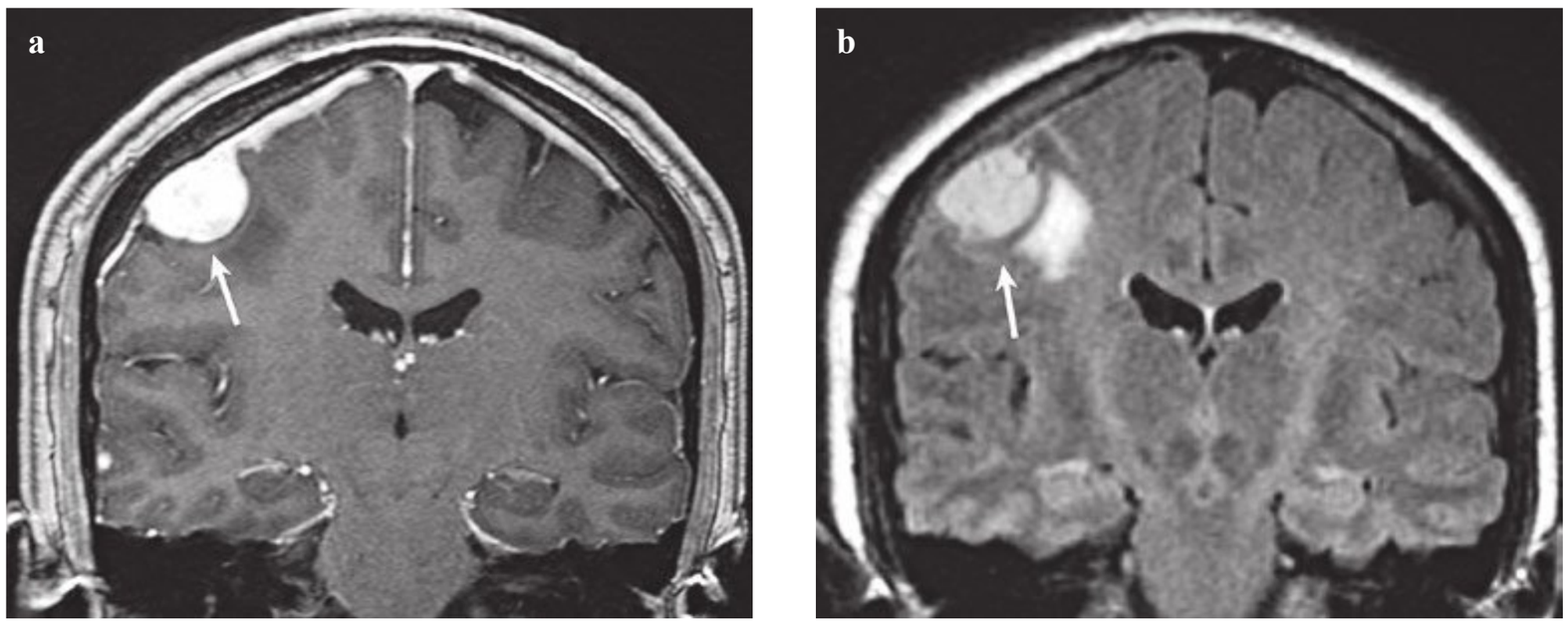

Fig. 3.17 A 35-year-old woman with a primary malignant fibrous histiocytoma involving the right frontal dura. **(a)** The tumor shows prominent gadolinium contrast enhancement on coronal T1-weighted imaging (arrow) as well as an enhancing dural tail medially. **(b)** The tumor has high signal on coronal FLAIR (arrow) and causes displacement and edematous changes in the adjacent brain parenchyma.

Table 3.1 (cont.) Solitary extra-axial mass lesions

Lesions	Imaging Findings	Comments
Chordoma (**Fig. 3.18**)	Well-circumscribed lobulated lesions along dorsal surface of clivus, vertebral bodies, or sacrum, + localized bone destruction. MRI: Lesions have low-intermediate signal on T1-weighted images and high signal on T2-weighted images, + gadolinium contrast enhancement (usually heterogeneous). Locally invasive, associated with bone erosion/destruction, encasement of vessels (usually without luminal narrowing), and nerves. Commonly located in skull base-clivus, usually in the midline. CT: Lesions have low-intermediate attenuation, ± calcifications from destroyed bone carried away by tumor, + contrast enhancement.	Chordomas are rare, locally aggressive, slow-growing, low to intermediate grade malignant tumors derived from ectopic notochordal remnants along the axial skeleton. Chondroid chondromas (5 to 15% of all chordomas) have both chordomatous and chondromatous differentiation. Chordomas that contain sarcomatous components are referred to as dedifferentiated chordoma or sarcomatoid chordoma (5%of all chordomas). Chordomas account for 2–4% of primary malignant bone tumors, 1–3%of all primary bone tumors, and less than 1%of intracranial tumors. The annual incidence has been reported to be 0.18 to 0.3 per million. Dedifferentiated chordomas or sarcomatoid chordomas account for less than 5%of all chordomas. For cranial chordomas, patients' mean age = 37 to 40 years.
Chondrosarcoma (**Fig. 3.19**)	Lobulated lesions with bone destruction at synchondroses. MRI: Lesions have low-intermediate signal on T1-weighted imaging, high signal on T2-weighted imaging, ± matrix mineralization with low signal on T2-weighted images, + gadolinium contrast enhancement (usually heterogeneous). Locally invasive, associated with bone erosion/destruction, encasement of vessels and nerves. Commonly located in skull base petro-occipital synchondrosis, usually off midline. CT: Lesions have low-intermediate attenuation associated with localized bone destruction, ± chondroid matrix calcifications, + contrast enhancement.	Chondrosarcomas are malignant tumors containing cartilage formed within sarcomatous stroma. Chondrosarcomas can contain areas of calcification/mineralization, myxoid material, and/or ossification. Chondrosarcomas rarely arise within synovium. Chondrosarcomas represent from 12 to 21%of malignant bone lesions, 21 to 26%of primary sarcomas of bone, 9 to14%of all bone tumors, 6%of skull base tumors, and 0.15%of all intracranial tumors. MRI is important for planning surgical approaches.
Osteogenic sarcoma (**Fig. 3.20**)	Destructive lesions involving the skull base or calvarium. MRI: Tumors often have poorly defined margins and commonly extend from the marrow through destroyed bony cortex into adjacent soft tissues. Tumors usually have low-intermediate signal on T1-weighted imaging. Zones of low signal often correspond to areas of tumor calcification/mineralization and/or necrosis. On T2-weighted imaging, zones of necrosis typically have high signal, whereas mineralized zones usually have low signal. Tumors can have variable MRI signal on T2-weighted imaging and fat-suppressed T2-weighted imaging depending upon the relative proportions, distributions, and locations of calcified/mineralized osteoid, chondroid, fibroid, and hemorrhagic and necrotic components. Tumors may have low, low-intermediate, and intermediate to high signal on T2-weighted imaging and fat-suppressed T2-weighted imaging. After gadolinium contrast administration, osteosarcomas typically show prominent enhancement in nonmineralized/noncalcified portions. CT: Tumors have low-intermediate attenuation, usually + matrix mineralization/ossification, and often show contrast enhancement (usually heterogeneous).	Osteosarcomas are rare malignant tumors comprised of proliferating neoplastic spindle cells that produce osteoid and/or immature tumoral bone. Occur in children as primary tumors, and in adults they are associated with Paget's disease, irradiated bone, chronic osteomyelitis, osteoblastoma, giant cell tumor, fibrous dysplasia. Locally invasive, with high metastatic potential.

(continued on page 532)

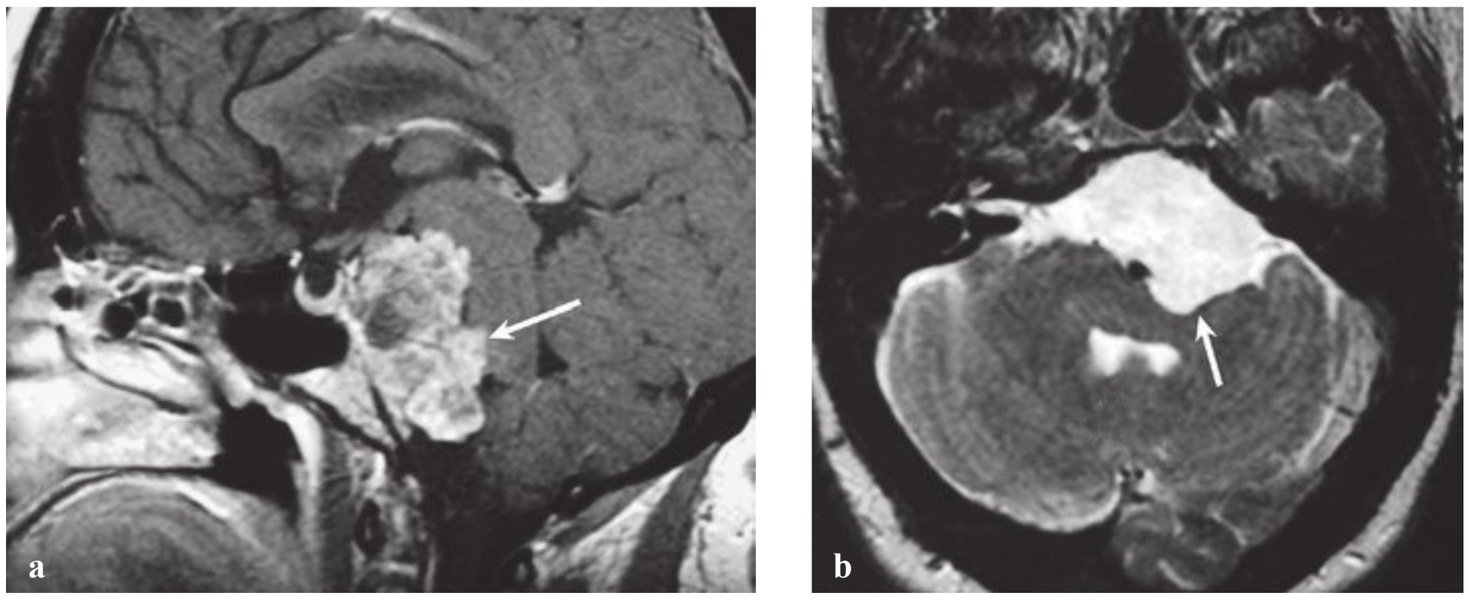

Fig. 3.18 A 55-year-old woman with a chordoma along the endocranial surface of the clivus that compresses and posteriorly displaces the brainstem and left middle cerebellar peduncle and left cerebellar hemisphere. **(a)** The tumor shows heterogeneous gadolinium contrast enhancement on sagittal T1-weighted imaging (arrow) and **(b)** has high signal on axial T2-weighted imaging (arrow).

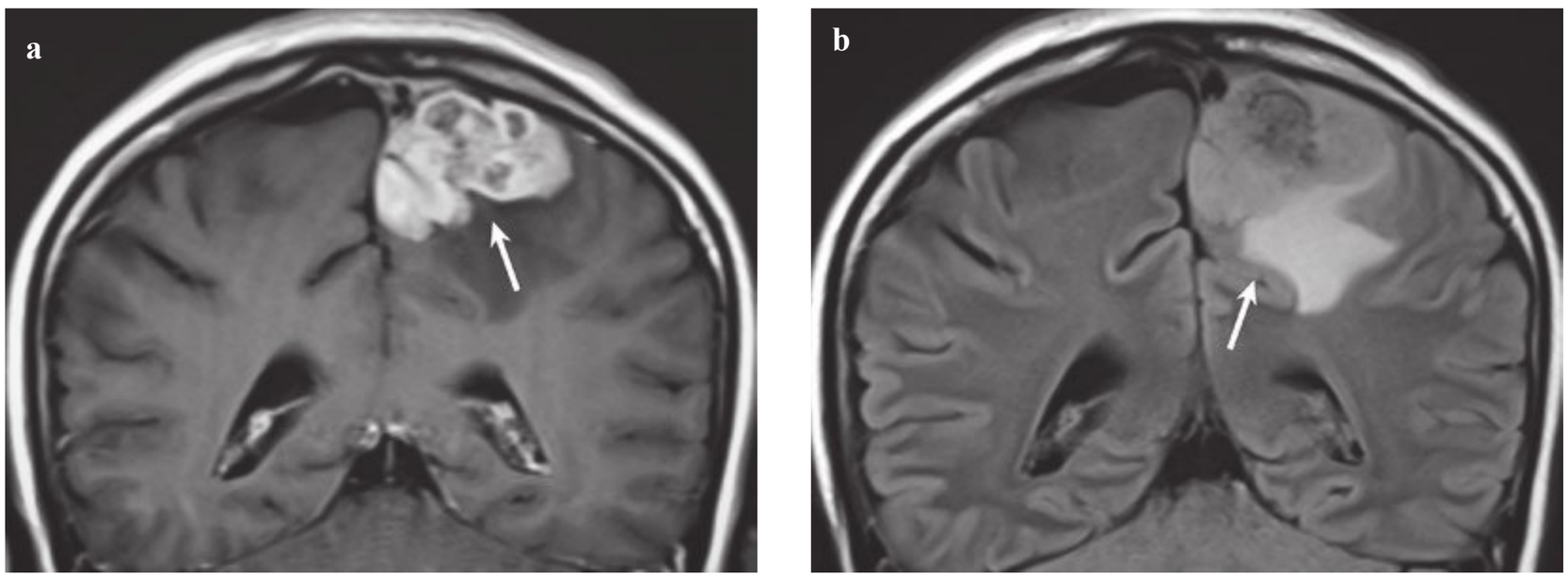

Fig. 3.19 A 30-year-old woman with a dura-based chondrosarcoma. **(a)** The tumor has lobulated margins and shows heterogeneous gadolinium contrast enhancement on coronal T1-weighted imaging (arrow) and **(b)** has mixed low and slightly high signal on coronal FLAIR (arrow). The tumor causes displacement and edematous changes in the adjacent brain parenchyma.

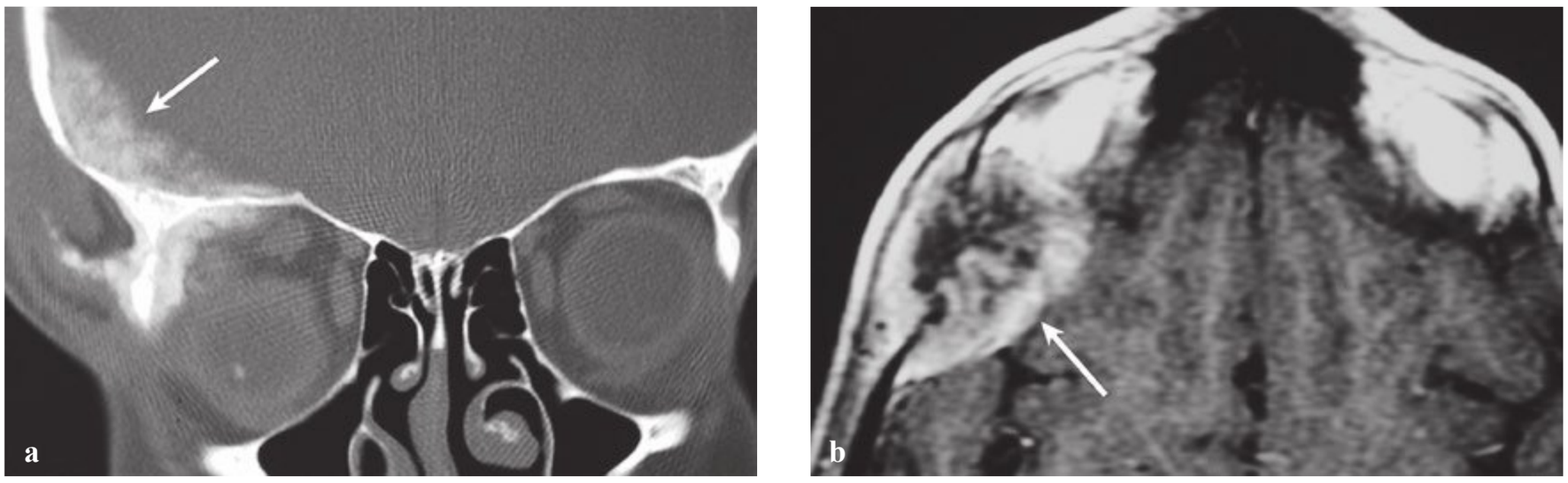

Fig. 3.20 A 10-year-old female with an osteogenic sarcoma involving the right frontal bone. **(a)** Coronal CT shows ossified tumor matrix within malignant tumor (arrow) that has extended into the anterior cranial fossa and upper right orbit. **(b)** The tumor shows heterogeneous gadolinium contrast enhancement and bone destruction with extraosseous extension and dural/intracranial involvement on axial T1-weighted imaging (arrow).

Table 3.1 (cont.) Solitary extra-axial mass lesions

Lesions	Imaging Findings	Comments
Ewing's sarcoma (**Fig. 3.21**)	MRI: Destructive lesion involving the skull base, with low-intermediate signal on T1-weighted imaging, mixed low, intermediate, and high signal on T2-weighted imaging, ± malignant periosteal reaction with low signal on T2-weighted imaging, + gadolinium contrast enhancement (usually heterogeneous). CT: Destructive lesion involving the skull base, with low-intermediate attenuation, and can show contrast enhancement (usually heterogeneous).	Malignant primitive tumor of bone comprised of undifferentiated small cells with round nuclei. Accounts for 6 to 11% of primary malignant bone tumors, 5 to 7% of primary bone tumors. Usually occurs between the ages of 5 and 30 years, in males > in females. Ewing's sarcomas commonly have translocations involving chromosomes 11 and 22: t(11;22) (q24:q12) which results in fusion of the FL1-1 gene at 11q24 to the EWS gene at 22q12. Locally invasive, with high metastatic potential. Rare lesions involve the skull base.
Sinonasal squamous cell carcinoma (**Fig. 3.22**)	Destructive lesions arising in the nasal cavity and paranasal sinuses, ± intracranial extension via bone destruction or perineural spread. MRI: Destructive lesions in the nasal cavity, paranasal sinuses, and nasopharynx, ± intracranial extension via bone destruction or perineural spread. Intermediate signal on T1-weighted imaging and intermediate-slightly high signal on T2-weighted imaging, often with gadolinium contrast enhancement. Large lesions (± necrosis and/or hemorrhage). CT: Tumors have intermediate attenuation and mild contrast enhancement and are large (± necrosis and/or hemorrhage).	Malignant epithelial tumors originating from the mucosal epithelium of the paranasal sinuses (maxillary, 60%; ethmoid, 14%; sphenoid and frontal sinuses, 1%) and nasal cavity (25%). Include both keratinizing and nonkeratinizing types. Account for 3% of malignant tumors of the head and neck. Occur in adults usually > 55 years old, and in males > females. Associated with occupational or other exposure to tobacco smoke, nickel, chlorophenols, chromium, mustard gas, radium, and material in the manufacture of wood products.
Nasopharyngeal carcinoma (**Fig. 3.23**)	MRI: Invasive lesions in the nasopharynx (lateral wall/fossa of Rosenmüller and posterior upper wall) ± intracranial extension via bone destruction or perineural spread. Intermediate signal on T1-weighted imaging and intermediate-slightly high signal on T2-weighted imaging, often with gadolinium contrast enhancement. Large lesions (± necrosis and/or hemorrhage). CT: Tumors have intermediate attenuation and mild contrast enhancement and are large (± necrosis and/or hemorrhage).	Carcinomas arising from the nasopharyngeal mucosa with varying degrees of squamous differentiation. Subtypes include squamous cell carcinoma, nonkeratinizing carcinoma (differentiated and undifferentiated), and basaloid squamous cell carcinoma. Occurs at higher frequency in Southern Asia and Africa than in Europe and the Americas. Peak ages are 40–60 years. Occurs two to three times more frequently in men than in women. Associated with Epstein-Barr virus, diets containing nitrosamines, and chronic exposure to tobacco smoke, formaldehyde, chemical fumes, and dust.

(continued on page 534)

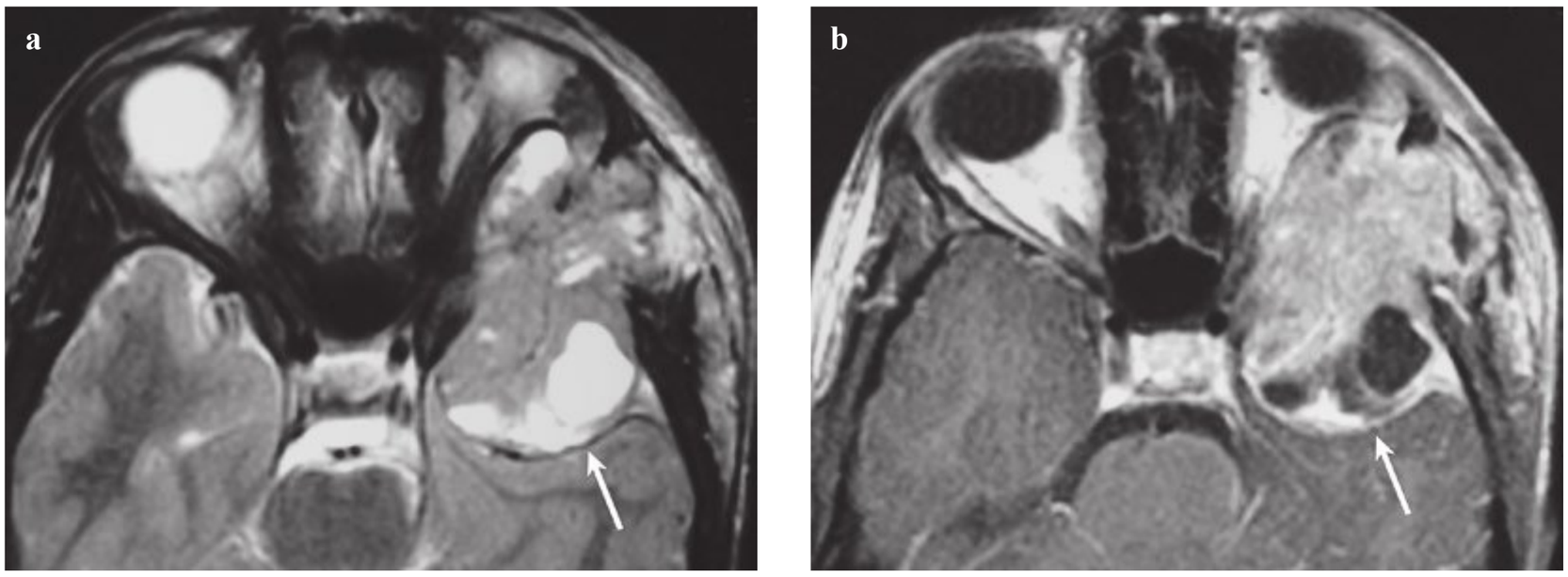

Fig. 3.21 An 11-year-old female with Ewing's sarcoma in the anterior portion of the left middle cranial fossa with bone destruction and intracranial tumor extension. **(a)** The tumor has mixed intermediate and high signal on axial T2-weighted imaging (arrow) and **(b)** heterogeneous gadolinium contrast enhancement on axial T1-weighted imaging (arrow).

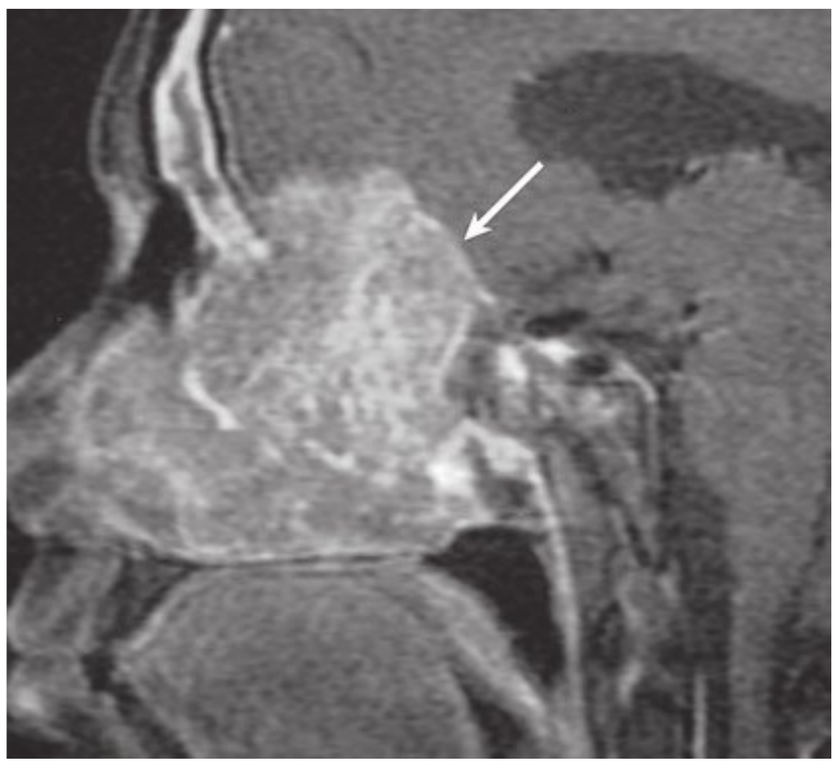

Fig. 3.22 A 37-year-old man with a gadolinium-enhancing sinonasal squamous cell carcinoma on sagittal fat-suppressed T1-weighted imaging in the ethmoid sinus associated with osseous destruction at the skull base and intracranial tumor extension displacing adjacent brain tissue (arrow).

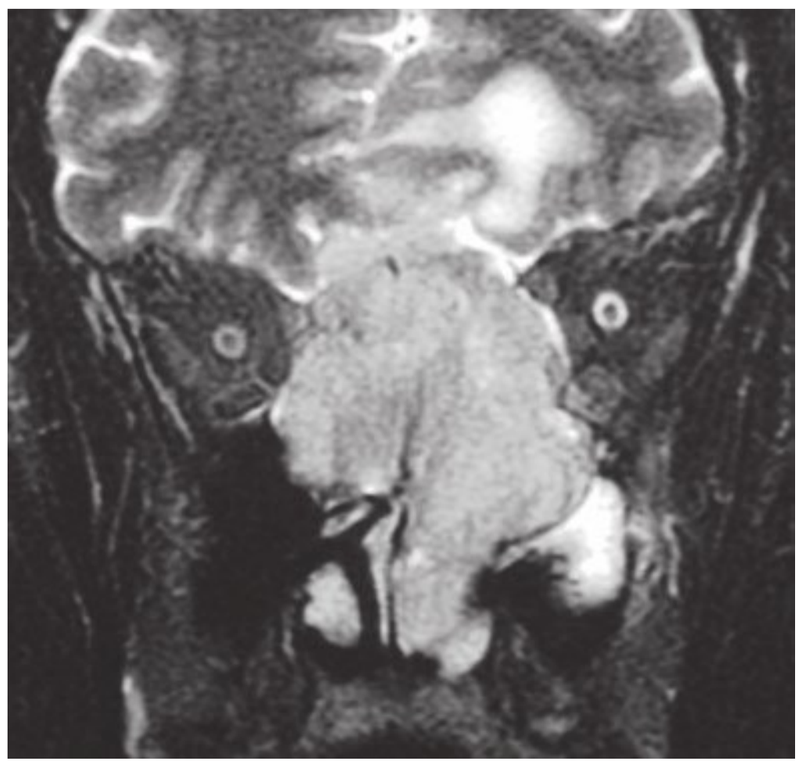

Fig. 3.23 A 48-year-old man with a nasopharyngeal carcinoma in the ethmoid sinus associated with bone destruction and tumor extension intracranially and into right orbit and right maxillary sinus. The tumor has slightly high signal on coronal STIR.

Table 3.1 (cont.) Solitary extra-axial mass lesions

Lesions	Imaging Findings	Comments
Adenoid cystic carcinoma (**Fig. 3.24**)	MRI: Destructive lesions in the paranasal sinuses, nasal cavity, and nasopharynx that can have intracranial extension via bone destruction or perineural spread. Intermediate signal on T1-weighted imaging and intermediate-high signal on T2-weighted imaging, with variable mild, moderate, or prominent gadolinium contrast enhancement. CT: Tumors have intermediate attenuation and variable mild, moderate, or prominent contrast enhancement.	Basaloid tumor comprised of neoplastic epithelial and myoepithelial cells. Morphologic tumor patterns include tubular, cribiform, and solid. Accounts for 10%of epithelial salivary neoplasms. Most commonly involves the parotid, submandibular, and minor salivary glands (palate, tongue, buccal mucosa and floor of the mouth, other locations). Perineural tumor spread common, ± facial nerve paralysis. Usually occurs in adults > 30 years old. Solid type has the worst prognosis. Up to 90%die within 10–15 years after diagnosis.
Esthesioneuroblastoma (**Fig. 3.25**)	MRI: Locally destructive lesions with low-intermediate signal on T1-weighted images and intermediate-high signal on T2-weighted images, + prominent gadolinium enhancement. Locations: superior nasal cavity, ethmoid air cells with occasional extension into the other paranasal sinuses, orbits, anterior cranial fossa, and cavernous sinuses. CT: Locally destructive lesions with low-intermediate attenuation, usually showing contrast enhancement. Locations: superior nasal cavity, ethmoid air cells with occasional extension into the other paranasal sinuses, orbits, anterior cranial fossa, and cavernous sinuses.	These tumors, also referred to as olfactory neuroblastoma, arise from olfactory epithelium in the superior nasal cavity. Tumors consist of immature neuroblasts with variable nuclear pleomorphism, mitoses, and necrosis. Tumor cells occur in a neurofibrillary intercellular matrix. Bimodal occurrence in adolescents (11–20 years old) and adults (50–60 years old), and occur in males more than in females.
Hemorrhage		
Epidural hematoma (**Fig. 3.26** and **Fig. 3.27**)	MRI: Biconvex extra-axial hematoma located between the skull and dura (displaced dura has low signal on T2-weighted imaging), ± edema (high signal on T2-weighted imaging involving the displaced brain parenchyma), ± subfalcine or uncal herniation. The signal of the hematoma itself depends on its age, size, hematocrit, and oxygen tension. Hyperacute: Intermediate signal on T1-weighted imaging and intermediate-high signal on T2-weighted imaging. Acute: Low-intermediate signal on T1-weighted imaging and high signal on T2-weighted imaging. Early Subacute: High signal on T1-weighted imaging and low signal on T2-weighted imaging. Subacute: High signal on T1- and T2-weighted imaging. CT: Biconvex extra-axial hematoma located between the skull and dura (displaced dura has high attenuation), ± low-attenuation edema involving the displaced brain parenchyma, ± subfalcine or uncal herniation. The CT attenuation of the hematoma depends on its age, size, hematocrit, and oxygen tension.	Epidural hematomas usually result from trauma/tearing of an epidural artery (often the middle meningeal artery) or dural venous sinus, ± skull fracture. Epidural hematomas do not cross cranial sutures.

(continued on page 536)

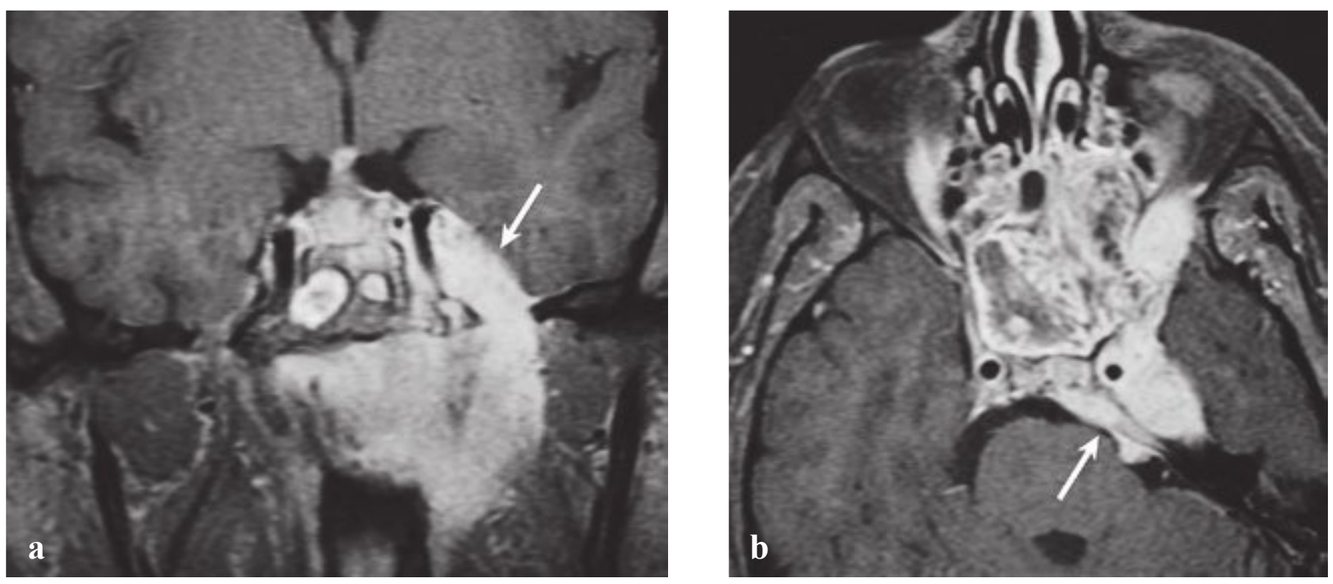

Fig. 3.24 A 46-year-old woman with a gadolinium-enhancing adenoid cystic carcinoma in the left nasopharynx extending through a widened left foramen ovale into the left trigeminal cistern/Meckel's cave, left cavernous sinus, and anteromedial portion of the left middle cranial fossa on **(a)** coronal (arrow) and **(b)** axial fat-suppressed T1-weighted imaging (arrow).

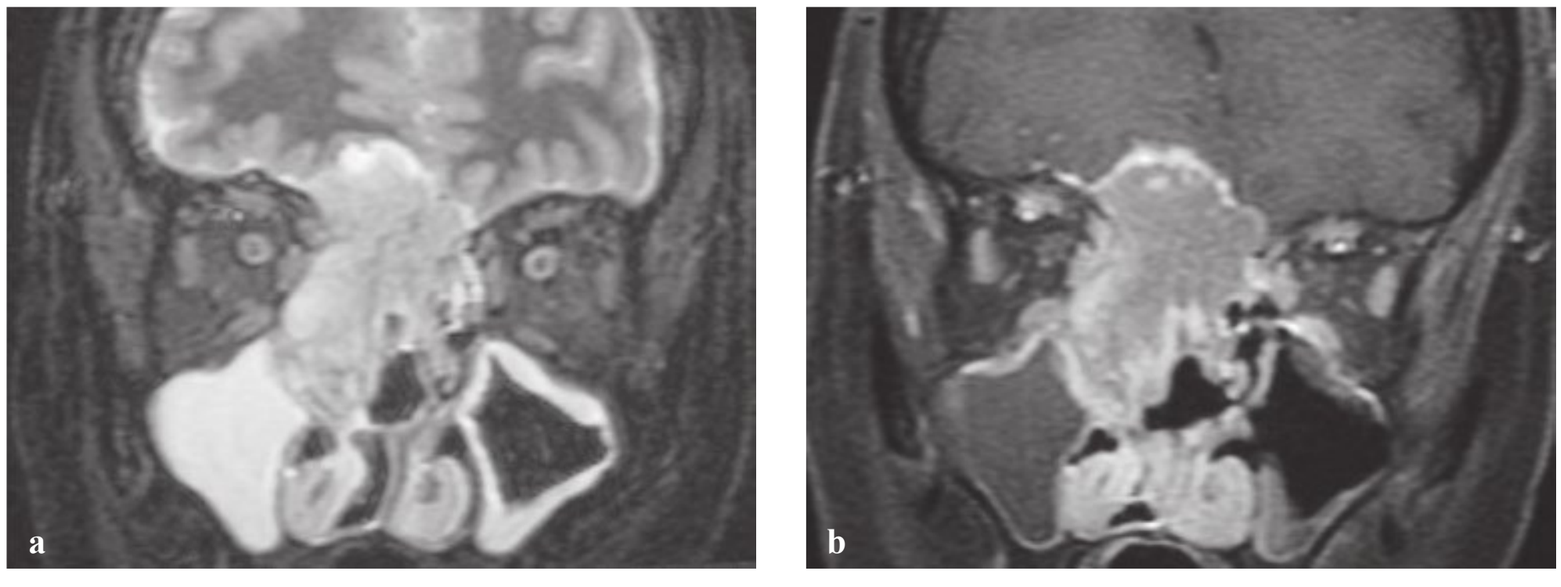

Fig. 3.25 A 30-year-old woman with an esthesioneuroblastoma in the ethmoid sinus associated with bone destruction and tumor extension intracranially and into the right orbit and the right maxillary sinus. **(a)** The tumor has slightly heterogeneous, slightly-high to high signal on coronal STIR and results in retained secretions with high signal in the right maxillary sinus from obstruction of the infundibulum of the right ostiomeatal complex. **(b)** The tumor shows gadolinium contrast enhancement on coronal fat-suppressed T1-weighted imaging.

Fig. 3.26 Epidural hematomas in two patients. **(a)** An epidural hematoma (arrow) with high attenuation on CT is seen in the right frontal region. **(b)** An epidural hematoma (arrow) is seen in the left temporal region on CT, as well as a scalp hematoma.

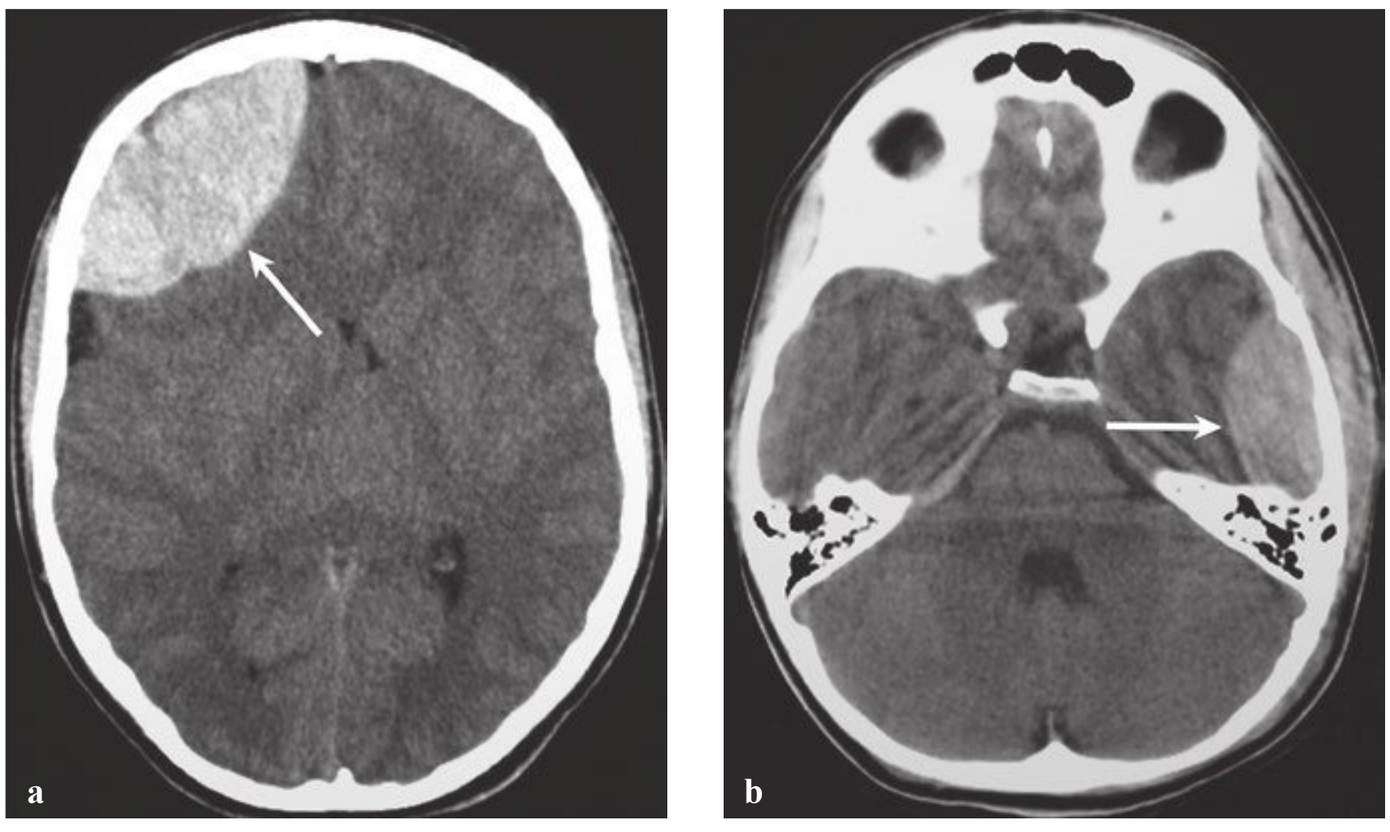

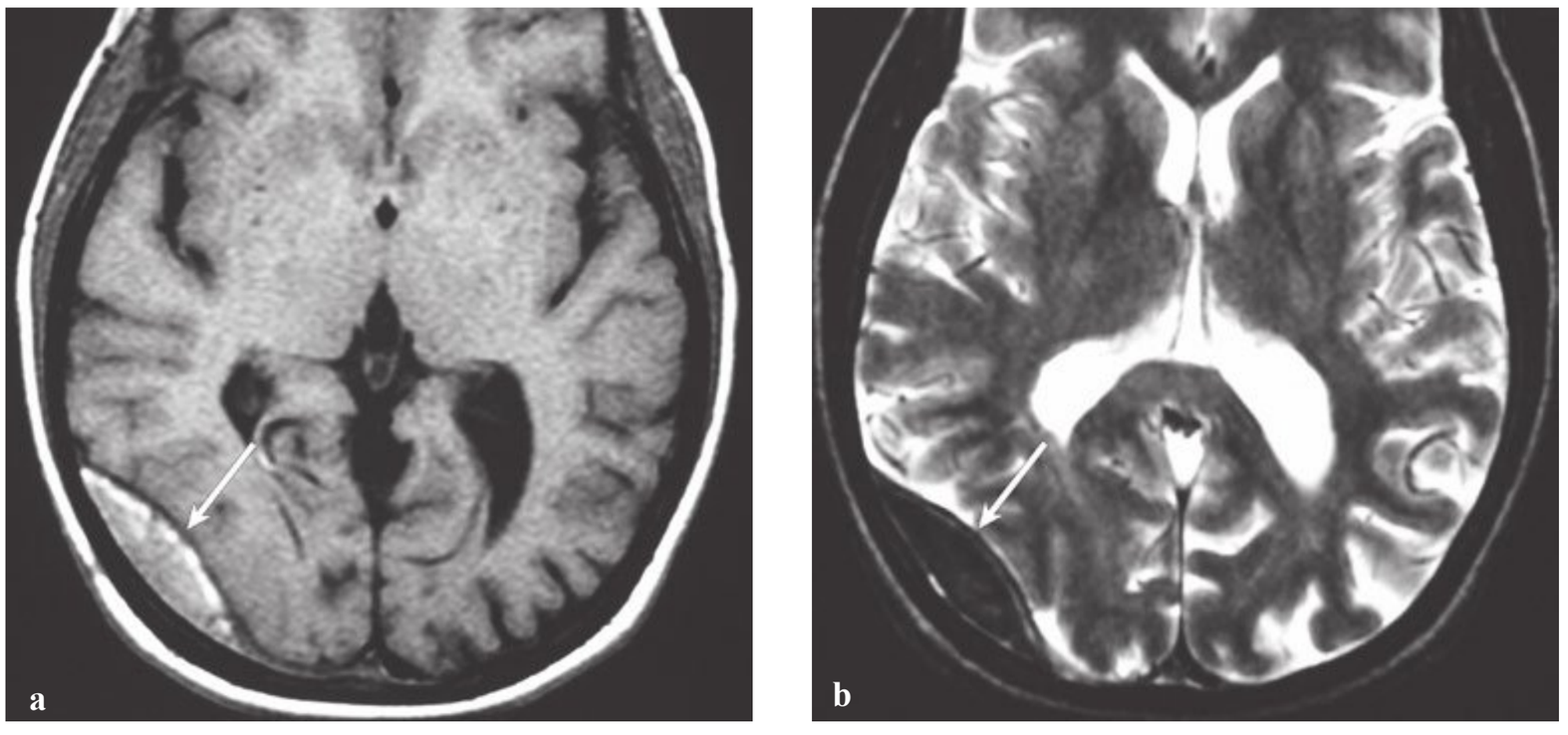

Fig. 3.27 Early subacute epidural hematoma in the right occipital region has **(a)** mixed slightly high and high signal on axial T1-weighted imaging (arrow) and **(b)** low signal on axial T2-weighted imaging (arrow).

Table 3.1 (cont.) Solitary extra-axial mass lesions

Lesions	Imaging Findings	Comments
Subdural hematoma (**Fig. 3.28** and **Fig. 3.29**) Hyperacute hematoma Acute hematoma Subacute hematoma Chronic hematoma	Crescentic extra-axial hematoma located in the potential space between the inner margin of the dura and outer margin of the arachnoid membrane, ± edema (low attenuation on CT and high signal on T2-weighted imaging) involving the displaced brain parenchyma, ± subfalcine and uncal herniation. The CT attenuation and MRI signal of the hematoma depend on its age, size, hematocrit, and oxygen tension. Hyperacute hematoma CT: Can have high or mixed high, intermediate, and/or low attenuation. MRI: Intermediate signal on T1-weighted imaging and intermediate-high signal on T2-weighted imaging. Acute hematoma CT: Can have high or mixed high, intermediate, and/or low attenuation. MRI: Low-intermediate signal on T1-weighted imaging, low signal on T2-weighted imaging. Subacute hematoma CT: Can have intermediate attenuation (isodense to brain) and/or low-intermediate attenuation. MRI: High signal on T1- and T2-weighted imaging. Chronic hematoma CT: Usually have low attenuation (hypodense to brain). MRI: Variable, often low-intermediate signal on T1-weighted imaging, high signal on T2-weighted imaging, ± gadolinium contrast enhancement of collection and organizing neomembrane. Mixed MRI signal can result if rebleeding occurs into chronic collection.	Subdural hematomas usually result from trauma/stretching/tearing of cortical veins where they enter the subdural space to drain into dural venous sinuses, ± skull fracture. Subdural hematomas do cross sites of cranial sutures.
Ossified hematoma	MRI: Thin or irregular peripheral zones with low signal from calcifications; peripheral and/or central ossification surrounding collections with variable low, intermediate, and/or high signal on T1- and T2-weighted imaging, ± gadolinium contrast enhancement of collection and organizing neomembrane. Mixed MRI signal can result if rebleeding occurs into chronic collection. CT: Usually has dense thin or irregular peripheral calcifications, and/or peripheral and central ossification surrounding collections with variable low, intermediate, and/or high attenuation.	Chronic subdural or epidural hematomas can rarely become calcified or ossified, and they are referred to as armored brain. Surgical removal of symptomatic lesions can be difficult because of dense adhesion to brain surface and/or dura.

(continued on page 538)

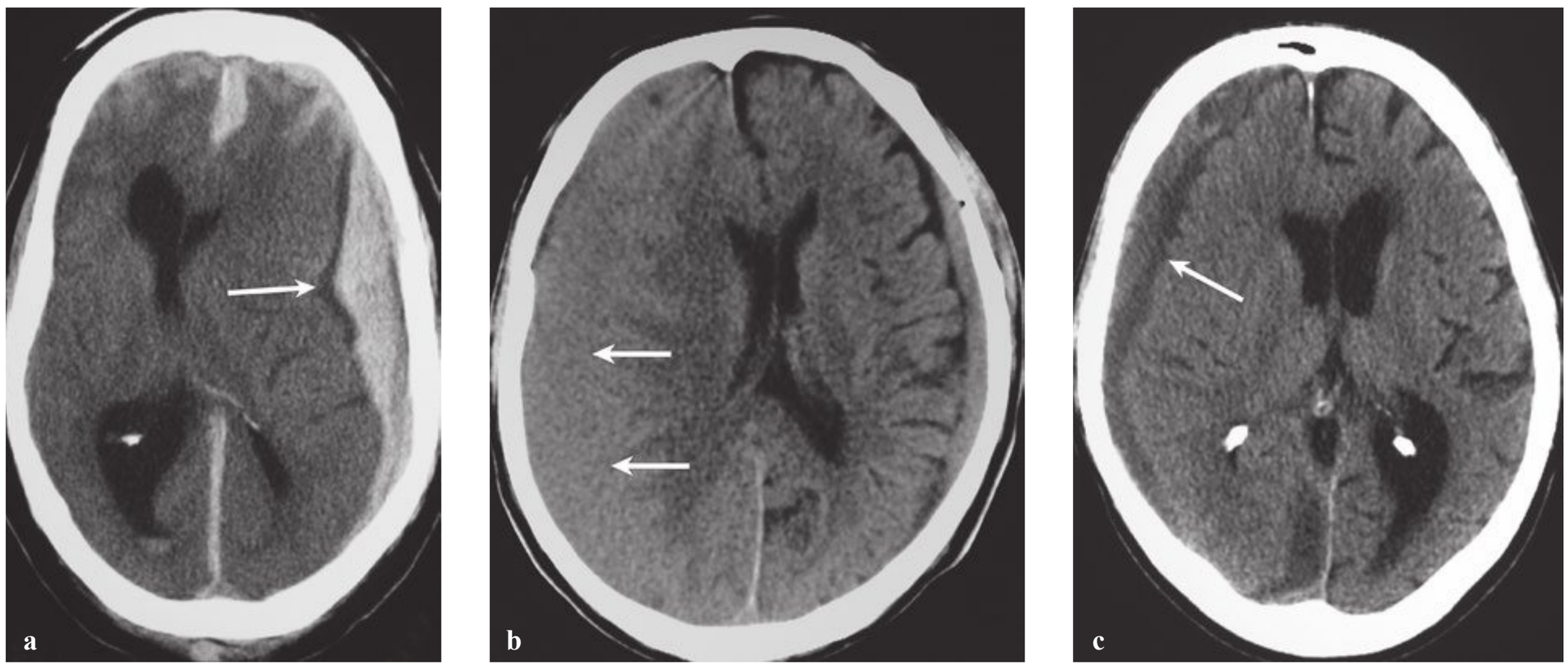

Fig. 3.28 Examples of subdural hematoma. Axial CT shows **(a)** an acute subdural hematoma (arrow) with high attenuation on the left and along the anterior falx as well as subarachnoid hemorrhage anteriorly; **(b)** an isodense subdural hematoma on the right (arrows), as well as a small isodense subdural hemtoma on the left; and **(c)** a subdural collection on the right (arrow) with mostly low attenuation, as well as irregular zones with higher attenuation representing recurrent hemorrhage into a chronic subdural hematoma.

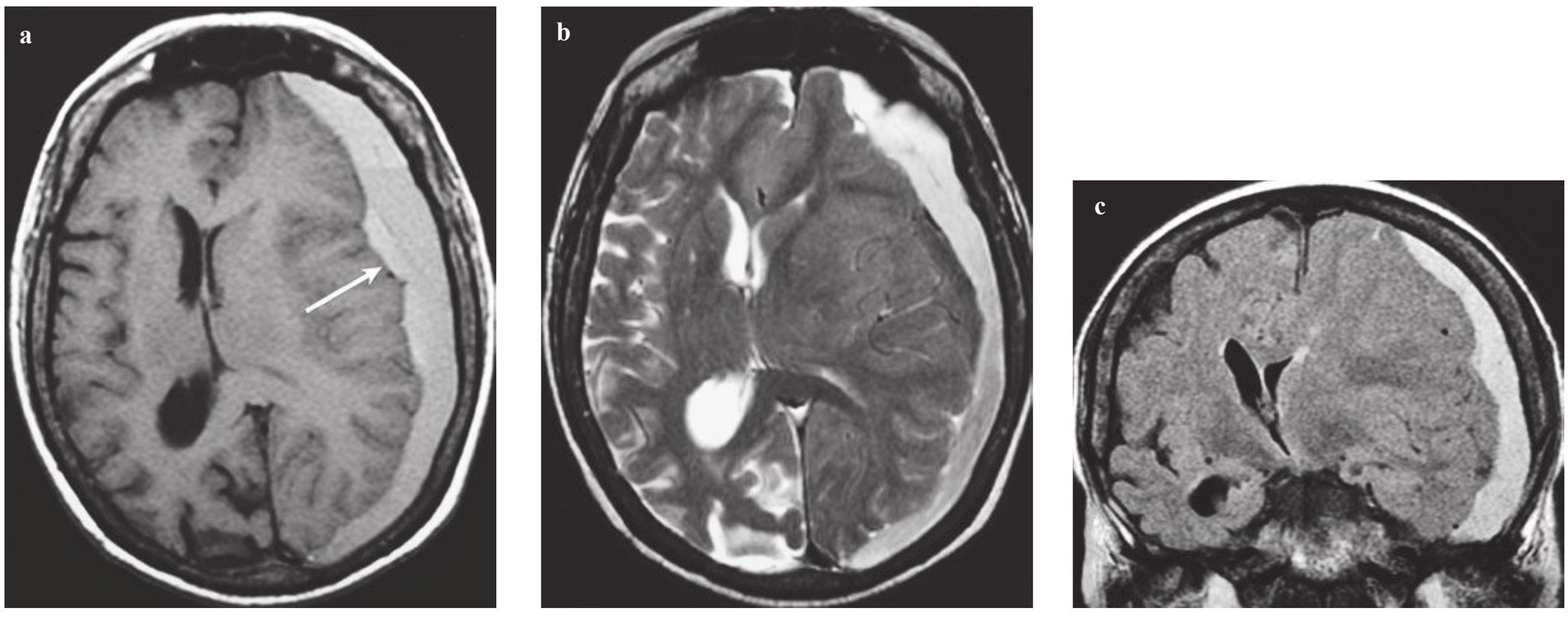

Fig. 3.29 Subdural hematoma on the left has **(a)** high signal on axial T1-weighted imaging (arrow), **(b)** heterogeneous slightly high and high signal on axial T2-weighted imaging, and **(c)** high signal on coronal FLAIR. The subdural hematoma has significant mass effect, with compression of the left lateral ventricle and leftward subfalcine herniation.

Table 3.1 (cont.) Solitary extra-axial mass lesions

Lesions	Imaging Findings	Comments
Infection/Inflammation		
Epidural abscess or subdural empyema (**Fig. 3.30** and **Fig. 3.31**)	MRI: Epidural or subdural collections with low signal on T1-weighted imaging, high signal on T2-weighted imaging, and thin linear peripheral zones of gadolinium contrast enhancement. CT: Epidural or subdural collections with low attenuation and linear peripheral zones of contrast enhancement.	Often results as a complication of sinusitis (usually frontal), meningitis, otitis media, ventricular shunts, or surgery. Can be associated with venous sinus thrombosis and venous cerebral or cerebellar infarctions, cerebritis, or brain abscess. Mortality is 30%
Langerhans' cell histiocytosis/ eosinophilic granuloma (**Fig. 3.32**)	MRI: Single or multiple circumscribed soft tissue lesions in the marrow of the skull associated with focal bony destruction/erosion with extension extracranially, intracranially, or both. Lesions usually have low-intermediate signal on T1-weighted imaging, mixed intermediate-slightly high signal on T2-weighted imaging, + gadolinium contrast enhancement, ± enhancement of the adjacent dura. CT: Single or multiple circumscribed soft tissue lesions in the marrow of the skull associated with focal bony destruction/erosion with extension extracranially, intracranially, or both. Lesions usually have low-intermediate attenuation, + contrast enhancement, ± enhancement of the adjacent dura.	Single lesion: Commonly seen in males > females, < 20 years old, with proliferation of histiocytes in medullary cavity and localized destruction of bone with extension in adjacent soft tissues. Multiple lesions: Associated with Letterer-Siwe disease (lymphadenopathy and hepatosplenomegaly) in children < 2 years old and Hand-Schüller-Christian disease (lymphadenopathy, exophthalmos, and diabetes insipidus) in children 5–10 years old.

(continued on page 540)

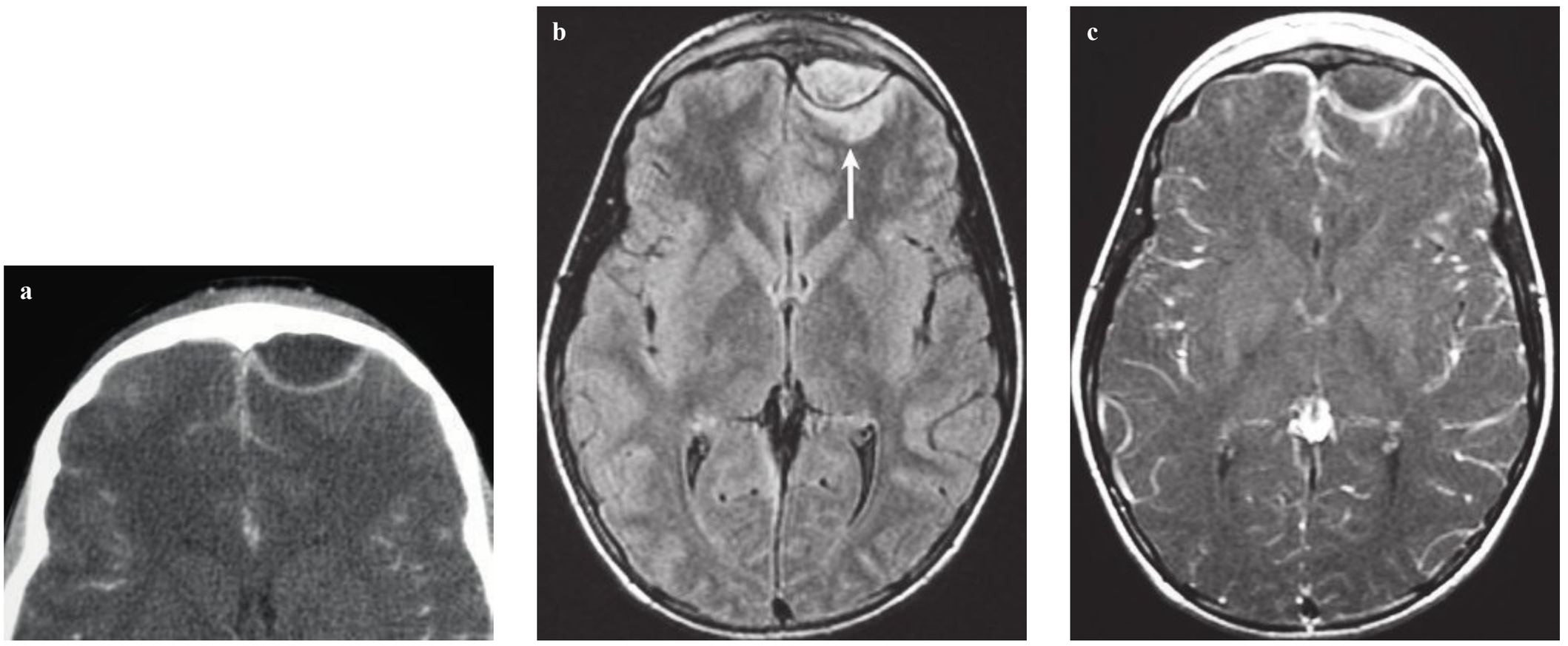

Fig. 3.30 Epidural empyema in a 9-year-old female as a complication of ethmoid sinus infection. **(a)** Axial CT shows a thin contrast-enhancing margin surrounding a low-attenuation collection at the left frontal region. **(b)** The epidural empyema has heterogeneous high signal centrally surrounded by a thin band of low signal representing displaced dura and edema in adjacent brain tissue on axial FLAIR (arrow). **(c)** The infected dura shows gadolinium contrast enhancement on axial T1-weighted imaging.

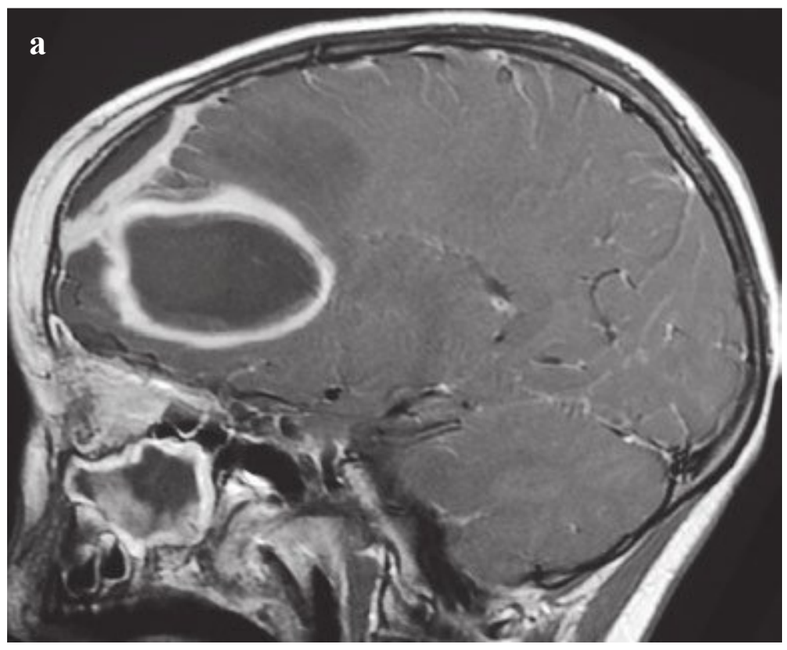

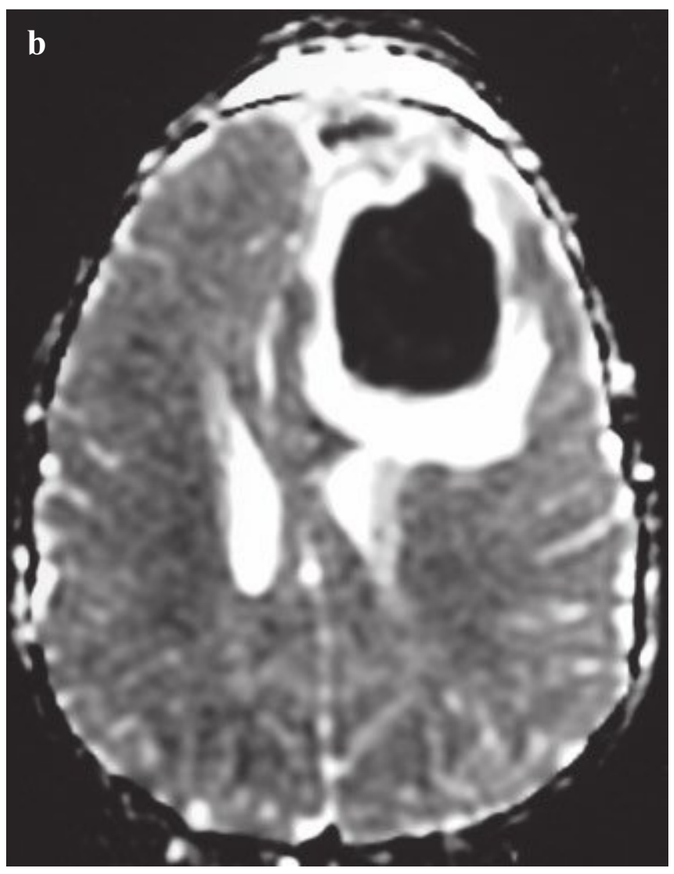

Fig. 3.31 An 8-year-old female with a subdural empyema in the left frontal region with associated complication of an abscess in the adjacent left frontal lobe. **(a)** Sagittal T1-weighted imaging shows thick peripheral gadolinium contrast enhancement at the subdural empyema and at the brain abscess. **(b)** The purulent material in the brain abscess and subdural empyema has restricted diffusion with low signal on axial ADC.

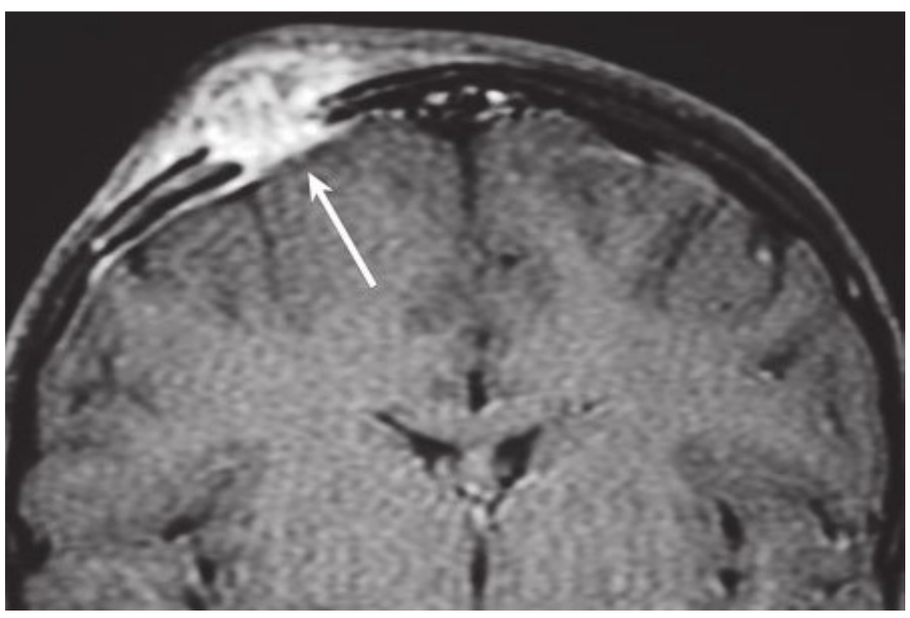

Fig. 3.32 A 7-year-old male with a gadolinium-enhancing eosinophilic granuloma (arrow) is seen in the marrow of the skull associated with localized destruction of both the inner and outer tables and with extraosseous extension, including dural thickening on coronal fat-suppressed T1-weighted imaging.

Table 3.1 (cont.) Solitary extra-axial mass lesions

Lesions	Imaging Findings	Comments
Vascular Lesions		
Arterial aneurysm (**Fig. 3.33** and **Fig. 3.34**) Saccular aneurysm Giant aneurysm Fusiform aneurysm	Saccular aneurysm MRI: Focal well-circumscribed zone of signal void on T1- and T2-weighted imaging, with variable mixed signal if thrombosed. CT: Focal well-circumscribed zone of intermediate-high attenuation, + contrast enhancement in nonthrombosed portion of aneurysm, easily visualized on CTA. Giant aneurysm MRI: Focal well-circumscribed structure with layers of low, intermediate, and high signal on T2-weighted imaging secondary to layers of thrombus of different ages, as well as a zone of signal void representing a patent lumen if present. On T1-weighted imaging, layers of intermediate and high signal can be seen as well as a zone of signal void. CT: Focal well-circumscribed structure with layers of low, intermediate, and/or high attenuation secondary to layers of thrombus of different ages, as well as a zone of contrast enhancement representing a patent lumen if present, ± wall calcifications present. Fusiform aneurysm MRI: Elongated and ectatic arteries, variable intraluminal MR signal related to turbulent or slowed blood flow or partial/complete thrombosis. CT: Elongated and ectatic arteries with intermediate attenuation, ± calcifications, variable contrast enhancement related to turbulent or slowed blood flow or partial/complete thrombosis.	Abnormal fusiform or focal dilatation of artery secondary to acquired/degenerative etiology, polycystic disease, connective tissue disease, atherosclerosis, trauma, infection (mycotic), oncotic involvement, arteriovenous malformation, vasculitis, and drugs. Focal aneurysms are also referred to as saccular aneurysms, which typically occur at arterial bifurcations and are multiple in 20% of cases. Saccular aneurysms > 2.5 cm in diameter are referred to as giant aneurysms. Fusiform aneurysms are often related to atherosclerosis or collagen vascular disease (Marfan syndrome, Ehlers-Danlos syndrome, etc.). Dissecting aneurysms form when hemorrhage occurs in the arterial wall from incidental or significant trauma.
Dural arteriovenous malformations (AVMs)	MRI: Dural AVMs contain multiple, tortuous, tubular flow voids on T1- and T2-weighted imaging. The venous portions often show gadolinium enhancement. Gradient echo MR images and MRA using time-of-flight or phase-contrast techniques show flow signal in patent portions of the vascular malformation and areas of venous sinus occlusion or recanalization. Usually not associated with mass effect unless there is recent hemorrhage or venous occlusion. CT: Dural AVMs contain multiple, tortuous, contrast-enhancing vessels on CTA at the site of a recanalizing thrombosed dural venous sinus. Usually not associated with mass effect.	Dural AVMs are usually acquired lesions resulting from thrombosis or occlusion of an intracranial venous sinus with subsequent recanalization resulting in direct arterial to venous sinus communications. Occur in transverse and sigmoid venous sinuses > cavernous sinus > straight and superior sagittal sinuses.
Vein of Galen aneurysm (**Fig. 3.35**)	MRI: Multiple, tortuous, tubular flow voids on T1- and T2-weighted imaging involving choroidal and thalamoperforate arteries, internal cerebral veins, vein of Galen (aneurysmal formation), straight and transverse venous sinuses, and other adjacent veins and arteries. The venous portions often show gadolinium enhancement. Gradient echo MR images and MRA using time-of-flight or phase-contrast techniques show flow signal in patent portions of the vascular malformation. CT: Multiple, tortuous, contrast-enhancing vessels involving choroidal and thalamoperforate arteries, internal cerebral veins, vein of Galen (aneurysmal formation), straight and transverse venous sinuses, and other adjacent veins and arteries. The venous portions often show contrast enhancement. CTA shows contrast enhancement in patent portions of the vascular malformation.	Heterogeneous group of vascular malformations with arteriovenous shunts and dilated deep venous structures draining into and from an enlarged vein of Galen, ± hydrocephalus, ± hemorrhage, ± macrocephaly, ± parenchymal vascular malformation components, ± seizures. High-output congestive heart failure in neonates.

(continued on page 542)

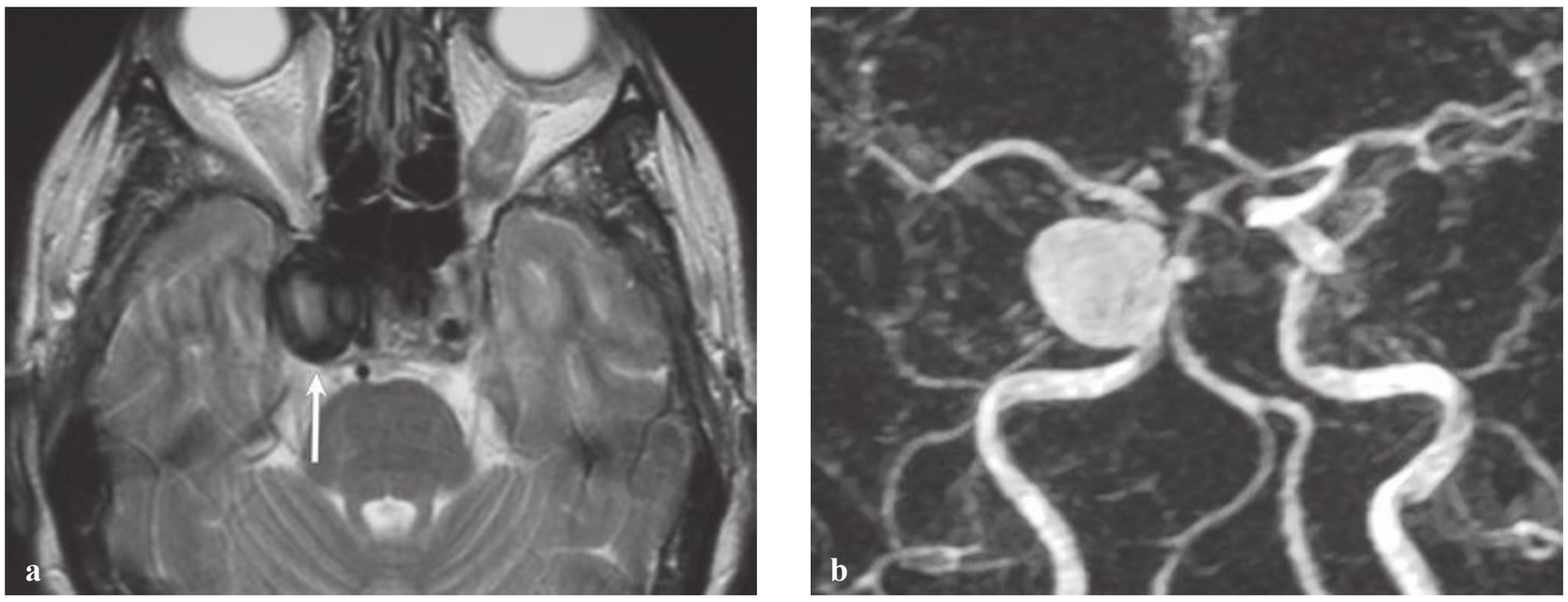

Fig. 3.33 Giant aneurysm of the right cavernous portion of the right internal carotid artery that has **(a)** a signal void with pulsation artifacts on axial T2-weighted imaging (arrow) and **(b)** flow signal on coronal MRA.

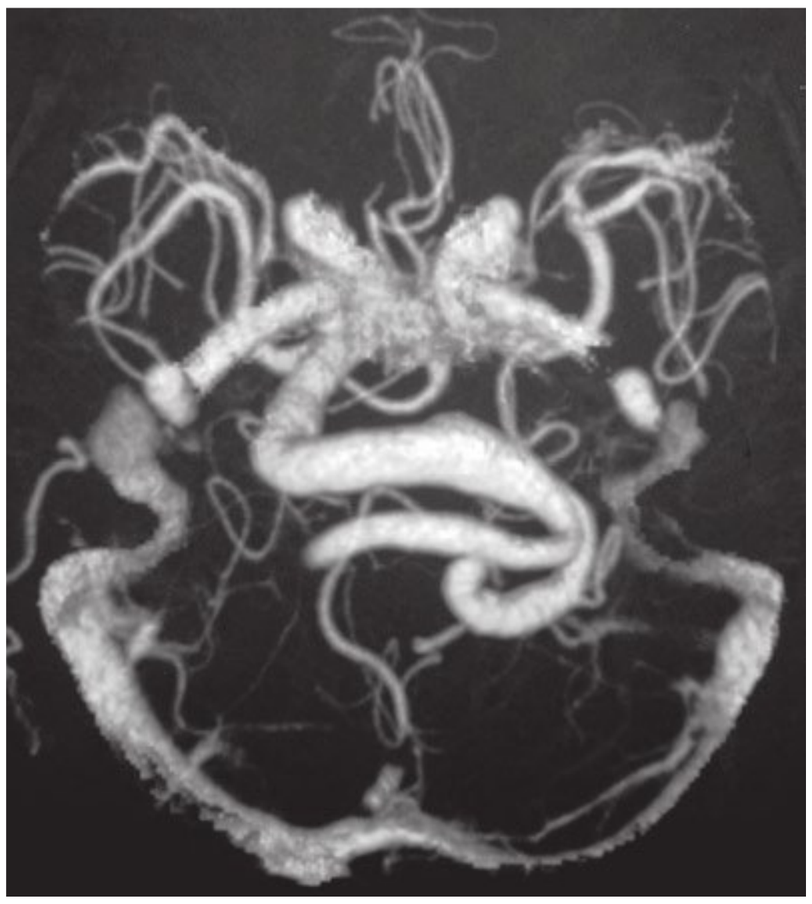

Fig. 3.34 Axial volume-rendered CTA shows a tortuous fusiform aneurysm of the basilar artery.

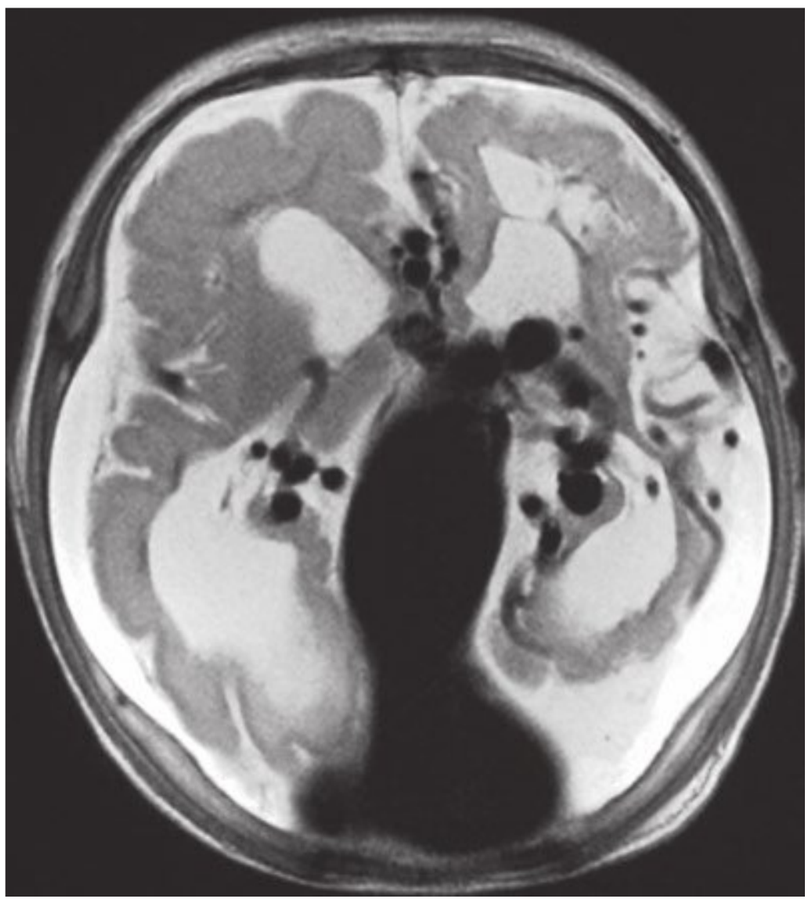

Fig. 3.35 Axial T2-weighted imaging of a neonate shows multiple intracranial flow voids as well as markedly dilated vein of Galen and straight venous sinus representing a vein of Galen aneurysm/malformation.

Table 3.1 (cont.) Solitary extra-axial mass lesions

Lesions	Imaging Findings	Comments
Tumorlike Lesions		
Arachnoid cyst (**Fig. 3.36**)	MRI: Well-circumscribed extra-axial lesions with low signal on T1-weighted imaging, FLAIR, and diffusion-weighted imaging and high signal on T2-weighted imaging similar to CSF, as well as no gadolinium contrast enhancement. Common locations: anterior middle cranial fossa > suprasellar/quadrigeminal cisterns > frontal convexities > posterior cranial fossa. CT: Well-circumscribed extra-axial lesions with low attenuation and no contrast enhancement.	Nonneoplastic congenital, developmental, or acquired extra-axial lesions filled with CSF, usually with mild mass effect on adjacent brain, in supratentorial > infratentorial locations, and in males > females, ± related clinical symptoms.
Leptomeningeal cyst (**Fig. 3.37**)	MRI: Well-circumscribed extra-axial lesions with low signal on T1-weighted imaging and high signal on T2-weighted imaging similar to CSF and no gadolinium contrast enhancement. Associated with erosion of the adjacent skull. CT: Well-circumscribed extra-axial lesions with low attenuation similar to CSF and no contrast enhancement.	Nonneoplastic extra-axial lesions filled with CSF thought to be secondary to trauma with dural tear/skull fracture, usually with mild mass effect on adjacent brain and progressive erosion of adjacent skull. Occasionally presents as a scalp lesion, and occurs in children > adults.
Rathke's cleft cyst (**Fig. 3.38**)	MRI: Well-circumscribed lesions with variable low, intermediate, or high signal on T1- and T2-weighted imaging. On T1-weighted imaging, two-thirds have high signal and one-third have low signal; on T2-weighted imaging, one-half have high signal, one-fourth have low signal, and one-fourth have intermediate signal, - gadolinium centrally, ± thin peripheral enhancement. Lesion locations: intrasellar, 50%; suprasellar, 25%; intra- and suprasellar, 25% CT: Well-circumscribed lesion with variable low, intermediate, or high attenuation and no contrast enhancement.	Uncommon sellar/juxtasellar benign cystic lesions containing fluid with variable amounts of protein, mucopolysaccharide, and/or cholesterol that arise from epithelial rests of the craniopharyngeal duct.

(continued on page 544)

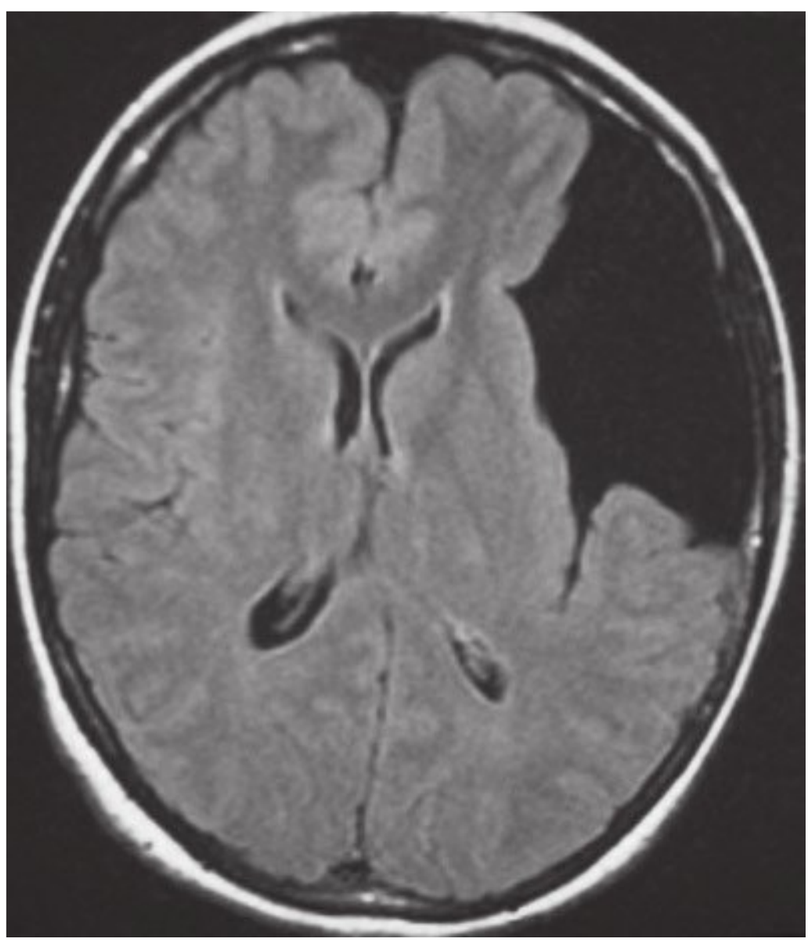

Fig. 3.36 A 29-year-old woman with an arachnoid cyst in the left frontal region that has CSF signal on axial FLAIR.

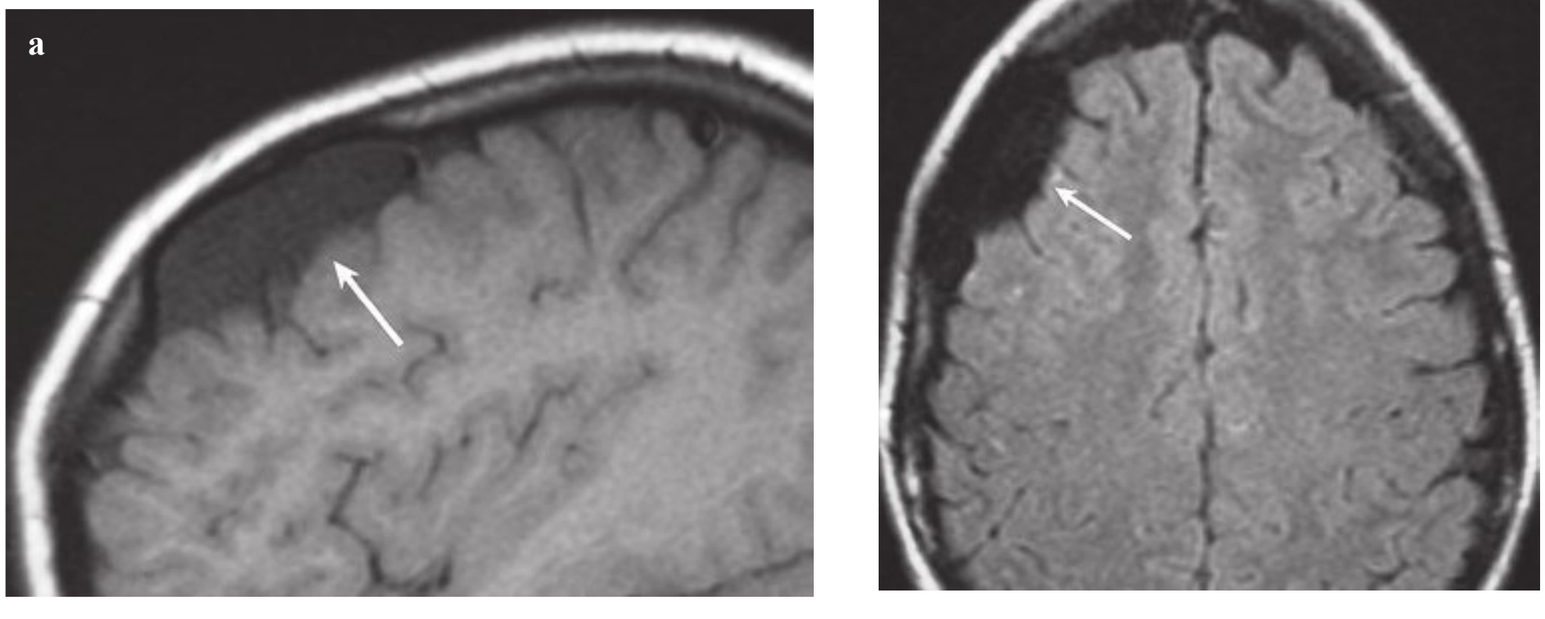

Fig. 3.37 A 16-year-old female with a leptomeningeal cyst that has CSF signal on **(a)** sagittal T1-weighted imaging (arrow) and **(b)** axial FLAIR and is associated with erosion and remodeling of the adjacent skull (arrow).

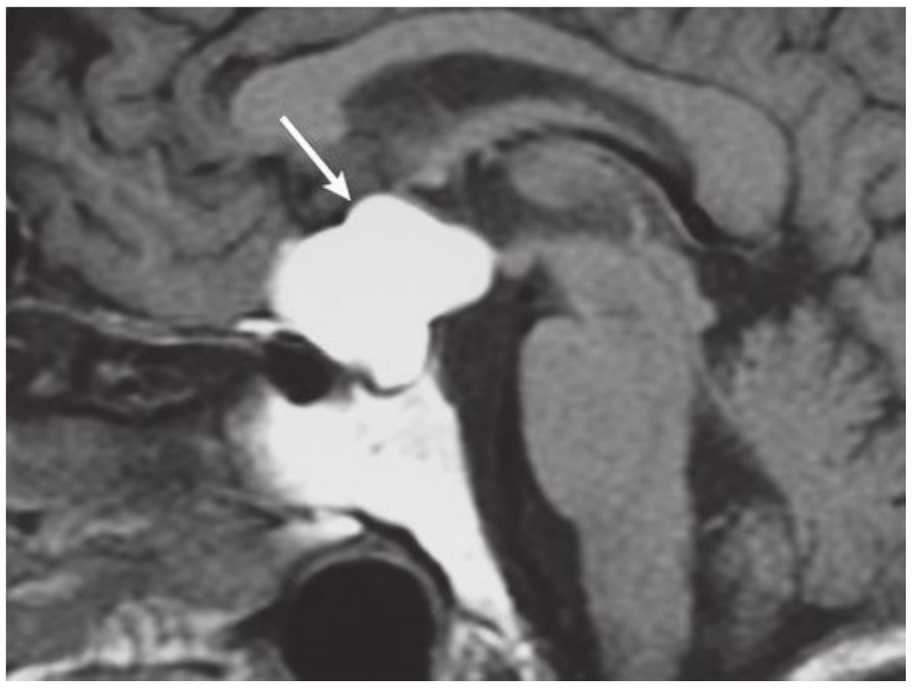

Fig. 3.38 A 60-year-old woman with a Rathke's cleft cyst (arrow) within the suprasellar cistern that has high signal on sagittal T1-weighted imaging.

Table 3.1 (cont.) Solitary extra-axial mass lesions

Lesions	Imaging Findings	Comments
Epidermoid (**Fig. 3.39**)	MRI: Well-circumscribed spheroid or multilobulated extra-axial ectodermal-inclusion cystic lesions with low-intermediate signal on T1-weighted imaging, high signal on T2-weighted imaging and diffusion weighted imaging (restricted diffusion), mixed low, intermediate, or high signal on FLAIR images, and no gadolinium contrast enhancement. Often insinuate along CSF pathways, causing chronic deformation of adjacent neural tissue (brainstem, brain parenchyma). CT: Well-circumscribed spheroid or multilobulated extra-axial ectodermal-inclusion cystic lesions with low-intermediate attenuation.	Nonneoplastic congenital or acquired extra-axial off-midline lesions filled with desquamated cells and keratinaceous debris, usually with mild mass effect on adjacent brain, and in infratentorial > supratentorial locations. Occur in adults, in males = females, ± related clinical symptoms. Commonly located in posterior cranial fossa (cerebellopontine angle cistern) > parasellar/middle cranial fossa.
Dermoid (**Fig. 3.40**)	MRI: Well-circumscribed spheroid or multilobulated extra-axial lesions, usually with high signal on T1-weighted images, variable low, intermediate, and/or high signal on T2-weighted imaging, and no gadolinium contrast enhancement, ± fluid/fluid or fluid/debris levels. CT: Well-circumscribed spheroid or multilobulated extra-axial lesions, usually with low attenuation, ± fat/fluid or fluid/debris levels.	Nonneoplastic congenital or acquired ectodermal-inclusion cystic lesions filled with lipid material, cholesterol, desquamated cells, and keratinaceous debris, usually with mild mass effect on adjacent brain. Occur in adults, in males slightly > females, ± related clinical symptoms. Can cause chemical meningitis if dermoid cyst ruptures into the subarachnoid space. Commonly located at or near midline, supra- > infratentorial.
Neurenteric cyst (**Fig. 3.41**)	MRI: Well-circumscribed, spheroid, intradural extra-axial lesions, with low, intermediate, or high signal on T1- and T2-weighted imaging, and usually no gadolinium contrast enhancement. CT: Circumscribed intradural extra-axial structures with low-intermediate attenuation. Usually no contrast enhancement,	Neurenteric cysts are malformations in which there is a persistent communication between the ventrally located endoderm and the dorsally located ectoderm secondary to developmental failure of separation of the notochord and foregut. Obliteration of portions of a dorsal enteric sinus can result in cysts lined by endothelium, fibrous cords, or sinuses. Observed in patients < 40 years old. Locations: thoracic > cervical > posterior cranial fossa > craniovertebral junction > lumbar; usually midline in position and often ventral to the spinal cord or brainstem. Associated with anomalies of the adjacent vertebrae and clivus.
Lipoma (**Fig. 3.42**)	MRI: Lipomas have signal isointense to subcutaneous fat on T1-weighted images (high signal); and on T2-weighted images. Signal suppression occurs with frequency-selective fat saturation techniques or with a short time to inversion recovery (STIR) method. Typically there is no gadolinium enhancement or peripheral edema. CT: Lipomas have CT attenuation similar to subcutaneous fat, typically with no contrast enhancement or peripheral edema.	Benign fatty lesions resulting from congenital malformation, often located in or near the midline, and may contain calcifications and/or traversing blood vessels.

(continued on page 547)

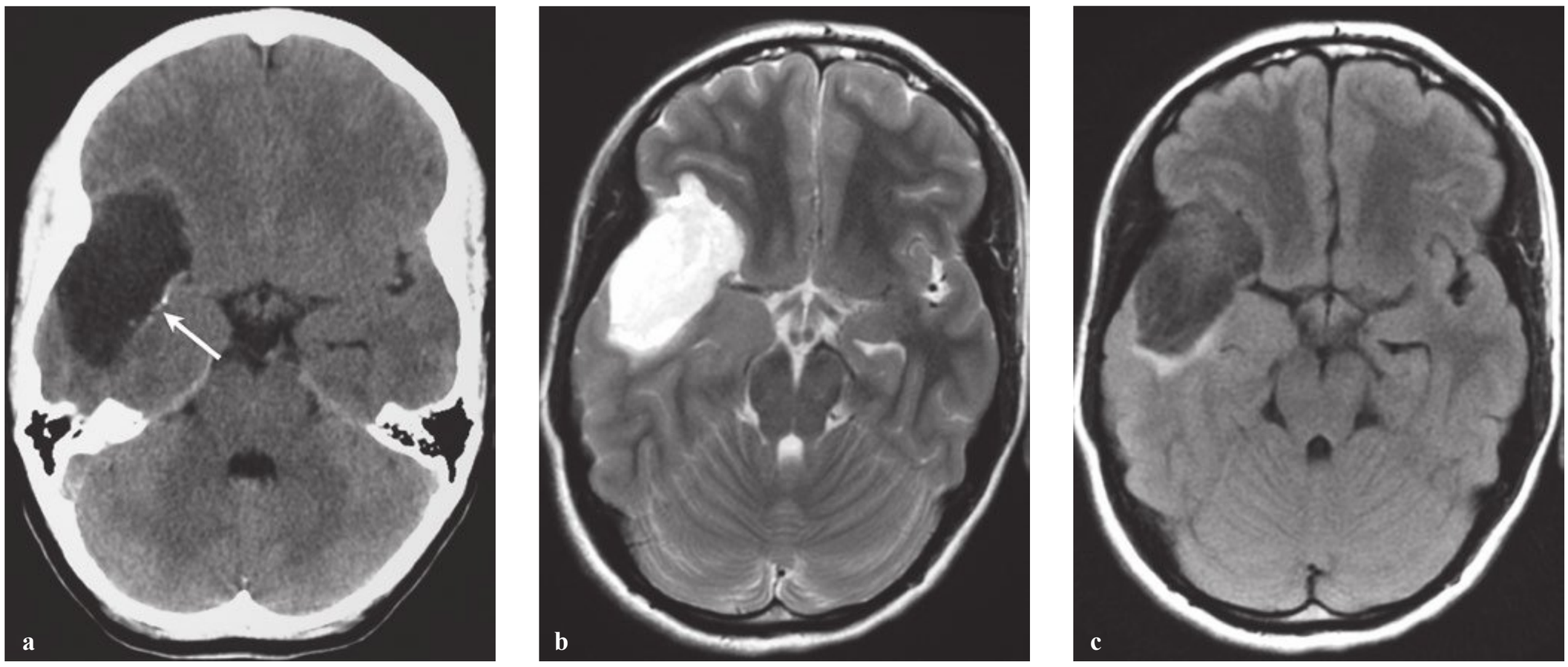

Fig. 3.39 An 18-year-old woman with an epidermoid cyst on the right that has **(a)** low attenuation on axial CT (arrow), **(b)** high signal on axial T2-weighted imaging, **(c)** mixed low and intermediate signal on axial FLAIR, and **(d)** restricted diffusion on axial diffusion-weighted imaging. **(e)** The epidermoid shows no gadolinium contrast enhancement on axial T1-weighted imaging.

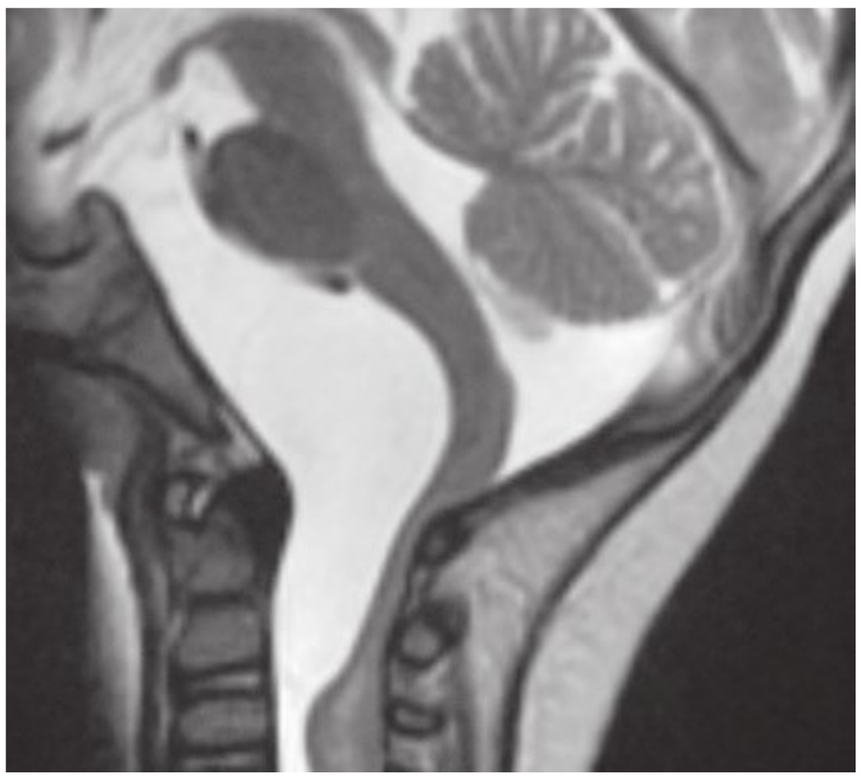

Fig. 3.40 A 2-year-old female with a neurenteric cyst with high signal on sagittal T2-weighted imaging and displacing the brainstem posteriorly.

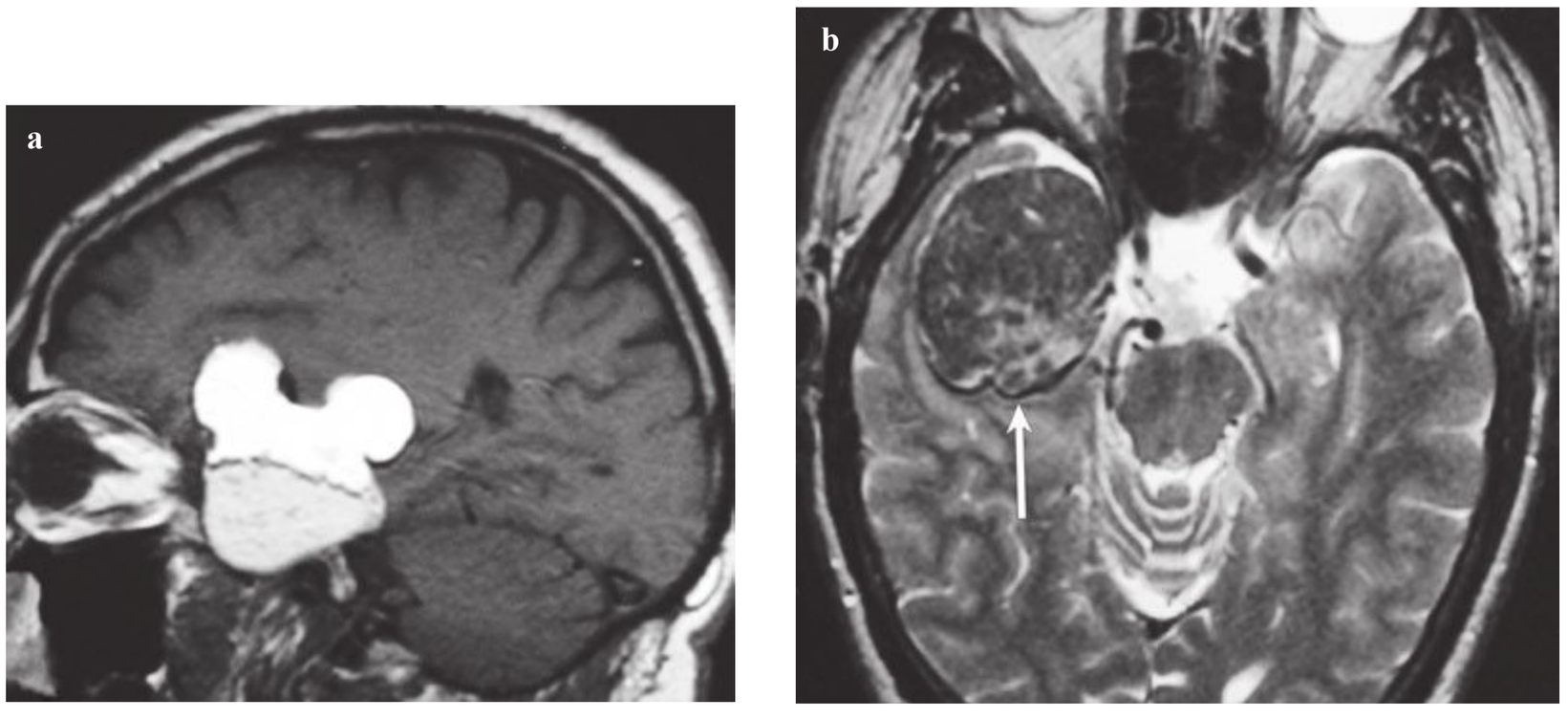

Fig. 3.41 A 55-year-old man with a dermoid cyst in the right middle cranial fossa that has **(a)** heterogeneous mostly high signal on sagittal T1-weighted imaging and **(b)** mixed low and high signal on axial T2-weighted imaging (arrow).

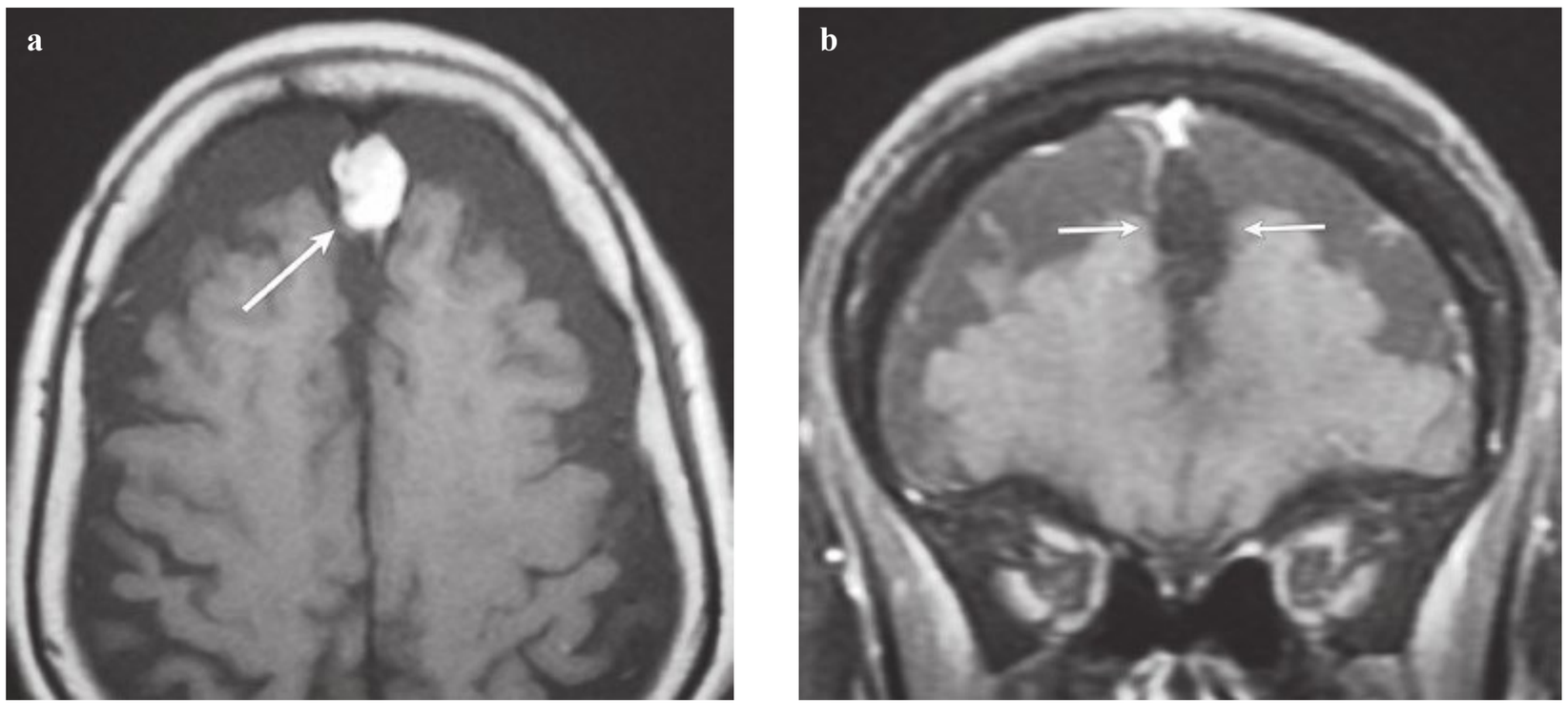

Fig. 3.42 **(a)** A 71-year-old woman with a lipoma at the anterior portion of the falx that has high signal on axial T1-weighted imaging (arrow). **(b)** The signal of the lipoma is nulled on fat-suppressed postcontrast coronal T1-weighted imaging (arrows).

Table 3.1 (cont.) Solitary extra-axial mass lesions

Lesions	Imaging Findings	Comments
Dural calcification and ossification (**Fig. 3.43**)	MRI: Zones of calcification usually have low signal on T1-weighted imaging, gradient recalled echo (GRE), and T2-weighted imaging. Zones of ossification can have a low-signal border on T1- and T2-weighted imaging and a central zone of fat marrow signal. CT: Calcification as well as zones of ossification can be seen in one or more sites of the intracranial dura.	Calcification and ossification can occur at single or multiple sites in the intracranial dura from metaplasia. Typically they are incidental findings.
Ecchordosis physaliphora (**Fig. 3.44**)	MRI: Circumscribed lesion ranging in size from 1 to 3 cm, with low signal on T1-weighted imaging, low to intermediate signal on FLAIR, and high signal on T2-weighted imaging. Typically shows no gadolinium contrast enhancement. CT: Lesions typically have low attenuation, ± remodeling/erosion of adjacent bone, ± small calcified bone stalk.	Congenital benign hamartoma composed of gelatinous tissue with physaliphorous cell nests derived from ectopic vestigial notochord. Incidence at autopsy ranges from 0.5 to 5% Usually located intradurally dorsal to the clivus and dorsum sella within the prepontine cistern, and rarely dorsal to the upper cervical spine or sacrum. Rarely occurs as an extradural lesion. Results from an ectopic notochordal remnant or from extension of extradural notochord at the dorsal wall of the clivus through the adjacent dura into the subarachnoid space. Typically are asymptomatic and observed as an incidental finding in patients between 20 and 60 years old.

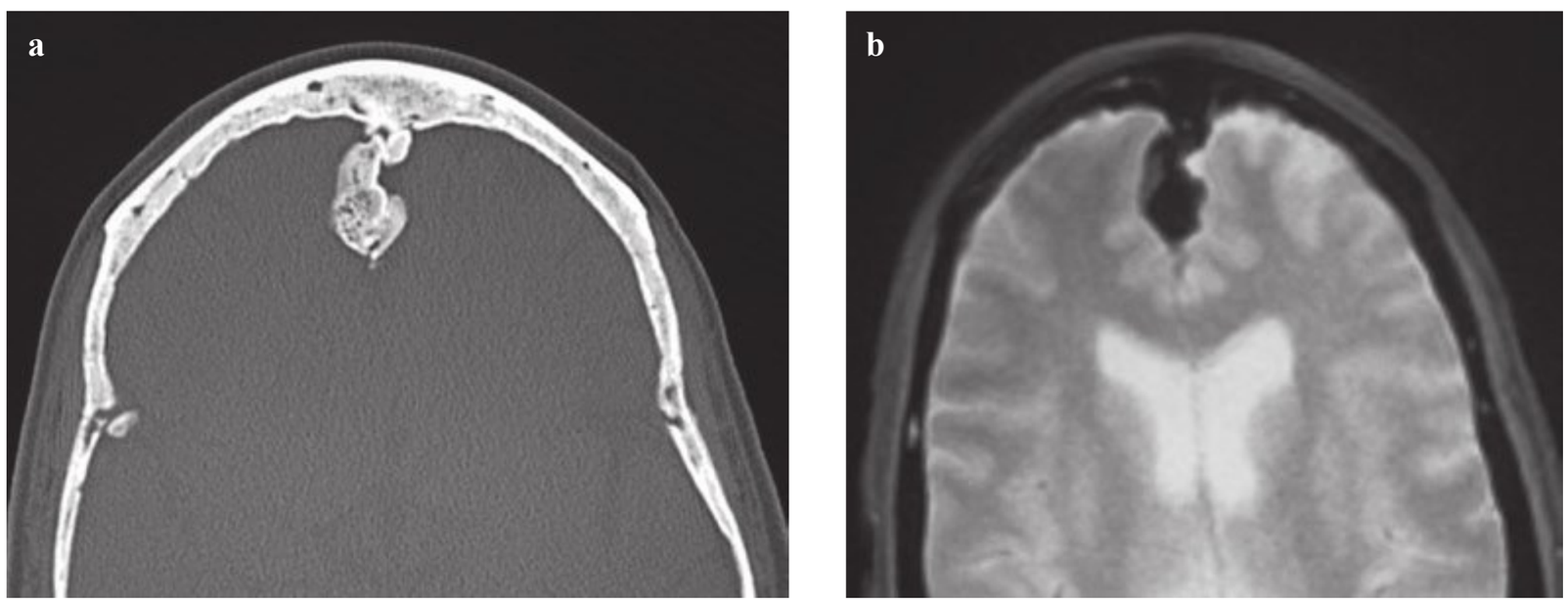

Fig. 3.43 **(a)** A 64-year-old woman with dural ossification at the anterior falx, as seen on axial CT. **(b)** The dural ossification has low signal on axial GRE.

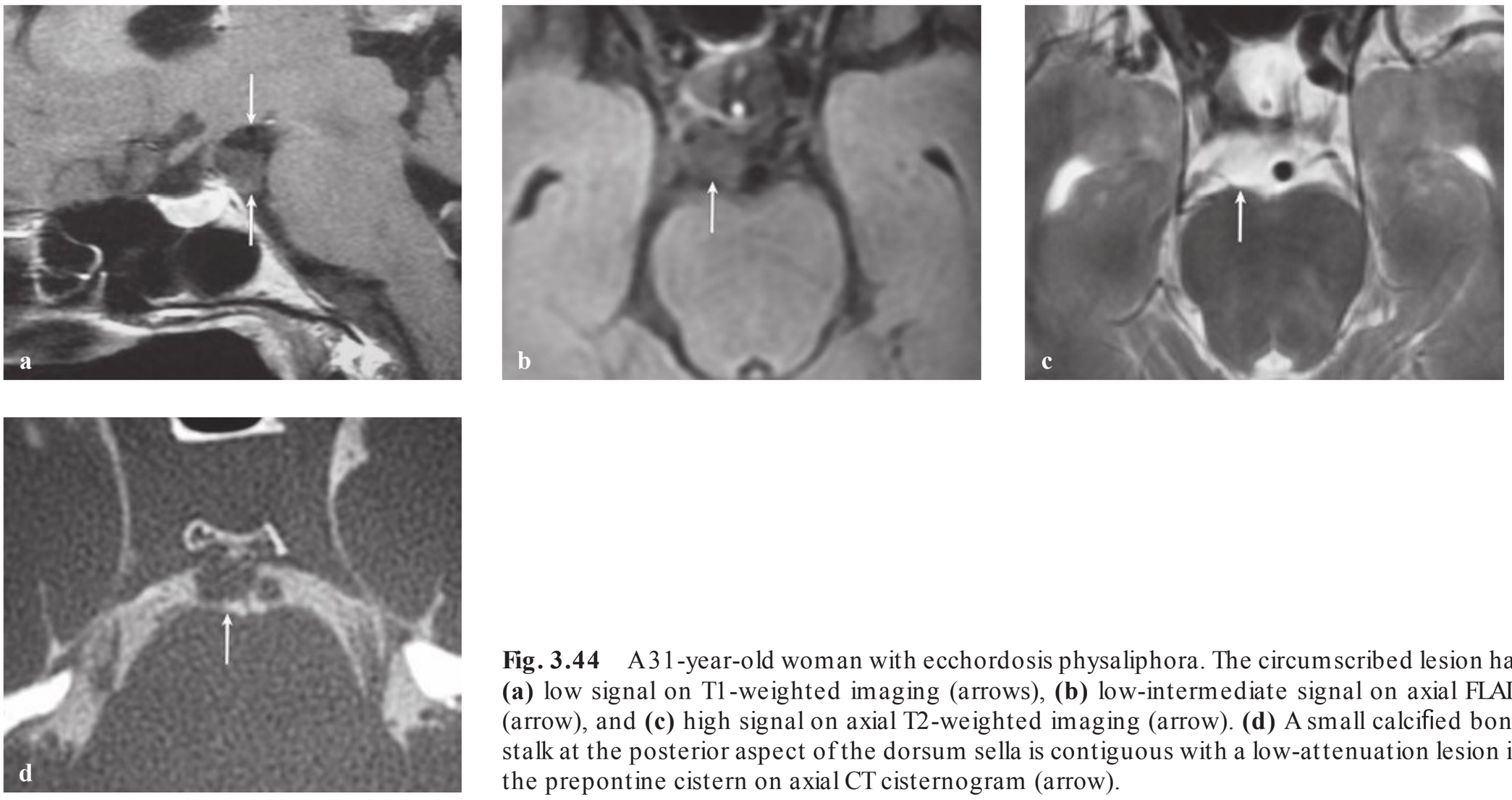

Fig. 3.44 A 31-year-old woman with ecchordosis physaliphora. The circumscribed lesion has **(a)** low signal on T1-weighted imaging (arrows), **(b)** low-intermediate signal on axial FLAIR (arrow), and **(c)** high signal on axial T2-weighted imaging (arrow). **(d)** A small calcified bone stalk at the posterior aspect of the dorsum sella is contiguous with a low-attenuation lesion in the prepontine cistern on axial CT cisternogram (arrow).

Table 3.2 Multifocal extra-axial lesions

- Benign Neoplasms
  - Meningioma
  - Schwannoma
  - Neurofibroma
- Malignant Neoplasms
  - Metastatic tumor
  - Lymphoma
  - Myeloma
- Hemorrhage
  - Epidural hematoma
  - Subdural hematoma
  - Ossified hematoma
- Infection/Inflammation
  - Subdural/epidural abscess or empyema
  - Eosinophilic granuloma, Langerhans' cell histiocytosis
  - Neurosarcoid
- Vascular Lesions
  - Arterial aneurysms (saccular aneurysms)
- Tumorlike Lesions
  - Ruptured dermoid cyst
  - Dural calcifications and ossifications

Table 3.2 Multifocal extra-axial lesions

Lesions	Imaging Findings	Comments
Benign Neoplasms		
Meningioma (**Fig. 3.45** and **Fig. 3.46**)	Well-circumscribed extra-axial dura-based lesions. Locations: supra- > infratentorial, parasagittal > convexity > sphenoid ridge > parasellar > posterior fossa > optic nerve sheath > intraventricular. MRI: Dura-based tumors with intermediate signal on T1-weighted imaging, intermediate to slightly high signal on T2-weighted imaging, usually with prominent gadolinium contrast enhancement, often with a dural tail, ± calcifications. Intratumoral hemorrhage and cystic or necrotic foci can occur in 15% Diffusion-weighted imaging/diffusion tensor imaging: ADC values vary among the different subtypes of meningioma. Some tumors can show restricted diffusion, although these findings can be seen with both benign and atypical or malignant tumors. Magnetic resonance spectroscopy can show elevated alanine (1.5 ppm), lactate, choline, and glutamine/glutamate levels, and reduced N-acetylaspartate (NAA). CT: Tumors have intermediate attenuation with or without calcifications, with or without hyperostosis, and usually show prominent contrast enhancement.	Meningiomas are the most common extra-axial tumors, accounting for up to 26%of primary intracranial tumors. Annual incidence is 6 per 100,000, typically in adults (>40 years old) and in women > men. Composed of neoplastic meningothelial (arachnoid or arachnoid cap) cells. Meningiomas are usually solitary and sporadic, but can also occur as multiple lesions in patients with neurofibromatosis type 2. Eighty percent of meningiomas are benign (WHO grade I), although 15%have atypical features (WHO grade II) and ~ 5%have anaplastic histologic features (WHO grade III). Can occur secondary to radiation treatment, with latencies ranging from 19 to 35 years. Classified into different subtypes, such as meningothelial, fibrous (fibroblastic), transitional (mixed), psammomatous, angiomatous, atypical, and anaplastic. The most common intracranial types of meningioma are meningothelial, fibrous, and transitional types. Usually show immunoreactivity to epithelial membrane antigen (EMA) and vimentin. Secretory meningiomas are typically immunoreactive to CEA. Associated cytogenetic findings of deletion of chromosome 22. Mutations in the NF2 tumor suppressor gene on chromosome 22 have been found in 60%of sporadic meningiomas.
Schwannoma (**Fig. 3.47** and **Fig. 3.48**)	MRI: Circumscribed or lobulated lesions with low-intermediate signal on T1-weighted imaging and high signal on T2-weighted imaging and fat-suppressed T2-weighted imaging. Usually show prominent gadolinium contrast enhancement. High signal on T2-weighted imaging and gadolinium contrast enhancement can be heterogeneous in large lesions due to cystic degeneration and/or hemorrhage. Schwannomas involving the temporal bone include those from CN V (trigeminal nerve cistern/Meckel's cave), CN VI (Dorello canal), CN VII and CN VIII (IAC and CPA cistern), CN IX, CN X, and CN XI (jugular foramen). CT: Circumscribed or lobulated lesions, intermediate attenuation, + contrast enhancement. Large lesions can have cystic degeneration and/or hemorrhage.	Schwannomas are benign encapsulated tumors that contain differentiated neoplastic Schwann cells. Most commonly occur as solitary sporadic lesions. Multiple schwannomas are often associated with neurofibromatosis type 2 (NF2), which is an autosomal dominant disease involving a gene at chromosome 22q12. In addition to schwannomas, patients with NF2 can also have multiple meningiomas and ependymomas. Schwannomas represent 8%of primary intracranial tumors and 29%for primary spinal tumors. The incidence of NF2 is 1/ 37,000 to 1/50,000 newborns. Age at presentation is 22 to 72 years (mean age = 46 years). Peak incidence is in the fourth to sixth decades. In NF2, many patients present in the third decade with bilateral vestibular schwannomas. Another syndrome with multiple schwannomas is schwannomatosis, in which patients have multiple schwannomas without involvement of CN VIII. The incidence of schwannomatosis ranges from 1/40,000 to 1/1.7 million. Peak age of incidence is between 30 and 60 years. Schwannomatosis is related to germline mutation of the SMARCB1 gene (also known as the INI tumor suppressor gene) on chromosome 22.

(continued on page 550)

Table 3.2 (cont.) Multifocal extra-axial lesions

Lesions	Imaging Findings	Comments
Neurofibroma	MRI: Circumscribed or lobulated extra-axial lesions with low-intermediate signal on T1-weighted imaging, intermediate-high signal on T2-weighted imaging, + prominent gadolinium contrast enhancement. High signal on T2-weighted imaging and gadolinium contrast enhancement can be heterogeneous in large lesions. CT: Ovoid or fusiform lesions with low-intermediate attenuation. Lesions can show contrast enhancement. Often erode adjacent bone.	Benign nerve sheath tumors that contain mixtures of Schwann cells, perineural-like cells, and interlacing fascicles of fibroblasts associated with abundant collagen. Unlike schwannomas, neurofibromas lack Antoni A and B regions and can not be separated pathologically from the underlying nerve. Most frequently occur as sporadic localized solitary lesions, less frequently as diffuse or plexiform lesions. Multiple neurofibromas are typically seen with neurofibromatosis type 1, which results as an autosomal dominant disorder (1/2500 births) from mutations involving the neurofibromin gene on chromosome 17q11.2. Represents the most common type of neurocutaneous syndrome and is associated with neoplasms of central and peripheral nervous system (optic gliomas, astrocytomas, plexiform and solitary neurofibromas) and skin (café-au-lait spots, axillary and inguinal freckling). Also associated with meningeal and skull dysplasias, as well as hamartomas of the iris (Lisch nodules).

(continued on page 552)

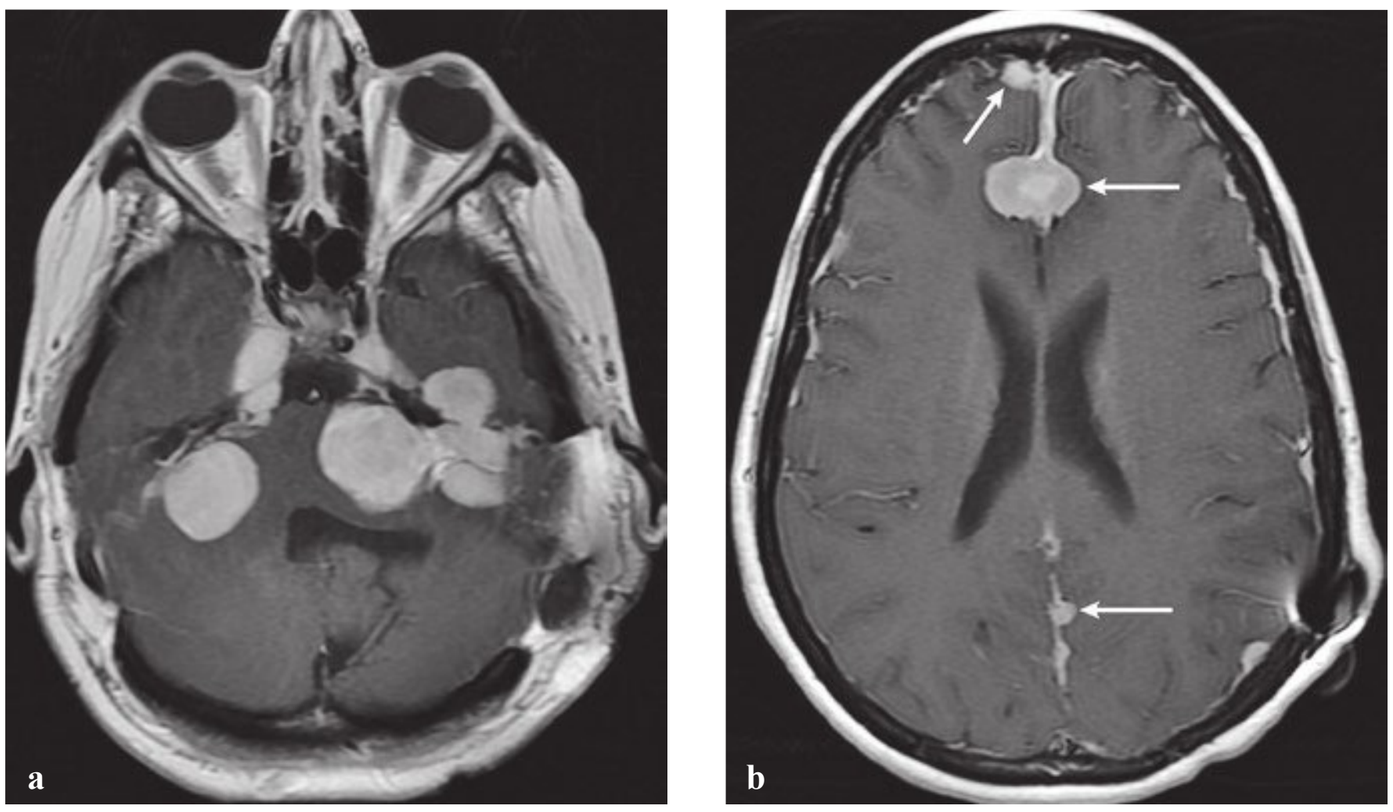

Fig. 3.45 **(a,b)** Patient with neurofibromatosis type 2 who has multiple gadolinium-enhancing meningiomas (arrows) and schwannomas on axial T1-weighted imaging.

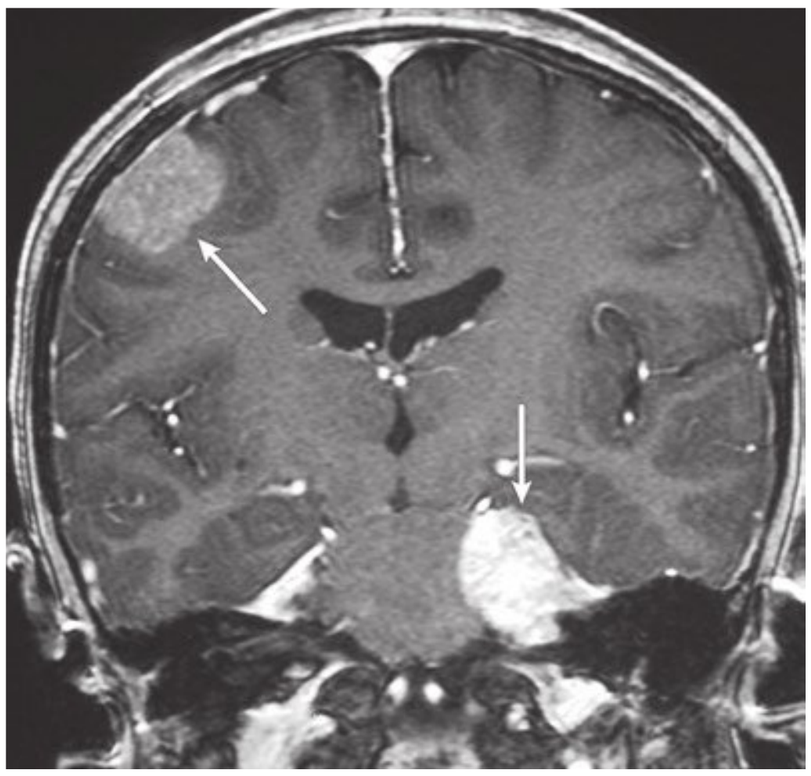

Fig. 3.46 A 25-year-old woman with neurofibromatosis type 2 with gadolinium-enhancing meningiomas (arrows) on coronal T1-weighted imaging.

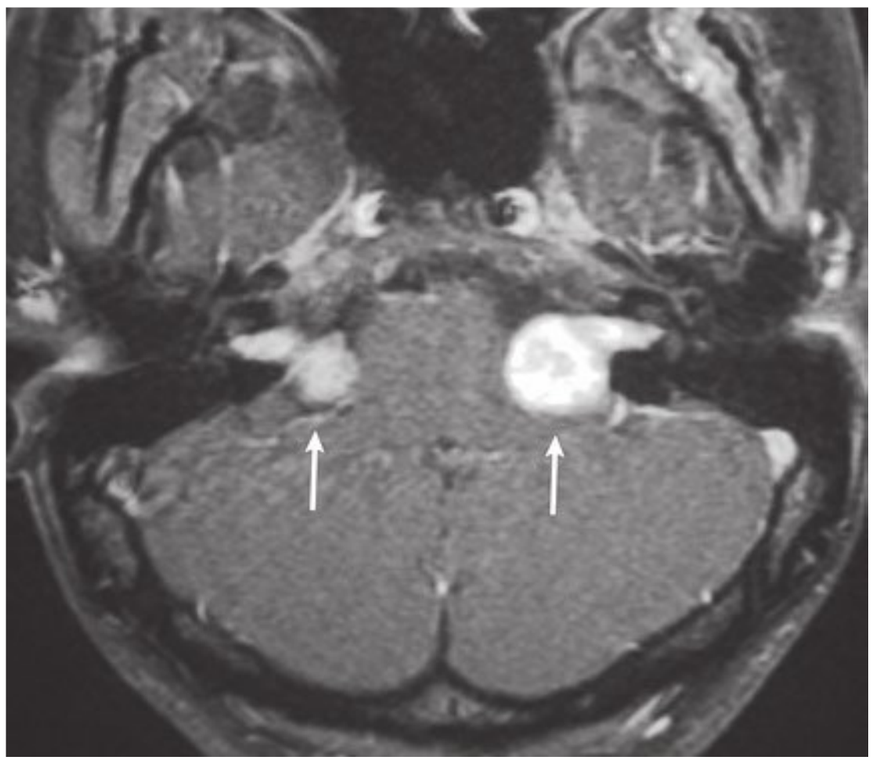

Fig. 3.47 Patient with neurofibromatosis type 2 with bilateral gadolinium-enhancing vestibular schwannomas/acoustic neuromas (arrows) seen on fat-suppressed T1-weighted imaging.

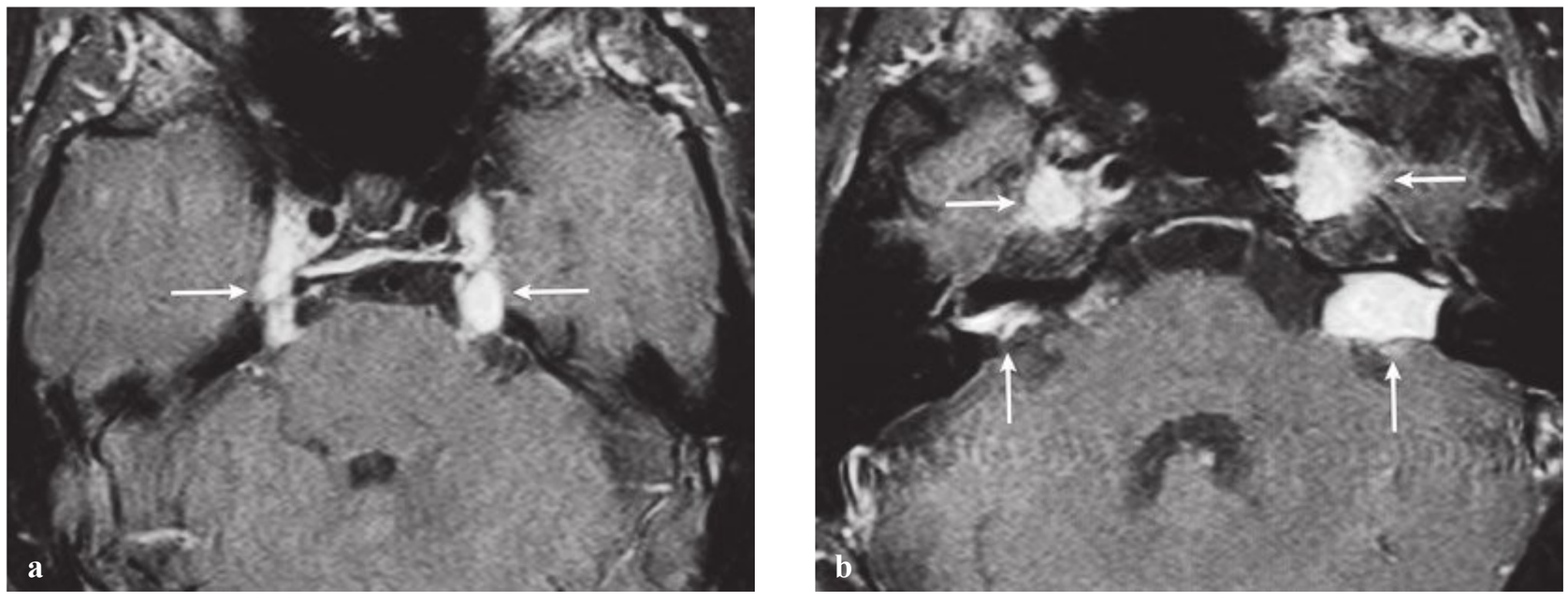

Fig. 3.48 **(a,b)** Patient with neurofibromatosis type 2 with bilateral gadolinium-enhancing vestibular and trigeminal schwannomas (arrows) seen on fat-suppressed T1-weighted imaging.

Table 3.2 (cont.) Multifocal extra-axial lesions

Lesions	Imaging Findings	Comments
Malignant Neoplasms		
Metastatic tumor (**Fig. 3.49** and **Fig. 3.50**)	MRI: Circumscribed spheroid lesion in dura, leptomeninges and/or choroid plexus. Often has low-intermediate signal on T1-weighted imaging and intermediate-high signal on T2-weighted imaging, ± hemorrhage, calcifications, and cysts. Variable gadolinium contrast enhancement. CT: Lesions usually have low-intermediate attenuation, ± hemorrhage, calcifications, and cysts. Variable contrast enhancement, ± bone destruction, ± compression of neural tissue or vessels. Leptomeningeal tumor often best seen on postcontrast images.	Represent ~ 33% of intracranial tumors, usually from extracranial primary neoplasm in adults > 40 years old. Primary tumor source: lung > breast > GI > GU > melanoma. Can occur as single or multiple well-circumscribed or poorly defined lesions involving the skull, dura, leptomeninges, and/or choroid plexus. Metastatic tumor may cause variable destructive or infiltrative changes in single or multiple sites.
Lymphoma	MRI: Single or multiple well-circumscribed or poorly defined lesions involving the skull, dura, and/or leptomeninges; low-intermediate signal on T1-weighted imaging, intermediate-high signal on T2-weighted imaging, usually + gadolinium contrast enhancement, ± bone destruction. Leptomeningeal tumor often best seen on postcontrast images. CT: CNS lymphoma can have intermediate attenuation or can be hyperdense related to a high nuclear/cytoplasm ratio. FDG PET/CT can show elevated uptake in PCNSL and in immunocompromised patients can be used to distinguish lymphoma from toxoplasmosis brain lesions, which have decreased FDG uptake.	Primary CNS lymphoma is more common than secondary, usually in adults > 40 years old. Accounts for 5% of primary brain tumors. Incidence currently ranges from 0.8 to 1.5% of primary intracranial tumors. Prior elevated incidence of 6% in patients with AIDS has been reduced with effective antiviral therapy. B-cell lymphoma is more common than T-cell lymphoma. MRI features of primary and secondary lymphoma of brain overlap. Intracranial lymphoma can involve the leptomeninges in secondary lymphoma > primary lymphoma.
Myeloma	Multiple (myeloma) or single (plasmacytoma) well-circumscribed or poorly defined lesions involving the skull and dura. MRI: Well-circumscribed or poorly defined lesions involving the skull and dura with low-intermediate signal on T1-weighted imaging and intermediate-high signal on T2-weighted imaging. Usually show gadolinium contrast enhancement, + bone destruction. CT: Lesions have low-intermediate attenuation, usually + contrast enhancement, + bone destruction.	In multiple myeloma, the malignant tumors are composed of proliferating antibody-secreting plasma cells derived from single clones. Multiple myelomas are primarily located in bone marrow. A solitary myeloma or plasmacytoma is an infrequent variant in which a neoplastic mass of plasma cells occurs at a single site of bone or soft tissue. In the United States, 14,600 new cases of multiple myeloma occur each year. Multiple myeloma is the most common primary neoplasm of bone in adults. Median age at presentation = 60 years. Most patients are older than 40 years. Tumors occur in the vertebrae > ribs > femur > iliac bone > humerus > craniofacial bones > sacrum > clavicle > sternum > pubic bone > tibia.

(continued on page 554)

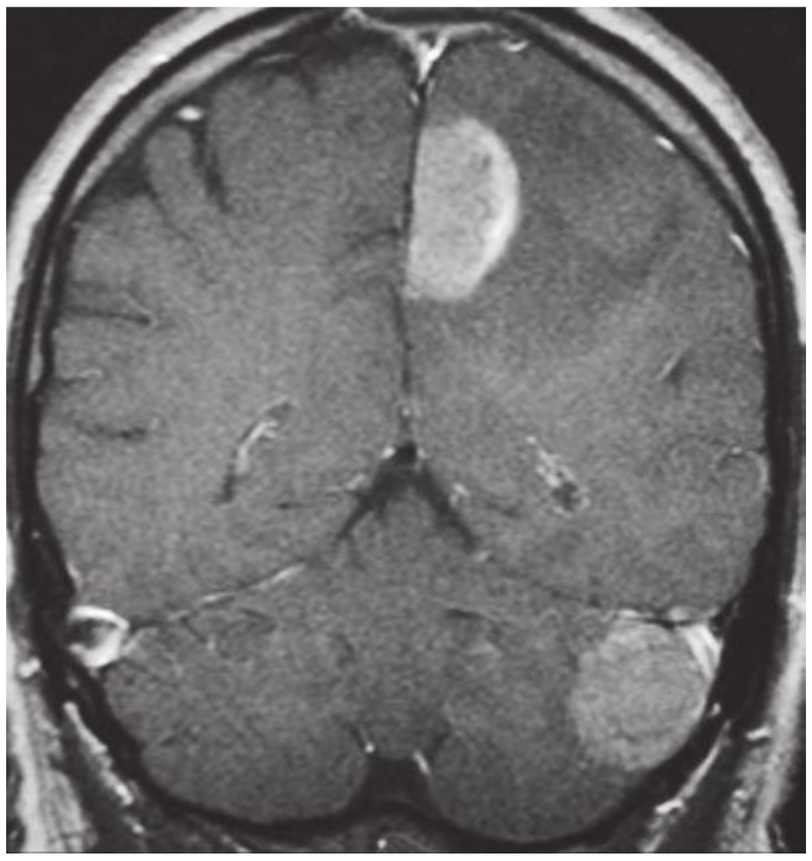

Fig. 3.49 A 56-year-old man with gadolinium-enhancing dural metastases from an extracranial malignant fibrous histiocytoma.

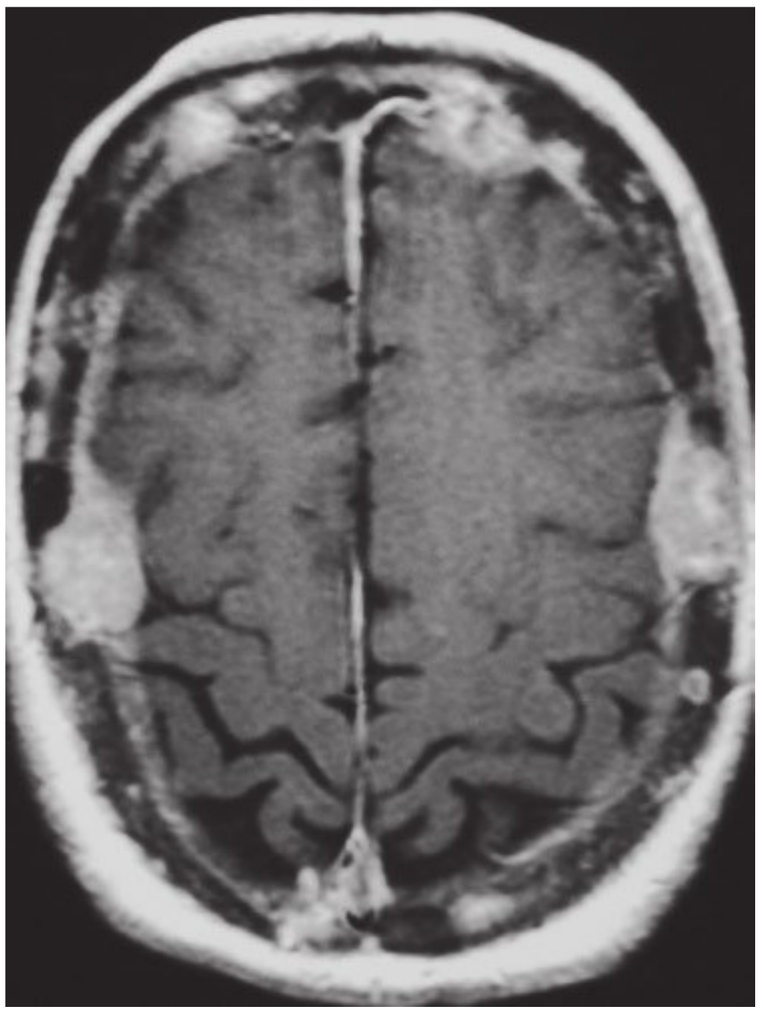

Fig. 3.50 Patient with breast cancer and multiple gadolinium-enhancing metastatic lesions involving the skull with associated bone destruction and dural invasion on axial T1-weighted imaging.

Table 3.2 (cont.) Multifocal extra-axial lesions

Lesions	Imaging Findings	Comments
Hemorrhage		
Epidural hematoma	MRI: Biconvex extra-axial hematoma located between the skull and dura (displaced dura has low signal on T2-weighted imaging), ± edema (high signal on T2-weighted imaging involving the displaced brain parenchyma), ± subfalcine or uncal herniation. The signal of the hematoma itself depends on its age, size, hematocrit, and oxygen tension. Hyperacute: Intermediate signal on T1-weighted imaging and intermediate-high signal on T2-weighted imaging. Acute: Low-intermediate signal on T1-weighted imaging and high signal on T2-weighted imaging. Early Subacute: High signal on T1-weighted imaging and low signal on T2-weighted imaging. Subacute: High signal on T1- and T2-weighted imaging. CT: Biconvex extra-axial hematoma located between the skull and dura (displaced dura has high attenuation), ± low-attenuation edema involving the displaced brain parenchyma, ± subfalcine or uncal herniation. The CT attenuation of the hematoma depends on its age, size, hematocrit, and oxygen tension.	Epidural hematomas usually result from trauma/tearing of an epidural artery (often the middle meningeal artery) or dural venous sinus, ± skull fracture. Epidural hematomas do not cross cranial sutures.
Subdural hematoma (**Fig. 3.51**) Hyperacute hematoma Acute hematoma Subacute hematoma Chronic hematoma	Crescentic extra-axial hematoma located in the potential space between the inner margin of the dura and outer margin of the arachnoid membrane, ± edema (low attenuation on CT and high signal on T2-weighted imaging) involving the displaced brain parenchyma, ± subfalcine and uncal herniation. The CT attenuation and MRI signal of the hematoma depend on its age, size, hematocrit, and oxygen tension. CT: Can have high or mixed high, intermediate, and/or low attenuation. MRI: Intermediate signal on T1-weighted imaging and intermediate-high signal on T2-weighted imaging. CT: Can have high or mixed high, intermediate, and/or low attenuation. MRI: Low-intermediate signal on T1-weighted imaging, low signal on T2-weighted imaging. CT: Can have intermediate attenuation (isodense to brain) and/or low-intermediate attenuation. MRI: High signal on T1- and T2-weighted imaging. CT: Usually have low attenuation (hypodense to brain). MRI: Variable, often low-intermediate signal on T1-weighted imaging, high signal on T2-weighted imaging, ± gadolinium contrast enhancement of collection and organizing neomembrane. Mixed MRI signal can result if rebleeding occurs into chronic collection.	Subdural hematomas usually result from trauma/stretching/tearing of cortical veins where they enter the subdural space to drain into dural venous sinuses, ± skull fracture. Subdural hematomas do cross sites of cranial sutures.
Ossified hematoma (**Fig. 3.52**)	MRI: Thin or irregular peripheral zones with low signal from calcifications; peripheral and/or central ossification surrounding collections with variable low, intermediate, and/or high signal on T1- and T2-weighted imaging, ± gadolinium contrast enhancement of collection and organizing neomembrane. Mixed MRI signal can result if rebleeding occurs into chronic collection. CT: Usually has dense thin or irregular peripheral calcifications, and/or peripheral and central ossification surrounding collections with variable low, intermediate, and/or high attenuation.	Chronic subdural or epidural hematomas can rarely become calcified or ossified, and they are referred to as armored brain. Surgical removal of symptomatic lesions can be difficult because of dense adhesion to brain surface and/or dura.

(continued on page 556)

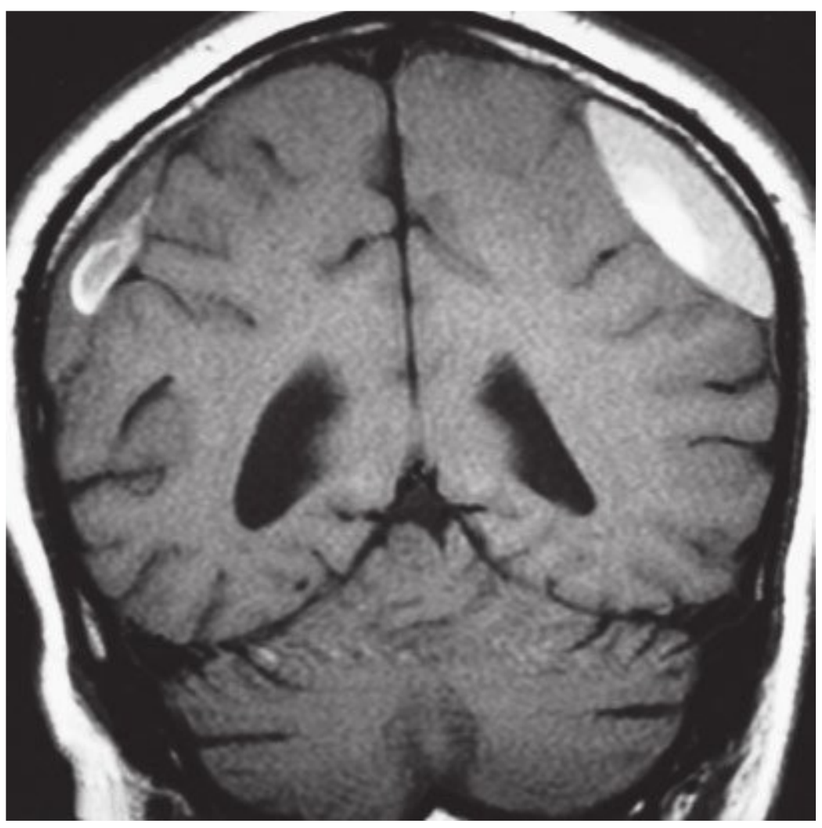

Fig. 3.51 A 63-year-old man with bilateral subdural hematomas with high signal on coronal T1-weighted imaging.

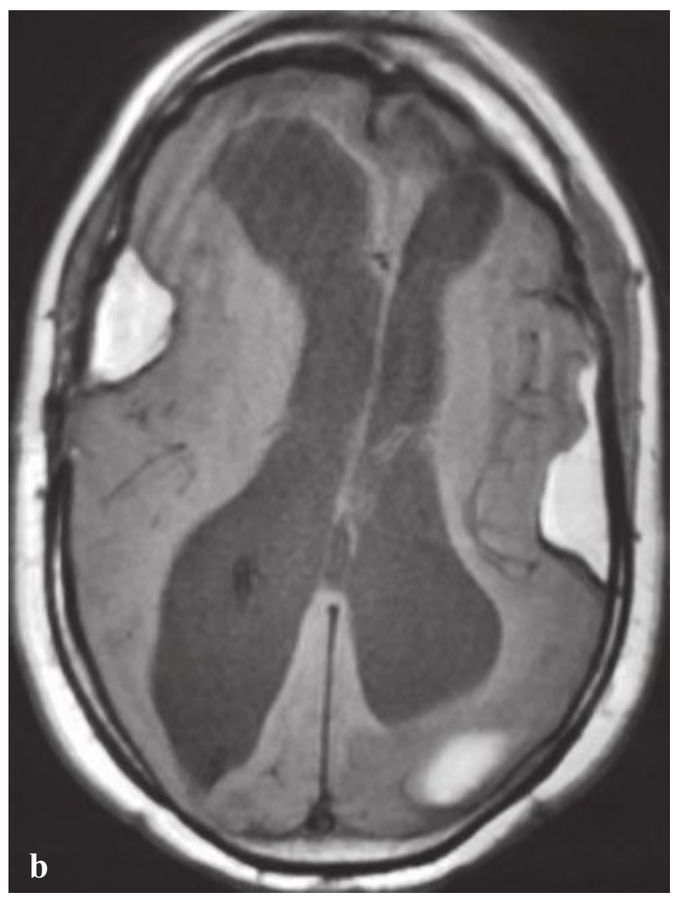

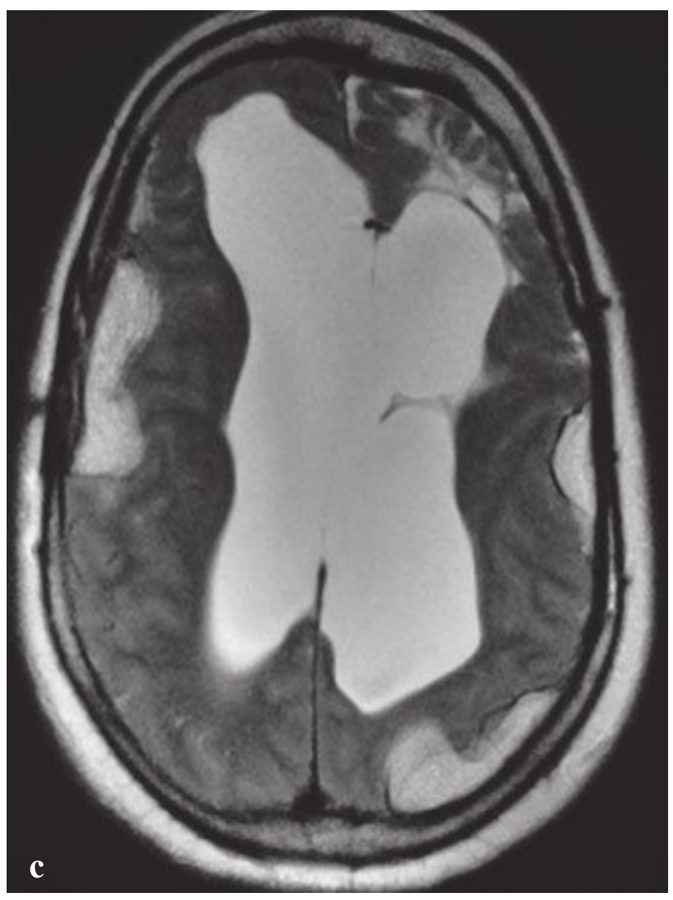

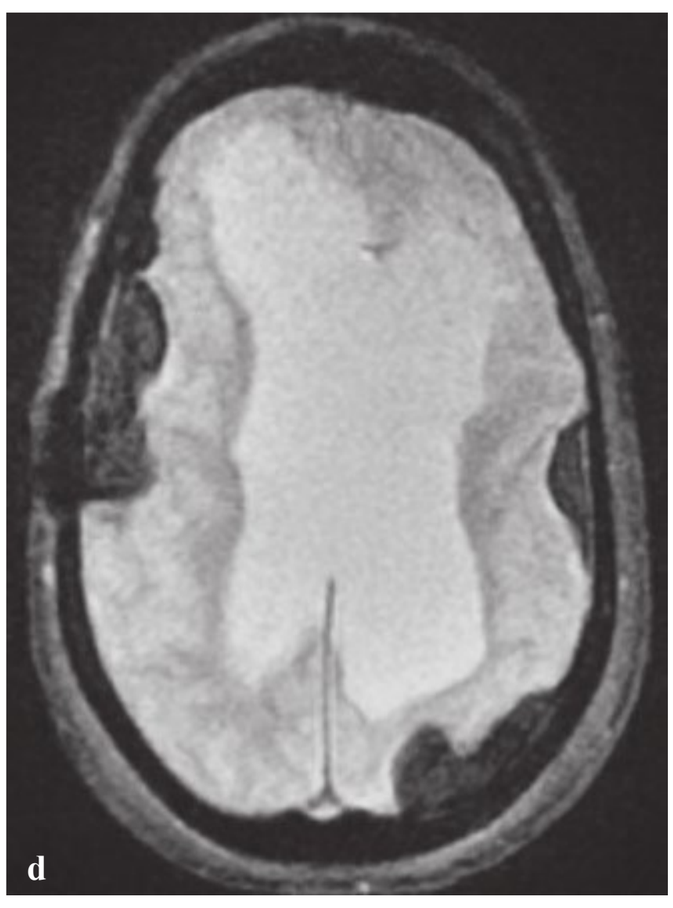

Fig. 3.52 **(a)** Patient with multifocal, ossified extra-axial hematomas on axial CT that have **(b)** high signal on axial T1-weighted imaging and **(c)** axial T2-weighted imaging, and **(d)** low signal on axial GRE.

Table 3.2 (cont.) Multifocal extra-axial lesions

Lesions	Imaging Findings	Comments
Infection/Inflammation		
Subdural/epidural abscess or empyema	MRI: Epidural or subdural collections with low signal on T1-weighted imaging, high signal on T2-weighted imaging, and thin or irregular peripheral zones of gadolinium contrast enhancement. CT: Epidural or subdural collections with low attenuation, thin or irregular peripheral zones of contrast enhancement.	Often results as a complication of sinusitis (usually frontal), meningitis, otitis media, ventricular shunts, or surgery. Can be associated with venous sinus thrombosis and venous cerebral or cerebellar infarctions, cerebritis, or brain abscess. Mortality is 30%
Eosinophilic granuloma, Langerhans' cell histiocytosis	CT: Single or multiple circumscribed soft-tissue lesions in the marrow of the skull associated with focal bony destruction/erosion with extension extra-, intra-cranially or both. Lesions usually have low-intermediate attenuation, + contrast enhancement, ± enhancement of the adjacent dura. MRI: Single or multiple circumscribed soft-tissue lesions in the marrow of the skull associated with focal bony destruction/erosion with extension extra-, intra- cranially or both. Lesions usually have low-intermediate signal on T1WI, mixed intermediate-slightly high signal on T2WI, + gadolinium contrast enhancement, +/- enhancement of the adjacent dura.	Benign tumorlike lesions consisting of Langerhans' cells (histiocytes), and variable amounts of lymphocytes, polymorphonuclear cells, and eosinophils. Account for 1%of primary bone lesions, and 8%of tumorlike lesions. Occur in patients with median age = 10 years (average age = 13.5 years) and peak incidence is between 5 and 10 years. Eighty to 85%occur in patients less than 30 years old. Single lesion: Commonly seen in males > females, < 20 years old, with proliferation of histiocytes in medullary cavity and localized destruction of bone with extension in adjacent soft tissues. Multiple lesions: Associated with Letterer-Siwe disease (lymphadenopathy and hepatosplenomegaly) in children < 2 years old and Hand-Schüller-Christian disease (lymphadenopathy, exophthalmos, and diabetes insipidus) in children 5–10 years old.
Neurosarcoid (**Fig. 3.53**)	MRI: Poorly marginated intra-axial zone or zones with low-intermediate signal on T1-weighted imaging and slightly-high to high signal on T2-weighted imaging and FLAIR, usually showing gadolinium contrast enhancement, + localized mass effect and peripheral edema. Often associated with gadolinium contrast enhancement in the leptomeninges and/or dura. CT: Poorly marginated intra-axial zone with low-intermediate attenuation, usually showing contrast enhancement, + localized mass effect and peripheral edema. Often associated with contrast enhancement in the leptomeninges.	Sarcoidosis is a multisystem noncaseating granulomatous disease of uncertain cause that can involve the CNS in 5 to 15%of cases. Associated with severe neurologic deficits, such as encephalopathy, cranial neuropathies, and myelopathy, if untreated. Diagnosis of neurosarcoid may be difficult when the neurologic complications precede other systemic manifestations in the lungs, lymph nodes, skin, bone, and/or eyes.

Fig. 3.53 A 53-year-old woman with neurosarcoid, seen as gadolinium-enhancing dural lesions (arrows) at the tentorium on coronal fat-suppressed T1-weighted imaging.

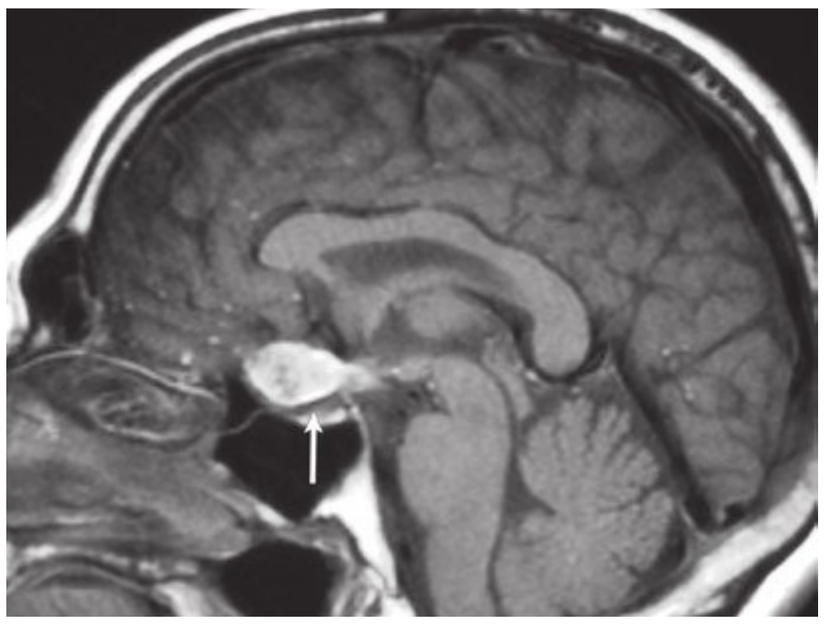

Fig. 3.54 A 53-year-old woman with a ruptured suprasellar dermoid. Sagittal T1-weighted imaging shows an extra-axial lesion (arrow) in the suprasellar cistern that has high signal. Multiple small foci with high signal seen in the subarachnoid space represent ruptured dermoid contents.

Lesions	Imaging Findings	Comments
Vascular Lesions		
Arterial aneurysms (saccular aneurysms)	MRI: Focal well-circumscribed zone of signal void on T1- and T2-weighted imaging, with variable mixed signal if thrombosed. CT: Focal well-circumscribed zone of intermediate-high attenuation, + contrast enhancement in nonthrombosed portion of aneurysm, easily visualized on CTA.	Focal dilatation of artery secondary to acquired/degenerative etiology, polycystic disease, connective tissue disease, atherosclerosis, trauma, infection (mycotic), oncotic involvement, arteriovenous malformation, vasculitis, and drugs. Focal aneurysms are also referred to as saccular aneurysms, which typically occur at arterial bifurcations, and are multiple in 20% of cases. Saccular aneurysms > 2.5 cm in diameter are referred to as giant aneurysms.
Tumorlike Lesions		
Ruptured dermoid cyst (**Fig. 3.54**)	MRI: Well-circumscribed spheroid or multilobulated extra-axial lesions, usually with high signal on T1-weighted images, and variable low, intermediate, and/or high signal on T2-weighted imaging, and no gadolinium contrast enhancement, ± fluid/fluid or fluid/debris levels. CT: Well-circumscribed spheroid or multilobulated extra-axial lesions, usually with low attenuation, ± fat/fluid or fluid/debris levels.	Nonneoplastic congenital or acquired ectodermal-inclusion cystic lesions filled with lipid material, cholesterol, desquamated cells, and keratinaceous debris, usually with mild mass effect on adjacent brain. Occur in adults, males slightly > females, ± related clinical symptoms. Can cause chemical meningitis if dermoid cyst ruptures into the subarachnoid space. Commonly located at or near midline, supra- > infratentorial.
Dural calcifications and ossifications (**Fig. 3.55**)	MRI: Zones of calcification usually have low signal on T1-weighted imaging, gradient recalled echo (GRE), and T2-weighted imaging. Zones of ossification can have a low signal border on T1- and T2-weighted imaging, and a central zone of fat marrow signal. CT: Calcification as well as zones of ossification can be seen in one or more sites of the intracranial dura.	Calcification and ossification can occur at single or multiple sites in the intracranial dura from metaplasia. Typically they are incidental findings.

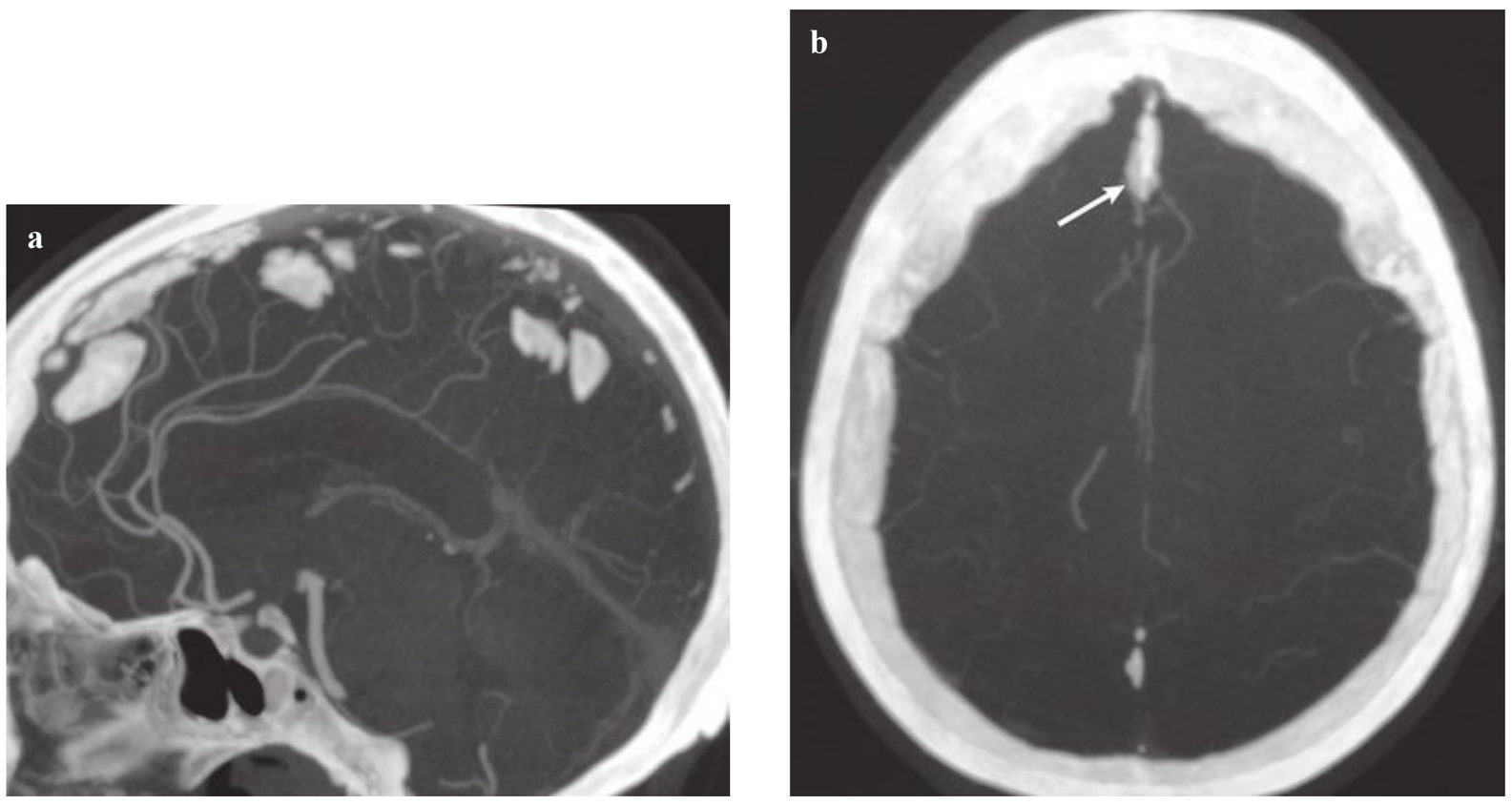

Fig. 3.55 **(a)** Sagittal and **(b)** axial CT show multiple dural ossifications involving the falx cerebri (arrow).

References

Craniopharyngioma

1. Rushing EJ, Giangaspero F, Paulus W, Burger PC. Craniopharyngioma. In: Louis DN, Ohgaki H, Wiestler OD, Cavenee WK, eds. World Health Organization Classification of Tumours of the Central Nervous System. 4th ed. Geneva: IARC Press; 2007:238–240

Dermoid Cyst

2. Indulkar S, Hsich GE. Spontaneous rupture of intracranial dermoid cyst in a child. Neurology 2011;77(23):2070
3. Orakcioglu B, Halatsch ME, Fortunati M, Unterberg A, Yonekawa Y. Intracranial dermoid cysts: variations of radiological and clinical features. Acta Neurochir (Wien) 2008;150(12):1227–1234, discussion 1234
4. Schneider UC, Koch A, Stenzel W, Thomale UW. Intracranial, supratentorial dermoid cysts in paediatric patients—two cases and a review of the literature. Childs Nerv Syst 2012;28(2):185–190
5. Wang YM, Chang TP, Lo CP, Tu MC. Spontaneous rupture of intracranial dermoid cyst with chemical meningitis. J Emerg Med 2013;44(2):e275–e276

Dural Calcification/Ossification

6. Al-Motabagani M, Haroun H, Meguid EA. Calcification and ossification of the convexity of the falx cerebri and related subdural space in human cadavers. Neurosciences (Riyadh) 2004;9(4):261–264
7. Xu Z, Su C, Xiao Y. A massive calcification and ossification of the transverse sinus and the neighbouring dura mimicking meningioma. BMC Neurol 2013;13:143

Ecchordosis Physaliphora

8. Krisht KM, Palmer CA, Osborn AG, Couldwell WT. Giant ecchordosis physaliphora in an adolescent girl: case report. J Neurosurg Pediatr 2013;12(4):328–333
9. Mehnert F, Beschorner R, Küker W, Hahn U, Nägele T. Retroclival ecchordosis physaliphora: MR imaging and review of the literature. AJNR Am J Neuroradiol 2004;25(10):1851–1855
10. Ng SH, Ko SF, Wan YL, Tang LM, Ho YS. Cervical ecchordosis physaliphora: CT and MR features. Br J Radiol 1998;71(843):329–331
11. Srinivasan A, Goyal M, Kingstone M. Case 133: Ecchordosis physaliphora. Radiology 2008;247(2):585–588

Epidermoid Cyst

12. Chen S, Ikawa F, Kurisu K, Arita K, Takaba J, Kanou Y. Quantitative MR evaluation of intracranial epidermoid tumors by fast fluid-attenuated inversion recovery imaging and echo-planar diffusion-weighted imaging. AJNR Am J Neuroradiol 2001;22(6):1089–1096
13. Hakyemez B, Aksoy U, Yildiz H, Ergin N. Intracranial epidermoid cysts: diffusion-weighted, FLAIR and conventional MR findings. Eur J Radiol 2005;54(2):214–220
14. Nagasawa D, Yew A, Safaee M, et al. Clinical characteristics and diagnostic imaging of epidermoid tumors. J Clin Neurosci 2011;18(9):1158–1162
15. Ren X, Lin S, Wang Z, et al. Clinical, radiological, and pathological features of 24 atypical intracranial epidermoid cysts. J Neurosurg 2012;116(3):611–621

Hemangiopericytoma

16. Giannini C, Rushing EJ, Hainfeller JA. Hemangiopericytoma. In: Louis DN, Ohgaki H, Wiestler OD, Cavenee WK, eds. World Health Organization Classification of Tumours of the Central Nervous System. 4th ed. Geneva: IARC Press; 2007:178–180
17. Zhou JL, Liu JL, Zhang J, Zhang M. Thirty-nine cases of intracranial hemangiopericytoma and anaplastic hemangiopericytoma: a retrospective review of MRI features and pathological findings. Eur J Radiol 2012;81(11):3504–3510
18. Righi V, Tugnoli V, Mucci A, Bacci A, Bonora S, Schenetti L. MRS study of meningeal hemangiopericytoma and edema: a comparison with meningothelial meningioma. Oncol Rep 2012;28(4):1461–1467
19. Rutkowski MJ, Jian BJ, Bloch O, et al. Intracranial hemangiopericytoma: clinical experience and treatment considerations in a modern series of 40 adult patients. Cancer 2012;118(6):1628–1636

Hemorrhage

20. Dainer HM, Smirniotopoulos JG. Neuroimaging of hemorrhage and vascular malformations. Semin Neurol 2008;28(4):533–547
21. Kubal WS. Updated imaging of traumatic brain injury. Radiol Clin North Am 2012;50(1):15–41
22. Parizel PM, Makkat S, Van Miert E, Van Goethem JW, van den Hauwe L, De Schepper AM. Intracranial hemorrhage: principles of CT and MRI interpretation. Eur Radiol 2001;11(9):1770–1783

Meningioma

23. Amirjamshidi A, Mehrazin M, Abbassioun K. Meningiomas of the central nervous system occurring below the age of 17: report of 24 cases not associated with neurofibromatosis and review of literature. Childs Nerv Syst 2000;16(7):406–416
24. Buetow MP, Buetow PC, Smirniotopoulos JG. Typical, atypical, and misleading features in meningioma. Radiographics 1991;11(6):1087–1106
25. Chen TY, Lai PH, Ho JT, et al. Magnetic resonance imaging and diffusion-weighted images of cystic meningioma: correlating with histopathology. Clin Imaging 2004;28(1):10–19
26. Chernov MF, Kasuya H, Nakaya K, et al. ^{1}H-MRS of intracranial meningiomas: what it can add to known clinical and MRI predictors of the histopathological and biological characteristics of the tumor? Clin Neurol Neurosurg 2011;113(3):202–212
27. Demir MK, Iplikcioglu AC, Dincer A, Arslan M, Sav A. Single voxel proton MR spectroscopy findings of typical and atypical intracranial meningiomas. Eur J Radiol 2006;60(1):48–55
28. Harting I, Hartmann M, Bonsanto MM, Sommer C, Sartor K. Characterization of necrotic meningioma using diffusion MRI, perfusion MRI, and MR spectroscopy: case report and review of the literature. Neuroradiology 2004;46(3):189–193
29. Majós C, Alonso J, Aguilera C, et al. Utility of proton MR spectroscopy in the diagnosis of radiologically atypical intracranial meningiomas. Neuroradiology 2003;45(3):129–136
30. Nakano T, Asano K, Miura H, Itoh S, Suzuki S. Meningiomas with brain edema: radiological characteristics on MRI and review of the literature. Clin Imaging 2002;26(4):243–249
31. Perry A, Louis DN, Scheithauer BW, Budka H, von Deimling A. Meningiomas. In: Louis DN, Ohgaki H, Wiestler OD, Cavenee WK, eds. World Health Organization Classification of Tumours of the Central Nervous System. 4th ed. Geneva: IARC Press; 2007:164–184
32. Santelli L, Ramondo G, Della Puppa A, et al. Diffusion-weighted imaging does not predict histological grading in meningiomas. Acta Neurochir (Wien) 2010;152(8):1315–1319, discussion 1319
33. Toh CH, Castillo M, Wong AMC, et al. Differentiation between classic and atypical meningiomas with use of diffusion tensor imaging. AJNR Am J Neuroradiol 2008;29(9):1630–1635
34. Ilica AT, Mossa-Basha M, Zan E, et al. Cranial intraosseous meningioma: spectrum of neuroimaging findings with respect to histopathological grades in 65 patients. Clin Imaging 2014;38(5):599–604
35. Watts J, Box G, Galvin A, Brotchie P, Trost N, Sutherland T. Magnetic resonance imaging of meningiomas: a pictorial review. Insights Imaging 2014;5(1):113–122
36. Yu XR, Jun-Zhang, Zhang BY, et al. Magnetic resonance imaging findings of intracranial papillary meningioma: a study on eight cases. Clin Imaging 2014;38(5):611–615
37. Yue Q, Isobe T, Shibata Y, et al. New observations concerning the interpretation of magnetic resonance spectroscopy of meningioma. Eur Radiol 2008;18(12):2901–2911

Meningioangiomatosis

38. Kashlan ON, Laborde DV, Davison L, et al. Meningioangiomatosis: a case report and literature review emphasizing diverse appearance on different imaging modalities. Case Rep Neurol Med 2011;2011:361203
39. Rokes C, Ketonen LM, Fuller GN, Weinberg J, Slopis JM, Wolff JE. Imaging and spectroscopic findings in meningioangiomatosis. Pediatr Blood Cancer 2009;53(4):672–674
40. Yao Z, Wang Y, Zee C, Feng X, Sun H. Computed tomography and magnetic resonance appearance of sporadic meningioangiomatosis correlated with pathological findings. J Comput Assist Tomogr 2009;33(5):799–804

Mesenchymal Non-Meningothelial Tumors of the Dura

41. Clarençon F, Bonneville F, Rousseau A, et al. Intracranial solitary fibrous tumor: imaging findings. Eur J Radiol 2011;80(2):387–394
42. Johnson MD, Powell SZ, Boyer PJ, Weil RJ, Moots PL. Dural lesions mimicking meningiomas. Hum Pathol 2002;33(12):1211–1226
43. Paulus W, Scheithauer BW, Perry A. Mesenchymal, non-meningothelial tumours. In: Louis DN, Ohgaki H, Wiestler OD, Cavenee WK, eds. World Health Organization Classification of Tumours of the Central Nervous System. 4th ed. Geneva: IARC Press; 2007:173–177

Metastatic Disease

44. Lee EK, Lee EJ, Kim MS, et al. Intracranial metastases: spectrum of MR imaging findings. Acta Radiol 2012;53(10):1173–1185
45. Mahendru G, Chong V. Meninges in cancer imaging. Cancer Imaging 2009;9 Spec No A:S14–S21
46. Smirniotopoulos JG, Murphy FM, Rushing EJ, Rees JH, Schroeder JW. Patterns of contrast enhancement in the brain and meninges. Radiographics 2007;27(2):525–551

Neurofibromatosis Type 2

47. Hoa M, Slattery WH III. Neurofibromatosis 2. Otolaryngol Clin North Am 2012;45(2):315–332, viii
48. Nandigam K, Mechtler LL, Smirniotopoulos JG. Neuroimaging of neurocutaneous diseases. Neurol Clin 2014;32(1):159–192

Ossified Subdural/Epidural Hematoma

49. Kaplan M, Akgün B, Seçer HI. Ossified chronic subdural hematoma with armored brain. Turk Neurosurg 2008;18(4):420–424
50. Moon HG, Shin HS, Kim TH, Hwang YS, Park SK. Ossified chronic subdural hematoma. Yonsei Med J 2003;44(5):915–918
51. Per H, Gümüş H, Tucer B, Akgün H, Kurtsoy A, Kumandaş S. Calcified chronic subdural hematoma mimicking calvarial mass: a case report. Brain Dev 2006;28(9):607–609

Neurenteric Cyst

52. Prasad GL, Borkar SA, Subbarao KC, Sharma MC, Mahapatra AK. Neurenteric cyst of the ventral cervicomedullary region. J Pediatr Neurosci 2012;7(3):188–190

Pituitary Adenoma

53. Ouyang T, Rothfus WE, Ng JM, Challinor SM. Imaging of the pituitary. Radiol Clin North Am 2011;49(3):549–571, vii
54. Rennert J, Doerfler A. Imaging of sellar and parasellar lesions. Clin Neurol Neurosurg 2007;109(2):111–124
55. Rumboldt Z. Pituitary adenomas. Top Magn Reson Imaging 2005; 16(4):277–288

Schwannomatosis

56. Ahlawat S, Chhabra A, Blakely J. Magnetic resonance neurography of peripheral nerve tumors and tumorlike conditions. Neuroimaging Clin N Am 2014;24(1):171–192
57. Koontz NA, Wiens AL, Agarwal A, Hingtgen CM, Emerson RE, Mosier KM. Schwannomatosis: the overlooked neurofibromatosis? AJR Am J Roentgenol 2013;200(6):W646-53

Chapter 4

Meninges

Introduction 562

4.1 Abnormalities involving the dura 563

4.2 Multifocal and/or diffuse leptomeningeal abnormalities 583

References 596

4 Meninges

Table 4.1 Abnormalities involving the dura

Table 4.2 Multifocal and/or diffuse leptomeningeal abnormalities

Introduction

Lesions Involving the Meninges (Dura/Leptomeninges)

The cranial and spinal meninges are three concentric contiguous membranes (dura mater, arachnoid, and pia mater) that surround the central nervous system **(Fig. 4.1)**. The outer intracranial meningeal layer is the dura mater (pachymeninx). The outermost layer of the dura mater is richly vascularized, with elongated fibroblasts and large intercellular spaces that contain arteries and veins, and represents the periosteum of the inner table of the calvaria. The arteries and veins in this layer form impressions on the inner table of the skull. The outer layer of the dura mater terminates at the foramen magnum. An inner layer of the dura arises from the meninx and consists of epithelial cells. This inner layer of the dura mater is contiguous with the spinal dura mater. The layers of the cranial dura separate at sites where there are large venous sinuses. Reflections of dura form the falx cerebri and tentorium cerebelli, which support the normal positions of the cerebrum and cerebellum.

The arachnoid and pia mater comprise the leptomeninges. The arachnoid membrane is immediately adjacent to the inner surface of the dura. A potential space exists between the dura and arachnoid, referred to as the subdural space. The arachnoid is thinner over the convexities than at the base of the skull. Deep to the arachnoid membrane is the subarachnoid space, which contains CSF. The inner boundary of the subarachnoid space is the cranial pia mater. The cranial pia mater is a thin layer adjacent to the surface of the brain and extending along the sulci. The cranial pia mater contains elastic fibers internally and collagenous fibers peripherally. Thin connective tissue strands and cellular septae extend across the arachnoid membrane to the pia, except at the base of the brain, where the arachnoid membrane and pia are widely separated. These regions are referred to as the basal subarachnoid cisterns. The spinal pia mater is thicker and more adherent to the nervous tissue than the cranial pia.

The meninges (dura, arachnoid, and pia) form the extra-axial compartments of the CNS. The epidural space exists when the dura is detached from the inner table, usually by trauma/fracture and injury to a meningeal artery/epidural hematoma, or occasionally by neoplasms involving the skull. The subdural space forms when a pathologic process is present, such as subdural hematoma from trauma/skull fracture and injury of large veins, inflammatory/infectious disease, or neoplasm. Unlike the epidural and subdural compartments, the subarachnoid space exists without the presence of a pathologic process. The presence of extravascular blood in the subarachnoid space usually is due to a ruptured intracranial aneurysm, vascular malformation, or trauma.

Blood vessels within dura mater do not have a blood–brain barrier. After intravenous gadolinium contrast administration, normal dura can show thin, linear, and discontinuous contrast enhancement. Thick or irregular gadolinium contrast enhancement of the dura can result from various causes, including neoplasms (primary and metastatic), inflammation/infection, or benign dural fibrosis secondary to intracranial surgery, transient hypotension (secondary to lumbar puncture or surgery), or evolving extra-axial hemorrhage. The dural enhancement follows the inner contour of the calvaria without extension into the sulci.

Gadolinium contrast enhancement in the intracranial subarachnoid space (leptomeninges) is nearly always associated with significant pathology (inflammation and/or infection or neoplasm). Inflammation and/or infection of the leptomeninges can result from pyogenic, fungal, or parasitic diseases, as well as tuberculosis. Complications of infectious meningitis include cerebritis, intra-axial abscess, ventriculitis, hydrocephalus, and venous sinus thrombosis/cerebral venous infarction. Neurosarcoid results in granulomatous disease in the leptomeninges, producing similar patterns of subarachnoid enhancement. Disseminated or metastatic disease involving the leptomeninges can result from CNS tumors or primary tumors outside of the CNS. Lymphoma and leukemia can also result in a similar pattern of leptomeningeal enhancement. Rarely, transient leptomeningeal enhancement can occur from chemical irritation caused by subarachnoid blood.

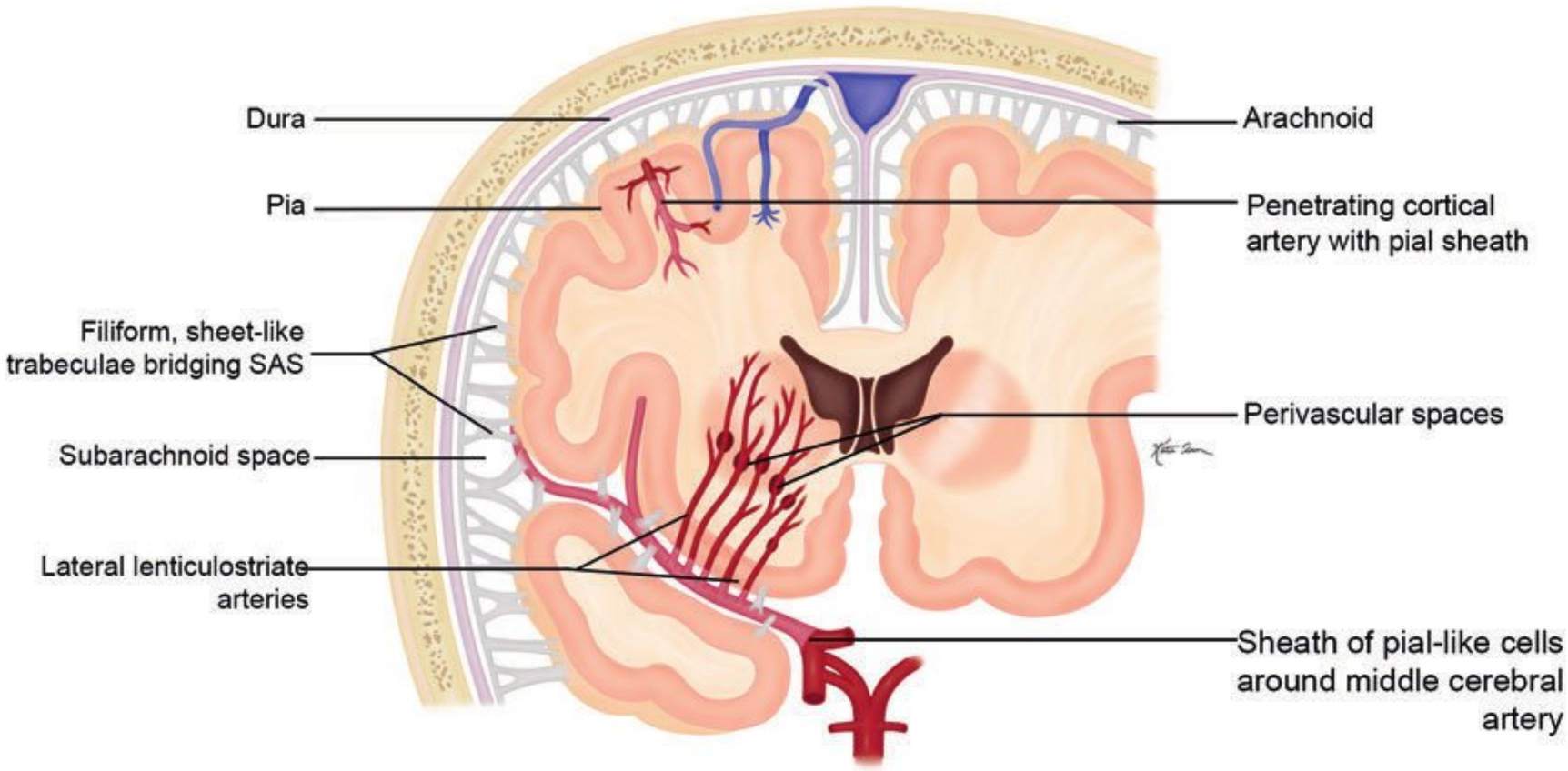

Fig. 4.1 Coronal view diagram of the layers of the meninges.

Table 4.1 Abnormalities involving the dura

- Congenital/Developmental
  - Cephaloceles (meningoceles or meningoencephaloceles)
  - Neurofibromatosis type 1—meningeal dyplasia/ectasia
- Neoplastic
  - Meningioma
  - Hemangiopericytoma
  - Solitary fibrous tumor
  - Epstein-Barr virus–associated smooth muscle tumors
  - Malignant meningioma
  - Anaplastic hemangiopericytoma
  - Metastatic tumor
  - Lymphoma
  - Leukemia
  - Melanocytic neoplasms
  - Malignant mesenchymal non-meningothelial tumors
  - Skull-base tumors
  - Perineural tumor spread from the sinuses and nasopharynx
- Vascular Lesions
  - Dural arteriovenous malformation (AVM)
- Traumatic/Postsurgical Abnormalities
  - Epidural hematoma
- Hemorrhagic Lesion
  - Subdural hematoma
  - Ossified hematoma
  - Postsurgical dural fibrosis
  - Intracranial hypotension
  - Postsurgical meningocele
- Inflammatory
  - Pachymeningitis from infection
  - Epidural/subdural abscess/empyema
  - Langerhans' cell histiocytosis
  - Erdheim-Chester disease
  - Rosai-Dorfman disease
  - Sarcoidosis
  - Granulomatosis with polyangiitis
  - Inflammatory pseudotumor
  - Idiopathic hypertrophic pachymeningitis

Table 4.1 Abnormalities involving the dura

Lesions	Imaging Findings	Comments
Congenital/Developmental		
Cephaloceles (meningoceles or meningoencephaloceles) (**Fig. 4.2**)	Defect in skull through which there is either herniation of meninges and CSF (meningocele) or of meninges, CSF/ventricles, and brain tissue (meningoencephalocele).	Congenital malformation involving lack of separation of neuroectoderm from surface ectoderm, with resultant localized failure of bone formation. Occipital location most common in patients in Western hemisphere, frontoethmoidal location most common site in Southeast Asians. Other sites include parietal and sphenoid bones. Cephaloceles can also result from trauma or surgery.
Neurofibromatosis type 1—meningeal dyplasia/ectasia (**Fig. 4.3**)	Neurofibromatosis type 1 (NF1) is associated with focal ectasia of intracranial dura, widening of internal auditory canals from dural ectasia, and dural and temporal lobe protrusion into orbit through bony defect (bony hypoplasia of greater sphenoid wing).	Autosomal dominant disorder (1/2,500 births) representing the most common type of neurocutaneous syndrome, associated with neoplasms of central and peripheral nervous system and skin. Also associated with meningeal and skull dysplasias.
Neoplastic		
Meningioma (**Fig. 4.4** and **Fig. 4.5**)	Extra-axial dura-based lesions that are well circumscribed. Locations: supra- > infratentorial, parasagittal > convexity > sphenoid ridge > parasellar > posterior fossa > optic nerve sheath > intraventricular. MRI: Dura-based tumors with intermediate signal on T1-weighted imaging, intermediate-slightly high signal on T2-weighted imaging, usually prominent gadolinium contrast enhancement often with a dural tail secondary to vasocongestion and interstitial dural edema, ± calcifications. Intratumoral hemorrhage and cystic or necrotic foci can occur in 15% of cases. Can result in compression of adjacent brain parenchyma, encasement of arteries, and compression of dural venous sinuses, rarely invasive/malignant types. Diffusion-weighted imaging/diffusion tensor imaging: ADC values vary among the different subtypes of meningioma. Some tumors can show restricted diffusion, although these findings can be seen with both benign and atypical tumors. Magnetic resonance spectroscopy: Can show elevated alanine (1.5 ppm), lactate, choline, and glutamine/glutamate levels, and reduced N-acetylaspartate (NAA). CT: Tumors have intermediate attenuation with or without calcifications, with or without hyperostosis, and usually show prominent contrast enhancement.	The most common extra-axial tumor, meningioma accounts for up to 26% of primary intracranial tumors. Annual incidence is 6 per 100,000, and it typically occurs in adults (> 40 years old) and in women > in men. Composed of neoplastic meningothelial (arachnoidal or arachnoid cap) cells. Meningiomas are usually solitary and sporadic, but can also occur as multiple lesions in patients with neurofibromatosis type 2. Eighty percent of meningiomas are benign (WHO grade I), although 15% have atypical features (WHO grade II) and ~ 5% have anaplastic histologic features (WHO grade III). Can occur secondary to radiation treatment, with latencies ranging from 19 to 35 years. Classified into different subtypes, such as meningothelial, fibrous (fibroblastic), transitional (mixed), psammomatous, angiomatous, atypical, and anaplastic. Meningothelial, fibrous, and transitional meningiomas are the most common intracranial types. Usually show immunoreactivity to epithelial membrane antigen (EMA) and vimentin. Secretory meningiomas are typically immunoreactive to CEA. Associated with cytogenetic findings of deletion of chromosome 22. Mutations in the NF2 tumor suppressor gene on chromosome 22 have been found in 60% of sporadic meningiomas.

(continued on page 566)

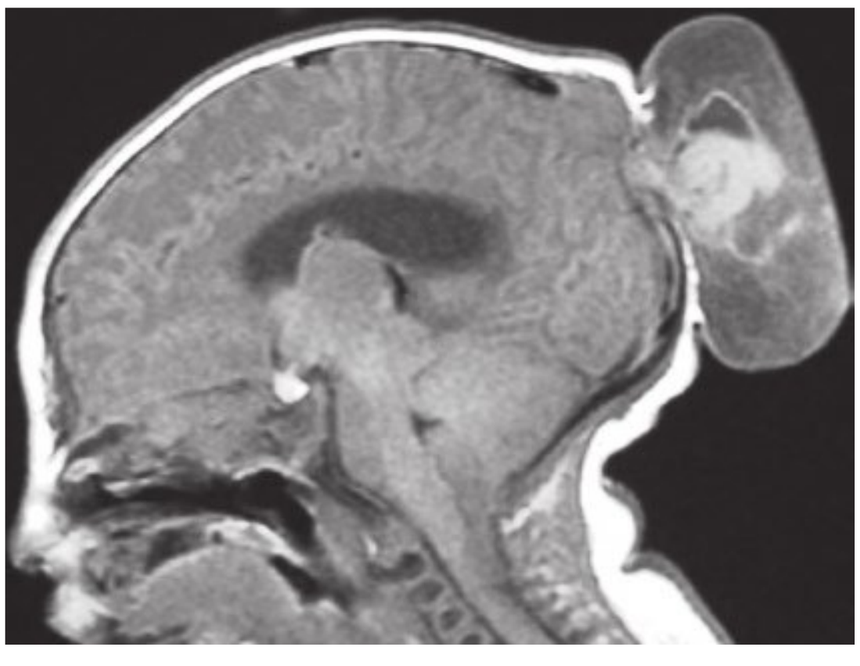

Fig. 4.2 Neonate with a parietal meningoencephalocele. Sagittal T1-weighted imaging shows a localized skull defect through which damaged brain and meninges extend.

Fig. 4.3 A 32-year-old woman with neurofibromatosis type 1 and aplasia of the greater wing of the right sphenoid bone (arrow), with dural protrusion into the right orbit on axial CT.

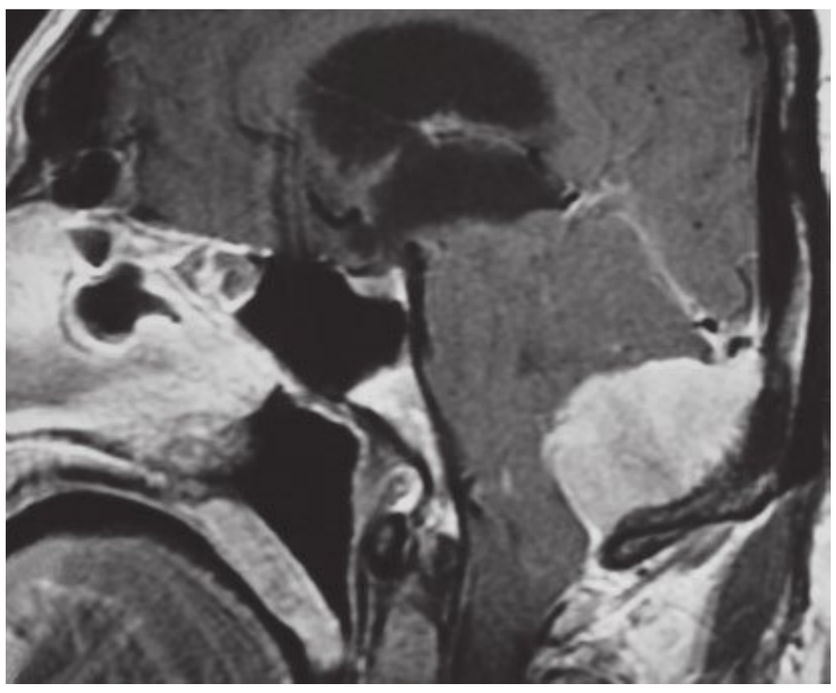

Fig. 4.5 A46-year-old man with a gadolinium-enhancing meningioma at the dorsal inferior posterior cranial fossa that compresses and displaces anteriorly the cerebellum and fourth ventricle and causes downward displacement of the cerebellar tonsils through the foramen magnum.

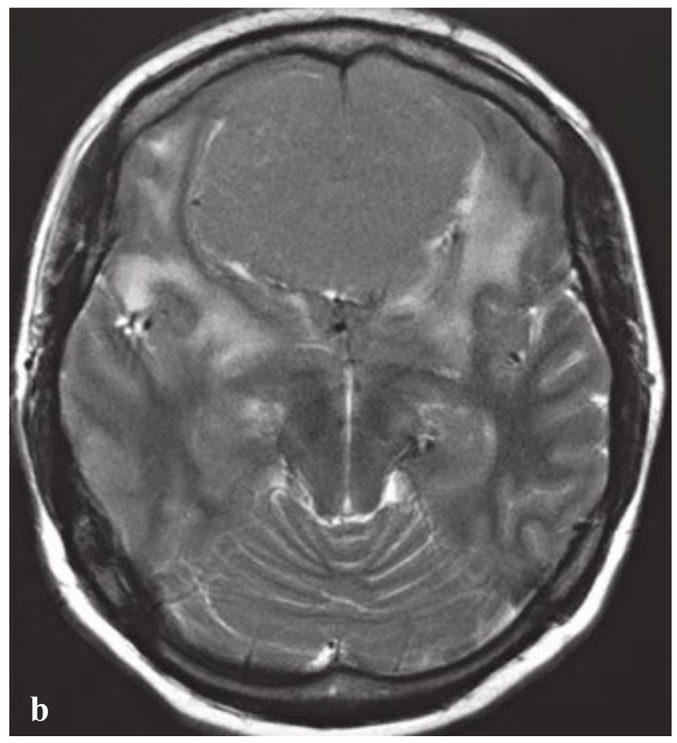

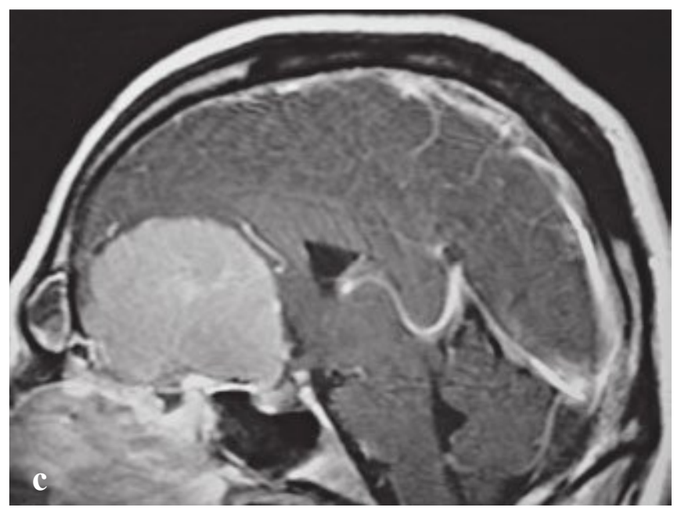

Fig. 4.4 **(a)** A 44-year-old woman with a contrast-enhancing meningioma arising from the dura along the floor of the anterior cranial fossa on axial CT; the tumor compresses and posteriorly displaces both frontal lobes. **(b)** The meningioma has intermediate signal on axial T2-weighted imaging and **(c)** shows gadolinium contrast enhancement on sagittal T1-weighted imaging. Edematous changes are seen in the displaced frontal lobes.

Table 4.1 (cont.) Abnormalities involving the dura

Lesions	Imaging Findings	Comments
Hemangiopericytoma (**Fig. 4.6**)	MRI: Solitary dura-based tumors ranging from 2 to 7 cm in diameter that have low-intermediate signal on T1-weighted imaging, intermediate-slightly high signal on T2-weighted imaging, and usually prominent gadolinium contrast enhancement often with a dural tail, ± calcifications, ± erosion of adjacent bone. Intratumoral hemorrhage and cystic or necrotic foci can occur in 30%of cases. MinADC with hemangiopericytoma is often higher than with most meningiomas (1.1×10^{-3} for hemangiopericytoma versus 0.88×10^{-3} for meningioma). Magnetic resonance spectroscopy: Relative ratios of myo-inositol (3.56 ppm), glucose, and glutathione with respect to glutamate are higher in hemangiopericytomas than in meningiomas. Absent or low alanine peak for hemangiopericytomas compared with meningiomas. CT: Tumors are extra-axial mass lesions, often well circumscribed, and have intermediate attenuation with or without calcifications and usually show prominent contrast enhancement.	Rare (WHO grade II) neoplasms, which account for 0.4%of primary intracranial tumors and are 50 times less frequent than meningiomas. Tumors are composed of closely packed cells with scant cytoplasm and round, ovoid, or elongated nuclei with moderately dense chromatin. Numerous slitlike vascular channels are seen in these tumors that are lined by flattened endothelial cells, ± zones of necrosis. Immunoreactive to vimentin (85%), factor XIIIa (80–100%), and variably to Leu-7 and CD34. Associated with abnormalities involving chromosome 12. Typically occur in young adults (mean age = 43 years) and in males > in females. Sometimes referred to as angioblastic meningioma or meningeal hemangiopericytoma, they arise from vascular cells—pericytes. Recur and metastasize more frequently than meningiomas.
Solitary fibrous tumor	MRI: Tumors often have low to intermediate signal on T1-weighted imaging, FLAIR, and proton density-weighted imaging; low, intermediate, and/or slightly high signal on T2-weighted imaging, and heterogeneous slightly high to high signal on fat-suppressed T2-weighted imaging, ± flow voids. After gadolinium contrast administration, solitary fibrous tumors can show prominent, slightly heterogeneous enhancement. Magnetic resonance spectroscopy: Can show elevated lipid, lactate and myo-inositol levels. CT: Intermediate to slightly high attenuation, ± calcifications, ± erosion of adjacent bone.	Rare, benign, spindle-cell mesenchymal neoplasms that occur in a wide range of anatomic sites, such as the pleura, liver, skin, orbits, paranasal sinuses, intracranial dura, and ventricles. Solitary fibrous tumors typically show a hemangiopericytoma-like branching vascular pattern. Mitotic activity is typically low and rarely exceeds 3 per 10 high-power fields. Patient ages range from 20 to 77 years (median age = 50–60 years).

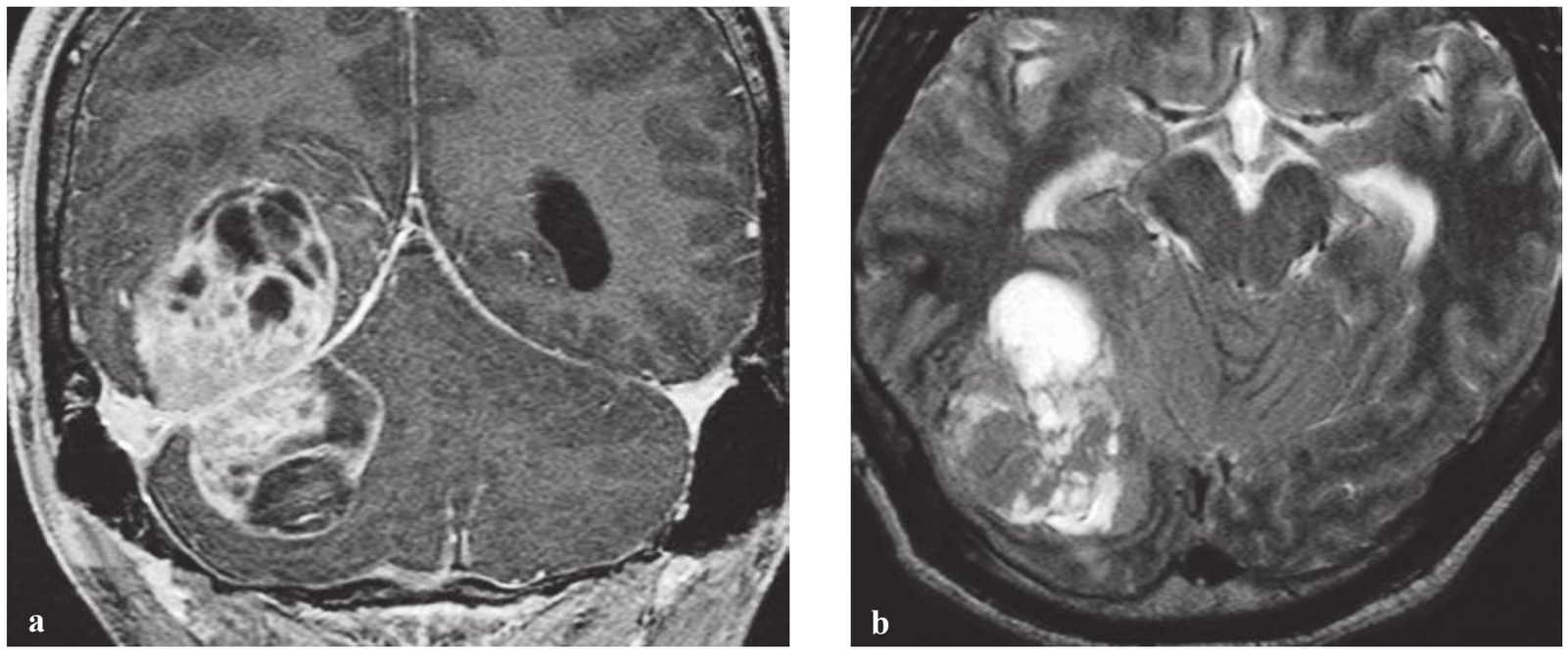

Fig. 4.6 **(a)** A 33-year-old man with a gadolinium-enhancing hemangiopericytoma arising from the tentorium that extends both superiorly and inferiorly on coronal T1-weighted imaging. **(b)** The tumor has mixed intermediate and high signal on axial T2-weighted imaging.

Lesions	Imaging Findings	Comments
Epstein-Barr virus–associated smooth muscle tumors	MRI: Tumors often have low to intermediate signal on T1-weighted imaging and proton density-weighted imaging; low, intermediate, and/or slightly high signal on T2-weighted imaging; and heterogeneous slightly high to high signal on fat-suppressed T2-weighted imaging. After gadolinium contrast administration, SFTs can show prominent slightly heterogeneous enhancement. CT: Tumors have intermediate attenuation, ± calcifications, ± erosion of adjacent bone.	In immunocompromised patients, Epstein-Barr virus (EBV) can cause development of smooth muscle tumors (such as leiomyoma and leiomyosarcoma) from mesenchymal cells in the dura or intracranial blood vessels. Tumors contain neoplastic spindle cells, with leiomyosarcomas having high mitotic activity. Immunoreactivity to myogenin, actin, and desmin.
Malignant meningioma (**Fig. 4.7**)	MRI: Dura-based tumors with intermediate signal on T1-weighted imaging and intermediate-slightly high signal on T2-weighted imaging, usually with prominent gadolinium contrast enhancement, ± calcifications. Malignant meningiomas are often large and may have irregular margins, with brain invasion and peritumoral edema. Diffusion-weighted imaging/diffusion tensor imaging: ADC values vary among the different subtypes of meningioma. Some tumors can show restricted diffusion, although these findings can be seen with both benign, atypical, and malignant tumors. Magnetic resonance spectroscopy (MRS): Can show elevated alanine (1.5 ppm), lactate, choline, and glutamine/glutamate peaks, and reduced N-acetylaspartate (NAA). MRS cannot reliably differentiate benign from malignant meningiomas. CT: Tumors have intermediate attenuation with or without calcifications, with or without hyperostosis, and usually show prominent contrast enhancement.	Eighty percent of meningiomas are benign (WHO grade I), although 15%have atypical features (WHO grade II) and ~ 5%have anaplastic/malignant histologic features (WHO grade III). Atypical and anaplastic/malignant meningiomas are associated with 5-year recurrence rates of 40%and 50–80%, respectively.

(continued on page 568)

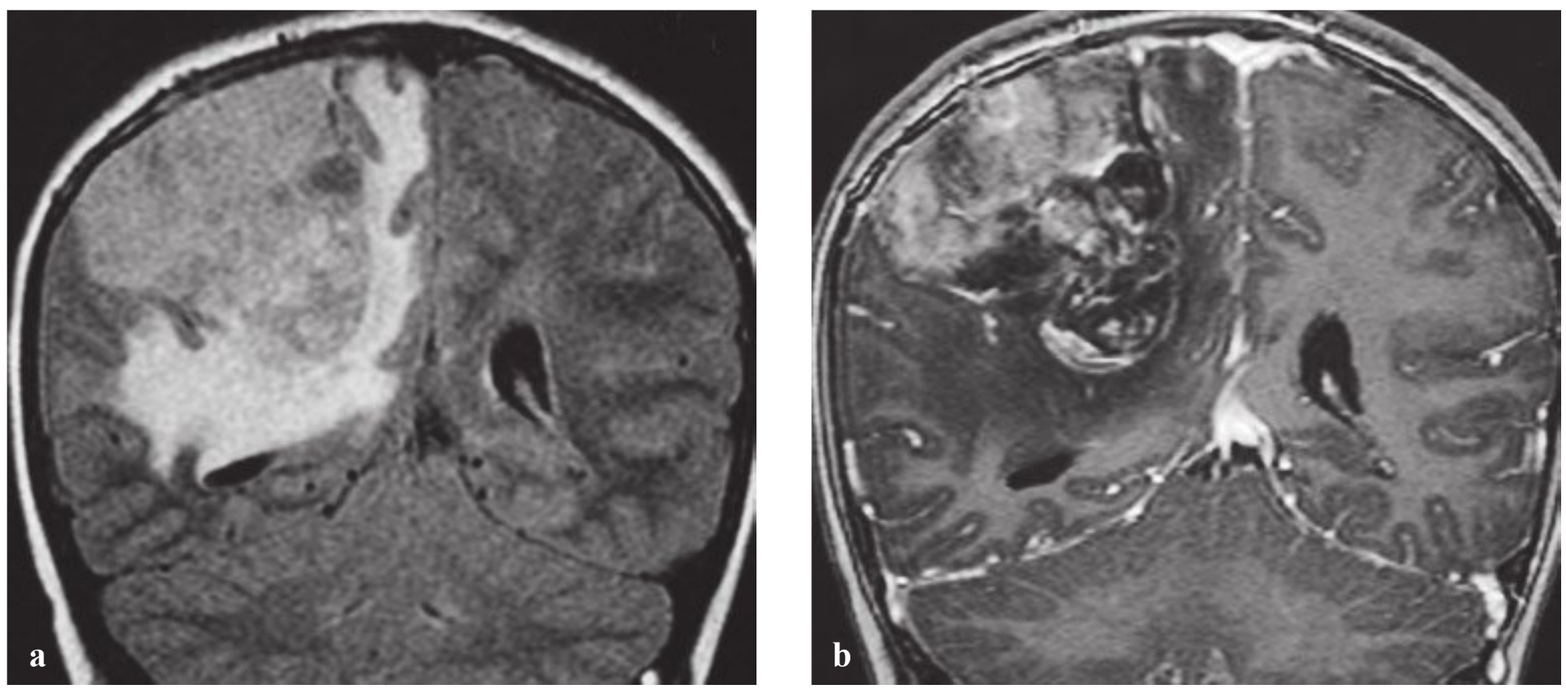

Fig. 4.7 **(a)** An 11-year-old male with a malignant meningioma in the upper right parietal region that has heterogeneous slightly high and high signal on coronal FLAIR with high signal in adjacent brain tissue. **(b)** The tumor shows heterogeneous gadolinium contrast enhancement with ill-defined margins on coronal T1-weighted imaging, representing invasion of adjacent brain tissue.

Table 4.1 (cont.) Abnormalities involving the dura

Lesions	Imaging Findings	Comments
Anaplastic hemangiopericytoma	MRI: Solitary, lobulated, dura-based tumors that have low-intermediate signal on T1-weighted imaging, mixed intermediate, slightly high, and high signal on T2-weighted imaging, and usually prominent heterogeneous gadolinium contrast enhancement. Intratumoral hemorrhage and cystic or necrotic foci are often present, ± dural tail, ± calcifications, ± bone destruction, ± peritumoral edema. CT: Tumors have intermediate attenuation with or without calcifications and usually show prominent contrast enhancement.	Anaplastic hemangiopericytomas (WHO grade III) have high degrees of nuclear atypia, with mitotic activities of greater than five mitoses per ten high-power fields. Ki-67 activity >15% Recurrence and metastases are more frequent than for WHO grade II hemangiopericytomas.
Metastatic tumor (**Fig. 4.8**)	MRI: Circumscribed spheroid lesion in dura, leptomeninges, and/or choroid plexus. Often has low-intermediate signal on T1-weighted imaging and intermediate-high signal on T2-weighted imaging, ± hemorrhage, calcifications, and cysts. Variable gadolinium contrast enhancement. CT: Lesions usually have low-intermediate attenuation; ± hemorrhage, calcifications, and cysts; variable contrast enhancement; ± bone destruction, ± compression of neural tissue or vessels. Leptomeningeal tumor often best seen on postcontrast images.	Represent ~ 33%of intracranial tumors, usually from extracranial primary neoplasm in adults > 40 years old. Primary tumor source: lung > breast > GI > GU > melanoma. Can occur as single or multiple well-circumscribed or poorly defined lesions involving the skull, dura, leptomeninges, and/or choroid plexus. Metastatic tumor may cause variable destructive or infiltrative changes in single or multiple sites of involvement.
Lymphoma (**Fig. 4.9**)	MRI: Single or multiple well-circumscribed or poorly defined lesions involving the skull, dura, and/or leptomeninges, with low-intermediate signal on T1-weighted imaging and intermediate-high signal on T2-weighted imaging, usually + gadolinium contrast enhancement, ± bone destruction. Leptomeningeal tumor is often best seen on postcontrast images. CT: CNS lymphoma can have intermediate attenuation or can be hyperdense related to a high nuclear/cytoplasm ratio. FDG PET/CT can show elevated uptake in PCNSL, and in immunocompromised patients it can be used to distinguish lymphoma from toxoplasmosis brain lesions, which have decreased FDG uptake. Usually + contrast enhancement, ± bone destruction. Dural and/or leptomeningeal tumor is usually best seen on postcontrast images.	Primary CNS lymphoma more common than secondary, usually in adults > 40 years old. Accounts for 5%of primary brain tumors. Incidence currently ranges from 0.8 to 1.5%of primary intracranial tumors. Prior elevated incidence of 6%in patients with AIDS has been reduced with effective antiretroviral therapy. B-cell lymphoma is more common than T-cell lymphoma. MRI features of primary and secondary lymphoma of brain overlap. Intracranial lymphoma can involve the dura and/or leptomeninges in secondary lymphoma > primary lymphoma. Extra-axial lymphoma may cause variable destructive or infiltrative changes in single or multiple sites of involvement.
Leukemia	MRI: Single or multiple well-circumscribed or poorly defined lesions involving the skull, dura, and/or leptomeninges with low-intermediate signal on T1-weighted imaging and intermediate-high signal on T2-weighted imaging, usually + gadolinium contrast enhancement, ± bone destruction. Leptomeningeal tumor often best seen on postcontrast images. CT: Dural and/or leptomeningeal tumor often best seen on postcontrast images.	Leukemias are neoplastic proliferations of hematopoietic cells. Myeloid sarcomas (also referred to as chloromas or granulocytic sarcomas) are focal tumors composed of myeloblasts and neoplastic granulocyte precursor cells and occur in 2%of patients with acute myelogenous leukemia. These lesions can involve the dura, leptomeninges, and brain. Intracranial lesions can be solitary or multiple.

(continued on page 570)

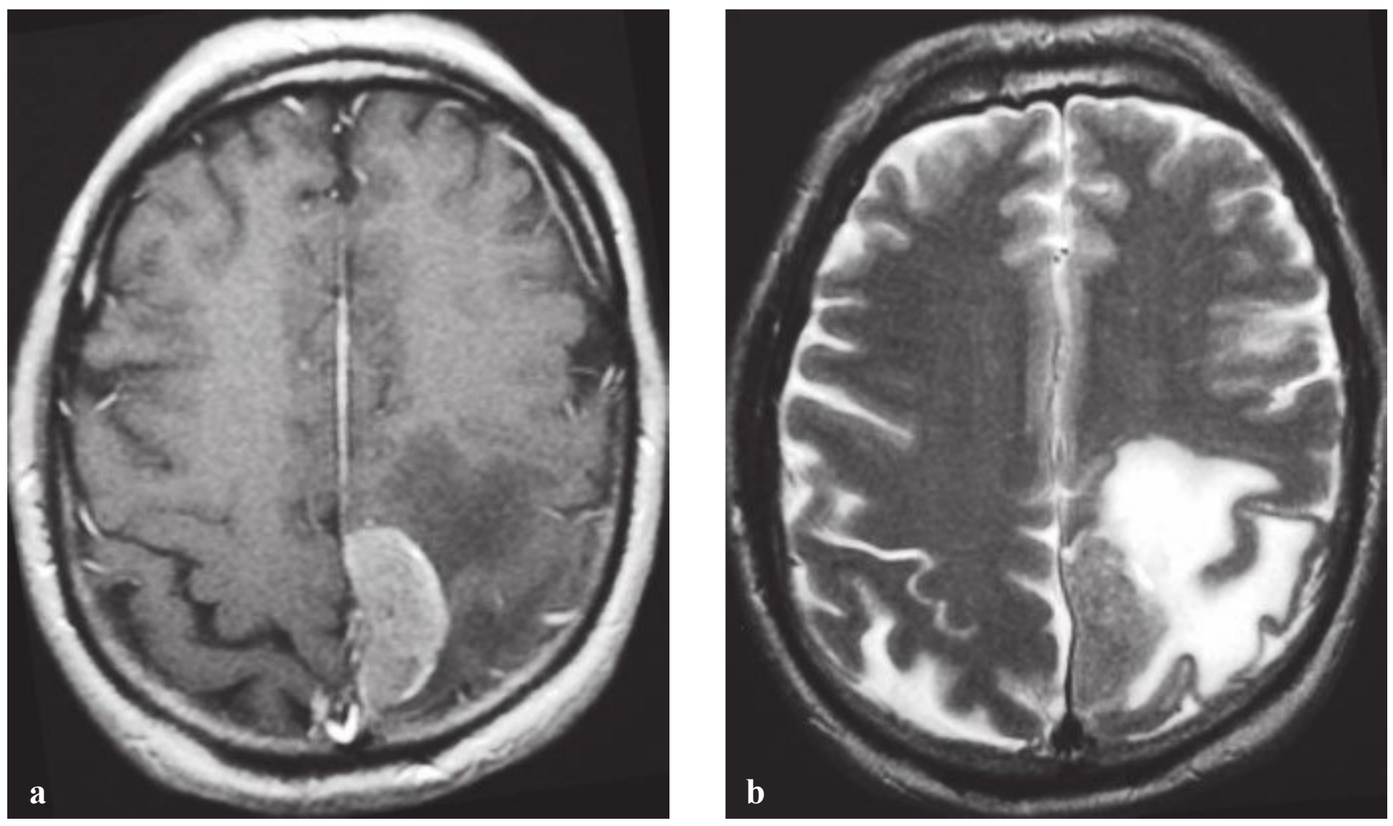

Fig. 4.8 A 56-year-old man with gadolinium-enhancing metastatic lung carcinoma in the posterior left side of the falx on **(a)** axial T1-weighted imaging and with intermediate signal on **(b)** axial T2-weighted imaging, with edema in the displaced adjacent brain tissue.

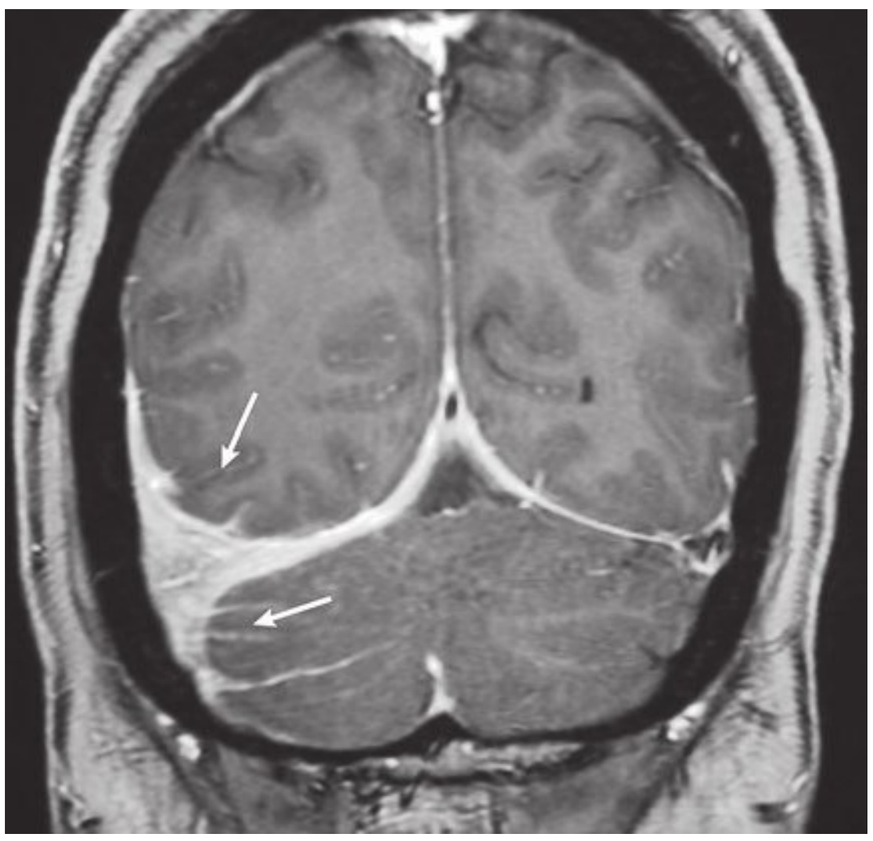

Fig. 4.9 A 51-year-old woman with gadolinium-enhancing non-Hodgkin lymphoma involving the dura of the right tentorium (upper arrow) as well as the adjacent leptomeninges (lower arrow) on coronal T1-weighted imaging.

Table 4.1 (cont.) Abnormalities involving the dura

Lesions	Imaging Findings	Comments
Melanocytic neoplasms	MRI: Lesions have low-intermediate or high signal (secondary to increased melanin) on T1-weighted imaging, intermediate-slightly high and/or low signal on T2-weighted imaging and FLAIR, and gadolinium contrast enhancement. CT: May show subtle hyperdensity secondary to increased melanin.	Melanocytoma is a rare benign tumor derived from melanocytes present within the leptomeninges. Tumors contain aggregates of cells with melanin in the cytoplasm. Immunoreactive to HMB-45, melan-A, and S-100. Treatment is surgery with or without radiation treatment. Local recurrence rate is 20% Localized primary dural melanoma with high mitotic activity, hemorrhage, and/or necrosis can have imaging features that overlap those of melanocytoma.
Malignant mesenchymal non-meningothelial tumors (**Fig. 4.10**)	MRI and CT findings of these lesions are dependent on their histologic features. Malignant tumors may be associated with invasion of adjacent brain, bone, and/or leptomeninges.	Malignant mesenchymal tumors (WHO grades III and IV) can rarely occur as solitary lesions involving the meninges and skull. Lesions include malignant fibrous histiocytoma, fibrosarcoma, rhabdomyosarcoma, leiomyosarcoma, liposarcoma, chondrosarcoma, osteosarcoma, Ewing's sarcoma, and angiosarcoma.
Skull-base tumors (**Fig. 4.11, Fig. 4.12,** and **Fig. 4.13**)	MRI: Destructive bone tumors extending intracranially can cause focal and/or diffuse dural thickening with gadolinium contrast enhancement.	Myeloma, primary bone tumors (chordoma, chondrosarcoma, osteogenic sarcoma, Ewing's sarcoma), and neoplasms from the sinuses and nasopharynx (squamous cell carcinoma, nasopharyngeal carcinoma, adenoid cystic carcinoma, and esthesioneuroblastoma) can invade the dura.

(continued on page 572)

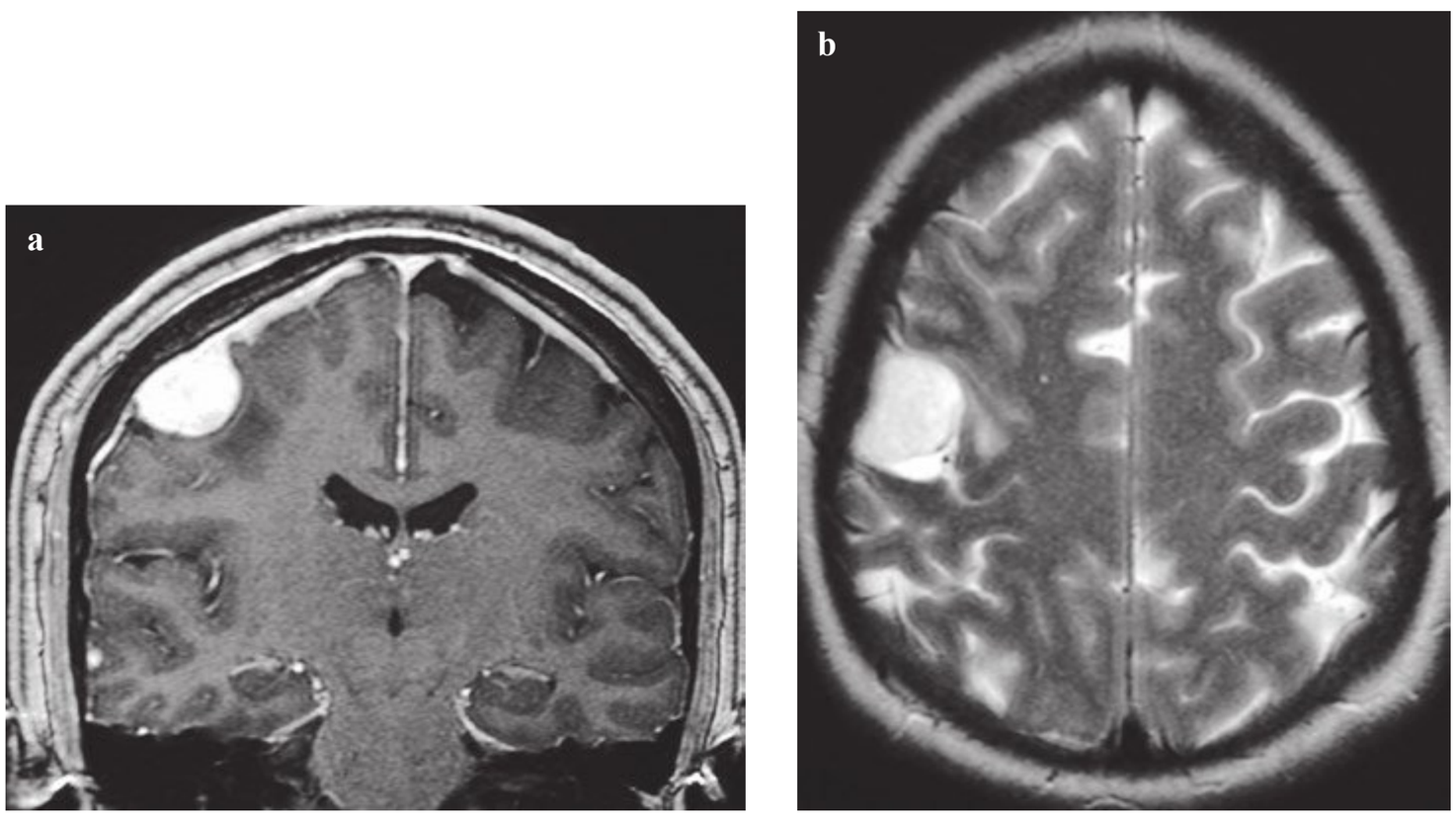

Fig. 4.10 A 35-year-old woman with a malignant fibrous histiocytoma in the dura that shows **(a)** gadolinium contrast enhancement on coronal T1-weighted imaging and **(b)** high signal on axial T2-weighted imaging.

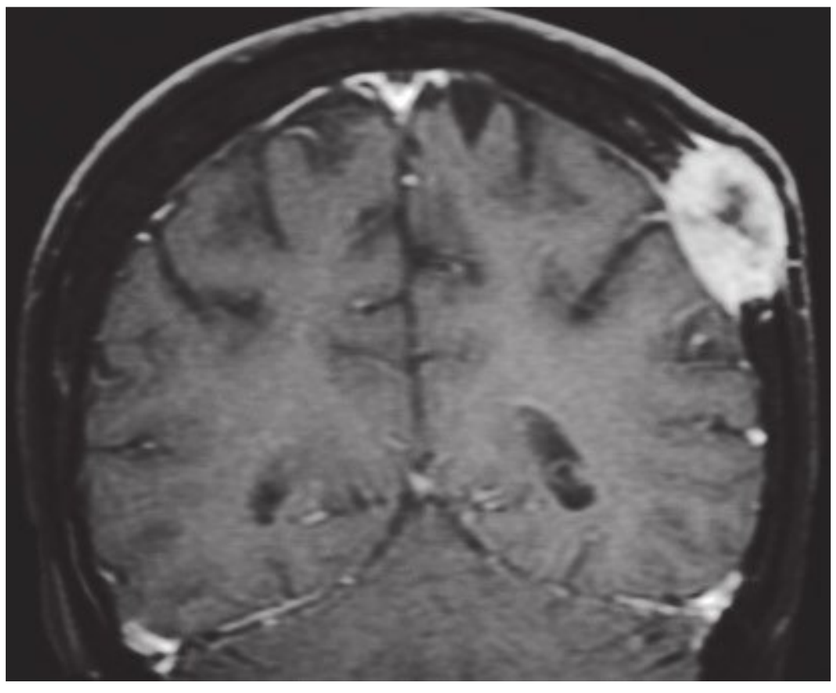

Fig. 4.11 Coronal fat-suppressed T1-weighted imaging shows a gadolinium-enhancing myeloma in the left calvarium associated with destruction of the inner and outer tables, with extraosseous tumor extension.

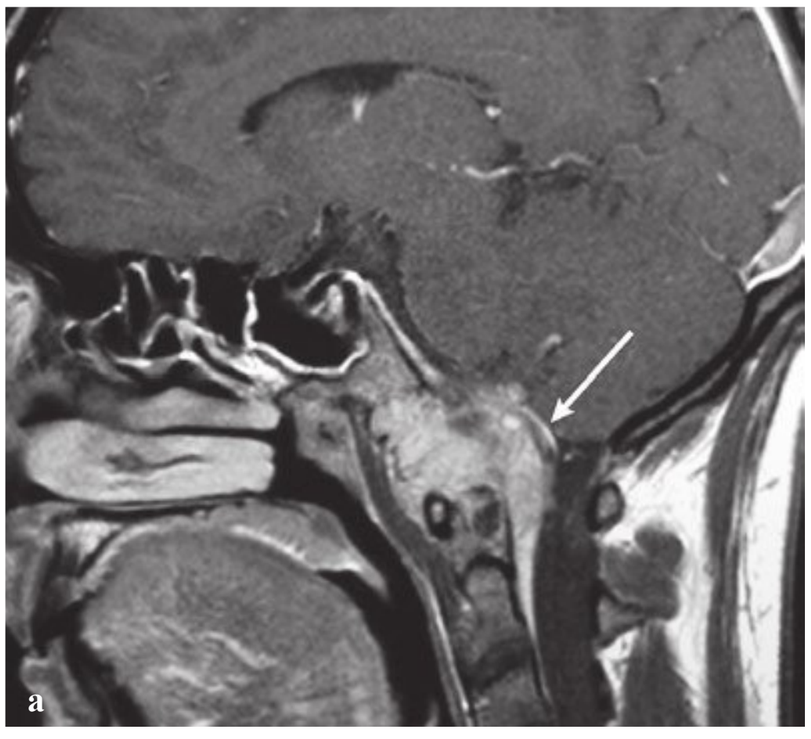

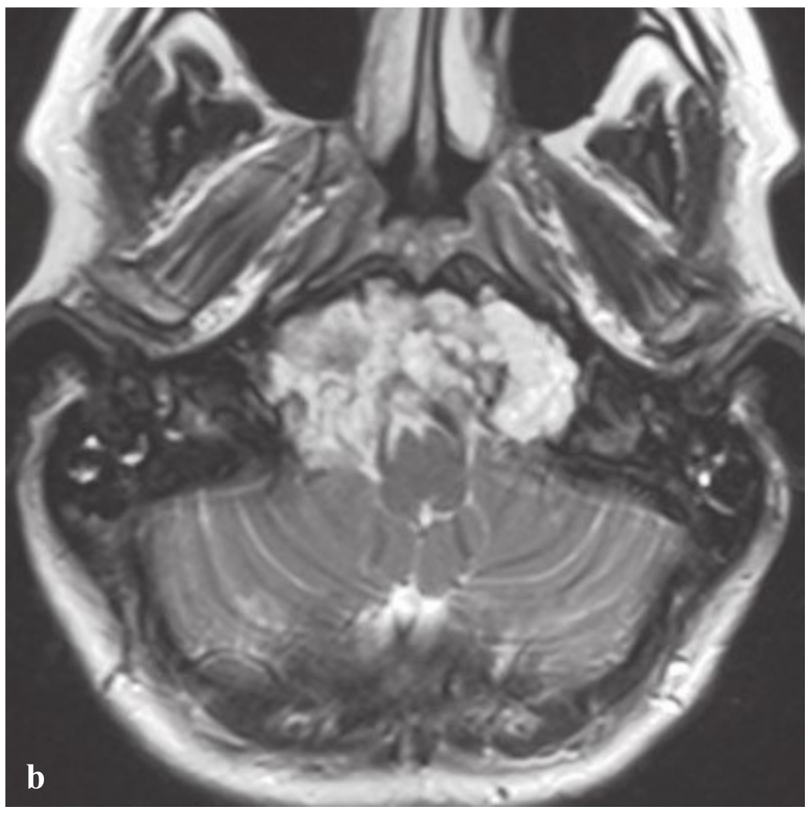

Fig. 4.12 A 44-year-old woman with a chordoma in the occipital portion of the clivus. The tumor shows **(a)** gadolinium contrast enhancement on sagittal T1-weighted imaging (arrow) and **(b)** heterogeneous high signal on axial T2-weighted imaging and is associated with bone destruction and extension into adjacent tissues.

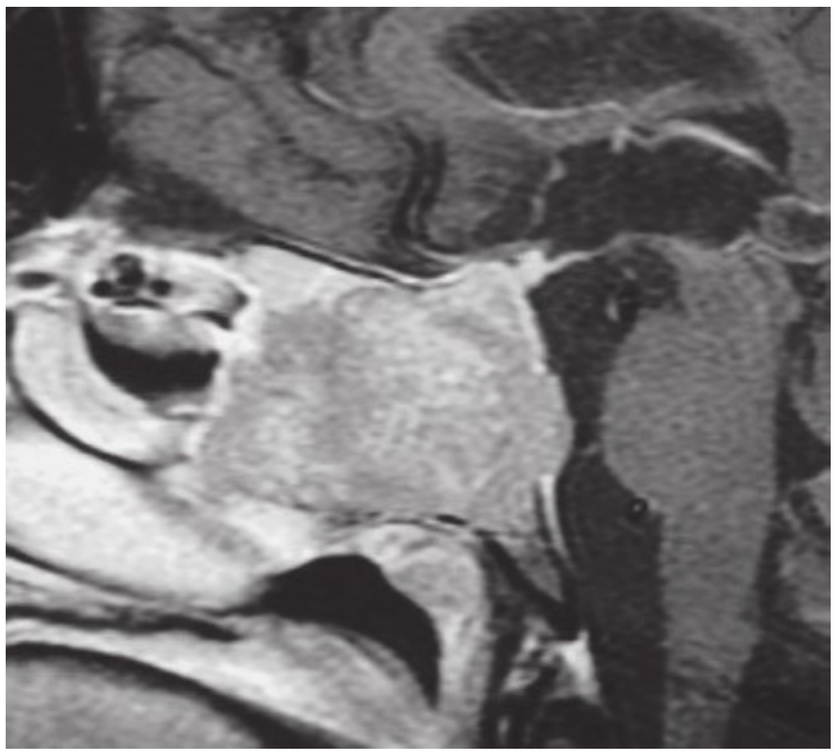

Fig. 4.13 A 48-year-old man with a gadolinium-enhancing esthesioneuroblastoma in the ethmoid and sphenoid sinuses as well as the clivus with intracranial extension involving dura of the skull base on sagittal fat-suppressed T1-weighted imaging.

Table 4.1 (cont.) Abnormalities involving the dura

Lesions	Imaging Findings	Comments
Perineural tumor spread from the sinuses and nasopharynx (**Fig. 4.14**)	MRI: Neoplasms can extend from below the skull base into the foramina to involve the dura, leptomeninges, brainstem, and/or brain. Typically show gadolinium contrast enhancement.	Malignant tumors like sinonasal squamous cell carcinoma, nasopharyngeal carcinoma, adenoid cystic carcinoma, and esthesioneuroblastoma can extend intracranially along the cranial nerves to involve the dura and/or leptomeninges.
Vascular Lesions		
Dural arteriovenous malformation (AVM) (**Fig. 4.15**)	Dural AVMs contain multiple, tortuous, tubular vessels. The venous portions often show contrast enhancement. MRA and CTA can show patent portions of the vascular malformation and areas of venous sinus occlusion or recanalization. Usually not associated with mass effect unless there is recent hemorrhage or venous occlusion.	Dural AVMs are usually acquired lesions resulting from thrombosis or occlusion of an intracranial venous sinus with subsequent recanalization resulting in direct arterial to venous sinus communications. Occur in transverse, sigmoid venous sinuses > cavernous sinus > straight, superior sagittal sinuses.
Traumatic/Postsurgical Abnormalities		
Epidural hematoma (**Fig. 4.16**)	The CT attenuation and MRI signal of the hematoma depend on its age, size, hematocrit, and oxygen tension. MRI: Biconvex extra-axial hematoma located between the skull and dura. Displaced dura has low signal on T2-weighted imaging, ± edema (high signal on T2-weighted imaging involving the displaced brain parenchyma), ± subfalcine or uncal herniation. Hyperacute: Intermediate signal on T1-weighted imaging, intermediate-high signal on T2-weighted imaging. Acute: Low-intermediate signal on T1-weighted imaging, high signal on T2-weighted imaging. Early Subacute: High signal on T1-weighted imaging and low signal on T2-weighted imaging. CT: Biconvex extra-axial hematoma located between the skull and dura. Displaced dura has high attenuation, ± low-attenuation edema involving the displaced brain parenchyma, ± subfalcine or uncal herniation.	Epidural hematomas usually result from trauma/tearing of an epidural artery (often the middle meningeal artery) or dural venous sinus, ± skull fracture. Epidural hematomas do not cross cranial sutures.

(continued on page 574)

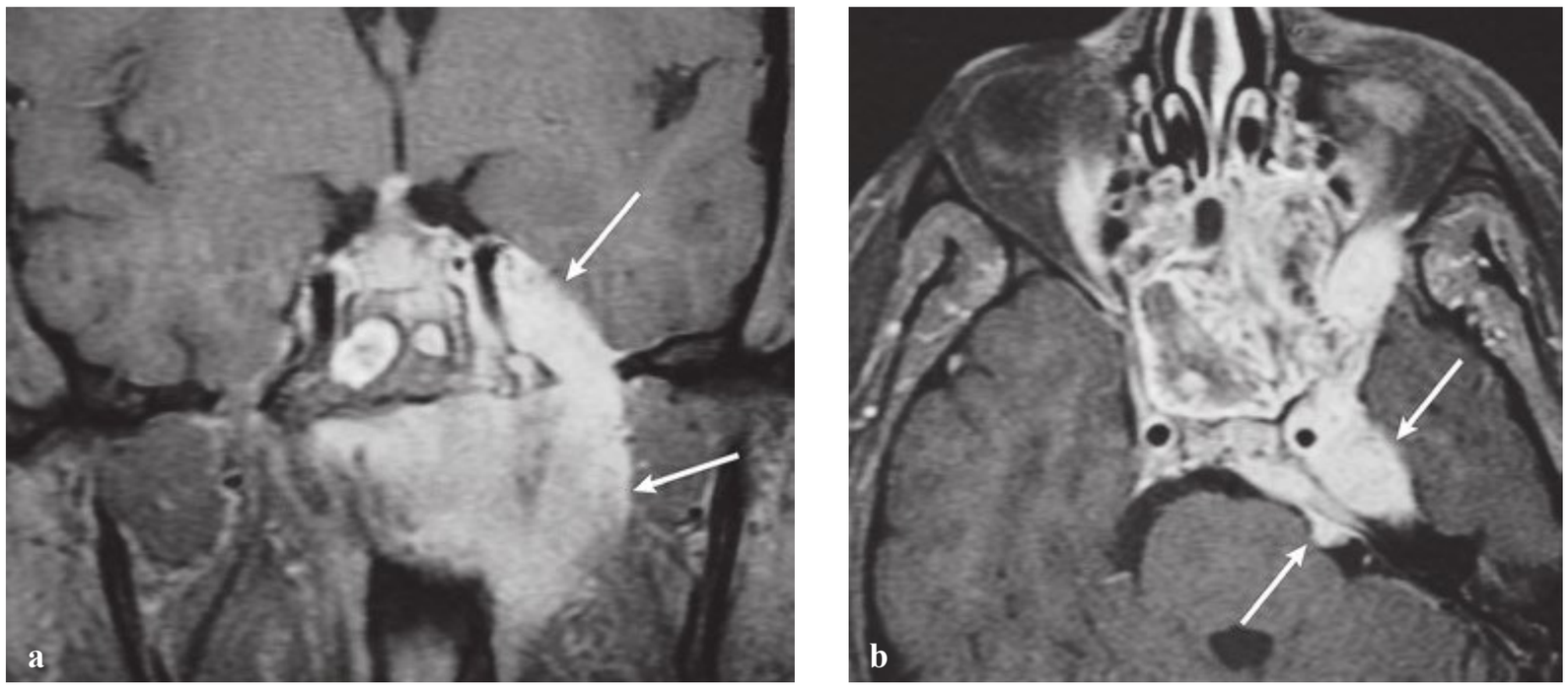

Fig. 4.14 A46-year-old woman with gadolinium-enhancing nasopharyngeal adenoid cystic carcinoma that extends intracranially through a widened foramen ovale to involve the left trigeminal cistern/Meckel's cave, left cavernous sinus, left foramen rotundum, and intracranial dura, as seen on postcontrast **(a)** coronal (arrows) and **(b)** axial fat-suppressed T1-weighted imaging (arrows).

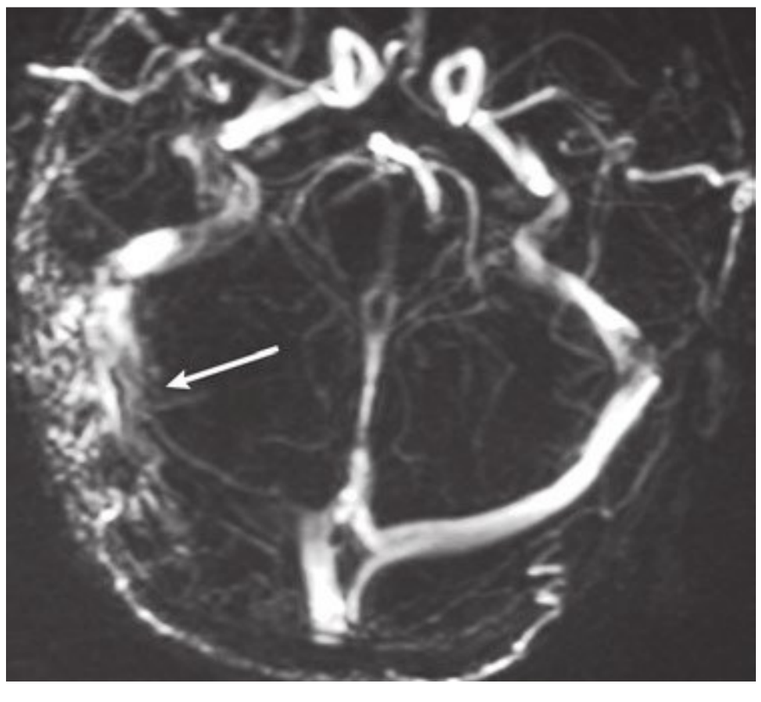

Fig. 4.15 A66-year-old woman with a dural arteriovenous malformation at the right transverse venous sinus. Two-dimensional phase-contrast image shows multiple, tortuous, tubular vessels (arrow) at the partially recanalized right transverse sinus.

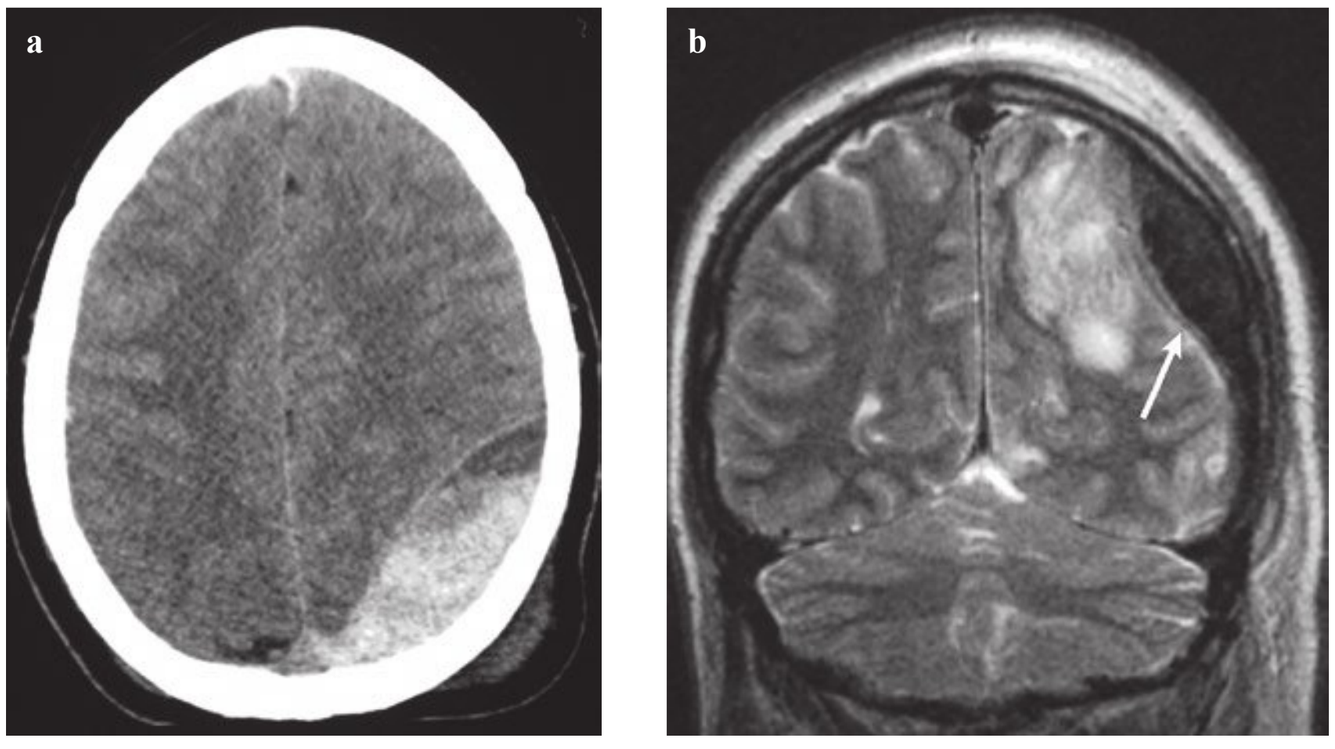

Fig. 4.16 Early subacute posterior left epidural hematoma has **(a)** heterogeneous high attenuation on axial CT and **(b)** low signal (arrow) on coronal T2-weighted imaging.

Table 4.1 (cont.) Abnormalities involving the dura

Lesions	Imaging Findings	Comments
Hemorrhagic Lesion		
Subdural hematoma (**Fig. 4.17**) Hyperacute hematoma Acute hematoma Subacute hematoma Chronic hematoma	Crescentic extra-axial hematoma located in the potential space between the inner margin of the dura and outer margin of the arachnoid membrane, ± edema (low attenuation on CT and high signal on T2-weighted imaging) involving the displaced brain parenchyma, ± subfalcine or uncal herniation. The CT attenuation and MRI signal of the hematoma depend on its age, size, hematocrit, and oxygen tension. Hyperacute hematoma MRI: Intermediate signal on T1-weighted imaging and intermediate-high signal on T2-weighted imaging. CT: Can have high or mixed high, intermediate, and/or low attenuation. Acute hematoma MRI: Low-intermediate signal on T1-weighted imaging and low signal on T2-weighted imaging. CT: Can have high or mixed high, intermediate, and/or low attenuation. Subacute hematoma MRI: High signal on T1-weighted imaging and T2-weighted imaging. CT: Can have intermediate attenuation (isodense to brain) and/or low-intermediate attenuation. Chronic hematoma MRI: Variable, often low-intermediate signal on T1-weighted imaging and high signal on T2-weighted imaging, ± gadolinium contrast enhancement of collection and organizing neomembrane. Mixed MRI signal can result if rebleeding occurs into chronic collection. CT: Usually has low attenuation (hypodense to brain).	Subdural hematomas usually result from trauma/stretching/tearing of cortical veins where they enter the subdural space to drain into dural venous sinuses, ± skull fracture. Subdural hematomas do cross sites of cranial sutures.
Ossified hematoma (**Fig. 4.18**)	MRI: Thin or irregular peripheral zones with low signal from calcifications; peripheral and/or central ossification surrounding collections with variable low, intermediate, and/or high signal on T1- and T2-weighted imaging, ± gadolinium contrast enhancement of collection and organizing neomembrane. Mixed MRI signal can result if rebleeding occurs into chronic collection. CT: Usually has dense thin or irregular peripheral calcifications, and/or peripheral and central ossification surrounding collections with variable low, intermediate, and/or high attenuation.	Chronic subdural or epidural hematomas can rarely become calcified or ossified, and are referred to as armored brain. Surgical removal of symptomatic lesions can be difficult because of dense adhesion to brain surface and/or dura.

(continued on page 576)

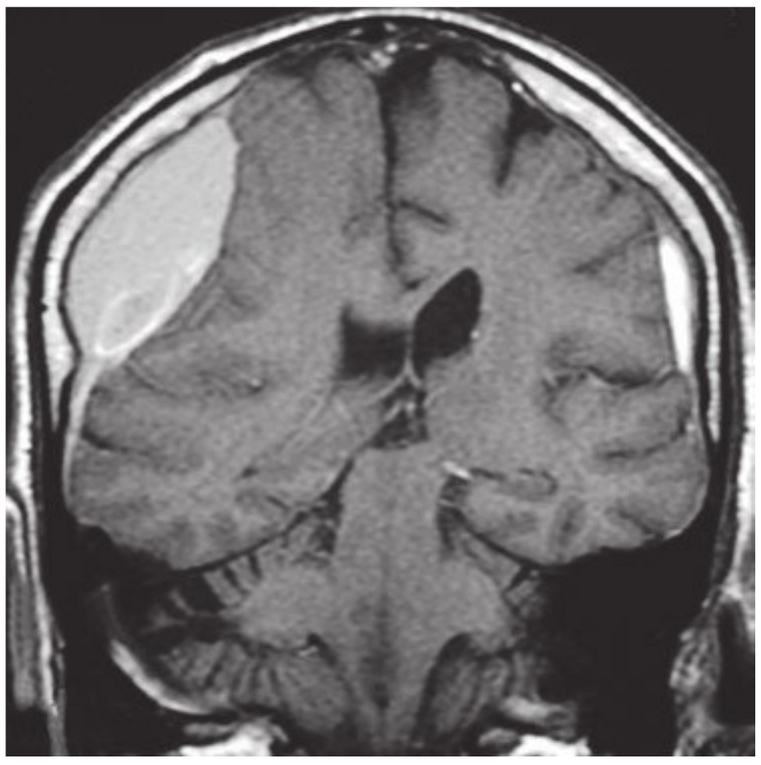

Fig. 4.17 A 71-year-old man with bilateral subdural hematomas that have high signal on coronal T1-weighted imaging.

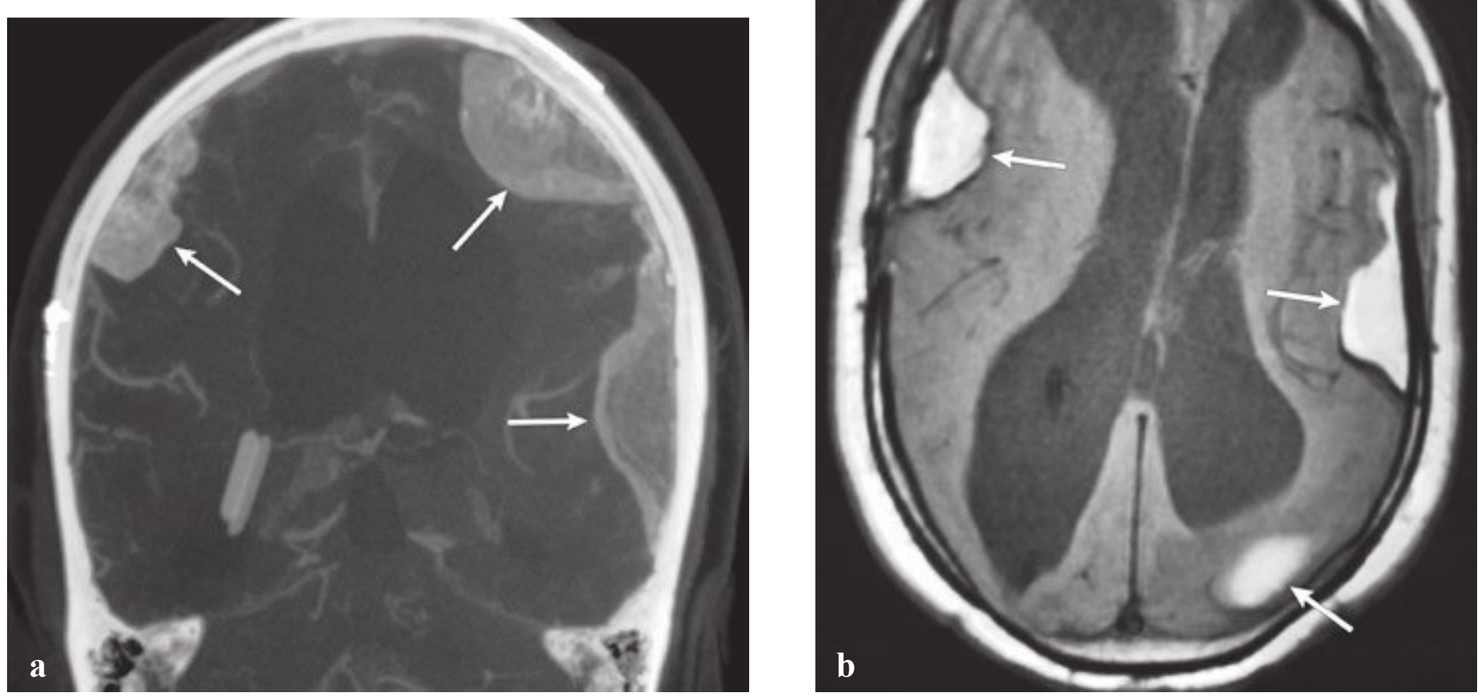

Fig. 4.18 Patient with multifocal, ossified extra-axial hematomas on **(a)** coronal CT (arrows) that have high signal on **(b)** axial T1-weighted imaging (arrows).

Table 4.1 (cont.) Abnormalities involving the dura

Lesions	Imaging Findings	Comments
Postsurgical dural fibrosis (**Fig. 4.19** and **Fig. 4.20**)	MRI: Diffuse thickened smooth gadolinium contrast enhancement of dura. The thickened dura can have intermediate signal on T1-weighted imaging and slightly high to high signal on T2-weighted imaging and FLAIR.	Thickened smooth pachymeningeal (dural) contrast enhancement can occur along the endocranial surface and/or dural reflections after surgery and can persist for years. Typically not associated with clinical signs.
Intracranial hypotension (**Fig. 4.21**)	MRI: Diffuse, thickened, smooth gadolinium contrast enhancement of dura; subdural fluid collections/hygromas; pituitary hyperemia; engorgement of intracranial veins and venous sinuses; "sagging" of the brainstem, with tonsillar descent below the foramen magnum; flattening of the ventral surface of the pons; decreased CSF in the interpeduncular and ambient cisterns; downward positioning of the optic chiasm and mamillary bodies with decreased mamillary body–pontine distances, which often measure approximately 4.5 mm (normal distance > 6–7 mm); downward positioning of the iter of the third ventricle below the incisural line; and decreased mean pontomesencephalic angle, which often measures approximately 41° (normal = 65°). The pontomesencephalic angle is the angle between a line drawn anteriorly from the junction of the midbrain and pons; and a line along the anterior margin of the midbrain. Mild cases of postoperative intracranial hypotension can have findings similar to those in spontaneous intracranial hypotension. In cases of rapid intraoperative and postoperative CSF loss, abnormal high signal on T2-weighted imaging in the bilateral thalami and basal ganglia can occur in association with impaired responsiveness/neurologic injury after surgery.	Can occur spontaneously with CSF leak, usually from the spinal canal, related to tears of the dura or nerve root sheaths. Associated with orthostatic headaches relieved by having the patient lie supine. Intracranial hypotension can also occur after lumbar puncture, myelogram, interventional procedure, or surgery. The exact site of CSF loss may not be clearly defined. Incidence is 5 per 100,000 cases per year, peak age of incidence is 40 years, and occurs in women two times more frequently than in men.
Postsurgical meningocele (**Fig. 4.22**)	CSF-filled collection contiguous with the subarachnoid space protruding through a surgical bony defect.	Usually are not clinically significant unless it becomes large or infected.

(continued on page 578)

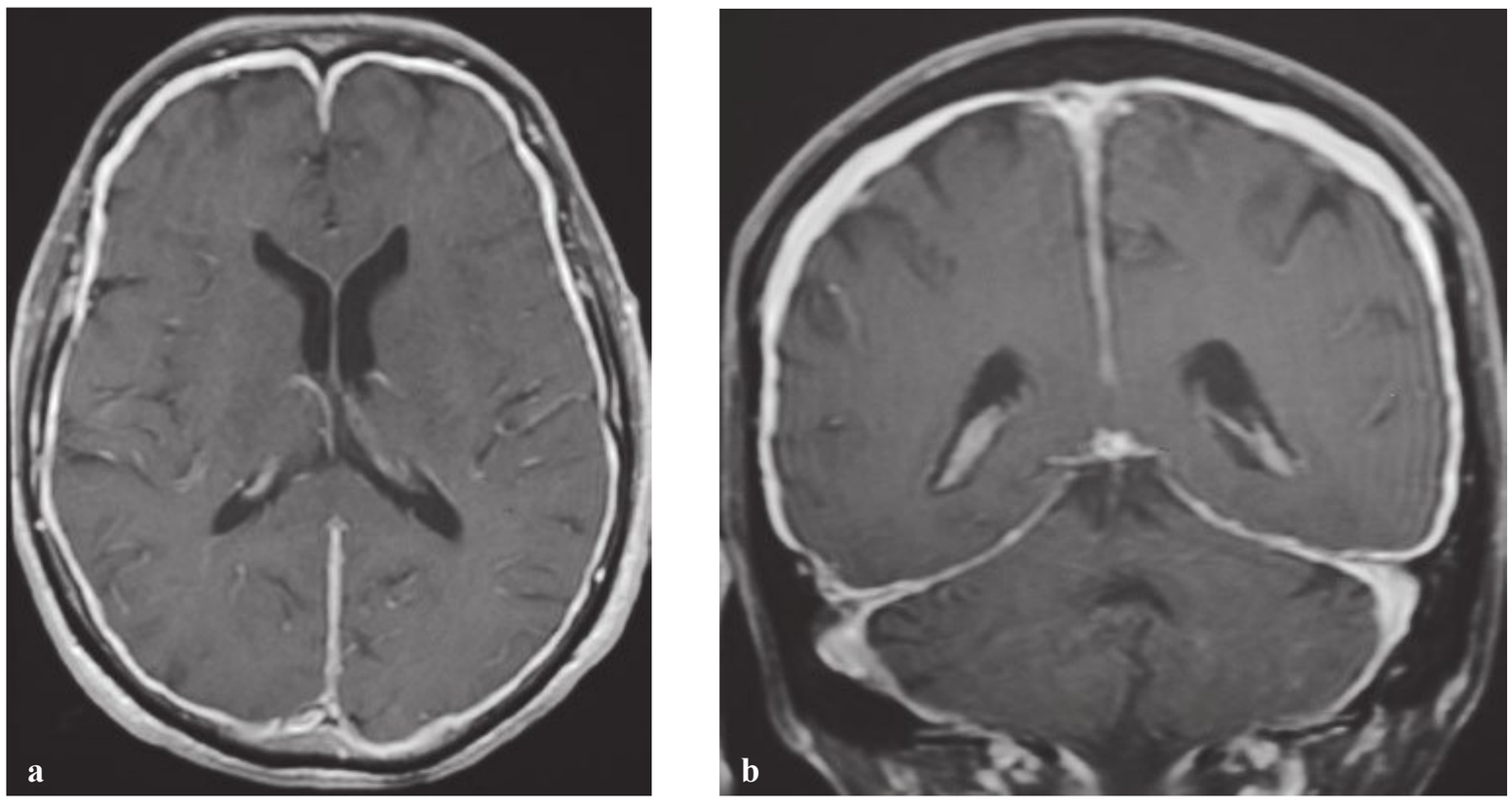

Fig. 4.19 An 89-year-old man with diffuse, thickened, smooth gadolinium contrast enhancement of intracranial dura as seen on **(a)** axial and **(b)** coronal T1-weighted imaging representing dural fibrosis.

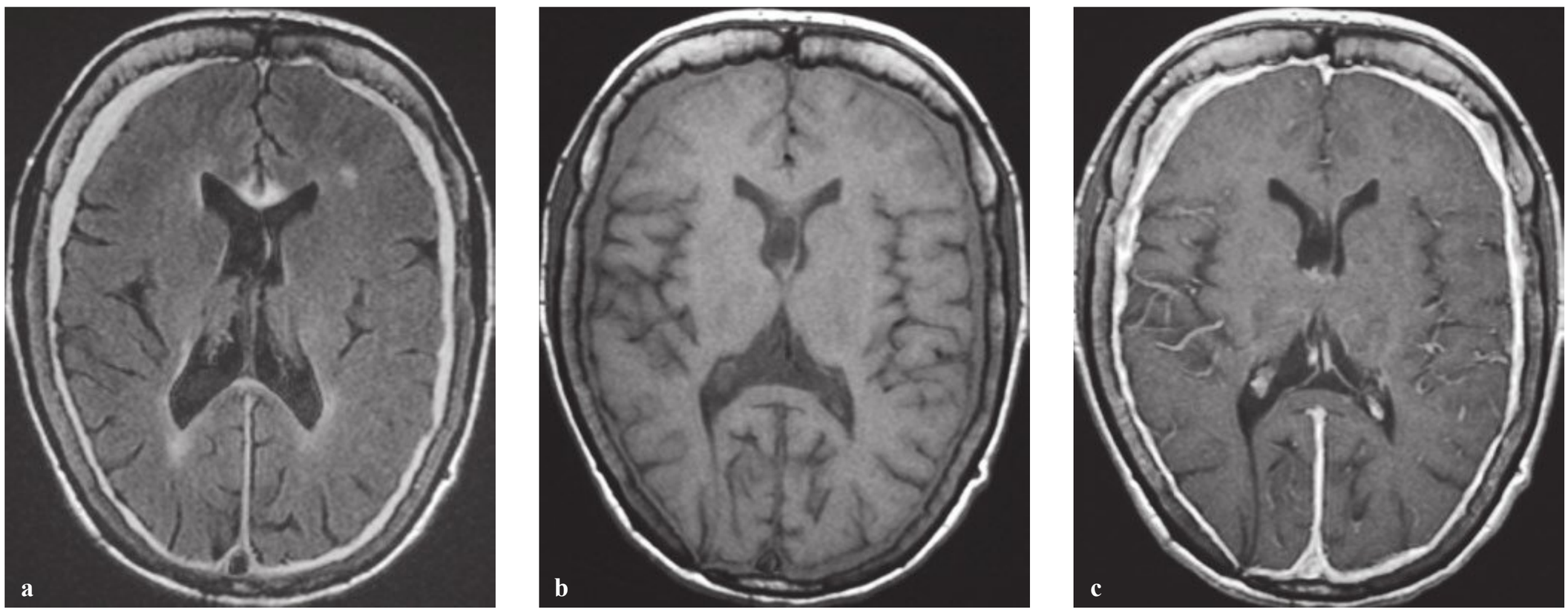

Fig. 4.20 Postshunt dural fibrosis in an 89-year-old man is seen as thickened dura with **(a)** high signal on axial FLAIR, **(b)** intermediate signal on axial T1-weighted imaging, **(c)** and diffuse gadolinium contrast enhancement on axial T1-weighted imaging.

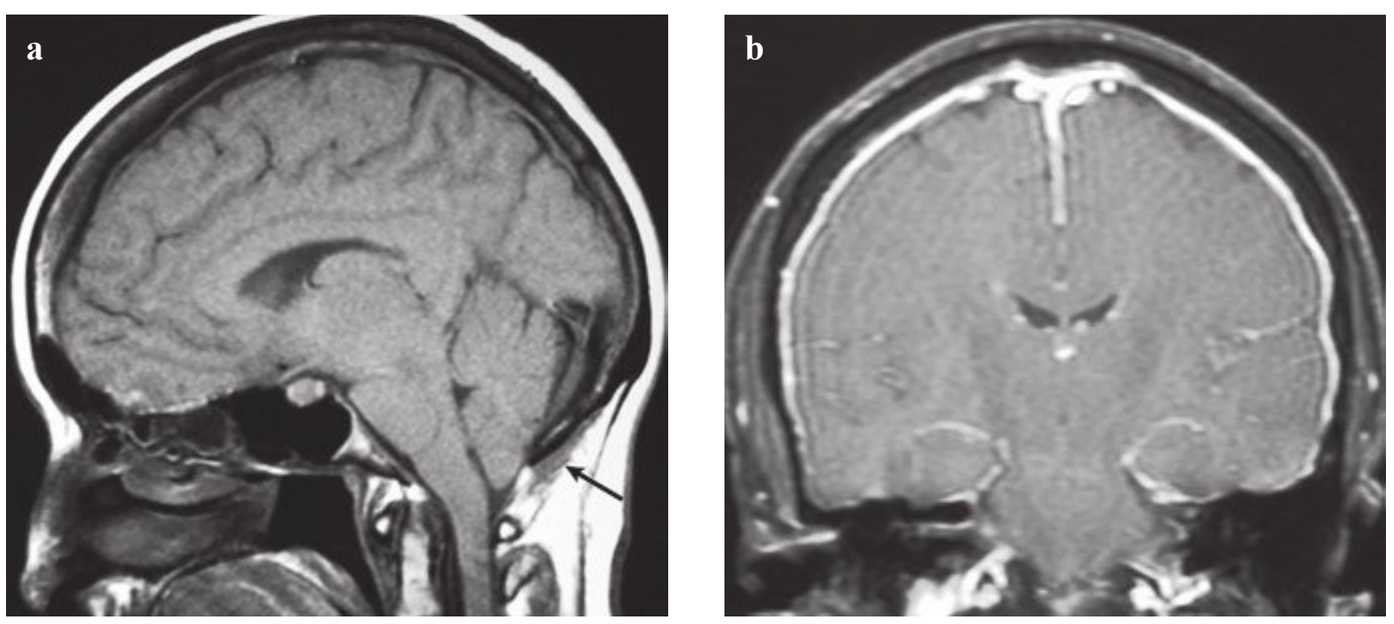

Fig. 4.21 Patient with history of intracranial hypotension. **(a)** Sagittal T1-weighted imaging shows "sagging" of the brainstem, with downward positioning of the cerebellar tonsils (arrow), flattening deformity of the ventral aspect of the pons, and decreased mamillary body–pontine distance. **(b)** Coronal fat-suppressed T1-weighted imaging shows diffuse, thickened, smooth gadolinium contrast enhancement of the intracranial dura.

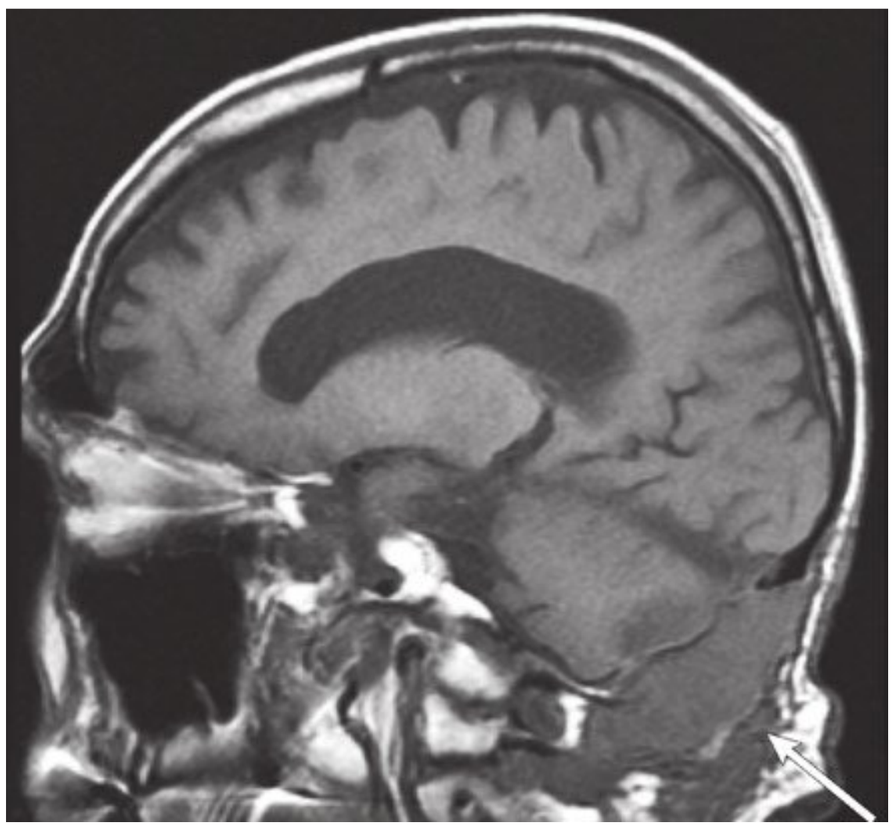

Fig. 4.22 Postsurgical meningocele is seen in the left occipital region (arrow) after occipital craniectomy on sagittal T1-weighted imaging.

Table 4.1 (cont.) Abnormalities involving the dura

Lesions	Imaging Findings	Comments
Inflammatory		
Pachymeningitis from infection (**Fig. 4.23**)	MRI: Usually shows gadolinium contrast enhancement of thickened dura, ± adjacent leptomeningeal gadolinium contrast enhancement, ± brain abscess and ventriculitis, ± skull osteomyelitis, ± sinus pyocele. Thickened dura can have intermediate signal on T1-weighted imaging and slightly high to high signal on FLAIR and T2-weighted imaging. CT: Zones of abnormal decreased attenuation, focal sites of bone destruction, ± complications, including subgaleal empyema, epidural empyema, subdural empyema, cerebritis, intra-axial abscess, and venous sinus thrombosis.	Infection of the dura can result from surgery, trauma, hematogenous dissemination from another source of infection, or direct extension of infection from an adjacent site, such as the brain, leptomeninges, skull, orbits paranasal sinuses, and nasopharynx. Intracranial extension of skull base infection typically involves the dura first, followed by the leptomeninges and brain.
Epidural/subdural abscess/empyema (**Fig. 4.24** and **Fig. 4.25**)	MRI: Epidural or subdural collections with low signal on T1-weighted imaging, high signal on T2-weighted imaging, and thin or irregular peripheral zones of gadolinium contrast enhancement. CT: Epidural or subdural collections with low attenuation and peripheral zones of contrast enhancement	Often results from complications related to sinusitis (usually frontal), meningitis, otitis media, ventricular shunts, or surgery. Can be associated with venous sinus thrombosis and venous cerebral or cerebellar infarctions, cerebritis, brain abscess; mortality 30%
Langerhans' cell histiocytosis (**Fig. 4.26**)	MRI: Fusiform or lobulated lesion with intermediate signal on T1- and T2-weighted imaging involving hypothalamus/pituitary stalk, skull, dura, and rarely the leptomeninges. Lesions in skull, dura, pituitary stalk, and leptomeninges usually show gadolinium contrast enhancement. CT: Intraosseous lesions usually have low-intermediate attenuation and are typically associated with localized bone destruction, + contrast enhancement of the adjacent dura, and rarely the leptomeninges. Thickening of the pituitary stalk may be seen.	Disorder of reticuloendothelial system in which bone marrow–derived dendritic Langerhans' cells infiltrate various organs as focal lesions or in diffuse patterns. Langerhans' cells have eccentrically located ovoid or convoluted nuclei within pale to eosinophilic cytoplasm. Lesions often consist of Langerhans' cells, macrophages, plasma cells, and eosinophils. Lesions are immunoreactive to S-100, CD1a, CD-207, HLA-DR, and β_2-microglobulin. LCH has been associated with BRAF or MAP2K1 mutations. Prevalence of 2 per 100,000 children less than 15 years old; only a third of lesions occur in adults. Localized lesions (eosinophilic granuloma) can be single or multiple in the skull with involvement of adjacent dura, usually at the skull base. Can also involve the dura without adjacent osseous disease. Intradural lesions occur at pituitary stalk/hypothalamus and can present with diabetes insipidus. Lesions rarely occur in brain tissue (<4% of patients with Langerhans' cell histiocytosis). Occur in patients with median age = 10 years, average = 13.5 years. Peak incidence is in patients between 5 and 10 years old; 80 to 85% occur in patients less than 30 years old.

(continued on page 580)

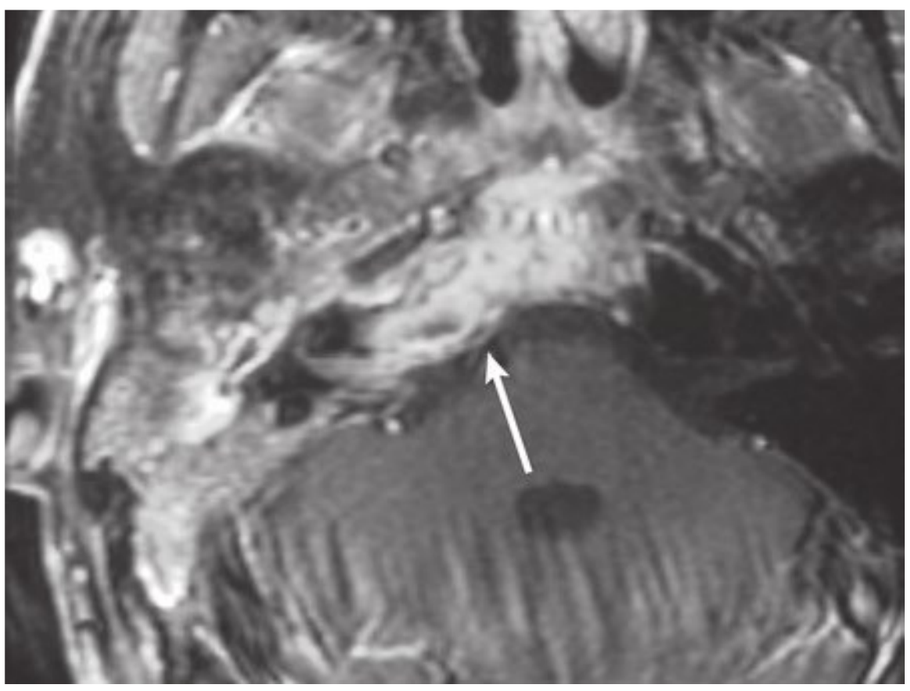

Fig. 4.23 Axial fat-suppressed T1-weighted imaging shows abnormal gadolinium contrast enhancement in the petrous apex due to skull-base infection with involvement of the adjacent endocranial dura (arrow).

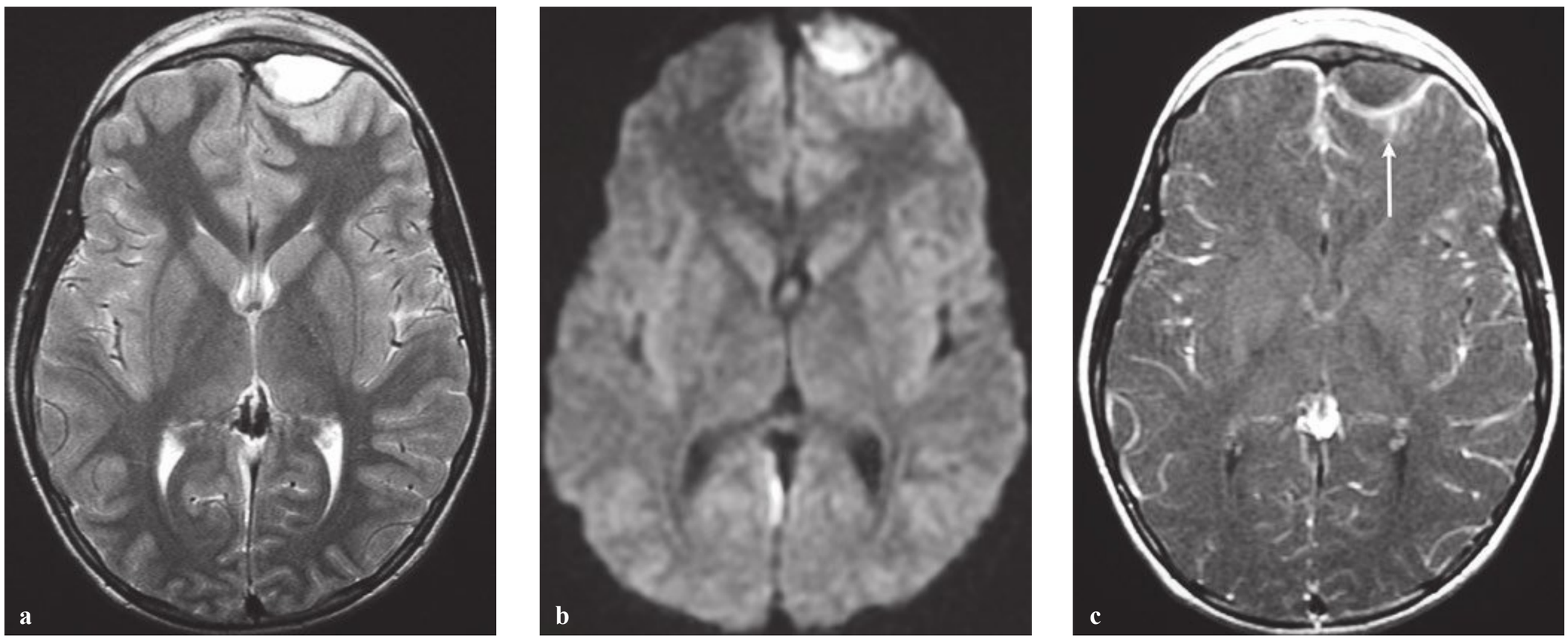

Fig. 4.24 **(a)** Left frontal epidural empyema in a 9-year-old female as a complication of ethmoid sinus infection. The epidural empyema has heterogeneous high signal centrally, surrounded by a thin band of low signal representing displaced dura, and associated with edema in adjacent brain tissue on axial FLAIR. **(b)** The epidural contents have restricted diffusion on axial diffusion-weighted imaging. **(c)** The infected and posteriorly displaced dura shows gadolinium contrast enhancement (arrow) on axial T1-weighted imaging.

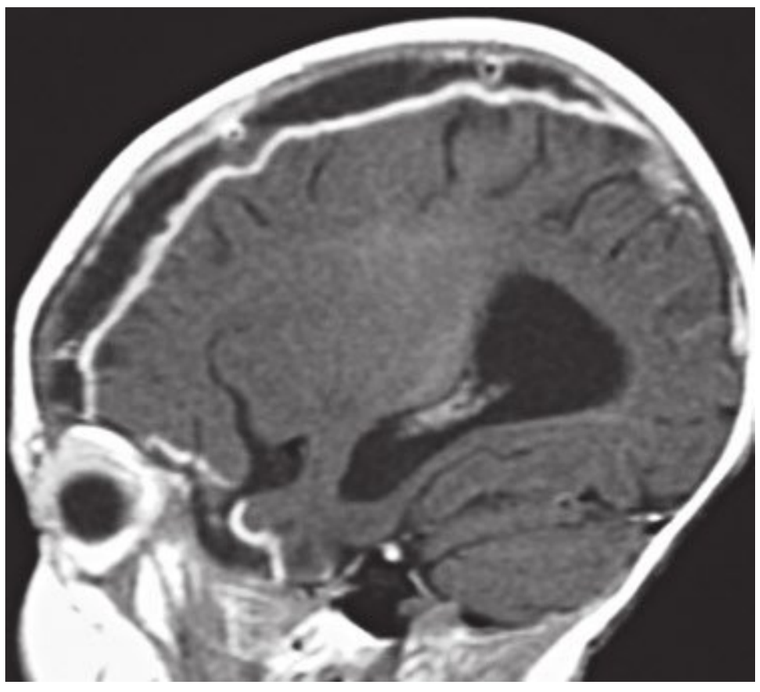

Fig. 4.25 Subdural empyema in a 3-month-old female resulting from sinus infection. Sagittal T1-weighted imaging shows thick peripheral gadolinium contrast enhancement at the inner margin of the subdural empyema and deep to the nonenhancing purulent material.

Fig. 4.26 A 13-year-old female with Langerhans' cell histiocytosis who has a gadolinium-enhancing eosinophilic granuloma in the left zygoma and adjacent skull, with intracranial extension seen as dural thickening with contrast enhancement on axial fat-suppressed T1-weighted imaging (arrow).

Table 4.1 (cont.) Abnormalities involving the dura

Lesions	Imaging Findings	Comments
Erdheim-Chester disease	MRI: Lesions in the CNS can occur in the cerebrum, hypothalamus, cerebellum, and choroid plexus, as well as in spinal or cranial dura. Single or multiple dura-based lesions can be seen with low to intermediate signal on T1-weighted imaging and proton density-weighted imaging and with low, intermediate, and/or slightly high signal on T2-weighted imaging. After gadolinium contrast administration, lesions usually show enhancement. Prolonged gadolinium contrast enhancement may occur from contrast retention by histiocytes. CT: Intermediate attenuation, ± osteosclerosis of craniofacial bones.	Rare multisystem non-Langerhans' cell histiocytic disorder of unknown etiology that usually affects adults. Collections are formed of foamy lipid-laden histiocytes with small bland nuclei, Touton-like giant cells, multinucleated giant cells, fibrosis/dense collagen, chronic inflammatory cells (lymphocytes and histiocytes), and occasional scattered eosinophils. Immunoreactive to the histiocytic antigen CD68 and show variable or no reactivity to S-100. Unlike Langerhans' cell histiocytosis, Erdheim-Chester disease lesions lack immunoreactivity to CD1a. Can involve the musculoskeletal, pulmonary, cardiac, gastrointestinal, and central nervous systems. Age range is 7 to 84 years. Most common in fourth to seventh decades. Prognosis depends on the extent and location of disease. Treatment includes surgical debulking, prednisone, cyclosporine, vincristine, vinblastine, cyclophosphamide, and/or doxorubicin. Radiation treatment may be useful for intracranial lesions in the brain parenchyma and other locations. Immunotherapy with agents like interferon-a_{2a} has also been used. Multisystem disease can progress to death from respiratory distress, pulmonary fibrosis, and renal and/or heart failure. Thirty-seven percent of patients had died after a mean follow-up interval of 32 months.
Rosai-Dorfman disease	MRI: Single or multiple dural lesions can be seen with intermediate signal on T1-weighted imaging and low-intermediate signal on T2-weighted imaging. Low signal centrally on T2-weighted imaging may be secondary to histiocytic release of free radicals. After gadolinium contrast administration, lesions usually show enhancement. CT: Dura-based lesion with intermediate attenuation, ± erosion of adjacent bone.	Rare benign histiocytosis in which collections of lymphoplasmacytic cells and histiocytes occur in fibrous stroma within various tissues, such as lymph nodes, bone, orbits, nasal cavity, and intracranial dura. Immunoreactive to S-100 protein and CD68 (macrophages) and lacks immunoreactivity to CD1a (Langerhans' cell marker). Occurs in children and young adults (peak age between 30 and 40 years).
Sarcoidosis (**Fig. 4.27**)	MRI: Smooth and/or nodular gadolinium contrast enhancement in the leptomeninges and/or dura are often seen. Lesions in the brain can show poorly marginated intra-axial zones with low-intermediate signal on T1-weighted imaging and slightly high to high signal on T2-weighted imaging and FLAIR, usually with gadolinium contrast enhancement, + localized mass effect and peripheral edema. CT: Smooth and/or nodular contrast enhancement in the leptomeninges and/or dura can be seen. Intra-axial lesions usually have poorly defined margins, low-intermediate attenuation, usually with contrast enhancement, + localized mass effect and peripheral edema.	Sarcoidosis is a multisystem noncaseating granulomatous disease of uncertain cause that can involve the CNS in 5 to 15% of cases. If untreated, it is associated with severe neurologic deficits, such as encephalopathy, cranial neuropathies, and myelopathy. Diagnosis of neurosarcoid may be difficult when the neurologic complications precede other systemic manifestations in the lungs, lymph nodes, skin, bone, and/or eyes.

(continued on page 582)

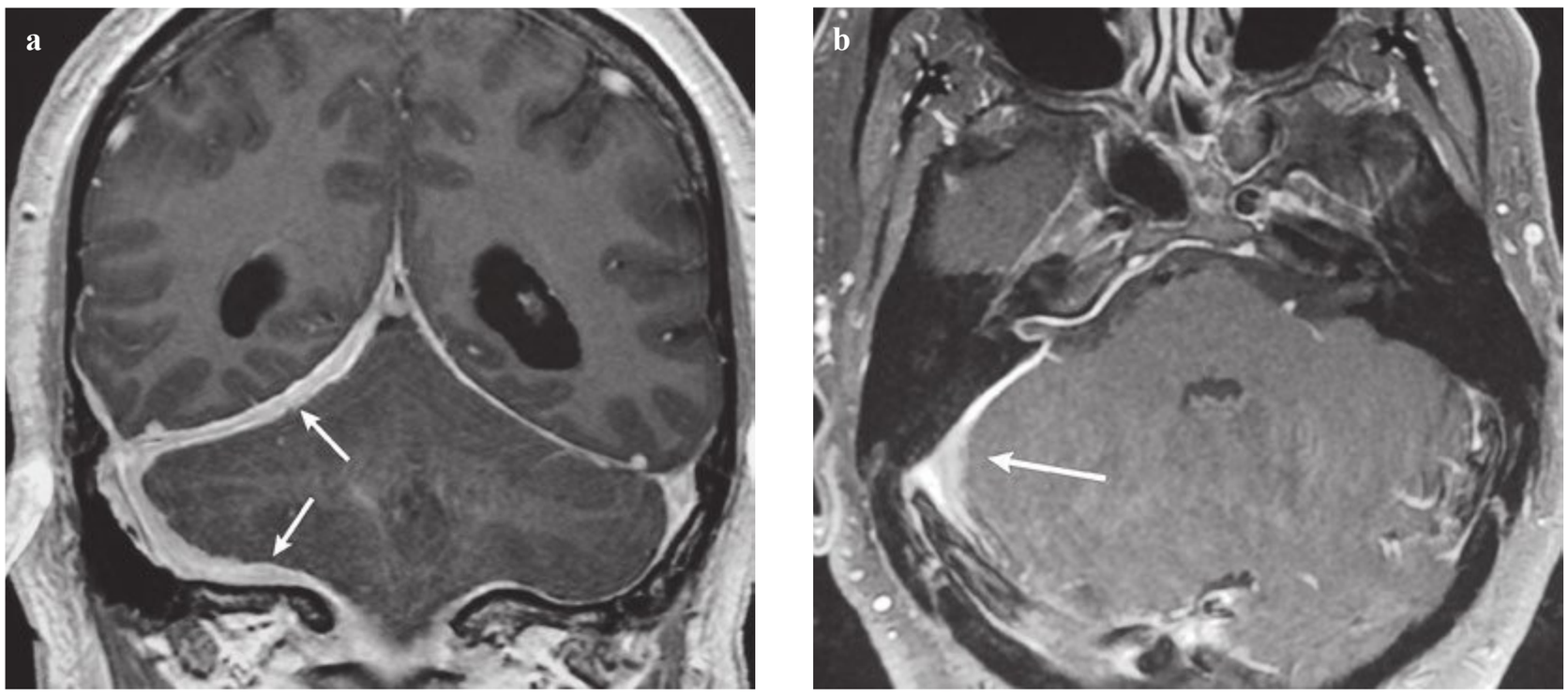

Fig. 4.27 Sarcoidosis with involvement of the intracranial dura. **(a)** Postcontrast coronal T1-weighted imaging and **(b)** fat-suppressed axial T1-weighted imaging show abnormal thickened dural contrast enhancement (arrows) in the tentorium and along the right posterior cranial fossa.

Table 4.1 (cont.) Abnormalities involving the dura

Lesions	Imaging Findings	Comments
Granulomatosis with polyangiitis	MRI: Poorly defined zones of soft tissue thickening with low-intermediate signal on T1-weighted imaging, slightly high to high signal on T2-weighted imaging, and gadolinium contrast enhancement within the nasal cavity, paranasal sinuses, infratemporal fossa, and external auditory canal, ± bone invasion and destruction, ± extension into the skull base. Intracranially, involvement of the dura, leptomeninges, brain, or venous sinuses can occur. CT: Zones with soft tissue attenuation, ± bone destruction.	Multisystem disease with necrotizing granulomas in the respiratory tract, focal necrotizing angiitis of small arteries and veins of various tissues, and glomerulonephritis. Often involves the upper respiratory tract, lungs, and kidneys, and can involve the paranasal sinuses, orbits, and temporal bone. Peak incidence is in the fifth decade, and annual incidence is 8 per million. Antibodies to neutrophil cytoplasmic antigens (ANCA) occur in 80–90% of patients and play a role in pathogenesis.
Inflammatory pseudotumor (**Fig. 4.28**)	MRI: Smooth and/or nodular gadolinium contrast enhancement in the dura and/or leptomeninges, ± extension from the skull base, infratemporal soft tissue, and/or orbits. Lesions in the brain can appear as poorly marginated intra-axial zones with low-intermediate signal on T1-weighted imaging and slightly high to high signal on T2-weighted imaging and FLAIR, usually with gadolinium contrast enhancement, + localized mass effect and peripheral edema. CT: Smooth and/or nodular contrast enhancement in the leptomeninges and/or dura can be seen. Intra-axial lesions usually have poorly defined margins and low-intermediate attenuation and usually show contrast enhancement, + localized mass effect and peripheral edema.	Chronic inflammatory disorder of unknown etiology with lesions composed of spindle cells, lymphocytes, and plasma cells. Lesions can occur in many locations, most commonly in the orbits and lungs. Rarely occur in the skull base, dura, and brain. Usually occur in children and young adults. Can be asymptomatic or associated with localized mass effect as well as systemic signs, such as weight loss and fever. Treatment of orbital inflammatory pseudotumor is typically with steroid medication. Surgery is often performed for lesions in other locations.
Idiopathic hypertrophic pachymeningitis	MRI: Thickened linear pattern of gadolinium contrast enhancement involving the dura. ± Lesions in the brain, which can appear as poorly marginated intra-axial zones with low-intermediate signal on T1-weighted imaging and slightly-high to high signal on T2-weighted imaging and FLAIR, usually with gadolinium contrast enhancement, + localized mass effect and peripheral edema. CT: Thickened linear pattern of contrast enhancement involving the intracranial dura can be seen. ± Intra-axial lesions in the brain with decreased attenuation and poorly defined margins.	Clinical disorder with diffuse and/or localized thickening and gadolinium contrast enhancement of dura without history of associated trauma, neoplasms, infection, or inflammatory diseases, such as rheumatoid arthritis, granulomatosis with polyangiitis, IgG4 disease, etc. Occurs more commonly in men than in women, age 39 to 88 years (mean age = 55 years). Clinical findings include headache, loss of vision, and diplopia. Dural biopsies show collections of small, mature lymphocytes, epithelioid histiocytes, and plasma cells, as well as absence of microorganisms, vasculitis, and neoplastic cells. Clinical symptoms like headaches and vision loss can progress. For these patients, treatment has consisted of steroids and other immunosuppressive drugs.

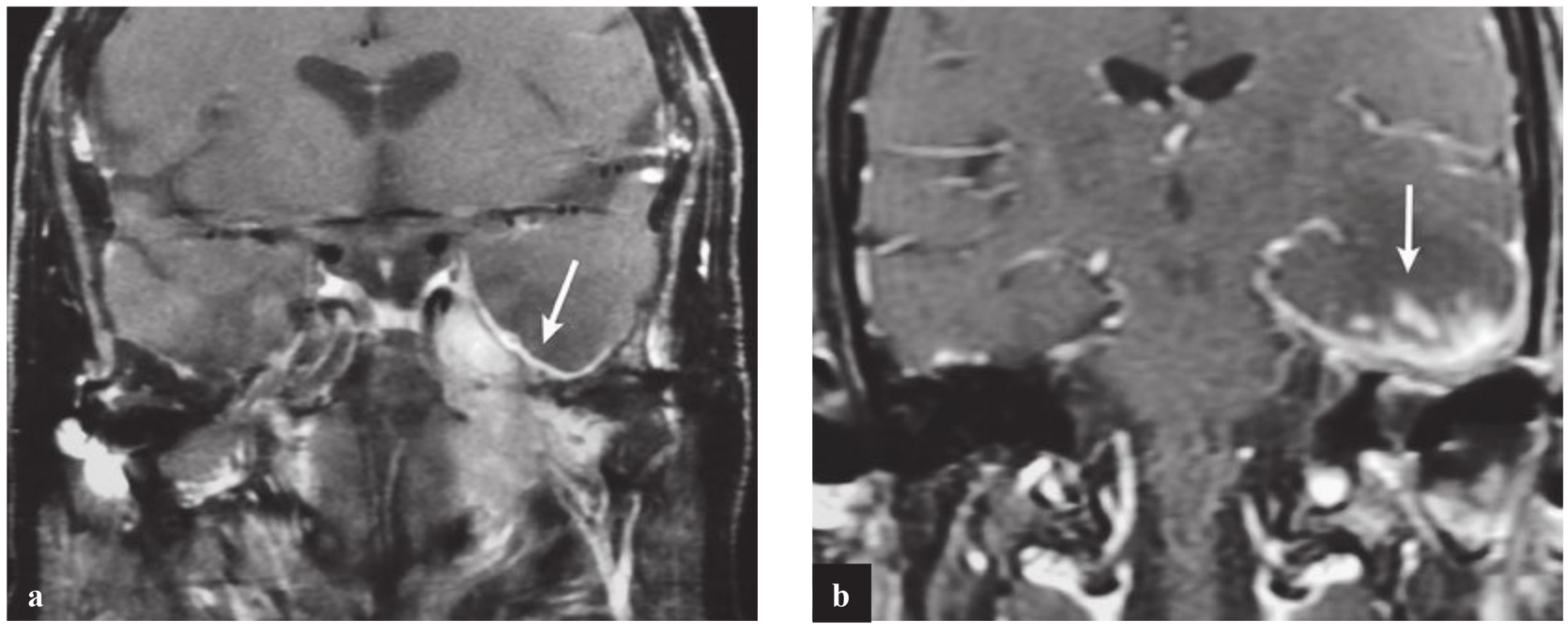

Fig. 4.28 A 53-year-old woman with inflammatory pseudotumor seen as abnormal gadolinium contrast enhancement in the left infratemporal fossa with invasion of the skull base, left foramen ovale, left trigeminal cistern/Meckel's cave, **(a)** left temporal dura (arrow), and **(b)** adjacent leptomeninges (arrow) on coronal fat-suppressed T1-weighted imaging.

Table 4.2 Multifocal and/or diffuse leptomeningeal abnormalities

- Neoplastic
  - Metastatic tumor
  - Lymphoma
  - Leukemia
  - Primary melanocytic tumors of the central nervous system
  - Myeloma
- Nonneoplastic Lesions
  - Ruptured dermoid
- Infection
  - Leptomeningeal infection
- Noninfectious Inflammatory Disorders
  - Sarcoidosis
  - Langerhans' cell histiocytosis
  - Granulomatosis with polyangiitis (formerly referred to as Wegener's granulomatosis)
  - Inflammatory pseudotumor
- Hemorrhage and Vascular Abnormalities
  - Subarachnoid hemorrhage
  - Superficial siderosis
  - Sturge-Weber syndrome
  - Moyamoya disease
- Developmental Abnormality
  - Benign enlargement of the subarachnoid space in infancy

Table 4.2 Multifocal and/or diffuse leptomeningeal abnormalities

Lesions	Imaging Findings	Comments
Neoplastic		
Metastatic tumor (**Fig. 4.29, Fig. 4.30**, and **Fig. 4.31**)	MRI: Irregular localized or diffuse gadolinium contrast enhancement within the subarachnoid space of sulci, cisterns; and/or ventricles, ± nodular and/or diffuse dural gadolinium contrast enhancement, ± intra-axial lesions in the brain. Subarachnoid tumor can have high signal on T2 FLAIR. May be associated with obstructive or communicating hydrocephalus. CT: Leptomeningeal tumor often best seen on postcontrast images. Associated intraosseous lesions with bone destruction may be seen.	Metastases represent ~ 33% of intracranial tumors, usually from extracranial primary neoplasm in adults > 40 years old. Primary tumor source: lung > breast > GI > GU > melanoma. Can also occur from tumor dissemination into the CSF from high-grade malignant brain tumors, including glioblastoma, primitive neuroectodermal tumors, pineoblastomas, and choroid pexus carcinomas. Subarachnoid tumor can occur as single or multiple well-circumscribed or poorly defined lesions involving the skull, dura, leptomeninges, and/or choroid plexus. Metastatic tumor may cause variable destructive or infiltrative changes in single or multiple sites.
Lymphoma (**Fig. 4.32**)	MRI: Irregular localized or diffuse gadolinium contrast enhancement within the subarachnoid space of sulci, cisterns; and/or ventricles, ± nodular and/or diffuse dural gadolinium contrast enhancement, ± intra-axial lesions in brain. Subarachnoid tumor can have high signal on T2 FLAIR. May be associated with obstructive or communicating hydrocephalus. CT: Leptomeningeal tumor often best seen on postcontrast images. Associated intraosseous lesions with bone destruction may be seen.	PCNSL is more common than secondary, usually in adults > 40 years old. Accounts for 5% of primary brain tumors. Incidence currently ranges from 0.8 to 1.5% of primary intracranial tumors. Prior elevated incidence of 6% in patients with AIDS has been reduced with effective antiretroviral therapy. B-cell lymphoma is more common than T-cell lymphoma. MRI features of primary and secondary lymphoma of brain overlap. Intracranial lymphoma can involve the dura and/or leptomeninges in secondary lymphoma > primary lymphoma. Extra-axial lymphoma may cause variable destructive or infiltrative changes in single or multiple sites.

(continued on page 586)

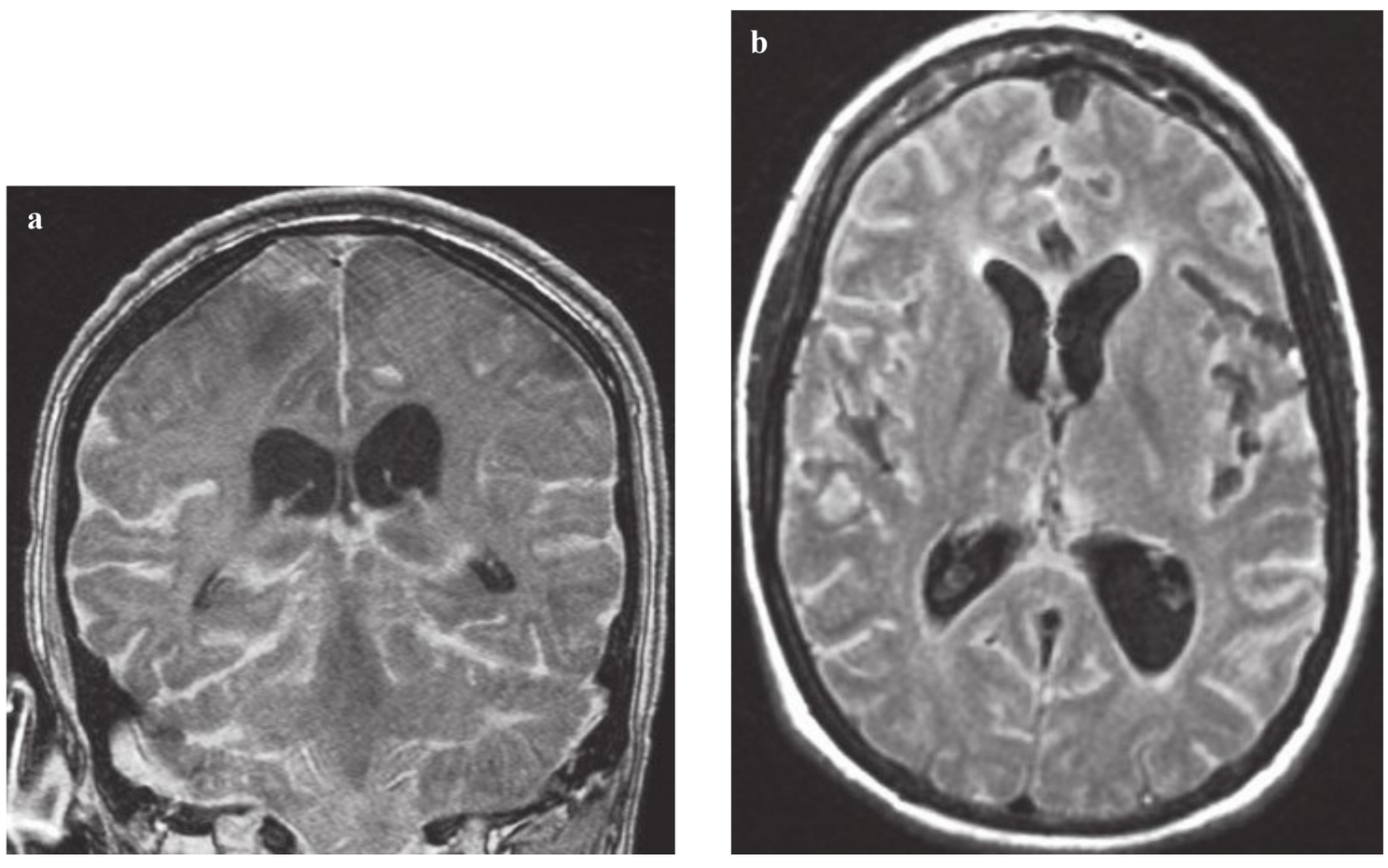

Fig. 4.29 **(a)** Coronal and **(b)** axial postcontrast T1-weighted imaging shows diffuse gadolinium contrast in the intracranial leptomeninges from metastatic melanoma.

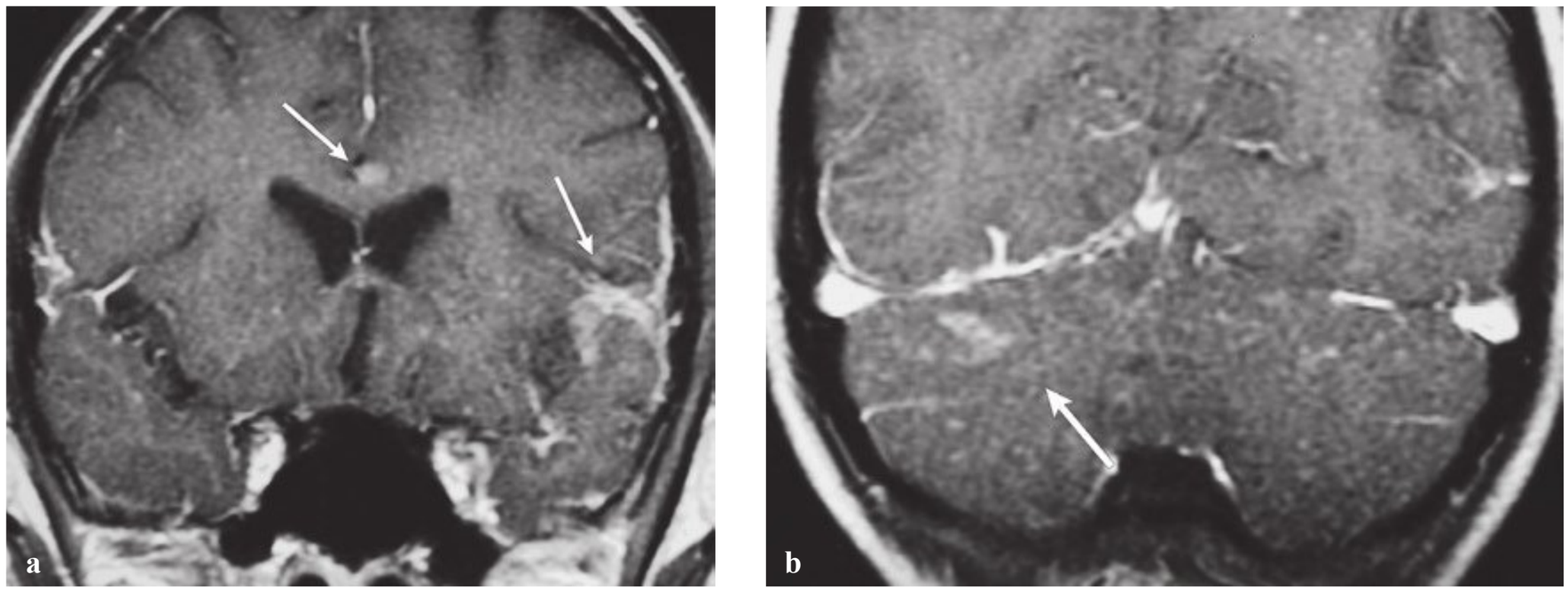

Fig. 4.30 **(a,b)** A 41-year-old woman with abnormal gadolinium contrast enhancement in the intracranial leptomeninges from metastatic breast carcinoma (arrows) as seen on coronal T1-weighted imaging.

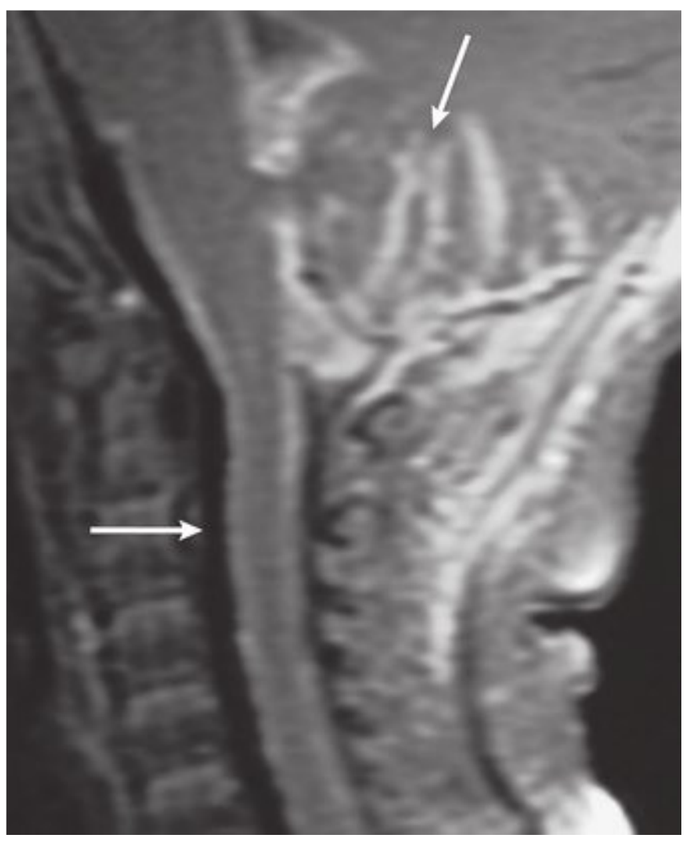

Fig. 4.31 Sagittal postcontrast T1-weighted imaging shows abnormal leptomeningeal gadolinium contrast enhancement within sulci and pial surface of the brainstem and spinal cord from disseminated medulloblastoma (arrows). Abnormal gadolinium contrast is also seen within the fourth ventricle.

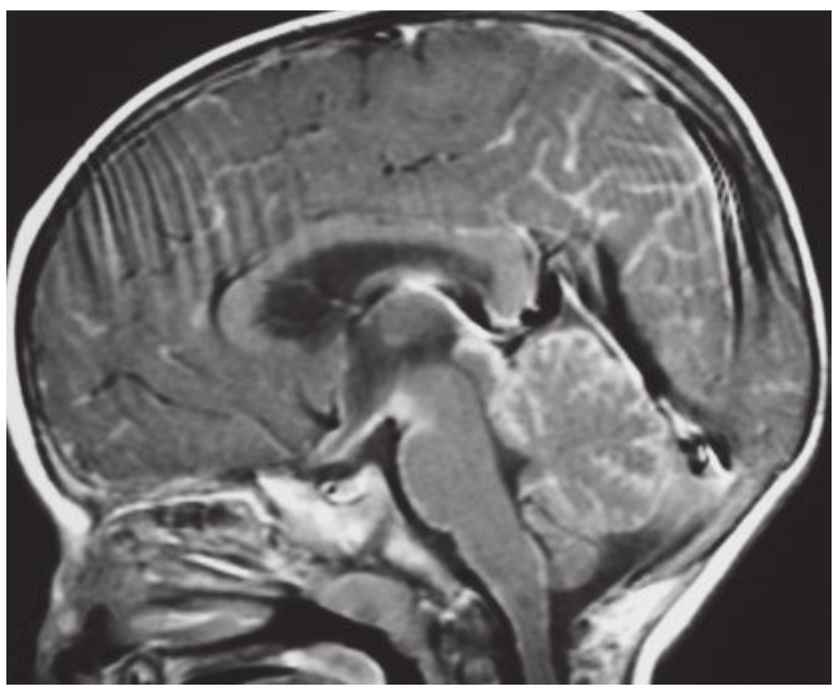

Fig. 4.32 Sagittal postcontrast T1-weighted imaging shows extensive abnormal leptomeningeal gadolinium contrast enhancement from non-Hodgkin lymphoma in a 1-year-old male.

Table 4.2 (cont.) Multifocal and/or diffuse leptomeningeal abnormalities

Lesions	Imaging Findings	Comments
Leukemia	MRI: Irregular localized or diffuse gadolinium contrast enhancement within the subarachnoid space of sulci, cisterns; and/or ventricles, ± nodular and/or diffuse dural gadolinium contrast enhancement, ± intra-axial lesions in brain. Subarachnoid tumor can have high signal on T2 FLAIR. May be associated with obstructive or communicating hydrocephalus. CT: Leptomeningeal tumor often best seen on postcontrast images. Associated intraosseous lesions with bone destruction may be seen.	Leukemias are neoplastic proliferations of hematopoietic cells. Myeloid sarcomas (also referred to as chloromas or granulocytic sarcomas) are focal tumors composed of myeloblasts and neoplastic granulocyte precursor cells and occur in 2% of patients with acute myelogenous leukemia. These lesions can involve the dura, leptomeninges, and brain. Intracranial lesions can be solitary or multiple.
Primary melanocytic tumors of the central nervous system (**Fig. 4.33**)	MRI: Neurocutaneous melanosis: Leptomeningeal lesions have irregular margins, intermediate or high signal (secondary to increased melanin) on T1-weighted imaging in the sulci, intermediate-slightly high signal on T2-weighted imaging, high signal on FLAIR, and leptomeningeal gadolinium contrast enhancement, ± hydrocephalus, ± vermian hypoplasia, ± arachnoid cysts, ± Dandy-Walker malformation. Intra-axial lesions usually < 3 cm in brain parenchyma/brainstem (anterior temporal lobes, cerebellum, thalami, inferior frontal lobes). Intra-axial lesions have intermediate-slightly high signal on T1-weighted imaging secondary to increased melanin, ± decreased signal on T2-weighted imaging, ± gadolinium contrast enhancement. Meningeal melanocytoma: Lesions have low-intermediate or high signal (secondary to increased melanin) on T1-weighted imaging in the sulci, intermediate-slightly high signal on T2-weighted imaging, high signal on FLAIR, and leptomeningeal gadolinium contrast enhancement. CT: May show subtle hyperdensity secondary to increased melanin, ± vermian hypoplasia, ± arachnoid cysts.	Primary melanocytic tumors of the CNS represents a spectrum of benign to malignant pigmented tumors in adults and children. In children, neurocutaneous melanosis is a rare nonfamilial disorder with focal and/or diffuse proliferation of melanocytes in leptomeninges associated with large and/or numerous cutaneous nevi. Presents in infants and young children. Immunoreactive to HMB-45, MART-1, and S-100. Can also occur in adults, referred to as diffuse meningeal melanocytosis or melanosis. Cutaneous nevi are typically benign. In patients with neurocutaneous melanosis, melanocytes in the leptomeninges change into CNS melanoma in 40–50% Meningeal melanocytoma is a benign rare pigmented tumor consisting of leptomeningeal melanocytes, which typically occur in the posterior cranial fossa or spinal canal in patients with a mean age of 42 years.
Myeloma	Multiple (myeloma) or single (plasmacytoma) are well-circumscribed or poorly defined lesions involving the skull and dura, and occasionally the leptomeninges. MRI: Well-circumscribed or poorly defined lesions involving the skull and dura with low-intermediate signal on T1-weighted imaging and intermediate-high signal on T2-weighted imaging, usually with gadolinium contrast enhancement, + bone destruction. Occasionally, gadolinium contrast enhancement may occur in the leptomeninges from subarachnoid tumor. CT: Lesions have low-intermediate attenuation, usually + contrast enhancement, + bone destruction.	Multiple myeloma is malignancy comprised of proliferating antibody-secreting plasma cells derived from single clones. Multiple myeloma is primarily located in bone marrow. A solitary myeloma or plasmacytoma is an infrequent variant in which a neoplastic mass of plasma cells occurs at a single site of bone or soft tissues. Myeloma may cause variable destructive or infiltrative changes in the axial and/or appendicular skeleton.

Lesions	Imaging Findings	Comments
Nonneoplastic Lesions		
Ruptured dermoid (**Fig. 4.34**)	MRI: Well-circumscribed spheroid or multilobulated extra-axial lesions, usually with high signal on T1-weighted images and variable low, intermediate, and/or high signal on T2-weighted imaging, no gadolinium contrast enhancement, ± fluid–fluid or fluid–debris levels. Ruptured dermoids are associated with multiple foci with high signal on T1-weighted imaging in the sulci, cisterns, and/or ventricles. CT: Well-circumscribed spheroid or multilobulated extra-axial lesions, usually with low attenuation, ± fat–fluid or fluid–debris levels. Can cause chemical meningitis if dermoid cyst ruptures into the subarachnoid space. Commonly located at or near midline, supra- > infra-tentorial.	Nonneoplastic congenital or acquired ectodermal-inclusion lesions filled with lipid material, cholesterol, desquamated cells, and keratinaceous debris, usually with mild mass effect on adjacent brain. Occur in adults and in males slightly more than in females, ± related clinical symptoms. Can cause chemical meningitis if dermoid cyst ruptures into the subarachnoid space. Commonly located at or near midline, supra- > infratentorial.

(continued on page 588)

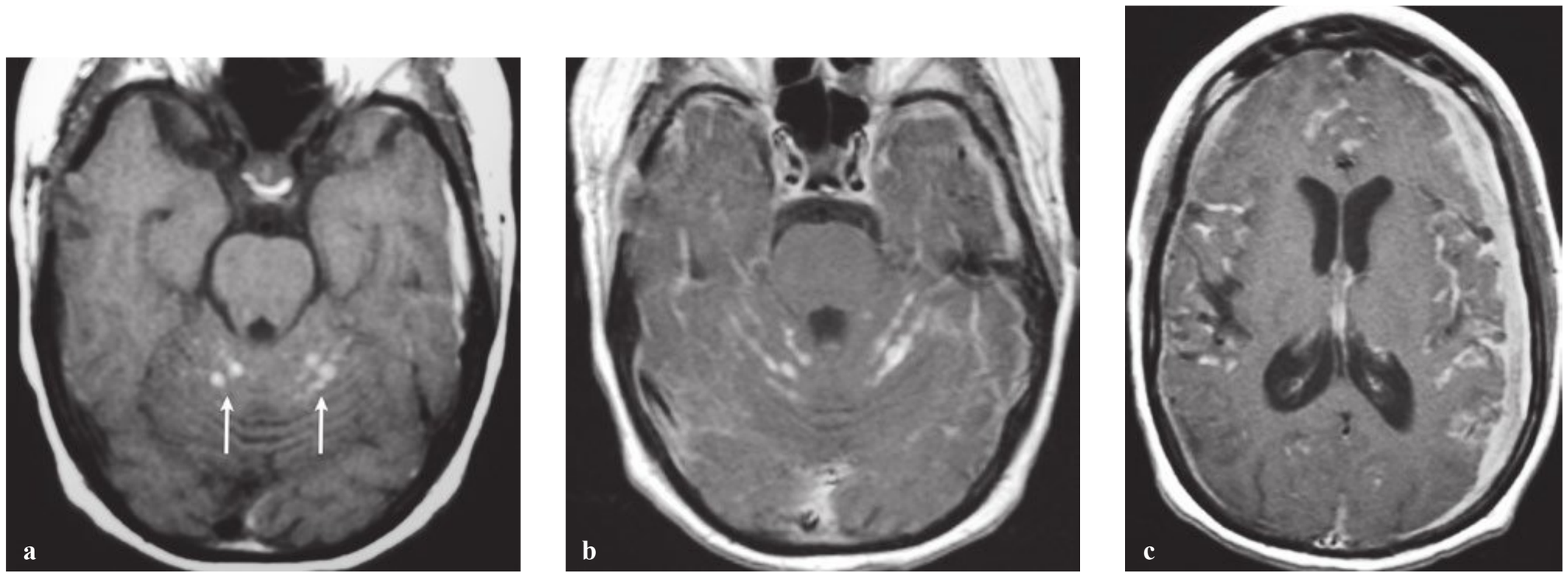

Fig. 4.33 **(a)** A 27-year-old woman with leptomeningeal melanocytosis who has foci with high signal on axial T1-weighted imaging from melanin along the sulci of the upper cerebellum (arrows). **(b,c)** Postcontrast axial T1-weighted imaging shows leptomeningeal and dural gadolinium contrast enhancement.

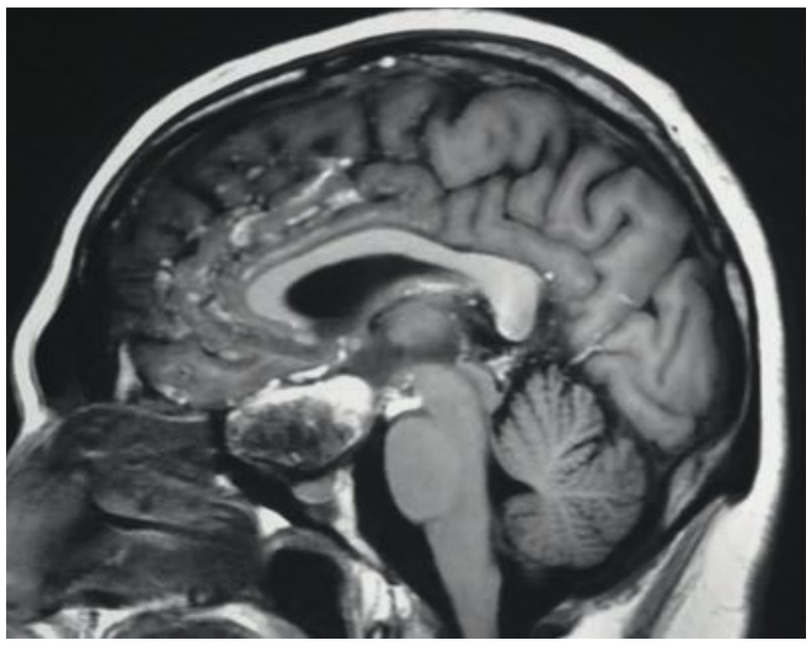

Fig. 4.34 A 23-year-old woman with a ruptured suprasellar dermoid. Sagittal T1-weighted imaging shows an extra-axial dermoid in the suprasellar cistern that has high signal. Multiple foci with high signal are also seen in the subarachnoid space and third ventricle, representing ruptured dermoid contents.

Table 4.2 (cont.) Multifocal and/or diffuse leptomeningeal abnormalities

Lesions	Imaging Findings	Comments
Infection		
Leptomeningeal infection (**Fig. 4.35, Fig. 4.36, Fig. 4.37, Fig. 4.38, Fig. 4.39,** and **Fig. 4.40**)	MRI: Irregular localized or diffuse gadolinium contrast enhancement within the subarachnoid space of sulci and cisterns and/or ventricles, ± nodular and/or diffuse dural gadolinium contrast enhancement, ± intra-axial lesions in the brain. Leptomeningeal gadolinium contrast enhancement is often thin and linear with bacterial or viral meningitis, and thick and irregular with fungal infection. Infection in the leptomeninges can have high signal on T2 FLAIR. May be associated with obstructive or communicating hydrocephalus. CT: Leptomeningeal infection often best seen on postcontrast images.	Subarachnoid infection by bacteria, fungi, viruses, and parasites can be seen as focal and/or diffuse zones of abnormal gadolinium contrast enhancement in the leptomeninges with or without dural involvement. Meningitis may result by direct extension (trauma, surgery, paranasal sinus infections, or osteomyelitis involving the skull) or hematogenously. Can occur in immuocompetent and immunocompromised patients. Gadolinium contrast enhancement results from breakdown of the blood–brain barrier without angiogenesis.

(continued on page 590)

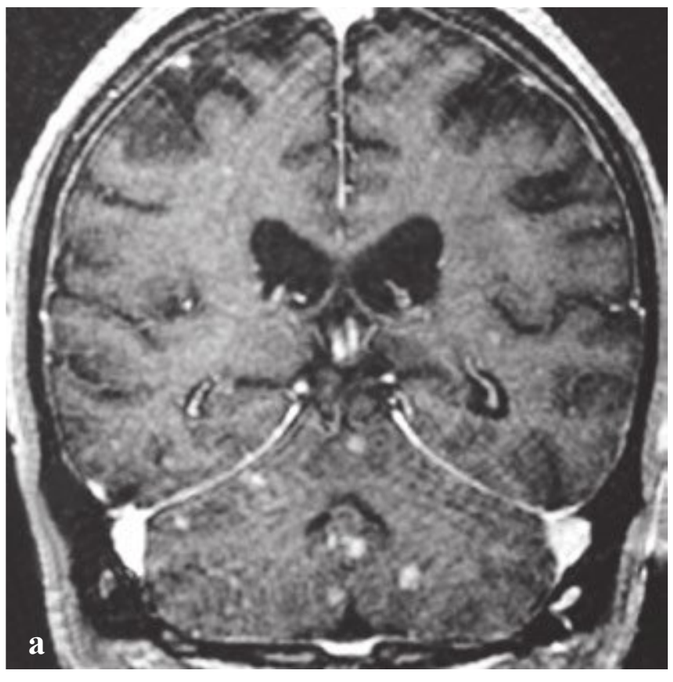

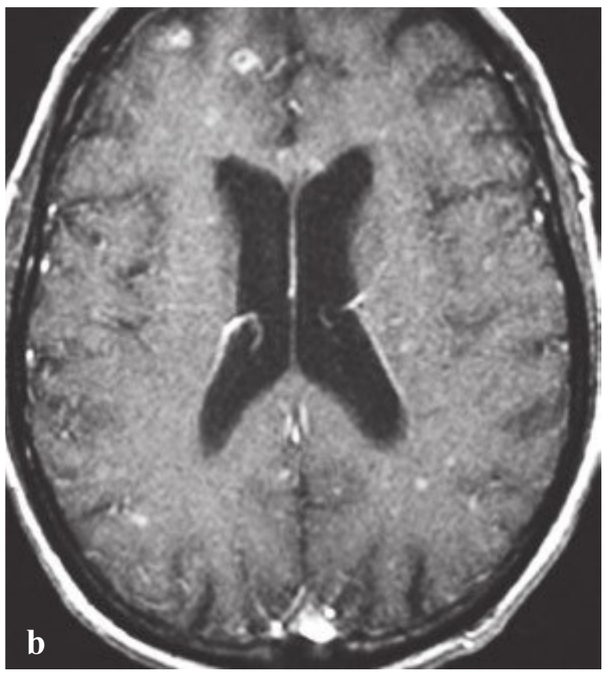

Fig. 4.35 A 57-year-old man with multiple foci of gadolinium contrast enhancement in the leptomeninges on **(a)** coronal and **(b)** axial T1-weighted imaging from bacterial meninigitis secondary to Nocardia infection.

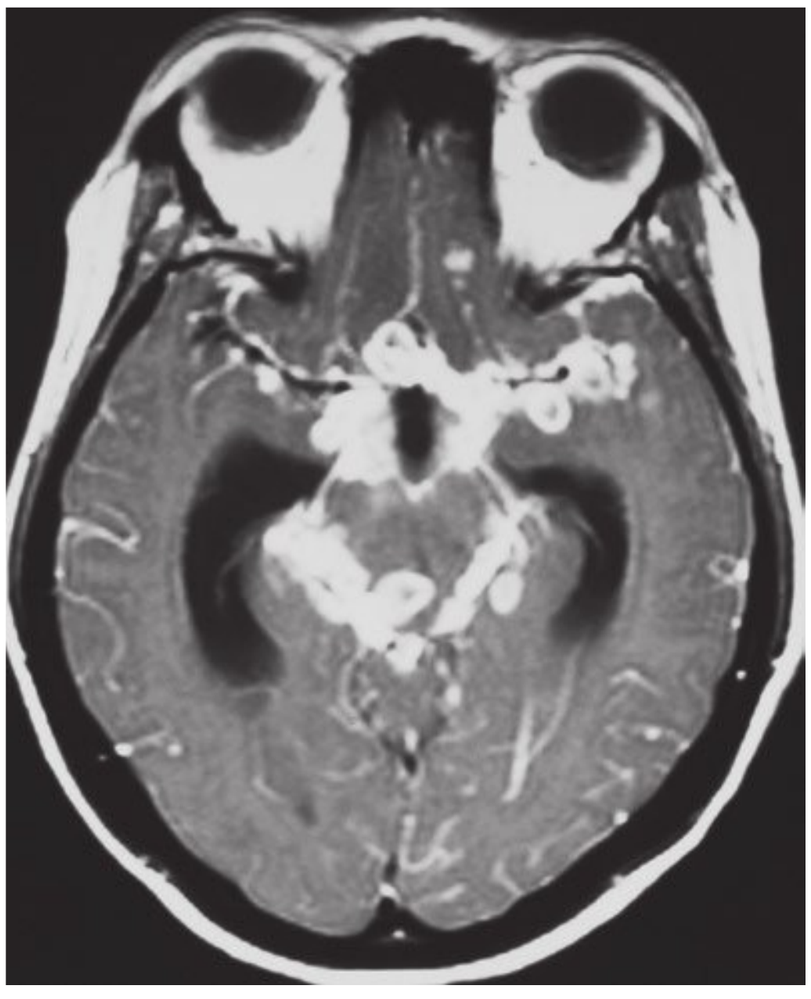

Fig. 4.36 Linear and ring-shaped zones of gadolinium contrast enhancement are seen in the basal meninges and sylvian fissures on axial T1-weighted imaging in a patient with tuberculous meningitis.

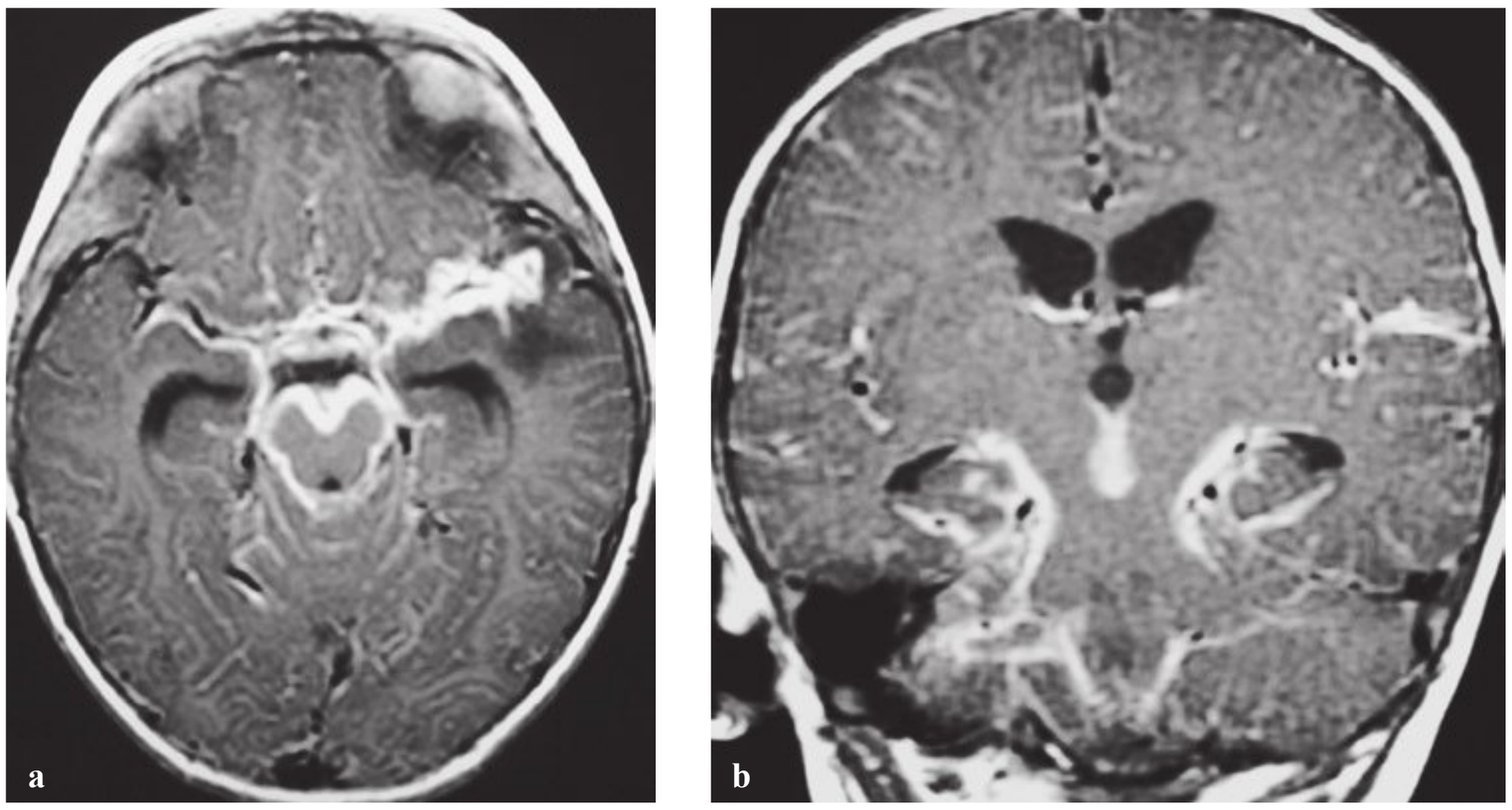

Fig. 4.37 A 14-month-old male with tuberculous meningitis seen as diffuse abnormal gadolinium contrast enhancement in the basal meninges, sylvian fissures, and infra- and supratentorial sulci on **(a)** axial and **(b)** coronal T1-weighted imaging.

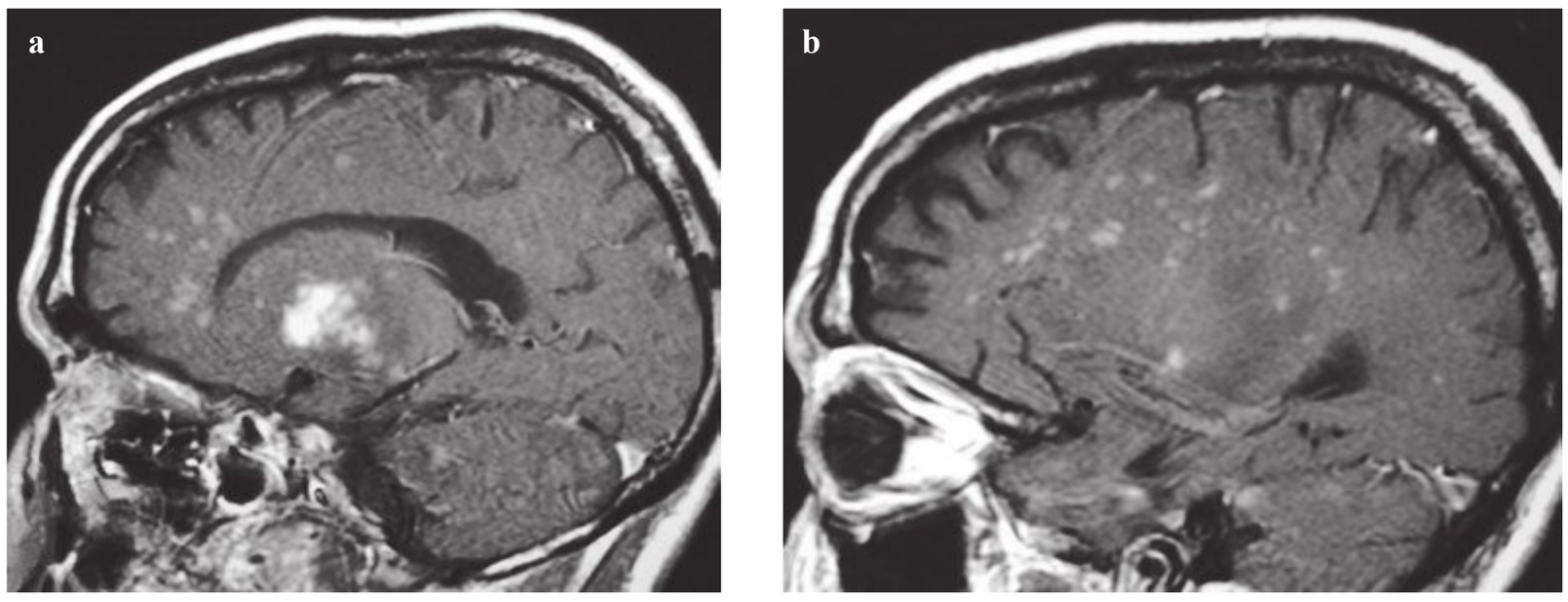

Fig. 4.38 Immunocompromised patient with intracranial Cryptococcus infection. **(a,b)** Sagittal T1-weighted imaging shows abnormal gadolinium contrast enhancement in the brain parenchyma and subarachnoid spaces of the sulci.

Fig. 4.39 A 76-year-old man with cysticercosis who has multiple small calcified granulomas in the sulci and brain on axial CT.

Fig. 4.40 Patient with toxoplasmosis who has multiple calcified granulomas in the sulci and brain on axial CT.

Table 4.2 (cont.) Multifocal and/or diffuse leptomeningeal abnormalities

Lesions	Imaging Findings	Comments
Noninfectious Inflammatory Disorders		
Sarcoidosis (**Fig. 4.41**)	MRI: Linear and/or nodular gadolinium contrast enhancement in the leptomeninges and/or dura are usually seen. Intra-axial lesions have poorly defined margins and usually have low-intermediate signal on T1-weighted imaging and slightly high to high signal on T2-weighted imaging and FLAIR, usually with gadolinium contrast enhancement, + localized mass effect and peripheral edema. CT: Linear and/or nodular gadolinium contrast enhancement in the leptomeninges and/or dura usually seen. Poorly marginated intra-axial zone(s) with low-intermediate attenuation can occur, which often show contrast enhancement, + localized mass effect and peripheral edema.	Sarcoidosis is a multisystem noncaseating granulomatous disease of uncertain cause that can involve the CNS in 5 to 15% of cases. If untreated, it is associated with severe neurologic deficits, such as encephalopathy, cranial neuropathies, and myelopathy. Diagnosis of neurosarcoid may be difficult when the neurologic complications precede other systemic manifestations involving the lungs, lymph nodes, skin, bone, and/or eyes.
Langerhans' cell histiocytosis	MRI: Fusiform or lobulated lesion with intermediate signal on T1- and T2-weighted imaging involving hypothalamus /pituitary stalk, skull, dura and rarely the leptomeninges. Lesions involving skull, dura, pituitary stalk, and leptomeninges usually show gadolinium contrast enhancement. CT: Intraosseous lesions usually have low-intermediate attenuation and are typically associated with localized bone destruction, + contrast enhancement of the adjacent dura and rarely the leptomeninges. Thickening of the pituitary stalk may be seen.	Disorder of reticuloendothelial system in which bone marrow-derived dendritic Langerhans' cells infiltrate various organs as focal lesions or in diffuse patterns. Langerhans' cells have eccentrically located ovoid or convoluted nuclei within pale to eosinophilic cytoplasm. Lesions often consist of Langerhans' cells, macrophages, plasma cells, and eosinophils. Lesions are immunoreactive to S-100, CD1a, CD-207, HLA-DR, and β_2-microglobulin. LCH has been associated with BRAF or MAP2K1 mutations. Prevalence of 2 per 100,000 children less than 15 years old; only a third of lesions occur in adults. Localized lesions (eosinophilic granuloma) can be single or multiple in the skull, usually at the skull base. Intradural lesions occur at pituitary stalk/hypothalamus and can present with diabetes insipidus, and lesions rarely occur in brain tissue (< 4% of patients with Langerhans' cell histiocytosis). Occur in patients with median age = 10 years, average age = 13.5 years, peak incidence is between 5 and 10 years, and 80 to 85% occur in patients less than 30 years old.

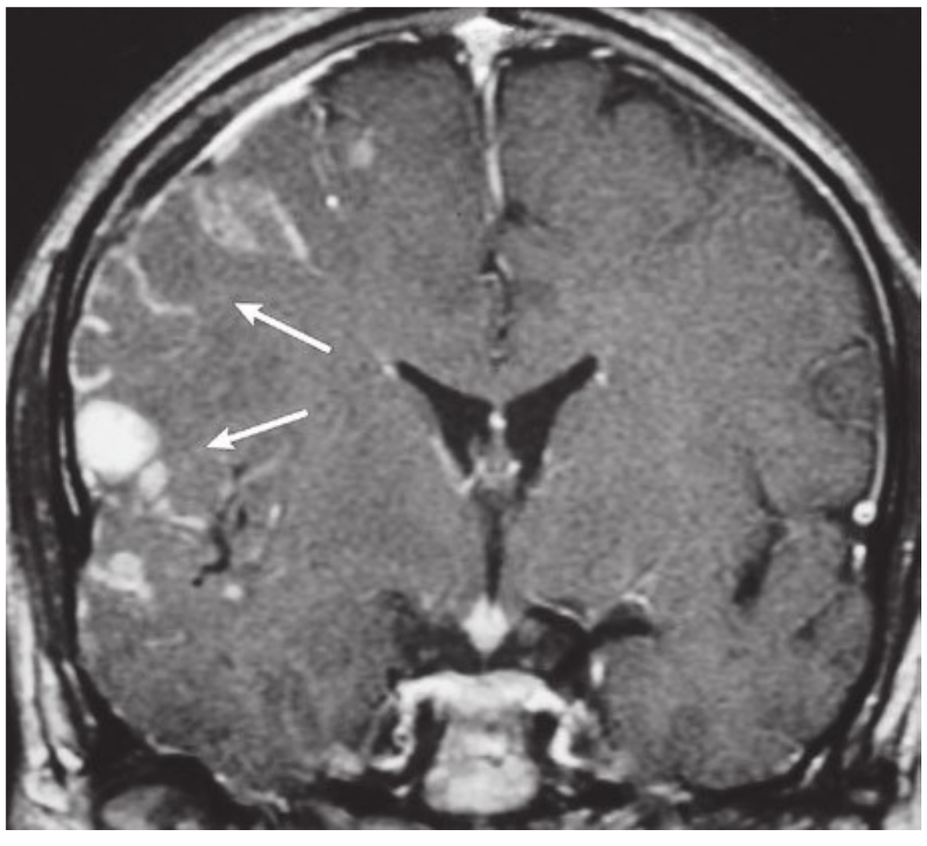

Fig. 4.41 A 33-year-old man with neurosarcoidosis who has abnormal gadolinium contrast enhancement in the leptomeninges (arrows), including the suprasellar cistern, on coronal T1-weighted imaging.

Lesions	Imaging Findings	Comments
Granulomatosis with polyangiitis (formerly referred to as Wegener's granulomatosis)	MRI: Poorly defined zones of soft tissue thickening with low-intermediate signal on T1-weighted imaging, slightly high to high signal on T2-weighted imaging, and gadolinium contrast enhancement within the nasal cavity, paranasal sinuses, infratemporal fossa, and external auditory canal, ± bone invasion and destruction, ± extension into the skull base. Intracranially, there can be involvement of the dura, leptomeninges, brain, or venous sinuses. CT: Zones with soft tissue attenuation, ± bone destruction.	Multisystem disease with necrotizing granulomas in the respiratory tract, focal necrotizing angiitis of small arteries and veins of various tissues, and glomerulonephritis. Can involve the paranasal sinuses, nasopharynx, orbits, skull base, dura, and rarely the leptomeninges. Peak incidence is in the fifth decade, and annual incidence is 8 per million. Antibodies to neutrophil cytoplasmic antigens (ANCA) occur in 80–90% of patients and play a role in pathogenesis.
Inflammatory pseudotumor (**Fig. 4.42**)	MRI: Smooth and/or nodular gadolinium contrast enhancement in the dura and/or leptomeninges, ± extension into the skull base, infratemporal soft tissue, and/or orbits. Lesions in the brain can appear as poorly marginated intra-axial zones with low-intermediate signal on T1-weighted imaging and slightly high to high signal on T2-weighted imaging and FLAIR, usually with gadolinium contrast enhancement, + localized mass effect and peripheral edema. CT: Smooth and/or nodular contrast enhancement in the leptomeninges and/or dura can be seen. Intra-axial lesions usually have poorly defined margins, low-intermediate attenuation, usually with contrast enhancement, + localized mass effect and peripheral edema.	Chronic inflammatory disorder of unknown etiology with lesions composed of spindle cells, lymphocytes, and plasma cells. Lesions can occur in many locations, most commonly in the orbits and lungs. Rarely occur in the skull base, dura, and brain. Usually occur in children and young adults. Can be asymptomatic or associated with localized mass effect as well as systemic signs, such as weight loss and fever. Treatment of orbital inflammatory pseudotumor is typically with steroid medication. Surgery is often performed for lesions in other locations.

(continued on page 592)

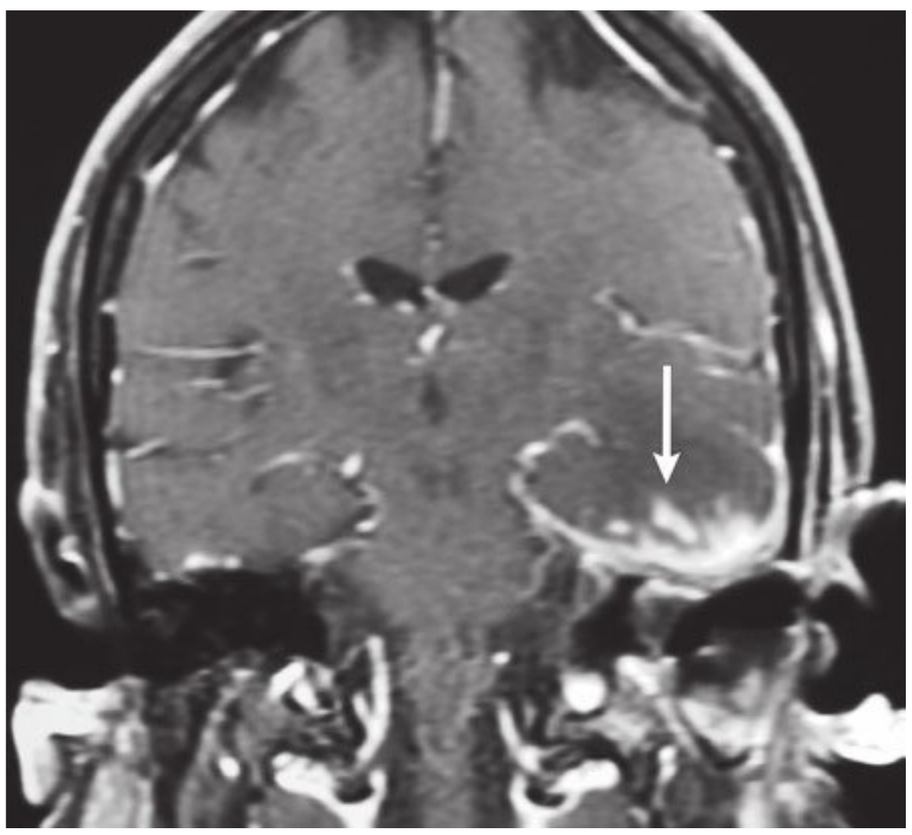

Fig. 4.42 A 53-year-old woman with inflammatory pseudotumor seen as abnormal gadolinium contrast enhancement involving the dura and leptomeninges (arrow) in the inferior left temporal region, as well as abnormal gadolinium contrast enhancement within the inferior left temporal lobe on coronal T1-weighted imaging.

Table 4.2 (cont.) Multifocal and/or diffuse leptomeningeal abnormalities

Lesions	Imaging Findings	Comments
Hemorrhage and Vascular Abnormalities		
Subarachnoid hemorrhage (**Fig. 4.43** and **Fig. 4.44**)	MRI: May not be seen on T1- or T2-weighted imaging, although may have intermediate to slightly high signal on FLAIR images, and occasionally has high signal on T1-weighted imaging. CT: Acute subarachnoid hemorrhage typically appears as poorly defined zones with high attenuation in the leptomeninges within the sulci and basal cisterns. Usually becomes isodense or hypodense after 1 week unless there is rebleeding.	Extravasated blood in the subarachnoid space can result from ruptured arterial aneurysms or dural venous sinuses, vascular malformations, hypertensive hemorrhages, trauma, cerebral infarcts, coagulopathy, etc.
Superficial siderosis (**Fig. 4.45**)	MRI: Low signal on T2-weighted imaging, GRE, and susceptibility-weighted imaging along the pial surfaces of the brain, brainstem, and cranial nerves, ± ependymal lining. May be associated with brain atrophy, which often involves the cerebellum.	Deposition of hemosiderin along the pial surfaces of the brain and brainstem results from episodes of hemorrhage within the subarachnoid space. Can be secondary to vascular malformations, amyloid angiopathy, trauma, hemorrhagic vasculopathy, hemorrhagic neoplasms, and ruptured aneurysms. Results in toxic effects on brain and cochleovestibular nerves, and can be associated with cranial neuropathies, including hearing loss, gait ataxia, and dysarthria.

(continued on page 594)

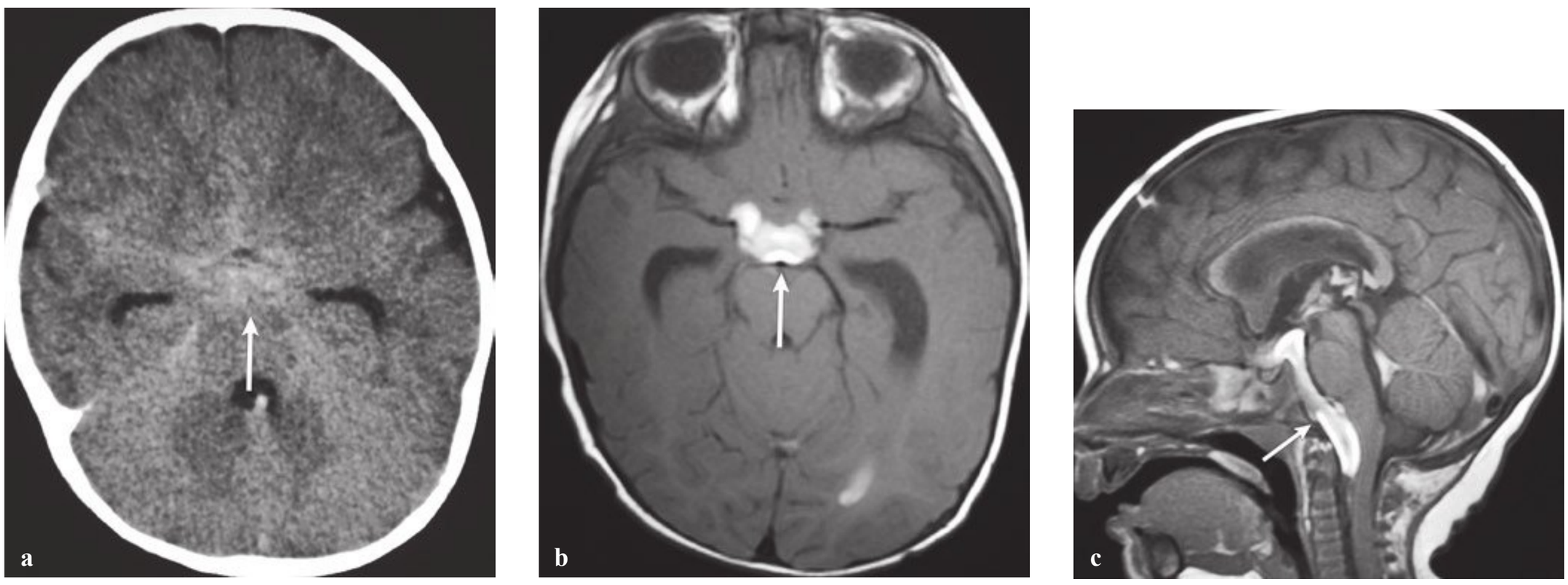

Fig. 4.43 **(a)** Subarachnoid hemorrhage with poorly defined increased attenuation in the suprasellar and basal cisterns (arrow) on axial CT. The subarachnoid hemorrhage has high signal on **(b)** axial (arrow) and **(c)** sagittal T1-weighted imaging (arrow). Intraventricular high signal is also seen in the left lateral ventricle and third and fourth ventricles **(b,c)**.

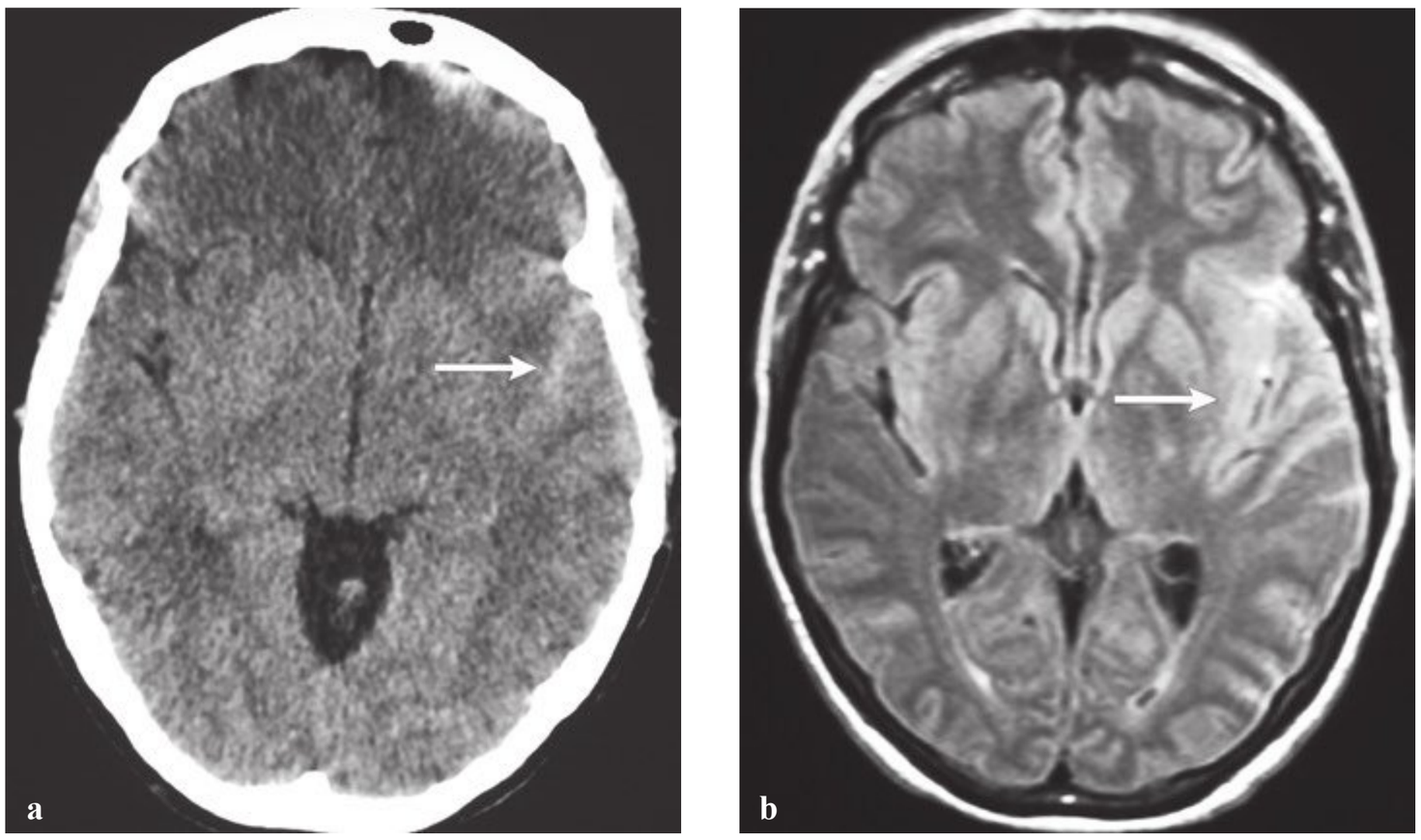

Fig. 4.44 Subarachnoid hemorrhage is seen as poorly defined increased attenuation in the subarachnoid space of the left sylvian fissure on **(a)** axial CT (arrow) and **(b)** corresponding high signal on axial FLAIR (arrow).

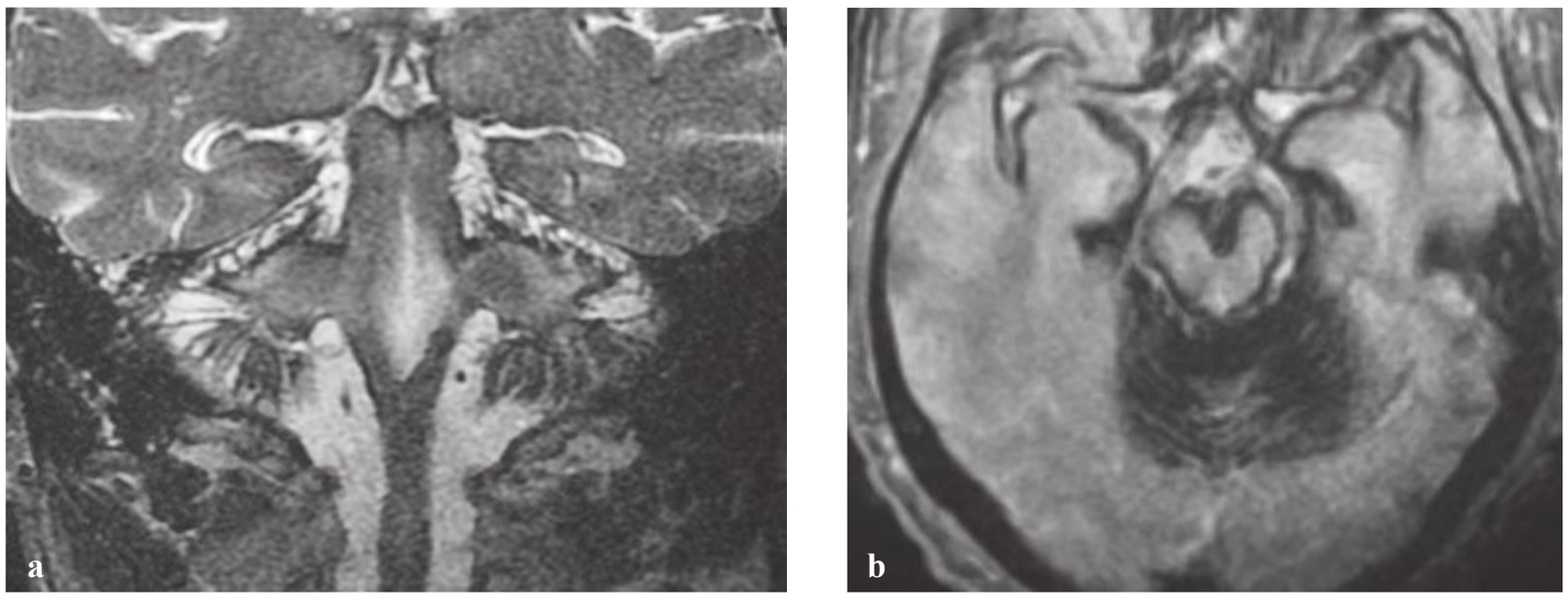

Fig. 4.45 Superficial siderosis seen as low signal on **(a)** coronal T2-weighted imaging and **(b)** axial GRE along the pial surface of the brainstem and pial surface of the cerebellum and cerebrum. Secondary atrophic changes are seen in the cerebellum.

Table 4.2 (cont.) Multifocal and/or diffuse leptomeningeal abnormalities

Lesions	Imaging Findings	Comments
Sturge-Weber syndrome (**Fig. 4.46** and **Fig. 4.47**)	MRI: Prominent localized unilateral leptomeningeal gadolinium contrast enhancement, usually in parietal and/or occipital regions in children, ± gyral enhancement, mild localized atrophic changes in brain with decreased signal on T2-weighted imaging adjacent to the pial angioma, ± prominent medullary and/or subependymal veins, ± ipsilateral prominence of choroid plexus. CT: Localized encephalomalacia adjacent to gyral calcifications > 2 years, progressive cerebral atrophy in region of pial angioma.	Also known as encephalotrigeminal angiomatosis, Sturge-Weber syndrome is a neurocutaneous syndrome associated with ipsilateral port wine cutaneous lesion and seizures and results from persistence of primitive leptomeningeal venous drainage (pial angioma) and developmental lack of normal cortical veins, producing chronic venous congestion and ischemia. Patients often present with progressive neurologic impairment.
Moyamoya disease (**Fig. 4.48**)	MRI: Multiple, tortuous, small, enhancing vessels may be seen in the basal ganglia and thalami secondary to dilated collateral arteries, + enhancement of the arteries related to slow flow within the collateral arteries versus normal-size arteries. Gadolinium contrast enhancement of the leptomeninges related to pial collateral vessels can be seen. MRA shows narrowed or occluded upper internal carotid arteries. Gadolinium-enhanced MRA can show enhancement of leptomeningeal and other small collateral vessels. CTA shows stenosis and occlusion of the distal internal carotid arteries with collateral arteries (lenticulostriate, thalamoperforate, and leptomeningeal) best seen after contrast administration, enabling detection of slow blood flow.	Progressive occlusive disease of the intracranial portions of the internal carotid arteries, with resultant numerous dilated collateral arteries arising from the lenticulostriate and thalamoperforate arteries as well as other parenchymal, leptomeningeal, and transdural arterial anastomoses. Moyamoya means "puff of smoke," which refers to the angiographic appearance of the collateral arteries (lenticulostriate, thalamoperforate). The disease usually has a nonspecific etiology but can be associated with neurofibromatosis, radiation angiopathy, atherosclerosis, or sickle-cell disease, and it usually occurs in Asians, in children more often than in adults.
Developmental Abnormality		
Benign enlargement of the subarachnoid space in infancy (**Fig. 4.49**)	MRI and CT: In the first year of life, subarachnoid spaces with CSF fluid attenuation and MRI signal are typically enlarged symmetrically in the frontal region, sylvian fissures, and anterior interhemispheric fissure. Slight enlargement of the lateral and third ventricles is often present.	Neurologically normal infants who have a developmental self-limited variation with transiently enlarged intracranial subarachnoid spaces and normal to slightly increased ventricular sizes, often with mild macrocephaly (high normal range, > 95th percentile in first 7 months). Head circumference and subarachnoid spaces return to normal sizes at 2 years. Can be idiopathic or familial. Persistent enlargement of the subarachnoid spaces beyond 3 years of age can be seen with disorders like the mucopolysaccharidoses, achrondroplasia, Sotos syndrome, and glutaric aciduria type 1.

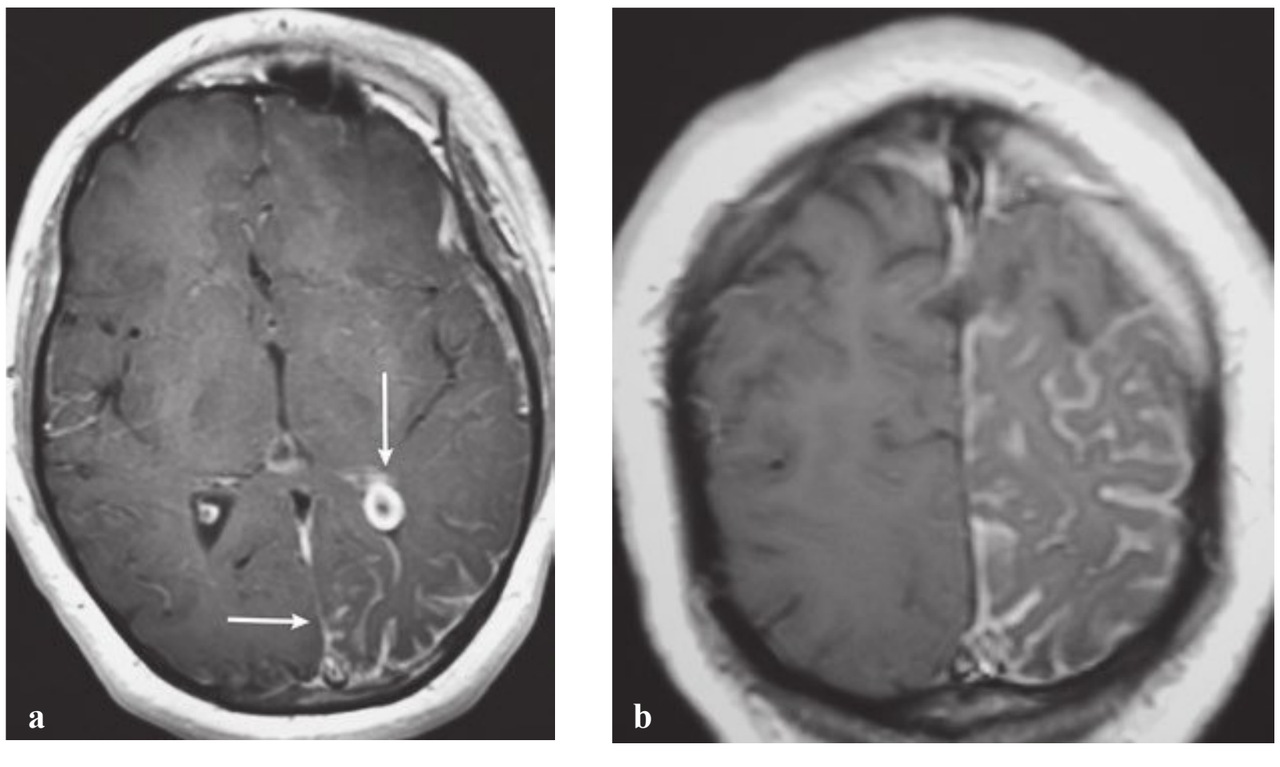

Fig. 4.46 Sturge-Weber syndrome with pial angioma seen as abnormal gadolinium contrast enhancement in the leptomeninges adjacent to the posterior left cerebral hemisphere on **(a)** axial (arrows) and **(b)** coronal T1-weighted imaging. Also seen is enlargement of the choroid plexus in the atrium of the left lateral ventricle **(a)**.

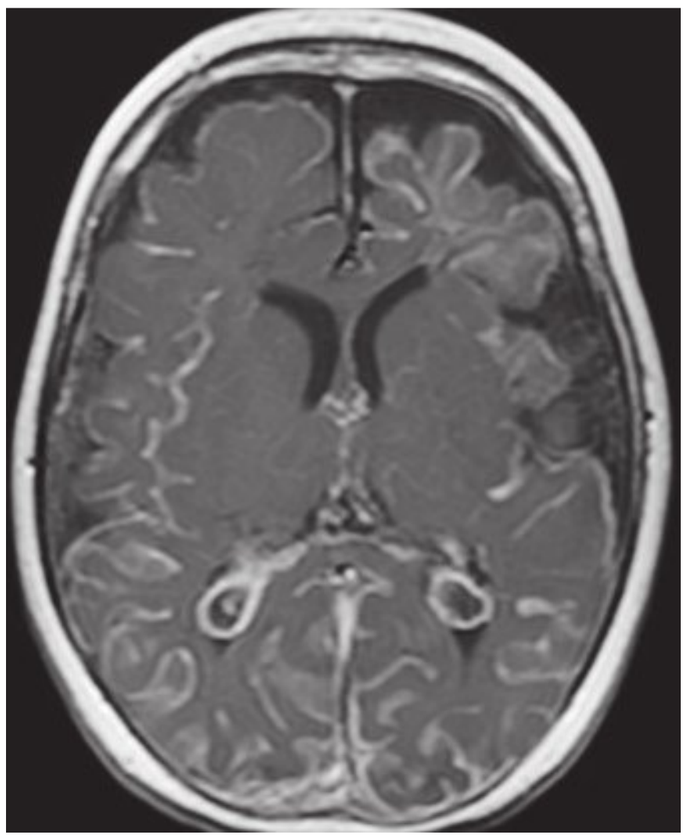

Fig. 4.47 A9-month-old female with Sturge-Weber syndrome, with extensive gadolinium contrast enhancement seen in the leptomeninges bilaterally on axial T1-weighted imaging. Also seen is enlargement of the choroid plexus in the atria of both lateral ventricles.

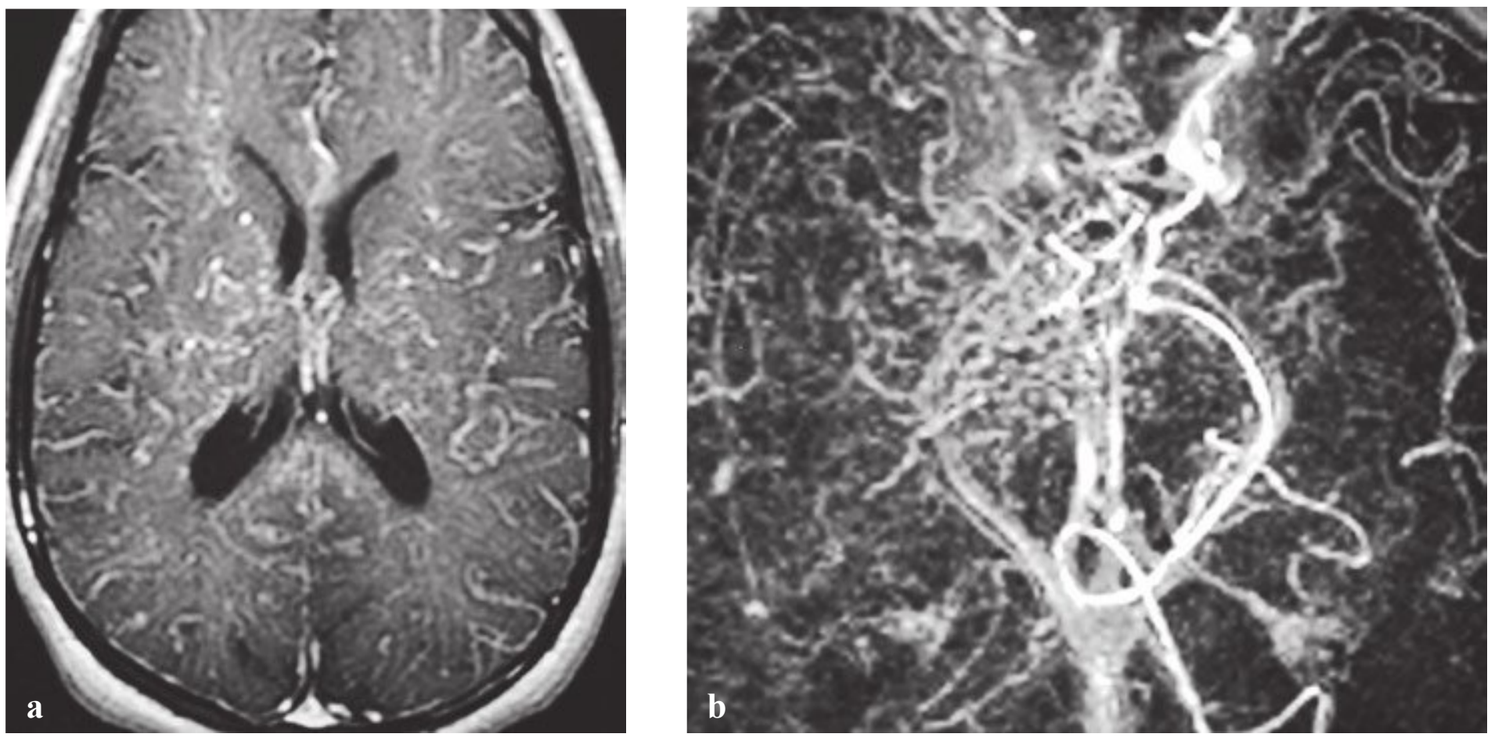

Fig. 4.48 A31-year-old man with moyamoya disease. **(a)** Postcontrast axial T1-weighted imaging shows multiple enhancing lenticulostriate collateral blood vessels in the basal ganglia and leptomeninges. **(b)** Postcontrast axial MRA shows multiple small enhancing leptomeningeal and lecticulostriate collateral blood vessels.

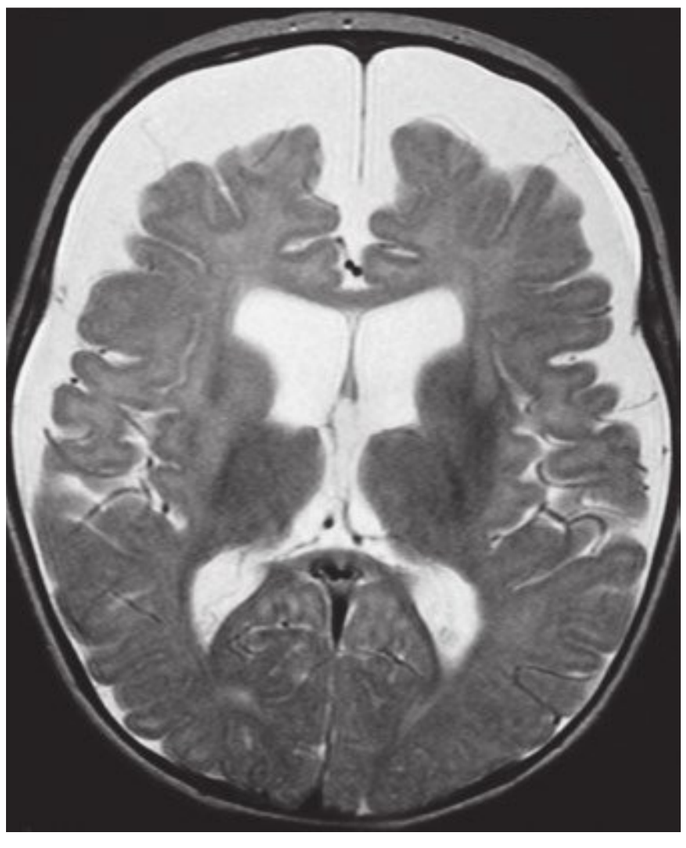

Fig. 4.49 A9-month-old female with benign enlargement of the subarachnoid spaces in the frontal regions on axial T2-weighted imaging.

References

Benign Enlargement of Subarachnoid Spaces in Infancy

1. Kuruvilla LC. Benign enlargement of sub-arachnoid spaces in infancy. J Pediatr Neurosci 2014;9(2):129–131
2. Paciorkowski AR, Greenstein RM. When is enlargement of the subarachnoid spaces not benign? A genetic perspective. Pediatr Neurol 2007;37(1):1–7

Contrast Enhancement of the Meninges

3. Smirniotopoulos JG, Murphy FM, Rushing EJ, Rees JH, Schroeder JW. Patterns of contrast enhancement in the brain and meninges. Radiographics 2007;27(2):525–551

Granulomatous Lesions

4. Razek AAKA, Castillo M. Imaging appearance of granulomatous lesions of head and neck. Eur J Radiol 2010;76(1):52–60

Granulomatosis with Polyangiitis (formerly Wegener's granulomatosis)

5. Di Comite G, Bozzolo EP, Praderio L, Tresoldi M, Sabbadini MG. Meningeal involvement in Wegener's granulomatosis is associated with localized disease. Clin Exp Rheumatol 2006;24(2, Suppl 41):S60–S64
6. Gajic-Veljic M, Nikolic M, Peco-Antic A, Bogdanovic R, Andrejevic S, Bonaci-Nikolic B. Granulomatosis with polyangiitis (Wegener's granulomatosis) in children: report of three cases with cutaneous manifestations and literature review. Pediatr Dermatol 2013;30(4):e37–e42
7. Pakrou N, Selva D, Leibovitch I. Wegener's granulomatosis: ophthalmic manifestations and management. Semin Arthritis Rheum 2006;35(5):284–292
8. Tarabishy AB, Schulte M, Papaliodis GN, Hoffman GS. Wegener's granulomatosis: clinical manifestations, differential diagnosis, and management of ocular and systemic disease. Surv Ophthalmol 2010;55(5):429–444
9. Trimarchi M, Sinico RA, Teggi R, Bussi M, Specks U, Meroni PL. Otorhinolaryngological manifestations in granulomatosis with polyangiitis (Wegener's). Autoimmun Rev 2013;12(4):501–505
10. Watanabe K, Tani Y, Kimura H, et al. Hypertrophic cranial pachymeningitis in MPO-ANCA-related vasculitis: a case report and literature review. Fukushima J Med Sci 2013;59(1):56–62

Idiopathic Hypertrophic Pachymeningitis

11. Kupersmith MJ, Martin V, Heller G, Shah A, Mitnick HJ. Idiopathic hypertrophic pachymeningitis. Neurology 2004;62(5):686–694

Inflammatory Pseudotumor

12. Häusler M, Schaade L, Ramaekers VT, Doenges M, Heimann G, Sellhaus B. Inflammatory pseudotumors of the central nervous system: report of 3 cases and a literature review. Hum Pathol 2003;34(3):253–262
13. Park SB, Lee JH, Weon YC. Imaging findings of head and neck inflammatory pseudotumor. AJR Am J Roentgenol 2009;193(4):1180–1186

Intracranial Hypotension

14. Hadizadeh DR, Kovács A, Tschampa H, Kristof R, Schramm J, Urbach H. Postsurgical intracranial hypotension: diagnostic and prognostic imaging findings. AJNR Am J Neuroradiol 2010;31(1):100–105
15. Haritanti A, Karacostas D, Drevelengas A, et al. Spontaneous intracranial hypotension: clinical and neuroimaging findings in six cases with literature review. Eur J Radiol 2009;69(2):253–259
16. Medina JH, Abrams K, Falcone S, Bhatia RG. Spinal imaging findings in spontaneous intracranial hypotension. AJR Am J Roentgenol 2010;195(2):459–464
17. Rahman M, Bidari SS, Quisling RG, Friedman WA. Spontaneous intracranial hypotension: dilemmas in diagnosis. Neurosurgery 2011;69(1):4–14, discussion 14
18. Schievink WI, Maya MM, Louy C, Moser FG, Tourje J. Diagnostic criteria for spontaneous spinal CSF leaks and intracranial hypotension. AJNR Am J Neuroradiol 2008;29(5):853–856
19. Shah LM, McLean LA, Heilbrun ME, Salzman KL. Intracranial hypotension: improved MRI detection with diagnostic intracranial angles. AJR Am J Roentgenol 2013;200(2):400–407
20. Urbach H. Intracranial hypotension: clinical presentation, imaging findings, and imaging-guided therapy. Curr Opin Neurol 2014;27(4):414–424

Mass Lesions Involving Dura

21. Smith AB, Horkanyne-Szakaly I, Schroeder JW, Rushing EJ. From the radiologic pathology archives: mass lesions of the dura: beyond meningioma-radiologic-pathologic correlation. Radiographics 2014;34(2):295–312

Metastases

22. Lee EK, Lee EJ, Kim MS, et al. Intracranial metastases: spectrum of MR imaging findings. Acta Radiol 2012;53(10):1173–1185
23. Mahendru G, Chong V. Meninges in cancer imaging. Cancer Imaging 2009;9 Spec No A:S14–S21
24. Pauls S, Fischer AC, Brambs HJ, Fetscher S, Höche W, Bommer M. Use of magnetic resonance imaging to detect neoplastic meningitis: limited use in leukemia and lymphoma but convincing results in solid tumors. Eur J Radiol 2012;81(5):974–978

Primary Melanoncytic Tumors

25. Islam MP, Neurocutaneous melanosis. Handb Clin Neurol. 2015; 132:111–117. doi: 10.1016/B978-0-444-62702-5.00007-X
26. Kusters-Vandevelde HVN, Kusters B, van Engen-van Grunsven A, Groenen PJTA, et al. Primary melanocytic tumors of the central nervous system: a review with focus on molecular aspects. Brain Path 2015;25:209–226
27. Matsumura M, Okudela K, Tateishi Y, Umeda S, et al. Leptomeningeal melanomatosis associated with neurocutaneous melanosis: an autopsy case report. Pathol Int 2015;65(2):100–105. doi: 10.1111/pin.12238
28. Sutton BJ, Tatter SB, Stanton CA, Mott RT. Leptomeningeal melanocytosis in an adult male without large congenital nevi: a rare and atypical case of neurocutaneous melanosis. Clin Neuropathol 2011;30:178–182
29. Yang C, Fang J, Li G, Jia W, et al. Spinal meningeal melanocytomas: clinical manifestations, radiological and pathological characteristics, and surgical outcomes. J Neurooncol 2016;127:279–286
30. Yang C, Fang J, Li G, Yang J, et al. Primary scattered multifocal melanocytomas in spinal canal mimicking neurofibromatosis. Spine J 2016; doi:10.1016/j.spinee.2016.03.007 [Epub ahead of print]

Chapter 5

Vascular Abnormalities

Introduction 598

5.1 Congenital and developmental vascular anomalies/variants 607

5.2 Acquired vascular disease 620

References 638

5 Vascular Abnormalities

Table 5.1 Congenital and developmental vascular anomalies/variants

Table 5.2 Acquired vascular disease

Introduction

Arterial Anatomy

The intracranial arterial system is divided into the anterior and posterior circulations. The *anterior circulation* includes the internal carotid artery and its branches as well the anterior and middle cerebral arteries and anterior and posterior communicating arteries. The *posterior circulation* includes the vertebral arteries, basilar artery, and posterior cerebral arteries (**Fig. 5.1**).

The internal carotid artery (ICA) is divided into seven segments corresponding to their embryonic precursor arteries (**Fig. 5.2** and **Fig. 5.3**). The first ICA segment extends from the bifurcation of the common carotid artery in the neck to the inferior level of the skull base. The second ICA segment is located within the petrous carotid canal of the temporal bone and has two small branches, the vidian artery (artery of the pterygoid canal), which anastomoses with branches of the external carotid artery (ECA), and the caroticotympanic artery to the middle ear. The third ICA segment is a short portion superior to the foramen lacerum that extends from the petrous apex to the cavernous sinus. The fourth ICA segment is located within the cavernous sinus and has two major branches (the meningohypophyseal trunk, which supplies the pituitary gland; clival dura; and tentorium via basal and marginal tentorial branch arteries, inferior hypophyseal artery, and trigeminal ganglion artery; and the inferolateral trunk, which supplies the cranial nerves and dura of the cavernous sinuses via cavernous sinus and meningeal branch arteries), which have anastomoses with branches of the ECA. The fifth ICA segment courses within the anterior portion of the cavernous sinus until it exits superiorly into the cranial cavity. The ophthalmic artery may occasionally arise from the fifth segment. The sixth ICA segment is the first segment in the intracranial subarachnoid space and has two branches (the ophthalmic artery and the superior hypophyseal artery, which supplies the adenohypophysis, pituitary stalk, and optic chiasm). The seventh ICA segment extends superiorly to the bifurcation of the ICA

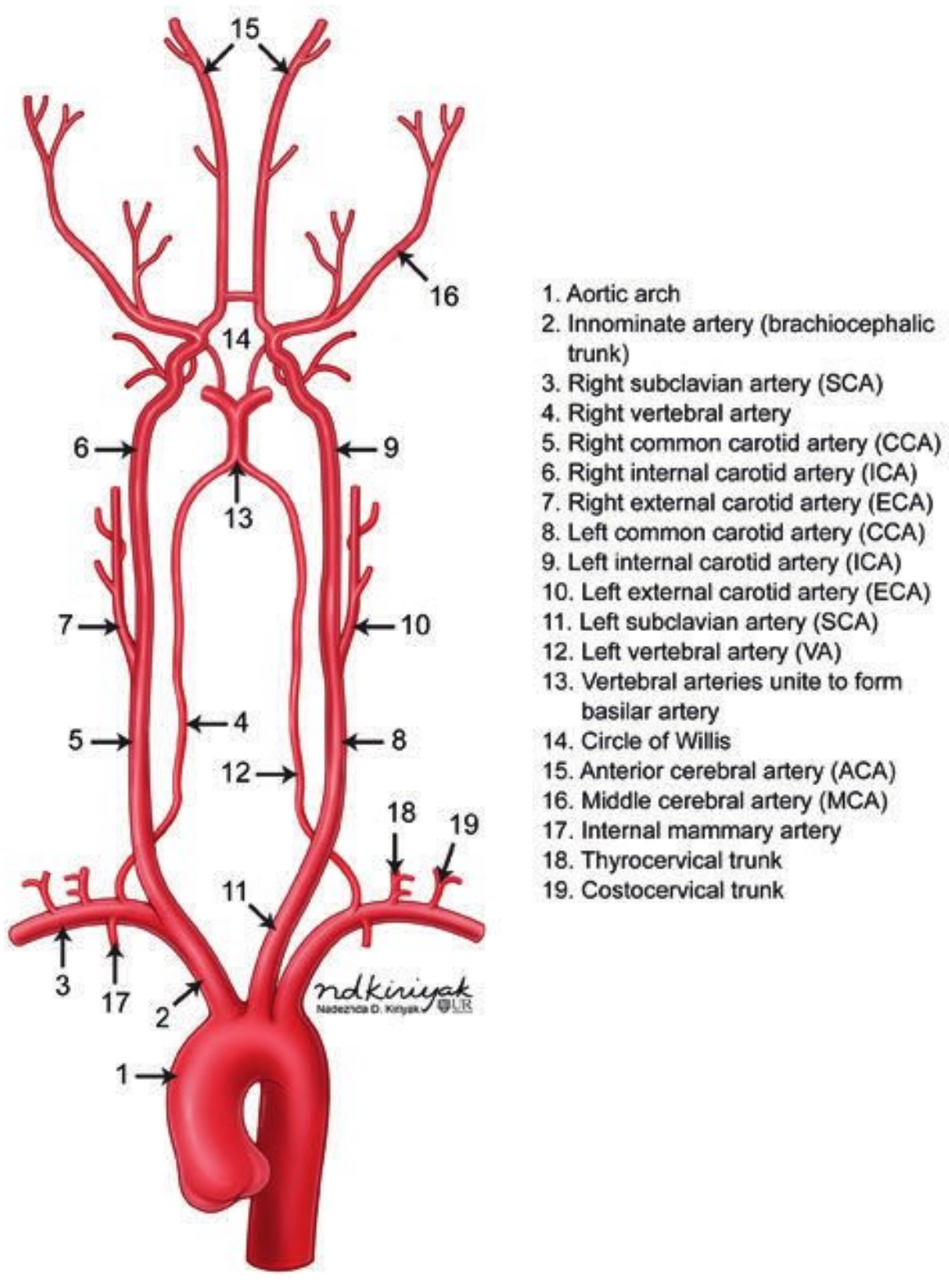

Fig. 5.1 Coronal view of the arteries from the aortic arch, which supply the brain.

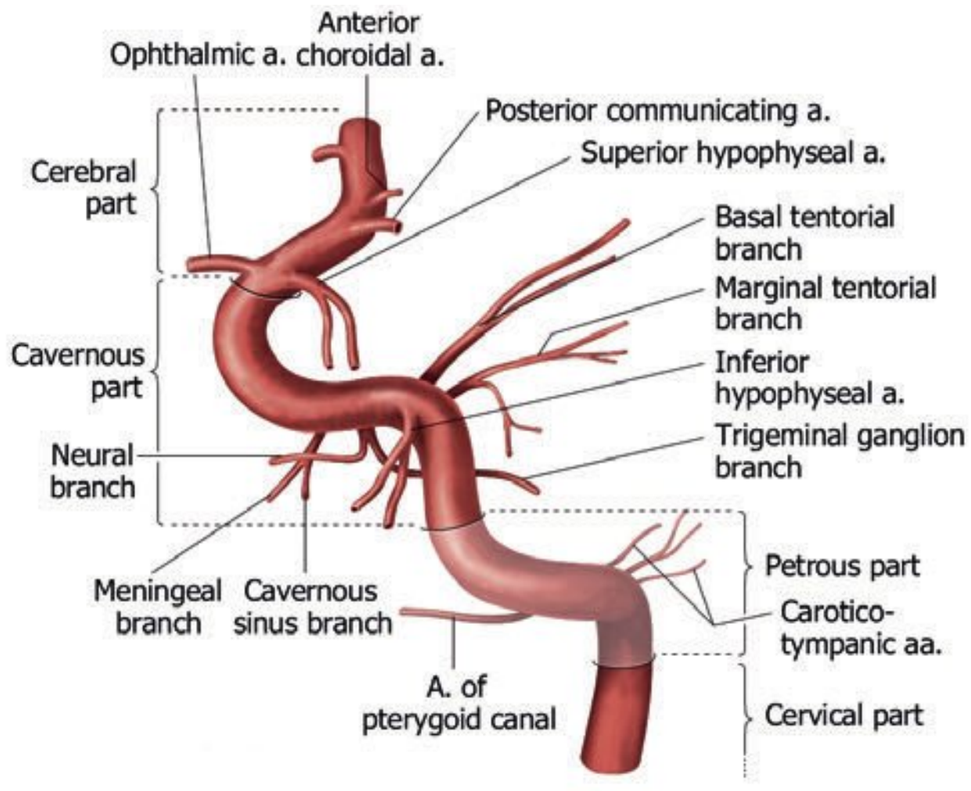

Fig. 5.2 Lateral view of the segments of the internal carotid artery and its branches. From THIEME Atlas of Anatomy, Neck and Internal Organs, © Thieme 2006, Illustration by Karl Wesker.

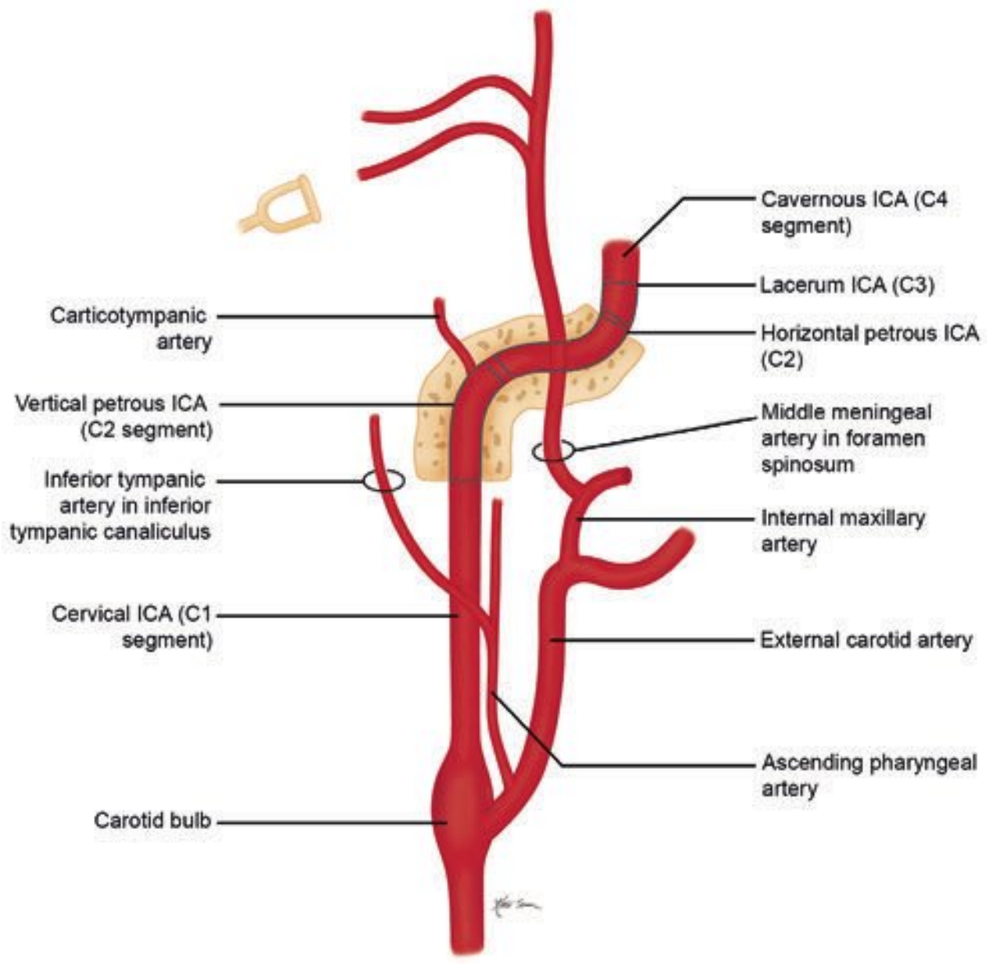

Fig. 5.3 Coronal view of the segments of the internal carotid artery and its branches.

into the anterior cerebral artery (ACA) and middle cerebral artery (MCA) and includes the posterior communicating artery (PCOM) as a branch.

The ACA has three segments (**Fig. 5.4** and **Fig. 5.5**). The A1 segment extends medially from the ICA to the midline and the origin of the anterior communicating artery (ACOM), which connects to the contralateral ACA. The A1 segment has branch arteries, such as the medial lenticulostriate arteries, that provide blood supply to the basal ganglia. The A2 segment extends superiorly within the interhemispheric fissure from the ACOM to the level of the rostrum of the corpus callosum. Branch arteries from the A2 segment include the orbitofrontal and frontopolar arteries, which supply the inferomedial portions of the frontal lobes. The recurrent artery of Heubner can also arise from the proximal portion of A2 providing blood to the basal ganglia in addition to the lenticulostriate arteries from the A1 segment. In some cases, the recurrent artery of Heubner may arise from the A1 segment or anterior communicating artery. The A3 segment extends around the corpus callosum and divides into the pericallosal and callosomarginal arteries, which course posteriorly over the corpus callosum and cingulate gyrus, respectively. The A2 and A3 segments provide blood to the medial portions of

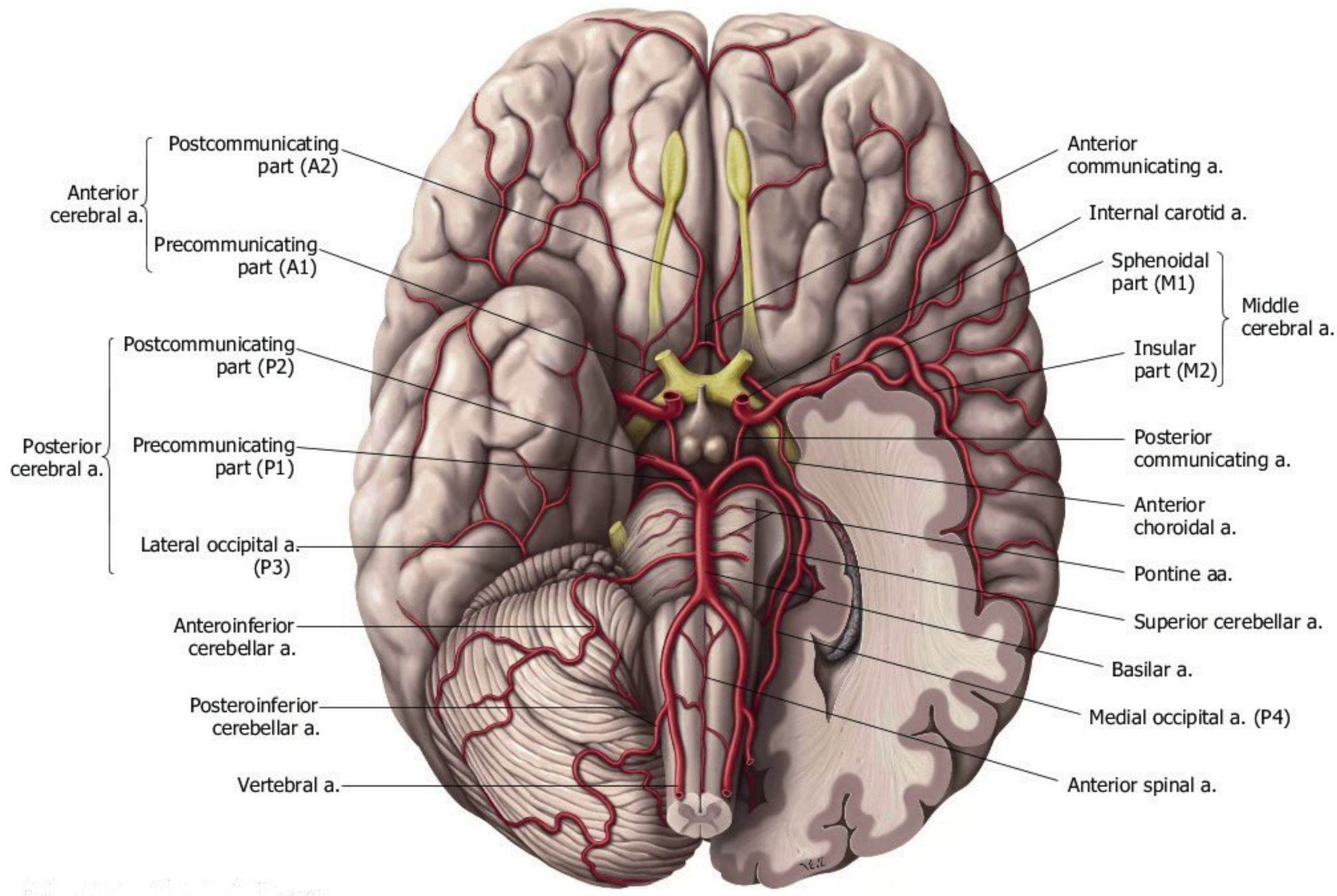

Fig. 5.4 Basal view of the anterior and middle cerebral arteries, basilar artery, and posterior cerebral arteries and their branches.

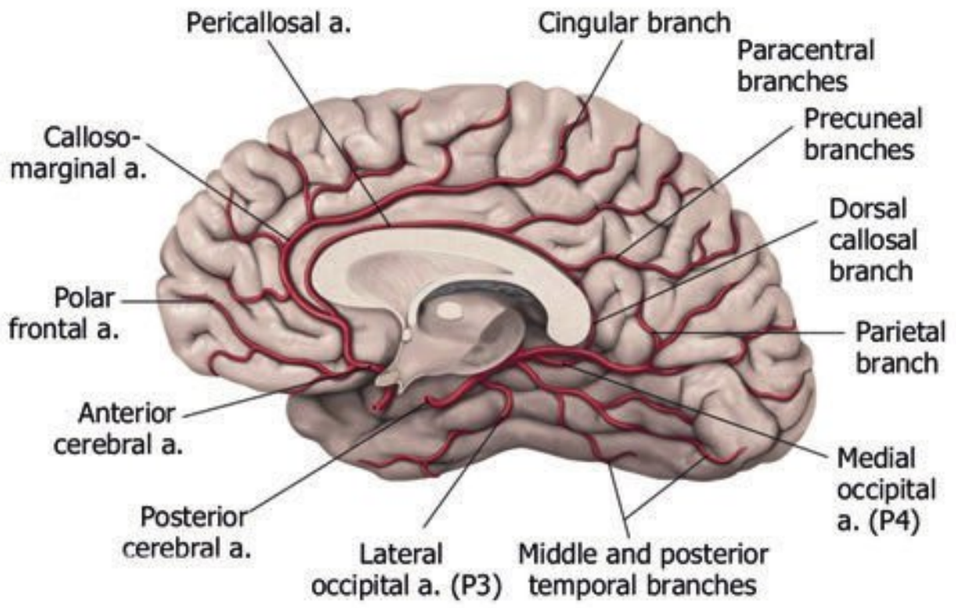

Fig. 5.5 Sagittal view of the anterior cerebral arteries and their branches. From THIEME Atlas of Anatomy, Neck and Internal Organs, © Thieme 2006, Illustration by Karl Wesker.

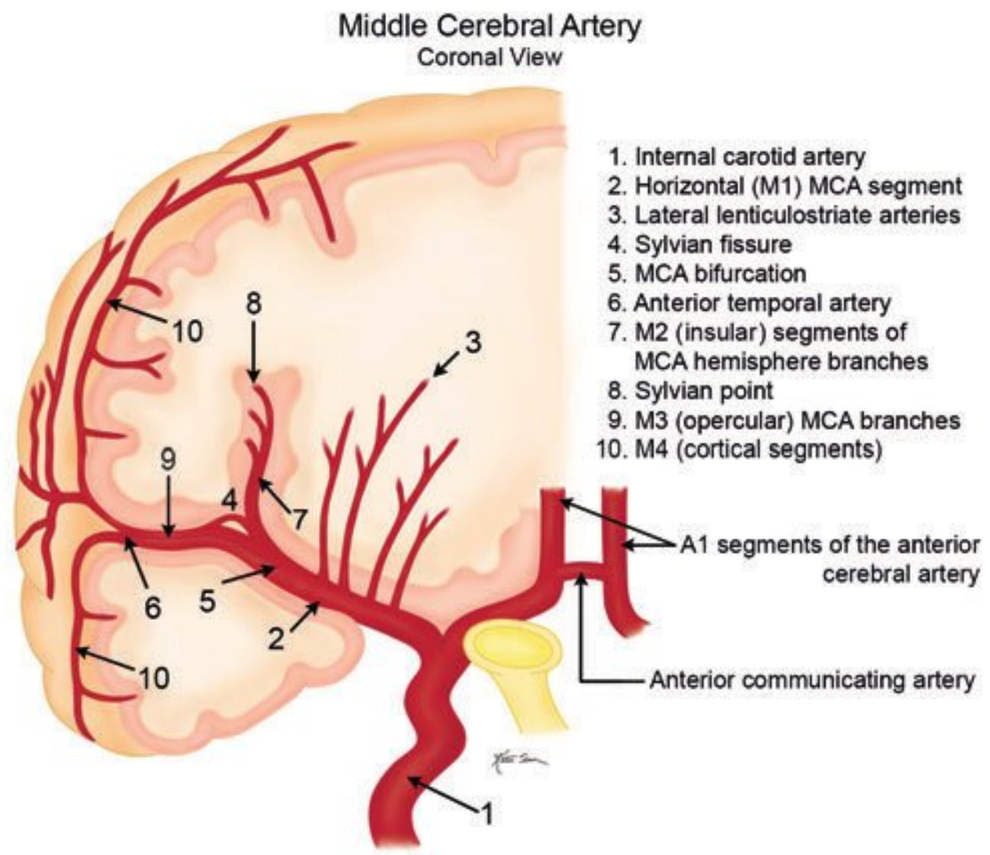

Fig. 5.6 Coronal view of the middle cerebral arteries and their branches.

the frontal and parietal lobes, corpus callosum, and anterior limbs of the internal capsules.

The MCA has four segments (**Fig. 5.6, Fig. 5.7**, and **Fig. 5.8**). The M1 (horizontal) segment extends laterally from the ICA to the sylvian fissure and has branch arteries, including the lateral lenticulostriate arteries, which supply the external capsule, caudate nucleus, and putamen, and the anterior temporal artery, which supplies the anterior portions of the temporal lobes. At the level of the sylvian fissure, the M1 segment bifurcates into the M2 (insular) segments, which extend upward and posteriorly along the insula. Branches from the M2 segments extend laterally along the overhanging or opercular portions of the cerebral hemispheres (M3 segments), providing blood to these locations. Continuation of the M3 segments after they exit the sylvian fissure are the M4 (cortical) segments, which supply the lateral portions of the cerebral hemispheres.

The upper terminal branches of the basilar artery are the posterior cerebral arteries (PCAs), which supply blood to the posteroinferior portions of the parietal lobes, occipital lobes, and thalami (**Fig. 5.9** and **Fig. 5.10**). The PCAs have four segments. The P1 segment extends laterally from the basilar artery to the level of the posterior communicating artery (PCOM). Branches from the P1 segment include the posterior thalamoperforating arteries, which supply the midbain and posterior portions of the thalami. The P2 segment extends posterolaterally from the P1 segment–PCOM junction around the midbrain above the tentorium. Arterial branches from the P2 segment include the anterior and posterior temporal arteries, which provide blood to the inferior portions of the temporal lobes not supplied by the anterior temporal artery from the M1 segment of the MCA. Other branches from the P2 segment include the medial and lateral posterior choroidal arteries, which supply the choroid plexus of the third and lateral ventricles, respectively; the thalamogeniculate arteries, which sup-

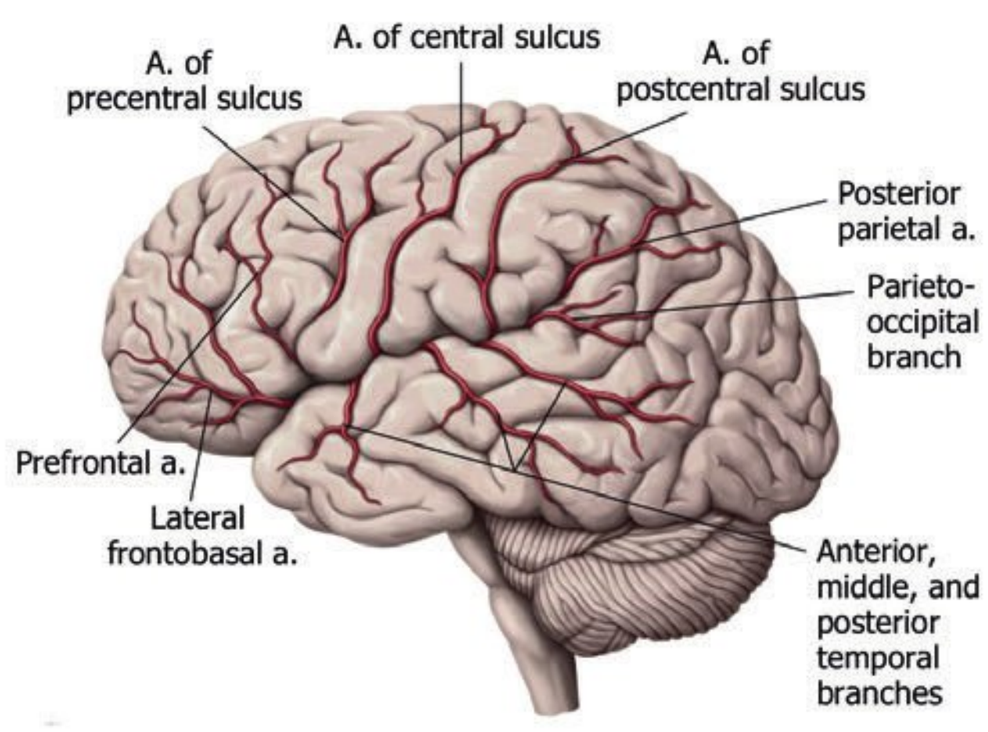

Fig. 5.7 Lateral surface view of the middle cerebral arteries and their superficial branches. From THIEME Atlas of Anatomy, Neck and Internal Organs, © Thieme 2006, Illustration by Karl Wesker.

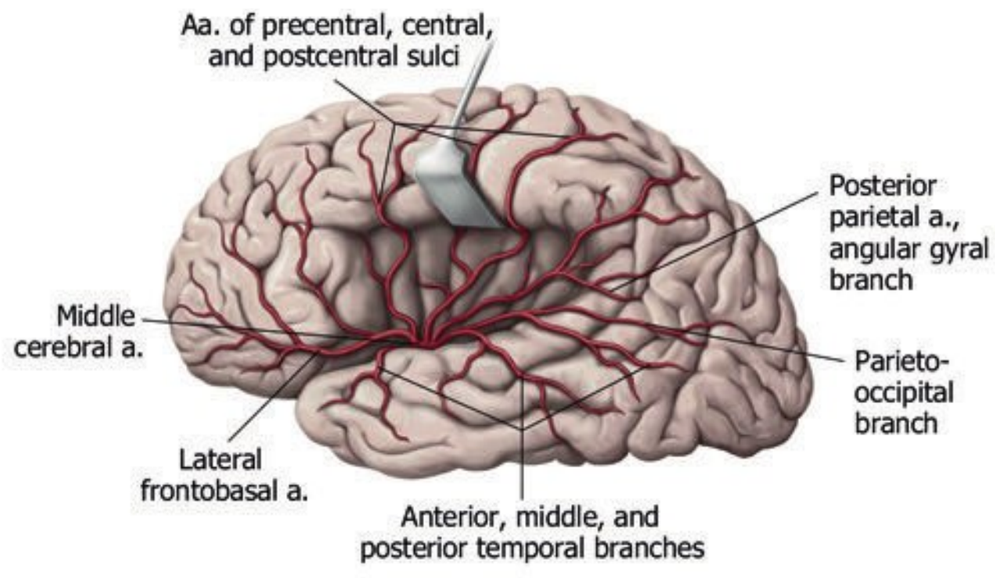

Fig. 5.8 Lateral view within the sylvian fissure shows the middle cerebral arteries and their proximal branches. From THIEME Atlas of Anatomy, Neck and Internal Organs, © Thieme 2006, Illustration by Karl Wesker.

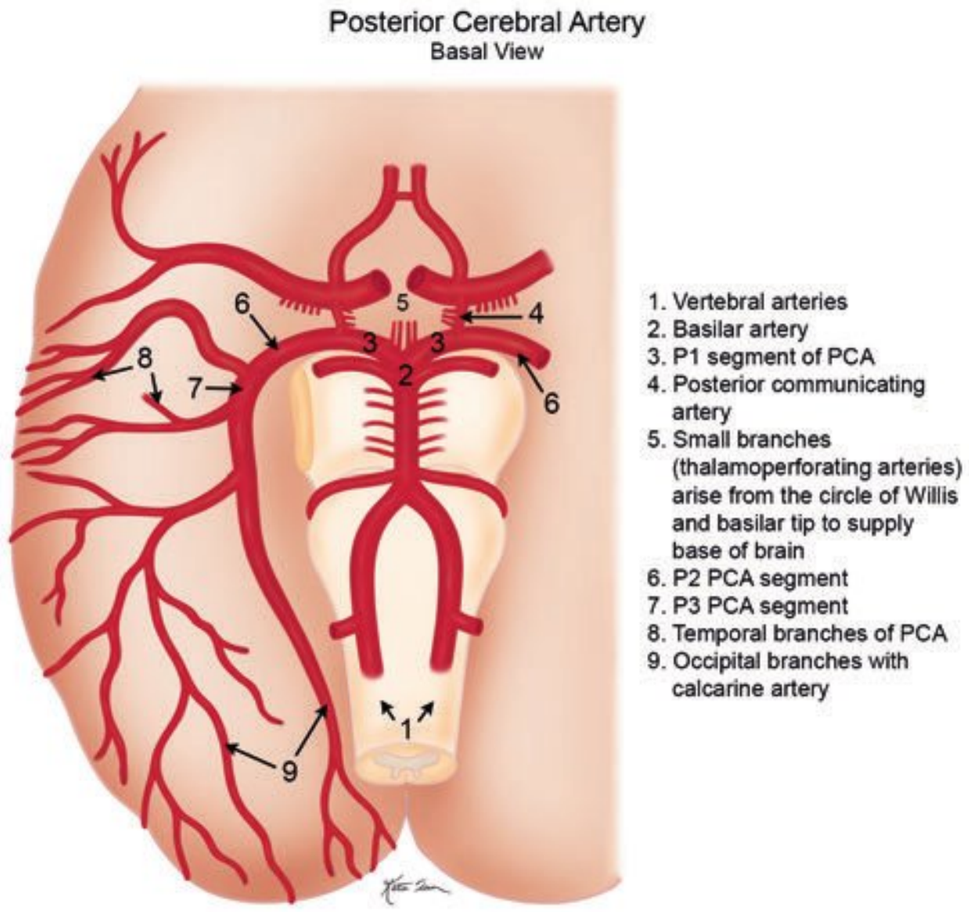

Fig. 5.9 Basilar view of the posterior cerebral artery and its branches.

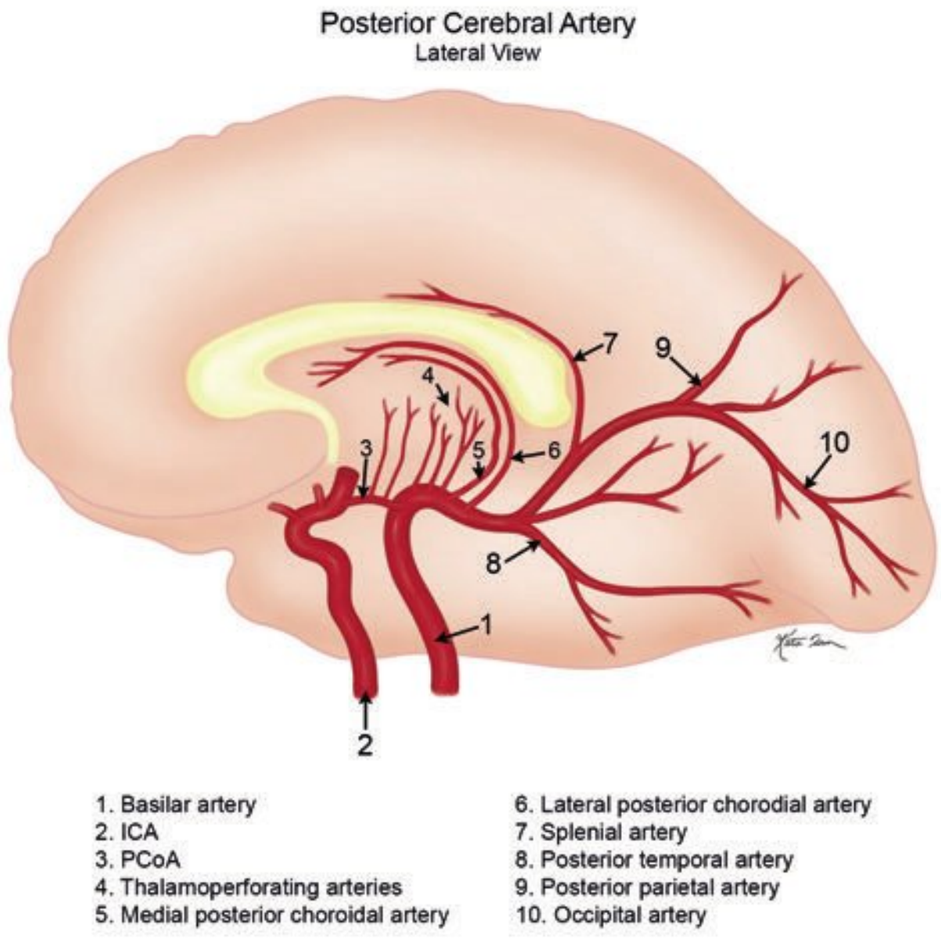

Fig. 5.10 Lateral view of the posterior cerebral artery and its branches.

ply the posterior thalamus; and the peduncular perforating arteries, which supply the midbrain. The P3 segment is the portion of the PCA located in the quadrigeminal cistern posterior to the midbrain prior to its entry into the calcarine fissure. The P4 segment of the PCA is located within the calcarine fissure and its branches include the parieto-occipital artery, calcarine artery, lateral occipital artery, and posterior splenial arteries, which supply the occipital lobe, posterior medial portions of the temporal lobes, and posterior corpus callosum.

Single vertebral arteries (VAs) arise from each subclavian artery and extend superiorly in the neck to eventually fuse intracranially to form the basilar artery anterior to the brainstem near the pontomedullary junction (**Fig. 5.1**). Each vertebral artery is divided into four segments. The V1 segment of the VA extends from its origin from the subclavian artery to its entry into the C6 foramen transversarium. The V1 segment supplies the lower portion of the cervical spinal cord and paraspinal musculature. The V2 segment extends upward through the C6 to C1 foramina tranversaria. The anterior meningeal artery is a branch from the V2 segment. The V3 segment is the portion of the VA from its exit from the C1 transverse foramen to the level of the outer dural margin at the foramen magnum. The posterior meningeal artery is a branch from the V3 segment. The V4 segment is the intradural portion of the VA from which the posterior inferior cerebellar artery arises. Other branches from the V4 segment include medullary perforating arteries and anterior and posterior spinal arteries. Both V4 segments fuse to form the basilar artery. Branches from the basilar artery include the anterior inferior cerebellar artery, superior cerebellar arteries, and basilar perforating arteries (**Fig. 5.11** and **Fig. 5.12**). The uppermost portion of the basilar artery terminates with a bifurcation into the right and left posterior cerebral arteries. The upper vertebral arteries and basilar artery provide blood supply to the upper spinal cord, brainstem, and cerebellum.

The circle of Willis is an important intracranial anastomotic arterial ring around the lower brain interconnecting the anterior and posterior circulations and includes the upper portions of both ICAs, the A1 segments of the ACAs, the anterior communicating artery (ACOM), the basilar artery, posterior communicating arteries (PCOMs), and P1 segments of both posterior cerebral arteries (PCA).

The external carotid artery (ECA) arises from the bifurcation of the cervical portion of the common carotid artery. The ECA has eight major branches (**Fig. 5.13**). The superior thyroid artery extends inferiorly to supply the larynx and thyroid gland. The ascending pharyngeal artery extends superiorly to supply the nasopharynx, oropharynx, dura, middle ear, and cranial nerves IX, X, and XI. The lingual artery supplies the oral cavity, tongue, and submandibular gland. The facial artery supplies the face, cheek, lips, and palate. The occipital artery supplies the meninges of the posterior cranial fossa as well as the upper cervical paraspinal muscles and scalp. The posterior auricular artery supplies the scalp and outer ear. The superficial temporal artery supplies the scalp. The maxillary artery supplies the deep soft tissues of the face and nose. A branch from the maxillary artery extends superiorly through the foramen spinosum as the middle meningeal artery to supply the intracranial meninges. Anastomoses between ECA branches (except for the superior thyroid and lingual arteries) and intracranial branches of the ICA and/or vertebral arteries can occur.

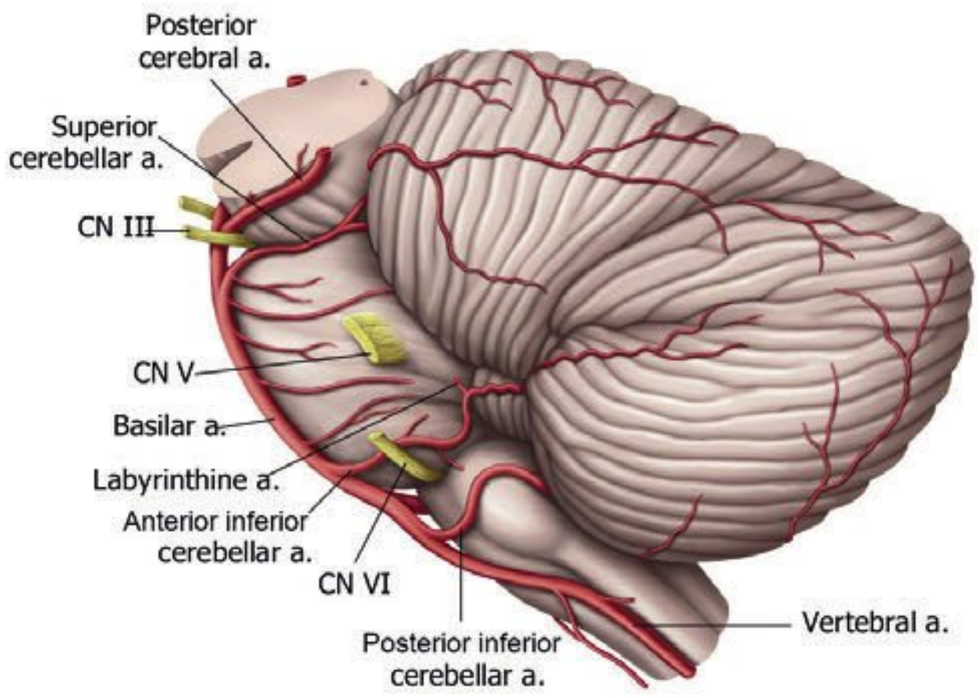

Fig. 5.11 Lateral view of the upper vertebral and basilar artery and their branches. From THIEME Atlas of Anatomy, Neck and Internal Organs, © Thieme 2006, Illustration by Karl Wesker.

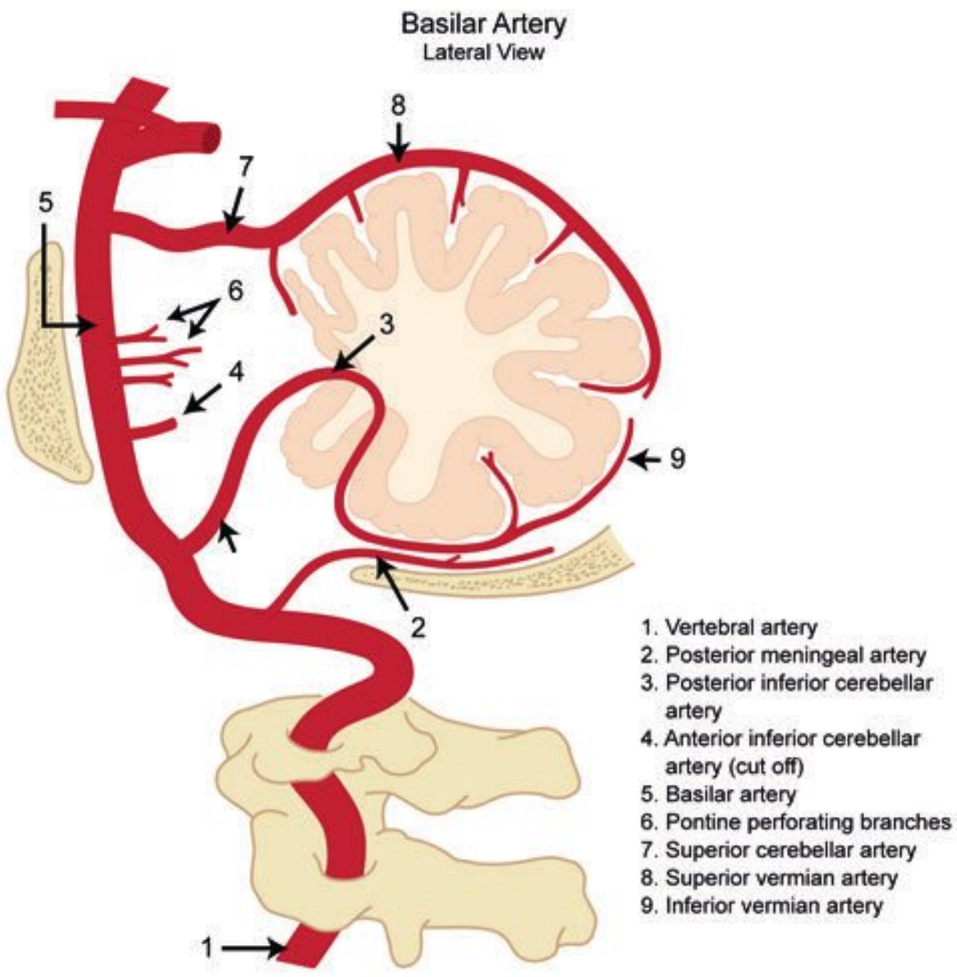

Fig. 5.12 Lateral view of the upper vertebral and basilar artery and their cerebellar branches.

Intracranial Venous Anatomy

The intracranial venous system consists of a *superficial system* that drains blood from the cerebral cortex and superficial white matter into cortical veins and eventually into the dural venous sinuses, and a *deep venous system* that drains blood from the deep white matter and basal ganglia (**Fig. 5.14**, **Fig. 5.15**, and **Fig. 5.16**). The deep venous system includes the paired internal cerebral veins in the roof of the third ventricle, the basal vein of Rosenthal, the vein of Galen, and the straight venous sinus. Also included in the deep venous system are transcerebral veins. The internal cerebral veins represent the confluence of septal, subependymal, ventricular, anterior caudate, thalomostriate, and choroidal veins at the foramen of Monro. The basal veins of Rosenthal are located at the medial aspects of the temporal lobes and drain blood from the adjacent temporal lobes, insula, and cerebral peduncles. These veins have anastomoses with the middle cerebral veins and petrosal veins. The basal veins course posteriorly around the cerebral peduncles, where they unite with internal cerebral veins to form the single midline great vein of Galen located below the splenium of the corpus callosum. The vein of Galen connects with the inferior sagittal sinus to drain venous blood into the straight venous sinus. Transcerebral veins are medullary veins that extend though the cerebral tissue and are not usually visualized on normal MRI or CT examinations.

The superficial venous system includes superficial cerebral veins along the surface of the brain that drain blood from the adjacent cerebral cortex and subcortical white matter. The superficial veins can have various configurations, including approximately 12 that drain into the superior sagittal sinus. A prominent superficial anastomotic vein of Trolard can be observed that connects to the superior sagittal sinus. A prominent inferior anastomotic

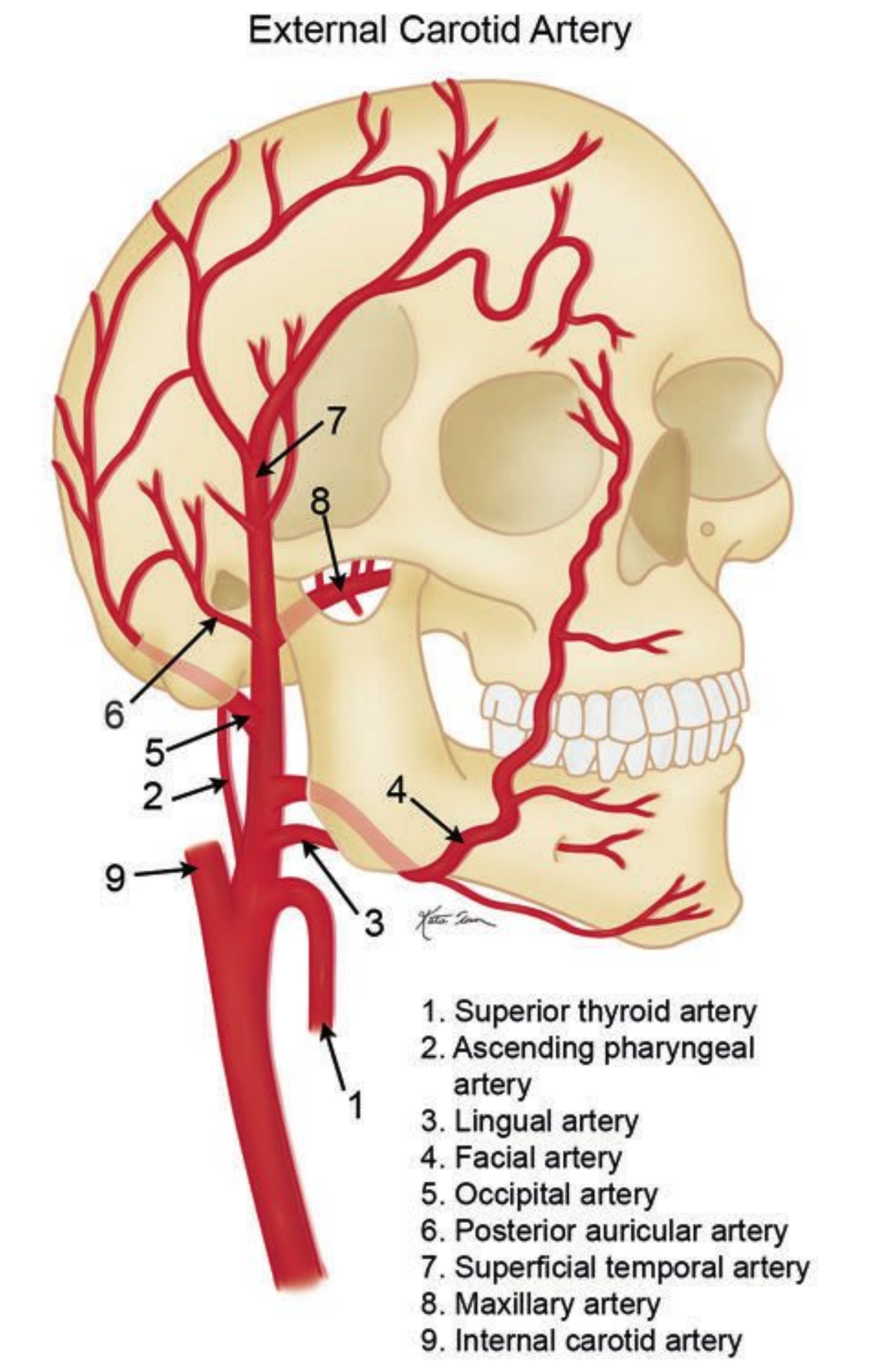

Fig. 5.13 Oblique coronal view of the external carotid artery and its branches.

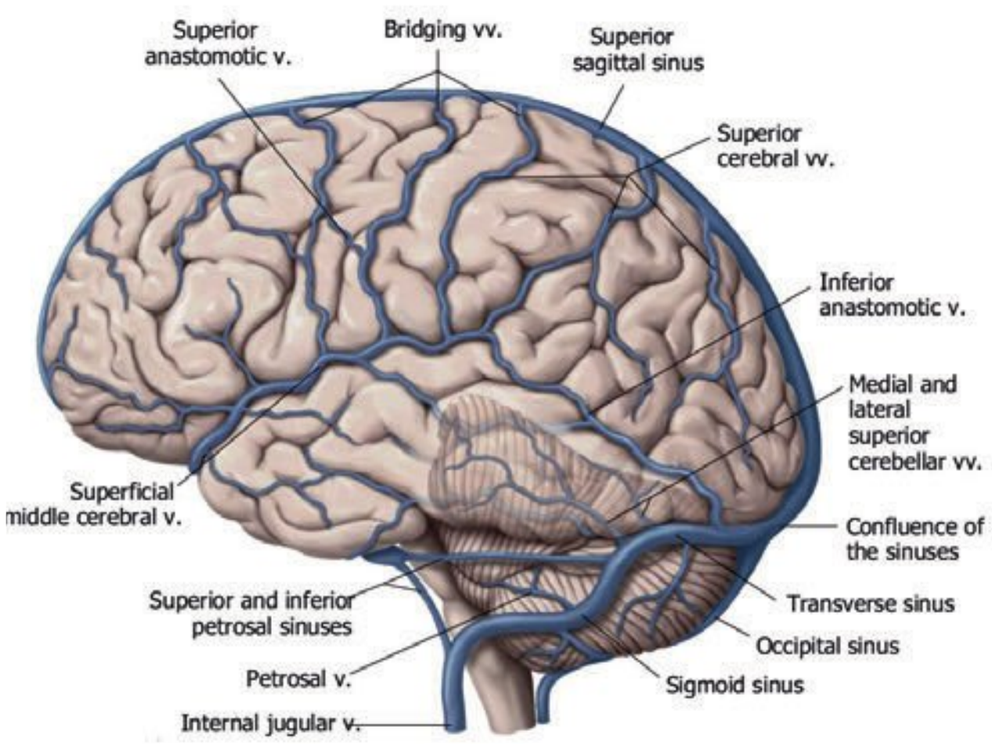

Fig. 5.14 Lateral view of the superficial and deep cerebral venous systems. From THIEME Atlas of Anatomy, Neck and Internal Organs, © Thieme 2006, Illustration by Karl Wesker.

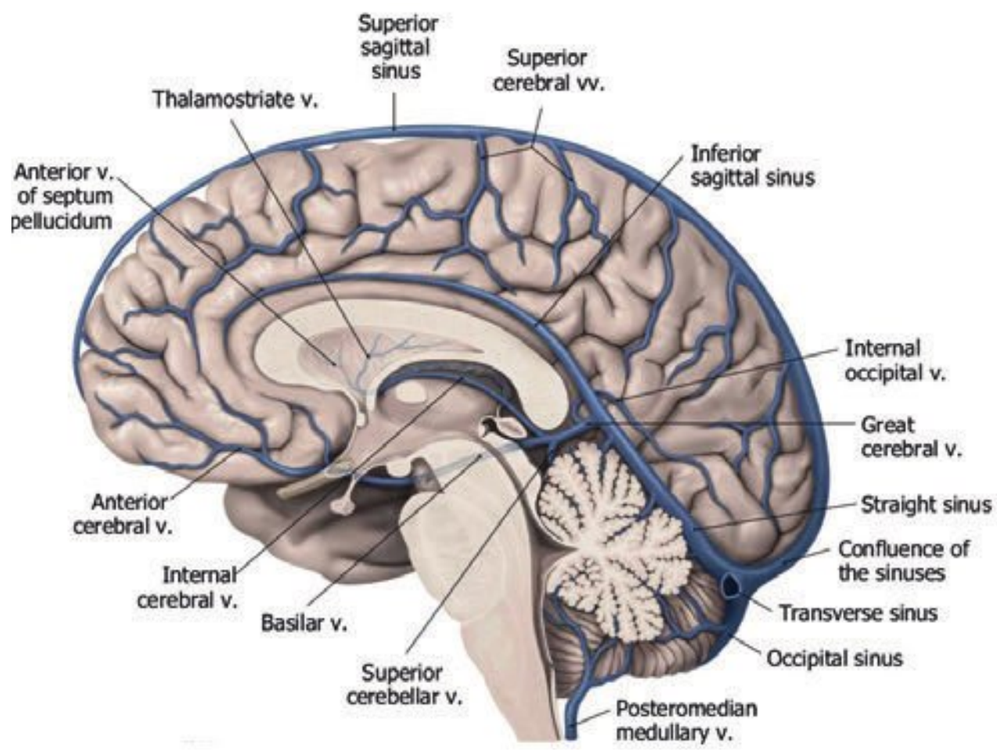

Fig. 5.15 Medial view of the superficial and deep cerebral venous systems. From THIEME Atlas of Anatomy, Neck and Internal Organs, © Thieme 2006, Illustration by Karl Wesker.

superficial vein of Labbé can also be seen that connects the transverse venous sinus. The superficial middle cerebral vein is another prominent vein that courses anteriorly in the sylvian fissure and drains blood from the adjacent lateral brain into the cavernous sinuses and/or pterygoid venous plexus.

Venous Sinuses

Veins from the superficial and deep venous systems drain into the dural venous sinuses (**Fig. 5.17**). The dural venous sinuses are endothelial channels located between the periosteal (outer) and meningeal (inner) layers of the dura. The dural venous sinuses can be subdivided into two groups: posterosuperior and anteroinferior. The posterosuperior group includes the superior and inferior sagittal sinuses, straight venous sinus, torcular herophili, transverse and sigmoid sinuses, and jugular bulbs. Arachnoid granulations can occur in all of the dural venous sinuses, although they are most frequently present in the superior sagittal and transverse venous sinuses.

The anteroinferior group of dural venous sinuses includes the cavernous sinus, superior and inferior petrosal sinuses, clival venous sinus, and sphenoparietal sinus. Blood from the cavernous sinuses drain into pterygoid venous plexuses via the foramen ovale or into the superior and/or inferior petrosal sinuses. Blood from the superior petrosal sinus drains into the sigmoid sinus, whereas blood from the inferior petrosal sinus drains into the jugular bulb. The clival venous plexus connects the cavernous sinus with the petrosal sinuses. The sphenoparietal sinus at the anterior portion of the middle cranial fossa connects the superficial veins adjacent to the temporal lobes to the inferior petrosal sinus (**Fig. 5.17**).

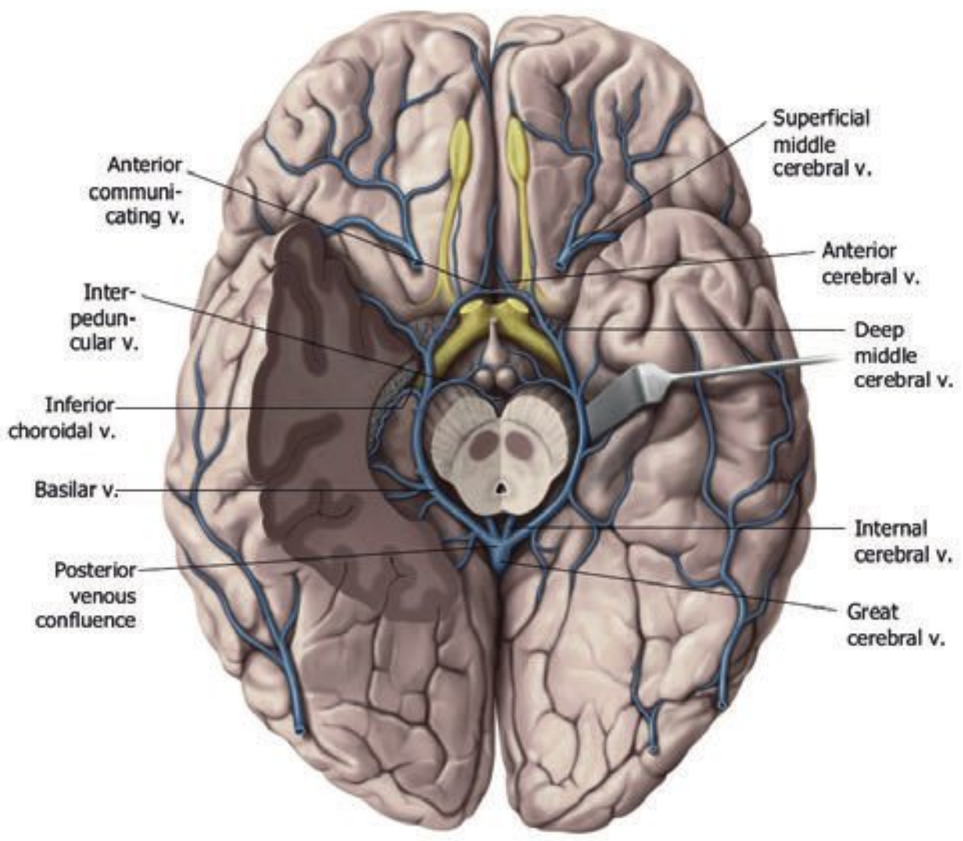

Fig. 5.16 Inferior basal view of the superficial and deep cerebral venous systems. From THIEME Atlas of Anatomy, Neck and Internal Organs, © Thieme 2006, Illustration by Karl Wesker.

The veins in the posterior cranial fossa can drain upward into the vein of Galen (superior vermian vein, precentral cerebellar vein, and anterior pontomesencephalic vein), anteriorly into the petrosal sinuses (petrosal veins), or posterolaterally into the transverse or sigmoid venous sinuses (inferior vermian veins) (**Fig. 5.18**).

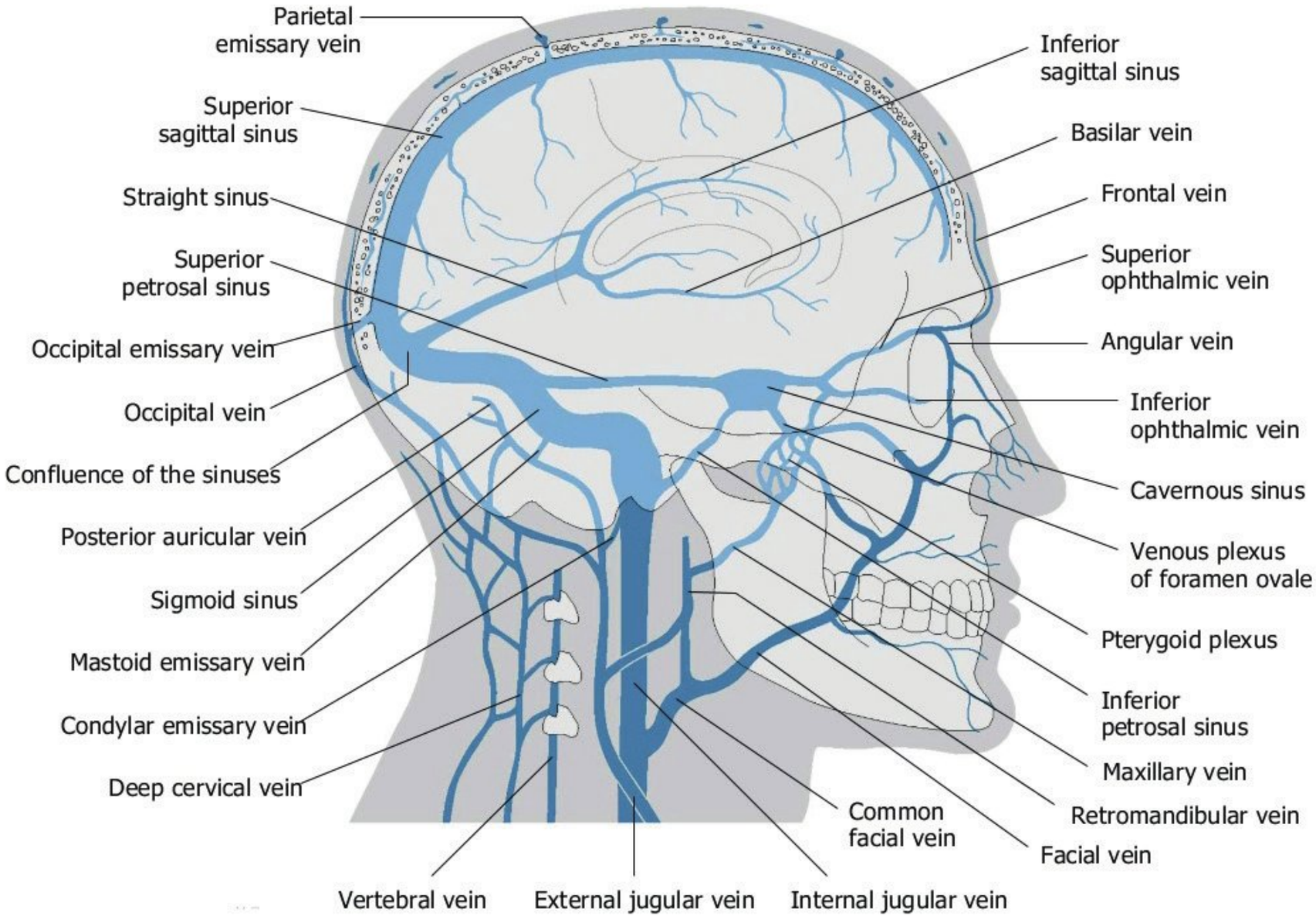

Fig. 5.17 Sagittal view of the intracranial venous drainage patterns, including the venous sinuses. From THIEME Atlas of Anatomy, Neck and Internal Organs, © Thieme 2006, Illustration by Markus Voll.

Cerebral Arterial and Venous Development

Arterial Development

There are six branchial arches during embryonic development. Derivatives of the third branchial arches form the internal carotid arteries. A portion of the left fourth branchial arch forms most the aortic arch, and the right fourth branchial arch forms the proximal segment of the right subclavian artery. Derivatives of the first arch form the vidian artery. Derivatives of the second arch form the pharyngeal artery, external carotid artery, stapedial artery, and caroticotympanic artery.

At 4 weeks of gestation, primitive, paired internal carotid arteries connected to the dorsal aorta and third aortic arch provide blood to the developing vesicles of the forebrain, midbrain, and hindbrain. The mature pattern of the cerebral arterial system develops by 8 weeks of gestation.

At 4 weeks of gestation, the developing hindbrain is supplied by paired longitudinal arteries that have transient anastomoses with the internal carotid arteries. These paired arteries progressively fuse in the midline to form

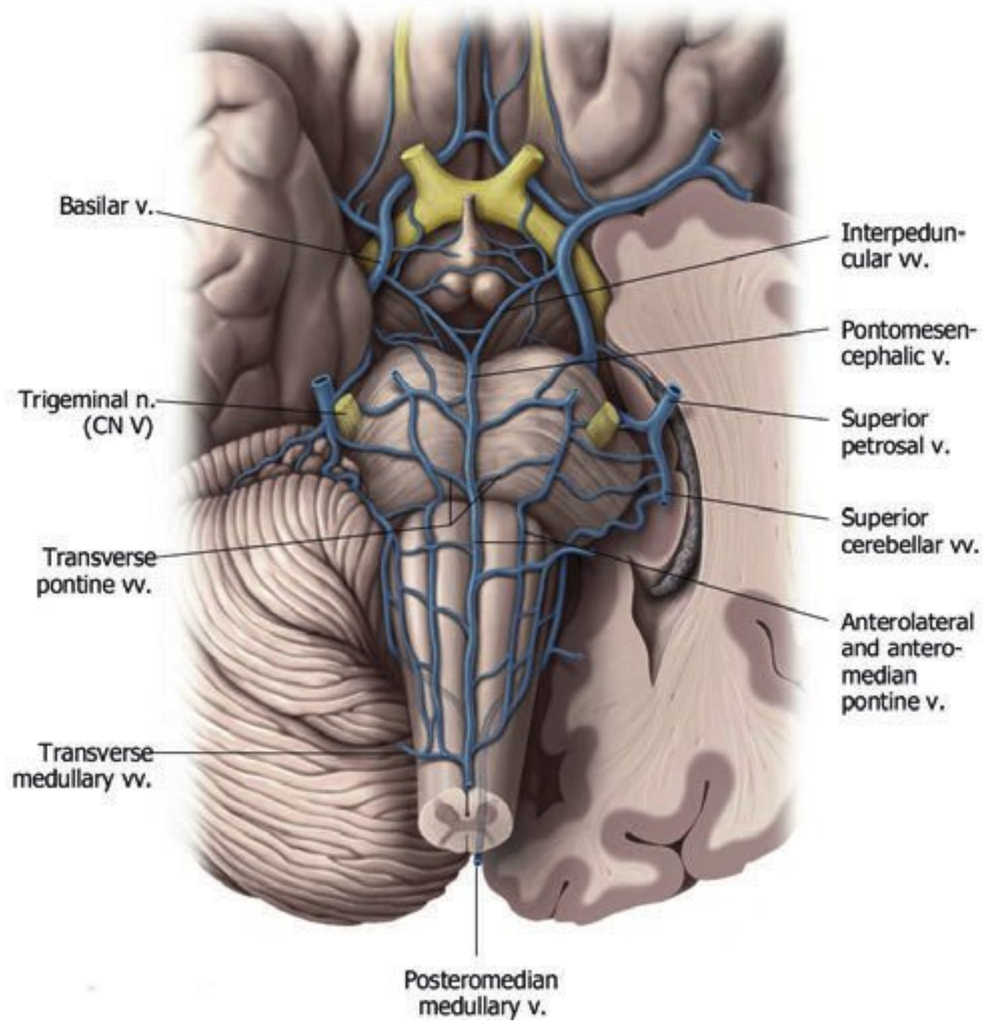

Fig. 5.18 Inferior basal view of the veins of the brainstem. From THIEME Atlas of Anatomy, Neck and Internal Organs, © Thieme 2006, Illustration by Karl Wesker.

the basilar artery around 5 weeks of gestation. Lack of normal fusion of the longitudinal arteries can result in arterial fenestrations. Lack of normal involution of some of the anastomoses between the internal carotid arteries and longitudinal arteries can result in anomalous connections between the internal carotid arteries and basilar artery, such as a persistent trigeminal artery (**Fig. 5.19**).

Venous Development

At the fifth week of gestation, three venous plexuses form around the posterolateral aspects of the developing brain. Progressive growth and connections between these plexuses result in eventual formation of the major dural venous sinuses over the next 6 months.

Development of cortical veins occurs after normal involution of early fetal transcerebral veins, and the primitive pial venous plexus develops by 11 weeks of gestation.

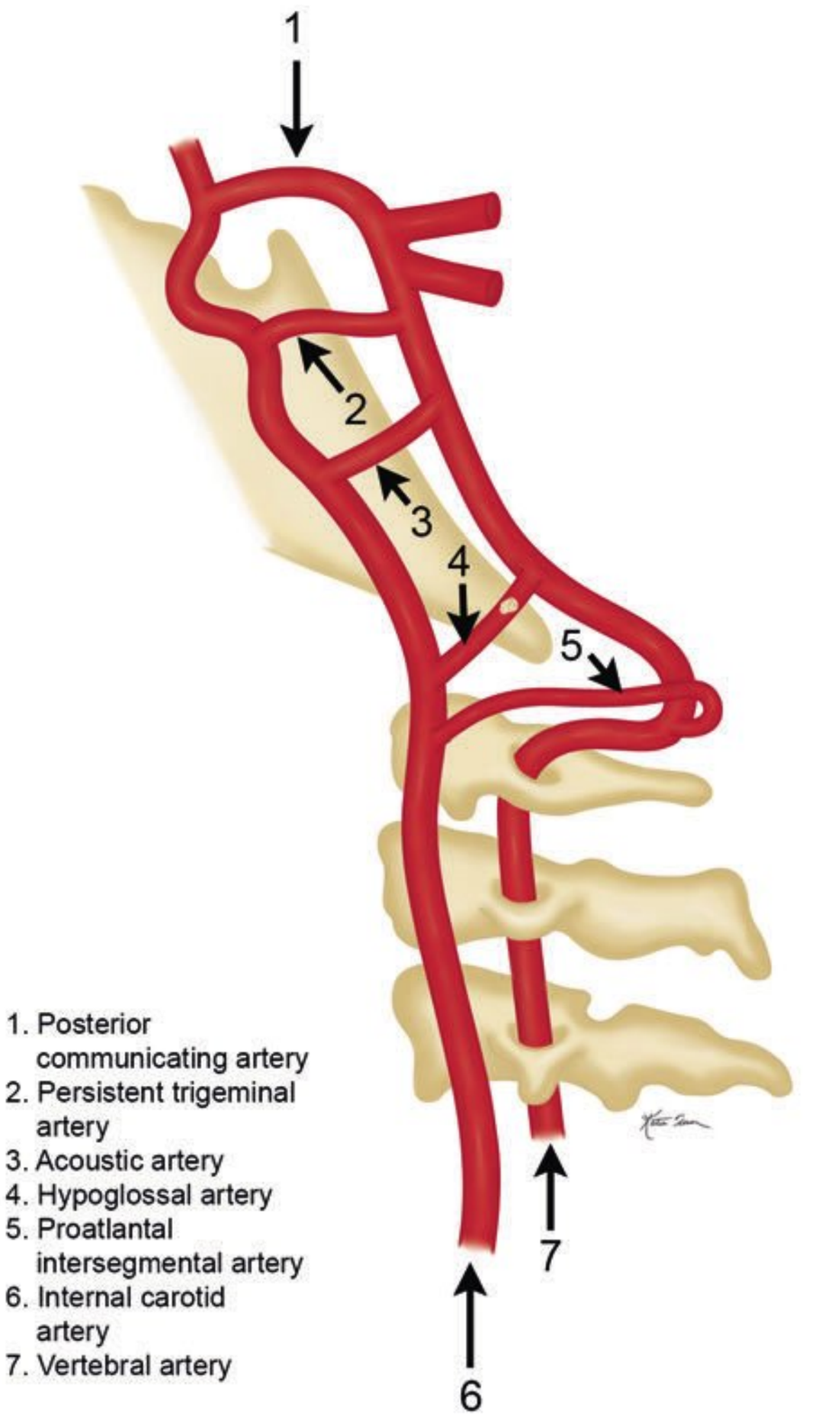

Fig. 5.19 Lateral diagram shows potential developmental anomalous connections between the internal carotid arteries and basilar artery.

CT Angiography and CT Perfusion

CT angiography (CTA) is a powerful imaging modality for evaluating normal and abnormal blood vessels. CTA has proven to be clinically useful in the evaluation of intracranial arteries, veins, and dural venous sinuses. Pathologic processes involving intracranial blood vessels, such as aneurysms, arteriovenous malformations, arterial occlusions, and dural venous sinus thrombosis, can be seen with CTA.

CT perfusion is a relatively new technique using dynamic intravenous infusion of contrast to measure cerebral blood flow (CBF), cerebral blood volume (CBV), and mean transit time of contrast enhancement (MTT) in selected volumes of interest in the brain. CT perfusion has major clinical application in the evaluation of cerebral infarcts and adjacent zones of decreased perfusion (penumbra and oligemic areas) at risk for progression to infarction. Maintenance of CBF is critical for neuronal function. With arterial occlusion, loss of normal neuronal electrical activity occurs within seconds after arterial occlusion. Cellular death is dependent on the duration and magnitude of ischemia, metabolic vulnerability of specific anatomic sites, and the oxygen content of blood. Normal CBF ranges from 50 to 60 mL/100 g/min. When CBF is reduced to 15 to 20 mL/100 g/min for several hours (mild–moderate hypoxia), spontaneous and evoked neuronal electrical activity decreases significantly secondary to ischemia, although it can be reversed by reperfusion with CBF above 50 mL/100 g/min. With severe hypoxia/anoxia resulting from CBF below 10 mL/100 g/min, cellular membrane depolarization and ischemia leading to brain infarction may occur within several minutes.

When thrombotic or embolic arterial occlusions occur, CBF in the involved brain tissue is usually heterogeneous, with a central core showing the greatest reductions in CBF that cause irreversible cell damage and infarction, and a surrounding zone (referred to as the *salvageable penumbra*) that may have moderate reduction in CBF, resulting in ischemia that may be reversible with reperfusion. The penumbra typically shows loss of neuronal electrical activity without immediate anoxic depolarization, as well as loss of autoregulation. If reperfusion does not occur, the penumbra will progress to infarction. An oligemic zone of mildly reduced CBF may also be seen surrounding the penumbra, and this zone is less vulnerable to infarction than the penumbra. Thrombolytic medication can be useful and beneficial when it results in timely reperfusion to the penumbra and oligemic zone. Estimating the sizes of the penumbra and oligemic zone can be done in the acute setting with dynamic contrast-enhanced CT. CT perfusion, utilizing iodinated contrast delivered as an intravenous bolus, can use the linear relationship between contrast concentration and attenuation to directly calculate and quantify CBF, CBV, and MTT for sites of ischemia and infarction in the brain prior to thrombolytic treatment.

Magnetic Resonance Angiography

Magnetic resonance imaging (MRI) is a powerful modality for evaluating normal and abnormal blood vessels. The appearance of blood vessels on MRI depends on various factors, such as the type of MRI pulse sequence, pulsatility and range of velocities in the vessels of interest, and size, shape, and orientation of the vessels relative to the image plane. Useful anatomic information about blood vessels can be gained by using spin echo pulse sequences, which can display patent vessels as zones of signal void (black-blood images), or gradient recalled echo (GRE) pulse sequences, which display the moving hydrogen atomic nuclei (protons) in blood as zones of high signal (bright-blood images).

The GRE technique is used to generate MR angiograms (MRA). The high signal from flowing blood on GRE images reflects movement patterns and velocities of hydrogen atomic nuclei rather than direct anatomic displays of the blood vessels. The operator of the MRI equipment can choose parameters to optimize the imaging of various arteries and veins. Two main types of GRE techniques are used for MRA. One is based on hydrogen signal amplitude and is referred to as the time-of-flight (TOF) method. The other method is based on the phase differences of the moving protons (hydrogen) in blood compared with stationary tissue and is referred to as phase-contrast (PC) MRA.

In TOF MRA, the GRE pulse sequence is optimized for demonstrating the inflow enhancement (high signal) of moving protons (hydrogen nuclei) in blood relative to the low signal of protons in stationary tissue. Phase-contrast (PC) MRA is a technique that differentiates flowing and stationary protons through the use of bipolar flow-encoding gradients. If the flow velocity is known, the flow sensitivity of the sequence can be selected to emphasize the vessels of interest. PC MRA can be optimized for detecting slow flow in veins and at areas of high-grade arterial stenosis.

The individual GRE images can be acquired in a sequential mode, also referred to as two-dimensional (2D) TOF or PC MRA, or as an entire volume of covered tissue, which is referred to as three-dimensional (3D) TOF or PC MRA. The acquired image data from either of these two methods are post-processed with computer algorithms to generate the MRA images in a display format similar to conventional arteriograms. Two commercially available types of post-processing are the maximum intensity projection (MIP) technique and surface rendering (SR). The former technique is more common, and the MIP MRA images can be displayed in any plane of obliquity on film or as a movie loop. Surface rendering is another post-processing method for MRA that shows 3D relationships by giving the displayed vessels shadowing and perspective. The MRA images are projected in a fashion similar to that used for the MIP method. Surface rendering has been demonstrated to be useful in showing spatial relationships between vessels on a single coronal image, allowing differentiation of adjacent and overlapping vessels.

MRA has proven to be clinically useful in the evaluation of the carotid arteries in the neck, intracranial arteries, intracranial veins, and dural venous sinuses. Disorders like aneurysms, arteriovenous malformations, arterial occlusions, dural venous sinus thrombosis, etc., can be seen with MRA.

References

1. Johnson MH, Thorisson HM, Diluna ML. Vascular anatomy: the head, neck, and skull base. Neurosurg Clin N Am 2009;20(3):239–258
2. Kathuria S, Chen J, Gregg L, Parmar HA, Gandhi D. Congenital arterial and venous anomalies of the brain and skull base. Neuroimaging Clin N Am 2011;21(3):545–562, vii
3. Kathuria S, Gregg L, Chen J, Gandhi D. Normal cerebral arterial development and variations. Semin Ultrasound CT MR 2011;32(3):242–251
4. Raybaud C. Normal and abnormal embryology and development of the intracranial vascular system. Neurosurg Clin N Am 2010;21(3):399–426
5. Scott JN, Farb RI. Imaging and anatomy of the normal intracranial venous system. Neuroimaging Clin N Am 2003;13(1):1–12

Table 5.1 Congenital and developmental vascular anomalies/variants

- Persistent fetal origin of posterior cerebral artery
- Hypoplasia of the A1 segment of the anterior cerebral artery
- Persistent trigeminal artery (PTA)
- Persistent otic artery
- Persistent hypoglossal artery
- Proatlantal artery
- Duplications of cerebral, carotid, vertebral, or basilar arteries
- Azygous anterior cerebral artery
- Hemiazygous anterior cerebral artery
- Arterial fenestration
- Aberrant position of the internal carotid artery
- Persistent stapedial artery (PSA)
- Unilateral agenesis, aplasia, and hypoplasia of the internal carotid artery
- Vein of Galen aneurysm
- Sturge-Weber syndrome
- Moyamoya disease
- *ACTA2* mutations with dolichoectasia of the proximal internal carotid arteries and stenosis of the upper internal carotid arteries
- Menkes' syndrome
- PHACES syndrome (posterior fossa malformations, facial hemangiomas, arterial anomalies, cardiac anomalies and aortic coarctation, eye abnormalities, and sternal clefts or supraumbilical raphe)
- Thoracic outlet syndrome
- Venous angioma (developmental venous anomaly)
- Dehiscence of the jugular bulb
- High position of the jugular bulb
- Sinus pericranii

Table 5.1 Congenital and developmental vascular anomalies/variants

Lesion	Imaging Findings	Comments
Persistent fetal origin of posterior cerebral artery (**Fig. 5.20**)	Large posterior communicating artery supplying the posterior cerebral artery, associated with hypoplasia or absence of connection between the basilar artery and the ipsilateral posterior cerebral artery.	Represents persistence of embryonic configuration, common vascular variant seen in ~ 20%of arteriograms.
Hypoplasia of the A1 segment of the anterior cerebral artery (**Fig. 5.21**)	Hypoplasia or absent A1 segment associated with a patent communicating artery supplying blood to ipsilateral A2 segment.	Anatomic variant seen in ~ 10%of arteriograms.

(continued on page 608)

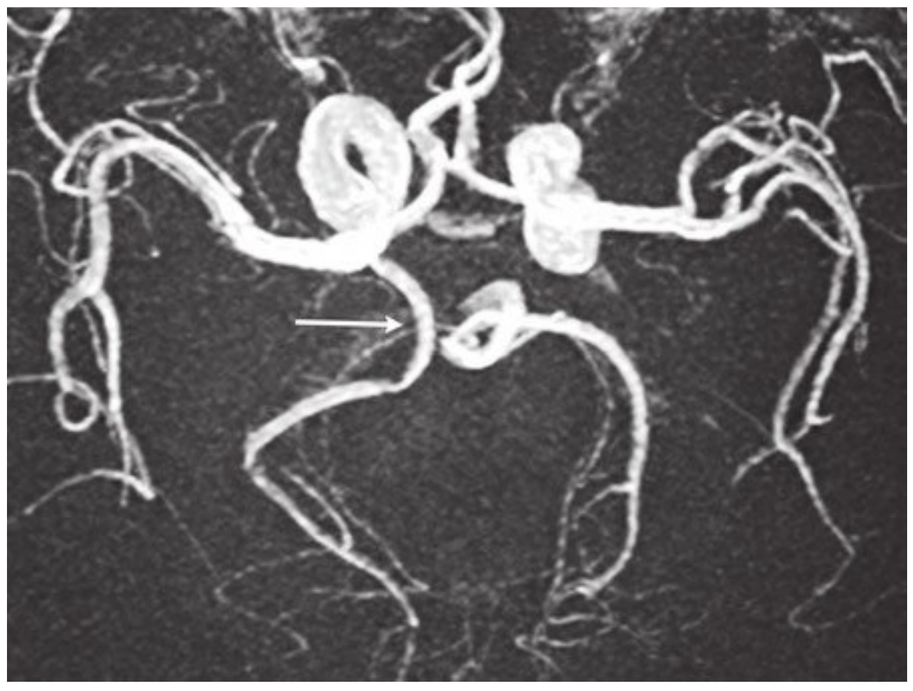

Fig. 5.20 Persistent fetal origin of posterior cerebral artery. Axial MRA shows the right posterior cerebral artery (arrow) receiving its blood flow directly from the right internal carotid artery via a large right posterior communicating artery with an absent P1 segment of the right posterior cerebral artery.

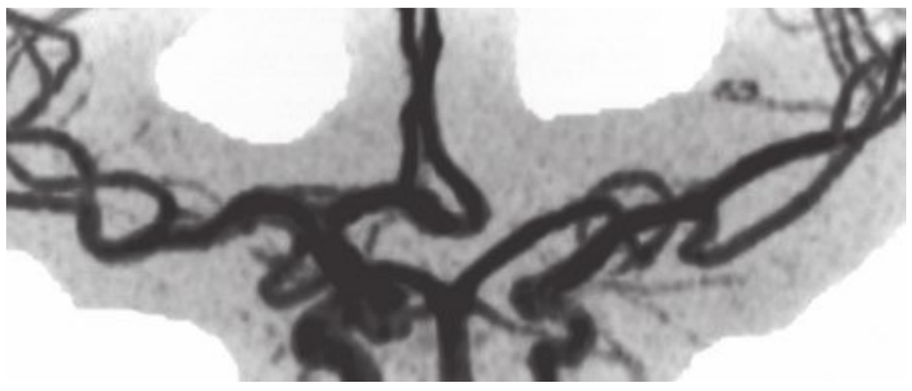

Fig. 5.21 Hypoplasia of the A1 segment of the anterior cerebral artery. Coronal MRA shows absent A1 segment of the left anterior cerebral artery. The A2 segment of the left anterior cerebral artery receives its blood supply via the anterior communicating artery.

Table 5.1 (cont.) Congenital and developmental vascular anomalies/variants

Lesion	Imaging Findings	Comments
Persistent trigeminal artery (PTA) (**Fig. 5.22** and **Fig. 5.23**)	Anomalous anastomosis connecting the internal carotid artery in cavernous sinus to the basilar artery at the level of the trigeminal nerve. Can pass posteriorly either lateral or medial to the sella turcica. The medially positioned PTA can indent the pituitary gland and needs to be reported if surgery is planned. The basilar artery below the anastomosis and the vertebral arteries are usually small.	Most common type of anomalous carotid-basilar anastomosis (0.5% of cerebral arteriograms), caused by failure of involution of persistent embryonic circulatory configuration. Associated with increased incidence of aneurysms and vascular malformations. Other less common types of anomalous carotid-basilar anastomosis include: persistent hypoglossal artery (adjacent to CN XII), persistent otic artery, and proatlantal intersegment artery.
Persistent otic artery	Anomalous anastomosis connecting the petrous portion of the internal carotid artery medially through the internal auditory canal to the lower basilar artery.	Rarest of anomalous carotid-basilar anastomoses, caused by failure of involution of persistent embryonic circulatory configuration. Associated with increased incidence of aneurysms and vascular malformations.
Persistent hypoglossal artery (**Fig. 5.24**)	Anomalous anastomosis connecting the posterior upper cervical portion of the internal carotid artery at the C1–C2 level to the basilar artery along the hypoglossal nerve within an enlarged hypoglossal canal. Often provides all of the blood flow to the basilar artery. Vertebral arteries are usually small.	Anomalous carotid-basilar anastomosis (0.1% of cerebral arteriograms), caused by failure of involution of persistent embryonic circulatory configuration. Associated with increased incidence of aneurysms and vascular malformations.

(continued on page 610)

Fig. 5.22 Persistent trigeminal artery. Lateral conventional arteriogram shows a persistent trigeminal artery (arrow), which is an arterial anastomosis between the internal carotid artery at the posteroinferior portion of the cavernous sinus and the basilar artery.

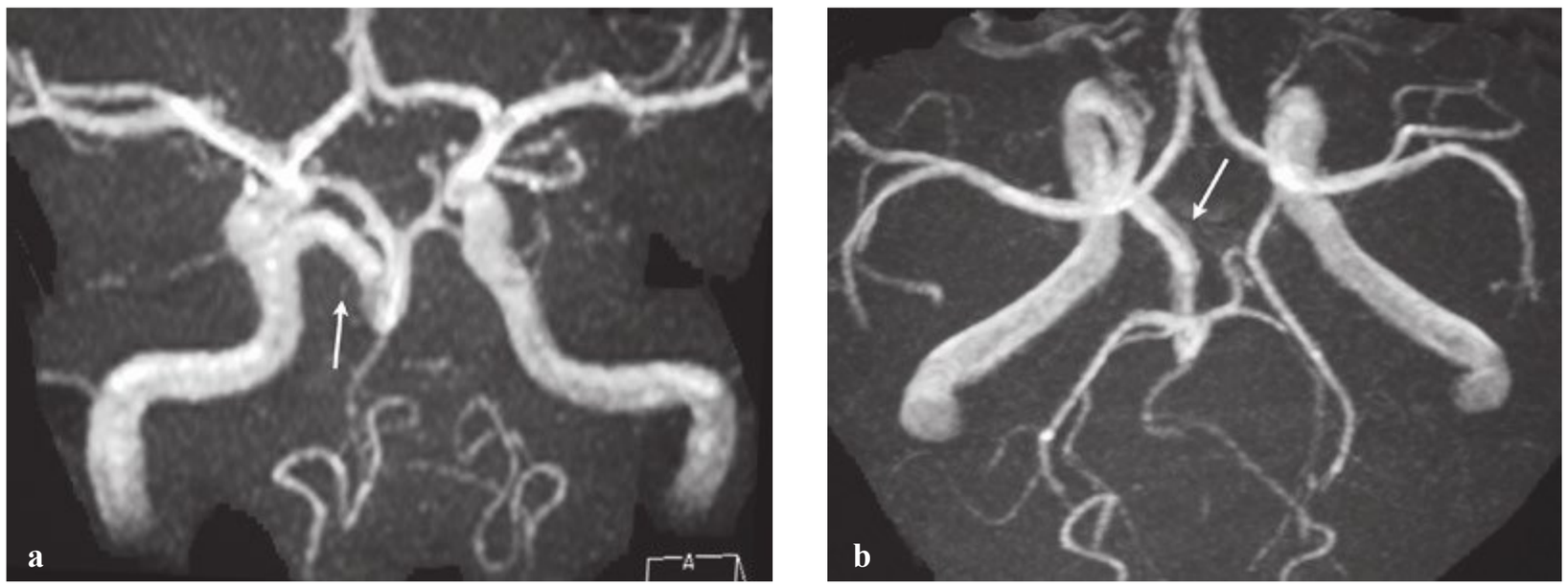

Fig. 5.23 Persistent trigeminal artery. **(a)** Coronal and **(b)** axial MRA show a persistent right trigeminal artery (arrows) supplying most of the blood to the basilar artery. The basilar artery below the trigeminal artery and both vertebral arteries are small in caliber.

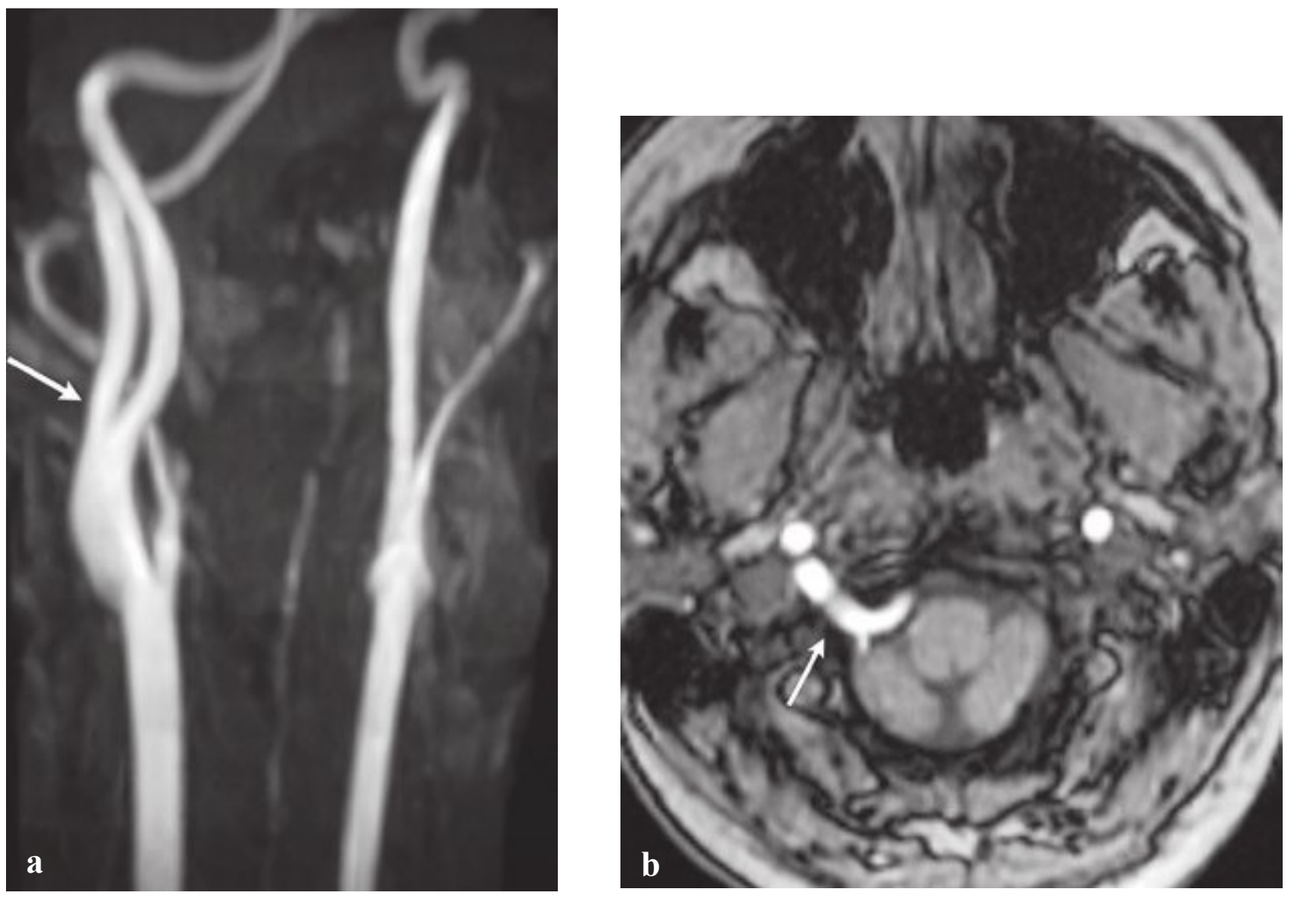

Fig. 5.24 Persistent hypoglossal artery. **(a)** Coronal MRA shows an anomalous anastomotic artery (arrow) arising from the posterior upper cervical portion of the internal carotid artery at the C1–C2 level, which connects to the basilar artery via an enlarged hypoglossal canal, as seen on **(b)** axial gradient recalled echo (GRE) imaging (arrow). Vertebral arteries are small.

Table 5.1 (cont.) Congenital and developmental vascular anomalies/variants

Lesion	Imaging Findings	Comments
Proatlantal artery	Anomalous anastomosis connecting the posterior cervical portion of the internal carotid artery at the C2–C3 level to the suboccipital vertebral artery prior to intracranial entry through the foramen magnum.	Failure of involution of persistent embryonic circulatory configuration. Associated with increased incidence of aneurysms and vascular malformations.
Duplications of cerebral, carotid, vertebral, or basilar arteries (**Fig. 5.25** and **Fig. 5.26**)	Duplication of arteries usually occurs as two parallel arteries from two separate origins, as seen on CTA, MRA, and/or conventional angiography.	Duplicated arteries have two origins and variable courses with or without eventual fusion. Duplications of intracranial or cervical arteries are less frequent than other anomalies of intracranial arteries. Other less common variants include fenestrations and accessory arteries.
Azygous anterior cerebral artery	Solitary A2 branch distal to the A1 segments of the anterior cerebral arteries.	Developmental variant with one A2 segment present distal to the A1 segments. Associated with holoprosencephaly.
Hemiazygous anterior cerebral artery (**Fig. 5.27**)	Both A2 segments of the anterior cerebral arteries arise from a more proximal solitary artery distal to the A1 segments.	Developmental variant with two A2 segments of the anterior cerebral arteries arising from a solitary proximal trunk.
Arterial fenestration (**Fig. 5.28**)	Duplication of a portion of an artery whose main trunk is derived from a single origin, as seen on CTA, MRA, or conventional angiography.	Developmental variation when there are double segments involving portions of the vertebral, basilar, or carotid arteries. With arterial fenestration, a vessel with a single origin divides into two parallel segments along its course with eventual re-anastomosis.
Aberrant position of the internal carotid artery (**Fig. 5.29**)	Abnormal position of the internal carotid artery (ICA), which enters the middle ear posteriorly through an enlarged inferior tympanic canaliculus lateral to the expected site of the petrous carotid canal. The anomalous artery courses anteriorly over the cochlear promontory to connect with the horizontal petrous ICA via a dehiscent carotid bone plate. The aberrant ICA in the middle ear is usually smaller in caliber than the contralateral normal ICA.	Congenital arterial variation related to altered formation of the extracranial ICA resulting from agenesis of the normal first embryonic segment of the ICA. A collateral alternative developmental pathway occurs where the proximal ICA originates from the ascending pharyngeal artery connecting to the inferior tympanic artery, which extends superiorly through the inferior tympanic canal into the middle ear where it anastomoses with the caroticotympanic artery, which connects to the lateral petrous portion of the ICA. As a result, the ICA is positioned laterally within the middle ear cavity. Also, a characteristic narrowing of the inferior tympanic artery occurs as it passes through the inferior tympanic canal at the skull base. Often an incidental finding with surgical planning implications.

(continued on page 612)

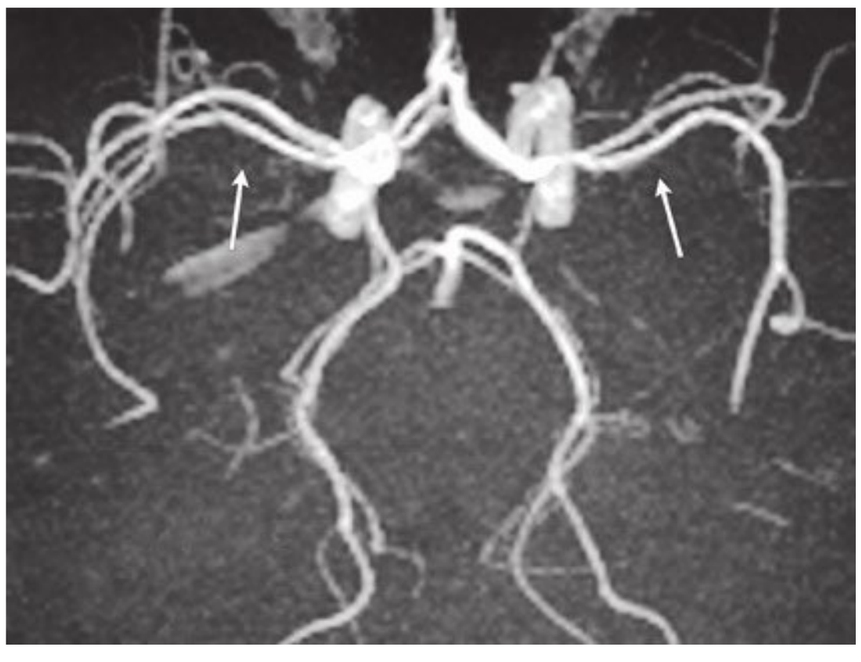

Fig. 5.25 Duplications of middle cerebral arteries. Axial MRA shows duplications of both middle cerebral arteries (arrows).

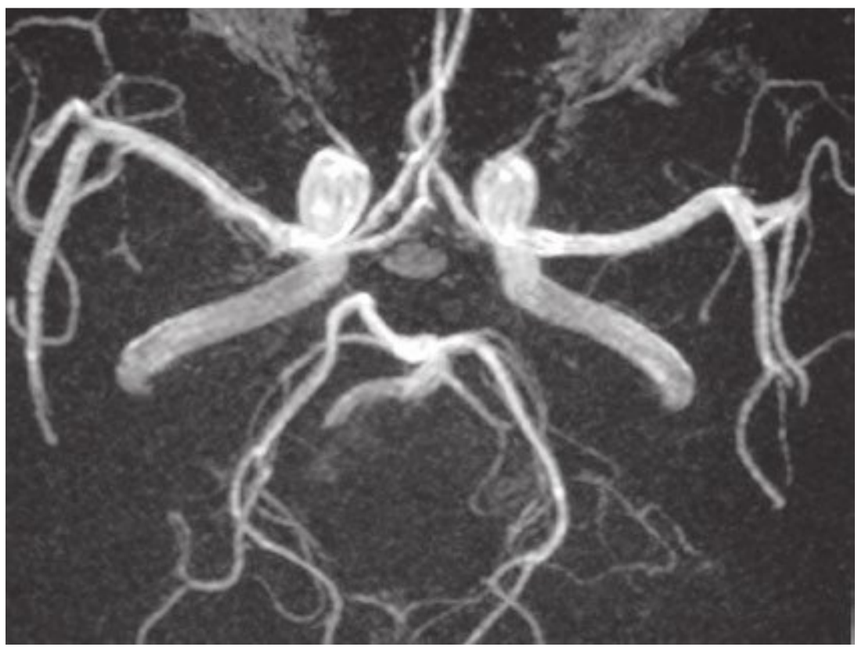

Fig. 5.26 Duplication of right anterior cerebral artery. Axial MRA shows duplication of the A1 segment of the right anterior cerebral artery.

Fig. 5.27 Hemiazygous artery. Coronal MRA shows both A2 segments of the anterior cerebral arteries arising from a more proximal solitary artery (arrow) distal to the A1 segments.

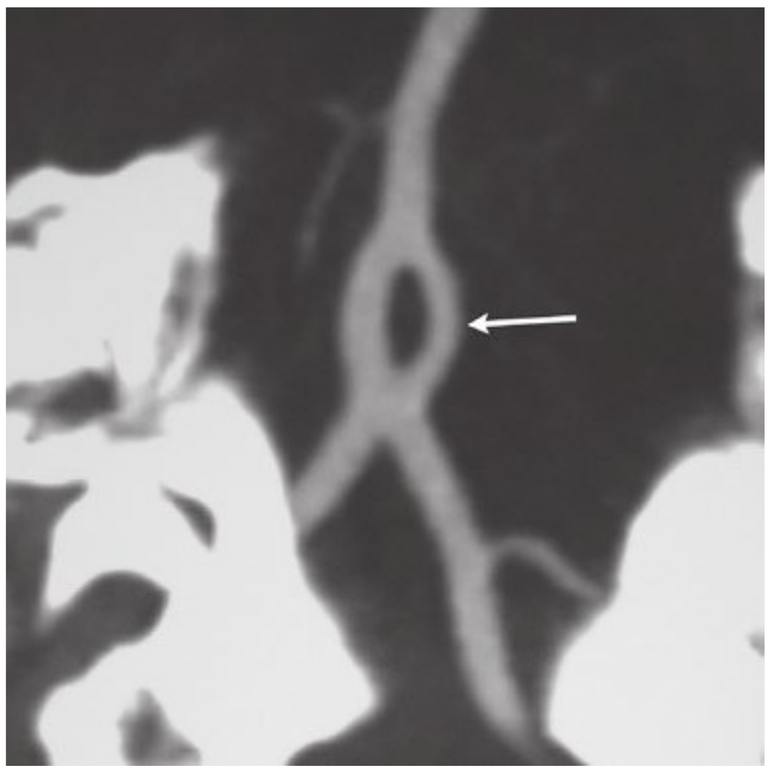

Fig. 5.28 Arterial fenestration. Coronal CTA shows a localized duplication and re-anastomosis of the basilar artery (arrow) representing an arterial fenestration.

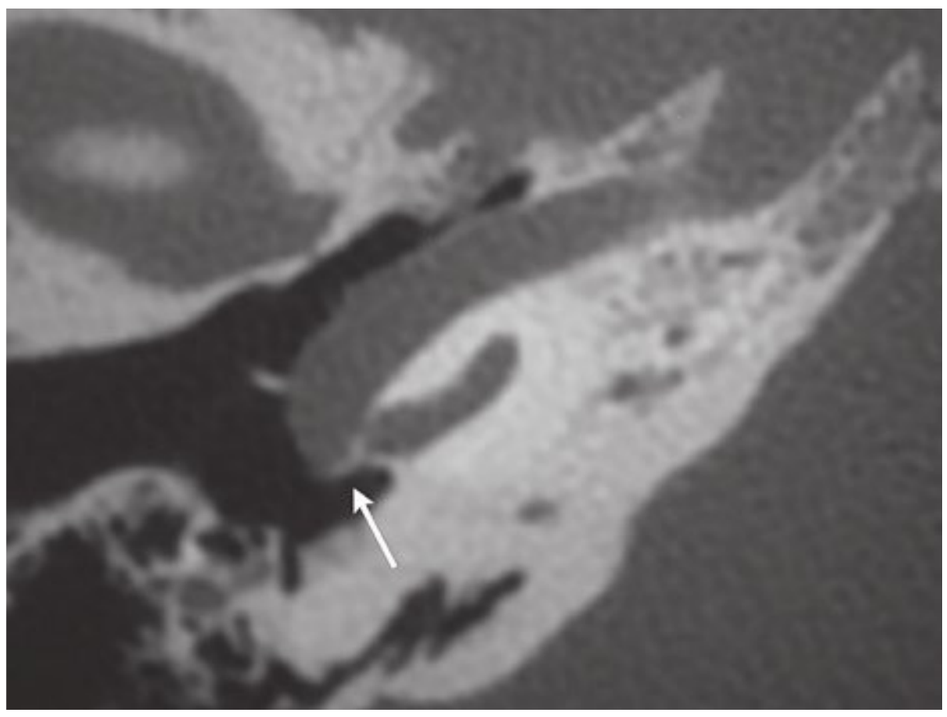

Fig. 5.29 Aberrant position of the internal carotid artery. Axial CT image shows the right internal carotid artery passing through the middle ear and positioned lateral to the basal turn of the cochlea (arrow).

Table 5.1 (cont.) Congenital and developmental vascular anomalies/variants

Lesion	Imaging Findings	Comments
Persistent stapedial artery (PSA) (**Fig. 5.30**)	Commonly occurs as an anomalous small artery associated with an aberrant internal carotid artery (ICA) or as an isolated anomaly. Findings include an absent ipsilateral foramen spinosum. The small tubular PSA extends from the ICA along the cochlear promontory through the stapes and then adjacent to the tympanic segment of CN VII to an enlarged tympanic facial nerve canal, where it enters the middle cranial fossa as the middle meningeal artery.	Rare vascular anomaly that is often associated with an aberrant ICA. Results from lack of normal evolution of the embryonic hyoid artery (from the second anterior embryonic aortic arch) into the stapedial artery, with eventual formation of the branches of the external carotid arteries (ECA) supplying the orbits, meninges, and lower face, as well as the small caroticotympanic and superior tympanic arteries. Lack of normal involution of the stapedial artery results in a persistent stapedial artery that extends from the ICA into the middle ear, passing through the stapes near the course of the tympanic portion of CN VII and extending intracranially to supply the middle meningeal artery. As a result, the middle meningeal artery is not supplied by the ECA and internal maxillary artery. There is no ipsilateral foramen spinosum.
Unilateral agenesis, aplasia, and hypoplasia of the internal carotid artery (**Fig. 5.31**)	Absence or near-complete absence of the internal carotid artery (ICA) and petrous carotid canal.	Congenital arterial variation that occurs in less than 0.01% of the population. Results from abnormal embryonic development of the third aortic arch and dorsal aorta from which the internal carotid artery arises. Collateral intracranial blood flow occurs via patent anterior and/or posterior communicating arteries.
Vein of Galen aneurysm (**Fig. 5.32**)	Multiple, tortuous, contrast-enhancing vessels involving choroidal and thalamoperforate arteries, internal cerebral veins, vein of Galen (aneurysmal formation), straight and transverse venous sinuses, and other adjacent veins and arteries. The venous portions often show contrast enhancement. CTA shows contrast enhancement in patent portions of the vascular malformation.	Heterogeneous group of vascular malformations with arteriovenous shunts and dilated deep venous structures draining into and from an enlarged vein of Galen, ± hydrocephalus, ± hemorrhage, ± macrocephaly, ± parenchymal vascular malformation components, ± seizures and high-output congestive heart failure in neonates.

(continued on page 614)

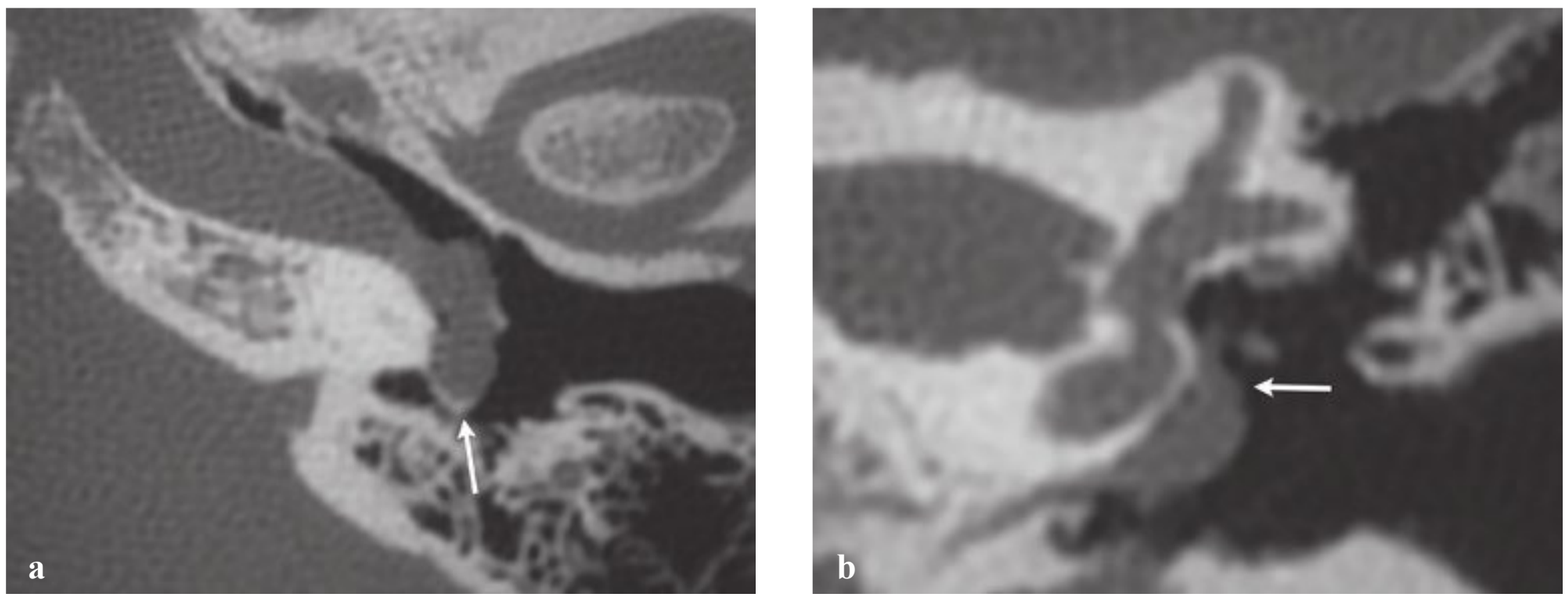

Fig. 5.30 Persistent stapedial artery (PSA) and aberrant position of the left internal carotid artery. **(a)** Axial CT image shows abnormal lateral position of the left internal carotid artery within the middle ear (arrow); the artery enters the posterior portion of the middle ear. **(b)** The PSA is seen as a small branch arising from the upper portion of the aberrant internal carotid artery (arrow) on coronal CT.

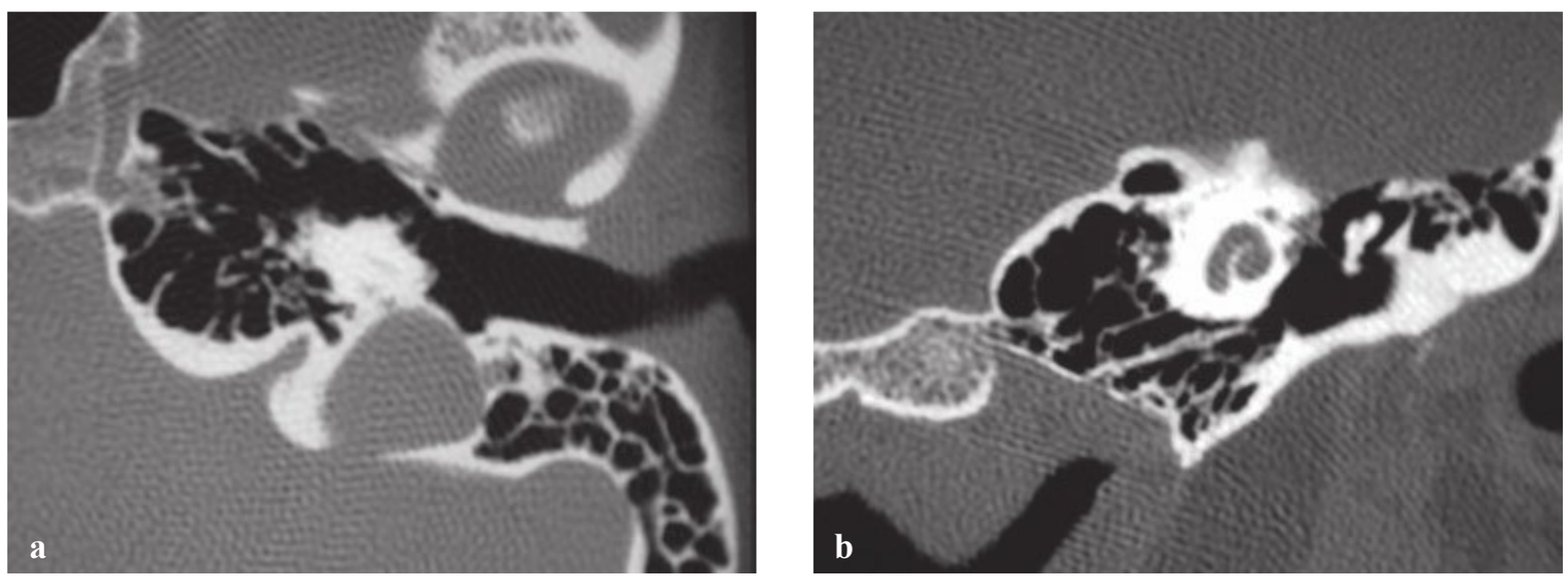

Fig. 5.31 Unilateral agenesis of the left internal carotid artery. The left internal carotid artery is completely absent **(a)** at the level of the jugular foramen on axial CT and **(b)** at the level of the cochlea on coronal CT.

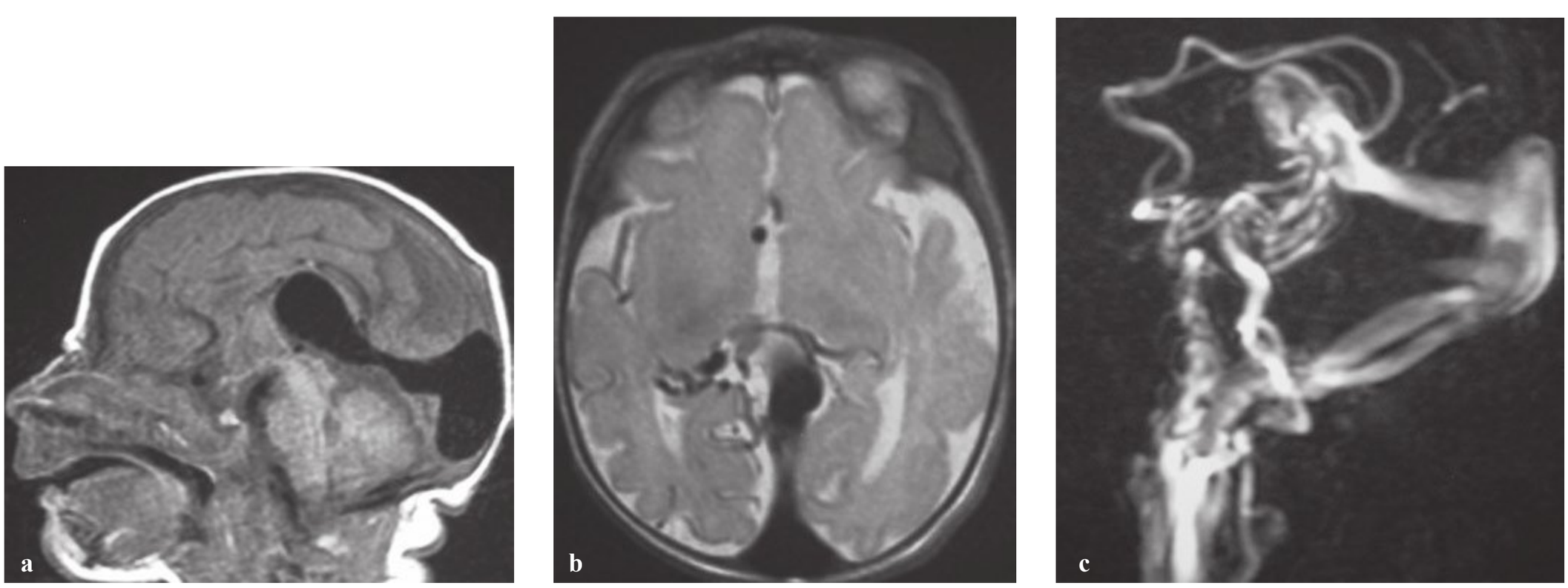

Fig. 5.32 A 2-day-old female with a vein of Galen aneurysm/malformation that is seen as abnormal enlargement of the flow voids of the basal veins, vein of Galen, straight venous sinus, and torcular herophili on **(a)** sagittal T1-weighted imaging and **(b)** axial T2-weighted imaging, with corresponding high venous flow signal on **(c)** sagittal 2D phase-contrast MRA.

Table 5.1 (cont.) Congenital and developmental vascular anomalies/variants

Lesion	Imaging Findings	Comments
Sturge-Weber syndrome (**Fig. 5.33** and **Fig. 5.34**)	Prominent, localized, unilateral leptomeningeal contrast enhancement usually in parietal and/or occipital regions in children, ± gyral enhancement, mild localized atrophic changes in brain adjacent to the pial angioma, ± prominent medullary and/or subependymal veins, ± ipsilateral prominence of choroid plexus. Gyral calcifications > 2 years, with progressive cerebral atrophy in region of pial angioma.	Also known as encephalotrigeminal angiomatosis, Sturge-Weber syndrome is a neurocutaneous syndrome associated with ipsilateral port wine cutaneous lesion and seizures. It results from persistence of primitive leptomeningeal venous drainage (pial angioma) and developmental lack of normal cortical veins, producing chronic venous congestion and ischemia.
Moyamoya disease (**Fig. 5.35**)	Multiple, tortuous, small, enhancing vessels may be seen in the basal ganglia and thalami secondary to dilated collateral arteries, + enhancement of these arteries related to slow flow within the collateral arteries versus normal-sized arteries. Contrast enhancement of the leptomeninges related to pial collateral vessels. Decreased or absent contrast enhancement in the supraclinoid portions of the internal carotid arteries and proximal middle and anterior cerebral arteries. MRA and CTA show stenosis and occlusion of the distal internal carotid arteries with collateral arteries (lenticulostriate, thalamoperforate, and leptomeningeal) best seen after contrast administration enabling detection of slow blood flow.	Progressive occlusive disease of the intracranial portions of the internal carotid arteries, with resultant numerous dilated collateral arteries arising from the lenticulostriate and thalamoperforate arteries as well as other parenchymal, leptomeningeal, and transdural arterial anastomoses. Moyamoya means "puff of smoke," referring to the angiographic appearance of the collateral arteries (lenticulostriate and thalamoperforate). The disease usually has a nonspecific etiology but can be associated with neurofibromatosis, radiation angiopathy, atherosclerosis, sickle-cell disease, and mutations in BRCC3/MTCP1 and GUCY1A3 genes. Usually occurs in children more than in adults, and in Asia more than other locations.
ACTA2 mutations with dolichoectasia of the proximal internal carotid arteries and stenosis of the upper internal carotid arteries (**Fig. 5.36**)	Conventional arteriography, MRA, CTA: Dilatation of the proximal internal carotid arteries (ICAs), severe narrowing of the upper ICAs, straightened patterns of the proximal ICAs, stenosis or occlusion of the M1 segments of the middle cerebral arteries without lenticulostriate collaterals, ± tortuous or corkscrew appearance of distal anterior, middle, and posterior cerebral arteries. MRI: Multiple small cerebral infarcts involving the cerebral cortex and/or white matter.	Arg179 missense mutation of the ACTA2 gene is associated with smooth muscle dysfunction resulting in dilatation of the proximal ICAs, severe narrowing of the upper ICAs, straightened patterns of the proximal ICAs, "moyamoya-type" collateral vessels, large artery occlusions, distal small distal aneurysms, dilated extradural arteries; as well as patent ductus arteriosus, mydriasis, pulmonary hypertension, and gastrointestinal and bowel dysfunction. Usual presentation is in children. ACTA2 mutations result in abnormal fibromuscular and/or smooth muscle proliferation in the intima and media of arteries.

(continued on page 616)

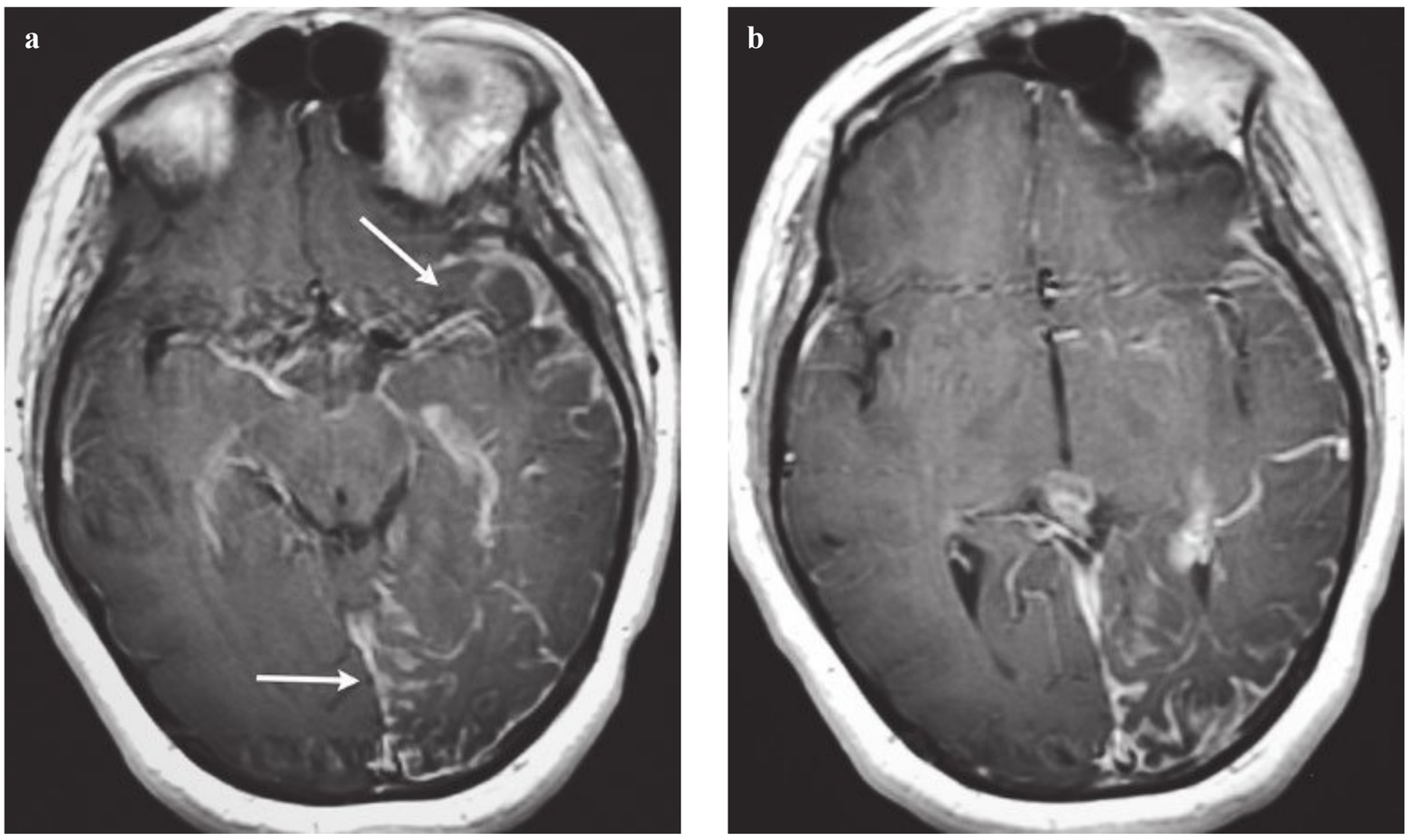

Fig. 5.33 **(a)** A 15-year-old male with Sturge-Weber syndrome who has gadolinium contrast enhancement in the leptomeninges on the left from the persistent fetal pial angioma (arrows) on axial T1-weighted imaging, as well as **(b)** an enhancing transmantle (medullary) vein that connects to the enlarged choroid plexus in the atrium of the left lateral ventricle on axial T1-weighted imaging.

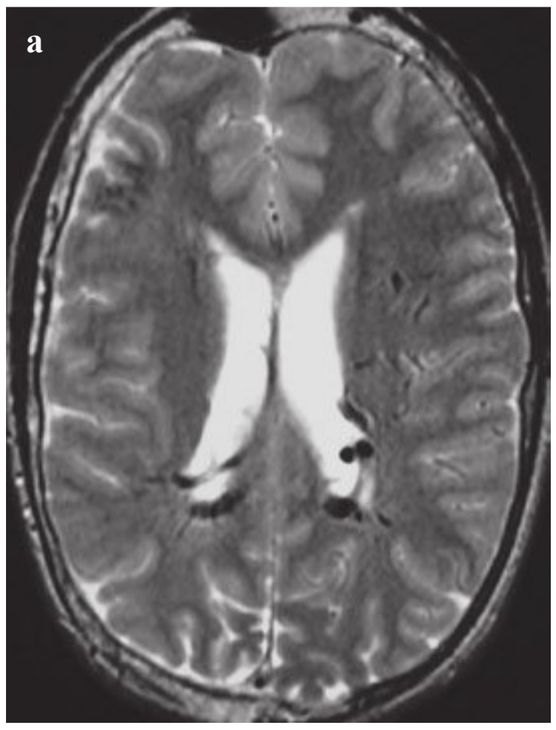

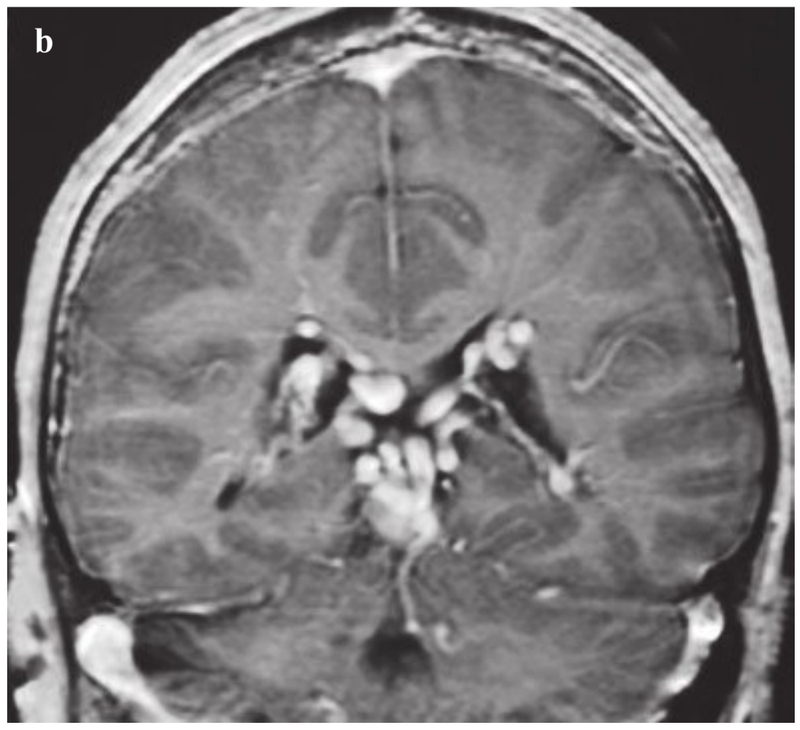

Fig. 5.34 **(a)** A 17-year-old male with an uncommon form of Sturge-Weber syndrome that is seen as flow voids along the ependymal lining of the lateral ventricles and within the cerebral white matter on axial T2-weighted imaging, with **(b)** corresponding gadolinium contrast enhancement on coronal T1-weighted imaging.

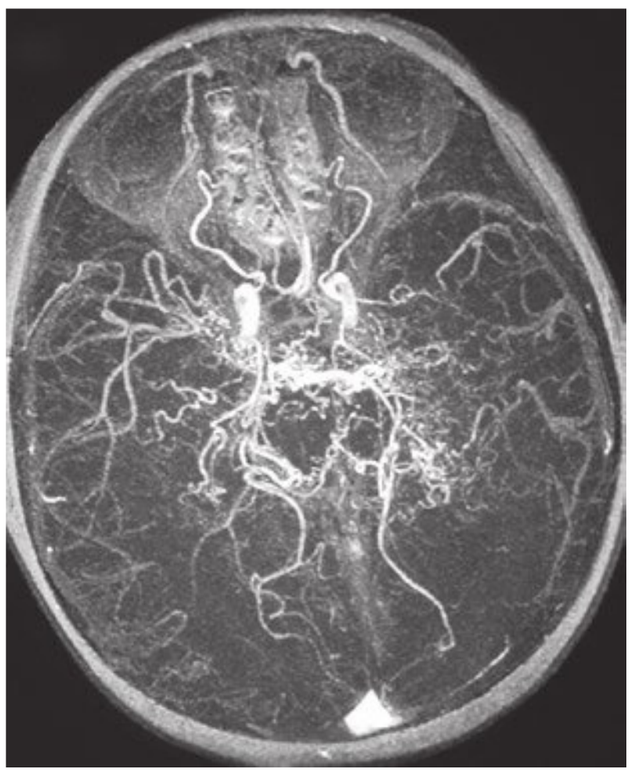

Fig. 5.35 A 3-year-old female with moyamoya disease. Postcontrast axial MRA shows stenosis and occlusion of the distal internal carotid arteries, with gadolinium contrast enhancement of many small, collateral lenticulostriate, thalamoperforate, and leptomeningeal arteries.

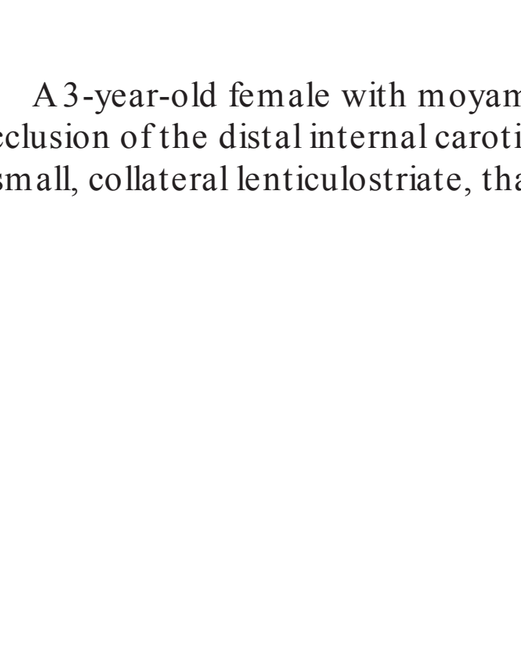

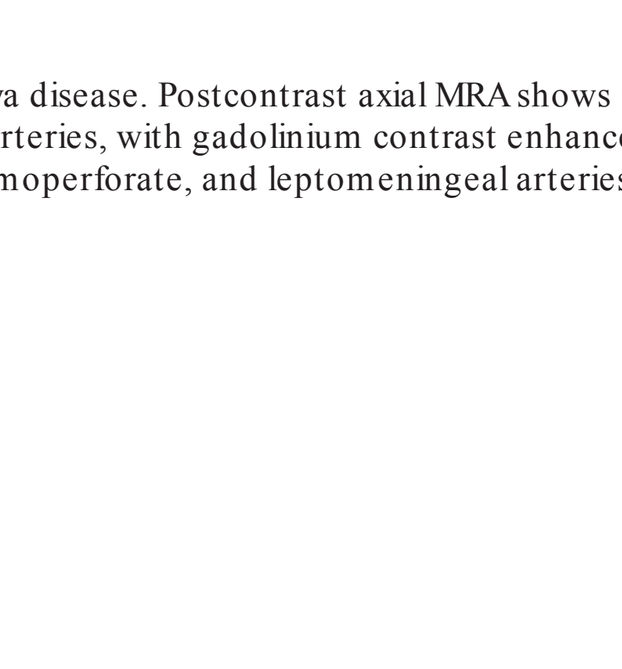

Fig. 5.36 A 14-year-old male with ACTA2 mutations and dolichoectasia of the proximal internal carotid arteries, with severe narrowing of the upper internal carotid arteries and M1 segments of the middle cerebral arteries and straightened patterns of proximal intracranial arteries, as seen on **(a)** coronal MRA and **(b)** conventional arteriogram. Tortuous corkscrew distal branches of the anterior and middle cerebral arteries are also seen **(b)**. **(c)** Axial FLAIR shows multiple intra-axial zones with high signal in the cerebral white matter related to small-vessel ischemia.

Table 5.1 (cont.) Congenital and developmental vascular anomalies/variants

Lesion	Imaging Findings	Comments
Menkes' syndrome (**Fig. 5.37**)	MRI: High signal on T2-weighted imaging can be seen in the cerebral white matter, putamen bilaterally, and/or caudate nuclei, with or without restricted diffusion. Delayed myelination involving the posterior limbs of the internal capsules can be seen. Progressive atrophy of the cerebrum, cerebellum, and brainstem. Small zones with high signal on T1-weighted imaging may be seen in the cerebral cortex. Large bilateral subdural hematomas can be seen with mixed signal on T1- and T2-weighted imaging. MRA and CTA show tortuous "corkscrew" arteries. CT: Rapid, progressive brain atrophy with large bilateral subdural hematomas.	X-linked recessive disorder from mutations of the ATP7A gene on Xq13.3, which encodes for the copper-transporting ATPase necessary for intestinal uptake of copper. Lack of adequate copper results in defective cytochrome c oxidase activity in mitochondria. Patients often have seizures, truncal hypotonia, hypothermia, failure to thrive, lack of reaching developmental milestones, hypermobile joints, hypopigmentation, and coarse, stiff, and broken hair—"kinky hair disease."
PHACES syndrome (posterior fossa malformations, facial hemangiomas, arterial anomalies, cardiac anomalies and aortic coarctation, eye abnormalities, and sternal clefts or supraumbilical raphe) (**Fig. 5.38**)	Vascular anomalies occur in 30% of patients. Arterial abnormalities include: absence or hypoplasia of the carotid, vertebral, and/or cerebral arteries; anomalous arteries; arterial stenoses and occlusions; moyamoya; aneurysms; and AVMs. Cavernous malformations can also occur. Malformations in the posterior cranial fossa can include Dandy-Walker malformation and dysgenesis/hypoplasia of the cerebellum, corpus callosum, or septum pellucidum.	Rare spectrum of anomalies of unknown etiology that includes facial hemangiomas that are present at birth and involve one trigeminal nerve division, as well as one or more of the following: arterial anomalies, coarctation of the aorta, malformations in the posterior cranial fossa, eye abnormalities (microphthalmos, cataracts, iris hypoplasia, and optic nerve hypoplasia or atrophy), cardiac defects, and/or sternal clefts. Occurs predominantly in females (up to 90% of cases).
Thoracic outlet syndrome (**Fig. 5.39**)	Cervical ribs or fibrous bands located adjacent to the subclavian artery, subclavian vein, and/or brachial plexus.	Signs and symptoms of the thoracic outlet syndrome (TOS) occur from compression of the brachial plexus (neurogenic TOS), subclavian artery (arterial TOS), and/or subclavian vein (venous TOS). Neurogenic TOS accounts for ~ 90% of cases. Compression of the thoracic outlet structures can be static or positional. Causes of the compression include cervical ribs, fibrous bands, or hypertrophy or anomalies of the scalene muscles.

(continued on page 618)

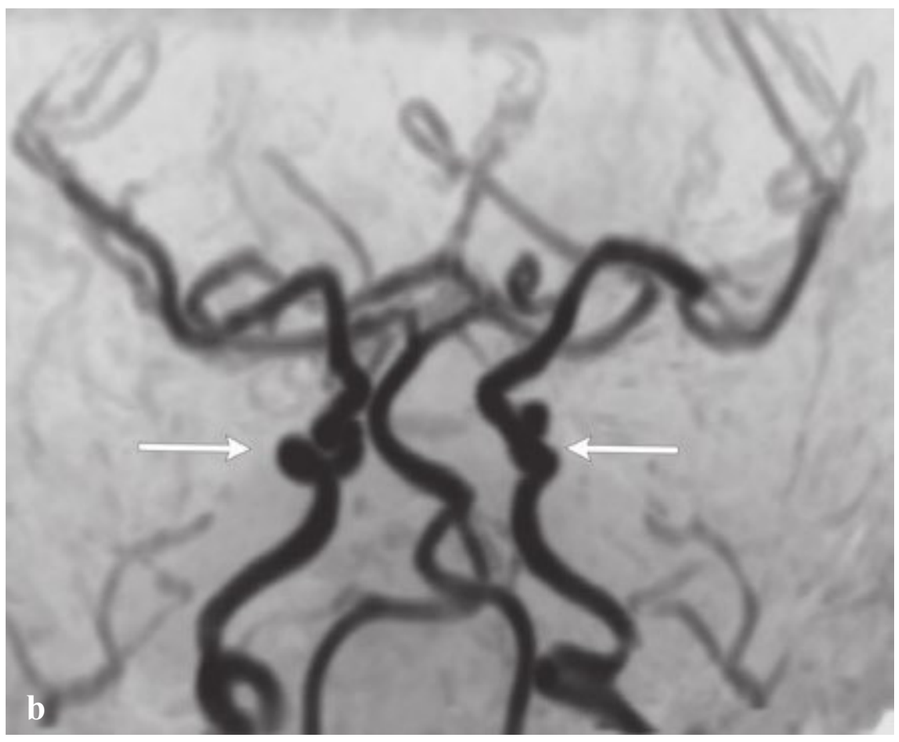

Fig. 5.37 **(a)** An 8-month-old female with Menkes' syndrome with bilateral complex subdural hematomas on axial CT. **(b)** Coronal MRA shows tortuous internal carotid arteries (arrows) that have a "corkscrew" appearance.

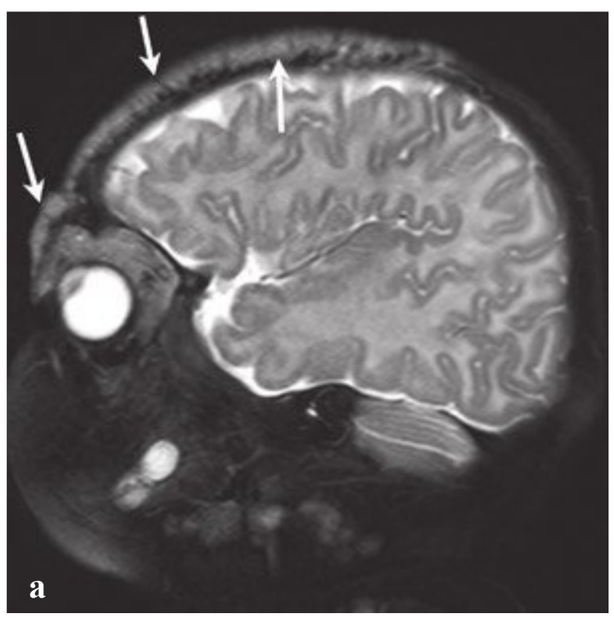

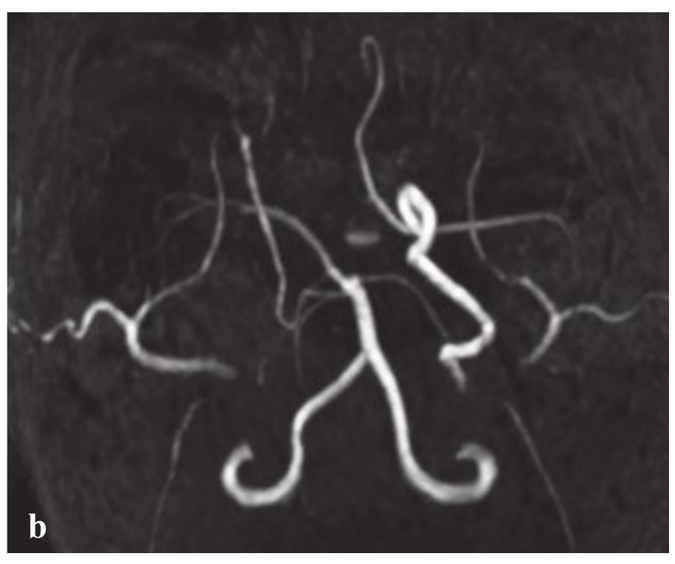

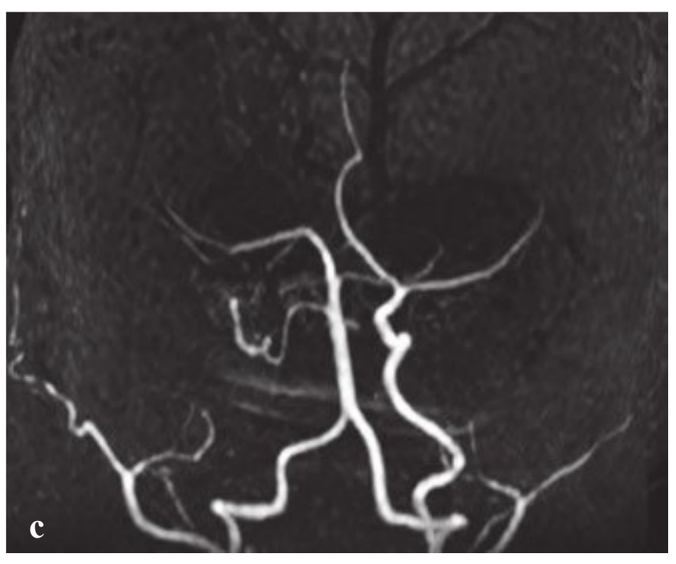

Fig. 5.38 **(a)** Patient with PHACES syndrome who has a superficial hemangioma involving the scalp at the top of the head on sagittal fat-suppressed T2-weighted imaging (arrows). **(b,c)** Coronal MRA shows occlusion of the cervical portion of the right internal carotid artery and anomalous arterial connection from the basilar artery to the right middle cerebral artery branches.

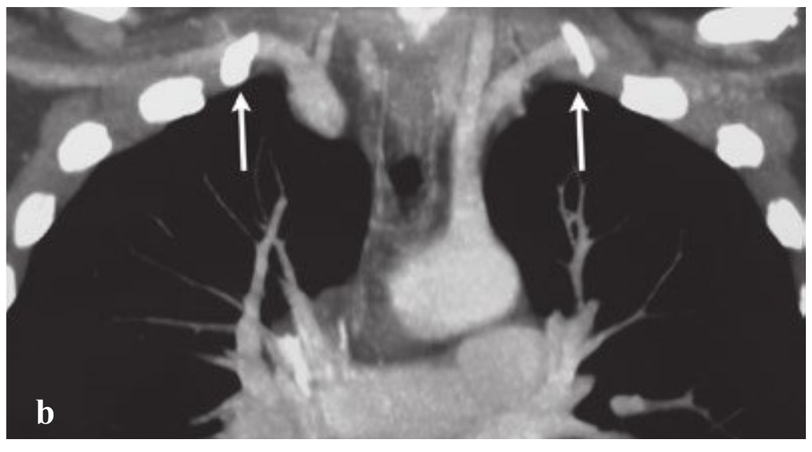

Fig. 5.39 Thoracic outlet syndrome. **(a)** Coronal CT shows bilateral cervical ribs at the C7 vertebra (arrow) that **(b)** impress on the subclavian arteries bilaterally (arrows) on coronal CTA.

Table 5.1 (cont.) Congenital and developmental vascular anomalies/variants

Lesion	Imaging Findings	Comments
Venous angioma (developmental venous anomaly) (**Fig. 5.40** and **Fig. 5.41**)	MRI: Gadolinium contrast enhancement of one or two prominent intra-axial vein(s) connected to a network of multiple small draining veins (caput medusae). Often no findings on T1- or T2-weighted imaging unless the vein is prominent. Some developmental venous anomalies have slightly high signal on T2-weighted imaging. Low signal on SWI can be seen at these venous anomalies. CT: No abnormality or small, slightly hyperdense zone prior to contrast administration. Contrast enhancement seen in a slightly prominent vein draining a collection of small veins on contrast-enhanced CT and CTA.	Considered an anomalous venous formation. Typically not associated with hemorrhage. Usually an incidental finding, except when it is associated with cavernous malformation (in ~ 25% of cases).
Dehiscence of the jugular bulb (**Fig. 5.42**)	Protrusion of the jugular bulb into the posteroinferior portion of the middle ear related to deficient or absent bone at the jugular plate.	Venous variant anatomy with the jugular bulb extending superiorly and laterally into the middle ear through localized bone deficiency/dehiscence of the jugular plate. May be associated with pulsatile tinnitus, Ménière disease, and hearing loss. Important to report for surgical planning.
High position of the jugular bulb	The upper portion of the jugular bulb is located above the base of the internal auditory canal/basilar turn of the cochlea. Does not protrude into the middle ear.	Developmental venous variant anatomy, with positioning of the upper portion of the jugular bulb above the level of the base of the internal auditory canal. Usually an incidental finding.
Sinus pericranii (**Fig. 5.43**)	Communication between dilated extracranial veins and the intracranial veins or dural venous sinuses through a skull defect or emissary veins.	Lesions are nonpulsatile, asymptomatic, soft tissue masses in the scalp near the midline calvarial sutures and often measure 15 mm. Can increase in size with Valsalva maneuver. Lesions are associated with intracranial anomalies, such as solitary DVAs (eight of 13 patients), vein of Galen hypoplasia (two of 13 patients), vein of Galen aneurysm (one of 13 patients), dural sinus malformation (one of 13 patients), and intraosseous arteriovenous malforamtion (one of 13 patients). Can be the cutaneous sign of an underlying venous anomaly.

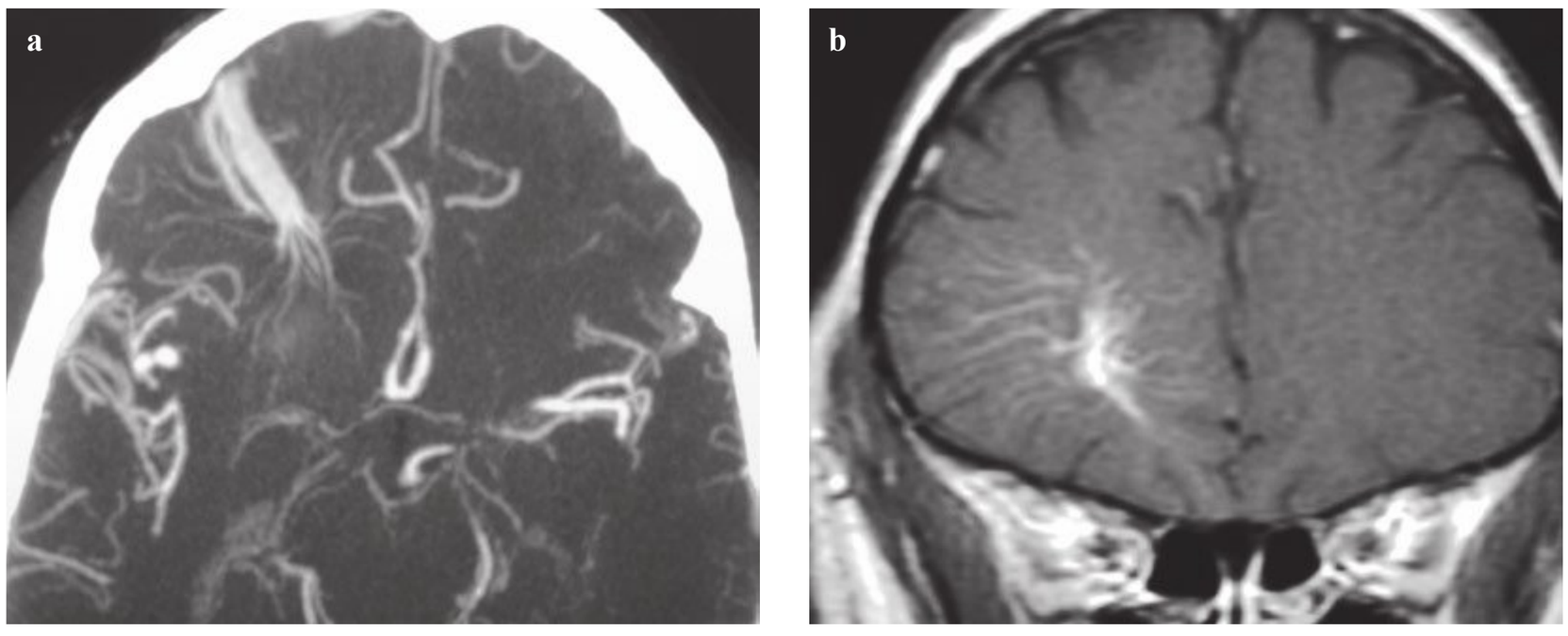

Fig. 5.40 A contrast-enhancing venous angioma (developmental venous anomaly) is seen in the anterior right frontal lobe on **(a)** axial CTA and **(b)** coronal T1-weighted imaging.

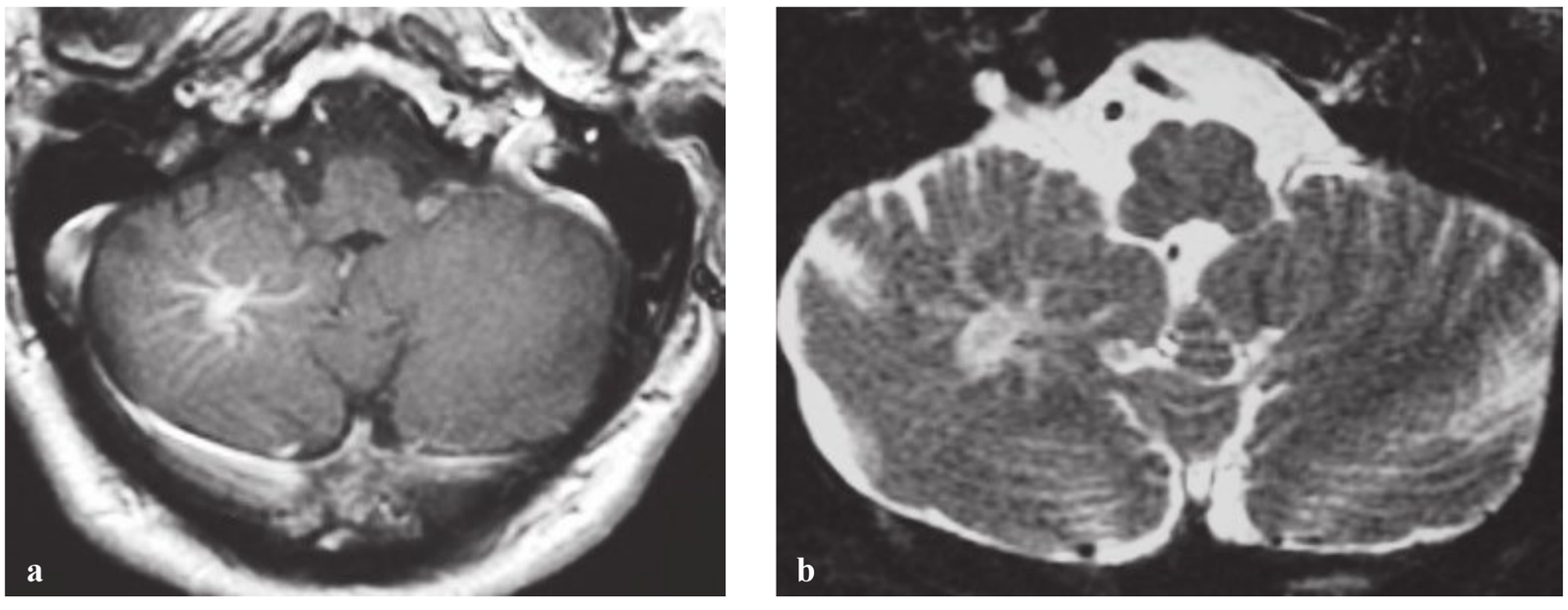

Fig. 5.41 A contrast-enhancing venous angioma (developmental venous anomaly) is seen in the right cerebellar hemisphere on **(a)** axial T1-weighted imaging and has high signal on **(b)** axial T2-weighted imaging.

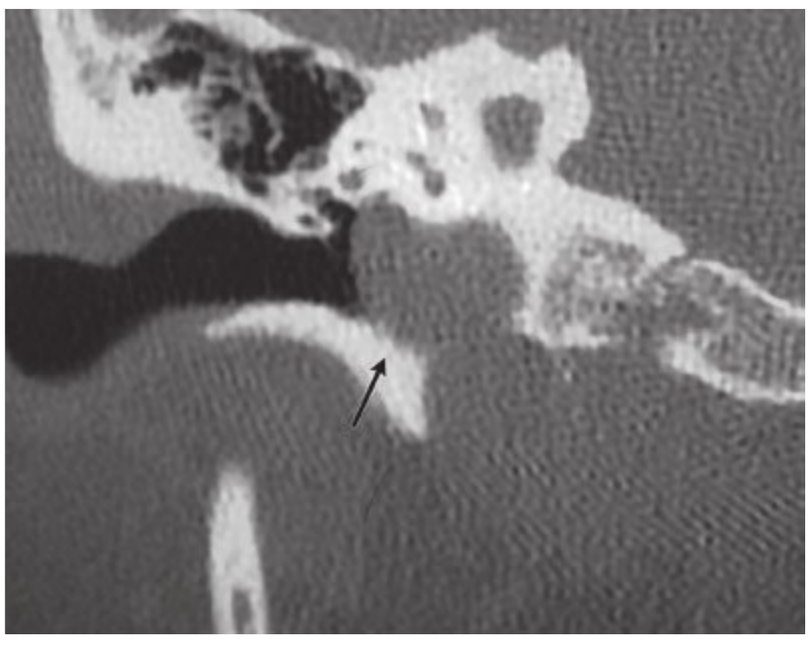

Fig. 5.42 Coronal CT shows dehiscence of the right jugular bulb (arrow), which protrudes into the right middle ear.

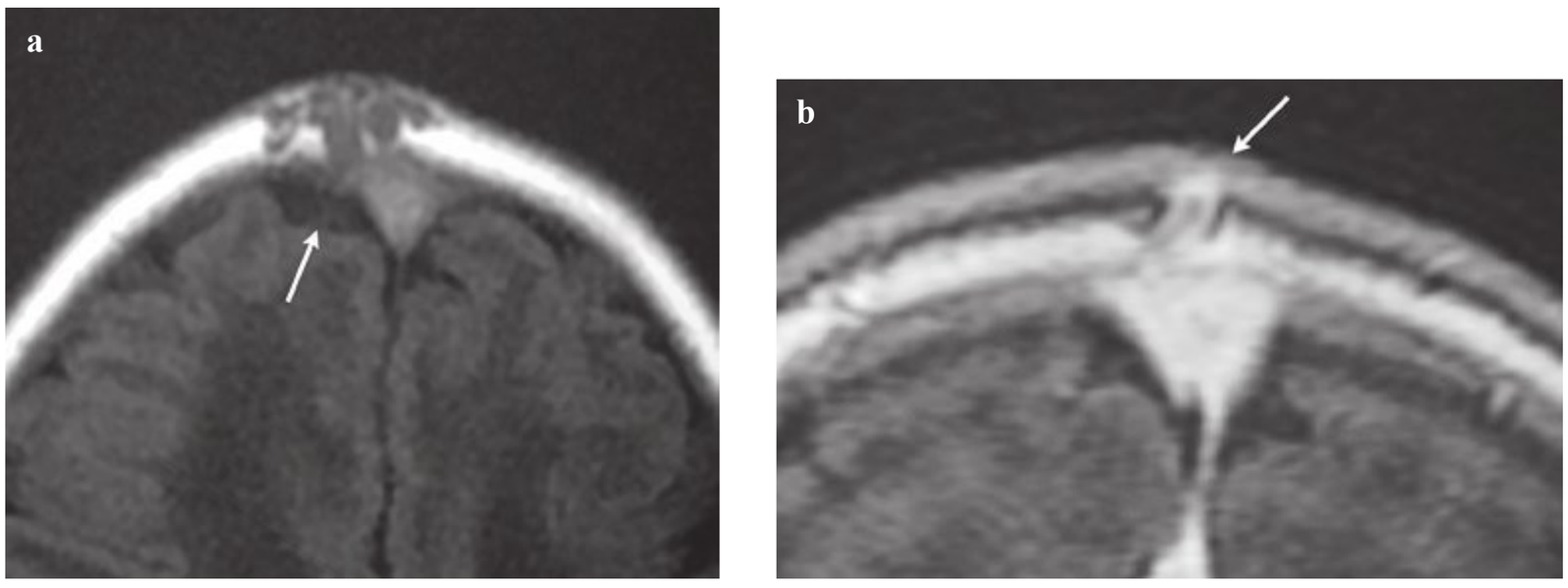

Fig. 5.43 A 4-week-old female with sinus pericranii, which is seen as communication between extracranial veins and the anterior portion of the superior sagittal sinus through a skull defect, as seen as on **(a)** axial T1-weighted imaging (arrow) and **(b)** postcontrast T1-weighted imaging (arrow).

Table 5.2 Acquired vascular disease

- Arterial stenosis/occlusion
- Subclavian steal syndrome
- Fibromuscular dysplasia
- Arterial dissection
- Vasculitis
- Intracranial venous sinus
- Thrombosis
- Arterial aneurysm
- Arterial-venous malformation
- Vein of galen aneurysm/malformation
- Dural arterial-venous malformation
- Carotid cavernous fistula
- Cavernous malformation
- Developmental venous anomaly (venous angioma)
- Capillary telangiectasia

Table 5.2 Acquired vascular disease

Lesions	Imaging Findings	Comments
Stenosis/Occlusive Vascular Disease		
Arterial stenosis/occlusion (**Fig. 5.44, Fig. 5.45, Fig. 5.46, Fig. 5.47, Fig. 5.48, Fig. 5.49**, and **Fig. 5.50**)	Focal narrowing (stenosis) or occlusion of artery on CTA, MRA, or conventional arteriography, ± narrowing of artery distal to site of stenosis.	Arterial stenosis or occlusion may result from atherosclerosis, emboli, fibromuscular disease/dysplasia, collagen vascular disease, coagulopathy, encasement by neoplasm, surgery, or radiation injury.
Subclavian steal syndrome (**Fig. 5.51**)	MRA, CTA, and conventional arteriography show occlusion of the proximal subclavian artery with reconstitution beyond the occlusion via reversed blood flow from the ipsilateral vertebral artery.	Stenosis or occlusion of the proximal subclavian artery can cause reversal of blood flow in the ipsilateral vertebral artery to supply the subclavian artery distal to the occlusion or stenosis. The reversed blood flow can result in signs of vertebrobasilar insufficiency (syncope, nausea, ataxia, vertigo, diplopia, headaches, etc.) elicited with exercise of the upper extremity on the same side where the stenosis/occlusion of the subclavian artery occurs.

(continued on page 623)

Fig. 5.44 Arterial stenosis. Sagittal CTA shows a mostly fatty atherosclerotic plaque (arrow) at the upper common carotid artery resulting in severe narrowing of the proximal internal carotid artery.

Fig. 5.45 Arterial stenosis. Sagittal CTA shows ulcerated fatty plaque (arrow) causing moderate stenosis of the proximal internal carotid artery.

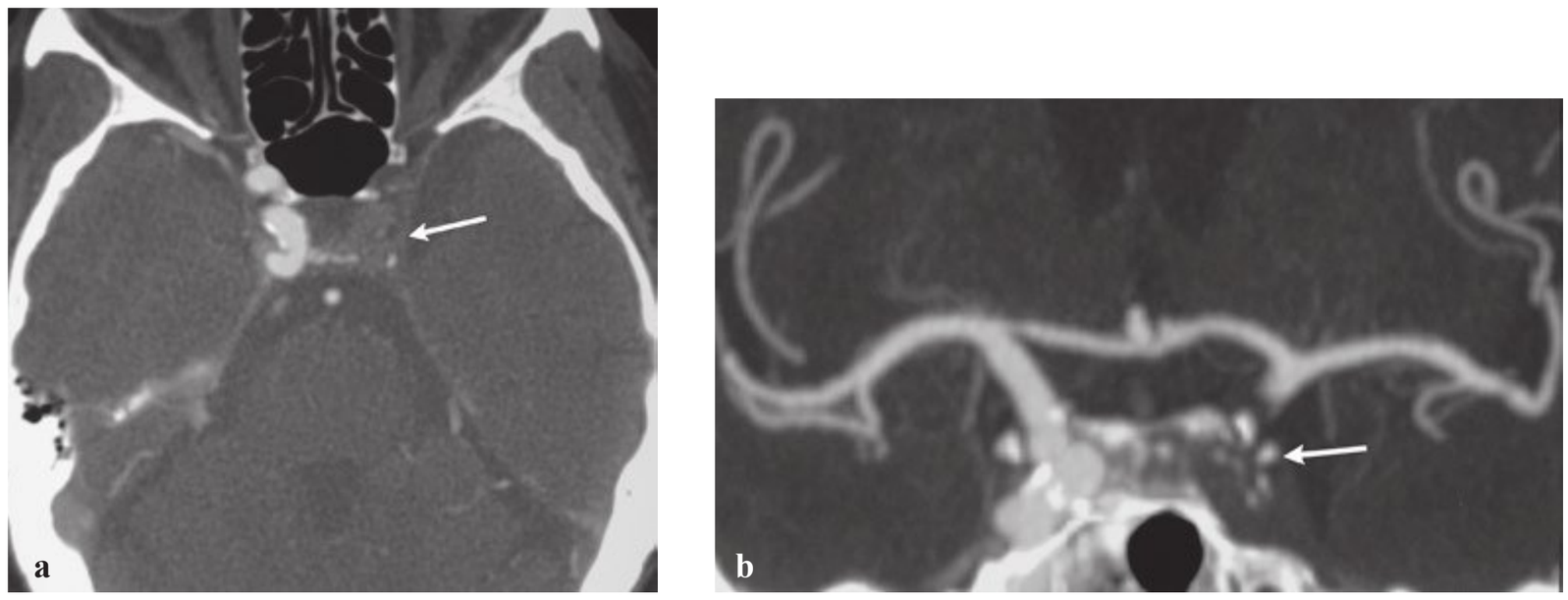

Fig. 5.46 **(a)** Axial and **(b)** coronal CTA shows occlusion of the left internal carotid artery, seen as absence of intra-arterial contrast enhancement (arrows).

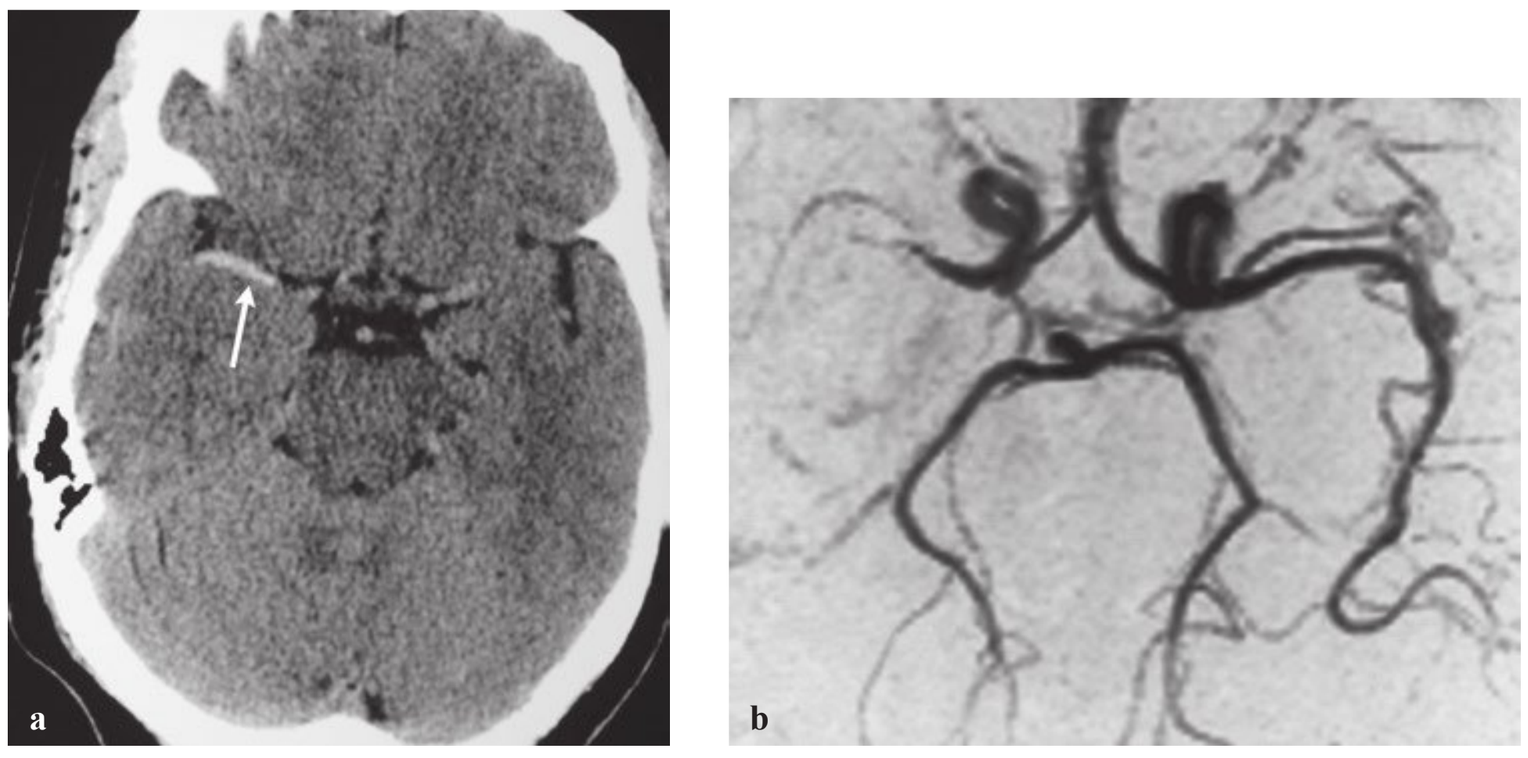

Fig. 5.47 **(a)** Axial CT shows a hyperdense M1 segment of the right middle cerebral artery (arrow) from intraluminal thrombus. **(b)** Axial MRA shows absent flow signal in the right middle cerebral artery resulting from the intraluminal thrombus.

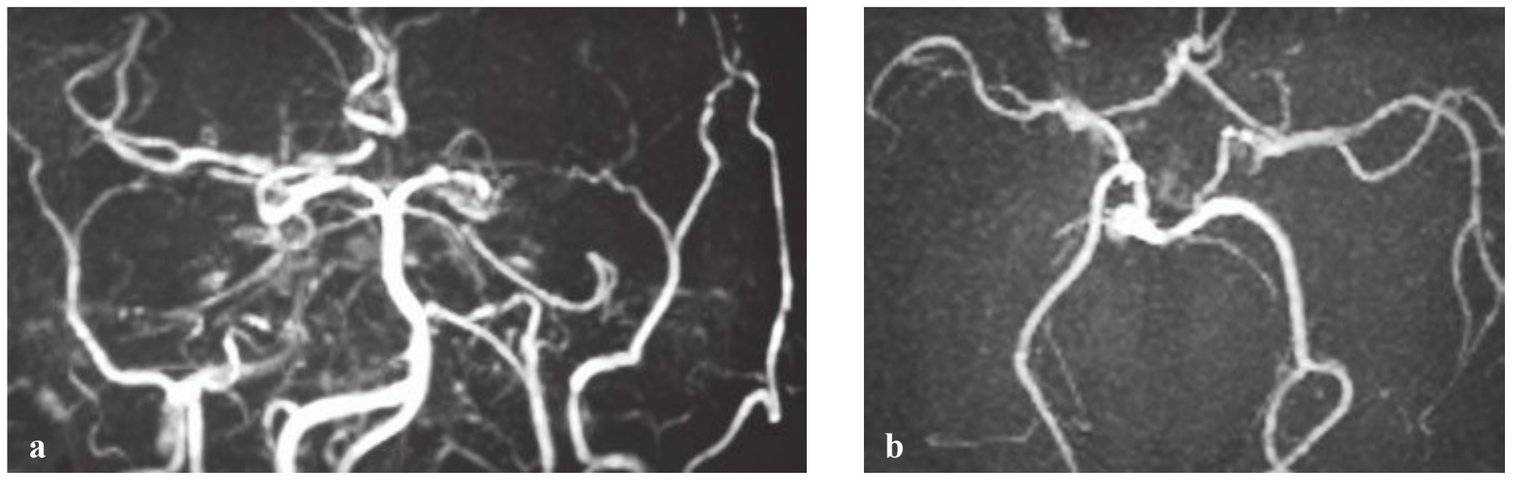

Fig. 5.48 **(a)** Coronal and **(b)** axial MRA shows absent flow signal in both internal carotid arteries from arterial occlusion. Flow signal is seen in the anterior and middle cerebral arteries from collateral flow via patent anterior and posterior communicating arteries **(b)**.

Fig. 5.49 MRA shows patent internal carotid arteries and near-complete occlusion of the basilar artery.

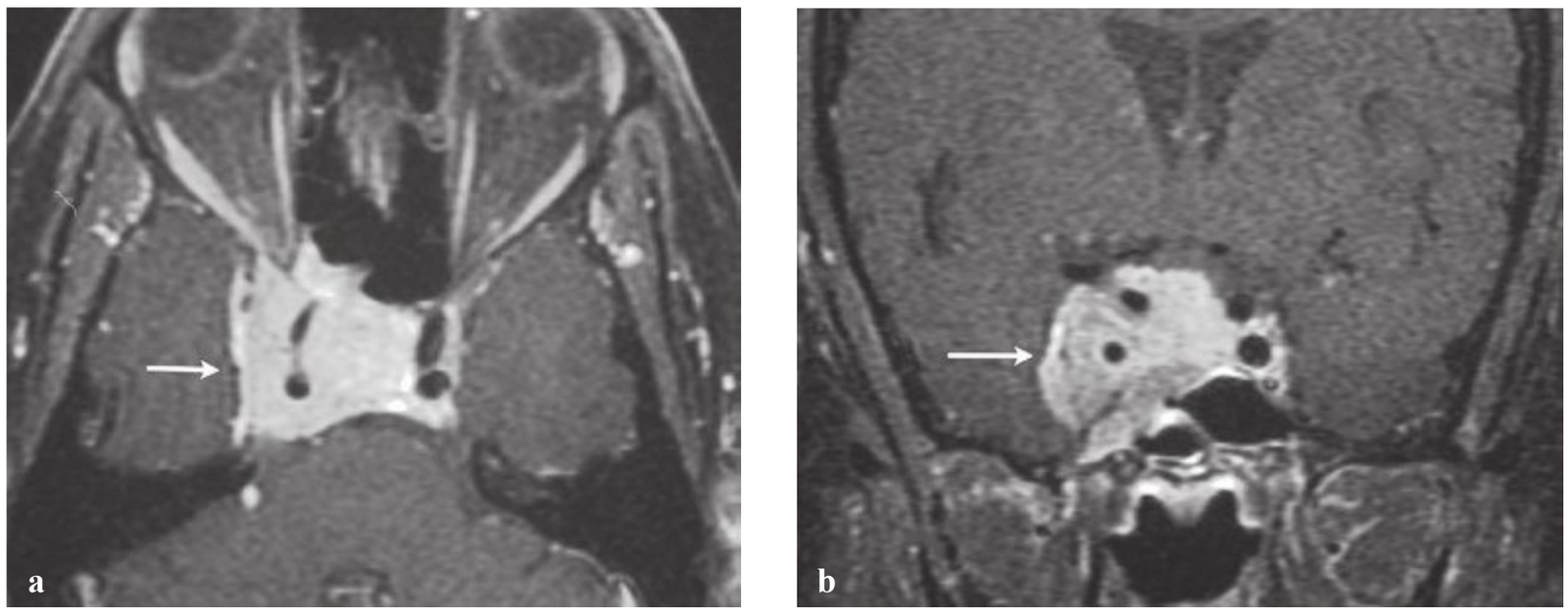

Fig. 5.50 **(a)** Axial and **(b)** coronal fat-suppressed T1-weighted imaging shows a gadolinium-enhancing meningioma in the medial portion of the right middle cranial fossa (arrows) and extending into the right cavernous sinus, encasing and narrowing the flow void of the right internal carotid artery.

Fig. 5.51 Subclavian steal syndrome. **(a)** CTA and **(b)** volume-rendered CTA show occlusion of the proximal left subclavian artery (arrows), with retrograde blood flow from the left vertebral artery into the subclavian artery.

Table 5.2 (cont.) Acquired vascular disease

Lesions	Imaging Findings	Comments
Fibromuscular dysplasia (**Fig. 5.52**)	CTA, MRA, and conventional arteriography: The medial *fi*broplasia subtype usually involves the middle and distal portions of the internal carotid arteries, and it can be bilateral and involve the vertebral arteries. The involved vessel has a "beaded" or "string of beads" appearance, with multiple small zone of stenosis and adjacent dilatation. The intimal subtype can show a focal bandlike constriction, with concentric narrowing or a long zone of tubular narrowing.	Noninflammatory, nonatherosclerotic segmental arteriopathy of unknown etiology that involves medium-sized arteries in the body, most commonly the cervical and intracranial arteries, and/or renal arteries. Most often occurs in women from 20 to 60 years old, but can also occur in men and children. Associated with increased risk of intracranial aneurysms, arterial dissection, transient ischemic attack, or stroke. The medial *fi*broplasia subtype accounts for up to 90% of cases and consists of alternating zones of thinned media and thick collagen ridges within the arterial wall. The intimal subtype has collagen deposition within the intima. Treatment includes antiplatelet therapy for asymptomatic patients and balloon angioplasty for symptomatic patients.

(continued on page 624)

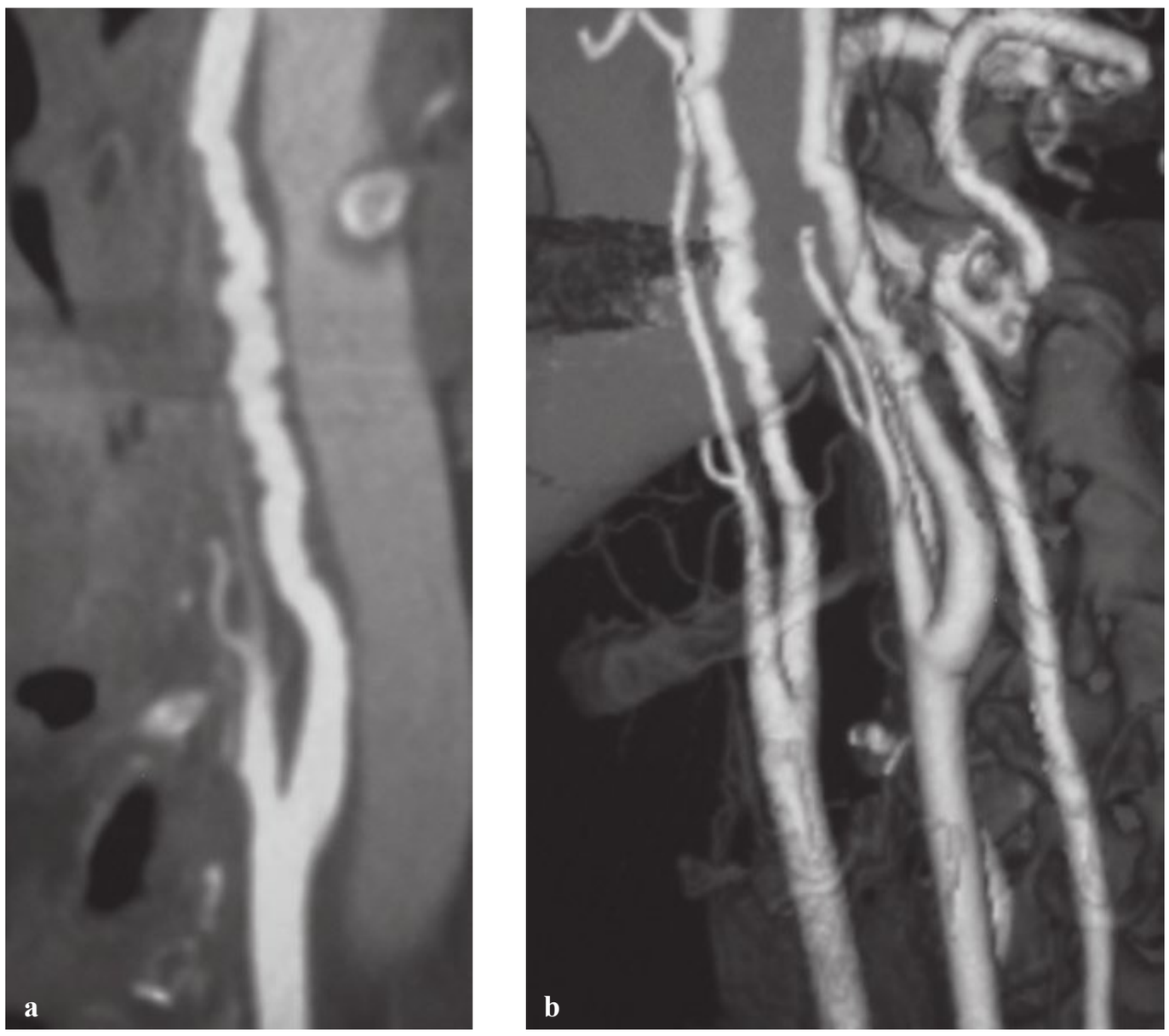

Fig. 5.52 Fibromuscular dysplasia. **(a)** CTA and **(b)** volume-rendered CTA show multifocal irregular wall thickening of the internal carotid arteries from fibromuscular dysplasia.

Table 5.2 (cont.) Acquired vascular disease

Lesions	Imaging Findings	Comments
Arterial dissection (**Fig. 5.53, Fig. 5.54**, and **Fig. 5.55**)	MRI: Crescentic zone with high signal on proton density-weighted imaging and fat-suppressed T1-weighted imaging involving the wall of a cervical carotid or vertebral artery, resulting in narrowing of the intraluminal flow void. The intramural hematoma can progress and fill to occlude the lumen, obliterating the flow void of the artery. MRA and CTA show narrowed or occluded arterial lumen. CT: The involved arterial wall is thickened in a circumferential or semilunar configuration and has intermediate attenuation. Lumen may be narrowed or occluded.	Arterial dissections are intramural hematomas that can be related to trauma, collagen vascular disease (Marfan syndrome, Ehlers-Danlos syndrome, etc.), or fibromuscular dysplasia, or they can be idiopathic. Hemorrhage in the arterial wall can cause stenosis, occlusion, and stroke.

(continued on page 626)

Fig. 5.53 Arterial dissection in a 36-year-old man. **(a)** Axial fat-suppressed T1-weighted imaging shows a thick crescent-shaped zone with high signal (arrow) involving the wall of the left internal carotid artery representing an intramural hematoma, which narrows the flow void of the left internal carotid artery. **(b)** Coronal MRA shows narrowing of the left internal carotid artery (arrows) from the arterial dissection.

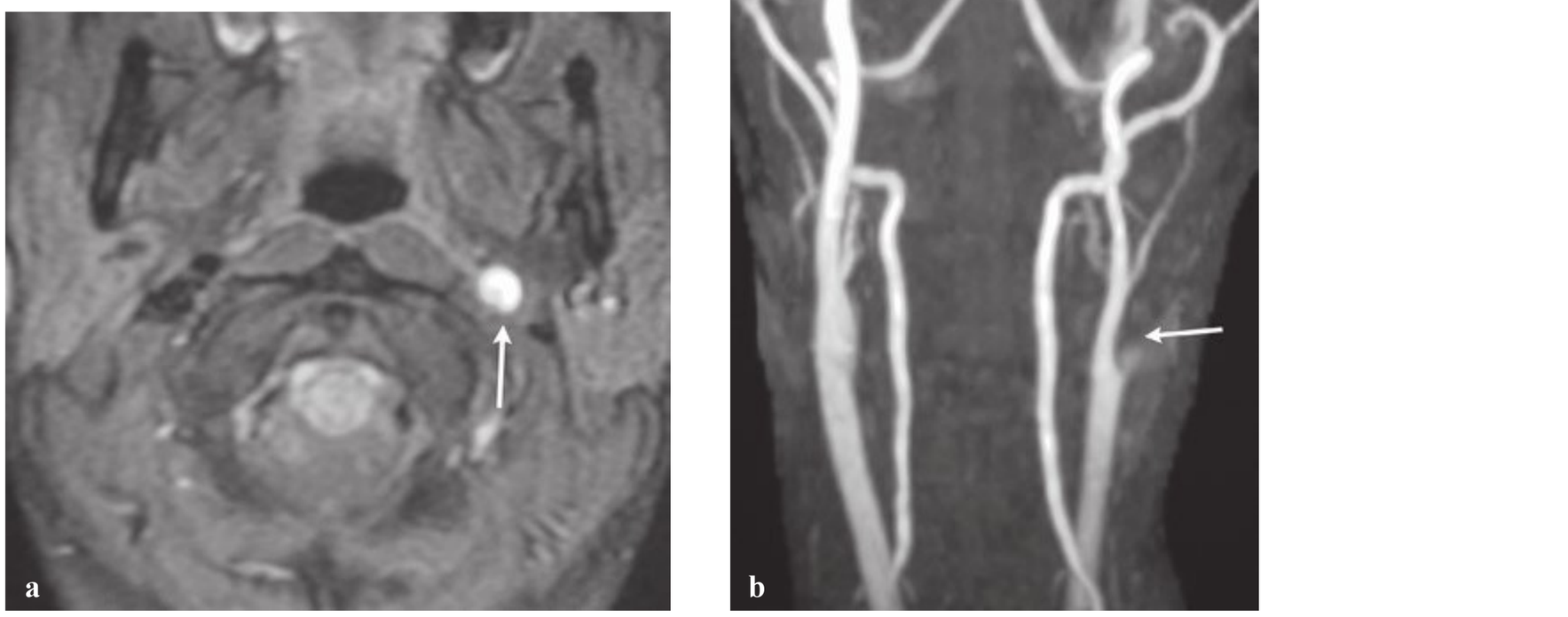

Fig. 5.54 Arterial dissection in a 37-year-old woman. **(a)** Axial fat-suppressed T1-weighted imaging shows a zone with high signal (arrow) filling the lumen of the left internal carotid artery representing a large intramural hematoma occluding the left internal carotid artery. **(b)** Coronal MRA shows abrupt tapering and occlusion of the proximal left internal carotid artery in the neck (arrow) from the arterial dissection.

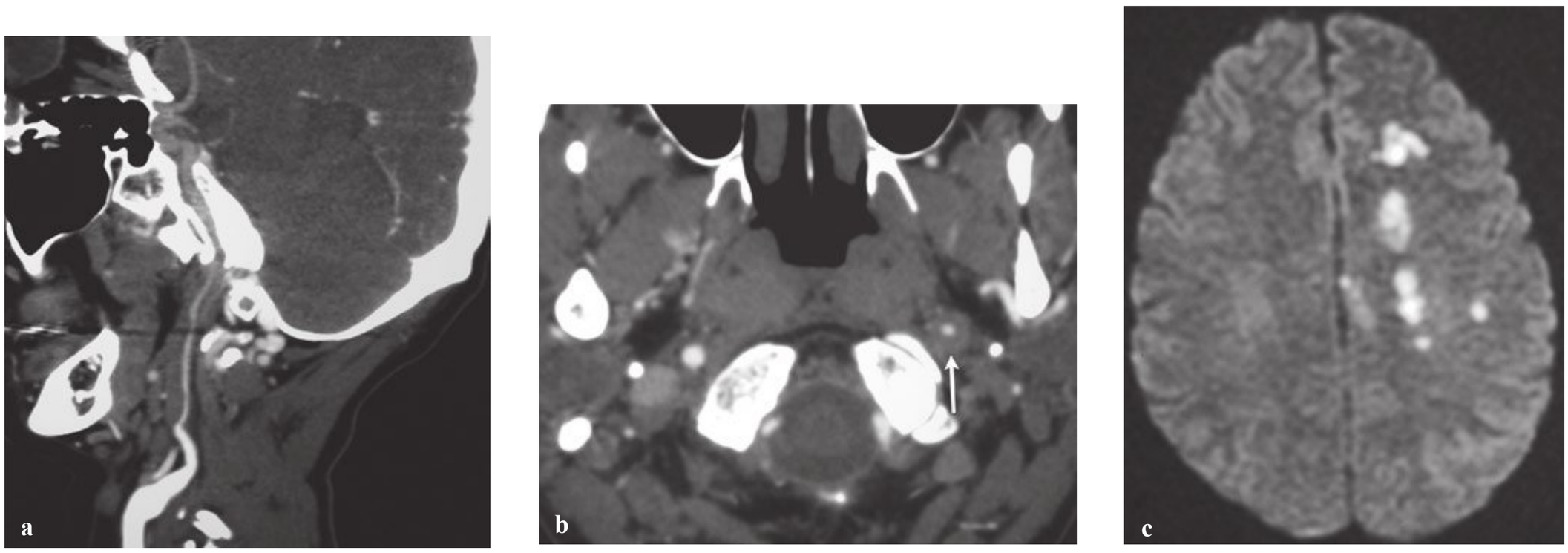

Fig. 5.55 A 42-year-old woman with fibromuscular dysplasia complicated by arterial dissection seen as a long segment of severe narrowing of the left internal carotid artery on **(a)** sagittal and **(b)** axial CTA (arrow). **(c)** The severe arterial stenosis resulted in acute infarcts in the watershed distal vascular distributions between the left anterior and middle cerebral arteries on axial diffusion-weighted imaging.

Table 5.2 (cont.) Acquired vascular disease

Lesions	Imaging Findings	Comments
Vasculitis (**Fig. 5.56** and **Fig. 5.57**)	MRI/MRA: Zones of arterial occlusion and/or foci of stenosis and poststenotic dilatation can be seen involving small or medium-sized intracranial and extracranial arteries. Cerebral and/or cerebellar infarcts can be seen in cortex and subcortical white matter and/or basal ganglia that have high signal on T2-weighted imaging and FLAIR, ± small zones of hemorrhage with low T2* signal on gradient echo imaging. Linear zones or foci of gadolinium contrast enhancement may be seen at the lesions. Acute lesions typically have restricted diffusion. CT: Multiple foci and/or confluent zones of decreased attenuation involving the subcortical and periventricular white matter, basal ganglia, and brainstem. There is no associated mass effect and minimal or no contrast enhancement. MRA, CTA, and conventional arteriography shows zones of arterial occlusion and/or foci of stenosis and poststenotic dilatation. May involve large, medium, or small intracranial and extracranial arteries.	Uncommon mixed group of inflammatory diseases/disorders involving the walls of cerebral blood vessels. Can involve small arteries (CNS vasculitis), small and medium-sized arteries (polyarteritis nodosa, Kawasaki disease), or large arteries with diameters of 7 to 35 mm, such as the aorta and its main branches (Takayasu arteritis, giant cell arteritis). Vasculitis can be a primary disease in which biopsies of meninges and brain show transmural vascular inflammation in the leptomeninges and brain parenchyma. Vasculitis can occur as a secondary disease in association with other disorders, such as systemic diseases (polyarteritis nodosa, granulomatosis with polyangiitis, giant cell arteritis, Takayasu arteritis, sarcoid, Behçet's disease, systemic lupus erythematosus, Sjögren's disease, dermatomyositis, mixed connective tissue disease), drugs (amphetamine, ephedrine, phenylpropaline, cocaine), or infections (viral, bacterial, fungal, or parasite).

(continued on page 628)

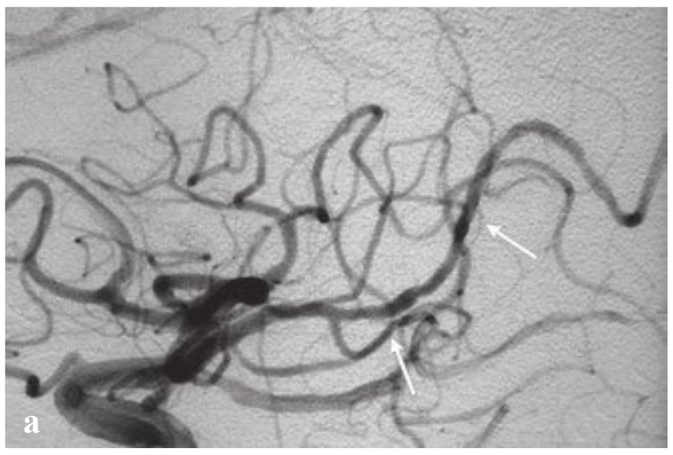

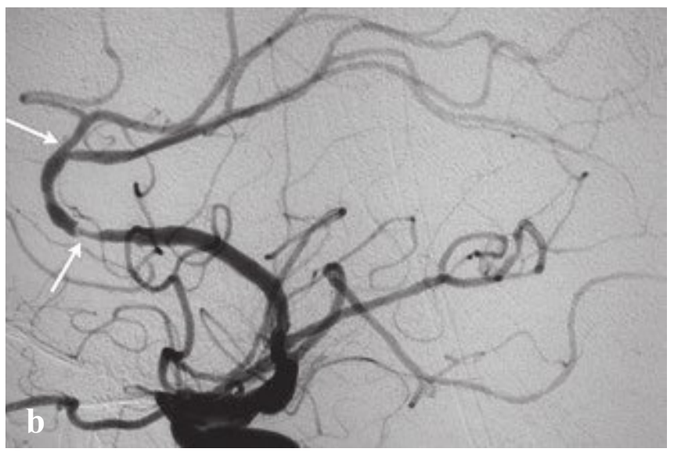

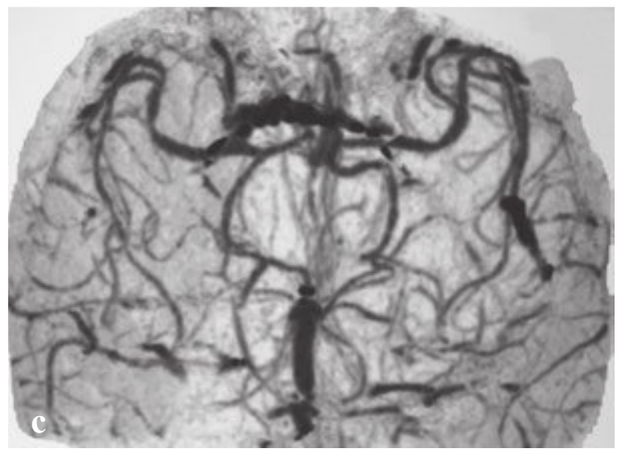

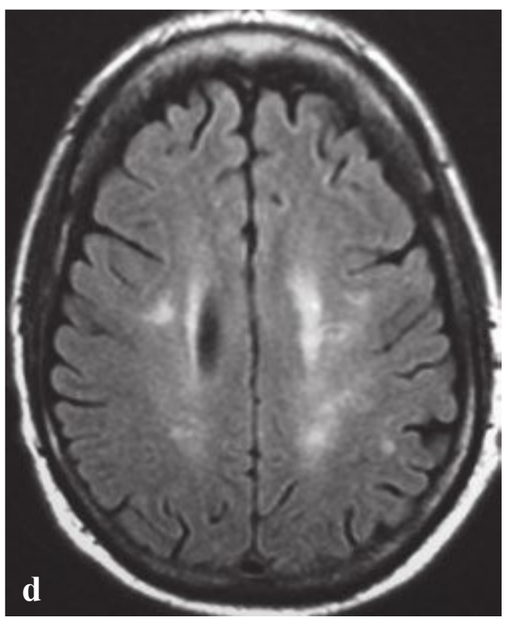

Fig. 5.56 A 50-year-old man with intracranial vasculitis. **(a,b)** Conventional arteriograms (arrows) and **(c)** CTA show zones of focal narrowing and dilatation of the anterior and middle cerebral arteries. **(d)** The vasculitis resulted in multiple zones of ischemic changes seen as intra-axial zones with high signal in the cerebral white matter on axial FLAIR.

Fig. 5.57 **(a)** A 59-year-old woman with intracranial vasculitis seen as zones of focal narrowing and dilatation of the middle cerebral arteries (arrows) on coronal MRA. **(b)** The vasculitis resulted in multiple zones of ischemic changes involving both cerebral hemispheres on axial FLAIR.

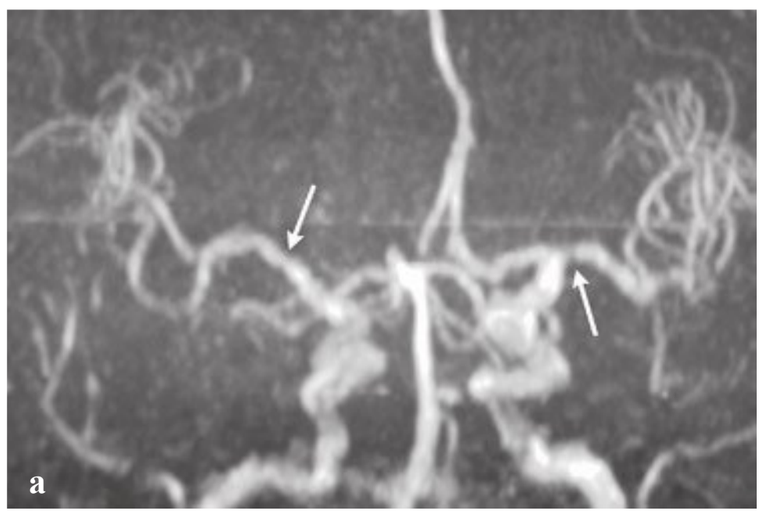

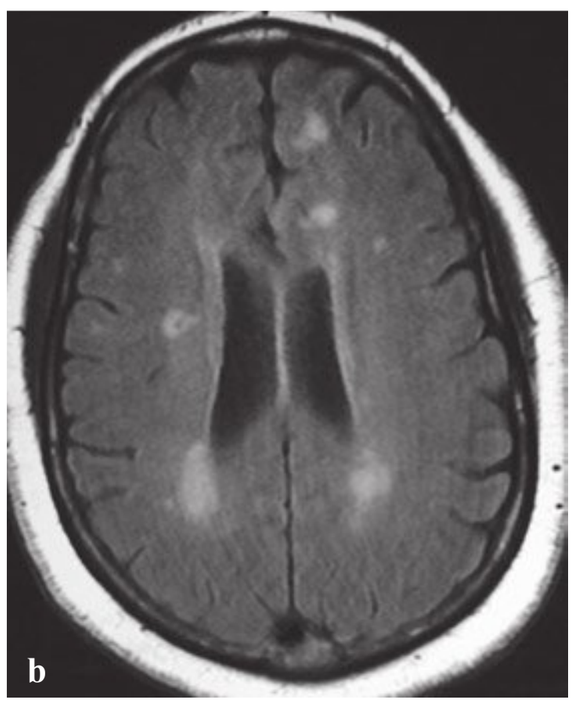

Table 5.2 (cont.) Acquired vascular disease

Lesions	Imaging Findings	Comments
Intracranial venous sinus thrombosis (**Fig. 5.58, Fig. 5.59**, and **Fig. 5.60**)	MRI: Thrombus in dural venous sinuses can have intermediate signal on T1-weighted imaging in the first 3 days, intermediate signal on T1-weighted imaging, low signal on FLAIR, and low signal on T2-weighted imaging from deoxyhemoglobin in the late acute phase (3–5 days), and high signal on T1- and T2-weighted imaging from methemoglobin in the subacute phase (6–30 days). In the chronic phase (> 30 days), thrombus can have intermediate signal on T1-weighted imaging and intermediate or high signal on T2-weighted imaging. In the first 7 days, T2* gradient echo (GRE) images and T2* susceptibility-weighted images (SWI) show low signal at the venous thrombus secondary to the paramagnetic effects of deoxyhemoglobin. Heterogeneous mixed signal may be seen be on diffusion-weighted imaging and ADC maps at acute venous infarcts related to sites with restricted diffusion from cytotoxic edema, hemorrhage, and interstitial or vasogenic edema. Impaired resorption of CSF at the arachnoid granulations may result from dural venous thrombosis. The extent of venous infarction may be related to the degree of abnormal dural venous pressures associated with venous thrombosis. MRA using time-of-flight or phase-contrast techniques shows loss of flow signal from venous occlusion. CTA shows patent veins and venous sinuses to have high attenuation from contrast enhancement compared to zones of thrombus that have lower attenuation and lack of contrast enhancement. Can be associated with venous brain infarcts with or without associated intra-axial and/or subarachnoid hemorrhage.	Venous sinus occlusion may result from coagulopathies, encasement or invasion by neoplasm, dehydration, adjacent infectious/inflammatory processes, and the chemotherapy agent L-asparaginase, which inactivates antithrombin III. The most frequently occluded/thrombosed dural venous sinus is the superior sagittal sinus, followed by the transverse, straight, and cavernous sinuses. With venous occlusion, there is an increase in venous and capillary pressure in the zone of affected venous drainage that can result in decreased resorption of interstitial CSF, interstitial edema, and congestion, leading to eventual venous brain infarction. Thrombosis of the cavernous sinuses can result from extension of sinonasal infections, with the potential for stenosis or occlusion of the cavernous portions of the internal carotid arteries. Cranial neuropathies involving V1 and V2 segments of the trigeminal nerve and CNs III, IV, and VI can also occur with thrombosis of the cavernous sinuses.

(continued on page 630)

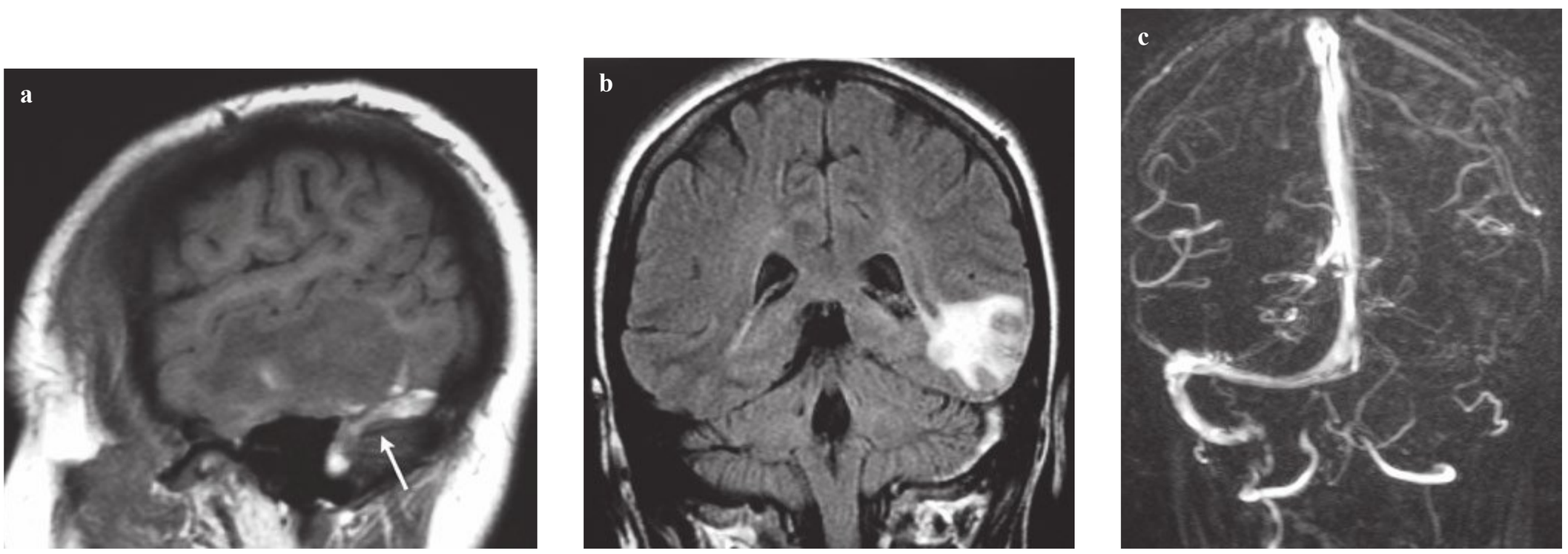

Fig. 5.58 A 33-year-old woman with thrombus filling the left transverse venous sinus that has high signal on **(a)** sagittal T1-weighted imaging (arrow) and **(b)** coronal FLAIR. The occlusion of the left transverse venous sinus resulted in a venous infarct with high signal on coronal FLAIR in the adjacent left temporal lobe. **(c)** Coronal MRA shows absent venous flow signal in the left transverse venous sinus.

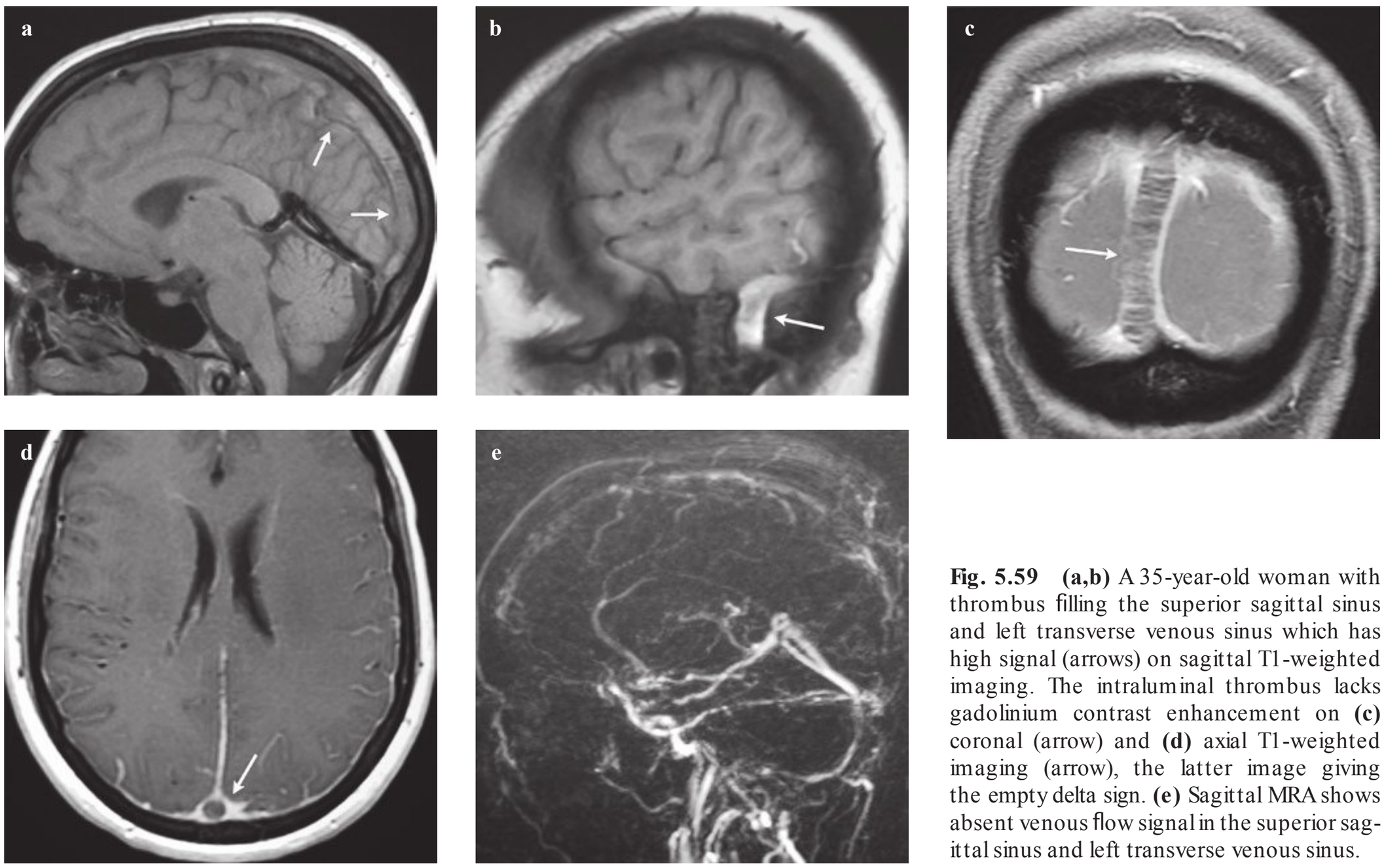

Fig. 5.59 **(a,b)** A 35-year-old woman with thrombus filling the superior sagittal sinus and left transverse venous sinus which has high signal (arrows) on sagittal T1-weighted imaging. The intraluminal thrombus lacks gadolinium contrast enhancement on **(c)** coronal (arrow) and **(d)** axial T1-weighted imaging (arrow), the latter image giving the empty delta sign. **(e)** Sagittal MRA shows absent venous flow signal in the superior sagittal sinus and left transverse venous sinus.

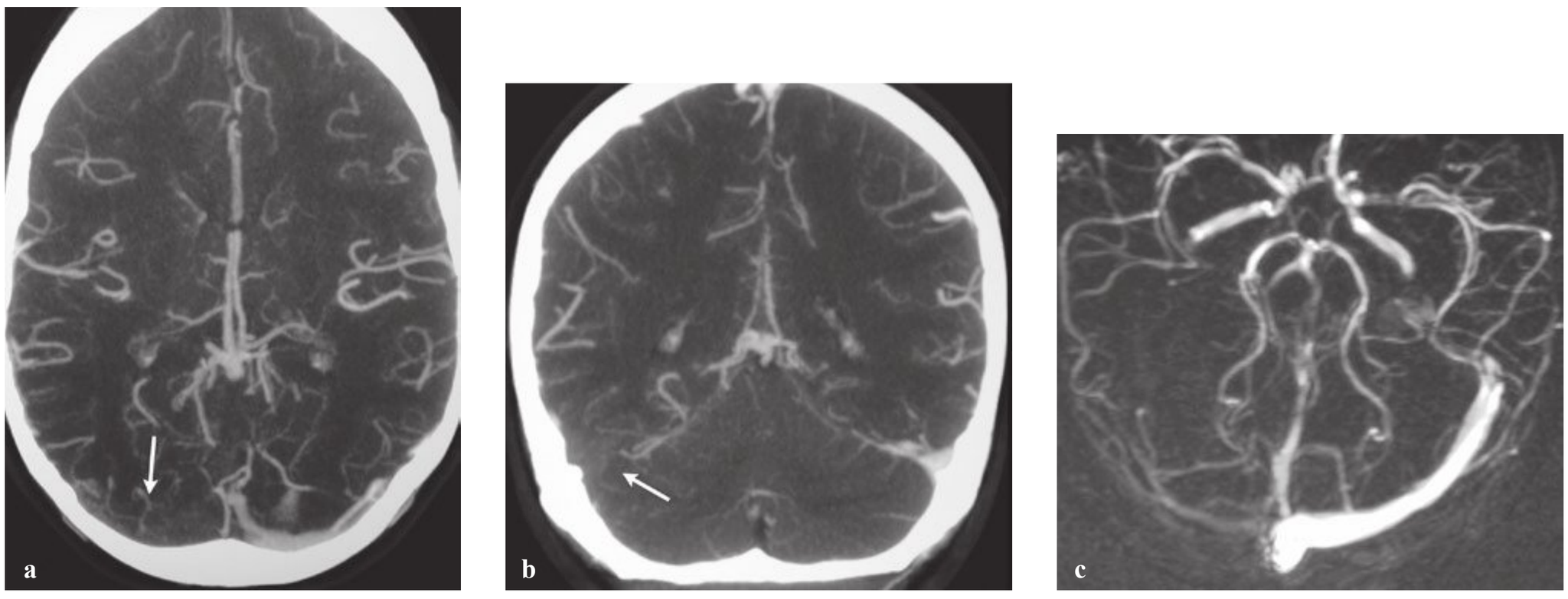

Fig. 5.60 **(a)** Axial and **(b)** coronal CTA shows lack of contrast enhancement in the right transverse venous sinus (arrows) due to occlusion by intraluminal thrombus. **(c)** Axial MRA shows absent blood flow signal in the right transverse venous sinus.

Table 5.2 (cont.) Acquired vascular disease

Lesions	Imaging Findings	Comments
Aneurysms		
Arterial aneurysm (**Fig. 5.61, Fig. 5.62, Fig. 5.63, Fig. 5.64, Fig. 5.65**, and **Fig. 5.66**)	Saccular aneurysm: Focal well-circumscribed zone of contrast enhancement seen on conventional arteriography, CTA, and MRA. Can also be seen on noncontrast MRI as a focal round or ovoid signal void. Fusiform aneurysm: Tubular dilatation of involved artery. Dissecting aneurysm (intramural hematoma): CT and CTA: Initially, the involved arterial wall is thickened in a circumferential or semilunar configuration and has intermediate attenuation with luminal narrowing. MRI: Initially, a crescentic zone with high signal can be seen on proton density-weighted imaging and fat-suppressed T1- weighted imaging involving the wall of a cervical carotid or vertebral artery, resulting in narrowing of the intraluminal flow void. Evolution of the intramural hematoma can lead to focal dilatation of the arterial wall hematoma. Giant aneurysm: Saccular aneurym that is more than 2.5 cm in diameter. Often contains mural thrombus, which has layers with intermediate to high attenuation on non-contrast enhanced CT, and intermediate to high signal on T1- and T2-weighted imaging. The patent portion of the aneurysm shows contrast enhancement on CT, CTA, MRI, and MRA.	Abnormal fusiform or focal saccular dilatation of artery secondary to acquired/degenerative etiology, polycystic disease, connective tissue disease, atherosclerosis, trauma, infection (mycotic), oncotic involvement, arteriovenous malformation, vasculitis, and drugs. Focal aneurysms are also referred to as saccular aneurysms, which typically occur at arterial bifurcations, and are multiple in 20% of cases. The chance of rupture of a saccular aneurysm causing subarachnoid hemorrhage is related to the size of the aneurysm. Saccular aneurysms > 2.5 cm in diameter are referred to as giant aneurysms. Fusiform aneurysms are often related to atherosclerosis or collagen vascular disease (Marfan syndrome, Ehlers-Danlos, etc.). Dissecting aneurysms arise when hemorrhage occurs in the arterial wall from incidental or significant trauma.

(continued on page 632)

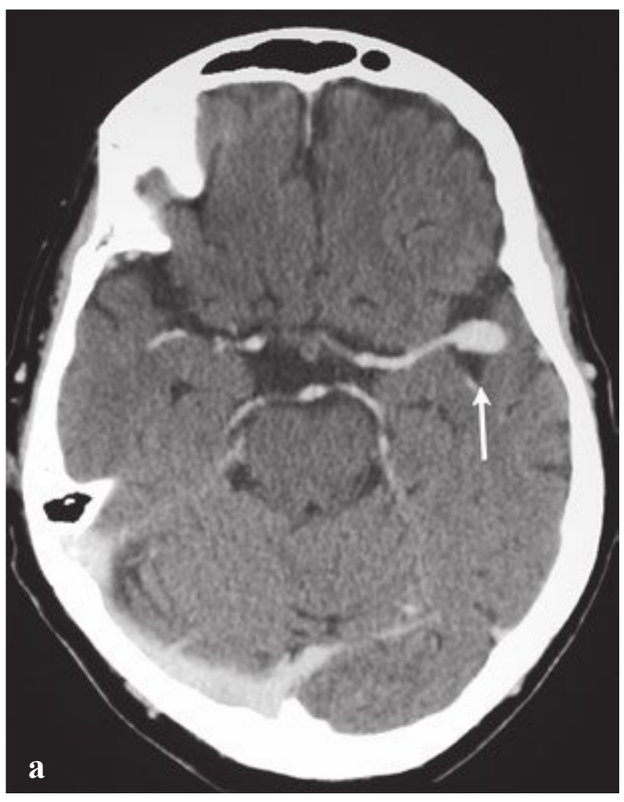

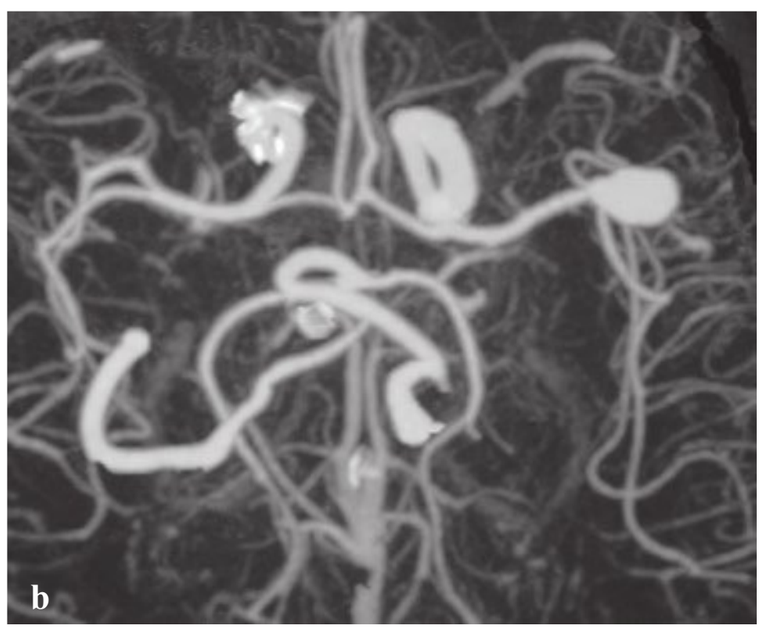

Fig. 5.61 Saccular arterial aneurysm. **(a)** Axial CT and **(b)** axial CTA show an enhancing aneurysm (arrow) at the lateral M1 portion of the left middle cerebral artery.

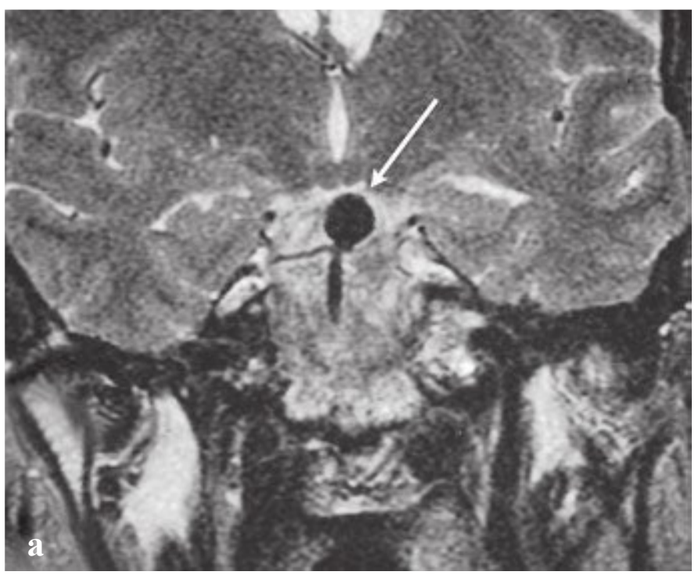

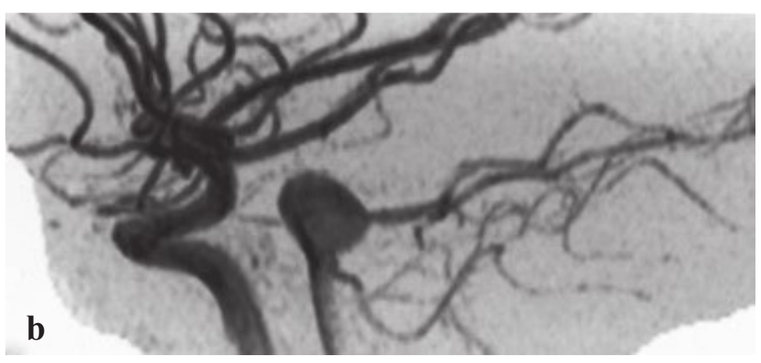

Fig. 5.62 A 44-year-old man with a saccular aneurysm at the basilar artery tip that has a flow void (arrow) on **(a)** coronal T2-weighted imaging and **(b)** flow signal on sagittal MRA.

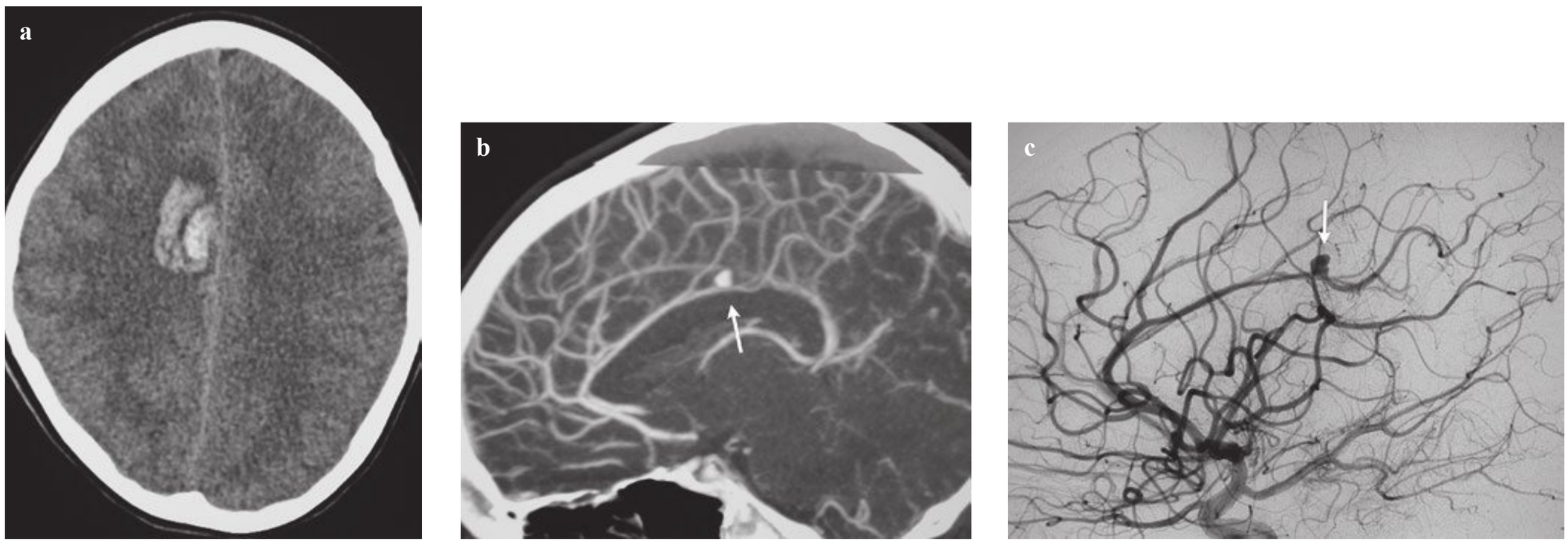

Fig. 5.63 A 12-year-old male with an intraparenchymal hemorrhage in the medial right frontal lobe on **(a)** axial CT resulting from a ruptured mycotic aneurysm involving the distal portion of the anterior cerebral artery on **(b)** sagittal CTA (arrow) and **(c)** conventional arteriogram (arrow).

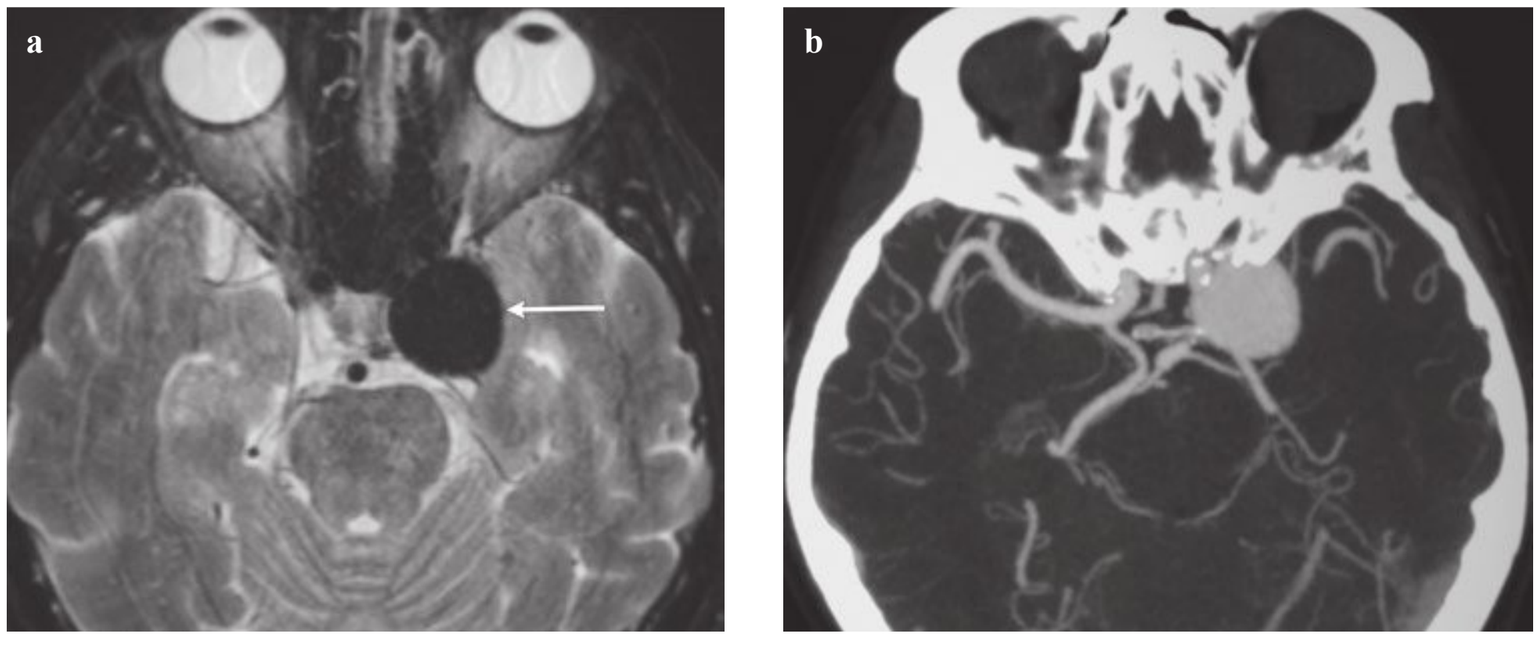

Fig. 5.64 Giant aneurysm of the cavernous portion of the left internal carotid artery is seen as a large flow void (arrow) on **(a)** axial fat-suppressed T2-weighted imaging, with corresponding contrast enhancement on **(b)** axial CTA.

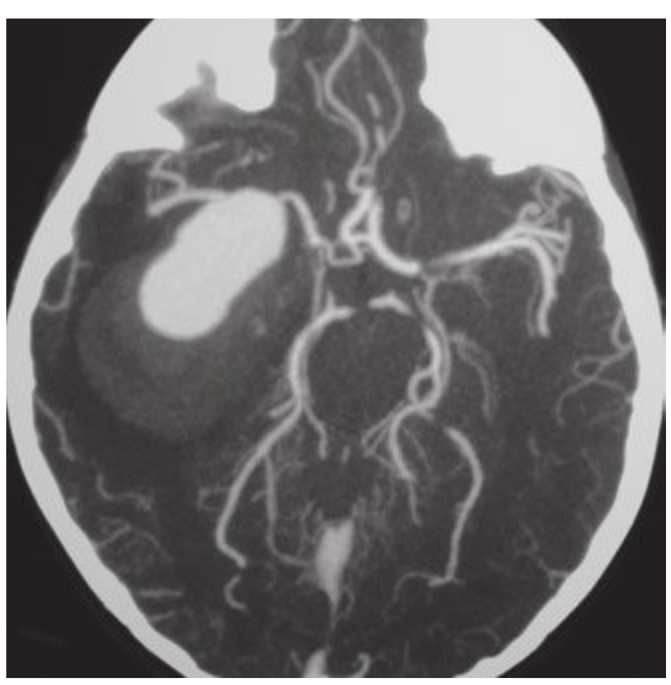

Fig. 5.65 A 2-year-old female with a giant arterial aneurysm involving the M1 segment of the right middle cerebral artery, with enhancement of the lumen and intermediate to slightly-high attenuation from peripheral thrombus on axial CTA.

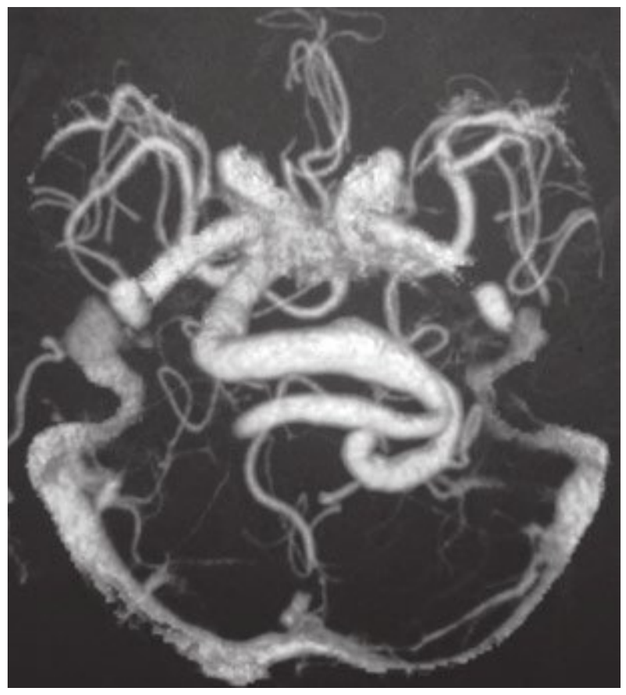

Fig. 5.66 Axial CTA with volume rendering shows a large fusiform aneurysm involving a tortuous basilar artery. Fusiform enlargement of the upper vertebral arteries is also present.

Table 5.2 (cont.) Acquired vascular disease

Lesions	Imaging Findings	Comments
Vascular Malformations		
Arteriovenous malformations (AVMs) (**Fig. 5.67** and **Fig. 5.68**)	MRI: Lesions with irregular margins that can be located in the brain parenchyma, pia, dura, and/or ventricles. AVMs contain multiple, tortuous, tubular flow voids on T1- and T2-weighted imaging secondary to patent arteries with high blood flow, as well as thrombosed vessels with variable signal, and areas of hemorrhage in various phases. Gradient echo MRI shows flow-related enhancement (high signal) in patent arteries and veins of the AVM. MRA using time-of-flight or phase-contrast techniques can provide additional detailed information about the nidus, feeding arteries, and draining veins, as well as presence of associated aneurysms. Usually not associated with mass effect unless there is recent hemorrhage or venous occlusion. CT: Lesions with irregular margins that can be located in the brain parenchyma, pia, dura, and/or ventricles. AVMs contain multiple tortuous vessels, ± calcifications. The venous portions often show contrast enhancement. Usually not associated with mass effect unless there is recent hemorrhage or venous occlusion. CTA can show the nidus and arterial and venous portions of the AVMs.	Vascular lesions with shunting of blood from arteries to veins without intervening capillaries within nervous tissue. Supratentorial AVMs occur more frequently (80–90%) than infratentorial AVMs (10–20%). Annual risk of hemorrhage. AVMs can be sporadic, congenital, or associated with a history of trauma. Multiple AVMs can be seen in Rendu-Osler-Weber syndrome (AVMs in brain and lungs and mucosal capillary telangiectasias) and Wyburn-Mason syndrome (AVMs in brain and retina, + cutaneous nevi).
Vein of Galen aneurysm (**Fig. 5.69**)	MRI: Multiple, tortuous, tubular flow voids on T1- and T2-weighted imaging involving choroidal and thalamoperforate arteries, internal cerebral veins, vein of Galen (aneurysmal formation), straight and transverse venous sinuses, and other adjacent veins and arteries. The venous portions often show gadolinium enhancement. Gradient echo MRI and MRA using time-of-flight or phase-contrast techniques show flow signal in patent portions of the vascular malformation. CT: Multiple, tortuous, contrast-enhancing vessels involving choroidal and thalamoperforate arteries, internal cerebral veins, vein of Galen (aneurysmal formation), straight and transverse venous sinuses, and other adjacent veins and arteries. The venous portions often show contrast enhancement.	Heterogeneous group of vascular malformations with arteriovenous shunts and dilated deep venous structures draining into and from an enlarged vein of Galen, ± hydrocephalus, ± hemorrhage, ± macrocephaly, ± parenchymal vascular malformation components, ± seizures and high-output congestive heart failure in neonates.

(continued on page 634)

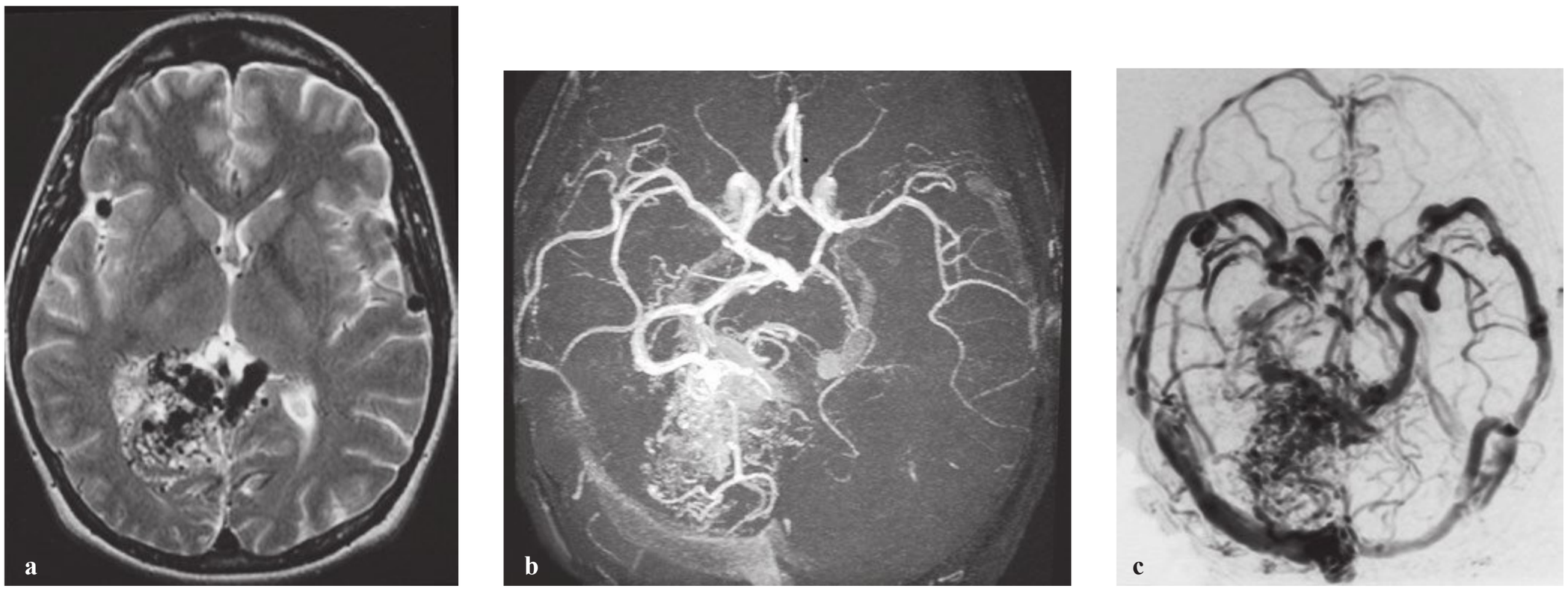

Fig. 5.67 **(a)** A 36-year-old woman with an arteriovenous malformation (AVM) involving the posterior brain that has multiple flow voids on axial T2-weighted imaging. **(b)** Axial 3D time-of-flight MRA shows an enlarged right posterior communicating artery and right posterior cerebral artery providing most of the arterial blood supply to the nidus of the AVM. **(c)** Axial phase-contrast MRV shows an enlarged right transverse venous sinus and bilateral cerebral veins from the AVM. Also seen is a venous aneurysm in the anterior right temporal region.

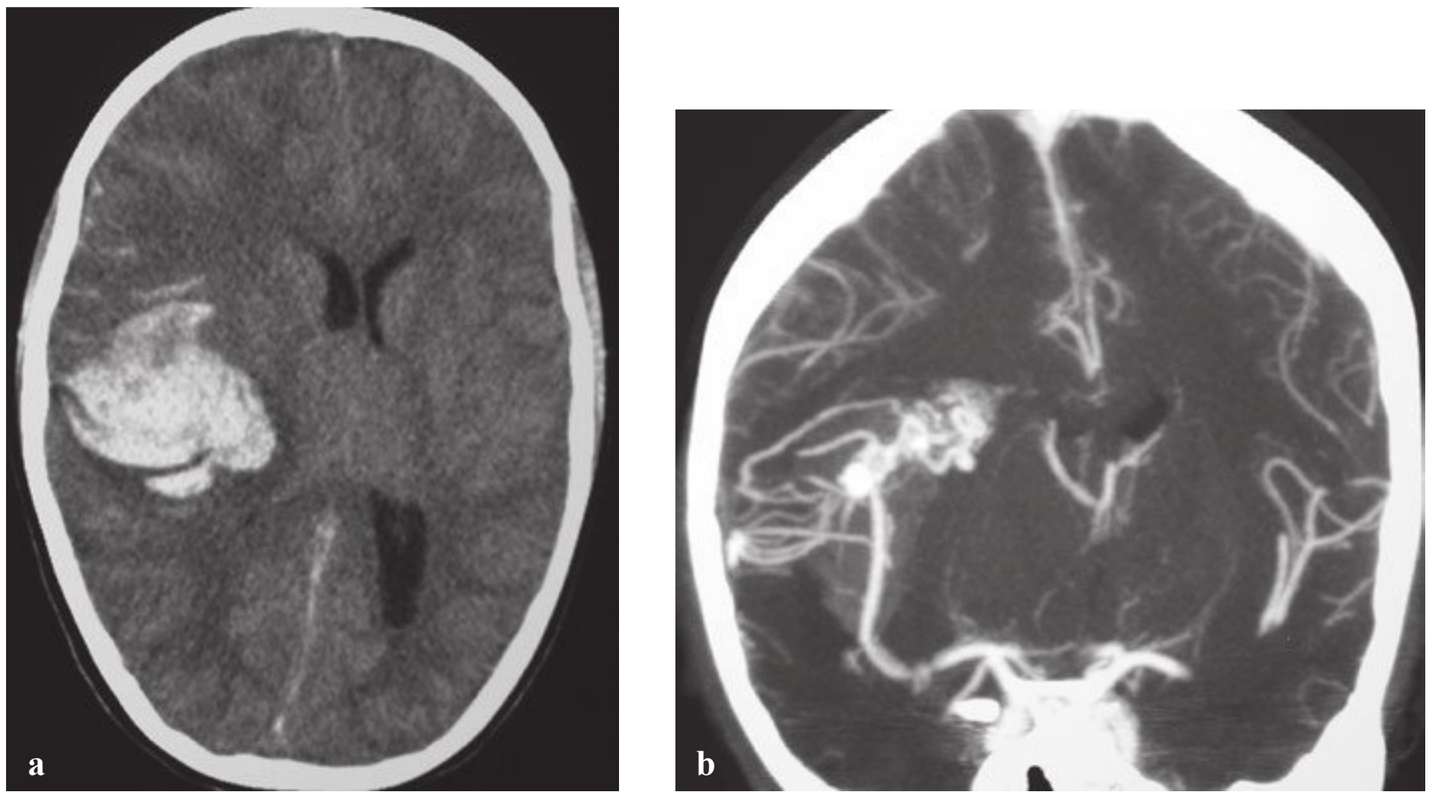

Fig. 5.68 An 11-year-old female with a right intra-axial hematoma and ipsilateral subarachnoid hemorrhage on **(a)** axial CT that resulted from an arteriovenous malformation, as seen on **(b)** corresponding coronal CTA.

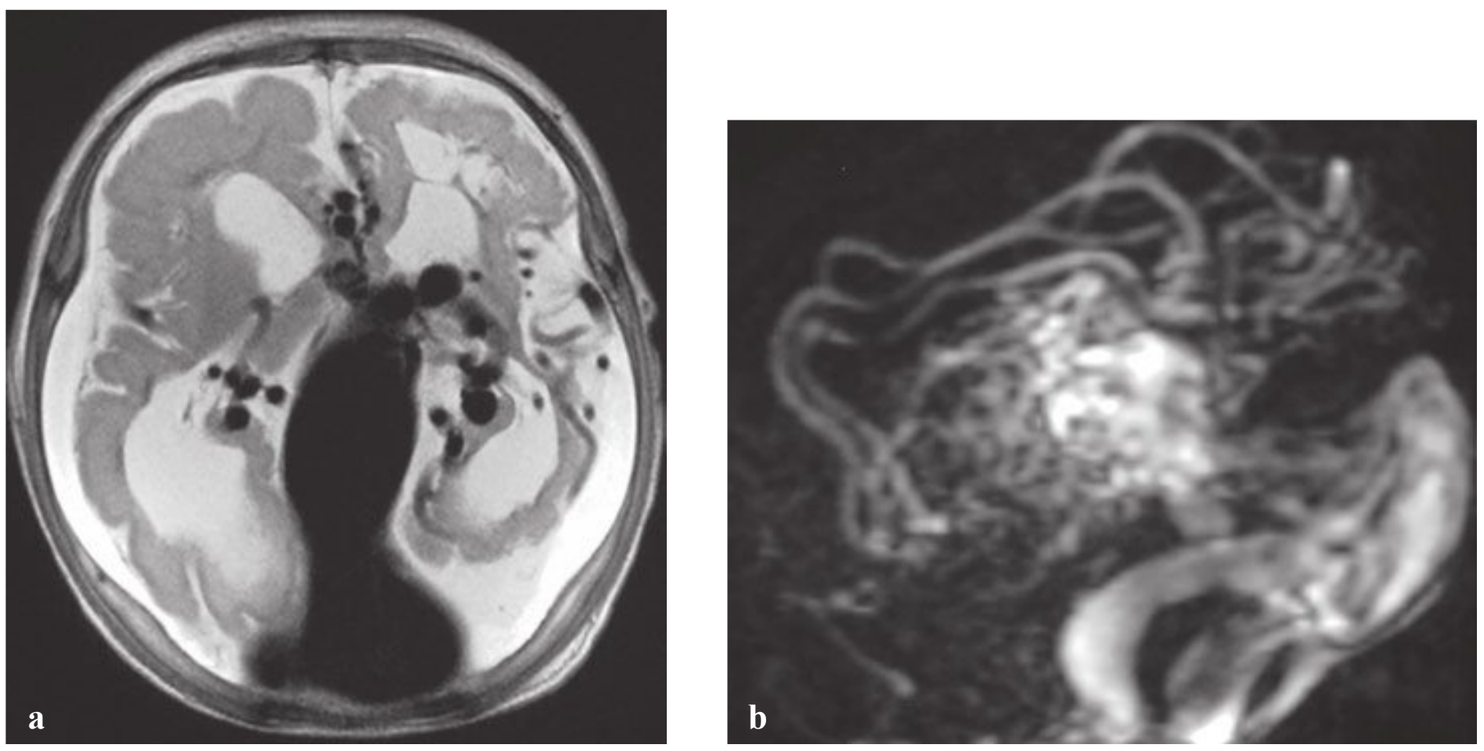

Fig. 5.69 **(a)** A 1-day-old male with a vein of Galen aneurysm/malformation that is seen as a large flow void at the vein of Galen, straight venous sinus, and torcular herophili, as well as multiple adjacent smaller flow voids on axial T2-weighted imaging. Prominent atrophic brain changes are present. **(b)** Sagittal MRA shows prominent blood flow within the vein of Galen aneurysm/malformation.

Table 5.2 (cont.) Acquired vascular disease

Lesions	Imaging Findings	Comments
Dural arteriovenous malformations (AVMs) (**Fig. 5.70** and **Fig. 5.71**)	MRI: Dural AVMs contain multiple, tortuous, tubular flow voids on T1- and T2-weighted imaging. The venous portions often show gadolinium enhancement. Gradient echo MRI and MRA using time-of-flight or phase-contrast techniques show flow signal in patent portions of the vascular malformation and areas of venous sinus occlusion or recanalization. Usually not associated with mass effect unless there is recent hemorrhage or venous occlusion. CT: Dural AVMs contain multiple, tortuous, contrast-enhancing vessels on CTA at the site of a recanalizing thrombosed dural venous sinus. Usually not associated with mass effect. MRA and CTA can show patent portions of the vascular malformation and areas of venous sinus occlusion or recanalization, ± venous brain infarction. Usually not associated with mass effect unless there is recent hemorrhage or venous occlusion.	Dural AVMs are usually acquired lesions resulting from thrombosis or occlusion of an intracranial venous sinus, with subsequent recanalization resulting in direct arterial to venous sinus communications. Transverse, sigmoid venous sinuses > cavernous sinus > straight, superior sagittal sinuses.
Carotid cavernous fistula (**Fig. 5.72** and **Fig. 5.73**)	MRI: Multiple flow voids are seen in dilated cavernous sinuses on T2-weighted imaging. Areas of brain contusion may also be seen. MRA and CTA show marked dilatation of the cavernous sinuses as well as the superior and inferior ophthalmic veins and facial veins. Conventional angiography: Shows early filling of the cavernous sinuses during the arterial phase, with dilated superior ophthalmic veins from retrograde blood flow from arterial to venous shunt.	Carotid artery to cavernous sinus fistulas usually occur as a result of blunt trauma causing dissection or laceration of the cavernous portion of the internal carotid artery. Patients can present with pulsating exophthalmos.

(continued on page 636)

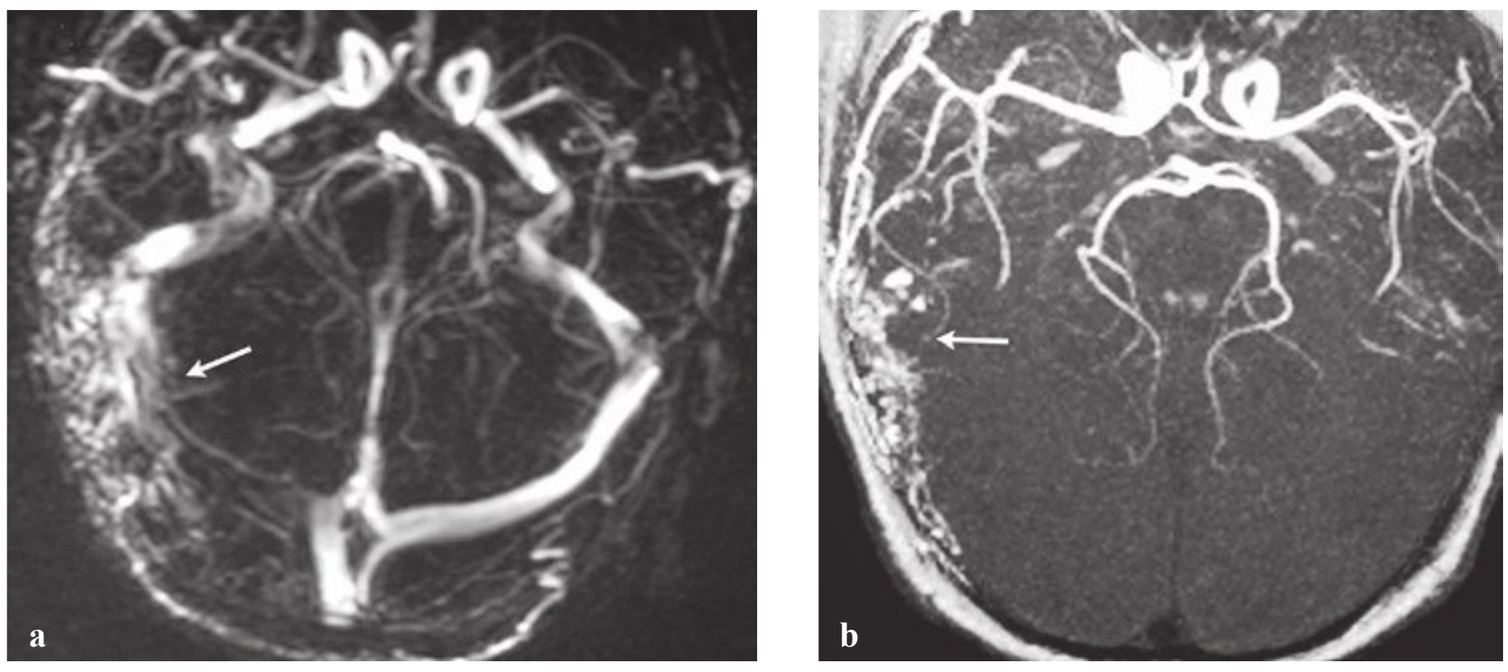

Fig. 5.70 A 66-year-old woman with a dural arteriovenous malformation (AVM) involving the previously thrombosed and partially recanalized right transverse venous sinus. **(a)** Axial MRV (arrow) and **(b)** axial MRA (arrow) show multiple small arteries with high flow at the dural AVM.

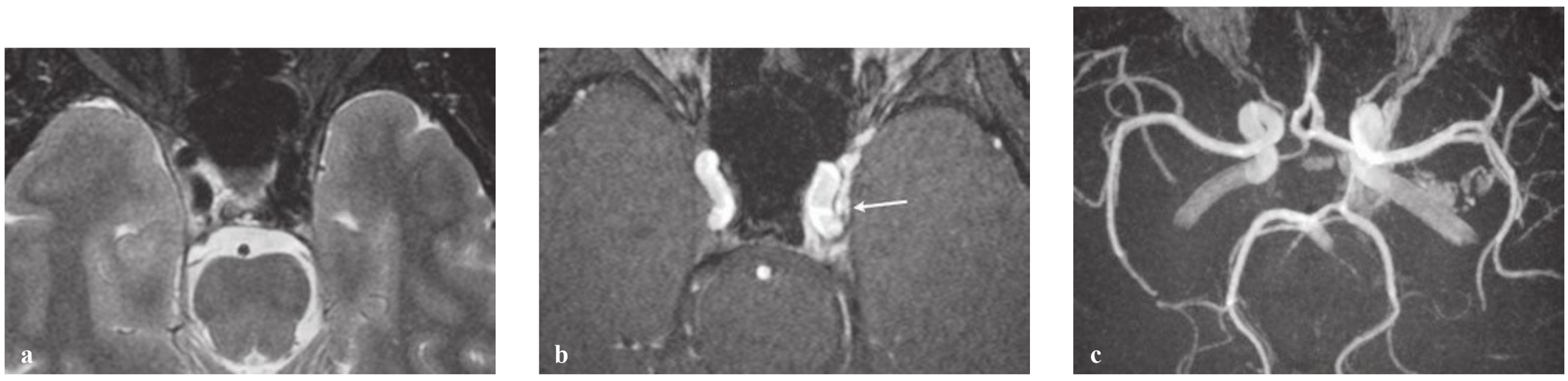

Fig. 5.71 A 43-year-old man with a dural arteriovenous malformation involving the left cavernous sinus, which is seen as multiple small flow voids on **(a)** axial fat-suppressed T2-weighted imaging and increased flow signal on **(b)** axial MRA source image (arrow) and **(c)** axial MRA.

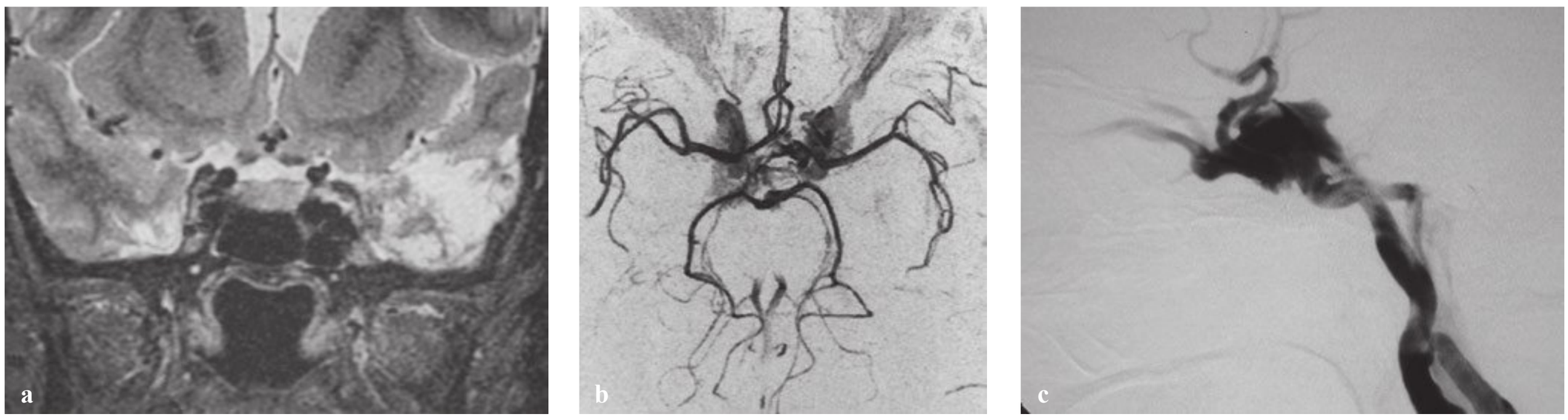

Fig. 5.72 A 50-year-old woman with a posttraumatic carotid cavernous fistula. **(a)** Coronal STIR shows multiple flow voids within both dilated cavernous sinuses as well as poorly defined zones with abnormal high signal in the anterior portions of both temporal lobes representing brain contusions. **(b)** Axial MRA shows patent intracranial arteries as well as faint flow signal in the cavernous sinuses and orbital veins. **(c)** Lateral conventional arteriogram shows early venous enhancement of the cavernous sinus and supraorbital vein during the arterial phase, representing the cavernous carotid fistula.

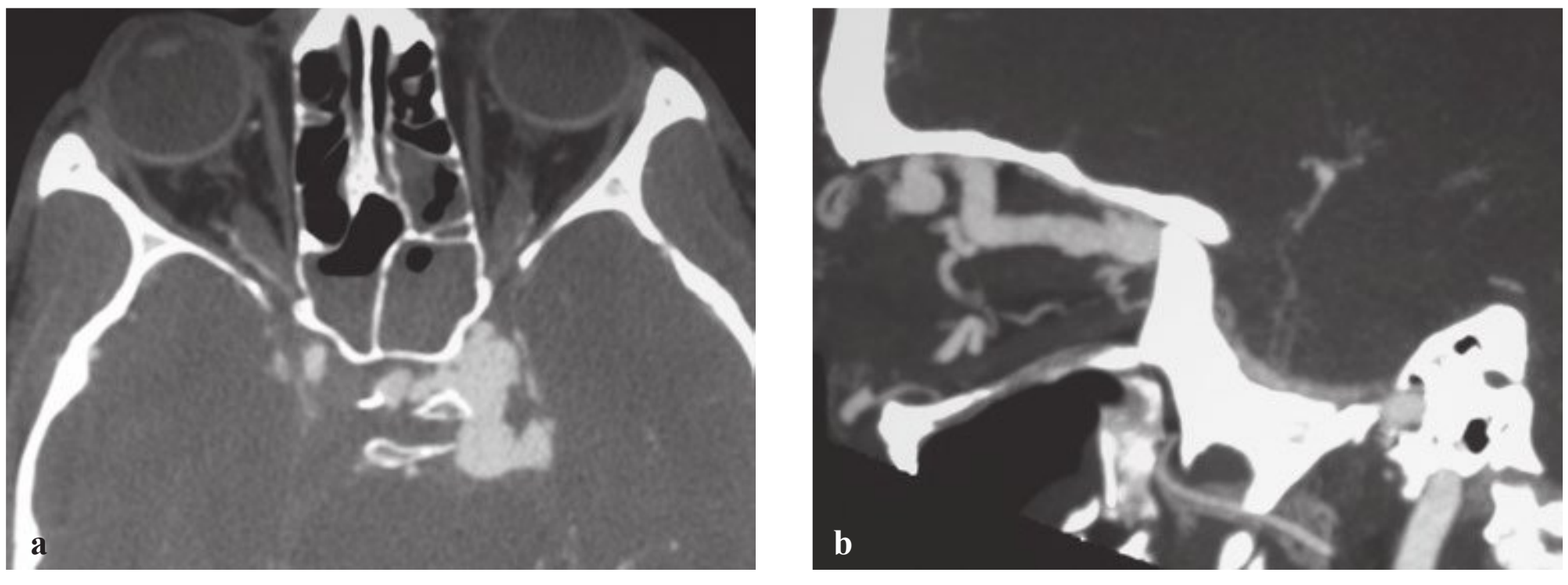

Fig. 5.73 A 20-year-old man with a posttraumatic carotid cavernous fistula. **(a)** Axial postcontrast CT shows abnormal enlargement and contrast enhancement involving the left cavernous sinus from a tear of the cavernous portion of the left internal carotid artery. **(b)** Sagittal CTA shows an enlarged superior ophthalmic vein from retrograde blood flow from the cavernous sinus secondary to the cavernous carotid fistula.

Table 5.2 (cont.) Acquired vascular disease

Lesions	Imaging Findings	Comments
Cavernous malformation (**Fig. 5.74** and **Fig. 5.75**)	MRI: Single or multiple multilobulated intra-axial lesions that have a peripheral rim or irregular zone of low signal on T2-weighted imaging secondary to hemosiderin, surrounding a central zone of variable signal (low, intermediate, high, or mixed) on T1- and T2-weighted imaging depending on ages of hemorrhagic portions. Gradient echo and magnetic susceptibility-weighted techniques are useful for detecting multiple lesions that have low T2* signal. Gadolinium contrast enhancement is usually absent, although some lesions may show mild heterogeneous enhancement. CT: Single or multiple multilobulated intra-axial lesions that have intermediate to slightly increased attenuation, minimal or no contrast enhancement, ± calcifications.	Cavernous malformations are hamartomas composed of thin-walled sinusoids and blood vessels without intervening neural tissue. Can be found in many different locations. Supratentorial cavernous malformations occur more frequently than infratentorial lesions. Lesions consist of epithelium-lined vascular channels within a collagenous stroma. Zones of thrombus and remote hemorrhage with hemosiderin are often present. Dystrophic calcifications may be present. Developmental venous anomalies occur in 25% of cases. Hereditary syndromes in which multiple cavernous malformations occur are associated with mutations of the CCM1/KRIT1, CCM2/MGC4608, and CCM3 PDCD10 genes, and have a higher risk of hemorrhage (up to 5% per year) than sporadic cavernous malformations.
Developmental venous anomaly (venous angioma) (**Fig. 5.76**)	MRI: Gadolinium-enhanced T1-weighted imaging shows a group of small veins in a "Medusa head" configuration that connect and drain into a slightly prominent enhancing vein. Can have low signal on GRE and SWI imaging. CT: No abnormality or small, slightly hyperdense zone prior to contrast administration. Contrast enhancement seen in a slightly prominent vein draining a collection of small veins.	Considered an anomalous venous formation typically not associated with hemorrhage, usually an incidental finding except when associated with cavernous malformation. Lesions consist of thin-walled venous channels within normal neural tissue. Can occur in association with cavernous malformations. Developmental venous anomaly accounts for more than 50% of cerebrovascular malformations.
Capillary telangiectasia (**Fig. 5.77** and **Fig. 5.78**)	MRI: Postcontrast MRI shows a small zone with enhancement without abnormal mass effect. Lesions may show slightly high signal on T2-weighted imaging and FLAIR, although they are often inconspicuous on precontrast T1- and T2-weighted imaging. Some capillary telangiectasias have slightly-high signal on T2WI. Lesions usually have low signal on susceptibility-weighted imaging. CT: Not usually seen on pre- or postcontrast examinations.	Asymptomatic, often incidental finding on gadolinium-enhanced MRI, which shows enhancement of a group of thin-walled vessels and capillaries within normal neural tissue of the brain or brainstem. Most are less than 1 cm in diameter. Can occur 10 years after radiation therapy. Common locations include the pons and cerebellum. Capillary telangiectasia accounts for up to 20% of vascular malformations in brain. Typically show no enlargement over time.

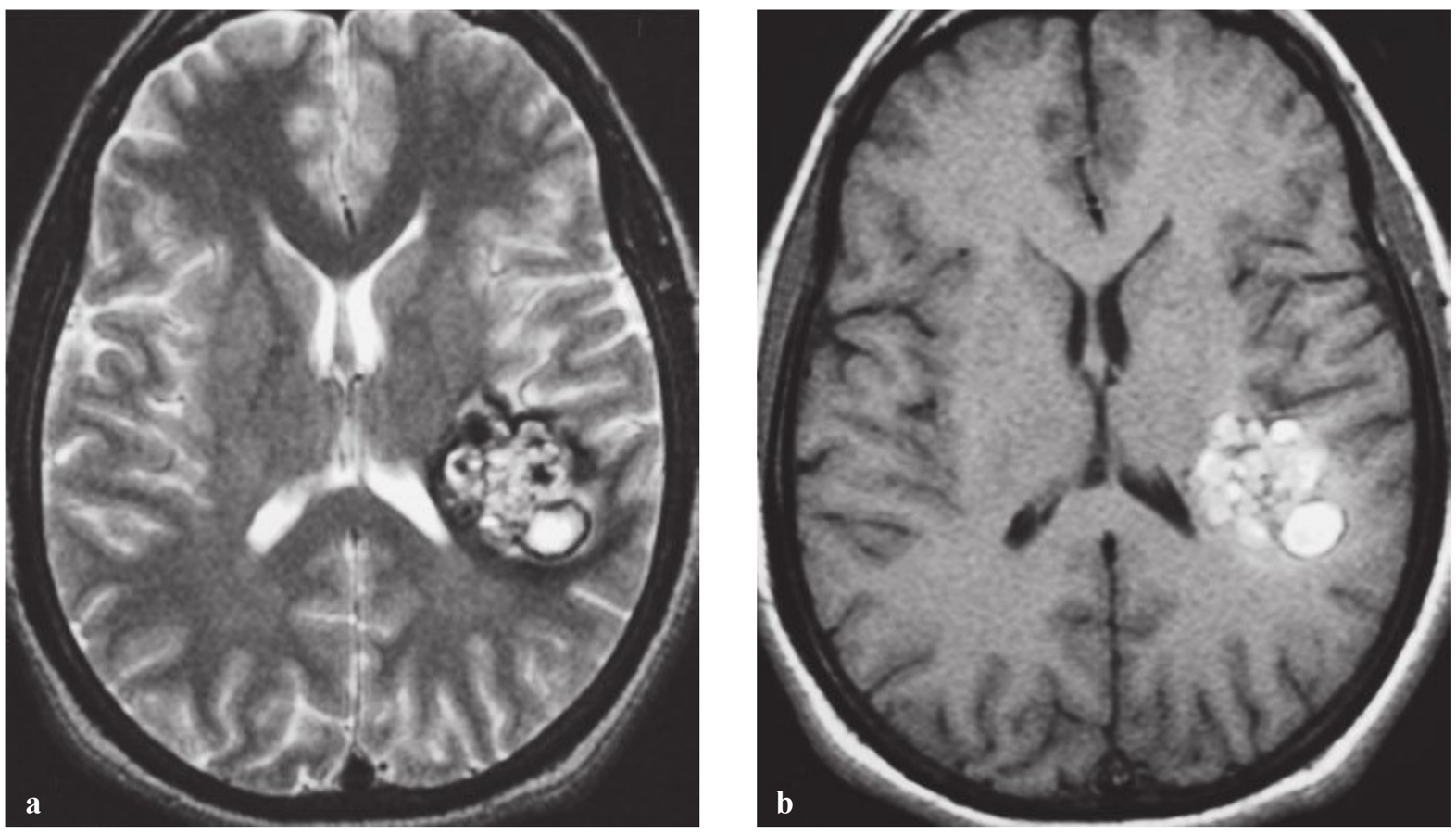

Fig. 5.74 **(a)** A 24-year-old man with a cavernous malformation in the left cerebral hemisphere that has multilobulated margins with a peripheral irregular zone of low signal on axial T2-weighted imaging secondary to hemosiderin that surrounds a central zone of mixed low, slightly high, and high signal. **(b)** The lesion has mostly high signal on T1-weighted imaging as well as thin rims of low signal.

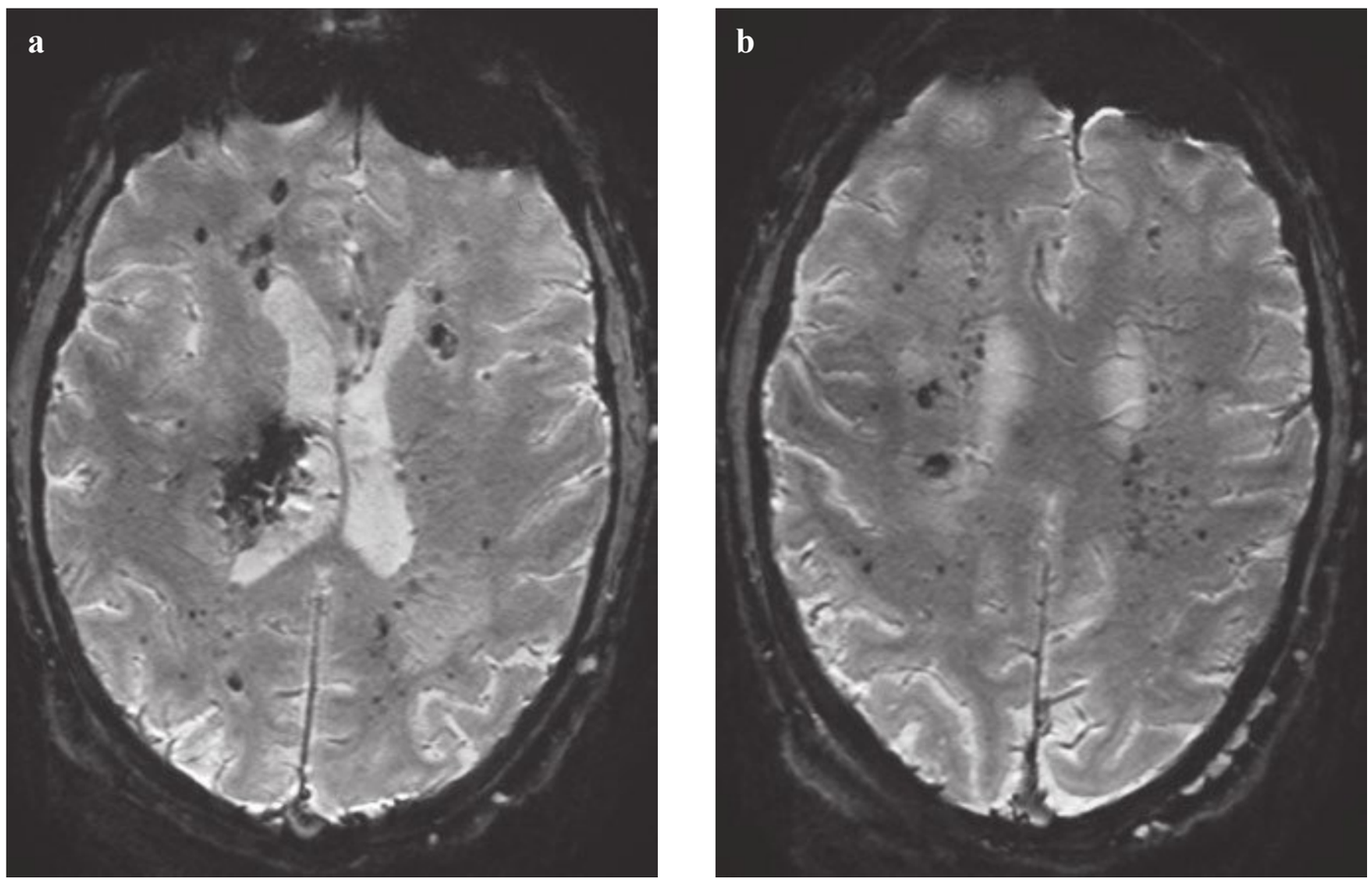

Fig. 5.75 **(a,b)** A 60-year-old woman with many cavernous malformations in the brain seen as low-signal foci on axial susceptibility-weighted imaging.

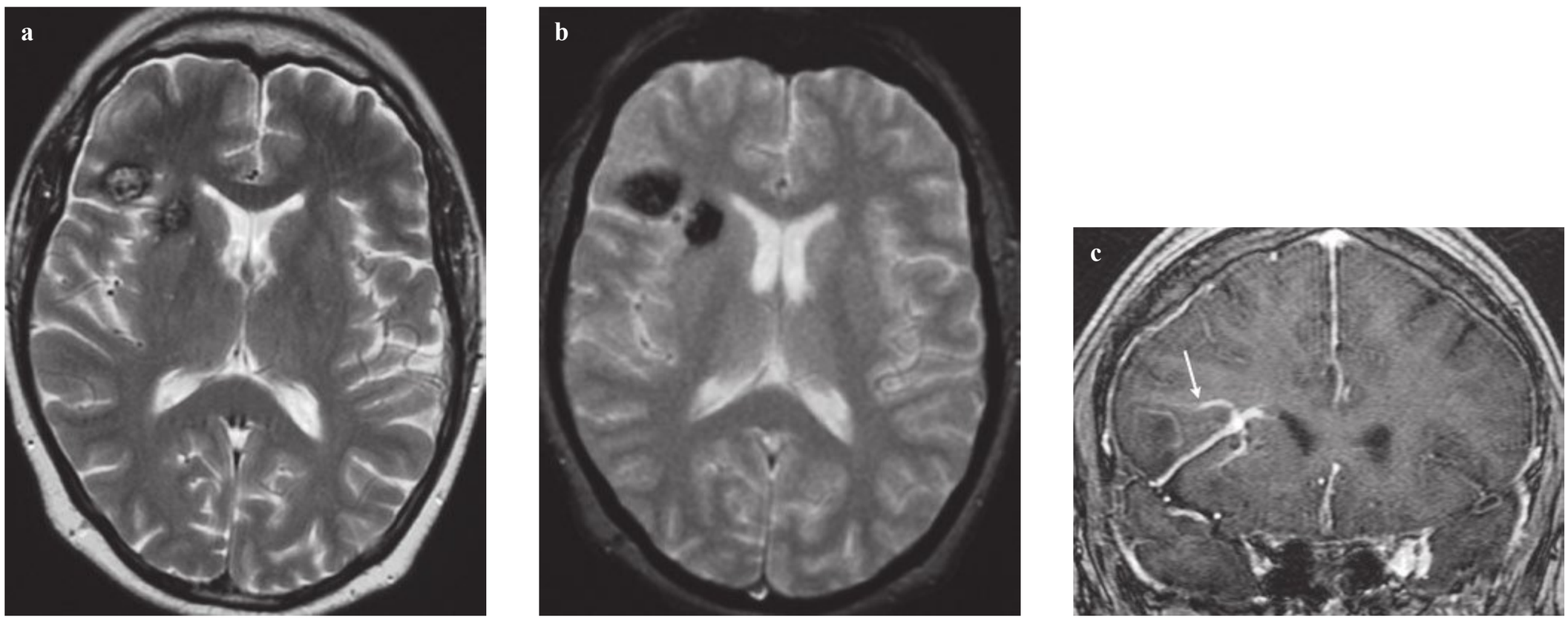

Fig. 5.76 A 50-year-old woman who has two cavernous malformations in the right frontal lobe as seen on **(a)** axial T2-weighted imaging and **(b)** axial gradient recalled echo (GRE) imaging. **(c)** One of the cavernous malformations is associated with a gadolinium-enhancing developmental venous anomaly (arrow) on coronal T1-weighted imaging.

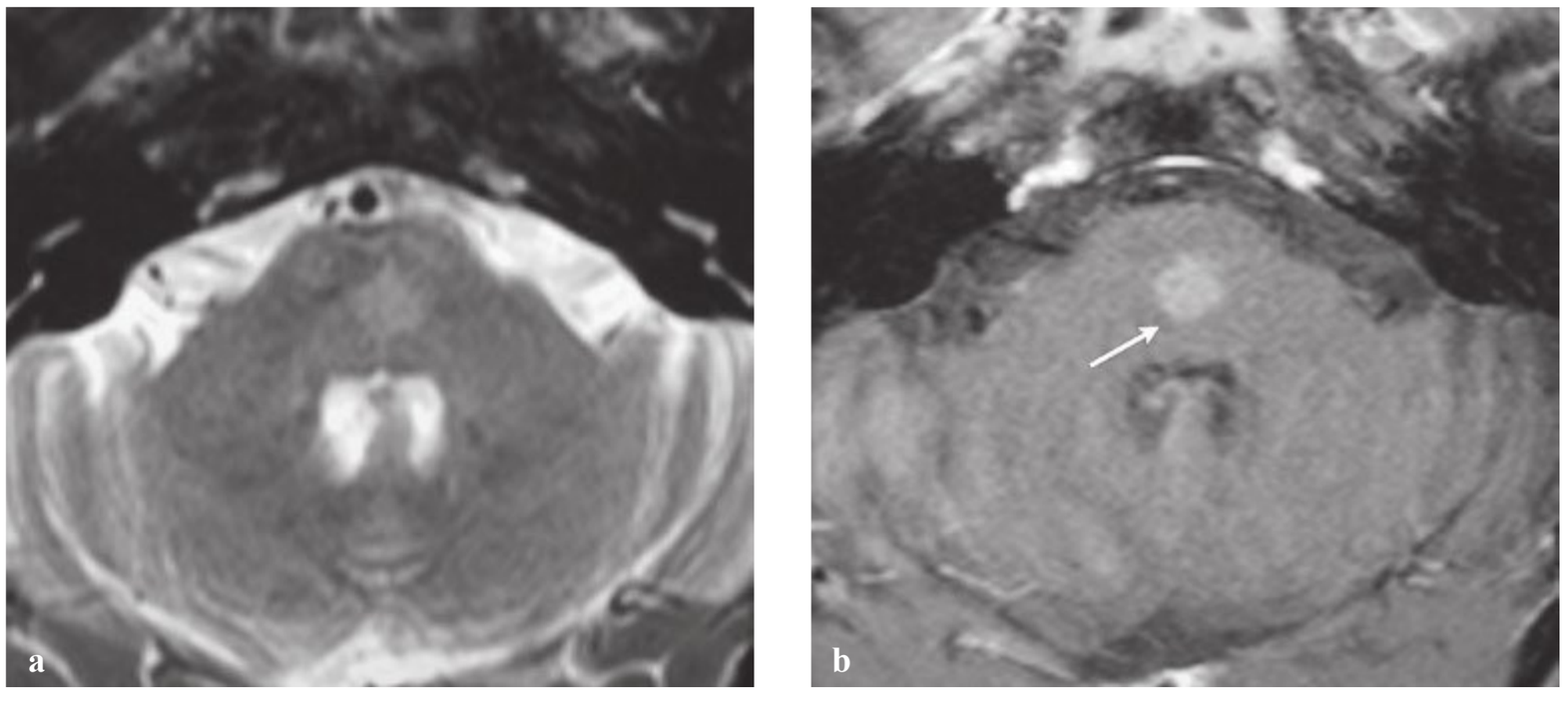

Fig. 5.77 A 79-year-old woman with a capillary telangiectasia within the pons that has faint slightly high signal on **(a)** axial fat-suppressed T2-weighted imaging and shows **(b)** mild gadolinium contrast enhancement on fat-suppressed T1-weighted imaging (arrow).

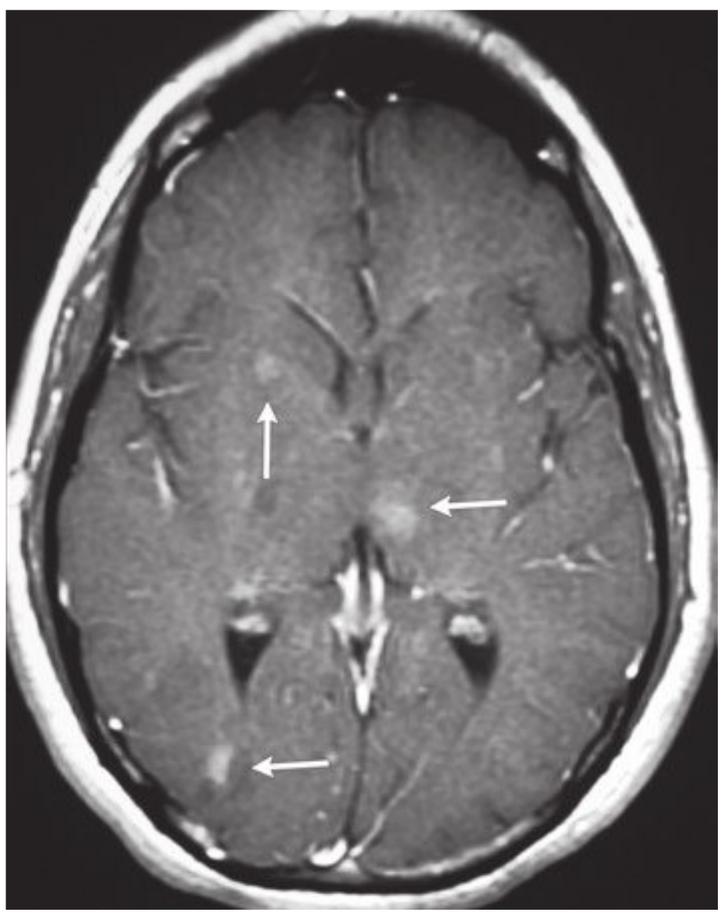

Fig. 5.78 A 40-year-old man with multiple capillary telangiectasias in the brain seen as small intra-axial lesions with mild gadolinium contrast enhancement on axial T1-weighted imaging without associated mass effect (arrows).

References

Aberrant Internal Carotid Arteries

1. Lo WW, Solti-Bohman LG, McElveen JT. Aberrant carotid artery: radiologic diagnosis with emphasis on high-reolution computed tomography. Radiographics 1985;5:985–993
2. Pfeiffer J, Becker C, Ridder GJ. Aberrant extracranial internal carotid arteries: new insights, implications, and demand for a clinical grading system. Head Neck 2016;38(Suppl1):E687–E693
3. Roll JD, Urban MA, Larson TC, Gailloud P, et al. Bilateral aberrant internal carotid arteries with bilateral persistent stapedial arteries and bilateral duplicated internal carotid arteries. AJNR 2003;24:762–765
4. Song YS, Yuan YY, Wang GJ, Dai P, et al. Aberrant internal carotid artery causing objective pulsatile tinnitus and conductive hearing loss. Acta Otolaryngol 2012;132(10):1126–1130

ACTA2 Mutations with Dolichoectasia of the Proximal Internal Carotid Arteries and Stenosis of the Upper Internal Carotid Arteries

5. Amans MR, Stout C, Fox C, et al. Cerebral arteriopathy associated with Arg179His *ACTA2* mutation. BMJ Case Rep 2013. 10.1136/bcr-2013-010997
6. Moosa ANV, Traboulsi EI, Reid J, Prieto L, Moran R, Friedman NR. Neonatal stroke and progressive leukoencephalopathy in a child with an *ACTA2* mutation. J Child Neurol 2013;28(4):531–534
7. Munot P, Saunders DE, Milewicz DM, et al. A novel distinctive cerebrovascular phenotype is associated with heterozygous Arg179 *ACTA2* mutations. Brain 2012;135(Pt 8):2506–2514
8. Yamada K, Hayakawa T, Ushio Y, Mitomo M. Cerebral arterial dolichoectasia associated with moyamoya vessels. Surg Neurol 1985;23(1):19–24

Aneurysms

9. Aryan HE, Giannotta SL, Fukushima T, Park MS, Ozgur BM, Levy ML. Aneurysms in children: review of 15 years experience. J Clin Neurosci 2006;13(2):188–192
10. Buis DR, van Ouwerkerk WJR, Takahata H, Vandertop WP. Intracranial aneurysms in children under 1 year of age: a systematic review of the literature. Childs Nerv Syst 2006;22(11):1395–1409
11. Huang J, McGirt MJ, Gailloud P, Tamargo RJ. Intracranial aneurysms in the pediatric population: case series and literature review. Surg Neurol 2005;63(5):424–432, discussion 432–433
12. Pradilla G, Wicks RT, Hadelsberg U, et al. Accuracy of computed tomography angiography in the diagnosis of intracranial aneurysms. World Neurosurg 2013;80(6):845–852

Arterial Stenosis

13. Khan S, Cloud GC, Kerry S, Markus HS. Imaging of vertebral artery stenosis: a systematic review. J Neurol Neurosurg Psychiatry 2007;78(11):1218–1225
14. Saba L, Anzidei M, Sanfilippo R, et al. Imaging of the carotid artery. Atherosclerosis 2012;220(2):294–309

Arteriovenous Malformations

15. Josephson CB, White PM, Krishan A, Al-Shahi Salman R. Computed tomography angiography or magnetic resonance angiography for detection of intracranial vascular malformations in patients with intracerebral haemorrhage. The Cochrane Library 2014, Issue 9. www.thecochranelibrary.com
16. March BT, Jayaraman MV. Aneurysms, arteriovenous malformations, and dural arteriovenous fistulas: diagnosis and treatment. Semin Roentgenol 2014;49(1):10–21

Capillary Telangiectasia

17. Castillo M, Morrison T, Shaw JA, Bouldin TW. MR imaging and histologic features of capillary telangiectasia of the basal ganglia. AJNR Am J Neuroradiol 2001;22(8):1553–1555
18. El-Koussy M, Schroth G, Gralla J, et al. Susceptibility-weighted MR imaging for diagnosis of capillary telangiectasia of the brain. AJNR Am J Neuroradiol 2012;33(4):715–720
19. Sayama CM, Osborn AG, Chin SS, Couldwell WT. Capillary telangiectasias: clinical, radiographic, and histopathologic features. J Neurosurg 2010;113:709–714
20. Yoshida Y, Terae S, Kudo K, Tha KK, Imamura M, Miyasaka K. Capillary telangiectasia of the brain stem diagnosed by susceptibility-weighted imaging. J Comput Assist Tomogr 2006;30(6):980–982

Cavernous Malformation

21. de Souza JM, Domingues RC, Cruz LCH Jr, Domingues FS, Iasbeck T, Gasparetto EL. Susceptibility-weighted imaging for the evaluation of patients with familial cerebral cavernous malformations: a comparison with T2-weighted fast spin-echo and gradient-echo sequences. AJNR Am J Neuroradiol 2008;29(1):154–158
22. Ozgen B, Senocak E, Oguz KK, Soylemezoglu F, Akalan N. Radiological features of childhood giant cavernous malformations. Neuroradiology 2011;53(4):283–289

23. Pinker K, Stavrou I, Szomolanyi P, et al. Improved preoperative evaluation of cerebral cavernomas by high-field, high-resolution susceptibility-weighted magnetic resonance imaging at 3 Tesla: comparison with standard (1.5 T) magnetic resonance imaging and correlation with histopathological findings—preliminary results. Invest Radiol 2007;42(6):346–351

Central Nervous System Vasculitis

24. Gowdie P, Twilt M, Benseler SM. Primary and secondary central nervous system vasculitis. J Child Neurol 2012;27(11):1448–1459
25. Salvarani C, Brown RD Jr, Hunder GG. Adult primary central nervous system vasculitis. Lancet 2012;380(9843):767–777
26. Schmidt WA. Imaging in vasculitis. Best Pract Res Clin Rheumatol 2013;27(1):107–118
27. Twilt M, Benseler SM. The spectrum of CNS vasculitis in children and adults. Nat Rev Rheumatol 2012;8(2):97–107

Developmental Venous Anomaly (Venous Angioma)

28. Abla A, Wait SD, Uschold T, Lekovic GP, Spetzler RF. Developmental venous anomaly, cavernous malformation, and capillary telangiectasia: spectrum of a single disease. Acta Neurochir (Wien) 2008;150(5):487–489, discussion 489
29. Aboian MS, Daniels DJ, Rammos SK, Pozzati E, Lanzino G. The putative role of the venous system in the genesis of vascular malformations. Neurosurg Focus 2009;27(5):E9
30. Pozzati E, Marliani AF, Zucchelli M, Foschini MP, Dall'Olio M, Lanzino G. The neurovascular triad: mixed cavernous, capillary, and venous malformations of the brainstem. J Neurosurg 2007;107(6):1113–1119

Dural Arteriovenous Malformations

31. Gandhi D, Chen J, Pearl M, Huang J, Gemmete JJ, Kathuria S. Intracranial dural arteriovenous fistulas: classification, imaging findings, and treatment. AJNR Am J Neuroradiol 2012;33(6):1007–1013
32. Kiyosue H, Hori Y, Okahara M, et al. Treatment of intracranial dural arteriovenous fistulas: current strategies based on location and hemodynamics, and alternative techniques of transcatheter embolization. Radiographics 2004;24(6):1637–1653
33. March BT, Jayaraman MV. Aneurysms, arteriovenous malformations, and dural arteriovenous fistulas: diagnosis and treatment. Semin Roentgenol 2014;49(1):10–21

Fibromuscular Dysplasia

34. Kirton A, Crone M, Benseler S, et al. Fibromuscular dysplasia and childhood stroke. Brain 2013;136(Pt 6):1846–1856
35. Olin JW, Sealove BA. Diagnosis, management, and future developments of fibromuscular dysplasia. J Vasc Surg 2011;53(3):826–36.e1
36. Stahlfeld KR, Means JR, Didomenico P. Carotid artery fibromuscular dysplasia. Am J Surg 2007;193(1):71–72
37. Touzé E, Oppenheim C, Trystram D, et al. Fibromuscular dysplasia of cervical and intracranial arteries. Int J Stroke 2010;5(4):296–305
38. Varennes L, Tahon F, Kastler A, et al. Fibromuscular dysplasia: what the radiologist should know: a pictorial review. Insights Imaging 2015;6(3):295–307

Intracranial Venous Sinus Thrombosis

39. Razek AA, Castillo M. Imaging lesions of the cavernous sinus. AJNR Am J Neuroradiol 2009;30(3):444–452
40. Chen JS, Mukherjee P, Dillon WP, Wintermark M. Restricted diffusion in bilateral optic nerves and retinas as an indicator of venous ischemia caused by cavernous sinus thrombophlebitis. AJNR Am J Neuroradiol 2006;27(9):1815–1816
41. Idbaih A, Boukobza M, Crassard I, Porcher R, Bousser MG, Chabriat H. MRI of clot in cerebral venous thrombosis: high diagnostic value of susceptibility-weighted images. Stroke 2006;37(4):991–995
42. Jonas Kimchi T, Lee SK, Agid R, Shroff M, Ter Brugge KG. Cerebral sinovenous thrombosis in children. Neuroimaging Clin N Am 2007;17(2):239–244
43. Leach JL, Fortuna RB, Jones BV, Gaskill-Shipley MF. Imaging of cerebral venous thrombosis: current techniques, spectrum of findings, and diagnostic pitfalls. Radiographics 2006;26(Suppl 1):S19–S41, discussion S42–S43

Menkes' Syndrome

44. Barnerias C, Boddaert N, Guiraud P, et al. Unusual magnetic resonance imaging features in Menkes disease. Brain Dev 2008;30(7):489–492
45. Bekiesińska-Figatowska M, Rokicki D, Walecki J, Gremida M. Menkes' disease with a Dandy-Walker variant: case report. Neuroradiology 2001;43(11):948–950
46. Ito H, Mori K, Sakata M, Naito E, Harada M, Kagami S. Transient left temporal lobe lesion in Menkes disease may influence the generation of tonic spasms. Brain Dev 2011;33(4):345–348
47. Jaspan T. Current controversies in the interpretation of non-accidental head injury. Pediatr Radiol 2008;38(Suppl 3):S378–S387
48. Koprivsek K, Lucic M, Kozic D, Djordjevic M, Kravljanac R. Basal ganglia lesions in the early stage of Menkes disease. J Inherit Metab Dis 2010;33(3):301–302
49. Moser FG, Sarnat HB, Maya MM, Menkes JH. Corkscrew basilar artery as an incidental finding on neuroimaging. Pediatr Neurol 2007;37(5):375–377
50. Nassogne MC, Sharrard M, Hertz-Pannier L, et al. Massive subdural haematomas in Menkes disease mimicking shaken baby syndrome. Childs Nerv Syst 2002;18(12):729–731

Moyamoya

51. Burke GM, Burke AM, Sherma AK, Hurley MC, Batjer HH, Bendok BR. Moyamoya disease: a summary. Neurosurg Focus 2009;26(4):E11
52. Guey S, Tournier-Lasserve E, Hervé D, Kossorotoff M. Moyamoya disease and syndromes: from genetics to clinical management. Appl Clin Genet 2015;8:49–68

PHACE Syndrome

53. Bayer ML, Frommelt PC, Blei F, et al. Congenital cardiac, aortic arch, and vascular bed anomalies in PHACE syndrome (from the International PHACE Syndrome Registry). Am J Cardiol 2013;112(12):1948–1952
54. Bracken J, Robinson I, Snow A, et al. PHACE syndrome: MRI of intracerebral vascular anomalies and clinical findings in a series of 12 patients. Pediatr Radiol 2011;41(9):1129–1138
55. Hess CP, Fullerton HJ, Metry DW, et al. Cervical and intracranial arterial anomalies in 70 patients with PHACE syndrome. AJNR Am J Neuroradiol 2010;31(10):1980–1986
56. Tangtiphaiboontana J, Hess CP, Bayer M, et al. Neurodevelopmental abnormalities in children with PHACE syndrome. J Child Neurol 2013;28(5):608–614

Sinus Pericranii

57. Gandolfo C, Krings T, Alvarez H, et al. Sinus pericranii: diagnostic and therapeutic considerations in 15 patients. Neuroradiology 2007;49(6):505–514
58. Morón FE, Morriss MC, Jones JJ, Hunter JV. Lumps and bumps on the head in children: use of CT and MR imaging in solving the clinical diagnostic dilemma. Radiographics 2004;24(6):1655–1674
59. Park SC, Kim SK, Cho BK, et al. Sinus pericranii in children: report of 16 patients and preoperative evaluation of surgical risk. J Neurosurg Pediatr 2009;4(6):536–542

Unilateral Agenesis of the Internal Carotid Artery

60. Naeini RM, DE J, Satow T, Benndorf G. Unilateral agenesis of internal carotid artery with ophthalmic artery arising from posterior communicating artery. AJR Am J Roentgenol 2005;184(2):571–573
61. Oz II, Serifoglu I, Yazgan O, Erdem Z. Congenital absence of internal carotid artery with intercavernous anastomosis: Case report and systematic review of the literature. Interv Neuroradiol 2016;pii: 1591019916641317 [Epub ahead of print]

Vein of Galen Malformation

62. Chow ML, Cooke DL, Fullerton HJ, et al. Radiological and clinical features of vein of Galen malformations. J Neurointerv Surg 2015;7(6):443–448
63. Hoang S, Choudhri O, Edwards M, Guzman R. Vein of Galen malformation. Neurosurg Focus 2009;27(5):E8
64. Li AH, Armstrong D, terBrugge KG. Endovascular treatment of vein of Galen aneurysmal malformation: management strategy and 21-year experience in Toronto. J Neurosurg Pediatr 2011;7(1):3–10

Index

Note: Page numbers followed by f indicate figures.

A

aberrant position of the internal carotid artery, 610, 611f
abscess
– epidural, 538, 538f, 539f, 556, 578, 579f
– fungal, 70, 71f, 112, 140, 141f, 209, 246, 247f
– pyogenic, 69, 69f, 110, 111f, 136, 137f, 208, 208f, 246
– subdural, 578, 579f
achrondoplasia, 594
acidemia, proprionic, 174, 194, 232, 233f
aciduria, arginosuccinic, 174, 194, 232
acquired hepatocerebral degeneration, 236, 237f, 290
ACTA2 mutations with dolichoectasia of the proximal internal carotid arteries and stenosis of the upper internal carotid arteries, 614, 615f
acute cerebellitis, 114, 115f
acute disseminated encephalomyelitis, 76, 77f, 116, 117f, 154, 155f, 212, 213f, 252, 253f
acute hypertensive crisis (malignant hypertension), 228, 229f
acute measles encephalitis, 72, 145, 209, 248
acute toxic leukoencephalopathy, 215, 216f
acyl-CoA oxidase 1 deficiency, 191
adenohypophysis (agenesis of the anterior pituitary lobe), 349, 349f
adenoid cystic carcinoma, 378, 379f, 534, 534f
adenoma, pituitary, 359, 359f, 360f, 361, 361f
– invasive, 361, 361f
adrenoleukodystrophy
– neonatal, 191
– X-linked, 191, 192, 193f
adrenomyeloneuropathy, 191, 192
agenesis
– of the anterior pituitary lobe (adenohypophysis), 349, 349f
– cerebellar, 31, 31f
– unilateral, of the internal carotid artery, 612, 613f
agyria or "smooth brain" (lissencephaly), 19, 19f
alcohol (ETOH) abuse, 290, 291f
Alexander disease (fibrinoid leukoencephalopathy), 198, 199f, 200f
ALS (amyotrophic lateral sclerosis), 271, 271f
Alzheimer's disease, 263, 263f, 452, 453f
amebiasis, 150, 151f
amebic encephalitis, granulomatous, 150
amebic meningoencephalitis, primary, 150
amyloid angiopathy, 156, 157f
amyloidoma, 90, 91f
amyotrophic lateral sclerosis (ALS), 271, 271f
anaplastic astrocytoma, 44, 45f, 96, 97f, 258, 434, 434f, 470, 471f, 490, 491f, 512f
anaplastic ependymoma, 52, 52f, 436, 437f, 492, 493f
anaplastic ganglioglioma, 54, 55f
anaplastic hemangiopericytoma, 526, 568
anaplastic oligoastrocytoma, 50, 50f
anaplastic oligodendroglioma, 48, 49f
aneurysms, 85, 119, 540, 541f
– arterial, 370, 371f, 540, 557, 630, 630f, 631f
– dissecting (intramural hematoma), 85, 119, 370
– giant, 370, 540, 541f
– ruptured, 85, 86f
– saccular, 85, 119, 370, 557
– vein of Galen, 485, 486f, 540, 541f, 612, 613f, 632, 633f
angioma, venous, 85, 122, 123f, 158, 515, 618, 618f, 619f, 636, 637f
angiopathy, amyloid, 156, 157f
anterior cerebral artery (ACA)
– anatomy, 599
– azygous, 610
– hemiazygous, 610, 611f
antiphospholipid syndrome, 164
aplasia, unilateral, of the internal carotid artery, 612, 613f
apoptosis, 9
aqueductal stenosis, 429, 429f
arachnoid cyst, 398, 399f, 542, 543f
– sellar/suprasellar, 372, 373f
arginosuccinic aciduria, 174, 194, 232
arhinia/arrhinencephaly, 18, 19f
armored brain, 536, 574
Arnold-Chiari malformation. *See* Chiari II malformation
arrhinencephaly/arhinia, 18, 19f
arterial anatomy, 598–602
arterial aneurysm, 370, 371f, 540, 557, 630, 630f, 631f
arterial development, 604–605
arterial dissection, 624, 624f, 625f
arterial fenestration, 610, 611f
arterial occlusion/stenosis, 620, 620f, 613f, 622f
– causing cerebral infarction, 87, 87f, 88
– causing ischemic stroke, 298
arteriovenous malformation (AVM), 158, 370, 371f, 485, 506, 515, 632, 633f
– dural, 540, 572, 573f, 634, 634f, 635f
– hemorrhage from, 84, 84f, 120, 121f
arteritis
– giant cell, 162, 228, 275, 626
– Takayasu's, 162, 228, 275, 626
Aspergillosis. *See* fungal brain abscess
astroblastoma, 47, 47f
astrocytoma, 429f
– anaplastic, 44, 45f, 96, 97f, 258, 434, 434f, 470, 471f, 490, 491f, 512f
– astroblastoma, 47, 47f
– desmotic infantile, 54, 55f
– diffuse, 40, 40f, 96, 97f, 434, 468, 469f, 488
– giant cell, subependymal, 38, 39f, 435, 468, 469f
– giant cell glioblastoma, 44, 46f
– glioblastoma multiforme, 44, 46f, 98, 99f, 133, 258, 434, 470, 471f, 490, 491f, 512f
– gliomatosis cerebri, 42, 43f, 96, 132, 132f, 258
– gliosarcoma, 47, 47f
– oligoastrocytoma, 50, 50f, 98
–– anaplastic, 50, 50f
– pilocytic, 38, 39f, 95, 95f, 259, 432, 433f, 468, 469f
– pilomyxoid, 40, 40f, 366, 367f
– pleomorphic xanthoastrocytoma, 42, 43f
– subependymal giant cell, 38, 39f
ataxia, Friedreich's, 288
ataxia telangiectasia, 286, 287f
atherosclerotic-embolic infarcts, 299, 299f, 300f, 301f, 302, 303f, 304f, 305f, 306, 307f
atherosclerotic-thrombotic infarcts, 299, 299f, 300f, 301f, 302, 303f, 304f, 305f, 306, 307f
atretic cephalocele, 12, 13f
atypical teratoid/rhabdoid tumor, 58, 59f, 104, 106f, 396, 397f, 436, 437f, 472, 473f
AVM. *See* arteriovenous malformation (AVM)
axonal injury, diffuse, 156, 156f
azygous anterior cerebral artery, 610

B

B cell lymphoma. *See* lymphoma
bacterial meningitis, 588f
barotrauma, 168, 168f
basal ganglia, 217, 218f
basal ganglia calcification, idiopathic, 220
basilar arteries, duplication of, 610
Batten disease, 191
Behcet's disease, 162, 164, 165f, 626
benign enlargement of the subarachnoid space in infancy, 594, 595f
benign family megalencephaly, 25
benign mesenchymal nonmeningothelial tumors, 522
Benson dementia (posterior cortical atrophy), 266, 267f
brain abscess, fungal, 70, 71f, 112, 140, 141f, 209, 246, 247f
brain abscess, pyogenic, 69, 69f, 110, 111f, 136, 137f, 208, 208f, 246
brain contusions, 154, 155f
brain development, 4–10
brainstem infarction, 124, 125f

C

CADASIL (cerebral autosomal dominant arteriopathy with subcortical infarcts and leukoencephalopathy), 162, 163f, 228, 229f, 266, 308, 309f
calcification and ossification, dural, 547, 547f, 557, 557f
calcifying pseudoneoplasm of the neuraxis (CAPNON), 66, 67f
Canavan disease (Canavan-van Bogaert-Bertrand disease), 200, 201f, 236, 237f
Canavan-van Bogaert-Bertrand disease (Canavan disease), 200, 201f, 236, 237f
Candidiasis. *See* fungal brain abscess
capillary telangectasia, 122, 123f, 158, 159f, 256, 636, 637f, 638f
CAPNON (calcifying pseudoneoplasm of the neuraxis), 66, 67f
CARASIL (cerebral autosomal recessive arteriopathy with subcortical infarcts and leukoencephalopathy), 162
carbon monoxide poisoning, 178, 180f, 240, 241f
carcinomas. *See specif c carcinomas*
cardioembolic stroke, 306, 307f
carotid arteries, duplication of, 610
carotid cavernous fistula, 370, 371f, 634, 635f
cavernous hemangioma, hemorrhage from, 85, 86f, 120, 121f
cavernous malformation, 158, 159f, 256, 372, 373f, 485, 486f, 506, 636, 636f, 637f
cavernous sinus hemangioma, 372, 373f
cavum septum pellucidum/cavum vergae, 464, 465f

cavum velum interpositum, 464, 465f
cavum vergae/cavum septum pellucidum, 464, 465f
CBF. See cerebral blood flow (CBF)
central neurocytoma, 56, 57f, 442, 443f, 478, 479f, 498, 499f
central pontine myelinolysis, 126, 127f
cephalocele, 12, 12f, 13f, 354, 355f, 564, 564f
– atretic, 12, 13f
cerebellar agenesis, 31, 31f
cerebellar contusion, 118
cerebellar cortical dysplasia, focal, 34, 36f
cerebellar dysplastic malformations, generally, 10
cerebellar hemisphere, hypoplasia of, 31, 31f
cerebellar hemorrhage, 118, 119f
cerebellar hypoplasia, 9–10
cerebellar infarction, 124, 125f
cerebellar malformations, generally, 9–10
cerebellitis, acute, 114, 115f
cerebral arteries, duplication of, 610, 610f
cerebral autosomal dominant arteriopathy with subcortical infarcts and leukoencephalopathy (CADASIL), 162, 163f, 228, 229f, 266, 308, 309f
cerebral autosomal recessive arteriopathy with subcortical infarcts and leukoencephalopathy (CARASIL), 162
cerebral blood flow (CBF), 296
– impaired, 297–298
– maintenance of, 296–297
cerebral contusion, 82, 83f
cerebral gigantism (Sotos syndrome), 25
cerebral infarction
– from arterial occlusion, 87, 87f, 88
– from venous occlusion, 88, 89f, 226, 227f
cerebral perfusion pressure (CPP), 296
cerebritis, 68, 136, 137f
cerebrohepatorenal syndrome (Zellweger syndrome), 191, 192, 193f
"chasing the dragon." *See* heroin toxicity
Chediak-Higashi syndrome, 212
chemodectoma (paraganglioma), 368
chemoradiation, tumor pseudoprogression within 3 months after chemoradiation, 90
Chiari I malformation, 13, 14f, 430, 430f
Chiari II malformation, 13, 14f, 430, 430f, 456, 457f
–with vanishing cerebellum, 31
Chiari III malformation, 13, 15f, 430
child abuse. *See* nonaccidental head injury (NAHI)
childhood ataxia with central nervous system hypomyelination (CACH), 196, 197f
childhood strokes, 318
chloromas (myeloid sarcoma), 65, 107, 132, 214, 568, 586
cholesteatoma, congenital (epidermoid), 354, 355f
chondrosarcoma, 376, 377f, 530, 531f, 570
chordoid glioma of the third ventricle, 500, 501f
chordoma, 376, 377f, 530, 531f, 570, 571f
choriocarcinoma, 392
choristoma, 362, 363f
choroid plexus carcinoma, 440, 441f, 478, 479f, 498, 499f
choroid plexus cyst, 484, 506, 507f
choroid plexus papilloma, 438, 439f, 476, 477f, 496, 497f, 524, 525f
chronic lymphocytic infiltration with pontine perivascular enhancement responsive to steroids (CLIPPERS), 116, 117f
circle of Willis anatomy, 601
cisterns, development of, 422–425
citrullinemia, 174, 194, 232
CLIPPERS (chronic lymphocytic infiltration with pontine perivascular enhancement responsive to steroids), 116, 117f
CLOVES syndrome (congenital lipomatous overgrowth, vascular malformation, epidermal nevi, scoliosis, and spine deformities), 22, 23f
CMV. *See* cytomegalovirus (CMV)
cocaine toxicity, 178, 240
Coccidioidomycosis. *See* fungal brain abscess
Cockayne syndrome, 202, 203f, 222, 223f
colloid cyst, 356, 444, 445f, 504, 504f, 505f
colpocephaly, 430, 431f
communicating hydrocephalus, 454, 455f
congenital cholesteatoma (epidermoid), 354, 355f
contusion
– brain, 154, 155f
– cerebellar, 118
– cerebral, 82, 83f
corpus callosum, dysgenesis of, 24, 24f
cortical dysplasia, 460, 461f
– focal cerebellar, 34, 36f
– focal, without balloon cells, 26, 27f
– transmantle, with balloon cells, 28
cortical hamartomas (tubers), 134, 135f
cortical organization, 9
cortical-subcortical hamartomas (tubers), 65
corticobasal degeneration, 266
corticobasilar syndrome, 264
Cowden syndrome, 34
cranial anatomy, 2
craniopharyngioma, 364, 365f, 480, 481f, 500, 501f, 524, 525f
Creutzfeldt-Jakob disease, 72, 146, 147f, 250, 251f, 266
crossed cerebellar diaschisis, 280, 281f
Cryptococcus. *See* fungal brain abscess
CSF flow, diagram, 424f
CT angiography (CTA), 605
CT perfusion, 605
CT, generally, 1–2
cyanide, 240
cyst
– arachnoid, 372, 373f, 398, 399f, 542, 543f
– choroid plexus, 484, 506, 507f
– colloid, 356, 444, 445f, 504, 504f, 505f
– dermoid, 398
–– ruptured, 556f, 557
– ependymal, 444, 445f, 484, 484f, 504, 505f
– epidermoid, 398
– hydatid, 74, 75f, 115, 150, 151f, 448, 449f
– leptomeningeal, 542, 543f
– neurenteric, 544, 546f
– neuroepithelial, 92, 93f, 260, 504, 505f
– neuroglial, 92, 93f, 260, 504, 505f
– pars intermedia, 354, 354f
– pineal, 392, 393f
_ porencephalic, 92, 93f, 278, 279f, 450, 451f, 462, 463f
– Rathke's cleft, 352, 353f, 542, 543f
cystic encephalomalacia, 320f
cysticercosis, 74, 75f, 114, 115f, 148, 149f, 210, 250, 446, 447f, 487, 508, 509f, 589f
cytomegalovirus (CMV), 72, 142, 142f, 143f, 145, 209, 248

D

D-bifunctional protein deficiency, 191
Dandy-Walker malformation, 32, 32f, 431, 431f, 462
Dandy-Walker variant (vermian hypoplasia), 33, 33f, 431, 431f, 462
de Morsier syndrome (septo-optic dysplasia), 18, 18f, 456, 458f
deep venous occlusion with hemorrhagic infarction, 254
dehiscence of the jugular bulb, 618, 619f
dementia
– Alzheimer's disease, 263, 263f, 452, 453f
– Benson (posterior cortical atrophy), 266, 267f
– frontotemporal, 264, 265f, 452, 453f
– with Lewy bodies, 264
– semantic, 264
– vascular/multi-infarct, 266, 267f
demyelinating disease. *See specif c diseases*
deoxyhemoglobin, 78
dermatomyositis, 162, 626
dermoid, 356, 357f, 544, 546f
– ruptured, 586, 587f
dermoid cyst, 398
– ruptured, 556f, 557
desmotic infantile astrocytoma (DIA), 54, 55f
desmotic infantile ganglioglioma (DIG), 54, 55f
developmental venous anomaly/venous angioma, 85, 122, 123f, 158, 515, 618, 618f, 619f, 636, 637f
DIA. *See* desmotic infantile astrocytoma (DIA)
diabetes insipidus, 358
diabetic ketoacidosis, 172f, 427f
diffuse astrocytoma, 40, 40f, 96, 97f, 434, 468, 469f, 488
diffuse axonal injury, 156, 156f, 204, 204f, 205f, 242, 253f
DIG. *See* desmotic infantile ganglioglioma (DIG)
dissecting aneurysm (intramural hematoma), 85, 119, 370
disseminated encephalomyelitis, acute, 76, 77f, 116, 117f, 154, 155f, 212, 213f, 252, 253f
dolichoectasia of the proximal internal carotid arteries and stenosis of the upper internal carotid arteries, from *ACTA2* mutations, 614, 615f
duplication of arteries, 610, 610f
dural arteriovenous malformation (AVM), 540, 572, 573f, 634, 634f, 635f
dural calcification and ossification, 547, 547f, 557, 557f
dural fibrosis, postsurgical, 576, 576f, 577f
durameninges, 562, 563f
Dyke-Davidoff-Masson syndrome, 278, 279f, 452, 453f
dysembryoplastic neuroepithelial tumor, 56, 57f
dysgenesis of the corpus callosum, 24, 24f, 460, 461f
dysplasia
– fibromuscular, 623, 623f
– fibrous, 380, 381f
– focal cerebellar cortical, 34, 36f
– focal cortical, without balloon cells, 26, 27f
– hemispheric, 28, 28f
– meningeal, 564, 565f
– septo-optic (de Morsier syndrome), 18, 18f, 456, 458f
– transmantle cortical, with balloon cells, 18
dysplastic cerebellar gangliocytoma (Lhermitte-Duclos disease), 34, 35f, 102, 103f
dysplastic white matter lesions/vacuolated myelin, 133, 133f, 260, 261f
dystroglycanopathies, 9
– Fukuyama congenital muscular dystrophy phenotype, 30, 202, 203f
– muscle-eye-brain phenotype, 30, 30f, 202, 203f
– Walker-Warburg phenotype, 29, 29f, 202

E

ecchordosis physaliphora, 547, 548f
Echinococcus granulosus. *See* hydatid cyst
Echinococcus multilocularis. *See* hydatid cyst
ectopic posterior pituitary gland, 350, 350f
Edwards syndrome, 456
Ehlers-Danlos syndrome, 540, 630
embolic disease infarction, 160, 161f
embryonal carcinoma, 392, 393f
embryonic brain development, 4–10

empty sella, 356, 357f
empyema
– epidural, 578, 579f
– subdural, 538, 538f, 539f, 556, 578, 579f
encephalitis/viral infections, 70, 71f, 112, 113f, 142, 142f, 143f, 144f, 209, 210f, 248, 249f
– acute measles, 72, 145, 209, 248
– cytomegalovirus (CMV), 72, 142, 142f, 143f, 145, 209, 248
– granulomatous amebic, 150
– herpes simplex virus, 70, 113f, 142, 142f, 209, 210f, 248, 273f
– human immunodeficiency virus (HIV) infection, 142, 143f, 145
– Japanese, 71, 142, 144f, 145, 248, 249f
– progressive multifocal leukoencephalopathy, 72, 113f, 142, 143f, 145, 248
– rabies, 72, 142, 144f, 145, 248, 249f
– Rasmussen's, 274f, 275, 448, 449f
– subacute sclerosing panencephalitis from measles, 72, 145, 209, 248
– West Nile virus, 72, 209, 248
encephalomalacia, 450, 451f
– cystic, 320f
encephalomyelitis, acute disseminated, 76, 77f, 116, 117f, 154, 155f, 212, 213f, 252, 253f
encephalopathy
– hypertensive (posterior reversible encephalopathy syndrome/PRES), 126, 127f
– toxic, late effects, 294, 295f
– Wernicke's, 238, 239f, 290
encephalotrigeminal angiomatosis (Sturge-Weber syndrome), 275, 485, 486f, 515, 515f, 594, 594f, 595f, 614, 614f, 615f
endocarditis, Libman-Sachs, 160, 161f, 306, 307f
eosinophilic granuloma, 538, 539f, 556
ependymal cyst, 444, 445f, 484, 484f, 504, 505f
ependymitis/ventriculitis, 446, 447f
ependymoma, 51, 51f, 100, 101f, 396, 397f, 436, 437f, 472, 473f, 492, 493f
– anaplastic, 52, 52f
epidermoid (congenital cholesteatoma), 354, 355f, 502, 503f, 544, 545f
epidermoid cyst, 398
epidural abscess, 538, 538f, 539f, 556, 578, 579f
epidural empyema, 578, 579f
epidural hematoma, 534, 535f, 554, 572, 573f
Epstein-Barr virus, 215, 567
Erdheim-Chester disease, 580
esthesioneuroblastoma (olfactory neuroblastoma), 378, 379f, 534, 535f, 570, 571f, 572, 573f
ethylene glycol toxicity, 240, 241f
Ewing's sarcoma, 378, 532, 533f, 570
excessively small ventricles, 426, 426f, 427f
external carotid artery (ECA) anatomy, 601, 602f
extrapontine osmotic myelinolysis, 182

F

Fabry disease, 170, 171f, 344
Fahr disease (familial cerebrovascular ferrocalcinosis/idiopathic basal ganglia calcification), 222, 223f, 286, 287f
familial cerebrovascular ferrocalcinosis/idiopathic basal ganglia calcification (Fahr disease), 222, 223f, 286, 287f
fenestration, arterial, 610, 611f
fetal brain development, 4–10
fetal brain MRI, generally, 10
fetal strokes, 318, 320, 321f
fibrinoid leukoencephalopathy (Alexander disease), 198, 199f, 200f
fibromuscular dysplasia, 623, 623f
fibrous dysplasia, 380, 381f
fissures and sulci, 10
fistula, carotid cavernous, 370, 371f, 634, 635f
focal cerebellar cortical dysplasia, 34, 36f
focal cortical dysplasia without balloon cells, 26, 27f, 460, 461f
Friedreich's ataxia, 288
frontotemporal dementia (FTD), 264, 265f, 452, 453f
– with motor neuron disease, 264
frontotemporal lobar degeneration (FTLD), 264, 452, 453f
FTD. *See* frontotemporal dementia (FTD)
FTLD. *See* frontotemporal lobar degeneration (FTLD)
Fukuyama congenital muscular dystrophy phenotype, 30, 202, 203f
fungal brain abscess, 70, 71f, 112, 140, 141f, 209, 246, 247f
fusiform aneurysm, 85, 119, 370, 540, 541f

G

gangliocytoma, 54, 54f, 102
– dysplastic cerebellar (Lhermitte-Duclos disease), 102, 103f
ganglioglioma, 53, 53f, 102, 103f
– anaplastic, 54, 55f
– desmotic infantile, 54, 55f
gangliosidoses (Sandhoff disease), 174, 187, 188, 190f
Gardner's syndrome, 522, 523f
germ cell tumors, 368, 369f, 390, 480, 481f, 500, 501f
– pineal, 60, 62f
germinal matrix hemorrhage, 276, 277f
– in preterm neonates, 255, 255f, 322f, 323
germinoma, 390, 390f, 391f. *See also* germ cell tumors
giant aneurysm, 370, 540, 541f
giant cell arteritis, 162, 228, 275, 626
giant cell astrocytoma, subependymal, 38, 39f, 435
giant cell glioblastoma, 44, 46f
glial cell proliferation, 9
glioblastoma multiforme, 44, 46f, 98, 99f, 133, 258, 434, 470, 471f, 490, 491f, 512f
glioblastoma, giant cell, 44, 46f
glioma
– of the hypothalamus, 364, 365f
– of the neurohypophysis, 362, 363f
– of the optic chiasm, 364, 365f
gliomatosis cerebri, 42, 43f, 96, 132, 132f, 258
glioneuronal tumor, papillary, 56, 498
gliosarcoma, 47, 47f
globoid cell leukodystrophy (Krabbe disease), 187, 188, 189f
glutaric acidemia/aciduria, 174, 177f, 194, 195f, 232, 234f, 594
gradient recalled echo (GRE), 606
granular cell tumor, 362, 363f
granulocytic sarcomas (myeloid sarcoma), 65, 107, 132, 214, 568, 586
granuloma, eosinophilic, 538, 539f, 556
granulomatosis with polyangiitis (Wegener's granulomatosis), 162, 228, 275, 384, 582, 591, 626
granulomatous amebic encephalitis, 150
granulomatous hypophysitis, 382
gray matter heterotopia, 13f, 14f, 20, 20f, 21f, 38, 129, 129f, 186, 459, 459f
Griscelli syndrome type 2, 212

H

Haltia-Santavuori disease, 191
hamartoma (tuberous sclerosis), 65, 65f, 108, 109f, 134, 134f, 135f, 187, 464, 464f, 512, 513f
– cortical, 134, 135f
– cortical-subcortical, 65
– hypothalamic, 66, 66f, 350, 351f, 482, 483f
– subependymal, 134, 135f, 512, 513f
Hand-Schuller-Christian disease, 538, 556
hemangioblastoma, 108, 109f, 134, 135f, 438, 474, 475f, 488, 489f
hemangioma
– cavernous, hemorrhage from, 85, 86f, 120, 121f
– cavernous sinus, 372, 373f
hemangiopericytoma, 442, 496, 497f, 519, 521f, 566, 566f
– anaplastic, 526, 568
hematoma, 506, 507f, 514, 514f
– epidural, 534, 535f, 554, 572, 573f
– intramural (dissecting aneurysm), 85, 119
– ossified, 536, 554, 555f, 574, 575f
– subdural, 2, 536, 537f, 554, 555f, 574, 575f
hemiazygous anterior cerebral artery, 610, 611f
hemimegalencephaly, unilateral, 22, 23f, 38, 130, 131f, 186, 460, 461f
hemispheric dysplasia, 28, 28f
hemophagocytic lymphohistiocytosis, 212, 213f
hemorrhage, 82, 82f, 484
– from arteriovenous malformation (AVM), 84, 84f, 120, 121f
– from cavernous hemangioma, 85, 86f, 120, 121f
– cerebellar, 118, 119f
– germinal matrix, 322f, 323
–– in preterm neonates, 255, 255f
– intracerebral, 3
– from intracranial aneurysm, 119
– intraparenchymal, 3
– from metastatic tumor, 82, 83f, 119, 156, 157f
– from ruptured aneurysm, 85, 86f
– subarachnoid, 2, 592, 592f, 593f
hepatocerebral degeneration, acquired, 236, 237f, 290
Hermansky-Pudlak syndrome type 2, 212
herniation
– subfalcine, 466, 467f
– transtentorial, 466, 467f
heroin toxicity, 178, 181f, 242, 243f
heroin-induced leukoencephalopathy (toxic spongiform encephalopathy). *See* heroin toxicity
herpes simplex virus, 70, 113f, 142, 142f, 209, 210f, 248, 273f
heterotopia, gray matter. 13f, 14f, 20, 20f, 21f, 38, 129, 129f, 186, 459, 459f
histiocytosis, Langerhans' cell, 382, 383f, 487, 538, 539f, 556, 578, 579f, 590
HIV. *See* human immunodeficiency virus (HIV) infection
holoprosencephaly, 15, 16f, 17f, 456, 457f, 458f
homocystinuria, 174, 194, 232
hormone regulation, 346f
human immunodeficiency virus (HIV) infection, 142, 143f, 145
Hunter syndrome (mucopolysaccharidosis type II), 178, 179f, 188, 189f, 236
Huntington disease, 242, 243f, 286, 287f, 454, 454f
Hurler syndrome (mucopolysaccharidosis type I), 178, 179f, 188, 189f, 236
hydatid cyst, 74, 75f, 115, 150, 151f, 448, 449f
hydranencephaly, 276, 277f, 450, 450f
hydrocephalus
– communicating, 454, 455f
– normal-pressure, 454, 455f
hyperglycemia, 172, 172f
– nonketotic, 238
hyperparathyroidism, 221
hyperplasia, pituitary, 358, 358f
hypertensive encephalopathy (posterior reversible encephalopathy syndrome/PRES), 126, 127f, 182, 183f, 215, 216f
hypertrophic olivary degeneration, 282, 283f
hypertrophic pachymeningitis, idiopathic, 582
hypertrophy, pituitary, 358, 358f
hypoglossal artery, persistent, 607, 609f
hypoglycemia, 172, 173f, 238
hypoparathyroidism, 221
hypophysitis
– granulomatous, 382
– lymphocytic, 382, 383f

hypopituitarism, 349f
hypoplasia
– of cerebellar hemisphere, 31, 31f
– of the A1 segment of the anterior cerebral artery, 607, 607f
– of the anterior pituitary lobe, 349, 349f
– unilateral, of the internal carotid artery, 612, 613f
hypotension, intracranial, 576, 577f
hypothalamic hamartoma, 66, 66f, 350, 351f, 482, 483f
hypothalamus, 345, 346f, 347f
hypothyroidism, 220
hypoxic-ischemic encephalopathy, 276, 277f
hypoxic-ischemic injury, 166, 166f, 167f, 204, 205f, 224, 225f
– in adults, 310, 311, 311f, 312f, 313f
– in children, 340f, 341
– in preterm neonates, 206, 320, 321, 322f
– in term neonates, 207, 324, 326, 327f, 328, 328f, 329, 330f

I

idiopathic basal ganglia calcification/familial cerebrovascular ferrocalcinosis (Fahr disease), 220, 222, 223f, 286, 287f
idiopathic hypereosinophilic syndrome, 313f
idiopathic hypertrophic pachymeningitis, 582
idiopathic intracranial hypertension (pseudotumor cerebri), 426, 427f
increased intracranial pressure, 426, 427f
infarct
– from arterial occlusion, 224, 225f
–– cerebral, 87, 87f, 88
–– in children, 336, 337f, 338, 339, 339f
–– in term neonates, 331, 331f, 332, 333, 333f
– atherosclerotic-embolic, 299, 299f, 300f, 301f, 302, 303f, 304f, 305f, 306, 307f
– atherosclerotic-thrombotic, 299, 299f, 300f, 301f, 302, 303f, 304f, 305f, 306, 307f
– brainstem, 124, 125f
– cerebellar, 124, 125f
– in children, generally, 318
– from embolic disease, 160, 161f
– lacunar, 308, 309f
– from vasculitis, 162, 163f
– from venous occlusion, 88, 89f
inflammatory pseudotumor, 582, 583f, 591, 591f
internal carotid artery (ICA)
– anatomy, 598, 599f
– aberrant position of, 610, 611f
– unilateral agenesis, aplasia, and hypoplasia of, 612, 613f
intracerebral hemorrhage, 3
intracranial hypotension, 576, 577f
intracranial pressure (ICP), 296
– increased, 426, 427f
intramural hematoma (dissecting aneurysm), 85, 119
intraparenchymal hemorrhage, 3
ischemia
– in children, generally, 318
– neonatal, from anoxia followed by hypoperfusion, 331
ischemic strokes from arterial stenosis or occlusion, 298

J

Jansky-Bielschowsky disease, 191
Japanese encephalitis, 71, 142, 144f, 145, 248, 249f
Joubert syndrome, 34, 34f, 462, 463f
jugular bulb
– dehiscence of, 618, 619f
– high position of, 618

K

Kawasaki disease, 162, 626
Kearns-Sayre syndrome, 170, 171f, 202, 203f, 230, 344
ketoacidosis, diabetic, 172f, 427f
Krabbe disease (globoid cell leukodystrophy), 187, 188, 189f
Kufs disease, 191

L

lacunar infarction, 308, 309f
Lambert-Eaton myasthenic syndrome, 184, 292
Langerhans' cell histiocytosis, 382, 383f, 487, 538, 539f, 556, 578, 579f, 590
Leigh's disease, 170, 171f, 230, 231f, 344
leptomeningeal cyst, 542, 543f
leptomeningeal infection, 382, 383f, 588, 588f, 589f
leptomeninges, 562, 563f
Letterer-Siwe disease, 538, 556
leucinosis (maple syrup urine disease), 174, 177f, 194, 195f, 232, 234f
leukemia, 65, 107, 132, 214, 568, 586
leukodystrophy
– globoid cell (Krabbe disease), 187, 188, 189f
– megalencephalic with subcortical cysts (MLC), 196, 197f
– metachromatic, 187, 187f
leukoencephalopathy
– acute toxic, 215, 216f
– fibroid (Alexander disease), 198, 199f, 200f
– progressive multifocal, 72, 113f, 248
– with vanishing white matter disease (VWMD), 196, 197f
leukomalacia, periventricular, 160, 161f, 206, 207f, 278, 279f
Lhermitte-Duclos disease (dysplastic cerebellar gangliocytoma), 34, 35f, 102, 103f
Libman-Sachs endocarditis, 160, 161f, 306, 307f
lipofuscinosis, neuronal ceroid, 174, 187, 191, 191f
lipoma, 92, 93f, 127, 127f, 398, 399f, 544, 546f
– of the sellar/hypothalamic region, 356, 357f
lissencephaly (agyria or "smooth brain"), 19, 19f, 186
– incomplete (pachygyria), 20, 20f, 186
lupus. *See* systemic lupus erythematosus
Lyme disease (spirochete infection), 138, 139f, 208
lymphocytic hypophysitis, 382, 383f
lymphohistiocytosis, hemophatocytic, 212, 213f
lymphoma, 64, 64f, 107, 130, 131f, 214, 257, 257f, 374, 375f, 490, 491f, 528, 529f, 552, 568, 569f, 584, 585f

M

magnetic resonance angiography (MRA), 606
malaria, 150, 151f, 211, 211f
malignant brain neoplasms with direct extension into the ventricles, 512, 512f, 513f
malignant hypertension (acute hypertensive crisis), 228, 229f
malignant meningioma, 567, 567f
malignant mesenchymal nonmeningothelial tumors, 528, 529f, 570, 570f
maple syrup urine disease (leucinosis), 174, 177f, 194, 195f, 232, 234f
Marchiafava-Bignami disease, 290, 291f
Marfan syndrome, 540, 630
MCAP (megalencephaly-capillary malformation), 22
McCune-Albright syndrome, 381f
mean arterial pressure (MAP), 296
measles encephalitis, acute, 72, 145, 209, 248
medulloblastoma (PNET), 104, 105f, 435, 435f, 470, 471f
megalencephalic leukodystrophy with subcortical cysts (MLC), 196, 197f
megalencephaly (Sotos syndrome), 25
– benign family, 15
melanocytic neoplasms, 570
melanoma, pineal, 394, 395f
melanosis, neurocutaneous, 68, 68f, 136, 137f, 586, 587f
MELAS (mitochondrial encephalopathy, lactic acidosis, and stroke-like events), 168, 169f, 230, 231f, 288, 289f, 344
meningeal dysplasia/ectasia, 564, 565f
meninges, 562, 563f
meningioangiomatosis, 66, 67f, 519, 521f
meningioma, 366, 367f, 394, 395f, 440, 441f, 482, 483f, 494, 495f, 519, 520f, 521f, 549, 550f, 564, 565f
– malignant, 526, 527f, 567, 567f
meningitis
– bacterial, 588f
– tuberculous, 588f, 589f. *See also* tuberculoma
meningocele, 12, 12f, 13f, 354, 355f, 564, 564f
– postsurgical, 576, 577f
meningoencephalitis, primary amebic, 150
meningoencephalocele, 12, 12f, 13f, 354, 355f, 564, 564f
Menkes' syndrome (trichopoliodystrophy), 235, 284, 616, 617f
MERRF (myoclonic epilepsy with ragged red fibers), 168, 169f, 230, 231f, 288, 289f, 344
mesenchymal nonmeningothelial tumors
– benign, 522
– malignant, 528, 529f, 570, 570f
metachromatic leukodystrophy, 187, 187f
metastases in the brain, 63, 63f, 104, 106f, 130, 131f, 214, 256, 394, 395f, 432, 433f, 474, 475f, 488, 489f, 510, 511f, 526, 527f, 552, 553f, 568, 569f, 584, 584f, 585f
– breast, 363f, 553f, 585f
– disseminated medulloblastoma, 585f
– extracranial malignant fibrous histiocytoma, 553f
– hemorrhage from, 82, 83f, 119, 156, 157f
– lung, 63f, 106f, 131f, 527f, 569f
– melanoma, 433f, 489f, 511f, 584f
– pituitary, 362, 363f
– renal cell carcinoma, 157f
– in the sphenoid bone and suprasellar cistern, 374, 375f
methanol intoxication, 240
methemoglobin, 78
methylmalonic aciduria, 174, 175f, 194, 232, 233f
microadenoma, pituitary, 359, 360f, 361, 361f
microcephaly
– from neonatal ischemia or infection, 25, 25f
– with simplified gyral pattern (microlissencephaly), 25, 25f
microlissencephaly (microcephaly with simplified gyral pattern), 25, 25f
middle cerebral artery (MCA) anatomy, 600–601
mitochondrial encephalopathy, lactic acidosis, and stroke-like events (MELAS), 168, 169f, 230, 231f, 288, 289f, 344
mixed connective tissue disease, 162, 626
Morquio syndrome (mucopolysaccharidosis type IV), 178, 179f, 188, 236
moyamoya disease, 226, 227f, 594, 595f, 614, 615f
MRA. *See* magnetic resonance angiography (MRA)
MRI, generally, 1–2
MS. *See* multiple sclerosis (MS)
mucopolysaccharidoses, 178, 179f, 187, 188, 189f, 190f, 236, 237f, 594
Mucor. *See* fungal brain abscess
multi-infarct/vascular dementia, 266, 267f
multiple sclerosis (MS), 76, 77f, 116, 117f, 153, 153f, 212, 213f, 252, 272, 274f
multiple system atrophy (MSA), 268
– olivopontocerebellar (MSA-C), 242, 268, 269f, 270f

– Shy-Drager syndrome (MSA-A), 242, 268, 269f, 270f
– striatonigral degeneration (MSA-P), 242, 268, 269f, 270f
muscle-eye-brain phenotype, 30, 30f, 202, 203f
myelinolysis
– central pontine, 126, 127f
– osmotic, 126, 127f, 182
– osmotic pontine, 291, 291f
myeloid sarcoma (chloromas, granulocytic sarcomas), 65, 107, 132, 214, 568, 586
myeloma, 552, 570, 571f, 586
myeloma/plasmacytoma, 374, 375f
myoclonic epilepsy with ragged red fibers (MERRF), 168, 169f, 230, 231f, 288, 289f, 344

N

NAHI. *See* nonaccidental head injury (NAHI)
nasopharyngeal carcinoma, 378, 379f, 532, 533f
necrosis, radiation, 90, 91f, 126, 182, 183f, 215, 216f, 294, 295f, 514
neonatal ischemia from anoxia followed by hypoperfusion, 331
neonatal sinovenous thrombosis and venous infarction, 324, 325f
neural plate formation, 5
neural tube formation, 6
neurenteric cyst, 544, 546f
neuroblastoma, olfactory (esthesioneuroblastoma), 534, 535f
neurocutaneous melanosis, 68, 68f, 136, 137f, 586, 587f
neurocytoma, central, 56, 57f, 442, 443f, 478, 479f, 498, 499f
neurodegeneration with brain iron accumulation (pantothenate kinase-associated neurodegeneration [PKAN disease]), 284, 285f
neuroectodermal tumor, primitive, 58, 59f
neuroepithelial (neuroglial) cyst, 92, 93f, 260, 504, 505f
neurofibroma, 522, 549
neurofibromatosis type 1 (NF1), 108, 109f, 133, 133f, 186, 260, 261f, 564, 565f
– and pilocytic astrocytoma, 259, 259f
neurofibromatosis type 2 (NF2), 549, 550f, 551f
neuroglial (neuroepithelial) cyst, 92, 93f, 260, 504, 505f
neurologic decompressive sickness, 168, 168f
neuronal ceroid lipofuscinosis, 174, 187, 191, 191f
neuronal migration, 5, 6–7
neuronal proliferation, 9
neurosarcoid, 116, 154, 155f, 252, 253f, 508, 509f, 556, 556f
NF1. *See* neurofibromatosis type 1 (NF1)
NF2. *See* neurofibromatosis type 2 (NF2)
non-Hodgkin's lymphoma. *See* lymphoma
nonaccidental head injury (NAHI), 204, 205f
nonketotic hyperglycemia, 238
normal-pressure hydrocephalus, 454, 455f

O

olfactory neuroblastoma (esthesioneuroblastoma), 534, 535f
oligoastrocytoma, 50, 50f, 98
– anaplastic, 50, 50f
oligodendroglioma, 48, 49f, 98, 99f
– anaplastic, 48, 49f
oncocytoma of the adenohypophysis, 362
ornithine transcarbamylase deficiency, 174, 176f, 194, 232, 233f
osmotic myelinolysis, 126, 127f, 182
– pontine, 291, 291f
ossification and calcification, dural, 547, 547f, 557, 557f
ossified hematoma, 536, 554, 555f, 574, 575f
osteogenic sarcoma, 376, 530, 531f, 570
osteoma, 380, 381f, 522, 523f
otic artery, persistent, 607
oxyhemoglobin, 78

P

pachygyria (incomplete lissencephaly), 20, 20f
pachygyria (nonlissencephalic cortical dysplasia), 20f, 186
pachymeningitis
– from infection, 578, 578f
– idiopathic hypertrophic, 582
Paget disease, 380
pallidotomy, 244, 245f
panencephalitis, subacute sclerosing, from measles, 71, 145, 209, 248
pantothenate kinase-associated neurodegeneration (PKAN disease), 232, 234f, 284, 285f
papillary glioneuronal tumor, 56, 498
papillary tumor of the pineal region, 60, 61f, 388, 388f
papilloma, choroid plexus, 438, 439f, 476, 477f, 496, 497f, 524, 525f
paraganglioma (chemodectoma), 368, 522, 523f
paragonimiasis, 152
paramagnetic property, 78
paraneoplastic syndrome, 184, 292, 293f
Parkinson-plus syndromes. *See* multiple system atrophy
Parkinson's disease, 268, 269f. *See also* multiple system atrophy
Pars intermedia cyst, 354, 354f
Patau syndrome, 456
Pelizaeus-Merzbacher disease, 196, 197f
perinatal-neonatal strokes, 318, 320
perineural tumor spread from the sinuses and nasopharynx, 572, 573f
periventricular leukomalacia, 160, 161f, 206, 207f, 278, 279f, 324, 325f
persistent craniopharyngeal canal, 352, 352f
persistent fetal origin of posterior cerebral artery, 607, 607f
persistent hypoglossal artery, 607, 609f
persistent otic artery, 607
persistent stapedial artery, 612, 613f
persistent trigeminal artery (PTA), 607, 609f
PHACES syndrome (posterior fossa malformations, facial hemangiomas, arterial anomalies, cardiac anomalies and aortic coarctation, eye abnormalities, and sternal clefts or supraumbilical raphe), 616, 617f
phenylketonuria, 174, 175f, 194, 195f, 232
phenytoin-related cerebellar atrophy, 292, 293f
Pick disease, 264, 265f
pilocytic astrocytoma, 38, 39f, 95, 95f, 259, 432, 433f, 468, 469f
pilomyxoid astrocytoma, 40, 40f, 366, 367f
pineal cyst, 392, 393f
pineal gland, 385
pineal tumors, 442, 443f, 502
– germ cell, 60, 62f
– pineoblastoma, 60, 62f, 388, 389f, 480, 481f
– pineocytoma, 60, 61f, 386
– pineal melanoma, 394, 395f
– pineal parenchymal tumor of intermediate differentiation, 60, 61f, 386, 387f
pituicytoma, 362, 363f
pituitary adenoma, 359, 359f, 360f, 524, 525f
– invasive, 361, 361f
pituitary apoplexy, 360f
pituitary carcinoma, 361, 361f
pituitary duplication, 350, 351f
pituitary gland, 345, 346f, 347f
– developmental pattern of, 347f
– ectopic posterior, 350, 350f
pituitary hypertrophy/hyperplasia, 358, 358f
PKAN disease (pantothenate kinase-associated neurodegeneration), 232, 234f, 284, 285f
plasmacytoma/myeloma, 374, 375f, 528, 529f
pleomorphic xanthoastrocytoma, 42, 43f
PNET (medulloblastoma), 58, 59f, 104, 105f, 396, 397f
polyarteritis nodosa, 162, 228, 275, 626
polyglandular autoimmune syndrome type I (PGA-I), 221
polymicrogyria, 26, 26f, 27f, 460, 461f
pontine osmotic myelinolysis, 182, 291, 291f
porencephalic cyst, 92, 93f, 278, 279f, 450, 451f, 462, 463f
porencephaly, 319f
posterior cerebral artery, persistent fetal origin of, 607, 607f
posterior cortical atrophy (Benson dementia), 266, 267f
posterior pituitary gland, ectopic, 350, 350f
posterior reversible encephalopathy syndrome (PRES) (hypertensive encephalopathy), 126, 127f, 182, 183f, 215, 216f, 297
postshunt change in the ventricles, 426, 426f, 427f
postsurgical dural fibrosis, 576, 576f, 577f
postsurgical meningocele, 576, 577f
posttransplant lymphoproliferative disorder (PTLD), 215
posttraumatic gliosis and encephalomalacis from brain contusions, 282, 283f
PRES. *See* posterior reversible encephalopathy syndrome (PRES) (hypertensive encephalopathy)
primary amebic meningoencephalitis, 150
primitive neuroectodermal tumor (PNET), 58, 59f, 396, 397f
prion disease, 72, 146, 147f, 250, 251f, 266
proatlantal artery, 610
progressive multifocal leukoencephalopathy, 72, 113f, 142, 143f, 145, 248
progressive multifocal leukoencephalopathy (PML)–immune reconstitution inflammatory syndrome (IRIS), 146, 147f
progressive nonfluent aphasia, 264
progressive supranuclear palsy, 264, 268, 270f
prominent perivascular spaces, 244, 245f
proprionic acidemia, 174, 194, 232, 233f
Proteus syndrome, 22
proton-electron dipole-dipole interaction, 78
pseudohypoparathyroidism, 221
pseudo-pseudohypoparathyroidism, 221
pseudotumor cerebri (idiopathic intracranial hypertension), 426, 427f
pseudotumor, inflammatory, 582, 583f, 591, 591f
PTLD. *See* posttransplant lymphoproliferative disorder (PTLD)
pyogenic brain abscess, 69, 69f, 110, 111f, 136, 137f, 208, 208f, 246

R

rabies, 72, 142, 144f, 145, 248, 249f
radiation necrosis, 90, 91f, 126, 182, 183f, 215, 216f, 294, 295f, 514
Rasmussen's encephalitis, 274f, 275, 448, 449f
Rathke's cleft cyst, 352, 353f, 542, 543f
Refsum disease
– adult, 191
– infantile, 191
Rendu-Osler-Weber syndrome, 158, 515, 632
retinocochleocerebral vasculopathy (Susac syndrome), 164, 165f
reversible cerebral vasoconstriction syndrome, 184

rhabdoid tumor. *See* teratoid/rhabdoid tumor, atypical
rhombencephalosynapsis, 34, 35f, 462, 463f
rickettsial infection. *See* Rocky Mountain spotted fever (rickettsial infection)
Rocky Mountain spotted fever (rickettsial infection), 138, 139f
Rosai-Dorfman disease, 384, 580
ruptured dermoid, 586, 587f

S

saccular aneurysm, 85, 119, 370, 557
Sandhoff disease (gangliosidoses), 174
Sanfilippo syndrome (mucopolysaccharidosis type III), 178, 179f, 188, 190f, 236
sarcoid, 162, 228, 275, 626
sarcoidosis, 116, 154, 252, 253f, 384, 508, 509f, 580, 581f, 590, 590f
sarcoma
– Ewing's, 378, 532, 533f, 570
– gliosarcoma, 47, 47f
– granulocytic, 65, 107, 132, 214, 568, 586
– myeloid, 65, 107, 132, 214, 568, 586
– osteogenic, 376, 530, 531f, 570
schistosomiasis, 152
schizencephaly (split brain), 22, 22f, 186, 460, 461f
schwannoma, 366, 367f, 522, 523f, 549, 551f
seizure, 168, 169f, 238, 239f, 292, 293f
sellar/hypothalamic lipoma, 356, 357f
semantic dementia, 264
septo-optic dysplasia (de Morsier syndrome), 18, 18f, 456, 458f
shunt placement, 514
Shy-Drager syndrome, 242, 268, 269f, 270f
sickle-cell disease, 206, 339f, 340, 340f
siderosis, superficial, 294, 295f, 592, 593f
sinonasal squamous cell carcinoma, 378, 379f, 532, 533f
sinovenous infarction
– in adults, 314, 315f, 316f, 317f
– in children, 342, 343f
– neonatal, 324, 325f
sinus pericranii, 618, 619f
Sjogren's disease, 162, 626
skull-base tumors, 570, 571f
small-vessel disease, 160, 161f, 226, 227f, 340
small-vessel infarction, 308, 309f
solitary fibrous tumor, 566
Sotos syndrome, 25, 594
sparganosis, 152
spindle-cell oncocytoma of the adenohypophysis, 362
spinocerebellar ataxia/degeneration, 288, 289f
spirochete infection. *See* Lyme disease (spirochete infection); syphilis (spirochete infection)
split brain (schizencephaly), 22, 22f
squamous cell carcinoma, sinonasal, 378, 379f, 532, 533f
stapedial artery, persistent, 612, 613f
stroke
– in children, 336
– cardioembolic, 306, 307f
– ischemic, from arterial stenosis or occlusion, 298
Sturge-Weber syndrome (encephalotrigeminal angiomatosis), 275, 485, 486f, 515, 515f, 594, 594f, 595f, 614, 614f, 615f
subacute sclerosing panencephalitis from measles, 72, 145, 209, 248
subarachnoid hemorrhage, 2, 592, 592f, 593f
subclavian steal syndrome, 620, 622f
subdural abscess, 578, 579f
subdural empyema, 538, 538f, 539f, 556, 578, 579f
subdural hematoma, 2, 536, 537f, 554, 555f, 574, 575f
subependymal giant cell astrocytoma, 38, 39f, 435, 468, 469f
subependymal hamartomas, 65, 134, 135f, 512, 513f
subependymoma, 52, 52f, 100, 101f, 440, 441f, 494, 494f, 495f
subfalcine herniation, 466, 467f
substantia nigra, 218
subthalamic nucleus, 217
sulci and fissures, 10
superficial siderosis, 294, 295f, 592, 593f
Susac syndrome (retinocochleocerebral vasculopathy), 164, 165f
syntelencephaly, 15, 17f
syphilis (spirochete infection), 138
systemic lupus erythematosus, 162, 164, 165f, 308, 309f, 626

T

T cell lymphoma. *See* lymphoma
T2-proton relaxation enhancement (T2-PRE), 78
Takayasu's arteritis, 162, 228, 275, 626
Tay-Sachs disease, 174, 188, 190f
telangectasia, capillary, 122, 123f, 158, 159f, 256, 636, 637f, 638f
teratoid/rhabdoid tumor, atypical, 58, 59f, 104, 106f, 396, 397f, 436, 437f, 472, 473f
teratoma, 368, 369f, 390, 391f, 502, 503f
thalamus, 218
thoracic outlet syndrome, 616, 617f
thrombosis, venous sinus, 628, 629f
time-of-flight (TOF) method, 606
TORCH and neonatal infections (toxoplasmosis, rubella, cytomegalovirus, and herpes), 272, 273f, 274f, 446, 447f
toxic encephalopathy, late effects, 294, 295f
toxic spongiform encephalopathy (heroin-induced leukoencephalopathy). *See* heroin toxicity
toxoplasmosis, 73, 114, 148, 149f, 250, 251f, 589f
transmantle cortical dysplasia with balloon cells, 28
transtentorial herniation, 466, 467f
traumatic brain injury. *See* diffuse axonal injury
trichopoliodystrophy (Menkes' syndrome), 235, 284
trigeminal artery, persistent, 607, 609f
trypanosomiasis, 152
tsetse fly (trypanosomiasis), 152
tuberculoma, 73, 73f, 112, 113f, 140, 141f
tuberculous meningitis, 588f, 589f. *See also* tuberculoma
tuberous sclerosis (hamartoma), 65, 65f, 108, 109f, 134, 134f, 135f, 187, 464, 464f
tumor pseudoprogression, within 3 months after chemoradiation, 90

U

unilateral agenesis, aplasia, and hypoplasia of the internal carotid artery, 612, 613f
unilateral hemimegalencephaly, 22, 23f, 38, 130, 131f, 186, 460, 461f

V

vacuolated myelin/dysplastic white matter lesions, 133, 133f, 260, 261f
van der Knaap disease, 196, 197f
vascular abnormalities, generally, 598–606
vascular/multi-infarct dementia, 266, 267f
vasculitis, 228, 229f, 275, 626, 627f
– infarction, 162, 163f
vein of Galen malformation/aneurysm, 485, 486f, 540, 541f, 612, 613f, 632, 633f
venous anatomy, 602–603
venous angioma/developmental venous anomaly, 85, 122, 123f, 158, 515, 618, 618f, 619f, 636, 637f
venous anomaly, developmental, 85, 636, 637f
venous development, 605
venous occlusion, causing cerebral infarction, 88, 89f, 226, 227f
venous sinus thrombosis, 628, 629f
venous sinuses, 603–604
ventricles, development of, 422–425
ventricular shunt failure, 454, 455f
ventriculitis, 446, 447f, 487, 508, 509f, 512, 513f, 514f
– chemical, 514
vermian hypoplasia (Dandy-Walker variant), 33, 33f, 431, 462
vertebral arteries
– duplication of, 610
– single, anatomy of, 601
vesicles, 5, 7f, 8f
VHL. *See* von Hippel-Lindau disease (VHL)
viral infections/encephalitis. *See* encephalitis/viral infections
von Hippel-Lindau disease (VHL), 108, 109f, 134, 135f, 474, 475f, 488, 489f
von Recklinghausen disease. *See* neurofibromatosis type 1 (NF1)

W

Walker-Warburg phenotype, 29, 29f, 202
Wallerian degeneration, 244, 280, 281f
Wegener's granulomatosis (granulomatosis with polyangiitis), 162, 228, 275, 384, 582, 591, 626
Wernicke's encephalopathy, 238, 239f, 290
West Nile virus, 72, 209, 248
Wilson's disease, 235, 235f, 284
Wyburn-Mason syndrome, 158, 515, 632

X

X-linked adrenoleukodystrophy, 191, 192, 193f
X-linked lymphoproliferative syndrome, 212
xanthoastrocytoma, pleomorphic, 42, 43f

Y

yolk sac tumor, 392, 393f

Z

Zellweger syndrome (cerebrohepatorenal syndrome), 191, 192, 193f